



fiv DUBLIN
IRELAND
2012

FLOW-INDUCED VIBRATION

EDITORS: C. MESKELL & G. BENNETT



Proceedings of the 10th International conference on
Flow-Induced Vibration (& Flow-Induce Noise)

FIV2012, Dublin, Ireland, 3-6 July 2012

FLOW-INDUCED VIBRATION

EDITED BY
C.MESKELL & G. BENNETT
SCHOOL OF ENGINEERING
TRINITY COLLEGE, DUBLIN

The papers in this volume have been typeset by the authors concerned, in some cases under supervision of the editors. The authors of each paper retain the copyright to their specific paper, and have granted a non-exclusive license to Trinity College, Dublin to distribute their paper as part of the FIV2012 proceedings. Any enquiries regarding the content of a paper in this volume should be addressed directly to the authors.

Cover design: Ex Ordo (www.exordo.com)

ISBN: 978-0-9548583-4-6

Preface

Flow-Induced Vibration and Noise, and the physical parameters which control them, are of significant importance to design engineers and operators of systems in a wide range of industries ranging from aerospace, automotive and civil engineering to marine structures, electricity generation and chemical processing. The potential of these phenomena to cause catastrophic failure to engineering systems and unacceptably high levels of environmental and occupational noise has motivated significant effort to understand and mitigate these problems in the interests of human safety.

FIV2012 is the tenth in a series of international conferences on Flow-Induced Vibration which started at Keswick in 1973 primarily in response to the needs of the nuclear industry. The conference is held every four years with the 7th and 8th international FIV conferences being held in Lucerne, Switzerland and École Polytechnique, Paris respectively. The most recent in the series was held in Prague in 2008. While many of the problems that appeared in the first FIV conference are still under investigation (e.g. flow induced vibration of tube arrays with cross flow or pipes with axial flow), subsequent conferences have evolved into major international events with a continually wider scope of papers in the field of flow-induced vibration and fluid structure interaction. Furthermore, over the past four decades, noise in confined or bluff body flows has emerged as a related and equally problematic issue to flow-induced vibration.

There has been an Irish contingent at FIV conferences from the outset; Prof. John Fitzpatrick, an Irishman of some renown, was one of the delegates at the very first meeting in 1973. Therefore, we have great pleasure in welcoming over one hundred delegates, coming from every continent, to Trinity College, Dublin to present and discuss their work. This is the proceedings of that meeting.

Craig Meskell, Gareth Bennett, Trinity College, Dublin

July 2012

LOCAL ORGANIZING COMMITTEE

Craig Meskell, Chair

Gareth Bennett, Chair

John Fitzpatrick

Petr Eret

Melanie Apied

INTERNATIONAL SCIENTIFIC COMMITTEE

Anthony D. Lucey, Australia

Marco Ambili, Canada

Petros Anagnostopoulos, Greece

Jose Antunes, Portugal

Christophe Bailly, France

Stavroula Balabani, UK

Peter Bearman, UK

Stefan Belfroid, Netherlands

Sofiane Benhamadouche, France

Hans Bodén, Sweden

Roberto Camussi, Italy

Michael Carley, UK

Ludovic Chatellier, France

Charles Dalton, USA

Emmanuel de Langre, France

Gunilla Efrainsson, Sweden

Yves Gervais, France

Hugh Goyder, UK

Marwan Hassan, Canada

Arne Henning, Germany

Mico Hirschberg, Netherlands

Jaromír Horáček, Czech Republic

Kerry Hourigan, Australia

Umberto Iemma, Italy

Peter Jordan, France

Lars Koop, Germany

Leonardo Lecce, Italy

Masaru Matsumoto, Japan

Atef Mohany, Canada

Scott Morris, USA

Pierre Moussou, France

Njuki Mureithi, Canada

Peter Oshkai, Canada

Michael P. Paidoussis, Canada

Michel J. Pettigrew, Canada

Michel Roger, France

Wolfgang Schröder, Germany

Sergio V. Möller, Brazil

Jean-François Sigrist, France

David B. Stephens, USA

Dave S. Weaver, Canada

Samir Ziada, Canada

Igor Zolotarev, Czech Republic

TABLE OF CONTENTS

1.1 Axial Flow and Thin Shells

Dynamics Of Fluid-Conveying Cantilevered Pipes With Additional Adornments 1

M. Haj Ghayesh, M. P. Paidoussis, M. Amabili

Low Order Resonance Of An Elastic Fluid-Conveying Tube 7

J. Richard, A. Steindl

Flow-Induced Oscillations Of A Cantilevered Pipe Conveying Fluid With Base Excitation 15

G. Chang, Y. Modarres-Sadeghi

1.2 Industrial Aeroacoustics

Experimental Analysis Of The Aeroacoustics Of Free And Impinging Jet 21

G. Sinibaldi, L. Marino, G. P. Romano

Fluid-Resonant Coupling In High-Speed Impinging Planar Jets 27

D. Arthurs, S. Ziada

Numerical Simulation And Analysis Of The Noise Generated By The Flow Over Rectangular Cylinders At Incidence 35

F. Margnat, A. Buitrago

2.1 Industrial Aeroacoustics

Countermeasures of Self-Sustained Tones by Baffle Plates in a Boiler Tube Bank 43

K. Ishihara

**On The Effect Of A Swirl On The Self-Sustained Oscillations In Compact
Axisymmetric Cavities** 49

G. Nakiboglu, O. Rudenko, A. Hirschberg, J. Golliard, S. Belfroid

Experimental Study of Interaction Between Pressure Pulsations and Piping Vibration 55

Y. Torigoe, T. Sakakibara, S. Kojima, E. Hirooka, M. Kato, T. Tsuji, A. Maekawa, T. Takahashi

2.2 Hydro- & Aeroelasticity

Low Speed Flutter And Limit Cycle Oscillations Of A Flat Plate Section In A Wind Tunnel 61

X. Amandolese, S. Michelin, M. Choquel

Numerical And Experimental Study Of Hydroelastic Behaviour Of A Hydrofoil 67

F. Gaugain, F. Deniset, J. Astolfi, J. Sigrist

Analysis of Vortex Shedding from a Wind Turbine Blade at High Angle of Attack 75

A. Pellegrino, C. Meskell

3.1 Tube Arrays

Modeling of the Phase Lag Causing Fluidelastic Instability in Tube Arrays 83

A. Khalifa, D. S. Weaver, S. Ziada

Measurement of surface pressure on neighbouring tubes in a deformed normal triangular tube array. 91

D. Keogh, C. Meskell

Study on In-Flow Fluidelastic Instability of Circular Cylinder Arrays 99

T. Nakamura, Y. Fujita, T. Oyakawa, Y. Ni

Unsteady Fluid Forces and the Time Delay in a Vibrating Tube Subjected to Cross Flow 107

M. Hassan, S. El Bouzidi

3.2 Bluff Bodies & VIV

Numerical Study On The Effects Of Particles On Damping The Vibration Of A Bluff Body Due To The Vortex Shedding 115

S. P. Omrani, S. Belfroid, A. Twerda, B. J. Boersma

Study Of Von Karman Vortex Shedding Robustness In The Wake Of A Fuzzy Coated Cylinder 123

B. Levy, Y. Z. Liu

Hilbert-Huang Transform – A Comparison With Fourier And Wavelet Transform For The Analysis Of The Shedding Process 131

R. S. Silveira, S. V. Möller

Numerical Predictions Of The Natural Frequencies Of Long Flexible Cylinders With A Form Of Damping That Includes The Effect Of The Current 139

F. Huera-Huarte, L. González

4.1 Hydro- & Aeroelasticity

- Numerical Simulation Of Influence Of A Gap Between The Main Lifting Surface
And The Aileron On Aeroelastic Behavior Of An Airfoil** 147

J. Horáček, M. Feistauer, P. Sváček

- Excitation Characteristics Of Dry Galloping Vibrations** 155

N. Nikitas, J. H. G. MacDonald

- Large Galloping Oscillations Of A Square Section Cylinder In Wind Tunnel** 165

P. Hémon

4.2 Industrial Aeroacoustics

- Experimental And Numerical Study Of The Fluid-Acoustic Interaction In
A T-Junction At Low Mach Number Flows** 171

A. Holmberg, M. Berton, A. Kierkegaard, M. Karlsson

- Flow-Induced Pulsations At T-Joints With Inserts: Experimental And Numerical Study** 179

J. Golliard, N. González Díez, G. Joost

- Acoustic Properties Of An In-Duct Orifice Subjected To Bias Flow And High
Level Acoustic Excitation** 187

H. Bodén, L. Zhou

5.1 Axial Flow and Thin Shells

Flow-Induced Vibration Tests of a Nuclear Reactor De Mountable Fuel Bundle 195

V. Janzen, B. A. W. Smith, Y. Han, T. Whan, D. F. Sears, M. R. Floyd

Stability Of A Structurally Inhomogeneous Flexible Plate In Uniform Axial Flow 203

B. H. Tan, A. D. Lucey, M. W. Pitman

Flow Energy Harvesting From Piezoelectric Flags 211

S. Michelin, O. Doaré

The Fluid-Structure Interaction Of A Spring-Mounted Cantilevered-Free Flexible Plate In A Uniform Flow 219

R. M. Howell, A. D. Lucey

5.2 Industrial Aeroacoustics

Does Reynolds Number Affect Lock-In of Aeroacoustic Resonance of Tandem Cylinders? 227

C. Paduano, C. Meskell

Direct Aeroacoustic Simulation of Merging Flow in T-duct 235

G. C. Y. Lam, R. C. K. Leung, S. Tang

Simulations Of Acoustic Scattering In Flow Ducts With The Frequency-Domain Linearized Navier-Stokes Equations 243

A. Kierkegaard, S. Boij, M. Åbom, G. Efraimsson

The spatial distribution of the acoustic sources in an inline tube array experiencing cross flow induced acoustic resonance. 251

S. Finnegan, C. Meskell

6.1 Industrial Aeroacoustics

- Audio Simulation And Analysis Of Noise Generated By Aircraft Engines Bearing
Contra-Rotating Open Rotor Fans** 259

L. Siozos-Rousoulis, A. I. Kalfas, K. Kritikos, E. Giordano, N. Tantot

- Partially Covered Cylindrical Cavity Flow: Resonance Identification** 267

F. Rodriguez Verdugo, D. B. Stephens, G. Bennett

- Partially Covered Cylindrical Cavity Flow: Application Of An Acoustic Analogy** 275

F. Rodriguez Verdugo, G. Bennett

6.2 Bluff Bodies & VIV

- On the Control of Flow past a Circular Cylinder via a Single Spanwise Protrusion** 283

A. Ekmekci, B. T. Aydin, A. Joshi

- Optimal Energy Harvesting By Vortex-Induced Vibrations In Cables** 291

C. Grouthier, S. Michelin, E. de Langre

- Optimal Control Cylinder Design For Vortex Suppression Behind A Circular Cylinder** 299

M. Subhash Reddy, B. S. V. Patnaik

- Drag Measurements Of A Circular Cylinder With Moving Surface Boundary-Layer Control** 307

I. Korkischko, J. R. Meneghini, R. Konrath

7.1 Tube Arrays

- Simple Shock Oscillator For Modelling A Loosely Supported Tube Subjected To Turbulence And Fluid-Elastic Forces** 313

L. Borsoi, P. Piteau, X. Delaune, J. Antunes

- Vibration Behavior of a Steam Generator Tube in Interaction with an Anti-Vibration Bar: Experimental Study** 321

V. Lalonde, A. Ross, M. J. Pettigrew

- Experimental Study of Fluidelastic Instability in a Rotated Triangular Tube Array Subjected to Two-Phase Cross-Flow** 329

T. Sawadogo, N. Mureithi

- Modelling of Fluidelastic Instability Inside an Inline Square Array** 337

J. B. Anderson, M. Hassan, A. Mohany

7.2 Bluff Bodies & VIV

- Active Control Of Flow Induced Vibrations Of A Bluff Body** 345

M. Sridhar, B. S. V. Patnaik

- A Numerical Investigation Of The Flow Around An Oscillating Circular Cylinder At Low Stokes Number** 353

J. Berland, L. Divaret, P. Moussou, O. Cadot

- Computation Of Flow Around A Circular Cylinder Undergoing Two-Degree-Of-Freedom Forced Motion At Low Reynolds Number** 361

L. Baranyi

- Two-Dimensional Simulation Of The Flow Around A Cylinder With Strakes** 369

B. Carmo

8.1 Axial Flow and Thin Shells

- A Consideration on Nonconservative Elastic Stability of a Beam Subjected to Axial Force Considered to be Fluid Force** 375

K. Fujita, A. Gotou

- On the Nonlinear Dynamics of Cantilevered Circular Cylindrical Shells Conveying Fluid** 383

M. Paak, M. P. Paidoussis, A. K. Misra

- Stiffening Of A Fuel Assembly Under Axial Flow** 391

G. Ricciardi, E. Boccaccio

8.2 Valves

- Study On Pressure Pulsations In Pump-Piping System: Acoustic Interaction Between Pump And Piping** 399

A. Maekawa, T. Tsuji, T. Takahashi, M. Kato

- Fluid-Structure Interaction At Water Hammer Events In Piping Systems** 407

S. Riedelmeier, S. Becker, E. Schlücker

- Experimental Investigation Of Flow-Acoustic Coupling In Gate Valves** 415

O. Barannyk, P. Oshkai

9.1 Tube Arrays

Numerical Study Of Cross-Flow Past Two Staggered Rows Of Cylinders 423

P. Anagnostopoulos, S. Seitanis

Numerical Study Of Tube-Bundle Flow-Induced Vibration With Multiphase-Pod Approach 431

M. Pomarède, E. Liberge, A. Hamdouni, E. Longatte, J. Sigrist

Homogenization Method For The Vibration Of Tube Bundle In A Fluid 439

Q. Desbonnets, D. Broc

9.2 Bluff Bodies & VIV

**Flow Around Circular Cylinder Submitted To Rotational Oscillation And Periodical
Cross Section Variation** 453

H. Oualli, M. Daou, M. L. Aouag, S. Hanchi, A. Bouabdallah

Limiting Amplitude In Vortex-Induced Vibration Of Elastically Mounted Circular Cylinders 457

E. Konstantinidis

Fluid Forces in Streamwise Vortex-Induced Vibrations 465

N. Cagney, S. Balabani

**Drag And Inertia Coefficients Of A Circular Cylinder In A Steady Plus
Low-Amplitude Oscillatory Flow** 473

E. Konstantinidis, A. Dedes, D. Bouris

10.1 Tube Arrays

The "Equivalent Spectrum" Concept For Turbulence Conveying Excitations 481

J. Antunes, L. Borsoi, P. Piteau, X. Delaune

A Model For Drag Coefficient In An Idealized Bubbly Two-Phase Flow 489

C. Béguin, S. Étienne, N. Mureithi, M. J. Pettigrew

State Space Reconstruction Of Experimental Time Series Of Bistable Flow On A Tube Bank 499

A. V. de Paula, S. V. Möller

Identification of mechanisms underlying periodic forces in a tube array subjected to two-phase cross-flow 507

N. Mureithi, M. J. Pettigrew

10.2 Axial Flow and Thin Shells

Flow-Induced Vibration In Subsea Pipework 515

A. Sanchis, K. G. Jakobsen

Flow Induced Vibration of Piping Downstream of Tee Connection 523

M. Nishiguchi, H. Izuchi, I. Hayashi, G. Minorikawa

On The Effects Of Particles Modulating The Acoustic Source Powers Generated In T-Joints 531

S. P. Omrani, J. Golliard, S. Belfroid, N. González Díez

Multiphase Fluid Structure Interaction In Pipe Systems With Multiple Bends 537

S. Belfroid, E. Nennie, E. van Bokhorst, D. Remans

11.1 Bluff Bodies & VIV

Experimental Investigation Of The Flow-Induced Vibration Of A Curved Circular Cylinder 543

G. R. S. Assi, C. M. Freire, I. Korkischko, N. Srinil

Vortex-Induced Vibrations of an Inclined Cylinder in Flow 555

A. Jain, Y. Modarres-Sadeghi

**Comparison Between Force Measurements Of One And Two Degrees-Of-Freedom
Viv On Cylinder With Small And Large Mass Ratio** 561

G. R. Franzini, J. R. Meneghini, R. T. Gonçalves, A. L. C. Fajarra

Modelling of Vortex-Induced Vibrations of Slender Marine Structures 569

A. Postnikov, E. Pavlovskaja, M. Wiercigroch

11.2 Industrial Aeroacoustics

**Experimental Evaluation of Acoustic Resonance at Single Stub Pipe in each Dry
and Wet Steam Flow** 577

Y. Uchiyama, R. Morita

Key Parameters for Noise Generation within Corrugated Pipes 585

H. Goyder

On Whistling Of Pipes With A Corrugated Pipe Segment 593

O. Rudenko, G. Nakiboglu, A. Hirschberg

**Modeling for Combustion Oscillation Experienced in Micro Gas Turbine Combustor
Fueled by Biomass Gas** 599

S. Kaneko, H. Hwang, D. Yamasaki, T. Watanabe, Y. Yamasaki

12.1 Valves

Steel Rod Breaking Excitation to Identify Full-Scale Tainter Gate Dynamics 607

K. Anami, N. Ishii, C. W. Knisely, T. Tsuji, T. Oku, T. Makihata

Mechanisms Of Instability Of Safety Relief Valves In Water Systems 615

H. Berro, P. Moussou

A Theoretical and Experimental Study of a Duckbill Valve 623

J. Wang, S. Tullis, D. S. Weaver

12.2 Axial Flow and Thin Shells

**Output-Only Identification Of An Elastic Panel Coupled To A Fluid: Model-Scale
And Full-Scale Investigations For Ships** 631

D. Dessì, D. D'Orazio

The Influence Of Channel Walls On Flag Flutter 639

O. Doaré, C. Eloy

Flow-Induced Vibrations Of A Flexible Panel In Boundary-Layer Flow 647

J. S. Kapor, A. D. Lucey

13.1 Bluff Bodies & VIV

**Experimental Investigation On Vortex-Induced Vibrations Of Yawed Cylinders
With One And Two Degrees-Of-Freedom**

655

G. R. Franzini, R. T. Gonçalves, A. L. C. Fajarra, J. R. Meneghini

**Karman vortex effect on cross flow response on non-yawed and yawed circular
cylinder in smooth flow**

663

M. Matsumoto, H. Ishizaki, M. Hashimoto

Vortex-Induced Vibrations Of A Flexible Cylinder In Inclined Flow

671

R. Bourguet, G. E. Karniadakis, M. S. Triantafyllou

13.2 High Speed Flow

Experimental Results Of A Fluttering Profile In The Wind Tunnel

677

I. Zolotarev, V. Vclek, J. Kozanek

Numerical Investigation Of Self-Sustained Shock Oscillation Acoustics

681

C. J. O'Reilly, G. Efrainsson, J. Hammar, U. Emborg

**Acoustic Resonances And Aerodynamic Interactions In An Axial Compressor
Stator Stage Test Rig**

689

B. Pardowitz, U. Tapken, L. Enghardt

14.1 Valves

Experimental Analysis Of Aerodynamic Noise Generation In A Rotary Control Valve 697

S. Malavasi, F. C. Bossi

**Experimental and Numerical Investigations of Self-Excited Vibration
of Steam Control Valves** 705

K. Yonezawa, Y. Tsujimoto, T. Endo, K. Tezuka

**Effects Of Internal Pipe Geometry On Acoustic Diametral Modes In
A Steam Control Valve** 713

O. Barannyk, P. Oshkai

14.2 Axial Flow and Thin Shells

Three-Dimensional Dynamics Of Long Pipes Towed Underwater 719

M. Kheiri, M. P. Paidoussis, M. Amabili, B. I. Epureanu

Normal Forces Exerted Upon A Long Cylinder Oscillating In An Axial Flow 727

L. Divaret, P. Moussou, O. Cadot, O. Doaré, J. Berland

Energy Harvesting From Axial Flow-Induced Instabilities In Slender Structures 735

K. Singh, S. Michelin, E. de Langre



Dynamics of fluid-conveying cantilevered pipes with additional adornments

Michael P. Païdoussis

Department of Mechanical Engineering
McGill University
817 Sherbrooke St. West, Montréal, Québec,
H3A 0C3 Canada
Email: michael.paidoussis@mcgill.ca

Marco Amabili

Department of Mechanical Engineering
McGill University
817 Sherbrooke St. West, Montréal, Québec,
H3A 0C3 Canada
Email: marco.amabili@mcgill.ca

Mergen H. Ghayesh

Department of Mechanical Engineering
McGill University
817 Sherbrooke St. West, Montréal, Québec, H3A 0C3 Canada
Email: mergen.hajghayesh@mail.mcgill.ca

ABSTRACT

The subject of this paper is the investigation of the three-dimensional dynamics of a fluid-conveying cantilevered pipe fitted with an end-mass and additionally supported by an array of four springs, attached at a point along its length. In the theoretical analysis, the nonlinear equations of motion are discretized via Galerkin's method, and the resulting equations are solved via Houbolt's finite difference scheme along with the Newton–Raphson method. Experiments were conducted and good qualitative and quantitative agreement with the analytical results was obtained.

INTRODUCTION

The linear dynamics of a plain fluid-conveying cantilevered pipe (i.e. without additional springs or other adornments) has been investigated for many years [1-6]. Some early studies on this system in the presence of additional adornments have been conducted [7, 8], considering the system with an intra-span spring, or a system fitted with additional point masses [9, 10, 11]. The first linear study on a cantilevered pipe with both intra-span spring support and an additional point mass has been conducted in [12], finding that in some cases there arise two Hopf bifurcations, involving different flutter modes, separated by a region of stability.

The first studies on the nonlinear dynamics of fluid-conveying pipes, in the 1980s [13, 14], coincide with the development of theoretical models for the study of 3-D motions of the pipe. Soon after, in the late 1980s and the 90s, the first nonlinear studies on the system with intra-span spring support [15-17] and an end-mass [18] started appearing. The work in [17] was later extended for 3-D motions of pipes fitted with an end-mass and an intra-span

spring support [19-22]. Building on the work in [19-22], here the nonlinear 3-D dynamics of the system is explored in the simultaneous presence of an end-mass and intra-span spring support. The incentive is the expectation that, since each of these added features engenders very interesting dynamics, the two together would do so even more.

PROBLEM STATEMENT, EQUATIONS OF MOTION, AND METHOD OF SOLUTION

Problem statement

A schematic representation of the system considered is shown in Fig.1 (a, b). The system consists of a tubular beam of length L , inner/outer diameter D_i / D_o , flexural rigidity EI , density ρ_p , and mass per unit length m , conveying fluid of density ρ_f and mass per unit length M , with flow velocity U . A concentrated mass m_e is attached to the free end of the pipe and an array of four springs of individual stiffness k , arranged at an angle θ with respect to the z axis, is attached to the pipe at a distance $s = L_s$, s being the distance along the generally deformed pipe, measured from the clamped end.

3-D nonlinear equations of motion

The three-dimensional (3-D) nonlinear equations of motion, for the system with additional intra-span spring support as well as an end-mass, have been derived previously in Ref. [19] via Hamilton's principle.

The resultant equations in dimensionless form in the two orthogonal directions y and z (Fig.1(b)) are given by

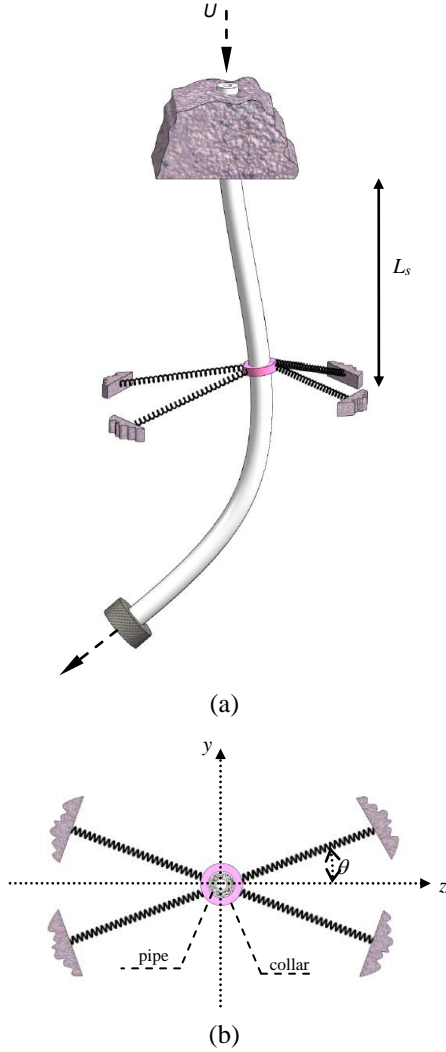


FIG.1. SCHEMATIC REPRESENTATION OF A FLUID CONVEYING CANTILEVERED PIPE WITH AN ARRAY OF INTERMEDIATE SPRINGS AND AN END-MASS: (a) DEFORMED SYSTEM; (b) TOP VIEW SHOWING THE FOUR-SPRING CONFIGURATION, LOCATED ALONG THE PIPE LENGTH AT $X = L_s$.

$$\begin{aligned}
 & \eta'''' + [1 + \Gamma \delta(\xi - 1)] \ddot{\eta} + 2u\sqrt{\beta} \dot{\eta}' + u^2 \eta'' \\
 & + \gamma [1 + \Gamma \delta(\xi - 1)] \eta' - \gamma \eta'' \int_{\xi}^1 [1 + \Gamma \delta(\xi - 1)] d\xi \\
 & + \gamma [1 + \Gamma \delta(\xi - 1)] \left(\frac{1}{2} \eta'^3 + \frac{1}{2} \eta' \zeta'^2 \right) \\
 & - \gamma \left(\frac{3}{2} \eta'^2 \eta'' + \frac{1}{2} \zeta'^2 \eta'' + \eta' \zeta' \zeta'' \right) \int_{\xi}^1 [1 + \Gamma \delta(\xi - 1)] d\xi \\
 & + 2u\sqrt{\beta} \left[\eta'^2 \dot{\eta}' + \eta' \zeta' \dot{\zeta}' - \eta'' \int_{\xi}^1 (\eta' \dot{\eta}' + \zeta' \dot{\zeta}') d\xi \right]
 \end{aligned}$$

$$\begin{aligned}
 & + u^2 \left[\eta'^2 \eta'' + \eta' \zeta' \zeta'' - \eta'' \int_{\xi}^1 (\eta' \dot{\eta}' + \zeta' \dot{\zeta}') d\xi \right] \\
 & + \left[\eta'^2 \eta'''' + 4\eta' \eta'' \eta'''' + \eta''^3 + \eta' \zeta' \zeta'''' \right. \\
 & \left. + 3\eta' \zeta'' \zeta'''' + \eta'' \zeta' \zeta'''' + \eta'' \zeta''^2 \right] \\
 & + \eta' [1 + \Gamma \delta(\xi - 1)] \\
 & \times \int_0^{\xi} (\dot{\eta}'^2 + \eta' \ddot{\eta}' + \dot{\zeta}'^2 + \zeta' \ddot{\zeta}') d\xi \\
 & - \eta'' \int_{\xi}^1 [1 + \Gamma \delta(\xi - 1)] \int_0^{\xi} (\dot{\eta}'^2 + \eta' \ddot{\eta}' + \dot{\zeta}'^2 + \zeta' \ddot{\zeta}') d\xi d\xi \\
 & + \left\{ (\kappa_{y1} \eta + \kappa_{yn1} \eta^3 + \kappa_{yz} \eta \zeta^2) \right. \\
 & \left. + \kappa_x \eta' \int_0^{\xi} (\zeta'^2 + \eta'^2) d\xi \right\} \delta(\xi - \xi_s) \\
 & - \kappa_x \eta'' \mu(0 \rightarrow \xi_s) \int_0^{\xi_s} (\zeta'^2 + \eta'^2) d\xi \\
 & + O(\varepsilon^4) = 0;
 \end{aligned} \tag{1}$$

$$\begin{aligned}
 & \zeta'''' + [1 + \Gamma \delta(\xi - 1)] \ddot{\zeta} + 2u\sqrt{\beta} \dot{\zeta}' + u^2 \zeta'' \\
 & + \gamma [1 + \Gamma \delta(\xi - 1)] \zeta' - \gamma \zeta'' \int_{\xi}^1 [1 + \Gamma \delta(\xi - 1)] d\xi \\
 & + \gamma [1 + \Gamma \delta(\xi - 1)] \left(\frac{1}{2} \zeta'^3 + \frac{1}{2} \zeta' \eta'^2 \right) \\
 & - \gamma \left(\frac{3}{2} \zeta'^2 \zeta'' + \frac{1}{2} \eta'^2 \zeta'' + \zeta' \eta' \eta'' \right) \int_{\xi}^1 [1 + \Gamma \delta(\xi - 1)] d\xi \\
 & + 2u\sqrt{\beta} \left[\zeta'^2 \dot{\zeta}' + \zeta' \eta' \dot{\eta}' - \zeta'' \int_{\xi}^1 (\zeta' \dot{\zeta}' + \eta' \dot{\eta}') d\xi \right] \\
 & + u^2 \left[\zeta'^2 \zeta'' + \zeta' \eta' \eta'' - \zeta'' \int_{\xi}^1 (\zeta' \dot{\zeta}' + \eta' \dot{\eta}') d\xi \right] \\
 & + \left[\zeta'^2 \zeta'''' + 4\zeta' \zeta'' \zeta'''' + \zeta''^3 + \zeta' \eta' \eta'''' \right. \\
 & \left. + 3\zeta' \eta'' \eta'''' + \zeta'' \eta' \eta'''' + \zeta'' \eta''^2 \right] \\
 & + \zeta' [1 + \Gamma \delta(\xi - 1)] \\
 & \times \int_0^{\xi} (\dot{\zeta}'^2 + \zeta' \ddot{\zeta}' + \dot{\eta}'^2 + \eta' \ddot{\eta}') d\xi \\
 & - \zeta'' \int_{\xi}^1 [1 + \Gamma \delta(\xi - 1)] \int_0^{\xi} \left(\dot{\zeta}'^2 + \zeta' \ddot{\zeta}' \right. \\
 & \left. + \dot{\eta}'^2 + \eta' \ddot{\eta}' \right) d\xi d\xi \\
 & + \left\{ (\kappa_{z1} \zeta + \kappa_{zn1} \zeta^3 + \kappa_{yz} \zeta \eta^2) \right. \\
 & \left. + \kappa_x \zeta' \int_0^{\xi} (\zeta'^2 + \eta'^2) d\xi \right\} \delta(\xi - \xi_s) \\
 & - \kappa_x \zeta'' \mu(0 \rightarrow \xi_s) \int_0^{\xi_s} (\zeta'^2 + \eta'^2) d\xi \\
 & + O(\varepsilon^4) = 0;
 \end{aligned} \tag{2}$$

where

$$\begin{aligned}
 \xi &= \frac{s}{L}, \quad \xi_s = \frac{L_s}{L}, \quad \xi_f = \frac{L_f}{L}, \quad \eta = \frac{v}{L}, \quad \zeta = \frac{w}{L}, \\
 \tau &= \left(\frac{EI}{m+M} \right)^{1/2} \frac{t}{L^2}, \quad u = \left(\frac{M}{EI} \right)^{1/2} UL, \\
 \gamma &= \frac{m+M}{EI} \dot{L}^3 g, \quad \beta = \frac{M}{m+M}, \quad \Gamma = \frac{m_e}{(m+M)L}, \\
 f_v &= \frac{F_v L^2}{EI}, \quad f_w = \frac{F_w L^2}{EI}, \quad \Omega = L^2 \sqrt{\frac{M+m}{EI}} \omega, \\
 \kappa_x &= \frac{K_x L^3}{EI}, \quad \kappa_{yl} = \frac{K_{yl} L^3}{EI}, \quad \kappa_{zl} = \frac{K_{zl} L^3}{EI}, \quad \kappa_{ynl} = \frac{K_{ynl} L^5}{EI}, \\
 \kappa_{znl} &= \frac{K_{znl} L^5}{EI}, \quad \kappa_{yz} = \frac{K_{yz} L^5}{EI},
 \end{aligned} \tag{3}$$

and

$$\begin{aligned}
 K_x &= 2k \left(1 - \frac{L_o}{R_o} \right), \quad K_{yl} = 4k \left(1 - \frac{L_o}{R_o} \cos^2 \theta \right), \\
 K_{ynl} &= 2k \frac{L_o}{R_o^3} \cos^2 \theta \left(\cos^2 \theta - 4 \sin^2 \theta \right), \\
 K_{yz} &= 2k \frac{L_o}{R_o^3} \left(15 \cos^2 \theta \sin^2 \theta - 2 \right), \\
 K_{zl} &= 4k \left(1 - \frac{L_o}{R_o} \sin^2 \theta \right), \\
 K_{znl} &= 2k \frac{L_o}{R_o^3} \sin^2 \theta \left(\sin^2 \theta - 4 \cos^2 \theta \right), \\
 K_{yz} &= 2k \frac{L_o}{R_o^3} \left(15 \cos^2 \theta \sin^2 \theta - 2 \right).
 \end{aligned} \tag{4}$$

In Eqs. (1)-(4), s is the dimensional and ξ the dimensionless distance along the pipe from the fixed end, ξ_s the dimensionless location of the attachment point of the springs, η and ζ the dimensionless transverse displacements in the y and z direction, respectively, and t and τ are the dimensional and dimensionless time, respectively; k is the linear stiffness of each spring of the four-spring array at $s = L_s$; L_o and R_o are, respectively, the unstretched and stretched length of each spring; the subscripted K s are constant coefficients related to the spring array, the subscripts identifying the direction to which they are related (x , y or z) and whether they are associated with the linear (l) or nonlinear (nl) components thereof, while the subscripted κ s are the corresponding dimensionless constants. Other than the spring- and force-related system parameters, β and γ are the dimensionless mass and gravimetric parameters, respectively, Γ is a dimensionless end-mass parameter, and u the dimensionless flow velocity. Moreover, δ , as in $\delta(\xi-\xi_s)$, is

the Dirac delta function, equal to 0 or 1 accordingly as $\xi \neq \xi_s$ and $\xi = \xi_s$; also, $\mu(0 \rightarrow \xi_s)$ stands for the Heaviside function, having a value of 1 in the interval $[0, \xi_s]$ and zero elsewhere.

Method of solution

The dimensionless equations of motion, Eqs.(1) and (2), are discretized via the Galerkin method using the eigenfunctions of a plain cantilevered beam as appropriate comparison functions. Houbolt's finite difference scheme along with the Newton-Raphson method are employed to solve the resultant discretized equations, yielding the time-varying generalized coordinates. From time histories of the generalized coordinates and the reconstructed η (ξ, τ) and ζ (ξ, τ) time histories, bifurcation diagrams, phase-plane plots, power spectral densities (PSDs), probability density functions (PDFs), and autocorrelations were constructed at points of interest in the parameter space. PSDs have been obtained via the Fast Fourier Transform technique.

In the results presented in this study, eight beam modes are employed in each transverse direction (η and ζ directions); totaling 16 beam modes. This is sufficient to give converged results. To make sure that this is true, 10 beam modes in each direction (totaling 20 beam modes) have been employed, and convergence was confirmed.

Of course, to obtain $\eta(\xi, \tau)$ and $\zeta(\xi, \tau)$, initial conditions must be utilized. If all initial conditions, for all generalized coordinates, are in one direction only, the resultant solution is 2-D in that direction, even if a set of initial conditions with components both in the y and z directions yields 3-D motion; obviously the latter is preferred. All results presented in this study have been obtained using the same initial conditions for all flow velocities.

In the theoretical calculations, the following parameters, corresponding to the system used in the experimental study, have been used: $L = 0.443$ m, $D_i = 6.4$ mm, $D_o = 15.7$ mm, $EI = 7.42 \times 10^{-3}$ N·m², $\rho_p = 1167$ kg/m³, $\rho_f = 999$ kg/m³, $m = 0.189$ kg/m, $M = 0.0320$ kg/m, $L_o = 0.0635$ m, $k = 17.63$ N/m, $R_o = 0.1160$ m and 0.1640 m (for $\theta = 0^\circ$ and 45° , respectively); $\gamma = 25.3$, $\beta = 0.145$ and $\Gamma = 0.1$.

THEORETICAL RESULTS

The spring-support is located at $\xi_s = 0.2$, near the clamped end of the pipe, and for the sample results presented in this paper all four springs are in the same plane; $\theta = 0^\circ$ (see Fig.1), two on each side. A point mass with $\Gamma = 0.1$ is attached at the free end.

The bifurcation diagram for this system, illustrating the dimensionless maximum and minimum free-end displacements η and ζ , respectively in the y and z directions, versus dimensionless flow velocity, u , is shown in Fig.2.

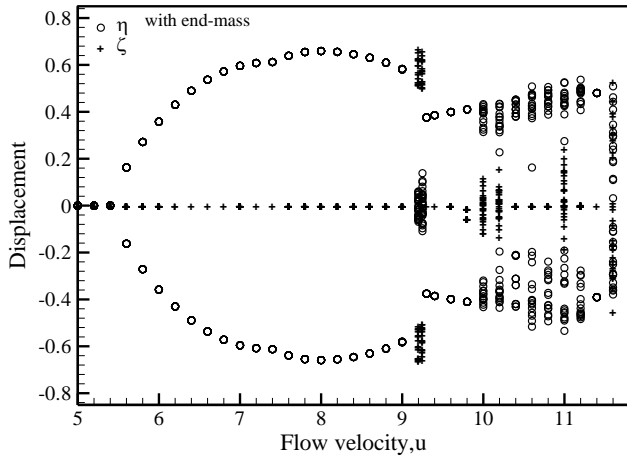


FIG.2. BIFURCATION DIAGRAM FOR THE PIPE WITH $\theta = 0^\circ$ (THE SPRINGS ARE ALIGNED ALONG THE Z-AXIS), $\xi_s = 0.2$, and $\Gamma = 0.1$.

As shown, the system remains at its original equilibrium position prior to losing stability by a supercritical Hopf bifurcation in the η direction at $u = 5.6$, giving rise to a periodic oscillation. Figure 3 shows (a) the time history, (b) the motion of the free end (tip) of the pipe in a plane perpendicular to the pipe, (c) the phase-plane portrait for the η motion, (d) a PSD plot for the η motion, showing the main frequency of oscillation $f = 2.93$ (in cycles per dimensionless second), as well as harmonics thereof, (e) the PDF of the η motion, displaying two prominent peaks at the extremes of the displacement as an identifier of periodic motion, and (f) the autocorrelation of the η motion, which is periodic with time.

At $u = 9.2$ (see Fig. 2), the motion is 3-D quasiperiodic, with larger amplitude in the ζ direction (in the plane of the springs and the pipe). The return to periodic flutter at $u = 9.3$ is accompanied by an amplitude jump, as shown very clearly in Fig.2. Before the amplitude jump, say at $u = 9.0$ the motion is periodic and it involves mainly first and second beam-mode travelling-wave¹ components, the latter being dominant; whereas, at $u = 9.3$, the motion is again periodic but of considerably smaller amplitude, with the third beam-mode dominant. This jump phenomenon is also accompanied by a frequency jump from $f = 3.42$ at $u = 9.0$ to $f = 6.65$ at $u = 9.3$.

At $u = 9.8$, the system oscillates in the ζ direction as well; the 3-D periodic oscillation displays a figure-of-eight-cross-sectional form. This periodic motion becomes 3-D quasiperiodic once again at $u = 10.0$, as seen in Fig.4 ($f_1 = 0.47$ and $f_2 = 6.47$; $f_3 = 2f_2 - f_1$ and $f_4 = 3f_2 - 2f_1$ et seq.).

The motion becomes chaotic in the range $10.2 \leq u \leq 11.6$, except for a window at $u = 11.4$, where the motion is periodic.

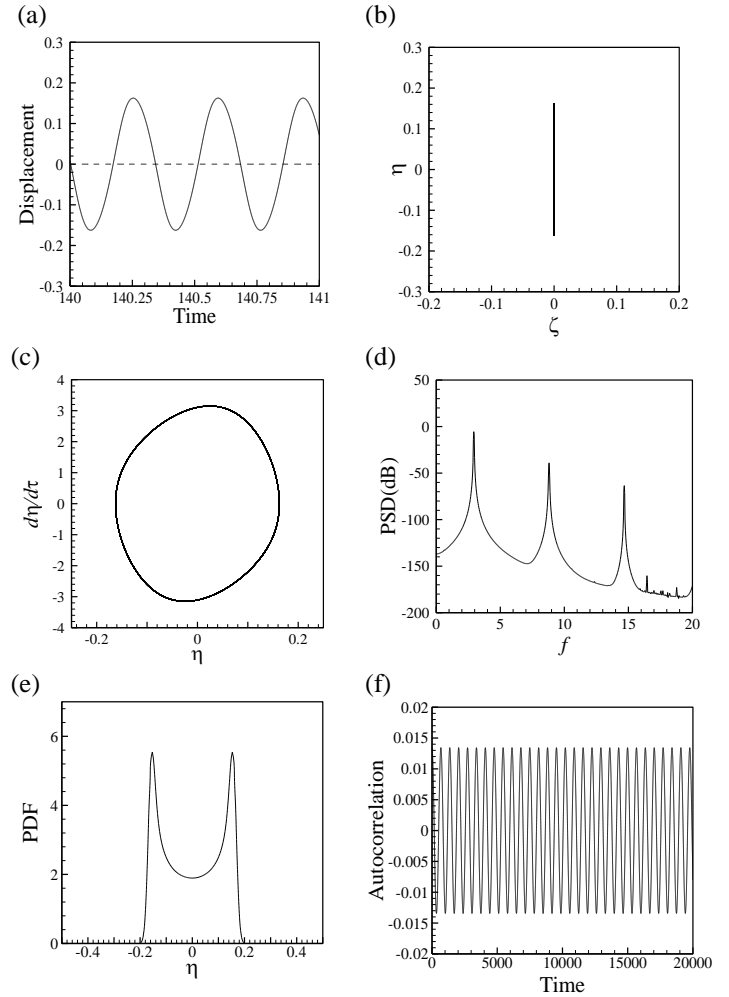


FIG.3. PLANAR OSCILLATIONS FOR THE SYSTEM WITH $\theta = 0^\circ$ AND $\xi_s = 0.2$ AT A DIMENSIONLESS FLOW VELOCITY OF $u = 5.6$: (a) TIME TRACE OF η (SOLID LINE) AND ζ (DASHED LINE); (b) THE MOTION OF THE FREE END (TIP) OF THE PIPE IN A PLANE PERPENDICULAR TO THE PIPE; (c-f) PHASE-PLANE DIAGRAM, PSD PLOT, PDF, AND AUTOCORRELATION OF THE η MOTION.

EXPERIMENTAL INVESTIGATION

Apparatus, procedure and data analysis

Experiments were conducted with a silicone rubber pipe and an aluminium end-mass with the geometrical and physical characteristics corresponding to the theoretical values mentioned in the previous section. A closed-circuit water circulation system, similar to the system utilized by Païdoussis et al. [20], was used; its description can be found therein.

The procedure in the experimental investigation and data analysis are described in what follows.

¹ A travelling-wave component is characterized by the instantaneous node(s) and antinode(s) moving with time along the pipe.

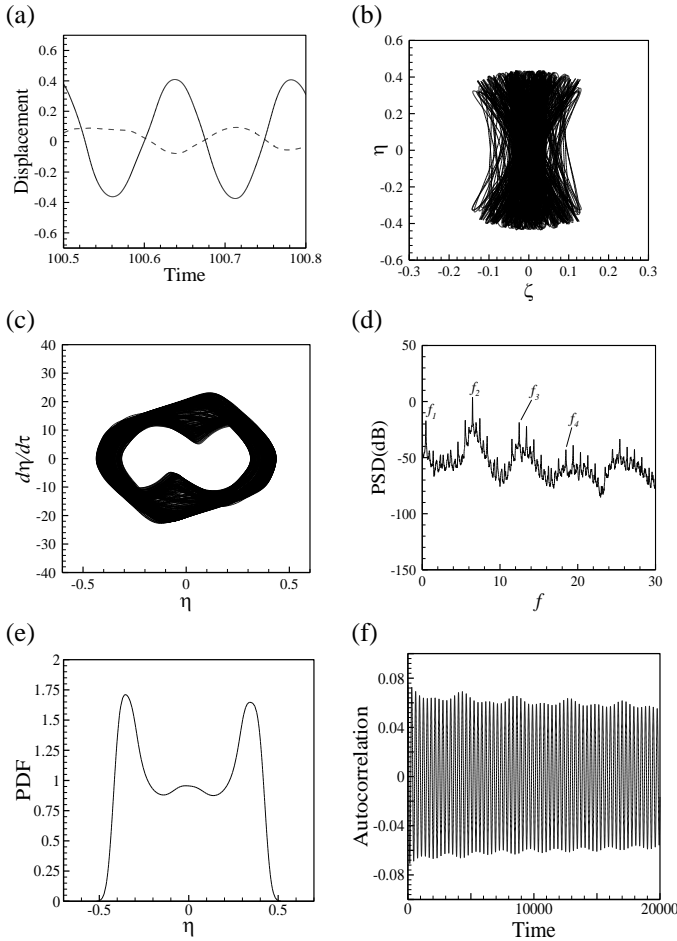


FIG.4. 3-D QUASIPERIODIC MOTION FOR THE SYSTEM WITH $\theta = 0^\circ$ AND $\xi_s = 0.2$ AT $u = 10.0$: (a) TIME TRACE OF η (SOLID LINE) AND ζ (DASHED LINE); (b) TOP VIEW OF THE TIP DISPLACEMENT; (c) PHASE-PLANE DIAGRAM OF THE η MOTION ; (d) PSD PLOT OF THE η MOTION, SHOWING THE DIMENSIONLESS FUNDAMENTAL FREQUENCIES $f_1 = 0.47$ AND $f_2 = 6.47$; (e, f) PDF AND AUTOCORRELATION OF THE η MOTION.

- (i) The flow rate was increased from zero gradually, allowing enough time for the transient motions to die out. The dynamical behaviour of the system was first observed qualitatively, before undertaking any measurements.
- (ii) The experiment was then repeated several times, this time recording the flow velocities at which the qualitative behaviour changed (higher order bifurcations occurred), along with video recordings of the observed motions.
- (iii) For each state, the displacement of a point along the pipe length was measured with the Optron 806-50-X instrument, which is a non-contacting optical tracking system, allowing

the measurement of the transverse displacement of that point of the pipe.

- (iv) The recorded signal (time trace) was filtered and stored in the computer by means of LabVIEW. An FFT spectral analysis was then made by implementing Welch's method in MATLAB. The FFTs, PDFs and autocorrelations helped in identifying periodic, quasiperiodic and chaotic oscillations.

The experimental results along with their theoretical counterparts are given in the form of a table for various bifurcations. The values of dimensionless flow velocities and frequencies are accurate to within ± 0.05 . It is also helpful to mention that, for quasiperiodic motions, the two fundamental frequencies have been chosen in a consistent manner in both the theoretical and experimental PSDs.

Experimental results showed that planar flutter involving only the η motion developed at $u = 5.4$ with frequency $f = 2.9$. As the flow rate was increased, the amplitude of flutter increased and the oscillation became quasiperiodic at $u = 9.9$, with fundamental frequencies $f_1 = 0.75$ and $f_2 = 2.11$. Increasing the flow velocity a little, an amplitude reduction occurred at $u = 10$ with $f = 5.9$ accompanied by η -motion flutter. The pipe ultimately developed to chaotic-like² motion at $u = 10.5$, with a dominant periodic component of $f = 6.1$. Before the amplitude reduction, the travelling-wave flutter was mainly associated with the second beam-mode travelling-wave component, and after that the third beam-mode.

As seen in Table 1, the experimental results are in good agreement with the theoretical ones, not only qualitatively but also quantitatively.

Other theoretical and experimental results, e.g. for $\theta = 45^\circ$, are available, displaying similarly good agreement between the two.

CONCLUSIONS

In this paper, the 3-D nonlinear dynamics of a cantilevered pipe fitted with an end-mass and additionally supported by an intra-span spring array has been investigated theoretically and experimentally.

As the flow velocity was increased, a succession of bifurcations occurred, with intervals of periodic, quasiperiodic and chaotic oscillations, involving two- or three-dimensional motions.

The same system was investigated experimentally and agreement with the theoretical predictions was found to be good. Thus, the theoretical model has been broadly validated.

² There is a strong periodic component plus a small chaotic component.

TABLE 1
FLOW VELOCITIES AND FREQUENCIES OF
BIFURCATION POINTS FOR
THE SYSTEM WITH $\xi_S = 0.2$, $\theta = 0^\circ$ AND $\Gamma = 0.1$:
THEORY VERSUS EXPERIMENT

	Values of u		Values of f^3	
	Theory	Experiment	Theory	Experiment
Planar flutter	5.6	5.4	2.93	2.9
First quasiperiodic motion (3D)	9.2	9.9	0.64 and 2.33	0.75 and 2.11
First planar oscillation after the amplitude reduction	9.4	10	6.7	5.9
Chaos (chaotic in theory and chaotic-like in experiment)	10.2	10.5	⁴	-

ACKNOWLEDGMENTS

The authors wish to express their appreciation to the Natural Sciences and Engineering Research Council (NSERC) of Canada for supporting this research, and the first author is also grateful for a MEDA Award awarded to him by McGill University.

REFERENCES

- [1, 2] Benjamin, T.B., 1961. "Dynamics of a system of articulated pipes conveying fluid, I and II". Proceedings of the Royal Society **A261**, pp. 457-486, 487-499.
- [3, 4] Gregory, R.W., Païdoussis, M.P., 1966. "Unstable oscillations of tubular cantilevers conveying fluid – Parts I and II". Proceedings of the Royal Society **A 293**, pp. 512-527, 528-542.
- [5] Herrmann, G., Nemat-Nasser, S., 1967. "Instability modes of cantilevered bars induced by fluid flow through attached pipes". *International Journal of Solids and Structures*, **3**, pp. 39-52.
- [6] Païdoussis, M.P., 1970. "Dynamics of tubular cantilevers conveying fluid". *Journal of Mechanical Engineering Science*, **12**, pp. 85-103.
- [7] Chen, S.S., 1971. "Flow-induced instability of an elastic tube", ASME Paper No. 71-Vibr-39.
- [8] Sugiyama, Y., Tanaka, Y., Kishi, T., Kawagoe, H., 1985. "Effect of a spring support on the stability of pipes conveying fluid". *Journal of Sound and Vibration*, **100**, pp. 257-270.
- [9] Hill, J. L., Swanson, C. P., 1970. "Effects of lumped masses on the stability of fluid conveying tubes". *Journal of Applied Mechanics*, **37**, pp. 494-497.
- [10] Chen, S.S., Jendrzejczyk, J.A., 1985. "General characteristics, transition, and control of instability of tubes conveying fluid". *Journal of the Acoustical Society of America* **77**, pp. 887-895.
- [11] Jendrzejczyk, J.A., Chen, S.S., 1985. "Experiments on tubes conveying fluid". *Thin Walled Structures*, **3**, pp. 109-134.
- [12] Sugiyama, Y., Kawagoe, H., Kishi, T., Nishiyama, S., 1988. "Studies on the stability of pipes conveying fluid (the combined effect of a spring support and a lumped mass)". *JSME International Journal, Series 1* **31**, pp. 20-26.
- [13] Rousselet, J., Herrmann, G., 1981. "Dynamic behaviour of continuous cantilevered pipes conveying fluid near critical velocities". *Journal of Applied Mechanics*, **48**, pp. 943-947.
- [14] Bajaj, A.K., Sethna, P.R., Lundgren, T.S., 1980. "Hopf bifurcation phenomena in tubes carrying fluid". *SIAM Journal of Applied Mathematics*, **39**, pp. 213-230.
- [15] Steindl, A., Troger, H., 1988. "Flow induced bifurcations to 3-dimensional motions of tubes with an elastic support". In *Trends in Applications of Mathematics to Mechanics* (eds J.F. Besserling & W. Eckhaus), pp. 128-138.
- [16] Steindl, A., Troger, H., 1995. "Nonlinear three-dimensional oscillations of elastically constrained fluid conveying viscoelastic tubes with perfect and broken O(2)-symmetry". *Nonlinear Dynamics*, **7(2)**, pp. 165-193.
- [17] Païdoussis, M.P., Semler, C., 1993. "Nonlinear dynamics of a fluid-conveying cantilevered pipe with an intermediate spring support". *Journal of Fluids and Structures*, **7**, pp. 269-298.
- [18] Copeland, G.S., Moon, F.C., 1992. "Chaotic flow-induced vibration of a flexible tube with end mass". *Journal of Fluids and Structures*, **6**, pp. 705-718.
- [19] Wadham-Gagnon, M., Païdoussis, M.P., Semler, C., 2007. "Dynamics of cantilevered pipes conveying fluid. Part 1: Nonlinear equations of three-dimensional motion". *Journal of Fluids and Structures*, **23**, pp.545-67.
- [20] Païdoussis, M.P., Semler, C., Wadham-Gagnon, M., Saaïd, S., 2007. "Dynamics of cantilevered pipes conveying fluid. Part 2: Dynamics of the system with intermediate spring support". *Journal of Fluids and Structures*, **23**, pp.569-87.
- [21] Modarres-Sadeghi, Y., Semler, C., Wadham-Gagnon, M., Païdoussis, M.P., 2007. "Dynamics of cantilevered pipes conveying fluid. Part 3: Three-dimensional dynamics in the presence of an end-mass". *Journal of Fluids and Structures*, **23**, pp.589-603.
- [22] Ghayesh, M.H., Païdoussis, M.P., 2010. "Three-dimensional dynamics of a cantilevered pipe conveying fluid, additionally supported by an intermediate spring array". *International Journal of Non-Linear Mechanics*, **45**, pp. 507-524.

³ f is dimensionless frequency (cycles per dimensionless second).

⁴ The experimental apparatus could not reach u greater than 11.8.

LOW ORDER RESONANCE OF AN ELASTIC FLUID-CONVEYING TUBE

Richard Jurisits*

Alois Steindl

Vienna University of Technology

Institute of Mechanics and Mechatronics

Wiedner Hauptstrasse 8/325, A-1040 Vienna, Austria.

Email: richard.jurisits@tuwien.ac.at

ABSTRACT

The two-dimensional motion of a slender elastic fluid-carrying tube is considered. The tube is clamped at the upper end, at its lower end a point mass is fixed, and at some intermediate position two springs support the tube in transversal direction. Adopting model equations for the tube-liquid system from previous works, the loss of stability of the trivial position of the tube is investigated. While a linear stability analysis indicates several possibilities of stability losses, special attention is paid to the Hopf-Hopf (coupled Flutter) instability where the occurrence of a (1 : 3) internal resonance is detected for distinct parameter values. In a non-linear analysis the post-bifurcation behaviour is investigated for the case of the (1 : 3) resonance. For limiting cases, the dynamics of the tube is shown to be described by Duffing's and by Mathieu's equation, respectively, associated with (quasi)periodic motions of the tube.

INTRODUCTION

Motivated by the article [1], we consider a slender elastic tube according to Fig.1, which is clamped at the upper end and has a point mass m fixed to its lower end $s=l$. Only two-dimensional motions are considered, where u and z denote the horizontal and the vertical displacement, respectively, of a tube element. The centerline of the tube is assumed to be inextensible, and the fluid being carried has a constant relative velocity U relative to the tube tangent to the centerline. Two springs with constants c are fixed to the tube at the position $s=l\xi$ (with $0 < \xi < 1$) and exert forces only in horizontal direction. The material of the tube obeys a Kelvin-Voigt material law [2], where the coefficient α describes the internal

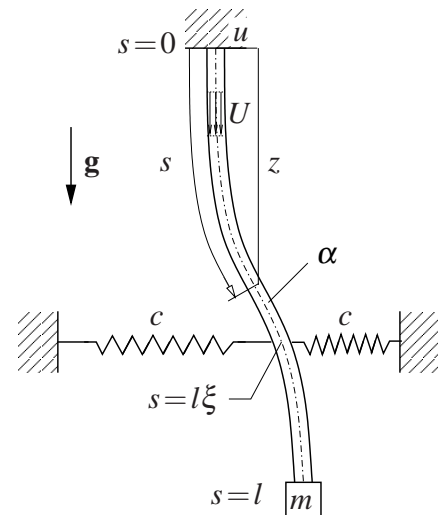


FIGURE 1: PROBLEM SKETCH: THE FLUID CARRYING TUBE.

damping. \mathbf{g} denotes the gravity acceleration vector.

We adopt the model equations for the tube system from the literature, see [2–4]. With m_T and m_F denoting the masses per unit length of the tube and the fluid, respectively, and EJ denoting the flexural rigidity of the tube, the model equations may be non-dimensionalized according to the following change of variables and definitions of parameters:

$$s \rightarrow \frac{s}{l}, \quad t \rightarrow \sqrt{\frac{EJ}{m_T + m_F}} \frac{t}{l^2}, \quad u \rightarrow \frac{u}{l}, \quad (1)$$

$$\alpha \rightarrow \sqrt{\frac{J}{(m_T + m_F)E}} \frac{\alpha}{l^2}, \quad c \rightarrow \frac{2l^3}{EJ} c, \quad (2)$$

*Address all correspondence to this author.

$$\beta := \frac{m_F}{m_T + m_F}, \quad \gamma := \frac{m_T + m_F}{EJ} l^2 g, \quad (3)$$

$$\Gamma := \frac{m}{(m_T + m_F)l}, \quad \rho := \sqrt{\frac{m_F}{EJ}} Ul, \quad (4)$$

The dimension-free governing equations then read in the standard form of a dynamical system:

$$\mathbf{w} = (w_1, w_2) = (u, \dot{u}), \quad \boldsymbol{\lambda} = (\rho, \Gamma, \alpha, \xi), \quad (5)$$

$$\dot{\mathbf{w}} = \mathbf{A}(\boldsymbol{\lambda})\mathbf{w} + \mathbf{g}(\mathbf{w}, \boldsymbol{\lambda}), \quad \mathbf{A}(\boldsymbol{\lambda}) = \begin{pmatrix} 0 & 1 \\ -C & -B \end{pmatrix}, \quad (6)$$

with the differential operators B and C given by

$$Cw_1 = w_1'''' + \rho^2 w_1'' - \gamma[(1 + \Gamma - s)w_1']', \quad (7)$$

$$Bw_2 = \alpha w_2'''' + 2\sqrt{\beta}\rho w_2'. \quad (8)$$

Here, primes denote partial derivatives with respect to s . The vector \mathbf{g} contains the non-linear part of the equations of motion, and the parameters collected in the vector $\boldsymbol{\lambda}$ are the distinguished parameters of the problem. The deflection z then follows with eq.(5) from the kinematic boundary condition

$$(u')^2 + (z')^2 = 1, \quad (9)$$

which represents the inextensibility constraint. It should be noted that neither the friction force between the tube and the fluid enters eqs.(5) and (6) as it is an inner force of the system, nor does the fluid pressure, which gives rise to a force on the tube element only in axial direction that can be eliminated by using D'Alembert's principle. The supplementary boundary and intermediate conditions in linearized form are

$$s=0: \quad w_1 = w_1' = 0, \quad (10)$$

$$s=\xi: \quad w_1'''(\xi+) + \alpha w_2'''(\xi+) - w_1'''(\xi-) - \alpha w_2'''(\xi-) = -cw_1(\xi), \quad (11)$$

$$s=1: \quad w_1''' + \alpha w_2''' = \Gamma(\gamma w_1' + \dot{w}_2), \\ w_1'' + \alpha w_2'' = 0, \quad (12)$$

The conditions (10)-(12) represent the clamping at the upper end of the tube, the intermediate force jumping due to the elastic support, the force due to the fixed point mass and the zero bending moment at the free end of the tube, respectively.

The equations of motion (6) as well as the boundary conditions (10)-(12) possess a \mathbf{Z}_2 symmetry which represents the symmetry of the system with respect to reflections at the vertical axis through the origin.

LINEAR STABILITY ANALYSIS

Performing a linear stability analysis of the straight downhanging (trivial) equilibrium position of the tube ($u = 0, \dot{u} = 0$) is achieved by quasistatically increasing one of the distinct parameters in $\boldsymbol{\lambda}$ with all the other parameters held fixed, until (at least) one real part of an eigenvalue of \mathbf{A} will become zero, in case of which the trivial position becomes unstable. Dependent on the parameter ranges, the following cases may be encountered (\mathbf{J}_c denotes the critical submatrix of the Jordan form of \mathbf{A}):

- (1) Static (steady-state) bifurcation: simple zero eigenvalue of \mathbf{A}

$$\mathbf{J}_c = (0) \quad (13)$$

- (2) Hopf bifurcation: purely imaginary eigenvalues $\pm i\omega$ of \mathbf{A}

$$\mathbf{J}_c = \begin{pmatrix} 0 & -\omega \\ \omega & 0 \end{pmatrix} \quad (14)$$

- (3) Takens-Bogdanov bifurcation: double zero eigenvalue of \mathbf{A}

$$\mathbf{J}_c = \begin{pmatrix} 0 & 1 \\ 0 & 0 \end{pmatrix} \quad (15)$$

- (4) Hopf-Hopf bifurcation coupling: two pairs of purely imaginary eigenvalues $\pm i\omega_1, \pm i\omega_2$ of \mathbf{A}

$$\mathbf{J}_c = \begin{pmatrix} 0 & -\omega_1 & & \\ \omega_1 & 0 & & \\ & & 0 & -\omega_2 \\ & & \omega_2 & 0 \end{pmatrix} \quad (16)$$

Although more degenerate cases of stability loss may be of interest (cf. [5], [3]), we will focus on case (4) in the present study.

Solving the equation of motions (6) for the different cases (1)-(4) leads to a three-point boundary value-inverse eigenvalue problem of a system of four 1st-order ordinary differential equations, which was solved numerically using the code BOUNDSCO [6] and a homotopy method [7]. The numerical values for the parameters were taken from measurements of [1]:

$$E = 2558 \text{ N/m}^2, \quad J = 0,290 \text{ cm}^4, \quad (17)$$

$$l = 44,3 \text{ cm}, \quad m_F = 0,0320 \text{ kg/m}, \quad (18)$$

$$m_T = 0,189 \text{ kg/m}, \quad g = 9,81 \text{ kg/ms}^2 \quad (19)$$

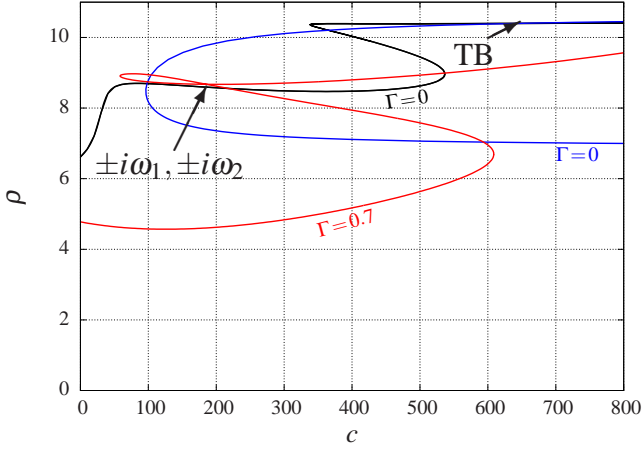


FIGURE 2: STABILITY DIAGRAM. FIXED PARAMETER VALUES $\xi = 0.78$ AND $\alpha = 2 \times 10^{-3}$. BLUE LINE: STATIC INSTABILITY (CASE (1), EQ.(13)), BLACK AND RED LINE: HOPF INSTABILITY (CASE (2), EQ.(14)).

In comparing with results in [1], it should be noted that no material damping has been included in [1], in contrast to the present study. This is of no concern for the instability boundaries with respect to steady-state bifurcations, but the Hopf instability boundaries may be influenced appreciably by the inclusion of material damping.

Figure 2 shows the resulting stability boundaries with respect to the static and to the Hopf instability for the parameter values indicated. While all the other parameters are fixed, Fig.2 shows the critical values of ρ in dependence on the value of c . As can be observed, for certain parameter constellations the coupled cases of a Takens-Bogdanov instability (case (3), eq.(15)), and of a Hopf-Hopf instability (case (4), eq.(16)) occur. The latter case is associated with a point at which the stability curve intersects with itself (“loop”), leading to an instability with two different eigenfrequencies ω_1 and ω_2 of the system. Such cases are of interest with respect to the dynamics, since if the two frequencies are multiples of each other, a so called internal resonance will occur, which leads to a different post-bifurcation behaviour compared to the non-resonant case, as we will show later in the non-linear analysis of the problem in the next section.

In Fig.3 the two black curves represent the instability boundaries with respect to a Hopf-instability for two different values of the parameter Γ . Now letting the parameter Γ vary (along with ρ and c), the red line shows the points at which the Hopf-instability curves intersect with themselves, starting (arbitrarily) from the point marked by the black cross and terminating in the point marked by the red cross. The red crossed point is the threshold

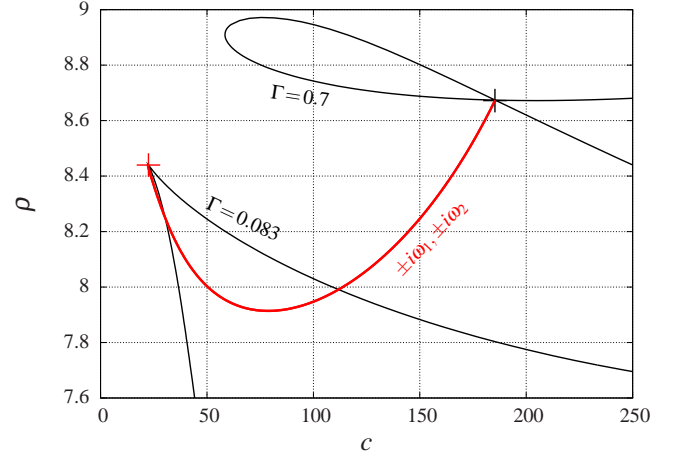


FIGURE 3: STABILITY DIAGRAM SHOWING HOPF-HOPF INSTABILITY COUPLING (RED LINE). FIXED PARAMETER VALUES $\xi = 0.78$ AND $\alpha = 2 \times 10^{-3}$.

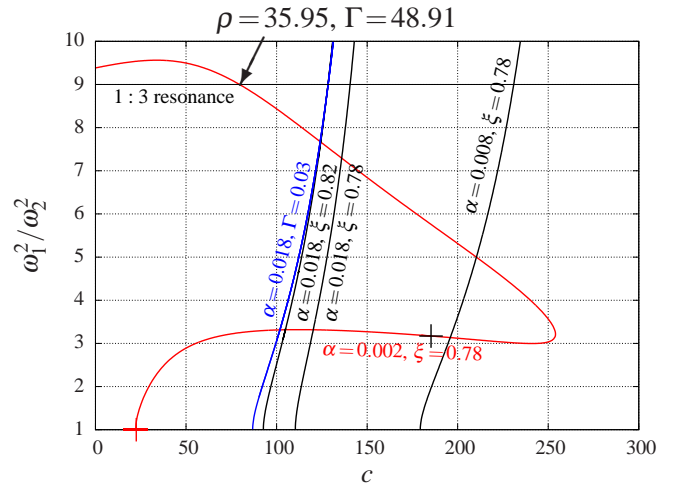


FIGURE 4: SQUARE OF THE FREQUENCY RATIO ALONG HOPF-HOPF STABILITY COUPLINGS FOR DIFFERENT BUT FIXED PARAMETER VALUES AS INDICATED.

beneath lower values of Γ no Hopf-Hopf couplings exist.

Figure 4 shows the squared fraction of the frequencies ω_1 and ω_2 as a function of c along Hopf-Hopf instability boundaries for the indicated parameter values held fixed. The red line in Fig.4 corresponds to the red line in Fig.3, where the red crossed point again marks the threshold for the existence of the Hopf-Hopf coupling. The black and blue curves correspond to different values of the same parameters held fixed. At that threshold, the two eigenfrequencies ω_1 and ω_2 merge for all the cases. As can be observed, the variation of the frequency fraction depends moderately on the parameter Γ but strongly on the parameter α .

Furthermore, the existence of an $(1 : 3)$ internal resonance for all the cases can be observed. The distinct parameter values for ρ and Γ on the occurrence of an $(1 : 3)$ internal resonance are indicated for the red curve. This low-order resonance is of specific interest because it is the lowest order resonance leading to a different (more complex) post-bifurcation behavior in case of a stability loss with respect to Hopf instabilities, as we will explain in the next section.

NON-LINEAR STABILITY ANALYSIS

Dimensional Reduction and Bifurcation Equations

To gain insight into the dynamics of the tube-liquid system in case of stability loss with respect to a Hopf (flutter) instability and the couplings therein, the techniques of dimensional reduction and the transformation to normal form is applied, see [3, 8]. By considering only the critical submatrix \mathbf{J}_c of \mathbf{A} , a near-identity but non-linear transformation on the variables is applied in a way such that as many of the (lowest order) non-linear terms can be eliminated. The resulting bifurcation equations still contain the complete dynamics of the system. This procedure is standard for the Hopf and Hopf-Hopf instability and can be found, e.g., in [3, 8]. In case of a simple Hopf bifurcation, the dimension of the critical submatrix is $\dim(\mathbf{J}_c) = 2 \times 2$, and the reduction process leads to two bifurcation equations, which can be summarized in one equation in complex notation $z_1 \in \mathbb{C}$

$$\dot{z}_1 = (\lambda + i\omega + A_1|z_1|^2)z_1 + \mathcal{O}(z_1^5) \quad (20)$$

Here, all quadratic terms and all cubic terms except for the one retained in eq.(20) have been eliminated. Higher order non-linearities, which are of $\mathcal{O}(z_1^5)$ in this case, will be omitted. This is justified as long as A_1 will not become zero. The parameter λ introduced in eq.(20) is a unfolding parameter needed to investigate the different cases of post-bifurcation behaviour in case of loss of stability. Since the co-dimension of this problem is one, only one unfolding parameter is involved.

In case of a Hopf-Hopf interaction bifurcation without low-order internal resonances, $\dim(\mathbf{J}_c) = 4 \times 4$ and the bifurcation equations are

$$\dot{z}_1 = (\lambda + i\omega_1 + A_1|z_1|^2 + A_2|z_2|^2)z_1 + \mathcal{O}(z_1^5, z_2^5), \quad (21)$$

$$\dot{z}_2 = (\mu + i\omega_2 + A_4|z_1|^2 + A_5|z_2|^2)z_2 + \mathcal{O}(z_1^5, z_2^5), \quad (22)$$

with $z_1, z_2 \in \mathbb{C}$ and two unfolding parameters λ and μ . Note that neither eq.(20) nor eqs.(21) and (22) contain even

TABLE 1: RESONANCE CONDITION FOR $m = 2$

eq.(23)	m_1	m_2	m_3	m_4	
	2	1	0	0	$ z_1 ^2 z_1$
	1	0	1	1	$ z_2 ^2 z_1$
	0	1	1	0	$\bar{z}_1 z_2$
eq. (24)	m_1	m_2	m_3	m_4	
	1	1	1	0	$ z_1 ^2 z_2$
	0	0	2	1	$ z_2 ^2 z_2$
	2	0	0	0	z_1^2

order non-linear terms, which is a consequence of the reduction process in which the \mathbf{Z}_2 symmetry is maintained in the bifurcation equations.

For the case of a Hopf-Hopf interaction bifurcation in presence of low-order resonances, the normal form can be calculated with the aid of the so called resonance condition. If a $(\omega_1 : \omega_2) = (1 : m)$ -resonance with given frequencies ω_1 and ω_2 of integer fraction m is present, the resonance condition reads (see [3])

$$m_1(i\omega_1) + m_2(-i\omega_1) + m_3(im\omega_1) + m_4(-im\omega_1) = i\omega_1 \quad (23)$$

$$m_1(i\omega_1) + m_2(-i\omega_1) + m_3(im\omega_1) + m_4(-im\omega_1) = im\omega_1. \quad (24)$$

If this condition can be fulfilled with certain integers m_1, m_2, m_3 and m_4 , the corresponding monomial non-linear term cannot be eliminated by the reduction process and therefore must be retained in the bifurcation equations.

Table 1 gives an overview of the smallest integers fulfilling the resonance conditions eqs.(23) and (23) for the case of a $(1 : 2)$ internal resonance, i.e. $m = 2$. The last column indicates the monomials which cannot be eliminated. As can be seen, some quadratic terms could not be eliminated, but such terms are not present in the critical equations, and some cubic terms must be retained. These cubic terms are already present in the non-resonant case, cf. eqs. (21) and (22). Hence, the dynamics (and the bifurcation equations) remain unchanged with respect to the non-linear behaviour in the case of a $(1 : 2)$ internal resonance compared to the non-resonant case.

This is different in the case of a $(1 : 3)$ internal resonance. Table 2 shows the resonance condition for that case, i.e. $m = 3$. Two new cubic terms, highlighted in red in Tab.2, have to be retained in the bifurcation equations compared to the non-resonant case. The $(1 : 3)$ resonance therefore is the lowest order internal resonance leading

TABLE 2: RESONANCE CONDITION FOR $m = 3$

eq.(23)	m_1	m_2	m_3	m_4	
	2	1	0	0	$ z_1 ^2 z_1$
	1	0	1	1	$ z_2 ^2 z_1$
	0	2	1	0	$\bar{z}_1^2 z_2$

eq.(24)	m_1	m_2	m_3	m_4	
	1	1	1	0	$ z_1 ^2 z_2$
	0	0	2	1	$ z_2 ^2 z_2$
	3	0	0	0	z_1^3

to a different post-bifurcation behaviour compared to the non-resonant case.

The resulting bifurcation equations for a Hopf-Hopf interaction bifurcation in case of an (1 : 3) internal resonance are

$$\dot{z}_1 = (\lambda + i\omega + A_1|z_1|^2 + A_2|z_2|^2)z_1 + A_3\bar{z}_1^2 z_2, \quad (25)$$

$$\dot{z}_2 = (\mu + 3i\omega + i\delta + A_4|z_1|^2 + A_5|z_2|^2)z_2 + A_6 z_1^3, \quad (26)$$

where the additional terms compared to the non-resonant case are highlighted in red.

Equations (25) and (26) can be conveniently rewritten in polar co-ordinates $z_i = r_i e^{i\varphi_i}$ ($i = 1, 2$)

$$\dot{r}_1 = (\lambda + \text{Re}A_1 r_1^2 + \text{Re}A_2 r_2^2)r_1 + \text{Re}[A_3 e^{-i(3\varphi_1 - \varphi_2)}]r_1^2 r_2, \quad (27)$$

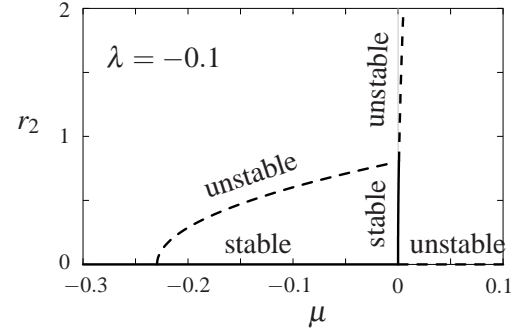
$$\dot{r}_2 = (\mu + \text{Re}A_4 r_1^2 + \text{Re}A_5 r_2^2)r_2 + \text{Re}[A_6 e^{i(3\varphi_1 - \varphi_2)}]r_1^3, \quad (28)$$

$$\begin{aligned} (3\varphi_1 - \varphi_2)' = & -\delta + (3\text{Im}A_1 - \text{Im}A_4)r_1^2 + \\ & (3\text{Im}A_2 - \text{Im}A_5)r_2^2 + \\ & 3\text{Im}[A_3 e^{-i(3\varphi_1 - \varphi_2)}]r_1 r_2 - \\ & \text{Im}[A_6 e^{i(3\varphi_1 - \varphi_2)}]r_1^3 r_2^{-1}, \end{aligned} \quad (29)$$

where again the additional terms compared to the non-resonant case are highlighted in red. The two equations resulting for the angles φ_1 and φ_2 have been added up to one eq.(29) for the resonance angle $(3\varphi_1 - \varphi_2)$. An additional unfolding parameter δ has been added in eq.(29) to account for the ‘‘detuning’’ of the resonance angle, yielding a co-dimension three problem. The values for the complex coefficients A_i ($i = 1, \dots, 6$) have to be computed numerically. This was done by discretizing the tube system into 16 rigid parts coupled to each other by rotational springs and dampers and solving the resulting algebraic problem by MATHEMATICA. The values for the parameters were taken as $\xi = 0.886$, $\Gamma = 0.099$,

TABLE 3: COMPLEX COEFFICIENTS A_i ($i = 1, \dots, 6$) IN THE BIFURCATION EQUATIONS (27)-(29) IN CASE OF A (1 : 3) INTERNAL RESONANCE

A_1	$14.4 + 22.7i$
A_2	$0.155 + 0.186i$
A_3	$-2.23 + 2.67i$
A_4	$33.0 - 2.19i$
A_5	$-0.00127 + -0.00122i$
A_6	$25.8 - 42.9i$


FIGURE 5: BIFURCATIONS OF r_1 FOR FIXED VALUE OF λ

$\beta = 0.146$, $\alpha = 0.018$ and $\gamma = 25.3$, where the resulting Hopf-Hopf interaction occurs for $c = 121$ and $\rho = 9.03$. Table3 shows the results for the complex coefficients A_i ($i = 1, \dots, 6$) in eqs.(27)-(29).

Unfolding and Bifurcation Diagrams - The Non-resonant Case

We first turn to the discussion of the non-resonant case, i.e. the case where all the terms in red in eqs.(27)-(29) are not present. In that case the eqs.(27) and (28) decouple from (29) to the order considered. This means that the solutions for r_1 and r_2 can be calculated independently of the dynamics of the phase angles. According to eq.(29), the phase velocities are $\dot{\varphi}_1 = \omega_1 = \text{const}$ and $\dot{\varphi}_2 = \omega_2 = \text{const}$ to leading order. Since the re-transformation to physical co-ordinates involves only rotations in variable space, one can immediately conclude that in case of stability loss with respect to a coupled Hopf-Hopf instability without low-order resonances, the tube will perform a quasi-periodic motion of two superimposed eigenfrequencies ω_1 and ω_2 , with amplitudes given by r_1 and r_2 .

Figure 5 shows the bifurcations of r_2 resulting from eqs.(27) and (28) for the plane $\lambda = -0.1$. From the bifurcation equations follows that up to four equilibrium points of r_1 and r_2 exist, dependent on the values of λ and μ .

As can be seen in Fig. 5, the stable trivial equilibrium undergoes two subcritical pitchfork bifurcations, where only the second bifurcation at $\mu = 0$ leads to stable non-trivial equilibria, whereas all other branches are unstable. The stability of the equilibria can be calculated from eqs.(27) and (28) by linearizing the equations around the equilibrium and calculating the corresponding eigenvalues. An analogous diagram can be obtained for r_1 , which shows two supercritical pitchfork bifurcations with non-trivial but all unstable branches for the equilibria of r_1 .

Figure 6 shows the stability diagram resulting from an unfolding of the bifurcation equations (27) and (28) for the non-resonant case, along with the corresponding solutions in phase space (r_1, r_2). The two solid lines separate regions of different numbers of equilibria of r_1 and r_2 (note that for visibility reasons the inclination of one of the lines has been enlarged by a factor of 100). The trivial equilibrium $r_1 = r_2 = 0$ is present in every region, but it is stable only in the lower left quadrant. The grey shaded area indicates the region where non-trivial values for the equilibria of both r_1 and r_2 exist. The dashed line shows a representative loading path, corresponding to quasistatically increasing one (or a linear combination of two) distinguished parameters, e.g. ρ . In region ①, two equilibria exist, from which only the trivial one is stable. Entering region ②, an additional third but unstable equilibrium appears. Proceeding to region ③ (which is very small), four equilibria are present, where the trivial equilibrium becomes a saddle point, and the only stable equilibrium is the one with ($r_1 = 0, r_2 \neq 0$), as was already concluded from Fig.5. Proceeding further to region ④, only three equilibria are present, all of which are unstable. The other phase portraits are self-explaining.

Since there is only one stable non-trivial equilibrium possible (the one in region ③), the tube performs quasi-periodic oscillations with almost constant frequency ω_2 and almost constant amplitude r_2 in that case.

Unfolding in the Case of an (1 : 3) Internal Resonance

As can be seen from eqs.(27)-(29) with the terms in red now included, the general solutions for the equilibria and the corresponding unfolding is much more complex, since the equations do not decouple any more. Nevertheless, one can conclude that the equilibria with r_1 are identical to the equilibria in the non-resonant case with $A_3 = A_6 = 0$.

In investigating the non-trivial equilibrium point ($r_1 \neq 0, r_2 \neq 0$), one can consider two limiting cases: First, we consider the limiting case of $r_2 \ll r_1$, which corresponds to the grey shaded area of Fig.6 close to the lower bound-

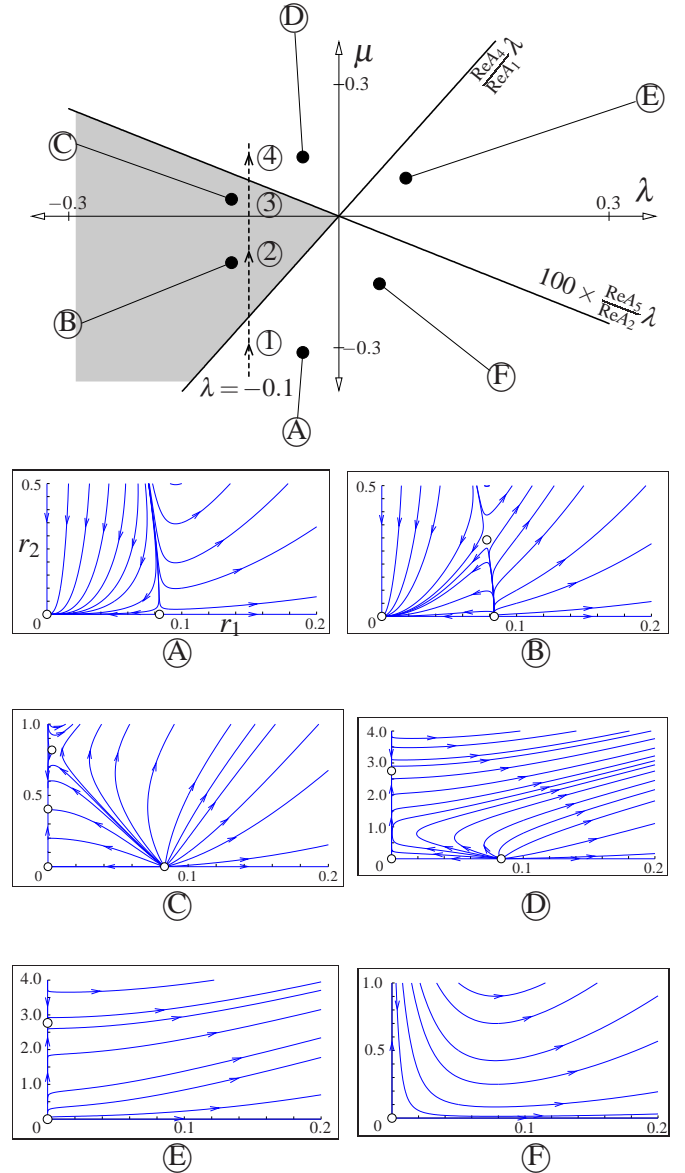


FIGURE 6: BIFURCATION DIAGRAM FOR THE NON-RESONANT CASE WITH PLATES SHOWING SOLUTIONS IN PHASE SPACE. THE DASEHD LINE IS A REPRESENTATIVE LOADING PATH.

ary $\frac{\text{Re}A_4}{\text{Re}A_1} \lambda$. Plugging into eqs.(25) and (25) an ansatz

$$z_1 = r_1 e^{i\Omega t}, \quad (30)$$

$$z_2 = r_2 e^{3i\Omega t + \varphi} \quad (31)$$

with $\Omega = \omega + \text{Im}A_1 r_1^2$ one observes that $r_1 \approx \text{const}$, as eq.(25) reduces to a decoupled equation as in the non-resonant case. The corresponding equations for r_2 and

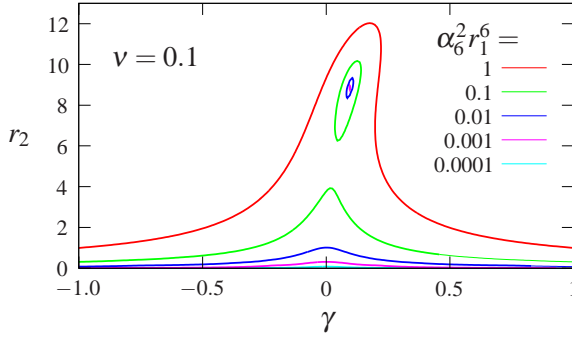


FIGURE 7: BIFURCATIONS OF r_2 IN CASE OF AN (1 : 3) INTERNAL RESONANCE IN THE LIMITING CASE $r_2 \ll r_1$.

the phase angle φ can be written as

$$\dot{r}_2 = \nu r_2 + \text{Re}A_5 r_2^3 + \alpha_6 \cos(\beta_6 - \varphi) r_1^3, \quad (32)$$

$$\dot{\varphi} = \gamma + \text{Im}A_5 r_2^2 + \alpha_6 \sin(\beta_6 - \varphi) r_1^3 r_2^{-1}, \quad (33)$$

with the shifted unfolding parameters

$$\nu = \mu + \text{Re}A_4 r_1^2, \quad (34)$$

$$\gamma = \delta + (\text{Im}A_4 - 3\text{Im}A_1) r_1^2 \quad (35)$$

and the polar representation for the complex coefficient $A_6 = \alpha_6 \exp(i\beta_6)$. Equations (32) and (33) are a phase space representation of Duffing's equation, see [8]. Therefore, the non-linear dynamics of r_2 is described by Duffing's equation in this limiting case. Figure 7 shows the unfolding of r_2 with respect to γ in the plane of the fixed value $\nu = 0.1$. It illustrates that up to three non-trivial equilibria for r_2 are possible, dependent on the values of ν , γ and $\alpha_6^2 r_1^6$.

Secondly, the opposite limiting case of $r_1 \ll r_2$ is considered. This case corresponds to the grey shaded area of Fig.6 close to the upper boundary $\frac{\text{Re}A_5}{\text{Re}A_2} \lambda$. Plugging into eqs.(25) and (25) the ansatz

$$z_2 = r_2 e^{3i\Omega t} \quad (36)$$

with $\Omega = \omega + \text{Im}A_5 r_2^2$ one finds that $r_2 \approx \text{const}$ and the dynamics of z_1 given by

$$\dot{z}_1 = (\lambda + i\omega + A_2 r_2^2 + A_1 |z_1|^2) z_1 + A_3 r_2 \bar{z}_1^2 e^{i\Omega t}. \quad (37)$$

Equation (37) is nothing else but the complex notation of a non-linear Mathieu's equation, see [8], which determines the dynamics of z_1 in case of an (1 : 3) internal resonance in the limiting case $r_1 \ll r_2$.

CONCLUSIONS

In investigating the stability behaviour of the liquid-tube system we have shown that Hopf-Hopf bifurcation interactions and the occurrence of low order internal resonances are present for distinct parameter values. The material damping of the tube, described by the parameter α , exhibits a strong influence on that behaviour. The (1 : 3) internal resonance is the lowest order resonance causing additional terms in the bifurcation equations to third order, leading to a much more complex dynamics of the tube compared to the non-resonant case. The motion of the tube in case of an (1 : 3) internal resonance was shown to be governed by a Duffing's and by a non-linear Mathieu's equation in limiting cases, corresponding to quasi-periodic oscillations of the tube.

REFERENCES

- [1] Ghayesh, M., Paidoussis, M., and Modarres-Sadeghi, Y. "Three-dimensional dynamics of a fluid-conveying cantilevered pipe fitted with an additional spring-support and an end-mass". *JSV*, **330**, pp. 2869–2899.
- [2] Paidoussis, M., 1998. *Fluid-structure interactions*. Academic Press, San Diego, California.
- [3] Troger, H., and Steindl, A., 1991. *Nonlinear stability and bifurcation theory*. Springer Verlag, Vienna, Austria.
- [4] Albrecht, B., 1997. "Dynamische Verzweigungen eines rotationssymmetrischen, flüssigkeitsdurchströmten Schlauches mit einer punktförmigen Masse". MS Thesis, TU Wien, Vienna, Austria.
- [5] Jurisits, R., and Steindl, A., 2012. "Degenerate cases of stability loss of an elastic fluid-conveying tube". In *GAMM - 83rd Annual Meeting of the International Association of Applied Mathematics and Mechanics, Proceedings in Applied Mathematics and Mechanics (PAMM)*. To be published.
- [6] Oberle, H., Grimm, W., and Berger, E., 1985. *BOUNDSCO, Rechenprogramm zur Lösung beschränkter optimaler Steuerungsprobleme*. TU München, Munich, Germany.
- [7] Seydel, R., 1977. "Numerische Berechnung von Verzweigungen bei gewöhnlichen Differentialgleichungen". PhD Thesis, TU München, Munich, Germany.
- [8] Guckenheimer, J., and Holmes, P., 1983. *Nonlinear oscillations, dynamical systems, and bifurcations of vector fields*. Springer, New York.



FLOW-INDUCED OSCILLATIONS OF A CANTILEVERED PIPE CONVEYING FLUID WITH A BASE EXCITATION

Gary Han Chang

Fluid-Structure Interactions Laboratory
Department of Mechanical and Industrial
Engineering
University of Massachusetts,
Amherst, MA 01003
Email: gary@engin.umass.edu

Yahya Modarres-Sadeghi

Fluid-Structure Interactions Laboratory
Department of Mechanical and Industrial
Engineering
University of Massachusetts,
Amherst, MA 01003
Email: modarres@engin.umass.edu

ABSTRACT

A plain cantilevered pipe conveying fluid loses its stability by a Hopf bifurcation, leading to either planar or non-planar flutter for flow velocities beyond the critical flow velocity for Hopf bifurcation. If a mass is attached to the end of the pipe (a so-called added mass), the resulting dynamics becomes much richer, showing 2-D and 3-D quasi-periodic and chaotic oscillations at high flow velocities. In this work, we consider a cantilevered pipe subjected to a periodic small-amplitude base excitation, and show that by selecting the right frequency and amplitude for an external base excitation, the non-planar periodic and quasiperiodic oscillations of the pipe can be reduced to planar ones.

INTRODUCTION

Pipes conveying fluid have been studied extensionally. Although the system is a rather simple one, with slight changes, it exhibits various complicated dynamical behavior, including quasi-periodic and chaotic motions. The initial models used to predict the behavior of a pipe conveying fluid were 2D linear models, which showed that the system would lose its original stability at a critical flow velocity, leading to periodic oscillations. The large amplitude as well as 3D oscillations observed in the experiments (Lundgren et al., 1979) initiated studies toward nonlinear and 3D models to predict the pipe's motion.

Bajaj and Sethna (1984) derived a nonlinear model for a plain pipe (i.e., with no additional mass or spring) conveying fluid. They used the centre manifold and normal form techniques and found that a horizontal pipe loses its original stability through a Hopf bifurcation and develops either 2-D (planar) or 3-D (orbital or rotary) flutter, depending on a mass parameter β (defined later, in Equation 3).

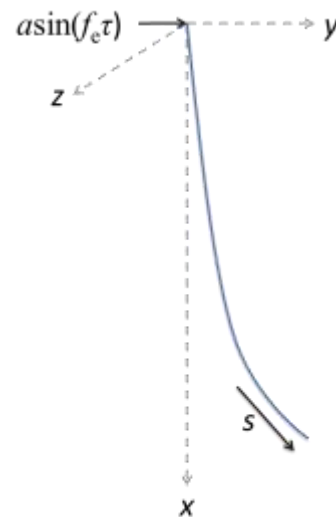


Fig. 1 A cantilevered pipe conveying fluid subjected to a periodic base excitation.

An additional mass or spring attached to the pipe can either stabilize or destabilize the system, depending on the system parameters and location of the additional mass or spring (Païdoussis, 1998). Copeland and Moon (1992) studied the three dimensional dynamics of a cantilevered pipe with an end-mass, and observed various planar and non-planar periodic, quasi-periodic and chaotic oscillations.

Wadham-Gagnon et al. (2007) derived a 3-D nonlinear model for a pipe conveying fluid with an additional mass and spring attached to it. They (Païdoussis et al., 2007) showed that an additional spring would lead to 2-D or 3-D periodic, quasi-periodic and chaotic oscillations after the initial planar flutter. The type of the motion depends on the spring array configuration, point of attachment and spring stiffness. In some configurations, the system loses stability by divergence, followed by oscillations in the plane of divergence or perpendicular to it, where these oscillations can be periodic, quasi-periodic

or chaotic. Using this model, Modarres-Sadeghi et al. (2007) studied the 3D oscillations of a pipe conveying fluid with an end-mass, and Ghayesh et al. (2011) studied the case with both an end-mass and an added spring. Again, using the same model, Modarres-Sadeghi et al. (2008) showed that a plain pipe oscillates mainly in a plane, for small mass parameters, β (except for $\beta=0.2$) and in a 3D circular way for larger values of β ($0.7 < \beta < 0.9$) where for the intermediate β values the oscillations switch between 2-D and 3-D as the flow velocity increases.

Furuya et al. (2010) studied the stability of a cantilevered pipe conveying fluid with an end-mass in the case of a horizontal excitation at the upper end, for a fluid velocity slightly over the critical value. By solving nonlinear equations of motion with base excitation numerically, they showed that the non-planar vibrations are reduced to planar vibrations when the excitation frequency is nearly equal to the frequency of the original flow-induced pipe vibrations.

In this work, we study the influence of base excitation on the oscillations of a cantilevered pipe conveying fluid. We examine the influence of a base excitation with various frequencies and amplitudes on the stability of a cantilevered pipe conveying fluid, for cases with or without an end-mass.

THE EQUATIONS OF MOTION AND THE METHOD OF SOLUTION

Three-dimensional equations of motion for a cantilevered pipe conveying fluid were derived by Wadham-Gagnon et al. (2007) for a pipe with extra mass added at the tip and springs attached somewhere along the length of the pipe. We modify these equations slightly in our model by introducing an external force acting at the base of the pipe, in a way similar to what Furuya et al. (2010) and Nayfeh and Pai (2002) have done.

The final form of the dimensionless equations of motion in the y -direction will become

$$\begin{aligned} & \eta'''' + [1 + \Gamma \delta(\xi - 1)] \ddot{\eta} + u^2 \eta'' + 2u\sqrt{\beta} \dot{\eta}' \\ & + \eta'^2 \eta'''' + 4\eta' \eta'' \eta'''' + \eta'^3 + \eta' \zeta' \zeta'''' \\ & + 3\eta' \zeta'' \zeta'''' + \eta'' \zeta' \zeta'''' + \eta'' \zeta''^2 \\ & + \eta'' [1 + \Gamma \delta(\xi - 1)] \int_0^\xi (\dot{\eta}'^2 + \eta' \ddot{\eta}' + \dot{\zeta}'^2 + \zeta' \ddot{\zeta}') d\xi \\ & - \eta'' \int_\xi^1 [1 + \Gamma \delta(\xi - 1)] \int_0^\xi (\dot{\eta}'^2 + \eta' \ddot{\eta}' + \dot{\zeta}'^2 + \zeta' \ddot{\zeta}') d\xi d\xi \\ & + \gamma [1 + \Gamma \delta(\xi - 1)] \eta' - \gamma \eta'' \int_\xi^1 [1 + \Gamma \delta(\xi - 1)] d\xi \\ & + \gamma \left(\frac{1}{2} \eta'^3 + \frac{1}{2} \eta' \zeta'^2 \right) \\ & - r \left(\frac{3}{2} \eta'^2 \eta'' + \frac{1}{2} \zeta'^2 \eta'' + \eta' \zeta' \zeta'' \right) \int_\xi^1 [1 + \Gamma \delta(\xi - 1)] d\xi \end{aligned}$$

$$\begin{aligned} & + u^2 \left[\eta'^2 \eta'' + \eta' \zeta' \zeta'' - \eta'' \int_\xi^1 (\eta' \eta'' + \zeta' \zeta'') d\xi \right] \\ & + 2u\sqrt{\beta} \left[\eta'^2 \dot{\eta}' + \eta' \zeta' \dot{\zeta}' - \eta'' \int_\xi^1 (\eta' \dot{\eta}' + \zeta' \dot{\zeta}') d\xi \right] \\ & = a f_e^2 \sin f_e t, \end{aligned} \quad (1)$$

with the boundary conditions of

$$\begin{aligned} & \eta(0) = \eta'(0) = \eta''(1) = 0, \\ & \zeta(0) = \zeta'(0) = \zeta''(1) = \zeta'''(1) = 0, \\ & \eta'''(1) = a f_e^2 \sin(w\tau), \end{aligned} \quad (2)$$

where,

$$\begin{aligned} & \xi = \frac{s}{L}, \quad \eta = \frac{w}{L}, \\ & \zeta = \frac{v}{L}, \quad u = \left(\frac{M}{EI} \right)^{1/2} LU, \\ & \beta = \frac{M}{M+m}, \quad \gamma = \frac{(M+m)L^3}{EI} g, \\ & \Gamma = \frac{m_e}{(m+M)L}, \quad \tau = \left[\frac{EI}{M+m} \right]^{1/2} \frac{t}{L}, \\ & a = \delta Y / L, \quad f_e = \omega \sqrt{(m+M)L^4 / (EI)}, \end{aligned} \quad (3)$$

in which η and ζ are dimensionless transverse displacements in the y - and z - directions, respectively; ξ is the dimensionless distance along the pipe; u is the dimensionless flow velocity; β is a mass parameter; γ is a dimensionless gravity parameter; τ is a dimensionless time; w and v are the transverse displacements in the y - and z -directions, respectively; a and f_e are the dimensionless amplitude and frequency of base excitation, respectively; s is the distance along the pipe, measured from the clamped end; L is the length of the pipe, D its diameter and EI its flexural rigidity; t is the time; ρ is the density of the fluid; m is the mass per unit length of the pipe; M is the mass per unit length of the fluid; U is the flow velocity; δY is the amplitude of the base excitation and ω its frequency.

The equation in the z -direction is obtained by exchanging ζ and η and removing the excitation force on the right hand side.

In order to analyze the equations of motion numerically, the nonlinear coupled partial differential equations are discretized by Galerkin's technique and eigenmodes of a cantilevered beam are used as the base functions. The resulting set of ordinary differential equations is solved using Houbolt's finite difference method (Semler et al., 1996). At least 6 modes are used in

each direction in these simulations, while higher modes are occasionally used to test the convergence of the results.

A THREE DIMENSIONAL PLAIN PIPE WITH BASE EXCITATION

For plain pipes, observing planar or non-planar oscillations depends on the mass parameter and flow velocity. The non-planar motions are usually observed at larger mass parameters ($\beta > 0.5$), while planar oscillations are more common for smaller mass parameters ($\beta < 0.5$) (Modarres-Sadeghi et al., 2008). In this section, we study the flow-induced oscillations of a 3D plain pipe with base excitation. In particular we examine the possibility of reducing the observed non-planar oscillations to planar ones by applying a low-amplitude low-frequency base excitation in the direction of the desired planar motion.

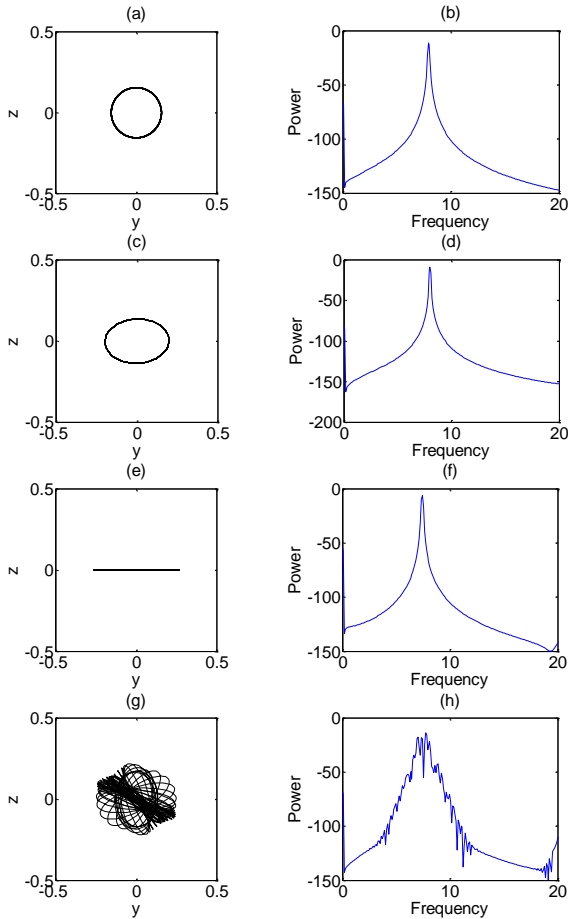


Fig. 2 Tip displacement and PSD plots for the system with $\beta = 0.7$, $u = 14.0$ (a,b) without base excitation, (c,d) with a base excitation of $a = 0.01$ and $f_e = 8.0$, (e,f) $f_e = 7.4$, and (g,h) $f_e = 7.0$.

Figure 2(a,b) shows that a plain cantilevered pipe with a mass parameter of $\beta = 0.7$ at a dimensionless flow velocity of $u=14$ and with no base excitation undergoes three-dimensional circular oscillations with a

dimensionless frequency of $f_0 = 8.0$ and a dimensionless amplitude of $\eta_M = \zeta_M = 0.16$.

If the base is excited periodically in the y -direction with a dimensionless frequency of excitation of $f_e = 8.0$ (a frequency equal to the frequency of oscillations with no base excitation) and a dimensionless amplitude of excitation of $a=0.01$, the tip of the pipe undergoes elliptical motion, with a dimensionless frequency of $f = 8.0$. The amplitude of oscillations increases in the y -direction, the same direction as the direction of the externally applied force, and reduces in the perpendicular direction: z -direction (Figure 2c,d).

When the frequency of base excitation is decreased slightly, e.g., $f_e = 7.4$ and with the same amplitude of base excitation, the free end undergoes a planar motion at a dimensionless frequency of $f = 7.8$, with an amplitude of oscillations larger than the original amplitude of oscillations with no base excitation (Figure 2e,f).

By further decreasing the frequency of base excitation to $f_e = 7.0$ at the same amplitude of excitation, $a = 0.01$, the planar motion is lost and the tip undergoes three-dimensional quasi-periodic motion (Figure 2g,h). A similar trend was observed for the other flow velocities.

In general, for a given amplitude of excitation and at a fixed flow velocity, if the pipe is excited at the frequency of its original oscillations (with no base excitation), $f_e = f_0$, an elliptical motion is observed. To observe a planar motion, the frequency of excitation should be lower than f_0 , but if it is much lower than f_0 , quasi-periodic motion is observed. Quasiperiodic motion is also observed for the frequencies of excitation larger than f_0 and between the frequency range for the elliptical and planar motion.

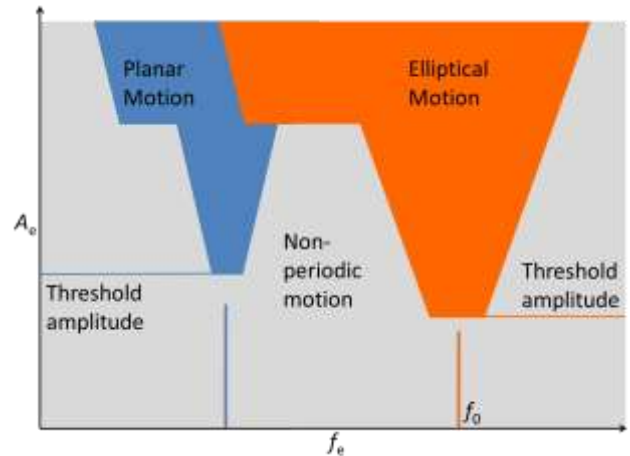


Fig. 3 A schematic of different kinds of motion observed for a fluid-conveying pipe with base excitation and their dependence on the frequency and amplitude of the base excitation.

Figure 3 shows a schematic of various kinds of motion that are observed when a plain pipe is subjected to a base excitation. The resulting planar or non-planar

oscillations depend not only on the frequency of excitation, but also on the amplitude of excitation. When the base is excited with a large-amplitude excitation, the planar motion is observed over a wide range of non-dimensional excitation frequencies. For the smaller excitation amplitude, both planar motion and elliptical motion are observed, while the elliptical motion is observed for the excitation frequency $f_e = f_0$. For excitation amplitudes smaller than a threshold amplitude, no planar motion is observed.

Generally, in order to obtain planar motion over a wider range of excitation frequencies, larger amplitude of excitation should be used. For larger amplitudes of excitation, quasi-periodic oscillation is not observed between the planar and elliptical motions. The promising fact is that the amplitude of excitation needed to observe the planar motion is not very large.

THE INFLUENCE OF BASE EXCITATION ON DYNAMICS OF A PIPE WITH AN END-MASS

So far we have observed that one can reduce the three-dimensional periodic oscillations of a pipe conveying fluid to two-dimensional ones by applying a proper base excitation. In this section we extend this analysis to the cases with quasiperiodic oscillations in the original pipe with no base excitation to see if such oscillations too can become two-dimensional by applying a proper base excitation.

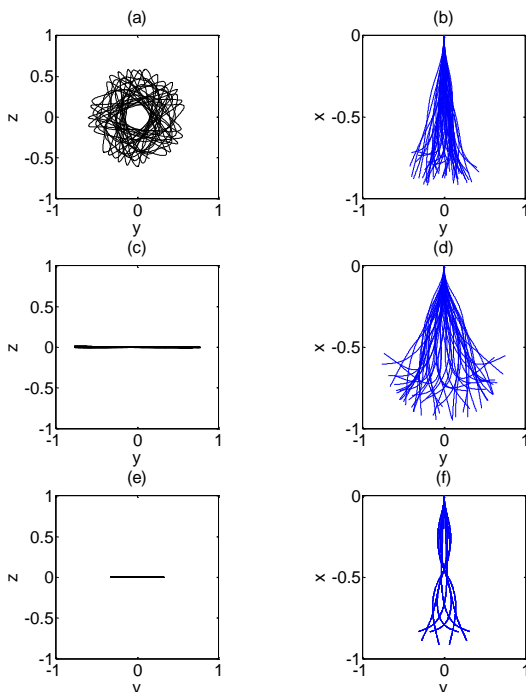


Fig. 4 Tip displacement and spatial plots for a pipe with an end-mass with $\beta = 0.2$, $\Gamma = 0.1$ and $u = 8.0$, (a,b) without base excitation, (c,d) with a base excitation of $a = 0.02$, $f_e = 2.5$, and (e,f) $f_e = 5.0$.

A pipe conveying fluid with an end-mass loses its original stability by a Hopf bifurcation leading to limit cycle oscillations, as the flow velocity increases. At higher flow velocities, the pipe can undergo period-doubling or torus instability, leading to period-2 or quasiperiodic oscillations, eventually leading to chaos (Modarres-Sadeghi et al., 2007). In this section, we study the influence of a base excitation on the resulting oscillations of a pipe with an end-mass.

A pipe with a mass parameter of $\beta = 0.2$ and an end-mass parameter of $\Gamma = 0.1$ (where $\Gamma = m_e / (m + M)L$ is a dimensionless end-mass parameter) loses its stability and undergoes 2-dimensional flutter at $u = 5.0$. At $u = 7.0$, the system's limit cycle oscillations become unstable through a torus, leading to quasiperiodic oscillations at higher velocities. Figure 4(a,b) shows the tip displacement and spatial plots of the quasiperiodic oscillations of this system at $u = 8$, where there is no external excitation. The dimensionless fundamental frequencies of this quasiperiodic motion can be chosen as $f_1 = 1.07$ and $f_2 = 2.73$.

The base is excited with a magnitude of $a = 0.02$ and a varying frequency. This amplitude is chosen because for smaller amplitudes (including $a = 0.01$) no planar motion was observed. If the base is excited at a dimensionless frequency of 2.5 (Figure 4c,d) a planar oscillation in the plane of excitation is observed. The oscillations are still quasi-periodic with the fundamental frequencies comparable with those of the original quasi-periodic oscillations, but they stay in a plane.

A base excitation at a higher dimensionless frequency, $f_e = 5$, (Figure 4 e,f) results in pure periodic oscillations of the third mode at a dimensional frequency of 5, resulting in a decrease in the magnitude of the tip displacement. These oscillations too stay in the plane of the base excitation.

Overall, in two ranges of excitation frequencies ($f_e = 2.5 - 2.55$ and $f_e = 5 - 5.5$), the pipe undergoes planar motion (i.e. $z = 0$). For the planar motions at the lower frequency range ($f_e = 2.5 - 2.55$), the amplitude of oscillations in the direction of the external force is larger than those for the original oscillations. In this range, the second mode of the pipe is excited. With the frequency of base excitation in the higher range, ($f_e = 5 - 5.5$), the 3rd mode of the pipe is excited, which naturally results in low-amplitude oscillations of the tip.

CONCLUSIONS

We study the influence of base excitation on the oscillations of a cantilevered pipe conveying fluid. We show that the non-planar oscillations of a pipe conveying fluid can be reduced to planar oscillations, when the pipe is subjected to a base excitation with a proper frequency and with relatively small amplitude. In general, the motion of the tip of a plain pipe conveying fluid with a base excitation can be classified as (i) planar periodic, (ii) elliptical periodic or (iii) non-planar quasiperiodic motion.

The observed motion depends on the frequency and amplitude of the base excitation.

Typically, if the pipe is excited with a frequency equal to the frequency of its original oscillations, the resulting motion will be an elliptical one. In order to force the non-planar motion into a planar one in the plane of the base excitation, the frequency of excitation must be slightly smaller than the frequency of original oscillation.

We have also studied the case of a cantilevered pipe with an added mass at the tip. With no base excitation, the pipe undergoes 3D quasi-periodic and chaotic oscillations. When we apply a small-amplitude base excitation at a frequency slightly smaller than the frequency of the original self-excited oscillations, the 3D quasiperiodic oscillations are reduced to 2D quasi-periodic oscillations.

REFERENCES

- Bajaj, A.K., Sethna, P.R., 1984. Flow induced bifurcations to three-dimensional oscillatory motions in continuous tubes. *SIAM Journal of Applied Mathematics* 44, 270–286.
- Copeland, G.S., Moon, F.C., 1992. Chaotic flow-induced vibration of a flexible tube with end mass. *Journal of Fluids and Structures*, 6, 705–718 (also in American Society of Mechanical Engineers AMD-vol. 152, Proceedings International Symposium on Flow-Induced Vibration and Noise, vol. 8, pp. 63–77).
- Furuya, H., Yamashita, K., Yabuno, H., 2010. Nonlinear stability of a fluid-conveying pipe with end mass in case of horizontal excitation at the upper end. ASME 2010 3rd Joint US-European Fluids Engineering Summer Meeting.
- Ghayesh, M. H., Païdoussis, M. P., Modarres-Sadeghi, Y., 2011. Three-dimensional dynamics of a fluid-conveying cantilevered pipe fitted with an additional spring-support and an end-mass. *Journal of Sound and Vibration* 330 2869–2899
- Lundgren, T.S., Sethna, P.R., Bajaj, A.K., 1979. Stability boundaries for flow induced motions of tubes with an inclined terminal nozzle. *Journal of Sound and Vibration* 64, 553–571.
- Modarres-Sadeghi, Y., Païdoussis, M.P., Semler, C. 2008. Three-dimensional oscillations of a cantilever pipe conveying fluid. *International Journal of Non-Linear Mechanics* 43 18-25
- Modarres-Sadeghi, Y., Semler, C., C., Wadham-Gagnon, Païdoussis, M. P., 2007. Dynamics of cantilevered pipes conveying fluid. Part3:three-dimensional dynamics in the presence of an end-mass, *Journal of Fluids and Structures* 23 589–603.
- Nayfeh, A. H., Pai, P. F., 2002. *Linear & Nonlinear Structural Mechanics*. WILEY-VCH, Verlag GmbH, Weinheim, Germany.
- Païdoussis, M. P., 1998. *Fluid-Structure Interactions: Slender Structures and Axial Flow* Academic Press, London.
- Païdoussis, M.P., Semler, C., Wadham-Gagnon, M., 2007. Dynamics of cantilevered pipes conveying fluid. Part 2: dynamics of the system with intermediate spring support. *Journal of Fluids and Structures* 23, 569-587
- Semler, C., Gentleman, W. C., Païdoussis, M. P., 1996. Numerical Solutions of second order implicit nonlinear ordinary differential equations. *Journal of Sound and Vibration* 195(4), 553-574
- Wadham-Gagnon, M., Païdoussis, M.P., Semler, C., 2007. Dynamics of cantilevered pipes conveying fluid. Part 1: Nonlinear equations of three-dimensional motion. *Journal of Fluids and Structures* 23, 545-567

EXPERIMENTAL ANALYSIS OF THE AEROACOUSTICS OF FREE AND IMPINGING JETS

Giorgia Sinibaldi

Luca Marino

Giovanni Paolo Romano

Department of Mechanical and Aerospace Engineering

University of Rome “La Sapienza”

Via Eudossiana 18, 00184 Rome, Italy

Email: sinibaldi.giorgia@gmail.com, luca.marino@uniroma1.it, romano@dima.ing.uniroma1.it

ABSTRACT

This paper is devoted to the experimental analysis of the aeroacoustics of free and impinging jets. The typical screech tones which characterize the acoustics of the free jets are measured and the results are compared with the data already published in the literature. The investigation is then focused on the effect on the screech tones of the impingement of the jet over a plate perpendicular to its axis. In particular the effect of the main geometrical and physical parameters is considered and discussed.

NOMENCLATURE

d	nozzle exit diameter
D	plate diameter
f	frequency
h	nozzle-to-plate distance
p_0	stagnation pressure
p_a	ambient pressure
St	Strouhal number
u	jet velocity
NPR	nozzle pressure ratio
$OASPL$	overall sound pressure level

INTRODUCTION

The aeroacoustics of free and impinging jets is an interesting and fundamental problem which received particular attention in the last decades. The phenomenon is relevant for several applications and for the physical processes which link the fluid dynamic field to the acoustic one. In many circumstances the noise of jets plays a fundamental role as, for example, for the jet issuing by rockets or by aeronautical engines. In these cases both

the free and the impinging configurations can be encountered. Electronic equipment cooling and paper drying devices are additional cases where high-pressure jets of gases are involved. These high-speed flows can develop several undesirable effects, in particular significant acoustic emissions, aerodynamic and thermal loads, high heat transfer coefficients, lift loss and surface erosion phenomena [1–4].

As pointed out by several authors [5–9], when the jet impinges on a surface the physical mechanism of the noise generation is not yet completely understood. The complex structure of the flow, characterized by the contemporary presence of subsonic and supersonic regions, shock-wave oscillations and instabilities, regions of turbulent shear and, eventually, a recirculation zone close to the impingement region, makes difficult to give a coherent and satisfactory model of the problem. An accurate review of the phenomena observed in experimental supersonic impinging jets studied from 1961 to 2000 is reported by Henderson [10].

More specifically, the acoustic properties of free and impinging jets are characterized by the presence of peaks at discrete frequencies, known as “screech” and “impinging” tones, which can induce an increase of more than 10 dB over the average broadband level. Likely, these discrete tones are due to a feedback mechanism [11–15] and represent one of the main problems encountered in the engineering applications. For an impinging jet in addition to these discrete tones, the broadband noise also becomes important, contributing to a significant increase of the OASPL (OverAll Sound Pressure Level).

These peculiar aspects motivated the content of the present paper which is devoted to an experimental evalu-

ation of the aero-acoustic field of a jet. The main goal is a better comprehension of the phenomenon by means of an accurate experimental analysis. The work was carried out in the laboratories of the Department of Mechanical and Aerospace Engineering, located at the University of Rome “La Sapienza”.

The study was organized as follow. The first step was devoted to the characterization of the anechoic chamber to test the quality of the acoustic insulation. A reference sound source calibrated both in intensity and frequency was adopted to evaluate the response of the test chamber to external noise sources and waves reflections. The work then focused on the collection of data related to the free jet behavior. In particular the acoustic measurements were carried out to the double purpose of tuning the experimental apparatus and observe the more referenced physical situations of the aeroacoustics of the free jet. The latter, in fact, has been extensively studied and provides a rich database to compare with. Finally the interaction of a jet and a surface was investigated. The research was aimed at evaluating different aspects of the flow and the acoustic field.

AEROACOUSTICS OF SUPERSONIC JETS

Under-expanded supersonic free jets produce noise through three main mechanisms. A first contribution, the turbulent mixing noise, is due to the large and fine scale structures of the turbulent flow. Moreover a broadband component and the discrete screech tones are present and are related to the shock cells structure in the jet [16].

The intensity of each component is strongly dependent on the observer position. In the downstream direction the most important component is the turbulent mixing contribution [17] while the broadband noise and the screech tones are the most significant upstream of the jet. The principal direction of radiation of the first harmonic of the screech tone is upstream of the nozzle exit at 90° with respect to the jet flow axis [18]. In the far field the measured frequency of the screech tone is almost constant regardless of the observer direction [19].

After the pioneering contribution of Powell in 1953 [11, 12], the screech phenomenon has been studied by several researchers and it is now recognized that these discrete tones are generated by a feedback loop. As clearly explained in [20, 21] the feedback loop is triggered by the large coherent vortical structures of the jet which are convected downstream and interact with the shock waves at the edge of the shock cells. The interaction produces strong acoustic waves that propagate upstream and excite the thin shear layer near the nozzle lip producing instabil-

ity waves. The instability waves propagate downstream growing in amplitude and the interaction with the shock cell structures produces the acoustic waves that travel upstream closing the feedback loop. The acoustic waves form the outer part of the loop and propagate outside the jet.

In presence of screech tones the jet exhibits different oscillation modes that are dependent on the nozzle geometry and the pressure ratio. For a supersonic circular jet Davies and Oldfield [22] found the four oscillation modes namely, with the increasing the pressure ratio, axisymmetric A1, axisymmetric A2, lateral B and helical C. Furthermore Powell [23, 24] found the lateral mode D at higher pressure ratios.

When the jet impinges on a solid surface, as a flat plate normal to its axis, the flow configuration becomes more complex. Following [25, 26] we can describe the flow field in terms of three different regions

- an upstream free jet region where the plate effect is almost negligible and where the behavior is like the free jet;
- an impingement region where the interaction of the jet with the solid surface changes the flow structure;
- a wall jet region with a radial flow close to the impingement surface.

From this brief description it is clear the complexity of the flow configuration.

For a given nozzle geometry, the main parameters that characterize the flow and consequently the sound emission are the nozzle pressure ratio *NPR* (ratio of the stagnation pressure p_0 to the ambient pressure p_a), the nozzle-to-plate distance h and the plate size D .

In the literature two different flows have been observed where a possible recirculating bubble can appear in the impingement region. Up to now it is not clear which conditions can lead to the presence of this stagnation bubble, as well as different mechanisms have been proposed to justify its presence. More details about this point can be found in the paper of Donaldson et al. [1], Carling and Hunt [27], Kalghatgi and Hunt [28], Lamont and Hunt [29], Alvi and Iyer [26] and Krothapalli et al. [7].

From the acoustical point of view the presence of the plate can induce additional discrete tones (“impinging tones”) which can dominate the noise spectrum. Some authors [7, 8, 10, 13–15, 26, 30–33] proposed a feedback loop similar to that of the screech tones to explain the origin of these tones. But as reported in more recent papers [8, 9] a satisfactory theory is still lacking and the issue is open.

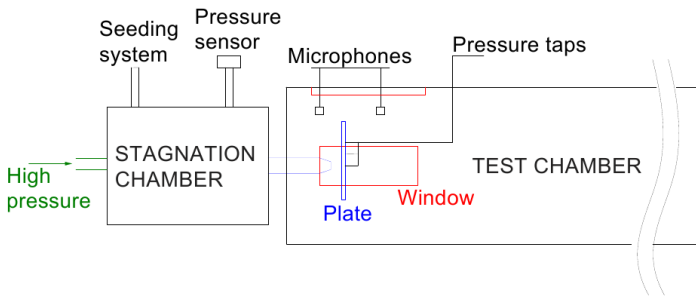


FIGURE 1: SKETCH OF THE EXPERIMENTAL SET-UP.

On the basis of our results we can observe that, in addition to this discrete tones, the presence of a solid surface lead to a significantly increase of the overall sound pressure level. This feature is also reported by Krothapalli et al. [7] who found an increase of about 8 dB of the overall sound pressure level with respect to the free jet. They also observed that the variation of the nozzle-to-plate distance doesn't produce a marked change of the OASPL.

EXPERIMENTAL SET-UP AND RESULTS

The acoustic measurements are obtained by a set of 8 free field 1/4 inch microphones type 3570, with a dynamic range of $(4 - 25000) Hz$, a sound analyzer Pulse-X3570 integrated with FFT and CPB analysis tools and a Nexus 2690 amplifier. All the acoustic instruments are produced by Brüel & Kjær.

The experimental apparatus consists of a cylindrical stagnation ambient (44 cm length x 29 cm diameter) connected to an high-pressure circuit and provided with a pressure sensor and a seeding system. Fig. 1 shows a sketch of the set-up.

The connection between the stagnation chamber and the test chamber is made by a round nozzle, with diameters d ranging from 0.4 to 1 cm. The test chamber (204 cm length x 40 cm diameter) is internally covered by anechoic materials and is provided of two windows for the PIV measurements.

For the impinging jet configuration the test chamber is provided with a circular plate downstream to the nozzle, equipped with the static pressure taps. Two plates of diameters $D = 15, 25 cm$ were adopted. The nozzle-to-plate distance h was changed between $h/d = 2 \div 10$ while the Mach number spans between 1.03 and 1.55. The jet Mach number was changed by setting proper values of the ratio between the pressure p_0 of the upstream stagnation chamber and the pressure p_a in the downstream ambient ($NPR = p_0/p_a$).

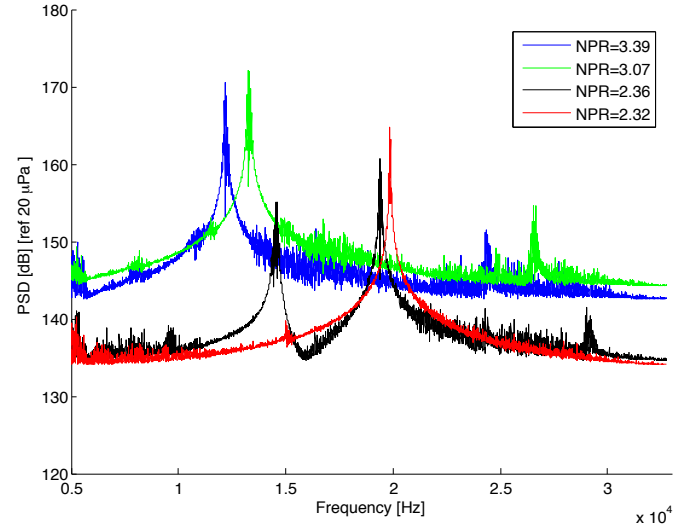


FIGURE 2: FREE JET. POWER SPECTRAL DENSITY PSD AT DIFFERENT VALUES OF NPR . $d = 1 cm$.

To complete the analysis when the plate is present, we used a set of static pressure taps coupled to a scan-valve system DSA3217 to measure the surface distribution of the pressure.

We present now some preliminary experimental results obtained in the apparatus described above. First we show the near field acoustic measurements for the free jet. The noise was measured with a microphone located two diameters upstream to the issuing jet and four diameters far from the jet axis in the radial direction. The angle between the microphone and the axis of the jet is 90° .

Fig. 2 reports an example of the power spectral density distribution at different values of NPR . It can be clearly recognized the existence of one or more screech tones. The main effect of the nozzle pressure ratio is to change the average value of the sound power level and the frequency and the number of the screech tones. In particular as the NPR increases the discrete tones shift toward lower frequencies. This effect was already observed in previous papers [24, 34, 35] but the scenery is complicated by the presence of multiple tones corresponding to different oscillating modes.

This last point is confirmed in the Fig. 3 where the distribution of the screech frequencies versus the nozzle pressure ratio is shown. The picture compares our experimental results against the experimental data of Powell [23, 24] for the same nozzle exit diameter. Both the dominant and secondary tones are reported and the agreement of the results is very good. We recall that a tone is called dominant when it corresponds to the maximum sound pressure level, usually more than 10 dB with respect to the mean value. At $NPR = 2.36$ it can be ob-

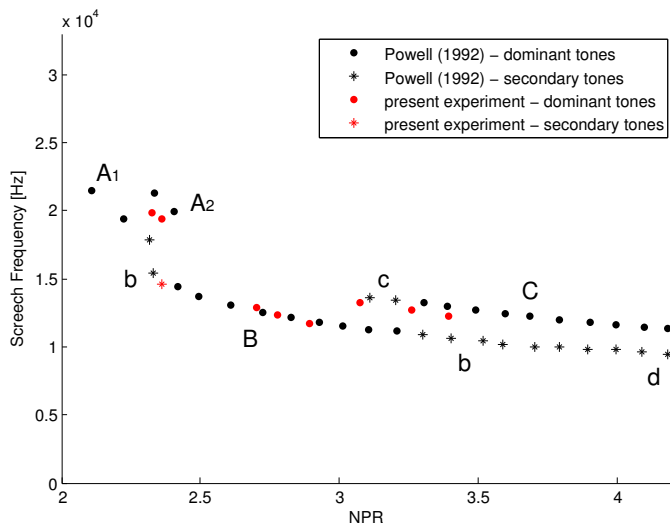


FIGURE 3: FREE JET. SCREECH FREQUENCY DISTRIBUTION AS FUNCTION OF NPR. $d = 1\text{ cm}$.

served in our data the presence of the two screech frequencies which, following the analysis of Powell, can be classified as a dominant tone related to the axisymmetric oscillation mode A2 and a secondary tone related to the lateral oscillation mode b. We want to point out that the satisfactory agreement with the data of Powell [23, 24] is a positive check of the quality of our experimental rig as well as the measurement set-up.

The effect of the plate on the noise of the jet is shown in the Figs 4 and 5 where a comparison of the power spectral distributions of the free and the impinging jet is shown. These initial experiments with the impinging jet are aimed at evaluating the effect of the presence of the plate on the screech tones.

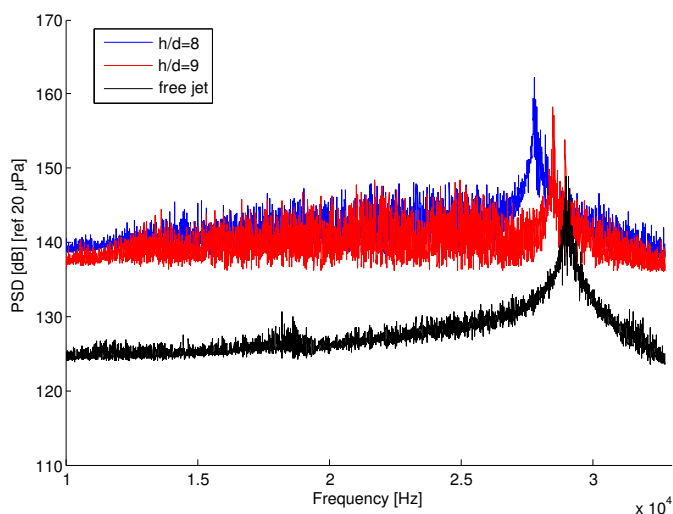


FIGURE 4: POWER SPECTRAL DENSITY PSD FOR FREE AND IMPINGING JET. $NPR = 2.9$, $d = 0.4\text{ cm}$.

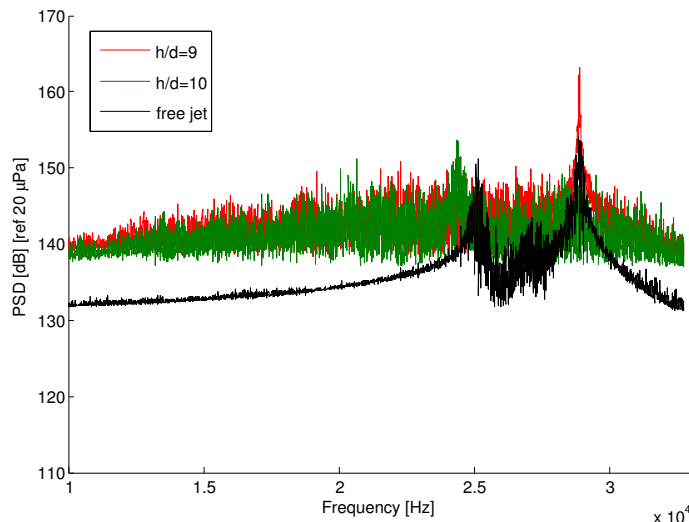


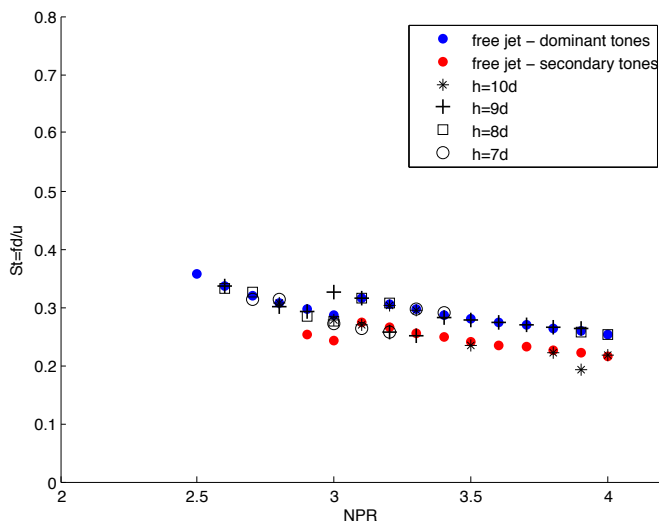
FIGURE 5: POWER SPECTRAL DENSITY PSD FOR FREE AND IMPINGING JET. $NPR = 3.6$, $d = 0.4\text{ cm}$.

Fig. 4 refers to $NPR = 2.9$ at two values of the nozzle-to-plate distance. As a general comment we note that, as expected from the data reported in [7], the average level of the noise of the impinging jet increases in all the cases investigated. The screech tone in the free configuration, located at frequency $f = 29\text{ kHz}$, shows a small shift toward lower frequencies as h/d decreases, while its maximum value increases. At a different pressure ratio, $NPR = 3.6$, the free jet shows two different screech tones with the dominant tone at higher frequency (Fig. 5). When the jet impinges on the plate at the same NPR the behavior of the screech tones is different. As the nozzle-to-plate distance changes, one of the tones cancel as an effect of the disappearing of the corresponding oscillation mode. This peculiar feature was found also for other values of NPR and h/d and denotes the complex effect of the presence of the plate on the acoustic field. Table 1 reports the comparison of the sound pressure level for the free and impinging jet and for the two nozzle pressure ratio. For each of the NPR values is evident a significantly increase of the OASPL in presence of the solid surface in front of the jet.

Finally Fig.6 summarizes the comparison between the free and impinging configurations in term of the Strouhal number $St = fd/u$ where the reference frequency is defined with the jet diameter d and its issuing speed u . It can be observed that the general trade off is almost the same, with exceptions in correspondence of some values of NPR and h/d . As a final comment we can note that though the free jet is largely investigated it is worthwhile to compare its characteristics to the screech tones that arise in the impinging configuration. Moreover with these first measurements we didn't observe the pres-

TABLE 1: OASPL [dB] FOR FREE AND IMPINGING JET. $d = 0.4\text{ cm}$.

	free jet	$h/d = 10$	$h/d = 9$	$h/d = 8$
$NPR = 2.9$	153.97	159.00	162.35	166.35
$NPR = 3.6$	160.32	161.80	167.20	162.90

**FIGURE 6:** SCREECH FREQUENCIES FOR FREE AND IMPINGING JET AS FUNCTION OF NPR . $d = 0.4\text{ cm}$

ence of the impinging tones. A further analysis is necessary to increase the data base and achieve a better comprehension of the phenomenon, in particular the effect of the presence of the plate on the oscillating modes of the jet. We are now planning to upgrade the experimental rig with a PIV system to have a quantitative details of the fluid dynamic field to complete the analysis of the jet and its correlation to the noise features.

REFERENCES

- [1] Donaldson, C.D., Snedeker, R.S., Margolis, D.P., 1971. "A study of free jet impingement. Part 2. Free jet turbulent structure and impingement heat transfer". *Journal of Fluid Mechanics*, **45**(3), pp. 477-512.
- [2] Gustavsson, J.P.R., Ragaller, P.A., Kumar, R., Alvi, F.S., 2010. "Temperature effect on acoustics of supersonic impinging jet". AIAA 2010-3785.
- [3] Margason, R.J., Arledge, T.K., Wardwell, D.A., Hange, C. Naumowicz, T., 1996. "Jet efflux characteristics and their influence on STOVL aircraft propulsion-induced effects". SAE transactions, **105**(1), pp. 1190-1197.
- [4] Levin, D.B., Wardwell, D.A., 1997. "Single jet-induced effects on small-scale hover data in ground effect". *Journal of Aircraft*, **34**(3), pp. 400-407.
- [5] Henderson, B., Powell, A., 1993. "Experiments concerning tones produced by an axisymmetric choked jet impinging on flat plates". *Journal of Sound and Vibration*, **168**(2), pp. 307-326.
- [6] Henderson, B., Powell, A., 1996. "Sound-production mechanisms of the axisymmetric choked jet impinging on small plates: The production of primary tones". *The Journal of the Acoustical Society of America*, **99**(1), pp. 153-162.
- [7] Krothapalli, A., Rajkuperan, E., Alvi, F., Lourenco, L., 1999. "Flow field and noise characteristics of a supersonic impinging jet". *Journal of Fluid Mechanics*, **392**, pp. 155-181.
- [8] Henderson, B., Bridges, J., Wernet, M., 2005. "An experimental study of the oscillatory flow structure of tone-producing supersonic impinging jets". *Journal of Fluid Mechanics*, **542**, pp. 115-137.
- [9] Yao, Z., Zhang, X., and Cui, X., 2012. "Relationship between vortex and sound in under-expanded supersonic impinging jets". *International Journal for Numerical Methods in Fluids*, **12**(9), pp. 1126-1141.
- [10] Henderson, B., 2002. "The connection between sound production and jet structure of the supersonic impinging jet". *The Journal of the Acoustical Society of America*, **111**(2), pp. 735-747.
- [11] Powell, A., 1953. "On the mechanism of choked jet noise". *Proceedings of the Physical Society*, **66**, pp. 1039-1057.
- [12] Powell, A., 1953. "On edge tones and associated phenomena". *Acustica*, **3**, pp. 233-243.
- [13] Ho, C.M., Nossier, N.S., 1981. "Dynamics of an impinging jet. Part 1. The feedback phenomenon". *Journal of Fluid Mechanics*, **105**(1), pp. 119-142.
- [14] Powell, A., 1988. "The sound-producing oscillations of round underexpanded jets impinging on normal plates". *The Journal of the Acoustical Society of America*, **83**, pp. 515-533.
- [15] Tam, C.K.W., Ahuja, K.K., 1990. "Theoretical model of discrete tone generation by impinging jets". *Journal of Fluid Mechanics*, **214**, pp. 67-87.
- [16] Tam, C.K.W., 1995. "Supersonic jet noise". *Annual Review of Fluid Mechanics*, **27**, pp. 17-43.
- [17] Seiner, J.M., Ponton, M.K., Jansen, B.J., Lagen, N.T., 1992. "The effects of temperature on supersonic jet noise emission". *14th DGLR/AIAA Aeroa-*

- oustics Conference*, **1**, pp. 295-307.
- [18] Norum, T.D., 1982. "Screech suppression in supersonic jets". *AIAA*, **1**, 82-0050.
- [19] Tam, C.K.W., Seiner, J.M., Yu, J.C., 1986. "Proposed relationship between broadband shock associated noise and screech tones". *Journal of Sound and Vibration*, **110**(2), pp. 309-321.
- [20] Yu, J.C., Seiner, J.M., 1983. "Nearfield observations of tones generated from supersonic jet flows". *AIAA paper*, 83-0706.
- [21] Umeda, Y., Ishii, R., 2001. "On the sound sources of screech tones radiated from choked circular jets". *The Journal of the Acoustical Society of America*, **110**(4), pp. 1845-1858.
- [22] Davies, M.G. Oldfield, D.E.S., 1962. "Tones from a choked axisymmetric jet. II. The self-excited loop and mode of oscillation". *Acustica*, **12**, pp. 267-277.
- [23] Powell, A., Umeda, Y., Ishii, R., 1990. "The screech of round choked jets, revisited". *AIAA paper*, 90-3980.
- [24] Powell, A., Umeda, Y., Ishii, R., 1992. "Observations of the oscillation modes of choked circular jets". *The Journal of the Acoustical Society of America*, **92**, pp. 2823-2836.
- [25] Donaldson, C.D., Snedeker, R.S., 1990. "A study of free jet impingement. Part 1. Mean properties of free and impinging jets". *Journal of Fluid Mechanics*, **45**(2), pp. 281-319.
- [26] Alvi, F.S., Iyer, K.G., 1999. "Mean and unsteady flowfield properties of supersonic impinging jets with lift plates". *AIAA paper*, 99-1829.
- [27] Carling, J.C. and Hunt, B.L., 1974. "The near wall jet of a normally impinging, uniform, axisymmetric, supersonic jet". *Journal of Fluid Mechanics*, **66**(1), pp. 159-176.
- [28] Kalghatgi, G.T., Hunt, B.L., 1976. "The occurrence of stagnation bubbles in supersonic jet impingement flows". *Aeronautical Quarterly*, **27**(3), pp. 169-185.
- [29] Lamont, P.J., Hunt, B.L., 1980. "The impingement of underexpanded, axisymmetric jets on perpendicular and inclined flat plates". *Journal of Fluid Mechanics*, **100**(3), pp. 471-511.
- [30] Wagner, F.R., 1971. "The sound and flow field of an axially symmetric free jet upon impact on a wall". NASA TT F-13942.
- [31] Neuwerth, G., 1974. "Acoustic feedback phenomena of the subsonic and hypersonic free jet impinging on a foreign body". NASA TT F-15719.
- [32] Nosseir, N.S.M., Ho, C.M., 1979. "On the feedback phenomenon of an impinging jet". DTIC Document.
- [33] Hourigan, K., Rudman, M., Brocher, E., 1996. "The feedback loop in impinging two-dimensional high-subsonic and supersonic jets". *Experimental thermal and fluid science*, **12**(2), pp. 265-270.
- [34] Massey, K.C., and Ahuja, K.K., 1997. "Screech frequency prediction in light of mode detection and convection speed measurements for heated jets". *AIAA paper*, 97-1625.
- [35] Panda, J., Raman, G., and Zaman, K., 1997. "Under-expanded screeching jets from circular, rectangular and elliptic nozzles". *AIAA paper*, 97-1623.

FLUID-RESONANT COUPLING IN A HIGH-SPEED IMPINGING PLANAR JET

David Arthurs[†]
Samir Ziada[‡]

Aeroacoustics Research Group
Department of Mechanical Engineering
McMaster University
Hamilton, ON, Canada
Email: arthurdg@mcmaster.ca[†]
Email: ziadass@mcmaster.ca[‡]

ABSTRACT

This paper examines aeroacoustic tone generation of a high-speed *planar* gas jet impinging normally on a flat, rigid surface. Experiments are performed over the complete range of subsonic jet velocities and impingement distance for which tones are generated for a single jet thickness of $h=3\text{mm}$. The behavior of the planar impinging jet case is compared to that of the axisymmetric case and found to be significantly different, with tones being excited at much larger impingement ratios and beginning at lower flow velocities. The acoustic tones have been found to be generated by both symmetric and anti-symmetric shear layer modes of the jet, which may also couple with resonant acoustic modes occurring between the nozzle and plate surfaces. The nature of the flow instabilities has been investigated using phase-averaged Particle Image Velocimetry measurements, and dimensionless analysis is performed in order to quantify the system behavior in terms of the appropriate length and velocity scales.

INTRODUCTION

High-speed impinging jet flows are known to be liable to excitation of very intense acoustic tones generated by a feedback mechanism between instabilities in the free shear layers of the jet, and pressure fluctuations produced by the flow at the impingement surface. These effects can limit the usefulness of these geometries in many applications, however work investigating the heat transfer of self-excited impinging planar jets has shown that heat transfer rates can be enhanced by as much as 75% [1] compared to equivalent steady flows, providing evidence of potentially useful effects of this phenomenon. Various forms of impinging jet flows have been the subject of a relatively intense research effort in the literature, and those which have been investigated to date can be broadly grouped as those using axisymmetric jets, and those using planar jets.

Of the geometries consisting of jets impinging on flat rigid surfaces, the majority of the research in the literature has been devoted to the axisymmetric case. Various aspects of the feedback excitation mechanism for the subsonic axisymmetric case have been investigated by a series of authors [2-5], and extensive work has also been performed on the axisymmetric case involving supersonic flows [6-7]. In addition, the planar impinging

jet case using supersonic jets has also received some attention in the literature [8]. In comparison to axisymmetric jets, the impinging planar jet case using *subsonic* flows has received relatively little attention in the literature [9], despite being widely used in a myriad of practical and industrial applications such as thermal processing in both heating and cooling applications, the production of sheet glass and polymer films, and coating control applications.

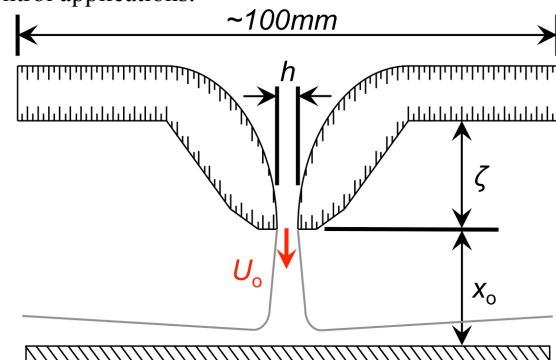


FIGURE 1: BASIC SCHEMATIC OF THE IMPINGING PLANAR JET FLOW SHOWING THE IMPINGEMENT DISTANCE AND THE GEOMETRY OF FLANGE, THE NOZZLE THICKNESS, AND THE FLOW VELOCITY AT THE NOZZLE OUTLET.

There has been considerable work performed on related geometries that use impinging planar jets, such as the jet-edge and jet-slot systems. Two recent studies of the jet-slot system [10-11] examined the coupling of a planar jet-slot oscillator with resonant longitudinal acoustic modes of the flow supply duct for Mach numbers up to $M=0.1$. In addition, there are many other studies in the literature documenting the response of the jet-slot oscillator [12-14] and numerous examples of work performed on the jet-edge system [15-17]. The response of the jet-edge and jet-slot systems is in some respects similar to that of the planar jet-plate system, however the range of flow velocity and impingement distance in the present investigation varies from these cases substantially. In addition, the change of momentum due to impingement on a plate, in comparison to the jet-edge and jet-slot cases, is bound to affect the flow dynamics at impingement and the resulting feedback mechanism which sustains the oscillations.

The current study focuses on experimental results of a high speed, subsonic planar jet impinging normally on a flat surface, as shown in Figure 1. A parametric study has been performed in which the impingement distance (x_0) and jet velocity (U_0) have been varied for a single jet thickness of $h=3\text{mm}$.

EXPERIMENTAL APPARATUS

A planar nozzle and impingement plate setup was carefully designed and constructed. The planar nozzle and plenum geometry, which has a span 100mm, was machined out of Aluminum, and allows for adjustment of jet thickness (h) from 1.0mm to 5.75 mm in increments of $\pm 0.25\text{mm}$. For the current study, results from a single jet thickness of $h=3\text{mm}$ are presented, for an overall aspect ratio of the nozzle of $L/h=33.3$. The nozzle is pressurized using compressed air, and several flow conditioning devices within the plenum such as a flow distribution tube and flow conditioning screens, are used to ensure an even flow distribution along the nozzle span, and a velocity profile at the exit consisting of a top-hat shaped velocity profile with thin shear layers. The jet nozzle uses an elliptical nozzle profile, and has a contraction ratio ~ 23 for a jet thickness of $h=3\text{mm}$. Static pressure in the plenum was measured at a location immediately upstream of the nozzle contraction at the centerline, and this supply pressure (P_s) was used to estimate the flow velocity of the jet exiting the nozzle using the following equation:

$$U_o = c \cdot \sqrt{\frac{2}{\gamma - 1} \left[\left(\frac{P_s + P_\infty}{P_\infty} \right)^{\frac{\gamma - 1}{\gamma}} - 1 \right]} \quad (1)$$

where P_∞ is the ambient pressure, c is the speed of sound in air (343 m/s) and γ is the ratio of specific heats of air. Subsequent PIV measurements confirmed that this expression, derived from equations of flow through a lossless nozzle, was accurate to within 1.5% for the conditions examined in this study.

The flat surface used for jet impingement consists of a large rigid plate machined out of Aluminum measuring 150mm \times 200mm and a thickness of 10mm. The plate surfaces have been machined using a single point fly-cut milling operation to provide the flattest surface possible. The plate has been machined to allow dynamic PCB 105C02 miniature dynamic pressure transducers to be flush mounted to the front surface of the plate at various locations to monitor fluctuating pressures at the plate surface.

Measurements in the acoustic free field were obtained using a GRAS 40BP 1/4" high-level microphone combined with a GRAS 26AC preamplifier and a GRAS 12AA power supply module. The microphone has a flat frequency response of 2Hz-70kHz ($\pm 1\text{dB}$) and were calibrated using a GRAS Type 42AB sound calibrator. The microphone was located at an angle of $\theta=60^\circ$ as measured from the jet plane, and at a microphone distance of $d=200\text{mm}$ as measured from stagnation point on the plate at the midpoint of the jet-span. Measurements were acquired using a National Instruments NI-4452 four channel data acquisition card

with hardware based anti-aliasing filters. Spectral analysis was performed acquiring data at a sample rate of 204.8kS/s for 15 seconds, breaking the time signal into 120 equally sized blocks of 51,200 samples with 50% overlap, calculating the amplitude spectrum of RMS acoustic pressure for each block, and averaging the 120 spectra to produce a final averaged spectrum. The resulting spectra were truncated to a frequency range of 0Hz to 70kHz, corresponding to the linear response range of the microphone.

In order to measure the velocity fields of the impinging jet flow, a 2-dimensional particle image velocimetry system was used. The system uses a single PowerView 4MP 12 bit digital camera with a resolution of 2048 \times 2048 pixels, along with a 532nm New Wave Solo 120XT pulsed Nd:YAG laser with a maximum output of 120mJ per pulse for flowfield illumination. Camera optics were determined by the required field of view for each flow field being captured, with a Sigma 105mm f 2.8 lens being used in combination with 1.4x and 2.0x teleconverters and extension tubes. Synchronization of the laser pulses and camera images was performed using a TSI LaserPulse Model 610035 synchronizer with external triggering and software adjustable time delay.

Acoustic tones produced by the impinging planar jet occur over a range of frequencies several orders of magnitude higher than the maximum image acquisition rate of the PIV system used in this study. In order to capture this relatively high-speed phenomenon using the traditional low-speed PIV system, a phase-locked PIV measurement technique was employed. Measurements performed using the phase-locked technique utilize the highly periodic pressure signal obtained at the plate surface to trigger flow velocity measurements at a particular instant in the flow oscillation cycle using a custom designed trigger generator. By adding and manipulating a time delay between the trigger point and the flow measurement, sets of images can be collected at any point in the phase of the cycle, to reconstruct the flow oscillation cycle.

Each PIV vector field was processed using a deformation based scheme incorporating 24 \times 24 pixel interrogation regions with 75% overlap in both the x and y -directions. All PIV measurements presented in this paper have a *minimum* validation rate of 99% for each instantaneous flow field before incorporating vector replacement or interpolation schemes. Seeding of the flow for PIV imaging was performed using a six-nozzle Laskin aerosol generator using olive oil as a seeding medium, producing 1 μm mean diameter droplets. The Stokes number of seeding particles for all PIV cases shown in present work falls below $Sk=0.1$ and fall within the range of $0.05 \leq Sk \leq 0.1$, which will result in tracking error of less than 2% [18].

AEROACOUSTIC RESPONSE

The high-speed impinging planar jet-plate system is known to produce large amplitude acoustic tones resulting from periodic flow oscillations over a range of impinging jet velocities and impingement distances. For the current study, sound measurements have been

performed in a grid for flow velocities from $U_o=150\text{m/s}$ to 343m/s (*choked flow*) in increments of $\pm 2.5\text{m/s}$, and for a range of impingement ratios, defined as the distance from the nozzle lip to the plate surface divided by the jet thickness, from $x_o/h=2.0$ to 32.0 in increments of ± 0.5 , a total of $\sim 4,800$ distinct acoustic measurements. This measurement domain represents all tone generating conditions for the jet thickness being examined.

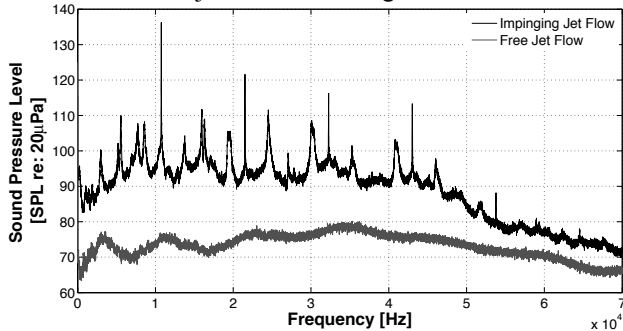


FIGURE 2: AEROACOUSTIC RESPONSE SHOWING THE SPECTRUM OF A FREE AND IMPINGING PLANAR JET IDENTICAL FLOW VELOCITIES OF $U_o=300\text{M/S}$ ($M=0.87$). $x_o/h=7.0$ FOR IMPINGING JET CASE.

Figure 2 shows a pair of acoustic spectra for a free and impinging planar jets at a flow velocity of $U_o=300\text{m/s}$, with the impinging jet case having an impingement ratio of $x_o/h=7$. The free planar jet contains only broadband noise, with no narrowband acoustic peaks, whereas the impinging jet case has a dominant acoustic tone at a frequency of $f=10.4\text{kHz}$ and an amplitude in sound pressure level of 137.4dB . Three super-harmonics of the dominant tone frequency are clearly visible on the spectrum, as well as one sub-harmonic, and a variety of other acoustic tones of smaller amplitudes. The dominant acoustic tone is more than 20 dB greater than the next largest acoustic tone amplitude, in this case the 1st super-harmonic of the dominant tone, and more than 40 dB greater than nearby broadband noise levels, and more than 60dB above levels of the free jet case. This behavior is indicative of the typical response of the planar jet-plate oscillator, which tends to generate an acoustic response with a large amplitude dominant acoustic tone, with a series of sub and super-harmonics of lesser amplitudes, and relatively high broadband noise levels. For the purposes of this paper, the threshold defining a “tone generating condition” shall be any configuration producing an acoustic spectrum having a spectral peak of greater than 20dB above nearby broadband noise levels.

Figure 3 shows a contour plot constructed using acoustic spectra taken for a range of flow velocities from $U_o=150\text{m/s}$ to $U_o=343\text{m/s}$ at a fixed impingement ratio of $x_o/h=7.0$. The contour plot clearly shows the presence of a distinct jet-staging phenomenon common to impinging shear layer flows, with the planar jet-plate oscillator switching between jet-stages at a flow velocity of $U_o\approx 265\text{m/s}$. Both the lower frequency jet-stage, which occurs for relatively low flow velocities, and the higher frequency stage show strong super-harmonics, although

the behavior of both the tone frequency and amplitude appears to be different for the two stages. The initial lower frequency jet-stage has tone frequencies that increase approximately linearly with increasing flow velocity, varying between 3.2kHz to 4.9kHz , and has relatively low acoustic pressure levels that increase with increasing flow velocity. In contrast, the higher frequency jet-stage has a tone frequency that is approximately constant and nearly invariant with increasing flow velocity, varying over a relatively small range of 10.2kHz to 10.6kHz . The acoustic pressures of this stage are significantly higher than those found in the lower jet-stage, and the difference in the behavior is thought to be attributed to the different mechanisms in the two regimes, with the lower jet-stage being produced by a traditional Rossiter mode, consisting only of upstream and downstream propagating disturbances between the nozzle lip and the plate surface, while the higher jet-stage is a Rossiter mode *coupled* with a resonant acoustic mode occurring between the nozzle and the plate, with the constant tone frequency corresponding to a fixed impingement distance. The nature of these resonant modes will be discussed in the final section of this paper.

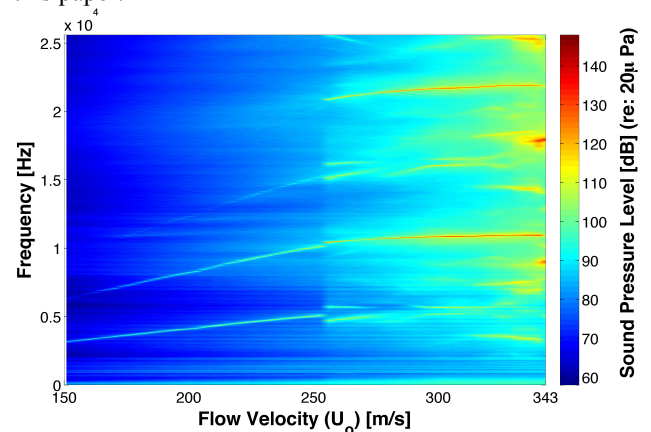


FIGURE 3: CONTOUR PLOT OF THE ACOUSTIC RESPONSE OF THE IMPINGING PLANAR JET AS A FUNCTION OF FLOW VELOCITY FOR $x_o/h=7.0$.

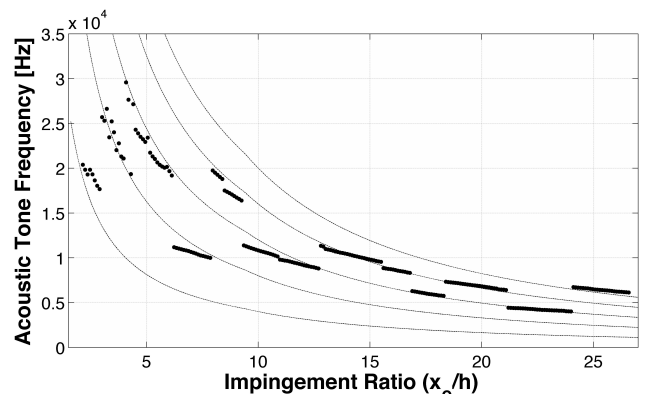


FIGURE 4: AEROACOUSTIC RESPONSE OF THE PLANAR IMPINGING JET-PLATE CASE AS A FUNCTION OF IMPINGEMENT RATIO FOR A CONSTANT FLOW VELOCITY OF $U_o=300\text{m/s}$ ($M=0.87$).

Figure 4 shows the frequency of the dominant acoustic tone as a function of varying impingement ratio, along with the predictions of the first five stages of a modified Rossiter model given in Eqn. (2), for a constant flow velocity of $U_o=300\text{m/s}$ ($M=0.87$).

$$f_n = \frac{n \cdot U_d \cdot c}{x_o (U_d + c)} \quad (2)$$

where n is the hydrodynamic mode number or jet-stage, U_d is the downstream velocity scale, c is the speed of sound and x_o is the impingement distance. The figure shows that the planar jet-plate oscillator responds in a large number of distinct jet-stages, which generate dominant acoustic tones over a wide range of frequencies, from $f \approx 3.0\text{kHz}$ to more than 30kHz . Furthermore, these tones occur over a large range of impingement ratios, from $x_o/h \approx 2$ up to $x_o/h \approx 28$, with frequent switching to both higher and lower jet-stages as the impingement ratio is increased, and there is an excellent agreement between the predictions of the modified Rossiter model and the experimental data.

This range of excitation is significantly wider than the impingement ratio range of similar geometries, such as the axisymmetric impinging jet case, which has been found to excite tones only over a relatively small impingement ratio range from $1.5 \leq x_o/D \leq 7.0$ [2,3,5,7-9], corresponding to the range of the potential core of a free axisymmetric jet. On the other hand, the planar impinging jet is found to excite tones over a range of both the jet's potential core in free planar jets, as well as the transition region, and the beginning of the self-similar regime. It also begins generating tones at lower flow velocities than the axisymmetric case, with the planar case exciting tones beginning at Mach numbers of $M=0.4$, compared to $M=0.6$ for the axisymmetric case.

$$St_{x_o} = \frac{f \cdot x_o}{U_{\text{eff}}} \quad (3)$$

$$U_d = \kappa_c \cdot U_o \quad \text{for } x_o/h < 10 \quad (4)$$

$$U_d = \kappa_c \cdot U_o \cdot 2.45 \cdot \left(x_o/h\right)^{-2/5} \quad \text{for } x_o/h \geq 10 \quad (5)$$

where $\kappa = 0.58$

$$U_{\text{eff}} = \frac{2 \cdot U_d \cdot c}{U_d + c} \quad (6)$$

In order gain greater insight into the mechanisms of acoustic tone generation and the form of jet instability driving acoustic tones, the data of the frequency of the dominant acoustic tone are non-dimensionalized in the form of an effective Strouhal number, given in Eqn. (3). The effective Strouhal number scale uses the impingement distance (x_o) as the relevant length scale, and an effective velocity (U_{eff}) as the velocity scale. The effective velocity scale is comprised of both an upstream and downstream velocity component which reflect the two portions of the feedback mechanism, with the downstream velocity scale being described by Eqn. (4) & Eqn. (5), each describing the downstream velocity over two distinct ranges of impingement ratio. These two

separate equations are required to account for the significant bulk slowing of the jet flow that occurs over the large range of impingement ratio for which the acoustic tones are excited, and the resulting variation in convection speed of coherent flow structures. The upstream velocity scale is simply the speed of sound (c), and the two scales are combined in Eqn. (6) that reflects the effective velocity of disturbances over a complete cycle.

When this effective Strouhal number scale is applied to the dominant tone frequency data for all tone generating conditions within the measurement domain ($0.4 \leq M \leq 1.0$ & $2 \leq x_o/h \leq 32$) as shown in both parts of Figure 5, a collapse of the data is observed. In part a) of the figure, the data points corresponding to the linear jet-stage collapse to a single mean Strouhal number of $St_{x_o} \approx 0.47$ at the low end of the Mach number range, while the data corresponding to the fluid-resonant stages, which occur at higher Mach numbers, also show a collapse to five distinct bands, with each representing the different jet-stages of the impinging jet flow, labeled $n=1$ through $n=5$ on the figure. The most prevalent of these fluid-resonant modes is the $n=3$ jet-stage, which occurs for Mach numbers as low as $M \approx 0.55$, with other modes occurring at a range of impingement ratios as the Mach number is increased. It is clear from inspection of part a) of the figure that for the higher Mach numbers tests, numerous jet-stages can occur depending on the impingement ratio, with the variation in data at each Mach number being attributed to the large variation in impingement ratio.

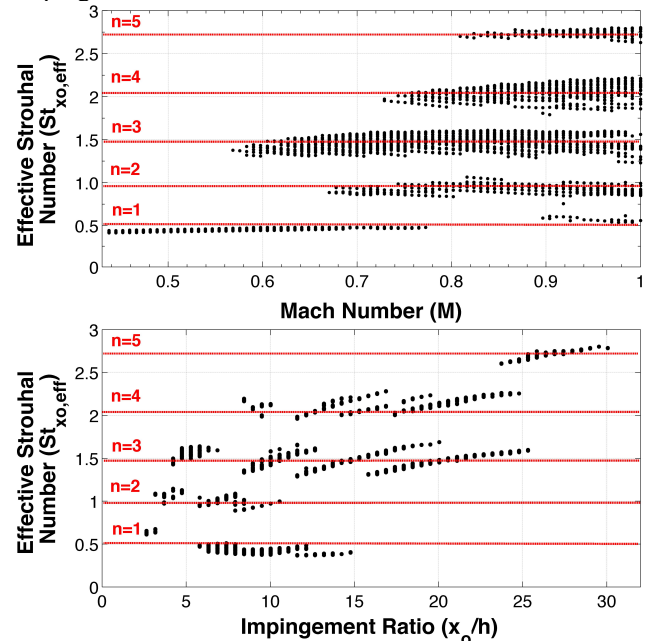


FIGURE 5: EFFECTIVE STROUHAL NUMBER AS A FUNCTION OF (TOP PLOT) MACH NUMBER AND (BOTTOM PLOT) IMPINGEMENT RATIO FOR ALL TONE GENERATING CONDITIONS.

Part b) of Figure 5 shows the same data as in part a) of the figure, but now plotted as a function of impingement ratio. Because the effective Strouhal number scale shown on the y -axis is identical to that of

part a), the data shows a collapse to the same mean Strouhal numbers for each of the five jet-stages however, viewing the data as a function of impingement ratio reveals a series of distinct clusters or bands related to the impingement ratio. The majority of these bands show a nominally linear upward sloping trend, with the spread of the data at each mean Strouhal number in part a) of the figure being attributed to these trends found within these clusters. As will be shown in a later portion of this paper, each of these separate clusters of data is produced as a result of a particular shear layer mode coupling with different resonant acoustic modes occurring between the nozzle flange and the impingement surface.

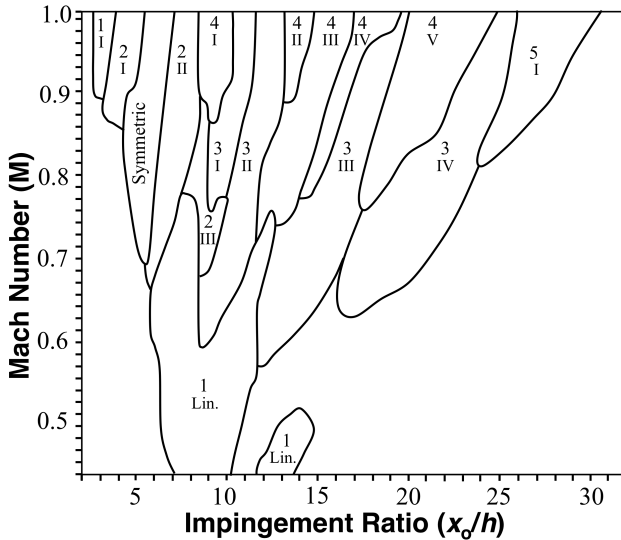


FIGURE 6: MODE DIAGRAM FOR THE IMPINGING PLANAR JET WITH THE SHEAR LAYER MODE OF THE JET DENOTED IN ARABIC NUMERALS, AND THE RESONANT MODES DENOTED BY ROMAN NUMERALS.

Figure 6 shows a contour plot illustrating the distribution of the various jet-stages as a function of both the Mach number and the impingement ratio obtained through a combination of the dimensionless analysis shown earlier, and confirmed with the results of phase-locked PIV measurements of the flow field for ~55 different combinations of Mach number and impingement ratio distributed over the measurement domain. This figure shows that the different jet-stages (n), corresponding to the number of structures occurring between the nozzle and the plate, and shown using Arabic numbers, are excited in a series of distinct bands occurring for concurrently increasing Mach number and impingement ratio. These jet-stage bands are further subdivided into smaller bands called sub-stages, denoted with roman numerals (m), with each corresponding to a different resonant acoustic mode occurring in the fluid volume between the nozzle and the plate, and different sub-stages correspond to different resonant acoustic modes with separate mode shapes. Variation of either the impingement ratio or Mach number may result in jumps between different jet-stages, between different sub-stages, or both, depending on the state of the system.

VISUALIZATION OF JET SHEAR LAYER MODES

In order to reveal the form of the flow oscillation driving acoustic tone generation, extensive flow measurements have been performed using phase-locked PIV measurement technique in which a series of images of the flow are captured at a series of specified points within the phase of the flow oscillation to produce a phase reconstruction of the flow oscillation cycle. Figure 7 shows a series of four phase-averaged velocity fields taken at phase angle increments of 90° . The figure shows the form of the flow oscillation for an impinging jet with an impingement ratio of $x_0/h=10.5$ and a flow velocity of $U_0=265\text{m/s}$, which produces an $n=3$ anti-symmetric flow oscillation at a frequency of $f \approx 10.5\text{kHz}$. Each flow field is composed using the average of 100 instantaneous velocity fields acquired at the same point in the phase of the flow oscillation. Coherent flow structures within the flow, shown with a single contour level superimposed on each flow field, have been identified using the velocity discriminant parameter given in the following Equation [19]:

$$d_2 = \left(\frac{\partial u}{\partial x} + \frac{\partial v}{\partial y} \right)^2 - 4 \left(\frac{\partial u}{\partial x} \frac{\partial v}{\partial y} - \frac{\partial u}{\partial y} \frac{\partial v}{\partial x} \right) \quad (7)$$

where u and v are the downstream and transverse velocity components respectively. This quantity, also commonly referred to as the “swirl” of the flow field, uses a non-linear combination of velocity derivative terms to identify areas of strong vorticity that have a particular shape characteristic, i.e. round or near-round structures.

Inspection of this figure shows that the impinging jet flow oscillates in a flapping instability mode, with the jet flow displaced from the centerline in a wave-like pattern, and with coherent flow structures positioned nominally at the saddle points of the wave pattern. The flapping oscillation propagates downstream as the phase of the oscillation progresses, with the structures also convecting downstream, and ultimately impinging on the downstream surface. The flow oscillation appears to have two structures in each shear layer on either side of the jet appearing between the nozzle and the plate, although this assessment is somewhat ambiguous as it is not entirely clear at which point in the cycle the structure has “impinged” on the plate surface, and detection of relatively small structures in the initial shear layer is difficult. A high-velocity pocket of flow occurs near the impingement surface in the wall-jet region between the plate and the vortex, with the rotation of the structure contributing to the increased velocity at these locations. These high velocity pockets propagate with the structure as it travels along the surface of the plate. For the current case, these periodic high-velocity pockets are more than 25% larger than the mean flow in this region, and represent a large fluctuating flow component at the surface of the plate.

Figure 8 shows a series of PIV flow fields obtained for some of the remaining modes of the jet, provided to the reader to illustrate the wide variety of self-excited oscillation patterns of the system. The figure shows the $n=2, 3$ and 4 anti-symmetric stages, as well the $n=2$ symmetric jet-stage.

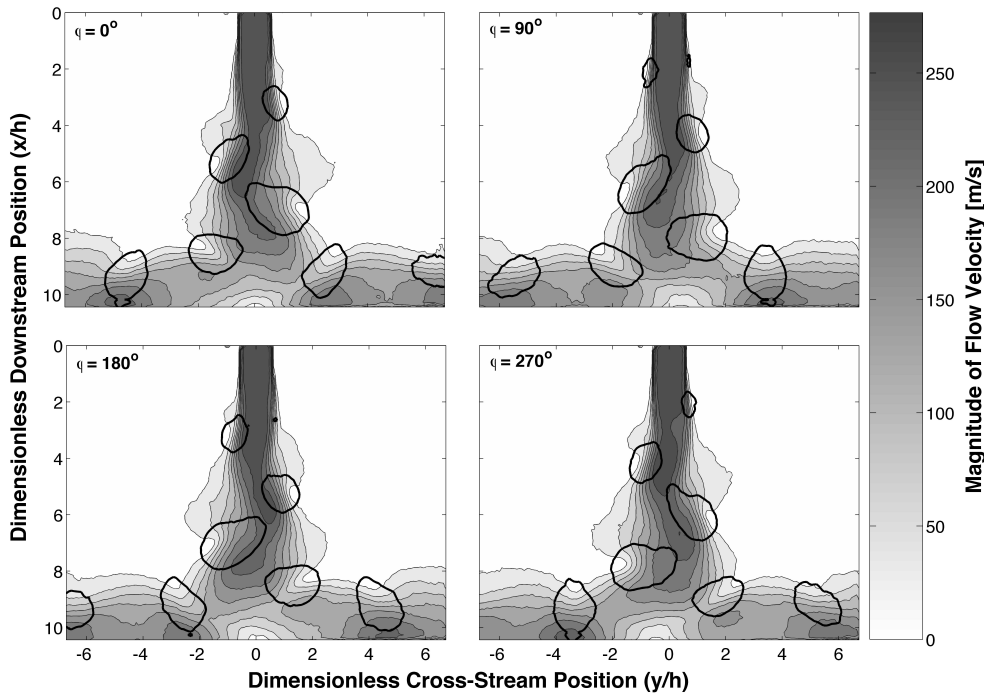


FIGURE 7: PHASE-LOCKED PIV FLOW FIELDS SHOWING THE OSCILLATING FLOW FIELD OF THE IMPINGING PLANAR JET. FLOW CONDITIONS: $x_0/h=10.5$, $U_0=265\text{m/s}$ ($M=0.77$), $f=10.5\text{kHz}$.

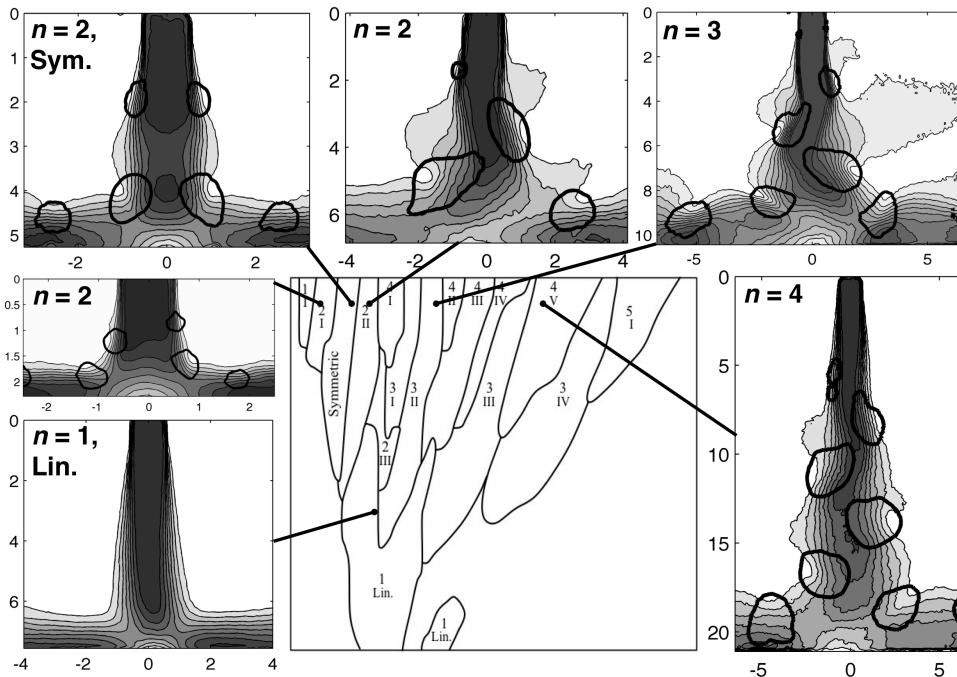


FIGURE 8: MODE DIAGRAM FOR THE IMPINGING PLANAR JET WITH PIV FLOW FIELDS OF THE VARIOUS SHEAR LAYER MODES.

FLUID RESONANT COUPLING

In this section, the nature of the fluid-resonant regime will be investigated, and the physical mechanisms responsible for the behavior of the various jet-stages will be explored. The current system is comprised of a planar jet nozzle with a large, flat flange set back $\zeta=30\text{mm}$ from the nozzle outlet and a large flat plate positioned at some distance downstream, as shown in Figure 1. This geometry forms an open acoustic system, with nominally

parallel solid surfaces at the plate and nozzle flange, and openings to surroundings at the either end of the nozzle span, as well as at the two edges of the plate and nozzle flange. This system is geometrically similar to a single occurrence of a flat plate cascade in an open environment and as a result, it is expected to possess trapped acoustic modes occurring between the nozzle and plate surface [20]. A number of authors have investigated the phenomenon of trapped modes in various geometries such

as ducts containing splitter plates and various bluff bodies [21], axisymmetric and rectangular cavities in ducts [22-23], as well as airfoils with leading-edge slats [24]. These geometries, which all represent relatively unconfined acoustic systems, have been found to be liable to the flow-excitation of trapped modes occurring between solid boundaries, especially at high frequencies as the acoustic wavelength becomes small and radiation to the surroundings diminishes.

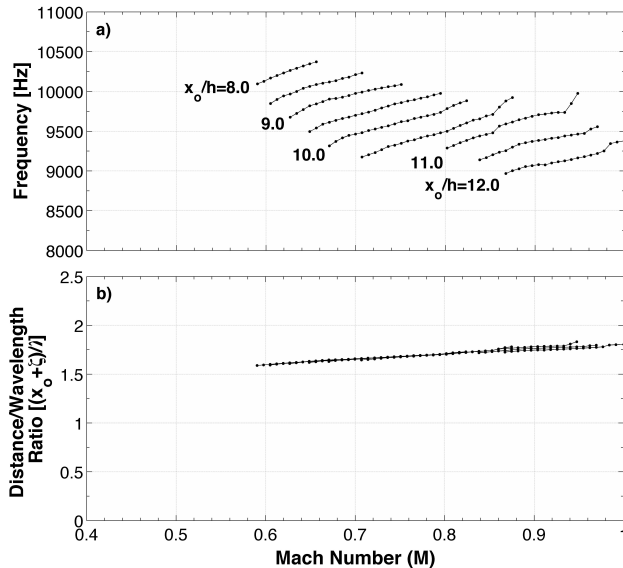


FIGURE 9: A) ACOUSTIC TONE FREQUENCY AND B) NUMBER OF ACOUSTIC WAVELENGTHS BETWEEN THE NOZZLE FLANGE AND THE IMPINGEMENT SURFACE FOR THE $n=3$, $m=II$ SUB-STAGE.

In order to investigate the fluid-resonant coupling of the shear layer mode of the jet with trapped acoustic modes between the nozzle and the plate, the acoustic tone data from the $m=II$ sub-stage of the $n=3$ anti-symmetric jet-stage is plotted in Figure 9. Part a) of the figure shows the tone frequency data as a function of Mach number for a variety of impingement ratios. At each fixed impingement ratio (x_0/h), the sub-stage is excited at frequencies which increase slightly as the Mach number of the jet is increased, with the total variation in resonant tone frequency as a function of Mach number at each particular impingement ratio is relatively small, typically less than 5% of the mean value. When the impingement ratio is increased, this qualitative trend is maintained, but the mean frequency for the sub-stage decreases, indicating that the impinging jet is coupled to acoustic mode between the nozzle flange and the impingement surface, with the frequency being tied to the length scale of the resonator.

Part b) of this figure shows same data in the form of a dimensionless parameter of the ratio of distance between the nozzle flange and the impingement surface ($x_0 + \zeta$) to the wavelength of the resonant acoustic mode, as a function of Mach number, which clearly shows a collapse of the frequency data to a well-defined increasing linear trend. The data shows an excellent collapse at Mach numbers below $M=0.9$, and a fair collapse at transonic Mach numbers, with approximately constant ratio between

the length scale and wavelength. The variation in the ratio of the length scale to the wavelength of the acoustic wave may be attributed to the effect of the mean flow on the frequency and mode shape of the resonant acoustic mode.

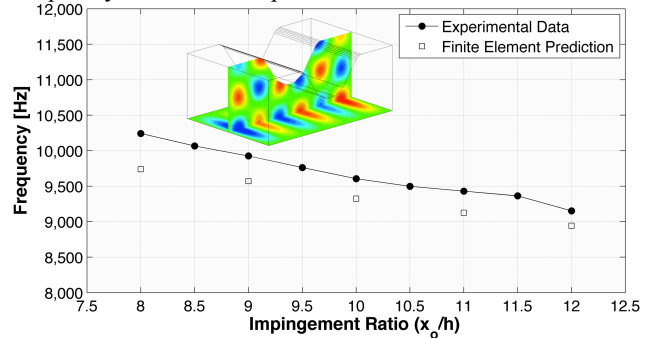


FIGURE 10: COMPARISON BETWEEN NUMERICAL AND EXPERIMENTALLY OBSERVED FREQUENCIES OF A RESONANT ACOUSTIC MODE BETWEEN THE NOZZLE FLANGE AND THE PLATE FOR THE $n=3$, $m=II$ FLUID-RESONANT MODE.

To investigate the possibility of trapped acoustic modes occurring between the nozzle and the plate surface, and to assess the effect of varying impingement ratio on resonant tone frequency, several acoustic simulations were carried out using Finite Element Analysis. Results were calculated using a 4-node tetragonal, unstructured mesh in a commercial FEA software package, with a minimum of 15 elements per acoustic wavelength, defined by the frequency range of interest. The finite element model treats the air volume within the domain as stagnant, and does not include the effects of the mean flow on the frequency or mode shape of the resulting modes.

Simulations were carried out using only the air volume between the nozzle and plate, as well as additional validation simulations that were performed with a large air volume surrounding all sides of the jet-plate geometry. It was found that the placement of the opening boundary condition at the edge of the nozzle and plate had a relatively small effect on both the frequency and mode shape of the resultant acoustic modes, with a difference in frequency of any given mode of less than 3% between simulations using the jet-plate air volume and those with additional air volumes placed at the openings.

The simulations confirmed the presence of a myriad of acoustic modes between the nozzle flange and the plate surface for the frequency range of interest. Figure 10 shows experimentally obtained average tone frequency for the $n=3$, $m=II$ sub-stage as shown in Figure 6, compared to the tone frequency prediction of the finite element model, along with the calculated dimensionless acoustic pressure distribution between the nozzle and the impingement surface. The prediction of the finite element model shows good agreement with the experimental data, with an average deviation of less than 5%. In addition, the good qualitative agreement in tone frequency as a function of impingement ratio between the experimental and the numerical model indicates that the sub-stage phenomenon is likely produced as a result of a fluid-resonant coupling.

It should be noted that the objective of computing the frequency of resonant acoustic modes was to validate the existence of trapped modes with frequencies and mode shapes consistent with results obtained during experiments within the fluid-resonant regime. A relatively simple model was therefore selected for this study because even if the boundary conditions were more accurately modeled, the resonance frequencies and mode shapes would still be approximate as the effects of the mean flow would not be captured.

CONCLUSIONS

A comprehensive experimental study of the high-speed planar jet-plate geometry has been performed for Mach numbers from $M=0.44$ to 1.0 and impingement ratios between $x_0/h=2.0$ and 32.0, for a single jet thickness of $h=3.0\text{mm}$. The planar jet-plate system has been shown to excite strong, narrow band acoustic tones over a wide range of Mach numbers and impingement ratios. These tones have been found to be excited within two distinct ranges, a lower speed linear regime, where tones are excited by a hydrodynamic mode of the jet consisting of downstream propagating flow structures and upstream propagating acoustic disturbances, and a higher-speed fluid-resonant regime, in which a hydrodynamic mode couples with a resonant acoustic mode occurring between the nozzle flange and the plate surface. The various jet-stages have been found to be excited in distinct recurring bands, with each band being associated with a particular resonant acoustic mode between the plate surface and the nozzle flange.

REFERENCES

- [1] Camci, C., Herr, F., 2002. Forced convection heat transfer enhancement using a self-oscillating impinging planar jet, *ASME J. Heat Trans.* 124(4), 770-782.
- [2] Ho, C., Nossier, N. S., 1981. Dynamics of an impinging jet. Part 1: The feedback mechanism. *J. Fluid Mech.* 105, 119-142.
- [3] Nossier, N. S., Ho, C., 1982. Dynamics of an impinging jet. Part 2: The noise generation. *J. Fluid Mech.* 116, 379-391.
- [4] Tam, C., Ahuja, K., 1990. Theoretical model of discrete tone generation by impinging jets. *J. Fluid Mech.* 214, 67-87.
- [5] Panicker, P., Raman, R., 2007. Criteria for the existence of helical instabilities in subsonic impinging jets. *Phy. Fluids*. 19, 106103-1.
- [6] Krothapelli, A., Rajkuperan, E., Alvi, F., Lourenco, L., 1999. Flow field noise characteristics of a supersonic impinging jet. *J. Fluid Mech.* 392, 155-181.
- [7] Henderson, B., 2001. The connection between sound production and jet structure of the supersonic jet. *J. Ac. Soc. Am.* 111 (2), 735-747.
- [8] Krothapelli, A., 1984. Discrete tones generated by an impinging under-expanded rectangular jet. *AIAA J.* 23 (12), 1910-1915.
- [9] Arthurs, D., Ziada, S., 2011. The planar jet-plate oscillator. *J. Fluids Struct.* 27, 105-120.
- [10] Billon, A. Valeau, A., Sakout, A., 2005. Two feedback paths for a jet-slot oscillator. *J. Fluids Struct.* 21, 121-132.
- [11] Glessner, M. Valeau, A., Sakout, A., 2008. Vortex Sound in unconfined flows: Application to the coupling of a jet-slot oscillator with a resonator. *Journal of Sound and Vibration*, 314, 635-649.
- [12] Rockwell, D., Naudasher, E., 1979. Self-sustained oscillations of impinging free shear layers. *Ann. Rev. Fluid Mech.* 11, 67-94.
- [13] Ziada, S., 1995. Feedback control of globally unstable flows: Impinging flows. *J. Fluids Struct.* 9, 907-923.
- [14] Ziada, S., 2001. Interaction of a jet-slot oscillator with a deep cavity resonator and its control. *J. Fluids Struct.* 15, 831-843.
- [15] Powell, A., 1961. On the edge tone. *J. Ac. Soc. Am.* 33, 395-409.
- [16] Ziada, S., 2002. Active stabilization of a planar jet impinging on a flexible wedge. *J. Fluids Struct.* 16, 613-626.
- [17] Ziada, S., Rockwell, D., 1982. Oscillations of an unstable mixing layer impinging upon an edge. *J. Fluid Mech.* 124, 307-334.
- [18] Melling, A., 1997. Tracer particles and seeding for particle image velocimetry. *Meas. Sci. Technol.* 8, 1406-1416.
- [19] Vollmers, H., 2001. Detection of vortices and quantitative evaluation of their main parameters from experimental velocity data. *Meas. Sci. Tech.* 12, 1199-1207.
- [20] Koch, W., 1983. Resonant acoustic frequencies of flat plate cascades. *J. Sound Vib.* 88(2), 233-242.
- [21] Hein, S., Hohage, T., Koch, W., 2004. On resonances in open systems. *J. Fluid Mech.* 506, 255-284.
- [22] Aly, K., Ziada, S., 2010. Flow-excited resonance of trapped modes of ducted shallow cavities. *J. Fluids Struct.* 26, 92-120.
- [23] Hein, S., Koch, W., 2008. Acoustic resonances and trapped modes in pipes and tunnels. *J. Fluid Mech.* 605, 401-428.
- [24] Hein, S., Hohage, T., Koch, W., 2007. Acoustic resonances in a high-lift configuration. *J. Fluid Mech.* 582, 179-202.
- [25] Graf, H., Ziada, S., 2010. Excitation source of a side-branch shear layer. *J. Sound Vib.* 329, 2825-2842.



NUMERICAL SIMULATION AND ANALYSIS OF THE NOISE GENERATED BY THE FLOW OVER RECTANGULAR CYLINDERS AT INCIDENCE

Florent Margnat*

Arts et Metiers ParisTech

DynFluid

151 bd de l'Hopital

75013 PARIS, France

Email: florent.margnat@ensam.eu

Arturo García Buitrago

Zahra Jalali Monfared

Arts et Metiers ParisTech

DynFluid

151 bd de l'Hopital

75013 PARIS, France

ABSTRACT

A hybrid noise prediction approach is proposed, validated and applied to study the acoustic emission by a 2D flow over a rectangular cylinder at $Re = 200$, and to investigate the influence of the angle of attack. In a first step, the unsteady incompressible flow is simulated. The presence of the bluff body is modelled through an immersed boundary method. In a second step, the acoustic field is evaluated using Curle's analogy and the compact source approximation. Ten values of the incidence are considered from 0° to 90° . A change in the vortex street topology around 20° of incidence is exhibited, whose trace is visible on the phase portrait of the aerodynamic force and, consequently, on the acoustic directivity.

1 INTRODUCTION

Thanks to past research efforts, the prediction of the noise radiated by unsteady flows has reached a state that is mature enough to provide efficient tools for industrial application. However, for some part, our understanding of the underlying physics remains fragmentary. For example, Curle's analogy [1] lead to an estimation of the acoustic pressure in far field as scaling on $M^{5/2}$ for its compact dipole in 2D. Such law needs the introduction of a characteristic length of the flow. As shown by Inoue & Hatakeyama [2, 3], Curle's power law describes correctly the case of the aeolian tone, for which the reference length is naturally the cylinder diameter. How the coefficient in front of $M^{5/2}$ is affected by the geometry of the body attacked by the flow is the issue addressed by the present contribution. In particular, the goal is to exhibit flows with the same reference length but with significantly dif-

ferent radiated power, for example whistling regimes with high acoustic efficiency.

For such purpose, the flow over a rectangular cylinder at incidence is a good configuration. Indeed, depending on the incidence angle, two shedding regimes are observed, as plotted in figure 1. For low angles, the vortex street is aligned downstream the body, while for angles higher than 45 degrees, positive and negative vortices form two alternate lines. In all likelihood, such change in the vortex dynamics may affect the acoustic emission mechanism and efficiency, despite the main cross section is kept constant. This will be studied in section 4.4.

Furthermore, it has been shown by different authors (Powell, Howe), and illustrated by Gloerfelt *et al* [4], that the surfacic source term derived by Curle should only be considered as an equivalent source, since it accounts for the diffraction by the body of acoustic waves generated inside the unsteady wake. The fact that an incompressible flow simulation is able to predict such effect does not contradict these theoretical results. Indeed, in the very near-field the wave operator reduces to the Laplacian which governs the incompressible pressure variations. However, exhibiting different shedding regimes provides a chance to improve our understanding of the link between the vortex dynamics and the associated noise.

The paper is organised as follows. In section 2, the flow configuration is presented as well as its numerical simulation. Then the noise estimation method is introduced in section 3, based on Curle's analogy and on the unsteady forces evaluation through the immersed boundary method. The validation of the method and the acoustic results are provided in section 4.

*Address all correspondence to this author.

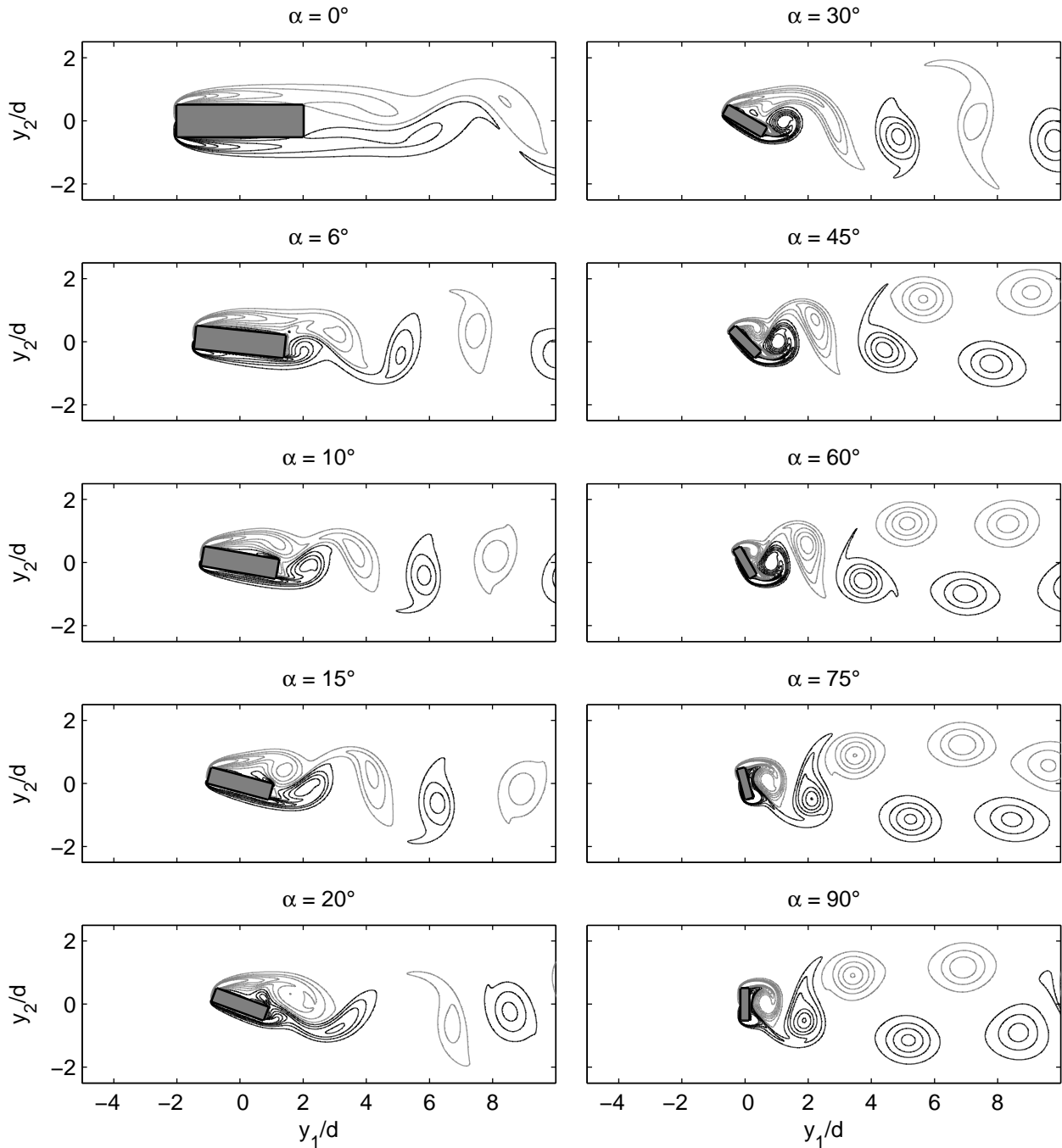


Figure 1: INSTANTANEOUS VORTICITY CONTOURS. THE LEVELS ARE FROM -5.5 TO 5.5 WITH AN INCREMENT OF 1. SOLID LINES: POSITIVE LEVELS; DASHED LINES: NEGATIVE LEVELS.

2 FLOW CONFIGURATION AND NUMERICAL TOOLS

Unsteady 2D numerical simulations of the viscous flow over a rectangular cylinder have been carried out, varying the incidence. The aspect ratio of the bluff body is kept constant, $B/A = 4$. The configuration is sketched in figure 2. The Reynolds number is 200, based on the upstream velocity U_∞ and on the main cross section, noted d , which are taken as characteristic velocity and length

in this study. The size of the computational domain in the transverse direction is also the same for every incidence, so that the blockage ratio has a constant value of 5%. Consequently, the size of the edges of the rectangular cylinder depends on the incidence. For example, for $\alpha = 0^\circ$, one have $A = d = 1$ and $B = 4$, while for $\alpha = 90^\circ$, A decreases to .25 while B becomes equal to the main cross section d . Beside, the projected length of the cylinder is noted L and is given by $L = B \cos \alpha + A \sin \alpha$.

Such conventions are followed in order to be consistent with the results presented by Sohankar *et al* [5]. Although this value of the Reynolds number may be critical for those flows, and that a 3D transition may have occurred (whilst it may depend on the incidence), the 2D simulations are well suited to the present aeracoustic issue of exhibiting and study whistling configurations.

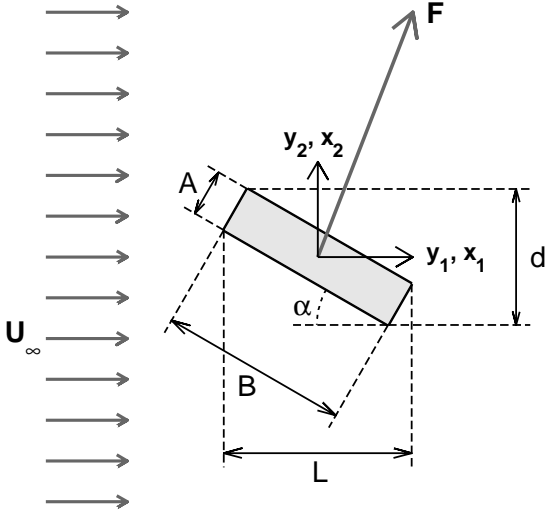


Figure 2: CONFIGURATION AND NOTATIONS.

Free-slip conditions are set on the lateral boundaries of the computational domain, while a convection condition is set outflow. The presence of the bluff body is modelled through a virtual boundary method, the behavior of which, in the case of sharp edged bodies, has been studied in [6]. The numerical code itself is described in details in [7]. It solves the incompressible Navier-Stokes equation, using 6th order compact centred finite difference scheme for the evaluation of space derivatives, and the 3rd order Runge-Kutta time marching. The cartesian grid is uniform streamwise, while, in the transverse direction, it is stretched from the cylinder center, the latter being taken as the origin of the reference frame.

3 NOISE ESTIMATION METHOD

Curle's analogy

The convected form of Curle's integral solution [1] to Lightill's analogy is computed here in the frequency domain. The acoustic pressure at an observer located in $\mathbf{x} = (x_1, x_2)$ is given by:

$$\tilde{p}_a(\mathbf{x}, \omega) = - \oint_{\partial D} [\tilde{p} \delta_{ij} - \tilde{\tau}_{ij}] \mathbf{n}_j \frac{\partial \tilde{G}_c(\mathbf{x}|\mathbf{y}, \omega)}{\partial y_i} d\Sigma(\mathbf{y}) \quad (1)$$

Where \tilde{f} is the Fourier transform of f , p is the pressure and τ_{ij} is the viscous stress tensor.

The 2D free-field convected Green function G_c is given in the frequency domain by:

$$\tilde{G}_c(\mathbf{x}|\mathbf{y}, \omega) = \frac{i}{4\beta} \exp\left(\frac{iMkr_1}{\beta^2}\right) H_0^{(2)}\left(\frac{kr_\beta}{\beta^2}\right) \quad (2)$$

where $\mathbf{y} = (y_1, y_2)$ is the source position, $r_i = x_i - y_i$, $i^2 = -1$, $H_\nu^{(m)}$ is the Hankel function of order ν of m^{th} kind, ω is the angular frequency under consideration and $k = \omega/c_0$. The Green function space derivatives are given in Gloerfelt *et al* [8].

$\beta^2 = 1 - M^2$, where M is the Mach number of the flow in the observer domain, is the Prandtl-Glauert factor, and $r_\beta = \sqrt{(x_1 - y_1)^2 + \beta^2(x_2 - y_2)^2}$.

In this application of Curle's analogy, which is devoted to low speed flows, the volumic source term has been neglected to get (1). Their quadrupolar character may *a priori* turn them insignificant with respect to the surfacic terms for low Mach number subsonic aeroacoustics. However, such assumption depends on the source compactness. This issue is postponed until a further study.

Assuming a compact source and a far field estimation, $\|\mathbf{x} - \mathbf{y}\|$ can be approximated by $\|\mathbf{x}\|$, that is $r_i \approx x_i$ and $r_\beta \approx \sqrt{x_1^2 + \beta^2 x_2^2}$. Consequently, the Green function and its derivatives does not depend on \mathbf{y} anymore, and Curle's solution reduces to:

$$\tilde{p}_a(\mathbf{x}, \omega) = - \frac{\partial \tilde{G}_c(\mathbf{x}|\mathbf{y}, \omega)}{\partial y_i} \tilde{F}_i(\omega) \quad (3)$$

where \tilde{G}_c stands for the approximation of \tilde{G}_c when $\|\mathbf{y}\| \ll \|\mathbf{r}\|$, and $\tilde{F}_i(\omega) = \oint_{\partial D} [\tilde{p} \delta_{ij} - \tilde{\tau}_{ij}] \mathbf{n}_j d\Sigma(\mathbf{y})$ is the i^{th} component of the unsteady aerodynamic force on the bluff body, here including its viscous component.

3.1 Unsteady aerodynamic force evaluation

The evaluation of the unsteady load, which is the source quantity in the present application of Curle's analogy, takes advantage of the modelling of the no-slip condition with the immersed boundary method. This method introduces an external force field in the following momentum equation:

$$\frac{\partial \mathbf{u}}{\partial t} + \mathbf{u}_j \frac{\partial \mathbf{u}_i}{\partial y_j} = - \frac{\partial p}{\partial y_i} + \frac{1}{Re} \frac{\partial^2 \mathbf{u}_i}{\partial y_j \partial y_j} + \mathbf{f} \quad (4)$$

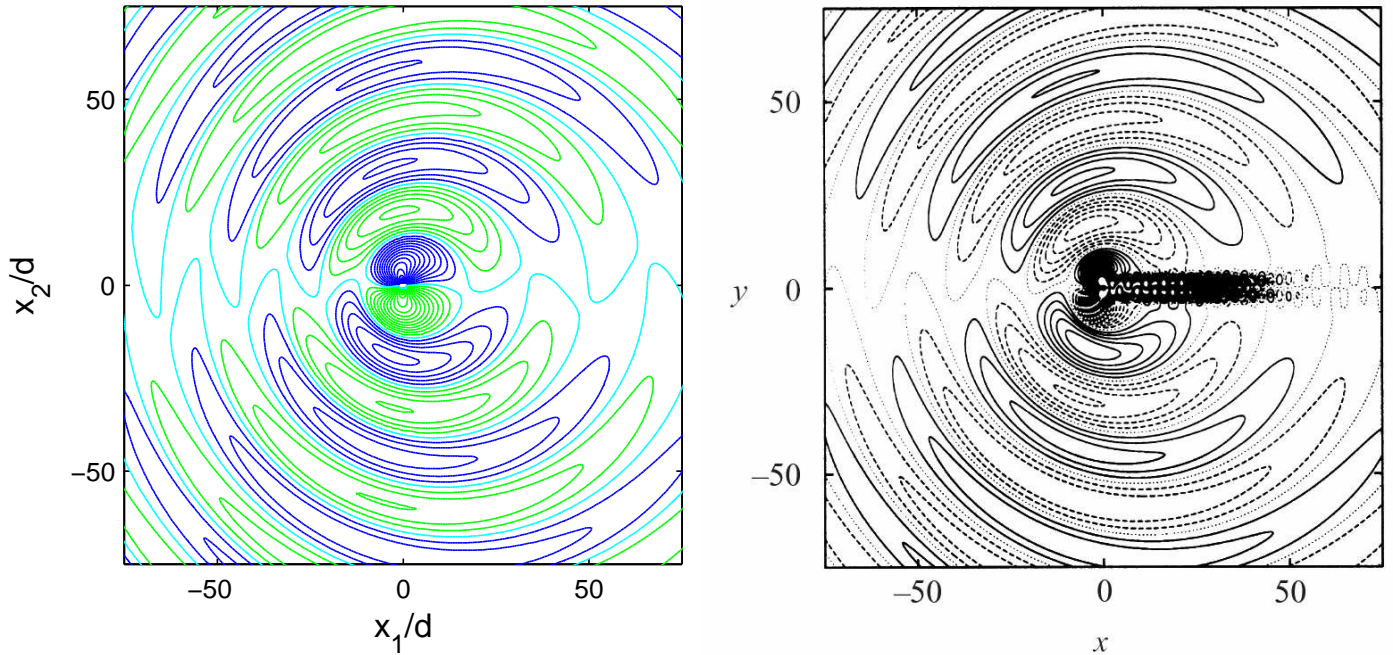


Figure 3: ACOUSTIC PRESSURE RADIATION FROM A CIRCULAR CYLINDER IN A FLOW AT $M = 0.2$. LEFT: PRESENT HYBRID METHOD; RIGHT: DNS FROM INOUE & HATAKEYAMA [2].

The feedback forcing method [9] defines \mathbf{f} as:

$$\mathbf{f}(\mathbf{y}, t) = -\varepsilon(\mathbf{y}) \left[\omega_n^2 \int \mathbf{u}(\mathbf{y}, t) dt + 2\zeta \omega_n \mathbf{u}(\mathbf{y}, t) \right] \quad (5)$$

where ω_n and ζ are the natural frequency and the damping coefficient of the second order controller thus introduced, which forces the velocity field \mathbf{u} to be zero everywhere ε is non zero. In the present case, this mask function is set to 1 for each grid point located inside the bluff body, and to 0 outside.

Integrating (4) over the solid domain ($\varepsilon = 1$) leads to:

$$\mathbf{F} = \frac{\partial}{\partial t} \int_{\varepsilon=1} \mathbf{u} dV(\mathbf{y}) + \oint_{\partial D} \mathbf{u}(\mathbf{u} \cdot \mathbf{n}) d\Sigma(\mathbf{y}) - \int_{\varepsilon=1} \mathbf{f} dV(\mathbf{y}) \quad (6)$$

Provided that the flow is effectively frozen in the solid domain thanks to the action of the force field, which is the case here, the two first terms on the right-hand side of (6) are insignificant. Thus, the immersed boundary method provides here a simple access to the aerodynamic force on the body through the integration of the forcing term over the solid domain.

4 RESULTS

4.1 Validation of the hybrid method

The hybrid method presented in the previous section is validated through the aeolian tone problem. In table 1, the aerodynamic quantities obtained using the incompressible solver combined with the immersed boundary method are compared with those obtained by Inoue & Hatakeyama [2] using a compressible solver for the direct noise computation, for the flow over a circular cylinder at $Re = 150$.

Table 1: AERODYNAMIC QUANTITIES FOR THE CIRCULAR CYLINDER FLOW AT $Re = 150$.

	Present	I & H [2]
Mean C_D	1.35	1.32
C_D amplitude	.026	.026
C_L amplitude	.52	.52
St	.189	.183

The amplitude of the lift and drag coefficients is perfectly evaluated using the forcing term as given by (6). The mean drag force is also in good agreement, while slightly overestimated by the immersed boundary method. The Strouhal number is 4% higher than the value reported in ref. [2]. However the latter also mention a value of .185 obtained with incompressible simulations, from which the present result is closer.

The comparison for the acoustic pressure field is presented in figure 3. The acoustic wave pattern predicted by the compact convected spectral form of the present application of Curle's analogy agrees qualitatively and quantitatively very well with the pressure field directly computed by Inoue & Hatakeyama [2]. The fluctuating aerodynamic wake is naturally lost in the hybrid computation since the Green formalism does not propagate the convective modes.

4.2 Validation of the rectangular cylinder flows

The flow over a rectangular cylinder is simulated for 10 values of the incidence, from 0° to 90° . Note that the main cross section is the same for all cases. The grid and domain extent are also kept constant. For each incidence, the Strouhal number, the mean drag and lift coefficients and the *rms* lift coefficient are evaluated once the periodic state is achieved, and compared to the results reported by Sohankar *et al* [5] in figure 4.

For all the aerodynamic quantities, the qualitative behavior with incidence is well recovered in the present simulation. In particular, the drag growth, the Strouhal number and the mean and *rms* lift peaks at 10° , and the secondary peaks of the Strouhal number and of the *rms* lift at higher incidences, are correctly tracked. The present values are globally overestimated, except the Strouhal number at incidences higher than 45° which is strongly underestimated. Note that for the mean drag coefficient, only the pressure drag is contained in the values communicated by Sohankar *et al* in [5]. A better agreement can be obtained with a finer grid and a larger domain streamwise. As a conclusion, the good prediction of the fluctuating force and its variation with incidence allows the study of the acoustic features of the flow.

4.3 Acoustic field for $\alpha = 30^\circ$

As an illustration, the noise radiated by the flow over the rectangular cylinder at 30 degrees of incidence is plotted in figure 7. Since the source quantities come from an incompressible simulation, the sound speed can be arbitrary defined. In order to respect the compact character in-

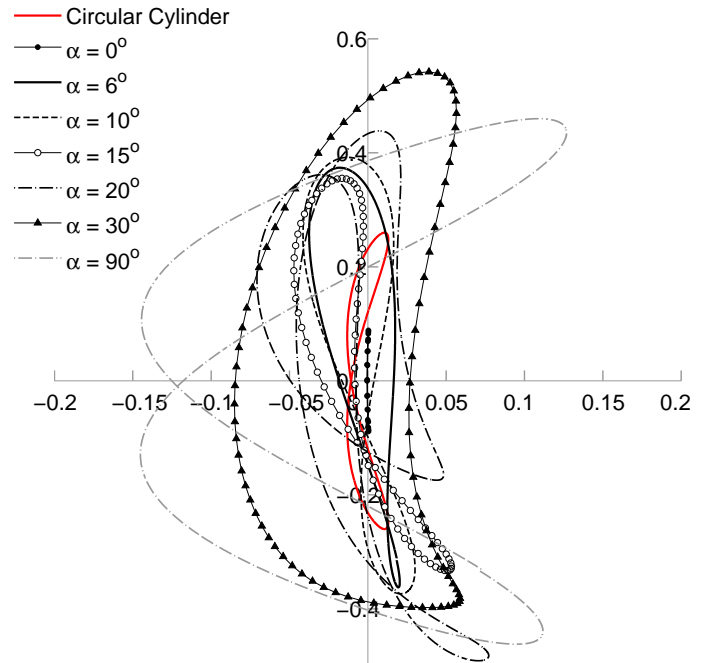


Figure 5: PHASE PORTRAIT OF THE AERODYNAMIC FORCE FOR THE TWO SHEDDING REGIMES: LOW INCIDENCE ($\alpha = 90^\circ$ FOR VISUAL AID).

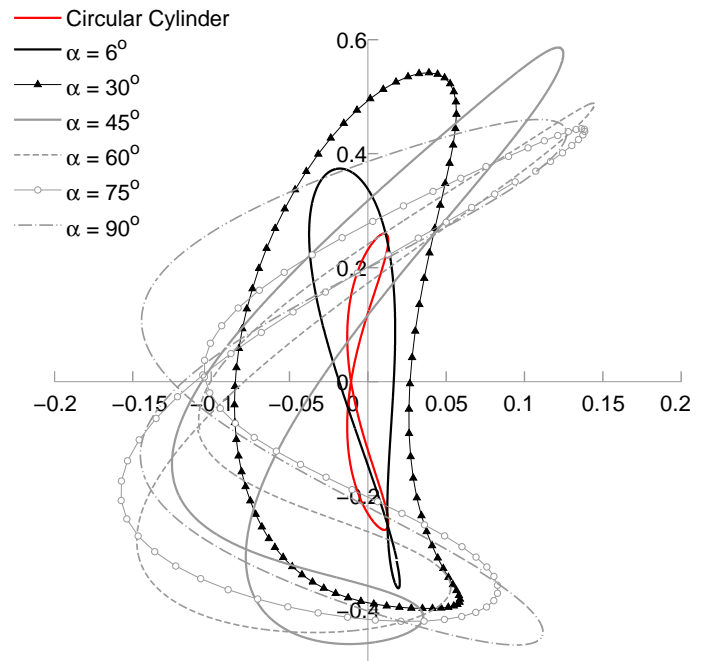


Figure 6: PHASE PORTRAIT OF THE AERODYNAMIC FORCE FOR THE TWO SHEDDING REGIMES: HIGH INCIDENCE ($\alpha = 6^\circ$ FOR VISUAL AID).

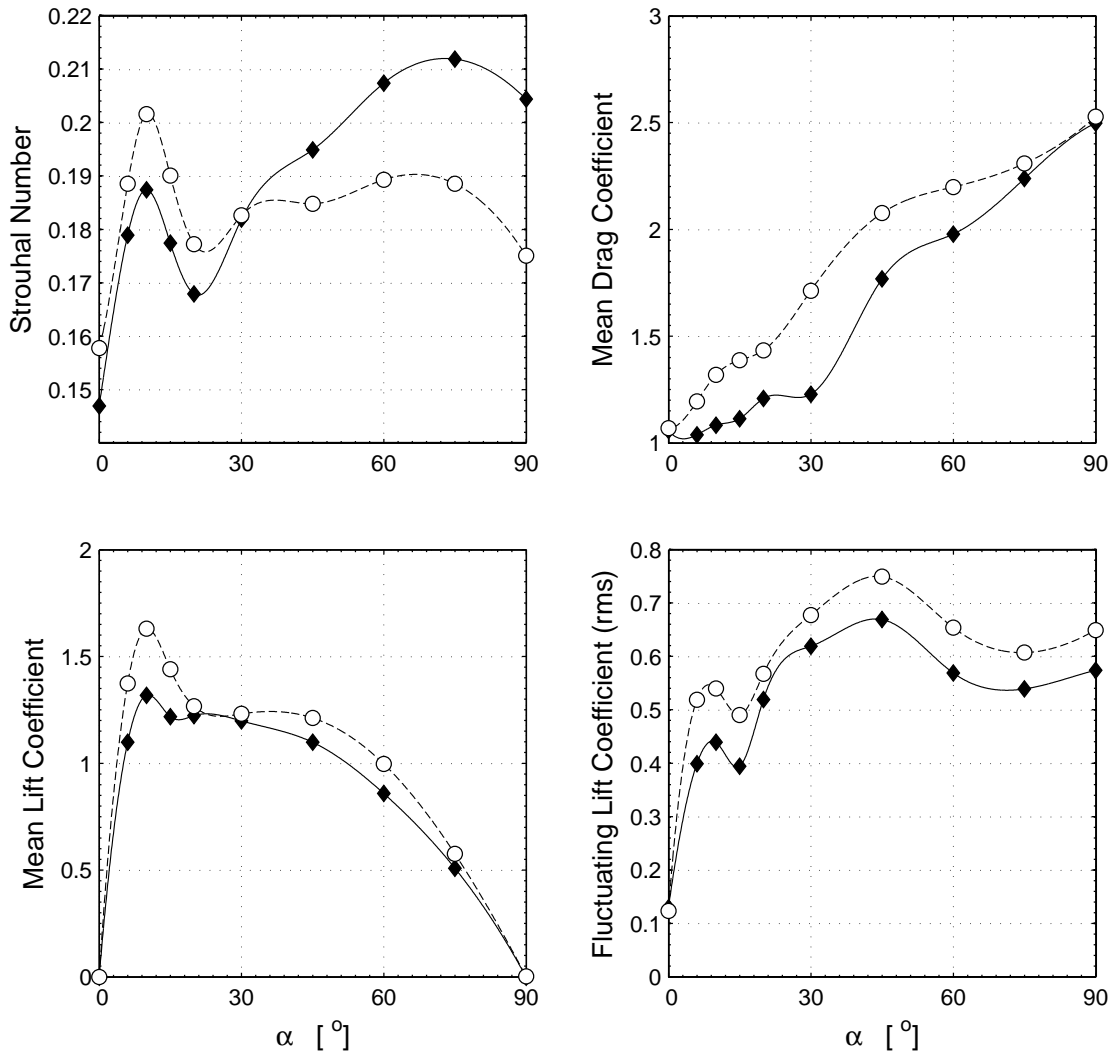


Figure 4: CIRCLES: RESULTS WITH THE IMMERSSED BOUNDARY METHOD; DIAMONDS: RESULTS FROM SOHANKAR *ET AL.* LINES FOR VISUAL AID ONLY.

cluded in the incompressible assumption and in the acoustic formulation, we take $c_0 = 10U_\infty$, that is $M = 0.1$. As a consequence, the wave pattern is less modified by convection effects than in the circular cylinder case at $M = 0.2$ presented in figure 3.

At that incidence, the lift contribution is strongly dominant, as in the aeolian tone, but the drag contribution becomes less negligible. The dipolar nature of the total noise is significantly modified by the drag contribution streamwise. Finally, the acoustic intensity at 90° is about 3 times higher (5dB) for the rectangular cylinder than for the circular cylinder.

4.4 Influence of the incidence

The phase portraits of the aerodynamic force (the fluctuating lift as a function of the fluctuating drag over one shedding period) are presented in figure 5 and 6.

They illustrate well how the transition of vortex shedding around $\alpha = 30^\circ$ affect the flow signature at the wall through the aerodynamic coefficients. There is a significant drag increase between 20° and 45° , and the phase loop shifts from a little North-West / South-East orientation to a strong South-West / North-East orientation.

The acoustic directivity pattern is plotted in figure 8 for every incidence. As expected, the acoustic intensity upward and downward follows closely the behavior of the *rms* lift coefficient, with a maximum of radiation for $\alpha = 45^\circ$. Except without incidence, the flow over the rectangular cylinder generates always more noise than the aeolian tone. The drag contribution increases with incidence, like the mean drag coefficient. For $\alpha = 90^\circ$, the intensity in the transverse direction is only five times higher (7dB) than the intensity streamwise, meaning that the latter direction can not be considered as quiet any-

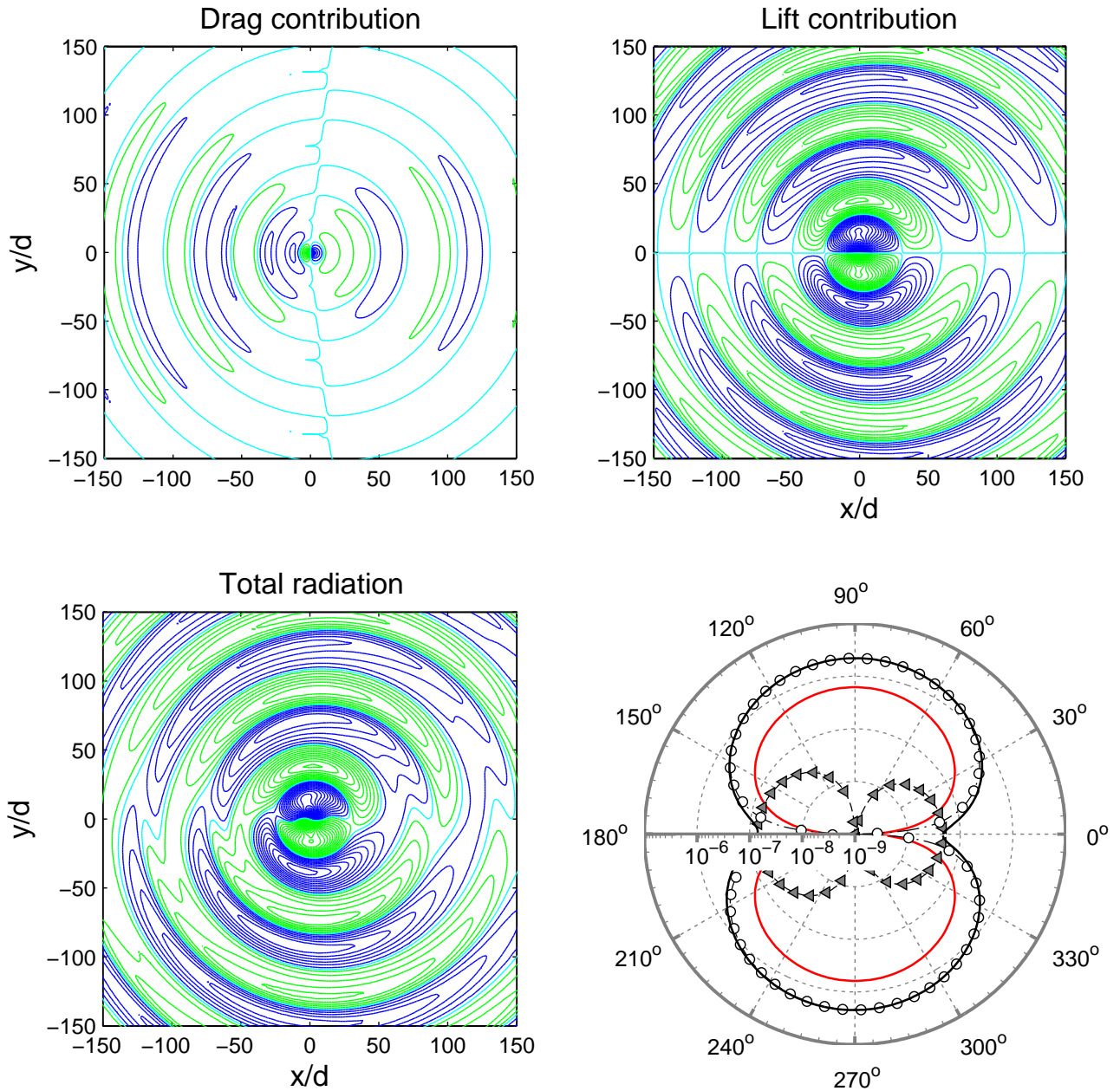


Figure 7: ACOUSTIC FIELD FOR $\alpha = 30^\circ$. DRAG, LIFT AND TOTAL CONTRIBUTION TO THE PRESSURE FIELD: LEVELS FROM 0.0004 TO 0.02 BY STEPS OF 0.0006, BLUE LINE: $p_a > 0$, GREEN LINE: $p_a < 0$, CYAN LINE: $p_a = 0$. DIRECTIVITY PATTERN AT $r/d = 250$, TRIANGLES: DRAG CONTRIBUTION, CIRCLES: LIFT CONTRIBUTION, FULL BLACK LINE: TOTAL NOISE, RED LINE: TOTAL AEOLIAN TONE.

more. Finally, the trace of the vortex regime change around $\alpha = 30^\circ$ is visible through a slight deviation of the directions of minimum or maximum acoustic intensity: for $\alpha \geq 30^\circ$, they are deviated clockwise, while they are deviated counterclockwise for small incidence.

5 CONCLUDING REMARKS

The present hybrid method, combining an incompressible simulation using the immersed boundary

method with Curle's formulation for a compact source, constitutes a kind of numerical aeroacoustic wind tunnel for low speed flows. It has been validated both aerodynamically and acoustically through the computation of the aeolian tone. Its flexibility with respect to geometry changes allowed to apply it to study the influence of incidence on the noise generated by a rectangular cylinder. The main result is the reduction of the dipolar nature of the aeroacoustic source, due to the drag increase with

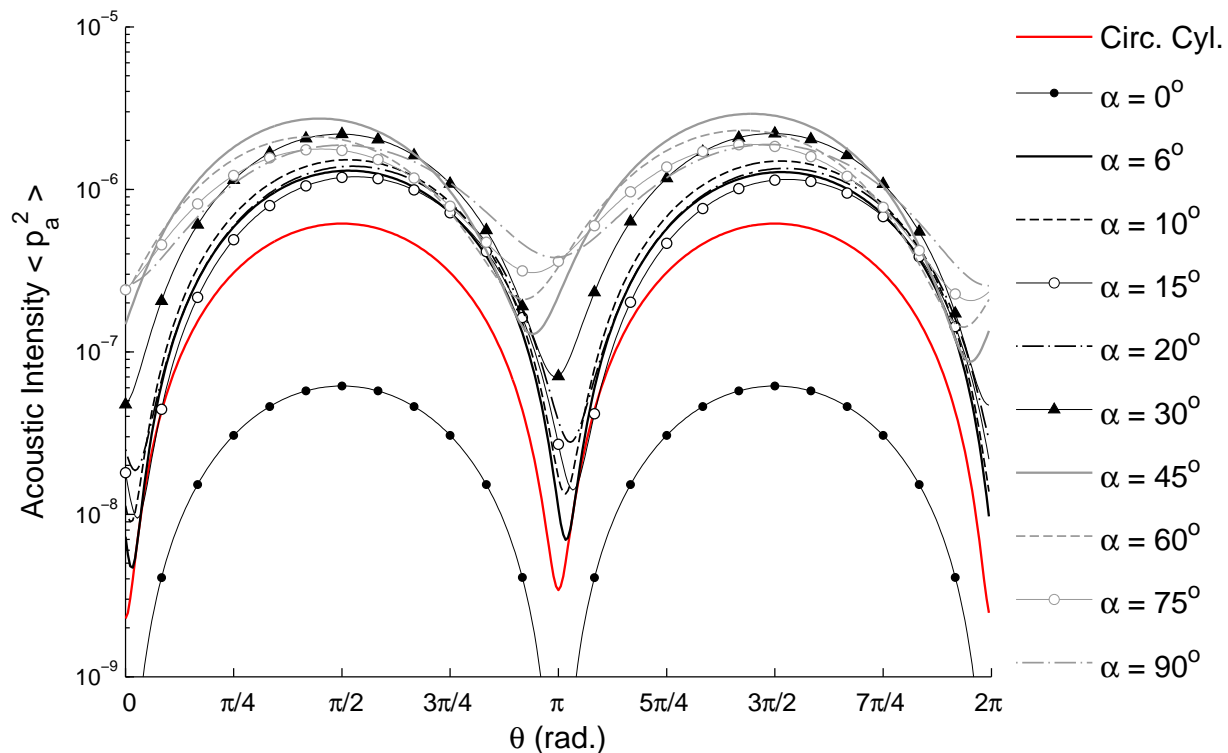


Figure 8: DIRECTIVITY OF THE ACOUSTIC INTENSITY AT $r/d = 250$ FOR VARIOUS INCIDENCES.

incidence.

Such database could serve as a catalog of aeroacoustic behaviors to support modelling. In an industrial context, models are missings which would be able to discriminate configurations from the aeroacoustic efficiency point of view, once the Mach Number, and thus Curle's power law, is given.

ACKNOWLEDGMENT

The authors gratefully acknowledge Pr. Eric Lamballais for allowing simulations with *Incompact3D* solver. We also would like to thank the referee of the abstract for helpful comments on the proposal.

REFERENCES

- [1] Curle, N., 1955. "The influence of solid boundaries upon aerodynamic sound". *Proc. Roy. Soc. A*, **231**, pp. 505–514.
- [2] Inoue, O., and Hatakeyama, N., 2002. "Sound generation by a two-dimensional circular cylinder in a uniform flow". *J. Fluid Mech.*, **471**, pp. 285–314.
- [3] Hatakeyama, N., and Inoue, O., 2004. "A novel application of Curle's acoustic analogy to aeolian tones in two dimensions". *Phys. Fluids*, **16**(5), pp. 1297–1304.
- [4] Gloerfelt, X., Pérot, F., Bailly, C., and Juvé, D., 2005. "Flow-induced cylinder noise formulated as a diffraction problem for low mach numbers". *J. Sound Vib.*, **287**, pp. 129–151.
- [5] Sohankar, A., Norberg, C., and Davidson, L., 1997. "Numerical simulation of unsteady low-reynolds number flow around rectangular cylinders at incidence". *J. of Wind Eng. and Ind. Aerodynamics*, **69-71**, pp. 189–201.
- [6] Margnat, F., and Morinière, V., 2009. "Behavior of the virtual boundary method in unsteady flows over sharp-edged bodies". *Computers and Fluids*, **38**(6), pp. 1065–1079.
- [7] Laizet, S., and Lamballais, E., 2009. "High-order compact schemes for incompressible flows: A simple and efficient method with quasi-spectral accuracy". *J. Comp. Phys.*, **228**, pp. 5989–6015.
- [8] Gloerfelt, X., Bailly, C., and Juvé, D., 2003. "Direct computation of the noise radiated by a subsonic cavity flow and application of integral methods". *J. Sound Vib.*, **266**, pp. 119–146.
- [9] Goldstein, D., Handler, R., and Sirovich, L., 1993. "Modeling a no-slip boundary condition with an external force field". *J. Comp. Phys.*, **105**, pp. 354–366.

ON COUNTERMEASURE OF SELF-SUSTAINED TONE BY BAFFLE PLATE IN BOILER TUBE BANK

Kunihiko Ishihara

The University of Tokushima.
Institute of Technology and Science
Minami-Jyosanjimacho 2-1, Tokushima-city,
Tokushima, 770-8506 Japan

ABSTRACT

Tube banks are set up in the duct of heat exchangers such as boilers etc. When the frequency of the Karman vortex behind the tube banks is close to the acoustic natural frequency of the duct, the self-sustained tone is generated. Generally, the method of inserting the baffle plate in tube banks is adopted as countermeasures of the self-sustained tone. However, when there is a space called a cavity between tube banks, the method of inserting the baffle plate has not been established. Then, to examine the generation mechanism and the countermeasure of the self-sustained tone for tube banks with a cavity, an experiment and analysis were carried out in this study.

INTRODUCTION

Tube banks are set up in the duct of heat exchangers such as boilers etc. When the frequency of the Karman vortex behind the tube banks is close to the natural frequency of the duct, the self-sustained tone is generated.

Generally, the methods of inserting the baffle plate in tube banks and sticking absorbents up on the duct wall are adopted as countermeasures of the self-sustained tone. The former is said to be due to the rising the acoustic natural frequency of the duct by inserting the baffle plate and a resonance can be avoided.

However the rising of the ducts natural frequency due to the insertion of the baffle plate could not be confirmed in this study. The mechanism of the countermeasure using the baffle plate has not been clarified yet. Also, the optimum inserting condition of the baffle plate has not been established in the case of two tube banks with a cavity as well.

In this paper, the effect of the insertion of the baffle plate on the acoustic natural frequency of the duct is examined experimentally and analytically. The suppression mechanism of the self-sustained tone due to the baffle plate is predicted by examining the relation between the inserting position and the suppression effect. Furthermore another countermeasure is also examined in which rubber sheets are applied to both sides of the walls of the duct.

CHANGE OF DUCT NATURAL FREQUENCY DUE TO BAFFLE INSERTION

According to the reference (4), the self-sustained tone is said to be able to be avoided by increasing the acoustic natural frequency of the duct due to the baffle plate insertion. However it was confirmed that the acoustic natural frequency of the duct was decreased by the baffle plate insertion in this study. The effect of the baffle plate insertion on the acoustic natural frequency of the duct will be examined in detail.

Experimental Method

Fig.1 shows the experimental setup. The size of the duct is shown in this figure. The tube bank is composed of many tubes and the array is 5 rows \times 18 tubes. The diameter of the tube is 6mm and the tube is made of the bronze. The array pattern is $T/D=L/D=2.0$. T and L are a transverse center-to-center spacing and a longitudinal center-to-center spacing respectively. The speaker and the microphone are set in the duct and the duct's natural frequency is measured. In addition, the measurement is also carried out in the case of the baffle insertion. The baffle plate length is as same as the width of the tube bank. The measurement is carried out by moving the baffle plate in the longitudinal direction. The center of the tube bank is defined as 0 points, the pitch of the tubes is defined as the unity, the upstream is defined as the minus position, and the downstream is defined as the positive position.

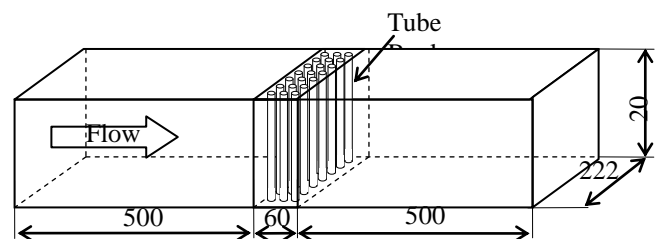


Fig.1 Experimental setup

Analytical Method

The two dimensional analytical model is shown in Fig.2 and the analysis is carried out by the finite element method. The boundary conditions are as follows: The

pressures of the inlet and the outlet of the duct are zero and the particle velocity is zero at both sides of the walls. The noise sources with anti-phase are put in order to excite the first wide direction mode of the duct. The tubes are modeled in two ways. One is modeled by the difference of the sound speed, which is the method by Blevins et.al. as shown in Fig.2. In the other, the tubes are modeled one by one in detail as shown in Fig.3.

The sound speed is unity anywhere in the sound field and is given by $c=340\text{m/s}$.

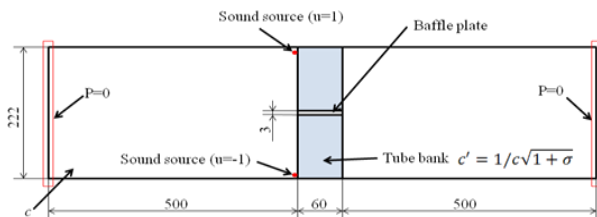


Fig.2 Analytical model (without tube bank)

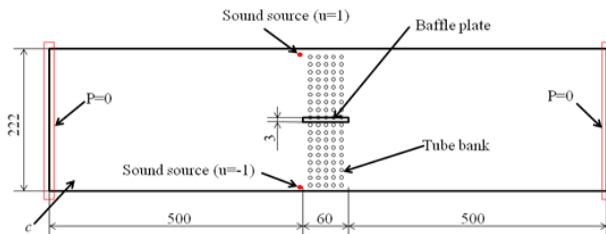


Fig.3 Analytical model

Experimental Result and Analytical Result

Fig.4 and Fig.5 show the acoustic natural frequencies of the combined mode with the first mode of width direction and the first longitudinal mode of the duct in two different models respectively. The horizontal axis shows the baffle plate position described before and the vertical axis shows the acoustic natural frequency of the duct. The small dotted line shows the experimental result and the large dotted line shows the analytical result in the case of no baffle plate

On the other hand, the real line shows the experimental result and the symbols shows the analytical result in the case of the baffle plate insertion. The baffle plate position is defined as unity of 12mm distance which is the space of two adjacent tubes. The minus (-) and the plus (+) show the upstream and the downstream directions respectively. It can be seen from Fig.4 that the acoustic natural frequency of the duct decreases when the baffle plate exists at the center of the duct and the analytical result is in good agreement with the experimental one. However the analytical result is different from the experimental one when the baffle plate exists in the tube bank.

On the other hand, it can be seen from Fig.5 that the analytical result is in good agreement with the

experimental one in detail even when the baffle plate exists in the tube bank. That is to say, the acoustic natural frequency of the duct becomes lower by inserting the baffle plate at the belly of the sound pressure in the longitudinal mode. In reverse, the decreasing of the acoustic natural frequency of the duct cannot yield in cases where the baffle plate is inserted at the node of the sound pressure in the longitudinal mode.

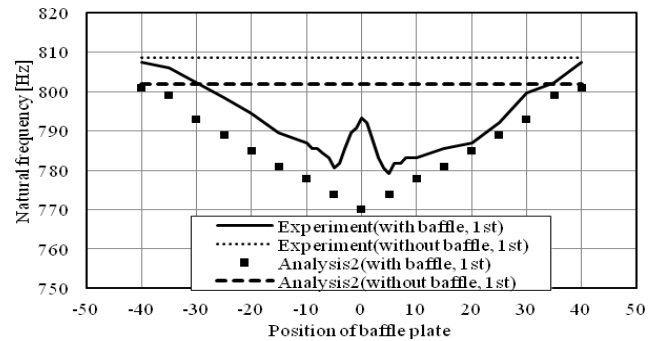


Fig.4 Comparison of experiment and analysis

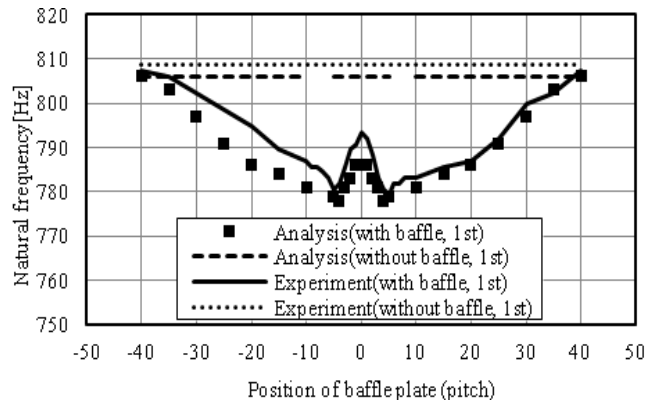


Fig.5 Comparison of experiment and analysis

EXAMINATION OF THE INSERTING POSITION OF BAFFLE PLATE IN BLOWING TEST

In the previous chapter, it could be understood that the suppression mechanism of the baffle plate insertion was not due to the change of the acoustic natural frequency of the duct because the baffle plate insertion makes the acoustic natural frequency lower. Then in this chapter, the relation between the onset velocity of the self-sustained tone and the baffle plate inserting position will be examined by the blowing test. There are two cases of examined items. One is the case of one bank, that is to say, no cavity and the other is two banks with a cavity. Here the effect of the baffle plate is defined to make the onset velocity high.

Experimental Setup and Method

Fig.6 shows the experimental setup. The size of the duct is shown in this figure. The duct is connected with the blower exit and the flow rate is changed by the inverter frequency. The inverter frequency range is 20Hz to 60Hz

and increases every 5Hz. The inverter frequency is changed every 1Hz in the neighborhood of the onset of the self-sustained tone. The experiments were carried out with and without baffle plates.

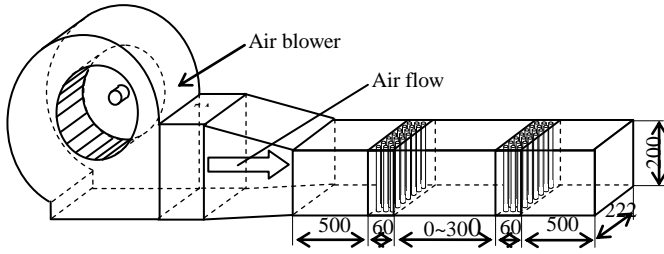


Fig.6 Experimental setup

Experimental Result (One Tube Bank)

Fig.7 shows the sound pressure distributions of the inner field of the duct in the cases of with/without insertion of the baffle plate. The left side of this figure shows the case without the baffle plate. It can be seen from this figure that the gradient of the sound pressure is the largest at the center in the width direction of the duct. In other words, it can be said that the particle velocity is the largest at the center in the width direction of the duct.

On the contrary, it can be seen from the right figure, which shows the case of insertion of the baffle plate, that the gradient of the sound pressure does not appear in the width direction of the duct and the particle velocity can be said to be small. From the velocity decreasing at the center of the width of the duct after an onset of the self-sustained tone and the sound pressure distribution shown in Fig.5, it can be considered that the particle velocity is large in the case of no insertion of the baffle plate and the particle velocity can be suppressed by the insertion of the baffle plate.

Also, the acoustic power $W(w)$ that the vortex gives to the sound field of the duct can be expressed by the Eq.(1)

$$W = \rho \int (\vec{\omega} \times \vec{v}) \cdot \xi dV \quad (1)$$

Where ρ is the gas density [kg/m³], $\vec{\omega}$ is the vorticity [rad/s], \vec{v} is the gap velocity [m/s], ξ is the particle velocity [m/s]. As mentioned above, it can be considered that the insertion of the baffle plate can suppress the

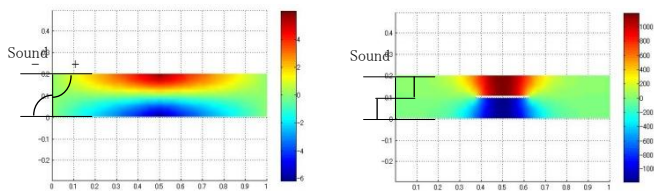


Fig.7 Sound pressure distribution

particle velocity. The particle velocity then becomes small in Eq.(1) in the case of the insertion of the baffle plate and it results in a large onset velocity.

Fig.8 shows the onset velocity of the self-sustained tone in each position when the baffle plate is moved in a longitudinal direction. The onset velocities in the case of the position of the baffle plate being -2~1 become larger than the one in the case of no baffle plate. This means the insertion of the baffle plate is effective in the suppression of the self-sustained tone. However the effect is not bilaterally symmetric and the inserting of the baffle plate upstream side is more effective. This may be considered as the vortex generating from the tube bank is also being suppressed by the baffle plate insertion.

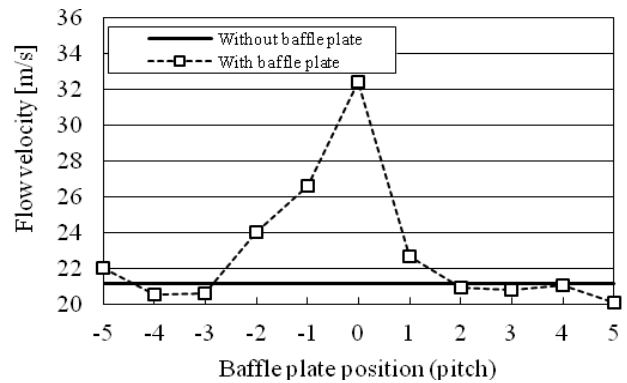


Fig.8 Flow velocity on generated sustained tone

Experimental Result (Two Tube Banks with Cavity)

Fig.9 shows the onset velocity of the self-sustained tone in the case of the two banks with a cavity. The horizontal line shows the cavity length and the result of one bank is also shown. The baffle plate is inserted into only the tube bank. Fig.9 shows the results of both cases which are with and without baffle plates. The self-sustained tone could not be observed at the places without a plot point.

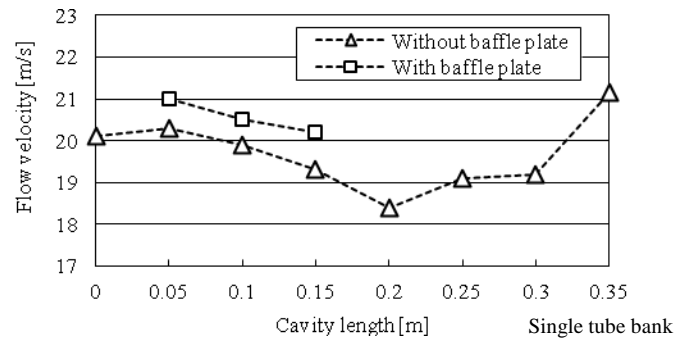


Fig.9 Flow velocity on generated sustained tone

The self-sustained tone generated in all cavity lengths in the case of no baffle plates and generated in the cavity length of 0.05m~0.15m in the case of baffle plate insertions. When the cavity length is small the two banks

behave like one large bank. When the cavity length is 0, the self-sustained tone does not generate. Because the baffle plate is inserted into all tube banks, it can be considered even as one bank. However when the cavity length is 0.05m~0.15m, the non-baffle plate part exists in a large bank which consists of two banks and a cavity part, and the self-sustained tone generated. On the contrary, when the cavity length becomes 0.2m or more, each bank becomes an independent state.

Thus, the self-sustained tone does not generate when the baffle plates are inserted into each tube bank.

SUPPRESSION OF SELF-SUSTAINED TONE DUE TO RUBBER SHEET

In order to examine the suppression effect of another countermeasure which is different from baffle plates and absorbents, the experiment using rubber sheets applied to both sides of the walls of the duct was carried out.

Fig.9 shows the outline of the experimental setup. The tube bank used here is as same as the one used in the previous chapter and its size is shown in this figure. Rubber sheets with 1mm thickness are inserted in the vicinity of both sides of the walls of the duct and they are fixed as shown in Fig.9.

The rubber sheets can be winded by the winder and the tension of the rubber can be changed. There are five patters in all as follows. The pattern 0 is the case of no rubber sheets and the pattern 1~4 are cases of the rubber sheets with four kinds of tension. The tension is the largest in pattern 4 and the smallest in pattern 1. The sound pressure level is measured with changing the flow velocity in each pattern.

Fig.10 shows the relation between the gap velocity of the tube bank and the sound pressure level in the case of the tube bank with 5 rows. The steep rising of the sound pressure can be seen in the cases of pattern 0, pattern 3 and pattern 4. The pattern 3 and the pattern 4 are the cases of comparatively larger tension. This steep rising of the sound pressure means the generation of the self-sustained tone. From this result, it can be clarified that the suppression effect of the self-sustained tone appears in the case of using rubber sheets with small tension.

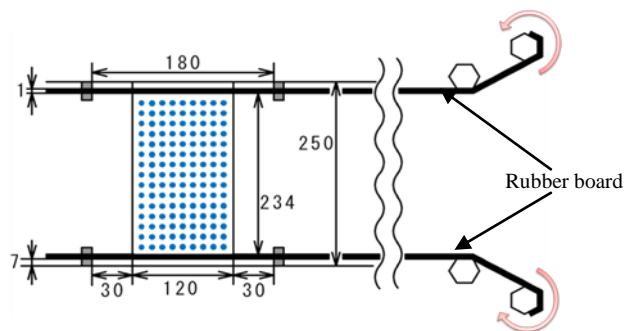


Fig.9 Experimental setup (outline drawing)

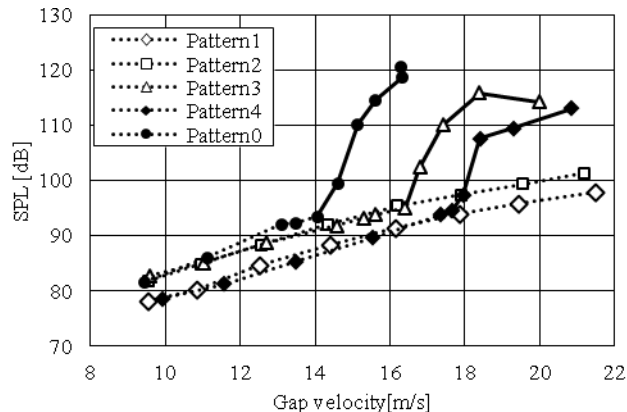


Fig.10 Relationship of gap velocity and SPL

CONCLUSIONS

The experiment and the analysis were carried out in order to examine the cause and the countermeasure for the self-sustained tone generated from the tube bank with a cavity. As a result, the following findings could be obtained.

- (1) The resonant frequency of the duct decreases when the baffle plate is inserted at the belly of the sound pressure distribution of the first longitudinal direction mode. Inversely, the resonant frequency does not decrease when the baffle plate is inserted at the node.
- (2) The insertion of the baffle plate suppresses the particle velocity of the width direction of the duct and its results in the suppression of the self-sustained tone.
- (3) It can be considered that the vortex shedding is suppressed by the insertion of the baffle plate. It also relates the suppression of the self-sustained tone.
- (4) It is important to focus the independency of each tube bank in the suppression of the self-sustained tone due to the insertion of the baffle plate in the tube bank duct with a cavity.
- (5) The new countermeasure which uses the rubber sheets at both sides of the walls of the duct is effective for the suppression of the self-sustained tone

REFERENCES

- (1) Kunihiko Ishihara, "Study on High SPL Sound of Gas Heater Composed of Two Parallel Located Ducts with Tube Bundles (1st Report, Understanding of Phenomenon)", *Transactions of JSME (Series B)*, Vol.70, No.689 (2004), pp. 126-132.
- (2) Kunihiko Ishihara, "Study on High SPL Sound of Gas Heater Composed of Two Parallel Located Ducts with Tube Bundles (2nd Report, Acoustic Damping of Perforated Baffle Plate and Its Effect)", *Transactions of JSME (Series B)*, Vol.70, No.689 (2004), pp. 133-139.
- (3) Hiromitsu Hamakawa, "Study on Suppression Method of Acoustic Resonance Phenomenon using Baffle Plates", *JSME Kyusyu Branch 57th*

Conference, No.48-1 (2004), pp. 126-132.

- (4) K. Shiraki, Noise Protection Design and Simulation, *Ohyo Gizyutu Syuppan*, 1987, p.188
- (5) M. S. Howe, "The Dissipation of Sound at an Edge" *Journal of Sound & Vibration*, 70(3), (1980), pp.407-411

ON THE EFFECT OF A SWIRL ON THE SELF-SUSTAINED OSCILLATIONS IN COMPACT AXISYMMETRIC CAVITIES

Güneş Nakiboğlu*

Oleksii Rudenko and Avraham Hirschberg

Laboratory of Fluid Dynamics,
Department of Applied Physics,
Eindhoven University of Technology
Eindhoven 5600 MB, The Netherlands
Email: g.nakiboglu@tue.nl

Joachim Golliard

Stefan P.C. Belfroid

TNO Science and Industry
Delft 2600 AD, The Netherlands

ABSTRACT

Axisymmetric cavities along pipes are commonly encountered construction in industrial applications, which can also be considered as a unit element of a corrugated pipe. At critical conditions, the flow through such an axisymmetric cavity-pipe system causes self-sustained oscillations that lead to high-amplitude sound generation, called whistling, and associated mechanical vibration. The current work studies the effect of a swirl on the whistling behaviour of single and double axisymmetric cavities in a pipe line. Experiments demonstrate that swirl has an effect both on the range of Strouhal numbers, in which the whistling is observed, and the respective whistling amplitudes.

INTRODUCTION

Pipe systems with axisymmetric cavities are often used in engineering applications. However, at critical conditions, the flow through such an axisymmetric cavity-pipe system causes self-sustained oscillations that lead to high-amplitude sound generation, called whistling and associated mechanical vibration. Whistling in such cavities has been a subject of extensive research [1–5]. The previous work in the literature discuss almost exclusively the case of grazing pipe flow over the cavity without swirl. However, swirl is very common in industrial applications e.g. an axisymmetric cavity at the downstream of a bending or a pipe splitting experiences an approach profile with a strong swirl. Helical corrugated pipe is another interesting application in which the flow has a strong swirl created by the helically corrugated wavy walls of the pipe.

In the current study aeroacoustic power generation

due to a self-sustained oscillation by an axisymmetric cavity exposed to a grazing flow with and without swirl is studied. The feedback effect is due to a fluid-resonant mechanism [6] produced by the velocity fluctuations resulting from a coupling of vortex shedding at the upstream cavity edge with an acoustic standing wave in a coaxial pipe [1, 7, 8].

EXPERIMENTAL CONDITIONS

Set-up and the test section

The set-up used for the experiments is shown in figure 1. The test section is composed of from upstream to downstream a long straight pipe segment, an axisymmetric cavity and a short straight pipe segment. The inner diameter of the straight pipe segments is $D = 44$ mm. The length of the long and the short segments are $L_{in} = 850$ mm and $L_{out} = 15$ mm, respectively. The width of the cavity is $W = 40$ mm. The cavity depth to width ratio is $H/W = 0.675$. The setup allows the placement of a second cavity and to vary the plateau (L_p) length, the constant diameter part between the two cavities. The radii of curvature of the upstream and downstream cavity edges are denoted by r_{up} and r_{down} , respectively. The upstream edge radius of the first cavity and the downstream edge radius of the last cavity is 5 mm, all the other edge radii are 2.5 mm. Experiments have been performed for three different plateau length to width ratios, namely $L_p/W = 0, 0.375$ and 0.875 . It should be noted that the plateau length does not include the edge radii of the cavities, see figure 1. Thus, when the plateau length is $L_p = 0$ mm there, still, exists a wall thickness ($r_{down} + L_p + r_{up}$) between the cavities, which is 5mm.

The upstream termination of the test section is con-

*Address all correspondence to this author.

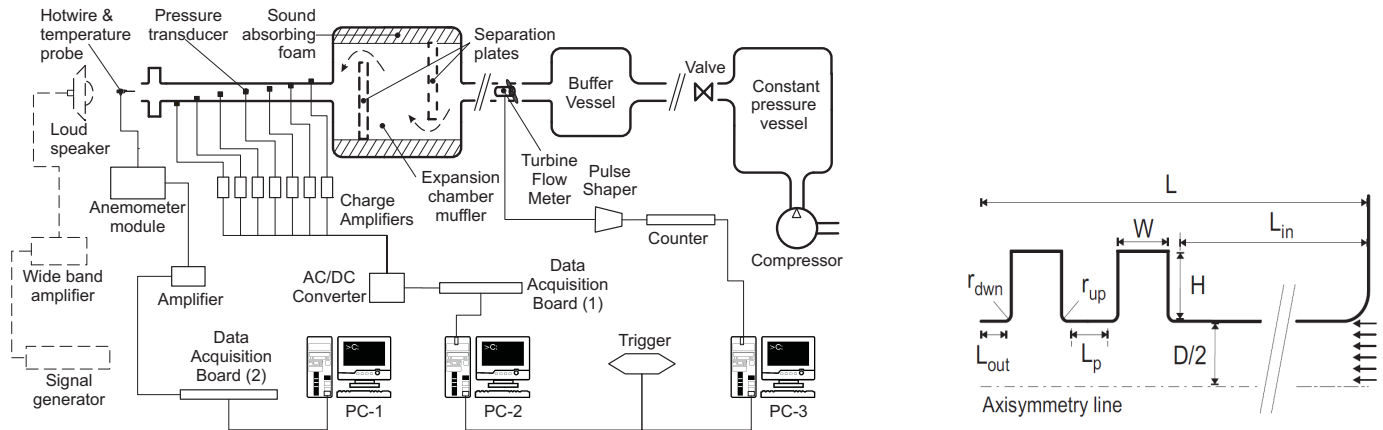


FIGURE 1: SCHEMATIC OF THE EXPERIMENTAL SETUP & RELEVANT GEOMETRIC PARAMETERS.

nected to a high-pressure air supply system, which is composed of, from upstream to downstream, a compressor, a constant pressure vessel, a control valve, a buffer vessel, a turbine flow meter and an expansion chamber muffler. Two different expansion chamber mufflers were used in the experiments. One of the expansion chamber mufflers was attached coaxially to the pipe for the reference case i.e. the flow does not have a swirl, as shown schematically in figure 1. For the case with the swirl the pipe tangentially connected to the second expansion chamber muffler also separation plates are installed in the expansion chamber to enhance swirl. Both of the expansion chamber mufflers have a length of 1.5 m and a diameter of 0.6 m and covered internally with sound absorbing foam with a thickness of 100 mm in order to avoid cavity resonances. The downstream termination is open to the laboratory, a large room of 15 m×4 m×4 m (not an anechoic chamber).

The details of the experimental setup are presented in earlier works of the authors [8,9].

Acoustic and mean flow conditions

Previous work on multiple side branch systems [10, 11] and corrugated pipes [12] has shown that the spatial position of the cavity with respect to the coupling longitudinal standing wave is important for the sound production. The cavity is placed close to the pipe termination, a pressure node, to maximize the sound production. All the experiments have been carried out at the first longitudinal acoustic mode. This is a standing wave of a half-wave length in the pipe ($L \approx \lambda/2$). The system whistles also for the higher acoustic modes (i.e. $L \approx \lambda, 3/2\lambda, \dots$). Experiments have been performed at the lowest possible whistling mode in order to keep the sound source as compact as possible ($W \ll \lambda$).

Velocity profile measurements are performed with a hotwire probe at 2 mm upstream of the cavity for both expansion chambers at a Reynolds number of $Re = 3.5 \times 10^4$. This Reynolds number corresponds to a mean flow velocity at which the system whistles at the first longitudinal acoustic mode. In figure 2 the velocity profiles measured with and without swirl are presented. It is seen that the swirl leads to a strong asymmetry in the velocity profile. Since the velocity profiles measurements are performed with a single-wire probe (55P11 - Dantec Dynamics) the azimuthal component of the mean flow velocity cannot be measured, as a result the strength of the swirl cannot be quantified. Thus, the paper should be considered as a preliminary work rather than a quantitative assessment of the effect of swirl on the whistling.

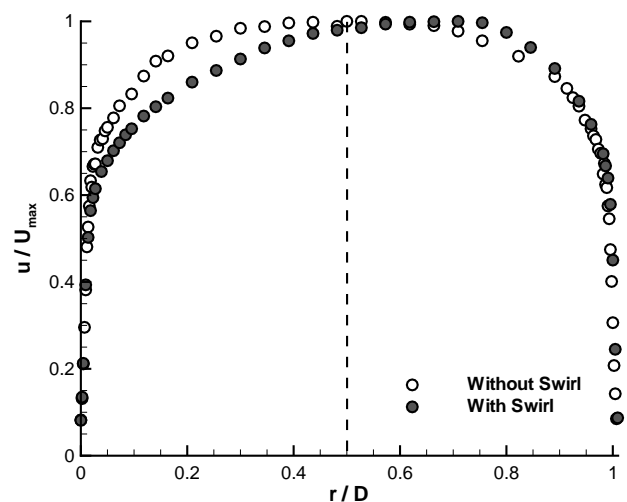


FIGURE 2: VELOCITY PROFILE UPSTREAM OF THE CAVITY WITH AND WITHOUT SWIRL.

Maximum dimensionless fluctuation amplitude

Knowing the pressure fluctuations at seven different spatial positions, using the multi-microphone method [13] traveling acoustic plane waves were reconstructed. In the paper the term *fluctuation amplitude* is used to specify the maximum dimensionless sound amplitude that is attained in the standing wave. The *fluctuation amplitude* is defined as:

$$\frac{|p'_{\max}|}{\rho_0 c_0 U} = \frac{|u'_{\max}|}{U} \quad (1)$$

where $|p'_{\max}|$ is the amplitude of the standing pressure wave at a pressure anti-node inside the pipe and $|u'_{\max}|$ is the amplitude of acoustic velocity at a pressure node. Since the term *fluctuation amplitude* always refers to this maximum dimensionless sound amplitude; the subscript *max* will be dropped for convenience. The details of the data processing is provided in an earlier work [9].

EFFECT OF A SWIRL ON THE WHISTLING

A single axisymmetric cavity

In figure 3 measured dimensionless fluctuation amplitude $|u'|/U$ is plotted against Strouhal number $Sr = f(W + r_{up})/U$ for a single axisymmetric cavity receiving two different velocity profiles, see figure 2. It is seen that swirl has an effect both on the Strouhal number and on the amplitude of the whistling. The difference in the Strouhal number is expected due to a variation in the velocity profile [14]. The drop in the fluctuation amplitude can be due to the disturbance of the 3D coherence of the vortex shedding due to the presence of swirl.

Double axisymmetric cavity configurations

In an earlier work of the authors [8] aeroacoustic sound generation due to self-sustained oscillations by a series of compact axisymmetric cavities exposed to grazing flow is studied. In the experiments cavities are coupled to the same standing wave. This synchronizes the vortex shedding among the cavities that are close to the same pressure node, which creates a collaborative sound production. The study demonstrated that there is also a strong hydrodynamic interference between adjacent cavities. Depending on the plateau length and the Strouhal number, the hydrodynamic interference can collaborate with the acoustic synchronization which amplifies the sound production or hydrodynamic interference can counteract with the acoustic synchronization which decreases the sound production. Here the effect of swirl on this phenomenon is addressed.

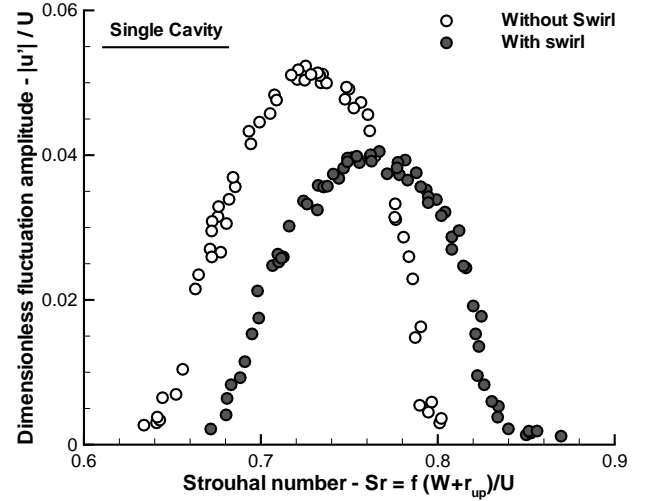


FIGURE 3: MEASURED DIMENSIONLESS FLUCTUATION AMPLITUDE, $|u'|/U$, PLOTTED AGAINST STROUHAL NUMBER, $Sr = f(W + r_{up})/U$, FOR A SINGLE AXISYMMETRIC CAVITY RECEIVING FLOW WITH AND WITHOUT SWIRL.

In figure 4 measured fluctuation amplitude is plotted against Strouhal number for 3 double axisymmetric cavity configurations with plateau lengths of $L_p/W = 0, 0.375, 0.875$, the left graph is flow without swirl (adopted from ref. [8]) and the graph on the right is flow with a swirl (see figure 2). It is seen that for $L_p/W = 0$ and $L_p/W = 0.375$ for both flow conditions (with and without swirl) there is a single peak for the fluctuation amplitude. Neither the peak-amplitude nor the range of whistling Strouhal numbers were altered significantly due to the presence of the swirl in the flow.

For $L_p/W = 0.875$, however, there are two peaks for the fluctuation amplitude for both flow conditions. The two peaks are merged to each other for the flow without swirl, whereas the flow with the swirl has distinctly separated peaks. It is clear that the swirl decreases the amplitude of the low Strouhal number peak considerably. These experiments indicate that swirl can have a strong effect on the whistling behaviour of double cavity systems. This is likely to be due to the effect of swirl on the hydrodynamic interference.

CONCLUSION

The effect of a swirl on the aeroacoustic sound generation due to self-sustained oscillations, whistling, by a single and double axisymmetric cavity configurations exposed the grazing flow has been studied. The feedback effect is produced by the velocity fluctuations result-

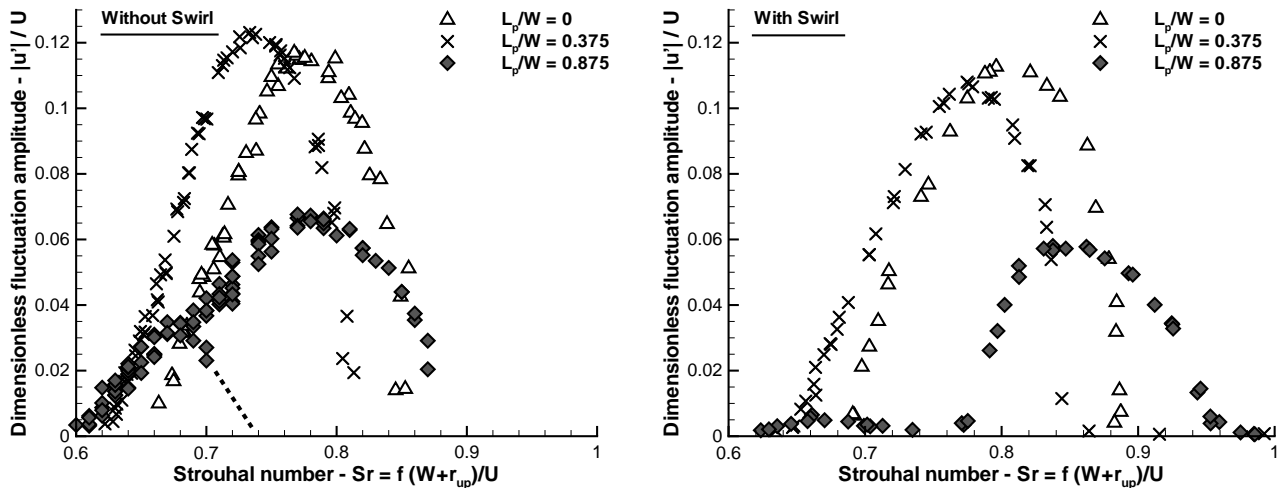


FIGURE 4: MEASURED DIMENSIONLESS FLUCTUATION AMPLITUDE, $|u'|/U$, PLOTTED AGAINST STROUHAL NUMBER, $Sr = f(W + r_{up})/U$, FOR 3 DOUBLE AXISYMMETRIC CAVITY CONFIGURATIONS WITH DIFFERENT PLATEAU LENGTHS ($L_p/W = 0, 0.375, 0.875$) RECEIVING FLOW WITH AND WITHOUT SWIRL. FIGURE WITHOUT SWIRL IS ADOPTED FROM REF [8].

ing from a coupling of vortex sheddings at the upstream cavity edges with acoustic standing waves in the coaxial pipe. By comparing experiments performed with and without the presence of a swirl in the flow, its effect on the whistling behaviour has been investigated.

The experiments performed on a single axisymmetric cavity show that swirl can decrease the amplitude of the acoustic fluctuations. It can also marginally affect the Strouhal range of whistling. Experiments performed on double axisymmetric cavity configurations with various plateau lengths demonstrate that the effect of the swirl depends on the plateau length and for some plateau lengths it can be pronounced particularly for the amplitude.

It should be noted that this work is a preliminary study on the effect of a swirl rather than an quantitative assessment. The findings indicate that swirl can play a significant role in the whistling behaviour of axisymmetric cavity pipe systems and calls for further research.

ACKNOWLEDGMENT

The work discussed in this paper was made possible by the contributions of STW Technologiestichting (Project STW 08126). The authors would like to acknowledge the contributions of H. B. M. Manders, A. Holten and F. M. R. van Uittert to the development of the experiments.

REFERENCES

- [1] Rockwell, D., and Schachenmann, A., 1982. "Self-generation of organized waves in an impinging turbulent jet at low mach numbers". *J. Fluid Mech.*, **117**, pp. 425–441.
- [2] Ziada, S., Ng, H., and Blake, C. E., 2003. "Flow excited resonance of a confined shallow cavity in low Mach number flow and its control". *J. Fluid. Struct.*, **18**, pp. 79–92.
- [3] Geveci, M., Oshkai, P., Rockwell, D., Lin, J. C., and Pollack, M., 2003. "Imaging of the self-excited oscillation of flow past a cavity during generation of a flowtone". *J. Fluid. Struct.*, **18**, pp. 79–92.
- [4] Oshkai, P., Rockwell, D., and Pollack, M., 2005. "Shallow cavity flow tones: transformation from large- to small-scale modes". *J. Sound Vib.*, **280**, pp. 777–813.
- [5] English, E. J., and Holland, K. R., 2010. "Aeroacoustic sound generation in simple expansion chambers". *J. Acoust. Soc. Am.*, **128**(5), pp. 2589–2595.
- [6] Rockwell, D., and Naudascher, E., 1978. "Review:self-sustaining oscillations of flow past cavities". *ASME J. Fluid Eng.*, **100**, pp. 152–165.
- [7] Schachenmann, A., and Rockwell, D., 1980. "Self-sustained oscillations of turbulent pipe flow terminated by an axisymmetric cavity". *J. Sound Vib.*, **73**, pp. 61–72.
- [8] Nakiboğlu, G., and Hirschberg, A., 2012. "Aeroacoustic power generated by multiple compact axisymmetric cavity: effect of hydrodynamic interac-

tion on the sound production”. *Phys. Fluids*, *Accepted for publication*.

- [9] Nakiboğlu, G., Manders, H. B. M., and Hirschberg, A., 2011. “Aeroacoustic power generated by a compact axisymmetric cavity: prediction of self-sustained oscillation and influence of the depth”. *J. Fluid Mech.*, *Submitted*.
- [10] Tonon, D., Landry, B. J. T., Belfroid, S. P. C., Willems, J. F. H., Hofmans, G. C. J., and Hirschberg, A., 2010. “Whistling of a pipe system with multiple side branches: comparison with corrugated pipes”. *J. Sound Vib.*, **329**, pp. 1007–1024.
- [11] Nakiboğlu, G., Belfroid, S. P. C., Willems, J. F. H., and Hirschberg, A., 2010. “Whistling behavior of periodic systems: corrugated pipes and multiple side branch system”. *Int. J. Mech. Sci.*, **52(11)**, pp. 1458–1470.
- [12] Golliard, J., Tonon, D., and Belfroid, S. P. C., 2010. “Experimental investigation of the source locations for whistling short corrugated pipes”. Proceedings of ASME 2010 3rd Joint US-European Fluids Engineering Summer Meeting and 8th International Conference on Nanochannels, Microchannels and Minichannels.
- [13] Åbom, M., and Bodén, H., 1988. “Error analysis of two-microphone measurements in ducts with flow”. *J. Acoust. Soc. Am.*, **83**, pp. 2429–2438.
- [14] Nakiboğlu, G., Belfroid, S., Golliard, J., and Hirschberg, A., 2011. “On the whistling corrugated pipes: effect of pipe length and flow profile”. *J. Fluid Mech.*, **672**, pp. 78–108.



Experimental Study of Interaction Between Pressure Pulsations and Piping Vibration

Yuichi Torigoe

torigoe.yuichi
@kki.kobelco.com

Takeo Sakakibara

sakakibara.takeo
@kki.kobelco.com

Shunsuke Kojima

kojima.shunsuke
@kki.kobelco.com

Eiko Hirooka

hirooka.eiko
@kki.kobelco.com

Minoru Kato

kato.minoru
@kki.kobelco.com

Kobelco Research Institute, Inc.

1-5-5 Takatsukadai, Nishi-ku, Kobe 651-2271, Japan

Takashi Tsuji

tsuji.takashi@inss.co.jp

Akira Maekawa

maekawa@inss.co.jp

Tsuneo Takahashi

takahashi.tsuneo@inss.co.jp

Institute of Nuclear Safety System, Inc.

64 Sata, Mihama-cho, Mikata-gun, Fukui-pref 919-1205, Japan

ABSTRACT

The purpose of this study was to experimentally examine the interaction between pressure pulsations and piping vibration to improve the accuracy of numerical simulation in predicting piping vibration. In this study, an experimental mock up of a piping system similar to an actual plant was designed so that the acoustic resonance frequency of the internal fluid would correspond with the natural frequency of the mechanical piping vibration. Then we experimentally studied the conditions of interaction between them. Our results show that in pump-piping systems where the internal fluid is liquid, an interaction between pressure pulsations and piping vibration appears in pressure pulsations above a certain level of piping vibration. In addition, we can confirm that interaction between pressure pulsations and piping vibration in the out-of-plane direction is observed. There has been little detailed experimental study of this interaction.

Our results show that when vibration in the pump-piping system is predicted, under some vibration conditions we must take the interaction of pressure pulsation into consideration to improve calculation accuracy.

INTRODUCTION

Piping systems attached to pumps or compressors are excited by pressure pulsations of fluid in the piping. In particular, systems are greatly vibrated when the natural frequency of the bending mode coincides with the acoustical resonance frequency of fluid, which may result in damage.

Therefore, simulation is often used in designing plants to predict pressure pulsations and piping vibration [1],[2]. Such preliminary analysis has been recommended in the API Standards [3], [4].

When piping vibration is predicted, it is important to take into account the interaction between piping vibration

and pulsations in order to improve accuracy. It is not necessary to take this interaction into consideration for gas in piping [5], however, for liquid, it is reported that the interaction sometimes occurs.

There are some detailed experimental studies of the interaction with piping vibration including bending modes and pressure pulsations. In the case of interaction in liquid systems, D'Souza [6], Washio [7], and Tanaka [8] have described it for longitudinal and shell mode vibrations of piping with a pump. Washio [9] and Tsuji [10], [11] also reported such phenomena.

In this study, we experimentally investigated the interaction between the piping vibrations, including bending modes and pressure pulsations in the piping system. A plunger pump-piping system was mocked up with a 40m piping. Then, our experiment was made with the natural frequencies of the piping coinciding with the acoustic resonance of liquid, and the resulting interaction phenomena were studied.

EXPERIMENTAL METHOD

EXPERIMENTAL EQUIPMENT

Figure 1 and Figure 2 show the test equipment that was used in this study. Table 1 outlines the equipment and test conditions. In our experimental piping system, approximately 40 m in length is connected to a triplex plunger pump. Pump speed is continuously varied from 75rpm to 450rpm with an inverter control. The piping system is stainless steel with an outside diameter of 27.2mm (3/4B sch40) and inside diameter of 21.4mm. As shown in Figure 2, there are seven bends (A-G), with movable supports near each bend to adjust the natural frequency of the piping system. Pressure is adjusted by a pressure control valve installed at the end of piping and ten pressure gauges measure pressure along the piping at positions P1-P10.

EXPERIMENTAL CONDITION

Table 2 shows the experimental conditions. Water was used as the internal fluid. The pump was operated from 100rpm to 460rpm and pressure pulsation and acceleration were measured by the pressure gauges installed along the piping and accelerometers attached at the bends. Line pressure was set to 1MPa, so that the boundary condition of the piping was “closed – open”. Two types of fixed conditions for the supports were used. One was a hard support using spacers as shown in Figure 3, so that the acoustic resonance frequency of the internal fluid would correspond with the natural frequency of the piping vibration. The other was a soft support using a coil spring as shown in Figure 4, so that the acoustic resonance frequency would not correspond with the natural frequency.

TABLE 1: OUTLINE OF TEST EQUIPMENT

Pump Specification	Type	Triplex Plunger Pump
	Discharge Pressure (MPa)	1~3
	Discharge Flow Rate (L/min)	24.3~149.0
	Rotating Speed (rpm)	75~460
Pipe Specification	Type	3/4B sch40
	Material	SUS304



FIG.1: TEST EQUIPMENT

TABLE 2: TEST CONDITION

Test Condition	Internal Fluid	Water
	Rotating Speed (rpm)	100~460
	Pressure (End)	1MPa
	Support of Bend	Hard, Soft

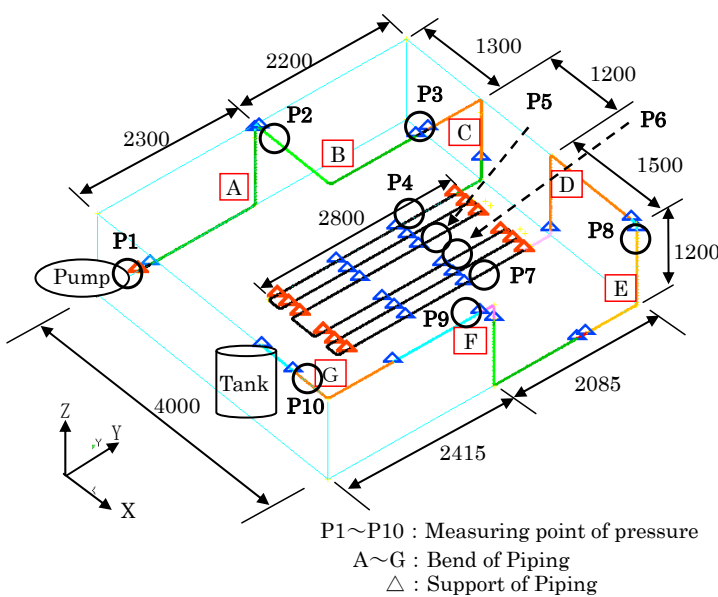


FIG.2: TEST EQUIPMENT

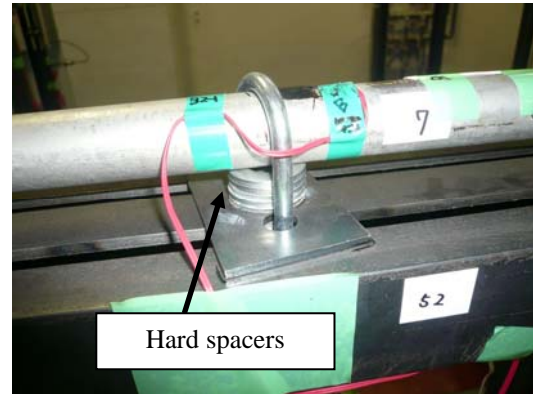


FIG.3: SUPPORT CONDITION (HARD)

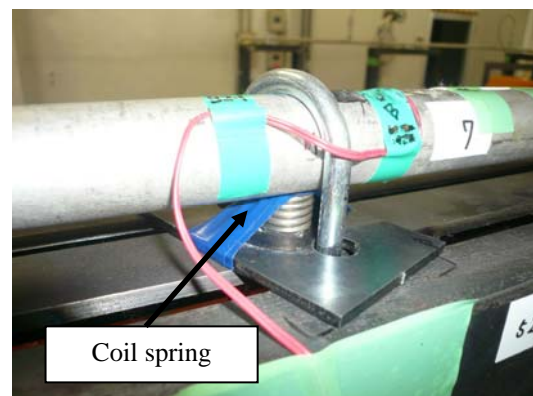


Fig.4: SUPPORT CONDITION (SOFT)

EXPERIMENTAL RESULTS

In the first part of the experiment, hard fixed conditions were used for the supports so that the acoustic resonance frequency of the internal fluid would correspond with the natural frequency of the piping vibration. Figures 5, 6 and 7 show pressure pulsations in the piping system when the pump was operated from 100rpm to 460rpm. In those figures the horizontal axis indicates the frequency and the vertical axis indicates the pressure. The third and sixth multiples of the basic rotating speed of the triplex plunger pump are shown.

In Figure 5, acoustic resonance phenomenon was observed at about 7Hz and 21Hz, where the length of the piping was 40.4m, the estimated sound velocity was about 1100m/s and the boundary condition of the piping was closed-open. It is notable that the pressure pulsation decreases at 19Hz and 22Hz, and increases at 16Hz, as shown in Figure 5-7. Figures 6 and 7 show the same phenomenon also appearing at all measurement points in the piping.

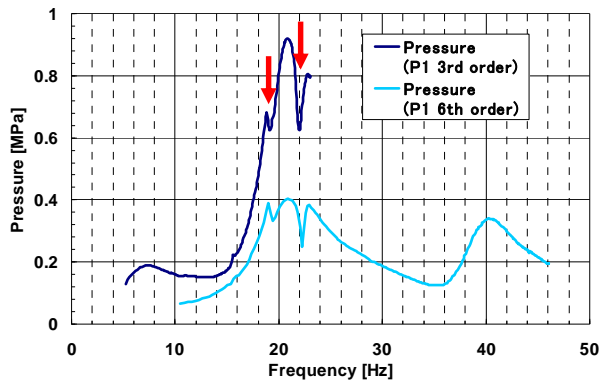


FIG.5: PRESSURE PULSATION AT POINT P1 (ROTATING SPEED: 100RPM~460RPM THE 3RD AND 6TH ORDERS SUPPORT CONDITION: HARD)

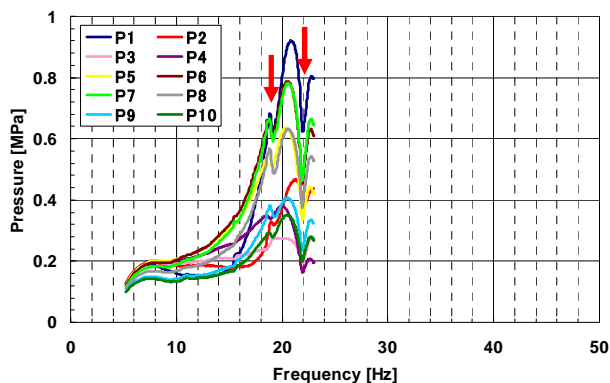


FIG.6: PRESSURE PULSATION AT P1-P10 (ROTATING SPEED: 100RPM~460RPM THE 3RD ORDER SUPPORT CONDITION: HARD)

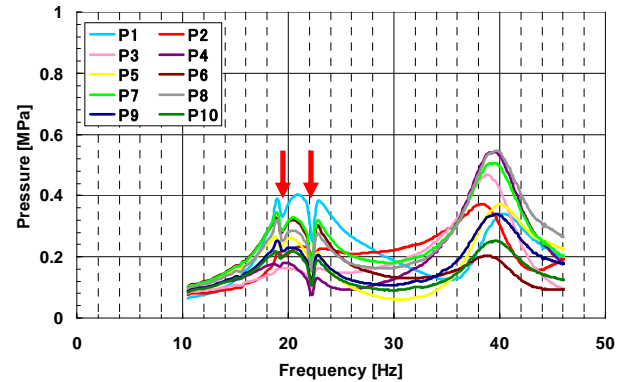


FIG.7: PRESSURE PULSATION AT P1-P10 (ROTATING SPEED: 100RPM~460RPM THE 6TH ORDER SUPPORT CONDITION: HARD)

PRESSURE DECREASE AT 22HZ AND 19HZ

Figure 8 shows pressure pulsations at P1 and acceleration at Bend B. The horizontal axis indicates frequency (Hz) and the vertical axes indicate acceleration (m/s^2) and pressure pulsation (MPa). In Figure 8, the pressure pulsation decreases at 22.1Hz, which is the natural frequency at Bend B section. Figure 9 shows another result of pressure pulsation and acceleration at Bend B when the pump speed is 150rpm-450rpm. In Figure 9, the same phenomenon was observed.

These fluctuations of pressure pulsations at 22Hz are affected by the mechanical resonance phenomenon at Bend B, particularly in the Y and Z directions of vibration.

Figure 10 shows pressure pulsation at P1 and acceleration at Bend C. Here, the pressure pulsation decreases at 22Hz, which is also the natural frequency at the Bend C section. The phenomenon is strongly affected by the piping vibration from Bend B to Bend C in the Y direction. The acceleration values are about $48-65m/s^2$ in the Y direction. Figure 11 shows pressure pulsation at P1 and acceleration at Bend F. Here, the pressure pulsation decreases at 19Hz, which is the natural frequency in the Y direction at Bend F. The phenomenon is strongly affected by the piping vibration at Bend F in the Y direction. The acceleration values are about $46m/s^2$ in the Y direction.

Figure 12 compares accelerations at Bend B between hard fixed supports and soft fixed supports. In the hard fixed supports the peak frequency is 22Hz and in the soft fixed supports the natural frequency is less than 20Hz and the peak value is smaller.

Figure 13 compares pressure pulsations at Bend B between hard and soft supports. In this case a decrease in pressure pulsation was not observed when the natural frequency of Bend B did not equal 22Hz. In Figure 12, another natural frequency at 17Hz was observed in the Z direction at Bend B, but it does not affect pressure pulsation in Figure 13.

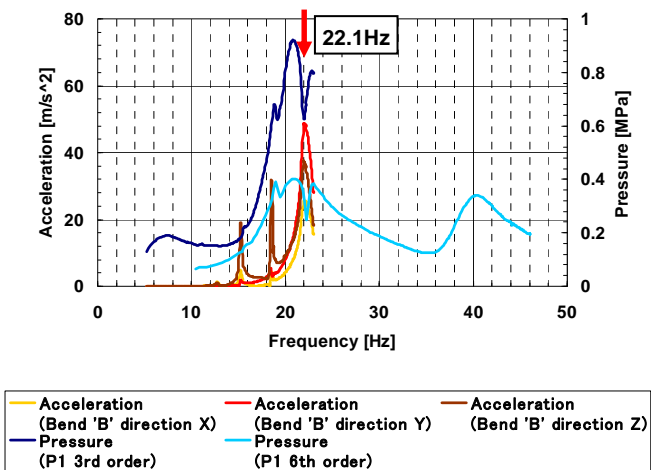


FIG.8: PRESSURE PULSATION AT P1 AND ACCELERATION AT BEND B (ROTATING SPEED: 100RPM~460RPM THE 3RD AND 6TH ORDERS SUPPORT CONDITION: HARD)

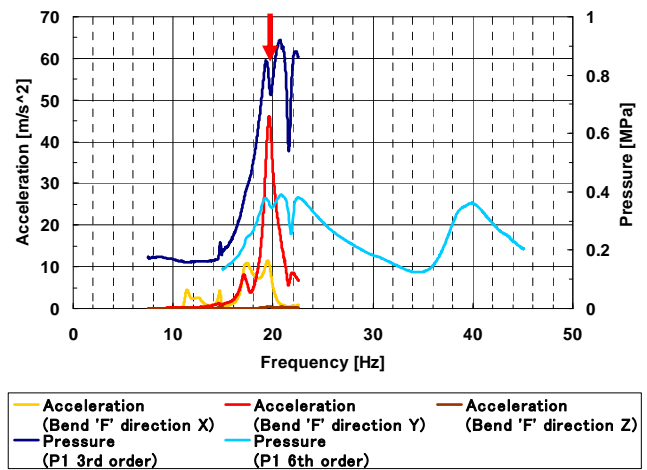


FIG.11: PRESSURE PULSATION AT P1 AND ACCELERATION AT BEND F (ROTATING SPEED: 150RPM~450RPM THE 3RD AND 6TH ORDERS SUPPORT CONDITION: HARD)

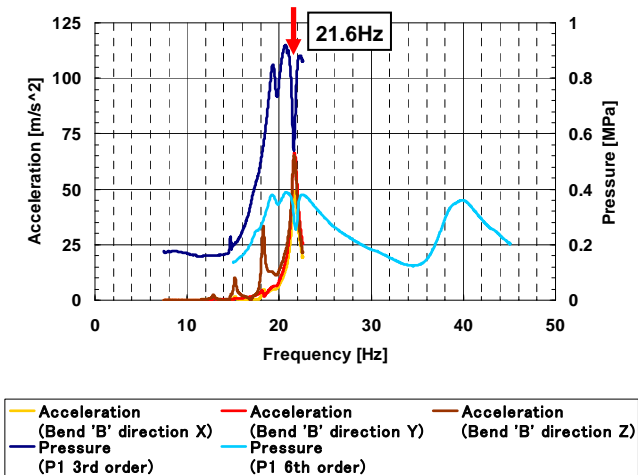


FIG.9: PRESSURE PULSATION AT P1 AND ACCELERATION AT BEND B (ROTATING SPEED: 150RPM~450RPM THE 3RD AND 6TH ORDERS SUPPORT CONDITION: HARD)

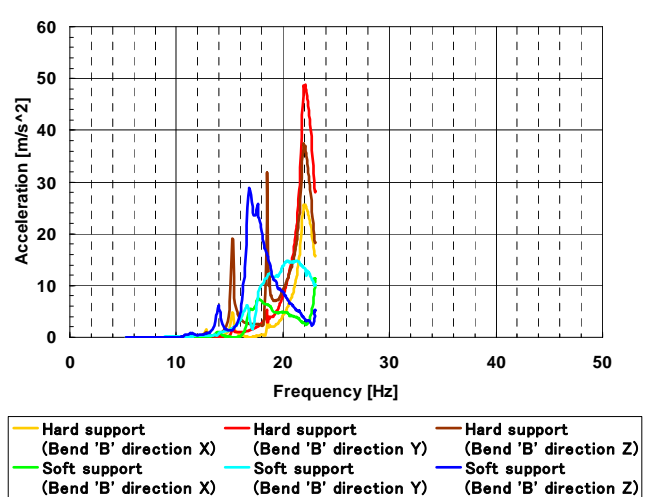


FIG.12: COMPARISON OF ACCELERATION AT BEND B (ROTATING SPEED: 100RPM~460RPM SUPPORT CONDITION: HARD VS. SOFT)

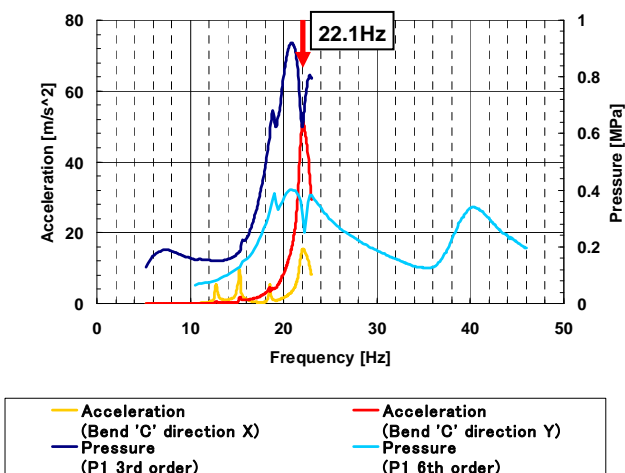


FIG.10: PRESSURE PULSATION AT P1 AND ACCELERATION AT BEND C (ROTATING SPEED: 100RPM~460RPM THE 3RD AND 6TH ORDERS SUPPORT CONDITION: HARD)

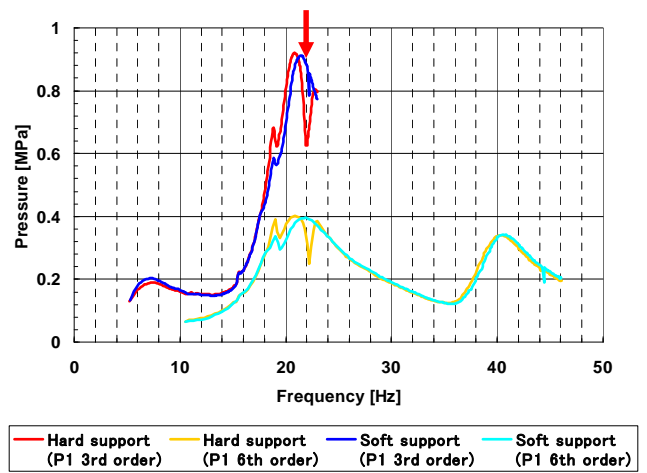


FIG.13: COMPARISON OF PRESSURE PULSATION AT P1 (ROTATING SPEED: 100RPM~460RPM THE 3RD AND 6TH ORDERS SUPPORT CONDITION: HARD VS. SOFT)

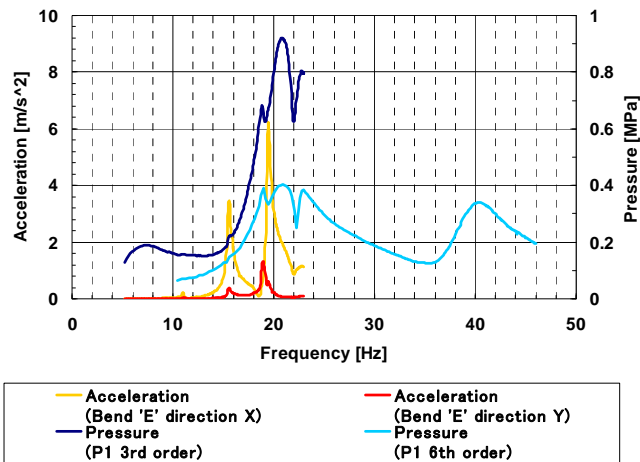


FIG.14: PRESSURE PULSATION AT MEASUREMENT POINT P1 AND ACCELERATION AT BEND E (ROTATING SPEED: 100RPM~460RPM THE 3RD AND 6TH ORDERS SUPPORT CONDITION: HARD)

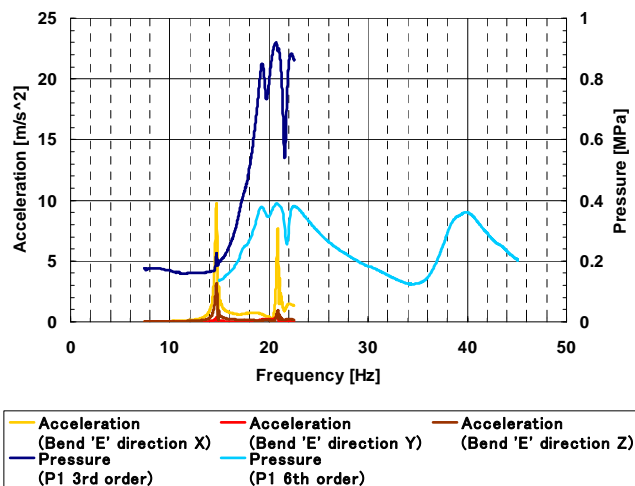


FIG.15: PRESSURE PULSATION AT MEASUREMENT POINT P1 AND ACCELERATION AT BEND E (ROTATING SPEED: 150RPM~450RPM THE 3RD AND 6TH ORDERS SUPPORT CONDITION: HARD)

PRESSURE INCREASE AT 16HZ

Figure 14 shows pressure pulsation at P1 and acceleration at Bend E. Here, the pressure pulsation increases at 16Hz, which is the natural frequency in the X direction, and which is the out-of-plane direction at Bend E. Figure 15 shows results of another experimental condition where the same phenomenon was observed. Therefore these increases of pressure pulsations around 16Hz appear to be affected by the mechanical resonance phenomenon in the X direction at Bend E.

CONCLUSION

(1) In pump-piping systems with liquid, an interaction occurs in pressure pulsation above a certain level of piping vibration.

Previous study showed that the piping vibration at 10-16 m/s^2 does not generate significant interaction with pressure pulsation [11]. In this study the interaction between pressure pulsation and piping vibration appears when the level is more than approximately 40 m/s^2 .

(2) The interaction between pressure pulsation and piping vibration in the in-plane direction results in a decrease of pressure pulsation. The interaction between pressure pulsation and vibration in the out-of-plane direction is observed, but in this case pressure pulsation increases. However interaction does not appear in other areas of the piping. Additional detailed study is needed to determine the mechanism of this interaction.

As already noted, to improve the accuracy of numerical simulation in predicting piping vibration it is important to take into account this interaction between pressure pulsations and piping vibration.

ACKNOWLEDGEMENT

We sincerely thank Institute of Nuclear Safety System, Inc. for giving us a permission to use their test equipment.

REFERENCE

- [1] Fujikawa, T. et al., 1987, Calculation of Pressure Pulsations in Piping System Attached to Reciprocating Compressor, KOBELCO Technology Review, Vol. 37, No.1, pp. 59.
- [2] Kato, M., et al., 1992, Calculation Method for Pressure Pulsations Including Interactions Between Reciprocating Compressors and Piping, ASME Winter Annual Meeting, Vol.6, pp.237-244.
- [3] API (American Petroleum Institute) Standard 618, 5th edition, Dec. 2007.
- [4] API (American Petroleum Institute) Standard 674, 3rd edition, Dec. 2010.
- [5] Kaneko, S. et al., 2008, Flow-Induced Vibration, Elsevier, pp.185.
- [6] D'Souza, A. F. and Oldenburger, R., 1964, Dynamic Response of Fluid Lines, Trans. ASME, J. Basic Engineering, 86, pp589-598.
- [7] Washio, S., et al., 1978, Trans. JSME, 44-384, pp.2781-2788. (in Japanese)
- [8] Tanaka, M. and Fujita, K., 1987, Vibration of Piping System by Pulsation of Containing Fluid (2nd Report), Trans. JSME, C, 53-491, pp.1363-1367. (in Japanese)
- [9] Washio, S., et al., 1978, Trans. JSME, 44-386, pp.3487-3495. (in Japanese)
- [10] Tsuji, T. et al., 2011, Experiment and Simulation on Pressure Pulsation Accompanied by Acoustic resonance and Piping Vibration, Proc. of ASME, PVP2011- 57221.
- [11] Tsuji, T. et al., 2011, Effect of Mechanical Resonance on Pressure Pulsation in Small-Bore Piping System, Proc. of JSME, D&D Conference 2011, 236. (in Japanese)



LOW SPEED FLUTTER AND LIMIT CYCLE OSCILLATIONS OF A FLAT PLATE IN A WIND TUNNEL

Xavier Amandolese¹

LadHyX, CNRS-Ecole Polytechnique
F-91128 Palaiseau, France
Département ISME, CNAM
F-75141, Paris, France

xavier.amandolese@ladhyx.polytechnique.fr

Sébastien Michelin

Maxime Choquel

LadHyX, CNRS-Ecole Polytechnique
F-91128 Palaiseau, France

Sebastien.michelin@ladhyx.polytechnique.fr

ABSTRACT

This paper focuses on the dynamical responses of a two degrees of freedom flat plate undergoing classical coupled-mode flutter in a wind tunnel at low Reynolds number $Re \sim 2.5 \cdot 10^4$. The flat plate model, at zero angle of attack, was flexibly mounted in heave and pitch in an experimental setup that allow high amplitude oscillations. At the critical velocity associated to the merging of frequencies, the system undergoes an unstable transient behavior before reaching a low amplitude limit-cycle oscillation regime with slow time varying amplitude. For higher velocity the system branches-off to a higher and more stable limit cycle oscillation regime. Amplitudes evolution with the flow velocity along with the phase lags between the pitch and heave response have been measured highlighting a hysteretic behavior in the LCO upper branch. In that context a by-pass transition to high limit cycle oscillations can be observed for hard perturbation below the critical velocity.

NOMENCLATURE

LCO	Limit Cycle Oscillations
O	Center of rotation
$\alpha(t)$	Pitch angle of attack about O (rad)
$z(t)$	Position in heave (m)
M_o	Aerodynamic momentum about O (N.m)
F_z	Lift force (N)
L, c, t	Span, chord and thickness of the plate model (m)
J_o	Inertia of the system about O (kg.m ²)
m	Mass of the system (kg)
d	distance between the centre of gravity and the center of rotation
k_α	Stiffness in rotation (N.m/rad)
k_z	Stiffness in bending (N/m)
f_α	Natural frequency in rotation (Hz)
f_z	Natural frequency in bending (Hz)
η_α	Reduced structural damping in rotation (%)
η_z	Reduced structural damping in bending (%)
U	Mean wind velocity (m/s)

Re	Reynolds number: $Re = U \times c / \nu$
ν	Kinematic viscosity (m ² /s)
U_c	Critical velocity (m/s)
U_r	Relative velocity: $U_r = U / U_c$
U_c^*	Reduced critical velocity: $U_c^* = U_c / f_c \times c$
f_c	merging frequency value at $U = U_c$
α_{LCO}	Amplitude in pitch at LCO (deg)
z_{LCO}	Amplitude in heave at LCO (m)
ϕ_{LCO}	Phase lag between the pitch and the heave at LCO (deg)

INTRODUCTION

Among the fluid-structure instabilities that can be experienced by a slender body in cross flow, classical flutter and stall flutter are probably the most thoroughly investigated. Classical flutter is a dynamic instability for which the energy transfer from the flow to the body relies on elastic and/or aerodynamic coupling between two structural modes [1]. Often referred to coupled-mode flutter, this instability can lead to high oscillations and then structural failures of slender structures such as wings or bridge decks if not properly designed. Fortunately, the critical parameters for the onset of classical flutter can be easily predicted using linear stability analysis [2-3].

On the other hand, stall flutter is known to be an instability not dependant on coupling for which a single mode body motion suffices to induce an aerodynamic loading in a way that energy is transferred from the flow to the body [4]. For slender structures such as wings or blades in stall flutter the most frequent mode of vibration involved is in torsion. The mechanism for energy transfer then relies on a dynamic stall process for which partial or complete detachment of the flow from the body occurs during each cycle of oscillation [5]. In that context, the essential feature of stall flutter is the non linear aerodynamic reaction of the body to the motion. This phenomenon is of particular importance for wing

Address all correspondence to this author¹

operating at high angle of attack [6-7], helicopter rotor blades [8] and more recently for wind turbine blades [9].

Due the non linear behavior of the aerodynamic load, stall flutter is also known to be limited in amplitude [10]. But limit cycle oscillations can also occur for aeroelastic systems in post critical flutter conditions due to structural nonlinearities [11]. In a recent work a link between classical flutter and stall flutter has also been pointed out by Razak *et al* [12] during tests performed on an aeroelastic wing model in wind tunnel, highlighting limit cycle oscillations around a mean angle of attack close to the static stall angle.

In that context, if the prediction for the onset of classical flutter is well understood the investigation of the non-linear flutter dynamics suffers from a lack of study. The aim of this paper is then to provide experimental evidences of the LCO for a simple aeroelastic flat-plate model undergoing classical coupled mode flutter. The present paper is then organized as follows: the experimental setup is first presented. Dynamical response of the system is then characterized below, at, and beyond the critical velocity associated to the merging of frequencies. The LCO amplitude evolution with the flow velocity is then highlighted along with the influence of the initial perturbation.

EXPERIMENTAL SETUP

The experiments were performed on a flat rectangular steel plate of span $L=0.225\text{m}$, chord length $c=0.035\text{m}$ and thickness $t=0.0015\text{m}$, which give a thickness-to-chord ratio of 4.3%. Dimensions of the model are shown in Fig. 1. This rectangular configuration has been chosen in order to limit the effect of the Reynolds number.

The flat plate model is flexibly mounted in heave and pitch in a in a small Eiffel wind tunnel with a closed rectangular test-section of 0.26 m width and 0,24 m high. The chord dimension of the model is then less than 15% of the height of the wind tunnel cross section in order to avoid blockage effects for high amplitude oscillations. Two end plates are also mounted at both the extremities of the flat-plate model in order limit end effects. The setup is shown in Fig. 1. The vertical stiffness of the system is set by two long steel laminated springs supporting the axis of rotation of the model. The rotational stiffness is set by two series of linear springs.

A particular attention has been paid to the design of a setup that can allow high amplitude linear response in pitch and heave. Moreover the rotation centre of the model O has been chosen between aerodynamic centre (i.e. the first quarter chord at zero angle of attack), and the centre of gravity G (i.e. the mid-chord) so the flat plate section can be subject to classical flutter in the velocity range of the wind tunnel.

Tests were performed for a mean velocity in the test-section varying from 5 to 13m/s, with a turbulence level less than 0.4% over this velocity range. In the present study the mean angle of attack of the model is set to zero.

The two degrees of freedom $z(t)$ and $\alpha(t)$ are measured using laser displacement sensors connected to an acquisition system.

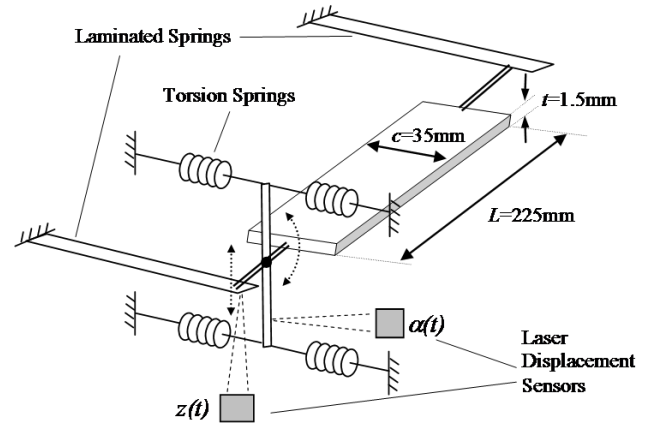


FIGURE 1: EXPERIMENTAL SETUP AND FLAT PLATE MODEL

Structural parameters

The linearized equations of motion for this structurally coupled two degrees of freedom system can be expressed as following [13]:

$$\begin{aligned} m \ddot{z} + 2m\eta_z \omega_z \dot{z} + k_z z + md \ddot{\alpha} &= F_z \\ J_o \ddot{\alpha} + 2J_o \eta_\alpha \omega_\alpha \dot{\alpha} + k_\alpha \alpha + md \ddot{z} &= M_o \end{aligned} \quad (1)$$

With $d = \overline{GO}$ the distance between the centre of gravity and the center of rotation ($d < 0$)

Structural parameters of the system are identified under zero-wind velocity. A static weight calibration technique is used to assess the stiffness k_z and k_α . Results reported in Fig. 2 show that the bending stiffness of the system behaves linearly in the range of $-0.3 \leq z/c \leq 0.3$.

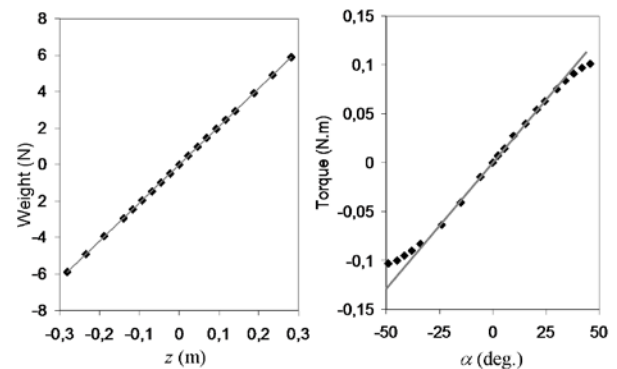


FIGURE 2: STIFFNESS STATIC WEIGHT CALIBRATION IN HEAVE AND PITCH

On the other hand the linearity of the stiffness in rotation is only guaranteed in the range of $-30 \text{ deg} \leq \alpha \leq 30 \text{ deg}$. For higher angles of rotation the rotational stiffness smoothly reduces until the critical limit angle of the ± 50 degrees. Above this critical angle the system is unable to properly restore a moment.

Free decay tests under zero wind conditions have been performed for each degree of freedom taken independently (the other one being locked). Natural frequencies f_z and f_α are then obtained by spectral analysis. Pure structural damping values η_z and η_α being determined using a standard decrement technique.

Assuming that the structural damping is small, the inertia J_O and mass m are then deduced, using

$$\begin{aligned} J_O &= k_\alpha / (2\pi f_\alpha)^2 \\ m &= k_z / (2\pi f_z)^2 \end{aligned} \quad (2)$$

Free decay tests have also been performed for the two-degrees of freedom system under zero wind conditions. This procedure allows the identification of the distance d between the centre of gravity and the center of rotation using the following expression (solution of the eigenvalue problem for the coupled system) [14]:

$$\frac{f_1^2 + f_2^2}{f_z^2 + f_\alpha^2} = \frac{1}{1 - md^2/J_O} \quad (3)$$

Structural parameters of the system are summarized in Table 1.

TABLE 1: STRUCTURAL PARAMETERS OF THE SYSTEM

f_α	f_z	k_α	k_z	J_O	m
9.0	7.05	0.149	595.6	$4.66 \cdot 10^{-5}$	0.304

η_α	η_z	d
0.015	0.002	-0.002

Aerodynamics of flat-plate

In situ measurements of the lift and moment coefficient has been performed using a static weight calibration technique under a wind velocity $U \approx 10 \text{ m/s}$ (i.e. a Reynolds number close to $2.3 \cdot 10^4$) at various angles of attack. Results are compared in Fig. 3 with the experiments of Fage and Johansen [15] (sharp-edged flat-plate model of thickness-to-chord ratio of 3% at Reynolds number $Re \approx 10^5$), along with those of Pelletier and Mueller [16] (flat-plate model of thickness-to-chord ratio of 1.93% at Reynolds number $Re \approx 8 \cdot 10^5$).

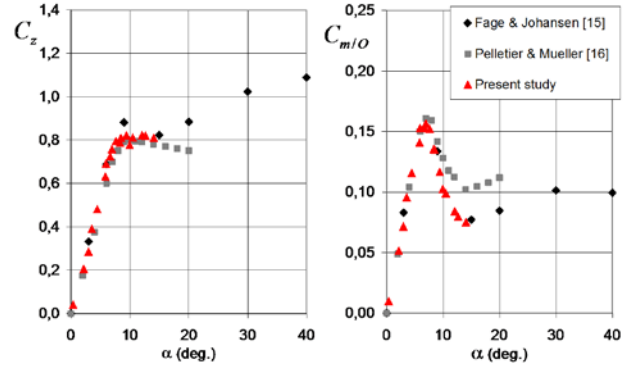


FIGURE 3: FLAT PLATE AERODYNAMIC CHARACTERISTICS VERSUS WIND VELOCITY

Those results show that the flat-plate model used in the present study follows the same trend with a lift-curve slope and moment-curve slope in the low-angle linear region respectively close to 6 and 1.5. The critical angle of attack at which the plate stalls can also be estimated between 7-8 degrees. As reported by Fage and Johansen [15] beyond this stall angle of attack the flow is completely separated from the upper surface.

LOW SPEED FLUTTER RESULTS

Experiments were performed with the flat plate model at zero mean angle of attack for wind tunnel velocity ranging from 5 up to 13 m/s. Increasing the velocity the system remains stable until a critical velocity $U_c \approx 10.5 \text{ m/s}$ is reached at which the merging of frequencies occurs. Beyond this critical velocity the system undergoes a flutter instability characterized by limit cycle oscillations that were studied up to $U/U_c \approx 1.2$. For higher velocities the dynamics of the system is corrupted by a static divergence in the pitching degree of freedom due to the structural limitation of the experimental setup.

Frequencies evolution with the flow-velocity

Free decay tests have been performed for various velocities in stable and post-stable condition. Spectral analysis of the dynamical responses then allows to identify the heaving and pitching frequencies evolutions versus the wind velocity. Results are reported in Fig. 4. For $U/U_c > 0.4$ both frequencies smoothly approach each other (the heaving frequency increasing while the pitching one decreases), until the critical condition $U/U_c = 1$ where the pitching frequency sharply reduces and merges the heaving frequency. Beyond that critical condition, the system dynamics adopts one dominant frequency close to $f_c \approx 8 \text{ Hz}$ which slightly reduces with the velocity.

For this flat-plate aeroelastic system characterized by a natural frequencies ratio $f_\alpha/f_z \approx 1.28$ the critical reduced velocity associated to flutter can then be approximated by $U_c^* = U_c/f_c \times c \approx 37.5$

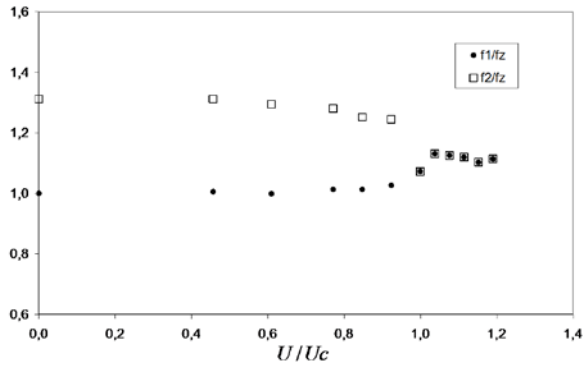


FIGURE 4: FREQUENCIES EVOLUTION IN HEAVE AND PITCH VERSUS RELATIVE VELOCITY

Analysis of the dynamical response

Below the critical velocity, i.e. for $U/U_c < 1$, heaving and pitching responses to any small initial perturbations are both damped to reach a small turbulence-induced vibration regime ($z/c < 0.0025$ & $\alpha < 0.1$ deg.).

At the critical velocity for which the frequency merging occurs, the system is unstable and any small initial perturbation is amplified. Heaving and pitching responses to a small initial deflection in heave ($z_0/c < 0.07$) are reported on Fig. 5. It clearly shows a transient growth in pitch and heave that is followed by a small decay and another growth. A low amplitude limit-cycle oscillations regime with slow time varying amplitude then occurs beyond reduced time $tU/c > 2$. Mean amplitudes in heave and pitch are then close to $z_{LCO}/c \approx 0.11$ and $\alpha_{LCO} \approx 6.5^\circ$.

In the LCO regime the mean phase angle ϕ_{LCO} by which the quasi-harmonic response in pitch lags the response in heave has been measured close to $\phi_{LCO} \approx -160^\circ$.

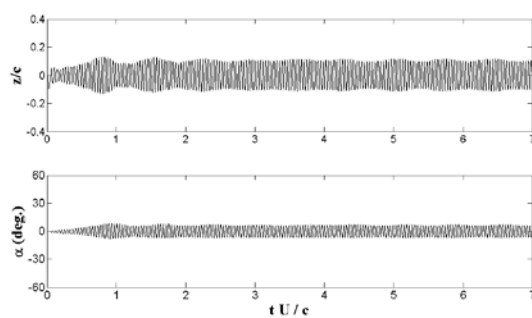


FIGURE 5: DYNAMICAL RESPONSE IN HEAVE AND PITCH AT THE CRITICAL VELOCITY

For higher velocity the dynamics of the response in heave and pitch change strongly. This can be seen in Fig 6. For $U/U_c \approx 1.08$ the initial transient growth of mechanical energy leads to a first regime of low amplitude oscillations in pitch ($\alpha < 11^\circ$) in the time

domain $1.1 < tU/c < 1.4$. In the same time the heaving response strongly decreases before growing again along with the pitching amplitude. The system then branches-off to a higher and more stable limit cycle oscillations regime characterized by high harmonic oscillations: $z_{LCO}/c \approx 0,2$ and $\alpha_{LCO} \approx 34^\circ$.

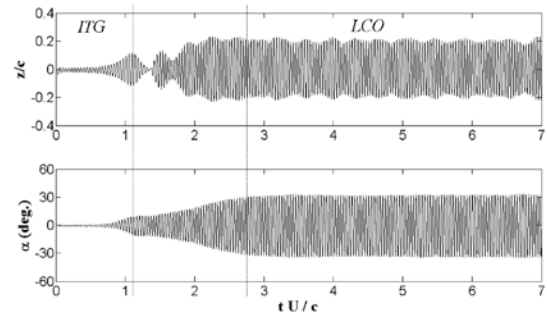


FIGURE 6: DYNAMICAL RESPONSE IN HEAVE AND PITCH IN THE POST-CRITICAL REGIME; $U/U_c \approx 1.08$

A phase diagram associated to each of the dynamical responses reported in Figs. 5 and 6 has been plotted in Fig. 7. For $U/U_c \approx 1$ the phase diagram shows the alternative occurrence of a phase angle regime of $\phi \approx -160^\circ$ which can be associated to the growth of mechanical energy, and an out of phase regime $\phi \approx -180^\circ$ where the oscillations decrease. For $U/U_c \approx 1.08$ the phase diagram shows that the first initial transient growth (ITG) regime is characterized by a mean phase lag between the pitch and the heave close to $\phi_{LCO} \approx -160^\circ$. Then the system branches-off to a more stable limit cycle oscillations regime characterized a mean phase angle $\phi_{LCO} \approx -36^\circ$.

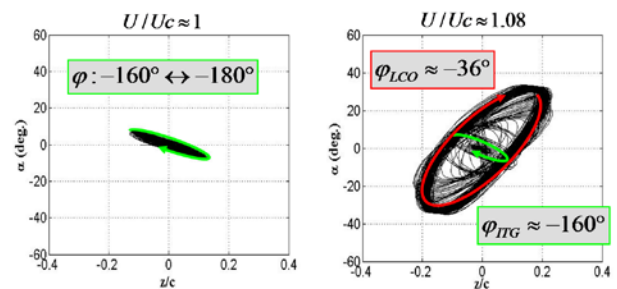


FIGURE 7: PHASE DIAGRAM OF THE DYNAMICAL RESPONSE FOR $U \approx U_c$ AND $U/U_c \approx 1.08$

For each velocity beyond the critical condition the amplitudes of oscillations associated to stable limit cycle oscillations have been checked along with the mean phase lag between the pitch and the heave response. Results are reported in Figs 8, 9 and 10. On those figures the first set of results has been obtained for the system undergoing flutter from rest. Additional tests have also been performed decreasing or increasing the flow velocity from a stable high amplitude LCO regime. The “decreasing

velocity” results clearly show a hysteretic behavior of the system which stay in a high amplitude LCO regime down to a relative velocity $U/U_c \approx 0.85$. For lower velocity the system is then damped. From $U/U_c \approx 0.85$ the heaving and pitching amplitudes of oscillations in the LCO branch also linearly increase with the relative velocity, reaching $z_{LCO}/c \approx 0.25$ and $\alpha_{LCO} \approx 44^\circ$ at $U/U_c \approx 1.2$.

As shown in Fig. 10 the negative phase lag between the pitch and the heave also changes with the velocity ratio. Following the “decreasing velocity” results one can see that $\varphi_{LCO} \approx -90^\circ$ for $U/U_c \approx 1.15$ and gradually increase to $\varphi_{LCO} \approx -11^\circ$ for the lower relative velocity $U/U_c \approx 0.85$

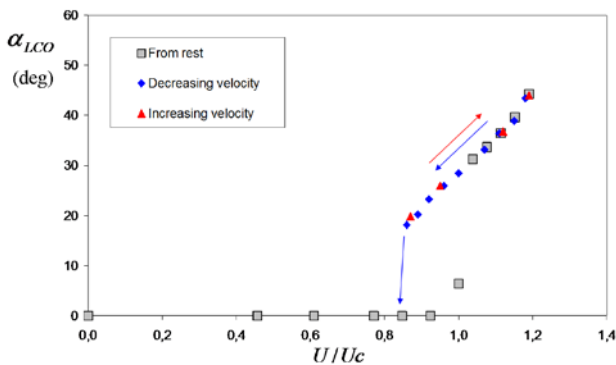


FIGURE 8: AMPLITUDE OF THE PITCHING RESPONSE VERSUS RELATIVE VELOCITY

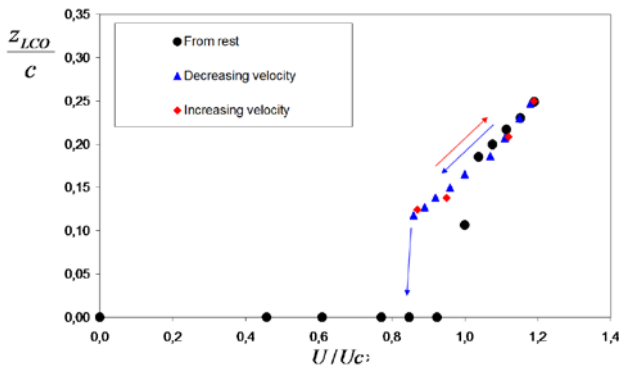


FIGURE 9: AMPLITUDE OF THE HEAVING RESPONSE VERSUS RELATIVE VELOCITY

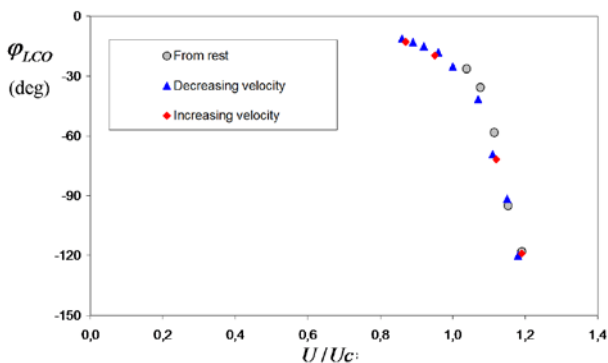


FIGURE 10: LCO PHASE LAG EVOLUTION WITH THE RELATIVE VELOCITY

Effect of the initial conditions

It is known that initial perturbations can significantly affect the dynamic response of system governed by non-linear behavior. Tests have then been performed below and beyond the critical velocity with different sets of initial conditions.

Below the critical velocity, the system remains stable (i.e. its dynamical response is damped) for different sets of low or moderate initial perturbations. On the other hand, for relative velocities $0.85 < U/U_c < 1$, a subcritical transition has been observed. Indeed, the onset of strong vibrations leading to the high limit cycle oscillations values reported on Figures 8 and 9 can be triggered by initial pitch angle and/or heave deflection such as : $\alpha_0 > \alpha_{LCO}$ and/or $z_0 > z_{LCO}$.

Above the critical velocity (i.e. for $U/U_c > 1$) different sets of low, moderate or strong initial conditions have been tested. They showed that even though the initial perturbations can significantly affect the transient regime, the same stable limit cycle oscillations regime is reached, with amplitudes and phase angle values in accordance with those reported in Figs 8-10.

CONCLUSIONS

Dynamical response of a two degrees of freedom flat plate undergoing classical coupled-mode flutter in a wind tunnel has been studied. Tests have been performed at low Reynolds number $Re \sim 2.5 \cdot 10^4$ using an experimental setup that allow high amplitude linear response in pitch and heave for relative velocity up to $U/U_c \approx 1.2$. In this study the frequency merging critical velocity (i.e. the onset of flutter), is such as the associated reduced velocity is close to $U_c^* = U_c / f_c \times c \approx 37.5$.

The results showed that beyond the critical velocity the system dynamical response is limited in amplitude. Indeed after a transient regime the system systematically branches off to a stable LCO regime characterized by high amplitudes in heave and pitch increasing linearly with the relative velocity, up to $z_{LCO}/c \approx 0.25$ and $\alpha_{LCO} \approx 44^\circ$ for $U/U_c \approx 1.2$. A hysteretic behavior has also been pointed out decreasing the velocity from a stable post-critical LCO regime. Indeed, the system dynamics remains in a high amplitude LCO regime down to a relative velocity $U/U_c \approx 0.85$, for which $z_{LCO}/c \approx 0.12$ and $\alpha_{LCO} \approx 18^\circ$.

In that context, a subcritical transition to high limit cycle oscillations can also be observed for hard perturbation of the system, starting from rest, for relative velocity $0.85 < U/U_c < 1$.

REFERENCES

- [1] Bisplinghoff, R.L. and Ashley, H., 1962. *Principles of aeroelasticity*. John Wiley and Sons, Inc., New-York, U.S.A.

- [2] Dowell, E.H., Crawley, E.F., Curtiss, H.C., Peters, D.A., Scanlan, R.H., and Sisto, F., 1995. *A modern course in aeroelasticity*. Ed. Kluwer, U.S.A.
- [3] Scanlan, R.H., and Tomko, J.J., 1971. "Airfoil and bridge flutter derivatives". *Journal of Engineering Mechanics*, ASCE. **109**(2), pp 586-603
- [4] Naudascher, E. and Rockwell, D., 1994. *Flow-induced vibrations: An engineering guide*. Ed. Balkema, Netherlands.
- [5] Carr, L.W., McAlister, K.W., McCroskey, W.J., 1977. "Analysis of the development of dynamic stall based on oscillating airfoil experiments". NASA-TN-D-8382.
- [6] Victory, M., 1943. "Flutter at High Incidence". Aeronautical Research Committee, Reports and Memoranda No. 2048.
- [7] Ericsson, L. E., and Peter Reding, J., 1971. "Unsteady Airfoil Stall and Stall Flutter," NASA, CR 111906.
- [8] Ham, N. D., and Young, M. I., 1966. "Limit Cycle Torsional Motion of Helicopter Blades due to Stall". *Journal of Sound and Vibration*, **4**(3), pp. 431-432.
- [9] Hansen, M.O.L., Sørensen, J.N. Voutsinas, S. Sørensen, N. Madsen, H.Aa. 2006. "State of the art in wind turbine aerodynamics and aeroelasticity". *Progress in Aerospace Sciences*, **42**(4), June, pp 285-330.
- [10] Li, J., and Dimitriadis, G., 2007. "Experimental Study of Stall Induced LCOS of Free-Vibrating Wings," in Proceedings of the CEAS International Forum on Aeroelasticity and Structural Dynamics, Paper IF-026, Stockholm.
- [11] Conner, M.D., Tang, D.M., Dowell, E.H., and Virgin, L.N., 1997. "Nonlinear behavior of a typical airfoil section with control surface freeplay". *Journal of Fluids and Structures*, **11**(1), January, pp 89-109.
- [12] Razak, N.A., Andrianne, T., and Dimitriadis, G., 2011. "Flutter and stall flutter of a rectangular wing in a wind tunnel". *AIAA Journal*, **49**(10), October, pp 2258-2271.
- [13] Fung, Y.C., 1993. *An Introduction to the Theory of Aeroelasticity*. Dover, New York.
- [14] P. Hémon, E. de Langre, P. Schmid. Experimental evidence of transient growth of energy before airfoil flutter. *Journal of Fluids and Structures*, 22:391-400, 2006
- [15] Fage, A., and Johansen, F.C., 1927. "On the flow of air behind an inclined flat plate of infinite span" in Proceedings of the Royal Society of London **116**(773) September, pp. 170-197
- [16] Pelletier, A., and Mueller, T.J., 2000. "Low Reynolds number aerodynamics of low-aspect-ratio thin/flat/cambered-plate wings", *Journal of Aircraft*, 37(5), September-October, pp 825-832.



NUMERICAL AND EXPERIMENTAL STUDY OF HYDROELASTIC BEHAVIOUR OF A HYDROFOIL

Fabien Gaugain¹
Jean-François Sigrist
 DCNS Research

Département Dynamique des Structures
 44620 La Montagne, France
 Email: fabien.gaugain@dcnsgroup.com

François Deniset
Jacques-André Astolfi

Institut de Recherche de l'Ecole Navale
 BCRM Brest CC600
 29240 Brest Cedex 9, France
 Email: françois.deniset@ecole-navale.fr

ABSTRACT

This paper presents a numerical and experimental study of the interaction between a deformable hydrofoil and a steady flow. The coupled problem is solved by an iterative sequential approach with fluid and structure domains calculated respectively with a FVM and FEM code. Stresses and displacements are predicted with a satisfactory accuracy. During test, the hydrofoil is instrumented with extensometric gauges and the displacement of the tip section is measured.

NOMENCLATURE

C_p	Pressure coefficient = $(p - p_{outlet}) / (1/2 \cdot \rho_f \cdot v_{inlet}^2)$
\mathbf{F}_e	Exterior forces vector applied to the structures
\mathbf{K}	Stiffness matrixes
Re	Reynolds number
\mathbf{U}	Nodal displacements vector
$\delta\mathbf{U}$	Virtual nodal displacements vector
d	Distance between mesh node and interface
k_{disp}	Mesh stiffness
p	Local pressure
p_{outlet}	Tunnel ambient pressure
\mathbf{u}	Structure displacements vector
$\delta\mathbf{u}$	Virtual structure displacements vector
\mathbf{v}	Fluid velocity vector
v_{inlet}	Fluid velocity at test section inlet
w_j	Component of mesh velocity vector
δ_{ij}	Kronecker tensor component
ε_{ij}	Strain tensor component
μ	Dynamic fluid viscosity
ρ_f	Fluid density
ρ_s	Structure density
σ_{ij}	Stress tensor component
ξ_i	Component of relative grid displacements vector

INTRODUCTION

Designing blades of propellers, rudders, or dynamic control lifting surfaces on a ship, or any lifting surface immersed in a fluid, requires an accurate knowledge of the loading conditions. In general, these conditions are defined by the flow which induces vibrations, deformations and stresses in the structure, and this deformed body modifies the flow. Taking into account this coupled phenomenon is important for increasing performance and life time of considered equipments. Indeed, considering interactions between noise generation, vibrations and cavitation inception and development will help to improve the equipment quality. For instance, [1] proposes to study the possibilities of designing propellers and lifting surfaces with adaptable geometry for improving the hydrodynamic performance and reducing the cavitation.

Reaching these goals needs numerical models able to solve fluid-structure coupled problems. At the moment, such methods are divided in two parts.

The first approach, so-called monolithic approach, consists in solving fluid and structure problems in one step. First, this process generally requires the reformulation of the fluid governing equations in a Lagrangian formulation or the inverse, the reformulation of the structure governing equations in an Eulerian formulation. Then, the problem is solved with a finite-volume method see e.g. [2], or a finite-element method, see e.g. [3]. This approach needs in general long computational times and is not economically optimal [4].

The second approach, so-called partitioned approach, consists in resolving each part of the problem, the fluid and the structure, with a specific solver. It requires a third code for driving the two solvers and exchanging information between them. The main advantage of this approach is the possibility of re-using current solver with different meshes for fluid and solid parts. But this technique requires accurate and robust coupling algorithms in time and space. This method has a lot of variants on the resolution method used for flow; for

¹ Address all correspondence to this author

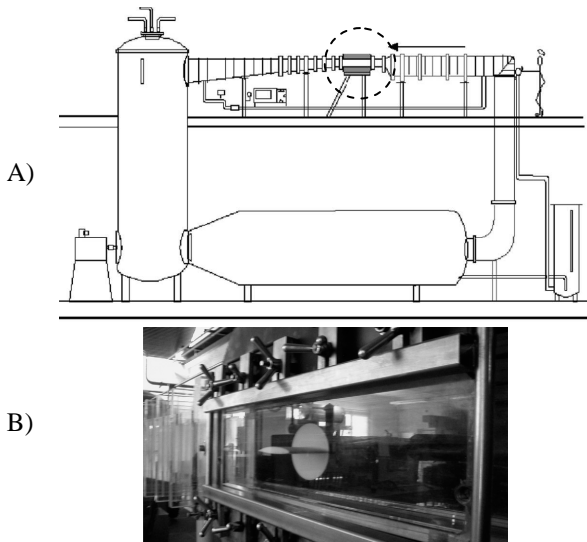


FIGURE 1: A) IRENAV TUNNEL SCHEME - B) PHOTO OF THE TEST SECTION WITH THE HYDROFOIL MOUNTED (FLOW IS COMING FROM THE RIGHT)

instance [5] resolves the problem with a finite-element method, [6] with a boundary-element method and [7] with a finite-volume method. The different coupling algorithms are discussed for example in [8].

In the following, the experimental process is first described, then, the formulation of the fluid-structure problem and the methods used for the resolution. The numerical results obtained are compared with numerical results of [7, 1] and with experimental results, both obtained in the same configurations.

EXPERIMENTAL SETUP

Experiments were conducted in the hydrodynamic tunnel of the French naval academy research institute. Figure 1 shows a scheme of the hydrodynamic tunnel where the dotted circle indicates the test section and a photo of the test section with the hydrofoil mounted. The test section is a square of 0.192 m sides and 1 m length.

The tested structure is a hydrofoil NACA66-312 with a camber ratio of 2 %, a relative thickness of 12 %, a chord length $C=150$ mm, and a span $B=191$ mm. It is made of polyacetate (POM); Table 1 gives the specification of this material. The hydrofoil theoretical zero lift angle is equal to 2.35° . Figure 2 shows the hydrofoil geometry.

The tests consist in determining hydrofoil displacements and stresses for a fixed angular position. For zero angle of incidence, the hydrofoil chord is located at mid-height of the test section.

Tests are performed for static angles of incidence located between 0 and 12 degrees. The hydrofoil rotation axis is located at mid-chord. The inlet velocity is equal to 5 m/s and the tunnel pressure is imposed equal to the atmospheric one.

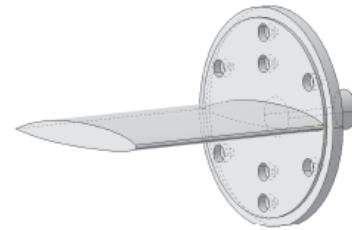


FIGURE 2: HYDROFOIL NACA66-312 GEOMETRY

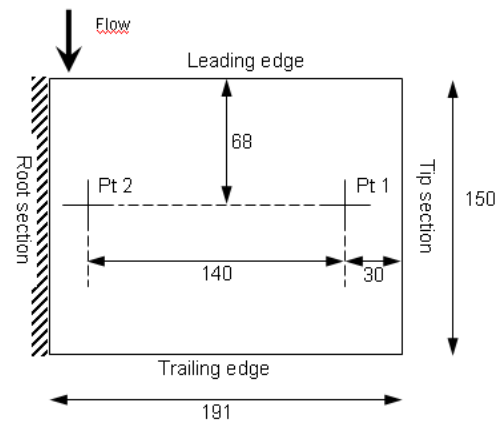


FIGURE 3: GAUGES LOCATIONS ON HYDROFOIL PRESSURE FACE (DIMENSIONS ARE IN MM)

TABLE 1: HYDROFOIL MATERIAL (POM) SPECIFICATIONS

Young modulus	3100 MPa
Density	1480 kg.m ⁻³
Poisson coefficient	0.35

GOVERNING EQUATIONS

To determine stresses, strains and tip section displacements in a such problem, a coupled system has to be solved. Flow causes deformations which induce flow modifications in terms of velocity and pressure fields. Equation (1) describes the structure behaviour in a displacements-like formulation,

$$\rho_s \frac{\partial^2 u_i}{\partial t^2} - \frac{\partial \sigma_{ij}(\mathbf{u})}{\partial x_j} = 0 \text{ in } \Omega_s \quad (1)$$

where \mathbf{u} is the structure displacement, ρ_s the structure density and $\boldsymbol{\sigma}$ the stresses tensor. At the clamped boundary Γ_{clamp} displacements are null:

$$u_i = 0 \text{ on } \Gamma_{\text{clamp}}$$

The incompressible fluid behaviour is modelled by Navier-Stokes equations. Equation (2) expresses the local momentum conservation and Eqn. (3) is the local mass conservation equation.

$$\frac{\partial \rho_f v_i}{\partial t} + \frac{\partial \rho_f v_i v_j}{\partial x_j} = - \frac{\partial p}{\partial x_i} + \frac{\partial}{\partial x_i} \left(\mu \left(\frac{\partial v_i}{\partial x_j} + \frac{\partial v_j}{\partial x_i} \right) \right) \quad (2)$$

$$\frac{\partial \rho_f}{\partial t} + \frac{\partial \rho_f v_j}{\partial x_j} = 0 \text{ in } \Omega_f \quad (3)$$

The fluid boundaries conditions are $p = p_{outlet}$ on Γ_{outlet} with p_{outlet} equals to atmospheric pressure and $v_i = v_{inlet} = 5 \text{ m/s}$ ($Re = 7.5 \times 10^5$).

The boundary conditions on the hydrofoil wall Γ_{fsi} are the fluid-structure conditions. First, a continuity of the velocity at the boundary is imposed:

$$v_i = \frac{\partial u_i}{\partial t} \text{ on } \Gamma_{fsi}$$

Second, stresses equality at the interface Γ_{fsi} is imposed:

$$\sigma_{ij}(\mathbf{u}) n_j = \left[-p \delta_{ij} + \mu \left(\frac{\partial v_i}{\partial x_j} + \frac{\partial v_j}{\partial x_i} \right) \right] n_j$$

NUMERICAL SIMULATION

A partitioned approach is used in this study with an iterative sequential process. Figure 4 presents the algorithm procedure. Once the flow field has been solved by ANSYS CFX, hydrodynamic forces are used to compute structure response in terms of displacements, strains and stresses. ANSYS Mechanical is employed for structure resolution. After that, interface displacements are transferred to the fluid mesh and the initial grid is deformed in consequence. Finally, a new fluid resolution loop is engaged, etc. The iterative process ends when the criteria of convergence are reached.

The fluid problem is solved by a finite-volume method [9] and the structure problem is solved by a finite-element method [10]. These methods are briefly described below followed by a presentation of the coupling algorithms.

Structure Problem

In stationary case Eqn. (1) becomes:

$$\frac{\partial \sigma_{ij}(\mathbf{u})}{\partial x_j} = 0 \text{ in } \Omega_s \quad (4)$$

The finite element method requires a weighted integral formulation which is obtained by multiplying Eqn. (4) by a virtual displacement field $\delta \mathbf{u}$. Then, integration on the structure domain and boundary conditions yields:

$$\int_{\Omega_s} \sigma_{ij}(\mathbf{u}) \varepsilon_{ij}(\delta \mathbf{u}) d\Omega_s - \int_{\Gamma_{fsi}} \sigma_{ij}(\mathbf{u}) n_j \delta u_i d\Gamma_{fsi} = 0$$

where ε is the linear strain tensor and \mathbf{n} the normal vector.

The finite element decomposition used with classic nodal interpolation functions yields to the stiffness matrix \mathbf{K} and the exterior forces vector applied to the structure \mathbf{F}_e . This last term contains the coupling condition in the structure equation.

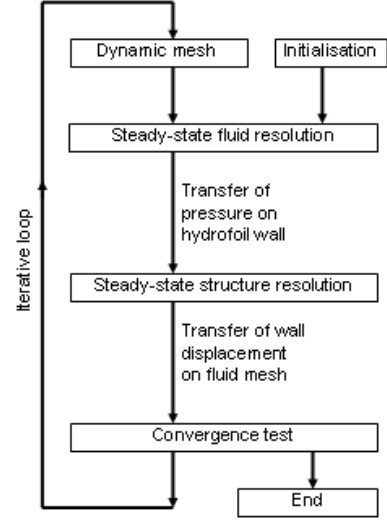


FIGURE 4: COUPLING ALGORITHM

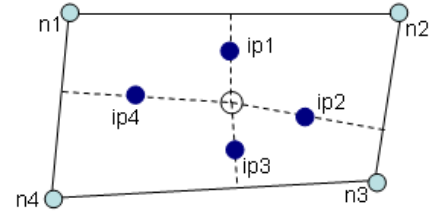


FIGURE 5: INTEGRATION POINTS FOR AN ELEMENT

$$\int_{\Omega_s} \sigma_{ij}(\mathbf{u}) \varepsilon_{ij}(\delta \mathbf{u}) d\Omega_s \rightarrow \delta \mathbf{U}^T \mathbf{K} \mathbf{U}$$

$$\int_{\Gamma_{fsi}} \sigma_{ij}(\mathbf{u}) n_j \delta u_i d\Gamma_{fsi} \rightarrow \delta \mathbf{U}^T \mathbf{F}_e$$

The discrete structure equation is:

$$\mathbf{K} \mathbf{U} - \mathbf{F}_e = \mathbf{0} \quad (5)$$

This equation is solved with an iterative technique so-called Preconditioned Conjugated Gradient (PGC). The criterion of convergence is reached when $\mathbf{K} \mathbf{U}$ is equal to $\mathbf{F}_e + \varepsilon$ with ε equal to 10^{-8} .

Fluid Problem

The finite volume method begins with an integration of Eqns. (2) and (3) over a control volume. In the present case, a steady-state formulation is used which eliminates inertial terms. The Arbitrary Lagrangian Eulerian (ALE) [11] formulation introduces a mesh velocity \mathbf{w} .

$$\int_{\Gamma} \rho_f (v_j - w_j) dn_j = 0 \quad (6)$$

$$\int_{\Gamma} \rho_f (v_j - w_j u_i) dn_j = - \int_{\Gamma} p dn_j + \int_{\Gamma} \mu_{eff} \left(\frac{\partial v_i}{\partial x_j} + \frac{\partial v_j}{\partial x_i} \right) dn_j \quad (7)$$

Surface integrals are replaced by sums at integration points (ip points on Fig. 5). Respecting local conservation,

the surface integrals are equal (in absolute value) and opposite for control volumes adjacent to the integration point. For transfer information between grid nodes and integration points, shape functions N are used.

Equations (6) and (7) become:

$$\sum_{ip} (\rho_f (v_j - w_j) \Delta n_j) = 0$$

$$\sum_{ip} (\rho_f (v_j - w_j v_i) \Delta n_j) =$$

$$- \sum_{ip} (p \Delta n_j) + \sum_{ip} \left(\mu_{eff} \left(\frac{\partial v_i}{\partial x_j} + \frac{\partial v_j}{\partial x_i} \right) \Delta n_j \right)$$

where the gradients of the diffusive term are replaced by a sum on the n nodes of the considered element:

$$\frac{\partial v}{\partial \mathbf{x}} \Big|_{ip} = \sum_n \frac{\partial N_n}{\partial \mathbf{x}} \Big|_{ip} \mathbf{v}_{ip}$$

The advection scheme uses the upwind velocity \mathbf{v}_{up} and a gradient of the velocity for approximating \mathbf{v}_{ip} :

$$\mathbf{v}_{ip} = \mathbf{v}_{up} + \beta \nabla \Delta \mathbf{r}$$

$\Delta \mathbf{r}$ is the vector from upwind node to integration point. β is a coefficient determined according to [12].

CFX uses a co-located grid, so a pressure-velocity coupling based on Rhie-Chow interpolation method [13] and Majumdar [14] improvement is employed. In this study, the turbulence is taken into account through a $k-\omega$ SST model [15] with a wall function.

Finally, a discrete equation system is obtained. Its resolution is performed with a coupled algebraic multi-grid method. Steady-state resolution in CFX uses a pseudo-time step for iteration process until convergence is reached. The residuals-based convergence criterion is fixed to 10^{-6} .

Coupling Algorithms

Since the problem under consideration is stationary, the coupling algorithms in this study are limited to space coupling techniques. These methods consist in first transferring hydrodynamic forces from fluid to structure meshes and displacements in the other way and second adapting the fluid meshes at the structure displacements.

The first point is the energy conservation at the interface. For a conformal mesh – structure and fluid nodes, edges and faces have the same location - the data of structure node corresponds exactly to the fluid node at the same point (or inverse). For a non-conformal mesh [16] uses the interface for projecting fluid and structure nodes. For interpolation [17] uses Gauss points or splines. [18] gives more information about projection and interpolation methods.

The transfer of displacements from ANSYS to CFX used a bucket method with a linear interpolation. [19] uses a similar interpolation method This kind of method is limited to non-conservative data because it only assures profil preservation but not global conservation.

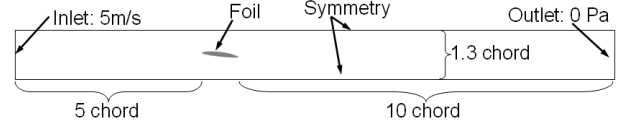


FIGURE 6: COMPUTATIONAL DOMAIN

Transferring forces from CFX to ANSYS requires a global conservation of the data. The projection of the elements is made on an interface and the interpolations use a weighted systems based on the surface of the projected elements. This method is described in details in [20].

In these two cases, the transferred data are under-relaxed in order to limit the possible numerical divergence between two steps.

The second point requires the definition of the grid velocity used in ALE formulation which is defined by the displacement of nodes. At the interface ξ , the grid displacement vector is equal to the structure displacement at this location. At the other fluid field boundaries, the grid displacement vector is null. Between them, it is defined by the diffusive equation below:

$$\frac{\partial}{\partial x_j} \left(k_{disp} \frac{\partial \xi_i}{\partial x_j} \right) = 0$$

where, k_{disp} is the mesh displacements stiffness which is a function of the interface distance d :

$$k_{disp} = \left(\frac{1}{d} \right)^{C_{stiff}}$$

In this study C_{stiff} default value is fixed to 10.

Fluid mesh displacement can be defined by some other methods. For example, [21] uses the spring analogy technique.

The last aim of the coupling algorithm is the control of convergence which is governed by a criterion of 10^{-3} on displacements and forces residuals.

GEOMETRIC MODELLING AND SPATIAL DECOMPOSITION

Geometric Modelling

The computational domain corresponds to the tunnel test section geometry. The length of the domain is equal to 5 hydrofoil chords upstream the hydrofoil leading edge and 10 chords downstream the hydrofoil trailing edge. Figure 6 shows the computational domain.

The hydrofoil geometry is reduced to the lift part, which is supposed to be clamped to the lateral tunnel wall at its root section.

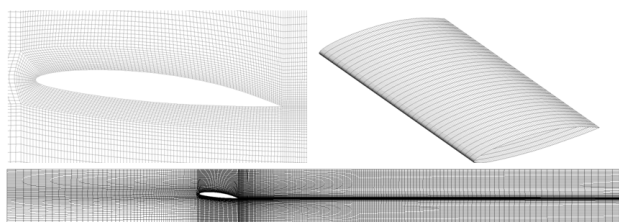


FIGURE 7: COARSE MESH AROUND THE HYDROFOIL, ON THE SPAN AND ON THE ENTIRE DOMAIN

TABLE 2: NUMBER OF ELEMENTS AND NODES ON THE FLUID MESHES

	Elements	Nodes	Chord \times Span
1	784,875	825,012	75 \times 35
2	1,569,750	1,627,107	75 \times 70
3	2,005,150	2,079,661	170 \times 70

Fluid Meshes

Three structured fluid meshes with hexahedrons are compared in this study. Table 2 gives their number of elements and nodes, as well as the number of nodes on one section of the hydrofoil and along the span.

Figure 7 displays the fluid meshes on the hydrofoil and around it for a vertical section. The 3D meshes are built from the extrusion along the span of the 2D meshes. The coarse mesh 1 and the mesh 2 have the same 2D original mesh. The fine mesh 3, is extruded with the same number of nodes than mesh 2.

All of them are designed to give a value of y^+ parameter between 30 and 300 on the hydrofoil wall. For this reason, the sizes of the first cells along the normal of the wall are the same on the three meshes.

Structure Meshes

Two structured meshes with quadrangular 20 nodes elements are carried out by extrusion along the span on 32 nodes for mesh A and on 70 nodes for mesh B. Figure 8 shows these two meshes.

Meshes Convergence

Figure 9 displays the influence of the mesh respectively on the maximum vertical displacement and the Von Mises stress. Table 3 presents the mesh configuration used in the different simulations.

The results of simulations 1 and 2 indicate the influence of the fluid meshes on Von Mises stress predictions. Comparison between calculations 2 and 3 reveals an insignificant influence of structure mesh density, because of the sufficiently fine mesh A. All the meshes give vertical displacements of the same order. These results demonstrate that stresses prediction requires a finer grid than displacement calculation.

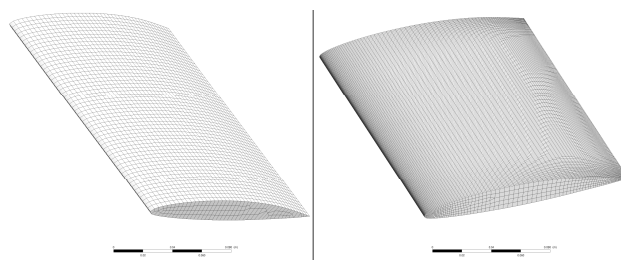


FIGURE 8: STRUCTURES MESHES A (LEFT) AND B (RIGHT)

TABLE 3: CONFIGURATION USED FOR MESH STUDY

Simulation number.	Structure mesh	Fluid mesh
1	A	1
2	A	2
3	B	2
4	B	3

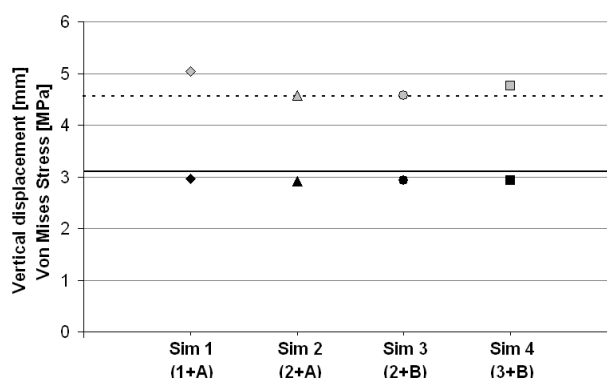


FIGURE 9: INFLUENCE OF MESHES ON THE MAXIMUM VERTICAL DISPLACEMENT (BLACK SYMBOLS) COMPARED TO EXPERIMENT (CONTINUOUS LINE) AND VON MISES STRESS AT THE GAUGE 2 (GREY SYMBOLS) COMPARED TO EXPERIMENTAL VALUES (DOTTED LINE) - ($Re=7.5 \times 10^5$, $U=5$ m/s, $\alpha=6^\circ$)

For this study, meshes A and 2 respectively for structure and fluid are sufficient to reach a good result. Nevertheless, meshes B and 3 are used in this study in prevision of future investigations about fluid-structure interaction on a cavitating hydrofoil.

RESULTS AND DISCUSSION

The numerical results are compared with experiments and with the numerical displacement obtained by [1]. The strains and stresses presented below are obtained from gauge 2 located close to the root section, the results at gauge 1 are too small for a correct exploitation.

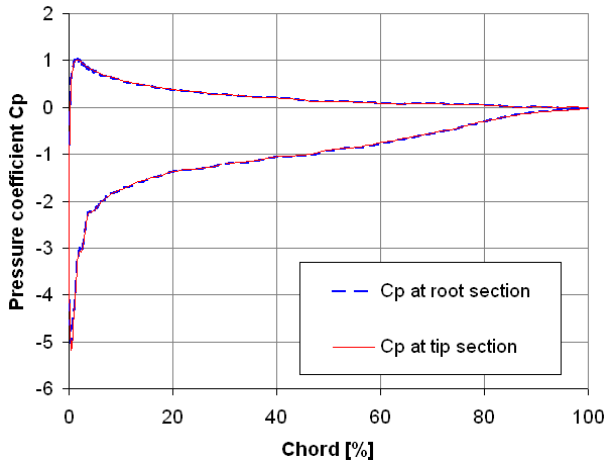


FIGURE 10: PRESSURE COEFFICIENT AT THE ROOT AND TIP SECTIONS ($Re=7.5 \times 10^5$, $U=5$ m/s, $\alpha=8^\circ$)

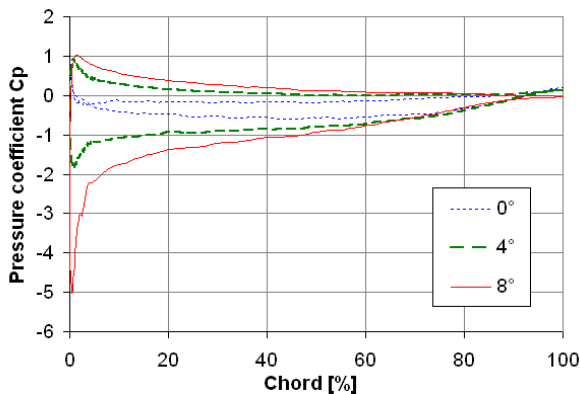


FIGURE 11: PRESSURE COEFFICIENT IN THE TIP SECTION FOR VARIOUS ANGLES OF INCIDENCE ($Re=7.5 \times 10^5$, $U=5$ m/s, $\alpha=0,2,8^\circ$)

Pressure Coefficient

Figure 10 shows the pressure coefficient calculated in the root and tip sections. It appears that deformation does not influence the pressure distribution on the hydrofoil. This is due to the fact that displacements are small. For higher deformations such as obtained in [7] for a flow velocity of 10 m/s, the pressure coefficient is strongly modified in the tip section leading to a higher local lift load due to the twist effect along the span. For a considered section along the hydrofoil span, its deformation is equivalent to a modification of the angle of incidence.

Figure 11 shows the impact of the angle of incidence on the pressure coefficient. Increasing the coefficient of pressure (or the incidence angle) induces an increase of the hydrodynamic forces and thus the deformation.

These results highlight the importance of a coupled resolution for an accurate prediction of pressure distribution around the hydrofoil. This accurate prediction of the local pressure is essential for cavitating studies and hydrodynamic forces calculations.

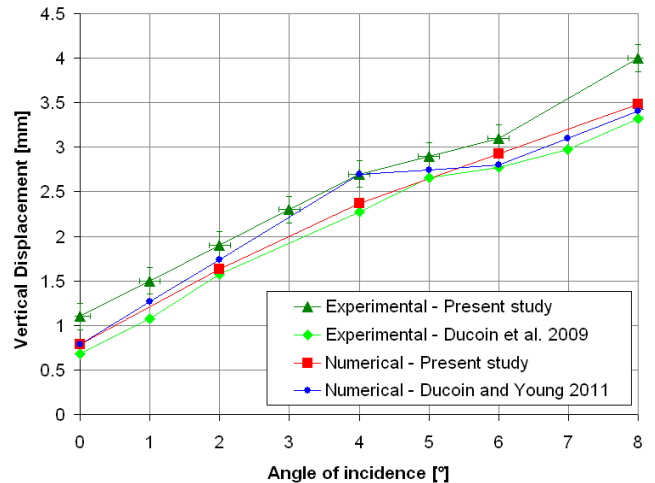


FIGURE 12: NUMERICAL AND EXPERIMENTAL DISPLACEMENTS OBTAINED FOR THE NACA66 - ($Re=7.5 \times 10^5$, $U=5$ m/s, $\alpha=8^\circ$)

Tip Section Displacement

Figure 12 shows the displacement at the tip section on the vertical axis versus the angle of incidence. The displacement increases with the angle of incidence, which is due to the hydrodynamic forces increase induced by the C_p increase. On this hydrofoil, the laminar to turbulent transition of the boundary layer occurs between 3 and 5 degrees of incidence. This transition explains the small slope variation observed at 5° .

The gap between numerical and experimental displacements can be explained by different reasons, for example, the non-use of low Reynolds resolution near the hydrofoil wall or the slip condition on the tunnel wall.

Figure 12 compares the numerical and experimental displacements of the tip section of this study with the work of [22] for experiments and with the numerical study of [1], which are performed with CFX coupled with a 2DOF structure code on the same case with the same conditions. The dispersion of experimental results shown in Fig. 14 can be accounted by small tunnel velocity fluctuations, the displacement being a function of the square of the velocity [7]. A second explanation can be an error on the angular position of the hydrofoil.

In light of these results, the calculations give accurate predictions of the displacements. The method with 2DOF coupling is faster than the finite element method but it cannot compute the stresses. It is a fine process for fast computation of hydrodynamic forces and displacements.

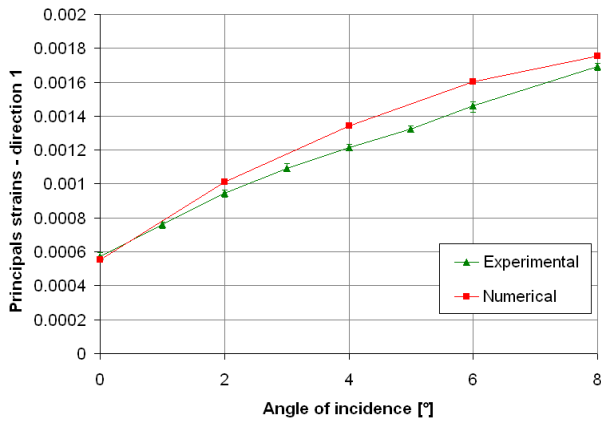


FIGURE 13: PRINCIPAL STRAINS ON DIRECTION 1 AT LOCATION 2 - ($Re=7.5 \times 10^5$, $U=5$ m/s, $\alpha=8^\circ$)

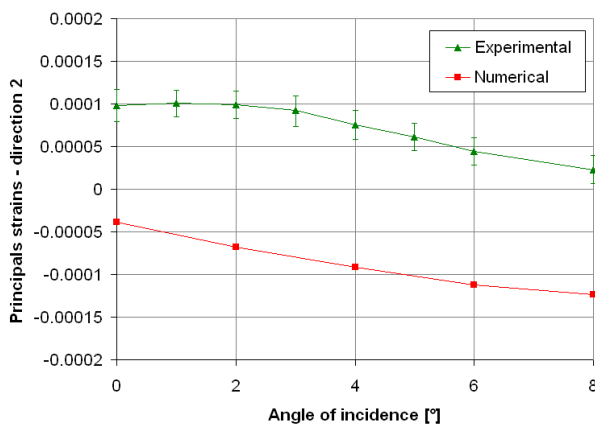


FIGURE 14: PRINCIPAL STRAINS ON DIRECTION 2 AT LOCATION 2 - ($Re=7.5 \times 10^5$, $U=5$ m/s, $\alpha=8^\circ$)

Principal Strains

The experimental principal strains are obtained from the extensometric gauges. The principal direction 1 is along the span and direction 2 is aligned with the chord. Figures 13 and 14 show the principal strains at location 2, the point located close to the root, for directions 1 and 2 respectively.

The values on direction 1 are 10 times higher than the ones on direction 2. This indicates the predominance of the flexion mode according to the experimental observation. The strains on direction 2 confirm the small torsion mode displacement of the hydrofoil.

On Fig. 14, the differences between experimental and numerical results are of the same order as the ones that are presented in Fig. 13.

Von Mises Stresses

The experimental Von Mises stresses are calculated with only principal strains on two directions. For a correct comparison, only two numerical principal strains on the two same directions are used.

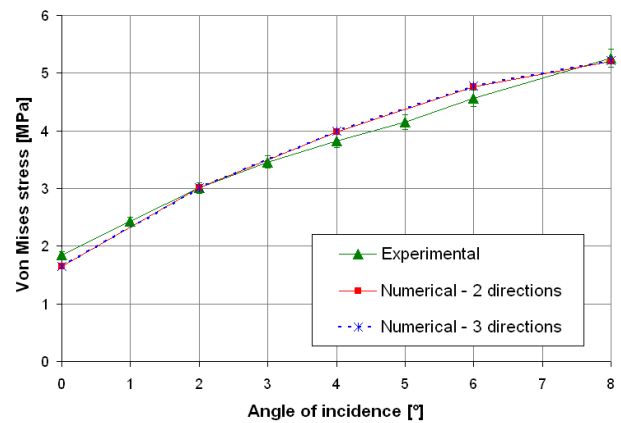


FIGURE 15: VON MISES STRESSES VERSUS ANGLE OF INCIDENCE - ($Re=7.5 \times 10^5$, $U=5$ m/s, $\alpha=8^\circ$)

As expected, a good agreement between the numerical and experimental results computed with the previous strains is obtained. The increases of the stresses with the angle of incidence are induced by the increase of the deformation.

On Fig. 15, the negligible gap between the Von Mises stresses computed with the three principal directions stresses and with two directions shows the very small influence of stresses along the hydrofoil thickness.

Computational Costs

The fluid and structure computations are performed respectively with 8 and 2 cores Xeon X5650 2.67 GHz with a total RAM of 24 GB. The CPU time repartition is 70% for fluid resolution, 10% for mesh and 20% for structure resolution. A similar repartition is obtained by [7] in hydroelasticity or by [23] in aeroelasticity.

The sequential process supposes a CPU time longer of 20% than for a parallel process. However, if the predictor was not very efficient, some supplementary coupling iterations would be necessary and the CPU time would be dramatically increased.

CONCLUSIONS

The present study shows that using a partitioned iterative sequential approach - with a finite volume method for the fluid part and a finite element method for the structure part - gives a robust enough method for solving fluid-structure steady cases with accuracy and an acceptable computing time with reasonable computing resources. As the simulations have shown, the displacements of the tip section are predicted with a maximum tolerance of 0.5 mm and this for angles of incidence from 0 to 8°. The strains and stresses present a very good agreement with experiments with a maximum relative error of 4.6 % on Von Mises stresses.

Future work will consist in investigating the fluid-structure interaction between a deformable hydrofoil and

an unsteady cavitating flow, both with numerical and experimental points of view.

Validating coupled calculations procedures improves the design of many systems like blades of propellers, rudders etc. and gives a satisfactory tool for future developments.

ACKNOWLEDGMENTS

The authors gratefully acknowledge the staffs of IRENav and DCNS Nantes for their contributions to this work.

REFERENCES

- [1] Ducoin, A., and Young, Y., 2011. "Hydroelastic Response and Stability of a Hydrofoil in Viscous Flow". Second International Symposium on Marine Propulsors SMP'11, Institute for fluid dynamics and ship theory – Hamburg University of Technology, German Society for Maritime Technologie, pp. 294-302. TB2-2.
- [2] Dermidžić, I., and Muzaferija, S., 1995. "Numerical method for coupled fluid flow, heat transfer and stress analysis using unstructured moving meshes with cells of arbitrary topology". *Computer Methods in Applied Mechanics and Engineering*, 125(1-4), September, pp. 235-255.
- [3] Hübner, B., Walhorn, E., and Dinkler, D., 2004. "A monolithic approach to fluid-structure interaction using space-time finite elements". *Computer Methods in Applied Mechanics and Engineering*, 193(23-26), June, pp. 2087-2104.
- [4] Piperno, S., and Farhat, C., 2000. "Design of efficient partitioned procedures for the transient solution of aeroelastic problem". *Revue Européenne des Eléments Finis*, 9(6-7), pp. 655-680.
- [5] Dettmer, W., and Perić, D., 2007. "A fully implicit computational strategy for strongly coupled fluid-solid interaction". *Archives of Computational Methods in Engineering*, 14(3), pp. 205-247.
- [6] Young, Y., 2008. "Fluid-structure interaction analysis of flexible composite marine propellers". *Journal of Fluids and Structures*, 24(6), pp. 799-818.
- [7] Ducoin, A., Astolfi, J.-A., Deniset, F., and Sigrist, J.-F., 2009. "Computational and experimental investigation of flow over a transient pitching hydrofoil". *European Journal of Mechanics B/Fluids*, 28(6), pp. 728-743.
- [8] Sigrist, J.-F., 2000. "Méthodes numériques de calculs couplés fluide/structure". *Techniques de l'Ingénieur*, BM5201.
- [9] Ferziger, J., and Perić, M., 2002. *Computational Method for Fluid Dynamics*. Springer-Verlag.
- [10] Zienkiewicz, O.C., and Taylor, R.L., 2000. *The Finite Element Method*, 5th edition. Butterworth-Heinemann.
- [11] Donea, J., Huerta, A., Ponthot, J.-P., and Rodriguez-Ferran, A., 2004. *Encyclopedia of Computational Mechanics*, chap. 14. John Wiley & Sons, pp. 413-437.
- [12] Bath, T.J., and Jespersion, D.C., 1989. "The design and application of upwind schemes on unstructured meshes". AIAA Paper 89-0366.
- [13] Rhie, C.M., and Chow, W.L., 1983. "A numerical study of the turbulent flow past an isolated airfoil with trailing edge separation". *AIAA Journal*, 21(11), pp.1525-1532.
- [14] Majundar, S., 1988. "Role of underrelaxation in momentum interpolation for calculation of flow with non staggered grids". *Numerical Heat Transfer*, 13(1), pp. 125-132.
- [15] Menter, F.R., 1994. "Two equation eddy-viscosity turbulence models for engineering applications". *AIAA Journal*, 32(8), pp. 1598-1605.
- [16] Farhat, C., Lesoinne, M., and Le Tallec, P., 1998. "Load and motion transfer algorithms for fluid/structure interaction problems with non-matching discrete interfaces: Momentum and energy conservation, optimal discretization and application to aeroelasticity". *Computer Methods in Applied Mechanics and Engineering*, 157(1-2), pp. 95-114.
- [17] De Boer, A., Von Zuijlen, A., and Bijl, H., 2007. "Review of coupling methods for non-matching meshes". *Computer Methods in Applied Mechanics and Engineering*, 196(8), pp. 1515-1525.
- [18] Maman, N., and Farhat, C., 1995. "Matching fluid and structure meshes for aeroelastic computations: A parallel approach". *Computers & Structures*, 54(4), February, pp. 779-785.
- [19] Piperno, S., 1997. "Explicit-Implicit Fluid-Structure Staggered procedures with a structural predictor and fluid subcycling for 2D inviscid aeroelastic simulations". *International Journal for Numerical Methods in Fluids*, 25(10), pp.1207-1226.
- [20] Galpin, P.F., Broberg, R.B. and Hutchinson, B.R., 1995. "Three-dimensional Navier-Stokes prediction of steady-state rotor/stator interaction with pitch change". 3rd Annual Conference of the CFD Society of Canada, pp. 294-302. TB2-2.
- [21] Markou, G.A., Mouroutis, Z.S., Charmpis, D.C., and Papadrakakis, M., 2007. "The ortho-semi-torsional (OST) spring analogy method for 3D mesh moving boundary problems". *Computer Methods in Applied Mechanics and Engineering*, 196(4-6), pp. 747-765.
- [22] Ducoin, A., Deniset, F., Astolfi, J.-A., and Sigrist, J.-F., 2009. "Numerical and experimental investigation of hydrodynamics characteristics of deformable hydrofoils". *Journal of Ship Research*, 53(4), pp. 1-13.
- [23] Farhat, C., Geuzaine, P., and Brown, G., 2003. "Application of a three-field nonlinear fluid-structure formulation to the prediction of the aeroelastic parameters of an F-16 fighter". *Computers & Fluids*, 32(1), January, pp. 3-29.

ANALYSIS OF VORTEX SHEDDING FROM A WIND TURBINE BLADE AT HIGH ANGLE OF ATTACK.

Alberto Pellegrino
School of Engineering
Trinity College,
Dublin
Ireland

Email address: albertopellegrino83@gmail.com

Craig Meskell*
School of Engineering
Trinity College,
Dublin
Ireland

Email address: cmeskell@tcd.ie

ABSTRACT

The unsteady flow around a stationary two-dimensional wind turbine blade (NREL S809) has been numerically simulated using unsteady RANS with the SST turbulence model at $Re = 10^6$ and high angles of attack. Vortex shedding frequency non-dimensionalised by the project area of the blade is in the range $0.11 < St < 0.14$. The fluctuating coefficients at the harmonics of the fundamental vortex shedding frequency for lift, drag and pitching moment are presented. The lift force is dominated by the fundamental vortex shedding frequency, but significant contributions at the second and third harmonics are also present. For the drag and pitching moment the second harmonic is as significant as the fundamental, with the third and fourth harmonics contributing to a lesser extent. From the results, it is inferred that the camber of the airfoil does not substantially affect the force coefficients, suggesting that the results presented are generally applicable to turbine blades of different geometry.

NOMENCLATURE

c Chord
 d Characteristic length
 f_v Vortex shedding frequency
 p Pressure
 C_f Generic force coefficient
 D Drag force per unit length
 L Lift force per unit length
 M Pitching moment per unit length
 U_∞ Freestream velocity
 α Angle of attack
 μ Flow dynamic viscosity
 ρ Flow density

ϕ Angular phase
 ω Angular frequency
 Re Reynolds number
 St Strouhal number
VIV Vortex-induced vibration

INTRODUCTION

In 2010, there were a total of 199.5 GW of wind generating capacity installed globally [1]. Throughout the world, national and regional policies designed to encourage the decarbonisation of the electricity supply, while also reducing dependency on energy imports, are encouraging the continuing rapid expansion of the wind generation sector [2]. The majority of the machines installed are horizontal axis design (HAWT). As with any technology that harvests ambient energy, wind turbines must be permanently exposed to environmental extremes. This coupled with the proportionately very large upfront capital cost [3] means that design for long term survival is a priority.

As a result, the minimum design requirements for wind turbines as defined by the international standard [4] includes specifications for extreme wind loading conditions (see section 6.3 of the standard). For example, the structure must be designed to withstand steady, turbulent and deterministic gusts which occur on average only every 50 years (i.e. a 50 year return period). As part of the transient wind (i.e. gust) environment a sudden change of wind direction of up to 180° must be considered. Consider a turbine blade, which will have either been feathered towards the prevailing mean wind in severe wind conditions, or will be at a low angle of attack relative to the local flow direction in operational conditions. In the extreme change of direction scenario, the blade will be

*Address all correspondence to this author.

suddenly inclined at high angle of attack to the local flow. Hence the section will behave more like a bluff body than a streamlined airfoil. Plus, complications may outcome under certain parked conditions (i.e. yaw mode). The design standard only requires calculation of ultimate loads, rather than fatigue loads in scenarios with extreme change of direction (see section 7 [4]). However, in these cases the blades will act as bluff bodies, and so periodic vortex shedding might be expected, which could cause damage or even failure due to increased fatigue.

The problem of vortex shedding from bluff bodies is well known, and still is a challenge for researchers. Furthermore, vortex shedding induced vibration, known as VIV, can be a problem for a wide range of structures exposed to a cross flow. The resulting vibration amplitudes can lead to catastrophic failure and so this field is still an active area of research. A clear presentation of the problem of VIV for a generic bluff body can be found in Paidoussis *et al.* [5]. For high Re the effect of viscosity is dominant only at a very small scale near the boundary, and the high level of vorticity is not dissipated in the vicinity of the body; hence the flow profile downstream shows two shear layers. These two shear layers of opposite vorticity are produced by the two edge of the body, interacting in a coupled instability. The resulting effect is the creation of alternating vortices (vortex shedding), defining a self sustained oscillation with a very well defined dominant vortex shedding frequency f_v . Vortex induced vibration is defined as a global instability since the whole wake is affected.

Gerrard [6] proposed an explanation of vortex formation mechanism related to a circular cylinder, nowadays still accepted. In his model, the forming vortex will continue to grow as long as it is fed by circulation from the separated shear layer until it is strong enough to draw the shear layer from the opposite side across the wake. The approaching, oppositely signed, vorticity from the other shear layer, with sufficient concentration, will cut off further supply of circulation to the vortex. At that point it sheds and convects downstream, completing half a cycle. As fluctuations of vorticity develop in the unstable wake, fluctuating forces and moments result on the body, leading to potential and unwanted vortex-induced vibrations (VIV). Since a dominant shedding frequency exists in the wake, it can be expected to be observed also in load fluctuations: the dominant frequency of the fluctuating lift coefficient is the same as that in the wake, while the frequency of the drag coefficient is twice [7]. Paidoussis *et al.* [5] present a classification of VIV models with different approaches depending on the grade of accuracy. The simplest one is the *forced system model* where forces are

independent of the body motion, and therefore only dependent on time (case of fixed body). The next step is the *fluidelastic system model* where the forces depend on both time and body's motion. The last and more accurate is the *coupled system model* where the forces depend on another variable related to the wake dynamics, the evolution of which depends on the body's motion. The first two models are limited since there is no relation to the physics of the wake, whereas the third one considers the fluid forces as the result of the wake dynamics itself influenced by the body motion, therefore considering VIV as resulting from the coupling of two systems (the bluff body and the unstable wake).

The most interesting phenomena in VIV are hysteresis and lock-in phenomena [8]. Lock-in phenomenon occurs when the vortex shedding frequency (deviated from its nominal value, i.e. referred to the fixed body case) approaches (or coincides with) the moving body frequency; synchronisation takes place and the structure undergoes severe VIV. The amplification of motion at lock-in condition observed in experiments can be understood as the consequence of an amplification of energy input caused by coupled-mode flutter.

The major amount of studies have been carried out on the circular cylinder body for its simple geometric shape. For other shapes, such as rectangular cylinders, long-span bridges section or blade section, there is limited knowledge about vortex shedding, even for many problems of practical importance. In fact, vortex shedding may occur in the wake of any bluff body, as it results from the instability of the flow profile created by the presence of the body itself, and therefore VIV can be expected in flexible slender bodies of any cross-section. Based on [9], Paidoussis *et al.* [5] give an overview of the vortex shedding regimes for rectangular cylinders, depending on the chord-to-thickness ratio. LEVS (i.e. leading-edge vortex shedding) is observed for small aspect ratio (below 3), whereas TEVS (i.e. trailing-edge vortex shedding) occurs when the aspect ratio is above 10. Between these two limiting cases, the pattern of vortex shedding is essentially the same, i.e. alternate vortices resulting from the wake instability. Plus, the evolution of St is much more complex. Here, a new kind of vorticity is involved (i.e. not belonging to the Benard-Karman group), the dynamics of which is then referred to as impinging leading-edge vortices (ILEV). It may be described qualitatively as interactions between vortices created by the shear layer at the leading edge and the downstream part of the bluff body.

Very few results can be found in the literature concerned with vortex shedding from wind turbine blades (or airfoil sections generally). Experiments have been con-

ducted for example by Medici & Alfredsson [10]. They found that the Strouhal number ($St \approx 0.12$) from the rotor disc is comparable with that reported for a solid disc. In addition, if the turbine is yawed (i.e. rotated with respect to the axis vertical-to-the-ground), the wake rotates in the opposite direction, with a consequent change in vortex shedding frequency (and therefore in loads on the turbine). Considering that aeroelastic instabilities have been found to be sensitive to rotor azimuthal and nacelle yaw positions [11], rotor disk orientation may be an issue for yawed-controlled turbines at standstill or operating in wind parks as the vortex shedding frequency may be more variable due to the wake's motion, .

The ultimate objective is to build a model of vortex induced vibration for wind turbine blades which can be used as part of a design or certification process. The current work represents a first step towards this goal. In this paper the simulation of vortex shedding from a wind turbine blade section is presented. In the next sections, methodology (i.e. fluid-dynamic and harmonic models) used will be presented, and results will be discussed.

METHODOLOGY

To meet our objectives, a series of two-dimensional transient simulations of the flow around the NREL S809 airfoil at different angles of attack were performed. Figure 1 shows the positive angular direction considered for the airfoil inclination with respect to the freestream direction. All calculations have been made at $Re = 10^6$. The software used is the commercial available URANS solver ANSYS-Fluent[®].

There is almost no detailed experimental data available for vortex shedding from airfoils at high angle of attack. Therefore, in order to have confidence in the modelling approach, the standard case of flow around a circular was calculated at the same Reynolds number and using the same meshing density and turbulence model. Once verified, the model has been used to perform simulations of the flow around the wind turbine blade section at 18 different angles of attack. Using the data obtained the non-dimensional shedding frequency (i.e. the Strouhal number) and non-dimensional loading coefficients have been obtained for each angle of attack.

Fluid-Dynamic Model

The fluid domain, illustrated in Fig. 2 has been created with the ANSYS[®] default meshing tool. The domain extends to $10c$ length from the body in the upstream direction, $40c$ in the downstream direction and $10c$ in both the vertical upward and downward directions. The ref-

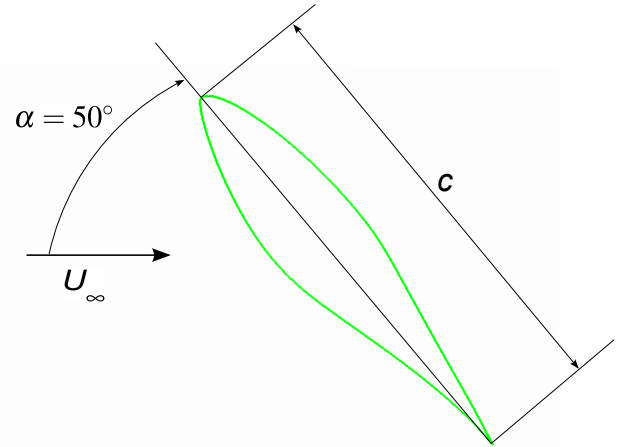


FIGURE 1: AIRFOIL POSITIVE ANGULAR POSITION WITH RESPECT TO THE FLOW DIRECTION

erence chord length is 1m. The fluid domain has been divided into different zones in which the mesh density is different, keeping it finer in the vicinity of the airfoil and fading in the far wake downstream. The inner zone has been modelled as a circle in order to facilitate the rotation of the airfoil with respect to the incoming flow. The mesh is unstructured, with triangular elements throughout except the quadratic elements in the boundary layer. The near wall mesh has 512 cells in the chord-wise direction and the overall mesh is composed in total of approximately 100,000 nodes.

Turbulence closure is modelled by the Shear Stress Transport (SST) eddy viscosity model. This transition turbulence model requires a very fine mesh in the vicinity of the airfoil: for that purpose, the height of the first cell has been tuned in order to obtain a y^+ value below 2 everywhere on the airfoil surface.

The airfoil throughout was specified by no-slip conditions. Inlet conditions was specified in the upstream boundary of the domain, with the following inflow conditions: flow speed $U_\infty = 14.607$ m/s, density $\rho = 1.225$ kg/m³, viscosity $\mu = 1.7894 \times 10^{-5}$ kg/ms. Flow speed has been calculated starting from the Re value of 10^6 . Outlet condition was specified in the downstream boundary of the domain with a reference pressure $p_{\text{gauge}} = 0$.

Computations have been made using the PISO resolving scheme, the Second Order Upwind discretisation scheme for the momentum and a time-step of 0.005s.

Harmonic description of forces

The lift for, L , is defined perpendicular to the flow direction, while the drag is parallel to the flow. When

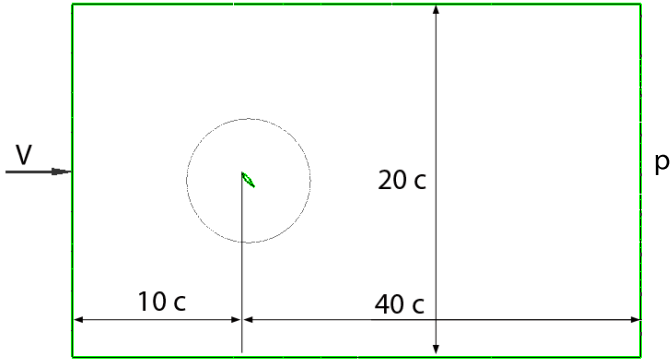


FIGURE 2: FLOW FIELD DOMAIN DIMENSIONS (NOT IN SCALE)

considering the loads on airfoils it is common to use the pitch moment, M , around the quarter chord (i.e. a point on the chord line, 25% of the chord from the leading edge) as this is theoretically the aerodynamic centre. However, as this airfoil is at such a high angle of attack and the behaviour as a bluff body is of most interest here, the pitching moment has been taken through the mid-chord point (i.e. equidistant from leading and trailing edge). The aerodynamic loads can be non-dimensionalised using the chord as the reference length:

$$\begin{aligned} C_l &= \frac{L}{\frac{1}{2}\rho U_\infty^2 c} \\ C_d &= \frac{D}{\frac{1}{2}\rho U_\infty^2 c} \\ C_m &= \frac{M}{\frac{1}{2}\rho U_\infty^2 c^2} \end{aligned} \quad (1)$$

The time series of the aerodynamic forces and moment coefficients have been decomposed into Fourier series, as shown in see Eqn. 2, in order to quantify the vortex induced excitation at higher frequencies.

$$C_f(t) = C_{f0} + \sum_i C_{fi} \sin(i2\pi f_v t + \phi_i) \quad (2)$$

Once the fundamental vortex shedding frequency has been obtained for each angle of attack, the Fourier coefficients at harmonics of this frequency are obtained. For the lift force, the first three harmonics are needed to fit the time data, whereas the first four harmonics are required for the drag force and the pitching moment.

The fundamental vortex shedding frequency f_v can be normalised using the characteristic length (d) and the local freestream speed (U_∞) as is usually done for bluff bodies, resulting in the non-dimensional frequency (Strouhal number) defined as:

$$St = \frac{f_v d}{U_\infty} \quad (3)$$

The choice of characteristic length will be considered below.

RESULTS AND DISCUSSIONS

In the first instance, a CFD simulation has been conducted on a cylinder section with the characteristic length equal to the airfoil chord ($d = 1$ m), to validate the fluid-dynamic model as explained before. Results were in good agreement with experiments for both the vortex shedding frequency and the amplitude of the aerodynamic forces. It must be said that the model needed to be tuned: reliable results required a residuals tolerance of at least $1 \exp^{-5}$; and a momentum relaxation factor value of 0.5 (the solver default value was 0.7) is needed to avoid residual divergence at the beginning of the simulation due to the high turbulence level associated with the relatively high Reynolds number ($Re = 10^6$).

Two ranges of angles of attack have been considered, positive $\alpha = [50^\circ \rightarrow 130^\circ]$ and negative $\alpha = [-50^\circ \rightarrow -130^\circ]$. The CFD simulations have been run for a physical time of 10s to allow the periodic wake associated with vortex shedding to become established.

In Fig. 3 the contour plot of the vorticity magnitude at $\alpha = 50^\circ$ at 10s is illustrated. Although the flow field in the immediate vicinity of the airfoil, which is effectively a bluff body, is specific to the geometry, in the downstream wake, a familiar vortex street can be seen.

The CFD simulations provide the temporal variation of the aerodynamic forces (lift, drag) and pitch moment. Figure 4 shows the time traces of these aerodynamic coefficients for $\alpha = 50^\circ$. For the sake of clarity only 1.2s has been shown. These plots are typical of what has been obtained. It is apparent that all three quantities are periodic, with significant higher harmonics, leading to signals which are not pure sinusoids. Furthermore, unlike a symmetric bluff body such as a circular cylinder, the mean of the lift and moment coefficients is non-zero. This is due to the asymmetric geometry of the blade section.

A spectral analysis of time-dependent data has been conducted to obtain the vortex shedding frequency values at all angles of attack. Figure 5 shows the Strouhal number trend against angle of attack. two normalisations are considered: the first uses the chord of the airfoil as the characteristic length ($d = c$), while the other uses the projection of the chord on the vertical axis ($d = c \sin \alpha$).

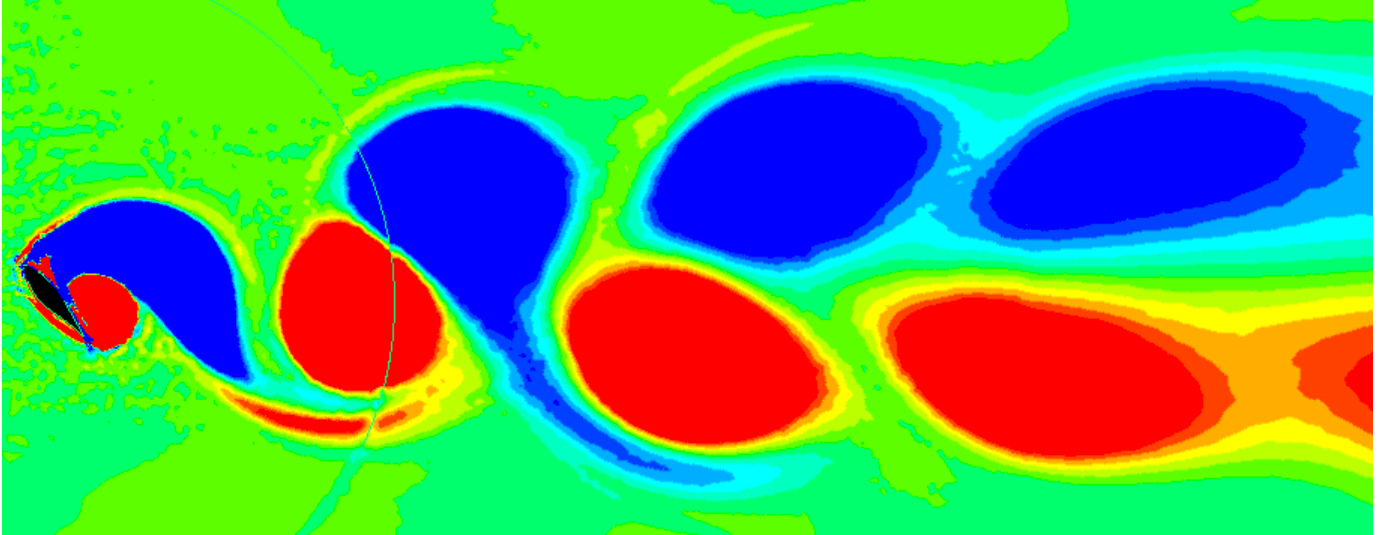


FIGURE 3: INSTANTANEOUS VORTICITY MAGNITUDE AT $\alpha = 50^\circ$, $t=10s$. BLUE INDICATES CLOCKWISE DIRECTION, RED COUNTERCLOCKWISE.

The St trend in the case of the projected chord shows less variation than with the simple geometric reference length.

No symmetry is present, with respect to the angular position of $\alpha = \pm 90^\circ$, due to the interchanging convex-concave as the upper-lower side of the airfoil. In general it can be noticed that the St takes higher values for the negative angle of attack compared with positive angles. This is probably to the presence in negative angular positions of a cusp (i.e. trailing edge) on the leeward upper side of the airfoil which strongly affects the vorticity in the near proximity of the body.

Figure 6 shows the variation of the mean forces and moment component coefficients (C_{l0} , C_{d0} , C_{m0}) with angle of attack. It can be seen that the lift and moment mean coefficients have a similar trend, changing in sign as they approach $\alpha = 90^\circ$. The lift coefficient is relatively high and is comparable to what would be expected at low angle of attack typical of the design operational range. However, unsurprisingly for a high angle of attack, this is accompanied by a very high mean drag coefficient, which is an order of magnitude greater than what would be found at low angles. There's no substantial difference in the mean coefficients between positive and negative angles of attack, indicating that the camber of the airfoil is not important at these high angles. Furthermore, the mean coefficients for angles in the range $\alpha = [50^\circ \rightarrow 90^\circ]$ and $\alpha = [-130^\circ \rightarrow -90^\circ]$ are comparable, indicating that the shape of the leading edge is unimportant as for $-90^\circ > \alpha > 90^\circ$ the sharp trailing edge is actually upwind of the rounded leading edge. These observations suggests that, at least for the mean force coef-

ficients the values obtained here may be generally applicable to a wide range of airfoil sections.

Figure 7 plots the variation with angle of attack of the coefficient of lift force components for the first three harmonics of the vortex shedding frequency (C_{l1} , C_{l2} , C_{l3}). The main characteristic is that the first harmonic dominates, as would be expected, for the whole range of angles considered. The second harmonic is greater than the third. The trend of each harmonic for positive and negative angles is similar. However, the Fig. 7(a) shows that at positive angles of attack the first harmonic of lift experiences a minimum around 70° , while for negative angles, Fig. 7(b), the trend is monotonic. This is due to the camber: geometrically, positive angles of attack present the oncoming flow with a concave shape, while negative angles present a convex profile. A more significant feature, in contrast to the mean coefficient, C_{l0} , for angles where the sharp trailing edge is upwind ($-90^\circ > \alpha > 90^\circ$), the fluctuating lift force at the vortex shedding frequency is substantially higher, than when the rounded leading edge is upwind ($90^\circ > \alpha > -90^\circ$).

Figure 8 shows the variation with angle of attack of the coefficient of drag force components for the first four harmonics of the vortex shedding frequency (C_{d1} , C_{d2} , C_{d3} , C_{d4}). In this case, the even harmonics are as important as the odd harmonics, with the second harmonic dominating in the region around $\alpha = \pm 90^\circ$. This is consistent with vortex shedding for circular cylinder [7]. The trends for all harmonics are similar for both positive and negative angles of attack, again suggesting that camber is unimportant. The coefficient for the second harmonic

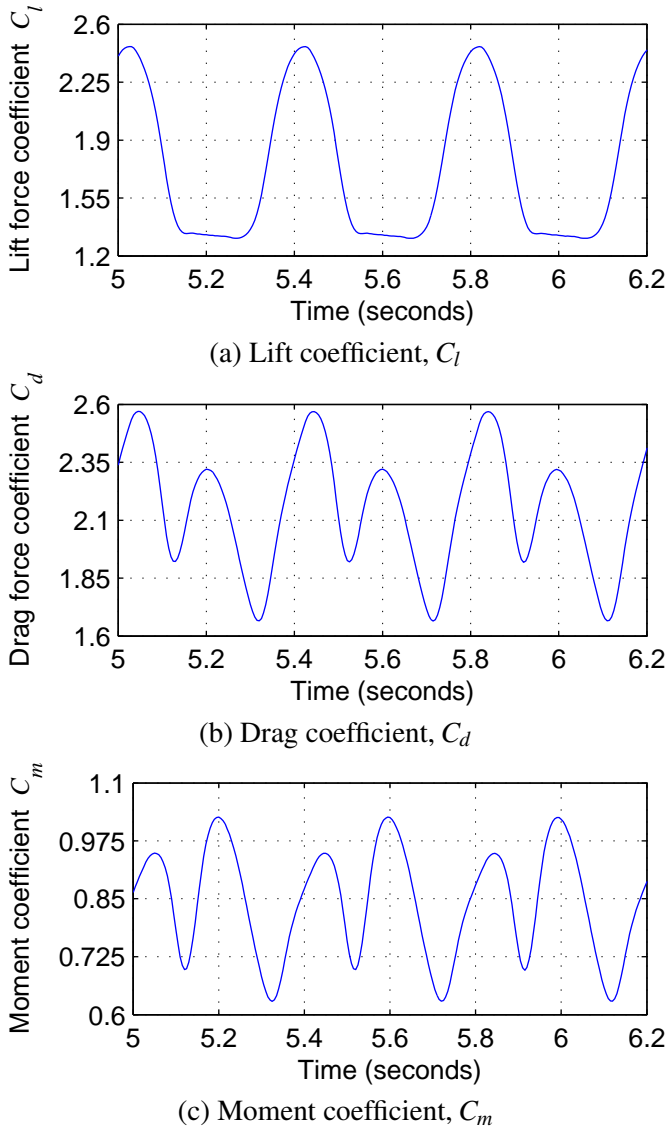


FIGURE 4: TIME TRACES OF THE AERODYNAMIC FORCES (LIFT, DRAG) AND MOMENT COEFFICIENTS AT $\alpha = 50^\circ$.

is lower when the sharp trailing edge is upwind, while the first harmonic is largely insensitive to this. Figure 9 shows the associated coefficients for the pitch moment about the mid-chord for the first four harmonics (C_{m1} , C_{m2} , C_{m3} , C_{m4}), which follow very similar behaviour to the drag coefficients.

CONCLUSIONS

At high angles of attack a wind turbine blade section (NREL S809) will behave primarily as a bluff body causing vortex shedding and hence will experience fluctuating loads. In general, the wake shape is consistent with what is seen in the literature for other bluff bodies, suggesting

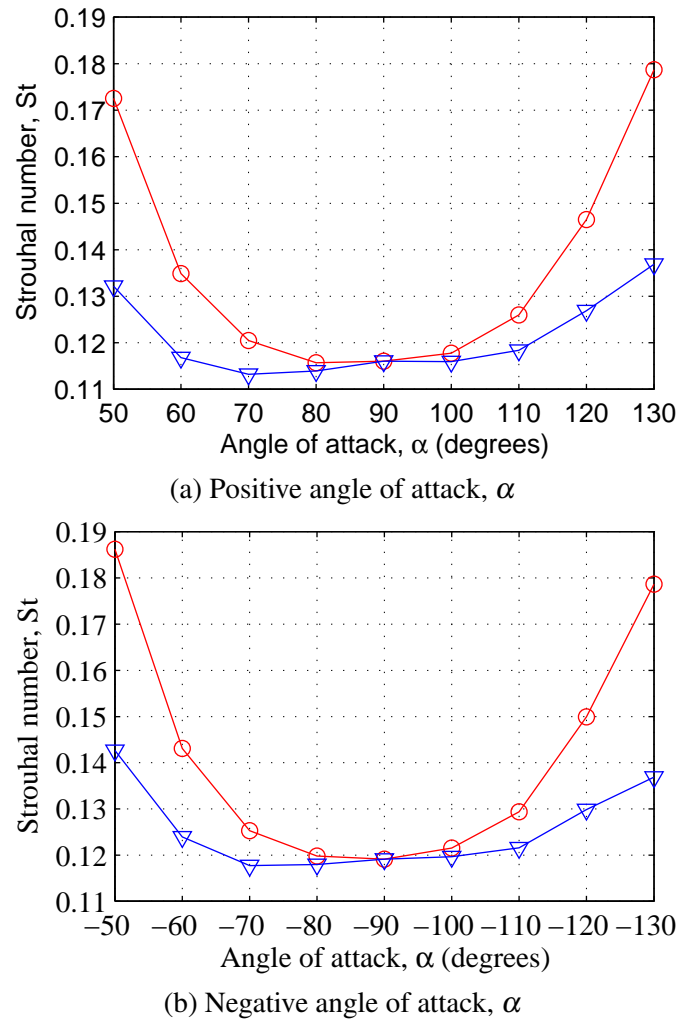


FIGURE 5: STROUHAL NUMBER AGAINST POSITIVE AND NEGATIVE ANGLE OF ATTACK WITH DIFFERENT CHARACTERISTIC LENGTH: $-\circ-$, AIRFOIL CHORD; $-\triangle-$, PROJECTED CHORD.

that the vortex shedding process has been correctly captured. When the projected area of the blade section is used to non-dimensionalise the vortex shedding frequency a Strouhal number varied from 0.12 to 0.14 for negative angles over the range of angles ($\alpha = [-50^\circ \rightarrow -130^\circ]$) and from 0.11 to 0.14 for positive angles ($\alpha = [50^\circ \rightarrow 130^\circ]$). The magnitude and harmonic content of the fluctuating forces depend on the angle of attack. Furthermore, the strength of the loading depends on whether the sharp trailing edge is upstream or downstream; when the trailing edge is upstream, the first harmonic of lift and drag are higher, but the second harmonic of drag and the pitching moment are lower. It has been found that the effect of camber on the fluctuating force coefficients is small, and so these results may be generally applicable to other airfoil sections. Further work is required to assess the effect

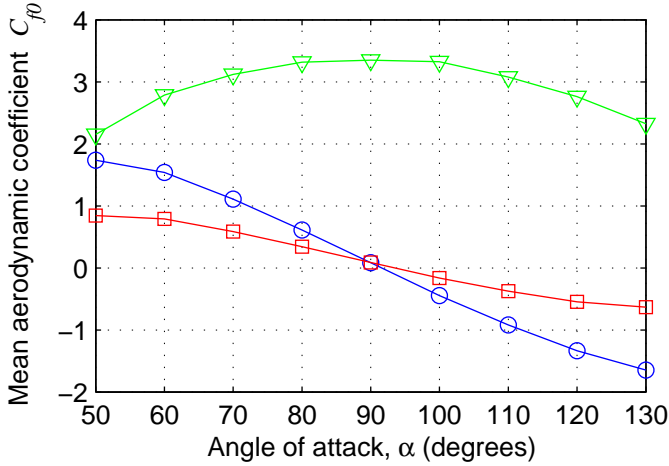
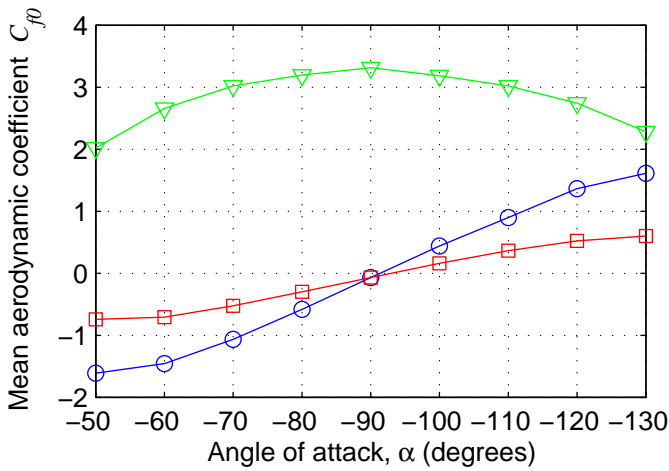

 (a) Positive angle of attack, α

 (b) Negative angle of attack, α

FIGURE 6: MEAN FORCES COMPONENT COEFFICIENTS AGAINST POSITIVE AND NEGATIVE ANGLE OF ATTACK: $-\circ-$, MEAN LIFT COEFFICIENT, C_{l0} ; $-\nabla-$, MEAN DRAG COEFFICIENT, C_{d0} ; $-\square-$, MEAN MOMENT COEFFICIENT, C_{m0} .

of Reynolds number, as only a single value was considered here ($Re = 10^6$), and the effect of three dimensionality caused by blade plan taper or low speed blade rotation. Perhaps the most important unanswered issue is the effect of structural motion on the vortex shedding, particularly the lock-in range. Nonetheless, this current study represents an initial step towards a full model of vortex induced vibration of wind turbine blades.

ACKNOWLEDGMENT

This research is carried out under the EU FP7 ITN project SYSWIND (Grant No. PITN-GA-2009-238325). TheSYSWIND project is funded by the Marie Curie Actions under the Seventh Framework Programme for Re-

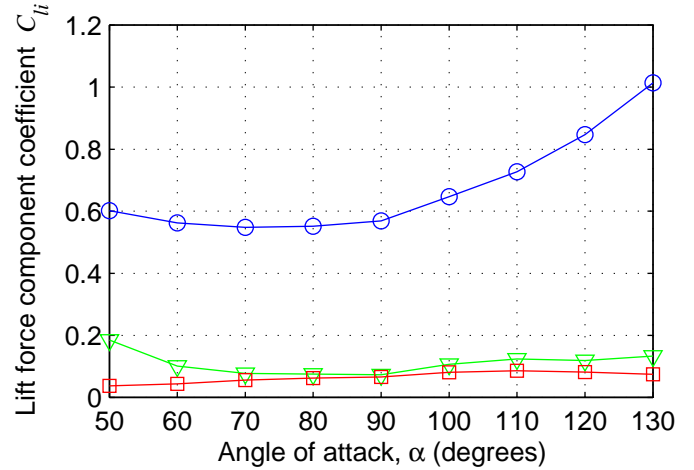
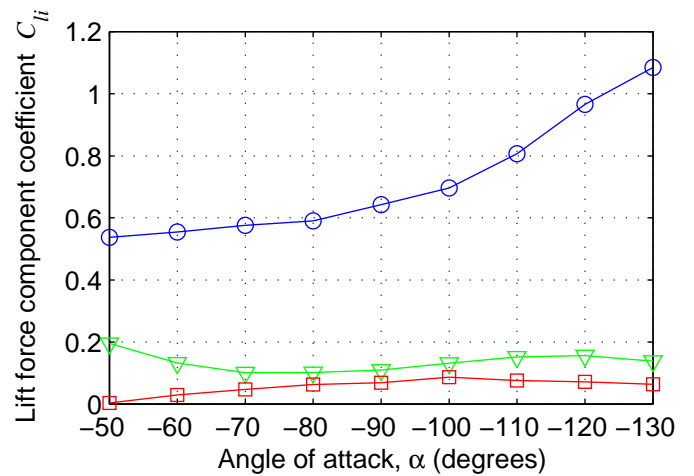
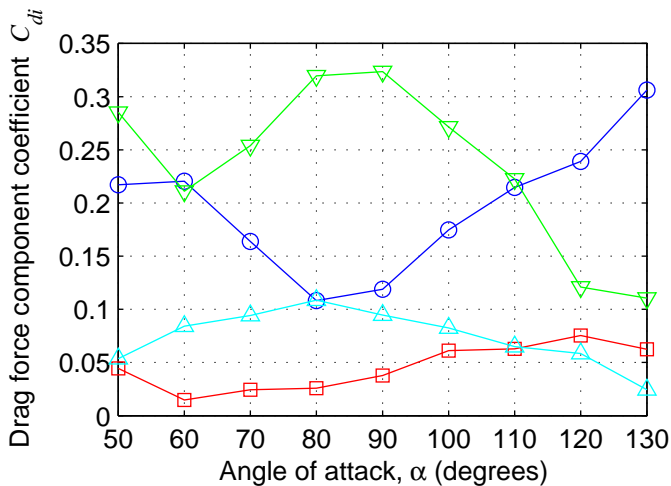

 (a) Positive angle of attack, α

 (b) Negative angle of attack, α

FIGURE 7: LIFT FORCE COMPONENT COEFFICIENTS AGAINST POSITIVE AND NEGATIVE ANGLE OF ATTACK: $-\circ-$, FIRST HARMONIC; $-\nabla-$, SECOND HARMONIC; $-\square-$, THIRD HARMONIC.

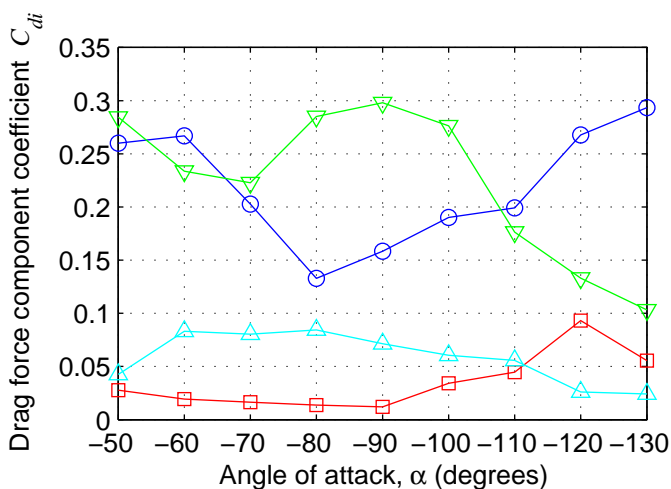
search and Technological Development of the EU. The authors are grateful for the support.

REFERENCES

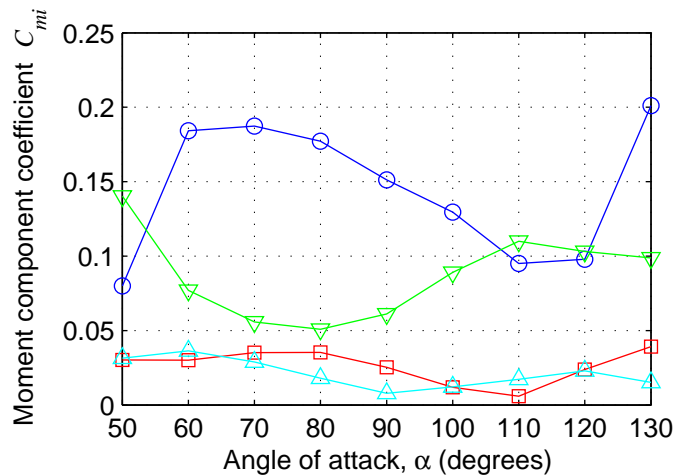
- [1] *BP Statistical Review of World Energy 2011*. BP.
- [2] Priddle, R., ed., 2010. *World Energy Outlook 2010*. International Energy Agency.
- [3] Ruffles, P., ed., 2004. *The Cost of Generating Elec-*



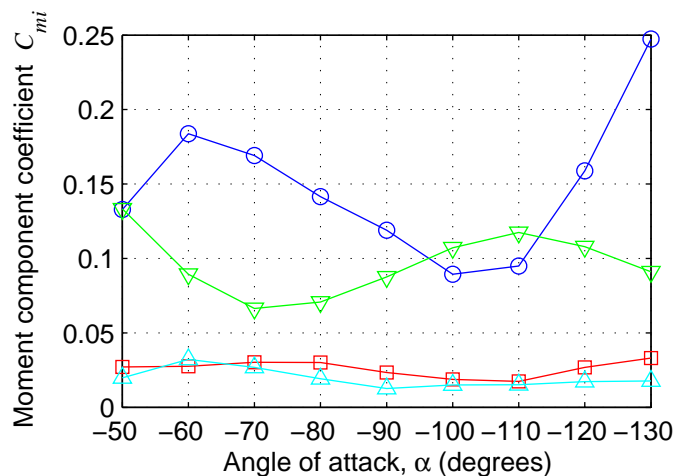
(a) Positive angle of attack, α



(b) Negative angle of attack, α



(a) Positive angle of attack, α



(b) Negative angle of attack, α

FIGURE 8: DRAG FORCE COMPONENT COEFFICIENTS AGAINST POSITIVE AND NEGATIVE ANGLE OF ATTACK: $-\circ-$, FIRST HARMONIC; $-\nabla-$, SECOND HARMONIC; $-\square-$, THIRD HARMONIC; $-\triangle-$, FOURTH HARMONIC.

FIGURE 9: MOMENT COMPONENT COEFFICIENTS AGAINST POSITIVE AND NEGATIVE ANGLE OF ATTACK: $-\circ-$, FIRST HARMONIC; $-\nabla-$, SECOND HARMONIC; $-\square-$, THIRD HARMONIC; $-\triangle-$, FOURTH HARMONIC.

tricity. The Royal Academy of Engineers.

[4] IEC, 61400-1:2005+A1:2010. *Wind turbines. Part 1: Design Requirements*.

[5] Paidoussis, M., Price, S., and De Langre, E., 2010. *Fluid-structure Interactions: Cross-flow-induced Instabilities*. Cambridge Univ Pr.

[6] Gerrard, J., 1966. "The mechanics of the formation region of vortices behind bluff bodies". *J. Fluid Mech*, **25**(2), pp. 401–413.

[7] Farell, C., 1981. "Flow around fixed circular cylinders: Fluctuating loads". *Journal of the Engineering Mechanics Division*, **107**(3), pp. 565–588.

[8] Sarpkaya, T., 2004. "A critical review of the intrinsic nature of vortex-induced vibrations". *Journal of Fluids and Structures*, **19**(4), pp. 389–447.

[9] Naudascher, E., and Wang, Y., 1993. "Flow-induced vibrations of prismatic bodies and grids of prisms". *Journal of Fluids and Structures*, **7**(4), pp. 341–373.

[10] Medici, D., and Alfredsson, P. H., 2006. "Measurements on a wind turbine wake: 3d effects and bluff body vortex shedding". *Wind Energy*, **9**, pp. 219–236.

[11] Bir, G., and Jonkman, J. "Aeroelastic instabilities of large offshore and onshore wind turbines". Vol. 75, IOP Publishing, p. 012069.



MODELING OF THE PHASE LAG CAUSING FLUIDELASTIC INSTABILITY IN TUBE ARRAYS

Ahmed Khalifa¹
McMaster University,
Hamilton, Ontario, Canada

David Weaver
McMaster University,
Hamilton, Ontario, Canada

Samir Ziada
McMaster University,
Hamilton, Ontario, Canada

ABSTRACT

Fluidelastic instability is considered a critical flow induced vibration mechanism in tube and shell heat exchangers. It is believed that a finite time lag between tube vibration and fluid response is essential to predict the phenomenon. However, the physical nature of this time lag is not fully understood. This paper presents a fundamental study of this time delay using a parallel triangular tube array with a pitch ratio of 1.54. Experimental measurements of the time delay between tube vibration and the associated flow disturbances were conducted over the range of reduced velocities ($U_r=6.2-8.5$). A Computational Fluid Dynamics (CFD) model was developed in an attempt to investigate the interaction between tube vibrations and flow perturbations at lower reduced velocities ($U_r=1-7$) and Reynolds numbers ($Re=2000-12000$). The numerical predictions of the phase lag are in reasonable agreement with the experimental measurements for the range of reduced velocities ($U_g/fd=6-7$). It was found that there is a fundamental change in the flow disturbance propagation mechanism at lower reduced velocity ($U_r \leq 2$). It seems that there are two propagation mechanisms; the first is associated with the acoustic wave propagation and the second mechanism is associated with the vorticity shedding and convection. An empirical model of the two mechanisms is developed and its predictions of the phase lag values are in reasonable agreement with the experimental and numerical measurements. The developed phase lag model is then coupled with the semi-analytical model developed by Lever & Weaver to predict the fluidelastic stability threshold which resulted in an improved prediction of the stability boundaries for the parallel triangular array. In addition, the present phase lag model has reduced the infinite number of stability loops predicted by the previous models to one stability loop only.

Keywords: Fluidelastic instability, time lag, tube bundle, heat exchanger, single flexible tube, theoretical model, CFD, Flow-induced vibrations.

NOMENCLATURE

C_p	Pressure coefficient.
D	Tube diameter.
f	Tube natural frequency (Hz).
f_s	Sampling frequency.
L_o	Modeled flow channel length.
m	Tube mass per unit length.
P_o	Tube surface pressure at the flow stagnation point.
P_θ	Tube surface pressure at an angle (θ).
P_r	Pitch ratio.
s^*	Scaled distance along the flow path.
s_s^*	Location of flow separation from the tube.
U_g	Mean gap velocity.
U_c	Flow disturbance convection velocity.
U_r	Reduced velocity = $U_g/(fD)$.
β	Transcendental function.
γ	Weight factor.
δ	Logarithmic decrement.
θ	Surface angle on the tube.
ρ	Fluid density.
φ	Phase lag function.
ω_n	Tube natural frequency (rad/s).

INTRODUCTION

Tube and shell heat exchangers are commonly used in many fossil and nuclear power plants. Therefore, the design process of such components has to account properly for all failure modes to ensure reliable service life. Flow-induced vibrations are a major design concern in nuclear power steam generators. Of the various flow excitation mechanisms, fluidelastic instability is considered the most critical [1]. The phenomenon of fluidelastic instability occurs when the fluid flowing across the tubes exceeds the critical velocity such that energy is transferred to the tubes from the flow and the vibration amplitudes rapidly increase [2;3]. Such large vibration amplitudes can lead to unexpected short-term failure which is extremely expensive and potentially dangerous especially in nuclear power steam generators [4].

¹ Corresponding author (khalifaa@aecl.ca). Present address:
Atomic Energy Canada Limited, Chalk River, Ontario, Canada

Due to the importance of fluidelastic instability in steam generators, significant research effort has been dedicated to understand and properly predict this phenomenon. A number of important reviews have been published over the few decades reporting the development of our understanding of the phenomenon [5;6]. While the several theoretical models developed to predict the fluidelastic instability have advanced our understanding of the phenomenon significantly [5], some issues remain unresolved [7-9]. One of these issues is the time lag between tube vibrations and flow response.

Fluidelastic instability in tube arrays subjected to cross flow is attributed to two fluid-structure interaction mechanisms [10;11]. The first mechanism is related to fluid coupling of neighboring tubes and called the "*stiffness mechanism*", and the second is related to a negative fluid damping mechanism i.e., fluidelastic forces in phase with tube velocity and called the "*damping mechanism*". In order for the damping instability mechanism to take place, there must be a finite time delay between structural motions and the induced fluid forces. The exact nature of this time delay or phase lag is not fully understood. However, it must be incorporated into any theoretical model to predict fluidelastic instability. Several models of the time delay between tube motion and fluid response have been introduced such as the finite fluid inertia model [12;13], the flow retardation model [14], and the vorticity shedding and convection model [15]. It seems that all these models offer different physical explanations for the same phenomenon. However, due to the difficulty of the problem and the lack of experimental observations, the developed models still require refinement. Recently, an attempt to measure this time delay has been published [16], yet more work is needed to understand and model this phenomenon.

This paper presents a fundamental study of the time delay between tube vibration and the associated flow perturbations in a tube array. A parallel triangular array was constructed with a pitch ratio of 1.54, and the flow-excited response of a single flexible tube located in the third row of the rigid array was monitored. Experimental measurements of the time delay were conducted over the range of reduced velocities ($U_g/fD=6-8.5$) [17]. A two dimensional CFD model of a parallel triangular array which has the same geometrical configuration and dimensions as the experimental setup was developed using ANSYS-CFX. The CFD model was validated using experimental results for surface pressure distribution by Mahon and Meskell [16]. The model was used to investigate the interaction between tube vibrations and flow perturbations at lower reduced velocities ($U_r=1-6$) and Reynolds numbers ($Re=2000-12000$). The experimental and numerical results were used to develop an empirical model for the time lag between tube vibrations and flow response. The developed phase lag model was then coupled the model of Lever & Weaver [12;13] to predict the fluidelastic instability threshold for a parallel triangular array.

EXPERIMENTAL SETUP

The parallel triangular array configuration was selected for the present study as this pattern has shown the most consistent behavior for a single flexible tube in a rigid array [18]. An array that consists of seven rows and five columns of tubes was constructed with a pitch ratio of 1.54 as shown in Fig.1. The tubes used in the array were made of aluminum and had a diameter of 57mm.

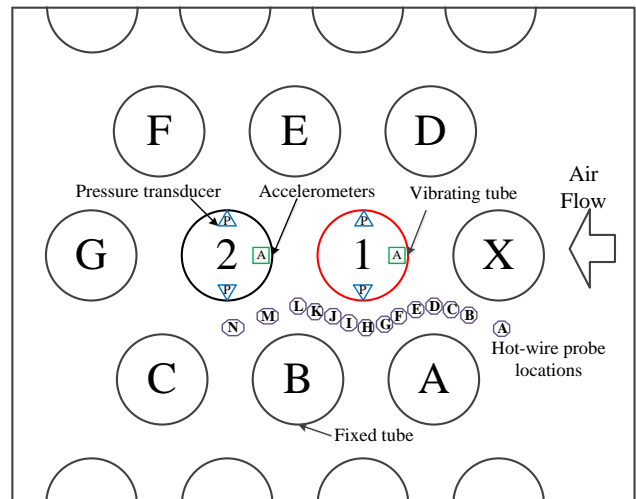


Figure 1. Array geometrical pattern and the locations of accelerometers (A), pressure transducers (P), and hot-wire measurements.

Each tube in the array was suspended on a piano wire arrangement and equipped with a spring mechanism and damping device to fine tune the tube natural frequency and the total damping. The middle third row tube, which is marked 1 in Fig.1, was free to vibrate in all directions while the other tubes in the array were held rigid. Tube 1 was instrumented with two uni-axial accelerometers to obtain the two normal components of tube motion. Two pressure transducers were mounted inside the tube and located along the cross-stream axis to monitor the surface pressures on both sides of the tube.

Hot-wire measurements of the flow disturbances were conducted in the flow channel along the locations (A) through (N) as shown in Fig.1. The flow path and locations of hot-wire measurements were selected based on previous flow visualization studies [19]. The instrumented tube was tuned to a natural frequency of 25 Hz and a total damping ratio of 0.36%. The mass ratio of tube 1 is $m/\rho D^2=70$, resulting in a mass damping parameter of $m\delta/\rho D^2=1.57$.

PHASE LAG EXPERIMENTAL RESULTS

Measurements of the interaction between tube vibrations and flow disturbances were performed, and the results shown in this section provide the validation data for the present study [17]. The phase lag between tube vibrations and the associated flow disturbances was measured along the flow path indicated in Fig.1 for the

range of reduced velocity ($U_r=6.2-8.5$). The phase lag between tube vibration and induced flow disturbances along the flow channel is shown in Fig.2(a) while Fig.2(b) shows the location of each measurement point and explains the location index scheme.

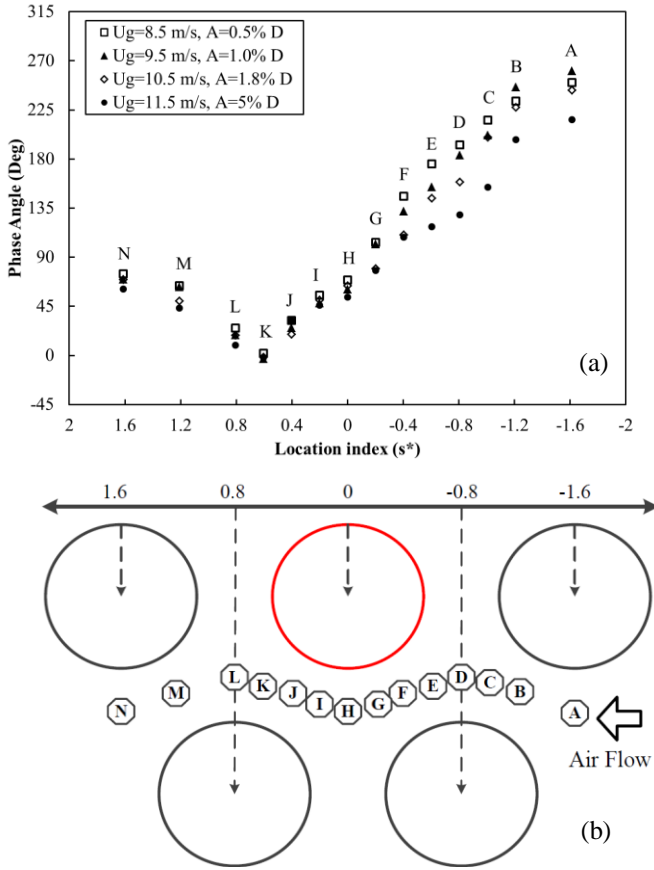


Figure 2. Phase lag measurements along the flow path. (a) Phase lag data, (b) Location index scheme.

The phase measurements along the flow path show that there are two distinct trends for the phase measurements; the first is taking place from location index of 1.6, i.e. two rows downstream, to location index of 0.6, while the second is taking place from location index of 0.6 to location index of -1.6, i.e. two rows upstream. It is important to note here that a positive phase angle means phase lag, in other words, it means that the flow perturbation takes place after the tube vibration by the time corresponding to this phase angle. The trends intersect at the point of location index 0.6 where the phase lag is almost zero. The phase lag trends shown in Fig.2(a) seem to be linear both upstream and downstream from the flow separation point. Linear phase lag trend means that the event is traveling at a constant speed in one direction.

The linear trends obtained in Fig.2(a) were analyzed to obtain the propagation velocity of flow disturbances for the regions discussed previously. The values for the flow disturbance propagation velocities upstream and downstream, U_c , normalized by the mean gap velocity are

shown in Table 1. The propagation velocity of the perturbations downstream is found to remain approximately constant at a value of 0.76 of the mean gap velocity. This ratio approximates the vorticity convection velocity obtained experimentally from a single cylinder subjected to cross flow as reported in the literature [20;21]. Thus the flow disturbances traveling downstream from the vibrating tube seem to be caused by the convection of vorticity which supports the time delay mechanism proposed by Granger and Paidoussis [15].

Table 1. Flow disturbance propagation velocities.

U_g (m/s)	Downstream	Upstream
	U_c/U_g	U_c/U_g
8.5	0.78	0.44
9.5	0.76	0.42
10.5	0.74	0.40
11.5	0.75	0.43

The normalized upstream propagation velocity was also found to be constant but less than the downstream propagation velocity by a factor of nearly 2. This behavior could be related to the fact that the perturbation is travelling upstream against the mean flow, which results in a larger time delay. The range of mean gap velocity investigated in this study was limited by the minimum tube vibration amplitude required to produce coherence level adequate for reliable phase measurements and by the fluidelastic instability onset beyond which measurements were not possible. Therefore, CFD modeling of the problem was used to extend the range of investigated reduced velocities

COMPUTATIONAL FLUID DYNAMICS MODEL

The CFD model was intended to examine, at least qualitatively, the ability to predict numerically the physical phase lag trends obtained experimentally. Precise quantitative agreement with the experimental results was not considered essential. Two dimensional tube array model was constructed using ANSYS-CFX. The flow response to harmonic tube vibrations in the cross-stream direction was monitored along the flow path shown in Fig.1. The surface pressures on the vibrating tube were monitored. The time-signals of the pressure on the tube and flow velocity perturbation at each monitored point were transferred to the frequency domain to estimate the amplitude and phase with respect to tube vibrations.

A parallel triangular array identical to the experimental array geometry was constructed. ANSYS CFX-Mesh module was used to produce the model meshing where tetrahedral and prism elements were used to capture the circular curvature of the tubes. The tube diameter (57 mm) was considered to be the length scale, and the standard element size was selected to be below 5% D. The elements were refined around the tubes and near the walls to about 1% of the tube diameter. An expansion factor of 1.2 between the fine and the standard elements was adopted.

Inflated boundary layer elements were used at the model walls and on the tubes surfaces to model the boundary layer development. The number and size of the inflated boundary layer elements were determined based on the non-dimensional distance from the wall (y^+), the Reynolds number (Re), and the length scale (D). Symmetry boundary conditions were assigned to the domain plans to handle the problem as two dimensional. The inlet region was set to have a uniform flow, while an opening boundary condition was assigned to the outlet region. The opening boundary condition allows the fluid to flow out or into the domain, and as such the flow is not forced to go in the outlet direction. The domain sides and the tube surfaces were treated as stationary no slip walls except for the third row central tube which was treated as a harmonically moving wall. The Reynolds numbers in the present simulations were in the range of ($Re = 2000-39000$). Figure 3 shows details of the model dimensions and boundary conditions.

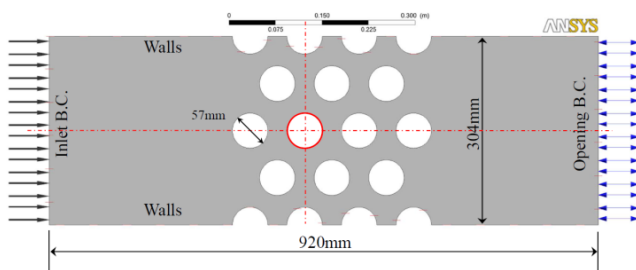


Figure 3. Boundary conditions and geometrical configurations of the CFD model.

A domain size independence study showed that at least eight length scales are required upstream of the tube array for the results to asymptote within 2%. A grid independence study was conducted to determine the minimum number of meshing elements without affecting the results. The time step was selected to maintain an RMS Courant number in the simulations below $Cr = 5$. The number of time steps was adjusted to provide about 100 cycles of tube vibrations which is enough for the frequency analysis. An investigation of the turbulence modeling effect showed that the Shear Stress Transport model (SST) performed best for the present geometry.

CFD RESULTS

The CFD model was validated first by comparing the predicted pressure distribution around the vibrating tubes to the experimental data reported by Mahon and Meskell [22]. The present CFD model provided reasonable agreement with the experimental results within 7%. Further simulations were carried out to predict the phase lag between tube vibrations and flow disturbances. Two flow conditions were examined which correspond to the lowest two flow velocities obtained experimentally. Simulations were conducted using air flow at reduced velocities ($U_r=6.2$ and 7) and Reynolds numbers ($Re=12000$ and 14000) respectively. The third row tube

was harmonically displaced in the cross-stream direction with amplitude of $1\%D$ at a frequency of $10Hz$. The flow velocities and pressures were monitored along the flow channel at comparable locations to the experimental data. The relative phase between tube velocity and flow velocity perturbations is compared to the experimental data for the same reduced velocities in Fig.4.

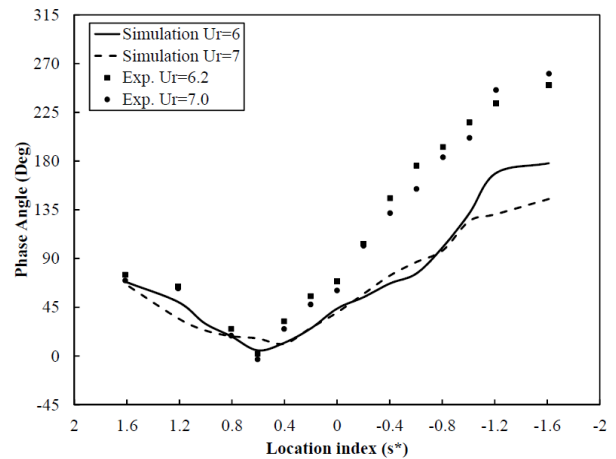


Figure 4. Comparison between the CFD phase prediction and the experimental data, $Re=12000$ and 14000 .

The numerical phase trend agreed qualitatively with the experimental data over the entire range of measurements. Two distinct phase trends were obtained from the numerical simulations and a minimum relative phase was observed at the flow separation point ($s^*=0.6$) which agrees with the experimental results reasonably well. The CFD model has captured the phenomenon physics quite well and further refinement of the CFD modeling might produce better agreement with the experimental data. As the CFD part of the present study was intended for qualitative analysis of the physics only, such refinement was not carried out and the model was employed in investigating the effect of reduced velocity on the phase trends.

Table 2. Reynolds numbers for the CFD simulations.

U_r	U_g (m/s)	Re
1	0.57	2000
2	1.14	4000
3	1.71	6000
4	2.28	8000
5	2.85	10000
6	3.43	12000

The effect of reduced velocity on the phase between tube vibrations and velocity perturbation was investigated over the range ($U_r=1-6$). In order to reduce the simulation time, the tube vibration frequency was reduced to $10Hz$ which resulted in a significant reduction of the flow velocities and Reynolds numbers. The details of this set of simulations are listed in Table 2. Phase trends were obtained from the CFD simulations for reduced velocities $U_r=1$ through $U_r=6$. For brevity purposes only, the cases for $U_r=2, 4,$ and 6 are shown in Fig.5.

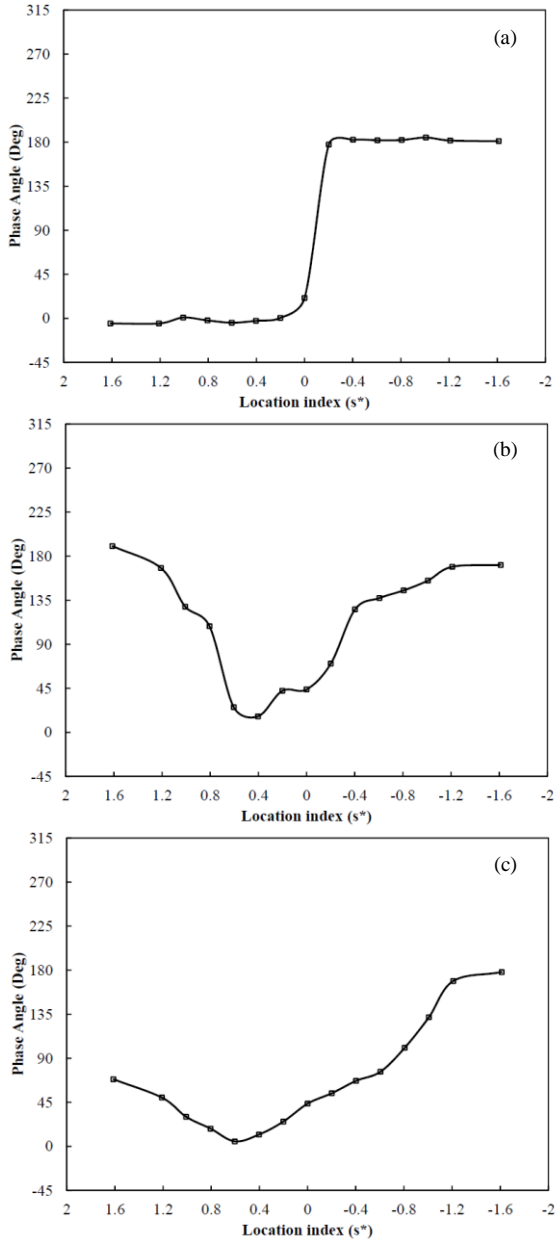


Figure 5. Development of the phase lag trends with the increase in reduced velocity. (a) $U_r=2$, (b) $U_r=4$, (c) $U_r=6$.

It was observed that the phase trend for $U_r=1$ is quite similar to that of $U_r=2$ as shown in Fig.5(a). The flow velocity perturbations at the upstream points, i.e. location index ($s^* < 0$), have a phase lag of about ($\varphi=180^\circ$) with the tube velocity, while the velocity perturbations at the downstream points, i.e. for location index ($s^* > 0$), are in-phase with the tube velocity ($\varphi=0^\circ$). Fundamental changes in the phase trends both upstream and downstream of the tube take place for $U_r > 2$ as shown in Fig.5(b). Physically the zero slope of the curves implies infinite disturbance propagation speed, while the 180° phase change at the disturbances source implies upstream and downstream propagation from this point. In reality, the propagation velocity would be the speed of a pressure wave as predicted by a compressible, inviscid flow model. Fig.5(c) shows that by $U_r=6$, the physics dominating the

propagation of disturbances has changed from acoustic to convection of vorticity as observed in the experiments. Fig.5(b) for $U_r=4$ shows a transitional case.

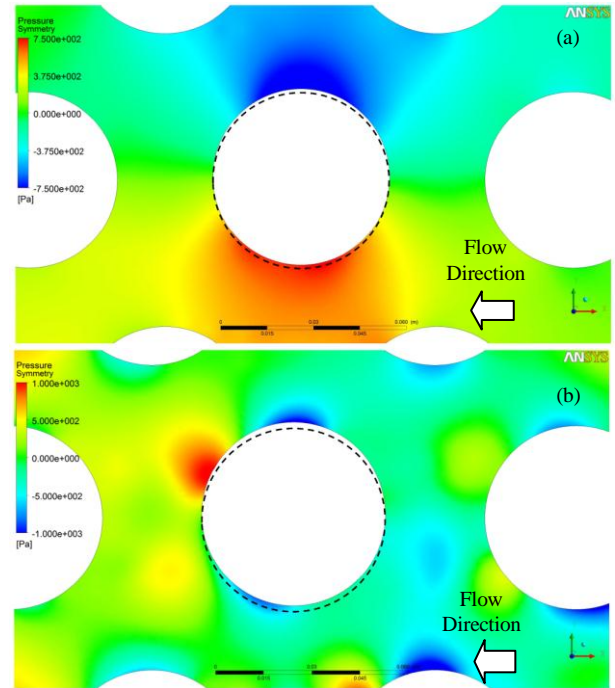


Figure 6. Instantaneous pressure fields around the vibrating tube at maximum displacement of 1%D. (a) $U_r=2$, (b) $U_r=4$.

In order to better understand the fundamental change in the phase behaviour between $U_r \approx 2$ and 4, the pressure fields in both cases were examined. The pressure images showed a fundamental change in the excitation and fluid response mechanisms as shown in Fig.6. At a reduced velocity of $U_r=2$, the flow follows a regular path in the array, no vorticity separation from the tube is detected and the flow field in this case is similar to the potential flow around a cylinder at relatively low Reynolds numbers. High and low pressure regions are formed as the tube vibrates as shown in Fig.6(a). It follows that, the flow perturbations are caused by the pressure pulse associated with the tube vibration and travel at the speed of sound. This propagation time is essentially instantaneous, which explains the zero slopes of the phase angle for upstream and downstream propagating disturbances. It is also observed that a phase shift of 180° takes place between the upstream and downstream directions. This behaviour is associated with the effect of tube vibration on the flow such that, when the tube moves in one direction, this reduces the interstitial gap area and thus the flow decelerates upstream and accelerates downstream of the vibrating tube. This opposite reaction results in a phase shift of 180° between the upstream and downstream.

Examining the flow pattern at $U_r=4$ as shown in Fig.6(b) reveals a fundamental change in the flow as vorticity shedding from the tube occurs. The pressure field images show that high and low pressure regions are associated with the flow separation from the tube. In this

case, the flow perturbation is caused by the flow separation and the associated vorticity shedding. Thus, the phase behaviour is governed by vorticity convection downstream and the associated effect upstream from the tube under consideration.

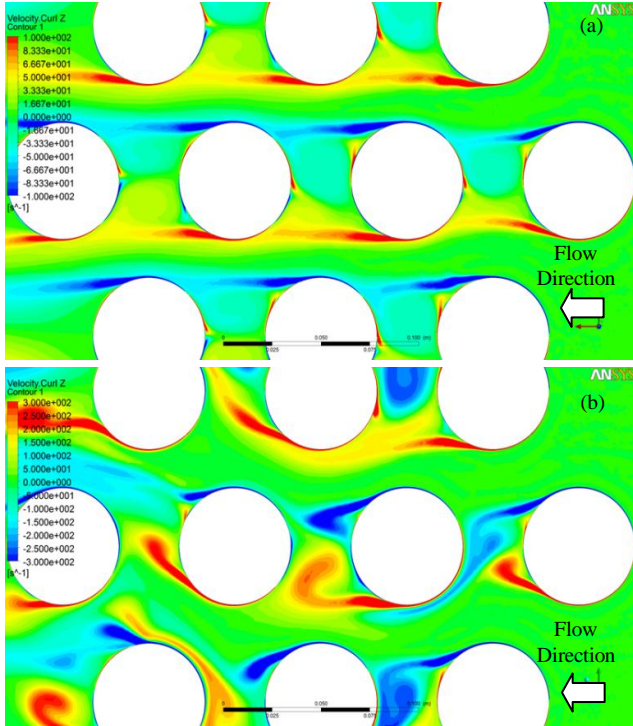


Figure 7. Instantaneous vorticity contours at maximum displacement 1%D. (a) $U_r=2$, (b) $U_r=4$.

In order to further investigate the flow disturbance propagation mechanisms, vorticity contours were obtained from the numerical simulations. Figures 7 (a) and (b) show the vorticity contours for reduced velocities of $U_r=2$ and $U_r=4$ respectively. In the case of $U_r=2$, as shown in Fig.7(a), the mean flow seems to have a clear path through the array which is not significantly affected by the wake regions. The vorticity contours for $U_r=4$ shown in Fig. 7(b) show the separation and formation of coherent vortex structures from the vibrating tube which cause significant disturbances to the flow path.

MODELING OF THE PHASE LAG FUNCTION

The numerical results reported in the present paper along with the experimental measurements [17] were used to develop an empirical expression for the phase lag between tube vibration and flow disturbance at any location along the flow path. The following assumptions were made in developing this empirical model:

- The source of flow disturbances due to tube vibration is located at the flow separation point which is denoted (s_s^*), and at this location the flow disturbances are in phase with tube vibration.
- The delay time between tube vibration and the flow perturbations at any location (s^*) is a function of the

distance between (s^*) and the disturbance source point (s_s^*). This delay time can be scaled with the tube natural frequency (ω_n), the mean gap velocity (U_g), and the modeled flow channel length (L_o) to produce the phase lag (φ) in radians.

- The flow disturbances propagate via two mechanisms. The pressure wave propagation mechanism dominates at lower reduced velocities ($U_r < 2$). Vorticity shedding and convection mechanism is dominant at higher reduced velocities resulting in a linear phase trend for ($U_r > 2$).

At lower reduced velocities ($U_r < 2$), the flow disturbances propagate in the form of a pressure wave at the speed of sound producing the phase trend shown in Fig.5(a). In order to model this sudden change from a phase of 180° upstream to a phase of 0° downstream, a transcendental function is adopted to provide a continuous transition as follows

$$\varphi_1(s^*) = \frac{\pi}{2} [\beta(50s^*) + 1] \quad (1)$$

where $\varphi_1(s^*)$ is the phase angle at any location due to the pressure wave propagation mechanism, and the function (β) can be defined as

$$\beta(s^*) = \frac{2}{\sqrt{\pi}} \int_0^{s^*} e^{-s^{*2}} ds^* \quad (2)$$

The phase lag measurements at higher reduced velocities ($U_r > 2$) show that the flow disturbances propagate at an essentially constant velocity of about $0.42U_g$ as shown in Table 1. Therefore, the phase lag between tube vibration and flow disturbances due to the vorticity shedding and convection mechanism can be expressed as

$$\varphi_2(s^*) = 2\pi \frac{s^* - s_s^*}{0.42U_r} \quad (3)$$

where (U_r) is a dimensionless reduced velocity in the form (U_g/fD). The modeled flow channel length (L_o) in the present case is considered to be the distance to two tube rows upstream where the effect of tube vibrations on the flow is considered to be negligible [23]. The pressure wave propagation mechanism is dominant at lower reduced velocities where no or little coherent vorticity is shed from the tube. The vorticity convection mechanism becomes dominant at higher reduced velocities, and the combination of these two mechanisms results in the total phase lag value. It follows that, the total phase lag at any location (s^*) in the array can be presented as

$$\Phi(s^*) = (1-\gamma)\varphi_1(s^*) + (\gamma)\varphi_2(s^*) \quad (4)$$

where (γ) is a weight factor in the form

$$\gamma = \frac{1}{2} [\beta(x) + 1] \quad (5)$$

$$x = 2U_r - 4$$

The weight function is designed to switch from the pressure wave mechanism to the vorticity convection mechanism continuously at about $U_r \approx 2$ which is selected based on the numerical results. The phase lag predictions using Eq. 5 agree reasonably with both the experimental and numerical results as shown in Fig.8.

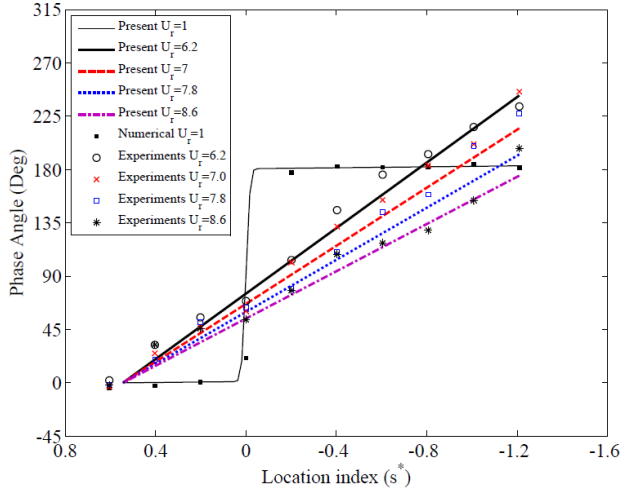


Figure 8. Comparison between the present prediction and the experimental and numerical results for phase lag.

FLUIDELASTIC STABILITY PREDICTION

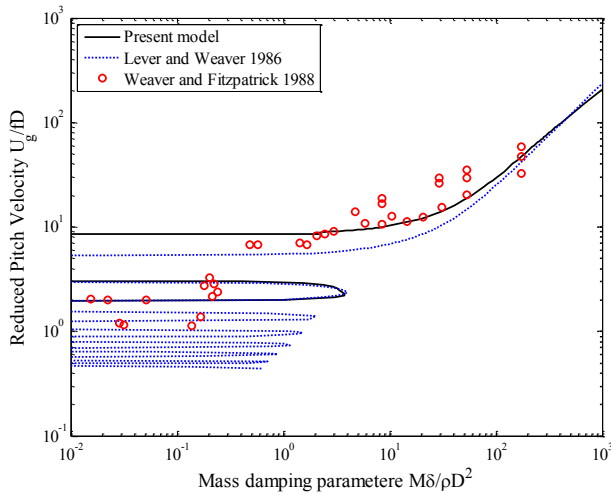


Figure 9. Present fluidelastic stability prediction for a parallel triangular array $P_r=1.375$.

The empirical phase lag expression discussed in the previous section was coupled with the semi-analytical model developed by Lever and Weaver [12;13] to predict the fluidelastic stability threshold for a parallel triangular array. The semi-analytical model is based on modeling the flow channels using the one dimensional unsteady Bernoulli's equation to obtain the pressures on the tube

surface. The tube vibrations are assumed to be in the transverse direction only, and result is a flow channel area perturbation. This disturbance is assumed to propagate at a certain rate which is obtained using the phase lag expression developed above. By solving the flow field, the pressures on the tube surface can be integrated to obtain the fluid forces acting on the tube. These forces are used as an input to the tube equation of motion. Solving the tube equation of motion provides the fluidelastic stability map as a function of the reduced velocity term (U_g/fD) and the mass damping parameter ($m\delta/\rho D^2$). The present prediction for the fluidelastic stability threshold is compared to the stability threshold of the original semi-analytical model and to the experimental data reported in the literature [6] in Fig.9.

The present stability boundaries follow reasonably well the experimental data [6] for mass damping parameter range ($m\delta/\rho D^2 \approx 0.6-200$). It is observed that the present stability boundary asymptotes as the experimental data asymptote for ($m\delta/\rho D^2 \leq 10$) at a reduced velocity of about ($U_g/fD \approx 9.5$). Only one instability loop is predicted by the present model in contrast with most of the theoretical models in the literature which predict an infinite number of instability loops. The instability loop occurs at reduced velocity range ($U_g/fD \approx 1.5-2$) and for mass damping parameters ($m\delta/\rho D^2 \leq 3$). It must be noted here that the existence of this stability loop is theoretical only, as once the tube becomes fluidelastically unstable, increasing the reduced velocity will not stabilize the tube. It follows that the practical stability boundaries should follow the lower bound of both loops. The prediction of a single stability loop as shown in Fig.9 may explain the sudden drop in the experimental data for a parallel triangular array at a mass damping parameter ($m\delta/\rho D^2 \approx 0.3$).

CONCLUSIONS

A fundamental study of fluidelastic instability (FEI) in a parallel triangular tube array with a pitch ratio of 1.54 has been carried out. Wind tunnel experiments were conducted to measure the propagation of flow disturbances associated with tube vibration. Additionally, a simple CFD study was conducted to determine whether such a numerical analysis could capture the physics of the perturbation propagation mechanism observed in the experiments. Good qualitative agreement between the CFD analysis and the experiments was found and the CFD model was then used to study the propagation of flow disturbances over a range of reduced velocities not achievable in the experiments. The results were used for physical insights as well as to develop an empirical model for the phase lag between tube motion and the propagating flow perturbations. This in turn was used in the semi-analytical model [12;13] for FEI to predict the stability threshold for parallel triangular tube arrays. The principal conclusions drawn from this study are:

1. The experiments indicate that the propagation of flow disturbances associated with tube vibration is related to the generation and convection of vorticity from the tube. This supports the phase lag mechanism for FEI proposed by Granger and Paidoussis [15].

2. The simple CFD study was able to replicate the phase lag behavior observed in the experiments, at least qualitatively, and was therefore considered a useful tool for gaining further insights into the disturbance propagation mechanisms.

3. The experimental and numerical studies revealed that there are two distinct disturbance propagation mechanisms. At low reduced velocities, there is little or no coherent vorticity shed into the tube wake and disturbances are propagated at the speed of sound. At higher reduced velocities, vorticity shedding and convection become the dominant mechanism for disturbance propagation. These observations help to explain why FEI is not observed in tube bundles at low reduced velocities.

4. An empirical phase lag function based on the present study, when used with the Lever and Weaver model for FEI, provides improved predictions of FEI for parallel triangular tube arrays and eliminates the infinite stability loops predicted by previous FEI models.

ACKNOWLEDGMENTS

The authors gratefully acknowledge the financial support of Natural Sciences and Engineering Research Council of Canada (NSERC).

REFERENCES

- [1] D. S. Weaver, S. Ziada, M. K. Au-Yang, S. S. Chen, M. P. Paidoussis, and M. J. Pettigrew, **2000**, "Flow-Induced Vibrations in Power and Process Plant Components- Progress and Prospect", *J. Pressure Vessel Technol.*, Vol. **122**, pp. 339-348.
- [2] M. J. Pettigrew and C. E. Taylor, **2003**, "Vibration analysis of shell-and-tube heat exchangers: an overview--Part 1: flow, damping, fluidelastic instability", *Journal of fluids and structures*, Vol. **18**, no. 5, pp. 469-483.
- [3] M. J. Pettigrew and C. E. Taylor, **2003**, "Vibration analysis of shell-and-tube heat exchangers: an overview--Part 2: vibration response, fretting-wear, guidelines", *Journal of fluids and structures*, Vol. **18**, no. 5, pp. 485-500.
- [4] M. P. Paidoussis, **2008**, "Real-life experiences with flow-induced vibration", *Journal of fluids and structures*, Vol. **22**, no. 6-7, pp. 741-755.
- [5] S. J. Price, **1995**, "A Review of Theoretical-Models for Fluidelastic Instability of Cylinder Arrays in Cross-Flow", *Journal of fluids and structures*, Vol. **9**, no. 5, pp. 463-518.
- [6] D. S. Weaver and J. A. Fitzpatrick, **1988**, "A review of cross-flow induced vibrations in heat exchanger tube arrays", *Journal of fluids and structures*, Vol. **2**, no. 1, pp. 73-93.
- [7] M. P. Paidoussis, **2005**, "Some unresolved issues in fluid-structure interactions", *Journal of fluids and structures*, Vol. **20**, no. 6, pp. 871-890.
- [8] M. J. Pettigrew, C. E. Taylor, N. J. Fisher, M. Yetisir, and B. A. W. Smith, **1998**, "Flow-Induced Vibration: Recent Findings and Open Questions", *Journal of Nuclear Engineering and Design*, Vol. **185**, pp. 249-276.
- [9] D. S. Weaver, **2008**, "Some Thoughts On The Elusive Mechanism Of Fluidelastic Instability In Heat Exchanger Tube Array", in Proceedings of the 9th International Conference On Flow-Induced Vibration, 1 ed Prague, Czech Republic: pp. 290-297.
- [10] S. S. Chen, **1983**, "Instability Mechanisms And Stability Criteria of a Group of Circular Cylinders Subjected to Cross Flow. I. Theory", *Journal of Vibration, Acoustics, Stress and Reliability in Design.*, Vol. **105**, pp. 51-58.
- [11] S. S. Chen, **1983**, "Instability Mechanisms And Stability Criteria of a Group of Circular Cylinders Subjected to Cross Flow. II. Numerical Results And Discussion", *Journal of Vibration, Acoustics, Stress and Reliability in Design.*, Vol. **105**, pp. 253-260.
- [12] J. H. Lever and D. S. Weaver, **1986**, "On the Stability of Heat-Exchanger Tube Bundles .2. Numerical Results and Comparison with Experiments", *Journal of Sound and Vibration*, Vol. **107**, no. 3, pp. 393-410.
- [13] J. H. Lever and D. S. Weaver, **1986**, "On the Stability of Heat-Exchanger Tube Bundles .1. Modified Theoretical-Model", *Journal of Sound and Vibration*, Vol. **107**, no. 3, pp. 375-392.
- [14] S. J. Price and M. P. Paidoussis, **1984**, "An improved mathematical model for the stability of cylinder rows subject to cross-flow", *Journal of Sound and Vibration*, Vol. **97**, no. 4, pp. 615-640.
- [15] S. Granger and M. P. Paidoussis, **1996**, "An Improvement to The Quasi-Steady Model With Application to Cross -Flow Induced Vibration of Tube Array", *Journal of Fluid Mechanics*, Vol. **320**, pp. 163-184.
- [16] J. Mahon and C. Meskell, **2010**, "Measurement of the Time Delay Associated with Fluid Damping Controlled Instability in a Normal Triangular Tube Array", in Proceedings of the 7th international symposium on fluid-structure interaction Montreal, Quebec, Canada: ASME.
- [17] A. Khalifa, D. S. Weaver, and S. Ziada, **2011**, "An Experimental Study of the Phase Lag Causing Fluidelastic Instability in Tube Bundles", in Proceedings of the ASME 2011 Pressure Vessel and Piping Conference PVP-2011 Baltimore, Maryland, USA: ASME.
- [18] A. Khalifa, D. S. Weaver, and S. Ziada, **2010**, "Fluidelastic Instability of a Single Flexible Tube in a Rigid Array", in Proceedings of the 7th international symposium on fluid-structure interaction Montreal, Canada: ASME.
- [19] A. Abd Rabbo and D. S. Weaver, **1986**, "A Flow Visualization Study of Flow Development in A Staggered Tube Array", *Journal of Sound and Vibration*, Vol. **106**, no. 2, pp. 241-256.
- [20] C. Lin and S. C. Hsieh, **2003**, "Convection Velocity of Vortex Structures in the Near Wake of a Circular Cylinder", *Journal of Engineering Mechanics*, Vol. **129**, no. 10, pp. 1108-1118.
- [21] Y. Zhou and R. A. Antonia, **1992**, "Convection Velocity Measurements in a Cylinder Wake", *Experiments in Fluids*, Vol. **13**, no. 1, pp. 63-70.
- [22] J. Mahon and C. Meskell, **2010**, "A Validation Database for Flow in a Parallel Triangular Heat Exchanger Tube Array", in Proceedings of the 7th international symposium on fluid-structure interaction Montreal, Quebec, Canada: ASME.
- [23] H. Tanaka and S. Takahara, **1980**, "Unsteady Fluid Dynamic Forces on Tube Bundle and Its Dynamic Effect on Vibration", *ASME Pressure Vessel and Piping Division*, Vol. **41**, pp. 77-92.

MEASUREMENT OF SURFACE PRESSURE ON NEIGHBOURING TUBES IN A DEFORMED NORMAL TRIANGULAR TUBE ARRAY.

Daniel Keogh *

School of Engineering
Trinity College,
Dublin
Ireland

Email: keoghd5@tcd.ie

Craig Meskell

School of Engineering
Trinity College,
Dublin
Ireland

Email: cmeskell@tcd.ie

ABSTRACT

A parametric study of the surface pressure on an instrumented cylinder positioned in 6 locations surrounding a displaced central cylinder has been performed. The tubes are arranged in a normal triangular tube array pattern with pitch-to-diameter ratio 1.32 which is subject to air cross-flow. Static tube displacements up to 10% of tube diameter were tested with cross-flow velocities in the range 3-9m/s. This corresponds to a Reynolds number range of 3.25×10^4 - 10^5 . Coefficients of lift and drag were calculated by integrating the surface pressure distributions with respect to angular position. The gradients of these forces with respect to the displacement of the neighbouring tube have been estimated, as these determine the onset of stiffness controlled fluidelastic instability in a flexible tube array. It has been found that these parameters are largely independent of Reynolds number.

NOMENCLATURE

\ddot{x}	In-flow acceleration (m/s^2)
\ddot{y}	Cross-flow acceleration (m/s^2)
\dot{x}	In-flow velocity (m/s)
\dot{y}	Cross-flow velocity (m/s)
C_f	Fluid damping matrix
C_s	Structural damping matrix
K_f	Fluid stiffness matrix
K_s	Structural stiffness matrix
M_f	Fluid mass matrix
M_s	Structural mass matrix
ρ	Density of fluid (kg/m^3)
C_D	Coefficient of drag
C_L	Coefficient of lift
d	Diameter of cylinder (m)

F_D	Lift force (N)
F_L	Drag force (N)
l	Length of cylinder (m)
P	Array pitch (m)
P_θ	Pressure at angle θ (Pa)
U_g	Gap velocity (m/s)
x	In-flow displacement (m)
y	Cross-flow displacement (m)

INTRODUCTION

Arrays of cylinders subject to fluid cross flow are very common in a number of engineering applications such as power lines, pipes connected to off-shore oil rigs and shell-and-tube heat exchangers. In heat exchangers the flow is highly turbulent and perpendicular to the axis of the tubes. This promotes heat transfer, however, the flow over these tubes may cause vibration which can, in extreme circumstances, cause these parts to fail.

Flow induced vibration can be categorized into four different mechanisms: turbulent buffeting, vortex shedding, acoustic resonance and fluidelastic instability. The first three mechanisms are reasonably well understood with a wealth of research having been done. Fluidelastic instability is potentially the most destructive oscillatory excitation mechanism in cross-flow heat exchangers. This phenomenon is particularly problematic in nuclear power stations where the heat generated by fission in the core is transferred to the turbines via a number of steam generators. The current solution to avoiding failures due to fluidelastic instability in steam generators is to adopt a conservative approach to operation by limiting flow rates through such heat exchangers. This leads to inefficiencies, with plants operating well below their maximum potential output due to this flow rate limitation [1]. Current

*Address all correspondence to this author.

predictive models of fluidelastic instability and related heat exchanger design guidelines are based on empirical evidence and tend to underestimate the critical velocity at which this phenomenon begins [2].

Recent computational fluid dynamics (CFD) models of fluidelastic instability [3–5] have proven successful in giving the time domain response of cylinders with loose supports vibrating in a tube array. It is believed that non-linear impacting forces are dominant in producing the complex dynamical behaviour rather than the fluid dynamics, which essentially just provides a source of energy to drive the system [6]. Understanding and experimentally validating the fluid dynamics models driving fluidelastic instability is vital to improving these CFD models.

Following on from the work of Mahon & Meskell [7]; this study presents surface pressure data from the flow field surrounding a displaced cylinder in a normal triangular tube array. This data can be used as input to a quasi-steady model similar to Price & Paidoussis [8]. Such a model would be useful in exploring the relationship between fluidelastic instability and Reynolds number.

There is now significant evidence [9–13] that there is a relationship between Reynolds number and fluidelastic instability - a point that current models have not significantly addressed [6]. From a practical point of view an understanding of this relationship would prove very useful to both plant designers and operators.

EXPERIMENTAL FACILITY

The experimental facility consists of a draw-down wind tunnel which has a tube array installed in the test section. The test-section is 750 mm long with a cross-section of 300 mm x 300 mm. The flow velocity in the wind tunnel test-section ranged from 3 to 9 m/s with a free stream turbulence intensity of less than 1%. The tubes in the array (38 mm diameter) are rigidly fixed, except for one tube which will be referred to as the displaced cylinder. The length of the displaced cylinder within the test section was 295 mm with a diameter of 38 mm. A normal triangular tube array with a pitch-to-diameter ratio (P/d) of 1.32 was used.

A custom built instrumented cylinder was used to gather surface pressure data. The instrumented cylinder (figure 2) has 36 pressure taps with a diameter of 1 mm and located at the mid-span around the circumference of the cylinder. The centre of the cylinder where the pressure taps are located was constructed from solid brass. Thirty six equispaced holes at 10° intervals were drilled around the circumference. The holes are 1 mm diameter and drilled in the direction of the origin (centre-axial di-

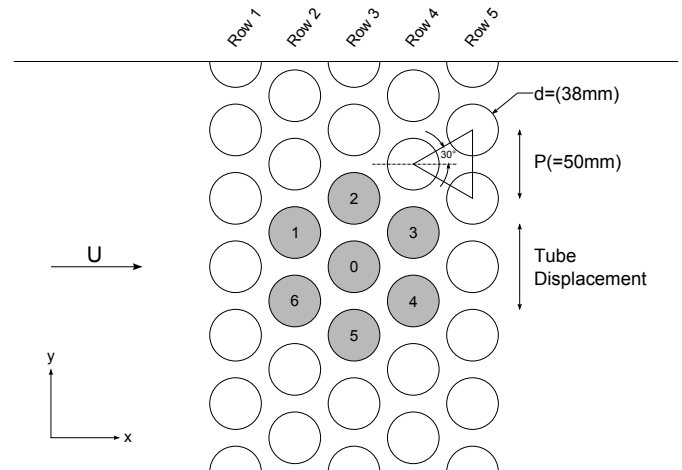


FIGURE 1: SCHEMATIC OF NORMAL TRIANGULAR TUBE ARRAY USED WITH MEASUREMENT LOCATIONS 0 - 6. $P/d = 1.32$.

rection) until the 1.59 mm diameter holes drilled in axial direction were reached. A 1.59 mm outer diameter brass tubing was fit into the axially drilled holes and air tightness was secured by brazing the connection. Two hollow brass tubes were fitted either side of the machined block. A solid cap and base were push fit.

The signal from the pressure transducer was acquired at a sample frequency of 1024 Hz and a mean value was obtained. A known pressure was applied to a single pressure transducer - the reference pressure transducer. The other pressure transducers were then calibrated with respect to this reference pressure transducer.

The instrumented cylinder was connected to the pressure transducers with short lengths (≈ 300 mm) of 2 mm internal diameter silicone tubing. Each pressure tap was monitored with a Micro Switch differential pressure transducer (24 PC Series). The other port of the pressure transducer was vented to atmosphere. In effect the gauge pressure was measured. The voltage from the pressure transducers was acquired using a 40 channel National Instruments data acquisition system (NI PXI-1044) with 5 PXI-4472B cards.

The displaced cylinder was mounted on horizontal traverse connected to a stepper motor. This assembly was then mounted on a bidirectional traverse (located outside the wind tunnel) to facilitate gross alignment of the cylinder. LabView was used to automate the experiment by simultaneously gathering data from the transducers, varying the flow velocity and displacing the cylinder in the cross-flow direction using a stepper motor.

Further details of the wind tunnel and other experimental equipment used in this study can be found in [14] and [15].



FIGURE 2: INSTRUMENTED CYLINDER FEATURING 36 CIRCUMFERENTIAL PRESSURE TAPS.

RESULTS

The flow conditions examined in this study can be seen in table 1. All Reynolds numbers are based on the gap flow velocity, $U_g = U[P/(P-d)]$, and the tube diameter as the characteristic dimension. Two sets of tests were performed. In the first test series, with reference to figure 1, the instrumented cylinder was placed in positions 1-6 while the cylinder in position 0 was displaced between $\pm 10\%$ of tube diameter in the cross-flow direction. The flow velocity was varied between 3-9 m/s in increments of 1.5 m/s. Measurements were acquired at a sample rate of 1024 Hz for 60 seconds with 100 seconds between tests to allow the flow to stabilise. This will be referred to as Test 1.

In the second test series, with reference to figure 1, the instrumented cylinder was placed in position 0 while another cylinder was placed in positions 1-6 and displaced between $\pm 10\%$ of tube diameter in the cross-flow direction. The flow velocity was varied between 3-9 m/s in increments between 0.5-1.0 m/s. Measurements were acquired at a sample rate of 1024 Hz for 30 seconds with 30 seconds between tests to allow the flow to stabilise. This will be referred to as Test 2.

The difference in measurement time and time between tests for Test 1 and Test 2 was to expedite the data gathering process.

Pressure Distributions

The pressure distributions were non-dimensionalised and the results are presented in terms of coefficient of pressure using equation (1) below:

$$C_p = 1 - \frac{P_{\theta_{max}} - P_{\theta}}{\frac{1}{2}\rho U_g^2} \quad (1)$$

The pressure coefficient was expressed in this way since taking the free stream static pressure as the reference pressure was not appropriate because the mean static pressure varies throughout the array. Figure 3 shows the sign convention adopted for the angular position of the pressure tappings on the instrumented cylinder.

TABLE 1: EXPERIMENT PARAMETERS. DISPLACEMENT $\pm 10\%$ IN INCREMENTS OF 2%.

U (m/s)	U_g (m/s)	Re ($\times 10^4$)	Test 1	Test 2
3.0	12.5	3.25	✓	✓
3.5	14.6	3.79	-	-
4.0	16.7	4.33	-	✓
4.5	18.8	4.88	✓	✓
5.0	20.8	5.42	-	✓
5.5	22.9	5.96	-	-
6.0	25.0	6.50	✓	✓
6.5	27.1	7.04	-	-
7.0	29.2	7.58	-	✓
7.5	31.3	8.13	✓	✓
8.0	33.3	8.67	-	✓
8.5	35.5	9.21	-	-
9.0	37.5	9.75	✓	✓

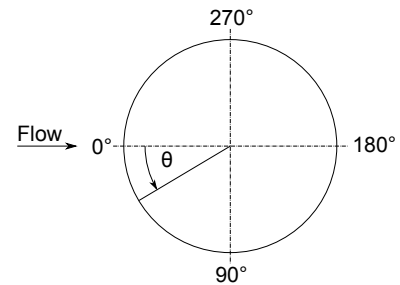


FIGURE 3: ANGULAR POSITION OF PRESSURE TAPS

The following indexing convention will be used: X_{ij} , where X is the property under examination, i is the position number of the cylinder (with reference to figure 1) being displaced and j is the position number of the cylinder measuring surface pressure. For Test 1 $i = 0$ and while for Test 2 $j = 0$

Figure 4 shows a pressure distribution from Test 1 against Test 2. Both distributions show the surface pressure on the instrumented cylinder when a cylinder 1 row upstream is displaced. It can be seen that the distributions are very similar, thus indicating that the data from Test 1 and Test 2 are consistent.

In figure 4 the pressure is at a maximum at 0° - the stagnation point - since the flow velocity is 0 m/s. The

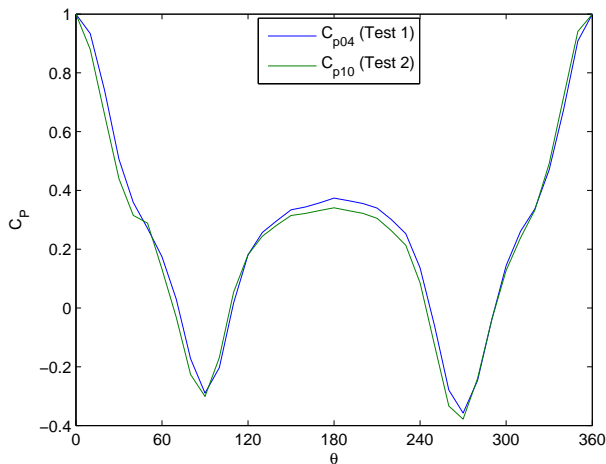


FIGURE 4: PRESSURE DISTRIBUTIONS OF TEST 1 AND TEST 2 AT 0% DISPLACEMENT. $U = 9$ M/S

flow velocity increases, thus creating a pressure drop on the surface of the cylinder, until it reaches 60° and 300° at which point there is a slight pressure recovery as the flow decelerates after passing through the inter-row gap. The flow velocity reaches a maximum and thus the pressure reaches a minimum at 90° and 270° where the streams from the upstream tube join and accelerate through these gaps. This pressure drop recovers between $90 - 270^\circ$, but does not recover completely due to viscous effects.

Figure 5 shows the pressure distributions from Test 1 for rows 2, 3 and 4. The distributions from rows 3 and 4 are very similar, suggesting that by the third row the flow is representative of the flow deep within an array. However, the pressure distribution for the cylinder in row 2 shows a sudden drop in pressure as the measurement location moves from the stagnation point. This is caused by the fact that the instrumented tube was at position 1 (row 2) and was therefore exposed to the free stream flow. This pressure distribution is not representative of a tube deep within an array. This is consistent with the results of Weaver & El-Kashlan [16]. Test 2 was performed to remedy these inconsistencies. The results proved more reliable because surface pressure data was only gathered when the instrumented cylinder was in the row 3 of the array.

In figure 6 pressure distributions are given at 3 displacements for the instrumented cylinder in position 0 and the displaced cylinder in position 2 (i.e. both in row 3 - see figure 1) at a free stream flow velocity of 9 m/s. Changes in these pressure distributions are especially noticeable at angles $270 - 360^\circ$ at -10% displacement, where the greatest blockage occurs, thus the greatest pressure drop. As the cylinder in position 2 is

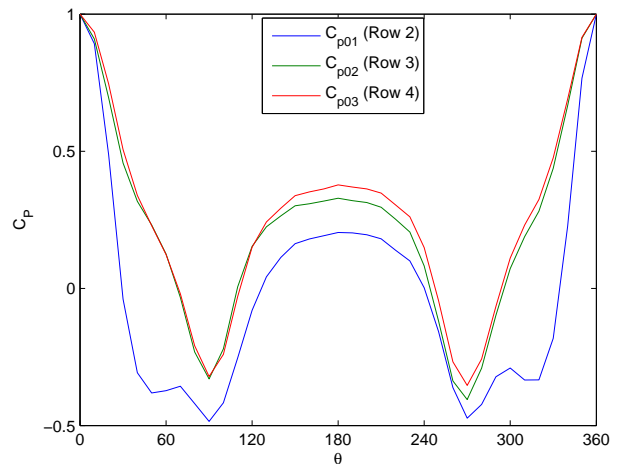


FIGURE 5: TEST 1 PRESSURE DISTRIBUTIONS IN ROWS 2-4 AT 0% DISPLACEMENT. $U = 9$ M/S

displaced from -10% to $+10\%$ the shape of the pressure distribution changes as can be seen at 270° where the minimum pressure recovers with increasing displacement (decreasing blockage). As the displacement is decreased to 0% , the pressure distribution is seen to be symmetrical showing a reduction in blockage. This blockage decreases further as the cylinder is displaced to $+10\%$ as can be seen at 270° where the minimum pressure becomes higher. Note that there is no change in pressure at 90° for the 3 displacements shown. This suggests that the flow is not splitting equally either side of the cylinder in a staggered array, which means that the use of the Bernoulli equation, as per the Lever & Weaver 'wavy wall' model [17], may be inappropriate in this type of array.

Symmetry

In figure 7 surface pressure measurements are shown for position 2 at $\Delta y_0 = +10\%$ displacement and compared to transposed measurements taken at $\Delta y_0 = -10\%$ displacement. This was done to determine whether the number of measurement positions could be reduced due to the symmetry of the array under analysis. With reference to figure 1, for Test 1 the pressure distributions around cylinders 1, 2 and 3 when subjected to a positive displacement of cylinder 0 are the same as the transposed (plotted from $360 - 0^\circ$) distributions of those around cylinders 4, 5 and 6 when subjected to a negative displacement of cylinder 0. The distributions from cylinders 4, 5 and 6 were transposed relative to cylinders 1, 2 and 3. The perturbation is symmetric about cylinder 0. This means that it is possible to analyse a kernel of 7

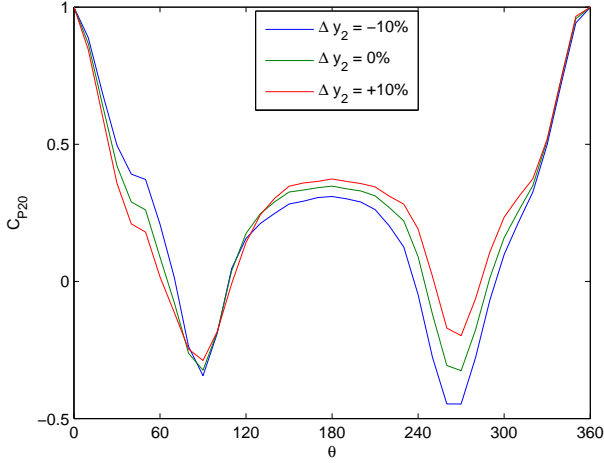


FIGURE 6: TEST 2. PRESSURE DISTRIBUTIONS AT 3 DISPLACEMENTS. $U = 9$ M/S

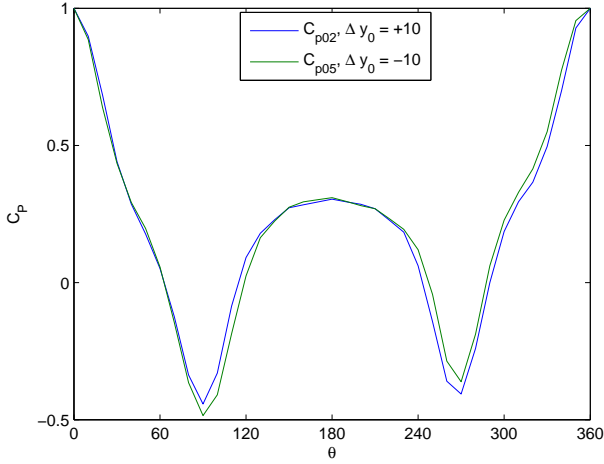


FIGURE 7: TEST 1 POSITION 2 AT $\Delta y_0 = +10\%$ DISPLACEMENT AGAINST POSITION 5 (TRANSPPOSED) AT $\Delta y_0 = -10\%$ DISPLACEMENT. $U = 9$ M/S

cylinders, using only pressure data from the cylinder in 4 positions (0, 1, 2 and 3). Thus surface pressure results presented in this study will be at either positions 1, 2 and 3.

Fluid Forces

The lift and drag on the cylinders were calculated by integrating the pressure distributions with respect to angle using equations (2) below:

$$F_D = \frac{1}{2} \int_0^{2\pi} P dl \cos \theta d\theta, \quad F_L = \frac{1}{2} \int_0^{2\pi} P dl \sin \theta d\theta \quad (2)$$

The coefficients of lift and drag were then determined using equations (3) below:

$$C_D = \frac{F_D}{\frac{1}{2} \rho d l U_g^2}, \quad C_L = \frac{F_L}{\frac{1}{2} \rho d l U_g^2} \quad (3)$$

The fluidelastic response of the tube array can be modelled using a linearized representation of the structural and fluid forces:

$$(\mathbf{M}_s + \mathbf{M}_f) \ddot{\mathbf{y}} + (\mathbf{C}_s + \mathbf{C}_f) \dot{\mathbf{y}} + (\mathbf{K}_s + \mathbf{K}_f) \mathbf{y} = 0 \quad (4)$$

The fluid added mass can be estimated using potential flow theory and in any case, will be negligible in gas flows, and so will be ignored here. The fluid damping and stiffness are dependent on structural motion, therefore fluid forces associated with fluidelastic instability on a static cylinder do not exist [6]. However, it is possible to estimate fluidelastic forces from measurements on a static cylinder by using the quasi-steady model [18]. For a fully flexible array at high mass-damping values, the dominant mechanism of instability is likely to be stiffness controlled. Therefore, the fluid damping will be ignored. As the system approaches instability the stiffness matrix becomes asymmetric. This means, for example $k_{01} \neq k_{10}$, where k_{01} represents the stiffness force acting on cylinder 1 due to displacement of cylinder 0. The coupling effect of the fluid can be estimated from the experimentally derived force-displacement gradient as shown in equation (5).

$$k_{ij} = \frac{1}{2} \rho d l U_g^2 \frac{\partial C_{Li}}{\partial y_j} \quad (5)$$

The $\frac{\partial C_{Li}}{\partial y_j}$ values are calculated by fitting a line to the graph in figure 10 between $\pm 2\%$ displacement as at the onset of fluidelastic instability the displacement will be below these levels.

Drag In Test 1 when the instrumented cylinder was in positions 2-5, the drag force behaved as expected - increasing with flow velocity for both positive and negative displacements. Figure 8 shows drag force against gap velocity velocity for the cylinders in positions 2 (row 3) and 3 (row 4). Note both scales are logarithmic. The data collapses well using a single line, thus indicating that the drag force is proportional to a power of the gap velocity.

Positions 1 and 6 are unusual in that they exhibit a negative drag force (a thrust acting upstream relative to

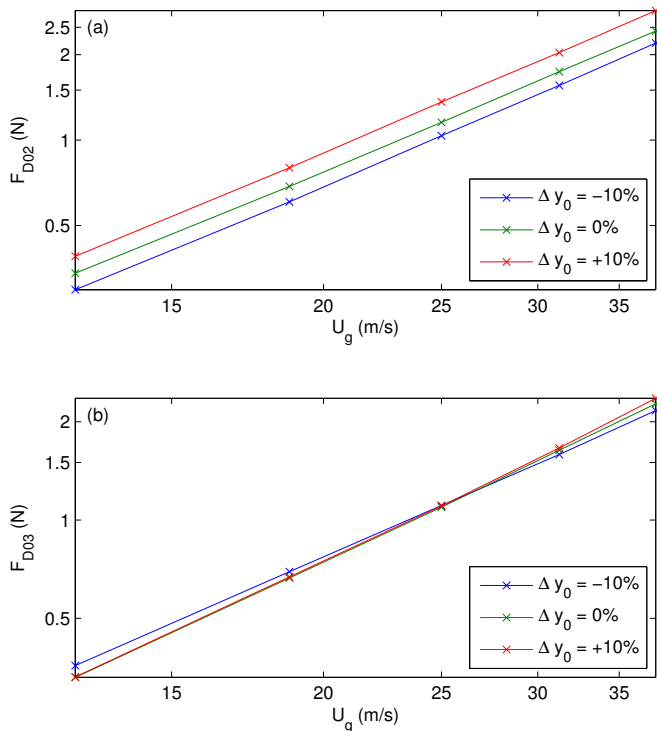


FIGURE 8: TEST 1 DRAG AGAINST GAP VELOCITY WITH INSTRUMENTED TUBE IN POSITIONS 2 AND 3. (a) POSITION 2 (ROW 3), (b) POSITION 3 (ROW 4)

the bulk flow direction) is seen at large displacements (2 – 10% of tube diameter) as can be seen in figure 9 (a). This is likely due to the fact that these surface pressure measurements were taken in row 2 and therefore the instrumented cylinder was exposed to the free stream, thus creating an unusual pressure distribution as can be seen in figure 9 (b). Also since the tube downstream of tubes 1 and 6 is being displaced, it is possible that recirculation behind these tubes is causing this thrust at extreme displacements (2-10%).

Lift The lift force is much more complex and has non-linear relationships with displacement, flow velocity and position. Figure 10 shows the coefficient of lift against displacement at various Reynolds numbers for Tests 1 and 2. The overall trend of the change in the coefficient of lift with displacement is the same between Test 1 (figure 10 (b), (f) and (j)) and Test 2 (figure 10 (a), (e) and (i)). Also shown in figure 10 is $\frac{\partial C_{Li}}{\partial y_j}$ against Reynolds number for Tests 1 and 2 at various measurement positions. The values for $\frac{\partial C_{Li}}{\partial y_j}$ are determined by measuring the change in coefficient of lift on a cylinder between $\pm 2\%$ displacement. The most significant changes in lift force, and thus coefficient of lift, occur at displacements

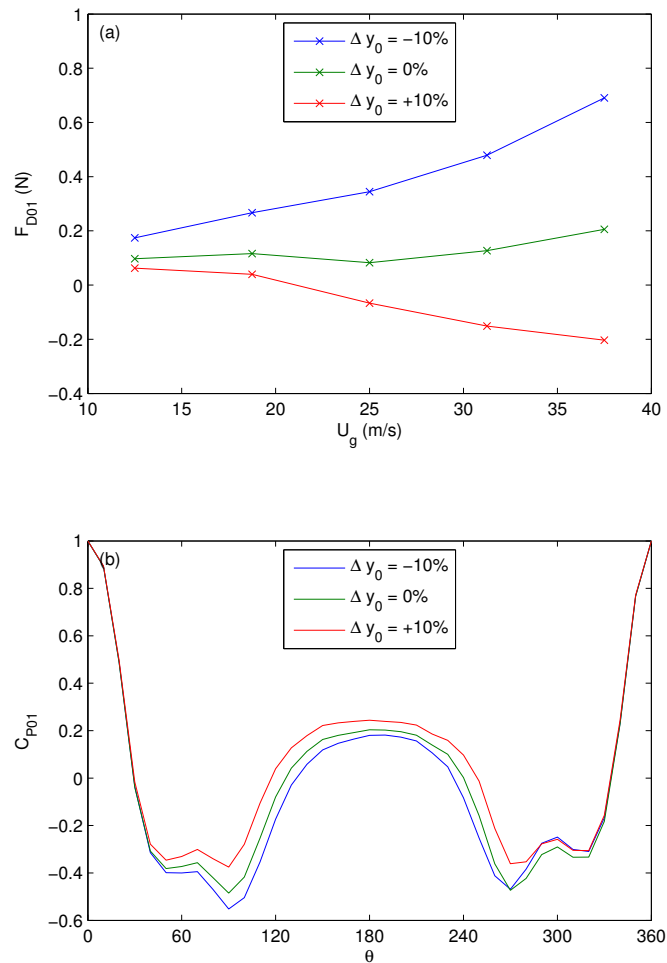


FIGURE 9: TEST 1 WITH INSTRUMENTED TUBE IN POSITION 1 (ROW 2). (a) DRAG AGAINST GAP VELOCITY AT 3 DISPLACEMENTS. (b) PRESSURE DISTRIBUTIONS AT 3 DISPLACEMENTS. $U = 9$ M/S

of $\pm 2\%$ of tube diameter as can be seen in figure 10 (a) and (b). The tests in this study were performed over the range of $\pm 10\%$ in order to see the overall trend of changes in lift force, or coefficient of lift, with displacement.

The coefficient of lift is approximately 0 at 0% displacement as would be expected. The deviation from 0 of the coefficient of lift at 0% displacement is caused by a combination of misalignment of the displaced cylinder (i.e. when the displaced cylinder was at the 0%, it was in fact at $\pm 1\%$), a DC offset in the pressure transducers and a rotational offset in the pressureappings of the instrumented cylinder. The misalignment of the displaced cylinder would have minimal effect on the change in coefficient of lift with displacement, since the tube is displaced between $\pm 10\%$ of tube diameter, meaning a misalignment will simply shift the result up or down, therefore the value of $\frac{\partial C_{Li}}{\partial y_j}$ will remain the same since the slope of the graph will be the same. The DC offset in the trans-

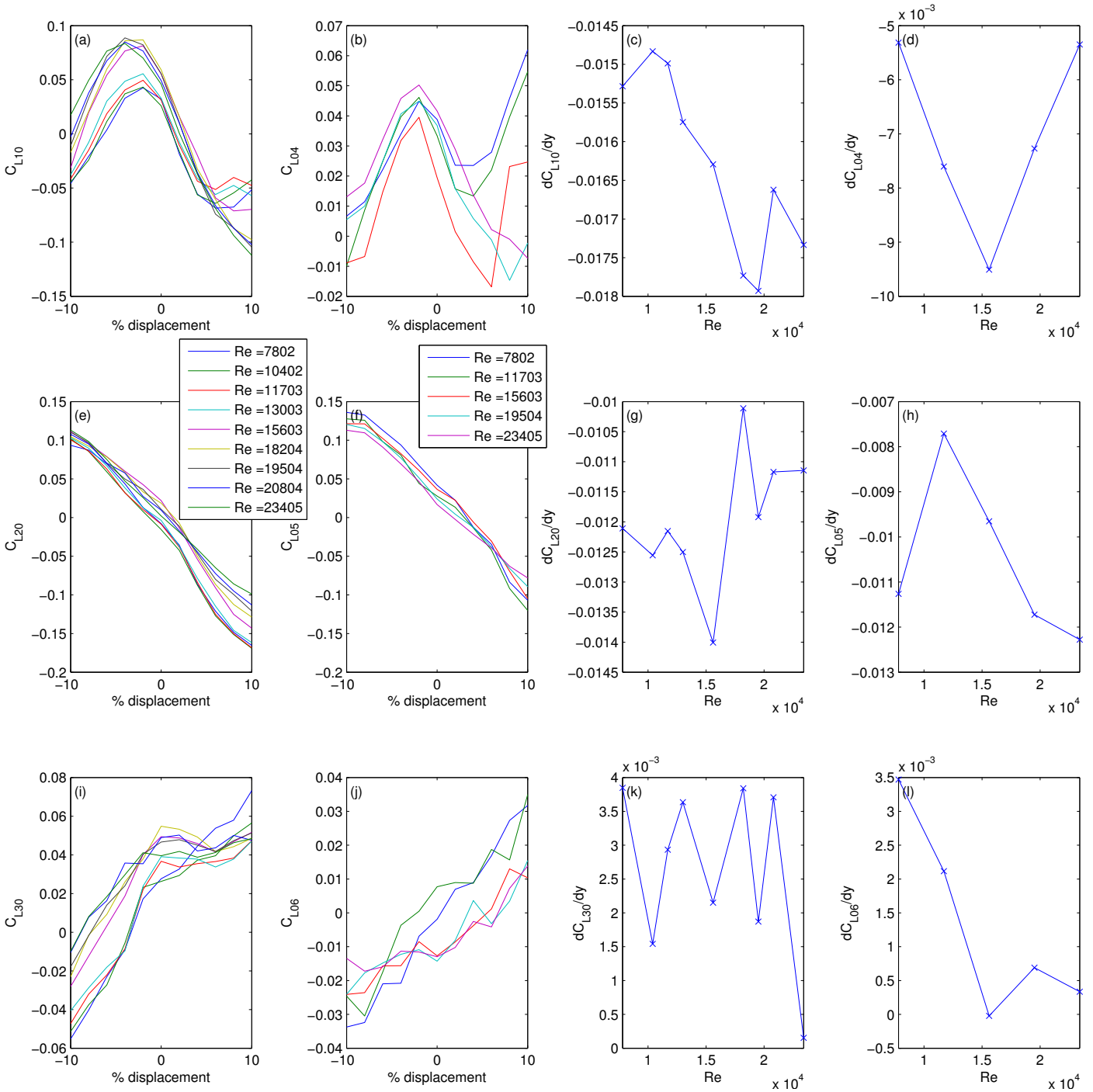


FIGURE 10: COEFFICIENT OF LIFT AGAINST DISPLACEMENT AT VARIOUS REYNOLDS NUMBERS AND MEASUREMENT POSITIONS. $\frac{\partial C_{L_i}}{\partial y_j}$ AGAINST REYNOLDS NUMBER AT VARIOUS MEASUREMENT POSITIONS

ducers has been accounted for in the calibration process. The rotational offset of the pressure taps is responsible for the slight asymmetry in the pressure distributions at 0% displacement as can be seen in figure 4, this gives a non-zero lift at 0% displacement.

Examining the estimates of the force-displacement gradient (figure 10 (c,d,g,h,k,i)) it is clear that Reynolds

number has a weak effect on the value for all coefficients except C_{L06} . In contrast, Mahon and Meskell [7] found that the force acting on a tube due to it's own motion is strongly dependent on Reynolds number. This suggests that while the Reynolds number affects damping controlled instability, it may be not important for the stiffness controlled regime.

CONCLUSION

The pressure field around a statically displaced cylinder has been acquired and analysed. The coefficients of lift and drag were determined for each cylinder by integrating the pressure data with respect to angle. This was done at a range of displacements and flow velocities.

ACKNOWLEDGMENT

This research was carried out thanks to funding from the Higher Education Authority

REFERENCES

- [1] Adobes, A., Pillet, J., David, F., and Gaudin, M., 2006. "Influence of steam generator tube bundle vibrations on the operating diagram of a nuclear plant during stretch out". *ASME Conference Proceedings*, **2006**(47551), Jan., pp. 147–156.
- [2] Price, S. J., 2001. "An investigation on the use of connors' equation to predict fluidelastic instability in cylinder arrays". *Journal of Pressure Vessel Technology*, **123**(4), Nov., pp. 448–453.
- [3] Hassan, M. A., Rogers, R. J., and Gerber, A. G., 2011. "Damping-controlled fluidelastic instability forces in multi-span tubes with loose supports". *Nuclear Engineering and Design*, **241**(8), Aug., pp. 2666–2673.
- [4] Hassan, M., and Hayder, M., 2008. "Modelling of fluidelastic vibrations of heat exchanger tubes with loose supports". *Nuclear Engineering and Design*, **238**(10), Oct., pp. 2507–2520.
- [5] Hassan, M., and Hossen, A., 2010. "Time domain models for Damping-Controlled fluidelastic instability forces in tubes with loose supports". *Journal of Pressure Vessel Technology*, **132**(4), pp. 041302–11.
- [6] Paidoussis, M. P., Price, S., and Langre, E. d., 2010. *Fluid-Structure Interactions: Cross-Flow-Induced Instabilities*. Cambridge University Press, Dec.
- [7] Mahon, J., and Meskell, C., 2009. "Surface pressure distribution survey in normal triangular tube arrays". *Journal of Fluids and Structures*, **25**(8), Nov., pp. 1348–1368.
- [8] Price, S., and Paidoussis, M., 1984. "An improved mathematical model for the stability of cylinder rows subject to cross-flow". *Journal of Sound and Vibration*, **97**(4), Dec., pp. 615–640.
- [9] Chen, S. S., and Srikantiah, G. S., 2001. "Motion-Dependent fluid force coefficients for tube arrays in crossflow". *Journal of Pressure Vessel Technology*, **123**(4), Nov., pp. 429–436.
- [10] Mureithi, N. W., Shahriary, S., and Pettigrew, M. J., 2008. "Flow-Induced vibration model for steam generator tubes in Two-Phase flow". *ASME Conference Proceedings*, **2008**(48140), Jan., pp. 365–374.
- [11] Mewes, D., and Stockmeier, D., 1991. "Fluid viscosity effects on flow induced vibrations of tube bundles in cross-flow". *Flow Induced Vibrations. London, United Kingdom*, pp. 231–242.
- [12] Gillen, S., and Meskell, C., 2008. "Variation of fluidelastic critical velocity with mass ratio and reynolds number in a densely packed normal triangular tube array". *Flow Induced Vibrations. Prague, Czech Republic*, pp. 193–198.
- [13] Hassan, M., Gerber, A., and Omar, H., 2010. "Numerical estimation of fluidelastic instability in tube arrays". *Journal of Pressure Vessel Technology*, **132**(4), pp. 041307–11.
- [14] Mahon, J., 2008. "Interaction between fluidelastic instability and acoustic resonance". PhD thesis, Trinity College Dublin, Department of Mechanical and Manufacturing Engineering, May.
- [15] Mahon, J., and Meskell, C., 2009. "Investigation of the underlying cause of the interaction between acoustic resonance and fluidelastic instability in normal triangular tube arrays". *Journal of Sound and Vibration*, **324**(1-2), July, pp. 91–106.
- [16] Weaver, D., and El-Kashlan, M., 1981. "On the number of tube rows required to study cross-flow induced vibrations in tube banks". *Journal of Sound and Vibration*, **75**(2), Mar., pp. 265–273.
- [17] Lever, J. H., and Weaver, D. S., 1982. "A theoretical model for Fluid-Elastic instability in heat exchanger tube bundles". *Journal of Pressure Vessel Technology*, **104**(3), p. 147.
- [18] Price, S. J., and Paidoussis, M. P., 1983. "Fluidelastic instability of an infinite double row of circular cylinders subject to a uniform Cross-Flow". *Journal of Vibration Acoustics Stress and Reliability in Design*, **105**(1), pp. 59–66.



Study on In-flow Fluid-elastic Instability of Circular Cylinder Arrays

Tomomichi NAKAMURA
Osaka Sangyo University, Daito, Japan

Yoshiaki FUJITA
Takanari OYAKAWA
Yikai NI
Osaka Sangyo University, Daito, Japan

ABSTRACT

The fluidelastic instability of cylinder arrays caused by cross-flow mainly occurs in the direction transverse to the flow due to the fluid force resulting from interaction between cylinders. However, in a recent study published by Canadian researchers, it was reported that an in-flow fluidelastic instability had been observed with their U-bend tube arrays. The present investigates the possibility and the parameter regimes of this in-flow instability in a simplified test setup.

A previous study using the cantilevered straight cylinder model showed that steady drag resulted in large cylinder static displacements which completely changed array geometry – in some cases leading to cylinder-cylinder contact at high flow velocities. In the present study, cylinders are supported at both ends. Tests are conducted in both water flow and air flow – the latter flow has lower drag forces.

1. INTRODUCTION

The stream-wise oscillation of a circular cylinder in cross-flow caused by alternate vortex shedding behind the cylinder is well known [1]. However, this phenomenon has not been well recognized in cylinder arrays. Recently inline fluid-elastic vibration of cylinder arrays has been reported for the U-bend tube array [2], where the array was found to oscillate in the stream-wise direction due to what is believed to be fluid-elastic instability.

This U-bend tube array is common in steam generators. Steam-generator tubes cannot be easily supported externally, particularly in the U-bend region. In the U-bend region tubes are supported with a loose support system using for example anti-vibration bars or other types of supports. For this reason, the U-bend tubes can easily vibrate in the so-called “in-plane direction,” which corresponds to the stream-wise direction, in-line with the flow. When fluid-elastic instability occurs in the in-plane direction, it can easily lead to excessive wear damage of the heat exchanger tubes in a short period of time.

In this paper, fluid-elastic instability in the stream-wise direction, which is expected at higher flow velocities, is the major issue of concern. The fluid-elastic instability is caused by the motion of cylinders in the array, under conditions where the cylinder movement results in net

energy transfer from the flow to the cylinders. There exists much research work on this problem [3]. However, fluid-elastic instability is believed to mainly occur in the cross-flow (or transverse) direction, although the motion of the cylinder-array may include both stream-wise direction and cross-stream direction displacements.

Our first study on inflow fluidelastic instability has been reported [4]. Although the results were interesting some were inconclusive on the question of occurrence of inflow fluidelastic instability. The water test loop has been modified based on these previous findings, and furthermore a new air test loop has been added; the latter air test loop makes it possible to avoid the excessive drag force effect, which changes the pitch of the set of cylinders.

The measurement results of unsteady fluid forces in cylinder arrays by Chen [5] indicate that there is a possibility of inflow fluidelastic instability in the case of small pitch staggered arrays. The first series of test is therefore done on a staggered array with the pitch-to-diameter ratio, $P/D=1.2$, in the water test loop. Further tests are then conducted based on the results of this initial test series.

2. WATER LOOP TEST

2.1 Test loop

Fig.1 shows the water test loop. The main flow is through a square cross sectional pipe of 90 mm section, where water flow is recirculated from a reservoir.

Flow straightening is achieved with a mesh unit composed of an array of circular tubes at the up-stream region of the test section. The flow velocity is controlled by a valve and an inverter power unit, and measured by an ultrasonic flow velocity sensor at the upstream region of the test section.

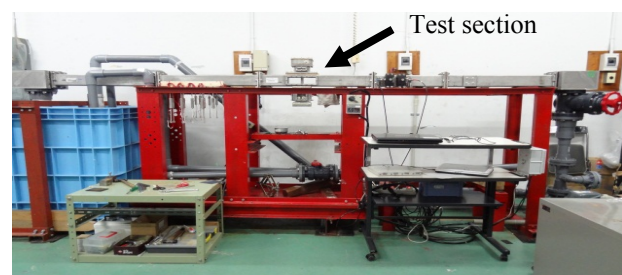


Fig.1 Test apparatus

2.2 Test cylinders

As indicated in Fig.1, the test section has a square geometry, where a maximum nine cylinders (3 by 3 in square array) can be installed. The cylinders are 20 mm in diameter, and 84 mm in length. The tubes are made of stainless steel. They are supported by a steel plate having 1 mm thickness and 6mm in width which runs through the center of the tube as shown in Fig.2. This provides symmetrical support at the upper and lower ends of the cylinders. Strain gages are mounted on the steel support plates to measure the cylinder response.

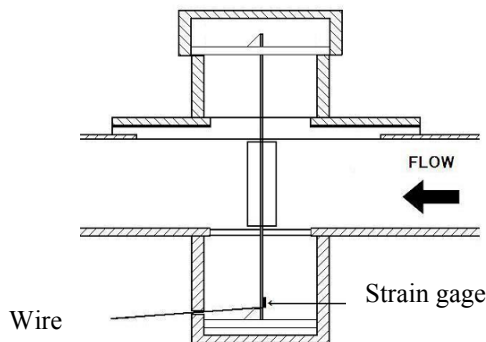


Fig.2 Concept of test cylinders

In the present series of tests, two types of basic cylinder arrays are tested, a staggered array and an in-line array. The pitch ratio of the staggered array is $P/D=T/D=1.2$ as shown in Fig.3(a). The pitch ratio of the in-line array is also $P/D=T/D=1.2$. In this array the tubes are set in a three-by-three square configuration as shown in Fig.3(b). As mentioned later, two additional tests have been conducted on the two configurations shown in Fig.3(c), (d). The additional tests were necessitated by interesting but inconclusive results from the square array of Fig.3(b). The results included inflow fluidelastic instability which was unexpected.

The frequencies of the tubes are approximately 20Hz in water while the damping ratio is nearly 2.5% in water. The initial vibrational characteristics are shown in Table 1 for the center cylinder in each case. Other cylinders are set to similar frequency and damping as in the table.

For each array, all cylinders are set flexible both in the direction transverse to the flow and in the stream-wise direction for comparison.

2.3 Test results

Fig.4 shows the root-mean-square response of instrumented cylinders in the case of the triangular array. The results are presented using the following dimensionless quantities:

$$Vr = \frac{V_{Gap}}{fD}, V_{Gap} = \frac{V_{Approaching} \times D}{P - D} \quad (1)$$

$$\eta = \frac{\text{Root - mean - dsplacement}}{D}$$

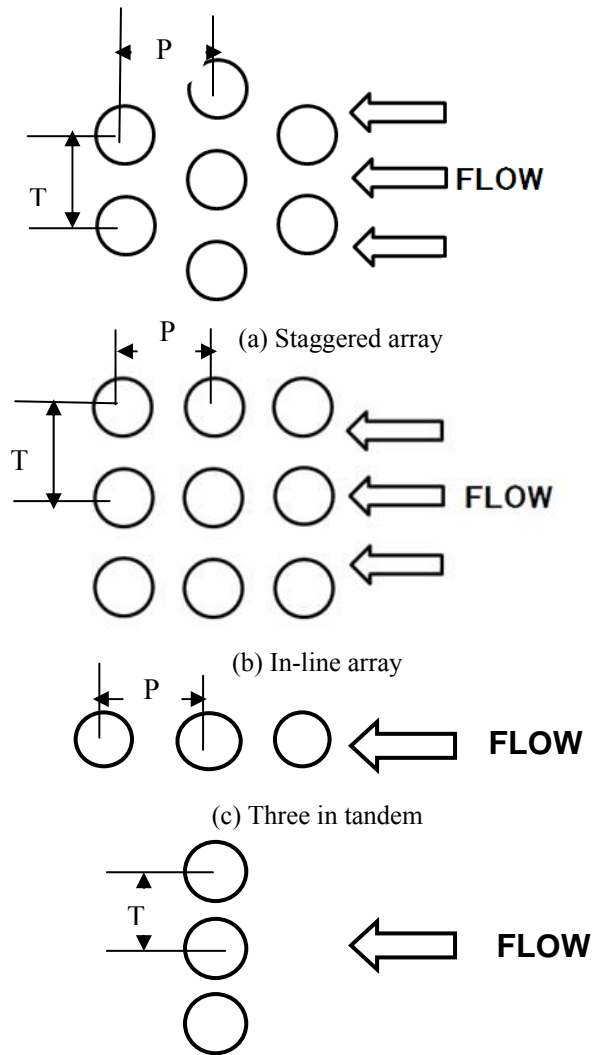


Fig.3 Test Pattern in water loop

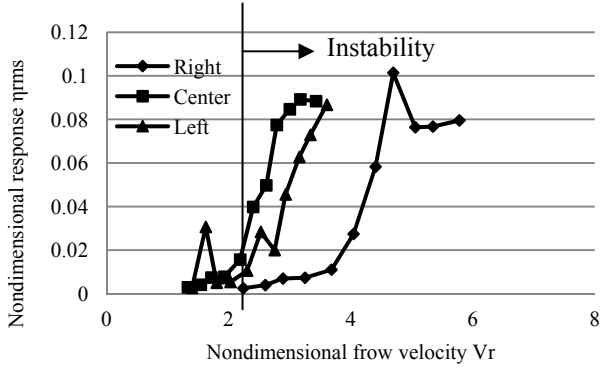
Table 1 Natural frequency and damping ratio

Cylinder array	Transverse direction		Inflow direction	
	Frequency	Damping	Frequency	Damping
Staggered	20.99 (23.61)	4.97 (2.61)	23.11 (24.55)	3.26 (1.4)
In-line	18.87 (19.92)	2.96 (2.46)	14.12 (19.1)	11.12 (3.33)
Three in tandem	19.08 (23.13)	7.01 (2.3)	15.15 (22.41)	3.94 (2.61)
Three in parallel	21.93 (22.78)	7.14 (2.2)	15.15 (23.87)	4.06 (2.22)

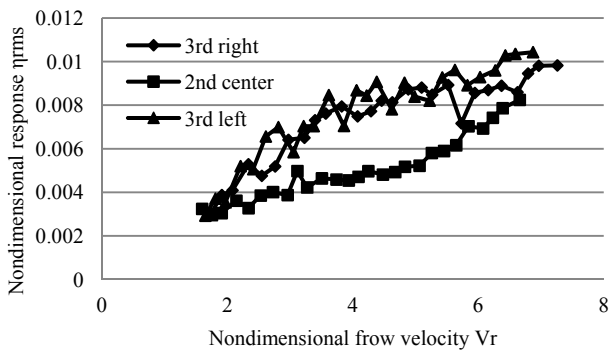
*Bracket means data in air

The cylinder responses increase rapidly near $Vr=3.8$ in the direction transverse to the flow. However, no clear increase was observed in the inflow direction. The magnitude of the response in the inflow direction also seems smaller than that in the transverse direction.

shown in Fig.5. A clear sharp peak appears when the cylinder becomes unstable, although the background turbulence noise level remains significant even for very high flow velocity in the inflow direction as indicated in Fig.5(b).

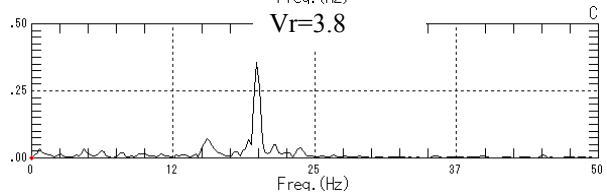
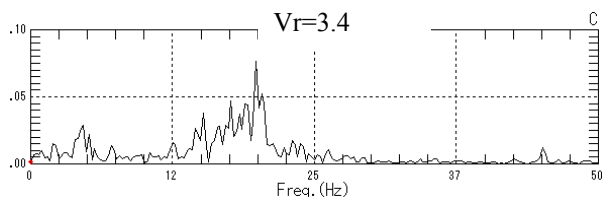


(a) Transverse direction

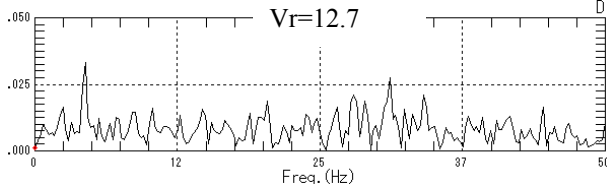


(b) In-flow direction

Fig.4 Response of cylinders (Staggered array P/D=1.2)



(a) Transverse direction



(b) In-flow direction

Fig.5 Example of frequency spectrum

Next, the response of cylinders in the case of the inline array is introduced in Fig.6. The occurrence of the

is easily discernible in Fig.6(a).

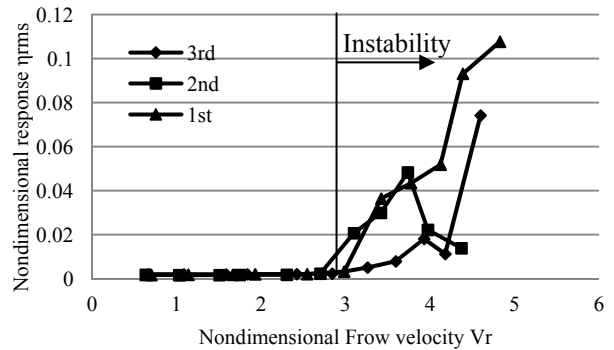
However, although the response in the inflow direction shown in Fig.6(b) is not as small as in Fig.4(b), it is not easily distinguishable from turbulence response.

In Fig.6(b), the fluidelastic vibration appears to occur starting at $V_r=8.0$, however, the frequency spectrum shown in Fig.7 indicates the occurrence of the instability to be closer $V_r=10$.

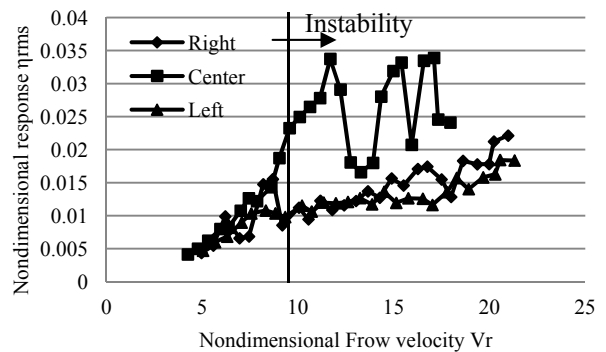
The spectral analysis introduces new insight into the behavior of the staggered array. Inflow instability can clearly be observed in in-line array. The details of the instability were, however, not fully clear based in the measurements in the square array. For this reason, new tests on the simpler array configurations in Fig.3(c,d) were performed.

Fig.8 shows the vibration in the case of three cylinders in tandem. This result is very interesting in that the instability occurs at almost the same non-dimensional flow velocity $V_r=3.8$ as in the case of the nine cylinder array.

In this test, the cylinders statically move in the in-flow direction due to the flow drag force. Fig.9 shows the static displacement of the three cylinders. Note that the



(a) Transverse direction



(b) In-flow direction

Fig.6 Response of cylinders (In-line array P/D=1.2)

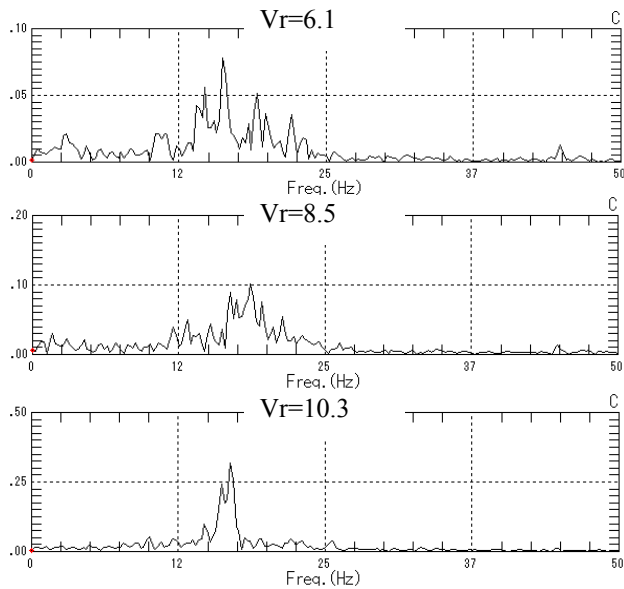
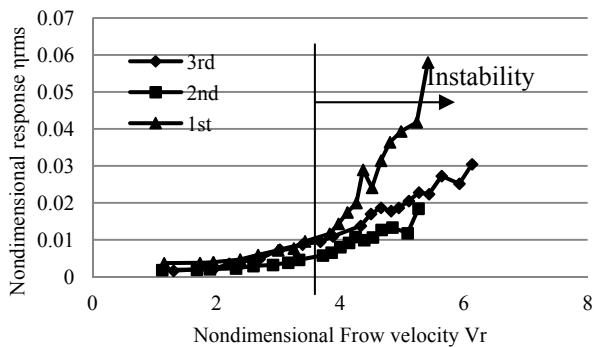
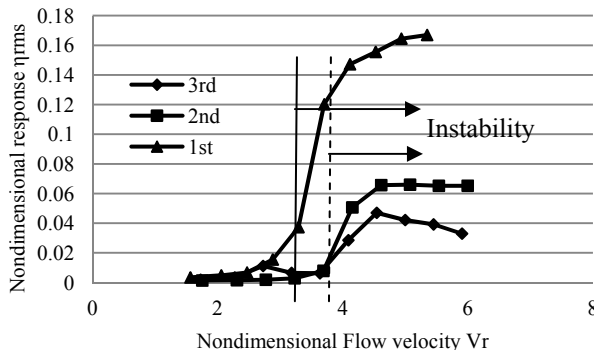


Fig.7 Example of frequency spectrum in in-flow direction



(a) Transverse direction



(b) In-flow direction

Fig.8 Response of cylinders (Three cylinders in tandem $P/D=1.2$)

center cylinder remains relatively in position while the upstream and downstream cylinders undergo significant static displacement.

The space between the first cylinder and the second one decreases with increasing flow velocity, while that

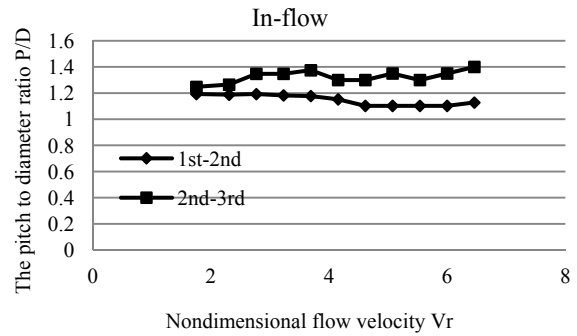
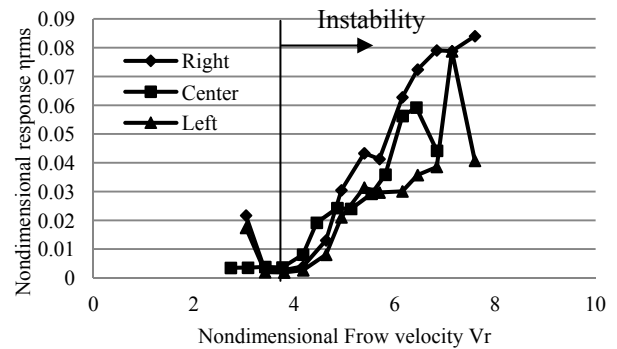


Fig.9 Static displacement (Three cylinders in tandem $P/D=1.2$)

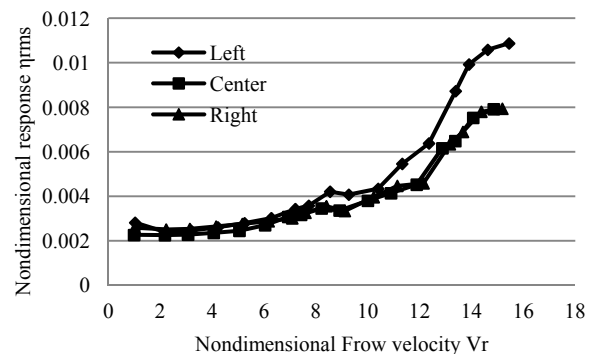
between the second cylinder and the third one increases. This may be the major reason that the first cylinder becomes unstable at the lower flow velocity, while the other cylinders destabilize at higher flow velocity.

During the test, the vibration response of the cylinders occasionally decreases, when the flow velocity increases, due to contact and impacting between the cylinders.

Fig.10 shows the response in the case of three cylinders in parallel. Fig.10(a) indicates that fluid-elastic instability occurs near $V_r=4.0$ in the transverse direction, while no clear instability is observed in the inflow direction.



(a) Transverse direction



(b) In-flow direction

Fig.10 Response of cylinders (Three cylinders in parallel $T/D=1.2$)

Table 2 Threshold of fluidelastic instability (P/D=1.2)

Cylinder array	Transverse		In-flow	
	Direction	K	Direction	K
Staggerd	V _r =2.1-3.7	2.4-4.2	V _r >7.3	-
In line	V _r =3.0	4.5	(V _r =8.6)	6.63
Three in tandem	(V _r =3.8)	3.7	V _r =2.9&3.7	3.0-4.7
Three in parellel	V _r =4.0	3.9	V _r >15	-

The spectral analysis also shows a similar trend as seen in Fig.5.

The results suggest that in-flow instability occurs due to the interaction between cylinders in the in-flow direction. The instability results in water flow are summarized in Table 2, indicating the constant K defined by Eq.(2).

$$\frac{Vc}{fD} = K \sqrt{\frac{m\delta}{\rho D^2}} \quad (2)$$

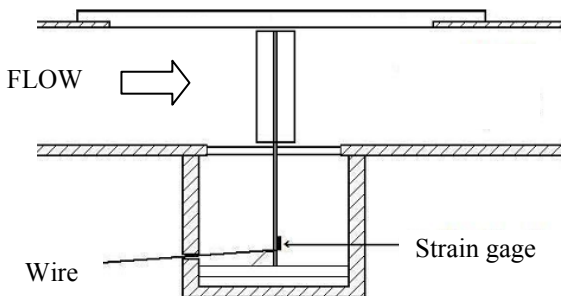
3. AIR FLOW TESTS

3.1 Test equipment

Similar tests have been done in air flow . Fig.11 shows the test equipment. The cylinders in the air flow test are similar to those used in the water flow test, but they are supported as a cantilevers as shown in Fig.11(b). The patterns of the cylinder array is basically the same as in Fig.3(a), (b), (c),(d).



(a) Test equipment



(b) Measured cylinder
Fig.11 Air test equipment

3.2 Test results

Fig.13 shows the response of cylinders in the case of the inline array. This array showed interesting behavior in water flow.. The response seems unstable behavior starting near the velocity, V_g=7. This can be confirmed from the example of the response time trace itself Fig.14. Instability occurs in both the lift and drag directions. However, in the flow direction vibration amplitudes are strongly limited by tube-tube impacting. There there is therefore no clear difference on the threshold of the instability, only the post instability behavior.

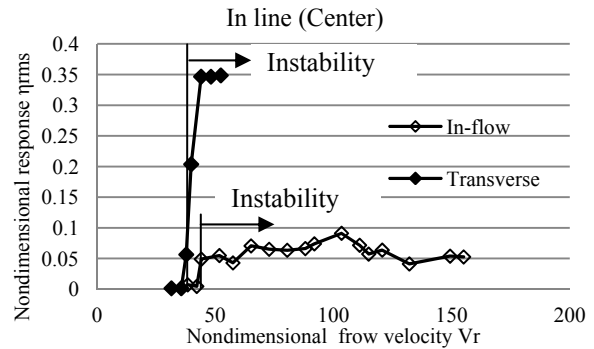


Fig.13 Response of cylinders (In-line array)

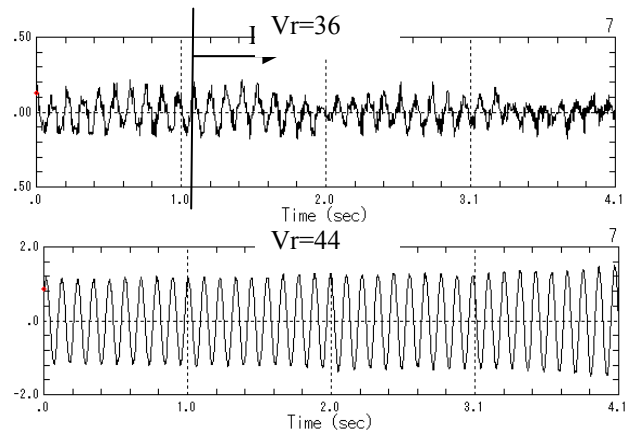


Fig.14 Example of response wave (In-line array)

Next, the cylinder in the case of the staggered array is shown in Fig.15. Fluid-elastic instability occurs near V_r=34 in the in-flow direction, while the instability is observed at the higher velocity of V_r=48 in the transverse direction. The response time trace indicates a similar trend as in Fig.14 even in this case, except for the amplitude modulation of the temporal response.

Fig.16 shows the results for the case of three cylinders in tandem. Contrarily with the result in water flow , no clear jump in the inflow direction is observed in air test, and the magnitude of the response in the inflow direction remains small. However, the response in the transverse direction shows a sharp increase near V_r=20, which indicates that fluidelastic instability occurs in the transverse direction only.

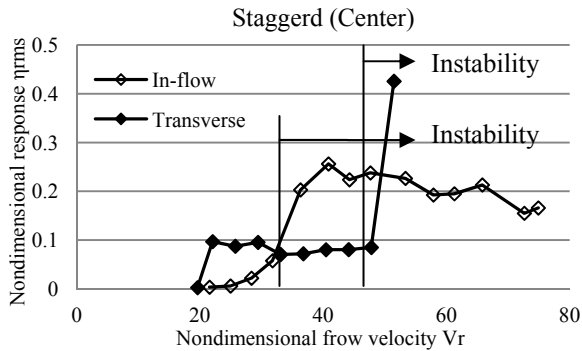


Fig.15 Response of cylinders (Staggered array)

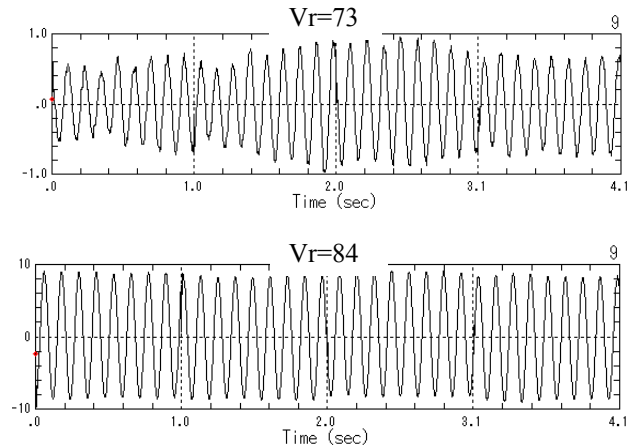


Fig.18 Example of response wave (Three cylinders in parallel)

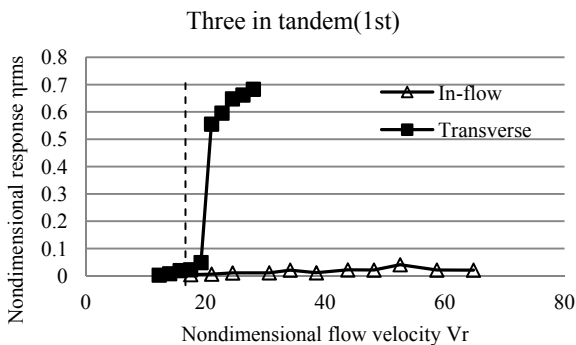


Fig.16 Response of cylinders (Three cylinders in tandem)

Another interesting result is observed in the case of three cylinders in parallel. In this case, fluidelastic instability is observed in the inflow direction and no instability is observed in the transverse direction as shown in Fig.17. This result is completely the opposite of the results found in the water flow tests.

The vibration response time trace shown in Fig.18 also shows a clear trend of the instability. The response amplitude in the transverse direction is modulated in time. The inflow vibrations, on the other hand, occur with a constant amplitude with no modulation.

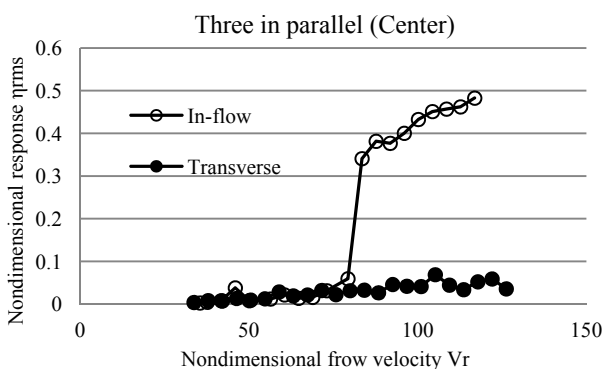


Fig.17 Response of cylinders (Three cylinders in parallel)

4. DISCUSSION

The phenomenon of the fluidelastic instability has been studied by many researchers over years since Connors' doctoral report [6] in 1969. Most of the research has been devoted to the investigation of generic issues, and the results have been compiled as design guidelines or vibration behavior overviews [7],[8]. Some papers have presented results on the effect of the tube vibration direction, in drag and/or in lift, however in most cases tubes are supported axisymmetrically; the result then being that the occurrence of instability is almost at the same flow velocity in the two directions [9]. When tubes are supported asymmetrically, it is the transverse direction that has been more flexible [10]. As this report highlights the difference between the inflow instability and the usual transverse instability, it is important to clarify the difference between the two cases.

The stability analysis using the fluidelastic force coefficients measured by Chen [5] indicates that instability usually occurs in cylinder arrays with small pitch-to-diameter ratio. His results do not directly correspond to the present test result, however, the observation that triangular arrays have a strong possibility of undergoing inflow instability is verified in the present work, at least for water flow. Gas flow, on the other hand, was shown to have more complex behavior relative to water flow. The results suggest that one might expect some effects related to tube pitch-to-diameter ratio. However, the reported effect attributed to pitch ratio has been relatively small in the case of rotated triangular array by two-phase flow [11].

With regard to inflow instability of the triangular array, references [12],[13] are two among the papers that have been published following the paper on U-tube tests [2]. The first paper [12] reports on the inflow instability of a parallel triangular array of $P/D=1.5$. The work shows that inflow instability occurs at a higher flow velocity in air-water two-phase flow compared to the transverse direction instability in the same two-phase flow mixture. The

suggested K value in Eq.(2) is $K=8$ for the in-flow direction, and $K=3$ for the transverse direction.

The second paper [13] reports similar results for a parallel triangular array of $P/D=1.37$ in air flow tests. In these tests a critical flow velocity in the in-flow direction of 2.7 m/s is obtained, while the velocity in the transverse direction is 1.7 m/s.

These results suggest that the ratio of the critical flow velocity in the in-flow direction to that in the transverse direction, κ ($=V_c(\text{in the in-flow direction})/V_c(\text{in the transverse direction})$), has an increasing trend with pitch-diameter ratio P/D . Fig.19 shows this trend in the case of triangular array, plotted using existing data; these data do not always correspond to the same fluid nor the same cylinder array.

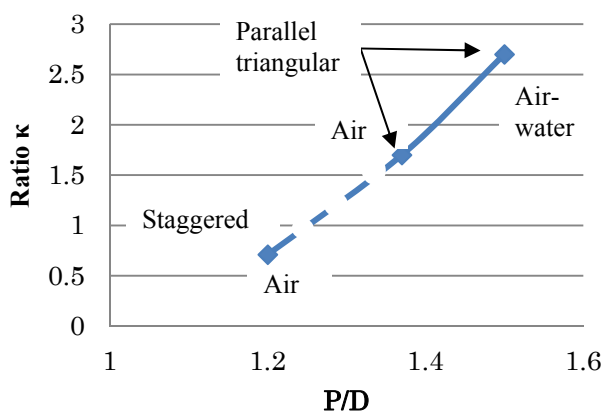


Fig.19 Ratio of critical flow velocity due to direction of movement (Staggered array)

In the case of in-line array, this trend is not easily confirmed even for air flow tests. The dynamic stability behavior is also quite complicated in the case of three cylinders, in tandem and parallel configurations. Further work is therefore needed for a better understanding of these cases.

To sum up, all the instability results obtained are plotted in the classical stability map and compared with Connors equation with $K=3.3$ in Fig.20. Based on the stability map of Fig.20, there is no clear trend in the experimental critical factor K , as depending on the cylinder array pattern for small pitch ratio, $P/D=1.2$, nor on the direction of movement. Further work is therefore required to clarify the physical mechanism underlying the observed stability behavior.

There is another discussion on the inflow instability [14], where the effect of the number of flexible cylinders is examined, and this report also indicates the further work is required.

5. CONCLUSION

In water flow tests it was generally not easy to confirm the inflow instability mainly due to the effect of the steady drag force. However, fluidelastic instability was

confirmed in the special case of three cylinders in tandem. The resulting K factor of Connors' equation was found to be almost the same as that for other arrays in the transverse direction. Water flow tests also show that the instability threshold is strongly affected by the pitch between cylinders.

Air flow tests confirmed the occurrence of in-flow instability for the staggered array of $P/D=1.2$. In this array, the critical flow velocity in the in-flow direction is smaller than that in the transverse direction. This trend is thought to depend the cylinder pitch spacing. The ratio of the critical flow in the in-flow direction to that in the transverse direction shows a clear trend with pitch spacing. This trend will be investigated in more detail in future tests.

The present work shows that there are significant differences between the air flow and water flow tests. This may come from the strong drag force effect in water flow, although there are some unknowns in the behavior of the cases of three cylinders in tandem and in parallel. Even in the case of the in-line array, air flow tests indicate the occurrence of in-flow instability, although its amplitude is suppressed due to the contact between the cylinders.

6. ACKNOWLEDGEMENT

This study is partially funded by the Japanese Society for the Promotion of Science. Our research work has greatly been inspired by late Shoei-Sheng Chen's work. Dr. Chen's encouragement and inspiration is greatly appreciated.

7. REFERENCES

- (1) JSME, 1998, "Guideline for Evaluation of Flow-Induced Vibration of a Cylindrical Structure in a Pipe", (in Japanese) JSME Standard S 012.
- (2) Janzen, V., et al., 2009, "Design specifications to ensure flow-induced vibration and fretting-wear performance in CANDU steam generators and heat exchangers", Proceedings of ASME's PVP conference, PVP2009-78078.
- (3) Paidoussis, M.P., 1987, "Flow Induced Instabilities of Cylindrical Structures", Applied Mechanics Reviews, Vol.40, pp.163-175. et al.
- (4) Nakamura, T., et al, 2011, "Study on in-flow vibration of cylinder arrays caused by cross flow", Proceedings of 2011 ASME Pressure Vessels & Piping Conference
- (5) Chen, S.S., et al., 1995, "Experimental Fluid-Force Coefficients for Wake-Induced Cylinder Vibration", Journal of Engineering Mechanics, Vol.121, No.9, pp.1003-1015.
- (6) Connors, Jr., H.J., 1969, "An Experimental Investigation of the Flow-Induced Vibration of Tube Arrays in Cross Flow", University of Pittsburg.
- (7) Paidoussis, M.P., 1982, "A Review of Flow-Induced Vibrations in Reactors and Reactor Components", Nuclear Engineering and Design, Vol.74, pp.31-60.
- (8) Pettigrew, M.J., Taylor, C.E., 1991, "Fluidelastic Instability of Heat Exchanger Tube Bundles: Review and Design Recommendations", ASME Journal of

- Pressure Vessel Technology, Vol.133, pp.242-256.
- (9) Pettigrew, M.J., et al., 1995, "Vibration of a Tube Bundle in Two-Phase Freon Cross-Flow", ASME Journal of Pressure Vessel Technology, Vol.117, pp.321-329.
- (10) Feenstra, P., et al., 2009, "Two-Phase Flow-Induced Vibration of Parallel Triangular Tube Arrays With Asymmetric Support Stiffness", ASME Journal of Pressure Vessel Technology, Vol.131, pp.031301-1-9.
- (11) Pettigrew, M.J., et al., 2001, "The effects of Bundle Geometry on Heat Exchanger Tube Vibration in Two-Phase Cross Flow", ASME Journal of Pressure Vessel Technology, Vol.123, pp.414-420.
- (12) Violette, R., et al., 2006, "Fluidelastic Instability of an Array of Tubes Preferentially Flexible in the Flow Direction Subjected to Two-Phase Cross Flow", ASME's Journal of Pressure Vessel Technology, Vol.128, pp.148-159.
- (13) Khalvati, A., et al., 2010, "Effect of Preferential Flexibility Direction on Fluidelastic Instability of a Rotated Triangular Tube Bundle", ASME's Journal of Pressure Vessel Technology, Vol.132, pp.041309-1-14.
- (14) Mureithi, N.W., et al., 2005, "Fluidelastic instability on an array of tubes preferentially flexible in the flow direction", Journal of Fluids and Structures, Vol.21, pp.75-87.

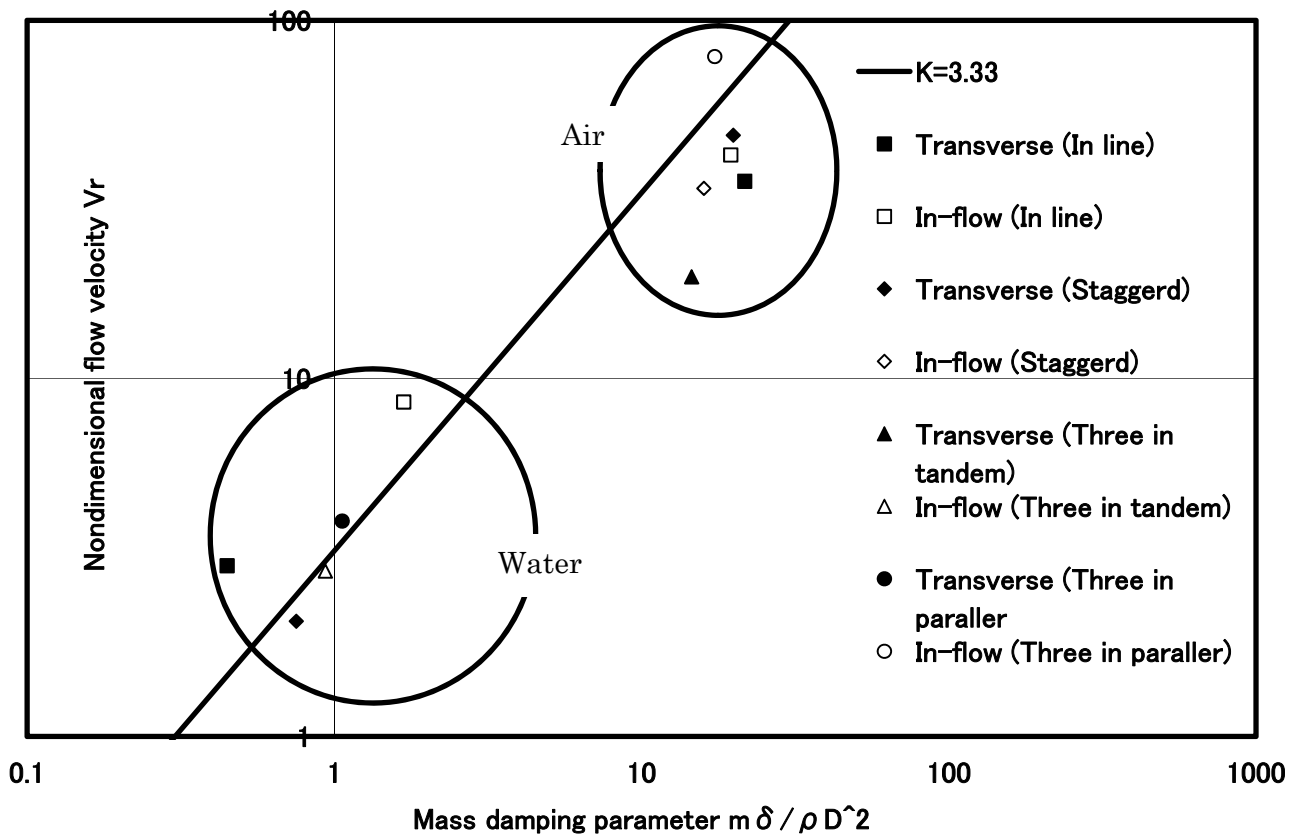


Fig.20 Stability map by obtained results



UNSTEADY FLUID FORCES AND THE TIME DELAY IN A VIBRATING TUBE SUBJECTED TO CROSS FLOW

Marwan Hassan *

School of Engineering
University of Guelph
Guelph, ON, Canada
Email: mahassan@uoguelph.ca

Salim El Bouzidi

School of Engineering
University of Guelph
Guelph, ON, Canada
Email: r04vg@unb.ca

ABSTRACT

Fluidelastic instability is generally regarded as the most severe type of flow excitation mechanism. When this mechanism prevails, it could cause serious damage to tube arrays in a very short period of time. This mechanism is characterized by a critical flow velocity beyond which the tubes undergo unstable oscillations. Several models were developed to predict this stability threshold. The common feature among the semi-analytical models is the use of time delay in the formulation. Although these models interpreted the nature of time lag differently, they captured the essence of the fluidelastic instability phenomenon and were successful in reproducing some features of the experimental data.

This paper will investigate the mechanism of time delay utilizing a numerical fluid model. The unsteady flow and the resulting fluidelastic forces, pressure, and velocity perturbations are investigated. Numerical simulations are presented for normal triangle tube arrays with a pitch to diameter (P/d) ratio of 1.35 utilizing a 2-dimensional model. In this model, a single tube was given a prescribed motion. Fluid forces acting on the oscillating tube and the surrounding tubes were estimated. In addition, the pressure and the velocity perturbations along the flow channels were predicted. The predicted forces, pressure, and velocity perturbations were utilized to estimate the time lag. The numerical model solves the Reynolds-Average Navier-Stokes (RANS) equations for unsteady turbulent flow, and is cast in an Arbitrary Lagrangian-Eulerian (ALE) form to mesh the motion associated with a moving boundary. The effect of Reynolds number on the displacement amplitude is also investigated.

NOMENCLATURE

- \bar{A} Steady state channel area.
- A_o Channel inlet area.
- a Channel area perturbation.
- d Tube diameter.
- f Tube frequency.
- \bar{U} Steady state flow velocity.
- U_o Inlet flow velocity.
- \bar{P} Steady state flow pressure.
- P_o Inlet pressure.
- p Pressure perturbation.
- s Curvilinear coordinate.

INTRODUCTION

In the past, plant equipment was made robustly and had rather modest performance demands. Flow-induced vibration problems were therefore rare. However, due to the higher performance demands and efficiencies required by modern facilities, structures became more flexible and were subjected to higher flow rates. As a result, flow-induced vibration problems became commonplace, making their study an important area of research. This is particularly true with regards to the nuclear industry and process chemical plants. Regulations, the enormous cost of plant shutdowns and repairs, and the potential for safety hazards generated intensive research activity. Shell and tube heat exchangers are integral parts of power and process plants and consist of a large number of tubes arranged in bundles. The integrity of these tubes is very important, especially in the case of nuclear steam generators. This makes the potential damage from flow induced vibration (FIV) a major concern. These vibrations can be attributed to several sources such as vortex shedding, turbulence, and fluidelastic instability mechanisms [1]. Turbulence is a random excitation mechanism that results in

*Address all correspondence to this author.

a low amplitude vibration (less than 2% of the tube diameter). Vortex shedding is a periodic excitation with a frequency that is proportional to the flow velocity. If the vortex shedding frequency coincides with one of the tube's natural frequencies, resonance takes place, leading to a large amplitude vibration. Fluidelastic instability (FEI) is characterized by the existence of feedback between the tube's motion and the resulting excitation forces. If the feedback is positive, the tube extracts energy from the flow. At a certain flow velocity, known as the critical flow velocity (U_c), the net damping of the system will vanish, leading to a higher tube displacement. This mechanism is potentially dangerous and, if unavoids, catastrophic failure of the operating unit can occur. This potential for catastrophic failure has led to several decades of intensive research to predict, understand and mitigate FEI effects. As a result, there is a large body of literature on the topic. Much of the research has been directed towards obtaining a reliable estimate of the critical flow velocity for the purpose of design [2]. To represent the stability behaviour of tube arrays, the Connors equation [3], in which a diagram depicting the reduced critical velocity as a function of the mass-damping parameter, is often used. Experimental investigation of the stability boundaries is required to establish these diagrams. The correlation of safe boundaries between the stable and unstable regions is essential for heat-exchanger tube bundle design. Numerous correlations of experimentally obtained critical flow velocities were developed. Excellent reviews providing design guidelines are provided by Weaver and Fitzpatrick [4]. The aforementioned efforts were devoted to obtaining more appropriate constants for the use of Connors-based models. These correlations presented the general trend of the instability phenomenon.

There are several models available to analyze FEI problems and the associated critical flow velocity [5–9]. These approaches, which includes Lever and Weaver [7], and Price and Païdoussis [8], are aimed at developing simple analytical models to describe the dynamic behaviour of tube bundles with limited (experimentally measured) input parameters. Based on the steady fluid forces measured on a tube positioned at various locations, a quasi-steady model was developed [8]. The forces are obtained from steady-state tests which are easy to perform. To account for the unsteadiness of fluid forces, a time delay is artificially introduced in the equation of motion. The time delay was postulated to be a result of a so-called flow retardation effect. Later, Granger and Païdoussis [10] modified the expression of time delay in a more intuitive manner. Rather than a constant value of the order of the tube diameter to velocity ratio ($\tau = O(d/U)$),

the time lag was described as a function.

A different approach was followed by Lever and Weaver [7]. They attempted to directly model the fluid forces rather than measuring them. This was done by simplifying the fluid mechanics such that an analytical expression that couples fluid forces and tube motion can be obtained. The flow through the tube array was divided into wake and channel regions. The flow was assumed to be incompressible and one dimensional. Fluidelastic excitation was considered to be independent of wake phenomena, and only perturbations in the free stream flow along either side of the tube were considered. Therefore the flow in the channels is shaped by the array geometry and can be modelled using the unsteady Bernoulli equation. The dimensions of the flow channels are a function of the tube array geometry only. It was postulated that the tube motion causes perturbations in the channel flow width. This in turn causes velocity and pressure perturbations. Fluid forces were obtained by integrating the pressure perturbation on the tube surface. A time delay was introduced to account for the flow redistribution effect, which leads to a fluid force with a component in phase with the velocity. The model resulted in a surprisingly good prediction of the stability threshold, which indicated that the model succeeded in capturing the essence of the phenomenon. The model was later modified to account for the effect of the neighbouring tubes [11]. Based on the same model, a time domain fluidelastic instability force model was developed where the nonlinear effect of the tubes' boundaries, such as gaps and frictional forces, were included [12].

Common among these two models [7, 8] is the use of time lag, which is a key element of the model. The choice of this time lag was found to affect the predicted results [12]. The exact nature of the time lag is not understood and further studies are needed to uncover its nature.

Tanaka and Takahara and Chen [6, 9] identified fluidelastic parameters by directly measuring the forces acting on the vibrating tube. An important aspect of these models is that the fluid parameters (fluid force coefficients) are expressed in terms of stiffness and damping coefficients. These force coefficients are strongly dependent on the reduced flow velocity ($U_r = U/fd$). The applicability of the unsteady flow models [6, 9] is restricted by the availability of the force coefficients on which these models depend. These force coefficients can be measured experimentally [6] or can be simulated using comprehensive numerical modelling [13].

Despite the considerable differences in the above mentioned theoretical models, there is an agreement in

the basic assumption that the flow is predominantly two-dimensional in nature. This assumption is justified by experimental results. It was shown that the correlation length of the fluid forces was found to increase suddenly to very large values. The interested reader is referred to the work of Romberg and Popp [14] which comprehensively examined the circumferential and axial correlation of fluid forces.

Since the early 1990s, there have been several avenues where computational fluid dynamics (CFD) has been extensively deployed to investigate flow induced vibration problems, with a particular emphasis on cylindrical tubes in various configurations. Considerable work was directed towards freely vibrating cylinders in which vortex structure and tube motion were coupled (see, for example, So et al. [15]). Moreover, several studies also embarked on attempting to directly predict critical flow velocities (leading to FEI) in flexible tube arrays [16–18]. This is a difficult task as it involves fully coupled fluid-structure interaction calculations. With respect to directly calculating critical flow conditions, the computational requirements are very high. Considering the many possible configurations of tube arrays including the fluid properties and state such as Reynolds number, at the current stage of development this approach appears to be infeasible for use in the context of practical heat exchanger configurations design.

A more pragmatic approach is to utilize CFD to predict parameters that can be integrated into the theoretical FEI models previously discussed. If applied intelligently, it would be possible to enhance the accuracy of the theoretical models. For example, Meskell et al. [19, 20] utilized numerical models to estimate the steady fluid forces as a function of both the velocity and the static tube displacement for a triangular tube array. They then used these force parameters in conjunction with the quasi-steady flow model. In another example, Hassan et al. [13] utilized CFD to simulate unsteady fluid forces and the corresponding force coefficient resulting from tube motion. The obtained coefficients were successfully utilized to predict the stability threshold of various arrays.

In this paper, CFD will be utilized to obtain the time lag information, which will be useful in shedding some light on the phenomenon. The obtained time lag will be integrated into the flow cell model to predict the stability threshold. In addition to this evaluation, and using the same approach, the effect of Reynolds number and vibration amplitude on the stability threshold will also be investigated.

1 The flow cell model

In its original form, the flow cell model of Lever and Weaver [7] idealizes the tube as a single degree of freedom system vibrating at its natural frequency. The fluid is assumed to flow through a series of flow channels passing between the tubes. The flow inside each channel is assumed to be one dimensional, inviscid and incompressible, and the fluidelastic excitation is independent of wake phenomena. Two flow channels are attached to the moving tube as shown in Fig. 1. The motion of the single flexible tube in a rigid array causes the dimensions of the flow channel to change. The channel width (A), flow velocity (U), and pressure (P) were decomposed into steady state (A_o , U_o , and P_o) and perturbation components (a , u , and p).

$$A(s,t) = \bar{A} + a(s,t) \quad (1)$$

$$U(s,t) = \bar{U} + u(s,t) \quad (2)$$

$$P(s,t) = \bar{P} + p(s,t) \quad (3)$$

This change in the flow channel's dimensions is postulated to lag behind the tube motion, which in turn leads to unsteadiness in the flow. A pressure perturbation that lags behind the tube motion is also produced. The resultant fluid forces have a component in-phase with the tube velocity which causes a destabilizing effect.

Each channel has a length of s_o and a cross sectional area of A , as shown in Fig. 1 for the normal triangle array. The geometry is simplified by assuming a constant steady state channel width which is $((P - D)/2)$ for this array. Consequently, the steady state velocity and pressure can be also be assumed to be constant and equal to the inlet velocity and pressure U_o and P_o . The curvilinear coordinates define the location along the channel. $-x_1$ and x_2 are the locations of the attachment and separation points. $-s_o$ is location of the next tube row. For each flow channel, the pressure at any point along the moving tube/channel interface is calculated by solving both the unsteady continuity and the momentum equations. The pressure is integrated along this tube/channel contact area to obtain the lift and the drag force per unit length ($F_L(t)$ and $F_D(t)$). The channel perturbation time lag is a very important parameter, which affects the quality of the predicted threshold. This parameter is dependent on the selection of the relevant fluid length (l_o). In the original model, the relevant fluid length was selected intuitively as $l_o = 2s_o$ (baseline value). Andjelc and Popp [21] recommended modified values for the relevant fluid length to achieve an acceptable agreement with their experimental stability thresholds for a normal triangle array. Hassan

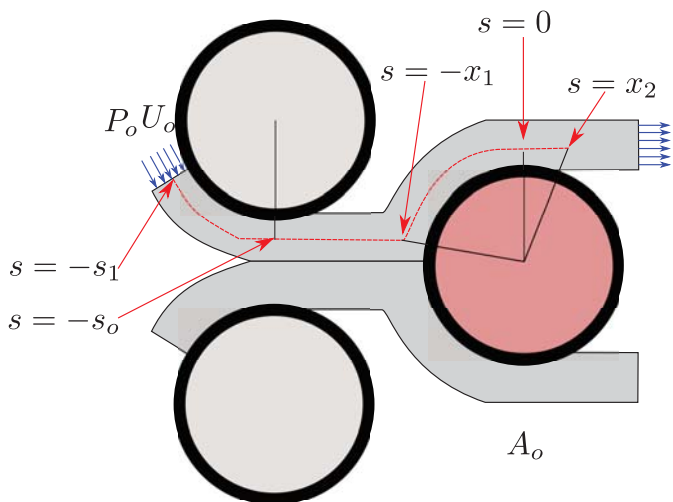


FIGURE 1: The flow cell mode [7]

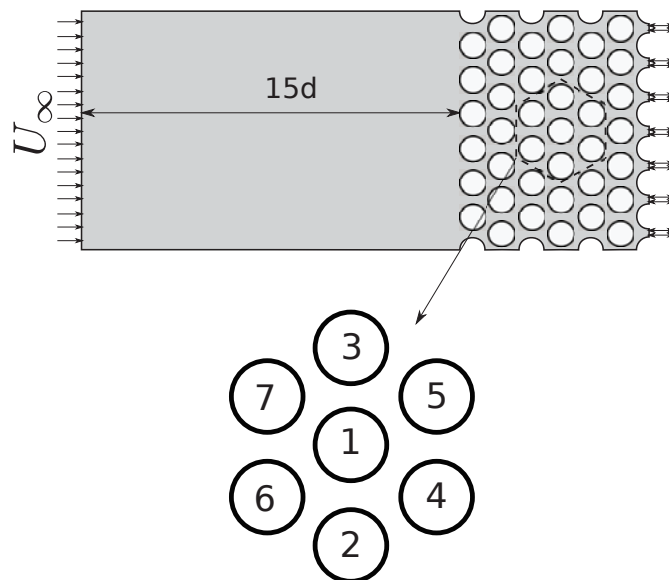


FIGURE 2: Schematic of the tube array geometry ($P/d = 1.35$)

and Hayder [12] conducted an investigation of the effect of variations in the relevant fluid length on the nonlinear response. They found minor effects on the lift response when the fluid length was increased by 200% of the baseline value.

2 Computational fluid dynamics model

The Reynolds Averaged Navier-Stokes (RANS) equations describing mass and momentum conservation are solved to obtain the time evolution of the velocity and pressure in the tube array. The interactions between fluid motion and moving structures is handled by casting the governing RANS equations in an Arbitrary Lagrangian-Eulerian (ALE) form which accommodates moving boundaries and any subsequent deformation of the underlying discrete mesh.

To include the influence of turbulent mixing, the Shear Stress Transport (SST) turbulence model is used [22]. For further details on the model choices, and a discussion on the turbulence modelling issues and justification, the reader is referred to the paper of Hassan et al. [13].

2.1 Solution strategy for generating unsteady fluid forces

Although a moving grid simulation is inherently a transient problem, the simulation is first run with a static tube bundle. This obtains a quasi steady-state solution to provide the initial flow conditions for the transient simulation. Following this preliminary process, a transient simulation is then started with one tube being forced to move at a specified frequency and amplitude. The mov-

ing tube is forced to first oscillate in the lift direction and then in the drag direction.

2.2 Tube array model

The normal triangle tube array contains 53 tubes arranged in 8 columns and 7 rows with $P/d = 1.35$ and a tube outside diameter (d) of 30mm, as shown in Fig. 2. The last row functioned as an exit. The Reynolds number is set by adjusting the value of the inlet velocity. Tube 1 (Fig. 2) was forced to oscillate in the lift and drag directions with various excitation frequencies. The excitation frequency (f_e) was used to obtain the required reduced flow velocity while fixing the upstream flow velocity. A uniform inlet velocity was applied with a turbulence intensity level of 5% (for medium-level turbulence). The gaps between the tubes in the last row were set as the exit. This was found to eliminate some of the periodicities in the force signal due to the wake oscillation behind the last row [13]. In addition, it also allowed the use of a smaller computation domain which resulted in a considerable savings in simulation time. The unsteady lift and drag forces acting on Tube 1 are obtained by integrating the pressure and the fluid shear stresses acting on these tubes. Once convergence in the steady flow solution is obtained, the transient solution commences.

Based on the steady state simulations, the shape of the flow channel was determined, as shown on Fig. 3. The space between any two adjacent tubes in a row was found to be divided into two separate flow channels. This is con-

sistent with the flow visualization of Scott [23]. Eighty nine monitoring points were placed along the upper flow channel associated with Tube 1. Forty-four monitoring points were placed along the upstream path, and a similar number of points were placed downstream. The flow velocity and pressure were obtained at each time step. The results at each monitoring point were processed to obtain the mean, the perturbation amplitude, and the phase.

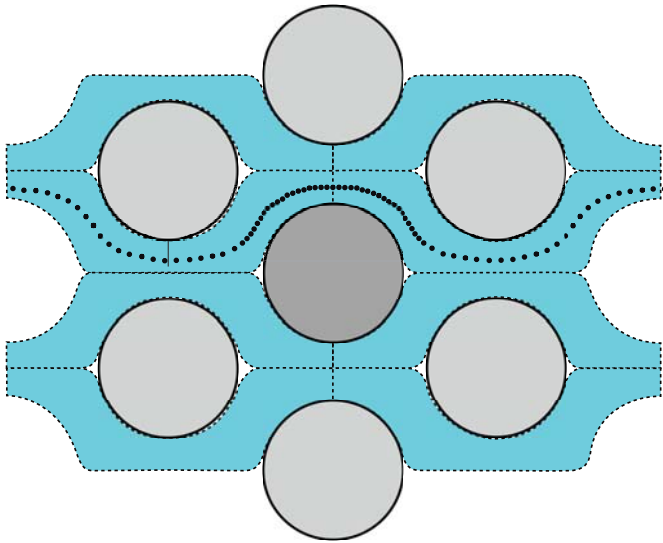


FIGURE 3: Locations of the monitoring points

The unsteady flow results include a dominant frequency which is associated with the prescribed tube motion. The mesh distribution around the moving tube is shown in Fig. 4. Detailed mesh resolution tests were performed to verify grid dependence. The effect of mesh resolution was conducted, and accordingly, a mesh with 160000 nodes was found to be suitable. A study of the time step resolution was conducted and found that a time step resolution of $\delta t = T/90$ (T is the oscillation period) provides not only reasonably accurate calculations, but also an efficient use of computational resources. Fifty tube oscillations, beginning from a quasi-steady initial solution, were simulated. This ensured steady statistics could be obtained when applying the Fast-Fourier Transform (FFT) process to the force data.

3 Results

The distribution of the mean velocity component (U_m) is shown in Fig. 5. The reduced mean velocity (U_m/U_o) has a value of 0.5 at $s/s_o = 0.6$. At $s/s_o = 0$ and $s/s_o = -1.0$ the reduced mean velocity is 1. This

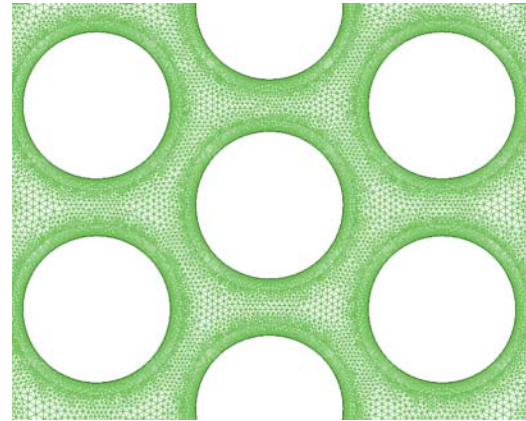


FIGURE 4: Mesh distribution for the moving and surrounding tubes

variation is attributed to the fact that two channels exist between the adjacent tubes at $s/s_o = 0$ and $s/s_o = -1.0$ while a single channel exists between adjacent tubes at $s/s_o = 0.6$. As mentioned earlier the original flow cell model simplifies the channel geometry as having a constant width which in turn results in a constant mean velocity and pressure along the channel length.

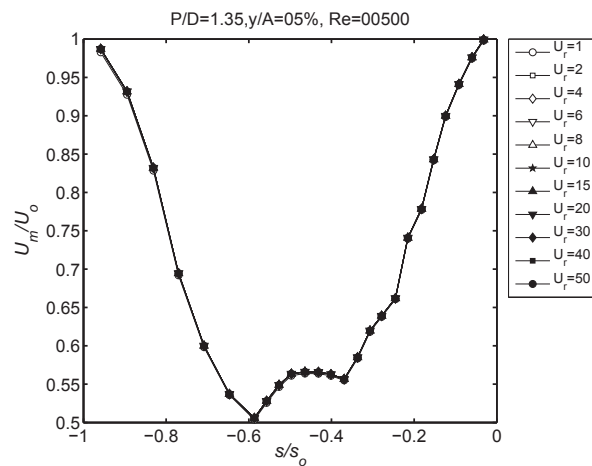


FIGURE 5: Mean Velocity perturbations for 5% displacement and $Re=500$

Figure 6 shows the velocity perturbation distribution along the channel for a reduced flow velocity of 1. The maximum velocity perturbation takes place at two locations $s/s_o \approx \pm 0.55$. The velocity perturbation becomes zero in the vicinity of the next tube row ($s/s_o \approx \pm 1.0$). For the moving tube attachment/separation region, the minimum velocity perturbation takes place at ($s/s_o \approx 0$).

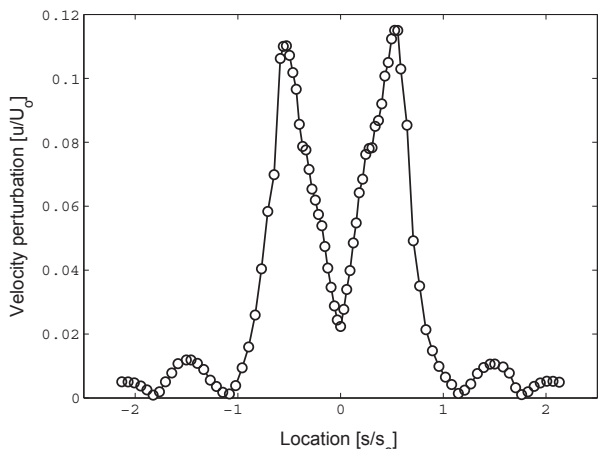


FIGURE 6: Mean Velocity perturbations for a reduced velocity ($U_r = 1$), 5% displacement and $Re=500$

In order to place these results in the context of the flow cell model of Lever and Weaver [7], the discussion will be restricted to the upstream portion only. The effect of the reduced flow velocity is shown in Fig. 7. The general trend was maintained for all reduced flow velocities with a maximum value at ($s/s_0 \approx 0.55$). It is also observed that the minimum velocity perturbation shifts slightly upstream for higher reduced flow velocities.

Figure 8 shows that the effect of the reduced flow velocity on the velocity perturbation at $s/s_0 \approx \pm 0.55$. The velocity perturbation ratio u/U_0 sharply decreases in the reduced flow velocity range of 1 to 4. The reduced flow velocity has an insignificant effect on the velocity perturbation for reduced flow velocities higher than 10. This is similar to the force coefficient trends reported experimentally [6] and numerically [13]. In addition, the same behaviour was observed for other Reynolds number values. Increasing the Reynolds number causes the velocity perturbation ratio to decrease.

The phase relationship between the tube displacement and the flow velocity perturbation was obtained for reduced flow velocities ranging from 1 to 50. The phase has two distinct trends depending on the range of reduced flow velocities. An example of the phase relationship for the low range of flow velocities (1 to 8) is shown in Fig. 9a. The phase of the velocity perturbations varies almost linearly with location (s) for $0.2 > s/s_0 > -0.2$ with a zero phase at $s/s_0 \approx 0$. For $s/s_0 < -0.2$ (upstream) and $s/s_0 > 0.2$ (downstream), the phase is relatively constant at about -100° and 100° , respectively. An example for higher reduced flow velocities is shown in Fig. 9b where the minimum velocity phase is located at $s/s_0 \approx 0$. The phase varies linearly both upstream and downstream in

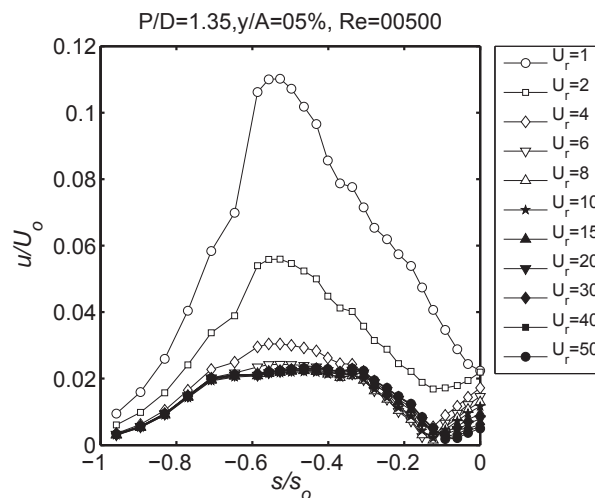


FIGURE 7: Velocity perturbations for 5% displacement and $Re=500$

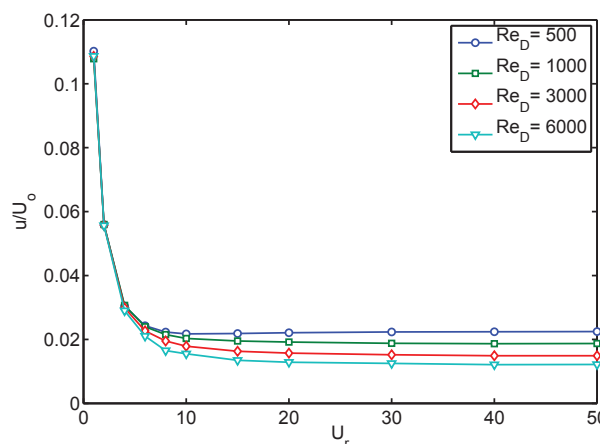


FIGURE 8: Effect of Re on the velocity phase for 5% displacement and $Re=500$

the vicinity of $s/s_0 = 0$. Further upstream and downstream the velocity phase levels off at constant values of 190° and 140° , respectively.

The velocity phase for all reduced flow velocities is shown in Fig. 10. The phase lag in this figure is presented in such a way to preserve a smooth variation in the trend. The general trend for all reduced flow velocities is preserved where a minimum phase exists at a location in the neighborhood of $s/s_0 \approx 0$ and levels off further downstream at $s/s_0 < -0.2$.

A further examination of the phase in the flat portion of the trend ($s/s_0 < -0.2$) was examined for various reduced flow velocities and Reynolds numbers and illustrated in Fig. 11. In the lower reduced velocity range

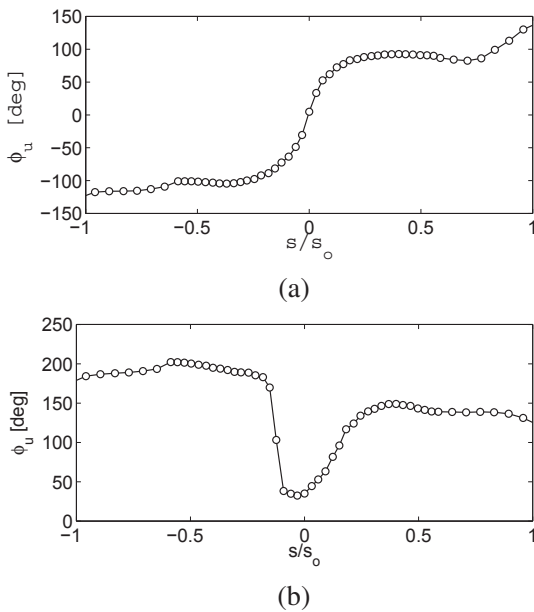


FIGURE 9: Velocity phase: (a) $U_r = 1$, (b) $U_r = 10$

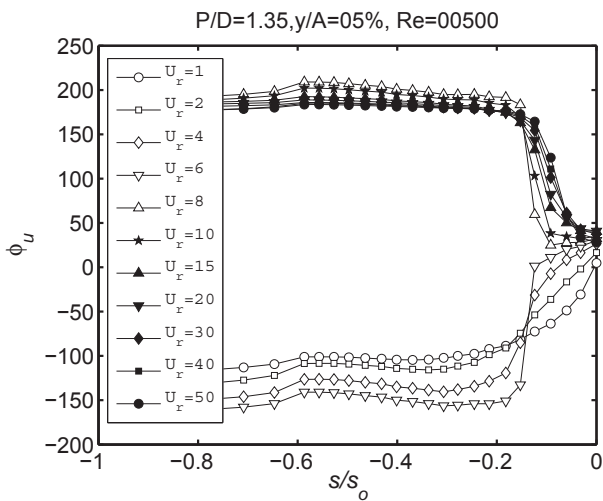


FIGURE 10: Velocity phase for 5% displacement and $Re=500$

(1-6), the phase sharply decreases from 270° and levels off approaching a value of 180° for reduced flow velocities greater than 10° . This behaviour is presented for all Re . For any reduced flow velocity, a higher Re results in a higher phase angle.

Conclusions

Numerical simulations for normal triangle tube array were conducted to investigate the time lag between the tube motion and the resulting flow perturbation. A RANS

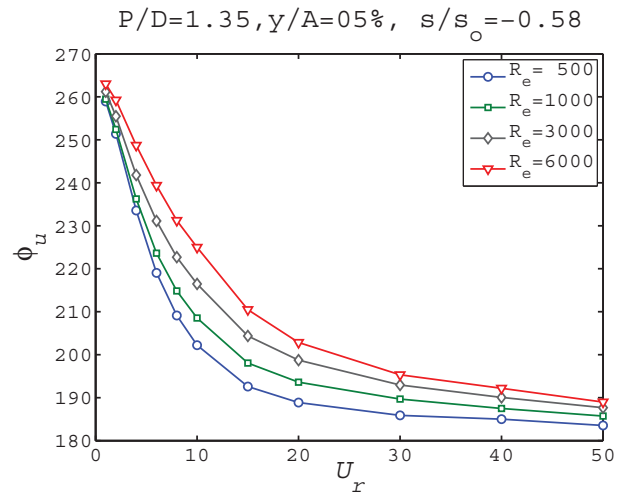


FIGURE 11: Effect of Re on the velocity perturbations for 5% displacement and $Re=500$

CFD solution using an arbitrary Lagrangian-Eulerian formulation with moving boundaries was utilized. A single tube was forced to oscillate at a fixed amplitude and frequency. The flow velocity amplitude and phase was obtained at 89 locations along the flow channel. The reduced flow velocity has no effect on the mean flow velocity distribution with a minimum value equal to half the pitch velocity. The maximum velocity perturbation amplitude was found to decrease as the reduced flow velocity increases. The velocity perturbation phase angle was found to increase with the location along the flow channel. The phase lag was also found to become constant beyond a certain point along the flow channel ($s/s_o < -0.2$). The current study provides valuable information regarding the time lag along the flow channel.

ACKNOWLEDGMENT

The authors thankfully acknowledge the financial support provided by the Natural Sciences and Engineering Research Council of Canada.

REFERENCES

- [1] Weaver, D., Ziada, S., Au-Yang, M., Chen, S., Païdoussis, M. P., and Pettigrew, M., 2000. "Flow-induced vibrations in power and process plant components - progress and prospects". *ASME Journal of Pressure Vessel Technology*, **122**, pp. 339–348.
- [2] Pettigrew, M., and Taylor, C., 2003. "Vibration analysis of shell-and-tube heat exchangers: An overview - part 1: Flow, damping, fluidelastic instability".

- Journal of Fluids and Structures*, **18**(5), Nov., pp. 469–483.
- [3] Connors, H. J., 1970. “Fluidelastic vibration of tube arrays excited by cross flow”. In *Flow-Induced Vibration in Heat Exchangers*, D. D. Reiff, ed., ASME, pp. 42–57.
- [4] Weaver, D., and Fitzpatrick, J., 1988. “A review of cross-flow induced vibrations in heat exchanger tube arrays”. *Journal of Fluids and Structures*, **2**, pp. 73–93.
- [5] Connors, H., 1981. “Flow-induced vibration and wear of steam generator tubes”. *Nuclear Technology*, **55**, pp. 311–331.
- [6] Tanaka, H., and Takahara, S., 1981. “Fluid elastic vibration of tube array in cross-flow”. *Journal of Sound and Vibration*, **77**, pp. 19–37.
- [7] Lever, J. H., and Weaver, D. S., 1982. “A theoretical model for the fluidelastic instability in heat exchanger tube bundles”. *ASME Journal of Pressure Vessel Technology*, **104**, pp. 104–147.
- [8] Price, S. J., and Païdoussis, M., 1983. “Fluidelastic instability of an infinite double row of circular cylinders subject to a uniform cross-flow”. *Journal of Vibration, Acoustics, Stress, and Reliability in Design, Transactions of the ASME*, **105**, pp. 59–66.
- [9] Chen, S. S., 1983. “Instability mechanisms and stability criteria of a group of cylinders subjected to cross-flow. Part 1: Theory”. *Journal of Vibration, Acoustics, Stress and Reliability in Design, Transactions of the ASME*, **105**, pp. 51–58.
- [10] Granger, S., and Païdoussis, M. P., 1996. “An improvement to the quasi-steady model with application to cross-flow-induced vibration of tube array”. *Journal of Fluid Mechanics*, **320**, pp. 163–184.
- [11] Yetisir, M., and Weaver, D., 1993. “An unsteady theory for fluidelastic instability in an array of flexible tubes in cross-flow. Part1: Theory”. *Journal of Fluids and Structures*, **7**, pp. 751–766.
- [12] Hassan, M., and Hayder, M., 2008. “Modelling of fluidelastic vibrations of heat exchanger tubes with loose supports”. *Nuclear Engineering and Design*, **238**(10), pp. 2507 – 2520.
- [13] Hassan, M., Gerber, A., and Omar, H., 2010. “Numerical estimation of fluidelastic instability in tube arrays”. *ASME Journal of Pressure Vessel Technology*, **132**(4), p. 041307.
- [14] Romberg, O., and Popp, K., 1998. “Influence of upstream turbulence on the fluidelastic instability of a parallel triangular tube bundle”. *Journal of Fluids and Structures*, **12**, pp. 153–169.
- [15] So, R., Liu, Y., Chan, S., and Lam, K., 2001. “Numerical studies of a freely vibrating cylinder in cross-flow”. *Journal of Fluids and Structures*, **15**, pp. 845–866.
- [16] Schröder, K., and Gelbe, H., 1999. “Two- and three-dimensional cfd simulation of flow-induced vibration excitation in tube bundles”. *Chemical Engineering and Processing*, **38**, pp. 621–629.
- [17] Kassera, V., and Strohmeier, K., 1997. “Simulation of tube bundle vibrations induced by cross-flow”. *Journal of Fluids and Structures*, **11**, pp. 909–928.
- [18] Longatte, E., Bendjeddou, Z., and Souli, M., 2003. “Methods for numerical study of tube bundle vibrations in cross-flows”. *Journal of Fluids and Structures*, **18**, pp. 513 – 528.
- [19] Meskell, C., and Fitzpatrick, J., 2003. “Investigation of the nonlinear behaviour of damping controlled fluidelastic instability in a normal triangular tube array”. *Journal of Fluids and Structures*, **18**(5), November, pp. 573–593.
- [20] Gillen, S., and Meskell, C., 2008. “Variation of fluidelastic critical velocity with mass ratio and Reynolds number in a densely packed normal triangular tube array”. In *Flow Induced Vibrations*, I. Zolotarev and J. Horáček, eds., pp. 193–198.
- [21] Andjelčić, M., and Popp, K., 1989. “Stability effects in a normal triangular cylinder array”. *Journal of Fluids and Structures*, **3**(2), pp. 165–185.
- [22] Menter, F. R., 1994. “Two-equation eddy viscosity turbulence models for engineering applications”. *AIAA Journal*, **32**(8), pp. 1598–1605.
- [23] Scott, P., 1987. “Flow visualization of cross-flow-induced vibrations in tube arrays”. Master’s thesis, McMaster University, Hamilton, Ontario, Canada.



Numerical study on the effects of particles on damping the vibration of a bluff body due to the vortex shedding

Pejman Shoeibi Omrani
 Fluid Dynamics Department,
 TNO Science and Industry,
 Stieltjesweg 1, 2628 CK Delft,
 The Netherlands
 Email: pejman.omrani@tno.nl

Stefan Belfroid, Aris Twerda
 Fluid Dynamics Department,
 TNO Science and Industry,
 Stieltjesweg 1, 2628 CK Delft,
 The Netherlands

Bendiks Jan Boersma
 Process and Energy
 Department, TU Delft
 The Netherlands

ABSTRACT

A Karman-vortex street is formed when a fluid passes a bluff body. This vortex shedding is altered by the presence of particles or droplets. In this paper we present numerical simulation results on the effect of particle mass loading on the vortex shedding frequency and the dynamic lift and drag forces on the bluff body. 2D simulations were done using ANSYS FLUENT software [1]. The Reynolds stress model was used to model the turbulence fluctuations and the Discrete Phase Model (DPM) for the particle tracking. We used one-way and two-way couplings between the continuous and the dispersed phases. A triangular shape was used for the bluff body as this mimics the shape of most vortex meters. The pressure fluctuations behind the bluff body and the forces acting on the bluff body were monitored. The results show that the presence of particles decrease the turbulent kinetic energy and intensity and it will lead to the decrease of the pressure fluctuations and the dynamic forces on the bluff body.

INTRODUCTION

The flow in a wake of bluff bodies has been a subject of study for many years. A summary of different regimes for the wake flow and the boundary layer is given in [2]. The regimes can differ from $Re \ll 1$ which is an unseparated flow (creeping flow) and dominates with viscous forces, to $Re > 3.5 \times 10^6$ which is a turbulent wake flow with turbulent boundary layer. It is important to note that the Reynolds number in this case is based on the bluff body diameter. For a range of Reynolds number a periodic vortex shedding occurs behind the bluff body.

For small Reynolds number ($Re < 40$), the flow will exert a static drag force on the body in the streamwise direction. For $Re > 40$ the vortices are formed and the vortex shedding will start and exert dynamic forces

(dynamic drag and lift forces) on the bluff body, due to the pressure asymmetry on the body.

The wake flow has extensive engineering applications. One of them is by relating the frequency of the vortex shedding to the flow velocity which is used in the flow meters and is called vortex meters [3-6]. A critical point about vortex shedding from the bluff body is that it can cause large vibration level or fatigue failure [7].

The periodic vortex shedding can be explained by its magnitude and frequency. The frequency of the vortex shedding is related to the non-dimensional Strouhal number, which is

$$Str = \frac{f d}{U}$$

In which Str is the Strouhal number [-], f is the shedding frequency [Hz], d is the diameter, in this case width, of the bluff body [m] and U is the free stream velocity [m/s]. The frequency of the shedding is equal to the frequency of the bluff body vibration in the direction perpendicular to the flow (dynamic lift force). The frequency of the shedding is half the dynamic drag force frequency. Strouhal number for different bluff body geometries and Reynolds numbers can be found experimentally and it is plotted in the Figure 1. Strouhal number is used in vortex flow meters to relate the vortex shedding frequency to the velocity.

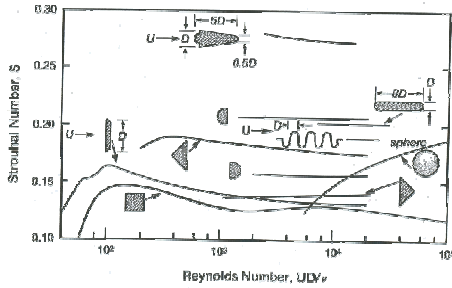


Figure 1- Strouhal number for different shapes of bluff body [9].

The presence of particles or droplets in the turbulent flows can enhance or damp the turbulent intensity [8]. The effects of particle inertia on the flow can be categorized by the non-dimensional Stokes number, which can be defined by the ratio of the particle response time to the fluid response time.

$$St = \frac{\tau_p}{\tau_f}$$

Where $\tau_p = \frac{\rho_p d_p^2}{18\mu}$ (particle response time) and

$\tau_f = \frac{L}{U}$ (fluid response time, L and U are the characteristic length [m] and velocity [m/s]).

In this study, the triangular geometry was chosen as a bluff body. The pressure downstream of the bluff body and the drag and lift force of the bluff body is monitored. In a preliminary step, the one-phase gas flow vortex shedding from the bluff body is investigated to verify the solver and the applied method in the calculations. From the Reynolds stress model, the effect of particles mass loading on the lift and drag coefficient of the bluff body is analyzed.

For the particle transport, a one-way coupling and two-way coupling approach was used. In one-way coupling the particles are following the flow without having any effect on the flow. In the two-way coupling, the particles will insert forces on the flow (momentum transfer). For a mass loading less than 10%, the one-way coupling assumption is valid [10]. This is the hypothesis that will be checked in this study. Particles with different mass loading (diameter) are injected into the gas flow.

SIMULATION APPROACH

Computational Domain

The computational domain is given in the Figure 2. The triangle has the width of $d = 1$ m and the height of $h = 2$ m. The velocity inlet boundary condition has the distance of 5 times the triangle width from the bluff body and the outlet boundary condition is located at 22 times the diameter (from the body). The symmetry lines are located about 5 times the triangle width from the domain centerline.

The structured grid is generated in Gambit package. The mesh was generated close to the walls with a fine aspect ratio to resolve the fluid flow close to the wall. The simulations were performed with the Reynolds numbers in the range of 1000 to 10000. For the Reynolds number of 10000, the wall unit ($y^+ = \frac{y}{\delta_v} = \frac{u_\tau y}{\nu}$) will be around 2 (u_τ is the friction velocity[m/s] and ν is the kinematic viscosity [m^2/s]).

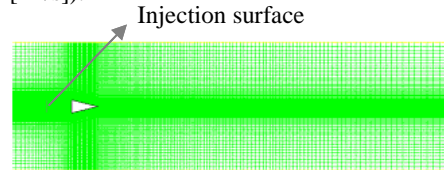


Figure 2- The computational domain.

For the calculation of the fluid response time, the width of the bluff body is taken as the characteristic length and the mean flow velocity as the characteristic velocity. The shedding frequency can be obtained by FFT (Fast Fourier Transform) of the dynamic lift force monitor.

The ANSYS FLUENT package was used for the numerical simulation. The unsteady Reynolds stress model which is a Reynolds-averaged Navier-Stokes model (RANS) was used for the turbulent modeling and the Discrete Phase Model (DPM) for the particle tracking. The point-particle approach is used in ANSYS FLUENT which means that the geometrical effect of the particles are neglected. The time step size is 0.01 sec in these simulations.

RESULTS

One-phase gas flow results

The Figure 3 shows the velocity magnitude contour in the computational domain. The periodic vortex shedding can be clearly detected in the downstream of the bluff body. The recirculating separation trailing edge. The recirculating separation trailing edge.

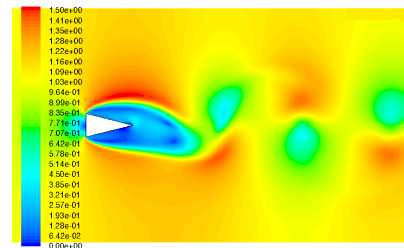


Figure 3- The velocity magnitude contour plot for Re =10000.

The comparison between the simulations and the experiment is given in the Figure 4. The figure shows the Strouhal number versus the Reynolds number. It can be seen that there is a small difference between the experimental and simulation data. The largest relative

error is about 4.2% at $Re = 10000$ which can be due to the turbulent structures and small eddies motion and they are not present in the simulation.

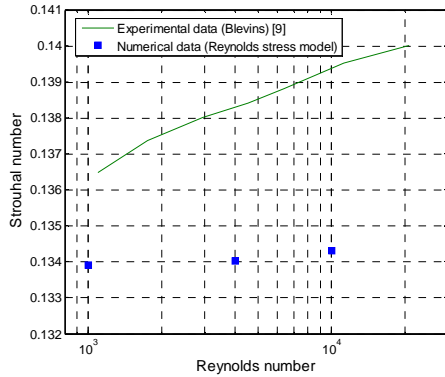


Figure 4- The comparison of Strouhal number as a function of Reynolds number (experimental data [9], numerical data (performed simulations)).

Effect of particles on the flow

In this section the air flow has the Reynolds number of 10^4 . The results are presented in two sections, one-way coupling and two-way coupling results. In the one-way coupling results, the effect of flow on the particles are resolved with neglecting the effect of particles on the flow. The goal of this part is to study the dispersion pattern of the droplets with different inertia in the wake flow. In the two-way coupling sections, the particles will exchange momentum with the continuous phase.

The number of particles injecting at each time step is equal to the number of cells at the injection surface which in our model is 350 particles. The density of the particles is 998 kg/m^3 . The choice of the time step in this case is dependent on both the shedding frequency and the particle velocities. In the simulations the particles are injected with the same velocity as the fluid flow ($u=1 \text{ m/s}$). In order to resolve the particle motion between the grids, we chose the time step size that the displacement of droplets in each time step is smaller than the size of two grid cells. This assumption is to make the simulation more accurate and prevents the particles jumping from one cell to another. Based on this assumption the time step was chosen to be 0.01 sec.

One-way coupling results

The particles are injecting into the fluid domain with constant diameter and they have no effect on the air flow. The only coupling between the air flow and droplets is the forces acting on the particles from the continuous phase. The results are shown in the Figure 5.

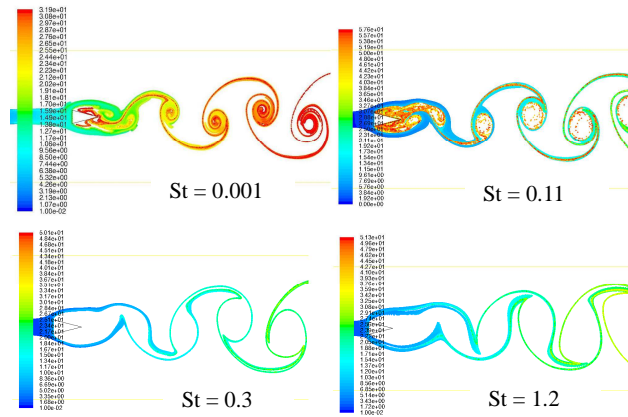


Figure 5- Unsteady droplet dispersion in the wake flow behind the bluff body, one-way coupling simulation with different Stokes number and $Re = 10000$.

It can be seen in the Figure 5 that the particles dispersion is greatly affected by the vortex-particle interaction. For very small particles ($St=0.001$), the particles will act as flow tracers and they follow the flow trajectories. By increasing the Stokes number, the particles residence time and inertia starts to increase and the balance of forces between the flow and particles will introduce a centrifugal force for particles. As it can be seen from the results, in larger Stokes numbers the particles tend to accumulate on the peripheries of the vortices.

It is important to note that the only force exerting on the droplets is the drag force (Stokes drag force). The Basset force, virtual mass and the lift forces are neglected. Thus, the drag force, or in this case centrifugal force from the center of vortices, push the droplets outward the vortices center and accumulate them on the outer boundary of the vortices. The results for the Strouhal number as a function of Stokes number are given in the Figure 6.

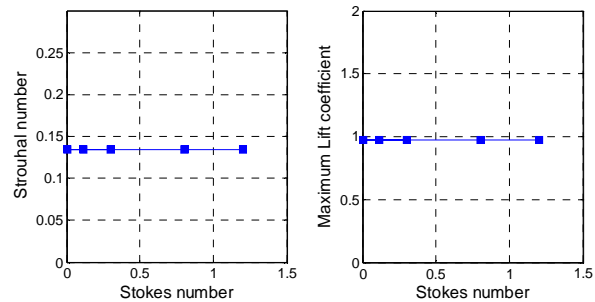


Figure 6- The Strouhal number and lift coefficient as function of Stokes number for the one-way coupling simulation.

It can be seen that there is no change in the Strouhal number and the maximum lift coefficient (also drag coefficient). In order to study the effect of particles on the flow, the two-way coupling simulations were performed which is given in the next part.

Two-way coupling results

In this part the effect of particles mass loading on the Karman vortex shedding is analyzed. The particle dispersion patterns are given in the Figure 7. The periodic vortex shedding is affected by the presence of the droplets.

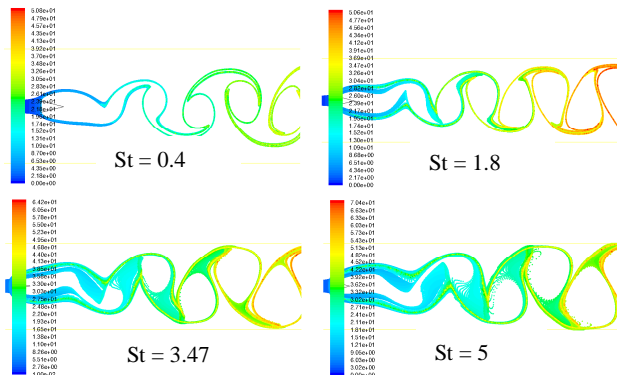


Figure 7- Unsteady droplet dispersion in the wake flow behind the bluff body, two-way coupling simulation with different Stokes number with Reynolds number of 10^4 .

It shows that the particles with very large Stokes number are starting filling the vortices core again and they fill the distance between the adjacent vortices. The particles with high Stokes number become unresponsive to the flow. The droplets decrease the turbulence intensity of the flow by exchanging momentum (Figure 8). Another effect that can be seen from the figure is that the large Stokes number particles change the vortices and braid their structures. Additionally, large Stokes number particles shift the formation of the vortex shedding further from the bluff body.

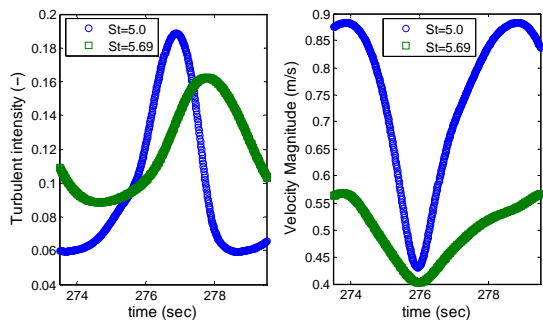


Figure 8- The changes of turbulent intensity and velocity magnitude in time in a point behind the bluff body (On the centreline and $x=6d$).

In order to analyze the effect quantitatively, the results for the Strouhal number and the bluff body lift and drag coefficients are presented in the figures 9 to 12. It is important to note that the Strouhal number in this case is equal to the shedding frequency ($U=1$ m/s, $d=1$ m).

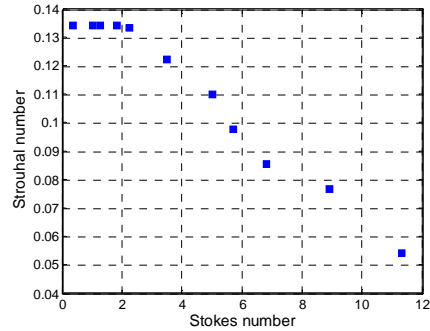


Figure 9- The Strouhal number as the function of Stokes number (two-way coupling results) with $Re=10000$.

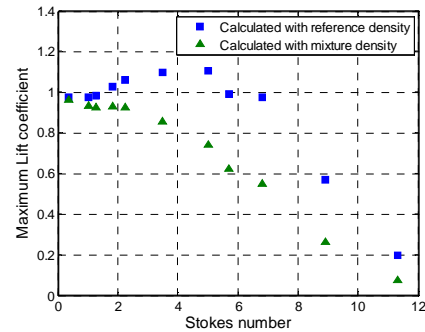


Figure 10- The bluff body maximum lift coefficient as the function of Stokes number (two-way coupling results for the mixture and reference density) with $Re=10000$.

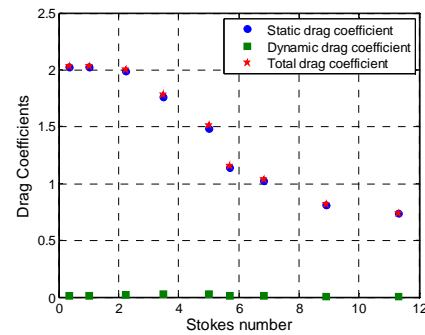


Figure 11- The Static, dynamic and total drag coefficients as function of the Stokes number, two-way coupling simulations with $Re = 10000$.

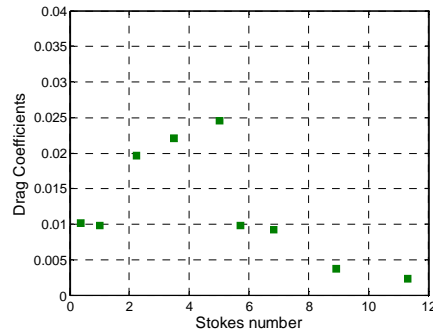


Figure 12- The dynamic drag coefficient of the bluff body versus the Stokes number, two-way coupling simulations $Re = 10000$.

The Figure 9 shows that higher Stokes number particles decrease the vortex shedding frequency and consequently, the Strouhal number. Large particles tend to stabilize the flow and decrease the turbulence intensity. The decrease in the Strouhal number starts at $St = 1.8$ which corresponds to the mass loading of 10.6%. This result show that the hypothesis on the effect of particles with mass loading of 10% or more is valid.

The increase in the lift coefficient is partly due to the mixture density. In Figure 10 the effect of the mixture density is shown on the reported value for lift coefficient from the FLUENT package. It can be seen that the particles inertia is decreasing the lift coefficient of the bluff body. However, for Stokes number less than 5 the effect of mixture density dominates the effect of particles stabilizing the flow. The decrease in the lift coefficient after $St = 5$ is corresponding to the dominant stabilizing effect of particles inertia on the vortex shedding.

Effect of the number of injected particles

In this section the discrete phase mass loading is changed by changing the number of injected particles. For this purpose the time step of the injection was doubled to decrease the number of droplets which are injecting per second ($\Delta t = 0.02$ s). Thus, the mass loading for this section case is half the mass loading of the previous case for each Stokes number.

The mass loading is calculated based on the injection area and the number of particles injecting into the domain. The equation for the mass loading is given below.

$$z = \frac{\dot{m}_p}{\dot{m}_F} = \frac{\rho_p V_p (\text{Particles} / s)}{\rho_f u_f A_{inj}}$$

where V_p, u_f, A_{inj} are the volume of each particle [m^3], velocity of the flow [m/s] and the injection area [m^2].

The results for the Strouhal number and the maximum lift coefficient (with and without considering the mixture density) is plotted in the Figure 13.

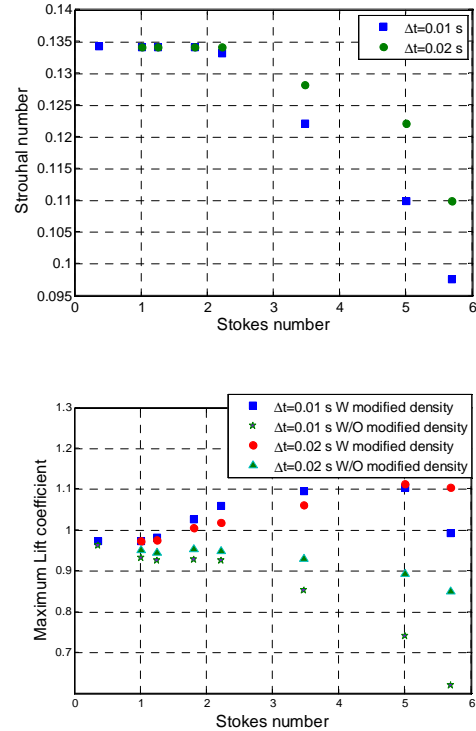


Figure 13- The Strouhal number and maximum lift coefficient as function of Stokes number for different number of injected particles.

The figure shows that lower mass loading can keep the vortex shedding without changing for higher Stokes number. The lower number of particles can shift the effect of particles to higher Stokes number. The decrease in the maximum lift coefficient for higher Stokes number without modified density can be seen in the Figure 13. The results for the lift coefficient without considering the mixture density show lower decrease in the lift coefficient for smaller mass loading.

VALIDATION

In this section the results are compared to the previous studies. There are couple of numerical studies on the effect of droplets or particles on the vortex shedding behind the bluff body with different numerical methods. One of them has been done by Tang *et al.* in which the experimental and numerical results were compared together [11]. Kun *et al.* [12] did the LES (Large Eddy Simulation) simulation of the particle-wake interaction of the circular cylinder bluff body. The comparison is given in the Figure 14.

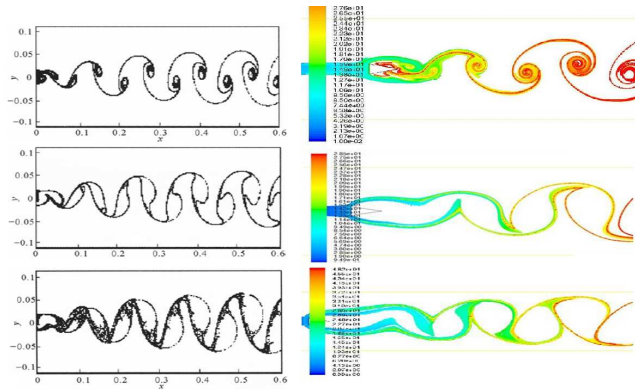


Figure 14- The comparison of particle dispersion in turbulent wake flows between LES results (left) [12] and Reynolds stress model (right).

The figure shows a good agreement between the LES data and our simulation ($St \approx 0.001$, $St \approx 1.8$, $St \approx 2.2$). It can be seen that in both simulations the particles starts connecting the vortices to each other from the connecting areas and the particles filling the connecting regions.

Time step and mesh sensitivity analysis

In this section of this study, the sensitivity of the results to the grid size and time step size is studied. For this purpose different time steps ($\Delta t = 0.005, 0.01, 0.02, 0.04$ s) were used for the simulations and the results for the Strouhal number are given in the Figure 15.

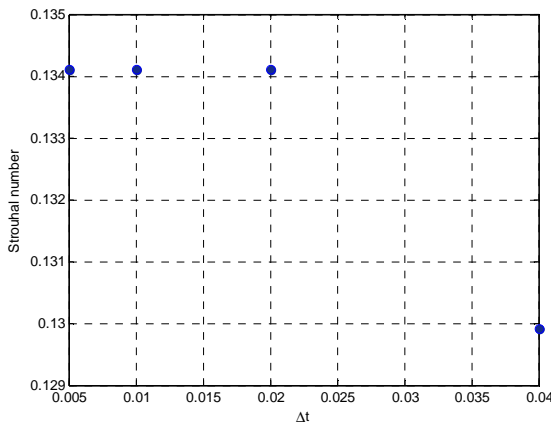


Figure 15- The Strouhal number for different time step size.

It can be seen that the results of the chosen time step ($\Delta t = 0.01$ s) is not sensitive to the smaller or larger time step. The same time of simulation was performed for different grid sizes. The grid cell sizes close to the wall are given in the Table 1. The grid size which was used in this study is number 2. The x is in the tangential direction of the wall and the y is in the normal direction.

Table 1- The different cases for mesh sensitivity analysis

Grid	$\Delta x (m)$	$\Delta y (m)$
Grid 1	0.04	0.0008
Grid 2	0.05	0.0017
Grid 3	0.06	0.0029

The results of the Strouhal number for different mesh sizes are given in the Figure 16.

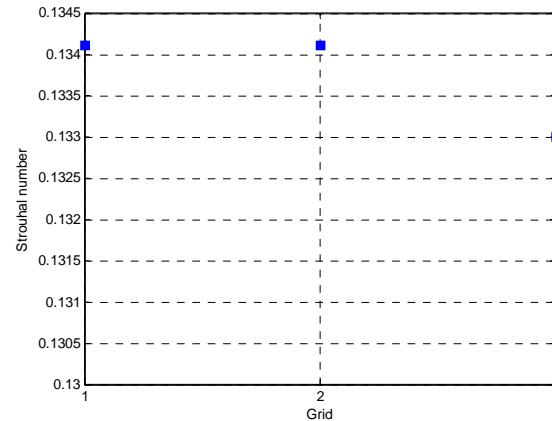


Figure 16- The Strouhal number for different grid sizes.

The results show the grid independency of the model. As it was mentioned before, the Grid 2 is the chosen grid for our simulations and it can generate an accurate result which takes less iteration.

CONCLUSIONS

The effect of particles on the vortex shedding behind the bluff body was investigated numerically. In the one-way coupling, higher Stokes number the particles tend to accumulate on the peripheries of the vortex structures. For higher Stokes number the effect of particles on the flow is not negligible and for this purpose two-way coupling simulations were performed. In the two-way coupling simulations, particles start to change the wake flow and by increasing the particles Stokes number (and consequently mass loading), the vortex shedding will be stabilized. In two-way coupling for high Stokes number, particles start filling the core of vortices and they decrease the turbulence intensity and the Strouhal number (which in our simulation is the same as vortex shedding frequency). The increase in the value of lift coefficient is due to the mixture density which is increasing for higher Stokes number particles.

The effect of particle mass loading on the vortex shedding was studied in two parts, by increasing the particles inertia and changing the number of injected particles. The larger the mass loading, the larger the changes of the vortices structures and it can make the vortices structures to get closer to each other from the center of the core region. It shows that the lower mass loading has less influence on the vortex shedding and it

can shift the transition of then vortex shedding stabilizing to a higher Stokes number.

REFERENCES

- [1] FLUENT 6.3 Documentation, user's guide.
- [2] Kundu, P. K. and Cohen, I. M., *Fluid Mechanics*, 2nd. Ed., Academic Press 2002.
- [3] B. K. Gandhi, S. N. Singh, V. Seshadri, J. Singh, *Effect of bluff body shape on vortex flow meter performance*, *Indian Journal of Engineering and Materials science*, Vol 11, 378-384, 2004.
- [4] A. L. Csiba, R. J. Martinuzzi, *Investigation of bluff body asymmetry on the properties of vortex shedding*, *Journal of wind Engineering and Industrial Aerodynamics*, Vol 96, 1152-1163, 2008.
- [5] R. C. Baker, *Flow measurement handbook*, Cambridge University Press, 2000.
- [6] K. J. Zanker, T. Cousins, *The Performance and Design of Vortex Meters*, *Fluid Flow Measurement*, 1975.
- [7] I. Giosan, *Vortex shedding induced loads on free standing structures*, *Structural Vortex Shedding Response Estimation Methodology and Finite Element Simulation*.
- [8] C. Crowe, M. Sommerfeld, Y. Tsuji, *Multiphase Flows with Droplets and Particles*, first ed. CRC Press, New York, 1998.
- [9] R.D. Blevins, *Flow-Induced Vibrations – 2nd ed.*, 1990.
- [10] Elghobashi, S. E., "On Predicting Particle-Laden Turbulent Flows," *J. Applied Scientific Research*, Vol. 52, 4, pp. 309-329, 1994.
- [11] L. Tang, F. Wen, Y. Yang, C. T. Crowe, J. N. Chung, T. R. Troutt, *Self-organizing particle dispersion mechanism in a plane wake*, *Physics of Fluids*, A 4(10), 1992.
- [12] L. Kun, J. Han-hui, F. Jian-ren, C. Ke-fa, *Large eddy simulation of the gas-particle turbulent wake flow*, *Journal of Zhejiang University Science*, Vol. 5, pp. 106-110, 2004.

STUDY OF VON KÁRMÁN VORTEX SHEDDING ROBUSTNESS IN THE WAKE OF A FUZZY COATED CYLINDER

Benjamin Levy*

Ying Zheng Liu

School of Mechanical Engineering

Shanghai Jiao Tong University

800 Dongchuan Road

China, Shanghai 200240

Email: benjamin.levy@hotmail.fr

ABSTRACT

We experimentally studied the effect of hairy/fuzzy/spined coating on the topology and dynamic of the flow past a cylinder at low Reynolds number. Primarily, the averaged topology is investigated for various configurations and compare to a reference smooth cylinder: all configurations increase the recirculation area (up to +400% in length) and decrease the fluctuating kinetic energy (up to -43%). Secondly, the dynamic of the wake is analyzed with the help of Time Resolved Particle Image Velocimetry (TR-PIV). Not only, some of the fuzzy coatings modify the vortex shedding frequency, moreover certain configurations are stopping the formation of contra rotative vortex structures, leading to a wake of chaotic structures. Finally, the abilities of coatings to alter the amplitude and the frequency of a freely vibrating cylinder is being investigated. The amplitude is decreased by nearly -90% and the frequency at which it vibrates by up to -51%.

NOMENCLATURE

- D Solide diameter of the cylinders.
 D_a Apparent diameter of cylinders including the thickness of the coating.
 Re Reynolds number based on the upstream velocity and the solide diameter.
 Re_a Reynolds number based on the upstream velocity and the apparent diameter.
 St Strouhal number based on the upstream velocity, the vortex shedding frequency and the solide diameter.
 St_a Strouhal number based on the upstream velocity, the

vortex shedding frequency and the apparent diameter.

L_f Length of the fuzzes.

d_f Diameter of the fuzzes.

θ_f Angle between the axis of the fuzzes and the surface of the cylinder.

ϕ Packing density of the coating material defined by the ratio of the volume occupied by hairs divided by the total volume of the coated layer.

Ω Symmetrical component of the velocity gradient tensor.

S Antisymmetrical component of the velocity gradient tensor.

λ_{1-3} Eigenvalues of $S^2 + \Omega^2$.

INTRODUCTION

Flow modification by mimicking our natural environment has been an uprising research field for some time now. Over the past decade, some researcher have focus on the particular effect of hairy/fuzzy coating. The numerical simulations by Favier [1] and more recently the experimental investigation by Niu [2] have demonstrated the ability of a self-adaptive hairy coating to significantly reduce the lift fluctuations by -44% and the drag by -15% through naturally adapting to counteract the near-wall separated flow. Gosselin [3] studied experimentally and theoretically the ability of poroelastic system to reduce drag. In some cases, solitary filament can even be sufficient to produce nonlinear phenomenon impacting the vortex shedding [4].

At first, the idea was to mimic a fuzzy geometry found in the nature and investigate whether it had any

*Address all correspondence to this author.

effects on the by-passing flow. The saguaro cactus and its spines seemed to be a good candidate and has already been partly investigated [5]. But the geometrical similitude was restraining the possibilities and was only answering the question whether spines were of any aerodynamic benefits for the survival of cactus. But what about other types of fuzzy coating? Can a fuzzy coating influence sufficiently the flow in order to reduced the induced vibrations past a cylinder? What would it take to have significant reductions in frequencies and amplitudes, if any? Therefor the idea is to investigate the effect of a coating layer on the vortices inducing vibrations past a cylinder with no restriction on it attributes beside having fuzzes no longer than $1 D$. The vibrations are not the only parameter analyzed, but also the averaged flow topology, the fluctuating kinetic energy, the shedding frequency, the pressure fluctuations and so on.

The reduction of VIV is of great concern in engineering, fuzzy coating may offer an innovating solution.

EXPERIMENTAL SETUP

In order to investigate the robustness of the von Kármán vortex shedding in the wake of fuzzy coated cylinders, three different coating materials were used. They are identified as F1, F2, F3 and depending on whether or not it is the version with the longer or the shorter fuzz, the attribute *long* or *short* is added to the name. The F1 coating is made of fuzzes considered rigid with 16 pairs of fuzzes periodically distributed along the cylinders circumference. Span-wise, the distance between each pair is $0.067 D$. The length of the fuzz is $0.1 D$ for F1_{short} and $0.2 D$ for F1_{long} (Fig. 1 (c)).

The F2 coating is made of fuzzes considered nearly rigid with the ability to rotate by a few degrees. The fuzzes are randomly scattered with a density of 310 fuzzes/cm². The length of the fuzz is $0.2 D$ for F2_{short} and $0.33 D$ for F2_{long}. The particularity of this coating is to have fuzzes which are not perpendicular to the surface of the cylinder, resulting in an asymmetric cross-section (Fig. 1 (d)).

The F3 coating is made of flexible bundles of fuzzes. Each bundle is made of approximately 100 microscopic fuzzes. The diameter of a fuzz is $0.0005D$. There are 28 bundles periodically distributed along the cylinders circumference. Span-wise, there is a bundle every $0.08D$. The length of the bundles is $1 D$ for F3_{long}; there is no F3_{short}. For commodity reasons, the bundles, will be considered as fuzz for the rest of the study. The particularity of this coating is its ability to deform itself and behave on a similar manner as the proelastic system studied by

TABLE 1: CHARACTERISTICS OF THE DIFFERENT COATINGS ($D = 1$ FOR ALL THE CASES).

Cylinder	D_a/D	L_f/D	d_f/D	θ_f	ϕ
Ref	1	0	0	0°	0
F1 _s	1.2	0.1	0.0093	90°	0.0095
F1 _l	1.4	0.2	0.0093	90°	0.0087
F2 _s	1.12	0.2	0.0037	18°	0.0231
F2 _l	1.2	0.33	0.0037	18°	0.0223
F3 _{lmax}	3	1	0.0005	90°	0.0120
F3 _{lmin}	1.2 - 2	1	0.0005	0° - 90°	0.0687

Gosselin [3]. It results on a significant variation of the characteristics of the coating: D_a is reduced, θ_f varies between 0° - 90°, ϕ increases and the cross-section is no longer circular. As a result, at any given time, the characteristic of this coating is between $F3_{lmin}$ and $F3_{lmax}$.

All those informations, as well as further details regarding diameters, orientation, packing density are summarized in Table 1.

The wake passed the cylinder is measured by Time Resolved Particle Image Velocimetry. Glassbeads ($\rho \approx 1.05 \text{ kg/m}^3$, $d \approx 10 \mu\text{m}$) are used as tracer particles and the middle plane is illuminated by a 1.8 Watt continuous-wave semiconductor laser (532nm). A high-speed CMOS camera is used to acquire the images at a frequency of up to 376 Hz for a resolution of 1280 x 1024 pixels. Series of 20000 consequential frames are recorded.

Fixed cylinder

The experimental studies are performed in a free surface water channel with the following test-section dimension: $10D$ (width) x $14D$ (height) x $70D$ (length). For each studied configuration, the cylinder spans the entire width of the test-section and is located in the water channel at mid-depth (Fig. 1 (a)). The aspect ratio of the experimental cylinders being 10, we made the approximation that the side effects due to the walls were negligible.

The laser sheet comes from below the channel and is perpendicular to the axis of the cylinder at half of the cylinder length. The camera is set aside the channel, in the axis of the cylinder.

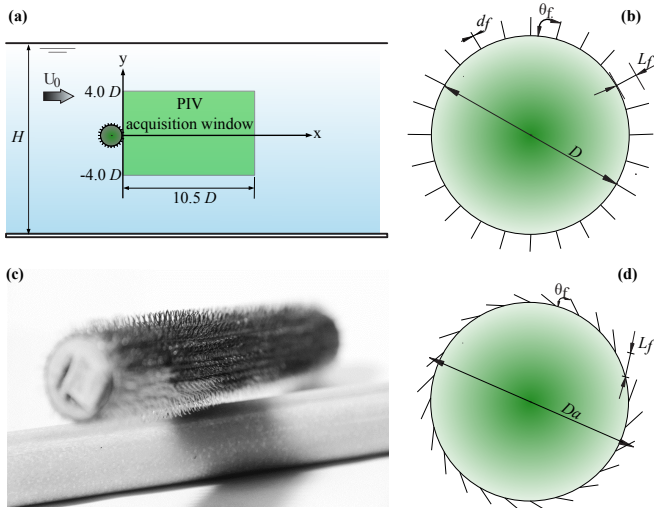


FIGURE 1: (A) SCHEMATIC OF THE EXPERIMENTAL SETUP; (B) SCHEMATIC OF A FUZZY CYLINDER; (C) PHOTOGRAPH OF THE REFERENCE AND THE $F1_{LONG}$ CYLINDERS; (D) SCHEMATIC OF THE CROSS-SECTION OF A CYLINDER WITH THE F2 COATING.

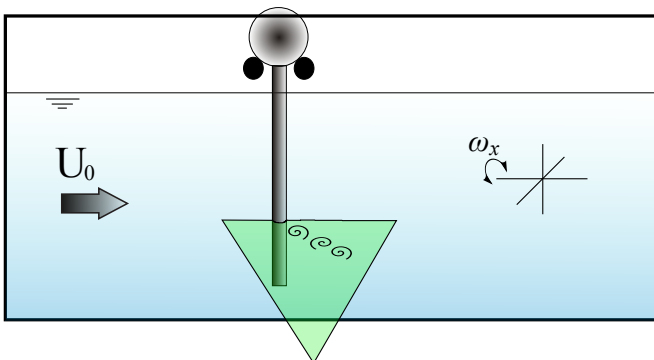


FIGURE 2: SETUP ALLOWING THE CYLINDER TO HAVE ONE DEGREE OF FREEDOM: ROTATION AROUND THE X-AXIS.

Oscillating cylinder, setting OM1

In order to be able to study the response of the cylinder to the vortex shedding, the cylinder needs to be given some degrees of freedom. The first setting, named OM1, allows the cylinder to oscillate in the cross-flow direction (ω_x) but refrain the cylinder to perform any translation or rotate around its axis (Fig. 2). Any oscillations in the in-line direction are being damped excepted for a slight inclination of the cylinder due to the drag. However, this inclination does not time evolved. This setting is quite similar to the one used by Flemming [6].

For the PIV data acquisition, the laser is set aside the channel with the sheet being perpendicular to the axis of

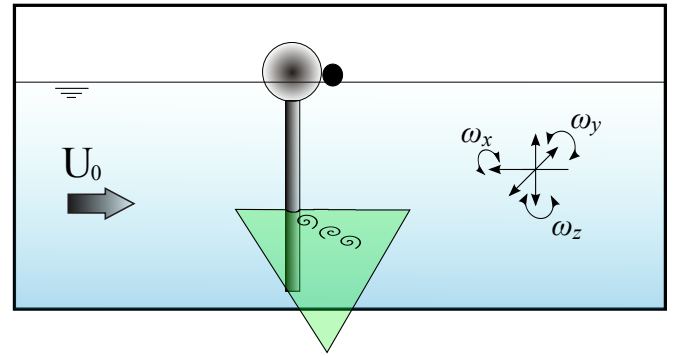


FIGURE 3: SETUP ALLOWING THE CYLINDER TO HAVE 5.5 DEGREES OF FREEDOM: ALL BUT TO TRANSLATE DOWNSTREAM.

the cylinder (without being inclined) at $2/3$ of the cylinder length toward the bottom. The camera is located below the channel.

Oscillating cylinder, setting OM2

It is known from the literature [7], that the motion of a cylinder under the effects of VIV is more complex than just a transverse displacement or rotation. For this reason, a second setup (OM2) was used to investigate the effect of the coating on a cylinder with almost unlimited degrees of freedom (Fig. 3). The only restriction for the cylinder is not being able to translate downstream if it hasn't performed an upstream translation prior to that. The major drawback of this setup is the ability to generate a fictional rotation around the axis of the cylinder due to the torque exercised on the mechanism by a strong cross-flow translation. Alike the setup OM1, the cylinder is slightly inclined due to the drag and the PIV setup is the same as for OM1.

EXPERIMENTAL RESULTS

Time averaged topology past a fix coated cylinder

Before investigating the effects of the coating on the VIV, it is important to have a better overview on how the coating effects the flow past a cylinder: what is the impact of the fuzz length and how those modifications evolves as the up stream velocity is increased. The analysis of the time averaged flow displays significant differences on the average topology. Looking at the recirculation area behind the cylinders, defined by $U_x = 0$, we can clearly see that its size is related to the length and the type of the fuzz (Fig. 4). At $Re = 390$, the recirculation area length for the reference cylinder is $1.58D$ and increases to $2.10D$ for $F1_{short}$ and $3.60D$ for $F1_{long}$. It represents a length increases of respectively +33% and +128%. An increase

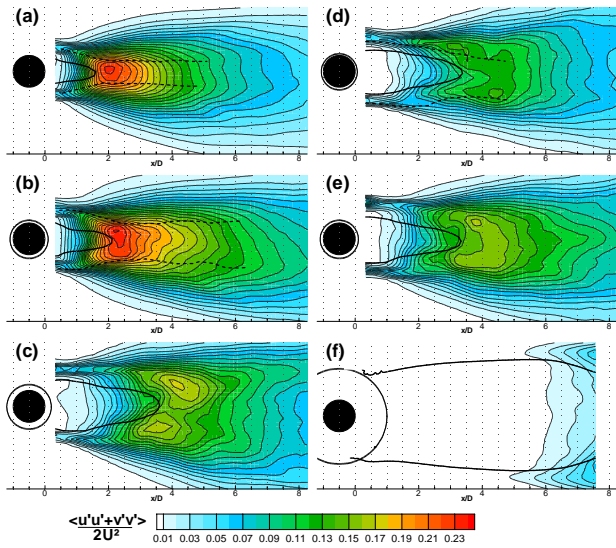


FIGURE 4: SUPERPOSITION OF THE FLUCTUATING KINETIC ENERGY INTENSITY, $\langle U'U' + V'V' \rangle / D^2$ (FLOOD) AND THE RECIRCULATION AREA DEFINED BY $U_X = 0$ (BOLD BLACK LINE); (A) REFERENCE CYLINDER, (B) $F1_{short}$, (C) $F1_{long}$, (D) $F2_{short}$, (E) $F2_{long}$, (F) $F3_{long}$. THE DASHED LINES ON (A), (B) AND (D) DEFINE THE APPROXIMATIVE TRAJECTORY OF A VORTEX CORE [8]. THE CYLINDERS OF DIAMETER D ARE IN BOLD BLACK AND THE BLACK DOTTED CIRCLE AROUND THEM DEFINES THE LIMIT EDGE OF THE APPARENT CYLINDER; $RE = 390$.

of the recirculation area means that the vorticity attached to the cylinder will move further downstream before to roll into an independent vortex. As a consequence, the fluctuating forces acting on the cylinders due to the forces exercised by the rotating vortices have to be reduced as the oscillations in the wake have more difficulties to travel upstream.

The material $F2$ is able to extend the length of the recirculation bubble by +114% with a coating layer thickness of only a third of $F1_{long}$ (Fig. 4(d)). However, by increasing the fuzz length of material $F2$, we do not achieve to increase the recirculation area any further.

The coating $F3_{long}$ has the most significant impact on the average recirculation area. With a size larger than the acquisition window, it is only possible to say that it is over $8D$ in length, representing an increase of over +400%.

At a fixed upstream velocity, the increase of a cylinder diameter results in an increase of the recirculation area. Therefore, it is important to verify that the coating does not simply act as a solid layer, by only increasing

TABLE 2: LENGTH OF THE RECIRCULATION AREA IN FUNCTION OF D AND D_a ; $RE = 390$.

	Ref	$F1_s$	$F1_l$	$F2_s$	$F2_l$	$F3_{lmax}$
r.a./ D	1.58	2.10	3.60	3.37	3.32	≥ 8
r.a./ D_a	1.58	1.67	2.43	2.95	2.68	≥ 2.17
Increase	0%	6%	54%	87%	70%	$\geq 37\%$

the solid diameter and therefore increasing the recirculation area (r.a.). That is why the apparent diameter also needs to be taken in consideration and the recirculation area measured from the edge of the coating layer in function of D_a . Table 2 summarizes the size of the r.a. in function of D_a and proves that coating layers do not simply act as a solid layer, which increases the diameter of the cylinder, but do have a significant impact on the wake.

Looking at the fluctuating kinetic energy, a reduction of the maximum intensity as well as a modification of the averaged topology can be observe. A significant reduction of the maximum intensity is recorded for the configurations with fuzzes $L_f \geq 0.2D$. The $F2_{short}$ coating displays the most significant results with a reduction of the maximum intensity by -43% compare to the reference cylinder ($F3_{long}$ not being included as maximum of fluctuating kinetic energy is so far downstream that it was out of the recording window) (Fig. 5(a)).

$F1_{long}$ and $F2_{long}$ show a similar magnitude of fluctuating kinetic energy, whereas $F1_{short}$, which has an apparent diameter equal to the one of $F2_{long}$, is merely affecting the fluctuating kinetic energy. This points out that the thickness of the coating should not be considered as an independent variable but as a variable depending on the characteristics of the fuzzes. Also, we can observe from the figure 5(a) that increasing the length of the fuzzes and therefore the thickness of the coating does not necessarily result in reducing the maximum fluctuating kinetic energy.

Increasing the Reynolds number to 1700 seems to be sufficient to overcome the benefits of the coatings in terms of reducing the maximum fluctuating kinetic energy (Fig. 5(b)). Nevertheless, the fuzzes are still able to move the maximum region away from the cylinder: +60%, +40%, +183% respectively for $F1_{long}$, $F2_{long}$, $F3_{long}$. Even by considering the apparent diameter, the coating has the same tendency.

The averaged topology is also noticeably changed,

the area of highest intensity, located just downstream of the recirculation region in the case of the reference cylinder, is divided into two as the recirculation length increases. Looking at an approximative spatial evolution of the vortex structures in the wake of the cylinders using the Q criterion [8]:

$$Q = \frac{1}{2}(\|\Omega\|^2 - \|S\|^2) = -\frac{1}{2}(\lambda_1 + \lambda_2 + \lambda_3) \quad (1)$$

$$Q = -\frac{\partial v}{\partial x} \frac{\partial u}{\partial y} - \frac{1}{2}\left(\left(\frac{\partial u}{\partial x}\right)^2 + \left(\frac{\partial v}{\partial y}\right)^2\right) \quad (2)$$

we can see that the longer the spines, the further apart are the trajectories of the vortex structures of opposite vorticity sign (Fig. 5(a-d), dashed line). If we set an arbitrary limit for the vortex core at $Q \geq 1$, then for the cylinder without spines, there is an area downstream of the cylinder ($x/D \in [1.42 - 3.18]$) and with an averaged width of $0.45D$, where part of the core of the counter-rotating vortical structures are alternatively passing by. This region encloses the area of greater fluctuating kinetic energy. In the case of the $F1_{short}$ coating, there is no area where the cores of the clockwise and counter-clockwise vortices superimpose over a shedding cycle. Yet, if we look at the boundary limit of the structure defined by $Q \geq 0$, the counter-rotating structures do pass over a common area. As the fuzzes are increased to a length of $0.2D$, coherent vortical structures are no longer identifiable. The area of maximum fluctuating kinetic energy is being reduced and split into two areas of lower intensities on each side of the recirculation region.

The material $F2$, due to a fuzz orientation differing from top and bottom generates a slightly asymmetric wake. This asymmetry is less important in the case of the longer fuzzes as it is more likely to adapt to the flow due to its lower stiffness.

High frequency analysis past a fix coated cylinder

The significant differences on the averaged topology emphasized previously can only be the result of a modified instantaneous flow field. At Reynolds number of a few thousands or less, the vortex shedding is the primary mechanisms of the flow and the main responsible for inducing fluctuating forces on the cylinder. The use of TR-PIV gives access to the vortex shedding frequency and the associated Strouhal number which can be compared to the results summarized by Williamson [9] (figure 6). If

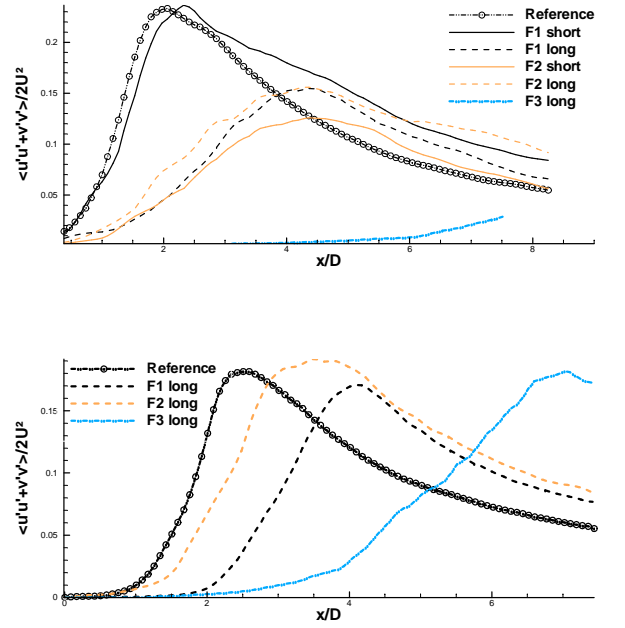


FIGURE 5: FLUCTUATING KINETIC ENERGY IN THE DIRECT WAKE OF THE CYLINDER, AT $y/D = 0$; (a) $RE = 390$, (b) $RE = 1700$.

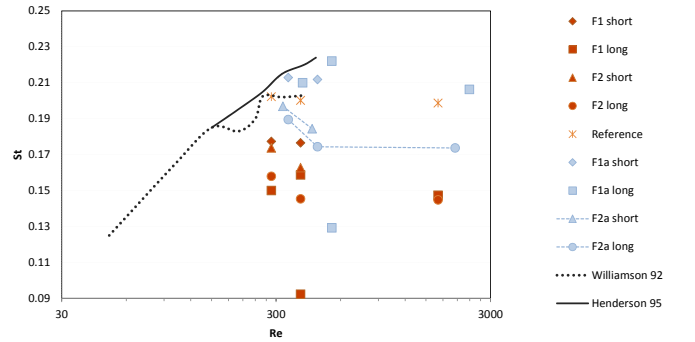


FIGURE 6: RE VS ST BASED ON THE SHEDDING FREQUENCIES. THE $F1_{short/long}$ AND $F2_{short/long}$ DATA WERE CALCULATED USING D ; THE $F1a_{short/long}$ AND $F2a_{short/long}$ DATA WERE CALCULATED USING D_a . THE DATA "WILLIAMSON 92" AND "HENDERSON 95" WERE TAKEN FROM A REVIEW [9].

we consider the solid diameter, we can see that the add of a fuzzy coating on the cylinder drastically reduces the vortex shedding frequency.

No von Kármán vortex street could be monitored in the wake of the $F3_{long}$ cylinder. It appears to have a dead water region where the recirculation area could be expected and the vorticity pattern past the cylinder is simi-

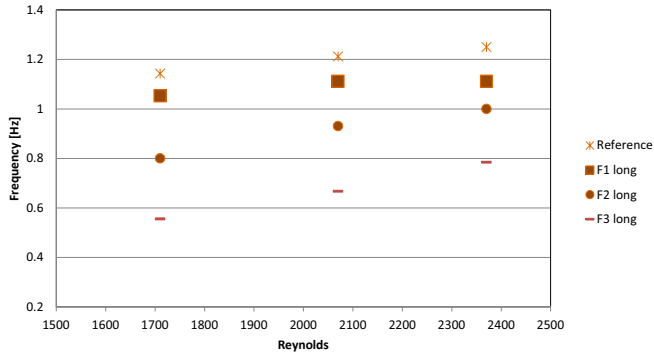


FIGURE 7: OSCILLATION FREQUENCY VS RE; SETTING OM1.

lar to Kelvin-Helmholtz instabilities observed in the wake of the reference cylinder at much higher Reynolds number. Otherwise, the coating $F2$, long or short, shows the best and most constant shedding frequency reduction: -15% to -30% for Reynolds number ranging from 280 to 2000. The $F1_{short}$ coating seems to have little effects on reducing the shedding frequency. This observation is in agreement with the one made on the average topology, that is: it has very little effect on the flow. However, it appears there is limit of fuzz length to overcome in order to make the $F1$ coating effective as the $F1_{long}$ coating does significantly destabilize the wake. There is no longer a single frequency measured but a double frequency, one of which is equivalent to a 55% reduction of the shedding frequency. Yet, if we use the apparent diameter we get a more complex picture. At $Re \sim 340$, the coating $F2_{short}$ only slightly decreases the associate Strouhal number (-10%). But as the Reynolds number increases, the associate Strouhal number decreases even more, going against the results of Henderson [10] for a smooth cylinder. This tendency is emphasized by $F2_{long}$. The coating $F1_{short}$ seems to have no influence on the St_a vs Re_a curve. With longer fuzzes, the tendency could be considered the same if it wasn't for the double frequency.

High frequency analysis past an oscillating cylinder

In order to quantify the effect of the coating layer on the VIV, it is best to have a setting in which the cylinder can react to the forces applied on it by the by-passing flow and the vortex structures. One of the usual setup for investigating the response is to mount the cylinder on a translation device with added springs [7, 11]. Unfortunately, such device does not give information on the rotations, therefore we have opted for the OM1 and OM2 settings.

The previous results have shown that a coating layer had the ability to modify the shedding frequency, its in-

TABLE 3: TENDENCY OF THE MAXIMUM AMPLITUDE OF THE CROSS-FLOW OSCILLATORY MOTION; OM1.

	Ref	$F1_l$	$F2_l$	$F3_l$
Re = 1700	-	-70%	-35%	-90%
Re = 2100	-	-60%	-26%	-82%
Re = 2400	-	-24%	+30%	-72%

tensity and the location where the accumulated vorticity was separating from the cylinder to form vortices. Therefore it is expectable to observe modified oscillatory response and amplitudes. With an increasing upstream velocity, a smooth cylinder oscillate more rapidly with a linear growth (Fig. 7). A similar result is also observed on the coated cylinders (only the *long* coatings have been investigated), but with reduced frequencies: up to -50% for the $F3_{long}$ coating. The least significant results are obtained with $F1_{long}$. This tendency is in agreement with the Re vs St plot for fixed cylinders (Fig. 6), which is understandable as the alternative formation and drop of vortices is creating oscillating stresses on the cylinder. Surprisingly, the greater the reduction of the oscillating frequency does not necessarily seems to mean the greater the amplitude reduction. The $F1_{long}$ coating, despite having less impact on the frequency as $F2_{long}$ coating, reduces the maximum amplitude by nearly twice as much as the later (Tab. 3). It is also important to notice that the $F3_{long}$ coating nearly stop the oscillation. The flexible coating may be absorbing the fluctuations beside moving the fluctuating kinetic energy away.

To have a better overview of what happens in the wake of the cylinders over time, the evolution of the vorticity along the axis at $x/D = 1 D$ and $x/D = 2$ can be recorded (Fig. 8). The phenomenon being periodical, a POD analyzes was made [12] and a phase averaging made based on the periodicity of the first eigenvectors [13]. The figure 8 displays the vorticity over one cycle.

The first important observation is that, with such setting (OM2), at 2/3 of the rotation point, the smooth cylinder present a vortex pattern that could be compared to a double 2T mode [6], meaning that over one cycle 12 vortices are dropped in the wake. In comparison, most of the vorticity recorded at $1D$ from the $F1_{long}$ cylinder stays attached during the entire cycle. The wake past $F3_{long}$ seems to be erratic with no coherent structures (Fig. 8(d)).

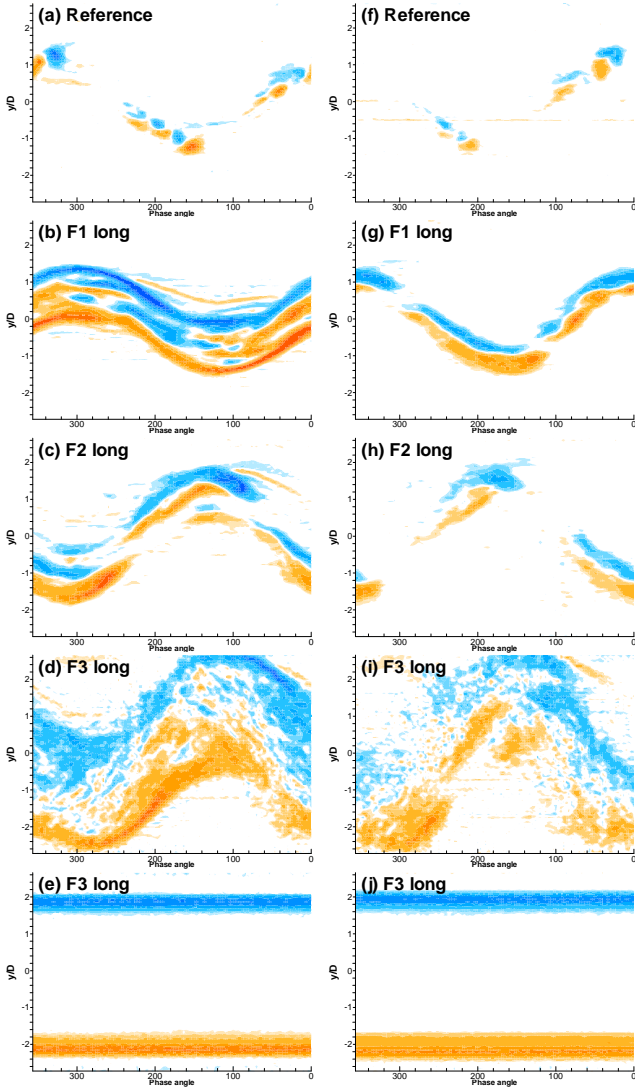


FIGURE 8: TEMPORAL EVOLUTION OF THE VORTICITY FOR A COMPLETE PHASE AVERAGED CYCLE ACROSS: THE AXIS $X/D = 1$ (a-e) AND THE AXIS $X/D = 2$ (f-j); SETTING $OM1$, $RE = 1700$ FOR (a-d,f-i), $RE_a = 1700$ FOR (e, j).

At $2D$ from the cylinder, the observation is the same for $F3_{long}$; $F2_{long}$ and $F1_{long}$ have each 2 pairs of contra rotative vortices over one cycle alike a 2P mode. Now however, if we are to consider D_a as the appropriate parameter for a coated cylinder, the upstream velocity has to be decreased in order to have $Re_a = 1700$. If doing so, the wake behind $F3_{long}$ shows no signs of fluctuations what so ever. There is positive vorticity and negative vorticity attached at each side of the cylinder, which is perfectly still, as if it was a steady wake (Fig. 8(e,j)).

CONCLUSIONS

With more than 5 parameters to play with (L_f , d_f , θ_f , ϕ , stiffness), the varieties of fuzzy coating are humongous. The aim of this study was not to identify an optimal configuration able to solve all problems linked to the flow past a cylinder, but to investigate whether or not a fuzzy coating was able to significantly alter the wake and the dynamic of a cylinder.

Five different coating configurations have been studied at moderate Reynolds number (280 to 2400) for various setups: with a fixed cylinder or a cylinder with 1 to 5 degrees of freedom; the averaged and instantaneous flow have been investigated. The points of investigation were whether the coatings were able to reduce the fluctuating kinetic energy in the vicinity of the cylinder, reduce the shedding frequencies and in fine reduce the VIV.

A coating with fuzzes too short seems to have little effect on the flow; flexible fuzzes seems to have a greater interaction with the flow; no tendencies were noticed regarding the packing density. Three of the investigated coatings produced results of interests. However, the use of the apparent diameter as the reference length instead of the solid diameter makes the variations be less significant. The results on the averaged flow tends to demonstrate that the coating does not simply act as a cylinder of greater diameter. However the shedding frequencies, for fixed cylinders, seem to be locked on the apparent diameter meaning it might be wrong to simply consider D or D_a . The dynamic might be governed by D_a but not the topology and intensity. This, however, is only true for fixed cylinders. As soon as some degrees of freedom are given to the cylinder, the dynamic parameters of a coated cylinder can not simply be normalized by the apparent diameter in order to have similar values to the reference case.

Quantitatively, the $F1_{long}$ coating is able to increase the recirculation area past a fix cylinder by +128% and in the mean time reduce the maximum of fluctuating kinetic energy by -35%. This must lead to a reduction of the stresses on the cylinder and may explain why the oscillating frequency and amplitudes are decreased by nearly -10% and -70% (at $Re = 1700$). The $F2_{long}$ coating is able to increase the recirculation area by +110% and reduce the maximum of fluctuating kinetic energy by -35% as well. The oscillating frequency is reduced by -23% for Reynolds ranging from 1700 to 2400 despite the fact that its amplitude is increased by +30% at $Re = 2400$. The $F3_{long}$ coating is able to increase the recirculation area by over +500% and dim any fluctuating kinetic energy in the vicinity of the cylinder to a negligible level. However, it does not laminarize the flow but rather damp the fluctua-

tions. As a results, the oscillating frequency is reduced by up to -50% and the amplitude is lowered by up to -90% (OM1, $Re = 1700$) or nearly completely depending on the setting (OM2, $Re_a = 1700$).

REFERENCES

- [1] Favier, J., Dauplain, A., Basso, D., and Bottaro, A., 2009. "Passive separation control using a self-adaptative hairy coating". *J. Fluid Mech.*, **627**, pp. 451–483.
- [2] Niu, J., and Hu, D., 2011. "Drag reduction of a hairy disk". *Phys. Fluids*, **23**(101701).
- [3] Gosselin, F., and de Langre, E., 2011. "Drag reduction by reconfiguration of a poroelastic system". *J. Fluid and Struct.* in press.
- [4] Shelley, J., and Zhang, J., 2011. "Flapping and bending bodies interacting with fluid flows". *Annu. Rev. Fluid Mech.*, **43**(449).
- [5] Levy, B., and Liu, Y., 2011. "Cactus spines and grooved cross-section, viv reducers or self-defense mechanisms?". In Blubof2011, IUTAM Symposium on Bluff Body Flows, pp. 201–205.
- [6] Flemming, F., and Williamson, C., 2005. "Vortex-induced vibrations of the pivoted cylinder". *J. Fluid Mech.*, **522**, pp. 215–252.
- [7] Jauvtis, N., and Williamson, C., 2004. "The effect of two degrees of freedom on vortex-induced vibration at low mass and damping". *J. Fluid Mech.*, **509**, pp. 23–62.
- [8] Jeong, J., and Hussain, F., 1995. "On the identification of a vortex". *J. Fluid Mech.*, **285**, pp. 69–94.
- [9] Williamson, C., 1996. "Vortex dynamics in the cylinder wake". *Annu. Rev. Fluid Mech.*, **28**, pp. 477–539.
- [10] Henderson, R., 1995. "Details on the drag curve near the onset of vortex shedding". *Phys. Fluids*, **7**(2102).
- [11] Morse, T., and Williamson, C., 2009. "Prediction of vortex-induced vibration response by employing controlled motion". *J. Fluid Mech.*, **634**, pp. 5–39.
- [12] Sirovich, L., 1987. "Turbulence and the dynamics of coherent structures". *Quarterly Applied Math.*, **45**, pp. 561–590.
- [13] Perrin, R., Cid, E., Cazin, S., Sevrain, A., Braza, M., Moradei, F., and Harran, G., 2007. "Phase averaged measurements of the turbulence properties in the near wake of a circular cylinder at high reynolds number by 2c-piv and 3-c piv". *Exp. in Fluids*, **42**, pp. 93–109.



HILBERT-HUANG TRANSFORM – A COMPARISON WITH FOURIER AND WAVELET TRANSFORM FOR THE ANALYSIS OF THE SHEDDING PROCESS

Rodrigo Santiago Silveira

Programa de Pós-Graduação em Eng. Mecânica
Universidade Federal do Rio Grande do Sul
Rua Sarmento Leite, 425
90050-170 Porto Alegre, RS, Brasil
Email: rodrigo.santiago@ufrgs.br

Sergio Viçosa Möller

Programa de Pós-Graduação em Eng. Mecânica
Universidade Federal do Rio Grande do Sul
Rua Sarmento Leite, 425
90050-170 Porto Alegre, RS, Brasil
Email: svmoller@ufrgs.br

ABSTRACT

Fourier and Wavelets transforms are important tools for signal analysis in many engineering applications, including turbulent flows around bluff bodies. In this case, the use of additional tools can improve the analysis of the parameters in the shedding process, including the vortex shedding frequency. In this paper, it is presented the use of the Hilbert-Huang transform, which can be applied to non-stationary and non-linear turbulent signals as an alternative method of data analysis. A comparison with the results from Fourier and Wavelets transforms is made, and the properties and application of each transform are discussed. For this comparison, the three tools are applied to the simple problem of the shedding process in the flow impinging on a cylinder. Results show that the use of Hilbert-Huang Transform can improve the analysis of the problem together with Fourier and wavelet analyses.

Keywords: Hilbert-Huang transform, turbulent flow, shedding process, wavelets, Fourier transform.

NOMENCLATURE

a	scale wavelet coefficient
b	position wavelet coefficient
$c_n(t)$	n-component of IMF
CWT	continuous wavelet transform
D	diameter – m
DWT	discrete wavelet transform
DWPT	discrete wavelet packet transform
f	frequency – Hz
$\bar{f}(t)$	mean frequency of the interval – Hz
$E(t)$	energy in time domain
$E(\omega)$	energy in frequency domain
F_s	sampling frequency – Hz
F_ν	pseudo frequency of the wavelet
$H[c_i(t)]$	Hilbert transform of i-component of IMF
$H(\omega, t)$	Hilbert spectrum
$h(\omega)$	Marginal spectrum

j, J	scale coefficients of the DWT and DWPT
k	position coefficient of the DWT and DWPT
m	modulation parameter of the DWPT
$P_{xx}(f)$	Fourier spectrum
$P_{xx}(a, b)$	continuous wavelets spectrum
$P_{xx}(j, k)$	discrete wavelets spectrum
$P_{xx}(\omega, t)$	Hilbert power spectral density
$P_{xx}(j, m, k)$	continuous wavelets spectrum
Re	Reynolds number (UD/ν)
RP	real part of complex number
$r_n(t)$	n-residue of IMF
S	Strouhal number (fD/U)
t	time – s
U	velocity – m/s
Ua	approaching velocity – m/s
$x(t)$	generic function in time domain
$x(f)$	generic function in Fourier domain
$\tilde{X}(a, b)$	generic function in wavelet domain (continuous)
$\tilde{X}(j, m, k)$	generic function in wavelet domain (discrete, packet)
$\tilde{X}(j, k)$	generic function in wavelet domain (discrete)
$\psi(t)$	generic wavelet function
$\phi(t)$	generic scaling function
$\Phi_i(t)$	instantaneous phase – rad
$\omega_i(t)$	instantaneous frequency – rad/s

INTRODUCTION

The use of mathematical tools for signal analysis is very common in many fields of engineering, in particular with regard to turbulent flow around bluff bodies in order to investigate the shedding process around these bodies. One of the most important parameters in the analysis of flow in a circular cylinder is the dimensionless frequency associated with vortex shedding, which is the Strouhal number, which depends on the shedding frequency, the cylinder diameter and the velocity of the free stream [1].

In experimental turbulence study, the RMS-values, auto spectral density functions, as well as auto and cross-correlation functions, are used, considering turbulence as a random phenomenon. Currently, this process is studied from the Fourier spectral analysis for stationary flows, and also by the wavelet analysis for non-stationary flows. Usually, random data are discrete time series.

The Fourier spectral analysis is a modification of the Fourier analysis, where it is more suitable for random time functions than for deterministic functions. Let us consider a generic time function $x(t)$ which is represented in Fourier domain by coefficients obtained from inner products of $x(t)$ with the Fourier basis. The auto spectral density function (PSD) of a random time series is the squared Fourier coefficients of that series smoothed over frequency intervals and over an ensemble of estimates [2].

To treat transient time series, the Wavelets analysis is similar to Fourier analysis in that the original function is expanded over an orthogonal basis. The wavelet basis is a set formed by dilatations and translations of a single function called wavelet. While the auto spectral density function or Fourier spectrum gives the energy for each frequency over the entire time domain, the wavelet spectrum provides the energy associated to each time and scale (or frequency). This characteristic of the wavelet transform allows the representation of the distribution of the energy of the transient signal over time-frequency domains [3].

The application of Fourier spectral analysis on stationary time series limits their use, while the use of wavelets analysis on non-stationary series represents a gain in turbulence analysis of this series, but its limitation is associated with the chosen wavelet according to the time series signal.

This work suggests the use of a tool that enables the analysis of non-stationary and non-linear turbulent signals named Hilbert-Huang Transform (HHT) [4], which is composed by Empirical Mode Decomposition (EMD), which is a direct and intuitive method, for the decomposition of the signal, and the Hilbert Spectral Analysis (HSA).

According to [5], the decomposition is based on the simple assumption that all the data consist of different simple intrinsic modes of oscillations, each of these modes of oscillation is called Intrinsic Mode Functions (IMF) and are obtained from the envelopment of the maxima and minima values and the average signal from this envelopment. Repeating this procedure iteratively, the decomposition of the original signal is obtained. The Hilbert transform is used to obtain a continuous spectral distribution of signal energy in the time frequency domain. This spectral analysis is made possible by applying the Hilbert transform to each of the intrinsic mode functions of the original signal.

In [6], a comparison between the wavelet transform and Hilbert-Huang transform to signals from earthquakes is made. The authors show that the Hilbert-Huang transform performs a direct decomposition of the original signal and can show

more clearly the intrinsic properties of the original signal.

BACKGROUND

The Fourier transform of a discrete time series representing a finite function $x(t)$ enables the study of spectral behavior of the random phenomenon from the series given by

$$\hat{x}(f) = \frac{1}{2\pi} \sum x(t)e^{-ift} \quad (1)$$

Thus, the Fourier spectrum gives the energy distribution of the signal in the frequency domain evaluated over the entire time interval. The Fourier spectrum is defined as

$$P_{xx}(f) = |\hat{x}(f)|^2 \quad (2)$$

The first attempt to deal with nonstationary processes was the Windowed Fourier Transform. However, due to the aliasing of high and low frequency components that do not fall within the frequency range of the window, the windowed Fourier transform is inaccurate for time-frequency location of transient features.

Wavelet analysis enables the treatment of transient series and it is based on idea of stretching and compressing the window of the windowed Fourier transform, according to the frequencies to be localized, allowing the definition of the scales of interest in time and frequency domains. The bases of wavelet transform are generated through dilatations and translations of a single function wavelet, $\psi(t)$ with finite energy and zero average.

Let be the function $\psi_{a,b}(t)$ the wavelets basis, the continuous wavelet transform (CWT) of a function $x(t)$ is given by:

$$\tilde{X}(a,b) = \int_{-\infty}^{+\infty} x(t)\psi_{a,b}(t)dt \quad a,b \in \mathbb{R} \quad (3)$$

The scale and position parameters a and b are related to the frequency and time of the analyzed function. The wavelet spectrum associated is the matrix of the squared wavelets coefficients, given by,

$$P_{xx}(a,b) = |\tilde{X}(a,b)|^2 \quad (4)$$

The continuous wavelet spectrum gives a general view of the distribution of a signal over time and scale and is able to emphasize the signal singularities. The CWT is very useful to pick out some features of the signal and the discrete wavelet transform (DWT) arises like a sub sampling of the CWT with dyadic scales, with no loss of information. The DWT is given by

$$\tilde{X}(j,k) = \sum_t x(t)\psi_{j,k}(t) \quad j,k \in \mathbb{Z} \quad (5)$$

where (j, k) are the dyadic scale and position coefficients.

The number of levels of the transformations which can be calculated is limited by the length of the time series. Unlike the Fourier transform, in the wavelets transform the remaining coefficients are related to the lower frequencies, including the mean value of the signal, and cannot be disregarded. So, the DWT of a series with more than 2^j elements is computed for $1 \leq j \leq J$, where J is a conveniently arbitrary choice, and the remaining information corresponding to mean values for a scale J is

$$\tilde{X}(J, k) = \sum_t x(t) \phi_{J,k}(t) \quad (6)$$

where $\phi(t)$ is the scaling function associated to the wavelet function. Thus, the representation of any discrete time series with a sampling frequency is given by,

$$x(t) = \sum_k \tilde{X}(J, k) \phi_{J,k}(t) + \sum_{j \neq J} \sum_k \tilde{X}(j, k) \psi_{j,k}(t) \quad (7)$$

where the first term is the approximation of the signal at the scale J , and the inner summation of the second term are details of the signal at the scales j ($1 \leq j \leq J$).

The discrete wavelet packed transform (DWPT) is a modification of the algorithm pyramidal where the DWT is computed [7]. Each detail series is wavelet transform in two series, with respectively lower and upper half bandwidth frequency interval. The DWPT basically is a modification of the DWT, in order to obtain the decomposition of the signal in successive intervals of equal bandwidth and is done by

$$\tilde{X}(j, m, k) = \int_{-\infty}^{+\infty} x(t) \psi_{j,m,k}(t) dt \quad (8)$$

The Hilbert-Huang Transform (HHT) is applied in the treatment of non-linear and non-stationary signals consisting of the Huang Transform and the Hilbert spectral analysis. The HHT is ruled by the empirical mode decomposition (EMD), known as the Huang Transform. The EMD assumes that any data set consists of different, simple, intrinsic modes of oscillation that need not be sinusoidal. Based on this assumption, each mode of oscillation from high frequency to low frequency is derived in an objective manner from the recorded complex data. We call each of these oscillatory modes an intrinsic mode function (IMF). As discussed in [4], the EMD method is necessary to deal with data from non-stationary and non-linear processes. This new method is intuitive, direct, and adaptive, with an *a posteriori*-defined basis, from the decomposition method, based on and derived from the data. The decomposition is made from the identification of all the local maxima, then connecting all the local maxima by a cubic spline to produce the upper envelop of $x(t)$, and repeat the procedures for the local minima to produce the lower envelop of $x(t)$.

All the data should be encompassed by the upper and lower envelopes. Their mean of these envelopes is designated by $m_1(t)$, and the difference between the data $x(t)$ and $m_1(t)$ provides the first component $h_1(t)$, i.e.,

$$h_1(t) = x(t) - m_1(t) \quad (9)$$

Ideally, $h_1(t)$ should be an IMF, but all the conditions of an IMF should be achieved; the conditions are [5]:

- (1) In the whole dataset, the number of maxima and minima and the number of zero-crossings must be either equal or differ at most by one, and
- (2) At any point, the mean value of the envelope defined by the local maxima and the envelope defined by the local minima is zero.

Not satisfied the condition of an IMF, the process is repeated. In the subsequent sifting process, $h_1(t)$ is treated as the data, then

$$h_{11}(t) = h_1(t) - m_{11}(t) \quad (10)$$

where $m_{11}(t)$ is the mean of the upper and lower envelopes of $h_1(t)$. Repeating k times until $h_{1k}(t)$ to satisfy the conditions of an IMF, we have

$$h_{1k}(t) = h_{1(k-1)}(t) - m_{1(k-1)}(t). \quad (11)$$

It is named the first IMF component $c_1(t)$ from the data, because $c_1(t) = h_{1k}(t)$. The component $c_1(t)$ will contain the finest-scale of the highest frequency component of the signal. The residue $r_1(t)$, given by

$$r_1(t) = x(t) - c_1(t) \quad (12)$$

contains longer-period components, is treated as new data and subjected to the same sifting process as described above. This procedure can be repeated to obtain all the subsequent $r_j(t)$'s

$$r_j(t) = r_{j-1}(t) - c_j(t) \quad (13)$$

The sifting process can be ended on any of the following predetermined criteria: a) either the component $c_n(t)$ or the residue $r_n(t)$ becomes so small that it is less than a predetermined value of consequence, or b) the residue $r_n(t)$ becomes a monotonic function from which no more IMFs can be extracted [5]. The original data can be expressed by the sum of the IMF components plus the final residue, thus we obtain

$$x(t) = \sum_{j=1}^n c_j(t) + r_n(t) \quad (14)$$

The components of EMD are usually physical meaningful, for the characteristic scale are defined by the physical data.

The HHT is completed by the Hilbert spectral analysis (HSA) which consists in the application of the Hilbert transform on each IMF components obtained. For one IMF $c_i(t)$ in Eq. (14), we can express the Hilbert transform as

$$H[c_i(t)] = \frac{1}{\pi} \int_{-\infty}^{\infty} \frac{c_i(t')}{t-t'} dt' \quad (15)$$

From this definition, an analytic signal may be given by

$$z_i(t) = c_i(t) + jH[c_i(t)] = a_i(t)e^{i\Phi_i(t)} \quad (16)$$

where

$$a_i(t) = \sqrt{c_i^2(t) + H^2[c_i(t)]} \quad (17)$$

$$\Phi_i(t) = \arctan \frac{H[c_i(t)]}{c_i(t)} \quad (18)$$

The instantaneous frequency is obtained from Eq. (18) as

$$\omega_i(t) = \frac{d\Phi_i(t)}{dt} \quad (19)$$

After applying the Hilbert transform to each IMF component, the original signal can be expressed as the real part (RP) in the following form [8]:

$$x(t) = RP \sum_{i=1}^n a_i(t)e^{i\Phi_i(t)} = RP \sum_{i=1}^n a_i(t)e^{i \int \omega_i(t) dt} \quad (20)$$

At this moment, the residue $r_n(t)$ is left out on purpose, for it is either a monotonic function or a constant. Equation (20) gives both amplitude and frequency of each component as functions of time. This frequency-time distribution of the amplitude is designated as the Hilbert spectrum $H(\omega, t)$:

$$H(\omega, t) = RP \sum_{i=1}^n a_i(t)e^{i \int \omega_i(t) dt} \quad (21)$$

Defined the Hilbert spectrum, we can also define the marginal spectrum $h(\omega)$ [5] as

$$h(\omega) = \int_0^T H(\omega, t) dt \quad (22)$$

where T is the total data length. The marginal spectrum offers a measure of the total amplitude (or energy) contribution from each frequency value.

We can use the Hilbert spectrum to obtain the local power spectral density, because $H(\omega, t)$ accurately describes the varying rule of signal amplitude

according time and frequency, so when energy is taken into account, the local power spectral density is given by [9]

$$P_{xx}(\omega, t) = \frac{|H(\omega, t)|^2}{2} \quad (23)$$

Based on the temporal-frequency feature of the HHT, the energy of random process or the samples has been localized. The energy is expanded on the plane of time and frequency, as Eq. (23), then, the local power spectral density is got.

The Hilbert energy spectrum is defined by $H^2(\omega, t)$ that describes the energy-frequency-time distribution. Leaving out the residue $r_n(t)$, the HHT of $x(t)$ should be energy conservation, namely, the relation could be obtained:

$$\int_{-\infty}^{\infty} |x(t)|^2 dt = \int_{-\infty}^{\infty} \int_{-\infty}^{\infty} H^2(\omega, t) d\omega dt \quad (24)$$

where $|x(t)|^2$ is the energy density of the signal $x(t)$. Thus, the instantaneous energy $E(t)$ is defined by [4]

$$E(t) = \int_{-\infty}^{\infty} H^2(\omega, t) d\omega \quad (25)$$

This $E(t)$ provides the energy distribution of the signal in the time domain. In frequency domain is given by [10]

$$E(\omega) = \int_{-\infty}^{\infty} H^2(\omega, t) dt \quad (26)$$

EXPERIMENTAL TECHNIQUE

Velocity measurements were made with DANTEC *StreamLine* hot wire anemometer in an aerodynamic channel to investigate the flow around a circular cylinder and the shedding process.

The test apparatus, shown on Fig. 1, with 146 mm height and width of 193 mm. Air, at room temperature, is the working fluid, driven by a centrifugal fan of 0,75 kW, passed by a diffuser and a set of honeycombs and screens, which reduce the turbulence intensity in the channel to about 1%. A frequency inverter controls the fan speed, where the flow velocity in the aerodynamic channel can be varied from 0 to 15 m/s. To measure the velocity reference a Pitot tube fixed before to the test section is used. The cylinder has a diameter of 32 mm and is rigidly mounted in vertical position inside the channel. The cylinder blockage ratio is 16.5% and the incidence angle of the flow on the cylinder is 90°. No attempt for correction of the effects of this blockage ratio was made. The experiment was performed with a Reynolds number $Re = 2.9941 \times 10^4$.

For the measurement of velocity and velocity fluctuations, a single hot wire probe was placed at the wake region in a location 20 mm downstream of the cylinder.

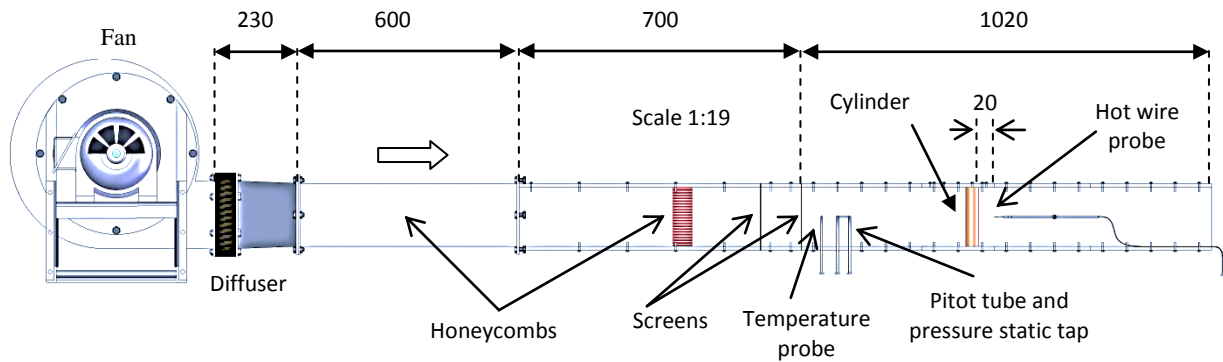


Figure 1. Schematic view of the aerodynamic channel (measures in mm)

Data acquisition was performed with a 16-bit A/D-board (NATIONAL INSTRUMENTS 9215-A) with USB interface, with a sampling frequency of 3000 Hz and a low pass filter at 1000 Hz.

With the purpose of comparing Fourier, Wavelet and HHT, the data set was acquired in steady state flows at same velocity value.

Computations of the Fourier transform, wavelet transform and HHT were performed using the MatLab © software.

The experimental data were analyzed by statistical, spectral, wavelet tools, where the time-frequency domain analysis of experimental signals by wavelets is compared with HHT results, which allows the detection of non-linear flow structures.

RESULTS

Figure 2 shows the signal obtained from the measurement with a single hot-wire. FFT of this signal gives the power spectral density in Fig. 3, where three peaks in the spectrum can be observed, the fundamental frequency of 105.5 Hz and two harmonics at 211 Hz and 316 Hz. The presence of the harmonics is inherent of the vortex shedding spectrum. The occurrence of a second peak (and, in this case, a third one) is an inherent feature of separated flows. According to nonlinear hydrodynamic stability theory and experimental findings, higher harmonics are generated when the amplitude of the fundamental component exceeds about 4% of the mean flow [11].

The Strouhal number corresponding to the fundamental frequency is 0.22, which is in accordance with the classic literature [1], considering the high blockage ratio in this study.

In the wavelet spectral analysis, Fig. 4a, the concentration of energy is observed only around the fundamental frequency, without a constant value along time. This slight oscillation around the shedding frequency is not depicted in the power spectral density, since it is averaged over the entire time interval. The presence of the first harmonic, however, is barely identified in the wavelet spectrum. Figure 4b shows the reconstruction of the original signal by means of the

Discrete Wavelet Transform. To the higher velocity values correspond the higher energy values in Fig. 4a, characterized by the clearest zones in time frequency representation.

From the original data signal, Fig. 2, was made the decomposition using the EMD algorithm of HHT, and eighteen IMFs are obtained, Fig. 5. Each component corresponds to a different oscillation mode with different amplitude and frequency content. The first IMF components have the highest-frequency, and the frequency content decrease with the increase IMF component. This frequency range is very useful to analyze any-frequency oscillation and it is used in HSA to obtain the instantaneous frequency.

The Fast Fourier Transform was performed for the first four IMF in Fig. 6 in order to determine the frequency of each IMF decomposition, from the highest to the lowest frequencies. The results show that those four IMFs have the principal contents of process shedding: the fourth IMF has the shedding frequency while the third contains the shedding frequency and the two harmonics. The first two decompositions present frequencies with a wide distribution and lower energy compared to the third and the fourth. The rest of the IMF components, from 5th to 18th, only have some lower frequencies and residues of the signal, not providing relevant information of the studied Phenomenon in particular.

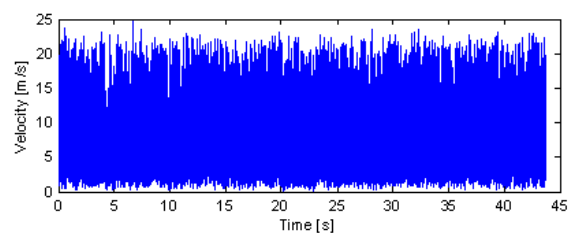


Figure 2. Data signal: shedding process measured with a hot wire.

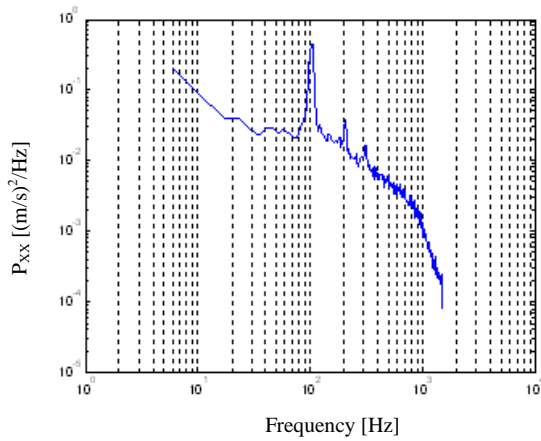


Figure 3: Power spectral density of the hot wire signal acquired at the wake of the cylinder.

From the decomposition of the signal using the Empirical Mode Decomposition by means of the Hilbert spectral analysis is shown on Fig. 7, and it can lead to a better visualization of the fundamental frequency and its one subsequent harmonics, with respect to the wavelet analysis. On the Fourier spectrum, Fig. 3, three peaks in the spectrum can be observed, the fundamental frequency and two harmonics. In the wavelet spectral analysis, Fig. 5 (a), the concentration of energy is observed only around the fundamental frequency, while in the HSA it is distributed around the three frequencies, which are those observed in Fourier spectrum.

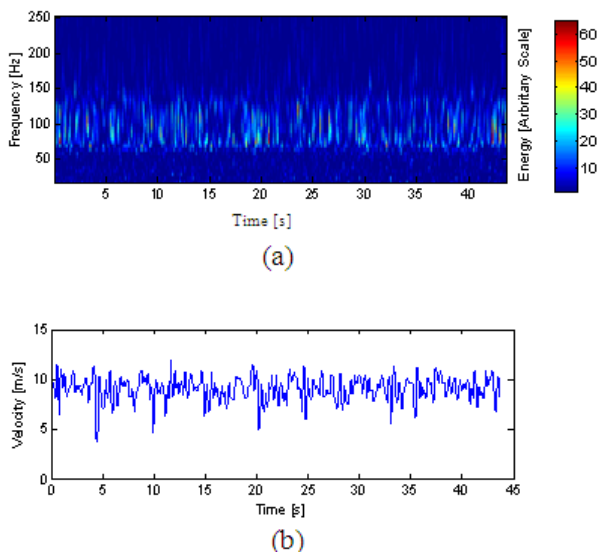


Figure 4: (a) Continuous wavelet spectrum of the hot wire signal at wake of the cylinder, (b) Reconstruction of the signal by discrete wavelet transform.

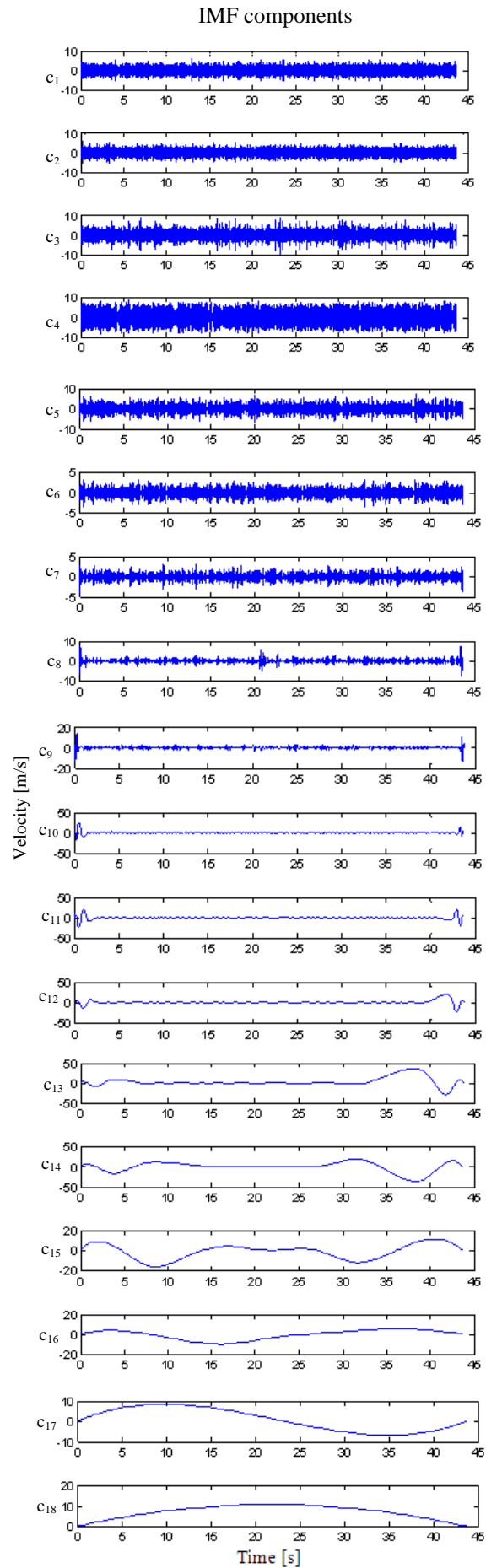


Fig. 5: All c_n IMFs of velocity data signal

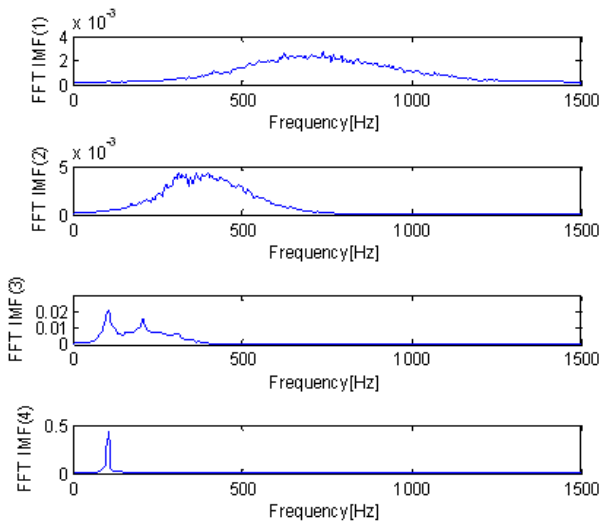


Figure 6: Fast Fourier Transform of 1st, 2nd, 3rd and 4th IMF components.

The Hilbert transform of second IMF (H(IMF2)) shows a scattered frequency distribution around 450 Hz, which is not observed in Fourier spectrum. This is associated to contents of second IMF, which has possibly a reminiscent noise of the original signal, which contaminates the frequency distribution, as seen also in FFT of IMF 2 in Fig. 6.

The Hilbert spectrum of first IMF shows the same features, but more scattered than in relation to H(IMF2) and this is in accordance with the FFT of IMF 1 on Fig. 6. In the other spectra, the distribution around the fundamental frequency, on Hilbert spectrum of 4th IMF (H(IMF4)) and these frequency and its harmonics on Hilbert spectrum of 3rd IMF (H(IMF3)) is observed. This one contains the three peaks observed in Fourier spectrum. Therefore, in the studied problem, the 3rd and 4th IMFs become the most important IMFs obtained since they carry the shedding process information.

That feature is only seen in HSA due to the presence of instant frequency obtained from application of Hilbert transform in each IMF with its respective frequency. Through the decomposition of the signal in IMFs the information is carried to the HSA time scale, providing a view of the vortex shedding frequency distribution and some harmonics, which represents an improvement in the signal analysis by HHT compared with wavelets. Furthermore, the distribution of the energy signal resultant of the Hilbert spectra obtained can also become more effective and detailed than the wavelet analysis, in this first study.

CONCLUSIONS

The Empirical Mode Decomposition from Hilbert-Huang transform leads to Intrinsic Mode Functions of the signal which reveals the features of oscillations of the data series, leading to obtain the instantaneous frequency from the Hilbert transform in each IMF. This

method can be more effective than wavelets, which depends on the wavelet mother to be applied on the signal, which has to be chosen by trial and error, according to the features of the signal analyzed. Since HHT is directly decomposed from original data, the intrinsic physical characteristics are shown clearly by each IMF and its application is simpler than wavelets. Both wavelets and HHT can reveal the main characteristics of signal.

The gain in use of HHT in respect to Fourier analysis is in the fact that HHT, like wavelets, can be applied to non-stationary signals, simply yet to verify its behavior on PSD or Fourier spectrum. In this work the comparison with Fourier spectrum leads us to analyses the frequencies obtained from the Hilbert spectrum and its possibility to compare the shedding frequency and its harmonics with the frequency distribution on Hilbert spectrum. Nevertheless, FFT had still to be used to identify the fundamental modes of the studied signal.

Therefore, the employed methods (Fourier, Wavelets and HHT) are complementary in interpreting the resulting data. In the case of use of FFT in some IMFs, this feature is very important in the methodology of a study since the conditions of applicability are satisfied.

In general, the analysis of the shedding process becomes more comprehensive with the aid of the Hilbert-Huang Transform to wavelet and Fourier transforms. HHT is a new technique and it can be a useful tool for the treatment of signals from turbulent flow studies.

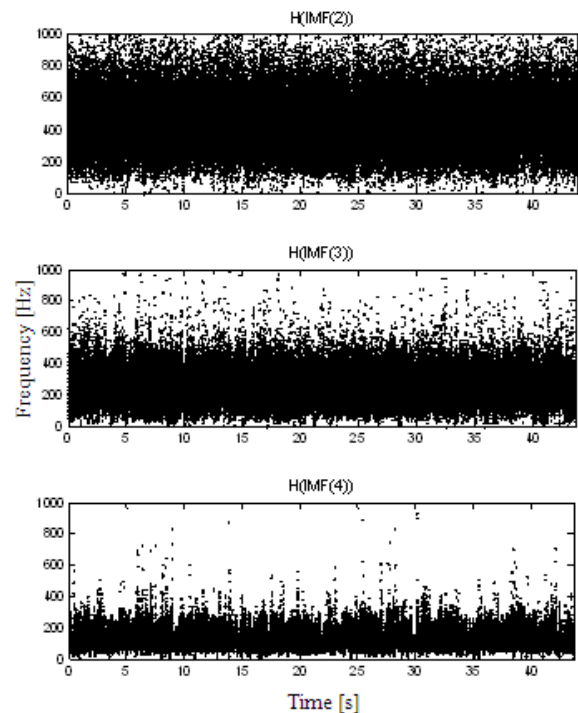


Figure 7: Results for Hilbert Spectral Analysis for second, third and fourth IMF.

ACKNOWLEDGMENTS

Authors gratefully acknowledge the support by the Brazilian Scientific and Technological Council – CNPQ.

Rodrigo Santiago Silveira thanks the CAPES, Ministry of Education, Brazil, for granting him a fellowship.

REFERENCES

- [1] BLEVINS, R.D., 1990. *Flow Induced Vibrations*, van Nostrand-Reinhold, New York.
- [2] BENDAT, J. S., PIERSOL, A. G., 1971. *Random Data: Analysis and Measurement Procedures*, Willey – Interscience, New York.
- [3] DAUBECHIES, I., 1992. *Ten Lectures on Wavelets*, SIAM – Society for Industrial and Applied Mathematics, Philadelphia.
- [4] HUANG, N.E.; SHEN, Z.; LONG, S.R.; WU, M.C.; SHIH, H.H.; ZHENG, Q.; YEN, N.C.; TUNG, C.C.; LIU, H.H., 1998 *The Empirical Mode Decomposition and the Hilbert Spectrum for Nonlinear and Non-stationary Time Series Analysis*, Proceedings of the Royal Society, v. 454, p. 903-995.
- [5] HUANG, N.E.; SHEN, S.S.P., 2005 *Hilbert-Huang Transform and Its Applications*, Word Scientific, v. 5, Singapore.
- [6] SHI, C.x.; LUO, Q.f., 2003 *Hilbert-Huang Transform and Wavelet Analysis of Time History Signal*, ACTA Seismologica Sinica, v. 16, no. 4, p. 422-429.
- [7] MALLAT, S., 2009. *A Wavelet Tour of Signal Processing - The Sparse Way*, 3rd ed., Academic Press, Burlington.
- [8] CHENG, J.; YU, D.; TANG, J.; YANG, Y., 2008 *Application of the frequency family separation method based upon EMD and local Hilbert energy spectrum method to gear fault diagnosis*, Mechanism and Machine Theory, v. 43, p. 712-723.
- [9] CAN-YANG, H.; QING-JUN, C.; TIAN-LI, H., 2008 *Estimation of Local Spectral Density of Seismogram by Orthogonal Hilbert-Huang Transform and Application of the Spectral Density*, The 14th World Conference on Earthquake Engineering, Beijing, China.
- [10] YU, D., CHENG, J., YANG, Y., 2003 *Hilbert Energy Spectrum and Its Application to Gear Fault Diagnosis*, Journal of Human University, v. 30, N°. 4, p. 47-50.
- [11] ZIADA, S., OENGÖREN, A. 1993. *Vortex Shedding in an in-line Tube Bundle with Large Tube Spacings*, Journal of Fluids and Structures, Vol. 7, p. 661-687.

NUMERICAL PREDICTIONS OF THE NATURAL FREQUENCIES OF LONG FLEXIBLE CYLINDERS WITH A FORM OF DAMPING THAT INCLUDES THE EFFECT OF THE CURRENT

F J Huera-Huarte*

Department of Mechanical Engineering
Universitat Rovira i Virgili (URV)
Avinguda Pasos Catalans, 26
43007 Tarragona, Spain
Email: francisco.huera@urv.cat

L M González

Naval Architecture Department (ETSIN)
Technical University of Madrid (UPM)
Arco de la Victoria s/n
28040 Madrid, Spain

ABSTRACT

We pose a quadratic eigenvalue problem (QEP) in order to study the dynamics of flexible cylinders in cross-flow. A structural model based on Euler-Bernoulli equation is used together with a fluid loading model yielding to a quadratic eigenvalue problem. The problem includes a form of damping dependent not only on the structural damping itself which is in advance known to be of very small effect in this type of problems, but also on the free stream velocity and the fluid force coefficients. The fluid force model is inspired by that used by Zhou et al. in [1].

We have validated the computations given by our QEP code, against a well known experimental set of data obtained back in 2003 by Chaplin et al. [2], in which a flexible circular cylinder model was used to model the dynamics of a long flexible cylinder undergoing multi-mode vortex-induced vibrations (VIV). QEP computed results are in very good agreement with the experimental ones. The code allows us to conclude the effect of the flow (force coefficients and current) showing for example that the inclusion of a mean lift coefficient in the eigenvalue problem, produce no variation in its result.

INTRODUCTION

Long flexible circular cylinders are often used as an idealisation of complex offshore structures such as marine cables, pipes, risers, tendons and catenaries. For the oil and gas industry, it is of extreme interest to predict the dynamics of offshore structures, as they are essential in their exploration activities. Other offshore industries that need moorings or tendons to gain stability in their structures, need better design tools. An example of this rela-

tively new applications can be found in the offshore wind turbines, which are considering the use of tendons, mooring lines, and other flexible systems in order to fix their floaters to the sea bed in relatively deep waters.

One of the main problems that arises when dealing with the design of such offshore systems is vortex-induced vibrations (VIV). They are the consequence of a very complex physics phenomena of interaction between the elasticity of the structure and the separated flow around it, in the presence of ocean currents. VIV leads to undesired structural motions and fatigue which can be dramatic in the harsh ocean environment. Excellent reviews on the topic of VIV can be found in [3–6] and [7]. VIV studies of long flexible cylinders are more scarce than rigid flexibly mounted ones, because the topic is intrinsically very challenging [8] and the simplification of the rigid cylinder section is often used. Numerically, the problem has been treated by many researchers such as in [9–13] and [14] just to mention some.

The aim of this work is the implementation of a quadratic eigenvalue solver that will be used to calculate the natural frequencies of flexible cylinders, taking into account a relatively complex description of the hydrodynamic loads. Natural frequencies can be obtained in many ways, and in fact there are simpler and easier ways to the one proposed here, still producing very good results when compared to experimental cases [2,15], but this one, specifically allows to study the influence of several important flow parameters on the natural frequencies. With it, we can study the influence of drag and lift coefficients in the dynamics of the cylinder. A structural model based on Euler-Bernoulli beam equation for both the parallel and the transverse to the flow motions, is coupled through a hydrodynamic loading model in this case. For the

*Address all correspondence to this author.

sake of completeness, the model also considers the presence of a tension applied at the top of the cylinder, which is a normal situation in offshore structures such as riser pipes or tendons. The code is validated with experiments performed by [2]. This method allows the simulation of more complicated situations such as the introduction in the loading model of a non zero mean lift coefficient, that could be used to study the modal characteristics of the cylinder, in a case of fluid-structure interaction with wake interference.

1 Governing equations

1.1 Structural model

We use a Cartesian reference with its origin at the bottom of the cylinder in which x axis is parallel to the flow velocity, y is transverse and z coincides with the vertical axis of the riser in its undeflected configuration. $u(z,t)$ and $v(z,t)$ are defined as the time variant in-line and cross-flow motions respectively. With these set of displacements, a point in the centreline of the beam can be spatially described. The states of bending are described by displacements and rotations around the two axes contained in the plane perpendicular to the beam axis. Geometric non-linearities are important when large deflections occur, introducing extra terms in the stress equations due to the effect of moments coming from the misalignment of the forces. When the first derivative in space of the transverse motions is small ($\frac{\partial u}{\partial z} \approx 0$ and $\frac{\partial v}{\partial z} \approx 0$), as in the cases modeled here, the non-linear terms in the stress equations disappear and both transverse and axial motions become uncoupled, [16]. Therefore, in problems involving small displacements, the motions in the the planes xz and yz can be treated independently.

With these conditions, the transverse motion of the cylinder using the Euler-Bernoulli or classical theory for beams, assumes: Planar surfaces orthogonal to the axis of the beam, remain planar and orthogonal to the axis after the deformation and therefore transverse shear is neglected; all the forces acting on the beam can be expressed by means of vectors parallel to the x or y axis (except the axial forces in our case of study); the transverse section of the beam is symmetric with respect to plane xz or yz . Therefore, the transverse deformation of a generic beam can be described with a fourth order differential equation which can be derived by applying force and momentum equilibrium to an infinitesimal section of the beam. The formulation works for any of the two transverse directions x or y with displacements u and v respectively.

$$EI \frac{\partial^4 u(z,t)}{\partial z^4} - \frac{\partial}{\partial z} \left(T(z) \frac{\partial u(z,t)}{\partial z} \right) + c \frac{\partial u(z,t)}{\partial t} + m(z) \frac{\partial^2 u(z,t)}{\partial t^2} = f(z,t) \quad (1)$$

In the above equation E is Young's modulus, I is the cross-sectional inertia, c is the structural damping coefficient, m is the mass per unit length of the cylinder and $f(z,t)$ is the hydrodynamic forcing applied to the cylinder. If the section is uniform along the length of the cylinder, I can be considered constant and equal in both planes. The mass of the cylinder is $m(z) = (c_m + 1)\rho_s A$ where ρ_s is the material density, A is the cross-section of the cylinder and c_m is the added mass coefficient. The tension $T(z)$ is expressed as

$$T(z) = T_t - w_s(L - z) \quad (2)$$

with T_t being the tension applied at the top of the riser, L the length of the riser and w_s the submerged weight per unit length. Equation (2) considers the effect of buoyancy on the riser because the submerged weight is used. In our case of study we will consider that our cylinder is pin-jointed at both ends and hence the boundary conditions for any of the two displacements u or v in the above differential equation are,

$$u(0,t) = 0, u(L,t) = 0 \quad \forall t$$

$$\frac{\partial^2 u(0,t)}{\partial z^2} = 0, \frac{\partial^2 u(L,t)}{\partial z^2} = 0 \quad \forall t \quad (3)$$

1.2 Fluid forcing model

In order to model the hydrodynamic loading on the cylinder $f(z,t)$, we will use:

$$f_x = \frac{1}{2} \rho U D \left[C_d \left(U_r - \frac{U_r}{U} \frac{\partial u}{\partial t} \right) + C_l \frac{U_r}{U} \frac{\partial v}{\partial t} \right] + \frac{1}{2} \rho U^2 D C'_d \sin(\omega_x t) \quad (4)$$

$$f_y = \frac{1}{2} \rho U D \left[C_l \left(U_r - \frac{U_r}{U} \frac{\partial u}{\partial t} \right) - C_d \frac{U_r}{U} \frac{\partial v}{\partial t} \right] + \frac{1}{2} \rho U^2 D C'_l \sin(\omega_y t) \quad (5)$$

where ρ is the fluid density, U is the free stream flow speed, D is the cylinder external diameter, C_d is the drag coefficient, C_l is the lift coefficient, U_r is the relative velocity between the cylinder and the fluid and ω_x and ω_y are the in-line and cross-flow fluid excitation frequencies, respectively. The hydrodynamic loading can be in general considered to be composed of three terms as in here: time-mean, periodical and random. The random part is neglected in this work as it is understood that the main fluid excitation comes from vortex shedding. The first term in equations (4) and (5) are for the time-mean forces whilst the second term accounts for the time-periodic term.

1.3 The resulting fluid-structural system

Substituting equations (4) and (5) into equation (1), yields the following coupled partial differential equations.

$$EI \frac{\partial^4 u(z,t)}{\partial z^4} - \frac{\partial}{\partial z} \left(T(z) \frac{\partial u(z,t)}{\partial z} \right) + c_{xx} \frac{\partial u(z,t)}{\partial t} + c_{xy} \frac{\partial v(z,t)}{\partial t} + m(z) \frac{\partial^2 u(z,t)}{\partial t^2} = \frac{1}{2} \rho U^2 D (C_d + C'_d \sin(\omega_x t)) \quad (6)$$

$$EI \frac{\partial^4 v(z,t)}{\partial z^4} - \frac{\partial}{\partial z} \left(T(z) \frac{\partial v(z,t)}{\partial z} \right) + c_{yy} \frac{\partial v(z,t)}{\partial t} + c_{yx} \frac{\partial u(z,t)}{\partial t} + m(z) \frac{\partial^2 v(z,t)}{\partial t^2} = \frac{1}{2} \rho U^2 D (C_l + C'_l \sin(\omega_y t)) \quad (7)$$

where c_{xx} , c_{xy} , c_{yx} and c_{yy} are in-line and transverse damping coefficients that will have different expressions depending on the assumptions made to solve the system.

A similar derivation was used in [1] to complement the study of an experimental arrangement of two cylinders side-by-side. They used a simplified version of Euler-Bernoulli equation in which the tension was not considered and fixed boundary conditions. The hydrodynamic loading model is the same as the one shown here, but they made different assumptions according to their experimental set-up. They considered the relative velocity in their system to be $U_r = \sqrt{(U - \frac{\partial u}{\partial t})^2 + (\frac{\partial v}{\partial t})^2} \approx U - \frac{\partial u}{\partial t}$ and $\frac{U_r}{U} \approx 1$, meaning that $U \gg \frac{\partial u}{\partial t}$ or $\frac{\partial v}{\partial t}$. In their experiments, this is acceptable as their cylinder had a very high mass ratio, very low L/D and high flexural stiffness,

yielding to very small motion amplitudes (order of tenths of mm) and therefore low velocities, even at high responding frequencies. Having all these assumptions into account, the damping coefficients are,

$$\begin{bmatrix} c_{xx} & c_{xy} \\ c_{yx} & c_{yy} \end{bmatrix} = \begin{bmatrix} c & 0 \\ 0 & c \end{bmatrix} + \rho U D \begin{bmatrix} C_d & -C_l/2 \\ -C_l & C_d/2 \end{bmatrix} \quad (8)$$

Equations (6) and (7) in [1] study are uncoupled and linear because they consider always C_l to be zero, therefore the damping matrix represented by the equation (8) is diagonal ($c_{xy} = c_{yx} = 0$) and the two equations of the system can be solved independently.

In Section 3, we compare the results of applying this derivation to the experimental results found in [2], obtained with a low mass-damping cylinder with high aspect ratio. In these experiments, relatively large amplitude of vibrations were observed with cylinder motion velocities of the order of the free stream velocity. All this makes the assumptions made in [1] not valid anymore. A better assumption for these cases is to consider $U \simeq \frac{\partial u}{\partial t}$ or $\frac{\partial v}{\partial t}$, which yields to $U_r = \frac{\partial v}{\partial t}$. We are also considering the applied tension and its variation along the axis of the cylinder, moreover the boundary conditions considered are those of pin-ended beams as in equations 3. The system ends up non-linear because of a term $\left(\frac{\partial v(z,t)}{\partial z}\right)^2$ that appears in the system of equations. We linearize the equations using $\left(\frac{\partial v(z,t)}{\partial z}\right)^2 \simeq U \left(\frac{\partial v(z,t)}{\partial z}\right)$, and our damping coefficients become:

$$\begin{bmatrix} c_{xx} & c_{xy} \\ c_{yx} & c_{yy} \end{bmatrix} = \begin{bmatrix} c & 0 \\ 0 & c \end{bmatrix} + \frac{\rho U D}{2} \begin{bmatrix} 0 & -C_l \\ 0 & C_d \end{bmatrix} \quad (9)$$

Moreover, in Section 3 we consider not only cases with $C_l = 0$ (uncoupled system) but also cases with $C_l \neq 0$ (coupled system), in order to see what is the effect of C_l on the natural frequencies of the system. In the following section we derive the quadratic eigenvalue problem that arises from this fluid-structural system, and we solve it using the finite element method.

2 The quadratic eigenvalue problem using the finite element method

We pose the quadratic eigenvalue problem (QEP) that allows the study of the natural frequencies of flexible cylinders in cross-flow, even for cases with interference,

when $C_l \neq 0$. Assuming that the general solution of the equations (6) and (7) is given by:

$$\begin{aligned} u(z,t) &= \hat{u}(z)e^{\lambda t} \\ v(z,t) &= \hat{v}(z)e^{\lambda t} \end{aligned} \quad (10)$$

where $\hat{u}(z)$ and $\hat{v}(z)$ are the amplitude functions that only depend on z and λ is a complex coefficient. When the ansatz represented by the equations (10) is substituted in equations (6) and (7), the following QEP can be deduced in the homogeneous case:

$$(\lambda^2 \mathbf{K} + \lambda \mathbf{C} + \mathbf{M}) \phi = 0 \quad (11)$$

where λ is the set of eigenvalues and $\phi = (\hat{u}, \hat{v})^T$ are the eigenvectors or eigenmodes. The physical meaning of the real part of the complex eigenvalue λ is the damping or growth rate of the mode, and the imaginary part is related with the frequency f of the mode by the equation $Im(\lambda) = 2\pi f$.

The solution of a QEP consists on finding scalars $\lambda \in \mathbb{C}$ and nonzero vectors $\phi \in \mathbb{C}^n$, given $n \times n$ matrices $\in \mathbb{R}$ that satisfy the homogeneous differential system of equations. Eigenvalue problems arise in many engineering disciplines and are of special importance in mechanical vibrations because if mass, stiffness and damping matrices (\mathbf{M} , \mathbf{K} and \mathbf{C} respectively) are used, their solution leads to the natural frequencies of the systems. A complete survey on QEP problems appear in [17]. Here, we solve the QEP derived from equations (6) and (7), where the operators are discretized using the finite element method (FEM) to obtain the matrices.

3 RESULTS

Here, we compute the natural frequencies for several cases of study, inspired by the experiments described in [2, 15]. We compare our numerical results with the dominant frequencies found in the experiments, in cases in which there was a current producing multi-mode VIV on the cylinder. For all these cases, the assumption is that the mean value of $C_l=0$, because the experiments were conducted with a single isolated cylinder, without any perturbation in the incoming flow.

Afterwards, we also compute situations with $C_l \neq 0$ as it would happen in conditions with wake interference in which the cylinder would see perturbed incoming flow being shed from another bluff body. Unfortunately, to

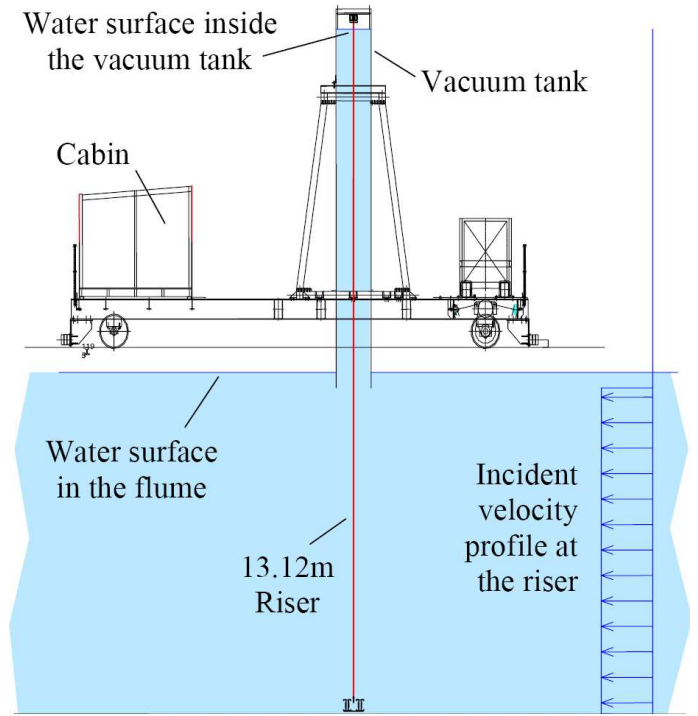


FIGURE 1: EXPERIMENTAL SET-UP USED IN [2] AT THE DELTA FLUME IN 2003.

the knowledge of the authors, there are not experimental results showing measured mean C_l in cases with self-excited multi-mode flexible cylinders in cross-flow, having wake interference (tandem, staggered or side-by-side), and therefore comparisons of the numerical results cannot be done. Recent results can be found in [18–20], but those are for low mode number. Finally, we compute as an example of the possibilities offered by the method, several natural frequency plots for a specific experimental cases obtained by varying U , C_d and c .

The main parameters of the cylinder model used in that experiments appear in table 1. The experiment layout can be seen in figure 1.

TABLE 1: MAIN PARAMETERS OF THE EXPERIMENT by [2].

External diameter	D	m	0.028
Length	L	m	13.12
Submerged Length	L_s	m	5.94
Flexural Stiffness	EI	Nm ²	29.9
Free stream flow speeds	U	m/s	≤ 1
Mass including water	m_w	kg/m	1.85
Mass including added mass	m_a	kg/m	2.46
Submerged weight	w_s	N/m	12.1
Structural damping coefficient	c	Ns/m	0.147

3.1 Effect of the current on the natural frequencies

Several experimental cases have been analyzed, for which the structural response, the top tension, the drag and the current were measured. The dominant modes and frequencies in the in-line and transverse directions were also obtained from the experiments by means of Fourier and modal analysis of the structural data [2, 15]. The cross-flow f_y and in-line f_x dominant responding frequencies from the experiments in [2], appear in table 2, besides the results computed with the QEP code described in this manuscript. A summary of all the results is presented in Figure 2, where the values from table 2 appear one against each other. The solid line indicates the place where all the points should fall if the numerical and experimental frequencies would be exactly the same. In general the results are in good agreement, meaning that the QEP is able to capture the modal characteristics of the cylinder model during the experiments.

3.2 Effect of a perturbation in the incoming flow leading to a $C_l \neq 0$

The last set of computations is for the case of a non zero a lift coefficient. In this section there is no data to compare the results with, because to the knowledge of the authors, there are no experiments showing the dynamic response of a flexible cylinder with wake interference at modes higher than the second. We have used the same cases as in table 2, but we have introduced a $C_l \neq 0$ for each case. The results given by the code are clear in the sense that no modifications in the natural frequencies of

TABLE 2: NATURAL FREQUENCIES f_x and f_y IN Hz FOR DOMINANT MODES OF VIBRATION FOR THE EXPERIMENTS CINDUCTED IN [2] FOR CASES WITH CURRENT ($U \neq 0$). QEP COMPUTED FREQUENCIES APPEAR BESIDES THE EXPERIMENTAL ONES.

T_t (N)	U (m/s)	C_d	f_{y_i} (Hz)		f_{x_i} (Hz)	
			exp.	QEP	exp.	QEP
416	0.207	2.68	1.325	1.349	1.325	1.357
518	0.403	1.50	2.676	2.641	5.376	5.243
685	0.602	1.48	3.876	3.707	7.727	7.612
743	0.648	2.24	4.074	3.857	8.149	7.878
755	0.700	2.13	4.526	4.631	9.027	8.847
1190	0.311	1.15	1.668	1.601	3.402	3.275
1199	0.412	1.81	2.568	2.426	5.168	5.006
1230	0.512	1.95	3.081	3.293	6.161	5.972
1273	0.612	2.19	3.601	3.333	7.221	7.011
1435	0.794	2.27	4.403	4.435	8.806	8.448

the cylinder have been observed when compared to the cases with $C_l = 0$. Differences only appear in the 5th representative digit. Physically, this means that any variation made respect to the case of an isolated single cylinder that introduces a $C_l \neq 0$, produces no variations in the natural frequencies of the system. According to this observation, a cylinder immersed in the wake of a bluff body, seeing a non zero mean lift steady incoming flow, would see no variation in its natural frequencies respect to the case of being isolated. Obviously, that does not mean that the dynamic response of a cylinder immersed in the wake of a bluff body will be the same as in the case of being isolated, it refers to its natural frequencies.

4 Conclusions

A QEP solver has been developed which is able to cope with the problem of finding the natural frequencies of long flexible cylinders in cross-flow, including the effect of the currents. The code can be used to study the dynamics of slender structures surrounded by a fluid or immersed in currents. It allows to input as a parameters not only the mechanical characteristics of the cylinder

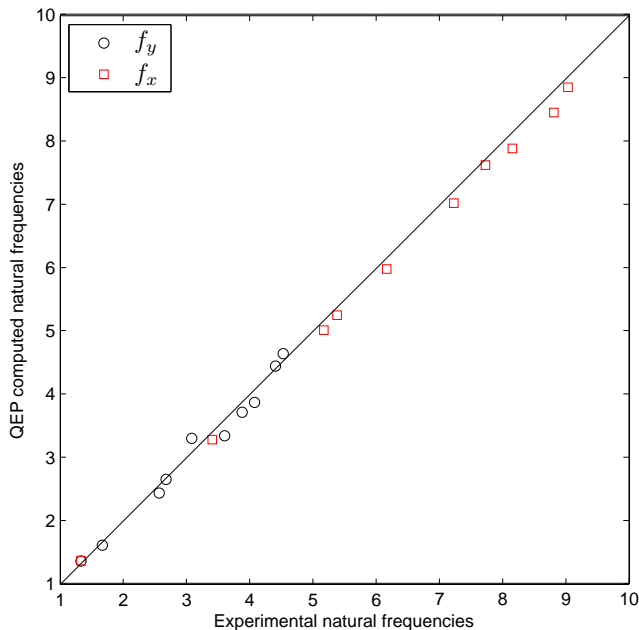


FIGURE 2: COMPARISON BETWEEN EXPERIMENTAL AND QEP COMPUTED NATURAL FREQUENCIES FOR CASES WITH THE CYLINDER MODEL EXPOSED TO CURRENT. DATA FROM TABLE 2. SOLID LINE INDICATES WHERE ALL THE POINTS SHOULD FALL FOR PERFECT QEP-EXPERIMENT AGREEMENT.

and the applied tension, which can be variable along the length of the cylinder, but also the free stream velocity, the expected mean drag and lift coefficients.

The code is also able to produce results which are in close agreement with previous experiments. It allows an important observation related to the effect of a non zero mean lift coefficient on the dynamics of a long flexible cylinder. This observation is of especial interest for situations in which a flexible cylinder is immersed in the wake of another bluff body, and hence affected by an incoming flow characterised by a $C_l \neq 0$. It is remarkable, that a non zero lift coefficient has practically no effect on the natural frequencies of the system, if a model such as the one in equations 4 and 5 is used.

ACKNOWLEDGMENT

The first author gratefully acknowledges the funding provided by Ministerio de Ciencia e Innovación (MICINN) through grant DPI2009-0714. The second author gratefully acknowledges MICINN for the support provided through grant TRA2010-16988. The authors want to thank Dr. Juan Miguel Sánchez for the valuable discussions during the development of this work.

REFERENCES

- [1] Zhou, Y., Wang, Z. J., So, R. M. C., Xu, S. J., and Jin, W., 2001. "Free vibrations of two side-by-side cylinders in a cross-flow". *Journal of Fluid Mechanics*, **443**, pp. 197–229.
- [2] Chaplin, J. R., Bearman, P. W., Huera-Huarte, F. J., and Pattenden, R., 2005. "Laboratory measurements of vortex-induced vibrations of a vertical tension riser in a stepped current". *Journal of Fluids and Structures*, **21**(1), pp. 3–24.
- [3] Sarpkaya, T., 1979. "Vortex-induced oscillations, a selective review". *Journal of Applied Mechanics*, **46**, pp. 241–258.
- [4] Bearman, P. W., 1984. "Vortex shedding from oscillating bluff bodies". *Annual Review of Fluid Mechanics*, **16**, pp. 195–222.
- [5] Sarpkaya, T., 2004. "A critical review of the intrinsic nature of vortex-induced vibrations". *Journal of Fluids and Structures*, **19**, pp. 389–447.
- [6] Williamson, C., and Govardhan, R., 2004. "Vortex-induced vibrations". *Annual Review of Fluid Mechanics*, **36**, pp. 413–455.
- [7] Bearman, P. W., 2011. "Circular cylinder wakes and vortex-induced vibrations". *Journal of Fluids and Structures*, **In Press**, p. doi:10.1016/j.jfluidstructs.2011.03.021.
- [8] Vandiver, J. K., 1998. "Research challenges in the vortex-induced vibration prediction of marine risers". In Offshore Technology Conference (OTC).
- [9] Evangelinos, C., Lucor, D., and Karniadakis, G. E., 2000. "Dns-derived force distribution on flexible cylinders subject to vortex-induced vibration". *Journal of Fluids and Structures*, **14**, pp. 429–440.
- [10] Willden, R. H. J., and Graham, J. M. R., 2004. "Multi-modal vortex-induced vibrations of a vertical riser pipe subject to a uniform current profile". *European Journal of Mechanics B/Fluids*, **23**, pp. 209–218.
- [11] Meneghini, J. R., Saltara, F., Fregonesi, R. A., Yamamoto, C. T., Casaprima, E., and Ferrari, J. A., 2004. "Numerical simulations of viv on long flexible cylinders immersed in complex flow fields". *European Journal of Mechanics B/Fluids*, **23**, p. 5163.
- [12] Lucor, D., Mukundan, H., and Triantafyllou, M., 2006. "Riser modal identification in cfd and full-scale experiments". *Journal of Fluids and Structures*, **22** (6-7), pp. 905–917.
- [13] Srinil, N., 2011. "Analysis and prediction of vortex-induced vibrations of variable-tension vertical risers in linearly sheared currents". *Applied Ocean Research*, **33** (1), pp. 41–53.

- [14] Bourguet, R., Karniadakis, G. E., and Triantafyllou, M. S., 2011. “Lock-in of the vortex-induced vibrations of a long tensioned beam in shear flow original research article”. *Journal of Fluids and Structures*, **In Press**, p. doi:10.1016/j.jfluidstructs.2011.03.008.
- [15] Huera-Huarte, F. J., 2006. “Multi-mode vortex-induced vibrations of a flexible circular cylinder”. PhD thesis, Imperial College London.
- [16] Reddy, J. N., 2004. *An introduction to the nonlinear Finite Element analysis*, second ed. Oxford University Press.
- [17] Tisseur, F., and Meerbergen, K., 2001. “The quadratic eigenvalue problem”. *SIAM REVIEW*, **43(2)**, p. 235286.
- [18] Huera-Huarte, F. J., and Bearman, P. W., 2011. “Vortex and wake-induced vibrations of two flexible circular cylinders in a tandem arrangement with near wake interference”. *Journal of Fluids and Structures*, **27(2)**, pp. 192–211.
- [19] Huera-Huarte, F. J., and Gharib, M., 2011. “Flow-induced vibrations of a side-by-side arrangement of two flexible circular cylinders”. *Journal of Fluids and Structures*, **27(3)**, pp. 354–366.
- [20] Huera-Huarte, F. J., and Gharib, M., 2011. “Vortex and wake-induced vibrations of two flexible circular cylinders in a tandem arrangement with far wake interference”. *Journal of Fluids and Structures*, **27(5-6)**, pp. 824–828.



NUMERICAL SIMULATION OF INFLUENCE OF A GAP BETWEEN THE MAIN LIFTING SURFACE AND THE AILERON ON AEROELASTIC BEHAVIOR OF AN AIRFOIL

Jaromír Horáček*

Institute of Thermomechanics
Academy of Sciences of the Czech Republic
Dolejškova 5, 182 00 Prague 8
Czech Republic
Email: jaromirh@it.cas.cz

Miloslav Feistauer

Charles University Prague
Faculty of Mathematics and Physics
Sokolovska 83, 186 75 Praha 8
Czech Republic
Email: feist@karlin.mff.cuni.cz

Petr Sváček

Czech Technical University Prague
Faculty of Mechanical Engineering
Karlovo nám. 13, 121 35 Praha 2
Czech Republic
Email: svacek@marian.fsik.cvut.cz

ABSTRACT

The contribution deals with numerical simulations of the interaction of two-dimensional (2D) incompressible viscous flow and a vibrating airfoil NACA 0012. The flexibly supported airfoil with three degrees of freedom (3-DOF) is performing rotation around the elastic axis, oscillations in the vertical direction and rotation of the aileron around the axis. The finite element (FE) solution of the Navier-Stokes equations is strongly coupled with a system of nonlinear ordinary differential equations describing the airfoil motion with large amplitudes. The time-dependent computational domain and a moving grid are treated by the Arbitrary Lagrangian-Eulerian (ALE) method. The developed method is used in the theoretical prediction of the aerodynamic damping, limit cycle oscillations (LCO) and the flutter instability of the airfoil, especially concerning the effects of the geometry and the size of the gap between the main lifting surface and the aileron.

NOMENCLATURE

$\mathbf{u}(x, t) = (u_1, u_2)$ fluid flow velocity,
 U_∞ far-field flow velocity,
 $P(x, t), p(x, t) = P/\rho$ pressure, kinematic pressure,
 ρ, ν fluid density, kinematic viscosity,
 t, τ time, time step,
 $h,$ airfoil vertical displacement,
 α, β airfoil and aileron rotation angles,
 c, l airfoil chord and depth of the segment,
 m airfoil mass,
 S_α, I_α airfoil static and inertia moments,
 S_β, I_β aileron static and inertia moments,
 $k_{hh}, k_{\alpha\alpha}, k_{\beta\beta}$ stiffness constants of the springs,

Address all correspondence to this author*

$D_{hh}, D_{\alpha\alpha}, D_{\beta\beta}$ structural damping coefficients,
 L_2, M_α, M_β lift force and torsional moments.

INTRODUCTION

The aeroelasticity problems of 3-DOF airfoils are usually associated with suppressing the vibration level in the subcritical flight speed range, increasing the flutter speed, and converting the unstable LCO to a stable one by a feedback mechanism and flow control.

A review of available control techniques related to time-dependent arbitrary motions of 2-DOF and 3-DOF airfoils featuring plunging-pitching and plunging-pitching-aileron deflection was published in [1]. The study [2] deals with the aeroelastic response and control of a 3-DOF flapped-wing system in an incompressible flow and exposed to external pressure pulse. The goal was to suppress the flutter instability. The vibration amplitudes were assumed small.

The aerodynamic forces for motions of an airfoil with 3-DOF subjected to a 2D incompressible flow were presented in [3]. Based on the Theodorsen's theory the equations of motion with piecewise linear characteristic for the airfoil with free play nonlinearity were established and the characteristics of LCO were predicted by numerical simulation. Analytical analysis and numerical simulations of the aeroelastic response of 3-DOF airfoil-flap system subjected to time-dependent loads in an incompressible flow were addressed in [4]. The paper is focused on feedback control methodology in order to suppress the flutter instability. The aerodynamic forces are derived from the Theodorsen's equations using Wagner's function. Flutter boundaries and LCO of 3-DOF aerofoil with structural stiffness nonlinearities in 2D compressible flow were studied in [5] by using the finite volume

solution of the Euler equations. Recently, the effects of a harmonically deflected trailing-edge flap on the dynamic load of an oscillating NACA 0015 airfoil were investigated experimentally [6] presuming applications in dynamic-stall flow control of rotor blades.

Some more studies on numerical modelling of the post-flutter behaviour of airfoils in laminar 2D incompressible flow were overviewed in the authors' preceding study [7], where a sufficiently accurate and robust FE method allowing the numerical simulation of large amplitude flow-induced vibrations of a 3-DOF airfoil was developed. The method was tested in good agreement with the available MSC.NASTRAN results by computing the critical flutter velocity and the flutter frequency.

In the present paper we are concerned with a numerical simulation of 2D viscous incompressible flow past a moving airfoil, which is considered as a solid flexibly supported body with three degrees of freedom, allowing its vertical and torsional oscillations and the rotation of an aileron. The formerly developed method [7] is used here for the theoretical prediction of dynamic behavior of the 3 DOF airfoil, especially concerning the effects of the geometry and the size of the gap between the main lifting surface and the aileron. The development of the vibration amplitudes is simulated in time domain in dependence on the various gaps and the far-field airflow velocities, from the lower airflow velocities up to the flutter and post flutter regimes, when the aileron rotation reached up to about 50 degrees. Such large vibration amplitudes are respected by a structural nonlinear mass matrix.

GOVERNING EQUATIONS

The motion of the airfoil is described by functions $\alpha(t)$, $\beta(t)$ and $h(t)$, representing the rotation of the airfoil around an elastic axis EA, the rotation of the aileron around an axis EF and the vertical displacement of the whole airfoil, respectively, as shown in Figure 1.

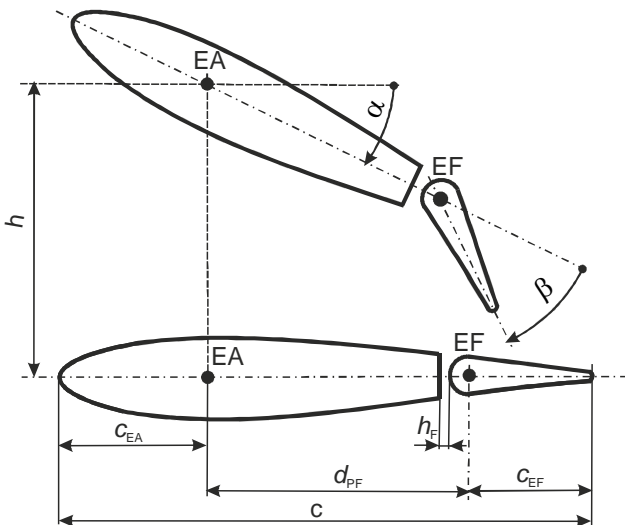


FIGURE 1: SCHEME OF THE 3-DOF AIRFOIL.

The nonlinear equations of the motion describing the vibrations with large amplitudes of the airfoil given by the functions α , β and h read

$$\begin{aligned}
 m\ddot{h} + \left[(S_\alpha - S_\beta) \cos \alpha + S_\beta \cos(\alpha + \beta) \right] \ddot{\alpha} \\
 + S_\beta \ddot{\beta} \cos(\alpha + \beta) - (S_\alpha - S_\beta) \dot{\alpha}^2 \sin \alpha \\
 - S_\beta (\dot{\alpha} + \dot{\beta})^2 \sin(\alpha + \beta) + D_{hh} \dot{h} + k_{hh} h = L_2, \\
 \left[(S_\alpha - S_\beta) \cos \alpha + S_\beta \cos(\alpha + \beta) \right] \ddot{h} \\
 + \left[(I_\alpha - 2d_{PF} S_\beta) + 2d_{PF} S_\beta \cos \beta \right] \ddot{\alpha} \\
 + \left[I_\beta + d_{PF} S_\beta \cos \beta \right] \ddot{\beta} - d_{PF} S_\beta \dot{\beta}^2 \sin \beta \\
 - 2d_{PF} S_\beta \dot{\alpha} \dot{\beta} \sin \beta + D_{\alpha\alpha} \dot{\alpha} + k_{\alpha\alpha} \alpha = M_\alpha, \\
 S_\beta \cos(\alpha + \beta) \ddot{h} + \left[I_\beta + d_{PF} S_\beta \cos \beta \right] \ddot{\alpha} \\
 + I_\beta \ddot{\beta} + d_{PF} S_\beta \dot{\alpha}^2 \sin \beta + D_{\beta\beta} \dot{\beta} + k_{\beta\beta} \beta = M_\beta.
 \end{aligned} \tag{1}$$

For the derivation, see [8]. The symbol L_2 denotes the lift, i.e. the component of the force acting on the whole airfoil in the vertical direction, M_α is the torsional moment of the force acting on the whole airfoil with respect to the axis EA, M_β is the torsional moment of the force acting on the aileron with respect to the axis EF, D_{hh} , $D_{\alpha\alpha}$, $D_{\beta\beta}$ are the coefficients of a structural damping, S_α , I_α and m denote the static moment of the whole airfoil around the elastic axis EA, the moment of inertia of the whole airfoil around the elastic axis EA and the mass of the whole profile, respectively. The coefficient S_β is the static moment of the aileron around the axis EF and I_β is the moment of inertia of the aileron around the axis EF. Constants k_{hh} , $k_{\alpha\alpha}$, $k_{\beta\beta}$ denote the spring stiffnesses of the flexible support of the airfoil and d_{PF} is the distance between the elastic axis EA and the aileron axis EF.

The unsteady 2D viscous incompressible flow is characterized by the velocity $\mathbf{u}(x,t)$ and the kinematic pressure $p(x,t)$ for $x \in \Omega_t$, where Ω_t denotes the computational domain occupied by the fluid at time $t \in [0, T]$.

The quantities \mathbf{u} and p satisfy the Navier-Stokes equations and the continuity equation

$$\begin{aligned}
 \frac{\partial \mathbf{u}}{\partial t} + (\mathbf{u} \cdot \nabla) \mathbf{u} - \nu \Delta \mathbf{u} + \nabla p = \mathbf{0}, \\
 \nabla \cdot \mathbf{u} = 0 \quad \text{in } \Omega_t, \quad t \in (0, T).
 \end{aligned} \tag{2}$$

By $\bar{\Omega}_t$ and $\partial\Omega_t$ we denote the closure and the boundary of the domain Ω_t . We assume that $\partial\Omega_t = \Gamma_D \cup \Gamma_O \cup \Gamma_{W_t}$, where the sets Γ_D , Γ_O and Γ_{W_t} are mutually disjoint and boundary conditions of different types are prescribed there. The part Γ_D represents the inlet, where the fluid flows into the domain Ω_t , Γ_O denotes the outlet, where the fluid leaves Ω_t and Γ_{W_t} is the moving airfoil boundary at time t . It consists of two parts - profile P_t and aileron F_t : $\Gamma_{W_t} = P_t \cup F_t$. We assume that Γ_D and Γ_O are independent of time in contrast to Γ_{W_t} . The shape of the domain Ω_t depends on the functions $\alpha(t)$, $\beta(t)$ and $h(t)$.

The interaction between the flow and the airfoil is given by the force component L_2 and the moments M_α and M_β defined by

$$\begin{aligned} L_2 &= -l\rho \int_{\Gamma_i \cup \Gamma_j} \sum_{j=1}^2 T_{2j} n_j ds, \\ M_\alpha &= -l\rho \int_{\Gamma_i \cup \Gamma_j} \sum_{i,j=1}^2 T_{ij} n_j (-1)^i (x_{1+\delta_{ii}} - x_{1+\delta_{ii}}^{EA}) ds, \\ M_\beta &= -l\rho \int_{\Gamma_i} \sum_{i,j=1}^2 T_{ij} n_j (-1)^i (x_{1+\delta_{ii}} - x_{1+\delta_{ii}}^{EF}) ds, \end{aligned} \quad (3)$$

where l is the depth of the considered segment of the airfoil, $\mathbf{n} = (n_1, n_2)$ is the outer unit normal to $\partial\Omega_t$ on Γ_{w_t} , δ_{ij} is the Kronecker symbol ($\delta_{ij} = 1$ for $i = j$ and $\delta_{ij} = 0$ for $i \neq j$), x_1 and x_2 are the coordinates of the point on Γ_{w_t} , x_i^{EA} , $i = 1, 2$, are coordinates of the current location of the elastic axis EA and x_i^{EF} , $i = 1, 2$, are the coordinates of the current location of the aileron elastic axis EF. The stress tensor is computed from the flow velocity and the pressure by the relation

$$T_{ij} = -p\delta_{ij} + \nu \left(\frac{\partial u_i}{\partial x_j} + \frac{\partial u_j}{\partial x_i} \right). \quad (4)$$

The Navier-Stokes equations are completed by the initial condition

$$\mathbf{u}(x, 0) = \mathbf{u}_0(x), \quad x \in \Omega_0 \quad (5)$$

and the following boundary conditions. On the inlet part Γ_D of sufficiently large computational domain we prescribe the Dirichlet condition

$$\mathbf{u}|_{\Gamma_D} = \mathbf{u}_D. \quad (6)$$

On the outlet Γ_O we consider the so-called do-nothing boundary condition

$$-(p - \bar{p})\mathbf{n} + \nu \frac{\partial \mathbf{u}}{\partial \mathbf{n}} = 0 \quad \text{on } \Gamma_O, \quad (7)$$

where \bar{p} is a reference value of the pressure and \mathbf{n} denotes the unit outer normal to $\partial\Omega_t$. On Γ_{w_t} we consider the condition

$$\mathbf{u}|_{\Gamma_{w_t}} = \mathbf{w}|_{\Gamma_{w_t}}, \quad (8)$$

where \mathbf{w} denotes the velocity of points on the profile, i.e. the domain velocity from the ALE mapping. Moreover, we equip the system of equations with the initial conditions

$$\begin{aligned} h(0) &= h_0, \dot{h}(0) = h_1, \alpha(0) = \alpha_0, \\ \dot{\alpha}(0) &= \alpha_1, \beta(0) = \beta_0, \dot{\beta}(0) = \beta_1, \end{aligned} \quad (9)$$

where $\alpha_0, \alpha_1, \beta_0, \beta_1, h_0, h_1$ are input parameters of the model.

The interaction of a fluid and an airfoil consists in the solution of the flow problem (2), (5) – (8) coupled by Eqs. (3) and (4) with the structural model described by Eqs. (1) and (9). This coupled problem represents a nonlinear dynamical system.

NUMERICAL SOLUTION OF THE COUPLED PROBLEM

The method of the numerical simulation is described in detail in [7, 9]. The method is based on the finite element solution of the Navier-Stokes equations (2) strongly coupled with a system of nonlinear ordinary differential equations (1) describing the airfoil motion with large amplitudes. The time-dependent computational domain and a moving grid are treated by the Arbitrary Lagrangian-Eulerian (ALE) formulation of the Navier-Stokes equations, which are discretized by the FE method in space and by the backward difference formula of second order (BDF2) in time. In order to avoid spurious numerical oscillations, the SUPG and div-div stabilization methods are applied. The solution of the ordinary differential equations is carried out by the fourth-order Runge-Kutta method. Special attention is paid to the construction of the ALE mapping of a reference domain on the computational domain at individual time instances. The resulting nonlinear discrete algebraic system is solved by the Oseen linearization. All components of the realization of the solution are assembled together by a strong coupling procedure, see [7]. Here we prescribed the calculation accuracy $\varepsilon = 10^{-6}$ and maximum 4 iterations in the coupling procedure and maximum 5 iteration steps in the Oseen linearization procedure.

NUMERICAL RESULTS

The numerical simulations were carried out for the airfoil NACA 0012 using the following structural parameters:

$$\begin{aligned} m &= 0.086622 \text{ kg}, & k_{hh} &= 105.109 \text{ N/m}, \\ k_{\alpha\alpha} &= 3.69558 \text{ N m/rad}, & k_{\beta\beta} &= 0.2 \text{ N m/rad}, \\ S_\alpha &= -0.000779598 \text{ kg m}, & S_\beta &= 0 \text{ kg m}, \\ I_\alpha &= 0.000487291 \text{ kg m}^2, & I_\beta &= 0.0000341104 \text{ kg m}^2, \\ c &= 0.3 \text{ m}, & c_{EA} &= 0.12 \text{ m}, \\ d_{PF} &= 0.12 \text{ m}, & l &= 0.079 \text{ m}. \end{aligned}$$

The damping coefficients $D_{hh}, D_{\alpha\alpha}, D_{\beta\beta}$ were assumed to be zero. The gap h_F between the main lifting surface and the aileron was varied between 0 % and 10.3 % of the aileron length and two different gaps geometries, denoted by CC and IC shaped gaps, were considered (see Fig. 2).

Figure 2 shows two examples of the meshes in the computational domain and the detailed triangulation around the airfoil near the CC and IC shaped gaps of the width 1.3 % and 3.8 %, respectively. We used an anisotropically adapted mesh designed in the open source software GMSH [10, 11]. The total number of fluid finite elements was approximately 60 000 depending on the gap size.

The initial conditions in all computations were set to

$$h(0) = -5 \text{ mm}, \alpha(0) = 3^\circ, \beta(0) = 0,$$

$$\dot{h}(0) = \dot{\alpha}(0) = \dot{\beta}(0) = 0. \quad (10)$$

The computational process started from the solution of the flow past a fixed airfoil at time $t = -0.01$ s. At time $t = 0$ the airfoil was released and the computation of the real interaction started. The total computer time for the

computation of the responses $h(t)$, $\alpha(t)$, $\beta(t)$ for $t = 0 - 3$ s on a PC with Intel i7 processor and 4GB memory was about 3 days. Computations were carried out with the time step $\tau = 0.01 c / U_\infty$ for the kinematic viscosity $\nu = 0.000015 \text{ m}^2/\text{s}$, the air density $\rho = 1.225 \text{ kg/m}^3$ and the far-field flow velocities $U_\infty = 6-12 \text{ m/s}$ corresponding to the Reynolds numbers $Re_\infty = U_\infty c / \nu$ between 1.2×10^5 and 2.4×10^5 .

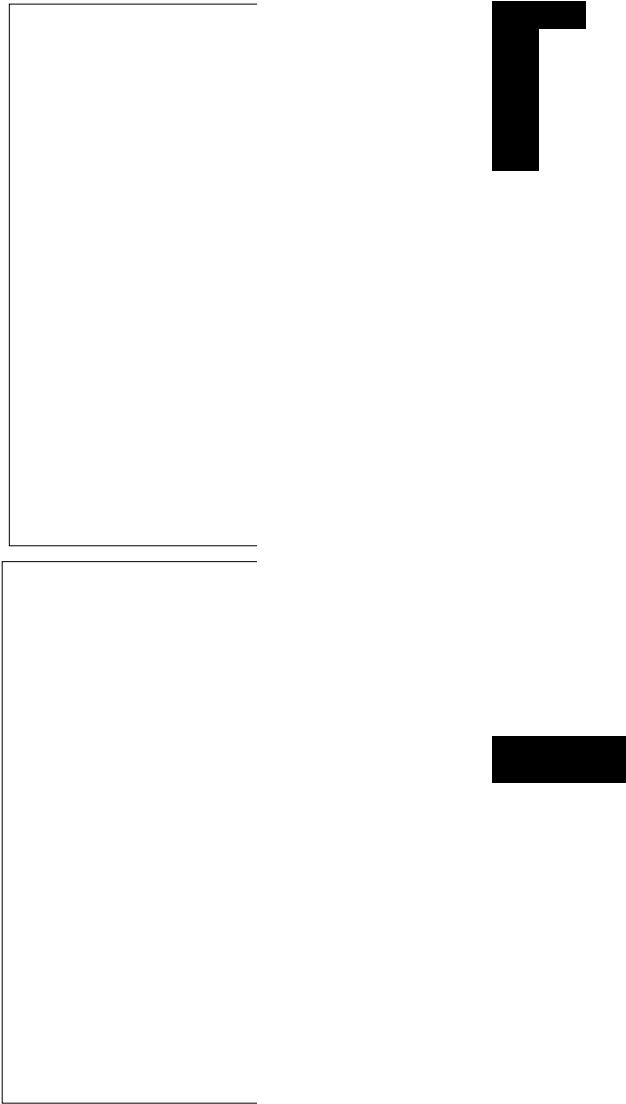


FIGURE 2: DETAILS OF THE FE MESHES NEAR THE GAP BETWEEN THE MAIN PART OF THE AIRFOIL AND THE AILERON FOR THE CC AND IC SHAPED GAPS.

Figures 3 - 5 show the examples of the computed graphs of the functions $h(t)$, $\alpha(t)$, $\beta(t)$ and Figures 6 - 7 show the corresponding phase diagrams for several flow velocities U_∞ . For small flow velocities the amplitudes for the vertical displacement h and the rotations α , β are decreasing in time (see Figure 3). The system is stable and

low level sustained vibrations are caused by vortex separation near the trailing edge of the airfoil.

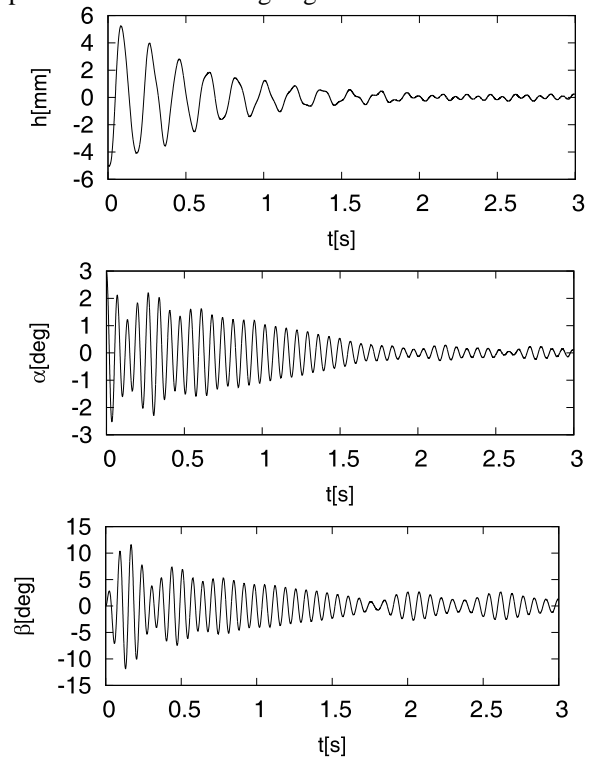


FIGURE 3: FUNCTIONS $h(t)$, $\alpha(t)$, $\beta(t)$ FOR $U_\infty = 8 \text{ m/s}$ AND THE IC SHAPED GAP OF THE WIDTH 3.8%.

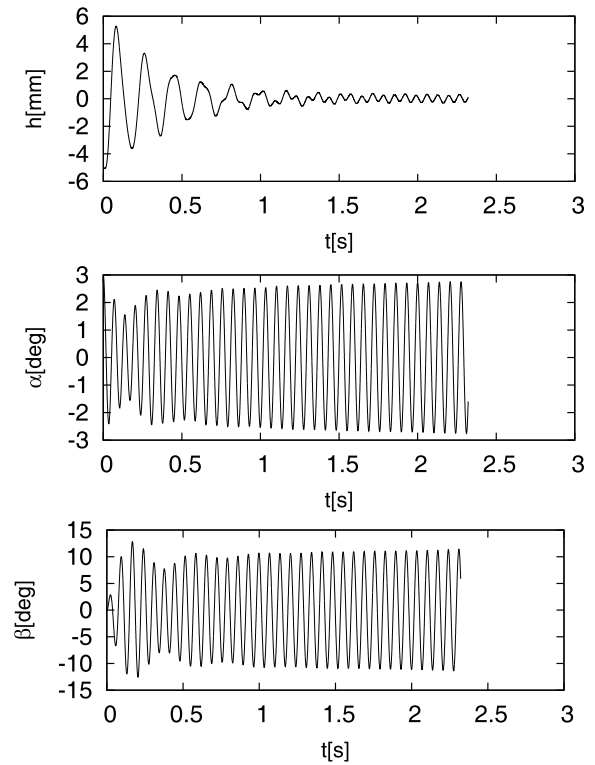


FIGURE 4: FUNCTIONS $h(t)$, $\alpha(t)$, $\beta(t)$ for $U_\infty = 10 \text{ m/s}$ AND THE IC SHAPED GAP OF THE WIDTH 3.8%.

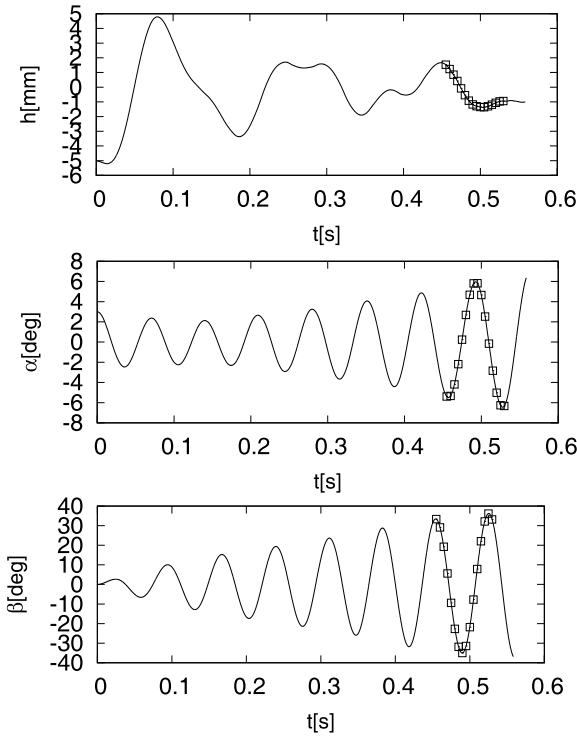


FIGURE 5: FUNCTIONS $h(t)$, $\alpha(t)$, $\beta(t)$ for $U_\infty=12$ m/s AND THE IC SHAPED GAP OF THE WIDTH 3.8%.

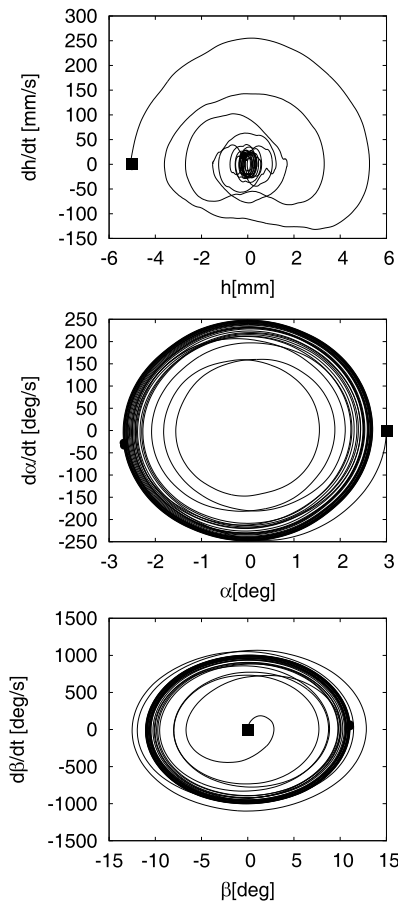


FIGURE 6: PHASE DIAGRAMS OF FUNCTIONS h , α , β FOR $U_\infty=10$ m/s AND THE IC SHAPED GAP OF THE WIDTH 3.8%.

By increasing the far-field flow velocity the vibration regime can be considered as a limit cycle oscillation (LCO) with the amplitude larger than 10 degrees for rotation β of the aileron (see Figures 4 and 6). For the higher flow velocity ($U_\infty = 12$ m/s), the system is becoming unstable by flutter, which would be catastrophic in this case due to an unstable LCO with the large amplitude for the rotation angle reaching values, up to about $\beta \approx 40$ degrees for the aileron (see Figures 5 and 7). These results are in agreement with the NASTRAN computations, according to which the system becomes unstable by flutter in $\alpha - \beta$ torsion for the far-field flow velocity at $U_{\infty, crit} = 11.32$ m/s and the flutter frequency $f_{cr} = 14.87$ Hz (see [7]).

For the far-field velocity $U_\infty = 12$ m/s, the computed velocity flow fields around the fluttering airfoil are shown in Figure 8 at several time instants marked in Figure 5. The shown velocity is defined as the magnitude of the velocity related to the far-field velocity. It is possible to see clearly the flow separation on the aileron surface, especially on the detailed snapshots viewing the velocity flow field around the aileron.

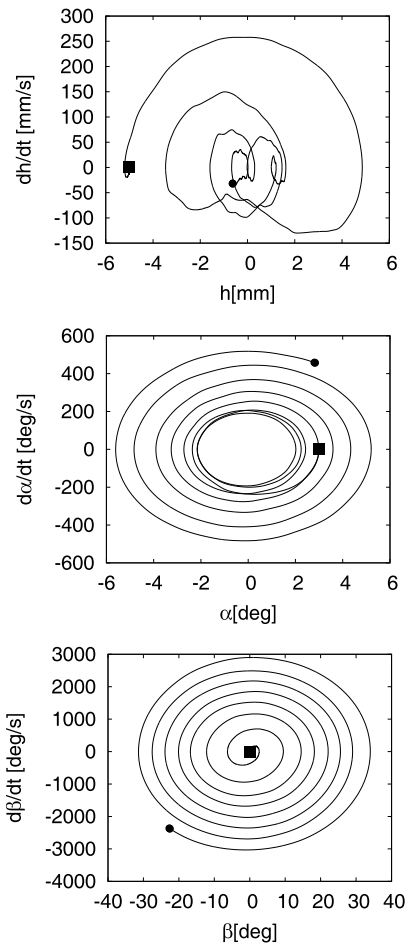


FIGURE 7: PHASE DIAGRAMS OF FUNCTIONS h , α , β FOR $U_\infty=12$ m/s AND THE IC SHAPED GAP OF THE WIDTH 3.8%.

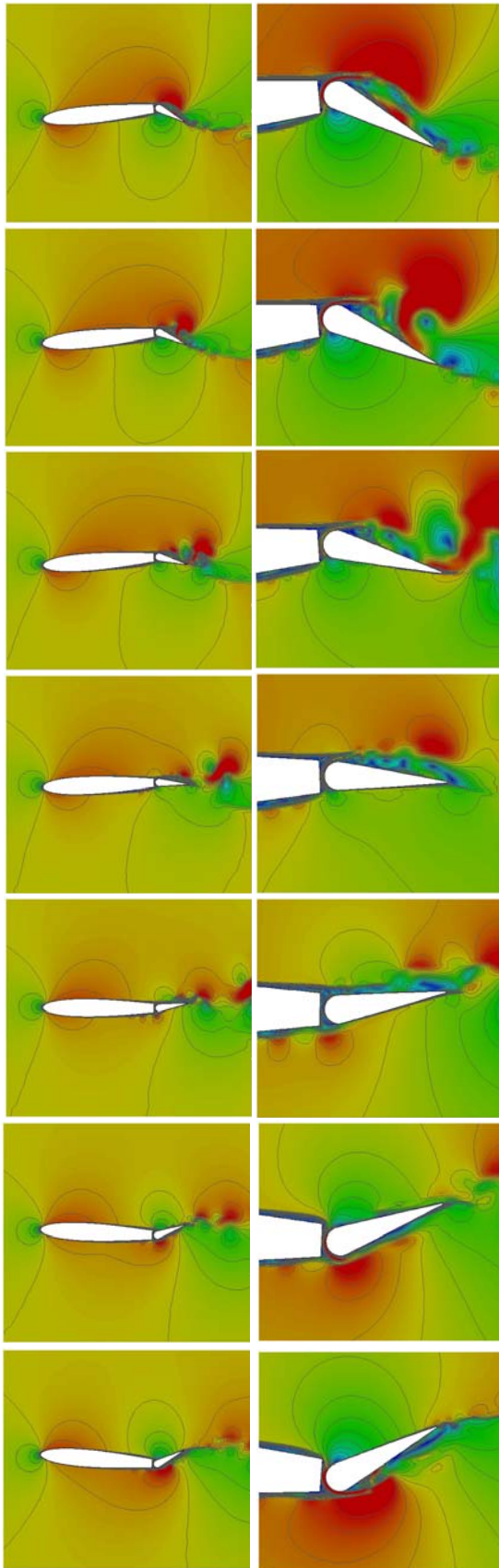


FIGURE 8: VELOCITY DISTRIBUTION AROUND THE FLUTTERING PROFILE FOR $U_{\infty}=12$ M/S AT SEVERAL TIME INSTANTS MARKED IN FIG. 5.

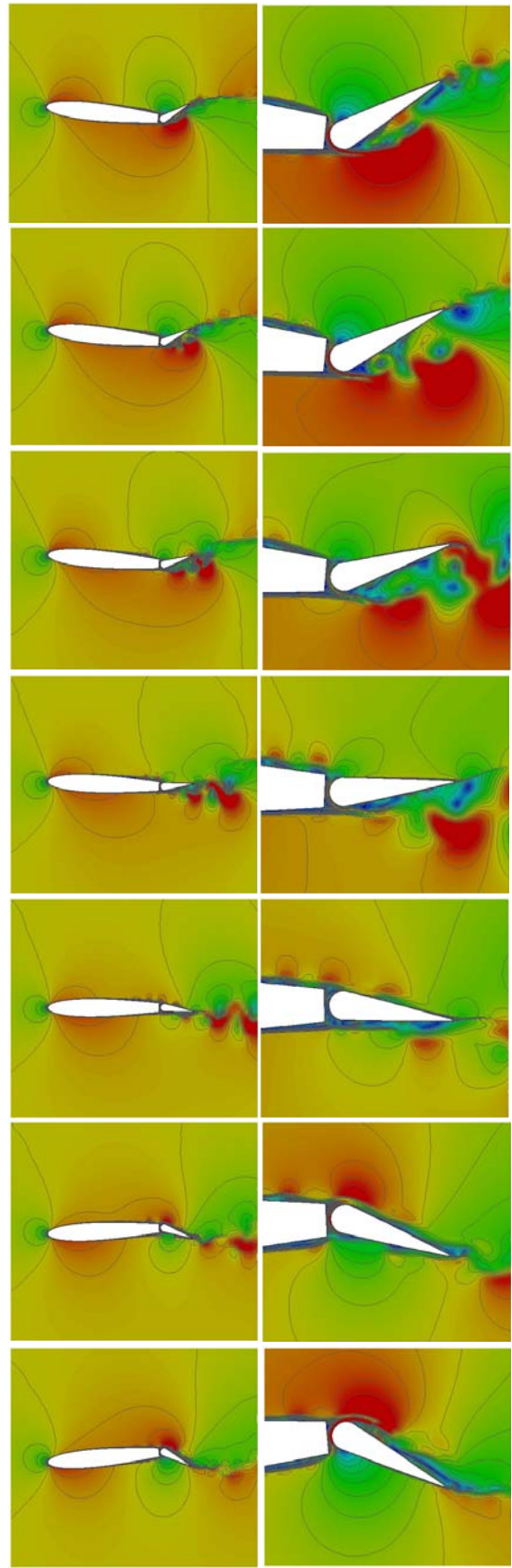


FIGURE 8 – continued.

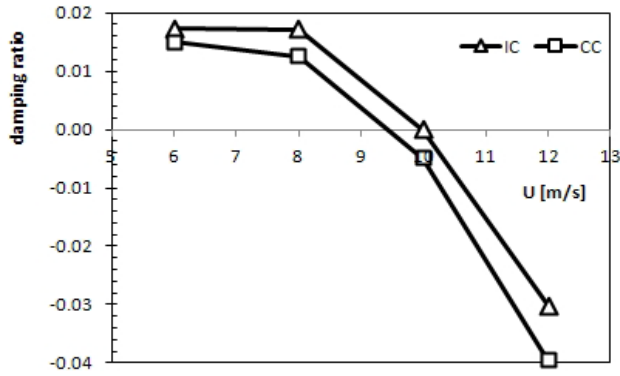


FIGURE 9: AERODYNAMIC DAMPING VERSUS FAR FIELD FLOW VELOCITY FOR THE IC AND CC SHAPED GAPS OF THE WIDTH 3.8 %.

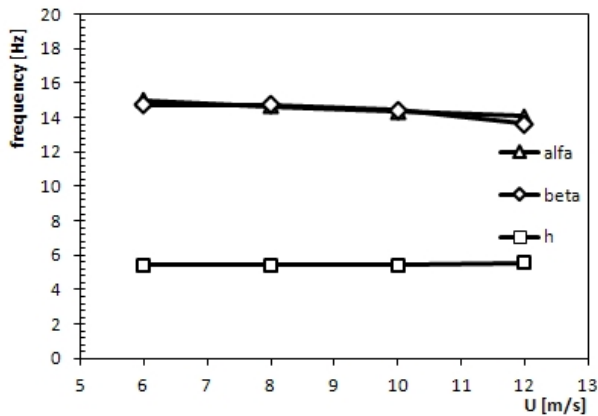


FIGURE 10: VIBRATION FREQUENCIES OF THE AIRFOIL VERTICAL MOTION h , THE AIRFOIL ROTATION α AND THE AILERON ROTATION β FOR THE IC SHAPED GAP OF THE WIDTH 3.8%.

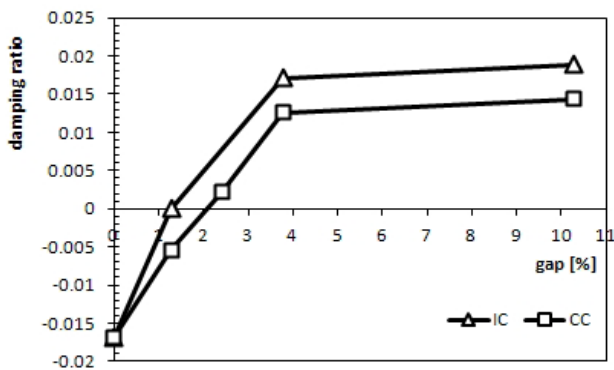


FIGURE 11: AERODYNAMIC DAMPING VERSUS GAP WIDTH FOR THE IC AND CC SHAPED GAPS AND $U_\infty = 8$ m/s.

Figure 9 shows the damping ratio $D = \ln(\alpha_0 / \alpha_n) / (2\pi n)$, calculated from n cycles of the time response of the airfoil for the rotation angle α , in

dependence on the far field air flow velocity for IC and CC shaped gaps of the same width 3.8 %.

The corresponding vibration frequencies are shown in Figure 10. The lowest frequency at about 5.5 Hz belongs to the vertical airfoil motion h and the two higher nearly identical frequencies at about 14 Hz belong to the airfoil and the aileron rotations α and β . If the damping ratio $D > 0$, the system is stable, and when $D < 0$, the system is unstable by coupled mode flutter for the rotations α and β . The aerodynamic damping is clearly higher for the IC shaped gap than for the CC shaped gap and similarly the critical flutter airflow velocity $U_F \approx 10.1$ m/s for flutter is higher for the IC shaped gap than $U_F \approx 9.5$ m/s for the CC shaped gap.

Similarly, Figure 11 shows the influence of the gap width on the aerodynamic damping flutter boundary for the IC and CC shaped gaps and for the constant airflow velocity $U_\infty = 8$ m/s. For both gap shapes the damping ration increases with the gap width and stabilizes the system. For zero gap the system is unstable by flutter ($D < 0$) getting to be stable at about the gap width 1.2% and 2% for IC and CC shaped gaps, respectively.

CONCLUSION

The results of the numerical simulations show that the flutter stability boundary of the airfoil with three degrees of freedom can be very sensitive to the gap shape and gap width between the aileron and the main lifting surface of the aileron. This is caused by an interaction of the main airstream with the airflow through the gap. This aside flow influences the vortex shedding at the airfoil trailing edge, the limit cycle oscillation amplitudes and the critical flutter velocity. However, the results have to be accepted with a caution, because the critical flutter flow velocity of the system studied was very low and the influence of the flow inside the gap on the aeroelastic behavior of the airfoil can be reduced in cases of higher far field airflow velocities.

ACKNOWLEDGMENTS

The authors acknowledge the financial support of the project of the Czech Science Foundation P101/11/0207 “Coupled problems of fluid and solid mechanics - nonlinear aeroelasticity”.

REFERENCES

- [1] Librescu, L. and Marzocca P., 2005. “Advances in the linear/nonlinear control of aeroelastic structural systems”. *Acta Mechanica*, **178**, pp. 147–186.
- [2] Na, S., Librescu, L., Kim, M. H., Jeong, I. J. and Marzocca, P., 2006. “Robust aeroelastic control of flapped wing systems using a sliding mode observer”. *Aerospace Science and Technology*, **10**(2), pp. 120–126.
- [3] Zhao, Y. H. and Hu, H. Y., 2003. “Aeroelastic analysis of two-dimensional airfoil with control surface free play nonlinearity “. *Acta Aeronautica et Astronautica Sinica*, **24**(6), pp. 521-524.

- [4] Shim, J. H., Na, S. and Chung, C. H., 2004. "Aeroelastic response of an airfoil-flap system exposed to time-dependent disturbances". *KSME International Journal*, **18**(4), pp. 560-572.
- [5] Jones, D. P., Roberts, I. and Gaitonde, A.L., 2007. "Identification of limit cycles for piecewise nonlinear aeroelastic systems". *Journal of Fluids and Structures*, **23**, pp. 1012–1028.
- [6] Lee, T. and Su Y.Y., 2011. "Unsteady airfoil with a harmonically deflected trailing-edge flap". *Journal of Fluids and Structures*, **27**, pp. 1411–1424.
- [7] Feistauer, M., Horáček, J., Růžička, M. and Sváček, P., 2011. "Numerical analysis of flow induced nonlinear vibrations of an airfoil with three degrees of freedom". *Computers and Fluids*, **49**, pp. 110-127.
- [8] Horáček, J., Sváček, P., Růžička, M. and Feistauer M., 2007. "Contribution to finite element modelling of airfoil aeroelastic instabilities". *Applied Computational Mechanics*, **1**, pp. 43–52.
- [9] Sváček, P., Feistauer, M., Horáček, J., 2007. "Numerical simulation of flow induced airfoil vibrations with large amplitudes". *Journal of Fluids and Structures*, **23**, pp. 391–411.
- [10] GMSH, <http://www.geuz.org/gmsh>.
- [11] Geuzaine C. and Remacle J. F., 2009. "Gmsh: a three-dimensional finite element mesh generator with built-in pre- and post-processing facilities". *International Journal for Numerical Methods in Engineering*, **79**(11), pp. 1309-1331.

EXCITATION CHARACTERISTICS OF DRY GALLOPING VIBRATIONS

Nikolaos Nikitas*

Department of Civil Engineering
University of Bristol
Queen's Building, University Walk
Bristol, BS8 1TR
Email: N.Nikitas@bristol.ac.uk

John H.G. Macdonald

Department of Civil Engineering
University of Bristol
Queen's Building, University Walk
Bristol, BS8 1TR
Email: John.Macdonald@bristol.ac.uk

ABSTRACT

This article attempts to highlight characteristics of the aerodynamic forcing on a circular cylinder experiencing dry galloping vibrations. Observations from a series of wind tunnel tests are studied comparatively with the literature on rain-wind cable vibrations and on flow past inclined lifting bodies, for drawing similarities. Unsteadiness and spatial variation of the flow, both previously undetermined, are significant during the large cylinder motions recorded. Thus, they are suspected to play a role in triggering unstable behaviour. Instabilities were restricted to specific ranges of cable-wind angles and Reynolds numbers. The transitional features identified refute the view of simple bursting separation bubbles that rhythmically produce lift and suggest that there is a multitude of paths for energetically feeding dry galloping. Finally explanations are provided and a mechanism incorporating unstable features is proposed for future modelling.

INTRODUCTION

Large vibrations of bridge cable stays have recently attracted much interest. Specifically the so-called rain-wind-induced vibrations [1, 2], which are very often observed on inclined cables, have become a matter of controversy. Different approaches have been proposed for explaining the complex fluid-structure interaction that emerges when rivulets develop on the cable surface due to rain. Modelling the rivulet formation and propagation has been a key element for understanding unwanted cable motions. Actually, two main branches have developed for the explanation of the phenomenon; the one assumes that the appearance of a still rivulet, if appropriately positioned, is adequate to transform the circular profile into an unstable section, as in Den Hartog gallop-

ing (e.g. [3]). The other suggests that it is primarily the motion of the formed rivulet that is central in developing large response [4, 5]. The role of influencing parameters such as the rainfall intensity, the cable inclination angle and roughness and the motion frequencies have been extensively studied and there is confidence in the knowledge of the combination of these contributions leading to the dynamic instability.

However, lately there is additionally growing concern over excessive vibrations of inclined cables that occur under dry conditions, exclusively due to wind, and their understanding seems more elusive. These so-called dry galloping events are believed to share common features with their rain-wind induced vibrations. Matsumoto et al. [3] first expressed the view that the functioning mechanism is the same for dry or rainy conditions, with rivulets contributing only as an amplifying factor. Further similarities were discussed by Macdonald & Larose [6]. A dedicated study that attempted to address the similarities between the two phenomena [7] was confined to static models and the comparison was limited to the assessment of the static lift that can be produced in different dry configurations. As a matter of fact the exciting force during dry galloping motion, which could be central to understanding, has rarely been recorded and analysed [8, 9]. This paper describes a series of large-scale wind tunnel tests which capture subtle forcing details of the dry galloping phenomenon. The objective is to present previously unknown characteristics regarding the unsteadiness of the aeroelastic loading. The well known case of an inclined cylinder with an ogive or conical nose, as for missiles [10, 11] provide this work with a very relevant precedent. Further connections are sought with rain-wind [4, 5, 12] and other flow-induced vibration phenomena [13], where unsteadiness is important.

*Address all correspondence to this author.

WIND TUNNEL TESTS

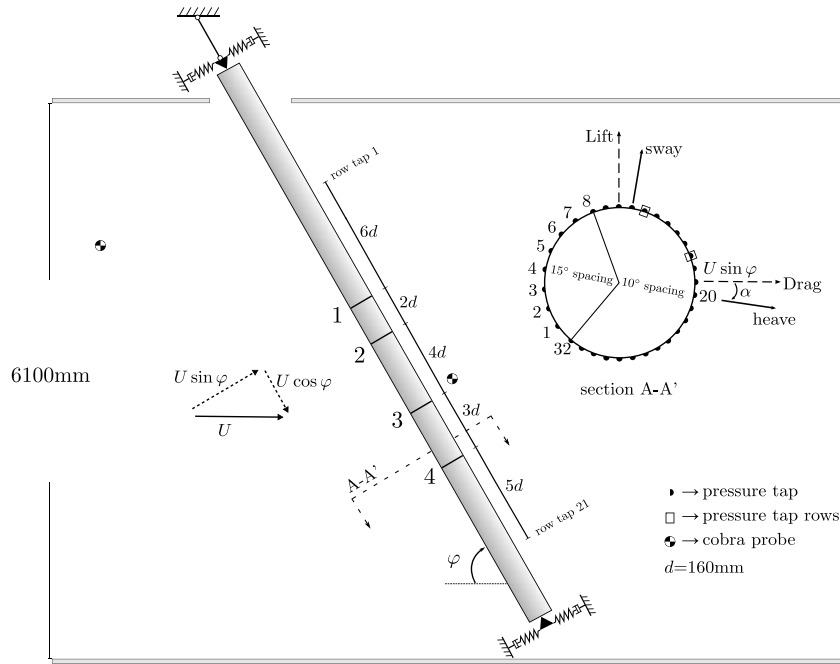
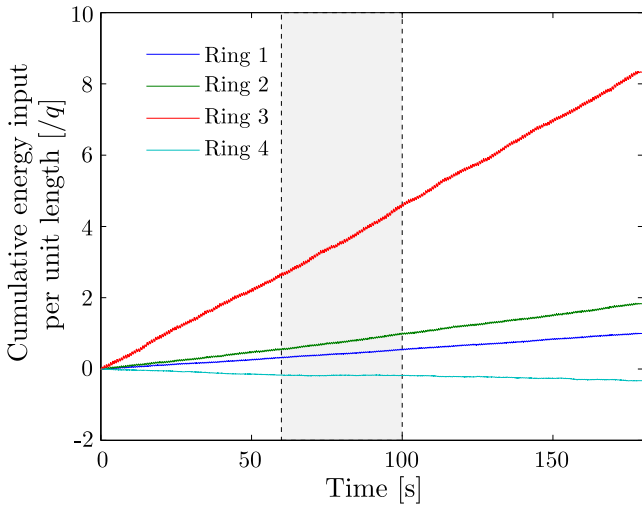
For the purpose of this experimental work an inclined rigid circular cable model replicating the parameters of a real bridge cable stay was tested in the 6m×3m open circuit wind tunnel at the National Research Council Canada (NRC). Typical free stream turbulence levels of the wind tunnel are of the order of 0.5%. A detailed illustration of the setup is provided in Fig. 1. More information about the testing was previously given in [8,9]. In short it should be noted that the model could oscillate in two perpendicular planes (denoted sway and heave) and was equipped with pressure measuring taps, arranged at four discrete cross-sections (termed rings) and two axial lines running along the lee side of the cylinder. The support springs could be rotated in order to give different relative orientations of the wind and principal structural axes, considering that the stiffnesses in the two planes were not identical. The model could also be locked in place, so as to quantify loads on the stationary cylinder and hence the motion-induced aerodynamic effect.

The wind speeds spanned the critical Reynolds (Re) number range and produced large dynamic responses in a number of cases. Interestingly, although a few different inclination and orientation angles were tested (φ , α in Fig. 1), only cables inclined at an angle of 60° to the wind exhibited large responses, mainly across-wind. The largest recorded amplitude was $0.75d$, where d is the cable diameter, although this was limited by the support arrangement. Vertical or near vertical configurations of the cable ($\varphi = 90^\circ$) showed only limited response, while the measured lift and drag forces on the individual pressure rings experienced large sudden jumps, connected with abrupt transitions between different flow states [8]. Specifically, the transition between subcritical and critical states was observed to occur intermittently on each side of the stationary cylinder under steady flow conditions. This could be an indication that there was no strong bias of the flow to give asymmetric lift in one direction or the other in these tests. In other similar studies Matteoni & Georgakis [14] and Flamand & Boujard [7] have observed that local lift and drag coefficients were very sensitive to even minute surface alterations, yet it was not possible to determine their global effect. Lamont [11], while testing ogive-nosed circular cylinders, captured a Reynolds number dependent roll effect very consistently. Still, he ascribed this to the asymmetry introduced by the ogive tip, disregarding any possible imperfection of the rest of the cylindrical body.

FLOW FEATURES AND EXCITATION MECHANISM

This section focuses on the pressure distributions that were acquired during large response records. The force evolution is mapped to the oscillation cycle and characteristics of the underlying mechanism of the dynamic instability are drawn out. An analytical description of the aeroelastic loading exerted on a cable undergoing dry-galloping vibrations was previously provided through a generalised quasi-steady framework [15]. In this analysis, for small amplitude vibrations the aeroelastic forces are equivalent to pure (negative) viscous damping forces that can possibly overcome the structural damping. However, this has its limitations and has not been validated. The energy input during each vibration cycle is given by integrating the product of applied force along the motion direction with velocity. Thus for the current dry galloping records, with predominantly across-wind vibrations, the local energy input can be assessed by the integral of lift on each ring with velocity. Fig. 2 provides such estimates and clearly indicates that different cross-sections contribute different energy inputs to the excitation mechanism. Specifically, Ring 3 contributes the most, while Ring 4 extracts energy from the cable (i.e. it acts to damp the response). This finding should not be confused with the observation by Matsumoto et al. [16] of excessive aerodynamic forces being confined to the near-end locations. Ring 3 is situated centrally and moreover the energy distribution presented in Fig. 2 was specific to the record examined. Other cases (e.g. different wind speeds or cable angles) produced different results (e.g. Ring 3 damping response and Ring 4 exciting response). These results indicate the complex 3D nature of the flow behaviour and its sensitivity to the test parameters (Reynolds number, cable inclination angle, etc.). The findings are in line with what was witnessed also by Lamont [11] on an inclined ogive cylinder. Such bodies exhibit through a wide range of Reynolds numbers high lift values (i.e. force out of the wind-cylinder plane), with a well defined distribution over their length. In transitional regimes though, the regular distribution breaks down with non repeatable lifting patterns emerging.

The actual evolution of the aerodynamic force with motion is now considered. For this purpose a mean cycle is extracted for Ring 3, corresponding to the time interval 60-100s in Fig. 2. The following discussion and figures, unless otherwise stated, refer to this specific period. Fig. 3 shows the phase-averaged lift force (dashed red line) over the averaged vibration cycle (black lines). Overlaid on these, are polar plots of the pressure coefficient (C_p) distributions, both phase-averaged over the cycle (lines over shaded areas) and averaged over the whole time pe-


FIGURE 1: ELEVATION OF CABLE MODEL.

FIGURE 2: ENERGY INPUT DURING LARGE RESPONSE (q DYNAMIC PRESSURE).

riod (grey dots). Scale-wise the radius of the drawn circles correspond to $C_p=1$. Evidently the averaged lift force shows clear periodic behaviour related to the motion, but it appears not to be in phase with the velocity. The specific waveforms of the two variables are not identical and the additional higher frequency forcing inputs do not entirely average out. Interestingly the phase lag of the Lift with respect to the velocity varies over the cycle. Instants of zero velocity are designated in the figure and the rel-

evant time delays τ_1 and τ_2 to instants of zero lift are evaluated at $1/12$ and $1/36$ of the vibration period T respectively. Indicatively the characteristic time associated with vortex-shedding $t = d/StU$, where St is the Strouhal number, could range from $T/28$ to $T/65$ depending on the value considered for St (0.2 to 0.48, [17]). For the studied record (i.e. $Re = 3.34 \times 10^5$, $U=31.5\text{m/s}$) no trace of vortex shedding could be identified. All these features are posing a hurdle for linearised quasi-steady theory, which can only perceive forces as linear products of the motion velocity.

Comparing pressure distributions from specific points in the vibration cycle with the overall mean, it is seen that two distinct mechanisms are operating on the different sides of the cylinder. The bottom part presents what seems to be a periodic motion around the cylinder circumference and a change in length of a laminar separation bubble. On the other hand the top seems to alternate between a subcritical-like state (i.e. weak suction on the across-wind pressure taps) to a critical one. However, both parts simultaneously contribute to the forcing throughout the oscillation cycle. Qualitatively the mechanism seems similar to what was put forward for rain-wind vibrations by Verwiebe [4] and Cosentino et al. [5]. According to Verwiebe a single underside rivulet can instigate large motion by causing an early underside separation and thus lift during upward movement. The resulting elliptical motion skews its top part windwards due to the concurrent drag force reduction that follows the lift

appearance. This was not the only elliptical behaviour in our tests where also opposite skewness was found depending on conditions. For Verwiebe's asymmetric excitation mechanism forcing occurs for a limited duration of the vibration cycle, contrary to what is seen in Fig. 3.

The agreement with the Cosentino et al. explanation is more profound. The forcing waveforms are similarly distorted and even the lift-velocity time lag distribution, varying over the vibration period, is much alike. Yet on the other hand this realisation necessitates for a single-sided asymmetry to develop and as was found herein the asymmetry was not necessary for the occurrence of dry-galloping. Cases existed where both cylinder sides were extracting energy from the wind through identical mechanisms. These were mostly cases of two laminar separation bubbles moving as in the bottom cylinder side in Fig. 3, with the main adverse forcing being from the apparent change in length of the bubble. Thus a critical transition and the intermittent formation of a separation bubble is not a necessary condition for instability as was previously thought.

The lift force was further examined to consider the forcing contributions from individual cycles (almost 60 in total). As seen in Fig. 4(a), there is large variation of the forcing over each cycle (black lines) and there are large fluctuations in the forces with time. When their ensemble is considered the result is Fig. 3, and it could be construed that the actual mean effect of the lift force is produced by the local unsteadiness (i.e. jumps). Considering randomly one individual cycle from the ensemble in Fig. 4(b) it is seen that lift coefficient jumps apparently randomly. Yet considering all cycles generally, the largest steps are located close to shortly after $T/4$ and $3T/4$ where the velocity (and the dynamic lift component) changes sign. Such characteristics seem traceable only through some integrate and fire type model. It is important to note that the time-mean behaviour is much more smooth, setting questions on the statistical interrelations of jumps between succeeding cycles. Actually the very linear shape over time of the energy input in Fig. 2 is a good indication of the smoothness of the time-mean behaviour.

The energy inputs in Fig. 2 however, are very different implying that the smoothness discussed greatly varies locally for the different rings. Evaluating the average phase lag between lift and velocity over each oscillation cycle for all rings though shows reasonable consistency over three rings. The results are shown in Fig. 5 and strikingly the phase lags for Rings 1-3 are all consistently around a value of 60° . Positive values for the phase lag add energy to the vibration, while negative values extract

energy. Ring 4, which acts to damp the motion seems to mainly jump between values around 60° , 0° and -60° , which could be representative of different states for the dry galloping motion. Comparing the results for the four rings, it is notable that the more consistent phase lag (Fig. 5), the greater the mean rate of energy input (Fig. 2).

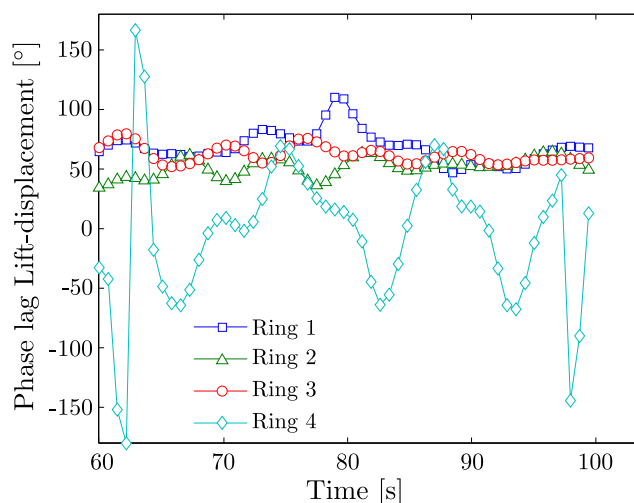


FIGURE 5: PHASE LAG BETWEEN THE LIFT FORCE AND DISPLACEMENT FOR THE RECORD IN Fig. 2.

Considering the spatial distribution of pressures further, data from the axial pressure taps, located at 100° and 150° behind stagnation line (Fig. 1), were used to identify the mean pressure profile during oscillation. This is illustrated in Fig. 6. Such information for dynamic models in the transitional Re range is not available in the literature. The relative positions of the two pressure tap lines allow some assessments regarding the state of the flow on the relevant side of the cylinder. At large negative value for pressure coefficients (around -1.5) on taps at 100° from the stagnation point indicate a leeward shift of the separation point, which simplistically implies reattachment of the flow and eventual turbulent separation. Pressure coefficients at 150° from the stagnation point are expected to coincide with the base pressure value, lying distant from the relevant 100° values. The small negative values (around -0.3) along the whole length are a sign that the flow is supercritical, if not necessary on this side of the cylinder definitely on one side. The 100° row pressure taps 17-21 seem to indicate a subcritical state on this side. Along the rest of the length there appears to be fairly regular spacing between positions where transition is not

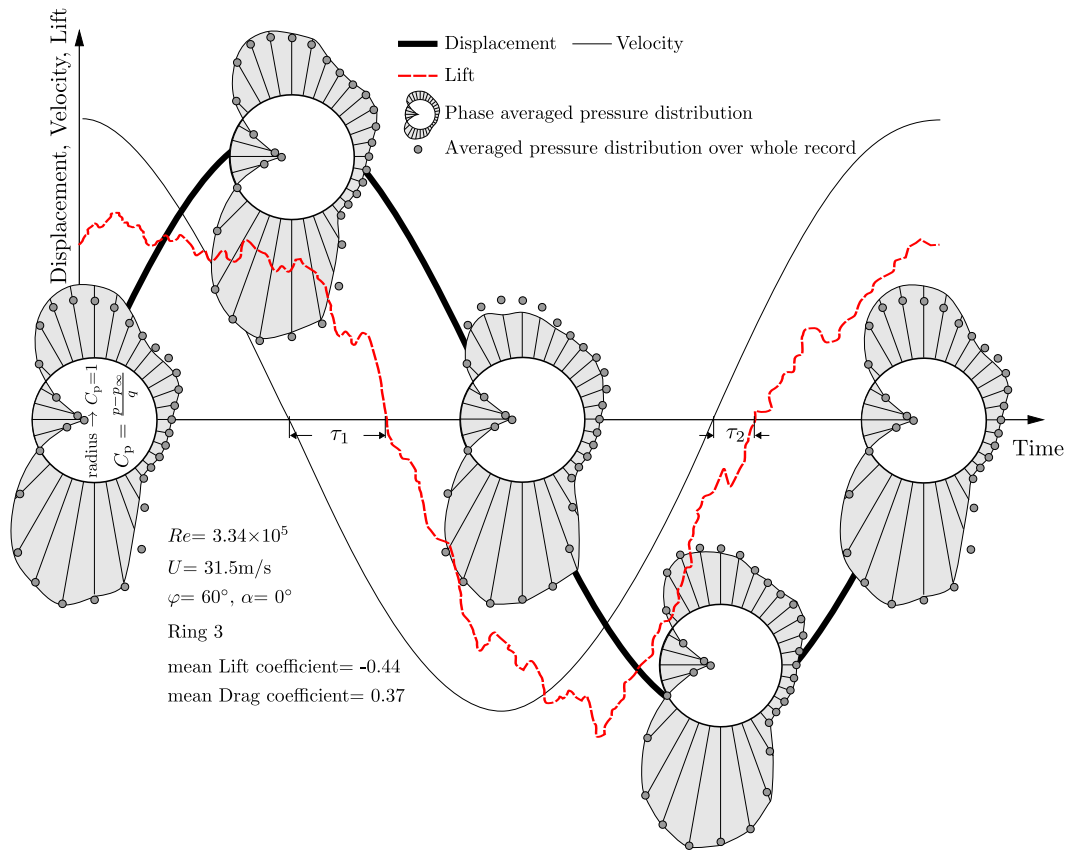


FIGURE 3: AVERAGED SECTIONAL AERODYNAMIC FORCING THROUGH A STEADY LARGE MOTION CYCLE (RING 3). THE TIME PERIOD USED CORRESPONDS TO THE SHADED AREA IN Fig. 2.

completed and others where it is. Thus it appears that cells may have formed with a characteristic length around $6d$, with variable separation lines along the length.

Considering the actual pressure distributions of the rings for the studied record there are features that do not fully comply with the description of the laminar to turbulent transition as this is put forward for non-inclined circular cylinders. In Fig. 7(a) it is seen that Rings 1, 2&4 are in very similar post-critical states with separation bubbles having formed on both sides (near 100° and 250° from the stagnation point respectively). Yet although in terms of mean pressure profiles they are so similar, as far as the dynamic instability is concerned they have opposite functions, with Rings 1&2 exciting motion and Ring 4 damping it. Thus it is apparent that the flow state alone is not enough to determine the propensity for dry galloping. Ring 3 on the other hand shows a distinct feature. Its profile is not normal with the plateau near 120° contributing to a sustained asymmetry between the two cylinder sides that protrudes far into the base pressure zone, contrary to classical transitional behaviour. Hence, what was earlier quoted as a subcritical-like state on the top side of the cylinder in Fig. 3 is definitely not just the product of

an intermittently bursting laminar separation bubble.

Sectional mean pressure profiles shown from other related cases in the literature, in Fig. 7(b), are used to help understand this behaviour. Cosentino et al. [5] studied rain-wind vibrations of an inclined stay (lower inclination to the one studied herein) and the recorded pressure data on one pressure ring during motion, similarly to this study. For the same conditions they also ran dry tests to address the effect of water on the cylinder surface. Their output in Fig. 7(b) interestingly shows asymmetries alike to those found here that extend into the base pressure region. The values on the other hand are quite different. In particular the minimum suction reaches almost -4 , lower than -3 that corresponds to potential flow which is a physical limit for circular cylinders normal to the wind.

Lamont [11], as previously quoted, worked on static ogive cylinders. He too recorded mean sectional pressures for transitional Reynolds numbers. For conditions close to our study, $\phi=55^\circ$ and $Re \approx 4 \times 10^5$, he identified two distinct interesting cases, illustrated in Fig. 7(b). In case 1 the pressure distribution is quantitatively almost identical to the one for Ring 3 in Fig. 7(a). The only difference is that the base pressure region lies on the level of

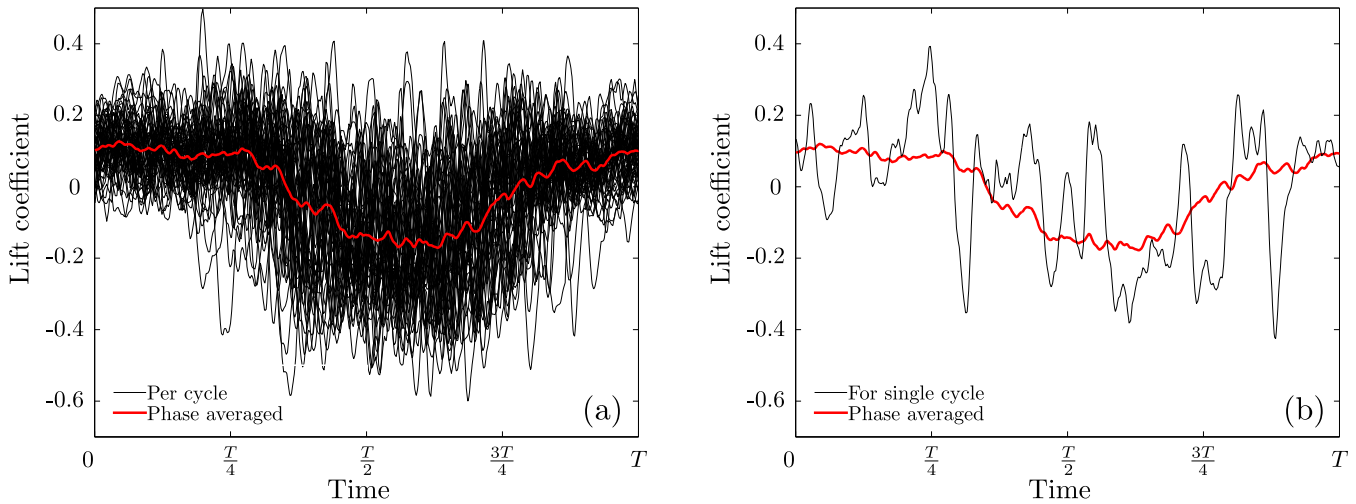


FIGURE 4: LIFT COEFFICIENTS FOR THE CASE ILLUSTRATED IN Fig. 3; a) ENSEMBLE OF THE LIFT VARIATIONS FOR EACH CYCLE ALONG WITH THEIR MEAN, b) LIFT VARIATION IN ONE RANDOMLY PICKED CYCLE ALONGSIDE THE MEAN OF THE ENSEMBLE.

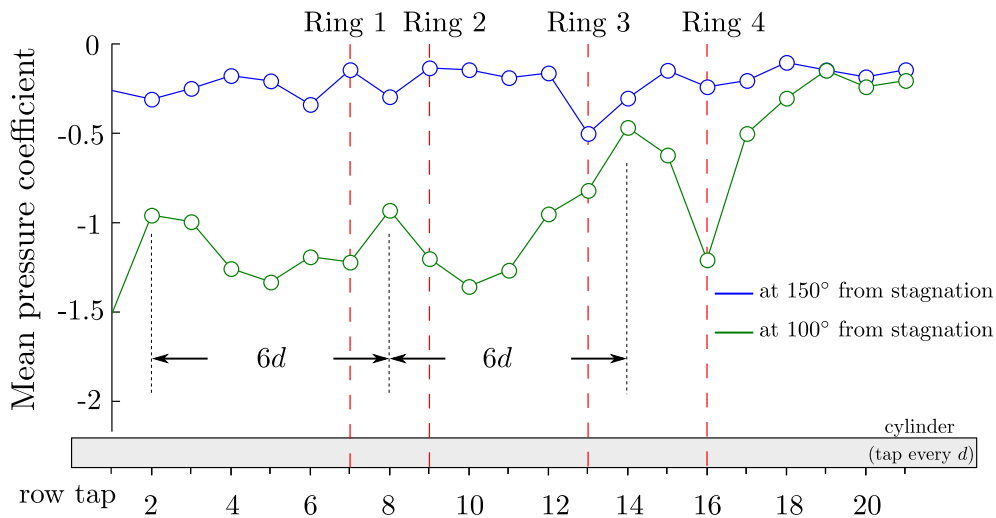


FIGURE 6: PRESSURE DISTRIBUTIONS ALONG THE CABLE MODEL FOR THE RECORD IN Fig. 2, INDICATING PATTERNING.

the unforeseen plateau of Ring 3 and is also symmetric. Such profiles according to Lamont were able to produce high lift values, although their repeatability and distribution were unpredictable. Thus all details match our observations well. In a second case Lamont, attempting to identify the effect of axial vortices originating from the expected nose asymmetry and propagating downstream, found what is presented in Fig. 7(b) as case 2. After the

early separation at around 80° a secondary vortex produces a second minimum pressure region. There is a great difference between the two sides of the cylinder and it seems there is some similarity with Ring 3 in the current study. Notably the value of the minimum pressure coefficient is again lower than -3, as found by Cosentino et al. This effect and similar pressure forms disappeared for larger inclinations ($> \sim 70^\circ$). From these comparisons it

seems that particular unusual features found during excessive dry galloping vibrations could also be relevant in other cases.

Lamont's tests were preceded by another series of similar tests by Lamont & Hunt [10] where it was shown that long abrupt pressure jumps were locally occurring repeatedly. It was then suspected that this was an effect of turbulence (of the order of 0.5% in the tests) and the subsequent series of tests [11] performed in a lower turbulence wind tunnel (0.05%) were thought to avoid this unstable feature that could make any reference to mean data inaccurate.

For the tests reported here, aerodynamic forcing during large vibrations was seen to be accompanied by erratic behaviour. This could in some respect average out, however the nature of the noise-like behaviour and moreover its time and spatial distribution (e.g. timing of jumps such as those in Fig. 4(b)) are entirely unknown. Although averages can hide unsteady features the contribution of such noise in the underlying mechanism of the dynamic instability could be significant. A different type of jump behaviour was recorded for non-inclined cylinders. The lift force for the dynamic cable model when in low amplitude response is presented in Fig. 8. The characteristic time of such a jump was found to be 0.068s. This is in good agreement with what was found for a static cylinder by Schewe [17]. For a transition of Lift coefficient from 0 to 1 (i.e. double the one in Fig. 8) he got a value of 0.15s. Strikingly the jumps in the shown case, appear as a succession of rectangular pulses with a regular time spacing between them. This corresponds to a frequency of $4.45\text{s}^{-1}=0.225\text{Hz}$. Therefore it is questionable whether a vertical cable with frequency close to this value will produce large response owing to some form of resonance loading.

CONCLUDING REMARKS

Summarising the main observations presented, it is believed that the effect of transitional behaviour is central for dry galloping. The inherent unsteadiness of the critical Re range and its interaction with turbulence and inclination are important in creating the conditions for dry galloping. Something similar was also seen for wake-induced vibrations [13], where quasi-steady features have to combine with unsteadiness to yield a dynamic response. Abrupt transitions and varying time delays are other characteristics in common between that case and the current one.

The features of the dry galloping mechanism captured in these tests do not involve simple bursting of a

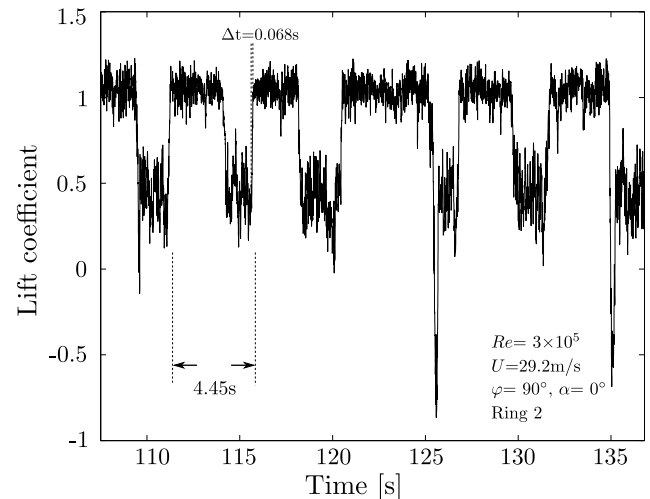


FIGURE 8: UNSTEADY FLOW TRANSITIONS DURING SMALL MOTION OF A NON-INCLINED CYLINDER.

laminar separation bubble. Characteristics related to axial vortices and previously seen in the study of inclined missiles appear to be present in the cable aerodynamic forcing and contribute towards the excitation mechanism. Although significant links were found with rain-wind vibrations it seems that one of the most interesting feature is something previously undiscussed even for them and lies in the contribution of noise-like unsteadiness. The current observations suggest that dry galloping is related to some kind of organisation of the noise that arises from both the transitional behaviour and the ambient turbulence. This type of mechanism can be seen to also cooperate with more conventional features, such as a consistent incidence dependence that its study seems to be getting growing interest.

ACKNOWLEDGMENT

The contributions of Jasna Jakobsen and Terje Andersen (University of Stavanger), Mike Savage, Guy Larose and Brian McAuliffe (NRC) and the technical staff at NRC are gratefully acknowledged. The tests were funded by NRC, EPSRC (via an Advanced Research Fellowship of the second author), the University of Stavanger and StatoilHydro ASA.

REFERENCES

- [1] Païdoussis, M. P., Price, S. J., and de Langre, E., 2011. *Fluid-Structure Interactions. Cross-Flow-*

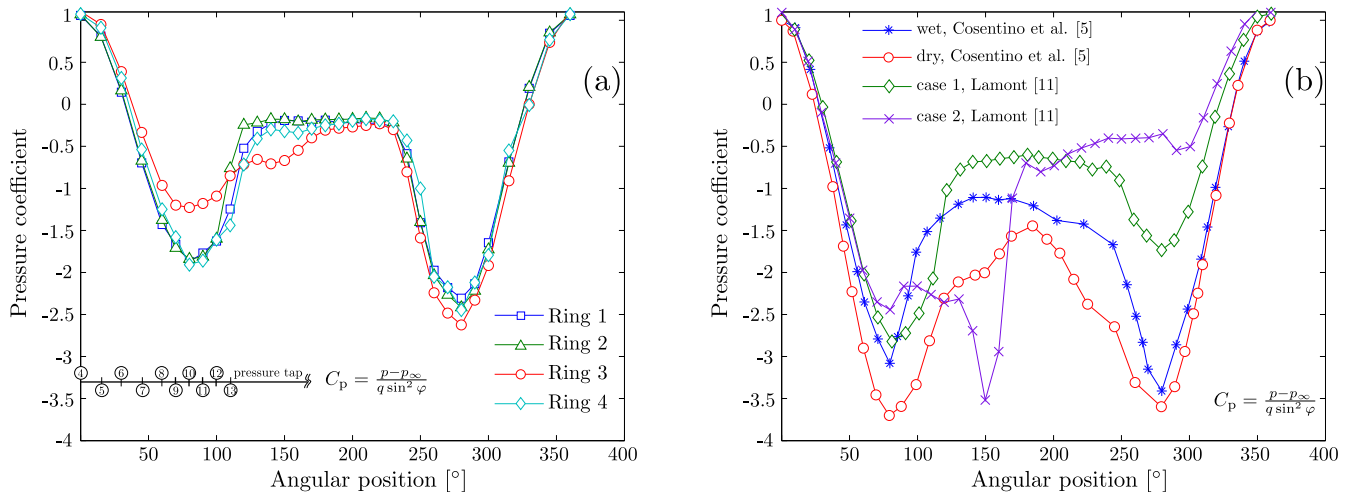


FIGURE 7: a) MEAN PRESSURE DISTRIBUTIONS ON ALL RINGS FOR THE RECORD IN Fig. 2, b) MEAN PRESSURE DISTRIBUTIONS FROM THE LITERATURE CORRESPONDING TO RAIN-WIND VIBRATION AND STATIC INCLINED OGIVE CYLINDERS.

Induced Instabilities. Cambridge University Press, New York.

- [2] Caetano, E., 2007. *Structural Engineering Documents 9; Cable Vibrations in Cable-Stayed Bridges.* IABSE-AIPC-IVBH, Zurich.
- [3] Matsumoto, M., Shiraishi, N., and Shirato, H., 1992. "Rain-wind induced vibration of cables of cable-stayed bridges". *J. Wind Eng. Ind. Aerodyn.*, **43**, pp. 2011–2022.
- [4] Verwiebe, C., 1998. "Exciting mechanisms of rain-wind-induced vibrations". *Struct. Eng. Int.*, **8**(2), pp. 112–117.
- [5] Cosentino, N., Flamand, O., and Ceccoli, C., 2003. "Rain-wind induced vibration of inclined stay cables. Part I: Experimental investigation and physical explanation". *Wind Struct.*, **6**(6), pp. 471–484.
- [6] Macdonald, J. H. G., and Larose, G. L., 2008. "Two-degree-of-freedom inclined cable galloping – Part 2: Analysis and prevention for arbitrary frequency ratio". *J. Wind Eng. Ind. Aerodyn.*, **96**, pp. 308–326.
- [7] Flamand, O., and Boujard, O., 2009. "A comparison between dry cylinder galloping and rain-wind induced excitation". In Proceedings of the 5th European & African Conference on Wind Engineering (EACWE5).
- [8] Nikitas, N., Macdonald, J. H. G., Jakobsen, J. B., Andersen, T. L., Savage, M. G., and McAuliffe, B. R. "Critical Reynolds number and galloping instabilities: experiments on circular cylinders". *Exp. Fluids*(in press).
- [9] Jakobsen, J. B., Andersen, T. L., Macdonald, J. H. G., Nikitas, N., Savage, M. G., and McAuliffe, B. R., 2009. "Wind tunnel testing of an inclined cable model-Pressure and motion characteristics, Part II". In Proceedings of the 5th European & African Conference on Wind Engineering (EACWE5).
- [10] Lamont, P. J., and Hunt, B. L., 1976. "Pressures and force distribution on a sharp-nosed circular cylinder at large angles of inclination to a uniform subsonic stream". *J. Fluid Mech.*, **76**, pp. 519–559.
- [11] Lamont, P. J., 1982. "Pressures around an inclined ogive cylinder with laminar, transitional, or turbulent separation". *AIAA J.*, **20**(11), pp. 1492–1499.
- [12] Flamand, O., Peube, J. L., and Papanikolas, P., 2001. "An explanation of the rain-wind induced vibration of inclined stays". In 4th International Symposium on Cable Dynamics, pp. 69–76.
- [13] Assi, G. R. S., Bearman, P. W., and Meneghini, J. R., 2010. "On the wake-induced vibration of tandem circular cylinders: the vortex interaction excitation mechanism". *J. Fluid Mech.*, **661**, pp. 365–401.
- [14] Matteoni, G., and Georgakis, C. T. "Effects of bridge cable surface roughness and cross-sectional distortion on aerodynamic force coefficients". *J. Wind Eng. Ind. Aerodyn.*(in press).
- [15] Macdonald, J. H. G., and Larose, G. L., 2006. "A unified approach to aerodynamic damping and drag/lift instabilities, and its application to dry inclined cable galloping". *J. Fluid Struct.*, **22**, pp. 229–252.

- [16] Matsumoto, M., Yagi, T., Shigemura, Y., and Tsushima, D., 2001. "Vortex-induced cable vibration of cable-stayed bridges at higher reduced wind velocity". *J. Wind Eng. Ind. Aerodyn.*, **89**, pp. 633–647.
- [17] Schewe, G., 1986. "Sensitivity of transition phenomena to small perturbation in flow round a circular cylinder". *J. Fluid Mech.*

LARGE GALLOPING OSCILLATIONS OF A SQUARE SECTION CYLINDER IN WIND TUNNEL

Pascal Hémon

LadHyX, Ecole Polytechnique - CNRS
Palaiseau, France

ABSTRACT

This paper reports an experimental study of galloping of a 2D square section cylinder flexibly mounted in a wind tunnel. The long term purpose deals with the evaluation of such a system for energy harvesting. Preliminary a deeper study is needed for large amplitude motions which are not well known. We present here two kinds of results, the oscillations amplitude measurements and the wake velocity investigation. An interesting feature is observed with the cylinder inclined by 10° from the axis: for high wind velocity the oscillation amplitude presents a saturation indicating the presence of a self-limited mechanism. Wake velocity profiles show that the vortex shedding remains present but independent of the galloping response due to the system design parameter.

NOMENCLATURE

D	width of the cylinder section, $D = 17.1\text{mm}$
f_1	frequency of vortex shedding (Hz)
f_2	natural frequency of cylinder motion (Hz)
f_r	reduced frequency, $f_r = f_2 D/U_{ref}$
h	vertical coordinate in the wind tunnel frame (m)
M	total mass of the cylinder (kg)
m	mass per unit length of the cylinder (kg/m)
Re	Reynolds number, $Re = U_{ref} D/\nu$
S	Span of the cylinder, $S = 170\text{mm}$
S_c	Scruton number, $S_c = 2\eta m/\rho D^2$
St	Strouhal number, $St = f_1 D/U_{ref}$
U	mean velocity (m/s)
U_{ref}	mean reference velocity of the wind tunnel (m/s)
U_r	reduced velocity, $U_r = 1/f_r$,
u	RMS velocity (m/s)
u_1	RMS velocity at vortex shedding frequency (m/s)
u_2	RMS velocity at cylinder motion frequency (m/s)
x	longitudinal coordinate in the wind tunnel frame,
$z(t)$	vertical displacement of the cylinder (m)
z	RMS vertical displacement of the cylinder (m)
θ	rotation angle of the cylinder ($^\circ$)
η	reduced damping, referred to critical damping
ρ	air density (kg/m^3)
ω	angular frequency, $\omega = 2\pi f$ rad/s

INTRODUCTION

Galloping is an aeroelastic coupling mechanism between an airflow and a flexible structure, often a cylinder normal to the flow. It is described as a one degree of freedom instability where the flow-structure coupling generates a negative added damping that induces the oscillations of the cylinder. This occurs above a critical velocity of the flow and oscillations amplitude may reach very large values, as for instance those observed on electric lines [1].

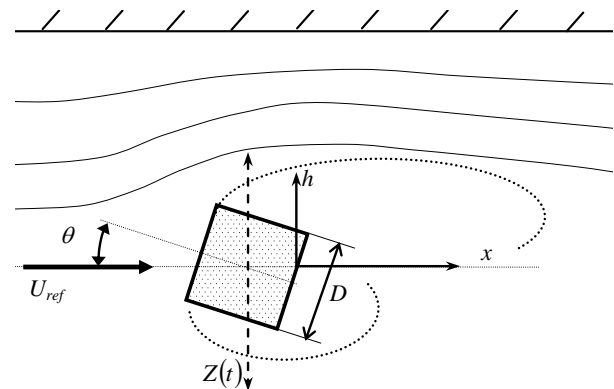


FIGURE 1. THE STUDIED CONFIGURATION.

The long term objective of the current project is to evaluate the energy harvesting potential of the galloping mechanism. Although it has been previously studied analytically [2, 3], the deep understanding of the phenomenon should be improved. Especially large amplitude galloping oscillations are not so well known in simple configuration such as a rigid cylinder, *i.e.* in an almost 2D configuration.

We present here the experiments performed with a square section cylinder as shown Fig. 1 and 2. First we describe the experimental setup, then the amplitude of oscillations are presented. Finally the wake investigation is shown, focusing on the unsteady characteristics.

1. EXPERIMENTAL SETUP

A flexibly mounted square cylinder is placed in a wind tunnel with a square test section (see Fig. 2 & 3).

The upstream velocity has a longitudinal turbulence intensity less than 1 % over a wide range of frequency. The reference velocity is measured with a Pitot tube connected to a pressure manometer. Corrections take into account atmospheric pressure and temperature and global accuracy is better than 1 %.

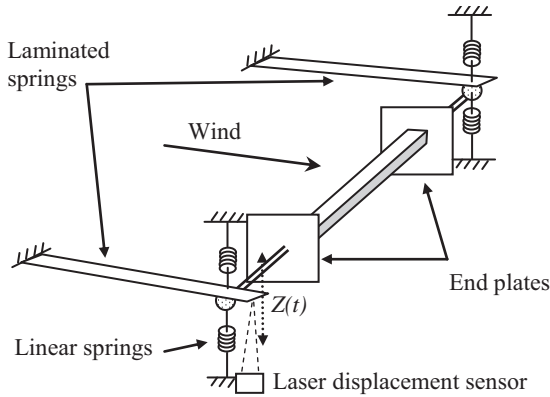


FIGURE 2. PRINCIPLE OF THE EXPERIMENTAL SETUP

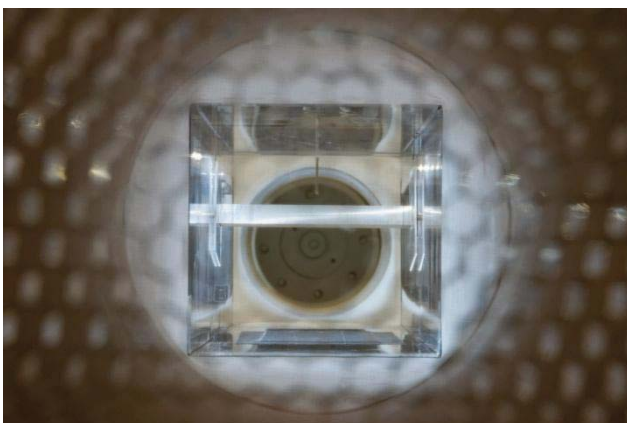


FIGURE 3. PHOTOS OF THE EXPERIMENTAL SETUP

The vertical displacement of the cylinder is measured by a laser sensor, *i.e.* without contact that could corrupt

damping of the system. All measured signals are connected to the acquisition system (resolution 24 bits, sampling frequency 512 Hz) providing time histories of the signal and simultaneous spectral analysis. Typically a record is 45 s long and the frequency resolution is 1/8 Hz.

The cylinder is equipped with two end plates which are supposed to keep the airflow 2D as much as possible. The shape has been adjusted on a milling machine ensuring very sharp edges. Stiffness is provided by combination of linear and laminated springs, suitably mounted in order to produce a very low structural damping. These springs are mounted outside the test section, via two vertical fences (see Fig. 2 & 3). Length of laminated springs is large (0.75 m) compared to the expected cylinder vertical displacement so that the system can be considered as linear in the range of use.

The structural data are determined experimentally without wind. First the stiffness is measured by static calibration using reference masses. Then the eigenfrequency is measured by spectral analysis. The total mass of the cylinder is deduced and expressed as a mass per unit length by dividing by the cylinder span. The damping is measured through the free decay of the vibrations after an initial excitation. The resulting Scruton number being large, the risk of vortex induced vibration is expected to be very small. Two cases have been studied by adding or not small masses on the cylinder. Summary of characteristics is given in Table 1.

TABLE 1. STRUCTURAL CHARACTERISTICS OF THE CYLINDER

	Case A	Case B
f_2 (Hz)	5.875	5.25
M (kg)	0.320	0.400
η (%)	0.177 ± 0.013	0.178 ± 0.006
k (N/m)	435.8	435.8
S_c	19.1	24.2

2. AMPLITUDE OF OSCILLATIONS

Amplitude of oscillations are measured for different wind velocities. As widely reported in the literature the square cylinder has a subcritical branch which leads to different limit cycles depending on the initial excitation or perturbation. In this study the high amplitudes are sought. In all results reported here, the hysteresis effect has been removed and the limit cycle amplitudes are obtained after an initial “strong” excitation manually operated. Each point in Figures 4 and 5 should be considered independent from each other.

To ensure that there is no transient effect, each record is started after the stabilization of the motion and at least one minute of stable oscillations. In all tests, the frequency of motion remained the one measured without wind.

Since Den Hartog it is well known that the galloping instability is possible when the lift derivative C_z' of the

cylinder is negative. In the case of square section this is true around $\theta = 0$ (see Fig. 1) up to a value about 15° depending on the free stream conditions [3, 4, 5]. When the upstream turbulence is low, as it is the case here, the steady lift gradient shows also a minimum around $\theta = 10^\circ$ which leads to larger sensitivity to galloping with this rotation angle.

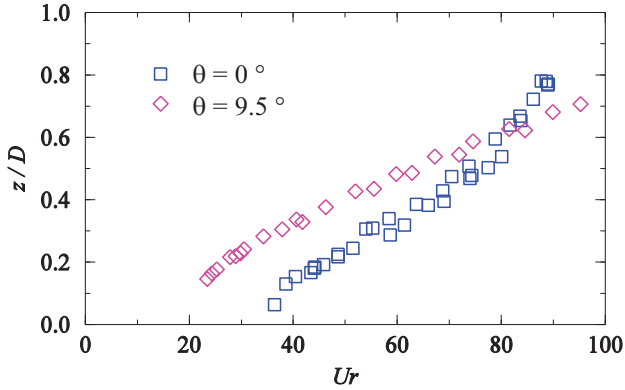


FIGURE 4. OSCILLATIONS AMPLITUDE VERSUS VELOCITY, CASE A.

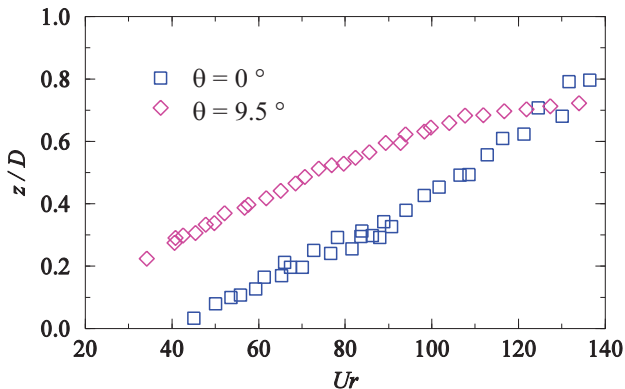


FIGURE 5. OSCILLATIONS AMPLITUDE VERSUS VELOCITY, CASE B.

Then the two cylinders A and B have been tested with two values of θ , 0 and 9.5° as reported in Fig. 4 and 5. Preliminary to these measurements the quasi-steady lift gradient of the cylinder has been estimated by measuring the total damping versus wind velocity. By remaining in stable conditions it is possible indeed by free decay tests to obtain the lift gradient Cz' using the quasi-steady relation of the added damping:

$$\eta_a = \frac{\rho D U}{2m 2\pi f_2} Cz' . \quad (1)$$

The resulting values listed in Tab. 2 are in good agreement with those encountered in the literature, especially for $\theta = 0^\circ$ [3, 6].

It is interesting to note that the amplitude response of the cylinder is much higher for $\theta = 9.5^\circ$ than for $\theta = 0^\circ$ at low wind velocities. However, for $\theta = 0^\circ$ the maximum

amplitude at high velocities is larger than for $\theta = 9.5^\circ$. Moreover one observes that the amplitude reaches a kind of saturation for $\theta = 9.5^\circ$ at high velocities, as clearly seen in Fig. 5. Even this was expected it is very interesting in the sense that such a system used as an energy harvesting starts to oscillate in low wind but is self-limited in amplitude in high wind. Note that the amplitude saturation is due to aeroelastic effect, not to the structural setup, as the oscillation amplitude for $\theta = 0^\circ$ reaches larger values without visible perturbation.

TABLE 2. AEROELASTIC CHARACTERISTIC OF THE SQUARE CYLINDER

	$\theta = 0^\circ$	$\theta = 9.5^\circ$
Cz'	-2.92 ± 0.3	-8.0 ± 0.3

Obviously the difference between the two cases $\theta = 0^\circ$ and $\theta = 9.5^\circ$ lies in the fact that geometrical symmetry is present for $\theta = 0^\circ$: during the oscillation the effective angle of attack seen by the cylinder in motion oscillates around its mean value $\theta = 0^\circ$. Since the lift curve is symmetric around 0° the galloping force is symmetric also.

But for $\theta = 9.5^\circ$ symmetry is lost which causes amplitude saturation because the effective angle of attack reaches large values for which the lift derivative becomes positive. Then saturation is the result of an equilibrium in which during one period of oscillation the cylinder gains energy for small effective angles of attack but losses energy at high angles of attack. Although this remark implies a kind of quasi-steady assumption, the present experiment proves that it is valid, at least qualitatively.

3. WAKE ANALYSIS

A single component hot wire sensor can be mounted in the wake of the cylinder. It can be moved vertically for measuring velocity profiles. Calibration was performed with a Pitot tube and a reference manometer. Accuracy is globally around 5 %. Length of records is typically 60 s with a sampling frequency of 1024 Hz. Accurate Fourier analysis of the signals provides the different components of the velocities due to vortex shedding (u_1) and to the cylinder oscillations (u_2) at the frequency f_2 .

First we measure the Strouhal number, as presented Fig. 6. It has a mean value of 0.147, which corresponds to a wind velocity of lock-in with the cylinder of 0.68 m/s. Agreement with [7] for instance is good.

Note that the blockage effect in the test section leads to a reference velocity lower than that around the cylinder. Geometrically this velocity is 10 % higher, resulting in a corrected Strouhal number 10% lower.

The important point here is that the frequency of vortex shedding is very different from the frequency of the cylinder oscillations due to galloping. Then during the measurements of wake velocity profiles, the reference

velocity was set to 8.5 m/s ($U_r = 85$ with cylinder A). Then the vortex shedding frequency, according to Strouhal law, is 73 Hz, to be compared to 5.875 Hz for the cylinder oscillations.

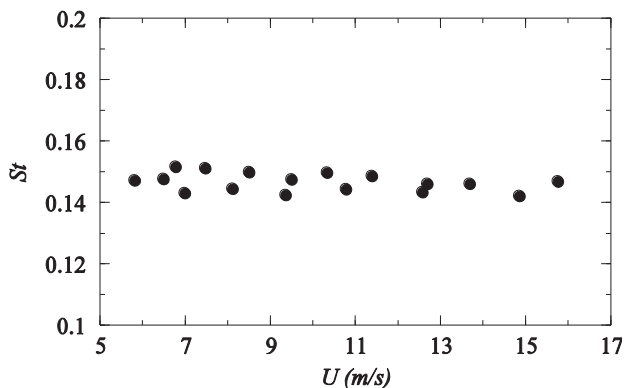


FIGURE 6. MEASURED STROUHAL NUMBER VERSUS VELOCITY FOR STATIC CYLINDER

The velocity profiles have been measured at three different distance from the cylinder rear face, $1.3 D$, $0.7 D$ and $0.23 D$. In the first position the entire wake has been investigated, showing symmetry along the axis, see Fig. 7, so that only one side has been measured for the two other distances Fig. 8 and 9.

In each case, the mean velocity U , its RMS value u and the two components u_1 and u_2 are plotted. In the case of u_2 it was found more significant and reliable to reduce the component by the oscillation velocity of the cylinder \dot{z} . Indeed these experiments were quite long and perfect stability of the oscillations was not exactly respected for such a long time. Then amplitude of u_2 , obviously related to oscillation amplitude, could have changed otherwise.

The first remark is that the oscillations of the cylinder do not modify the main characteristics of the wake. Mean and RMS velocities remain the same in amplitude and distribution. This is also the case for the component at the frequency of vortex shedding, although more noisy signals. It means that the cylinder motion, at a frequency much lower than that of vortex shedding does not perturb the natural shed of vortices which remains present during oscillations. It can be explained by the quasi-steady assumption for which the cylinder motion is so slow that its aerodynamic behaviour remains the same than if there were no motion at all.

But a difference in the phenomena can be observed when considering the expansion of the wake along the distance behind the cylinder. The spatial evolution of the unsteady wake is shown in Fig. 10 where the positions of the maxima of the two velocities u_1 and u_2 are plotted versus the distance x / D behind the cylinder. The expansion of the wake width due to the cylinder oscillation is clear, with a rate of 0.19 (corresponding to an angle 10.75°), although the wake resulting from the

alternate vortex shedding remains parallel in the observed region.

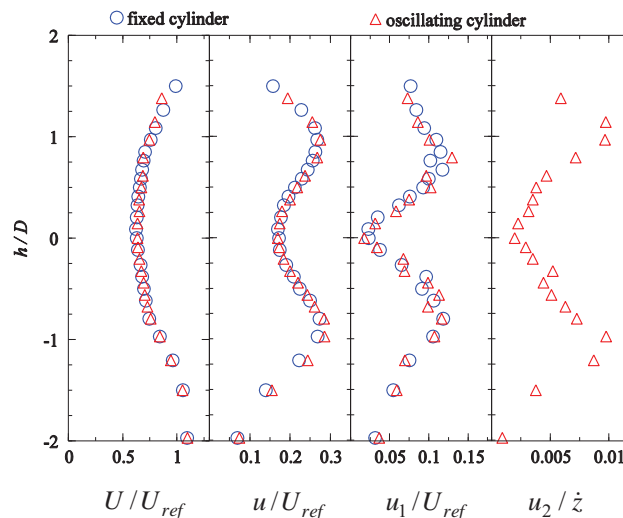


FIGURE 7. VELOCITY PROFILES IN THE WAKE AT $x = 1.3D$ FOR FIXED AND OSCILLATING CYLINDER AT $U_r = 85$, CASE A WITH $\theta = 0$.

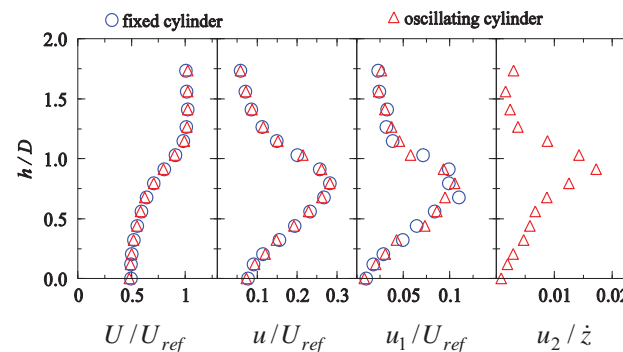


FIGURE 8. VELOCITY PROFILES IN THE WAKE AT $x = 0.7D$ FOR FIXED AND OSCILLATING CYLINDER AT $U_r = 85$, CASE A WITH $\theta = 0$.

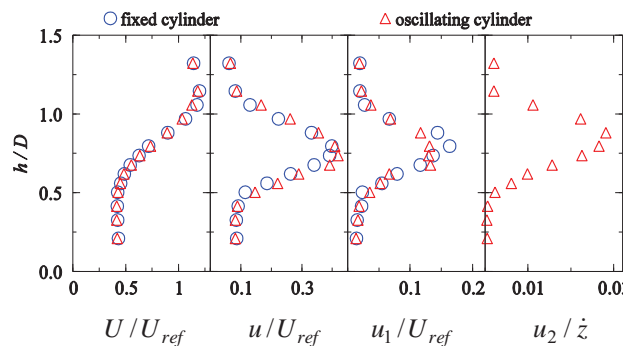


FIGURE 9. VELOCITY PROFILES IN THE WAKE AT $x = 0.23D$ FOR FIXED AND OSCILLATING CYLINDER AT $U_r = 85$, CASE A WITH $\theta = 0$.

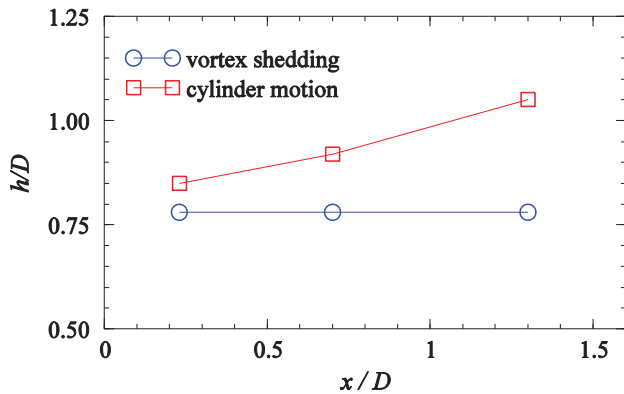


FIGURE 10. VERTICAL POSITIONS h/D OF THE MAXIMA OF THE FLUCTUATING VELOCITIES VERSUS THE DISTANCE x/D BEHIND THE VIBRATING CYLINDER AT $U_r = 85$.

CONCLUSION

Experiments have been conducted with a mostly 2D square section rigid cylinder flexibly mounted in wind tunnel. The setup allows large amplitude oscillations due to galloping instability. Vortex shedding, although always present, does not lead to excitation because of its very different frequency from the cylinder natural frequency.

Results of oscillations amplitude shows that it is possible to design a system that can start to oscillate at a low wind velocity. Moreover the same system in high wind presents a saturation of oscillations amplitude, suggesting that it is self-limited naturally by its aeroelastic properties. Then the long term objective of the study which is the development of an energy harvesting simple system is still valid and needs further investigations.

Experimental results presented can serve for instance for the validation of analytical models including large nonlinear amplitude features.

REFERENCES

- [1] DEN HARTOG J.P. 1985. Mechanical Vibrations. Dover, New York.
- [2] BARRERO-GIL A., ALONSO G., SANZ-ANDRES A. 2010 Energy harvesting from transverse galloping. *J. Sound and Vibration* **329**, p. 2873-2883.
- [3] NOVAK, M. 1969 Aeroelastic galloping of prismatic bodies. *Journal of the Engineering Mechanics Division of the ASCE* **95**, 115-142.
- [4] SAATHOFF, P., MELBOURNE, W.H. 1999 Effects of freestream turbulence on streamwise pressure measured on a square-section cylinder. *Journal of Wind Engineering and Industrial Aerodynamics* **79**, 61-78.
- [5] HEMON P. & SANTI F. 2002 On the aeroelastic behaviour of rectangular cylinders in cross-flow. *J. Fluids and Structures* **16**(7), p. 855-889.

- [6] LUO S.C., YAZANI Md.G., CHEW Y.T., LEE T.S. 1994. Effect of incidence and afterbody shape on flow past bluff cylinders. *Journal of Wind Engineering and Industrial Aerodynamics* **53**, 375-399.
- [7] NORBERG, C. 1993 Flow around rectangular cylinders: pressure forces and wake frequencies. *Journal of Wind Engineering and Industrial Aerodynamics* **49**, 187-196.

EXPERIMENTAL AND NUMERICAL STUDY OF THE FLUID-ACOUSTIC INTERACTION IN A T-JUNCTION AT LOW MACH NUMBER FLOWS

Andreas Holmberg*

The Marcus Wallenberg Laboratory
The Linné Flow Centre
Department of Aeronautical and
Vehicle Engineering
Royal Institute of Technology
Stockholm, Sweden
Email: anholmbe@kth.se

Marion Berton

Axel Kierkegaard

The Marcus Wallenberg Laboratory
Department of Aeronautical and
Vehicle Engineering
Royal Institute of Technology
Stockholm, Sweden
berton@kth.se
axelk@kth.se

Mikael Karlsson

Swenox AB
Västra Frölunda,
Sweden
mikael.karlsson@swenox.com

ABSTRACT

Experiments and numerical simulations of the aeroacoustic response of a T-junction, subject to grazing and bias flow is presented in this paper. Specifically, the regions of acoustic amplification and attenuation are studied, via the scattering matrix. The experiments are based upon plane wave-decomposition, using flush mounted loudspeakers to excite the acoustic fields. The numerical method is based upon frequency-domain linearized Navier-Stokes equations, which has been shown both efficient and accurate for studies of flow duct constrictions with two ports.

A main point addressed in this paper is whether 2D RANS can be used to calculate the mean flow of the T-junction, which is needed as input to the acoustic calculations. For this reason, at grazing inflow of Mach 0.1, three different cases are calculated; a closed sidebranch end, an open sidebranch end, and bias inflow of Mach 0.01. Comparing with the experiments, it is found that the agreement is good up to about half the plane wave region of the experiments, beyond which the calculations overpredicts the amplification regions. This is believed to be due to 3D effects in the experiments, not captured by the 2D RANS.

INTRODUCTION

T-junctions (see Fig. 1) and similar elements with orifices are common in e.g. automotive intake and exhaust systems, ventilation systems and pipelines. The aero-

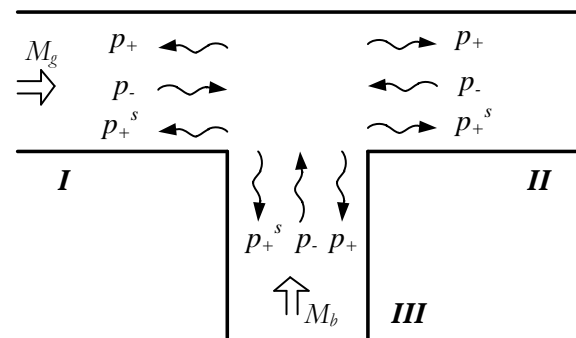


FIGURE 1: A T-junction. Definitions of coordinate systems, positive directions for the Mach numbers and numbering of side branches used in the paper.

acoustics of T-junctions have therefore attracted much attention, see e.g. [1-9]. Both the active and passive aeroacoustic responses of such elements are strongly influenced by the mean flow configuration in the system. The interaction between the acoustic field and hydrodynamic instabilities, which are convected across the orifice, can lead to either attenuation or amplification of the incident acoustic power. If the T-junction is connected to a strongly resonant system, e.g. a tailpipe or a quarter-wave resonator, a self-sustained oscillation can occur, leading to intense noise and even mechanical failure.

Unfortunately, analytical models of single orifices generally produce results which correlate poorly with experimental data, as is shown by Peat et al. [10] and Jing et al. [11]. Furthermore, the versatility of existing empirical models with respect to the geometry and flow con-

*Address all correspondence to this author.

ditions is limited [12]. Bias flow, i.e. flow through the orifice, is an example of a flow case, for which high fidelity predictions generally are unattainable using existing models. Thus, experiments or simulations must be used to obtain the frequency regions and magnitudes of amplification and attenuation, for a given flow case and geometry. This can be done by determining the scattering matrix [13], from which the attenuation and amplification potentiality can be obtained [7, 14]. For a T-junction, the scattering matrix can be written as

$$\mathbf{p}_+ = \mathbf{S}\mathbf{p}_- + \mathbf{p}_+^S \quad (1)$$

where \mathbf{p}_+^S is the source vector, \mathbf{p}_+ and \mathbf{p}_- contains the outgoing and incoming (complex) pressure amplitudes of all ports, and \mathbf{S} is the (complex) scattering matrix, which for a three-port system is given by [7]

$$\mathbf{S} = \begin{pmatrix} R_I & T_{II,I} & T_{III,I} \\ T_{I,II} & R_{II} & T_{III,II} \\ T_{I,III} & T_{II,III} & R_{III} \end{pmatrix} \quad (2)$$

R_m has the physical meaning of reflection of waves propagating towards the three-port in branch m , and $T_{m,n}$ is the transmission of acoustic pressure from branch m to branch n , see Fig. 1. A main feature of the scattering matrix is that it generally can be obtained from 50 Hz say, to the cut-on of the first non-planar wave in the duct. The main drawback is that the model functions as a black box, giving no details as of how the output was obtained.

In this work, both experiments and numerical simulations of scattering matrices are performed. The aim in the long run is to obtain a prediction model for the linear scattering matrix valid for a wide range of flow conditions and geometries, with focus on the mixed grazing/bias cases, i.e. when there is a net flow in all three branches. However, in this paper, the focus is on validating the numerical procedure. Concerning acoustic investigations of T-junctions subject to a combination of bias and grazing flow, the literature consists of the recent experimental works [7, 15]. Here, the experimental procedure and test facilities presented in [7, 15] are used to add more flow cases to said work.

The method chosen for the numerical simulations was recently developed and tested for a few internal flow objects [16, 17], with good agreement to experimental data. It is a hybrid method, where the mean flow is obtained using a RANS solver, and used as input to a linearized Navier-Stokes frequency domain solver for the

perturbed quantities. The scattering matrix is then obtained from planar waves in a way similar to the experimental methods.

MEASUREMENT METHOD

The analysis of the experimental data is based upon the ability to decompose the sound field in planar waves. For flow ducts the microphone methods consists of the two-microphone method [18, 19], multi-microphone methods [20, 21] or the full wave-decomposition method [22]. In a recent study [23] it was investigated how to best utilize a microphone array of 5 microphones per port. The best method found was that described in [20] if combined with a routine optimizing the number of microphones used per frequency. This is also done in this paper, for an array of 4 microphones per port.

Theory

The microphone data collected at a port side, is used input on the right hand side of the equation system

$$\begin{pmatrix} e^{-ik_+x_1} & e^{-ik_-x_1} \\ e^{-ik_+x_2} & e^{-ik_-x_2} \\ \vdots & \vdots \\ e^{-ik_+x_j} & e^{-ik_-x_j} \end{pmatrix} \begin{pmatrix} p_+ \\ p_- \end{pmatrix} = \begin{pmatrix} p_1 \\ p_2 \\ \vdots \\ p_j \end{pmatrix} \quad (3)$$

where k_+ and k_- are the wavenumbers in the positive and negative directions respectively, x_j is the position and p_j is the complex pressure of microphone j . The sound field is obtained by having external loudspeakers mounted on the test rig, and the three port source part, which is independent on the acoustic field, is suppressed by averaging over the cross spectra between the microphone pressure and the loudspeaker signal.

Now, to solve for \mathbf{S} , measurements of three linear independent acoustic fields are required. Here, the method of using flush mounted loudspeakers [24] is used in order to excite the fields. The scattering matrix is then solved via the equation

$$\mathbf{S} = \mathbf{P}_+ \mathbf{P}_-^{-1} \quad (4)$$

with

$$\mathbf{P}_+ = (\mathbf{p}_+^{L_1} \mathbf{p}_+^{L_2} \mathbf{p}_+^{L_3}), \quad \mathbf{P}_- = (\mathbf{p}_-^{L_1} \mathbf{p}_-^{L_2} \mathbf{p}_-^{L_3}) \quad (5)$$

where the superscripts L_1 , L_2 and L_3 refer to vectors obtained from three differently excited sound fields. The wave numbers in Eqn. (3) are obtained from a model proposed by Dokumaci [25], which includes the effects of visco-thermal damping

$$k_{\pm} = \frac{\omega}{c_0} \frac{K_0}{1 \pm K_0 M} \quad (6)$$

where ω is the angular frequency, c_0 the adiabatic speed of sound, M the averaged Mach number over the cross section, and K_0 is given by

$$K_0 = 1 + ((1-i)/s)(1 + (\gamma-1)/\sqrt{Pr})/\sqrt{2} \quad (7)$$

with γ being the ratio of specific heats, Pr the Prandtl number, and s the shear wavenumber

$$s = r\sqrt{\rho_0\omega/\mu} \quad (8)$$

where ρ_0 is the ambient density, μ the dynamic viscosity and r is the duct radius. In this work, since the duct cross section is rectangular, the radius is defined as that of a circle with the same circumference as that of the rectangular duct.

Measurement setup

The measurement rig consists of three rectangular ducts, each terminated by a lined expansion chamber, filled with mineral wool. The rig, which is depicted in Fig. 2, was connected to the MWL wind tunnel. The rectangular ducts have the inner dimensions 25x120 mm, the walls made of 15 mm thick steel. The T-junction is constructed so that the length of the opening is 25 mm in the grazing flow direction.

The velocity in each branch was tuned by the use of two valves, and monitored via Prandtl-tubes in circular ducts, one put upstream of the lined expansion chamber of branch *III* but downstream of the valve, and one put upstream of the junction where the flow is separated into the main duct and into the side branch duct. The Mach numbers are calculated by considering the difference in mass flow at the two velocity measurement points, indicated in Figure 2. Since both measurements are conducted in circular ducts, it is possible to use the 1/7th power law [26] to predict the ratio between mean and maximum velocity, which for the Reynolds numbers found in this work are approximately 0.82.

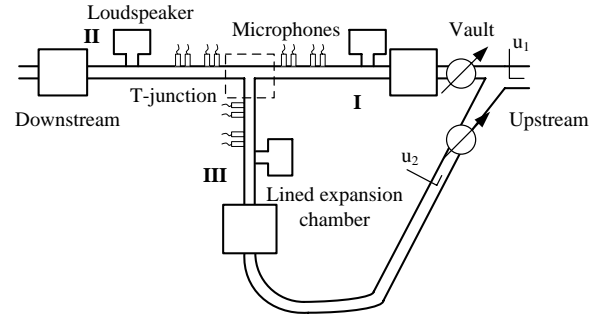


FIGURE 2: Schematic drawing of the test rig, showing positions of velocity measurements.

The microphone array on each side consists of four microphones, placed in order for the wave-decomposition to be valid from 100 Hz up to the cut-on of the first non-plane mode in the test rig.

A stepped sine signal is used to map the aeroacoustic response of the T-junction in steps of 12.5 Hz, with a frequency resolution of 1.25 Hz. The measurement time for each loudspeaker and flow velocity case was about two hours, which from experience is short enough to ensure an approximately constant temperature. However to validate this, the temperature was measured in all three branches before and after the measurement, and the maximum increase in temperature was about 2°C, thus increasing the speed of sound by less than 0.4%.

NUMERICAL METHOD

To calculate acoustic scattering in the duct, the linearized Navier-Stokes equations for the frequency domain [16] are adopted. They are capable of capturing acoustic dissipation due to vorticity shedding, as well as acoustic amplification due to acoustic-vorticity feedback, and should thus be well suited for the phenomena studied here. The equations are here expressed in the form

\hat{p} :

$$(u_0 \ v_0) \nabla \hat{p} + \left(\frac{\partial u_0}{\partial x} + \frac{\partial v_0}{\partial y} - i\omega \right) \hat{p} = - \left(\frac{\partial \rho_0 \hat{u}}{\partial x} + \frac{\partial \rho_0 \hat{v}}{\partial y} \right) \quad (9)$$

\hat{u} :

$$\nabla^T \left(- \left(\frac{4}{3} \mu \ 0 \right) \nabla \hat{u} \right) + \rho_0 (u_0 \ v_0) \nabla \hat{u} + \rho_0 \left(\frac{\partial u_0}{\partial x} - i\omega \right) \hat{u} =$$

$$= \rho_0 \hat{F}_x - \left(u_0 \frac{\partial u_0}{\partial x} + v_0 \frac{\partial u_0}{\partial y} \right) \hat{\rho} - c^2 \frac{\partial \hat{\rho}}{\partial x} + \frac{1}{3} \mu \frac{\partial^2 \hat{v}}{\partial x \partial y} - \rho_0 \frac{\partial u_0}{\partial y} \hat{v} \quad (10)$$

\hat{v} :

$$\nabla^T \left(- \begin{pmatrix} \mu & 0 \\ 0 & \frac{4}{3} \mu \end{pmatrix} \nabla \hat{v} \right) + \rho_0 (u_0 \ v_0) \nabla \hat{v} + \rho_0 \left(\frac{\partial v_0}{\partial y} - i \omega \right) \hat{v} =$$

$$= \rho_0 \hat{F}_y - c^2 \frac{\partial \hat{\rho}}{\partial y} - \left(u_0 \frac{\partial v_0}{\partial x} + v_0 \frac{\partial v_0}{\partial y} \right) \hat{\rho} - \rho_0 \frac{\partial v_0}{\partial x} \hat{u} + \frac{1}{3} \mu \frac{\partial^2 \hat{u}}{\partial x \partial y} \quad (11)$$

where $\nabla = (\partial/\partial x \ \partial/\partial y)^T$, and the superscript $\hat{\cdot}$ refers to an acoustic quantity. The mean flow quantities u_0 , v_0 and ρ_0 are obtained a priori, here via RANS calculations.

Mean flow methodology

The mean flow is calculated using incompressible RANS equations with $k - \varepsilon$ turbulence modeling. Due to computational cost, the computational realm is set to 2D, both for the RANS solution and the acoustic solution. This is a significant limitation which will be discussed further in the discussion section of this paper.

Wall functions [27] are used in two consecutive pre-steps; first, starting from a uniform inflow velocity profile, the flow is calculated in a duct of 30 m in order to obtain the outlet flow velocity, pressure, turbulence kinetic energy k , and the dissipation rate of turbulence energy ε . The outlet properties are then used as inlet condition in the main branch I , see Fig. 1.

The second step involving wall-functions is a T-junction mean flow calculation, where the objective is to generate an initial condition of the flow, used to setup calculations without wall functions. The reason for using the $k - \varepsilon$ turbulence model is that it is one of the most common and simplest turbulence models found in commercial software. The computations are performed in the commercial finite element method code Comsol Multiphysics v4.2.

Acoustic methodology

The numerical approach used here to study the T-junction, are in many aspects similar to the experimental methods performed. The 3-port scattering matrix is obtained by decomposing three differently excited sound fields, into propagating waves. Once solved for, the scattering matrix obtained from the numerical simulations can be analyzed as if it was determined experimentally. The wave-decomposition is made by solving Eqn. (3) for two complex amplitudes and two real wavenumbers in

each duct. Thus, losses are omitted. The input to the resulting non-linear equation system is the cross section average acoustic density (here, 30 equidistant data-points are used for this purpose), at 150 cross sections per duct. The equation system is solved using the MatLab built-in function `lsqcurvefit`.

In theory, the results obtained using the methodology suggested here, will not be influenced by the end reflections in the duct. However, for numerical stability reasons, the reflections should be kept to a minimum. For this reason, an additional duct length of 0.5 m with artificial viscosity is placed after each duct end. The mean flow is not calculated for this region, instead the values of the mean flow quantities at the duct ends are extended to hold for the entire additional duct. This is done in order to avoid acoustic scattering at the interface.

The sound fields are excited by applying the source terms F in Eqn. (10) and (11) to one duct branch at a time. The maximum for the continuous function for F is set at the interface between the original duct end, and the additional length, and the function is non-zero in a region of 0.05 m in both directions.

The acoustic boundary layers are assumed to have negligible effect on the simulated field. Therefore, a slip condition for the acoustic particle velocity is implemented at all walls.

Computational domains

For the RANS calculations of the T-junction, each main branch is 1.5 m long, while the sidebranch length is 1 m. The pre-study with applied wall-functions, used to obtain an initial condition, is calculated on an unstructured mesh consisting of linear triangular elements, the largest with a size of 5 mm. At the edges the element size was set to 0.109 mm, and the maximum element growth rate was 1.3.

For the calculations without wall-functions the mesh near the wall was refined. In the wall normal direction, the mesh consisted of 25 linear quadrilateral elements ranging from a height of 30 μm (closest to the wall) to 50 μm , see Fig. 3. The $y+$ value based upon the center of a wall adjacent element was expected to be below unity for all walls. The obtained $y+$ value was 0.5 and below everywhere except in a 2 mm proximity of the T-junction edges, where $y+$ as high as 2.8 was found. For one flow-case the mesh was refined in order to study the mesh convergence. In the refined mesh, the number of elements closest to the wall was increased from 25 to 40. However, the maximum $y+$ value was only lowered to about 2.7. For both meshes, the remaining domains consisted of unstructured linear triangular elements, with a maxi-

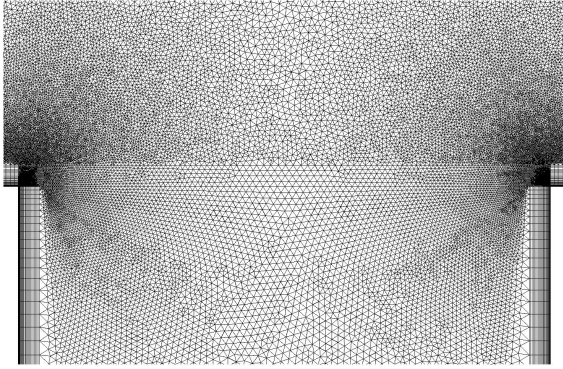


FIGURE 3: A close-up around the T-junction of the unrefined mesh used for RANS calculations.

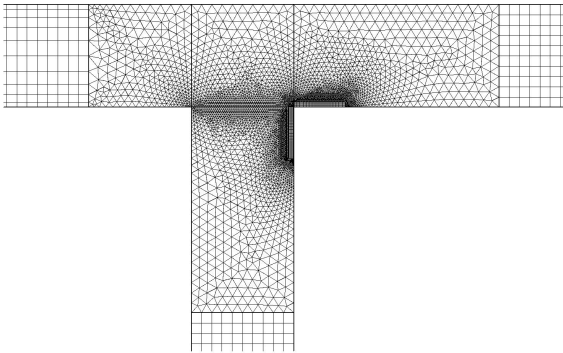


FIGURE 4: A close-up around the T-junction of the mesh used for acoustic calculations.

mum stretching factor of 1.025 and a maximum size of $h/15$, where h is the duct height.

For the acoustic calculations, the mesh consists of cubic elements. In the ducts, a distance h away from the T-junction in duct *I*, and $2h$ away from the junction in the other ducts, the mesh consisted of a structured quadrilateral elements with a size of $h/10$. This corresponds to approximately 91 elements per wavelength at the highest frequency calculated for. Over the junction, an unstructured mesh of triangular elements was used, also with a maximum size of $h/10$, and with a maximum element growth rate of 1.1. The number of elements across the junction was set to 50. At the downstream edge, a structured mesh of quadrilateral elements with a size of $h/100$ was utilized in a region $h/20$ in the wall normal direction, and $h/2$ in the axial direction, see Fig. 4

RESULTS

In this paper we have chosen to limit the number of scattering matrix elements shown, in order to have room for all flow combinations investigated.

Measurements conducted

The grazing-bias flow combinations presented in this paper consists of

- A Zero mean inflow (in towards the T-junction) in the sidebranch, (referred to as bias flow). The mean inflow Mach number in branch *I* (from now on referred to as the grazing Mach number), see Fig. 1, was for this case varied between 0.05 to 1.25, in steps of 0.0125.
- B Constant grazing Mach number of 0.1. The bias inflow Mach number was varied from 0 to 0.05 in steps of 0.01.

Calculations performed

In this paper, three different mean flow cases are calculated, all with a grazing flow of Mach 0.1. The flow cases consist of

- C Zero bias flow
- D Mach 0.01 bias inflow (in towards the T-junction)
- E Opened ends at both branch *II* and *III*

Measurement results

The experimentally determined scattering matrix element $T_{I,III}$ is shown in Fig. 5 for flow combinations A, and in Fig. 6 for flow combinations B.

Calculation results

The velocity magnitude obtained using the original mesh, see Fig. 3, is shown in Fig. 7 for flow combination C, while flow combinations D and E are shown in Fig. 8 and Fig. 9 respectively.

The calculated scattering matrix element $T_{I,III}$ is shown in Fig. 10 for all flow combinations C and E, where it is compared to the experimental result obtained at flow combination C. In Fig. 11 the calculated and the measured scattering matrix element $T_{I,III}$ is shown for flow case D.

DISCUSSION

The experimental results show that the magnitude of amplification and dissipation regions, is strongly influenced by both grazing and bias Mach numbers. Comparing with experiments performed on ducts with circular

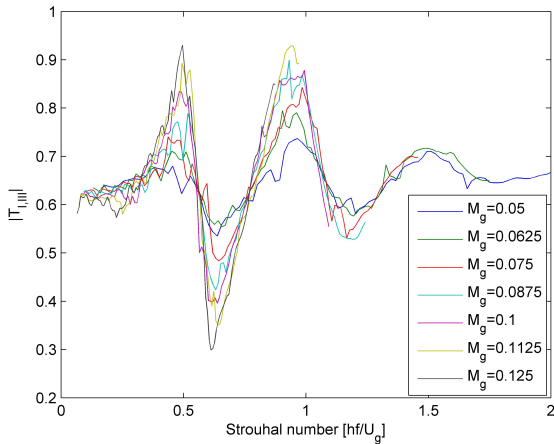


FIGURE 5: Magnitude of the transmission from branch *I* to branch *III*, as function of the Strouhal number for various grazing Mach numbers.

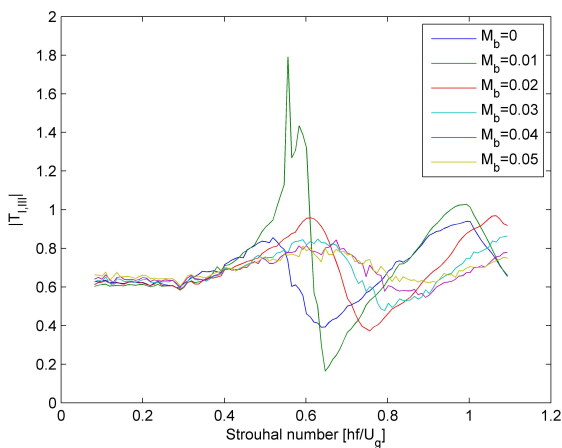


FIGURE 6: Magnitude of the transmission from branch *I* to branch *III*, as function of the Strouhal number for a grazing Mach number of 0.1 and various bias Mach numbers.

cross sections [7], these regions are stronger for the rectangular duct. This is likely due to a stronger velocity gradient in the shear layer across the junction. The influence of the momentum thickness on the stability of an inviscid parallel free shear layer was described by Michalke [28], the shear layer having the shape of a hyperbolic-tangent velocity profile. A quick glance at the calculated velocity fields presented in this paper, shows that the shear layer over the junction differs in shape between the three different flow cases. Thus, the results in [28] does not generally apply to the T-junction. If the amplitude and frequency are to be normalized into non-dimensional numbers, valid

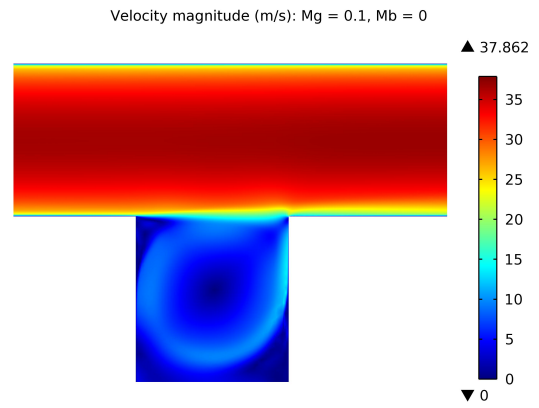


FIGURE 7: Velocity magnitude obtained using the unrefined mesh, for $M_g = 0.1$ and $M_b = 0$ (flow combination C).

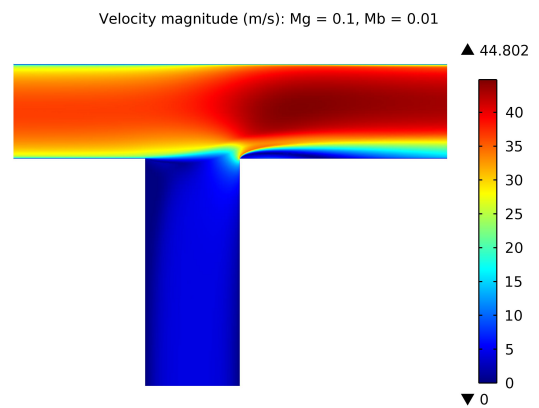


FIGURE 8: Velocity magnitude obtained using the unrefined mesh, for $M_g = 0.1$ and $M_b = 0.01$ (flow combination D).

for a wide range of flow combinations and geometries, a large amount of these cases must first be studied. One possible way to obtain enough data is to perform RANS calculations for a wide range of parameters, and validate a few of them experimentally. A main point of this paper is therefore to address the possibility to use 2D RANS in these studies.

The RANS mesh refinement results indicate that the quality of the mean flow solution is crucial for the acoustic results. Whether or not this quality can be achieved with 2D RANS remains an open question. Inspecting the comparison between experiments and calculations, there is good agreement up to a certain Strouhal number, beyond which the calculations predict an amplification region several times that of the experimental result. A possible reason for this is differences in the upstream velocity profile, caused by 3D-effects in the experiments. For

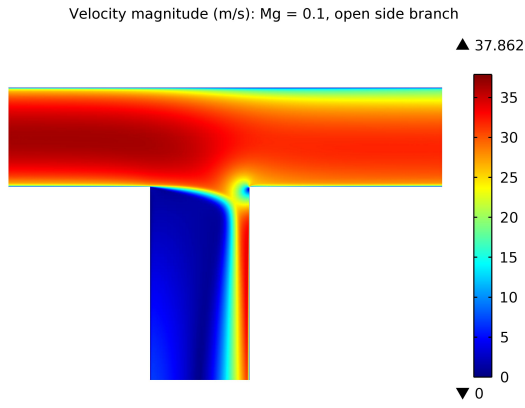


FIGURE 9: Velocity magnitude obtained using the unrefined mesh, for $M_g = 0.1$ and open end in branch *III* (flow combination E).

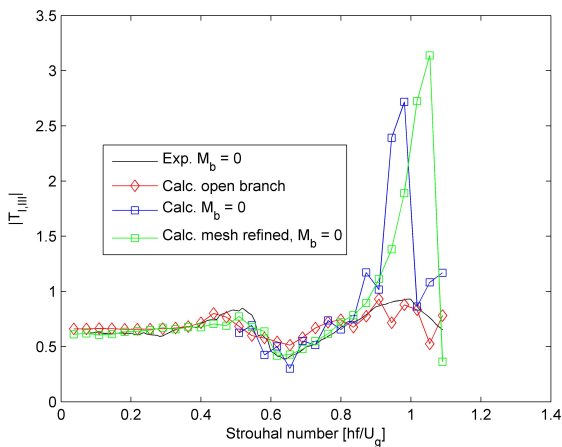


FIGURE 10: Calculations vs Experiments: Magnitude of the transmission from branch *I* to branch *III*, as function of the Strouhal number, at experimental $M_g = 0.1$ and $M_b = 0$, and calculation flow combinations C and E.

instance, rectangular duct flows are subject to secondary flows in the corners [26].

The calculation result for the open end shows an amplification which agrees surprisingly well with the result of the experiments for zero bias flow and Mach 0.1 grazing flow. If there was a leak in the sidebranch during the experiments, a small outflow of Mach 0.01 could exist in the sidebranch, while the air was quiescent at the Prandtl tube measurement point, some distance away. Another, perhaps more likely reason is that bias outflow has been observed to dampen the amplification regions [7], which here would mean that the overprediction of the amplification in the calculated result is dampened to fit the experiments at zero bias flow.

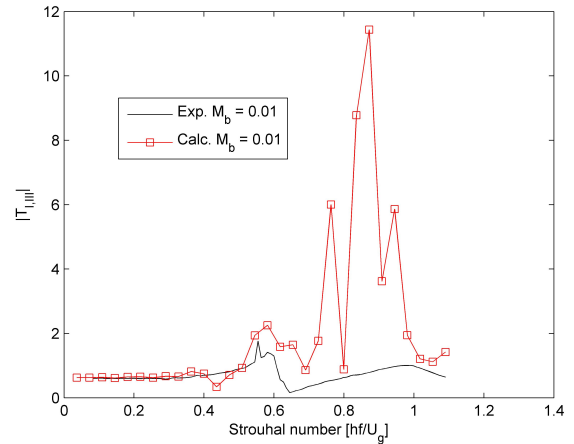


FIGURE 11: Calculations vs Experiments: Magnitude of the transmission from branch *I* to branch *III*, as function of the Strouhal number, at experimental $M_g = 0.1$ and $M_b = 0.01$, and calculation flow combination D.

REFERENCES

- [1] Bruggeman, J. C., Hirschberg, A., and van Dongen, M. E. H., 1991. "Self-sustained aero-acoustic pulsations in gas transport systems: experimental study of the influence of closed side branches". *J. Sound. Vib.*, **150**, pp. 371-393.
- [2] Hofmans, G. C. J., 1998. "Vortex Sound in Confined Flows". Phd Thesis, Eindhoven University of Technology
- [3] Dequand, S., Hulshoff, S. J., and Hirschberg, A., 2003. "Self-sustained oscillations in a closed side branch system". *J. Sound. Vib.*, **256**, pp. 359-386.
- [4] Koojiman, G., Hirschberg, A., and Golliard, J., 2008. "Acoustical response of orifices under grazing flow: effect of boundary layer profile and edge geometry". *J. Sound. Vib.*, **315**, pp. 849-874.
- [5] Testud, P., Aurégan, Y., Moussou, P., and Hirschberg, A., 2009. "Acoustical response of orifices under grazing flow: effect of boundary layer profile and edge geometry". *J. Sound. Vib.*, **325**, pp. 769-780.
- [6] Martínez-Lera, P., Schram, C., Fller, S., Kaess, R., and Polifke, W., 2009. "Identification of the aeroacoustic response of a low Mach number flow through a T-joint". *J. Acoust. Soc. Am.*, **216**(2), pp. 582-586.
- [7] Karlsson, M., and Åbom, M., 2010. "Aeroacoustics of T-junctions-An experimental investigation". *J. Sound. Vib.*, **329**, pp. 1793-1808.
- [8] Graf, H. R., and Ziada, S., 2010. "Excitation source of a side-branch shear layer". *J. Sound. Vib.*, **329**,

- pp. 2825-2842.
- [9] Tonon, D., 2011. "Aeroacoustics of shear layers in internal flows: closed branches and wall perforations". Phd Thesis, Eindhoven University of Technology
- [10] Peat, K. S., Ih, J. -G., and Lee, S. -H., 2003. "The acoustic impedance of a circular orifice in grazing mean flow: comparison with theory". *J. Sound. Vib.*, **114**, pp. 3076-3086.
- [11] Jing, X., Sun, X., Wu, J., and Meng, K., 2001. "Effect of grazing flow on the acoustic impedance of an orifice". *AIAA Journal*, **39**, pp. 1478-1484.
- [12] Lee, S. -H., and Ih, J. -G., 2003. "Empirical model of the acoustic impedance of a circular orifice in grazing mean flow". *J. Acoust. Soc. Am.*, **114**, pp. 98-113.
- [13] Åbom, M., 1991. "Measurement of the scattering-matrix of acoustical two-ports". *Mech. Sys. and Sign. Proc.*, **5**, pp. 89-104.
- [14] Aurégan, Y., and Starobinski, R., 1999. "Determination of acoustical dissipation/production potentiality from the acoustical transfer function of a multiport". *Acta Acustica*, **85**, pp. 788-792.
- [15] Holmberg, A., and Karlsson, M., 2010. "The effect of grazing-bias flow on the self sustained oscillations in a side branch". *Proceedings of the 20th International Congress on Acoustics (Sydney, Australia)*.
- [16] Kierkegaard, A., Boij, S., and Efraimsson, G., 2010. "A frequency domain linearized Navier-Stokes equations approach to acoustic propagation in flow ducts with sharp edges". *J. Acoust. Soc. Am.*, **127**(2), pp. 710-719.
- [17] Kierkegaard, A., 2010. "Frequency Domain Linearized Navier-Stokes Equations Methods for Low Mach Number Internal Aeroacoustics". Phd Thesis, Royal Institute of Technology, Stockholm
- [18] Schmidt, W. E., and Johnston, J. P., 1975. "Measurement of Acoustic Reflection from Obstructions in a Pipe with Flow". *NSF Report*, PD-20
- [19] Seybert, A. F., and Ross, D. F., 1997. "Experimental determination of acoustic properties using a two-microphone random-excitation technique". *J. Acoust. Soc. Am.*, **61**, pp. 1362-1370.
- [20] Fujimoro, T., Sato, S., and Miura, H., 1989. "An automated measurement system of complex pressure reflection coefficients". *Internoise 84*, pp. 1009-1014.
- [21] Jones, M. G., and Parrott, T. L., 1989. "Evaluation of a multi-point method for determining acoustic impedance". *Mech. Sys. and Sign. Proc.*, **3**, pp. 15-35.
- [22] Allam, S., and Åbom, M., 2006. "Investigation of damping and radiation using full plane wave decomposition in ducts". *J. Sound. Vib.*, **292**, pp. 519-534.
- [23] Holmberg, H., Åbom, M., and Bodén, H., 2011. "Accurate experimental two-port analysis of flow generated sound". *J. Sound. Vib.*, **330**, pp. 6336-6354.
- [24] Munjal, M. L., and Doige, A. G., 1990. "Theory of a two source-location method for direct experimental evaluation of the four-pole parameters of an aeroacoustic element". *J. Sound. Vib.*, **141**, pp. 323-333.
- [25] Dokumaci, E., 1997. "A note on transmission of sound in a wide pipe with mean flow and viscothermal attenuation". *J. Sound. Vib.*, **208**, pp. 653-655.
- [26] Schlichting, H., 1968. *Boundary-Layer Theory*. McGraw-Hill.
- [27] Kuzmin, D., Mierka, O., and Turek, S., 2007. "On the Implementation of the $k - \epsilon$ Turbulence Model in Incompressible Flow Solvers Based on a Finite Element Discretization". *Int. J. Comp. Sci. and Math.*, **1**, pp. 193-206.
- [28] Michalke, A., 1965. "On spatially growing disturbances in an inviscid shear layer". *J. Fluid. Mech.*, **23**(3), pp. 521-544.



FLOW-INDUCED PULSATIONS AT T-JOINTS WITH INSERTS: EXPERIMENTAL AND NUMERICAL STUDY

J. Golliard*

TNO
P.O. Box 155
2611 AD
Delft, The Netherlands
Email: joachim.golliard@tno.nl

**N. Gonzalez-Diez
J.S. Groen**

TNO
P.O. Box 155
2611 AD
Delft, The Netherlands

ABSTRACT

In this paper, the influence of an sawtooth insert on the pulsations measured in a double side-branch pipe system is investigated. The single-vortex approach, a basically two dimensional method to compute the generated acoustic power, is extended to include basic three dimensional effects. On the other hand, experimental results measured in a flow test rig with a good whistling double-side branch system without and with sawtooth inserts are presented. Yet the model is a crude approximation accounting only partially for the three dimensional effects, it gave a reasonable indication of both the frequency shift and the decrease in amplitude due to the inserts.

INTRODUCTION

The goal of this study is to investigate the effect of inserts at T-joints on Flow-Induced Pulsations. In gas transport pipe systems, Flow-Induced Pulsations can for example occur when a grazing flow is grazing on a closed side branch. This kind of situations is typically found in metering or mixing stations in natural gas transport and distribution networks, and at the connection of anti-surge lines in compressors. These pulsations can induce large forces on the piping, in some cases resulting in pipe failures. The geometry of the Tee connection is critical for the amplitude of the source. It has for example been demonstrated [1,2] that a connection with rounded edges can produce larger flow-induced pulsations than a connection with sharp edges.

When this problem is foreseen at the design phase, it is possible to search for remedies, for example by detuning the acoustical resonator by modifying the pipe routing

and the pipe length. In some cases, it is also possible to reduce the pulsation sources. Indeed, Tee connections in gas transport systems are sometimes equipped with gratings, grids, or with so-called "scraper guides", which are meant to guide the cleaning device (pig) towards the export piping. The motivation of this study was to investigate the effect of various inserts at Tee connections on the pulsation, so that the best choice can be made to avoid or reduce pulsations. In this article, we focus on one single type of insert, with a sawtooth upstream edge, which is expected to destroy the coherence of the vorticity in the opening and thus to reduce the source strength. Furthermore an attempt is presented to extend the single-vortex method to include some three-dimensional effect.

In next section, the basic mechanisms of flow-induced pulsations in a closed side branch are reminded. Then, the pseudo three dimensional approach is described. Last, the experimental setup is presented and the results are discussed.

MECHANISM OF FLOW-INDUCED TONAL NOISE IN CLOSED SIDE BRANCH SYSTEMS

Pulsations in a pipe system with closed side branches is generated by the instability of the shear layers separating the main flow from the stagnant fluid in the side branch(es). The instabilities are triggered by the acoustic oscillation and result into the formation of discrete vortices. The acoustic oscillation frequencies correspond to acoustic resonances of the system which are close to the resonances predicted without flow.

One general condition for acoustic oscillations to occur is that a resonance frequency of the pipe system should coincide with a frequency range of energy pro-

*Address all correspondence to this author.

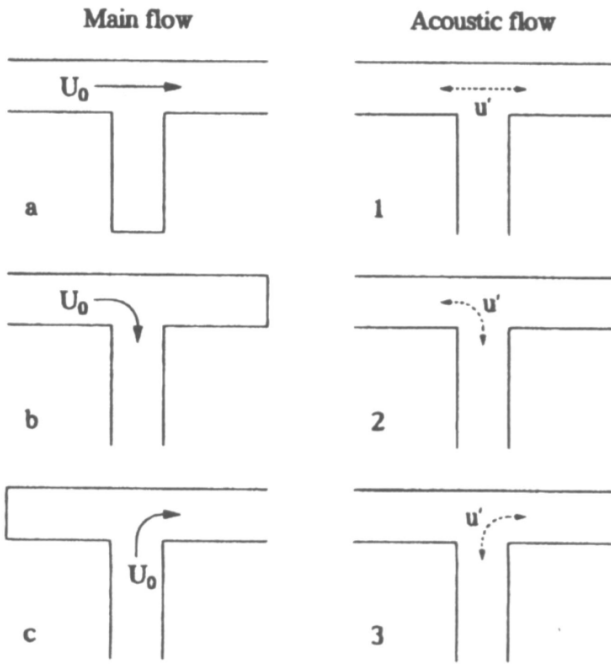


FIGURE 1: Definition of source configurations in Tee-joints, based on the mean flow and the acoustic field [4].

duction of the flow instabilities at the Tees. In this case, distinct tones are observed close to the resonance frequencies of the piping. These pulsations are furthermore observed to collapse around certain optimal Strouhal numbers $Sr = fD_{sb}/U$ based on the diameter D_{sb} of the side branch and on the flow velocity in the main pipe. The Strouhal number of maximum pulsation amplitude depends on the geometry and the flow path. In figure 1, the different combinations of acoustic resonances with main flow direction are given. For resonances in side branches due to a flow on the main pipe (modes a2 and a3), typical values for the Strouhal number are around $Sr = 0.5$. See for example Tonon et al. [3] for a review of flow-induced pulsations in pipe systems.

PSEUDO-THREE DIMENSIONAL MODEL FOR SOURCE STRENGTH AT TEE-JOINTS

In this section, a simple model is presented to evaluate some of the three-dimensional effects involved at the Tee-joints. It is based on summing-up the acoustic source contributions of streamwise strips of the opening of the side branch in the main pipe. For each strip, a two-dimensional approach to the problem is used. In figure 2, the crosswise discretization in twenty strips is illustrated for the standard Tee without insert. The computations are actually done with a discretization in fifty strips.

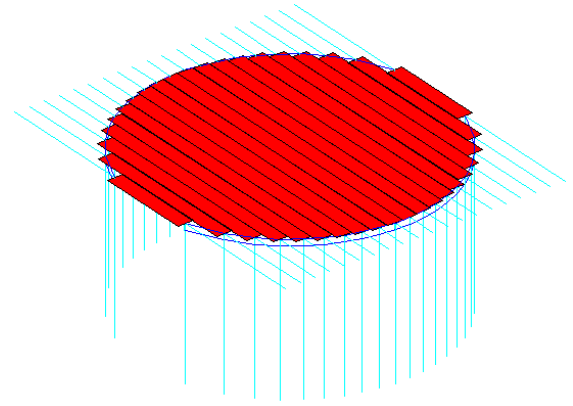


FIGURE 2: Crosswise discretization in 20 strips of the Tee-joint opening. Each red area represents the area of the strip while the light blue line represents the 2D geometry used for the computation of each strip.

For each strip, the time-averaged power of the acoustic source is computed using the formula suggested by Howe [1, 5] for low Mach number flows. This formula enables the computation of the sound power generated by a compact vortex traversing an acoustic field:

$$P = -\rho \int_V \langle (\vec{\omega} \wedge \vec{v}) \cdot \vec{u}_{ac} \rangle d\vec{y}, \quad (1)$$

with $\langle \rangle$ denoting the averaging over one acoustic period, \vec{u}_{ac} the acoustic velocity, $\vec{\omega}$ the vorticity vector and \vec{v} the total velocity.

To evaluate this formula, a crude single-vortex approximation is used. It is assumed that all the vorticity shed at the separation point (the upstream edge) is accumulated in a single vortex shed every acoustic period. The vortex is assumed to follow a straight path p_{vortex} between the upstream and downstream edges of the orifice at a convection velocity equal to half the main-flow velocity. This approximation holds for low to medium acoustic amplitudes, but will fail for very large amplitudes, when the vortex path becomes longer. To compute the acoustic field, with is locally incompressible at low frequencies, the Laplace equation is solved with a conformal mapping technique. The Swartz-Christoffel transformation is used here. It can be analytically solved for simple geometries, or numerically for more complicated configurations. For each geometry, two geometries are considered, corresponding to the a2 and a3 modes (see figure 1).

An example of the potential field in the opening of a standard Tee is given in figure 3. In this figure, the streamlines and potential lines of the acoustic field are plotted, as well as the path of the vortex (red dotted line)

and the acoustic velocity along this path (plain red line).

In figure 4, the power computed with the 2D single-vortex method for an equal-diameter Tee is plotted. Both the a2 and a3 modes are presented. In this figure, the power is nondimensionalized with $\frac{1}{2}\rho U_0^2 q_{ac}$, where the acoustic flux q_{ac} is defined as $\int_{p_{vortex}} u_{ac} dy_1$. In frequency ranges where $P > 0$, sound production by the shear layer is possible. The curves are plotted thicker in these regions in the figure. As expected, the shear layer only absorbs acoustic energy at low frequency, and starts to be a source for larger frequencies. For this purely 2D computation, the first two regions of possible noise production are centered around Strouhal numbers of 0.35 and 0.76.

In figure 5, the power computed with the pseudo 3D method (as the sum of the contribution of all the strips) is plotted. In this figure, the acoustic flux q_{ac} is defined as $\int_{S_{op}} u_{ac} dy_1 dy_2$, with S_{op} the area of the opening. Note important differences between the 2D computation of figure 4 and the pseudo 3D computation of figure 5. The Strouhal number of the production regions increase, while the amplitude of the produced power decreases. Both effects are due to the loss of coherence between the sources due to the different strips. The first effect is usually accounted for, when using a 2D method for 3D circular pipes, by replacing the diameter D by an effective diameter $W_{eff} = \frac{\pi}{4}D$. Using a purely 2D method, it is not possible to account for the reduction of amplitude. For this geometry, the effect is limited, but it becomes larger when opening has large length variations in the stream-wise direction. This is the case for some of the inserts used in the experiments reported in this paper. For example, the pseudo 3D approach has been used to compute the

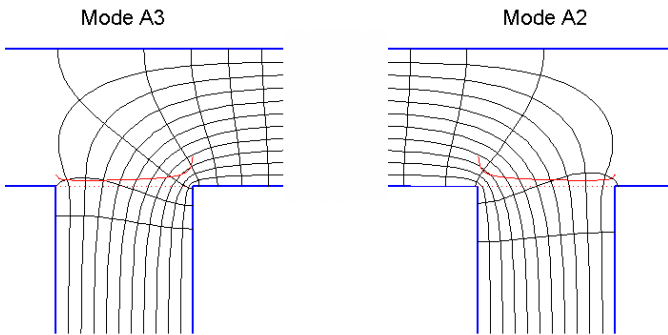


FIGURE 3: Acoustic field computed with potential method at low frequencies for a standard Tee geometry for acoustic modes a2 (right) and a3 (left). The potential field is given in black, the path of the vortex is illustrated with red dots and the acoustic velocity along this path is plotted in red.

acoustic power from the shear layer in a Tee joint with a sawtooth insert, as illustrated in figure 6.

However, it should be kept in mind that this approach does not account for all the three-dimensional effects, both on the acoustic point of view as on the hydrodynamic point of view. Indeed, the acoustic field is computed for each slice in the crosswise direction independently from the other slices. Furthermore, for the sake of simplicity, the diameter of the main pipe is taken identical for all the slices. A more accurate method would require solving the 3D Laplace equation for the locally incompressible acoustic field, which is a simple task. On the hydrodynamic point of view, the assumption that vortices travel at

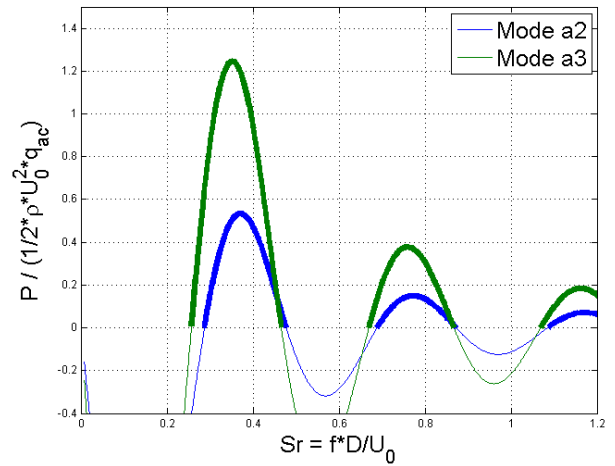


FIGURE 4: Non-dimensional acoustic power computed with the 2D single-vortex method for an equal-diameter Tee.

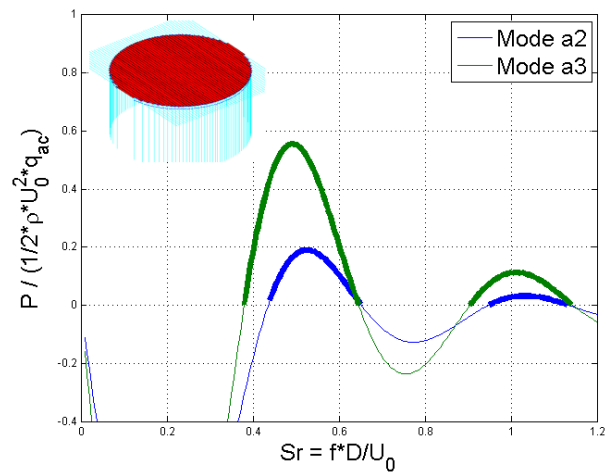


FIGURE 5: Non-dimensional acoustic power computed with the pseudo 3D single-vortex method for an equal-diameter Tee.

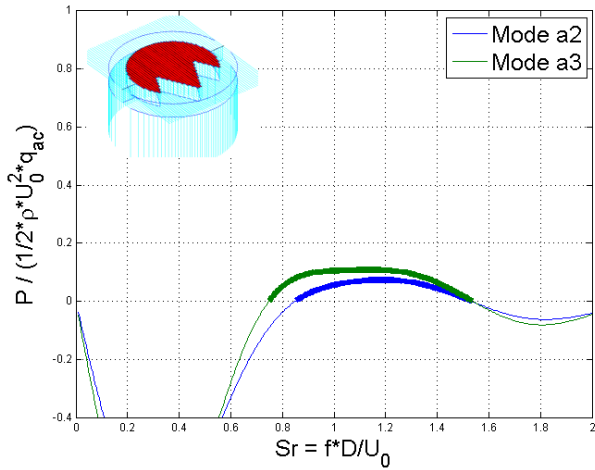


FIGURE 6: Non-dimensional acoustic power computed with the pseudo 3D single-vortex method for Tee with sawtooth insert.

a constant speed along a rectilinear path between the upstream and downstream edge of each slice is very crude, since discontinuities in the upstream edge are expected to destroy the crosswise coherence and to push upwards or downwards parts of the remaining vortex tube. These two effects would typically occur for a sawtooth upstream edge.

EXPERIMENTAL SETUP

A photograph of the experimental setup is given in figure 7. The flow through the main pipe is maintained by a high pressure supply system. The pressure in the pipe is atmospheric and the flow is controlled by a regulation valve. An expansion chamber muffler is located upstream of measuring section to reduce the noise due to the control valve.

Resonator configuration

For the tests, a double-side branch system configuration combining a good acoustic resonator to sources located at optimal location has been chosen. The main pipe has a diameter of 52.5 mm and the side branches have a diameter of 46.9 mm. The two side branches have equal length $L_{sb} = 0.21$ m and are separated on the main pipe at a distance equal to $2L_{sb} = 0.42$ m. The upstream and downstream pipes are also 0.42 m. Both the upstream and downstream pipes are connected via a 2"x3" reducer to a muffler.

Let us consider the acoustic resonator consisting of the two side branches and the main pipe between these

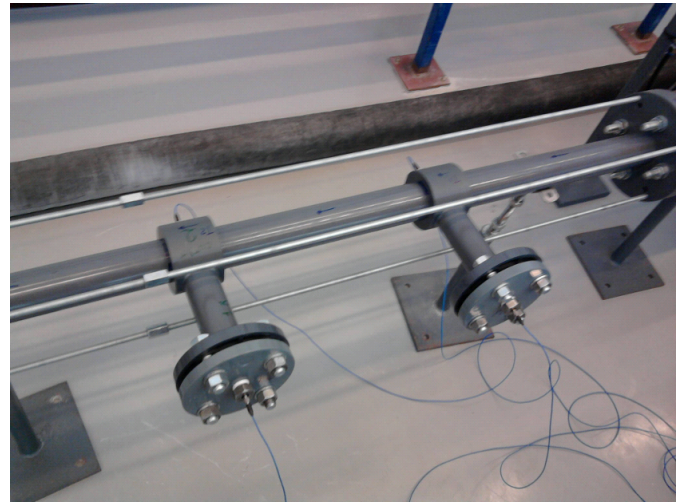


FIGURE 7: Photograph of the double side branch resonator, showing the pressure transducers mounted at the closed end of the side branches.

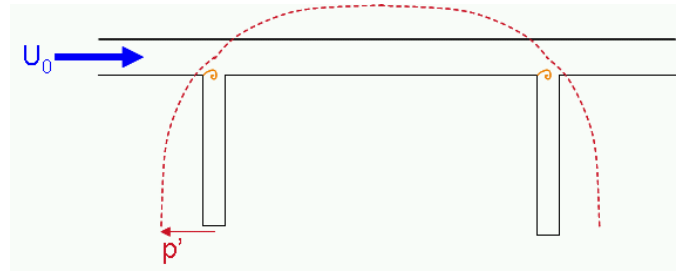


FIGURE 8: Sketch of the experimental setup and pressure standing wave for the second acoustic mode.

two. In this configuration, the pressure nodes for the standing wave at the second acoustic mode (one wave length fitting exactly between the two closed ends of the side branches), are located exactly at the Tee connections on the main pipe. This is illustrated in figure 8. Since these points are also the connection of the resonator to the rest of the system, this mode does not dissipate acoustic energy to the rest of the piping. This is also true for all other $L_{sb} = n\lambda/4$ modes, with n integer larger or equal than 1.

In this configuration, the sources are located at maxima of acoustic velocity, where they couple the most efficiently with the acoustic resonator [3]. Furthermore, the T-joints are rounded at the upstream edges and the downstream edges are sharp. This configuration was chosen to increase the amplitude of the Flow-Induced Pulsations.

This configuration can thus be seen as a worst-case scenario for Flow-Induced Pulsations. This was chosen in order to ensure good quality, reproducible measurements.

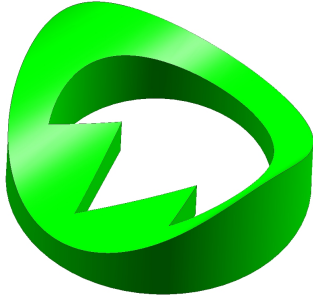


FIGURE 9: Sketch of the tested sawtooth insert.

Instrumentation

The sound in the resonator is measured with pressure transducers located at the closed ends of the side branches. Since pressure maxima are located at the pipe ends, the pressure measured there is also the amplitude of the standing waves at the resonances. The flow rate is measured by means of a mass-flow meter upstream of the control valve. The pressure and temperature of the gas are monitored continuously. The flow velocity is computed with the density ratio between the location of the flow meter upstream of the control valve and the test section.

Inserts

A series of inserts have been tested. The geometry of the inserts range from scaled down scrapper guides to geometries meant to understand the physical phenomena. The inserts were produced with a rapid-prototyping system, allowing for production of complicated geometries at this small scale. In figure 9, a sketch of the sawtooth insert, for which the results are reported in the following, is presented.

EXPERIMENTAL RESULTS AND DISCUSSION

In figure 10, the pressure amplitude measured in the side branches in the basis configuration (no insert) is plotted as function of the Mach number. The pressure is made non-dimensional as $p'/(\rho c U) = u'/U$, with u' the amplitude of the acoustic velocity in the Tee. As expected, tones are observed at close-to discrete frequencies, corresponding to odd multiples of the quarter-wavelength resonance frequency of the side branch. All the tones are also concentrated around two Strouhal numbers ($Sr = 0.46$ and $Sr = 1.1$). The length L used here to compute the Helmholtz number He is the distance from the opening to the end of the side branch: $L = L_{sb} - D_{pipe}/2$.

In figure 11, the same data measured with the sawtooth inserts installed in both Tee connections are plotted.

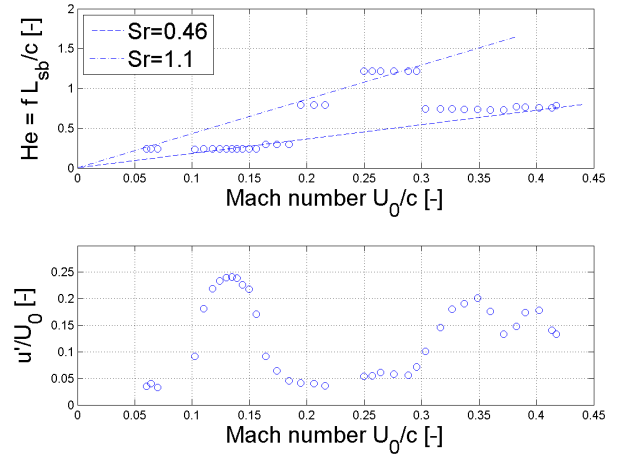


FIGURE 10: Plot of the non-dimensional frequency (above) and pressure (below) measured in the side branches without insert.

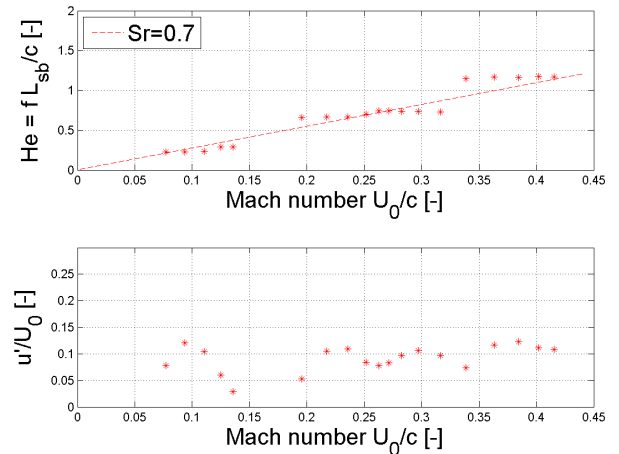


FIGURE 11: Plot of the non-dimensional frequency (above) and pressure (below) measured in the side branches with the sawtooth insert.

It appears that the amplitude of the tones is reduced by a factor 2. Furthermore, the tones only occur in one range of Strouhal numbers. This range is around $Sr = 0.7$, but wider than without insert.

This is more apparent in figure 12, where the non-dimensional amplitude measured both without and with the inserts is plotted versus the Strouhal number.

In table 1, the results of the experiments in terms of Strouhal numbers of the peaks are summarized, and compared to the whistling Strouhal number predicted by the pseudo 3D single vortex approach. For the model, the strength and the Strouhal number of the strongest mode (mode a3) are summarized. The strength cor-

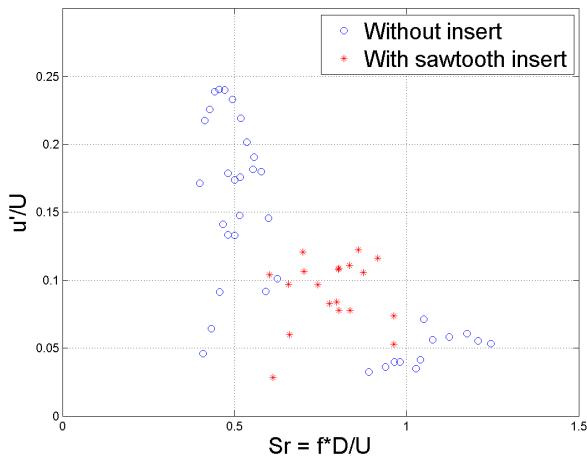


FIGURE 12: Plot of the non-dimensional pressure measured in the side branches without insert (blue circles) and with the sawtooth inserts (red stars) versus the Strouhal number.

responds to the non-dimensional time-averaged acoustic power $P/(1/2 * \rho * U_0^2 * q_{ac})$. For the experiments, the reported amplitude is the non-dimensional amplitude $p'/(\rho c U_0) = u'/U_0$.

The measured amplitude (u'/U_0 between 0.07 and 0.24) correspond to moderate to large pulsation amplitudes [1, 3].

In this amplitude range, the single vortex assumption used in the model is reasonable. However, the assumption that the path of the vortices is not influenced by the acoustic field becomes questionable for $u'/U_0 > 0.1$. The strength of the sources and the amplitude of the pulsations are not directly related in this case, as the amplitude also depends on the losses, which are subject to different mechanism depending on the amplitude range.

Given all the limitations of the model, particularly not including three dimensional deformation of the vortex tubes as expected at these amplitudes, the match between the model and the experimental results is surprisingly good. The model can help predict the effect of the insert on the frequency range of the whistling, and if the insert has a positive or a negative effect on the amplitude. To have a better evaluation of the effect of the inserts on the amplitude, one should also include the modification of the damping due to the inserts.

CONCLUSIONS

In this paper, an experimental investigation of effect of inserts in Tee connections on Flow-Induced Pulsations is presented. The choice of the resonator reproduces a worst-case pulsating gas transport pipe system and enables reproducible measurements. The results show that a sawtooth insert can at best reduce the amplitude of the pulsations, but not completely prevent the pulsations. Furthermore, the pseudo three-dimensional model based on single-vortex formulation of Howe's formula provides a reasonable prediction of the effect of this insert.

REFERENCES

- [1] Bruggeman, J.C. *Flow-Induced Pulsations in Pipe Systems*. PhD thesis, Technical University of Eindhoven, 1987.
- [2] Peters, M.C.A.M. and van Bockhorst, E. *Flow-Induced Pulsations in Pipe Systems with Closed Branches, Impact of Flow Direction*. 7th Flow-Induced Vibration Conference, Lucerne, Switzerland, 2000.
- [3] Tonon, D., Hirschberg, A., Golliard, J. and Ziada, S. *Aeroacoustics of pipe systems with closed side branches*. International Journal of Aeroacoustics, volume 10, number 2&3, 2011.
- [4] Belfroid, S.P.C., Peters, M.C.A.M., Schiferli, W and Buffing, J. *Flow induced pulsations caused by split flow in T-branch connections*. 6th FSI, AE and FIV Symposium, Vancouver, Canada, 2006.
- [5] Howe, M.S. *Contribution to the theory of the aerodynamic sound, with application to excess jet noise and the theory of the flute*. Journal of Fluid Mechanics, volume 71, number 4, 1975

TABLE 1: Comparison of the Whistling behaviour without and with insert, as measured and predicted by the pseudo three dimensional approach.

	Model		Experiments	
Standard Tee without insert	Sr	Strength	Sr	Amplitude
1 st Peak	0.50 [0.38–0.65]	0.56	0.46 [0.40–0.62]	0.24
2 nd Peak	1.01 [0.90–1.13]	0.11	1.1 [0.90–1.2]	0.07
Tee with sawtooth insert	Sr	Strength	Sr	Amplitude
1 st Peak	1.12 [0.75–1.53]	0.11	0.70 [0.60–0.96]	0.12
2 nd Peak	-	-	-	-

ACOUSTIC PROPERTIES OF AN IN-DUCT ORIFICE SUBJECTED TO BIAS FLOW AND HIGH LEVEL ACOUSTIC EXCITATION

Hans Bodén*

Linné Flow Centre
 Marcus Wallenberg Laboratory
 Aeronautical and Vehicle Engineering
 KTH -The Royal Institute of Technology
 MWL,AVE,KTH,Stockholm,SE-10044
 Email: hansbod@kth.se

Lin Zhou

CCGEx-Competence Centre for IC-Engine Gas Exchange
 Marcus Wallenberg Laboratory
 Aeronautical and Vehicle Engineering
 KTH -The Royal Institute of Technology
 MWL,AVE,KTH,Stockholm,SE-10044
 Email: linzhou@kth.se

ABSTRACT

This paper experimentally investigates the acoustic properties of an orifice with bias flow under medium and high sound level excitation. The test included no bias flow and two bias speeds for three different frequencies. Experimental results are compared and discussed with theory. It is shown that bias flow makes the acoustic properties much more complex compared theory and with the no bias flow case, especially when velocity ratio between acoustic particle velocity and mean flow velocity is near unity.

NOMENCLATURE

c Speed of sound
 C_c Discharge coefficient
 d Orifice diameter
 D Diameter of pipe
 J Bessel function
 \bar{l} Variable effective length
 l_w Orifice thickness
 l_0 End correction on one side of orifice
 L Jet length
 M_b Bias flow Mach number
 M_g Grazing flow Mach number
 k Wave number
 K_R Rayleigh conductivity
 U Mean flow velocity in the orifice
 P Sound pressure amplitude
 P_0 Mean flow pressure drop
 dP Sound pressure difference
 ΔP Measured mean flow pressure drop
 R Orifice radius

U Mean flow velocity in the orifice
 V Acoustic particle velocity in the hole
 Z_R Acoustic resistance
 Z_I Acoustic reactance
 Z Acoustic impedance
 $\beta = d/D$
 μ Adiabatic dynamic viscosity
 ν Kinematic viscosity
 ω Radian frequency
 ρ_0 Air density
 σ Porosity
 τ Time for ejection of air flow orifice

Superscripts

$\hat{\quad}$ Denotes a peak value

Subscripts

u On source side of orifice
 d On downside of orifice
 $+$ Mean flow direction
 $-$ Opposite direction of mean flow
 $1,2$ Microphones on source side
 $3,4$ Microphones on the downstream side

INTRODUCTION

Orifice plates and perforates appear in many technical applications where they are exposed to a combination of high acoustic excitation levels and either grazing or bias flow or a combination. Examples are automotive mufflers and aircraft engine liners. Taken one by one the effect of high acoustic excitation levels, bias flow and grazing flow are reasonably well understood. The nonlinear effect of high level acoustic excitation has for instance

*Address all correspondence to this author.

been studied in [1–11]. It is well known from this literature that perforates can become non-linear at fairly low acoustic excitation levels. The non-linear losses are associated with vortex shedding at the outlet side of the orifice or perforate openings [9, 10]. The effect of bias flow has for instance been studied in [12–17]. Losses are significantly increased in the presence of bias flow, since it sweeps away the shed vortices and transforms the kinetic energy into heat, without further interaction with the acoustic field. Grazing flow has also received a lot of attention see for instance [18–24]. The combination of bias flow and high level acoustic excitation has been discussed and studied in [25] and some experimental investigations have been made in [26]. Luong [25] derived a simple Rayleigh conductivity model for cases when bias flow dominates and no flow reversal occurs.

The purpose of the present paper is to make a detailed experimental study of the transition between the case when high level nonlinear acoustic excitation is the factor determining the acoustic properties to the case when bias flow is most important. As discussed in [25] it can from a theoretical perspective be expected that this is related to if high level acoustic excitation causes flow reversal in the orifice or if the bias flow maintains the flow direction. Acoustic properties, such as impedance, Rayleigh conductivity and absorption coefficient are discussed.

Semi-empirical impedance model

Starting for instance from [4] a number of semi-empirical models have been developed to include the effect of high level acoustic excitation, grazing flow and bias flow have been suggested. One example is the model presented in [8] where the normalised impedance of a perforate is expressed as

$$Z_R = \text{Re}\left(\frac{ik}{\sigma C_c} \left[\frac{l_w}{F(\mu')} + \frac{\delta_{re}}{F(\mu)} f_{int} \right] \right) + \frac{1}{\sigma} \left[1 - \frac{2J_1(kd)}{kd} \right] + \left(\frac{1 - \sigma^2}{\sigma^2 C_c^2} \right) \frac{1}{2c} \hat{V} + \frac{0.5}{\sigma} M_g + \frac{1.15}{\sigma C_c} M_b \quad (1)$$

$$Z_I = \text{Im}\left(\frac{ik}{\sigma C_c} \left[\frac{l_w}{F(\mu')} + \frac{0.5d}{F(\mu)} f_{int} \right] \right) - \left(\frac{1 - \sigma^2}{\sigma^2 C_c^2} \right) \frac{1}{2c} \hat{V} - \frac{0.3}{\sigma} M_g \quad (2)$$

where Z_R is the normalized resistance and Z_I is the normalized reactance, k is the wave number, σ is the porosity (percentage open area), C_c is the discharge coefficient,

l_w is the plate thickness, μ is the adiabatic dynamic viscosity, $\mu' = 2.179\mu$ is the dynamic viscosity close to a conducting wall, $\nu = \mu/\rho_0$ is the kinematic viscosity, J is the Bessel function, d is the hole diameter, c is the speed of sound, M_g is the mean flow Mach number grazing to the liner surface, M_b is the bias flow Mach number inside the holes of the perforate and \hat{V} is the peak value of the acoustic particle velocity in the hole. The rest of the parameters are defined as

$$K = \sqrt{-\frac{i\omega}{\nu}} \quad (3)$$

$$F(\mu) = 1 - \frac{4J_1(Kd/2)}{Kd \cdot J_0(Kd/2)} \quad (4)$$

$$\delta_{re} = 0.2d + 200d^2 + 16000d^3 \quad (5)$$

$$f_{int} = 1 - 1.47\sqrt{\sigma} + 0.47\sqrt{\sigma^3} \quad (6)$$

Using Eqn. (1) and Eqn. (2) the magnitude of the terms related to high level nonlinear effects and bias flow, as well as grazing flow, can be compared. It should be noted that these terms are based on studies of the effect of nonlinearity and flow separately and not simultaneously.

The Cummings Equation

Consider orifice with bias flow, one of the most important models to study the acoustic properties is Cummings [6] empirical equation. It is based on Bernoulli equation for unsteady flow, which in [25] is written as

$$\bar{l}(t) \frac{dV}{dt} + \frac{1}{2C_c^2} (U+V)|U+V| = \frac{P_0 + d\hat{P}e^{i\omega t}}{\rho_0} \quad (7)$$

where P_0 is the steady pressure drop; $d\hat{P}e^{i\omega t}$ is the sound pressure difference over the orifice; $\bar{l}(t)$ is variable effective length of the fluid plug in the hole; V is oscillating velocity averaged over the plane of the orifice; U is the mean bias flow velocity in the orifice. For irrotational flow, the length $\bar{l}(t)$ is $2l_0 + l_w$, where $l_0 \approx (\pi/8)d$ is the end-correction on one side of the orifice plane. When a jet is formed, it according to Cummings [6] becomes a function of the effective length L :

$$L(\tau) = \int_0^\tau |U+V| dt \quad (8)$$

where the time τ is measured from the previous flow “changeover” during the sign of $U + V(t)$ is constant. The empirical coefficient $\varepsilon = \bar{l}(t)/L_0$, where $L_0 = 0.425d + l_w$ in [6] is the maximum possible lost end correction, were expressed as

$$\varepsilon = 1 - [1 + (L/d)^{1.585}/3]^{-1} \quad (9)$$

This function is a little different in [25] when considering cases with bias flow. In the paper the effective length is divided into two parts: where the end correction on the inflow side remains constant as l_0 but on the outflow side decreases according to the jet length, as follows

$$\bar{l}(t) = l_0 + \frac{l_0 + l_w}{1 + (L/d)^{1.585}/3} \quad (10)$$

Thus, in the cases of $U \gg \hat{V}$, Cummings equation can be expressed as

$$\bar{l}(t) \frac{dV}{dt} + \frac{V}{C_c^2} \left(U + \frac{V}{2} \right) = \frac{d\hat{P}e^{i\omega t}}{\rho_0} \quad (11)$$

here $\bar{l}(t) \rightarrow l_0$ for the jet length is large enough. At high frequency ($\omega R/U > 1$), $\bar{l}(t)$ revert to the value $2l_0 + l_w$, for unsteady volume flux through the aperture causes pulsations in the jet cross-sectional area in or just downstream of the aperture. Using an effective hole thickness (l) which can vary between l_0 and $2l_0 + l_w$ we get a normalized impedance

$$Z = \frac{d\hat{P}}{\rho_0 c \hat{V}} = ikl + \frac{U}{cC_c^2} + \frac{\hat{V}}{2cC_c^2} \quad (12)$$

This gives a Rayleigh conductivity

$$K_R = \frac{ik\pi R^2}{Z} = \frac{\pi R^2}{l} \frac{\omega l/U}{(\omega l/U) + \frac{i}{C_c^2} \left(1 + \frac{\hat{V}}{2U} \right)} \quad (13)$$

If this is linearized a Rayleigh conductivity model was in [25] developed as

$$K = \frac{K_0(\omega l/U)}{(\omega l/U) + i/C_c^2} \quad (14)$$

where $K_0 = \pi R^2/l$, $l = 2l_0 + l_w$

EXPERIMENTAL SETUP

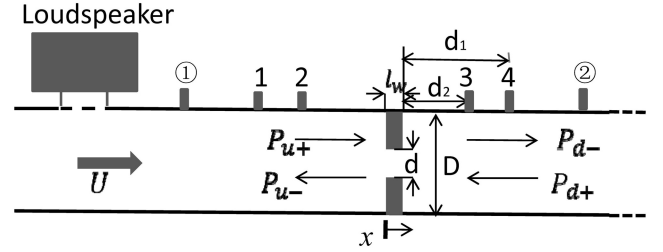


FIGURE 1: Experimental configuration

The experimental configuration is illustrated in Fig. (1). The test object was an orifice plate with 3 mm thickness and 6 mm hole diameter. The orifice plate was mounted in a rigid tube with a diameter of 40 mm. On the left hand side, a high quality loudspeaker was mounted as the excitation source. Pure tone excitation was used and it was checked make sure that nonlinear harmonics generated at the loudspeaker were sufficiently small. Two microphones (1-4) were mounted on each side of the sample so that we could use two-microphone wave decomposition to identify the sound wave components on each side.

In order to get the mean flow velocity passing through the orifice, two steady pressure sensors (1, 2) were mounted to measure the steady pressure drop ΔP . The calculation is according to ISO5167-1:2003 [27], as follows

$$U = C_c \sqrt{\frac{2\Delta P}{\rho_0(1 - \beta^4)}} \quad (15)$$

where $\beta = d/D$. According to [27] the discharge coefficient C_c should be a function of β , Reynolds number and etc.. Here we suppose it is 0.75 recommended by Cummings [6]. In the study we consider two mean flow cases: one is with $\Delta P = 14\text{Pa}$ and the mean flow velocity in the orifice is 3.65 m/s; the other is $\Delta P = 40\text{Pa}$ and the mean flow velocity is 6.17 m/s.

Under the plane wave assumption, sound wave components on both sides the orifice can be expressed as

$$\begin{bmatrix} P_{u+} \\ P_{u-} \end{bmatrix} = \begin{bmatrix} e^{ik_+d_1} & e^{-ik_-d_1} \\ e^{ik_+d_2} & e^{-ik_-d_2} \end{bmatrix}^{-1} \begin{bmatrix} P_1 \\ P_2 \end{bmatrix} \quad (16)$$

$$\begin{bmatrix} P_{d+} \\ P_{d-} \end{bmatrix} = \begin{bmatrix} e^{ik_-d_2} & e^{-ik_+d_2} \\ e^{ik_-d_1} & e^{-ik_+d_1} \end{bmatrix}^{-1} \begin{bmatrix} P_3 \\ P_4 \end{bmatrix} \quad (17)$$

where $k = \omega/c$, $M = U/c$, $k_+ = k/(1+M)$, $k_- = k/(1-M)$. With acoustic waves amplitudes P_{u+} , P_{u-} , P_{d+} , P_{d-} , the oscillating velocity in the orifice \hat{V} and acoustic properties, such as normalized impedance Z , Rayleigh conductivity K_R can be given as

$$\hat{V} = \frac{P_{u+} - P_{u-}}{\rho_0 c \sigma} \quad (18)$$

$$Z = \frac{P_{u+} + P_{u-} - P_{d+} - P_{d-}}{\rho_0 c \hat{V}} \quad (19)$$

$$K_R = 2R \cdot \frac{ik \cdot \pi R/2}{Z} \quad (20)$$

RESULTS AND DISCUSSION

Effects of in incident pressure level

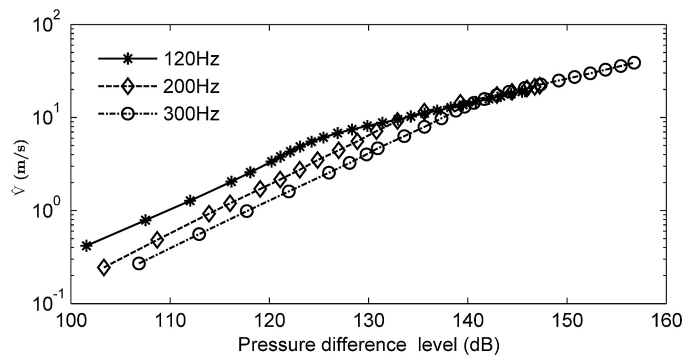


FIGURE 2: Acoustic particle velocity in the orifice as a function of pressure difference level without bias flow

Fig. (2) shows the acoustic particle velocity for different levels of pressure difference over the orifice. The

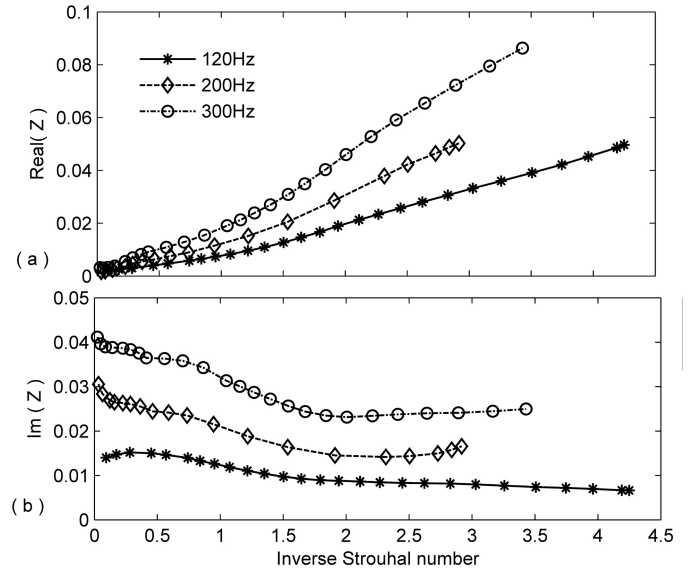


FIGURE 3: Normalized impedance in the orifice as a function of inverse Strouhal number $\hat{V}/\omega d$

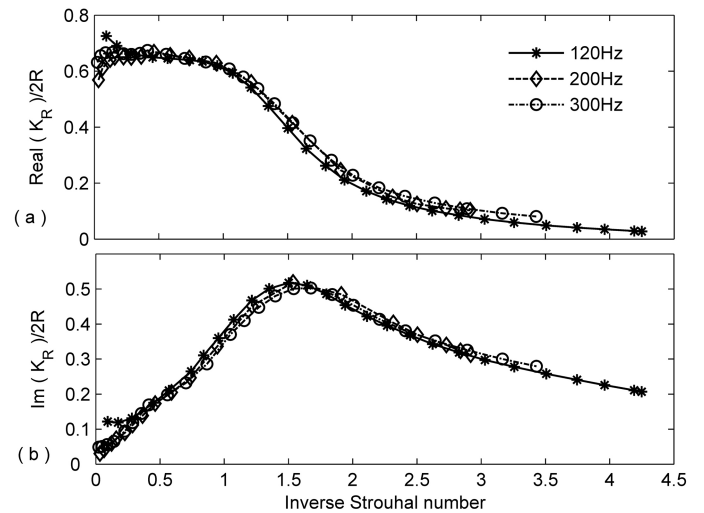


FIGURE 4: Rayleigh conductivity in the orifice as a function of inverse Strouhal number $\hat{V}/\omega d$

nonlinear behavior at higher levels of excitation can be clearly seen. The corresponding normalized impedance is shown in Fig. (3), and we can see the non-linearity at fairly low acoustic excitation levels. Instead plotting the Rayleigh conductivity makes the curves for different frequencies collapse, as can be seen in Fig. (4). The real part approaches the value $K_0/2R = 0.61$ at low levels. The real part decrease when the inverse Strouhal number is near 1 and goes to a very low value at high inverse Strouhal numbers; while the imaginary part first increases and reaches a maximum at an inverse Strouhal number around 1.5.

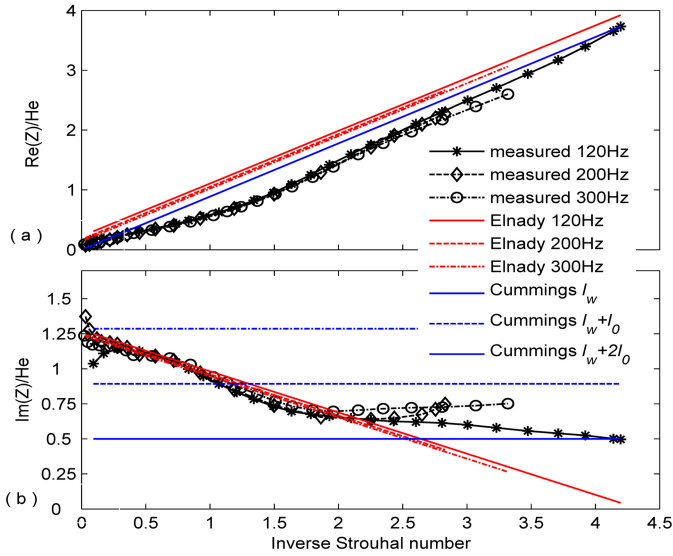


FIGURE 5: Normalised hole impedance divided by the Helmholtz number plotted against inverse Strouhal number $\hat{V}/\omega d$

It can be seen from Fig. (5) that dividing the normalized impedance by the Helmholtz number makes the curves for different frequencies collapse which is consistent with the result for the Rayleigh conductivity. There is also a fairly good agreement between experimental resistance and the results from both the Elnady and Cummings models. These two models for the resistance only differs on two points: The Cummings model does not include any linear resistance term and the slope of the non-linear term is reduced by a factor $1 - \sigma^2$ in the Elnady model compared to the Cummings model. The slope can in both models be changed by choosing another value for the discharge coefficient. Here the discharge coefficient has been set to 0.75 for both models. For the reactance term there is a reasonable agreement between experimental results and the Elnady model at lower inverse Strouhal numbers. Higher up the model does not catch the fact that the reactance does not continue to decrease with the increase in particle velocity. The Cummings model, as it is presented in Eqn. (12) does not include any nonlinear effect on the reactance term. In the article by Cummings [6] it is however discussed that the reactance may vary with time and with the effective jet length caused by the high level acoustic excitation. The effective thickness would at low acoustic levels take the value $l = l_w + 2l_0$ and would then decrease at higher acoustic excitation levels. It can be seen that this agrees fairly well with the results in Fig. (5), the experimental reactance results start close to the curve for effective thickness $l = l_w + 2l_0$ and approaches the curve for effective thickness $l = l_w$ at high acoustic excitation levels.

Effects of bias flow velocity

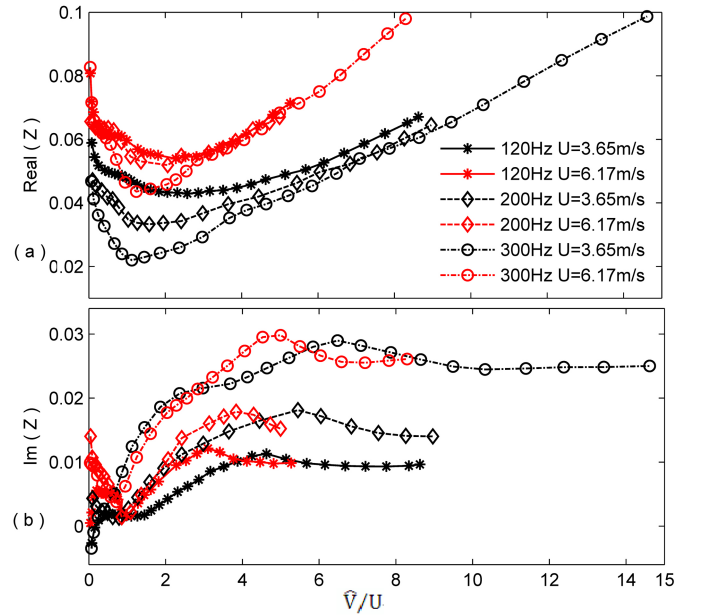


FIGURE 6: Measured normalized impedance in the orifice as a function of ratio between a acoustic particle velocity and mean flow velocity

When there is a flow through the orifice the acoustic properties become more complex. Fig. (6) shows the normalized impedance as a function of the ratio of oscillating velocity to flow velocity. We divide the results into three parts according to the value of the velocity ratio: much less than unity (I), near unity (II) and much larger than unity (III). The resistance reduces as the velocity ratio increases in region I, has a minimum in region II and then increases in region II where the acoustic particle velocity dominates the behavior. The reactance has a more complex behavior and can either initially increase or decrease with increasing velocity ratio in region I. It then has a minimum in region II and the increases in region III to finally approach a constant value at high velocity ratios.

Fig. (7) compares the measured result with Elnady and Cummings models calculated by Eqn. (12). Neither resistance nor reactance is consistent with experimental data, especially near the ratio of unity. It seems the mechanism is much more complex and further works should focus on the interaction of frequency, acoustic particle velocities and mean flow velocity.

In the conclusions of [25] it was mentioned that the Rayleigh conductivity for the case without flow reversal ($\hat{V} \ll U$) should approach the result in Eqn. (14). In order to check this experimental results for the Rayleigh

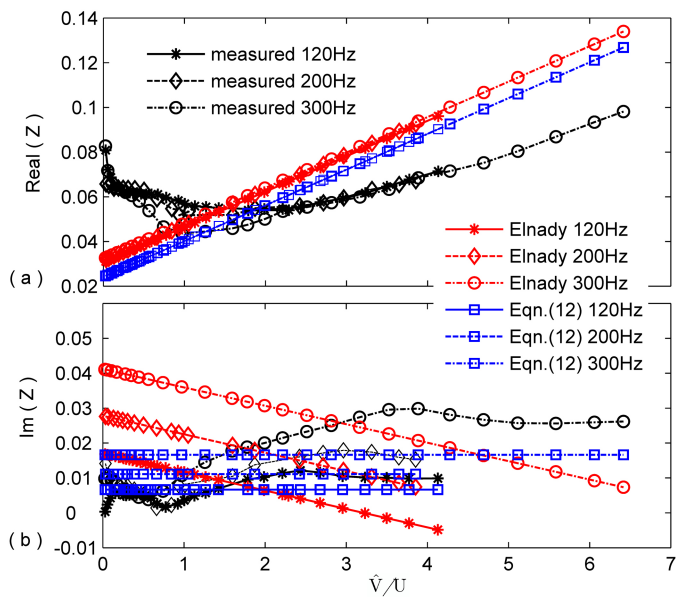


FIGURE 7: Normalized impedance in the orifice as a function of ratio between a acoustic particle velocity and mean flow velocity ($U=6.17$ m/s)

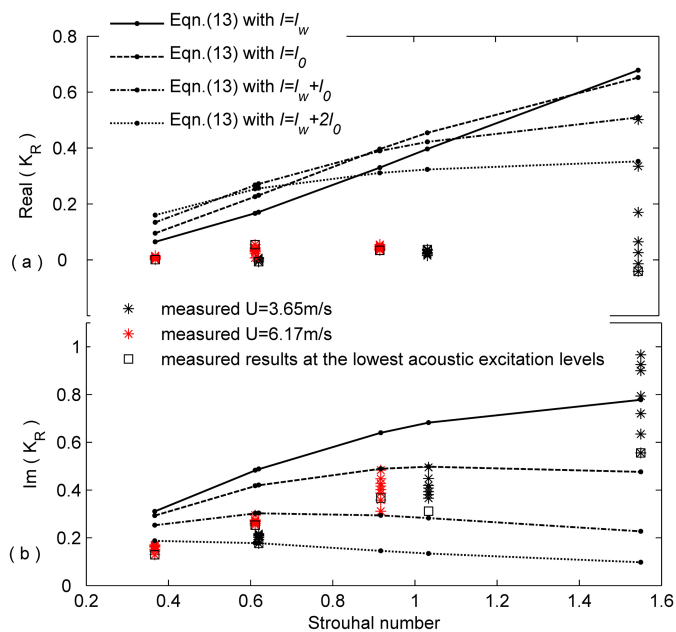


FIGURE 8: Rayleigh conductivity plotted against flow Strouhal number $\omega R/U$

conductivity has been compared to the model results. Fig. (8) shows the Rayleigh conductivity plotted against flow Strouhal number ($\omega R/U$). This means that at each Strouhal number there are a number of experimental data points representing different acoustic particle velocity levels. It can be seen that the Rayleigh conductivity

does not exhibit a linear behavior since the results vary with acoustic excitation level at each flow Strouhal number point. The agreement with the model result is also not very good. It can be seen that by varying the effective hole thickness results of the right order of magnitude can be obtained but it seems that the Rayleigh conductivity has a more complicated dependence on both mean flow velocity and acoustic excitation level than indicated by Eqn. (14).

CONCLUSIONS

An experimentally study of the acoustic properties for an orifice plate under high acoustic excitation levels and bias flow conditions has been made. Comparisons have been made with a semi-empiric impedance model [7, 8] and the Cummings model as described in [25]. It was seen that without bias flow there is a reasonably good agreement between model results and measurements for the resistance. For the reactance the model according to [7, 8] catches the initial decrease with increasing excitation level but not the subsequent behavior at high excitation levels. The Cummings [6] model as described in [25] discusses the possibility of an end correction which varies with both bias flow and high level acoustic excitation. It can be seen that the measured reactance is within the range predicted by the suggested variations in end corrections. For the case with bias flow three regions were identified in terms of the ratio between acoustic particle velocity and mean flow velocity being: (I) smaller than unity, (II) around unity and (III) larger than unity. For region I there was a decrease in resistance and a variation in reactance with velocity ratio. In region II both parts of the impedance had a minimum. In region III resistance increases while the reactance first has an increase and the approaches a constant value. Compared with experimental data, it seems neither the Elnady nor the Cummings model gives a good prediction result since the nonlinear acoustic mechanism with bias flow is much more complex than that without. In [25] it was predicted that the Rayleigh conductivity would go to the linearized value according to Eqn. (14) for cases when the acoustic particle velocity is smaller than the mean flow velocity in the orifice so that no flow reversal occurs. Comparisons with experimental results shows that this is not the case there is still a nonlinear variation in Rayleigh conductivity even when the velocity ratio is small.

REFERENCES

[1] Sivian, L. J., 1935. "Acoustic impedance of small orifices". *Journal of the Acoustical Society of Amer-*

- ica, **7**, pp. 94–101.
- [2] Ingrd, U., and Labate, S., 1950. “Acoustic circulation effects and the nonlinear impedance of orifices”. *Journal of the Acoustical Society of America*, **22**, pp. 211–219.
- [3] Ingrd, U., and Ising, H., 1967. “Acoustic nonlinearity of an orifice”. *Journal of the Acoustical Society of America*, **42**, pp. 6–17.
- [4] Melling, T., 1973. “The acoustic impedance of perforates at medium and high sound pressure levels”. *Journal of Sound and Vibration*, **29**(1), pp. 1 – 65.
- [5] Zinn, B., 1970. “A theoretical study of non-linear damping by helmholtz resonators”. *Journal of Sound and Vibration*, **13**(3), pp. 347 – 356.
- [6] Cummings, A., 1986. “Transient and multiple frequency sound transmission through perforated plates at high amplitude”. *Journal of the Acoustical Society of America*, **79**, pp. 942–951.
- [7] Elnady, T., and Boden, H., 2003. “On semi-empirical liner impedance modeling with grazing flow”. *AIAA*, pp. 1–11.
- [8] Elnady, T., 2004. “Modelling and characterization of perforates in lined ducts and mufflers”. PhD Thesis, Department of Aeronautical and Vehicle Engineering, KTH, Stockholm, Sweden.
- [9] Ingrd, U., 1970. “Nonlinear distortion of sound transmitted through an orifice”. *The Journal of the Acoustical Society of America*, **48**(1A), pp. 32–33.
- [10] TAM, C., and KURBATSKII, K., 2000. “Microfluid dynamics and acoustics of resonant liners”. *AIAA Journal*, **38**, pp. 1331–1339.
- [11] C.K.W. TAM, K.A. KURBATSKII, K. A., and JR, R. G., 2001. “A numerical and experimental investigation of the dissipation mechanisms of resonant acoustic liners”. *Journal of Sound and Vibration*, **245**(3), pp. 545 – 557.
- [12] D. Bechert, U. M., and Pfizenmarier, E., 1977. “Experiments on the transmission of sound through jets”. In American Institute of Aeronautics and Astronautics, Aeroacoustics Conference, 4th, Atlanta.
- [13] Howe, M., 1979. “On the theory of unsteady high reynolds number flow through a circular aperture”. *Royal Society of London Proceedings A*, **366**, pp. 205–233.
- [14] Howe, M., 1980. “The dissipation of sound at an edge”. *Journal of Sound and Vibration*, **70**, pp. 407–411.
- [15] Howe, M., 1998. *Acoustics of Fluid-structure interactions*. Cambridge University Press.
- [16] Hughes, I. J., and Dowling, A. P., 1990. “The absorption of sound by perforated linings”. *Journal of Fluid Mechanics*, **218**, pp. 299–335.
- [17] Eldredge, J. D., and Dowling, A., 2003. “The absorption of axial acoustic waves by a perforated liner with bias flow”. *Journal of Fluid Mechanics*, **485**, pp. 307–335.
- [18] Ronneberger, D., 1972. “The acoustical impedance of holes in the wall of flow ducts”. *Journal of Sound and Vibration*, **24**, pp. 133–150.
- [19] Ronneberger, D., 1980. “The dynamics of shearing flow over a cavity a visual study related to the acoustic impedance of small orifices”. *Journal of Sound and Vibration*, **71**, pp. 565–581.
- [20] Walker, B., and Charwat, A., 1982. “Correlation of the effects of grazing flow on the impedance of helmholtz resonators”. *Journal of the Acoustical Society of America*, **72**, pp. 550–555.
- [21] Nelson, N. H., and Doak, P., 1981. “Fluid dynamics of a flow excited resonance, part i: Experiment”. *Journal of Sound and Vibration*, **78**, pp. 15–38.
- [22] Nelson, N. H., and Doak, P., 1983. “Fluid dynamics of a flow excited resonance, part ii: Flow acoustic interaction”. *Journal of Sound and Vibration*, **91**, pp. 375–402.
- [23] Worraker, W., and Halliwell, N., 1985. “Jet engine liner impedance: An experimental investigation of cavity neck flow/acoustics in the presence of a mach 0.5 tangential shear flow”. *Journal of Sound and Vibration*, **103**, pp. 573–592.
- [24] Goldman, A., and Panton, R., 1976. “Measurement of the acoustic impedance of an orifice under a turbulent boundary layer”. *Journal of the Acoustical Society of America*, **60**, pp. 1397–1404.
- [25] T. Luong, M. H., and McGowan, R., 2005. “On the rayleigh conductivity of a bias-flow aperture”. *Journal of Fluids and Structures*, **21**(8), pp. 769 – 778.
- [26] J. Rupp, J. C., and Spencer, A., 2010. “Interaction between the acoustic pressure fluctuations and the unsteady flow field through circular holes”. *Journal of Engineering for Gas Turbines and Power*, **132**(6), p. 061501.
- [27] Iso5167-1:2003 measurement of fluid flow by means of pressure differential devices inserted in circular cross-section conduits running full.



FLOW-INDUCED VIBRATION TESTS OF A NUCLEAR-REACTOR DE-MOUNTABLE FUEL BUNDLE

V.P. Janzen, B.A.W. Smith, Y. Han, T. Whan, D.F. Sears and M.R. Floyd

Atomic Energy of Canada Ltd.
Chalk River Laboratories,
Chalk River, ON, Canada K0J 1J0
Email: janzenv@aecl.ca

ABSTRACT

A series of out-reactor flow tests has been carried out with a prototypical 42-element De-Mountable-Element (DME) CANDU[®]-type fuel bundle in the Chalk River VIBFLO loop, in order to assess the vibration and pressure-drop characteristics of the new bundle in flow and compare them to those of a standard 36-element DME bundle. Vibration amplitudes and frequencies of selected fuel elements at various flow rates were measured by displacement probes mounted on an acrylic flow tube surrounding the fuel bundle and with accelerometers mounted on the test bundle itself. Measured root-mean-square (RMS) displacement values were typically of the order of 5 μm , comparable to those from previous tests with stand-alone fuel elements. Somewhat higher vibration levels – and more defined response peaks – were observed for one of the fuel elements; this difference was related to larger than-expected clearances between the element and its mount(s). Based on a comparison between results from the reference 36-element and prototypical 42-element DME fuel bundles in the test rig, the vibration levels and pressure drop associated with the prototypical DME bundle were acceptable, and from that point of view, the bundle was judged to be suitable for irradiation testing in the NRU reactor loops.

NOMENCLATURE

CANDU	CANada Deuterium Uranium
DME	De-Mountable Element
FIV	Flow-Induced Vibration
NRU	National Research Universal
PWR	Pressurized Water Reactor
RMS	Root Mean Square
VIBFLO	VIBration in FLOW

INTRODUCTION

CANDU[®] pressurized heavy water reactors use cylindrical fuel bundles, approximately 500 mm long and 100 mm in diameter that contain individual fuel elements

held together by two circular endplates. Primary coolant is pumped through the fuel channels that contain the bundles, at a typical rate of 23 kg/s per channel. The fuel bundles are subject to hydrodynamic forces due to turbulence, and hydro acoustic disturbances (such as pressure pulsations from primary coolant pumps). These can lead to stress on bundle components, and to vibration of the bundles and fuel elements [1-3]. If sufficiently large, these forces lead to unreasonably high levels of stress, vibration and wear damage to the fuel and/or fuel channel [4-6].

The possibility of excessive fluid excitation forces is a particular concern for “demountable element” (DME) fuel bundles used for irradiation tests of advanced fuels in the NRU reactor. These bundles closely resemble those used in CANDU power reactors, but are designed to have interlocking components that allow the bundles to be disassembled underwater (or in hot cells) so that individual fuel elements can be examined and reused. The concern is that, at high flow rates, flow-induced vibration (FIV) could cause interlocking components to move against each other and to wear, particularly during long residence times.

Figure 1 shows the bottom end-plate of a partially assembled DME bundle, with the central tie rod and several fuel elements attached. The elements are arranged in three concentric rings. Each element has a vertically oriented “spigot” that fits into a circular hole in the end-plate assembly. At the other end of the fuel bundle (not shown), each element has a “nailhead” that mates with a slot in the top end-plate. During assembly, a retaining ring is placed over and around the perimeter of the end-plate to clamp the elements in place.

In terms of the potential for fretting-wear, experience with previous DME-type bundles has shown that the critical locations are the top and bottom ends of the de-mountable elements, where they come into contact with the endplates. Of the two ends, the spigot end is considered to be the more susceptible to wear because there is a clearance fit between the pin and circular hole into which it fits, with no screw-on retaining ring to hold it tight as is the case at the nailhead end.

Under operational conditions, CANDU fuel elements (and the bundle assemblies) can be characterized as

CANDU[®] (CANada Deuterium Uranium) is a registered trademark of Atomic Energy of Canada Ltd. (AECL).

slender cylindrical structures in axial flow. Much work has gone into analyzing the associated flow-induced dynamics, [1,7,8] and applying that knowledge to model FIV characteristics of nuclear fuel, e.g., [9]. Nevertheless, previous efforts to solve FIV-related problems with nuclear fuel in CANDU [3] and pressurized-water reactor (PWR) [10] power plants underscored the need for hydraulic tests, to assess the design of fuel and fuel-channel components before they are placed into operation. Therefore, before performing irradiation tests of a prototypical 42-element DME bundle in AECL's NRU reactor, it was decided to perform out-reactor hydraulic tests at low pressure and temperature. The purpose of the tests was to assess the vibration response and pressure-drop characteristics of the prototypical bundle, and compare them with those of a reference 36-element DME bundle and with vibration levels measured in previous tests.

DESCRIPTION OF TESTS

The tests were carried out in a vertical single-channel test section of the Chalk River Laboratories VIBFLO hydraulic loop, designed to accommodate a fuel carriage approximately 2 m in length loaded with three standard-length fuel bundles, plus a 5 m head of water above the fuel string. Figure 2 shows a diagram of the test section enclosing the fuel string. The vertical flow tube consisted of an acrylic tube with a smooth inner surface of diameter $4.100 \pm 0.015''$ (104.1 ± 0.4 mm; representative of a pressure tube in the NRU-reactor test loops (and a CANDU-reactor pressure tube). Pressure taps were located at six locations along the fuel string, as shown in Figure 2, and just upstream and downstream of the fuel string.

The string comprised three standard length fuel bundles placed vertically end-to-end, loaded in the same type of fuel carriage used during irradiation tests in the NRU reactor test loops. The carriage consisted of upper and lower flux suppressors and a central axial rod running through the bundles connecting the two flux suppressors.

To hold the fuel string rigidly together, an axial force was applied using a spring mechanism to obtain a specified spring force of 1400 lb (6227 N). The bottom end of the fuel string was supported by bolting the bottom flux suppressor axially to a supporting flange at the base of the test section. The other end of the fuel string was left unattached and free to centre itself in flow, as is the case in NRU reactor tests.

The DME test bundle included 42 elements loaded with Pb/Sn pellets, fabricated to replicate the dimensions and density of standard natural uranium dioxide pellets. Because the structural damping – and, therefore, vibration amplitude – of fuel elements depends strongly on the internal motion of the fuel pellets, special consideration was given to selecting a realistic fit of the pellets within the sheath. To simulate reactor conditions, a pellet size was selected which gave a “light snug” fit within the sheath, such that the pellets did not slide through the

sheath under their own weight but did if a light pressure was applied. This type of fit was intended to minimize damping and avoid increasing bending stiffness.

One of the inner-ring elements was replaced by an instrumented element in which three miniature accelerometers were installed. The remaining space inside the element was filled with Pb/Sn pellets, as described above.

The reference 36-element DME bundle included 32 slightly-enriched-uranium fuel elements, and four demountable elements containing a combination of natural uranium/dysprosium and Pb/Sn pellets.

The first and last bundles in the string were identical standard 36-element fuel bundles of the type used in NRU tests but having “dummy” elements filled with steel.

Hydraulic conditions were monitored by the standard VIBFLO loop vortex flowmeter and temperature sensor. The flow rate and temperature were set and then automatically maintained by a programmable logic controller process control system. These pressures and the flow rate were logged continuously in a computer database.

For all flow tests, the radial motions of selected outer-ring fuel elements in the test bundle were measured by five displacement probes mounted in the flow tube. The locations of these probes are shown in Figure 2. Three of them were aimed towards an outer-ring fuel element, at the bottom, middle, and top of the element. The other two were aimed at the endplates just above and below the fuel element. To assess the vibration of an inner ring element, three miniature accelerometers were installed inside an element oriented in such a way as to measure radial and circumferential accelerations at the bottom of the element and axial acceleration at the middle. Horizontal motion of the test rig was monitored with two accelerometers attached to the outside of the flow tube.

Vibration and pressure data were acquired with a 16-channel data-acquisition system built around National Instruments PC boards and customized LabVIEW™ software, using standard techniques.

Test Conditions

For the purposes of these measurements, it was unnecessary to match pressure and temperature between reactor and test rig. In terms of fuel-element vibration, it is more important to match (to a reasonable extent) the dynamic flow conditions. To that end, 100% flow in the test rig was defined as the mass flow rate at a temperature of 30°C, which gave the same dynamic pressure, $\frac{1}{2} \rho V_i^2$ as an NRU flow rate of 20.0 kg/s at 270°C and a static pressure of 10 MPa. This results in an equivalent 100% flow rate of 22.7 kg/s in the test rig. Measurements were taken at selected flow rates from zero to 27.3 kg/s (zero to 120%) flow.

The tests were carried out in two parts: one set of tests with a 36-element DME reference bundle and the second set with the 42-element DME bundle. Note that the

azimuthal orientations of the fuel bundles relative to each other are expected to have an effect on bundle vibration and pressure drop. Therefore, information was obtained with the fuel-string components both aligned and misaligned. Within each set of tests, the fuel string components were initially misaligned, since this was considered to be more likely to produce higher turbulence – and thus higher vibration levels – than an aligned fuel string.

Vibration levels for three or four different outer ring elements were recorded and monitored on-line, over a range of flow rates, and a worst case was selected. The fuel string was then dismantled, re-assembled in the aligned configuration, and measurements were taken of the “worst-case” element from 0 to 120% flow. In total, the in-flow measurements involved 39 different combinations of bundle type, alignment, element, and flow rate.

A series of modal vibration tests was also carried out partway through the tests, to help interpret the vibration spectra and to check instrument calibrations.

The DME fuel bundle was inspected for obvious marks and general surface appearance before and after the tests. Although these tests could not quantifiably measure wear rates, particular attention was paid to locations where contact might be expected, namely, the points where the fuel elements mate with the endplates, and individual fuel element spacer pads, which are typically in contact with pads from neighbouring elements. In addition, clearances between interfacing spacer pads were measured.

Data Analysis

For each test condition, 65.5 seconds of data were filtered to avoid aliasing and digitally sampled at a rate of 4000 Hz with a customized LabVIEW computer program. Vibration of the ends of the fuel elements relative to the bundle endplates was obtained by calculating the difference between signals from adjacent displacement probes in the time domain.

The resulting time-history files were Fourier transformed into frequency spectra over the frequency range 0-to-2000 Hz. Accelerometer data were double integrated in the frequency domain to produce displacement spectra.

For the modal tests, displacement spectra were obtained in the same manner. These spectra were then fitted to one or more damped-resonance response functions, using standard least-squares techniques (e.g., Figure 3). The solid line represents a “global” fit to the spectrum, consisting of the summed response functions associated with the three damped-resonance peaks at 35, 124 and 281 Hz. The fit also includes a “background” term proportional to $1/f^2$.

Previous studies of fuel element vibration have focused on frequency ranges spanning 20-to-125 Hz, with fuel element natural frequencies of vibration falling in the range 29-to-67 Hz, depending on the type of fuel element and reactor operating conditions, primarily pressure and

power production [2]. In the present study, spectra taken with the accelerometers mounted on the flow tube show that the majority of test rig vibration occurs at frequencies below 20 Hz. Therefore, RMS-displacement values for fuel element vibration were calculated for frequency bands above 20 Hz: namely, 20-to-200 Hz, 30-to-39 Hz and 41-to-200 Hz.

For the displacement probes, the 20-to-200 Hz Band-RMS values were used to compare vibration levels amongst the different tests.

RESULTS & DISCUSSION

Typical vibration spectra from in-flow tests are shown in Figure 4, for the displacement probes at the bottom, middle and top of Element #21 (outer ring of the 42-element DME bundle), as a function of mass flow rate. Acceleration and displacement spectra obtained from the circumferential (transverse) and radial accelerometers mounted inside the instrumented element in the inner ring are shown in Figure 5, for a flow rate of 22.7 kg/s.

Spectra obtained from the miniature instrumented element accelerometers used with the 42-element DME bundle have the following characteristics (Figure 5):

- generally broad-band acceleration spectra, nearly constant with frequency over the range 20-to-100 Hz,
- acceleration amplitudes near the transducer threshold of 0.15 m/s^2 (equivalent to $60 \mu\text{V}$),
- 60-Hz interference from the line voltage because of the relatively low signal levels, especially in the circumferential accelerometer spectra, and
- a sharp rise in the displacement spectra at low frequency, due to broad-band noise, a poor low-frequency response and the double integration in the frequency domain (a $1/f^2$ factor).

Consequently, it is unreasonable to make direct, detailed comparisons between displacement Band-RMS values obtained from accelerometers in the inner instrumented element and values obtained from displacement probes for the outer elements. While not ideal, the data allow a limit to be placed on vibration amplitudes; if the inner element were to vibrate at its natural frequency with the same amplitude as outer Element #21 in flow (see Figure 4), then the motion would be clearly reflected as a peak in the accelerometer spectra in the 30-to-39 Hz frequency range.

Flow-test spectra obtained from the mid-plane displacement probe for Element #21 were the only flow test results for either type of DME bundle to show damped-resonance peaks (see Figure 6).

Note that these tests were designed to provide a direct comparison between vibration amplitudes for the 42-element DME bundle and the standard 36-element bundle at low temperature and pressure.

In terms of absolute vibration amplitudes, previous tests with standard DME elements showed that vibration levels obtained from in-reactor and out-reactor tests differed by, at most, a factor of two over a wide range of temperatures and pressures. Given that the 42-element

fuel elements were designed with realistic pellet-to-sheath contact properties, the absolute vibration levels in NRU are not expected to be more than a factor of two higher than those in the test rig.

Damping Ratios

Measured damping ratios as a function of flow rate are shown in Figure 7. Compared to previous tests of unconstrained single fuel elements of similar design, the general trend seems to be the same over the range of flow rates covered by both tests, where the damping ratio is approximately 2% at low flow and increases to nearly 10% at the highest flow rate used in this study. The simplest approach to turbulence-induced vibration predicts that flow-dependent damping is proportional to the flow velocity - and thus flow rate. The present data suggest a somewhat stronger dependence on flow rate, although more data at higher flow rates would be needed to corroborate this. A value of 1.9% for the viscous damping measured in earlier tests would appear to be an overestimate, as the measured structural damping already accounts for most of the observed damping at low flow rates.

Vibration Frequencies and Amplitudes

For a 42-element DME outer element mounted vertically in the bundle, the vibration frequency measured for the first bending mode in air was 35.4 Hz (see Figure 3) – very similar to the frequencies observed in previous tests of unconstrained fuel elements of similar design (31.5-36.1 Hz). The vibration spectrum shown in Figure 3 is well described by the summed response functions associated with the three damped resonance peaks at 35, 124 and 281 Hz. These frequencies are interpreted as corresponding to the first three fuel-element bending modes. The 2nd and 3rd bending-mode frequencies suggest end conditions that are closer to pinned-pinned than fixed-fixed. This is consistent with earlier tests of a standard fuel element that was radially unconstrained but otherwise mounted conventionally.

Spectra for 42-element DME Element #21 at its midplane offer the only examples of relatively unconstrained fuel element vibration in flow, for the test with a misaligned fuel string (e.g., Figure 4, Disp 3 and Figure 6). In this case, the first-mode frequencies varied from 32.1 to 37.7 Hz, at zero flow, to 38 Hz, at the highest flows recorded. The 2nd and 3rd modes are also visible in Figure 6, although a mid-plane displacement probe is particularly insensitive to 2nd-mode vibration. This damped resonant type of vibration only occurred with the fuel string misaligned, suggesting that fuel bundle alignment has an effect on either the level of turbulent excitation forces or, more likely, the structural boundary conditions of Element #21. Remaining displacement probe vibration spectra do not exhibit pronounced peaks in the frequency range of interest (e.g., Figure 4, Disp 2 and Disp 4).

At a flow rate of 22.7 kg/s (mass flux of 6135 kg/m²-s), the averaged RMS displacements are 4.1 μm for the reference DME bundle and 4.7 μm for the prototypical 42-element DME bundle, within experimental uncertainty at these low vibration levels. By comparison, RMS amplitudes of between 5.8 and 6.5 μm were measured at the same mass flux for a single element in liquid flow. Vibration levels measured by the miniature accelerometers inside the instrumented inner element were higher than those measured for outer elements. The 30-to-39 Hz Band-RMS values are likely the most accurate and focus on any vibration at the fuel element natural frequency. These values ranged between 5 μm and 10 μm at 22.7 kg/s flow; higher than the 1-to-3 μm typical for the displacement probes over that narrow frequency range, but less than the 13 μm measured for the mid-plane vibration observed in the 42-element DME tests with Element #21. As discussed earlier, there are no indications of resonant peaks in the spectra near the fuel element natural frequency.

Fretting-Wear Considerations

In terms of the potential for fretting wear, experience with previous DME bundles has shown that the critical locations are the top and bottom ends of the de-mountable elements, where they come into contact with the endplates. The vibration levels measured during these tests are not considered high enough to cause serious fretting-wear damage, especially since they are comparable to levels measured for the reference DME bundle, which has not been susceptible to undue wear. Nevertheless, bundle components were inspected for wear and sample photographs were taken of wear surfaces before and after the test. Any marks visible on the nailhead or spigot ends of the fuel elements were due to machining or handling, not wear (as expected). There is some evidence of slight wear due to surface contact on some of the midplane spacer pads, as shown in Figure 8. Some of the clearest examples of such surface markings occurred on or next to outer Element #21, which also exhibited the largest midplane clearance (0.71 mm) between its spacer pads and those of its nearest neighbour. This is consistent with midplane displacement spectra that are characteristic of a relatively unconstrained fuel element undergoing flow-induced vibration.

CONCLUSIONS & RECOMMENDATIONS

The measured levels of flow-induced vibration for outer elements in the two types of DME bundles tested, the 42-element prototype and the 36-element standard, were generally low: less than 6 μm RMS at 22.7 kg/s flow at the nailhead and spigot ends of the elements, and were comparable with each other.

Somewhat higher outer element vibration levels, approximately 15 μm RMS at 22.7 kg/s flow, were observed at the midplane location of Element #21 of the 42-element prototype bundle, in a misaligned fuel string

configuration. This result is probably related to a larger-than-average clearance between inter-element spacer pads for this element. Mid-plane vibration amplitudes were low for this element in an aligned fuel string configuration, except at the maximum flow rate of 27.3 kg/s. At the nailhead and spigot ends of the element, where there is more concern regarding fretting wear than at the midplane, vibration levels were low, below 5 μm RMS in all cases.

The vibration amplitudes measured at 22.7 kg/s flow for an inner element in the 42-element DME bundle ranged from 5-to-10 μm RMS over the frequency range 30-to-39 Hz. It was concluded that the measured levels for broader frequency bands are inaccurate due to the accelerometers' instrument response. The accelerometer data were used to search for high levels of vibration at the elements' natural frequencies in the 30-to-39 Hz range, for which no evidence was found.

The damping ratio measured for a 42-element DME dummy outer fuel element in air were typically 2%, compared to approximately 3-to-23% previously measured for a standard fuel element. This result is probably related to the pellet characteristics chosen for the DME dummy elements. Damping ratios measured for Element #21 in water ranged between 2% at low flow and 10% at 27.3 kg/s flow, comparable to previous results.

Recommendations

Based on the comparison of vibration levels measured for the two types of bundles, the 42-element DME bundle was judged to be suitable for irradiation testing in the NRU-reactor test loops.

Concerning in-reactor tests with this bundle, it was recommended that normal prudent inspection practices be followed, namely that the bundle be inspected for undue wear after one (or at most two) reactor operating cycles, and subsequently at longer intervals as considered necessary. In particular, it was recommended that the nailhead ends, spigot ends, bearing pads and inter-element spacer pads of the fuel elements be examined. It was also recommended that the clearances between inter-element spacers in an assembled bundle be assessed before placing the bundle into the reactor.

A prototype 42-element DME bundle (DME-222) is currently being irradiated in the NRU loops. The irradiation is planned for 1000 days, with interim inspections after 50, 150, 300, 500 and 700 days. To date, DME-222 has been successfully irradiated for 90 days.

An interim inspection was completed after 50 days of irradiation. The core components showed no evidence of fretting wear: no end-plate wear was observed at the locations interfacing with the nailheads and spigots of the de-mountable elements, nor was any wear observed on the fourteen intermediate elements and their spacer pads; the spin-on ring that holds the assembled bundle together showed no evidence of wear or distortion. Minimal spacer-pad wear was observed on four of the twenty-one de-mountable outer elements. One outer element

exhibited minor fretting wear on its nailhead, while another exhibited minor wear on its spigot. The extent of outer-element fretting wear did not affect the integrity or performance of the elements. The seven demountable inner elements did not exhibit any spacer pad, nailhead or spigot wear.

Similar wear assessments will be conducted during future planned inspections.

ACKNOWLEDGMENTS

The authors wish to thank J. Fraser, for providing the 42-element bundle and related information, K. Hagen, for machining test-rig components, B. Luloff, in handling fuel logistics, I. Lusk, B. Surette and J. Sullivan, for providing fuel carriage components, conditioning bundles, 36-element DME bundles and fuel elements, L. Lyall, for assistance with instrumentation and with the hardware and software systems used with the test rig, and T. Prins, for assistance with the VIBFLO loop preparations.

REFERENCES

- [1] Pettigrew, M.P., 1981, "Flow-Induced Vibration Phenomena in Nuclear Power Station Components", *Power Industry Research* **1**, p. 97.
- [2] Pettigrew, M.J., 1993, "The Vibration Behaviour of Nuclear Fuel Under Reactor Conditions", *Nuclear Science and Engineering* **114**, p. 179.
- [3] Smith, B.A.W., Derksen, D.D., 1998, "Measurement of Steady and Unsteady Hydro-Dynamic Loads on a Nuclear Fuel Bundle", *Journal of Fluids and Structures* **12**, p. 475.
- [4] Fisher, N.J., Tromp, J.H., Smith, B.A.W., 1996, "Measurement of Dynamic Interaction between a Vibrating Fuel Element and Its Support", *ASME Journal of Pressure Vessel Technology* **328**, p. 271.
- [5] Ko, P.L., 1997, "Wear of Power Plant Components due to Impact and Sliding", *Applied Mechanics Reviews* **50**, p.387.
- [6] Yetisir, M., Fisher, N.J., 1997, "Prediction of Pressure Tube Fretting-Wear Damage due to Fuel Vibration", *Nuclear Engineering and Design* **176**, p. 261.
- [7] Paidoussis, M.P., 1976, "Dynamics of Cylindrical Structures Subjected to Axial Flow", *Journal of Sound and Vibration* **29**, p. 365.
- [8] Paidoussis, M.P., 2004, *Fluid-Structure Interactions* Vol. 2, Chap. 8, Elsevier.
- [9] Zhang, X., Yu, S.D., 2011, "Large Eddy Simulation of Turbulent Flow surrounding Two Simulated CANDU Fuel Bundles", *Nuclear Engineering and Design* **241**, p. 3553.
- [10] Haslinger, K.H., Joffe, P.F., Nordström, L., and Andersson, S., 2001, "Flow Induced Vibration Testing of a PWR Fuel Assembly", In Proceedings of the 16th International Conference on Structural Mechanics in Reactor Technology (SMiRT 16), Washington, DC, Paper #1514.

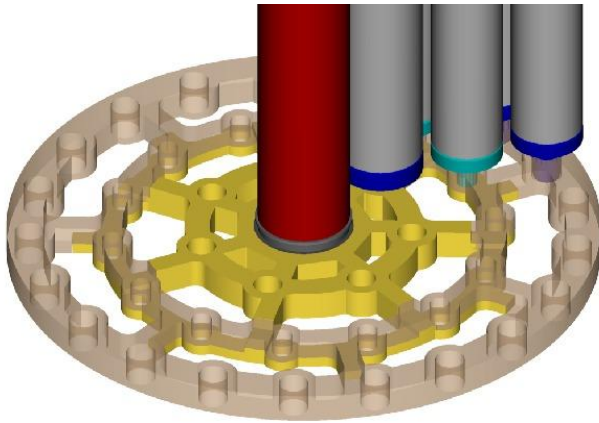


FIGURE 1: EXPANDED VIEW OF THE END-PLATE OF A PARTIALLY ASSEMBLED DME BUNDLE (THE RED CENTRAL COMPONENT IS THE FUEL CARRIAGE TIE ROD).

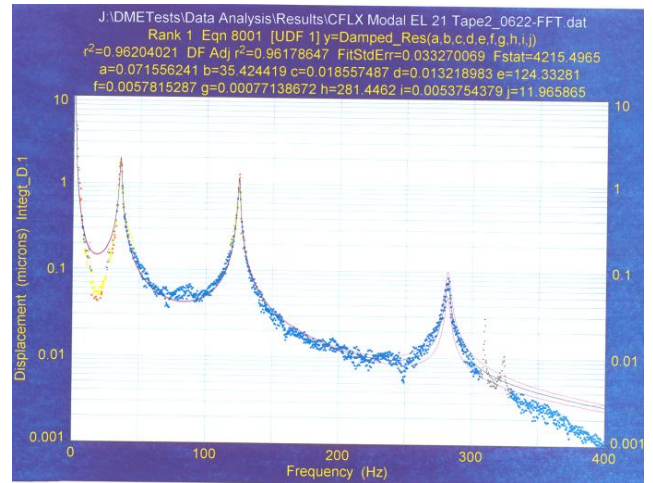


FIGURE 3: MODAL RESPONSE FOR ELEMENT #21 (42-ELEMENT DME BUNDLE), IN AIR.

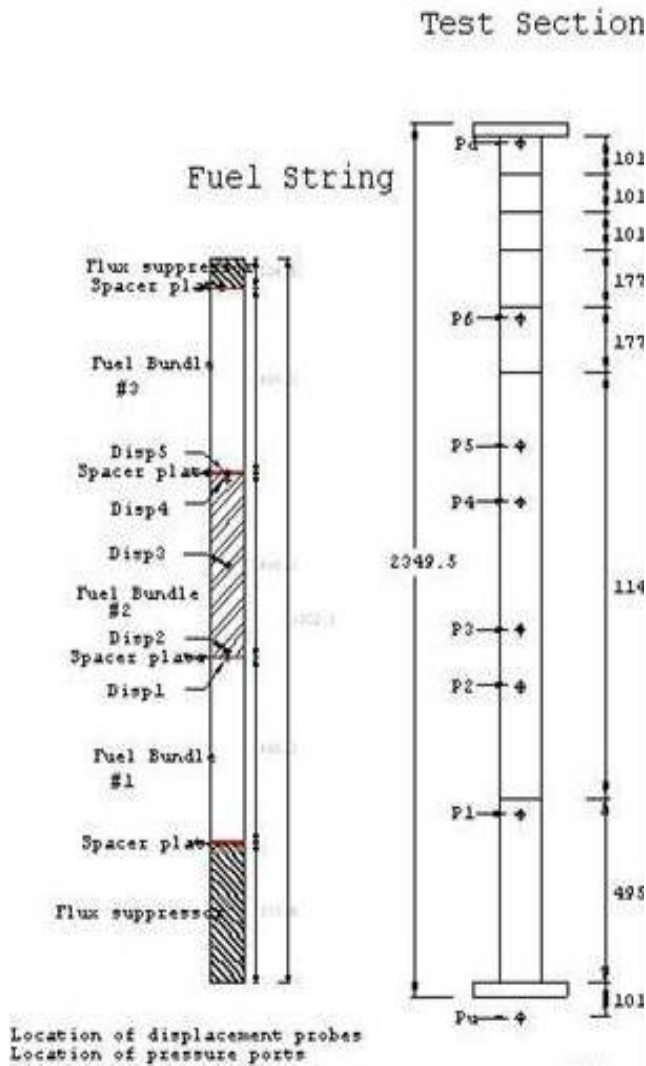


FIGURE 2: TEST-SECTION LAYOUT.

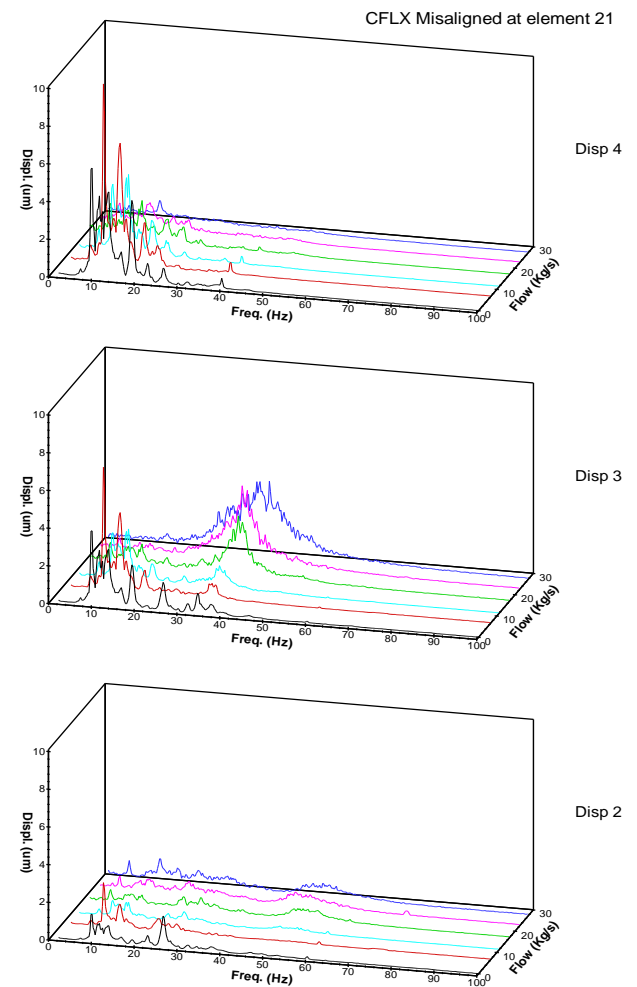


FIGURE 4: RMS-DISPLACEMENT FREQUENCY SPECTRA FROM PROBES FACING THE BOTTOM (DISP 2), MIDDLE (DISP 3) AND TOP (DISP 4) OF OUTER-RING ELEMENT #21 (42-ELEMENT DME BUNDLE, MISALIGNED FUEL STRING).

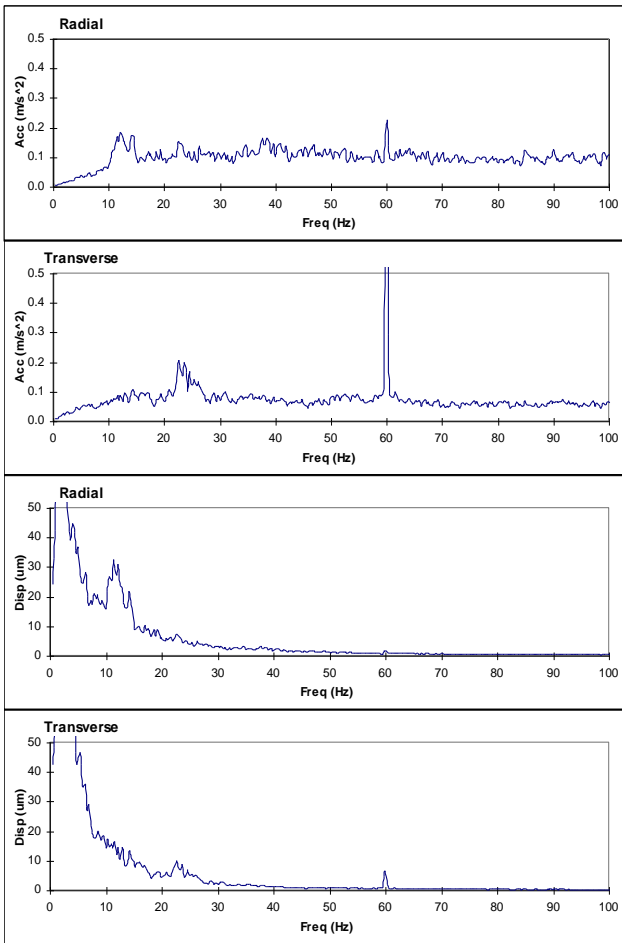


FIGURE 5: TRANSVERSE AND RADIAL ACCELERATION AND DISPLACEMENT VIBRATION SPECTRA OBTAINED FROM INTERNAL ACCELEROMETERS (42-ELEMENT DME BUNDLE, MISALIGNED FUEL STRING).

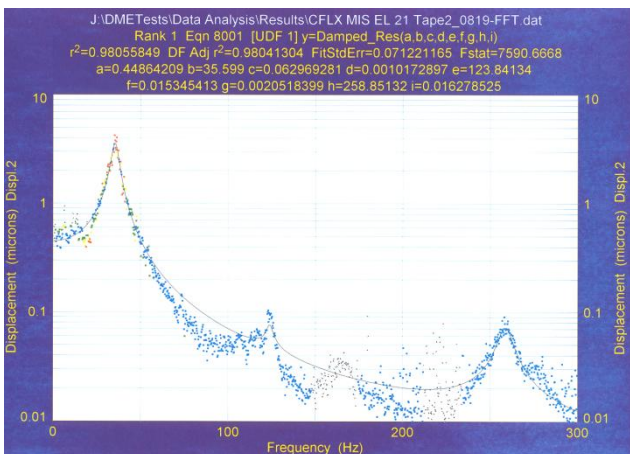


FIGURE 6: FREQUENCY RESPONSE OF OUTER-RING ELEMENT #21 IN FLOW (42-ELEMENT DME BUNDLE, MISALIGNED FUEL STRING, FLOW RATE 22.7 KG/S).

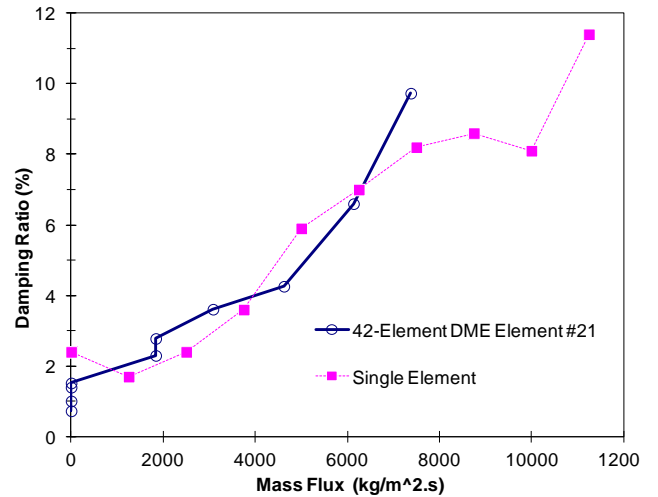


FIGURE 7: DAMPING RATIO FOR FIRST-MODE VIBRATION OF ELEMENT #21 IN THE 42-ELEMENT DME BUNDLE (SMALL SQUARES) AND A SINGLE ELEMENT OF A SIMILAR DESIGN (LARGE SQUARES), AS A FUNCTION OF MASS FLUX.

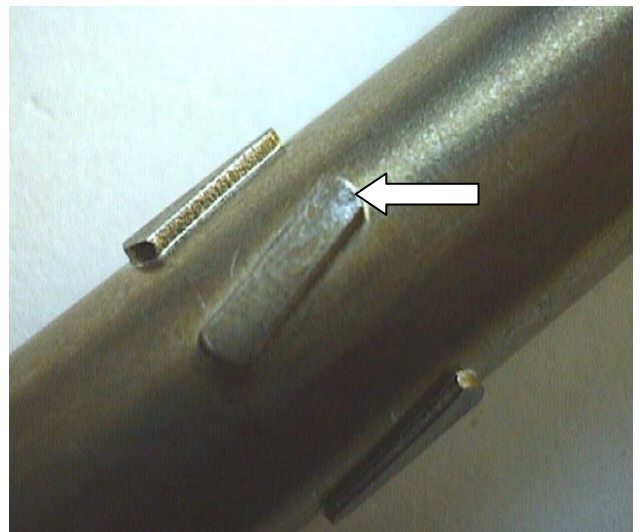


FIGURE 8: PHOTOGRAPH OF ELEMENT #7 MID-PLANE SPACER PAD FOLLOWING FLOW TESTS, SHOWING THE WORST WEAR MARK OBSERVED (ARROW).

STABILITY OF A STRUCTURALLY INHOMOGENEOUS FLEXIBLE PLATE IN UNIFORM AXIAL FLOW

Ben H. Tan

Anthony D. Lucey*

Mark. W. Pitman

Fluid Dynamics Research Group

Curtin University

Perth, WA 6845, Australia

Email: A.Lucey@curtin.edu.au

ABSTRACT

This paper considers the hydro-/aero-elastic linear stability of a finite elastic plate held along all four of its edges and subjected to an ideal axial flow. A combination of theoretical and computational modeling is used to frame an eigen-value problem for the fully coupled fluid-structure system. A particular advantage of the method is that it copes readily with structural inhomogeneity. The method is used to predict the behaviour of both homogeneous panels and panels to which localized stiffening has been added as a stabilization strategy. Such stiffening is shown to be very effective for the increasing divergence-onset flow speeds and, in the aero-elastic problem, as a means to suppress flutter. Finally, it is shown that two-dimensional analyses are able to provide a close representation of the phenomenology of the full three-dimensional system.

INTRODUCTION

This paper considers the classical hydro-/aero-elastic system comprising a flexible panel exposed to a one-sided incompressible uniform flow; previous linear studies include [1-6]. The system is representative of the high Reynolds number situations found in many engineering applications that range from the hydrodynamic loading of panels making up the hull of a ship through to the axial wind loading of glass panels of curtain walls that have become a feature of contemporary high-rise buildings for both aesthetic and thermal-control reasons. In such applications, the concern is that at some critical speed the panel loses stability, usually through divergence that can lead to a buckled nonlinearly saturated state, e.g. [7-10], or a highly destructive flutter instability at higher flow speeds.

Strategies to postpone critical flow speeds to values beyond the speed for which a panel is designed are usually based upon material selection or uniform thickening of the panel that results in increased cost and dead weight. By contrast, the goal of the present paper is to control instability through the judicious use of highly localised structural inhomogeneity (stiffening) based upon a full

understanding of instability modes. Our previous work [11-13] has demonstrated the utility of this stabilization strategy for the two-dimensional system of Fig. 1a where an isolated spring is included as an additional support. Herein, we extend the hybrid of theoretical and computational methods of [5] to conduct an eigen-analysis of the three-dimensional model system depicted in Fig. 1b wherein a transverse stiffening strip replaces the spring-support of our two-dimensional studies; however, we also show that the much simpler two-dimensional spring-supported configuration does provide an excellent guide to the phenomenology of the more realistic three-dimensional model.

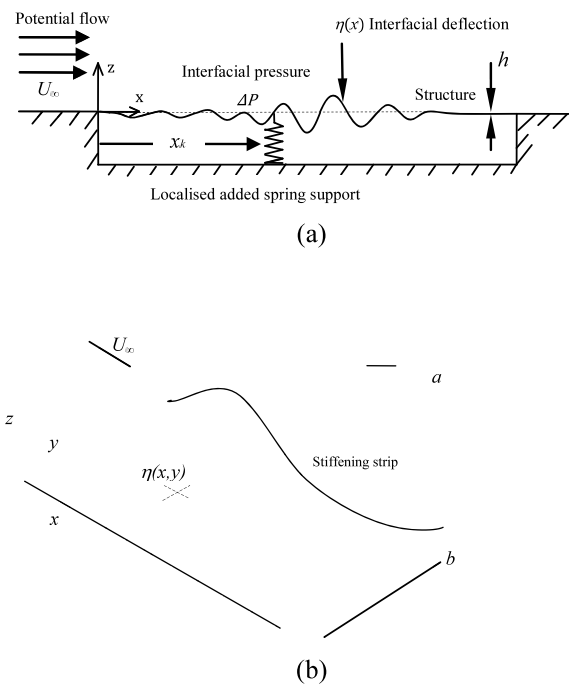


FIGURE 1: SCHEMATICS OF THE (a) TWO-DIMENSIONAL (SIDE VIEW) AND (b) THREE-DIMENSIONAL (ISOMETRIC VIEW) PROBLEMS.

THEORETICAL AND COMPUTATIONAL MODELS

A linear ideal-flow model is developed based on the two-dimensional computational modelling of [5] and utilized in [11-13] for the system depicted in Fig. 1(a). The first objective of the present paper is to model and solve the corresponding three-dimensional system shown in Figure 1(b), so that system eigenvalues can be extracted to determine and predict the behaviour of the plate and, in particular, identify parameter values that result in its instability. The second objective is to determine the effect of localized structural inhomogeneity introduced as a stiffening strip (or rib on the underside of the panel) on the stability of the panel.

The development of the model is broken into three main sections. An overview of the plate mechanics is presented and then the potential-flow solution methodology and pressure determination is described. Finally, the coupling that yields the fully interactive three-dimensional FSI system is presented and the resulting governing equation is cast in state-space form so that eigenmodes describing the system at infinite time after some form initial excitation can be calculated.

The small-amplitude motion of a homogeneous thin flexible plate as shown in Fig. 1(b), fixed along all of its four edges, in the presence of a fluid flow is

$$\rho_m h \frac{\partial^2 \eta}{\partial t^2} + d \frac{\partial \eta}{\partial t} + B \nabla^2 \nabla^2 \eta = -\Delta p(x, y, 0, t), \quad (1)$$

where $\eta(x, y, t)$, ρ_m , h , d and B are respectively, the plate's deflection, density, thickness, damping coefficient and flexural rigidity of the flexible panel. $\nabla^2 \nabla^2$ is the biharmonic operator. On the right-hand side, $\Delta p(x, y, z, t)$ is the unsteady perturbation fluid pressure.

The plate is discretised into $M \times N$ equidistantly spaced points at which the mass is lumped. Equation (1) is then written in finite-difference form to yield the plate-motion equation

$$\rho_m h [I] \{\ddot{\eta}\} + d [I] \{\dot{\eta}\} + B [D_4] \{\eta\} = -\{\Delta p\}, \quad (2)$$

where $[I]$ and $[D_4]$ are the identity and fourth-order biharmonic spatial differentiation matrices respectively with order $P = M \times N$. $\{\ddot{\eta}\}$, $\{\dot{\eta}\}$ & $\{\eta\}$ are column vectors of size P of the acceleration, velocity and deflection of plate respectively, while $\{\Delta p\}$ is the pressure column vector with size P . The boundary conditions for Eqns. (1) and (2) used herein are that the plate has four hinged edges enforced as zero deflection and bending moment.

The fluid is assumed to be incompressible and its flow is irrotational and unsteady. A velocity potential can therefore be introduced as a linear combination of uniform flow and a perturbation due to the plate motion. The total velocity potential Ψ is the sum of velocity-perturbation potential ϕ and uniform velocity potential with mean flow U_∞ in x-direction

$$\Psi(\mathbf{r}, t) = \phi(\mathbf{r}, t) + U_\infty x, \quad (3)$$

where $\mathbf{r} = (x, y, z)$. Each of the total velocity potential Ψ and the velocity-perturbation potential ϕ satisfy the Laplace equation that incorporates the irrotationality of the flow and enforces mass conservation

$$\begin{aligned} \nabla^2 \Psi &= 0, \\ \nabla^2 \phi &= 0. \end{aligned} \quad (4)$$

The flow field can be written as

$$\mathbf{u}(\mathbf{r}, t) = \nabla \phi(\mathbf{r}, t) + U_\infty \mathbf{i}. \quad (6)$$

The perturbation potential ϕ is generated by integrating a distribution of sources of intensity σ over the wall-flow interface S , thereby giving

$$\phi(\mathbf{r}_Q, t) = \iint_S \frac{\sigma(\mathbf{r})}{|\mathbf{r}_Q - \mathbf{r}|} dS. \quad (7)$$

The solution of the Laplace equation must satisfy the kinematic boundary condition that enforces no flow through the impermeable boundary. Accordingly, the velocity of fluid normal to the flexible-plate must equal the flexible-plate velocity in that direction

$$(U_\infty \mathbf{i} + \nabla \phi(x, y, z, t)) \cdot \mathbf{n} = u^p. \quad (8)$$

Here \mathbf{n} and u^p are the unit vector and wall speed in the direction of outward normal of the wall-flow interface respectively.

The solution of the Laplace equation can then be used to determine the pressure on the panel through the unsteady Bernoulli equation

$$\rho \frac{\partial \psi}{\partial t} + \frac{1}{2} \rho \bar{\mathbf{U}} \cdot \bar{\mathbf{U}} + p = \frac{1}{2} \rho U_\infty^2 + p_\infty, \quad (9)$$

in which ρ and $\bar{\mathbf{U}}$ are the fluid density and velocity vector respectively. By assuming that the wall motion is of small amplitude, Eqn. (9) can be linearised to give

$$\Delta p = -\rho \frac{\partial \phi}{\partial t} - \rho U_\infty \frac{\partial \phi}{\partial x}, \quad (10)$$

having substituted for the velocity perturbations using the derivatives of their velocity potential.

As in the structure discretization of Eqn. (2), the solid-fluid interface is discretised into an array of panels numbered $i: 1 \rightarrow M$ and $j: 1 \rightarrow N$. These panels form the basis for the application of a zero-order boundary-element method using source(-sink) singularities. By applying standard panel-method techniques [14] and their adaptation to numerical simulations of the present problem [15], the disturbance normal velocity, velocity-perturbation potential and tangential velocity induced at each panel can be obtained. Consistent with the foregoing linearization, the source-strength distribution remains in the undisturbed plane, $z=0$. We then have the straightforward determination of source strengths on any panel i, j through

$$\sigma_{ij} = \frac{1}{2\pi}(U_\infty \alpha_{ij} + u_{ij}^v), \quad (11)$$

where α_{ij} and u_{ij}^v are the slope in x -direction and the vertical velocity of the control point respectively. By expressing α_{ij} and u_{ij}^v in terms of wall deflection and wall velocity respectively, the source strength on each panel is related to wall motion only by

$$\sigma_{ij} = \frac{1}{2\pi}(U_\infty [D_1']\{\eta_{ij}\} + [D^+']\{\dot{\eta}_{ij}\}), \quad (12)$$

where $[D^+']$ is a matrix operator for the interfacial vertical speed and $[D_1']$ is the first order spatial differentiation finite-difference matrix operator. Furthermore, the perturbation potential ϕ_{ij} and tangential perturbation velocity in the x -direction u_{ij} can be derived and are related to the source strength σ_{ij} through

$$\phi_{ij} = [\Phi']\{\sigma_{ij}\}, \quad (13)$$

$$u_{ij} = [T']\{\sigma_{ij}\}, \quad (14)$$

where $[\Phi']$ and $[T']$ are the potential influence coefficient and the tangential velocity influence matrices.

The pressure perturbation at any panel's control point can now be found using a discretized form of the linearized unsteady Bernoulli equation

$$\{\Delta p_{ij}\} = -\rho \dot{\phi}_{ij} - \rho U_\infty u_{ij}. \quad (15)$$

By substituting Eqns. (12), (13), and (14) into Eqn. (15), the perturbation pressure is found and seen to be related to wall deflection. $[D_1']$, $[D^+']$, $[\Phi']$ and $[T']$ are transformed into their corresponding square coefficient matrices $[D_1]$, $[D^+]$, $[\Phi]$ and $[T]$ of size P . The matrices of system variables are transformed into variable column vectors of size P . Thus the interfacial pressure can be written as

$$-\{\Delta p\} = \frac{\rho}{2\pi}[\Phi][D^+]\{\dot{\eta}\} + \frac{\rho}{2\pi}U_\infty([T][D^+] + [\Phi][D_1])\{\dot{\eta}\} + \frac{\rho U_\infty^2}{2\pi}[T][D_1]\{\eta\}. \quad (16)$$

We now assemble the coupled FSI system equation. The interfacial fluid pressure of Eqn. (16) is substituted into the plate-motion equation (2) and re-arranging, we obtain

$$[A]\{\ddot{\eta}\} + [B]\{\dot{\eta}\} + [C]\{\eta\} = 0, \quad (17)$$

where

$$[A] = -\rho_m h[I] + \frac{\rho}{2\pi}[\Phi][D^+],$$

$$[B] = -d[I] + \frac{\rho}{2\pi}U_\infty([T][D^+] + [\Phi][D_1]),$$

$$[C] = -B[D_4] + \frac{\rho}{2\pi}U_\infty^2[T][D_1].$$

Re-arranging Eqn. (17) so that the left-hand side is the acceleration term gives

$$\{\ddot{\eta}\} = -[A]^{-1}[B]\{\dot{\eta}\} - [A]^{-1}[C]\{\eta\}. \quad (18)$$

We now define $[E] = -[A]^{-1}[B]$ and $[F] = -[A]^{-1}[C]$, so that Eqn. (18) becomes

$$\{\ddot{\eta}\} = [E]\{\dot{\eta}\} + [F]\{\eta\}. \quad (19)$$

Introducing state variables $x_i = \eta_i$ and $x_{P+i} = \dot{\eta}_i$ for i from 1st to the P^{th} point, the $2P$ output vector for the state-space model is

$$\begin{Bmatrix} \{\eta\} \\ \{\dot{\eta}\} \end{Bmatrix} = \{x\}. \quad (20)$$

Using these definitions, equation (18) is then converted into the state differential equation

$$\{\dot{x}\} = \begin{bmatrix} 0 & I \\ F & E \end{bmatrix} \{x\}, \quad (21)$$

and letting

$$[H] = \begin{bmatrix} 0 & I \\ F & E \end{bmatrix},$$

noting that matrix H is $2P \times 2P$, the final form of the state differential equation (21) is

$$\{\dot{x}\} = [H]\{x\}. \quad (22)$$

The long-time response is found by first assuming single-frequency response in the time domain, and then extracting the resulting eigenvalues of $[H]$. The single-frequency response is proportional to e^{st} where s is a complex variable; the imaginary part is the vibration frequency while the real part indicates growth or decay of the system disturbance. Finally, the system eigenvectors can then be used to assemble the deflection, $\eta(x,t)$, of the panel.

To incorporate the effect of a stiffening strip notionally attached to the underside to the panel a transverse (thin) beam is conceived, straddling the panel, as depicted in Fig. 1b. The beam has second moment of area I and elastic modulus E ; in this paper it is aligned with the y -direction and thus contributes an additional restoring force (per unit area) of

$$(EI) \frac{\partial^4 \eta}{\partial y^4} \quad (23)$$

that acts over a single line of boundary-element panels, $j:1 \rightarrow N$, and which, when discretised, generates a further, η -dependent term in the left-hand side Eqn. (2). Clearly a similar approach could be used to incorporate one or more stiffeners in a combination of either the x - and/or y -directions. In the present investigation, only a transverse stiffener located at the plate mid-line, $x = a/2$, is used and we neglect its inertial effects. In support of the latter assumption, it was shown in [15] that significant added mass – of the order of the plate mass – is necessary to

modify the flutter behaviour in the related problem of a cantilevered-free flexible plate.

RESULTS

The results presented in this paper serve first to demonstrate the integrity of the new modelling for the case of a homogenous plate and show how its phenomenology is similar to that of the antecedent two-dimensional model. Thereafter, the stabilization of the flexible plate through the addition of a stiffener is addressed.

The homogenous-plate system can be shown [3, 4, 11, 12] to be governed by two non-dimensional control parameters, the fluid-to-solid mass ratio (or non-dimensional plate length) and the fluid-to-solid stiffness ratio (or non-dimensional flow speed), each based on the stream-wise panel length, a , and respectively defined by

$$L' = \rho a / (\rho_m h) \quad \text{and} \quad \Lambda^F = \rho U_\infty^2 a^3 / B \quad (24a,b)$$

in addition to which the aspect ratio (b/a) needs to be defined. Hereinafter we will, for convenience, to the terms in Eqn. (24a,b) as the mass ratio and flow speed. Consistency with these non-dimensional parameters requires that time be non-dimensionalised using a/U_∞ . In the results that follow, we also provide physical examples to give an engineering feel for types of systems to which the results are applicable. Throughout this paper we consider only elastic plates, hence $d = 0$ in Eqn. (1); the effect of energy dissipation in the structure has been addressed in [5].

As a reference, Fig. 2 shows the computed variation of eigenvalues with flow speed for the well-known two-dimensional analysis (e.g. [2,3,5]). Although all 400 system eigenvalues are calculated, only the two with the lowest frequencies have been plotted for clarity. Two distinct values of mass ratio are presented that, for a plate of given length and thickness, could represent water ($\rho = 1000 \text{ kg/m}^3$) and air ($\rho = 1.27 \text{ kg/m}^3$) flow over an aluminum panel of length 1 m and thickness 1 cm. These two cases respectively yield mass ratios of 38.5 and 0.049. For both water and air flows, divergence sets in at a non-dimensional flow speed of 40.1; this is in excellent agreement with the Galerkin-method based analyses of [2,3]. As the flow speed is increased, the high-mass ratio results (water) evince divergence recovery and then modal-coalesce flutter occurs. This solution morphology, and the flow-speed values at which these events occur agree well with previous studies [2,3,5]. For the mass-ratio case (air) this sequence is very different: instead of first-mode divergence recovery, the second mode also undergoes divergence instability and at higher flow speeds, these two non-oscillatory modes coalesce to give flutter. This somewhat surprising result – that could also occur for very short panels with a water flow having the same mass ratio as the present air case – arises from the dominance of the aero-/hydro-dynamic stiffness in the

fluid pressure loading; it is explained in more detail in [13].

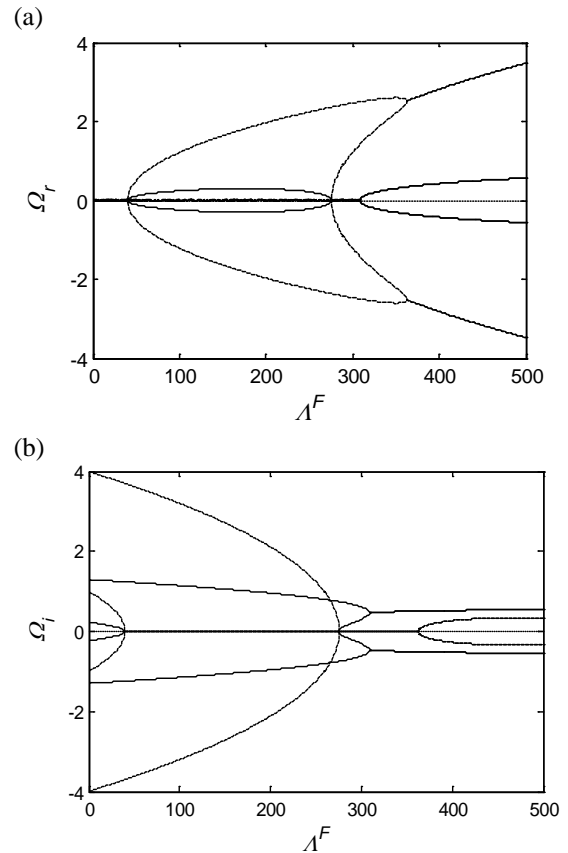


FIGURE 2. TWO-DIMENSIONAL ANALYSIS: VARIATION OF SYSTEM EIGENVALUES WITH NON-DIMENSIONAL FLOW SPEED FOR ----- HIGH MASS RATIO = 38.5 (WATER OVER ALUMINUM) AND - - - - LOW MASS RATIO = 0.049 (AIR OVER ALUMINUM): (a) REAL PART (GROWTH/DECAY) AND (b) IMAGINARY PART (OSCILLATION FREQUENCY) OF EIGENVALUES.

Results of the corresponding (to Fig. 2) three-dimensional analysis are shown in Fig. 3 for a panel of aspect ratio unity; i.e. a 1 m x 1 m aluminum panel (for which 3,200 system eigenvalues are calculated). The non-dimensional divergence-onset flow speed is seen to be much higher than that of the two-dimensional analysis. This is because the fixed side edges contribute additional structural restraint to the system as well as contributing to a transverse scaling of the flow pressure that is responsible for destabilization; the latter also features in the destabilisation of cantilevered-free plates of finite width [16]. The present value of divergence-onset flow speed and the solution morphology for the high mass-ratio case (water) agrees well with that of the Galerkin analysis for the same system [4] and serves to validate the present methods. What these results show is that the sequence of destabilisation events - from divergence through to flutter - is the same as for the two-dimensional analysis. Qualitatively, a two-dimensional analysis can be used to

predict the physics of the FSI system, while the three-dimensional analysis must be used for the quantification of divergence and flutter instability onset flow speeds.

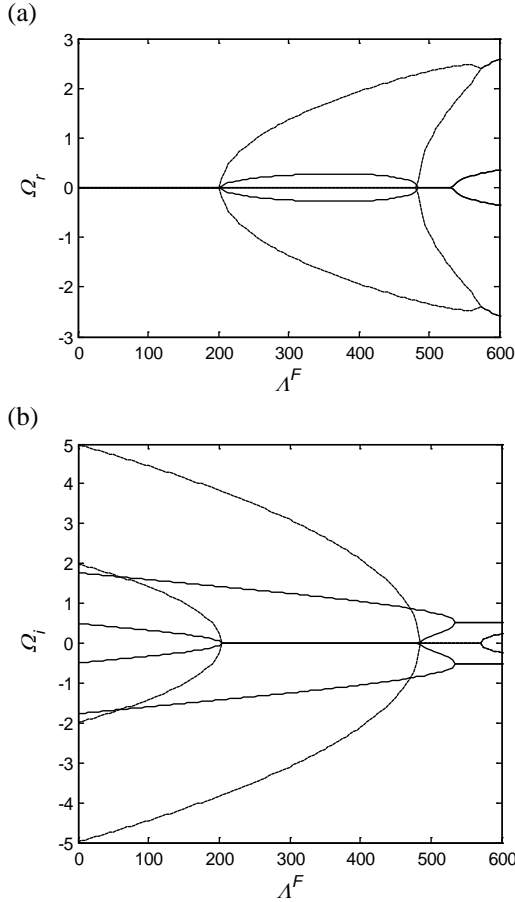


FIGURE 3. THREE-DIMENSIONAL ANALYSIS: VARIATION OF SYSTEM EIGENVALUES WITH NON-DIMENSIONAL FLOW SPEED FOR A PANEL WITH ASPECT RATIO UNIT. LEGEND AND SUB-FIGURE TITLE AS IN FIG. 2.

We now present results for a strategy of stabilization by adding additional localized stiffness to the flexible plate. For the two-dimensional analysis, additional stiffnesses is incorporated by the inclusion of a localized spring support at the panel mid-point as shown in Fig. 1a. Figure 4a shows the variation of divergence-onset, divergence-recovery and modal-coalescence flutter-onset flow speeds with the coefficient of the added spring support for a high value of mass-ratio, 92.3, representing water flow over an aluminum panel of length 0.6 m and thickness 2.5 mm (hence $B = 76.6$ Nm). The spring coefficient, k , is non-dimensionalised through division by $(\rho_m h)^3 / (\rho^3 B)$. Figure 4b shows the same variations for a low mass ratio 0.226, representing air flow over a glass panel of length 1.7 m and thickness 4 mm (hence $B = 381$ Nm) typical of that found in curtain walls of high-rise buildings.

(a)

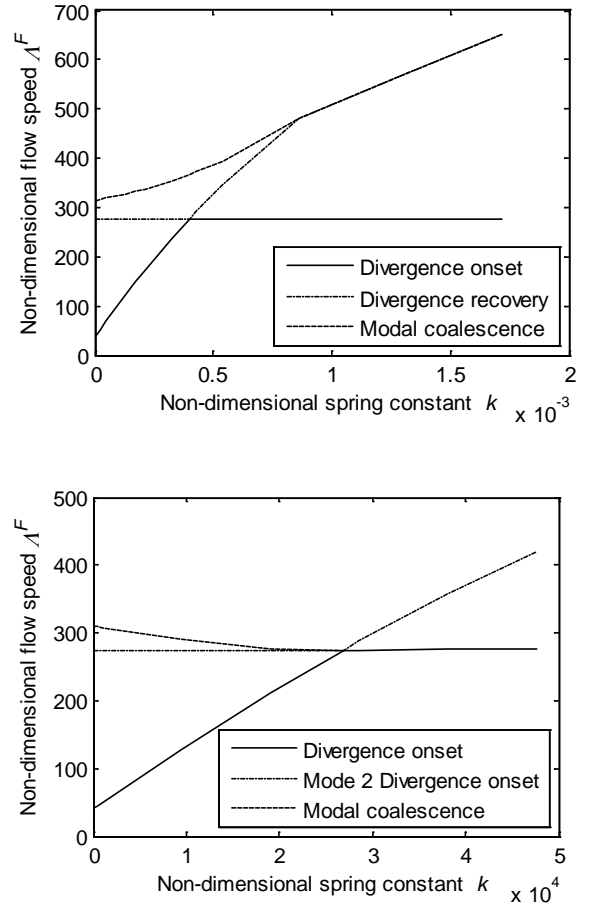


FIGURE 4. TWO-DIMENSIONAL ANALYSIS: THE EFFECT OF AN ADDED SUPPORT SPRING ON DIVERGENCE-ONSET, DIVERGENCE-RECOVERY / MODE-2 DIVERGENCE-ONSET, AND MODAL-COALESCENCE FLUTTER-ONSET FLOW SPEEDS FOR (a) HIGH MASS RATIO = 92.3 (WATER OVER ALUMINUM), AND (b) LOW MASS RATIO = 0.226 (AIR OVER GLASS).

In both high and low mass-ratio cases, the addition of a spring support is seen to be very effective in increasing the critical flow speed of (Mode 1) divergence-onset. However, there is a limit to this strategy because at a threshold value of spring stiffness, Mode 2 takes over as being critical. This is understandable because Mode 2 has a (quasi) node at the panel mid-point where the spring has been located. At higher values of spring stiffness than this threshold the solution morphologies between the high and low mass-ratio cases differ. For the former, the standard sequence of divergence recovery followed by modal-coalescence flutter (seen in Fig. 2) continues to hold although the neutral-stability flow-speed range between divergence recovery and flutter onset reduces to zero for a very stiff spring. However, for low mass ratio, values of spring stiffness above the threshold value yield concurrent Mode 1 and Mode 2 divergence that replaces modal-coalescence flutter. For glass panels this may be advantageous as it is flutter that is the most destructive instability.

Clearly the introduction of an isolated spring support would require some form of additional structure on which to mount its base; as such, it can only be regarded as an idealization of panel stiffening for two-dimensional analyses. The practicable way to stiffen a flexible panel is to introduce a stiffening rib that straddles the panel in the transverse direction as shown in Fig. 1b to which we now turn in the three-dimensional analysis.

Thus the discussions of the phenomenology for each of Figs. 4a and 4b respectively carry across to the three-dimensional systems of Figs. 5a and 5b. Most importantly, it is shown how and why even a single stiffening rib can be used very effectively to control the hydro-/aero-elastic stability of a flexible panel.

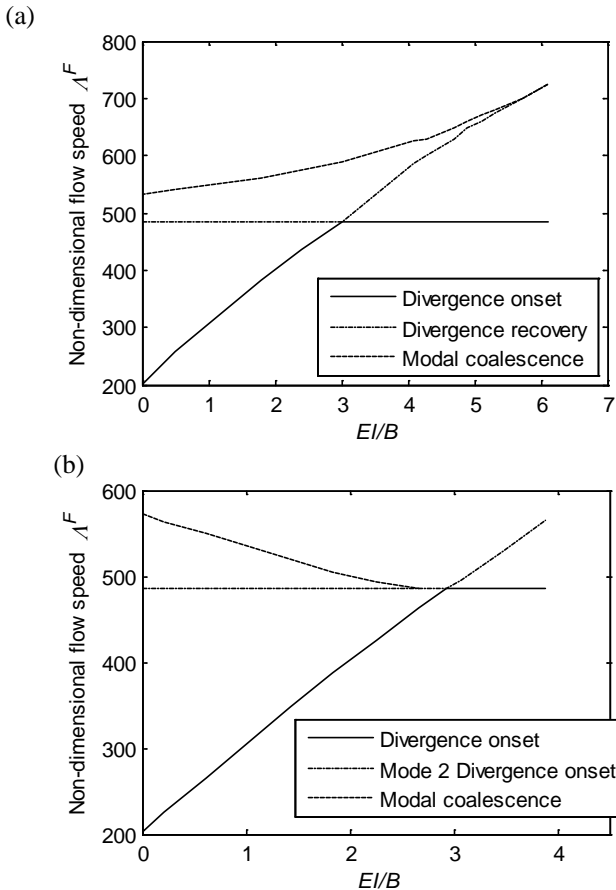


FIGURE 5. THREE-DIMENSIONAL ANALYSIS: THE EFFECT OF A TRANSVERSE STIFFENING STRIP AT THE PANEL MID-LINE ON DIVERGENCE-ONSET, DIVERGENCE-RECOVERY /MODE-2 DIVERGENCE-ONSET, AND MODAL-COALESCENCE FLUTTER-ONSET FLOW SPEEDS ON A PANEL OF ASPECT RATIO UNITY FOR (a) HIGH MASS RATIO = 38.5 (WATER OVER ALUMINUM), AND (b) LOW MASS RATIO = 0.049 (AIR OVER ALUMINUM).

Figures 5a and 5b respectively show the variation of divergence-onset, divergence-recovery or Mode-2 divergence onset, and modal-coalescence flutter-onset flow speeds with the flexural rigidity, EI (non-dimensionalised using the plate flexural rigidity B) of the stiffener located at the panel mid-line for the two cases of high (water) and low (air) mass ratio that generated the results in Fig. 3 for an aluminum panel of aspect ratio unity. Comparing these with the results in Figs. 4a and 4b – the two-dimensional analysis of added stiffness – indicates that the qualitative effects are almost identical.

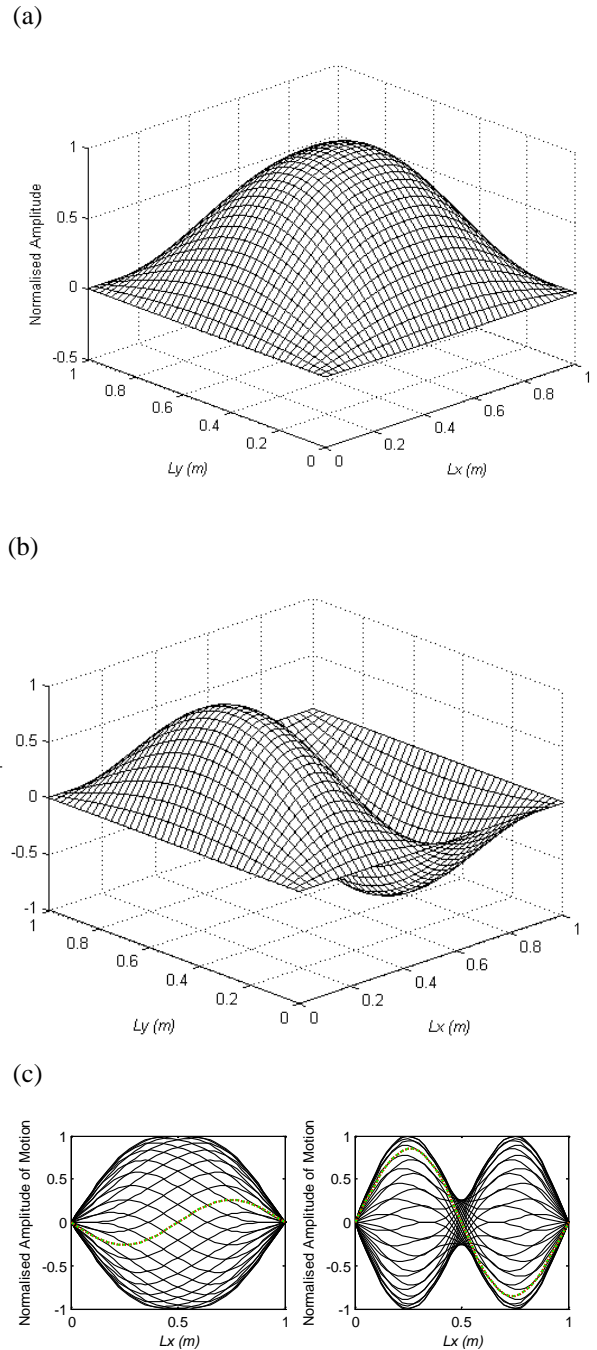


FIGURE 6. NEUTRALLY-STABLE FLEXIBLE-PANEL MODES FOR HIGH MASS RATIO (38.5) WITH A STIFFENING STRIP ($EI/B = 2$) ACROSS ITS MIDLINE AT A PRE-DIVERGENCE NON-DIMENSIONAL FLOW SPEED, 380: (a) MODE 1, (b) MODE 2, AND (c) CENTRELINE PROFILES OF MODES 1 AND 2 OVER ONE CYCLE OF OSCILLATION.

To give qualitative feel for the types of deformation that would result when a transverse stiffening strip (or rib) is added to the mid-line of an otherwise homogeneous flexible plate, we present a series of mode shapes in Figs. 6-8. Each of these is for the case of high mass ratio (water over aluminum) and with the stiffener having $EI/B = 2$; the sequence of results pertains to points in the stability map of Fig. 5a at different flow speeds on the vertical line $EI/B = 2$.

Figure 6 illustrates panel behaviour typical in the neutrally stable pre-divergence range of flow speeds. The effect of the stiffening strip can especially be seen in the shape of Mode 1 that features a strong (*in vacuo*) Mode-2 type content.

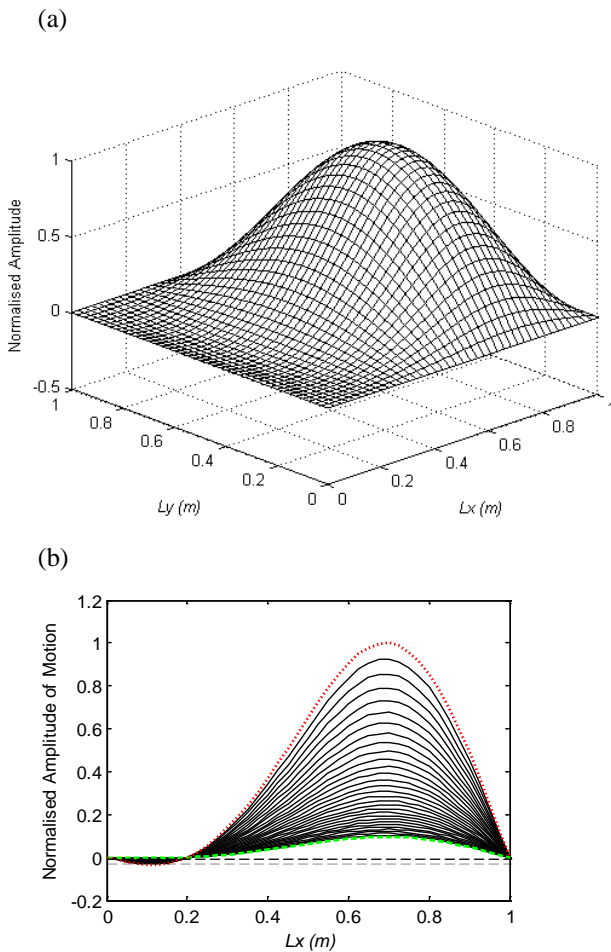


FIGURE 7. FLEXIBLE-PANEL DIVERGENCE MODE FOR HIGH MASS RATIO (38.5) WITH A STIFFENING STRIP ($EI/B = 2$) ACROSS ITS MIDLINE AT NON-DIMENSIONAL FLOW SPEED 450: (a) ISOMETRIC VIEW, AND (b) CENTRELINE PROFILES OVER A SEQUENCE OF TIME-STEPS FROM GREEN TO RED LINES.

Figure 7 illustrates panel behaviour typical in the divergence range of flow speeds. The effect of the stiffening strip is to reduce the mid-point deflection and thereby introduce a second-mode content to the unstable

mode. Finally, Fig. 8 shows a typical modal-coalescence flutter. While the modal coalescence has occurred between systems Modes 1 and 2 (see Fig. 3), non-negligible elements of (*in vacuo*) Modes 3 and 4 are seen; the stiffening strip tends to advance the order of basis modes that contribute to the panel's behaviour.

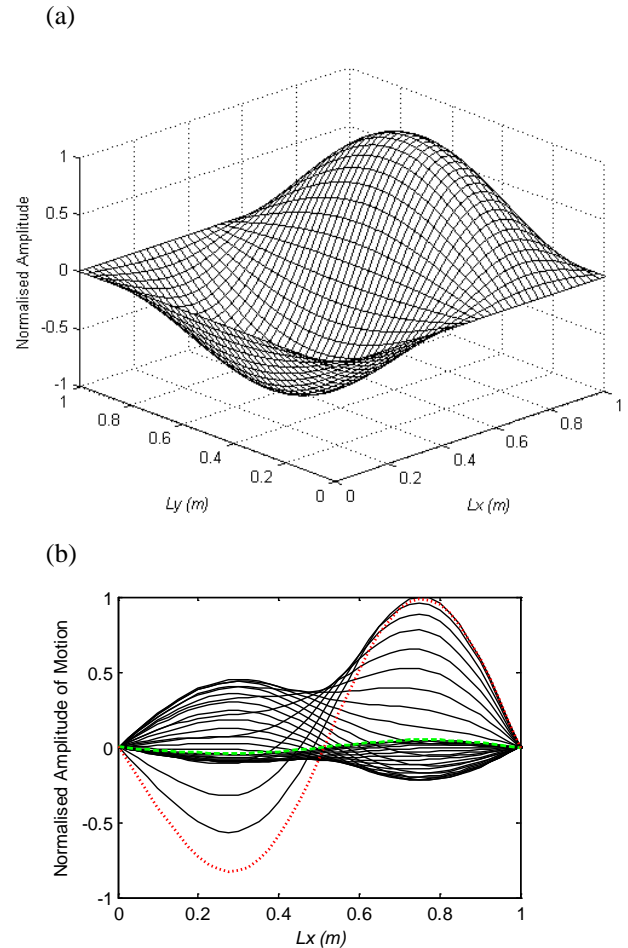


FIGURE 8. FLEXIBLE-PANEL MODAL-COALESCENCE FLUTTER MODE FOR HIGH MASS RATIO (38.5) WITH A STIFFENING STRIP ($EI/B = 2$) ACROSS ITS MID-LINE AT NON-DIMENSIONAL FLOW SPEED 600: (A) ISOMETRIC VIEW, AND (B) CENTRELINE PROFILES OVER A SEQUENCE OF TIME-STEPS FROM GREEN TO RED LINES.

CONCLUSION

A hybrid of theoretical and computational methods has been developed to study the linear three-dimensional hydro-/aero-elasticity of a flexible panel held along all four of its edges. The main merit of this method is that it can be used to analyse the FSI of panels having arbitrary structural inhomogeneity.

The investigations of this paper has used the method to determine the effect of localized added stiffness on a panel's behaviour, in particular the instability boundaries of divergence and modal-coalescence flutter. It has been shown that a transverse stiffening rib can yield significant

increases to the divergence-onset flow speed up to a certain threshold value of rib stiffness. This finding would be of engineering benefit in such applications as the panels of high-speed ship hulls.

For low fluid-to-solid density ratios (the mass ratio for given panel length and thickness), sufficiently high stiffness of the added rib eliminates the coalescence of the first two modes, replacing flutter with divergence of both of these modes. This effect would be of benefit in applications such as wind-loaded glass panels of curtain walls of high-rise buildings given that divergence, which would statically saturate at finite amplitude, is far less destructive than flutter.

Finally, the present study has shown that a two-dimensional analysis of the system using an isolated spring to represent the transverse rib of a flexible panel is able to capture qualitatively all of the phenomenology of the full three-dimensional FSI system.

REFERENCES

1. Dugundji, J., Dowell, E. & Perkin, B., 1963, "Subsonic flutter of panels on a continuous elastic foundation", *AIAA Journal* **1**, pp. 1146-1154.
2. Weaver, D.S. & Unny, T.S., 1971, "The hydroelastic stability of a flat plate", *ASME: Journal of Applied Mechanics* **37**, pp 823-827.
3. Ellen, C.H., 1973, "The stability of simply supported rectangular surfaces in uniform subsonic flow", *ASME: Journal of Applied Mechanics* **95**, pp 68-72.
4. Lucey, A.D. & Carpenter, P.W., 1993, "The hydroelastic stability of three dimensional disturbances of a finite compliant wall", *Journal of Sound and Vibration* **165**, pp.527-552.
5. Pitman, M.W. & Lucey, A.D., 2009, "On the direct determination of the eigenmodes of finite flow-structure system", *Proceedings of the Royal Society A* **465**, 257-281.
6. Lucey, A.D., 1998, "The excitation of waves on a flexible panel in a uniform flow", *Philosophical Transactions of the Royal Society of London A* **356**, pp. 2999-3039.
7. Ellen, C.H. 1977, "The non-linear stability of panels in incompressible flow". *Journal of Sound and Vibration* **54**, pp. 117-121.
8. Reynolds, R.R. & Dowell, E.H. 1993. "Nonlinear aeroelastic response of panels". Collection of Technical Papers -- AIAA/ASME Structures, Structural Dynamics and Materials Conference, Part 5, pp. 2566-2576.
9. Lucey, A.D., Cafolla, G.J. Carpenter, P.W. and Yang, M. 1997. "The nonlinear hydroelastic behaviour of flexible walls". *Journal of Fluids and Structures* **11**, pp. 717-744.
10. Peake, N., 2001. "Nonlinear stability of a fluid-loaded elastic plate with mean flow". *J. Fluid Mechanics* **434**, pp. 101-118.
11. Tan, B.H., Lucey, A.D., & Pitman, M.W., 2010, "Hydroelastic stability of flexible panel: eigen-analysis and time-domain response", Proceedings of ASME 2010 3rd Joint US-European Fluids Engineering Summer Meeting, Montreal, Canada, Paper no. FEDSM-ICNMM2010-30057.
12. Tan, B.H., Lucey, A.D., and Pitman M.W., 2011, "Controlling hydroelastic instability of hull panels through structural inhomogeneity", In: RINA, Royal Institution of Naval Architects – International Conference, High Speed Marine Vessels, 2-3 March 2011, Fremantle, pp. 51-60.
13. Tan, B.H., Lucey, A.D. & Pitman, M.W., 2011, "Controlling aero-elastic instability of curtain wall systems in high-rise buildings". In: Chan, F., Marinova, D. and Anderssen, R.S. (eds) MODSIM2011, 19th International Congress on Modelling and Simulation. Modelling and Simulation Society of Australia and New Zealand, December 2011, pp. 601-607.
14. Hess, J.L. & Smith, A.M.O., 1966, "Calculation of potential flow about arbitrary bodies", *Vol. 8 of Progr. Aeronaut. Sci.*, Pergamon Press, New York pp1-138.
15. Lucey, A.D. & Carpenter, P.W. 1992. "A study of the hydroelastic stability of a compliant panel using numerical methods". *International Journal of Numerical Methods for Heat and Fluid Flow* **2**, pp. 537-553.
16. Howell, R.M., Lucey, A.D. & Pitman M.W. 2011. "The effect of inertial inhomogeneity on the flutter of a cantilevered flexible plate". *Journal of Fluids and Structures*, **27**(3), pp. 383-393.
17. Eloy, C., Souilliez, C. & Schouveller, L. 2007. "Flutter of a rectangular plate". *Journal of Fluids and Structures* **23**, pp. 904-919.

FLOW ENERGY HARVESTING FROM PIEZOELECTRIC FLAGS

Sébastien Michelin*

LadHyX – Department of Mechanics
Ecole polytechnique
Route de Saclay
91128 Palaiseau, France

Email: sebastien.michelin@ladhyx.polytechnique.fr

Olivier Doaré

Unité de Mécanique (UME)
ENSTA, ParisTech
Chemin de la Hunière
91761 Palaiseau, France

Email: olivier.doare@ensta-paristech.fr

ABSTRACT

The present work investigates the possibility to produce electrical energy from the flutter oscillations of a flexible plate placed in an axial flow and covered with piezoelectric patches that convert bending and stretching of the plate's surface into electric charge displacement. A fully-coupled nonlinear model for the dynamics of the fluid-solid-electric system is presented and used to determine the influence of the different system parameters on the stability, nonlinear dynamics and energy harvesting efficiency of the system. In particular, the role of the tuning between the fluid-solid and electrical systems is investigated as well as the impact of the flow velocity and fluid-solid mass ratio.

INTRODUCTION

Global climate change and scarcity of traditional fossil fuels motivate the development of innovative and renewable energy sources with low environmental impact. Converting the kinetic energy associated with geophysical flows such as winds, rivers, oceanic and tidal currents is particularly attractive, given the wide availability of this resource. Classical fluid-solid instabilities such as Vortex-Induced Vibrations, galloping and flutter in axial flows effectively extract energy from the flow and transform it into solid mechanical energy that can then be used to produce electricity using either displacement-based (e.g. electromagnetic converters) or deformation-based energy converters (e.g. piezoelectric materials) [1–5]

In the present work, we are interested in the feasibility and performance of flow energy harvesting using piezoelectric flexible plates, or flags. Thin flexible plates placed in a steady axial flow are known to become unstable to flutter at a critical velocity [6–8], above which

a large amplitude flapping regime can develop, characterized by the propagation of deformation waves along the flag [9]. When a piezoelectric patch is attached on the deforming flag surface, its periodic bending can be converted into electric charge transfers [10]. Use of piezoelectric materials is not adapted to large scale harvesters, but such materials show competitive and promising performances in the domain of small-power devices [11].

Classically, energy harvesting is represented in the fluid-solid system as an additional damping [12], but this approach overlooks the possible coupling between the harvesting circuit and the fluid-solid system powering it. In this study, an explicit description of the harvesting system is introduced in terms of piezoelectric patches, and following Refs. [13, 14], the equations for the fully-coupled fluid-solid-electrical nonlinear dynamics are derived. This approach provides insight on the double impact of energy harvesting, namely producing electrical energy and modifying the behavior of the fluid-solid system. For example, increasing the coupling coefficient might lead to a better energy transfer to the output circuit but could also eventually result in the restabilization of the system due to its damping effect. Considering the model problem of a slender flexible plate in axial flow, we analyze the energy harvesting efficiency of the system in terms of the different fluid-solid-electric parameters.

The present paper is organized as follows: the fluid-solid-electric model is first presented in Section 1. The effect of the piezoelectric coupling on the stability of the system is then analyzed using linear analysis (Section 2). Section 3 finally focuses on the nonlinear dynamics of the system to determine the amplitude and frequency of the saturated flapping motion and assess the energy harvesting efficiency.

*Address all correspondence to this author.

1 MODEL

1.1 Presentation of the piezoelectric flag

In this work, we consider a rectangular inextensible flexible plate of length L and span l , and negligible thickness h . The plate is clamped at its leading edge and placed in a steady incoming inviscid flow of velocity U_∞ and density ρ . The surface of the plate is covered by pairs of piezoelectric patches (one patch on each side) whose negative electrodes have been shunted through the plate and whose positive electrodes are connected to an output resistive circuit (Figure 1). We neglect here any spanwise plate deformation and charge transfer so that the mechanical and electrical state variables are only functions of the streamwise curvilinear coordinate s and time t . In the following, for any function $a(s,t)$, its derivatives with respect to t and s are noted \dot{a} and a_s , respectively.

The deformation and position of the cantilevered plate are characterized by the local orientation $\theta(s,t)$ of the unit tangent vector $\boldsymbol{\tau}(s,t)$ with the flow direction \mathbf{e}_x . The difference of potential between the free electrodes on each side of the plate and the charge transfer between those electrodes are respectively noted $v(s,t)$ and $q(s,t)$ (Figure 1). In the limit of continuous coverage by patches of infinitesimal length in the streamwise direction [14], the piezoelectric effect results in an additional torque inside the plate imposed by the voltage between the electrodes, namely

$$\mathcal{M}_{\text{piezo}} = -\chi v, \quad (1)$$

with χ the piezoelectric coupling, and in a charge transfer q resulting from the plate's deformation:

$$q = cv + \chi \theta_s \quad (2)$$

with c the characteristic capacity of the piezoelectric patch pair. Noting g the lineic conductivity of the output circuit, q and v are related through Ohm's law

$$\dot{q} + gv = 0. \quad (3)$$

1.2 Non-linear solid dynamics

The system {plate + piezo} is represented as an Euler–Bernoulli beam, and large amplitude displacements of the beam are considered. The beam is inextensible and, taking into account the piezoelectric torque in

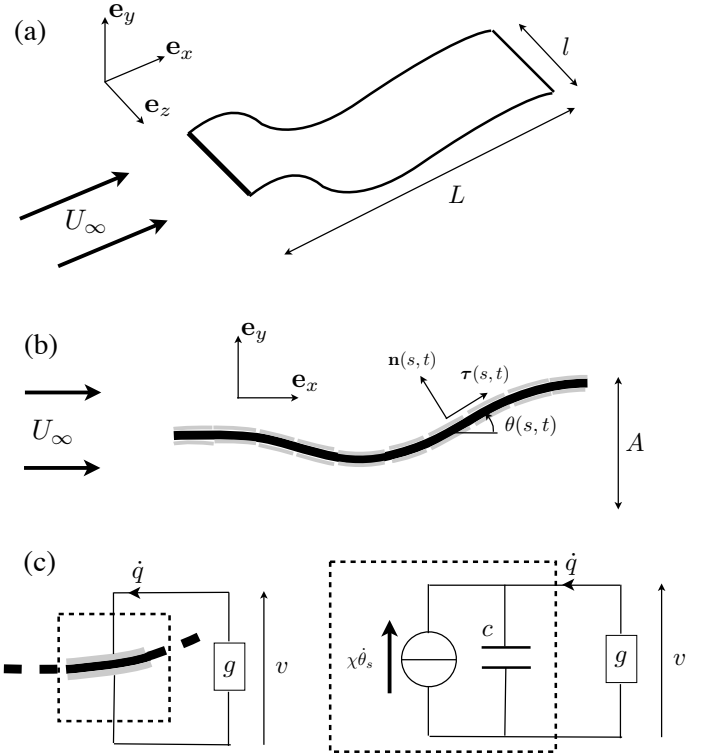


FIGURE 1: (a) Two-dimensional motion of a cantilevered slender flexible plate in axial flow. (b) Piezoelectric flag: the flexible plate (black) is covered on each side by piezoelectric patches (grey). (c) each piezoelectric patch pair is connected to a dissipative circuit and the electrical equivalent is given on the right.

Eq. (1), its position $\mathbf{x}(s,t)$ satisfies

$$\mu \ddot{\mathbf{x}} = \left[T \boldsymbol{\tau} - (B \theta_{ss} - \chi v) \mathbf{n} \right]_s + \mathbf{f}_{\text{fluid}}, \quad (4)$$

$$\mathbf{x}_s = \boldsymbol{\tau}, \quad (5)$$

where B and μ are respectively the uniform rigidity and lineic mass of the piezoelectric flag, $T(s,t)$ is the plate's tension and acts as a Lagrangian multiplier to enforce the inextensibility of the plate, and $\mathbf{f}_{\text{fluid}}$ is the fluid force per unit length on the flag. Clamped-free boundary conditions are used so that

$$\mathbf{x} = 0, \quad \theta = 0 \quad \text{at } s = 0, \quad (6)$$

$$B \theta_s - \chi v = B \theta_{ss} - \chi v_s = 0 \quad \text{at } s = L. \quad (7)$$

1.3 Fluid model

We focus here on the slender body limit ($l \ll L$), when the fluid force applied to the plate can be decomposed into two distinct parts: a reactive force [15], resulting from the added inertia of the fluid put in motion by

each cross-section of the plate, and a resistive force [16] accounting for inertial drag and dissipative effects:

$$\mathbf{f}_{\text{fluid}} = -m_a \rho l^2 \left(\dot{u}_n - (u_\tau u_n)_s + \frac{1}{2} u_n^2 \theta_s \right) \mathbf{n} - \frac{1}{2} \rho l c_d |u_n| u_n \mathbf{n}, \quad (8)$$

where m_a and c_d are the non-dimensional added mass and drag coefficient associated with the plate's cross-section, respectively, and $u_\tau \boldsymbol{\tau} + u_n \mathbf{n} = \dot{\mathbf{x}} - U_\infty \mathbf{e}_x$ is the local relative velocity of the solid to the fluid at rest. The validity of this approach, initially developed to evaluate flow forces created by the motion of a fish body in large amplitude deformations, was recently confronted to and found in good agreement with Reynolds-Averaged Numerical Simulations (RANS) at high Reynolds number [17]. Although limited, in theory, to asymptotically small aspect ratios l/L , it was also shown recently that predictions using this approach provide satisfying results even up to $O(1)$ aspect ratio [18]. In the following, the aspect ratio is taken as $H^* = l/L = 0.5$, and we focus on thin flat plates so that $m_a = \pi/4$ and $c_d = 1.8$.

1.4 Harvesting efficiency

The total power $\mathcal{P}(t)$ harvested by the system is equal to the energy actually transferred to the output circuit and dissipated in the useful load g :

$$\mathcal{P}(t) = \int_0^L g v(s,t)^2 ds. \quad (9)$$

The efficiency of the system is defined as the ratio of the harvested energy to the fluid kinetic energy flux through the section occupied by the system:

$$\eta = \frac{\langle \mathcal{P} \rangle}{\frac{1}{2} \rho U_\infty^3 \mathcal{A} l}, \quad (10)$$

with \mathcal{A} the peak-to-peak flapping amplitude, and $\langle \mathcal{P} \rangle$ the time-average of the output power.

1.5 Non-dimensional parameters

Equations (1)–(9) are non-dimensionalized using L , L/U_∞ and ρL^3 as reference length, time and mass, respectively. v and q are non-dimensionalized by $U_\infty \sqrt{\mu/c}$ and $U_\infty \sqrt{\mu c}$, respectively. The system is then characterized by five non-dimensional coefficients:

$$M^* = \frac{\rho l L}{\mu}, \quad U^* = U_\infty L \sqrt{\frac{\mu}{B}}, \quad H^* = \frac{l}{L} \quad (11)$$

$$\alpha = \frac{\chi}{\sqrt{Bc}}, \quad \beta = \frac{c U_\infty}{gL}, \quad (12)$$

corresponding to the fluid-solid inertia ratio, the non-dimensional flow velocity, the aspect ratio, the piezoelectric coupling and the tuning of the output circuit, respectively. β is indeed the ratio of the non-dimensional time-scale associated with the output RC -loop. In the following, all quantities are non-dimensionalized, unless specified otherwise.

2 LINEAR STABILITY ANALYSIS

We first consider the impact of the piezoelectric coupling on the linear stability of the flexible plate. In the absence of any coupling ($\alpha = 0$), the plate becomes unstable to flutter for a flow velocity U^* greater than a threshold value $U_c^0(M^*)$ [8, 9, 19].

2.1 Linearized equations

In the limit of small vertical displacement $y(s,t)$ of the plate, the linearized equations for y and v are obtained from Eqs. (2)–(4) as

$$(1 + m_a M^* H^*) \ddot{y} + 2m_a M^* H^* \dot{y}_s + m_a M^* H^* y_{ss} + \frac{1}{U^{*2}} y_{ssss} - \frac{\alpha}{U^*} v_{ss} = 0, \quad (13)$$

$$\beta \dot{v} + v + \frac{\alpha \beta}{U^*} \dot{y}_{ss} = 0. \quad (14)$$

Assuming $[y, v] = \text{Re}([Y(s), V(s)]e^{i\omega t})$ with ω complex, Eqs (13)–(14), together with the boundary conditions

$$Y(0) = Y_s(0) = 0, \quad (15)$$

$$Y_{ss}(1) - \frac{\alpha}{U^*} V(1) = Y_{ssss}(1) - \frac{\alpha}{U^*} V_s(1) = 0, \quad (16)$$

become an eigenvalue problem for $[Y, V]$ and ω , solved numerically using a collocation method on N Chebyshev-Gauss-Lobatto points (typically $N \approx 60$ – 120).

2.2 Impact of the piezoelectric coupling on the instability threshold

For a given output circuit (fixed β), an increase in the piezoelectric coupling α impacts the dynamics of the system in two ways: (i) it increases the effective rigidity of the system and (ii) it increases the energy transfer to the output circuit where it is dissipated. One therefore expects an increase of the critical velocity (i.e. a stabilization) due to the piezoelectric coupling. In Fig. 2, the critical velocity is represented for increasing values of α . A stabilization is indeed observed for low M^* (light fluid or short flag), while a destabilization of the higher

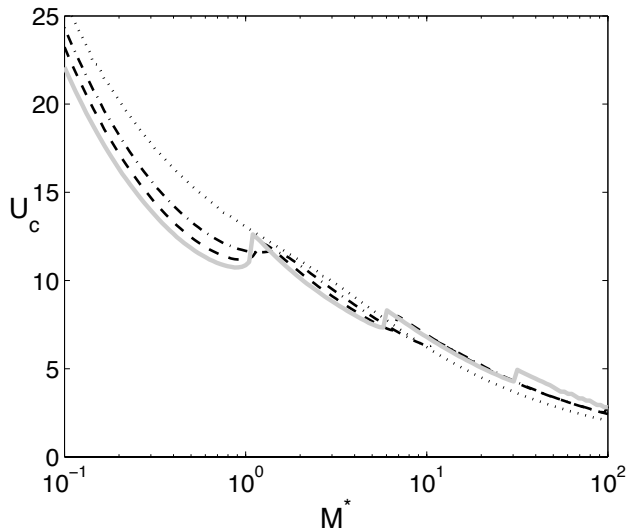


FIGURE 2: Critical velocity threshold $U_c(M^*)$ for $\beta = 0.1$ and $\alpha = 0$ (uncoupled, thick light grey), $\alpha = 0.3$ (dashed), $\alpha = 0.5$ (dash-dotted) and $\alpha = 0.9$ (dotted).

order dominant modes is observed for higher M^* (typically heavier fluid or long flag). This effect was observed recently for a purely two-dimensional model (flag of infinite span), and can be related to the destabilization by damping of negative energy waves in the local stability analysis [14]. One should emphasize that the influence of the piezoelectric coupling is highly dependent on the tuning β of the fluid-solid and electric systems. The results presented in Fig. 2 are obtained when both systems have similar fundamental time-scales.

For a fixed piezoelectric coupling α , the frequency tuning of the fluid-solid and electrical systems, β , is a measure of the resistance in the output circuit. For $\beta \ll 1$, the piezoelectric patches' electrodes are short-circuited: no electric potential is applied to the piezoelectric element and the piezoelectric torque in Eq. (1) vanishes. The flag dynamics is not modified by the piezoelectric, and the critical velocity threshold is that of a flag with no piezoelectric coupling, U_c^0 (Figure 3). On the other hand, when $\beta \gg 1$, the conductivity of the output circuit is negligible and no charge transfer can occur between the electrodes. Equations (1)–(2) impose that the potential v , and therefore $\mathcal{M}_{\text{piezo}}$ are proportional to curvature and effectively, the piezoelectric coupling acts as an increase in the flag's rigidity. As a result, the critical velocity threshold in this open-circuit limit is obtained directly as $U_c^0 \sqrt{1 + \alpha^2}$ (Figure 3). Between these two limit cases, the impact described above is recovered: the fluid-solid-electric coupling induces a destabilization of the system at large M^*

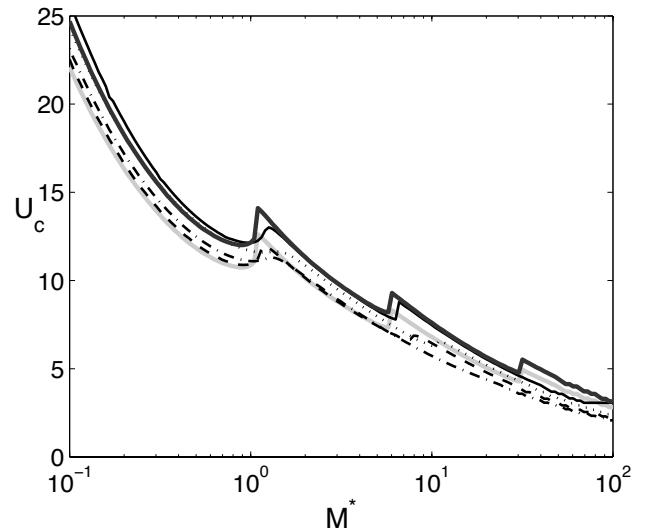


FIGURE 3: Critical velocity threshold $U_c(M^*)$ for $\alpha = 0.5$ and $\beta = 0$ (short circuit, thick light grey), $\beta = 0.1$ (dashed), $\beta = 0.3$ (dash-dotted), $\beta = 1$ (dotted), $\beta = 3$ (solid) and $\beta = \infty$ (open circuit, thick dark grey)

and a stabilization for small M^* .

This destabilization by damping is particularly interesting from the point of view of harvesting energy from a flow. In general, the optimal operating regime of the device should be a trade-off between adding enough damping on the system to dissipate energy in the output circuit while maintaining sufficiently high flapping amplitude. When the system is destabilized by damping, initially at least, the addition of damping to the system satisfies both constraints: it increases the energy transfer while maintaining, or possibly enhancing, the flapping dynamics.

3 NON-LINEAR DYNAMICS

Studying the nonlinear dynamics of the fully coupled fluid-solid-electric system is necessary in order to determine the characteristics of the limit-cycle oscillations of the system (amplitude and frequency) and assess the amount of power that can be harvested by such a device. The non-dimensional form of Eqs. (1)–(8) is solved numerically using a Chebyshev collocation in space and a second order implicit time-stepping method [20]. The flag is initially at rest, with the piezoelectric patches in their reference configuration ($q = v = 0$). At $t = 0$, a small vertical perturbation is added to the horizontal flow to initiate the flag motion.

For $U^* > U_c$, the small perturbation results in an exponential growth of the flapping amplitude that eventually saturates (Figure 4). Two different behaviors can

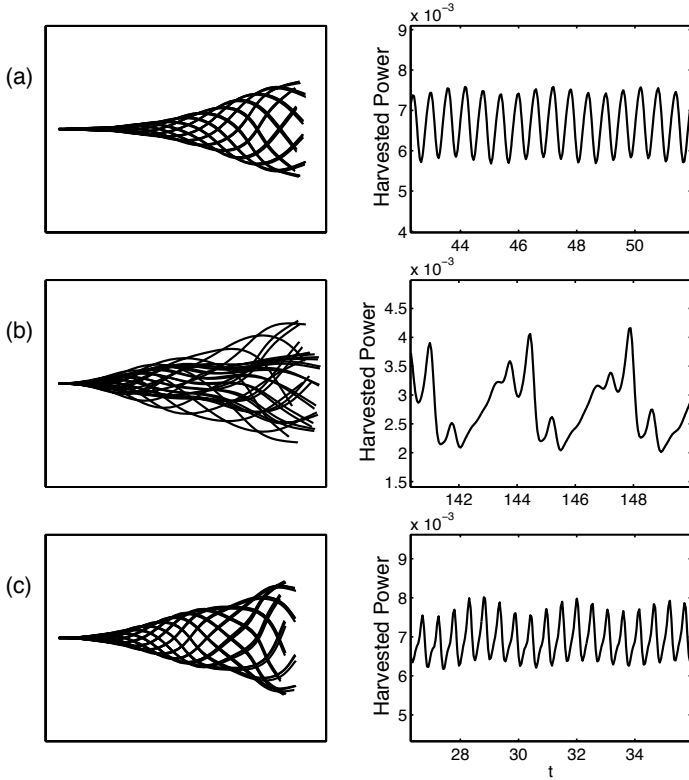


FIGURE 4: Flapping dynamics of the piezoelectric flag for $\alpha = 0.5$, $M^* = 10$, $\beta = 0.158$ and (a) $U^* = 10.5$, (b) $U^* = 11$ and (c) $U^* = 14.5$. (Left) Successive position of the piezoelectric flag and (Right) evolution in time of the instantaneous harvested power.

then be observed: (i) the flag enters a strongly periodic regime with a limit cycle oscillation clearly identified or (ii) the flag dynamics is more complex, suggesting some nonlinear interactions between different modes, and some chaotic-looking motion.

A complete discussion of the properties of the latter behavior is beyond the scope of the present work, but it is worth noting that such complex behavior was reported in experimental and numerical studies on the flapping flag dynamics [9, 18, 21, 22], and is not specific to the piezoelectric coupling problem. For fixed M^* , α and β , as U^* is increased beyond the critical velocity U_c and more modes become unstable, the system shows different mode switching events, one being illustrated on Figures 4 and 5. The impact of such events on the harvesting performance is important as the amplitude, frequency and curvature distributions are modified.

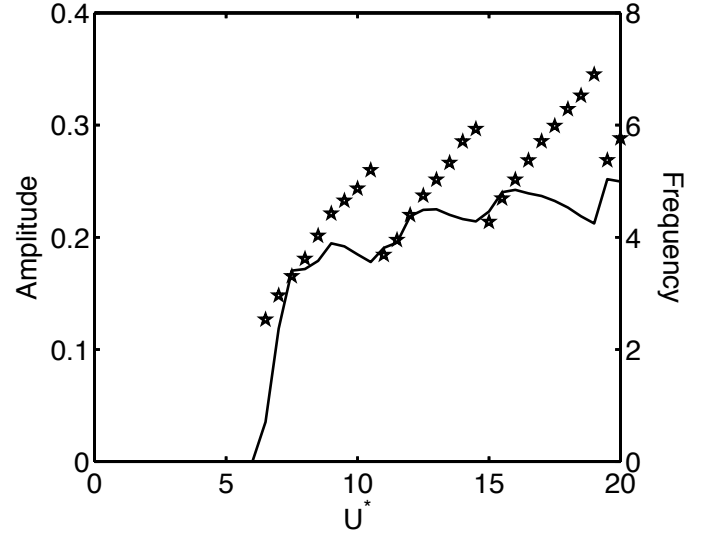


FIGURE 5: Evolution with U^* of the amplitude (solid) and frequency (stars) of the limit-cycle oscillations for $M^* = 10$, $\alpha = 0.5$ and $\beta = 0.158$.

4 HARVESTED ENERGY AND EFFICIENCY OF THE SYSTEM

For a given set of parameters $(M^*, U^*, \alpha, \beta)$ the dynamics of the piezoelectric system is obtained using the numerical method presented above, and the harvesting efficiency is computed using Eq. (9). When a limit cycle is detected, the efficiency is simply obtained by taking the time-average of $\mathcal{P}(t)$ over one period, and the non-dimensional flapping amplitude $A = \mathcal{A}/L$ is computed as

$$A = \sqrt{\langle 2y_e(t)^2 \rangle}, \quad (17)$$

with $y_e(t)$ the deflection of the trailing edge of the flag.

In the case where a limit cycle can not be identified, the computation is carried over a long enough time frame to ensure that a stationary flapping state has been reached. The efficiency is then obtained using statistical averages over this interval in order to define A and $\langle \mathcal{P} \rangle$.

We are interested here in the influence of the different parameters on the system's performance, measured here by the efficiency η , the ratio of the energy used in the output circuit (i.e. dissipated in the resistive elements) and of the flow kinetic energy flux through the cross-section occupied by the device. In Figure 6, the evolution of η with β and U^* is represented for two different values of M^* .

One first observes that η vanishes for both $\beta \ll 1$ and $\beta \gg 1$ and is only significant in the intermediate range $\beta \sim 0.1-1$, a direct result from the filtering properties of the RC-loop: for $\beta \ll 1$, the circuit's resis-

tance is infinitesimal, resulting in negligible energy dissipation despite the charge transfers between the piezoelectric electrodes; for $\beta \gg 1$, the resistance is too large for any charge transfer to be possible. The dissipated power is maximum when the frequency of the forcing on the electrical circuit (here, the flapping flag frequency) is close to the circuit's fundamental frequency g/c . This is confirmed by comparing the results for $M^* = 1$ and $M^* = 10$: for larger M^* , higher order modes are known to become dominant and have typically higher frequencies [9]. The maximum efficiency is then obtained for a higher characteristic frequency of the electrical circuit, namely a smaller value of β (Figure 6).

For a fixed β and increasing U^* , successive optimal regions are observed separated by low-efficiency transition regions. This behavior can be interpreted from the mode switching events observed on Figure 4 and 5: as U^* is increased, the efficiency of the system increases while the dynamics of the system remains locked on the same mode, because the frequency of that mode is increasing with U^* . However, as more modes become unstable the limit cycle oscillations can lock onto a different mode with lower frequency resulting in a drop in the system's efficiency. One observes that when the fluid inertia is increased (greater M^*), mode switching events occur at more closely-spaced values of U^* .

The effect of β can also be observed on the stability threshold: for small M^* , the critical velocity increases monotonically with β between the short-circuit and open-circuit limits, while destabilization by damping is observed for larger M^* . Figure 6(b) also shows that the impact of β on the mode switching thresholds is similar to that on the stability threshold.

The performance of the system can therefore be optimized by tuning the output circuit to the frequency of the flag dynamics. This frequency is however not constant but is itself modified by the fluid-solid-electric coupling. In Fig. 7, we consider the evolution of the efficiency of the optimally-tuned system with M^* and U^* : for a given value of these two parameters, the maximum achievable efficiency (over all possible values of β) is represented. One observes that the efficiency is in general an increasing function of U^* (as seen previously) and M^* . This higher efficiency of the high-fluid loading limit (large M^*) confirms the linear analysis in Ref. [14], where the energy transfer from the fluid-solid system to the electrical circuit was shown to be more efficient on configurations destabilized by damping. Maximum efficiencies above 10% are achievable, but it must be pointed out that the efficiency is strongly dependent on U^* at higher M^* as critical flow velocities leading to mode switching events get closer as

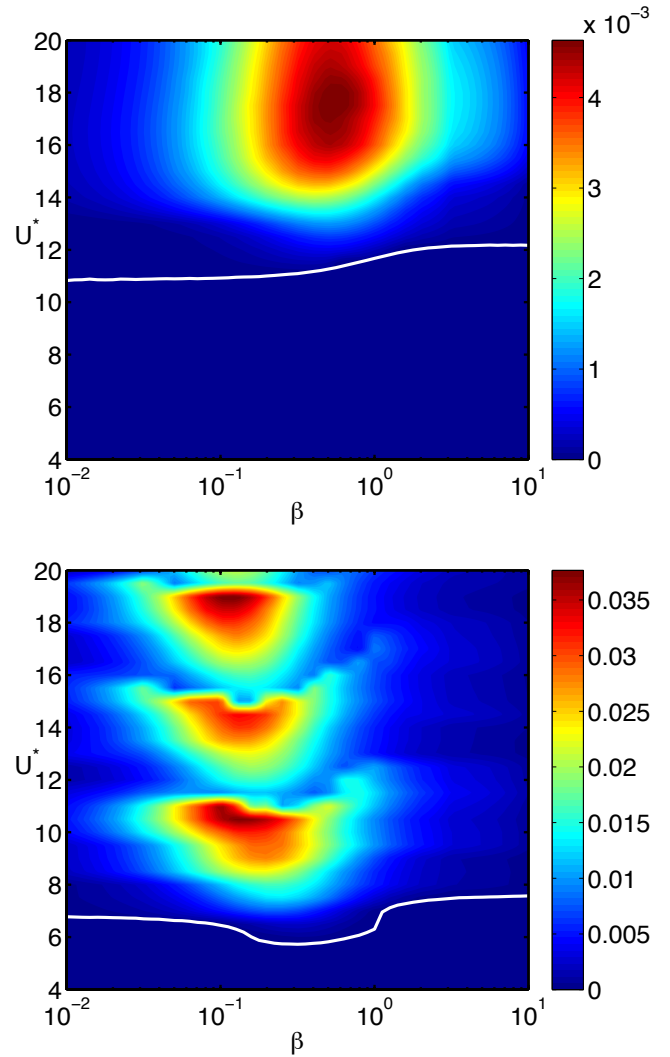


FIGURE 6: Evolution of the harvesting efficiency with the tuning ratio β and flow velocity U^* for $\alpha = 0.5$ and $M^* = 1$ (top) and $M^* = 10$ (bottom). the white line corresponds to the stability threshold.

M^* is increased (Figure 6). This results in an increased sensitivity of the device's performance with the flow velocity.

CONCLUSIONS

The present study provides some important insight on the coupled dynamics of a classical fluid-solid system (a fluttering flag) and an output circuit producing electrical energy from the deformation of the structure. It was shown that the coupling can lead to a destabilization of the system, corresponding to an increase in the operating range of the device. The destabilized range of fluid loading M^* also corresponds to the highest harvesting efficiencies. The role of the tuning of the output circuit to

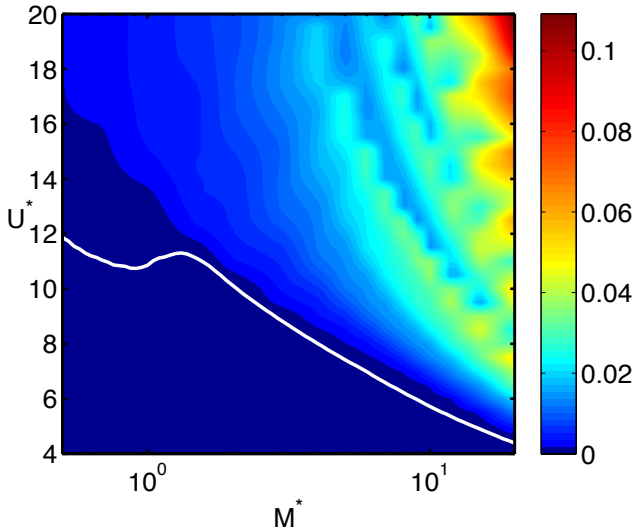


FIGURE 7: Optimal energy harvesting efficiency as a function of M^* and U^* for $\alpha = 0.5$. For each value of (M^*, U^*) , the maximum efficiency obtained for the optimal value of β is represented. The white line corresponds to the minimum stability threshold over all β .

the fluid-solid frequency is here essential: only carefully-tuned system can harvest a significant amount of energy.

Here, we illustrated the critical role played by the nonlinear flapping mode selection on the energy harvesting efficiency of the system. The locking of the flag on a particular dynamics is a strongly nonlinear phenomenon, and it is expected that it is also influenced by the output circuit behavior. Further investigation is therefore necessary to understand more completely the factors determining the nonlinear dominant mode in order to ensure an increased robustness to the harvesting system with respect to the flow conditions.

ACKNOWLEDGMENT

S. M. would like to acknowledge the support of a Marie Curie International Reintegration Grant within the 7th European Community Framework Program.

REFERENCES

- [1] Bernitsas, M. M., Raghavan, K., Ben-Simon, Y., and Garcia, E. M. H., 2008. "VIVACE (Vortex Induced Vibration Aquatic Clean Energy: a new concept in generation of clean and renewable energy from fluid flow". *J. Offshore Mech. Arct. Eng.*, **130**, p. 041101.
- [2] Barrero-Gil, A., Alonso, G., and Sanz-Andres, A., 2010. "Energy harvesting from transverse galloping". *Journal of Sound and Vibration*, **329**(14), pp. 2873–2883.
- [3] Peng, Z., and Zhu, Q., 2009. "Energy harvesting through flow-induced oscillations of a foil". *Phys. Fluids*, **21**, p. 123602.
- [4] Singh, K., Michelin, S., and de Langre, E., 2012. "Energy harvesting from axial fluid-elastic instabilities of a cylinder". *J. Fluids Struct.*, **30**, pp. 159–172.
- [5] Grouthier, C., Michelin, S., and de Langre, E., 2012. Energy harvesting using vortex-induced vibrations of tensioned cables. submitted to *J. Fluids Struct.*, preprint available at <http://arxiv.org/abs/1203.0236>.
- [6] Paidoussis, M. P., 2004. *Fluid-Structure Interactions, Slender Structures and Axial Flows*, Vol. 2. Academic Press, London.
- [7] Shelley, M. J., and Zhang, J., 2011. "Flapping and bending bodies interacting with fluid flows". *Ann. Rev. Fluid Mech.*, **43**, pp. 449–465.
- [8] Eloy, C., Lagrange, R., Souilliez, C., and Schouveiler, L., 2008. "Aeroelastic instability of a flexible plate in a uniform flow". *J. Fluid Mech.*, **611**, pp. 97–106.
- [9] Michelin, S., Llewellyn Smith, S. G., and Glover, B. J., 2008. "Vortex shedding model of a flapping flag". *J. Fluid Mech.*, **617**, pp. 1–10.
- [10] Allen, J. J., and Smits, A. J., 2001. "Energy harvesting eel". *J. Fluids Struct.*, **15**, pp. 629–640.
- [11] Sodano, H., Inman, D., and Park, G., 2004. "A review of power harvesting from vibration using piezoelectric materials". *The Shock and Vibration Digest*, **36**(3), pp. 197–205.
- [12] Tang, L., and Paidoussis, M. P., 2009. "The coupled dynamics of two cantilevered flexible plates in axial flow". *J. Sound Vib.*, **323**, pp. 214–231.
- [13] Bisegna, P., Caruso, G., and Maceri, F., 2006. "Optimized electric networks for vibration damping of piezoactuated beams". *Journal of Sound and Vibration*, **289**(4-5), pp. 908–937.
- [14] Doaré, O., and Michelin, S., 2011. "Piezoelectric coupling in energy-harvesting fluttering flexible plates: linear stability analysis and conversion efficiency". *J. Fluids Struct.*, **27**, pp. 1357–1375.
- [15] Lighthill, M., 1971. "Large-amplitude elongated-body theory of fish locomotion". *Proc. Roy. Soc. B*, **179**, pp. 125–138.
- [16] Taylor, G., 1952. "Analysis of the swimming of long and narrow animals". *Proc. Roy. Soc. Lon. A*, **214**, pp. 158–183.
- [17] Candelier, F., Boyer, F., and Leroyer, A., 2011. "Three-dimensional extension of lighthill's large-

- amplitude elongated-body theory of fish locomotion”. *J. Fluid Mech.*, **674**, pp. 196–226.
- [18] Eloy, C., Kofman, N., and Schouveiler, L., 2012. “The origin of hysteresis in the flag instability”. *J. Fluid Mech.*, **691**, pp. 583–593.
- [19] Eloy, C., Souilliez, C., and Schouveiler, L., 2007. “Flutter of a rectangular plate”. *J. Fluids Struct.*, **23**, pp. 904–919.
- [20] Alben, S., 2009. “Simulating the dynamics of flexible bodies and vortex sheets”. *J. Comp. Phys.*, **228**, pp. 2587–2603.
- [21] Connell, B. S. H., and Yue, D. K. P., 2007. “Flapping dynamics of a flag in uniform stream”. *J. Fluid Mech.*, **581**, pp. 33–67.
- [22] Alben, S., and Shelley, M. J., 2008. “Flapping states of a flag in an inviscid fluid: bistability and the transition to chaos”. *Phys. Rev. Lett.*, **100**, p. 074301.

THE FLUID-STRUCTURE INTERACTION OF A SPRING-MOUNTED CANTILEVERED-FREE FLEXIBLE PLATE IN A UNIFORM FLOW

R.M. Howell*

A.D. Lucey

Fluid Dynamics Research Group
Curtin University of Technology
GPO Box U1987, Perth, WA 6845, Australia
Email: richard.howell@curtin.edu.au

ABSTRACT

We study a new fundamental system comprising a cantilevered thin flexible plate aligned with a uniform flow in which its upstream end is attached to a spring-mass system. This allows the entire system to oscillate perpendicularly to the flow direction as a result of the mounting's dynamic interaction with the flow-induced oscillations of the flexible plate. The long-term goal of the study is the development of an energy harvesting system whereby the reciprocating motion of the support system can be tapped for energy production. Here we formulate and deploy a hybrid of theoretical and computational models for the system and map out its linear stability characteristics. Compared to a fixed cantilever, the introduction of the dynamic support system yields lower flutter-onset flow speeds and a reduction of the order of the mode that yields the critical flow speed, effects that are desirable for energy harvesting.

INTRODUCTION

Recent practical motivation for the renewed study of cantilevered-free flexible plates in axial flow - a problem first studied in the modern era by [1] - is the potential to use flow-induced oscillations, or flutter, of the flexible plate to capture kinetic energy from the mean flow. Vortex-shedding from an upstream cylinder can be used to drive the dynamic deformation of the flexible plate [2, 3] that principally operates at frequencies determined by the Strouhal number of the cylinder flow. Perhaps more versatile are the recent ideas of [4–6] wherein it is the fluid-structure interaction of the flexible plate that is the source of its motions; these exploit the naturally

occurring flutter instability of the flexible plate above a critical flow speed. In most of these studies the mechanical energy of the flexible-plate is converted to electrical energy via a piezoelectric material adhered to the surface of the flexible plate. This is both less convenient and robust than energy-harvesting systems in which the pitching and heaving of a rigid aerofoil drive reciprocating motion that can readily be converted into rotary motion of a shaft; for example see [7–9].

The long-term goal of the present work is the development of an energy-harvesting system that combines the merits of the flexible-plate flutter systems with the robust energy transmission principles of rigid-aerofoil systems. We therefore conceive the system illustrated in Fig. 1 wherein the flow-induced oscillations of the flexible plate drive vertical oscillatory motion of a mass-spring support system having its own dynamics that can clearly be tuned. The extraction of power could readily be modelled by the inclusion of a linear damping at the support. However, the first step towards our goal is to understand the stability characteristics of this new fundamental FSI system.

In this paper we therefore develop a theoretical and computational model of the two-dimensional system,

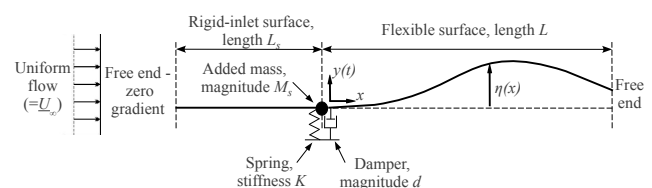


FIGURE 1: THE FLUID-STRUCTURE SYSTEM UNDER CONSIDERATION.

*Address all correspondence to this author.

leave damping to one side, and map out the dynamics of the remaining parameter space that we find has the usual non-dimensional control parameters, mass ratio \bar{L} and flow speed \bar{U} , for a fixed cantilever, in addition to which there are the natural frequency of the spring-mass support system, $\bar{\omega}_s$, and the length and mass of the rigid-inlet \bar{L}_s and M_s . To this end, the methods of [10, 11] that mixed numerical simulation with eigenvalue analysis are built upon in the present paper. Thus, ideal two-dimensional flow is assumed wherein the rotationality of the boundary-layers is modelled by vortex elements on the solid-fluid interface and the imposition of the Kutta condition at the plate's trailing edge. The Euler-Bernoulli beam model is used for the structural dynamics. The latter is appropriate because it is our overall objective to design and optimise an energy-harvesting system that operates for low-amplitude deformations - to reduce material fatigue effects - of the flexible plate by tuning the support system such that the available wind speed coincides with the critical speed of flutter onset of the flexible plate. The results presented in this paper demonstrate that this strategy is practicable.

THEORETICAL AND COMPUTATIONAL MODELLING

The essential modelling is described in detail in [10] wherein the system of Fig. 1 was mounted symmetrically within a channel with its walls located at $y = \pm H$; the present system is obtained by letting $H \rightarrow \infty$. For the present paper, we also neglect the effects of the wake that were modelled in the precursor paper.

Simply supported free beams where the support can move vertically and actuate the system have been analysed in studies of insect flight, for example see [12], and constrain that the leading edge must follow (i) the heaving motion and (ii) the pitching motion of the actuating force. In our study we allow that as well as applying an actuating force due to the reaction of the spring, the motion of the leading edge can also be actuated upon by the motion of the flexible plate; we therefore modify these constraints so that they are applied through the inclusion of (i) a non-zero normal velocity at all panel control points equal to the velocity of the first mass point (upstream end of the flexible plate), and (ii) a shear-force balance condition at the leading edge that transmits the shear force that drives the vertical motion of the mounting system and the rigid, upstream splitter-plate whilst also enforcing that neither free nor controlled rotation of the beam about its leading edge is permitted; this means that the support mechanism can provide, without deformation, any level of moment reaction to the flexible plate at its upstream end.

We now summarise the approach of [10] as applied to the present investigation and show how these two conditions for the spring mass system are readily incorporated in the model. J_s and J are the number of panels on the rigid central-surface and the flexible plate respectively. At the centre of each panel is a control point where properties relating to the fluid pressure calculated for each panel are assumed to be located. In contrast, the flexible plate is discretised into a set of $N(=J-1)$ mass points where the mechanical properties of the plate will be assumed centred. The flow field is found using a linearised boundary-element method (BEM) with first-order vortex panels on the flexible plate because of the discontinuity of tangential fluid velocity across this surface that makes it a lifting surface; the distributed lift drives the motion of the flexible plate. The singularity strengths are determined by enforcing the no-flux boundary condition at every panel control point and continuity of the distributed vorticity between adjacent panels used to discretise the flexible plate. However, enforcing condition (i) from above requires that the no-flux condition be modified to reflect that all the panels now move with an additional component of normal velocity $\dot{\eta}_1$. Thus the vector of singularity strengths is given by

$$\{\Gamma_m\} = [I_{im}^N]^{-1} \{U_\infty \theta_m + \dot{\eta}_m + \dot{\eta}_1\}, \quad (1)$$

where Γ_m contains the zero- and first-order coefficients of the singularity distributions on the panels in the BEM; U_∞ is the free-stream flow speed. $[I_{im}^N]^{-1}$ contains, in addition to the normal influence-coefficients of the singularities, the boundary conditions of: a) vortex strength continuity at panel end points; and b) zero vorticity at the plate's trailing edge, thus enforcing the standard Kutta condition of zero pressure difference at the trailing edge for linear displacements. The panel's angle to the horizontal is θ_m which in the linear framework is the stream-wise spatial derivative of the deformed interface, η_m .

The unsteady Bernoulli equation is used to determine the pressure distribution on the flexible plate. The transmural pressure is then used as the forcing term in the one-dimensional thin flexible-plate equation couched in finite-difference form. The motions of the plate and the fluid flow are fully coupled through deflection, vertical velocity and acceleration of the two media at their interface. This allows the following single system (matrix) equation to be written

$$\begin{aligned} & \rho h [\mathbf{I}] \{\ddot{\eta} + \dot{\eta}_1\} + d [\mathbf{I}] \{\dot{\eta}\} + B [\mathbf{D}_4] \{\eta\} + K [\mathbf{I}] \{\eta\} \\ & = 2\rho_f U_\infty^2 \frac{1}{\delta x} [\mathbf{B}_1^+] \{\eta_m\} + \rho_f U_\infty [\mathbf{B}_1^-] \{\dot{\eta}_m\} \end{aligned}$$

$$\begin{aligned}
 & + \rho_f U_\infty [\mathbf{B}_{1^*}^-] \{\dot{\eta}_1\} + \rho_f U_\infty \frac{1}{\delta x} [\mathbf{B}_{2^*}^+] \{\dot{\eta}_m\} \\
 & + \rho_f [\mathbf{B}_2] \{\ddot{\eta}_m\} + \rho_f [\mathbf{B}_{2^*}] \{\ddot{\eta}_1\}, \quad (2)
 \end{aligned}$$

where $[\mathbf{B}]$ are matrices of singularity influence coefficients, $[\mathbf{D}_4]$ is a fourth-order spatial-differentiation matrix and $[\mathbf{I}]$ is the identity matrix. The $[\mathbf{B}]$ matrices marked with a + or - have been suitably rearranged to have the equations in terms of η instead of θ ; those marked with an asterisk * are the additional affects of the system mobile mounting and only contain values in their first column. ρ , h , d and B are respectively, the material density, thickness, dashpot-type damping coefficient and flexural rigidity of the plate, the dynamics of which appear on the left-hand side of the equation. The extra $\ddot{\eta}_1$ in the first mass term on the left-hand side reflects the extra inertia of the system owing to the moving neutral axis. Uniform discretisation of the plate length L into N collocation points defines $\delta x = L/N$. The pressure perturbation that drives the plate motion appears on the right-hand side, where ρ_f is the fluid density. The pressure terms that depend on plate displacement, velocity and acceleration in Eqn. (2) can be interpreted as the hydrodynamic stiffness, damping and inertia respectively.

Equation (2) above applies to the mass points from 2 through to N . For $N = 1$ condition (ii) will be applied as the upstream end condition where the shear force drives the vertical motion of the mounting system and the rigid upstream splitter plate. Thus, the shear force in the flexible plate is calculated exactly from the enforcement of the following force-balance condition at its leading edge where it connects to the spring-mass support mechanism that has displacement $\eta_1(t)$,

$$M \frac{\partial^2 \eta_1}{\partial t^2} + K \eta_1 = \frac{Eh^3}{12} \frac{\partial^3 \eta}{\partial x^3} \Big|_{x=0} + \int_{-L_s}^0 \delta p_s dx, \quad (3)$$

and where $\eta(x,t)$ is the flexible-plate vertical-displacement field; δp_s is the pressure difference across the moving splitter plate that generates an additional vertical force driving the motion of the support system. The shear condition is therefore joining two separate systems: a vertically oscillating flat plate joined to a vertically oscillating flexible plate.

It is also noted that the first mass point in the system is at the exact same height as the cantilever leading to a flat panel in the BEM and therefore an absence of hydrodynamic stiffness on this panel as well as along the rigid inlet; it is effectively an extension of the rigid inlet and therefore the pressure on this panel is included the

value of δp_s on the right hand side of Eqn. (3). We therefore have the following values for the boundary condition mass points

$$\eta_{-1} = \eta_0 = \eta_1, \quad \dot{\eta}_0 = \dot{\eta}_1 \quad \text{and} \quad \ddot{\eta}_0 = \ddot{\eta}_1. \quad (4a, b, c)$$

The values in Eqn. (4) are applied in the first columns of the $[\mathbf{B}]$ matrices and the matrix $[\mathbf{D}_4]$.

To model the mass of the inlet we introduce a point mass at the first mass point; its value is given in quanta, n_s^+ , of total flexible plate mass (per unit width), $M^T = \rho h L$. To effect this, the plate mass M in Eqn. (3) becomes $M + n_s^+ M^T$. It is noted that the rigid inlet surface is totally rigid and so only exists in the plate model owing to this added mass: it does physically exist on the fluid side of the model to capture its aerodynamic effects.

We take two approaches to the solution of the system comprised of Eqns. (2) and (3). In the first we reduce the second-order ordinary differential equation in $\{\eta\}$ to first-order using the state-space variables $w_1(t) = \eta(t)$ and $w_2(t) = \dot{\eta}(t)$. Rearranging in companion-matrix form then yields the system equation

$$\dot{w} = [H]w \quad \text{where} \quad w = \{w_1, w_2\}^T. \quad (5)$$

Single-frequency time-dependent response is assumed at ω which is a complex eigenvalue of $[H]$. Positive ω_r and ω_R respectively represent the oscillatory and amplifying parts of the response.

Alternatively, we perform a time-discretisation of the system comprised of Eqns. (2) and (3) and then numerically time-step, using a semi-implicit method, the equation to determine the system response to some form of initial perturbation. In doing so we are able to study transient behaviour and reveal localised flow-structure dynamics that when summed contribute to the system response.

RESULTS

Our results are presented in non-dimensional form having used the scheme of [13], and derived more explicitly in [14], whereby reference time and length are given by

$$t_r = (\rho h)^{\frac{5}{2}} / (\rho_f^2 B^{\frac{1}{2}}) \quad \text{and} \quad L_r = \rho h / \rho_f, \quad (6a, b)$$

and therefore

$$\bar{t} = t / t_r \quad \text{and} \quad \bar{U} = U_\infty t_r / L_r. \quad (7a, b)$$

The non-dimensional streamwise coordinate, the length (or mass ratio) of the flexible plate and the non-dimensional rigid inlet length are defined by

$$\bar{x} = x/L, \quad \bar{L} = L/L_r \quad \text{and} \quad \bar{L}_s = L_s/L. \quad (8a, b, c)$$

This scheme permits \bar{U} and \bar{L} to be interpreted respectively as the physical flow speed and plate length for given fluid and plate properties.

Instead of using the non-dimensional form of \bar{K} associated with the foregoing scheme, we use the following property from systems analysis

$$\bar{\omega}_s = \sqrt{\frac{K}{M_s}} t_r, \quad (9)$$

where $\bar{\omega}_s$ is the non-dimensional natural frequency of the spring-mass system. M_s is defined as

$$M_s = (n_s^+ + 1)\rho hL, \quad (10)$$

the whole mass of the plate being critical to the spring-mass system's natural frequency; the effect of the fluid mass along the flexible and rigid surfaces on the natural frequency is compensated for in the non-dimensional scheme.

In summary, we find that the critical velocity of the system \bar{U}_c takes the functional dependence

$$\bar{U}_c = f(\bar{L}, \bar{L}_s, n_s^+, \bar{\omega}_s), \quad (11)$$

on the system's control parameters. We discretise the flexible plate into N mass points, following the study in [10] wherein the present methods were validated, and extract all N system eigenmodes.

Stability Characteristics

We first review the results for a homogeneous, or 'standard', short plate at $\bar{L} = 1$ presented in [10] for $\bar{H} = 1$ (for which the channel walls were shown to exert negligible effect) with $\bar{L}_s = 0$. Figure 2a shows the variation of system eigenvalues with applied flow speed. In this and subsequent eigenvalue plots the broken lines denote the oscillatory (imaginary) part of the eigenvalue, ω_I , while the solid lines show the associated growth/decay (real) part of the eigenvalue, ω_R . The modes are numbered in the plots following their order of increasing frequency at zero flow speed. Instability sets in at the lowest flow

speed (the critical flow speed, \bar{U}_c) for which ω_R becomes positive, *i.e.* that at which the ω_R locus crosses the horizontal axis to move into the upper positive quadrant of the plot. In Fig. 2a it is seen that single-mode flutter of the second system mode - highlighted by a thicker line type - is the critical instability at a non-dimensional flow speed $\bar{U} = \bar{U}_c = 5.452$. Figure 2b shows the numerical simulation of the critical mode at this flow speed. The simulation was started by releasing the plate from an applied deformation - the thick black line - in the shape of the second *in-vacuo* mode. The critical mode, seen to contain strong contributions from the first and second *in-vacuo* modes, then evolves from the initial excitation.

Figure 3 shows the effect on these results of the now oscillating mounting support of the cantilever. Contrasting with Fig. 2b, Fig. 3b shows that the critical mode shape loses most of its second-order mode content and becomes more first-mode dominated. The reason for this is seen in Fig. 3a as the stronger real component of the first mode just below the x -axis. For this reason the simulation was started by releasing the plate from an applied deformation in the shape of the first *in-vacuo* mode enabling the system to settle more quickly into its limit cycle. It is noted that the mobile cantilever instability is more severe as shown by a steeper gradient of the real part of Mode 2 when it becomes positive.

We now review the results presented in [10] for $\bar{H} = 1$ with a rigid, upstream splitter-plate that gives $\bar{L}_s = 1$. In Fig. 4a it is seen that modal-coalescence flutter of the second and third system modes - highlighted by a thicker line type - is the critical instability at a non-dimensional flow speed $\bar{U} = \bar{U}_c = 13.48$. Figure 4b shows that the critical mode, containing strong contributions from the second and third *in-vacuo* modes, then evolves from the initial excitation.

Figure 5 shows the effect on these results of the now oscillating mounting support of the cantilever. Figure 5b shows that the critical mode shape loses some of its third-order mode content as the first node becomes absorbed into the movement of the mobile cantilever. This allows the second-order mode content to become greater than in the fixed cantilever case. Figure 5a shows that the frequency of oscillation is much lower as seen in the much lower imaginary part of the third mode at the critical velocity. It also shows that the instability is less severe because the gradient of the real part of Mode 3 is milder where it crosses the axis and that the modal coalescence between Modes 2 and 3 is less pronounced as compared with the corresponding features in Fig. 4a. The spring mounting has reduced the difference in frequency between the system modes at zero flow speed: thus, the

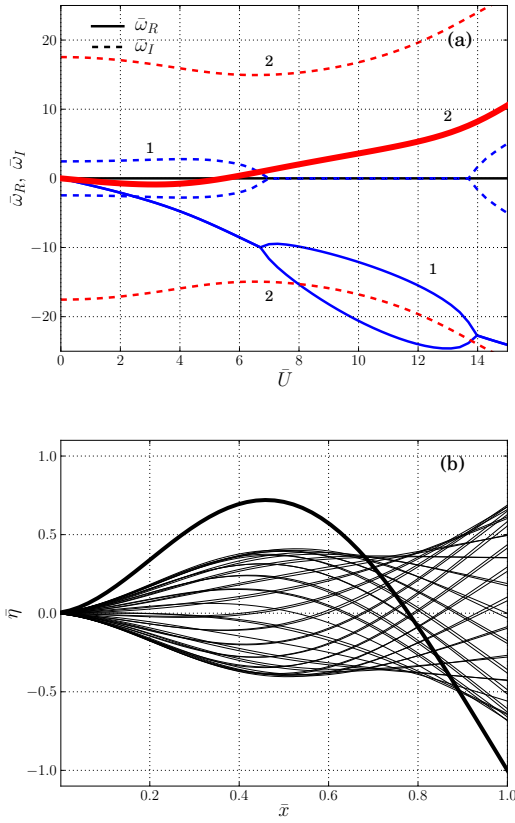


FIGURE 2: SYSTEM DYNAMICS FOR $\bar{L} = 1$ AND $\bar{L}_s = 0$: (a) VARIATION OF NUMBERED EIGENVALUES WITH FLOW SPEED (OSCILLATORY AND GROWTH/DECAY PARTS REPRESENTED BY BROKEN AND FULL LINES RESPECTIVELY) WITH THE REAL PART OF MODE 2 THAT BECOMES UNSTABLE HIGHLIGHTED THROUGH A THICKER LINE TYPE, (b) TIME-SEQUENCE OF INSTANTANEOUS PLATE POSITION AT CRITICAL SPEED $\bar{U}_c = 5.452$ (OF MODE 2 IN (a), THE THICK LINE BEING THE INITIAL DEFLECTION WITH EARLY OSCILLATIONS REMOVED). ADAPTED FROM [10].

gap between the frequencies of Modes 2 and 3 to achieve modal coalescence through the fluid loading is substantially less. This type of instability is sensitive to the magnitude of the applied fluid pressure (that scales with flow speed) and thus for the spring-mounted case the instability first occurs at a lower value of flow speed than for a fixed cantilever.

Figures 6a and 7a show how the critical speeds of instability onset vary with the spring-mounting characterised by $\bar{\omega}_s$ for fixed \bar{L} , with $n_s^+ = 0$ and $\bar{L}_s = 0$ and 1 respectively while Figs. 6b and 7b show the corresponding variation of the frequencies of the critical modes. The vertical dashed lines show the \bar{U}_c and $\bar{\omega}$ values for the fixed cantilever case. In Figure 6 the system is destabilised by

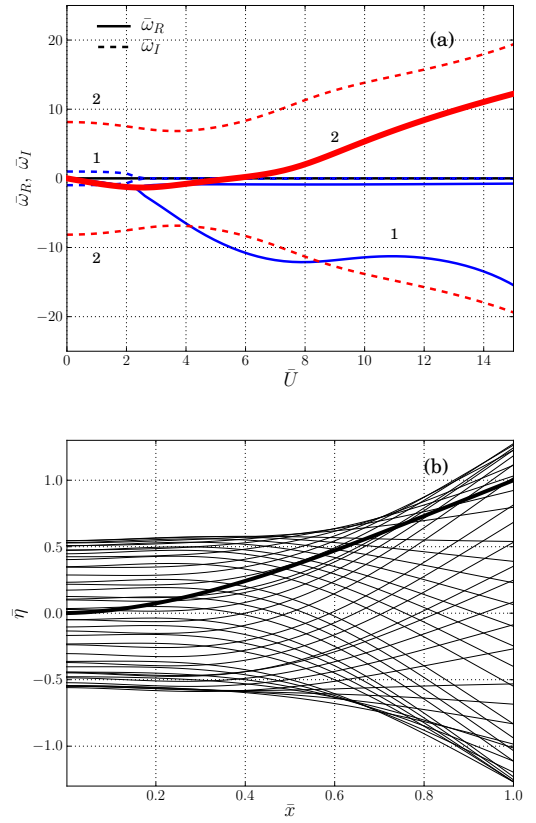


FIGURE 3: THE EFFECT OF A MOBILE CANTILEVER ON THE FLUID STRUCTURE INTERACTION AT $\bar{L} = 1$ AND $\bar{L}_s = 0$ WITH $\bar{\omega}_s = 1$: SYSTEM GIVING FIG. 2 MODIFIED BY A MOBILE CANTILEVER GIVING $\bar{U}_c = 5.6$ OF MODE 2. SUB-FIGURE TITLES AND LEGENDS AS IN FIG. 2.

single-mode flutter while in Fig. 7 the instability is due to a modal-coalescence of system Modes 2 and 3. We remark that the detailed results of Figs. 3 and 5 respectively appear as the data points for $\bar{\omega}_s^{-1} = 1$ in Figs. 6 and 7. Figures 6a and 7a show that the spring-mounted cantilever is typically less stable - critical flow speeds are lower - than the fixed cantilever. Figures 6b and 7b show that the introduction of the spring-mounting generally decreases the oscillation frequencies of the critical mode as compared with the fixed-cantilever although an unusual region appears in Fig. 7b for high mounting spring stiffness wherein the frequency actually exceeds that of the fixed case. The onset flow speeds and frequencies of the critical mode are seen to approach those of the fixed cantilever as $\bar{\omega}_s$ is increased ($\bar{\omega}_s^{-1}$ is decreased) although a very small numerical difference between the new mobile and previous [4] fixed cantilever models appears in Fig. 6a. This is most probably due to ill-conditioning of the system stiffness matrix as the value of the spring-support coefficient is made extremely large. The most significant

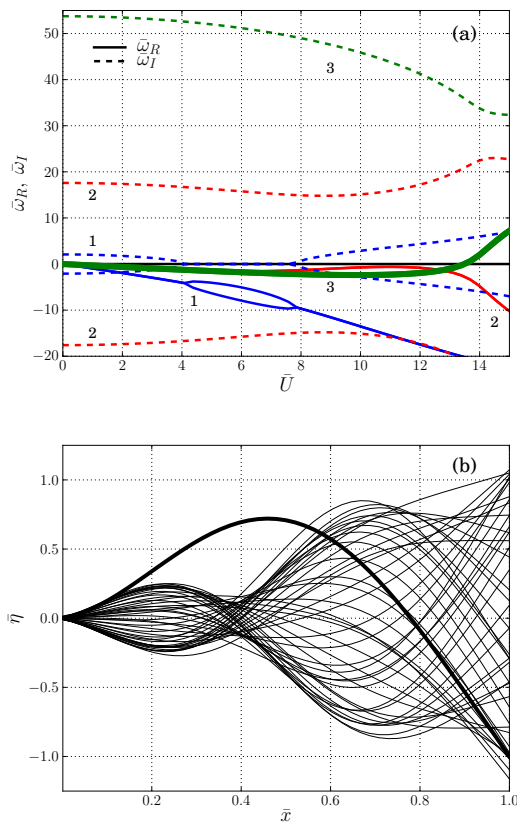


FIGURE 4: SYSTEM DYNAMICS FOR $\bar{L} = 1$ AND $\bar{L}_s = 1$: SYSTEM GIVING FIG. 2 MODIFIED BY A RIGID-INLET SURFACE UPSTREAM OF THE FIXED CANTILEVER GIVING $\bar{U}_c = 13.48$ OF MODE 3. SUB-FIGURE TITLES AND LEGENDS AS IN FIG. 2. ADAPTED FROM [10].

feature of Figs. 6a and 7a is that there exists a minimum value of critical speed. This is due to switching of the critical mode. Thus, as $\bar{\omega}_s$ is decreased in Fig. 6a the lower branch is principally characterised by Mode-2 content typified by Fig. 2b whereas the upper branch is dominated by Mode-1 content as typified by Fig. 3b. A similar effect occurs for modal-coalescence flutter in Fig. 7a; the lower branch mode strongly features Mode 3 content while the upper branch is principally a Mode-2 deformation, these being typified by Figs. 4b and 5b respectively. These effects - the reduction of critical-mode order - are reflected in the reduction of critical mode frequency seen in Figs. 6b and 7b as $\bar{\omega}_s$ is reduced.

CONCLUDING REMARKS

We have developed a model for predicting the two-dimensional linear-stability characteristics of a spring-mounted cantilevered flexible plate in a uniform flow. The basic stability characteristics of the system have

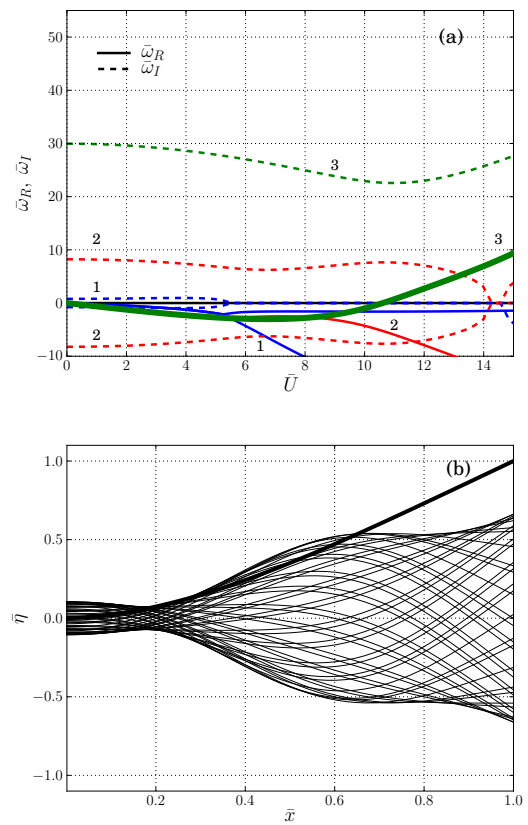


FIGURE 5: THE EFFECT OF A MOBILE CANTILEVER ON THE FLUID STRUCTURE INTERACTION AT $\bar{L} = 1$ AND $\bar{L}_s = 1$ WITH $\bar{\omega}_s = 1$: SYSTEM GIVING FIG. 2 MODIFIED BY A RIGID-INLET SURFACE UPSTREAM OF THE MOBILE CANTILEVER GIVING $\bar{U}_c = 10.6$ OF MODE 3. SUB-FIGURE TITLES AND LEGENDS AS IN FIG. 2.

been investigated for cases without and with a rigid upstream splitter plate that, for a rigid mounting, would succumb to single-mode and modal-coalescence flutter respectively. It has been shown that the introduction of a spring-mounting is generally destabilising in that it leads to lower values of the critical flow speed of the onset of both types of flutter. As the natural frequency of the mounting system is reduced, a value is reached for which the critical speed is a minimum. This minimum exists because the critical mode evolves from one of a higher to a lower order that can then become more stable with further decreases to the mounting stiffness. In effect the flexible plate becomes very stiff as compared with the mounting system and the entire system then asymptotes towards rigid-body motion of the plate and support. These stability findings augur well for the introduction of means to extract power from the reciprocating motion of the support; this is readily modelled by introducing a dashpot damper alongside the spring. The present methods can

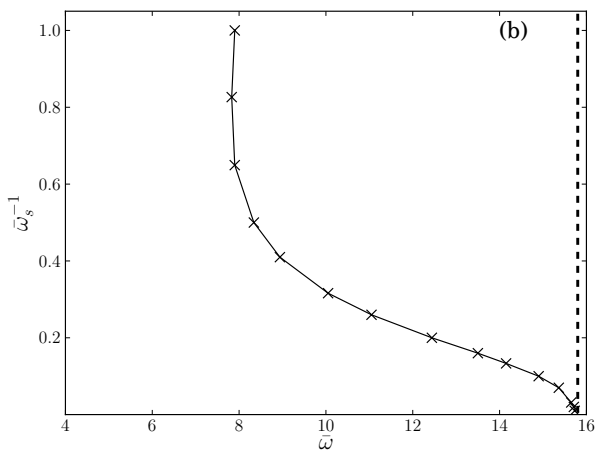
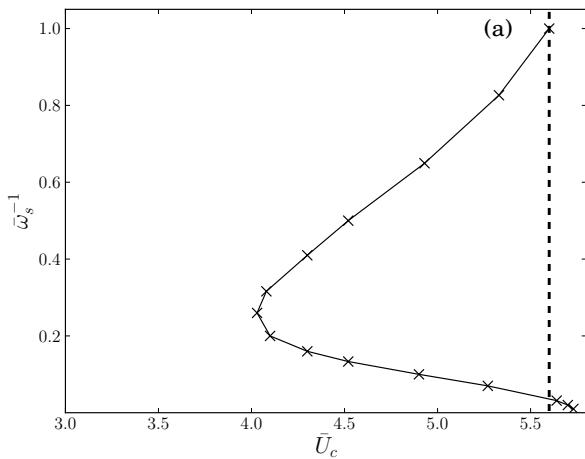


FIGURE 6: ZERO-GRADIENT-FREE BEAM AT $\bar{L} = 1$ AND $\bar{L}_s = 0$: PLOTS OF $\bar{\omega}_s^{-1}$ AGAINST (a) \bar{U}_c AND (b) $\bar{\omega}$. SINGLE-MODE FLUTTER; DASHED LINES DENOTE \bar{U}_c AND $\bar{\omega}$ AT \bar{U}_c FOR THE FIXED CANTILEVER CASE.

then be used to determine optimal system parameters for energy harvesting.

ACKNOWLEDGMENT

We express our gratitude to Dr. M. W. Pitman for many discussions in which he has contributed to this research.

REFERENCES

- [1] Kornecki, A., Dowell, E. H., and O'Brien, J., 1976. "On the aeroelastic instability of two-dimensional panels in uniform incompressible flow". *Journal of Sound and Vibration*, **47**(2), pp. 163–178.
- [2] Allen, J. J., and Smits, A. J., 2001. "Energy harvest-

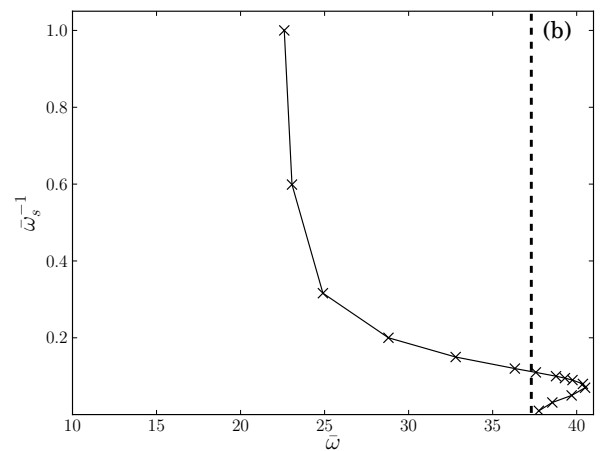
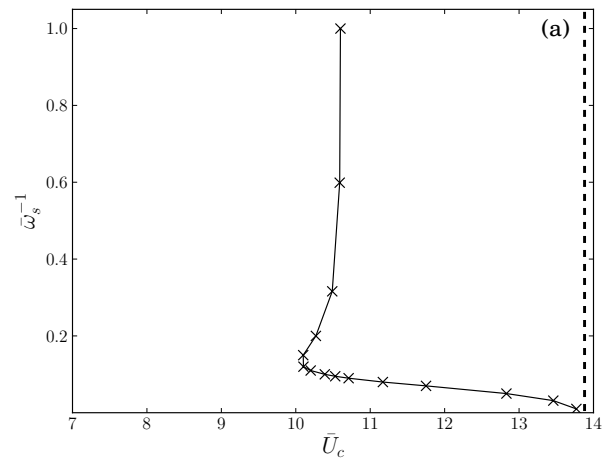


FIGURE 7: ZERO-GRADIENT-FREE BEAM AT $\bar{L} = \bar{L}_s = 1$: PLOTS OF $\bar{\omega}_s^{-1}$ AGAINST (a) \bar{U}_c AND (b) $\bar{\omega}$. MODAL COALESCENCE; DASHED LINES DENOTE \bar{U}_c AND $\bar{\omega}$ AT \bar{U}_c FOR THE FIXED CANTILEVER CASE.

ing eel". *Journal of Fluids and Structures*, **15**(4), pp. 629–640.

- [3] Kuhl, J. M., and DesJardin, P. E., 2012. "Power production locality of bluff body flutter mills using fully coupled 2d direct numerical simulation". *Journal of Fluids and Structures*, **28**, pp. 456–472.
- [4] Tang, L., Païdoussis, M. P., and Jiang, J., 2009. "Cantilevered flexible plates in axial flow: Energy transfer and the concept of flutter mill". *Journal of Sound and Vibration*, **326**(2), pp. 263–276.
- [5] Dunmon, J. A., Stanton, S. C., Mann, B. P., and Dowell, E. H., 2011. "Power extraction from aeroelastic limit cycle oscillations". *Journal of Fluids and Structures*, **27**(8), pp. 1182–1198.
- [6] Doaré, O., Sauzade, M., and Eloy, C., 2011. "Flutter of an elastic plate in a channel flow: Confinement

- and finite-size effects”. *Journal of Fluids and Structures*, **27**(1), pp. 76–88.
- [7] Zhu, Q., and Peng, Z., 2009. “Mode coupling and flow energy harvesting by a flapping foil”. *Physics of Fluids*, **21**, p. 033601.
- [8] Zhu, Q., Haase, M., and Wu, C. H., 2009. “Modeling the capacity of a novel flow-energy harvester”. *Applied Mathematical Modelling*, **33**, pp. 2207–2217.
- [9] Young, J., Ashraf, M. A., Lai, J. C. S., and Platzer, M. F., 2010. “Numerical simulation of flow-driven flapping-wing turbines for wind and water power generation”. In Proceedings 17th Australasian Fluid Mechanics Conference.
- [10] Howell, R. M., Lucey, A. D., Carpenter, P. W., and Pitman, M. W., 2009. “Interaction between a cantilevered-free flexible plate and ideal flow”. *Journal of Fluids and Structures*, **25**, pp. 544–566.
- [11] Howell, R. M., Lucey, A. D., and Pitman, M. W., 2011. “The effect of inertial inhomogeneity on the flutter of a cantilevered flexible plate”. *Journal of Fluids and Structures*, **27**, pp. 383–393.
- [12] Manela, A., 2012. “Vibration and sound of an elastic wing actuated at its leading edge”. *Journal of Sound and Vibration*, **331**(3), pp. 638–650.
- [13] Crighton, D. G., and Oswell, J. E., 1991. “Fluid loading with mean flow. i. response of an elastic plate to localized excitation”. *Philosophical Transactions of the Royal Society of London A*, **335**, pp. 557–592.
- [14] Lucey, A. D., Sen, P. K., and Carpenter, P. W., 2003. “Excitation and evolution of waves on an inhomogeneous flexible wall in a mean flow”. *Journal of Fluids and Structures*, **18**(2), pp. 251–267.

DOES REYNOLDS NUMBER AFFECT LOCK-IN OF AEROACOUSTIC RESONANCE OF TANDEM CYLINDERS?

Cristina Paduano¹

Craig Meskell

Department of Mechanical Engineering
Trinity College,
Dublin
Ireland
Email: paduanoc@tcd.ie

ABSTRACT

Lock-in is a critical aspect of aeroacoustic resonance and consists in the ability of the acoustic field to modify the hydrodynamic vortex shedding frequency to self-excite and self-sustain acoustic resonance. Experimental studies have demonstrated that lock-in depends on the amplitude of the acoustic field and the frequency ratio. This paper investigates the effect of the Reynolds number on the ability of a system to achieve lock-in. Lock-in is modeled with CFD for a configuration of two cylinders in tandem. A hydrodynamic analogy is used which represents the acoustic excitation as an oscillating velocity boundary condition applied to the incompressible flow. Two lock-in conditions are simulated: a pre-coincidence resonance at a frequency ratio of 1.2; and coincidence resonance at a frequency ratio of 0.85. Both conditions are simulated at 12 Reynolds numbers in the range 1.1×10^4 to 3.6×10^4 . The results have shown that lock-in occurs only at the higher Reynolds numbers above a threshold of 2.7×10^4 .

NOMENCLATURE

A	acoustic wave amplitude
D	cylinder diameter
f_a	acoustic frequency
f_v	natural frequency of vortex shedding
P	pressure distribution
Re	Reynolds number $\rho V D / \mu$
St	Strouhal number $f_v D / V_\infty$
t	time
U_a	acoustic particle velocity
V	hydrodynamic velocity
V_∞	mainstream velocity
Π	acoustic power
\mathfrak{R}	integration volume
ω	hydrodynamic vorticity
ρ	mean air density
μ	mean air viscosity

INTRODUCTION

Ducted air flows may experience acoustic resonance, especially if the configuration includes a rapid change in duct cross section or bluff bodies. The sound is instigated by the instability in the flow due to the presence of the bluff body [1, 2]. As the flow passes the body, vortices are shed periodically at a frequency f_v that increases linearly with the flow velocity V_∞ . This relationship is characterised by a constant Strouhal number. Aeroacoustic resonance is experienced in ducted flows when the frequency of the flow periodicity (i.e. vortex shedding) approaches the acoustic frequency of the duct [3,4].

If vortex shedding simply acted as a periodic excitation force, then the occurrence of resonance at frequency coincidence (i.e. $f_v = f_a$) would not be remarkable. However, the acoustic field modifies the hydrodynamic field so that the vortex shedding frequency coincidences with the acoustic resonant frequency not at a single flow velocity, but over a range of flow velocities. This is called lock-in. During lock-in the shedding frequencies remain constant as flow velocity is increased until resonance subsides and the vortex shedding process reverts to the frequency indicated by the Strouhal number. This behaviour is shown schematically in figure 1.

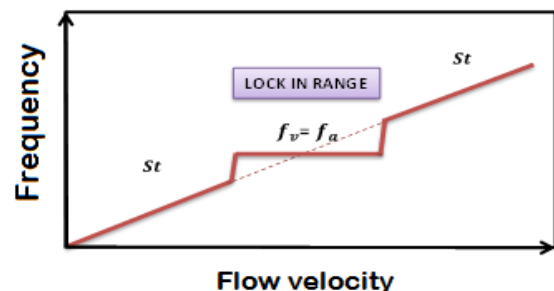


FIGURE 1: SCHEMATIC OF LOCK-IN CONDITION.

Behavior of frequency of vortex shedding at the increasing of flow velocity and synchronization of frequencies at the excited acoustic frequency (lock-in).

¹Address all correspondence to this author

While the basic phenomenon is well known, predicting the flow velocity at which lock-in starts is not yet possible, and hence it is difficult to assess *a priori* the degree to which a particular system may be prone to acoustic resonance.

Aeroacoustic resonance can be found in many engineering systems such as in heat exchangers which often consist of long slender pipes orientated in some regular pattern. It can also be a problem in heating, ventilating and air conditioning (HVAC) systems and environmental control system (ECS) installations in aircraft. It is a concern for the designers because the sound pressure levels (SPL) can exceed 140dB [5]. Furthermore, the resulting acoustic pressure can exceed the dynamic head of the flow [6] which could even lead to fatigue failure.

The requirement to avoid lock-in is therefore enforcing an upper limit to the practicable flow velocities [7, 8]. Figure 2 shows a typical aeroacoustic behavior of a heat exchanger. The data refer to Finnegan's [9,10] experiments where he measured the sound pressure and the vortex shedding from a tube array exposed at different flow velocities within a duct having a natural acoustic frequency of 322 Hz. Figure 2(a) shows the associated spectra of a point velocity measurements with a hot wire. Figure 2(b) shows the sound pressure level as a cross flow velocity increases. The lock-in region (16m/s-21m/s) is apparent in both data sets. The peak SPL is over 154dB (1000Pa).

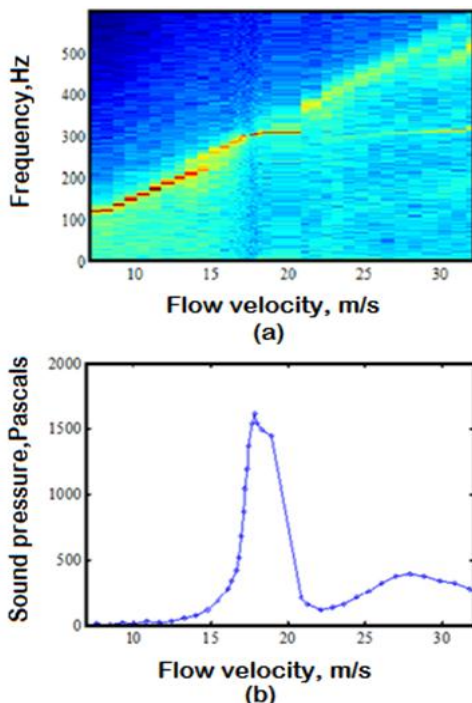


FIGURE 2: AEROACOUSTIC BEHAVIOR OF A TUBE BUNDLES IN CROSS FLOW. Figure 2(a).frequencies obtained with hot wire measurements of flow velocity showing lock-in range between 16 to 21 m/s. Figure 2(b) sound pressure at resonance achieving 1400 Pa. Finnegan [9].

Many of the investigations conducted until to date have focused on the definition of the extends of the lock in range using as case studies configurations of single and tandem cylinders. Blevins and Blesser [3, 11] conducted experiments using single cylinders in cross flow trying to develop a model to predict the resonant sound pressure level in heat exchangers tube bundles. They founded that for a single cylinder the lock-in range appeared over one set of flow velocities and was excited by the vortex shedding process observed in absence of resonance. Hall *et al.* [12] analyzed the effect of sound on the vortex shedding frequency for single and tandem cylinders at a spacing ratios, L/D , of 2.5 and 1.75; they varied the amplitude of the excitation in relation to the mean flow velocity and observed that, sound shifted the vortex shedding frequency to the frequency of excitation even when the excitation amplitude was as low as 0.5% of the mean flow velocity. Figure 3 shows the results of their tests: the shadowing indicates, for each case the amplitude and the frequency ratios for which lock-in occurred. As it can be seen for the two cylinders configuration, the lock-in range was wider than for a single cylinder case and this behavior was also seen as the cylinders spacing ratio was reduced. Mohany and Ziada [13] conducted experiments over a single cylinder to study the dependency of the lock-in from the cylinder diameter.

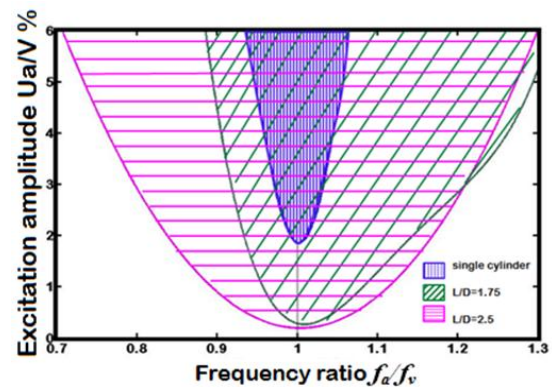


FIGURE 3: EXPERIMENTAL LOCK-IN MAP. Dependency of lock-in condition from the amplitude and frequency ratio of the excitation for a single and two tandem cylinders. Hall *et al* [12].

They noticed that, as the cylinder diameter was increased, the reduced flow velocity required to instigate resonance decreased and the lock-in range was wider. Furthermore the sound pressure level measured for the bigger cylinder diameter was strongly intensified. The acoustic pressure in fact increased by an order of magnitude as the cylinder diameter was doubled. The authors also considered a configuration of two cylinders in tandem to define the dependency of the lock-in range from the spacing ratio, L/D , between them. During their experiments they recognized that, when the cylinders spacing ratio was less than 3.5, in contrast to a single cylinder case, the resonance mechanism occurring at lock-in velocities

before the frequencies coincidence ($f_v < f_a$) was different from the resonance phenomenon occurring at lock-in velocities after frequency coincidence ($f_v > f_a$). During the *first resonance*, which they defined as *pre-coincidence resonance*, the sound pressure level (SPL) was reported to be higher than the one emitted after coincidence was achieved, and more remarkably, that the causes which instigated pre-coincidence resonance appeared diverse from the ones which instigated coincidence resonance. This was confirmed also by the experiments of Finnegan *et al* [10] In this investigation of the distribution of the acoustic sources around two cylinders in tandem, it was found that there was a positive net acoustic power in the wake of the downstream cylinder for coincidence resonance which, similar to the single cylinder case, confirmed the vortex shedding in the wake as the process responsible for this type of resonance. For the pre-coincidence resonance, the strongest source appeared instead in the gap between the cylinders.

These experimental studies have demonstrated that the ability of the acoustic field to modify the hydrodynamic vortex shedding frequency depends on the amplitude of the acoustic field and the frequency ratio f_a/f_v . However, practically, the vortex shedding frequency depends on the flow velocity, and so for a given duct geometry, quite a narrow range of velocities, and hence Reynolds numbers, have been examined. In this study, the effect of Reynolds number on the ability of the system to achieve lock-in is investigated. The condition of lock-in is modeled numerically through CFD for a configuration of two cylinders in tandem. Two lock-in conditions are simulated: a pre-coincidence resonance at a frequency ratio of 1.2; and coincidence resonance at a frequency ratio of 0.85. Both conditions are simulated at 12 Reynolds numbers in the range 1.1×10^4 to 3.6×10^4 .

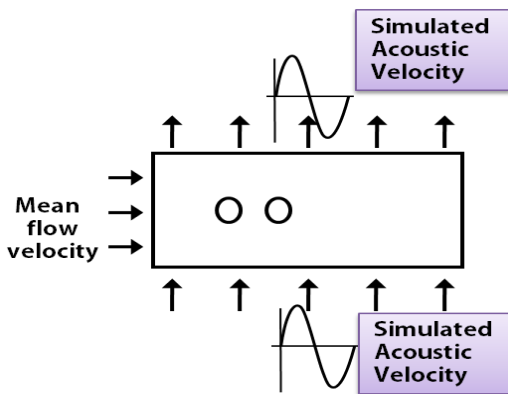


FIGURE 4: SCHEMATIC OF OSCILLATING CROSS FLOW BOUNDARY CONDITION. Sinusoidal velocity applied at the flow boundary to simulate acoustics.

USE OF HYDRODYNAMIC ANALOGY TO MODEL AEROACOUSTIC RESONANCE

The primary flow induced acoustic mode in a rectangular section duct consists of a transverse standing wave (i.e. normal to flow direction). Tan *et al.* [14] proposed an hydrodynamic analogy in which the acoustic

field is represented as an oscillating cross flow velocity boundary condition applied to an incompressible flow. A sinusoidal velocity of the form $A \sin(2\pi f_a t)$ is applied perpendicularly to the flow direction as shown in figure 4; A represents the acoustic particles velocity amplitude and f_a is the acoustic frequency. This has two advantages. Firstly, the compressibility associated with acoustics does not have to be modeled directly; and secondly, a RANS calculation is sufficient.

Mohany and Ziada [15] have used this analogy to model resonance for a single and two cylinders at a spacing ratio L/D of 2.5 using a Reynolds number of 2.5×10^4 . In their work they have simulated the acoustic resonance for different lock-in velocity by changing the frequency of the cross-flow oscillation f_a relative to that of the vortex shedding, f_v . Frequency ratio was in the range of 0.9-0.8 to model cases of coincidence resonance; and in the range of 1.1-1.35 for pre-coincidence resonance. For the single cylinder case they have varied the oscillation amplitude of the acoustic wave and have found a lock-in map similar to that obtained experimentally by Hall *et al.* [12] Reyes *et al.* [16] used the same two cylinder configuration of Mohany and Ziada [15] including the Reynolds number of 2.5×10^4 , the amplitude and frequency range to simulate lock-in condition.

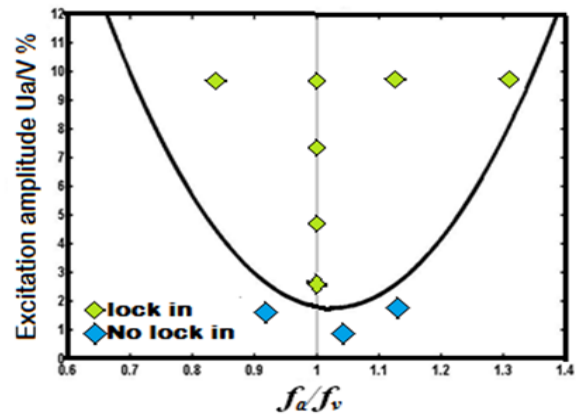


FIGURE 5: LOCK-IN MAP OBTAINED FROM NUMERICAL SIMULATIONS. Dependence of lock-in on the amplitude and frequency of the cross flow oscillation for a single cylinder as obtained numerically by Reyes *et al* [16].

They have investigated the dependency of the lock-in condition from the acoustic amplitude and frequency ratio for the two cylinders configuration obtaining a lock-in map for this configuration in agreement to that obtained by Hall *et al.* [12] for a similar case and shown in figure 5. Mohany and Ziada [15] and Reyes *et al.* [16] used the numerical flow field to calculate the acoustic power spatial distribution around a single and two tandem cylinder following the formula of Howe. Accordingly to Howe's theory of aerodynamic sound [17], at low Mach numbers the instantaneous Acoustic Power Π generated by an unsteady vorticity field $\vec{\omega}$ embedded within an acoustic field of particles velocity \vec{U}_a can be expressed as the triple product of $\vec{\omega} \cdot (\vec{U}_a \times \vec{V})$ with \vec{V} as the flow velocity. The

integration of the instantaneous acoustic power over a flow volume \mathfrak{R} for a complete acoustic cycle gives the net acoustic energy that the sound and the flow are exchanging:

$$\Pi = -\rho \int \vec{\omega} \cdot (\vec{U}_a \times \vec{V}) d\mathfrak{R} \quad (1)$$

The flow regions where Π is positive imply that acoustic resonance is enhanced and sustained as the flow field is transferring energy to the sound field, indicating an acoustic source. Regions with negative value of Π correspond instead to an energy transferring from the sound field to the flow indicating an acoustic sinks. Thus the numerical model of resonant flows obtained through the hydrodynamic analogy of Tan *et al.* [14] can be used to extract the variables $\vec{\omega}, \vec{V}$ which enter in the integral calculation together with the acoustic particles velocity \vec{U}_a obtained experimentally going to excite the acoustic mode of a test duct. The acoustic particles velocity is calculated by mean of the Euler's formula:

$$U_{a(x,y)} = \frac{A}{\rho 2\pi f_a} \cos(2\pi f_a t) \cdot \nabla P \quad (2)$$

For the two cylinder configuration, Mohany and Ziada [15] obtained net acoustic power between the cylinders and in the near wake. This acoustic source distribution is qualitatively similar to that obtained empirically by Finnegan, Meskell and Ziada [10].

Considering the success in predicting lock-in dependency on amplitude and acoustic source distribution, it appears that the hydrodynamic analogy is a useful tool.

MODEL DESCRIPTION AND SIMULATIONS ASSUMPTIONS

Twelve different velocities are simulated with Reynolds numbers in the range 1.1×10^4 – 3.6×10^4 . This is a similar range of Reynolds numbers to that considered experimentally by Finnegan *et al.* [10]. The flow is simulated with and without acoustic excitation at all flow velocities. The vortex shedding frequencies obtained without excitation are used to define the frequency of the oscillating velocity. The ratio between the frequency f_a , to that of the vortex shedding, f_v , is defined as 0.85 for the coincidence resonance and as 1.2 for the pre-coincidence resonance.

The amplitude A of the oscillation is 10% of the flow velocity V_∞ . The unsteady flow was simulated using the commercial CFD code ANSYS Fluent 12.1 [18]. The flow is assumed to be incompressible standard air with $\rho = 1.225 \text{ kg/m}^3$ and $\mu = 1.78 \times 10^{-5} \text{ kg/m}\cdot\text{s}$.

Table 1 specifies the uniform inlet flow velocities simulated, and the associated acoustic excitation frequencies applied in the pre-coincidence and coincidence scenarios.

The cylinders have a diameter (D) of 13 mm and a pitch ratio (L/D) of 2.5. The computational domain extends $5D$ upstream and $20D$ downstream of the centre of the leading cylinder. The domain is $5D$ wide on both sides, see figure 6. The flow is solved using uRANS.

TABLE 1. SIMULATED FLOW CONDITIONS AND EXCITATION FREQUENCIES.

Inlet flow velocity	Reynolds number	Fz. Vortex shedding simulated	Acoustic fz. simulated Preinc. $f_a/f_v=1.2$	Acoustic fz. simulated Coinc. $f_a/f_v=0.85$
12.23 m/s	10900	170 Hz	204 Hz	144 Hz
15.29 m/s	13679	218 Hz	262 Hz	185 Hz
18.85 m/s	16864	252 Hz	303 Hz	214 Hz
21.76 m/s	19467	304 Hz	365 Hz	258 Hz
24.91 m/s	22286	340 Hz	408 Hz	289 Hz
27.65 m/s	24737	380 Hz	456 Hz	323 Hz
30.90 m/s	27645	456 Hz	547 Hz	387 Hz
33.55 m/s	30015	482 Hz	579 Hz	410 Hz
35.27 m/s	31554	507 Hz	609 Hz	431 Hz
37.38 m/s	33442	536 Hz	643 Hz	456 Hz
39.13 m/s	35008	557 Hz	668 Hz	473 Hz
40.41 m/s	36153	580 Hz	696 Hz	493 Hz

The inlet boundary has a constant velocity. The outlet boundary is defined with a constant static reference pressure. The cylinder surfaces are defined as no slip walls. The upper and lower boundaries are maintained as slip walls for the simulations where no acoustic excitation is provided; when the acoustic excitation is imposed, these boundaries are normal velocity inlets/outlet with an instantaneous spatially invariant velocity which is temporally periodic and with a zero mean.

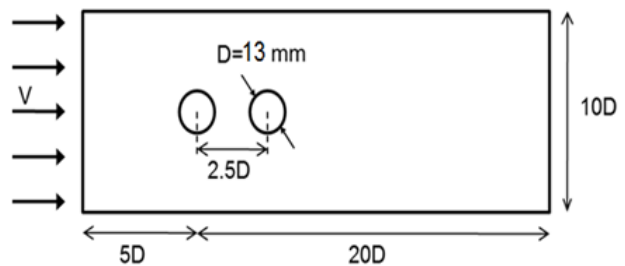


FIGURE 6: SCHEMATIC OF COMPUTATIONAL FLOW DOMAIN.

The time discretization scheme is of the second-order for the momentum, PISO scheme is used for the pressure-velocity coupling. Turbulence closure in the RANS scheme is achieved with two-equation SST model. The near wall flow is resolved with a “low Reynolds number” approach (i.e. the $y^+ \approx 1$). The convergence criteria for all normalized residuals is 1×10^{-5} . The calculations are executed in parallel mode.

SIMULATION RESULTS

Simulated Vortex Shedding Phenomena without Acoustic Excitation

The first set of simulations is executed with no acoustic excitation to reproduce the vortex shedding phenomena for each Reynolds number tested. The contours of velocity showed a clear vortex street for each simulation. The frequency of vortex shedding is obtained from the lift coefficient of the downstream cylinder [19, 20]. The periodic nature of the flow is obvious in the time series of lift coefficient for a Reynolds number of 10,600 as shown in figure 7.

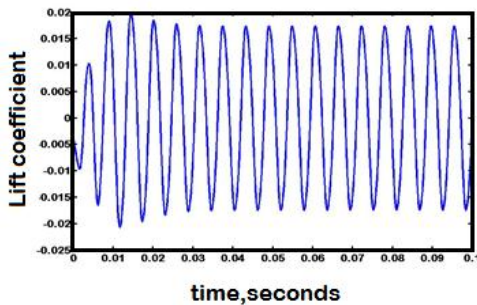


FIGURE 7: LIFT COEFFICIENT IN THE TIME. Lift coefficient of the downstream cylinder in the time, data refer to simulation of the $Re=10900$.

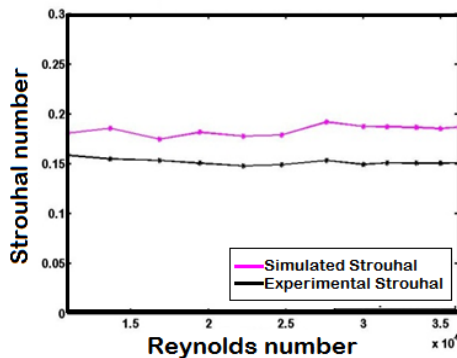


FIGURE 8: STROUHAL NUMBER AT DIFFERENT REYNOLDS NUMBERS. Strouhal numbers simulated (magenta) and Strouhal numbers obtained experimentally by Finnegan's [10] for two tandem cylinders.

Figure 8 compares the Strouhal number obtained at each velocity (i.e. Reynolds number) with experimental values [10]. An average value of $St = 0.18$ was obtained. The simulations systematically over-estimate the vortex shedding frequency by $\sim 20\%$. This can be attributed to increased blockage in the experimental setup. Furthermore, the 2D nature of the simulation may also contribute to the discrepancy.

Lock-in at pre-coincidence ratio $f_a/f_v = 1.2$

Figure 9 presents two spectra of lift coefficient on the downstream cylinder when acoustic excitation is applied at a frequency ratio $f_a/f_v = 1.2$. This is a pre-coincidence

condition. The frequency is normalized by the appropriate vortex shedding frequency to allow a direct comparison. Two Reynolds number cases are presented; $Re=10,900$ and $Re=36,000$, corresponding to an inlet velocity of 12.23 m/s and 40.41 m/s, respectively. The effect of acoustic excitation has been visible in the spectra of all the Reynolds numbers simulated, with nonzero content around the imposed excitation frequency. It is clear that at the lower Reynolds number, the fluctuating transverse flow velocity, which is modelling acoustic excitation, is causing a fluctuating lift at a normalized frequency, f/f_v , of 1.2. This coexists with vortex shedding at the normal vortex frequency ($f/f_v=1$). When the mean flow velocity is increased so that the Reynolds number is 3.6×10^4 , it is apparent that the excitation frequency is still in evidence in the lift coefficient, but the normal vortex shedding frequency is not. Thus, at a Reynolds number of 10^4 the system is not locked in, but at a Reynolds number of 3.6×10^4 the vortex shedding frequency is now locked in to the acoustic frequency. Examining the spectra for all the pre-coincidence cases ($f_a=1.2f_v$) shows that lock-in does not occur at Reynolds numbers below 27,600 which corresponded to a mean flow velocity of 30.9 m/s. Above this value, lock-in always occurs at this frequency ratio and excitation amplitude. This is shown in figure 10(a) which indicates whether a local maxima in the spectrum at the frequencies of f_v and f_a are observed.

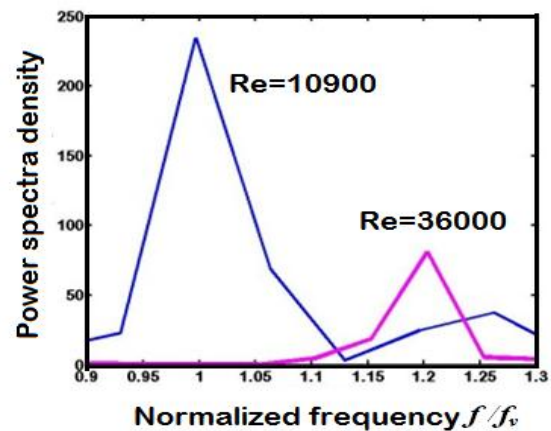


FIGURE 9: SPECTRA AT PRE-COINCIDENCE AT $Re=10,900$ AND $Re=36,000$. Graphics of the frequency spectra with excitation frequency ratio of 1.2 applied showing lock-in achieved at $Re=36,000$.

Lock-in at coincidence ratio $f_a/f_v = 1.2$

Similarly to the pre-coincidence cases, the introduction of the acoustic excitation has been visible in all the spectra, but above a Reynolds number of 27,600 lock-in again occurs, with vortex shedding suppressed at the normal shedding frequency. This is shown schematically in figure 10(b) which depicts the presence or not of peaks in the spectra at the vortex shedding and acoustic excitation frequencies.

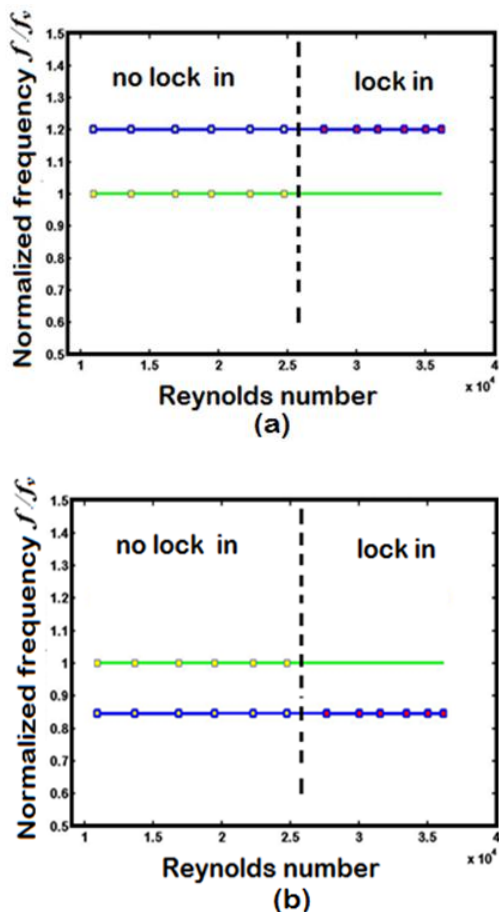


FIGURE 10: LOCK-IN AT DIFFERENT REYNOLDS NUMBERS. Figure 10(a) frequencies obtained in the spectra normalized to vortex shedding frequencies for simulations with excitation at a pre-coincidence ratio $f_a/f_v=1.2$ for the 12 Reynolds numbers modeled. Figure 10(b) frequencies obtained in the spectra normalized to vortex shedding frequencies for simulations with excitation at a coincidence ratio $f_a/f_v=0.85$ for the 12 Reynolds numbers modeled.

LOCK-IN MAP AT REYNOLDS=27600

There appears to be a critical Reynolds number between 2.5×10^4 and 2.8×10^4 ; there is no lock-in below $Re=2.5 \times 10^4$, while there is always lock-in at $Re=2.8 \times 10^4$. In order to verify the validity of the results obtained, the case of $Re=27,600$ has been further analysed. The excitation amplitude has been modified in range from 1% to 10% of the mean flow velocity and the frequency ratio has been varied from pre-coincidence at $f_a/f_v=0.75$ to coincidence $f_a/f_v=1.3$.

The results of these simulations are presented as a “lock-in map” in figure 11. As can be seen, the results are similar to that one obtained experimentally by Hall *et al.*¹² The numerical results predict lock-in at a lower excitation amplitude than experimentally observed. This can be attributed to the fact that there is no acoustic damping in the simulation, nor is there acoustic leakage

(i.e. radiation from the duct) as is experienced experimentally. Both of these factors would necessitate in effect a minimum energy to be overcome before acoustic resonance can be self-sustaining. Nonetheless, the qualitative agreement lends some confidence to the integrity of the main finding above: that lock-in depends on Reynolds number.

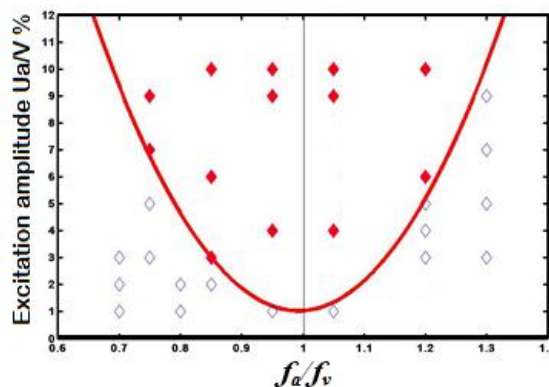


FIGURE 11: LOCK-IN MAP AT RE=27,600. Dependency of lock-in condition from frequency ratio and excitation amplitude.

FLOW VISUALISATION

Examining the flow field at pre-coincidence for Reynolds numbers of 1.1×10^4 and 3.6×10^4 shows clear qualitative differences in the flow when it is locked in to the acoustic excitation frequency.

Figure 12 and figure 13 show the instantaneous velocity magnitude fields, normalized by free-stream velocity for these two cases at the same phase of the vortex shedding cycle. It is clear that lock-in causes the width of the far wake to narrow, reducing the size of the vortex structures, and the magnitude of the velocity perturbation associated with them. Furthermore, the mean velocity in the near wake is reduced by approximately one third. Similar observations can be made for the coincidence case. This is somewhat counter intuitive: the onset of lock-in is actually reducing the velocity fluctuations.

The investigations of the phenomenon of aeroacoustic resonance in ducted flows conducted by Hall and Ziada[12].

Wolfe and Ziada [4] have reported that the lock-in ability, shown by an acoustic field to synchronize the vortex shedding frequency, depends on the amplitude of the acoustic wave and the ratio between the frequency of sound and the frequency of vortex shedding. However, the Reynolds number could not be controlled for directly as the vortex shedding frequency is determined by the flow velocity, while the acoustic ratio is defined by the duct geometry, and so a given frequency ratio defined the Reynolds number indirectly.

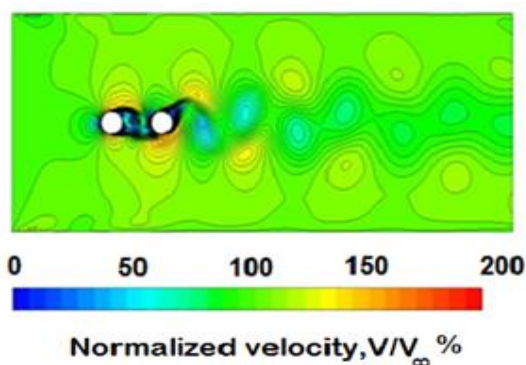


FIGURE 12: VELOCITY MAGNITUDE AT RE=10,900 AT PRE-COINCIDENCE. Velocity contour taken at Re=10900 for the pre-coincidence resonance 1.2, case which did not show "lock in."

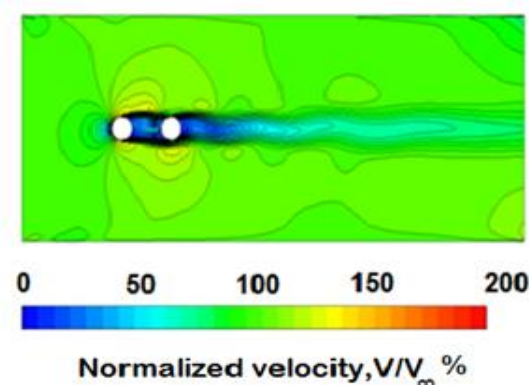


FIGURE 13: VELOCITY MAGNITUDE AT RE=36,000 AT PRE-COINCIDENCE. Velocity contour taken at Re=36000 for the pre-coincidence resonance 1.2, case which did show "lock in."

COMMENTS

The numerical investigation conducted in this work has shown that the Reynolds number of the flow has an effect on the likelihood of acoustic resonance establishing lock-in. This result has been obtained by using uRANS of incompressible flow with an hydrodynamic analogy to represent aeroacoustic resonance in ducted flow by substituting the acoustic wave with the oscillating velocity perturbation that it causes. The hydrodynamic system has been simulated in CFD by imposing the excitation amplitude and frequency ratios at which lock-in could occur.

The results have shown the phenomenon of lock-in has occurred only at the higher Reynolds numbers. A critical Reynolds number has been found to be approximately 2.7×10^4 , but this is likely to be specific to the geometry under investigation here. Without doubt, given the modeling assumptions necessary, this result must be verified with careful experiments. Further study is required to better understand the mechanisms at work.

REFERENCES

- [1]. Gerrard, J. H. "The mechanics of the formation region of vortices behind bluff bodies" *Journal of Fluid Mechanic* Vol. 25, 1966, pp. 401-413.
- [2]. Hirschberg, A. "Introduction to Aeroacoustics of internal flows" Revised version of the chapter from the course "Advances in Aeroacoustics", 2001, 12-16 March.
- [3]. Blevins R.D. "The effect of sound on vortex shedding from cylinders," *Journal of Sound and Vibration* Vol. 161, 1985, pp. 217-237.
- [4]. Wolfe, D., and Ziada, S. "Feedback control of vortex shedding from two tandem cylinders," *Journal of Fluids and Structures* Vol. 17, No. 4, 2003, pp. 579-592.doi: 10.1016/s0889-9746(02)00147-0
- [5]. Ziada, S. "Flow-excited acoustic resonance in industry," *Journal of Pressure Vessel Technology, Transactions of the ASME* Vol. 132, No. 1, 2010, pp. 0150011-0150019.
- [6]. Ziada, S. "Vorticity shedding and acoustic resonance in tube bundles," *J. of the Braz. Soc. of Mech. Sci. & Eng.* Vol. XXVIII, No. 2 / 199, 2006.
- [7]. Feenstra, P. A., Weaver, D. S., and Eisinger, F. L. "A study of acoustic resonance in a staggered tube array," *Journal of Pressure Vessel Technology, Transactions of the ASME* Vol. 128, No. 4, 2006, pp. 533-540.
- [8]. Eisinger, F. L. "Acoustic resonance in a package boiler and its solution-A case study," *Journal of Pressure Vessel Technology, transactions of ASME* Vol. 129, 2007, pp. 759-762.
- [9]. Finnegan, S. L. "Resonant aeroacoustic source localisation in ducted bluff body flows," Dept. of Mechanical and Manufacturing engineering. Trinity College Dublin, 2011.
- [10]. Finnegan, S. L., C.Meskell,S.Ziada. "Experimental investigation of the acoustic power around two tandem cylinders," *Journal of Pressure Vessel Technology, transactions of ASME* Vol. 132, 2010, pp. 041306-1-041306-11.
- [11]. Blevins R.D, B. M. M. "Experiments on acoustic resonance in heat exchanger tube bundles," *Journal of Sound and Vibration*, 1993, pp. 164,503-533.
- [12]. Hall, J. W., Ziada, S., and Weaver, D. S. "Vortex-shedding from single and tandem cylinders in the presence of applied sound," *Journal of Fluids and Structures* Vol. 18, No. 6, 2003, pp. 741-758.doi: 10.1016/j.jfluidstructs.2003.06.003
- [13]. Mohany, A., and Ziada, S. "Flow-excited acoustic resonance of two tandem cylinders in cross-flow," *Journal of Fluids and Structures* Vol. 21, No. 1 SPEC. ISS., 2005, pp. 103-119.
- [14]. Tan B.T, Thompson. M. C., Hourigan K., "Sources of acoustic resonance generated by the flow around a long rectangular plate in a duct " *Journal of Fluids and Structures* Vol. 18, 2003, pp. 729-740.

- [15]. Mohany, A., and Ziada, S. "Numerical simulation of the flow-sound interaction mechanisms of a single and two-tandem cylinders in cross-flow," *Journal of Pressure Vessel Technology, Transactions of the ASME* Vol. 131, No. 3, 2009, pp. 0313061-03130611.
- [16]. Ryes,E., "*Simulation of flow induced acoustic resonance of bluff bodies in ducted flows,*" Dept. of Mechanical and Manufacturing engineering. Trinity College Dublin, 2010.
- [17]. Howe, M.S., *Theory of vortex sound.* Cambridge University Press., 2003.
- [18]. ANSYS Workbench, FLUENT, Software Package. 12.1 ed., ANSYS Inc., Southpointe, Canonsboug, PA.
- [19]. Farell,C., "Flow around fixed circular cylinders: fluctuating loads " *Proceedings of ASCE Engineering Mech. Division* Vol. 107 EM3, 1981, pp. 565-588.
- [20]. Mohany, A., and Ziada, S. "Measurements of the dynamic lift force acting on a circular cylinder in cross-flow and exposed to acoustic resonance," *Journal of Fluids and Structures* Vol. 27, No. 8, 2011, pp. 1149-1164.

DIRECT AEROACOUSTIC SIMULATION OF MERGING FLOW IN T-DUCT

Garret C. Y. Lam

Randolph C. K. Leung*

Department of Mechanical Engineering,
The Hong Kong Polytechnic University,
Hong Kong, PR China
Email: mmrleung@polyu.edu.hk

S. K. Tang

Department of Building Services Engineering,
The Hong Kong Polytechnic University,
Hong Kong, PR China
Email: besktang@polyu.edu.hk

ABSTRACT

This paper reports an aeroacoustic investigation of the two dimensional turbulent merging flow in a T-duct. The numerical investigation is conducted by solving the unsteady compressible Navier-Stokes (N-S) equations and the perfect gas equation of state simultaneously with CE/SE method. Implicit LES strategy by combining the MILES approach and wall modeling is included to account for the effects of flow turbulence. The Reynolds number (Re) based on duct width and maximum inlet flow velocity at side branch is set equal to 10^5 . Simulations of two velocity ratios ($= 1.0, 2.0$) were performed. An approach is also proposed to extract the acoustic contribution in the mixed flow and acoustic disturbances. The flow unsteadiness is dominated by the recirculating zone downstream of the duct junction, rather than the shear layer formed between the two inlet flows. Furthermore, both the vortex interactions and the acoustic efficiency are observed to be higher in velocity ratio of 2.0.

INTRODUCTION

T-duct is commonly found in various fluid transporting systems such as a large air-ventilation system in building or small intake system in automobiles. When air streams flow inside a T-duct, sound are generated through aerodynamic processes. Therefore, in order to minimize the sound generated inside T-duct, it is essential to understand the underlying mechanism of aeroacoustic generation. Regarding the aeroacoustics of T-duct, previous research mainly focused the effects of the grazing flow on the resonance behavior of T-duct [1, 2]. However, the merging flow in T-duct, which is another type of flow commonly encountered, receives comparatively little attentions. These researches usually focused on the mixing

behavior of the merging flow rather than the aeroacoustics [3, 4]. When the two flows merge at the junction of a T-duct, a shear layer is created between them due to the velocity gradient across the flow. This kind of shear layer may roll up to form vortices as a result of growing flow instability. In addition, a recirculating region is also created by the merged flow near the downstream edge of duct junction. It may be so unstable such that vortices are also shed here. Since these vortices are believed to be the acoustic sources, it is essential to understand the effects of their evolution on aeroacoustics occurred in a T-duct.

Therefore, this paper aims at investigating the aeroacoustics of the high Reynolds number (10^5) merging flow in a T-duct numerically with two different velocity ratios between the inlet flows. The numerical approach adopted is the direct aeroacoustic simulation (DAS) for the readiness for educing the flow structures and the acoustics, which are not easy to differentiate experimentally. In this paper, the formulation of the flow problem is first discussed in the next section. This is followed by the numerical method and turbulence modeling adopted. Then, the results are discussed together with the effect of the velocity ratio based on the simulations highlighted.

FORMULATION OF FLOW PROBLEM

Figure 1 shows the schematic of the merging flow problem under investigation and the reference parameters are given in Tab. 1. The computational domain of the T-duct consists of three branches with length 20 and width 1. Buffer zones with length 10 are appended to each end of branch. Two flows enter the domain at Inlets I_1 and I_2 while the merged flow exits the domain through outlet at the right hand side. The origin is located at the upstream edge of the duct junction. The vertical branch is termed as side-branch and the horizontal duct is the main duct. The

*Address all correspondence to this author.

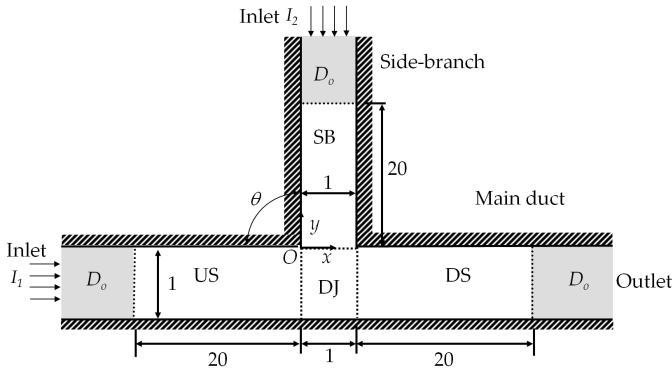


FIGURE 1: SCHEMATIC OF THE MERGING FLOW PROBLEM WITH VARIABLES NORMALIZED BY PARAMETERS IN TAB. 1.

TABLE 1: DEFINITIONS OF REFERENCE PARAMETERS.

Reference parameters	Physical variables
Length, \hat{L}_o	Width of duct, \hat{W}
Velocity, \hat{u}_o	Maximum velocity at I_2 , $\hat{u}_{2,max}$
Time, \hat{t}_o	$\hat{W} / \hat{u}_{2,max}$
Density, $\hat{\rho}_o$	Density at inlets, $\hat{\rho}_{in}$
Pressure, $\hat{\rho}_o \hat{u}_o^2$	Inlet pressure, $\hat{\rho}_{in} \hat{u}_{2,max}^2$

Reynolds number Re studied is 2.3×10^5 and the Mach number M is 0.1. These parameters corresponds to a typical flow values encountered in the air ventilation system. In the present study, the velocity ratio VR between two inlet flows is defined as

$$VR = \frac{\hat{u}_{2,max}}{\hat{u}_{1,max}} = \frac{u_{2,max}}{u_{1,max}}, \quad (1)$$

where $\hat{u}_{1,max}$ and $\hat{u}_{2,max}$ are the maximum velocity at inlet I_1 and I_2 respectively. The VR simulated are 1.0 and 2.0 in the present study. To ease the forthcoming discussion, four regions, namely US, SB, DJ and DS, are defined in Fig. 1.

DIRECT AEROACOUSTIC SIMULATION

Unlike conventional hybrid approach, the direct aeroacoustic simulation (DAS) solves the compressible

Navier-Stokes equations and the equation of state simultaneously, thus allowing the interactions between the flow field and the acoustic field to be properly resolved. Various researches [5–7] have demonstrated its success in aeroacoustic investigation. In the investigation of turbulent flows, large eddy simulation (LES) has been recognized as an appropriate numerical tool for DAS [8]. An efficient implementation of LES, Monotonically Integrated Large Eddy Simulation (MILES), was proposed by Boris [9], in which the turbulent dissipation in the flows is mimicked by the dissipation of the numerical scheme without invoking any subgrid scale (SGS) model. Various aeroacoustic researches, e.g., free shear jet in Ref. [10] and flow past deep cavity in Ref. [11], demonstrated its success. Thus, it is adopted in the current investigation. In order to further reduce the mesh requirement for reasonably accurate turbulent simulation, wall modeling [12,13] is also adopted to accommodate the viscous effect near the wall.

Governing equations

The present aeroacoustic problem is governed by the two dimensional compressible Navier-Stokes (N-S) equations and the ideal gas law for calorically perfect gas. As mentioned, MILES formulation is applied to the N-S equations for the calculation of the turbulent flow. Therefore, in the following discussion, the pressure p , the density ρ , the temperature T and the heat q are spatial filtered variables while all other variables are the Favre variables (density weighted). Furthermore, the variables with hat denote the variables with dimensions. Taking the reference scales such as length \hat{L}_o , velocity \hat{u}_o , time, \hat{t}_o , $\hat{\rho}_o$, $\hat{\rho}_o \hat{u}_o^2$, \hat{T}_o and $\hat{\mu}_o$ from the problem, the non-dimensionalized N-S equations in two dimensions are expressed in the strong conservation form as

$$\frac{\partial U}{\partial t} + \frac{\partial (F - F_v)}{\partial x} + \frac{\partial (G - G_v)}{\partial y} = \text{SGS}, \quad (2)$$

where

$$U = \begin{bmatrix} \rho \\ \rho u \\ \rho v \\ \rho E \end{bmatrix}, \quad F = \begin{bmatrix} \rho u \\ \rho u^2 + p \\ \rho uv \\ (\rho E + p)u \end{bmatrix}, \quad G = \begin{bmatrix} \rho v \\ \rho uv \\ \rho v^2 + p \\ (\rho E + p)v \end{bmatrix},$$

$$F_v = \frac{1}{Re} \begin{bmatrix} 0 \\ \tau_{xx} \\ \tau_{xy} \\ \tau_{xx}u + \tau_{xy}v - q_x \end{bmatrix}, G_v = \frac{1}{Re} \begin{bmatrix} 0 \\ \tau_{xy} \\ \tau_{yy} \\ \tau_{xy}u + \tau_{yy}v - q_y \end{bmatrix},$$

with $\tau_{xx} = \frac{2}{3}\mu \left(2\frac{\partial u}{\partial x} - \frac{\partial v}{\partial y} \right)$, $\tau_{xy} = \mu \left(\frac{\partial u}{\partial y} + \frac{\partial v}{\partial x} \right)$, $\tau_{yy} = \frac{2}{3}\mu \left(2\frac{\partial v}{\partial y} - \frac{\partial u}{\partial x} \right)$, $E = \frac{p}{\rho(\gamma-1)} + \frac{u^2+v^2}{2}$, $p = \frac{\rho T}{\gamma Ma^2}$, $q_x = -\frac{\mu}{(\gamma-1)PrMa^2} \frac{\partial T}{\partial x}$, $q_y = -\frac{\mu}{(\gamma-1)PrMa^2} \frac{\partial T}{\partial y}$, the specific heat ratio $\gamma = 1.4$, Mach number $Ma = \hat{u}_o/\hat{c}_o$, $\hat{c}_o = \sqrt{\gamma \hat{R} \hat{T}_o}$, the specific gas constant for air $\hat{R} = 287.058 J/(kg \cdot K)$, Reynolds number $Re = \hat{\rho}_o \hat{u}_o \hat{L}_o / \hat{\mu}_o$ and Prandtl number $Pr = \hat{c}_{p,o} \hat{\mu}_o / \hat{k}_o = 0.71$. SGS denotes all subgrid terms of the turbulent flow [11] and are taken as zero following MILES formulation [9, 10]. The wall modeling is based on the classical logarithm law of wall with van Driest compressibility correction [12, 13]. The friction velocity u_τ are first determined by an iterative Newton process with the known u adjacent to the wall. Then, the turbulent viscous dissipations are estimated from u_τ .

Numerical method

The adopted numerical method is the conservation element and solution element (CE/SE) method, whose details can be referred to the works of Chang [14] and Lam *et al.* [15].

In CE/SE method, ghost cell approach is applied for setting the boundary condition. Fully developed turbulent profile is taken as the inlet velocity profile with $\rho_{I_1} = \rho_{I_2} = 1$ and $p_{I_1} = p_{I_2} = 1/\gamma M^2$ for I_1 and I_2 . The no-slip wall boundary condition [15] with aforementioned wall modeling is adopted for all the walls. Furthermore the non-reflecting boundary condition [15] is adopted for the outlet boundary condition.

The mesh is so designed to meet the requirement for correct turbulent simulations where all the mesh points are clustered near the wall. The minimum mesh size $\Delta x_{min} = 0.001$ near the walls while the maximum mesh size $\Delta x_{max} = 0.015$ at the center of the duct. Δx_{min} corresponds to the wall unit, $y^+ = y\rho_w u_\tau Re / \mu_w = 16$ at $Ma = 0.1$, where u_τ is the friction velocity, ρ_w is the fluid density at wall and μ_w is the fluid viscosity at wall. There are roughly 20 meshes inside each turbulent boundary layer at $Ma = 0.1$. Thus, the boundary layers are sufficiently captured by the mesh distribution. Furthermore, the time step adopted is between $5 \times 10^{-4} \leq \Delta t \leq 6.25 \times 10^{-4}$. A time stationary solution with coarser mesh is taken as the initial condition. Solutions are then obtained by simulating a duration of 20 after the solutions reaches time stationary state.

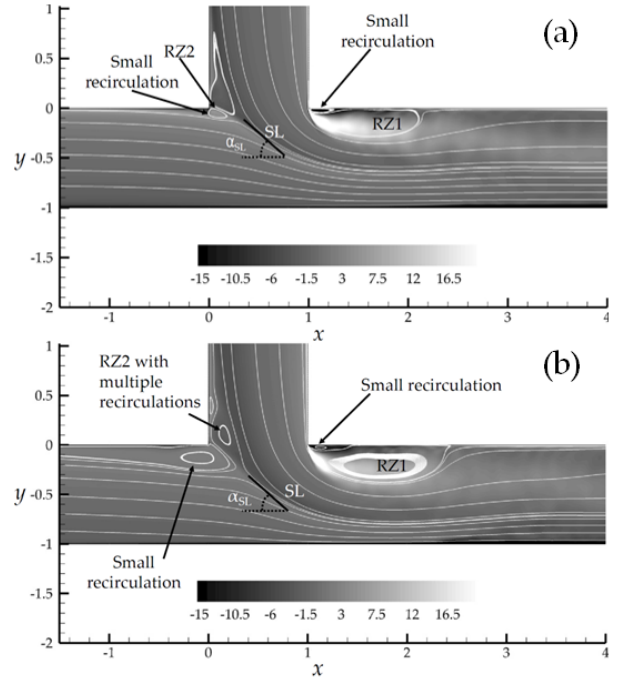


FIGURE 2: ω_{mean} NEAR THE DUCT JUNCTION (DJ). (a) $VR = 1.0$; (b) $VR = 2.0$.

RESULTS AND DISCUSSIONS

Flow dynamics

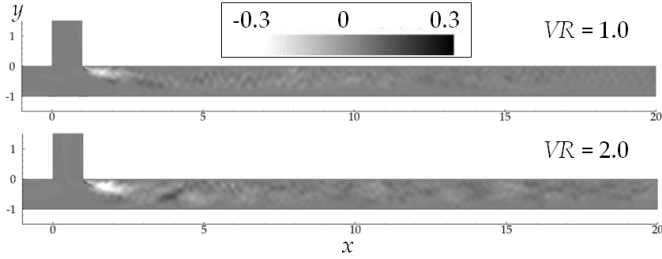
Mean flows The mean flow features can be readily observed from the mean vorticity ω_{mean} near DJ as shown in Fig. 2 with streamlines presented. Three distinct mean flow features can be observed. The first one is the recirculating zone RZ1 formed near the downstream edge of DJ. The second one is the curved shear layer (SL) generated between the two inlet flows in DJ. The last flow feature observed is another recirculating zone RZ2 at the upstream edge of DJ. Such kind of flow pattern is in good agreement with that reported in previous literature [4].

RZ1 consists of two counter-rotating zones which contains the highest vorticity among the observed flow features. When the two inlet flows meet at DJ, the y -momentum of side-branch flow presses on the main flow, creating a separation region from the downstream edge of DJ. The merged flow then covers up this region later and creates the recirculating zone RZ1, which can be characterized by the reattachment length L_{RZ1} . The variation of L_{RZ1} with VR is shown in Tab. 2. L_{RZ1} increases with VR in general.

The second key feature is the thin, curved shear layer SL generated between the two merging flows in DJ. Its characteristics can be described with an inclined angle α_{SL} measured from main duct axis. Table 2 illustrates that α_{SL} increases with VR as a result of the increased ratio of y -momentum to x -momentum of the merging flow.

TABLE 2: CHARACTERISTIC LENGTHS OF MEAN FLOW FEATURES.

Velocity ratio, VR	L_{RZ1}	α_{SL}	L_{RZ2}
1.0	1.170	38.15°	1.461
2.0	1.469	41.78°	0.903


FIGURE 3: MEAN REYNOLDS SHEAR STRESS.

The last feature of the merging flow, RZ2 in Fig. 2, consists of recirculating zones attached to the upstream edge of DJ. Furthermore, a small recirculating zone in US also exists as a result of the high flow velocity in the side branch. Generally, RZ2 is caused by an early separation of flow in SB and US before reaching DJ, which is induced by the impinging flow at DJ. This zone can also be characterized by the separation length of the flow in the side branch L_{RZ2} as shown in Tab. 2.

Flow unsteadiness The mean resolved Reynolds shear stress $\overline{u'v'}/u_{eq}^2$, where $u_{eq}^2 = u_{1,max}^2 + u_{2,max}^2$, is calculated over the entire domain. Here the fluctuating quantities, denoted by the superscript t , are defined by $\phi^t(x, y, t) = \phi(x, y, t) - \overline{\phi}(x, y)$, where ϕ denotes the flow variables and the over bar denotes the time averaged quantity. The distributions of mean Reynolds shear stresses $\overline{u'v'}/u_{eq}^2$ for $VR = 1.0$ and 2.0 are shown in Fig. 3. It illustrates that the region near RZ1 contains the highest Reynolds shear stress, implying that localized strong flow fluctuations occur there. The Reynolds shear magnitude drops significantly upon moving to the upstream end of DS, i.e. in US, SB and DJ. Moreover, the stress levels in $VR = 2.0$ is higher than those in $VR = 1.0$. Similar stress distribution of both VR s are also observed for $\overline{u'u'}/u_{eq}^2$ and $\overline{v'v'}/u_{eq}^2$, so they are not shown here. All these observations also demonstrate that the merging flow fluctuations are localized downstream near the junction. Hence, the discussion on the flow dynamics are focused near the junction.

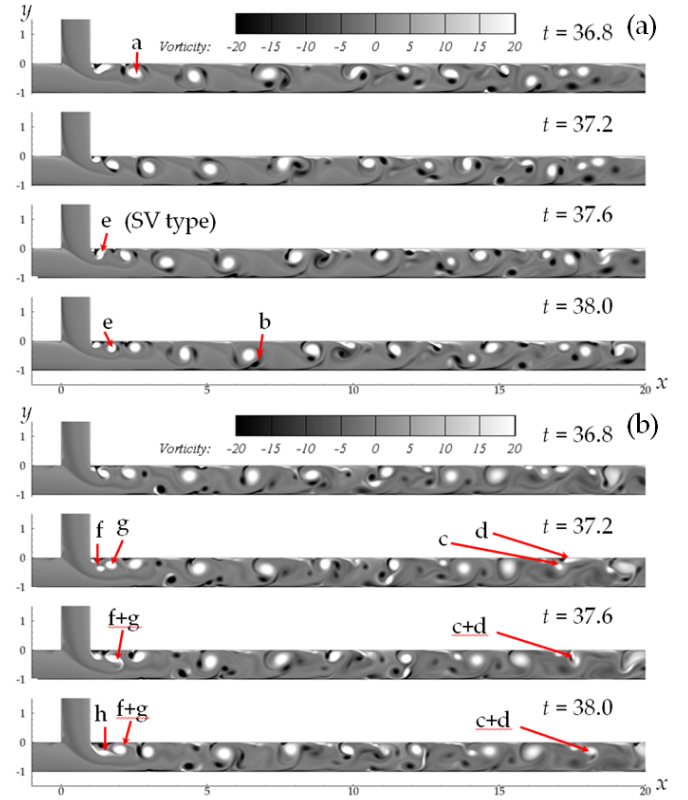

FIGURE 4: SNAPSHOTS OF INSTANTANEOUS VORTICITY, ω .

Figure 4 shows the snapshots of instantaneous vorticity distribution near the duct junction for $VR = 1.0$ and 2.0 . In both cases, only vortex shedding at RZ1 is observed. There is no vortex roll-up or shedding at SL, which instead is entrained by the vortex shed at RZ1 to form a larger vortex (e.g. Vortex a at $VR = 1.0$). This observation further confirms the fact that the dominant flow unsteadiness is generated from the recirculating zone RZ1, rather than SL. This implies that the recirculating zone occurred in internal flow play an important role in the development of the vortical structures. When the vortex shed at RZ1 approaches the lower wall, secondary vortices of opposite rotation are induced at the lower wall (e.g. Vortex b at $VR = 2.0$). All these vortices undergo vigorous coalescence further downstream in DS (e.g., Vortical Structures c and d forming c+d at $VR = 2.0$). In general, the flow pattern becomes irregular as flow convects to downstream of the junction. Comparing these two VR s, the irregularity of flow pattern in DS is increased with VR possibly due to the increased occurrence of bouncing of the vortices shed at RZ1. This explains higher mean Reynolds stresses levels observed in $VR = 2.0$. Furthermore, the size and vorticity of the vortices in the further downstream (e.g. $x = 20$) are com-

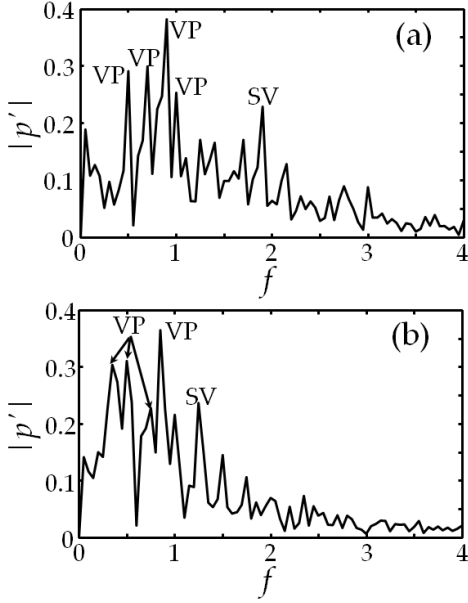


FIGURE 5: SPECTRA OF PRESSURE FLUCTUATIONS OBTAINED AT $(x_{dj} + 2, -0.2)$. (a) $VR = 1.0$; (b) $VR = 2.0$.

parable to those near RZ1.

The evolution of vortical structures at RZ1 can be generally divided into two types. The first type (SV) involves the shedding of a single vortex (e.g. Vortex e at $VR = 1$). The second type (VP) is the formation of a relatively large vortex, which is evolved from the pairing of vortices just rolled up (e.g. Vortex f+g formed by Vortex f and g at $VR = 2.0$) at RZ1. Note that both types of flow development occur in both VRs. In order to determine the frequencies of both types at RZ1 for each VR, the snapshots of their instantaneous vorticity and their pressure spectra at $(3, -0.2)$ lying on the paths of the vortices shed at RZ1 are inspected and compared. These spectra are illustrated in Fig. 5. Several observations can be made from this figure. Firstly, multiple dominant peaks are observed in the spectra. This echoes to the aforementioned vortical development and shows its complexity. Secondly, the frequency of SV is higher than that of VP in all cases because VP can occur only after the roll-up of at least two single vortices, which requires a longer time to evolve. Thirdly, VP is the dominant type of structures for both cases and may consist of several peaks in the pressure spectra. This corresponds to the multiple vortex pairings of VP observed, e.g. Vortex f+g and h in Fig. 4.

Acoustic generation

Differentiation of near field and far field for acoustic evaluation In Lighthill's aeroacoustic theory [16], the aerodynamics dominated region is always

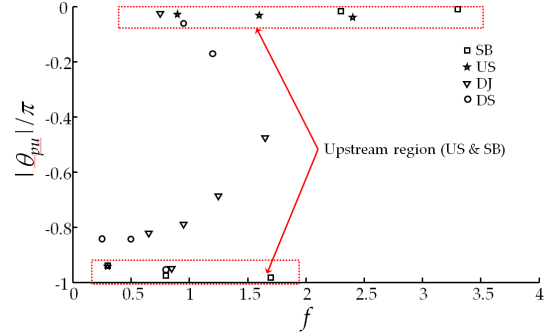


FIGURE 6: PHASE DIFFERENCE BETWEEN u AND p AT SELECTED LOCATIONS IN US, SB, DJ AND DS.

treated as the near field, where the acoustic generation occurs and both aerodynamic and acoustic fluctuations are mixed. On the other hand, the far field is dominated by the acoustic propagation only, which is described by linear acoustic theory. According to Morse [17], for a simple harmonic point acoustic source, the velocity and the pressure are related by $u(x) = \frac{p}{\rho c_0} \left(1 + i \frac{\lambda}{2\pi x}\right)$, where x is the distance from the source, λ is the wavelength of the source and c_0 is the acoustic speed. In the far field ($x \rightarrow \infty$), $\frac{\lambda}{2\pi x} \rightarrow 0$ and u and p are in phase. In the Cartesian coordinates, they are out of phase if the propagating direction is in the negative x direction. On the other hand, in the near field ($x \rightarrow 0$), $\frac{\lambda}{2\pi x} \gg 1$ and the phase difference between u and p , θ_{pu} , are close to $\frac{\pi}{2}$. Figure 6 shows the phase difference between the velocity and the pressure at $(-17, -0.5)$ in US, $(-0.6, -0.5)$ in DJ, $(x_{dj} + 17, -0.5)$ in DS and $(0.5, 17)$ in SB for $VR = 2.0$. One should note that same peaks occur simultaneously in the spectra of u' and p' . The values of θ_{pu} are very close to either 0 or $-\pi$ in US and SB while $0 < |\theta_{pu}| < \pi$ in the other two regions, especially in DJ, whereas $|\theta_{pu}|$ at nearly all peaks are far from 0 and π . This observation indicates that the disturbances in US and SB reaches the far field while those in DJ and DS are still in the near field. This also shows that even at a very long distance downstream from the duct junction available, the fluctuations there are still dominated by the flow dynamics, leading to the inapplicability of the acoustic theory. Therefore, the analysis of the fluctuations obtained in DJ and DS requires additional efforts to distinguish the acoustic and the flow disturbances.

Extraction of acoustic contribution in mixed disturbances Since the acoustic and flow disturbances are mixed in DS, this leads to another challenge in analyzing the DAS results. An approach utilizing the two di-

dimensional wave number to frequency spectrum [18] is adopted to extract the acoustic contribution in mixed disturbances. Such spectral analysis has been successfully applied to the jet-noise experimental data [18] for the disturbance differentiation. A brief description of this approach is given in this paper. The pressure fluctuating field $p'(x, t)$ along a straight line mesh with uniform mesh size Δx is first selected and transformed to a wave number - frequency spectrum $p'(k_x, f)$ by

$$p'(k_x, f) = \frac{1}{2\pi} \iint p'(x, t) W(x) e^{-i(k_x x + 2\pi f t)} dx dt, \quad (3)$$

where $W(x)$ is the window function, f is the frequency, $k_x = 2\pi f / v_p$ is the wave number and v_p is the phase speed of the disturbances. The straight line mesh is so chosen that aligns with the dominant traveling direction of disturbances. Based on Eqn. (3), the fluctuations with the same frequency but different propagating speeds are decomposed into different phase speeds. When the phase speed of the disturbance increases, k_x decreases for the same frequency. In the present calculations, the pressure fluctuations are recorded in a uniform line mesh along $y = -0.2$ and -0.5 , with $\Delta x = 0.2$, in DS. This mesh overlaps on the paths of the vortices and cuts through RZ1. No windowing is applied for the present case, i.e. $W(x) = 1$.

Figure 7 shows the $p'(k_x, f) / \rho_0 u_{eq}^2$ spectra at $y = -0.2$ for all VR studied together with the loci of acoustic speed and other flow speeds. The region below the line $v_p = c_o$ is regarded as the incompressible zone as all the disturbances there travel with speeds close to incompressible limit (higher than the acoustic speed c_o). On the other hand, the region above this solid line is regarded as the subsonic zone, whereas the disturbances travel at subsonic speeds. This figure indicates that the dominant disturbances in DS propagates with $v_p \sim 0.5 - 0.6 u_m$, where $u_m = (u_{max} + u_{min}) / 2$. Here, u_{max} and u_{min} are respectively the maximum and minimum velocities in the separated flow at RZ1 and u_{min} is found to be zero. This observation generally agrees with previous experimental results of mixing layers [19]. Furthermore, the acoustic disturbances are revealed in the spectra when the dominant flow disturbances are filtered out, e.g., Fig. 7c with $VR = 1.0$ at $y = -0.2$. The relatively weak acoustic disturbances are clearly illustrated in this spectrum. Therefore, this two dimensional Fourier transformation is capable of differentiating the mixed acoustic and flow dynamic signals in our DAS results and helping us to analyze the effects of individual disturbances passing through

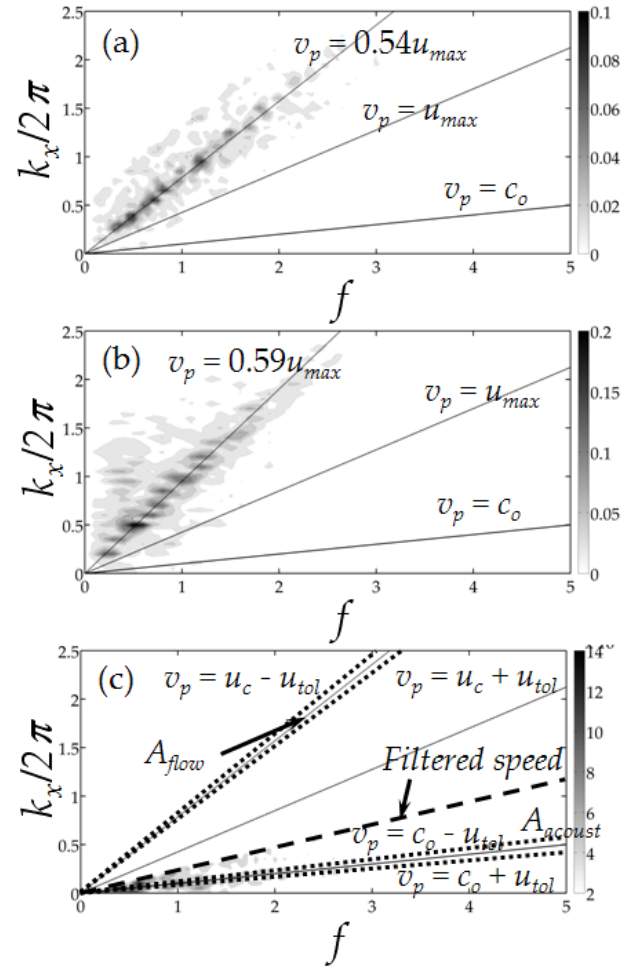


FIGURE 7: $p'(k_x, f) / \rho_0 u_{eq}^2$ AT $y = -0.2$ IN DS. (a) $VR = 1.0$; (b) $VR = 2.0$; (c) FILTERED $p'(k_x, f) / \rho_0 u_{eq}^2$ AT $y = -0.2$ FOR $VR = 1.0$.

the T-duct.

Such signal differentiation can be also adopted to extract the acoustic contribution in the mixed disturbance energy inside DS. The $p'(k_x, f) / \rho_0 u_{eq}^2$ spectra along the centerline of DS ($y = -0.5$) with $\Delta x = 0.2$ are first calculated. Integrations are then performed in the spectra within the areas A_{flow} and A_{acoust} marked in Fig. 7c. Both areas are bounded by $v_{p,flow} \pm v_{tol}$ and $v_{p,acoust} \pm v_{tol}$ respectively, where $v_{tol} = 0.1$ is the tolerance applied, $v_{p,flow}$ and $v_{p,acoust}$ are the phase speeds of flow and acoustic disturbances respectively. Thus, the contribution of acoustic component in mixed signals AR can be estimated by $AR = A_{acoust} / (A_{acoust} + A_{flow})$.

Table 3 lists AR for different VR in this investigation. Evidently the acoustic contribution in each case is three to four orders of magnitude smaller than the flow dynamic contribution, which is typical in low Mach number aero-

TABLE 3: VARIATION OF AR WITH VR IN DS.

VR	AR
1.0	6.88×10^{-4}
2.0	3.7×10^{-3}

coustics. AR can then be used to estimate the acoustic power when the overall fluctuating power is obtained.

Acoustic power The overall acoustic power generated W_{acoust} by a flow through a duct cross-section can be calculated from the instantaneous acoustic intensity along that section using the definition given by Morfey [20]. With the presence of a mean flow, the instantaneous acoustic intensity $\mathbf{I}_a(t)$ at a point is given by

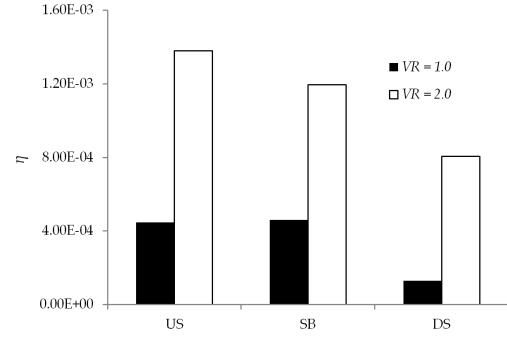
$$\mathbf{I}_a(t) = p' \mathbf{u}' + (\mathbf{M} \cdot \mathbf{u}') (\mathbf{M} p' + \bar{\rho} c \mathbf{u}') + \mathbf{M} \left(\frac{p'^2}{\bar{\rho} c} \right), \quad (4)$$

where c is the local acoustic speed, $\mathbf{u}' = (u', v')$ is the fluctuating velocities, p' is the fluctuating pressure, $\mathbf{M} = |\bar{\mathbf{u}}|/c$, $|\bar{\mathbf{u}}|$ is the mean velocity and $\bar{\rho}$ is mean density. By integrating across the duct cross-section, the instantaneous acoustic power $W_i(t)$ per unit length is calculated by $W_i(t) = \int \mathbf{I}_a(t) \cdot \mathbf{n} ds$, where \mathbf{n} is the unit outward normal of the section. The overall acoustic power per unit length in the z direction W_{acoust} is then given by

$$W_{acoust} = \frac{1}{T} \int_0^T W_i(t) dt, \quad (5)$$

where the duration T is chosen such that at least one period of the lowest dominant frequency is covered. In the present calculations, the chosen cross-sections are $x = -9$ in US, $y = 9$ in SB and $x = 10$ in DS. For each cross-section, the line integral only covers the region so chosen that the influence of duct boundary layer is excluded. Furthermore, in order to eliminate the bias of inlet flow variations on assessing acoustic generation capability in the different cases attempted, a term acoustic efficiency $\eta = W_{acoust}/W_{inlet}$ is defined. W_{inlet} is determined by

$$W_{inlet} = \sum_i \int \frac{1}{2} \rho (\mathbf{u} \cdot \mathbf{u}) \mathbf{n} \cdot \mathbf{v} ds, \quad (6)$$


FIGURE 8: Variation of η in $VR = 1.0$ and 2.0 .

where i is the number of inlet duct section, \mathbf{u} is the flow velocity. The acoustic efficiency η indicates the level of acoustic generation per unit flow power injected into the T-duct. The calculation of W_i are usually done along a cross-section in the duct acoustic far field; otherwise the result consists of both acoustic and flow dynamic fluctuations, e.g. in DS. Therefore, in DS, the acoustic efficiency can be estimated by $\eta_{DS} = AR \times \eta_{DS,overall}$, where AR is calculated from the last section, $\eta_{DS,overall}$ is calculated by Eqn. (5) and Eqn. (6).

The acoustic efficiency η is found to be increased with VR as shown in Fig. 8, i.e., larger portion of the flow power input is transformed to the acoustic power for $VR = 2.0$. This may be explained with the flow unsteadiness observed in Fig. 4. Previous discussions have indicated that most acoustic generating flow unsteadiness mainly occurs around RZ1. At $VR = 2.0$, the unsteady vortical structures created at RZ1 appear to be larger and carrying higher circulation. Their interactions are stronger than their counterparts at $VR = 1.0$, leading to a more effective acoustic generation. In fact the higher level of localized flow unsteadiness at $VR = 2.0$ is revealed in the distribution of mean Reynolds stress (Fig. 3). Thus, the acoustic production are enhanced when VR is increased. Furthermore, η_{DS} is smaller than η_{US} and η_{SB} for both VR s. This may imply that the acoustic propagation in the merging flow has an upstream preference.

CONCLUSIONS

A two dimensional aeroacoustic investigation of a merging flow in a T-duct was performed numerically. Two velocity ratios were attempted. From the numerical results, three distinct flow features are observed for the merging flow in T-duct– the recirculating zone at downstream edge of duct junction, the shear layer between the two inlet flows and another recirculating region upstreams of the duct junction. Among these features, the vortex shedding at the flow region is found to be the dom-

inant flow unsteadiness and thus the dominant acoustic generation in the flow. This shows that the unstable recirculating zone is an efficient acoustic source in internal flow. Due to the mixed nature of the disturbances in the downstream of T-duct, a two dimensional spectral analysis is employed to differentiate them. These results are then applied to extract the acoustic contribution in these regions. Generally, the acoustic power generated increase with the velocity ratio between the main and side-branch flows, which is perhaps caused by the increased vortex interactions. Therefore, this interaction plays an important role in the acoustic generation. Furthermore, only acoustic propagation prevails in regions upstream of the duct junction.

ACKNOWLEDGMENT

Funding support received from the Research Grants Council of the HKSAR Government (through Grant No. PolyU 5278/06E and No. PolyU 5230/09E) and from the Hong Kong Polytechnic University (through Grant No. J-BB2C) is gratefully acknowledged.

REFERENCES

- [1] Dequand, S., Hulshoff, S. J., and Hirschberg, A., 2003. "Self-sustained oscillations in a closed side branch system". *Journal of Sound and Vibration*, **265**(2), Aug., pp. 359–386.
- [2] Karlsson, M., and Åbom, M., 2010. "Aeroacoustics of T-junctions - An experimental investigation". *Journal of Sound and Vibration*, **329**(10), May, pp. 1793–1808.
- [3] Wu, H., 2003. "Influence of sleeve tube on the flow and heat transfer behavior at a T-junction". *International Journal of Heat and Mass Transfer*, **46**(14), July, pp. 2637–2644.
- [4] Hirota, M., Asano, H., Nakayama, H., Asano, T., and Hirayama, S., 2006. "Three-dimensional structure of turbulent flow in mixing T-junction". *JSME International Journal Series B*, **49**(4), pp. 1070–1077.
- [5] Freund, J. B., 2001. "Noise sources in a low-Reynolds-number turbulent jet at Mach 0.9". *Journal of Fluid Mechanics*, **438**, July, pp. 277–305.
- [6] Rowley, C. W., Colonius, T., and Basu, A. J., 2002. "On self-sustained oscillations in two-dimensional compressible flow over rectangular cavities". *Journal of Fluid Mechanics*, **455**, Apr., pp. 315–346.
- [7] Leung, R. C. K., So, R. M. C., Wang, M. H., and Li, X. M., 2007. "In-duct orifice and its effect on sound absorption". *Journal of Sound and Vibration*, **299**(4-5), Feb., pp. 990–1004.
- [8] Wagne, C., Hüttl, T., and Sagaut, P., eds., 2007. *Large-Eddy Simulation for Acoustics*. Cambridge University Press, Cambridge, New York.
- [9] Boris, J. P., Grinstein, F. F., Oran, E. S., and Kolbe, R. L., 1992. "New insights into large eddy simulation". *Fluid Dynamics Research*, **10**(4-6), Dec., pp. 199–228.
- [10] Fureby, C., 2002. "Large eddy simulation of high-Reynolds-number free and wall-bounded flows". *Journal of Computational Physics*, **181**(1), Sept., pp. 68–97.
- [11] Larchevêque, L., Sagaut, P., Mary, I., Labbé, O., and Comte, P., 2003. "Large-eddy simulation of a compressible flow past a deep cavity". *Physics of Fluids*, **15**(1), pp. 193–210.
- [12] Huang, P. G., Bradshaw, P., and Coakley, T. J., 1993. "Skin friction velocity profile family for compressible turbulent boundary layers". *AIAA Journal*, **31**(9), pp. 1600–1604.
- [13] Huang, P. G., and Coleman, G. N., 1994. "Van Driest transformation and compressible wall-bounded flows". *AIAA Journal*, **32**(10), pp. 2110–2113.
- [14] Chang, S. C., 1995. "The method of space-time Conservation Element and Solution Element-A new approach for solving the Navier-Stokes and Euler equations". *Journal of Computational Physics*, **119**(2), July, pp. 295–324.
- [15] Lam, G. C. Y., Leung, R. C. K., Tang, S. K., and Seid, K. H., 2011. "Simplified Courant number insensitive CE/SE Scheme for low Mach number direct aeroacoustic simulation". *Computers and Fluids (Submitted)*.
- [16] Lighthill, M. J., 1952. "On sound generated aerodynamically. I. General theory". *Proceedings of the Royal Society A: Mathematical, Physical and Engineering Sciences*, **211**(1107), Mar., pp. 564–587.
- [17] Morse, P. M., 1986. *Theoretical Acoustics*. Princeton University Press.
- [18] Tinney, C. E., and Jordan, P., 2008. "The near pressure field of co-axial subsonic jets". *Journal of Fluid Mechanics*, **611**, Aug., pp. 175–204.
- [19] Thomas, F. O., 1991. "Structure of mixing layers and jets". *Applied Mechanics Reviews*, **44**(3), pp. 119–153.
- [20] Morfey, C. L., 2001. "Acoustic Power". In *Dictionary of Acoustics*. Academic Press, London, p. 199.



SIMULATIONS OF ACOUSTIC SCATTERING IN FLOW DUCTS WITH THE FREQUENCY-DOMAIN LINEARIZED NAVIER-STOKES EQUATIONS

Axel Kierkegaard*
Susann Boij
Mats Åbom

MWL The Marcus Wallenberg Laboratory for
Sound and Vibration Research
KTH Royal Institute of Technology
Stockholm
Sweden

Gunilla Efraimsson

Department of Aeronautical and Vehicle Engineering
KTH Royal Institute of Technology
Stockholm
Sweden

ABSTRACT

A method is presented for numerical simulations of flow duct aeroacoustics. The method aims specially at predictions of acoustic scattering in complex duct systems with fine geometrical details with presence of acoustic boundary layers and sound-vorticity interaction. The method has been shown both very time efficient and accurate.

A frequency-domain linearized Navier-Stokes equations methodology has been developed to simulate sound propagation and acoustic scattering in flow duct systems. The performance of the method has been validated to experimental data and analytical solutions for several cases of in-duct area expansions and orifice plates and other geometries at different flow speeds. Good agreement has generally been found, suggesting that the proposed methodology is suitable for analyzing internal aeroacoustics.

Introduction

Common to existing commercial duct acoustics software is the lack of satisfying inclusion of flow-acoustic interaction effects on the acoustic propagation. One obvious way to overcome this limitation would be to solve the full non-linear compressible Navier-Stokes equations for entire duct systems. This is however prohibitively computationally expensive and will be out of reach for industrial use in many years to come. Hence, improved, but still efficient methods are needed.

Since most research efforts have been aimed at jet noise generation, where unsteady simulations are needed, few studies have paid attention to the possibilities of frequency-domain aeroacoustics for duct scattering. Examples of sound wave propagation simulations in frequency domain are, e.g. [1, 2] where the Linearized Euler Equations were used, and [3] which implemented the Linearized Lileys equation. In [4], a frequency domain LEE solver was implemented in axisymmetry and applies to an intake geometry. The LEE solver was later applied to bypass outlet sound radiation [1, 5, 6] and good agreement to measurements was found, concluding that frequency domain LEE captures all relevant physics involved in sound radiation from turbo fan engine ducts. In [7, 8], a DGM framework was developed for LEE in frequency domain.

Neither of these studies has however included viscous effects. However, since viscous losses are non-negligible in duct acoustics due to viscous dissipation along walls and at sharp edges, modeling of viscous aeroacoustics might be relevant.

The frequency domain linearized Navier-Stokes equations

In order to achieve reliable results with least possible computational effort, strong knowledge of relevant involved physical mechanisms is needed. For example, in flow duct acoustics it is necessary to include convective effects and effects of refraction due to inhomogeneous mean flows and shear layers. This latter requirement limits the use of for example convected wave equa-

*Address all correspondence to this author. Email: axelk@kth.se

tions based on potential flow theory where all motion is assumed rotation-free. On the other hand, the influence of small-scale turbulent eddies on propagation of sound waves is in most cases negligible, and the use of for example DNS or LES is excessively resource-demanding to these applications.

Many acoustic studies deal with statistically stationary sound fields. In such cases, time-harmonic time dependence can be assumed and calculations be carried out in frequency domain. This is also computationally more efficient than time-domain simulations, since only one calculation is needed per frequency instead of a long time series as in time-domain simulations.

To derive the equations, the full compressible Navier-Stokes equations are chosen as a starting point. Due to the high computational demands associated with three-dimensional simulations, all simulations are here carried out in two dimensions. We first assume that the solution can be written as a sum of a time-independent mean flow term and a time-dependent perturbation term. Furthermore we assume that the relation between pressure and density can be regarded as isentropic. This is however not applicable for all flows, e.g. combustion. A frequency domain approach is taken by prescribing harmonic time-dependence of the perturbed quantities.

The method consists of two stages. In the first step, the steady-state mean flow field in the flow duct is solved with a Reynolds-Averaged Navier-Stokes (RANS) solver. This mean flow field is used as input in the second step, where it is used for linearization of the Navier-Stokes equations. The linearized Navier-Stokes equations solve for the perturbations of density and vorticity around the mean flow, and are capable of capturing acoustic dissipation due to vorticity shedding, as well as acoustic amplification due to acoustic-vorticity feedback.

Methodology

The full compressible Navier-Stokes equations are chosen as a starting point. Due to the high computational demands associated with three-dimensional simulations, all simulations in this paper are carried out in two dimensions.

We first assume that the solution can be written as a sum of a time-independent mean flow term and a time-dependent perturbation term and assume that quadratic and higher order perturbation terms are sufficiently small to be neglected. Furthermore we assume that the relation between pressure and density can be regarded as isentropic. With this relation, the fluctuating pressure becomes redundant and can be removed from the system,

and the continuity and momentum equations are decoupled from the energy equation, which in turn can be omitted. In this way, the size of the computational problem is considerably reduced.

Finally, a frequency domain approach is taken by prescribing harmonic time-dependence of the perturbed quantities. For implementational aspects we write the dimensional linearized Navier-Stokes equations on the form:

$\hat{\rho}$:

$$(u_0 \ v_0) \nabla \hat{\rho} + \left(\frac{\partial u_0}{\partial x} + \frac{\partial v_0}{\partial y} - i\omega \right) \hat{\rho} = - \left(\frac{\partial \rho_0 \hat{u}}{\partial x} + \frac{\partial \rho_0 \hat{v}}{\partial y} \right) \quad (1)$$

\hat{u} :

$$\begin{aligned} \nabla^T \left(- \begin{pmatrix} \frac{4}{3}\mu & 0 \\ 0 & \mu \end{pmatrix} \nabla \hat{u} \right) + \rho_0 (u_0 \ v_0) \nabla \hat{u} + \rho_0 \left(\frac{\partial u_0}{\partial x} - i\omega \right) \hat{u} = \\ = \rho_0 \hat{F}_x - \left(u_0 \frac{\partial u_0}{\partial x} + v_0 \frac{\partial u_0}{\partial y} \right) \hat{\rho} - c^2 \frac{\partial \hat{\rho}}{\partial x} + \frac{1}{3} \mu \frac{\partial^2 \hat{v}}{\partial x \partial y} - \rho_0 \frac{\partial u_0}{\partial y} \hat{v} \end{aligned} \quad (2)$$

\hat{v} :

$$\begin{aligned} \nabla^T \left(- \begin{pmatrix} \mu & 0 \\ 0 & \frac{4}{3}\mu \end{pmatrix} \nabla \hat{v} \right) + \rho_0 (u_0 \ v_0) \nabla \hat{v} + \rho_0 \left(\frac{\partial v_0}{\partial y} - i\omega \right) \hat{v} = \\ = -c^2 \frac{\partial \hat{\rho}}{\partial y} - \left(u_0 \frac{\partial v_0}{\partial x} + v_0 \frac{\partial v_0}{\partial y} \right) \hat{\rho} - \rho_0 \frac{\partial v_0}{\partial x} \hat{u} + \frac{1}{3} \mu \frac{\partial^2 \hat{u}}{\partial x \partial y} \end{aligned} \quad (3)$$

where $\nabla = (\partial/\partial x \ \partial/\partial y)^T$.

This formulation of the frequency-domain linearized Navier-Stokes equations will be used throughout this paper. The equations has also been implemented in axial symmetry, but is not presented here.

The scattering matrix formalism

The scattering matrix formulation is derived to efficiently model networks with both serial and parallel element connections. Often scattering matrices are obtained from analytical solutions or measurement data. Analytical solutions are however often difficult to find, and measurements are expensive to carry out for a large number of components of varying geometrical parameters and flow speeds. The aim here is to develop a fast and efficient yet physically realistic simulation methodology such that the acoustical performance of individual network elements

may be numerically predicted. A general 2-port element can, in the frequency domain, be written as

$$\begin{pmatrix} \hat{\rho}_{1+} \\ \hat{\rho}_{2+} \end{pmatrix} = \underbrace{\begin{pmatrix} R^+ & T^- \\ T^+ & R^- \end{pmatrix}}_{\text{Passive part}} \begin{pmatrix} \hat{\rho}_{1-} \\ \hat{\rho}_{2-} \end{pmatrix} + \underbrace{\begin{pmatrix} \hat{\rho}_{1+}^S \\ \hat{\rho}_{2+}^S \end{pmatrix}}_{\text{Active part}} \quad (4)$$

where the waves are defined as in Figure 1. In the general case, all quantities are complex functions of frequency. The scattering matrix S describes how incoming acoustic waves are transmitted and reflected through the acoustic network element.

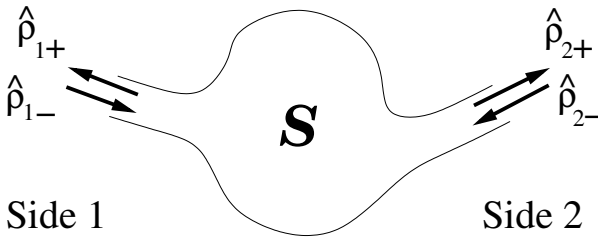


FIGURE 1: A GENERIC ACOUSTIC NETWORK ELEMENT WITH DEFINITION OF WAVE DIRECTION, WHERE $\hat{\rho}_{\pm}$ ARE THE COMPLEX VALUED DENSITY PERTURBATIONS. POSITIVE WAVES ARE PROPAGATING OUT FROM THE ELEMENT WHEREAS NEGATIVE WAVES ARE PROPAGATING INTO THE ELEMENT.

To determine the four unknown quantities in S , two linearly independent acoustic fields, denoted I and II , are needed [9]. This is most commonly realized using either the two-load method [10] or the two source-location method [11], of which the latter is used here. In the two source-location method, a time-harmonic body force is applied first at the inflow and then at the outflow to obtain two independent acoustic cases. The scattering matrix can then be calculated from

$$S = \begin{bmatrix} R^+ & T^- \\ T^+ & R^- \end{bmatrix} = \begin{bmatrix} \hat{\rho}_{a+}^I & \hat{\rho}_{a+}^{II} \\ \hat{\rho}_{b+}^I & \hat{\rho}_{b+}^{II} \end{bmatrix} \begin{bmatrix} \hat{\rho}_{a-}^I & \hat{\rho}_{a-}^{II} \\ \hat{\rho}_{b-}^I & \hat{\rho}_{b-}^{II} \end{bmatrix}^{-1} \quad (5)$$

where R^+ and R^- represents the upstream side and downstream side plane wave reflection coefficients, re-

spectively, and T^+ and T^- represents the upstream-to-downstream side and downstream-to-upstream side plane wave transmission coefficients, respectively.

Plane wave decomposition methods

In order to characterize the acoustic scattering caused by the geometries, it is necessary to know the magnitudes and phases of the up- and downstream propagating waves on both sides of the geometry, i.e. $\hat{\rho}_{\pm}$ of Figure 1. The method used here is based on a non-linear curve-fitting algorithm to the numerical solutions of Eqs (1-3) to determine the magnitudes, phases and wave numbers of the up- and downstream propagating waves, respectively. The two up- and downstream propagating plane waves can be written as $\hat{\rho}(x) = |\hat{\rho}_+|e^{i\phi_+}e^{ik_+x} + |\hat{\rho}_-|e^{i\phi_-}e^{-ik_-x}$ where $|\hat{\rho}_{\pm}|$, k_{\pm} and ϕ_{\pm} are real quantities representing the amplitudes, wave numbers and phases of the up- and downstream propagating waves, respectively. A plus sign denotes propagation in the positive x -direction, and a minus sign denotes propagation in the negative x -direction.

Two postprocessing zones are chosen, upstreams and downstream of the acoustic network element under consideration. About hundred points in the x -direction is taken in each zones and used in an overdetermined non-linear least-squares curve fitting to find the amplitudes and phases of the up- and downstream propagating waves on both sides of the area expansion.

One downside of this wave decomposition technique is that the plane wave assumption is no longer valid in the presence of vortical waves, as it is based on acoustic wave propagation solely. If the evaluation zones are chosen sufficiently large, the acoustic waves and the vorticity waves will not be correlated in space over this region, and vorticity will not significantly affect the performance of the decomposition method. However, in the cases of low frequencies and at high Mach numbers, the length scales of the vortical waves are larger, and might be correlated over the evaluation zone, and will thus yield less accurate results from the wave decomposition method.

Once the up- and downstream propagating waves on both sides of the area expansion are known, the scattering matrix can be calculated as described by Eq. (5).

Validation

In order to evaluate the proposed methodology from both a modeling as well as computational point of view, investigations of the scattering of acoustic plane waves in several duct configurations were carried out. The geometries consist of straight two-dimensional ducts with thin

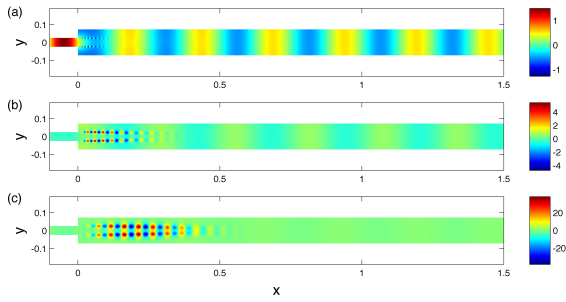


FIGURE 2: PLANE WAVE SCATTERING AT AN AREA EXPANSION. DENSITY PERTURBATIONS AT 1500 HZ FOR MACH NUMBERS 0.08, 0.19 AND 0.29. BOTH PLANE WAVE PROPAGATION AND VORTEX SHEDDING CAN BE SEEN.

and thick orifice plates mounted inside, and of area expansions and other geometries.

Area expansion

An area expansion geometry has been simulated and the scattering matrix and end corrections calculated and validated to experiments [12] and analytical solutions [13, 14, 15]. Figure 2 shows density perturbations at 1500 Hz for three different Mach numbers. Several Mach number cases were investigated, and both scattering matrices as well as end corrections were calculated. In the experiments, a cylindrical duct with diameter 50 mm upstream and 85 mm downstream was used, yielding an area expansion ratio of $\eta = 0.346$. The upstream duct height in the two dimensional rectangular geometry is chosen to be equal to the upstream duct diameter in the experiments, i.e. 50 mm. The downstream height then becomes $50 \text{ mm}/\eta = 144.5 \text{ mm}$.

In Figure 3 the magnitude for the four scattering matrix elements for the $M = 0.08$ Mach number mean flow case are shown. As can be seen, the simulated results agree well with experimental data, indicating that the frequency domain Navier-Stokes methodology manages to capture the relevant physical phenomena of the scattering of acoustic waves by the area expansion. At higher Mach numbers, larger errors were found, although this is partly believed to be due to difficulties in the postprocessing when vorticity is present in the measurement zone, and partly due to errors in the mean flow since at high Mach numbers the incompressibility assumption of the mean flow may not be justified.

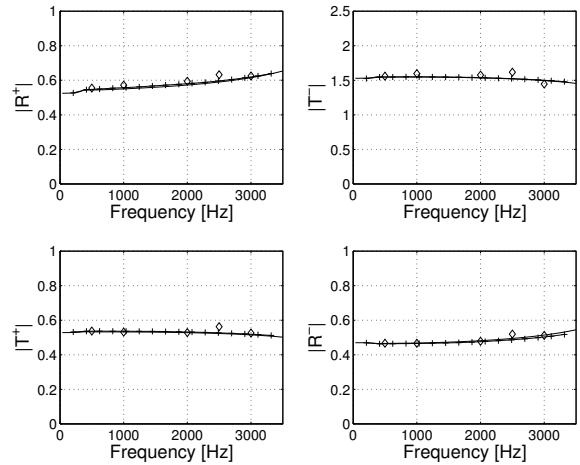


FIGURE 3: MAGNITUDE OF THE SCATTERING MATRIX AT A $M = 0.08$ MACH NUMBER MEAN FLOW. SOLID LINE: ANALYTIC SOLUTION, DIAMONDS (\diamond): EXPERIMENTS, PLUS (+): SIMULATIONS.

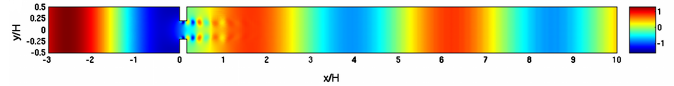


FIGURE 4: SCATTERING IN A DUCT WITH AN ORIFICE PLATE. THE SOUND-VORTICITY INTERACTION AT THE ORIFICE MAY LEAD TO AN AMPLIFICATION OF IMPINGING SOUND WAVES.

Orifice plate

Orifice plates of different thickness have been simulated. Figure 4 shows density perturbations including plane wave propagation and vorticity shedding. The sound-vorticity interaction may in this case either attenuate or amplify impinging sound waves depending on frequency. In Figure 6, the so-called whistling potentiality [16] is shown for experiments [16] and simulations with and without viscosity taken into account. It is clearly seen that viscosity is needed to correctly simulate amplification of sound waves by an orifice.

A critical issue in flow duct configurations is the potential risk of flow-acoustic coupling leading to whistling, which counteracts the performance of installed mufflers, and must be avoided. Although whistling itself is a non-linear phenomena, the onset from a linear state is not, and can therefore be simulated with linear aeroacoustics. By calculating a so-called power balance over an individual duct component it can be seen that for certain configurations, for certain frequency ranges, more acoustical power is emitted than put into the system. This is due to an in-

teraction between the acoustical and the vorticial modes in the fluid, where an amount of acoustical power is transferred into vorticity which may be amplified in mean flow shear layers, and if interacting with for example an edge, emits more acoustic energy than that which to start with triggered the vorticity instability. In that case a net power amplification can be caused. If this acoustic power amplification occurs in a frequency range corresponding to any acoustical resonance frequencies of the system, it may lead to a resonant feedback loop yielding very large amplitudes such that transition from the linear state into a non-linear regime occurs.

The net attenuation or amplification of sound waves in a duct element is characterized by its scattering properties. From the scattering properties, the acoustical power output to a unit acoustical power input can be calculated [17, 16]. Frequency ranges with a net power amplification are identified as potential causes of whistling.

The linearized Navier-Stokes equations are used due to their inclusion of the viscous terms, which are assumed to be of fundamental relevance at boundaries and sharp edges, as is the case with most in-duct geometry.

Geometry The geometry studied here corresponds to that of [16], and consists of an in-duct orifice. In the experiments carried out in [16] the thickness of the orifice plate was 5 mm, the diameter of the orifice was 19 mm and the duct diameter was 30 mm, yielding an area expansion ratio of $19^2/30^2 \approx 0.4$. The area expansion ratio is a crucial parameter to the acoustic scattering, which needs to be maintained in the simulations. In the simulations presented here, we use a 2D approximation of the geometry which thus needs to be modified to acoustically agree with the geometry of the experiments. If the height of the duct is set to be equal to the duct diameter of the experiments, i.e. $H = 30$ mm, the height of the orifice section needs to be $h = 11.9$ mm to ensure an expansion ratio of $h/H \approx 0.4$. The orifice thickness does not need to be modified, and is set to $t = 5$ mm.

Mean flow The first step in the simulation methodology is to calculate the mean flow in the duct section, which later is used to linearize around. The flow is simulated with an incompressible, non-linear, steady-state Reynolds-Averaged Navier-Stokes (RANS) method, with a $k - \epsilon$ turbulence model.

The inflow Mach number is $M = 0.042$, which corresponds to a Reynolds number $Re_H \approx 2.5 \cdot 10^4$ based on the duct height. The magnitude of the velocity of the mean flow field is dominated by the formation of a jet

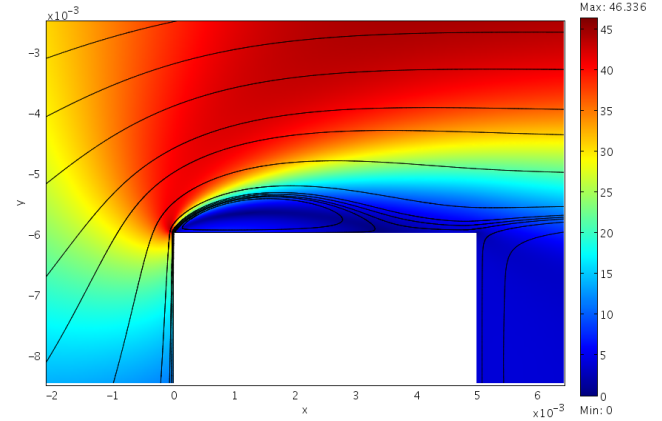


FIGURE 5: MAGNITUDE OF THE VELOCITY FIELD [M/S] AND STREAMLINES OF THE STEADY-STATE MEAN FLOW.

with a maximum flow speed of $M = 0.14$ in the region at the orifice, expanding further downstream and develops into channel flow within 3-5 duct diameters. A large recirculation zone is formed, with reattachment point at about 1.5 duct diameters downstream of the orifice plate. A close-up of the mean flow in the vicinity of the lower orifice edge is shown in Figure 5, which reveals the formation of a smaller recirculation zone just downstream of the leading edge of the orifice plate.

It should be pointed out that the recirculation zone within the cavity seemed to be sensitive to properties of the RANS modeling and computational mesh used. As this recirculation zone influence the acoustic scattering, care should be taken when calculating the mean flow.

Whistling potentiality In [17], a theoretical criterion for a flow duct element's ability to amplify impinging sound waves, the so-called whistling potentiality, was proposed. Starting at a pre-calculated scattering matrix, this can be reformulated into a power balance equation to find frequency regimes where energy amplification is present.

Following [17], the dissipated power is calculated as the difference between the incident and the scattered sound power yielding an eigenvalue problem as

$$\lambda_{1,2} = E - \text{eig}(S_e^* S_e) \quad (6)$$

where E is the unit matrix and the scattering matrix S_e is

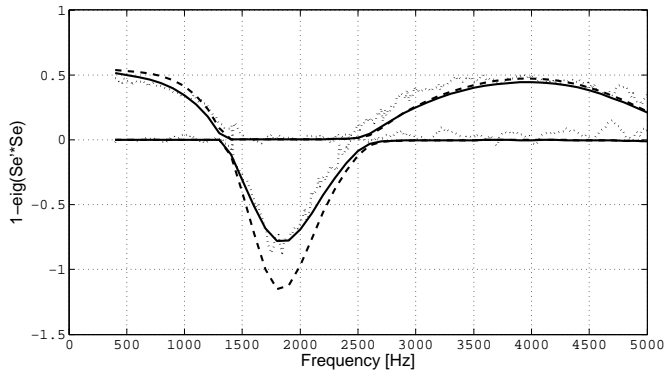


FIGURE 6: WHISTLING POTENTIALITY CALCULATED WITHOUT VISCOUS EFFECTS (DASHED) AND WITH VISCOUS EFFECTS (SOLID) TAKEN INTO ACCOUNT ON THE ORIFICE PLATE, COMPARED TO EXPERIMENTS [CITE] (DOTTED). AS CAN CLEARLY BE SEEN, THE CASE WITHOUT VISCOUS EFFECTS (LEE) OVERPREDICTS THE WHISTLING POTENTIALITY.

defined as

$$\begin{pmatrix} (1+M)\hat{p}_{2-} \\ (1-M)\hat{p}_{1-} \end{pmatrix} = \underbrace{\begin{pmatrix} T^+ & R^- \\ R^+ & T^- \end{pmatrix}}_{S_e} \begin{pmatrix} (1+M)\hat{p}_{1+} \\ (1-M)\hat{p}_{2+} \end{pmatrix} \quad (7)$$

which is modified to take convective effects into account, compared to the scattering matrix defined in Eq. (5) where this is not included. Following the definition of Eq. (6), a positive eigenvalue indicates a net dissipation whereas a negative indicates a net amplification of sound power.

In Figure 6, the eigenvalues are plotted as a function of frequency. For comparison, the eigenvalues based on measured data from [16] are plotted in the same figure. As can be seen, the frequency domain linearized Navier-Stokes methodology accurately predicts the magnitudes as well as the frequency ranges of net production and dissipation of incident sound when compared to experimental data.

To investigate the influence of viscous boundary layers on the whistling potentiality, a second simulation was carried out with slip boundary conditions on the orifice plate, mimicking the behavior of a Linearized Euler Equations (LEE) simulation. The results are included in Figure 6 as well, showing an overprediction of whistling potentiality due to an increased vortical strength in the absence of boundary layers. This clearly demonstrates that a methodology based on LEE would be insufficient

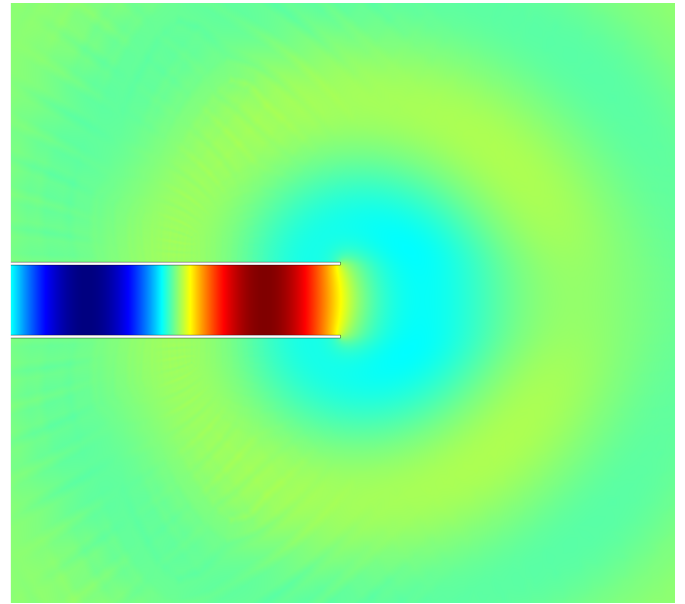


FIGURE 7: SOUND WAVES AT A DUCT TERMINATION WITH A LOW MACH NUMBER MEAN FLOW AT 400 °C.

for this application.

Reflections from an open duct with a hot jet

Another example of simulations successfully simulated with the frequency-domain linearized Navier-Stokes equations include sound wave reflections at an open duct termination with a hot jet. The diameter of the jet was 41 mm, following the experiments carried out in [18]. The purpose of the study was to investigate the effects of temperature on the reflection coefficient, and the mean flow speed was set low, at 2.5 m/s to avoid significant convective effects. Temperatures of 21 °C (ambient temperature), 200 °C and 400 °C were studied and compared to experiments [18] and Munt's theory [19].

Figure 7 shows the sound field inside the duct, and radiation to the surrounding air at a temperature of 400 °C and a frequency of 2500 Hz.

In Figure 8, the simulated reflection coefficients are shown for the three temperatures as a function of frequency, and compared to experiments and analytical solutions, with good agreement.

Summary

A simulation methodology based on a frequency domain formulation of the linearized Navier-Stokes equations have been developed and evaluated with applications related to the prediction of scattering of sound in flow ducts and whistling. The method solves the propaga-

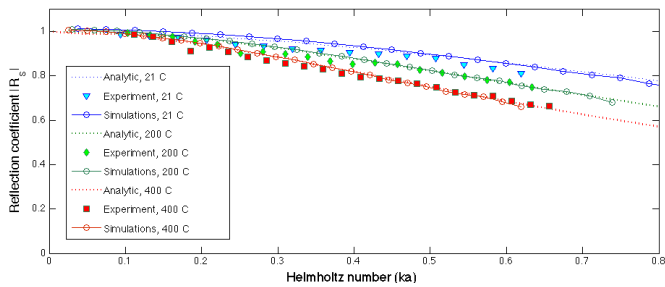


FIGURE 8: REFLECTION COEFFICIENT OF AN OPEN DUCT DEPENDING ON MEAN FLOW TEMPERATURE. BLUE: 21 °C, GREEN: 200 °C, RED: 400 °C. CIRCLES: SIMULATIONS, DOTTED LINE: ANALYTICAL SOLUTION, SHAPES: EXPERIMENTAL RESULTS.

tion of sound waves directly by solving the compressible governing equations for the perturbations about a mean flow state. The method consists of two stages. In the first step, the steady-state mean flow field in the flow duct is solved with a Reynolds-Averaged Navier-Stokes (RANS) solver. This mean flow field is used as input in the second step, where it is used for linearization of the Navier-Stokes equations. A frequency-domain approach is taken to prevent unbounded growth of hydrodynamic instabilities, and for efficiency reasons. Both acoustic and vortical perturbations are included and thus enables studies of vortex-sound interaction in cases of acoustic dissipation or amplifications due to vortex shedding. The method was applied to test cases of in-duct thin and thick orifice plates as well as area expansions and open duct terminations with good agreement to experimental results. To improve the method, implementations full three dimensional geometries are needed. An implementation of the energy equation is needed in cases when the isentropic relation between density and pressure does not hold. Further validation on more complex geometries are needed, as for example geometries with curved boundaries. In all, the frequency-domain linearized Navier-Stokes method has shown great potential both for research and as a practical industrial tool.

REFERENCES

- [1] Özyörük, Y., 2009. “Numerical prediction of aft radiation of turbofan tones through exhaust jets”. *J. Sound Vib.*, **325**(1-2), pp. 122–144.
- [2] Rao, P. P., and Morris, P. J., 2006. “Use of finite element methods in frequency domain aeroacoustics”. *AIAA J.*, **44**(7), pp. 1643–1652.
- [3] Casalino, D., and Genito, M. Solution of linearized Lilley’s equation in the frequency domain for turbofan aft noise prediction. AIAA Paper 2007-3705, 13th AIAA/CEAS Aeroacoustics conference, Rome, Italy, 2007.
- [4] Özyörük, Y., Alpman, E., Ahuja, V., and Long, L. N., 2004. “Frequency-domain prediction of turbofan noise radiation”. *J. Sound Vib.*, **270**(4-5), pp. 933–950.
- [5] Özyörük, Y., Dizemeny, E., Kayay, S., and Aktürkçz, A. A frequency domain linearized Euler solver for turbomachinery noise propagation and radiation. AIAA Paper 2007-3521, 13th AIAA/CEAS Aeroacoustics conference, Rome, Italy, 2007.
- [6] Özyörük, Y., and Tester, B. J., 2010. “Assessment of a frequency-domain linearised Euler solver for turbofan aft radiation predictions and comparison with measurements”. *Procedia Engineering*, **6**, pp. 153–162.
- [7] Gabard, G. Wave-based discontinuous Galerkin methods for the linearized Euler equations in the frequency domain. AIAA Paper 2007-3476, 13th AIAA/CEAS Aeroacoustics Conference, Rome, Italy, 2007.
- [8] Gabard, G., 2007. “Discontinuous Galerkin methods with plane waves for time-harmonic problems”. *J. Comp. Phys.*, **225**(2), pp. 1961–1984.
- [9] Åbom, M., 1991. “Measurement of the scattering-matrix of acoustical two-ports”. *Mechanical Systems and Signal Processing*, **5**(2), pp. 89–104.
- [10] Lung, T. Y., and Doige, A. G., 1983. “A time-averaging transient testing method for acoustic properties of piping systems and mufflers with flow”. *J. Acoust. Soc. Am.*, **73**(3), pp. 867–876.
- [11] Munjal, M. L., and Doice, A. G., 1990. “Theory of a two source-location method for direct experimental evaluation of the four-pole parameters of an aeroacoustic element”. *J. Sound Vib.*, **141**(2), pp. 323–333.
- [12] Ronneberger, D., 1987. Theoretische und experimentelle untersuchung der schallausbreitung durch querschnitts-sprünge und lochplatten in strömungskanälen. Tech. rep., DFG-Abschlussbericht, Drittes Physikalisches Institut der Universität Göttingen.
- [13] Boij, S., and Nilsson, B., 2003. “Reflection of sound at area expansions in a flow duct”. *J. Sound Vib.*, **260**(3), pp. 477–498.
- [14] Boij, S., and Nilsson, B., 2006. “Scattering and absorption of sound at flow duct expansions”. *J. Sound Vib.*, **289**(3), pp. 577–594.
- [15] Boij, S., 2009. “Flow effects on the acoustic end

- correction of a sudden in-duct area expansion”. *J. Acoust. Soc. Am.*, **126**(3), pp. 995–1004.
- [16] Testud, P., Aurégan, Y., Moussou, P., and Hirschberg, A., 2009. “The whistling potentiality of an orifice in a confined flow using an energetic criterion”. *J. Sound Vib.*, **325**(4-5), pp. 769–780.
- [17] Aurégan, Y., and Starobinsky, R., 1999. “Determination of acoustic energy dissipation/production potentiality from the acoustic transfer functions of a multiport”. *Acustica*, **85**, pp. 788–792.
- [18] Rämmal, H., and Lavrentjev, J., 2008. “Sound reflection at an open end of a circular duct exhausting hot gas”. *Noise Control Eng. Journal*, **56**(2), pp. 107–114.
- [19] Munt, R. M., 1990. “Acoustic transmission properties of a jet pipe with subsonic jet flow: I. the cold jet reflection coefficient”. *J. Sound Vib.*, **142**(3), pp. 413–436.
- [20] Karlsson, M., and Åbom, M., 2011. “On the use of linear acoustic multiports to predict whistling in confined flows”. *Acta Acoustica united with Acoustica*, **97**(1), pp. 24–33.



THE SPATIAL DISTRIBUTION OF THE ACOUSTIC SOURCES IN AN INLINE TUBE ARRAY EXPERIENCING CROSS FLOW INDUCED ACOUSTIC RESONANCE.

Shane L. Finnegan
School of Engineering
Trinity College,
Dublin
Ireland

Craig Meskell
School of Engineering
Trinity College,
Dublin
Ireland

ABSTRACT

The flow induced acoustics in an inline tube bank ($P/d=3$) subject to cross flow, indicative of a generic heat exchanger geometry, are examined over a range of flow velocities using Particle Image Velocimetry (PIV) coupled with acoustic analysis. In this way, the spatial and temporal aeroacoustic source distribution has been determined experimentally. It is found that the acoustic sources are most intense behind the first row due to the compactness of the vortices. However, a strong negative source (i.e. a sink) is also present in this location, so that the effect of the first row wake is actually to suppress the acoustic resonance. In subsequent rows, the sources are weaker and more dispersed, but the sink is reduced dramatically. The result is that after the first row the entire array contributes energy to the acoustic field.

1 Introduction

Acoustic resonance can occur when gas flow within a cavity or duct exhibits periodic vortex structures. If the frequency of flow periodicity is similar to an internal acoustic mode of the cavity, then a feedback can occur whereby energy is transferred from the flow into the acoustics, causing large pressure fluctuations. This acoustic resonance can lead to excess vibration and hence failure of components.

Interaction between the resonant acoustic field and the unsteady flow field around bluff bodies (flow-acoustic coupling) has been thoroughly investigated experimentally, for various configurations. For example, Mohany and Ziada [1,2], Hall *et al.* [3] and Finnegan *et al.* [4] have examined two tandem cylinders. Blevins and Bressler [5], Fitzpatrick [6], Oengoren and Ziada [7], [8] and Ziada *et al.* [9] for tube arrays. While these studies have high-

lighted the mechanisms of acoustic resonance, they have not provided much empirical insight into the global distribution of acoustic sources in the flow field. Knowledge of the distribution of acoustic sources for a particular geometry of tube bundle could improve the design of a heat exchanger or possibly help improve acoustic resonance mitigation techniques. Furthermore, flow induced acoustic resonance is not completely understood, especially in complex geometries. This means that the conditions for the onset and the intensity of any resonance cannot be well predicted a priori. Nor can the effect of mitigation measures be easily assessed. Ideally, the compressible flow would be modelled so as to provide a predictive tool for the onset of lock-in, as well as the amplitude of the acoustic resonance. However, while the field of computational aeroacoustics (CAA) is advancing rapidly, much of the research effort is focused on exterior flows. Furthermore, simulation of the coupled fluid flow and acoustic systems in the complex geometry of a heat exchange system appears to be some way off. In this context, the current work attempts to provide a rich data set for a reference configuration which can be used as an interim validation of simulation tools, while also providing some physical insight into the mechanism of acoustic resonance in tube bundles. The paper outlines the basic analysis approach and the experimental procedure before presenting the key results of the study.

2 Calculating the instantaneous aeroacoustic power.

Experimental method used to calculate the spatial distribution of the acoustic energy has previously been developed for arrangements of two and four cylinders [4, 10]. The basic approach is based on a formulation de-

veloped by Howe [11] which calculates the dissipation of acoustic energy by the generation of vorticity at a rigid boundary in a low sub-sonic mean flow with uniform density and is an extension of his theory of vortex sound [12].

The instantaneous local acoustic power, λ , is given by Eq. 1:

$$\lambda(x, y, z, t) = -\rho \boldsymbol{\omega}(x, y, z, t) \cdot (\mathbf{V}(x, y, z, t) \times \mathbf{U}_a(x, y, z, t)). \quad (1)$$

A positive value of λ indicates that the location (x, y, z) is amplifying the instantaneous system acoustic power (i.e. the point is acting as an acoustic source), while a negative value indicates that acoustic power is being dissipated (i.e. a sink). The total instantaneous acoustic power in the flow field can be obtained simply by integrating over the region \mathfrak{R} , to yield the familiar formulation of Howe:

$$\Lambda(t) = -\rho \int_{\mathfrak{R}} \boldsymbol{\omega}(x, y, z, t) \cdot (\mathbf{V}(x, y, z, t) \times \mathbf{U}_a(x, y, z, t)) d\mathfrak{R} \quad (2)$$

This equation was derived from the kinetic energy of the incompressible velocity field in a divergence-free, isentropic mean flow. It predicts that the acoustic power flux of the vortical structures is equal to the rate at which work is performed by the Coriolis force density experienced by the vortical structures [11]. Equation 2 states that acoustic power $\Lambda(t)$ can be calculated from the spatial integral of the triple product between the vorticity vector $\boldsymbol{\omega}$, the local hydrodynamic flow velocity vector \mathbf{V} and the acoustic particle velocity vector \mathbf{U}_a , where ρ is the mean density of air and \mathfrak{R} is the control volume. A central assumption is that the hydrodynamic and acoustic components in the flow field can be decoupled from each other, resolved separately and then re-coupled to calculate the acoustic sources. This requires a low Mach number.

The system under investigation here is geometrically two dimensional (i.e. it can be considered to be an extruded shape). The fluid mechanics (i.e. the vortical structures) may still be highly three dimensional in these types of geometries, but it will be assumed that the flow field is two dimensional, and so the vorticity is a scalar, as only the component normal to the plane will be non-zero. Thus, the local instantaneous acoustic power is

$$\lambda(x, y, t) = -\rho \omega_z(x, y, t) (\mathbf{V}(x, y, t) \times \mathbf{U}_a(x, y, t)). \quad (3)$$

The assumption of two dimensionality is justified for two reasons. Firstly, it has been shown that the spanwise correlation length of vortex shedding in a tube array at moderate Reynolds numbers is approximately 6 diameters (see

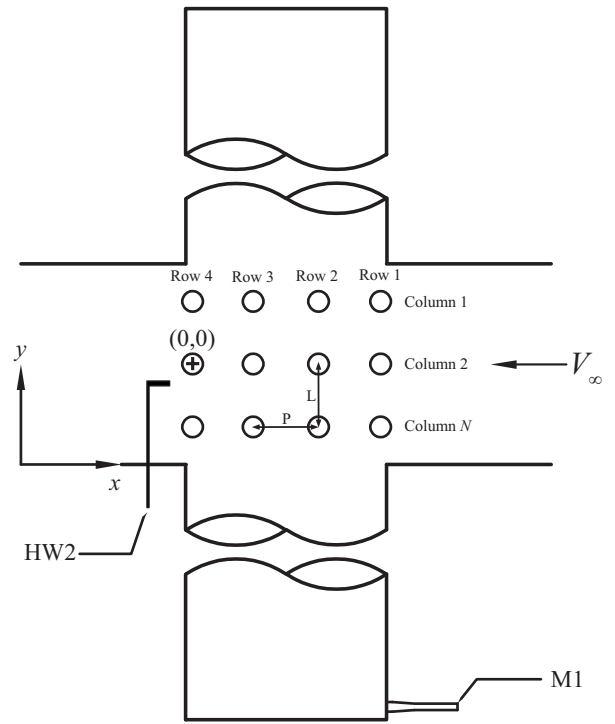


FIGURE 1: Schematic of experimental geometry. Tube array geometry is $P/d = L/d = 3.0$. Tube diameter, $d = 13\text{mm}$. Position of microphone and hotwire are indicated by M1 and HW2, respectively.

for example Zdravkovich [13] or Mahon *et al.* [14]). The second reason is that the presence of the acoustic resonance will enhance the spanwise correlation.

3 Experimental facility

The target geometry was a four row in-line square tube array ($P/d = L/d = 3.0$). The tube diameter, d , was 13mm. Tests were conducted in a small scale, draw down wind tunnel with a test section of $125\text{mm} \times 125\text{mm}$. Figure 1 shows a schematic of the experimental geometry. The position of the roving hotwire probe and fixed reference microphone are shown as HW2 and M1 respectively. Note that side branches were added to reduce the resonant acoustic frequency, f_a , to approximately 300Hz. The side branches are sufficiently wide that the acoustic mode shape only differs from what would be expected in an infinite array in a straight duct at the four corner locations in the array. Many aspects of the setup are similar to previous test campaign with two tandem cylinders [4].

The tube array spacing is larger than would be ex-

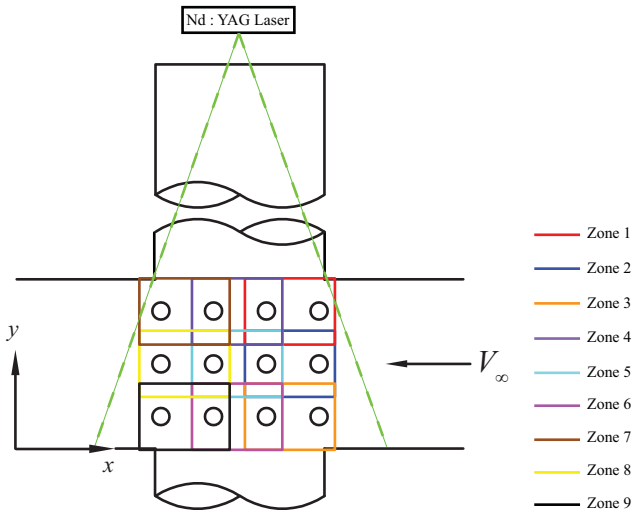
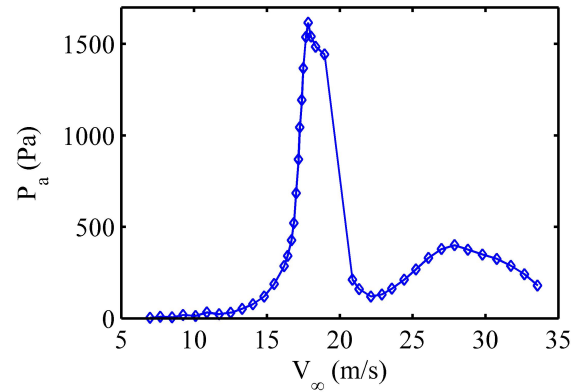


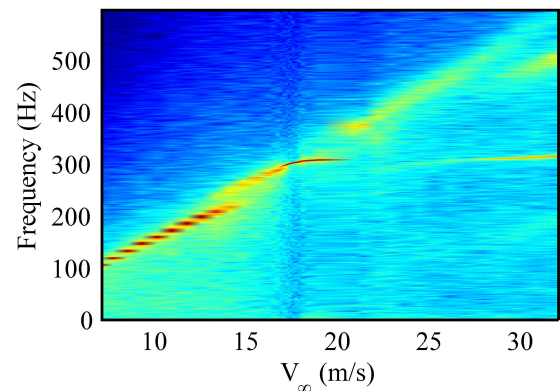
FIGURE 2: Schematic of the nine overlapping interrogation zones used for PIV measurements.

pected in nuclear installations. In fact it is classified as large streamwise spacing ratio according to [7]. This large spacing was chosen to facilitate PIV measurements. However, it should be remembered that the current test campaign is intended to provide validation data for a reference case, rather than target a particular operational design.

Sound pressure was monitored using a flush mounted G.R.A.S. Type 40BH microphone and location M1. The hotwire and the microphone data was digitized using an NI PXI 4472B data acquisition card. The seeding particles of diethyl-hexylsebacate (DEHS) with a diameter of approximately $1\mu\text{m}$ were illuminated by a Nd:YAG pulsed laser. A Davis Flowmaster 3 CCD camera was used to capture the PIV images and the PIV post processing was completed with LaVision DAVIS 7.2. In order to maintain sufficient spatial resolution to ensure good quality vector maps, which are unbiased by peak locking, the field of view of the PIV had to be restricted to $50\text{mm}\times 40\text{mm}$. As a result, the entire array was decomposed into nine overlapping zones, shown in Figure 2. Data for each zone was phase locked to the microphone signal and ensemble averaged, allowing a composite velocity map of the entire array to be obtained. Even if a much higher resolution camera was used, so that the interrogation area could be increased to capture the entire array in a single image, it would still be desirable to decompose the region into these nine zones so as to minimize the effect of parallax.



(a) Acoustic pressure measured at M1.



(b) Velocity spectra (magnitude on arbitrary logarithmic scale).

FIGURE 3: Aeroacoustic behaviour of the tube array at various flow velocities measured by microphone M1 and hotwire HW2

4 Flow-acoustic coupling.

Figure 3 shows the aeroacoustic response of this tube array configuration. Figure 3(a) shows the acoustic pressure measured with microphone M1 whilst fig. 3(b) shows a waterfall plot of the streamwise velocity spectra measured by the hotwire HW2. Acoustic excitation is triggered by vortex shedding at acoustic-Strouhal coincidence. The increase in acoustic pressure is gradual as f_v approaches f_a but accelerates at acoustic-Strouhal coincidence. Hence this square array would be classified as experiencing coincidence resonance. The system remains locked-in for approximately 4 m/s. When lock-in is broken, the vortex shedding frequency f_v jumps up to a higher frequency and increases with flow velocity. However, at these higher velocities, the vortex shedding gradually diminishes into broadband turbulent structures.

This is apparent in the waterfall plot as the strength of the Strouhal peak after lock-in is much lower com-

pared to the dependency before lock-in. Closer inspection of the waterfall plot reveals that the f_v suddenly jumps to a higher frequency at $V_\infty = 14\text{m/s}$ and follows a slightly different Strouhal dependency before lock-in occurs. This occurs at approximately the same velocity as the onset of the acoustic pressure increase in fig. 3(a). This may represent the switch between global jet instability excitation and local wake instability excitation discussed by [15]. The frequencies before the jump yield a Strouhal number based on gap velocity of $St_g = 0.14$ while the frequencies after the jump yield a Strouhal number of $St_g = 0.15$. [15] reported Strouhal numbers of 0.14 and 0.16 respectively in their water tunnel tests.

5 Spatial distribution of acoustic power

As discussed above, in order to resolve the entire flow field, the setup was decomposed into 9 zones, the nature of the phase locked PIV measurement means that testing and post-processing is very time consuming. For this reason, the full field acoustic power was investigated for only one flow velocity ($V_\infty = 18.2\text{m/s}$; $V_g = 27.8\text{m/s}$) which corresponded to acoustic-Strouhal coincidence. The pressure measured by microphone M1 at acoustic-Strouhal coincidence was $P_a = 1376\text{Pa}$ (156.75 dB) which meant that the dimensionless acoustic particle velocity was $U_a/V_\infty = 0.18$; $U_a/V_g = 0.12$.

Triggered PIV acquisition, enabled phase locked ensemble averaging. The microphone signal was used as a time reference. The velocity field was resolved using 100 image pairs, at phase increments of 22.5° . Thus the acoustic cycle was resolved with 16 full field maps. When the net acoustic power at all 16 phases are examined, it is found that maximum acoustic power is generated at $\phi = 22.5^\circ$ and $\phi = 202.5^\circ$, while at $\phi = 112.5^\circ$ and $\phi = 292.5^\circ$ acoustic power is absorbed. Figure 4 plots the vorticity and the corresponding acoustic power calculated using Eq. 2 at $\phi = 22.5^\circ, 112.5^\circ, 202.5^\circ, 292.5^\circ$. Each tube exhibits a white halo. In this region there is no data available because of parallax; the tubes themselves obscure the view of the flow field adjacent to the surface.

Inspection of the vorticity plots in Fig. 4(a-d) shows that well defined vortices form from the first row of cylinders, propagate in the wake and impinge onto the second row. The vortices formed from one shear layer are out-of-phase with the vortices formed in the adjacent shear layer of the neighbouring column. As the vortex impinges, it induces a second, weaker vortex to form from the second row. This vortex forms on the other side of the cylinder from which the impinging vortex was shed and so has opposite polarity. The shedding of this second vortex

is contemporaneous with the shedding of a strong vortex of similar sense from the first row. That is to say, the structures are highly synchronised across the bundle. The vortices formed in the second row are spread out over a larger area than the vortices shed from the first but have a smaller magnitude. Moreover, they also seem to be less coherent. When the vortices formed from the second row impinge on the third row, even less coherent vortices form in their wake. At this stage, the flow has become mostly turbulent which is apparent from the noisy vorticity contours. Even though the structures in the deeper rows are less defined and much more turbulent compared to upstream rows, they continue to form alternatively in the wakes of the cylinders and synchronisation of the flow seems to remain between both the rows and the columns. The structure of the phased averaged flow field agree well with the findings of [15].

Figure 4(e-h) shows the acoustic power at each phase. Much stronger sources and sinks are generated at phase of 22.5° and 202.5° (Fig. 4(e) and (g), respectively) compared to $\phi = 112.5^\circ$ and 292.5° (Fig. 4(f) and (h), respectively) because the magnitudes of the acoustic particle velocities (negative and positive) are much greater at these phases. Concentrating on the phases that generate most acoustic power, inspection of Fig. 4(e, g) reveals that the sources generated at $\phi = 22.5^\circ$ are associated with structures shed from the top sides of the cylinders whilst sources generated at $\phi = 202.5^\circ$ correspond to structures shed from the bottom sides of the cylinders. One can see that at both of these phases, the vortices are still developing behind rows 1 and 2 and have not quite fully formed. They have a significant contribution to Eq. 2 because they possess a high level of vorticity due to their attachment to the shear layer. On the other hand, for the phases that absorb acoustic power, it can be seen that the sinks generated at $\phi = 112.5^\circ$ correspond to vortex structures shed from the top sides of the cylinders whilst sinks generated at $\phi = 292.5^\circ$ correspond to structures shed from the bottom sides of the cylinders. One can see that at both of these phases, the vortices (which were previously still forming) are now fully developed and just about to impinge on a downstream cylinder. Even though the acoustic particle velocity at these phases has reduced, the fact that the vortices are fully developed and cover a large area means their contribution is still significant and hence absorption occurs. It seems that the generation of acoustic power in this in-line tube bundle is due to the generation and formation of new structures from the cylinders whilst the absorption of acoustic power seems to be due to their interaction with a downstream cylinder in the wake.

The spatial distribution of the net acoustic energy per

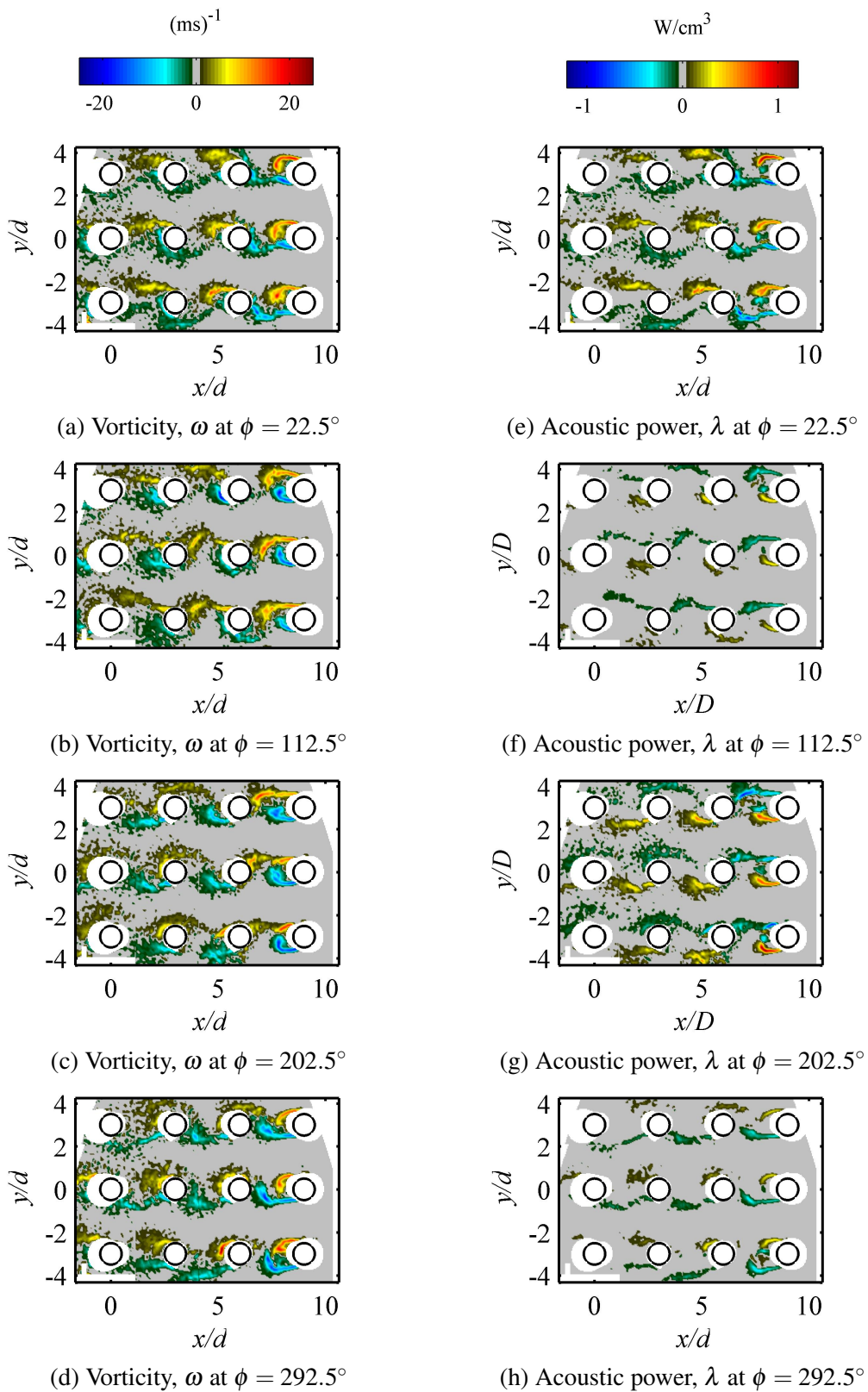


FIGURE 4: The full field hydrodynamic vorticity and acoustic power for different phases of the acoustic wave cycle at acoustic-Strouhal coincidence, $f_a = 311\text{Hz}$, $\frac{U_a}{V_\infty} = 0.18$.

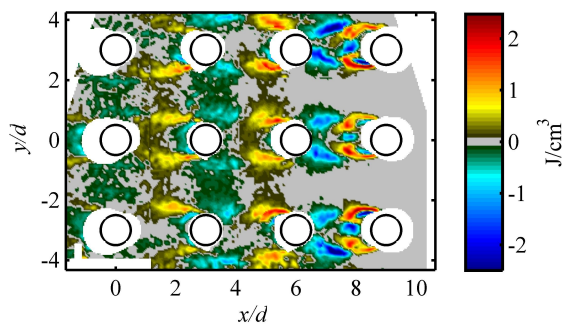


FIGURE 5: Total acoustic energy per cycle generated at acoustic-Strouhal coincidence.

cycle generated by the tube bundle can be seen in Fig. 5. It should be noted that due to parallax, there is a substantial portion of the flow field for which there is no information available; these areas appear as white voids in Fig. 5. The result is that while the spatial distribution of time averaged acoustic power offers quantitative information locally, only qualitative information is available globally. Nonetheless, some useful observations can be made. The generation/absorption of acoustic energy occurs in a periodic fashion from the first row of the array to the last. Moreover, the distributions of the sources and sinks around each column are almost identical, at least for the first three rows. The generation of acoustic energy seems to be largely due to the formation of vortices behind the first and second rows, whilst the absorption of energy seems to be due to the vortices impinging on the cylinders. Fitzpatrick and Donaldson[15] concluded that vortex shedding from the first few rows of a shallow in-line tube bundle (no. rows < 5) is the primary source of acoustic resonance. Indeed, the region near the second row seems to be particularly important as there are very large sinks situated just before it and very strong sources situated just aft of it. The sinks just in front of the second row cylinders have the strongest magnitudes of all the structures. The first and second rows have the strongest sources and sinks as they have the best defined hydrodynamic structures. However, as can be seen, the less defined turbulent structures behind the third row are significant in the generation of acoustic power. A general observation is that the strength of the sources/sinks decreases from row to row. This is not thought to be due to the drop off in the acoustic particle velocity but rather to the breakdown in coherent vortex structures as the flow travels deeper into the array. In fact, the net contribu-

tion in each inter-cylinder gap is comparable, so that, although the strongest acoustic sources are without doubt to be found between row 1 and 2, the entire array contributes significantly to the generation of sound.

6 Comparison with two tandem cylinders.

The coupled flow-acoustic resonance of two tandem cylinders in a duct has been extensively studied in the literature, and is reasonably well understood. In order to build on this knowledge base, Figure 6 compares the normalised net acoustic energy transfer at a streamwise location per cycle E^* (as a function of the distance from the upstream cylinder) generated around the cylinders in column 2 of the array with that generated by the two tandem cylinders with pitch ratio (P/d) of 2.5 during pre-coincidence resonance[6]. Note that the reduced velocities are similar in these two cases. The normalised energy E^* was defined by [10] as:

$$E^* = \frac{E}{P_a d} \quad (4)$$

where E is net acoustic energy at a stream-wise location, per unit tube span, per cycle, P_a is the sound pressure level, and d is the cylinder diameter. This is obtained from integrating eqn. 3:

$$E(x) = \int_0^T \int_{-\infty}^{\infty} \lambda(x, y, t) dy dt \quad (5)$$

The distributions of the sources and sinks between the two cases are remarkably similar suggesting that the mechanisms generating and absorbing acoustic power are similar. As can be seen, the strongest sinks form at $x = -2.5d$ for the tandem cylinder case and at $x = -2.2d$ for the tube bundle. The biggest difference between the two plots is the relative magnitudes of the sources and sinks in the wake of the first row. This is due to the extra stream-wise spacing between the cylinders for the in-line tube bundle. For the tandem cylinder configuration, the downstream cylinder is located at $x = -2.5d$ and the vortices in this are stretched by the downstream cylinder. Hence, they are not developing or strengthening. For column 2 of the in-line tube bundle, the cylinder in the second row is at $x = -3d$ which means the vortices can still grow and strengthen. The added space has afforded the vortex more time to develop which is why it has a stronger contribution. For the two tandem cylinder case, it was found that pre-coincidence acoustic resonance is generated by the formation of vortices in the gap between

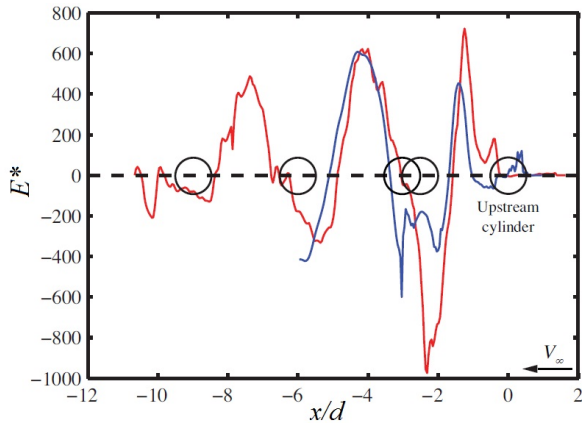


FIGURE 6: Comparison of normalized acoustic energy per cycle E^* as a function distance from the first upstream cylinder: — Inline tube bundle ($P/d = 3$), current study; — two tandem cylinders during pre-cocidence resonance ($P/d = 2.5$) from [4].

the two cylinders and that absorption of acoustic power is related to the impingement of the vortices on the downstream cylinder. This is largely the case here. However, it is interesting how changing the spacing of the gap between two cylinders by only a small amount can drastically change the relative contribution of the sources and sinks. Finnegan et al. [10] reported a similar effect for a four cylinder configuration with a pitch ratio $P/d = 3$.

As previously mentioned, the effect of parallax will be to make the acoustic power in the region of the tubes uncertain, and so the net acoustic power for the entire system does not give a reliable metric of whether the system would tend to be locked in. This problem will not be present in numerical simulations, which can be validated against the local spatial distribution of acoustic power measured in this paper.

7 Conclusions

The most general conclusion to be drawn is that the combined PIV, FEA and microphone approach, previously applied to tandem and four cylinders, is applicable to the geometrically more challenging configuration of a tube array, although the practical obstacles to overcome in implementing the experimental protocol are significant.

Nonetheless, detailed information has been obtained for a square in-line array with a pitch ratio of 3.0 at acoustic-Strouhal frequency coincidence. The behaviour of the array is broadly consistent with that of similar geometry reported in the literature. The principal physical insights to be gained in this study are:

1. The flow structure between the first three rows of the array during lock-in is highly synchronous despite its geometric complexity and moderate Reynolds number.
2. The mechanisms of acoustic resonance for the tested array are similar to those observed in the tandem cylinder and four cylinder configurations previously reported.
3. Vortex shedding in the wake of the first and second rows provide the dominant sources in the flow field. The strength of the sources diminishes with each row as the vortex structures become less coherent. However, the net sound generated by these relatively diffuse structures is not insignificant.
4. The absorption of acoustic resonance in this particular array is largely associated with the vortices shed from the first row of cylinders impinging on the second row. The large stream-wise spacing allows more time for the vortices to develop which means their contribution will be more significant.

The effect of parallax means that there are gaps in the data at important locations in the field. However, the data provides a useful reference case which will allow deep validation of any numerical simulation of flow-acoustic resonance in tube arrays.

8 Acknowledgements

This publication has emanated from research conducted with the financial support of Irish Research Council for Science Engineering and Technology (IRCSET).

REFERENCES

- [1] Mohany, A., and Ziada, S., 2005. "Flow-excited acoustic resonance of two tandem cylinders in cross-flow". *Journal of Fluids and Structures*, **21**(1), pp. 103–119.
- [2] Mohany, A., and Ziada, S., 2009. "A parametric study of the resonance mechanisms of two tandem cylinders in cross-flow". *Journal of Pressure Vessel Technology*, **131**(2).
- [3] Hall, J. W., Ziada, S., and Weaver, D. S., 2003. "Vortex-shedding from single and tandem cylinders in the presence of applied sound". *Journal of Fluids and Structures*, **18**(6), pp. 741–758.
- [4] Finnegan, S. L., Meskell, C., and Ziada, S., 2010. "Experimental investigation of the acoustic power around two tandem cylinders.". *Journal of Pressure Vessel Technology*, **132**, August.
- [5] Blevins, R., and Bressler, M., 1993. "Experi-

- ments on acoustic resonance in heat exchanger tube bundles”. *Journal of Sound and Vibration*, **164**, pp. 502–534.
- [6] Fitzpatrick, J. A., 1985. “The prediction of flow-induced noise in heat exchanger tube arrays”. *Journal of Sound and Vibration*, **99**(3), pp. 425–435.
- [7] Oengoren, A., and Ziada, S., 1992. “Vorticity shedding and acoustic resonance in an in-line tube bundle- part ii: Acoustic resonance”. *Journal of Fluids and Structures*, **6**, pp. 293–309.
- [8] Oengoren, A., and Ziada, S., 1998. “An in-depth study of vortex shedding, acoustic resonance and turbulent forces in normal triangular tube arrays”. *Journal of Fluids and Structures*, **12**, pp. 717–758.
- [9] Ziada, S., Oengoren, A., and Buhlmann, E. T., 1989. “On acoustical resonance in tube arrays part ii: Damping criteria”. *Journal of Fluids and Structures*, **3**(3), pp. 315–324.
- [10] Finnegan, S., Meskell, C., and Oshkai, P., 2010. “Aeroacoustic source distribution around four cylinders orientated in a square”. In ASME 2010 3rd Joint US-European Fluids Engineering Summer Meeting Collocated with 8th International Conference on Nanochannels, Microchannels, and Minichannels, ASME, pp. 735 – 744.
- [11] Howe, M. S., 1980. “The dissipation of sound at an edge”. *Journal of Sound and Vibration*, **70**(3), pp. 407–411.
- [12] Howe, M. S., 1975. “Contributions to theory of aerodynamic sound, with application to excess jet noise and theory of flute”. *Journal of Fluid Mechanics*, **71**(4), pp. 625–673.
- [13] Zdravkovich, M., 2003. *Flow around circular cylinders : a comprehensive guide through flow phenomena, experiments, applications, mathematical models, and computer simulations Volume 2. Applications*. Oxford University Press.
- [14] Mahon, J., Cheeran, P., and Meskell, C., 2010. “Spanwise correlation of surface pressure fluctuations in heat exchanger tube arrays”. In ASME 2010 3rd Joint US-European Fluids Engineering Summer Meeting Collocated with 8th International Conference on Nanochannels, Microchannels, and Minichannels, ASME, pp. 533–542.
- [15] Ziada, S., and Oengoren, A., 1992. “Vorticity shedding and acoustic resonance in an in-line tube bundle- part i: Vortex shedding”. *Journal of Fluids and Structures*, **6**, pp. 271–292.



AUDIO SIMULATION AND ANALYSIS OF NOISE GENERATED BY AIRCRAFT ENGINES BEARING CONTRA-ROTATING OPEN ROTOR FANS

Leonidas Siozos - Roussoulis¹

Laboratory of Fluid Dynamics and Turbomachines,
Department of Mechanical Engineering,
Aristotle University of Thessaloniki,
Thessaloniki, Greece
Email: leonidassr@windowslive.com

Anestis I. Kalfas

Laboratory of Fluid Dynamics and Turbomachines,
Department of Mechanical Engineering,
Aristotle University of Thessaloniki,
Thessaloniki, Greece

Kosmas Kritikos

Department of Mechanical Engineering,
Aristotle University of Thessaloniki,
Thessaloniki, Greece

Emidio Giordano

Department of Mechanical Engineering,
Aristotle University of Thessaloniki,
Thessaloniki, Greece

Nicolas Tantot

SNECMA, Safran Group
Centre de Villaroche,
Moissy-Cramayel, France

ABSTRACT

Aircraft engines equipped with contra-rotating open rotor (CROR) fans have been the subject of recent study, as they can provide adequate reduction of fuel consumption and emissions. Due the use of an unducted fan, the issue of extensive noise generation has to be taken into account. This paper presents the simulation and analysis of noise generated by CROR engines, while investigating tonal noise directivity patterns.

The audio simulation was based on numerical sound pressure level versus frequency results for computations realized during the sideline validation stage and resulted in the generation of a digital audio file. A spectrum analysis of the audio signal was also obtained. Tonal noise components were located, while their directivity patterns were plotted and compared to empirical and experimental data.

The directivity patterns of the numerical data well duplicated the experimental results, thus validating the original modeling procedure, and enhancing the value of the simulated audio files, in future research.

NOMENCLATURE

B_1	number of blades of rotor 1
B_2	number of blades of rotor 2
M_{adv}	advancing Mach number
N_1	rotation speed of rotor 1
N_2	rotation speed of rotor 2
R	rotor radius
f	tone frequency
f_1	harmonic frequency of rotor 1
f_2	harmonic frequency of rotor 2

f_{12}	interaction tone between the rotors
k	tone wave number
m	circumferential mode of tone
n_1	positive integer
n_2	positive integer
a	speed of sound
θ	engine noise emission angle

INTRODUCTION

During the last decade, aircraft engine manufacturers have initiated research on innovative engine architectures, thus aiming to reduce emissions and fuel consumption. The growing concern on CO₂ emissions, as well as the constantly rising cost of jet fuel have imposed this alteration of needs and market demand. Contra-rotating open rotor engines fulfill the standards stated above, due to their high propulsive efficiency, and have thus been the subject of constant research. Despite their undisputed qualities, the use of CROR engines is confined by certain drawbacks. Reduced cruise Mach number and increased noise emissions, are potential issues that need to be addressed. The latter, in particular, is due to the engine's unducted fan architecture, which allows fan rotor noise to propagate unobstructed. Consequently, control and optimization of CROR sound emissions has evolved into an exceptionally challenging objective. Several research projects have focused on rendering CROR engines compliant with the severe noise regulation context, governing civil aviation. The outcome of the aforementioned investigations was the basis for this paper.

The generation of noise emanating from CROR engines has been studied by a number of research groups

¹Address all correspondence to this author

on an experimental and numerical basis. During the late 1980's, experimental study on CROR engines was at its peak. General Electric's GE-36 Unducted Fan [1] (Fig. 1) was tested in flight on a Boeing 727 (1986) and on a McDonnell Douglas MD-80 (1988). Additionally, R.P. Woodward [2] obtained noise measurements from a model CROR in NASA's Lewis Research Center (1987), extensively investigating tonal noise levels and their correlation to design characteristics and test conditions. Work on that subject decreased during the early 1990s, as the measured noise emissions were considered to be unacceptably high. However, research on CROR engines has lately known a renewed interest, due to the constantly increasing cost of jet fuel. Recently, Kritikos et al. [3] developed a numerical tool which allows fast estimation of noise emissions generated by CROR engines. The emissions were calculated throughout the time domain, for different engine specifications and flight conditions, thus providing sufficient data, that could be studied in respect to Woodward's experimental results.

The current paper presents the development of an audio file which simulates the noise emissions of a CROR engine. A spectrum analysis of the audio signal was additionally obtained in order to locate tonal noise components and investigate their origin. Finally, rotor-alone and interaction tone directivity patterns were determined, according to the original numerical data. These directivities were then compared to empirical results and actual experimental measurements of CROR engine noise emissions. The comparison of computational and experimental data would provide further validation of the initial numerical method, which was utilized in order to obtain the input data for this paper.

INPUT DATA ANALYSIS

Files containing calculated noise emissions of a CROR engine were obtained from earlier research work, in order to achieve accurate simulation of aircraft engine noise. These files also sufficed for the latter stage of the investigation, which included extensive study of tonal noise directivity patterns.

The input data for this paper was derived by Kritikos et al [3], while developing a numerical model which could predict noise levels generated by CROR engines, thus optimizing noise emissions. A number of cases of engine operation were processed and investigated, each differing in operating conditions and structural specifications of the engine. The calculated noise emissions of one of these cases was adequate for developing the final sound simulation and analyzing the generation of tonal noise. The effect of airframe noise and the upstream pylon interaction were not taken into account, while the aircraft incidence angle was considered to be 0 degrees during the investigated case. The CROR engine which was studied was equipped with a 12-blade front rotor and a 10-blade aft rotor.

The data files resulting from [3] comprise of effective perceived noise level (EPNL), versus frequency results



FIGURE 1: GENERAL ELECTRIC GE-36 UDF MOUNTED ON A MCDONELL-DOUGLAS MD-80 [4].

for calculative measurements realized during three different stages of flight (approach, sideline and takeoff). Only sideline noise was investigated in this paper, as the experimental reference data [2] was also derived from a sideline measurement procedure. The extraction of the computational noise levels was realized by a microphone virtually located at a sideline of 450 m from the aircraft's path, as is dictated by the ICAO validation regulations [5]. The aircraft's speed was considered to be constant and equal to 0.2 Mach.

In Fig. 2 the location of the 41 computational reference points (named "observers") of the sideline stage, is typified. The 39 points located on the horizontal plane represent the computational extraction of sound levels realized by a microphone, during the aircraft's flight from (-1020, 450, 0) to (273, 450, 0) (observers 1 to 39), while retaining zero altitude. Additionally, two further observers (40 and 41) are depicted in Fig. 2, which are located at (136.5, 450, 150) and (273, 450, 300), and were assigned to monitor noise levels in respect to the circumferential sound emission angle. The microphone "M" was supposedly located at a sideline, 450 m away from the aircraft's route (and from all 41 observers), being theoretically positioned at the origin (0, 0, 0).

The computational process was initiated when the aircraft had reached the point (-1020, 450, 0) and therefore, this reference value was assigned to the first temporal observer. The aircraft was considered to travel in a straight line, on the horizontal plane, till it reached the point (273, 450, 0) and thus the 39th temporal observer. Accordingly, two further observers, 40 and 41, which were not located on the horizontal plane, were taken into account. The reference value of observer 41 was considered to be the last temporal observer. Each one of the observers can be defined either temporally or spatially, as all 41 observers correspond to specific points on the aircraft's route which are determined by the aircraft's constant speed (0.2 Ma) [3].

The time interval between consecutive observers in the time domain was set to 0.5 seconds. Due to the number of observers (41) and the time step between them (0.5

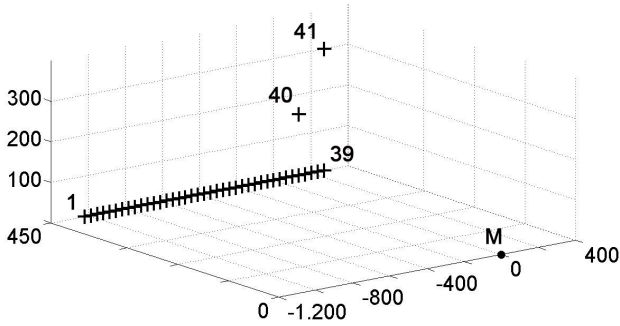


FIGURE 2: SIDELINE NOISE LEVEL EXTRACTION REFERENCE POINTS.

seconds), the final time length of the audio file simulating the sideline stage would subsequently be 20.5 seconds. The microphone extracted the predicted sound pressure levels throughout the time domain and the reference data was then transferred into the frequency domain, via a Fast Fourier Transformation (FFT).

Each temporal observer provided an instantaneous spectrum analysis of the emitted noise. The frequency range stretched from 19.69 Hz to 5039.37 Hz, while the frequency step was set to 19.69 Hz. Thus, the data file corresponding to each observer consisted of 256 discrete tones, all differing in EPNL. The upper limit of the frequency range was proved to be sufficiently high.

AUDIO SIMULATION AND SPECTRUM ANALYSIS

The outcome of the audio simulation of the noise generated during the sideline validation stage, was a 20.5 second long digital audio file. Moreover, a spectrum analysis of the final audio signal was obtained in order to locate tonal components and aid the study of the variation of tone noise levels, throughout the time domain. Finally, the creation of a time dependent series which included audio and visual elements, was considered necessary for achieving a comprehensible visual representation of the audio output.

The simulation procedure, as well as the method of obtaining the spectrum analysis and the time dependent series, were described extensively in [6].

Spectrum Analysis of Sideline Validation Stage

The computational measurement procedure, as well as the location of the microphone were described in Fig. 2. The spectrum analysis of all 41 reference points of the sideline stage, is depicted in Fig. 3 and 4. It graphically illustrates the computed effective perceived noise levels in respect to the 256 discrete tones which constitute the frequency spectrum. Each separate curve represents the spectrum analysis of one temporal observer and therefore Fig. 3 and 4 depict the overall fluctuation of noise levels throughout the time and frequency domain.

A thorough examination of Fig. 3 and 4 leads to certain conclusions regarding tone noise generation as will be further analyzed in the following section of the paper. It should be noted that high frequencies tend to be attenuated more effectively by ambient air, in contrast to lower frequencies. Thus, noise levels remain low for frequencies above 1500 Hz, during the first temporal observers, when the aircraft is supposedly located the furthest away from the microphone. Sound transmission loss is mainly affected by atmospheric humidity, temperature and pressure, parameters which were defined by the initial numerical model [3].

TONAL NOISE DIRECTIVITY

The directivity patterns of rotor-alone and interaction tones, were determined, after analyzing the initial data. These patterns were then compared to the theoretically expected directivities and experimentally derived results.

Main Characteristics of Tonal Noise

The blade passing frequencies (BPF) of the front and aft rotor are derived from Eqn. (1) and (2) [4], respectively:

$$f_1 = n_1 B_1 N_1 \quad \text{in Hz,} \quad (1)$$

$$f_2 = n_2 B_2 N_2 \quad \text{in Hz,} \quad (2)$$

The frequencies of the interaction tones between the two rotors are calculated from Eqn. (3) [4], while the circumferential mode of a tone f_{12} is derived from Eqn. (4) [4]:

$$f_{12} = |n_1 B_1 N_1 + n_2 B_2 N_2| \quad \text{in Hz,} \quad (3)$$

$$m = n_2 B_2 - n_1 B_1 \quad (4)$$

Where N_1 and N_2 are the rotation speeds of each rotor (in Hz), while n_1 and n_2 are positive integers. In addition, B_1 and B_2 are the number of blades in each rotor. The second row of blades is taken as reference for the rotation direction for the sign of m [4].

Empirical Directivity Patterns

The directivity patterns of the noise emissions computed in [3] were initially studied in respect to empirically predicted directivities.

According to [4], the levels of sound radiated at a tone of wave-number $k = 2\pi f/\alpha$ and of mode m , is governed by the Bessel function of first kind and order m :

$$J_m \left(\frac{kR \sin \theta}{1 - M_{adv} \cos \theta} \right) \quad (5)$$

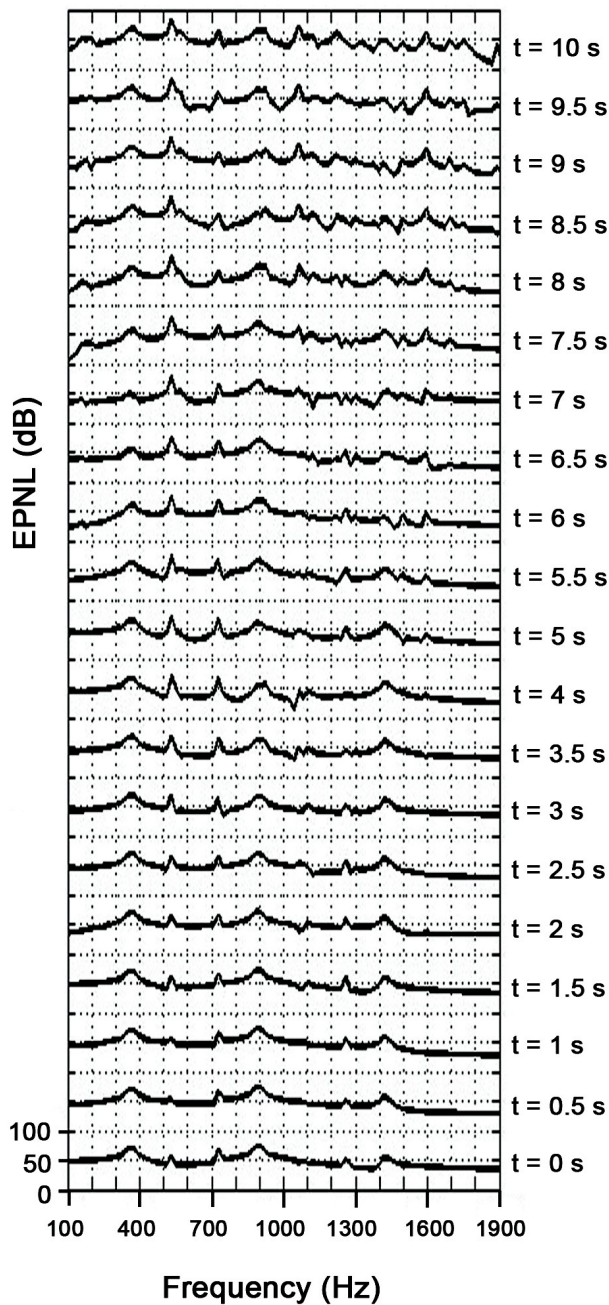


FIGURE 3: SPECTRUM ANALYSIS OF TEMPORAL OBSERVERS 1 TO 20 DURING SIDELINE STAGE

Where R is the rotor radius, M_{adv} is the advancing Mach number and θ is the noise emission angle in the horizontal plane ($\theta = 0$, on the upstream axis). Frequencies are divided by $(1 - M_{adv}\cos\theta)$, in order to take into account the Doppler effect, when the microphone is fixed to the ground.

Figure 5 depicts the plots of the Bessel functions corresponding to a numerical test case where $m = B_1 = 11$ at $kR = 8.888$ for the front rotor BPF (BPF1), $m = B_2 = 9$ at $kR = 7.272$ for the BPF of the aft rotor (BPF2) and $m = -2$ at $kR = 16.16$ for the first interaction tone (BPF1 +

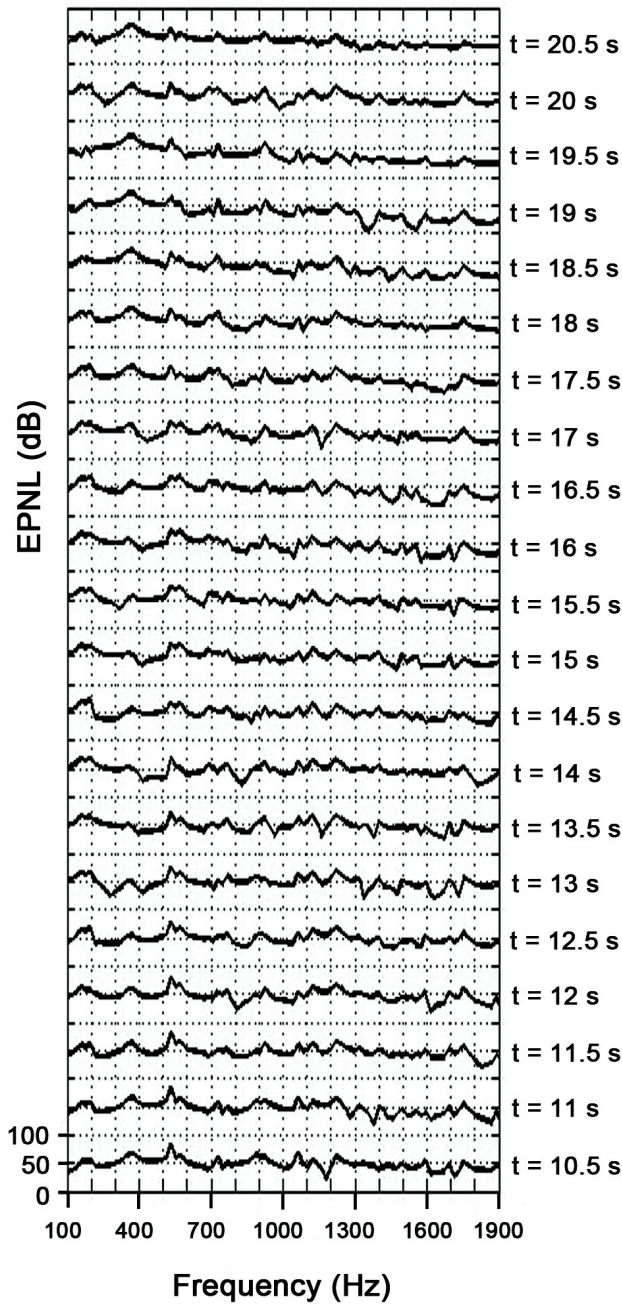


FIGURE 4: SPECTRUM ANALYSIS OF TEMPORAL OBSERVERS 21 TO 41 DURING SIDELINE STAGE

BPF2). The computed Bessel functions were additionally multiplied by $\sin\theta$, in order to take into account the variation of distance. Three curves were thus plotted, each corresponding to one of the aforementioned frequencies. The curves illustrate the correlation between tone noise levels and the emission angle.

Additional study of analytic prediction of tone noise radiation was presented in [7]. Figure 6 typifies the results of the analytic method described in [7], regarding the directivity of the rear rotor BPF (BPF₂) and the first interaction tone. Again, the two curves depict the

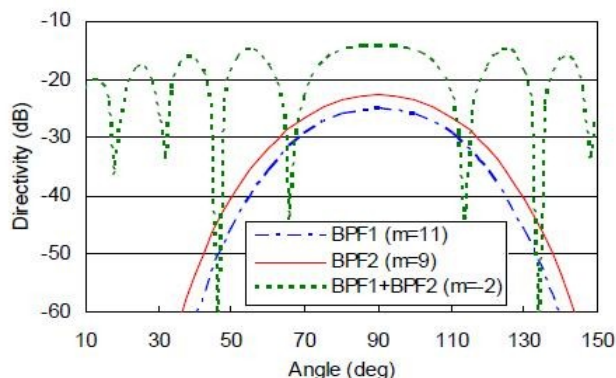


FIGURE 5: DIRECTIVITY PATTERNS DESCRIBED BY BESSEL FUNCTIONS [4].

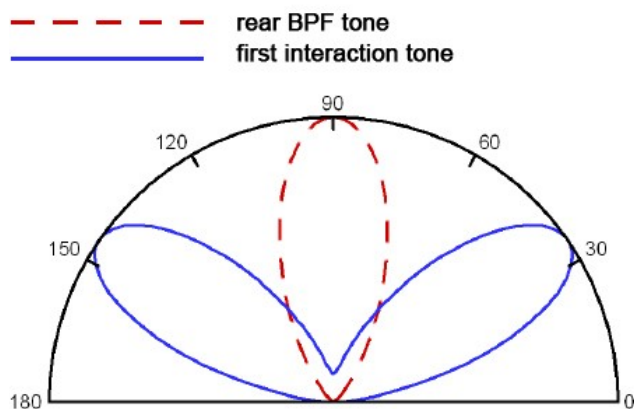


FIGURE 6: DIRECTIVITY OF REAR ROTOR BPF TONE AND FIRST INTERACTION TONE DERIVED FROM AN ANALYTIC PREDICTION MODEL [7].

correlation between tone noise levels and the emission angle.

Despite some divergences, mainly due to the different approach of each study, the similarities between Fig. 5 and 6 are evident. It is apparent that the radiation of rotor-alone tones is restricted to the angles near the propeller plane. On the other hand, the first interaction tone appears to maintain high levels throughout the sideline directivities, while tending to radiate mostly in the forward and rearward arc.

Experimental Directivity Patterns

The empirical directivity patterns were studied in order to provide a guideline for the analysis of experimental tone noise directivities, thus aiding the final comparison of experimental and numerical results.

The experimental data were obtained by R. P. Woodward [2], during the investigation of a model CROR engine in NASA's Lewis Research Center. The tested CROR engine (F7/A7) was equipped with an 11-blade front rotor and a 9-blade aft rotor. The measurement

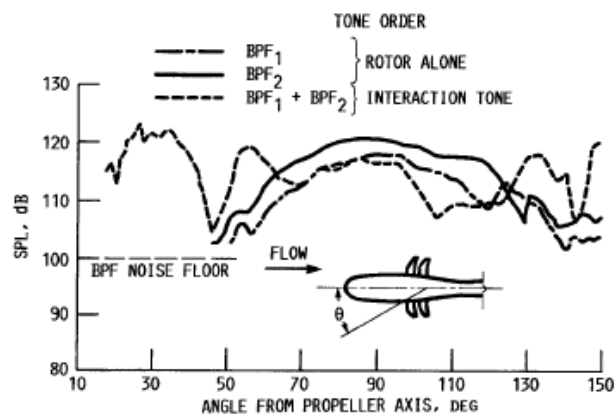


FIGURE 7: TONE DIRECTIVITY MEASURED ALONG A SIDELINE [2].

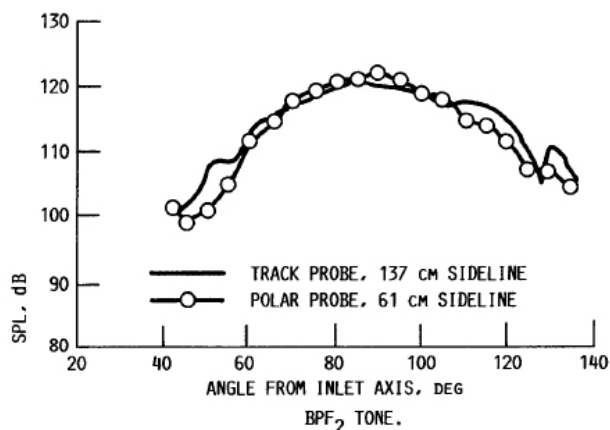


FIGURE 8: SIDELINE DIRECTIVITY OF AFT ROTOR BPF TONE MEASURED BY TWO PROBES [2].

procedure included sideline measurements realized by a track probe, located 137 cm from the propeller axis. The probe traversed 6.5 m, in a straight line parallel to the propeller axis, thus surveying sideline angles ranging from 18 to 150 degrees. Further sideline measurements were obtained by a polar probe which was located 61 cm from the propeller axis, and was initially intended for determining circumferential directivity patterns.

Figure 7 presents the sideline directivities of the front and aft rotor BPF tones (BPF_1 and BPF_2 respectively), as well as the first interaction tone ($BPF_1 + BPF_2$), measured by the track probe in the aircraft flyover plane.

Additionally, Fig. 8 depicts the sideline directivity patterns of the aft rotor BPF tone, obtained from measurements realized by both the track and polar probe, at different distances from the propeller axis. Having taken into account the expected spherical decay, the application of the inverse square law, was considered necessary in order to reduce the results obtained from the microphone closer to the engine. Final comparison of data originating from measurements realized by the track and polar probe, proved that the corrected polar probe measurements well

duplicated the data recorded by the track probe. Therefore, far-field measurements can be rather accurately estimated by a microphone positioned at a distance of one propeller diameter from the propeller axis.

A thorough study of Fig. 7 and 8 lead to apparent conclusions, regarding the directivity patterns of rotor-alone and interaction tone noise. Evidently, sideline measurements proved that the rotor plane is dominated by first order rotor-alone tones, BPF₁ and BPF₂. Additionally, the first interaction tone (BPF₁ + BPF₂) maintains high levels throughout the sideline directivities, while the maximum noise levels are observed near the propeller axis.

The conclusions derived above, well duplicate the outcome of the empirical prediction methods, of tonal noise directivity, described in [4] and [7]. The first order rotor-alone tone directivities depict undisputed similarities. On the other hand, the experimental directivity pattern of the first interaction tone despite appearing complicated, shows some overall resemblance to the empirical models. Note, for instance, the trough at approximately 45 degrees in both Fig. 5 and 7, as well as the maximum noise level values located at approximately 30 and 150 degrees in both Fig. 6 and 7.

Computed Directivity Patterns

After having investigated noise directivity patterns obtained from empirical methods and experimental measurements, a clear guideline was set in order to realize a comprehensive comparison of experimental and numerical results. Therefore, noise level versus emission angle plots of first order rotor-alone tones, as well as the first interaction tone, were derived from the sideline reference data [3].

The emission angle of the radiated engine noise corresponding to each one of the 41 observers, of the sideline validation stage, can accurately be computed, as the microphone retained a fixed position during all 41 numerical noise level extractions. The coordinates of each observer were predefined in [3], therefore, 41 radiation angles were determined during the sideline validation stage. The angle value range stretched from 23.81 to 121.24 degrees and was predefined by the specifications of the noise level extraction procedure.

In Fig. 9 the directivities of first order rotor-alone tones are depicted, according to numerical results derived from [3], during the sideline calculation stage. As was described above, 41 reference points provided sufficient data, in order to plot two curves, which present the directivity patterns of tones corresponding to the BPF of the front rotor (BPF₁ = 198.94 Hz, for $n_1 = 1$ and $n_2 = 0$, mode order $m = -12$) and the BPF of the aft rotor (BPF₂ = 165.78 Hz, for $n_1 = 0$ and $n_2 = 1$, mode order $m = 10$). The directivity patterns approximate a parabola, which reaches its maximum value between 80 and 90 degrees. The curves thus illustrate that the noise of first order rotor-alone tones is mostly restricted to angles near the propeller plane, as was expected. Therefore, despite a slight divergence

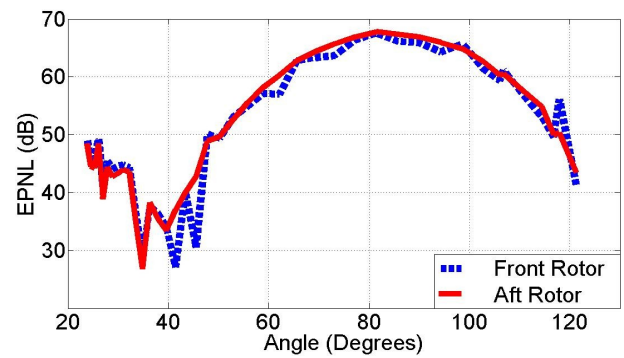


FIGURE 9: COMPUTED FIRST ORDER ROTOR-ALONE TONE DIRECTIVITY PATTERNS.

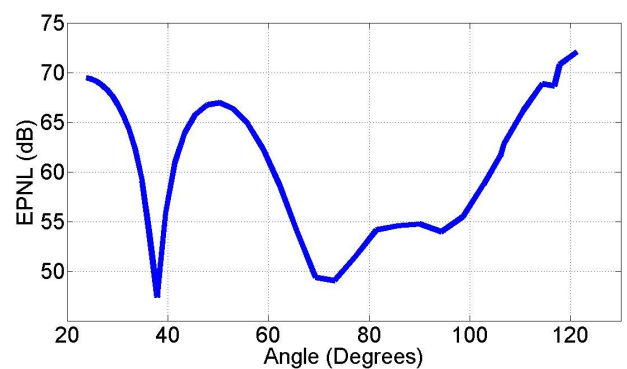


FIGURE 10: COMPUTED INTERACTION TONE DIRECTIVITY PATTERNS.

regarding the location of the maximum noise level value on the horizontal axis, both curves are in absolute accordance to the empirical and experimental data cited in previous sections of this paper.

The directivity of the first interaction tone ($f_{12} = 364.72$ Hz, for $n_1 = 1$ and $n_2 = 1$, mode order $m = -2$) is presented in Fig. 10. The curve shows great resemblance to the experimental measurements presented in Fig. 7, especially in the region between 30 and 80 degrees. Additionally, the trough at 38 degrees well compares to the trough located at both Fig. 5 and 7, and is therefore in accordance to both empirical and experimental results. Further comparison can be realized with Fig. 6, thus proving the tendency of the first interaction tone to radiate mostly near the propeller axis, while maintaining overall high noise level values throughout the angle domain. Again, the directivity patterns of the first interaction tone, which were derived from [3], well duplicate the empirical and experimental results, investigated previously.

Despite not being able to obtain the same range of angle values, as was realized in the experimental case [2], the data from [3] still suffice to provide a clear aspect of the directivities of certain tones. The directivity patterns derived from the numerical data show undisputed resemblance to the experimental measurements, while being in overall accordance to the patterns dictated by

empirical methods. Therefore, the outcome of this comparison provides additional validation of the numerical method applied in [3].

CONCLUSIONS

In this paper, the audio simulation of noise generated by an aircraft engine equipped with a CROR fan was presented. A spectrum analysis of the final audio signal was obtained, in order to provide accurate visualization of the audio file, thus aiding the analysis of tonal noise contribution to overall engine noise. Further investigation was focused on the directivity patterns of rotor-alone and interaction tones, which were determined by the initial numerical data. The directivities underwent comparison with patterns resulting from empirical methods, as well as actual experimental measurements. The computed directivities compared exceptionally well to both empirical and experimental results, thus providing validation of the original numerical model, while encouraging future research on tonal noise directivity.

In conclusion, the undisputed similarities between tonal noise directivities of the actual experimental measurements and the numerical results, enhance the importance of the simulated audio file. This file can be therefore utilized in research procedures focused on aircraft engine noise and its impact on human hearing. A combination of audio and visual elements can significantly aid the acoustic perception of noise generated by engines of innovative architecture, while leading to an intuitive understanding of aircraft noise and its components. Additionally, the outstanding resemblance between experimental measurements and numerical data, provides proof of the correctness of the method utilized by Kritikos et al. [3], thus further validating the computed results, as well as the developed numerical tool. The efficiency of the procedure, encourages further extensive study of the numerical data in respect to experimental measurements, in order to set an accurate basis that outlines the correlation of actual and calculated results.

ACKNOWLEDGMENTS

The authors would like to acknowledge SNECMA, for the kind permission to publish this paper, and particularly Dr. Rasika Fernando, for providing his expert advice. The paper was realized within the frame of the European wide DREAM project (validation of Radical Engine Architecture systems).

REFERENCES

- [1] Taylor, J. B., 1990, "Unducted Counterrotating Gearless Front Fan Engine", *U.S. Patent No. 4,976,102*.
- [2] Woodward, R. P., 1987, "Noise of a Model High Speed Counterrotation Propeller at Simulated Takeoff/Approach Conditions (F7/A7)", *NASA Technical Memorandum 100206, AIAA-87-2657*.
- [3] Kritikos, K., Giordano, E., Kalfas, A. I., and Tantot, N., 2012, "Prediction of Certification Noise Levels Generated by Contra-Rotating Open Rotor Engines", *ASME Turbo Expo 2012, GT2012-69232*.
- [4] Lewy, S., 2010, "Semi-Empirical Prediction of Tone Noise Due to Counter-Rotating Open Rotors", *20th International Congress on Acoustics, ICA 2010*.
- [5] ICAO, 2005, "Annex 16, Environmental Protection: Volume 1, Aircraft Noise", *International Civil Aviation Organization*.
- [6] Siozos-Roussoulis, L., Kalfas, A. I., Kritikos, K., Giordano, E., Tantot, N., 2012, "Noise Modelling and Analysis of Aircraft Engines with Contra-Rotating Open Rotors", *15th International Conference on Fluid Flow Technologies, Conference on Modelling Fluid Flow, CMFF 2012*.
- [7] Brouwer, H., "Analytic Description of the Noise Radiation from Single- and Contra Rotating Propellers", *20th International Congress of the Aeronautical Sciences, ICAS 2010*.
- [8] Everest, F. A., and Pohlmann, K. C., 2009, "Master Handbook of Acoustics, Fifth Edition", *McGraw-Hill*.
- [9] Williams, J. F. F., and Hawkings, D. L., 1969, "Sound Generation by Turbulence and Surfaces in Arbitrary Motion", *Philosophical Transactions of the Royal Society of London, Series A, 264, pp. 321-342*.
- [10] Deconick, T., Hoffer, P. A., Hirsch, C., De Meulenaere, A., Bonaccorsi, J. C., and Ghorbaniasl, G., 2010, "Prediction of Near-Field and Far-Field Noise Generated by Contra-Rotating Open Rotors", *16th AIAA/CEAS Aeroacoustics Conference, AIAA 2010-3794*.
- [11] ICAO, 2008, "Doc 9829 AN/451: Guidance on the Balanced Approach to Aircraft Noise Management (2nd Edition)", *International Civil Aviation Organization*.
- [12] ICAO, 2007, "Doc 9501 AN/929: Environmental technical manual on the use of procedures in the noise certification of aircraft". *International Civil Aviation Organization*.
- [13] ACARE, 2001, "European Aeronautics: A Vision for 2020", *European Communities*.
- [14] Rhodes, D. D. P., 2005, "Document 29 3rd edition: Report on standard method of computing noise contours around civil airports". *ECAC.CEAC, Vol. 1: Applications Guide*.
- [15] Rhodes, D. D. P., 2005, "Document 29 3rd edition: Report on standard method of computing noise contours around civil airports". *ECAC.CEAC, Vol. 2: Technical Guide*.
- [16] Beranek, L., 1993, "Acoustics", *Acoustical Society of America*.
- [17] Pinelli, L., Poli, F., Marconcini, M., Arnone, A., Spano, E., and Torzo, D., "A Linearized Method for Tone Noise Generation and Propagation in a Multistage Contra-Rotating Turbine".
- [18] Woodward, R. P., Gordon, E. P., 1988, "Noise of a Model Counterrotation Propeller with Reduced Aft Rotor Diameter at Simulated Takeoff/Approach

Conditions (F7/A3)", *NASA Technical Memorandum 100254, AIAA-88-0263*.

- [19] Dittmar, J. H., Gordon E. B., Jeracki, R. J., 1988, "The Effect of Front-to-Rear Propeller Spacing on the Interaction Noise of a Model Counterrotation Propeller Having a Reduced Diameter Aft Propeller", *NASA Technical Memorandum 101329*.
- [20] Whitfield, C., Gliebe, P., 1990, "Predicted Vs. Scale Model and Flight Test UDFR Engine Noise", *AIAA 13th Aeroacoustics Conference, AIAA-90-3936*.



PARTIALLY COVERED CYLINDRICAL CAVITY FLOW: RESONANCE IDENTIFICATION

Francisco Rodriguez Verdugo

Dipartimento di Ingegneria Meccanica Industriale
 Universit degli Studi Roma Tre
 Rome, Italy
 frodriguezverdugo@uniroma3.it

David B. Stephens

NASA Glenn Research Centre
 Cleveland
 Ohio, USA
 David.Stephens@nasa.gov

Gareth J. Bennett*

School of Engineering
 Trinity College Dublin
 Dublin 2, Ireland
 gareth.bennett@tcd.ie

ABSTRACT

This is the first of two companion papers concerned with the study of partially covered cylindrical cavities. These geometries can be found in the transportation industry: window buffeting in cars/trains, aircraft landing gear wheel wells; in musical instruments: jug bands; or in duct applications: side branches. Partially covered cavity oscillations have been investigated previously [1–4] but little attention has been devoted to the description of the shear-layer dynamics [5, 6]. In addition, the excitation of higher order acoustic modes in cavities has gone largely unreported. The aim of these two papers is to investigate the interaction between the shear layer spanning a rectangular opening and the flow-excited acoustic response of the cylindrical cavity. In this first paper, the excited resonant modes are predicted and measured by the use of an acoustic numerical simulation and a wall mounted microphone respectively. The influence of the position of the rectangular opening is analysed.

INTRODUCTION

Shear layer driven cavity flows can exhibit several types of features generally described as resonance. The review paper of Rockwell and Naudascher [7] categorized self-sustaining oscillations into three groups: fluid-dynamic; fluid-resonant; and fluid-elastic. Of these, self-sustaining cavity oscillations which are strongly coupled with resonant waves within the cavity may be classified as fluid-resonant oscillations. Oscillations of this class occur at sufficiently high frequencies such that the corresponding acoustic wavelength is of the same order of magnitude, or smaller, than the cavity characteristic length—considered here to be the height of the cylindrical cavity, H . For ideal organ pipe conditions, these oscillations

are predicted to have an acoustic wavelength of $\lambda \leq 2H$ for a closed cavity end condition. The exact frequency at which these longitudinal modes (standing waves along the height of the cavity) occur for shear layer driven oscillations is complicated by the very presence of the shear layer. Within the fluid-dynamic category, a highly cited work is for high Mach number ($M > 0.5$) flow over a shallow cavity known as a Rossiter cavity. In this system, the feedback mechanism is an upstream-travelling acoustic wave generated by turbulent structures hitting the downstream edge of the cavity. These acoustic waves have a wavelength close to the cavity opening dimension, or length, L . Resonance occurs if this acoustic frequency can excite the shear layer oscillation. The fluid-elastic category occurs when one or more wall of the cavity undergoes a displacement that exerts a feedback control on the shear layer perturbation. For cavities with rigid boundaries, the fluid-resonant category may contribute significantly to unwanted noise: from aircraft landing gear for example; or to undesirable pressure pulsations such as may be experienced in vehicles with open windows. A recent study by Langtry and Spalart [8] used computational methods to predict the unsteady pressure inside a landing gear wheel well on a commercial aircraft geometry. Balasubramanian et al. [9] have recently considered sun-roof buffeting on a simplified vehicle geometry. Tonon et al. [10] have studied a series of side branch resonators as a model for flow in a corrugated pipe. Height modes were also studied by Yang et al. [11] who specifically analyzed the effect of the stream wise dimension of the cavity. A coaxial side branch configuration was studied by Oshkai and Yan [12]. Kook and Mongeau [13] and Ma et al. [5] have both recently studied Helmholtz resonators and accurately predicted the magnitude of the interior cavity pressure, when adequate information about the shear layer is available. Higher order acoustic modes

*Address all correspondence to this author.

have been explored for an axisymmetric shallow cavity configuration in a work by Awny and Ziada [14], and the work of Oshkai et al. [15] illustrates well how PIV can be used to gain further insight into the study of shear layer flows. To date, within the fluid-resonant category, almost no consideration has been given to higher order acoustic modes which might resonate in cavities. In this paper we are particularly interested in exploring the test case where a number of different types of resonant behavior can be excited depending on flow speed or orifice geometry. In practical cases, such as for aircraft take-off and landing where the flow speed varies, it is important to be able to predict these modes so that mitigation measures can be implemented.

EXPERIMENTAL RIG DESIGN

A cavity resonance experiment that incorporates a number of the above feedback mechanisms has been designed and constructed. As the rig was to be built using a small, low speed wind tunnel, preliminary analysis was required in order to optimally design the cavity given the imposed limitations. In each of the three fluid-resonant oscillations considered in this paper, viz. Helmholtz Resonance, Longitudinal Resonance and Azimuthal Resonance, the acoustic excitation is assumed to be due to instability in the shear layer of flow over the cavity opening. The shear layer excitation frequency can be estimated using the empirical relationship suggested by Rossiter [16]. Given the low Mach number under consideration in the current paper ($M < 0.15$), the upstream-propagating acoustic feedback mechanism usually associated with Rossiter is not expected to occur in the present experiment, because the acoustic frequency corresponding to the cavity opening length would be in the order of 8kHz, far higher than any expected shear layer oscillation frequency. Rossiter's equation for the shear layer excitation frequency, however, has been used by many authors to accurately model other feedback mechanisms [5, 17]. This equation is given as

$$St \equiv \frac{fL}{U} \approx \frac{n - \alpha}{M + \frac{1}{\kappa}} \quad (1)$$

where α describes the phase delay and κ is the convection velocity of the shear layer normalized by the free stream velocity and $n = 1, 2, 3, \dots$ is the order of the shear layer mode. For the low subsonic speeds considered here, $\alpha = 0$ was found to be appropriate, and has been used by other authors [5, 18, 19], who argued that there is no

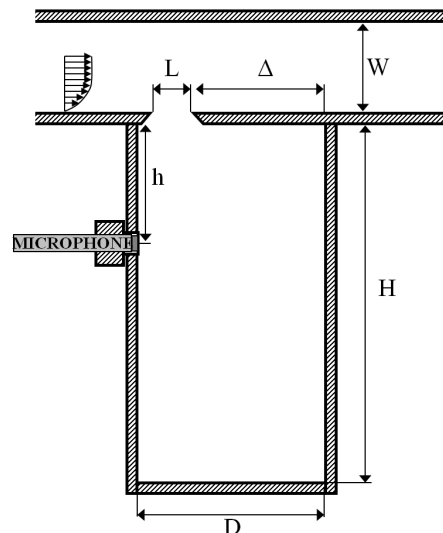


FIGURE 1: Schematic of the wind tunnel test section and the cavity. Section taken in the central plane. Not to scale.

need to consider a phase delay when the convection speed is much less than the speed of sound. The typical value of $\kappa = 0.5$ is the average of the free stream speed and the flow in the cavity, and does not include effects of the boundary layer which acts to retard the apparent free stream velocity.

As can be seen in Eqn. (1), decreasing the characteristic length of the cavity opening, L , increases the excitation frequency for a given flow speed. Similarly, from knowledge of duct acoustics [20], increasing the cavity diameter will result in lower cut-on frequencies for the higher order modes. Thus for the low tunnel speeds available, a large diameter and small orifice was required to achieve the test objectives allowing excitation of the three different fluid-resonance categories considered. Schematics of the cavity and opening can be seen in Fig. 1 and Fig. 2. The large diameter of the cylinder was selected in order to accommodate higher-order azimuthal acoustic modes. The first azimuthal mode should cut-on at 846Hz for this diameter assuming closed/closed end conditions. Initially, a 40mm square opening with sharp edges connected the cavity to the wind tunnel, however, openings of different length and location relative to the cavity centerline were also tested.

Numerical Analysis Wave Expansion Method (Wem)

In order to verify the cavity design prior to construction, a series of numerical simulations were performed on a meshed domain of equal dimensions to the proposed design, see Fig. 3. A highly efficient finite difference method originally introduced by Caruthers et al. [21] was

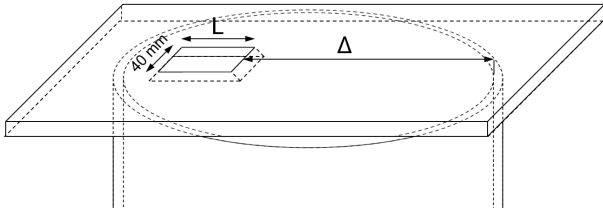


FIGURE 2: Schematic of the cavity opening

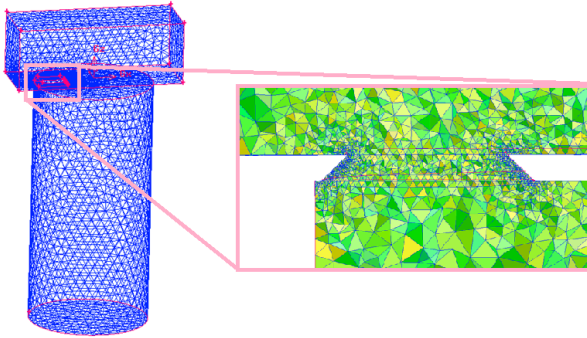


FIGURE 3: Computational domain meshed for the WEM calculation. Detail of the mesh in the opening area (section taken in the middle plane).

used for the analysis. The approach uses wave functions which are exact solutions of the governing differential equation. The wave expansion method (WEM) code used for this study was further developed by Ruiz and Rice [22] and has been examined by Bennett et al. [23] for its applicability in ducts. In order to simulate an oscillation in the shear layer, a numerical monopole volume source was located at the orifice opening mid-point. The complex pressure is solved in the domain as a function of source frequency and the amplitude can be plotted on the mesh to give an indication of the pressure field in the cavity/windtunnel rig set-up. Some examples of the solution are given in Fig. 4.

The Helmholtz numbers chosen illustrate: the first plane wave depth/height or longitudinal mode (AZ1) and a combination azimuthal/longitudinal mode (AZ1H1). An awareness and understanding of these modes is necessary if a comprehensive understanding of the acoustic behavior of cavities is to be reached. Based on the results of this analysis, it was confirmed that this cavity geometry would allow all three fluid-resonant category configurations to be excited by a cavity orifice of approximately 40mm in the flow range of the wind tunnel available for the tests.

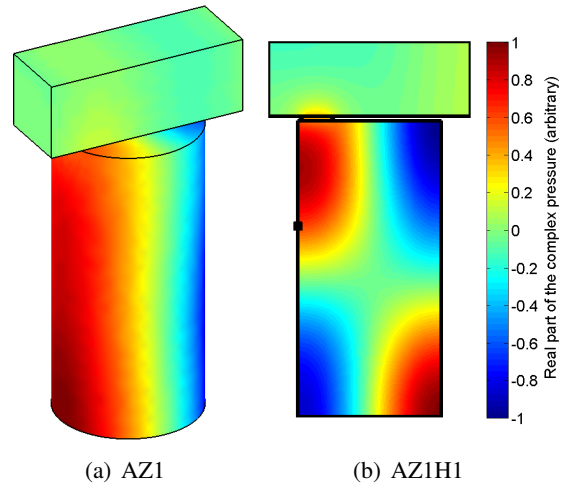


FIGURE 4: Numerical WEM results: normalized real pressure of the cavity to monopole excitation at orifice opening of cavity and windtunnel test section. Two acoustic resonances are given: (a) first azimuthal mode AZ1 ($He=1.85$); (b) first azimuthal-longitudinal combination mode AZ1H1 ($He=2.0$); The position of the microphone is indicated by a black square.

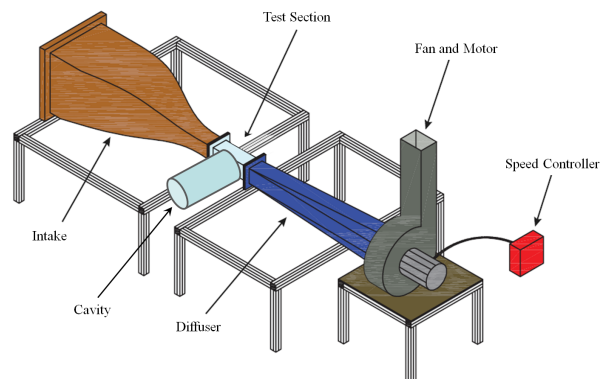


FIGURE 5: Schematic of the wind tunnel, adapted from [24].

Test-Set Up

A draw-down wind tunnel with an elliptical bell-mouth inlet was used with a square test section (125mm x 125mm) 335mm in length, see Fig. 5. The cavity height is 493mm and 119.25mm in radius. The orifice spanned the test section with a real depth of 7.75mm and a sharp chamfer at 45 degrees - see Fig. 2.

Boundary Layer Characterization The knowledge of the boundary layer's nature is of special interest when dealing with wall bounded flows. For the boundary layer characterization, the panel with a rectangular orifice was replaced by a panel without orifice. The boundary layer was measured in a position corresponding to the

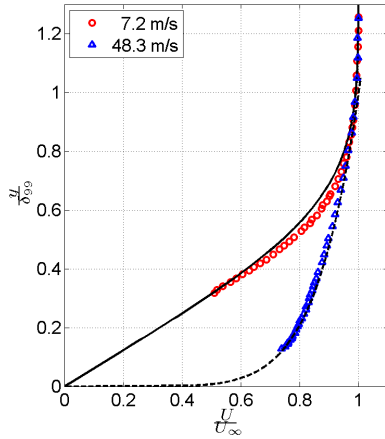


FIGURE 6: Boundary layer profiles for two different flow velocities: 7.2 and 48.3 m/s. The Blasius (plain line) and 1/7 power profiles (dashed line) are also represented.

upstream edge of the orifice openings. Two different free stream velocities were investigated: 7.2 m/s and 48.3 m/s. Velocity profiles are reported in figure 6. At low velocities, the boundary layer was found to be laminar whereas for high flow speed it becomes turbulent. Table 1 gives the characteristics of the boundary layer.

TABLE 1: BOUNDARY LAYER PROPERTIES FOR 2 FREE STREAM VELOCITIES: 7.2 AND 48.3 m/s. BOUNDARY LAYER THICKNESS $\delta(99\%)$, DISPLACEMENT THICKNESS δ^* AND MOMENTUM THICKNESS θ .

U_∞ (m/s)	δ (mm)	δ^* (mm)	θ (mm)
7.2	3.98	1.34	0.50
48.3	3.6	0.51	0.40

EXPERIMENTAL RESULTS

Due to the presence of the nodal lines associated with higher order modes it was hypothesised that some modes would respond more when excited at antinodes and less or not at all when the excitation region coincided with a nodal position. In order to perform a parametric study, a number of different cover plates were manufactured, each with openings of differing characteristics. Table 2 lists some of the openings tested.

TABLE 2: CAVITY OPENING PARAMETERS. STREAMWISE LENGTH AND POSITION FROM DOWNSTREAM EDGE.

L (mm)	40				
Case	L40EU	L40HU	L40CC	L40HD	L40ED
Δ (mm)	189	159	99	39	9
L (mm)	45				
Case	L45EU	L45HU	L45CC	L45HD	L45ED
Δ (mm)	184	157	97	37	9

Preliminary Results

Once the rig was built, some preliminary tests were performed to verify the cavity’s response to excitation. An initial test was performed with a small loudspeaker radiating broadband noise located in the tunnel test section in the proximity of the orifice. A transfer function between the speaker input signal and a microphone flush mounted with the inside surface of the cavity was calculated and its magnitude is plotted in Fig. 7 (black). Qualitatively, this compares extremely closely to a similar analysis performed on the numerical WEM data (red), where the transfer function was calculated between the monopole source and a location equivalent the microphone position. Each of the longitudinal, azimuthal and combination modes are identified. The exception to this is the Helmholtz resonance in the numerical data which poorly models the compressibility effect. In addition there is a small (4Hz) frequency shift between the WEM peaks and those measured with the speaker experiment. As the numerical solution has been found to be very sensitive to changes in the duct geometry, it is thought that this may be due to the difference in location of the monopole source and the equivalent acoustic source due to the loudspeaker.

Similarly, the response from the same microphone located in the cavity is plotted for a tunnel flow velocity of approximately 21m/s (blue). Again there is excellent qualitative agreement with no frequency difference between these results and those when using the loudspeaker. There is however, a significant amount of low frequency noise which is presumed to originate from the centrifugal blower and ducting of the wind tunnel.

A summary of these results are given in Tab. 3 where the peak frequencies are tabulated with the analytical results for a closed/closed duct. Overall the results concur well with the most significant deviation being between the three “real” sets of data viz. WEM, Speaker and Flow, which include the orifice, and the analytical model which

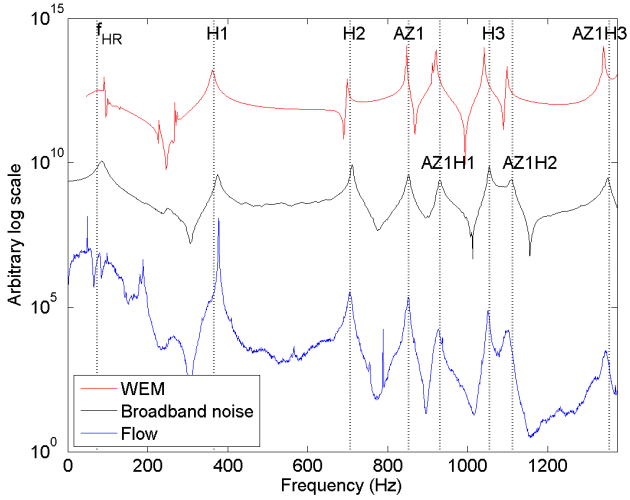


FIGURE 7: Response of the cavity to different excitations: monopole acoustic source (WEM, red), broadband noise (experimental, black) and flow (experimental, blue).

TABLE 3: FREQUENCIES, IN HERTZ, OF THE ACOUSTIC MODES OF A CYLINDRICAL CAVITY ($D = 238$ mm AND $H = 493$ mm) AT 22° C. MODE ORDER (m, n, q) : AZIMUTHAL, RADIAL, LONGITUDINAL.

Mode	H1	H2	AZ1	AZ1H1	H3	AZ1H2	AZ1H3
(m, n, q)	(0,0,1)	(0,0,2)	(1,0,0)	(1,0,1)	(0,0,3)	(1,0,2)	(1,0,3)
Analytical	350	699	846	915	1049	1097	1347
WEM	365	706	842	930	1054	1111	1354
Speaker	375	712	852	930	1054	1110	1350
Flow	377	706	851	927	1050	1102	1345

does not. The disparities are most noticeable for H1 and AZ1H1.

Baseline opening: case L45EU

Following the initial tests, an automated velocity sweep of the tunnel was performed using LabView to control the centrifugal blower motor speed controller. These results are presented in Fig. 8 with shear layer modes calculated according to Eqn. (1) superimposed onto the plot. A range of convection speed coefficients are to be found in the literature [5, 16, 17] although often at a value of approximately $\kappa = 0.38$. A value of $\kappa = 0.42$ has been used here as a best fit to the measured data.

Audible tones in the region of the Helmholtz frequency were clearly heard and are seen in Fig. 8 to be excited at low flow speeds by the first shear layer instability mode (approx. 7m/s). Given the thin wall forming the neck of the resonator, an equivalent neck approach is used to calculate the Helmholtz resonance frequency as developed by Ma et al. [5];

$$f_{HR} = \frac{c}{2\pi} \sqrt{\frac{S}{Vl_s}}, \quad (2)$$

where S is the plan-view cross sectional opening of the orifice, V is the volume of the cavity, c is the speed of sound and l_s is the length of the slug of air that oscillates in the opening, or neck of the cavity. For the cavity under consideration, the neck length is essentially zero, so an “effective” neck length equal to the opening length ($l_s = L$) was used. For the geometry of this test case the theoretical value of 68Hz superimposed on Fig. 8 compares extremely well with the measurements

For higher flow speeds, an intense lock-in with the first cavity longitudinal mode (H1) is generated, again by the first shear layer instability mode. The amplitude of this tone is so great that a non-linear response is generated which results in the first and second harmonics to be excited and is seen in the plot at higher frequencies. The lock-on subsequently drops out at higher velocities as the shear layer mode increases in frequency above the first longitudinal mode frequency. At higher velocities, the second shear layer mode locks on to the third longitudinal mode (H3) and switching between the two frequencies was audible. A time/frequency domain analysis on this data has been performed to further examine this process [25]. The second and third shear layer modes also cause lock on with the H1 mode and amplification of the azimuthal and azimuthal combination modes (AZ1 and AZ1H1) is clearly evident at high velocities. Also identified in Fig. 8 is the combination longitudinal mode of wind tunnel width and cavity height (HW1). As the shear layer is bounded, transverse to the flow direction, by the wind tunnel wall on one side and by the cavity termination on the other, the first shear layer mode excites a standing wave which is formed between these two surfaces and can be seen to lock on at approximately 27m/s.

Strength of lock-on

The receptivity of the cavity to shear layer excitation was quantified using a “strength of lock-on” parameter, as suggested by [26] and described by [11]. The parameter chosen was the amplification of the cavity pressure level above the background noise level, as defined by a linear scaling in log-log space. For each frequency, a linear fit was made to the spectral density in decibels. The magnitude of the pressure above this linear fit was designated as the “strength of lock-on” (SoL). At the flow speed U_∞ , the SoL of the frequency f can be calculated through:

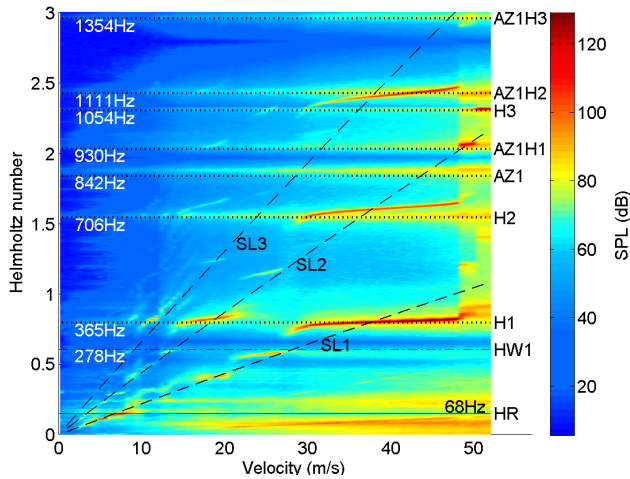


FIGURE 8: Acoustic response inside the cavity as a function of tunnel flow-speed. Superimposed on the plot are the theoretical shear layer modes (SL), the WEM acoustic modes (H1, AZ1...) and the Helmholtz resonance (HR). The first longitudinal cavity/test section mode (HW1) calculated analytically is also reported. Frequencies are given in non-dimensional form (Helmholtz number = $2\pi Rf/c$).

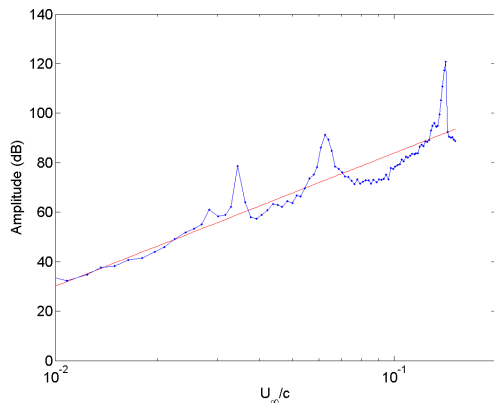


FIGURE 9: Pressure amplitudes at 376 Hz as a function of the wind tunnel flow speed. Opening L45ED.

$$SoL(M_\infty, f) = p_{dB}(M_\infty, f) - [p_{dB}(1, f) + 20n \log(M_\infty)] \quad (3)$$

where p_{dB} denotes the pressure amplitude (in dB) function of the frequency f and the Mach number of the flow ($M_\infty = U_\infty/c$) and n the exponential at which the broadband turbulent noise grows. An example of the linear fitting is given in Fig. 9.

Influence of the location of the opening

The effect of the opening location was quantified using the SoL parameter previously introduced. Three dif-

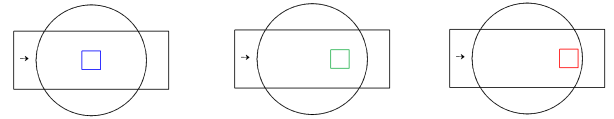


FIGURE 10: Orifice locations: L40CC, L40HD and L40ED.

ferent positions were explored: $\Delta = 99, 39$ and 9 mm (L40CC, L40HD and L40ED respectively), refer to figure 10. The results are summarized in figures 11, 12 and 13, where the contour lines encircle values of SoL higher than 13 dB. The threshold criterion is an useful and straightforward technique to identify the resonance conditions in a flow excited cavity.

There are some interesting differences between the three opening analysed. It is clear that the resonance lock-on for H1 is much stronger when the opening is in the center of the cavity (L40CC): the first shear layer hydrodynamic mode remains locked-on H1 for a wider range of velocities than for the other two orifice positions. Especially noteworthy is the cut-on of the azimuthal mode AZ1H1 at velocities above 45 m/s for L40ED and L40HD, which does not occur for L40CC. When the opening is off-center, the shear layer pressure fluctuations tend to excite AZ1H1 because they are closer to an acoustic anti-node. On the contrary, the central location is a pressure node for this acoustic mode as seen in Fig. 4(b). The third longitudinal mode is excited by the shear layer mode II from 50.3 m/s to 52.3 m/s for L40HD while this resonance occurs only for the highest tested flow speed for L40ED.

It is interesting to note that, whereas the azimuthal combination mode AZ1H1 tends to be excited by the off-center orifice locations, the pure AZ1 azimuthal modes tends not to be. The vortex sound theory developed by Howe [27] is a good start in order to explain the predilection for certain specific eigenmodes for a flow-acoustic coupling. In Howe's acoustic analogy, the Coriolis density forces $\rho_0 \vec{w} \times \vec{u}$ are identified as the principal source of sound. The acoustic power generated by the vortical field Π can be calculated by equation

$$\Pi = -\rho_0 \int_V (\vec{w} \times \vec{v}) \cdot \vec{u}_{acoust} dV \quad (4)$$

which states that the Π is proportional to the triple $\vec{u}_{acoust} \cdot (\vec{w} \times \vec{u})$. From this formula it is clear that if the acoustic particle velocity at the opening has the same orientation as the velocity or the vorticity, there is no acoustic

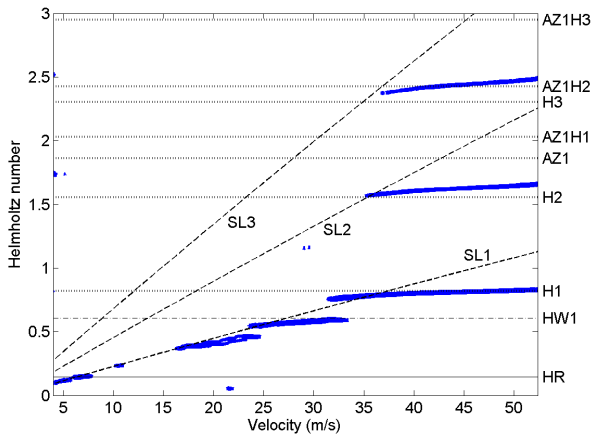


FIGURE 11: Contour of strength of lock-on higher than 13 dB. L40CC.

power generated. Let us now take the example of the first azimuthal mode (AZ1). It has been shown numerically, Fig. 4(a), that this mode is symmetrical about plane Oyz (it could have been symmetrical about any other vertical plane; however the opening location imposes the symmetry plane). The mode AZ1 does not radiate sound because the acoustic particle velocity has the same orientation as the mean flow. This is a very simplistic explanation especially because it assumes the directions of \vec{u}_{acoust} , \vec{w} and \vec{u} to be known a priori.

CONCLUSIONS

A cylindrical cavity experiment which allows different modes of resonant behaviour to be excited depending on flow speed and orifice geometry has been designed and constructed. Specifically, modes falling into the fluid-resonant category, viz., Helmholtz resonance, Longitudinal resonance and Azimuthal resonance, have all been excited by different shear layer oscillation modes. Lock on between these different resonant modes and shear layer excitation has been clearly measured and observed to occur upon adjusting only the flow speed. The effect of the cavity opening location on the internal resonance was also studied, and found to be a major factor in determining which modes were excited. Specifically, azimuthal modes were only found when the excitation was not located at the center of the cavity, which would be a node for the azimuthal mode.

REFERENCES

[1] Helmholtz, H., 1860. "Theorie der luftschwingungen in röhren mit offenen enden". *Crelle's Journal*,

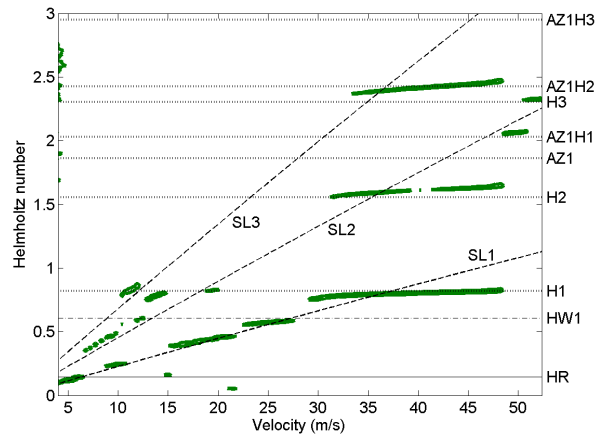


FIGURE 12: Contour of strength of lock-on higher than 13 dB. L40HD

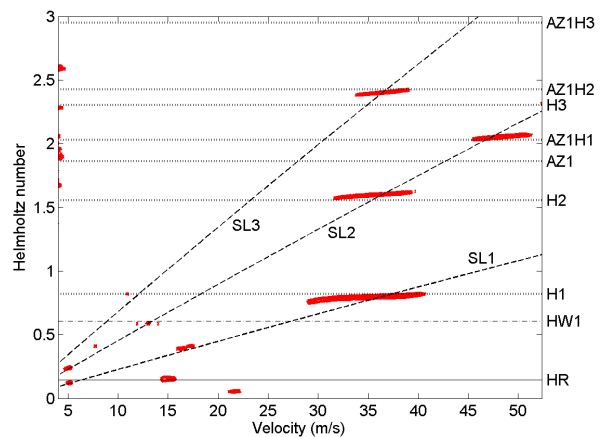


FIGURE 13: Contour of strength of lock-on higher than 13 dB. L40ED.

57, pp. 1–72.

- [2] Panton, R. L., and Miller, J. M., 1975. "Resonant frequencies of cylindrical helmholtz resonators". *Journal of Acoustical Society of America*, **57**(6), pp. 1533–1535.
- [3] De Metz, F. C., Farabee, T. M., and David, W., 1977. "Laminar and turbulent shear flow induced cavity resonances". In 4th AIAA Aeroacoustics Conference, no. 77-1293.
- [4] Elder, S. A., 1978. "Self-excited depth-mode resonance for a wall-mounted cavity in turbulent flow". *Journal of Acoustical Society of America*, **64**, pp. 877–890.
- [5] Ma, R., Slaboch, P. E., and Morris, S. C., 2009. "Fluid mechanics of the flow-excited helmholtz resonator". *Journal of Fluid Mechanics*, **623**, pp. 1–26.

- [6] Nelson, P. A., Halliwell, N. A., and Doak, P. E., 1981. "Fluid dynamics of a flow excited resonance, part i: experiment". *Journal of Sound and Vibration*, **78(1)**, pp. 15–38.
- [7] Rockwell, D., and Naudascher, E., 1978. "Review - self-sustained oscillations of flow past cavities". *Journal of Fluids Engineering*, **100**, pp. 152–165.
- [8] Langtry, R. B., and Spalart, P. R., 7 - 10 January 2008. "Des investigation of a baffle device for reducing landing-gear cavity noise". *46th AIAA Aerospace Sciences Meeting and Exhibit, Reno, Nevada, USA*.
- [9] Balasubramanian, G., Crouse, B., and Freed, D., 11-13 May 2009. "Numerical simulation of leakage effects on sunroof buffeting of an idealized generic vehicle". *15th AIAA/CEAS Aeroacoustics Conference, Miami, Florida, USA*.
- [10] Tonon, D., Hirschberg, A., Golliard, J., and Ziada, S., 2011. "Aeroacoustics of pipe systems with closed branches". *International Journal of Aeroacoustics*, **10**, pp. 201–276.
- [11] Yang, Y., Rockwell, D., Lai-Fook Cody, K., and Pollack, M., 2009. "Generation of tones due to flow past a deep cavity: effect of streamwise length". *Journal of Fluids and Structures*, **25**, pp. 364–388.
- [12] Oshkai, P., and Yan, T., 2008. "Experimental investigation of coaxial side branch resonators". *Journal of Fluids and Structures*, **24**, pp. 589–603.
- [13] Kook, H., and Mongeau, L., 2002. "Analysis of the periodic pressure fluctuations induced by flow over a cavity". *Journal of Sound and Vibration*, **251(5)**, pp. 823–846.
- [14] Awny, K., and Ziada, S., 2008. "Effect of cavity depth on diametral mode excitation". *9th International Conference on Flow-Induced Vibrations (FIV2008)*, Prague, Czech Republic.
- [15] Oshkai, P., Geveci, M., Rockwell, D., and Pollack, M., 2005. "Imaging of acoustically coupled oscillations due to flow past a shallow cavity: effect of cavity length scale". *Journal of Fluids and Structures*, **20**, pp. 277–308.
- [16] Rossiter, J. E., 1964. Wind-tunnel experiments on the flow over rectangular cavities at subsonic and transonic speeds. Tech. Rep. R&M 3438, Aeronautical Research Council.
- [17] Rodriguez Verdugo, F., Guitton, A., Camussi, R., and Grottaurea, M., 2009. "Experimental investigation of a cylindrical cavity". In 15th AIAA/CEAS Aeroacoustics Conference, no. 2009-3207.
- [18] Chatellier, L., Laumonier, J., and Gervais, Y., 2004. "Theoretical and experimental investigations of low mach number turbulent cavity flows". *Experiments in Fluids*, **36**, pp. 728–740.
- [19] El Hassan, M., Labraga, L., and Keirsbulck, L., 2007. "Aero-acoustic oscillations inside large deep cavities". In 16th Australasian Fluid Mechanics Conference.
- [20] Bennett, G. J., Verdugo, F. R., and Stephens, D. B., 2010. "Shear layer dynamics of a cylindrical cavity for different acoustic resonance modes". In 15th International Symposium on Applications of Laser Techniques to Fluid Mechanics.
- [21] Caruthers, J. E., Engels, R. C., and Ravinprakash, G. K., 1996. "A wave expansion computational method for discrete frequency acoustics within inhomogeneous flows". In 2nd AIAA/CEAS Aeroacoustic Conference.
- [22] Ruiz, G., and Rice, H. J., 2002. "An implementation of a wave-based finite difference scheme for a 3-d acoustic problem". *Journal of Sound and Vibration*, **256**, pp. 373–381.
- [23] Bennett, G. J., O'Reilly, C. J., and Liu, H., 2009. "Modelling multi-modal sound transmission from point sources in ducts with flow using a wave-based method". In 16th Congress on Sound and Vibration.
- [24] Finnegan, S. L., 2011. "Resonant aeroacoustic source localisation in ducted bluff body flows". PhD thesis, University of Dublin.
- [25] Stephens, D. B., Rodriguez Verdugo, F., and Bennett, G. J., 2010. "Shear layer driven acoustic modes in a cylindrical cavity (AIAA 2010-3903)". In 16th AIAA/CEAS Aeroacoustics Conference.
- [26] Mendelson, R. S., 2003. "Methods of measuring lock-in strength and their application to the case of flow over a cavity locking into a single side-branch". In 9th AIAA/CEAS Aeroacoustics Conference, no. 2003-3106.
- [27] Howe, M. S., 1975. "Contributions to theory of aerodynamic sound, with application to excess jet noise and the theory of the flute". *Journal of Fluid Mechanics*, **71,4**, pp. 625–673.



PARTIALLY COVERED CYLINDRICAL CAVITY FLOW: APPLICATION OF AN ACOUSTIC ANALOGY

Francisco Rodriguez Verdugo

Dipartimento di Ingegneria Meccanica Industriale
 Universit degli Studi Roma Tre
 Rome, Italy
 frodriguezverdugo@uniroma3.it

Gareth J. Bennett*

School of Engineering
 Trinity College Dublin
 Dublin 2, Ireland
 gareth.bennett@tcd.ie

ABSTRACT

This is the second of two companion papers concerned with the study of partially covered cylindrical cavities. These geometries can be found in the transportation industry: window buffeting in cars/trains, aircraft landing gear wheel wells; in musical instruments: jug bands; or in duct applications: side branches. Partially covered cavity oscillations have been investigated previously [1–4] but little attention has been devoted to the description of the shear-layer dynamics [5, 6]. In addition, the excitation of higher order acoustic modes in cavities has gone largely unreported. The aim of these two papers is to investigate the interaction between the shear layer spanning a rectangular opening and the flow-excited acoustic response of the cylindrical cavity. In this second paper, a methodology to extract the acoustic power generated by the shear layer is proposed. The velocity and the vorticity fields are found experimentally and the acoustic field is calculated numerically.

INTRODUCTION

Shear layer driven cavity flows can exhibit several types of features generally described as resonance. The review paper of Rockwell and Naudascher [7] categorized self-sustaining oscillations into three groups: fluid-dynamic; fluid-resonant; and fluid-elastic. Of these, self-sustaining cavity oscillations which are strongly coupled with resonant waves within the cavity may be classified as fluid-resonant oscillations. Oscillations of this class occur at sufficiently high frequencies such that the corresponding acoustic wavelength is of the same order of magnitude, or smaller, than the cavity characteristic length—considered here to be the height of the cylindrical cavity, H . For ideal organ pipe conditions, these oscillations

are predicted to have an acoustic wavelength of $\lambda \leq 2H$ for a closed cavity end condition. The exact frequency at which these longitudinal modes (standing waves along the height of the cavity) occur for shear layer driven oscillations is complicated by the very presence of the shear layer. Within the fluid-dynamic category, a highly cited work is for high Mach number ($M > 0.5$) flow over a shallow cavity known as a Rossiter cavity. In this system, the feedback mechanism is an upstream-travelling acoustic wave generated by turbulent structures hitting the downstream edge of the cavity. These acoustic waves have a wavelength close to the cavity opening dimension, or length, L . Resonance occurs if this acoustic frequency can excite the shear layer oscillation. The fluid-elastic category occurs when one or more wall of the cavity undergoes a displacement that exerts a feedback control on the shear layer perturbation. For cavities with rigid boundaries, the fluid-resonant category may contribute significantly to unwanted noise: from aircraft landing gear for example; or to undesirable pressure pulsations such as may be experienced in vehicles with open windows. A recent study by Langtry and Spalart [8] used computational methods to predict the unsteady pressure inside a landing gear wheel well on a commercial aircraft geometry. Balasubramanian et al. [9] have recently considered sun-roof buffeting on a simplified vehicle geometry. Tonon et al. [10] have studied a series of side branch resonators as a model for flow in a corrugated pipe. Height modes were also studied by Yang et al. [11] who specifically analyzed the effect of the stream wise dimension of the cavity. A coaxial side branch configuration was studied by Oshkai and Yan [12]. Kook and Mongeau [13] and Ma et al. [5] have both recently studied Helmholtz resonators and accurately predicted the magnitude of the interior cavity pressure, when adequate information about the shear layer is available. Higher order acoustic modes

*Address all correspondence to this author.

have been explored for an axisymmetric shallow cavity configuration in a work by Awny and Ziada [14], and the work of Oshkai et al. [15] illustrates well how PIV can be used to gain further insight into the study of shear layer flows. To date, within the fluid-resonant category, almost no consideration has been given to higher order acoustic modes which might resonate in cavities. In this paper we are particularly interested in exploring the test case where a number of different types of resonant behavior can be excited depending on flow speed or orifice geometry. In practical cases, such as for aircraft take-off and landing where the flow speed varies, it is important to be able to predict these modes so that mitigation measures can be implemented.

OVERVIEW OF THE EXPERIMENTAL RIG

Experiments were performed in the Fluids Laboratory of the Mechanical and Manufacturing Engineering Department at Trinity College Dublin. The rig consists of a 493 mm (H) deep cylindrical cavity with a 238 mm internal diameter (D) mounted on the lateral wall of a 335 mm long test section with a 125 mm \times 125 mm cross section ($W \times W$). A rectangular orifice connects the interior of the cavity to the test section of the elliptical bell-mouth inlet draw-down wind tunnel. The flow was generated by a centrifugal blower driven by a motor. A photograph of the Perspex cavity is given in figure 1 showing also the PIV camera. Additionally, a schematic of the wind tunnel (figure 2) gives an overview of the experimental rig. Further description of the rig can be found in the companion paper.

Instrumentation and Data Processing

Pitot-static tube The flow speed was measured with a Pitot-static tube located at the end of the test section and connected to a micromanometer Furness Controls FCO 510. The probe was introduced in the wind tunnel through a small hole on the upper wall of the diffuser section. During the PIV measurements, the Pitot tube was removed from the test section in order to avoid flow disturbances. The micromanometer internally calculates the velocity; a verification of the calculated mean velocity was done with a pressure transducer connected to a liquid column manometer. The mean velocity given by the FCO 510 was found in good agreement with the liquid column manometer measurements.

Hot wire anemometry A Dantec CTA Module 90C10 with a Dantec 50P11 single component hot-wire (HW) probe was used for the boundary layer characteriza-

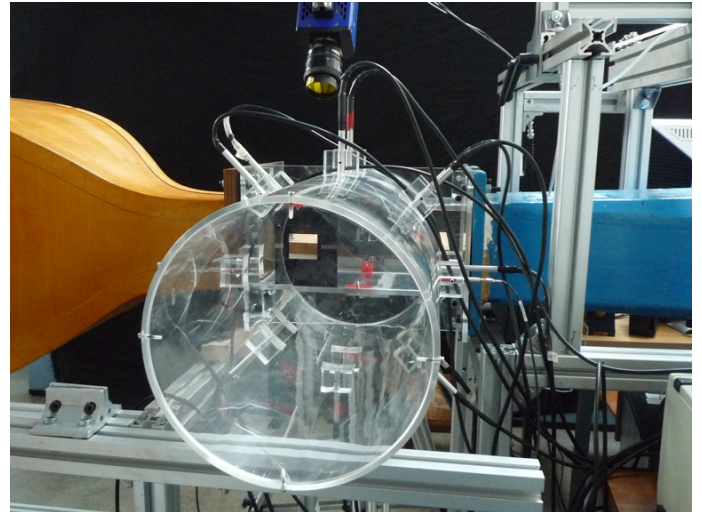


FIGURE 1: Photograph of the experimental rig. One can see the digital camera for the PIV measurements and two rings of eight microphones each.

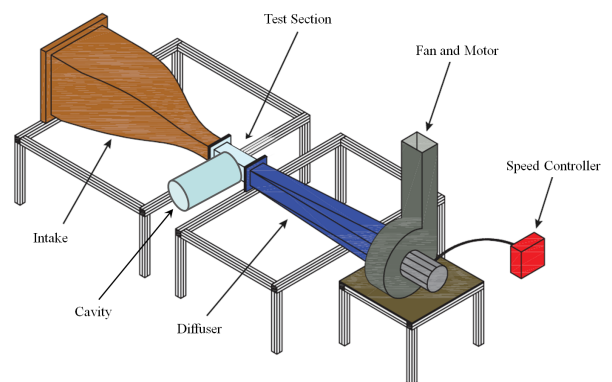


FIGURE 2: Schematic of the wind tunnel, adapted from [16].

tion. The velocity measurements are automatically compensated for flow temperature changes through a thermocouple based system.

The HW probe was directly calibrated inside the test section and the procedure is described hereafter. The probe mounted on its holder was introduced in the test section at the position desired for the BL characterization. A Pitot tube was also introduced in the wind tunnel and placed near the HW probe. The location of the Pitot tube in the same plane that the HW probe was not always possible because of the finite number of holes to introduce the Pitot tube. After the calibration, the Pitot tube was removed from the wind tunnel and the BL characterization was done straight after. The main advantage to this procedure is that the calibration and the measurements are done with the same conditions (temperature, pressure, HW ori-

entation).

Particle image velocimetry The flow in the orifice region was explored with a low speed LaVision PIV system. The seeding particles of Di-Ethyl-Hexyl-Sebacat (DEHS), which had a typical particle size of $1 \mu\text{m}$, were produced by an LaVision aerosol generator. A double pulsed Nd:YAG laser was used to illuminate the plane of interest. Images were taken with a digital Flow Master CCD camera equipped with a 1279×1023 pixel CCD sensor and a 28 mm focal length lens. The images were processed using Davis 7.2 software. The computed velocity fields were then exported into Matlab for further post processing. The PIVMat Toolbox (www.fast.u-psud.fr/pivmat) developed by Frédéric Moisy from the Université Paris-Sud was used for the production of the vector field figures.

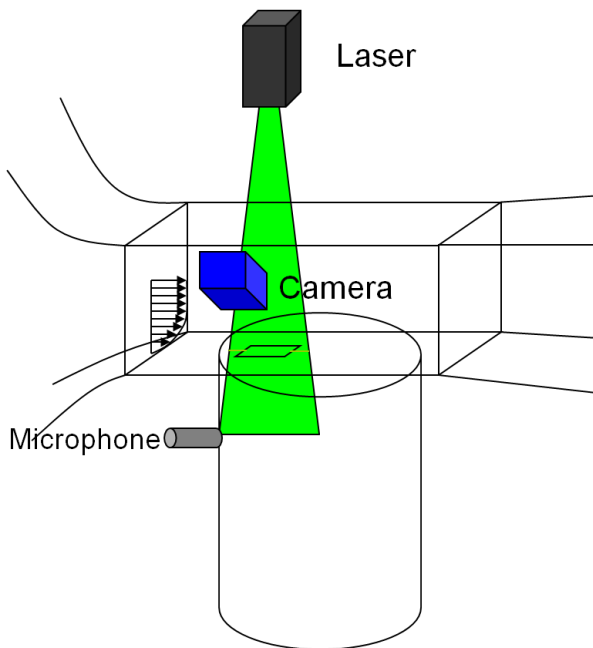


FIGURE 3: Schematic the PIV configuration

Data acquisition card The output signals from the instruments were acquired using a National Instrument PXI-4472B Data Acquisition Card. The three signals were sampled at a frequency of $F_s = 40 \text{ kHz}$ for 8 seconds. The pressure signals were processed in Matlab using a Fast Fourier Transform (FFT) technique. The number of points per segment was 8192, therefore the frequency resolution was 2.44 Hz. The 19 data sets were then averaged.

Phase-averaging technique The highest recording rate of the camera is 4.03 Hz. This value is far below the range of frequency of the shear layer modes [0 - 1500 Hz] predicted. In order to provide an average view of the velocity fluctuations, a phase-averaging technique was used. This method is applicable only when the pressure signal has a single dominant peak in the spectrum. To identify the phase of the PIV images, the wall pressure fluctuations and the laser trigger signal were recorded simultaneously. The $\Phi = 0^\circ$ condition was chosen at an arbitrary location during the pressure evolution (one quarter of period previous to the position of the local maxima). The phase in degrees is defined as $\Phi = 360^\circ \tau/T$ (figure 4(a)) where τ is the relative time at which the velocity is measured and T is the local period of the pressure fluctuations. In practice, the signal from the microphone was filtered to reduce temporal disturbances. For every velocity studied, 1000 PIV images were acquired and divided in 8 different bins according on their phases. Each bin contains between 100 and 150 PIV realizations as reported in figure 4(b). All the velocity fields of each bin are then averaged in order to obtain a phase-averaged velocity field.

EXPERIMENTAL RESULTS

Shear layer dynamics

Velocity measurements in the orifice region allow greater insight into the fluid dynamics of the shear layer to be obtained. The four different velocities explored (7.4, 46.3, 48.4 and 51.5 m/s) have already been presented in the companion paper. They correspond to: the first shear layer mode locked on the Helmholtz resonance (figure 6), the first shear layer mode locked on the first longitudinal mode (figure 7), the second shear layer mode locked on AZ1H1 (figure 8) and the second shear layer mode locked on H3 (figure 9) for the baseline opening (L45EU). The phase-averaged velocity and vorticity fields are reported. Eight different phases were calculated during the processing but 45° , 135° , 225° and 315° were omitted for brevity's sake.

First shear layer mode

Helmholtz resonance At a velocity of 7.4 m/s, the first shear layer hydrodynamic mode locks on the Helmholtz resonance. The phase average velocity and vorticity fields are reported in figure 6. In the upstream portion of the opening ($-1 < x/L < 0$), the shear layer appears to flap whereas in the downstream portion ($0 < x/L < 1$) it rolls up into a single vortex. As the vortex is convected downstream along the cavity opening, it grows

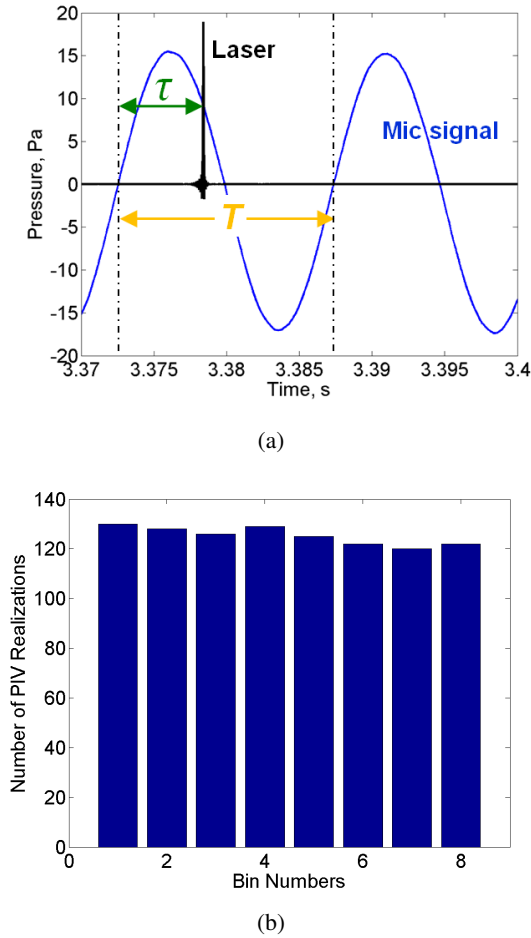


FIGURE 4: (a) Temporal evolutions of the pressure signal and the laser trigger electric signal. The relative time of the PIV realization τ and the local period of the pressure fluctuations T . (b) Histogram of 1000 PIV realizations distributed into height different phase bins

and when it reaches the downstream edge, it splits in two parts: one part is captured by the cavity while the other part escapes from it. The splitting mechanism is not very clear mainly because the area under the edge is not correctly illuminated by the laser.

Acoustic mode H1 The phase averaged velocity and vorticity fields are given in figure 7 for $U_\infty = 46.3$ m/s. During an acoustic cycle, a single vortex is generated as in the previous case. In fact, the 7.4 m/s and the 46.3 m/s cases are very similar even if the nature of the resonant acoustic mechanism is different: periodic compression of the fluid inside the cavity in the former case as opposed to a standing acoustic wave in the second case. For both velocities however the predominant instability in the shear layer is the first hydrodynamic mode.

Second shear layer mode

Acoustic mode AZ1H1 The phase averaged velocity and vorticity fields are given in figure 8. The dynamics is less clear than for the two velocities formerly presented where the shear layer was rolling up into one single vortex per acoustic cycle. Here instead, it seems to roll-up into two smaller vortices. The flapping noticed for the first hydrodynamic mode is not discernible here. Furthermore, the air does not appear to enter into the cavity, not even near the downstream edge.

Acoustic mode H3 In figure 9 the phase averaged velocity and vorticity fields are reported. During an acoustic cycle, two vortices are generated in the shear layer. From the velocity fields, the rolling-up appears to take place in the first half of the orifice, sooner than when the shear layer mode I is dominant. Again, the flow does not seem to enter into the cavity at any phase of the cycle. The main difference between AZ1H1 and H3 is the phase of the velocity fields: the $\phi = 180^\circ$ for a flow speed of 48.4 m/s corresponds to the $\phi = 0^\circ$ at 51.5 m/s. This change of phase is due to the position of the microphone (figure 5): the acoustic oscillations at the opening are in phase with the fluctuations at the microphone location for the mode AZ1H1 and out of phase for the mode H3.

Acoustic power

In this section vortex sound theory [17] is applied to the opening region for the baseline orifice (L45EU). In Howe's acoustic analogy, the Coriolis density forces $\rho_0 \vec{w} \times \vec{u}$ are identified as the principal source of sound. The acoustic power generated by the vortical field Π can be calculated by Howe's integral

$$\Pi = -\rho_0 \int_V (\vec{w} \times \vec{v}) \cdot \vec{u}_{acoust} dV \quad (1)$$

which states that the Π is proportional to the triple $\vec{u}_{acoust} \cdot (\vec{w} \times \vec{v})$.

The velocity and the vorticity fields were extracted from the PIV data and the particle velocity numerically from the WEM simulation. An important assumption in the development followed is that the hydrodynamic and to acoustic fields can be computed independently. This assumption is motivated by the fact that the orifice, i.e the region where the acoustics is generated, is compact compared to the acoustic wavelengths.

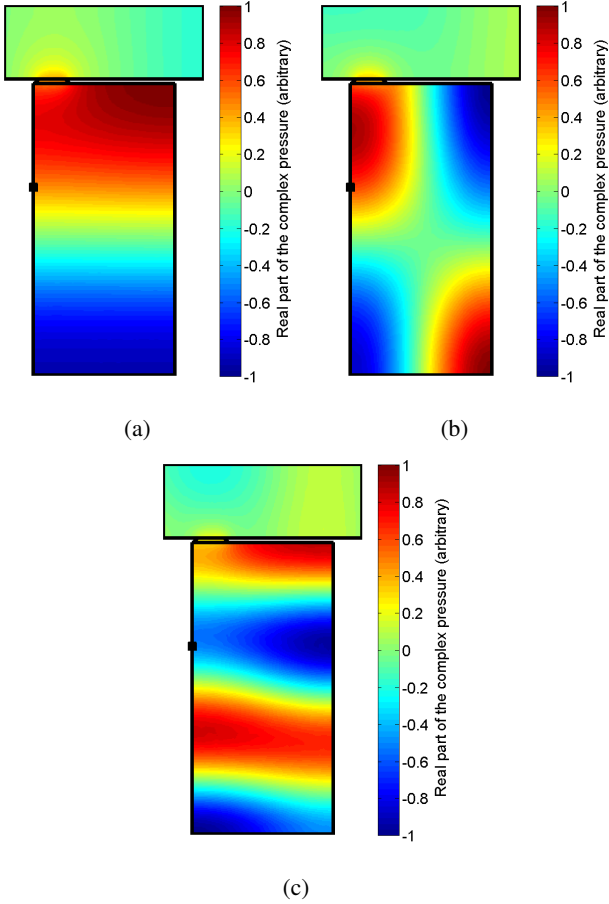


FIGURE 5: Normalized real pressure on the middle plane of the cavity: WEM results. Three acoustic resonance are given: (a) first longitudinal mode H1; (b) first azimuthal-longitudinal mode AZ1H1; (c) third longitudinal mode H3. The position of the microphone for the PIV campaign is indicated by a black square.

Computation of the acoustic particle velocity

As seen in the companion paper, the acoustic simulation gives a complex pressure field whose amplitude depends on the intensity of the monopole source. In order to scale the pressure, the experimental data acquired with a flush-mounted microphone was used. It is assumed that the pressure inside the cavity has a simple harmonic behaviour. This assumption is good for strongly resonant states. Therefore, the pressure P_{acoust} at any point inside the cavity (x, y, z) and at any moment of time (t) can be expressed as:

$$P_{acoust}(x, y, z, t) = cst P_{WEM}(x, y, z, f_{acoust}) \sin(2\pi f_{acoust} t) \quad (2)$$

where, P_{WEM} is the pressure from the numerical simulation, f_{acoust} is the frequency of the dominant acoustic mode during the experimental testing and cst a constant

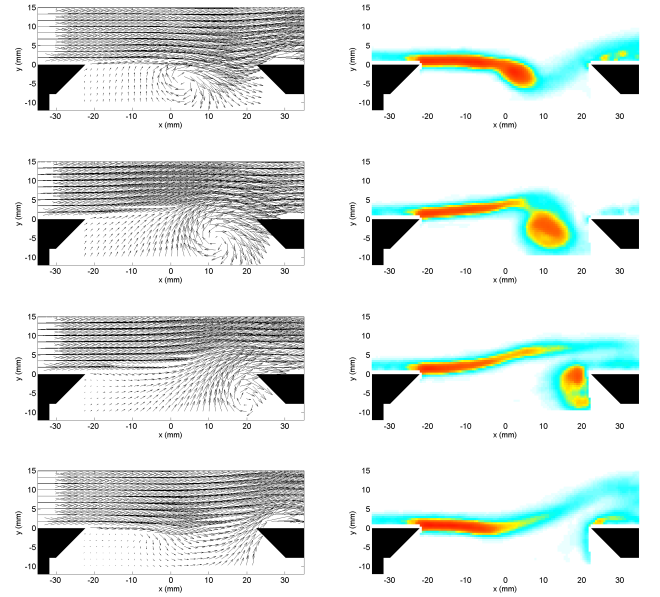


FIGURE 6: Phase-averaged velocity (left) and vorticity (right) fields at the opening of the cavity. Four phases are given: 0° , 90° , 180° and 270° . Flow speed 7.4 m/s. Predominant shear layer mode: SL1. Predominant acoustic mode: Helmholtz resonance.

necessary to match the experimental pressure measurements. The calculation of the particle velocity field was done by integrating the linearized Euler momentum equation:

$$\rho_0 \frac{\partial \vec{u}_{acoust}}{\partial t} + \nabla P_{acoust} = 0 \quad (3)$$

The integration is straightforward because the field is time harmonic. As an example, pressure and velocity fields in the orifice region are given in figure 10 for the modes H1, AZ1H1 and H3. The area of interest for this study is delimited by a rectangle. Even if inside the cavity the acoustic modes have very different shapes (figure 5), locally, around the opening the acoustic velocity fields are very similar for the three cases (figure 10).

Time-averaged acoustic power

Three free stream velocities were chosen for the study: 46.3, 48.4 and 51.5 m/s. These velocities correspond respectively to the first shear layer mode (SL1) locked-on with the first longitudinal mode (H1), the second shear layer mode (SL2) exciting the first azimuthal-longitudinal mode (AZ1H1) and the second shear layer mode (SL2) amplified by the third longitudinal mode H3. The shape of these three acoustic modes is displayed in

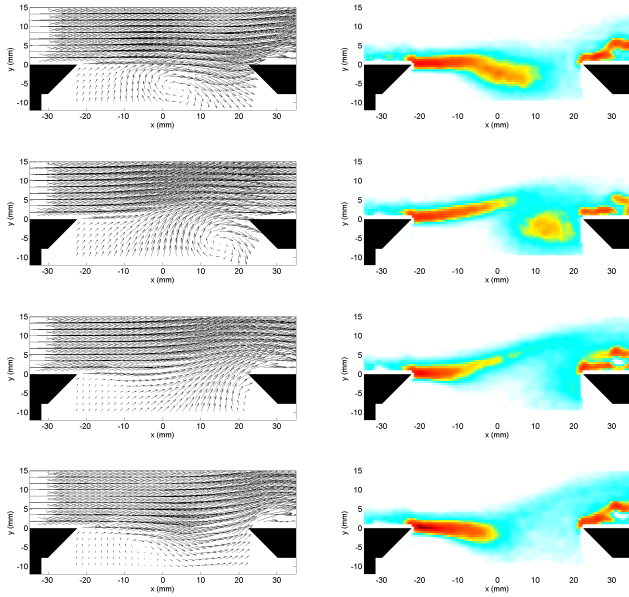


FIGURE 7: Phase-averaged velocity (left) and vorticity (right) fields at the opening of the cavity. Four phases are given: 0° , 90° , 180° and 270° . Flow speed 46.3 m/s. Predominant shear layer mode: SL1. Predominant acoustic mode: the first longitudinal resonance (H1).

figure 5 and 10. The instantaneous acoustic power was found for 8 different phases by computing the integrand of equation 1. This intermediate result, even if essential for understanding of the sound production, is not presented here for sake of brevity.

The acoustic power generated by the vortices in the orifice region over an entire acoustic period can be obtained by averaging the computed instantaneous acoustic powers:

$$\langle \Pi \rangle = \left\langle -\rho_0 \int_V \vec{u}_{acoust} \cdot (\vec{\omega} \times \vec{u}) dV \right\rangle \quad (4)$$

where $\langle \rangle$ denotes the time averaging over one period of oscillation.

The net acoustic energy $E = \langle \Pi \rangle / f$ produced by a free stream during an acoustic cycle of 46.3 m/s (SL1-H1) is given in figure 11(a). The spatial distribution of the acoustic energy is characterized by a distinct source-sink pair. This corresponds to the fact that when the first shear layer mode predominates, a single large-scale vortex is generated during an acoustic period.

The two cases for which the second shear layer mode is dominant are presented in figure 11(b) and 11(c). It is interesting to observe the degree of similarity between these two patterns: two source-sink pairs are found above

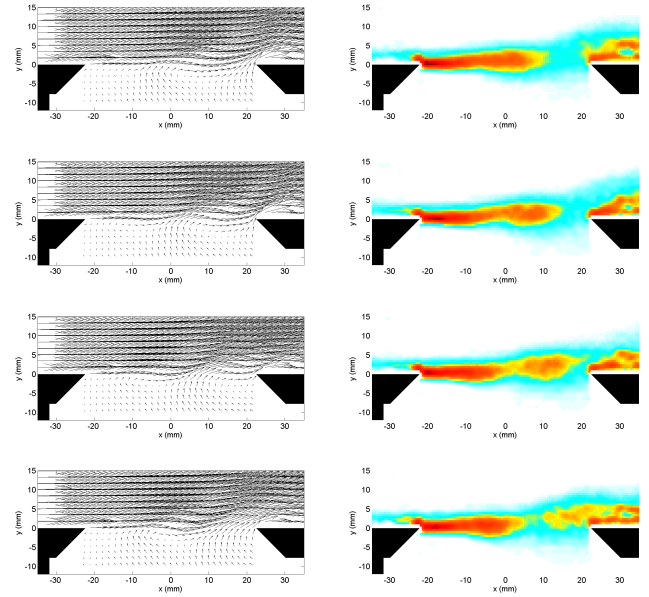


FIGURE 8: Phase-averaged velocity (left) and vorticity (right) fields at the opening of the cavity. Four phases are given: 0° , 90° , 180° and 270° . Flow speed 48.4 m/s. Predominant shear layer mode: SL2. Predominant acoustic mode: AZ1H1.

the opening. Again, the shear layer rolling up into large-scale vortices generates this pattern: the second shear layer mode produces two vortices during an acoustic cycle. Oshkai et al. [18] (alternatively Velikorodny et al. [19]) also reported two source-sink pairs when calculating the acoustic power for coaxial side branches for a dominant second shear layer mode. The major difference between both cases is the sign of the source-sink pairs. It is important to say that the sign of the computed acoustic power depends on the origin of the time axis. The determination of the phase of each PIV realization was done with reference to the pressure measured with the microphone at the upstream wall of the cavity. Therefore the acoustic pressure fluctuations in the orifice region (upstream) are in phase with the fluctuations recorded by the microphone for the AZ1H1 case and out of phase when H3 is dominant (figure 5 b, c).

CONCLUSIONS

A cylindrical Helmholtz resonator was experimentally studied by wall pressure measurements and 2D PIV. The designed experiment allows different resonant modes to be excited depending on both flow speed and orifice location.

At low flow speeds, the Helmholtz resonance was found to be excited by the first shear layer hydrodynamic mode at the frequency predicted by an improved

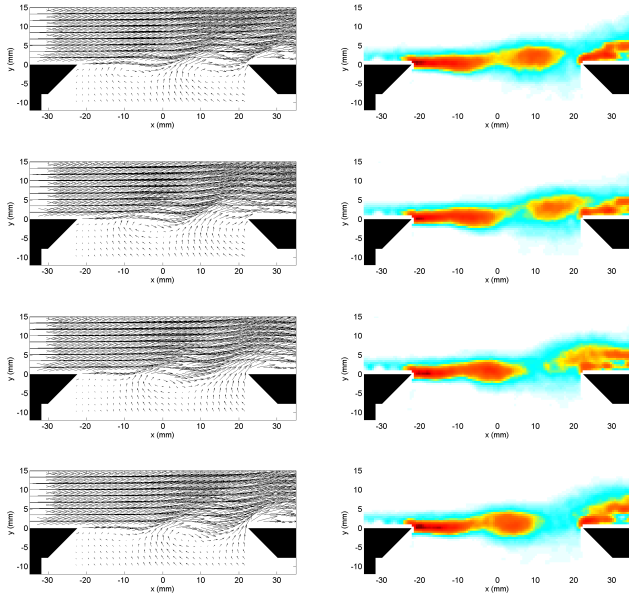


FIGURE 9: Phase-averaged velocity (left) and vorticity (right) fields at the opening of the cavity. Four phases are given: 0° , 90° , 180° and 270° . Flow speed 51.5 m/s. Predominant shear layer mode: SL2. Predominant acoustic mode: the third longitudinal resonance (H3).

Helmholtz resonance formulation.

For higher velocities, lock-on between the first two shear layer hydrodynamic modes and different eigenmodes of the cavity was observed. The location of the cavity's opening was found to be a major factor in determining which acoustic mode is excited. Specifically, a combination mode (azimuthal and longitudinal) was found to generate lock-on only when the opening was located off-center. This was ascribed to the fact that the main axis of the cavity is a pressure node for the first azimuthal mode.

The dynamics of the shear layer were then explored through PIV measurements for four flow speeds corresponding to strongly resonant cases. Phase averaged PIV allowed the coherent structures present in the shear layer to be examined and the interaction between the cavity resonances and the shear layer to be analysed. The first hydrodynamic mode is characterized by a flapping movement in the upstream portion of the resonator's opening and by the rolling up of the shear layer in a single vortex in the downstream portion of the orifice. The number of vortices generated per acoustic cycle increases to two when the second hydrodynamic instability becomes dominant. This observation is consistent with previous studies. The experimental results show that the order of the dominant acoustic resonant mode does not affect the organization of the shear layer. A possible explanation is

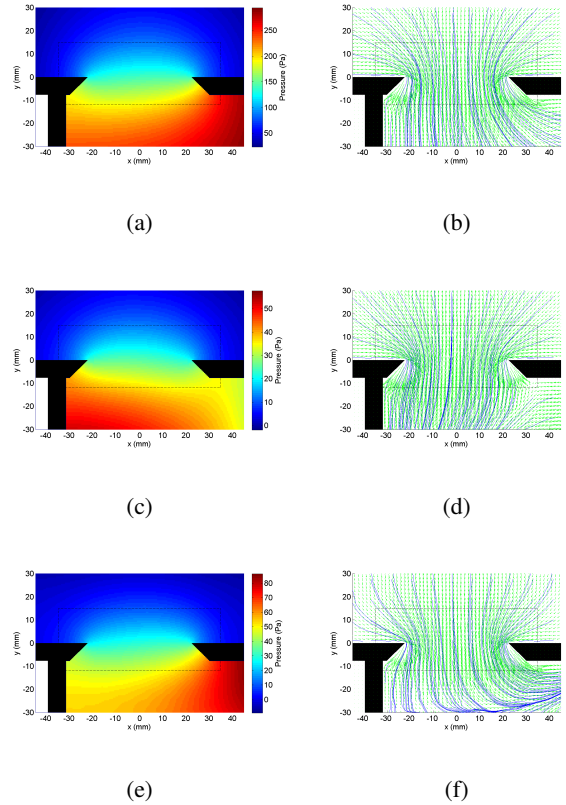


FIGURE 10: Acoustic pressure field P_{acoust} (left), acoustic velocity field \vec{u}_{acoust} in green and streamlines in blue (right) at the orifice region calculated with the WEM simulation and scaled by the experimental data. From top to bottom: H1, AZ1H1 and H3. Pressure fields are given at $\phi = 90^\circ$ whereas velocity fields at $\phi = 0^\circ$.

that in the opening region, the acoustic velocity fields are similar.

The vortex sound theory of Howe was applied in order to characterize the energy transfer mechanisms on the orifice region. The velocity and the vorticity fields were extracted from the PIV data and the particle velocity was calculated using a Wave Expansion Method (WEM) simulation. Three different flow conditions generating acoustic resonance were analysed. For each case, the acoustic sources were localized revealing that the spatial organization of the sound production depends exclusively on the predominant shear layer hydrodynamic mode.

REFERENCES

- [1] Helmholtz, H., 1860. "Theorie der luftschwingungen in rhren mit offenen enden". *Crelle's Journal*, 57, pp. 1–72.
- [2] Panton, R. L., and Miller, J. M., 1975. "Resonant frequencies of cylindrical helmholtz resonators".

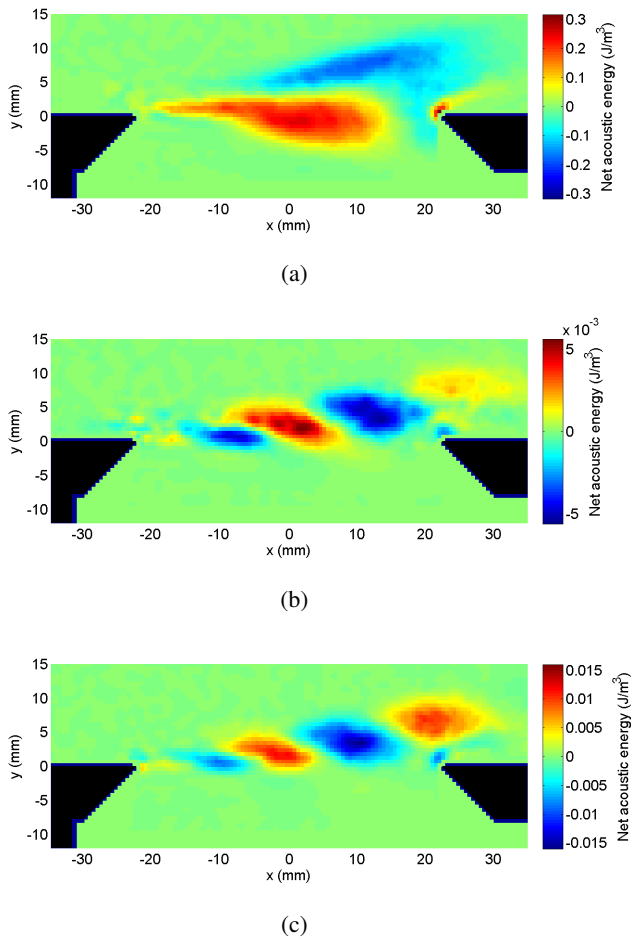


FIGURE 11: Distribution of the net acoustic energy generated per acoustic cycle on the orifice. (a): 46.3 m/s, SL1-H1. (b): 48.4 m/s, SL2-AZ1H1. (c): 51.5 m/s, SL2-H3.

Journal of Acoustical Society of America, **57(6)**, pp. 1533–1535.

- [3] De Metz, F. C., Farabee, T. M., and David, W., 1977. “Laminar and turbulent shear flow induced cavity resonances”. In 4th AIAA Aeroacoustics Conference, no. 77-1293.
- [4] Elder, S. A., 1978. “Self-excited depth-mode resonance for a wall-mounted cavity in turbulent flow”. *Journal of Acoustical Society of America*, **64**, pp. 877–890.
- [5] Ma, R., Slaboch, P. E., and Morris, S. C., 2009. “Fluid mechanics of the flow-excited helmholtz resonator”. *Journal of Fluid Mechanics*, **623**, pp. 1–26.
- [6] Nelson, P. A., Halliwell, N. A., and Doak, P. E., 1981. “Fluid dynamics of a flow excited resonance, part i: experiment”. *Journal of Sound and Vibration*, **78(1)**, pp. 15–38.
- [7] Rockwell, D., and Naudascher, E., 1978. “Review - self-sustained oscillations of flow past cavities”. *Journal of Fluids Engineering*, **100**, pp. 152–165.
- [8] Langtry, R. B., and Spalart, P. R., 7 - 10 January 2008. “Des investigation of a baffle device for reducing landing-gear cavity noise”. *46th AIAA Aerospace Sciences Meeting and Exhibit, Reno, Nevada, USA*.
- [9] Balasubramanian, G., Crouse, B., and Freed, D., 11-13 May 2009. “Numerical simulation of leakage effects on sunroof buffeting of an idealized generic vehicle”. *15th AIAA/CEAS Aeroacoustics Conference, Miami, Florida, USA*.
- [10] Tonon, D., Hirschberg, A., Golliard, J., and Ziada, S., 2011. “Aeroacoustics of pipe systems with closed branches”. *International Journal of Aeroacoustics*, **10**, pp. 201–276.
- [11] Yang, Y., Rockwell, D., Lai-Fook Cody, K., and Pollack, M., 2009. “Generation of tones due to flow past a deep cavity: effect of streamwise length”. *Journal of Fluids and Structures*, **25**, pp. 364–388.
- [12] Oshkai, P., and Yan, T., 2008. “Experimental investigation of coaxial side branch resonators”. *Journal of Fluids and Structures*, **24**, pp. 589–603.
- [13] Kook, H., and Mongeau, L., 2002. “Analysis of the periodic pressure fluctuations induced by flow over a cavity”. *Journal of Sound and Vibration*, **251(5)**, pp. 823–846.
- [14] Awny, K., and Ziada, S., 2008. “Effect of cavity depth on diametral mode excitation”. *9th International Conference on Flow-Induced Vibrations (FIV2008)*, Prague, Czech Republic.
- [15] Oshkai, P., Geveci, M., Rockwell, D., and Pollack, M., 2005. “Imaging of acoustically coupled oscillations due to flow past a shallow cavity: effect of cavitylength scale”. *Journal of Fluids and Structures*, **20**, pp. 277–308.
- [16] Finnegan, S. L., 2011. “Resonant aeroacoustic source localisation in ducted bluff body flows”. PhD thesis, University of Dublin.
- [17] Howe, M. S., 1975. “Contributions to theory of aerodynamic sound, with application to excess jet noise and the theory of the flute”. *Journal of Fluid Mechanics*, **71,4**, pp. 625–673.
- [18] Oshkai, P., Yan, T., Velikorodny, A., and VanCaeseele, S., 2008. “Acoustic power calculation in deep cavity flow: a semiempirical approach”. *Journal of Fluids Engineering*, **130(5)**.
- [19] Velikorodny, A., Yan, T., and Oshkai, P., 2010. “Quantitative imaging of acoustically coupled flows over symmetrically located side branches”. *Experiments in Fluids*, **48**, pp. 245–263.



ON THE CONTROL OF FLOW PAST A CIRCULAR CYLINDER VIA A SINGLE SPANWISE PROTRUSION

Alis Ekmekci¹

Institute for Aerospace Studies
University of Toronto
Toronto, Ontario, Canada
ekmekci@utias.utoronto.ca

Tayfun Aydin

Institute for Aerospace Studies
University of Toronto
Toronto, Ontario, Canada

Antrix Joshi

Institute for Aerospace Studies
University of Toronto
Toronto, Ontario, Canada

ABSTRACT

An experimental study is conducted in the near wake of a circular cylinder with a single, large-scale spanwise protrusion on its surface. In a range of Reynolds numbers, $5,000 \leq Re_D \leq 15,000$, varying the angular location θ of the protrusion, the critical angles for its implementation are investigated via hot-film anemometry. Emphasis was on the question if critical states, defined in previous findings [6-8], exist when the Re_D is varied in the subcritical range.

For each Re_D , two critical θ are shown to exist. The peak amplitude of velocity spectra significantly attenuates when the protrusion is at the first critical angle θ_{c1} , whereas it amplifies at the second critical angle θ_{c2} .

Time traces of velocity show notable irregularities at θ_{c1} . Hydrogen-bubble visualization at θ_{c1} depict recurrent occurrence of periods during which no order or rhythm is detectable in vortex shedding, and times when the regular Karman shedding resumes. During the times when coherency of Karman shedding is disrupted at θ_{c1} , the near-wake bubble significantly extends.

NOMENCLATURE

d	Diameter of the surface wire
D	Diameter of the cylinder
f	Frequency
f_K	Characteristic Karman frequency
f_L	Low frequency
L	Length along the wetted span of the cylinder
Re_D	Reynolds number based on the cylinder diameter
St	Strouhal number
S_u	Autospectral density of streamwise velocity component
δ	Boundary-layer thickness
θ	Angular position of the wire from the forward stagnation point of the cylinder, in degrees

θ_{c1}	First critical angle
θ_{c2}	Second critical angle
t	Time
u	Streamwise velocity component
U_o	Free-stream velocity
$\langle * \rangle$	Time-averaged value of *

INTRODUCTION

Certain forms of protrusions, such as helical strakes and helical ribs, staggered separation wires, and fairings, have been widely employed in many applications of wind and ocean engineering on cylindrical or near-cylindrical structures to suppress or at least subdue the intensity of vortex-induced vibrations [1,2]. Among these protrusions, helical patterns are the most commonly employed, owing to their proven success in suppression. Previous research has shown that the effectiveness of suppression for helical protrusions alters with the number, pitch and size of the protrusion(s) [2]. However, the reason why certain helical configurations optimize the suppression under certain conditions, while other helical configurations turn out to be detrimental, has remained unresolved. At this point, little is understood with regard to the basic physics involved, despite the physical importance. This is mostly because the three-dimensionality of helical protrusions increases the complexity of the associated flow phenomena. In search of a physical understanding, a number of investigators have turned their attention to two-dimensional models with spanwise (straight) surface protrusion.

Previous related research on stationary cylinders with spanwise protrusions in the subcritical flow regime have shown strong dependence of the vortex shedding frequency, and the mean drag and lift loads on the wire size [3-6], the wire location θ [4-8], and the Reynolds number [3,5]. (Conventionally, θ values on a cylinder are

¹Address all correspondence to this author¹

measured from its forward stagnation point.) A single spanwise wire was found to affect the shedding frequency of Karman vortices from a circular cylinder only when the wire, on the cylinder surface, is located over a certain range of angular locations θ . Within this range of θ , shedding frequency was found to typically show a gradual decrease and then an increase as θ is increased [5-7].

Recently, Ekmekci (2006) and Ekmekci & Rockwell (2010, 2011) provided an in-depth quantitative insight into the effects induced by a single wire, glued spanwise on the outer surface of a circular cylinder, utilizing the cinema technique of Particle Image Velocimetry (PIV) [6-8]. On the cylinder surface, they revealed two angular locations θ that are critical for the implementation of a surface wire. When the wire is attached at those critical angles, either the most significant extension or the most significant contraction occurred in the streamwise length of the near-wake bubble. Ekmekci & Rockwell (2011) has shown that these critical angles depend on the scale of the wire: the smaller the wire, the larger the critical angles [8]. Ekmekci (2006) and Ekmekci & Rockwell (2010, 2011) also reported bistable oscillations of the shear layer between two separation modes when the wire is located at the critical angle that yields the maximum near-wake extension [6-8]. One separation mode involved shear-layer reattachment and the other mode involved no reattachment after the separation of the flow at the wire. Bistable oscillations of the shear layer between these two modes have been shown to involve broad frequencies, centered around a value that is one order of magnitude smaller than the characteristic Karman frequency. This broad low frequency was found to be predominant in the vicinity of separation toward the surface wire [6,7]. As a major breakthrough, Ekmekci & Rockwell (2010) has shown for the first time that, in specific cases, a spanwise wire can attenuate the Karman instability when attached at the critical angle associated with the maximum near-wake extension; while, it can significantly intensify the Karman instability when attached at the critical angle correlated with the maximum near-wake contraction [6,7].

In the works of Ekmekci (2006) and Ekmekci & Rockwell (2010, 2011), consideration was given to wires having wire-to-cylinder-diameter ratio $d/D = 0.029, 0.012$ and 0.005 at a fixed Reynolds number of 10,000. The present investigation evaluates the effect of a much larger-size wire, having $d/D = 0.059$, over a range of Reynolds numbers from 5,000 to 15,000. The purpose here is to investigate the Reynolds number dependence of the effects of a large-scale spanwise wire. A major issue is whether analogous changes in flow can be induced when the Reynolds number is varied in the subcritical regime.

EXPERIMENTAL SETUP AND METHODOLOGY

Experiments were conducted in a free-surface water channel, located at the University of Toronto. Through its recirculating design, the water channel provided continuous flow in the horizontal direction along its 5,000-mm-long test section. The wetted cross-section of

the main test section had a width of 680 mm and a height of 670 mm. The test-section walls were made of Plexiglas material to allow optical access to the flow. Prior to the test-section inlet, flow passed through a settling chamber, composed of a honeycomb and a set of screens, and then a 6:1 contraction to reduce potential non-uniformities in the flow. This arrangement yielded free-stream turbulence intensity of less than 0.5% and a flow uniformity better than 0.3%.

In each experiment, a circular wire, made of nylon fishing line, was stretched tight and glued on the outer surface of a circular cylinder, parallel to its span. The wires in consideration had diameters $d = 1.48$ mm and 3.0 mm, and the main cylinder had a diameter $D = 50.8$ mm, producing two different experimental configurations having wire-to-cylinder-diameter ratios of $d/D = 0.029$ and 0.059. Each cylinder-wire model was set up in the vertical orientation on a rectangular endplate within the water channel. All arrangements had an aspect ratio of $L/D = 12.3$. The wire was placed on the surface of the main cylinder at various angular locations, ranging from $\theta = 0^\circ$ to 180° , with respect to the forward stagnation point of the cylinder. To change the angular location of the wire on the cylinder, the cylinder-wire arrangement was simply rotated around the longitudinal axis of the cylinder. During the course of investigation, time traces of the streamwise velocity component u was measured through hot-film anemometry at $Re_D = 5,000, 10,000$ and 15,000, based on the main cylinder diameter. The hot-film probe, in these measurements, was placed $3D$ downstream and $2.5D$ lateral to the cylinder axis on the wire side of the wake. It gave 8,192 discrete streamwise velocity signals at an acquisition rate of 50 Hz. Autospectral density S_u of the streamwise velocity was then calculated using fast Fourier transformation. Long-time visualization of streaklines in the near-wake was carried out with the hydrogen bubble technique at $Re_D = 10,000$ over the range of θ .

RESULTS AND DISCUSSIONS

Comparison with Previous Findings

Before discussing the results of the present paper, we would like to point out two key findings, taken from Ekmekci and Ekmekci & Rockwell [6-8], presented herein in Figures 1 and 2.

Figure 1 shows the contour patterns of the time-averaged streamwise velocity $\langle u \rangle / U_o$, obtained from PIV measurements in the near-wake of a circular cylinder with a spanwise wire, having wire-to-cylinder-diameter ratio $d/D = 0.029$ at $Re_D = 10,000$. This wire had a scale larger than the thickness of the boundary layer forming around a smooth cylinder, and hence, was referred to as a large-scale wire. In Figure 1, the dashed contour lines distinguish the pockets of negative streamwise velocity in the near wake, i.e., the near-wake bubble. $\langle u \rangle / U_o$ patterns in Figure 1 show a gradual variation in the streamwise length of the near-wake bubble as a function of θ .

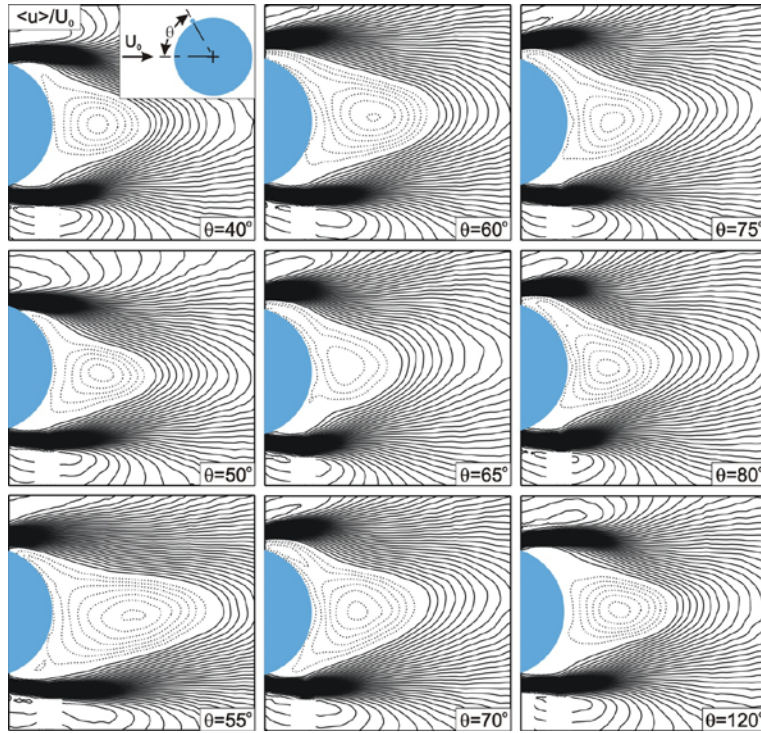


FIGURE 1: PATTERNS OF TIME-AVERAGED STREAMWISE VELOCITY $\langle u \rangle / U_o$ CONTOURS FOR THE WIRE WITH $d/D = 0.029$ AT $Re_D = 10,000$. ANGULAR POSITION OF THE WIRE RANGE FROM $\theta = 40^\circ$ TO $\theta = 120^\circ$. MINIMUM AND INCREMENTAL VALUES ARE AS FOLLOWS: $|\langle u \rangle / U_o|_{min} = 0.04$ AND $\Delta[\langle u \rangle / U_o] = 0.04$. FIGURE IS TAKEN FROM EKMEKCI (2006) AND EKMEKCI & ROCKWELL (2011).

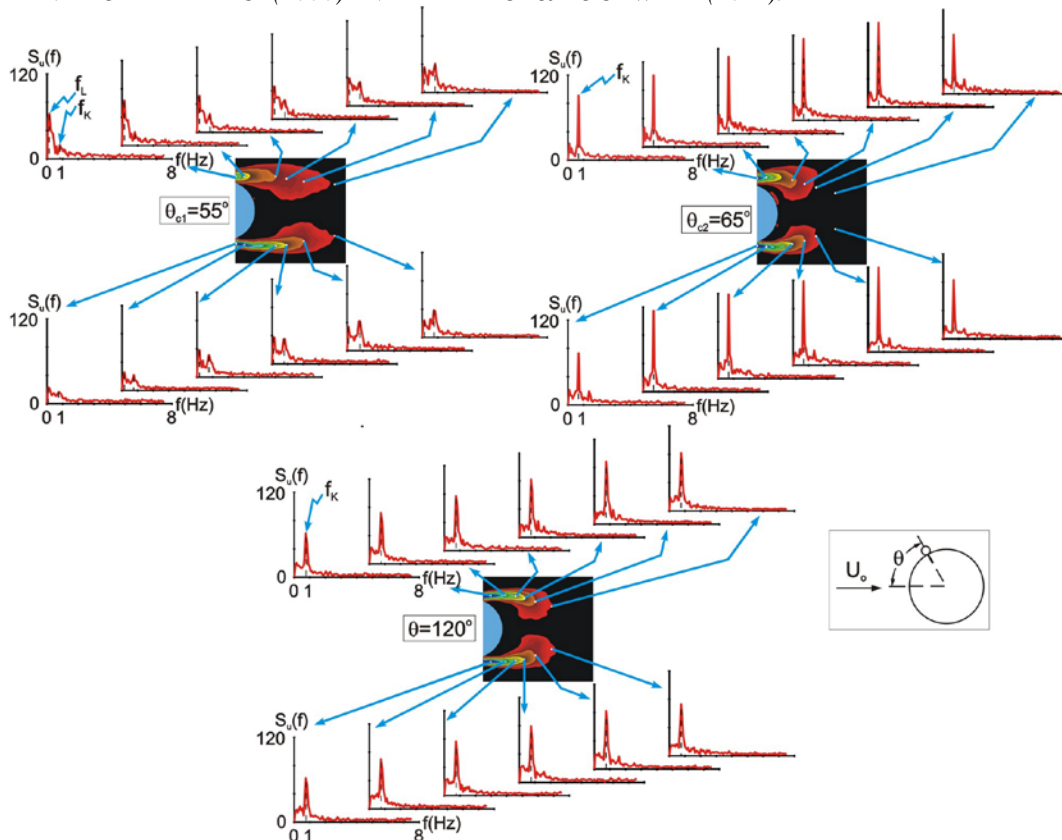


FIGURE 2: AUTOSPECTRAL DENSITY $S_u(f)$ OF THE STREAMWISE VELOCITY FLUCTUATIONS OVER SEVERAL POINTS IN THE NEAR WAKE FOR THE CRITICAL SURFACE WIRE LOCATIONS $\theta_{c1} = 55^\circ$ and $\theta_{c2} = 65^\circ$, AND THE REFERENCE CASE AT $\theta = 120^\circ$ ($d/D = 0.029$, $Re_D = 10,000$). FIGURE IS TAKEN FROM EKMEKCI (2006) AND EKMEKCI & ROCKWELL (2010).

Based on the length of the near-wake bubbles, Ekmekci and Rockwell [6,7] distinguished two angular locations on the cylinder surface as being critical for the implementation of this surface wire. The angular location that yields the largest extension of the near wake was denoted as the first critical angle θ_{c1} , whereas the one leading to the most significant contraction of the near wake was discerned as the second critical angle θ_{c2} . These critical angles were determined to be $\theta = 55^\circ$ and $\theta = 65^\circ$ for the large-scale wire with $d/D = 0.029$ at $Re_D = 10,000$ [6-8].

Figure 2, taken from Ekmekci (2006) and Ekmekci & Rockwell (2010), shows how the autospectral density $S_u(f)$ of the streamwise velocity component varies over a number of points in the near wake for the two critical angles $\theta_{c1} = 55^\circ$ and $\theta_{c2} = 65^\circ$ of the wire with $d/D = 0.029$ at $Re_D = 10,000$. The $S_u(f)$ variation for $\theta = 120^\circ$ is also included in the figure as a reference case for comparison, since the influence of a wire when placed in the base region was found to be insignificant [5-7]. The locations where the spectra are displayed in the near wake are marked by arrows for each case on a corresponding pattern of time-averaged vorticity. The reference case ($\theta = 120^\circ$) shows at all points a pronounced spectral peak at the characteristic Karman frequency, which is designated as f_K in the figure. The critical states, on the other hand, reveal some unexpected features [6,7]: Firstly, at the critical angle associated with the maximum near-wake extension, i.e., at θ_{c1} , the large-scale wire considerably attenuates the spectral amplitude at f_K . On the other hand, at the critical angle associated with the significant near-wake contraction, i.e., at θ_{c2} , the spectral amplitude at f_K is increased. Comparison of the spectral amplitudes at f_K for θ_{c1} and θ_{c2} with the reference case at $\theta = 120^\circ$ in Figure 2 clearly shows their attenuation and the amplification at θ_{c1} and θ_{c2} , respectively. Secondly, for the critical state of near-wake extension (encountered at θ_{c1}), a broad spectral peak with a low value of center frequency, designated as f_L , is found to be predominant especially near the separation region from the wire. Note that the upper shear layer in Figure 2 corresponds to the wire-side shear layer. With increasing distance from the location of separation, the peak at f_L gradually diminishes. The physical origin of the broad, low-frequency fluctuations centered at f_L near the separation region from the wire has been revealed to be associated with bistable switching of the shear layer between two separation modes: one involving the reattachment and the other involving no reattachment of the shear layer after the separation at the wire.

Ekmekci and Rockwell [6-8] studied the effects of a large-scale wire ($d/D = 0.029$) as well as small-scale wires ($d/D = 0.012$ and 0.005) at a fixed Reynolds number of 10,000, using the cinema technique of PIV. Space-time imaging of velocity fluctuations through this non-intrusive optical technique provided immense insight into the underlying flow physics. Consideration was not given to Reynolds number dependence at those studies, and the

present investigation questions this point, employing hot-film measurements of velocity at a single point and hydrogen bubble visualization in the wake region. PIV technique used in the studies of Ekmekci and Rockwell [6-8] allowed the acquisition of 200 image pairs at a rate of 15 Hz; whereas, the hot-film measurements in the present investigation provided 8,192 data points at a rate of 50 Hz. Longer-time records of velocity signals with much higher acquisition rate attainable through the hot-film velocimetry as well as longer-time records of streakline patterns through the hydrogen bubble visualization can further our understanding in this realm.

Before assessment of the Reynolds number effect, the present study first compares the spectral trends of the streamwise velocity fluctuations with the previous spectral findings [6,7] at $Re_D = 10,000$ for the same large-scale spanwise wire with $d/D = 0.029$.

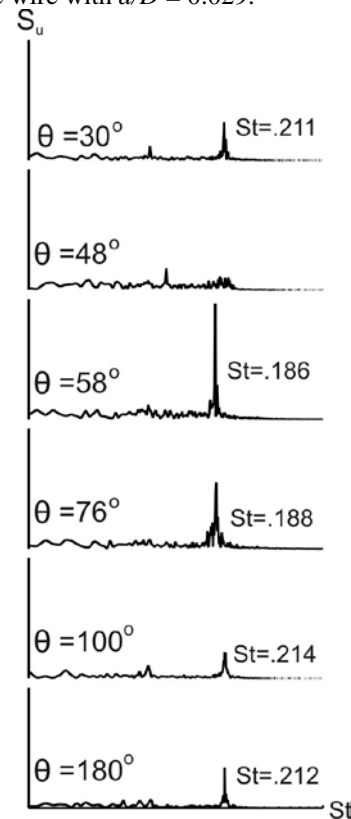


FIGURE 3: AUTOSPECTRAL DENSITY S_u OF THE STREAMWISE VELOCITY COMPONENT FOR $d/D = 0.029$ AT $Re_D = 10,000$ ARE SHOWN FOR DIFFERENT ANGULAR POSITIONS θ OF THE WIRE. HEREIN, THE VALUE OF THE PREDOMINANT STROUHAL NUMBER St ARE ALSO INDICATED FOR EACH θ . (St AXIS IS PLOTTED IN LOG SCALE.)

Figure 3 shows the autospectral density S_u of the streamwise velocity fluctuations for the large-scale wire with $d/D = 0.029$ at $Re_D = 10,000$ (same conditions as in [6,7]), obtained from hot-film velocity measurements at a point on the wire-side of the wake. This point was located a distance of $3D$ downstream and $2.5D$ lateral from the cylinder center. During the course of hot-film

measurements, the angular position of the wire was varied to a number of θ values. Especially near the critical states, the θ increments were selected to be 2° . As θ of the wire was increased starting from 0° , significant attenuation of the spectral amplitude at Karman frequency f_K was observed at θ values near 48° . It, therefore, was concluded that $\theta = 48^\circ$ corresponds to the first critical angle θ_{c1} defined by Ekmekci (2006) and Ekmekci & Rockwell (2010). After 48° , as the value of θ increased, the peak spectral amplitude was observed to increase, finally reaching the highest amplitude at $\theta = 58^\circ$. Therefore, $\theta = 58^\circ$ was determined to be the second critical angle θ_{c2} , after which an increase in θ , resulted in a gradual decrease of the peak amplitude of S_u to the levels observed at $\theta = 100^\circ$ and 180° , i.e., the cases where the wire is in the base of the cylinder, showing no significant influence on the wake.

The first thing to be noticed when the findings of the present study thus far are compared with those of the previous published literature is that Ekmekci and Rockwell reported higher values of critical angles ($\theta_{c1} = 55^\circ$ and $\theta_{c2} = 65^\circ$, as shown in Figure 2), compared to those found in the present study ($\theta_{c1} = 48^\circ$ and $\theta_{c2} = 58^\circ$). This difference in the exact values of the critical angles between the two studies might arise due to a number of reasons: First of all, the experiments were conducted in different water channel facilities, having dissimilar free stream turbulence characteristics, which might affect the values of the critical θ . Secondly, both studies measure the angular location θ of the wire referencing the forward stagnation point of the cylinder. Since this stagnation point was determined merely through visual investigation, it is estimated that both studies had approx. $\pm 4^\circ$ human error in the determination of its location. Also, Ekmekci and Rockwell studied θ variation in coarser (5°) increments. Despite the difference in exact values of the critical angles, however, the overall variation trend of the peak spectral amplitudes of velocity fluctuations, and the significant attenuation of the spectral amplitude at a critical angle and the intensification of it at a second critical angle are all in accord with the observations reported by Ekmekci and Rockwell [6,7].

Another point is that, in Figure 3, the velocity spectra at the first critical angle $\theta_{c1} = 48^\circ$ does not show a significantly pronounced peak at low frequencies. This is, in fact, expected, because the low frequency fluctuations were detected to be pronounced toward the separation region close to the wire as shown in Figure 2 [6,7]. The location of the hot-film probe ($3D$ downstream and $2.5D$ lateral from the cylinder center) is far downstream of the separation region to detect prominently the frequencies related to the bistable shear-layer oscillations reported by Ekmekci and Rockwell [6,7].

In Figure 3, the predominant frequency of velocity fluctuations are also indicated in terms of Strouhal number (St) in each S_u plot. These values vary depending on θ . Figure 4 presents this variation over a wide range of θ . The crater-like trend, observed in Figure 4, is in perfect

agreement with the findings of Nebres & Batill (1993) and Ekmekci & Rockwell (2010).

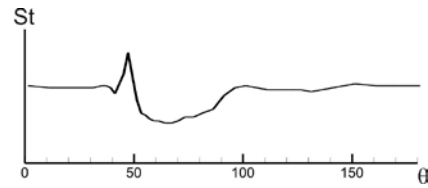


FIGURE 4: VARIATION OF THE PREVAILING STROUHAL NUMBER (St) OF VELOCITY FLUCTUATIONS WITH THE ANGULAR POSITION (θ) OF THE WIRE; $d/D = 0.029$, $Re_D = 10,000$.

When compared to related findings in the literature, it can be concluded from all the discussions so far that hot-film measurements can provide a means to determine the critical flow states.

Effect of the Reynolds Number

Now, we would like to turn our attention to the effects of a much larger-size wire, having $d/D = 0.059$ and question if similar critical states can be observed at varying Reynolds numbers. Consideration is given to a Reynolds number range from $Re_D = 5,000$ to $15,000$.

Prior to any further discussion, let's identify the scale of the wire that has $d/D = 0.059$. In Figure 5, the size of this wire (d/D) is compared to the thickness of the boundary layer (δ/D) developing around a smooth cylinder at $Re_D = 5,000$ and $10,000$. The laminar boundary-layer thickness around smooth cylinders, therein, are estimated based on the Blasius method described by Schlichting [9]. These calculations required the acquisition of the surface pressure distribution around a smooth cylinder. This was achieved using a pressure tap, connected to a pressure transducer, on the model and rotating the cylinder around its axis to vary the angular location of the tap. The plot in Figure 5 clearly shows that at those Re_D (as well as higher Re_D values), the wire is always larger than δ/D at all circumferential locations between 10° to 75° . Hence, the wire with $d/D = 0.059$ is a large-scale wire over the Re_D range studied in the present investigation.

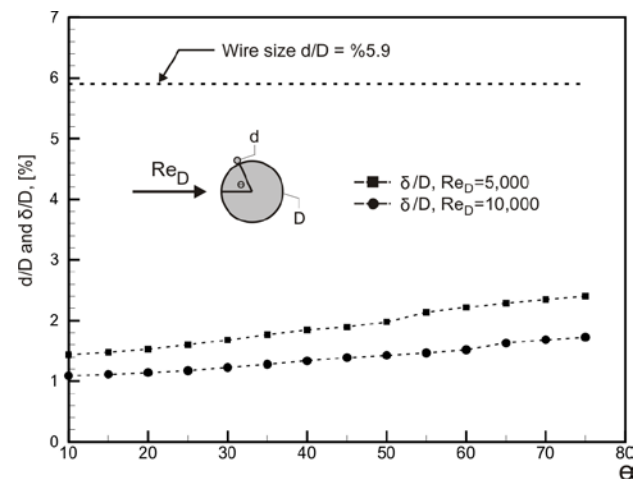


FIGURE 5: WIRE SCALE (d/D) COMPARED TO THE BOUNDARY LAYER THICKNESS (δ/D), FORMING AROUND A SMOOTH CYLINDER AT $Re_D = 5,000$ AND 10,000.

For the cylinder with this large-scale spanwise wire, Figure 6 shows the autospectral density S_u of the streamwise velocity fluctuations, determined through the hot-film measurements, for $Re_D = 5,000$ in the first column, $Re_D = 10,000$ in the second column, and $Re_D = 15,000$ in the third column. For all the Reynolds numbers investigated herein, as the angular location θ of the wire is increased, a critical θ producing significant attenuation of the spectral amplitude at the Karman frequency is encountered. The second row in Figure 6 presents the spectra at this first critical angle for each Re_D . After this critical position (θ_{c1}) of the wire, as the value of θ is increased further, the spectral amplitude increases, eventually resulting in the highest spectral peak at the second critical angle θ_{c2} . The spectra associated with this second critical angle are given in the third row for each Re_D . Past the second critical angle θ_{c2} , the spectral amplitude of the Karman instability gradually decreased to moderate levels, as observed at $\theta = 180^\circ$, which was shown to have no detectable effect on the flow [5-7]. This trend is in accord with the previous observations found when the large-scale wire having $d/D = 0.029$ was used at a fixed Reynolds number of 10,000.

At this point, one can conclude that the critical angular locations θ_{c1} and θ_{c2} exist for all the subcritical Reynolds numbers studied herein. The value of θ_{c1} changes markedly depending on Re_D . However, the change in θ_{c2} is not notable.

It should be emphasized here that since the location of the stagnation point, that is, the reference for the measurements of θ , on the cylinder surface was determined visually, the exact values of θ might contain a certain level of human error. Therefore, for increased accuracy of the exact values of the critical angles, one should determine the stagnation point for each experiment with increased precision. Nevertheless, the experiments in this investigation provides valuable preliminary understanding of the Reynolds number effect.

In addition, previous studies has shown that the wake width changes as a function of the angular location θ of the wire [5,6]. Depending on θ , a decrease or increase of the distance between the hot-film probe and the shed vortices behind the cylinder would cause a change in the strength of the signals. However, the global velocity spectra (from [6,7]), as shown in Figure 2, suggests that an attenuation and amplification in velocity fluctuations physically exist when the wire is at the critical locations θ_{c1} and θ_{c2} , respectively.

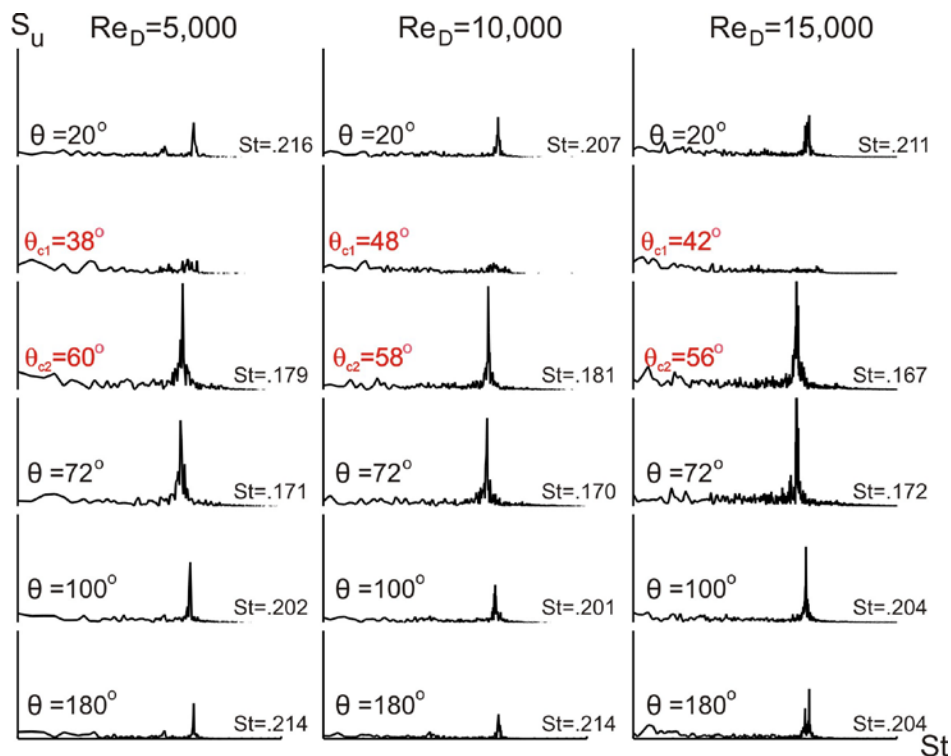


FIGURE 6: AUTOSPECTRAL DENSITY S_u OF THE STREAMWISE VELOCITY COMPONENT FOR $d/D=0.059$ AT $Re_D=5,000$ TO 15,000 FOR DIFFERENT ANGULAR POSITIONS (θ) OF THE WIRE. THE PREDOMINANT STROUHAL NUMBER (St) ARE INDICATED FOR EACH θ . (St AXIS IS PLOTTED IN LOG SCALE.)

Unsteady Characteristics of the Near Wake

In Figure 7, for the case of $d/D = 0.059$ at $Re_D = 10,000$, the time traces of the streamwise velocity component are presented. These time traces directly correspond to the velocity data of the spectra provided in Figure 6.

Figure 7 clearly depicts what was observed previously by Ekmekci and Rockwell [6-8]: the velocity fluctuations lose their ordered periodicity, exhibiting large amount of irregularities at the first critical angle θ_{c1} , compared to the velocity signals at other angular locations of the wire.

In Figure 8, representative streakline images, from the hydrogen bubble visualization, are provided at the two critical angles (θ_{c1} and θ_{c2}) and at the reference case of $\theta = 180^\circ$ for $d/D = 0.059$ at $Re_D = 10,000$. Inspection of the long-time records of the hydrogen-bubble-visualization images at the first critical angle θ_{c1} shows that there are recurrent periods during which no indication of rhythmic development of clusters are evident, that is, ordered and consistent shedding of Karman vortices are not detected, and there are times when the regular shedding resumes again. Representative streaklines are provided in Figure 8 (a) and (b) from the times when the regular shedding of

Karman vortices ceases and times when it resumes, respectively. In short-time movies (13.3 s long) obtained from PIV imaging, Ekmekci and Rockwell [6, 7] showed clearly the attenuation phase of the Karman vortex shedding. This animation is available online in Ekmekci & Rockwell (2010). Figure 8 (a) shows that, at the first critical angle, when the coherent formation of Karman vortex shedding is disrupted, significant extension in the streamwise length of the near-wake bubble arises. This explains the reason why maximum near-wake extension was observed at θ_{c1} in the time-averaged patterns, given in Figure 1. Figure 8 (c) clearly depicts that the wire at the second critical angle θ_{c2} brings about contraction in the streamwise length of the near-wake bubble. This same observation (maximum near-wake contraction) at θ_{c2} was reported by Ekmekci and Rockwell [6-8], as shown in the time-averaged $\langle u \rangle / U_o$ pattern in Figure 1.

All the observations presented in this investigation not only correlates well with the findings of the previous pertinent investigations but also provides further understanding on the effects of a spanwise protrusion on the flow past a circular cylinder.

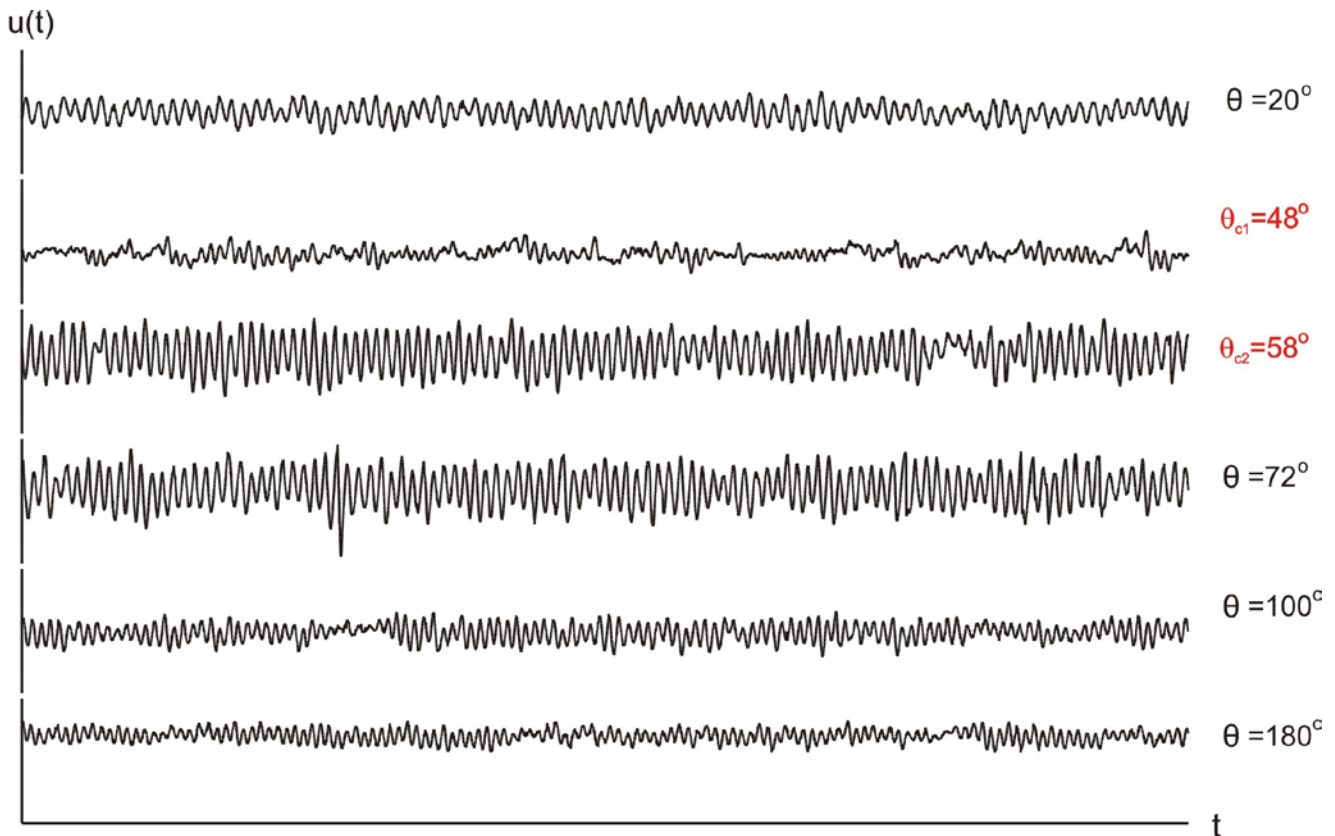


FIGURE 7: TIME TRACES OF STREAMWISE VELOCITY COMPONENT u FOR $d/D = 0.059$ AT $Re_D = 10,000$. HOT-FILM PROBE IS LOCATED $3D$ DOWNSTREAM AND $2.5D$ LATERAL FROM THE CYLINDER CENTER.

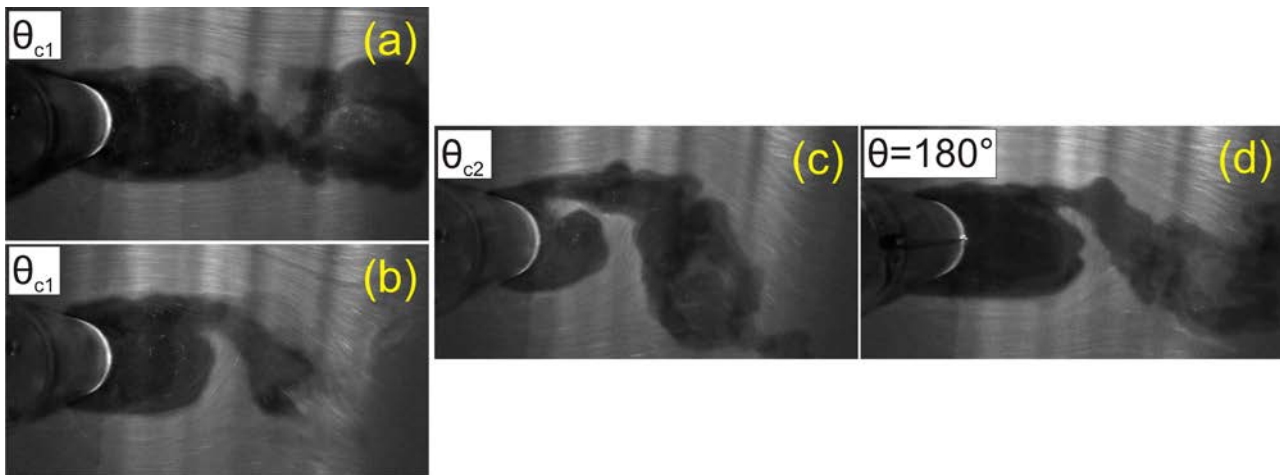


FIGURE 8: HYDROGEN BUBBLE VISUALIZATION OF THE NEAR WAKE FOR $d/D = 0.059$ AT $Re_D = 10,000$. (a) AT THE FIRST CRITICAL ANGLE θ_{c1} WHEN THE REGULAR KARMAN VORTEX SHEDDING IS INTERRUPTED, (b) AT THE FIRST CRITICAL ANGLE θ_{c1} WHEN THE KARMAN VORTEX SHEDDING RESUMES, (c) AT THE SECOND CRITICAL ANGLE θ_{c2} , AND (d) WHEN THE WIRE IS AT THE BASE, i.e., AT $\theta = 180^\circ$.

CONCLUDING REMARKS

The scope of the investigation is to evaluate the effects of a single spanwise protrusion on the flow past a circular cylinder. Consideration is given to protrusions (wires) having larger scales than the thickness of the unperturbed boundary layer forming around a smooth cylinder. The study involved varying the value of the Reynolds number over the subcritical range from $Re_D = 5,000$ to $15,000$ and evaluating if critical states exist.

Hot-film velocimetry provided means to determine the critical angular locations of the wire. It has been found that over the range of Reynolds numbers, for the application of the wire, two critical angular locations exist on the cylinder surface for each Re_D . The first critical angle θ_{c1} results in significant attenuation of the spectral amplitudes of velocity fluctuations; whereas, the second critical angle θ_{c2} leads to an amplification. Time traces of velocity fluctuations also confirm large amount of irregularities at θ_{c1} .

Long-time records of hydrogen-bubble-visualization images show at the first critical angle θ_{c1} repeated appearance of periods with no detectable order in Karman vortex shedding and periods with regular formation of Karman shedding. At times when the coherent formation of Karman vortex shedding is disrupted at θ_{c1} , a significant amount of extension in the streamwise length of the near-wake bubble arises. This results in a significant amount of extension in the time-averaged near-wake bubble, which was reported previously in [6-8]. When the wire is at the second critical angle, a contraction in the streamwise length of the near-wake bubble is apparent from the streakline patterns of hydrogen bubble visualization.

ACKNOWLEDGMENTS

The authors are pleased to acknowledge the support of NSERC, Canada Foundation for Innovation (CFI) and the Ministry of Research and Innovation (MRI).

REFERENCES

- [1] Naudascher, E. and Rockwell, D., 2005. *Flow-Induced Vibrations: An Engineering Guide*, Dover Publications, Inc., Mineola, New York.
- [2] Zdravkovich, M. M., 1981. Review and Classification of Various Aerodynamic and Hydrodynamic Means for Suppressing Vortex Shedding, *Journal of Wind Engineering and Industrial Aerodynamics*, Vol. 7, pp. 145-189.
- [3] Fage, A. and Warsap, J., 1929. The Effects of Turbulence and Surface Roughness on the Drag of a Circular Cylinder, *British Aero. Res. Comm. R. & M.*, No. 1283.
- [4] James, D. F. and Truong, Q. S., 1972. Wind Load on Cylinder with Spanwise Protrusion, *Journal of the Engineering Mechanics Division*, Proceedings of ASCE, Vol. 98, pp. 1573-1589.
- [5] Nebres, J. and Batill, S., 1993. Flow about a Circular Cylinder with a Single Large-Scale Surface Perturbation, *Experiments in Fluids*, Vol. 15, pp. 369-379.
- [6] Ekmekci, A., 2006. "Control of the Near Wake of a Circular Cylinder: Effects of Surface Disturbances". PhD Dissertation, Lehigh University, PA, USA.
- [7] Ekmekci, A. and Rockwell, D., 2010. Effects of a Geometrical Surface Disturbance on Flow past a Circular Cylinder: A Large Scale Spanwise Wire, *Journal of Fluid Mechanics*, Vol. 665, pp. 369-379.
- [8] Ekmekci, A. and Rockwell, D., 2011. Control of Flow past a Circular Cylinder via a Spanwise Surface Wire: Effect of the Wire Scale, *Experiments in Fluids*, Vol. 51, Number:3, pp. 753-769.
- [9] Schlichting, H., 1968. *Boundary-Layer Theory*, 6th edition, McGraw-Hill, New York.

OPTIMAL ENERGY HARVESTING BY VORTEX-INDUCED VIBRATIONS IN CABLES

Clément Grouthier*

Sébastien Michelin

Emmanuel de Langre

LadHyX

Department of Mechanics

Ecole Polytechnique

91128 Palaiseau, France

Email: clement.grouthier@ladhyx.polytechnique.fr

ABSTRACT

The issue of global climate change and the growing energy demand induce a need for innovative energy harvesting devices. The possibility to harvest energy using VIV of a long tensioned cable or of an elastically-mounted rigid cylinder is investigated throughout this paper. A simple wake-oscillator model is used to represent the major characteristics of the complex dynamics of such structures. The optimal efficiency of the two devices are similar and are reached when the solid and its fluctuating wake are in lock-in condition. The sensitivity of the optima of such energy harvesters with flow velocity is also discussed.

INTRODUCTION

Geophysical flows represent a widely available source of clean energy, useful to tackle the global energy demand using for example wind turbines, marine turbines or wave energy converters.

An original way to extract energy from these flows is to take advantage of flow-induced vibrations, reviewed for example in Ref. [1]. For instance, several devices based on fluid-elastic instabilities like transverse galloping or flutter have already been introduced in Refs. [2–5]. Another kind of flow-induced oscillations that can be useful to harvest energy from a flow is the vortex-induced vibrations (VIV) of a bluff body [6]. The strong coupling between a solid and its fluctuating wake may lead to a lock-in phenomenon between the solid dynamics and the vortex shedding, resulting in high amplitude oscillations,

that can be used for energy harvesting [7, 8].

Yet, the energy density in geophysical flows is small, and large systems are required in order to harvest significant amount of energy. Besides, VIV of long cables like oil rigs anchors or risers have been extensively investigated since they are of capital importance for offshore industry [9]. The possibility to harvest energy from a flow using VIV of long tensioned cables is consequently studied in this paper [10].

Extensive experimental and numerical analysis have shown that the dynamics of slender structures in VIV are very rich and complex [11–13]. The most important features of these dynamics (frequencies, wavenumbers) are however well predicted by a simple wake oscillator approach [14–16]. This approach is used in the present paper to investigate the energy harvesting using VIV of long tensioned cables.

In a first section, the model is presented and the generic case of energy extraction using VIV of an elastically-mounted short rigid cylinder is analyzed. Energy harvesting using VIV of an infinite tensioned cable is investigated in a second section.

THE ELASTICALLY-MOUNTED RIGID CYLINDER

The energy harvesting from an elastically-mounted rigid cylinder VIV is first investigated, see Fig. 1. The fluid density and velocity are respectively noted ρ and U , while D and m_s stand for the rigid cylinder diameter and mass per unit length. Let also r and h be the damping and stiffness coefficients of the elastic support.

*Address all correspondence to this author.

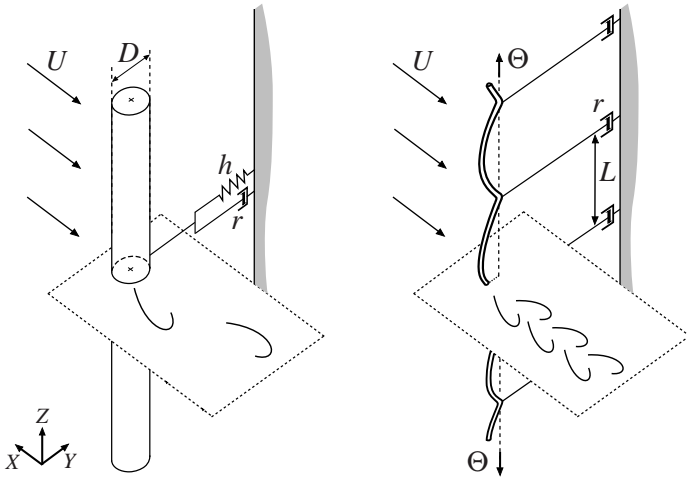


FIGURE 1. ENERGY HARVESTING FROM VIV OF (LEFT) AN ELASTICALLY-MOUNTED RIGID CYLINDER AND (RIGHT) AN INFINITE TENSIONED CABLE.

The fluid-solid model for energy harvesting

The cross-flow displacement Y of the cylinder is described by

$$m_t \frac{\partial^2 Y}{\partial T^2} + (r + r_a) \frac{\partial Y}{\partial T} + hY = F_{wake}, \quad (1)$$

where $m_t = m_s + m_a$, $m_a = \pi \rho D^2 C_{M0} / 4$ being the added mass per unit length and C_{M0} the added mass coefficient. The fluid added damping is defined by $r_a = \rho D U C_D / 2$, where C_D is the cylinder drag coefficient and F_{wake} denotes the wake forcing on the body [14]. Two frequencies appear : (i) the natural frequency of the solid in still fluid $\omega_s = \sqrt{h/m_t}$ and (ii) the vortex shedding frequency behind a fixed cylinder, $\omega_f = 2\pi St U / D$, St being the Strouhal number [1]. Using $y = Y/D$ and $t = \omega_f T$, the dimensionless equation for the solid motion reads

$$\ddot{y} + \left(\xi + \frac{\gamma}{\mu} \right) \dot{y} + \delta^2 y = f_{wake}, \quad (2)$$

where $\delta = \omega_s / \omega_f$ is the frequency ratio and $\xi = r / m_t \omega_f$ the damping coefficient. The dimensionless fluid added damping coefficient γ / μ is defined by the stall parameter $\gamma = C_D / 4\pi St$ [17] and the mass ratio $\mu = m_t / \rho D^2$ [14]. As far as the cylinder is concerned, harvesting energy from its motion comes to a loss of energy, which is modelled by the damping term $r \partial Y / \partial T$, or $\xi \dot{y}$ in dimensionless form. The efficiency of such an harvesting device is

defined as the ratio between the time-averaged extracted power and the energy flux through the section of the cylinder $\rho D U^3 / 2$ [3, 8, 10, 18]. In dimensionless form, it reduces to

$$\eta = 16\mu\pi^3 St^3 \langle \xi \dot{y}^2 \rangle. \quad (3)$$

Following [14], a wake-oscillator approach is used to model f_{wake} . The fluctuating load due to the wake is assumed to be proportional to a fluctuating lift coefficient $q = 2C_L / C_{L0}$, which satisfies a Van der Pol oscillator equation, C_{L0} being a fluctuating lift coefficient. This second equation is then coupled with Eqn. (2) by an inertial forcing to define the fluid-solid model

$$\ddot{y} + \left(\xi + \frac{\gamma}{\mu} \right) \dot{y} + \delta^2 y = Mq, \quad (4a)$$

$$\ddot{q} + \varepsilon (q^2 - 1) \dot{q} + q = A\dot{y}, \quad (4b)$$

where $(\dot{})$ denotes derivation with respect to dimensionless time t , coefficient M being defined as $M = C_{L0} / 16\mu\pi^2 St^2$ and A and ε are parameters based on experiments. In all the paper, the values $A = 12$, $\varepsilon = 0.3$, $C_D = 2$, $C_{L0} = 0.8$, $St = 0.17$, $\mu = 2.79$ and $C_{M0} = 1$ are fixed as in [10, 16], so that $M = 0.06$ and $\gamma / \mu = 0.34$. Equations (4) are integrated using finite differences and the limit cycle is analyzed in terms of efficiency.

Optimal energy harvesting and lock-in

The map of the efficiency as a function of the frequency ratio δ and the damping coefficient ξ is displayed on Fig. 2.

There is an optimal harvesting configuration leading to maximum efficiency, corresponding to a frequency ratio of $\delta = 0.89$ and a damping coefficient of $\xi = 0.20$. The corresponding optimal efficiency $\eta_{2D}^{opt} = 0.23$ is close to the value found in [7] for a similar system.

The efficiency vanishes for both small and large damping, as expected. For small damping, the amplitude saturates according to the Skop-Griffin diagram [6] and η thus varies linearly with ξ . On the other hand, large damping inhibits the solid motion leading to an amplitude varying as $1/\xi$: the efficiency $\eta \propto \xi \dot{y}^2$ consequently also vanishes as $1/\xi$ for large values of ξ .

The optimal frequency ratio $\delta = \omega_s / \omega_f = 0.89$ is close to 1, which corresponds to the synchronization of the wake and solid natural frequencies or lock-in [6],

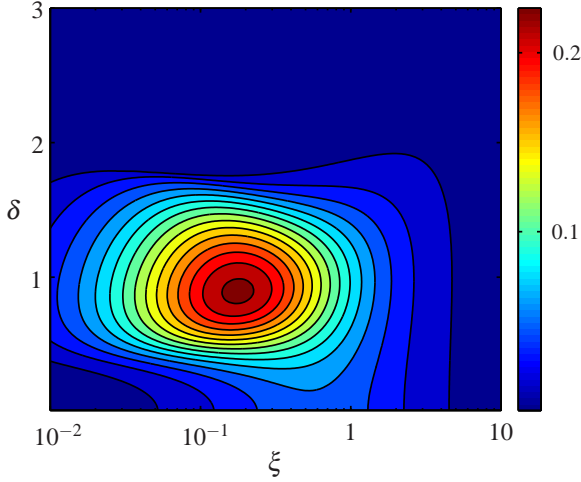


FIGURE 2. (a) HARVESTING EFFICIENCY AS A FUNCTION OF THE TWO HARVESTING PARAMETERS δ AND ξ (LEVEL STEP : 0.015).

known to lead to high amplitude oscillations. The optimal configuration for energy harvesting from VIV of an elastically-mounted short rigid cylinder corresponds to a lock-in condition for the frequency ratio δ and a well-balanced value of the damping coefficient, or harvesting intensity, ξ .

THE INFINITE TENSIONED CABLE

The possibility to harvest energy from a flow using VIV of an infinite tensioned cable is now investigated [10]. The same approach as in the previous section is followed, the vortex-induced vibrations of the structure are modelled by a wake-oscillator. This model is identical to the one used for the rigid cylinder case, except that the stiffness force hY is now replaced by the stiffness induced by the uniform tension Θ of the cable : $-\Theta \partial^2 Y / \partial Z^2$. The spanwise coordinate Z is scaled using a characteristic length based on the waves phase velocity $z = Z \omega_f \sqrt{m_t / \Theta}$ and the dimensionless form of the model reads

$$\ddot{y} + \frac{\gamma}{\mu} \dot{y} - y'' = Mq, \quad (5a)$$

$$\ddot{q} + \varepsilon (q^2 - 1) \dot{q} + q = A\ddot{y}, \quad (5b)$$

where $(\cdot)'$ denotes derivation with respect to dimensionless spanwise coordinate z . The extraction of energy from a flow is still modelled by damping. In this configuration, discrete harvesters/dashpots are periodically distributed over the span of the cable, see Fig. 1, with a distance L between two harvesters of damping coefficient R . This

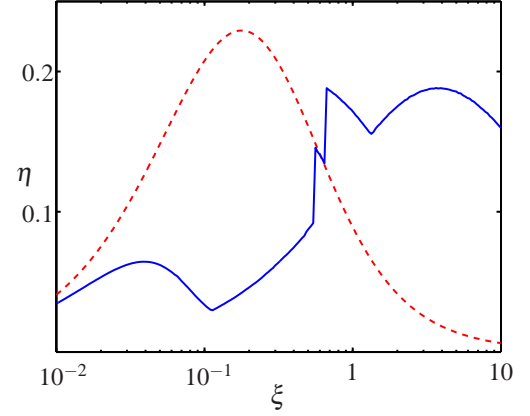


FIGURE 3. COMPARISON OF EFFICIENCIES OF (RED - DASHED) THE ELASTICALLY-MOUNTED RIGID CYLINDER CASE $\eta_{2D}(\xi)$ AND (BLUE - SOLID) THE INFINITE TENSIONED CABLE $\eta_{3D}(\xi)$.

introduces a damping condition at each damper location which reads in dimensionless form

$$y'(0, t) - y'(l, t) = l\xi \dot{y}(l, t), \quad (6)$$

where $\xi = R/Lm_t\omega_f$ is the dimensionless damping per unit length and $l = L\omega_f\sqrt{m_t/\Theta}$ the dimensionless distance between two harvesters.

The efficiency is again defined as the ratio between the time-averaged power extracted by a dashpot and the energy flux through a length L of the cable, which is still written using the dimensionless variables as Eqn. (3). The system of Eqns. (5) and (6) is integrated in space and time using finite differences on a spatially periodic domain, with the cable initially at rest $y = 0$ and a small random perturbation of the fluctuating lift q . The harvesting is studied as a function of the length between two dampers l and the damping per unit length ξ .

Optimal efficiency

In order to compare the energy harvesting using either an elastically-mounted rigid cylinder or an infinite tensioned cable, two optimal efficiency curves are derived, giving the maximum achievable efficiency for any value of the damping density ξ . For the two-dimensional case of the rigid cylinder, $\eta_{2D}(\xi)$ corresponds to the efficiency obtained for an optimal value of the frequency ratio δ at a given damping density ξ , whereas for the infinite tensioned cable case, $\eta_{3D}(\xi)$ is the optimal efficiency given by the choice of an optimal value of l at a given ξ . The two curves are shown on Fig. 3.

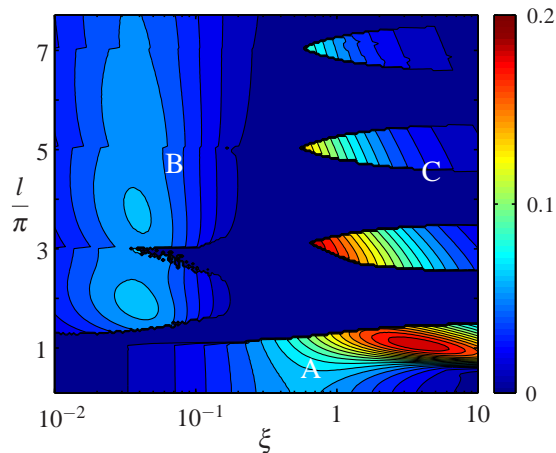


FIGURE 4. HARVESTING EFFICIENCY AS A FUNCTION OF THE LENGTH BETWEEN TWO HARVESTERS l AND THE DAMPING PER UNIT LENGTH ξ (LEVEL STEP : 0.01).

The optimal performances of these two systems are similar, $\eta_{2D}^{opt} = 0.23$ while $\eta_{3D}^{opt} = 0.19$, justifying a deeper investigation of the new concept of energy harvesting using a tensioned cable.

The differences in the shape of the two curves η_{2D} and η_{3D} are yet striking. Contrary to the case of the rigid cylinder, the efficiency of energy harvesting via an infinite tensioned cable in VIV is far from a classical bell-shape curve. The optimal damping per unit length is also very different for the two configurations as, for the elastically-mounted rigid cylinder $\xi_{2D}^{opt} = 0.20$, whereas in the case of an infinite tensioned cable, $\xi_{3D}^{opt} = 3.65$. A deeper analysis of the efficiency dependence of the latter configuration with the two harvesting parameters l and ξ is thus necessary. Figure 4 displays the map of the efficiency as a function of these two parameters.

This map is actually much more complex than that of Fig. 2. Three zones may be defined to explain its structure.

The first one, zone A, corresponds to small distances between two dashpots for any damping. Within this zone, the classical influence of damping on the efficiency is retrieved. Actually, η vanishes for small and large damping, even if the peak is not at the same location for every values of l . Moreover, the overall optimal harvesting configuration lies in this zone : $\xi = 3.65$ and $l = 1.09\pi$ lead to $\eta = 0.19$. As shown on Fig. 5, this zone explains most of the efficiency curve $\eta_{3D}(\xi)$.

The second zone, zone B, corresponds to the left part of the map, typically $\xi < 0.4$, and larger values of l . The efficiency within this zone is rather small, it corresponds to the left low peak of the efficiency curve, Fig. 5. Within

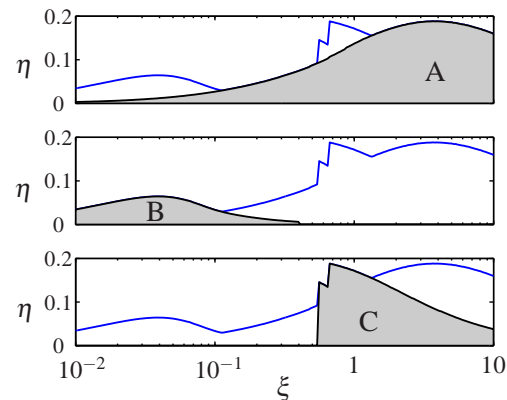


FIGURE 5. CONTRIBUTION OF EACH ZONE TO THE EFFICIENCY CURVE $\eta_{3D}(\xi)$.

this zone, the motion of the cable is close to travelling waves of wavelength $\lambda = 2\pi, 4\pi, 6\pi, \dots$. Yet, the efficiency is low in zone B so it shall not be discussed any further.

Within zone C, the efficiency depends very strongly on the two parameters, especially on l . High efficiency tongues are surrounded with inefficient harvesting configurations, resulting in the discontinuities that can be seen on the efficiency curve, Fig. 5.

Mode shapes and efficiency

To gain some understanding of the efficient part of this complex energy map (zone A and C), the dynamics of the cable in these two zones are compared and shown on Fig. 6. Contrary to zone B, the motion of the cable is close to stationary waves.

The optimal cable displacement for energy harvesting is shown on Fig. 6(a), and the corresponding values of the parameters are reported in Tab. 1. The motion resembles a mode 1 vibration of a tensioned cable, with slight displacement of the dashpots.

If a fixed value of the damping ξ is considered, the cable motion evolves with an increasing length l , but it is always close to one of the classical harmonics of a tensioned cable. The cable dynamics actually jumps from even modes in zones where the harvesting efficiency is very low, Fig. 6(b), to odd modes in the high efficiency regions of zone C, Fig. 6(c).

The motion of the dashpot is forced by the jump in the cable slope between the two sides of the harvester, Eqn. (6). Odd modes are thus more likely than even ones to lead to high jumps in the cable slope, then to high efficiency, Fig. 7.

The mode number is defined as $n = 2l/\lambda$, where λ denotes the wavelength of the cable motion. This mode

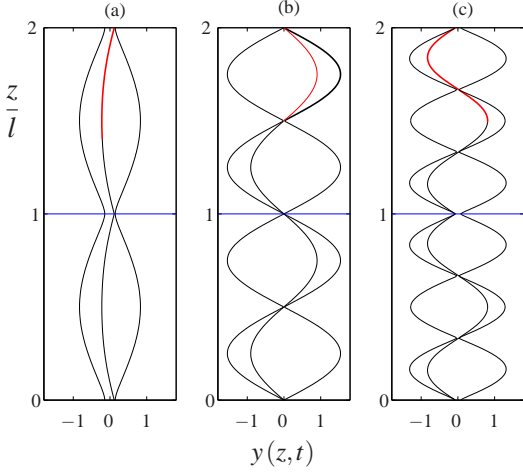


FIGURE 6. DYNAMICS OF THE CABLE IN ZONES A AND C, THE RED LINE STANDS FOR THE INSTANTANEOUS DISPLACEMENT OF THE CABLE, THE BLUE ONE FOR THE POSITION OF ONE OF THE DASHPOTS AND THE BLACK LINE REPRESENTS THE ENVELOPE OF THE CABLE MOTION : (a) $l = 3.43$, $\xi = 3.65$, $\eta = 0.19$, ZONE A (OPTIMAL CASE), (b) $l = 6.80$, $\xi = 3.65$, $\eta = 9.10^{-7}$, ZONE C, (c) $l = 9.56$, $\xi = 3.65$, $\eta = 0.07$, ZONE C.

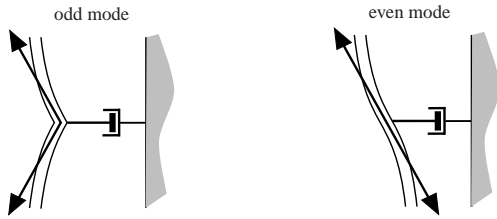


FIGURE 7. LOCAL MECHANISM OF FORCING OF AN HARVESTER BY STATIONARY MODES. LEFT : ODD MODES, HIGH EFFICIENCY, RIGHT : EVEN MODES, LOW EFFICIENCY.

number may not be an integer, in that case, the closest integer is used. Following Ref. [16], the linearized version of the model is used to derive the characteristics of the most unstable linear mode which will dominate the non-linear response of the model. The linearized version of the model reads

$$\ddot{y} + \frac{\gamma}{\mu}\dot{y} - y'' = Mq, \quad (7a)$$

$$\ddot{q} - \varepsilon\dot{q} + q = A\dot{y}. \quad (7b)$$

The dominance zones of every mode number n are reported on the efficiency map of the infinite tensioned ca-

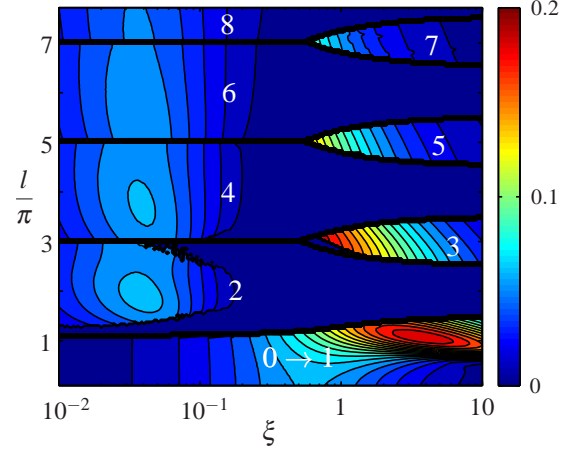


FIGURE 8. MODE NUMBERS ZONES REPORTED ON THE EFFICIENCY MAP (LEVEL STEP : 0.01).

ble, see Fig. 8. There is a very good agreement between the discontinuities of the efficiency map and the frontiers between the dominance zones of two different mode numbers. In particular, the high efficiency tongues indeed correspond with regions where the dominant mode number is odd. In zone B, only even modes exist, which are expected to be less efficient.

Finally, the damping coefficient plays a double role in energy harvesting from VIV of an infinite tensioned cable as it controls both the local dynamics of the harvesters and the global mode shape of the solid displacement.

DISCUSSION

Energy harvesting using VIV of (i) an elastically-mounted rigid cylinder and (ii) an infinite tensioned cable was investigated in this paper and exhibit similar optimal efficiencies, of the order of 0.2.

Optimal harvesting and lock-in

For the two devices, the optimal harvesting configuration corresponds to a lock-in condition. For an elastically-mounted rigid cylinder, this lock-in condition takes the classical form of synchronization between the vortex shedding frequency and the solid natural frequency, $\delta = \omega_s/\omega_f = 1$.

In the case of an infinite tensioned cable, Refs. [15, 16] showed that lock-in corresponds to the highest growth rates of the fluid/solid coupled mode instability. The modes dominance zones shown on Fig. 8 can then also be regarded as the lock-in regions of each mode. The dispersion relation between frequency ω and wavenumber k derived from Eqn. 7 consequently results in a lock-in condition for an infinite cable, $k = 1$. This condi-

tion is yet modulated by the periodic boundary condition, Eqn. (6), leading to a lock-in condition for each mode. The solid adapts its own dynamics via its wavenumber in order to be always at lock-in, under the restrictions of the periodic harvesting boundary conditions. Considering an ideal lock-in condition $k = 1$ and the definition of the wavenumber, one may nevertheless derive optimal lengths corresponding with the lock-in condition for every mode. For the odd modes, which were shown to be the efficient ones, this results in the lock-in conditions $l = (2n + 1)\pi$, which agree well on the location of the several peaks on Fig.5. For each mode number $2n + 1$, it also defines a frequency ratio $\delta_{2n+1} = (2n + 1)\pi/l$, playing a similar role as the frequency ratio $\delta = \omega_s/\omega_f$ of the rigid cylinder case. Reminding that the exact optimal configurations differ slightly from the exact lock-in conditions, see Tab. 1, the optimal frequency ratio indeed reads for the elastically-mounted rigid cylinder

$$\delta = \left(\frac{D}{2\pi S_t U} \right) \omega_s = 0.89, \quad (8)$$

and for the infinite tensioned cable

$$\delta_1 = \frac{\pi}{l} = \left(\frac{D}{2\pi S_t U} \right) \frac{\pi}{L} \sqrt{\frac{\Theta}{m_t}} = 0.92. \quad (9)$$

These two conditions are of the same form and actually correspond to lock-in between the vortex shedding frequency and the natural frequency of the solid motion, the natural frequency of the rigid cylinder ω_s being replaced by the natural frequency of the cable vibrations

$$\omega_c = \frac{\pi}{L} \sqrt{\frac{\Theta}{m_t}}. \quad (10)$$

The major difference between the two optimal configurations lies in the values of the optimal damping intensity ξ , which differ by more than an order of magnitude between the two analyzed devices. This is due to the fact that for the tensioned cable with periodically distributed harvesting devices, ξ does not only drive the local dynamics of the dashpots, as it is the case for the short rigid cylinder, but it also controls the choice of the overall dynamics of the cable. This double role of the harvesters is of capital importance since the harvesting efficiency depends a lot on the cable overall motion, especially on the selected mode number.

TABLE 1. OPTIMAL CONFIGURATIONS FOR THE TWO CONSIDERED ENERGY HARVESTING DEVICES USING VIV.

	Rigid cylinder	Tensioned cable
η	0.23	0.19
ξ	0.20	3.65
δ	0.89	0.92

Optimal design of a real energy harvester

The present study may then be used to design an energy harvester based on VIV, using Tab. 1. The definition of the efficiency η provides an estimation of the maximum power extracted by a cable of length $L_{tot} = 100$ m and diameter $D = 4$ cm in a flow of mean velocity $\bar{U} = 1.5$ m.s⁻¹, namely $P = 1282.5$ W. It is interesting to note that this is far from being negligible and that it can be achieved for many different triplets (Θ, L, R) .

For an elastically-mounted rigid cylinder of diameter $D = 4$ cm and mass ratio $\mu = 2.79$ placed in a flow of mean velocity $\bar{U} = 1.5$ m.s⁻¹, the dimensional optimal damping and stiffness are $r = 35.8$ kg.s⁻¹.m⁻¹ and $h = 5673.2$ kg.s⁻².m⁻¹. For the tensioned cable mentioned above ($L_{tot} = 100$ m), under a tension $\Theta = 10$ kN, the damping coefficient of each dashpot is $R = 2645$ kg.s⁻¹ and they are separated by a distance $L = 4.05$ m.

Influence of the velocity variations on the efficiency in real operating conditions

The dimensional parameters are fixed once and for all, but the operating conditions may drift from the optimal ones because of a varying flow velocity U . The influence of a varying flow speed on the performances of a harvesting device is now discussed. Three cases are considered : (i) an elastically-mounted rigid cylinder, (ii) an infinite cable with constant tension and (iii) an infinite cable with drag-induced tension. The values of the harvesting parameters are derived so that the optimal is reached for the mean flow speed \bar{U} . The evolution of the efficiency with the flow speed for each case is then plotted on Fig.9. In order to quantify the influence of flow speed fluctuations on the actual efficiency, the peak width w is defined as the ratio between the length of the velocity interval for which the efficiency is above 75% of the peak efficiency ΔU and the mean velocity \bar{U} , see Tab. 2.

For the rigid cylinder, it comes from the dimensionless parameters definitions that $\delta \propto 1/U$ and $\xi \propto 1/U$.

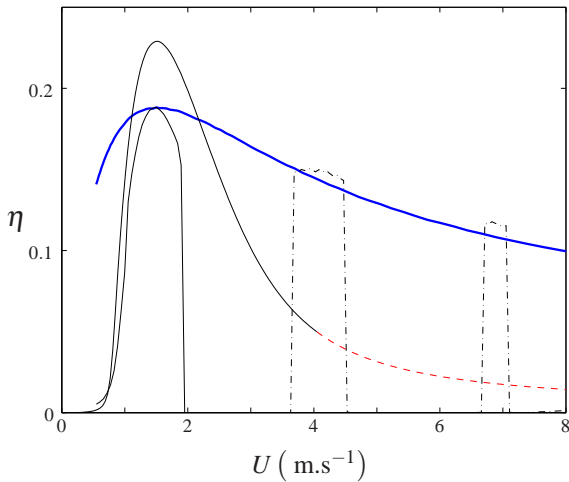


FIGURE 9. EVOLUTION OF THE EFFICIENCY WITH FLOW VELOCITY. (RED - DASHED) RIGID CYLINDER, (BLUE - SOLID) CABLE WITH DRAG-INDUCED TENSION AND (BLACK - DASH-DOT) CABLE WITH FIXED TENSION.

The curve of the evolution of η with U hence corresponds to the values of η along a curve $\delta \propto \xi$ passing through the optimal configuration. Even if the best efficiency is achieved as expected by this configuration, the width of the peak is small, see Tab. 2. The efficiency dramatically drops down as the current speed drifts away from its mean value.

For the long tensioned cable, if the tension is constant (induced for instance by a buoy on top of a cable anchored at its bottom), $\xi \propto 1/U$ and l varies linearly with U . The efficiency depends a lot on the flow speed, Fig.9. The peak width is even smaller than for the rigid cylinder, $w = 0.54$, and η even falls down to zero for some velocities. This solution should be avoided because of this high sensitivity to current velocity.

In the last case considered, the tension is due to a drag force acting on a well-chosen area A , which may differ from the cable area DL_{tot} . The area A has here been chosen so that the optimal harvesting parameters are identical to the constant tension case in order to compare this configuration with previous ones ($\Theta = 10$ kN for $U = \bar{U}$). In that case, $\Theta \propto U^2$, $\xi \propto 1/U$ and l is constant ($l = 3.43$), which sounds a valuable option as the efficiency depends a lot more on l than on ξ , Fig. 4. It actually appears as the best solution since the efficiency stays high for a wide range of velocity, Fig. 9. The peak value is lower than for the rigid cylinder, but the peak width is much larger, $w = 2.47$, see Tab. 2. The efficiency decrease as U deviates from \bar{U} is slow, it even overtakes the rigid cylinder efficiency for $U \leq 1.1$ m.s⁻¹ and $U \geq 2.2$ m.s⁻¹.

TABLE 2. WIDTH OF THE PEAK AROUND THE OPTIMAL FLOW VELOCITY $w = \Delta U / \bar{U}$.

Configuration	Peak width w
Rigid cylinder	0.73
Cable - constant tension	0.54
Cable - drag-induced tension	2.47

As a conclusion, the analysis performed throughout this paper has shown that energy harvesting using vortex-induced vibrations of a long tensioned cable seems, at least, as promising as using those of an elastically-mounted short rigid cylinder as in [7] or [8]. This new configuration may even have some advantages like the possibility to imagine very long cables able to harvest large amounts of energy, and to adapt their dynamics so that they are always near lock-in conditions, if their tension is induced by drag.

ACKNOWLEDGMENT

S. Michelin would like to acknowledge the support of a Marie Curie International Reintegration Grant within the 7th European Community Framework Program. Clement Grouthier is also supported by a Gaspard Monge scholarship of the Ecole Polytechnique.

REFERENCES

- [1] Blevins, R., 1990. *Flow-induced vibration - Second edition*. Van Nostrand Reinhold, New York.
- [2] Tang, L., Padoussis, M. P., and Jiang, J., 2009. "Cantilevered flexible plates in axial flow : Energy transfer and the concept of flutter mill". *Journal of Sound and Vibration*, **326**, pp. 263–276.
- [3] Barrero-Gil, A., Alonso, G., and Sanz-Andres, A., 2010. "Energy harvesting from transverse galloping". *Journal of Sound and Vibration*, **329**, pp. 2873–2883.
- [4] Doaré, O., and Michelin, S., 2011. "Piezoelectric coupling in energy-harvesting fluttering flexible plates : linear stability analysis and conversion efficiency". *Journal of Fluids and Structures*, **27**, pp. 1357–1375.
- [5] Singh, K., Michelin, S., and de Langre, E., 2012. "Energy harvesting from axial fluid-elastic instabilities of a cylinder". *Journal of Fluids and Structures*, **30**, pp. 159–172.

- [6] Williamson, C., and Govardhan, R., 2004. “Vortex-induced vibrations”. *Annual review of fluid mechanics*, **36**, pp. 413–455.
- [7] Bernitsas, M. M., Raghavan, K., Ben-Simon, Y., and Garcia, E. M. H., 2008. “Vivace (vortex-induced vibration aquatic clean energy) : A new concept in generation of clean and renewable energy from fluid flow”. *Journal of Offshore Mechanics and Arctic Engineering*, **130**(041101), pp. 1–15.
- [8] Barrero-Gil, A., Pindado, S., and Avila, S., 2011. “Extracting energy from vortex-induced vibrations : a parametric study”. *Applied mathematical modelling*, p. *In press*.
- [9] Baarholm, G., Larsen, C., and Lie, H., 2006. “On fatigue damage accumulation from in-line and cross-flow vortex-induced vibrations on risers”. *Journal of Fluids and Structures*, **22**, pp. 109–127.
- [10] Grouthier, C., Michelin, S., and de Langre, E., 2012. “Energy harvesting using vortex-induced vibrations of tensioned cables”. *Under review*, p. <http://arxiv.org/abs/1203.0236>.
- [11] Newman, D. J., and Karniadakis, G. E., 1997. “A direct numerical simulation study of flow past a freely vibrating cable”. *Journal of Fluid Mechanics*, **344**, pp. 95–136.
- [12] Bourguet, R., Karniadakis, G. E., and Triantafyllou, M. S., 2011. “Vortex-induced vibrations of a long flexible cylinder in shear flow”. *Journal of fluid mechanics*, **677**, pp. 342–382.
- [13] Modarres-Sadeghi, Y., Chasparis, F., Triantafyllou, M., Tognarelli, M., and Beynet, P., 2011. “Chaotic response is a generic feature of vortex-induced vibrations of flexible risers”. *Journal of Sound and Vibration*, **330**, pp. 2565–2579.
- [14] Facchinetti, M. L., de Langre, E., and Biolley, F., 2004. “Coupling of structure and wake oscillators in vortex-induced vibrations”. *Journal of Fluids and Structures*, **19**, pp. 123–140.
- [15] de Langre, E., 2006. “Frequency lock-in is caused by coupled-mode flutter”. *Journal of Fluids and Structures*, **22**, pp. 783–791.
- [16] Violette, R., de Langre, E., and Szydlowski, J., 2010. “A linear stability approach to vortex-induced vibrations and waves”. *Journal of Fluids and Structures*, **26**(3), pp. 442–466.
- [17] Skop, R., and Balasubramanian, S., 1997. “A new twist on an old model for vortex-excited vibrations”. *Journal of Fluids and Structures*, **11**, pp. 395–412.
- [18] Zhu, Q., Haase, M., and h. Wu, C., 2009. “Modeling the capacity of a novel flow-energy harvester”. *Applied Mathematical Modelling*, **33**, pp. 2207–2217.

OPTIMAL CONTROL CYLINDER DESIGN FOR VORTEX SUPPRESSION BEHIND A CIRCULAR CYLINDER

M Subhash Reddy

Fluid Mechanics Laboratory
Department of Applied Mechanics
Indian Institute of Technology, Madras
Chennai, India
Email: subhash27july@gmail.com

B S V Patnaik*

Fluid Mechanics Laboratory
Department of Applied Mechanics
Indian Institute of Technology, Madras
Chennai, India
Email: bsvp@iitm.ac.in

ABSTRACT

We propose to control flow induced oscillations of a circular cylinder by suppression of vortex shedding past it. This was achieved by placing two small rotating control cylinders in the proximity of the main cylinder which inject momentum into the boundary layer. Identification of the position and circulation strengths of the control cylinders are the important aspects of our study. Solving the complete Navier-Stokes (NS) equations would lead to a large number of cases for the simulation. To avoid such expensive computations, a reduced order model (ROM) has been used instead of solving the complete NS model. Reduced order models are approximations to the full NS equations and can be effective under appropriate conditions. In the present study, we try to achieve potential flow like behavior through optimum positioning of the control cylinders and hence potential flow analysis is carried out with different analytical methods like Föppl vortex model and conformal mapping techniques. For these optimum values, the analytical solution obtained is compared against the numerical viscous flow simulations.

INTRODUCTION

The control of vortex shedding behind a circular cylinder is of practical interest in a wide range of technological applications. Flow past chimneys, cooling towers, marine risers, spar type platforms etc will be benefited by such developments. Both active and passive flow control strategies have been developed in the literature [1]. There have been a number of efforts to understand wake vortices analytically. Tang and Aubry [2] have shown that vortex shedding can be suppressed by introducing two small point vortices in the far wake of the cylinder. Gal-

vao et al [3] have shown that vortices can be suppressed by placing hydrofoils around the cylinder by achieving potential flow like behaviour. In the present study, we make an attempt to suppress vortex shedding by placing two small counter rotating cylinders very close to the main cylinder as shown in Fig. 1. These control cylinders prevent or delay flow separation to produce streamlines that resemble potential flow like patterns. To this end, finding the optimum position of the control cylinders around the main cylinder is important. Positioning them too far upstream will not delay flow separation by much and positioning them too far downstream will not be able to energize the boundary layer to delay flow separation. Also the optimum rotation rate (circulation strength) of the control cylinders need to be investigated as a lower value will not affect flow separation and a very high value may not be beneficial, as it consumes power.

Solving the complete Navier-Stokes equations can be time consuming while performing parametric investigation of the position and circulation strength of the control cylinders. Instead, reduced order models (ROM) can be employed. Reduced order modeling includes many of the techniques for modeling and simplification commonly used in fluid dynamics analysis such as potential flow analysis, vortex methods etc. Each of these are approximations to the full Navier-Stokes equations and each can serve as an effective ROM under appropriate conditions.

In the present investigation, we focus on the point vortex model known as the Föppl vortex model to obtain the optimum position of control cylinders. The optimum circulation strength of the control cylinders is obtained by using conformal mapping techniques proposed by Crowdy [4]. For these optimum values, a comparison of the analytical solution against numerical viscous flow

*Address all correspondence to this author.

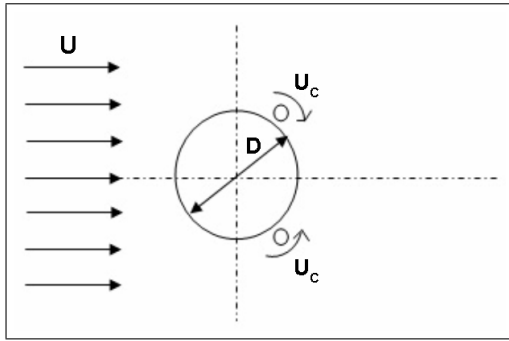


FIGURE 1: SCHEMATIC OF THE MAIN CYLINDER WITH TWO SMALL COUNTER ROTATING CONTROL CYLINDERS. THE RATIO OF THE MAIN CYLINDER, CONTROL CYLINDER AND GAP BETWEEN THEM ARE FIXED AS $D : 0.1D : 0.01D$ RESPECTIVELY, WHERE D IS THE DIAMETER OF THE MAIN CYLINDER.

simulation is presented.

THE FÖPPL VORTEX MODEL

In unsteady viscous flows, a pair of vortices are formed underneath an envelope encompassing the top and bottom separation points of the main cylinder. They extend downstream and then roll up tightly into two counter rotating vortices behind the body. These vortices are fed by circulation from the upstream shear layers. Since these tightly rolled vortices have much higher circulation strength than the distributed vortex sheets, influence of the latter can be neglected. Although the fundamental mechanism for the generation of such vortices is of viscous origin, the basic flow features can be represented by an inviscid model with concentrated point vortices, when the wake vortices are established. The concentrated vortices behind the circular cylinder or a similar bluff body establishes the recirculatory flow behind the body and co-exists with the two separation points. In this section we study the various positions of control cylinders in influencing flow separation.

Basic Föppl model

In the Föppl model [5], two point vortices are symmetrically positioned behind the circular cylinder with positions (x_1, y_1) and (x_2, y_2) , such that $x_1 = x_2 = x$ and $y_1 = -y_2 = y$ (see Fig. 2). The upper vortex is imparted with a clockwise circulation strength $-\Gamma$, while the lower vortex with a counterclockwise circulation strength $+\Gamma$. The circular boundary is centered at the origin and has a unit radius. The free stream velocity (U) encountered

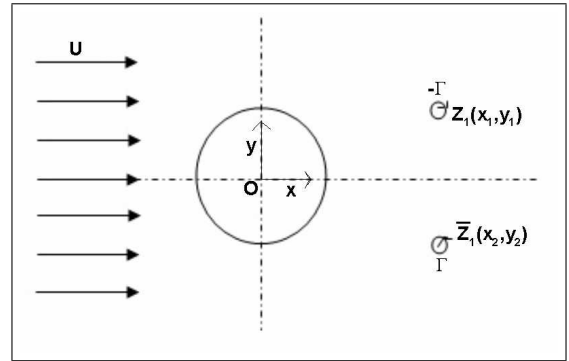


FIGURE 2: SCHEMATIC OF THE FÖPPL VORTEX MODEL. z_1 AND z_2 (OR \bar{z}_1) ARE THE LOCATIONS OF THE POINT VORTICES OF STRENGTH $-\Gamma$ AND $+\Gamma$ RESPECTIVELY.

by the main cylinder is known. The boundary conditions are enforced by making use of the circle theorem [6], in which the velocity field due to each single-point vortex includes the influence of an image vortex located inside the boundary which ensures that the circular boundary remains a streamline.

The complex potential of the Föppl model at any point $z = x + iy$ in the domain is given by

$$W(z) = U \left(z + \frac{1}{z} \right) + \frac{\Gamma}{2\pi i} \left[\ln \left(z - \frac{1}{\bar{z}_1} \right) - \ln \left(z - \frac{1}{\bar{z}_2} \right) \right] + \frac{\Gamma}{2\pi i} [-\ln(z - z_1) + \ln(z - z_2)] \quad (1)$$

where $z_1 = x_1 + iy_1$ and $z_2 = x_2 + iy_2$ are the complex positions for the upper and lower vortices respectively. The stream function is then given by

$$\Psi = \text{imag}(W(z)) \quad (2)$$

from which the streamlines can be plotted.

Without loss of generality free stream velocity (U) can be assumed as unity. The velocities at $z = z_1$ and $z = z_2$ are given by

$$\frac{d\bar{z}_1}{dt} = \frac{dW(z)}{dz} \Big|_{z=z_1} = 1 - \frac{1}{z_1^2} + \frac{\Gamma}{2\pi i} \left(\frac{1}{z_1 - 1/\bar{z}_1} - \frac{1}{z_1 - 1/\bar{z}_2} \right) + \frac{\Gamma}{2\pi i} \frac{1}{z_1 - z_2} \quad (3)$$

$$\frac{d\bar{z}_2}{dt} = \frac{dW(z)}{dz} \Big|_{z=z_2} = 1 - \frac{1}{z_2^2} + \frac{\Gamma}{2\pi i} \left(\frac{1}{z_2 - 1/\bar{z}_1} - \frac{1}{z_2 - 1/\bar{z}_2} \right) - \frac{\Gamma}{2\pi i} \frac{1}{z_1 - z_2} \quad (4)$$

To solve for the Föppl equilibria, Eqn. (3) and (4) are set to zero. From these conditions, we get

$$y = (r^2 - 1)/2r \quad (5)$$

$$\Gamma = 2\pi(r^2 - 1)^2(r^2 + 1)/r^5 \quad (6)$$

where $r = r_1 = r_2 = \sqrt{x^2 + y^2}$

The family of Föppl equilibria can be parameterized by x , y and Γ and specification of one of these values fixes the other two. Thus for a given strength of circulation for the Föppl pair, velocity at any point in the domain at z_0 can be calculated as,

$$\frac{d\bar{z}_0}{dt} = \frac{dW(z)}{dz} \Big|_{z=z_0} = 1 - \frac{1}{z_0^2} + \frac{\Gamma}{2\pi i} \left(\frac{1}{z_0 - 1/\bar{z}_1} - \frac{1}{z_0 - 1/\bar{z}_2} \right) + \frac{\Gamma}{2\pi i} \left(-\frac{1}{z_0 - z_1} + \frac{1}{z_0 - z_2} \right) \quad (7)$$

$$u = \text{real} \left(\frac{d\bar{z}_0}{dt} \right) \quad (8)$$

$$v = -\text{imag} \left(\frac{d\bar{z}_0}{dt} \right) \quad (9)$$

Using the above equations, both streamwise and cross-stream components of velocity (u , v) on the cylinder surface can be calculated and the separation point can be obtained. The condition for flow separation on the body used here is that, the velocity at the separation point vanishes and the velocities on both sides of the separation point are towards the point (i.e. velocity sign changes on either side of the separation point) (see Cai et al [7]). Let the flow velocity be zero at a separation point $z_0 = e^{i\theta_0}$ on

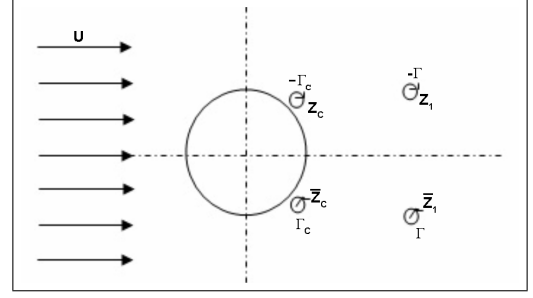


FIGURE 3: SCHEMATIC OF THE FÖPPL VORTEX MODEL ALONG WITH TWO VORTEX PERTURBATIONS OF STRENGTHS $-\Gamma_c$ AND Γ_c LOCATED AT z_c AND \bar{z}_c RESPECTIVELY.

the cylinder surface. The angle θ_0 can be obtained from Eqn. (7). Each circulation value of the Föppl vortex pair corresponds to a different separation point on the surface of the cylinder. The results obtained from this are compared with those in the literature [8] and were found to be accurate.

Föppl model with two control cylinders

Let the rotation parameter (ξ) be defined, as the ratio of the velocity of the control cylinder (U_c) to that of free stream velocity (U). The circulation strength (Γ_c) is given as,

$$\Gamma_c = 2\pi r U_c \quad (10)$$

where r is the radius of the control cylinders. If U_c is normalized with the free stream velocity (U), the circulation strength (Γ_c) of the control cylinders is related to the rotation parameter (ξ) as,

$$\Gamma_c = 2\pi r \xi \quad (11)$$

Two control cylinders are introduced in the basic Föppl model as shown in Fig. 3. Let the circulation strengths of the control cylinders be $-\Gamma_c$ and $+\Gamma_c$ for the vortices located at z_c and \bar{z}_c respectively. Due to the small size of the control cylinders compared to the main cylinder, they can be assumed as two vortex perturbations (Tang and Aubry [2]). In the presence of two small vortex perturbations (control cylinders), the complete complex potential can be written as,

$$\begin{aligned}
 W(z) = & \left(z + \frac{1}{z} \right) + \frac{\Gamma}{2\pi i} \left[\ln \left(z - \frac{1}{\bar{z}_1} \right) - \ln \left(z - \frac{1}{\bar{z}_2} \right) \right] \\
 & + \frac{\Gamma}{2\pi i} [-\ln(z - z_1) + \ln(z - z_2)] \\
 & + \frac{\Gamma_c}{2\pi i} \left[\ln \left(z - \frac{1}{\bar{z}_c} \right) - \ln \left(z - \frac{1}{z_c} \right) \right] \\
 & + \frac{\Gamma_c}{2\pi i} [-\ln(z - z_c) + \ln(z - \bar{z}_c)]
 \end{aligned} \tag{12}$$

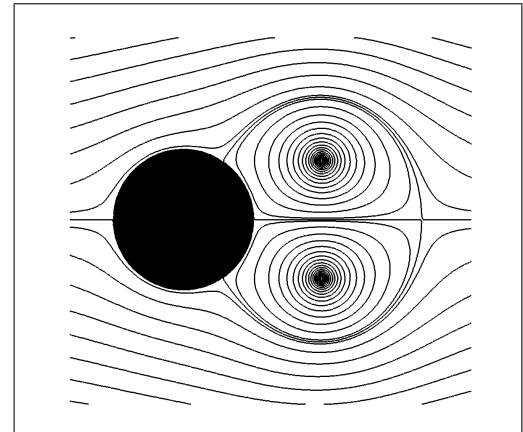
The velocity at any point $z = z_0$ is given by

$$\begin{aligned}
 \frac{d\bar{z}_0}{dt} = \frac{dW(z)}{dz} \Big|_{z=z_0} = & 1 - \frac{1}{z_0^2} + \frac{\Gamma}{2\pi i} \left(\frac{1}{z_0 - 1/\bar{z}_1} - \frac{1}{z_0 - 1/\bar{z}_2} \right) \\
 & + \frac{\Gamma}{2\pi i} \left(-\frac{1}{z_0 - z_1} + \frac{1}{z_0 - z_2} \right) \\
 & + \frac{\Gamma_c}{2\pi i} \left[\frac{1}{z_0 - 1/\bar{z}_c} - \frac{1}{z_0 - 1/z_c} \right] \\
 & + \frac{\Gamma_c}{2\pi i} \left[-\frac{1}{z_0 - z_c} + \frac{1}{z_0 - \bar{z}_c} \right]
 \end{aligned} \tag{13}$$

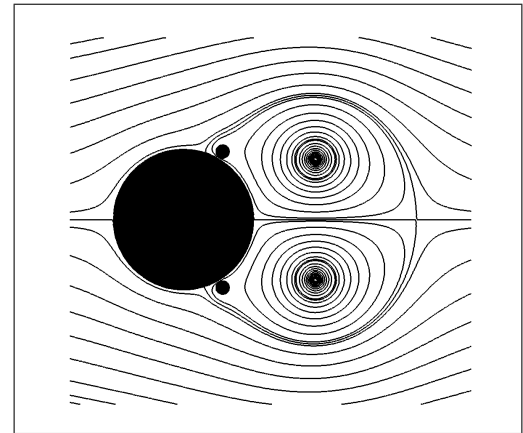
The velocities at z_1 and z_2 (i.e. \bar{z}_1) can be obtained from Eqn. (13) by neglecting the term due to velocity induced by the same vortex. These can be set to zero for Föppl equilibria as mentioned in the previous section. Hence, the equilibrium positions of the Föppl pair are obtained for the given circulation strengths of Föppl vortices and control cylinders. Furthermore, the stream-wise and cross stream velocities (u , v), along the cylinder surface can be obtained from Eqn. (8) and Eqn. (9) respectively. Hence, the separation point on the main cylinder can be found for different positions of the control cylinders. The separation point in the presence of control cylinders changes from the single cylinder case. This new separation point indicates range of influence of control cylinders and their impact. Figure 4 depicts the flow patterns immediately after the introduction of control cylinders at 120° around the main cylinder. Results and discussion section elaborates these simulations.

POTENTIAL FLOW ANALYSIS BY CONFORMAL MAPPING

The potential flow lines for uniform flow past an isolated single circular cylinder can be readily obtained by the superposition of uniform flow and a doublet flow [9].



(a) Single cylinder



(b) 120°

FIGURE 4: INFLUENCE OF POSITION OF THE CONTROL CYLINDERS ON THE FLOW SEPARATION POINT OF THE MAIN CYLINDER FOR $\theta = 120^\circ$

However, an extension to flow past multiple cylinders either in tandem or transverse is not trivial. The stream lines for flow past three cylinders can be achieved by conformal mapping technique. The solution for flow past a multi-cylinder configuration in a planar flow was originally developed by Crowdy [11]. Detailed description of their method is available in [11–13].

After finding the optimum position of the control cylinders from the Föppl vortex model, the right quantum of circulation strengths need to be determined. As the circulation strength of the control cylinders is increased, it affects the pressure distribution on the surface of the main cylinder and in turn the forces acting on the cylinder. The pressure distribution and drag force on the main cylinder are calculated for different circulation strengths and the optimum value of circulation strength is obtained. This is further discussed in Results section.

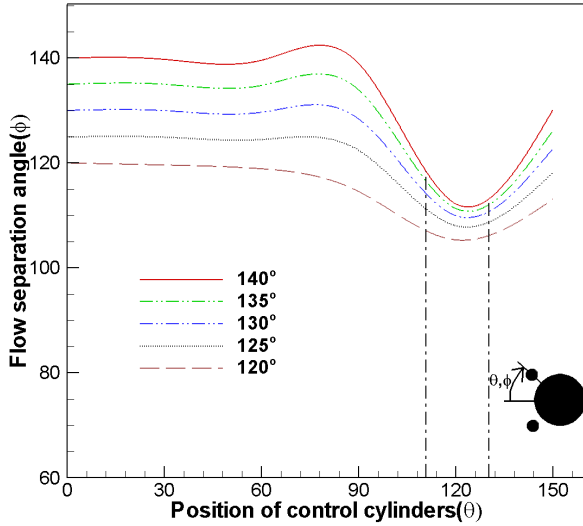


FIGURE 5: INFLUENCE OF THE POSITION OF CONTROL CYLINDERS ON THE POINT OF FLOW SEPARATION FROM THE MAIN CYLINDER.

RESULTS AND DISCUSSION

The optimum position and circulation strength of control cylinders for the potential flow can be obtained by investigating various parameters. The forces on the main cylinder, pressure coefficient (C_p), flow pattern and other design parameters are discussed. The control cylinders are initially rotated at a specific speed and the influence of their position on the flow separation is studied. Once the optimum position is obtained, the rotation rates are varied to obtain an optimum value.

Optimum position of control cylinders

In this section, the effect of placing control cylinders at different positions around the main cylinder is discussed. The influence of control cylinder rotations will be felt within a certain region around them. The control cylinders are initially rotated at constant speed and the influence of their position (θ) on the flow separation point (ϕ) is studied. The separation point on the cylinder surface is indeed a function of Reynolds number. However, in the present study, circulation strength (Γ) of the Föppl vortices is chosen such that typical flow separation angles (ϕ) of 120° to 140° is covered where both θ and ϕ are measured as shown in Fig. 5. In Fig. 5, $\theta = 0^\circ$ position refers to the case where control cylinders are absent (i.e. single main cylinder case). The control cylinders are introduced at different angles 30° , 60° , 90° , 120° , 150° around the main cylinder and their effect on the separation angle (ϕ) was studied for different flow separation angles. It can be seen that the position of the control cylinders

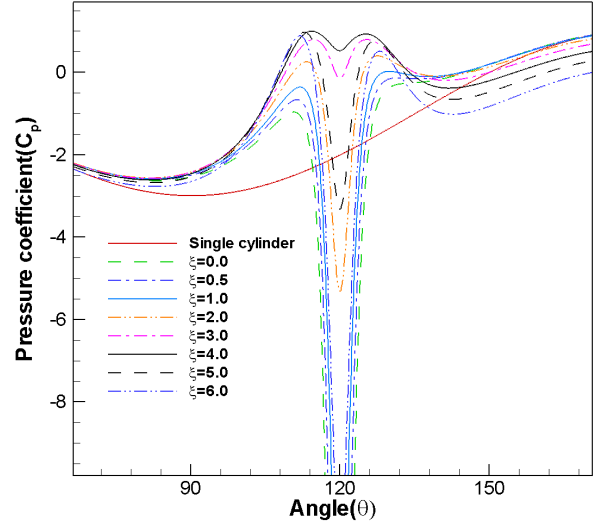


FIGURE 6: VARIATION OF SURFACE PRESSURE DISTRIBUTION ON THE MAIN CYLINDER IN THE VICINITY OF THE CONTROL CYLINDERS AT 120° .

in the range of 0° to 60° does not affect flow separation. However, the maximum effect is felt when the control cylinders are placed at 120° . Hence, the optimum position for the control cylinders is around 120° .

Optimum circulation strength of control cylinders

Using conformal mapping techniques, the complex potential and hence the stream function have been found for different circulation strengths of control cylinders in Section 3. In this section, we present the influence of circulation strength (rotation parameter) of control cylinders by plotting the pressure coefficient (C_p) and drag force on the main cylinder.

Pressure coefficient (C_p) on the cylinder surface

In this section, we investigate the existence of an optimum value by plotting the pressure coefficient (C_p) on the surface of the main cylinder for different circulation strengths of control cylinders.

The pressure coefficient is defined as

$$\begin{aligned} C_p &= 1 - \frac{V^2}{U^2} \\ &= 1 - (u^2 + v^2) \end{aligned} \quad (14)$$

where U is the free stream velocity, V is the total velocity at a point in the domain and u, v are its x and y components respectively which can be calculated from stream

function using

$$u = \frac{\partial \psi}{\partial y} \quad v = -\frac{\partial \psi}{\partial x} \quad (15)$$

The variation of the pressure coefficient (C_p) along the cylinder surface has been plotted in the vicinity of the optimum position of control cylinders (120°) for $\xi = 0$ to $\xi = 6$ as shown in Fig.6. A dip in the value of surface pressure can be noticed at 120° due to the presence of control cylinders. As the circulation strength of the control cylinders is increased, there is a pressure recovery until a value of $\xi = 4$ after which the static pressure starts to dip again. This indicates the existence of an optimum value for the circulation strength of control cylinders.

Forces on the main cylinder In the previous section, the existence of an optimum value of circulation strength for the control cylinders was presented. In this section, the influence of the circulation strength (rotation parameter) of the control cylinders on the drag force experienced by the main cylinder is presented. The drag and lift forces can be calculated from the complex potential ($W(z)$) and are given by

$$F_x - iF_y = -\frac{i\rho}{2} \oint_{\partial D_0} \left(\frac{dW}{dz} \right)^2 dz \quad (16)$$

where F_x , F_y are the drag and lift forces respectively and ∂D_0 is the main cylinder surface.

Lift force on the main cylinder is found to be zero as expected from potential flow theory. Drag force on the main cylinder is calculated for different circulation strengths of control cylinders with all other parameters remaining fixed. Drag force variation against rotation parameter (ξ) is plotted in Fig. 7. It can be seen that the drag force is minimum at $\xi = 2.7$ which indicates the optimum circulation strength for the control cylinders.

Comparison with viscous flow simulations

The potential flow analysis is complemented through numerical calculations for a two-dimensional, incompressible, laminar flow. Detailed viscous flow calculations are shown in Ref. [10].

From our earlier investigations [10], it can be noticed that rate of rotation plays an important role in the suppression of vortex shedding. To this end, positioning the control cylinders at five different combinations (θ values

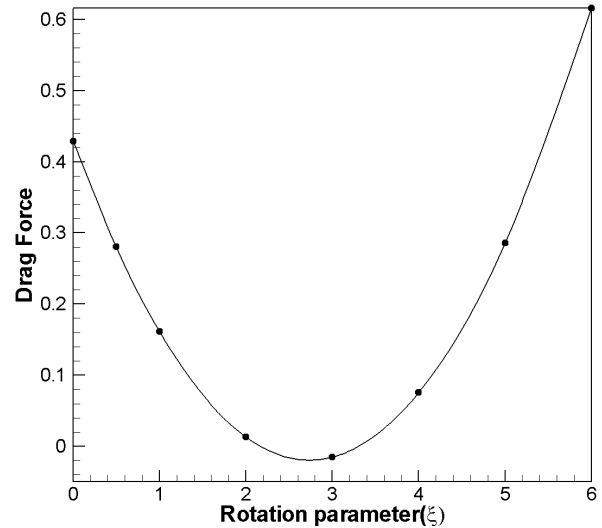


FIG. 7: DRAG FORCE VARIATION AGAINST ROTATION PARAMETER (ξ). NOTE IN PARTICULAR THE POSSIBLE PRESENCE OF AN OPTIMAL ROTATION SPEED AT $\xi = 2.7$

in steps of 30° each) have been assessed. Temporal evolution of fluid flow features are simulated and time averaged over 10 - 12 vortex shedding cycles. The streamlines thus obtained are plotted for different θ values in Fig. 8. When the control cylinders are imparted with a constant rate of rotation at $\xi = 2.0$, the wake region could be completely controlled only for $\theta = 120^\circ$ (see Fig. 8). Time averaged streamlines depict viscous effects in Fig. 8. The fluid flow features for the inviscid patterns can be seen in Fig. 8[f-j]. The latter are generated by means of conformal mapping technique discussed in the earlier sections. According to these qualitative visuals, the presence of control cylinders are best suited for $\theta = 120^\circ$, which is reflective of optimal control cylinder position. For $\theta = 90^\circ$, wake formation length is much longer, although the wake width is reduced. From Fig. 8, it can be observed that the potential flow like behaviour could be achieved for viscous flow for optimum position and circulation strength of the control cylinders. Hence, we can justify the use of potential flow theory to obtain the design parameters of the control cylinders.

CONCLUSIONS

The influence of momentum injection through the control cylinder rotations on flow past a circular cylinder is investigated. Optimum control cylinder position and strength of circulation have been analytically determined. The analytical approach enables rapid prototyping of the parametric space, which is crucial in identifying an op-

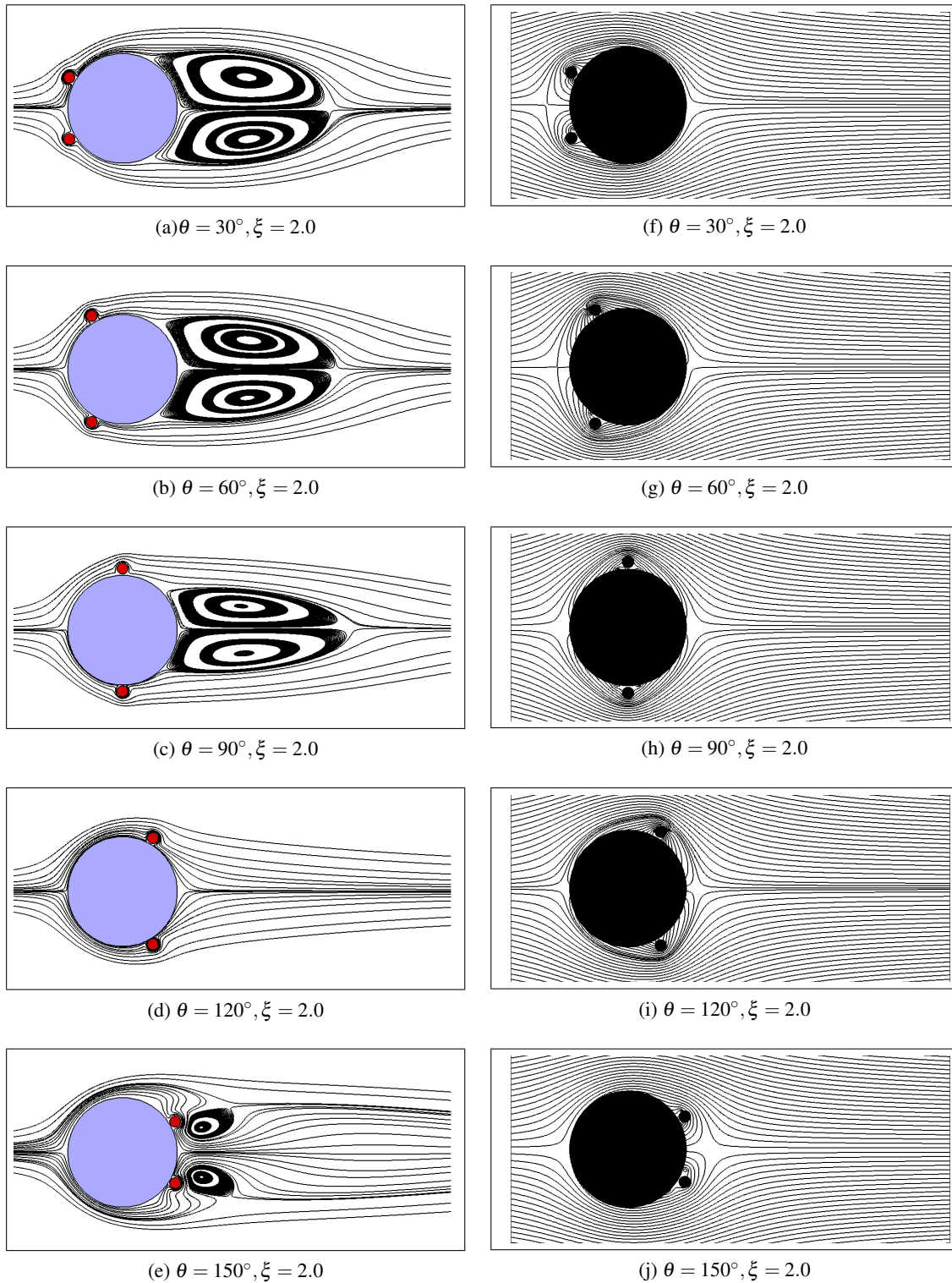


FIGURE 8: FLOW PATTERNS FOR $Re = 100$ AND $\xi = 2.0$. (a - e) TIME AVERAGED STREAMLINES. (f - j) STREAMLINES GENERATED USING CONFORMAL MAPPING METHOD.

timum solution. The analytical frame work carried out simulates the Reynolds number range, where in the flow separation angles are in the range of $120^\circ - 140^\circ$. It is shown that for optimum position, and circulation strength of control cylinders, we are able to eliminate wake vor-

tices and achieve potential flow like behavior. The analytical solution obtained is complemented with the aid of a numerical study of the real flow patterns. The flow patterns generated using viscous flow calculations further confirm 120° cylinder position for optimal control cylin-

der design. By conformal mapping technique, the optimum circulation strength for which drag force on the main cylinder is minimum was determined.

REFERENCES

- [1] Gad-el-Hak, M., ed., 2000. *Flow control*, Cambridge University Press, Cambridge.
- [2] Tang, S., and Aubry, N., 2000. "Suppression of vortex shedding inspired by a low dimensional model". *Journal of Fluids and Structures*, **14**, pp. 443 - 468.
- [3] Galvao, R., Lee, E., Farrell, D., Hover, F., Triantafyllou, M., Kitney, N., and Beynet, P., 2008. "Flow control in flowstructure interaction". *Journal of Fluids and Structures*, **24**, pp. 1216 - 1226.
- [4] Crowdy, D., 2006. "Analytical solutions for uniform potential flow past multiple cylinders". *European Journal of Mechanics B/Fluids*, **25**, pp. 459 - 470.
- [5] Föppl L. Wirbelbewegung hinter einem Kreiscylinder. Sitzb. d. k. Bayer. Akad. d. Wiss 1913; (1): 1.
- [6] Milne-Thomson, 1996. *Theoretical Hydrodynamics*. Dover publications Inc., New York.
- [7] Cai, J., Liu, F., and Luo, S., 2003. "Stability of symmetric vortices in two dimensions and over three-dimensional slender conical bodies". *J. Fluid Mech*, **480**, pp. 65 - 94.
- [8] Protas, B., 2004. "Linear feedback stabilization of laminar vortex shedding based on a point vortex model". *Physics of Fluids*, **16(12)**, pp. 44-73.
- [9] Kundu, P., K., and Cohen, I., M., 2004. *Fluid Mechanics*. Elsevier Academic Press, San Diego, California.
- [10] Muddada, S., Patnaik, B., S., V., 2010. "An active flow control strategy for the suppression of vortex structures behind a circular cylinder". *European Journal of Mechanics B/Fluids*, **29**, pp. 93-104.
- [11] Crowdy, D., 2006. "Calculating the lift on a finite stack of cylindrical aerofoils". *Proc.R. Soc. A*, **462**, pp. 1387-1407.
- [12] Crowdy, D., and Marshall, J., 2005. "Analytical formulae for the KirchhoffRouth path function in multiply connected domains". *Proc. R. Soc. A*, **461**, pp. 2477-2501.
- [13] Crowdy, D., and Marshall, J., 2007. "Computing the Schottky - Klein Prime Function on the Schottky Double of Planar Domains". *Computational Methods and Function Theory*, **7**, pp. 293-308.

DRAG MEASUREMENTS OF A CIRCULAR CYLINDER WITH MOVING SURFACE BOUNDARY-LAYER CONTROL

Ivan Korkischko

Email: ivan.korkischko@gmail.com

Julio R. Meneghini*

Email: jmeneg@usp.br

NDF, Dept. of Mechanical Engineering
POLI, University of São Paulo, Brazil

Robert Konrath

Email: robert.konrath@dlr.de

Inst. of Aerodynamics and Flow Technology
German Aerospace Center (DLR)
Göttingen, Germany

ABSTRACT

Experimental results of flow around a circular cylinder with moving surface boundary-layer control (MSBC) are presented. Two small rotating cylinders strategically located inject momentum in the boundary layer of the cylinder, which delays the separation of the boundary layer. As a consequence, the wake becomes narrower and the fluctuating transverse velocity is reduced, resulting in a recirculation free region that prevents the vortex formation. The control parameter is the ratio between the tangential velocity of the moving surface and the flow velocity ($\Omega = U_c/U$). The main advantage of the MSBC is the possibility of combining the suppression of vortex-induced vibration (VIV) and drag reduction. The experimental tests are performed at a circulating water channel facility. In order to verify the effectiveness of the MSBC regarding drag reduction, two different techniques were employed to measure the mean drag of the cylinder with and without MSBC. The first method used a load cell to measure the drag, while the second one was based on the integration of velocity data along a line located on a averaged velocity field obtained through particle image velocimetry (PIV).

INTRODUCTION

The flow around a circular cylinder has shown its theoretical and applied importance throughout the great amount of analytical, experimental and numerical investigations found in the literature. Along with the study of the flow characteristics [1], the control of the flow over a circular cylinder has received special attention from researchers [2], mainly for purposes of drag reduction

and suppression of vortex-induced vibration (VIV) [3,4]. Among the huge amount of flow control devices, the moving surface boundary-layer control (MSBC) was investigated in this study due to its effectiveness in drag reduction and VIV suppression [5–8]. The MSBC relies on the injection of momentum in the boundary layer of the body by rotating elements, which usually are small circular cylinders. The momentum injection in the boundary layer postpones the effects of the adverse pressure gradient generated by the bluff body geometry, moving the separation point of the boundary layer to a more advanced position. As a result, the wake becomes narrower and the recirculation region behind the body is suppressed or drastically reduced. Figure 1 shows a schematic of the MSBC system, which consists of two small rotating cylinders strategically located that inject angular momentum in the boundary layer of the cylinder, delaying separation. The control parameter is the ratio between the tangential velocity of the moving surface and the flow velocity ($\Omega = U_c/U$).

In order to verify the effectiveness of the MSBC regarding drag reduction, two different techniques were employed to measure the mean drag of the cylinder with and without MSBC. The first method used a load cell to measure the drag, while the second one was based on the integration of velocity data along a line located on a averaged velocity field obtained through particle image velocimetry (PIV). The theory for aero- and hydrodynamic forces and moments is developed through a rigorous analysis of the viscous flow equations [9], and the formulation of the profile drag in steady flow has already been successfully applied in the mean drag measurements of a wing profile using PIV velocity fields [10].

This experimental investigation is a parametric study

*Address all correspondence to this author.

based on three different configurations: plain cylinder, $\Omega = 0$ and $\Omega = 5$. In order to verify the drag reduction efficiency of the MSBC, drag measurements are presented using the two different techniques previously mentioned. As one of the advantages of the MSBC is VIV suppression, the amplitude response is also shown. PIV velocity fields are presented in order to identify the modifications of the wake flow introduced by the MSBC.

EXPERIMENTAL ARRANGEMENT

The experimental tests were performed at the Fluid-Dynamics Research Group Laboratory (NDF) of the University of São Paulo (USP). The test-section of the circulating water channel facility has the following dimensions: 0.70m (width) \times 0.80m (height) \times 7.50m (length). The maximum flow velocity is 1.0m/s. The channel operates at a turbulence level $< 2\%$.

The circular cylinder models are made of rigid acrylic with smooth surface. Figure 1 shows the main geometric characteristics of the circular cylinder with moving surface boundary-layer control (MSBC). The main cylinder external diameter is $d = 50\text{mm}$ and the immersed length $l = 500\text{mm}$, giving an aspect ratio $l/d = 10$. The control cylinder diameter is $d_c = 0.06d$ and the gap between the main and the controlling cylinders is $g = 0.07d$. The control cylinders are made of carbon fiber and they move along with the main cylinder. The main cylinder without MSBC is called plain cylinder in the following results. The mass parameter, which is the ratio between the moving structural mass and the displaced fluid mass, is $m^* = 1.8$. The structural damping coefficient in air is $\zeta = 0.01$, resulting in a mass-damping parameter $m^*\zeta = 0.018$, which is valid to the plain and the MSBC cylinders. The $\Omega = U_c/U$ ratio is the control parameter of the cylinder rotation, where U_c is the tangential velocity of the control cylinders and U is the water channel flow velocity. Each control cylinder is actuated by one dc electric motor with maximum voltage equal to 12V supplied by a single dc power supply.

For the VIV experiments, the cylinders are rigidly attached beneath a platform on an elastic air-bearing system with one degree of freedom in the direction transverse to the flow. [4] give a more complete description of the elastic base. The Reynolds number is in the range of 1600 to 7500, and the reduced velocity varies from 3.7 to 17. The reduced velocity is defined as $V_r = U/f_n d$, where U is the water channel flow velocity, f_n is the natural frequency in still water, and d is the diameter of the plain cylinder. The natural frequency f_n is obtained through decay tests in still water, while the structural damping

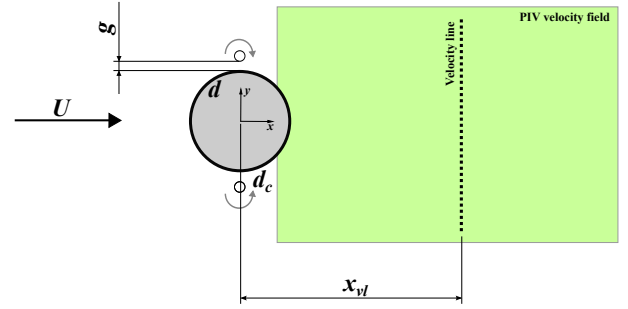


FIGURE 1: CIRCULAR CYLINDER WITH MSBC.

coefficient is obtained from decay tests performed in air. The cylinders were kept static for the drag measurements ($Re = 2700 - 9800$). The Reynolds number range for the load cell measurements was 2700 – 9800 and the PIV measurements were taken at $Re = 3000$.

The PIV velocity fields were measured at $Re = 3000$ for the main cylinders rigidly mounted at $\Omega = 0$ and 5. The PIV measurements were obtained by seeding the liquid with polyamide particles about $11\mu\text{m}$ in diameter. A Quantel (Brilliant Twins) double-cavity pulsed Nd:YAG laser with a 532 nm wavelength illuminated the flow. One workstation, the DaVis 7.2 software and one Imager Pro X 2 Megapixel camera compose the LaVision PIV system. One Nikon (AF Nikkor f/2.8D) lens of 28-mm focal length was used in the measurements. The PIV velocity fields were measured at a rate of 15 Hz and at half the distance of the immersed span. The vector calculation employed a two-pass windowing process with decreasing size: the first correlation used a 64×64 pixel interrogation window followed by the second correlation with a 32×32 pixel window. The field of view is $5.4d \times 7.2d$ (width \times length), resulting in a 75×100 point grid. Each PIV data set contains 345 velocity fields that are sampled for 23 s, which is the maximum capacity of the camera buffer. The analysis provided an uncertainty of $2 \times 10^{-3}\text{m/s}$ (3%) in velocity.

PROFILE DRAG IN STEADY FLOW

The profile drag per unit length of a solid body in steady flow is given by the following equation [9],

$$D = \rho U \int_{-\infty}^{\infty} (U - u) dy, \quad (1)$$

where ρ is the specific mass of water, U is the water channel flow velocity, u is the streamwise velocity at the velocity line and the integration is performed at an x_{PIV} location

far from the body. Equation (1) is a formula derived by using the momentum theorem.

Two important geometrical aspects will be taken in consideration for the usage of Eqn. (1). The first one is the effect of the variation of the integration domain length, as the equation is initially defined with an infinity domain. The second aspect is the definition of the x_{vl} position where the integration will be performed. Both aspects will be considered in this paper prior to the presentation of the mean drag measurements.

SUPPRESSION OF VORTEX-INDUCED VIBRATION

This section presents the results of a parametric VIV investigation regarding the moving surface boundary-layer control (MSBC) applied to a circular cylinder. The control parameter is the ratio between the tangential velocity of the moving surface and the fluid flow velocity, defined as $\Omega = U_c/U$.

Figure 2 shows the amplitude response of isolated cylinders with and without MSBC. The nondimensional amplitude is defined as $A^* = \sqrt{2}y_{rms}/d$, where y_{rms} is the root-mean-square of the transverse displacement. The amplitude response of the plain cylinder presents the classical response [11], which includes the initial, upper and lower branches, as well as, a de-synchronization region. For the present configuration, the maximum amplitude is $A^* \approx 0.7$ at the reduced velocity $V_r \approx 7$.

The amplitude response is completely different for the static control cylinders ($\Omega = 0$), when compared to the plain cylinder. The oscillating motion starts before ($V_r \approx 4$), where it reaches the maximum amplitude ($A^* = 0.6$) and slowly decreases along the V_r range tested, reaching asymptotic values slightly below $A^* = 0.4$. When the control cylinders are actuated, one can verify a substantial reduction of the oscillating amplitude for $\Omega = 5$. The maximum amplitude does not surpass $A^* = 0.2$.

WAKE FLOW VELOCITY FIELDS

The wake velocity fields of cylinders with and without MSBC were measured by the PIV technique. The magnitude of velocity is presented as a nondimensional, $\sqrt{u^2 + v^2}/U$. The main cylinders were rigidly mounted and the Reynolds number was 3000. The nondimensional mean fields of velocity magnitude of the plain cylinder and cylinder with MSBC are presented in Fig. 3. Each mean field is the time-average of 345 instantaneous fields.

Initially, the recirculation region has a length of around two diameters for the plain and $\Omega = 0$ configurations, but its length is reduced by the MSBC. The comparison between the plain and the $\Omega = 0$ cylinders shows

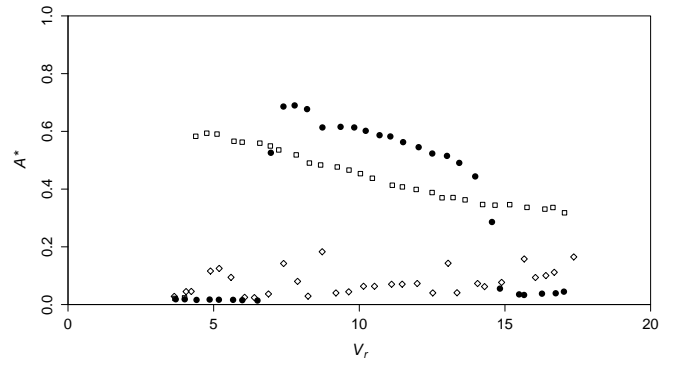


FIGURE 2: AMPLITUDE RESPONSE FOR CYLINDERS WITH AND WITHOUT MSBC: ●, PLAIN; □, $\Omega = 0$; ◇, $\Omega = 5$.

a wider wake to the latter, which results from the control cylinders. Activating the MSBC ($\Omega = 5$), there is a notable change in the wake structure of the circular cylinder. The injection of momentum in the boundary layer by the rotating control cylinders moves the separation point further back on the cylinder surface when compared to the plain cylinder, which results in a narrower wake with smaller velocity gradients for $\Omega = 5$.

Figure 3 also shows the mean streamwise velocity profiles at three positions ($x/d = 2, 4$ and 6) obtained from the wake velocity fields of the cylinders with and without MSBC. The solid black lines represent the velocity profiles at each one of the positions considered. The origin of the distances x/d and y/d is located at the cylinder centre. To begin with, one can observe the characteristic wake velocity profile for the plain cylinder, which presents a region of low velocity between $y/d = -1$ and 1 . With the increasing of the x/d distance, the mean profile gets more uniform. The $\Omega = 0$ configuration shows a general behaviour similar to the plain cylinder's. However, there is a perceivable difference in the wake width, which is greater to $\Omega = 0$; a fact already observed and justified by the presence of the control cylinders. For $\Omega = 5$, one can observe that the wake flow becomes more uniform. A wake region of low velocity is still observed, but it is smaller and narrower than the plain and $\Omega = 0$ cases. The wake velocity profiles show that one of the main MSBC effects is turning the wake flow uniform.

Figure 4 presents the distribution of the streamwise mean velocity (\bar{u}) normalized with the water channel flow velocity (U) along the wake centreline. The recirculation bubble is defined as the region of reversed flow that exists close to the cylinder base. The velocity reaches a minimum value near the cylinder and then increases

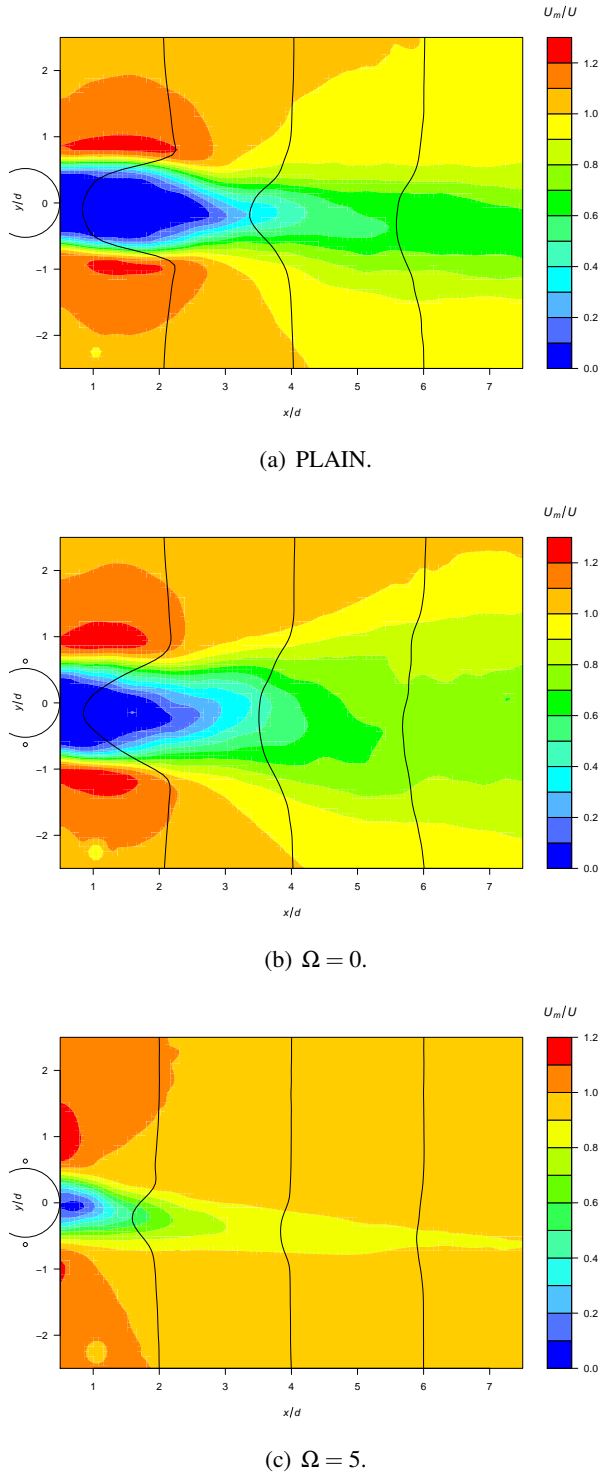


FIGURE 3: TIME-AVERAGED WAKE FLOW VELOCITY FIELDS.

abruptly to positive values before reaching an asymptotic tendency in a farther downstream position. The recirculation bubble (region) length (x_b) is a characteristic length scale of the wake, which is the downstream position where the mean velocity equals zero. The value

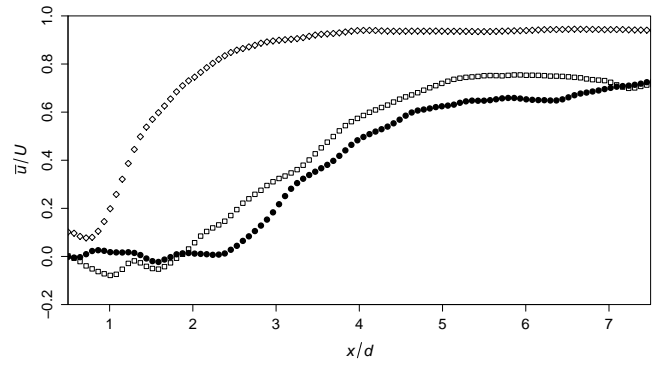


FIGURE 4: MEAN STREAMWISE VELOCITY ALONG THE WAKE CENTRE LINE: ●, PLAIN; □, $\Omega = 0$; ◇, $\Omega = 5$.

obtained through the PIV velocity fields for the plain cylinder was $x_b/d = 2.3$, which compares well with the measurements using the same definition, $x_b/d = 2.3$ at $Re = 2750$ [12]. The recirculation bubble length is reduced for $\Omega = 0$ ($x_b/d = 1.8$) and is less than 1 for $\Omega = 5$ considering the beginning of the abrupt increase of the mean velocity. Another important effect of the MSBC ($\Omega = 5$) is that the asymptotic value is reached before the plain and $\Omega = 0$ and the mean velocity recovers almost 100% of the mean flow velocity.

MEAN DRAG MEASUREMENTS

Validation Test

The determination of the profile drag through Eqn. 1 was validated using the mean velocity field of the plain cylinder. Two geometrical characteristics of the wake flow were investigated: the integration domain length (w) and the x location where the integration is performed. Figure 5 presents the effect of the variation of the w and x parameters on the value of the mean drag ($\overline{C_D}$).

Firstly, the $\overline{C_D}$ value strongly depends on the variation of the integration domain length, specially for $x/d < 3$. One can note that the convergence is obtained for greater lengths. As a result, the integration domain corresponds to the maximum length allowed by the PIV field of view, which is $w/d = 5.4$.

Experimental measurements of airfoil profile drag [10, 13] indicate a small variation of the drag value as a function of the streamwise position of the line integration, as can be seen from the Fig. 5 at the maximum integration domain length. Finally, the $\overline{C_D}$ presented is the average of 100 values calculated at different streamwise (x_{vl}) positions at the range $x/d = 0.05 - 7.7$. The drag uncertainty is estimated by the standard deviation of the $\overline{C_D}$ values

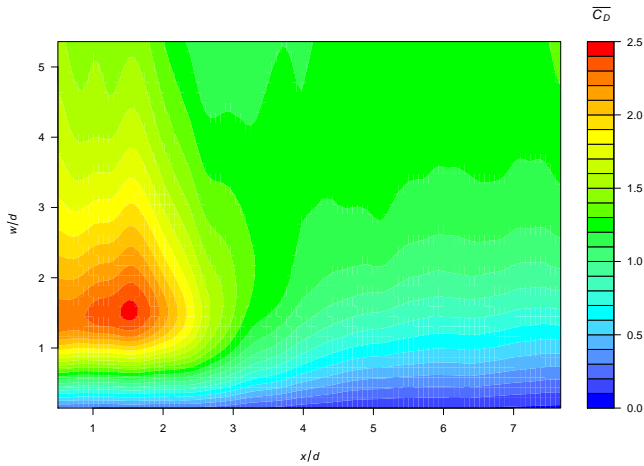


FIGURE 5: MEAN DRAG AS A FUNCTION OF THE VELOCITY LINE LENGTH (w/d) AND THE STREAMWISE POSITION (x/d) FOR THE PLAIN CYLINDER.

calculated along the wake. The spanwise variation in the profile drag was not investigated in this paper, as the results were obtained in the middle spanwise position.

Mean Drag Results

Table 1 shows the mean drag coefficient for the main cylinders rigidly mounted. Firstly, one can note the good agreement between the different techniques employed to measure the drag. Regarding the different configurations tested, the addition of static control cylinders ($\Omega = 0$) generates the increasing of the mean drag coefficient compared to the plain cylinder. For a slightly different configuration ($Re = 10000$, $d_c/d = 0.05$ and $g/d = 0.075$), [6] found $\overline{C_D} \approx 1.6$ for $\Omega = 0$, which is close to the experimental measurement. When the control cylinders are activated, the cylinder rotation leads to the reduction of the mean drag. For $\Omega = 5$, $\overline{C_D} = 0.5$, which represents a substantial reduction (60%) from the mean drag of the plain cylinder. [6] obtained $\overline{C_D} = 0.47$ for the same velocity ratio. These results allow the validation of the numerical simulations and experimental measurements of the MSBC.

CONCLUSIONS

The drag measurements presented in this paper show that the MSBC is effective in reducing drag, as well as suppressing VIV. The injection of momentum in the boundary layer by the rotating control cylinders moves the separation point further back on the cylinder surface when compared to the plain cylinder, which results in a

TABLE 1: MEAN DRAG COEFFICIENT OF A CIRCULAR CYLINDER WITH AND WITHOUT MSBC ($\overline{C_D}$).

	Load cell	PIV
Plain	1.21 ± 0.13	1.28 ± 0.13
$\Omega = 0$	1.51 ± 0.15	1.49 ± 0.15
$\Omega = 5$	0.49 ± 0.10	0.52 ± 0.05

narrower wake. The wake velocity profiles show that one of the main MSBC effects is turning the wake flow uniform. The validation of the profile drag using PIV velocity fields was obtained through the comparison with load cell measurements. The paper presented an analysis of the effect of the streamwise distance of the velocity line used for calculating the mean drag. The variation of the integration domain length was also investigated, showing that the mean drag has a strong dependence with this parameter. Further investigations will account for the spanwise variation of the calculated mean profile drag.

ACKNOWLEDGMENT

I.K. would like to acknowledge FAPESP for the fellowship provided during the development of this work. All experimental resources were provided by NDF-USP.

REFERENCES

- [1] Williamson, C. H. K., 1996. "Vortex dynamics in the cylinder wake". *Annual Review of Fluid Mechanics*, **28**, pp. 477–539.
- [2] Choi, H., Jeon, W.-P., and Kim, J., 2008. "Control of flow over a bluff body". *Annual Review of Fluid Mechanics*, **40**, pp. 113–139.
- [3] Bearman, P. W., 1984. "Vortex shedding from oscillating bluff bodies". *Annual Review of Fluid Mechanics*, **16**, pp. 195–222.
- [4] Korkischko, I., and Meneghini, J. R., 2010. "Experimental investigation of flow-induced vibration on isolated and tandem circular cylinders fitted with strakes". *Journal of Fluids and Structures*, **26**, pp. 611–625.
- [5] Modi, V. J., 1997. "Moving surface boundary-layer control: a review". *Journal of Fluids and Structures*, **11**, pp. 627–663.
- [6] Mittal, S., 2001. "Control of flow past bluff bodies

- using rotating control cylinders”. *Journal of Fluids and Structures*, **15**, pp. 291–326.
- [7] Muddada, S., and Patnaik, B. S. V., 2010. “An active flow control strategy for the suppression of vortex structures behind a circular cylinder”. *European Journal of Mechanics B/Fluids*, **29**, pp. 93–104.
- [8] Korkischko, I., and Meneghini, J. R., 2011. “Suppression of vortex-induced vibration using moving surface boundary-layer control”. *Journal of Fluids and Structures*, p. under revision.
- [9] Wu, J. C., 1981. “Theory for aerodynamic force and moment in viscous flows”. *AIAA Journal*, **19**, pp. 432–441.
- [10] van Oudheusden, B. W., Casimiri, E. W. F., and Scarano, F., 2007. “Aerodynamic load measurement of a low speed airfoil using Particle Image Velocimetry”. In *AIAA 45th Aerospace Science Meeting and Exhibit*.
- [11] Khalak, A., and Williamson, C. H. K., 1999. “Motions, forces and mode transitions in VIV at low mass-damping”. *Journal of Fluids and Structures*, **13**, pp. 813–851.
- [12] Konstantinidis, E., Balabani, S., and Yianneskis, M., 2003. “The effect of flow perturbations on the near wake characteristics of a circular cylinder”. *Journal of Fluids and Structures*, **18**, pp. 367–386.
- [13] Goett, H. J., 1939. “Experimental investigation of the momentum method for determining profile drag”. *National Advisory Committee for Aeronautics*, **660**, pp. 365–371.



SIMPLE SHOCK OSCILLATOR FOR MODELLING A LOOSELY SUPPORTED TUBE SUBJECTED TO TURBULENCE AND FLUID-ELASTIC FORCES

Laurent Borsoi¹
Philippe Piteau
Xavier Delaune

Laboratoire d'études de dynamique
Commissariat à l'énergie atomique
et aux énergies alternatives
CEA, DEN, DM2S, SEMT, DYN
F-91191, Gif-sur-Yvette Cedex, France
Email: laurent.borsoi@cea.fr

José Antunes

Applied Dynamics Laboratory
Instituto Tecnológico e Nuclear
Instituto Superior Técnico
Universidade Técnica de Lisboa
2686-953 Sacavem, Portugal
Email: jantunes@itn.pt

ABSTRACT

Heat-exchanger tubes, when loosely supported and subjected to cross flow, may exhibit vibro-impacting responses due to both turbulence and fluid-elastic forces.

The authors recently addressed the prediction of such regimes using, i) an experimental rig (a rigid square bundle surrounding a flexible tube moving along the lift direction) ; ii) numerical simulations in the time domain where an “instantaneous” frequency of the vibro-impacting tube was continuously determined for taking into account the linear fluid-elastic coupling coefficients which are frequency dependent.

In complement to these sophisticated computations, this paper reports a deliberately simplified analysis based on a simple modal shock oscillator in the frequency domain. The central frequency of the oscillator response is directly apprehended from an iterative process ensuring that the four items - stops penetration, fluid-damping, fluid-stiffness and turbulence excitation - are consistent in frequency. So the “mean value of the instantaneous response frequency” and thus the preponderant vibro-impacting regime of the tube are captured.

The iterative process and outputs involve analytical formulations derived from the Fokker-Planck equation which provides the probability density function of the shock oscillator response in the phase space.

Although extremely reduced, this shock oscillator model permits to instantly recover, at least in order of magnitude, essential features of experiments and previous time-history calculations: Rice and impact frequency, mean impact force, power balance.

NOMENCLATURE

c viscous damping term

c_d dimensionless fluid-elastic damping coefficient
 c_k dimensionless fluid-elastic stiffness coefficient
D tube diameter

$\text{erf}()$ error function, $\text{erf}(y) = \frac{2}{\sqrt{\pi}} \int_0^y \exp(-t^2) dt$

$\text{erfc}()$ complementary error function, $\text{erfc}(y) = 1 - \text{erf}(y)$

$E()$ mathematical expectation

f frequency

f_{c1} left contact force,
 $f_{c1} = (k_1(x + j_1) + c_1 \dot{x})H(-x - j_1)$

f_{c2} right contact force,
 $f_{c2} = (k_2(x - j_2) + c_2 \dot{x})H(x - j_2)$

f_{\max} impact force (local maximum)

f_{Ri} Rice frequency

f_r reduced frequency, $f_r = f \cdot D / V$

f_s fluid-structure index

$f_t(z, t)$ turbulent force per unit of length

$H()$ Heaviside's step function

j gap (positive)

j^* reduced gap, $j^* = j / \sigma_{x0}$

j_0 index for shock oscillator with zero gaps

k stiffness term

K factor, $K = 2 \cdot L \cdot \frac{(1/2 \cdot \rho_f \cdot V^2 \cdot D)^2}{V/D}$

L tube length under flow

L_e equivalent length, $L_e = \int_0^L \varphi_1^2(z) dz$

m mass term

Address all correspondence to this author¹

- m_n tube modal mass, $m_n = \rho S \int_0^L \varphi_n^2(z) dz$
 p probability density
 S tube cross section
 $\tilde{S}_{ff}^{eq}(f_r)$ dimensionless equivalent spectrum (see [3])
 $\tilde{S}_{ref}^{eq}(f_r)$ dimensionless envelope reference spectrum
 t time, $(dx/dt = \dot{x}$, time derivative)
 t_c single contact duration
 T total time
 T_c total contact duration
 U elastic potential energy
 $U(x) = \frac{1}{2} \{ k_0 x^2 + k_1 (x + j_1)^2 H(-x - j_1) + k_2 (x - j_2)^2 H(x - j_2) \}$
 V flow velocity
 $x(t)$ displacement of the mass
 z abscissa along the tube
 0 associated linear oscillator index (without stop)
 1 left stop index
 2 right stop index
 α stiffness ratio, $\alpha = k_1/k_0 = k_2/k_0$
 $\varphi_n(z)$ tube modeshape (mode n , $\max_z |\varphi_n(z)| = 1$)
 φ_s $\varphi_s = \varphi_1(z_s)$ (z_s stops location)
 v_0^+ zero crossing rate with positive slope
 v_a^+ crossing rate of level a with positive slope
 ρ tube density (with fluid added mass)
 ρ_f flow density
 σ standard deviation
 ω circular frequency
 ω_n modal circular frequency (mode n , without stop)
 ξ_n reduced modal damping (mode n)

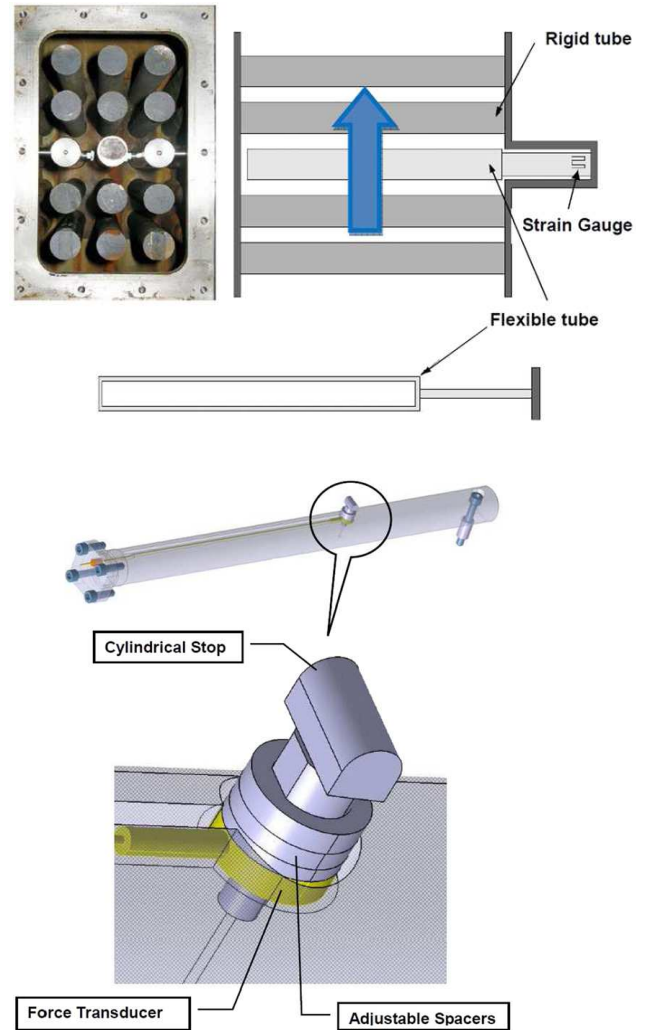


FIGURE 1: EXPERIMENTAL RIG
 (Top: General View - Bottom: Stop Detail)

INTRODUCTION

In recent papers [1,2], the authors addressed the problem of predicting the nonlinear vibro-impacting responses of loosely supported heat-exchanger tubes subjected to both turbulence and fluid-elastic coupling forces under cross-flow. These works were based on analytical experiments and numerical simulations.

The test rig is shown in Fig. 1. It consists of a rigid square bundle (3 x 5) surrounding a flexible tube vibrating along the lift direction ($D=30$ mm, $L=0.3$ m, reduced pitch $P/D=1.5$) and impacting its neighbours. The experiments were carried out with water and air-water mixture to cope with single and two-phase flows. First, the tube is unsupported (without loosely support) and the linearized fluid-elastic coupling coefficients, as well as the turbulence excitation, were identified for a significant range of reduced velocity using an active control method.

Then nonlinear experiments were performed under the same flow conditions (without active control) after installing an instrumented loose support in the rig (Fig. 1-

Top), composed of two impact stops (one on each side) fixed on the adjacent rigid tubes and whose gap is adjusted with spacers (Fig. 1-Bottom). For each test configuration, both the tube response and the impact forces were measured.

Moreover the experimental vibro-impacting responses of the flexible tube were numerically simulated in the time domain using a nonlinear modal superposition technique encapsulating the linear fluid-elastic coupling coefficients and the turbulent excitation previously identified. A delicate aspect of such a calculation is the real time estimation of a representative “instantaneous” response frequency of the vibro-impacting tube, which is required since the fluid-elastic coefficients depend on the local reduced response frequency. The simple method proposed by the authors to identify such an “instantaneous” frequency through the continual adjustment of a 1-DOF linear system, on a short moving time-window, was found efficient and sufficient, given the satisfying comparison between the experimental results and nonlinear computed

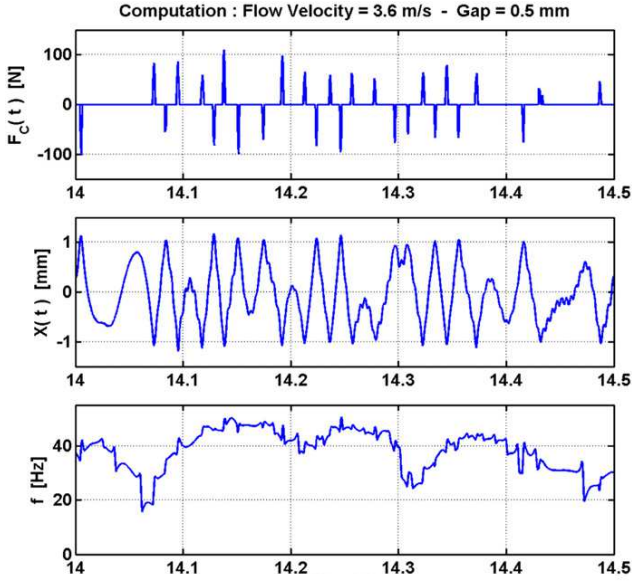


FIGURE 2: TIME-HISTORY COMPUTATION
(Impact Force, Tube End Displacement and
“Instantaneous” Frequency)

predictions, an example of which is shown Fig. 2. All the details about experimental and computational methods can be found in reference [1].

In complement to these sophisticated but CPU-time consuming calculations, this paper reports a deliberately simplified analysis based on a simple 1-DOF modal shock oscillator, addressed in the frequency domain. One of the motivations of this work is a better understanding of the underlying physics, especially about the dynamic equilibrium which tends to stabilize the fluid-elastically unstable vibro-impacting tube, in connection with the increase in the apparent frequency of the system with the impacts (see [1]).

As a first step, the current analysis is focused on the single-phase experiments under water cross-flow.

SHOCK OSCILLATOR MODEL

The shock oscillator (see Fig. 3) is composed of a linear mass-spring-dashpot oscillator restrained by two stops with gap (one on each side). Each intermittently acting stop is made of a linear spring and viscous dashpot in parallel. The shock oscillator displacement corresponds to the lateral displacement of the flexible tube in front of the loosely support.

The components of the linear oscillator act for the mass, damping and stiffness of the fluid-structure coupled system that constitutes the “dry” tube under the action of the fluid-elastic forces (added mass included).

The stop spring models the impact rigidity mainly due to the local shell stiffness of the tube, whereas the associated dashpot should express the whole dissipation mechanisms due to impacts: high modes excitation, radiation damping, local plasticity...

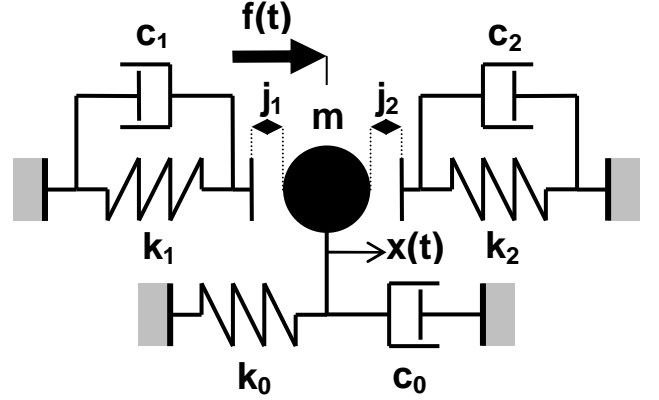


FIGURE 3: SHOCK OSCILLATOR MODEL

The external force, which is assumed to be a white noise, represents the turbulence excitation generated by the cross-flow.

Modal Shock Oscillator

Assuming 1-DOF behaviour, the lateral motion of the flexible tube is projected on its first cantilever beam mode (without stop); one obtains:

$$\frac{m_1}{\varphi_s^2} \ddot{x} + \frac{c_{fs}}{\varphi_s^2} \dot{x} + \frac{k_{fs}}{\varphi_s^2} x = \frac{\int \varphi_1(z) f_t(z, t) dz}{\varphi_s} - f_{c1} - f_{c2}, \quad (1)$$

where $x(t)$ is the tube displacement at the stops location; the modal mass m_1 includes the added mass due to still water (without flow); the modal fluid-structure factors c_{fs} and k_{fs} take into account the fluid-elastic coefficients:

$$c_{fs} = 2.m_1.\xi_1.\omega_1 + 1/2.\rho_f.D.V.c_d.L_e ;$$

$$k_{fs} = m_1.\omega_1^2 + 1/2.\rho_f.V^2.c_k.L_e ;$$

the first right term corresponds to the turbulence excitation, while the last ones, f_{c1} and f_{c2} , represent the intermittent action of stops.

The force balance of Eqn. (1) is dimensional and gives the physical motion of the tube under the 1-DOF assumption. The transposition with Fig. 3, the equation of which is: $m.\ddot{x} + c_0.\dot{x} + k_0.x = f(t) - f_{c1} - f_{c2}$, is direct.

Turbulence Excitation

The turbulence excitation generated by the water cross-flow has been found in the experiments [1] very close to the logarithmic bi-slope envelope spectrum proposed by Axisa et al. [3]:

$$\tilde{S}_{ref}^{eq}(f_r) = 4.10^{-4}.f_r^{-0.5} \text{ for } 0.01 \leq f_r \leq 0.2, \quad (2-a)$$

$$\tilde{S}_{ref}^{eq}(f_r) = 3.10^{-6}.f_r^{-3.5} \text{ for } 0.2 \leq f_r \leq 3. \quad (2-b)$$

So the reference spectrum of Eqn. (2) has been taken in the analysis, more precisely the equivalent spectrum: given by $\tilde{S}_{ff}^{eq}(f_r) = (L_{ref}/L) \cdot (D/D_{ref}) \cdot \tilde{S}_{ref}^{eq}(f_r)$; (see [3] for detail).

Associated Linear Oscillator (ALO)

The ALO is defined from Fig. 3 by suppressing the stops or considering infinite gaps. It is characterized by the following eigenfrequency and reduced damping:

$$\omega_0^2 = \frac{k_{fs}}{m_1}, \quad f_0 = \frac{\omega_0}{2\pi}, \quad \xi_0 = \frac{c_{fs}}{2 \cdot m_1 \cdot \omega_0}.$$

Under the white noise approximation at the reduced frequency, $f_{r0} = f_0 \cdot D/V$, the ALO displacement response has the following variance:

$$\sigma_{x0}^2 = K \cdot L_e \cdot \frac{\tilde{S}_{ff}^{eq}(f_{r0})}{8 \cdot \xi_0 \cdot m_1^2 \cdot \omega_0^3} \cdot \phi_s^2. \quad (3)$$

FOKKER-PLANCK EQUATION

The Fokker-Planck equation (also named forward Kolmogorov eqn.) is a partial derivatives equation which drives the probability density function (PDF) of stochastic diffusion processes, a class of homogeneous Markov processes. It can be applied to mechanical systems on the strict conditions of white excitations ($\underline{\dot{W}}$) and description in the phase space (\underline{X}), [4,5].

By writing the associated stochastic differential equation, $d\underline{X}(t) = \underline{b}(\underline{X}(t)) \cdot dt + \underline{\sigma} \cdot d\underline{W}(t)^2$, where the first right term acts for the deterministic drift and the second one for the stochastic diffusion, the Fokker-Planck equation is expressed as [5]:

$$\frac{\partial p(\underline{x}, t)}{\partial t} = - \sum_{i=1}^n \frac{\partial}{\partial x_i} [b_i(\underline{x}, t) \cdot p(\underline{x}, t)] + \frac{1}{2} \sum_{i=1}^n \sum_{j=1}^n \frac{\partial^2}{\partial x_i \partial x_j} [a_{ij}(\underline{x}, t) \cdot p(\underline{x}, t)]$$

with $\underline{a} = \underline{\sigma} \cdot \underline{\sigma}^t$, and the left term $\partial p / \partial t$ equal to zero for stationary regimes.

But this equation, when derived for the shock oscillator of Fig. 3, has no analytical solution and must be numerically solved.

Shock Oscillator With Undamped Stops

When stops are undamped ($c_1 = c_2 = 0$), there is a simple analytical solution for the stationary regime [6]:

$$p(x, \dot{x}) = C \cdot \exp \left\{ - \frac{1}{2 \cdot \sigma_{x0}^2} \cdot \frac{2 \cdot U(x)}{k_0} - \frac{\dot{x}^2}{2 \cdot \sigma_{\dot{x}0}^2} \right\}, \quad (4)$$

with C the PDF normalization constant given in Appendix A. Equation (4) permits to derive analytical formulations for the shock oscillator [7].

Crossing Rate. By applying the well-known Rice formula, $v_a^+ = \int_0^\infty \dot{x} \cdot p(a, \dot{x}) \cdot d\dot{x}$, one obtains:

$$v_a^+ = v_0^+ \cdot \exp \left\{ - \frac{1}{2 \cdot \sigma_{x0}^2} \cdot \frac{2 \cdot U(a)}{k_0} \right\}, \quad (5)$$

with $v_0^+ = \frac{f_0}{A}$ (see Apx. A for A). Therefore, the frequency

impact of the right stop is: $v_{j2}^+ = v_0^+ \cdot \exp \left\{ - \frac{j_2^{*2}}{2} \right\}$.

Rice Frequency. One has (with G given in Apx. A):

$$f_{Ri} = \frac{1}{2\pi} \cdot \sqrt{\frac{\sigma_{\dot{x}}^2}{\sigma_x^2}} = f_0 \cdot \sqrt{\frac{A}{G}}. \quad (6)$$

Impact Mean Force. Under a ‘‘narrow band assumption’’ - one single peak, i.e. only one local maximum of the impact force, per stop contact - one has for a symmetrical shock oscillator:

$$\frac{E[f_{\max}]}{k_0 \cdot \sigma_{x0}} = \sqrt{\frac{\pi}{2}} \cdot \frac{\alpha}{\sqrt{1+\alpha}} \cdot \exp \left(\frac{j^{*2}}{2 \cdot (1+\alpha)} \right) \cdot \operatorname{erfc} \left(\frac{j^*}{\sqrt{2 \cdot (1+\alpha)}} \right). \quad (7)$$

Equivalent Linear Damping

The above formulations are only available for undamped stops. But the stop damping is the only way to dissipate energy in the shock oscillator model as the flow-coupled system becomes linearly unstable. So, for keeping an analytical frame, a crude equivalent linear damping, taking into account the stop damping in pro rata of contact duration has been adopted. For symmetrical oscillators ($c_1 = c_2$, $k_1 = k_2$, $j_1 = j_2$), $c_{eq} = c_0 + (T_c/T) \cdot c_1$, or:

$$c_{eq} = c_0 + \frac{\exp(-j^{*2}/2)}{A \cdot \sqrt{1+\alpha}} \cdot E[t_c^*] \cdot c_1. \quad (8)$$

In first approximation, $E[t_c^*] = \frac{E[t_c]}{T_{j0}/2} \approx 1$, in which

$T_{j0} = 2\pi \sqrt{m/(k_0 + k_1)}$ is the period of the shock oscillator with zero gaps.

² Notation: matrix, vector, n dimension of the phase space.

ITERATIVE PROCESS

The displacement response of a weakly damped linear oscillator under stationary white noise is characterized by a peaked power spectral density (PSD) and time envelope with large fluctuations. On the contrary, a shock oscillator exhibits a relatively flat time envelope due to stop limitation, but an enlarged PSD given the nonlinear relation between the response amplitude and the apparent or “instantaneous” frequency [6].

The fluctuation of the “instantaneous” frequency, which is specific to any system with stops, is here complicated by the frequency dependence of the fluid-elastic damping and stiffness coefficients, $c_d(f_r)$ and $c_k(f_r)$, but also by the frequency content of the random excitation given by Eqn. (2), the slope of which is very abrupt. Such a fluctuation is shown in Fig. 2 as finally resulting from strong and complex interaction between tube motion, stops penetration, fluid-damping, fluid-stiffness and turbulence excitation, that only time-history calculations can capture.

Nevertheless, in addition to the 1-DOF assumption about tube motion, it is supposed in the current analysis that the central or “equivalent” frequency, around which the “instantaneous” frequency fluctuates, may be directly apprehended from an iterative process in the frequency domain ensuring the four items - stops penetration, fluid-damping, fluid-stiffness and excitation level - are consistent in frequency. Equation (1) is used for this, in the frequency domain, with convergence on the reduced frequency constructed on the Rice frequency. In other words, at the end of the iterative process, the Rice frequency f_{Ri} given by Eqn. (6), the fluid-elastic damping and stiffness coefficients $c_d(f_r)$ and $c_k(f_r)$ extracted from the linear experiments [1] and the random excitation level $\tilde{S}_{ff}^{eq}(f_r)$ given by Eqn. (2) are coherent, i.e. one has:

$$f_r = f_{Ri} \cdot D / V .$$

For practical reasons the iterative process is “temporized” as: $A_u^+ = (\eta_u \cdot A_u^- + \eta_p \cdot A_p) / (\eta_u + \eta_p)$, with A the quantity of interest, p index for previous value, u for updated one (- before, + after), η the weight coefficients.

The “equivalent” frequency approximates the time average of the “instantaneous” frequency. So the stationary dynamic equilibrium implied by Eqn. (1) under this “equivalent” frequency should capture the preponderant vibro-impacting regime of the tube.

RESULTS

The analysis is conducted for the single-phase tests in water cross-flow for two gap sizes: 0.5 mm and 1.0 mm (gap on each side). Results are provided in function of the flow velocity from 0.5 to 4.0 m/s with a step of 0.1 m/s. They are compared to the experimental ones and previous time-history (TH) calculations, both given in reference [1]. They are shown in Figs. 4-11 and commented in the

following sub-sections. The fluid-elastic stiffness and damping coefficients as a function of the reduced frequency, as well as the turbulence spectrum used in the computations, are shown in Figs 9-11.

Model Data

The first mode of the cantilever tube (in still water, without stop) has a measured frequency $f_0 = 18$ Hz with a reduced damping $\xi_1 \approx 1\%$.

The stops system is assumed to be fully symmetrical, $k_1 = k_2 = k_j$, $c_1 = c_2 = c_j$, $j_1 = j_2 = j$. The stop stiffness is $k_j = 10^6$ N/m, while a reduced damping of the mass-stop system, $\xi_j = c_j / 2\sqrt{k_j \cdot m} = 2\%$, has been taken.

Rice Frequency (Fig. 4)

One notices in Fig. 4 the general good agreement even if the experimental slope is slightly weaker. The evolution with flow velocity is quite a straight line and the apparent frequency at $V=4$ m/s is approximately twice the cantilever tube frequency whatever the gap size; (a little higher for $j=0.5$ mm than for $j=1.0$ mm).

Impact Frequency (Fig. 5)

Although correct in order of magnitude, the 1-DOF analysis fails in capturing the precise slope and values of experiments and time-history calculations especially for $V \geq 2.5$ m/s. The impact frequency, which is provided by $v_j^+ = 2 \cdot v_0^+ \cdot \exp(-j^{*2} / 2)$, is overestimated and tends to twice the zero crossing frequency given the very low reduced gaps obtained for high flow velocity; e.g. $j^* \approx 0.3$ for $V=4$ m/s.

Mean Impact Force (Fig. 6)

The 1-DOF analysis is close to the time-history calculations (with same slopes) but overestimates the experimental results up to 45% for $V=4$ m/s.

Power Balance (Fig. 7)

The comparison is only made with the time-history calculations as this information is not available through the experiments. The trends are qualitatively correct. Turbulence always injects energy into the system while structural damping (tube and stops) always dissipates it, which is obvious. But the sign of the fluid-elastic power is gap dependent. The fluid-elastic damping force is always dissipative for the gap size of 0.5 mm, whereas it is slightly dissipative then injective when the flow velocity increases ($V > 3$ m/s) for the larger gap size of 1.0 mm. This is illustrated in Fig. 10 where the 1-DOF calculation points are circled on the $c_d(f_r)$ experimental curve, from right to left as the flow velocity increases.

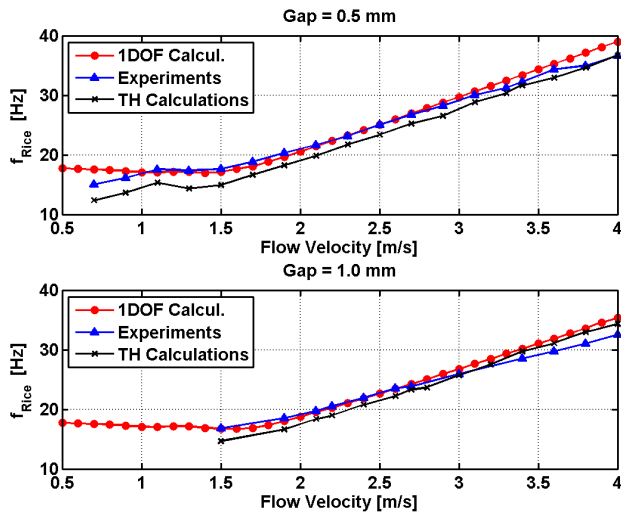


FIGURE 4: RICE FREQUENCY EVOLUTION

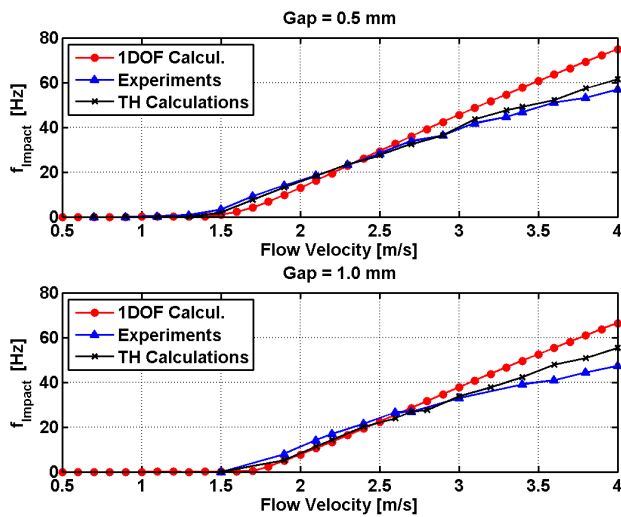


FIGURE 5: IMPACT FREQUENCY EVOLUTION

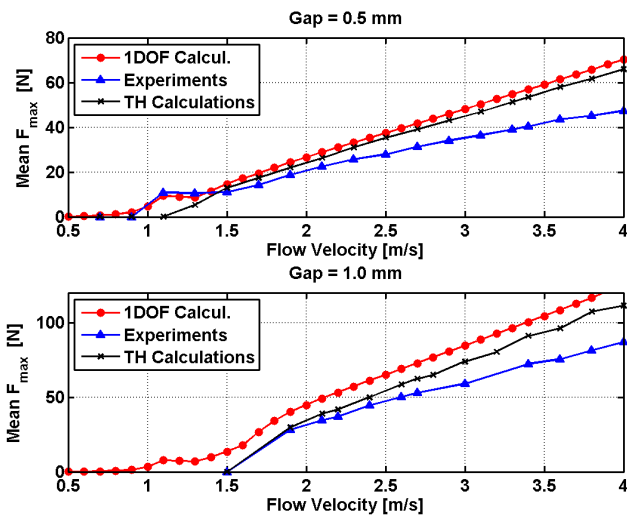


FIGURE 6: MEAN IMPACT FORCE EVOLUTION

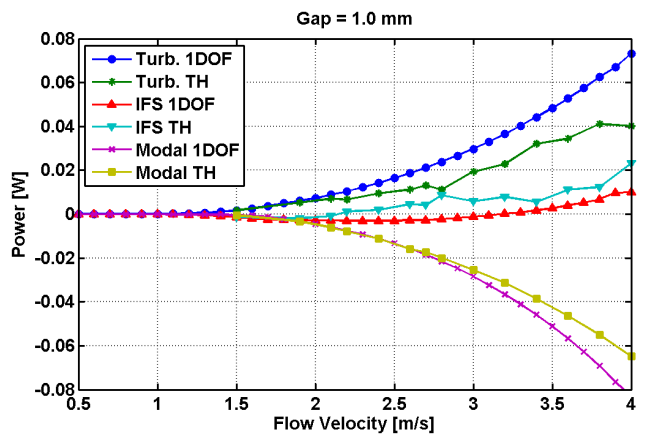
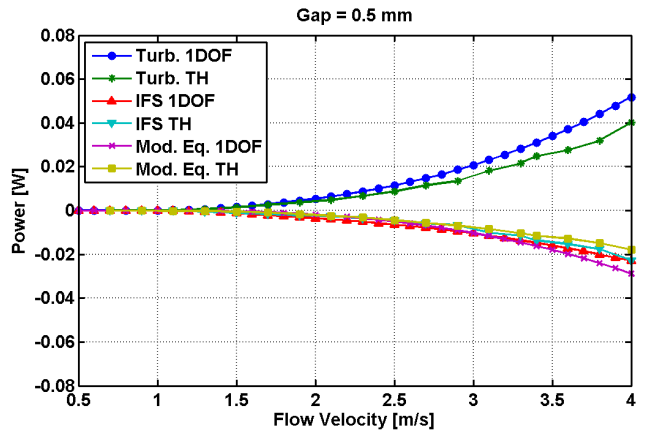


FIGURE 7: POWER BALANCE EVOLUTION

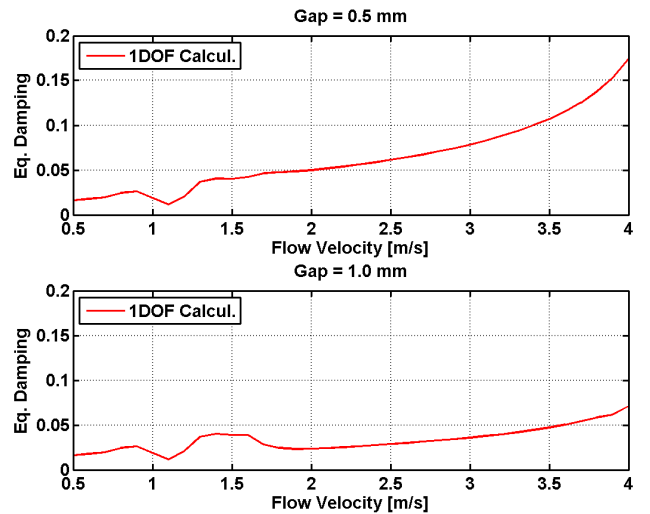


FIG. 8: ALO REDUCED DAMPING EVOLUTION

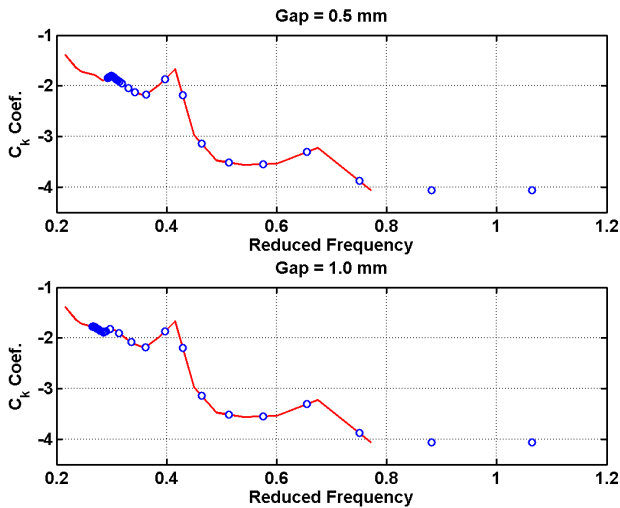


FIGURE 9: Ck FLUID-STIFFNESS COEFFICIENT

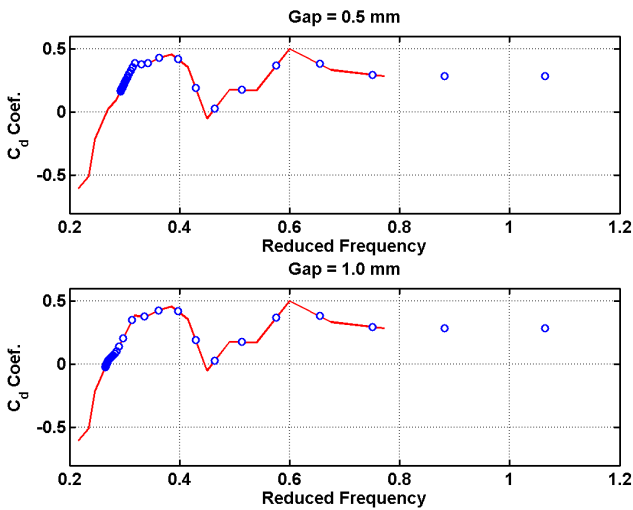


FIGURE 10: Cd FLUID-DAMPING COEFFICIENT

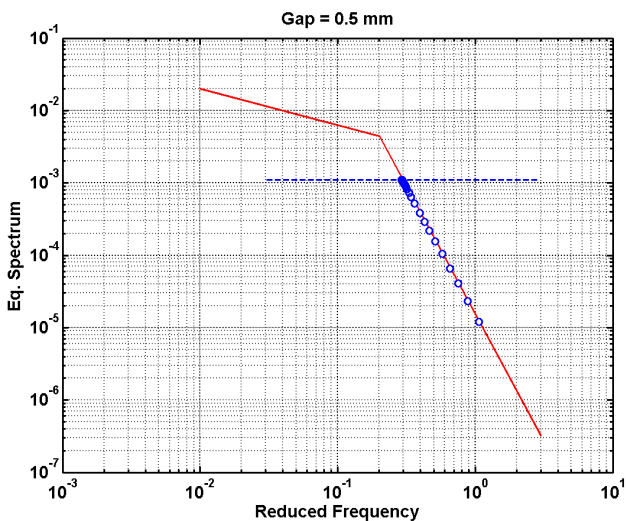


FIGURE 11: EQUIVALENT SPECTRUM

Nevertheless the power balance produced by the 1-DOF analysis is relatively imprecise: too much power is injected by turbulence (up to 30%) and not enough by fluid-damping force when injective.

DISCUSSION

The above results must be judged with respect to the simplified method that has been adopted and the severity of the initial problem. For example not only the fluid-damping acts a lot for high flow velocity, but also the fluid-stiffness (Fig. 9), which produces an eigenfrequency drop up to 45% leading to very large stiffness ratios in the shock oscillator, $\alpha \sim 500$.

First the 1-DOF, i.e. 1-MODE, behaviour of the tube motion is a very crude assumption given the large impact forces which are well known for exciting higher modes. Secondly the dynamic problem reduction to frequency coherence in Eqn. (1) may be controversial depending on the gap size.

Gap size j=0.5 mm

The smaller gap, $j=0.5$ mm, is the easiest case as the fluid-elastic damping force is always dissipative (Fig. 7 & 10). The ALO reduced damping is shown in Fig. 8 where the final high value ($\xi_0 = 18\%$ for $V=4$ m/s) must be noted. More than the stop damping, this is mainly due to the fluid-damping (see Fig.10 to be multiplied by V) and the previously evoked frequency drop.

Finally the main criticism lies here in the white noise approximation. Under this required assumption, the power injected by the turbulence excitation is [7]:

$$P_t = K.L_e \cdot \frac{\tilde{S}_{ff}^{eq}(f_r)}{4.m_1}, \tag{9}$$

with the reduced frequencies, $f_r = f_{Ri}.D/V$, located on the abrupt logarithmic slope of -3.5 according to Fig. 11 and Eqn. (2). The injected power is very sensitive to f_r given this slope. But above all, higher is the slope and less good is the white noise approximation for moderate damping. As easily demonstrable, the power injected into a linear oscillator by a coloured noise of slope -2 is equal to the one of a white noise (hold at the oscillator frequency) since the low frequency power excess exactly compensates the high frequency deficit. But “above” -3, it is not true at all [7]. More than a question of power, the coloured excitation is then very far from a white noise excitation, especially through its low frequency content which creates significant forced responses.

In other words, given the turbulence DSP slope, the white noise approximation which is required for using the Fokker-Planck equation introduces a major bias that should be corrected.

Gap size $j=1.0$ mm

This case is more complicated as fluid-damping injects energy at high flow velocity. This injection is found too weak in the 1-DOF analysis as the converged reduced frequencies are a little too high (see Fig.4 & 10). The ALO equivalent damping may be suspected in such a result in addition to the white noise approximation. Equation (8) is just an artifice for “saving” the Fokker-Planck analytical approach but has no solid foundation. The damping value reaches $\xi_0 = 7\%$ for $V=4$ m/s (Fig. 8), which shows the stops solicitation.

For the cases of negative fluid-structure damping, an alternative approach, outside the Fokker-Planck frame, has also been tested but is not reported due to lack of space. It was built on a simple energy balance between the injective part (turbulence and fluid-structure damping) and the dissipative one (stops damping) during one harmonic limit cycle. Results are in the same order of magnitude, the “apparent” frequency is well in continuity of the previous Rice frequency but the impact frequency is too high (twice the zero crossing rate by construction) and the “mean” impact force too low as no fluctuation is present in the cycle amplitude.

CONCLUSION

The objective of this study was to analyze in the first order the dynamics of tubes loosely supported and subjected to turbulence and fluid-elastic forces. The simplified method that has been adopted is based on a “double” drastic reduction: 1-DOF shock oscillator under 1-Frequency (the predominant “apparent” frequency). All formulations are analytical. Results are instantaneous and relatively satisfactory given the hardness of the initial problem.

Nevertheless the biases inherent to the method must be classified by order of importance. Among them, the 1-DOF reduction, the white noise approximation, the equivalent linear damping due to stops, the model parameters, the way of “averaging” the instantaneous frequency... Time-history calculations and numerical resolutions of the Fokker-Planck equation should be performed for this purpose. But concerning the Fokker-Planck equation, the task is complicated by the stop stiffness and white noise filters required to recover the DSP slope (-3.5).

It is the firm belief of the authors the consolidation of the current results can significantly aid for the deep understanding and quantification of the stabilization process of linearly unstable tubes which occurs with the increase in the apparent frequency due to impacts. This understanding is currently only qualitative, for example the quasi-straight line of Fig. 8 (the “apparent” frequency is proportional to the flow velocity) is not fully explained.

ACKNOWLEDGMENTS

This study has been performed in the framework of a joint research program co-funded by AREVA NP, EDF and CEA. The authors acknowledge financial support for this work.

REFERENCES

- [1] Piteau, P., Delaune, X., Antunes, J., Borsoi, L., 2012. “Experiments and computations of a loosely supported tube in a rigid bundle subjected to single-phase flow”. *Journal of Fluids and Structures*, 28 (2012), pp. 56-71.
- [2] Delaune, X., Antunes, J., Piteau, P., Borsoi, L., 2011. “Experiments and computations of a loosely supported tube under two-phase buffeting and fluid-elastic coupling forces”. Transactions, SMIRT 21 (New Dehli). Div-I, Paper 134.
- [3] Axisa, F., Antunes, J., Villard, B., 1990. “Random excitation of heat-exchanger tubes by cross-flow”. *Journal of Fluids and Structures*, 4 (1990), pp. 321-341.
- [4] Lin, Y., K., (Reprint 1976). “Probabilistic Theory of Structural Dynamics”. Robert E. Krieger Publishing Company.
- [5] Krée, P., Soize, C. (1983). “Mécanique aléatoire”. Dunod, Paris.
- [6] Guihot, P., 1990. “Analyse de la réponse de structures non linéaires sollicitées par des sources d’excitation aléatoires - Application au comportement des lignes de tuyauteries sous l’effet d’un séisme”. PhD Thesis. Université de Paris VI.
- [7] Borsoi, L., (2011). “Analyse 1-DDL des essais TGV_ICE - 1) éléments théoriques, 2) application”. CEA Reports.

Appendix A: Constants from Fokker-Planck Formulations

The following constants are given for symmetrical shock oscillators: $k_1 = k_2$, $j_1 = j_2$. Similar formulations exist for non symmetrical oscillators.

$$C^{-1} = 2.\pi.\sigma_{x0}.\sigma_{\dot{x}0}.A \quad (10)$$

$$(11)$$

$$A = \left\{ \operatorname{erf} \frac{j^*}{\sqrt{2}} + \frac{1}{\sqrt{1+\alpha}} \cdot \exp\left(\frac{-j^{*2} \cdot \alpha}{2 \cdot (1+\alpha)}\right) \cdot \operatorname{erfc}\left(\frac{j^*}{\sqrt{2 \cdot (1+\alpha)}}\right) \right\} \quad (12)$$

$$G = \left\{ \operatorname{erf} \frac{j^*}{\sqrt{2}} - \sqrt{\frac{2}{\pi}} \cdot j^* \cdot \frac{\alpha^2}{(1+\alpha)^2} \cdot \exp\left(\frac{-j^{*2}}{2}\right) + \operatorname{erfc}\left(\frac{j^*}{\sqrt{2 \cdot (1+\alpha)}}\right) \cdot \frac{1}{(1+\alpha)^{3/2}} \cdot \left(1 + j^{*2} \cdot \frac{\alpha^2}{(1+\alpha)}\right) \cdot \exp\left(\frac{-j^{*2}}{2} \frac{\alpha}{1+\alpha}\right) \right\}$$



VIBRATION BEHAVIOR OF A STEAM GENERATOR TUBE IN INTERACTION WITH AN ANTI-VIBRATION BAR: EXPERIMENTAL STUDY

Valérie Lalonde

BWC/AECL/NSERC Chair of Fluid-Structure Interaction
 Dep. of Mechanical Engineering
 École Polytechnique de Montreal
 Montreal, Quebec, Canada, H3C 3A7
 valerie.lalonde@polymtl.ca

Annie Ross¹

CREPEC
 Dep. of Mechanical Engineering
 École Polytechnique de Montreal
 Montreal, Quebec, Canada, H3C 3A7
 annie.ross@polymtl.ca

Michel J. Pettigrew

BWC/AECL/NSERC Chair of Fluid-Structure Interaction
 Dep. of Mechanical Engineering
 École Polytechnique de Montreal
 Montreal, Quebec, Canada, H3C 3A7
 michel.pettigrew@polymtl.ca

ABSTRACT

Fretting-wear of steam generator tubes is an important issue in the nuclear power industry. The two-phase cross-flow induces vibration of the U-tubes causing impacts and rubbing against the anti-vibration bars (AVB) and leading to premature fretting-wear damage. The objective of this project is to study experimentally the tube dynamics by reproducing the tube/AVB configuration as encountered in steam generators. The vibration response of the tube and the fretting-wear work-rate are measured in terms of displacement and contact force. For random excitation forces around the first and second modes of the tube, results show sliding and impacts of the tube against the AVB. This study also shows similar behavior of the fretting-wear work-rate as a function of clearance and preload for excitation forces around the first and second modes. In both cases, the work-rate is low for all clearances and high when there is a preload between the tube and the AVB.

INTRODUCTION

In steam generators of CANDU nuclear reactors, thermal energy is transferred from a primary loop to a secondary loop to convert water into steam. The primary loop contains high pressure heavy water heated by the nuclear fission reaction. The heavy water circulates inside U-tubes contained in the steam generator. The secondary loop is a flow of water that passes through the U-tube bundles. Heat transfer takes place to convert water of the secondary loop into steam. Steam is then used to run turbines that provide electricity.

Two-phase steam/water cross flow of the secondary loop induces vibration of the U-tubes. To prevent large vibration amplitudes, the tubes are supported by anti-vibration bars (AVB) in the U-bend region. Minimum clearances between the tubes and the AVBs are set to allow thermal expansion of the tubes and to prevent fretting-wear damage. Unfortunately, larger clearances occur in some steam generators causing significant impacts and rubbing of the U-tubes against the AVB. Premature fretting damage often leads to tube failure, resulting into power plant shut-downs and costly repairs. Therefore, to avoid such damage it is necessary to understand the dynamic behavior of the tubes subjected to two-phase cross flow.

The dynamic behavior of the tubes depends on vibration excitation mechanisms and damping. Several studies were conducted regarding two-phase cross-flows and their resulting mechanisms [1-6]. One of the most important excitation mechanisms is fluid-elastic instability which occurs from the interaction between flow-induced dynamic forces and tube motion. When fluid velocity is critical, instability occurs; the vibration response of the tubes increases drastically, causing large impacts and rubbing against the AVB. Random excitation forces due to turbulent flow and periodic wake shedding mechanisms can also contribute to vibration excitation forces.

To predict the service life of steam generator U-tubes, normal fretting-wear work-rate is the parameter used [7]. This variable was introduced in literature in 1984 to quantify the rate of dissipated energy at the contact point of two parts [8]. It depends on operating conditions within the steam generator and the characteristics of the dynamic interaction between the tubes and the AVBs, such as

Address all correspondence to this author¹

excitation frequency and amplitude as well as contact force and sliding distance. Normal fretting-wear work-rate is defined as the product of normal contact force F_N and sliding distance s averaged over time, as described by the following equation:

$$\dot{W}_N = \frac{1}{T} \int_0^T F_N(t) ds \quad (1)$$

To meet recommended service life of steam generator tubes, the normal fretting-wear work-rate should be less than 1mW [9]. Many numerical models were developed to predict the dynamic behavior of the tubes in interaction with the AVBs and to estimate the fretting-wear work-rate [10-13]. These models are evolving as they are developed from experimental knowledge. Experimental studies are conducted to understand the vibration mechanisms encountered in steam generators [14].

In the present experimental study, the vibration behavior of a tube in interaction with an AVB is studied by reproducing the tube-to-support configuration as encountered in steam generators of nuclear reactors. Time responses of tube displacement and contact force at the AVB are measured in order to analyze the vibration response of the tube and to compute the normal fretting-wear work-rate.

In the following sections, an overview of the experimental setup and procedure is first presented. Then, the vibration response of the tube is analyzed from time signals and frequency spectra. Finally, the fretting-wear work-rate is calculated as a function of clearance or preload between the tube and the AVB for different excitation forces.

EXPERIMENTAL SETUP

The objective of the experimental setup, shown in Fig. 1, is to study the dynamic behavior of a tube in interaction with an AVB by duplicating a realistic steam generator tube-to-support configuration. To simplify the experimental model, a simply supported straight tube replicates a steam generator U-tube with the largest radius of curvature. A fixed flat bar at mid-span is used as a steam generator AVB. The tube (1) is provided with extension links at both ends, and is fixed to an I-beam mounting post (2) with bottom and top supports (3). The AVB displacement assembly (4) is also fastened to the I-beam mounting post which is fixed to a structural concrete column of the building. Electromagnetic shakers (5) are used to simulate the flow induced vibration excitation forces. The test-rig is also instrumented with laser position sensors and force sensors.

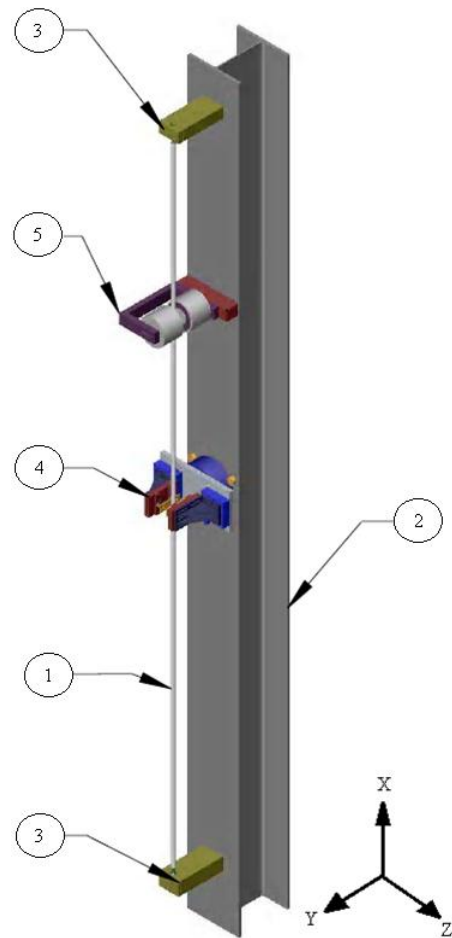


FIGURE 1: EXPERIMENTAL SETUP.

The tube extension links and supports are shown in Fig. 2.

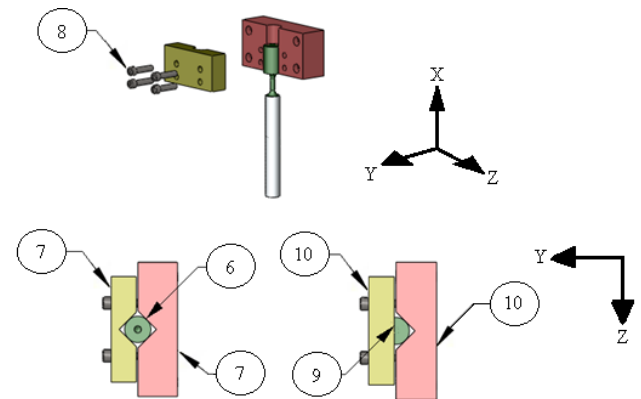


FIGURE 2: EXTENSION LINKS AND SUPPORTS ASSEMBLY.

The Inconel 690 tube is 2,5m long, has a 15,9mm outer diameter and a 0,965mm wall thickness. The stainless steel extension links at both ends of the tube are bone shaped to allow tube bending at natural frequencies close to those of simple support conditions. The bottom extension link (6) has a circular neck. One end is bonded

inside the tube with Loctite while the other end is squeezed between two parts of the bottom support (7) with screws (8). The top extension link (9) has one end bonded inside the tube while the other end is clamped inside the top support (10). A square neck is provided to uncouple the displacement of the tube in the Y and Z directions. Consequently, the tube is preferentially flexible in those two principal directions. It also has a flat surface to prevent rotation of the tube inside the support and to ensure a consistent position of the tube for each assembly of the test rig.

The AVB displacement assembly, shown in Fig. 3, allows varying the position of the AVB relative to the tube. The 410SS AVB (11) (56mm x 25,3mm and 3,7mm thick) is mounted on a translation stage (12) through a 90° bracket (13). The position of the stage is changed by a micrometer screw which has an accuracy of 1µm. Different clearances or preloads between the tube and the AVB can be set. For example, a tube deflection of -100µm corresponds to a preload of 0,149N.

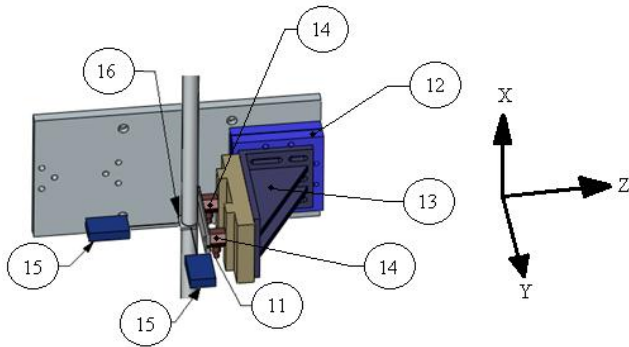


FIGURE 3: AVB DISPLACEMENT ASSEMBLY.

The electromagnetic shakers are located 0,88m above the center of the tube. They attract a ferromagnetic target located inside the tube. An excitation signal is generated by a signal analyzer and transmitted to an amplifier. The amplified signal then passes through a diode bridge that separates the positive and the negative portions of the wave. The positive portion is transmitted to one of the electromagnet while the negative portion is transmitted to the other, so that the tube is successively attracted by each of the electromagnet. The excitation is applied along the Y direction, parallel to the flat bar, as seen in Fig. 1.

In Fig. 3, two piezoelectric force sensors (14) are positioned between the AVB and the 90° bracket. They measure the dynamic contact force of the tube against the AVB at mid-span along Z. The force sensors are discharged in about 5 seconds when a static force is applied, therefore only dynamic loads are measured. The output voltage is 0,494V/N ± 0,1% and the optimal operating range is from 0,979N to 9,790N.

Finally, two laser sensors (15) measure the position of the tube at mid-span along Y and Z as shown in Fig. 3. The beams are directly pointing on the flat surfaces of a ring (16) around the tube, so that the curvature of the tube

does not generate reading errors. One side of the ring is cut off to avoid interference between the tube and the AVB when interacting. The output voltage of the laser sensors is 0,2V/mm ± 0,1%, the measuring range is 50mm and they have a resolution of 8µm.

EXPERIMENTAL PROCEDURE

In a previous experimental study, it was shown that the use of random noise in a 10Hz bandwidth around each natural frequency of the tube is suitable to approximate flow-induced excitation in steam generators [15]. This study also revealed that all odd bending modes have similar dynamic behavior. However, a different behavior was observed for all even modes. For those reasons, random excitation forces in a 10Hz bandwidth around the first and second modes of the tube are used. Fig. 4 shows bending mode shapes of the tube.



FIGURE 4: MODE SHAPES OF THE TUBE
A) MODE 1 B) MODE 2.

Excitation Frequencies

The natural frequencies of the tube were obtained by conducting an impact test on the tube to excite a large frequency range. In Table 1, the first four experimental natural frequencies obtained are compared to the theoretical values of a tube simply supported at both ends. The experimental versus theoretical natural frequencies confirm that the configuration of a simply supported tube is an adequate representation since the relative errors are less than 10% for each mode. The natural frequencies of the first and second modes are respectively 7,25Hz and 26,50Hz. Random excitation forces will then be applied in a 10Hz bandwidth around those two frequencies.

TABLE 1: NATURAL FREQUENCIES OF THE TUBE AND EXCITATION FREQUENCY RANGE.

Mode	Theoretical	Experimental	Relative errors	Excitation range
	Hz	Hz	%	Hz
1	6,62	7,25	9,52	2,25-12,25
2	26,49	26,50	0,04	21,50-31,50
3	59,60	55,40	7,05	---
4	105,95	98,60	6,94	---

Excitation Amplitudes

The random forces induced by a two-phase cross flow can be evaluated by the equivalent power spectral density (EPSD) recommended in steam generators of nuclear reactors [16]. This method is therefore used to calculate

tube displacements similar to those found in steam generators.

Assuming a void fraction of 80% in the U-bend section of the tubes, a flow rate of 5m/s and mechanical and geometric properties of the Inconel tube, the mid-span RMS displacement should not exceed 3,79mm. The supplied electromagnetic voltage used to obtain a displacement of 3,79mm at the center of the tube is 8,06V. This voltage is supplied to the electromagnetic shakers in a 10Hz bandwidth around 7,25Hz and 26,50Hz.

Experimental Protocol

Time signals of mid-span position and contact force are obtained using the real time frequency analyzer OROS via the graphical user interface NVGate. Sampling frequency and acquisition window are respectively set to 32 768Hz and 100 seconds.

The AVB is positioned manually at a distance of $0\mu\text{m}$ relative to the surface of the tube. The desired clearance or preload is then adjusted relative to $0\mu\text{m}$. Three data acquisitions are conducted for each position of the AVB: 1) using no excitation force, 2) using a supplied voltage of 8,06V in the 2,25Hz to 12,25Hz bandwidth and 3) using a supplied voltage of 8,06V in the 21,50Hz to 31,50Hz bandwidth. Data acquisitions are performed for clearances between $-4000\mu\text{m}$ and $4000\mu\text{m}$ (80 positions). Recall that a tube deflection of $-100\mu\text{m}$ corresponds to a preload of 0,149N. The full procedure is then repeated four times for a total of 1200 tests lasting 100 seconds each.

Finally, noise reduction processing is performed by a Matlab code to attenuate the noise in displacement and contact force time signals. Band-cut filters are applied around specific frequencies to reduce the mechanical noise originating from the vibration of the supporting structure. Electromagnetic noise originating from the measuring system components is eliminated from the signals by applying upper and lower noise thresholds, which are estimated from the sensors noise levels.

VIBRATION RESPONSE ANALYSIS

The vibration analysis aims to study the system response regarding the trajectory of the tube and the contact force spectra. Since a significant number of tests were conducted, the vibration analysis is only presented for a targeted sample of results, which represent all the distinctive behaviors in the experiments. For all 80 configurations, the analysis is exclusively shown for clearances $0\mu\text{m}$, $500\mu\text{m}$, $2000\mu\text{m}$ and $4000\mu\text{m}$ and for preloads corresponding to tube deflections $-50\mu\text{m}$, $-150\mu\text{m}$, $-250\mu\text{m}$ and $-500\mu\text{m}$.

Tube Trajectory

The trajectory of the tube is observed using Lissajous figures. In those figures, the position of the tube along Y is plotted as a function of the position along Z. The Y-axis is

in the same direction as the excitation force and parallel to the AVB, and Z-axis is normal to the excitation force, as shown in Figs. 1 to 3.

For excitation force around the first mode, the mode shape of the tube has an antinode at mid-span as seen in Fig. 4. Displacement is then maximal at this location. Figure 5 shows the trajectory of the tube in the YZ plane for different clearances between the tube and the AVB. The curves represent the trajectories of the tube and the thick vertical lines indicate the location of the AVB. For clearances $0\mu\text{m}$ and $500\mu\text{m}$, the displacement is mainly parallel to the AVB. The AVB guides the movement of the tube in the Y direction and prevents whirling. However, at $500\mu\text{m}$, the movement of the tube is slightly oblique, likely due to a small offset in the excitation direction with respect to the AVB. The contact consists of sliding combined with impacts. The vibration amplitude increases as the clearance enlarges. Beyond $500\mu\text{m}$, whirling of the tube is observed. The displacement along Z increases, but it decreases in the Y direction. Compared to a clearance of $4000\mu\text{m}$ where there is no contact between the tube and the AVB, sliding and impacts are still present for a clearance of $2000\mu\text{m}$. At $4000\mu\text{m}$, the tube rotates around its initial position without touching the AVB.

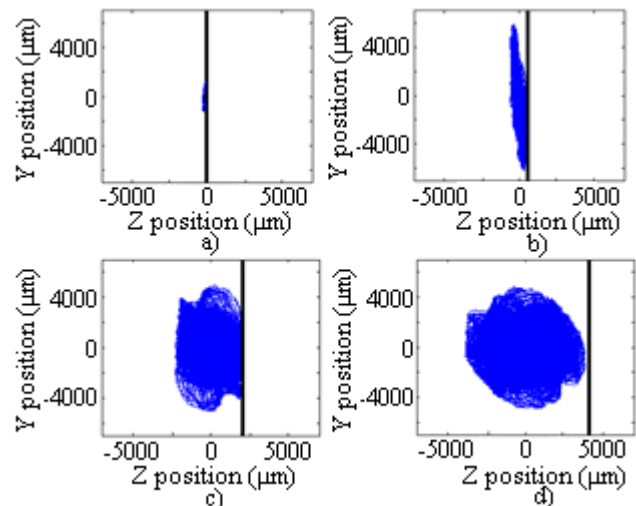


FIGURE 5: TRAJECTORY OF THE TUBE FOR EXCITATION AROUND MODE 1 FOR CLEARANCES: A) $0\mu\text{m}$ B) $500\mu\text{m}$ C) $2000\mu\text{m}$ D) $4000\mu\text{m}$.

In Fig. 6, the same analysis is presented for different preloads between the tube and the AVB. For comparison purposes, the trajectory of the tube for a clearance of $0\mu\text{m}$ is showed with a smaller scale. For preloads corresponding to tube static deflections $0\mu\text{m}$, $-50\mu\text{m}$, $-150\mu\text{m}$ and $-250\mu\text{m}$, the dynamic displacement of the tube is essentially parallel to the AVB, along Y. The vibration amplitude decreases as the preload increases. Indeed, when there is a preload, the movement along Z is restricted by the AVB through normal static force. The contact between the tube and the AVB is sliding only. When the preload is set to $-500\mu\text{m}$, the displacement of

the tube is almost zero. The friction force due to preload is high enough relative to the excitation force to prevent any vibration.

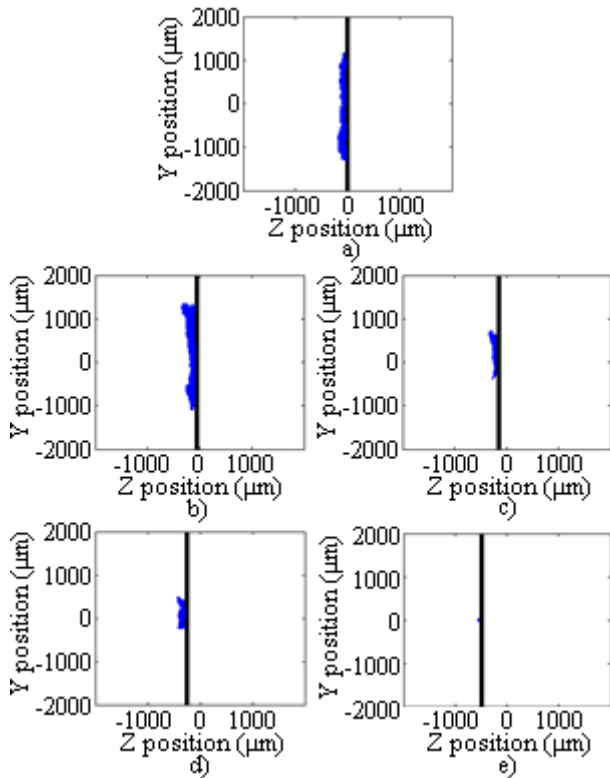


FIGURE 6: TRAJECTORY OF THE TUBE FOR EXCITATION AROUND MODE 1 FOR PRELOADS: A) 0µm B) -50µm C) -150µm D) -250µm E) -500µm.

When the excitation force is around the second mode of the tube, there is a node at mid-span as seen in Fig. 4. The displacement should then always be zero at this location of the tube regardless of clearance or preload. For clearances above 10µm, practically no displacement and no contact force were observed. Thus, only preload configurations are shown in this analysis. Figure 7 presents the tube trajectory at different preloads for an excitation force around the second mode. Compared to the expected behavior, displacements are relatively high. At -150µm, the maximum displacement along Y and Z are respectively about 300µm and 100µm. Moreover, compared to an excitation force around the first mode, the tube has a small two-dimension random motion rather than a displacement along Y. Finally, the tube response decreases as the preload increases.

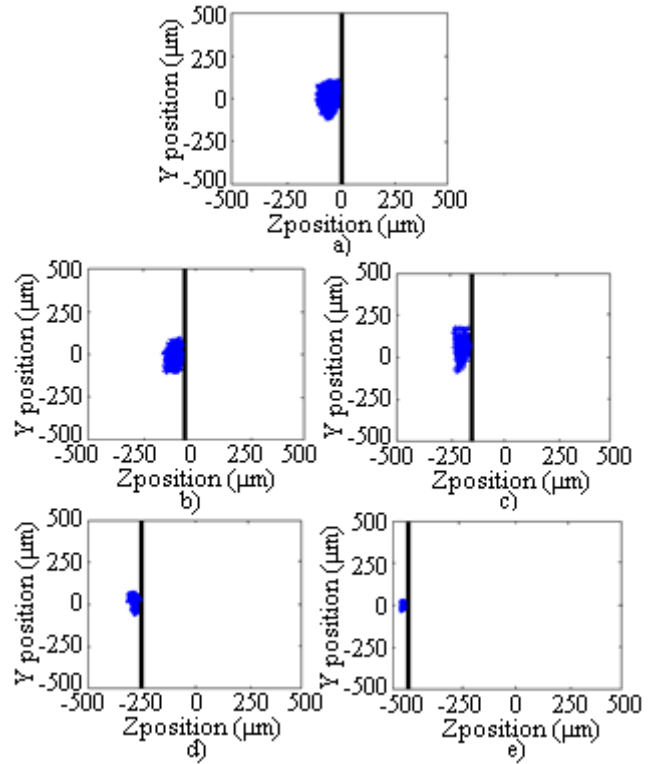


FIGURE 7: TRAJECTORY OF THE TUBE FOR EXCITATION AROUND MODE 2 FOR PRELOADS: A) 0µm B) -50µm C) -150µm D) -250µm E) -500µm.

Contact Force

The contact force between the tube and the AVB is analyzed by inspecting some of the time signals and frequency spectra. Recall that the contact forces are measured in the Z direction, normal to the AVB. The total force is obtained by adding time signals of the two force sensors and the static preload force when applicable.

For excitation forces around the first mode, the tube has an antinode at mid-span. The contact between the tube and the AVB consists of sliding combined with impacts. For a clearance of 500µm, Fig. 8a) shows the contact force time signal zoomed on several impacts.

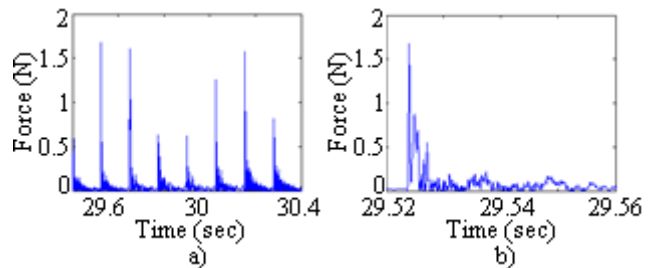


FIGURE 8: TIME SIGNAL OF THE CONTACT FORCE FOR EXCITATION AROUND MODE 1 AND A CLEARANCE OF 500µm.

A) OVERVIEW B) MAGNIFIED

There are approximately seven impacts over a period of 1 second, which corresponds to the first natural frequency of the tube (7,25Hz). After an impact, the force does not drop immediately to zero due to a short period of rubbing between the tube and the AVB. To visualize the shape of an impact, Fig. 8b) shows the signal zoomed on one impact. Multiple impacts over a short period of 0,002 second are observed during the interaction. This can be explained by higher modes being excited when the tube is impacting against the AVB.

For an excitation force around the first mode, contact force spectra are calculated from time signals for different clearances as seen in Fig. 9. For a clearance of 0µm, force magnitude is low for all frequencies. However, the spectral content is mainly located at low frequencies. There is a small peak at 7,25Hz which corresponds to the first natural frequency of the tube. For clearances 500µm and 2000µm, harmonics of the first natural frequency of the tube are present in the spectra. This is caused by the discontinuous and triangular shape of the impacts seen in Fig. 8. Finally, at 4000µm, there is no contact between the tube and the AVB as it was also observed in the trajectory of the tube of Fig. 5d).

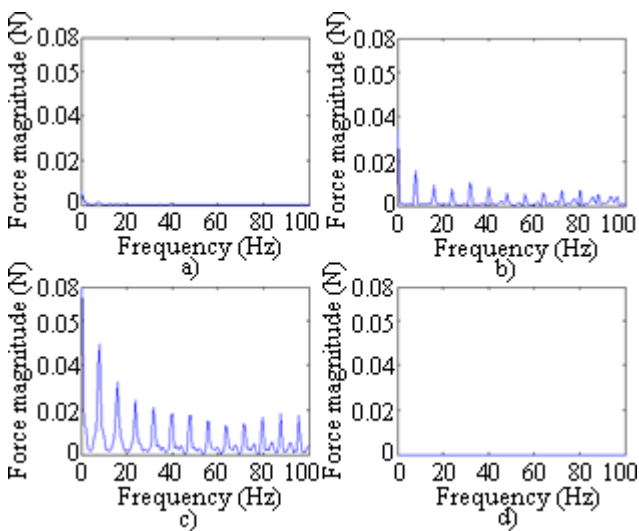


FIGURE 9: SPECTRA OF THE CONTACT FORCE FOR EXCITATION AROUND MODE 1 FOR CLEARANCES: A) 0µm B) 500µm C) 2000µm D) 4000µm.

For preloads, the tube rubs against the AVB. No impacts are detected, but only sliding of the tube against the AVB. For a preload corresponding to a tube deflection of -250µm, Fig. 10 shows time signal magnifications of the contact force. Compared to Fig. 8 when there is a clearance, the waveform illustrates a complete different behavior. Discontinuous segments of near-sinusoidal waves combined with flat segments corresponding to the static preload force are noticed. This alternating behavior is consistent with the «stick-slip» phenomenon often observed during relative sliding of two bodies [17]. «Stick-slip» can be explained by the Coulomb friction

laws which involve static and dynamic friction. When there is no sliding, static friction occurs. Otherwise, if the tube is in motion, dynamic friction occurs. Since the static friction coefficient is greater than the dynamic friction coefficient, larger effort is required to provoke tube displacement from rest than to maintain its motion.

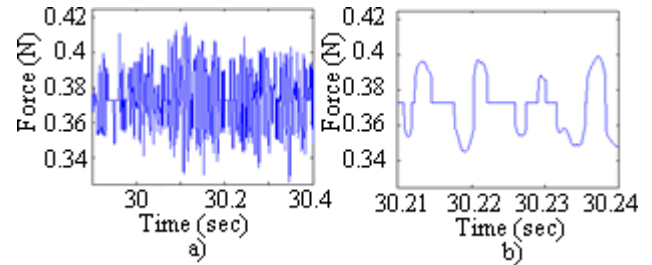


FIGURE 10: TIME SIGNAL OF THE CONTACT FORCE FOR EXCITATION AROUND MODE 1 AND A PRELOAD OF -250µm. A) OVERVIEW B) MAGNIFIED

By inspecting the spectra in Fig. 11 for an excitation force around the first mode, we notice an important spectral component at the first natural frequency for preloads 0µm, -50µm and -150µm.

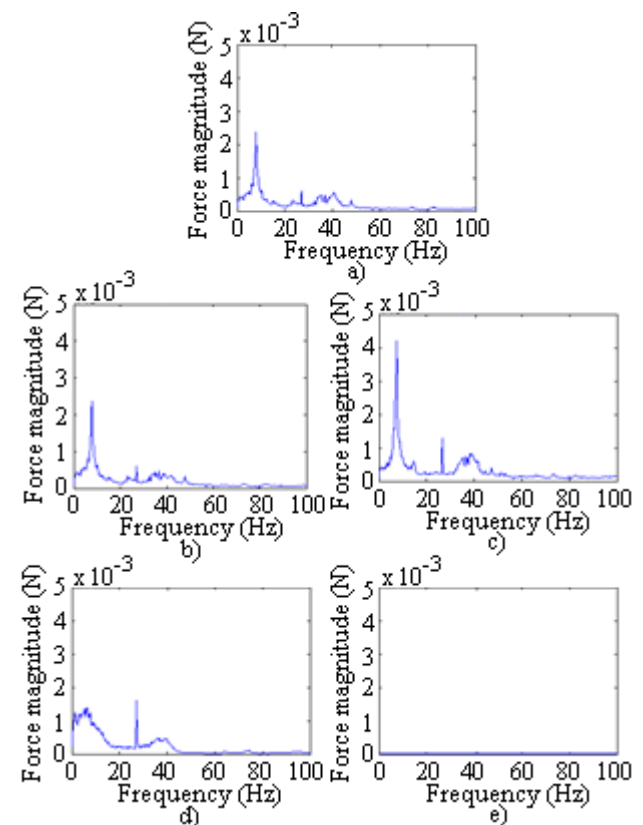


FIGURE 11: SPECTRA OF THE CONTACT FORCE FOR EXCITATION AROUND MODE 1 FOR PRELOADS: A) 0µm B) -50µm C) -150µm D) -250µm E) -500µm.

A lower peak at the second natural frequency (26,50Hz) is also observed. Even if the excitation force is around the first mode, impacts excite all modes to different degrees. For a higher preload corresponding to a tube deflection of $-250\mu\text{m}$, the magnitude at the first natural frequency is reduced while the second natural frequency is amplified. Finally, for a preload of $-500\mu\text{m}$, there is no dynamic force between the tube and the AVB.

For an excitation force around the second mode, Fig. 12 shows the contact force spectra for different preloads. At $0\mu\text{m}$, $-50\mu\text{m}$ and $-150\mu\text{m}$, predominant spectral contents are seen at 26,50Hz, 53,50Hz and 81,25Hz. Those frequencies represent respectively the second natural frequency of the tube and its harmonics. The presence of harmonics is due to the time signals of the contact force which are not perfect sinusoids. For a higher preload of $-250\mu\text{m}$, both harmonics are attenuated. Finally, when the preload is increased to $-500\mu\text{m}$, the dynamic force between the tube and the AVB is zero for all frequencies.

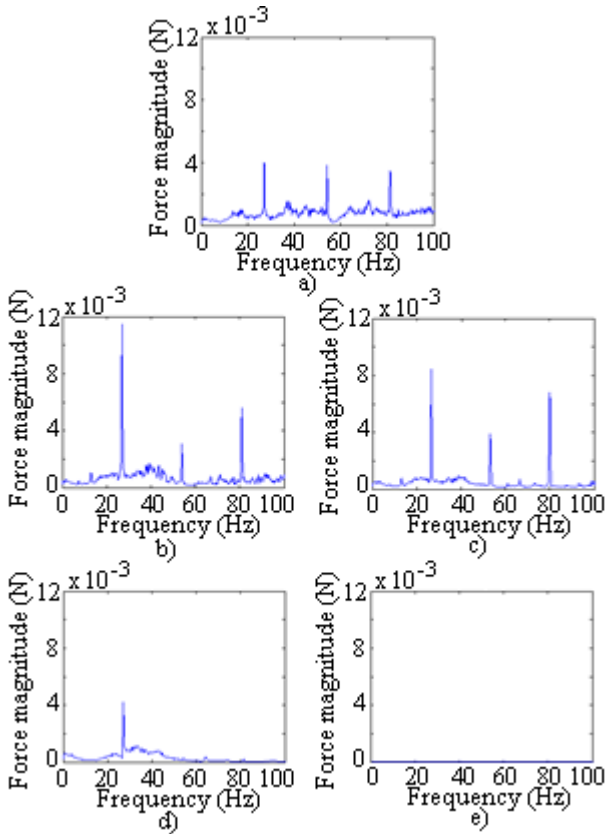


FIGURE 12: SPECTRA OF THE CONTACT FORCE FOR EXCITATION AROUND MODE 2 FOR PRELOADS:
 A) $0\mu\text{m}$ B) $-50\mu\text{m}$ C) $-150\mu\text{m}$ D) $-250\mu\text{m}$ E) $-500\mu\text{m}$.

FRETTING-WEAR WORK-RATE

Since data acquisition converts the analog signal into a series of discrete points, the integral of Eq. 1 is modified into a summation to compute the work-rate. Moreover, as

the laser sensors measure the mid-span position of the tube, positions are converted into displacements.

For the position time signal $y(t) = \{y_1, y_2, y_3, \dots, y_n\}$, where n is the number of points contained in the signal, the displacement of the tube can be obtained as follows:

$$ds(t) = \{ds_1, ds_2, ds_3, \dots, ds_{n-1}\} \\ = \{y_2 - y_1, y_3 - y_2, y_4 - y_3, \dots, y_n - y_{n-1}\} \quad (2)$$

By multiplying the contact force time signal $F(t) = \{f_1, f_2, f_3, \dots, f_n\}$ with the displacement signal $ds(t)$, the fretting-wear work-rate can be evaluated as:

$$W_N = \frac{1}{T} \sum_{i=1}^{n-1} f_i (y_{i+1} - y_i) \quad (3)$$

In Fig. 13, fretting-wear work-rate is computed as a function of clearance or preload for excitation forces around the first and second modes.

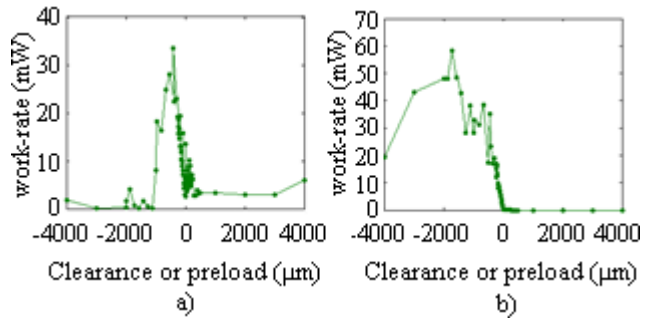


FIGURE 13: FRETTING-WEAR WORK-RATE AS A FONCTION OF CLEARANCE OR PRELOAD FOR EXCITATION FORCE AROUND:
 A) MODE 1 B) MODE 2

For excitation force around the first mode, the mode shape of the tube indicates an antinode at mid-span. As seen in Fig. 13a), the fretting-wear work-rate increases linearly for preloads corresponding to tube deflections between $0\mu\text{m}$ and $-650\mu\text{m}$. Even if the displacement of the tube and the dynamic force are small, the work-rate is high due to a constant static force caused by preload. For higher preloads, the work-rate decreases as the friction force becomes greater than the excitation force, and the displacement of the tube tends to zero. A preload of $1,64\text{N}$ corresponding to a tube deflection of $-1100\mu\text{m}$ is required to avoid work-rate higher than 1mW . For clearances above $0\mu\text{m}$, the work-rate is lower compared to a preload because the contacts are of short duration and the static force is zero. However, the work-rate is higher than 1mW for all clearances.

When the tube is excited around mode 2, there is a node at mid-span. Therefore, the displacement of the tube is practically zero regardless of clearance or preload. For clearances above $10\mu\text{m}$, the work-rate seen in Fig. 13b) is

zero because there is virtually no displacement and no contact force. For small preloads, the work-rate increases linearly, similar to the first mode. It confirms that the static force due to preload has the most significant influence on the work-rate. We also observe higher work-rates when the tube is excited around the second mode. Indeed, for a given preload, the contact force signals are higher for excitation force around mode 2. For all preloads, the work-rate is greater than 1mW.

CONCLUSION

The main objectives of this paper were to study experimentally the vibration behavior of a tube in interaction with an AVB and to compute the fretting-wear work-rate. A test rig that replicates the tube/support configuration as encountered in steam generators was used to measure the mid-span displacement of the tube and the contact force against the AVB.

For an excitation force around the first mode of the tube, the mode shape has an antinode at mid-span. When there is a clearance between the tube and the AVB, the contact consists of combined sliding and impacts. However, for high preloads, there is only sliding because the tube is restricted by the AVB at its center. For an excitation force around the second mode with a clearance, there is no contact force between the tube and the AVB as the mode shape indicates a node at mid-span. When a preload is applied, the contact force is however higher than for an excitation force around the first mode.

From the results obtained in this paper, to ensure the effectiveness of AVBs and to maintain low fretting-wear work-rate, a high preload between the tube and the AVB is recommended if the excitation forces are around the first mode. On the other hand, for excitation forces around the second mode of the tube, a small clearance is recommended.

ACKNOWLEDGMENTS

The authors gratefully acknowledge the financial support of BWC, AECL and NSERC.

REFERENCES

- [1] Janzen, V. P., Hagberg, E. G., Pettigrew, M. J., & Taylor, C. E. (2005). Fluidelastic Instability and Work-Rate Measurements of Steam-Generator U-Tubes in Air-Water Cross-Flow. *Journal of Pressure Vessel Technology*, 127, 84-91.
- [2] Pettigrew, M. J., Taylor, C. E., & Kim, B. S. (1989). Vibration of Tube Bundles in Two-Phase Cross-Flow: Part 1-Hydrodynamic Mass and Damping. *Journal of Pressure Vessel Technology*, 111, 466-477.
- [3] Pettigrew, M. J., Tromp, J. H., Taylor, C. E., & Kim, B. S. (1989). Vibration of Tube Bundles in Two-Phase Cross-Flow: Part 2-Fluid-Elastic Instability. *Journal of Pressure Vessel Technology*, 111, 478-487.
- [4] Taylor, C. E., Currie, I. G., Pettigrew, M. J., & Kim, B. S. (1989). Vibration of Tube Bundles in Two-Phase Cross-Flow: Part 3-Turbulence-Induced Excitation. *Journal of Pressure Vessel Technology*, 111, 488-500.
- [5] Pettigrew, M. J., Tromp, J. H., & Mastorakos, J. (1985). Vibration of Tube Bundles Subjected to Two-Phase Cross-Flow. *Journal of Pressure Vessel Technology*, 107, 335-343.
- [6] Pettigrew, M. J., & Taylor, C. E. (2003). Vibration Analysis of Shell-and-Tube Heat Exchangers. *Journal of Fluid and Structures*, 18, 469-500.
- [7] Fisher, N. J., Chow, A. B., & Weckwerth, M. K. (1995). Experimental Fretting-Wear Studies of Steam Generator Materials. *ASME Journal of Pressure Vessel Technology*, 117, 312-320.
- [8] Frick, T. M., Sobek, T. E., & Reavis, J. R. (1984). Overview on the Development and Implementation of Methodologies to Compute Vibration and Wear of Steam Generator Tubes. *ASME Symposium on Flow-Induced Vibrations*, 3, 149-161.
- [9] Yetisir, M., & Fisher, N. J. (1997). Prediction of Pressure Tube Fretting-Wear Damage Due to Fuel Vibration. *Nuclear Engineering and Design*, 176, 261-271.
- [10] Fisher, N. J., Olesen, M. J., Rogers, R. J., & Ko, P. L. (1989). Simulation of Tube-to-Support Dynamic Interaction in Heat Exchange Equipment. *Journal of Pressure Vessel Technology*, 111, 378-384.
- [11] Hassan, M. A., & Rogers, R. J. (2005). Friction Modelling of Preloaded Tube Contact Dynamics. *Nuclear Engineering and Design*, 235, 2349-2357.
- [12] Hassan, M. A. (2006). Simulation of Fluidelastic Vibrations of Heat Exchanger Tubes with Loose Supports. *ASME Pressure Vessels and Piping Division Conference*, July, 621-631.
- [13] Hassan, M., & Hayder, M. (2008). Modeling of Fluidelastic Vibrations of Heat Exchanger Tubes with Loose Supports. *Nuclear Engineering and Design*, 238, 2507-2520.
- [14] P. L. Ko. (1979). Experimental Studies of Tube Fretting in Steam Generators and Heat Exchangers, *ASME Journal of Pressure Vessel Technology*, 101, 125-134.
- [15] Nowlan, I. (2008). *Étude expérimentale du comportement vibratoire d'un tube de générateur de vapeur en interaction avec une barre plate*, Masters Thesis (École Polytechnique de Montréal), 136p.
- [16] Axisa, F., Antunes, J., & Villard, B. (1990). Random Excitation of Heat Exchanger Tubes by Cross-Flows. *Journal of Fluid and Structures*, 4, 321-341.
- [17] Berman, A. D., Ducker, W. A., & Israelachvili, J. N. (1996). Origin and Characterization of Different Stick-Slip Friction Mechanisms. *Langmuir*, 12, 4559-4563.



EXPERIMENTAL STUDY OF FLUIDELASTIC INSTABILITY IN A ROTATED TRIANGULAR TUBE ARRAY SUBJECTED TO TWO-PHASE CROSS-FLOW

Teguewinde Sawadogo

Njuki Mureithi

BWC/AECL/NSERC Chair of Fluid-Structure Interaction
 Department of Mechanical Engineering
 École Polytechnique de Montréal
 C.P. 6079 Succursale Centre-ville, Montréal, H3C 3A7, Canada
 Email: teguewinde-pierre.sawadogo@polymtl.ca
 Njuki.mureithi@polymtl.ca

ABSTRACT

Fluidelastic instability induced by two-phase cross-flow in a rotated triangular tube array is investigated in this article. Quasi-static fluid forces in the lift direction were measured in two-phase flow for various void fractions at a Reynolds number $Re_\infty = 2.8 \times 10^4$. The derivative of the lift coefficient with respect to the non-dimensional displacement in the lift direction was calculated from the measured fluid force coefficients. This derivative is the most important parameter in studying fluidelastic instability in the lift direction.

This derivative was found to be positive in liquid flow and negative in two-phase flow. Interestingly, this derivative seems to vanish at around 5% void fraction. In fact, the tube behaves as in liquid flow when it is close to the equilibrium position and, as in two-phase flow when it is far from the equilibrium position.

The quasi-steady model with a time retardation parameter of order 1 as suggested by Price & Païdoussis (1982, 1983) cannot predict fluidelastic instability for a single flexible tube in a rigid tube bundle when the derivative of the lift coefficient is zero. However, a stability test conducted for 5% void fraction showed that the tube was subjected to fluidelastic instability. A measurement of the time delay inherent to the quasi-steady model for this void fraction is necessary to better understand the instability mechanism.

Stability tests were also carried out for various values of the mass-damping parameter. The damping was varied using viscoelastic rubber. The fluid damping and the added mass were also measured. The fluid damping was found to increase linearly up to a peak of approximately 4% at 70% void fraction. The added mass was compared to the Pettigrew *et al.* (1989) expression. It was found that this formula underestimates the added mass for void fractions higher than 20% by a large factor. The stability test results show that for a given void fraction, the reduced critical velocity does not vary significantly with the mass damping parameter. The Connors model was also tested

against the experimental data which were generally above the Connors curve with $K = 4$.

NOMENCLATURE

C_D, C_L	Drag and lift coefficients based on free stream velocity, respectively.
$C_{L,Y/D}$	Derivative of the lift coefficient with respect to the non-dimensional displacement in the lift direction.
C_{D0}, C_{L0}	Steady drag and lift coefficients based on free stream velocity, respectively.
D	Tube diameter.
D_e/D	Confinement parameter.
f, f_0, f_c, f_r	Tube frequency, tube natural frequency in air, tube frequency at instability, tube frequency in the flow, respectively.
K	Constant of Connors.
m, m_a	Tube total mass per unit length, hydrodynamic mass.
P	Pitch between tubes.
Re_∞	Reynolds number based on upstream velocity.
Q_G, Q_L	Volumetric flow rate of gas, liquid phase, respectively.
U, U_∞, U_G, U_P	Fluid velocity, upstream velocity, gap velocity and pitch velocity, respectively $\left(U_G = U_\infty \frac{T}{T - 0.5D}, U_P = U_\infty \frac{P}{P - D} \right)$.
T	Center to center distance between tubes in the cross-flow direction.
x	Gas mass quality.
Y/D	Non-dimensional displacement in the lift direction.

β	Homogeneous void fraction.
δ	Damping logarithmic decrement.
μ	Dynamic viscosity (Pa s ⁻¹).
ρ, ρ_h	Fluid density, homogeneous density, respectively.
τ	Time lag between the tube displacement and the resulting fluid force.
ω	Angular frequency.
ζ	Damping ratio.

INTRODUCTION

Tube bundles in steam generators and heat exchangers are subjected to several types of flow induced excitations including turbulence buffeting, periodic excitations and fluidelastic instability. Among these flow induced excitation mechanisms, fluidelastic instability is considered to be the most severe type of excitation and consequently, has attracted a great deal of investigation. However, this research effort has been carried out mostly for single phase flow whereas tube bundles operate generally in two-phase flow.

By measuring the quasi-static fluid forces acting on a tube statically displaced in a tube row and balancing the energy in the in-flow and cross-flow directions, Connors (1970) derived his famous equation, relating the reduced critical velocity to the mass-damping parameter:

$$\frac{U}{fD} = K \left(\frac{m\delta}{\rho D^2} \right)^{0.5} \quad (1)$$

where U is the fluid velocity, f the tube natural frequency, D the tube diameter, m the tube mass per unit length including the hydrodynamic mass, δ the logarithmic decrement and ρ the fluid density. K is the Connors constant which is determined experimentally.

Price and Païdoussis (1982, 1983) improved the Connors model under the name of quasi-steady model by taking into consideration the relative flow velocity and the time lag between the fluid forces and the tube displacement. They showed that fluidelastic instability is governed by two different mechanisms: i) a damping controlled mechanism for low mass-damping parameters and ii) a fluid stiffness controlled mechanism or displacement controlled mechanism for high values of the mass-damping parameter. Chen (1983a, b) also brought these two mechanisms into evidence with his unsteady model.

Both Chen (1983a) and Païdoussis & Price (1988) showed that the criterion for a damping controlled mechanism could be written as:

$$\frac{U}{fD} = K \left(\frac{m\delta}{\rho D^2} \right) \quad (2)$$

while for the displacement controlled mechanism the criterion would be the same as the Connors equation:

$$\frac{U}{fD} = K \left(\frac{m\delta}{\rho D^2} \right)^{0.5} \quad (3)$$

The stiffness controlled mechanism can occur only in multiple degrees-of-freedom systems while the damping controlled instability can occur in a single degree-of-freedom system. This means that the Connors model is relevant only for multiple degrees-of-freedom systems.

It is well known (Violette et al., 2006) that the instability threshold in the lift direction is usually much lower than that in the drag direction. For this reason, we have focused on the study of fluidelastic instability in the lift direction.

In the present work, measurements of the quasi-static fluid force coefficients in the lift direction in a rotated triangular tube bundle for various void fractions are presented. Fluidelastic instability measurements for a single tube, flexible only in one direction (the lift direction) are also presented for various void fractions and mass damping parameters. The fluid damping and the added mass were also measured and compared with data available in the literature.

QUASI-STATIC FLUID FORCE COEFFICIENTS

Expression of the Fluid Force in the Quasi-Steady Model

Considering a single flexible tube, flexible only in the lift direction, the quasi-steady fluid force expression in the lift direction adopted from Païdoussis & Price (1988) may be rewritten as (Sawadogo & Mureithi, 2011):

$$F_y = \frac{1}{2} \rho D U_\infty^2 \left[\begin{array}{l} C_{L0} - \left(\frac{C_{D0}}{U_G} + \frac{\sin \omega \tau}{\omega} \frac{\partial C_L}{\partial y} \right) \dot{y} \\ + \cos \omega \tau \left(\frac{\partial C_L}{\partial y} y \right) \end{array} \right] \quad (4)$$

where C_{L0} and C_{D0} are the steady lift and drag coefficients, respectively; U_∞ and U_G are the fluid upstream velocity and gap velocity, respectively; ω is the tube natural angular frequency; τ is the time lag between the tube displacement and the resulting fluid force.

In the quasi-steady model, the fluid damping comes from the term:

$$\left(\frac{C_{D0}}{U_G} + \frac{\sin \omega \tau}{\omega} \frac{\partial C_L}{\partial y} \right) \dot{y} \quad (5)$$

For negative damping to occur the quantity $\frac{\sin \omega \tau}{\omega} \frac{\partial C_L}{\partial y}$

must be negative and the derivative of the lift coefficient with respect to the displacement in the lift direction has to be large enough to overcome the structural damping and the fluid positive damping (C_{D0}/U_G). The most important parameter in the study of fluidelastic instability in the lift direction is therefore $\frac{\partial C_L}{\partial y}$. In the following, experimental measurements of this lift force coefficient are presented.

Experimental Setup

The fluid force measurements were conducted with the experimental setup presented in Figures 1-2. It includes a compressed air source capable of delivering up to 250 l/s and a water loop powered by a centrifugal pump able to deliver up to 28 l/s. The air is injected in the loop at an upstream location with respect to the test section and the homogenization is done using a mixer.

The air flow rate is measured through two distinct orifice plates, one for low flow and the other for high flow, situated at a distant location from the test section and connected to a differential pressure transducer. The pressure was measured in the tube array and the air flow rate was corrected accordingly. The measurements were conducted at room temperature (approximately 22°C).

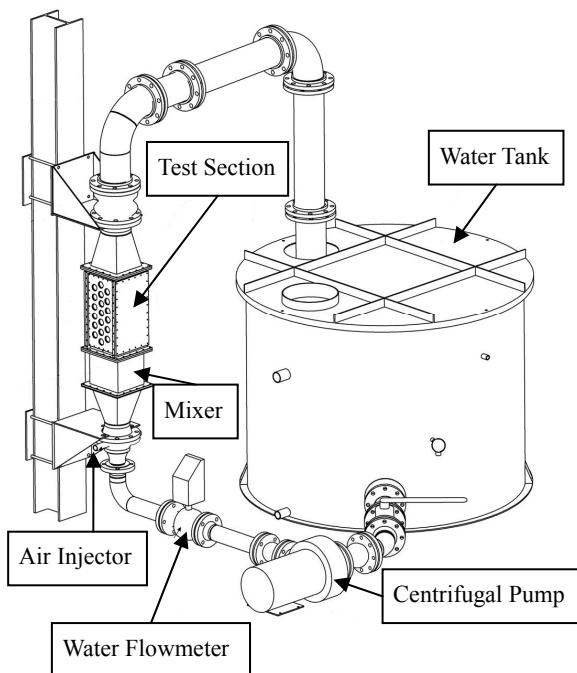


FIGURE 1 - TWO-PHASE FLOW LOOP.

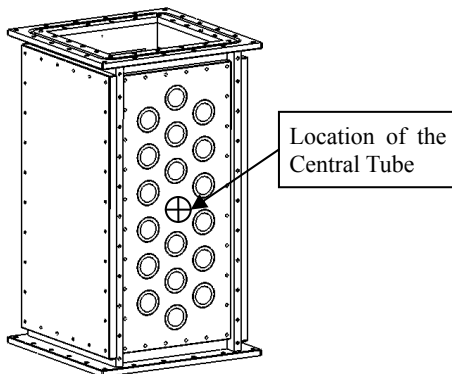


FIGURE 2 – TEST SECTION.

The tube array is a rotated triangular tube array (see Figure 3) composed of three columns of tubes and two columns of half-tubes attached to the walls, all arranged in seven rows. The diameter of the tubes is 38 mm and the pitch-to-diameter ratio $P/D = 1.5$. The tube length is 0.188 m. All the tubes were fixed except the central tube for which finite displacements were applied.

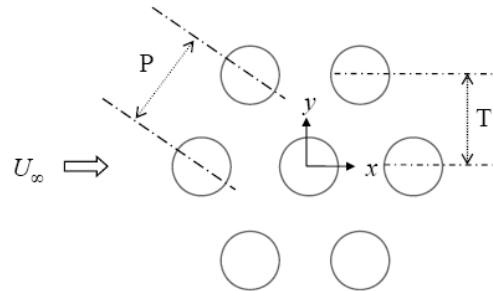


FIGURE 3 – TUBE BUNDLE CONFIGURATION.

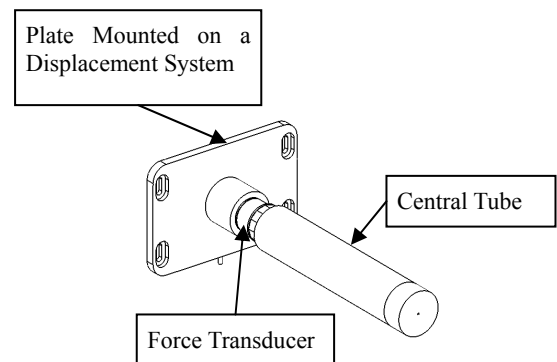


FIGURE 4 – INSTRUMENTED CENTRAL TUBE.

The central tube was mounted on an ATI Nano25 force transducer mounted on a plate attached to a displacement mechanism as shown in Figure 4. The resolution of the force transducer was 0.04 N and the RMS of the white noise was less than 0.01 N.

Fluid Force Coefficients

The test procedure involved applying finite displacements in increments of 1 mm ($0.026D$) to the central tube using the displacement mechanism, and, waiting for the flow to attain steady state, before starting the fluid force measurement. The fluid force data were acquired at a sampling rate of 2000 samples per second and averaged over 50 s. For some measurements, an averaging time of 80 s was necessary to obtain the steady force value. For each flow condition, two different measurements were taken and averaged.

The fluid force coefficient was non-dimensionalized using the flow upstream velocity, the tube diameter, the tube length and the homogeneous flow mass density. The variation of the lift coefficient with the non-dimensional displacement in the lift direction is presented in Figure 5 for various void fractions. These measurements have been conducted at a Reynolds number $Re_\infty = 2.8 \times 10^4$. The Reynolds number was calculated based on the upstream flow velocity, the tube diameter and the following homogeneous flow properties:

$$\beta = \frac{Q_G}{Q_G + Q_L}; \quad \rho_h = \beta \rho_G + (1 - \beta) \rho_L$$

$$x = \frac{\rho_G Q_G}{\rho_G Q_G + \rho_L Q_L} = \frac{\beta}{\beta + (1 - \beta) \frac{\rho_L}{\rho_G}} \quad (6)$$

$$\frac{1}{\mu_h} = \frac{x}{\mu_G} + \frac{(1-x)}{\mu_L}; \quad Re_\infty = \frac{\rho_h U_\infty D}{\mu_h}$$

where β is the homogeneous void fraction, Q the volumetric flow rate, ρ the mass density, x the gas mass quality, μ the dynamic viscosity, U_∞ the fluid upstream homogeneous velocity, and D the tube diameter. The subscripts G, L and h denote the value of the physical quantity for the gas phase, the liquid phase, and the homogeneous mixture, respectively.

It should be noted that there is no exact equation for the homogeneous mixture viscosity. The expression used here is the McAdams formula, which is expressed similarly to the homogeneous density. The Reynolds number of the two-phase flow is considered to be the sum of the Reynolds numbers of the two separate phases. As a result, the Reynolds number of the two-phase flow is only an approximate value.

In water flow and for void fractions higher than 50%, the lift coefficient varies abruptly in the vicinity of the zero position, but it becomes almost constant beyond $0.05D$. For this reason, the fluid lift coefficient was measured only from -4 mm to 4 mm for these flow conditions. This corresponds to $\pm 0.11D$.

For 10% and 20% void fraction, the variation of the lift coefficient with the position is quite linear within $0.05D$ of the equilibrium position.

From 5% to 40% void fraction, the lift coefficient was measured from -5 mm to $+5$ mm ($\pm 0.13D$) since its variation seems to continue at relatively distant positions.

As mentioned before, the most important parameter for the study of fluidelastic instability in the lift direction is the slope of the lift coefficient at the equilibrium position of the central tube.

This slope goes from a positive value in water flow to negatives values in two-phase flow as shown in Figures 5. The derivative of the lift coefficient with respect to the non-dimensional displacement in the lift direction ($C_{L,Y/D}$) is presented in Figure 6 as a function of the void

fraction. The slope $C_{L,Y/D}$ varies linearly from 5% to 50% void fraction and from 50% to 70% void fraction. From 70% to 80% this slope is constant.

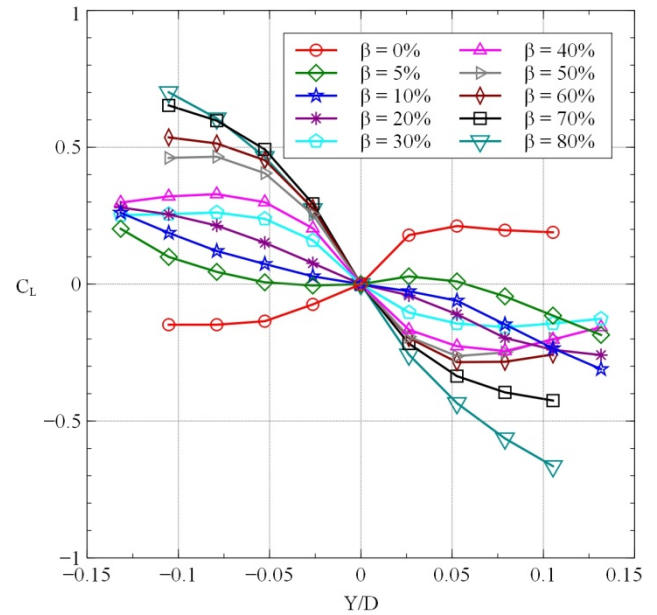


FIGURE 5 – VARIATION OF THE LIFT COEFFICIENT AT A REYNOLDS NUMBER $Re_\infty = 2.8 \times 10^4$.

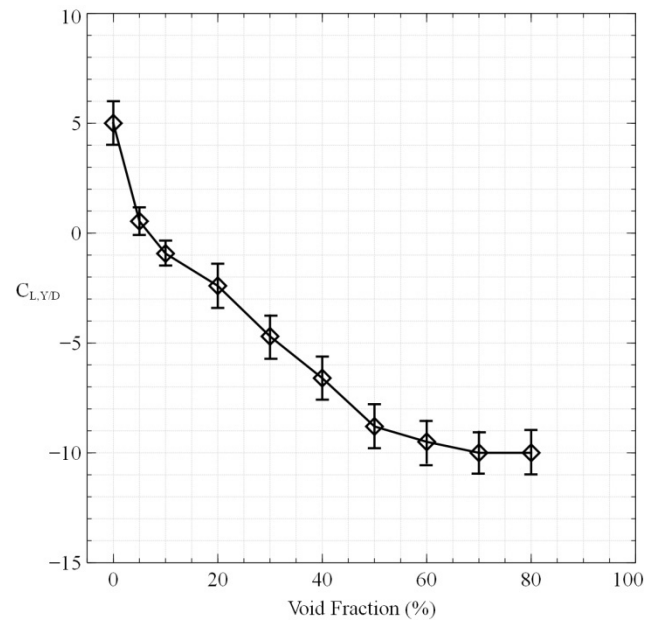


FIGURE 6 – VARIATION OF $C_{L,Y/D}$ WITH THE VOID FRACTION AT REYNOLDS NUMBER $Re_\infty = 2.8 \times 10^4$.

Something interesting happens at around 5% void fraction. The slope seems to vanish, suggesting that there will be no fluidelastic instability for this void fraction (at least based on the quasi-steady model). A closer look at

the variation of the lift coefficient with respect to the non-dimensional displacement in the lift direction is presented in Figure 7. Three different measurements were conducted at the same flow velocity.

From Figure 7, it can be seen that the fluid force varies as in water flow in the vicinity of the zero position, but beyond $0.05D$, it behaves as in two-phase flow. This may come from the void fraction distribution in the tube array at this void fraction. A visual observation shows that the gas phase on the one hand is more present in the flow path between tube columns, while the liquid phase on the other hand is more concentrated in the tube wakes.

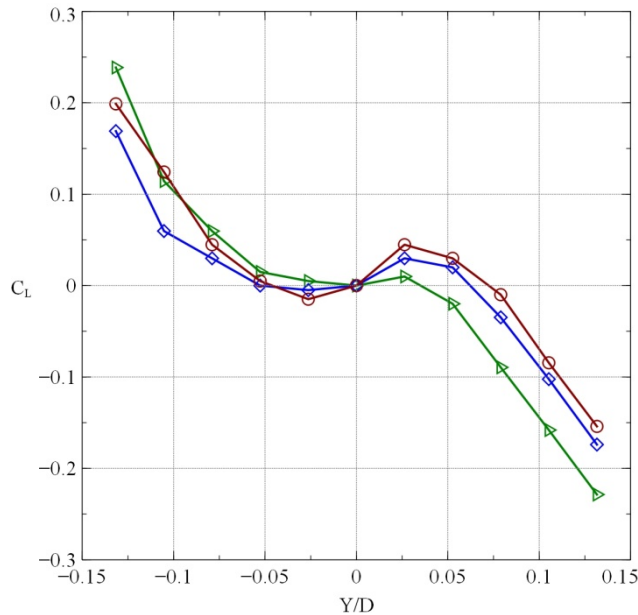


FIGURE 7 – VARIATION OF THE LIFT COEFFICIENT FOR 5% VOID FRACTION AT A REYNOLDS NUMBER $Re_{\infty}=2.8 \times 10^4$.

The data of Figure 7 suggest that for a flexible tube, the fluidelastic forces will be insignificant when the turbulence induced vibrations are limited to below $\pm 5\%D$. Beyond that, the tube will behave as in two-phase flow and it should be subjected to fluidelastic instability.

DYNAMIC STABILITY TESTS

The data available in the literature on fluidelastic instability concern mainly single phase flow whereas tube bundles operate mostly in two-phase flow. Recently, unsteady and quasi-static fluid forces in two-phase flow were made available (Mureithi et al., 2002, Shahriary et al., 2007) but stability tests are still needed to validate the theoretical models.

In the following experiment stability tests are performed for various mass-damping parameters. The tests were conducted for various void fractions and various damping ratios.

Experimental Setup

The same test section and flow loop as presented in the previous sections are used to perform these experiments. In this case, a fixed-free tube is used as a central tube. The tube is mounted on a flexible plate, and some viscoelastic damping rubber is placed between the flexible plate and the wall as shown in Figure 8. The dimensions of the rubber damper are changed to vary its damping effect.

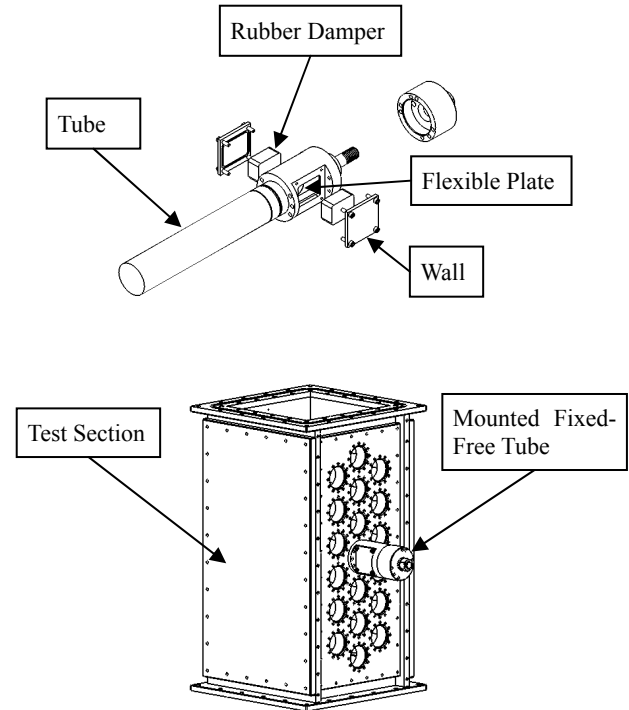


FIGURE 8 – FLEXIBLE TUBE AND DAMPING MECHANISM.

The whole assembly is mounted in the test section within the array. Strain gages mounted on the flexible plate are calibrated to measure the displacement at the free end of the tube.

TABLE 1 - TUBE FREQUENCY AND DAMPING RATIO OBTAINED BY VARYING THE RUBBER DIMENSIONS.

Case	Frequency (Hz)	Damping ratio (%)
No rubber	13.8	0.3
Rubber 1	14.8	1.6
Rubber 2	15.6	2.2

Changing the dimensions of the rubber changes also the tube natural frequency but this variation was relatively small and does not affect the purpose of the experiment which is to vary the mass damping parameter. The tube natural frequencies and damping ratios are presented in Table 1.

Data Analysis Technique

For each flow condition, the tube displacement at the free end was acquired through Labview via a National Instrument data acquisition card. Data were acquired during 16 s at a sampling rate of 500 samples per second and averaged 15 to 30 times depending on the magnitude of the vibration compared to the noise. This allowed a frequency resolution of 0.0625 Hz.

The tube damping in flow and its frequency at instability were estimated using its frequency response, approximated by the frequency response of a single degree-of-freedom system given by:

$$|H(\omega)| = \frac{1}{\left[\left(1 - \left(\frac{\omega}{\omega_n} \right)^2 \right)^2 + \left(2\zeta \frac{\omega}{\omega_n} \right)^2 \right]^{1/2}} \quad (7)$$

The damping and the frequency are estimated using a least square curve fitting technique. The curve given by Equation (7) is fitted to the experimental data as shown in Figure 9, and, the damping ratio and the frequency are extracted. The damping ratio may also be estimated using the quality factor. The damping estimated using the two methods was found to be in quite good agreement.

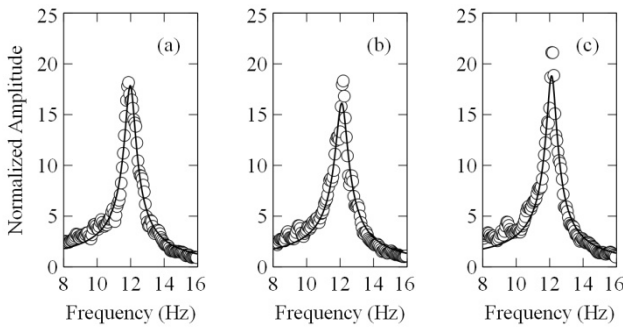


FIGURE 9 – CURVE FIT OF THE DATA FOR 50% VOID FRACTION. (A) $U_p = 0.3$ M/S, (B) $U_p = 0.4$ M/S, (C) $U_p = 0.5$ M/S.

Added Mass

The added mass was estimated for various void fractions since it is an important parameter for both the quasi-steady and the unsteady models.

The added mass was estimated from the variation of the tube natural frequency in flow at relatively low velocities. Considering a one degree-of-freedom system of stiffness, mass per unit length and added mass k , m , and m_a , respectively; the natural frequency in air $f_0 = \sqrt{k/m}$ and in flow $f_r = \sqrt{k/(m+m_a)}$ are related by:

$$\frac{f_0^2}{f_r^2} = \frac{(m+m_a)}{m} = 1 + \frac{m_a}{m} \quad (8)$$

The added mass is deduced from Equation (8) as:

$$m_a = \left(\frac{f_0^2}{f_r^2} - 1 \right) m \quad (9)$$

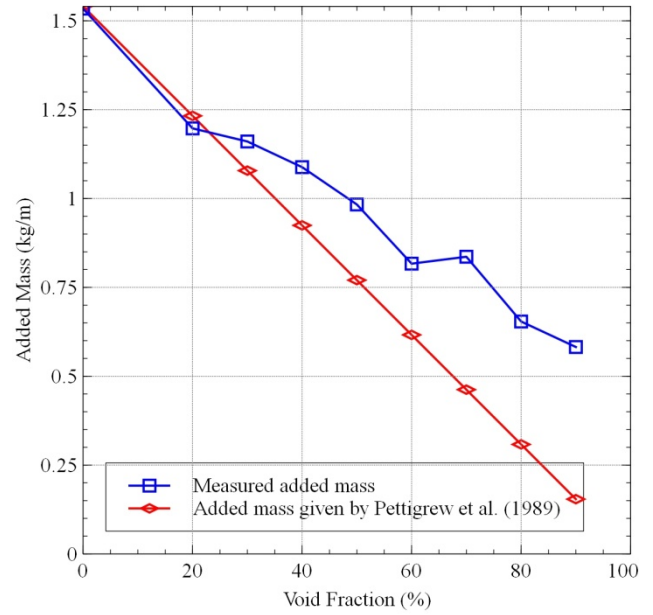


FIGURE 10 – MEASURED ADDED MASS AND COMPARISON WITH THE FORMULA SUGGESTED BY PETTIGREW ET AL. (1989).

The measured added mass is presented in Figure 10 along with the added mass suggested by Pettigrew et al. (1989). The authors suggested an added mass expression that varies linearly with the flow density and consequently the void fraction, as the mass density of the air phase is negligible compared to the water mass density:

$$m_a = \frac{\pi}{4} \rho_h D^2 \left[\frac{(D_e/D)^2 + 1}{(D_e/D)^2 - 1} \right] \quad (10)$$

where ρ_h is the fluid homogeneous density. The confinement parameter is given by $D_e/D = (0.96 + 0.5P/D)P/D$ for a tube within a triangular tube bundle. The agreement might be good for low void fractions (0% to 20%) but for higher void fractions, the formula underestimates the added mass by a large margin, as seen in Figure 10.

Damping

The flow dependent damping is inherent to both the quasi-steady and the unsteady model. Therefore, only the structural damping is needed as a damping input to these models. However, it is a common practice to include this damping in the mass damping parameter when presenting the instability results. For this reason, its measurement is useful.

The damping presented here was measured at relatively low flow velocities (typically around 30% of the critical velocity). The damping was measured at three different but close velocities and averaged as its value was found to be nearly constant as shown in Figure 11.

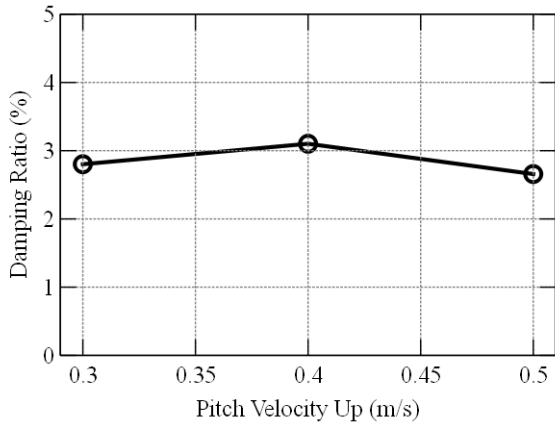


FIGURE – 11 DAMPING VS. PITCH VELOCITY FOR 50 % VOID FRACTION.

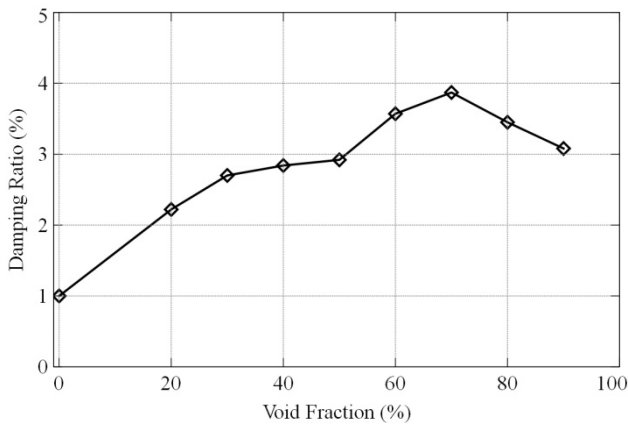


FIGURE 12 – DAMPING VS. VOID FRACTION.

The variation of the measured damping with void fraction is presented in Figure 12. The damping increases approximately linearly with void fraction up to a maximum at 70% void fraction and then decreases once again approximately linearly. Pettigrew *et al.* (1989) have found the same trend for the damping in a rotated triangular array of $P/D = 1.47$. In axial internal flow, the maximum damping was found to be between 30% and 40% void fraction for low flow velocities (Gravelle *et al.*, 2007).

Fluidelastic Instability

In this experiment, the “structural” damping was varied by changing the dimensions of the rubber damper. Stability tests were conducted for various void fractions. For each stability test, the flow velocity was increased

progressively and the RMS of the displacement at the free end of the tube was measured. The damping was also measured as a function of the flow velocity. It was found that the damping generally decreased with the flow velocity.

The critical velocity is defined as the point where the increase in the RMS response is drastic.

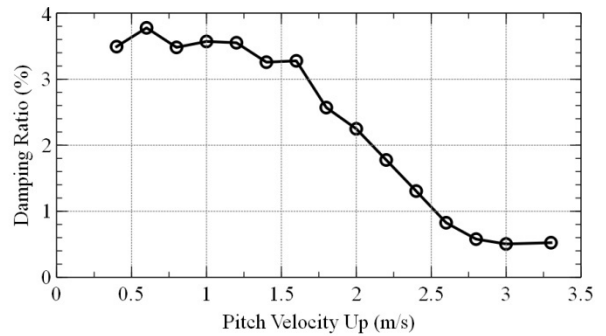
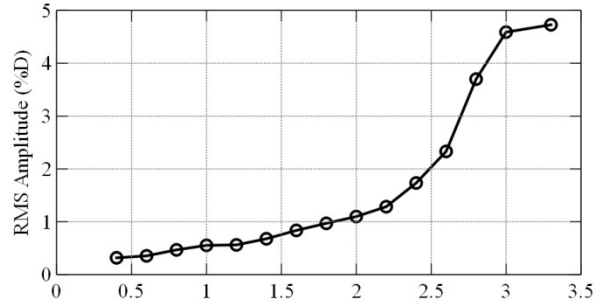


FIGURE 13 – RMS RESPONSE AND DAMPING VS. PITCH VELOCITY FOR 60% VOID FRACTION.

The damping value becomes very small (theoretically zero or negative) at instability. In some cases where the instability is not well defined by the RMS response, the sudden decrease of the damping is used to detect the critical velocity. For instance, the critical velocity in Figure 13 is 2.6 m/s.

A stability test was done for 5% void fraction where a change in the sign of the lift coefficient derivative was observed. As shown in Figure 14, the tube was subjected to fluidelastic instability at $U_{pc} = 1.1$ m/s. This value is close to the critical velocity of the same tube in water flow ($U_{pc} = 1.0$ m/s). For 20% void fraction the critical velocity is $U_{pc} = 1.5$ m/s. The question remains to know if this instability is governed by the negative or the positive slope of the lift coefficient, that is to say, if the instability is generated by the liquid flow or the two-phase flow. A measurement of the time delay is necessary to assess the instability mechanism for this case.

All the results of the stability tests are summarized in Figure 15. The Connors expression is also plotted in the same Figure for $K = 3$ and $K = 4$. As is seen in the figure, $K = 4$ fits the data best although some data are still above this curve. The tests also show that for a given void fraction, the reduced critical velocity does not vary much

with the mass damping parameter. The quasi-steady model will be tested against these experimental data in future work where the time delay in two-phase flow will be measured.

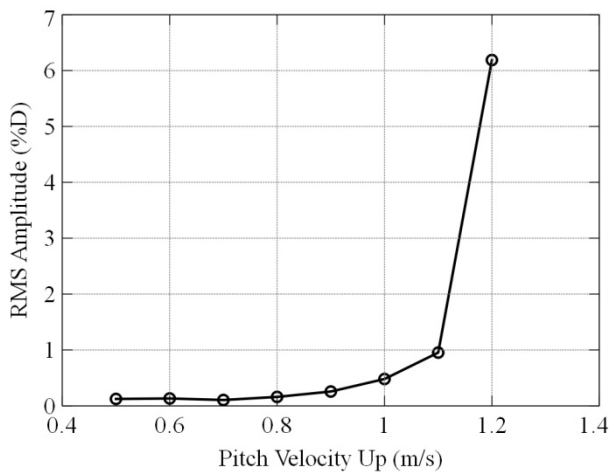


FIGURE 14 – STABILITY TEST FOR 5% VOID FRACTION SHOWING FLUIDELASTIC INSTABILITY.

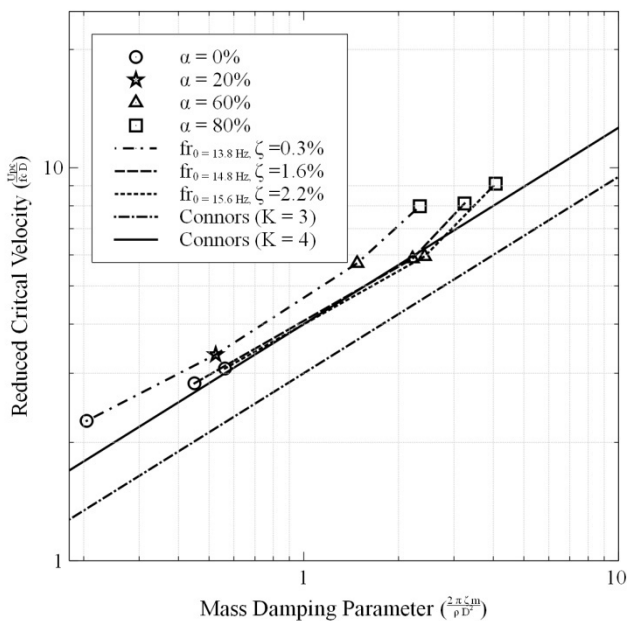


FIGURE 15 – REDUCED CRITICAL VELOCITY VS. MASS DAMPING PARAMETER.

CONCLUSION

Experiments were conducted on a single flexible tube in a rotated triangular tube bundle, subjected to two-phase flow. The fluid damping, the added mass and the critical velocity for fluidelastic instability were measured. The fluid damping was found to vary linearly with the void fraction with a peak of approximately 4% at 70% void fraction.

The added mass was compared to the added mass expression given by Pettigrew *et al.* (1989); it was found that this formula underestimates the added mass for void fraction higher than 20%.

The variation of the fluid lift coefficient with the non-dimensional tube displacement in the lift direction was also measured for various void fractions. The lift coefficient derivative goes from a positive value in liquid flow to negative values in two-phase flow. A change in the sign of this derivative was found near 5% void fraction, challenging the ability of the quasi-steady model to predict fluidelastic instability in this case. A measurement of the time delay is, however, necessary to answer this question. The present work is a first step toward that goal.

REFERENCES

Chen, S. S. (1983a). Instability Mechanisms and Stability Criteria of a Group of Circular Cylinders Subjected to Cross-Flow. Part I: Theory. *Journal of Vibration, Acoustics, Stress, and Reliability in Design*, 105(1), 51-58.

Chen, S. S. (1983b). Instability Mechanisms and Stability Criteria of a Group of Circular Cylinders Subjected to Cross-Flow. Part II: Numerical Results and Discussion. *Journal of Vibration, Acoustics, Stress, and Reliability in Design*, 105(2), 253-260.

Connors, H. J., Jr. (1970). Fluidelastic Vibration of a Tube Array Excited by Cross-Flow. *Paper presented at the symposium on Flow-Induced Vibration in Heat Exchanger*, New York, 1970.

Gravelle, A., Ross, A., Pettigrew, M. J., & Mureithi, N. W. (2007). Damping of Tubes Due to Internal Two-Phase Flow. *Journal of Fluids and Structures*, 23(3), 447-462.

Mureithi, N. W., Nakamura, T., Hirota, K., Murata, M., Utsumi, S., Kusakabe, T., et al. (2002). Dynamics of an Inline Tube Array Subjected to Steam-Water Cross-Flow. Part 2: Unsteady Fluid Forces. *Journal of Fluids and Structures*, 16(2), 137-152.

Païdoussis, M. P., & Price, S. J. (1988). The Mechanisms Underlying Flow-Induced Instabilities of Cylinder Arrays in Cross-Flow. *Journal of Fluid Mechanics*, 187, 45-59.

Price, S. J., & Païdoussis, M. P. (1982). A Theoretical Investigation of the Parameters Affecting the Fluidelastic Instability of a Double Row of Cylinders Subject to a Cross-Flow. *Paper presented at the Vibration in Nuclear Plant Conference. Proceedings of the 3rd International Conference, Keswick, UK.*

Price, S. J., & Païdoussis, M. P. (1983). Fluidelastic Instability of an Infinite Double Row of Circular Cylinders Subject to a Uniform Cross-Flow. *Journal of Vibration Acoustics Stress Reliability in Design* 105(1), 59-66.

Violette, R., Pettigrew, M. J., & Mureithi, N. W. (2006). Fluidelastic Instability of an Array of Tubes Preferentially Flexible in the Flow Direction Subjected to Two-Phase Cross Flow. *Transactions of the ASME. Journal of Pressure Vessel Technology*, 128(1), 148-159.

Sawadogo, T. & Mureithi, N. (2011). Simulation of The Vibration of a Steam Generator Tube Subjected to Fluidelastic Forces Induced by Two-Phase Cross-Flow. *Paper presented at the ASME 2011 Pressure Vessels and Piping Conference July, 17-21, 2011 Baltimore, Maryland, USA.*

Shahriary, S., Mureithi, N. W., & Pettigrew, M. J. (2007). Quasi-Static Forces and Stability Analysis in a Triangular Tube Bundle Subjected to Two-Phase Cross-Flow. *Paper presented at the 2007 ASME Pressure Vessel and Piping Division Conference, July 22-26, 2007, San Antonio, TX, USA.*



MODELLING OF FLUIDELASTIC INSTABILITY INSIDE AN INLINE SQUARE ARRAY

J. Burns Anderson

University of New Brunswick
Fredericton, New Brunswick, E3B 5A3
Canada
Email: JBurns.Anderson@unb.ca

Marwan Hassan*

University of Guelph
Guelph, Ontario, N1G 2W1
Canada
Email: mahassan@uoguelph.ca

Atef Mohany

University of Ontario Institute of Technology
Oshawa, Ontario, L1H 7K4
Canada
Email: atef.mohany@ouit.ca

ABSTRACT

This paper presents a time domain model to predict the fluidelastic instability forces in a tube array. The proposed model accounts for temporal variation in the flow attachment and separation. The unsteady boundary layer is solved numerically and coupled with the structure and far field flow models. It is found that the proposed model predicts instability at lower values of reduced flow velocity compared to the original flow cell model due to larger fluidelastic forces. The increase in the fluidelastic forces is a direct result of the motion of the separation point of the boundary layer, which in turn, changes the area of interaction between the flow field and the flexible tube. It is also observed that a non-linear limit cycle is predicted by the proposed model.

NOMENCLATURE

A, \bar{A}, a Flow channel area; unsteady, steady state, perturbation
 b Effective viscosity
 δ Log decrement
 D Tube Diameter
 f, f_n Frequency, natural frequency
 L Length scale used to normalize position
 P, \bar{P}, p Pressure; unsteady, steady state, perturbation
 ρ Fluid density
 s_o, s_a, s_s Flow channel inlet, attachment point, separation point
 s Position along flow channel
 t, T time, Non-dimensional time
 τ time lag
 X, η Dimensionless boundary layer coordinates
 U, \bar{U}, u Flow velocity; unsteady, steady state, perturbation

\hat{U}, \hat{U}_o Normalized flow velocity; current, initial
 U_p Pitch velocity, inlet flow velocity
 w Tube displacement

Introduction

Historically, heat exchangers have been among the most failure prone components in nuclear power plants. Most of these failures are due to corrosion, fatigue and fretting wear of the tubes. Fatigue and fretting wear is a result of dynamic loading caused by three cross-flow excitation mechanisms; turbulent buffeting, Strouhal periodicity and fluidelastic instability (FEI) [1]. Of the three mechanisms FEI has the greatest potential for destruction [1] and because of this a large amount of research has been conducted on this mechanism. FEI is a self excitation mechanism caused by the interaction of the flexible tubes and the fluid forces. The motion of the tubes alters the flow field, which in turn, creates fluid forces that further excites the tube and thereby transfers energy from the flow to the tube. Problems arise when more energy is extracted from the fluid flow than can possibly be dissipated by the arrays own internal damping. This causes large amplitude vibrations that can result in mid-span collisions between tubes and accelerated wear at the tube supports. However predicting tube response at the onset of the instability or at the pre-stability is still far from realistic. Without an estimation of the tubes motion, a heat exchangers life cycle can not be accurately predicted. This inaccuracy is most relevant in nuclear power generation where any leak causes a radiation hazard and the offending tube must be plugged. Over time several tubes can be plugged reducing the overall efficiency, requiring the heat exchanger to be replaced which is very costly.

Several theoretical models have been proposed such

*Address all correspondence to this author.

as that of Tanaka and Takahara [2], Chen [3], Lever and Weaver [4] and Price and Paidoussis [5]. These models provide vital tools for predicting the critical flow velocity. Many of these models rely on experimentally determined inputs. The model proposed by Weaver et al. [4, 6] is a semi-analytical model, which requires fewer empirical coefficients. Hassan et al. [7, 8] reformulated the model for time domain simulations and demonstrated its validity in estimating the fretting wear analysis of loosely supported bundles.

This paper formulates a semi-analytical model based on the original flow cell model developed by Lever & Weaver [4] that accounts for temporal variations in the boundary layer development over the moving tube. The effect of the reduced flow velocity and response amplitude on the boundary layer motion and the tube response is also investigated.

1 Model Description

1.1 Flow Channel Subdomain

Using the flow cell model proposed by Lever & Weaver [4], the complex flow through a tube array is approximated through the use of a flow cell. Referring to Fig. 1, the flow cell is comprised of a number of rigid tubes (2-6), a single flexible tube (1) and two flow channels. The rigid tubes act only to define the flow channels through the flow cell. The position along the length of a flow channel is described using the curvilinear coordinate s , which originates at the centre of the single flexible tube and decreases in the direction of the flow cell inlet. The flow channel interacts with the single flexible tube over the attached region ($s_a \leq s \leq s_s$), where s_a and s_s are the flow attachment and separation points respectively.

In the original formulation the system is prescribed to oscillate harmonically at its natural frequency to simplify the calculations. This is realistic only at the onset of the instability where the response frequency approaches the natural frequency for a linear system. However, tubes are usually loosely supported without a well defined natural frequency which complicates the response prediction. This was accounted for by Hassan & Hayder [7] and Hassan & Hossen [9], where the fluidelastic forces are formulated to account for any arbitrary tube response.

The flow field of the flow cell is divided into two subdomains, the first is flow channel subdomain which replicates the velocity and pressure fields as a result of deformation to the flow channels caused by motion of the tube. The second replicates the boundary layer development as a result of the far field velocities and pressures determined in the flow channel subdomain.

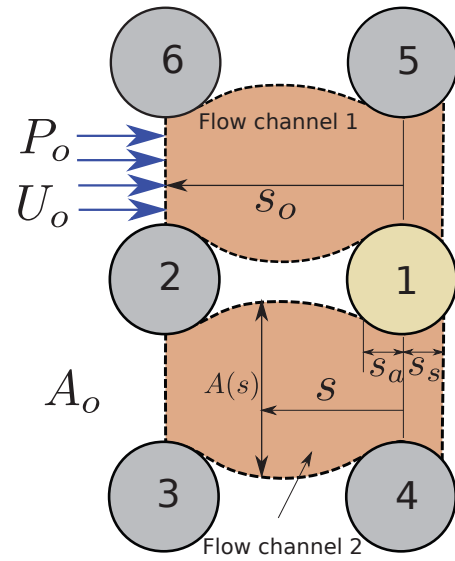


FIGURE 1: Flow cell comprised of five rigid tubes (2-6), a single flexible tube (1) and two flow channels.

The parameters of the flow channel subdomain being modelled are the flow channel cross-sectional area (A), flow velocity (U) and pressure (P) along the length of the flow channel. These parameters are the summation of a steady state terms ($\bar{A}, \bar{U}, \bar{P}$) and perturbations about the steady state terms (a, u, p). The steady state terms are related to the geometry of the flow cell and the inlet conditions while, the perturbations is related to the motion of the flexible tube.

$$A(s, t) = \bar{A}(s) + a(s, t) \quad (1)$$

$$U(s, t) = \bar{U}(s) + u(s, t) \quad (2)$$

$$P(s, t) = \bar{P}(s) + p(s, t) \quad (3)$$

The conservation of mass given by:

$$\frac{\partial A(s, t)}{\partial t} + \frac{\partial (A(s, t) \cdot U(s, t))}{\partial s} = 0 \quad (4)$$

The flow channel subdomains are divided into three regions; an upstream region ($s \leq s_a$), an attached region ($s_a \leq s \leq s_s$) and a downstream region ($s \geq s_s$). In the attached region any motion of the tube instantaneously affects the flow channel area without a time lag. Due to the finite inertia of the fluid the channel flow response will lag behind the motion of the tube. The channel area perturbation is expressed as:

$$a(s, t) = w(t - \tau(s)) \cdot f(s) \quad (5)$$

where w is the transverse displacement of the tube, τ is the time lag and $f(s)$ is an arbitrary decay function to meet the boundary conditions of the flow cell. Due to the rigid tubes at the inlet of the flow cell $a(-s_o, t)$ must always be zero, while in the attached region $a(s, t)$ must be equal to the displacement of the flexible tube.

Lever & Weaver [4] postulated that the time lag can be derived in a fashion similar to a thin plate transient problem.

$$\tau(s) = \frac{2s}{U(-s_o)} \quad (6)$$

There have been other interpretations of the time lag presented in literature, such as that presented by Price & Paidoussis [5] in which the concept of flow retardation was assumed. The experimental investigations of Kalifa & Weaver [10] has shed more light on the physics of the time lag. The current work follows the original time lag analogy developed by Lever & Weaver [4] until a more generally accepted expression can be determined. By integrating the one dimensional continuity and momentum equations along the length of the flow channel an expression describing the flow velocity and pressure perturbations can be derived.

$$u(s, t) = \frac{-1}{A + a(s, t)} \left[\bar{U}(-s_o) \cdot a(s, t) + \int_{-s_o}^s \frac{\partial a(s, t)}{\partial t} ds \right] \quad (7)$$

$$p(s, t) = P(-s_o) + \rho \left\{ \frac{1}{2} \bar{U}(-s_o)^2 - \frac{1}{2} U^2 - \int_{-s_o}^s \frac{\partial U}{\partial t} ds \right\} - \rho \left\{ \frac{h}{2s_o} \cdot \int_{-s_o}^s U^2 ds \right\} \quad (8)$$

The (s, t) have been dropped off the U terms, $\bar{U}(-s_o)$ and $P(-s_o)$ are the inlet flow velocity and pressure of the flow channel, ρ is the fluid density and h is the resistance coefficient. It is assumed that h is constant over a large range of Reynolds numbers and held constant at a value of 0.275. Based on the time history the flow channel area and velocity are numerically integrated using five point Gauss quadrature and the results added to the appropriate steady state value to replicate the far field parameters used to solve the boundary layer subdomain.

1.2 Boundary Layer subdomain

So far the effect of viscosity has been neglected. However, at the tube wall where the no slip condition

must be maintained, the effect of viscosity can no longer be neglected. This requires the implementation of the Navier-Stokes equations. By introducing the stream function and dimensionless similarity variable (η) for a cylinder, the Navier-Stokes equations for a boundary layer take the non-dimensional form of:

The dimensionless similarity variable perpendicular to the surface of the tube is presented as:

$$\eta = \frac{y}{R} \sqrt{\frac{U(s, t) \cdot R}{\nu}} \quad (9)$$

where y is the vertical position perpendicular to the tube wall, R is the radius of the tube, $U(s, t)$ is the far field flow velocity defined by Eqn. (2) and ν is the kinematic viscosity of the fluid.

$$(bf'')' + P_1 f f'' - P_2 (f')^2 + P_3 = X \left(f' \frac{\partial f'}{\partial X} - f'' \frac{\partial f}{\partial X} + \frac{1}{\hat{U}_o} \frac{\partial f'}{\partial T} \right) \quad (10)$$

where $'$ indicates differentiation with respect to η , b is the effective viscosity term, X is the normalized horizontal position (s/L), f, f', f'' represent the dimensionless stream function, horizontal and vertical velocity respectively, \hat{U}_o is normalized initial flow velocity and T is non-dimensional time determined by;

$$T = \frac{t \cdot U(-s_o)}{L} \quad (11)$$

where $U(-s_o)$ is the flow channel inlet flow velocity and L is the length scale used to normalize the horizontal position. The terms P_1, P_2 , and P_3 in Eqn. (10) represent the non-dimensional pressures determined by:

$$P_1(s) = \frac{1}{2} [1 + P_2(s)] + P_c(s, t) \quad (12)$$

$$P_2(s) = \frac{X}{\hat{U}_o} \frac{\partial \hat{U}(s, t)}{\partial X} \quad (13)$$

$$P_3(s, t) = \frac{X}{\hat{U}_o^2} \left[\hat{U}(s, t) \frac{\partial \hat{U}(s, t)}{\partial X} + \frac{\partial \hat{U}(s, t)}{\partial T} \right] \quad (14)$$

where \hat{U}_o is normalized initial flow velocity, $\hat{U}(s, t)$ is the normalized current flow velocity, P_c is the normalized far field pressure.

The viscosity term, b , previously mentioned in Eqn. (10) is the summation of the fluid viscosity and the eddy

viscosity. Due to the large number of tubes inside a shell and tube heat exchanger the turbulence intensity is quite high. This high level of turbulence tends to cause the boundary layer transition to occur shortly after becoming fully developed. A boundary layer is unable to transition to turbulent without fully developing as laminar first. With this in mind the length required for full laminar development exceeds the expected attachment lengths for inline square arrays. For simplicity the effect of this transition from a laminar to turbulent has been neglected and only a laminar boundary layer has been modelled.

The non-dimensional Navier-Stokes Eqn. (10) is solved using a central difference scheme known as Keller's box method [11]. The box method belongs to a family of methods for obtaining exact solutions of the boundary layer equations using finite differences which yields a tridiagonal system. This method allows for the use of a non-uniform mesh that allows for mesh refinement at key areas of interest such as the region directly beside the surface of the tube and the point of flow separation. To use this scheme known boundary conditions must be applied to the inlet of the mesh. In the case of parallel triangular, normal triangular and rotated square arrays, the two flow channels attaches to the tube at two points near the -90° location. The same sign convention used by Lever & Weaver [6] is maintained in this model, where the angle is measured from the curvilinear coordinate s equal to zero. This allows for the use of stagnation models to determine the point of flow channel attachment and the appropriate velocity profile to be used as an inlet condition. For the case of an inline square array the wakes created by the upstream tubes extend between tube rows causing the flow channels to attach at some point on the upstream side of the tube with a somewhat developed velocity profile.

Using available flow visualization studies Lever & Weaver [6] found that the attachment and separation points can be related to the array geometry. For an inline square array it was found that s_a and s_s occur at $\mp 10^\circ$ respectively. Thus Lever & Weaver were able to approximate the point of attachment but not the initial velocity profile. Thus to achieve a solution and to simplify the computations, it is assumed that the boundary layer is fully developed at the point of attachment.

As stated the solution process is initiated at the attachment point and progressively marches downstream till the wall shear crosses zero, which represents the separation point. This approach is similar to that of other boundary layer models such as that of Cebeci & Carr [12]. Unlike the model of Cebeci & Carr the formal solution process is terminated at the point of flow separation and

the boundary layer is approximated for a few steps downstream to account for possible downstream motion of the boundary layer. This approach does not account for reattachment of the boundary layer after separation. To account for this a more complex differencing scheme such as the "zig-zag" box method must be employed. This methods tends to be very sensitive to conditions and prone to error, for this reason the zig-zag box method is not employed in this iteration of the model.

Once the separation point is determined the pressure field is integrated over the attached region to determine the fluidelastic forces acting on the tube. Due to the curvature of the tube the fluidelastic forces act in both the lift and drag direction, because the instability is known to be predominantly in the transverse direction of the flow [13] only the lift component is imposed on the single flexible tube.

2 Structural Response

The geometry of a shell and tube heat exchanger is quite complex with a large number of tubes, but by using the flow cell only the response of one tube needs to be modelled. This greatly simplifies the structure but does not make it a trivial problem. Due to the tube length of heat exchangers, supports in the form of either baffles or anti-vibration bars are used to maintain the array pattern. Due to the tolerances used in the fabrication process gaps occur between tubes and supports, while anti-vibration bars might not contact the tubes evenly. As the tube vibrates this will allow for the tube to leave contact with the support producing a non-linear response. This non-linear response is very difficult to model and there have been models such as those of Hassan et al. [7, 14], which predict the non-linear response of a tube as result of loose supports. For simplicity it is assumed that the response of the tube is linear with no interaction with supports by modelling a cantilevered tube with a length of 1000 mm, 12.7 mm outer diameter and a tube thickness 0.5 mm. The effective mass per unit length and modules of elasticity are taken to be 0.078 kg/m and 108 GPa, respectively. Hassan & Hayder [7] found that to fully capture the fluidelastic forces for a linear system a time step of the order of 0.01 ms is required.

The complete solution is constructed considering satisfying the compatibility conditions between subdomains. As discussed in Section 1.1, the flow through each channel is assumed to be one-dimensional, and the subdomain dimensions are calculated approximately from the array geometry. Changes in fluid forces are caused by a change in the width of the channel as a result of tube vibration.

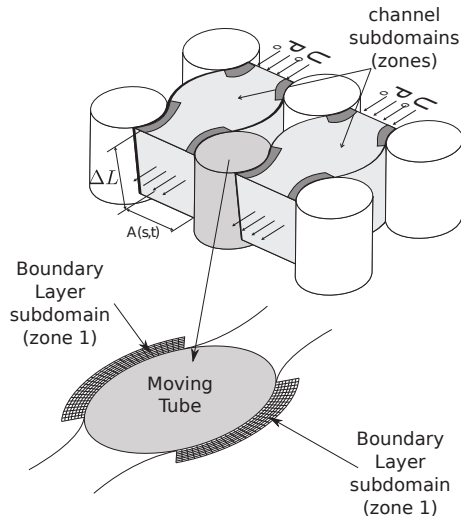


FIGURE 2: The flow cell indicating the boundary layer subdomains

Using the unsteady continuity and momentum equations, the pressure Eqn. (8) and velocity Eqn. (7) can be estimated in the channel and are used to solve the boundary layer subdomain.

As mentioned earlier the box method is utilized to solve the boundary layer. Solving this system involves starting from the attachment point and progressing downstream until separation. The lift force is calculated by integrating the pressure over the attached region. Due to tube motion, the pressure field will change but the boundary layer will require time to develop. This will result in a delay between the tube motion and the motion of s_s . This in turn will govern the phase relationship between tube motion and the flow adjustment [15] and will control the time lag in the resulting fluid force.

As stated FEI is a feedback mechanism meaning tube motion is required to initiate the interaction between the tube motion and the flow field. Turbulence in the flow and/or Strouhal periodicity generally provides this initial motion but for simplicity these mechanisms are neglected. The tube is released from rest with an initial displacement.

The solution strategy, at each time step can be summarized as follows: firstly, evaluate structure response as a result of tube motion; secondly, the channel flow is computed, then the velocity and the pressure fields, which are used to match the interface between each subdomain zone; thirdly, the boundary layer solution will yield an identification of an adverse streamwise pressure gradient, which define s_s . The pressure is integrated over the attached region, resulting in a net lift force used to compute the updated response and the process is repeated un-

til convergence is attained.

3 Results

Based on a mesh study it was determined that a uniform mesh comprised of 105 streamwise and 61 vertical computation points is sufficient to resolve the boundary layer and the motion of the separation points (Fig. 3). It was found that increasing the number of streamwise computation points had little effect on increasing the accuracy while, drastically increasing the computation time.

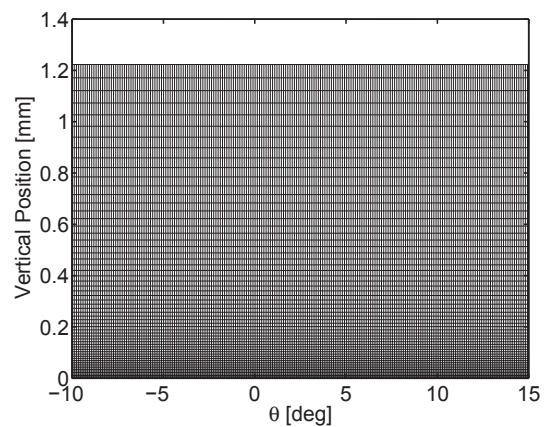


FIGURE 3: Boundary layer mesh.

3.1 Prescribed Motion

A study was performed with a prescribed tube motion with constant vibration amplitudes and excitation frequency. A number of simulations was conducted using a single inlet flow velocity while the excitation frequency was changed to produce the desired reduced flow velocity ($U_r \equiv U_p/fd$). The amplitude of the separation angle variation ($\Delta\beta$) and its phase with respect to the tube motion was investigated. Figure 4 shows the time history of the tube prescribed displacement and the resulting separation angle motion for a reduced flow velocity of 2.

The tube displacement amplitude was set to 5% of tube diameter. The separation angle oscillates at the same frequency of the tube motion with a constant amplitude of $\Delta\beta = 3.5^\circ$ about a mean value of 7.5° . It can be also observed that the separation movement leads the tube motion by a phase angle of 108° . The effect of the reduced flow velocity on the separation phase is shown in Fig.5. The separation phase angle sharply varies from 147° to 42° in the reduced flow velocity range of 1 to 6 then levels off and approaches a zero phase for higher reduced

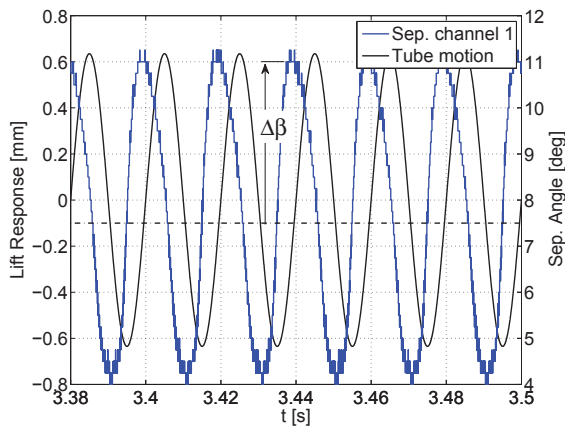


FIGURE 4: Tube motion plotted with the resulting motion of the separation point for flow channel 1.

flow velocities. Similar trend was found regarding the amplitude of the separation angle where the reduced flow velocity has its greatest effect in the lower range (Fig. 5).

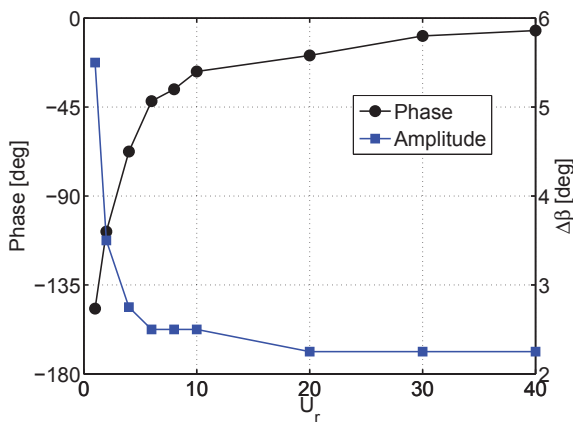


FIGURE 5: Phase difference and $\Delta\beta$ for the separation point as a function of reduced flow velocity.

To investigate the effect of the oscillation amplitude on the separation angle variation and phase, simulation were conducted for a reduced velocity of 40 and oscillation amplitude was varied in the range of 5 to 20%. The increase of the oscillation amplitude was found to cause an increase in the separation angle amplitude as shown in Fig. 6. It should be noted that a slight decrease was found in the mean separation angle as the amplitude of vibration increased. At this reduced flow velocity the smaller oscillation amplitude allowed the separation movement to closely follow the tube motion and the phase angle is

small (5°). Increasing the oscillation amplitude causes the separation phase difference to increase. This is attributed to the fact that the tube velocity is increased relative to the flow velocity.

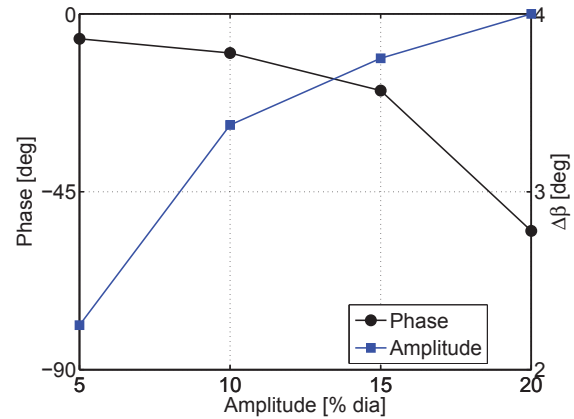


FIGURE 6: Phase difference and $\Delta\beta$ for the separation point as a function of excitation amplitude.

3.2 Vibration Response Case

Simulations were conducted for vibrations cases with an initial displacement of 0.2 mm and subjected to cross-flow. Simulations were conducted for a mass damping parameter of 80 and covered the stable and post-stable regions. The results of a typical stable system are shown in Fig. 7. The initial displacement was set to 1 mm. The system is stable and the vibration amplitude decays to a steady state value. It is important to note that because the effect of turbulent buffeting and Strouhal periodicity are neglected the vibration amplitude will decrease to zero as shown in Fig. 7. This causes the RMS response of the system to approach zero as simulation time increases.

The motion of the separation points follows a similar patten as that of the response, in that if the system is stable the separation point will decay to a steady state value as shown in Fig. 8. The steady state value of the separation point is within 15% of the Lever & Weaver’s suggested value (10°).

Similar simulations were performed at various flow velocities, with the RMS response determined and plotted as a function of the reduced flow velocity (Fig. 9). The critical flow velocity is identified as the flow velocity at which the damping ratio becomes zero. Using this method the original flow cell model predicts instability at a reduced flow velocity of 119, while the proposed model predicts instability at a reduced flow velocity of 88.3 or

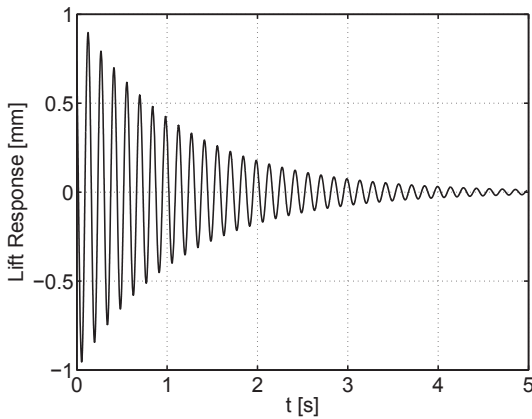


FIGURE 7: Tube response for a stable system; $P/D = 1.5$, $MDP = 80$, $U_r = 54.1$.

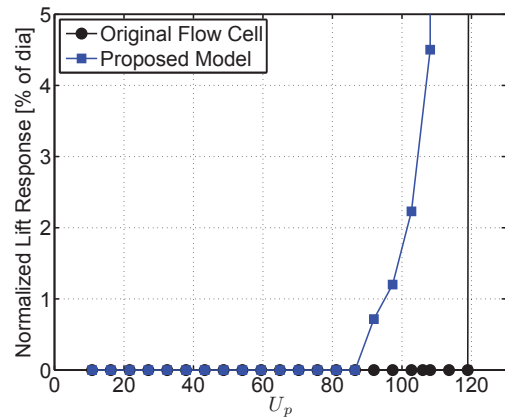


FIGURE 9: Normalized lift response for a single flexible tube inside an inline square array with a P/D ratio of 1.5 as a function of reduced flow velocity.

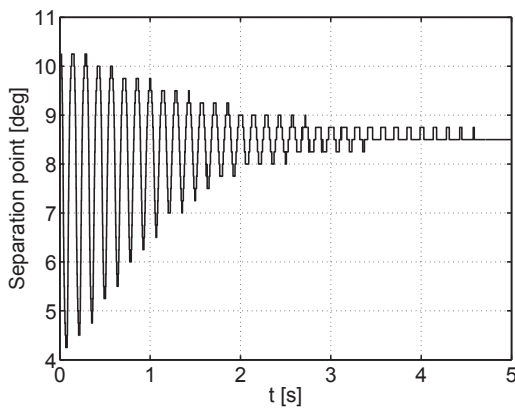


FIGURE 8: Motion of the separation point for flow channel one as a result of the motion in Fig. 7.

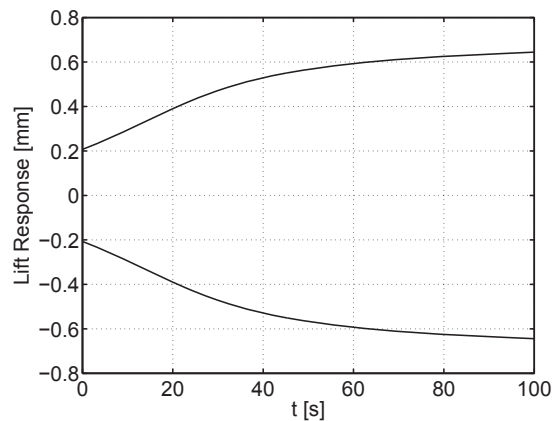


FIGURE 10: The envelope of the lift response predicted by the proposed model; $P/D = 1.5$, $MDP = 80$, $U_r = 92$.

roughly 26% lower. It can be seen that the RMS unstable response of the two models is very different. The original flow cell model becomes unstable and the amplitudes of vibration grows without bounds. This is not the case for the proposed model where the RMS response grows within bounds (nonlinear limit cycle) as the reduced flow velocity is increased beyond the threshold of instability. This is shown Fig. 10, where the envelope of the tube response is plotted. It can be seen that the response of the tube is initially unstable resulting in growth of the vibration amplitude. Over time this growth slows until the system appears to regain some stability. The response was analyzed by dividing it up into five bins of five seconds each for determining the damping ratio. The bins were selected such that the first and last five seconds were analyzed as well as a section at a quarter, half and three quarters of the simulation time.

It was found that as time progressed the damping ra-

tio of the system increased towards zero indicating that the system is regaining stability. This behaviour can be attributed to the motion of the boundary layer separation phase. Examining the phase of the boundary layer separation revealed that the phase decreases and approaches zero as the tube amplitude increases. This is similar to the results presented earlier in Fig. 6. Very few studies investigated the non-linear behaviour of FEI [16–18]. Lever & Rzentkowski [17] postulated that a limit cycle was the root cause behind the hysteretic behaviour of FEI while, Meskell & Fitzpatrick [18] developed a non-linear model capable of predicting the amplitude of a limit cycle in the post stable response using experimental force coefficients. The current model reproduces a limit cycle behaviour and it is thought that the limit cycle predicted by the proposed model is a result of the boundary layer and the fluidelastic forces interacting with the tube mo-

tion.

4 Conclusions

This paper presents a time domain model which introduces the effect of boundary layer motion on the fluidelastic stability forces and the resulting tube response. The model utilizes the flow cell approach to calculate the far field flow velocity and pressure. The Keller box method was utilized to resolve the temporal variations of the boundary layer separation motion. It was found that by accounting for boundary layer motion causes the system to become unstable at lower values of reduced flow velocity. The system exhibits limit cycle oscillations in the post-stable region. The new model offers some insight into the fluidelastic mechanism and offers a step towards developing a comprehensive FEI model.

ACKNOWLEDGMENT

The authors thankfully acknowledge the financial support provided by the Natural Sciences and Engineering Research Council of Canada.

REFERENCES

- [1] Weaver, D., and Fitzpatrick, J., 1988. "A review of cross-flow induced vibrations in heat exchanger tube arrays". *Journal of fluids and structures*, **2**(1), pp. 73–93.
- [2] Tanaka, H., and Takahara, S., 1981. "Fluid elastic vibration of tube array in cross flow". *Journal of sound and vibration*, **77**(1), pp. 19–37.
- [3] Chen, S., 1983. "Instability mechanisms and stability criteria of a group of circular cylinders subjected to cross-flow. part i: theory". *Journal of Vibration, Acoustics, Stress, and Reliability in Design*, **105**.
- [4] Lever, J., and Weaver, D., 1982. "A theoretical model for fluid-elastic instability in heat exchanger tube bundles". *Journal of Pressure Vessel Technology*, **104**, p. 147.
- [5] Price, S., and Paidoussis, M., 1984. "An improved mathematical model for the stability of cylinder rows subject to cross-flow". *Journal of Sound and Vibration*, **97**(4), pp. 615–640.
- [6] Lever, J., and Weaver, D., 1986. "On the stability of heat exchanger tube bundles, part ii: Numerical results and comparison with experiments". *Journal of Sound and Vibration*, **107**(3), pp. 393–410.
- [7] Hassan, M., and Hayder, M., 2008. "Modelling of fluidelastic vibrations of heat exchanger tubes with loose supports". *Nuclear Engineering And Design*, **238**, pp. 2507–2520.
- [8] Hassan, M., and Mohany, A., 2011. "Numerical characterization of flow-induced vibration and fretting wear potential in nuclear steam generator tube bundles". In *Flow-induced vibration in heat exchanger tube arrays I: presented at the Pressure Vessels and Piping Conference*, Baltimore, Maryland, July 17–21, 2011.
- [9] Hassan, M., and Hossen, A., 2010. "Time domain models for damping-controlled fluidelastic instability forces in tubes with loose supports". *Journal of Pressure Vessel Technology*, **132**, p. 041302.
- [10] Khalifa, A., Weaver, D., and Ziada, S., 2011. "An experimental study of the phase lag causing fluidelastic instability in tube bundles". In *Proceedings of the ASME 2011 Pressure Vessel & Piping Division Conference*.
- [11] Keller, H., 1978. "Numerical methods in boundary-layer theory". *Annual Review of Fluid Mechanics*, **10**(1), pp. 417–433.
- [12] Bradshaw, P., Cebeci, T., and Whitelaw, J., 1981. *Engineering calculation methods for turbulent flow*.
- [13] Price, S., 1995. "A review of theoretical models for fluidelastic instability of cylinder arrays in cross-flow". *Journal of Fluids and Structures*, **9**(5), pp. 463–518.
- [14] Hassan, M., Weaver, D., and Dokainish, M., 2002. "A simulation of the turbulence response of heat exchanger tubes in lattice-bar supports". *Journal of fluids and structures*, **16**(8), pp. 1145–1176.
- [15] Hara, F., 1987. "Unsteady fluid dynamic forces acting on a single row of cylinders vibrating in a cross flow". *Flow-induced Vibrations*, pp. 51–58.
- [16] Price, S., and Valerio, N., 1990. "A non-linear investigation of single-degree-of-freedom instability in cylinder arrays subject to cross-flow". *Journal of sound and vibration*, **137**(3), pp. 419–432.
- [17] Lever, J., and Rzentkowski, G., 1993. "Dependence of post-stable fluidelastic behavior on the degrees of freedom of a tube bundle". *Journal of fluids and structures*, **7**(5), pp. 471–496.
- [18] Meskell, C., and Fitzpatrick, J., 2003. "Investigation of the nonlinear behaviour of damping controlled fluidelastic instability in a normal triangular tube array". *Journal of fluids and structures*, **18**(5), pp. 573–593.

ACTIVE CONTROL OF FLOW INDUCED VIBRATIONS OF A BLUFF BODY

M.Sridhar

Offshore Structures Group
National Institute of Ocean Technology
Chennai 600 100, INDIA
Email: sridhar@niot.res.in

B.S.V.Patnaik*

Fluid Mechanics Laboratory,
Department of Applied Mechanics,
Indian Institute of Technology Madras,
Chennai 600 036, INDIA
Email: bsvp@iitm.ac.in

ABSTRACT

A simple active flow control strategy is implemented to suppress vortex induced oscillations behind a circular cylinder. The approach consists of sensors, actuators and a control algorithm. Based on zero net mass injection strategy two types of actuators have been devised. First one, is a three actuator system which consists of a blowing slot and two suction slots on the cylinder surface. In the second one, two simple rotary type control cylinders are located at 120° , behind the main cylinder. The control cylinders are rotated (top one clock-wise and bottom one counter clock-wise) to enable momentum injection. The fluid flow features are modeled by assuming a two dimensional, unsteady and incompressible flow. The study of vortex induced vibrations entails the computation of forces for flow past the cylinder and its temporal evolution. This in turn necessitates calculation of the cylinder displacement which is triggered by the fluctuating lift force acting on the structure. The most common model used to describe the motion of the structure is through the idealizations for a lumped parameter model involving mass, spring and damper system. The governing equation for momentum injection is coupled with the mass and momentum equations and a dynamical evolution equation for the structure. The fluid forces and flow visualization is obtained to investigate the efficacy of the actuators and the closed loop feed back algorithm on the self excited oscillations. All the simulations are carried out at $Re = 100, 200$ and 3900 . The flow induced oscillations due to turbulent wake at $Re = 3900$ are effectively controlled with suction and blowing actuators.

INTRODUCTION

Flow past a flexibly mounted bluff body is prone to flow induced vibrations caused by the *kármán* vortex shedding behind the body. These vortex induced oscillations impact the vortex dynamics, even leading to structural failure, when the shedding frequency is in the neighborhood of the natural frequency of the body [1]. The suppression of vortex shedding and control of flow induced oscillations is of great practical significance in a number of applications such as, riser tubes, off shore structures, chimneys, buildings, bridges, stacks, transmission lines, mooring cables, heat exchanger tubes etc ([2, 3]). Control of these vibrations can be attained by modifying the fluid forces responsible for oscillation, either through active or passive means ([4]).

Generally reduction of flow induced vibrations is achieved by changing the natural frequency of the body (or) by increasing the stiffness (or) redistributing its mass [1] etc. The rapid advances in materials, is making the structures more flexible and lighter, this necessitates analysis of vortex induced vibrations. Therefore the ability to manipulate and control the flow field to reduce flow induced oscillations is gaining importance. Control of these vibrations can be attained by modifying the fluid forces responsible that are responsible for these oscillations. A wide variety of active and passive control strategies have been reported in the literature [5]. Recently, Baek and Karniadakis [6] have introduced a slit along the streamwise direction, which passes through the cylinder to create a jet that interacts with the wake to suppress vortex shedding. Chen and Aubry [7] have developed a closed loop algorithm to suppress vortex induced vibrations by means of direct numerical simulations (DNS). They have used Lorentz forces to control the cylinder oscillations based on partial flow information available on the surface of the cylinder. However, in practical appli-

*Corresponding author

cations, blowing and suction [8], acoustic acutations [9] and cylinder rotations [10] are some of the widely known active flow control techniques. Inspired by the pioneering work on chaos control by OGY [11], Patnaik and Wei [12] have proposed the stabilization of unstable periodic orbits (UPO) through synchronization based coupling between driver system and target system. By this coupling, complete annihilation of wake vortices behind a D-cylinder was achieved. The strategy of momentum injection control was further extended by Muddada and Patnaik [13] to control vortex shedding behind a circular cylinder by means of two symmetric rotating elements.

In the present study, we investigate the performance of two types of actuator systems for annihilating the flow induced oscillations at $Re = 100$ and 3900 . The numerical simulations employ the active control algorithm presented in Muddada and Patnaik [13]. To start with, the influence of forced cylinder oscillations on the vortex structures behind a circular cylinder is validated by generating $P + S$ wake pattern for the frequency, $f^* = 0.8$ and amplitude, $A^* = 0.65$ combinations. We then, solve the structural equation along with Navier-Stokes equations to set free vibrations in the cylinder and further investigate the performance of (a) one blowing and two suction actuator slot and (b) two small rotating control cylinders. The effectiveness of blowing and suction in suppressing free vibrations for high Reynolds number turbulent wakes also examined vis - á - vis the momentum injection using the two control cylinders.

SIMULATION DETAILS

Governing equations

The fluid flow is assumed to be incompressible, Newtonian and two-dimensional. In the context of wake behind a cylinder, three-dimensionality effects set in around $Re \approx 200$ [14]. For high Reynolds number turbulent flows, resorting to statistical averaging techniques leads to Reynolds averaging on the instantaneous mass, momentum conservation equations. The unsteady Reynolds averaged Navier-Stokes (URANS) version of equations are given as:

$$\frac{\partial \bar{u}_i}{\partial x_i} = 0, \quad (1)$$

$$\frac{\partial \bar{u}_i}{\partial t} + \bar{u}_j \frac{\partial \bar{u}_i}{\partial x_j} = -\frac{1}{\rho} \frac{\partial \bar{p}}{\partial x_i} + \frac{\partial (\bar{\tau}_{ij} + \tau_{ij}^R)}{\partial x_j}. \quad (2)$$

Where,

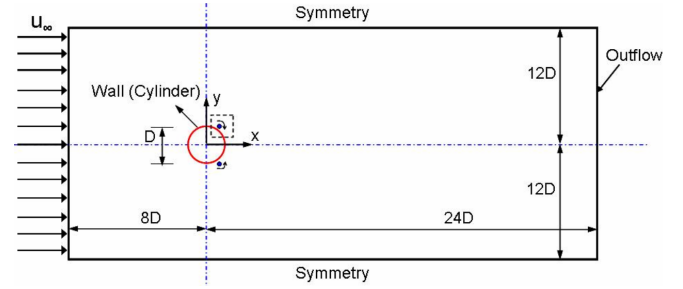


FIGURE 1: COMPUTATIONAL DOMAIN OF INTEREST WITH DIFFERENT BOUNDARY CONDITIONS.

$$\tau_{ij}^R = -\rho \overline{u'_i u'_j}; \quad \bar{\tau}_{ij} = \frac{\mu}{\rho} \left(\frac{\partial \bar{u}_i}{\partial x_j} + \frac{\partial \bar{u}_j}{\partial x_i} \right) \quad (3)$$

Here, τ_{ij}^R and $\bar{\tau}_{ij}$ are the Reynolds stress and mean shear stress tensors respectively. For high Re flows, τ_{ij}^R need to be suitably approximated through closure modelling strategies. However, when simulations are performed for low Re range, τ_{ij}^R is set to zero and additional equations need not be invoked as it simplifies to a non-statistical approach. All geometrical length scales are normalized with the size of cylinder diameter (D), streamwise and cross stream velocities with the inlet velocity (U_∞), physical time (t) with ($\frac{D}{U_\infty}$), and pressure (p) with (ρU_∞^2), where ρ refers to the fluid density. The flow domain of interest with second type of actuator is shown in Figure 1, where all the dimensions indicated are based on the cylinder diameter D . The overall size of the domain is $32D$ in the streamwise direction and $16D$ along the cross-streamwise direction. The centre of the cylinder is $8D$ from the left boundary. The left boundary is imposed with *velocity inlet* boundary condition, where u , is specified as U_∞ and $v = 0$. The right boundary is assigned with an *outflow* boundary condition with normal gradients $\frac{\partial u}{\partial x}$ and $\frac{\partial v}{\partial x}$ set to zero. The upper and lower boundaries are assigned with *symmetry* boundary condition ($\frac{\partial u}{\partial y} = 0; v = 0$). The cylinder surface is assigned a no-slip *wall* ($u = v = 0$) boundary condition.

The popular finite volume based SIMPLE family of schemes [15], which is incorporated in FLUENT [16] is used in our numerical calculations. A second order accurate semi-implicit scheme is chosen for the time integration. The spatial discretization is performed on a standard collocated grid using finite volume method. Further details related to the flow solver and spatial discretization are available in reference [15].

Turbulence modeling

Navier-Stokes equations in their standard form are sufficient to resolve the wide spectrum of eddy scales by enabling a fine grid resolution. Such a route is pop-

ularly called direct numerical simulations (DNS). However, in DNS the computational expenditure shoots up approximately as Re^3 [17]. Therefore, statistical averaging, via URANS with the aid of standard two-equation turbulence models are popular in industrial practice. These models rely on turbulent eddy viscosity hypothesis which assumes a linear approximation between Reynolds stress tensor and the strain rate tensor. In the present investigation, Reynolds stresses $\overline{u'_i u'_j}$ are approximated by solving an evolution equation for turbulent kinetic energy (k) and its rate of dissipation (ε). The standard k - ε model of Launder and Spalding [18] uses the eddy viscosity hypothesis of Boussinesq:

$$\overline{u'_i u'_j} = \nu_t \left(\frac{\partial \bar{u}_i}{\partial x_j} + \frac{\partial \bar{u}_j}{\partial x_i} \right) - \frac{2}{3} k \delta_{ij}. \quad (4)$$

This concept works on the assumption that the Reynolds stresses are linearly related to the mean velocity gradients through a proportionality constant, given by the turbulent eddy viscosity ν_t . In the k - ε model, the turbulent eddy viscosity is related to the turbulent kinetic energy (k) and to the rate of its dissipation (ε), as,

$$\nu_t = c_\mu \frac{k^2}{\varepsilon}. \quad (5)$$

k - ε model [19] The spatial and temporal distribution of k and ε is governed by the differential form of the transport equations for these quantities, considering the history and transport effects of turbulence

$$\frac{\partial k}{\partial t} + \frac{\partial [\bar{u}_l k]}{\partial x_l} = \frac{\partial}{\partial x_l} \left(\left(\mathbf{v} + \frac{\mathbf{v}_t}{\sigma_k} \right) \frac{\partial k}{\partial x_l} \right) + P_k - \varepsilon, \quad (6)$$

$$\frac{\partial \varepsilon}{\partial t} + \frac{\partial [\bar{u}_l \varepsilon]}{\partial x_l} = \frac{\partial}{\partial x_l} \left(\left(\mathbf{v} + \frac{\mathbf{v}_t}{\sigma_\varepsilon} \right) \frac{\partial \varepsilon}{\partial x_l} \right) + C_{\varepsilon 1} P_k \frac{\varepsilon}{k} - C_{\varepsilon 2} \frac{\varepsilon^2}{k}, \quad (7)$$

with P_k referring to production of turbulent kinetic energy, which is given as,

$$P_k = \nu_t S^2 \quad \text{where,} \quad S = \sqrt{\frac{1}{2} \left[\frac{\partial \bar{u}_i}{\partial x_j} + \frac{\partial \bar{u}_j}{\partial x_i} \right]^2} \quad (8)$$

Here, S refers to the symmetric mean strain rate tensor. The model constants used in the above equations are: $c_\mu = 0.09$, $C_{\varepsilon 1} = 1.44$, $C_{\varepsilon 2} = 1.92$, $\sigma_k = 1.0$ and $\sigma_\varepsilon = 1.3$.

k - ε model of Kato and Launder [20] The standard k - ε model is modified by Kato and Launder to control and regulate the over production of the turbulent kinetic energy in the stagnation regions. Kato and Launder [20] introduced the following ad-hoc model relation for the production term in the turbulent kinetic energy equation:

$$P_k = \nu_t S \Omega \quad \text{instead of} \quad P_k = \nu_t S^2 \quad (9)$$

The quantity Ω is an antisymmetric rotation tensor and is proportional to the magnitude of the local vorticity and is given as,

$$\Omega = \sqrt{\frac{1}{2} \left[\frac{\partial \bar{u}_i}{\partial x_j} - \frac{\partial \bar{u}_j}{\partial x_i} \right]^2} \quad ; \quad S = \sqrt{\frac{1}{2} \left[\frac{\partial \bar{u}_i}{\partial x_j} + \frac{\partial \bar{u}_j}{\partial x_i} \right]^2} \quad (10)$$

In simple shear flows, the behavior of the production term remains unchanged as $\Omega \approx S$, while spurious turbulence production is eliminated as $\Omega \approx 0$ in stagnation regions. Here, the model constants used are same as that in the standard k - ε model. However, these model constants need not be recalibrated owing to the fact that production term is identical both in standard k - ε and Kato and Launder's modification for simple shear flows.

Fluid-structure coupling

The study of vortex induced vibrations entails the computation of forces for flow past the cylinder and its temporal evolution. This in turn necessitates calculation of the cylinder displacement which is triggered by the fluctuating lift force acting on the structure. The most common model used to describe the motion of the structure is through the idealizations involving mass, spring and damper system. Motion is enabled only along the y -direction by virtue of its connectivity to linear springs. The governing equation for the structure is given by,

$$m\ddot{y} + c\dot{y} + ky = F_L(t) \quad (11)$$

where $F_L(t)$ refers to the fluctuating lift force. The parameters associated with the structure, viz., mass (m), damping (c) and stiffness (k), are chosen inline with earlier experimental studies. Once the lift force ($F_L(t)$) is determined by solving the Navier - Stokes equations, the ordinary differential equation (11) can be solved to find the position of the cylinder. At the end of each time step,

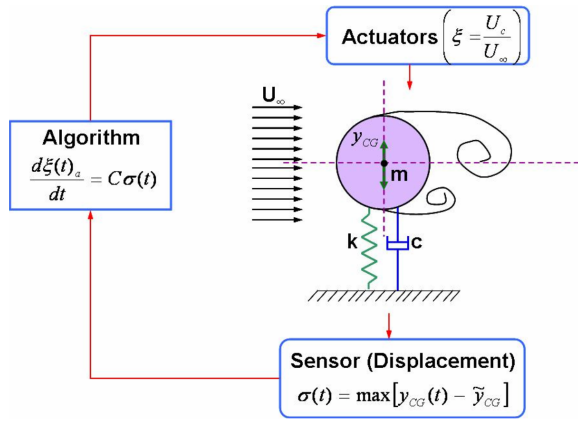


FIGURE 2: GENERIC FRAME WORK OF THE CLOSED-LOOP ACTIVE FLOW CONTROL ALGORITHM

lift force on the structure is obtained from the flow solver. The current position of the centre of gravity of the cylinder is updated and its position at the next time step is obtained.

Control algorithm and actuators

To investigate the dynamic nature of the vortex induced oscillations and its suppression, a sensitivity check is carried out by designing a simple control equation as suggested in Refs. [12] and [13]. The approach consists of sensors, actuators and a control algorithm (see Fig. 2). Based on the displacement which is reported by the sensors, the maximum standard deviation ($\sigma(t)$) against time in each cycle of oscillation is constructed as follows:

$$\sigma(t) = \max |y_{CG}(t) - \tilde{y}_{CG}(t)| \quad (12)$$

where y_{CG} denotes the position of the centre of gravity of the vibrating cylinder about its desired equilibrium position \tilde{y}_{CG} , which is free from oscillations. This is coupled to the actuators by means of a control parameter $\xi = \frac{U_c}{U_\infty}$ and is given by the equation (13) below.

$$\frac{d\xi}{dt} = C\sigma(t) \quad (13)$$

Here, the coefficient C is proportionality constant and can be varied like a fuzz factor.

To evaluate the efficacy of flow control, two types of actuators have been tested. First one, is a three actuator system which consists of a blowing slot and two suction slots on the cylinder surface as shown in Fig 3(a). These

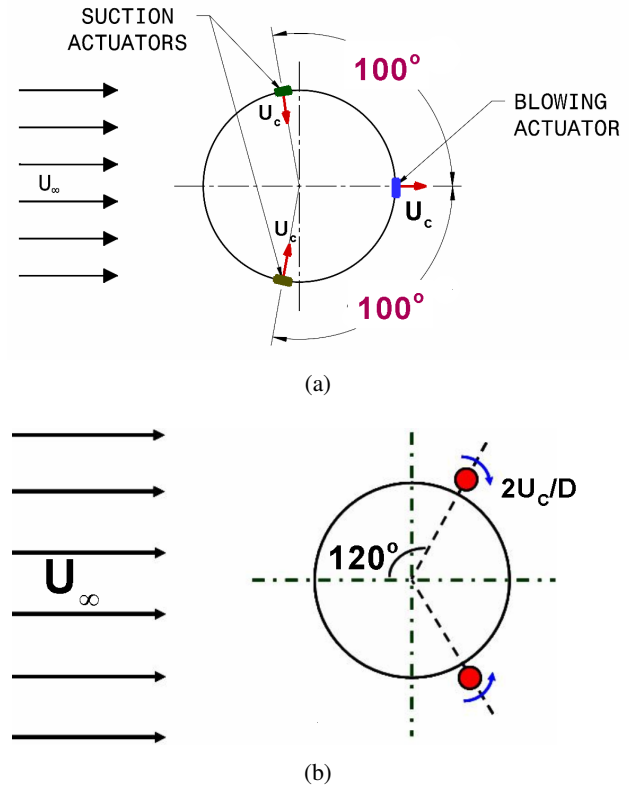


FIGURE 3: FLOW PAST A CIRCULAR CYLINDER WITH (a) THREE ACTUATORS SYSTEM AND (b) TWO ACTUATORS SYSTEM.

surfaces are assigned a *mass flow* boundary condition to enable suction with zero net mass injection. In the second one, two simple rotary type control cylinders are located at 120° , behind the main cylinder (see Fig 3(b)). The control cylinders are rotated (top one clock-wise and bottom one counter clock-wise) to enable momentum injection. The U_c which is used in the definition of control parameter is a normal velocity at the slots and a tangential velocity on the control cylinder for the first and second type of actuator systems respectively. Furthermore, this control equation is incorporated along with the equation of structure and solved with mass and momentum conservation equations.

RESULTS AND DISCUSSION

Before we proceed to study the vortex induced vibrations and its control, flow past a circular cylinder with external excitation is numerically investigated. In the context of forced vibrations the coupling between the flow field and structural oscillations is unidirectional where both amplitude and frequency of oscillation are chosen at will and superimposed on the structure. The influence these vibrations on the wake vortices is often easier to categorize. Cylinder displacements are imposed and do not have a bearing on the actual force exerted by the fluid.

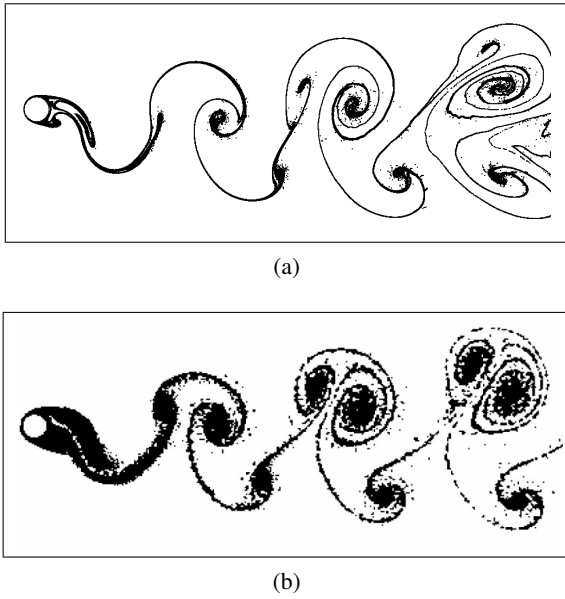


FIGURE 4: P+S WAKE PATTERN BEHIND CIRCULAR CYLINDER UNDER CONTROLLED VIBRATIONS AT $Re = 200$. (a) PRESENT STUDY AND (b) MENEGHINI AND BEARMAN [21].

The motion of a the cylinder is idealized as, $y = A \sin(\omega t)$, where, A is the maximum amplitude of oscillation and ω , refers to the imposed circular excitation frequency on the structure. For the purpose of comparison the amplitude, $A^* = 0.65$, and frequency, $f^* = 0.8$, combinations were chosen, to investigate the flow patterns behind the cylinder. Here, the amplitude of oscillation (A^*) is normalized with cylinder diameter and cylinder excitation frequency with the Strouhal frequency (f_{St}). Results from the present investigation are compared with those obtained by Meneghini and Bearman [21] at the same amplitude and frequency for $Re = 200$, in Figures 4. The P+S wake pattern is well captured by the present numerical setup which is used in further studies.

To investigate the performance of two types of actuators, the control equation described in the section is coupled with the governing equations of both structural motion and fluid flow. The control equation (13) described above is a generic one that determines the actuation parameter, which is implemented as a user defined function (UDF). Actuators are switched *on* (indicated by A in Fig.5 and 10), only after reaching the full blown form of steady periodic oscillations.

In the case of first actuator system which consists of two suction slots and a blowing slot on the cylinder surface starts suction and blowing of the fluid with zero net mass injection at A where actuators are switched *on* (see Fig. 5). In the Fig. 5, we can observe the amplitude of vortex induced oscillations are droops down to zero with

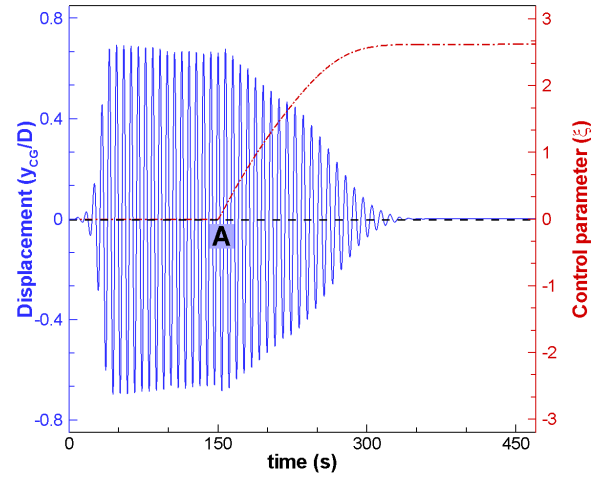


FIGURE 5: GRADUAL SUPPRESSION OF FREE VIBRATIONS, WHEN CONTROL WAS SWITCHED ON AT $t = 150$. THE CONTROL INPUT REACHES A DYNAMICALLY STEADY STATE

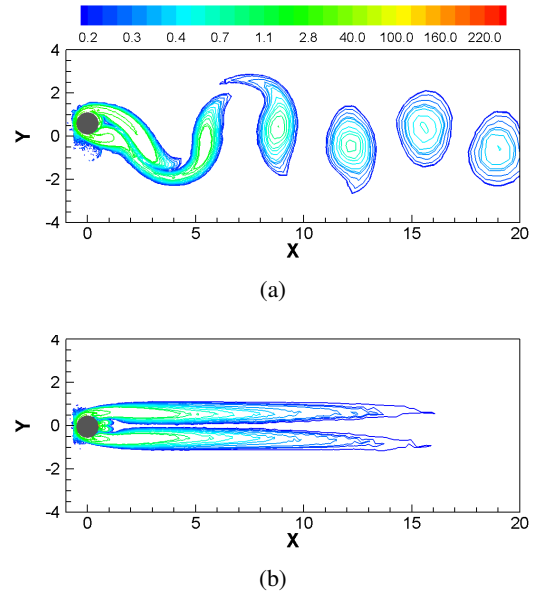


FIGURE 6: WAKE PATTERNS (a) BEFORE CONTROL AT $t = 150$, (b) AFTER CONTROL AT $t = 450$.

gradual increment of control parameter $\xi(t)$. The complete suppression of oscillations and vortex shedding (as shown in Fig. 6) are observed at study state value of control parameter, $\xi = 2.6$ at $Re = 100$.

To investigate the performance of three actuator system for turbulent wake, we carried out the simulations at $Re = 3900$. At Reynolds number 3900 the wake is fully turbulent, although the boundary layer is laminar. Resolving features of the turbulent fluctuations in the wake region by URANS approach is limited by the approximation capability of the turbulent eddy viscosity hypothesis employed for the Reynolds stress tensor. So, the accu-

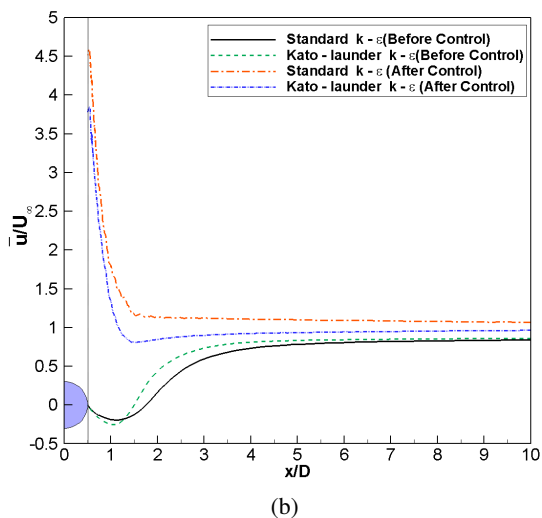
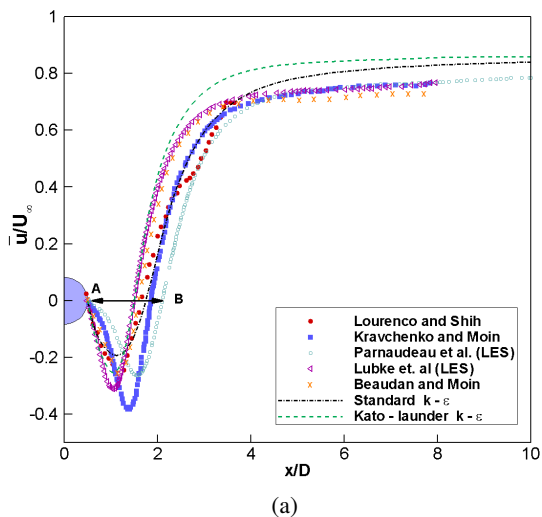


FIGURE 7: MEAN STREAMWISE VELOCITY ALONG THE WAKE CENTER LINE FOR $Re = 3900$. (a) VALIDATION WITH LOURENCO AND SHIH (from Ref. [22]), KRAVCHENKO AND MOIN [23], PARNAUDEAU et. al [22], LÜBCKE et. al [24], BEAUDAN AND MOIN (from Ref. [24]) AND (b) BEFORE AND AFTER CONTROL.

racy of these turbulence models in predicting the forces and flow parameters influence (i) the calculation of structural oscillations and (ii) the efficacy of suction - blowing control. In the Present study, the control equation and the governing equation of the structure are coupled and solved simultaneously along with a chosen two equation turbulence model. The time averaged mean and turbulence characteristics are obtained over ten vortex shedding cycles, after reaching steady periodic state. The location of the centre of mean vortex and length of formation region (L_f) is quantified by plotting normalized mean streamwise velocity (\bar{u}_{cl}) against the wake centreline as

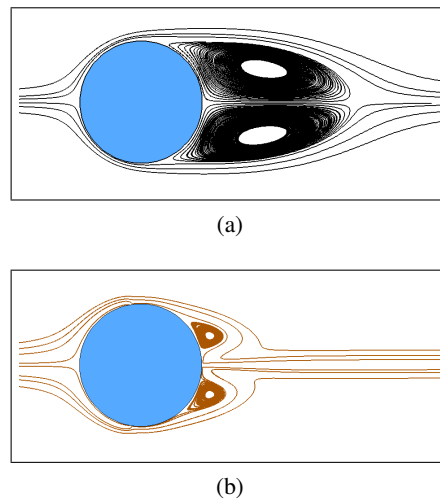
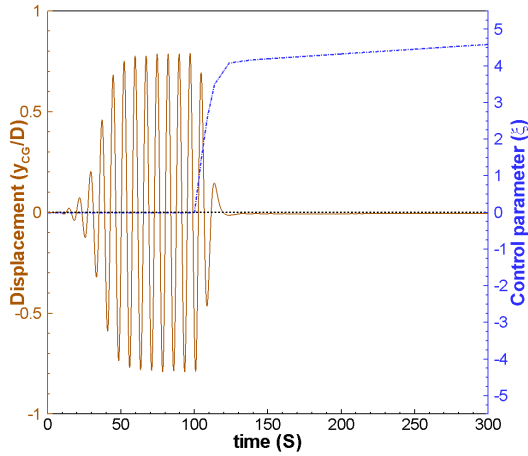


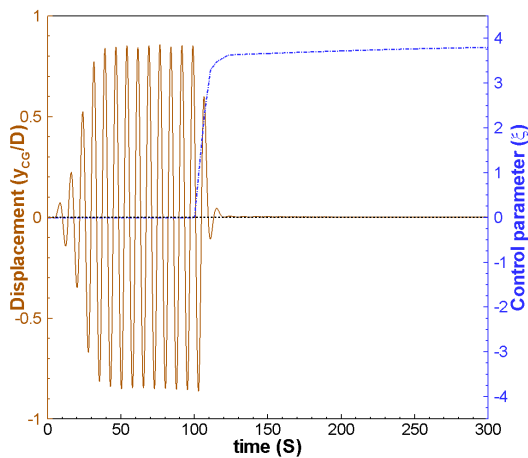
FIGURE 8: TIME AVERAGED STREAMLINES IN THE WAKE BEHIND THE MAIN CIRCULAR CYLINDER WITH STANDARD $k - \epsilon$ MODEL AT $Re = 3900$. (A) WITHOUT CONTROL AND (B) WITH CONTROL.

shown in Fig. 7(a). The plot signifies the predictive capability of two models vis-à-vis other numerical and experimental investigations. The models tested have a better comparison with both PIV and LES data in the far wake region. However, there is a clear under prediction on the location of centre of mean vortex, length of the wake formation region (L_f) and the corresponding magnitude of velocity (as indicated by AB). The influence of suction-blowing control averaged over a long time period is shown in Fig. 7(b). Corresponding vortex formation length under the influence of adaptive control is shown in Fig. 8. Here, the streamline topology involves two large counter-rotating eddies in the near-wake region. However, under the influence of control the eddies get shrunk very close to the cylinder surface, indicating a tighter and a tiny wake formation region. Note in particular, the fluid is able to reach the rear stagnation point and contain the absolute instability region. This is a typical signature of the complete annihilation of wake vortices. Thus, flow induced oscillations are effectively controlled even for turbulent flow conditions as depicted in Fig. 9. Therefore, the coupled control strategy is found to be effective when τ_{ij}^R modelling is achieved either through standard $k - \epsilon$ or Kato-Laundner $k - \epsilon$ models.

In the present study, simulations are carried out for the actuator system (second type) which contains the two simple rotary type control cylinders are located at 120° , behind the main cylinder to enable momentum injection. Control cylinder rotations are switched *on* (indicated by A), only after reaching the full blown form of steady pe-



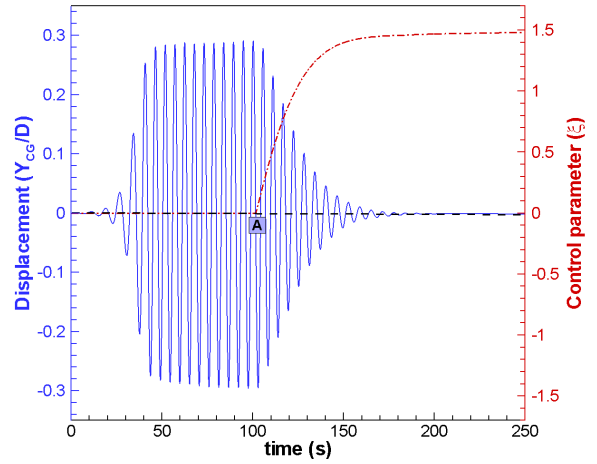
(a)



(b)

FIGURE 9: GRADUAL SUPPRESSION OF FREE VIBRATIONS AT $Re = 3900$, WHEN CONTROL WAS SWITCHED ON AT $\tau = 100$. THE CONTROL INPUT REACHES A DYNAMICALLY STEADY VALUE. (a) STANDARD $k - \varepsilon$ and (b) $k - \varepsilon$ OF KATO-LAUDER.

riodic oscillations as shown in Fig.10. The rate of injection of momentum (through $\xi(t)$) gradually picks up and reaches a steady state value, while the amplitude of the oscillations droops down (see the Fig. 10). We observed the complete suppression of oscillations at study state value of $\xi(t) = 1.48$ at $Re = 100$. The temporal evolution of wake stabilization process is presented in the form of streakline visuals as shown in Fig. 11. A wide and fully developed wake is observed in the Fig.11 (a) at $t = 100$ where control cylinders start rotating. Once the control is switched on, the actuators start injecting the momentum into the wake and a quiescent state of wake is achieved through gradual changes as depicted in Fig 11 (b)-(d). The complete suppression of vortex shedding and flow induced oscillations is achieved at $t = 250$ where the rotation parameter (ξ) reached the steady state value.



(a)

FIGURE 10: TEMPORAL HISTORY OF DISPLACEMENT (Y/D) AND ITS ASSOCIATED ROTATION PARAMETER OF THE OSCILLATING CYLINDER WITH CONTROL TWO CONTROL CYLINDERS WHILE CONTROL ALGORITHM IS ACTING AT $Re = 100$.

CONCLUSIONS

Two types of actuator systems are investigated in a closed loop feedback system. These two approaches have successfully demonstrated control of vortex induced oscillations at $Re = 100$ and 3900 . Validations are performed for forced cylinder oscillation cases. The two suction and one blowing actuator system completely suppressed the flow induced oscillations at study control parameter $\xi = 2.6$. At $Re = 3900$, this three actuator system effectively controlled the free vibrations of the turbulent wake and the wake formation length is effectively zero indicating complete suppression of vortex shedding. It is observed that the second type of actuator system, which consists of two small rotating control cylinders kept behind the main cylinder at an angle of 120° , is completely controlled the vortex induced oscillations and the corresponding study control parameter is, $\xi(t) = 1.48$.

REFERENCES

- [1] Blevins, R. D., 1990. *Flow Induced Vibrations*. Von Nostrand Reinhold, New York.
- [2] Williamson, C. H. K., and Govardhan, R., 2004. "Vortex-induced vibrations". *Annu. Rev. Fluid Mech.*, **36**, pp. 413–455.
- [3] Bearman, P. W., 1984. "Vortex shedding from oscillating bodies". *Annu. Rev. Fluid Mech.*, **16**, pp. 195–222.
- [4] Modi, V. J., 1997. "Moving surface boundary-layer

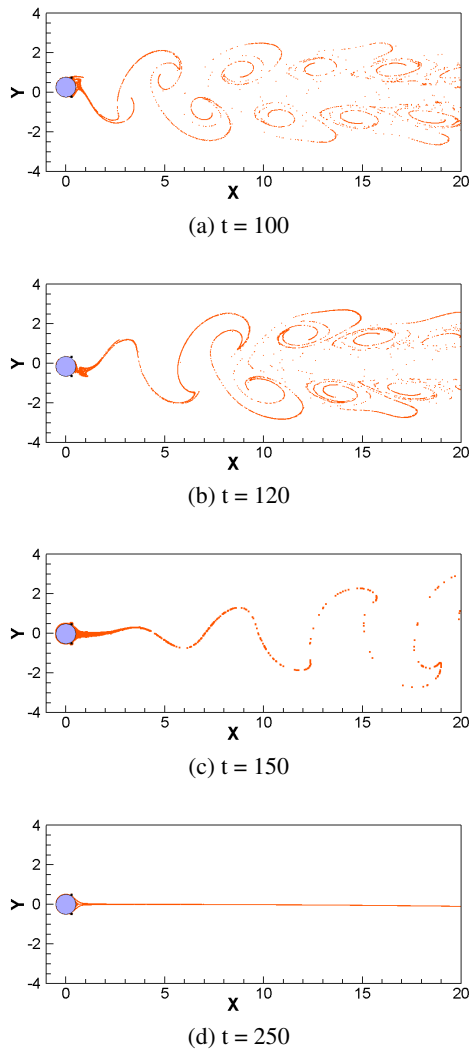


FIGURE 11: TEMPORAL EVOLUTION OF STREAK-LINE PATTERNS AT DIFFERENT TIME LEVELS BY COUPLING CONTROL CYLINDER ROTATIONS TO MAIN CYLINDER OSCILLATION.

- control: A review". *J. Fluids and Struct.*, **11**, pp. 627–663.
- [5] Kumar, A. R., Chan-Hyun, S., and Gowda, B. H. L., 2008. "Passive control of vortex-induced vibrations: An overview". *Recent Patents on Mech. Engg.*, **1**, pp. 1–11.
- [6] Baek, H., and Karniadakis, G. E., 2009. "Suppressing vortex-induced vibrations via passive means". *J. Fluids Struct.*, **25**, pp. 848–866.
- [7] Chen, Z., and Aubry, N., 2005. "Closed-loop control of vortex-induced vibration". *Comm. Nonlinear Science and Num. Simulation*, **10**, pp. 287–297.
- [8] Li, Z., Navon, I. M., Hussaini, M. Y., and Dimet, F.-X. L., 2003. "Optimal control of cylinder wakes via suction and blowing". *Comp. Fluids.*, **32**, pp. 149–171.

- [9] Fujisawa, N., and Takeda, G., 2003. "Flow control around a circular cylinder by internal acoustic excitation". *J. Fluids and Struct.*, **17**, pp. 903–913.
- [10] Tokumar, P., and Dimotakis, P., 1991. "Rotary oscillation control of a cylinder wake". *J. Fluid Mech.*, **224**, pp. 77–90.
- [11] Ott, E., Grebogi, C., and Yorke, J. A., 1990. "Controlling chaos". *J. Fluids Struct.*, **64**, pp. 1196–1199.
- [12] Patnaik, B. S. V., and Wei, G., 2002. "Controlling wake turbulence". *Phy. Rev. Lett.*, **88**, p. 054502.
- [13] Muddada, S., and Patnaik, B. S. V., 2010. "An active flow control strategy for the suppression of vortex structures behind a circular cylinder". *Eur. J. Mech. B - Fluids*, **29**, pp. 93–104.
- [14] Williamson, C. H. K., 1996. "Vortex dynamics in the cylinder wake". *Annu. Rev. Fluid Mech.*, **28**, pp. 477–539.
- [15] Patankar, S. V., 1980. *Numerical Heat Transfer and Fluid Flow*. Hemisphere, Washington, DC.
- [16] Fluent Inc., 2006. *Fluent 6.2 Users Guide*. Canonsburg, Pennsylvania, USA.
- [17] Davidson, P. A., 2005. *Turbulence: an introduction for scientists and engineers*. Oxford University Press, Great Clarendon Street, Oxford ox2 6DP.
- [18] Launder, B. E., and Spalding, D. B., 1974. "The numerical computation of turbulent flow". *Comput. Methods Appl. Mech. Eng.*, **3**, pp. 269–289.
- [19] Launder, B. E., and Sharma, B., 1974. "Application of the energy-dissipation model of turbulence to the calculation of flow near a spinning disc". *Lett. Heat and Mass Tran.*, **1**, pp. 131–138.
- [20] Rodi, W., 1997. "Comparison of les and rans calculations of the flow around bluff bodies". *J. Wind Engg. Ind. Aerodyn.*, **69**, pp. 55–75.
- [21] Bearman, J. R. M. P. W., 1995. "Numerical simulation of high amplitude oscillatory flow about a circular cylinder". *Journal of Fluids and Structures*, **9**, pp. 435–455.
- [22] Parnaudeau, P., Carlier, J., Heitz, D., and Lamballais, E., 2008. "Experimental and numerical studies of the flow over a circular cylinder at reynolds number 3900". *Physics of Fluids.*, **20**, p. 085101.
- [23] Kravchenko, A. G., and Moin, P., 2000. "Numerical studies of flow over a circular cylinder at $re_d = 3900$ ". *Journal of Fluids and Structures*, **12**, pp. 403–417.
- [24] Lübbeke, H., Schmidt, S., Rung, T., and Thiele, F., 2001. "Comparison of les and rans in bluff-body flows". *Journal of Fluids and Structures*, **89**, pp. 1471–1485.

A NUMERICAL INVESTIGATION OF THE FLOW AROUND AN OSCILLATING CIRCULAR CYLINDER AT LOW STOKES NUMBER

Julien Berland*

Lise Divaret

Pierre Moussou

LaMSID

UMR CNRS/EDF/CEA 2832

Clamart, France

Email: julien-j.berland@edf.fr

Olivier Cadot

Unité de Mécanique

ENSTA ParisTech

Palaiseau, France

ABSTRACT

The flow around an oscillating cylinder in a medium at rest is simulated for various Stokes and Keulegan-Carpenter numbers in order to design guidelines to properly adjust the simulation parameters to the flow configuration. Criteria for mesh requirements and minimum time steps are thus provided. The range of Stokes and Keulegan-Carpenter numbers on which 2D or 3D simulations is also determined. URANS turbulence modelling is finally shown to fail to capture the flow features around an oscillating body.

INTRODUCTION

Solid bodies undergoing forced motions in an otherwise quiescent medium are of significant practical and academic interest. In the present work the scope shall be narrowed to flows developing around oscillating cylinders, which have received great attention in the field of flow-induced vibrations [1–3].

In practice the prediction of flow-induced forces acting upon a cylinder is based on an equation due to Morrison *et al.* [1]. They proposed the in-line force acting on a cylinder to be the sum of a drag and of an inertial force. Based on this decomposition, the fluid force per unit length is determined by two non-dimensional coefficients:

$$F = -\frac{1}{2}\rho d C_d |U|U - \frac{1}{4}\pi\rho d^2 C_m \frac{dU}{dt} \quad (1)$$

where ρ is the fluid density, d the cylinder diameter and U its velocity. The non-dimensional coefficients C_d and

C_m are the drag and inertia coefficients, respectively. In the case of a cylinder oscillating with a frequency f , they depend on the Keulegan-Carpenter number $KC = U/fd$, on the Stokes number $\beta = d^2 f/\nu$ and on the frequency f in a rather complex manner.

An extensive database of the drag and inertia coefficients is available for a relatively large range of both Stokes and Keulegan-Carpenter numbers. Among others, Bearman *et al.* [4], Obasaju *et al.* [5], Dütsch *et al.* [6], as well as Sarpkaya [2] provided experimental data on flow-induced forces acting on an oscillating cylinder.

More recently numerical simulations also led to complementary results. Several numerical solutions of the unsteady Navier-Stokes equations for flows around a circular cylinder at various Keulegan-Carpenter and Stokes numbers have been reported in the literature. A sum-up of these calculations is proposed in Table 1. A striking point is that oscillating flows are much more encountered than oscillating cylinders as performed by Dütsch *et al.* [6] or Duclercq *et al.* [7]. The Stokes numbers are generally lower than 10^3 to avoid high Reynolds number flow, except for Suthon & Dalton [8] who have been able to reach Stokes numbers as high as 10^4 . In the works presented in Table 1, turbulent motions are taken into account through Direct Numerical Simulation (DNS), Large-Eddy Simulation (LES) as well as the vortex method. It is also worth noting that both two- and three-dimensional calculations have been successfully used for the same task.

It turns out that the interplay between the modeling choice and the accuracy of such calculations is still not clear. Consequently, it may be valuable to propose ground rules on the topic. Numerical parameters may indeed be adjusted in several manners:

- when dealing with numerical simulations of oscillat-

*Address all correspondence to this author.

TABLE 1: PARAMETER RANGE AND FLOW CONFIGURATION OF THE PREVIOUS NUMERICAL SIMULATIONS OF THE FLOW AROUND AN OSCILLATING CYLINDER, OR OF THE OSCILLATING FLOW AROUND A CYLINDER.

Reference	Year	β	KC	Geometry	Turbulence model
Oscillating flow (fixed cylinder)					
Justesen [9]	1991	196 ; 483	0-26 ; 0.5-3	2D	DNS
Lin <i>et al.</i> [10]	1991	76	0.1-30	2D	Vortex method
Wang & Dalton [11]	1991	451	5-20	2D	DNS
Lu <i>et al.</i> [12]	1997	1035	0.5-10	3D	LES
Zhang & Dalton [13]	1997	7.4-730	0.2-18	2D	Vortex method
Iliadis & Anagnostopoulos [14]	1998	34; 53	1-10	2D	DNS
Zhang & Dalton [15]	1999	196	1-4	3D	DNS
Nehari <i>et al.</i> [16]	2004	20	5-8.5	2D; 3D	DNS
Scandura <i>et al.</i> [17]	2009	20; 50	10	3D	DNS
An <i>et al.</i> [18]	2010	100-600	1.75-2.5	3D	DNS
Suthon & Dalton [8]	2011	1035; 6815; 9956	0.1-20	3D	DNS
Oscillating cylinder (medium at rest)					
Dutsch <i>et al.</i> [6]	1998	35	0.5-15	2D	DNS
Duclercq <i>et al.</i> [7]	2011	4-50	10	2D	DNS

ing flows one must keep in mind that there are two basic approaches to deal with them: (i) oscillate the medium past a fixed cylinder in a harmonic motion, or (ii) oscillate the cylinder in a harmonic motion in a medium at rest. The methods are actually equivalent and will produce the same results. However, method (i) is easier to implement in a solver since the cylinder is static, and numerical methods commonly encountered in computational fluid dynamics can be used. On the other hand, being able to increase the complexity of the system is a great asset and only methods (ii) offers the opportunity to investigate for instance the effect of confinement, the influence of non-harmonic motions or of detuning for cylinder arrays.

- concerning turbulence modeling, choices are also multiple. DNS strives to resolve all the important scales directly using very large degrees of freedom. Alternatively, the LES method computes the most energetic larger scales while the smaller ones are modeled so that the resolution barrier is considerably relaxed. At last, turbulence models based on the Reynolds-Averaged Navier-Stokes (RANS) equations require few computational resources. All scales present in the flow are modeled.
- as pointed out in Table 1, two- and three-dimensional calculations may be performed to evaluate flow-induced forces acting upon an oscillating cylinder. Such modeling choice is driven by the flow physics: turbulent structures at low Reynolds number may be dominated by two-dimensional vortices but at

higher flow speed vortex breakdown and flow three-dimensionalization are likely to occur.

- mesh design is also a key parameters. Mesh size close to the solid surfaces are expected to have a great influence on the solution quality. Criteria on mesh size requirements for oscillating flows are still to be proposed.
- finally, time stepping influence, particularly when using a moving mesh, must be thoroughly investigated.

In the present work special attention is therefore paid to the link between numerical modeling and calculation accuracy in order to design guidelines to properly adjust the simulation parameters to the flow configuration. The flow development around a single oscillating cylinder is determined with a finite-volume solver, coupled with a moving mesh technique, for various Stokes numbers and using different turbulence modeling strategies: two-dimensional DNS, three-dimensional quasi-DNS, and two-dimensional URANS (Unsteady RANS). The approach (ii), as denoted earlier, is only treated here (oscillating cylinder in a medium at rest). The objectives are to determine on which range of Stokes and Keulegan-Carpenter numbers 2D or 3D simulations must be used, to assess the ability of URANS turbulence models to capture the flow features around an oscillating body, and to propose guidelines for the mesh design and the time stepping parameters.

With this aim in view, the incompressible Navier-Stokes equations are solved using the collocated finite-volume solver *Code_Saturne* [19]. The displacement of

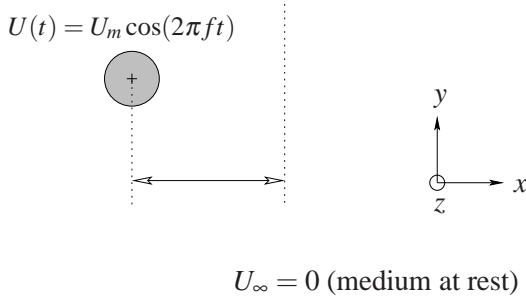


FIGURE 1: SCHEMATIC VIEW OF THE FLOW CONFIGURATION.

the cylinder is taken into account using the Arbitrary-Lagrangian-Eulerian (ALE) procedure [20], which permits to solve the flow equations with a moving mesh. Two Stokes numbers ($\beta = 483; 1035$) are considered and the Keulegan-Carpenter number ranges from 1 to 20. As pointed out, 2D DNS, 3D quasi-DNS and 2D URANS simulations are performed to determine their possible range of use. LES capabilities have not been assessed. The solution quality is evaluated by estimating the drag and inertia coefficients throughout a least square method and comparing them to available experimental data.

The simulation apparatus is first detailed. The results are then presented and discussed and concluding remarks are finally drawn.

SIMULATION APPARATUS

Flow configuration

As shown in figure 1 a single circular cylinder placed in a medium at rest is considered. The axis of the cylinder coincides with the z -axis and harmonic oscillations are imposed in the in-line direction, *i.e.* following the x -axis in the present setup. The velocity $U(t)$ of the solid body then reads $U(t) = U_m \cos(2\pi ft)$ where U_m is the velocity amplitude and f the oscillation frequency. Introducing the diameter d of the rod permits to introduce the so-called Keulegan-Carpenter number $KC = U_m/fd$ in order to characterize the motion amplitude, and the Stokes number β , or “frequency parameter”, with $\beta = d^2 f/\nu$, where ν is the kinematic viscosity.

In the present investigation, two Stokes numbers are studied, $\beta = 483$ and $\beta = 1035$, and the Keulegan-Carpenter number is in-between 0.4 and 20. The Reynolds number consequently spans over two decades, from 10^2 to 10^4 . Drag and inertia coefficients are available in the experiments of Bearman *et al.* [4] and Obasaju *et al.* [5] for $\beta = 483$, and in those of Sarpkaya [2] for $\beta = 1035$.

Numerical methods

Flow motions are solved here using *Code_Saturne*, an EDF in-house open CFD tool [19] based on a collocated finite volume approach. Moving boundaries are modelled using the Arbitrary Lagrangian-Eulerian (ALE) approach which is based on a moving reference frame [21].

As concern the boundary conditions, a no slip condition is enforced on the cylinder wall. Periodicity is imposed in the spanwise direction while free outlets are implemented on the other frontiers of the calculation domain.

Calculations based on 2D DNS, 3D quasi-DNS and URANS are assessed. Three-dimensional calculations are here referred to as “quasi-DNS” since all the turbulent scales, especially those away from the walls, are not fully resolved in order to reduce computational cost. URANS simulations are also performed based on the $k - \epsilon$, the $k - \omega$ and the $\overline{v^2} - f$, whose derivations may be found in Archambeau *et al.* [19].

Grid design

Wall resolution. A key parameter directly acting on the solution quality is the element size Δ in the vicinity of the solid surfaces. Mesh resolution at the wall is commonly reformulated in terms of wall units Δ^+ for aerodynamic applications [22]: when Δ^+ is smaller than 1 the simulation is ensured to capture all the turbulent scales developing at the wall. In the case of the oscillating cylinder different criteria as those retained for bodies in uniform translation may be however needed.

For a cylinder in harmonic motions, the thickness δ_v of the Stokes layer can be a relevant quantity. For instance Iliadis & Anagnostopoulos [14] proposed to evaluate the required minimum spatial resolution based on the thickness δ_v , which can be approximated by $\delta_v \propto 4\sqrt{\nu/\omega}$ where the pulsation reads $\omega = 2\pi f$. Note however that this criterion is only valid under the assumption that the flow is purely viscous and is consequently expected to be relevant only at very small Reynolds number.

Alternatively, when flow separation is likely to occur, *e.g.* for large Keulegan-Carpenter numbers and moderate Stokes numbers, one could propose a wall resolution requirement relying on the thickness δ_c of the laminar boundary layer at separation. Unfortunately, this quantity can hardly be predicted without the help of a full numerical simulation. Nonetheless, an order of magnitude can still be evaluated based on the experimental data of Bloor [23], obtained for a circular cylinder in a uniform cross-flow. Bloor [23] indeed suggested that the boundary layer thickness at separation would vary as $\delta_c \propto \sqrt{\nu d/U_m}$. It is proposed here to use these convective

tive thickness to determine the minimum space resolution at higher Reynolds number flows.

In terms of non-dimensional parameters, it is straightforward to demonstrate that the viscous thickness reads $\delta_v/d \propto 4/\sqrt{2\pi\beta}$ and the thickness obtained when the flow is dominated by convective phenomenon is given by the relationship $\delta_c/d \propto 1/\sqrt{\beta \cdot KC} = 1/\sqrt{Re}$.

It is worth noting that the viscous thickness only depends on the Stokes number whereas the convective thickness is a function of the Reynolds number only. Relevancy and practical use of these quantities to build up resolution criteria are further discussed in the result section where quantitative data are presented.

Meshes. All meshes used in the present study are build based on quadrangle elements only. Two- and three-dimensional grids have been designed with several wall resolution in order to assess the relevancy of the mesh resolution requirements proposed above.

Grids are parametrized according to the number of nodes N around a fourth of the circumference of the cylinder. Cells in addition have an aspect ratio close to 1 at the wall so that the mesh size Δr in the radial direction is given by $\pi d/4N$. For the three-dimensional mesh the spanwise extent, $L_z = 4d$, has been chosen to be the same of the one commonly used for static cylinders in a uniform flow.

Time stepping. The time step Δt is based on the Courant-Friedrichs-Lewy (CFL) condition, $CFL = U_m \Delta t / \Delta r$, where Δr is the smallest mesh size. Further requirements related to the ALE procedure are further discussed in the remainder of the paper.

RESULTS

Two-dimensional DNS simulations

The drag and inertia coefficients, C_d and C_m , are presented in figures 2.a and 2.b, respectively, as functions of the Keulegan-Carpenter number KC , for a Stokes number β equal to 1035. Two-dimensional DNS results obtained with three mesh sizes are provided: $4\Delta r = \pi d/80$, $4\Delta r = \pi d/160$ and $4\Delta r = \pi d/320$. For all these calculations the time steps are deduced only based on a CFL number equal to 0.5. The theoretical predictions of Wang & Dalton [24] as well as the experimental data of Sarpkaya [2] are also depicted for comparison.

A large scatter of the simulation results is first observed. The trend is particularly obvious for the drag coefficient in figure 2.a. For Keulegan-Carpenter numbers above 5, the calculations indeed underestimate the

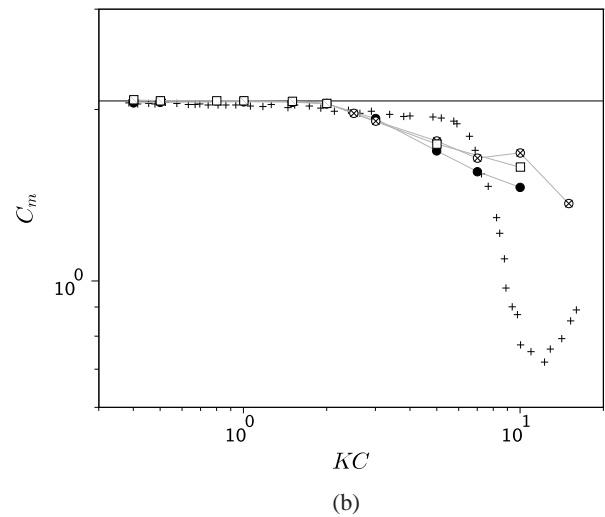
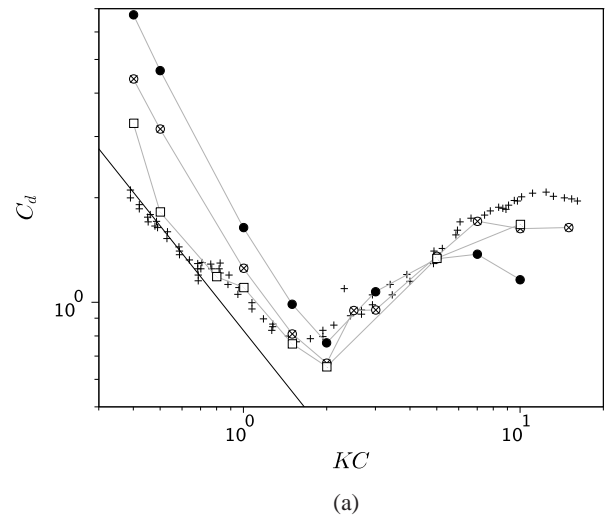


FIGURE 2: (a) DRAG COEFFICIENT C_d , AND (B), INERTIA COEFFICIENT C_m , OBTAINED WITH THE 2D DNS CALCULATIONS, AS FUNCTIONS OF THE KEULEGAN-CARPENTER NUMBER KC , FOR VARIOUS MESH SIZES AND FOR A STOKES NUMBER β EQUAL TO 1035. —, THEORY OF WANG & DALTON [24]; +, EXPERIMENTS OF SARPKAYA [2]; •, ⊗ AND □, PRESENT SIMULATION FOR $4\Delta r = \pi d/80$, $4\Delta r = \pi d/160$, $4\Delta r = \pi d/320$, RESPECTIVELY.

drag coefficient and discrepancies are seen on the inertia coefficient. This could be explained by the fact that for such oscillation amplitudes the flow is likely to be fully turbulent and three-dimensional. Two-dimensional simulations are consequently not able to reproduce the force coefficients.

For intermediate Keulegan-Carpenter numbers, with KC between 2 and 5, the amplitude of the forced motion

of the cylinder appears to be small enough to ensure a good collapse between the 2D simulations and the experiments.

Surprisingly, for smaller KC numbers, below 2, most of the simulations fail to predict the drag coefficient and tend to overestimate it.

Mesh convergence nonetheless seems to occur: in this range of motion amplitudes, reducing the mesh size seem to narrow the gap between the numerical data and the experiments. For instance, for $KC = 0.5$ and $KC = 1$, a mesh convergence is clearly visible, the finest grid ($4\Delta r = \pi d/320$) eventually provides a coefficient in good agreement with the one obtained by Sarpkaya [2]. However, for the smallest Keulegan-Carpenter, $KC = 0.4$, the finest mesh again overestimates the drag coefficient. Another numerical effect is probably responsible for the present discrepancies.

Two-dimensional DNS simulations with adjusted time step

Based on the results presented in section it seems that another numerical bias must be taken into account in order to explain the discrepancies observed for small motion amplitudes of the cylinder.

The ALE procedure itself may have an effect on the flow development. Time convergence is nonetheless granted and using a small enough time step ensures a negligible influence of the mesh motions on the flow field. In the present work, using at least 1000 time steps per oscillation period of the cylinder provides force coefficients in much better agreement with the reference values, especially for small Keulegan-Carpenter numbers.

The drag and inertia coefficients, C_d and C_m , are presented again in figures 3.a and 3.b, respectively, as functions of the Keulegan-Carpenter number KC , for a Stokes number β equal to 1035. For these simulations the time step has however been chosen so that it is always very small compared to the time scale of the cylinder motions. For both coefficients, a good collapse with the experiments is now seen for Keulegan-Carpenter numbers up to 3. Above this limit, the flow is probably fully turbulent and the 2D-DNS calculations thus fail to yield accurate predictions.

Consequently, an additional constraint on the time step, only related to the ALE procedure, may be formulated as $\Delta t \ll 1/f$ where $1/f$ is the period of the cylinder oscillations. Unfortunately, this criterion cannot be expressed in a quantitative manner. The maximum acceptable level of spurious dissipation introduced by the ALE procedure is indeed likely to depend on the numerical methods employed or on the flow configuration.

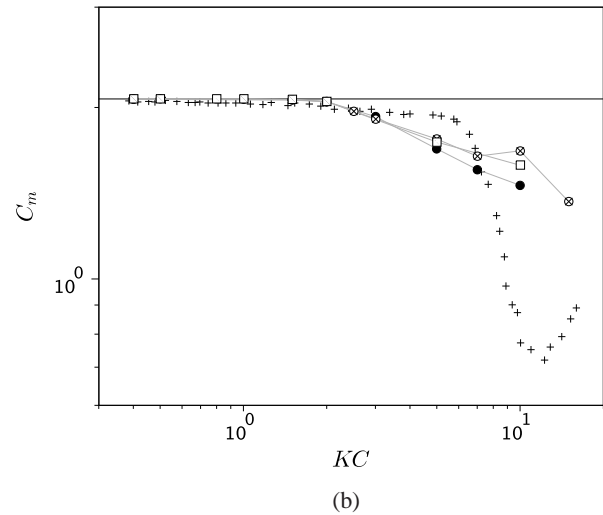
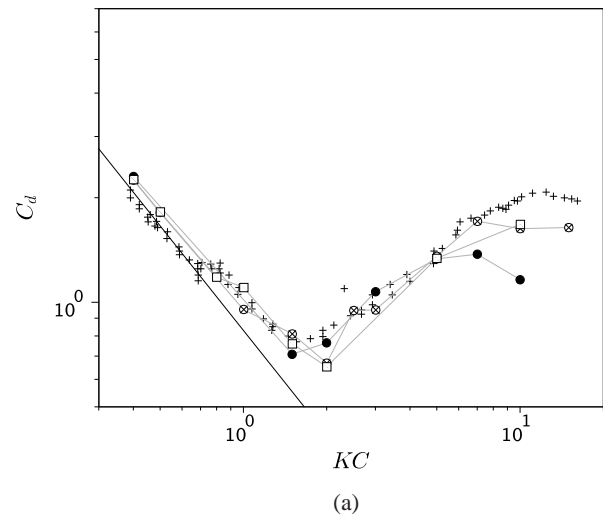


FIGURE 3: COEFFICIENTS OBTAINED WITH THE 2D DNS CALCULATIONS WITH ADJUSTED TIME STEPS. SEE CAPTION OF FIGURE 2 FOR DETAILS.

2D vs. 3D simulations

As emphasized in the previous sections, increasing the Keulegan-Carpenter numbers concurrently increases the Reynolds number. At large amplitude oscillations the flow is expected to be fully turbulent and to exhibit a three-dimensional structure.

In figures 3.a and 3.b it was shown that two-dimensional simulations fail to correctly predict the drag and inertia for Keulegan-Carpenter above 3. This upper limit for two-dimensional simulations corresponds to a Reynolds number close to 3100.

At a lower Stokes number, the same behavior is observed but on different intervals of Keulegan-Carpenter

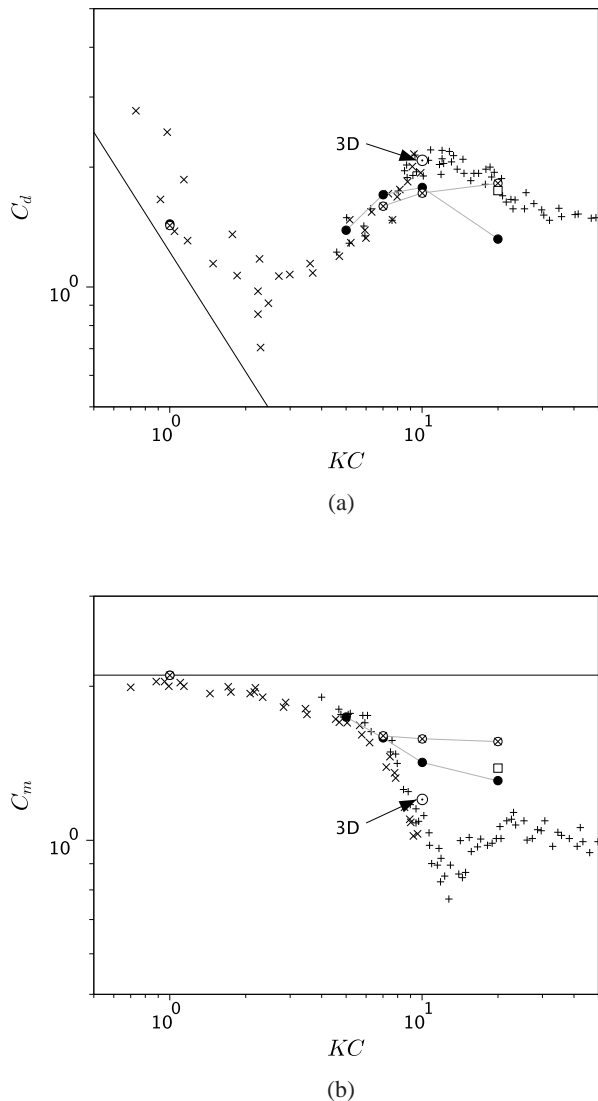


FIGURE 4: (a) DRAG COEFFICIENT C_d , AND (b), INERTIA COEFFICIENT C_m , OBTAINED WITH THE 2D DNS AND 3D QUASI-DNS CALCULATIONS WITH ADJUSTED TIME STEP, AS FUNCTIONS OF THE KEULEGAN-CARPENTER NUMBER KC , FOR VARIOUS MESH SIZES AND FOR A STOKES NUMBER β EQUAL TO 483. —, THEORY OF WANG & DALTON [24]; \times , EXPERIMENTS OF OBASAJU *et al.* [5]; $+$, EXPERIMENTS OF BEARMAN *et al.* [4]; \bullet , \otimes and \square , PRESENT SIMULATION FOR $4\Delta r = \pi d/80$, $4\Delta r = \pi d/160$, $4\Delta r = \pi d/320$, RESPECTIVELY. \odot , 3D QUASI-DNS SIMULATION FOR $4\Delta r = \pi d/80$, ALSO SHOWN BY THE ARROWS.

numbers. In figures 4.a and 4.b, the drag and inertia coefficients are presented as functions of the Keulegan-Carpenter number KC , for a Stokes number β equal to 483, for 2D DNS calculations. Mesh sizes such as $4\Delta r = \pi d/80$, $4\Delta r = \pi d/160$ and $4\Delta r = \pi d/320$ are depicted here, and the experiments of Bearman *et al.* [4] and

Obasaju *et al.* [5] are used as references. Above $KC = 7$, limitations of the two-dimensional geometry lead to large gaps between the simulation and the experiments. The discrepancies are especially visible for the inertia coefficient. The Reynolds number is then around 3400 which is close to the value obtained for the other Stokes number $\beta = 1035$.

A three-dimensional quasi-DNS simulation has been carried out above this limit, for $\beta = 483$ and a motion amplitude $KC = 10$, leading to a Reynolds number of approximately 4800. Three-dimensional quasi-DNS and the experiments are depicted in figures 4.a and 4.b. For a Keulegan-Carpenter of 10, an offset is visible between the 2D DNS data and the reference. Switching to a 3D configuration however greatly improved the numerical results: a better collapse is seen for both drag and inertia coefficients.

Three-dimensional simulations are thus required for large amplitude motions of the cylinder. The Reynolds number seems to be a relevant indicator of the frontier between 2D and 3D calculations. Based on the present numerical data, for $Re < 3000$, two-dimensional modeling is enough to provide accurate drag and inertia coefficient, but above this limit, three-dimensional mesh configurations need to be used to fully capture turbulence features.

Mesh convergence

Mesh convergence is now considered in order to propose quantitative values for the criteria introduced in section .

A careful examination of the numerical data collected for the Stokes numbers $\beta = 483$ and $\beta = 1035$ demonstrated that in the purely viscous range the criterion based on the thickness of the Stokes layer is indeed relevant. For small Keulegan-Carpenter numbers, grids with sizes such as the constraint $\Delta r < \delta_v/8$ is fulfilled provide results in good agreement with the experiments.

For larger amplitudes of oscillations flow separation occurs and the resolution requirements at the wall seem to be given by the convective thickness. It turns out that grids with $\Delta r < \delta_c/2$ yield force coefficients close to the reference data.

These two criteria are of primary interest since they allow to design *a priori* the features of the mesh. It should be kept in mind that such upper limits of the wall resolution are most likely to depend on the discretization tools employed. Nonetheless, they still can be used to provide an order of magnitude of the minimum grid size.

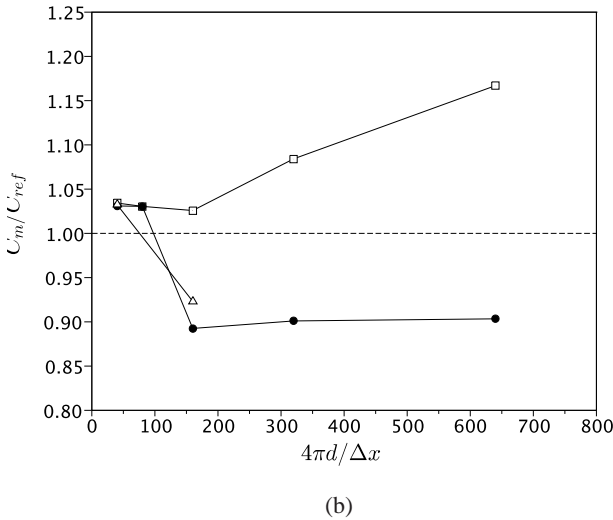
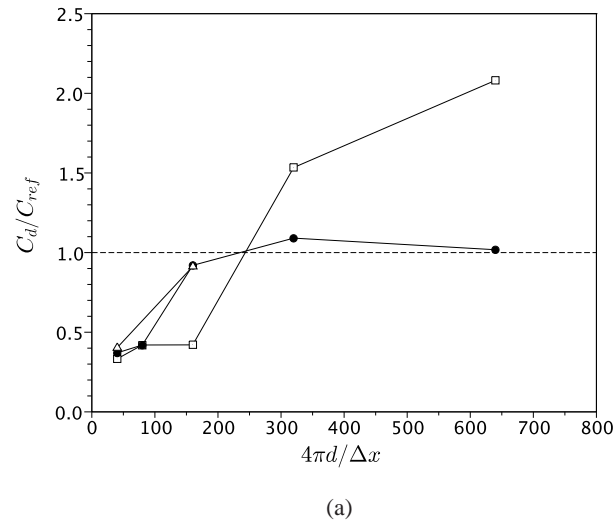


FIGURE 5: MESH CONVERGENCE FOR THE 2D-URANS, FOR $KC = 5$ AND $\beta = 1035$. (a), DRAG COEFFICIENT C_d , AND (b), INERTIA COEFFICIENT C_m , AS FUNCTIONS OF THE NUMBER OF CELLS $\pi d/\Delta r$ IN THE AZIMUTHAL DIRECTION. THE COEFFICIENTS ARE NORMALIZED BY THE REFERENCE VALUE C_{ref} DEDUCED FROM THE EXPERIMENTAL DATA OF SARP-KAYA [2]. \square , $k-\varepsilon$; \bullet , $k-\omega$; Δ , $\overline{v^2}-f$; - - -, EXPERIMENTS.

URANS turbulence modeling

The ability of URANS simulations to predict the force coefficients is finally assessed. The basic hypothesis underlying the use of RANS models is that the flow is fully turbulent. Comparisons are therefore carried out for a Stokes number equal to $\beta = 1035$ and a Keulegan-Carpenter number of 5. The Reynolds number is then close to 5×10^4 .

RANS calculations are performed on two-dimensional meshes and the computed drag and inertia coefficients are presented in figure 5.a and 5.b as functions of the grid resolution. The data are normalized by the experimental value of Sarpkaya [2]. A large scatter is first observed, especially concerning the inertia coefficient with a failure of the various models to provide convergence to the reference value. In particular, the $\overline{v^2}-f$ calculations had some stability issue with simulations that could not be completed on the finest grid. For the $k-\omega$ model, refining the grid tends to increase the gap between the simulations and the experiments with for instance a drag coefficient two times larger than the expected value for the finest grid. As for the $k-\varepsilon$, convergence seems to occur for both coefficients. Unfortunately, even if the drag coefficient eventually reaches the correct value, the inertia coefficient is significantly underestimated.

URANS simulations consequently fail to provide consistent force coefficients.

CONCLUSION

In the present work special attention has been paid to the link between numerical modeling and calculation accuracy in order to design guidelines to properly adjust the simulation parameters to the flow configuration. Two Stokes numbers ($\beta = 483; 1035$) have been considered with Keulegan-Carpenter number ranging from 1 to 20, using 2D DNS, 3D quasi-DNS and 2D URANS simulations.

Comparison of the drag and inertia coefficients to experimental data permits to draw some practice guidelines:

- an additional constraint on the time step, related to the spurious dissipation introduced by the ALE approach, has been highlighted: the time step must indeed be small compared to the oscillation period of the cylinder to avoid any interplay between the moving mesh procedure and the flow physics.
- two-dimensional DNS simulations accurately predict the force coefficients as long as the Reynolds number is lower than 3000. Above this limit the three-dimensional structure of the flow must be taken into account. Three-dimensional quasi-DNS calculations must then be performed.
- mesh resolution requirements depend on the flow physics. For viscous flow (e.g. small Keulegan-Carpenter numbers) the minimum grid size at the wall can be evaluated using the Stokes layer thickness $\delta_v/d \propto 4/\sqrt{2\pi\beta}$ while at higher amplitudes it is driven by the convective thickness defined defined

here as $\delta_c/d \propto 1/\sqrt{\text{Re}}$.

- RANS-based simulations fail to provide accurate prediction the force coefficients.

LES capabilities have not been assessed in the present work even though it may interested to analyze the influence of the subgrid-scale models on the resulting force coefficients.

REFERENCES

- [1] Morison, J., O'Brien, M., Johnson, J., and Schaf, S., 1950. "The force exerted by surface waves on piles". *Petroleum Trans.*, **189**, pp. 149–157.
- [2] Sarpkaya, T., 1986. "Force on a circular cylinder in viscous oscillatory flow at low Keulegan-Carpenter numbers". *J. Fluid Mech.*, **165**, pp. 61–71.
- [3] Williamson, C., 1985. "Sinusoidal flow relative to circular cylinders". *J. Fluid Mech.*, **155**, pp. 141–174.
- [4] Bearman, P., Downie, M., Graham, J., and Obasaju, E., 1985. "Forces on cylinders in viscous oscillatory flow at low Keulegan-Carpenter numbers". *J. Fluid Mech.*, **154**, pp. 337–356.
- [5] Obasaju, E., Bearman, P., and Graham, J., 1988. "A study of forces, circulation and vortex patterns around a circular cylinder in oscillating flow". *J. Fluid Mech.*, **196**, pp. 467–494.
- [6] Dütsch, H., Durst, F., Becker, S., and Lienhart, H., 1998. "Low-Reynolds-number flow around an oscillating circular cylinder at low Keulegan-Carpenter numbers". *J. Fluid Mech.*, **260**, pp. 249–271.
- [7] Duclercq, M., Broc, D., and Cadot, O., 2011. "Characterization of long time fluctuations of forces exerted on an oscillating circular cylinder at $\text{KC}=10$ ". *J. Fluid Struct.*, **312**(1-2), pp. 19–38.
- [8] Suthon, P., and Dalton, C., 2011. "Streakline visualization of the structures in the near wake of a circular cylinder in sinusoidally oscillating flow". *J. Fluid Struct.*, **27**(7), pp. 885–902.
- [9] Justesen, P., 1991. "A numerical study of oscillating flow around a circular cylinder". *J. Fluid Mech.*, **222**, pp. 157–196.
- [10] Lin, X., Bearman, P., and Graham, J., 1996. "A numerical study of oscillatory flow about a circular cylinder for low values of beta parameter". *J. Fluid Struct.*, **10**(5), pp. 501–526.
- [11] Wang, X., and Dalton, C., 1991. "Oscillating flow past a rigid circular cylinder: a finite-difference calculation". *J. Fluid Eng.*, **113**(3), pp. 377–383.
- [12] Lu, X., Dalton, C., and Zhang, J., 1997. "Application of large eddy simulation to an oscillating flow past a circular cylinder". *J. Fluid Eng.*, **119**(3), pp. 519–526.
- [13] Zhang, H.-L., and Zhang, X., 1997. "Flow structure analysis around an oscillating circular cylinder at low KC number: a numerical study". *Comput. Fluids*, **26**(1), pp. 83–106.
- [14] Iliadis, G., and Anagnostopoulos, P., 1998. "Viscous oscillatory flow around a circular cylinder at low Keulegan-Carpenter numbers and frequency parameters". *Int. J. Num. Meth. Fluids*, **26**(4), pp. 403–442.
- [15] Zhang, J., and Dalton, C., 1999. "The onset of three-dimensionality in an oscillating flow past a fixed circular cylinder". *Int. J. Num. Meth. Fluids*, **30**(1), pp. 19–42.
- [16] Nehari, D., Armenio, V., and Ballio, F., 2004. "Three-dimensional analysis of the unidirectional oscillatory flow around a circular cylinder at low Keulegan-Carpenter and β numbers". *J. Fluid Mech.*, **520**, pp. 157–186.
- [17] Scandura, P., Armenio, V., and Foti, E., 2009. "Numerical investigation of the oscillatory flow around a circular cylinder close to a wall at moderate Keulegan-Carpenter and low Reynolds numbers". *J. Fluid Mech.*, **627**, pp. 259–290.
- [18] An, H., Cheng, L., and Zhao, M., 2010. "Direct numerical simulation of oscillatory flow around a circular cylinder at low Keulegan-Carpenter number". *J. Fluid Mech.*, **666**, pp. 77–103.
- [19] Archambeau, F., Sakiz, M., and Namane, M., 2004. "Code Saturne: a finite volume code for turbulent flows". *Int. J. Finite Vol.*, **1**(1), pp. 1–62.
- [20] Hirt, C., Amsden, A., and Cook, J., 1974. "An arbitrary Lagrangian-Eulerian computing method for all flow speeds". *J. Comp. Phys.*, **14**(3), pp. 227–253.
- [21] Souli, M., Ouahsine, A., and Lewin, L., 2000. "ALE formulation for fluid-structure interaction problems". *Comput. Meth. Appl. Mech. Eng.*, **190**(5-7), pp. 659–675.
- [22] Schlichting, H., 1955. *Boundary layer theory*. McGraw-Hill, New York.
- [23] Bloor, M., 1964. "The transition to turbulence in the wake of a circular cylinder". *J. Fluid Mech.*, **19**, pp. 290–304.
- [24] Wang, X., and Dalton, C., 1968. "On high frequency oscillating viscous flows". *J. Fluid Mech.*, **32**(1), pp. 55–68.



COMPUTATION OF FLOW AROUND A CIRCULAR CYLINDER UNDERGOING TWO-DEGREE-OF-FREEDOM FORCED MOTION AT LOW REYNOLDS NUMBER

László Baranyi¹

Department of Fluid and Heat Engineering
University of Miskolc
Miskolc
Hungary
Email: arambl@uni-miskolc.hu

ABSTRACT

This study investigates flow around a circular cylinder in forced two-degree-of freedom motion at four different phase angles between the transverse and in-line cylinder motion, at a Reynolds number of 250. Time-mean and rms values of force coefficients and mechanical energy transfer are investigated against frequency ratio in the lock-in domain. Computations were carried out by an in-house finite difference code developed by the author. Results reveal that an increase in phase angle, by bending the figure-eight cylinder path downstream, can reduce drag. Mechanical energy transfer was mostly positive, meaning that energy is transferred from the fluid to the cylinder, leading to a potentially dangerous VIV situation. The change in the initial conditions resulted in hardly any changes in the results.

NOMENCLATURE

$a_{0x,y}$	the dimensionless x and y components of cylinder acceleration
$A_{x,y}$	amplitude of oscillation in x or y directions, respectively, non-dimensionalised by d
C_D	drag coefficient, $2F_D / (\rho U^2 d)$
C_L	lift coefficient, $2F_L / (\rho U^2 d)$
d	cylinder diameter (m)
E	mechanical energy transfer
f	oscillation frequency, non-dimensionalised by U/d
f_v	vortex shedding frequency, non-dimensionalised by U/d
F_D	drag per unit length of cylinder (N/m)
F_L	lift per unit length of cylinder (N/m)
R	radius, non-dimensionalised by d
Re	Reynolds number, Ud/ν
St	non-dimensional vortex shedding frequency, $f_v d/U$
t	time, non-dimensionalized by d/U
T	motion period, $1/f_y$
U	free stream velocity, velocity scale (m/s)
$v_{0x,y}$	the dimensionless x and y components of cylinder velocity

x,y	Cartesian coordinates, non-dimensionalised by d
θ	phase angle difference between transverse and in-line cylinder motion
ρ	fluid density

Subscripts

D	drag
fb	fixed body
L	lift
rms	root-mean-square value
v	vortex shedding
x, y	components in x and y directions
0	for cylinder motion; for stationary cylinder at same Re; for initial condition
1	on the cylinder surface
2	on the outer boundary of the physical domain

INTRODUCTION

The flow past a single circular cylinder has been studied as a prototype of bluff body flows theoretically, experimentally and numerically. Some examples of these in real life are silos or smokestacks in wind or underwater pipes in a current. When vortices are shed from the structure a periodic force is generated which might lead to the vibration of the structure especially if the damping is small. The motion resulting from this force usually has either one or two degrees of freedom. The most frequently investigated type of one-degree-of-freedom (1-DoF) cylinder motion is the transverse cylinder oscillation. Both experimental and numerical studies have dealt with pure transverse cylinder motion (e.g., Williamson and Roshko, 1988; Lu and Dalton, 1996; Blackburn and Henderson, 1999). Less often investigated is pure in-line cylinder motion (e.g., Cetiner and Rockwell, 2001; Al-Mdallal et al., 2007; Mureithi et al., 2010).

However, far fewer investigations have been carried out for combined, two-degree-of-freedom (2-DoF) cylinder motion. In reality, however, both motions are often present, leading to a Lissajous-type path. The vortex-

¹Address all correspondence to this author¹

induced vibration (VIV) arising in such cases can lead to problems such as fatigue and damage of structures.

Kheirkhah and Yarusevych (2010) suggest that where the mass ratio (the ratio of the mass of the vibrating system to the mass of the displaced fluid) is high, as mainly occurs when a structure is oscillating in air, then the frequency of oscillation in in-line and in transverse directions are approximately equal to each other. This can lead to an elliptical path, such as that observed in tube bundles in heat exchangers (Blevins, 1990). Studies by Didier and Borges (2007), Baranyi (2008) and Kheirkhah and Yarusevych (2010), among others, look at elliptical cylinder motion. The occurrence of vortex switches at certain amplitude values was noted (Baranyi, 2008).

A more typical Lissajous-type path, on the other hand, occurs with a low mass ratio, typically found when a cylinder is moving in liquid: cables and pipes submerged in flowing water may undergo fatigue or damage due to this kind of motion. In this case the frequency of the cylinder motion in in-line direction is approximately twice its frequency in transverse direction, as for example found by Jeon and Gharib (2001), Jauvtis and Williamson (2004), and Sanchis et al. (2008). The phase angle difference between in-line and transverse motion θ results in different cylinder paths (Jeon and Gharib, 2001). One typical Lissajous curve is a figure-eight-shaped path, while a path in the shape of an arc, or C-shape, has also been observed in the experimental study for an elastically supported cylinder of Sanchis et al. (2008) in the Reynolds number domain of $Re=(1.3 \text{ to } 1.9) \times 10^4$ and in the numerical work of Prasanth and Mittal (2009).

Figure-eight paths have been studied to some extent in numerical investigations with forced cylinder motion (e.g., Baranyi, 2011; Peppas et al., 2010). Both studies looked at the influence of the direction of motion along the figure-eight path; i.e., when the path is traced in a clockwise direction in the upper half or lobe of the figure (and naturally anticlockwise in the lower lobe), or vice versa. It was found that the orientation influenced the mechanical energy transfer: anticlockwise motion in the upper lobe (acw) resulted in positive energy transfer, meaning that the fluid tends to amplify the cylinder oscillation, which can easily lead to VIV. Force coefficients were also affected, with higher drag values for acw. Sanchis et al. (2008) found acw orientation in their free vibration study.

In their experimental study of flow around a forced 2-DoF cylinder motion, Jeon and Gharib (2001) investigated regular figure-eight paths and figure-eight patterns with the lobes bent slightly downstream. They state that the phase angle differences found ranged between $\theta = 0^\circ$ and -45° . Similar distorted figure-eight paths were also found in Sanchis et al. (2008).

Based on the results of the above-mentioned experimental studies, a numerical simulation can be designed in order to investigate the effect of phase angle difference on the flow past a cylinder in 2-DoF figure-eight motion. Mechanical oscillation is used to simulate

flow around the cylinder as a preliminary study, without carrying out a full fluid-structure interaction (FSI) study. While it is true that a direct relationship between results of investigations of free and of forced vibration is difficult to ascertain (e.g., Williamson, 2004), this is a first step towards considering FSI, with special attention to the energy transfer between the cylinder and fluid.

Low-Reynolds number simulation is sometimes criticised for being irrelevant to real-life cases, which almost always involve higher Reynolds (Re) numbers. However, as Newman and Karniadakis (1995) argue, since many phenomena in flow-induced vibrations are only weakly dependent on Re , they can be fairly accurately simulated even at relatively low Re .

In this numerical study a circular cylinder is placed in a uniform flow at Reynolds number $Re=250$ and mechanically oscillated in two directions, yielding various figure-eight paths (all anticlockwise in the upper lobe) for four phase angle differences. Mechanical energy transfer and the time-mean and root-mean-square (rms) values of force coefficients are investigated.

COMPUTATIONAL METHOD

A non-inertial system fixed to the accelerating cylinder is used to compute 2D low-Reynolds number unsteady flow around a circular cylinder placed in a uniform stream. The governing equations are the non-dimensional Navier-Stokes equations for incompressible constant-property Newtonian fluid in a non-inertial system fixed to the accelerating cylinder, the equation of continuity and the Poisson equation for pressure.

On the cylinder surface, no-slip boundary condition is used for the velocity and a Neumann type boundary condition is used for the pressure. At the far region, potential flow is assumed. Computational results show that this approximation results in some inaccuracies near the outer boundary only, and in practice it has no influence on the results of the near-wake flow and forces acting on the cylinder.

Boundary-fitted coordinates are used to impose the boundary conditions accurately. The physical domain bounded by two concentric circles with radii R_1 and R_2 is mapped into a rectangular computational domain with equidistant spacing in both directions (see Fig. 1). In the physical domain logarithmically spaced radial cells are used, providing a fine grid scale near the cylinder wall and a coarse grid in the far field. The transformed governing equations and boundary conditions are solved by finite difference method. Space derivatives are approximated by fourth order central differences, except for the convective terms for which a third order modified upwind scheme is used. The Poisson equation for pressure is solved by the successive over-relaxation (SOR) method. The Navier-Stokes equations are integrated explicitly and continuity is satisfied at every time step. For further details see Baranyi (2003; 2008).

The 2D code developed by the author has been extensively tested against experimental and computational

results with good agreement being found, (Baranyi, 2008). A systematic comparison with results from the commercial software package Ansys Fluent also yielded very good agreement (Baranyi et al., 2011).

In this study the dimensionless time step is 0.0005, the number of grid points is 481x451, and a relatively large physical domain of $R_2/R_1=360$ has been chosen to enhance accuracy.

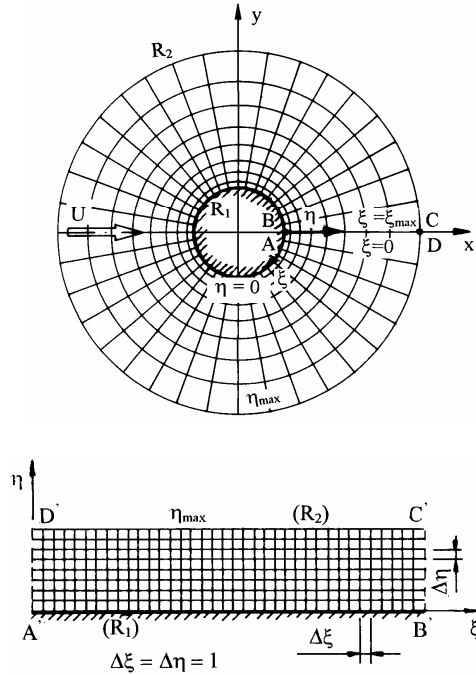


Figure 1. Physical and computational domains

This study investigates the behaviour of flow past a cylinder placed in a uniform stream with its axis perpendicular to the main flow. The cylinder is oscillated mechanically in both in-line and transverse directions in relation to the uniform stream. The dimensionless displacement of forced cylinder motion given in the experimental study of Jeon and Gharib (2001) is adopted here, defined as

$$x_0 = A_x \sin(4\pi f_y(t-t_0) + \Theta); \quad y_0 = A_y \sin(2\pi f_y(t-t_0)), \quad (1)$$

where A_x and A_y are the dimensionless oscillation amplitudes and f_y is the frequency of oscillation in transverse direction. Here t and t_0 are non-dimensional time, with t_0 being the initial condition, and Θ is the phase angle difference between the two oscillations. The second time derivatives of x_0 and y_0 give the accelerations that occur in the Navier-Stokes equations.

Jeon and Gharib (2001) suggest that the value of phase angle Θ tends to drift for free-vibration cases, but is usually in the range of 0 to -45° . Different phase angle values result in different cylinder paths. Based on the suggestion of Jeon and Gharib (2001) $\Theta = 0^\circ, -15^\circ, -30^\circ$, and -45° are investigated here. As shown in Fig. 2, $\Theta = 0^\circ$

gives a symmetric figure-8-path; whereas at $\Theta = -45^\circ$ the path is a figure-8 pattern with the lobes bent downstream. The dimensionless oscillation amplitudes in this study are fixed at $A_x=0.1$ and $A_y=0.4$ throughout the study, ensuring slender cylinder paths. The Reynolds number is fixed at $Re=250$. The independent variable for the investigation is the frequency ratio of f_y/St_0 ranging from around 0.7 to 1.1 (in the vicinity of the natural vortex shedding frequency $f_y/St_0=1$), but limited to within the lock-in domain. Here St_0 is the dimensionless vortex shedding frequency for a stationary cylinder at the same Reynolds number. For $Re=250$ the value $St_0=0.20355$ was used (from Posdziech and Grundmann, 2007).

Since initial condition was earlier found to influence the number and/or location of jumps in the TM and rms values of force coefficients for a cylinder in 2-DoF motion (Baranyi, 2008), computations were carried out for three different initial conditions ($t_0=0, 0.5, 1.0$) for $\Theta = -15^\circ$. For the other Θ values the initial condition was $t_0=0$.

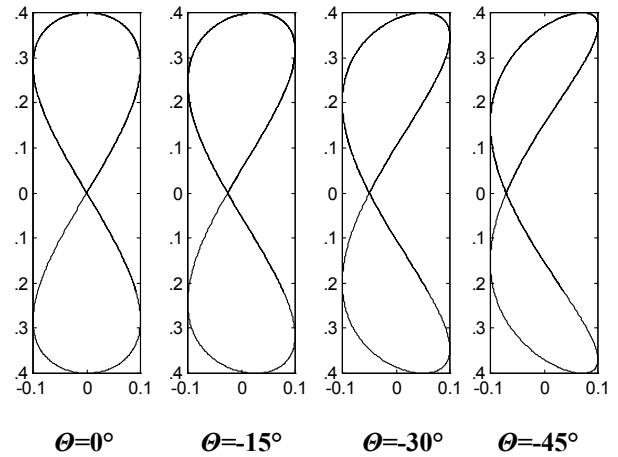


Figure 2. Cylinder paths for different phase angles Θ

The time-history of force coefficients (lift, drag, base pressure and torque), pressure and velocity field are computed. From these data, time-mean (TM) and root-mean-square (rms) values of force coefficients, streamlines, and vorticity contours can be obtained. Where jumps are found when force coefficients are plotted against frequency ratio, pre- and post-jump analysis is carried out by investigating limit cycle curves, time history curves, FFT spectra and vorticity contours.

Throughout this paper the lift and drag coefficients used do not contain the inertial forces originated from the non-inertial system fixed to the accelerating cylinder, except for the determination of the mechanical energy transfer E . Coefficients obtained by removing the inertial forces are often termed ‘fixed body’ coefficients (see Lu and Dalton, 1996). The relationship between the two sets of coefficients can be written as

$$C_D = C_{D,fb} + \pi a_{0x}/2, \quad C_L = C_{L,fb} + \pi a_{0y}/2 \quad (2)$$

where a_{0x} and a_{0y} are the cylinder acceleration components and subscript 'fb' refers to the fixed body (understood in an inertial system fixed to the stationary cylinder), Baranyi (2005). Since the inertial terms are periodic functions, their TM values vanish, resulting in identical TM values for lift and drag in the inertial and non-inertial systems. Naturally the rms values of C_L and C_D will be somewhat different in the two systems.

Investigation was restricted to lock-in cases. Lock-in, or the synchronization between vortex shedding and cylinder motion, produces a periodic solution for each of the force coefficients. In this paper, we consider lock-in to be when the vortex shedding frequency is identical to f_y , the frequency of transverse cylinder oscillation.

The non-dimensional mechanical energy transfer originally introduced by Blackburn and Henderson (1999) for transversely oscillated cylinder was extended for a general 2-DoF motion of the cylinder by Baranyi (2008):

$$E = \frac{2}{\rho U^2 d^2} \int_0^T \mathbf{F} \cdot \mathbf{v}_0 dt = \int_0^T (C_D v_{0x} + C_L v_{0y}) dt, \quad (3)$$

where $T=1/f_y$ is the motion period chosen, v_{0x} and v_{0y} are the x and y components of cylinder velocity. Note that Eq. (3) is valid for 1-DoF cylinder motion as well.

RESULTS

In this study, computations are carried out for the flow past a cylinder following a distorted figure-8-path at $Re=250$ against frequency ratio f_y/St_0 within the lock-in domain. Mechanical energy transfer E between the cylinder and the fluid, time-mean (TM) and rms values of lift C_L , drag C_D , base pressure and torque coefficients are investigated, but for the sake of simplicity only C_L , C_D and E values will be shown in the paper. Sudden jumps between state curves were found in some cases; these indicate a sudden change in the vortex structure (Baranyi, 2008). Values just before and just after a jump (vortex switch) are presented in a pre- and post-jump analysis.

Time-mean and rms values

At all four phase angle values investigated, the TM of lift and torque coefficients was zero throughout the locked-in frequency domain (not shown here). This has also been found for all transversely oscillated cases investigated by the author. The rms of fixed-body lift, shown in Fig. 3, generally increases with frequency ratio for all θ values. A tendency that can be observed in Fig. 3 above the frequency ratio of 0.84 is that the absolute value of θ increases with f_y/St_0 . Some jumps can be seen in the curves. The curve belonging to $\theta = -45^\circ$ is not even continuous, because – in accordance with the findings of Gharib (1999) – for $\theta = -45^\circ$ a not-locked-in domain exists that is bounded by two lock-in domains.

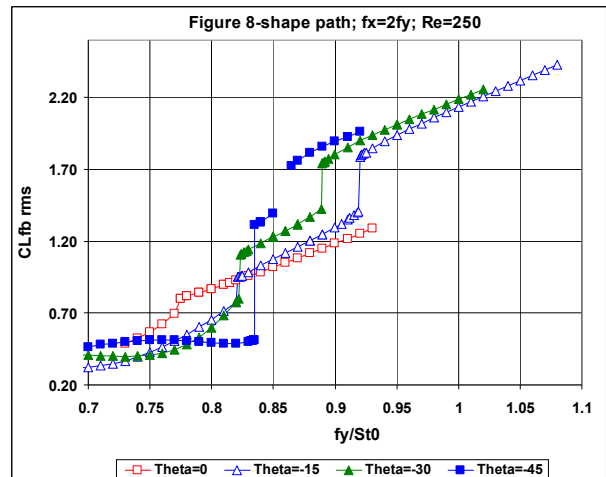


Figure 3. Rms of lift versus frequency ratio for phase angles $\theta=0^\circ$, -15° , -30° and -45°

The TM of drag versus frequency ratio for the four phase angle values is shown in Fig. 4 in the lock-in domain. It can be seen that the TM of drag decreases with larger absolute values of the phase angle over most of the lock-in frequency ratio domain for the given parameters. Clear changes in behaviour are seen between $\theta=0^\circ$ and the other θ values; as the path is bent downstream, the drag is drastically reduced, while sudden jumps in the curve appear, indicating an abrupt switch in vortex structure (see e.g. Baranyi, 2008).

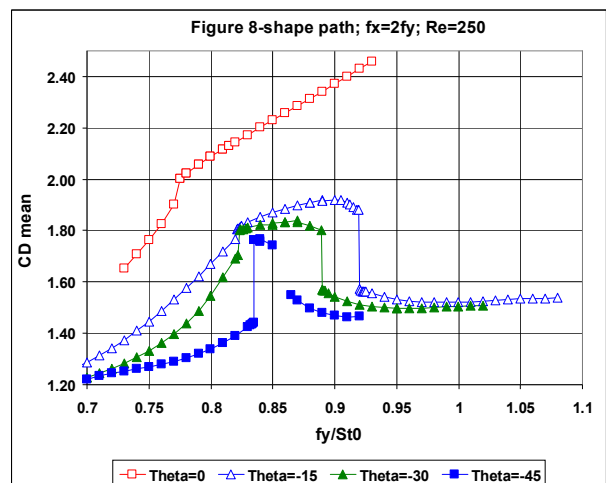


Figure 4. Time-mean of drag versus frequency ratio for phase angles $\theta=0^\circ$, -15° , -30° and -45°

The rms of fixed body drag against frequency ratio can be seen in Fig. 5. It seems that the values for $\theta=0^\circ$ are much higher than $C_{Dfb rms}$ values belonging to other θ values. As can be seen in the figure, the curves belonging to $\theta = -15^\circ$, -30° and -45° are grouped together. As no substantial jump can be observed in the figure, it seems that vortex switches do not have much effect on $C_{Dfb rms}$ values, probably due to symmetry.

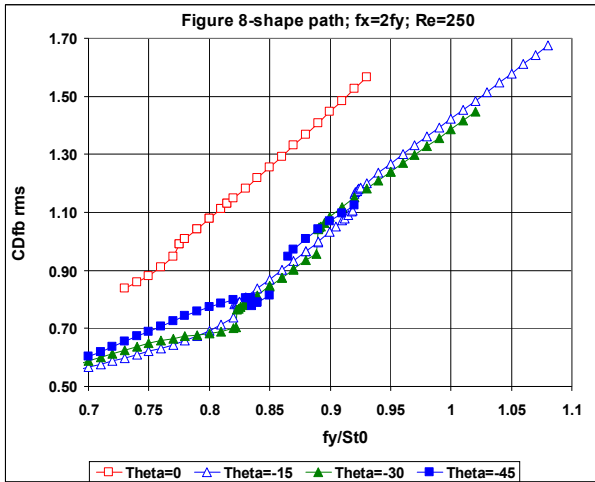


Figure 5: Rms of drag versus frequency ratio for phase angles $\Theta=0^\circ$, -15° , -30° and -45°

Mechanical energy transfer

Figure 6 shows the mechanical energy transfer E between the fluid and cylinder. For $\Theta=0^\circ$ and at the amplitudes of A_x and A_y investigated, E remained positive throughout the lock-in domain, and practically constant from 0.77 to 0.93. For the other three values, although the largest part of the lock-in domain exhibits positive mechanical energy transfer values, there are some sub-domains where E is negative. Positive E means that energy is introduced into the cylinder and in the case of free vibration, this could well lead to VIV. It can also be seen in the figure that E decreases with larger phase angle differences.

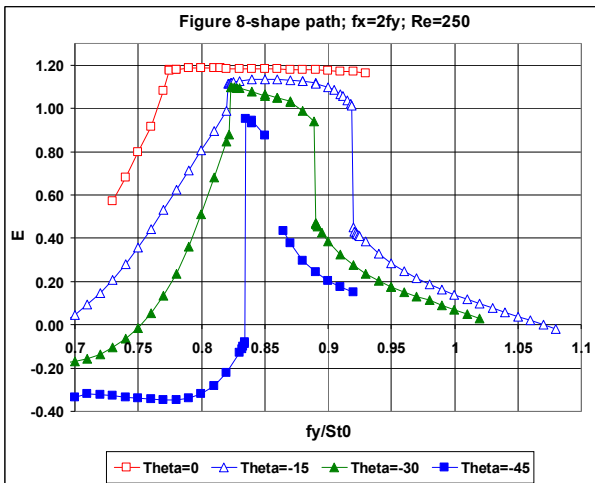


Figure 6. Mechanical energy transfer vs. frequency ratio for phase angles $\Theta=0^\circ$, -15° , -30° and -45°

Effect of initial condition

As is well known, a main feature of non-linear systems is that their solutions can be very sensitive to the initial condition. A very small change in the initial conditions can result in a drastic change in the solution. To check whether this is the case here computations for $\Theta= -15^\circ$, first carried

out at $t_0=0$, were repeated for $t_0=0.5$ and 1.0 (see Eq. (1)). In contrary to previous findings in Baranyi (2008) for an elliptical path, where the location of jumps was affected strongly by the initial condition, here the solutions basically were independent of the initial conditions: the three curves collapse into one, as can be seen in Figs. 7 and 8. Note that the curve for the TM of drag in Fig. 7 is the same as that denoted by blue empty triangles in Fig. 4, while the mechanical energy transfer curve shown in Fig. 8 is seen also in Fig. 6. Curves for all other variables also coincided for the three different t_0 values. For these parameters, it can thus be stated that the initial condition has essentially no effect on the flow.

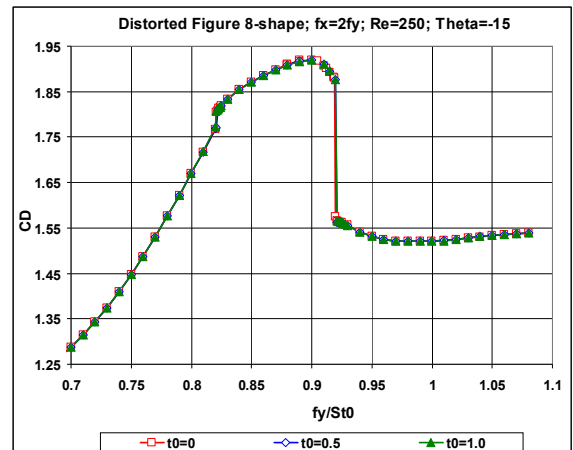


Figure 7. Time-mean of drag vs. frequency ratio for phase angle $\Theta=-15^\circ$ and $t_0=0, 0.5, 1.0$

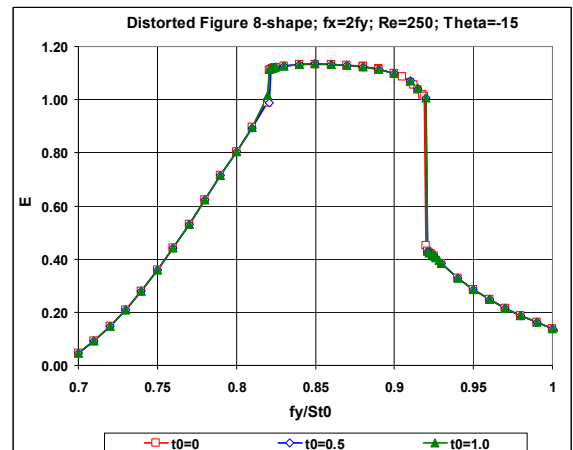


Figure 8. Mechanical energy transfer vs. frequency ratio for phase angle $\Theta=-15^\circ$ and $t_0=0, 0.5, 1.0$

Pre- and post-jump analysis

As can be seen in most of the figures, sudden jumps in the curves can be seen at some frequency ratio values, which can probably be attributed to vortex switches. The vicinity of a jump is investigated by different means, such as the time history of fixed body lift, limit cycle curves and vorticity contours before and after a jump. Due to lack

of space pre- and post-jump results will be shown only for the single case of $\Theta = -45^\circ$, with frequency ratios on the two sides of the jump of $(f_y/St_0)_1 = 0.8345$ and $(f_y/St_0)_2 = 0.835$.

The time histories of the periodic part of the fixed body lift for the two frequency ratios are shown against the dimensionless time t in Fig. 9. Pre-jump curves are denoted by red lines and post-jump curves by blue lines in Figs. 9 and 10. As can be seen in the figure, despite the tiny difference in the frequency ratios, the two time-history curves are substantially different.

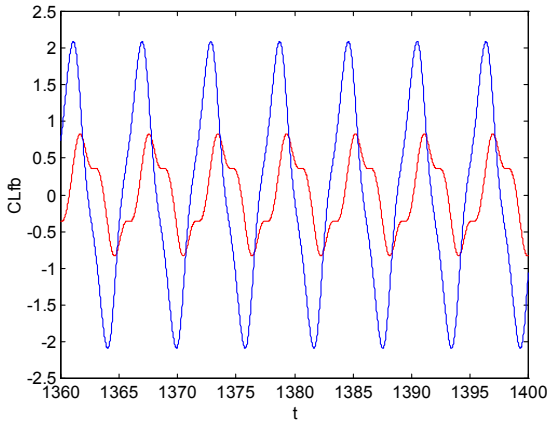


Figure 9. Time history of fixed body lift (red line: $f_y/St_0=0.8345$; blue line: $f_y/St_0=0.835$)

The limit cycle curves (C_{Dfb}, C_{Lfb}) can be seen in Fig. 10 for the pre-jump and post-jump frequency ratios. The very small difference in frequency ratio results in a drastic change in the shape of the two limit cycle curves. Interestingly, both curves have reflection symmetry. This is true for the drag-lift limit cycle curves of every computational point with a periodic solution. This symmetry originates from the fact that the drag is the same for both positive and negative y_0 displacement values.

When C_{Lfb} and its time derivative \dot{C}_{Lfb} are plotted only at the multiples of the motion period T a Poincaré map is obtained, which can be interpreted as a discrete dynamical system. Here, we investigate the limit cycle curves (C_{Lfb}, \dot{C}_{Lfb}) containing all the points in the phase plane as a continuous function of time, for pre-jump (Fig. 11) and post-jump (Fig. 12) frequency ratios. Again, noticeable differences occur. The curve in Fig. 11 exhibits two cusps, and is much smaller than the post-jump curve in Fig. 12, which is a relatively smooth curve.

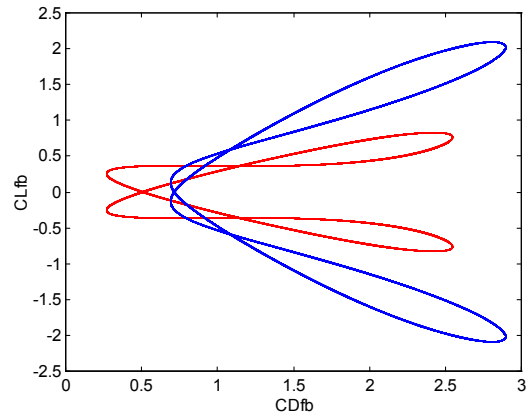


Figure 10. Limit cycle (C_{Dfb}, C_{Lfb}) for $\Theta = -45^\circ$; $f_y/St_0 = 0.8345$ (red) and 0.835 (blue)

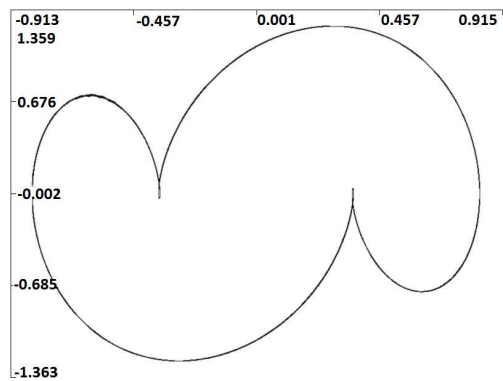


Figure 11. Limit cycle (C_{Lfb}, \dot{C}_{Lfb}) for $\Theta = -45^\circ$; $f_y/St_0 = 0.8345$ (pre-jump)

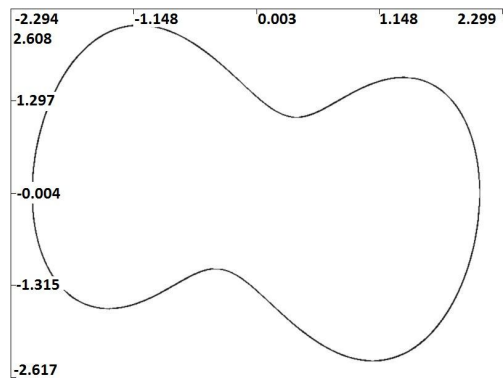


Figure 12. Limit cycle (C_{Lfb}, \dot{C}_{Lfb}) for $\Theta = -45^\circ$; $f_y/St_0 = 0.835$ (post-jump)

Vorticity contours are presented for pre-jump (Fig. 13) and post-jump (Fig. 14) frequency ratio values. The blue lines indicate negative vorticity values (clockwise rotation), and the red lines show positive values (anticlockwise rotation). The contours belong to the same

cylinder position, at $t=240T$, by which time the solution is fully periodic.

With pure in-line oscillation mirror image switches have been observed, so the pattern remains the same type (in the cases investigated, one pair of vortices is shed in one cycle) (Baranyi et al., 2010). This was probably caused by symmetry-breaking bifurcation (see e.g. Crawford and Knobloch, 1991). For transverse cylinder oscillation no switches were found, and the 2S pattern (a single vortex shed from each side of the cylinder within a single cycle; see Williamson and Roshko, 1988) appears to be typical around $Re=250$ (Baranyi et al. 2011). With elliptical motion, the solution flips but appears to move further from the mirror image solution as the transverse component increases (Baranyi, 2008). In this case, the flow patterns do not seem to flip in the vicinity of the cylinder, but a striking difference in flow structure can be seen. Figure 13 shows what appears to be 2P shedding (a pair shed from each side of the cylinder in one cycle), while the post-jump pattern seems to be 2S, rather similar to the Kármán vortex street but with a broader wake.

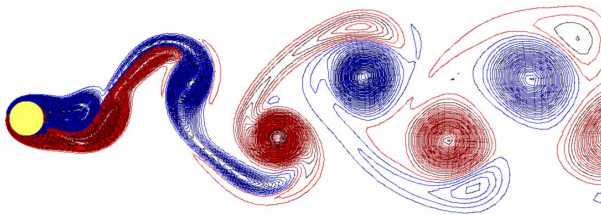


Figure 13. Vorticity contours at $t=240T$ for $\Theta=-45^\circ$; $f_y/St_0=0.8345$ (pre-jump)

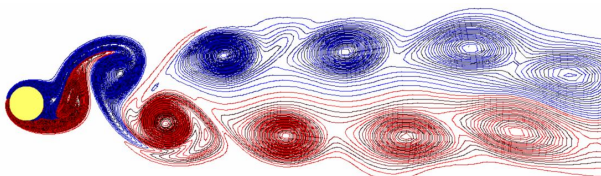


Figure 14. Vorticity contours at $t=240T$ for $\Theta=-45^\circ$; $f_y/St_0=0.835$ (post-jump)

CONCLUSIONS

Low-Reynolds number flow around a circular cylinder in two-degree-of-freedom forced motion is investigated numerically at the Reynolds number of 250. Computations were carried out at four different phase angles of $\Theta=0^\circ$, -15° , -30° and -45° , ranging from a symmetrical to a distorted figure-eight shape, with an anticlockwise direction of orientation in the upper lobe.

The numerical investigation revealed that larger phase angle differences can reduce drag by bending the figure-eight cylinder path further downstream.

Mechanical energy transfer also decreases with increasing phase angle difference, but remains mostly in the positive domain, meaning that energy is transferred from the fluid to the cylinder, thus leading to a potentially dangerous VIV situation.

At all four phase angle values investigated, the time-mean of lift and torque coefficients was zero throughout the locked-in frequency domain.

The initial condition had scarcely any effect on the solution for $\Theta=-15^\circ$.

Where jumps in time-mean or rms values representing vortex switches were identified, pre- and post-jump analysis was carried out, revealing different time-history and limit cycle curves, vorticity contours and even different vortex shedding patterns.

As this study investigated only an anticlockwise direction of orbit, further investigation could include repeating computations for the clockwise case or at other Reynolds numbers or oscillation amplitude values.

ACKNOWLEDGMENTS

The support provided by the Hungarian Scientific Research Fund under contract No. OTKA K 76085 is gratefully acknowledged. The author thanks Mr. L. Daróczy for designing the flow visualization software used in Figs. 11-14. The work was carried out as part of the TÁMOP-4.2.1.B-10/2/KONV-2010-0001 project in the framework of the New Hungarian Development Plan. The realization of this project is supported by the European Union, co-financed by the European Social Fund.

REFERENCES

- Al-Mdallal, Q.M., Lawrence, K.P. and Kocabiyik, S., 2007, "Forced streamwise oscillations of a circular cylinder: Locked-on modes and resulting fluid forces," *Journal of Fluids and Structures* **23**, 681-701.
- Baranyi, L., 2003, "Computation of unsteady momentum and heat transfer from a fixed circular cylinder in laminar flow," *Journal of Computational and Applied Mechanics* **4**(1), 13-25.
- Baranyi, L., 2005, "Lift and drag evaluation in translating and rotating non-inertial systems," *Journal of Fluids and Structures* **20**(1), 25-34.
- Baranyi, L., 2008, "Numerical simulation of flow around an orbiting cylinder at different ellipticity values," *Journal of Fluids and Structures* **24**, 883-906.
- Baranyi, L., Huynh, K. and Mureithi, N.W., 2010, "Dynamics of flow behind a cylinder oscillating in-line for low Reynolds numbers," Proc. *7th International Symposium on Fluid-Structure Interactions, Flow-Sound Interactions, and Flow-Induced Vibration and Noise, (within FEDSM2010-ICNMM2010 ASME Conference 2010)*, Montreal, Québec, Canada, on CD ROM, pp. 1-10, Paper No. FEDSM-ICNMM2010-31183
- Baranyi, L., 2011, "Low-Reynolds number flow around a cylinder following a figure-8 path -- effect of direction

- of orbit,” Proc. *IUTAM Symposium on Bluff Body Flows*, Kanpur, India, pp. 21-24.
- Baranyi, L., Bolló, B. and Daróczy, L., 2011, “Simulation of low-Reynolds number flow around an oscillated cylinder using two computational methods,” Proc. *ASME 2011 Pressure Vessels and Piping Division Conference PVP2011*, Baltimore, Maryland, USA, pp. 1-9, Paper No. PVP2011-57554
- Blackburn, H.M. and Henderson, R.D., 1999, “A study of two-dimensional flow past an oscillating cylinder,” *Journal of Fluid Mechanics* **385**, 255-286.
- Blevins, R.D., 1990, *Flow-Induced Vibrations*. Van Nostrand Reinhold, New York.
- Cetiner, O. and Rockwell, D., 2001, “Streamwise oscillation of a cylinder in a steady current. Part 1. Locked-on states of vortex formation and loading,” *Journal of Fluid Mechanics* **427**, 1-28.
- Crawford, J.D. and Knobloch, E., 1991, “Symmetry and symmetry-breaking bifurcations in fluid dynamics,” *Annual Review of Fluid Mechanics* **23**, 341-387.
- Didier, E. and Borges, A.R.J., 2007, “Numerical predictions of low Reynolds number flow over an oscillating circular cylinder,” *Journal of Computational and Applied Mechanics* **8**(1), 39-55.
- Gharib, M.R., 1999, “Vortex-induced vibration, absence of lock-in and fluid force deduction,” *PhD dissertation*, GALCIT, California Institute of Technology, Pasadena, CA, U.S.A.
- Jauvtis, N. and Williamson, C. H. K., 2004, “The effect of two degrees of freedom on vortex-induced vibration and at low mass and damping,” *Journal of Fluid Mechanics* **509**, 23–62.
- Jeon, D. and Gharib, M., 2001, “On circular cylinders undergoing two-degree-of-freedom forced motions,” *Journal of Fluids and Structures* **15**, 533-541.
- Kheirkhah, S. and Yarusevych, S., 2010, “Two-degree-of-freedom flow-induced vibrations of a circular cylinder with a high moment of inertia ratio,” Proc. *ASME 2010 3rd Joint US-European Fluids Engineering Summer Meeting and 8th Int. Conference on Nanochannels, Microchannels, and Minichannels (FEDSM-ICNMM2010)*, Montreal, Québec, Canada, on CD ROM, pp. 1-10, Paper No. FEDSM-ICNMM2010-30042
- Lu, X.Y. and Dalton, C., 1996, “Calculation of the timing of vortex formation from an oscillating cylinder,” *Journal of Fluids and Structures* **10**, 527-541.
- Mureithi, N.W., Huynh, K., Rodriguez, M. and Pham, A., 2010, “A simple low order model of forced Karman wake,” *International Journal of Mechanical Sciences* **52**(11), 1522-1534.
- Newman, D.J., and Karniadakis, G.E., 1995, “Direct numerical simulation of flow over a flexible cable”, Proc. *6th Int. Conference on Flow-Induced Vibration*, London, pp. 193-203 .
- Peppas, S., Kaiktsis, L. and Triantafyllou, G.S., 2010, “The effect of in-line oscillation on the forces of a cylinder vibrating in a steady flow,” Proc. *7th International Symposium on Fluid-Structure Interactions, Flow-Sound Interactions, and Flow-Induced Vibration and Noise, (within FEDSM2010-ICNMM2010 ASME Conference 2010)*, Montreal, Québec, Canada, on CD ROM, pp. 1-8, Paper No. FEDSM-ICNMM2010-30054
- Prasanth, T.K. and Mittal, S., 2009, “Flow-induced oscillation of two circular cylinders in tandem arrangement at low Re,” *Journal of Fluids and Structures* **25**, 1029-1048.
- Posdziech, O. and Grundmann, R., 2007, “A systematic approach to the numerical calculation of fundamental quantities of the two-dimensional flow over a circular cylinder,” *Journal of Fluids and Structures* **23**, 479-499.
- Sanchis, A., Sælevik, G., Grue, J., 2008, “Two-degree-of-freedom vortex-induced vibrations of a spring-mounted rigid cylinder with low mass ratio,” *Journal of Fluids and Structures* **24**, 907-919.
- Williamson, C.H.K. and Roshko, A., 1988, “Vortex formation in the wake of an oscillating cylinder,” *Journal of Fluids and Structures* **2**, 355-381.
- Williamson, C.H.K., 2004, “Vortex-induced vibrations,” *Annual Review of Fluid Mechanics* **36**, 413-455.

TWO-DIMENSIONAL SIMULATION OF THE FLOW AROUND A CYLINDER WITH STRAKES

Bruno S. Carmo

Department of Mechanical Engineering, POLI
University of São Paulo
Av. Prof. Mello Moraes, 2231
São Paulo/SP – Brazil. 05508-030
Email: bruno.carmo@usp.br

ABSTRACT

Two-dimensional simulations of the flow around straked cylinders are presented. We set the geometry of the strakes and tested five different angles of rotation of the cylinder with respect to the free stream. The simulations were performed for fixed cylinders and for cylinders mounted on elastic bases. The Reynolds number was kept constant and equal to 150 for all simulations, and the mass ratio was equal to 10. The results were compared to those obtained from the simulation of the flow around a bare cylinder under the same conditions. We observed that the two-dimensional strakes are not effective in suppressing the vibration of the cylinders, but also noticed that the responses were completely different even with a slight change in the angle of rotation of the body. Although the simulations do not reproduce what happens with cylinders fitted with three-dimensional helical strakes, it provides some insights of the physical mechanisms responsible for the vibration suppression.

INTRODUCTION

In the last two decades, offshore oil exploration on the Brazilian coast has significantly increased, and nowadays the high importance of this economical activity to the country is undisputed. One of the challenges in the design of offshore systems is to cope with the vortex-induced vibration (VIV) of risers, which can cause serious damage by fatigue. There are many devices that are employed to mitigate and/or suppress VIV; amongst the most common of them are strakes. Strakes are ribbons that are attached to the riser forming a helix around it. They were first employed in wind engineering [1], but have proved efficient also in marine applications. The

usual design is to use three ribbons equally spaced along the riser circumference, so the cross-section of the final product is a circle with three small protrusions, spaced 120 degrees from each other.

Although the suppression of VIV is crucial for the offshore industry and strakes are by far the most used device to achieve this goal, the number of papers about the flow around straked cylinders published so far is not large. Almost all of them are experimental [2–4]; [5] published the only computational work that investigates the flow around straked cylinders we are aware of. These papers and the experience in the oil industry shows that strakes are indeed efficient in suppressing VIV. However, little is understood about the physics of how it works. The Centre for Fluids and Dynamics (NDF) of the Department of Mechanical Engineering at the University of São Paulo has recently started an initiative to elucidate the physical mechanisms of the VIV suppression by strakes. The first approach was experimental, and resulted in the publication of a paper in an international journal [4]. Currently, we are approaching the problem with computational tools. [6] presents an investigation using the Lattice-Boltzmann Method, while here we use the Spectral/*hp* Element Method [7]. The goal of this initiative is to understand the mechanism that damps the VIV, so more efficient designs can be proposed. Besides that, it is known that strakes increase the drag on the cylinder; a secondary objective of this study is to find ways to lessen this downside of the device.

We carry out two-dimensional simulations to investigate the dynamics of the shear layers that separate from the body, and compare to what is observed for a plain cylinder. The Reynolds number tested is 150, which is well below that characteristic of offshore structures, but

high enough to allow the observation of the interaction of the shear layers that separate from the body. We believe that the physical insights obtained in this work will be valid for higher Reynolds numbers.

METHODOLOGY

We ran simulations for the flow around a fixed cylinder and around a rigid cylinder mounted on an elastic base. For the simulations around movable cylinders, the computational results were obtained by coupling the solution of the flow with the solution of the structural response. To simulate the oscillatory movement of the body, an oscillatory cross-flow around circular cylinder in a frame of reference fixed to the body has been employed. The uniform flow is superimposed on a cross-flow representing the transverse movement of the body, modifying the Dirichlet boundary conditions (upstream boundary) and adding the oscillatory component (α), like in [8]. The flow is governed by the incompressible Navier-Stokes equations, which can be written in non-dimensional form, for a non-inertial frame of reference, as:

$$\frac{\partial \mathbf{u}}{\partial t} = -(\mathbf{u} \cdot \nabla) \mathbf{u} - \nabla p + \frac{1}{Re} \nabla^2 \mathbf{u} + \alpha, \quad (1)$$

$$\nabla \cdot \mathbf{u} = 0. \quad (2)$$

The cylinder diameter D is the reference length and the free-stream speed U_∞ is the reference speed used in the non-dimensionalisation. $\mathbf{u} \equiv (u, v, w)$ is the velocity field, t is the time, p is the static pressure, $Re = \rho U_\infty D / \mu$ is the Reynolds number and μ is the dynamic viscosity of the fluid. The pressure was assumed to be scaled by the constant density ρ . The numerical solution of these equations was calculated using a Spectral/ hp discretisation as described in [7], which is high order and has been extensively validated in previous works.

On the structural side, we assumed that the moving cylinder was rigid and mounted on an elastic base with zero damping that allows displacement in only one direction; the behaviour of such an oscillating structure is described by the equation of a linear mass-spring system forced by the fluid load. This equation can be written in non-dimensional form as

$$\frac{\pi m^*}{4} \ddot{y}_c^* + \frac{\pi^3 m^*}{V_r^2} y_c^* = F_y^*(y_c^*, y_c^*, t^*). \quad (3)$$

The non-dimensional parameters $m^* = \frac{4M}{\rho \pi D^2 L}$ and $V_r = \frac{U_\infty}{f_n D}$ are the mass ratio and reduced velocity respectively

and $F_y^* = \frac{C_L}{2} = \frac{F_y}{\rho U_\infty^2 D L}$ is the non-dimensional force imposed by the fluid in the direction of motion. The corresponding dimensional structural parameters are the dimensional mass M and the structural stiffness K . f_n is the natural frequency of the structure in vacuum ($f_n = \sqrt{K/M}/(2\pi)$), L is the (axial) length of the cylinder and C_L is the lift coefficient. The structural equation was integrated using Newmark's scheme [9].

Equations (1), (2) and (3) have to be solved in a coupled manner. The fluid load F_y^* in eq. (3) is calculated from the solution of the flow equations (1)-(2), and the velocity of the flow on the boundaries, which are necessary for the solution of Eqns. (1)-(2), is determined by the solution of the structure equation (3). In this work, the structure and flow solvers were loosely coupled, similar to the work of in [10], since the time step size necessary for the solution of the flow equations (i.e. the CFL restriction) was sufficiently small to yield convergent loosely-coupled schemes.

RESULTS

We have simulated the flow around a bare cylinder with diameter D , to serve as a benchmark case, and around a cylinder with three strake ribbons, each one with a cross section of $0.2D$ of height and $0.05D$ of width. We have tested five different configurations of the straked cylinder: the first had one of the strakes aligned with the flow, pointing in the upstream direction, and the four other configurations were obtained rotating the cylinder in steps of 15 degrees in the anti-clockwise direction, as illustrated in Fig. 1. We employed circular meshes to run the simulations. This choice was made because we intend to extend the code to run three-dimensional simulations, and we envisage a way of dealing with helical geometry that will require circular meshes. The radius of the circular domain was $30D$ for all configurations but that with 60° rotation, for which a domain with a radius of $60D$ had to be employed due to numerical stability problems. The meshes were very refined close to the cylinder and strakes and had coarser elements away from the body. We have employed velocity inlet boundary conditions on the left-hand border of the mesh: ($u = 1, v = 0$) and a high-order boundary condition for the pressure as explained in [11]. On the right-hand border outflow conditions were employed, i.e., ($\partial u / \partial n = 0, \partial v / \partial n = 0, p = 0$). No-slip boundary conditions were imposed on the cylinder and strakes surfaces. A 8th degree Jacobi polynomial was employed as test function in all mesh elements. This discretization was chosen after a rigorous convergence test that analysed the variation of the most important integral

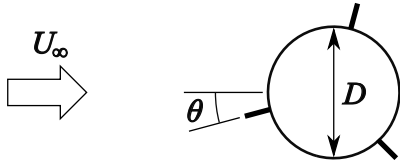


FIGURE 1: SCHEMATIC DRAWING OF THE STRAKED CYLINDER. THE CONFIGURATIONS INVESTIGATED ARE IDENTIFIED BY THE ANGLE θ INDICATED, WITH RESPECT TO THE DIRECTION OF THE FREE STREAM.

quantities (mean drag coefficient, Strouhal number and RMS of the lift coefficient), and ensured a relative error of less than 0.1% in these quantities for fixed cylinders.

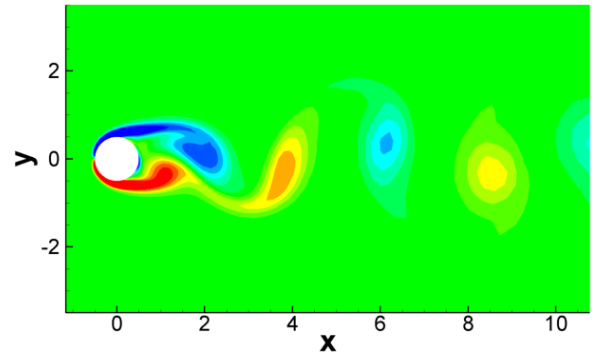
First, we show the results from the simulations with fixed cylinders. Next, we present simulations for cylinders mounted on an elastic base, with mass ratio equals to 10.0 and zero structural damping, and vary the reduced velocity from 2.0 to 15.0, keeping the Reynolds number constant, i.e. changing the stiffness of the structure. All the simulations were run for more than 1000 non-dimensional time units.

Fixed cylinders

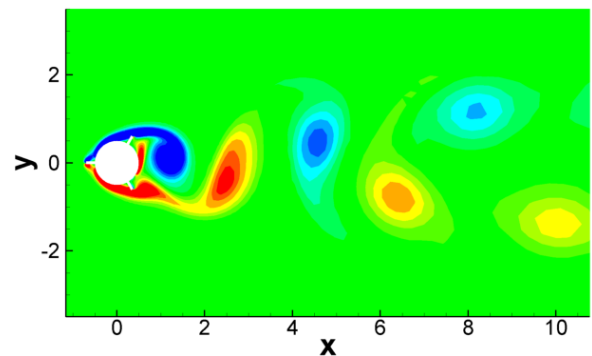
Table 1 shows the force coefficients obtained from the simulations of the flow around the fixed configurations. Some instantaneous vorticity fields obtained with these simulations are shown in Fig. 2, in which one of the most important features of the flow around straked cylinders can be clearly seen: the fixed separation points on the strakes. We can see, though, that the presence of strakes in a two-dimensional simulation does not prevent the interaction of the separating shear layers and vortex shedding.

It can be seen in Tab. 1 that the value of all the quantities vary significantly from one geometry to the other. The bare cylinder shows the highest Strouhal number and the narrower wake, as evinced in Fig. 2(a). Among the straked cylinders, the lowest Strouhal numbers are those obtained with the rotations 45° and 60° , which exhibit separation in the upstream half of the cylinder due to the strakes, as illustrated in Fig. 2(d). The fact that the opposite shear layers are farther apart from each other in those cases explain the lower Strouhal numbers and wider wakes obtained.

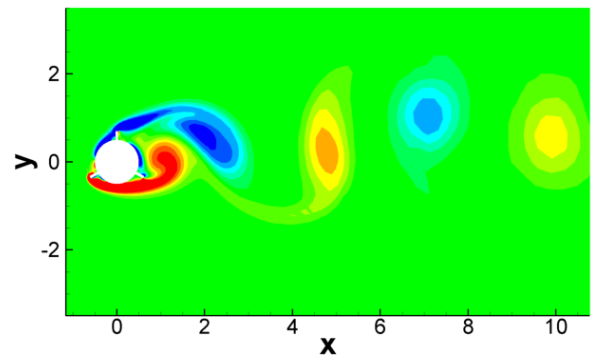
It is also remarkable the increase in drag when the cylinders are fitted with strakes, reaching values almost twice as large as that of the bare cylinder. Even for the flow around the configuration with rotation 0° , illustrated



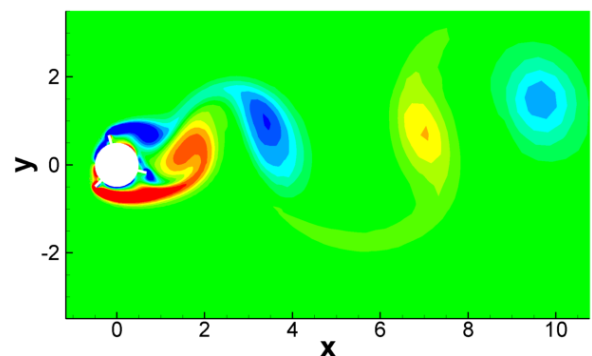
(a) BARE CYLINDER



(b) STRAKES 0°



(c) STRAKES 30°



(d) STRAKES 45°

FIGURE 2: INSTANTANEOUS NON-DIMENSIONAL VORTICITY CONTOURS FOR FIXED CYLINDERS, SELECTED CONFIGURATIONS. VALUES RANGE FROM -3.3 (BLUE) TO 3.3 (RED).

TABLE 1: FORCE COEFFICIENTS OBTAINED FROM THE SIMULATIONS AROUND FIXED CYLINDERS.

Geometry	St	\bar{C}_D	C_L RMS	\bar{C}_L
Bare Cylinder	0.185	1.323	0.365	0.000
Strakes 0°	0.171	2.009	0.602	0.000
Strakes 15°	0.170	1.968	0.616	-0.789
Strakes 30°	0.161	1.969	0.694	-1.281
Strakes 45°	0.135	2.371	1.060	-0.718
Strakes 60°	0.136	2.568	1.183	-0.001

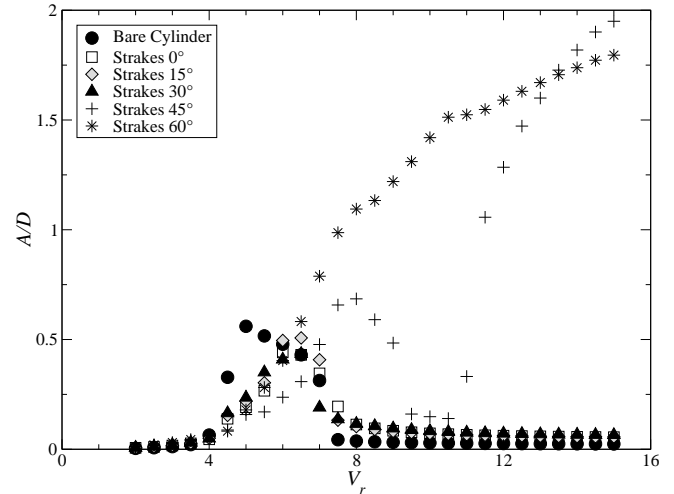
in Fig. 2(b), which has the strakes in the “more streamlined” position of all, the drag coefficient is already 65% larger than in the bare cylinder case. In general, the larger frontal area of the straked cylinders and the poor pressure recovery due to the early separation of the flow decisively contribute to this higher drag.

The presence of strakes also increases the fluctuation of the lift coefficient, as can be seen in the column with C_L RMS data. Besides that, a nonzero mean lift is observed for the asymmetric configurations (with respect to the streamwise direction), 15°, 30° and 45°. Figures 2(c) and 2(d) show examples of asymmetric wakes produced by such configurations.

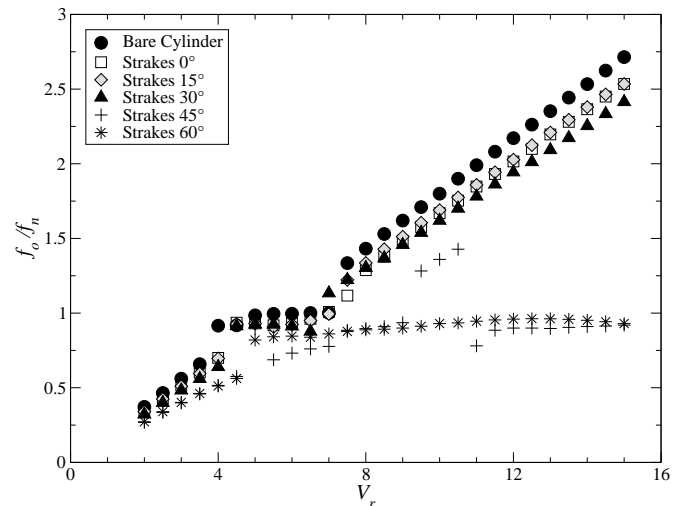
Cylinders mounted on elastic bases

Figure 3(a) shows the amplitude vibration of the cylinder as a function of the reduced velocity, for all configurations. It can be seen that the bare cylinder exhibits a typical low Reynolds number VIV response, with significant amplitudes located on a limited range, which is the synchronisation range. Within this range, the frequency of vortex shedding is approximately equal to the natural frequency of the structure, as can be seen in Fig. 3(b). For the parameters studied here ($Re = 150$ and $m^* = 10$), the maximum amplitude of vibration is about $0.56D$ and the synchronisation occurs for $4.0 < V_r < 7.5$.

The straked cylinders show different responses. For the configurations with 0°, 15° and 30° rotations, the responses are similar to that obtained with the bare cylinder: there is a synchronisation range for which the amplitude of vibration is significant and outside this range the amplitude is small. This reduced velocity range is the same as that of the bare cylinder. However, the amplitudes are smaller within the synchronisation range when compared to the bare cylinder, reaching a maximum of about $0.51D$. In contrast, the configurations with 45° and 60° rotations



(a) AMPLITUDE OF VIBRATION



(b) FREQUENCY OF OSCILLATION

FIGURE 3: STRUCTURAL RESPONSES OF THE CONFIGURATIONS MOUNTED ON ELASTIC BASES.

show a strikingly different behaviour. For 45° rotation, there is a synchronisation range too, but it is wider than for the previous cases, starting at $V_r = 4.0$ and finishing at $V_r = 10.0$, reaching amplitude values of about $0.69D$. After this synchronisation range, there is a region of very high amplitudes, for $V_r > 11.0$. In this region, the cylinder is vibrating due to *galloping*. Figure 3(b) shows that during galloping, the structure vibrates at the natural frequency. This is different from what happens to the other configurations, since for those at high reduced velocities the cylinder vibrates at the Strouhal frequency. For the configuration with 60° the galloping range merges with the synchronisation range, there is no clear separation between them.

Figure 4 shows some examples of instantaneous vor-

ticity contours obtained with configurations mounted on elastic bases at reduced velocities for which the amplitude of vibration was large. The bare cylinder, shown in Fig. 4(a), exhibits the typical Kármán wake, while the other configurations present different vortex patterns. For 15° rotation within the synchronisation range (Fig. 4(b)), the vortex wake is regular, with vortices of opposite vorticity on different sides of the wake, but the wake itself is much wider than in the bare cylinder case. Figure 4(c) shows contours for 45° rotation at the peak amplitude of the synchronisation range. We see that the wake is not regular and the vortices interact in a manner completely different from the previous two cases. Finally, a galloping case is illustrated in Fig. 4(d), in which the separation and reattachment of the boundary layer, typical from galloping responses, can be seen on the lower part of the cylinder. The vortex wake is not regular in this case either.

CONCLUSION

The results show that two-dimensional strakes are not effective in suppressing VIV, so we conclude that the helical geometry is a prime feature of this device. Although the simulations do not reproduce what happens with helical strakes, the results presented here give some insights of the mechanisms involved in the suppression. We could see that the flow fields and response of the structure changes dramatically with just a slight change of the angle of the geometry with respect to the incoming flow direction. For example, we could see VIV or galloping happening at the same reduced velocity, depending on the straked cylinder rotation. Therefore we expect that the flow will be completely de-correlated along the span, and this certainly contributes to the vibration suppression. In the next stages of the research, we are going to extend the computational code in order for it to be able to simulate the flow around a three-dimensional helical geometry.

ACKNOWLEDGMENT

The author would like to acknowledge the support from FAPESP through grant 2011/00131-2.

REFERENCES

- [1] Zdravkovich, M. M., 1981. "Review and classification of various aerodynamic and hydrodynamic means for suppressing vortex shedding". *Journal of Wind Engineering and Industrial Aerodynamics*, 7(2), pp. 145 – 189.

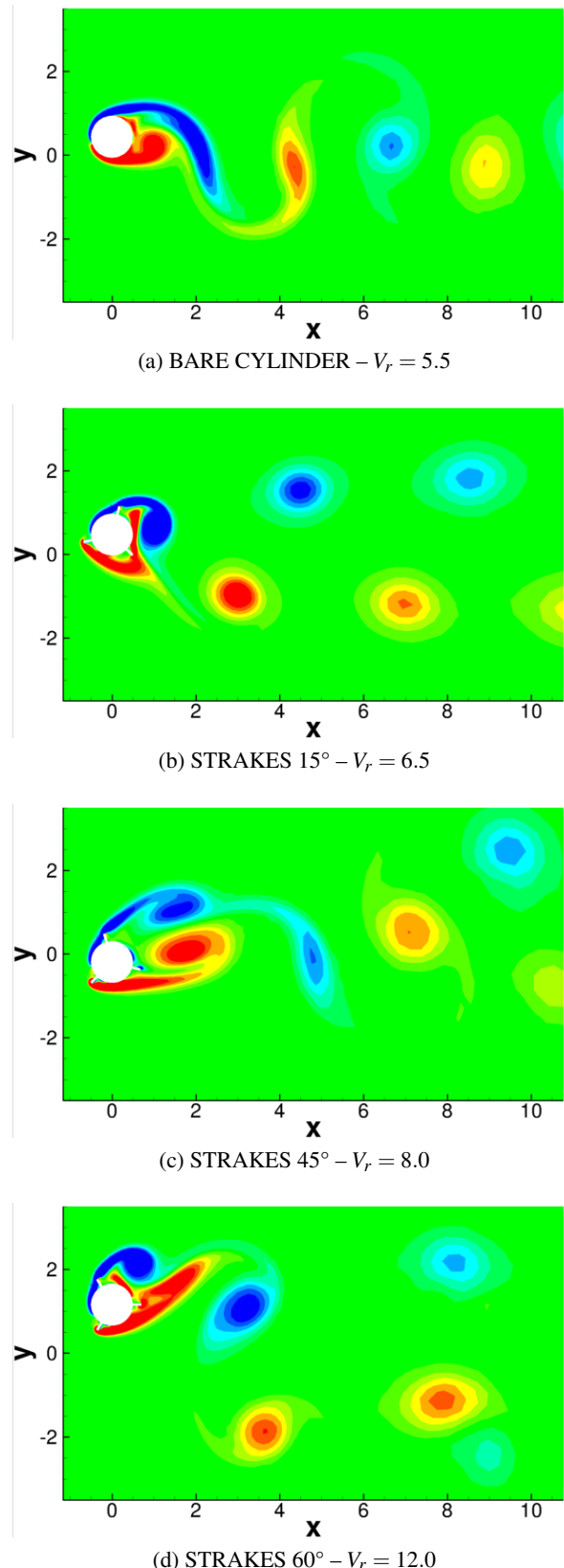


FIGURE 4: INSTANTANEOUS NON-DIMENSIONAL VORTICITY CONTOURS FOR CYLINDERS MOUNTED ON AN ELASTIC BASE, SELECTED CONFIGURATIONS AND REDUCED VELOCITIES. VALUES RANGE FROM -3.3 (BLUE) TO 3.3 (RED).

- [2] Trim, A. D., Braaten, H., Lie, H., and Tognarelli, M. A., 2005. “Experimental investigation of vortex-induced vibration of long marine risers”. *Journal of Fluids and Structures*, **21**(3), pp. 335–361.
- [3] Branković, M., and Bearman, P. W., 2006. “Measurements of transverse forces on circular cylinders undergoing vortex-induced vibration”. *Journal of Fluids and Structures*, **22**(6-7), pp. 829–836.
- [4] Korkischko, I., and Meneghini, J. R., 2010. “Experimental investigation of flow-induced vibration on isolated and tandem circular cylinders fitted with strakes”. *Journal of Fluids and Structures*, **26**(4), 5, pp. 611–625.
- [5] Constantinides, Y., and Oakley Jr, O. H., 2006. “Numerical prediction of bare and straked cylinder viv”. In Proceedings of OMAE2006, W. L. Kuehnlein and D. Valentine, eds., no. 92334.
- [6] Gioria, R. S., Korkischko, I., and Meneghini, J. R., 2011. “Simulation of flow around a circular cylinder fitted with strakes”. In Proceedings of COBEM 2011.
- [7] Karniadakis, G. E., and Sherwin, S. J., 2005. *Spectral/hp Element Methods for Computational Fluid Dynamics*, 2nd ed. Oxford University Press, Oxford-UK.
- [8] Li, L., Sherwin, S. J., and Bearman, P. W., 2002. “A moving frame of reference algorithm for fluid/structure interaction of rotating and translating bodies”. *International Journal for Numerical Methods in Fluids*, **38**, pp. 187–206.
- [9] Newmark, N. M., 1959. “A method of computation for structural dynamics”. *Journal of the Engineering Mechanics Division of ASCE*, **85**, pp. 67–94.
- [10] Jester, W., and Kallinderis, Y., 2004. “Numerical study of incompressible flow about transversely oscillating cylinder pairs”. *Journal of Offshore Mechanics and Arctic Engineering - Transactions of the ASME*, **126**, pp. 310–317.
- [11] Karniadakis, G. E., Israeli, M., and Orszag, S. A., 1991. “High-order splitting methods for the incompressible Navier–Stokes equations”. *Journal of Computational Physics*, **97**, pp. 414–443.



A CONSIDERATION ON NONCONSERVATIVE ELASTIC STABILITY OF A BEAM SUBJECTED TO AXIAL FORCE CONSIDERED TO BE FLUID FORCE

Katsuhisa FUJITA¹

Osaka City University
Mechanical and Physical Engineering,
Graduate School of Engineering,
3-3-138 Sugimoto, Sumiyosi-ku, Osaka
558-8585, Japan
E-mail: fujita@mech.eng.osaka-cu.ac.jp

Akihide GOTOU

Osaka City University
Mechanical and Physical Engineering,
Graduate School of Engineering,
3-3-138 Sugimoto, Sumiyosi-ku, Osaka
558-8585, Japan
E-mail: akihide.gotou@gmail.com

ABSTRACT

The dynamic stability problem of machines and structures is one of the important subjects for a long time. By the way, in the conventional dynamic stability analysis, many problems of the structural analysis have been dealt with as a conservative system. However, as it is thought that some problems may be affected by the deflections of a structure, the treatment of a nonconservative system such as a follower force becomes important. In this paper, the stability of nonconservative system of a beam is investigated when the fluid force acting on a beam subjected to the axial flow is considered to be an axial force. The fundamental study is performed by using the discrete model of 2 degree of freedom systems. Moreover, this is expanded to the continuous models of a cantilever, a simply supported beam and a free-free beam. And, the physical consistency between a discrete model and a continuous one and the effect of damping are discussed.

INTRODUCTION

The dynamic stability problem of a machine and a structure is one of the problems important for a long time. Recently in particular, when a machine and a structure become large size and weighted lightly, it is considered that they become flexible structures relatively to the force. So, the dynamic stability problem becomes important more and more.

In the conventional dynamic stability analysis, they are analyzed assuming that the acting direction of a force is not affected by their deflections. In other words, the many problems which have been dealt with are corresponding to a conservative system in which the force is considered to be conservative. However, the technical problems which are affected by fluids such as air or water increase recently. It is often thought that the acting direction of the force subjected to these fluids forces changes according to the deflection of the structure. That

is, the handling the force to be nonconservative such as follower forces is considered to be important.

As examples that the examination of a follower force is necessary, a rocket subjected to the thrust of burners, a submarine to the thrust of screws or water jets and the Guillotine shaped break of a large-scale piping, and so forth are enumerated. In addition, in the accident of a machine and structure which were occurred in the past, it is thought that there are some examples in which the unstable vibration caused by follower forces was a main cause although the detailed elucidation has not been done. Under such situation, as for the study of this field, the submission of the problem has been already accomplished relatively for a long time [1]-[4], and some studies have been accomplished continuously [5]-[9]. However, it cannot be necessarily said that they are enough. The studies which focused on a nonconservative system become very important to send a safer machine and structure off to the world.

Here, a fluid force is considered to be axial force about a beam subjected to the axial flow, and a nonconservative stability problem of a beam is investigated. At first, the fundamental study is performed using a discrete model consisted of two degree of freedom systems. Next, the study is developed by using the continuous model of the cantilever. Then, the physical consistency between the discrete model and the continuous model and the effect of damping so on are investigated. Moreover, the stability of a simply supported beam and a free-free beam are also studied.

THEORY

Modeling of a conservative system and a non-conservative system

The drag forces of a fluid acting on a structure are divided into frictional drag and pressure drag. When a

Address all correspondence to this author¹

fluid flows on the surface of a structure, the structure is subjected to the friction drag due to the viscosity of a fluid. When a structure is streamlined, this friction drag becomes dominant. Of course, by a vortex shedding and a flow separation from the surface of a structure, the structure is subjected to the pressure drag based on the differences in the pressure of a fluid. When a structure is bluff, this pressure drag becomes dominant. Here, when the above-mentioned fluid forces are acted on the cantilever, the elastic stability problem of a beam is studied by assuming approximately the force to be a concentrated force or the uniform distributed force tangentially. At first, let us study a model shown in Fig.1 as a general elastic stability problem.

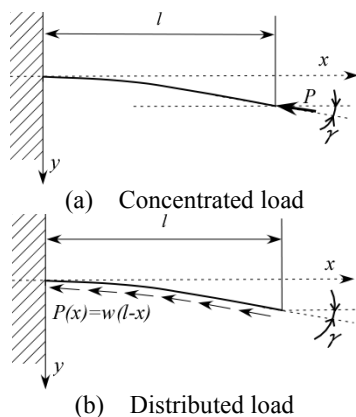


Fig. 1 Modeling on elastic stability of structure

Here, l is length of the cantilever, P , $P(x)$ show a concentrated force and a distributed axial force, respectively. γ shows the angle between the direction of a force and the tangential direction of a beam.

Figure 1(a) shows the case in which a concentrated force acts on the free end of a cantilever. In the case of $\gamma = 0$, it is the Euler buckling of a beam in statics. In addition, it is the problem of Beck where a nonconservative force acts on a beam in case of $\gamma > 0$. On the other hand, Fig. 1(b) shows the case that a tangential uniform distributed force acts on a beam. In the case of $\gamma = 0$, a uniform distributed force acts axially on a beam in the direction which is the tangential one before a beam deflects, and it is a problem of Euler as the model where the conservative force acts on a beam. In addition, in the case of $\gamma > 0$, a uniform distributed force acts on a beam to the tangential direction of the beam as a follower force, and it is a problem of Leipholz as the model where the non-conservative force acts on a beam.

Discrete model of 2 degree of freedom systems

Concerning with the models subjected to a conservative force and a nonconservative one (follower force), the discrete model of 2 degree freedom systems can be adopted in stead of a continuous model of a uniform beam according to Ziegler[2]. These models are called as

Euler model and Herrmann model respectively, as shown in Fig. 2.

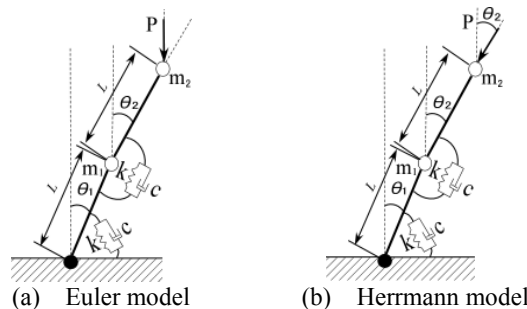


Fig. 2 Discrete model of two-degree-of-freedom

As for 2 degree of freedom systems, a uniform elastic beam is assumed to consist of 2 rigid bars, and springs and dampers, and the rigid bars which connect the mass points are mass-less. In Fig. 2, m_1, m_2 are the concentrated mass, L is the length of a beam, and θ_1, θ_2 are the angular displacement. And, k denotes the rotational spring constant, c the coefficient of rotational viscous damper.

Governing equation

Discrete model of 2 degree freedom subjected to a concentrated force at the free end

When a conservative force acts on the model, the governing equation corresponding to Euler model of Fig 2(a) is obtained as follows by using Lagrange's equation.

$$\begin{bmatrix} (m_1 + m_2)L^2 & m_2L^2 \\ m_2L^2 & m_2L^2 \end{bmatrix} \begin{Bmatrix} \ddot{\theta}_1 \\ \ddot{\theta}_2 \end{Bmatrix} + \begin{bmatrix} 2c & -c \\ -c & c \end{bmatrix} \begin{Bmatrix} \dot{\theta}_1 \\ \dot{\theta}_2 \end{Bmatrix} + \begin{bmatrix} 2k - PL & -k \\ -k & k - PL \end{bmatrix} \begin{Bmatrix} \theta_1 \\ \theta_2 \end{Bmatrix} = \begin{Bmatrix} 0 \\ 0 \end{Bmatrix}, \quad (1)$$

Next, when a nonconservative force acts on the model, the governing equation corresponding to Herrmann model of Fig 2(b) is obtained as follows as well as the case of a conservative force.

$$\begin{bmatrix} (m_1 + m_2)L^2 & m_2L^2 \\ m_2L^2 & m_2L^2 \end{bmatrix} \begin{Bmatrix} \ddot{\theta}_1 \\ \ddot{\theta}_2 \end{Bmatrix} + \begin{bmatrix} 2c & -c \\ -c & c \end{bmatrix} \begin{Bmatrix} \dot{\theta}_1 \\ \dot{\theta}_2 \end{Bmatrix} + \begin{bmatrix} 2k - PL & PL - k \\ -k & k \end{bmatrix} \begin{Bmatrix} \theta_1 \\ \theta_2 \end{Bmatrix} = \begin{Bmatrix} 0 \\ 0 \end{Bmatrix}, \quad (2)$$

Continuous model subjected to a concentrated force at the free end

When a conservative concentrated force P acts on the continuous model (cantilever) as shown in Fig 1(a), it becomes Euler's buckling problem. Then, the following value is obtained.

$$P_{cr} = \frac{\pi^2 EI}{(2l)^2}, \quad (3)$$

where P_{cr} is the critical force for buckling.

Next, when the concentrated force P as a nonconservative force (follower force) acts on the continuous model (cantilever), the following governing equation can be obtained as shown in references [1]-[4].

$$\rho A \frac{\partial^2 y}{\partial t^2} + EI \frac{\partial^4 y}{\partial x^4} + P \frac{\partial^2 y}{\partial x^2} + c \frac{\partial y}{\partial t} = 0, \quad (4)$$

where the damping term due to material damping and structural damping is assumed to be displayed by the forth term in Eq. (4).

Continuous model subjected to a uniform distributed force

When a conservative uniform distributed force w acts on the continuous model (beam) as shown in Fig 1(b), the following governing equation can be obtained as proposed by Leipholz [3].

$$\rho A \frac{\partial^2 y}{\partial t^2} + EI \frac{\partial^4 y}{\partial x^4} + w(l-x) \frac{\partial^2 y}{\partial x^2} - w \frac{\partial y}{\partial x} + c \frac{\partial y}{\partial t} = 0, \quad (5)$$

Next, when a uniform distributed load w which is a nonconservative force (follower force) acts on the continuous model (beam) tangentially, the following governing equation can be obtained by using $w(l-x)$ in stead of $P(x)$ in Eq. (4) as proposed by Leipholz [3].

$$\rho A \frac{\partial^2 y}{\partial t^2} + EI \frac{\partial^4 y}{\partial x^4} + w(l-x) \frac{\partial^2 y}{\partial x^2} + c \frac{\partial y}{\partial t} = 0. \quad (6)$$

Thus, the uniform distributed force is corresponding to the friction drag mainly when a beam is subjected to an axial flow.

Numerical solutions

In this section, how to get the dynamical solution of a uniform beam subjected to an axial force is explained. Let us consider the case where the uniform distributed load acts on a continuous model (cantilever) as a nonconservative force (follower force) which is assumed to be a fluid force approximately.

Applying the Gelarkin's method, the displacement of a uniform cantilever $y(x, t)$ is expressed by the Fourier's expansion of the function $\phi_i(x)$ which satisfies the boundary conditions of a cantilever in the followings.

$$y(x, t) = \sum_{i=1}^{\infty} \phi_i(x) q_i(t), \quad (7)$$

where $q_i(t)$ is the function of time. When Eq. (7) is substituted into Eq. (6) which is the governing equation when a uniform distributed load w as a nonconservative force (follower force) acts on the a continuous model (cantilever) tangentially, the following equation is obtained.

$$\rho A \sum_{i=1}^{\infty} \phi_i(x) \ddot{q}_i(t) + EI \sum_{i=1}^{\infty} \frac{d^4 \phi_i(x)}{dx^4} q_i(t) + w(l-x) \sum_{i=1}^{\infty} \frac{d^2 \phi_i(x)}{dx^2} q_i(t) + c \sum_{i=1}^{\infty} \phi_i(x) \dot{q}_i(t) = 0. \quad (8)$$

When $\phi_i(x)$ is the eigen function of a beam in vacuum, the following equation is given.

$$\frac{d^4 \phi_i(x)}{dx^4} - \kappa_i^4 \phi_i(x) = 0, \quad (9)$$

where $\kappa_i^4 = \frac{\rho A}{EI} \omega_i^2$, and ω_i is the eigen circular frequency for $\phi_i(x)$. Applying the relationship of Eq. (9) to Eq. (8) and arranging the equation, the following equation is obtained.

$$\sum_{i=1}^{\infty} \phi_i(x) \ddot{q}_i(t) + \frac{c}{\rho A} \sum_{i=1}^{\infty} \phi_i(x) \dot{q}_i(t) + \sum_{i=1}^{\infty} \omega_i^2 \phi_i(x) q_i(t) + \frac{w(l-x)}{\rho A} \sum_{i=1}^{\infty} \frac{d^2 \phi_i(x)}{dx^2} q_i(t) = 0. \quad (10)$$

Multiplying the eigen function $\phi_k(x)$ with the eigen circular frequency ω_k for the both sides of Eq. (10) and integrating from 0 to l on the whole length of a beam, the following equations are obtained by applying the orthogonality of the eigen functions.

$$\left\{ \int_0^l \phi_k^2(x) dx \right\} \ddot{q}_k(t) + \left\{ \frac{c}{\rho A} \int_0^l \phi_k^2(x) dx \right\} \dot{q}_k(t) + \omega_k^2 \left\{ \int_0^l \phi_k^2(x) dx \right\} q_k(t) + \sum_{i=1}^{\infty} \left(\frac{w}{\rho A} \int_0^l (l-x) \phi_k(x) \frac{d^2 \phi_i(x)}{dx^2} dx \right) q_i(t) = 0 \quad (k=1 \sim \infty), \quad (11)$$

where, as n is the truncation number of the mode, $i, k=1 \sim n$. Rewriting Eq. (11) in the matrices expression, it becomes as follows.

$$\begin{bmatrix} \ddots & & 0 \\ & M_k & \\ 0 & & \ddots \end{bmatrix} \{\ddot{q}_k(t)\} + \begin{bmatrix} \ddots & & 0 \\ & C_k & \\ 0 & & \ddots \end{bmatrix} \{\dot{q}_k(t)\} + \left(\begin{bmatrix} \ddots & & 0 \\ & K_k & \\ 0 & & \ddots \end{bmatrix} + [D_{i,k}] + [E_{i,k}] \right) \{q_k(t)\} = 0, \quad (12)$$

where

$$\begin{aligned} M_k &= \int_0^l \phi_k^2(x) dx \\ C_k &= \frac{c}{\rho A} \int_0^l \phi_k^2(x) dx \\ K_k &= \omega_k^2 \int_0^l \phi_k^2(x) dx \\ D_{i,k} &= \frac{wl}{\rho A} \int_0^l \phi_k(x) \frac{d^2 \phi_i(x)}{dx^2} dx \\ E_{i,k} &= \frac{-w}{\rho A} \int_0^l x \phi_k(x) \frac{d^2 \phi_i(x)}{dx^2} dx. \end{aligned} \quad (13)$$

Besides, the damping is assumed to be the modal damping approximately.

Changing the uniform distributed load w in Eq. (12), the complex eigen value analysis is performed and the root locus is calculated. When the real part $\text{Re}(\lambda)$ of the eigen value λ is positive and $\text{Im}(\lambda)$ is not 0, the flutter phenomenon occurs. And, when $\text{Re}(\lambda)$ is positive and $\text{Im}(\lambda)$ equals 0, the divergence phenomenon appears. Besides in this section, although only Eq. (6) in which the uniform distributed load as a nonconservative force (follower force) acts on the continuous model tangentially is considered, Eq. (4) in which a concentrated load as a nonconservative force (follower force) acts on the continuous model, and further Eq. (5) in which a uniform distributed load acts on the continuous model as a conservative force can be also analyzed by the similar treatment.

ANALYSIS RESULTS AND CONSIDERATIONS

Specifications of numerical analysis

Table 1 shows the physical specifications of a beam. The value of Young modulus is adopted for the copper material. In this analysis, the dimensionless treatment is not performed for the experiments in the future.

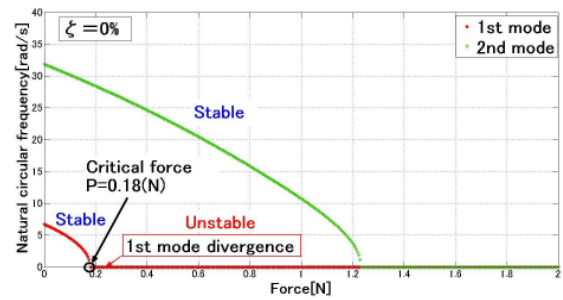
Table 1 Specifications of a beam

ρ : Density [kg/m ³]	8.92×10^3	R : Radius of beam [m]	1.00×10^{-3}
E : Young modulus [Pa]	1.00×10^{11}	l : Length of beam [m]	1.00

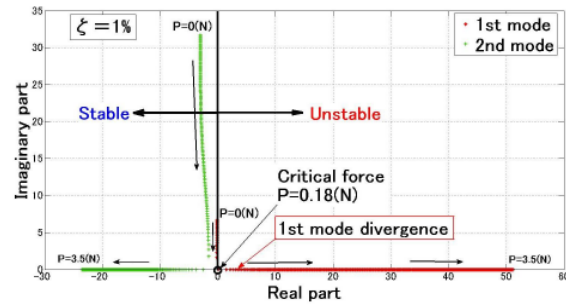
Discrete model of 2 degree freedom systems

Case of Euler model (conservative force)

Figure 3 shows the root locus for both undamped system and damped system concerning Euler model. Besides, in case of the undamped system, the relationship between the force of the abscissa and the eigen circular frequency of the ordinate is shown instead of the root locus of complex eigenvalue. Furthermore, the relationship between the force and the real part of eigenvalue which can govern the stable and unstable phenomena is shown in Fig. 4 changing the damping ratio.



(a) No damping



(b) 1 % critical damping

Fig. 3 Euler model

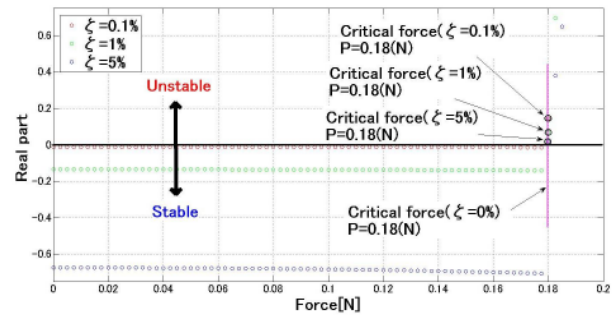


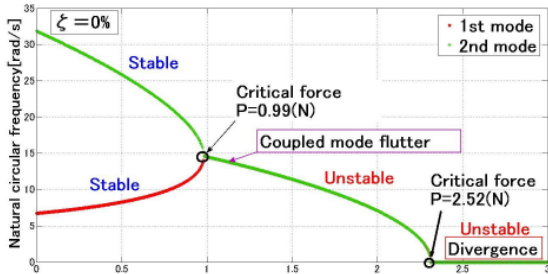
Fig. 4 Effect of damping on instability of Euler model

Case of Herrmann model (nonconservative force)

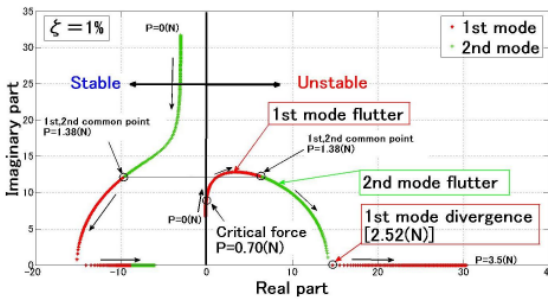
Figure 5 shows the root locus for both undamped system and damped system concerning Herrmann model as well as Euler model. In case of the undamped system, the relationship between the force and the eigen circular

frequency is shown instead of the root locus. Furthermore, the relationship between the force and the real part of eigenvalue is shown in Fig. 6 changing the damping ratio.

Comparing Euler model in Fig. 4 with Herrmman model in Fig. 6, the damping is found to have an effect of destabilization in Herrmman model.



(a) No damping



(b) 1 % critical damping
Fig. 5 Herrmman model

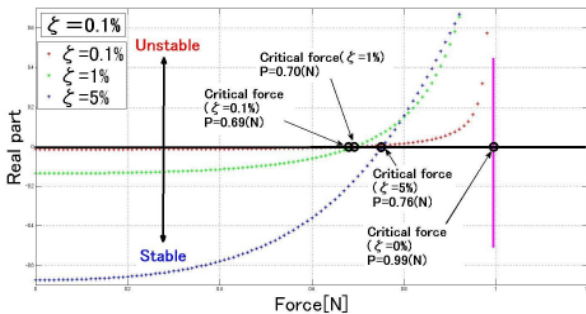
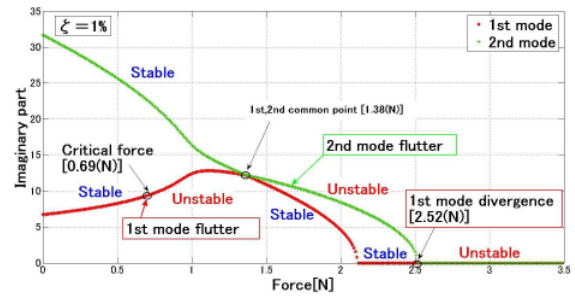


Fig. 6 Effect of damping on instability of Herrmman model

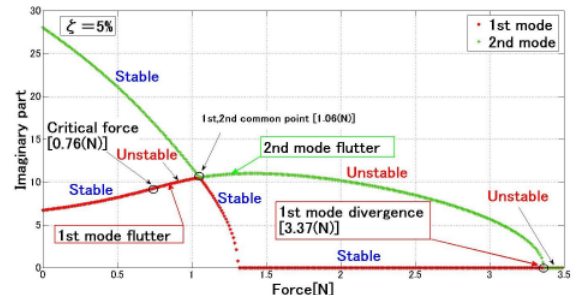
In order to consider this destabilization effect more, the relationship between the critical force and the imaginary part of eigenvalue is investigated in Fig. 7 as for the flutter of Herrmman model by changing the damping ratio. In this figure, the horizontal axis shows the force, and the vertical axis shows the imaginary part which is the eigen circular frequency, and the circles denote the beginning position of flutter and the coalescing position between 1st mode and 2nd mode. Observing Fig. 5(a) and Fig. 7 simultaneously, it is found that the flutter occurs at the coalescing position of 1st and 2nd modes in case of the undamped system, and the beginning point of the flutter appears on the way of 1st mode in case of the damped

system. That is, although the coupled mode flutter in Fig. 5(a) is found to appear in the undamped system, the single (1st) mode flutter in Fig. 7 appears in the damped system.

However, in case of Euler model, it is found that there is no difference between the undamped system and the damped system from comparing the critical force of Fig. 3 (a) for the undamped system and that of Fig. 3 (b) for the damped system. Besides, the 1st, 2nd common point in Fig. 7 denotes the coalescing position of 1st and 2nd modes.



(a) 1 % critical damping



(b) 5 % critical damping

Fig. 7 Relationship between damping and critical load on flutter of Herrmman model

Continuous model

In modeling, the specifications of the discrete model and the continuous model have been selected to keep the dynamic equivalency between both models.

Continuous model (cantilever) subjected to a conservative concentrated force

The dynamic difference between Euler model and Herrmman model as for two degree freedom systems is investigated more by using a continuous model. The continuous model, which is a cantilever, subjected to a conservative force is corresponding to Euler model of two degree freedom systems. The dynamic equivalency between the discrete model of two degree freedom systems and the continuous model is kept in the numerical calculation.

When the continuous model is subjected to a conservative force, it becomes Euler buckling in structural mechanics. When the critical buckling force P_{cr} is calculated using Eq. (3), it is obtained as $P_{cr} = 0.18 N$. This is corresponding to the Euler model which is the

discrete model of 2 degree freedom systems as shown in Fig. 3 (a).

Continuous model (cantilever) subjected to a nonconservative concentrated force

The continuous model subjected to a nonconservative force (follower force) is equivalent to Herrmman model of two degree freedom systems. Figure 8 shows the root locus for both undamped system and damped system. In the undamped system, the relationship between the force and the eigen circular frequency is shown in stead of the root locus. Figure 9 shows the relationship between the concentrated force and the real part of root locus by changing the damping ratio as well as in Fig. 6. Besides, the value of the point where the curve of Fig. 8(a) intersects the vertical axis denotes the 1st and 2nd eigen circular frequencies when the force is zero. For example, when these values are compared with those in Fig. 3(a), a few differences are recognized. This means the differences in the modeling accuracy between the analytical solutions of the continuous model and the discrete model of two degree freedom systems.

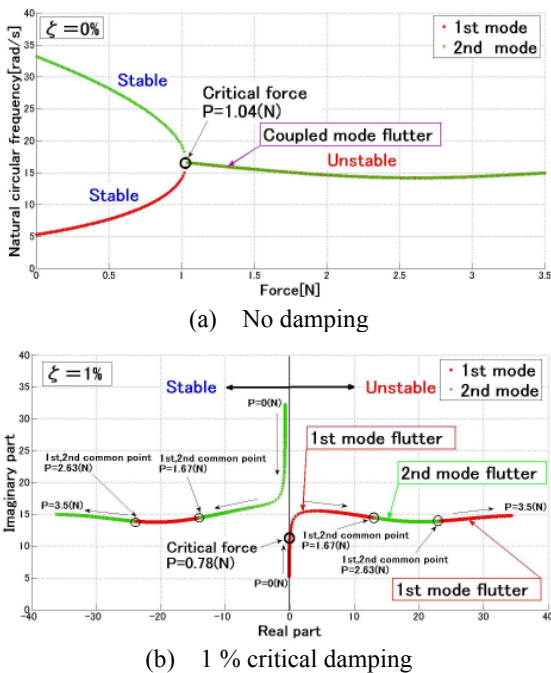


Fig. 8 Continuous model (cantilever) subjected to nonconservative concentrated force

Observing Fig. 6 and Fig. 9, it is found that the existence of damping gives a effect of destabilization to the system subjected to a nonconservative force for both the discrete model of two degree freedom and the continuous model. In order to study this effect moreover, the relationship between the critical force and the imaginary part of root locus is investigated by changing the damping ratio for the flutter of the continuous model subjected to the nonconservative force as shown in Fig. 10. Considering about Fig. 8 (a) and Fig. 10 simultaneously,

the coupled mode flutter in Fig. 8(a) generates at the coalescing position of 1st and 2nd modes for the undamped system. On the other hand, the single (1st) mode flutter appears in Fig. 10 on the way of 1st mode for the damped system. Then, when the force increases further, 1st mode and 2nd mode become unstable alternately.

Although the undamped system subjected to a nonconservative force continues being stable until the 1st mode and 2nd mode coalesce, it is found that the damped system subjected to a nonconservative force goes into a flutter before the 1st and 2nd modes coalesce. This difference is thought one of reasons to generate the destabilization effect of damping.

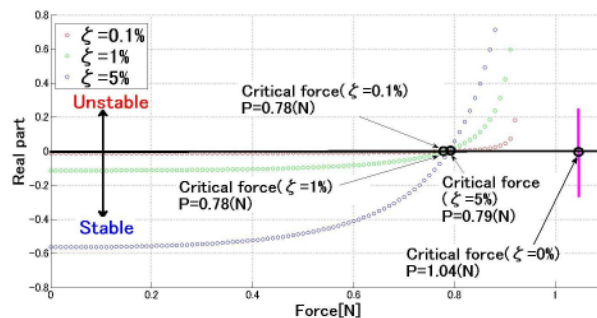


Fig. 9 Effect of damping on instability of continuous model subjected to nonconservative concentrated force

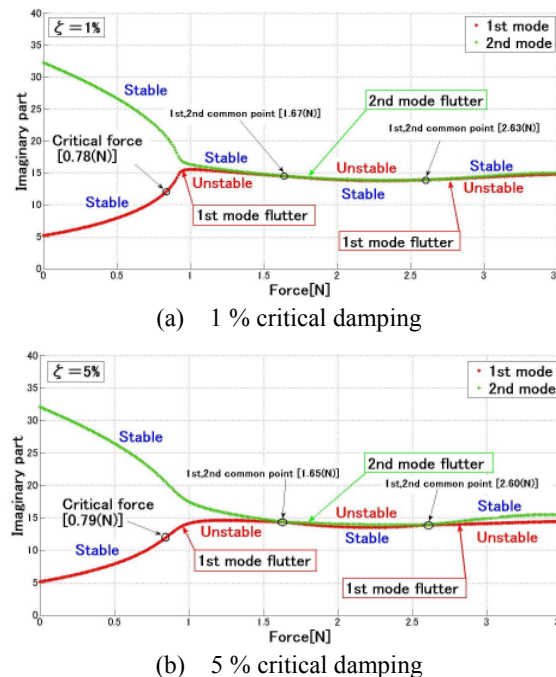


Fig. 10 Effect of critical force on flutter of continuous model (cantilever) subjected to nonconservative concentrated force

Figure 11 and 12 show the variation of modes before and after the outbreak of flutter. Figure 11 shows the vibration mode of the coupled mode flutter shown in Fig. 8 (a) for the undamped system. On the other hand, Fig. 12

shows the vibration mode of the single (1st) mode flutter shown in Fig. 10 (a) for the damped system.

Besides, the truncating number of modes in numerical calculations is 10 as for the continuous model. It is similar in the subsequent numerical computation.

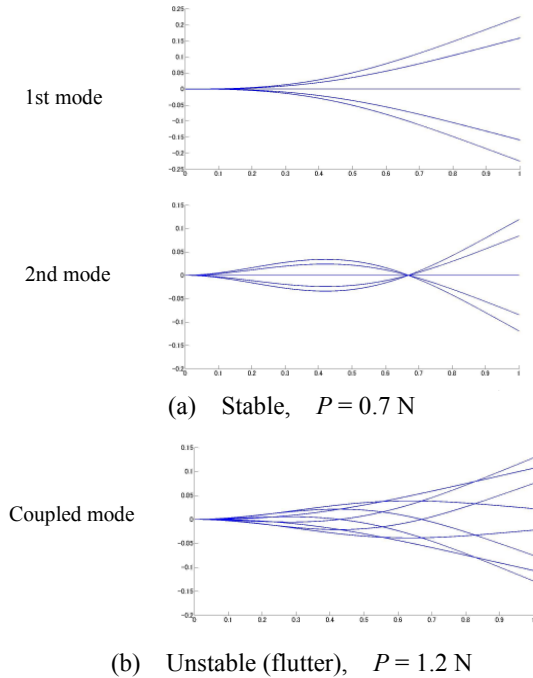


Fig. 11 Mode shape before and after coupled mode flutter of continuous model (cantilever) subjected to nonconservative concentrated force (Undamped system)

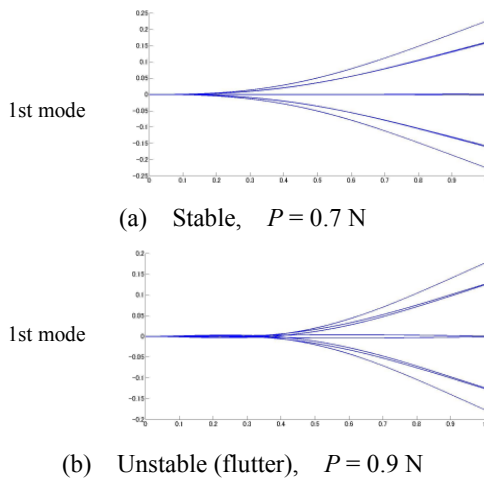


Fig. 12 Mode shape before and after single (1st) mode flutter of continuous model (cantilever) subjected to nonconservative concentrated force (Damped system, 1% of critical damping)

Continuous model (cantilever) subjected to a nonconservative distributed force

Figure 13 shows the root loci for both undamped system and damped system when a nonconservative force (follower force) acts on a cantilever tangentially. In case

of the undamped system, the relationship between the force and the eigen circular frequency is shown in stead of the root locus. The same phenomena are recognized as well as in Fig. 8.

From Fig. 13, it is found that the existence of damping gives an effect of destabilization to the system subjected to a nonconservative force (follower force).

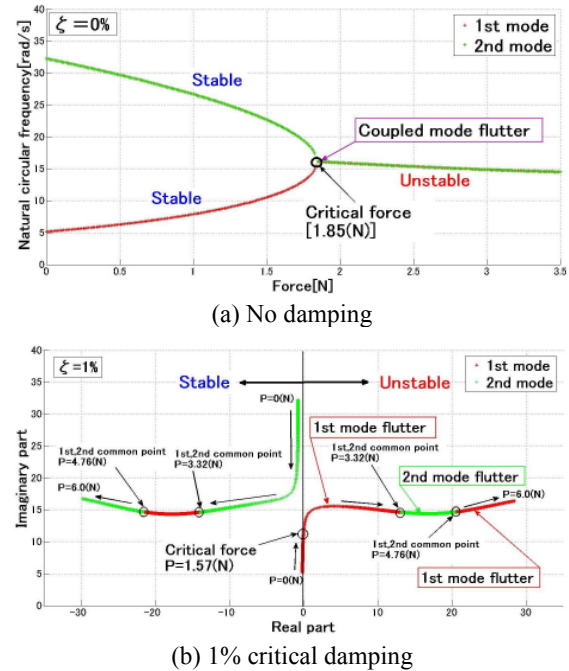


Fig. 13 Continuous model (cantilever) subjected to nonconservative distributed force

Continuous model (simply supported beam) subjected to a nonconservative distributed force

Figure 14 shows the root locus for the damped system of 1% critical damping when a nonconservative force (follower force) acts on a simply supported beam.

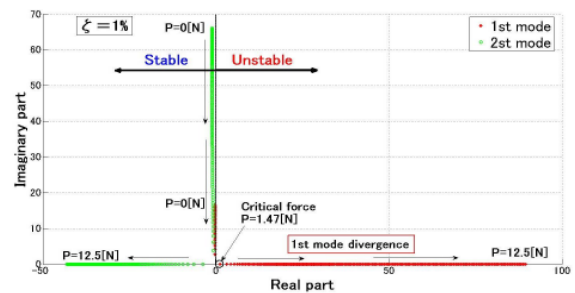


Fig. 14 Root locus of continuous model (simply supported beam) subjected to nonconservative distributed force

Continuous model (free-free beam) subjected to a nonconservative distributed force

Figure 15 shows the root locus for the damped system of 1% critical damping when a nonconservative force (follower force) acts on a free-free beam.

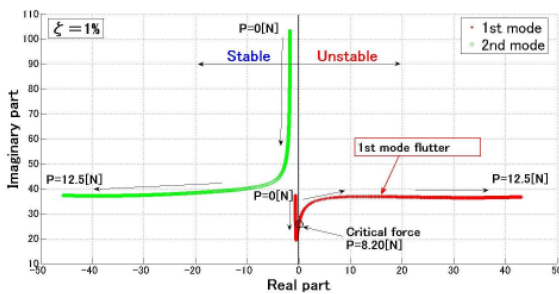


Fig. 15 Root locus of continuous model (free-free beam) subjected to nonconservative distributed force

Comparing Fig. 13(b), Fig. 14 and Fig. 15, it is found that there are some differences in the behavior of instability among the supported conditions. It is thought that a further study on these differences is necessary.

CONCLUSIONS

- (1) The numerical solutions of the continuous model corresponding to that of the discrete model consisted of Euler model and Herrmman model are confirmed, and the physical agreement between both models is confirmed. It is found that the continuous model and the discrete model show a good agreement at the lower force. However at the higher force, it is found that the continuous model continues showing a coupled mode flutter phenomenon sequentially without 2nd mode being separated from 1st mode although the discrete model shows a divergence phenomenon after a flutter one.
- (2) In case of the cantilever subjected to a compressive force axially, it is confirmed that a flutter appears first when the force is nonconservative although the critical force become high, on the other hand a divergence appears first when the force is conservative.
- (3) The destabilization effect of the damping is shown to be recognized in the damped system subjected to a nonconservative force. The coupled mode flutter is confirmed to generate in the undamped system, and the single mode flutter to generate in the damped system. The damped system subjected to a nonconservative force goes into a flutter before the 1st mode and 2nd mode coalesce although the undamped system subjected to a nonconservative force continues being stable until the 1st mode and the 2nd mode coalesce. This difference is thought one of reasons to generate the destabilization effect of damping.
- (4) It is understood that the same dynamic instability as the concentrated force is recognized when the uniform distributed force acts on a cantilever.
- (5) It is found that there are some differences in the behavior of instability among a cantilever, a simply supported beam and a free-free beam. It is thought that a further study on these differences is necessary.

ACKNOWLEDGMENTS

We received much support by Professor Tadao Kawai of Osaka City University in performing our study. We thank him deeply here.

REFERENCES

1. Bolotin, V. V., 1963, "Nonconservative Problems of the Theory of Elastic Stabilities, Pergamon press.
2. Ziegler, H., 1968, "Principles of Structural Stability", Blaisdell Publishing Company, A Division of Ginn and Company.
3. Leipholz, H., 1980, "Stability of elastic systems", The Universities Press, Belfast, Samsom-Sijthoff, Alphen aan den Rijn.
4. Sugiyama Y., Sekiya T., 1970, "Stability Problem of Nonconservative Elastic Systems", *Journal of the Japan Society of Mechanical Engineers*, Vol. 73, No. 620, pp.1238-1245 (in Japanese).
5. Honma T., Tosaka N., 1997, "Dynamic Stability Analysis for an Elastic Rod Subjected to Conservative and Nonconservative Forces by Integral Equation Method", *Transactions of Japan Society of Mechanical Engineers*, 63-614, A, pp.2180-2187 (in Japanese).
6. Langthjem, A. M., 2002, "Optimum Design of Cantilevered Columns Subjected to Non-conservative Loading by Rocket Thrust", *Doctoral Thesis at Osaka Prefecture University*.
7. Kounadis, A. N., Gantes, and C. j., Bolotin, V. V., 2001, "An Improved Energy Criterion for Dynamic Buckling of Imperfection Sensitive Nonconservative Systems", *International Journal of Solids and Structures*, Vol. 38, pp.7487-7500.
8. Schmid, P. J., Langre, E. de., 2003, "Transient Growth Before Coupled-Mode Flutter", *Transactions of the ASME, Journal of Applied Mechanics*, Vol. 70, pp.894-901.
9. Fazelzadeh, S. A., Kalantani, H., and Mazidi, A., 2008, "Aeroelastic Instability of Bending-Torsion Wings Containing a Mass Subjected to Follower Force", *Proc. of the 9th International Conference on Flow-Induced Vibration*, pp.477-482.
10. Fujita, K., Gotou A., 2012, "A Consideration on Nonconservative Elastic Stability of a Beam Subjected to Axial Force Considered to be Fluid force", *Transactions of Japan Society of Mechanical Engineers*, 78-789, C (in Japanese).



ON THE NONLINEAR DYNAMICS OF CANTILEVERED CIRCULAR CYLINDRICAL SHELLS CONVEYING FLUID

Mehdi Paak*

Department of Mechanical Engineering
McGill University
Montreal, Canada H3A 2K6
Email: mehdi.paak@mail.mcgill.ca

M. P. Païdoussis

Department of Mechanical Engineering
McGill University
Montreal, Canada H3A 2K6
Email: michael.paidoussis@mcgill.ca

A. K. Misra

Department of Mechanical Engineering
McGill University
Montreal, Canada H3A 2K6
Email: arun.misra@mcgill.ca

ABSTRACT

In this paper, the nonlinear behaviour of thin-walled clamped-free shells conveying fluid is studied for the first time. The stability of the structure is analyzed and bifurcation analyses are performed. Also, a parametric study of both linear and nonlinear models is performed. The nonlinear shell model is based on Flügge's assumptions, taking into account in-plane inertia terms and retaining all nonlinear terms of mid-surface stretching. The fluid is assumed to be incompressible and inviscid, and the flow irrotational. Therefore, fluid-structure interaction may be described by linear potential flow theory. The fluid flow beyond the free end of the shell is described by an "out-flow" model through which a fluid boundary condition is characterized. Equations of motion are derived using Hamilton's principle, and discretized by taking a direct variational approach. The discretized equations are then integrated numerically, and bifurcation diagrams obtained by using the software AUTO. Results are compared with existing experimental data, and good agreement is observed.

INTRODUCTION

For a long time, the focus of attention, insofar as the dynamics of cylindrical shells conveying fluid is concerned, has been on supersonic compressible flows which can have profound effects on the structure; the ensuing dynamical behaviour is very rich and of high importance in the aerospace industry. On the other hand, the dynamics associated with subsonic or incompressible fluid flows was considered to be relatively uninteresting: no more than a mild (small amplitude) divergence was thought to be possible. Nevertheless, the work of Païdoussis

and Denise [1] showed that this is not always the case, and thereafter there has been increased interest in the analysis of thin shells subjected to incompressible fluid flows. Païdoussis and Denise developed the first analytical linear model for thin shells with clamped-clamped and clamped-free boundary conditions, and also performed experiments. It was shown that cantilevered shells subjected to axial flow lose stability via a Hopf bifurcation, and that the structure undergoes an oscillatory type of instability (single-mode flutter). This observation was in agreement with experiments. The work on different aspects of the dynamics of cantilevered shells in contact with flowing fluid continued both theoretically and experimentally. Païdoussis et al. [2] carried out a comprehensive theoretical study of the stability of cantilevered coaxial shells conveying fluid, taking into account viscous effects of the mean flow, while obtaining the perturbation pressure by means of potential flow theory. They used the Fourier transform technique in conjunction with the extended Galerkin method to solve the coupled fluid-structure equations. It should be noted that the authors utilized an outflow model to describe how the flow perturbation dies out some distance after the fluid exits the shell. The concept of an outflow model was first introduced in [3]; Later on, other outflow models have been proposed [4]. Nguyen et al. [5] have also carried out an experimental study of cantilevered "coaxial shells" conveying fluid in which they measured (i) the critical flow velocities of the shells for various length-to-radius and annular-gap-to-radius ratios and (ii) frequencies of oscillation of the shell at different subcritical flow velocities. Their results indicate both divergence and flutter for the case of annular flow, whereas only flutter was observed for internal flow. Their experimental results agree well with the theoretical results obtained by the same au-

*Address all correspondence to this author.

thors [6].

Comparatively fewer studies have been conducted using nonlinear models; the subject is quite young. The work on the nonlinear dynamics and stability of circular cylindrical shells conveying fluid was initiated in a series of papers by Amabili et al. [7,8]. In their work, Donnell's nonlinear shallow-shell theory was used for the structure and potential flow theory for the fluid to describe the nonlinear behaviour of simply-supported shells containing flowing fluid. Later on, Karagiozis et al. [9] studied the nonlinear stability of clamped-clamped shells conveying fluid both theoretically and experimentally. A thorough account of the nonlinear behaviour of thin shells in contact with fluids is given in the book by Amabili [10]. However, to the best of the authors' knowledge, the nonlinear analysis of cantilevered shells conveying fluid has not been addressed yet, and therein lies the motivation for this research. In this paper, the mathematical model of the system is briefly outlined and some results are presented. Readers should notice that the works cited, here, are of immediate interest to the subject of this paper. For a wider bibliography, refer to Paidoussis [11,4].

THEORETICAL MODEL

Assumptions

Figure 1 shows a schematic diagram of the system considered. It consists of a circular cylindrical shell

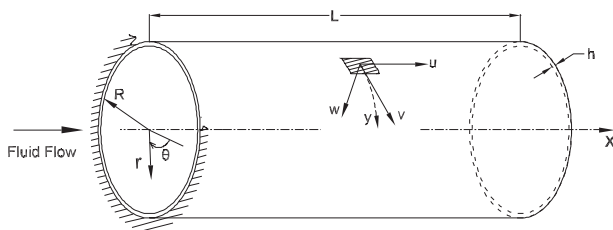


FIGURE 1: CANTILEVERED SHELL GEOMETRY

clamped at the upstream end ($x = 0$) and free at the downstream end ($x = L$). The shell is thin ($h/R \ll 1$) and assumed to be homogeneous, isotropic, and linearly elastic with density ρ_s , Young's modulus E and Poisson ratio ν . The shell nonlinearity is geometric (i.e., deformations are of the order of the shell thickness); thus, finite strain theory is used to describe the displacement field. The displacement vector of a point on the shell middle surface is denoted by $\mathbf{u} = (u, v, w)$, where u , v and w are its components in the axial, circumferential and radial directions, respectively, in general functions of the mid-surface co-

ordinates and time, i.e., (x, y, t) . The shell and fluid are in full contact assuming there is no cavitation.

The fluid is considered to be inviscid and incompressible with density ρ_F , flowing with velocity U in the x -direction. The flow is assumed to be isentropic and irrotational. Therefore, potential flow theory is utilized to obtain the fluid dynamic forces. The effect of hydrostatic pressure on the shell is neglected. Finally, it is assumed that the flow perturbations (induced by shell motion) decay to zero far upstream and downstream of the shell.

Formulation

Shell. The nonlinear shell model is based on Flügge's assumptions [12]. This shell theory does not have the limitations of shallow shell models (e.g., Donnell-Mushtari), in which the in-plane displacements and their derivatives are omitted from the expressions of mid-surface curvatures and twist. Moreover, in Flügge's shell theory, unlike many other classical theories, the thinness assumption is applied only when the stress resultants are calculated; in that, terms of order $\mathcal{O}((h/R)^3)$ and smaller are neglected. Hence, the strains and stresses remain in their original form, resulting in more reliable equations of motion. To obtain the nonlinear equations, the Green strain tensor and Kirchhoff's stress tensor are used, so that calculations can be performed in the undeformed configuration.

To formulate the model, the extended Hamilton's principle is invoked:

$$\int_{t_1}^{t_2} [(\delta T - \delta U + \delta W_D) + \delta W_F] dt = 0, \quad (1)$$

where δ is the variational operator, and T , U and δW_D are the kinetic energy, potential energy (strain energy) and the work done by damping force, respectively. These terms are associated with only the structural part of the system (i.e., the shell); fluid flow, on the other hand, manifests its effect through δW_F , which is the virtual work associated with the hydrodynamic force. The kinetic and potential energy of the shell may be expressed as

$$T = \frac{1}{2} \int_S \rho_s h (\dot{u}^2 + \dot{v}^2 + \dot{w}^2) dS, \quad (2)$$

$$U = \frac{1}{2} \int_V (\sigma_x \epsilon_x + \sigma_y \epsilon_y + \sigma_{xy} \epsilon_{xy}) dV. \quad (3)$$

Damping in the shell is modelled via Rayleigh's dissipation function

$$F = \frac{1}{2} \int_S ch (\dot{u}^2 + \dot{v}^2 + \dot{w}^2) dS, \quad (4)$$

where c is the viscous damping coefficient. In energy-based approaches, the structural boundary conditions naturally appear in the equations of motion and are satisfied in the mean.

Fluid. As alluded earlier, the equations of motion of the shell and that of fluid are coupled through the term δW_F , which is the virtual work done by the perturbation pressure at the fluid structure interface. Hence, the fluid pressure field should be calculated. According to potential flow theory, the fluid velocity field can be written as the gradient of the potential function Ψ (i.e., $\vec{V} = \nabla\Psi$). Ψ has two components: (i) the perturbation potential, Φ , due to the motion of the shell, (ii) the potential of the mean flow, related to the undisturbed axial flow velocity U ; thus, $\Psi = \Phi + Ux$, and the velocity components may be written as

$$V_x = U + \Phi_{,x}, \quad V_\theta = \frac{1}{r}\Phi_{,\theta}, \quad V_r = \Phi_{,r}. \quad (5)$$

The conservation of mass requires that Ψ and accordingly Φ satisfy the Laplace equation,

$$\nabla^2\Phi = \frac{\partial^2\Phi}{\partial x^2} + \frac{\partial^2\Phi}{\partial r^2} + \frac{1}{r}\frac{\partial\Phi}{\partial r} + \frac{1}{r^2}\frac{\partial^2\Phi}{\partial\theta^2}. \quad (6)$$

Using Bernoulli's equation for unsteady flows, the perturbation pressure, after neglecting the nonlinear terms of the dynamic pressure, is obtained as

$$p = -\rho_F \left(\frac{\partial\Phi}{\partial t} + U\frac{\partial\Phi}{\partial x} \right). \quad (7)$$

In fact, the fluid displacement is of the order of the shell thickness and is justifiably considered to be small; thereby, allowing a linear formulation for the fluid. Equation (6) is solved via the Fourier transform technique along with the method of separation of variables. The fluid boundary conditions imposed are periodicity in the circumferential direction, finiteness of the solution at $r = 0$, and the impermeability condition at $r = R$,

$$\frac{\partial\Phi}{\partial r}\Big|_{r=R} = - \left(\frac{\partial w}{\partial t} + U\frac{\partial w}{\partial x} \right). \quad (8)$$

In addition, the flow perturbation is zero at the inlet and vanishes smoothly over a distance beyond the free end of the shell. The latter condition is empirical and is introduced into the equations through an "outflow model".

Fundamentally, the notion is to extend the control surface enclosing the fluid past the structure domain, assuming a specified form of decay of the perturbation for $x > L$.

Performing the necessary mathematical manipulations, Eqn. (1) leads to

$$\int_0^L \int_0^{2\pi R} (L_1(\mathbf{u})\delta u + L_2(\mathbf{u})\delta v + [L_{3S}(\mathbf{u}) + L_{3F}(\mathbf{u})]\delta w) dy dx - \int_0^{2\pi R} [R_1(\mathbf{u})\delta u + R_2(\mathbf{u})\delta v + R_3(\mathbf{u})\delta w + R_4(\mathbf{u})\delta w_{,x}] \Big|_{x=L} dy = 0, \quad (9)$$

where L_1 , L_2 , and L_{3S} are the nonlinear differential operators associated with shell motion, and L_{3F} is the linear differential operator acting in the radial direction due to the fluid flow. The natural boundary conditions of the shell at the free end are accounted for by the nonlinear operators R_i , $i = 1, 2, 3, 4$. Operators L_{3S} , L_{3F} and R_3 , in dimensional form, are given in Appendix A.

METHOD OF SOLUTION

Equation (9), in its original form, leads to a set of coupled nonlinear partial differential equations, which to-date elude an exact analytical solution. Approximate solutions, however, are possible; one technique is the global discretization of the assumed solution in space, using an appropriate set of shape functions. In this analysis, the following expansion is used:

$$\begin{aligned} u &= \sum_{n=1}^N \sum_{m=1}^M \left[A_{u,mn}(t) \cos\left(n\frac{y}{R}\right) + B_{u,mn}(t) \sin\left(n\frac{y}{R}\right) \right] u_m(x), \\ v &= \sum_{n=1}^N \sum_{m=1}^M \left[A_{v,mn}(t) \cos\left(n\frac{y}{R}\right) + B_{v,mn}(t) \sin\left(n\frac{y}{R}\right) \right] v_m(x), \\ w &= \sum_{n=1}^N \sum_{m=1}^M \left[A_{w,mn}(t) \cos\left(n\frac{y}{R}\right) + B_{w,mn}(t) \sin\left(n\frac{y}{R}\right) \right] w_m(x), \end{aligned} \quad (10)$$

where the $A(t)$ and $B(t)$ are the generalized coordinates (unknown time-dependent amplitude functions) and u_m, v_m and w_m are the basis functions in the axial direction. Any complete set of independent functions can be utilized to form the solution space, provided that they satisfy the essential (geometric) boundary conditions $u|_{x=0} = v|_{x=0} = w|_{x=0} = 0$, $w_{,x}|_{x=0} = 0$; here, the cantilevered beam eigenfunctions, $\phi_m(x)$, are employed:

$$u_m(x) = \phi'_m(x), \quad v_m(x) = \phi_m(x), \quad \text{and} \quad w_m(x) = \phi_m(x). \quad (11)$$

Nevertheless, when incorporating the outflow model, $w_m(x)$ is extended beyond the shell end (see [4]).

Discretized equations are obtained by substituting Eqns (10) and (11) into (9) and performing the surface integrations analytically, using the Mathematica computer software [13]. The resulting nonlinear ODEs are then rendered nondimensional by using

$$\bar{t} = \frac{t}{T}, \bar{A}_{,mn} = \frac{A_{,mn}}{R}, \bar{B}_{,mn} = \frac{B_{,mn}}{R}, \bar{U} = \frac{U}{\mathcal{U}}, \beta = \frac{R}{L},$$

$$\varepsilon = \frac{h}{R}, \gamma = \frac{\rho_F}{\rho_s}, T = R\sqrt{\frac{(1-\nu^2)\rho_s}{E}}, \mathcal{U} = \frac{R}{T}. \quad (12)$$

The ODEs are next converted to state-space form and integrated numerically employing the Runge-Kutta 4th order method. Bifurcation diagrams are computed with AUTO software [14].

RESULTS AND DISCUSSION

Theoretical results are obtained for shells of various L/R and h/R with $\nu = 0.5$. To be consistent with the experimental data in [1], the fluid is considered to be air with density ratio $\gamma = 0.00136$. In the linear investigation six axial modes ($M = 6$) are included in the expansions. The dimensionless damping value $c = 0.0001$ is used in all calculations (i.e., linear and nonlinear models).

Linear Analysis

The linear calculations here are based on the formulations given in [2]; however, the equations are slightly modified to include the effect of viscous damping. Unlike shells with supported ends, cantilevered shells lose stability through flutter. Figure 2 shows the dimensionless critical velocity of flutter for various L/R . It is observed that for relatively long shells ($L/R \geq 12$) instability occurs with $n = 2$, while for shorter shells it occurs with $n = 3$. The discrepancy between theory and experiment is more significant for short shells. This is speculated to be a boundary effect, which becomes more pronounced in the case of short shells. In the linear model circumferential modes, n , are decoupled; for each n , instability occurs when the fluid centrifugal force overcomes the shell restoring force. The value of n with the lowest critical flow velocity depends on the system parameters, viz., L/R and h/R ; see, e.g., Fig. 3 for $L/R = 7$ and a few values of h/R . It can be seen that for $h/R = 0.005$ the circumferential mode with lowest critical velocity is at $n = 4$; whereas, for higher thickness-to-radius ratios it is at $n = 3$. For thicker shells instability occurs at higher flow velocities.

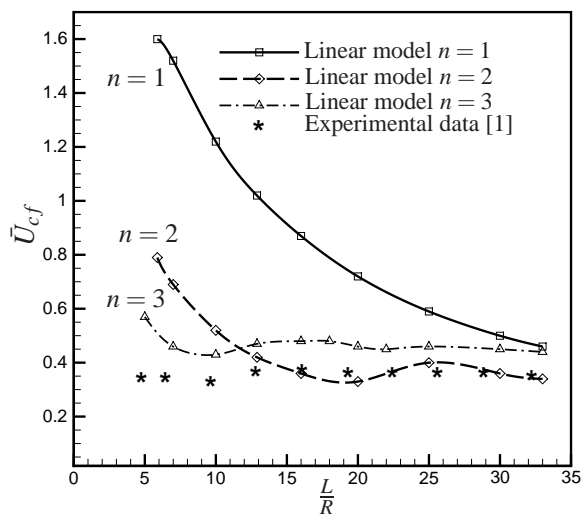


FIGURE 2: DIMENSIONLESS CRITICAL FLOW VELOCITY VERSUS LENGTH-TO-RADIUS RATIO, $\frac{h}{R} = 0.0227$.

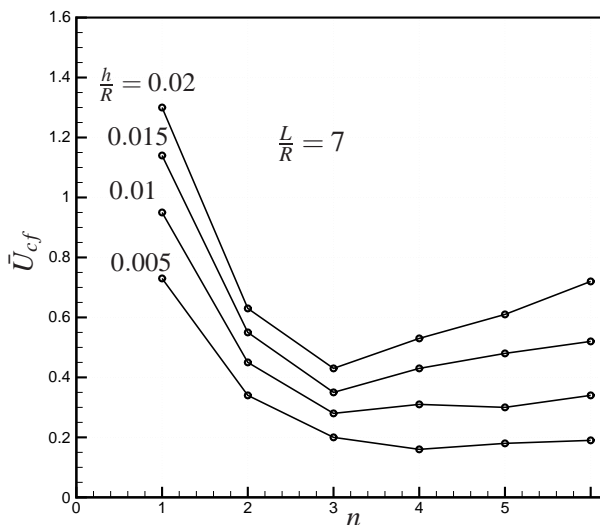


FIGURE 3: DIMENSIONLESS CRITICAL FLOW VELOCITY VERSUS CIRCUMFERENTIAL MODE NUMBER n ; $\frac{L}{R} = 7$.

Nonlinear Analysis

Stationary Solution. The linear model is only valid up to the onset of instability. Therefore, to study the post-instability behaviour a nonlinear model is required. In this study, the nonlinear differential equations contain quadratic and cubic nonlinear terms. The former arise from both bending and stretching of the shell mid-surface, whereas the latter is solely due to stretching. As opposed to the linear case, the nonlinearity cou-

ples the circumferential modes together. The strength of this coupling, however, depends on the system parameters. To verify the nonlinear model, the stability of the equilibrium position is analyzed and compared with linear theory. To this end, the dimensionless flow velocity \bar{U} is used as the bifurcation parameter, and the stationary solution (i.e., equilibrium) is followed by means of the AUTO software, which implements a pseudo-arclength continuation algorithm. Convergence of the solutions is carefully studied by experimenting with different values of N and M [Eqn. (10)]. It turns out that for shells of $L/R \leq 12$ several circumferential modes (e.g., $N \geq 3$) are necessary, while for longer shells high axial modes are important (e.g., $M \geq 2$). In general, for each set of shell geometric parameters, the circumferential mode at which the linear instability occurs should be included. For instance, for a shell with $L/R = 7$ at $h/R = 0.02$, $n = 3$ and for $h/R = 0.005$, $n = 4$ must be included (Fig. 3). In this analysis, for the most part, inclusion of three circumferential modes (i.e., $N = 3$) and three axial modes (i.e., $M = 3$) proved to be enough for convergence. Figure 4 shows \bar{U}_{cf} predicted by the nonlinear theory, versus length-to-radius ratio. It is seen that for relatively short shells results converge when $n = 3$ is included; for longer shells, $n = 2$ is enough. Also, the nonlinear model is in better agreement with the experiment than the linear one. The effect of thickness-to-radius ratio, h/R , on the value

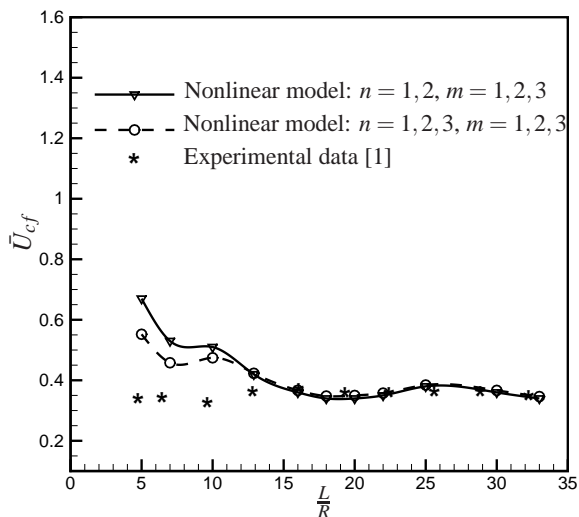


FIGURE 4: DIMENSIONLESS CRITICAL FLOW VELOCITY VERSUS LENGTH-TO-RADIUS RATIO PREDICTED BY NONLINEAR MODEL.

of critical flow velocity, predicted by both linear and non-

linear models, is shown in Fig. 5.

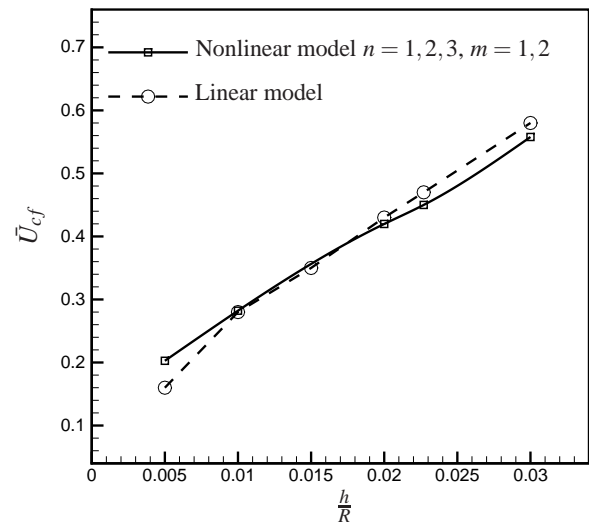


FIGURE 5: DIMENSIONLESS CRITICAL FLOW VELOCITY VERSUS THICKNESS-TO-RADIUS RATIO PREDICTED BY LINEAR AND NONLINEAR MODELS, $L/R = 7$.

Periodic Solution. In the preceding section, the validity of the nonlinear model was established through comparison with linear theory and existing experimental data. In this section, the post-instability behaviour of the system is analyzed. Results are presented for a shell with $L/R = 7$, $h/R = 0.02$ and $n = 3$. Figure 6 shows the bifurcation diagram of the maximum radial displacement of a point at the shell tip versus dimensionless flow velocity. It is seen that at $\bar{U} = 0.42$ the stationary solution loses stability through a supercritical Hopf bifurcation (solid square) giving birth to a family of stable periodic solutions (see Fig. 7). The amplitude of the periodic oscillation rapidly grows with the flow velocity and, eventually, becomes unstable via a Neimark-Sacker (torus) bifurcation (solid diamond) at $\bar{U} = 0.95$. After this flow velocity, there is no stable limit cycle, and the system behaves nonperiodically.

Nonperiodic Solution. The AUTO software is not capable of following nonperiodic solutions *viz.*, quasiperiodic and chaotic orbits. Hence, in order to unfold the dynamics for $\bar{U} > 0.95$, the time response of the system is investigated with the Poincaré maps and FFT analysis. To this end, the system of nonlinear ODEs are

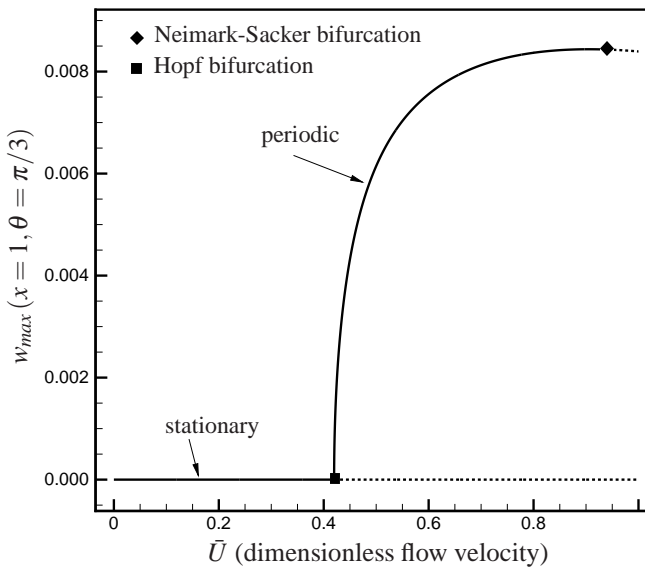


FIGURE 6: BIFURCATION DIAGRAM OF THE MAXIMUM RADIAL DEFLECTION, w , AT SHELL TIP AND $\theta = \frac{\pi}{3}$; ———, STABLE SOLUTIONS; ·······, UNSTABLE SOLUTIONS; $\frac{L}{R} = 7$, $n = 3$ and $m = 1, 2$.

PSD plot (Fig. 11) shows a broad frequency band, which is an indication of chaos. The Poincaré map in Fig. 12

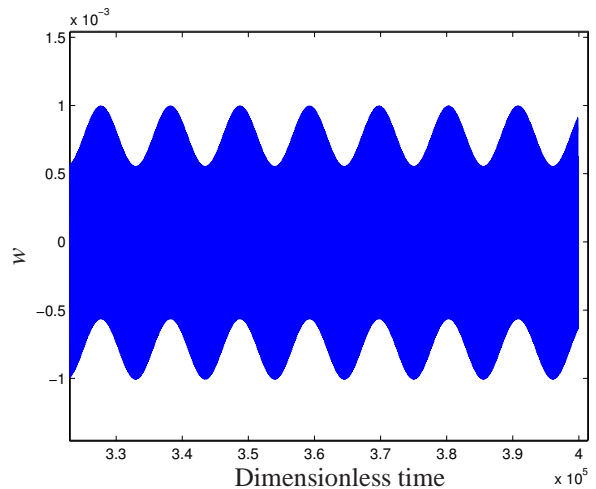


FIGURE 8: TIME TRACE OF \dot{w} VERSUS w AT POINT $(x = 1, \theta = \pi/3)$, AND $\bar{U} = 0.953$.

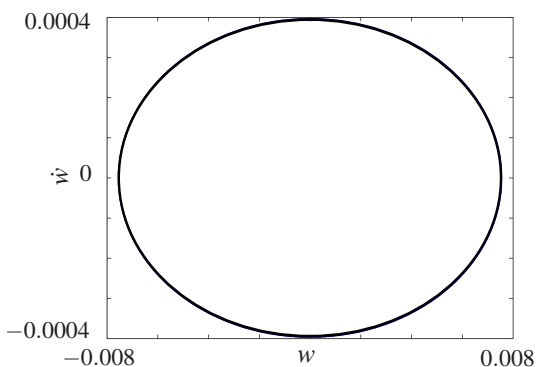


FIGURE 7: PHASE-PLANE PLOT OF \dot{w} VERSUS w AT POINT $(x = 1, \theta = \pi/3)$, AND $\bar{U} = 0.60$.

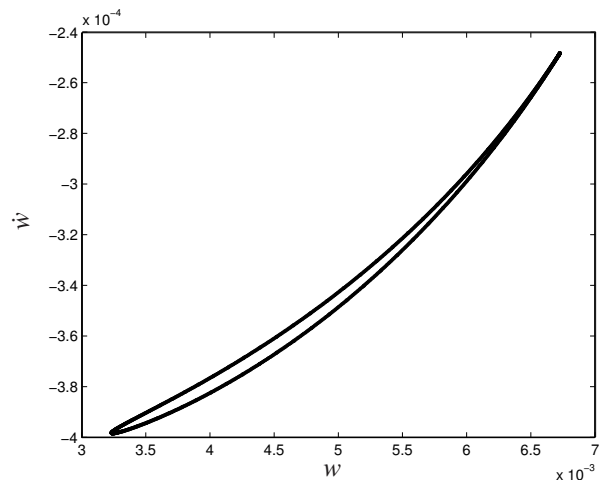


FIGURE 9: ONE-SIDED POINCARÉ MAP; \dot{w} VERSUS w AT POINT $(x = 1, \theta = \pi/3)$, AND $\bar{U} = 0.953$.

numerically integrated for $\bar{U} = 0.953, 0.99$, and 1 . The time trace for $\bar{U} = 0.953$, which is immediately after the torus bifurcation, is shown in Fig. 8; it is seen that the amplitude of the oscillation is modulated, which implies that the response can be quasiperiodic. In addition, the Poincaré map is a closed curve, which indicates that the solution is quasiperiodic; topologically, the solution is attracted to a stable 2-torus (\mathbb{T}^2) in the phase space (Fig. 9). The stable quasiperiodic oscillation grows with the flow velocity, until it loses stability at a certain value of \bar{U} ; in other words, the stable torus breaks up and results in a chaotic motion on a strange attractor. Figure 10 shows the time trace of the system at $\bar{U} = 0.99$; the corresponding

shows a section of the strange attractor at $\bar{U} = 0.99$. At a slightly higher flow velocity (e.g., $\bar{U} = 1$), the chaoticity of the response increases, and the motion trajectories visit a wider region of the phase space. The time trace and the corresponding PSD plot of the system for $\bar{U} = 1$ are shown in Figs 13 and 14. It is observed that the frequency spectrum for $\bar{U} = 1$ is broader than that for $\bar{U} = 0.99$; thus it can be said that in the former case the chaos is stronger. The fractal structure of the strange attractor for $\bar{U} = 1$ can be seen in Fig 15.

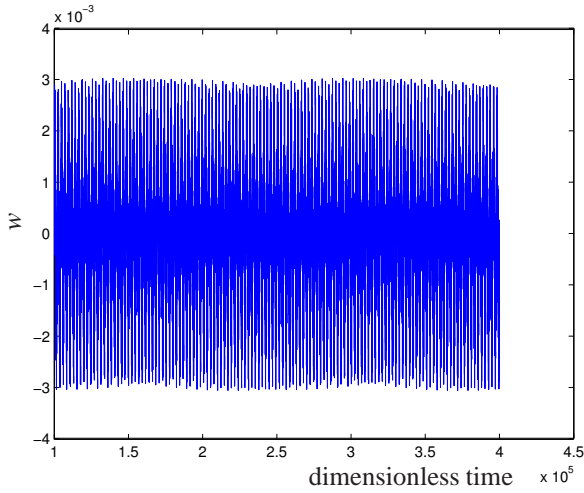


FIGURE 10: TIME TRACE OF \dot{w} VERSUS w AT POINT $(x = 1, \theta = \pi/3)$, AND $\bar{U} = 0.99$.

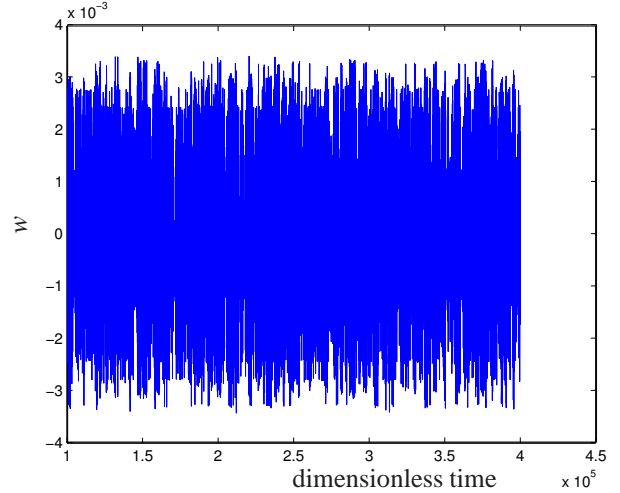


FIGURE 13: TIME TRACE OF \dot{w} VERSUS w AT POINT $(x = 1, \theta = \pi/3)$, AND $\bar{U} = 1$.

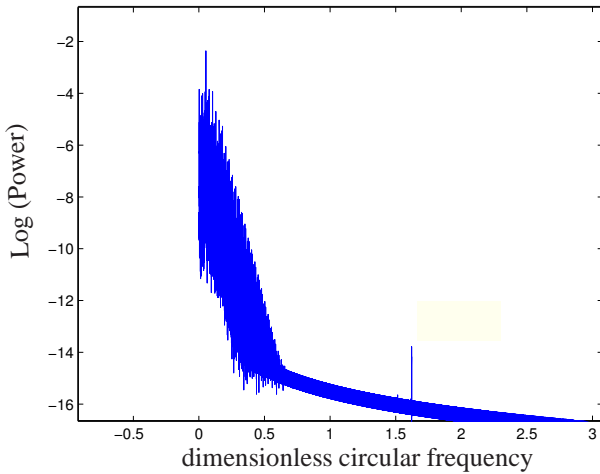


FIGURE 11: PSD PLOT FOR $\bar{U} = 0.99$.

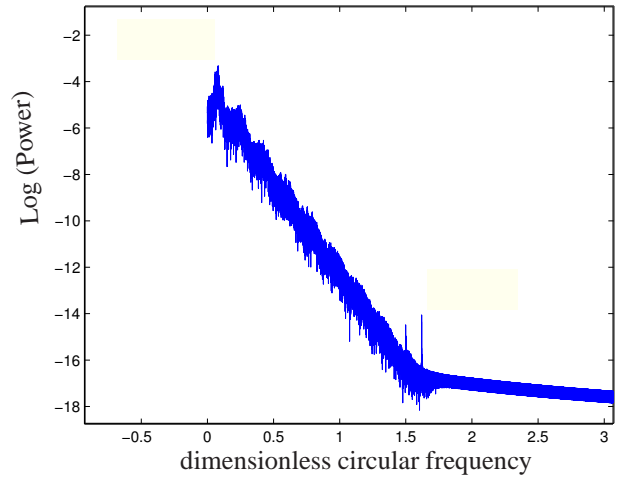


FIGURE 14: PSD PLOT FOR $\bar{U} = 1$.

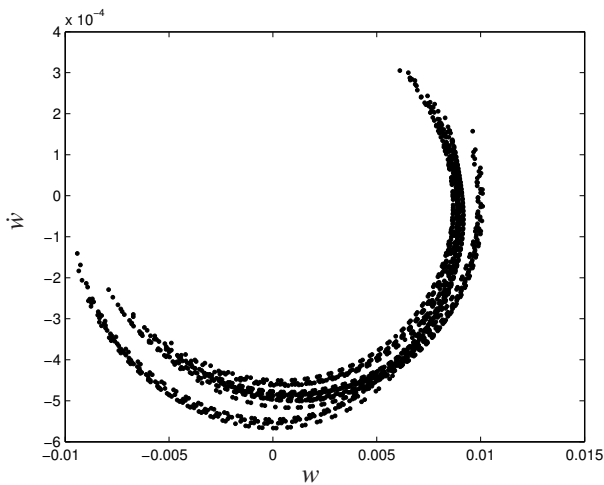


FIGURE 12: ONE-SIDED POINCARÉ MAP; \dot{w} VERSUS w AT POINT $(x = 1, \theta = \pi/3)$, AND $\bar{U} = 0.99$.

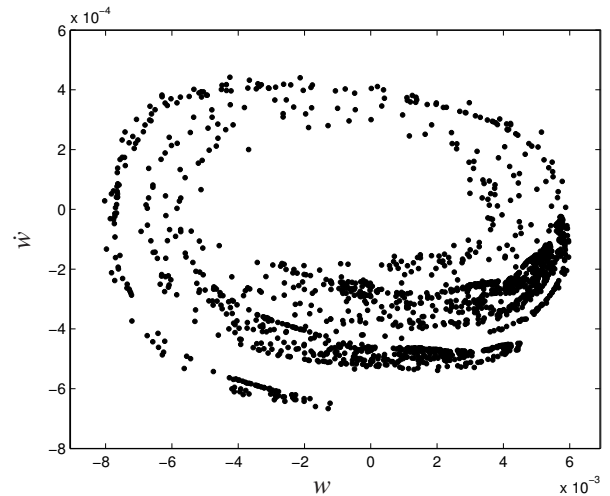


FIGURE 15: ONE-SIDED POINCARÉ MAP; \dot{w} VERSUS w AT POINT $(x = 1, \theta = \pi/3)$, AND $\bar{U} = 1$.

CONCLUSION

In this paper, for the first time, the nonlinear dynamics of a cantilevered shell conveying fluid is analysed. A theoretical nonlinear model is developed and its validity is established. In terms of the values of the critical flow velocity, a good agreement is observed between the nonlinear theory and the existing experimental data. The effect of parameters h/R and L/R on the value of the critical flow velocity obtained from the nonlinear model is studied.

It is shown that the system possesses rich dynamical behaviour in the post-instability regime. According to nonlinear theory, the system loses stability through a supercritical Hopf bifurcation. As the flow velocity is increased, the resulting family of limit cycles become larger in amplitude until they lose stability via a torus bifurcation. The resulting stable quasiperiodic orbits survive over a small range of \bar{U} ; then, they lose stability to strange chaotic attractors. Hence, the system undergoes a quasiperiodic route to chaos.

REFERENCES

- [1] Païdoussis, M. P., and Denise, J. P., 1972. "Flutter of thin cylindrical shells conveying fluid". *Journal of Sound and Vibration*, **20**, pp. 9–26.
- [2] Païdoussis, M. P., Nguyen, V. B., and Misra, A. K., 1991. "A theoretical study of the stability of cantilevered coaxial cylindrical shells conveying fluid". *Journal of Fluids and Structures*, **5**, pp. 127–164.
- [3] Shayo, L. K., and Ellen, C. H., 1978. "Theoretical studies of internal flow-induced instabilities of cantilever pipes". *Journal of Sound and Vibration*, **56**, pp. 463–474.
- [4] Païdoussis, M. P., 2004. *Fluid-Structure Interactions, Vol 2*. Elsevier Academic Press, London.
- [5] Nguyen, V. B., Païdoussis, M. P., and Misra, A. K., 1993. "An experimental study of the stability of cantilevered coaxial cylindrical shells conveying fluid". *Journal of Fluids and Structures*, **7**, pp. 913–930.
- [6] Nguyen, V. B., Païdoussis, M. P., and Misra, A. K., 1994. "A CFD-based model for the study of the stability of cantilevered coaxial cylindrical shells conveying viscous fluid". *Journal of Sound and Vibration*, **176**, pp. 105–125.
- [7] Amabili, M., Pellicano, F., and Païdoussis, M. P., 1999. "Non-linear dynamics and stability of circular cylindrical shells containing flowing fluid. Part I: Stability". *Journal of Sound and Vibration*, **225**, pp. 655 – 699.
- [8] Amabili, M., Pellicano, F., and Païdoussis, M. P.,

1999. "Non-linear dynamics and stability of circular cylindrical shells containing flowing fluid. Part II: Large-amplitude vibrations without flow". *Journal of Sound and Vibration*, **228**, pp. 1103 – 1124.

- [9] Karagiozis, K. N., Païdoussis, M. P., Amabili, M., and Misra, A. K., 2008. "Nonlinear stability of cylindrical shells subjected to axial flow: Theory and experiments". *Journal of Sound and Vibration*, **309**, pp. 637–676.
- [10] Amabili, M., 2008. *Nonlinear Vibrations and Stability of Shells and Plates*. Cambridge University Press, Cambridge.
- [11] Païdoussis, M. P., 1998. *Fluid-Structure Interactions, Vol 1: Slender Structures and Axial Flow*. Academic Press, London.
- [12] Leissa, A. W., 1973. *Vibration of Shells*. NASA.
- [13] Wolfram Research, I., 2008. *Mathematica*, version 7.0 ed. Wolfram Research, Inc., Champaign, Illinois.
- [14] Doedel, E. J., Champneys, A. R., Fairgrieve, T. F., Kuznetsov, Y. A., Sandstede, B., and Wang, X., 1997. "Auto97 continuation software".

Appendix A: Additional expressions

$$\begin{aligned}
 L_{3S}(\mathbf{u}) &= \partial_{x,x} M_x + \partial_{x,y} (M_{xy} + M_{yx}) + \partial_{y,y} M_y \\
 &\quad + \partial_x \left(N_x \partial_x w + N_{xy} \left(\partial_y w + \frac{v}{R} \right) \right) \\
 &\quad + \partial_y \left(N_{xy} \partial_x w + N_y \left(\partial_y w + \frac{v}{R} \right) - \frac{M_y}{R} \left(\frac{v}{R} + \partial_y w \right) \right) \\
 &\quad + \frac{N_y}{R} \left(1 + \partial_y v - \frac{w}{R} \right) + \frac{N_{xy} \partial_x v}{R} + \frac{M_y}{R^2} \left(\frac{w}{R} - \partial_y v \right) \\
 &\quad - \rho h \partial_{t,t} w - ch \partial_t w,
 \end{aligned}$$

$$L_{3F}(\mathbf{u}) = p(\mathbf{u}, r)|_{r=R},$$

$$R_3(\mathbf{u}) = \partial_x M_x + \partial_y (M_{xy} + M_{yx}) + N_x \partial_x w + N_{xy} \left(\partial_y w + \frac{V}{R} \right), \quad (13)$$

where N_x , M_x , etc. are stress resultants and stress couples, respectively; $p(\mathbf{u}, r)$ is the fluid perturbation pressure. The operators $\partial_{x,y}$, ∂_x , and ∂_y denote the partial derivatives $\partial(\cdot)/\partial x \partial y$, $\partial(\cdot)/\partial x$, and $\partial(\cdot)/\partial y$, respectively.



STIFFENING OF A FUEL ASSEMBLY UNDER AXIAL FLOW

Guillaume Ricciardi

Eric Boccaccio

DEN/DTN/STRI/LHC, CEA CADARACHE
13108, Saint-Paul-Lez-Durance Cedex, France
Email : guillaume.ricciardi@cea.fr

ABSTRACT

Nuclear industry needs tools to design reactor cores in case of earthquake. Models simulating the response of the core to a seismic excitation have been developed. Full scale tests considering one fuel assembly are performed to identify coefficients (added mass and damping) that will be used as inputs in the models. Tests showed that the axial water flow induced an added stiffness. In the paper, an expression of the fluid force responsible for the added stiffness is proposed. Numerical simulations are compared to experiments and showed good agreement.

INTRODUCTION

Earthquakes can irreversibly damage nuclear power plants especially in the core, where the fuel assemblies containing enriched uranium have to be particularly resistant. Before building a nuclear power plant, it is necessary to make sure that the core will resist the worst possible earthquake conditions liable to occur at the site. Therefore when Pressurized Water Reactors (PWR) are subjected to seismic loading, the spacer grids strike each other, and safety measures are required to prevent the spacer grids from buckling. Engineers need special tools for designing and maintaining reactor cores.

The core made of fuel assemblies is subjected to an axial water flow to cool the reactor. The flow strongly modifies the dynamical behaviour of the fuel assemblies by damping and added mass effect. Most of the models developed for industrial purpose account for the added mass and damping induced by the axial flow, and need to identify the related coefficients [1]. Therefore, experiments on full scale fuel assemblies need to be performed. The LHC (Laboratory of Core and Circuit Hydrodynamics) has facilities to perform dynamical tests on a fuel assembly under axial flow. The displacement of one grid of the fuel assembly is imposed by a hydraulic jack with a force sensor, and the displacements of the other grids are measured. LDV measurements are also performed to give a description of the flow distribution in

the fuel assembly. The flow conditions are close to those of a PWR.

The tests give access to dynamical characteristics of the fuel assembly in air, in still water and under various flow rates between 0 and 5 m/s. Results show that the flow induced damping increases with the flow rate. An added mass effect is also observed. First observations seem to testify that added mass depends on the flow rate, which is counterintuitive and moreover contradict the knowledge available about added mass effect [2]. It is also observed that the stiffness increases with the flow rate. The stiffening can be explained by the by-pass at each side of the fuel assembly. In these by-passes the flow velocity increases depending on the displacement of the fuel assembly and generates extra fluid forces.

In this paper authors propose to analyse the experimental results by comparisons with numerical simulations. A model is proposed to account for the induced stiffening. Simulations and experimental results are compared.

EXPERIMENTAL APPARATUS

HERMES T loop

HERMES T is a one phase hydraulic loop that can handle one or two full scale PWR fuel assemblies. The pump can debit 1200 m³/h in axial flow and 400 m³/h in cross-flow, at 35 bar and 170°C. Therefore, the flow rate is similar to the PWR condition, the lower temperature (PWR operates at 315°C) allows to provide accurate measurement devices to the test section. In the present study one fuel assembly is considered under axial flow at 50°C.

Test section

The test section is 40 mm larger than the fuel assembly in the excitation direction and 10 mm larger in the orthogonal direction (Fig. 1). Grids of the fuel assembly are around 200 mm width. The displacement of the fifth grid is imposed with a hydraulic jack, a force

sensor between the fuel assembly and the hydraulic jack gives the force applied to the fifth grid. A plexiglass window allows to make optical fluid measurements. The grids displacements are measured with LVDT sensors.

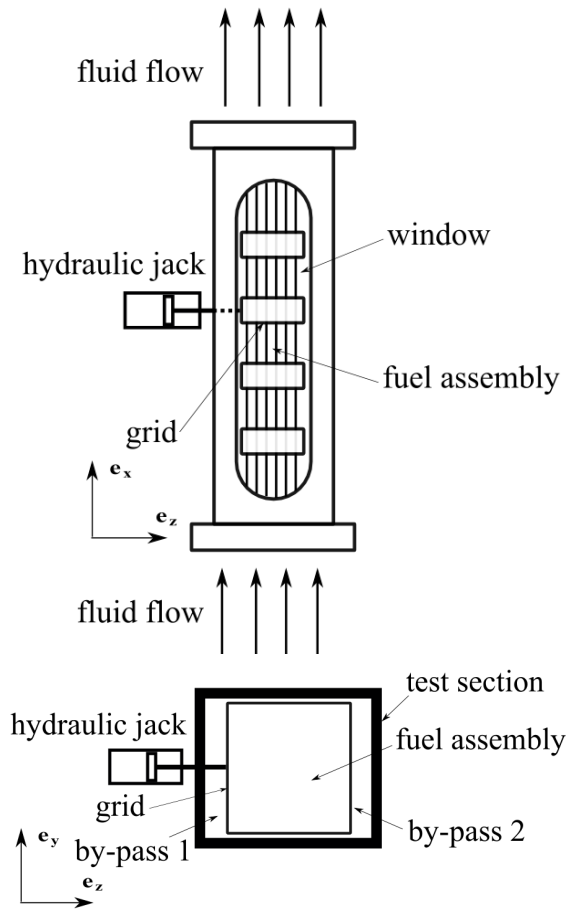


FIGURE 1 : TEST SECTION

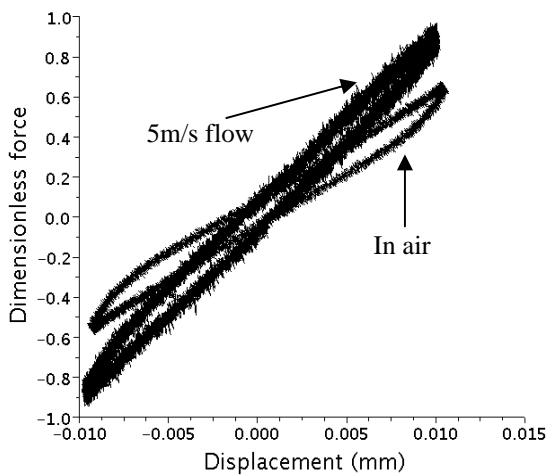


FIGURE 2 : QUASI-STATIC TESTS

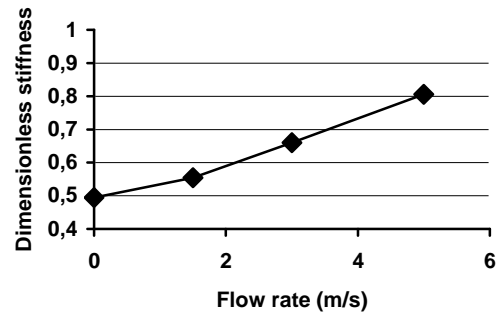


FIGURE 3 : STIFFNESS IDENTIFIED FROM QUASI-STATIC TESTS FOR VARIOUS FLOW CONDITIONS

Experiments

Quasi-static tests and dynamic tests are carried out. For dynamic tests the movement imposed on the fifth grid is a swept sine ranging from 0Hz to 2,5Hz. The fuel assembly resonant frequency is located at around 2Hz. The displacement amplitude reaches 10 mm. Tests are performed in air, in still water, and under axial flow for three flow rates (1,5 m/s, 3m/s and 5m/s).

RESULTS

For confidential reasons most of the results are given dimensionless.

Quasi-static tests

Figure 2 shows the force applied to the fifth grid versus its displacement for quasi-static tests. Tests in air show a hysteretic behaviour due to friction between the rods and the grids cells. One can observe that the stiffness increases with the flow rate (Fig. 3).

Dynamic tests

Figure 4 shows the modulus and the phase of the transfer function H between the fifth grid displacement and the force applied by the jack:

$$H = \frac{FFT(displacement)}{FFT(force)}, \tag{1}$$

where FFT is for Fast Fourier Transform.

As the quasi-static tests, the dynamic tests show that the stiffness increases with the flow rate. One can also observe the added mass effect due to the fluid, and that the damping increases with the flow rate. These are well known classical results already observed [2].

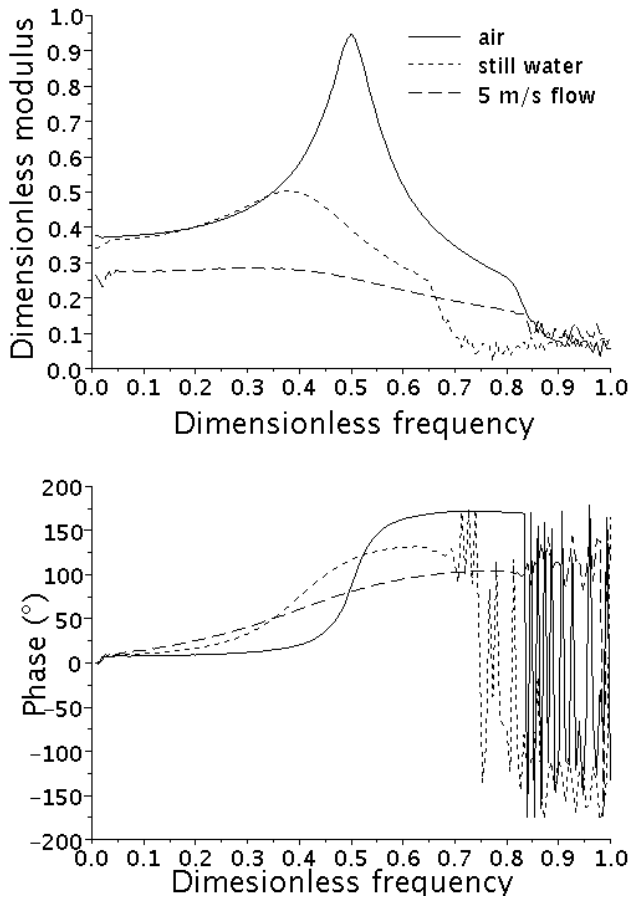


FIGURE 4 : MODULUS AND PHASE OF THE TRANSFER FUNCTION H, IN AIR, IN STILL WATER AND UNDER 5M/S AXIAL FLOW

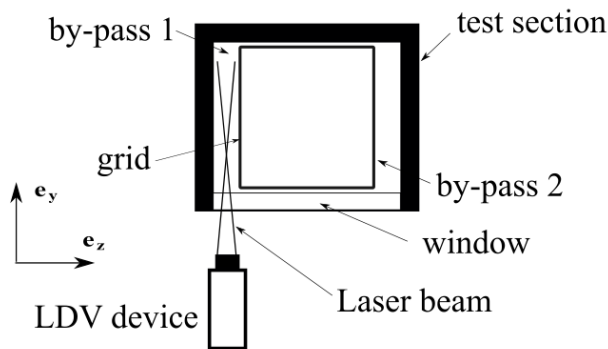


FIGURE 5 : FLOW MEASUREMENT

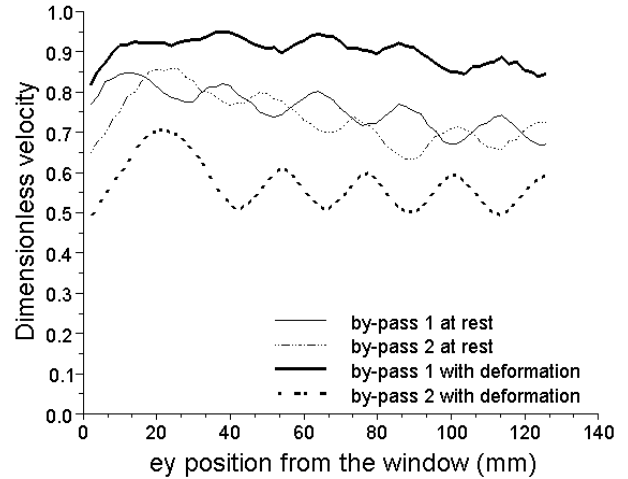


FIGURE 6 : LDV FLOW MEASUREMENTS IN THE BY-PASSES FOR TWO POSITIONS OF THE FUEL ASSEMBLY

Flow measurements

A Laser Doppler Velocimetry (LDV) device allows use to make fluid velocity measurements in the by-passes (Fig. 5). Flow measurements are performed for two positions of the fuel assembly; centred at rest and with a displacement of 10 mm of the fifth grid. In each position the fuel assembly is maintained still under axial flow. Measurements give the mean value of the fluid velocity in the x direction.

At rest, the test section is symmetric; the by-passes have the same size, and the flow rate is the same (Fig. 6). When a deformation is imposed to the fuel assembly, the by-passes have no more the same size and the flow rates change. The size of the by-pass 1 increases and so does the flow rate, whereas in the by pass 2 the flow rate decreases since it is smaller.

PARAMETERS IDENTIFICATION AND DISCUSSION

Stiffness k , damping c and mass m are identified by fitting a linear one degree of freedom dynamical system to the experimental transfer function. By comparing in air, in still water and under axial flow identified parameters, one can have access to the added mass and damping. These coefficients will be used as inputs in codes to simulate the response of a PWR core to a seismic excitation.

The damping seems to increase linearly as the flow rate increases (Fig. 7) this result was expected [3] On the other hand the mass seems also to increase with the flow rate, this result was unexpected. The mass should increase with the presence of fluid but it should not depend on the flow rate [4]. To the authors knowledge this has never been observed.

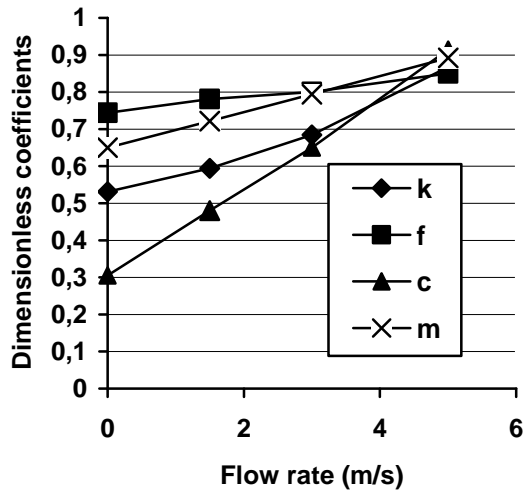


FIGURE 7 : NATURAL FREQUENCY, MASS, DAMPING AND STIFFNESS IDENTIFIED FROM DYNAMICAL TESTS.

The mass shows almost the same evolution than the stiffness. In the identification process the mass is given by the formula:

$$m = \frac{k}{4\pi^2 f^2}, \quad (2)$$

where f , is the natural frequency. Since the frequency does not depend on the flow rate, the mass is proportional to the stiffness.

The added stiffness is due to the difference of fluid velocity in the by-passes when a displacement is imposed to the fuel assembly (Fig. 6). The deformation of the fuel assembly modifies the hydraulic diameter of the by-passes, when the size of the by-pass increases the fluid velocity increases. Thus the difference of velocity induces a difference of pressure. The resulting pressure force depends on the fuel assembly displacement. This force tends to pull the fuel assembly back to its initial position, and can be seen as an added stiffness.

The velocity difference in the by-passes is a steady state flow that takes a certain time to establish. Let us note τ the duration of the transient flow. If τ is negligible compared to the oscillating period as in quasi-static tests the resulting force are in phase with the fuel assembly displacement and may be seen as an added stiffness. On the other hand if τ is not negligible compared to the oscillating period the resulting force will be delayed compared to the fuel assembly displacement. In the latter case the resulting force may not be consider as an added stiffness. Therefore, the added stiffness may depend on the oscillating frequency. In the parameter identification it

is assumed that the stiffness is constant over the broad band excitation. The consequence of it would be that the identification of the mass is wrong.

Nevertheless these assumptions need to be verified by measuring or simulating the delay between the fuel assembly displacement and the oscillations of the fluid in the by-passes.

MODELLING OF ADDED STIFFNESS

In this section we propose to give an expression for the added stiffness.

Fluid force

Let us consider the fluid velocities (Fig. 8); V_1 in the by-pass number 1, V_2 in the by-pass number 2 and V_{fa} in the fuel assembly. The linear fluid force is the consequence of a difference of pressure P_1 and P_2 in the by-passes:

$$dF = (P_1 - P_2)dS, \quad (3)$$

where dS is the fuel assembly surface over which the force is applied. Pressures can be related to fluid velocities by the Bernoulli's principle:

$$\frac{V_1^2}{2} + \frac{P_1}{\rho} = \frac{V_2^2}{2} + \frac{P_2}{\rho}. \quad (4)$$

By replacing Eqn. (4) in Eqn. (3), we can give an expression for the fluid force depending on the velocities in the by-passes:

$$dF = 2\rho(V_2^2 - V_1^2)dS. \quad (5)$$

It is now needed to give the velocities as an expression of the fuel assembly displacement.

Pressure drop

The pressure drop ΔP in the test section can be given by the empirical expressions:

$$\Delta P = \lambda_1 \rho \frac{V_1^2}{2} \frac{L}{D_1}, \quad (6)$$

$$\Delta P = \lambda_2 \rho \frac{V_2^2}{2} \frac{L}{D_2}, \quad (7)$$

$$\Delta P = \lambda_{fa} \rho \frac{V_{fa}^2}{2} \frac{L}{D_{fa}}, \quad (8)$$

where L is the length over which the pressure drops, D_1 , D_2 and D_{fa} are respectively the hydraulic diameters of the

by-pass number 1 and 2, and of the flow section in the fuel assembly, λ_1 , λ_2 and λ_{fa} are respectively the Darcy friction factor of the by-pass number 1 and 2, and of the flow section in the fuel assembly.

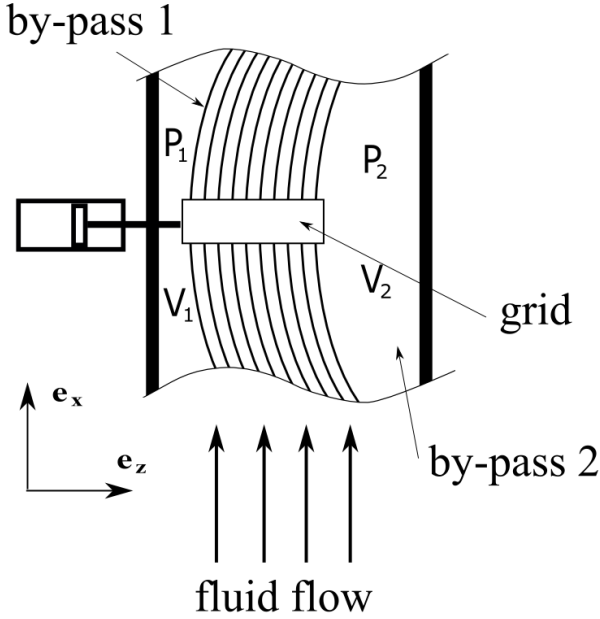


FIGURE 8: VELOCITY AND PRESSURE DEFINITION.

We assume that Darcy friction factors are equals:

$$\lambda = \lambda_1 = \lambda_2 = \lambda_{fa}. \quad (9)$$

D_1 and D_2 depend on the fuel assembly displacement:

$$D_1 = \frac{4w_{fa}(w_g + u_{fa})}{2(w_{fa} + w_g + u_{fa})}, \quad (10)$$

$$D_2 = \frac{4w_{fa}(w_g - u_{fa})}{2(w_{fa} + w_g - u_{fa})}, \quad (11)$$

where w_{fa} is the fuel assembly width, w_g is the by-passes width when the fuel assembly is not deformed, and u_{fa} is the fuel assembly displacement. We make the assumption that w_g and u_{fa} are negligible compared to w_{fa} , which gives the simplifications:

$$D_1 = 2(w_g + u_{fa}), \quad (12)$$

$$D_2 = 2(w_g - u_{fa}), \quad (13)$$

Considering Eqn. (9) we note K defined by:

$$K = \frac{2\Delta P}{\lambda \rho L}, \quad (14)$$

thus Eqn. (6), Eqn. (7) and Eqn. (8) become :

$$\frac{V_1^2}{D_1} = K, \quad (15)$$

$$\frac{V_2^2}{D_2} = K, \quad (16)$$

$$\frac{V_{fa}^2}{D_{fa}} = K. \quad (17)$$

Introducing Eqn. (12) and Eqn. (13) in Eqn. (15) and Eqn. (16), and replacing it in Eqn. (5) give:

$$dF = -8\rho K u_{fa} dS. \quad (18)$$

We need to give an expression of K depending on input parameters.

Continuity equation

We note Q the flow in the test section, the continuity equation gives:

$$Q = V_1 S_1 + V_2 S_2 + V_{fa} S_{fa}, \quad (19)$$

where S_1 , S_2 and S_{fa} are the flow areas of the by-pass number 1 and 2, and in the fuel assembly.

Using Eqn. (15), Eqn. (16) and Eqn. (17) in Eqn. (19) give:

$$K = \frac{Q^2}{\left(\sqrt{D_{fa}} S_{fa} + \sqrt{D_1} S_1 + \sqrt{D_2} S_2\right)^2}. \quad (20)$$

After several mathematical operations K can be approximated by:

$$K = \frac{Q^2}{C_{fa1}} \left(1 - C_{fa2} u_{fa}^2\right), \quad (21)$$

where C_{fa1} and C_{fa2} are geometrical coefficients defined by:

$$C_{fa1} = \left(\sqrt{D_{fa}} S_{fa} + 2\sqrt{2} w_{fa} w_g^{3/2}\right)^2, \quad (22)$$

$$C_{fa2} = \frac{2\sqrt{2}w_{fa}w_g^{3/2}}{\sqrt{D_{fa}S_{fa} + 2\sqrt{2}w_{fa}w_g^{3/2}}w_g^2} \cdot 1 \quad (23)$$

Replacing Eqn. (21) in Eqn. (18) gives the final expression of the fluid force:

$$dF = -8\rho \frac{Q^2}{C_{fa1}} (1 - C_{fa2}u_{fa}^2) u_{fa} dS \quad (24)$$

The fluid force is opposed to the fuel assembly displacement; this confirms the experimental observations that it can be seen as an added stiffness. Moreover, this added stiffness is nonlinear and decreases as the displacement increases.

Delay

As explained in the discussion about experimental results we make the assumption that the fluid force is delayed of a time noted τ compared the fuel assembly displacement. Thus, it gives the expression:

$$dF(t) = \dots - 8\rho \frac{Q^2}{C_{fa1}} (1 - C_{fa2}u_{fa}^2(t-\tau)) u_{fa}(t-\tau) dS \quad (25)$$

COMPARISON EXPERIENCE THEORY

Ricciardi et al [1] proposed a modelling for the dynamical behaviour of fuel assemblies under axial flow. The modelling is based on a porous medium approach. The fluid-structure interaction force is based on theory of Paidoussis [2], and account for added mass effect and damping. Nevertheless, it does not reproduce the added stiffness effect observed in the present study.

We introduced the fluid force established in the previous section (Eqn. (25)) in the modelling developed by Ricciardi et al. [1]. For confidential reasons coefficients used in the simulations are not given.

The modelling reproduces the added mass effect and shows a good agreement with experiments in still water (Fig. 9). The damping in air is overestimated by the simulation.

The fluid force expression proposed in the present study reproduces the added stiffness effect. Quasi-static simulations are in good agreement with experiments (Fig. 10).

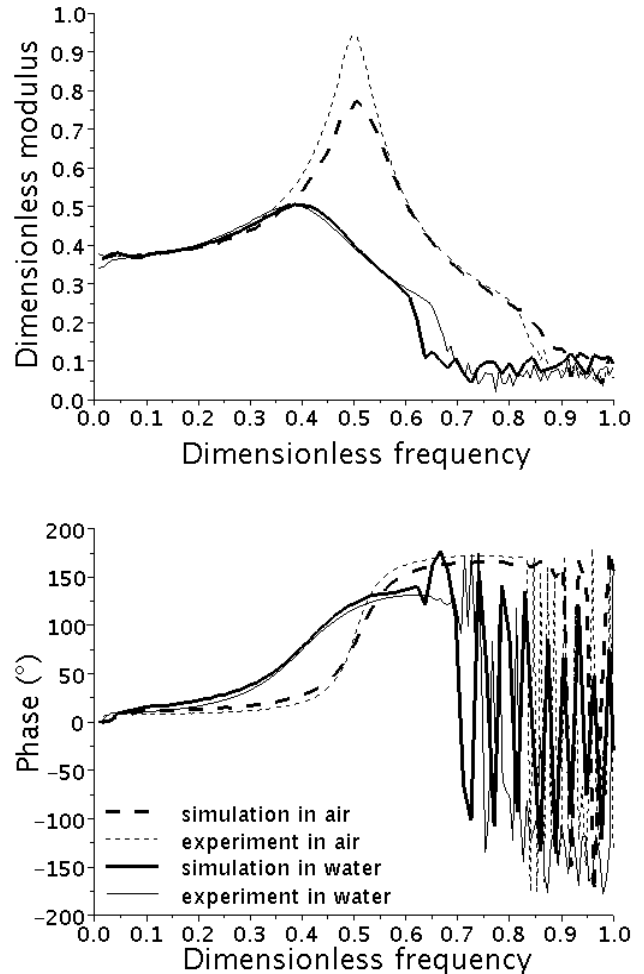


FIGURE 9: MODULUS AND PHASE OF THE TRANSFER FUNCTION H, IN AIR AND STILL WATER; COMPARISON EXPERIMENTAL DATA AND SIMULATIONS.

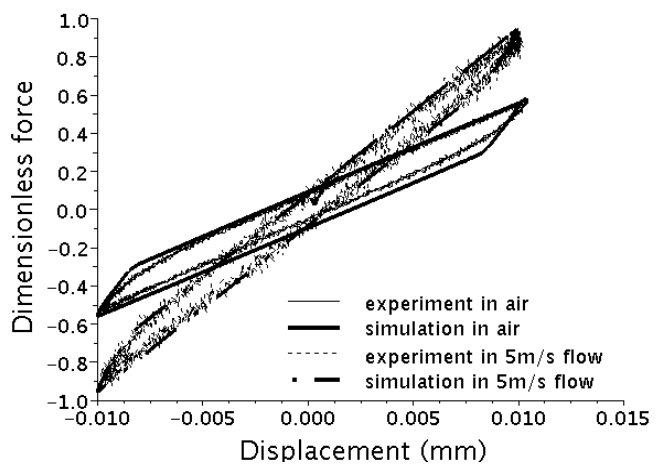


FIGURE 10 : QUASI-STATIC TESTS IN AIR AND UNDER 5M/S FLOW; COMPARISON EXPERIMENTS SIMULATIONS.

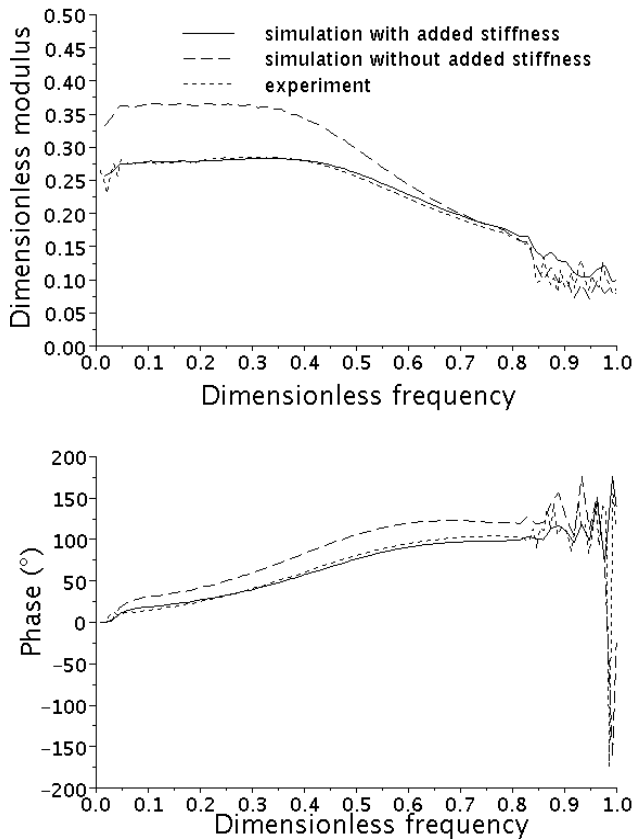


FIGURE 11 : MODULUS AND PHASE OF THE TRANSFER FUNCTION H , UNDER 5 M/S AXIAL FLOW; FOR EXPERIMENTAL DATA, SIMULATION WITH AND WITHOUT ADDED STIFFNESS MODELLING.

Figure 11 compares simulations with and without the modelling of added stiffness (Eqn. (25)). The classical Paidoussis model does not fit with experimental data. In the Paidoussis theory the flow is assumed to be homogeneous whereas in the present case, the flow rate increases at the boundaries of the structures and depends on the structure position. This is due to the narrow confinement of the fuel assembly.

The modelling is in good agreement with the experimental data. It reproduces well the added mass effect, damping in still water and under axial flow, and the added stiffness effects. Therefore, the theory seems to be confirmed by the fitting of simulations with experimental data. Nevertheless, the modelling is based on assumptions that need to be verified. It is assumed that there is a delay between the fuel assembly displacement and the fluid force; this could be verified by measuring the fluid velocity in the by-pass during dynamic tests. Moreover, the possibility for the fluid to cross the fuel assembly is not accounted for in the pressure drop consideration (Eqn. (6-8)), thus the real flow behaviour may be more complicated than what is assumed in the modelling.

CONCLUSION

The mechanical behaviour of a fuel assembly under axial flow has been investigated. Tests showed classical added mass and damping effects. An unexpected added stiffness under axial flow has been observed. An explanation has been proposed, and the modelling resulting was compared to experimental data. Simulations are in good agreement with experiments. Nevertheless, the modelling is based on assumptions that need to be verified by further measurements.

REFERENCES

- [1] G. Ricciardi, S. Bellizzi, B. Collard, B. Cochelin. Modelling Pressurized Water Reactor cores in terms of porous media. *Journal of Fluids and Structures*, Volume 25, Issue 1, January 2009, Pages 112-133
- [2] Paidoussis, M.P., 2003. *Fluid-Structure Interactions : Slender Structures and Axial Flow*, Vol 2. Elsevier Academic Press, London.
- [3] Pisapia, S., Collard, B., Bellizzi, S., Mori, V., 2003. Modal testing and identification of a PWR fuel assembly. In: Vejvoda, S. (Ed.), *Transactions of the 17th International Conference on Structural Mechanics in Reactor Technology (SMIRT 17)*, Prague, Czech Republic, Paper C01-4.
- [4] C. Conca, A. Osses, J. Planchard Added mass and damping in fluid-structure interaction. *Computer Methods in Applied Mechanics and Engineering*, 146 (1997), pp. 387–405.



STUDY ON PRESSURE PULSATION IN PUMP-PIPING SYSTEMS: ACOUSTIC INTERACTION BETWEEN PUMP AND PIPING

Akira Maekawa

maekawa@inss.co.jp

Takashi Tsuji

Institute of Nuclear Safety System, Inc.
64 Sata, Mihama-cho, Mikata-gun,
Fukui-pref, 919-1205 Japan
tsuji.takashi@inss.co.jp

Tsuneo Takahashi

takahashi.tsuneo@inss.co.jp

Minoru Kato

Kobelco Research Institute, Inc.
1-5-5 Takatsukadai, Nishi-ku,
Kobe, 651-2271 Japan,
kato.minoru@kki.kobelco.com

ABSTRACT

In this study, factors to improve the analysis accuracy of pressure pulsation behavior in pump-piping systems were examined. First, pressure pulsation behavior was measured using an experimental apparatus with a plunger pump – three-dimensional complex piping system to mock an actual plant. Next, the measured data were compared with numerical simulation results derived from two different kinds of input conditions in terms of pump discharge flow waveform. There were obvious differences between the simulation results using a discharge flow waveform assumed from pump specifications and the results using a discharge flow waveform modified assumed from the pressure pulsation measured at the pump outlet. This comparison indicates that an acoustic interaction between the pump and discharge piping dealing with liquid was caused for the experimental conditions of this study. Although such an acoustic interaction between the pump and discharge piping dealing with liquid can usually be ignored in analysis, an acoustic interaction was actually generated in the operation conditions of this study. Furthermore, the operation conditions to consider the acoustic interaction in the compressor-piping system dealing with gas, which were proposed in the literature, were judged to be applicable to the operation conditions of pump-piping systems dealing with liquid.

INTRODUCTION

Dynamic devices such as pumps and compressors are used in many fields such as electricity generating plants and industrial plants for such tasks as water intake or discharge. In piping systems including dynamic devices, large amplitude vibration on piping derived from pressure pulsation often leads to destruction of piping, leakage from the valves or flange portions, or failure of system

instruments such as meters. As a result, the large amplitude vibration occasionally affects the plant operation.

Reciprocating pumps and compressors cause periodic flow fluctuation due to intermittent fluid flow at pump suction or discharge associated with pump movement, and that leads to pressure pulsation. Centrifugal pumps and compressors cause periodic flow fluctuation due to movement of the blades and vanes of a diffuser, and that leads to pressure pulsation. When the frequencies of these pressure pulsations correspond to the natural frequencies or the liquid column resonance frequencies, large amplitude vibration of piping systems is caused.

In piping system design, it is fundamental that natural frequencies and liquid column resonance frequencies of piping system should not match frequencies by exciting forces such as pressure pulsation of the pumps or compressors.

In order to avoid large amplitude vibration of piping system, solutions preventing pressure pulsation behavior have been developed and methods for its prediction have been proposed. Several groups have proposed a method for evaluating pressure pulsation in piping considered acoustic interaction between reciprocating compressor and piping system dealing with gas [1]-[3]. Hayashi and Kaneko [4] proposed a practical method for analyzing pressure pulsation by assuming damping of all piping systems was a concentrated coefficient for the excitation part of a centrifugal compressor. Although the vibration property has been clarified experimentally and accuracy verification of analysis methods has been conducted, it is still important that analysis methods should be further improved to better reflect the plant operation.

Maekawa et al. [5] produced an actual-size three-dimensional complex apparatus and conducted a pressure pulsation experiment using water under severe conditions with mechanical resonance and liquid column resonance.

Their results provided some understanding of the pressure pulsation behavior and validated the accuracy of behavior reproduction by computational analysis. Almost the same group of authors has also considered the boundary condition of liquid column resonance [6] and the interaction between piping vibration and liquid column resonance [7], [8].

In this study, acoustic interaction between a pump and discharge piping dealing with liquid was investigated. The results of pressure pulsation behavior obtained using an experimental apparatus with reciprocating pump-three dimensional complex piping and the numerical simulation results of pressure pulsation behavior derived from two different kinds of input conditions were compared. One of the simulations adopts the discharge flow waveform assumed from pump specifications as the input condition, and the other adopts the discharge flow waveform assumed from pressure pulsation measured at the pump outlet as the input condition. In addition to comparing the results of the two simulations with experimental results from the present study, and the acoustic interaction between a pump and discharge piping is described.

Numerical simulation procedure

In this study, numerical simulations for pressure pulsation in piping were conducted using the method of characteristics. The method of characteristics estimates pressure and flow rate at different positions using the theoretical formula shown in Eq.(1). Pressure pulsation analysis was done using the Flowmaster code [9], which is a one-dimensional network thermal-hydraulic analysis application.

$$\lambda \frac{dH}{dt} + \frac{1}{gA} \frac{dQ}{dt} + \frac{f}{2gDA^2} Q|Q| - \frac{\lambda \sin \alpha}{A} Q = 0 \quad (1)$$

λ : undetermined coefficient

H : hydraulic head (m)

Q : flow quantity rate (m³/h)

D : pipe diameter (m)

A : pipe cross-sectional area (m²)

α : angle of inclination (radian)

f : friction coefficient

g : gravitational acceleration (m/s²)

t : time (s)

The analysis model was made using one-dimensional elements, and the piping configuration and elbow geometry were established in consideration of pressure loss. Pump rotation number and opening ratio of pressure control valve were set in accordance with experimental conditions. The pump discharge flow waveform, which was an input condition of the simulation analysis, was obtained by assuming two different types of conditions. Simulation results derived from these two types of pump

discharge flow waveforms were compared with experimental results.

At first, the pump discharge flow waveform which was made by using pump specifications such as cylinder configuration and crank radius is given. A discharge waveform is shown in Eq.(2). Numerical simulation was conducted using this discharge waveform.

$$\left. \begin{aligned} y &= \max(y_1, y_2, y_3) \\ y_1 &= A \omega r \left| \sin \theta + \frac{1}{2} \rho \sin 2\theta \right| \\ y_2 &= A \omega r \left| \sin \left(\theta + \frac{2}{3} \pi \right) + \frac{1}{2} \rho \sin 2 \left(\theta + \frac{2}{3} \pi \right) \right| \\ y_3 &= A \omega r \left| \sin \left(\theta + \frac{4}{3} \pi \right) + \frac{1}{2} \rho \sin 2 \left(\theta + \frac{4}{3} \pi \right) \right| \end{aligned} \right\} \quad (2)$$

y : pump discharge flow rate (m³/h)

y_1, y_2, y_3 : plunger-specific flow rate (m³/h)

A : cylinder cross sectional area (m²)

ω : crank shaft angular velocity (rad/s)

r : crank radius (m)

ρ : ratio of crank length to connecting rod length (m)

θ : phase (rad)

$y_1, y_2,$ and y_3 were discharge flow rates for each plunger, and their phases differed by 120 deg from each other. The pump discharge flow waveform consisted of three plunger-specific flows. Since a part of the plunger-specific flow returned to the cylinder, the pump discharge flow waveform did not adopt the sum of the quantity of each plunger; rather it adopted the largest quantity of each plunger at each time. The cylinder configuration inside the pump structure was modeled with the same configuration of piping. In this analysis, the open-closed status of the pump discharge valve was not modeled. So, acoustic interaction between the pump and discharge piping was not considered in this analysis model.

Next, the discharge flow waveform which was constructed from the pressure pulsation measured at the pump outlet is shown in Eq.(3).

$$y = F_1 + F_2 \cdot \sum_i^n a_i \cdot \sin 2\pi f_i (t - \phi_i) \quad (3)$$

y : pump discharge flow rate (m³/h)

F_1 : constant flow rate (m³/h)

F_2 : non-constant flow rate (m³/h)

a_i : ratio of amplitude in i-th harmonics

f_i ($f_i = i f_1$): frequency of i-th pulsation mode (Hz)

ϕ : phase (rad)

t : time (s)

F_1 was measured with a flowmeter at the tank inlet. The other parameters were obtained by pressure pulsation. F_2 which is the ratio of non-constant flow rate to constant flow rate was obtained as the ratio of the non-constant pressure rate to the constant pressure rate. A_i , f_i and φ were obtained by frequency analysis of pressure pulsation. Numerical simulation was done using this discharge waveform. Acoustic resonance between the pump and discharge piping was considered to be taken into account in the analysis.

Experimental procedure

The pressure pulsation experiment was conducted using the three-dimensional complex piping system (total length, about 40m) in order to mock the pressure pulsation of a piping system in an actual plant. A photograph and schematic diagram of the experimental apparatus are shown in Figs.(1) and(2), respectively. The apparatus consisted of a three-cylinder plunger pump, tank, piping and pressure control valve. Table 1 shows the major pump specifications. The piping was made of type 304 stainless steel, with an outside diameter of 27.2mm and wall thickness of 2.9mm. The pressure pulsation was measured at 10 positions (P1 to P10 in Fig. 2). The internal fluid was water which had been sufficiently degassed.

The opening ratio of the pressure control valve installed at the tank inlet was adjusted so that the pressure at the end of the piping system would be 1MPa at the pump rotation number of 150rpm. The pressure control valve was also used as a relief valve. The boundary condition of liquid column resonance at the pump was closed, and the boundary condition at the end of piping system was open since there was a tank there and the opening ratio of the pressure control valve was sufficiently large. Response of pressure pulsation was measured by varying flow rate as pump rotation numbers of 150rpm, 342rpm, and 450rpm.



Fig.1 Photograph of experimental apparatus

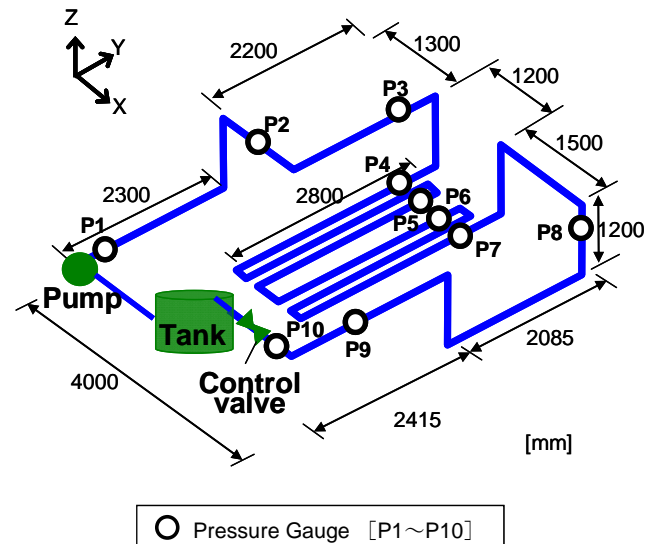


Fig.2 Diagram of experimental apparatus

Table 1 Pump specifications

Item	Specification
Number of cylinders	3
Rotation speed (rpm)	75-460
Discharge flow rate (L/min)	24.3-149.0
Discharge pressure (MPa)	1-3

Experimental results

When the boundary condition of the pump outlet and tank inlet is respectively "closed" and "open", frequency of liquid column resonance caused by pressure pulsation could be estimated by the following theoretical formula. Acoustic velocity was 1300m/s which was determined from the average value of pressure pulsation measured by pressure gauges shown in Fig.2.

$$f_0 = (c/4L) \cdot (2n-1) \quad (n=1,2,3,4) \quad (4)$$

f_0 : frequency of liquid column resonance (Hz)

c : acoustic velocity (m/s)

L : piping length (m)

n : order

Table 2 lists theoretical frequencies obtained by Eq.(4) and measured experimental frequencies. The measured frequencies are 7.75Hz for the first order mode at 150rpm, 23.0Hz for the first order at 450rpm and 45.75Hz for the second order at 450rpm which almost correspond to the theoretical frequencies for the first, second and third orders of 8.4Hz, 25.3Hz and 42.2Hz.

So the condition of liquid column resonance is occurring when the pump rotation speed was 150rpm and 450rpm.

Table 2 Theoretical and measured frequencies

		Theoretical (closed-open) [Hz]	Measured [Hz]		
			150	342	450
Pump rotation speed (rpm)		—	150	342	450
Order mode	1	8.4	7.75	17.25	23.00
	2	25.3	15.75	34.50	45.75
	3	42.2	23.50	51.75	68.75
	4	59.1	31.50	69.00	91.75

Comparison of experiment and simulation

At first, the pressure pulsation obtained by the simulation analysis which used the discharge flow waveform assumed as Eq. (2) (based on the pump specifications) was compared with the experimentally measured pressure pulsation.

Fig.3 plots the constant pressure comparison of results and Fig.4 plots the fluctuating pressure comparison of results. Fig.3 shows that constant pressure decreases as the distance from pump outlet is longer, and the simulation results are in close correspondence to the experimental results. Fig.4 shows the distribution of all pressure pulsations along the piping axis direction. Despite the difference in pump rotation speeds, the simulation results correspond well to the experimental results in terms of the mode shape such as the node and anti-node positions. But when the pump rotation speed was 450rpm, the simulation results do not correspond to the experimental results in terms of the amplitude of pressure. The simulated amplitude of pressure is larger than from the experiment when the pump rotation speed was 450rpm. Figs.5, 6, and 7 compare experimental and simulation results of Fig.4 using modal analysis. Figs.5, 6, and 7 show good agreement between the experimental and simulation results in terms of the mode shape. But at the pump speed of 450rpm, for the first order, there is a large difference between simulation and experiment in terms of amplitude of pressure. Therefore, the analysis method cannot duplicate the experiment sufficiently using the discharge flow waveform assumed as Eq. (2).

Next, pressure pulsation obtained by the simulation analysis which used the discharge flow waveform assumed as Eq. (3) (based on the pressure pulsation measured at the pump outlet) was compared with the experimentally measured pressure pulsation.

Fig.8 plots the comparison of constant pressure results and shows that the simulation results almost correspond to the experimental results. Fig.9 plots the comparison of fluctuating pressure results and shows that good agreement in terms of both mode shape and amplitude of pressure. Figs.10, 11, and 12 compare experimental and simulation results of Fig.9 using modal analysis. All of the simulation results reasonably correspond to the experimental results in terms of both mode shape and amplitude of pressure. Therefore, the analysis method can duplicate the experiment using discharge flow waveform assumed as Eq. (3).

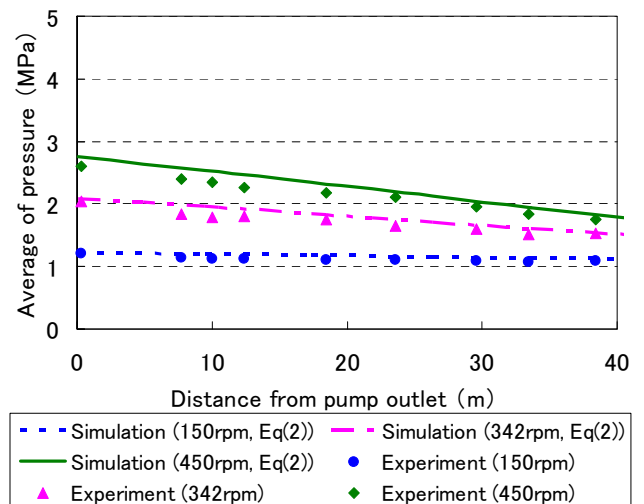


Fig.3 Comparison of constant pressure (Eq.(2))

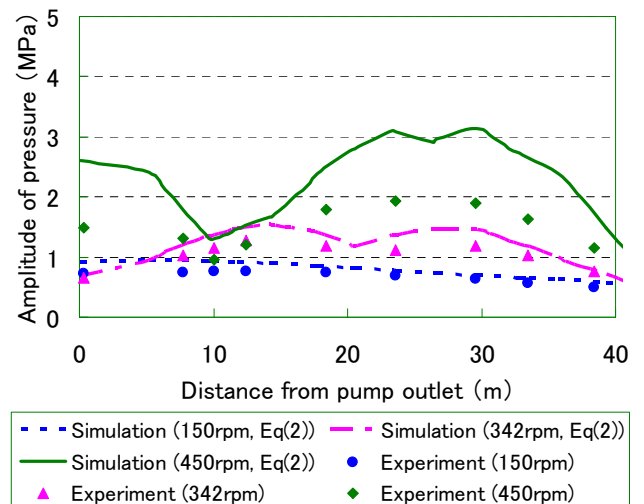


Fig.4 Comparison of amplitude of pressure(Eq.(2))

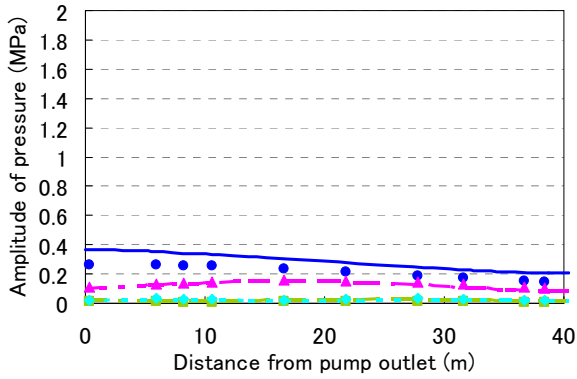


Fig.5 Comparison of mode analysis (Eq.(2))
(Pump rotation speed: 150rpm)

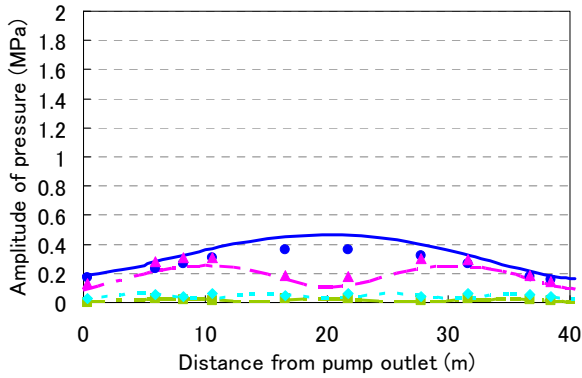


Fig.6 comparison of mode analysis (Eq.(2))
(Pump rotation speed: 342rpm)

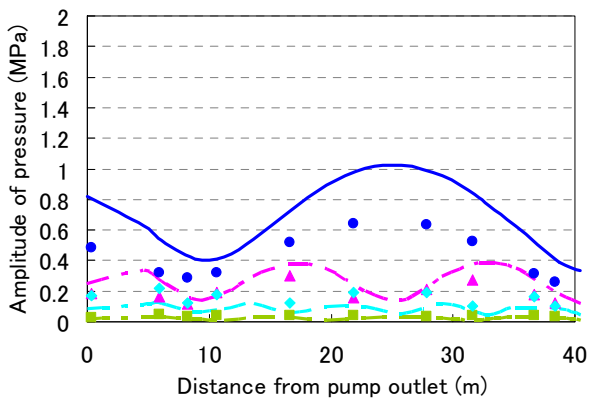


Fig.7 comparison of mode analysis (Eq.(2))
(Pump rotation speed: 450rpm)

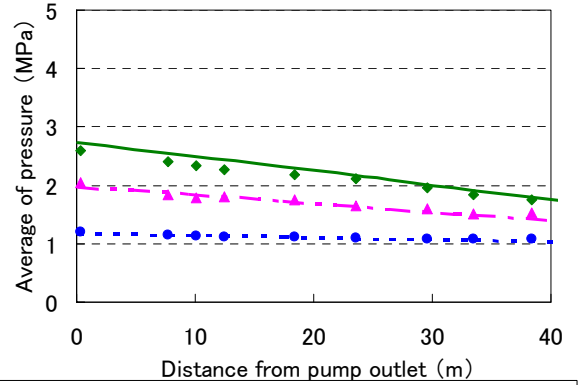


Fig.8 Comparison of constant pressure (Eq.(3))

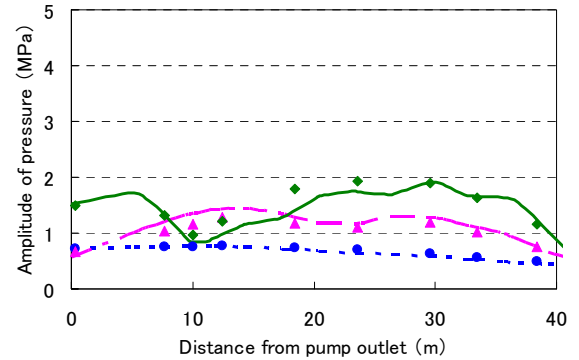


Fig.9 Comparison of amplitude of pressure (Eq.(3))

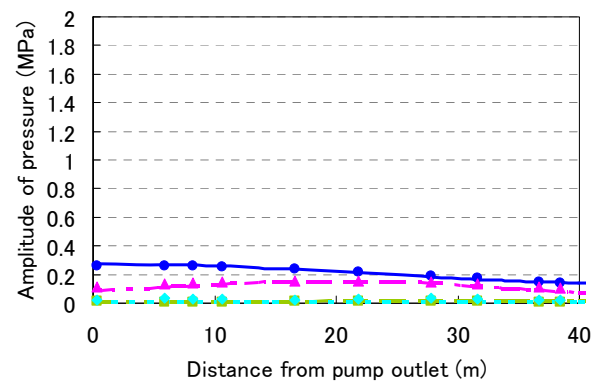


Fig.10 comparison of mode analysis (Eq.(3))
(pump rotation speed: 150rpm)

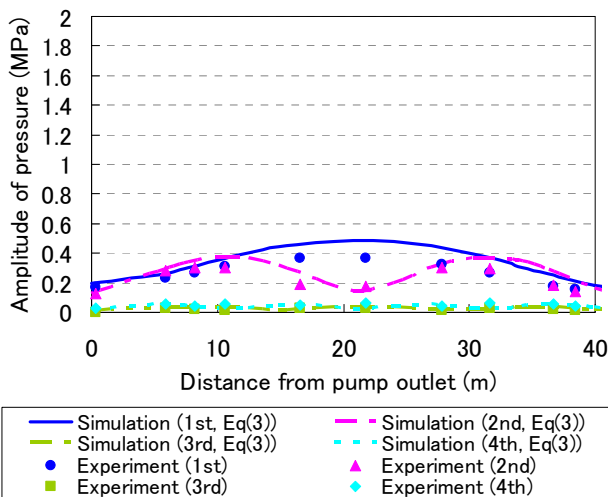


Fig.11 Comparison of mode analysis (Eq.(3)) (pump rotation speed: 342rpm)

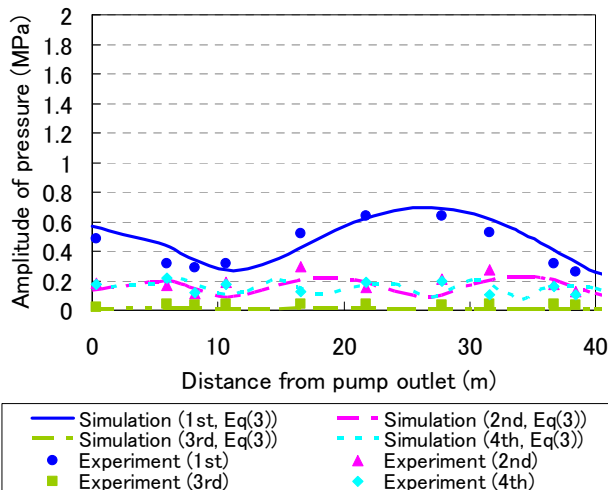


Fig.12 Comparison of mode analysis (Eq.(3)) (pump rotation speed: 450rpm)

Consideration

Pressure pulsation obtained by the analysis using the discharge flow waveform constructed by Eq. (2) (based on the pump specifications) differed from the measured values at the high pump rotation speed. Pressure pulsation obtained by the analysis using the discharge flow waveform by Eq. (3) (based on the pressure pulsation measured at the pump outlet) closely corresponded to the measured values. In this way, it was possible to improve the accuracy of analysis by using the measured pressure pulsation waveform and modifying the pump discharge flow waveform. From this result, it was judged that acoustic resonance occurred between the reciprocating pump and the discharge piping and impedance of the piping system was changed for the experimental apparatus with the experimental conditions of this study. Generally,

pump discharge (suction) flow dealing with a liquid is said not to be influenced by pressure pulsation of the piping side and open-closed status of the pump discharge valve is independent from fluid flow in the piping. But this result indicated that acoustic resonance could occur depending on the operation conditions.

Figs.13 and show the relationship between the ratio of the pressure amplitude to the flow and frequency obtained by frequency analysis of the time history of the pressure waveform at position P10 in Fig.2. Fig.13 shows the results at pump rotation speed of 342rpm and Fig.14 shows them at 450rpm. For the results at 342rpm, system impedance obtained by the analysis result based on Eq.(2) was estimated to be a little larger than that based on Eq. (3) at the first order mode of pressure pulsation. There was little difference in the simulation results between Eq.(2) and Eq.(3) at the higher harmonics. Therefore, the analysis result of Eq.(2) almost corresponded to the result of Eq.(3) as a whole. For the results at 450rpm, system impedance obtained by simulation results based on Eq. (2) was estimated to be larger than that based on Eq. (3) at the first and second order modes of pressure pulsation which had a larger amplitude of pressure pulsation in the case of using the pump discharge flow waveform assumed as pump specifications.

Thus, the first order of impedance was remarkably influenced by considering acoustic interaction.

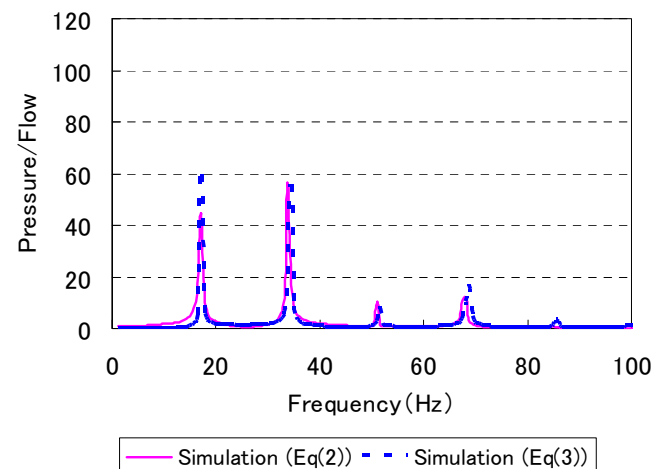


Fig.13 Relation between ratio of pressure amplitude to flow and frequency (pump rotation: 342rpm)

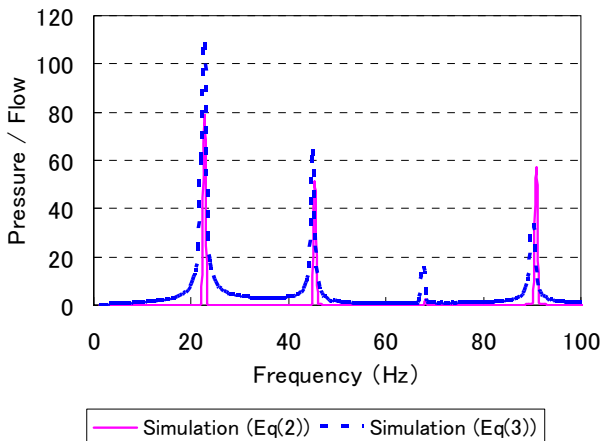


Fig.14 Relation between ratio of pressure amplitude to flow and frequency (pump rotation: 450rpm)

Fujikawa [10] and Kato et al. [11] proposed operation conditions of a compressor-piping system in the case of causing acoustic interaction between a reciprocating compressor and a piping system dealing with gas. They [10],[11] proposed five operation conditions which caused acoustic interaction. Their proposed conditions and the conditions of this study in which acoustic resonance was caused are listed in Table 3. The operation conditions of this study which caused acoustic interaction are almost satisfied as the operation conditions shown by Fujikawa [10] and Kato et al. [11].

This result indicated that pressure pulsation of the pump-piping systems dealing with liquid incidentally caused acoustic interaction and the occurrence of acoustic interaction depended on the operation condition. In order to improve analysis accuracy of pressure pulsation of pump-piping systems dealing with liquid, considering the acoustic interaction between the pump and discharge piping is required. Furthermore, the operation conditions to consider the acoustic interaction for compressor-piping systems dealing with gas, which were proposed to consider the acoustic interaction by Fujikawa and Kato et al., were found to be applicable to the operation conditions of pump-piping systems dealing with liquid.

Table 3 Comparison of the conditions by Fujikawa [10] and Kato et al. [11] (dealing with gas) and the conditions of this study (dealing with liquid)

Conditions by authors of [10] and [11] (dealing with gas)	Condition of this study at 450rpm (dealing with liquid)
Frequency of pressure pulsation: high	Frequency of pressure pulsation: higher due to high pump rotation speed
Pump rotation speed: high	Pump rotation speed: high (450rpm)
Boundary condition of acoustic resonance: closed at the pump side	Boundary condition of acoustic resonance: closed at the pump side
Pump size: large	Plunger pump size: medium
Constant part of pressure: low	Constant part of pressure: as low as 1.74 MPa

Conclusion

Compared with the pressure pulsation analysis which was carried out using the discharge flow waveform assumed from the pump specifications, the pressure pulsation analysis which was carried out using the discharge flow waveform assumed from the pressure pulsation measured at the pump outlet was in better agreement with measured values. Thus, since the discharge flow waveform of the pump was modified using the measured pressure pulsation, it was thought that acoustic interaction between the pump and discharge piping was caused.

Depending on the operation conditions, pressure pulsation of the pump-piping system dealing with liquid incidentally caused acoustic interaction in the same way as the system dealing with gas.

Furthermore, the operation conditions to consider the acoustic interaction for the compressor-piping system dealing with gas, which were proposed by Fujikawa and Kato et al., was judged to be applicable to the operation conditions of the pump-piping system dealing with liquid.

Acknowledgements

Sincere thanks are extended to Mr. Yuichi Torigoe and Mr. Takeo Sakakibara of Kobelco Research Institute, Inc. for their assistance in the pressure pulsation experiment.

References

- [1] Steyer, G. C. and Harvey, R., 1984, "Computer Simulation of a Reciprocating Compressor - Compressor / Valves / Piping Interaction," American Gas Association Operating Section, 84-DT-94, pp.546-551.
- [2] Matsuda, H. and Hayama, S., 1985, "A Method for Calculating the Pressure Pulsations Taking Dynamic Compressor-Piping Interaction into Consideration: Part 1 Formulation and Experiments in Simple Piping System," Bulletin of JSME, **28** (245), pp.2797-2714.
- [3] Kato, M., Inoue, Y., Fujikawa, T., and Aoshima, M., 1986, "A Digital Simulation Method of Pressure Pulsations in Reciprocating Compressor-Piping Systems," Proceeding of the International Conference on Vibration Problems in Engineering, pp.447-452.
- [4] Hayashi, I. and Kaneko, S., 2007, "Pressure Pulsations by a Centrifugal Compressor at Blade Passing Frequency," Proceedings of ASME PVP Conference, PVP2007-26212.
- [5] Maekawa, A., Takahashi, T., Tsuji, T., Noda, M., Kato, M. and Fujita, K., 2010, "Vibration Experiments and Numerical Simulations of Pulsation Behavior in Actual Size Mock-Up Piping," Proceedings of the ASME 3rd Joint US-European Fluids Engineering Summer Meeting and 8th International Conference on Nanochannels, Microchannels, and Minichannels, FEDSM-ICNMM2010-30280.
- [6] Maekawa, A., Takahashi, T., Tsuji, T., Noda, M., Kato, M. and Fujita, K., 2011, "Pressure Pulsation Behavior in Actual Size Mock-Up Piping System," Journal of System Design and Dynamics, **5** (4), pp.603-611.
- [7] Tsuji, T., Maekawa, A., Takahashi, T., Noda, M., Kato, M. and Fujita, K., 2011, "Experiment and Simulation on Pressure Pulsation Accompanied by Acoustic Resonance and Piping Vibration," Proceedings of the ASME 2011 Pressure Vessels and Piping Division Conference, PVP2011-57221.
- [8] Torigoe, Y., Sakakibara, T., Kojima, S., Hirooka, E., Kato, M., Tsuji, T. and Maekawa, A., 2012, "Experimental Study of Interaction between Pressure Pulsations and Piping Vibration," Proceedings of 10th International Conference on Flow-Induced Vibration.
- [9] Flowmaster Reference Help, 2002, Flowmaster, Ltd.
- [10] Fujikawa, T., 1991, A Digital Simulation of a Pulsation System Taking the Interaction between Reciprocating Compressor and Pipelines into Consideration, Transactions of the Japan Society of Mechanical Engineers, Series C, **57** (533), pp.148-153 (in Japanese)
- [11] Kato, M., Hirooka, E., Murai, K., Fujikawa, T., 1992, "Calculation Method for Pressure Pulsations Including Interaction between Reciprocating Compressors and Piping", Symposium on Flow-Induced Vibration and Noise, ASME Winter Annual Meeting, Vol.6, pp.237-244.



FLUID-STRUCTURE INTERACTION AT WATER HAMMER EVENTS IN PIPING SYSTEMS

Stefan Riedelmeier
Stefan Becker
Eberhard Schlücker

Institute of Process Machinery and Systems Engineering iPAT
 Friedrich-Alexander University of Erlangen-Nuremberg
 Cauerstr. 4, D-91058 Erlangen
 Email: rie@ipat.uni-erlangen.de

ABSTRACT

In order to examine the effects of fluid-structure interaction (fsi) in piping systems, a test facility was built at the University in Erlangen. The research objective is to identify the conditions under which fsi has to be taken into account for water hammer events.

Resonance experiments with movable bends in two piping system configurations were carried out. The displacement of the bend and the pressure inside the pipe were measured for various free oscillating lengths of the bend. The results were displayed in resonance curves and frequency spectra for the different configurations. In both a correlation between the pressure and the displacement spectrum showed a transfer of momentum from the fluid to the structure, but only in one configuration a reaction of the fluid onto the structural movement could be observed. Frequency shifts of the pressure outside the resonance area and a splitting of the pressure peak inside the resonance area were obvious.

NOMENCLATURE

DN	nominal diameter
H	pressure head
\mathbb{N}	natural numbers
PN	nominal pressure
c	water hammer propagation velocity
d_i	inner diameter
g	acceleration of free fall
f_f	fluid frequency
f_s	structural frequency
l	length of the piping system
n	mode number

p	pressure
p_{max}	maximum allowable pressure
x	displacement
x_{max}	mean maximum displacement

INTRODUCTION

Water hammer analysis is a fundamental part in the design process of piping systems. In most cases this calculation does not consider fluid-structure interaction (fsi). In the following fsi stands for a two-way interaction in contrast to an one-way interaction where there is only a load transmission from the fluid onto the structure. In the analysis of pipe oscillations the two-way fsi generally is not considered. There is no reaction from the fluid on the calculated results of the structure. If the piping system is rigidly anchored, the method is justified [1]. If not, the introduction of fsi can show an effect. As a consequence there could be changes in the amplitudes and the frequencies [2]. Fsi comprises three different coupling types. Poisson coupling is related to the radial movement of the pipe wall and causes a variation of the speed of sound in the fluid. This is often integrated in the calculation of the fluid system by considering the mentioned reduction of the propagation velocity. Friction coupling is a result of the wall shear stresses. The last type is called junction coupling and occurs at movable bends or tees etc. [3] [4]. The general opinion is that a consideration of fsi has either no influence or leads to lower loads [5]. So the calculation of a piping system without fsi is conservative. The general validity of this statement should be investigated in detail.

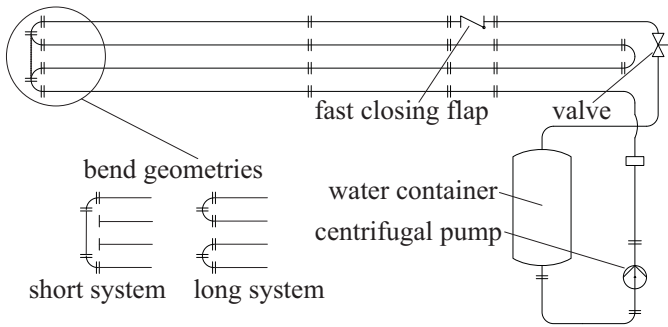


FIGURE 1: FLOW DIAGRAM OF THE TEST FACILITY

TEST FACILITY

The test facility consists of a piping system and measurement equipment.

Piping System

The piping system for water hammer experiments is sketched in Figure 1. It consists of a water container, a centrifugal pump, a fast closing flap and a valve to regulate the flow rate. The pressure level is PN 63 ($p_{max} = 63$ bar) and the diameter is DN 100 ($d_i = 106,3$ mm). For this investigation two different piping configurations have been used. In the short system the distance between the container and the flap is $l = 35$ m, in the long one the distance is $l = 63$ m. Along with the variation of the pipe length the frequency of the water hammer oscillation changes. The water container has a volume of 5 m³ (tap water). A frequency converter regulates the pump frequency, which allows to change the pressure level. The maximum pressure head is $H = 150$ m. The mean velocity in the piping system can be varied between 0 m/s and 4 m/s. The fast closing flap produces a water ham-



FIGURE 2: WATER HAMMER TEST FACILITY IN ERLANGEN

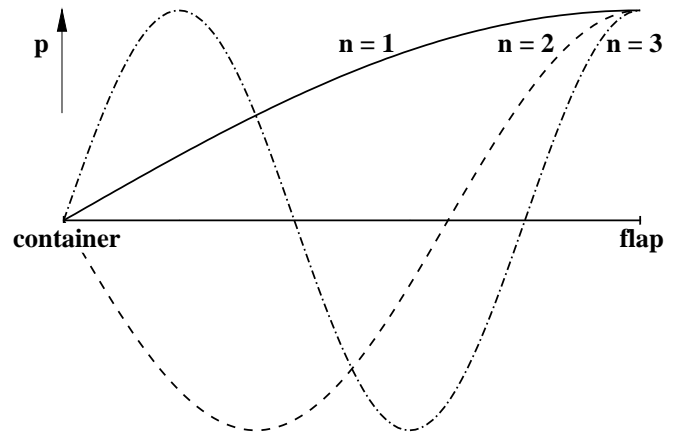


FIGURE 3: FIRST THREE EIGENMODES OF THE PIPING SYSTEM

mer. It is optimized for short closing times and therefore an inhouse construction.

In order to get an impression of the water hammer test facility, a picture is shown in Figure 2.

Hydraulic modes

The length of the piping system, the propagation velocity of the water hammer and the boundary conditions at both ends fix the fluid frequency. At the flap the velocity of the fluid is zero (hydraulically closed) and at the water container the pressure is constant (hydraulically open). With these boundary conditions the fluid frequency f_f is calculated by equation (1) where n defines the mode number, l is the length of the piping system and c is the propagation velocity of the water hammer which is lower than the speed of sound of the fluid due to the elasticity of the pipe wall.

$$f_f = (2n - 1) \cdot \frac{c}{4l} \quad , \quad n \in \mathbb{N} \quad (1)$$

The first eigenmodes of the piping system are sketched in Figure 3. For the calculation of the fluid frequencies of both configurations it is necessary to measure the propagation velocity of the water hammer because it is dependent on various parameters like temperature and solute gas. Previous investigations of water hammer at the depicted piping system identified a propagation velocity between 1276 m/s and 1325 m/s [6]. With given length of the piping system it is possible to calculate the frequencies of the first eigenmodes analytically (Table 1).

Measurements at the rigidly anchored system showed in both configurations that the base frequency of the water hammer oscillation ($n = 1$) is dominant (Figure 4). The

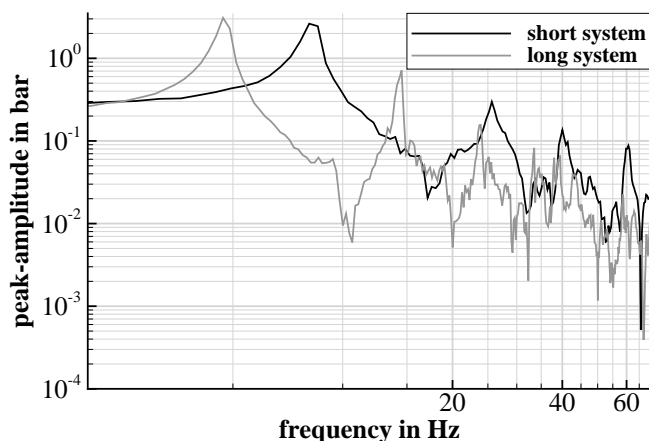
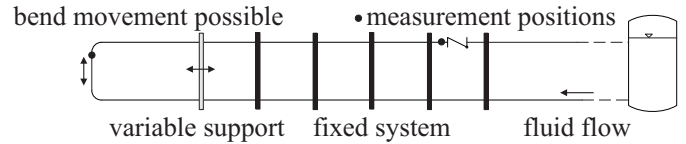
TABLE 1: FREQUENCIES OF THE EIGENMODES FOR BOTH CONFIGURATIONS

mode	short system	long system
$n = 1$	9.1 Hz - 9.5 Hz	5.1 Hz - 5.3 Hz
$n = 2$	27.3 Hz - 28.4 Hz	15.2 Hz - 15.8 Hz
$n = 3$	45.6 Hz - 47.3 Hz	25.3 Hz - 26.3 Hz
$n = 4$	63.8 Hz - 66.3 Hz	35.4 Hz - 36.8 Hz

excitation frequency of the short system is 8.3 Hz and of the long system 4.6 Hz. But also higher modes were excited. Comparing the analytically calculated frequencies with measured ones it is obvious that for the long system the frequencies fit well. For the short configuration differences in the frequencies occur.

Measurement Equipment

25 possible measuring positions are distributed over the whole piping system. In this investigation six sensors with a measurement range of 200 bar (Kistler type 4043A200) and one with a range of 10 bar (Kistler type 4045A10) were installed. The latter was used in the suction side of the pump. Additional piezocapacitive acceleration sensors measured the pipe vibration. There were six uniaxial sensors (Kistler type 8702B500M1T) and one triaxial sensor (Kistler type 8793A500). All of them have a measurement range of 500 g. A magnetic-inductive measurement system (Endres + Hauser Proline Promag 50W) determined the flow rate. The movement of a bend

**FIGURE 4: FREQUENCY SPECTRA OF THE PRESSURE SIGNAL IN FRONT OF THE FLAP FOR BOTH CONFIGURATIONS WHEN THE PIPING SYSTEM IS RIGIDLY ANCHORED****FIGURE 5: SUPPORT SYSTEM SHOWN AT THE BEND OF THE SHORT CONFIGURATION**

was measured by an inductive displacement transducer (HBM W10). Additionally rotary encoders (Leine Linde RSA 670/671 analog) were used for the determination of the rotation angles of the pump and the fast closing flap.

EXPERIMENTAL PROCEDURE

Water hammer experiments with oscillating bends were carried out. The water hammer was produced with the fast closing flap. The whole piping system was rigidly anchored with the exception of a single bend. The geometry of this bend depends on the system configuration (Figure 1). The piping system was excited by a water hammer at a mean velocity of 0.5 m/s. Due to the fixed length of the hydraulic system, the frequency of the pressure oscillation respectively the excitation frequency was kept constant. The support position of the movable bend and thus the natural frequency was varied (Figure 5). The displacement of the bend, the pressure as well as the acceleration at various positions were recorded. At each support position the measurement was repeated five times.

RESULTS

The results are divided into resonance curves, frequency spectra and time signals.

Resonance Curves

The resonance curves show at which support position the system is in resonance.

For the determination of the structural frequency f_s or rather the bend frequency a Fourier transformation of the displacement signal was performed. In Figure 6 the mean maximum displacement of the bend x_{max} is depicted over the structural frequency f_s . The results show that the resonance point of each system is at the excitation frequency of the water hammer. For high frequencies the displacement of the bend is low, towards the resonance point the displacement rises, reaches a maximum and afterwards decreases. This characteristic is similar to the forced oscillation of a single mass or the free oscillation of two coupled masses. The displacements of the bend of the short configuration are higher due to the higher ex-

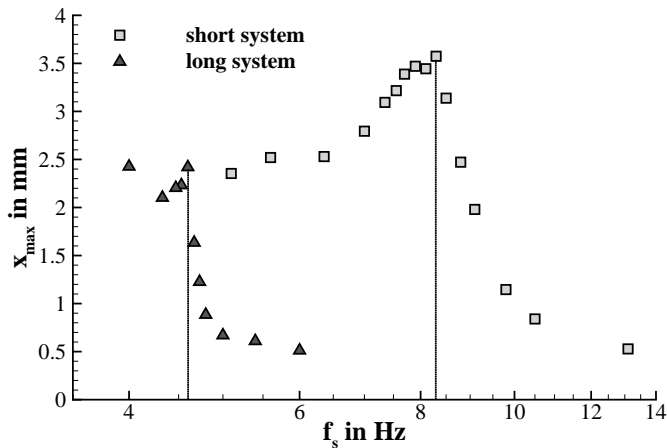


FIGURE 6: MEAN MAXIMUM DISPLACEMENT x_{max} OVER THE FREQUENCY OF THE STRUCTURE f_s FOR THE SHORT AND THE LONG CONFIGURATION

citation. Owing to the longer vertical pipe section of the bend of the short configuration the excitation force produced by the water hammer affects the bend longer but the amplitude of the force is the same in both configurations.

Frequency Spectra

In order to analyse the effects of fsi the signals were examined in the frequency domain.

For every support position a Fourier transformation of the pressure signal in front of the flap and of the displacement signal of the bend was performed. The spectra were averaged over the five repeated measurements. Additionally to the pictured spectra in the following graphs the frequency spectrum of the pressure in front of the flap for a rigidly anchored system is plotted as reference (*pressure reference*). This would be a result of an analysis without fsi respectively of an analysis with one-way interaction. For an oscillating bend differences in the pressure signal are expected because the movement of the pipe causes secondary pressure waves.

The diagrams in Figure 7 show the spectra for the short system for various support positions. The longer the free oscillating length of the bend respectively the more distant the support position the lower is the structural frequency of the bend. In the resonance area fsi is obvious. At the frequency of the displacement a local minimum in the spectrum of the pressure occurs. There is a transport of momentum from the fluid onto the structure. The reaction of the bend causes a minimum in the fluid spectrum. The peak of the pressure is split into two peaks. Moreover there are frequency shifts of the pressure near the

resonance area (Figure 7 e.g. support positions 1652 mm, 1777 mm, 2902 mm and 3137 mm).

In Figure 8 the frequency spectra for the long system are depicted. In the resonance area no splitting of the pressure peak appears. There is only a wide reduction in the amplitudes of the fluid peak and a rise of the amplitudes of the displacement. The transport of momentum is just one way. The movement of the bend has little effect on the fluid. Also no striking frequency shifts can be noticed.

In summary two different oscillation characteristics occur. This is a consequence of the unequal bend geometries (Figure 1). In the short system the bend has a long vertical pipe section, in the long one this section is small. The mass of fluid inside this vertical pipe section and the length itself are a measure for the coupling of the structure and the fluid. The longer this section the longer the excitation force acts on the bend. The greater the mass of the fluid the greater is the potential momentum of the fluid onto the structure.

Far from the resonance area the influence of the movement of the bend on the fluid is relatively small. Here no effect of the introduction of fsi would be expected. In the resonance area the above mentioned differences are obvious. It is remarkable that the spectra of the pressure do not always lie under the reference spectrum for a completely fixed system. That means that a one-way calculation is not conservative without exception. For example at a fluid resonance in a branch pipe under disadvantageous but very rare conditions it is possible that a movable pipeline causes higher loads than a fixed one.

Time Signals

The pressure in front of the flap and the displacement of the bend are plotted for both configurations. Each diagram includes the distributions for two support positions - in and out of the resonance between fluid and structure.

Figure 9 shows the graphs for the short system. The influence of fsi is obvious in form of a beat in the resonance case. Here in the first phase of the oscillation primarily there is a transfer of momentum from the fluid onto the structure. The amplitudes of the pressure decrease and those of the displacement increase. There is a little phase shift between the minimum of the pressure and the maximum of the structure which is caused by the distance between the measurement positions. Afterwards the amplitudes of the pressure increase and the distribution of the displacement shows a dent. This indicates a transport of momentum from the structure back to the fluid. Out of resonance there is a little transport of momentum from

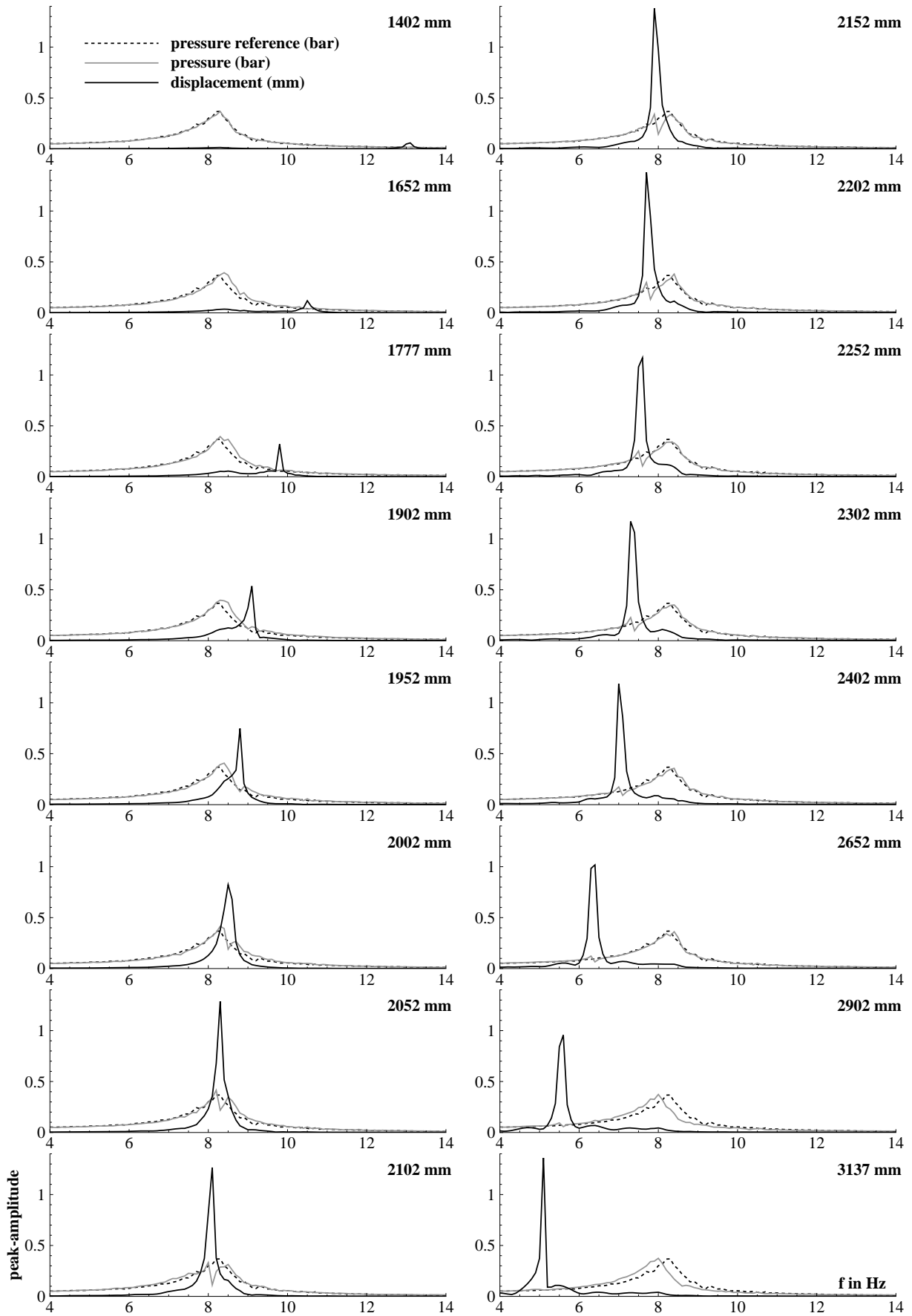


FIGURE 7: AVERAGED FREQUENCY SPECTRA FOR VARIOUS SUPPORT POSITIONS (SHORT SYSTEM)

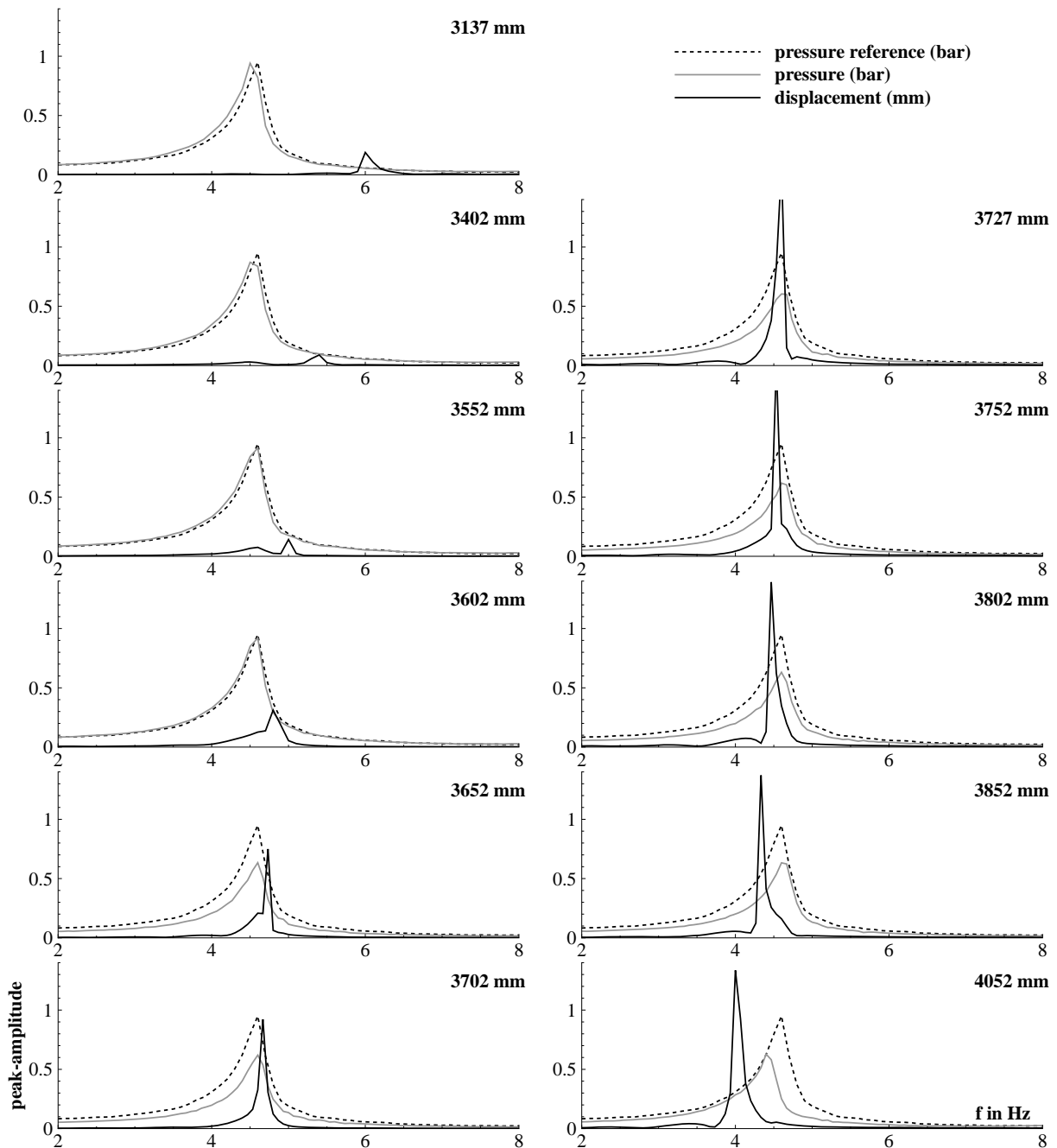


FIGURE 8: AVERAGED FREQUENCY SPECTRA FOR VARIOUS SUPPORT POSITIONS (LONG SYSTEM)

the fluid onto the structure, but no beat is apparent.

Figure 10 includes the distributions of the long system in and out of the resonance. No beats occur. The pressure signals in and out of the resonance are nearly identical. Only the distributions of the displacement illustrate the resonance state.

The results of the time signals coincide with the findings of the frequency spectra, that two different oscillation characteristics occur. A two-way interaction can only be observed for the short system due to the different bend geometries.

CONCLUSION

In order to examine the effects of fsi water hammer experiments at bends near resonance were performed. Measurements at the rigidly anchored system identified the base frequencies to be dominant. Resonances of the different bends depending on the system configuration appeared at the base frequencies of the water hammer. For the long system the excitation of the bend was smaller due to the short vertical pipe section of the bend. The frequency spectra of the pressure in front of the flap and of the displacement of the bend identified differences in the

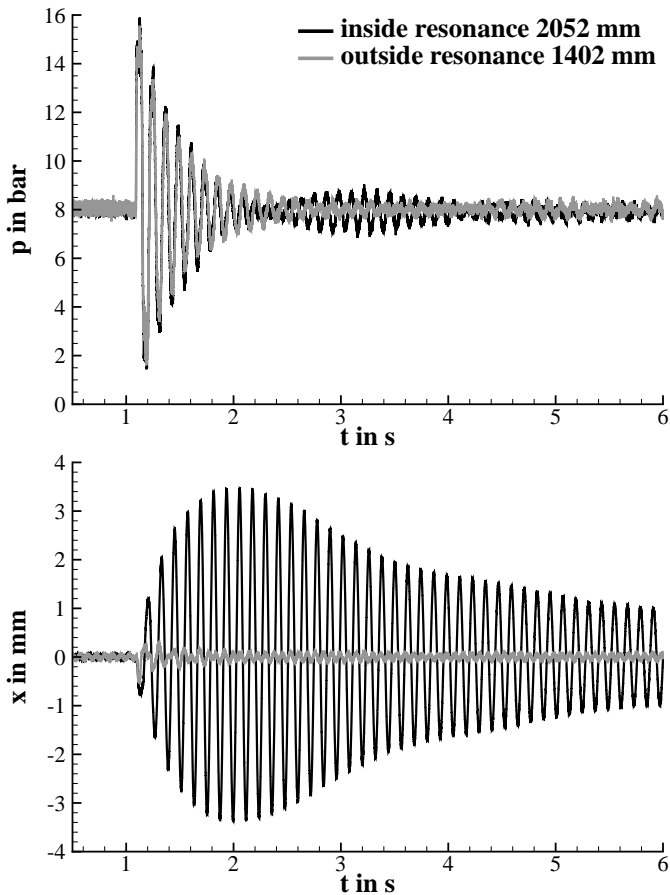


FIGURE 9: PRESSURE AND DISPLACEMENT DISTRIBUTION FOR THE SHORT SYSTEM AND TWO SUPPORT POSITIONS

oscillation characteristics. These are caused by the various bend geometries. The coupling between the structure and the fluid is dependent on the bend geometry or rather the length of the vertical pipe section. So the effects of fsi are more dominant in the short system, which also showed the time signals.

Outside of the resonance area fsi has little influence on the spectra. Here a two-way interaction wouldn't show a noticeable effect. Inside the resonance area the analysis identified frequency shifts and a splitting of the peak in the pressure spectrum. In some cases the spectrum of the pressure lies over the reference spectrum. That means a calculation with one-way interaction wouldn't be conservative in all cases. In some seldom and disadvantageous situations the consideration of fsi can lead to higher loads.

ACKNOWLEDGMENT

I would like to thank AREVA NP GmbH (section Fluid Dynamics PEPR-G Erlangen) for the long lasting cooperation and the funding. Additionally I'm grateful

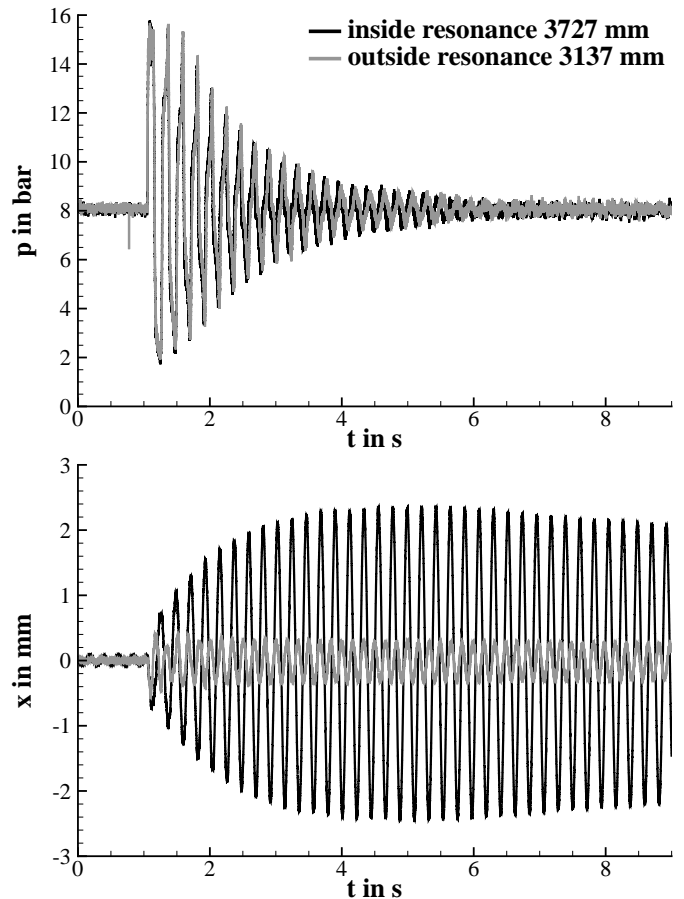


FIGURE 10: PRESSURE AND DISPLACEMENT DISTRIBUTION FOR THE LONG SYSTEM AND TWO SUPPORT POSITIONS

for the expertise assistance and the possibility to benefit from decades of experience.

REFERENCES

- [1] Lavooij, C. S. W.; Tijsseling, A. S., 1991. "Fluid-structure interaction in liquid-filled piping systems". *Journal of Fluids and Structures*, **5**, pp. 573–595.
- [2] Heinsbroek, A. G. T. J.; Tijsseling, A. S., 1994. "The influence of support rigidity on water hammer pressures and pipe stresses". In 2nd International Conference on Water Pipeline Systems.
- [3] Tijsseling, A. S., 1996. "Fluid-structure interaction in liquid-filled pipe systems: A review". *Journal of Fluids and Structures*, **10**, pp. 109–146.
- [4] Wiggert, D. C. ; Tijsseling, A. S., 2001. "Fluid transients and fluid-structure interaction in flexible liquid-filled piping". *Applied Mechanics Reviews*, **54**, pp. 455–481.

- [5] Verein Deutscher Ingenieure, 2004. *VDI-Richtlinie 3842: Schwingungen in Rohrleitungssystemen (Vibrations in piping systems)*, July.
- [6] Ismaier, A., 2011. “Untersuchung der fluidodynamischen Wechselwirkung zwischen Druckstößen und Anlagenkomponenten in Kreiselpumpensystemen”. PhD thesis, Lehrstuhl für Prozessmaschinen und Anlagentechnik, Friedrich-Alexander Universität Erlangen-Nürnberg.



EXPERIMENTAL INVESTIGATION OF FLOW-ACOUSTIC COUPLING IN GATE VALVES

Oleksandr Barannyk¹

Institute for Integrated Energy Systems
Department of Mechanical Engineering
University of Victoria
Victoria, BC V8W 3P6,
Canada
Email: barannyk@me.uvic.ca

Peter Oshkai

Institute for Integrated Energy Systems
Department of Mechanical Engineering
University of Victoria
Victoria, BC V8W 3P6,
Canada
Email: poshkai@me.uvic.ca

ABSTRACT

The objective of the present study is to provide insight into mechanism of coupling between turbulent pipe flow and partially-trapped diametral acoustic modes associated with a shallow cavity formed by the seat of a gate valve. The experiments were performed using a scaled model of a gate valve mounted in a pipeline that contained a converging-diverging section in the vicinity of the valve. Acoustic pressure measurements at three azimuthal locations at the floor of the cavity were performed for a range of geometries of the converging-diverging section and inflow velocities. The resonant response of the system corresponded to the second diametral mode of the cavity. Excitation of the dominant acoustic mode was accompanied by pressure oscillations corresponding to other acoustic modes. Increase of the convergence angle leads to a moderate decrease in the amplitude of the resonant acoustic mode.

INTRODUCTION

Gate valves that are commonly deployed in the pipelines of power plants can disrupt the gas flow and can lead to the coupling of flow oscillations with the acoustic modes of the internal valve and pipeline geometry. On a small scale, this phenomenon can pose an environmental hazard for plant personnel [1]. However, in extreme cases, high level of flow-induced noise and vibrations can lead to serious accidents, such as 80% reduction of nominal power in Unit 3 on Chernobyl nuclear power plant (NPP) (Chernobyl, Ukraine) due to intensive vibrations of the main steam pipelines [2] or the accidents in Mihama NPP (Mihama, Japan) in 1991 and 2004 that led to the injury and death of several plant workers.

In references [1, 3], a scale-model investigation of reducing the steam line noise and vibration at a thermal power plant was reported. During preliminary tests, it was confirmed that the source of acoustic excitation leading to excessive pipe vibration in the cold reheat steam lines of the power plant was vortex shedding related directly to the geometry of the cold-reheat gate valves. Based on measurements at the site, it was concluded that the inline gate valves were the most probable source of the problem. A variety of practical cavity, gate and seat modifications were tested in a 0.115-scale model using air as the flowing fluid. During initial tests, it was shown that the model reproduced the tonal noise generating mechanism seen in the plant and that filling in the valve seat cavity eliminated this noise. The noise generating mechanism was found to be associated with vortex shedding over the valve seat cavity coupled with an acoustic cross mode in the valve throat.

There exists a large body of work dedicated to deeper understanding of control of shear flows over cavities in walls and external cavities in axisymmetric bodies of revolution [4-8]. Because of the inherent instability of a free shear layer, small disturbances at the upstream edge of the cavity result in the formation of large-scale vortices in the shear layer over the cavity. Each vortex will convect downstream until it impinges on the downstream edge of the cavity where it causes a pressure perturbation. This pressure perturbation will then be acoustically transmitted back to the upstream edge where it can initiate the formation of another vortex. The time required for the vortex to move across the mouth of the cavity plus the time required to transmit the pressure back to initiate the formation of a new vortex will determine the preferred vortex shedding frequencies.

Address all correspondence to this author¹

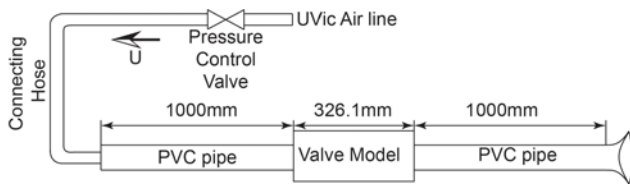


Figure 1: Schematics of the experimental layout

There had been several reports [9-11], where it was stated that vortex shedding instabilities over a cavity can be significantly reduced if the flow is prevented from impinging on the downstream edge of the cavity either by moving the downstream edge out of the flow or deflecting the flow at the upstream edge. Alternatively, pressure amplitudes can be reduced by rounding and inclining the downstream corner. These approaches were examined for the gate valve geometry in [1], where downstream seats that had rounded or chamfered corners with the minimum sealing face height were implemented. While these configurations all reduced the maximum unsteady pressure coefficients, the reductions were generally small.

Also related to the present study are investigations in [12-14], where a simplified system consisting of a shallow axisymmetric cavity mounted in a pipeline with a circular cross-section was considered. Those studies were aimed to understand excitation mechanism of the trapped acoustic diametral modes, present in an axisymmetric internal cavity-duct system, and their azimuthal behavior. It was shown by the authors, that for the all tested configurations, flow coupling with acoustic diametral modes was a dominant phenomenon at relatively low Mach number. It was found that the pulsation amplitude during resonance was increased as the cavity got deeper or shorter. The authors also concluded that the acoustic diametral modes, coupled with the flow, are likely to be spinning when the cavity-duct system has a perfectly axisymmetric geometry.

The objective of the current work is to develop an effective methodology for efficient control of flow-induced noise and vibration caused by gate valves in a wide variety of piping systems. The outcome of these experiments will lead to a development of a method for prediction of acoustic power and identification of regions within the flow system where the acoustic noise is generated.

EXPERIMENTAL SYSTEM AND TECHNIQUES

Flow system

The flow system consisted of two 1m-long PVC pipe sections of the circular cross-section connected by the gate valve sub-system, as shown in Figure 1.

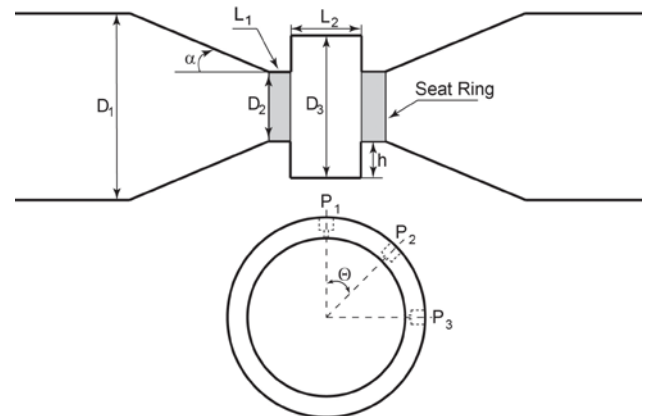


Figure 2: Cavity subsystem

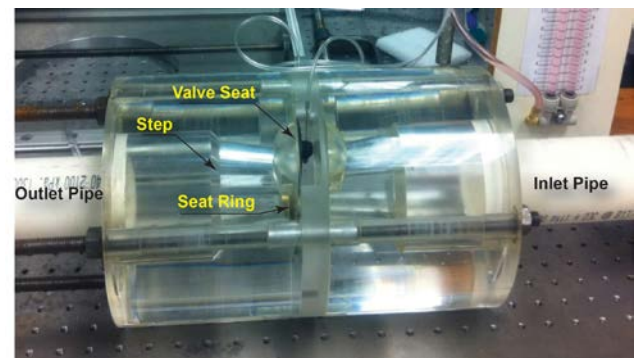


Figure 3: Experimental system

Air was used as a working fluid in this experimental study. It was supplied by an air compressor located in a separate room. The test section was isolated from flow pulsations induced by the compressor by employing a long connecting hose that served as a damper for the incoming flow oscillations. The inlet chamber was located upstream of the experimental apparatus and incorporated honeycomb flow straighteners and a contracting section in order to provide well-conditioned inflow to the test section. The outlet pipe was outfitted with a diffuser in order to reduce losses due to the flow.

The air compressor was able to provide a constant air supply at 60psi which corresponded to a maximum velocity of 29.4 m/s immediately upstream of the cavity, verified by a pitot tube measurement. The velocity in each test section was calibrated with respect to the inlet pressure measured at the location of the control valve shown in Figure 1.

Valve model

A scaled model of a gate valve assembly mounted in a pipeline with a circular cross-section was designed and constructed in order to investigate the flow-acoustic coupling and to quantify the effect of contraction and expansion of the pipeline immediately upstream and downstream of the valve. The experimental apparatus consisted

of four different valve models. The model shown in Figure 3 is the small-scale model of a gate valve assembly that was used in the previous studies by the Atomic Energy of Canada Limited (AECL) research team [1, 3]. Its characteristic dimensions are defined in Figure 2.

Each model contained three major parts: an upstream converging section, a downstream diverging section with a constant divergence angle α , and a central insert that represented the valve seat cavity. All three parts were interfaced with O-rings and were tightly clamped together by four threaded rods. In this paper, the four geometries used in the current study, are referred to as follows: G_1 : $\alpha=5^\circ$, G_2 : $\alpha=8^\circ$, G_3 : $\alpha=11.2^\circ$, G_4 : $\alpha=11.2^\circ$ (the AECL original geometry). In contrast to the geometries G_1 through G_3 , the geometry G_4 featured a secondary contraction/expansion step between the main pipeline and the contracting/diverging section around the valve. This step is indicated in Figure 3. As it is discussed below, this geometric feature resulted in substantial changes in the acoustic response of the system. In all four cases, the following parameters were kept constant as follows: $D_1=72\text{mm}$, $D_2=47.2\text{mm}$, $D_3=54.3\text{mm}$, $L_1=6.2\text{mm}$, $L_2=21.3\text{mm}$, $h=3.55\text{mm}$.

Valve seat

The valve seat, modeled by a central disk-shaped insert, was represented by a shallow axisymmetric cavity with the length-to-depth ratio of $L_2/h = 6$. The cavity was located 152.4 mm from the inlet of the main pipeline. Brass seat rings with the internal diameter of 47.2 mm and width of 6.2 mm were located immediately upstream and downstream of the cavity [1].

Acoustic pressure measurements

Each model was designed to allow acoustic pressure measurements. Three piezoelectric pressure transducers (PCB model 103A02) were flush mounted into the bottom wall of the valve's cavity using technique of [15]. This mounting adjustment ensured, for the range of frequencies in the current investigation, that no acoustic resonant effect will be generated in the region between the face of the transducer and the surface of the pressure tap at the interior of the pipe. The transducers were separated by angle $\Theta=45^\circ$ from each other, as shown in Figure 2. With this setup, the system provided an opportunity to investigate azimuthal orientation of the partially trapped diametral modes [12, 13].

The transducers were connected to the National Instruments (NI) PXI-4472 board, which had eight analog input channels that could perform simultaneous sampling at a maximum rate of 102.4 kHz with 24-bit resolution.

	G1	G2	G3	G4
f_1^D (Hz)	4125	4191	4181	4167
f_2^D (Hz)	6648	6644	6632	6665
f_3^D (Hz)	8984	8996	8985	8964

Table 1: Frequencies corresponding to the first three diametral modes, obtained numerically for geometries G_1 - G_4 .

During the experiments, the analog pressure signals were converted to digital form at the time of acquisition at a sampling rate of 70 kHz. That sampling rate was ten times higher than the maximum resonant frequency present in the current investigation. The NI 4472 board contained a built-in two-pole anti-alias filter for each channel.

Custom Labview and Matlab routines were used to process the pressure data and to characterize it in time and frequency domain.

RESULTS AND DISCUSSION

Effect of the inflow velocity

Figure 4 shows experimentally obtained pressure spectra as the inflow velocity was increased from 8 m/s to 29.4 m/s. The data corresponds to the case of the shallow axisymmetric cavity and the geometry G_4 with $\alpha=11.2^\circ$ that was used in the original AECL study [1]. The measurements were obtained at the bottom wall of the cavity from three pressure transducers P1, P2, and P3 simultaneously. Unless stated otherwise, the results presented here correspond to the data sets obtained from pressure transducer P1. The dominant spectral peaks correspond to acoustically-coupled flow regimes that occurred when the frequencies of the hydrodynamic shear layer oscillations matched the frequencies of the diametral acoustic mode of the axisymmetric cavity.

In order to identify which acoustic diametral mode was excited, a finite element numerical simulation [12] was employed to obtain frequencies and shapes of various acoustic modes for each of the geometries. The mode shapes were calculated numerically by solving a Helmholtz equation in a 3D domain corresponding to the internal geometry of the pipe and the cavity. The boundary condition at the inlet and the outlet of the pipe corresponded to zero acoustic pressure to simulate the open ends of the pipe. All other surfaces were modeled as solid boundaries. The results are shown in Table 1.

These results indicate that the highest peak in Figure 4 corresponds to the second acoustic diametral mode ($f = 6665$ Hz). The corresponding mode shape is shown in Figure 5 in terms of contours of acoustic pressure.

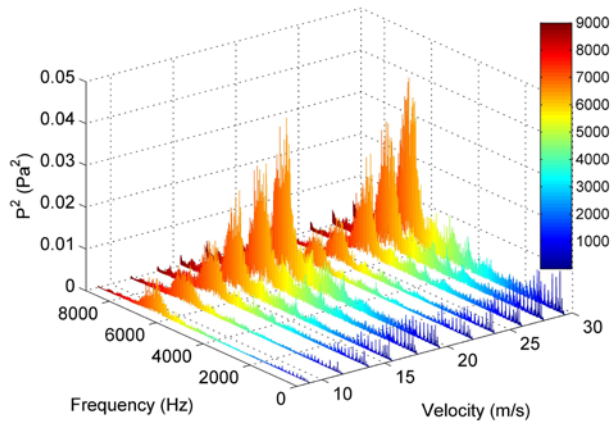


Figure 4: Power spectrum of pressure as a function of the inflow velocity for geometry G₄

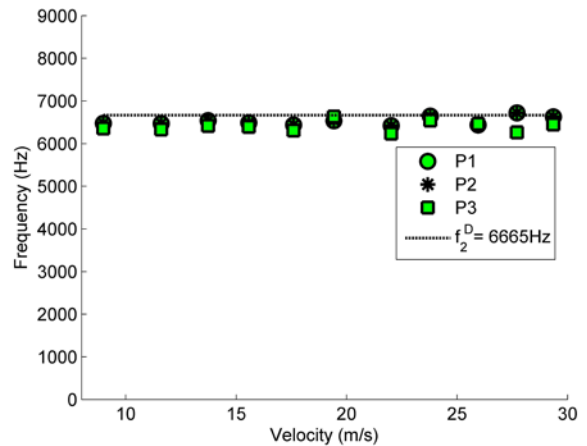


Figure 7: Frequency of the dominant pressure peak as a function of the inflow velocity and the azimuthal position (represented by three pressure transducers). Geometry G₄.

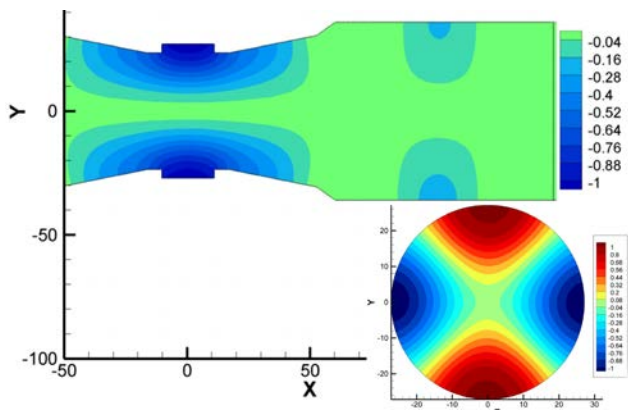


Figure 5: Mode shape of the second diametral mode of the geometry G₄. The inset shows the cross-section at the center of the cavity, $f = 6665$ Hz

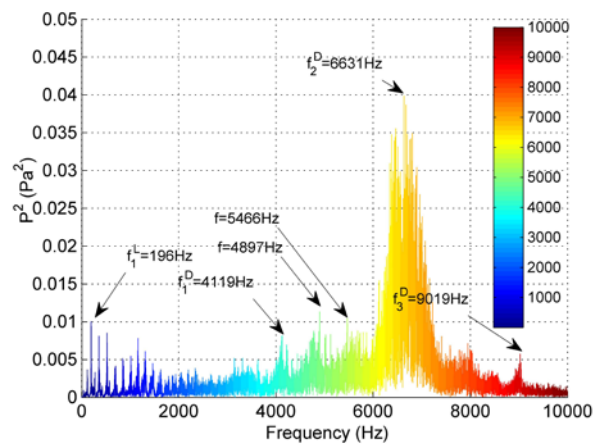


Figure 8: Power spectrum of pressure for geometry G₄ at $U = 29.4$ m/s

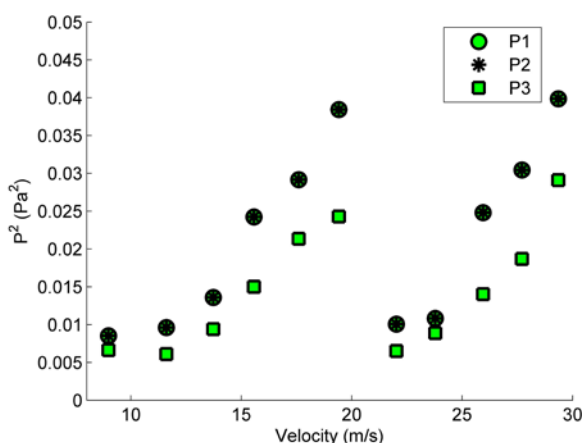


Figure 6: Maximum pressure as a function of the inflow velocity and the azimuthal position (represented by three pressure transducers). Geometry G₄.

Figure 4 indicates that the maximum amplitude of acoustic oscillation increased as the mean flow velocity increased up to $U = 19.4$ m/s, followed by a rapid decrease at $U = 22$ m/s. The pressure amplitude increased again as the inflow velocity increased from 22 m/s to 29.4 m/s. Thus, the maximum pressure amplitudes for the geometry G₄ were observed at the inflow velocities of $U = 19.4$ m/s and $U = 29.4$ m/s.

The measured frequency of the pressure peaks was within $\pm 0.5\%$ of the predicted acoustic resonance frequencies. Moreover, the lock-on frequency remained approximately constant throughout the entire velocity range employed in this experiment, as shown in Figure 8.

Figure 6 indicates that the amplitude of acoustic oscillations, measured by three pressure transducers varied with respect to the azimuthal position in the cavity. In fact, the amplitudes obtained from P₁ and P₂ coincided

with each other, while the amplitude obtained from P_3 followed a similar trend but was generally lower. The differences observed in this particular case could be attributed to the spatial orientation of the acoustic diametral mode. The pressure transducers P_1 and P_2 corresponded to the same acoustic pressure level, while P_3 measured pressure data at a different position with respect to the mode shape shown in Figure 5.

Figure 9 shows the power spectrum of the acoustic pressure corresponding to the inflow velocity $U=26.4$ m/s, at which the acoustic pressure amplitude reached its maximum. For the geometry G_1 , pronounced pressure peaks are evident and can be clearly classified into two major groups. The first group contains secondary modes, represented by longitudinal acoustic modes, with the resonant frequency of $f=196$ Hz, and its harmonics, separated by $\Delta f=163$ Hz. The second group contains primary modes, and it is represented by partially trapped acoustic diametral modes, $f_1^D=4119$ Hz, $f_2^D=6631$ Hz, $f_3^D=9019$ Hz. It can be seen from Figure 4 that as velocity increased from its minimum value of $U=8$ m/s, the first mode to be excited was the second diametral mode f_2^D . As velocity increased, one can clearly see sequential excitation of the secondary, longitudinal modes of the pipe-cavity system. At the inflow velocities of up to 15 m/s the peaks of the amplitudes corresponding to these modes were low. However, as velocity increased, at approximately 16 m/s, the amplitudes of the acoustic pressure became comparable to those of the first and the third diametral modes. In particular, in Figure 8, one can see that the amplitude of the first longitudinal mode is slightly higher than that of the partially trapped acoustic diametral modes f_1^D and f_3^D . This feature is typical to excitation of flow tones in resonant systems that have multiple resonant modes [4].

Effect of the angle of divergence of the pipeline

The main objective of the following set of experiments was to explore the effect of internal geometry change on partially-trapped acoustic diametral modes of an axisymmetric pipeline-cavity system.

The governing parameter for the geometry variations considered in this study is the angle of the converging/diverging pipe section α , which is defined in Figure 2. Geometries G_1 through G_3 were tested, and the cavity dimensions were chosen to be constant. Figure 9 through Figure 14 illustrate the acoustic response of the system as the angle of the converging/diverging section increased from 5° to 11.2° .

For the case of the smallest angle of the converging/diverging section, $\alpha=5^\circ$, the peaks shown in

Figure 9 and Figure 12 show slightly different behaviour than those previously described for G_4 . The waterfall plot of Figure 9 clearly shows the sequential excitation of various modes of the resonant pipeline-cavity system. The maximum acoustic pressure amplitude was reached at $U=22$ m/s. In addition, at $U=19.4$ m/s and 29.4 m/s, the acoustic pressure amplitude was very close to its maximum value.

Compared to G_1 , the pressure variation for the geometry G_2 as a function of the inflow velocity also showed pronounced peaks of pressure amplitudes at $U=22$ m/s, and $U=19.4$ m/s. In addition to that, the second largest pressure amplitude was achieved at $U=17.6$ m/s. At $U=29.4$ m/s, the acoustic pressure amplitude of G_2 was approximately 25% lower than that of G_1 . Both geometries G_1 and G_2 resulted in the maximum acoustic pressure amplitude at $U=22$ m/s.

In the case of geometry G_3 , there is a qualitative similarity with the spatial distribution of pressure spectrum to that of G_4 . This is not surprising as both cases have the same value of the convergence/divergence angle $\alpha=11.2^\circ$. Addition of the secondary convergence/divergence step in the geometry G_4 resulted in the decrease of the maximum acoustic pressure of 10% to 15%, compared to the case of G_3 . In particular, the maximum acoustic pressure amplitude reached at $U=29.4$ m/s, was approximately 15% higher in the case of G_3 , with the maximum acoustic pressures for the geometries G_1 through G_4 were achieved at the values of the inflow velocity of $U^{CR}_1=17.6$ m/s, $U^{CR}_2=19.4$ m/s, $U^{CR}_3=22$ m/s, and $U^{CR}_4=29.4$ m/s, respectively. The maximum acoustic pressure amplitude decreased as the angle of the converging/diverging section increases from 5° to 11.2° as it can be seen in Figures 6 and 12 through 14. One of the possible implications of these results is that as the angle of the converging/diverging section is increased, the acoustic energy associated with the diametral modes begins to radiate into the pipeline, thus decreasing the strength of the flow tone lock-on.

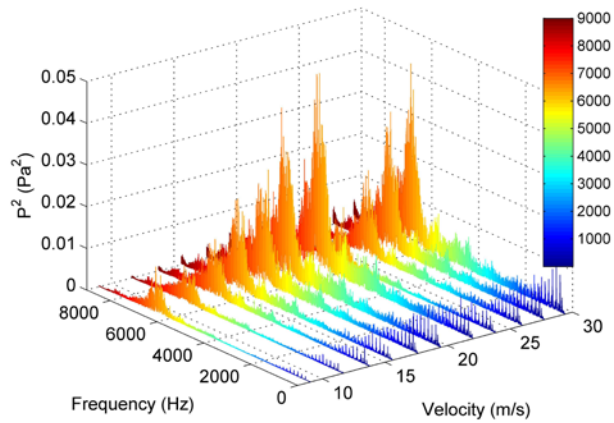


Figure 9: Power spectrum of pressure as a function of the inflow velocity for geometry G_1

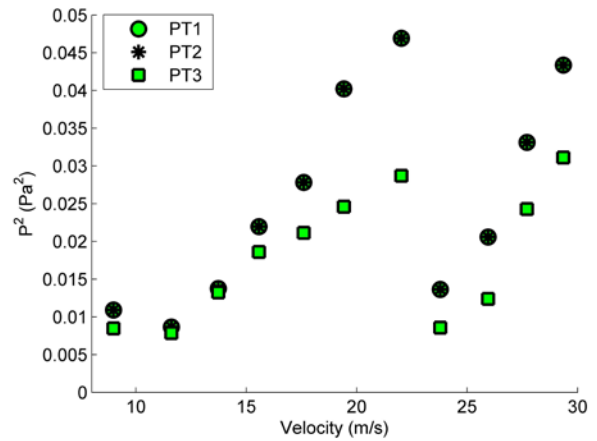


Figure 12: Maximum pressure as a function of the inflow velocity and the azimuthal position (represented by three pressure transducers). Geometry G_1 .

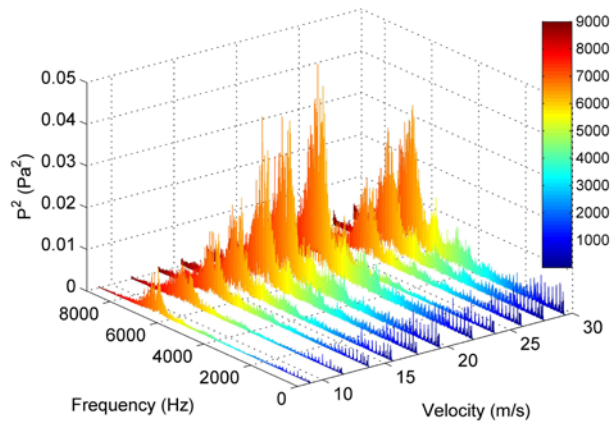


Figure 10: Power spectrum of pressure as a function of the inflow velocity for geometry G_2

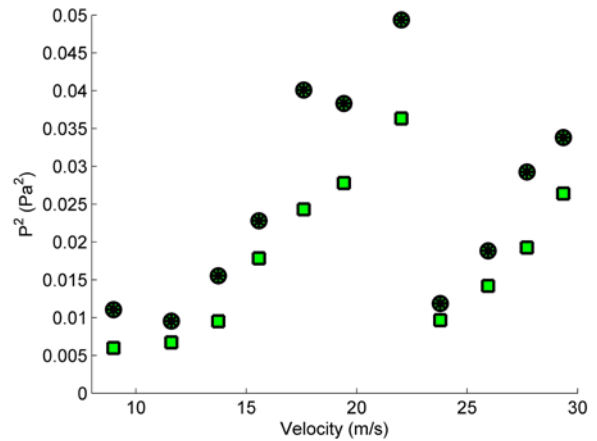


Figure 13: Maximum pressure as a function of the inflow velocity and the azimuthal position (represented by three pressure transducers). Geometry G_2 .

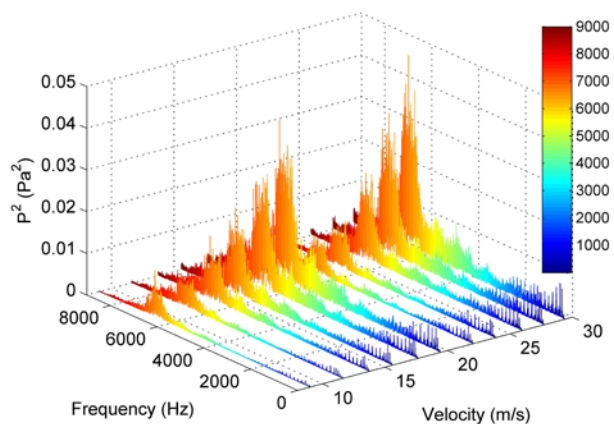


Figure 11: Power spectrum of pressure as a function of the inflow velocity for geometry G_3

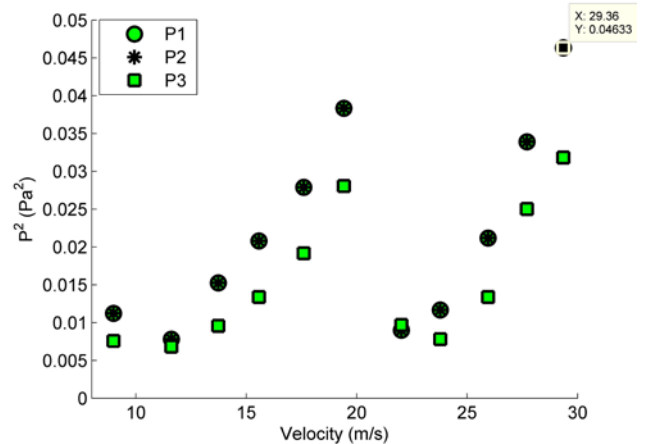


Figure 14 Maximum pressure as a function of the inflow velocity and the azimuthal position (represented by three pressure transducers). Geometry G_3 .

CONCLUSIONS

It was confirmed that flow across a shallow axisymmetric cavity can strongly excite the acoustic diametral modes. The flow tone lock-on was observed for a range of inflow velocities up to 29.7 m/s. It was shown that the acoustic response corresponded to the partially-trapped second diametral acoustic mode of the cavity. Simultaneous excitation of other acoustic modes was also observed.

All considered geometries showed qualitative similarity for all values of angle of the converging/diverging pipe section. In particular, the mode switching from diametral acoustic modes to longitudinal modes of pipe-cavity system was observed at low velocities. At the higher inflow velocities, simultaneous excitation of both diametral and longitudinal acoustic modes was observed.

For larger values of the angle of the converging/diverging pipe section, the noticeable decrease in the values of maximum pressure was achieved. The flow tone lock-on can also be avoided by operating the system at a particular value of the inflow velocity U .

ACKNOWLEDGMENTS

The authors wish to thank the Atomic Energy of Canada Limited (AECL) for providing the original experimental model of the gate valve and the Natural Sciences and Engineering Research Council of Canada (NSERC) for providing funding for financial support.

Keywords: *inline gate valve, shallow cavity, acoustic power, flow-acoustic coupling*

REFERENCES

- Smith, B.A.W. and B.V. Luloff, *The effect of seat geometry on gate valve noise*. Journal of Pressure Vessel Technology-Transactions of the Asme, 2000. **122**(4): p. 401-407.
- Fomin, V., V. Kostarev, and K. Reinsch, *Elimination of Chernobyl NPP Unit 3 Power Output Limitation Associated with High Main Steam Piping Flow Induced Vibration*. Proceedings of the 16th International Conference on Structural Mechanics in Reactor Technology, 2001.
- Janzen, V.P., et al., *Acoustic noise reduction in large-diameter steam-line gate valves*. Proceedings of the Asme Pressure Vessels and Piping Conference 2007, Vol 4: Fluid-Structure Interaction, ed. M. Moatamedi. 2008. 513-522.
- Rockwell, D., et al., *Shallow cavity flow tone experiments: onset of locked-on states*. Journal of Fluids and Structures, 2003. **17**(3): p. 381-414.
- Erdem, D., et al., *Flow tones in a pipeline-cavity system: effect of pipe asymmetry*. Journal of Fluids and Structures, 2003. **17**(4): p. 511-523.
- Ziada, S., *Flow-Excited Acoustic Resonance in Industry*. Journal of Pressure Vessel Technology-Transactions of the Asme, 2010. **132**(1).
- Michaud, S., S. Ziada, and H. Pastorel, *Acoustic fatigue of a steam dump pipe system excited by valve noise*. Journal of Pressure Vessel Technology-Transactions of the Asme, 2001. **123**(4): p. 461-468.
- Verdugo, F.R., A. Guitton, and R. Camussi, *Experimental investigation of a cylindrical cavity in a low Mach number flow*. Journal of Fluids and Structures, 2012. **28**: p. 1-19.
- Rockwell, D. and C. Knisely, *The organized nature of flow impingement upon a corner*. Journal of Fluid Mechanics, 1979. **93**(03): p. 413-432.
- Willmarth, W.W., et al., *Management of turbulent shear layers in separated flow*. Journal of Aircraft, 1978. **15**(7): p. 385-386.
- Blevins, R.D., *Flow-induced vibration*. 1990: Van Nostrand Reinhold.
- Aly, K. and S. Ziada, *Flow-excited resonance of trapped modes of ducted shallow cavities*. Journal of Fluids and Structures, 2010. **26**(1): p. 92-120.
- Aly, K. and S. Ziada, *Azimuthal behaviour of flow-excited diametral modes of internal shallow cavities*. Journal of Sound and Vibration, 2011. **330**(15): p. 3666-3683.
- Duan, Y.T., et al., *Complex resonances and trapped modes in ducted domains*. Journal of Fluid Mechanics, 2007. **571**: p. 119-147.
- Peters, M.C.A.M., *Aeroacoustic sources in internal flows*. 1993, Technical University of Eindhoven.



NUMERICAL STUDY OF CROSS-FLOW PAST TWO STAGGERED ROWS OF CYLINDERS

P. Anagnostopoulos¹

S. Seitanis

Department of Civil Engineering

University of Thessaloniki

Thessaloniki

Greece

Email: anagnost@civil.auth.gr

ABSTRACT

The results of a numerical study of cross-flow past two staggered rows of cylinders are presented, at a fixed Reynolds number equal to 200. The upstream row comprised three and the downstream row four cylinders, for centre-to-centre pitch ratio in the streamwise direction, S/D , equal to 1. The centre-to-centre pitch ratio between adjacent cylinders on the same row, T/D , was equal to 3.

The mathematical model of the problem consists of the well-known Navier-Stokes equations. In the present investigation the finite element technique was favored for the solution of the Navier-Stokes equations, in the formulation where the stream function and the vorticity are the field variables. The pressure distribution throughout the flow field was obtained from the solution of Poisson's equation. The in-line (drag) and transverse (lift) forces exerted on the cylinders were evaluated from the pressure and shear distribution around the cylinder surfaces.

The vorticity contours were used for the numerical flow visualization, whereas the time histories of the drag and lift forces exerted on the cylinders are presented. Although the time histories of the hydrodynamic forces, especially in the in-line direction, appears almost chaotic, systematic attempt was made for the classification of the various flow regimes with the aid of flow visualization.

INTRODUCTION

The investigation of flow through bundles of cylinders is a problem of growing engineering interest, since it is related to various engineering applications, such as heat exchangers, boilers, nuclear reactors, etc. Apart from the extensive experimental effort devoted to the problem, numerical investigations of flow through arrays of cylinders have been undertaken during the last years, using various computational techniques. Ganoulis *et al.* [1] used Laser-Doppler anemometry for the measurement of flow velocity through a periodic array of cylinders and compared the experimental measurements with results obtained numerically at similar conditions. Tezduyar and

Liou [2] used the stream function and vorticity formulation for the finite element solution of flow through arrays of cylinders. Rasoul *et al.* [3] used the finite difference technique for the solution of laminar flow through a staggered bundle of cylinders of infinite depth, considering a unit cell in the streamwise direction. Rorris *et al.* [4] extended the solution to the full configuration of five staggered cylinder rows, at different pitch ratios. Braun and Kudriavtsev [5] investigated numerically the flow structure past a single row and staggered banks of cylinders located in a channel, at Reynolds numbers ranging between 86 and 869. Sweeney and Meskell [6] used a discrete vortex method to simulate vortex-shedding in tube arrays for $Re=2,200$, whereas Huang *et al.* [7] used FLUENT solver for the numerical simulation of flow around rows of cylinders for $Re \leq 100$. Lam *et al.* [8] conducted a numerical simulation of cross-flow past a row of rigid and flexible cylinders at $Re=2.67 \times 10^4$. More recently Liang and Papadakis [9] presented a large eddy simulation of cross-flow through a staggered tube bundle at $Re=8,600$.

Although the literature through deep rows of cylinder is extensive, cross-flow past one or two rows of cylinders has received less attention. A significant contribution is that of Roberts [10], who conducted an experimental study in order to investigate the vibratory motion of a cascade of closely spaced circular cylinders. He measured the drag coefficients on two half cylinders and found that the cylinder with the narrow wake (upstream cylinder) experiences a greater drag than the cylinder with the wide wake (downstream cylinder). Zdravkovich and Stonebanks [11] examined the flow past a single row and two staggered rows of tubes. They found that the biased gap flows could intermittently switch direction (metastable flows). They also noticed that the drag forces on the cylinders of the upstream row were higher than those of the downstream row, in agreement with the measurement conducted by Roberts. More recently, Seitanis *et al.* [12] examined experimentally the vibratory motion of a flexible row of three circular cylinders in the streamwise direction,

¹Address all correspondence to this author

placed alternately between four cylinders of a fixed row. The flexible row was oscillating upstream of the fixed row and the oscillation amplitude was not constant at different cycles for the same reduced velocity.

The objective of this study is the numerical solution of cross-flow past two staggered rows of cylinders in tandem, for longitudinal pitch ratio equal to 1, at a fixed Reynolds number equal to 200. The upstream row comprised three and the downstream row four cylinders, while the distance between adjacent cylinders on the same row was equal to 3 cylinder diameters. The arrangement of the two rows and the numbering of cylinders are illustrated in Fig. 1. The finite element technique was employed for the solution of the Navier-Stokes equations, in the formulation where the stream function, Ψ , and the vorticity, ζ , are the field variables. The vorticity contours were employed for the numerical flow visualization, whereas the time histories of the drag and lift forces exerted on three of the cylinders are presented.

THE COMPUTATIONAL TECHNIQUE

In the present study the formulation of the Navier-Stokes equations is employed, in which the stream function, Ψ , and the vorticity, ζ , are the field variables. In this formulation the Navier-Stokes equations are written as:

$$\nabla^2 \Psi = -\zeta \quad (1)$$

$$\frac{\partial \zeta}{\partial t} + \frac{\partial \Psi}{\partial y} \frac{\partial \zeta}{\partial x} - \frac{\partial \Psi}{\partial x} \frac{\partial \zeta}{\partial y} = \nu \nabla^2 \zeta \quad (2)$$

Application of the ‘‘characteristic-Galerkin’’ technique, described by Zienkiewicz and Taylor [131 for the time-discretization of Eq. (2) yields

$$\begin{aligned} \frac{\Delta \zeta}{\Delta t} + \frac{\partial \Psi}{\partial y} \frac{\partial \zeta}{\partial x} - \frac{\partial \Psi}{\partial x} \frac{\partial \zeta}{\partial y} &= \nu \nabla^2 \zeta + \frac{\partial}{\partial x} \left(\frac{u^2 \Delta t}{2} \frac{\partial \zeta}{\partial x} \right) + \\ &\frac{\partial}{\partial y} \left(\frac{v^2 \Delta t}{2} \frac{\partial \zeta}{\partial y} \right) + uv \Delta t \frac{\partial^2 \zeta}{\partial x \partial y} \end{aligned} \quad (3)$$

The pressure distribution throughout the solution domain was obtained from the solution of Poisson's equation

$$\nabla^2 p = -2\rho \left(\frac{\partial u}{\partial y} \frac{\partial v}{\partial x} - \frac{\partial u}{\partial x} \frac{\partial v}{\partial y} \right) \quad (4)$$

where ρ is the fluid density and u , v are the two components of the fluid velocity.

The solution of equations (1), (3) and (4) yields the distribution of stream function, vorticity and pressure in the solution domain. From the distribution of pressure and shear on each cylinder the in-line (drag) and transverse (lift) forces were evaluated

APPLICATION - RESULTS

The first task of the solution is the generation of a suitable computational grid. An unstructured mesh was employed for the solution, consisting of three-node triangular elements. The mesh was refined near the cylinders and coarser in the remaining part of the solution domain.

The values of both the free-stream velocity and the cylinder diameter were taken equal to 1, and the Reynolds number was determined by adjusting the kinematic viscosity of the fluid. Thus, the real time yielded directly the dimensionless time, $t^* = tUI/D$, and the non-dimensional frequency, $f^* = fD/U$, was coincident with the real frequency, f . Moreover, considering the fluid density, ρ , equal to 2, the dimensionless drag and lift coefficients, $C_D = F_x / 0.5 \rho U^2 D$ and $C_L = F_y / 0.5 \rho U^2 D$ were equal to the drag and transverse forces, F_x and F_y . The solution was started assuming zero vorticity throughout the solution domain. In the early stages of computation the flow pattern remained symmetrical with respect to the horizontal axis of symmetry, yielding zero lift on cylinder 4. After an interval small asymmetries developed, which were eventually amplified and lead finally to an entirely asymmetric and aperiodic flow pattern. The vorticity contours at $t=20$, when the last symmetrical flow pattern was observed, are depicted in Fig. 1.

The non-dimensional values of mean drag, mean lift, r.m.s. deviation of drag from the mean drag and r.m.s. lift for cylinders 1 to 4 are summarized in Table 1. For the determination of these values the initial transient from irrotational flow was excluded. Due to symmetry the corresponding values for cylinders 5, 6 and 7 are equal to those of cylinders 3, 2 and 1. The mean lift that is negative for cylinders 1, 2 and 3 is positive for cylinders 5, 6 and 7. Although the time-histories of drag and lift forces for all cylinders were produced, only those for cylinders 3, 4 and 5 will be presented.

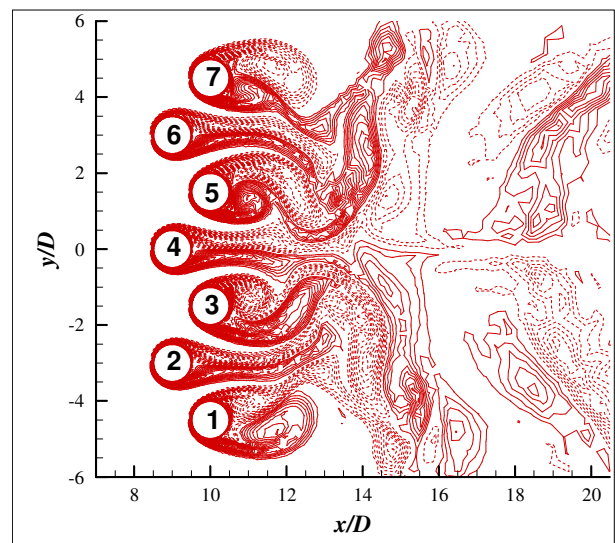


FIGURE 1: VORTICITY CONTOURS AT T=20.

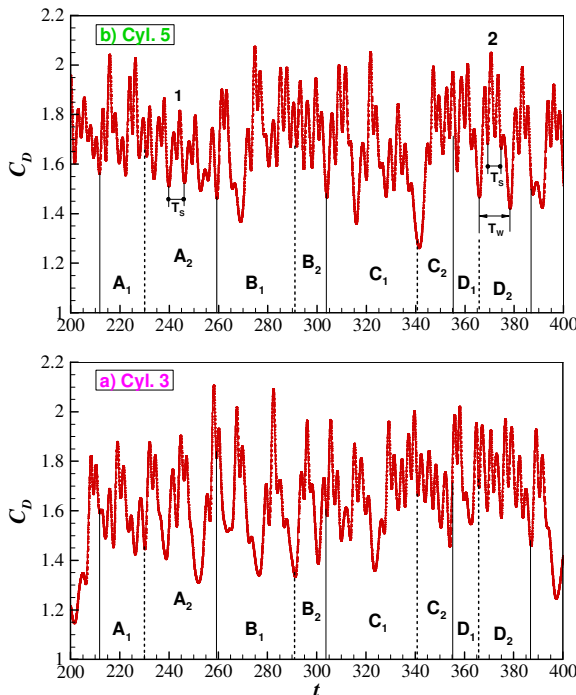


FIGURE 2: TIME HISTORY OF THE DRAG COEFFICIENT ON CYLINDERS 3 AND 5.

The time-histories of the drag coefficients exerted on cylinders 3 and 5 and of the lift coefficients on cylinders 3, 4 and 5 in the interval between 200 and 400 are illustrated in Figs. 2 and 3 respectively. A first observation reveals that the hydrodynamic forces have an aperiodic character. From Table 1 is concluded that the fluctuations of the drag forces on cylinders 3 and 5 are more intense than the fluctuations of the drag force on cylinder 4. In addition, the r.m.s. lift exerted on cylinder 4 is very small compared to the r.m.s. lift on cylinders 3 and 5 (note the reduced range of the axis of C_L for cylinder 4 in Fig. 3). This constitutes a strong indication of suppression of vortex shedding behind cylinder 4 that belongs to the upper row. A closer observation of the traces of the lift forces reveals that apart from the fluctuations of amplitude at different cycles there also exist fluctuations of frequency. The situation in the trace of the drag force exerted on these cylinders is more complicated. We see in Fig. 2b that for cylinder 5 the cycle marked as “1” has frequency, determined from the time interval between successive

TABLE 1: MEAN DRAG, MEAN LIFT, R.M.S. DRAG AND R.M.S. LIFT ON CYLINDERS 1-4.

Cylinder number	Mean drag	Mean lift	R.m.s. drag	R.m.s. lift
1	1.57	-0.21	0.15	0.57
2	1.67	-0.49	0.10	0.029
3	1.65	-0.03	0.18	0.59
4	1.82	0	0.09	0.021

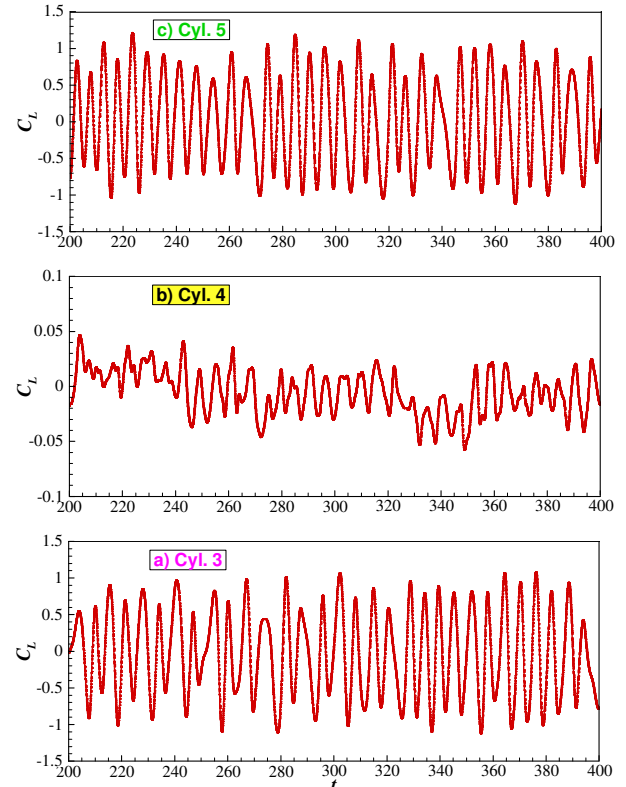


FIGURE 3: TIME HISTORY OF THE LIFT COEFFICIENT ON CYLINDERS 3, 4 AND 5.

minima, equal to 0.156, which approximates very closely the frequency of the lift force. However, after the beginning of the cycle a local maximum followed by a local minimum are observed before the absolute maximum; thus the drag trace diverges considerably from that of an isolated cylinder, which is purely sinusoidal with frequency twice the frequency of the lift force. On the other hand, we can detect cycles of lower frequency or greater period, T_w , like the cycle marked as “2”, on which fluctuations of higher frequency are superimposed. Twice the frequency of these fluctuations approximates closely the frequency of the lift force, f_s , thus these fluctuations are associated with the shedding of vortices behind the cylinders. It is evident that each cycle of period T_w contains two shedding cycles. In the beginning of cycle “2” the drag is low. It increases in the first shedding cycle in the second half of which acquires its maximum value, and decreases in the second shedding cycle, in the first half of which a local peak is observed. In what follows for reasons of brevity the cycles like cycle “2” of Fig. 2 will be denoted as “W” type cycles.

We can identify regions A, B, C and D in the time-record of the drag forces exerted on cylinders 3 and 5. Each of these regions is subdivided in two parts, 1 and 2. For example, region A is divided in two subregions, A_1 and A_2 . In A_1 , B_1 , C_1 and D_1 , the “W” cycles exist simultaneously in both cylinders. In regions A_2 and B_2 the “W” cycles can be seen only in the trace of cylinder 3,

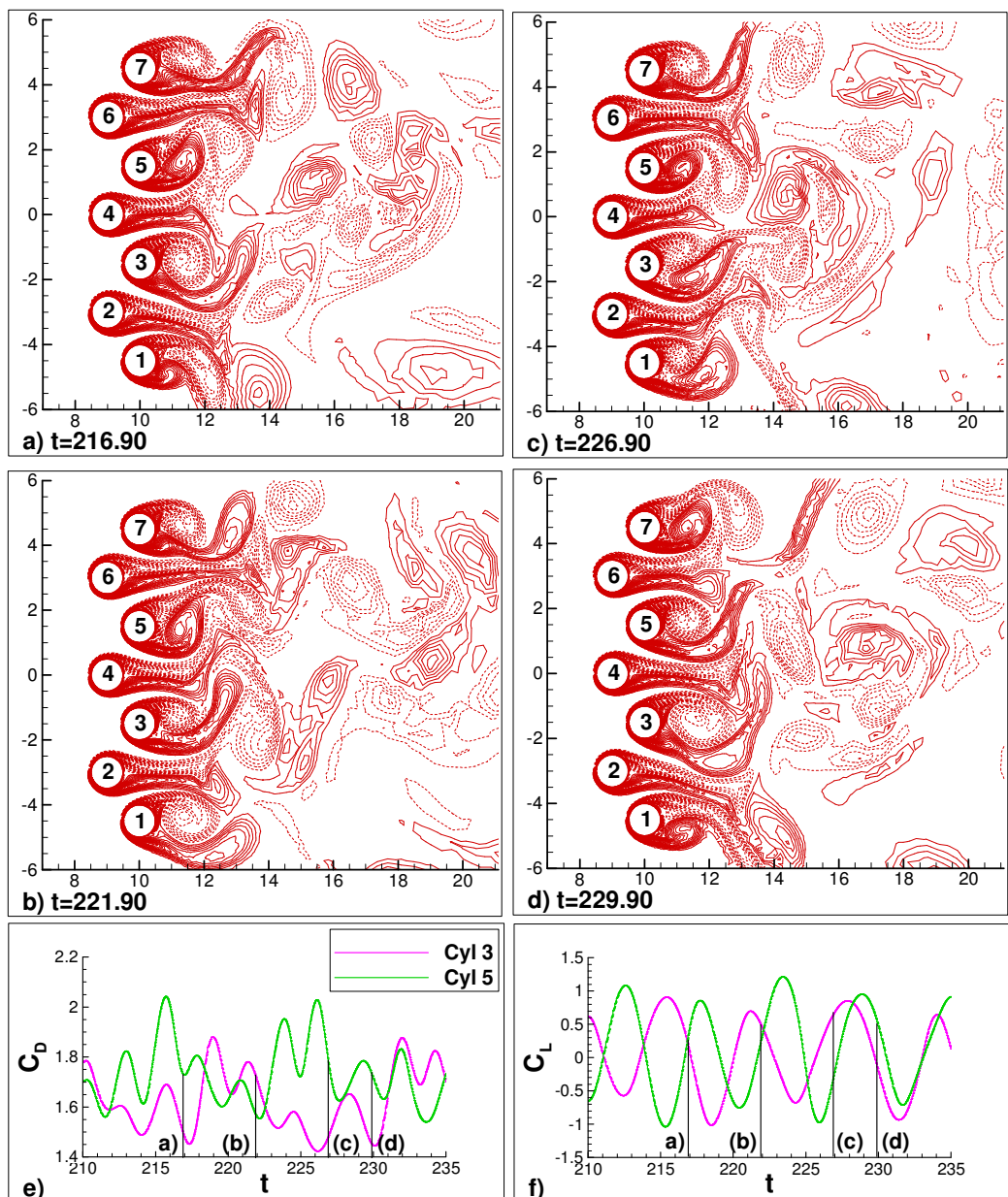


FIGURE 4: VORTICITY CONTOURS AT FOUR INSTANTS IN THE INTERVAL BETWEEN 216.9 AND 229.9, WITHIN SUBREGION A_1 OF FIG. 2.

whereas in the drag trace of cylinder 5 only fluctuations characteristic of vortex-shedding are present. In regions C_2 and D_2 cycles of type “W” exist in the trace of cylinder 5 and vortex-shedding fluctuations in the trace of cylinder 3.

An explanation of these intriguing phenomena was attempted with the aid of flow visualization. Vorticity contours at four characteristic time instants in the interval between 216.90 and 229.90 (within subregion A_1) are presented in Fig. 4. The time histories of the drag and lift forces on cylinders 3 and 5 in and around this interval are also shown (Fig. 4e and 4f respectively) and the four instants in which vorticity contours are presented are clearly marked with the corresponding letter. We notice

that at $t=216.90$ (Fig. 4a) the wake behind cylinder 3 is wider than that behind cylinder 5 and the shedding of vortices past these cylinders close to anti-phase. Referring to Fig. 4e, we notice at this instant a low drag on cylinder 3, that marks approximately the beginning of a “W” cycle, and a high drag on cylinder 5. The anti-phase timing of vortex shedding behind cylinders 3 and 5 is compatible to the anti-phase character of the lift signal of these cylinders. At $t=221.90$ (Fig. 4b), approximately one shedding cycle after the instant depicted in Fig. 6a, the wake behind cylinder 5 is wider than the wake behind cylinder 3, and the drag on cylinder 5 is lower than that on cylinder 3. At $t=226.90$ (Fig. 4c) a wide wake has been restored behind

cylinder 3 and a narrow wake behind cylinder 5, similarly to Fig. 4a. However, the shedding of vortices past cylinders 3 and 5 does not remain close to anti-phase as in Fig. 4a. In Fig. 4c the shedding of vortices past cylinder 3 appears retarded compared to the case in Fig. 4a.

As time increases the timing of vortex shedding past cylinders 3 and 5 becomes more synchronized, until, at $t=229.90$ (Fig. 4d), which marks the boundary between subregions A_1 and A_2 , the shedding of vortices behind these cylinders is very close to in-phase. This can be interpreted from the traces of the lift forces at this instant. The reason for the change in timing of vortex shedding past cylinders 3 and 5 is the different shedding frequency past these two cylinders. For cylinder 5, one shedding cycle after $t=221.90$ is completed approximately at $t=226.90$. For cylinder 3, one shedding cycle after $t=221.90$ is completed approximately at $t=228.90$ (the corresponding instant is not shown in Fig. 4). The wake of cylinder 3 at $t=229.90$ is wider than that of cylinder 5, which results in a lower drag on cylinder 3. This confirms that “W” cycles are associated with the fluctuations of the wake width behind a cylinder in two successive shedding cycles, which provides justification for their notation. There is also agreement with experimental evidence, that a wide wake results in a low drag on the corresponding cylinder and a narrow wake to a high drag.

Hence, flow visualization reveals that in subregion A_1 a wide wake behind cylinder 3 coexists with a narrow wake behind cylinder 5 and vice versa, which is in agreement to the traces of the drag forces on the two cylinders. The anti-phase timing of vortex shedding behind cylinders 3 and 5 in region A_1 at $t=216.90$ is compatible to the anti-phase character of the lift signal of these cylinders, whereas the in-phase timing at $t=229.90$ agrees with the in-phase character of the traces of the lift forces.

Vorticity contours in subregion A_2 are presented in Fig. 5 in the interval between 238.90 and 251.90, which corresponds to a “W” cycle for cylinder 3. At $t=238.90$ (Fig. 5a) a wide wake is observed behind cylinder 3, which provides justification for the low drag on this cylinder ($C_D=1.40$), whereas a narrow wake can be seen behind cylinder 5. At $t=242.90$ (Fig. 5b), approximately a half of a shedding cycle after $t=238.90$, the wake behind cylinder 3 is narrower than in Fig. 5a, which is in agreement to the higher drag on this cylinder ($C_D=1.55$). The wake behind cylinder 5 is similar to the wake behind cylinder 3 although somewhat narrower, which results in a slightly higher drag ($C_D=1.63$). Fig. 5c depicts the vorticity contours at an instant one shedding cycle after $t=238.90$ (Fig. 5a) for cylinder 3. The wake behind cylinder 3 at $t=245.90$ is narrow, giving rise to a higher drag ($C_D=1.73$) than that at $t=238.90$. Fig. 5d corresponds to an instant one shedding cycle after that of Fig. 5c and two shedding cycles after that of Fig. 5a. The wake behind cylinder 3 at $t=251.90$ is wider than that at $t=238.90$, yielding a dimensionless drag as low as 1.31. The shedding of vortices past cylinders 3 and 5 remains close to in-phase throughout the interval of Fig. 5, although the

shedding frequency is not the same for both cylinders. The shedding frequency for cylinder 5 remains almost constant, whereas significant variations of the shedding frequency past cylinder 3 can be detected from the lift trace of Fig. 5f.

Hence in subregion A_2 approximately the same wake pattern is repeated in each shedding cycle behind cylinder 5, whereas the wake behind cylinder 3 switches from wide to narrow in a shedding cycle and from narrow to wide in the following cycle. However, the width of the wake of cylinder 5 increases slightly in successive cycles, accompanied by a small decrease of the drag force. In the drag trace of cylinder 3 we detect lower frequency (“W”) cycles on which fluctuations at the vortex shedding frequency are superimposed, whereas in the trace of the drag force exerted on cylinder 5 no “W” cycles are visible. At $t=260$ the wake past cylinder 3 becomes substantially narrower than that past cylinder 5. After that subregion B_1 begins, in which switch of wake width for both cylinders 3 and 5 is observed.

Other parts of the record are identified, in which the wake behind cylinder 3 remains very close to periodic at consecutive shedding cycles, whereas it switches from wide to narrow and vice-versa behind cylinder 5. This is the case in the interval $365 < t < 387$ for example, characterized as subregion D_2 . In this interval the fluctuations due to vortex shedding in the trace of the drag force on cylinder 5 are more discernible than those in the trace of the drag force of cylinder 3 in subregion A_2 .

A conclusion drawn from Fig. 2 and the visualization of flow patterns is that a subregion like A_2 (switch of wake width behind only one cylinder) is always preceded by a subregion like A_1 , in which the switch of wake width occurs at both cylinders. When the vortex pattern past both cylinders is close to in-phase, like in Fig. 4d, subregion A_1 gives its position to subregion A_2 . The cylinder whose wake width switches is the one with wider wake at the upper boundary of region A_1 . For example, in Fig. 4d ($t=229.90$) the wake of cylinder 3 is wider, and this is the cylinder whose wake width switches in region A_2 that follows. Conversely at $t=365.65$ (upper boundary of region D_1) the wake behind cylinder 5 is wider, thus wake switch occurs in the wake of that cylinder.

In all cases a narrow wake is formed behind each of the three cylinders of the upstream row, and the vorticity generated on these cylinders enters through the gap and is conveyed behind the downstream cylinders. The vorticity generated on the upstream cylinders switches direction (up and down), which is controlled by the wakes of the downstream cylinders. In Fig. 4b, for example, the vorticity generated on cylinder 4 is tilted downwards due to the wide wake of cylinder 5, whereas in Fig. 4c the wide wake of cylinder 3 displaces upwards the vorticity generated on cylinder 4. The almost symmetrical wake pattern close to the upstream cylinders is compatible to the very low lift force exerted on them. The mean drag on the upstream cylinders is higher than that of the downstream cylinders, in agreement with experimental evidence.

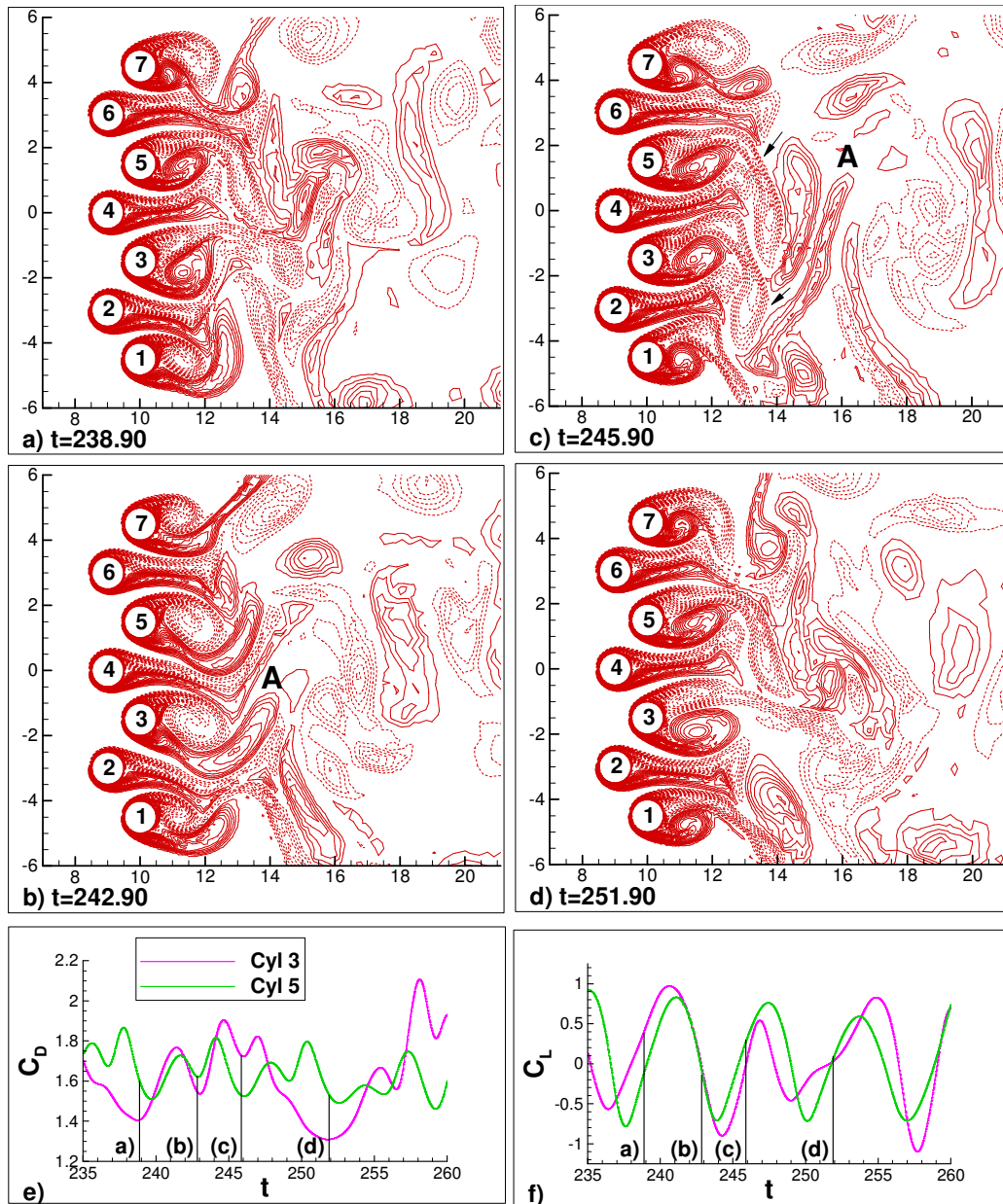


FIGURE 5: VORTICITY CONTOURS AT FOUR INSTANTS IN THE INTERVAL BETWEEN 238.9 AND 251.9, SPANNING A “W” CYCLE FOR CYLINDER 3 WITHIN SUBREGION A_2 OF FIG. 2.

Detailed flow visualization and examination of the lift traces confirmed that a wide wake behind any of cylinders 3 or 5 results in a lower frequency of the lift force in the corresponding interval and a narrow wake in a higher frequency. In region A_1 , for example, when a wide wake behind cylinder 3 coexists with a narrow wake behind cylinder 5, the frequency of the corresponding lift cycle is lower for cylinder 3 than for cylinder 5. The same observation is valid in region A_2 , for cylinder 3 whose wake width switches. The frequency of the lift force of cylinder 5 in this region does not vary substantially in different cycles, although it does not remain absolutely constant. Although the present situation is different from

the flow past a single cylinder, the phenomena are compatible to the definition of Roshko’s [14] universal Strouhal number. According to this definition a large wake width compared to the cylinder diameter is associated to a lower shedding frequency and vice-versa.

The sequence of vorticity contours displayed in Fig. 5 reveals the procedure of formation of vortex structures, quite different from those observed for flow past a single cylinder. The negative vortices formed at the upper side of cylinders 3 and 5 at $t=242.90$ are convected at a substantial distance transversely below the wake central-line of the corresponding cylinder at $t=245.90$ (Fig. 5c), as shown with the arrows. It is reminded that Fig. 5c depicts

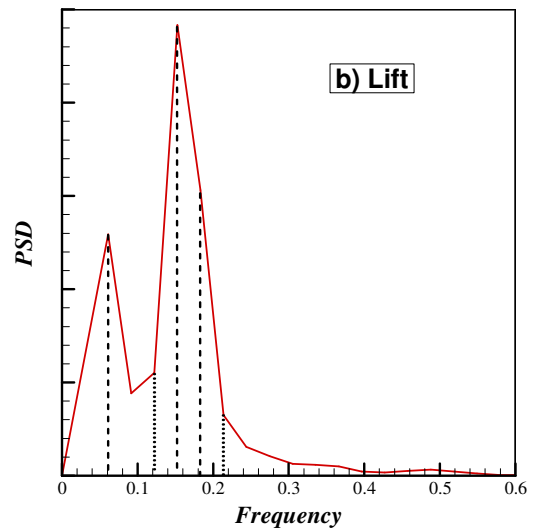
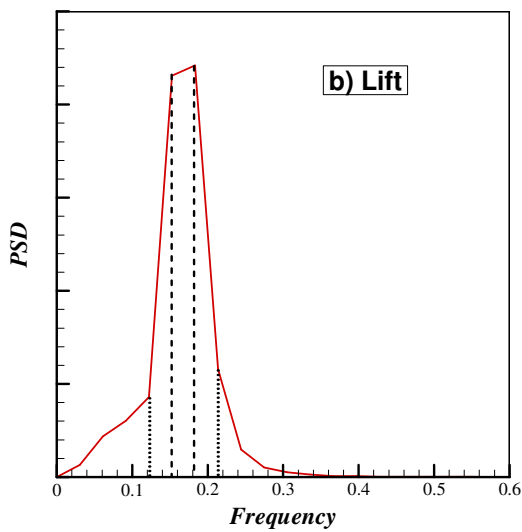
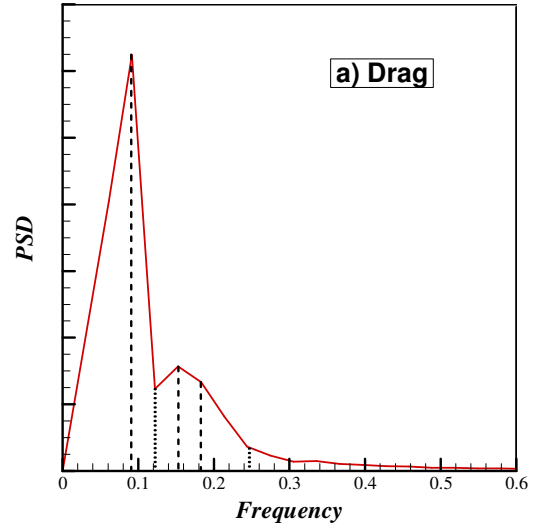
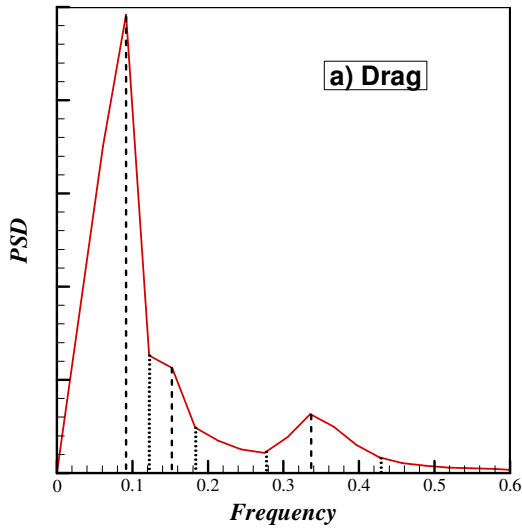


FIGURE 6: POWER SPECTRA OF DRAG AND LIFT FORCES FOR CYLINDERS 3 AND 5

FIGURE 7: POWER SPECTRA OF DRAG AND LIFT FORCES FOR CYLINDER 4.

the instant in which the wake behind cylinder 3 has switched to narrow. We can also observe vortex “A” formed at the lower side of cylinder 3 at $t=242.90$. The cross-wake motion of the negative vortex formed at the upper side of this cylinder causes complete detachment of vortex “A”, which at $t=245.90$ appears long and narrow and has merged with the vortex shed from the lower side of cylinder 2.

Power spectra generated from the force traces of Fig. 2 and 3 are presented in Fig. 6 for cylinders 3 and 5 and in Fig. 7 for cylinder 4. The spectra of the lift forces for cylinders 3 and 5 display an almost constant peak in the band of frequencies between 0.152 and 0.182. The lower of these frequencies (0.152) is the dominant vortex-shedding frequency associated with a wide wake, and the higher (0.182) the dominant frequency associated with a narrow wake. These values are lower than 0.196, which was obtained by Meneghini and Bearman [15] for 2-D flow past a single cylinder at $Re=200$. The lift frequency

for the cylinder whose wake width does not switch in subregions like A_2 varies between 0.152 and 0.17 in most cases. The frequencies 0.12 and 0.21 (marked with dotted lines) that bound the region in which the frequency varies linearly to the peak values are compatible to the minimum and maximum frequency detected in the traces of the lift force. The spectra of the drag forces for the same cylinders display a peak at $f=0.091$, which results from the “W” cycles in the traces of the drag forces due to the wake switch. It should be noted that the value 0.091 is the half of 0.182, which is the value of the higher of the two dominant shedding frequencies. We can also detect the increased contribution in the band of frequencies between 0.28 and 0.42, which clearly results from the fluctuations of the drag force at a frequency twice of a shedding cycle. Interestingly, the local peak in this band occurs at the frequency 0.334, which is the sum of the dominant vortex-shedding frequencies (0.152+0.182). There also exists a local increase of spectral densities in the band of

frequencies between 0.12 and 0.182, with a local peak at $f=0.152$. This band results evidently from cycles like cycle 1 in Fig. 2b, in which the drag fluctuation at the shedding frequency is more pronounced than its double value.

The peak at the lower of the dominant vortex-shedding frequencies, equal to 0.152, can be seen in the spectrum of the lift force exerted on cylinder 4, whereas there is an inflexion at $f=0.182$. This can be explained from the fact that vortex shedding from the cylinders of the upstream row does not occur. The fluctuations of the lift forces on these cylinders result from the motion of their wakes up and down, which is controlled by the wakes of the cylinders of the downstream row. As already explained, the wider wakes, associated with frequency equal to 0.152 seem to have the first role. A local peak at a frequency equal to 0.061 is also present. The peak in the spectrum of the drag force of cylinder 4 occurs at $f=0.091$, which is the dominant frequency of the “W” cycles. A local peak can be seen at $f=0.152$ and an inflexion at $f=0.182$. The drag force exerted on cylinder 4 fluctuates at the same frequency as the lift force, contrary to the vortex-shedding case past a single cylinder. This is compatible to the fact that vortex-shedding behind the cylinders of the upstream row does not occur. The spectra of the drag and lift forces for the other two cylinders of the upstream row, 2 and 6, are not appreciably different from the corresponding for cylinder 4.

CONCLUSIONS

The finite element study conducted herein revealed interesting aspects of cross-flow past two staggered rows of cylinders. Although, at a first glance, the flow pattern looks chaotic, a systematic attempt was made for the flow classification. Focusing our attention on the two inner cylinders of the downstream row, switch of wake width in two successive shedding cycles was observed, simultaneously for both cylinders or at least for one of these cylinders. When wake switch occurred on both cylinders, a wide wake behind one of the cylinders coexisted with a narrow wake behind the other cylinder and vice versa. The formation of a wide wake behind a cylinder is associated with a lower drag and a lower shedding frequency and vice-versa. The mean drag forces exerted on the cylinders of the upstream row were higher than those on the cylinders of the downstream row, in agreement with experimental evidence. Vortex shedding does not occur behind the cylinders of the upstream row, yielding a negligible lift force on these cylinders.

REFERENCES

- [1] Ganoulis, J., Brunn, P., Durst, F., Holweg, J., and Wunderlich, A., 1989. “Laser measurements and computations of viscous flow through cylinders”. *ASCE Journal of Hydraulic Engineering*, 115, pp. 1223-1239.
- [2] Tezduyar, T.E., and Liou, J., 1990. “Computation of spatially periodic flows based on the vorticity-stream function formulation”. *Computer Methods in Applied Mechanics and Engineering*, 83, pp. 121-142.
- [3] Rasoul, J., Anagnostopoulos, P., and Ganoulis, J., 1994. “Numerical and experimental investigation of laminar flow through a staggered bundle of cylinders”. *Zeitschrift Angewandte Mathematik und Mechanik (ZAMM)*, 74, pp. 333-340.
- [4] Rorris, L., Rasoul, J., Anagnostopoulos, P., and Ganoulis, J., 1994. “Finite difference analysis of transient flow through a staggered bundle of cylinders”. In Proceedings of the 5th Conference on Hydraulic Engineering Software (HYDROSOFT V), W.R. Blain and K. Katsifarakis, eds., Vol. 2, Chalkidiki, Greece, WIT Press, pp. 67-74.
- [5] Braun, M.J. and Kudriavtsev, V.V., 1995. “Fluid flow structures in staggered banks of cylinders located in a channel”. *ASME Journal of Fluids Engineering*, 117, pp. 36-44.
- [6] Sweeney, C., and Meskell, C., 2003. “Fast numerical simulation of vortex shedding in tube arrays using a discrete vortex method”. *Journal of Fluids and Structures*, 18, pp. 501-512.
- [7] Huang, Z., Olson, J.A., Kerekes, R.J., and Green, S.I., 2006. “Numerical simulation of the flow around rows of cylinders”. *Computers and Fluids*, 35, pp. 485-491.
- [8] Lam, K., Jiang, G.D., Liu, Y., and So, R.M.C., 2006. “Simulation of cross-flow-induced vibration of cylinder arrays by surface vorticity method”. *Journal of Fluids and Structures*, 22, pp. 1113-1131.
- [9] Liang, C., and Papadakis, G., 2007. “Large eddy simulation of cross-flow through a staggered tube bundle at subcritical Reynolds number”. *Journal of Fluids and Structures*, 23, pp. 1215-1230.
- [10] Roberts, B.W., 1966. “Low frequency, aeroelastic vibrations in a cascade of circular cylinders”. Mechanical Engineering Science Monograph No 4, IMechE.
- [11] Zdravkovich, M.M., and Stonebanks, K.L., 1990. “Intrinsically nonuniform and metastable flow in and behind tube arrays”. *Journal of Fluids and Structures*, 4, pp. 305-319.
- [12] Seitanis, S.A., Anagnostopoulos, P., and Bearman, P.W., 2005. “An experimental study of the in-line oscillations of a closely spaced row of cylinders in cross-flow”. *Journal of Fluids and Structures*, 21, pp. 211-226.
- [13] Zienkiewicz, O.C., and Taylor, R.L., 1991. “The Finite Element Method”. 4th Ed., McGraw-Hill, London.
- [14] Roshko, A., 1955. “On the wake and drag of bluff bodies”. *Journal of the Aeronautical Sciences*, 22, pp. 124-132.
- [15] Meneghini, J.R., and Bearman, P.W., 1995. “Numerical simulation of high amplitude oscillatory flow about a circular cylinder”. *Journal of Fluids and Structures*, 9, pp. 435-455.



NUMERICAL STUDY OF TUBE-BUNDLE FLOW-INDUCED VIBRATIONS WITH MULTIPHASE-POD APPROACH

Marie Pomarède

LaMSID - UMR CNRS # 8193
1 Avenue du Général de Gaulle
92141 Clamart
FRANCE

Erwan Liberge

LaSIE - FRE CNRS 3474
Avenue Michel Crépeau
17042 La Rochelle
FRANCE

Aziz Hamdouni

LaSIE - FRE CNRS 3474
Avenue Michel Crépeau
17042 La Rochelle
FRANCE

Email: marie-externe.pomarede@edf.fr

Elisabeth Longatte

LaMSID - UMR CNRS # 8193
1 Avenue du Général de Gaulle
92141 Clamart
FRANCE

Jean-François Sigrist

DCNS Research
Dept. Dynamique des Structures
CESMAN
44620 La Montagne
FRANCE

ABSTRACT

Flow-induced vibrations occurring in nuclear steam generators (of nuclear power plants or nuclear on-board stokeholds) are the cause of damages that have to be avoided to ensure a long life to exploitations. The numerical study of such mechanisms is thus crucial and, in order to proceed to even more efficient calculations in terms of time, the use of reduced-order models has now become an essential method. In this paper, we propose to apply the so-called “Multiphase-POD”, which is the adaptation of the well-known POD method to the case of fluid-structure interactions. We focus on the case of large displacements in tube bundle-like configurations. Results are encouraging to open this technique to systematic FIV studies and to real-time control.

NOMENCLATURE

ρ Global density ($kg.m^{-3}$)
 μ Global dynamic viscosity ($kg.m^{-1}.s^{-1}$)
 \mathbf{u} Global velocity field
 p Global pressure field
 σ Constraints tensor
 g_f A variable g in the fluid domain
 g_s A variable g in the solid domain
 D Cylinder diameter
 P Pitch ratio in tube bundle

INTRODUCTION

Nuclear power plants and nuclear on-board stokeholds are containing very complex installations where flow-induced vibrations are present at various levels. Particularly, tube bundle systems in the steam generator part are prone to fretting-wear or even breaking, mainly due to transverse flow-induced vibration problems [1–8]. But, as well as experiments, numerical simulations of fluid-structure interactions in a tube bundle system remain very costly [9–11] : in order to give a relevant description of the flow and of the structure displacements, it is necessary to construct a system with a large number of degrees of freedom. The three-dimensional aspect of the flow and of the fluid-structure interactions added to the large number of tubes and their reciprocal interactions force us to lead long-time calculations, in order to be as precise as possible.

One of the existing alternatives to these restrictive situations from an industrial point of view is to have recourse to reduced-order models [12–17] such as POD (Proper Orthogonal Decomposition) [18–20]. It is thus possible to make numerical calculations in a very short time, and this paves the way to lead parametric studies or even real-time control. Here, the challenge consists in the adaptation of POD to the case of fluid-structure interaction problems. Liberge & Hamdouni [16,21] proposed an efficient

way to cope with the moving fluid-structure interface; this method is called ‘‘Multiphase-POD’’ : the idea is to consider the whole system (fluid and structure domains) as a unique multiphase domain. The advantages of this technique are numerous. First, the data can be extracted from any way (experiments, moving grid techniques, etc.), it is only necessary to know how data are organized to proceed to the interpolation. Here, we show its ability to reproduce large structure displacements, which is often, to the author’s knowledge, not so easy with other reduced-order models. The first part of this paper is dedicated to the description of the Multiphase-POD method. Then, its application to the case of large displacements of a single circular cylinder under cross-flow (lock-in phenomenon) is presented in a second part. Finally, a 2D tube-bundle configuration is considered with one moving cylinder under cross-flow.

MULTIPHASE-POD

We consider here that POD-Galerkin method is well known (see for example [19]) and we are interested on its adaptation to FSI through Multiphase-POD. Complete calculations are leaded with a classic ALE approach [22]. Thus, in this case of Flow Induced Vibrations, classic POD-Galerkin method cannot be used because of the presence of a moving interface : POD modes are only spatial and consequently, they do not contain any dynamic information, although snapshots, in the case of an ALE calculation, have been taken for several positions of mesh nodes.

To get round this problem, Liberge & Hamdouni [16] proposed an original method that treats the case of a fluid-structure interaction problem with an adaptation of the POD-Galerkin technique, which is called ‘‘Multiphase-POD method’’, where a non-moving mesh is used. The description of the Multiphase-POD method is the following : lets consider a global domain Ω containing the fluid domain $\Omega_f(t)$ and the solid domain $\Omega_s(t)$ at each time step t , where the solid domain is considered as a particular fluid with its own physical characteristics (density, viscosity). We have $\Omega = \Omega_f(t) \cup \Omega_s(t) \cup \Gamma_i(t)$, where $\Gamma_i(t)$ is the interface between fluid and solid domains. A global velocity field $u \in H(\Omega)$ (with H a Hilbert space) is considered :

$$u(x, t) = u_f(x, t)\chi_{\Omega_f}(x, t) + u_s(x, t)\chi_{\Omega_s}(x, t) \quad (1)$$

where χ_{Ω_f} and χ_{Ω_s} are respectively characteristics functions defining if the considered point position is in the

fluid or in the solid domain :

$$\chi_{\Omega_s}(x, t) = \begin{cases} 1 & \text{if } x \in \overline{\Omega_s} \\ 0 & \text{if } x \notin \overline{\Omega_s} \end{cases} \quad (2)$$

and $\chi_{\Omega_f}(x, t) = 1 - \chi_{\Omega_s}(x, t)$. Taking into account this notations, a global weak form of Navier-Stokes equations on Ω is made possible to formulate :

$$\int_{\Omega} \rho \frac{\partial u(x, t)}{\partial t} u^* dx + \int_{\Omega} (u \cdot \nabla) u \cdot u^* dx = \int_{\Omega} (\nabla \cdot \sigma) u^* dx \quad (3)$$

where u^* is a test-function defined as $u^* \in H(\Omega)$ with the non-deformable solid constraint :

$$D(u^*) = 0 \text{ in } \Omega_s(t) \quad (4)$$

Each field or variable is defined on the global domain Ω as described below:

$$\begin{cases} u(x, t) = u_f(x, t)\chi_{\Omega_f}(x, t) + u_s(x, t)\chi_{\Omega_s}(x, t) \\ \sigma(x, t) = \sigma_f(x, t)\chi_{\Omega_f}(x, t) + \sigma_s(x, t)\chi_{\Omega_s}(x, t) \\ \rho(x, t) = \rho_f(x, t)\chi_{\Omega_f}(x, t) + \rho_s(x, t)\chi_{\Omega_s}(x, t) \\ \mu(x, t) = \mu_f(x, t)\chi_{\Omega_f}(x, t) + \mu_s(x, t)\chi_{\Omega_s}(x, t) \end{cases} \quad (5)$$

Lets define both components of the constraints tensor σ :

$$\sigma_{f,ij}(x, t) = -p\delta_i^j + 2\mu_f D_{ij}(u_f) \quad (6)$$

where δ_i^j is the Kroenecker symbol and D_{ij} is the deformation velocity tensor. The definition of the structural compotent $\sigma_s(x, t)$ allows taking into account that the solid has its specific viscosity and the non-deformable structural condition. For the viscosity, a penalization term is used: in order to specify that the domain $\Omega_s(t)$ is solid, the viscosity is artificially increased. To insure the non-deformable condition, a Lagrange multiplier Λ is added. Thus, the structural component of the constraints tensor is:

$$\sigma_{s,ij}(x, t) = -p\delta_i^j + \Lambda + 2\mu_s D_{ij}(u_s) \quad (7)$$

Developing the global weak form with these definitions and making the Proper Orthogonal Decomposition on the global velocity flow field leads to the construction of a dynamical system for the whole domain Ω which is fixed

all over the studied time interval. Taking into account the space-time decomposition of the global velocity field as:

$$u(x,t) = \sum_{i=1}^N a_i(t) \Phi_i(x) \quad (8)$$

where Φ_n , $n = 1, \dots, N$ are elements of the POD basis and $a_n(t)$, $n = 1, \dots, N$ are time coefficients, the final dynamical system is the following :

$$\begin{cases} \sum_{i=1}^N \frac{da_i}{dt} A_{in} = \sum_{i=1}^N \sum_{j=1}^N B_{ijn} a_i a_j + \sum_{i=1}^N C_{in} a_i + E_n \\ D(u) = 0 \text{ on } \Omega_s(t) & \text{(non deformability)} \\ \frac{\partial \chi_{\Omega_s}}{\partial t} + u \cdot \nabla \chi_{\Omega_s} = 0 & \text{(characteristic function transfer)} \end{cases} \quad (9)$$

for each $n = 1, \dots, N$ where N is the number of modes in the POD basis. Coefficients $A_{in}, B_{ijn}, C_{in}, E_n$ are not detailed here, but a very important point to notice is that they are not all exclusively spatial coefficients, because some of them contain the physical characteristics $\rho(x,t)$ and $\mu(x,t)$. Thus, they have to be re-calculated at each time step: the time calculation is increased in comparison with a classic POD model without moving structure. But this time calculation is still less than a complete calculation. Another approach consists in making the proper orthogonal decomposition of the characteristic function $\chi_{\Omega_f}(x,t)$ also, which allows avoiding the time dependence of all coefficients of the dynamical system. For more precisions, see [21]. Practical implementation of the Multiphase-POD technique is described below.

1. Lead a complete ALE calculation of the fluid-structure interaction problem during a time interval $[0,T]$
2. Extract enough snapshots from this complete calculation
3. Create a unique Cartesian fixed mesh containing both fluid and solid domains
4. Interpolate each extracted snapshot onto the fixed reference mesh: new fixed snapshots are created
5. Apply the classic POD approach for the new snapshots constructed on the reference mesh
6. Construct the dynamical system following (9) and resolve it with a classic method (Runge-Kutta for example).

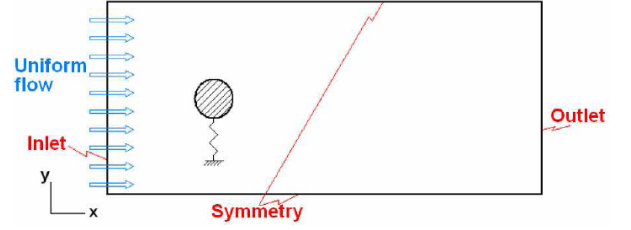


FIGURE 1: CASE OF A SINGLE CIRCULAR CYLINDER AND BOUNDARY CONDITIONS

APPLICATION TO LOCK-IN PHENOMENON OF A SINGLE CIRCULAR CYLINDER

In a first time, we propose a simple application of the Multiphase-POD technique, which is the case of a circular cylinder under cross-flow (see Fig.1). The cylinder is submitted to transverse displacements (y -direction) due to the presence of the flowing fluid. The case of small displacements of the structure has already been tested with Multiphase-POD in [16]. Here, we consider the lock-in phenomenon [23–25], where amplitudes of the structure displacement are of the order of the cylinder radius. The fluid domain is considered as infinite, as boundaries are far enough from the structure. The effects that the flow exerts on the structure are modeled through a restoring force. Reynolds number is $\mathcal{R}_e = 100$, fluid is water. Cylinder displacement maximal amplitude is $A^* = 0.58D$, where D is the cylinder diameter: the frequency lock-in mechanism is reached. Complete calculations are leaded with the CFD code *Code_Saturne* [26] and data at the interface are interpolated to the cylinder gravity center. The reduced-order model is constructed with the following characteristics: 250 snapshots are extracted from the complete ALE calculation, 6 POD modes are constituting the POD basis. The fixed reference mesh contains 200×250 points. The dynamical system resolution in the present case is simplified: indeed, the penalization term is sufficient to guarantee the non-deformable condition. Time integration scheme is Runge-Kutta 4.

The two first time coefficients are represented on Fig.2, they are well reconstructed by the reduced model. And, as they are containing the main part of the system energy, this good reproduction allows a good reconstruction of the velocity flow field and the cylinder displacement is also well reproduced (Fig.3), which is confirming that 1) the Multiphase-POD method is able to reproduce a structure displacement and a fluid flow with its global formulation and 2) the Multiphase-POD method is able to reproduce large displacements of the structure. The latter point is interesting for the willingness of studying instability behaviors.

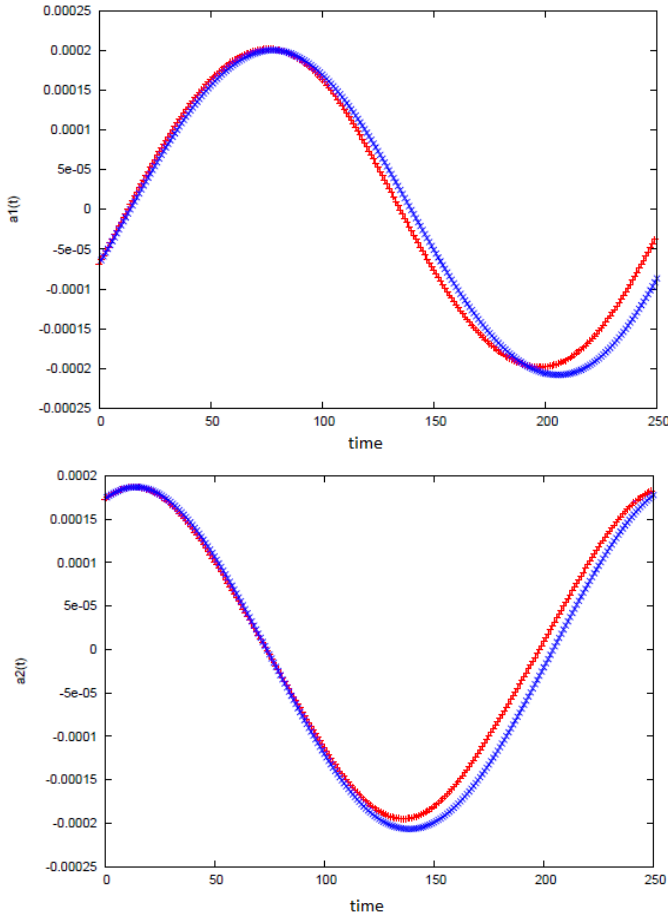


FIGURE 2: TWO FIRST TIME COEFFICIENTS OF THE VELOCITY FIELD FOR THE SINGLE CYLINDER. +++ DIRECT COEFFICIENT ; xxx MULTIPHASE-POD RECONSTRUCTION

APPLICATION TO FIV IN TUBE-BUNDLE CONFIGURATION

In order to consider a configuration close to the case of a tube bundle of heat exchanger, we consider a circular cylinder in a confined configuration. Non-dimensional numbers are adapted to this configuration, here Reynolds number is defined as $Re = \frac{\rho U_p D}{\mu}$. The step fluid velocity U_p takes into account the tube confinement and is defined as: $U_p = U_\infty \frac{P}{P-D}$ where U_∞ is the equivalent mean flow velocity that would have been imposed in an infinite domain and P is the pitch ratio (distance between two neighbouring cylinders centres). Geometry and boundary conditions are depicted on Fig.4: a 2D domain and only one tube and its neighbors are considered, with inlet/outlet boundary conditions. Thus, the domain is not representing a whole tube bundle but a confined case. Reynolds number is fixed to $Re = 2000$, complete calcu-

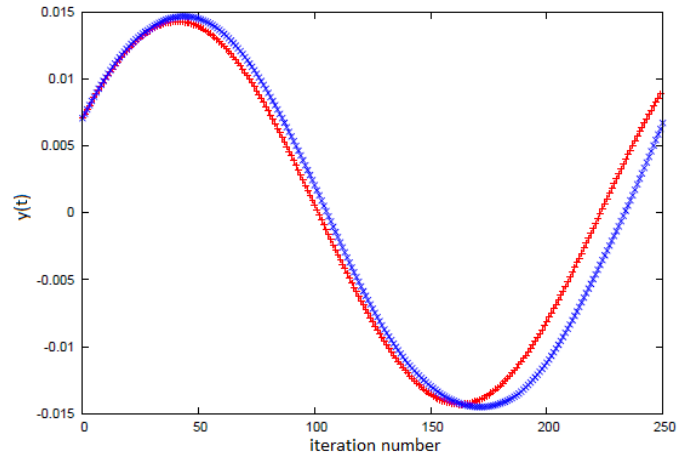


FIGURE 3: GRAVITY CENTER DISPLACEMENT RECONSTRUCTION OF THE CYLINDER. +++ DIRECT CALCULATION ; xxx MULTIPHASE-POD RECONSTRUCTION

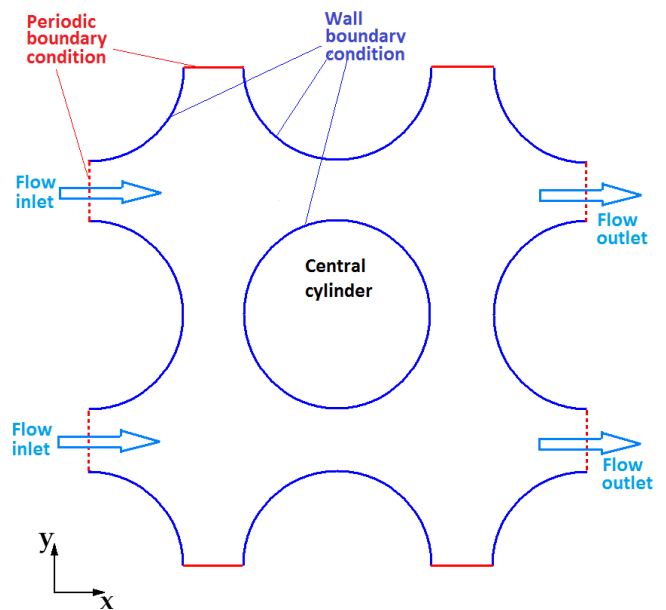


FIGURE 4: BOUNDARY CONDITIONS FOR THE CONFINED TUBE

lation is also leaded with *Code_Saturne* which has been validated in various FSI studies in tube bundle systems [9, 10, 27]. Large displacements in the y -direction (see Fig.4) of the central cylinder are considered ($A^* = 0.35D$ when $P/D = 0.44D$). The reference fixed mesh contains 200×200 points.

Figure 5 represents the comparison between the global velocity flow field from the complete calculation and the interpolated velocity flow field. It allows to check the precision of the snapshots interpolation algo-

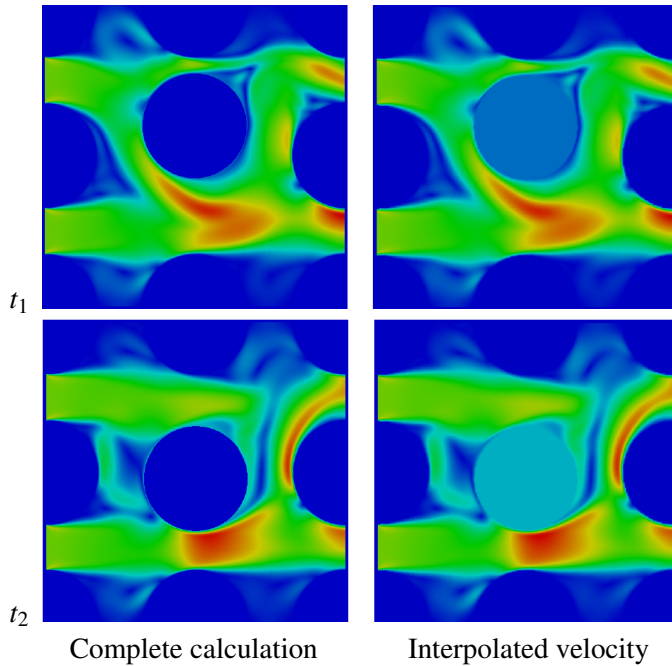


FIGURE 5: COMPARISON BETWEEN COMPLETE AND INTERPOLATED VELOCITY FIELD AT TWO DATES t_1 AND t_2

rithm: velocity levels are well reproduced after interpolation. In the interpolated case (right-hand side), the non-zero velocity in the cylinder zone is representative of the structure velocity, which is now considered as the second phase of the flow. Figure 6 shows the comparison between the central cylinder displacement calculated by complete calculation and by Multiphase-POD. The reconstruction gives very satisfying results, which is confirmed by the observation of the two first time coefficients of the global velocity flow field (Fig.7). The reconstruction of large displacements with Multiphase-POD in the case of a confined tube bundle is very interesting. It allows to plan for its implementation to unstable fluid-structure interactions like fluid-elastic instability occurring in tube bundle systems [5, 6, 28–30].

CONCLUSION

In this paper, the Multiphase-POD method is presented and applied to the case of a single circular cylinder moving under cross-flow and a confined cylinder in tube bundle under cross-flow. The method was already shown to be efficient in the case of small displacements of a structure under flow solicitations and here, we show its efficiency in the case of large displacements of the structure. This is a very interesting point in order to treat instabilities that can appear in a large number of industrial

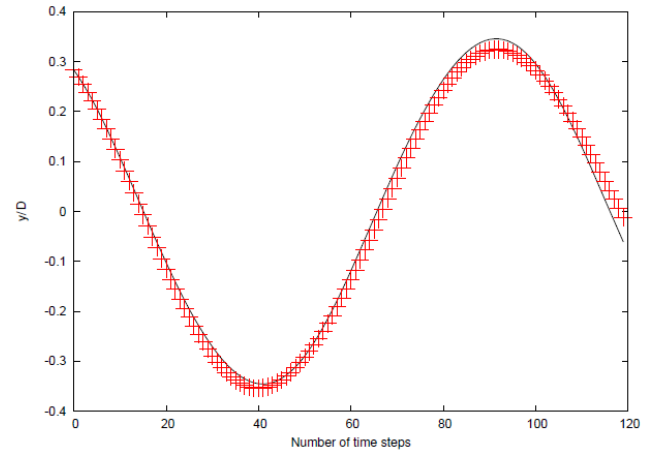


FIGURE 6: COMPARISON BETWEEN COMPLETE AND MULTIPHASE-POD RECONSTRUCTION OF THE CENTRAL CYLINDER DISPLACEMENT. — COMPLETE CALCULATION, +++ MULTIPHASE-POD RECONSTRUCTION

systems. Moreover, a simple case of tube bundle has been successfully past with Multiphase-POD, which is encouraging for reducing calculation times in this context. An on-going work is the application of parametric studies with the help of POD: the main interest of reduced-order models consists in their ability to reconstruct various solutions of a system where one or several parameters have been changed. Indeed, the reconstruction of a solution for which we already have the complete calculation is not sufficient. Further work will consist in the application of these methods to the case of FSI.

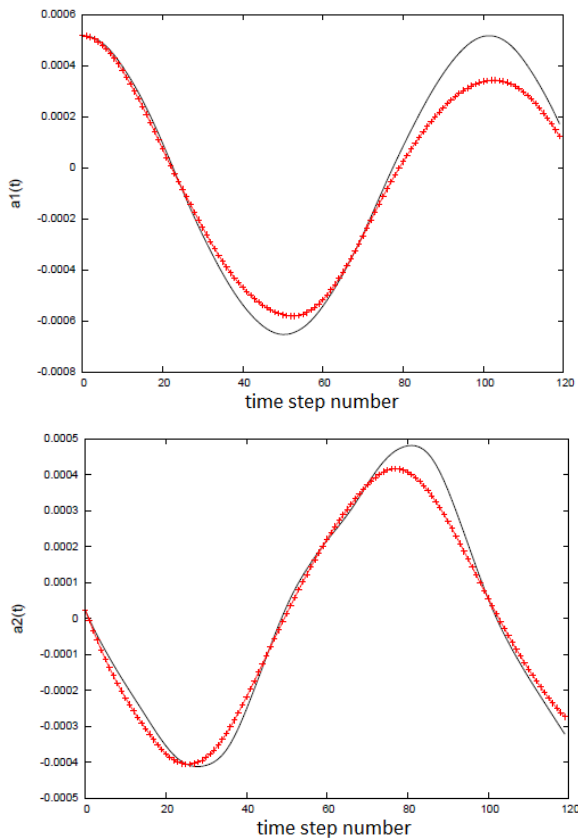


FIGURE 7: COMPARISON BETWEEN COMPLETE AND MULTIPHASE-POD RECONSTRUCTION OF TIME COEFFICIENTS. +++ DIRECT COEFFICIENT; — MULTIPHASE-POD RECONSTRUCTION

REFERENCES

- [1] Axisa, F., Antunes, J., and Villard, B., 1990. “Random excitation of heat exchanger tubes by cross-flows”. *Journal of Fluids and Structures*, **4**, pp. 231–341.
- [2] Blevins, R., 1990. *Flow-Induced Vibrations*. Van Nostrand Reinhold.
- [3] Blevins, R., and Bressler, M., 1987. “Acoustic resonances in heat exchangers, Part II: Prediction and suppression of resonance”. *ASME Journal of Pressure Vessel Technology*, **109**, pp. 282–288.
- [4] Feenstra, P., Weaver, D., and Nakamura, T., 2003. “Vortex shedding and fluidelastic instability in a normal square tube array excited by two-phase cross-flow”. *Journal of Fluids and Structures*, **17**, pp. 793–811.
- [5] Lever, J., and Weaver, D., 1986. “On the stability of Heat Exchanger Tube Bundles, Part II: Numerical results and comparison with experiments”. *Journal of Sound and vibration*, **107**(3), pp. 393–410.
- [6] Pettigrew, M., and Taylor, C., 1991. “Fluidelastic Instability of heat exchanger tube bundle: review and design recommendations”. *Journal of Pressure Vessel Technology*, **113**, pp. 242–256.
- [7] Paidoussis, M.P., 1982. “A review of flow-induced vibrations in reactors and reactor components”. *Nuclear Engineering and Design*, **74**, pp. 31–60.
- [8] Pettigrew, M., and Gorman, D., 1981. “Vibration of heat exchanger tube bundles in liquid and two-phase cross-flow”. *Flow-induced vibration design guidelines P.Y. Chen edition, ASME PVP*, **52**, pp. 89–110.
- [9] Benhamadouche, S., and Laurence, D., 2003. “LES, coarse LES, and transient RANS comparisons on the flow across a tube bundle”. *International Journal of Heat and Fluid Flow*, **24**, pp. 470–479.
- [10] Huvelin, F., 2008. “Couplage de codes en interaction fluide-structure et application aux instabilités fluide-élastiques”. PhD Thesis, Ecole des Sciences Pour l’Ingénieur de Lille.
- [11] Sigrist, J., and Abouri, D., 2006. “Numerical simulation of a non-linear coupled fluid-structure problem with implicit and explicit coupling procedures”. ASME, ed., *Pressure Vessel and Piping*. Vancouver.
- [12] Allery, C., Guerin, S., Hamdouni, A., and Sakout, A., 2004. “Experimental and numerical POD study of the Coanda effect used to reduce self-sustained tones”. *Mechanics Research Communications*, **31**, January-February, pp. 105–120.
- [13] Couplet, M., Basdevant, C., and Sagaut, P., 2005. “Calibrated reduced-order POD-Galerkin system for fluid flow modelling”. *Journal of Computational Physics*, **207**, pp. 192–220.
- [14] Anttonen, J., King, P., and Beran, P., 2005. “Application of Multi-POD to a pitching and plunging airfoil”. *Mathematical and Computer Modelling*, **42**, pp. 245–259.
- [15] Bogaers, A., 2010. “Reduced Order Modeling Techniques for Mesh Movement Strategies as Applied to Fluid Structure Interactions”. Master of engineering, University of Pretoria.
- [16] Liberge, E., and Hamdouni, A., 2010. “Reduced-order modelling method via Proper Orthogonal Decomposition (POD) for flow around an oscillating cylinder”. *Journal of Fluids and Structures*, **26**(2), pp. 292–311.
- [17] Lieu, T., Farhat, C., and Lesoinne, M., 2006. “Reduced-order fluid/structure modelling of a complete aircraft configuration”. *Computer Methods in Applied Mechanics and Engineering*, **195**, pp. 5730–5742.
- [18] Sirovich, L., 1987. “Turbulence and the dynamics of coherent structures, Parts I-III”. *Quarterly of Ap-*

- plied Mathematics*, **45**(3), pp. 561–590.
- [19] Holmes, P., Lumey, J., and Berkooz, G., 1996. *Turbulence, Coherent Structures, Dynamical Systems and Symmetry*. Cambridge Monographs on Mechanics, Cambridge University Press.
- [20] Kunisch, K., and Volkwein, S., 2001. “Galerkin Proper Orthogonal Decomposition methods for parabolic systems”. *Numerische Mathematik*, **90**, pp. 117–148.
- [21] Liberge, E., Pomarède, M., and Hamdouni, A., 2009. “Reduced-order modelling method by POD-multiphase approach for fluid-structure interactions”. *European Journal of Computational Mechanics*, **19**, pp. 41–52.
- [22] Donea, J., Huerta, A., Ponthot, J., and Rodriguez-Ferran, A., 2004. *Arbitrary Lagrangian-Eulerian Methods*. Wiley & Sons, Encyclopedia of Computational Mechanics Vol. 1: Fundamentals, Chap. 14.
- [23] Khalak, A., and Williamson, C., 1999. “Motions, Forces and Mode Transitions in Vortex-Induced Vibrations at Low Mass Damping”. *Journal of Fluids and Structures*, **13**, pp. 813–851.
- [24] Pomarède, M., Longatte, E., and Sigrist, J.-F., 2009. “Benchmark of numerical codes for coupled csd/cfd computations on an elementary vortex induced vibration problem”. ASME, ed., Pressure Vessel and Piping, Prague.
- [25] Williamson, C., and Roshko, A., 1988. “Vortex formation in the wake of an oscillating cylinder”. *Journal of Fluids and Structures*, **2**, pp. 355–381.
- [26] Archambeau, F., Mechtoua, N., and Sakiz, M., 2004. “Code_Saturne: a finite volume code for the computation of turbulent incompressible flows Industrial applications”. *International Journal of Finite Volumes*, [www.latp.univ-mrs.fr/IJFV/], **1**.
- [27] Longatte, E., Bendjeddou, Z., and Souli, M., 2003. “Methods for numerical study of tube bundle vibrations in cross-flows”. *Journal of Fluids and Structures*, **18**, pp. 513–528.
- [28] Blevins, R., 1974. “Fluidelastic whirling of a tube rows”. *ASME Journal of Pressure Vessel Technology*, **96**, pp. 263 – 267.
- [29] Chen, S., 1983. “Instability mechanisms and stability criteria of a group of circular cylinders subject to cross-flow, Part I Part II”. *Journal of vibration, acoustics, stress and reliability in design*, **105**, pp. 51–58.
- [30] Price, S., 2001. “A review of theoretical models for fluidelastic instability of cylinder arrays in cross-flow”. *Journal of Fluids and Structures*, **9**, pp. 3147–3170.



HOMOGENIZATION METHOD FOR THE VIBRATION OF TUBE BUNDLE IN A FLUID.

Quentin Desbonnets

CEA/DEN/DANS/DM2S/SEMT/EMSI
Laboratoire d'Études de Mécanique Sismique
F-91191 Gif-sur-Yvette, France
Email: quentin.desbonnets@cea.fr

Daniel Broc

CEA/DEN/DANS/DM2S/SEMT/EMSI
Laboratoire d'Études de Mécanique Sismique
F-91191 Gif-sur-Yvette, France
Laboratoire de Mécanique des Structures Industrielles Durables
UMR CNRS-EDF-CEA 2832
1 avenue du Général de Gaulle, F-92141 Clamart, France
Email : dbroc@cea.fr

ABSTRACT

This paper takes place in the problematic of numerical simulation of complex tubular systems in presence of fluid. The feasibility of set up an homogenized model based on the incompressible Navier-Stokes equations is investigated. Numerical simulations of a bundle oscillating in a fluid, for various condition of Keulegan-Carpenter numbers and Reynolds numbers, are analysed to identify the mechanisms to homogenize. Bases of the model are explained, and the model is finally proposed. Numerical implementation of the model is developed. Coupling schemes used are detailed. Cases of validation are presented and results are discussed.

NOMENCLATURE

$\tilde{\alpha}/\alpha$ Dimensionless variable / Dimensional variable.
 v Fluid velocity field.
 p Fluid pressure field.
 v^* Homogenized fluid velocity field.
 p^* Homogenized fluid pressure field.
 σ Stress tensor.
 ρ Fluid density.
 μ Fluid dynamic viscosity.
 Ω_f Fluid volume.
 Ω^* Homogenized fluid-structure domain.
 Γ_{cyl} Cylinders boundaries.
 Γ_{ext} External boundaries.
 \vec{n}, \vec{t} Boundaries normal and tangential vectors.
 d Cylinders diameter.
 m Cylinders mass.
 k Cylinders stiffness.
 N Number of cylinders in the bundle.

X Bundle displacement.
 e Spacing coefficient.

INTRODUCTION

Multiple fields are concerned about interaction fluid-structure problems. In the nuclear industry, for problematic of nuclear safety, the behaviour of fluid assemblies in the nuclear core or steam generator submitted to seismic solicitation must be controlled. These structures are slender. It has been widely pointed out that the surrounding fluid significantly affect their behaviours. Fluid flow leads to inertial and dissipative effects and affects eigenfrequencies and damping. Due to their complex geometry numerical simulations of such systems could lead to very huge sizes and times of calculation. For example, a pressure water reactor core is composed of 157 assemblies. Each fuel assemblies is an array composed of 17 by 17 tubes (264 fuel rods and 25 guide rods). A rod is a 4-meters high and 1-centimetre diameter cylinder. That gives a system to simulate composed of 45373 of these cylinders immersed in a 5-meters diameter tank full of fluid. To solve these problems, homogenized models have been built [1]. These models have been developed based on the linearised Euler equations for the fluid. In this case calculation times and sizes have been effectively reduced. However, only inertial effects and small structure displacement are taken into account. In order to build more accurate homogenized models, they have to be based on the Navier-Stokes equations.

At first, the feasibility of building a homogenized model is investigated. Bi-dimensional numerical simulations are done with the finite element modelling code

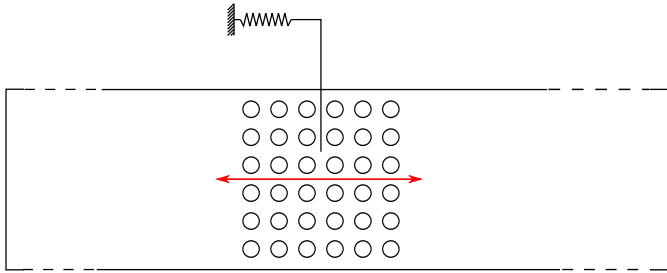


FIGURE 1: REPRESENTATION OF THE CALCULATION DOMAIN. THE BUNDLE IS CONFINED ON ITS LATERAL SIDES. THE MOTION IS SUBMITTED TO AN 1 D.O.F. OSCILLATOR EQUATION.

CAST3M [2]. They are made for various fluid conditions depending on the Keulegan-Carpenter number and the Reynolds number. These parameters are taken in low-range ($Kc \leq 10$ and $Re \leq 1000$). Identification of the homogenization mechanism in the bundle are made by force analyses. Only results of a few numerical simulations are presented in this paper. The notion of representative equivalent volume is highlighted. Setting up a model requires some approximations and hypotheses. They are detailed. Added mass and viscous related coefficients are calculated and compared to numerical and experimental results. The numerical implementation is detailed. Simulations for fluid-structure problem require the use of some coupling method that are presented. Cases of validation are introduced. Drop cases are made in confined and half-confined configurations. The dynamic of the bundle obtained with classic CFD and the homogenized model is compared for various conditions.

DESCRIPTION OF CONSIDERED CASE

The system is a cylinder bundle in square arrangement, immersed in a viscous fluid. All tubes are supposed to be rigid, circular and smooth. The global behaviour of the system is focused, all the tubes have the same motion. The bundle motion is submitted to an 1 d.o.f. oscillator equation. The structure is either confined or half-confined as presented in Fig. 1 and Fig. 2. This system is described by the incompressible Navier-Stokes equations and boundaries conditions in Eqn. (1).

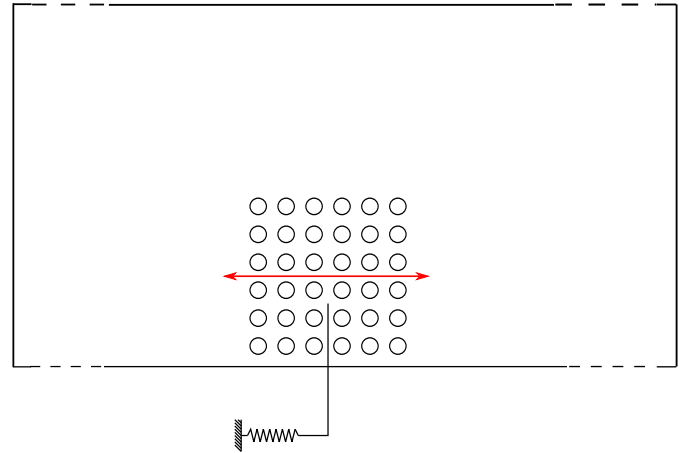


FIGURE 2: REPRESENTATION OF THE CALCULATION DOMAIN FOR AN HALF-CONFINED BUNLDE. LEFT AND RIGHT TANK SIDES ARE SIGNIFICANTLY DISTANT FROM THE BUNDLE.

$$\left\{ \begin{array}{ll} \nabla \cdot (\tilde{v}) = 0 & \text{in } \Omega_f \\ \rho \frac{\partial \tilde{v}}{\partial \tilde{t}} + \rho \tilde{v} \cdot \nabla \tilde{v} = -\nabla \tilde{p} + \mu \Delta \tilde{v} & \text{in } \Omega_f \\ Nm\ddot{\tilde{X}} + Nk\dot{\tilde{X}} = \tilde{F}_{f \rightarrow s} = \int_{\Gamma_{cyl}} \tilde{\sigma} \cdot n d\tilde{\Gamma} & (1) \\ \tilde{v} = \dot{\tilde{X}} & \text{on } \Gamma_{cyl} \\ \tilde{v} = 0 \text{ or } \tilde{\tau} \cdot \tilde{\sigma} \cdot \tilde{n} = 0 & \text{on } \Gamma_{ext} \\ \tilde{v} \cdot \tilde{n} = 0 \text{ and } \tilde{\tau} \cdot \tilde{\sigma} \cdot \tilde{n} = 0 & \end{array} \right.$$

The problem is defined by 6 characteristic dimension (m , k , d , ρ , μ and V the maximum bundle velocity). From this, it is deduced :

$$\begin{aligned} \omega_0 &= \sqrt{\frac{k}{m}}, f_0 \text{ the angular and natural structure frequencies,} \\ T &= \frac{2\pi}{\omega_0}, \\ D &= VT \text{ magnitude order of the structure displacement,} \\ P &= \rho V^2 \text{ magnitude of the dynamic pressure.} \end{aligned}$$

Thus the system is made dimensionless in Eqn.2 and is described by the 3 parameters

$$Kc = \frac{VT}{d}, \quad Re = \frac{\rho V d}{\mu} \quad \text{and} \quad \mathcal{M} = \frac{\rho \pi \frac{d^2}{4}}{m}.$$

$$\left\{ \begin{array}{ll} \nabla \cdot (v) = 0 & \text{in } \Omega_f \\ \frac{1}{Kc} \frac{\partial v}{\partial t} + v \cdot \nabla v = -\nabla p + \frac{1}{Re} \Delta v & \text{in } \Omega_f \\ \ddot{X} + \omega_0^2 T^2 X = \frac{4\mathcal{M}Kc}{\pi} F_{f \rightarrow s} = \frac{4\mathcal{M}Kc}{\pi} \int_{\Gamma_{cyl}} \sigma n d\Gamma & \text{on } \Gamma_{cyl} \\ v = \dot{X} & \text{on } \Gamma_{cyl} \\ v = 0 \text{ or} & \text{on } \Gamma_{ext} \\ v \cdot \vec{n} = 0 \text{ and } \vec{\tau} \cdot \sigma \cdot \vec{n} = 0 & \text{on } \Gamma_{ext} \end{array} \right. \quad (2)$$

In this paper, the spacing between two cylinders is fixed at 1.7 and \mathcal{M} is fixed at $\frac{1}{4}$.

HIGHLIGHTING THE NOTION OF "REPRESENTATIVE ELEMENTARY VOLUME"

In Eqn. (2) the displacement comes from the oscillation equation. For now, the displacement is not solved and replaced by a forced oscillating motion $\dot{X}(t) = \sin(2\pi t)$. The bundle is confined on its lateral sides. The purpose is to analyse the behaviour of the fluid in the bundle and to highlight the existence of a representative elementary volume of this behaviour in a bundle. Parameters of the system are the Kc and the Re numbers. They influence the flow. This dependence has been well identified by [3], [4] or [5] in the case of a single tube oscillating in a large domain. It has been shown for low range of Kc and Re that there are different domain of flow behaviour (from symmetrical regime to transverse vortex street regime [3]). This diversity of flow is also present for a bundle of tube as shown in [6]. An example of flow is done in Fig. 3. The pattern is composed of complex vortices which are not identical for each one of them. However, a global behaviour is observed. This point is confirmed by calculating the force exercised by the fluid on each tube in the bundle. This analysis is made for various configuration of Kc and Re . In this paper only the effect of the Kc is developed, the Reynolds number is fixed at 250 for the simulations presented.

For very small range of Kc (≤ 1) the pattern and the flow around each tube is symmetrical, periodic and identical. Drag forces applied of all the cylinders in the bundle are globally sinusoidal and equal, Fig. 4. The lift forces are null due to the symmetry. In this range of Kc the force is mainly inertial. Thus the maximum of drag forces is on the order of $\frac{\pi^2}{Kc}$.

As the Kc increase to 5 some asymmetries appear in Fig. 3. The new created vortices affect the forces ap-

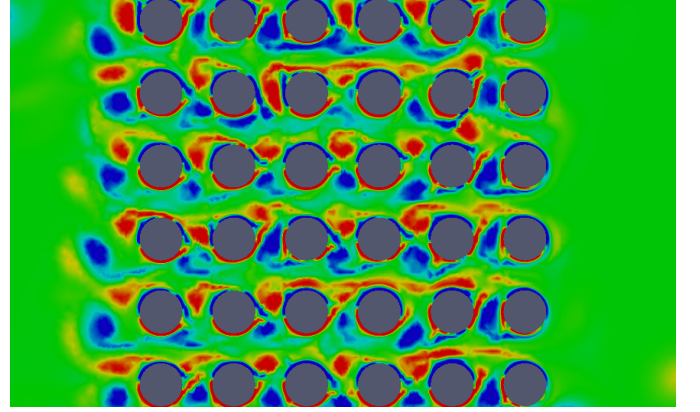


FIGURE 3: VORTICITY FIELD INDUCED BY A OSCILLATING BUNDLE WITH $Kc = 5$ AND $Re = 250$.

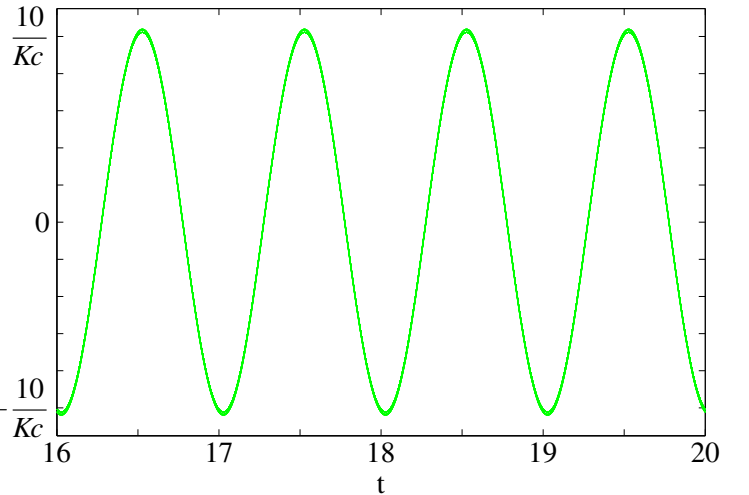


FIGURE 4: DRAG FORCES APPLIED ON EACH OF THE 36 CYLINDERS OF A CONFINED BUNDLE OSCILLATING IN FLUID (—) DURING SEVERAL PERIOD FOR $0.01 \leq Kc \leq 1$.

plied on each cylinders Fig. 6 and 7. The drag forces aren't sinusoidal and identical anymore and important lift forces appear. Although a global behaviour is observed, the difference between each cylinder is important. These differences are well reduced by considering groups of 4 closed tubes and more with groups of 9 tubes Fig. 5. The mean amplitude of lift forces is 3 times reduced and become closed to their mean value 0. The same conclusions are observed when the Kc is increased to 10, Fig. 8 and 9. This analysis highlights the existence of a REV, which shows the feasibility of the homogenisation.

INTEGRATION OF THE SYSTEM OVER THE REV

The representative elementary volume I is composed by a fluid volume I_f and a structure volume I_s . The oper-

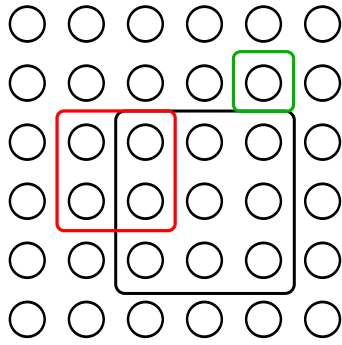


FIGURE 5: EXAMPLE OF A VOLUME WHERE THE DRAG AND LIFT FORCES ARE CALCULATED FOR A CYLINDER (—), A GROUP OF 4 TUBES (—) AND A GROUP OF 9 TUBES (—). THUS IN THIS BUNDLE, 25 GROUP OF 4 TUBES AND 16 GROUP OF 9 TUBES COULD BE ANALYSED.

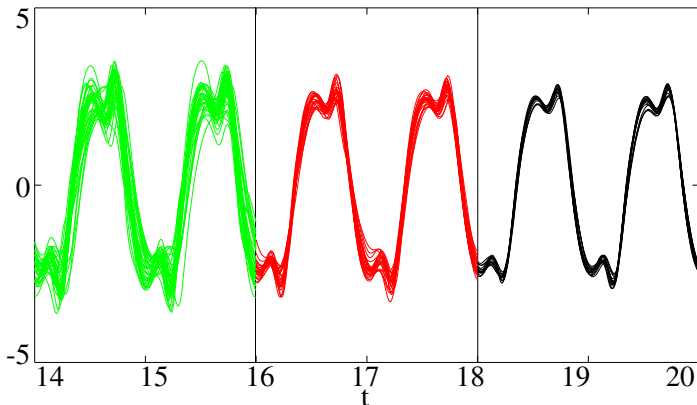


FIGURE 6: DRAG FORCES APPLIED ON ALL THE TUBES (—), ALL THE GROUPS OF 4 TUBES (—) AND ALL THE GROUPS OF 9 TUBES (—) FOR $Kc = 5$ AND $Re = 250$.

ator $\alpha \rightarrow \frac{1}{|I|} \int_{I_f} \alpha d\Omega$ is applied to the fluid mass continuity and fluid momentum equations of Eqn. (2).

$$\frac{1}{|I|} \int_{I_f} \left(\begin{array}{c} \nabla \cdot (v) = 0 \\ \frac{1}{Kc} \frac{\partial v}{\partial t} + (v \cdot \nabla)v = -\nabla p + \frac{1}{Re} \Delta v \end{array} \right) d\Omega \quad (3)$$

The fluid velocity is defined over I_f and is extended by continuity to $v = \begin{cases} v & \text{on } I_f \\ \dot{X} & \text{on } I_s \end{cases}$. Thereafter the notation

$\bar{\alpha} = \frac{1}{|I|} \int_{I_f} \alpha d\Omega$ is used. The integration of Eqn. (3) gives

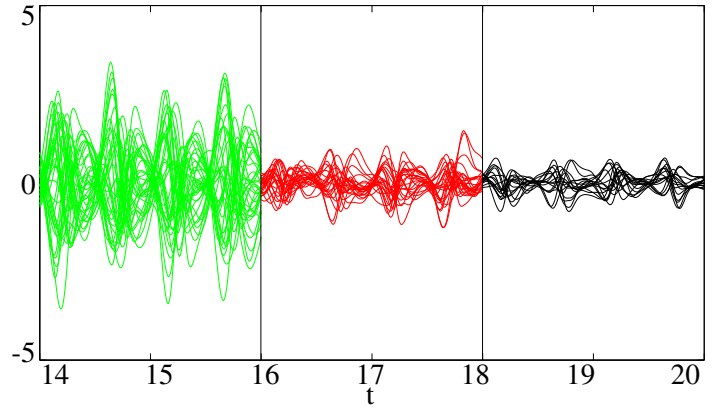


FIGURE 7: LIFT FORCES APPLIED ON ALL THE TUBES (—), ALL THE GROUPS OF 4 TUBES (—) AND ALL THE GROUPS OF 9 TUBES (—) FOR $Kc = 5$ AND $Re = 250$.

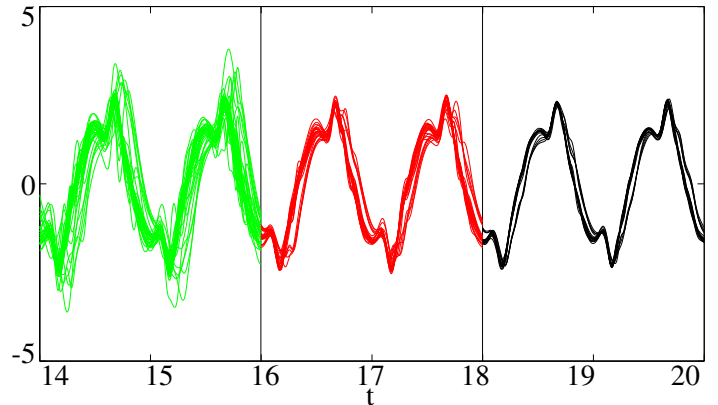


FIGURE 8: DRAG FORCES APPLIED ON ALL THE TUBES (—), ALL THE GROUPS OF 4 TUBES (—) AND ALL THE GROUPS OF 9 TUBES (—) FOR $Kc = 10$ AND $Re = 250$.

Eqn. (4).

$$\begin{cases} \nabla \cdot \bar{v} = 0 \\ \frac{1}{Kc} \frac{\partial \bar{v}}{\partial t} + (\bar{v} \cdot \nabla) \bar{v} = -\frac{1}{|I|} \int_{\partial I_{ext}} pn d\Gamma + \frac{1}{Re} \Delta \bar{v} + \frac{\eta}{Kc} \ddot{X} + \vec{r} \\ \quad + \frac{1}{|I|} \int_{\partial I_s} \left[p - \frac{1}{Re} (\nabla v + {}^t \nabla v) \right] n d\Gamma \end{cases} \quad (4)$$

where $\vec{r} = (\bar{v} \cdot \nabla) \bar{v} - \frac{1}{|I|} \int_{I_f} (v \cdot \nabla)v d\Omega$ is a corrective

term and $\eta = \frac{|I_s|}{|I|}$ is the solid volume fraction. There is no assumption about the form of I . So it is likely that the contour will pass alternately through the fluid and the solid part. Otherwise the integration over the solid contours is equal to the force exercised by the fluid on the cylinders and the integration over the fluid external contour will be resume as a pressure gradient. Based on the

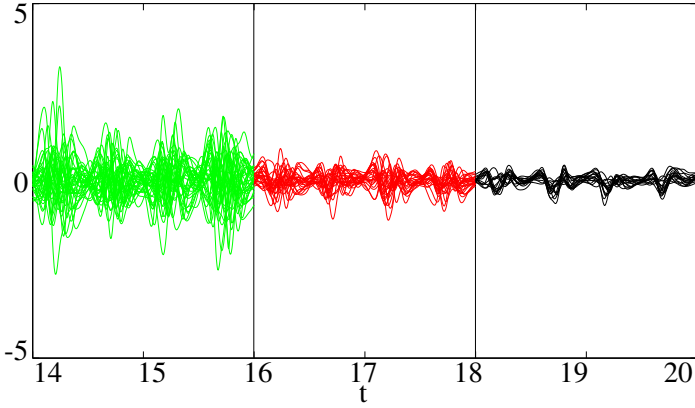


FIGURE 9: LIFT FORCES APPLIED ON ALL THE TUBES (—), ALL THE GROUPS OF 4 TUBES (—) AND ALL THE GROUPS OF 9 TUBES (—) FOR $Kc = 10$ AND $Re = 250$.

repetitiveness of the behaviour system, these approximations are made for the whole domain.

Hence, the integrated system is obtained (adding the oscillator equation motion) in Eqn. (5).

$$\begin{cases} \nabla \cdot \bar{v} = 0 \\ \frac{1}{Kc} \frac{\partial \bar{v}}{\partial t} + (\bar{v} \cdot \nabla) \bar{v} = -\nabla \bar{p} + \frac{1}{Re} \Delta \bar{v} - \frac{1}{|I|} F_{f \rightarrow s} + \frac{\eta}{Kc} \ddot{X} + \vec{r} \\ \ddot{X} + \omega_0^2 T^2 X = \frac{4 \mathcal{M} Kc}{\pi} F_{f \rightarrow s} \end{cases} \quad (5)$$

Order of magnitude of the corrective vector

The corrective term \vec{r} is still expressed with the variable v . Its importance is detailed by looking at the order of magnitude. It could be shown that

$$(\bar{v} \cdot \nabla) \bar{v} = \frac{1}{|I|} \int_{\partial I_{ext}} v (\bar{v} \cdot n) d\Gamma \quad (6)$$

The term \vec{r} is then calculated. Figure 10 represent the value of this term during 10 period of oscillation calculated on a fluid volume around 1 cylinder, 4 cylinders and 9 cylinders for a configuration of $Kc = 5$ and $Re = 250$. By increasing the volume of integration the importance of this corrective term is well reduced. Moreover, it is shown in Fig. 11 that it is low compared to the other term of Eqn. (5). Thus this term is not taken into account for the homogenized model.

Expression of the force

An expression of the drag force exercised by the fluid on a cylinder oscillating in a large domain of fluid is given

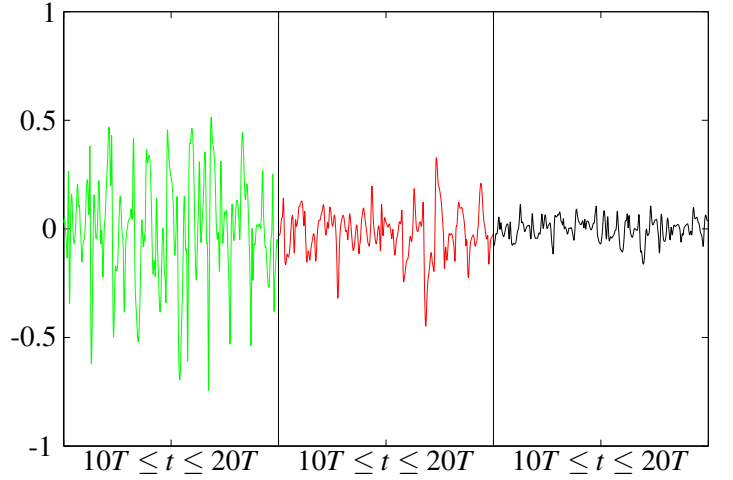


FIGURE 10: CONVECTIVE TERM (AXIAL COMPONENT) CALCULATED ON THE FLUID AROUND A TUBE —, A GROUP OF 4 TUBES — AND A GROUP OF 9 TUBES —, FOR $Kc = 5$ AND $Re = 250$.

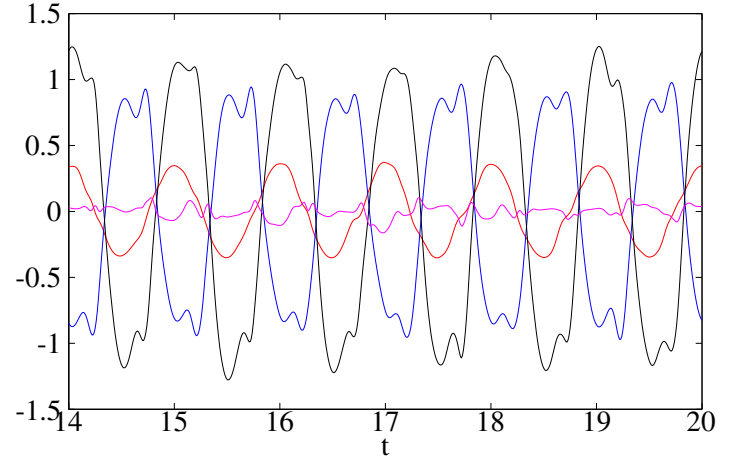


FIGURE 11: COMPARISON OF THE AXIAL COMPONENT OF THE TERM IN EQN.10 CALCULATED FOR AN INTEGRATION VOLUME OF 9 TUBES. THE CURVES REPRESENT $\left(\frac{1}{Kc} \frac{\partial \bar{v}}{\partial t} - \frac{\eta}{Kc} \right)$ (—), $F_{f \rightarrow s}$ (—), $\left(-\nabla \bar{p} + \frac{1}{Re} \Delta \bar{v} \right)$ (—) AND \vec{r} (—).

by Morison type approximation [7], given in Eqn. (7).

$$\tilde{F}_{f \rightarrow s} = -m_a \ddot{X} - C |\dot{X}| \dot{X} \quad (7)$$

with $m_a = C_m m_d = C_m \frac{\rho \pi d^2}{4}$ and $C = C_d \frac{\rho d}{2}$. Those expressions are useful in industrial context because they well transcript the loss of frequency and the damping effect. Such approximations are valid when the cylinder is oscillating in a non-moving fluid (or to determine the force exercises by waves on a cylinder). However, in the

presence of a global fluid movement, these forces are generalised in Eqn. (8) (if the viscous effect are not considered).

$$\tilde{F}_{f \rightarrow s} = -m_a \ddot{\tilde{X}} + (m_a + m_d) \frac{\partial \tilde{v}}{\partial \tilde{t}} \quad (8)$$

This expression is introduced in [8] and used in [1] to set up a model based on the linearised Euler equations. It should be noticed that if $\ddot{\tilde{X}} = \frac{\partial \tilde{v}}{\partial \tilde{t}} = \gamma$ the force exercised on a cylinder is the Archimedes force. Thus, the Morison type expression of the force exercised on N cylinder in a bundle in presence of global fluid movement and viscous effect is formulated in Eqn. (9).

$$\tilde{F}_{f \rightarrow s} = -m_a \ddot{\tilde{X}} + (m_a + m_d) \frac{\partial \tilde{v}}{\partial \tilde{t}} - NC |\dot{\tilde{X}}| (\dot{\tilde{X}} - \tilde{v}) \quad (9)$$

Dividing this expression by $|I|$ (the representative elementary volume that contains the N tubes), a force density is obtained, which dimensionless form is given in Eqn. (10).

$$f_{f \rightarrow s} = \frac{F_{f \rightarrow s}}{|I|} = -\frac{C_m \eta}{Kc} \ddot{\tilde{X}} + \frac{(C_m + 1) \eta}{Kc} \frac{\partial \tilde{v}}{\partial \tilde{t}} - \frac{NC_d}{2|I|} (\dot{\tilde{X}} - \tilde{v}) \quad (10)$$

Values of parameters η and $\frac{|I|}{N}$ have to be fixed. η is the solid volume fraction. In homogenisation this parameter generally tends to a limit as the REV grows. In our case $\eta \rightarrow \frac{\pi}{4e^2}$. In the same way, the fraction $\frac{|I|}{N} = \frac{\pi}{4\eta} \rightarrow e^2$.

In the case of the bundle oscillating in a confined tank, it could be shown that \tilde{v} and $\frac{\partial \tilde{v}}{\partial \tilde{t}}$ are null which simplified Eqn. (10). By multiplying this force density with the bundle velocity or acceleration (which are both periodic) the coefficient C_m and C_d are determined, Eqn. (11).

$$C_d = \frac{\int_T f_{f \rightarrow s} \dot{\tilde{X}} dt}{\frac{1}{2e^2} \int_T \dot{\tilde{X}}^2 dt} \quad (11)$$

$$C_m = \frac{\int_T f_{f \rightarrow s} \ddot{\tilde{X}} dt}{\frac{\eta}{Kc} \int_T \ddot{\tilde{X}}^2 dt}$$

These coefficient are represented in Fig. 12 and 13. Their values are detailed in Tab. 1 and Tab. 2. At these values are added the calculation of coefficients C_m for a bundle less confine on his lateral size in [5]. Those results

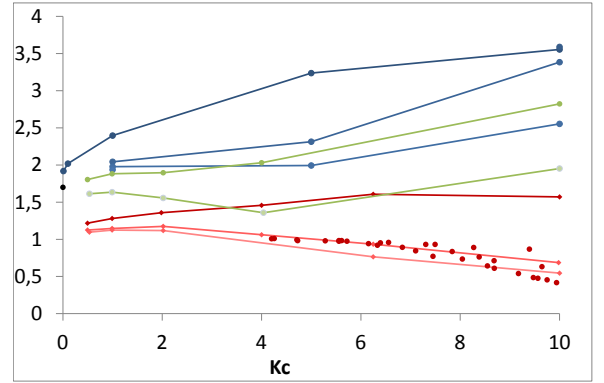


FIGURE 12: C_m VERSUS Kc FOR VARIOUS VALUES OF Re CALCULATED FROM THE CASE OF A BUNDLE OSCILLATING IN A FLUID (-●-, EQN.11) AND (-●-, [5]) COMPARED WITH THE LINEARISED EULER APPROXIMATION (●, [1]). THE RESULT FOR A SINGLE CYLINDER (●, [9]) AND (-●-, [5]) ARE ADDED FOR A COMPARISON.

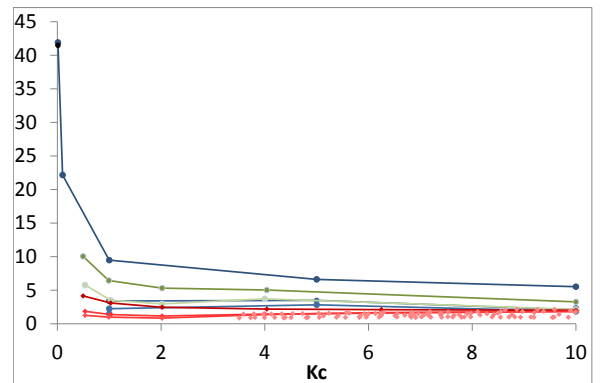


FIGURE 13: C_d VERSUS Kc FOR VARIOUS VALUES OF Re CALCULATED FROM THE CASE OF A BUNDLE OSCILLATING IN A FLUID (-●-, EQN.11) AND (-●-, [5]) COMPARED WITH THE STOKES APPROXIMATION IN EQN.12 (●). THE RESULT FOR A SINGLE CYLINDER (●, [9]) AND (-●-, [5]) ARE ADDED FOR A COMPARISON.

are obtained using the same numerical method. They give complementary informations. For very small value of Re , the fluid equations are reduced to the Stokes equations, and a value of C_d could be analytically estimated using

$Kc \backslash Re$	40	200	250	500	1000	Eul. lin.
$\rightarrow 0$	—					1.7
0.01	1.98	—	—	—	—	
0.1	2.02	—	—	—	—	
1	2.4	—	2.04	1.98	1.94	
5	3.24	—	2.31	1.99	—	
10	3.55	3.59	3.38	2.55	—	

TABLE 1: VALUES OF C_m FOR VARIOUS VALUES OF Kc AND Re , AND FROM THE LINEARISED EULER APPROXIMATION [1].

$Kc \backslash Re$	$\rightarrow 0$	40	200	250	500	1000
Stokes	41.49					
0.01		41.91	—	—	—	—
0.1		22.17	—	—	—	—
1		9.48	—	3.39	2.25	1.48
5		6.62	—	3.49	2.83	—
10		5.52	2.28	2.06	1.85	—

TABLE 2: VALUES OF C_d FOR VARIOUS VALUES OF Kc AND Re , AND FROM THE STOKES APPROXIMATION [10].

the formula of [10] in Eqn. (12).

$$C_d = \frac{3\pi^3}{2Kc} \left[(\pi\beta)^{-1/2} + (\pi\beta)^{-1} - \frac{1}{4}(\pi\beta)^{-3/2} \right] \quad (12)$$

Where the Stokes number $\beta = \frac{Re}{Kc}$. Moreover, for very high value of Re and small structure displacement, which tend toward to the linearised Euler equations, the C_m coefficient is estimated by [8]. The profuse values of C_m and C_d determined by [9] for a single cylinder are also represented for high range of Re (from 2000 to 60000). They are compared to the ones obtained by a finite element method in [5] for more moderate Re (100, 500 and 1000). Thus, except for the case of the lowest Re , numerical method tally with experimental data. Values for small Kc tend toward the theoretical value of C_m for a single tube in infinite fluid domain [8], which is 1. In both

study, there is a decrease of this force coefficients with growing Kc . But this has been shown in [9] to be a local effect.

When the case of the bundle is considered, values of C_m rise. Both results presented are simulation of a bundle oscillating in a tank. In this paper the bundle is strictly confined while in [5] the lateral side are lightly spaced. It result that a global motion of fluid appears (due to the recirculation outside the bundle). \bar{v} and $\frac{\partial \bar{v}}{\partial t}$ are not null anymore. Thus, the definition of C_m are not exactly the same and the coefficient calculated in this paper are more important that in [5]. The theoretical value of C_m for the bundle presented in Fig. ?? is 1.7 and bound the results of this paper (Tab. 1). As the Kc grows, the coefficient increase. However, at a fixed Kc , the growing Re significantly reduce the C_m .

For both case of the single tube and the bundle, it is assumed that the evolution of the C_d follows a vertical asymptote for $Kc \rightarrow 0$. It is in agreement with Eqn. (12). A value from this approximation of C_d is given in Tab. 2 (labelled as Stokes) and could be compared to the value calculated for $Kc = 10^{-2}$ and $Re = 40$. As the Kc increases the coefficient decreases and tend to a limit. When $Kc \rightarrow \infty$, i.e. the structure moves with a constant velocity, it is well know that the C_d tend to 1 for values of Re higher than a few thousands. It corresponds to a dimensional force of $\frac{1}{2}\rho d\dot{X}^2$.

THE HOMOGENIZED MODEL

An expression of the force density exercised by the fluid on the bundle has been proposed. It has been shown that the corrective term \vec{r} could be neglected. Thus, the homogenized model is introduced. To underline the fact that the homogenized variables are not linked any-more to the complete simulation fluid variables, they are now labelled v^* and p^* . $(v^*, p^*) \neq (\bar{v}, \bar{p})$, they are not defined in the same domain. However, they are built to transcribe a similar physics and influence in the same way the bundle motion. Finally, the homogenized model is expressed

in Eqn. (13).

$$\left\{ \begin{array}{ll} \nabla \cdot v^* = 0 & \text{in } \Omega^* \\ \frac{1}{Kc} \frac{\partial v^*}{\partial t} + (v^* \cdot \nabla) v^* = -\nabla p^* + \frac{1}{Re} \nabla v^* & \text{in } \Omega^* \\ + (C_m + 1) \frac{\eta}{Kc} \left(\ddot{X} - \frac{\partial v^*}{\partial t} \right) + \frac{C_d}{2e^2} (\dot{X} - v^*) & \\ \ddot{X} + 4\pi^2 X = -C_m \mathcal{M} \ddot{X} + (C_m + 1) \mathcal{M} \frac{\partial v^*}{\partial t} & \\ - \frac{2C_d \mathcal{M} Kc}{\pi} (\dot{X} - v^*) & \end{array} \right. \quad (13)$$

where Ω^* represent the fluid-structure homogenized domain.

Now that the model has been proposed, it has to be compared with CFD simulations of the system in Eqn.(2). This system is a fluid-structure interaction problem and requires some coupling method.

FLUID-STRUCTURE INTERACTION COUPLING

The motion of the bundle generates or disturbs the fluid flow. And the fluid flow exercises forces on the bundle. These actions are simultaneous. For the numerical simulation of FSI systems, two methods are generally used : Monolithic method (or strong coupling method) and partitioned method (or weak coupling method). The first one is useful to solve at the same time the fluid system, the structure system and the position of their interface as a single system. But the implementation of such method is difficult for complex geometry. Weak coupling method are more appropriate to the case of moving cylinders. The principle is to mutually exchange informations between both systems. Thus, each one can be solved separately. Other methods could be used. Particle-mesh methods, first set up for two-phase flow problems and level-set based methods for the interface follow up can be adapted for fluid-structure interaction problems. In this paper only partitioned methods are used. The principle of these methods is to solve iteratively both systems using a coupling scheme. Basically, in a time step the fluid system is solved. A new state of fluid is known. Forces exercised by the fluid on the structure are calculated. Then the solid motion is solved. It has been shown in [11] that first solving the fluid system leads to better energy balance at the fluid-structure interface. Several coupling scheme can be used. In this paper a staggered algorithm is used. It has been introduced by [12]. Its bases are illustrated in Fig. 14. It is composed of 4 steps :

1. A prediction of the structure position or velocity is made. In our case a velocity prediction is used as in

Eqn. (14).

$$\dot{X}_{n+1}^p = \dot{X}_n + \frac{1}{2} \Delta t \ddot{X}_n \quad (14)$$

2. The structure prediction changes the fluid boundaries conditions. The fluid system is solved.
3. The new fluid state exercises local forces on the structure.
4. The structure system is submitted to these forces and is solved. The time step is done.
5. The coupling scheme is repeated.

Other schemes have been developed. Staggered algorithm schemes can be used with smaller time step for one of the systems (generally the fluid temporal resolution is smaller than the structural one). Thus some sub-cycling are made for the concerned system. Semi-Implicit Algorithm or Implicit Algorithm (also called Iterative Algorithm) can be used. With these schemes, a convergence is reached for the fluid-structure interface behaviour.

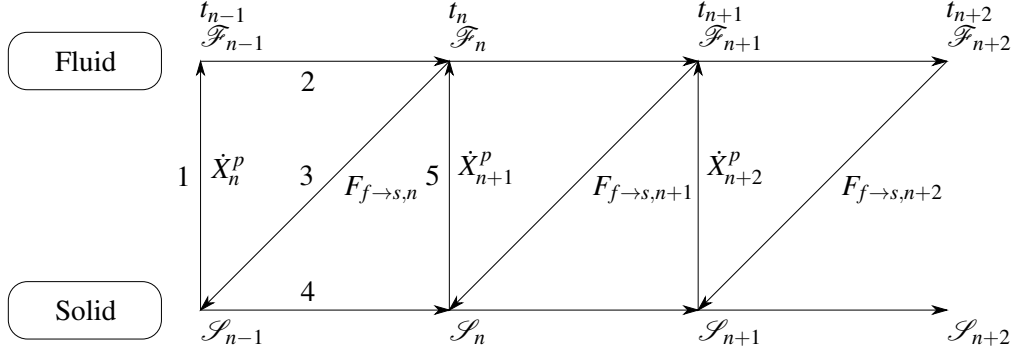
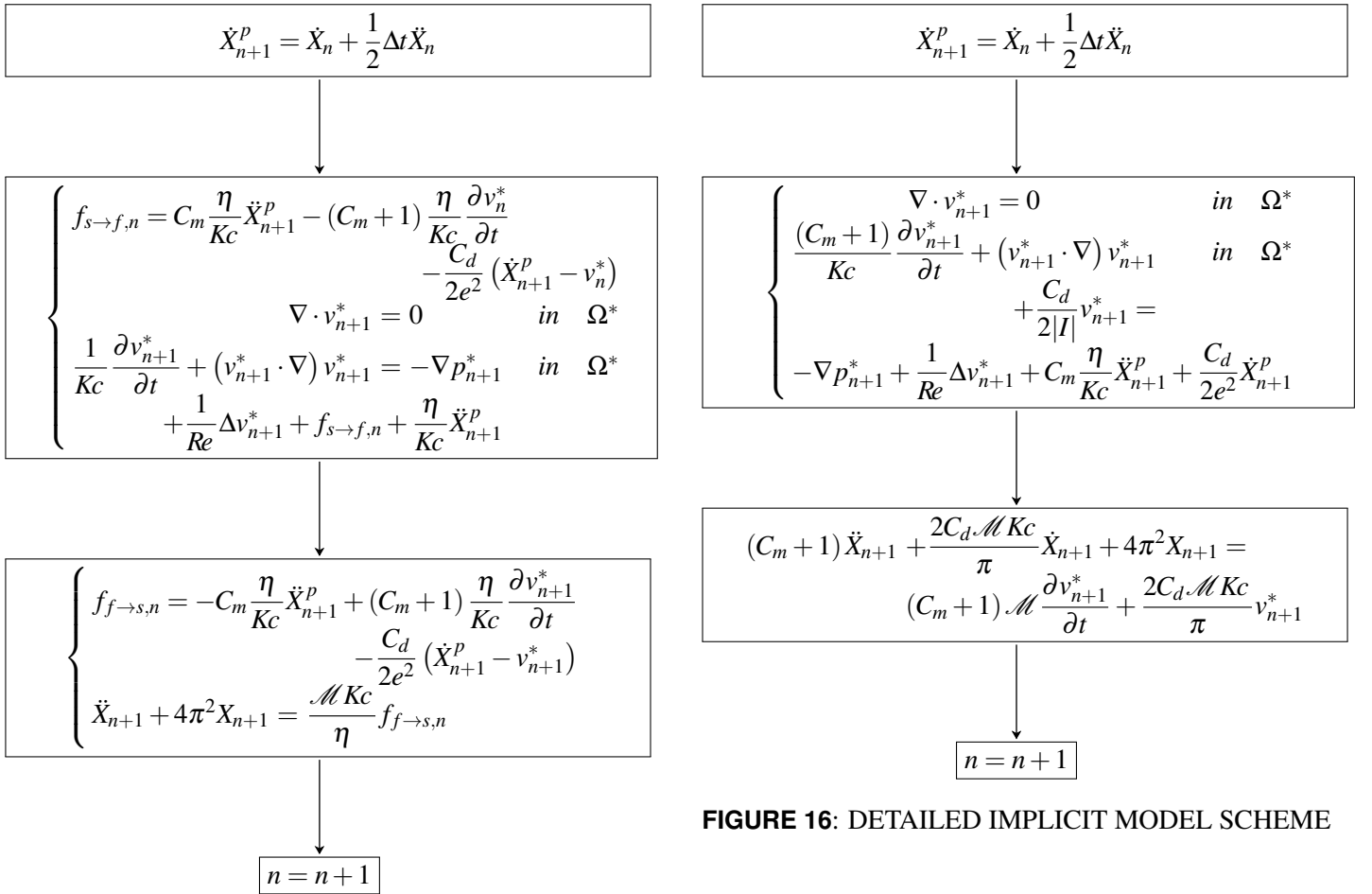
The system in Eqn.(13) is not a classical fluid-structure interaction problem. The homogenized fluid system exercises a force density on the structure system. However, it doesn't induced perturbation to the fluid by changing its boundaries conditions. In the model the structure exercises the same force density on the fluid. Moreover, this force density is expressed using both homogenized fluid and structural variables. In order to compare with CFD results without being influenced by the choice of the fluid-structure interaction coupling method employed, a staggered algorithm is also used to solve the homogenized model in this paper. Depending on whether the fluid terms of the force (or the structure terms) are treated in an explicit or implicit way in the fluid equation (respectively in the oscillator equation), two models are obtained.

HOMOGENIZED COUPLING SCHEME

The models described below are labelled explicit and implicit model schemes. The explicit or implicit notations refer to the treatment of the force density in the model (not to be confused with implicit algorithm).

Explicit model scheme

The first way is to consider the force density as a source term in both homogenized fluid and structure systems. Moreover, there is a difference between the force density exercised by the homogenized fluid on the structure and the force density exercised by the structure on


FIGURE 14: SCHEMATIC REPRESENTATION OF A STAGGERED ALGORITHM.

FIGURE 16: DETAILED IMPLICIT MODEL SCHEME

Implicit model scheme

An second scheme can be used where the force density is split and treated in a implicit way to obtain the time integration scheme in Fig. 16.

CASES OF VALIDATION

Cases of validation are made with drop cases with an initial displacement and zero initial velocity. Drop cases are chosen because of their easy implementation and also because they illustrate how the model reacts when it is

the fluid. Thus, the time integration scheme is obtained in Fig. 15. In this scheme, the force density is updated twice in a time step. This scheme have the advantage to not be restricted to a specific form of the force density. It could be easily improved.

shortly perturbed and let free right after. The bundle is either confined or half-confined as shown in Fig. 1 and Fig. 2. The initial displacement of the bundle is $\frac{Kc}{2\pi}$. That correspond to a maximum dimensionless speed of 1 if the bundle is in air. Then the bundle is dropped. Added mass parameters C_m and viscous parameter C_d values are taken from *Part I* where they are calculated from the case of an oscillating confined bundle and depend on the Kc and the Re . Due to the fluid viscosity, the bundle velocity magnitude will be reduced. Thus the parameters chosen are not adapted to long time behaviour of drop cases.

CONFINED CASES

Drop cases in a confined tank are presented in this paper for a few couple of (Kc, Re) . As in *Part I*, the Re is fixed to 250 and the Kc is set to 1, 5 and 10. Results on the dynamic of the bundle are presented in Fig. 17-19. Displacement, velocity, acceleration are represented for the explicit and implicit scheme models and are compared to the classic CFD simulation results. The force density applied by the fluid on the structure is also calculated and compared to the total force exercised on the cylinder divided by the total volume of the bundle $\frac{1}{Ne^2} \sum F_{f \rightarrow s}$.

For $Kc = 1$, the homogenized model gives good results Fig. 17a-d, especially when the implicit model scheme is used. With the explicit treatment of the force density in the explicit model scheme, numerical dissipation appears. However, in this case the maximum displacements are small and the fluid behaviour is well predictable.

For higher Kc , such as $Kc = 5$ Fig. 18 or $Kc = 10$ Fig. 19, the bundle behaviour is more complicated. The displacement becomes strongly damped Fig. 18a and 19a. Its amplitude is significantly reduced. At $t \sim 1.5$ it has been reduced by more than a half. The added mass and damping parameters are not adapted for long time simulation, thus a growing phase difference and a overestimated damping is observed.

HALF-CONFINED CASE

An half confined case is made to validate the model in presence of global fluid motion. Figure 20 and Fig. 21 show the comparison of the field pressure and the velocity norm in the fluid domain calculated by the classic CFD and by the homogenized model for $Kc = 5$ and $Re = 250$. The black square represents the equivalent volume where the model's equations are applied. The rest of the domain

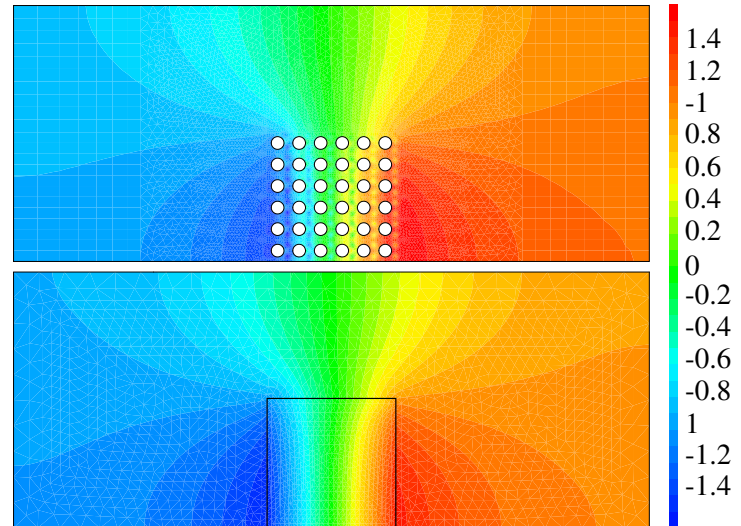


FIGURE 20: COMPARISON BETWEEN THE CFD AND THE HOMOGENIZED MODEL PRESSURE FIELDS AT $t = 0.5$.

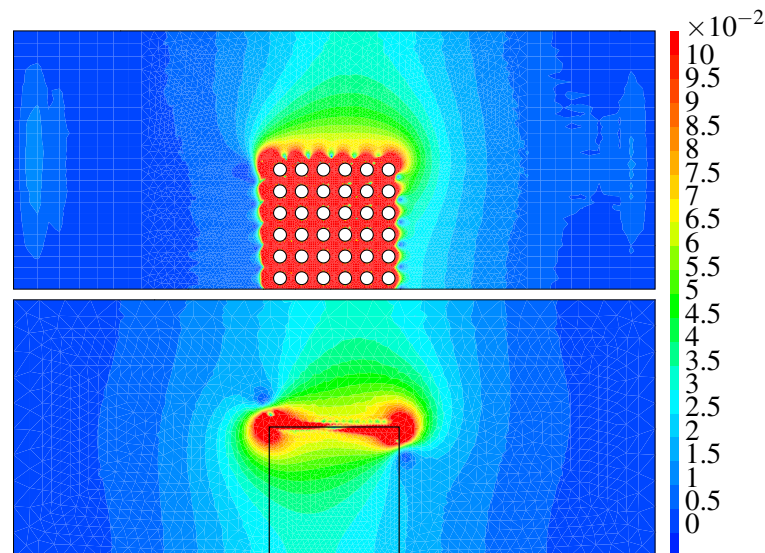


FIGURE 21: COMPARISON BETWEEN THE CFD AND THE HOMOGENIZED VELOCITY NORMS AT $t = 1.1$.

is ruled by classic Navier-Stokes equations. In Fig. 20, the pressure field is shown at $t = 0.5$, when the force density applied by the fluid is almost maximum, Fig. 22d. At $t = 1.1$ the mean homogenized velocity is maximum in the bundle equivalent domain, which means that the global motion of fluid reaches its maximum speed. Thus, in free fluid domain (where $v^* \sim v$) the fluid velocity is maximum. Figure 21 shows that the model retrieves this global motion.

As in confined cases, the bundle dynamics is presented in Fig. 22a-d. The force density is slightly overes-

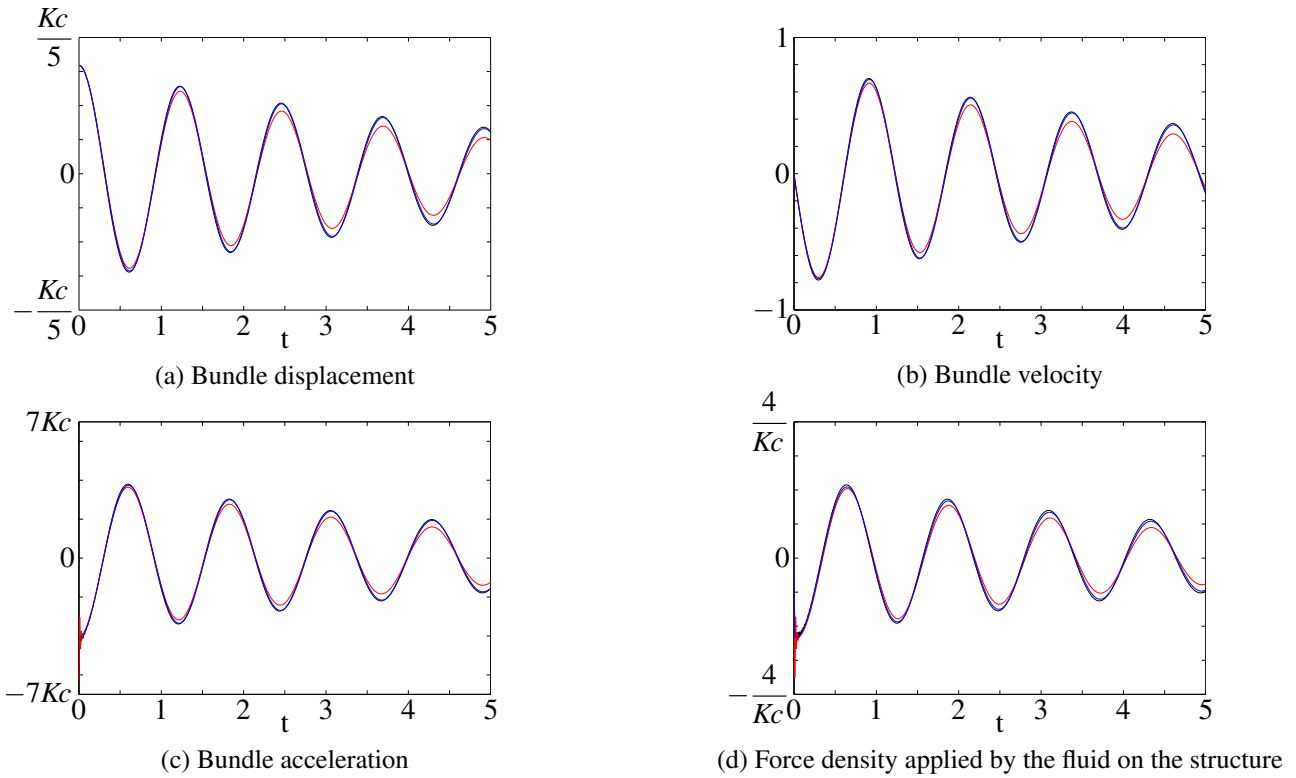


FIGURE 17: EVOLUTION OF THE BUNDLE DYNAMICS FOR $Kc = 1$, $Re = 250$, CALCULATED WITH THE HOMOGENIZED EXPLICIT SCHEME MODEL (—), HOMOGENIZED IMPLICIT SCHEME MODEL (—) AND COMPARED TO THE CFD SIMULATION (—).

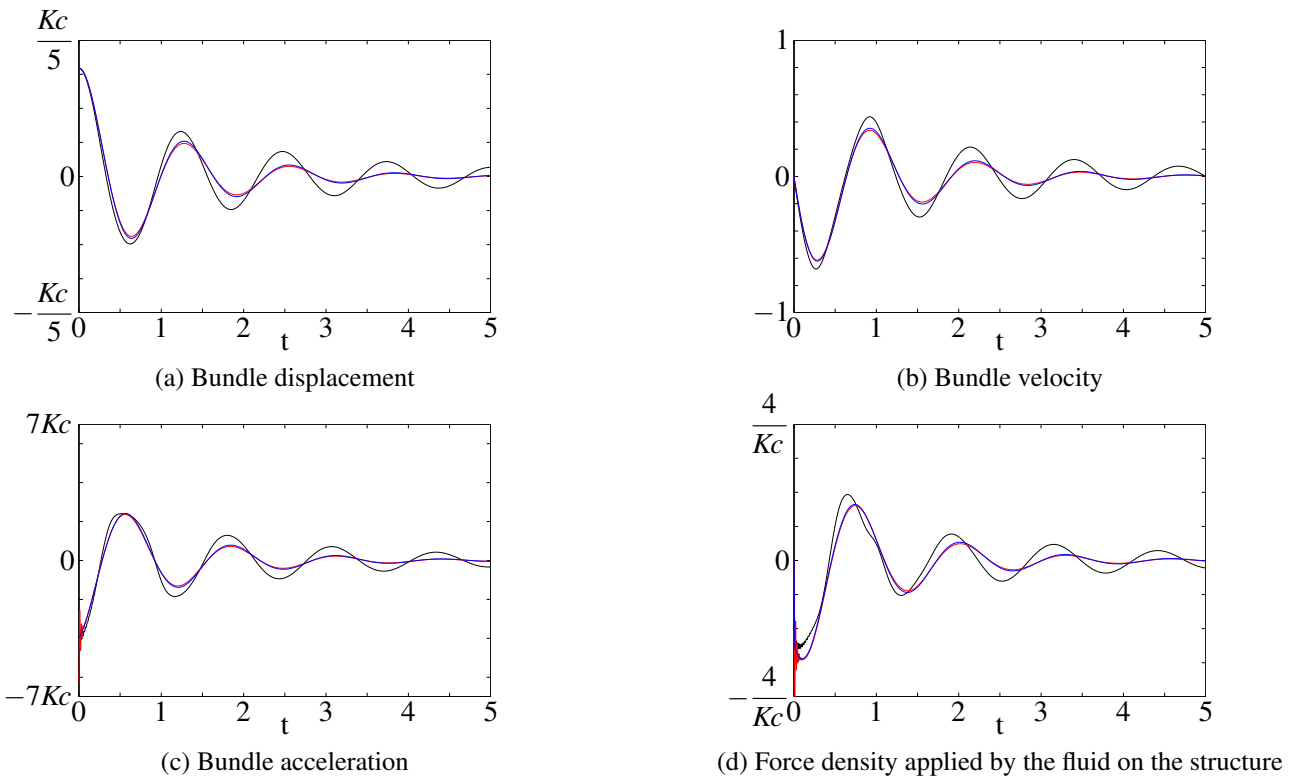


FIGURE 18: EVOLUTION OF THE BUNDLE DYNAMICS FOR $Kc = 5$, $Re = 250$, CALCULATED WITH THE HOMOGENIZED EXPLICIT SCHEME MODEL (—), HOMOGENIZED IMPLICIT SCHEME MODEL (—) AND COMPARED TO THE CFD SIMULATION (—).

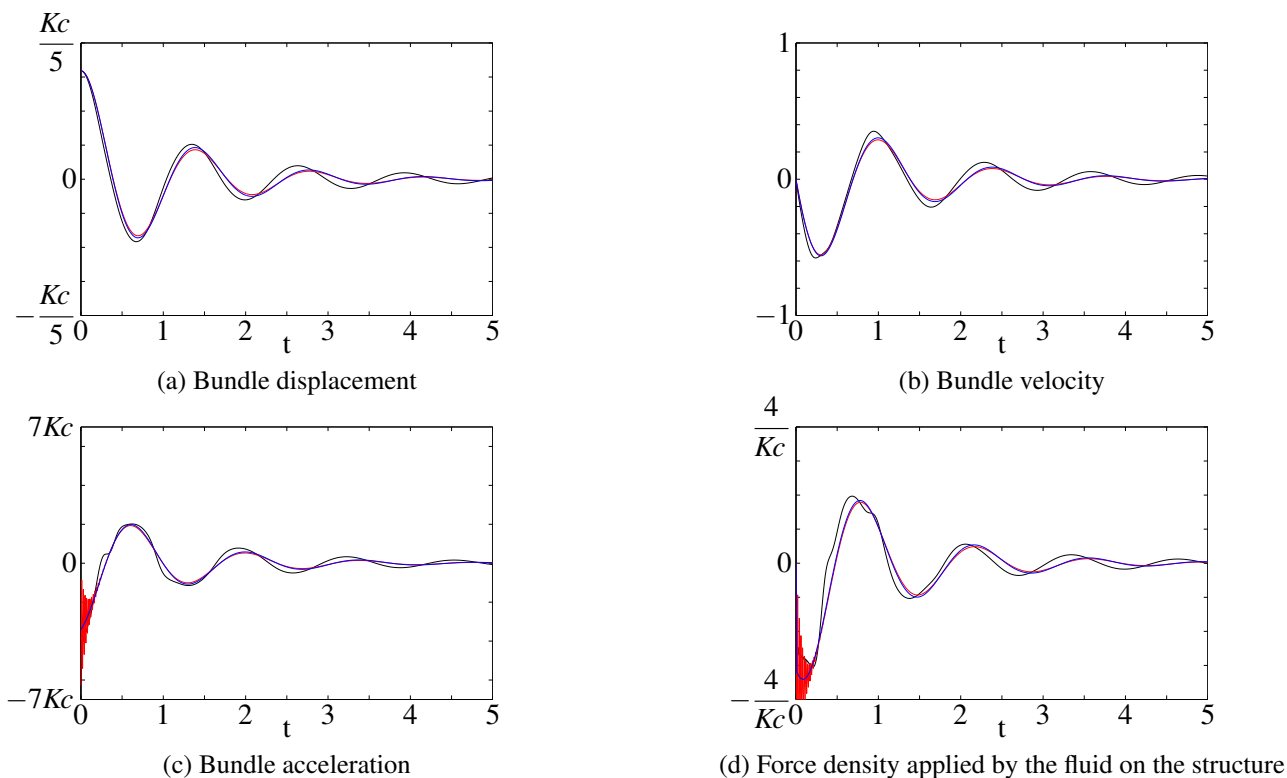


FIGURE 19: EVOLUTION OF THE BUNDLE DYNAMICS FOR $Kc = 10$, $Re = 250$, CALCULATED WITH THE HOMOGENIZED EXPLICIT SCHEME MODEL (—), HOMOGENIZED IMPLICIT SCHEME MODEL (—) AND COMPARED TO THE CFD SIMULATION (—).

timated on the first maximum, which cause the displacement, velocity and acceleration to be underestimated too.

CONCLUSION

The feasibility of building an homogenized model based on Navier-Stokes equations for the vibration of bundles of tubes in a fluid is investigated. Forces exercised on a 6x6 square bundle by the fluid are calculated in the case of an oscillating bundle for various conditions of Kc and Re . Low range of these parameters are focused. The existence of a representative elementary volume in our system is shown. Over the REV the dynamics of mean forces are identical in the whole bundle. An integration over the fluid domain ruled by the Navier-Stokes equations leads to a new system. Some terms in this system are not taken into account after looking at their order of magnitude and compared to major terms as fluid-structure forces. These forces are modelled by using some Morison-type approximations and the formula of a force density exercised by the fluid on the structure is introduced. The added mass coefficients and the damping coefficients of these forces are identified. Results in this paper agree with numerical and experimental results. The expression of the force density is set up to take into account global motion of fluid. The final model is finally

presented and is compared to a classic CFD method. A partitioned method is used to simulate the fluid-structure interaction. A staggered algorithm is chosen to solve the system. For the model part, the approximation of the force density chosen lead to two possible numerical solving scheme. One treats the force as a source term in an explicit way, the other integrates the term of the force density in the fluid and structural system. Validation and application cases are simulated and compare to the CFD results. Comparison are mostly qualitative analyses. Application cases with a seismic solicitation applied to the structure will be considered in further works.

In this paper, the feasibility and the accuracy of the homogenized model based on the Navier-Stokes equations have been presented. Some improvements can be made. The bundle has been taken not deformable. Some large scale differential movements can be considered. The interest of such model is to predict structural instabilities as breathing or ovalisation instabilities. Moreover, the model, in its current version could be extend to a bi-dimensional one.

REFERENCES

- [1] Sigrist, J.-F., and Broc, D., 2008. "Dynamic analysis of a tube bundle with fluide-structure interaction

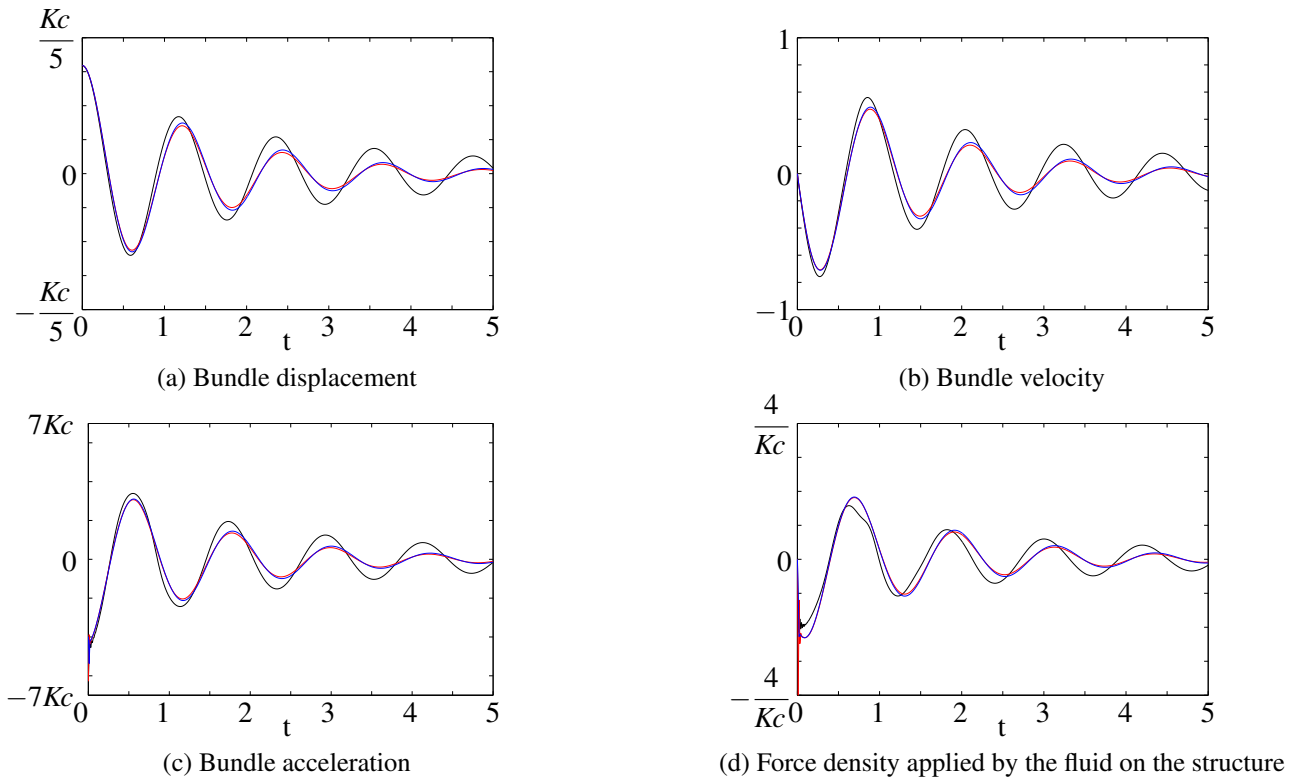


FIGURE 22: EVOLUTION OF THE BUNDLE DYNAMICS IN A HALF-CONFINED DOMAIN, CALCULATED WITH THE HOMOGENIZED EXPLICIT SCHEME MODEL (—), HOMOGENIZED IMPLICIT SCHEME MODEL (—) AND COMPARED TO THE CFD SIMULATION (---).

modelling using a homogenisation method”. *Computer Methods in Applied Mechanics and Engineering*, **197**(9-12), pp. 1080 – 1099.

[2] <http://www-cast3m.cea.fr>.

[3] Tatsuno, M., and Bearman, P. W., 1990. “A visual study of the flow around an oscillating circular cylinder at low keulegan-carpenter numbers and low stokes numbers”. *Journal of Fluid Mechanics*, **211**, pp. 157–182.

[4] Nehari, D., Armenio, V., and Ballio, F. “Three-dimensional analysis of the unidirectional oscillatory flow around a circular cylinder at low keulegan-carpenter and β numbers”.

[5] Duclercq, M., 2010. “Étude de l’interaction entre un fluide et une structure oscillante : régimes d’écoulement et de forces, du cylindre isolé au réseau de cylindres”. PhD Thesis, École Polytechnique, December.

[6] Anagnostopoulos, P., and Dikarou, C., 2011. “Numerical simulation of viscous oscillatory flow past four cylinders in square arrangement”. *journal of Fluids and Structures*, **27**, pp. 212–232.

[7] Morison, J. R., O’Brien, M. P., Johnson, J. W., and Schaaf, S. A., 1950. “The forces exerted by surface waves on piles”. *Petroleum transactions, AIME*,

189, pp. 149 – 154.

[8] Fritz, R. J., 1972. “The effect of liquids on the dynamic motions of immersed solids”. *Journal of Engineering for Industry*, **94**(1), pp. 167–173.

[9] Sarpkaya, T., 1976. “In-line and transverse forces on smooth and sand-roughened cylinders in oscillatory flow at high reynolds numbers”. *Naval postgraduate school*.

[10] Wang, C.-Y., 1968. “On high-frequency oscillatory viscous flows”. *Journal of Fluid Mechanics*, **32**(01), pp. 55–68.

[11] Piperno, S., 1995. “Simulation numérique de phénomènes d’interaction fluide-structure”. PhD Thesis, École nationale des ponts et chaussées, June.

[12] Farhat, C., Lesoinne, M., and Maman, N., 1995. “Mixed explicit/implicit time integration of coupled aeroelastic problems: Three-field formulation, geometric conservation and distributed solution”. *International Journal for Numerical Methods in Fluids*, **21**(10), pp. 807–835.



Flow around circular cylinder submitted to rotational oscillation and periodical cross section variation

Hamid Oualli¹

Fluid Mechanics Laboratory, EMP BP17,
Bordj El Bahri, 16111, Algiers, Algeria,
houalli@gmail.com

Med Lotfi Aouag

Med Daou

Samir Hanchi

Fluid Mechanics Laboratory, EMP BP17,
Bordj El Bahri, 16111, Algiers, Algeria.

Ahcene Bouabdallah

LTSE Laboratory, Faculty of
Physics, USTHB, 16111
Bab Ezzouar, Algiers, Algeria.
abouab2002@yahoo.fr

ABSTRACT

In this study we describe the near wake structure and flow dynamics associated with experimentally simulated flow around a circular cylinder that is either stationary, in simple rotative oscillation or simple harmonic cross-section variation combined to rotative oscillation. Results are examined for a Reynolds number of $Re \approx 3000$ and a fixed vibrating amplitude equal to 5% of the cylinder diameter. A large domain of forcing Strouhal number, up to twice the natural shedding frequency of the cylinder is considered. Results are interpreted using an analysis of visualizing snapshots focused on the cylinder near wake response. The obtained results suggest that the investigated nonlinear combination of rotative oscillation and cross-section variation favorably plaid for the fineness optimization and drastic aeroacoustic noise reduction using the present controlling strategy.

INTRODUCTION

The importance of the so called bluff body wakes and the role they play in the design of the major engineering structures and industrial applications is ubiquitous. This explains the abundance of the studies devoted to understanding the underlying involved phenomenology. Such intricate problems are almost omnipresent in hydro and aerodynamics, heat exchangers, offshore structures, turbomachinery...etc.

Control of vortex shedding leads to decreasing the unsteady forces acting on the body and can substantially reduce its vibrations. The emitted structures are inherently linked to the generated acoustic noise which can be significantly decreased if the vortices intensity and scale are weakened. Flow control may be executed by controlling

the boundary layer separation, the shear layers structures and / or the coherent structures dynamics in the body near wake. The evolution of the flow past a circular cylinder superimposed simultaneously to rotative oscillation and a radial pulsatile motion—cross section variation—is considered by visualizing the flow patterns using smoke streaklines and by analyzing qualitatively the corresponding snapshots. The researched objective consists in investigating the possibility of developing a technique for increasing the cylinder fineness—lift to drag ratio—by combining the Magnus effect with the drag drop induced by the cross section variation. The suggested controlling strategy contributes to largely decreasing both the intensity and the scale of the shedded vortices. These are prevented from further vorticity supply by cutting the links with the cylinder boundary layer. The structures are thus forced to disengage from the cylinder wake in the early stage of the shedding cycle. The resulting von Karman eddy street is thus weakened and correlatively the acoustic noise as well, Oualli et al. (2004, 2005a and 2005b).

EXPERIMENTAL SETUP

The main constitutive element of the experimental device is depicted in figure 1(a and b). The deforming mechanism is inserted in the cylinder wall to generate the pulsatile motion avoiding thus any disturbance of the evolving flow. The cylinder made of PVC (Polyvinyl Chlorine) walls, figure 1, is mounted horizontally traversing the test section with the ends linked to two external motors destined to deliver rotating motion of the cylinder shaft and cylinder walls as well. The inserted mechanism consists in a cylinder shaft entrained into a rotation motion using an external motor, rotating cams transform the entering rotating motion into diameter variation movement

Address all correspondence to this author¹

of the test cylinder walls according the following sinus law:

$$D = D_0 (1 + A_s \left| \sin(2\pi \times f \times t) \right|)$$

Where D is the variable cylinder diameter, D_0 is the initial cylinder diameter, A_s is the deformation amplitude set equal to 5% of the cylinder diameter, f is the cylinder forcing frequency in Hertz and t is time in seconds.

Considering the cylinder dimensions, the above relation becomes:

$$D = 0.08(1 + 0.005 \left| \sin(2\pi \times f \times t) \right|) \quad (1)$$

The flow behavior is thus controlled by the sinusoidal variation law of the cylinder cross-section applied uniformly along the span.

The rotative oscillation of the cylinder is executed as in Tokumaru and Dimotakis (1991) according to the law:

$$\theta = \theta_0 \sin(2\pi \times f_{osc} \times t) \quad (2)$$

Where θ is the instantaneous rotative oscillation angle, θ_0 is the maximum amplitude of the cylinder oscillation and f_{osc} is the superimposed frequency for the rotative oscillating dynamic.

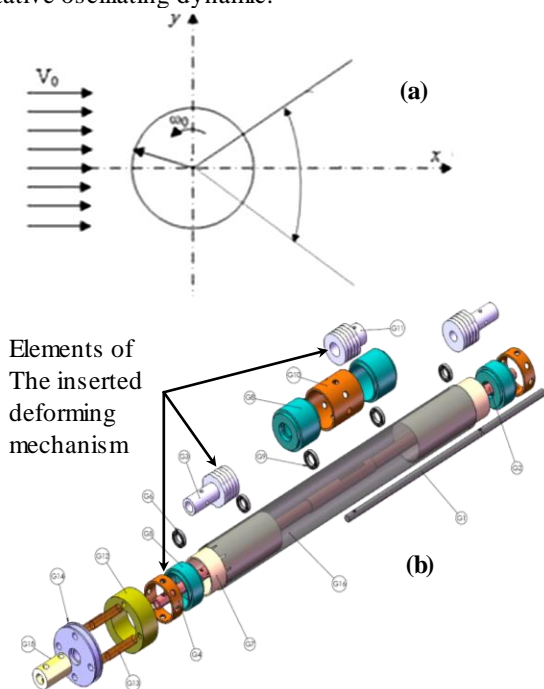


Figure 1: (a) Schematic view of the cylinder rotative oscillation coordinates
(b) Exploded view of the circular cylinder maquette

IMPORTANT RESULTS

The flow regime considered in this study corresponds to the moderate Reynolds number range ($Re \approx 3000$)

belonging to the so called ‘subcritical regime’ for the flow around a circular cylinder. The non-dimensional rotatively oscillating rate considered in this study, $\alpha = f_{osc}/f_0$, with f_{osc} is the rotatively oscillating frequency and f_0 is the cylinder natural shedding frequency, increases from 0.46 to 1.95 and the length along which the wake is tackled limits to the recirculating bubble corresponding to the cylinder near wake. The non-dimensional radial vibrating rate considered, $\beta = f_{vib}/f_0$, where f_{vib} is the superimposed radial vibrating frequency to the cylinder is in the range of 0 to 10 with the pulsating amplitude A_s reported to the cylinder diameter is fixed equal to 5%. The rotative oscillating amplitude θ is fixed to $\theta = 30^\circ$ and $\theta = 60^\circ$ for this study. The details of the near wake response mechanism are particularly examined and the flow asymmetry induced by the cylinder rotative oscillation is found to be apparent from $\alpha = 1.95$ and $\theta = 30^\circ$. The von Karman eddy street for a naturally evolving flow (with non-actuation) is depicted in the figure 2 where the primary vortices are alternatively shed from the cylinder and evolve in an anti-symmetrical fashion along the near and far wake.

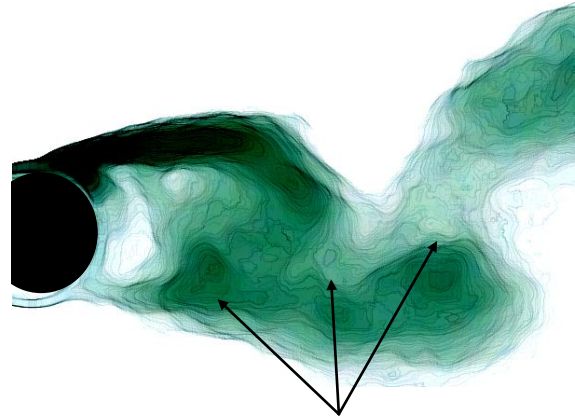
When the rotative oscillation is applied it is established that the acceleration and deceleration phases of the rotative oscillating cycle make the cylinder primary vortices to “smash” into smaller scale vortices before travelling in the von Karman street. The formation length substantially drops and the recirculating region fairly vanishes, figures 3 and 4. When increasing the rotative oscillating amplitude $\theta = 60^\circ$, the near wake is slightly deviated in the upper direction, the cylinder shear layers emit the vortices separately without penetrating the recirculation zone leading to two vortices parallel emitted rows. These emitted vortices rapidly diffuse in the eddy street and are not discernible when the distance from the cylinder is around 3 to 4D, figure 4. When the value of α is increased to 1.95 with θ maintained equal to 60° the flow exhibits a lock-in configuration as the one reported by Cheng (2001). The formation length completely disappears and the near wake length and width are considerably reduced around the cylinder tightened by the surrounding flow. The emitted vortices in smaller scales diffuse immediately after being shed in the eddy street, figure 5.

A central result obtained from visualisations of the upper primary and secondary interacting zone, consists in the fact that the cylinder cross-section variation (decreasing and increasing) greatly influences the primary and secondary structures interaction, Oualli et al. (2008), and that the so-called α and β phenomena, as identified by Coutenceau and Ménard (1985), are profoundly altered. In fact, during the cylinder cross-section decreasing phase, the near wake is subject to a radial attraction towards the cylinder surface leading thus to the near wake premature separation from the eddy street (far wake) which keeps travelling freely from the cylinder near wake. During the cylinder cross-section increasing phase, the cylinder near wake reduced to smaller smashed vortices by the rotative oscillations, Tokumaru and Dimotakis (1991) and Shields

and Leonard (1996), are subject to simultaneous further dislocations and radially pulled out from the cylinder in such a way that they are forced to early disengage from the cylinder surface, Oualli et al. (2008). The cylinder near and far wakes rupture is also induced at an early flow stage for this increasing phase of the cylinder diameter. This explanation is the underlying phenomenon for the Strouhal frequency increasing reported in the figure 6. It is noteworthy to notice that the aforementioned induced modifications (reduction of the near wake dimensions, shedding frequency increasing...) favourably contribute to the drag reduction around the circular cylinder.

CONCLUSIONS

The present study analyses the flow response around a circular cylinder submitted to simultaneous uniform spanwise cross-section vibrating motion and rotative oscillation. It is established that the flow topology is deeply altered in terms of the near wake and the global von Karman eddy street behavior. The shed primary vortices, and thus the Bénard-Karman eddy street, are strongly affected by the proposed controlling strategy. The global response show that the primary structures break into smaller scale weakened substructures which diffuse rapidly in the flow. The cylinder cross-section variation enhances the vortices dislocations and increases the shedding frequency by forcing the nascent neighboring vortices to prematurely disengage from the cylinder vicinity. The near and far wakes link is permanently cut by this boundary pulsatile motion, figure 7. All these feature favorably plaid for important drag coefficient and acoustic noise reduction, Williamson (1996) et Gad-El-Hak (2003).



Vortices shed in smaller scale

Figure 4: Flow configuration for $\theta=60^\circ$ and $\alpha=1.95$

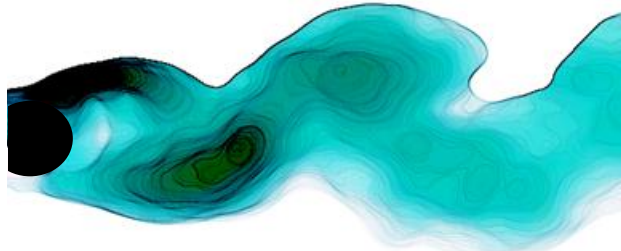


Figure 2: Natural eddy street behind a non-actuated cylinder

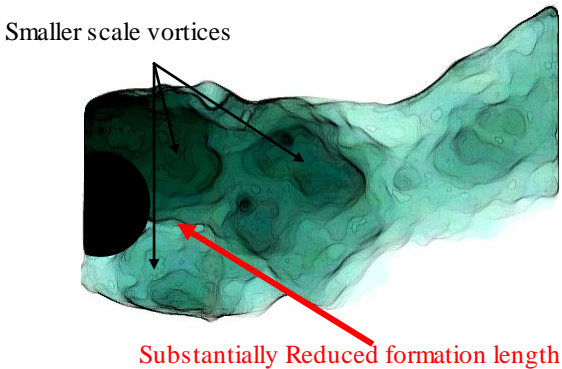


Figure 3: Flow configuration for $\theta=30^\circ$ and $\alpha=1.95$

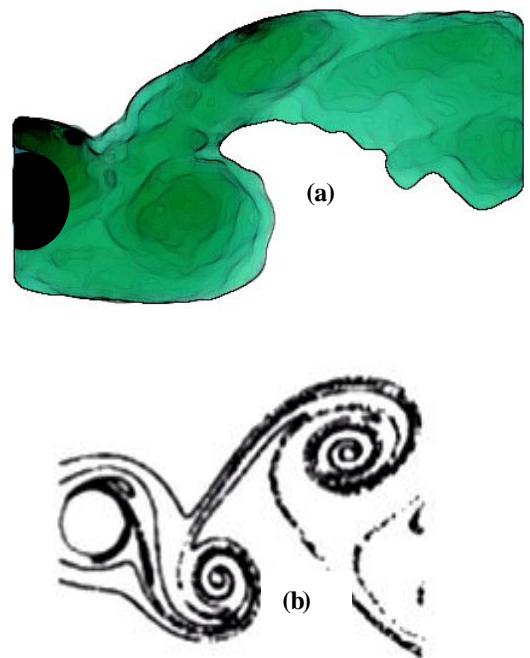


Figure 5: Flow configuration for lock-in conditions:
 (a) Present results
 (b) Cheng (2001)

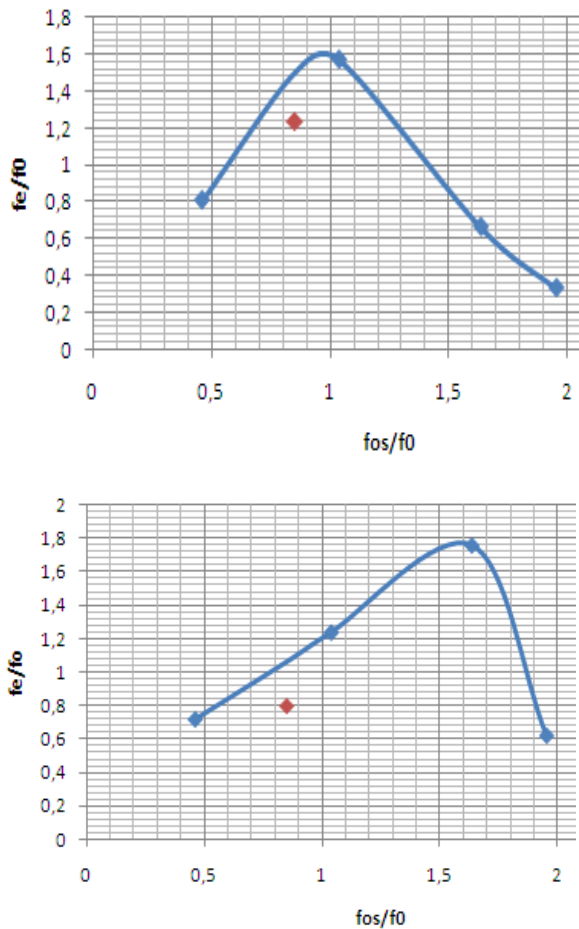
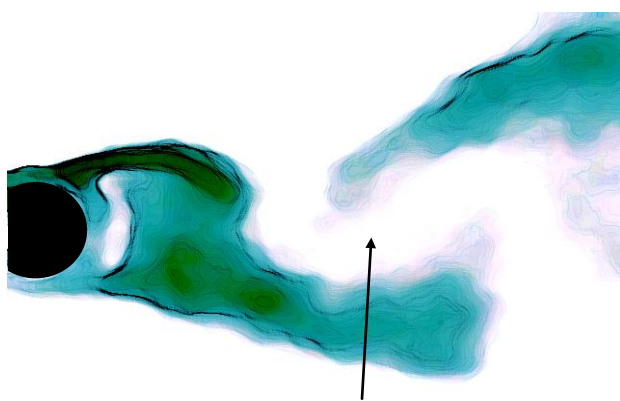


Figure 6: Evolution of the shedding frequency versus the oscillating frequency for a cylinder executing a cross-section variation:
 (a) $\theta=30^\circ$ and $\beta=2$
 (b) $\theta=60^\circ$ and $\beta=2$



Wake dislocation by radial pulsatile motion

Figure 7: Flow configuration for $\theta=60^\circ$, $\alpha=1.95$ and $\beta=2$

REFERENCES

- Oualli H., Hanchi S., Bouabdallah A., Asković R., 2004. Experimental investigation of the flow around a radially vibrating circular cylinder, *Experiments in fluids* 37, 789-801.
- Oualli H., Hanchi S., Bouabdallah A., Askovic R., 2005a. Influence of the circular cylinder cross-section variation on the near wake behaviour, 21st Int. Congress of Theoretical and applied Mechanics, Springer Acad. Press, id. FSM4_13050, ICTAM, August 15-21, 2004-Warsaw, Poland.
- Oualli H., Hanchi S., Bouabdallah A., Asković R., Gad-El-Hak M., 2005b. Drag reduction in a radially pulsating cylinder at moderate Reynolds number, *Bulletin of the American Physical Society*, vol. 50, N°9, 56.
- Cheng M. Numerical investigation of a rotationally oscillating cylinder in mean flow, *Journal of fluids and Structures*, 15 981-1007, 2001.
- Oualli H., Hanchi S., Bouabdallah A., Asković R., Gad-El-Hak M., 2008. Interaction between the near wake and the cross-section variation of a circular cylinder in uniform flow, *Experiments in fluids* 44:807-818.
- Badr, H., Coutenceau, M., Denis, S. C. R and Ménard, C. Unsteady flow past a rotating circular cylinder at Reynolds numbers 10^3 and 10^4 , *J. Fluid Mech.* 220, 459-484, 1990.
- Tokumar P. T. and Dimotakis P. E. Rotary oscillation control a cylinder wake. *Journal of Fluid Mechanics*, 244:77-90, 1991.
- Shiels D. and Leonard A. Investigation of drag reduction on a rotationally oscillating cylinder, *Journal of Fluid Mechanics*, 408 :275-300, 1996.
- Williamson C. H. K. Vortex dynamics in the cylinder wake. *Ann. Rev. Fluid. Mech.*, 28:477-539, 1996.
- Gad-El-Hak M. Flow control: passive, active and reactive flow management. *Cambridge University Pres, United Kingdom*, 2003.

LIMITING AMPLITUDE IN VORTEX-INDUCED VIBRATION OF ELASTICALLY MOUNTED CIRCULAR CYLINDERS

Efstathios Konstantinidis

Department of Mechanical Engineering
University of Western Macedonia
Bakola & Sialvera, Kozani 50100 Greece
ekonstantinidis@uowm.gr

ABSTRACT

A heuristic criterion is proposed for estimation of the maximum allowable amplitude of elastically mounted cylinders freely vibrating transverse to a free stream derived for the limiting case of zero structural damping. The criterion is based on Morison's equation to represent the reaction force which comprises components due to fluid inertia (added mass) and fluid damping (drag). It is presumed that vibrations are restricted in the inertia-dominated regime in the amplitude-frequency parameter space. This assumption along with the introduction of the relative velocity magnitude in Morison's equation results in an inequality for maximum amplitude. Comparison against experimental data from the published literature shows that the proposed criterion captures intrinsic features of the actual response found in free vibration tests with low structural damping.

INTRODUCTION

One of the basic excitation mechanisms of flow-induced vibration is the periodic formation and shedding of vortices alternatively from each side of bluff structures immersed in a stream of fluid, thereof termed vortex-induced vibration. A notable feature of this phenomenon is that the fluid force is directly related to the shed vortices. If the structure is lightly damped and flexibly mounted, or flexible itself, it may be excited into vibration when the vortex shedding frequency is close to a natural frequency of the system. In turn, the ensuing cylinder motion affects substantially the process of vortex formation and different shedding modes are attainable in the wake. The fundamentals of the vortex-induced vibration have been studied in innumerable studies for, perhaps, over 50 years but research on the subject is still very active.

This reflects the highly non-linear dynamics of unsteady separated flows in bluff body wakes. Progress has been summarized, among others, in recent review papers [1–3].

The present study is concerned with vortex-induced vibrations of an elastically mounted, rigid circular cylinder allowed to oscillate transverse to a free stream. This is one of the simplest possible arrangements in terms of fluid mechanics. Another is when the cylinder is allowed to oscillate only along the free stream, which offers a more clear case-study to this author's opinion. The two arrangements exhibit markedly different response characteristics, i.e. frequencies and amplitudes of vibration, but have a common thread in the basic excitation mechanism, that is vortex shedding.

It is well known that cylinder wakes exhibit three-dimensional flow structures above a Reynolds number of 189 approximately [4]. The Reynolds number encountered in most practical applications such as offshore risers in sea currents and civil structures in turbulent winds, is orders of magnitude above that value. However, the flow remains statistically homogeneous along the spanwise direction if the incident stream is always perpendicular to the cylinder axis. Hence, it is deemed appropriate to deal with a cross section of the cylinder. In the following, all related variables refer to per unit length of the cylinder.

Previous works on the subject have shown that the response of freely-vibrating cylinders depends primarily on three parameters: the reduced velocity, $U_\infty/f_N D$ (here U_∞ is the free stream velocity, f_N the natural frequency of the mechanical oscillator, either in vacuum or in still fluid, and D the diameter of the cylinder), the ratio of mass of the cylinder to the mass of the displaced fluid, m^* , and the fraction of critical damping, or damping ratio, ζ . There is some controversy between researchers whether ζ should incorporate the effect of the surrounding fluid. This point

TABLE 1: PEAK RESPONSE DATA.

Ref.	m^*	ζ	A_{\max}/D	$U/f_N D$	Re
[5]	78.3	0.0012	0.66	5.2	1000
[6]	1.19	0.005	1.01	6.2	3000
[7]	10.0	0	0.90	6.0	4000
[8]	0.82	0.0002	1.18	4.3	8000
[9]	6.39	0.002	1.16	6.2	30000
[10]	142	0.002	1.25	6.9	50000
[11]	1.14	0.019	1.78	9.6	90000

needs not further consideration here as attention is drawn to the limiting case of $\zeta \rightarrow 0$. However, attention to this limiting case might not be expected to diminish the generality of the present study as experimental results indicate that the basic response characteristics remain essentially the same for finite, but low, levels of damping.

In the vast majority of the previous investigations mechanical systems with very low structural damping were employed. This makes vibration possible over wide ranges of reduced velocities as the free stream velocity is varied, either increasing or decreasing, in a typical experiment. Traditionally, the peak response amplitude over the entire range of reduced velocities has been expressed as a function of a combined mass-damping parameter, known in variants such as the ‘stability parameter’, Scruton number, or the Skop–Griffin number, which are all proportional to each other. Empirical fits to experimental data suggest that the response approaches a limiting amplitude of 1.3, approximately, as m^* approaches zero which corresponds to $\zeta \rightarrow 0$ since the cylinder mass need be finite in all real circumstances. Sarpkaya [2] argues that there is no compelling reason to combine m^* with ζ into a single parameter. He also notes the potential variations in the determination of the damping factor which arise from tests in still air rather than in vacuum. Yet, he also provides an empirical equation of the peak response amplitude as a function of $M^*\zeta$ which, at the limit of zero damping, indicates a limiting amplitude of 1.12.

It is now recognized that, the peak amplitude depends strongly on Reynolds number and higher peak amplitudes might be anticipated at high subcritical (before the drag crisis) Reynolds numbers [7, 12]. Table 1 provides a short collection of peak response data selected from various

free vibration studies. Their common characteristic is that the response jumps abruptly from relatively low to much higher amplitude at some ‘critical’ reduced velocity. In this table, some of the figures were estimated while f_N is the natural frequency measured in still fluid (mostly water). The trends in the data indicate that the most influential (governing) parameter is the Reynolds number irrespectively of the mass and damping, combined or separately. This observation might suggest that the peak response amplitude is limited by purely fluid dynamic factors rather than the mass and/or damping parameters.

The objective of the present work to develop a criterion for the limiting response amplitude (not just the peak amplitude) based on purely fluid-dynamic considerations. Initially, it is shown that it is necessary to supplement the equation of motion with an additional condition in order to make the problem fully-determined. This analysis is based on the classical harmonic model which is described in the next section. Subsequently, Morison’s equation is introduced and a criterion for the limiting amplitude is derived. Finally, predictions using this criterion are compared against experimental data and conclusions are drawn.

HARMONIC MODEL

Consider an elastically mounted cylinder of rigid length which undergoes vortex-induced motion $y(t)$ under fluid forcing $F_y(t)$ both assumed to be, within reasonable approximation, harmonic functions of time t :

$$y(t) = A \sin(2\pi ft) \quad (1)$$

$$F_y(t) = \frac{1}{2} \rho U_\infty^2 D C_y \sin(2\pi ft + \phi) \quad (2)$$

where A and f are the cylinder’s oscillation amplitude (maximum displacement) and frequency, respectively, ρ the fluid density, D the cylinder diameter, and U_∞ the free stream velocity. C_y is the magnitude of the total transverse force acting on the cylinder and ϕ its phase with respect to the cylinder motion. Bearman notes that C_y “accounts for the component in the y direction of the total instantaneous fluid force acting on a cross section of the oscillating body and embodies elements that could be considered as fluid inertia and damping forces” [13].

The cylinder is part of a mechanical oscillator (mass–spring–dashpot system) of given mass, m , stiffness, k , and damping, c . The equation of cylinder motion reads

$$m\ddot{y} + c\dot{y} + ky = F_y \quad (3)$$

where the overdot ($\dot{\cdot}$) denotes differentiation with respect to time. A solution for the response amplitude under the above said assumptions may be obtained by substitution of the harmonic functions (1) and (2) into (3) and equating cosine terms on both sides, which yields

$$\frac{A}{D} = \frac{C_y \sin \phi}{4\pi^3 \zeta} \left(\frac{\rho \pi D^2}{4m} \right) \left(\frac{U_\infty}{f_N D} \right)^2 \left(\frac{f}{f_N} \right)^{-1} \quad (4)$$

In the above equation f_N is the undamped natural frequency of the mechanical oscillator and ζ its damping ratio in vacuum as measured by free decay tests in still air. Clearly, the above result is problematic in the limit of zero damping as it accepts $C_y \sin \phi = 0$ as the only possibility. Hence, the component of the total force in phase with the velocity of the cylinder, or excitation force, is zero. This is oxymoron since there must be some fluid excitation for finite vibrations to realize. Furthermore, this condition appears to be very strict physically as it must be satisfied over the entire range of response, which generally involves different modes of vortex shedding and possible jumps between them. Figure 1 shows the response amplitude from an experiment with very low damping together with the contour of zero fluid excitation determined from a series of free vibration tests with the same facility [9, 14]. The abscissa is the true reduced velocity. It may be seen that the two lines do not precisely overlap in the amplitude–frequency parameter space as required by Eq. (4). This might be partly attributed to averaging of the data in producing the contours of $C_y \sin \phi$ but it is not clear if that can fully compensate the differences. For the moment, this point does not need more concern as Eq. (4) may be discarded altogether.

Another result for the response amplitude may be obtained by equating the sine terms on both sides of the equation of motion (3) after substitution of (1) and (2), which yields

$$\frac{A}{D} = \frac{C_y \cos \phi}{2\pi^2} \left(\frac{\rho \pi D^2}{4m} \right) \left(\frac{U_\infty}{f_N D} \right) \left[1 - \left(\frac{f}{f_N} \right)^2 \right]^{-1} \quad (5)$$

The last equation is typically solved for the response frequency but, unequivocally, it may be solved for the amplitude as above. In fact, for the case of zero damping, this single equation need be solved for both amplitude and frequency! But there are two unknown response variables and only one equation. This brings up the question: how does the fluid-mechanical oscillator select its response in the $A : f$ parameter space? This implies that an additional

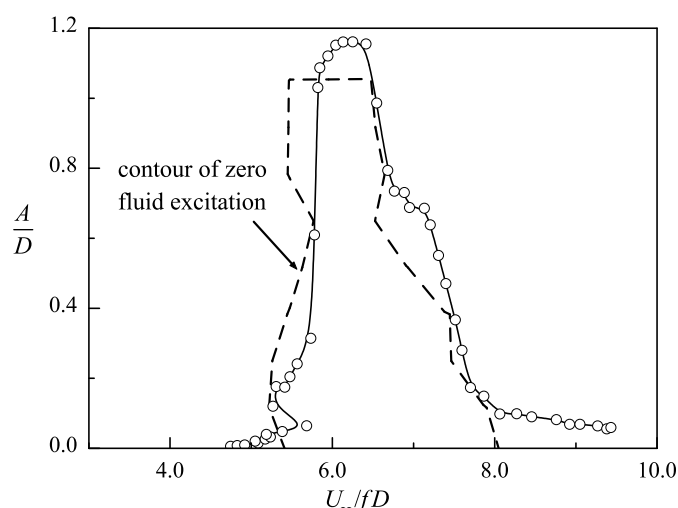


FIGURE 1: RESPONSE AMPLITUDE OF FREELY VIBRATING CYLINDER AND CONTOUR OF ZERO FLUID EXCITATION [9, 14].

condition need be satisfied if a unique solution to this problem exists. To make things even more complicated, there is evidence that the fluid-oscillator (wake flow) is admissible to different dynamical states, or marginally different stable states, corresponding to a single point in the $A : f$ space [15].

REACTION FORCE AND MORISON'S EQUATION

The total force acting on an oscillating structure may be split into excitation, F_L , and reaction, $-F_R$, components as suggested by Griffin and Koopmann [16]. In their original study, each component was written in terms of a magnitude coefficient and a phase-angle as in (2). It was later shown in a review article by Griffin that the two components are orthogonal [17]. Hence, inserting the two components in the equation of motion (3) is equivalent to the classical harmonic model discussed in the previous section. However, their decomposition has a fundamental bearing. The reaction force comprises the fluid inertia, or added mass, and fluid damping; these are the same whether the cylinder undergoes self-excited vibrations or it is forced to oscillate. In fact, the components of the reaction force are no different than those represented in the well-known Morison's equation,

$$F_R = \underbrace{\frac{1}{4}\rho\pi D^2 C_A \dot{U}}_{\text{inertia}} + \underbrace{\frac{1}{2}\rho D C_D U^2}_{\text{damping}} \quad (6)$$

where C_A and C_D are the added mass (inertia) and drag (damping) coefficients, respectively. The equation

was originally developed to understand wave loading on offshore structures [18]. Note that the equation above does not include the Froude-Krylov force induced by pressure gradients in unsteady flows. The drag and inertia coefficients are assumed constant over a cycle of oscillation but empirical data show that these depend on the flow parameters, e.g. the nondimensional amplitude and frequency as well as the Reynolds number. Despite its empirical use, Morison's equation is based on theoretical considerations. The inertia term can be predicted from potential flow theory, which yields $C_A = 1.0$ for a circular cylinder. The damping term accounts for the effects of viscosity and C_D may be assumed the same as for steady flow (quasi-steady approach), possibly taking into account the Reynolds number. Although these assumptions may appear oversimplifying, there is evidence to suggest that hold approximately true. For instance, it was recently shown that the above simplified-model predictions do not fall astray from the actual total in-line force for cylinders immersed in a perturbed fluid stream [19]. Further results from numerical simulations at low Reynolds numbers over a wide range of parameters for the same configuration, show that the simple model performs correspondingly with Morison's equation with coefficients which were determined by least-squares fits to the data [20]. The latter configuration is analogous to a cylinder oscillating in-line with the free stream. In the present study, it is hypothesized that Morison's equation is applicable to transverse oscillations of the cylinder in a free stream by introducing the relative velocity between the fluid and the moving cylinder.

CRITERION FOR LIMITING AMPLITUDE

Consider an elastically-mounted circular cylinder that is excited into transverse vibration by vortices shed in its wake. As the cylinder oscillates transverse to the free stream, an unsteady relative velocity $\mathbf{U}(t) = U_\infty \mathbf{i} - \dot{y}(t) \mathbf{j}$ is induced where \mathbf{i} and \mathbf{j} are the unit vectors in a Cartesian frame of reference, U_∞ the free stream velocity, and $\dot{y}(t)$ the time-dependent velocity of the cylinder. Assuming that the motion is sinusoidal $y = A \sin(2\pi ft)$, the relative velocity magnitude is

$$U(t) = U_\infty \sqrt{1 + \alpha^2 \cos^2(2\pi ft)} \quad (7)$$

where the alpha parameter $\alpha = 2\pi fA/U_\infty$ is the ratio of maximum velocity of the cylinder to the free stream velocity. Figure 2 shows that, for a typical value of $\alpha = 1.0$ encountered in vortex-induced vibrations, the

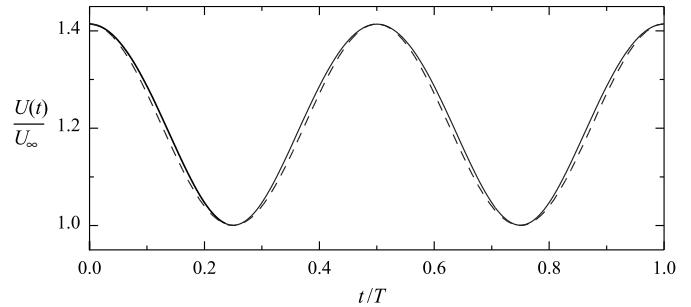


FIGURE 2: RELATIVE VELOCITY MAGNITUDE FOR A CYLINDER OSCILLATING TRANSVERSE TO A FLUID STREAM.

waveform of the relative velocity from Eq. 7 (denoted by a solid line), can be approximated by a simple sinusoidal oscillation (dashed line) of the following form

$$U(t) \approx U_0 + \Delta U \cos(4\pi ft). \quad (8)$$

An immediate observation is that the frequency of the unsteady relative velocity is twice that of the cylinder's oscillation. For $\alpha = 1.0$, the root-mean-square (rms) deviation between the actual and approximate velocities is 4.3% of the rms value of the actual unsteady velocity itself whereas the percentage increases to 9.7% for an extremely high value of $\alpha = 2.0$. Equation 8 will be employed here forth as the relative velocity because it is much easier to cope with mathematically, rather than the punctual instantaneous velocity in (7). Note that both U_0 and ΔU are complex functions of free stream velocity, U_∞ , and alpha parameter, α .

The tactic here is to introduce the relative velocity into Morison's equation. Expansion of the squared velocity term and rejecting the second-order term in the perturbation velocity leads to $U^2 \approx U_0^2 + 2U_0\Delta U \cos(4\pi ft)$, while differentiation yields $\dot{U} = -4\pi f\Delta U \sin(4\pi ft)$. Substitution into Morison's equation yields

$$F_R = \frac{1}{2}\rho DC_D U_0^2 + \rho DC_D U_0 \Delta U \cos(4\pi ft) - \rho \pi^2 D^2 f \Delta U C_A \sin(4\pi ft). \quad (9)$$

The first term in the reaction force is a steady drag component as if the cylinder is stationary. Its action is expended in the mechanical supports since the streamwise position of the cylinder is fixed. If the cylinder is stationary then there is only a steady drag term. When the cylinder actually vibrates in a steady or quasi-steady periodic state, F_R has additionally two unsteady components, in and out

of phase with the velocity of the oscillating cylinder. It is proposed here that the amplitude of the vibrations is limited by purely fluid-dynamical factors in the range where the fluid inertia dominates over the fluid damping, otherwise vibrations would decay. Mathematically, this means that the ratio of the multiplier in front of the cosine to that of the sine in Eq. 9 must be equal or greater than unity, i.e.

$$\pi^2 \left(\frac{fD}{\mu_1(\alpha)U_\infty} \right) \frac{C_A}{C_D} \geq 1.0 \quad (10)$$

where $\mu_1(\alpha)$ is the ratio of the mean relative velocity to the free stream velocity, U_0/U_∞ . Using the analytic form of the function $\mu_1(\alpha)$ leads to the following result

$$\left(\frac{A}{D} \right)_{\zeta=0} \leq \frac{1}{2\pi} \left(\frac{U}{fD} \right) \left\{ \left[2\pi^2 \left(\frac{fD}{U} \right) \frac{C_A}{C_D} - 1 \right]^2 - 1 \right\}^{\frac{1}{2}} \quad (11)$$

The last equation is a criterion for the limiting amplitude in vortex-induced vibration transverse only to the free stream. It should be emphasized that it is not a solution to the equation of motion. Strictly speaking, it holds for the limiting case of zero damping. However, it might be expected that its validity might be extended since experimental observations indicate that the response is similar for finite, but low, levels of the damping ratio [7]. A major consequence of Eq. 11 is that the limiting amplitude depends primarily on the drag coefficient and its variation as a function of two nondimensional parameters, U_∞/fD and A/D .

RESULTS AND DISCUSSION

An equation for the limiting amplitude was derived in the previous section based solely on theoretical considerations. Although the derivation was based on the assumption of zero fluid excitation, or zero structural damping, it is deemed that it might be applicable in configurations involving very low levels of damping as in most experiments of free vibration. Its merits will be assessed by comparison of its predictions against experimental data. A complete comparison requires knowledge of C_A and C_D for known pairs $U_\infty/fD : A/D$ that are realized in free vibration experiments at fixed m^* and ζ . Direct measurement of the added mass and drag coefficients is virtually impossible. As already discussed, there are strong indications that a universal value of the added mass coefficient in the relative frame of reference is that predicted from potential flow theory,

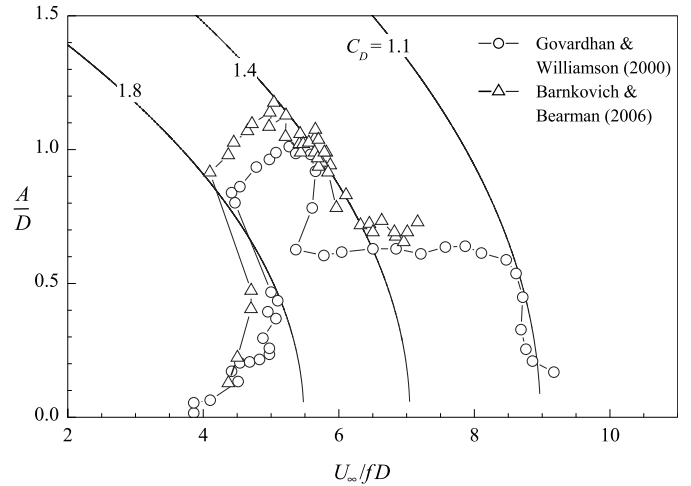


FIGURE 3: COMPARISON BETWEEN LIMITING AMPLITUDE CRITERION AND ACTUAL RESPONSE OF FREELY VIBRATING CYLINDERS [6, 8].

i.e. $C_A = 1.0$ [19]. A complete set of the required data is seldom reported in a single source but one [9]. Most of the experimental studies only report on the response amplitude and frequency in terms of A/D and f/f_N as functions of the reduced velocity, $U_\infty/f_N D$. Apparently, it is necessary to transform such data into an appropriate form so as to make useful comparisons.

Figure 3 shows a comparison of predictions using the equality in Eq. 11 for different constant values of C_D against two sets of experimental data from well-known laboratories at Cornell and Imperial [6, 8]. It is important to note that the data points were carefully reproduced using digitization techniques from different figures presented in their publications. Hence, it was necessary to interpolate the data in order to combine data for the response amplitude and frequency. As a consequence, the data shown are not exactly at the original measurement points. For both sets of data, $m^* \sim 1$ (see Table 1 for the pertinent parameters). Three lines are shown for three different values of the drag coefficient which capture the data trends in different parts of the response curve in Fig. 3. The inequality in Eq. 11 suggests that amplitudes above the lines are not possible given the value of the drag coefficient. $C_D = 1.1$ corresponds to a fixed cylinder in the range of Reynolds numbers of the experiments. The corresponding line in the plot delineates markedly well the response curve in the so-called ‘desynchronization’ range. The line for $C_D = 1.8$ follows the jump between low and high amplitudes (jump between ‘initial’ and ‘upper’ branches in the terminology of Ref. [3]). This suggests that the drag force varies in a continuous

fashion across the jump, a finding which is consistent with physical intuition. An isoline for $C_D = 1.4$ passes through the data points near the maximum response amplitude. This isoline represents well the actual data trend for one set of data [8] but not the other [6]. This difference will be accounted for further below.

The value of the drag coefficient at peak response in the preceding analysis, $C_D \approx 1.4$, is much lower than expected; for instance, a value of around 3.8 was measured at peak response for $m^* = 3.3$ and $\zeta = 0.0026$ in a previous study at Cornell [21]. However, it should be emphasized that, C_D as employed in the derivation of Eq. 11, is not equal to the time-averaged value of the total force in-line with the free stream, which is what one actually measures in the laboratory. Instead, C_D refers to the true drag coefficient experienced by the oscillating cylinder in **relative** motion to the free stream. Hence, it is necessary to correct for this effect. As a first approximation, the true mean velocity of the relative flow may be employed. In this case, it can be shown that the measured drag increases by a factor of μ_1^2 . However, it is deemed more appropriate to correct the result by considering that the rate of energy dissipation in the flow must be the same in relative flow as the one associated with the total force, which equals $\frac{1}{2}\rho DC_D U_\infty^3$. In this case, it can be shown that the correction factor becomes μ_1^3 . Applying the latter correction factor to the data from the group at Cornell [6], the estimated value for the total in-line force at peak response is 3.7. This value is unexpectedly close to the one measured directly in the laboratory [21].

It was recently shown that the response for reduced velocities past the peak amplitude is markedly higher in the absence of an end-plate than when an end-plate is employed to promote parallel vortex shedding [22]. Indeed, the different free-end conditions is possibly the reason for the differences in the two sets of data shown in Fig. 3. The criterion put forward in this study can account for these differences; it is well known that parallel vortex shedding is associated with a higher drag, which according to Eq. 11, effectively dampens the vibrations. This can be readily seen in Fig. 3 for reduced velocities between 5.5 and 6.5.

Blevins [14] provides a database of the forces on a elastically-mounted circular cylinder from free vibration tests in tabulated format. The database comprises the components of the transverse force in-phase with velocity and acceleration and the time-averaged total in-line force as functions of parameter pairs $(U_\infty/fD)St : A/D$ where St is the Strouhal number for a fixed cylinder. With this information in hand, one may look for solutions to the

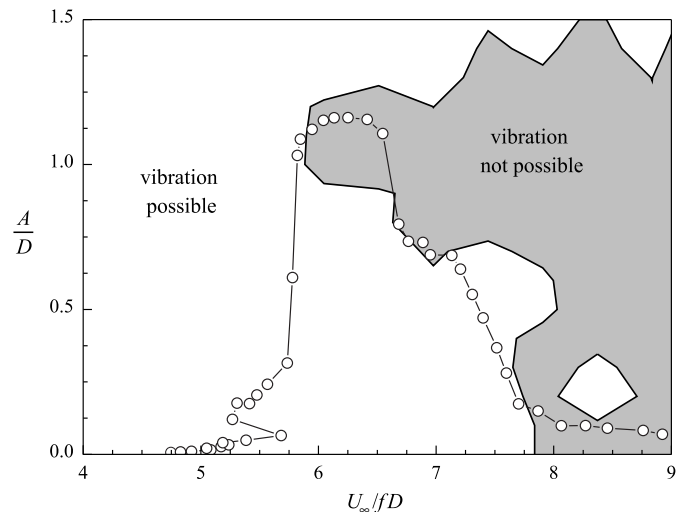


FIGURE 4: COMPARISON BETWEEN LIMITING AMPLITUDE CRITERION AND ACTUAL RESPONSE OF FREELY VIBRATING CYLINDERS [9].

following nonlinear equation (Eq. 10)

$$C_D \left\{ \left(\frac{U_\infty}{fD} \right) St, \frac{A}{D} \right\} \leq \frac{\pi^2}{\mu_1(\alpha)} \left(\frac{fD}{U_\infty} \right) C_A \quad (12)$$

where the curly brackets on the left-hand-side indicate a functional relationship. Vibration is possible only in those regions in the amplitude–frequency parameter space in which the above condition is satisfied, i.e. in the inertia-dominated regime.

Figure 4 shows worked-out solutions of Eq. 12 juxtaposed with the actual response of an elastically-mounted cylinder with low damping ($\zeta = 2 \times 10^{-3}$) [9]. There is a region (gray-shaded) in the non-dimensional parameter space where vibration is not possible according to the criterion proposed here. Outside this region, vibration is theoretically possible anywhere as long as there is some kind of interaction (broadly put, synchronization) between fluid excitation from shed vortices and induced motion of the cylinder. Clearly, this is possible only in a limited region in the parameter space as numerous forced oscillation studies have demonstrated. Attention is now directed to the actual response in Fig. 4. It is seen that, as the true reduced velocity increases the vortex-induced forces ‘drive’ or ‘regulate’ the motion of the cylinder in the initial response around $U_\infty/fD \approx 5.0$. Subsequently, a critical reduced velocity is succeeded in which a jump occurs in the response amplitude. From this point onward, the actual response rests on the margin (or remarkably close to it) between drag and inertia dominated regimes. This can be interpreted as vortex shedding providing the

prerequisite fluid excitation but does not regulate the motion. The differentiation between ‘regulation’ and ‘excitation’ capability of the wake vortices was first-noted by Sarpkaya [2] but there has been no theoretical attack to this issue so far, to this author’s knowledge. The level of agreement between the ‘theoretical’ predictions and the actual response is very encouraging.

CONCLUSION

A criterion for the limiting amplitude of vibration of an elastically mounted circular cylinder placed normal to a fluid stream and excited by periodic separation of vortices in its wake, has been proposed. The criterion has been derived based on purely fluid dynamic considerations; its premise is that vibrations are limited to the regions in the nondimensional amplitude–frequency parameter space where there is a balance between the fluid inertia and fluid damping, which comprise the reaction force exerted on the moving cylinder. In other words, a freely vibrating cylinder needs to overcome its own induced drag (fluid damping) as it moves relative to the free stream provided that shedding of vortices can provide the necessary fluid excitation. This approach also provides a rational explanation as to why the cylinder is more prone to vibrations transverse to free stream rather than in-line. Verification of this hypothesis is not straightforward due to the lack of detailed empirical data for the drag coefficient (actually lack of reporting the values in detail) and some complications that arise as to which is the appropriate value to use. Those selected results presented, indicate that self-excited vibration of an elastically mounted circular cylinder occurs at amplitudes surrounding those predicted by the proposed criterion except for the initial response at low true reduced velocities and amplitudes. This provides support for the hypothesis put forward.

ACKNOWLEDGMENT

The author would like to express his gratitude to R. D. Blevins for making the force database employed in the present study, widely available in [14].

REFERENCES

- [1] Bearman, P. W., 2011. “Circular cylinder wakes and vortex-induced vibrations”. *Journal of Fluids and Structures*, **27**(5–6), pp. 648–658.
- [2] Sarpkaya, T., 2004. “A critical review of the intrinsic nature nature of vortex-induced vibrations”. *Journal of Fluids and Structures*, **19**, pp. 389–447.
- [3] Williamson, C. H. K., and Govardhan, R., 2004. “Vortex-induced vibrations”. *Annual Review of Fluid Mechanics*, **36**, pp. 413–455.
- [4] Williamson, C. H. K., 1989. “Oblique and parallel modes of vortex shedding in the wake of a circular cylinder at low Reynolds numbers”. *Journal of Fluid Mechanics*, **206**, pp. 579–627.
- [5] Klamo, J. T., Leonard, A., and Roshko, A., 2006. “The effects of damping on the amplitude and frequency response of a freely vibrating cylinder in cross-flow”. *Journal of Fluids and Structures*, **22**(6–7), pp. 845–856.
- [6] Govardhan, R., and Williamson, C. H. K., 2000. “Modes of vortex formation and frequency response of a freely-vibrating cylinder”. *Journal of Fluid Mechanics*, **420**, pp. 85–130.
- [7] Govardhan, R., and Williamson, C. H. K., 2006. “Defining the modified Griffin plot in vortex-induced vibration: revealing the effect of Reynolds number using controlled damping”. *Journal of Fluid Mechanics*, **561**, pp. 147–180.
- [8] Branković, M., and Bearman, P. W., 2006. “Measurements of transverse forces on circular cylinders undergoing vortex-induced vibration”. *Journal of Fluids and Structures*, **22**, pp. 829–836.
- [9] Blevins, R. D., and Coughran, C. S., 2009. “Experimental investigation of vortex-induced vibration in one and two dimensions with variable mass, damping, and Reynolds number”. *Journal of Fluids Engineering, Transactions of the ASME*, **131**(10), pp. 1–7. 101203.
- [10] Zasso, A., Belloli, M., Giappino, S., and Muggiasca, S., 2008. “Pressure field analysis on oscillating circular cylinder”. *Journal of Fluids and Structures*, **24**(5), pp. 628–650.
- [11] Lee, J. H., and Bernitsas, M. M., 2011. “High-damping, high-Reynolds VIV tests for energy harnessing using the VIVACE converter”. *Ocean Engineering*, **38**(16), pp. 1697–1712.
- [12] Klamo, J. T., Leonard, A., and Roshko, A., 2005. “On the maximum amplitude for a freely vibrating cylinder in cross-flow”. *Journal of Fluids and Structures*, **21**(4), pp. 429–434.
- [13] Bearman, P. W., 1984. “Vortex shedding from oscillating bluff bodies”. *Annual Review of Fluid Mechanics*, **16**, pp. 195–222.
- [14] Blevins, R. D., 2009. “Models for vortex-induced vibration of cylinders based on measured forces”. *Journal of Fluids Engineering, Transactions of the ASME*, **131**(10), pp. 1–9. 101203.
- [15] Konstantinidis, E., and Bouris, D., 2009. “Effect of

- nonharmonic forcing on bluff-body vortex dynamics". *Physical Review E*, **79**(4). 045303.
- [16] Griffin, O. M., and Skop, R. A., 1976. "The vortex-induced oscillations of structures". *Journal of Sound and Vibration*, **44**(2), pp. 303–305.
- [17] Griffin, O. M., 1981. "OTEC cold water pipe design for problems caused by vortex-excited oscillations". *Ocean Engineering*, **8**(2), pp. 129–209.
- [18] Morison, J. R., O'Brien, M. P., Johnson, J. W., and Schaaf, S. A., 1950. "The force exerted by surface waves on piles". *Petroleum Transactions AIME*, **189**, pp. 149–154.
- [19] Konstantinidis, E., and Liang, C., 2011. "Dynamic response of a turbulent cylinder wake to sinusoidal inflow perturbations across the vortex lock-on range". *Physics of Fluids*, **23**(7). art. no 075102.
- [20] Konstantinidis, E., Dedes, A., and Bouris, D., 2012. "Drag and inertia coefficients for a circular cylinder in a steady plus low-amplitude oscillatory flow". In *Flow-Induced Vibration*, C. Meskell and G. Bennett, eds. 10th International Conference on Flow-Induced Vibration, Trinity College, Dublin, Ireland, 2-6 July 2012.
- [21] Khalak, A., and Williamson, C. H. K., 1997. "Fluid forces and dynamics of a hydroelastic structure with very low mass and damping". *Journal of Fluids and Structures*, **11**(8), pp. 973–982.
- [22] Morse, T. L., Govardhan, R. N., and Williamson, C. H. K., 2008. "The effect of end conditions on the vortex-induced vibration of cylinders". *Journal of Fluids and Structures*, **24**(8), pp. 1227–1239.

FLUID FORCING IN STREAMWISE VORTEX INDUCED VIBRATIONS

Neil Cagney

Department of Mechanical Engineering
University College London
London, UK
Email: neil.cagney.11@ucl.ac.uk

Stavroula Balabani*

Department of Mechanical Engineering
University College London
London, UK
Email: s.balabani@ucl.ac.uk

ABSTRACT

Time-resolved Particle-Image Velocimetry measurements were performed of the flow past a cylinder experiencing Vortex-Induced Vibrations in the streamwise direction for a range of reduced velocities. These were used to estimate the dominant wake modes, cylinder displacement signals, and the drag and lift forces. The response regime consisted of two branches, separated by a low amplitude region at resonance between the cylinder motion and natural vortex shedding frequency. The vortices were found to be shed symmetrically before resonance, while the vortex shedding was alternate during the low amplitude region and the second branch.

Symmetric shedding was found to be associated with a large amplitude, narrow-band drag force, and a weak, irregular lift signal, while the inverse was observed for alternate vortex shedding. At resonance, the drag signal was dominated by low frequency fluctuations, and did not have a significant component occurring at the response frequency, which is thought to be the cause of the low amplitude response observed in this region.

NOMENCLATURE

U_0 Freestream velocity
 D Cylinder diameter
 ν Kinematic viscosity of the fluid
 ρ Density of the fluid
 f_n Cylinder natural frequency (measured in still water)
 f_x Cylinder response frequency (in flowing water)
 f_{St} Predicted frequency of vortex shedding frequency of fixed cylinder
 f^* Frequency ratio
 $St = f_{St}D/U_0$ Strouhal number
 $U_r = U_0/f_nD$ Conventional reduced velocity
 U_rSt/f^* 'True' reduced velocity

$Re = U_0D/\nu$ Reynolds number

C_d Sectional drag force

C_l Sectional lift force

$\bar{\mathbf{u}}$ Velocity vector

$\bar{\mathbf{n}}$ Normal unit vector

$\bar{\mathbf{C}}_f$ Sectional force coefficient vector

INTRODUCTION

Vortex-Induced Vibrations (VIV) is a highly complex problem, which can lead to significant damage in industrial applications such as heat exchangers, offshore structures and tall buildings. Despite the extensive range of research that has been performed in this area, relatively little is known about VIV occurring in the streamwise, or flow, direction, which is known to play a crucial role in the overall response of multi-degree-of-freedom structures [1].

The response of a cylinder undergoing free streamwise VIV can be expressed as a function of the 'true' reduced velocity, U_rSt/f^* , hereafter referred to simply as the reduced velocity, which accounts for variations in the cylinder response frequency due to added mass effects. The amplitude response of a cylinder in the streamwise direction is characterised by two response branches, separated by a low amplitude region at $U_rSt/f^* = 0.5$ [2, 3]. This region corresponds to the predicted point at which the unsteady fluid forces caused by the vortex shedding coincides with the response frequency, which for transverse VIV and classical resonance corresponds to increased levels of vibration. Nishihara et al. [4] forced a cylinder to oscillate in the streamwise direction with an amplitude of $A/D = 0.05$ for a range of reduced velocities, and measured the forces acting on the cylinder. They concluded that the low amplitude region was caused by a change in phase between the cylinder motion and the drag force, such that the drag acted as a damping force, which

*Address all correspondence to this author.

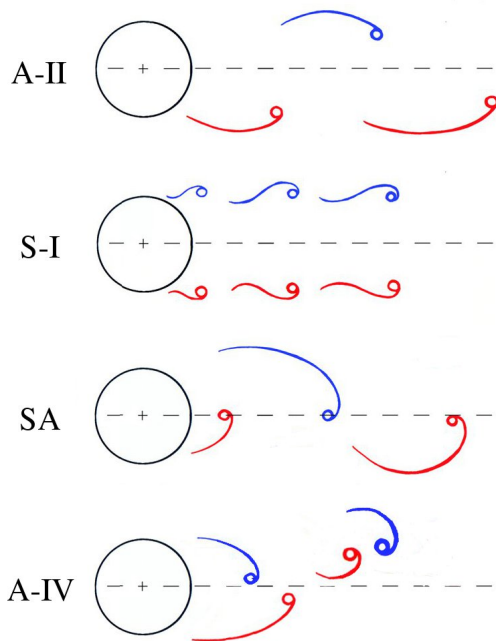


FIGURE 1: SKETCH OF WAKE MODES ASSOCIATED WITH STREAMWISE VIV.

would act to suppress vibrations in this region.

In the same study, the vortices were found to be in an alternate pattern similar to that observed in the wake of a stationary body (referred to as the A-II mode) for $U_r St/f^* \geq 0.5$, while for $U_r St/f^* \lesssim 0.4$ the vortices were shed simultaneously from either side of the cylinder (known as the S-I mode). The symmetry of this mode is known to be unstable, and the wake tends to rearrange into an alternate structure downstream, similar to that of the A-II mode [5, 6].

A special case of the A-II mode has been observed when the vortex shedding is synchronised to the streamwise motion of the cylinder, in which the vortices are shed alternately, but are formed in the very near wake and are convected downstream along the wake centreline [2, 7]. To aid discussion, this case is referred to as the SA mode. The A-IV mode has also been observed in the wake of a cylinder experiencing forced vibrations [6], but has not previously been noted in the free response case, in which two pairs of counter-rotating vortices are shed per cycle. The wake modes discussed here are sketched in Fig. 1.

It is not clear what effect these different modes will have on the fluid forces acting upon the cylinder. In particular; how will the forcing in the drag and lift directions differ for cases of symmetric and alternate shedding? Similarly, what will be the effect of the breakdown

of the S-I mode into asymmetry downstream? What is the cause of the low response region at $U_r St/f^* \approx 0.5$.

This paper seeks to address these questions, by providing simultaneous measurements of the cylinder displacement and wake dynamics using time-resolved Particle-Image Velocimetry. The fluid forces are estimated directly from the velocity fields, and are related to the dominant shedding mode throughout the response regime.

EXPERIMENTAL DETAILS

The experiments were performed in a closed loop water tunnel, which had a $72\text{mm} \times 72\text{mm}$ test-section, previously described in [8]. The cylinder was 7.1mm in diameter, 71mm in length, had a specific density (mass ratio) of 1.17, and was supported within the flow using fishing wires such that it was free to move only in the streamwise direction. A series of tap tests indicated that the damping coefficient was 0.0198, and the natural frequency (in still water) was 23.70Hz . As the cylinder mass ratio was low, the effects of the added mass were large, and at high reduced velocities the response frequency, f_x , was found to be considerably larger than the still water natural frequency (by up to 30%). To account for this, all frequencies are normalised with respect to f_x . The Strouhal number was 0.2 and the Reynolds number varied from 1000 - 5000.

Time-resolved Particle-Image Velocimetry (PIV) measurements were acquired for a range of reduced velocities spanning the streamwise response regime. The measurements were performed using a pulsed Nd:Yag laser and a high-speed CMOS camera, which were controlled using Dynamic Studio (Dantec). For each reduced velocity examined, 1000 image-pairs were acquired at 200Hz , spanning approximately 120 cylinder oscillations. A three-pass cross-correlation scheme was used to estimate the velocity fields, which had a final vector spacing of 12 pixels, which corresponded to approximately 18 vectors per cylinder diameter. The cylinder motion was tracked directly from the PIV images using a template-matching algorithm. The mean cylinder position was used to define the origin of the coordinate system, in which x and y are measured in the streamwise and transverse directions respectively. The experimental set-up and procedures are described in more detail elsewhere [9].

FORCE ESTIMATION

Given the means by which the cylinder was supported and the magnitude of the unsteady drag forces the cylinder was likely to experience in this study (of the order of

0.01 - 1N), it was not possible to measure the forces acting on the cylinder directly. Instead, the forces were estimated from the PIV fields using the relations proposed by Noca et. al. [10]. Using algebraic manipulations to remove the pressure term from the integral form of the momentum equation, the forces acting on any body within a volume V can be expressed as:

$$\bar{\mathbf{C}}_{\mathbf{f}} = -\frac{1}{\frac{1}{2}\rho U_0^2 D} \frac{d}{dt} \int_V \bar{\mathbf{u}} dV + \frac{1}{\frac{1}{2}\rho U_0^2 D} \int_S \bar{\mathbf{n}} \cdot \boldsymbol{\gamma}_{mom} dS \quad (1)$$

where S is the surface surrounding the control volume V , and $\boldsymbol{\gamma}_{mom}$ is a matrix dependent on the local flow velocity, acceleration, vorticity, and position, as well as some viscous terms. Due to the Reynolds number range in this study, the viscous terms were not found to have a noticeable effect on the force estimates, and were neglected.

The flow is assumed to be two-dimensional, and all out-of-plane terms (which could not be measured in this study) are assumed to be zero. The terms in Eqn. 1 then become area and line integrals. As the flow is in fact three-dimensional at this Reynolds number, it is not guaranteed that the two-dimensional equations will be fully closed. As a result, at certain reduced velocities, the choice of integration boundary affected the resulting force signals. To counteract this effect, the force signals were computed for a number of integration boundaries surrounding the cylinder and averaged. The final estimates of the forces were computed from over 50 such signals. It was found that averaging over 30 signals was sufficient for the peak frequency, phase and amplitude of the final estimate of the force to converge.

A fixed reference frame was employed, and the integration boundary did not move depending on the cylinder motion. Thus, the force estimates are of the fluid forces only, and do not include any terms due to the motion of the cylinder.

RESULTS

Amplitude Response

The cylinder amplitude response is shown in Fig. 2a (blue circles) as a function of reduced velocity. The displacement signals were band-pass filtered with cut-off frequencies of $f_{St}/3$ and $1.5f_x$, and the mean peak height was used to define the amplitude. Two response branches are clearly visible, as well as the low amplitude region at $U_r St / f^* \approx 0.5$, as has previously been observed [2, 3].

Figure 2b shows the variation of the dominant frequency of the estimated lift force (red triangles) and the

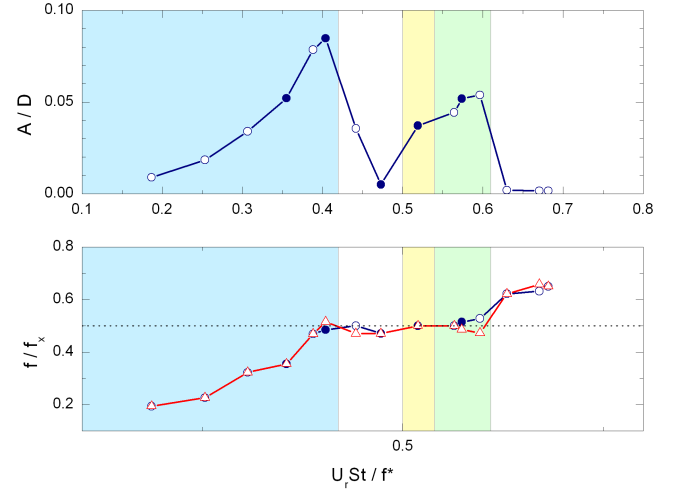


FIGURE 2: (A) AMPLITUDE RESPONSE OF CYLINDER AS A FUNCTION OF REDUCED VELOCITY. (B) DOMINANT FREQUENCY OF TRANSVERSE VELOCITY FLUCTUATIONS AT $(x/D, y/D) = (3, 0.5)$ (BLUE CIRCLES) AND ESTIMATED LIFT FORCE (RED TRIANGLES) THE SHADED REGIONS DENOTE THE DOMINANT SHEDDING MODE, AS OUTLINED IN TABLE 1. CLOSED SYMBOLS INDICATE THE REDUCED VELOCITIES FOR WHICH THE PHASE-AVERAGED VORTICITY FIELDS AND SPECTRA OF THE FLUID FORCES ARE DISCUSSED IN THE FOLLOWING SECTIONS.

transverse velocity measured at $(x/D, y/D) = (3, 0.5)$, with reduced velocity. The frequency of the lift force appears to match that of the downstream fluctuations reasonably closely throughout the response regime. Both signals tend to follow the Strouhal relation, but become locked in to the cylinder motion for $U_r St / f^* = 0.39 - 0.6$.

The amplitude is also shown in Fig. 3, this time as a function of the conventional reduced velocity in order to facilitate comparison with the results of Jauvtis and Williamson, for the case of a cylinder free to move in both the streamwise and transverse directions (red circles). The damping coefficient of the cylinder used by Jauvtis and Williamson was an order of magnitude smaller than that used in the present study, and thus their peak amplitude response is larger. Aside from this, the response of both systems are quite similar, suggesting that the results presented in this paper are applicable to the general, multi-degree-of-freedom response in this reduced velocity range, not just streamwise-only VIV.

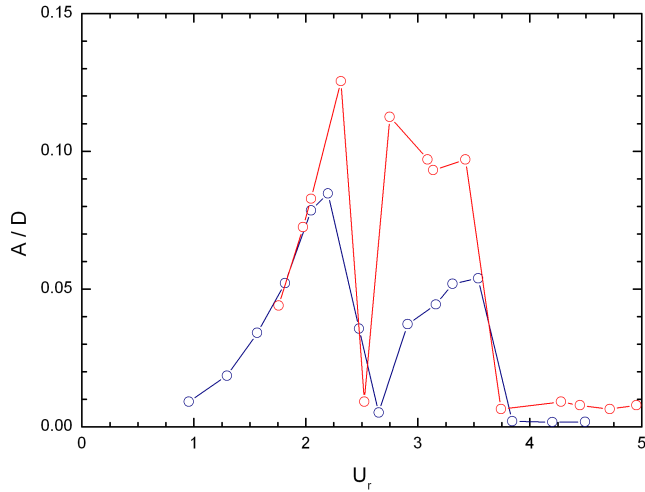


FIGURE 3: AMPLITUDE RESPONSE OF CYLINDER AS A FUNCTION OF CONVENTIONAL REDUCED VELOCITY, FOR PRESENT STUDY (BLUE CIRCLES) AND THE RESULTS OF JAUVTIS AND WILLIAMSON [7] FOR CYLINDER WITH TWO DEGREES OF FREEDOM.

TABLE 1: ESTIMATED REDUCED VELOCITY RANGE OVER WHICH EACH WAKE MODE IS DOMINANT, AND COLOUR USED TO IDENTIFY MODE IN FIG. 2

Mode	Reduced Velocity Range	Colour
S-I	< 0.42	Blue
A-II	$0.42 - 0.5, > 0.61$	White
SA	$0.5 - 0.54$	Yellow
A-IV	$< 0.54 - 0.61$	Green

Wake Modes

The shaded regions in Fig. 2 denote the dominant shedding mode at each reduced velocity, as listed in Table 1. Phase-averaged vorticity fields representing each of the four observed modes, as well as the breakdown of the S-I mode, are shown in Fig. 4a-e for the five reduced velocities indicated by the closed symbols in Fig. 2. The transverse velocity signal extracted from the PIV was used as a reference signal in the phase-averaging process. For $U_r St/f^* < 0.42$, when the wake exhibited the S-I mode and the shedding was synchronised to the cylinder motion, the reference signal was measured at

$(x/D, y/D) = (2, 0.5)$, while for reduced velocities above this, when the shedding no longer occurred at the response frequency, the reference signal was measured at $(x/D, y/D) = (3, 0.5)$. This choice of reference signal ensured that the phase-averaged fields accurately captured the shedding mode which was apparent throughout the instantaneous fields. Each phase shown corresponds to the cylinder in its most downstream position.

The symmetric arrangement of vortices which characterises the S-I mode is clear in Fig. 4a ($U_r St/f^* = 0.35$). Two simultaneously shed vortices are visible in the near wake, and the general symmetry of the wake is maintained until $x/D \approx 3$, after which the vorticity field becomes unclear. The symmetric shedding is also visible in the near wake of the phase-averaged field for $U_r St/f^* = 0.4$ (Fig. 4b). However, at this reduced velocity the vortices are found to decay downstream into an alternate structure. The point at which the breakdown occurred was found to be variable, as was also noted by Konstantinidis and Balabani [5] who observed this mode in the wake of a fixed cylinder in sinusoidally perturbed flow. The symmetrical wake structure was found to be most stable at $U_r St/f^* = 0.35$, and tended to decay into asymmetry closer to the cylinder as the reduced velocity was increased above and below this point.

This rearrangement increases the wavelength of the wake, and causes the frequency of velocity fluctuations to decrease accordingly. Although the vortices are formed at the response frequency for $U_r St/f^* < 0.42$, the breakdown of symmetry in the wake causes the fluctuations occurring downstream to occur at a different frequency. For $U_r St/f^* < 0.39$ the wake reverts to the natural, or Strouhal, frequency, while for $U_r St/f^* = 0.39 - 0.42$, the wake continues to decay into an alternate structure, but one which is synchronised to half the response frequency. This causes the wake in this region to have a slightly shorter wavelength than would occur in the wake of a stationary cylinder.

At the onset of the low amplitude region, $U_r St/f^* = 0.47$, the vortex shedding is alternate (Fig 4c), and the wake resembles that seen behind a stationary cylinder. The shear layers extend relatively far into the wake, before rolling up to form vortices at approximately $x/D = 1.5$. At a slightly higher reduced velocity, $U_r St/f^* = 0.52$, the SA modes dominates (Fig. 4d); the vortex shedding remains alternate, but the vortices are now formed very close to the cylinder and are convected downstream along the wake centreline. The onset of this wake mode coincides with a partial recovery of the levels of cylinder vibration observed during the first response branch.

The shedding mode is also alternate at $U_r St/f^* =$

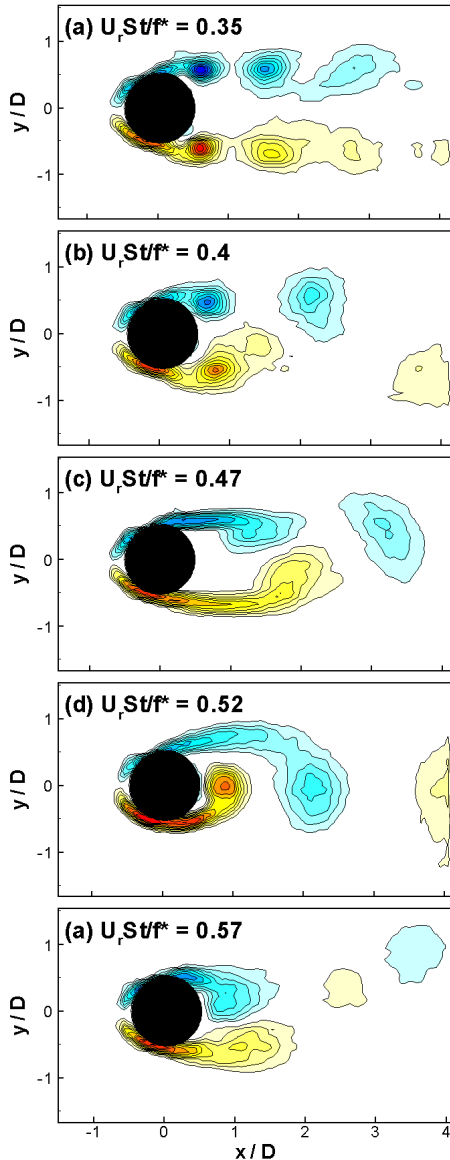


FIGURE 4: PHASE AVERAGED VORTICITY FIELDS SHOWING THE S-I MODE (A); THE S-I MODE WITH BREAKDOWN OCCURRING IN THE NEAR WAKE (B); A-II MODE OCCURRING IN THE LOW AMPLITUDE REGION (C); THE SA MODE (D); AND THE A-IV MODE (E). ALL FIELDS CORRESPOND TO THE CYLINDER IN ITS MOST DOWNSTREAM POSITION. CONTOUR LEVELS ARE $\omega_z D/U_0 = \pm 0.75, \pm 1.5, \dots$

0.57 (Fig 4e), but four vortices are now shed per cycle, forming the A-IV mode. A vortex pair is visible in the top right of the field, convecting away from the cylinder. It appears that the increased number of vortices shed per cycle causes a reduction in the magnitude of vorticity within each vortex; the positive and negative vortices at

$x/D = 2.5$ and 3.5 appear to be considerably weaker than those observed in the same region for the A-II and SA modes.

Fluid Forces

The variation in the amplitude of the unsteady lift and drag coefficients with reduced velocity is shown in Fig. 5. The force signals were filtered and the amplitudes estimated in the same manner as the displacement signals (i.e. with cut-off frequencies of $f_{St}/3$ and $1.5f_x$).

The unsteady drag is large for $U_r St/f^* \lesssim 0.4$ while the S-I mode dominates. The increased tendency of the wake to rearrange into an alternate structure as the reduced velocity nears 0.5 does not appear to reduce the levels of the the drag force in this region, with a local maximum occurring at $U_r St/f^* = 0.38$. As the wake switches to an alternate shedding pattern, there is a dramatic reduction in the drag force, reaching a local minimum in the low cylinder response region at $U_r St/f^* = 0.47$. This is recovered somewhat at the onset of the SA mode, and there is a further increase during the region of A-IV shedding. Beyond the second response branch, the unsteady drag coefficient remains constant at approximately 0.23. This is notably smaller than the value seen before the onset of the first branch, and it would appear that for a body free to move only in the streamwise direction, there is a marked difference between the cases of a cylinder before and after resonance. This is likely to be associated with the tendency for the symmetric shedding mode to dominate at reduced velocities before resonance, $U_r St/f^* < 0.5$, as it would appear that the S-I mode is associated with comparatively large amplitude fluctuating drag, while the alternate shedding modes coincide with low levels of forcing in this direction.

The lift coefficient amplitude is roughly constant for $U_r St/f^* < 0.4$, but increases as the reduced velocity nears 0.5, as the wake has an increasing tendency to breakdown into asymmetry. It is notable that a local minimum occurs at $U_r St/f^* = 0.35$ where the S-I mode is found to be most stable. Despite the alternate shedding which occurs at $U_r St/f^* = 0.47$, the unsteady lift force reaches another local minimum. The sudden decrease in both the drag and lift forces at this reduced velocity are likely to be caused by formation of vortices quite far from the cylinder base, as can be seen in the vorticity fields in Fig 4; as the vortices form farther downstream, they will have a reduced effect on the pressure and velocity fields in the near wake, and as a result the cylinder will experience lower levels of vortex-induced forcing.

There is a sudden increase in the lift coefficient at the onset of the SA mode, $U_r St/f^* = 0.52$, where the forces

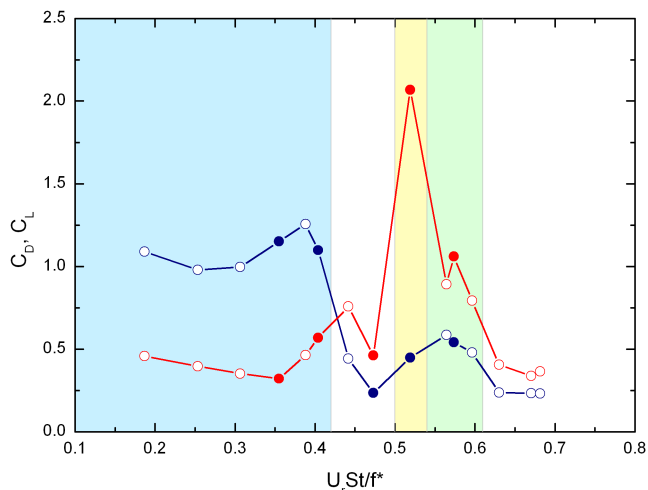


FIGURE 5: AMPLITUDES UNSTEADY LIFT (RED) AND DRAG (SIGNALS) ESTIMATES AS FUNCTION OF REDUCED VELOCITY.

in this direction reach a maximum. Examination of the phase averaged vorticity field in this region (Fig. 4d) indicates that there is also a sudden decrease in the vortex formation length. The vortices are now formed very close to the cylinder, as was observed for $U_r St / f^* < 0.4$. However, the vortex shedding is now alternate, not symmetric, and the primary component of the fluid forcing now acts in the transverse rather than streamwise direction. The A-IV mode coincides with a reduction in the amplitude of the lift force, which reaches a peak at $U_r St / f^* = 0.57$, although these levels remain above those observed while the A-II mode occurs.

In general, the levels of transverse forcing are relatively low during the symmetric shedding region, but increase as the alternate shedding modes become dominant. This distinction is discussed further in the following section with regards to the frequency spectra of the force signals associated with each mode.

Frequency Spectra

The frequency spectra of the fluid forces for the five reduced velocities discussed in the previous section, are shown in Fig. 6. The spectra were estimated using Welch's method and had a resolution of 0.78Hz, or approximately $0.03 f_x$.

At $U_r St / f^* = 0.35$, the vortices are shed at the response frequency, but rearrange downstream, and the fluctuations downstream occur at the Strouhal frequency. In spite of the bi-modal nature of the wake, the spectrum of the drag signal at this reduced velocity (Fig. 6a) contains only one peak, at f_x . It appears the loss of symmetry

downstream has little impact on the drag forces experienced by the cylinder. In contrast, it is this breakdown which, by introducing asymmetry into the wake, is the origin of the forcing in the transverse direction. The lift spectrum (Fig. 6b) has peaks at f_{St} and f_x , as well as smaller secondary peaks at $f_{St}/2$ and $2f_{St}$. The position at which the breakdown of symmetry occurs in the wake varies with time, which is likely to be the cause of the wide distribution of energy in this signal.

At $U_r St / f^* = 0.4$, the wake tends to lose its symmetrical structure closer to the cylinder; this appears to have little effect on the spectrum of the drag force (Fig. 6c), but causes the lift spectrum to become slightly more ordered (Fig. 6d), with large twin peaks occurring at f_{St} and f_x , and less low frequency fluctuations.

The spectrum of the drag coefficient in the low amplitude region, $U_r St / f^* = 0.47$ is no longer well-ordered (Fig 6e) compared to those calculated for the first branch. The signal is dominated by low frequency fluctuations and shows no significant component occurring at the response frequency. As only the component of the force acting at the frequency of the structural motion is capable of providing a net energy transfer, this implies that the wake is incapable of imparting any excitation to the cylinder in this reduced velocity region, and explains the negligible levels of vibration observed here.

In contrast, the lift spectrum at this reduced velocity (Fig 6f) is more ordered than that seen previously, with only one large peak occurring at $f_x/2 \approx f_{St}$.

The onset of the SA mode causes the drag signal to have a significant component at the response frequency, although several subharmonic peaks are also present (Fig. 6g). The alternate shedding causes the lift force signal to become increasingly narrow-band, with no secondary peaks (Fig. 6h). The spectrum of the drag signal becomes slightly more ordered at $U_r St / f^* = 0.57$ (Fig. 6i), as the A-IV mode dominates, with the maximum component of the signal occurring at f_x once more. The lift spectrum (Fig. 6j) is again well-ordered, with only one peak at $f_x/2$.

In general, when the dominant shedding mode is symmetric ($U_r St / f^* \lesssim 0.5$), the drag signal tends to be narrow-band and have a large amplitude, while the lift signal is relatively weak and disorganised, tending to be dominated by low frequency fluctuations and harmonic peaks. However, when the shedding is alternate, the opposite is true; the lift spectra are well ordered while the drag signals have an increased irregularity. As the majority of the response regime of a cylinder free to move in both the streamwise and transverse directions is characterised by alternate shedding [7], it is not surprising that

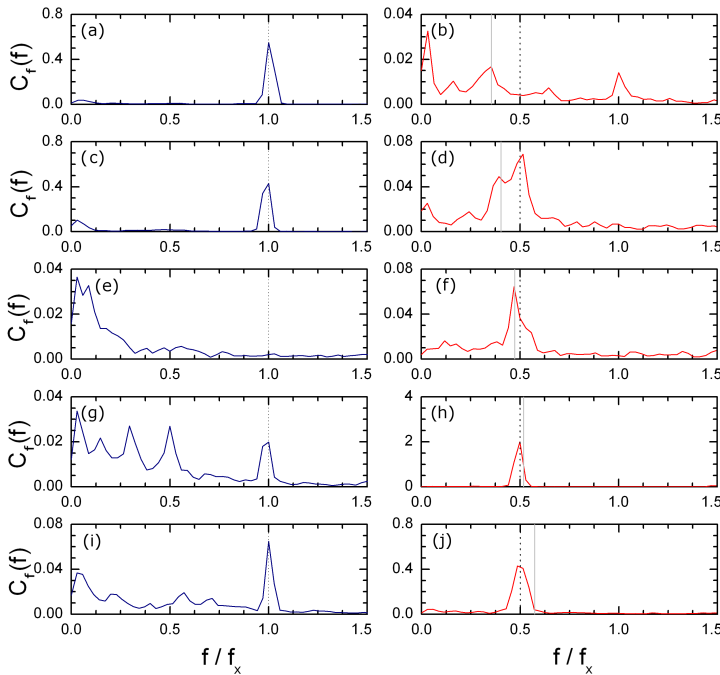


FIGURE 6: SPECTRA OF UNSTEADY DRAG (LEFT COLUMN, SHOWN IN BLUE) AND LIFT (RIGHT COLUMN, SHOWN IN RED) FOR $U_r St / f^* = 0.35$ (A, B), 0.4 (C, D), 0.47 (E, F), 0.52 (G, H) AND 0.57 (I, J). THE GREY LINE IN THE LIFT SPECTRA DENOTES THE STROUHAL FREQUENCY.

only a relatively small component of the overall cylinder response occurs in the streamwise direction [1].

However, the effects of streamwise oscillations of a cylinder are similar to those of sinusoidal pulsations in the freestream velocity, as may occur due to wave loading in offshore structures; these findings indicate that when the frequency of the wave loading exceeds twice the Strouhal frequency (which is equivalent to $U_r St / f^* < 0.5$), the wake will tend to be asymmetrical and will provide low levels of transverse forcing or excitation. In contrast, when the loading occurs at a frequency below this (i.e. $U_r St / f^* > 0.5$) the wake forcing will occur primarily in the lift direction.

Similarly, a cylinder free to move in both the streamwise and transverse direction will experience significant excitation only in the drag direction below resonance ($U_r St / f^* < 0.5$) and negligible motion normal to the flow, while above this value it is likely to experience both lift and drag forcing. As the lift force occurs at a frequency half that of the drag, this is likely to cause the cylinder to exhibit streamwise-only motion during the first branch, and to follow a figure-of-eight orbit during the second branch, as was observed by Jauvtis and Williamson [7].

CONCLUSIONS

The response amplitude and dominant shedding mode of a cylinder experiencing streamwise-only VIV were measured using time-resolved PIV. These measurements were used to estimate the unsteady lift and drag forces acting on the cylinder. The response regime contained two branches, and a low amplitude region at $U_r St / f^* = 0.5$. For reduced velocities below this region, the vortices were shed symmetrically, while at higher reduced velocities the vortex shedding was alternate, and the A-II, SA and A-IV wake modes were all observed.

The symmetric shedding modes tended to coincide with a large amplitude drag, but a weak and irregular lift force. In contrast, when the shedding was alternate, the lift force tended to be narrow-band, while the drag became irregular. At $U_r St / f^* \approx 0.5$, the drag signal was dominated by low frequency fluctuations, and the component occurring at the response frequency was negligible, which is thought to be the cause of the reduced levels of vibration which occurred in this region.

REFERENCES

- [1] Williamson, C. H. K., and Jauvtis, N., 2004. "A high-amplitude 2T mode of vortex-induced vibration for a light body in XY motion". *European Journal of Mechanics B/Fluids*, **23**, pp. 107–114.
- [2] Aguirre, J. E., 1977. "Flow induced, in-line vibrations of a circular cylinder". PhD thesis, Imperial College of Science and Technology.
- [3] Okajima, A., Nakamura, A., Kosugi, T., Uchida, H., and Tamaki, R., 2003. "Flow-induced in-line oscillation of a circular cylinder". *European Journal of Mechanics B/Fluids*, **23**, pp. 115–125.
- [4] Nishihara, T., Kaneko, S., and Watanabe, T., 2005. "Characteristics of fluid dynamic forces acting on a circular cylinder oscillating in a streamwise direction and its wake patterns". *Journal of Fluids and Structures*, **20**, pp. 505–518.
- [5] Konstantinidis, E., and Balabani, S., 2007. "Symmetric vortex shedding in a near wake of a circular cylinder due to streamwise perturbations". *Journal of Fluids and Structures*, **23**, pp. 1047–1063.
- [6] Ongoren, A., and Rockwell, D., 1988. "Flow structure from an oscillating cylinder Part 2. Mode competition in the near wake". *Journal of Fluid Mechanics*, **191**, pp. 225–245.
- [7] Jauvtis, N., and Williamson, C. H. K., 2003. "Vortex-induced vibration of a cylinder with two degrees of freedom". *Journal of Fluids and Structures*, **17**, pp. 1035–1042.

- [8] Konstantinidis, E., Balabani, S., and Yianneskis, M., 2003. "The effect of flow perturbations on the near wake characteristics of a circular cylinder". *Journal of Fluids and Structures*, **18**, pp. 367–386.
- [9] Cagney, N., and Balabani, S., 2012. Wake modes of a cylinder undergoing free streamwise vortex-induced vibrations. *Journal of Fluids and Structures* (submitted February 2012), February.
- [10] Noca, F., Shiels, D., and Jeon, D., 1999. "A comparison of methods for evaluating time-dependent fluid dynamic forces on bodies, using only velocity fields and their derivatives". *Journal of Fluids and Structures*, **13**, pp. 551–578.

DRAG AND INERTIA COEFFICIENTS FOR A CIRCULAR CYLINDER IN A STEADY PLUS LOW-AMPLITUDE OSCILLATORY FLOW

Efstathios Konstantinidis *

Alexis Dedes

Demetri Bouris

Department of Mechanical Engineering

University of Western Macedonia

Bakola & Sialvera, Kozani 50100 Greece

ABSTRACT

Numerical computations of steady plus low-amplitude oscillatory flow about a circular cylinder are reported at a fixed Reynolds number of 150 based on the steady component. The conventional Keulegan–Carpenter number based on the oscillatory component was held at a constant value of $\pi/5$. The main parameter varied was the excitation frequency so as to study a wide spectrum of flows where inertial forces dominate at one end, and viscous drag forces at the other. The total force on the cylinder in-line with the flow direction is represented by Morison's equation and an extended version with three terms. The drag and inertia coefficients in Morison's equation are determined by least-squares fits to data directly computed by integration of skin friction and pressure distributions around the periphery of the cylinder. The root-mean-square value of the residue of reconstructed minus directly-computed forces varies between 2 and 41% depending on the flow parameters. Physical explanations for the variation of the force coefficients are provided.

INTRODUCTION

Practical considerations require engineering analysis of structures subjected to a fluid stream against flow-induced vibration. In turn, this calls for comprehension of the basic mechanisms that are responsible for such vibration from the fundamental point of view. Whenever a structure, or body, immersed in a fluid stream vibrates, a time-dependent relative velocity between the body and the flow is induced and non-linear interactions take place.

It is often the case, that such non-linear dynamics need be interpreted and embodied in simple mathematical models that can be used in engineering analysis. A widely employed model for the forces on cylindrical structures in time-dependent flows is the so-called 'Morison's equation' [1].

The present study is concerned with time-dependent flows about a circular cylinder. This may be viewed as a generalized configuration encompassing the principal mechanisms of flow-structure interactions, whether these are externally posed, self-excited, or both. The circular cylinder, in addition to its wide-spread use as a structural element in engineering, has been employed as a paradigm in fluid dynamics for the study of unsteady separated flows. In many practical flow problems, flow separation is inevitable. As a consequence, vortices that separate periodically in the wake are responsible for generation of time-dependent fluid forces on structures. If the structure has natural frequencies close to that of the applied forces, reciprocal coupling takes place which may lead to substantial vibrations. At the origin of this mechanism, is the existence of a region of absolute flow instability in the very-near wake [2]. Because of the two-dimensional nature of the absolute instability, numerical simulations of the Navier–Stokes equations limited to a cross-section of the cylinder provide satisfactory results of the flow around real structures.

Planar unsteady flows about cylinders may be classified in three broad categories: purely oscillatory (tidal) flows with zero mean, combined steady plus oscillatory flows where both components are of the same order (flow reversal is possible), and steady flows with low-amplitude oscillatory perturbations superimposed (no flow reversal). It should be noted that a time-dependent flow about a

*Address all correspondence to this author.
E-mail: ekonstantinidis@uowm.gr

fixed cylinder is kinematically equivalent to a cylinder that oscillates in still fluid or in-line with a steady flow. The present study is concerned with perturbed flows. Two prominent phenomena are associated with perturbed flows. Firstly, the regular formation of vortices can be captured by the imposed perturbation frequency, a condition which is often called ‘vortex lock-on’ and typically leads to enhancement of flow organization and wake fluctuations. Secondly, the alternating mode of vortex formation from each side of the cylinder may be modified and give place to a symmetric mode. The reader is referred to the introductory sections of previous publications for more information [3–5].

Despite the fact that perturbed flow over an isolated cylinder has been studied to a great extent, data for the drag and inertia coefficients in Morison’s equation seem to be lacking. This contrasts the plethora of available information for purely oscillatory and combined steady plus high-amplitude oscillatory flows. Instead, force components in phase with acceleration and velocity were determined in order to yield ‘effective added-mass’ and ‘added-damping’ coefficients for an oscillating cylinder in a relatively recent experimental study [6]. To achieve this, measured forces were introduced in the equation of motion of a cylinder hypothetically excited into oscillations due to vortex shedding. It is deemed that, although this approach is useful in identifying regions in the parameter space where such oscillations are possible, it masks the physical understanding of the fluid forcing. This is partly due to the incomplete understanding of the physics of the added mass and, particularly, whether the structural mass and/or damping in the equation of motion should take into account the added mass, or not. This issue remains inadequately resolved for cylinders oscillating either transversely or in-line with a fluid stream, e.g., see recent reviews in vortex-induced vibrations [7, 8]).

The purpose of the present study is to examine the effect of steady plus low amplitude oscillatory (perturbed) flows on the wake dynamics and resulting forces on a circular cylinder over a wide spectrum of parameters ranging from, one end where inertial forces dominate, to the other where viscous drag forces are dominant. Numerical computations of these flows in two dimensions are carried out using an in-house code in order to provide data for the time-dependent forces on, and flow structures around the cylinder. Morison’s equation is employed to reconstruct the total in-line force and the unknown force coefficients are fitted to the directly-computed force. Inevitably, there will be some overlap with previous related studies. However, one is forced to replicate some results in order to enhance the understanding of the basic flow

mechanisms, extend them to wider ranges in parameter space and, hopefully, be able to extrapolate the findings to other regions in the multi-parameter space based on physical reasoning.

MORISON’S EQUATION

Consider a fixed circular cylinder placed normal to a steady plus oscillatory flow, $U(t) = U_c + U_w \sin(\omega t)$. The total force per unit length of the cylinder in-line with the flow can be expressed as the sum of two components,

$$F_x(t) = \frac{1}{2}\rho D C_d |U(t)| U(t) + \frac{1}{4}\rho \pi D^2 C_m \frac{dU}{dt}, \quad (1)$$

where ρ is the fluid density, D is the cylinder diameter, C_m and C_d are the mass (inertia) and drag coefficients, respectively. The equation was originally developed to compute wave loading on offshore structures, now is widely known as Morison’s equation [1]. The inertial force accounts for two different mechanisms: (a) a component due to the pressure waves induced by the unsteady flow (a.k.a. Froude–Krylov term), and (b) a component due to the added (or hydrodynamic) mass. The coefficients C_m and C_d in (1) are assumed constant over a cycle but these will generally be functions of three independent non-dimensional parameters.

To a first approximation, the inertial term may be assumed the same for both inviscid and viscous fluids, in which case C_m can be predicted from potential flow theory; $C_m = 1 + C_a$ where C_a is the added mass coefficient which depends on the geometry of the cylinder. For a circular cylinder, $C_a = 1.0$. Then, the drag term accounts for all effects of viscosity and may be further assumed the same as for steady flow (quasi-steady approach), taking into account the Reynolds number. When the perturbation velocity is small, the Reynolds number does not change appreciably and the drag coefficient is effectively constant. This approach has the advantage that only the variation of the mean drag coefficient as a function of Reynolds number $C_{D_s}(Re)$ for steady flow is required. This can be useful in determining roughly the regimes where the drag or inertia terms dominate the response. As previously shown [5], for low-amplitude perturbed flows this boils down to the following criterion:

$$\frac{1}{\pi^2} \left(\frac{U_c}{f_e D} \right) \frac{C_d}{C_m} \begin{cases} \gg 1 & \text{drag-dominated regime} \\ \ll 1 & \text{inertia-dominated regime} \end{cases} \quad (2)$$

Alternatively, the drag coefficient in Morison’s equation may be computed from empirical data as the time-

averaged value of the total in-line force over an integer number of flow cycles,

$$C_D = \frac{\langle F_x \rangle}{\frac{1}{2} \rho D U_c^2} \quad (3)$$

where $\langle \cdot \rangle$ is the time averaging operator. It should be emphasized that the mean drag coefficient C_D above is fundamentally different to the drag coefficient C_d , which is an empirical constant in Morison's equation. Using $C_d \approx C_D$ is a test hypothesis under consideration.

Substitution of the unsteady flow velocity $U(t)$ and its derivative into the Morison equation yields

$$F_x(t) = \frac{1}{2} \rho D C_{d2} U_c^2 g_1(t) + \frac{1}{4} \rho \pi D^2 C_m U_w \omega g_2(t) \quad (4)$$

where $g_1(t) = (1 + \varepsilon \sin \omega t)^2$ and $g_2(t) = \cos \omega t$ if the flow is assumed to be non-reversing. An extended Morison's equation which comprises steady and oscillatory drag terms and an inertial term was proposed to account for the effect of a current [9]. The 3-term equation reads

$$F_x(t) = \frac{1}{4} \rho \pi D^2 C_m U_w \omega \cos(\omega t) + \frac{1}{2} \rho D C_{dc} U_c^2 + \frac{1}{2} \rho D C_{do} U_w^2 |\sin(\omega t)| \sin(\omega t). \quad (5)$$

Empirical data may be used along with (4) and (5) to determine the numerical values of the coefficients in the equations. A number of different methodologies can be employed for this purpose, either in the time or frequency domain (see [10] for a comprehensive description). Frequency domain methods have mostly been developed for forces on structures in random waves and will not be considered here. Time domain methods can be cast into two broad categories: Fourier averaging and least-squares fitting. The former is considered more appropriate when the force signal is approximately monochromatic. This is clearly not the case over the entire range of parameters examined in the present study. Therefore, the method of least squares was employed so that useful comparisons can be made. This involves minimization of the mean squared error between empirical and reconstructed forces,

$$\sigma^2 = \frac{1}{N} \sum_{i=1}^N [F_x(t_i) - F_x^*(t_i)]^2, \quad (6)$$

where F_x is the empirically-determined force and F_x^* is the reconstructed force. This leads to two equations,

$$\frac{\partial \sigma^2}{\partial C_d} = \frac{\partial \sigma^2}{\partial C_m} = 0, \quad (7)$$

with two unknowns in the case of the 2-term equation (4), and three equations,

$$\frac{\partial \sigma^2}{\partial C_{dc}} = \frac{\partial \sigma^2}{\partial C_{do}} = \frac{\partial \sigma^2}{\partial C_m} = 0. \quad (8)$$

with three unknowns for the 3-term equation (5). The solution of the systems of equation gives the values of the unknown force coefficients (final result is omitted for brevity).

NUMERICAL METHOD

The finite-volume method is employed to solve the continuity and Navier–Stokes equations for unsteady flow about a circular cylinder. The equations can be written in generalized form as

$$\begin{aligned} \frac{\partial}{\partial t}(\rho \Phi) + \frac{1}{l_\xi l_\eta} \frac{\partial}{\partial \xi}(\rho u l_\eta \Phi) + \frac{1}{l_\xi l_\eta} \frac{\partial}{\partial \eta}(\rho v l_\xi \Phi) = \\ \frac{1}{l_\xi l_\eta} \frac{\partial}{\partial \xi} \left(\mu \frac{l_\eta}{l_\xi} \frac{\partial \Phi}{\partial \xi} \right) + \frac{1}{l_\xi l_\eta} \frac{\partial}{\partial \eta} \left(\mu \frac{l_\xi}{l_\eta} \frac{\partial \Phi}{\partial \eta} \right) + S_\Phi \end{aligned} \quad (9)$$

where ρ and μ are the density and viscosity of the fluid, respectively, l_ξ and l_η are the spatially varying metric coefficients related to the orthogonal curvilinear coordinates (ξ, η) , and (u, v) the corresponding velocities in local coordinates. The variable $\Phi = 1, u, v$ for the continuity and momentum equations, respectively, and S_Φ are the source terms, including pressure terms. The method is based on the discretization of the governing equations on an orthogonal curvilinear grid in two dimensions. Volume averaging is performed in physical space and the metric coefficients are replaced by the physical distances. All variables are collocated at the grid cell centers so that the original SIMPLE algorithm can be combined with the Rhie and Chow modification to avoid checker board oscillations in the pressure coupling [11, 12]. A fully-implicit first-order Euler discretization of the temporal term is used while for the convection and diffusion terms, a higher-order bounded upwind scheme and central differencing is employed, respectively [13].

The solution domain is rectangular and extends $10D$ upstream, $25D$ downstream and $10D$ above and below the cylinder. The curvilinear mesh consists of 299×208 nodes, which is sufficiently dense for mesh-independent results. A time-dependent uniform velocity is specified at the inflow whereas a convective boundary condition is employed at the outflow. Symmetry conditions are employed at the lateral boundaries whereas the no-slip

TABLE 1: REFERENCE DATA FOR STEADY FLOW

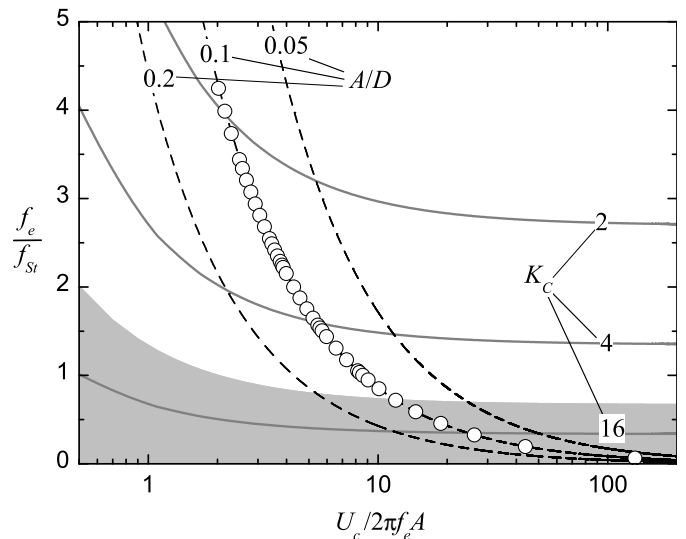
Re	St	C_{Ds}	C_{Dos}	C_{Ls}
150	0.185	1.331	0.018	0.380

condition is applied on the cylinder surface. The time step is of the order of $\delta t U_c/D = 10^{-2}$. The system of discretized equations is solved using a Tri-Diagonal Matrix Algorithm (TDMA) with an iterative Alternating Direction Implicit (ADI) method.

The instantaneous in-line and transverse forces on the cylinder are computed by suitably integrating the pressure and skin friction distributions around its circumference. The history of the in-line force is subsequently processed to yield the drag and inertia coefficients by the method of least squares.

FLOW PARAMETERS

For the present simulations, the steady velocity component is fixed so that the corresponding Reynolds number has a constant value of $U_c D/\nu = 150$. Table 1 lists the main flow characteristics in steady flow at this Reynolds number, for reference. No detailed comparison is provided here for economy of space, suffice it to say that the reported values are in agreement to other published data. The main variable in unsteady flow is the frequency of the oscillatory component while its amplitude is adjusted so that $U_w/\omega D = 0.1$. The latter parameter is equal to the non-dimensional amplitude of a cylinder oscillating in-line with a steady current, A/D . There is a multitude of other parameters that can be employed to describe the problem in hand. For purely oscillatory flows with zero mean, it is conventional to organize the results in terms of the Keulegan–Carpenter number, $K_C = U_w/f_e D = 2\pi A/D$ and the Stokes number, $\beta = f_e D^2/\nu$. However, Zdravkovich showed that if the conventional Keulegan–Carpenter number is replaced by a modified version, as originally suggested by Sarpkaya and his coworkers, the regimes of vortex patterns can be described in a more orderly fashion for combined mean plus oscillatory flows [14]. The modified version, $K_C = (U_c + U_w)/f_e D$, is employed in the present study as more relevant. It represents the ratio of the inertial to drag forces. Note that it can also be written as $K_C = 2\pi A/D + U_c/f_e D$ where the first term on the right-hand-side is the conventional Keulegan–Carpenter number and the second term is often referred to as the reduced velocity, V_r . For the present study, $K_C = \frac{\pi}{5} + V_r$.


FIGURE 1: PARAMETER SPACE EXAMINED IN THE PRESENT STUDY.

The above non-dimensional parameters, although widely employed in related studies, they generally fail to separate the effects of excitation frequency and amplitude. From the fundamental point of view, the excitation frequency is the key variable that governs flow-structure interactions in terms of the wake response and the resulting forces acting on the cylinder. The magnitude of the imposed perturbation acts as an amplifier to the basic modes that are excited at different frequencies. Such effects become more clear if the excitation frequency is normalized by the frequency of vortex shedding in the absence of flow perturbations, i.e. $f_{St} = St U_c/D$ (where St is the Strouhal number). The effects of amplitude may be succinctly described in terms of the velocity ratio of the oscillatory to steady components, $\varepsilon = U_w/U_c$, or its inverse, $U_c/2\pi f_e A$ as in [15]. A useful relationship among the various parameters above is

$$\frac{f_e}{f_{St}} = \frac{1 + \varepsilon}{K_C St}. \quad (10)$$

The parameter space examined in the present study is illustrated in Fig. 1. The gray-shaded area indicates the parameter space in which the drag component is expected to be higher than the inertial one based on the Morison equation with coefficients, $C_d = 1.33$ and $C_m = 2.0$. The dividing line corresponds to $K_C = 8.05$.

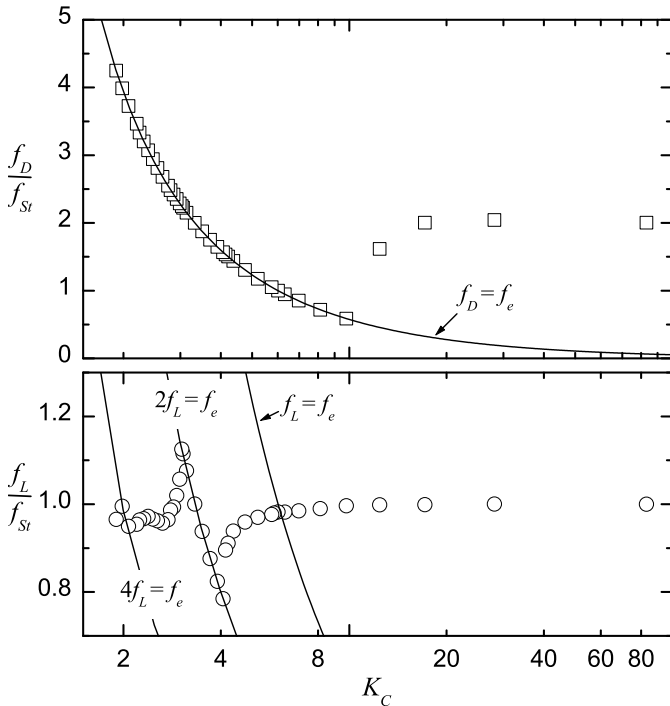


FIGURE 2: FREQUENCY OF DRAG AND LIFT.

RESULTS AND DISCUSSION

In-Line and Transverse Force

Figure 2 shows the frequency response of the in-line (drag) and transverse (lift) forces. The frequency was inferred from the force signals by computing the time between peaks and/or zero-crossings. This method was found to be more accurate and straightforward than Fourier analysis. The drag frequency is locked at the excitation frequency but for the higher K_C values when it is almost equal to twice the Strouhal frequency as it would be expected in steady flow. In contrast, the lift exhibits a markedly different response. For $K_C \approx 2$, f_L is locked at $\frac{1}{4}f_e$. For $2.2 < K_C < 2.7$, it remains nearly constant at a frequency approximately 4% lower than the Strouhal frequency. Then increases until it is locked to $\frac{1}{2}f_e$ over the range $3.0 < K_C < 4.1$. Subsequently, the lift frequency gradually increases towards the Strouhal frequency up to $K_C = 8.0$ whereupon it remains constant.

Figure 3 shows the magnitude of the mean drag and rms lift. Both vary in a very similar fashion as a function of K_C . Outside the gray-shaded area, both mean drag and rms lift are almost equal to their corresponding values in steady flow without perturbations. Inside the lock-on range in which vortex shedding is locked at $\frac{1}{2}f_e$ (indicated by the shaded area), both exhibit a peak amplification where the mean drag coefficient increases by 20% and the rms lift coefficient by 100% compared to their steady

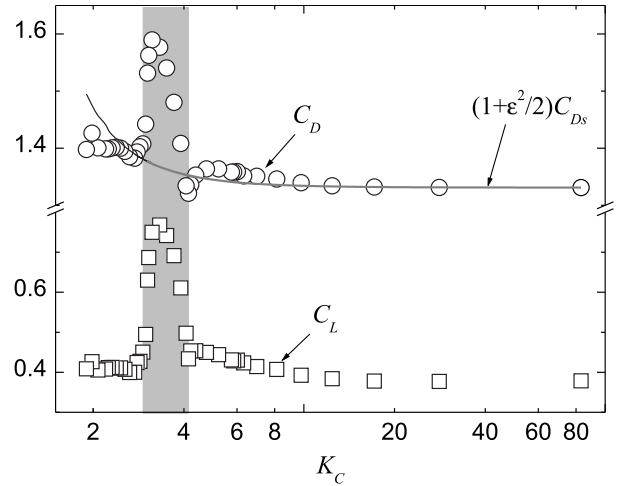
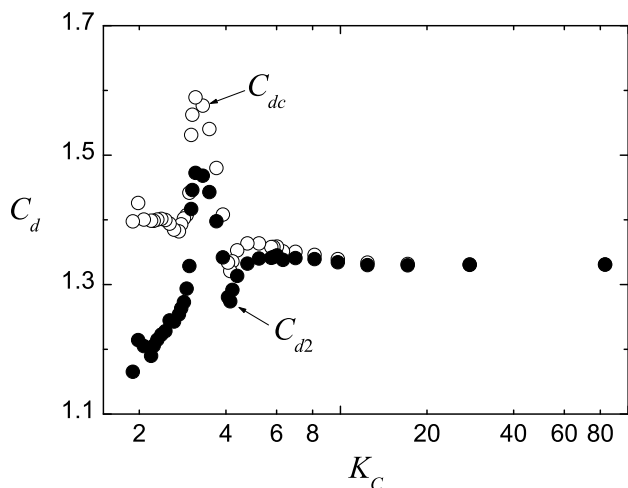
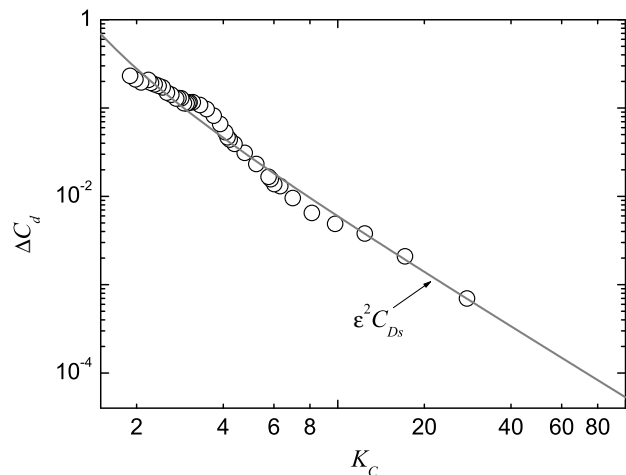


FIGURE 3: MEAN DRAG AND RMS LIFT.

flow counterparts. A small increase in magnitude can be also noted for $K_C \approx 2.0$ when vortex shedding locks-on at $\frac{1}{4}f_e$. The solid line in Fig. 3 indicates the expected variation of the mean drag from a quasi-steady approach, i.e. $C_D = C_{Ds}(1 + \epsilon^2/2)$. The corresponding line follows the data trend but for the lock-on response at $\frac{1}{2}f_e$ and for $K_C < 2.4$. This deviation might be attributed to the modification of the vortex formation mechanism (vortex patterns not shown here due to lack of space). In the middle of the lock-on range ($f_e/f_{St} \approx 2$), the alternating mode of vortex formation is strongly amplified. On the other hand, a symmetrical mode of vortex formation is induced for low K_C values ($f_e/f_{St} \approx 4$).

The forces and vortex patterns from the present study at $Re = 150$ agree very well, both qualitatively and quantitatively, with two-dimensional simulations for a cylinder oscillating in-line with a steady flow (e.g., 1-2% difference in C_D over the range $0.5 < f_e/f_{St} < 3$ for $A/D = 0.1$ and $Re = 200$) [16]. This verifies that the two cases, oscillating cylinder or flow, are kinematically equivalent; dynamically differ in the Froude-Krylov term.

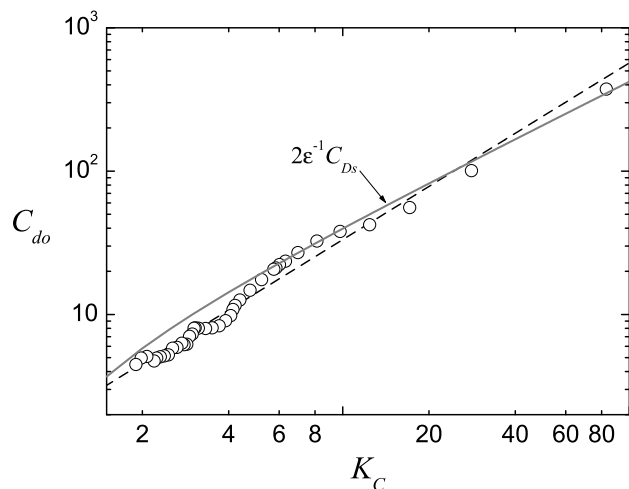
Furthermore, the present findings are qualitatively very consistent with the effect of small-amplitude harmonic flow perturbations ($\epsilon \approx 2 - 5\%$) on vortex formation patterns and forces of circular cylinders observed from laboratory experiments and numerical simulations at Reynolds number an order of magnitude higher [4, 5, 17, 18]. Similar effects have also been observed for rectangular cylinders examined in a wind tunnel albeit at much higher Reynolds numbers of the order of 10^4 , and smaller perturbations ($\epsilon \approx 1\%$) [19]. In the latter experiment, it was noted that symmetric vortex formation was observed for $f_e = 4f_{St}$ when the amplitude exceeded some undetermined threshold value.


FIGURE 4: DRAG COEFFICIENTS.

FIGURE 5: DIFFERENCE BETWEEN DRAG COEFFICIENTS.

Drag and Inertia Coefficients

Figure 4 shows the drag coefficients C_d and C_{dc} in the 2- and 3-term model equations, respectively, computed from least-squares fits to the time-dependent in-line force. It turns out that the steady drag in the 3-term equation is essentially the same as the mean drag coefficient, i.e. $C_{dc} = C_D$, over the entire K_C range as might be expected. The drag coefficient C_{d2} in the 2-term equation is nearly equal to C_{dc} for $K_C > 8$ (drag-dominated regime) but deviates for $K_C < 8$ (inertia-dominated regime). Interestingly, it was noted that the difference $\Delta C_d = C_{dc} - C_d$, can be approximated well by $\varepsilon^2 C_{Ds}$ as illustrated in Fig. 5. The reason for this behavior is not clear at present. The variation of the oscillatory drag coefficient C_{do} is shown in Fig. 6. Its magnitude increases almost linearly with K_C in log-log scale (dashed line is a straight-line fit). A solid line indicates the expected variation from quasi-steady approach $C_{do} = 2\varepsilon^{-1} C_{Ds}$, which also follows the data trend.

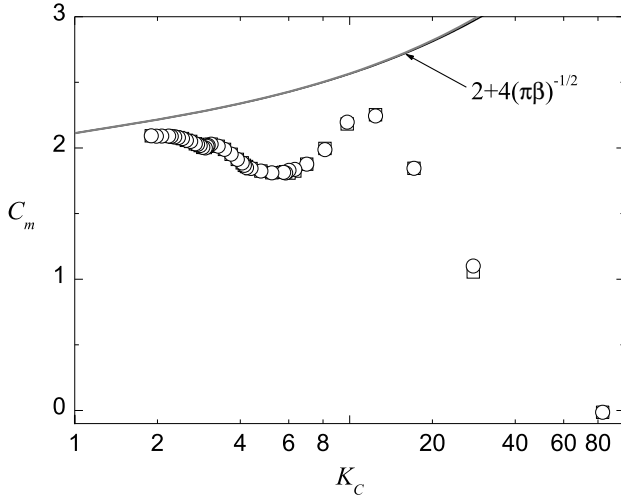
Figure 7 shows the best-fit inertia coefficient as a function of K_C . There is little difference in C_m results for the 2- and 3-term equations. For low K_C , C_m approaches the values predicted from Stokes solution, $C_m = 2 + 4(\pi\beta)^{-1/2}$ as it might be expected in the limit of $K_C \rightarrow 0$. For K_C around 3.7, i.e. $f_e/f_{St} \approx 2.0$, the inertia coefficient is very close to its value predicted from potential flow theory, $C_m \approx 2.0$. As K_C increases above that point, C_m starts to decrease reaching a minimum value of 1.81 at $K_C = 5.2$. Then it increases again up to a maximum of $C_m = 2.24$ at $K_C = 12.4$. With a further increase in K_C , the inertia coefficient drops to virtually zero. The behavior in the drag-dominated regime ($K_C > 8$) might be explained from the quasi-steady approach as follows:


FIGURE 6: OSCILLATORY DRAG COEFFICIENTS.

trigonometric expansion leads to $g_1(t) = 1 + 2\varepsilon \sin(\omega t) + \frac{1}{2}\varepsilon^2(1 + \cos(2\omega t))$. The last term induces a component in phase with acceleration which is proportional to ε^2 . As the drag starts to dominate the force relative to the inertia terms, this component causes an increase in C_m . Since $K_C \propto \varepsilon^{-1}$, its contribution diminishes with increasing K_C until both inertia and ε become negligible at the upper end.

Morison's Equation

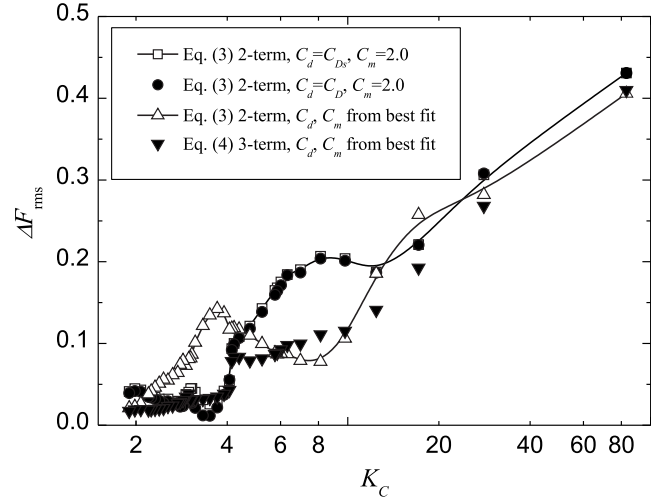
The force coefficients in the previous section, alone do not allow comparisons between directly-computed and reconstructed total in-line forces. For this purpose, the root-mean-square value of the residue of various reconstructed forces with Morison's equation less the actual


FIGURE 7: INERTIA COEFFICIENTS.

(directly-computed) in-line force,

$$\Delta F_{\text{rms}} = \frac{2}{F_{x_{\text{max}}} - F_{x_{\text{min}}}} \sqrt{\frac{\sum_{i=1}^N [F_x^*(t_i) - F_x(t_i)]^2}{N}}, \quad (11)$$

where F_x^* is the reconstructed force, is calculated. The results for the entire K_C range are shown in Fig. 8. It is seen that, the value of ΔF_{rms} generally increases as K_C increases. This behavior has been previously associated with the formation and shedding of more vortices per cycle as K_C increases and the fact that equations (2) and (3) with cycle-averaged coefficients are not able to model the high harmonics generated by the vortex shedding in the drag-dominated regime [9]. It is also seen that, the 3-term equation (5) with best-fitted coefficients performs better overall with an average (unweighted over all points) value of the r.m.s. error of 7.0%. In contrast, the 2-term equation (4) with best-fitted coefficients is the poorest performer, particularly near the vortex lock-on range ($2.2 < K_C < 4.2$), with an average value of the r.m.s. error of 10.3%. This might be attributed to the fact that there are only two degrees of freedom in the 2-term equation, thus it cannot cope with simultaneous variations in both magnitude and phase of the total force that take place when lock-on occurs. Interestingly, the minimum value of the error (1.2%) is found for the 2-term equation with $C_d = C_D$ and $C_m = 2.0$ for $K_C = 3.5$, i.e. in the middle of the lock-on range. Furthermore, the performance of the 2-equation with $C_d = C_{D_s}$ and $C_m = 2.0$ is no-much worse than that of the 3-term equation with best-fitted coefficients, which is surprising to find this level of agreement. This might suggest that the mechanism of vortex formation and ensuing forces are not


FIGURE 8: R.M.S. RESIDUE OF RECONSTRUCTED LESS ACTUAL IN-LINE FORCE.

strongly modified by the oscillatory flow component for the parameters investigated in the present study, except perhaps for the lock-on range and lower K_C range where symmetric formation is observed. However, even in the latter case the near wake tends to maintain an asymmetric pattern similar to the classical alternating Karman mode.

CONCLUSION

The main conclusions drawn from this study are the following:

For $K_C < 3.0$, the effect of the addition of an oscillatory component to a steady flow about a circular cylinder is to induce symmetric formation of vortices on both sides of the cylinder. Once formed, vortices rearrange in the near wake to an asymmetric pattern similar to the classical alternating Karman mode. The effect is most pronounced at the lowest K_C values for which the velocity perturbation is highest and gradually diminishes as K_C increases. The use of Morison's equation in order to predict the in-line force with reasonable accuracy seems appropriate in this inertia-dominated regime.

For $3.0 < K_C < 4.1$, the shedding frequency is locked to $\frac{1}{2}f_e$ and vortices form alternatively from each side. This is accompanied by considerable increase in the magnitude of mean drag and r.m.s. lift coefficients. Inertial forces are dominant in this range. Predictions using Morison's equation have an r.m.s. error of about 3% but for the 2-term equation with best-fitted coefficients.

For $4.1 < K_C < 12.4$, the mechanism of vortex formation is modulated by the imposed velocity perturbation. Both inertial and viscous drag forces are important but the

total in-line force is masked by the former component; although the frequency of vortex shedding is not phase-locked to the perturbation, the unsteady drag remains locked on. The error associated with the use of Morison's equation increases to about 10%.

For $K_C > 12.4$, vortex formation is hardly affected and the flow can be considered as superposition of quasi-steady drag and ideal inertial forces. The error in the reconstructed force raises quickly with K_C due to the existence of harmonics at the vortex shedding frequency which are not taken into account in Morison's equation.

In corollary, Morison's equation can provide reasonable estimates of the total in-line force acting on fixed cylinders in time-dependent flows, or more generally in relative motion, within the inertia-dominated regime. In all of the above ranges but the second (lock-on), Morison's equation cannot capture the nonlinear flow-structure interactions involving vortex shedding at different frequencies. This presents a major drawback in modeling self-excited vibrations of flexibly-mounted cylinders.

REFERENCES

- [1] Morison, J. R., O'Brien, M. P., Johnson, J. W., and Schaaf, S. A., 1950. "The force exerted by surface waves on piles". *Petroleum Transactions AIME*, **189**, pp. 149–154.
- [2] Bearman, P., 1997. "Near wake flows behind two- and three-dimensional bluff bodies". *Journal of Wind Engineering and Industrial Aerodynamics*, **71**, pp. 33–54.
- [3] Griffin, O. M., and Hall, M. S., 1991. "Vortex shedding lock-on and flow control in bluff body wakes – Review". *ASME: Journal of Fluids Engineering*, **113**(4), pp. 526–537.
- [4] Konstantinidis, E., and Balabani, S., 2007. "Symmetric vortex shedding in the near wake of a circular cylinder due to streamwise perturbations". *Journal of Fluids and Structures*, **23**, pp. 1047–1063.
- [5] Konstantinidis, E., and Liang, C., 2011. "Dynamic response of a turbulent cylinder wake to sinusoidal inflow perturbations across the vortex lock-on range". *Physics of Fluids*, **23**(7). art. no 075102.
- [6] Nishihara, T., Kaneko, S., and Watanabe, T., 2005. "Characteristics of fluid dynamic forces acting on a circular cylinder oscillated in the streamwise direction and its wake patterns". *Journal of Fluids and Structures*, **20**, pp. 505–518.
- [7] Sarpkaya, T., 2004. "A critical review of the intrinsic nature nature of vortex-induced vibrations". *Journal of Fluids and Structures*, **19**, pp. 389–447.
- [8] Williamson, C. H. K., and Govardhan, R., 2004. "Vortex-induced vibrations". *Annual Review of Fluid Mechanics*, **36**, pp. 413–455.
- [9] Zhou, C. Y., and Graham, M. R., 2000. "A numerical study of cylinders in waves and currents". *Journal of Fluids and Structures*, **14**, pp. 403–428.
- [10] Wolfram, J., and Naghipour, M., 1999. "On the estimation of Morison force coefficients and their predictive accuracy for very rough circular cylinders". *Applied Ocean Research*, **21**(6), pp. 311–328.
- [11] Patankar, S., and Spalding, D., 1972. "A calculation procedure for heat, mass and momentum-transfer in three-dimensional parabolic flows". *International Journal of Heat and Mass Transfer*, **15**(10), pp. 1787–1806.
- [12] Rhie, C., and Chow, W., 1983. "Numerical study of the turbulent - Flow past an airfoil with trailing edge separation". *AIAA Journal*, **21**(11), pp. 1525–1532.
- [13] Papadakis, G., and Bergeles, G., 1995. "A locally modified 2nd-order upwind scheme for convection terms discretization". *International Journal of Numerical Methods for Heat and Fluid Flow*, **5**(1), pp. 49–62.
- [14] Zdravkovich, M. M., 1996. "Inadequacy of a conventional Keulegan–Carpenter number for wave and current combination". *Journal of Offshore Mechanics and Arctic Engineering*, **118**, pp. 309–311.
- [15] Cetiner, O., and Rockwell, D., 2001. "Streamwise oscillations of a cylinder in a steady current. Part 1. Locked-on states of vortex formation and loading". *Journal of Fluid Mechanics*, **427**, pp. 1–28.
- [16] Al-Mdallal, Q. M., Lawrence, K. P., and Kocabiyik, S., 2007. "Forced streamwise oscillations of a circular cylinder: Locked-on modes and resulting fluid forces". *Journal of Fluids and Structures*, **23**, pp. 681–701.
- [17] Konstantinidis, E., Balabani, S., and Yianneskis, M., 2005. "The timing of vortex shedding in a cylinder wake imposed by periodic inflow perturbations". *Journal of Fluid Mechanics*, **543**, pp. 45–55.
- [18] Konstantinidis, E., Balabani, S., and Yianneskis, M., 2007. "Bimodal vortex shedding in a perturbed cylinder wake". *Physics of Fluids*, **19**(1), p. 011701.
- [19] Knisely, C., Matsumoto, M., and Menacher, F., 1986. "Rectangular cylinders in flows with harmonic perturbations". *Journal of Hydraulic Engineering-ASCE*, **112**(8), pp. 690–704.



THE "EQUIVALENT SPECTRUM" CONCEPT FOR TURBULENCE CONVEYING EXCITATIONS

Jose Antunes¹

Applied Dynamics Laboratory
 Instituto Tecnológico e Nuclear
 Instituto Superior Técnico
 Universidade Técnica de Lisboa
 IST/ITN/ADL
 2686 Sacavem codex, Portugal
 Email: jantunes@itn.pt

**Laurent Borsoi
 Philippe Piteau
 Xavier Delaune**

Laboratoire d'Etudes de Dynamique
 Commissariat à l'Energie Atomique
 et aux Energies Alternatives
 CEA, DEN, DM2S, SEMT, DYN
 F-91191, Gif-sur-Yvette Cedex, France
 Email: laurent.borsoi@cea.fr
 philippe.piteau@cea.fr
 xavier.delaune@cea.fr

ABSTRACT

Turbulence is an important vibration excitation mechanism and a component life controlling factor. Characterization of the flow turbulence excitation by axial flows has often been addressed, Corcos model still standing as a sound basis for formulating the vibratory responses of tubes subjected to turbulence conveying flows. Classically, turbulence excited vibrations are formulated in terms of a local excitation spectrum weighted by acceptance integrals, which account for the correlation length and convection velocity of the random field. However, significant incertitude exists concerning the actual values of these parameters and their dependence on frequency, for each specific configuration. Axisa et al. circumvented this difficulty, for transverse flows, by proposing an "Equivalent Spectrum" encapsulating the correlation length, whatever its (small) value. In the present paper we extend this concept to axial flows, by proposing a new Equivalent Spectrum which additionally encapsulates the effects of turbulence convection. The suggested approach leads to the same predictive formulation for both transverse and axial flows.

NOMENCLATURE

A Subscript/superscript for axial flow.
 C_{nm}^2 Joint- and cross-acceptance integrals of the simplified "equivalent" formulation.
 D Tube diameter.
 f Frequency.
 f_n Modal frequency.
 \bar{f}_R Reduced frequency.
 $F(x, t)$ Random turbulence field.
 $H_n(f)$ Modal term of the transfer function (excluding mode shape coefficients).

k_x Streamwise wavenumber.
 k_y Spanwise wavenumber.
 L Tube length.
 $L_{nm}^2(\bar{f}_R)$ Joint- and cross-acceptance integrals.
 $\tilde{L}_{nm}^2(\bar{f}_R)$ Reduced joint- and cross-acceptance integrals.
 m, n Modal indexes.
 m_n Modal mass.
 q_n Modal responses.
 $S_{FF}(x_1, x_2, f)$ Flow turbulence cross-spectrum.
 $S_{F_n F_m}(f)$ Cross-spectra of the modal excitations.
 $S_{q_n q_m}(f)$ Cross-spectra of the modal responses.
 t Time.
 T Subscript/superscript for transverse flow.
 $u(x)$ Dimensionless velocity profile.
 $V(x)$ Flow velocity field.
 \bar{V} Space-averaged velocity.
 $V_c(\bar{f}_R)$ Convection velocity.
 x Axial coordinate.
 \bar{x} Reduced axial coordinate.
 $\tilde{X}_c(\bar{f}_R)$ Reduced convection distance.
 $Z(x, t)$ Tube vibratory response.
 α Transformed coordinate (mean location).
 α_x Streamwise coherence decay rate.
 α_y Spanwise coherence decay rate.
 $\alpha_c(\bar{f}_R)$ Dimensionless correlation length (with respect to the tube diameter).
 β Transformed coordinate (point separation).

¹Address all correspondence to this author¹

- $\beta_c(\bar{f}_R)$ Dimensionless convection velocity (with respect to the average flow velocity).
 $\gamma(x_1, x_2, \bar{f}_R)$ Space-frequency coherence of the turbulence field.
 $\lambda_c(\bar{f}_R)$ Axial correlation length of the random force field along the tube.
 $\hat{\lambda}_c(\bar{f}_R)$ Reduced correlation length.
 $\lambda_x(\omega)$ Correlation length of the pressure field along the axial direction.
 $\lambda_y(\omega)$ Correlation length of the pressure field along the transverse direction.
 $\varphi_n(x)$ Tube mode shape.
 $\phi_n(x)$ Mode shape weighted by the square of $u(x)$.
 $\hat{\Phi}_{EQ}(\bar{f}_R)$ Dimensionless "equivalent" excitation spectrum.
 $\hat{\Phi}_{FF}(\bar{f}_R)$ Dimensionless excitation spectrum of the random forces per unit tube length.
 $\Phi_{pp}(\omega)$ Local pressure excitation spectrum.
 $\Phi_{pp}(\xi_x, \xi_y, \omega)$ Pressure excitation cross-spectrum.
 ω Circular frequency.
 ρ Fluid density.
 ζ_n Modal damping.
 ξ_x Streamwise coordinate difference $x_2 - x_1$ between two locations.
 ξ_y Spanwise coordinate difference $y_2 - y_1$ between two locations.

INTRODUCTION

Turbulence is one of the main vibration excitation mechanisms and a component life controlling factor, in the long range. Phenomenological characterization of the excitation by turbulence conveying flows has been addressed by many authors, since the pioneering work of Corcos in the early 60s, see for instance [1-5], but also in more recent times, see [6-11] for relevant research and review work. These authors mainly focused on linear vibratory analysis in the frequency domain, for boundary layer turbulence excitation of plates, pipes and tubes. Although the bulk of their findings is well established, important points are still open to debate, such as the behavior of the turbulence correlation lengths as a function of frequency and of the flow velocity, see [7,9]. Concerning the industrial components of power producing facilities, it has been argued that boundary layer turbulence is remote from the actual turbulence excitation mechanism which is relevant for tubular bundles, in particular nuclear fuel rods. However, recent CFD results presented by Moussou et al. [12] suggest that a classical Corcos-type formulation may well also apply to the higher level space-time random force fields generated along fuel rods downstream of mixing grids. Therefore, this model appears to be a sound basis when establishing

formulations for the vibratory responses of tubes subjected to realistic turbulence conveying flows.

Classically, in the frequency domain, the modal vibration excitations stemming from a turbulence force field are formulated in terms of a local excitation spectrum weighted by correlation integrals, the so-called joint- and cross-acceptances, which express the effectiveness of the force field to excite the various modes of the tube, accounting for the correlation length and convection velocity of the random force field. However, as pointed, significant uncertainty still exists concerning the actual values of these parameters, as function of frequency, for each specific bundle configuration. To circumvent this difficulty for the turbulence excitation by transverse flows, Axisa et al. [13] suggested the use of a so-called "Equivalent Spectrum", instead of the common local spectrum, which conveniently encapsulates the correlation length whatever its value, provided it is small with respect to the length-scales of the relevant excited modes. In the present paper we extend this concept in order to deal with axial flows, and show how the "Equivalent Spectrum" depends on the convection velocity. Through some illustrative calculations, we highlight the features of the proposed simplified formulation. Among the results presented, it emerges that the suggested approach leads to the very same predictive formulation for both transverse and axial flows.

THE ORIGINAL "EQUIVALENT SPECTRUM" CONCEPT

Under linear conditions, the tube vibratory responses $Z(x, t)$ to a given excitation field $F(x, t)$ can be written using modal superposition:

$$Z(x, t) = \sum_{n=1}^N \varphi_n(x) q_n(t) \quad (1)$$

and similarly in the frequency domain, through Fourier transformation of (1). It is well established [13] that the modal responses of a tube (with length L and diameter D) stemming from a space-time random excitation $F(x, t)$ are expressed, in the frequency domain, as ($m = 1, 2, \dots, N$; $n = 1, 2, \dots, N$):

$$S_{q_n q_m}(f) = H_n(f) H_m^*(f) \times \int_0^L \int_0^L \varphi_n(x_1) \varphi_m(x_2) S_{FF}(x_1, x_2, f) dx_1 dx_2 \quad (2)$$

where $H_n(f) = [4\pi^2 m_n (f_n^2 - f^2 + 2if_n \zeta_n)]^{-1}$, $\varphi_n(x)$ are the modeshapes, while the excitation field $F(x, t)$ is entirely described in terms of its cross-spectrum $S_{FF}(x_1, x_2, f)$ modeled by:

$$S_{FF}(x_1, x_2, f) = \left(\frac{1}{2} \rho \bar{V}^2 D \right)^2 \frac{D}{\bar{V}} \hat{\Phi}_{FF}(\bar{f}_R) \times [u(x_1)u(x_2)]^2 \gamma(x_1, x_2, \bar{f}_R) \quad (3)$$

where \bar{V} is the average flow velocity, ρ is the fluid density, $\bar{f}_r = fD / \bar{V}$, $u(x) = V(x) / \bar{V}$ is the velocity profile, $\hat{\Phi}_{FF}(\bar{f}_r)$ is the dimensionless excitation spectrum and $\gamma(x_1, x_2, \bar{f}_r) \approx \gamma(\xi_x, \bar{f}_r)$ is the space coherence function, which typically depends on the distance $\xi_x = x_2 - x_1$. Then, it can be shown that the modal excitations are given as:

$$S_{F_n F_m}(f) = \left(\frac{1}{2} \rho \bar{V}^2 D \right)^2 \frac{D}{\bar{V}} \hat{\Phi}_{FF}(\bar{f}_r) L_{nm}^2(\bar{f}_r) \quad (4)$$

with the correlation integrals (joint- and cross-acceptances) $L_{nm}^2(f)$ given as:

$$L_{nm}^2(\bar{f}_r) = \int_0^L \int_0^L \phi_n(x_1) \phi_m(x_2) \gamma(x_2 - x_1, \bar{f}_r) dx_1 dx_2 \quad (5)$$

where $\phi_n(x) = \varphi_n(x) [u(x)]^2$ is a velocity profile weighted modeshape. For pure transverse flows, there is no axial convection of the turbulence, and the space coherence is modeled as:

$$\gamma(x_2 - x_1, \bar{f}_r) = \exp\left(-\frac{|x_2 - x_1|}{\lambda_c(\bar{f}_r)}\right) \quad (6)$$

where $\lambda_c(\bar{f}_r)$ is the axial correlation length of the turbulence field. Defining reduced quantities $\hat{x} = x / L$, $\hat{\lambda}_c(\bar{f}_r) = \lambda_c(\bar{f}_r) / L$ and $\hat{L}_{nm}^2(\bar{f}_r) = L_{nm}^2(\bar{f}_r) / L^2$, the correlation integrals (5), with coherence (6), read:

$$\hat{L}_{nm}^2(\bar{f}_r) = \int_0^1 \int_0^1 \phi_n(\hat{x}_1) \phi_m(\hat{x}_2) \exp\left(-\frac{|\hat{x}_2 - \hat{x}_1|}{\hat{\lambda}_c(\bar{f}_r)}\right) d\hat{x}_1 d\hat{x}_2 \quad (7)$$

Expressions (7) cannot in general be solved without a detailed knowledge of the correlation length $\lambda_c(\bar{f}_r)$, however it is safe to assume in physical grounds that $\hat{\lambda}_c(\bar{f}_r) \ll 1$. As detailed in the following, under such assumption this allows a good approximation of (7) by the expression:

$$\hat{L}_{nm}^2(\bar{f}_r) \approx 2 \hat{\lambda}_c(\bar{f}_r) \int_0^1 \phi_n(\hat{x}) \phi_m(\hat{x}) d\hat{x} \quad (8)$$

Then, from (4) and (8), the modal excitations are given by:

$$S_{F_n F_m}(f) \approx \left(\frac{1}{2} \rho \bar{V}^2 D \right)^2 \frac{D}{\bar{V}} \hat{\Phi}_{FF}(\bar{f}_r) L^2 \times \left[2 \hat{\lambda}_c(\bar{f}_r) \int_0^1 \phi_n(\hat{x}) \phi_m(\hat{x}) d\hat{x} \right] \quad (9)$$

and, as suggested by Axisa et al. [13], the imperfect knowledge of $\hat{\lambda}_c(\bar{f}_r)$ can be circumvented by defining the dimensionless "Equivalent Spectrum":

$$\hat{\Phi}_{EQ}^T(\bar{f}_r) = \left[\hat{\Phi}_{FF}^T(\bar{f}_r) \hat{\lambda}_c(\bar{f}_r) \right] \quad (10)$$

or equivalently:

$$\hat{\Phi}_{EQ}^T(\bar{f}_r) = \left[\hat{\Phi}_{FF}^T(\bar{f}_r) \alpha_c(\bar{f}_r) \frac{D}{L} \right] \quad (11)$$

where the correlation length is now embedded in the spectral excitation information. In the second definition (11), the correlation length is assumed to be proportional to the tube diameter, $\alpha_c(\bar{f}_r) = \lambda_c(\bar{f}_r) / D$. Formulation (9) can then be written as:

$$S_{F_n F_m}(f) \approx \left(\frac{1}{2} \rho \bar{V}_T^2 D \right)^2 \frac{D}{\bar{V}_T} \hat{\Phi}_{EQ}^T(\bar{f}_r) L^2 C_{nm}^2 \quad (12)$$

where the correlation integrals C_{nm}^2 are now independent of any frequency effects:

$$C_{nm}^2 = 2 \int_0^1 \phi_n(\hat{x}) \phi_m(\hat{x}) d\hat{x} \quad (13)$$

Notice that, if the local spectrum $\hat{\Phi}_{FF}(\bar{f}_r)$ and $\hat{\lambda}_c(\bar{f}_r)$ are both known, then the equivalent spectrum can be computed from (10) or (11). However, if $\hat{\lambda}_c(\bar{f}_r)$ is unknown, then $\hat{\Phi}_{EQ}^T(\bar{f}_r)$ can be directly identified from the modal response measurements, thus bypassing the need for an explicit identification of $\hat{\lambda}_c(\bar{f}_r)$. This renders formulation (12)-(13) very practical and attractive, the reason why it has been used in lots of laboratories for many years.

"EQUIVALENT SPECTRUM" FOR TURBULENCE CONVEYING FLOWS

For turbulence conveying axial flows, the space-frequency empirical model used for describing the random force field is typically based on the classical Corcos formulation. For plates subjected to boundary layer turbulence, the cross-spectrum of the pressure field is formulated as [1]:

$$\Phi_{pp}(\xi_x, \xi_y, \omega) = \Phi_{pp}(\omega) \gamma(x_2 - x_1, y_2 - y_1, \omega) \quad (14)$$

where $\xi_x = x_2 - x_1$ and $\xi_y = y_2 - y_1$ are distances between two locations respectively along the axial and the transverse directions, the excitation being expressed in terms of the local spectrum by the turbulence pressure fluctuations $\Phi_{pp}(\omega)$ and the space coherence:

$$\gamma(\xi_x, \xi_y, \omega) = \exp\left(-\frac{|\xi_x|}{\lambda_x(\omega)}\right) \exp\left(-\frac{|\xi_y|}{\lambda_y(\omega)}\right) \exp\left(-i \frac{\omega \xi_x}{V_c(\omega)}\right) \quad (15)$$

where $V_c(\omega)$ is the convection velocity, while $\lambda_x(\omega)$ and $\lambda_y(\omega)$ are the axial and transverse correlation lengths of the pressure field, which are in general frequency dependent. In the original Corcos formulation, the correlation lengths have been established in terms of the ratio $V_c(\omega) / \omega$ as:

$$\lambda_x(\omega) = \frac{V_c(\omega)}{\alpha_x \omega} \quad ; \quad \lambda_y(\omega) = \frac{V_c(\omega)}{\alpha_y \omega} \quad (16)$$

α_x and α_y are experimental parameters expressing the coherence decay rates with distance [1], hence:

$$\gamma(r_x, r_y, \omega) = \exp(-\alpha_x k_c(\omega) |\xi_x|) \exp(\alpha_y k_c(\omega) |\xi_y|) \times \exp(-ik_c(\omega) \xi_x) \quad (17)$$

where the vortical structures are convected at the wavenumber $k_c(\omega) = \omega / V_c(\omega)$. An often used variant of formulation (14), in terms of the wavenumber-frequency spectrum, is obtained by Fourier transforming (17) in space. One obtains [6,11]:

$$\gamma(k_x, k_y, \omega) = \frac{\alpha_x \alpha_y}{\pi^2} \left\{ \alpha_x^2 + \left(\frac{k_x}{k_c(\omega)} - 1 \right)^2 \right\} \left\{ \alpha_y^2 + \left(\frac{k_y}{k_c(\omega)} \right)^2 \right\}^{-1} \quad (18)$$

where k_x and k_y are respectively, the streamwise and spanwise wavenumbers. In spite of the Corcos approach wide use, accumulated experimental evidence suggests that it overpredicts levels at wavenumbers below the convection peak defined in (18) at $k_x \approx k_c$. This justified a number of refined versions of Corcos model, those proposed by Ffowcs Williams [14], Chase [15] and Smolyakov & Tkachenko [16], among others. For the interested reader, their works are reviewed and compared by Graham [6] and Hwang et al. [11].

For simplicity, we will stick here to the basic formulation (15), which in the case of tubular systems subjected to axial flows simplifies to:

$$\gamma(x_2 - x_1, \bar{f}_r) = \exp\left(-\frac{|x_2 - x_1|}{\lambda_c(\bar{f}_r)}\right) \exp\left(-i \frac{x_2 - x_1}{V_c(\bar{f}_r)/2\pi f}\right) \quad (19)$$

When replaced in (5), this leads to the dimensionless correlation integrals:

$$\widehat{L}_{mm}(\bar{f}_r) = \int_0^1 \int_0^1 \phi_n(\bar{x}_1) \phi_m(\bar{x}_2) \exp\left(-\frac{|\bar{x}_2 - \bar{x}_1|}{\widehat{\lambda}_c(\bar{f}_r)}\right) \exp\left(-i \frac{\bar{x}_2 - \bar{x}_1}{\widehat{X}_c(\bar{f}_r)}\right) d\bar{x}_1 d\bar{x}_2 \quad (20)$$

where $\widehat{X}_c(\bar{f}_r) = V_c(\bar{f}_r) / (2\pi fL)$ is a dimensionless convection parameter. In general (20) leads complex values of the cross-acceptance integrals:

$$\begin{aligned} \text{Re}[\widehat{L}_{mm}(\bar{f}_r)] &= \\ &= \int_0^1 \int_0^1 \phi_n(\bar{x}_1) \phi_m(\bar{x}_2) \exp\left(-\frac{|\bar{x}_2 - \bar{x}_1|}{\widehat{\lambda}_c(\bar{f}_r)}\right) \cos\left(-\frac{\bar{x}_2 - \bar{x}_1}{\widehat{X}_c(\bar{f}_r)}\right) d\bar{x}_1 d\bar{x}_2 \quad (21) \end{aligned}$$

$$\begin{aligned} \text{Im}[\widehat{L}_{mm}(\bar{f}_r)] &= \\ &= \int_0^1 \int_0^1 \phi_n(\bar{x}_1) \phi_m(\bar{x}_2) \exp\left(-\frac{|\bar{x}_2 - \bar{x}_1|}{\widehat{\lambda}_c(\bar{f}_r)}\right) \sin\left(-\frac{\bar{x}_2 - \bar{x}_1}{\widehat{X}_c(\bar{f}_r)}\right) d\bar{x}_1 d\bar{x}_2 \quad (22) \end{aligned}$$

Notice that, even if we may still assume that $\widehat{\lambda}_c(\bar{f}_r)$ in axial flow is small, the convection parameter $\widehat{X}_c(\bar{f}_r)$ may vary widely in the range $[0, \infty]$, depending on the

convection velocity and frequency. This fact must be accounted for, if - similarly to (7)-(8) - one wishes to approximate the correlation integrals (21) and (22) by more convenient simplified expressions. For small values of the reduced correlation length $\widehat{\lambda}_c(\bar{f}_r)$, as detailed in Appendix A, the correlation integrals (21) and (22) may be approximated by the following expressions:

$$\text{Re}[\widehat{L}_{mm}(\bar{f}_r)] \approx 2\widehat{\lambda}_c(\bar{f}_r) \left[1 + \left(\frac{\widehat{\lambda}_c(\bar{f}_r)}{\widehat{X}_c(\bar{f}_r)} \right)^2 \right]^{-1} \int_0^1 \phi_n(\bar{x}) \phi_m(\bar{x}) d\bar{x} \quad (23)$$

$$\text{Im}[\widehat{L}_{mm}(\bar{f}_r)] \approx -2 \frac{(\widehat{\lambda}_c(\bar{f}_r))^3 (\widehat{X}_c(\bar{f}_r))^3}{[\widehat{X}_c(\bar{f}_r)^2 + (\widehat{\lambda}_c(\bar{f}_r))^2]^2} \int_0^1 \left[\phi_n(\bar{x}) \phi'_m(\bar{x}) - \phi'_n(\bar{x}) \phi_m(\bar{x}) \right] d\bar{x} \quad (24)$$

where $\phi'_n(\bar{x}) = \partial \phi_n(\bar{x}) / \partial \bar{x}$. The approximate integral (8) has been often quoted and used for transverse flow excitations, however the mathematical rationale behind (8) is seldom explained. Notice that such result is obtained as a particular case from (23) when there is no convected turbulence.

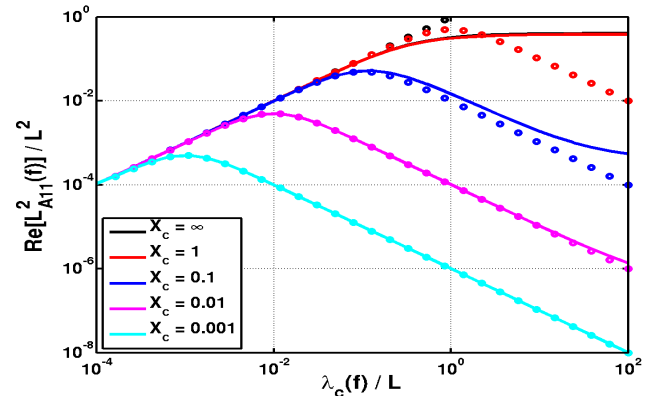


FIGURE 1: EXACT AND APPROXIMATE JOINT-ACCEPTANCES FOR $m = n = 1$ (UNIFORM VELOCITY PROFILE).

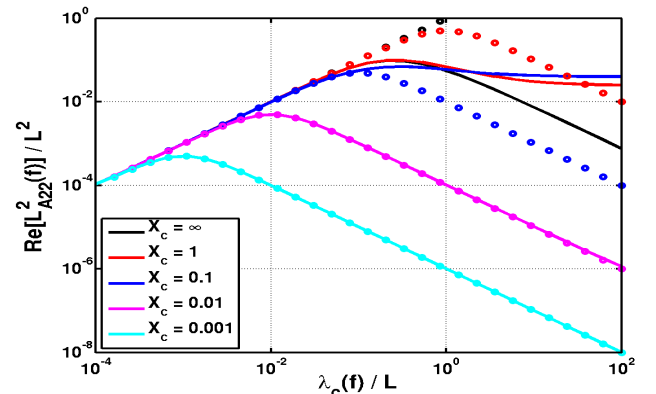


FIGURE 2: EXACT AND APPROXIMATE JOINT-ACCEPTANCES FOR $m = n = 2$ (UNIFORM VELOCITY PROFILE).

As an illustration, for a pinned-pinned tube with $\phi_n(\bar{x}) = \sin(n\pi\bar{x})$, $0 \leq \bar{x} \leq 1$, Figs. 1 and 2 show the

exact numerical (*lines*) and approximate analytical (*dots*) results for joint acceptances, computed from expressions (21) and (23), respectively for $m = n = 1$ and $m = n = 2$, for a uniform velocity profile $u(\hat{x}) \equiv 1$ ($\forall \hat{x}$). In these figures, the values of the dimensionless correlation integrals are plotted as a function of the dimensionless correlation length $\hat{\lambda}_c(\bar{f}_R)$, for several very different values of the convection parameter $\hat{X}_c(\bar{f}_R)$. One can see that the simplified formulation perfectly agrees with the exact results in the range $\hat{\lambda}_c(\bar{f}_R) \ll 1$, and often well beyond. As expected, for the joint-acceptances $m = n$, the imaginary part (24) is always nil, which is not the case for the cross-acceptances $m \neq n$.

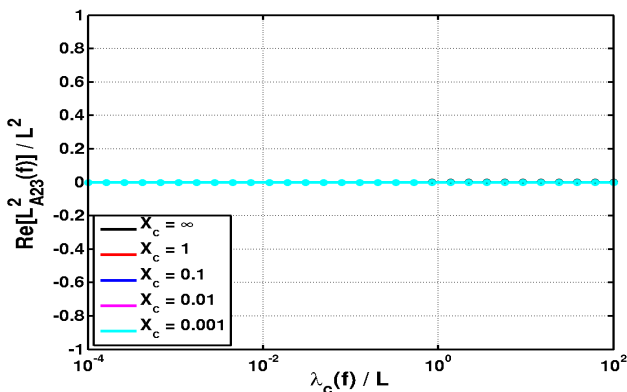


FIGURE 3: EXACT AND APPROXIMATE REAL PART OF THE CROSS-ACCEPTANCES FOR $m = 2, n = 3$ (UNIFORM VELOCITY PROFILE).

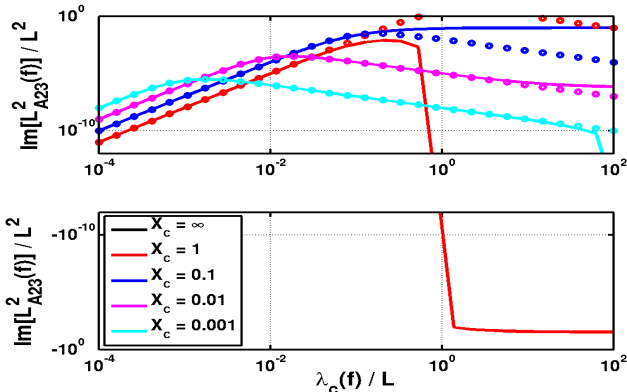


FIGURE 4: EXACT AND APPROXIMATE IMAGINARY PART OF THE CROSS-ACCEPTANCES FOR $m = 2, n = 3$ (UNIFORM VELOCITY PROFILE).

In Figs. 3 and 4 we illustrate the exact numerical (*lines*) and approximate analytical (*dots*) results for the real and imaginary parts of a sample cross-acceptance, with $m = 2, n = 3$, for the uniform velocity profile. In this case the real part is nil, but not the imaginary part. It should be mentioned that, for very low values of $\hat{\lambda}_c$ the

numerical integration schemes may experience difficulties on the double integrations. As a last illustration, the cross-acceptance results with $m = 2, n = 3$ are also shown in Figs. 5 and 6, but this time for an very localized flow velocity profile, such that $u(\hat{x}) = 0$ for $0 \leq \hat{x} < 0.6$ and $0.8 < \hat{x} \leq 1$, $u(\hat{x}) = 1$ for $0.6 \leq \hat{x} \leq 0.8$. Notice that both the real part and the imaginary part of the cross-acceptance are non-zero.

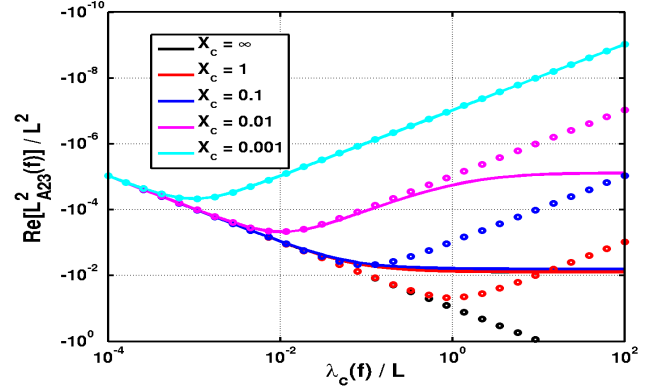


FIGURE 5: EXACT AND APPROXIMATE REAL PART OF THE CROSS-ACCEPTANCES FOR $m = 2, n = 3$ (LOCALIZED VELOCITY PROFILE).

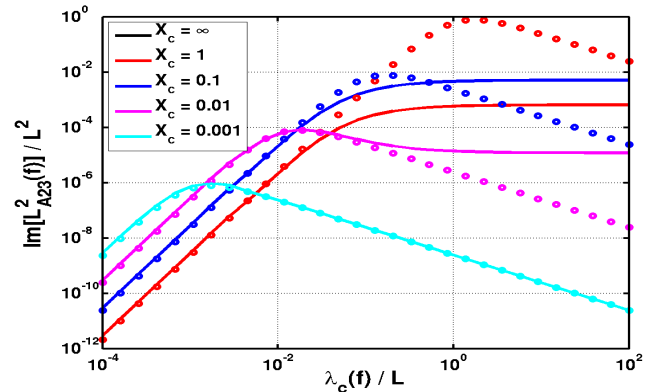


FIGURE 6: EXACT AND APPROXIMATE IMAGINARY PART OF THE CROSS-ACCEPTANCES FOR $m = 2, n = 3$ (LOCALIZED VELOCITY PROFILE).

As a final comment on the joint- and cross-acceptance computations, it is worth mentioning that the order of magnitude of the imaginary part of the cross-acceptances was found, in the range of interest $\hat{\lambda}_c(\bar{f}_R) \ll 1$, to be consistently lower than the non-zero real part of the joint- and cross acceptances.

From the previous arguments and results, similarly to formulation (10)-(13) for transverse excitations, we now suggest that an "Equivalent Spectrum" for axial turbulent flows may be defined. From the simplified real part of the correlation integrals (23), which dominates the vibratory responses, we can now write:

$$\widehat{\Phi}_{EQ}^A(\bar{f}_r) = \left[\widehat{\Phi}_{FF}^A(\bar{f}_r) \widehat{\lambda}_c(\bar{f}_r) \left[1 + \left(\frac{\widehat{\lambda}_c(\bar{f}_r)}{\widehat{X}_c(\bar{f}_r)} \right)^2 \right]^{-1} \right] \quad (25)$$

or, assuming that $\alpha_c(\bar{f}_r) = \lambda_c(\bar{f}_r) / D$ and defining $\beta_c(\bar{f}_r) = V_c(\bar{f}_r) / \bar{V}_A$:

$$\widehat{\Phi}_{EQ}^A(\bar{f}_r) = \left[\widehat{\Phi}_{FF}^A(\bar{f}_r) \alpha_c(\bar{f}_r) \left[1 + \left(\frac{2\pi \alpha_c(\bar{f}_r)}{\beta_c(\bar{f}_r)} \bar{f}_r \right)^2 \right]^{-1} \frac{D}{L} \right] \quad (26)$$

These definitions of $\widehat{\Phi}_{EQ}^A(\bar{f}_r)$, not only encapsulate the effects of the correlation length, but also (explicitly or implicitly) those of the convection term. When (25) or (26) are used with the general formulation (4), one obtains for turbulence conveying flows:

$$S_{F_n F_m}(f) \approx \left(\frac{1}{2} \rho \bar{V}_A^2 D \right)^2 \frac{D}{\bar{V}_A} \widehat{\Phi}_{EQ}^A(\bar{f}_r) C_{nm}^2 \quad (27)$$

with:

$$C_{nm}^2 = 2 \int_0^1 \phi_n(\hat{x}) \phi_m(\hat{x}) d\hat{x} \quad (28)$$

which are entirely similar to expressions (12)-(13) used for transverse flows. Furthermore, definitions (25) or (26) of the Equivalent Spectrum for axial turbulence excitations lead to correlation integrals C_{nm}^2 that are independent of any frequency and convection effects. These two aspects appear as significant advantages of the proposed formulation.

As a side remark, notice that the ratio D/L might have been "extracted" from the original expression (11), and *a fortiori* from expression (26), thus avoiding that "Equivalent Spectra" be defined with respect to arbitrary "reference" values of the tube length and diameter, see Axisa et al. [13]. Such convenience would entail the transfer of the ratio D/L into expressions (12) and (27), respectively. Although a minor point, this formal change might prove a convenient decision in practice, as some feel the need for "reference" values on the Equivalent Spectra - as well as the need for the spectrum scaling with respect to the actual values of D and L used on each specific application - somewhat as a nuisance. However, a strong reason militates against such change: the well-known reference equivalent spectrum proposed by Axisa et al. [13], for transverse flows, was defined according to (11) and has been in use for many years.

More important, remember that introduction of D in formulations (11) and (26) is based on the *assumption* that $\lambda_c(\bar{f}_r) / D$ is near invariant, which is debatable, to say the least, and even more for axial turbulence. Nevertheless, spectral scaling based on this assumption is obviously convenient, even if lacking a firm physical or experimental ground.

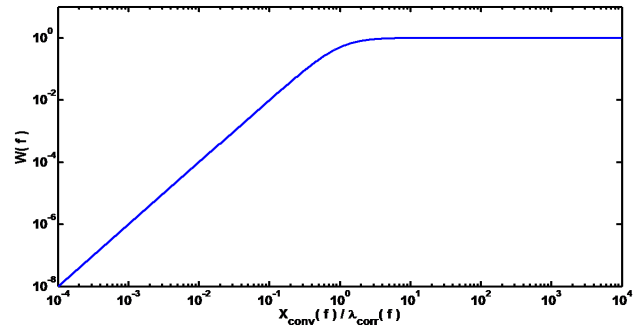


FIGURE 7: WEIGHTING FUNCTION FOR THE EQUIVALENT SPECTRUM IN TURBULENT AXIAL FLOW.

One may notice from (25) that, when compared to the transverse excitation case, the proposed equivalent spectrum introducing the following weighting term, which stands for the convection effects:

$$W(\bar{f}_r) = \left[1 + \left(\frac{\widehat{\lambda}_c(\bar{f}_r)}{\widehat{X}_c(\bar{f}_r)} \right)^2 \right]^{-1} \quad (29)$$

The corresponding plot in Fig. 7 shows that this term always lowers the value of the equivalent spectrum. It also shows that the convective term significantly affects the spectrum in the range $\widehat{X}_c(f) / \widehat{\lambda}_c(f) < 1$ and that excitation tends to zero when $\widehat{X}_c(f) \rightarrow 0$.

EQUIVALENT EXCITATION SPECTRUM FOR A FUEL ROD DOWNSTREAM OF A MIXING GRID

We will now proceed by applying the previous formulation in order to infer an "Equivalent Spectrum" from the valuable computational data recently offered by Moussou et al. [12], for the specific case of a fuel rod subjected to axial flow with an upstream mixing grid. The results shown in the following were obtained by processing Moussou's data, extracted from Ref. [12], in order to apply the scaling of formulation (26). Notice that this grid-generated turbulence data is quite remote from the boundary layer turbulence on which Corcos model is anchored. Nevertheless, Moussou et al. convincingly show that their computed pressure field fits the essential features of Corcos formulation. Computations were based on a cell with 8 "half-rods" at the boundaries, a central rod with $D \approx 9$ mm, the reduced pitch being 1.3 and the hydraulic diameter 11.8 mm. The computed flow length was about $L \approx 40D$, with an axial velocity $\bar{V}_A = 5$ m/s.

The basic results obtained by Moussou et al. are shown in Fig. 8. In this dimensionless local spectrum we collapsed data from both orthogonal directions and the scaling by the hydraulic diameters was replaced by using D . To get a feeling of the amplitude of this data, it was first reduced according to formulation (11) and compared to the reference equivalent spectrum proposed by Axisa et al. [13] for transverse excitation, as shown in Fig. 9. At low reduced frequencies, the transverse spectrum is two

orders of magnitude higher than the axial excitation data, something that does not conflict with some practitioners experience. At higher frequencies, amplitude differences become progressively lower. Finally, in Fig. 10 we compare the axial excitation data in two "Equivalent Spectrum" forms, by reducing respectively according to formulation (11) (black dots) and to formulation (26) (red dots). The amplitude lowering by virtue of the weighting factor $W(\bar{f}_R)$, Eq. (29), is quite obvious.

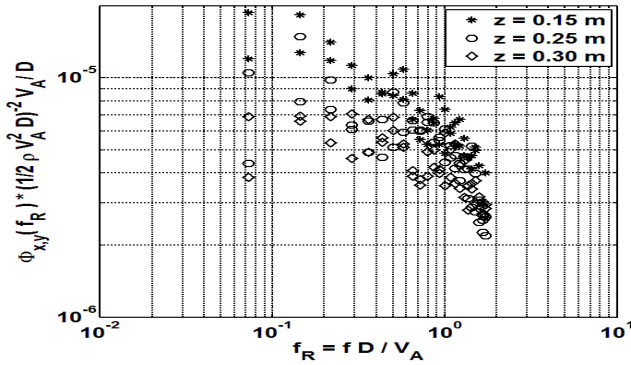


FIGURE 8: DIMENSIONLESS LOCAL EXCITATION SPECTRUM, REDUCED FROM THE DATA BY MOUSSOU ET AL. [12].

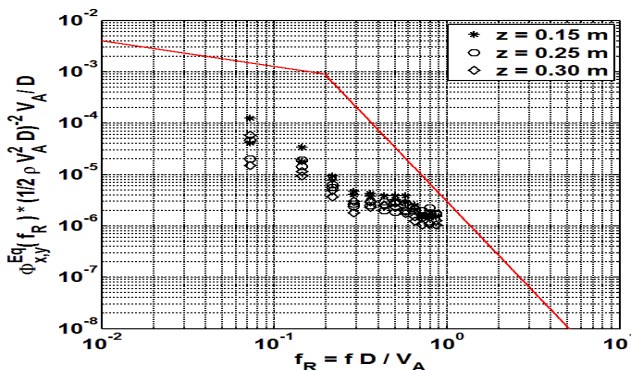


FIGURE 9: EQUIVALENT SPECTRUM OF EXCITATION, REDUCED FROM THE DATA BY MOUSSOU ET AL. [12] ACCORDING TO THE "TRANSVERSE" FORMULATION, EQ. (11).

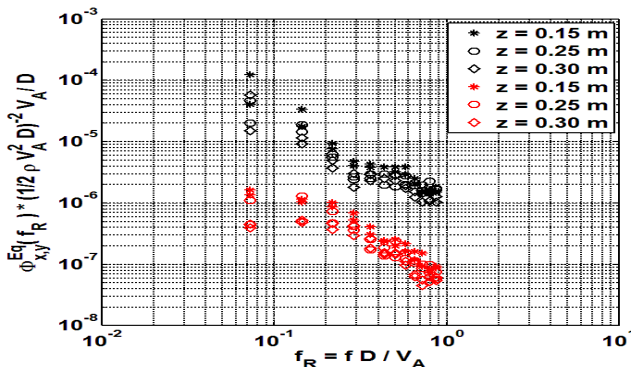


FIGURE 10: EQUIVALENT SPECTRUM OF EXCITATION, REDUCED FROM THE DATA BY MOUSSOU ET AL. [12] ACCORDING TO THE "TRANSVERSE" AND "AXIAL" FORMULATIONS, EQS. (11) AND (26).

CONCLUSION

In this paper we develop a simplified formulation for the vibration of tubular systems subjected to axial flow turbulence. Expanding the work by Axisa et al. [13] for transverse flows, we propose a new "Equivalent Spectrum" scaling method to deal with turbulence conveying axial flows. This formulation conveniently encapsulates the effects of both the turbulence correlation length and the convection, leading to identical predictive formulations for both transverse and axial flows. As an illustration, the recent excitation data computed by Moussou et al. [12] for a rod downstream of a turbulence grid is processed here in the light of the present approach.

REFERENCES

- [1] Corcos, G. M. (1964) "The structure of the turbulent pressure field in boundary layer flow". *Journal of Fluid Mechanics*, Vol. 18, pp. 353-378.
- [2] Clinch, J. M. (1969) "Measurement of the wall pressure field at the surface of a smooth-walled pipe containing turbulent water flow". *Journal of Sound and Vibration*, Vol. 9, pp. 398-419.
- [3] Willmarth, W., Wooldridge, C. (1962) "Measurements of the fluctuating pressure at the wall beneath a thick turbulent boundary layer". *Journal of Fluid Mechanics*, Vol. 14, pp. 187-210.
- [4] Bull, M. K. (1967) "Wall-pressure fluctuations associated with subsonic turbulent boundary layer flow". *Journal of Fluid Mechanics*, Vol. 28, pp. 719-754.
- [5] Bakewell, H. P. (1968) "Turbulent wall pressure fluctuations on a body of revolution". *Journal of the Acoustical Society of America*, Vol. 43, pp. 1358-1363.
- [6] Graham, W. R. (1997) "A comparison of models for the wavenumber-frequency spectrum of turbulent boundary layer pressures". *Journal of Sound and Vibration*, Vol. 206, pp. 541-565.
- [7] Durant, C., Robert, G., Filippi, P., Mattei, P.-O. (2000) "Vibroacoustic response of a thin cylindrical shell excited by a turbulent internal flow: Comparison between numerical prediction and experimentation". *Journal of Sound and Vibration*, Vol. 229, pp. 1115-833.
- [8] Au-Yang, M. K. (2001) "Flow-induced vibration of power and process plant components : A practical workbook". ASME Press, New York, USA.
- [9] Leclercq, D. J., Bohineust, X. (2002) "Investigation and modelling of the wall pressure field beneath a turbulent boundary layer at low and medium frequencies". *Journal of Sound and Vibration*, Vol. 257, pp. 477-501.
- [10] Païdoussis, M. P. (2004) "Fluid-Structure Interactions: Volume 2 – Slender Structures and Axial Flow". Elsevier, London, UK.
- [11] Hwang, Y. F., Bonness, W. K., Hambric, S. A. (2009) "Comparison of semi-empirical models for turbulent

boundary layer wall pressure spectra". *Journal of Sound and Vibration*, Vol. 319, pp. 199-217.

- [12] Moussou, P., Bodel, C., Benhamadouche, S. (2011) "CFD estimation of the unsteady fluid force along a fuel rod downstream a mixing grid". Paper PVP2011-57337. ASME Pressure Vessels & Piping Conference (PVP2011), 17-21 July 2011, Baltimore, USA.
- [13] Axisa, F., Antunes, J., Villard, B. (1990) "Random excitation of heat-exchanger tubes by cross-flows". *Journal of Fluids and Structures*, Vol. 4, pp. 321-341.
- [14] Ffowcs Williams, J. E. (1982) "Boundary layer pressures and the Corcos model: A development to incorporate low wavenumber constraints". *Journal of Fluid Mechanics*, Vol. 125, pp. 9-25.
- [15] Chase, D. (1987) "The character of the turbulent wall pressure spectrum at subconvective wavenumbers and a suggested comprehensive model". *Journal of Sound and Vibration*, Vol. 112, pp. 125-147.
- [16] Smolyakov, A. V., Tkachenko, V. M. (1991) "Model of a field of pseudosonic turbulent wall pressures and experimental data". *Soviet Physics - Acoustics*, Vol. 37, pp. 627-631.

Appendix A: Computation of the simplified correlation integrals for convective flows

To convert the double integrals of (21) and (22) into single integrals, the following classical coordinate transformation, illustrated in Fig. 11, is used:

$$\alpha = (\bar{x}_2 + \bar{x}_1) / \sqrt{2} \quad ; \quad \beta = (\bar{x}_2 - \bar{x}_1) / \sqrt{2} \quad (30)$$

and, from (21), one obtains:

$$\begin{aligned} \operatorname{Re}[\tilde{L}_{mm}(\bar{f}_R)] &\approx \\ &\approx \int_0^{\sqrt{2}\varepsilon} \int_0^{\varepsilon} \phi_n\left(\frac{\alpha-\beta}{\sqrt{2}}\right) \phi_m\left(\frac{\alpha+\beta}{\sqrt{2}}\right) \exp\left(-\frac{\sqrt{2}\beta}{\hat{\lambda}_c(\bar{f}_R)}\right) \cos\left(\frac{\sqrt{2}\beta}{\hat{X}_c(\bar{f}_R)}\right) d\beta d\alpha + \\ &+ \int_0^{\sqrt{2}\varepsilon} \int_{-\varepsilon}^0 \phi_n\left(\frac{\alpha-\beta}{\sqrt{2}}\right) \phi_m\left(\frac{\alpha+\beta}{\sqrt{2}}\right) \exp\left(\frac{\sqrt{2}\beta}{\hat{\lambda}_c(\bar{f}_R)}\right) \cos\left(\frac{\sqrt{2}\beta}{\hat{X}_c(\bar{f}_R)}\right) d\beta d\alpha \end{aligned} \quad (31)$$

where $\pm\varepsilon$ is a parameter expressing the integration boundary normal to the α axis. Notice that, as shown in Fig. 11, because of the fast decreasing of the exponential integrand when $\hat{\lambda}_c \ll 1$, the boundary ε can take any value between a few $\hat{\lambda}_c$ and ∞ without affecting significantly the result.

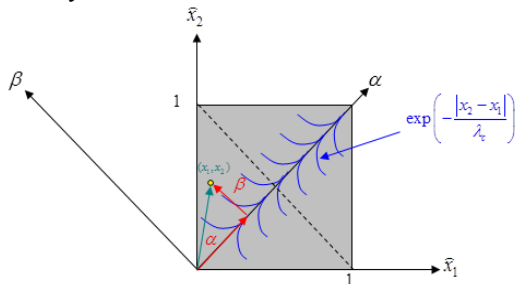


FIGURE 11: COORDINATE CHANGE FOR THE INTEGRALS COMPUTATION.

Then, because the $\phi_{n,m}(x)$ change slowly within the narrow strip of effective integration, a Taylor series development of these functions is allowable within $|\beta| \leq \varepsilon$, leading to the approximate first term of the "internal" integral in (31):

$$\begin{aligned} &\int_0^{\varepsilon} \phi_n\left(\frac{\alpha-\beta}{\sqrt{2}}\right) \phi_m\left(\frac{\alpha+\beta}{\sqrt{2}}\right) \exp\left(-\frac{\sqrt{2}\beta}{\hat{\lambda}_c(\bar{f}_R)}\right) \cos\left(\frac{\sqrt{2}\beta}{\hat{X}_c(\bar{f}_R)}\right) d\beta \approx \\ &\approx \int_0^{\varepsilon} \left\{ \left[\phi_n\left(\frac{\alpha}{\sqrt{2}}\right) - \frac{\beta}{\sqrt{2}} \phi_n'\left(\frac{\alpha}{\sqrt{2}}\right) + \dots \right] \left[\phi_m\left(\frac{\alpha}{\sqrt{2}}\right) + \frac{\beta}{\sqrt{2}} \phi_m'\left(\frac{\alpha}{\sqrt{2}}\right) + \dots \right] \right. \\ &\quad \left. \times \exp\left(-\frac{\sqrt{2}\beta}{\hat{\lambda}_c(\bar{f}_R)}\right) \cos\left(\frac{\sqrt{2}\beta}{\hat{X}_c(\bar{f}_R)}\right) \right\} d\beta \end{aligned} \quad (32)$$

and similarly for the second term. Then, neglecting terms beyond first order, while computing the integrals in the convenient limit $\varepsilon \rightarrow \infty$, we obtain:

$$\begin{aligned} &\int_0^{\varepsilon} \phi_n\left(\frac{\alpha-\beta}{\sqrt{2}}\right) \phi_m\left(\frac{\alpha+\beta}{\sqrt{2}}\right) \exp\left(-\frac{\sqrt{2}\beta}{\hat{\lambda}_c(\bar{f}_R)}\right) \cos\left(\frac{\sqrt{2}\beta}{\hat{X}_c(\bar{f}_R)}\right) d\beta = \\ &= \int_{-\varepsilon}^0 \phi_n\left(\frac{\alpha-\beta}{\sqrt{2}}\right) \phi_m\left(\frac{\alpha+\beta}{\sqrt{2}}\right) \exp\left(\frac{\sqrt{2}\beta}{\hat{\lambda}_c(\bar{f}_R)}\right) \cos\left(\frac{\sqrt{2}\beta}{\hat{X}_c(\bar{f}_R)}\right) d\beta \approx (33) \\ &\approx \frac{\hat{\lambda}_c(\bar{f}_R)}{\sqrt{2}} \left[1 + \left(\frac{\hat{\lambda}_c(\bar{f}_R)}{\hat{X}_c(\bar{f}_R)} \right)^2 \right]^{-1} \phi_n\left(\frac{\alpha}{\sqrt{2}}\right) \phi_m\left(\frac{\alpha}{\sqrt{2}}\right) \end{aligned}$$

which is valid for $\hat{\lambda}_c(f) \ll 1$, in the full range $0 \leq \hat{X}_c(f) \leq \infty$. Then, one obtains from (31) and (33), after reversion to the original coordinate system:

$$\operatorname{Re}[\tilde{L}_{mm}(\bar{f}_R)] \approx 2\hat{\lambda}_c(\bar{f}_R) \left[1 + \left(\frac{\hat{\lambda}_c(\bar{f}_R)}{\hat{X}_c(\bar{f}_R)} \right)^2 \right]^{-1} \int_0^1 \phi_n(\bar{x}) \phi_m(\bar{x}) d\bar{x} \quad (34)$$

which is the result (23).

A similar approach is now applied to the imaginary part (22) of the correlation integral, leading to:

$$\begin{aligned} \operatorname{Im}[\tilde{L}_{mm}(\bar{f}_R)] &\approx \\ &\approx \int_0^{\sqrt{2}\varepsilon} \int_0^{\varepsilon} \phi_n\left(\frac{\alpha-\beta}{\sqrt{2}}\right) \phi_m\left(\frac{\alpha+\beta}{\sqrt{2}}\right) \exp\left(-\frac{\sqrt{2}\beta}{\hat{\lambda}_c(\bar{f}_R)}\right) \sin\left(\frac{\sqrt{2}\beta}{\hat{X}_c(\bar{f}_R)}\right) d\beta d\alpha + \\ &+ \int_0^{\sqrt{2}\varepsilon} \int_{-\varepsilon}^0 \phi_n\left(\frac{\alpha-\beta}{\sqrt{2}}\right) \phi_m\left(\frac{\alpha+\beta}{\sqrt{2}}\right) \exp\left(\frac{\sqrt{2}\beta}{\hat{\lambda}_c(\bar{f}_R)}\right) \sin\left(\frac{\sqrt{2}\beta}{\hat{X}_c(\bar{f}_R)}\right) d\beta d\alpha \end{aligned} \quad (35)$$

and we obtain from (35):

$$\operatorname{Im}[\tilde{L}_{mm}(\bar{f}_R)] \approx -2 \frac{(\hat{\lambda}_c(\bar{f}_R))^3 (\hat{X}_c(\bar{f}_R))^3}{[(\hat{X}_c(\bar{f}_R))^2 + (\hat{\lambda}_c(\bar{f}_R))^2]^2} \int_0^1 \left[\phi_n(\bar{x}) \phi_m(\bar{x}) \right] d\bar{x} \quad (36)$$

which corresponds to result (24).

A MODEL FOR DRAG COEFFICIENT IN AN IDEALIZED BUBBLY TWO-PHASE FLOW

C. Béguin*, S.Étienne, N.W. Mureithi & M. J. Pettigrew

BWC/AECL/NSERC Chair of Fluid-Structure Interaction

Department of Mechanical Engineering, École Polytechnique,

P.O.Box 6079, succ. Centre-Ville, Montréal (Québec), Canada, H3C 3A7

* cedric.beguin@polymtl.ca

ABSTRACT

In the present work, the forces on a spherical inclusion of one phase within a second are determined. This information is essential to completely characterize dispersed flows. Most of these two-phase flow models are empirically obtained from experiments involving single bubbles (or droplets). Their applicability to systems with high void fraction is questionable. Moreover correlations that take into account the effect of local void fraction are rare. This paper explores the drag on spherical bubbles (or droplets) inside an idealized homogeneous bubbly flow (identical bubbles rising at the same speed). In the present work, a general relation for the drag coefficient of spherical bubbles (or droplets) depending on Reynolds number, void fraction, viscosity ratio and density ratio is developed. Analytical numerical results are compared with previous studies including experimental measurements. The results lead to a proposal for a general relation of the drag coefficient for a cloud of spherical bubbles. It is shown that in the idealized bubbly flow considered, void fraction has a major effect on drag essentially through confinement and that wake effects are comparatively small. The proposed relation can be used to construct a two-phase flow model for bubbly or annular flows. This work proposes an improvement of the closure relations for the drag coefficient compared to previous works. The main conclusion is that void fraction pushes to higher Re the limit at which Stokes flow represents accurately the flow around bubbles.

INTRODUCTION

In the nuclear and chemical process industries, 50% of components and piping elements operate with two-

phase flows, (see *e.g.* [1]). The associated flow-induced vibrations can lead to structural degradation, process malfunction and component failure. Two-phase flow can create significant damping or vibration excitation forces. In the present work, the forces on a spherical inclusion of one phase in the other are determined. This information is essential to completely characterize dispersed flows. Most two-phase correlation are empirically obtained from experiments involving single bubbles (or droplets), making their applicability to systems with high void fraction questionable [2]. Moreover very few correlations available in the literature take into account the effect of the local void fraction.

This paper will explore the drag on spherical bubbles (or droplets) inside an idealized homogeneous bubbly flow. For simplicity, spherical bubbles (or droplets) corresponding to the dispersed phase will be named “gas” or “bubbles” and the continuous phase “liquid” with the respective subscripts g and l . A priori, the drag coefficient (C_D) depends on fluid viscosity (μ_l, μ_g), fluid density (ρ_l, ρ_g), bubble size (radius : a), void fraction (ε - ratio of gas volume to total volume) and bubble velocity (U_b). Assuming there are no other parameters involved such as the presence of impurities and according to the Buckingham- π theorem, the drag coefficient (C_D) is a function of four independent dimensionless numbers. We choose :

$$\mu^* = \frac{\mu_g}{\mu_l}, \rho^* = \frac{\rho_g}{\rho_l}, Re = \frac{2\rho_l U_b a}{\mu_l} \text{ and } \varepsilon$$

The goal of the present work is to find a general relation $C_D = F(\mu^*, \rho^*, Re, \varepsilon)$. This relation is then compared with previous studies. The paper is divided into four sections. In the first section, we will present a brief literature review of drag coefficient models. In Section 2, analytical solutions for Stokes and Euler flows are presented. In

*Address all correspondence to this author.

Section 3, a numerical experiment is presented. Finally, Section 4 result are compared to an experiment. The results lead to a proposal for a general relation of the drag coefficient for a cloud of spherical bubbles. The main results are summarized in the conclusion section.

DRAG COEFFICIENT CORRELATION

When bubbles are small (small Bond number $Bo = 4\Delta\rho ga^2/\gamma \ll 1$), they are spherical and their velocities depend only on density, gravity, bubble size and liquid viscosity. For a single spherical bubble, C_D is inversely proportional to Reynolds number, as proposed by Mei et al. [3]:

$$C_D = \frac{16}{Re} \left[1 + \frac{2}{\frac{16}{Re} + \frac{3.315}{\sqrt{Re}} + 1} \right] \quad (1)$$

The bubble terminal velocity is determined by the equilibrium between the buoyancy force on the bubble ($\Delta\rho ga^3$) and the drag force on the bubble :

$$\frac{1}{2} C_D \rho_l \pi a^2 U_b^2 = \frac{4}{3} \pi \Delta\rho ga^3$$

$$U_b = \frac{1}{3} \frac{16}{C_D Re} \frac{\Delta\rho ga^2}{\mu_l} = \frac{1}{3} \frac{16}{C_D Re} U_0 \quad (2)$$

where $\Delta\rho = \rho_l - \rho_g$ represents the density difference and U_0 is a "typical" bubble velocity. The Stokes approximation ($Re \ll 1$) leads to $U_b/U_0 = 1/3$ while the Euler approximation ($Re \gg 1$) leads to $U_b/U_0 = 1/9$.

For low Reynolds numbers, Taylor and Acrivos [4] have proposed a relation that takes into account the viscosity ratio (μ^*) dependence for a bubble in an infinite liquid domain ($\varepsilon = 0$), meaning no surrounding bubbles. The relation is :

$$C_D = \frac{16}{Re} \frac{2+3\mu^*}{2+2\mu^*} \left[1 + \frac{1}{8} \frac{2+3\mu^*}{2+2\mu^*} Re + \frac{1}{40} \left(\frac{2+3\mu^*}{2+2\mu^*} \right)^2 Re^2 \ln Re \right] \quad (3)$$

This equation gives the correct drag coefficient for a solid sphere at the limit $\mu^* \rightarrow \infty$. The drag coefficient for a solid sphere is also given by the following correlation of

[5] for $Re < 3.7 \times 10^5$:

$$C_D = \frac{24}{Re} \left[1 + 0.15 Re^{0.687} + \frac{0.0175}{1 + \frac{42500}{Re^{1.16}}} \right] \quad (4)$$

Ishii et al. [6] have proposed a relation for a droplet or small bubble at low Reynolds numbers which includes void fraction dependence :

$$C_D = \frac{24}{Re} \left(\frac{1}{1-\varepsilon} \right)^{\frac{2+5\mu^*}{2+2\mu^*}} \quad (5)$$

Equations (3) and (5) are in agreement for $\mu^* \gg 1$ and $\varepsilon = 0$. It is known that very small bubbles, probably due to impurities, usually behave as solid particles (equivalent to $\mu^* \gg 1$).

STOKES AND EULER FLOW ANALYTICAL SOLUTIONS

This section attempts to derive analytical expressions for the drag coefficient taking into account void fraction. Analytical results from a simple model representing one bubble in a bubbly flow are presented. In order to model the effect of void fraction, in the bubble reference frame, we consider the stationary solution for a gas bubble of radius (a) centered in a liquid sphere of radius (l) (see Figure 1). The void fraction, which is the ratio of gas to total volume, can easily be calculated in this case as $\varepsilon = a^3/l^3$. We consider an incompressible fluid flow governed by :

$$\begin{aligned} \nabla \cdot \vec{u}_g &= 0 & (a) \\ \rho_g \vec{u}_g \nabla \vec{u}_g &= -\nabla P_g + \mu_g \Delta \vec{u}_g & (b) \end{aligned} \quad (6)$$

and

$$\begin{aligned} \nabla \cdot \vec{u}_l &= 0 & (a) \\ \rho_l \vec{u}_l \nabla \vec{u}_l &= -\nabla P_l + \mu_l \Delta \vec{u}_l & (b) \end{aligned} \quad (7)$$

The actual pressures would include a hydrostatic pressure component and would thus be $P_l + \rho_l gz$ and $P_g + \rho_g gz$. However, the effect of the hydrostatic pressure results in the well known buoyancy force $\frac{4}{3} \Delta\rho g \pi a^3$. Thus the hydrostatic pressure component effects is already taken into account and does not have to be included explicitly. We

consider the following boundary conditions :

$$\begin{aligned}
 (1) \quad r = l : & \quad u_{rl} = -U_b(1 - \varepsilon) \cos \theta \\
 (2) & \quad u_{\theta l} = U_b(1 - \varepsilon) \sin \theta \\
 (3) \quad r = 0 : & \quad u_{rg} \text{ and } u_{\theta g} \text{ have a finite value} \\
 (4) \quad r = a : & \quad u_{\theta l} = u_{\theta g} \\
 (5) & \quad \tau_{(r\theta)l} = \tau_{(r\theta)g} \\
 (6) \quad P_l + \Delta\rho g a \cos \theta - \tau_{(rr)l} = P_g - \tau_{(rr)g} - 2\gamma/a & \quad (8)
 \end{aligned}$$

Conditions (1) and (2) are chosen in order to have $\langle u_l \rangle = U_b$. This is important for the closure relations of the averaged Navier-stokes equations. The proposed closure relations model is expressed using unknown factors of the averaged Navier-stokes equations. In this case, U_b is not necessarily the actual relative velocity of the bubbles but rather the velocity obtained from the unknown factors of the averaged Navier-Stokes equation ($\langle u_g \rangle$ and $\langle u_l \rangle$) see e.g. [6–8].

The case $l \rightarrow \infty$ ($\varepsilon \rightarrow 0$) corresponds to the case of a single bubble in an infinite liquid volume. The influence of neighboring bubbles is set through the distance l , which represents the average half distance between the bubbles and its neighbors. Condition (6) in equation (8) is never valid because the assumption of a spherical bubble was made. This condition is replaced by $u_{rl}|_{r=a} = u_{rg}|_{r=a} = 0$. However, the condition (6) can be used to verify the validity of the spherical shape assumption. Surface tension contributes to maintain the spherical shape against other forces. We are able to solve this problem analytically only for Stokes and Euler flows. In the case of Euler flow, the analytical solution of the equations cannot satisfy all boundary conditions. Conditions (1) and (2) are therefore replaced by $\langle u_l \rangle = U_b$.

INTERNAL FLOW

For the internal flow, a Navier-Stokes solution exists known as the Hill vortex.

$$\begin{aligned}
 u_{rg} &= 2B_0(r^2 - a^2) \cos(\theta) \\
 u_{\theta g} &= -2B_0(2r^2 - a^2) \sin(\theta) \\
 P_g &= 20B_0\mu_g r \cos \theta \\
 &+ \underbrace{\rho_g B_0^2 [(4r^4 - 6a^2r^2) \sin^2 \theta - 2r^4 + 4a^2r^2]}_{\text{Euler or convective component}} \quad (9)
 \end{aligned}$$

Note that the difference between Stokes and Navier-Stokes solutions lies in the pressure component due to the convective terms.

EXTERNAL STOKES FLOW ($Re \ll 1$)

In the case of external Stokes flow, considering incompressibility and symmetry and using spherical coordinates (r, θ, ϕ) , and variable separation, we deduce the following solution from the vorticity equation and the boundary condition :

$$\begin{aligned}
 u_{rl} &= 2(C_0(r^2 - a^2) + C_2(\frac{1}{r} - \frac{1}{a}) + C_3(\frac{1}{r^3} - \frac{1}{a^3})) \cos \theta \\
 u_{\theta l} &= -(2C_0(2r^2 - a^2) + C_2(\frac{1}{r} - \frac{2}{a}) - C_3(\frac{1}{r^3} + \frac{2}{a^3})) \sin \theta \\
 P_l &= \mu_l \left(20C_0r + \frac{2C_2}{r^2} \right) \cos \theta \\
 a^2 B_0 &= -\frac{U_b}{2} \frac{1 - \varepsilon}{F(\varepsilon)} (2 - 5\varepsilon + 3\varepsilon^{5/3}) \\
 a^2 C_0 &= \frac{U_b}{2} \frac{1 - \varepsilon}{F(\varepsilon)} (2\varepsilon + 3\mu^*(\varepsilon - \varepsilon^{5/3})) \\
 \frac{C_2}{a} &= U_b \frac{1 - \varepsilon}{F(\varepsilon)} (2 + 3\varepsilon^{5/3} + 3\mu^*(1 - \varepsilon^{5/3})) \\
 \frac{C_3}{a^3} &= -U_b \frac{1 - \varepsilon}{F(\varepsilon)} (\varepsilon + \mu^*(1 - \varepsilon)) \\
 F(\varepsilon) &= (1 - \varepsilon^{1/3})^3 ((4 + 6\varepsilon^{1/3} + 6\varepsilon^{2/3} + 4\varepsilon) \\
 &\quad + \mu^*(4 + 3\varepsilon^{1/3} - 3\varepsilon^{2/3} - 4\varepsilon)) \quad (10)
 \end{aligned}$$

Using equation (10), the force on the bubble may be evaluated from surface stress integration :

$$\begin{aligned}
 \vec{f} &= \int_{\varphi=0}^{2\pi} \int_{\theta=0}^{\pi} (-P_l \bar{\bar{1}} + \bar{\bar{\tau}}_l) \cdot \vec{n} a^2 \sin \theta d\theta d\varphi \\
 &= -4\pi\mu_l U_b a \frac{1 - \varepsilon}{F(\varepsilon)} (2 + 3\varepsilon^{5/3} + 3\mu^*(1 - \varepsilon^{5/3})) \vec{e}_z \quad (11)
 \end{aligned}$$

The terminal velocity (U_b) of the bubble is obtained from the balance between drag and buoyancy forces while the drag coefficient C_D is given by $C_D = f/(1/2\rho_l\pi a^2 U_b^2)$. The resulting expressions for U_b and C_D are :

$$\begin{aligned}
 U_b &= \frac{1}{3} \frac{\Delta\rho g a^2}{\mu_l} \left[\frac{F(\varepsilon)}{(1 - \varepsilon)(4 + 6\varepsilon^{5/3} + 6\mu^*(1 - \varepsilon^{5/3}))} \right] \\
 C_D &= \frac{16}{Re} \left[\frac{(1 - \varepsilon)(4 + 6\varepsilon^{5/3} + 6\mu^*(1 - \varepsilon^{5/3}))}{F(\varepsilon)} \right] \quad (12)
 \end{aligned}$$

In the limiting case of one bubble in an infinite liquid domain ($\varepsilon = 0$), the above expression reduces to

$$C_D = \frac{16}{Re} \frac{2 + 3\mu^*}{2 + 2\mu^*} \quad (13)$$

This result is in accordance with equation (3) proposed by [4] for $\varepsilon = 0$. Equation (12) is a new result for the drag coefficient of a bubble in a two-phase mixture, as-

suming an external Stokes flow. This result extends the expression for C_D to all values of the void fraction (ε).

EXTERNAL EULER FLOW WITH BOUNDARY LAYER CORRECTION ($Re \gg 1$)

The case of external Euler flow is considered next. Similarly to the approach taken for the Stokes flow solution, the stationary Euler vorticity equation is used. Considering boundary condition : $u_{rl} |_{r=a} = 0$ and the condition $\langle u_l \rangle = U_b$ we deduce the following radial and tangential velocities and pressure :

$$\begin{aligned} u_{rl} &= -U_b \left(1 - \frac{a^3}{r^3}\right) \cos \theta \\ u_{\theta l} &= U_b \left(1 + \frac{a^3}{2r^3}\right) \sin \theta \\ P_l &= -\rho_l U_b^2 \left[\left(\frac{3a^3}{2r^3} - \frac{3a^6}{8r^6} \right) \sin^2 \theta - \frac{a^3}{r^3} + \frac{a^6}{2r^6} + C_2 \right] \end{aligned} \quad (14)$$

We cannot satisfy both the boundary conditions (8-(1) and (2)). We choose to respect only the condition $\langle u_l \rangle = U_b$, since it is a central condition for the averaged Navier-Stokes equations. Moore [9] proposed a boundary layer correction for $\varepsilon = 0$ and found :

$$C_D = \frac{48}{Re} \left[1 - \frac{2.2}{\sqrt{Re}} + 0(Re^{-5/6}) \right] \quad (15)$$

Following the same procedure as Moore a new boundary layer correction is derived, a new boundary layer correction valid only for $\mu^* \ll Re$ is proposed

$$\begin{aligned} u_{rl}^* &= \frac{U_b}{Re} \frac{4\chi(\theta)}{3} \left[\tau F(\tau) - \left(1 - \frac{\cos \theta}{2}\right) (6 + 9\mu^*) \operatorname{erf}(\tau) \right] \\ u_{\theta l}^* &= U_b \sqrt{\frac{2\chi(\theta)}{Re}} F(\tau) \sin \theta \\ \text{with :} \\ \tau &= \sqrt{\frac{Re}{8\chi(\theta)}} \left(\frac{r}{a} - 1 \right) \\ F(\tau) &= -(6 + 9\mu^*) \left[\frac{1}{\sqrt{\pi}} e^{-\tau^2} - \tau (1 - \operatorname{erf}(\tau)) \right] \\ \chi(\theta) &= \frac{1}{18} \left(\frac{\cos(3\theta) - 9\cos \theta + 8}{\sin^4 \theta} \right) \end{aligned} \quad (16)$$

To be able to follow the procedure by Moore, some assumptions about the pressure needed to be made. This leads to an incorrect value of the pressure field especially at the interface. The force on the bubble can then only be deduced through the total dissipation in the liquid domain which needs to be equal to the power of the drag forces (see [10]). We can finally deduce the velocity of the bub-

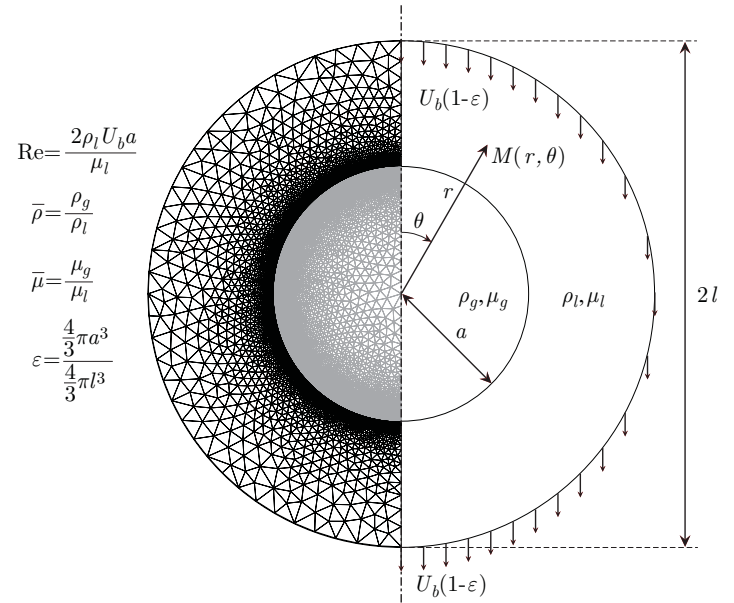


FIGURE 1: Geometry of the problem of a single bubble.

ble from the balance between drag and buoyancy forces and the drag coefficient C_D :

$$C_D = \frac{48}{Re} \left[1 - \varepsilon^{5/3} - \frac{5.35(1 + 1.5\mu^*) - 3.44(1 + 1.5\mu^*)^2}{\sqrt{Re}} \right] \quad (17)$$

This relation is in accordance, for $Re \gg 1$ and $\varepsilon = 0$, with the relation (1). For $\varepsilon = \mu^* = 0$:

$$C_D = \frac{48}{Re} \left[1 - \frac{1.9}{\sqrt{Re}} \right] \quad (18)$$

This result is in accordance with Moore for $\varepsilon = \mu^* = 0$ except for the factor 1.9 instead of 2.2. We probably do not have the same integral resolution. The new relation (17) extends the drag formulation for $\varepsilon \neq 0$ and $\mu^* \neq 0$.

NUMERICAL SOLUTIONS

In order to confirm and even improve the new relation we have proposed for the drag coefficient (C_D), numerical experiments have been carried out by varying Reynolds number Re (from 0.01 to 300), void fraction ε (from 10^{-6} to 0.6), viscosity ratio μ^* (from 0.02 to 50) and density ratio ρ^* (from 10^{-3} to 10^3).

NUMERICAL SOLUTION STRATEGY

Figure 1 shows the geometry of the problem solved both numerically and analytically. Figure 2 shows the geometry of a more realistic case of a five bubble train. This

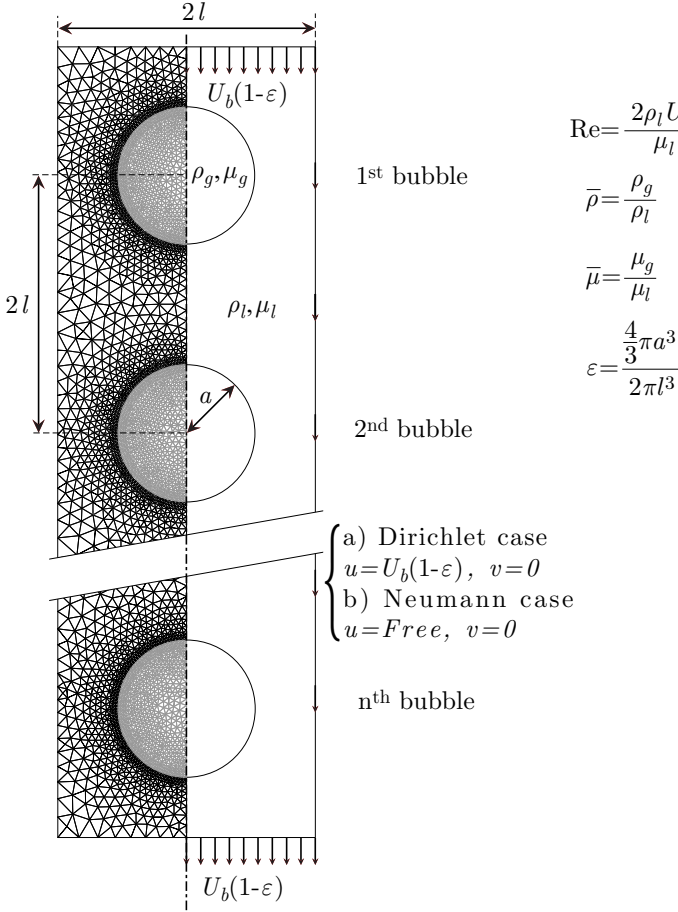


FIGURE 2: Geometry of the problem of a n bubbles train.

problem was solved with two types of boundary conditions, one with $u = U_b(1 - \varepsilon), v = 0$ for $r = l$ named later on the “Dirichlet case” and one with $u = \text{“Free”}, v = 0$ for $r = l$ named later on the “Neumann case”. Both cases have for inlet and outlet condition : $u = U_b(1 - \varepsilon), v = 0$. A finite element code was used to solve the incompressible Navier-Stokes equations in an axisymmetric frame of reference (the central axis of rotation is noted by a dash-dot line). A Taylor-Hood element was selected for both domains (external flow and flow within the bubble). The fluid velocity is discretized using 6-node quadratic elements, while fluid pressure is discretized by piecewise linear continuous functions. The mixed method is used in which the pressure is a Lagrange multiplier.

The tangential condition is satisfied via another Lagrange multiplier which enforces the non-penetration of fluid across the bubble boundary. An interface allows matching of the inner bubble boundary velocity to the outer bubble boundary velocity (Eq. (8)-4). Similarly, continuity of interface tangential loads is also enforced, (Eq. (8)-5).

Dirichlet boundary conditions are imposed on the

$$\begin{aligned} Re &= \frac{2\rho_l U_b a}{\mu_l} \\ \bar{\rho} &= \frac{\rho_g}{\rho_l} \\ \bar{\mu} &= \frac{\mu_g}{\mu_l} \\ \varepsilon &= \frac{\frac{4}{3}\pi a^3}{2\pi l^3} \end{aligned}$$

nb of nodes	C_D	nb of bubbles	C_D
219	1.37657	1	1.22008
2018	1.14649	3	1.10543
6948	1.10445	5	1.10505
24662	1.10505	7	1.10496
94148	1.10516	9	1.10513
188891	1.10517	11	1.10503

TABLE 1: Left: convergence with respect to the number of nodes, right: convergence with respect to the number of bubbles.

outer boundary of the domain. This means that the pressure needs to be set at only one point in the fluid domain. Symmetry conditions are imposed on all axial boundaries (dash-dot line). Finally, for all cases, we extract the total drag by integrating reactions on the outer boundary of the bubble.

Linearization of the flow equations accounts for all implicit dependencies to ensure quadratic convergence of Newton’s method [11]. The resulting sparse matrix system is solved using the PARDISO software, [12, 13].

A convergence study has been performed to ensure that the results are obtained with sufficient numerical accuracy. Simulations were performed for a representative case corresponding to $\varepsilon = 20\%$ for a multi-bubble configuration, with $Re = 100$, $\mu^* = 0.02$ and $\rho^* = 10^{-3}$, and Dirichlet conditions $u = U_b(1 - \varepsilon), v = 0$. Results, in terms of drag coefficient values, are summarized in Table 1. From this table we deduced that taking a bubble train of 5 bubbles and 24662 nodes is sufficient to ensure accuracy to 3 or 4 significant digits while keeping the computational time reasonable.

COMPARARISON WITH ANALYTICAL RESULTS FOR THE CASE OF ONE BUBBLE (cf. fig. 1)

The non dimensionalization process allows us to choose $a = 0.5$, $U_b = 1$ and $\mu_l = 1$, which means : $Re = \rho_l$, $\rho^* = \rho_g/Re$, $\mu^* = \mu_g$ and $\varepsilon = 0.5^3/l^3$. We choose to seek solutions for the following combinations of parameters :

$$\begin{aligned} \rho^* &= 10^{-3}, 1, 10^3 \\ \mu^* &= 0.02, 0.1, 0.5, 2.5, 12.5, 50 \\ Re &= 0.01, 0.1, 1, 10, 100, 300 \\ l &= 0.59(60\%), 0.68(40\%), 0.79(25\%), 1(12.5\%), \\ &2.5(0.8\%), 5(0.1\%), 10(0.0125\%), 50(0.0001\%) \end{aligned}$$

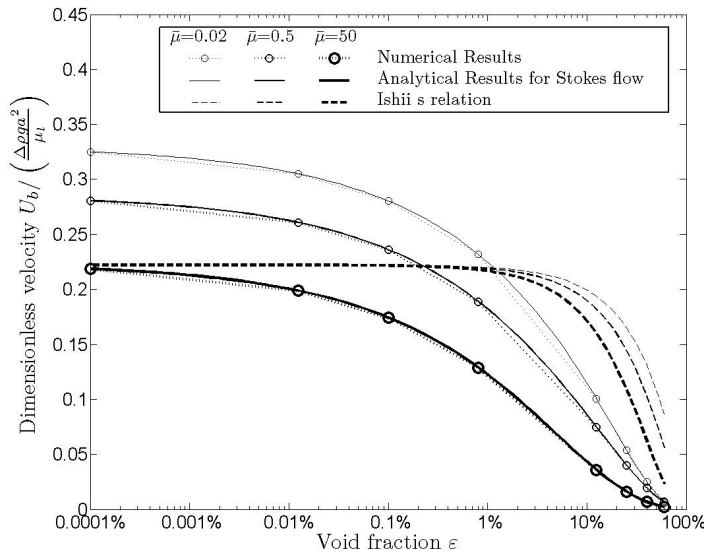
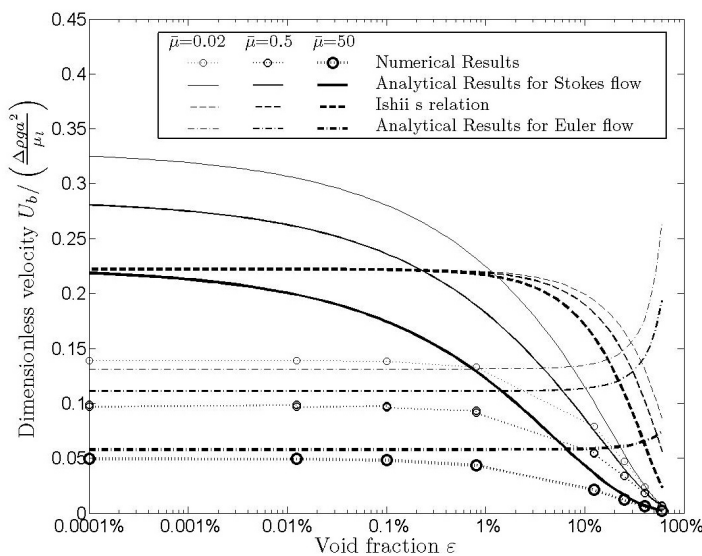

 (a) $Re=0.01$.

 (b) $Re=100$.

FIGURE 3: Numerical and analytical comparison of dimensionless velocity versus void fraction for (a) $Re=0.01$ (b) $Re=100$ (cf. Eq.(12) for analytical results and Eq. (5) for Ishii's relation).

The corresponding void fraction (ε) is indicated in the brackets.

The drag coefficient is inversely proportional to the Reynolds number while the terminal velocity varies according to the product of the drag coefficient and Reynolds number. For this reason we present the results of the dimensionless terminal velocity as expressed on Eq. (2).

For a bubble surrounded by an outer infinite liquid domain, very good agreement is obtained between the numerical Navier-Stokes solutions and the relations of Mei et al. [3] and the relation of Taylor and Acrivos [4]. In order to evaluate the maximum Reynolds number for which Stokes assumption remains valid, computational results and analytical results are compared in Figures 3(a), 3(b). Very good agreement with analytical results for Stokes flow is achieved for $Re < 10$ and for all Reynolds number (0.01 to 300) in the case of void fractions higher than 10% ($\varepsilon > 0.1$). In each graph, the results for the three different density ratios are presented. They are so close that we are not able to distinguish the different points except for $Re = 100$ where we can see a small difference.

As shown on Figure 3(b), the new relation (17) is a good model for low void fractions and takes into account relatively well the influence of μ^* while viscosity ratio remains small relative to Reynolds number ($\mu^* \ll Re$) and for sufficiently high Reynolds number $Re \geq 100$. For high Reynolds number flows ($Re \geq 100$), the influence of void fraction is not important when $\varepsilon < 1\%$, which was not the case for low Reynolds number flows.

As suggested by the results presented in Figures 3(a),3(b), even for high Reynolds number, if the void fraction is higher than 10%, Stokes flow is more representative of reality than Euler flow. When the flow is confined, viscous effects are generally more important than inertial effects. Even a low void fraction corresponds to a relatively small average distance between bubbles, consequently liquid flow is closer to liquid film flow between the bubbles rather than infinite liquid domain flow. This explains why the Stokes flow model is a better approach than the Euler flow model.

NUMERICAL RESULTS OF DRAG COEFFICIENT FOR MORE REALISTIC CASES

The agreement between numerical and analytical results gives confidence in the accuracy of both the numerical and the analytical calculations. We can therefore now study more realistic cases. The previous case allows us to obtain an analytical solution but does not take into account the wakes of surrounding bubbles. To investigate this, the problem presented in Figure 2 was solved. Several computations were done varying the number of bubbles in a bubble train. The bubbles are separated by a distance $2l$ inside a tube of radius l . As shown in Table 1, a train of five bubbles is sufficient to eliminate any variation of the C_D of the central bubble by adding more bubbles in the train. Solutions for a train of five bubbles were obtained for the following combinations of parameters :

$$\begin{aligned} \mu^* &= 0.02, 0.1, 0.5, 12.5, 25, 50 \\ Re &= 0.01, 0.1, 1, 10, 100, 300 \\ \varepsilon &= 0, 0001\%, 1\%, 2\%, 5\%, 10\%, 20\%, 30\%, \\ &40\%, 45\%, 50\% \end{aligned}$$

To evaluate the wake effect, numerical results of the drag coefficient obtained for a single bubble and those for the central bubble of a five bubble train were compared. The wake effect on the drag coefficient for the Dirichlet cases is fairly small except for high Reynolds numbers and high viscosity ratios. The effect in Neumann case is larger than for the Dirichlet case, but remains 30% below for Reynolds numbers lower than 10 and never exceed 50%. Since the effect of confinement is much larger than the wake effect, we conclude that confinement is the main effect governing drag variation. It follows that a model with one bubble will therefore represent reality quite well. Adding additional terms to take into account high Reynolds numbers, we arrive at the following newly proposed correlation :

$$C_D = \frac{16}{Re} \left(1 + \frac{2 \left(\frac{2+3\mu^*}{2+2\mu^*} \right)^2}{1 + \frac{Re_c}{Re}} \right) \frac{1-\varepsilon}{(1-\varepsilon^{1/3})^3} \left[\frac{P_1 + \mu^* P_2}{P_3 + \mu^* P_4} \right] \quad (19)$$

with :

$$\begin{aligned} P_1 &= 4 + 6\varepsilon^{5/3} \\ P_2 &= 6 - 6\varepsilon^{5/3} \\ P_3 &= 4 + 6\varepsilon^{1/3} + 6\varepsilon^{2/3} + \varepsilon \\ P_4 &= 4 + 3\varepsilon^{1/3} - 3\varepsilon^{2/3} - 4\varepsilon \\ Re_c &= 33 + 50000\varepsilon \end{aligned}$$

The transition from Stokes flow like to Euler flow like behavior occurs at the critical Reynolds number Re_c . The proposed formula takes into account the void fraction dependence. Figure 4 shows the agreement between correlation (19) and the numerical results for Neumann cases. The value of the drag coefficient from the correlation gives a maximal relative error of 47% compared to numerical values and an average relative error of 18%. For the Dirichlet cases (fixed boundary condition), the effect of confinement is more important and we obtain a good correlation by multiplying the void fraction by 1.5 in the previous relation. For the Dirichlet cases, the value of the drag coefficient from the correlation (19) gives a maximum error of 36% relative to numerical values and an average relative error of 16%. Figure 5 shows the agreement between the correlation (eq. (19)) and numerical results for the Dirichlet cases. As we can see the correlation is more accurate in the Dirichlet cases. Generally the error increases with void fraction, reflecting the difficulty in estimating the effect of surrounding bubbles on the drag

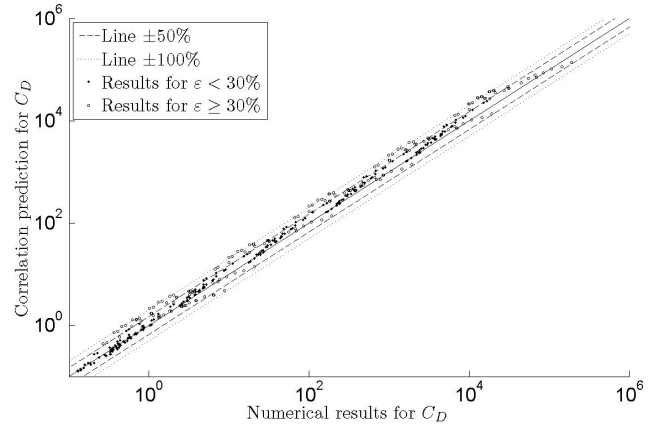


FIGURE 4: Comparison of the Correlation (19) and numerical computation for the Neumann cases.

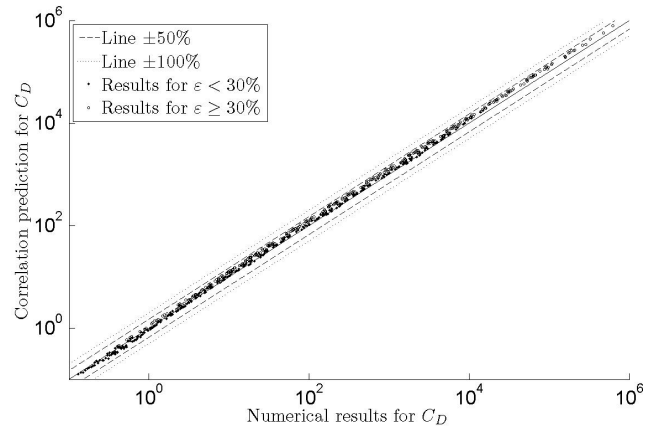


FIGURE 5: Comparison of the Correlation (19) and numerical computation for the Dirichlet cases.

Figure 6 presents, respectively, the influence of Reynolds number (Re), void fraction (ε) and viscosity ratio (μ^*) on the bubble terminal velocity (U_b) in the Dirichlet cases. The drag coefficient rises dramatically with void fraction, essentially due to confinement and consequently the terminal velocity decreases significantly. The previous comparison between one bubble and five bubbles leads to the conclusion that the wake influence is most of the time less than 10% of total drag. The drag coefficient rises with viscosity ratio. The value of $\mu^* \sim 1$ corresponds to the transition between an approximately free surface condition and an essentially solid surface condition (no slip). The dimensionless terminal velocity decreases with Reynolds number. For void fractions $\varepsilon \geq 1\%$, transition between Stokes and Euler flow occurs for $Re_c > 300$. For very low void fractions $Re_c \sim 33$ is the transition from Stokes to Euler flow. As the previous results suggest, gas density has no effect on drag coefficient and consequently none on the dimensionless terminal ve-

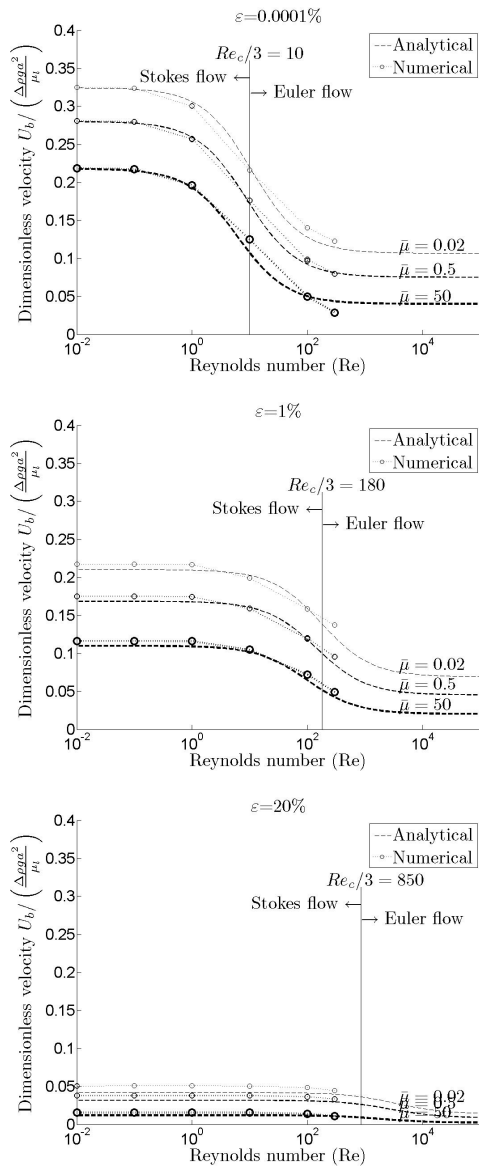


FIGURE 6: Numerical and Correlation (cf. Eq. (19)) comparison of dimensionless terminal velocity for different void fraction for Dirichlet case.

locity.

COMPARISON WITH EMPERICAL RESULTS

The only experimental study of an idealized bubbly flow (same size bubble) with sufficient small bubble, that we are aware of in the open literature, is the study of Roig et al. [14]. In their experiment, the mean bubble diameter varies from 1.14mm to 2.38mm and the void fraction from 0.3% to 14%. For a single air bubble in water, bubbles bigger than 1.3mm are deformed and their terminal velocities do not vary much with their diameter. The figure 7 show the comparison of terminal velocity expected by the new model cf. eq. (19) and their experiments.

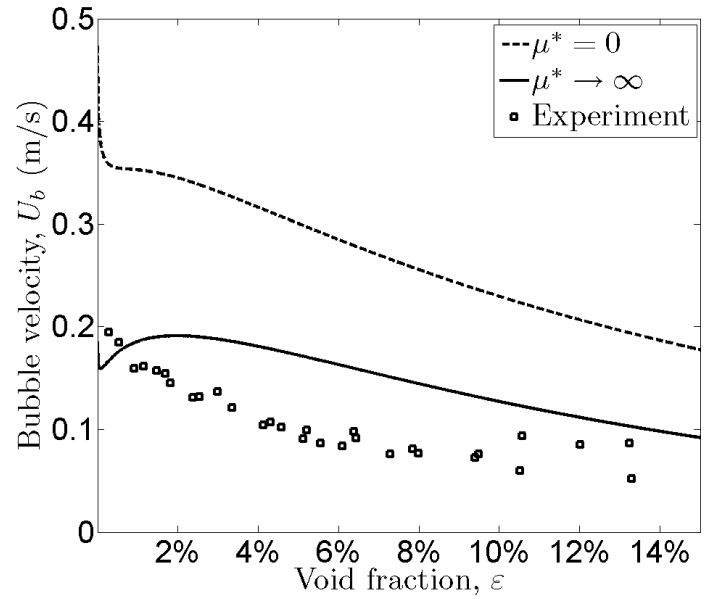


FIGURE 7: Bubble terminal velocity for bubble of 1.3 mm diameter and experiment from Roig et al. [14]

CONCLUSION

This paper proposes a relation for the drag coefficient of spherical bubbles or droplets for Reynolds numbers, Re , less than 300, void fractions ϵ up to 50%, and viscosity and density ratios (μ^*, ρ^*) between 10^{-3} and 10^3 . For simplicity the term 'gas' has been used to described the fluid in the dispersed phase. However, considering the ratios of density and viscosity studied, liquid droplets are also taken into account in the new relations proposed in the paper. For practical cases, only solid spheres are able to reach Reynolds numbers significantly larger than 1 000 while remaining spherical. The proposed relations is therefore useful for all fluid-fluid cases.

More work remains to be done to evaluate the drag coefficient for larger bubbles. However, the present work shows that the slip ratio is very small for bubbly flow. Moreover, even if the boundary condition in the present work were idealized, we think that in almost all practical cases of bubbly flow, the flow around a bubble can be considered as Stokes flow. The void fraction, ϵ , has a major effect on the drag essentially through confinement. The proposed relation can be used to construct a two-phase flow model for bubbly flow.

The present work proposes an improvement of the closure relation for the drag coefficient (C_D) compared to previous works. Previous work generally deduced forces on bubbles from potential flow, which as we have shown is not realistic. In Stokes flow the variation of forces due to void fraction have a much stronger effect than for Euler flow conditions (previous models). The dependence of in-

terface forces with void fraction is of utmost importance because it drives the variation of void fraction. Void fraction variation and flow pattern are known to be the major causes on severe fluid structure interaction in two-phase flows.

REFERENCES

- [1] Pettigrew, M., and Taylor, C., 2004. “Damping of heat exchanger tubes in two-phase flow: Review and design guidelines”. *ASME Journal of Pressure Vessel Technology*, **126**, p. 523.
- [2] Darmana, D., Deen, N., Kuipers, J., Hartevelt, W., and Mudde, R., 2009. “Numerical study of homogeneous bubbly flow: influence of the inlet conditions to the hydrodynamic behavior”. *International Journal of Multiphase Flow*, **35**, pp. 1077–1099.
- [3] Mei, R., Klausner, J., and Lawrence, C., 1994. “A note on the history force on a spherical bubble at finite Reynolds number”. *Physics of fluids*, **6**, pp. 418–420.
- [4] Taylor, T., and Acrivos, A., 1964. “On the deformation and drag of a falling viscous drop at low Reynolds number”. *Journal of Fluid Mechanics*, **18**, pp. 466–476.
- [5] Clift, R., Grace, J., and Weber, M., 1978. *Bubbles, drops and particles*. Academic Press, New York.
- [6] Ishii, M., and Zuber, N., 1979. “Drag coefficient and relative velocity in bubbly, droplet or particulate flows”. *American Institute of Chemical Engineers Journal*, **25**, pp. 843–855.
- [7] Park, J., Drew, R., and Lahey, R., 1998. “The analysis of void wave propagation in adiabatic monodispersed bubbly two-phase flows using an ensemble-averaged two-fluid model”. *International Journal of Multiphase Flow*, **24**, pp. 1205–1244.
- [8] Leon-Becerril, E., and Liné, A., 2001. “Stability analysis of a bubble column”. *Chemical Engineering Science*, **56**, pp. 6135–6141.
- [9] Moore, D., 1963. “The boundary layer on a spherical gas bubble”. *Journal of Fluid Mechanics*, **16**, pp. 161–176.
- [10] Batchelor, G., 1971. *An Introduction to Fluid Dynamics*, 2nd ed. Cambridge University Press.
- [11] Étienne, S., and Pelletier, D., 2005. “A general approach to sensitivity analysis of fluid-structure interactions”. *Journal of fluids and structures*, **21**, pp. 169–186.
- [12] Schenk, O., and Gärtner, K., 2004. “Solving unsymmetric sparse systems of linear equations with PARDISO”. *Journal of Future Generation Computer Systems*, **20(3)**, pp. 475–487.
- [13] Schenk, O., and Gärtner, K., 2006. “On fast factorization pivoting methods for symmetric indefinite systems”. *Electronic Transactions on Numerical Analysis*, **23**, pp. 158–179.
- [14] Roig, V., and Larue de Tourmelaine, A., 2006. “Measurement of interstitial velocity of homogeneous bubbly flows at low to moderate void fraction”. *Journal of Fluid Mechanics*, **572**, pp. 87–110.



STATE SPACE RECONSTRUCTION OF EXPERIMENTAL TIME SERIES OF BISTABLE FLOW ON A TUBE BANK

Alexandre Vagtinski de Paula

Programa de Pós-Graduação em Eng. Mecânica
Universidade Federal do Rio Grande do Sul
Rua Sarmento Leite, 425, 90050-170
Porto Alegre, RS, Brazil
Email: vagtinski@mecanica.ufrgs.br

Sergio Viçosa Möller¹

Programa de Pós-Graduação em Eng. Mecânica
Universidade Federal do Rio Grande do Sul
Rua Sarmento Leite, 425, 90050-170
Porto Alegre, RS, Brazil
Email: svmoller@ufrgs.br

ABSTRACT

This paper presents a study of the bistable phenomenon which occurs in the turbulent flow impinging on a tube bank. Time series are obtained with the constant temperature hot wire anemometry technique in an aerodynamic channel. The state space of the simplified geometry of two side-by-side circular cylinders is reconstructed with both axial and transversal velocity components, and show that, although distorted, the resultant geometric object are similar in appearance. The flow after two rows tube bank of triangular arrangement are also studied and its experimental time series present a bistable characteristic, where the state space reconstruction presents a similar behavior with the simplified geometry of two side-by-side circular cylinders.

NOMENCLATURE

A_c	Critical limit
$C_L(\tau)$	Autocorrelation function
d	Dimension
d_E	Embedding dimension
D	Diameter - m
f	Frequency - Hz
f_s	Sampling frequency - Hz
j	Index
k	Data point
P	Pitch - m
R_A	Typical size of the attractor
$R_d(k)$	Distance between a given point and its nearest
Re	Reynolds number ($u \cdot D / \nu$)
R_T	Critical distance
S	Strouhal number ($f \cdot D / u$)
$s(n)$	Scalar measurement
\bar{s}	Mean value
t	Time - s
u	Reference velocity - m/s
ν	Kinetic viscosity - m^2/s

x Generic distance of measurement - m
 $x(n), y(n), z(n)$ Coordinates

INTRODUCTION

Banks of tubes or rods are found in several engineering applications, like nuclear and process industries, being the most common geometry used in heat exchangers. Tube banks are the usual simplification for fluid flow and heat transfer in the study of shell-and-tube heat exchangers, where the coolant is forced to flow transversely to the tubes by the action of baffle plates. The cross flow passing a tube in a bank is strongly influenced by the presence of the neighboring tubes. The turbulent flow impinging on two circular cylinders placed side-by-side presents a floppy and random phenomenon that changes the flow mode. This behavior is called in the literature as bistable flow and is characterized by a wide near-wake behind one of the cylinders and a narrow near-wake behind the other, which generates two dominant Strouhal numbers, each one associated with one of the two wakes formed: the wide wake is associated with a lower Strouhal number and the narrow wake with a higher one.

New studies performed with new techniques are justified to better understand this complex phenomenon, since the flow induced vibration and structure-fluid interaction are very dependent of the arrangement or configuration of the cylinders and since bistability can be an additional excitation mechanism on the tubes.

Inside tube banks with square arrangements was observed the presence of instabilities, generated after the second row of the tube bank, which propagates to the interior of the bank [1, 2]. This study were performed by using wavelets transforms and flow visualizations, and the three-dimensional behavior of the flow is responsible for a mass redistribution inside the bank that leads to velocity values not expected for the studied geometry, according to the known literature. This behavior was also observed after the second row of a tube bank with triangular

Address all correspondence to this author¹

arrangement [3]. This process is associated to the phenomenon of bistability known in the flow on two cylinders side-by-side.

Experimental investigations on normal triangular tube arrays has been explored in literature [4, 5, 6], and a series of different techniques has been applied to understand the complex and unsteady behavior of the turbulent flow impinging on the tubes. The structure of the flow on this configuration for $P/D=1.58$ is unstable and the jet switching is observed even when geometric symmetry is broken. The surface pressure fluctuations observed in a jet switching is correlated along the cylinder, although, the special behavior is complex. However, vortex shedding and acoustic resonance are well correlated.

Chaotic time series are observed routinely in experiments on physical systems and in observations in the field [7]. Although unknown, the study of the dynamic process of bistability can reveal new features about the chaotic behavior of these time series, and the first step of this process is to reconstruct the state space of the phenomenon in an appropriate embedding dimension.

A way to reconstruct a near-equivalent attractor from single-variable time series was suggested from their derivatives to know the dynamics of a system [8]. Another theorem shows that it is not necessary to calculate the derivatives to form a coordinate system to capture the structure of orbits in phase space [9]. It could directly use lagged variables to create a vector in d dimensions [7]. Although the new geometric object is distorted, it is similar in appearance, and the topological properties are preserved.

A method to calculate the average exponential rates of divergence or convergence of nearby orbits in state space is through the Lyapunov exponents of the state space reconstructed [10]. Any system containing at least one positive Lyapunov exponent is defined to be chaotic, with the magnitude of the exponent reflecting the time scale on which system dynamics become unpredictable, and the technique of state space reconstruction with time delay coordinates can provide a basis to obtain from such a time series an attractor whose Lyapunov spectrum is defined to that of the original attractor.

THE BISTABLE EFFECT

According to the literature, the cross steady flow trough circular cylinder with same diameter (D) placed side-by-side can present a wake with different modes, depending on the pitch-to-diameter ratio P/D [11]. For intermediate pitch ratios ($1.2 < P/D < 2.0$), the flow is characterized by a wide near-wake behind one of the cylinders and a narrow near-wake behind the other, as shown schematically in Fig. 1a and Fig. 1b. This phenomenon generates two dominants vortex-shedding frequencies, each one associated with a wake: the wide wake is associated with a lower frequency and the narrow wake with a higher one. The switching of the gap flow, which is biased toward the cylinder, from one side to other

at irregular time intervals, is therefore known as a flip-flopping regime or bistable flow regime [12].

Figure 1 presents a link between the wakes patterns (Figs. 1a and 1b) and a velocity measurement technique, performed by the hot wire anemometry technique (Fig. 2). The velocity signals are measured downstream the cylinders, along the tangent to their internal generatrices, where one switching mode can be observed (modes 1 and 2). Previous studies show that this pattern is independent of Reynolds number, and it is not associated to cylinders misalignment or external influences, suggesting that bistability is an intrinsically feature of the flow. The transition between the asymmetric states is completely random and it is not associated with a natural frequency. Through dimensional analysis, it was observed that the mean time between the transitions is on order 10^3 times longer than vortex shedding period, and the mean time intervals between the switches decreases with the increasing of Reynolds number. There is no correlation between the bistable feature and the vortex shedding, due to the fact that Strouhal numbers are relatively independent from the Reynolds numbers [13].

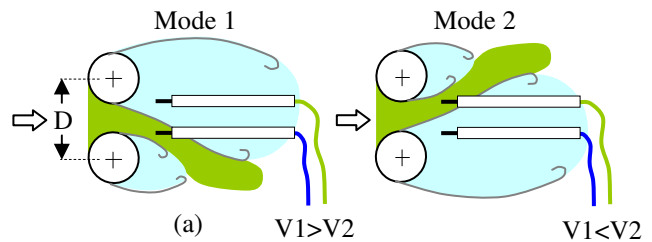


FIGURE 1: BISTABILITY SCHEME FOR (a) MODE 1 AND (b) MODE 2.

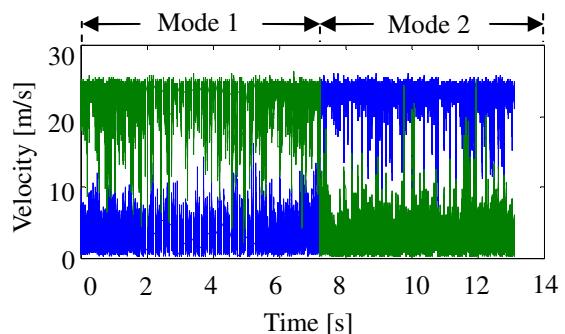


FIGURE 2: CHARACTERISTIC HOT WIRE ANEMOMETRY SIGNALS OF FIG. 1.

FUNDAMENTALS

Experimental data typically consist of discrete measurements of a single observation. In the literature [14, 9, 15], a state space reconstruction of experimental time series can be performed using time-delay coordinates, from scalar measurements $s(n) = s(t_0 + n\tau)$.

The main idea is that the lagged variables $s(n+T) = s(t_0 + (n+T)\tau)$ can be used to form a coordinate system to capture the structure or orbits in phase space, where T is some integer to be determined.

The required coordinates can be provided by using a collection of time lags to create a vector in d dimensions $y(n) = [s(n), s(n+T), s(n+2T), \dots, s(n+(d-1)T)]$.

By selecting a variable, e.g. $x(n)$, of an attractor with coordinates $[x(n), y(n), z(n)]$, and using a 3-vector of time delayed variables $[x(n), x(n+dT), x(n+2dT)]$ in R^3 , a geometric object similar in appearance to the original geometric portrait of the attractor is observed, though somewhat distorted. This distortion is due to the difference between $[x(n), x(n+dT), x(n+2dT)]$ and $[x(n), y(n), z(n)]$.

The procedure of choosing sufficiently large dimension d is called as embedding, and the selected dimension is called an embedding dimension d_E . For any large enough dimension achieved ($d \geq d_E$) will also provide an embedding.

By using delay coordinates to reconstruct an attractor, an embedding of the original attractor is obtained for any sufficiently large dimension d and almost any choice of time delay τ [9]. However, to obtain accurate properties of the attractor and to extract physics from the data, this estimation requires some care in choosing these two parameters.

a) Selecting the time delay

If the time delay T is chosen too small, the coordinates $s(n+jT)$ and $s(n+(j+1)T)$ will not be distinguished from each other, since their numerical values are closed, and the reconstructed attractor will be compressed around the diagonal $y = x$. In other words, there will be a linear dependence between the delayed values, which does not occur with the real components x and y . On the other hand, if T is chosen too large, the lagged coordinates will be completely independent of each other in a statistical sense, and the reconstructed attractor will cover the whole phase space. A time delay T of the order of the *autocorrelation function* $C_L(\tau)$ can be computed, and looking for the time lag where $C_L(\tau)$ first passes through zero.

The autocorrelation function is defined as

$$C_L(\tau) = \frac{\frac{1}{N} \sum_{m=1}^N [s(m+\tau) - \bar{s}][s(m) - \bar{s}]}{\frac{1}{N} \sum_{m=1}^N [s(m) - \bar{s}]^2}, \quad (1)$$

where $\bar{s} = \frac{1}{N} \sum_{m=1}^N s(m)$.

This criterion ensures that the next coordinate points are linearly independent, but not completely uncorrelated, providing a good hint of a choice for T . However, this only expresses the independence of the coordinates in a linear fashion.

b) Selecting the embedding dimension

The goal of the reconstruction theorem is to provide a Euclidean space R^d large enough, so that the set of points of dimension d_A can be unfolded without ambiguity [7].

However, depending on the characteristics of the attractor, a reconstruction in a space dimension smaller than R^d may be sufficient to reveal all its metric structure.

Since the dimension of an attractor associated with an experimental data is not known *a priori*, a dose of experimentation is necessary to evaluate and interpret the obtained results.

A method was proposed to determine the minimum size necessary to embed an attractor [16]. This task can be performed by counting the number of false neighbors for each of its points. When the number of false neighbors drops to zero, the attractor will have been sufficiently "unfolded", and it is possible to identify the smaller immersion able to represent it adequately.

In this work, this method called *false nearest neighbors* was applied to choose the embedding dimensions of the reconstructions. False neighbors are identified by two concurrent tests. Let $R_d^2(k)$ be the square of the distance between a given point k and its nearest $k^{(1)}$ in a reconstructed attractor with dimension d . If $k^{(1)}$ is a false neighbor, $R_d^2(k)$ probably greatly increase when going from dimension d to dimension $d+1$. Thus, $k^{(1)}$ is a false neighbor if

$$\left[\frac{R_{d+1}^2(k) - R_d^2(k)}{R_d^2(k)} \right]^{1/2} > R_T, \quad (2)$$

where R_T is a critical distance.

However, this criterion is a necessary condition but not sufficient to identify the false neighbors. Due to the finite number of points used in practice, the distance to the nearest neighbor point may be on the order of size of the attractor. Let R_A be a typical size of the attractor, then $R_d(k) \sim R_A$ and $R_{d+1}(k) \sim 2R_A$ for a false neighbor. Thus, a further condition may be established, so that

$$\frac{R_{d+1}(k)}{R_A} > A_C, \quad (3)$$

where A_C is a critical limit.

A neighbor is considered false if it satisfies both conditions (2) and (3).

EXPERIMENTAL APPARATUS

The aerodynamic channel used in the experiments is made of acrylic, with a rectangular test section of 0.146 m height, width of 0.193 m and 1.02 m of length (Fig. 3a). The air is impelled by a centrifugal blower of 0.64 kW, and passes through two honeycombs and two screens, which reduce the turbulence intensity to about 1% in the test section. Upstream the test section, placed in one of the side walls, a Pitot tube measures the reference velocity of the non-perturbed flow. Data acquisition is performed by a 16-bit A/D-board (NATIONAL INSTRUMENTS 9215-A) with USB interface. The acquisition frequency of time series was of 1 kHz, and a low-pass filter of 300 Hz was used to avoid aliasing. The circular cylinders, with external diameter of 25.1 mm, are made of Polyvinyl chloride (PVC), are rigidly attached to the top wall of test section and their extremities are closed. The probe support is positioned with 3D transverse system placed 200 mm

downstream the outlets. The measurements were performed aligning the probes along the tangent to the external generatrices of the tubes. The mean error of the flow velocity determination with a hot wire was about +/- 3%. The Reynolds number of the experiment is 21,000, computed with the tube diameter and the reference velocity of 12.9 m/s. The velocity of the flow and its fluctuations are measured by means of a DANTEC StreamLine constant hot-wire anemometry system. One double straight/slant hot wire probe (type DANTEC 55P71 Special) and a single hot wire probes (type DANTEC 55P11) were used in the experiments, where their positions are show in Fig. 3b and Fig. 3c, respectively. The double probe has a straight wire perpendicular to the main flow, and a slant wire 45° with the probe axis. The single probe has the wire perpendicular to the main flow.

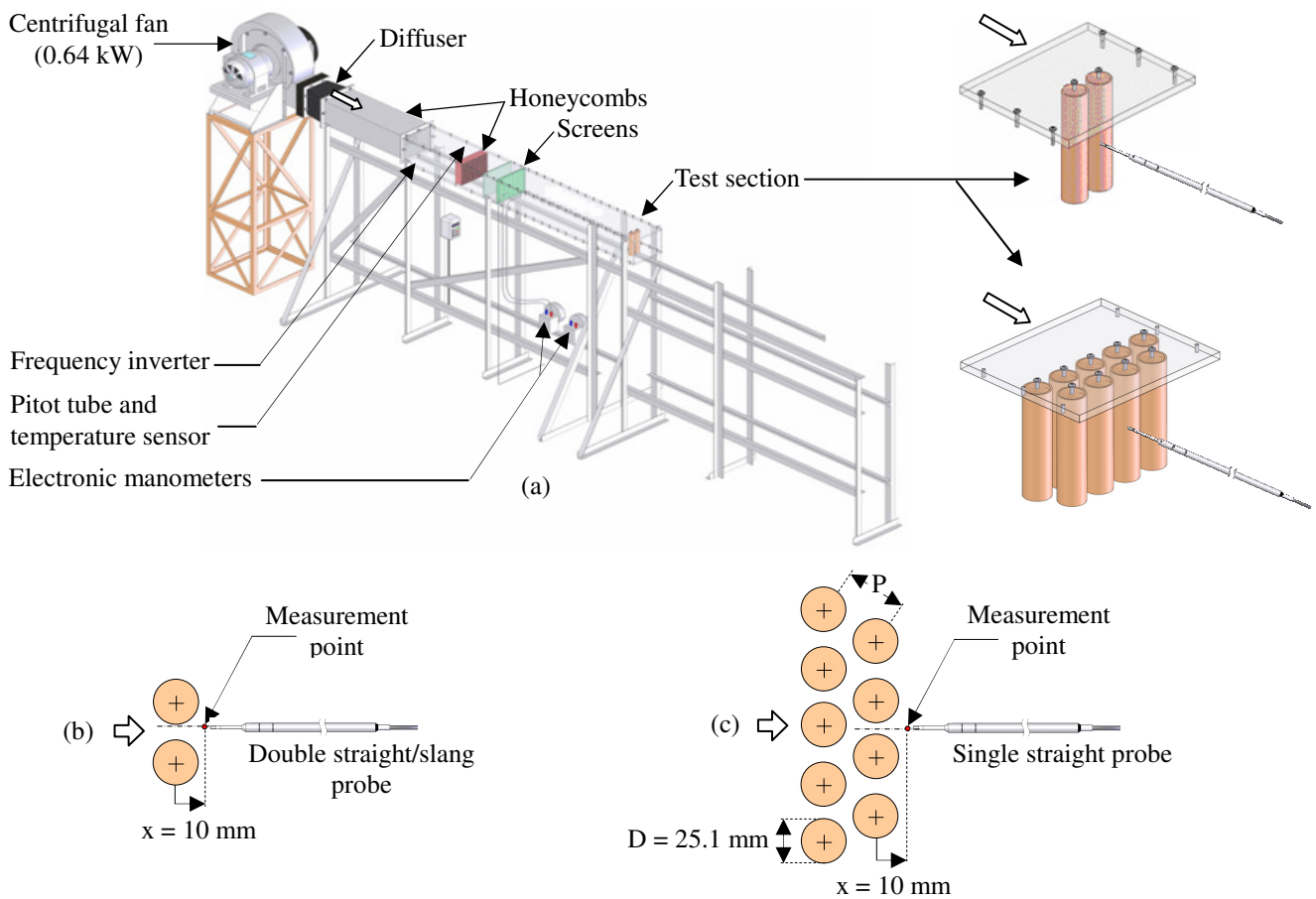


FIGURE 3: SCHEMATIC VIEWS: (a) AERODYNAMIC CHANNEL. PROBE POSITIONS FOR: (b) TWO SIDE-BY-SIDE CIRCULAR CYLINDERS AND (c) TWO ROWS TUBE BANK.

RESULTS

The time series of axial velocity and transversal velocity of the flow on the simplified geometry of two side-by-side circular cylinders are shown in Fig. 4a and Fig. 4b, respectively, where some changes between two distinct velocity levels are observed. The autocorrelation function for both velocity signals are shown in Fig. 4c and Fig. 4d, respectively, where a similar behavior is observed. In addition, the numerical values when these functions first

passes through zero are nearly equal. The state space reconstructions of the axial velocity for $d = 2$ and $d = 3$ are presented in Fig. 5a and Fig. 5b, respectively. For the transversal velocity component, the reconstructions for the same embedding dimensions are presented in Fig. 6a and Fig. 6b, respectively. Although distorted, the resultant geometric objects are similar in appearance, what suggests that the target attractor is well reconstructed.

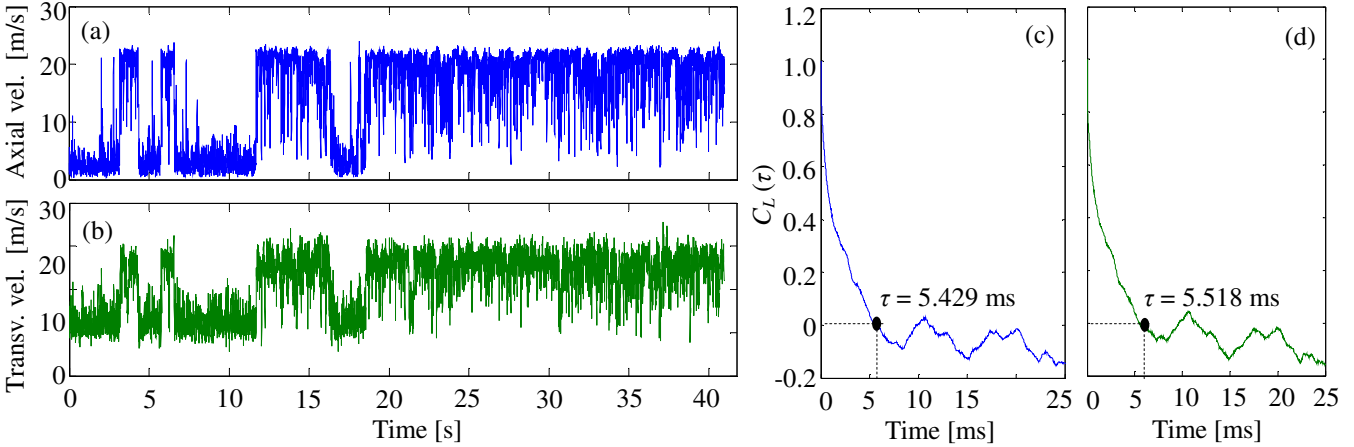


FIGURE 4: EXPERIMENTAL TIME SERIES OF BISTABLE FLOW FOR TWO SIDE-BY-SIDE CIRCULAR CYLINDERS: (a) AXIAL VELOCITY AND (b) TRANSVERSAL VELOCITY. CHOOSING THE AUTOCORRELATION FUNCTIONS FOR THE TIME DELAY: (c) AXIAL VELOCITY AND (d) TRANSVERSAL VELOCITY.

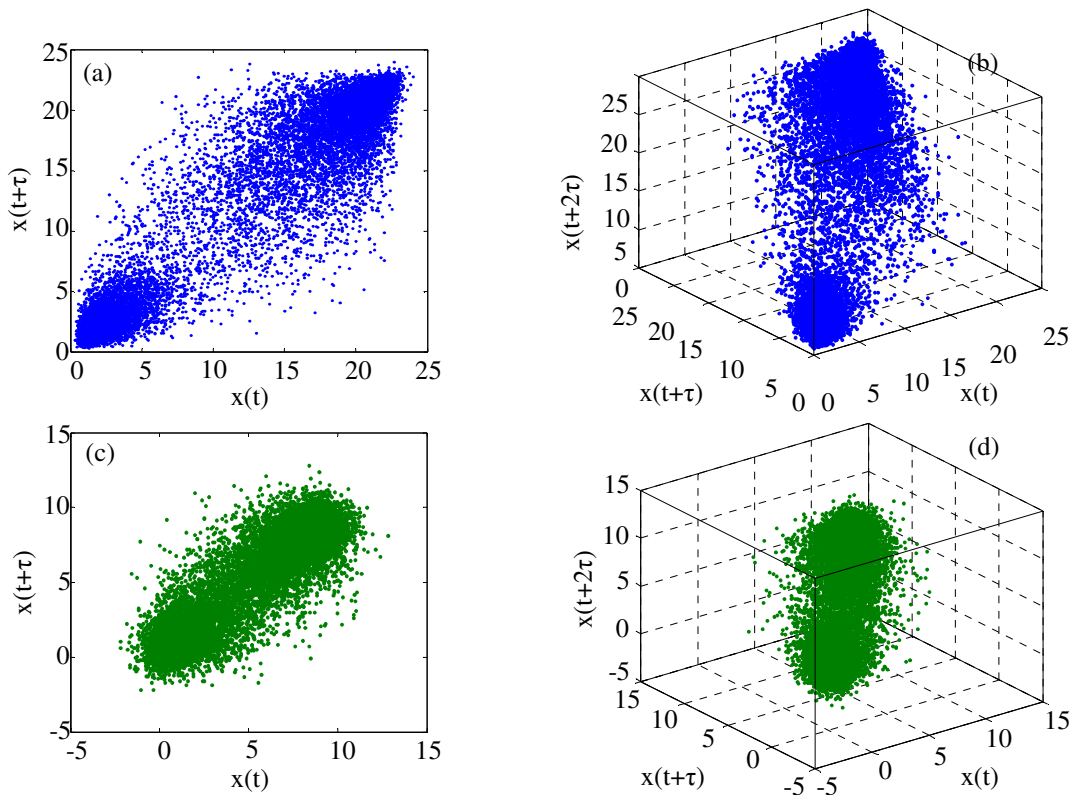


FIGURE 5: STATE SPACE RECONSTRUCTIONS FOR TWO SIDE-BY-SIDE CIRCULAR CYLINDERS: (a) AXIAL VELOCITY WITH $d = 2$, (b) AXIAL VELOCITY WITH $d = 3$, (c) TRANSVERSAL VELOCITY WITH $d = 2$ AND (d) TRANSVERSAL VELOCITY WITH $d = 3$.

A comparison between the reconstructions of the state space of both velocity components with $d = 2$ (Fig. 5a and Fig. 5d) and the components observed as an ordered pair of data (Fig. 6) show a qualitatively similar. Although the points are dispersed over a large area, two concentrations are observed in all cases, showing that the bistable

characteristic of the flow is preserved not only in the phase space reconstructions performed, but also when the velocity components are observed together. In this case, the path or temporal trajectory of the flow in the measurement plan is observed.

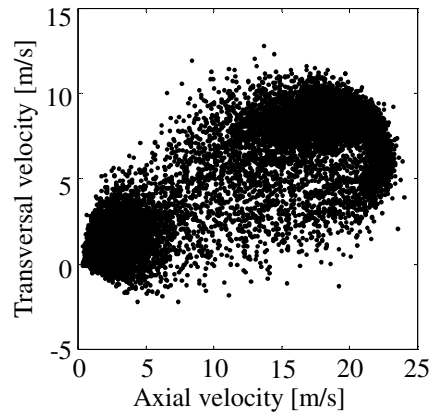


FIGURE 6: AXIAL AND TRANSVERSAL VELOCITY COMPONENTS OBSERVED AS AN ORDERED PAIR OF DATA.

The flow after two rows tube bank of triangular arrangement is also studied and its experimental time series present a bistable characteristic (Fig. 7a), with changes in the mean velocity levels. The autocorrelation function for the signal is shown in Fig. 7b. The state space reconstructions of the axial velocity for $d = 2$ and $d = 3$ are shown in Fig. 8a and Fig. 8b, respectively, and presents a

similar behavior with the simplified geometry of two side-by-side circular cylinders.

Two areas of concentration points are observed in all reconstructions.

A sensible dependence in the choice of time delay was observed in the reconstruction process.

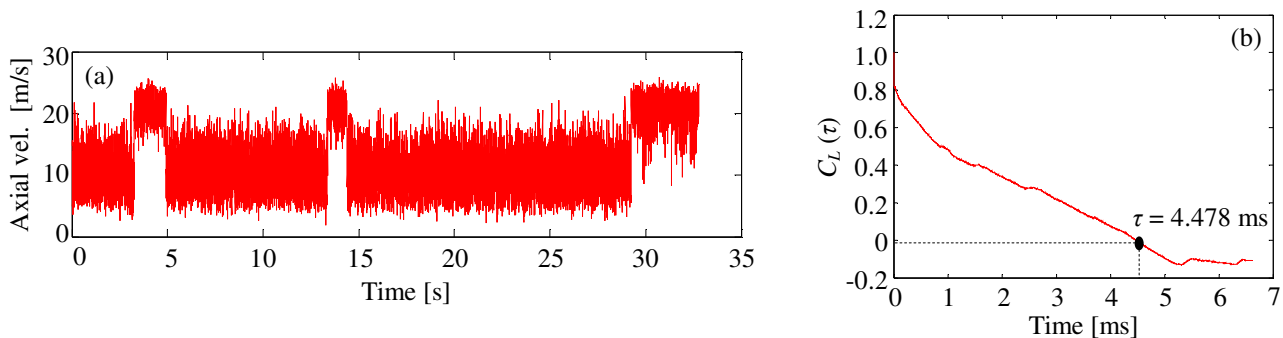


FIGURE 7: (a) EXPERIMENTAL TIME SERIES OF BISTABLE FLOW FOR TWO ROWS TUBE BANK. (b) CHOOSING THE TIME DELAY FROM THE AUTOCORRELATION FUNCTIONS.

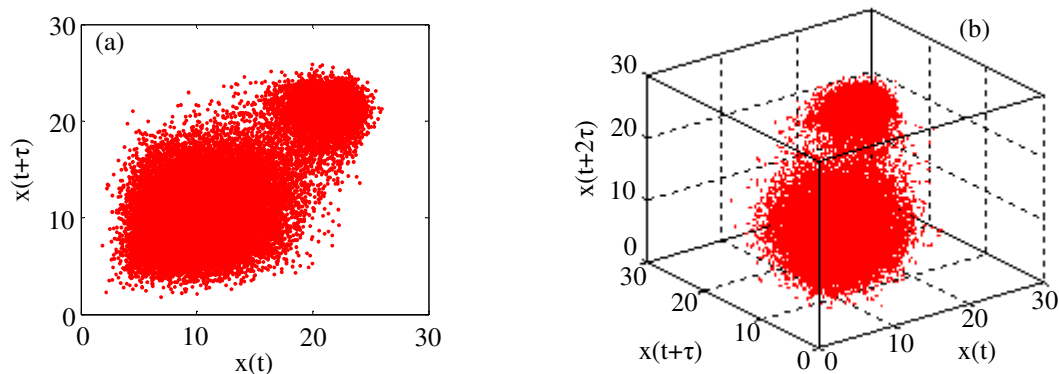


FIGURE 8: STATE SPACE RECONSTRUCTIONS FOR TWO ROWS TUBE BANK: (a) AXIAL VELOCITY WITH $d = 2$ AND (b) AXIAL VELOCITY WITH $d = 3$.

CONCLUSIONS

This work presents a study about the bistable phenomenon on the simplified geometry of two side-by-side circular cylinders and on two rows tube bank. Time series of the phenomenon under study are obtained with an experimental technique and used as input data to perform a state space reconstruction.

The state space of the simplified geometry of two side-by-side circular cylinders is reconstructed with both axial and transversal velocity components, and show that, although distorted, the resultant geometric object are similar in appearance. A comparison between the reconstructions of the state space of both velocity components with $d = 2$ and the components observed as an ordered pair of data, to observe the path or temporal trajectory of the flow in the measurement plan, showed that they are qualitatively similar.

The flow after two rows tube bank of triangular arrangement show the present of bistability, and the state space reconstruction presents a similar behavior with the simplified geometry of two side-by-side circular cylinders.

Two areas of concentration points are observed in all reconstructions, and a sensible dependence in the choice of time delay was observed in the reconstruction process.

ACKNOWLEDGMENTS

Authors gratefully acknowledge the support by The National Council for Scientific and Technological Development (CNPq), Ministry of Science and Technology (MCT), Brazil.

Alexandre V. de Paula thanks also the CNPq for granting him a fellowship.

REFERENCES

- [1] Olinto, C. R.; Indrusiak, M. L. S.; Endres, L. A. M. and Möller, S. V., 2006, "Experimental Study of the Bistable Flow in Tube Arrays". *Journal of the Brazilian Society of Mechanical Engineering*, São Paulo, v. XXVIII, p. 221-229, 2006.
- [2] Olinto, C. R.; Endres, L. A. M. and Möller, S. V., 2009, "Experimental study of the characteristics of the flow in the first rows of tube banks". *Nuclear Engineering and Design*, v. 239, p. 2022-2034, 2009.
- [3] De Paula, A.V.; Endres, L.A.M. and Möller, S.V., 2009, "Some features of the turbulent flow in tube banks of triangular arrangement", In: *SMiRT 20 - 20th International Conference on Structural Mechanics in Reactor Technology*, 2009, Toronto. *Transactions of SMiRT 20*.
- [4] Mahon, J., Meskell, C. 2008, Effect of acoustic resonance on fluidelastic instability in normal triangular tube arrays, *Proceedings of Flow Induced Vibration, 9th International Conference on Flow-Induced Vibrations*, Prague, Czech Republic.
- [5] Mahon, J., Meskell, C. 2009, Surface pressure distribution survey in normal triangular tube arrays, *Journal of Fluids and Structures*, Vol. 25, pp. 1348-1368.
- [6] Mahon, J., Cheeran, P., Meskell, C. 2010, Spanwise correlation of surface pressure fluctuations in heat exchanger tube arrays, *Proceedings of the ASME 2010 Fluids Engineering Summer Meeting*, Montreal, Canada.
- [7] Abarbanel, H.D.I., Brown, R., Sidorowich, J.J. and Tsimring, L.S., 1993, "The analysis of observed chaotic data in physical systems", *Reviews of Modern Physics*, Vol. 65, pp. 1331-1392.

- [8] Packard, N.; Crutchfield, J.; Farmer, D. and Shaw, R., 1980, "Geometry from a time series". *Physical Review Letters*, Vol. 45, pp. 712-715.
- [9] Takens, F., 1981, "Detecting strange attractors in turbulence", *Lecture Notes in Mathematics*, Vol. 898, pp. 366-381.
- [10] Wolf, A., Swift, J., Swinney, H., Vastano, J., 1985, "Determining lyapunov exponents from a time series", *Physica 16D*, North-Holland, Vol. 285, pp. 285-317.
- [11] Sumner, D., Wong, S.S.T., Price, S.J. and Païdoussis, M.P., 1999, "Fluid behavior of side-by-side circular cylinders in steady cross-flow", *Journal of Fluids and Structures*, Vol. 13, pp. 309-338.
- [12] Bearman, P.W. and Wadcock, A.J., 1973, "The interaction between a pair of circular cylinders normal to a stream", *Journal of Fluid Mechanics*, Vol. 61, Part 3, pp. 499-511.
- [13] Kim, H.J. and Durbin, P.A., 1988, "Investigation of the flow between a pair of circular cylinders in the flopping regime", *Journal of Fluid Mechanics*, Vol. 196, pp. 431-448.
- [14] Mañé, R., 1981, "On the dimension of the compact invariant sets of certain nonlinear maps", *Lecture Notes in Mathematics*, Springer-Verlag, Vol. 898, pp. 230-242.
- [15] Sauer, T., Yorke, J.A. and Casdagli, M., 1991, "Embedology", *Journal of Statistical Physics*, Vol. 65, pp.579-616.
- [16] Kennel, M.B., Brown, R. and Abarbanel, H D I., 1992, "Determining embedding dimension for phase-space reconstruction using a geometrical construction", *Physical Review A*, Vol. 45, No 6, pp. 3403-3411.



IDENTIFICATION OF MECHANISMS UNDERLYING PERIODIC FORCES IN A TUBE ARRAY SUBJECTED TO TWO-PHASE CROSS-FLOW

Eddy S. Perrot

BWC/AECL/NSERC Chair of Fluid-
Structure Interaction, Department of
Mechanical Engineering
École Polytechnique
Montréal, QC, Canada

Njuki Mureithi¹

BWC/AECL/NSERC Chair of Fluid-
Structure Interaction, Department of
Mechanical Engineering
École Polytechnique
Montréal, QC, Canada

Michel Pettigrew

BWC/AECL/NSERC
Chair of Fluid-Structure
Interaction Department of
Mechanical Engineering,
École Polytechnique,
Montréal, QC, Canada

ABSTRACT

The present work addresses the question of the fluid dynamics origin of period forces measured in a normal triangular array subjected to two-phase cross-flow. The question of the origin of periodicities in two-phase cross-flow is an important fundamental question. Knowledge of the origin of these forces is an important starting point for the development of correlations or models for the estimation of force frequencies and magnitudes. In single phase flow, periodic forces are commonly associated with vorticity shedding or shear layer oscillations within the tube array. These mechanisms are, however, absent or only poorly defined for two-phase flows.

Detailed flow measurements, employing multiple optical probes, have been conducted in a normal triangular tube array having pitch spacing $P/D=1.5$. Correlation analysis with simultaneously measured fluid forces confirmed the existence of two fundamental excitation mechanisms generating (nearly) period forces. The first is a quasi-constant frequency bundle scale mechanism while the second we call a slug 'shedding' mechanism having a frequency dependent on flow velocity.

INTRODUCTION

Flow periodicities in tube arrays are known to be an important source of excitation in cross-flow. For single phase flows, the flow periodicities have been extensively measured and maps of associated Strouhal numbers

drawn, [1]. For a given tube array, the risk of periodicity induced excitation can be estimated by investigating the possibility of resonance between tube natural frequencies and the measured frequencies. It is interesting to note that the origin and nature of these flow periodicities has not been investigated in detail although it is generally known that they must be related to vorticity shedding and/or free shear layer oscillations or instabilities for single phase flows.

Until recently, it was believed that two-phase cross-flows could not generate well defined periodicities – for which a Strouhal number can be defined – as in the case of single phase flows; (we remark, however, that internal two-phase flows are known to undergo transition into the highly periodic slug flow pattern following a destabilization of the bubbly flow regime). Two-phase cross-flow induced-vibration has mainly been attributed to two mechanisms – random turbulence excitation and fluidelastic instability, [2]. Recently, however, a third mechanism, associated with quasi-periodic excitations has been observed in triangular tube bundles [3,4]. These quasi-periodic forces were also shown to be the mechanism driving the flexible tube dynamics in the normal triangular tube bundle [4,5]. Although these forces were precisely characterized, e.g. in [6], their exact origin is not yet understood. A goal of the present work is to shed some light on the nature and origin of these quasi-periodic forces. To this end, detailed experiments using a normal triangular tube bundle are carried out. Fluid force and flow measurements are carried out and a correlation

Address all correspondence to this author¹

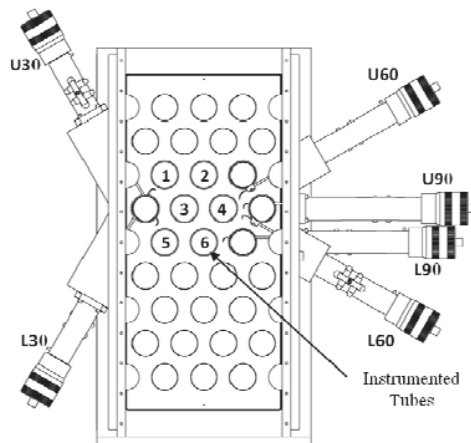


FIGURE 1: TEST SECTION AND OPTICAL PROBES.

analysis done. Flow visualization is additionally done employing high speed photography for additional insight into the nature and structure of the flow field under different flow conditions.

EXPERIMENTAL SETUP AND TEST PROCEDURE

To precisely define the two-phase flow several important parameters are first defined here. To identify the flow conditions in the experimental study, the homogeneous void fraction β was primarily used. However, the local void fraction ε was also measured using optic probes. The latter defines more precisely the local two-phase flow. The homogeneous void fraction β and the void fraction ε are defined as:

$$\beta = \frac{Q_g}{Q_g + Q_l} \quad (1)$$

$$\varepsilon = \frac{V_g}{V_g + V_l} \quad (2)$$

where Q_g and Q_l are, respectively, the gas and liquid volumetric flow rates and V_g and V_l the gas and liquid volumes. The pitch velocity U_p which is a convenient reference velocity for tube bundles is also defined as

$$U_p = U_\infty \frac{P}{P - D} \quad (3)$$

where U_∞ is the homogeneous free-stream velocity, P the tube pitch and D the tube diameter.

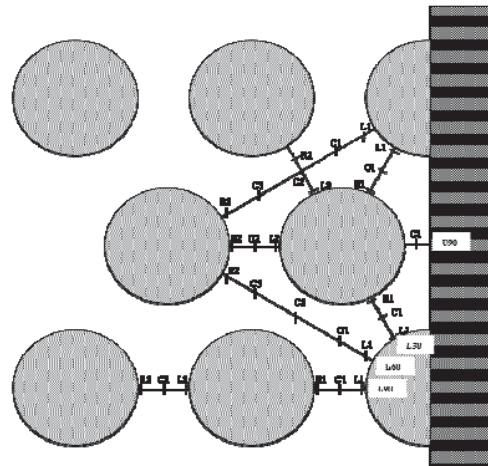


FIGURE 2: OPTICAL PROBE POSITIONS.

The experimental air-water test loop is described in detail in [6]. The key components of the loop include a 30 l/s variable speed pump and a compressed air system supplying up to 500 scfm. The rectangular test section (229x191mm) contains 25 fixed tubes, 10 fixed half-tubes, 6 instrumented tubes and 6 optical fiber probes as shown in Fig. 1. The tubes have a relatively large diameter (38 mm) to allow for detailed flow measurements. The pitch-to-diameter ratio is 1.5 and the array configuration normal triangular. The tubes instrumented with strain gauges are located close to the optical fiber probes to allow measurement of the correlation in the interstitial gaps. The optical fiber probes were installed in six directions, Fig.1. The probe angular positions relative to the drag direction are identified as, lower and upper 60° probes (L60 and U60), lower and upper 90° probes (L90 and U90) and lower and upper 30° probes (L30 and U30). For brevity, primarily results for the L90 position will be presented. Upper and lower correspond to the location of probes in the test section. As the test section is symmetrical the flow path is the same for the probes located in the right or left side of the test section.

Flow measurements using fiber-optic probes were taken at the left position (L), the center position (C), and the right position (R) as shown in Fig.2. Lift and drag forces were simultaneously measured making it possible to compute the correlations between the flow and force measurements. Detailed flow measurements have also been taken every millimeter for the six probes.

Local void fraction, bubble size and bubble velocity are measured using dual fiber optical probes. The local void fraction ε is the ratio of the sum of gas phase immersion time t_{air} to the total measurement time t_{total} ,

$$\varepsilon = \frac{\sum t_g}{t_{total}} \quad (4)$$

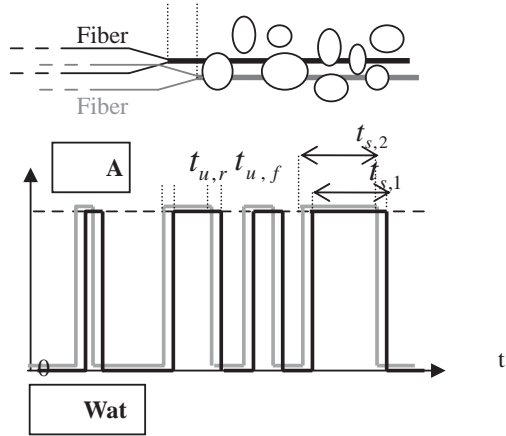


FIGURE 3. BUBBLE VELOCITY (U_b) AND BUBBLE SIZE (s) MEASUREMENTS.

The bubble velocity U_b is the ratio of the distance d between the two fibers (approximately $100 \mu\text{m}$) to the bubble transit time $t_{u,r}$ as illustrated in Fig.3.

$$U_b = \frac{d}{t_{u,r}} \quad (5)$$

In addition to the measurements above, a Mikrotron high speed camera having a frame rate of 2200 frames/s was used for flow visualization.

TWO-PHASE FLOW STRUCTURE FOR 50% VOID FRACTION

For 50% homogeneous void fraction, two tube scale flow regimes were observed. For low velocities (from 0.6 to 1.8 m/s), the flow pattern within the array is bubbly as shown in Fig. 4. Close observation shows that the bubbly flow regime is coupled with a void wave observable at a larger scale.

The void fraction, bubble size and bubble velocity are shown in Fig. 5 for the L90 probe (A1) for the 50% void fraction. The local void fraction reaches a maximum value at the approximate positions $y/D=0.08$ and $y/D=0.42$ from the tube wall. Bubble size and bubble velocity follow approximately the same trend. This suggests that there are two paths preferentially followed by the gas (air) phase. In these paths, the bubble velocity is close to 2 m/s and the bubble size larger than 2 mm.

The observed flow paths are schematically shown in Fig.6. In the figure the spatial distribution of the local void fraction is also shown. The void fraction is seen to be

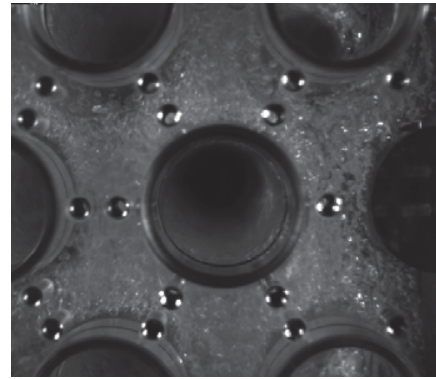


FIGURE 4: LOCAL BUBBLY FLOW for $U_p=1.8 \text{ m/s}$, $\beta=50\%$.

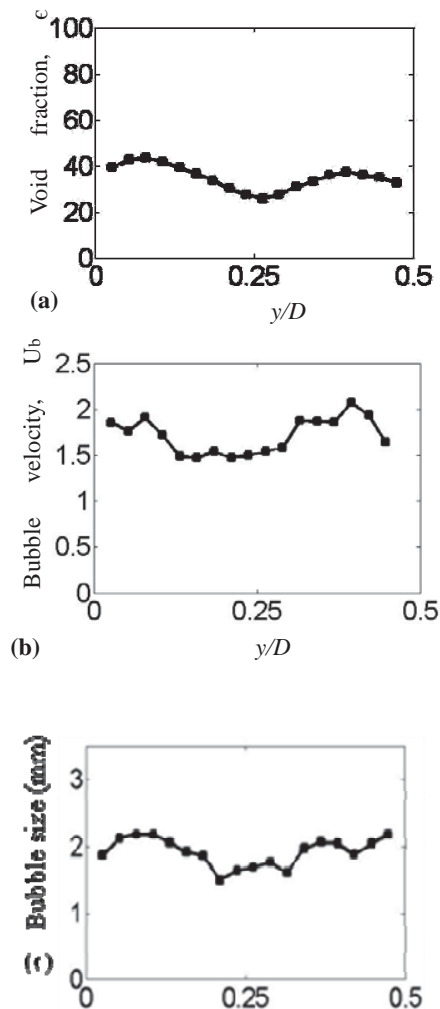


FIGURE 5: (a) VOID FRACTION (b) BUBBLE VELOCITY AND (c) BUBBLE SIZE FOR 1.8 M/S AND $\beta=50\%$, AT POSITION L90.

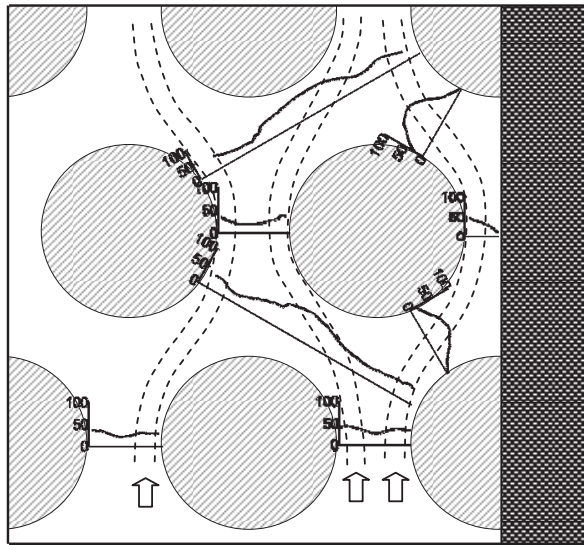


FIGURE 6: DETAILED LOCAL VOID FRACTION MEASUREMENTS AND BUBBLE FLOW PATHS FOR 1.8 M/S AND $\beta=50\%$.

locally higher indicating that the gas (air) phase preferentially flows along these paths.

Fig.7 shows the spatial profiles of the void fraction, bubble size and bubble velocity measured by the L30 probe (A1) along the 30° direction. The void fraction profile shows a single maximum at the approximate position $y/D=0.21$. In this maximum void fraction zone the bubble size is also maximum. The bubble velocity on the other hand decreases from a maximum 0.75 m/s at $y/D=0$ to near zero at the position 0.5 y/D . Hence, the bubbles are faster (up to 0.9 m/s) in the intrados of the flow path and larger in the middle of the flow path (up to 2.0 mm).

The second flow regime observed at 50% homogeneous void fraction may be roughly described as a ‘slug flow’ where the slugs are formed within the open flow lanes in the array. This flow regime was found for instance for a pitch velocity of 3.6 m/s. The flow path of the liquid slugs is sketched together with the detailed void fraction measurements in Fig. 8. While the void fraction profile is similar to that found at 1.8 m/s (Fig.6) the gas flow paths are wider here. Note also that the liquid slugs are travel within the ‘high void fraction’ flow paths.

In Fig. 9 the void fraction, bubble size and bubble velocity are shown for the flow speed of 3.6 m/s for the L90 probe. The void fraction reaches its maximum value for positions close to the wall. Recall that for the velocity of 1.8 m/s, the maximum was observed for the positions $y/D=0.08$ and $y/D=0.42$. Consequently, the air flow is closer to the cylinder walls with the increasing pitch velocity. The bubble size follows a similar trend and

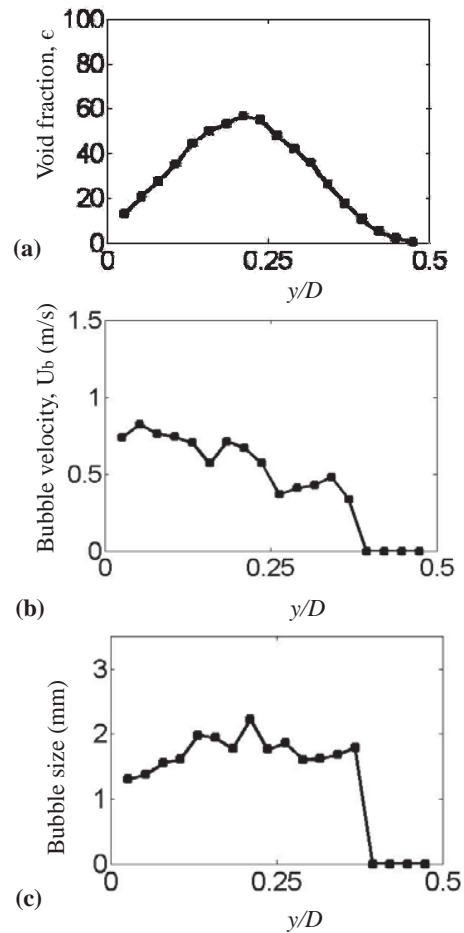


FIGURE 7: (a) VOID FRACTION, (b) BUBBLE VELOCITY AND (c) BUBBLE SIZE FOR L30-A1 FOR 1.8 M/S AND $\beta=50\%$.

reaches a maximum diameter near 1.7 mm. For the L30 probe, the general at 3.6 m/s trend was found to be quite similar to that observed at 1.8 m/s.

We consider next the detailed two-phase flow characteristics for 50% homogeneous void fraction. Bubble size and velocity are shown versus pitch velocity in Fig.10 and Fig.11, respectively. Data for all 90° position measurements are plotted and the average trend shown as a solid line. For homogeneous flow velocities between 0.6 m/s and 3.6 m/s the average bubble size decreases from 2.5 mm to 1.2 mm. The increase in velocity causes a more homogeneous flow and the higher shear forces result in smaller bubbles. Between 0.6 m/s and 3.6 m/s pitch velocity, the bubble velocity increases from 0.5 m/s to 1.7 m/s. For low pitch velocities (up to 1.2 m/s), the average bubble velocity is close to but slightly below the pitch flow velocity, U_p . However, for higher

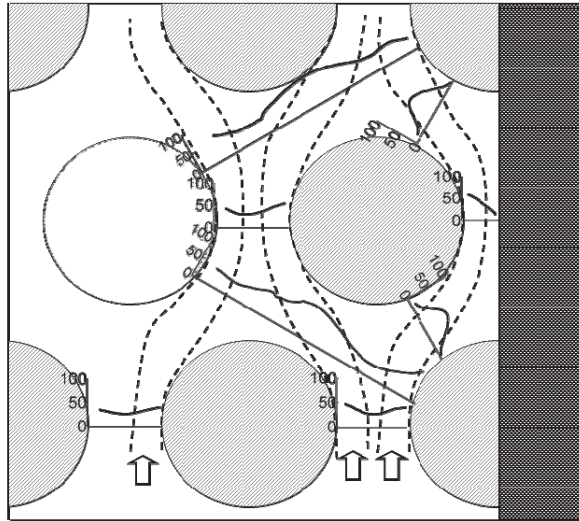


FIGURE 8: DETAILED LOCAL VOID FRACTION MEASUREMENTS AND WATER DROP FLOW PATHS.

flow rates, the bubble velocity is up to two times lower than U_p . This result mainly attests to the complex flow paths within the array where the flow must change direction at every tube row. Note also that the optical probe measurement only captures the component of the bubble velocity normal to the probe – hence an underestimation of the absolute bubble velocity can be expected.

Secondly, for all the test conditions, a peak caused by void waves is observed at low frequencies. The wave velocity seems to be higher than the pitch velocity. These waves consist mainly large air bubbles which appear at higher flow velocities due to increased flow non-uniformity. These large bubbles are not correctly captured by the optical probes because their size is much larger than the average bubble size. The measured bubble velocity may therefore not be fully representative of the average gas phase velocity particularly for high flow rates.

Fluid force measurements were also carried out simultaneously with the flow measurements. Typical PSDs of the lift and drag forces acting on a tube within the bundle are presented in Fig.12. The flow conditions are $\beta=50\%$ and velocity range 0-3.6 m/s. Two well-defined groups of peaks are identifiable. The first is significant from 0.6 m/s to 3.6 m/s and occurs at low and quasi-constant frequencies. The second occurs from 2.4 m/s to 3.6 m/s, and the frequencies are higher and are linearly dependent on flow velocity.

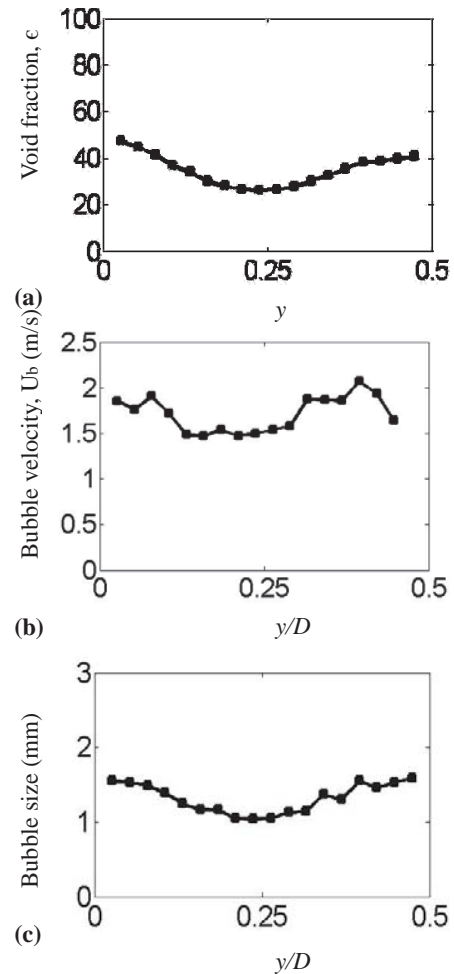


FIGURE 9: (a) VOID FRACTION, (b) BUBBLE VELOCITY AND (c) BUBBLE SIZE FOR L90-A1 AT 3.6 M/S FOR 50% HOMOGENEOUS VOID FRACTION.

For comparison, PSDs of the optical probe signals were also computed. The dominant frequencies in the force and flow spectra are compared in detail in Fig.13. Previous measurements in the same array, [4], are also included as an indicator of repeatability. The frequency data are plotted in two ranges for clarity; a low frequency range in Fig.13(a) and a high frequency range in Fig.13(b), which also corresponds to the two mechanisms suggested above. In Fig.13(a), in the drag direction, the frequencies show a decreasing trend (from 7 Hz to 4 Hz) for velocities up to 1.8 m/s and remain constant at higher velocities up to 3.6 m/s. In the lift direction, the frequencies decrease (from 10 Hz to 5 Hz) up to 1.8 m/s. However, above 1.8 m/s, the frequencies increase up to approximately 20 Hz. The latter increasing trend suggests

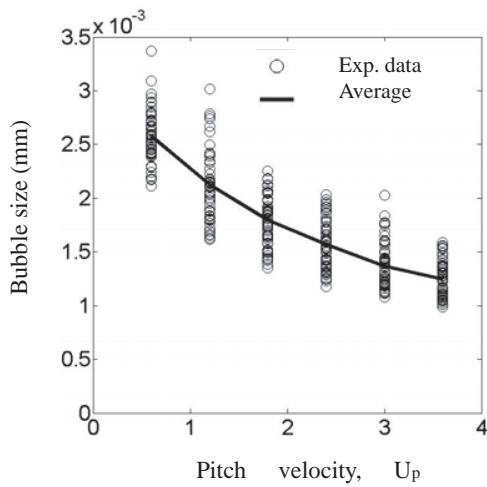


FIGURE 10: BUBBLE SIZE VERSUS PITCH VELOCITY AT 50% HOMOGENEOUS VOID FRACTION FOR 90° PROBES.

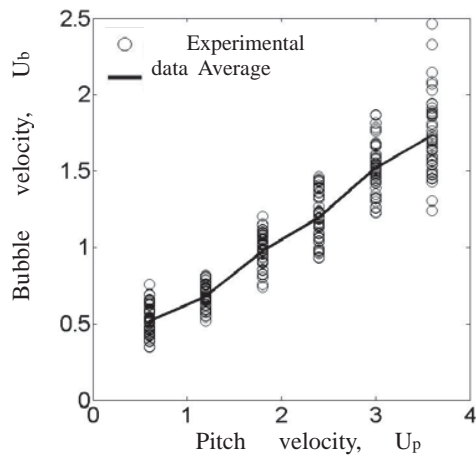


FIGURE 11: BUBBLE VELOCITY VERSUS PITCH VELOCITY AT 50% HOMOGENEOUS VOID FRACTION FOR 90° PROBES.

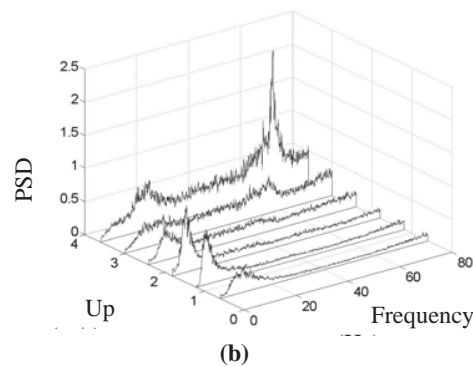
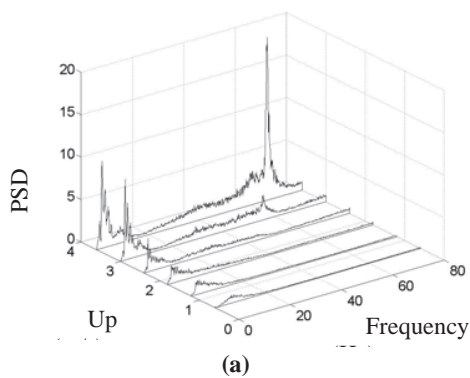


FIGURE 12: TYPICAL PSD SPECTRA FOR 50% HOMOGENEOUS VOID FRACTION (a) IN THE DRAG AND (b) IN THE LIFT DIRECTIONS.

a different mechanism in the lift direction above 1.8 m/s. The dominant frequencies found in the flow spectra are constant around 4 Hz for all velocities. Above 1.8 m/s, the flow frequencies show the same trend as the force frequencies in the drag direction. In the high frequency range, Fig.13(b), all the peak frequencies in the force and flow spectra are essentially identical and show a linear dependence on pitch velocity.

The results of Fig.13 support the observation of both localized and bundle scale flow mechanisms underlying the measured fluid force fluctuations. This was further confirmed by computations of spectral coherence between the fluid forces and flow fluctuations which showed the highest coherence at the peak frequencies identified above.

TWO-PHASE FLOW STRUCTURE FOR 80% HOMOGENEOUS VOID FRACTION

A second series of measurements was conducted for 80% homogeneous void fraction. For this higher void fraction, two main flow regimes were also observed. For low velocities (from 1.5 to 3.6 m/s), the flow regime is intermittent and dominated by bundle scale void wave fluctuations. For higher velocity (from 4.5 to 8.0 m/s), the flow structure at the tube scale is highly random. However, a large liquid recirculation zone is observed in the tube wakes. This recirculation zone is found to exhibit nearly periodic fluctuations similar to those associated with free shear layers.

The spatial distribution of the averaged void fraction within the array for 80% void fraction and 3.6 m/s pitch velocity is shown in Fig. 14. The flow path of the void waves is also sketched in the figure. In all the void fraction graphs, the void fraction is significant (above 80%) for most positions.

The flow becomes more non-uniform at the higher velocity of 8 m/s as shown in void fraction profiles of Fig.15. The large wake recirculation regions are indicated by dashed lines. The void fraction shows a decrease in

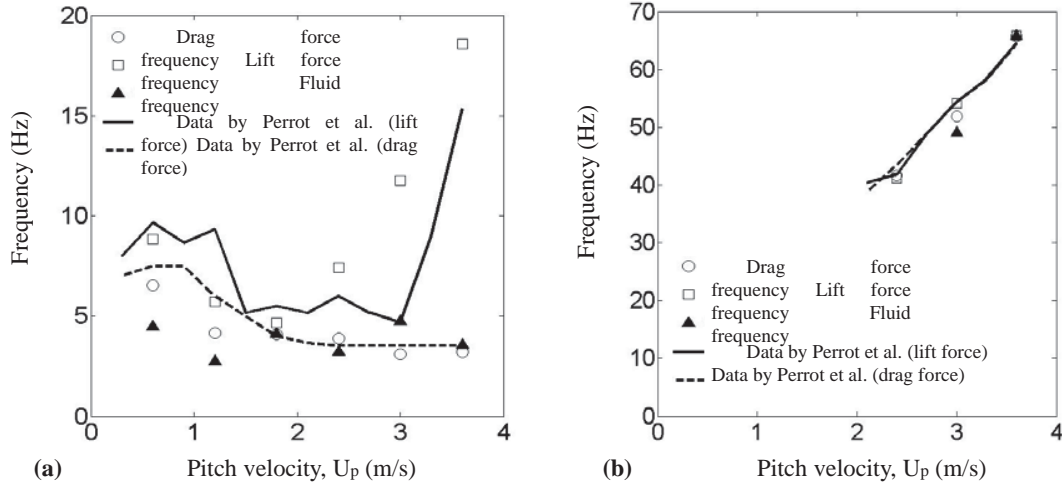


FIGURE 13: DOMINANT FREQUENCIES FOR 50% HOMOGENEOUS VOID FRACTION (a) AT LOW FREQUENCIES AND (b) AT HIGHER FREQUENCIES.

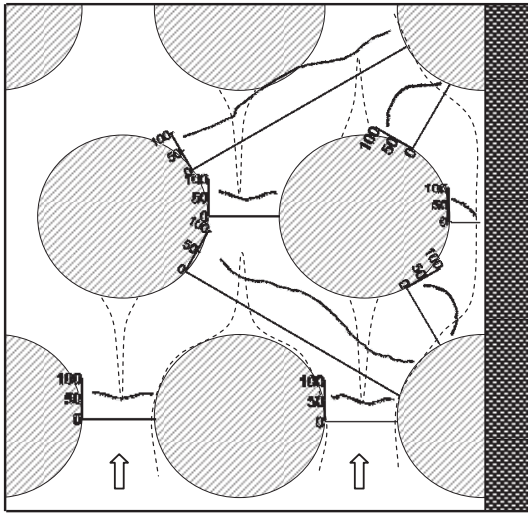


FIGURE 14: LOCAL VOID FRACTION AND FLOW PATHS 3.6 M/S FOR $\beta=80\%$.

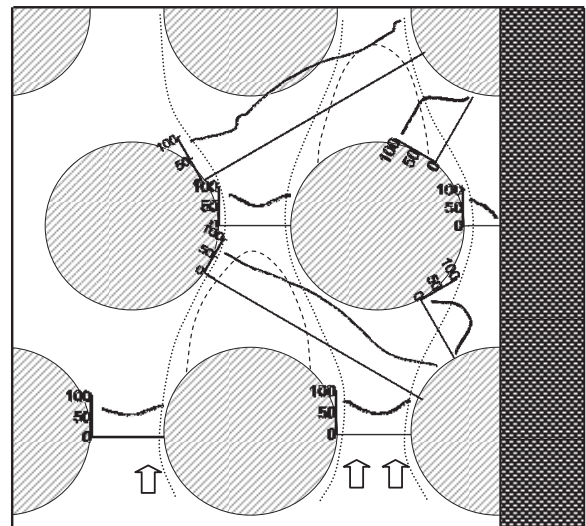


FIGURE 15 LOCAL VOID FRACTION AND FLOW PATHS FOR 8 M/S, $\beta=80\%$.

these zones. The flow path primarily followed by the gas phase, on the other hand, very well-defined as shown with the dotted line in the figure.

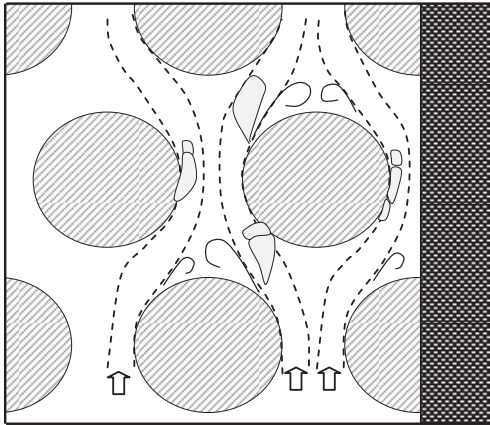


FIGURE 16: FLOW STRUCTURE AND SLUG 'SHEDDING' MECHANISM, $\beta=80\%$.

DISCUSSION

Two flow phenomena have been identified which are closely linked to the unsteady lift and drag forces measured in the tube array. The associated forces can be expected to govern flow induced vibrations in the array. One is a bundle scale fluid force and the other a tube scale fluid force. In this section we discuss further these forces and the possible underlying mechanisms. Observations with a high speed camera helped to clarify the physical origin of the bundle scale fluid forces. Video imaging showed that the low frequency forces are generated by void waves generated in a cycle involving liquid accumulation – pressure build-up and then liquid 'ejection' due to gas over-pressurization. This cycle is repeated nearly periodically at a low frequency proportional to the test section dimensions. From a practical point of view, this phenomenon should not be of much concern since the main frequency will be even lower at prototypical plant component scales.

Periodic excitations related to tube scale fluctuations, the second mechanism, should be of greater concern. Flow visualization tests show that the fluid force originates from the impact of large water slugs on the tubes. The tube wakes contain large mainly liquid recirculation zones. Instead of vortex shedding as in a single-phase flow, liquid slugs are 'shed' approximately periodically from this zones and propagated downstream along the main flow paths. Unable to follow the torturous flow path due to liquid inertia, the liquid slugs impact the tube downstream and further replenish the downstream

tubes recirculation zone in the process as depicted in Fig.16. The shedding process is then repeated at the downstream tube and so forth throughout the array. The frequency of this phenomenon is closely related to the distance between two tubes (along the flow direction) and with the pitch velocity.

CONCLUSION

Periodic forces have been measured in a triangular tube bundle subjected to two-phase cross flow. Some of the forces have a quasi-constant and low dominant frequency. Other forces have a dominant frequency proportional to flow velocity. The low frequency forces are associated by bundle scale void waves. The higher frequency forces are associated with a slug 'shedding' mechanism where slugs shed from an upstream cylinder impacts the downstream neighbor at approximately periodic time intervals. These forces depend on the pitch-to-diameter ratio and on the void fraction.

REFERENCES

- [1] Blevins, R. D., 1991. Flow-Induced Vibration. 2nd ed. New York.
- [2] Pettigrew, M.J., Taylor, C.E., 1994. Two-Phase flow-Induced vibration : An overview. *ASME Journal of Pressure Vessel Technology*, **116**, pp. 233-253.
- [3] Zhang, C., 2007. Correlation between vibration excitation forces and the dynamics characteristics of two-phase flow in a rotated triangular tube bundle. Ph.D. Thesis, Mechanical Engineering Department, Ecole Polytechnique Montreal, Montreal.
- [4] Perrot, E., Mureithi, N.W., Pettigrew, M.J., Ricciardi, G., 2011. Vibration excitation forces in a normal triangular tube bundle subjected to two-phase cross-flow. Paper 57102, FIV Symposium, proceedings of the ASME Pressure Vessels and Piping Division Conference, Baltimore.
- [5] Ricciardi, G., Pettigrew, M.J. and Mureithi, N.W., 2011, Fluidelastic instability in a normal triangular tube bundle subjected to air-water cross-flow, *ASME, Journal of Pressure Vessel Technology*, **130**, (061301).
- [6] Zhang, C., Pettigrew, M. J., Mureithi, N. W., 2008. Correlation between vibration excitation forces and the dynamic characteristics of two-phase cross flow in a rotated-triangular tube bundle. *ASME, Journal of Pressure Vessel Technology*, **130**(1), pp.567-575.



FLOW-INDUCED VIBRATIONS IN SUBSEA PIPEWORK

Arnaud Sanchis*

PPS - Flow Assurance CompetenceCenter
FMC Kongsberg Subsea AS
NO-1373 Asker, Norway
Email: arnaud.sanchis@fmcti.com

Ken-Robert G. Jakobsen

PPS - Flow Assurance CompetenceCenter
FMC Kongsberg Subsea AS
NO-1373 Asker, Norway
Email: ken-robert.jakobsen@fmcti.com

ABSTRACT

In this paper single- and multi-phase CFD U-RANS simulations of the flow in a sharp 1D bend at moderately high Reynolds number are presented. The capability of the two-equation SST turbulence model to resolve the flow induced pressure loading on the pipe walls is addressed. It is found that for single-phase flow, the SST model is able to correctly predict the frequency and location of the wall pressure fluctuations but neither their amplitude nor the associated large-scale unsteady flow features. This work is part of a project aiming at developing a methodology for the prevention of FIV-related issues in subsea production systems.

NOMENCLATURE

BC Boundary Condition
CFD Computational Fluid Dynamics
FEA Finite Element Analysis
FIV Flow-Induced Vibration
GVF Gas Volume Fraction
ID Inner Diameter
JAEA Japanese Atomic Energy Agency
LOF Likelihood of Failure
PPS Production Performance Services
 r Bend radius of curvature
RANS Reynolds Averaged Navier-Stokes
Re Reynolds number
RSM Reynolds Stress Model
SPS Subsea Production System
SST Shear Stress Transport
St Strouhal number
 U_b Bulk velocity
U-RANS Unsteady-RANS
 y^+ Dimensionless wall distance

INTRODUCTION

An increasing number of subsea developments today concern gas fields characterized by high flow velocities, which is the governing parameter for the occurrence of Flow-Induced Vibration. FIV can impose restrictions on the allowed maximum flow rates and severely limit an installations production capabilities.

Excessive vibration in the flow lines of subsea production systems may cause fatigue fracture in the piping, support structures and welds. Due to the particular challenges posed by the subsea environment, this a major concern for contractors and their clients. A failure in the process piping of a deepwater installation will lead to long production down-time, extreme costs of intervention and significant environmental hazards. As a result, an increasing demand has developed among oil companies towards a more accurate assessment of the risks posed by FIV.

Present studies in the industry often follow the methodology of [1], which is a screening method that relies on calculating a so-called Likelihood of Failure for single pipe elements of the flow line as a function of flow velocities, pipe dimensions and support arrangement. Basically, this represents an estimate of the likelihood for the excitation frequencies to coincide with the fundamental natural frequencies of the system. The LOF values are to be used as a form of scoring for screening purposes, not as an absolute probability of failure. The results of these studies are based on simplified models and are necessarily conservative.

During the last couple of years, there has been an increasing need for more detailed studies focused on sections of the piping identified as “hot spots” for FIV, such as sharp bends, tees or expanding sections. The screening methodology may often be too conservative resulting in mitigations that are hard to implement in compact subsea equipment, such as adding pipe support to increase the stiffness of the system. Consequently, there has been

*Address all correspondence to this author.

an interest in developing a combined CFD and FEA approach applicable to the mechanical models and flow conditions encountered in a typical subsea production system. Here, the present paper focuses on the CFD capability of accurately capturing the excitation loading from the internal pipe flow. The work is part of a bigger project aiming at establishing a method for one-way coupling between cyclic wall pressure loading from the flow and the mechanical response. As for benchmarking, we are using the results of a large project conducted by the Japanese Atomic Energy Agency and described in [2]. JAEA has studied in detail the unsteady flow structure, wall pressure loading and associated structural response of a pipe element with a sharp bend (one diameter radius) at high Reynolds numbers. Their work rely on extensive numerical and experimental results obtained at different scales. The flow in the pipe bend is characterized by separation immediately downstream of the bend and the alternate shedding of streamwise vorticity which cause the separation bubble to oscillate sidewise. At the edges of the separation bubble large oscillations of the wall pressure are observed at a Strouhal number close to 0.5.

The present paper presents U-RANS simulations where the capability of the two-equation SST turbulence model to accurately capture practical FIV flow scenarios in subsea production systems is addressed. The latter also involves simulating flow conditions with more than one phase. For initial validation, the results will be compared to the experimental data from [3] and [4], and the numerical simulations from [5].

PROBLEM FORMULATION

Bending of a flow in curved tubes and channels results in the appearance of centrifugal forces directed from the center of curvature to the outer wall of the tube. This causes an increase of the pressure at the outer wall and its decrease at the inner wall, when the flow passes from the straight to the curved section of the pipe. Therefore, the flow velocity will correspondingly be lower at the outer wall and larger at the inner wall [6].

Figure 1 shows the geometry of the pipe element considered here. Strictly speaking, the curved section is defined as a “bend” if the center of curvature of both the inner and outer walls is the same (or in other words, if both walls are arcs of concentric circles). The geometry is different for an elbow, although both terms are often used interchangeably in the literature.

Only right-angled bends will be considered here and the main flow parameters are thus the bulk velocity U_b , pipe inner diameter ID and the relative radius of curvature

r/ID . The Reynolds number Re is defined from the bulk velocity and the pipe internal diameter:

$$Re = \frac{\rho U_b ID}{\mu}, \quad (1)$$

where ρ is the fluid density and μ is the dynamic viscosity. For all Reynolds numbers of practical interest ($Re > 1 \times 10^4$) the flow is characterized by the following features:

1. Permanent flow separation occurs at the inner wall for radii of curvature $r/ID \leq 1$. The separation bubble extends past the bend exit and the exact location of the point of re-attachment depends on the Reynolds number. For $r/ID = 1.5$ separation was observed only intermittently by [4]. The formation of eddies at the inner wall is a considerable source of pressure loss in the bend.
2. The appearance of centrifugal forces and the presence of boundary layers on the walls generate a secondary flow in the circumferential direction formed of counter-rotating vortex pairs. Time-resolved experiments showed that these vortices flow towards the inside wall alternately. This periodical inflow at the bend inner wall affects the behavior of the separation region near the inside wall and causes periodic pressure fluctuations at a Strouhal frequency close to 0.5.
3. A local acceleration in the axial direction is observed just downstream of the reattachment point, due to the lateral secondary flow adding momentum to the axial component of the velocity at the inner wall.

SINGLE PHASE CFD

In this section an attempt is made to reproduce the above observations using some of the available experimental data as reference. A 15 cm ID pipe is considered with oil flowing at 3.21 m/s, yielding a Reynolds number of 5.4×10^5 . The liquid properties can be found in Tab. 3. Tests with water yielded the exact same results as shown in this section. The objective is to obtain an accurate description of both the time-averaged and periodic flow components, where particularly the dominant frequency of the wall pressure fluctuations is of interest. The ANSYS-CFXTM solver is used with the Shear Stress Transport (SST) turbulence model. In the numerical study by [5] the 7-equations Reynolds Stress Model (RSM) was tested with success at Reynolds numbers above 1×10^6 ; however, the computational cost associated with the RSM model is impractical for the large models involved in the FIV analysis of subsea production piping.

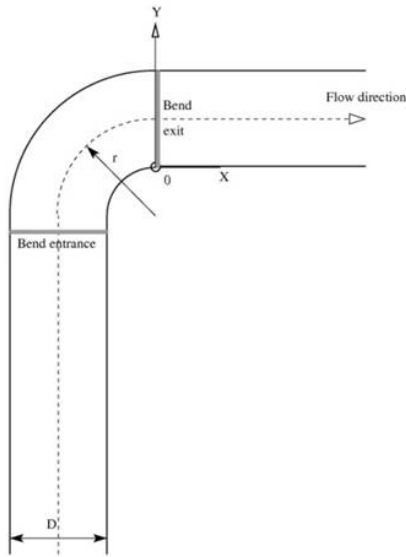


FIGURE 1: COMPUTATIONAL DOMAIN.

Model description

The model geometry is based on the sketch in Fig. 1. The distance from the pipe inlet plane to the bend entrance is 11 diameters. The distance from the bend exit plane (defined as $x/ID = 0$) to the outlet is 5 diameters. Sensitivity tests indicated that the position of the outlet section does not influence the flow field close to the bend. The mesh structure is presented in Fig. 2. The pipe model is split into three segments, with the mesh axial size varying from $0.125ID$ in the two outer segments to $0.05ID$ in the bend. In the circumferential direction each element covers an angle of 5° (72 divisions). Close to the wall the first layer thickness is adjusted in order to yield a value of $y^+ = 1$ at the pipe inlet. Due to the flow acceleration in the bend the maximal value of y^+ in the whole model is 2. The total number of elements is 500 000.

Numerical options used for the simulations were determined by a preliminary parametric study and are summarized in Tab. 1. The flow was found to be particularly sensitive to the inlet boundary conditions and the advection scheme.

The wall pressure was monitored at locations given in Fig. 3 which correspond to the position of the wall pressure sensors in the experimental setup of [3].

Steady-state results

Transverse distributions of the axial velocity component at different locations downstream of the bend exit are shown in Fig. 4. The numerical solution of the steady-state runs is compared to the time-averaged experimental data of [4]. Two inlet boundary conditions are tested:

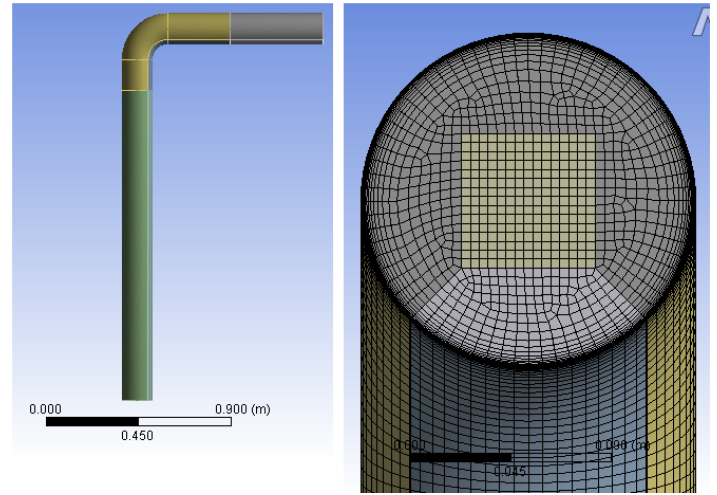


FIGURE 2: MESH STRUCTURE (LEFT: SIDE VIEW, RIGHT: CROSS-SECTION).

TABLE 1: ANSYS-CFX™ SIMULATION SETTINGS, SINGLE PHASE.

Properties	Settings
Inlet BC	Normal velocity, 5% turb. intensity
Outlet BC	Zero area-averaged pressure
Wall BC	No-slip
Turbulence model	SST
Simulation time	5 seconds
Time step	Fixed = 0.005 s
Inner-loop iterations	2 - 5
Precision	Double
Time scheme	2nd order backward Euler
Advection scheme	High resolution
Turbulence numerics	First order

- fully-developed profiles of the velocity and turbulent kinetic energy (continuous line)
- flat velocity profile and 5% turbulence intensity (dashed line).

The numerical solution overestimates the transverse extent of the separation bubble and fails to predict the correct position of the point of reattachment in both cases. The flow is found to be sensitive to the inlet boundary conditions and for comparison with the numerical results of [5] the inlet BC of Tab. 1 have been used in the paper.

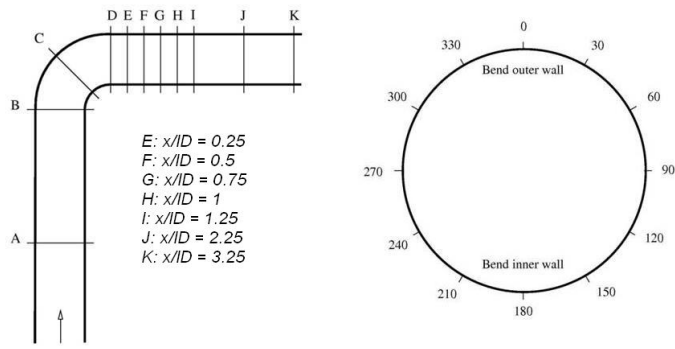


FIGURE 3: LOCATION OF WALL PRESSURE MEASUREMENT POINTS.

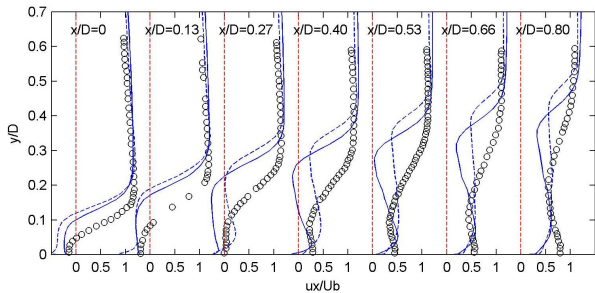


FIGURE 4: AXIAL VELOCITY PROFILES. CONTINUOUS LINE: FULLY-DEVELOPED INLET BC, DASHED LINE: TAB. 1 INLET BC, CIRCLES: EXPERIMENTAL DATA FROM [4].

Transient results

The velocity field downstream of the bend does not reveal any major difference with the steady-state results: the alternate vortex shedding described in the PIV experiments by [4] and [5] is not observed. In the pipe cross-section the flow field is found to be almost symmetric, with two counter-rotating vortex structures of equivalent strength coexisting at all times (Fig. 6). Clearly, the two-equation SST model fails to reproduce the unsteady flow features obtained by [5] with the more advanced RSM model.

An analysis of the wall pressure signal around section E (see Fig. 3) reveals periodical oscillations at a frequency corresponding to $St = 0.45$, with maximum standard deviation of 45 Pa obtained at 150° and 210°. The oscillation frequency is in agreement with the experimental results of [3] and [4]. When scaled with the flow param-

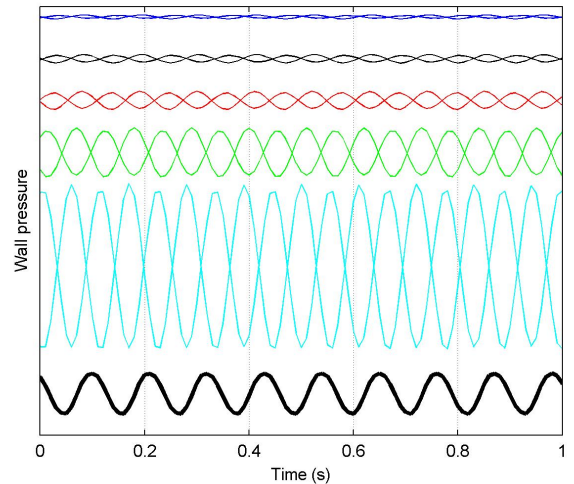


FIGURE 5: TIME SIGNALS OF THE WALL PRESSURE AROUND SECTION E. FROM TOP TO BOTTOM: 30°/330°, 60°/300°, 90°/270°, 120°/240°, 150°/210° AND 180°.

eters, this amplitude is found to be three orders of magnitude weaker than in the experiments by [3]. The time signals at different circumferential locations around section E are plotted in Fig. 5 for one second of simulation. The pressure fluctuations at symmetric locations around the pipe are in phase opposition. Along each side of the pipe the phase of the time pressure fluctuations thus varies progressively. Both the phase shift and amplitude variations around the pipe circumference suggests that these oscillations are produced by the sidewise displacement of the separation bubble, as confirmed in Fig. 6.

A contour plot of the wall pressure standard deviation downstream of the bend at various locations (see Fig. 3 for reference) is shown on Fig. 7. Results were obtained from 5 seconds of data sampled at 200 Hz. A small asymmetry appears in the results, with stronger fluctuations on one side of the bend.

Similar observations have been obtained for Reynolds numbers comprised between 1×10^5 to 3×10^6 , by changing the inlet velocity or the pipe diameter. For these sensitivity runs the Strouhal number varies between 0.44 and 0.52. At Reynolds numbers higher than 3×10^6 an asymmetric flow solution is obtained, with one of the vortices shown in Fig. 6 dominating its counterpart. Larger, random variations of the wall pressure are recorded and the numerical convergence is poor compared to the results at lower Re.

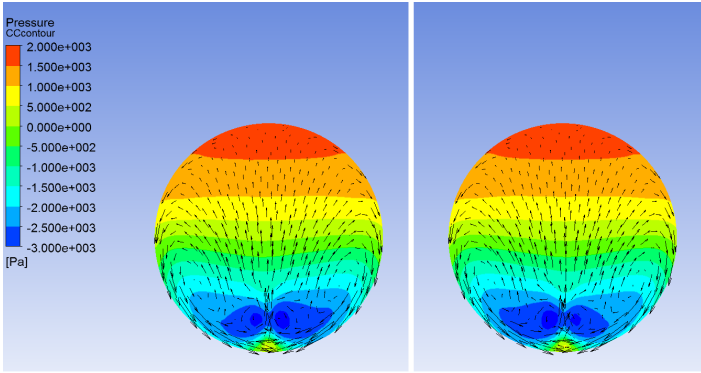


FIGURE 6: PROJECTIONS OF THE INSTANTANEOUS VELOCITY (ARROWS) AND CONTOUR PLOTS OF PRESSURE IN THE CROSS-SECTION E. IMAGES ARE SEPARATED BY HALF A PERIOD OF OSCILLATION.

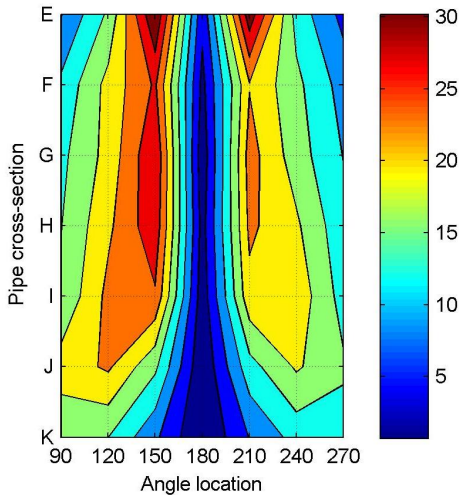


FIGURE 7: STANDARD DEVIATION OF THE WALL PRESSURE DOWNSTREAM OF THE BEND, SINGLE-PHASE SIMULATION.

MULTI-PHASE CFD

In order to approach a more practical scenario in a typical SPS, the following section introduces multiphase CFD simulations consisting of one gas phase and one liquid phase. The geometry and flow conditions together with the experience and results gained from the single phase investigation will be used as a natural starting point for the present study.

Models

There are two phases present in the multiphase simulations discussed here: one continuous liquid

TABLE 2: ANSYS-CFX™ SIMULATION SETTINGS, MULTI-PHASE.

Properties	Settings
Inlet BC	Mass bulk flow, fully mixed 5% turb. intensity
Outlet BC	Pressure = 0
Wall BC	No-slip
Turbulence model	SST
Simulation time	5 seconds
Time step	Fixed = 0.005s
Inner-loop iterations	1 - 10
Precision	Double

phase and one dispersed gas phase. Each of the phases possesses its own flow field through the inhomogeneous Eulerian-Eulerian multiphase model. Interphase transfer terms are modeled using the so-called Particle Model (default when having a dispersed phase), in which the Schiller-Naumann model is used to calculate the interphase drag. Here, the particle drag coefficient is defined as:

$$C_D = \frac{24}{Re} (1 + 0.15Re^{0.687}), \quad (2)$$

where Re is the particle Reynolds number.

A homogeneous turbulence field is applied in the present simulations, meaning that both phases share the same turbulence field that is being modeled using one single turbulence model. The model used is the SST U-RANS turbulence model. It is referred to the single phase calculations for details on the latter.

The general simulation settings including the specifics of the transient simulation setup are summarized in Tab. 2.

Fluid properties

A fully mixed flow, typically found in subsea piping with high velocities and complex piping routing, is applied at the inlet of the computational domain. This implies a homogeneous mixture of gas bubbles into the continuous liquid phase at the specified gas volume fraction, where the liquid properties have been kept equal as for the single phase case. The latter is true for the bulk

TABLE 3: FLUID PROPERTIES.

Properties	Settings
<i>Gas</i>	
Density [kg/m ³]	99.9
Dynamic viscosity [cP]	0.0166
Bubble size [micron]	500
<i>Liquid</i>	
Density [kg/m ³]	692.7
Dynamic viscosity [cP]	0.65
<i>General</i>	
GVF [-]	0.3
Bulk mass flow [kg/s]	41.1
Surface tension [mN/m]	4.6

mass flow (gas + liquid) as well in order to keep a close resemblance to the single phase case. However, by introducing the lighter gas phase the average inlet velocity will increase slightly compared to the single phase case.

The gas bubbles are assumed to be spherical with a diameter of 500 microns, for simplicity. In a practical situation there exists a wide range of particle sizes in the fluid stream. A surface tension coefficient between the phases was estimated and applied in the numerical model.

The fluid properties are given in Tab. 3. The density, viscosity and volume fraction of the two phases have been taken from an actual subsea development.

Results

The results from the multi-phase simulations will be presented in the following. These have been obtained from a transient calculation in ANSYS-CFXTM preceded by a steady-state simulation to generate the proper initial conditions. The simulation settings have been summarized in Tab. 2 and Tab. 3.

The GVF plot in Fig. 8 taken at the midplane of the pipe shows that the fully mixed flow condition specified at the inlet of the computational domain is maintained through to the bend. This is mainly due to geometrical reasons, whereby the piping upstream of the bend sees a vertical orientation and does not allow for the gas and liquid phases to separate. Test simulations in a horizontal pipe were also conducted, which showed a rather slow separation of the gas and liquid phases for the given flow condition. The latter can be explained by the given fluid

properties such as the GVF and density difference between the two phases.

When the gas and liquid mixture enters the bend, centrifugal effects forces the liquid towards the outer part of the pipe, while the gas phase makes out the inner part. This can be seen in Fig. 8 as well as at the transverse sections E and K in Fig. 9 (see definition in Fig. 3). Noticeably, there is a huge separation zone consisting mainly of gas starting slightly upstream of the bend outlet. This is illustrated by the vector plot in Fig. 10. By comparing with the single-phase results a similar flow behaviour can be found as the flow approaches the outlet of domain (section K in Fig. 9). Two counter-rotating vortices (now separated by a liquid layer in dark blue) coexist and their position oscillates slightly with time, which generates pressure fluctuations at the pipe walls. Also, the gas moves to the top of the pipe and mixes with the liquid as the flow moves downstream the horizontal part of the domain. An illustration is given in Fig. 11 showing an isosurface with a GVF equal 0.3.

The level and spatial distribution of the wall pressure fluctuations is shown on Fig. 12. Compared to the single-phase case (Fig 7) much stronger fluctuations are obtained everywhere downstream of the bend, with a maximum at section J. The pressure signals at section J are plotted in Fig. 13 as a function of time. Contrary to the single-phase case, there is no phase shift between the different angular locations. In fact, an analysis of the wall pressure signals at all planes shows that the signals are in phase everywhere, except for section K. The variations are also more irregular, even though a peak in the power spectrum is still obtained at $St \approx 0.5$ (Fig. 14). For section K a much broader peak is obtained.

Based on these observations, differences with the single-phase case can be summarized as follows:

- the separation bubble extends up to two diameters downstream of the bend exit and consists mainly of gas.
- with the intrusion of liquid at the pipe inner wall (secondary flow), counter-rotating streamwise vorticity structures are formed. Their sidewise position oscillates in a similar pattern as shown in Fig. 6, creating wall pressure fluctuations with a Strouhal number close to 0.5.
- wall pressure fluctuations are of much higher magnitude than for single-phase and also more spatially correlated downstream of the bend, thereby increasing the risk for flow-induced vibration.

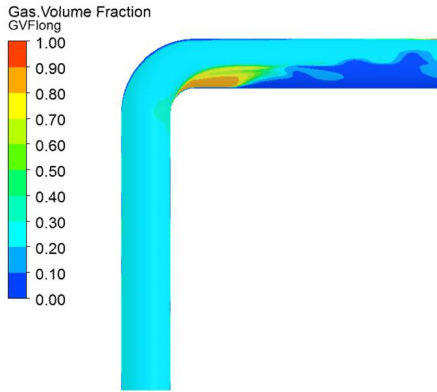


FIGURE 8: GVF AT MIDPLANE, T = 4 S.

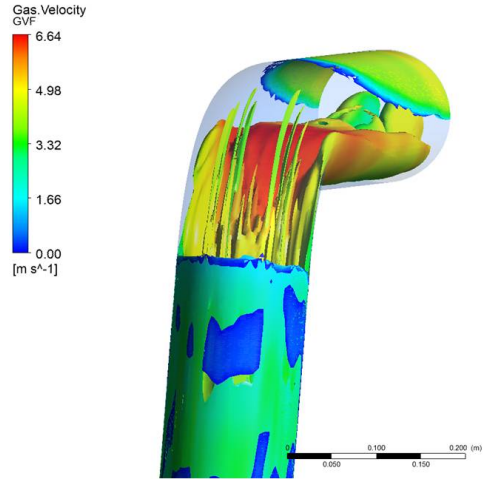


FIGURE 11: ISOSURFACE OF GVF=0.3 COLORED BY GAS VELOCITY.

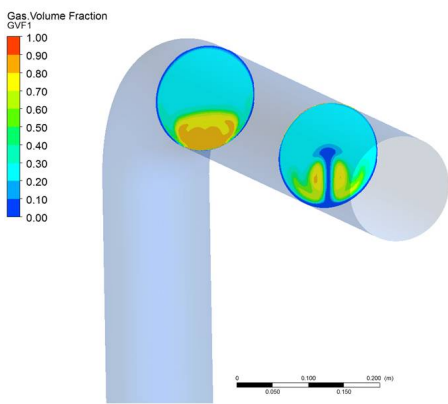


FIGURE 9: GVF AT SECTIONS E AND K, T = 4 S.

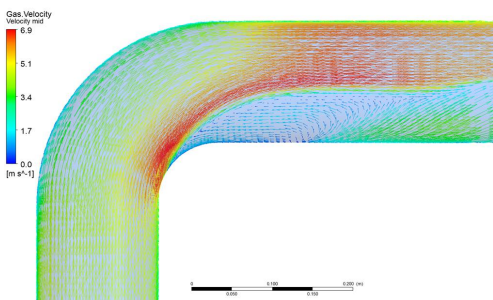


FIGURE 10: GAS VELOCITY VECTORS AT MID-PLANE, T = 4 S.

Conclusions

A single phase CFD analysis of the flow at moderately high Reynolds numbers into a sharp bend has been presented. Compared to the numerical simulations of [5] a simpler, two-equation turbulence model has been chosen, which is more suited to our engineering applications where time is critical. With this setup the location and frequency of the wall pressure fluctuations downstream

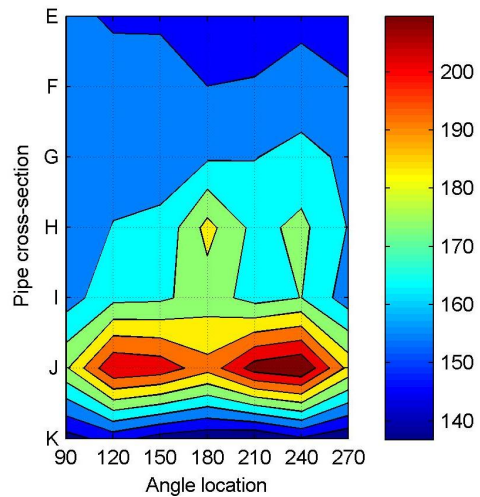


FIGURE 12: STANDARD DEVIATION OF THE WALL PRESSURE DOWNSTREAM OF THE BEND, MULTI-PHASE SIMULATION.

of a sharp bend can be predicted over a wide range of Reynolds number. However, neither the amplitude of those fluctuations nor the associated large-scale flow features (vortex shedding) can be obtained and the flow field remains essentially steady. The generalization of these results to more complex geometries (multiple bends, blind tees) would provide a valuable input to the FIV screening of subsea production systems.

CFD calculations of multi-phase flow through a 1D bend have been presented, where the flow consisted of one continuous liquid phase and one dispersed gas phase. An inhomogeneous Eulerian-Eulerian model im-

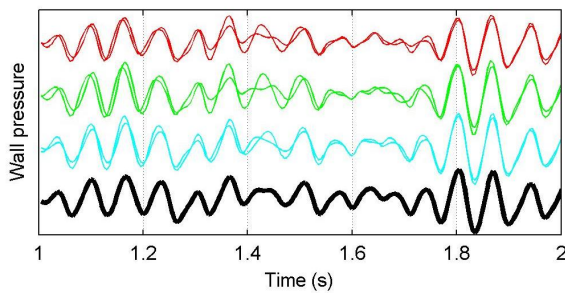


FIGURE 13: PRESSURE SIGNALS, SECTION J. BLACK=180°, BLUE=210/150°, GREEN=240/120°, RED=270/90°.

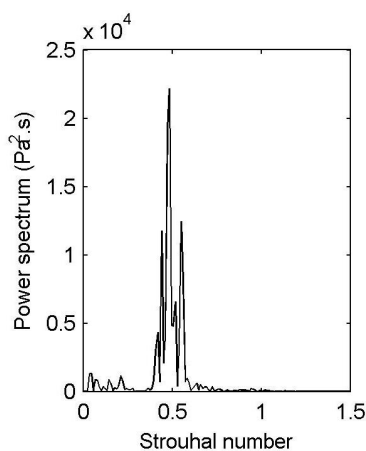


FIGURE 14: DOMINANT FREQUENCY, SECTION J.

plemented in the ANSYS-CFXTM software was used to solve the conservation equations, while the two-equation SST model was used to capture the turbulent field.

With the given fluid properties and volume representation of the phases, the results indicate the presence of wall pressure fluctuations occurring at the same dominating frequency as for the single phase flow, but with much higher pressure amplitudes. Depending on the upstream geometrical layout and the fluid properties, the flow enters the bend as a homogeneous mixture of gas and liquid, and the centrifugal force brings the liquid out of the mixture and towards the outer wall, while the separation zone located at the inner wall consists of mainly gas. The size of the separation zone is significantly larger than for single-phase flow.

Future work

The FIV investigations using multi-phase CFD will be continued. First and foremost, it will be necessary to

look into different geometries as well as fluid properties in order to approach the changing flow conditions that a SPS represents. From a numerical point of view, the impact of different simulation settings such as the choice of multi-phase models on the computed flow field should be looked into.

Eventually, the excitation frequencies extracted from the flow field will be coupled with structural analyses. This ultimate step requires an accurate description of the wall pressure loading.

ACKNOWLEDGMENT

Acknowledgment is given to the PPS department at FMC Kongsberg Subsea AS for sponsoring the present work.

REFERENCES

- [1] *Guidelines for the avoidance of vibration induced fatigue failure in process pipework (2nd Edition)*. Energy Institute, London, 2008.
- [2] Yamano, H., Tanaka, M., Kimura, N., Ohshima, H., Kamide, H., and Watanabe, O., 2011. "Development of flow-induced vibration evaluation methodology for large-diameter piping with elbow in Japan sodium-cooled fast reactor". *Nuclear Engineering and Design*, **241**(11), November, pp. 4464–4475.
- [3] Shiraishi, T., Watanabe, H., Sago, H., and Yamano, H. "Pressure fluctuation characteristics of the short-radius elbow pipe for FBR in the post-critical Reynolds regime". *Journal of Fluid Science and Technology*, **4**(2).
- [4] Ono, A., Kimura, N., Kamide, H., and Tobita, A., 2011. "Influence of elbow curvature on flow structure at elbow outlet under high Reynolds number condition". *Nuclear Engineering and design*, **241**(11), November, pp. 4409–4419.
- [5] Tanaka, M., Ohshima, H., Yamano, H., Aizawa, K., and Fujisaki, T. "U-RANS simulation of unsteady eddy motion in pipe elbow at high Reynolds number conditions".
- [6] Idelchik, I., 2003. *Handbook of hydraulic resistance (3rd Edition)*. Jaico Publishing House, Mumbai, India.



Flow Induced Vibration of Piping Downstream of Tee Connection

Masato NISHIGUCHI

CHIYODA ADVANCED SOLUTIONS CORPORATION
1-25, Shin-Urashima-cho 1-chome, Kanagawa-ku, Yokohama 221-0031, Japan
Email: masato.nishiguchi@chas.chiyoda.co.jp

Hisao Izuchi

CHIYODA ADVANCED
SOLUTIONS
CORPORATION
Yokohama, KANAGAWA
Pref., Japan

Itsuro HAYASHI

CHIYODA ADVANCED
SOLUTIONS
CORPORATION
Yokohama, KANAGAWA
Pref., Japan

Gaku MINORIKAWA

HOSEI UNIVERSITY
Department of Mechanical
Engineering
Koganei-shi, TOKYO, Japan

ABSTRACT

In the process plant, random vibrations excited by the turbulence generated at tee connection might cause problems such as piping damage. In general, the beam mode piping vibration is known to be excited when the piping is subjected to the severe turbulent conditions. However, the shell mode piping vibration could occur when the piping stiffness of the circumferential direction is relatively low. In this study, a new evaluation index is proposed in order to evaluate the integrity of the piping system for the tee connection against flow induced random vibration. This evaluation index is based on the excitation force of the fluid and the mechanical properties of the piping. Experiments and numerical analysis were executed in order to evaluate the validity of the new evaluation index. As a result, it was confirmed that the new evaluation index tends to be proportional to the shell mode stress of the random vibration. Therefore, the proposed index is effective to evaluate the extent of the vibration.

NOMENCLATURE

A :Flow Area of Brach Pipe (1-1/2inch) [m²]
 A_0 :Excitation Area in FEA Analysis [m²]
 c :Damping Constant [kg/s]
 d :Branch Pipe Inside Diameter[m]
 D :Main Pipe Diameter[m]
 E :Young's Modulus [Pa]
 f :Frequency [Hz]
 f_g :Excitation Frequency Range of Fluid Flow [Hz]
 f_n :Natural Frequency of Fundamental Shell Mode of Main Pipe [Hz]
 F :Excitation Force [N]
 H :Transfer Function [-]

I :Second Moment of Area [m⁴]
 k :Spring Constant [N/m]
 m :Mass [kg]
 n :Mode Number [-]
 Δp :Pressure Discontinuity through Tee in Case of Critical Condition [Pa]
 Δp_0 : ΔP at 25barg of RO Upstream (TP1) [Pa]
 Δp_1 : ΔP corresponding to Q_1 [Pa]
 P_{rms} :Overall RMS of Pressure Fluctuation [Pa]
 Q_0 :PSD of Vibration Stress Obtained by FEA at 25barg of RO Upstream (TP1) [Pa²/Hz]
 Q_1 :PSD of Stress Calculated by FEA at Each Upstream Pressure (TP1) [Pa²/Hz]
 R :Pipe Radius [m]
 St :Strouhal Number [m]
 S_x :Power Spectrum Density of Vibration Displacement [m²/Hz]
 S_w :Power Spectrum Density of Excitation Force [N²/Hz]
 t :Pipe Wall Thickness [m]
 v_0 :Fluid Velocity at End of Branch at 25barg of RO Upstream (TP1) [m/s]
 v_l :Fluid Velocity at End of Branch [m/s]
 V_n :Vibration Velocity Number [m/s]
 V_{rms} :Overall RMS of Vibration Velocity [m/s]
 W_0 :Power Spectrum Density of Excitation Force [Pa²/Hz]
 x :Vibration Displacement [m]
 \dot{x} :Vibration Velocity [m/s]

- \ddot{x} :Vibration Acceleration [m/s²]
- X_{rms} :Overall RMS of Vibration Displacement [m]
- ρ_g :Fluid Density [kg/m³]
- ρ_p :Pipe Material Density [kg/m³]
- σ_{rms} :RMS Value of Vibration Stress [Pa]
- ω :Angular Frequency [rad/s]
- ζ :Damping Ratio [-]

INTRODUCTION

In the process plant, random vibrations excited by the turbulence generated at tee connections might cause problems such as piping damages. In general, the beam mode piping vibration is known to be excited when the piping is subjected to the severe turbulent conditions. However, the shell mode piping vibration could occur when the piping stiffness for the circumferential direction is relatively low.

In the past investigations, the random vibrations caused by turbulence were examined for several piping configurations or structures. Au-Yang expressed the evaluation method of the random pressure fluctuation caused by flow turbulence for a nuclear vessel based on the measurement [1]. The evaluation method of the random vibration caused by the turbulence has been reported for cylindrical structures [2]. The evaluation method of the random vibration caused by the turbulence has been reported for baffle plate [3]. The vibration response for the baffle plate in the duct is calculated by the random vibration analysis based on the pressure fluctuation obtained by the experiment [4]. The vibration response for the elbow is calculated by the random vibration analysis based on the pressure fluctuation obtained by the experiment [5] [6]. The random vibration response of the simple straight pipe caused by turbulence is calculated by the combined analysis with CFD and FEA [7]. However, the characteristic of the random vibration of the shell mode at the tee connection would not have been reported.

In order to investigate the characteristic of the random vibration of the shell mode at the tee connection, experiments and numerical analysis were executed in this study. As a result of the experiment, it was confirmed that the random pressure fluctuation of the pipe inner surface is proportional to the total pressure change through the tee, $(1/2)\rho_g Av^2 + \Delta pA$, hear, Δp is the discontinuous pressure change in case of choking flow occurrence at the end point of the branch. This term of Δp expresses the effect of shock wave caused by the critical flow. It was also confirmed that the piping vibration stress of the shell mode caused by the pressure fluctuation is proportional to the overall RMS (Root Mean Square) of the random pressure fluctuation. This means that the vibration stress is proportional to the total pressure change in through the tee, $(1/2)\rho_g Av^2 + \Delta pA$.

A numerical analysis by random vibration analysis was performed by the 3-dimensional structural analysis. The excitation force of this FEA analysis is obtained by the

experiment. As a result of this analysis, it was confirmed that the tendency of the random vibration stress can be evaluated by the random vibration analysis with this 3-dimensional structural analysis.

In this study, a new evaluation index (Vn: Vibration Velocity Number) is proposed in order to evaluate the integrity of the piping system against the flow induced random piping vibration of the shell mode. This Vn is based on the excitation force of the fluid and the mechanical properties of the piping structure. Since the Vn was almost proportional to the vibration stress in the experimental result, it is concluded that the Vn can be an useful index to evaluate the vibration stress of the random piping vibration caused by turbulence.

Outline of Random Vibration Theory

In order to evaluate the random vibration, statistical processing is required [8]. In this processing, the overall RMS (Root Mean Square) of the vibration is equivalent to the standard deviation. When the single DOF (Degree Of Freedom) vibration system is assumed and excited by a random external force as shown in Equation (1), the PSD (Power Spectrum Density) of the displacement can be written by Equation (2).

$$m\ddot{x} + c\dot{x} + kx = F(t) \tag{1}$$

$$S_x(\omega) = |H(\omega)|^2 \cdot S_w(\omega) \tag{2}$$

The transfer function, H (ω) can be written by Equation (3).

$$H(\omega) = \frac{1}{\sqrt{(k - m\omega^2)^2 + (c\omega)^2}} \tag{3}$$

The RMS of the displacement can be written by Equation (4) which is integration of Equation (2) [9].

$$X_{rms}^2 = \int_{-\infty}^{\infty} S_x(\omega) d\omega = \int_{-\infty}^{\infty} |H(\omega)|^2 \cdot S_w(\omega) d\omega = \frac{W_0}{4kc} \tag{4}$$

The relation of Equation (7) can be derived from Equation (4), Equation (5) and Equation (6).

$$k = (2\pi f_n)^2 m \tag{5}$$

$$c = 2\zeta \sqrt{mk} = 2\zeta m \omega_n = 4\pi \zeta m f_n \tag{6}$$

$$X_{rms} \propto \frac{\sqrt{W_0 f_n}}{m \sqrt{\zeta f_n^2}} \propto \frac{\sqrt{W_0 f_g}}{m \sqrt{\zeta f_n^2}} \tag{7}$$

The symbol f_g expresses the frequency range of the excitation force and the numerator of the right-hand side expresses the excitation force. Since the stress is basically proportional to the vibration velocity in the pipe, the

characteristic of the vibration stress caused by random vibration can be written by Equation (8)

$$\sigma_{rms} \propto V_{rms} = 2\pi f_n \times X_{rms} \propto \frac{\sqrt{W_0 f_g}}{m\sqrt{\zeta} f_n} \quad (8)$$

Excitation force is generally proportional to the pressure fluctuation that would be proportional to the total fluid momentum $\rho_g Av^2$. Once the velocity at the end of the branch reaches the sonic condition, this velocity becomes to be equal to the sound speed even though the mass flow rate increases. This situation is so called the critical flow condition and the discontinuity of the pressure occurs between the end of the branch and the main pipe and it might generate shock wave accompanied by additional pressure fluctuations. This discontinuous pressure effect of the critical flow may be proportional to the total pressure change through the tee connection, $(1/2)\rho_g Av^2 + \Delta pA$. From the considerations described above, pressure fluctuation after the combining point of the tee would be proportional to the total pressure change as expressed by Equation (9).

$$P_{rms} = \sqrt{W_0 f_g} \propto \rho_g Av^2 + 2\Delta pA \quad (9)$$

In Equation (8), the mass of the pipe could be expressed as $\pi\rho_p D^2 t$. Therefore, Equation (10) could be derived from Equation (8) and Equation (9). In equation (10), a new index, V_n (Vibration Velocity Number) is introduced which expressed the extent of the vibration stress.

$$\sigma_{rms} \propto V_n = \frac{\rho_g AV^2 + 2\Delta pA}{\pi\rho_p D^2 t f_n} \quad (10)$$

Experimental System and Method

In order to investigate the characteristics of the shell mode vibration caused by the random excitation force occurred in the tee connection, the pressure fluctuation of the pipe inner surface and the shell mode vibration strain were measured by the experimental system shown in Figure 1 and Figure 2. In order to measure the maximum vibration stress and vibration mode, 21 strain gauges were attached to the half side of the test pipe. The static pressure of the pipe inner surface was measured by pressure sensors with the strain gauge type. The pressure fluctuation was measured by pressure fluctuation sensors with the piezoelectric type. The experimental procedure is shown below.

1. The air inside air chamber is pressurized to 29barg.
2. The ball valve is opened and the pressurized air flows to the downstream.
3. The pressure of the air is reduced through the RO (Restriction Orifice) as shown in Figure 4 and Table 2.

4. The pressure fluctuations and the vibration strains were measured.

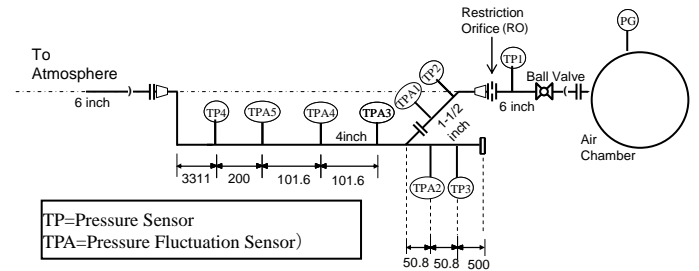


Fig.1 Experimental Setup

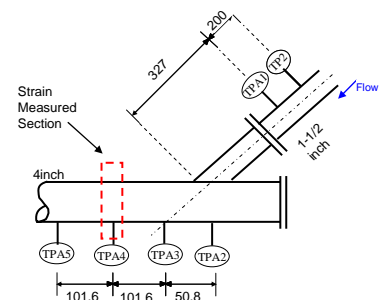


Fig.2 Experimental Setup around Tee

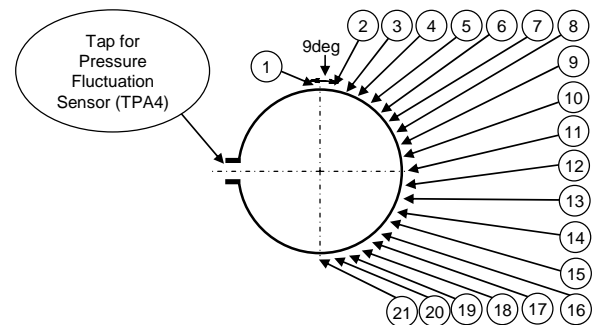


Fig.3 Measuring Point for Strain

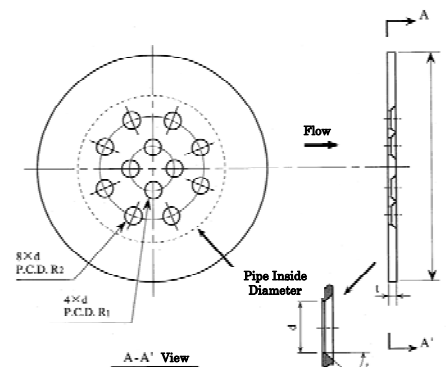


Fig.4 Configuration of RO

Table 1 Experimental Condition

Inside Diameter of Main Pipe [mm]	110.1
Wall Thickness of Main Pipe [mm]	2.1
Inside Diameter of Branch Pipe[mm]	45.2
Wall Thickness of Branch Pipe[mm]	1.7
Fluid	Air
Upstream Pressure of RO (TP1) [barg]	1.0 – 29.0
Velocity at End of Branch* [m/sec]	313
Pressure at End of Branch* [kPaA]	509
Fluid Density at End of Branch* [kg/m ³]	7.52
Pressure Discontinuity through Tee in Case of Critical Condition* [kPa]	283

*In case upstream pressure of RO (TP1) is 25barg

Table 2 Specification of RO

Pipe Inside Diameter [mm]	151.0
Thickness, t [mm]	8.0
Edge Thickness, h [mm]	0.8
Hole Dia. D [mm]	8.66
P.C.D. R1 [mm]	39.1
P.C.D. R2 [mm]	87.4

Numerical Analysis Method

Figure 5 shows the numerical analysis model for the tee connection. Firstly, CFD analysis using the commercial code, STAR-CCM+ V5.2 is executed to examine the high turbulence area where high pressure fluctuation occurs. Figure 6 shows the CFD results and high turbulence area is a little downstream of the tee connection. Corresponding to this high turbulence area the exciting force area is determined as shown in Figure 7. Figure 8 shows the PSD (Power Spectrum Density) of the pressure fluctuation at TPA4 obtained by the experiment for 25 barg condition at the RO upstream. This pressure fluctuation is loaded to the exciting force area shown in Figure 7 and the random vibration analysis is executed by the commercial FEA code, ABAQUS V6.10.

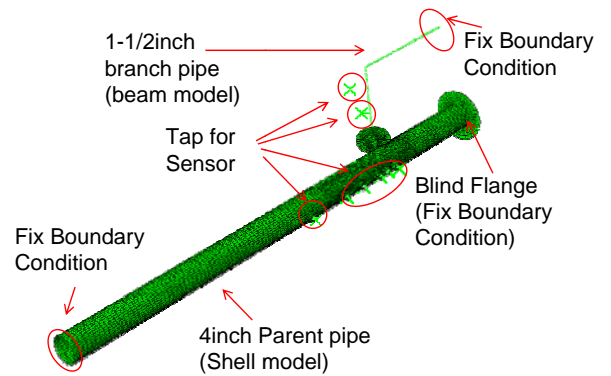


Fig.5 Numerical Analysis Model with FEA Boundary Conditions

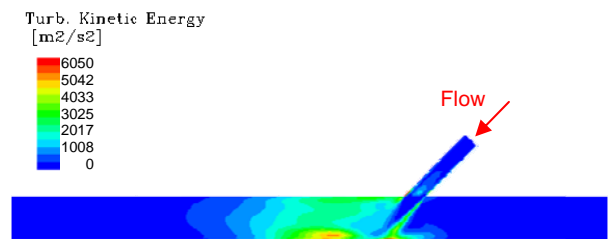


Fig.6 Turbulence Energy Obtained by CFD Analysis (Upstream Pressure of RO (TP1) is 25barg)

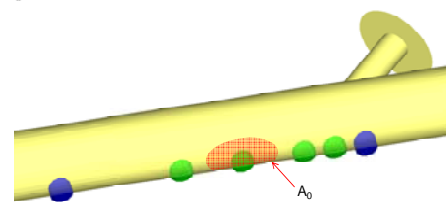


Fig.7 Exciting Force Area

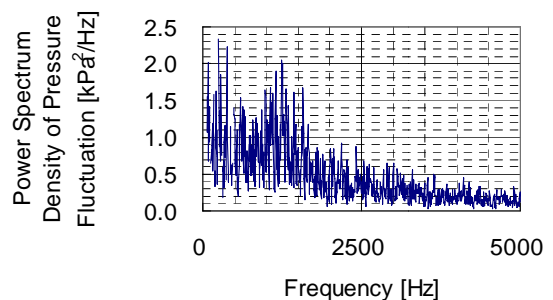


Fig.8 Power Spectrum Density of Pressure Fluctuations (TPA4) (Upstream Pressure of RO (TP1) is 25barg)

In the structural analysis the vibration stress is basically evaluated at the condition of 25barg at RO upstream. For the other pressure condition, vibration stress is obtained by the relation of Equation (11), where process conditions are obtained by the experiment.

$$Q_1(\omega) = Q_0(\omega) \times \left(\frac{\rho_{g1}v_1^2 + 2\Delta p_1}{\rho_{g0}v_0^2 + 2\Delta p_0} \right)^2 \quad (11)$$

Results and Discussions

Random Characteristic of Measured Data

Figure 9 and Figure 10 show the time history examples of the measured pressure fluctuation and strain, respectively. From these figures, the history data seems to have the random characteristics. Figure 11 and Figure 12 show the probability distribution obtained by the measured pressure fluctuation and strain, respectively. From these figures, it was confirmed that the shape of the measured probability distributions were almost close to the normal probability distribution. This is one of the typical characteristics of the random vibration [8]. Table 3 shows the comparison between the instantaneous maximum value and the 3σ value, here σ is the standard deviation. Table 3 shows the instantaneous value is almost close to the 3σ in both of the measured pressure fluctuation strain. Therefore the maximum stress can be obtained the three times of the overall RMS of the stress obtained by the random vibration analysis.

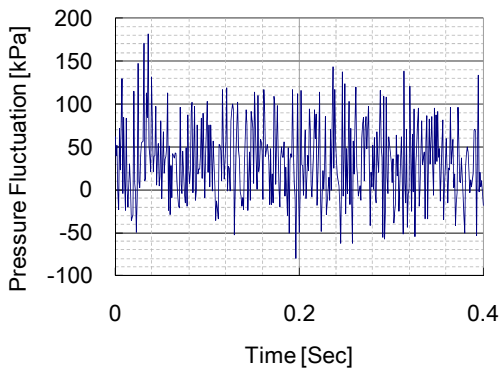


Fig.9 Time History of Measured Pressure Fluctuation (TPA4: Upstream Pressure of RO (TP1) is 27barg)

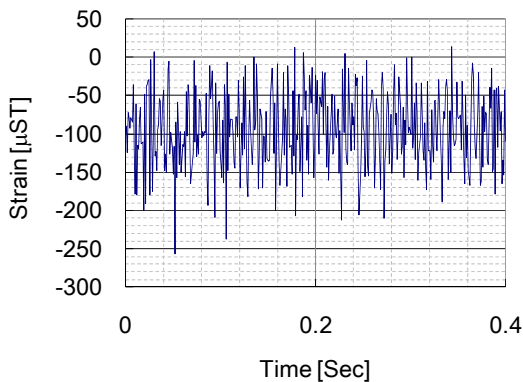


Fig.9 Time History of Measured Pressure Fluctuation (ST2y: Upstream Pressure of RO (TP1) is 27barg)

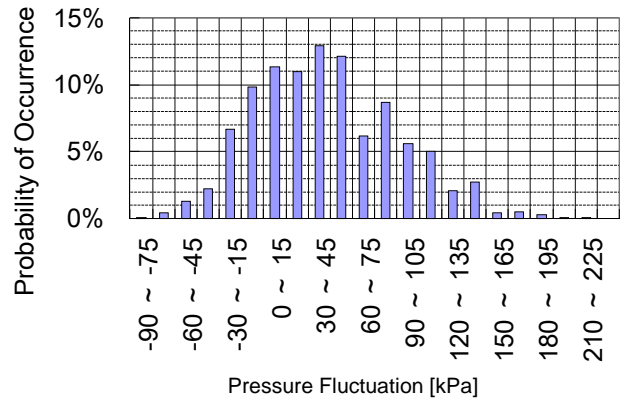


Fig.11 Probability Distribution of Measured Pressure Fluctuation (TPA4: Upstream Pressure of RO (TP1) is 27barg)

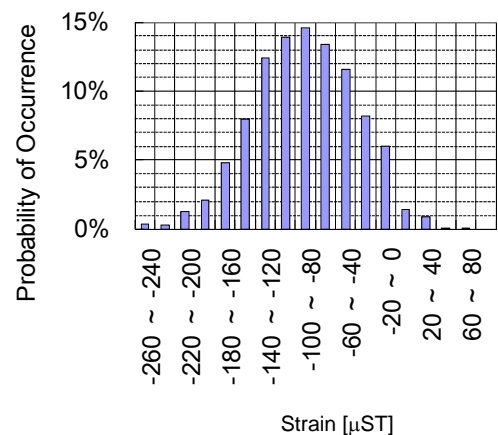


Fig.12 Probability Distribution of Measured Strain (ST2y: Upstream Pressure of RO (TP1) is 27barg)

Table 3 Comparison between 3σ and Instantaneous Maximum Value

	3σ Value	Instantaneous Maximum Value
Pressure Fluctuation (TPA4)	144 kPa	149 kPa
Strain (ST2y)	154 μST	164 μST

Pressure Fluctuation in the Pipe

(1) Dominant Factor of Pressure Fluctuation

Figure 13 shows the comparison between the pressure fluctuation at the just upstream of the tee connection (TPA1) and the pressure fluctuation at the just downstream of the tee connection (TPA4). From Fig. 13, it was confirmed that the pressure fluctuation at the downstream of the tee (TPA4) is considerably larger than

that at the upstream of the tee (TPA1). If the effect of the AIV (Acoustically Induced Vibration) generated by the RO is large, the pressure fluctuation at the upstream of the tee would be large. However, such kind of tendency is not observed. Therefore, it is confirmed that the dominant factor of the pressure fluctuation in this experimental system is the turbulence occurred at the downstream of the tee connection.

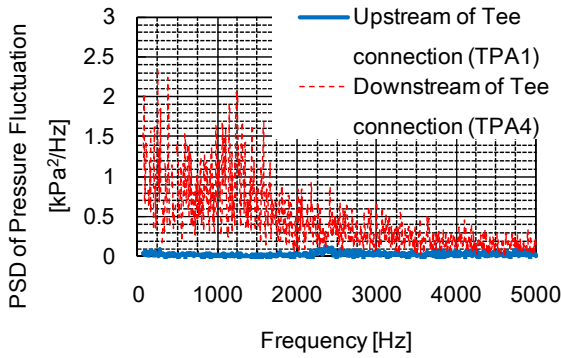


Fig.13 Power Spectrum Density of Pressure Fluctuations at Upstream and Downstream of Tee

(2) Relation between Pressure Fluctuation and $\rho_g Av^2 + 2\Delta pA$

Figure 14 shows the comparison between the upstream pressure of RO and RMS of the pressure fluctuation measured at downstream of the tee connection. From Figure 14, it is observed that the pressure fluctuation increases as the upstream pressure of RO increases. Figure 15 shows the pressure fluctuation divided by $\rho_g Av^2 + 2\Delta pA$ (fluid momentum + pressure change in case of critical condition) as a function of RO upstream pressure. Here, the term of $\rho_g Av^2 + 2\Delta pA$ expresses the effect of the total pressure change through the tee as explained before. From Figure 15, the pressure fluctuation is almost proportional to $\rho_g Av^2 + 2\Delta pA$ since the ratio of the pressure fluctuation to $\rho_g Av^2 + 2\Delta pA$ is almost constant within the deviation of 4% for wide range of the upstream pressure condition.

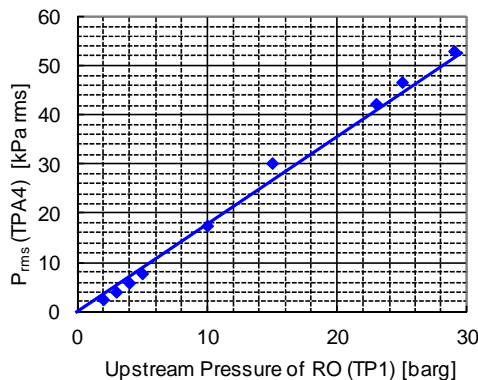


Fig.14 Overall RMS of Pressure Fluctuation in Pipe

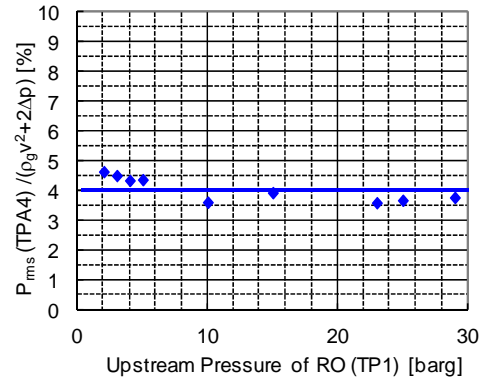


Fig.15 Ratio of Pressure Fluctuation to $\rho_g v^2 + 2\Delta P$

Random Vibration Analysis

(1) Vibration Mode

Figure 16 shows the shape of the shell mode vibration obtained by the strain measurement taking the phase difference at each measurement point into account. The vibration levels at the points from 22 to 40 are assumed to be equal to the measured vibration levels at the points from 1 to 21. In the experiment, the 2nd and 3rd shell modes are observed at 400Hz and 1170Hz, respectively, as shown in Figure 16. Figure 17 shows the 2nd and 3rd mode shapes of the shell mode vibration obtained by the FEA analysis. From the comparison between Figure 16 and Figure 17, the vibration modes and its natural frequencies are good agreement between the experimental results and the FEA analysis results.

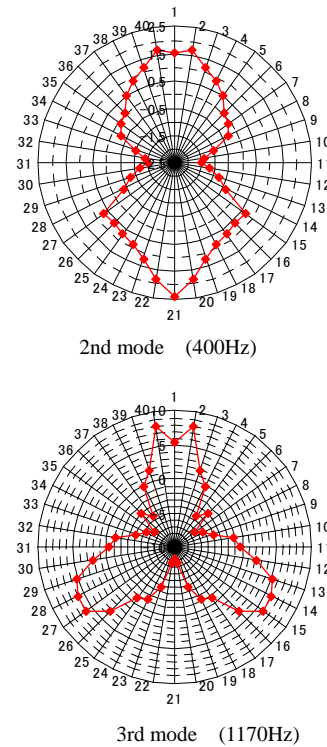


Fig.16 Shell Mode Vibration (Experiment)

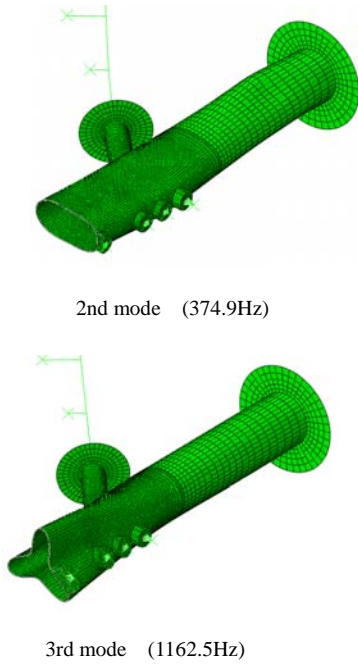


Fig.17 Shell Mode Vibration (FEA Analysis)

(2) Frequency Response

Figure 18 shows the PSD of the random vibration stress at the measurement point “15” shown in Fig.3. From Figure 18, on the peak frequencies (375Hz, 1160Hz, and 2450Hz) and their components, it is observed that the FEA and experimental results has same tendency, even though the complete agreement is not observed. Since the random vibration caused by the turbulence is quite complicated, it is quite difficult to predict the vibration characteristic precisely by the analysis. However, the FEA analysis would be useful to predict the basic characteristics of the random vibration from Figure 18.

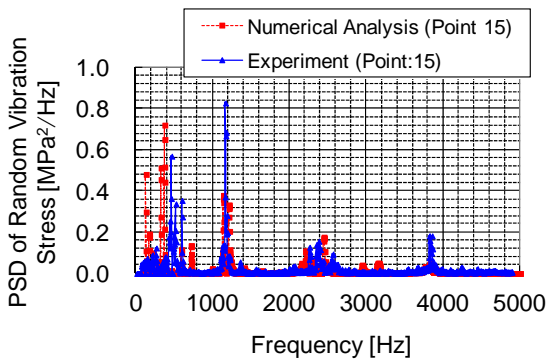


Fig.18 Spectrum of Random Vibration Stress (Upstream Pressure of RO is 25barg)

(3) RMS Value of Vibration Stress

Figure 19 shows the comparison between FEA and experimental results on the overall vibration stress. From Figure 19, it was confirmed that the overall RMS value of the random vibration stress of the experimental results almost agreed with that of the FEA results. Therefore, the FEA analysis in this study is useful to evaluate the random vibration stress at the tee connection.

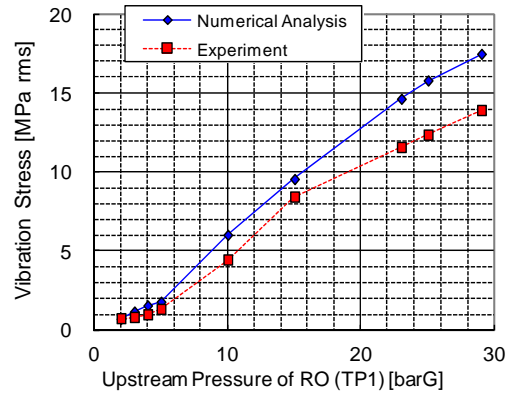


Fig.19 Comparison of Vibration Stress between Analysis and Experiment

(4) Evaluation with Vn (Vibration Velocity Number)

Figure 20 shows the relation between the Vn (Vibration Velocity Number) and the overall RMS of the random vibration stress. Figure 20 shows that the overall RMS of the random vibration stress is almost proportional to the Vn. Therefore, the integrity of the piping structure against the shell mode vibration at the combined tee can be evaluated by the proposed evaluation index, Vn.

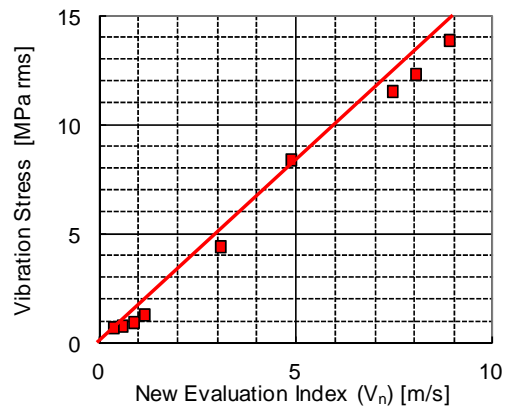


Fig.20 Comparison between Vibration Stress and Vn (Vibration Velocity Number)

Conclusion

In order to investigate the characteristic of the shell mode vibration at the downstream of the tee connection caused by the turbulence, experiments and numerical analysis were executed. As a result, the following conclusions are drawn:

1. The overall RMS of the pressure fluctuation caused by the turbulence at the tee connection is proportional to the total pressure change through the tee expressed by $\rho_g Av^2 + 2\Delta p A$.
2. The random vibration of the piping shell mode caused by the turbulence at the tee connection can be evaluated by FEA approach with the random vibration analysis.
3. The random vibration stress can be evaluated by the evaluation index of the random vibration stress, V_n proposed in this study.

REFERENCES

- [1] Au-Yang, M.K., Dynamic Pressure inside a PWR-A Study based on Laboratory and Field Test Data, Nuclear Engineering and Design, Vol.58, pp.113-125., 1980
- [2] JSME Standard, "Guideline for Evaluation of Flow-Induced Vibration of a Cylindrical Structure in a Pipe" JSME S 012, 1998. (in Japanese)
- [3] Blevins, R.D., Flow-Induced Vibration 2nd ed., Van Nostrand Reinhold. 1990.
- [4] Arihara, Okada, Dynamics and Design Conference 2009 Collection of Papers (in Japanese)
- [5] T.Nakamura et al., Flow-Induced Vibration of a Large-Diameter Elbow Piping Based on Random Force Measurement Caused by Conveying Fluid (Visualization Test Results), PVP2005-71277
- [6] Kazuo Hirota et al., Flow-Induced Vibration of a Large-Diameter Elbow Piping in High Reynolds Number Range; Random Force Measurement and Vibration Analysis, Flow Induced Vibration 2008
- [7] Thomas Shurtz et al., Analysis of Induced Vibrations in Fully-Developed Turbulent Pipe Flow Using a Coupled LES and FEA Approach, FEDSM-ICNMM2010-30477, ASME 2010
- [8] Fatigue Analysis for Random Vibration, Ansys Advantage, Vol.2 Issue-3, 2008 (In Japanese)
- [9] Paul H. Wirsching et al., "Random Vibrations Theory and Practice", DOVER Books



On the effects of droplets modulating the acoustic source powers generated in T-joints

Pejman Shoeibi Omrani
 Fluid Dynamics Department,
 TNO Science and Industry,
 Stieltjesweg 1, 2628 CK Delft,
 The Netherlands
 Email: pejman.omrani@tno.nl

Joachim, Golliard,
Stefan Belfroid,
Nestor Gonzales Diez
 Fluid Dynamics Department,
 TNO Science and Industry,
 Stieltjesweg 1, 2628 CK Delft,
 The Netherlands

ABSTRACT

High Reynolds number gas flows in pipelines with pipe elements, such as orifices and T-joints, can induce pulsations which can lead to piping vibration. In these cases, the acoustic waves in the pipes are intensified or attenuated by an interaction with the shear layer at the restrictions or T-joint. In this study, the effect of droplets on the acoustic source terms generated from the T-joints is presented.

Experiments are performed in which different liquid rates and different droplet sizes are injected in a double T-joint system.

INTRODUCTION

In piping systems with T-joints, the shear layer at the edge of the joint can interact with acoustical waves present in the duct and cavity and lead to production or absorption of acoustic power. Sound production leads to the generation of flow induced pulsations, which can itself result in piping vibrations. As this is a safety issue, prediction of the possible occurrence, frequency and amplitude of the flow induced pulsation and vibrations (FIP and FIV, respectively) is of prime importance.

The whistling frequency can be related to the flow velocity with the non-dimensional Strouhal number, which is defined as:

$$Sr = \frac{f d_{sidebranch}}{U_{flow}}$$

with f the frequency [Hz], U_{flow} the average velocity in the main pipe [m/s] and $d_{side-branch}$ the diameter of the side branch [m].

A large number of both numerical and experimental work has been done [1-5] on the sound production in

different T-joint configurations. A review is given in Tonon *et. al.* [2].

In gas production or transport lines small traces of liquid are often present. Liquid can influence the sound production in different ways. The presence of small amount of droplets in the main flow will cause a small shift in the speed of sound and increase the acoustic damping. The presence of droplets/liquid at or near the wall can disturb the shear layer directly, by the presence of small droplets present in the shear layer, or indirectly via the presence of droplets, rivulets or a film at the wall upstream of the T-joint and at the separation point.

The effects of particle inertia on the flow can be categorized by the non-dimensional number Stokes number, which can be defined by the ratio of the particle response time to the fluid response time.

$$St = \frac{\tau_p}{\tau_F}$$

Where $\tau_p = \frac{\rho_p d_p^2}{18\mu}$ (particle response time) and

$\tau_F = \frac{L}{U}$ (fluid response time, with L and U the characteristic length [m] and velocity [m/s]).

From experience, large amount of liquid will prevent the formation of a stable shear layer and therefore the occurrence of FIPS for cylinders. A critical liquid volume content (void fraction) of 15% is given in literature [10] which means no FIPS can occur in the void fraction between 15% to 95%. Although high liquid loads can induce themselves large dynamic forces. However, at this stage it is unknown, at which liquid mass or volume fraction, the possibility of the presence of FIPS in T-joints must still be considered. Furthermore, the influence of

droplet size and liquid distribution (droplets, rivulets, film) is unknown.

The goal of the study is to evaluate the influence of the presence of a small amount of liquids on both the Strouhal number and on the amplitude of the produced pressure pulsations for a T-joint configuration

In this study, a double-T configuration was chosen, as it is shown in the Figure 2. The configuration was chosen as it was known from literature to generate clear tones in case of gas only. This configuration consist of an A3 mode in combination with an A2 mode (Figure 1).

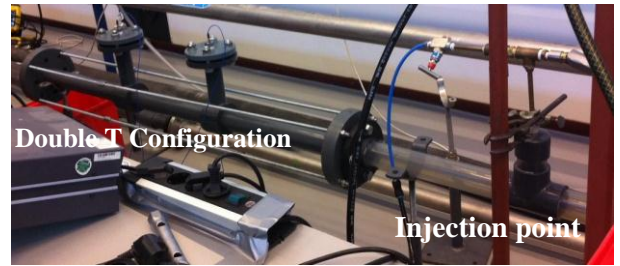


Figure 2- Experimental setup.

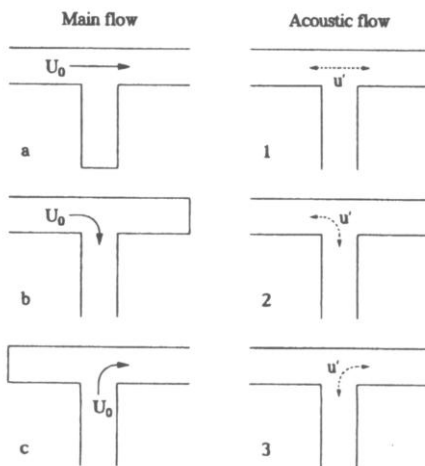


Figure 1- Definition of source conditions in T-joints, via the direction of mean flow and acoustic field [3].

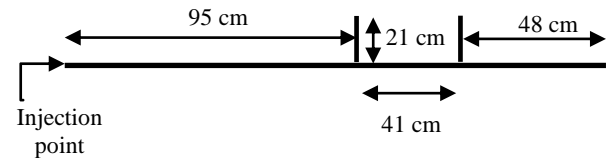


Figure 3- The dimensions of the setup.

Liquid injection is done via injection nozzles (BETE type: PJ 8, 20, 28, 40). The injection is achieved by mounting the nozzles on a probe inserted into the main tube via a T-joint with a diameter of 12 mm. The injector is situated 950 mm upstream of the first side branch.

Different nozzles allowed for a variation of the droplet size and the injection rate. For a given nozzle, the injection rate is controlled via control of the upstream nozzle pressure using a bypass from the water pump. The different nozzles produce fine droplets, in the order of 50 to 100 μm with an initial 90° spreading angle cone. Different injector nozzles can generate the same liquid mass loading either by injecting a large amount of small droplets or injecting a small amount of large droplets. These droplets sizes were measured for the spray nozzles outside the tube but not during the experiments (due to the confinement of the pipe walls and the deposition on the walls).

The calibration curves of the different nozzles are given in Figure 4. For a given nozzle the droplet diameter will decrease with an increase injection rate as the droplet size changes can be approximately related to the changes of the pressure by the following equation [9].

$$\frac{d_{p2}}{d_{p1}} = \left(\frac{P_2}{P_1} \right)^{-0.3}$$

EXPERIMENTAL SETUP

The experiments were conducted at the TNO Fluid Dynamics lab in Delft. The experimental setup is given in the Figure 2. The setup is an open-open system with a main pipe diameter of 0.0525 m and the diameter of the side branches are 0.0469 m with a length of 0.21 m (measured from the center of tube). The test section is 1.84m. The downstream end of the pipe is an open end. The upstream of the pipe section is connected to a muffler with a length of 1005 mm and a reducer from 3 to 2 inches with the length of 185 mm which can result in an effective open end. The T-joints are positioned upwards to avoid the liquid trapping inside the branch. The flow direction in Figure 2 is from right to left. The dimension of the setup is presented in the Figure 3. The T-joints were rounded (5 mm) at the upstream edge and at the downstream side they were sharp edges. This configuration was again chosen to increase the FIP amplitude.

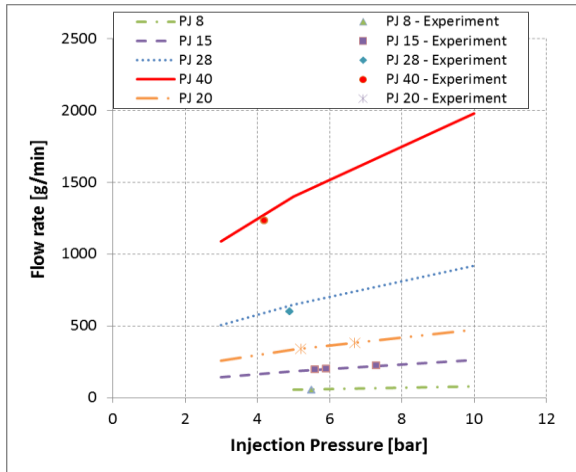


Figure 4- Calibration curves for the different injection nozzles [9].

The pressure fluctuations are measured via the piezoelectric pressure transducers with sensitivity of 0.001 mv/Pa at the ends of the T-joints. The T-joints are located at the top of the setup to avoid the liquid trapping inside the cavity. The gas flow rate and temperature are monitored with the turbine flow meter and temperature probe (PT-100). A gas velocity range of 15 to 65 m/s was used with a liquid injection rate varying from 0 to 1.2 l/min. It must be noted that a large part of the injected droplets deposit on the walls.

The deposition rate of the droplets on the wall was estimated from the McCoy and Hanratty study [7] and the entrainment rate of the droplets from the wall film was approximated from the Kataoka *et al.* study [8]. Based on the approximation for the gas velocity range of 15 to 60 m/s and the liquid rate of 50 to 1230 g/min, the droplets entrainment rate from the wall film will be in the range of 0.04 to 0.1. The deposition rate in this range will also be between 5×10^{-5} to 3.3×10^{-3} per unit area [kg/s.m^2]. The deposition rate estimation is based on the droplets with the diameter between 50 to 100 μm . It is important to note that higher deposition rate will be caused by the low gas velocity and high liquid injection rate.

A series of base line experiments are done without liquid injecting. The acoustic whistling frequency is obtained by FFT (Fast Fourier Transform) of the pressure signals from the pressure transducers in the cavity.

In evaluating the influence of liquid, three sets of experiments are done. In the first, gas flow sweeps are done at a fixed injection rate. In the second a sweep of the liquid injection rate is done at a fixed gas velocity. The final step is to keep the gas-liquid loading constant. These sets of experiments are done using different nozzle sizes to be able to vary the liquid rate and the droplet sizes independently.

RESULTS

Without liquid injection

For the experiments without liquid, the measured pulsation amplitude is plotted as function of Strouhal number in the Figure 5. The Strouhal number is defined with the side branch diameter and the average velocity at the inlet of the pipe. The amplitude is made dimensionless with the acoustic amplitude based on the gas density (ρ) and gas speed of sound (c).

Two modes are measured. The lowest measured mode is at a Strouhal number of $Sr = 0.4$, the second at a Strouhal number of $Sr = 0.95$. The repeatability of the base experiments was good with a maximum deviation of 8%.

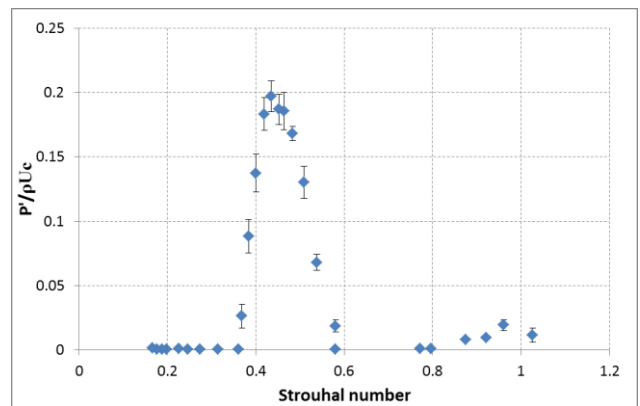


Figure 5- The dimensionless pressure pulsation amplitude versus the Strouhal number of a double T-joint configuration without liquid injection. The pulsation amplitude is made dimensionless with the gas density (ρ), average gas velocity (U) and the speed of sound (c).

With liquid injection

In Figure 6, the dimensionless time-averaged pressure pulsation amplitude for different liquid injection rates is plotted as a function of gas velocity. The different liquid mass flow rates are obtained by using different injector nozzles. The liquid flow rates are presented in grams of water per minute. At a typical gas velocity of 50 m/s, the maximum rate of 1230 g/min corresponds to a (no-slip) mass loading of 16%.

The visual observations show that the flow regime below the gas velocity of approximately 38 m/s (with the liquid rate of 1230 g/min) is dominated by the stratified flow. By increasing the gas velocity, the flow pattern will be dominated by the mist flow. This velocity is marked in the Figure 6 with the dashed line.

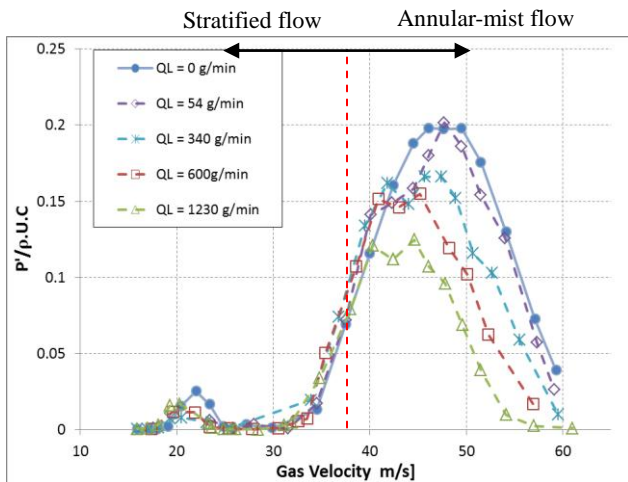


Figure 6- Dimensionless pressure pulsation amplitude versus the gas velocity for different liquid mass flow rates. The dashed line show the region where the flow regime will change from the stratified flow to the mist flow.

At increasing injection rates the amplitude decreases for both the modes measured. The maximum pressure amplitude decreased with a factor of two for the lower mode. For the higher mode the influence is much smaller.

Aside the amplitude also the Strouhal number changes. The same experiments are plotted in Figure 8 as function of Strouhal number. A shift in the Strouhal number (at maximum amplitude) from $Sr = 0.46$ to 0.49 is measured.

The whistling frequency is also plotted versus the gas velocity (Figure 7). The turning point in the Figure 8 indicated the peak of pressure pulsations. It can be seen that the presence of the liquid can shift the frequency in the same gas velocity.

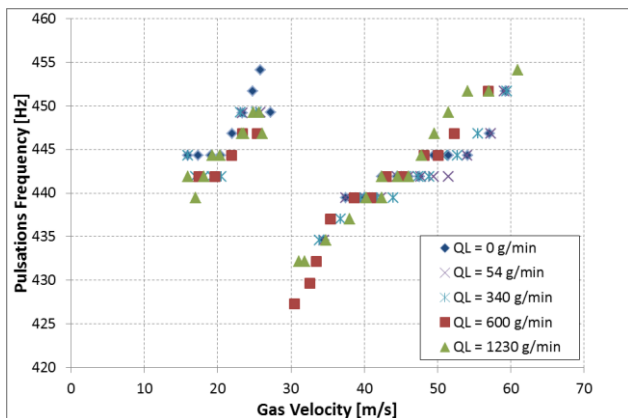


Figure 7- The pulsation frequency versus the gas velocities for different liquid mass flow rates.

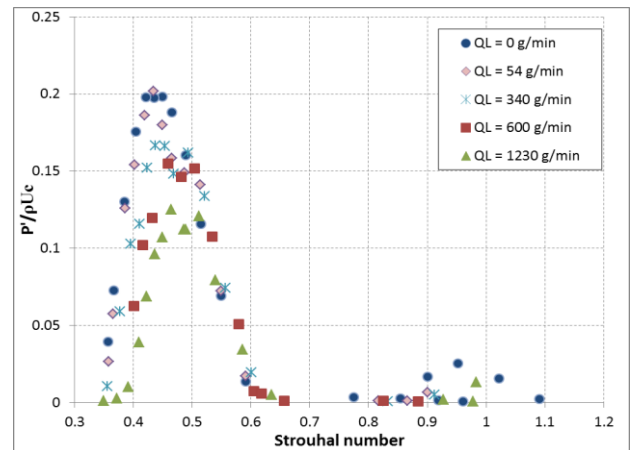


Figure 8- dimensionless pressure pulsations versus the Strouhal number for different liquid injection rates.

In a second series of experiment the gas velocity was kept constant at 47 m/s (corresponding to the maximum for dry gas) and the liquid injection rate was increase from 0 to $Q_L=1200 \text{ g/min}$. The results in terms of Strouhal number are plotted in the Figure 9. In the same graph the results of the dry gas and the highest liquid injection rate of the gas sweep experiments are included. The deviation of the liquid loading line from the straight vertical line is partly due to the difference in the velocity caused by different experimental conditions (compressor load fluctuations, etc.)

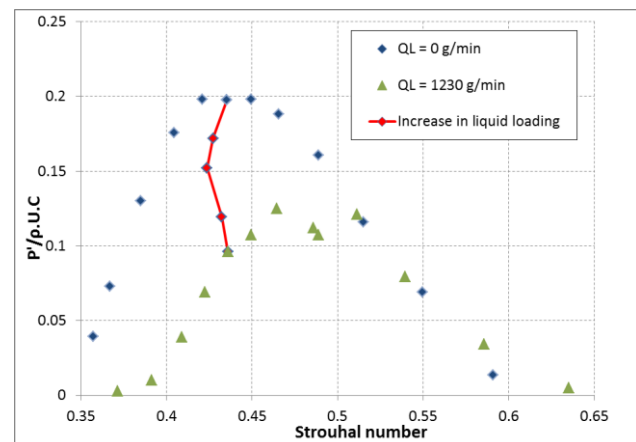


Figure 9- The effect of liquid injection on the pressure pulsations peak value.

In the next part of the study, the changes in the pressure pulsations are studied by keeping the liquid mass loading constant. The liquid mass loading is defined as

$$z = \frac{Q_l}{Q_g} = \frac{Q_l [\text{kg/s}]}{\rho_g u_g A_p}$$

For this reason, a higher gas velocity will require larger liquid injection. The mass loading was kept at the value of 5% and two different injection nozzles were used at different injection pressure. Thus, there will be a difference in the droplets size. The changes of

dimensionless pressure pulsation amplitude compared to reference case (no liquid injection case) are plotted versus the Strouhal number in Figure 10. The changes are given as a relative and absolute value, defined by:

$$\Delta_{abs} = \left| \left(\frac{P'}{\rho U c} \right)_{noliquid} - \left(\frac{P'}{\rho U c} \right)_{withliquid} \right|$$

$$\Delta_{relative} = \left| 1 - \frac{\left(\frac{P'}{\rho U c} \right)_{noliquid}}{\left(\frac{P'}{\rho U c} \right)_{withliquid}} \right|$$

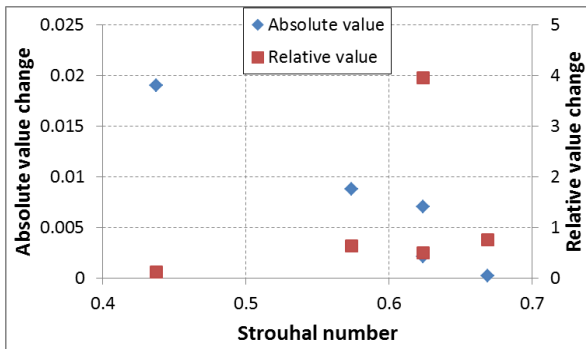


Figure 10- The dimensionless pressure pulsations changes (relative and absolute value) as a function of Strouhal number.

It was shown that at low velocities the effect is less dominant and it can be due to the low droplets fraction in the shear layer and the vortices.

DISCUSSION

The influence of the liquid on the amplitude and frequency can be due to:

- Lower source strength due to the influence of liquid directly on the shear layer.
- Enhanced acoustic damping in the main pipe.
- Influence on the speed of sound resulting in a less effective resonance.

Effect of liquid on the shear layer

The presence of the particles or droplets with high inertia in the shear layer can attenuate the vortices. In the study of Shoeibi Omrani *et al.* [11] the effect of solid particles inertia and mass loading on the periodic vortex shedding was determined. It was found that the particles with larger Stokes number and mass loading can damp the vortex shedding. As the shear layer interaction with the acoustic waves is the main mechanism of the sound production in the cavity, the shear layer damping might alter the pressure pulsations in side branches.

The observation in this study shows that at lower air velocities, the flow regime is closer to annular flow and by increasing the gas velocities, the flow will become

annular-mist or dispersed flow. Note that the T-joints are installed upwards and they will not be affected by the wall liquid film at the bottom of the pipe. Thus, in low air velocities there will be less droplets entrained close to the cavity and consequently the shear layer will be less effected by the presence of the liquid, specifically droplets.

Effect of liquid fraction on the sound velocity

Another important factor is the effect of the liquid on the sound velocity. The mixture sound velocity can affect the dimensionless pulsation level by changing the amplitude of the pulsations or shifting the frequency of the pulsations. In this analysis only the effect of mixture sound velocity on the amplitude of the dimensionless pressure pulsations is discussed.

Small amounts of droplets lowers the speed of sound significantly. For a mixture, the effective speed of sound is given by

$$c_{mixture} = \frac{1}{\sqrt{\left(\frac{\alpha_L}{\rho_L c_L^2} + \frac{1 - \alpha_L}{\rho_G c_G^2} \right) \rho_{mixture}}}$$

with c_G and c_L are the speed of sound for the gas and liquid phase [m/s], ρ_G and ρ_L are the gas and liquid density [kg/m^3] and α_L the liquid hold-up. For the experiments no hold-up measurements were done and no information on the entrained fraction is present. The speed of sound is estimated assuming all injected liquid is present in the form of droplets which move at the same velocity as the gas.

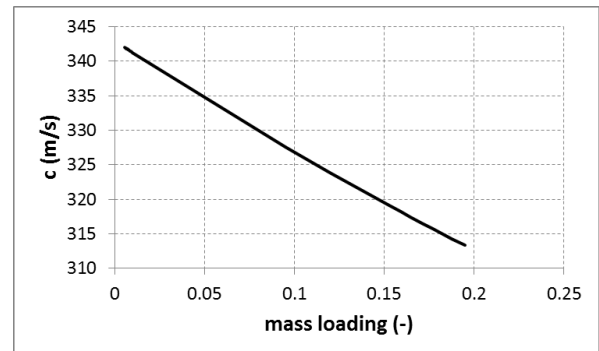


Figure 11- The mixture sound velocity as a function of mass loading.

It is important to note that this sound velocity is just an approximation and it cannot be exactly determined, because there is no information available about the percentage of the liquid that are present in the form of droplets or film. The results made dimensionless with the mixture speed of sound are plotted in Figure 12. From this graph it is concluded that the direct influence of the speed of sound, due to the velocity fluctuations is expected to be minor.

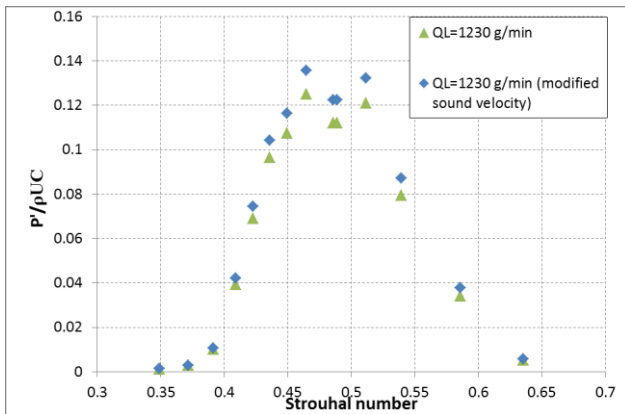


Figure 12- The effect of mixture sound velocity on the dimensionless pressure pulsations.

The figure shows that the effect of mixture sound velocity is more significant at the peak values. It can shift the data on the y-axis to a higher value (in this liquid loading between 6 to 13 percent increase) for larger liquid flow rates but the value is not significant. This does not explain the amplitude deduction observed in the Figure 6.

Effect of liquid on the acoustic damping

In an ongoing project the acoustic damping is measured in a pipeline for different liquid loads. The work is still in progress and no definite conclusion is available. The preliminary results show relatively low added acoustic damping for the air-water mixture.

CONCLUSIONS

This study focuses on the effect of liquid on the acoustic source power in the T-joints cavities. The double T-joint was used in this study and the liquid with different mass loading was injected to the system. The results show that the presence of liquid can alter the amplitude and the frequency of the pressure pulsations in the cavities. The effect is more dominant when the gas velocity and the liquid mass loading is larger. The peak of pressure pulsations level can be altered by injecting droplets.

The effect of the liquid on the sound velocity scaling was approximated and it shows the increase in the dimensionless pulsations levels.

REFERENCES

- [1] A. Powel, *Theory of vortex sound*, *Journal of the acoustical Society of America*, Vol. 33, pp. 395-409, 1961.
- [2] D. Tonon, A. Hirschberg, J. Golliard, S. Ziada, *Aeroacoustics of pipe systems with closed branches*, *Journal of Aeroacoustics*, pp. 201-276, 2011.
- [3] S. P. C. Belfroid, M.C.A.M. Peters, W. Schiferli, J. Buffing, *Flow induced pulsations caused by split flow in*

T-branch connections, 6th FSI, AE and FIV Symposium, Vancouver, Canada, 2006.

[4] P. Martinez-Lera, J. Golliard, C. Schram, *Numerical study of flow-induced pulsations in pipe systems with closed branches*, *American Institute of Aeronautics and Astronautics*, Stockholm, 2010.

[5] D. Tonon, G. Nakiboglu, J. F. H. Willems, A. Hirschberg, R. E. Leandro, W. Polifke, H. J. Riezebos, *Self-sustained aeroacoustic oscillations in multiple side branch pipe systems*, *Proceeding of 15th AIAA conference*, 2009.

[6] M.C.A.M. Peters, E. Van Bokhorst, *Flow-induced pulsations in pipe systems with closed branches, impact of flow direction*, 7th International conference on Flow-Induced Vibration, Lucerne, Switzerland, 2000.

[7] D. D. McCoy, T. J. Hanratty, *Rate of deposition of droplets in annular two-phase flow*, *Int. J. Multiphase flow*, Vol. 3, pp. 319-331, 1977.

[8] I. Kataoka, M. Ishii, A. Nakayama, *Entrainment and deposition rates of droplets in annular two-phase flow*, *Int. Journal of Heat and Mass transfer*, Vol. 43, pp. 1573-1589, 2000.

[9] BETE, *nozzles for industry, pollution control and fire protection catalogue*.

[10] S. Kaneko, T. Nakamura, F. Inada, M. Kato, *Flow-Induced Vibrations, Classifications and lessons from practical experiences*, Elsevier Publications, 2008.

[11] P. Shoeibi Omrani, S.P.C. Belfroid, A. Twerda, B. J. Boersma, *Numerical study on the effects of particles on damping the vibration of a bluff body due to the vortex shedding*, 10th International Conference on Flow-Induced Vibration, 2012.



Multiphase Fluid Structure Interaction in pipe systems with multiple bends

David Remans

TNO technical sciences
Department of Fluid Dynamics
Delft, The Netherlands
david.remans@tno.nl

Evert van Bokhorst

TNO technical sciences
Department of Fluid Dynamics
Delft, The Netherlands
evert.vanbokhorst@tno.nl

Erik Nennie

TNO technical sciences
Department of Fluid
Dynamics
Delft, The Netherlands
erik.nennie@tno.nl

Stefan Belfroid

TNO technical sciences
Department of Fluid
Dynamics
Delft, The Netherlands
stefan.belfroid@tno.nl

ABSTRACT

Two-phase flow occurs in many situations in the process industry. Under certain circumstances this can be a source of flow-induced vibration forces. Although the occurrence of such forces is well known, not much is known about their magnitudes.

Previously a set of experiments was carried out at small scales (6 mm and 25 mm diameter). In these experiments the dynamic forces on bends and T-joint structures were measured and simple estimation models were setup. In these experiments only fully developed flow was used and a single geometrical component (bend or T-joint) [1][2][5][9].

In this paper a set of experiments are discussed in which the previous experiments are repeated at 4" scale. Dynamic forces and pressures are measured at the bends. Furthermore the upstream flow condition was verified visually. The results are compared to the previous small scale experiments and a scaling rule has been derived.

NOMENCLATURE

A	Tube cross sectional area	[m ²]
D	Tube diameter	[m]
F _{rms}	RMS value of F _R	[N]
Rem	Mixture Reynolds number	[-]
We	Weber number	[-]
u _m	Mixture velocity	[m/s]
u _{s,g}	Superficial gas velocity	[m/s]
u _{s,l}	Superficial liquid velocity	[m/s]
α _l	Liquid hold-up	[-]
ρ _l	Liquid density	[kg/m ³]
σ	Surface tension	[N/m]
Q _{liquid}	Liquid mass flow	[kg/h]
Q _{gas}	Gas mass flow	[kg/h]

INTRODUCTION

Flow assurance is often taken to include mostly events occurring inside a flow line or well, such as wax deposition or the formation of hydrates. However, structural integrity of a piping system is obviously a basic requirement for flow assurance. This can become an issue in many situations. In single phase flow, water hammer waves caused by fast valve closures may cause high loads. In multiphase flows these problems may be exacerbated: in slug flow, for example, slugs of water move at high velocities dictated by the gas flow, resulting in high momentum and consequently high forces in locations where the flow changes direction.

Previous experiments to determine the multiphase forces were primarily on smaller scale (0.25 – 1") [2][9]. Based on these experiments, no clear conclusion could be drawn on the effect of the tubing size. Therefore a set of experiments was setup on a 100 mm scale. In this paper in particular the three sets of the experiments by the authors are compared to each other:

- 6mm, air-water, atmospheric conditions, glass tube, horizontal setup [9]
- 25mm (sometimes referred to as 1"), air-water, atmospheric conditions, Perspex and PVC, horizontal setup [2]
- New 100mm (sometimes referred to as 4"), air-water near atmospheric, Perspex, PVC, large height differences in setup.

EXPERIMENTAL SETUP

The experimental setup consists of a 19m long pvc pipe, including two transparent sections and the bend under investigation. The diameter of the pipe is 100mm. The water used is normal tap water, treated to prevent corrosion and the grow of algae. The treatment did not

change the relevant physical properties, such as surface tension viscosity or density.

Mixing of the air and water occurs in an Y-piece with air being injected from the top. The injection of pressurized air is controlled by a set of flow control valves. After passing some bends, the mixture enters a long horizontal section (length 124 D) to develop a stable flow condition. After this straight section the bend under investigation is located. After this bend the mixture will leave the setup to a large separator vessel (volume 7m³) at atmospheric conditions.

The gas flow was varied from a superficial velocity of 0.1 to 20 m/s and the liquid flow rate was varied from 0.15 up to 3.0 m/s. The water was circulated using two pumps connected to a large vessel at atmospheric conditions. A schematic view of the setup can be found in Figure 1. In Figure 2 a photograph of this setup can be found.

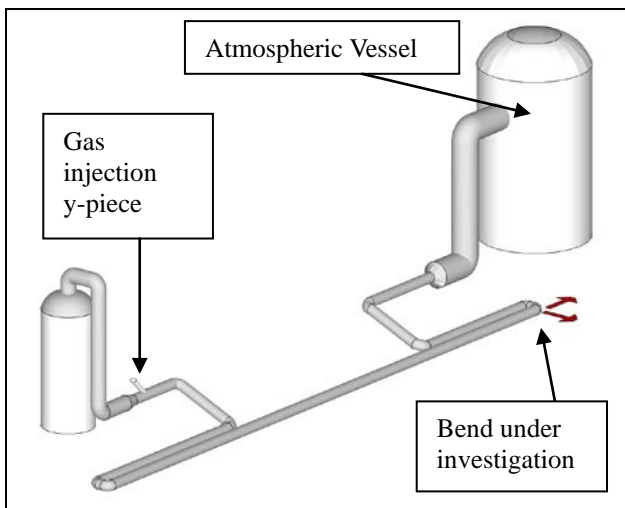


Figure 1 Schematic overview of the setup

The force on the bend was measured in two directions using force transducers (Brüel & Kjør type 8230-003). To be able to measure the forces in two directions independent of each other a set of stingers was used that only contains significant stiffness in one direction (see Figure 3).

The dynamic and static pressure is measured at three locations upstream the bend. One of the pressure transducers is located just before the bend. Pressures are measured using a strain-gauge pressure transducer (HBM type P3). The flow is measured using standard flow meters present in the water and air rigs at TNO flow lab facilities.

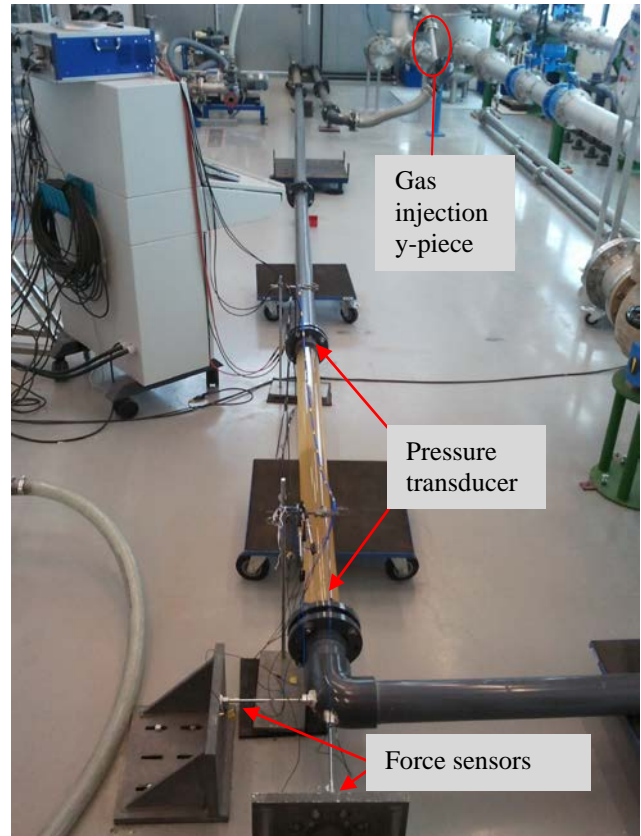


Figure 2 Photograph of the measurement setup.

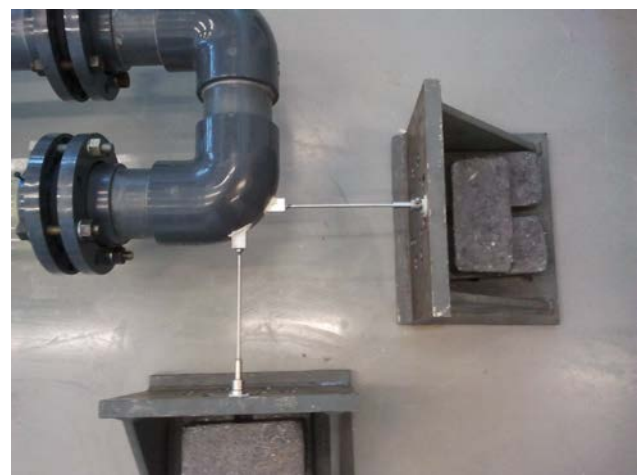


Figure 3 Connection of the force transducers to the bend under investigation (Bend 1)

The Bends under investigation are a 180 degree bend with a distance of 0.3 m, and a 90 degree bend with a bending radius equal to the diameter of the pipe. They will be referred to as Bend 1 and Bend 2, respectively. Bend 2 is a large U-bend with a spacing between the two bends of 2.5m. In Figure 4 a photograph of the two bends are presented.



Figure 4 Photographs of Bend 1 (left) and Bend 2 (right), respectively

In the presentation of the results in this paper, the resulting force is calculated by adding the force measured in the two horizontal directions (see formula 1)

$$F_R = \sqrt{F_1^2 + F_2^2} \quad (1)$$

Before the experiment started the mechanical coupling of the piping to the supporting structure was tested by simultaneously measuring the accelerations on both the supports and the piping on a given input. During the experiments, these accelerations are continuously monitored.

FLOW CHARACTERISTICS – FLOW MAP

In Figure 5, the experimental flow regime map is compared to the classic flow maps of Mandhane and Baker [6], [7]. Mandhane's flow map is based on pipe diameters ranging from 12.7 mm to 165.1 mm. The Baker flow map is also based on a large number of experiments. The flow map derived from the visual observations in these experiments shows agreement with the classical flow maps. This is an indication that the inflow length of this set-up is sufficiently long to produce fully developed slug flow. Due to practical limitations in the setup there are a limited amount measurement points outside the slug regime area.

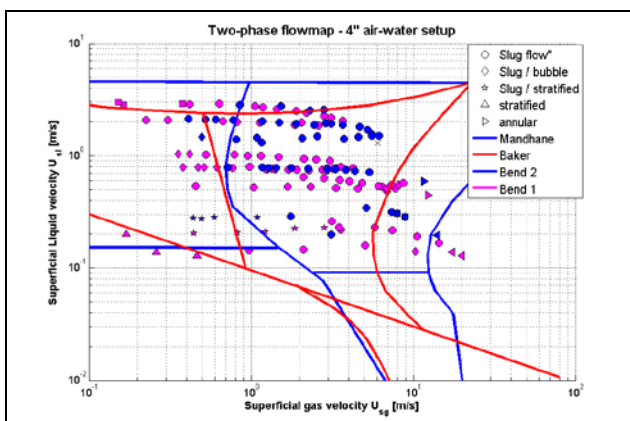


Figure 5 Experimental two-phase flow regime map, compared to Mandhane [6] and Baker [7]

The visual flow regime observations were done on the transparent parts in the piping. Images of a slug passing the transparent section can be found in Figure 6 and Figure 7

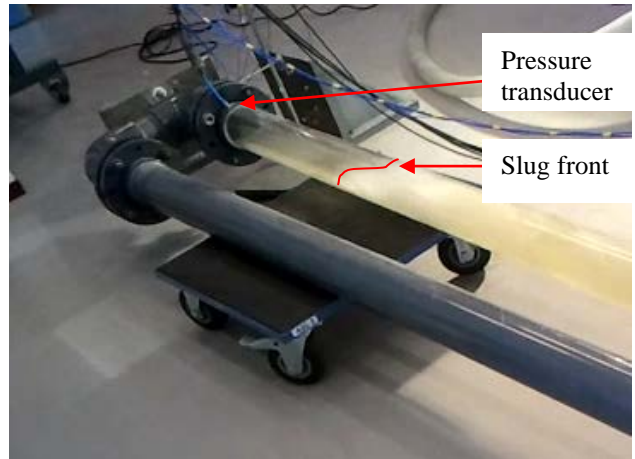


Figure 6 Photograph of a slug just before arriving at the bend under investigation.

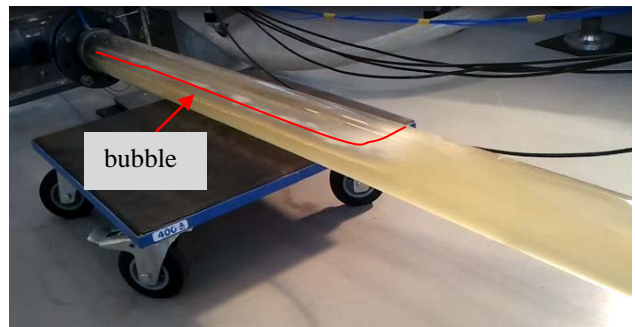


Figure 7 Photograph of a slug in the straight section of the pipe

FLOW CHARACTERISTICS – SLUG FLOW

The flow behaviour between the slugs formed in the 4" setup are very different from slugs in a small 6mm setup. Hydrodynamic slugs in a 6mm setup are almost completely consisting of liquid. There is almost no gas entrained in the liquid slug. At larger diameter the slug is much more aerated. At 6mm a liquid content of the slug of 92% is expected whereas for a 4" pipe this is only 47%. [8] This large difference in gas content in the slugs is a primary reason why there might be a scaling mismatch in the forces. The change in liquid hold-up and therefore momentum is much less for the larger tube sizes compared to the smaller tube sizes. Therefore, less dynamic force are expected.

Furthermore, in the 4" setup, there is a significant height difference between the measurement section and the upstream gas inlet and the downstream separator (Figure 1). These height differences result that not only hydrodynamic slugging can occur, but also more terrain induced slugging is encountered in the experiments. Finally, there is another large difference between the setups. In the 6mm and 1" setup, the outlets to the atmosphere were close to the measurements section, which means that for these small scale experiments never more than one slug was present in the setup.

These differences result that the slug flow encountered in the 4" setup is less regular than was measured for the smaller setups.

FORCES

An example of the measured force for the two positions is given in Figure 8. Included in the same figure is the pressure just upstream of the bend.

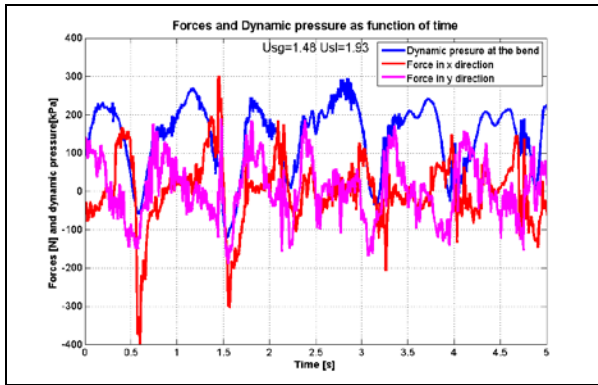


Figure 8 Forces [N] as function of time for force sensor 1 and 2. Included is the pressure measurement just upstream of the bend

The different experiments are compared to each based on the rms value of the total force (combined force sensor 1 and force sensor 2). It must be noted, that for the analysis of the mechanical integrity the absolute maximum and the shape of force transient are important.

Based on experiments on vertical U-bends with tubing size $D = 20.6$ mm, Riverin proposed a relation for the dimensionless force on a bend:

$$\overline{F_{rms}} = \frac{F_{rms}}{\rho_l u_m^2 A} = C We^{-0.4} \tag{2}$$

with We being the Weber number defined as

$$We = \rho_l u_m^2 D / \sigma \tag{3}$$

In his experiments Riverin found a good fit with a constant of $C=10$. In previous experiments on a 6 mm setup the constant C was corrected to $C=3.51$ in order to match with the experiments [9] in the experiments on a 25 mm setup the dimensionless force was under predicted when using $C=10$.

EFFECT OF MULTIPLE BENDS

The results of bend 1 and bend 2 are also evaluated to see what the effect would be of having multiple bends in one setup. Bend 1 is considered to be a combination of two 90 degree bends and bend 2 is considered to be a single 90 degree bend.

The flow regimes are similar for the two set-ups as can be seen in Figure 5. Which means that in both cases it was considered that the same flow patterns arrive at the upstream bend. In Figure 9, the forces on the upstream bend for the two configurations are compared to each. The differences between the two experiments is marginal. This means that in the experiments, the influence of the downstream piping can be considered to be very small. This indicates also that it is likely that each bend can be evaluated independently even in close proximity of other bends. In future experiments, it must be evaluated whether this also holds for the downstream bend.

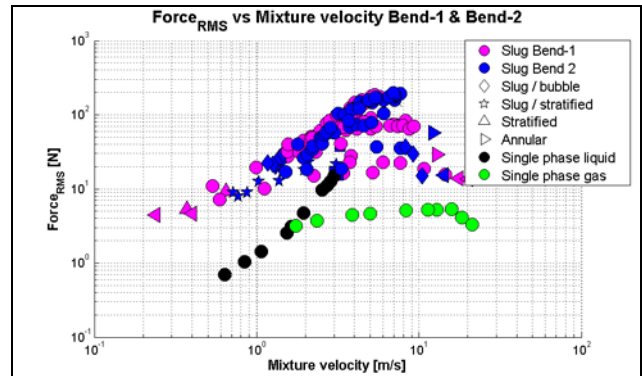


Figure 9 Real rms forces 4" bend 1 & Bend 2

EFFECT OF SCALING

In Figure 10 the total rms forces of the 1" and 4" experiments are compared to each other (note that the results presented in [1][2] contained an error and are a factor 100 lower than previously presented). The 4" experiments are the approximately one order higher, which fits with a direct scaling with the tube area.

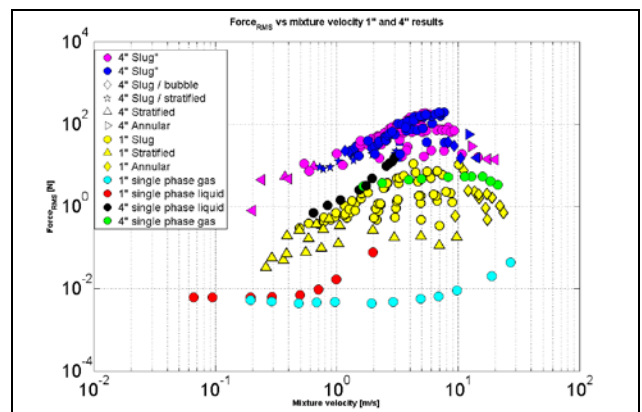


Figure 10 RMS forces of 4 inch setup compared to the 1 inch setup

From the smaller scale experiments it was concluded that the main component in the forces on the bend can be described by a change in mixture momentum when the fluid passes the bend [2]. This seemed valid independently of flow regime.

Therefore rather than making the force dimensionless with the liquid momentum, the force is made dimensionless with mixture momentum. In case of the mixture momentum ($\rho_m u_m^2$) the no slip liquid hold-up is used to calculate the mixture density. That is:

$$\rho_m = \left(\frac{Q_{liquid}}{Q_{liquid} + Q_{gas}} \right) \rho_{liquid} + \left(\frac{Q_{gas}}{Q_{liquid} + Q_{gas}} \right) \rho_{gas} \quad (4)$$

In Figure 11, the dimensionless force is plotted as a function of the no-slip liquid hold-up for the two 4” bend experiments, the 1” experiments and the 6mm experiments. As with the 1” experiments, the scaling with the mixture momentum fails for the single phase conditions but at two-phase conditions, the results are almost independently of tube diameter. It can be concluded that the influence of the amount of liquid on the forces on the bend are equal for scales investigated.

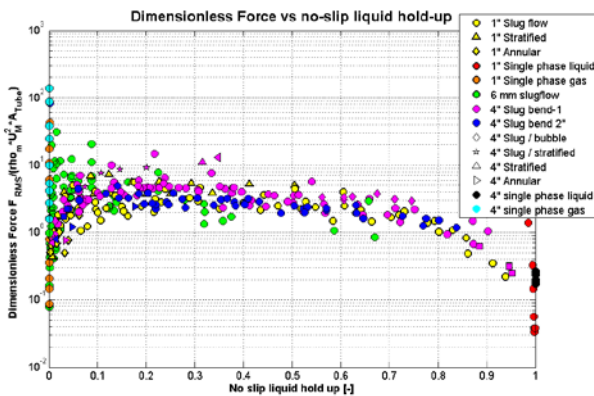


Figure 11 Dimensionless force as function of no-slip liquid hold-up. Results of 6mm, 1” and 4” geometry.

These results confirm that the expression for the resulting rms force, F_R , is given by the following formula:

$$F_R = \sqrt{2} \rho_m U_m^2 A \quad (5)$$

Riverin found that for his specific setup a good fit between the dimensionless forces and the weber number could be made using a constant of $C=10$ (see equation 2) results from a setup with a diameter of 6mm showed a good fit with $C=3.51$ In Figure 12 The results of the 4 inch setup are plotted against the weber number and this time a best fit is made using Riverin criteria with a constant of $C=50$. From this we can say that the weber number, as proposed by Riverin, is not a practical non dimensional number to use for determining the resulting rms forces on a bend due to slug flow.

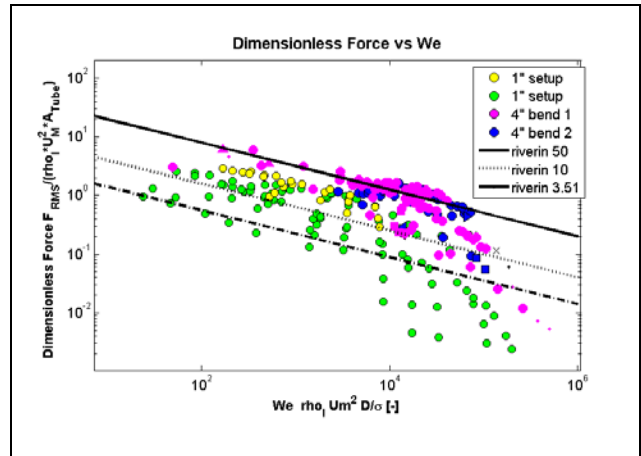


Figure 12 Dimensionless forces as function of the Weber number. Results from the 1 inch and 4 inch setup are displayed.

CONCLUSION

Combining the results and observations from this investigation leads to the following conclusions:

- The flow characteristics of an air-water flow through a 4 inch pipe has been analyzed. The flow regime map corresponds to the classical flow maps. This confirms the validity of the experimental set-up.
- The effect of multiple bends on the resultant force appears to be negligible. A second bend located directly after the bend under investigation does not seem to influence the resultant force on the first bend.
- The criteria described by Riverin is not practical for determining the resultant force since the scaling factor needs to be scaled too when the diameter of the setup is changed.
- The real rms forces do scale linear with the increase of the cross sectional area, when seen as a function of the mixture velocity.
- The dimensionless resulting force as a function of mixture velocity describes the experiments well, because the dimensionless force as a function of no-slip liquid hold-up is similar for the different small scale experiments (ranging from $D=6$ mm to $D=100$ mm). Despite the differences in the setup and the non-controlled hydrodynamic flow regimes, the scaling with mixture momentum works.

REFERENCES

[1] S.P.C. Belfroid, M.F. Carnelutti, W. Schiferli, M. v Osch, Multiphase fluid structure interaction in bends and t-joints, PVP 2010-25696
 [2] S.P.C. Belfroid, M.F. Carnelutti, W. Schiferli, M. v Osch, Forces on bends and t-joints due to multiphase flow FEDSM-ICNMM2010-30756

- [3] Riverin, J.L., De Langre, E., Pettigrew, M.J., 2006, "Fluctuating forces caused by internal two-phase flow on bends and tees", JSV 298, pp. 1088-1098.
- [4] Tay, B.L. and Thorpe, R.B., 2004, "Effects of Liquid Physical Properties on the Forces Acting on a Pipe Bend in Gas-Liquid Slug Flow", Chemical Engineering Research and Design, 82(3), pp. 344-356.
- [5] Carnelutti M.F., e.a, 'Two-phase flow-induced forces on bends in small scale tubes', PVP2009-77708, ASME PVP conference Prague, 2009
- [6] Mandhane, J.M., Gregory, G.A., and Aziz, K., 1974, "A Flow Pattern Map for Gas-Liquid Flow in Horizontal Pipes", Int. J. Multiphase Flow, 1(4), pp. 537-553.
- [7] Chiaasiaan S.M. , 'Two-phase Flow, boiling, and condensation' (1st edition, 2008)
- [8] P.Andreussi and K. Bendiksen, an investigation of void fraction in liquid slugs for horizontal and inclined gas/liquid pipeflow. Int. J. Multiphase Flow, 15, (1989) 937-946
- [9] M.F. Carnelutti, S.P.C. belfroid W. Schiferli, Two Phase flow induced forces on bends in small scale tubes, PVP2009-77708

EXPERIMENTAL INVESTIGATION OF THE FLOW-INDUCED VIBRATION OF A CURVED CIRCULAR CYLINDER

Gustavo R.S. Assi*

Dept. Naval Arch. & Ocean Eng. – NDF Group
University of São Paulo, Brazil

Cesar M. Freire

Dept. Mechanical Eng. – NDF Group
University of São Paulo, Brazil

Ivan Korkischko

Dept. Mechanical Eng. – NDF Group
University of São Paulo, Brazil

Narakorn Srinil

Dept. Naval Arch. & Marine Eng.
University of Strathclyde, Glasgow, UK

ABSTRACT

Experiments have been conducted to investigate the vortex-induced vibration (VIV) response of a rigid section of a curved circular cylinder. Two curved configurations, a concave and a convex, were tested regarding the direction of the flow, in addition to a straight cylinder that served as reference. Amplitude and frequency response are presented versus reduced velocity for a Reynolds number range between 750 and 15,000. Results showed that the curved cylinders presented significant less vibration for both concave and convex configurations when compared to the typical VIV response of a straight cylinder. The concave configuration presented relatively high amplitudes of vibration that are sustained beyond the typical synchronisation region. We believe this distinct behaviour between the convex and the concave configurations is related to the wake interference happening in the lower half of the curvature due to perturbations generated in the horizontal section when it is positioned upstream. Particle-image velocimetry (PIV) measurements of the separated flow along the cylinder highlight the effect of curvature on vortex formation and excitation revealing a complex fluid-structure interaction mechanism.

NOMENCLATURE

D Cylinder external diameter
 h Cylinder vertical length below the water line
 m^* Mass ratio

ζ Structural damping ratio
 f_0 Natural frequency in air
 U Flow speed
 U/Df_0 Reduced velocity
 \hat{x} Streamwise harmonic amplitude of vibration
 \hat{y} Cross-flow harmonic amplitude of vibration
 f_x Streamwise oscillating frequency
 f_y Cross-flow oscillating frequency
 Re Reynolds number
 St Strouhal number

INTRODUCTION

Ongoing deep-sea exploration, installation and production of hydrocarbon energy need the development of new viable technologies. One of these is the requirement of a robust and reliable analysis tool for the prediction of vortex-induced vibration (VIV) of marine structures exposed to ocean currents. Because VIV can cause high cyclic-loading fatigue damage of structures, it is now widely accepted to be a crucial factor that should be taken into account in the preliminary analysis and design. However, many insightful VIV aspects are still unknown and far from fully understood; these render the structural design quite conservative with the use of a large factor of safety. For offshore structures with initial curvatures and high flexibility such as catenary risers, mooring cables and free-spanning pipelines, the theoretical, numerical or experimental VIV research is still very lacking.

Risers are very long pipes used to carry oil from the sea bed to offshore platforms floating on the water surface. Under the effect of sea currents, these flexible structures are especially susceptible to flow-induced vibrations, particularly since they have a relatively low

*Corresponding author: g.assi@usp.br. Address: PNV Dept. Eng. Naval e Oceânica, Escola Politécnica da Universidade de São Paulo, Av. Prof Mello Moraes 2231, 05508-030, São Paulo - SP, Brazil. www.ndf.poli.usp.br.

mass compared to the mass of the displaced fluid. Generally, an offshore floating platform accommodates more than 40 riser pipes together with many other cylindrical structures. The interaction of these flexible structures can produce an even more complex problem, resulting in vibrations with rather unexpectedly higher amplitudes [1]. Flow interference from the platform hull, the soil on sea bed and the pipe itself can also increase the complexity of the flow, generating complex responses.

The riser may respond with different amplitudes and frequencies depending on the flow excitation and structural stiffness along the length of the pipe. Consequently, several modes of vibration with varying curvature appear along the span resulting in a very rich fluid-structure interaction mechanism [2]. In addition to that, flexible risers can be laid out in a catenary configuration which results in high curvature close to the region where it touches the bottom of the ocean, called the touchdown point.

In an attempt to understand and model the fluid-dynamic behaviour around curved sections of risers we have performed experiments with a curved section of rigid cylinder in a water channel. This idealised experiment is far from reproducing the real conditions encountered in the ocean, nevertheless it should throw some light on understanding how the vortex shedding mechanism is affected by the curvature of the pipe.

An investigation into the vortex shedding patterns and the fundamental wake topology of the flow past a stationary curved circular cylinder has been carried out by Miliou et al. [3] based on computational fluid dynamics studies. As a result of pipe initial curvatures, flow visualizations highlight different kinds of wake characteristics depending on the pipe (convex or concave) configuration and its orientation with respect to (aligned with or normal to) the incoming flow. When the flow is uniform and normal to the curvature plane, the cross-flow wake dynamics of curved pipes behave qualitatively similar to those of straight pipes. This is in contrast to the case of flow being aligned with the curvature plane where wake dynamics change dramatically. However, these scenarios are pertinent to a particular stationary cylinder case in a very low-Reynolds number range. The VIV behaviour will further transform if the structure oscillates and interacts with the fluid wakes, depending on several fluid-structure parameters.

EXPERIMENTAL ARRANGEMENT

Experiments have been carried out in the Circulating Water Channel of the NDF (Fluids and Dynamics Research Group) at the University of São Paulo, Brazil. The

NDF-USP water channel has an open test section 0.7m wide, 0.9m deep and 7.5m long. Good quality flow can be achieved up to 1.0m/s with turbulence intensity less than 3%. This laboratory has been especially designed for experiments in flow-induced vibrations and more details about the facilities are described in Assi et al. [4].

A rigid section of a curved circular cylinder, with an external diameter of $D = 32\text{mm}$, was made of ABS plastic and Perspex tubes according to the dimensions shown in Figure 1. The curved cylinder was composed of a horizontal section with $10D$ in length, a curved section with a $10D$ radius and a vertical section with length h/D that could be varied with reference to the water line. The water level was set to 700mm from the floor of the channel, which meant that the $10D$ -long horizontal part of the cylinder was not close enough to the floor to suffer interference from the wall.

The model was connected by its upper end to a long pendulum rig (length $H = 3.0\text{m}$) that allowed the system to oscillate in two degrees of freedom (2dof) in the cross-flow and streamwise directions. The model was attached to two pairs of coil springs that provided the stiffness of the system. The springs were set to provide the same natural frequency (f_0 , measured in air) in both the cross-flow and streamwise directions. The design and construction of the pendular elastic rig was made by Freire et al. [5] based on a previous idea employed by Assi et al. [6,7] for experiments with VIV suppressors. The present apparatus has been validated for VIV experiments by Freire et al. [8,9].

Two laser sensors measured the cross-flow and streamwise displacements of the pendulum referring to the displacement of the bottom tip of the models. A load cell was installed before the springs to allow for instantaneous measurements of lift and drag acting on the cylinder. (Hydrodynamic forces will not be discussed in this paper.) A particle-image velocimetry (PIV) system was employed to analyse the wake along the span.

Regarding the flow direction, two orientations were investigated: a convex and a concave configuration according to the direction of the flow approaching the curvature. The flow direction in the test section of the water channel was not changed; naturally the curved cylinder was rotated by 180 degrees to allow for both concave and convex arrangements. This is also illustrated in Figure 1.

Decay tests have been performed in air in order to determine the natural frequencies of the system in both directions as well as the level of structural damping. The apparatus with one universal joint and four springs turned out to present a very low structural damping of $\zeta = 0.2\%$, measured as a fraction of the critical damping. The to-

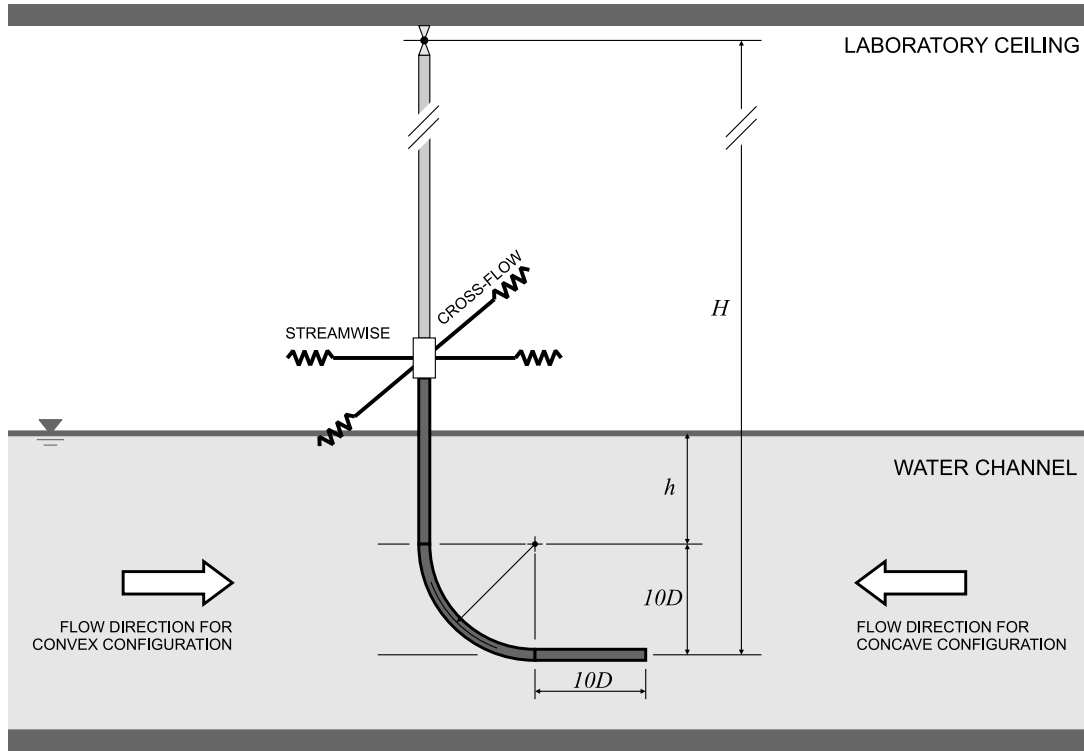


FIGURE 1: Experimental arrangement in the NDF-USP circulating water channel. The cylinder was rotated by 180 degrees to arrange concave and convex configurations.

TABLE 1: Structural properties.

	m^*	ζ	$m^*\zeta$
Straight cylinder	2.8	0.2%	0.0056
Curved cylinders	2.1	0.2%	0.0042

tal oscillating mass of the system was measured in air, resulting in a non-dimensional mass ratio m^* , defined as the ratio between the total mass and the mass of displaced fluid. Consequently, the mass-damping parameter $m^*\zeta$ of the system was kept to the lowest possible value in order to amplify the amplitude of response.

Table 1 presents a summary of the structural parameter for both the straight and curved cylinder.

RESULTS OF A STRAIGHT CYLINDER

A preliminary VIV experiment was performed with a straight cylinder in order to validate the set-up and generate data for comparison. The same pendulum rig was employed, only replacing the curved model by a straight cylinder with the same diameter. This time, the straight cylinder was long enough to reach the bottom wall only

leaving a 3mm clearance to allow for free movement of the pendulum in any direction.

The dynamic response of the straight cylinder covered a reduced velocity range from 1.5 to 12, where reduced velocity (U/Df_0) is defined using the cylinder natural frequency of oscillation measured in air. The only flow variable changed during the course of the experiments was the flow velocity U , which, as for full-scale risers, alters both the reduced velocity and the Reynolds number between 750 and 15,000 for a maximum reduced velocity of 20.

Throughout the study, cylinder displacement amplitudes (\hat{x}/D for the streamwise and \hat{y}/D for the cross-flow directions) were found by measuring the root mean square value of response and multiplying by the square root of 2 (the so called harmonic amplitude). This is likely to give an underestimation of maximum response but was judged to be perfectly acceptable for assessing the general behaviour of VIV, since the response is mostly harmonic. Results presented in the present study correspond to the displacement of the lowest point of the model, i.e., the end of the cylinder closer to the section floor, thus representing the maximum displacement developed by each model. Displacements are non-dimensionalised by the cylinder diameter D .

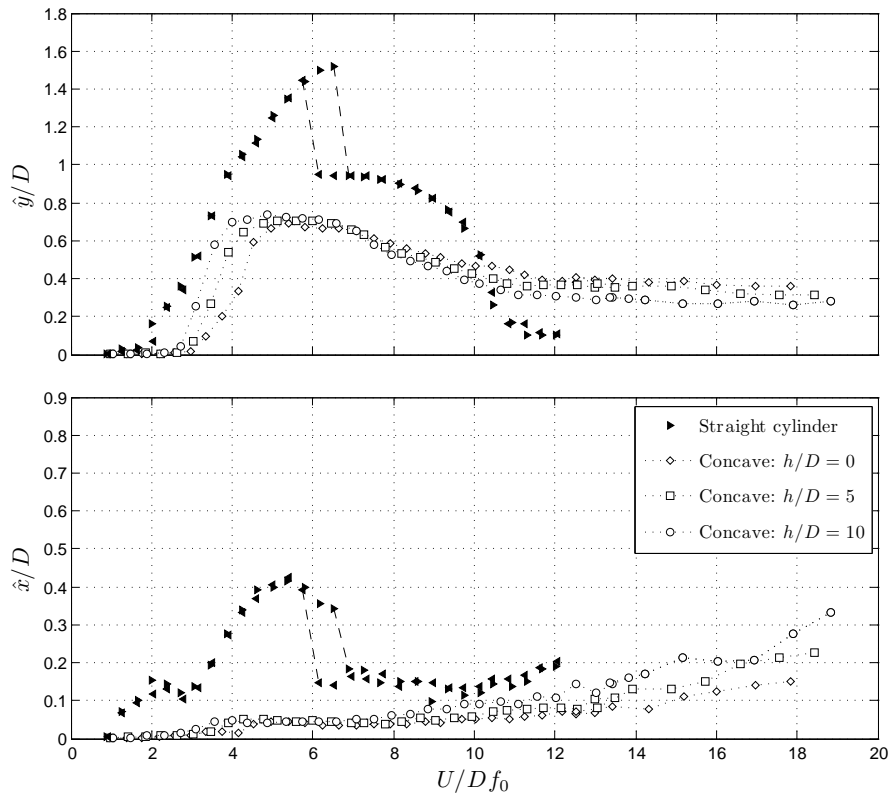


FIGURE 2: Cross-flow (\hat{y}/D) and streamwise (\hat{x}/D) amplitude of vibration versus reduced velocity for a straight cylinder and concave configurations varying the vertical section length (h/D).

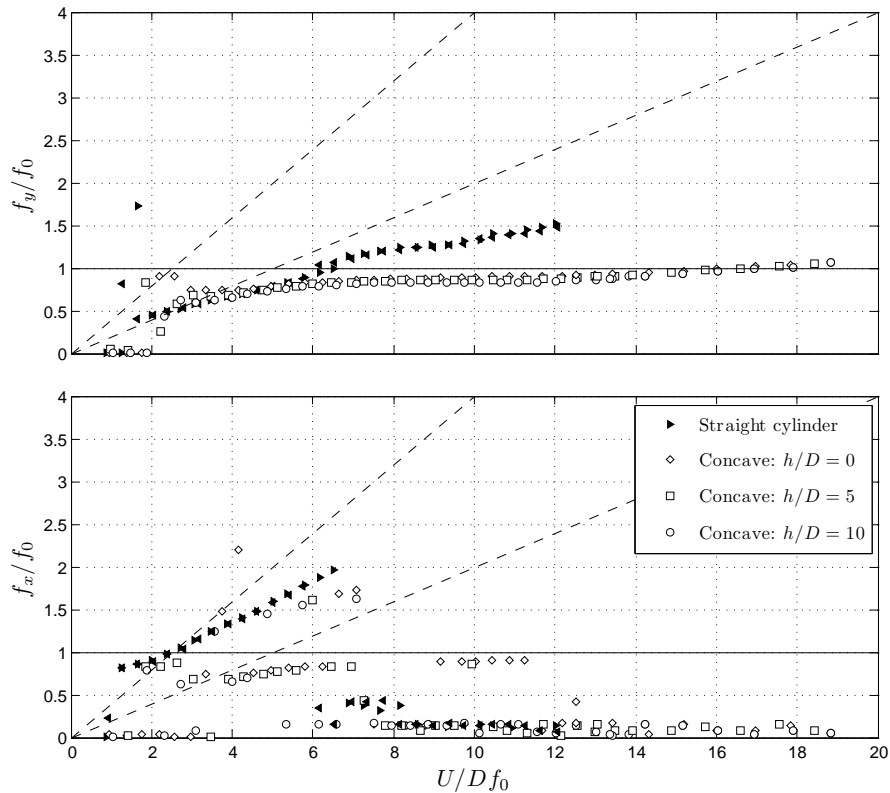


FIGURE 3: Cross-flow (\hat{y}/D) and streamwise (\hat{x}/D) dominant frequency of response versus reduced velocity for a straight cylinder and curved concave configurations varying the vertical section length (h/D).

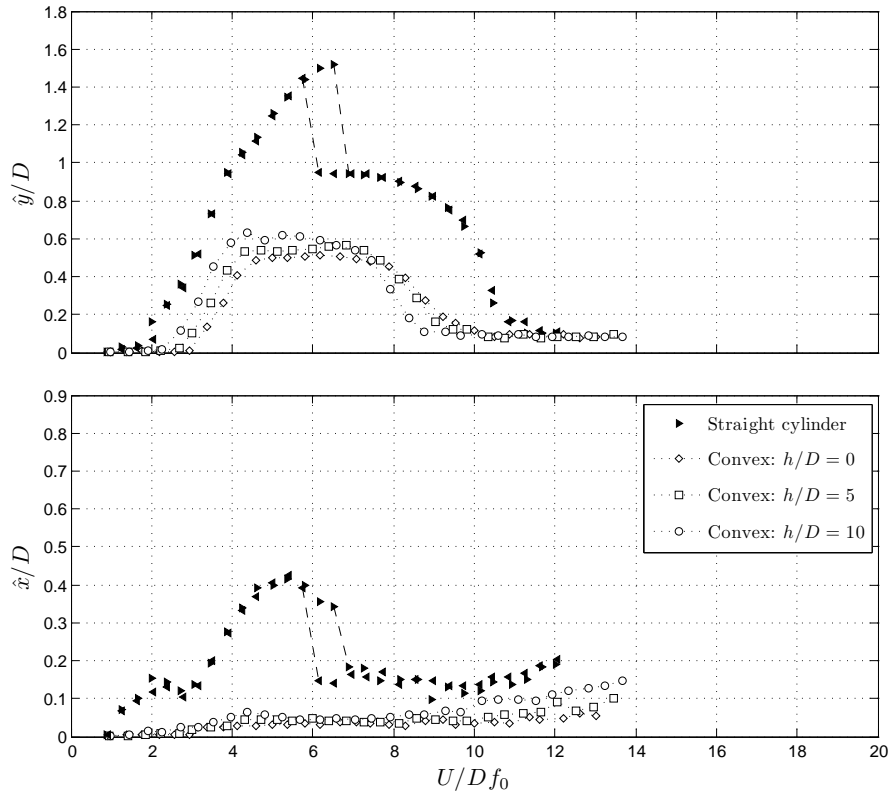


FIGURE 4: Cross-flow (\hat{y}/D) and streamwise (\hat{x}/D) amplitude of vibration versus reduced velocity for a straight cylinder and convex configurations varying the vertical section length (h/D).

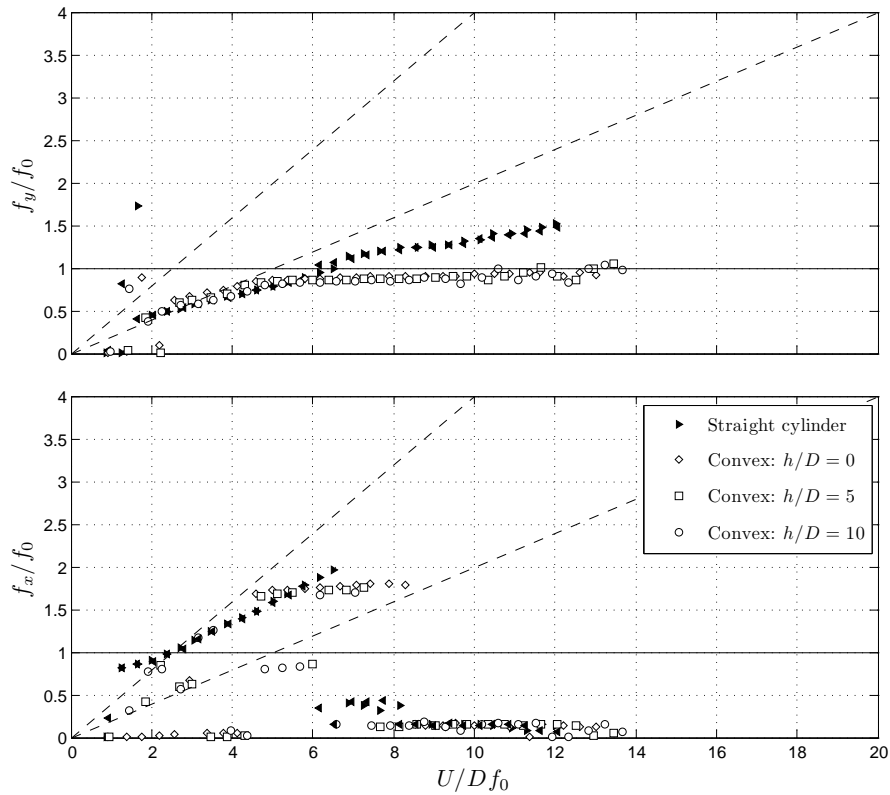


FIGURE 5: Cross-flow (\hat{y}/D) and streamwise (\hat{x}/D) dominant frequency of response versus reduced velocity for a straight cylinder and curved convex configurations varying the vertical section length (h/D).

Figures 2 and 4 compare the reference cross-flow and streamwise responses obtained from two different runs with the straight cylinder. In the first one, flow speed was increased in 30 steps from zero to a maximum, while in the second it was decreased from the maximum to zero. Both data sets overlap rather well for all the reduced velocity range except for a region around $U/Df_0 = 6$ where the well-known phenomenon of hysteresis in the VIV response has been observed. The streamwise VIV response also seems to occur in two resonance ranges ($U/Df_0 = 2$ and 6), the so-called second and third instability ranges involving asymmetric vortices.

Although the observed peak amplitude of $\hat{y}/D = 1.5$ around $U/Df_0 = 6$ is slightly higher than other results found in the literature for similar values of $m^*\zeta$ (for example, Assi et al. [6]) the general behaviour of both curves show a typical response for 2-dof VIV. The higher amplitude found here could be explained by the very low mass-damping characteristics of the system and the geometric projection of the amplitude at the tip of the model and not at mid-length as usual.

Although the cylinder was initially aligned in the vertical position, in flowing water the mean drag displaces the cylinder from its original location reaching a slightly inclined configuration from the vertical. This was judged not to be detrimental to the experiment; hence the inclination of the cylinder was not corrected between each step. The same procedure was adopted for the curved cylinder.

Figures 3 and 5 present the dominant frequency of response versus reduced velocity. The dataset for the straight cylinder is repeated in both figures to serve as reference. Two dashed lines inclined with different slopes represent the region for a Strouhal number of 0.2 and 0.4, i.e., an estimation of the vortex shedding frequency for a straight cylinder in the cross-flow and streamwise direction respectively. It is clear that the straight cylinder presents a typical VIV response oscillating in the cross-flow direction with a frequency following the $St = 0.2$ line up to the beginning of the upper branch. Eventually, f_y/f_0 departs from $St = 0.2$ towards the unity value around $U/Df_0 = 6$. The behaviour observed for the streamwise vibration is also typical of VIV with the difference that the frequency of response is twice as that for the cross-flow direction during much of the synchronisation range.

RESPONSE OF THE CURVED CYLINDERS

As mentioned above, experiments with the curved cylinder were performed taking into account two distinct configurations as far as the flow direction is concerned. In the concave configuration the flow approaches

the model reaching first the horizontal section. As opposed to that, in the convex configuration the horizontal section is placed downstream of the curved and vertical parts.

Amplitude of vibration

In general terms, as presented in Figures 2 and 4, the curved cylinders showed significantly less vibration for both concave and convex configurations when compared to the typical VIV response of the straight cylinder. Such a reduction is noticeable in both the cross-flow and streamwise responses. This clearly shows that the curvature of the cylinder modifies the vortex shedding mechanism in a manner that the structure extracts less energy from the flow. We shall return to this point when investigating the velocity flow field with PIV.

For each concave and convex configuration, the vertical section of the cylinder close to the free surface was varied in three different lengths: $h/D = 0, 5$ and 10. The overall response for the three values of h/D is very similar, showing only minor differences at the beginning of the synchronisation range between $U/Df_0 = 3.0$ and 5.0. Apart from that, no distinct behaviour was observed as far as a variation in h/D is concerned for both concave and convex configurations.

The cross-flow displacement does not reveal distinct upper and lower branches of vibration such as those observed for a straight cylinder, but it produces a smooth curve that spans the whole synchronisation region with maximum amplitude around $\hat{y}/D = 0.75$ for the concave and 0.65 for the convex configurations. No hysteresis is found.

However, the most interesting feature of such a behaviour is found when the convex response is compared to the concave one (Figures 2 and 4). While the convex curve for \hat{y}/D drops immediately between $U/Df_0 = 8$ and 10 to a level of $\hat{y}/D \approx 0.1$, the response for the concave case does not diminish, but is sustained for higher reduced velocities around $\hat{y}/D = 0.3$ until the end of the experiment. Apparently there must be a fluidelastic mechanism occurring for reduced velocities above 8.0 for the concave configuration capable of extracting energy from the flow to sustain vibrations around $\hat{y}/D = 0.3$. We shall discuss this point later while analysing the PIV flow fields.

In the streamwise direction the responses of the curved cylinders are different from the typical VIV developed by the straight cylinder. Streamwise vibrations in the first and second resonance regions are totally suppressed, probably owing to the hydrodynamic damping effect induced by the cylinder's horizontal part. At the same time, the streamwise vibration \hat{x}/D for the concave

case also shows increasing amplitude taking off for reduced velocities higher than 10 and reaching $\hat{x}/D \approx 0.35$ for the highest flow speed. It coincides with the increased amplitude observed in the cross-flow direction and should be related to the same excitation mechanism. Once more, no distinct difference in the streamwise response was observed while varying h/D .

Frequency of vibration

Figures 3 and 5 present the dominant frequency of oscillation non-dimensionalised by the natural frequency for both cross-flow and streamwise directions of motion. Results for the curved cylinder show a consistent behaviour in the cross-flow direction, with data points following the Strouhal line up to the upper branch peak but remaining closer to $f_y/f_0 = 1.0$ for the rest of the reduced velocity range. In the streamwise direction, we find data points following both Strouhal lines and also very low frequencies indicating random drifts instead of periodic oscillations. Since the displacements in the streamwise direction are much smaller for the curved cylinder than the straight one, we should expect broader frequency spectra dominating over the response.

One might remember that the straight and curved cylinder should have very similar values of added mass in the cross-flow direction, but slightly different values in the streamwise direction due to the geometric properties relative to the flow. We have not taken such effect into account in this paper, but it might be playing an important role defining the frequencies of oscillation in water.

Trajectories of motion

Figure 6 qualitatively compares samples of displacement trajectories obtained for three experiments performed with the straight cylinder and the curved cylinders with $h/D = 10$. The straight cylinder presents distinct eight-shape figures typical of 2dof VIV owing to the 2:1 ratio on the streamwise to cross-flow frequency of excitation. On the other hand, trajectories for both configurations of the curved cylinder reveal that the streamwise displacement is greatly reduced when compared to the straight cylinder. Both concave and convex cases show very little movement in the streamwise direction for the whole range of reduced velocity.

Another interesting observation relates the movement of both curved cylinders. It is clear that for reduced velocities greater than 10 the convex cylinder shows little displacement in both direction, while vibrations are sustained until the end of the experiment for the concave case as shown in Figures 2 and 4.

VELOCITY FIELDS

PIV measurements of the flow around the cylinder were performed for both concave and convex configurations as presented in Figures 7 to 10. Four visualisation areas for each configuration, labelled A1 to A4, were conveniently distributed along the length of the cylinder in order to evaluate as much as possible to flow pattern around the body. All four areas are in the same plane illuminated by the laser, which is parallel to the plane of curvature only dislocated by $1D$ from the centre of the cylinder in order to capture the highest velocities induced by the vortex tubes. Figures 8 and 10 show the location of each area composing the flow field along the cylinder. It is important to note that each velocity field was obtained from a different acquisition; hence A1, A2, A3 and A4 are not correlated in time.

All PIV measurements were performed for a static cylinder at $Re \approx 1000$. Of course the wake pattern for the static cylinder is expected to be different from the wake of an oscillating cylinder, but even an analysis of a fixed body can contribute to the understanding of the complex vortex-structure interaction occurring during the response. A similar approach was employed by Miliou et al. [3] who performed numerical simulations for a static, curved cylinder between $Re = 100$ and 500.

With that in mind, let us analyse first the flow pattern around the concave configuration in Figures 7 and 8. The overall flow around the body can be divided in two parts:

(I) Areas A1 and A2 show the region where the flow is mostly parallel to the axis of the cylinder. Therefore, no clear vortex tubes are observed with concentrated axial vorticity. Instead, the flow along the horizontal length is disturbed by the separation occurring at the tip of the cylinder. Area A1 shows the flow approaching the disk facing upstream and separating into a recirculation bubble. The periodicity of the shedding associated with this region is also related to the flow speed and the diameter D , but no coherent vortices parallel to the cylinder are able to form. As a consequence, a cascade of small vortices is convected downstream along the horizontal length (see area A2) reaching the beginning of the curved section.

(II) Areas A3 and A4 show the region where the flow is mainly perpendicular to the axis of the cylinder. Coherent vortex tubes tend to form following the curvature of the body, but further downstream they are stretched and rapidly breakdown into smaller vortices that are convected by the flow. Area A3 show the instant when a vortex tube is shed almost tangent to the curvature, while area A4, around the vertical section, reveal a formation region more or less aligned with the axis of the cylinder. Streamlines drawn in areas A3 and A4 reveal a non-negligible

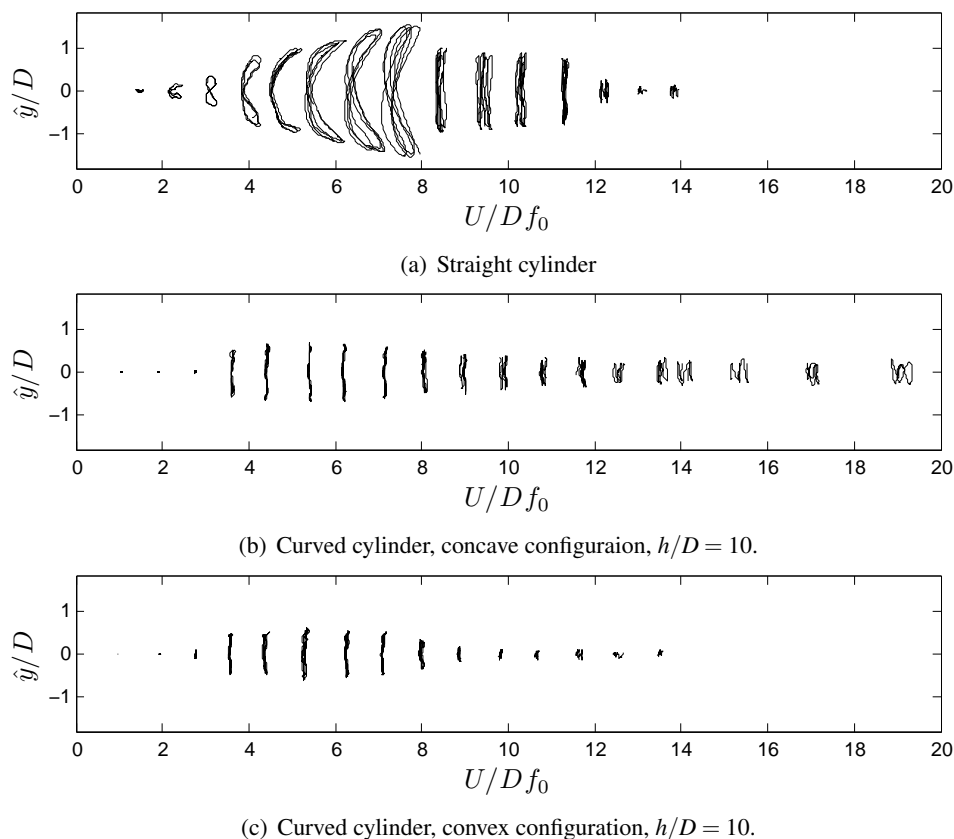


FIGURE 6: Response trajectories of motion for a (a) straight cylinder and a curved cylinder in (b) concave and (c) convex configurations.

velocity component deflecting the flow downwards immediately after the vortex formation region. As we move along the cylinder towards the water line from A3 to A4 the downward component is gradually reduced until it eventually disappears towards the upper half of A4. This region marks the competition between two wake modes existent along the transition from curved to straight cylinder. This looks similar to Figure 15 in Miliou et al. [3], with $Re = 100$, although without the cylinder horizontal section therein.

Analysing the flow pattern for the convex configuration in Figures 9 and 10 we notice two striking differences:

(I) Because the flow approaching the convex body does not encounter a blunt disk facing upstream, no strong separation or recirculation bubble is formed. As a consequence, the horizontal section seen in areas A1 and A2 is not exposed to a disturbed, unsteady flow parallel to the axis of the cylinder. In fact, A1 and A2 reveal that the upper half of the horizontal length is exposed to a periodic flow formed by a regular wake, while the bottom half experiences almost no perturbation, with streamlines showing a well behaved flow field parallel to the axis.

(II) Now, looking at the upper half of the body (A3 and A4) we notice much stronger and coherent vortex tubes when compared to the flow around the concave configuration. Area A3 reveals some kind of vortex dislocation after a formation region that increases in length as we move upwards. Because the convex geometry does not encourage the vortex tubes to stretch and break, a periodic wake seems to be sustained farther downstream. In contrast with the flow around the concave configuration, the velocity field around the curved section has a non-negligible vertical component upwards. It is stronger in A2 and is gradually reduced as we move upwards along the curvature in A3. This looks similar to Figure 3 in Miliou et al. [3] for $Re = 100$.

THE EXCITATION MECHANISMS

The main question to be answered by the present study is concerned with the fact that the amplitude in the cross-flow direction for the convex configuration is able to drop down to 0.1 for high reduced velocities while the concave configuration sustains vibration around 0.35. We believe this distinct behaviour between the convex and the concave configurations is related to the wake interference

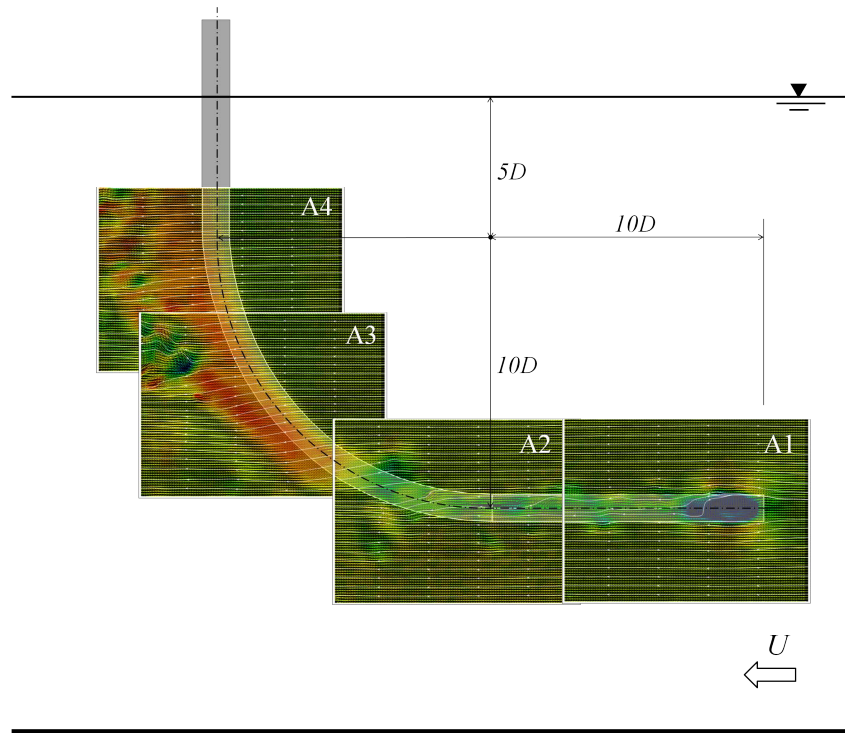


FIGURE 7: Composition of PIV velocity fields for concave configuration with $h/D = 5$.

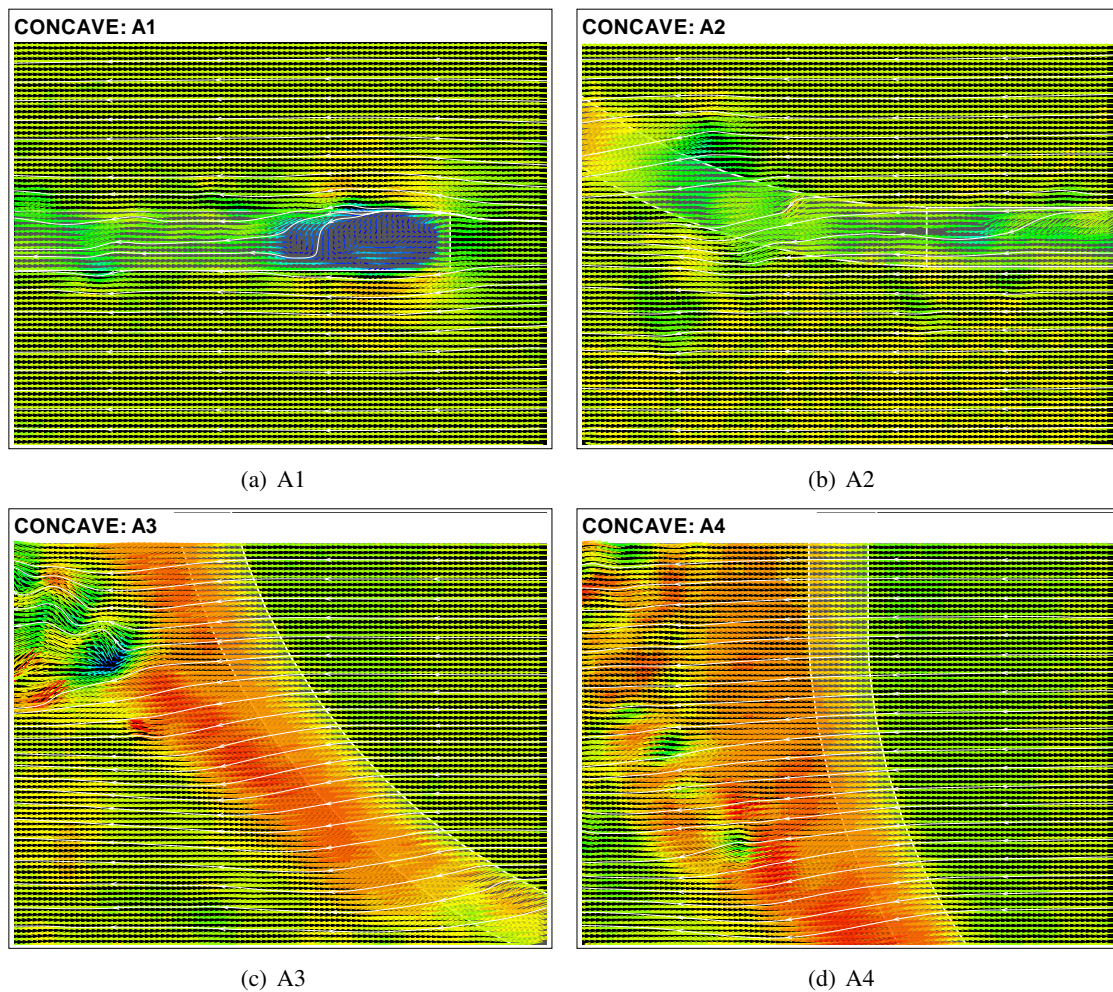


FIGURE 8: Detailed velocity fields from Figure 7. Flow direction is from right to left and vectors are coloured by velocity magnitude. $Re = 1000$.

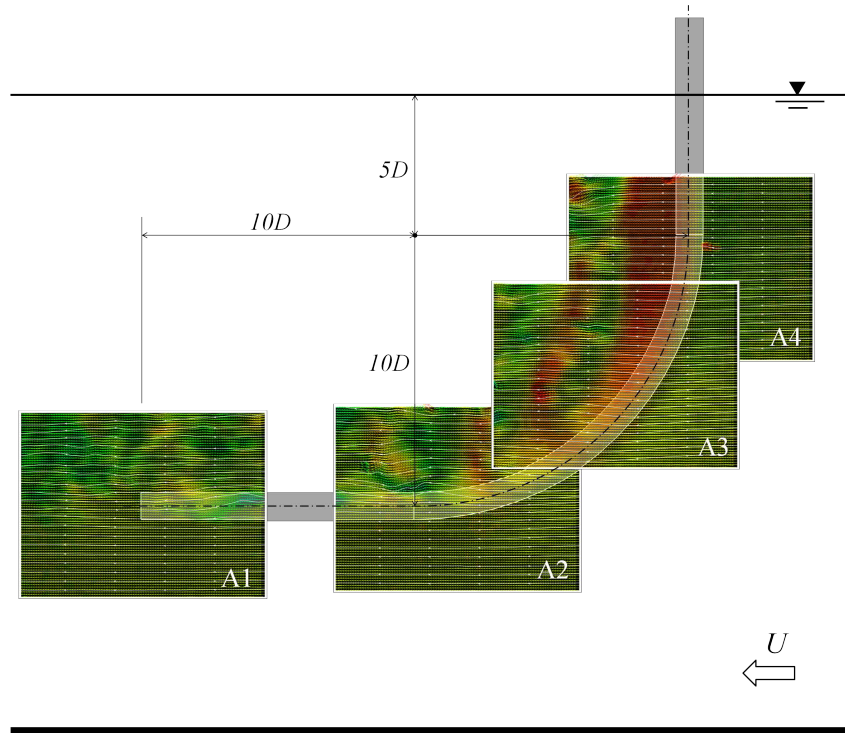


FIGURE 9: Composition of PIV velocity fields for convex configuration with $h/D = 5$.

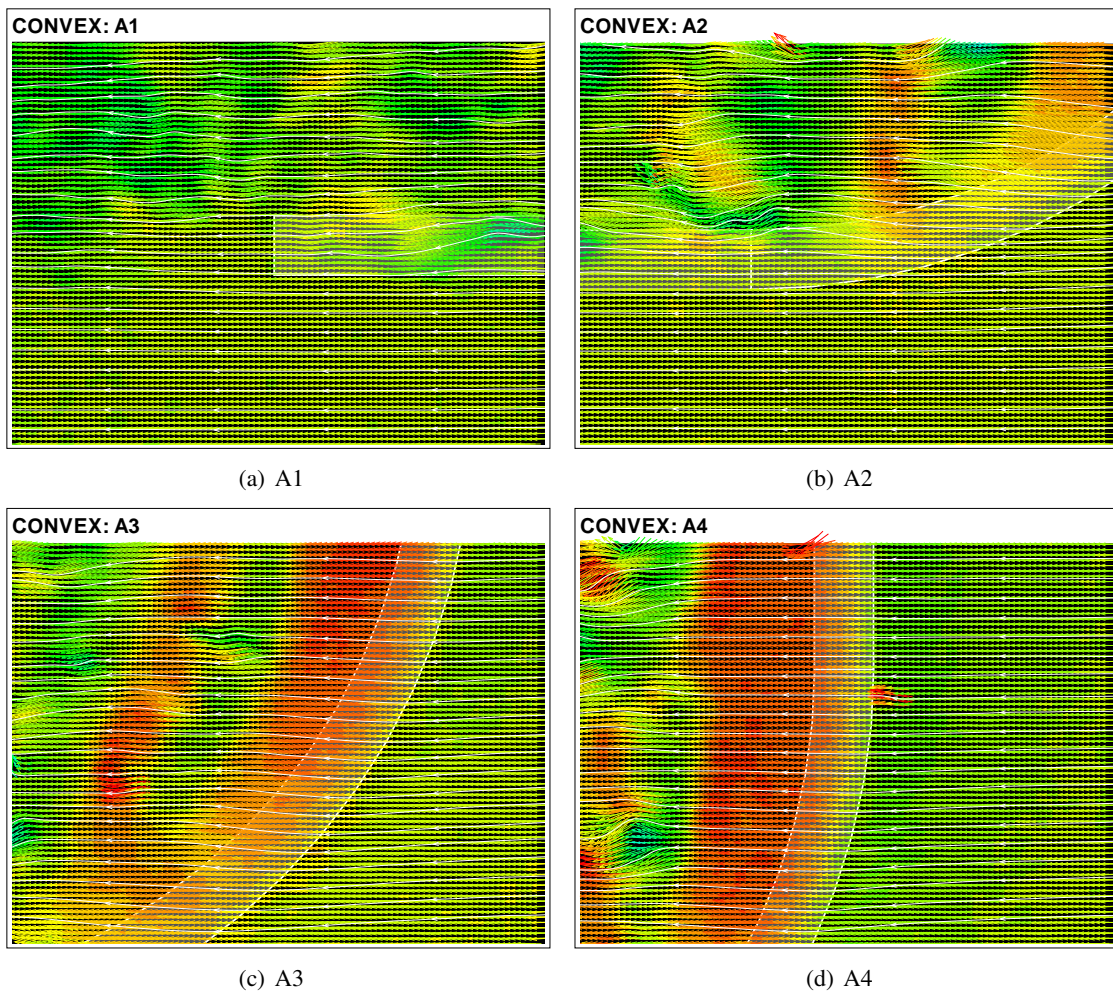


FIGURE 10: Detailed velocity fields from Figure 9. Flow direction is from right to left and vectors are coloured by velocity magnitude. $Re = 1000$.

happening in the lower half of the cylinder due to perturbations generated in the horizontal section when it is positioned upstream.

In the concave configuration the horizontal part of the cylinder is located upstream of the curved and vertical parts. The approaching flow encounters a circular blunt leading edge with a clear separation region around the circumference (Figure 8(a)). The flow that separates at the leading edge tends to create a separation bubble and latter reattaches along the horizontal section of the cylinder. Because the cylinder already presents cross-flow and streamwise vibrations, the three-dimensional separation bubble will not find a stable configuration nor a definite reattachment region, instead it will develop a periodic behaviour that may result in three-dimensional vortices being shed downstream, reaching the other parts of the cylinder. This is very clear in areas A1 and A2 of Figures 7 and 8 for the static cylinder.

The fluid-elastic mechanism behind the response may be a composition of different phenomena acting at the same time. We believe this interaction between the disturbed flow from the upstream horizontal part with the curved and vertical parts is responsible for sustaining the level of vibration around $\hat{y}/D = 0.35$ and $\hat{x}/D = 0.35$. We suggest such an interaction may be occurring in the following forms:

(i) Vortices generated along the horizontal section may impinge on the curved part generating impulses in the same manner that large eddies of turbulence induce buffeting on elastic structures. Because the concave configuration has a longer section immersed in such a disturbed wake it is more susceptible to buffet. Evidence that a buffeting-like phenomenon might be occurring is that the streamwise vibration shows a considerable increase in amplitude with increasing flow speed further out of the synchronisation range. Figure 6(b) also reveals that these vibrations are not harmonic and may even be chaotic, another evidence supporting the buffeting-excitation hypothesis.

(ii) The disturbed flow from the horizontal part may be disturbing and disrupting the vortex shedding mechanism from the curved and vertical sections, for example uncorrelating the vortex shedding mechanism in a curved region of the cylinder near the horizontal part. Also, the vortex wake along the curved-vertical half of the concave cylinder showed less correlation along the span, resulting in a lower peak of vibration during the synchronisation range.

(iii) Because the concave configuration has a fixed separation ring at the circle facing upstream, there might be some galloping-like instability related to the separa-

tion and reattachment of the three-dimensional bubble. This could generate non-resonant forces that could sustain some level of vibration for reduced velocities above the synchronisation range.

(iv) Finally, the concave configuration might experience some kind of instability related to the geometric arrangement of the experiment. Because the centre of pressure is located upstream of the vertical axis of the pendulum a minute deflection (or torsion) of the cylinder may result in a resolved force that will increase displacement. The opposite is true for the convex configuration in which the centre of pressure downstream of the vertical axis of the pendulum can only generate stabilising forces.

Of course all four mechanisms suggested above may also be occurring simultaneously or it may not even be possible to explain them separately. In addition, they might as well be very dependent on Reynolds number and amplitude of vibration.

CONCLUSIONS

We have investigated the VIV response of a curved cylinder for a concave and convex configurations regarding the approaching flow. We conclude that:

(i) In general terms, a curved cylinder presents a lower peak of amplitude of vibration in both the cross-flow and streamwise direction when compared to a straight cylinder. Nevertheless, a considerable level of streamwise vibration, not attributed to VIV, was observed for reduced velocity as high as 18.

(ii) Although the peak amplitude is reduced, a curved cylinder may present a significant level of vibration that is sustained for higher values of reduced velocity beyond the end of the typical synchronisation range.

(iii) The concave configuration shows a considerable level of cross-flow vibration around $\hat{y}/d = 0.35$ up to the highest reduced velocity performed in this experiment.

(iv) The overall response showed little dependency on the vertical length immediately below the water line, at least for a section varying between $h/D = 0$ and 10.

(v) We suggest that the flow-structure interaction mechanism that differentiates the concave form the convex response has its origin in the disturbed flow that separates from the horizontal part located upstream. This could be related to buffeting, galloping, disturbed VIV or geometric instabilities.

Future work should concentrate on correlated PIV analyses of the vortex formation along the curvature as well as on measurements of the flow field on planes perpendicular to the plane of curvature. An investigation of the interference effect generated by the separation at the

tip of the horizontal section could also help towards understanding the response. PIV measurements for an oscillating cylinder, especially at high reduced velocities, could throw some light into the actual mechanism of excitation.

ACKNOWLEDGEMENTS

G.R.S. Assi wishes to acknowledge the support of FAPESP (São Paulo State Research Foundation) through the research grant 2011/00205-6. N. Srinil is grateful to “The Sir David Anderson Award” from the University of Strathclyde.

REFERENCES

- [1] Assi, G.R.S., Bearman, P.W., Meneghini, J.R. **2010** On the wake-induced vibration of tandem circular cylinders: the vortex interaction excitation mechanism *J. Fluid Mech.*, 661, 365-401.
- [2] Srinil, N. **2010** Multi-Mode Interactions in Vortex-Induced Vibrations of Flexible Curved/Straight Structures with Geometric Nonlinearities *J. Fluids and Structures*, 26, 1098-1122.
- [3] Miliou, A., De Vecchi, A., Sherwin, S.J., Graham, M.R. **2007** Wake dynamics of external flow past a curved circular cylinder with the free stream aligned with the plane of curvature *J. Fluid Mech.*, 592, 89-115.
- [4] Assi, G.R.S., Meneghini, J.R., Aranha, J.A.P., Bearman, P.W., Casaprima, E. **2006** Experimental investigation of flow-induced vibration interference between two circular cylinders. *J. Fluids and Structures*, 22, 819-827.
- [5] Freire, C.M., Meneghini, J.R. **2010**. Experimental investigation of VIV on a circular cylinder mounted on an articulated elastic base with two degrees-of-freedom. *In the proceedings of BBVIV6 – IUTAM Symposium on Bluff Body Wakes and Vortex-Induced Vibrations*, 2010, Capri, Italy.
- [6] Assi, G.R.S., Bearman, P.W and Kitney, N **2009** Low Drag Solutions for Suppressing Vortex-Induced Vibration of Circular Cylinders. *J. Fluids and Structures* 25, 1-10.
- [7] Assi, G.R.S., Bearman, P.W., Kitney, N., Tognarelli, M.A. **2010** Suppression of Wake-Induced Vibration of Tandem Cylinders with Free-to-Rotate Control Plates. *J. Fluids and Structures*, 26, 1045-1057.
- [8] Freire, C.M., Korkischko, I., Meneghini, J.R. **2009** Development of an elastic base with tow degrees of freedom for VIV studies. *In the proceedings of COBEM 2009 – 20th International Congress of Mechanical Engineering*, 2009, Gramado, Brazil.
- [9] Freire, C.M., Korkischko, I., Meneghini, J.R. **2011** Defining a parameter of effectiveness for the suppression of vortex-induced vibration. *In the proceedings of OMAE2011 – 30th International Conference on Ocean, Offshore and Arctic Engineering*, 2011, Rotterdam, The Netherlands.



Vortex-Induced Vibrations of an Inclined Cylinder in Flow

Anil Jain

Fluid-Structure Interactions Laboratory
Department of Mechanical and Industrial
Engineering
University of Massachusetts
Amherst, MA 01003
Email: abjain@engin.umass.edu

Yahya Modarres-Sadeghi

Fluid-Structure Interactions Laboratory
Department of Mechanical and Industrial
Engineering
University of Massachusetts
Amherst, MA 01003
Email: modarres@engin.umass.edu

ABSTRACT

We study the Vortex-Induced Vibrations (VIV) of a flexibly-mounted cylinder inclined to the oncoming flow by conducting a series of experiments. For a fixed inclined rigid cylinder, there have been various experimental and numerical studies and it is believed that, at least up to a critical angle of inclination, the cylinder behaves similarly to a vertical one if the component of the flow velocity normal to the cylinder axis is considered. We conduct a series of experiments on a flexibly-mounted rigid cylinder placed inclined to the oncoming flow with various angles of inclination and we examine how various angles of inclination result in various lock-in regions (large-amplitude vibrations). In our experiments, a rigid cylinder is mounted on springs, and is placed in the test section of a recirculating water tunnel. We use air bearings to reduce the structural damping of the system. Even at high angles of inclination, large-amplitude oscillations are observed, and the onset of lock-in increases with increasing angle of inclination. If the normal component of the oncoming flow is used, the onset of lock-in is observed at a normal reduced velocity of around 4.0, but the width of the lock-in range decreases as the angle of inclination increases. At the maximum angle of inclination tested (65 degrees), a second range for the high-amplitude oscillations is observed at higher normal reduced velocities.

NOMENCLATURE

St : Strouhal number
 Re : Reynolds number
 L : Immersed length of the cylinder
 D : Diameter of the cylinder
 m : Total moving mass
 m^* : Mass ratio
 ζ : Structural damping ratio
 U^* : Reduced velocity
 U^*_{N} : Normal reduced velocity
 f : Oscillating frequency of the cylinder
 f_N : Natural frequency of the system
 f_S : Vortex shedding frequency
 f^* : Non-dimensional frequency
 A^* : Non-dimensional amplitude

INTRODUCTION

The Vortex-Induced Vibrations (VIV) of a rigid cylinder inclined to the oncoming flow is not studied as extensively as the normal-incidence case, despite its applications in the riser tubes, cables under sea, mooring lines of floating offshore wind turbines and subsea pipelines, where the direction of the flow may not always be perpendicular to the long axis of the structure. An existing hypothesis, called the Independence Principle (IP), which is mainly used for the fixed cylinders inclined to flow, states that the inclined cylinders can be treated as normal-incidence ones, if only the component of the free stream velocity normal to the cylinder axis is considered. This approach neglects the effect of the axial component of the flow velocity, which is legit for small angles of inclination but becomes dominant as the angle of inclination increases.

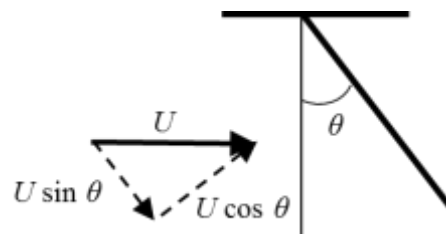


Figure 1. An inclined cylinder placed in flow along with the normal and tangential components of flow velocity

The angle of inclination is defined as the angle between the cylinder axis and the plane normal to the incoming flow (θ in Figure 1). Zero angle of inclination corresponds to a cylinder perpendicular to the incoming flow (cross-flow). A cylinder inclined away from the incoming flow is considered to have a positive angle of inclination and otherwise.

For a fixed inclined rigid cylinder, studies conducted by Surry and Surry (1967), Van Atta (1968), Ramberg (1983), Kozakiewicz et al. (1995), Zhao et al. (2009) among others suggest that the cylinder behaves similarly to a normal cylinder up to an inclination of around 40° to 50° . But in the case of a flexibly mounted inclined

cylinder, very few experimental (Hanson, 1966; Ramberg, 1983, and Franzini et al., 2009) and numerical studies (Lucor and Karniadakis, 2003; Willden and Guerbi, 2010) have been conducted to study the IP based on the Strouhal number (St), drag coefficient (C_D) and the angle of vortex shedding.

Van Atta (1968) investigated a higher inclination range ($50^\circ \leq \theta \leq 75^\circ$) on hot wires. He confirmed that large oscillations could be seen for such high angles and that the maximum-amplitude region lies in the normalized reduced velocity ($U^*_N = U \cos\theta / f_N D$) range of 5.8 – 6.4. King (1977) justified taking the component of the flow velocity ($U \cos\theta$) to calculate the reduced velocity and drag forces by performing flow visualization tests. He demonstrated that flow over -34° in-line oscillating inclined cylinder was normal to the cylinder axis. The existence of the axial flow was also evident and it was different in the case of positively and negatively inclined cylinders. Positive angles of inclination lead the flow to move down the back face of cylinder and negative angles caused the flow move up the back face of the cylinder (Figure 2). Ramberg (1983) studied the effect of the angle of inclination on circular cylinders forced to vibrate in a Reynolds number range of 160 to 460. He observed parallel vortex shedding till $\theta = 50^\circ$ (condition for IP validity) and summarized that the end conditions dominate the flow around an inclined cylinder.

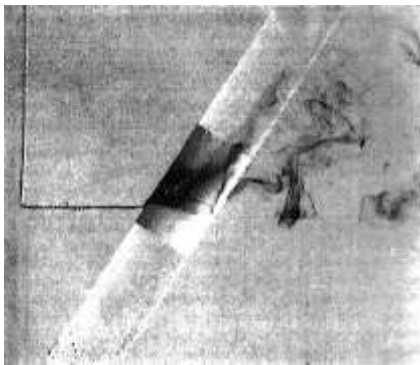


Figure 2. Flow visualization in the wake of an inclined cylinder with an angle of inclination of -34° , oscillating in the in-line direction (King, 1977)

Lucor and Karniadakis (2003) performed direct numerical simulation (DNS) to validate the IP for stationary and freely vibrating rigid cylinders for $\theta = -60^\circ$ and -70° with $m^*\zeta = 0.006$ and an aspect ratio (L/D) of 22 at a constant Reynolds number: $Re = 1000$. They observed that the maximum amplitude response decreases with the increase in the inclination ($A^* = 0.63$ for -60° and $A^* = 0.52$ for -70°) and the maximum amplitude lies in the U^*_N range stated by King (1977) and Ramberg (1983). For a freely vibrating cylinder, the vortex shedding was parallel to the cylinder axis. In addition, they found that the drag forces were higher than predicted by IP and the lift forces

were correlated along the length of the cylinder in the case of -70° compared to -60° .

Franzini et al. (2009) performed experiments on inclined cylinders free to oscillate in the cross-flow direction till $\theta = 45^\circ$ and observed that the amplitude, lift and drag coefficients lie in the same normalized reduced velocity range as stated by King (1977) and Ramberg (1983). Finally, Willden and Guerbi (2010) performed forced oscillation tests across a range of oscillating frequencies (f/f_s) at a fixed oscillation amplitude ($A/D = 0.3$), emphasizing on the variation of the component of the lift coefficient in phase with the cylinder's velocity C_{L_v} , which is calculated as:

$$C_{L_v}(t) = C_{L_v} \sin\phi \quad (1)$$

where ϕ is the phase angle by which $C_{L_v}(t)$ leads the displacement $y(t)$. For $\theta = 60^\circ$, they observed two excitation regimes: The first wider regime around $f/f_s = 0.75$ resulted in parallel vortex shedding, and the second small regime around $f/f_s = 1$ resulted in slantwise vortex shedding.

In this study, we conduct a series of experiments on a flexibly mounted inclined rigid cylinder up to an angles of inclination of 65° in the subcritical Reynolds range of $Re = 500-10,000$.

EXPERIMENTAL SETUP

The experiments were performed in a re-circulating water tunnel with a test section of $1.27 \text{ m} \times 0.50 \text{ m} \times 0.50 \text{ m}$ with turbulence intensity of less than 1% RMS up to 0.3 m/s flow velocity. To achieve a low mass-damping coefficient, two air bearings were mounted on rigid parallel shafts located atop the water tunnel test section, resulting in one-degree-of-freedom oscillations in the cross-flow direction. The structural damping coefficient (ζ) of the system is around 0.0045 and the mass ratio ($m^* = 4m / \pi\rho D^2 L$) of the cylinder is 6.5, leading to a mass-damping coefficient of $m^*\zeta = 0.029$. The mass of the system includes the mass of the cylinder and the moving objects such as the air bearings and the supporting plate. The 12.7 mm diameter solid aluminum cylinders were machined to achieve the desired inclination such that for each cylinder, the lower end was cut parallel to the test section floor. The immersed aspect ratio (L/D) of the cylinders was kept constant at 29 for every angle of inclination. The natural frequency (f_N) of the system was measured by performing a decay test in air and was 1.0 Hz (Figure 3).

The end conditions of the cylinder play an important role in the observed VIV response as demonstrated by King (1977) and Ramberg (1983). For a vertically mounted cylinder partially submerged in water, the upper end of the cylinder is in contact with the free surface and the lower end is submerged in water. The free surface does not influence the parallel vortex shedding (Khalak and Williamson, 1996) but the lower end of the cylinder can induce three-dimensionality into the flow. We

performed experiments with two different scenarios: First a cylinder with no end plate and then a cylinder with an unattached streamlined end plate with varying gap. The gap size used was 1 mm ($0.08D$) and 3 mm ($0.23D$). Flow visualization was conducted on the endplate to make sure no major separation was resulted by the endplate's leading edge. The displacement was measured using a Micro-Epsilon (ILD 1402-600) non-contacting laser sensor.

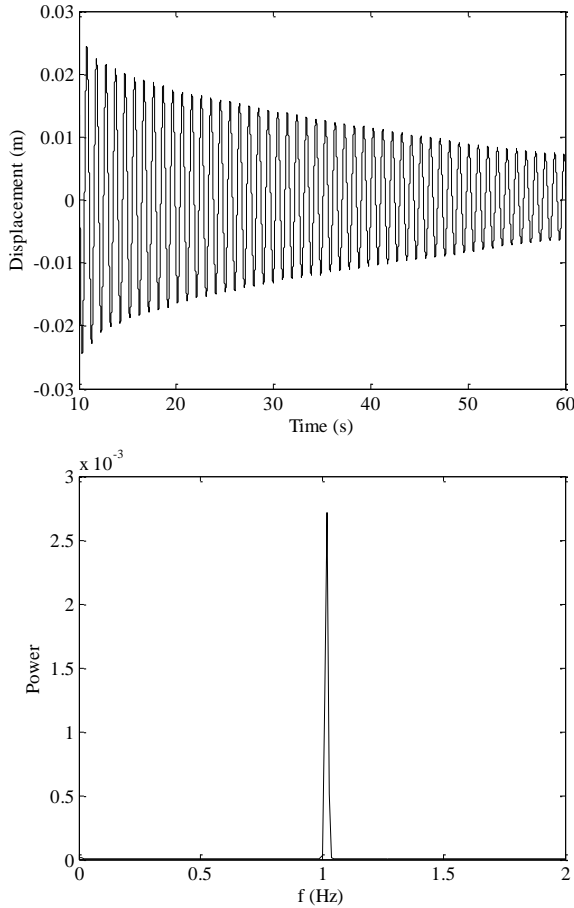


Figure 3. Damping and natural frequency calculations by performing a decay test in air

EXPERIMENTAL RESULTS

For each inclination, the water level was held constant and the flow velocity was increased from zero in small steps. At each step the amplitude and frequency were calculated by recording the displacement time series and the reduced velocity was calculated using $U^* = U/f_N D$.

One set of experiments was performed on a normal-incidence cylinder (crossflow oscillations) to have a base for comparison. These results were in agreement with those of Khalak and Williamson (1999) in terms of the onset and width of the lock-in region as well as the amplitude of oscillations as shown in Figure 4. The upper branch was not observed in our tests due to the difference in the mass-damping coefficient ($m^*\zeta$) compared with the Khalak and Williamson's tests. Figure 5 shows the non-

dimensional frequency ($f^* = f/f_N$) plotted against the reduced velocity. As the flow velocity increases, the oscillating frequency (f) approaches the natural frequency (f_N) of the system in the lock-in region and the cylinder starts oscillating in the crossflow direction.

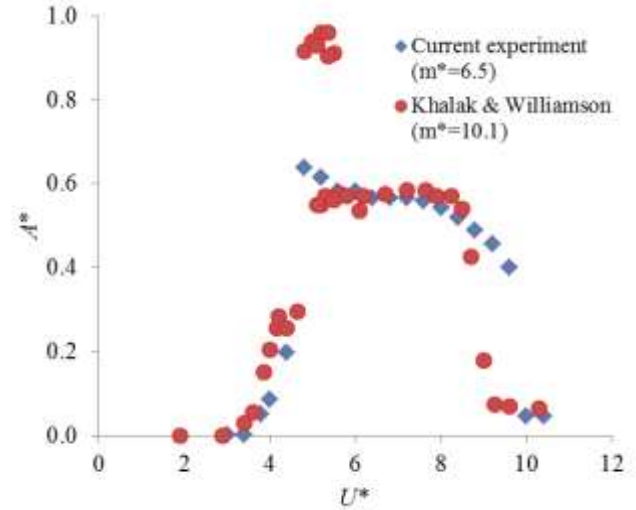


Figure 4. Comparison of our results for a normal incidence cylinder ($m^*\zeta = 0.029$) with Khalak & Williamson's (1999) results ($m^*\zeta = 0.013$).

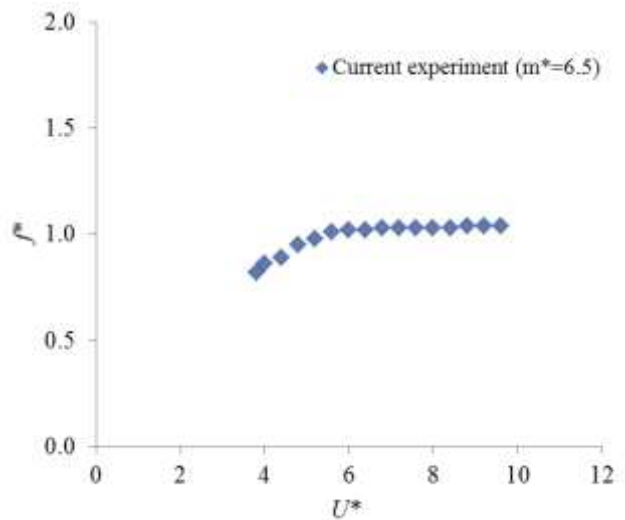


Figure 5. Frequency response for a normal-incidence cylinder ($m^*\zeta = 0.029$)

A set of experiments was performed on a 45° -inclined cylinder with a 1 mm gap ($0.08D$). Following Morse et al. (2008) work on a normal incidence cylinder, three gap sizes were chosen. A gap size of 1 mm ($0.08D$) was chosen because for a normal-incidence cylinder, a gap size smaller than 15% of the cylinder diameter results in a behavior similar to a cylinder with an attached endplate – i.e., negligible three-dimensional effects due to the end

condition – without increasing the added mass due to the attached endplate (Morse et al., 2008). The amplitude and frequency response of a 45°-inclined cylinder are shown in Figure 6, together with the results of a similar test from Franzini et al. (2009).

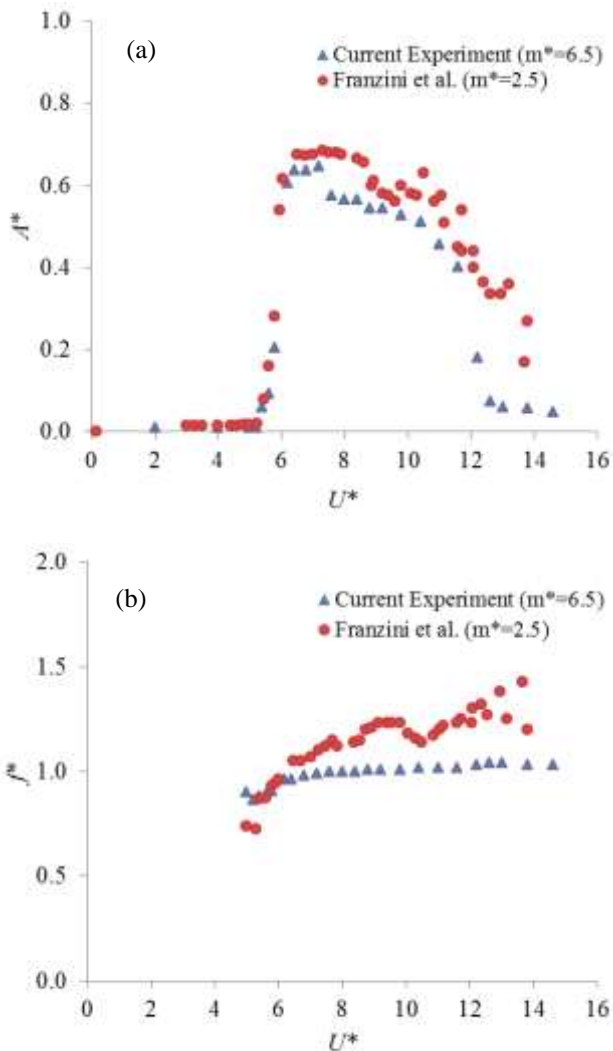


Figure 6. (a) Amplitude and (b) frequency response of a 45°-inclined cylinder from the current experiments and from Franzini et al. (2009). The mass-damping coefficient ($m^*\zeta$) is 0.029 for the current experiments and 0.0125 for Franzini et al. (2009).

Three sets of experiments were performed on the 65°-inclined cylinder with varying gap between the lower end of the cylinder and the endplate. The results for a 65°-inclined cylinder with a 1 mm gap are shown in Figure 7. The Reynolds number, Re , is shown on the secondary horizontal axis of the figure. Two regions of large-amplitude oscillations are observed: one in the range of $U^* = 7-13$ and other in the range of $U^* = 35-52$. In both regimes, the maximum amplitude is around $0.5D$, while the second region is three times wider than the first one. We call these two regions, the two lock-in regions. The first one, corresponding to the smaller reduced velocities

is very similar to what we have observed for the case of 45°-inclined cylinder. The second lock-in region, however, was not observed in the smaller angles of inclination. The frequency response shown in Figure 7b shows that the oscillating frequency gets locked in with the natural frequency at a dimensionless frequency of around 1.0 in the first lock-in region, and a dimensionless frequency of around 0.85 in the second lock-in region.

The displacement time histories at two different speeds are shown in Figures 8 and 9. At $U^*=10$, where the peak amplitude of the first lock-in occurs, we observe a periodic response with a constant amplitude. The oscillating frequency is 0.99 Hz, very close to the natural frequency of the system (1.0 Hz). At $U^*=41$, in the second lock-in region, some modulation in the amplitude of response are observed and the frequency of oscillations reduces to around 0.85 Hz. It is worth mentioning that the free surface waves were present throughout the second lock-in region because of the high flow velocity.

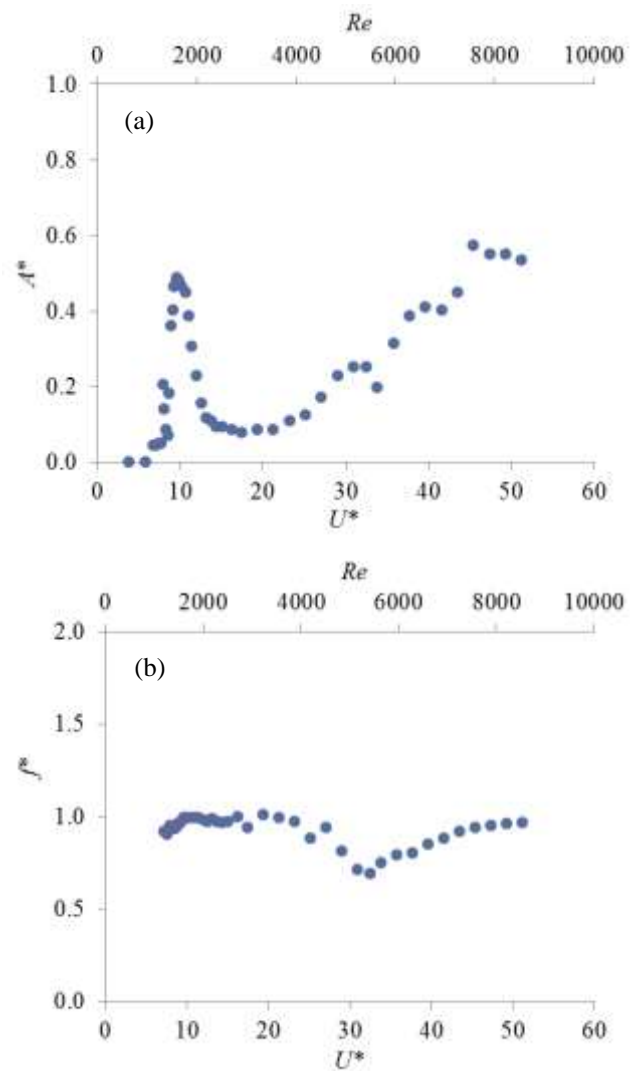


Figure 7. (a) Amplitude and (b) frequency response of a 65°-inclined cylinder with a gap size of 1 mm between the cylinder and the end plate.

Furthermore, the 3 mm (0.23D) gap and the no-endplate cases were tested to observe the influence of the end condition on the cylinder's response. From Figure 10, it can be seen that the end plate does not seem to have a significant influence on the first lock-in region as the onset and the peak amplitudes are unchanged in the three cases. But there seems to be a significant effect of on the second lock-in region. The peak amplitude in the second lock-in region is the same for the 1 mm and 3 mm gap and decreases for the case with no endplate.

In order to validate IP, the amplitude response was plotted against the normalized reduced velocity U_n^* in Figure 11. The lock-in region for all the inclinations begins at a normal reduced velocity of around 4.0 but the lock-in width is much smaller for the 65°-inclination case compared with the 45°-inclination. The maximum amplitude for all the inclinations lie in the U_n^* range of 4 – 6, in agreement with Lucor and Karniadakis (2003). The response for the 65°-inclination has a very wide second lock-in range, which is absent for the other angle of inclination.

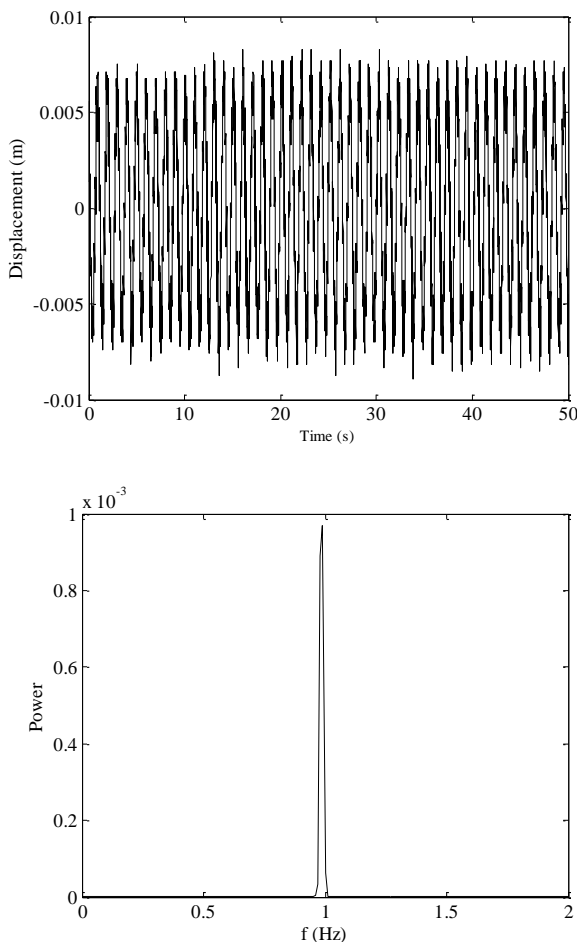


Figure 8. Time history and PSD plots of the displacement for a 65°-inclined cylinder with 1 mm gap at $U^* = 10$

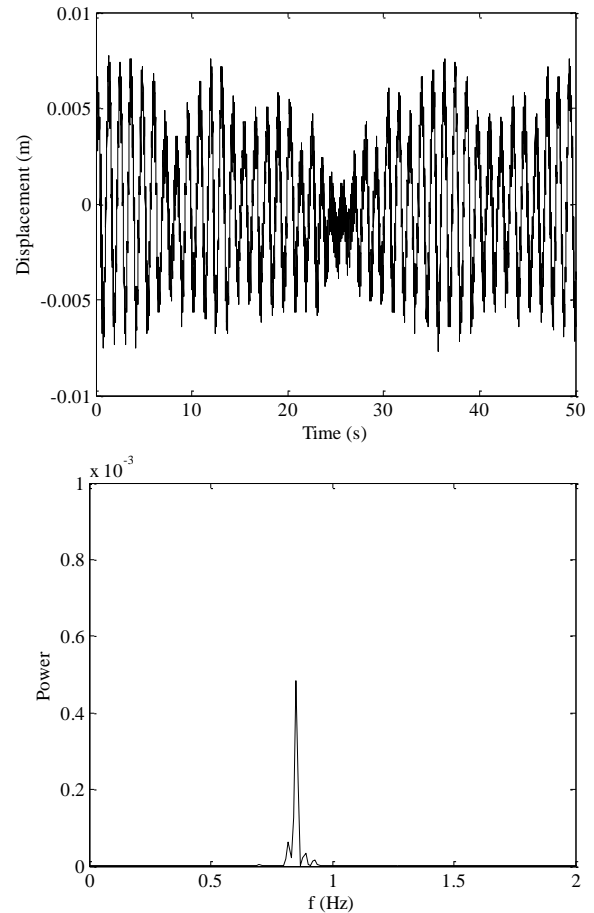


Figure 9. Time history and PSD plots of the displacement for a 65°-inclined cylinder with 1 mm gap at $U^*=41$

CONCLUSIONS

We have conducted a series of experiments to study vortex-induced vibrations of an inclined cylinder placed in flow. We have considered angles of inclination of 45° and 65°. For the case of a 65°-inclined cylinder with a low mass-damping parameter and one degree of freedom – transverse to the incoming flow – we have observed two lock-in regions. The first lock-in region was observed when the oscillating and the natural frequencies were close to 1 and the second lock-in region was characterized by a smaller lock-in frequency of around 0.85. The time histories show a periodic oscillation in the first lock-in region and a modulating response in the second lock-in region. The endplate and the gap between the cylinder and the endplate does not influence the first lock-in region much, but have a major influence on the second lock-in region. If only the normal component of the oncoming flow is considered, the onset of the first lock-in region for both inclinations coincides with that for the normal-incidence cylinder. The width of this lock-in range, however, is much smaller for the case of 65°-inclination.

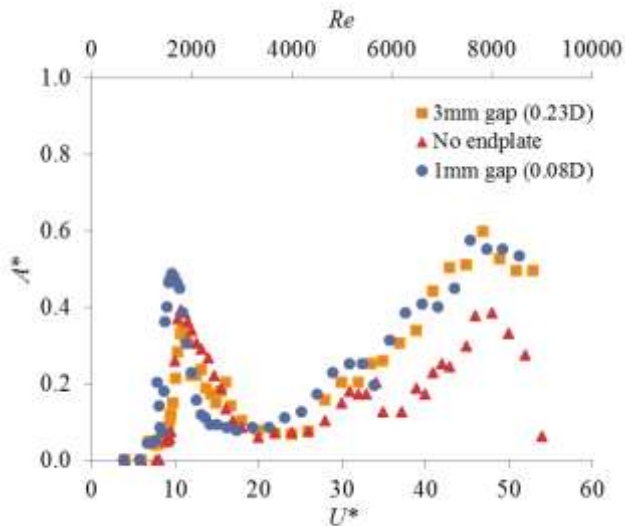


Figure 10. Amplitude response of a 65°-inclined cylinder with various gap sizes of 1mm (0.08D), 3mm (0.23D) and with no endplate.

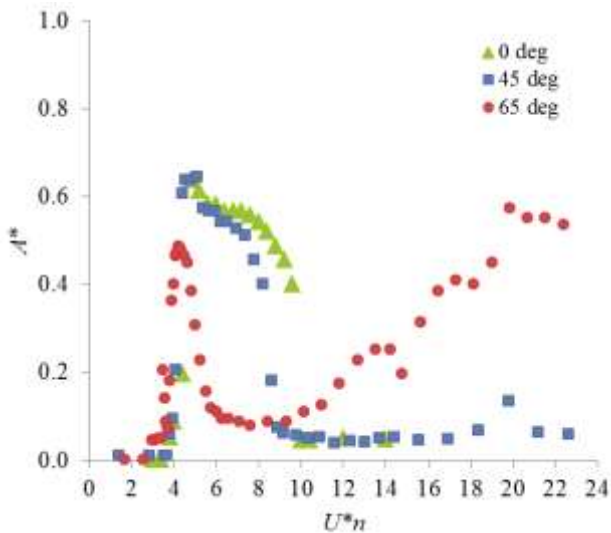


Figure 11. Amplitude versus the normalized reduced velocity after applying the IP for various inclinations.

ACKNOWLEDGMENTS

The authors are grateful to Mr. Al Rakouskas and Mr. Rick Winn of the Department of Mechanical and Industrial Engineering of University of Massachusetts, Amherst for their valuable help in setting up the experiments.

REFERENCES

Franzini, G.R., Fugarra, A.L.C., Meneghini, J.R., Korkischko, I., Franciss, R., 2009. Experimental investigation of Vortex Induced Vibration on rigid, smooth and inclined cylinders. *Journal of Fluids and Structures* 25 (2009) 742-750.

Hanson, A.R., 1966. Vortex-shedding from yawed cylinders. *AIAA Journal* 4(4) 738-740.

Khalak, A., Williamson, C.H.K., 1996. Dynamics of a hydro elastic cylinder with very low mass and damping. *Journal of Fluids and Structures* 10, 455-472.

Khalak, A., Williamson, C.H.K., 1999. Motions, forces and mode transitions in vortex-induced vibrations at low mass damping, *Journal of Fluids and Structures* 13 (7-8) (1999) 813-851.

King, R., 1977. Vortex excited oscillations of yawed circular cylinders. *ASME, Journal of Fluids Engineering* (1977) 495-502.

Kozakiewicz, A., Fredsøe, J., Sumer, B., 1995. Forces on Pipelines in Oblique Attack: Steady Current and Waves, Vol. II. The Hague, Netherlands, pp. 174-183.

Lucor, D., Karniadakis, G.E.M., 2003. Effects of oblique inflow in vortex-induced vibrations. *Flow, Turbulence and Combustion* 71, 375-389.

Morse T. L., Govardhan R., Williamson C. H. K., The effect of end conditions on the vortex-induced vibration of cylinders, *Journal of Fluids and Structures*, 24 (2008) 1227- 1239.

Ramberg, S., 1983. The effects of yaw and finite length upon vortex wakes of stationary and vibrating circular cylinders. *Journal of Fluid Mechanics* 128, 81-107.

Surry, J., Surry, D., 1967. The effect of inclination on the Strouhal number and other wake properties of circular cylinders at subcritical Reynolds numbers. Technical Report, UTIAS Technical note No. 116, Institute for Aerospace Studies, University of Toronto.

Van Atta, C. W., 1968. Experiments on vortex shedding from yawed circular cylinders. *AIAA Journal* 6, 931-933.

Willden R. H. J., Guerbi M., 2010. Vortex dynamics of stationary and oscillating cylinders in yawed flow. The proceedings of the 6th symposium on bluff body vortex induced vibrations (BBVIV-6), Capri, Italy, June 2010.

Zhao, M., Cheng, L., Zhou, T., 2009. Direct numerical simulation of three-dimensional flow past a yawed circular cylinder of infinite length. *Journal of Fluids and Structures* 25 831-847.

COMPARISON BETWEEN FORCE MEASUREMENTS OF ONE AND TWO DEGREES-OF-FREEDOM VIV ON CYLINDER WITH SMALL AND LARGE MASS RATIO

Guilherme R. Franzini*

Julio R. Meneghini

Fluids and Dynamics Research Group - NDF
POLI
University of São Paulo, Brazil

Rodolfo T. Gonçalves

André L. C. Fajarra†

Numerical Offshore Tank - TPN
POLI
University of São Paulo, Brazil

ABSTRACT

Experimental results of Vortex-Induced Vibrations (VIV) with one and two degrees-of-freedom obtained (1DOF and 2DOF respectively) with the same apparatus are shown. A rigid cylinder is mounted on a very low damped leaf-spring system and time-series of displacement and forces are acquired. Two values of mass ratio parameter m^* are tested, $m^* = 2.6$ and $m^* = 8.1$. The Reynolds number range is $3 \times 10^3 < Re < 1.3 \times 10^4$. The focus is to compare results of forces coefficients, including added mass results, as well as amplitudes and frequency values for both experimental conditions.

The results showed a marked difference in behavior between 1DOF and 2DOF at the “*super upper branch*” and at the in-line synchronization range for $m^* = 2.6$. For $m^* = 8.1$, the difference is constrained to the in-line synchronization range. An interesting feature of the in-line synchronization is the fact that the increase in the mass ratio parameter does not lead to significant differences in the amplification of forces coefficients.

Considering the $m^* = 2.6$ 2DOF experiments, the cross-flow added mass coefficient results differs from the ones obtained with the 1DOF system only at the “*super upper branch*” range. On the other hand, no difference was observed in the added mass plot for $m^* = 8.1$.

Keywords: Vortex-induced vibration, Experiments, One degree-of-freedom, Two degrees-of-freedom, Forces measurements, Added mass coefficient

INTRODUCTION

The Vortex-Induced Vibrations (VIV) is a self-excited and self-limited phenomenon that occurs when the vortex-shedding frequency f_s is close to one of the natural frequencies of the structure. The phenomenon plays an important role in the behavior of offshore structures, such as risers. Despite maximum amplitudes of oscillation with order of one diameter, VIV can be important in the prediction of fatigue problems.

Besides its practical importance, VIV consists on a puzzling fluid-structure resonant problem and has motivated several studies during the last decades. As a result of these studies, there are numerous research works into the subject. The comprehensive papers written by [1, 2], [3], [4, 5] and [6] are classical examples of surveys regarding the theme.

Up to the early 2000's, most of the works, both theoretical and experimental, concerned the problem of a rigid cylinder, free to oscillate only in the cross-flow direction, consisting of an elastic system with one degree-of-freedom (1DOF). Considering 1DOF systems, some aspects are extensively studied, such as the effects of structural mass ([7]), the maximum amplitude of response ([8]) and the hydrodynamic forces ([9], [10] and [11]).

Motivated by the technological demands, especially those related to the oil and gas exploration in the offshore environment, a great amount of effort has been employed on the study of the VIV both on a rigid cylinder with two degrees-of-freedom (2DOF) and on a flexible cylinder. Some papers regarding these conditions are those written by [12], [13], [14], [15] and [16].

The fundamental studies developed by [17, 18] enlightened some unrevealed aspects concerning the 2DOF VIV phenomenon and its governing parameters were bet-

*Corresponding author. Email: gfranzini@usp.br

†Presently at MARIN - Maritime Research Institute Netherlands as visiting researcher.

ter understood according to an enhanced phenomenological fundament. A key-point aspect is the influence of the mass ratio parameter m^* . Through experiments in water, the authors proposed two dynamical behaviors for the cylinder. One of them was verified for “*moderate to large mass ratio parameter*” ($m^* > 6$), in which the in-line oscillations are negligible in the cross-flow amplitude of response.

The second dynamic behavior, observed for “*moderate to small mass ratio parameter*” ($m^* < 6$) is characterized by a strong presence of the in-line oscillations. The concomitant presence of in-line and cross-flow oscillations can lead the system to a new stable branch of response, named by the authors as “*super upper branch*” and defined by a $2T$ pattern of vortex shedding, in which two triplets of vortex are shed in each cycle. At the “*super upper branch*” range, the frequency of in-line oscillations are twice the ones observed in the cross-flow ones. Most of the features observed for a rigid cylinder at “*super upper branch*” can be extent to a flexible cylinder, as stressed by [19].

Despite the growing number of works discussing amplitude and frequency for 2DOF VIV, there are a few works that present results about force coefficients. Forces measurements described by [18] reported the presence of a 3ω component in the lift force at the “*super upper branch*” range. The published papers by [20] and [21] showed experimental 2DOF VIV results about the mean drag coefficient.

In spite of the numerous papers concerning the VIV, the concept of added mass m_a and its definition within the phenomenon context still keep some discussion points in Conferences, as can be found in the Preface written by [22]. There are two ways of defining the added mass; the first one is the term of the hydrodynamic force in-phase with the body acceleration and the second one is based on the definition of the kinetic energy of the fluid.

The added mass is a key point of hydroelastic problems in which the kinetic energy of the fluid is not negligible compared to the structural kinetic energy, such as the natural frequencies of floating units and risers. In numerical studies carried out using the Iwan & Blevins phenomenological model, [23] observed that the variation of the added mass coefficient with the reduced velocity allows to capture the lower branch in the amplitude response curve. Another investigation concerning the added mass is the one presented in [24], in which the general behavior of the added mass curve was observed for different types of phenomenological models.

In circular cylinders subjected to VIV, the added mass coefficient $C_a = m_a/m_d$ can be significantly differ-

ent from the potential value $C_a = 1$ as stressed in several works, such as those by [3], [25] and [26].

The added mass coefficient for 1DOF VIV can be evaluated from experiments using both the time domain ([26]) and the frequency domain ([27]) approaches. In these works, C_a curve crosses zero value at reduced velocity equal to 8 monotonically and presents an asymptotic value $C_a = -1$ outside the lock-in region.

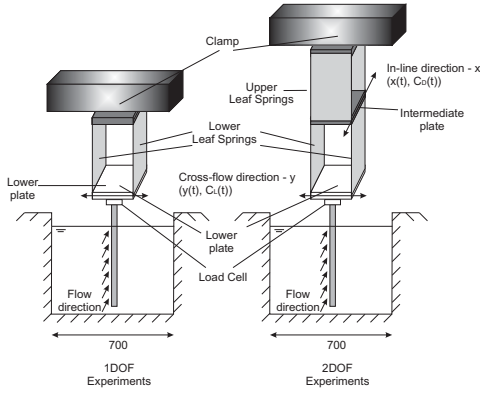
There are a few works of added mass coefficient for 2DOF VIV. The paper by [25] shows in-line and cross-flow added mass coefficients for a large m^* experiment. For the cross-flow added mass coefficient $C_{a,y}$, a marked similarity is observed between 1DOF and 2DOF experiments, except for an inflection behavior in the range $5.6 < V_R < 6.8$, which corresponds to the region with the higher amplitudes of oscillation.

The objectives of the present work are to present and discuss aspects about hydrodynamic forces and added mass coefficients for 1DOF and 2DOF VIV experiments carried out with the same apparatus, aiming at minimizing behaviors that can be associated to different set-ups. Two values of mass ratio parameter m^* were chosen, being one of them lower and the other higher than the critical value $m_c^* \approx 6$ proposed by [18]. It is worth mentioning that the results of added mass for two 2DOF system, at small value of m^* , are not found in the literature, at least to the authors knowledge.

EXPERIMENTAL ARRANGEMENT AND ANALYSIS METHODOLOGY

All the experiments were carried out at the NDF Circulating Water Channel facility of the University of São Paulo (USP). The dimensions of the test section is $7500 \times 700 \times 700\text{mm}$ and the flow has low levels of turbulence (less than 2%). The pump system can operate with good quality with free-stream velocities up to 0.40m/s . Further details concerning the Circulating Water Channel can be found in [28].

The leaf-spring elastic base can be assembled for experiments with 1DOF or 2DOF. In the later case, two orthogonal leaf-springs must be employed. The models are made of aluminium with external diameter $D = 44.45\text{mm}$. A schematic representation of the experimental arrangement is shown in Figure 1.


FIGURE 1: Experimental Arrangement.

Laser position sensors LEUZE model ODSL 8/V4 were employed to measure the in-line and cross-flow displacements. A load cell ATI, model Mini40 was used to acquire the lift and drag forces. The sample frequency was 100Hz and all the data were acquired on a HBM system.

Free-decays tests in air allowed identifying a very low structural damping coefficient ($\zeta_s < 0.1\%$). The aspect ratio (L/D) for all the experiments was kept constant and equal to 15. The gap between the lower tip of the model and the bottom of the channel was less than $0.5D$ in order to minimize the influence of the flow around this region. No end-plates were employed. Table 1 presents the experimental parameters.

TABLE 1: Experimental parameters.

$m^* = \frac{4m_s}{\rho\pi D^2 L}$	$\zeta_s [\%]$	$\zeta = \zeta_s \sqrt{\frac{m^*}{1+m^*}}$	$m^* \zeta$	L/D
2.6	0.08	0.07	0.0018	15
8.1	0.07	0.07	0.0057	

The oscillation amplitudes were taken by computing the average of the 10% highest peaks in the time series. The dominant frequency f_d refers to the frequency that contains the highest amount energy in the power spectrum density function (PSD).

The concept of added mass adopted in this paper is the component of the hydrodynamic force in-phase with the acceleration. Using an analogous approach to the one described in the papers by [27] and [29], the drag and lift forces are decomposed according to the equations:

$$F_D(t) = -m_{a,x}\ddot{x} - c_{v,x}\dot{x} \quad (1)$$

$$F_L(t) = -m_{a,y}\ddot{y} - c_{v,y}\dot{y} \quad (2)$$

Where m_a and c_v refer to the added mass and the hydrodynamic damping respectively. Applying the Fourier Transform F on both sides of the Equations 1 and 2, the following equations are obtained:

$$\frac{F[F_D]}{F[x]} = m_{a,x}\omega^2 - ic_{v,x}\omega \quad (3)$$

$$\frac{F[F_L]}{F[y]} = m_{a,y}\omega^2 - ic_{v,y}\omega \quad (4)$$

The added mass coefficient for the in-line and cross-flow directions can be obtained from Equations 3 and 4. For each direction, the value of added mass was taken considering the spectral component at the dominant frequency of the displacement spectrum (f_{dx} or f_{dy}).

RESULTS AND DISCUSSION

The experimental results will be presented in the next four subsections. Firstly, the results related to displacement (amplitude and frequency) and to the hydrodynamic forces for $m^* = 2.6$ will be compared to those discussed in the papers by [7] and [18]. Following, a direct comparison between 1DOF and 2DOF results will be discussed for both values of the m^* tested. Finally, the results of cross-flow and in-line added mass coefficients will be presented.

COMPARISON WITH PREVIOUS RESULTS - $m^* = 2.6$

Figure 2 presents the comparison between the experimental 1DOF results from the present work and the results obtained by [7]. One can note that both the amplitude of oscillation (Figure 2(a)) and the root-mean-square (RMS) lift coefficient (Figure 2(d)) very well match with the previous results. The frequency response, shown in Figure 2(b) does not follow either the curve for a fixed cylinder (Strouhal number $St \approx 0.20$) or the classical lock-in response $f_{dy} \approx f_N$. Figure 2(c) shows the drag amplification, although there is a difference in the maximum value of C_D when compared with the literature.

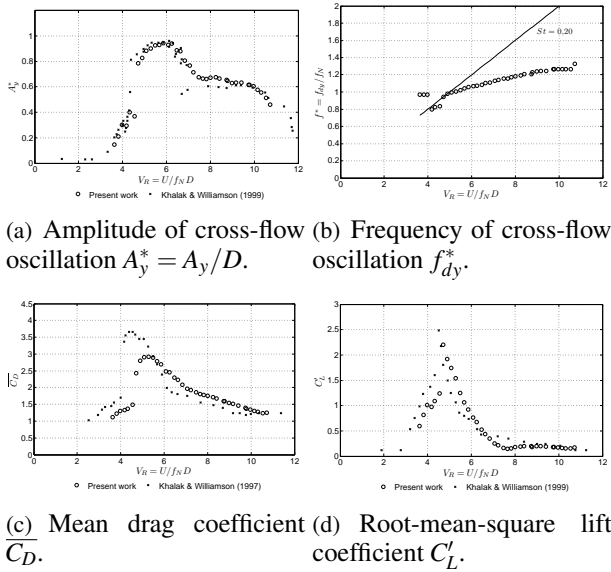


FIGURE 2: Experimental Results 1DOF - $m^* = 2.6$.

The comparison between the present results from 2DOF experiments and those published in [18] are shown in Figure 3. The amplitude of oscillation matches with the previous results very well, including the in-line resonance observed in $2 < V_R < 4$. The frequency plot (Figure 3(b)) shows the well known result regarding the twice in-line frequency of oscillation. The results for force coefficients are presented in Figures 3(c) and 3(d). The good agreement with previous results for the RMS lift coefficient can be observed. The mean drag coefficient follows the same trend, in spite of a slightly higher value obtained in the present study.

COMPARISON BETWEEN 1DOF and 2DOF RESULTS
- $m^* = 2.6$

Figure 4 presents the direct comparison between 1DOF and 2DOF results. For the values of reduced velocities $V_R < 4.5$, i.e., before the range characterized by the “upper branch” (1DOF) and the “super upper branch” (2DOF), the amplitude of oscillation, shown in Figure 4(a), is independent of the in-line degree-of-freedom. Considering the results in the “lower branch” range, the amplitudes for the 2DOF system are slightly higher than those for the 1DOF case. Notice that the onset of desynchronization occurs for the same reduced velocity for both conditions $V_R \approx 11$.

Besides the higher amplitudes of oscillation at the “lower branch”, the frequency of oscillation shows no distinction between 1DOF and 2DOF experiments at this range, as shown in Figure 4(b). Considering the range $4 < V_R < 8$ in the frequency plot, the 1DOF curve is

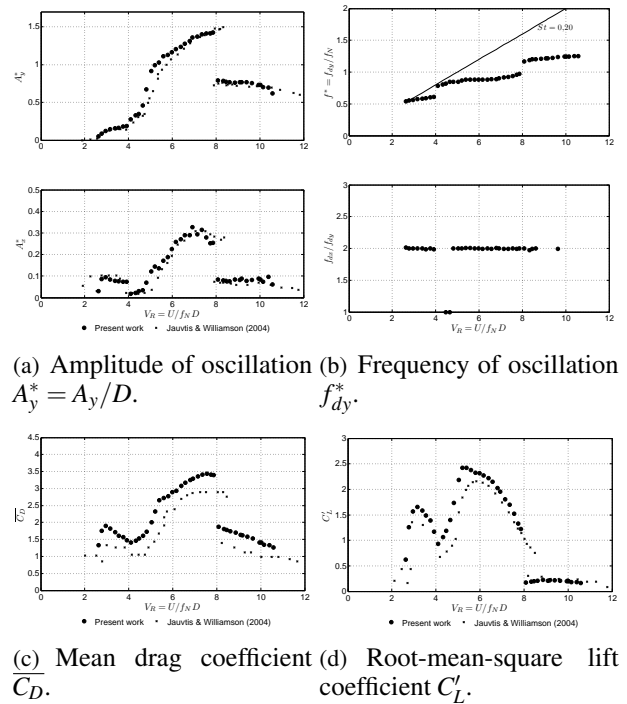


FIGURE 3: Experimental Results 2DOF - $m^* = 2.6$.

monotonically crescent and higher than the 2DOF results.

Figures 4(c) and 4(d) present the results for the mean drag coefficient and RMS lift coefficient respectively. Notice, also, the asymptotic value $\overline{C_D} \approx 1.2$ at $V_R \approx 10.5$, corresponding to the mean drag coefficient observed in a stationary circular cylinder.

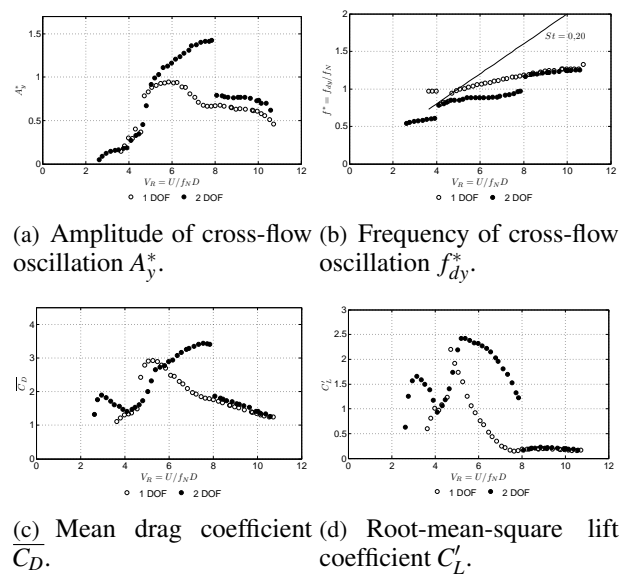


FIGURE 4: Comparison between 1DOF and 2DOF results - $m^* = 2.6$.

Some interesting aspects should be highlighted in the force coefficients plots. The first one is the marked amplification in both $\overline{C_D}$ and C'_L observed in the in-line resonance, despite the small cross-flow amplitudes $A_y^* \approx 0.1$. This fact demonstrates a dependence on the hydrodynamic forces not only with the amplitude, but also with the presence of synchronization.

The second aspect that must be emphasized is the similar maximum value of C'_L , although the maximum cross-flow amplitude for 2DOF case is 50% higher than for 1DOF system. Another feature regarding the 2DOF results is the broader range of synchronization at the “*super upper branch*” range.

Additionally to the classical curves of response discussed above, the Lissajous figures shown in Figure 5 were plotted aiming at enhancing the comparative analysis. A first aspect that can be better understood with the Lissajous plot is the increase in the forces coefficients, for 2DOF system, at the in-line synchronization range, characterized by a symmetric vortex-shedding pattern (see [18]). At $V_R = 3.4$, the well defined eight-shaped xy Lissajous plot indicates a highly correlated wake along the span, and thus higher hydrodynamic forces can be expected in comparison with the case in which there is no spanwise wake correlation. At the same reduced velocity, the 1DOF system presents amplitude of oscillation lower than $1D$, which is an indicative of lower correlation length.

Another aspect that can be discussed through the Lissajous plot is related to the spectral distribution of both the lift force and the cross-flow oscillations. As pointed out by [18], the “*super upper branch*” range is characterized by the $2T$ vortex shedding pattern and by the presence of a third subharmonic (3ω) component on the lift force coefficient. Analyzing reduced velocities $V_R = 5.6$ and $V_R = 6.4$, the xy plot presents the classical 8-shape and the $y^*(t) \times C'_L(t)$ clearly reveal the presence of the referred subharmonic.

Focusing on the reduced velocity immediately before the jump to the “*lower branch*” ($V_R = 7.9$), the in-line amplitude is $A_x^* \approx 0.3$ although the xy figure does not follow the classical 8-shape pattern, whereas the $y^*(t) \times C'_L(t)$ clearly does not presents the 3ω harmonic. Therefore, the 3ω component on the lift force is related to the twice in-line frequency of oscillation, despite the non negligible in-line amplitude.

COMPARISON BETWEEN 1DOF and 2DOF RESULTS

- $m^* = 8.1$

The results for the condition with moderate to large mass ratio is presented in Figure 6. As mentioned in pre-

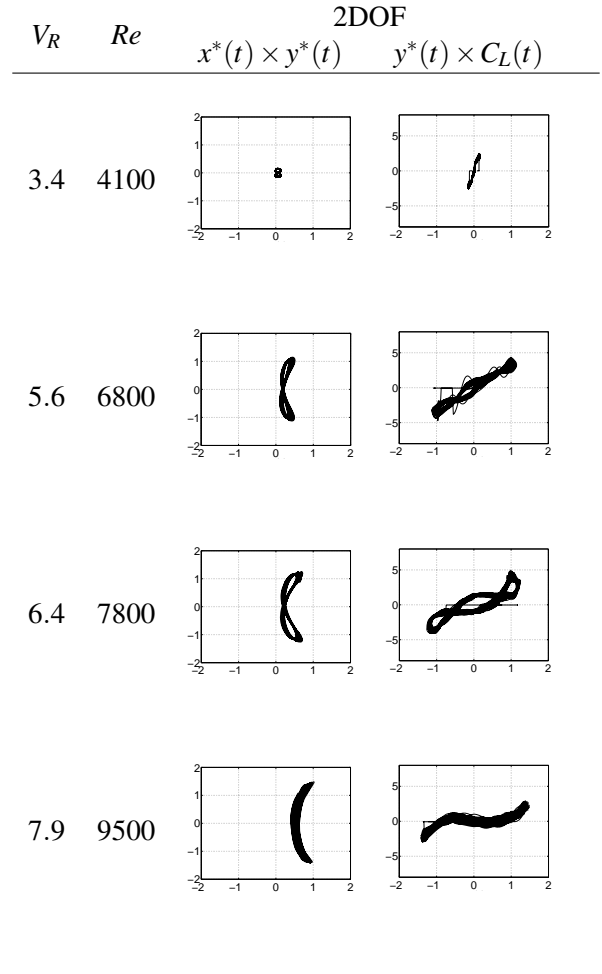


FIGURE 5: Lissajous plot - $m^* = 2.6$.

vious works, the amplitude of cross-flow oscillations for the 2DOF system very well agrees with that observed in the 1DOF experiments, even though some minor differences are shown in the “*upper branch*”, as presented in Figure 6(a). The review by [4] reported the narrowing of the “*lower branch*” for 1DOF systems, fact in total agreement with the present 2DOF results.

The non-dimensional frequency of response, shown in Figure 6(b), is closer to the unity than the results for the experiments with $m^* = 2.6$. This feature was also discussed, for 1DOF experiments in [7].

The analysis of the forces coefficients results deserves a more detailed discussion. Considering the range $V_R > 4$, both the C'_L (Figure 6(d)) and the $\overline{C_D}$ (Figure 6(c)) plots show a very good agreement 1DOF and 2DOF experiments. This aspect extends, to the forces coefficients, the assertion that for moderate to large mass ratio parameter, the in-line oscillations are negligible; there is thus no difference between one or two degrees-of-freedom systems.

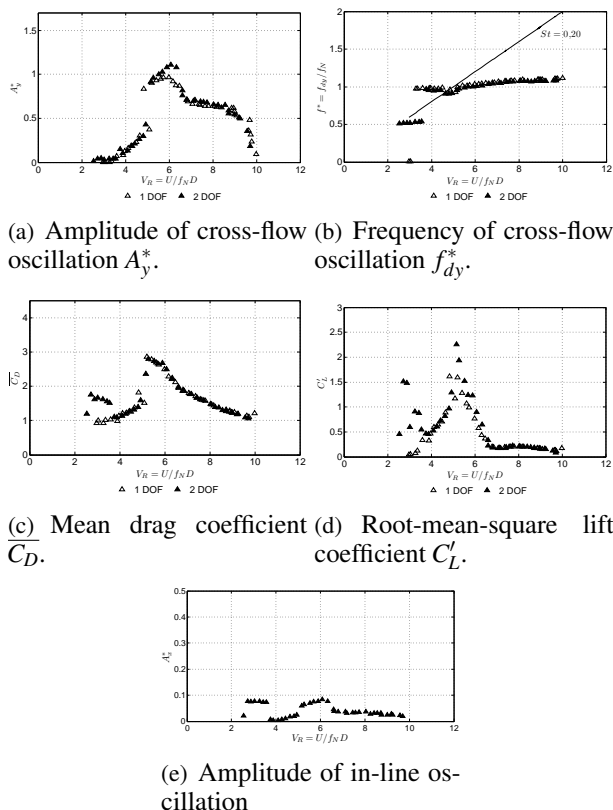


FIGURE 6: Comparison between 1DOF and 2DOF results - $m^* = 8.1$.

However, for the range in which the in-line synchronization is observed ($2 < V_R < 4$), the marked increase in both forces coefficients is observed. Moreover, the maximum values in this range very well agree with those observed for moderate to small mass ratio parameter experiments; therefore, the effects of the larger values m^* are more evident in the “super upper branch” range than in the in-line synchronization range.

ADDED MASS COEFFICIENT

The added mass coefficient results for both mass ratio parameters tested are presented in Figure 7. Considering $m^* = 2.6$ and 2DOF, the results for in-line, as well as cross-flow added mass (Ca_x and Ca_y respectively) are found in Figure 7(a). In the Ca_x plot, the zero-crossing result occurs at $V_R \approx 4$, which corresponds to the end of the in-line synchronization. Analyzing the “super upper branch” range of reduced velocities, both Ca_x and Ca_y show an inflection behavior at $V_R \approx 6.4$, although the decreasing rate of the cross-flow results are more noticeable in the Ca_y plot.

Figure 5 shows that, at $V_R = 6.39$ the 2DOF Lissajous plots are more pronouncedly coupled, in agreement with the results described by [25] for moderate to large m^* ex-

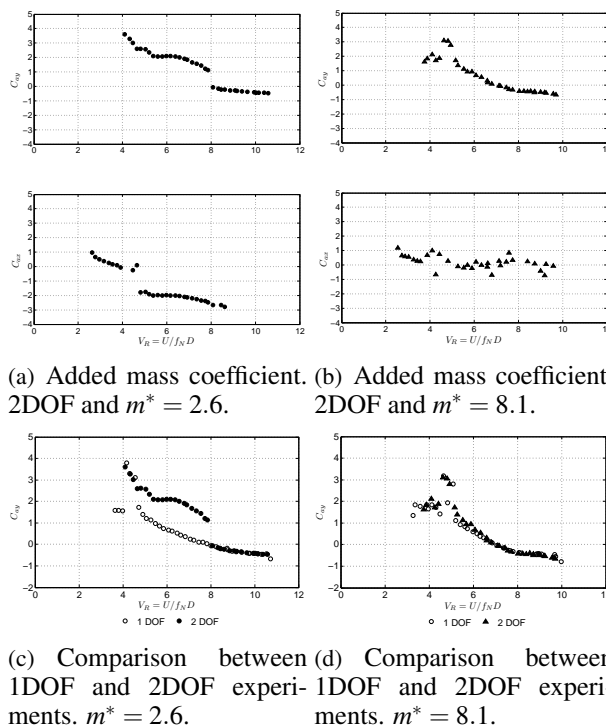


FIGURE 7: Added mass coefficient.

periments. In [25], the authors pointed out that the inflection in Ca_y plot could be an effect of the in-line oscillations, and consequently to change in the vortex shedding pattern. At the range $5 < V_R < 7$, the Ca_y is constant and the 3ω component is present in the lift force spectrum; hence the $2T$ vortex shedding pattern is observed. The inflection occurs when the 3ω component is no longer observed, implying a change in the vortex shedding pattern, as previously pointed out, with no significant change in the in-line amplitude of oscillation, though.

The present results show the same trend in spite of the higher value of in-line oscillations compared to those presented in the cited work ($A_x \approx 0.30$ in present work, $A_x^* \approx 0.05$ in [25]). Also notice the marked similarity of the values of Ca_y at the “lower branch” for both 1DOF and 2DOF systems (see Figure 7(c)).

Conversely to the $m^* = 2.6$ results, the cross-flow added mass coefficient for 2DOF very well agrees with those from 1DOF experiments for the whole range of reduced velocities, as presented in Figure 7(d). Because of the very small oscillations, specially at the “lower branch”, the in-line oscillations, as well as the corresponding accelerations, are not well defined thus, through Equation 3, the in-line added mass is poorly defined for moderate to large m^* .

FINAL REMARKS

Experiments of vortex-induced vibrations (VIV) were carried out with a circular cylinder free to oscillate in one or two directions using the same apparatus. Two conditions of structural mass were tested, allowing studying either the effects of moderate to small or moderate to large mass ratio parameter. A direct comparison of results was discussed, enabling to identify differences in amplitudes of oscillation, forces and added mass coefficients between 1DOF and 2DOF for both values of mass ratio parameter.

For moderate to small mass ratio parameter $m^* = 2.6$, the results showed that at the “lower branch”, there are no differences between 1DOF or 2DOF systems, except for slightly higher amplitudes for 2DOF. At the “super upper branch” the in-line degree of freedom introduces a marked difference in the plots. It is worth mentioning the fact that the maximum value of RMS lift force coefficient is similar for both 1DOF and 2DOF, even though the maximum cross-flow amplitude differs by 50%.

Considering moderate to large values of m^* , the results for amplitude, frequency and forces coefficients show very good agreement between 1DOF or 2DOF systems for both the “upper branch” and “lower branch” ranges. At the range in which the in-line synchronization is observed $2 < V_R < 4$, both the 2DOF RMS lift force and mean drag coefficients showed a marked increase if compared with the 1DOF results. Moreover, both the cross-flow and the forces magnification in this range were less influenced by the effects of the mass ratio parameter.

Results of in-line and cross-flow added mass coefficient were also presented. The discontinuities at the $m^* = 2.6$ curves are associated to the end of the in-line synchronization for the Ca_x and to the end of the “super upper branch” and the onset of the “lower branch” for cross-flow added mass coefficient. The Ca_y plot for $m^* = 8.1$ very well agreed of the results for 1DOF system. For this value of mass ratio parameter, the in-line added mass is poorly defined.

Further works will include the study of force and added coefficients for different ratio of in-line and cross-flow stiffness.

ACKNOWLEDGMENT

The authors acknowledge FAPESP (São Paulo State Research Foundation), CNPq (National Council of Research), Petrobras (Brazilian company of oil and gas) and FINEP (National agency for research sponsoring) for the financial support on Vortex-Induced Vibrations (VIV) projects at USP. G.R.F. is also grateful to FAPESP for

his PhD scholarship, process 2008/066 – 88. Special thanks to César Monzu Freire, Ivan Korkischko, Douglas Silva and Reinaldo Marcondes Orselli for their help with the experiments. Prof. Fujarra is grateful to the Brazilian Navy and Maritime Research Institute Netherlands for all support provided during his sabbatical period, 2011 – 2012.

REFERENCES

- [1] Bearman, P. W., 1984. “Vortex shedding from oscillating bluff bodies”. *Annual Review of Fluids Mechanics*, **16**, Jan, pp. 195–222.
- [2] Bearman, P. W., 2011. “Circular cylinders wake and vortex-induced vibrations”. *Journal of Fluids and Structures*, **27**, pp. 648–658.
- [3] Sarpkaya, T., 2004. “A critical review of the intrinsic nature of vortex-induced vibrations”. *Journal of Fluids and Structures*, **19**, pp. 389–447.
- [4] Williamson, C. H. K., and Govardhan, R. N., 2004. “Vortex-induced vibrations”. *Annual Review of Fluids Mechanics*, **36**, pp. 413–455.
- [5] Williamson, C. H. K., and Govardhan, R. N., 2008. “A brief review of recent results in vortex-induced vibrations”. *Journal of Wind Engineering and Industrial Aerodynamics*, **96**, pp. 713–735.
- [6] Gabbai, R., and Benaroya, H., 2005. “An overview of modeling and experiments of vortex-induced vibration of circular cylinders”. *Journal of Fluids and Structure*, **282**, pp. 575–616.
- [7] Khalak, A., and Williamson, C. H. K., 1999. “Motions, forces and modes transitions in vortex-induced vibration at low reynolds number”. *Journal of Fluids and Structures*, **13**, pp. 813–851.
- [8] Govardhan, R. N., and Williamson, C. H. K., 2006. “Defining the “modified griffin plot” in vortex-induced vibration: reavealing the effect of reynolds number using controlled damping”. *Journal of Fluid Mechanics*, **561**, pp. 147–180.
- [9] Hover, F. S., Miller, S. N., and Triantafyllou, M. S., 1997. “Vortex-induced vibration of marine cables: Experiments using force feedback”. *Journal of Fluids and Structures*, **11**, pp. 307–326.
- [10] Khalak, A., and Williamson, C. H. K., 1997. “Fluid forces and dynamics of a hydroelastic structure with very low mass and damping”. *Journal of Fluids and Structures*, **11**, pp. 973–982.
- [11] Sarpkaya, T., 1995. “Hydrodynamic damping, flow-induced oscillations and biharmonic response”. *Journal of Offshore Mechanics and Artic Engineering*, **117**, pp. 232–238.

- [12] Pesce, C. P., and Fujarra, A. L. C., 2000. "Vortex-induced vibrations and jump phenomenon: Experiments with a clamped flexible cylinder in water". *International Journal of Offshore and Polar Engineering*, **10**, pp. 26–33.
- [13] Fujarra, A., Pesce, C., Flemming, F., and Williamson, C., 2001. "Vortex-induced vibration of a flexible cantilever". *Journal of Fluids and Structures*, **15**, pp. 651–658.
- [14] Sanchis, A., Sælevik, G., and Grue, J., 2008. "Two-degrees-of-freedom vortex-induced vibrations of a spring-mounted rigid cylinder with low mass ratio". *Journal of Fluids and Structures*, **24**, pp. 907–919.
- [15] Stappenbelt, B., and Lalji, F., 2008. "Vortex-induced vibration super-upper branch boundaries". *International Journal of Offshore and Polar Engineering*, **18**, pp. 99–105.
- [16] Freire, C. M., and Meneghini, J. R., 2010. "Experimental investigation of viv on a circular cylinder mounted on an articulated elastic base with two degrees-of-freedom". In IUTAM Symposium on Bluff Bodies Wakes and Vortex-Induced Vibrations - BBVIV6.
- [17] Jauvtis, N., and Williamson, C. H. K., 2003. "Vortex-induced vibration of a cylinder with two degrees of freedom". *Journal of Fluids and Structures*, **17**, pp. 1035–1042.
- [18] Jauvtis, N., and Williamson, C. H. K., 2004. "The effect of two degrees of freedom on vortex-induced vibration at low mass and damping". *Journal of Fluid Mechanics*, **509**, pp. 23–62.
- [19] Pesce, C. P., and Fujarra, A. L. C., 2005. "The "super-upper branch" viv response of flexible cylinders". In 4th Bluff-Bodies Wakes and Vortex-Induced Vibrations Conference - BBVIV4.
- [20] Assi, G. R. S., Bearman, P. W., and Kitney, N., 2009. "Low drag solutions for suppressing vortex-induced vibration of circular cylinders". *Journal of Fluids and Structures*, **25**, pp. 666–675.
- [21] Blevins, R. D., and Coughran, C. S., 2009. "Experimental investigation of vortex-induced vibration in one and two dimensions with variable mass, damping, and reynolds number". *Journal of Fluids Engineering*, **131**.
- [22] Leweke, T., Bearman, P. W., and Williamson, C. H. K., 2001. "Preface of the special issue on iutam symposium on bluff bodies wakes and vortex-induced vibrations, bbviv2.". *Journal of Fluids and Structures*, **15**, pp. 375–386.
- [23] Fujarra, A. L. C., and Pesce, C. P., 2002. "Added mass variation and van der pol models applied to vortex-induced vibrations". In Proceedings of the 5th FSI, AE, FIV & N - 5th International Symposium on Fluid-Structure Interactions, Aeroelasticity, Flow-Induced Vibrations and Noise, New Orleans.
- [24] Cunha, L. D., Pesce, C. P., Wanderley, J., and Fujarra, A. L. C., 2006. "The robustness of the added mass in viv models". In Proceedings of OMAE 06 , 25th Int. Conference on Offshore Mechanics and Arctic Engineering.
- [25] Fujarra, A. L. C., and Pesce, C. P., 2004. "Vortex-induced vibration with a 2-dof elastically mounted cantilevered cylinder in water: Some results on cross and stream-wise added mass". In Proceedings of the International Conference on Flow-Induced Vibrations, Paris.
- [26] Vikestad, K., Vandiver, J. K., and Larsen, C. M., 2000. "Adde mass and oscillation frequency for a circular cylinder subjected to vortex-induced vibrations and external disturbances". *Journal of Fluids and Structures*, **14**, Jan, pp. 1071–1088.
- [27] Fujarra, A. L. C., and Pesce, C. P., 2002. "Experiments on viv added mass with elastically mounted cylinder in water". In Proceedings of OMAE 02 , 21th Int. Conference on Offshore Mechanics and Arctic Engineering.
- [28] Assi, G. R. S., Meneghini, J. R., Aranha, J. A. P., and Coletto, W. G. P., 2005. "Design, assembling and verification of a circulating water channel facility for fluid dynamics experiments". In Proceedings of COBEM05 - 18th International Congress of Mechanical Engineering.
- [29] Franzini, G. R., Fujarra, A. L. C., Meneghini, J. R., Korkishcko, I., and Franciss, R., 2009. "Experimental investigation of vortex-induced vibration on rigid, smooth and inclined cylinders". *Journal of Fluids and Structures*, **25**, pp. 742–750.

MODELLING OF VORTEX-INDUCED VIBRATIONS OF SLENDER MARINE STRUCTURES

Andrey Postnikov*

Ekaterina Pavlovskaja

Marian Wiercigroch

Centre for Applied Dynamics Research
School of Engineering, University of Aberdeen,
Aberdeen, AB24 2FX
United Kingdom
Email: a.postnikov@abdn.ac.uk

ABSTRACT

In this paper we study VIVs of a slender marine structure using low dimensional models. Specifically, this work aims to use CFD simulations of VIV of low-mass ratio cylinders in order to calibrate existing reduced-order models based on nonlinear self-excited oscillators of van der Pol type (so-called wake oscillator models). The onset to lock-in region will be examined and the results will be presented together with the details of CFD analysis.

NOMENCLATURE

D	Diameter of the cylinder, m
A_y/D	Transverse amplitude, dimensionless
A_x/D	Inline amplitude, dimensionless
C_L	Lift coefficient ($= 2F_L/\rho U^2 D$), dimensionless
C_D	Drag coefficient ($= 2F_D/\rho U^2 D$), dimensionless
f_n	Natural frequency of the structure, Hz
f_s	Vortex shedding frequency, Hz
U	Flow velocity, m/s
Re	Reynolds number ($= UD/\nu$), dimensionless
St	Strouhal number ($= f_s D/U$), dimensionless
U_{red}	Reduced velocity ($= U/f_n D$), dimensionless
m	Mass per unit length, kg/m
m^*	Mass ratio (total mass, includes hydrodynamic added mass) ($= m/\rho D^2$), dimensionless

INTRODUCTION

Slender marine structures such as risers, mooring cables, umbilicals and tethers play crucial roles in global

offshore exploration, installation and production activities. As offshore oil and gas fields are moving into deeper waters, the nonlinearities in the system and the fluid-structure interaction phenomena such as vortex induced vibrations (VIVs) become more and more important. Many of VIV aspects are far from being understood and advanced modelling is required to investigate the impact of the phenomenon which significantly affects the service life of marine structures.

It is well known that when the vortex shedding frequency matches natural frequency of the structure, a lock-in phenomenon can be observed. This results in higher cross-flow oscillations which can inflict a significant amount of damage to the riser.

In the current work to investigate VIV phenomenon, we study vibrations of a rigid cylinder in a two-dimensional flow. A series of 2D CFD calculations is performed where the flow is analysed for the forced harmonic oscillations of the cylinder in transversal directions, then for the elastically supported cylinder capable of moving in transversal direction only and finally for the cylinder capable of moving in transversal and inline directions.

Motivation

The motivation behind this work is coined by the need of industry in effective toolkit that allows predicting loads and fatigue damage on riser systems, especially most common Top Tensioned Risers (TTRs) and Steel Catenary Risers (SCRs), which represent a crucial part of offshore facilities. Accurate prediction of VIVs can help to produce more robust structural design and lead to

*Address all correspondence to this author.

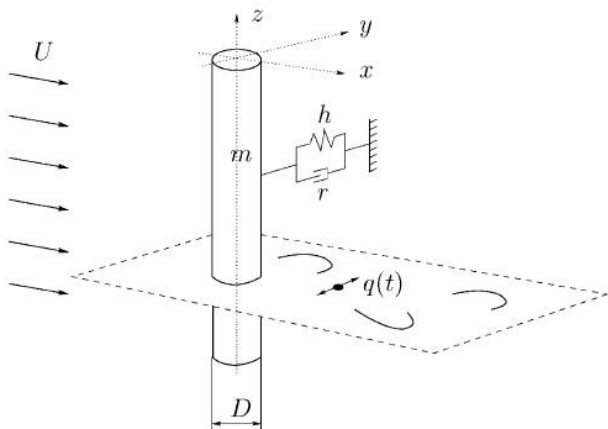


FIGURE 1. ILLUSTRATION OF WAKE OSCILLATOR MODEL. [9]

substantial savings in the offshore applications.

Wake Oscillator Models

The nature of the vortex shedding process behind cylindrical structure suggests that the forces acting on the structure from the fluid might be modelled by a non-linear, self-excited oscillator called wake oscillator. This idea was first proposed by Bishop and Hassan in 1964 [1] and then pursued by Skop and Griffin [2], and Blevins and Iwan [3]. In wake oscillator models the system is usually described by two coupled ordinary differential equations. One of the equations is the equation of motion of the rigid cylinder. The second equation is a semi-empirical description of fluid: the nonlinear self-excited fluid oscillator.

In the last ten years, models based on wake oscillators were once again considered to be useful in describing such problems. A number of wake oscillator models were developed and applied to slender flexible structures undergoing VIV. The original form of van der Pol equation has been reinterpreted by Balasubramanian and Skop [4], Skop and Luo [5], Krenk and Nielsen [6], Mureithi et al. [7] and Plaschko [8], and then applied in its 3D version.

Skop and Balasubramanian [4] proposed the new model where they introduced two terms for the lift force. In previous models, the van der Pol equation has been employed as the governing equation for the entire lift force on the cylinder. The Skop-Balasubramanian model included a van der Pol equation driven by the local transverse motion of the cylinder as a governing equation for one component of the fluctuating lift force and a so-called stall term which is linearly proportional to the local transverse velocity of the cylinder. Because of the stall term

they were able to capture an asymptotic, self-limiting structural response at zero structural damping, a kind of behaviour that has not been previously captured by the old models.

A critical analysis on this class of low-order models in terms of the fundamental behaviour was made by Facchinetti et al. [9] in 2003 where the transverse VIV of one degree-of-freedom structures in stationary uniform flow was investigated in 2003. Illustration of the model is shown on Fig. 1.

Three coupling models have been examined and compared in their ability to describe, qualitatively and quantitatively, the main phenomena observed in 2D vortex-induced vibrations. The models were referred to as displacement, velocity and acceleration coupling models. The analysis has been done by first estimating the values of all parameters from comparison with experimental data on forced vortex shedding and then by deriving analytical and numerical results on the fully coupled system. These results have been systematically compared with experimental data from the literature such as oscillation amplitude at lock-in, extension of lock-in and effective added mass. It was found that the acceleration coupling provided the best match for the experimental results qualitatively and, in some aspects, quantitatively.

In 2006 Violette et al. [10] investigated the wake dynamics represented using a distributed wake oscillator coupled to the dynamics of the slender structure, a cable or a tensioned beam and then compared the model with Direct Numerical Simulations (DNS) and experiments in order to show that wake oscillator model can be used as a simple computational tool in prediction of some aspects of vortex-induced vibrations of long flexible structures.

Coupled Reduced-Order Model

The primary objective of the following work is calibration of reduced-order models with Computational Fluid Dynamics. One of these reduced-models was proposed by Keber and Wiercigroch [11] in 2008 and is based on mathematical description of interaction between fluid and structure with two separate equations coupled at the forcing terms. The coupled model includes equation of the structure (1) and semi-empirical wake oscillator (2) as the fluid equation that models vortex shedding process:

$$m \frac{\partial^2 v(z,t)}{\partial t^2} + EI \frac{\partial^4 v(z,t)}{\partial z^4} - T \frac{\partial^2 v(z,t)}{\partial z^2} = F_F \quad (1)$$

$$\frac{\partial^2 q(z,t)}{\partial t^2} + \lambda \Omega_R (q(z,t)^2 - 1) \frac{\partial q(z,t)}{\partial t} + \Omega_R^2 q(z,t) = F_S \quad (2)$$

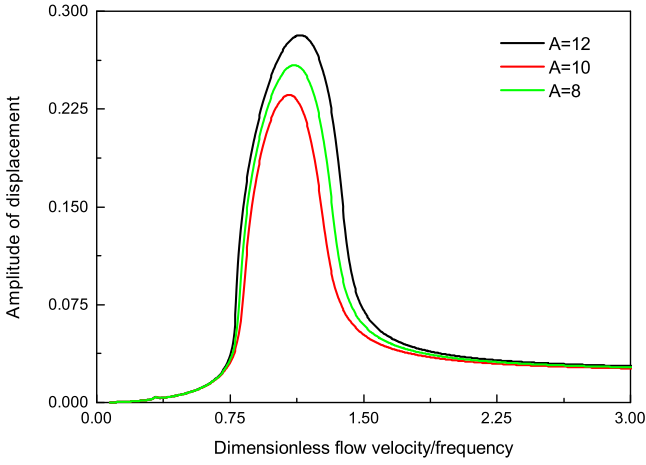


FIGURE 2. SINGLE MODE APPROXIMATION.

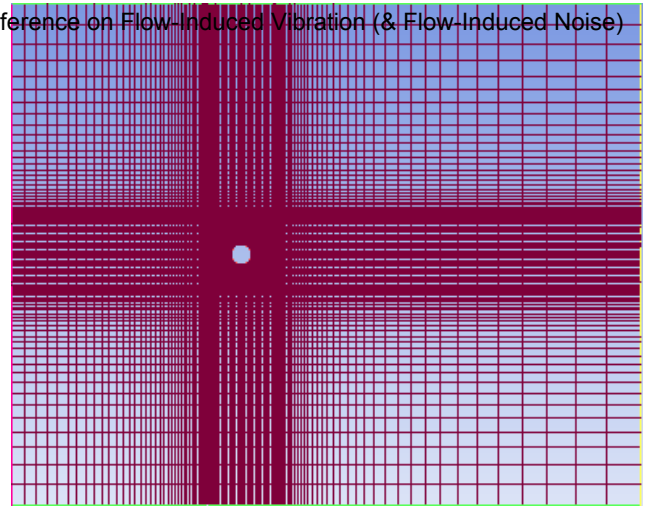


FIGURE 3. COMPUTATIONAL DOMAIN.

and the forcing terms are:

$$F_F = \frac{1}{4} C_{L0} \rho_F D U_0^2 q(z, t) - \frac{1}{2} C_D \rho_F D U_0 \frac{\partial v(z, t)}{\partial t} \quad (3)$$

$$F_S = A \frac{\partial^2 v(z, t)}{\partial t^2} \quad (4)$$

for fluid and structure respectively with coupling through the acceleration term as proposed in the Facchinetti model. The approximate solution of these equations can be constructed using modal expansion where the linear normal modes of the simply supported tension beam are used, i.e. $v(z, t) = \sum_{n=1}^N v_n(t) \sin kz$ and $q(z, t) = \sum_{n=1}^N q_n(t) \sin kz$. Single mode approximation is then described in non-dimensional form by two coupled equations given below:

$$\frac{d^2 v_1(\tau)}{d\tau^2} + \alpha \Omega_R \frac{dv_1(\tau)}{d\tau} + \omega_{R1} v_1(\tau) = b \Omega_R^2 q_1(\tau) \quad (5)$$

$$\begin{aligned} \frac{d^2 q_1(\tau)}{d\tau^2} + \lambda \Omega_R (\gamma q_1(\tau)^2 - 1) \frac{dq_1(\tau)}{d\tau} + \Omega_R^2 q_1(\tau) \\ = A \frac{d^2 v_1(\tau)}{d\tau^2} \end{aligned} \quad (6)$$

Numerical solution for single mode approximation allows to track the response of the coupled system as a function of vortex shedding frequency to natural frequency ratio. The example of the solution for a single mode is shown on a Fig. 2

From that point, a certain interest is observing different modes of vibration and detecting a resonating frequency ranges for each mode of vibration. Most simulations using CFD are done on either full scale risers, both Steel Catenary and Top Tensioned, or single degree-of-freedom rigid cylinders, but there is significantly less

information available about behaviour of reduced-order system with a relatively small amount of degrees-of-freedom. Analytical investigations on this problem including the results obtained by modelling vortex shedding with a self-excited oscillator of van der Pol type demonstrate that ranges of frequencies which correspond to modes of vibration exceeding the first one can be wider, at the same time retaining a high amplitude vibration. Low-scale CFD models could provide important calibration of these low-dimensional approximate models and allow to gain fundamental understanding of VIVs phenomenon using less costly computational approach.

CFD MODELLING

Two dimensional numerical simulations of vortex-induced vibrations of a cylindrical structure are presented in this section where two main sets of results are described.

Simulations have been performed in ANSYS FLUENT 12.0.16 for static case of a fixed rigid cylinder and dynamic case of an oscillating cylinder to observe the time history of lift and drag coefficients and the amplitudes of oscillations inside and outside the lock-in region. The fluid flow computations are run using Finite Volume Method in order to solve Navier-Stokes equations. Relatively low Reynolds numbers (500 to 2000) were considered without additional turbulence modelling. As it is a well-known fact that after a Reynolds number of 300 the wake is turbulent, a high quality grid is a necessary condition for solution to converge.

The forces acting on the cylinder have been calculated by integration of the wall pressure on the cylinder surface, and the drag and lift coefficients have been obtained as corresponding non-dimensional components of these forces. Transversal oscillations of the cylinder are studied under varying system parameters including the

TABLE 1. MESH SMOOTHING METHOD SETTINGS.

Parameter	Value
Spring Constant Factor	0.05
Boundary Node Relaxation	1
Convergence Tolerance	0.001
Number of Iterations	1500

velocity of the flow. Then the role of the inline vibrations and their overall impact on transverse amplitudes at resonance are investigated. On each set of simulations the fluid density and viscosity are constant and represents the properties of water.

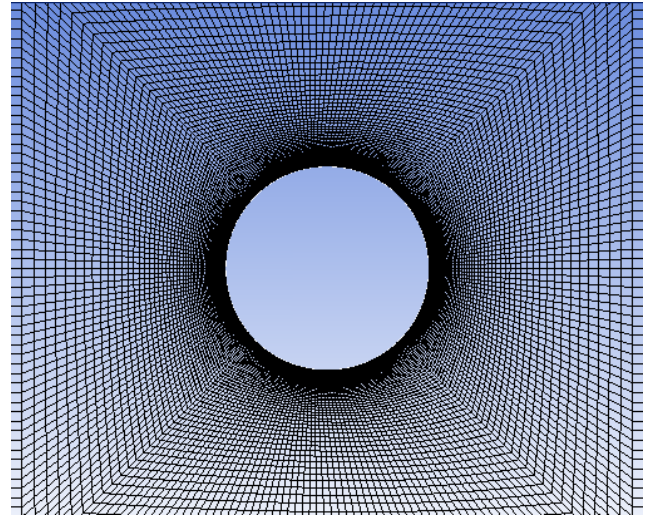
Data Grid and Numerical Method

A cylinder of a unit diameter was considered on the computational domain (Fig. 3). The domain consists of an upstream of 11.5 times the diameter to downstream of 20 times the diameter of the cylinder and 12.5 times on each cross stream direction. The data grid contains 15380 quadrilateral cells and 15659 nodes (Fig. 4). A fine grid is created near the boundary layer around the cylinder and gets coarser at far flow field, especially outside the wake region. The inlet region is on the left and the outlet is on the right side of the grid.

In order to capture displacement of the cylinder the spring-based smoothing method has been applied to all cells of the dynamic mesh. Parameters for mesh smoothing are provided in Tab. 1. The model uses the full feedback from the fluid. It was achieved by including the 'Compute Force and Moment' function into the motion equation of the cylinder, providing lift force directly from the solver on each time step and resulting in a coupled fluid-structure model.

The PISO (Pressure Implicit solution by Split Operator method) Pressure-Velocity coupling scheme was chosen as a solution method as it allows the use of higher time step size without affecting the stability of the solution. In the PISO scheme, in comparison to the SIMPLE scheme, the same decomposition of velocity and pressure corrections is made, however, a second corrector stage is added, in an attempt to account for the neglected components in the first stage. PISO algorithm performs two additional corrections: neighbour correction and skewness correction.

The time step size was chosen with regard to Strouhal number that relates shedding frequency to stream veloc-

**FIGURE 4.** QUADRILATERAL MESH AROUND THE CYLINDER.

ity and diameter of the cylinder. The vortex shedding frequency is defined as the frequency of a complete vortex shedding circle.

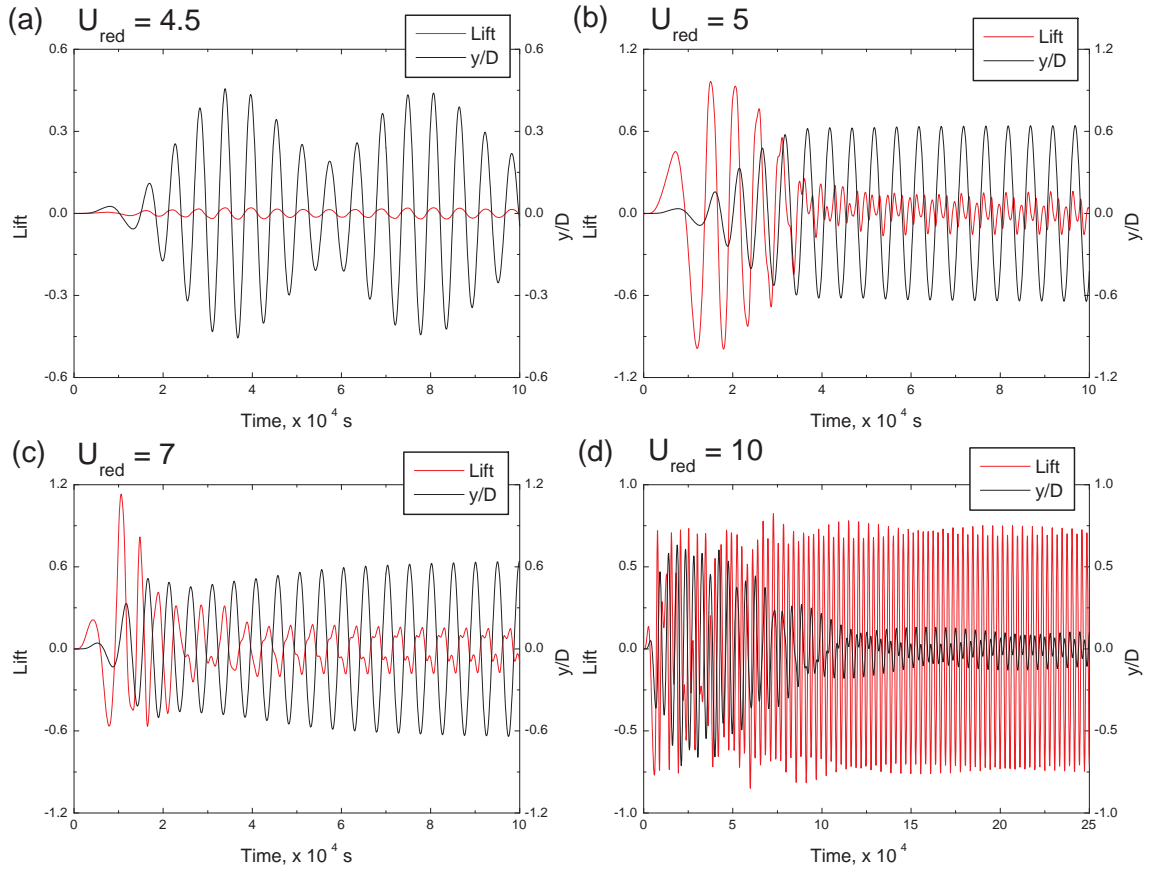
NUMERICAL RESULTS

Two sets of simulations were performed: vibrations of a single degree-of-freedom coupled system (transversal vibration of the rigid cylinder only) and, of a special interest, vibrations of low-mass ratio two degrees-of-freedom coupled system (transversal and inline vibrations of the cylinder). While the natural frequency of the structure was held constant, change of the reduced velocity was achieved by altering the flow velocity and, as consequence, the Reynolds number. The cylinder was at rest in its initial equilibrium position. Initial conditions for cylinder's transversal and inline displacements and velocities are $y(0) = 0$ and $\dot{y}(0) = 0$, and $x(0) = 0$ and $\dot{x}(0) = 0$.

Apart from coupled models, the preamble of the CFD modelling of VIV has included static and prescribed motion simulations (where the cylinder was moving in transversal direction harmonically at various frequencies) in order to observe the flow regimes and test the cylinder displacement in computational domain. In case of stationary cylinder the sinusoidal pattern was observed, which is a sign of a sustained vortex shedding process. The obtained Karman vortex streets on various Reynolds numbers corresponded well to the existing literature [12].

Fluid-Structure Coupling

The first set of simulations was carried out when fluid force is coupled with the equation of motion of the cylinder through the lift coefficient obtained numerically on each time step of the simulation process. For transversal


FIGURE 5. LIFT COEFFICIENT AND DIMENSIONLESS AMPLITUDE.

motion the non-dimensionalized equation for the cylinder motion is

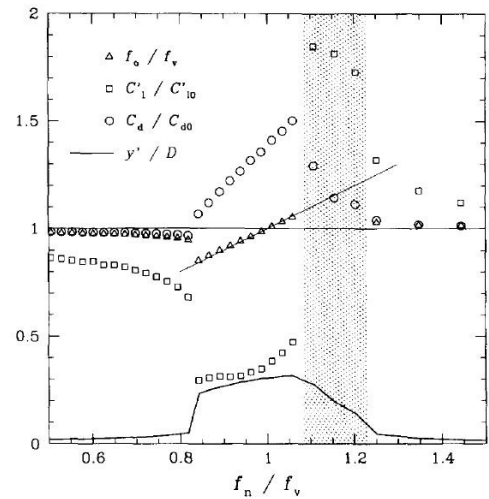
$$\ddot{y} + \frac{4\pi\zeta}{U_{red}} \dot{y} + \frac{4\pi^2}{U_{red}^2} y = \frac{C_L(t)}{2m^*} \quad (7)$$

where $C_L(t)$ is lift coefficient. The physical parameters of the structure are $\zeta = 0.01$ and $m^* = 6.4$. The natural frequency of the structure in water is

$$f_n^\omega = f_n \sqrt{\left(\frac{m^*}{m^* + C_A} \right)} \quad (8)$$

where C_A is added mass coefficient, which can be considered as 1.

The frequency of cylinder vibration is tightly related to the vortex shedding frequency. As the flow velocity is increased or decreased so that the vortex shedding frequency approaches to the natural frequency of structure, the shedding frequency locks onto the structural natural frequency. The lock-in resonant oscillations occur at or


FIGURE 6. LIFT COEFFICIENT DROP DURING LOCK-IN. BLACKBURN AND HENDERSON. [13]

near the natural frequency of the structure and have significantly larger amplitude. The set of simulations has been carried out in order to observe the entry to and

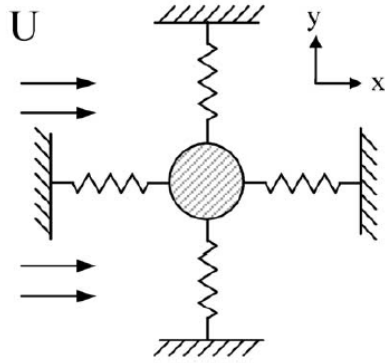


FIGURE 7. TWO DEGREE-OF-FREEDOM MOTION. [14]

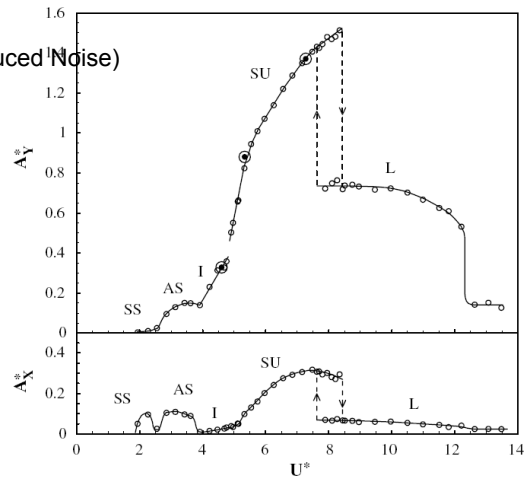


FIGURE 9. "SUPER-UPPER" BRANCH. [15]

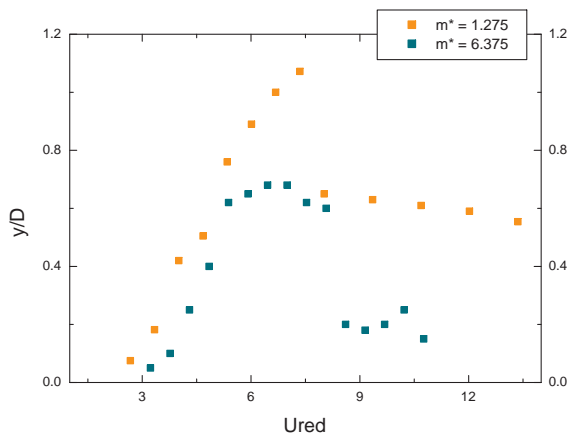


FIGURE 8. AMPLITUDE RESPONSE FOR VARIOUS MASS RATIOS.

exit from the lock-in condition at the range of reduced velocities from 3 to 10 (Reynolds number from 600 to 2000) with a step of 0.5. The most notable result is a significant drop of lift coefficient and amplitude modulation (Fig. 5a) at $U_{red} = 4.5$ near the entry to lock-in condition. While amplitude exhibited stable large values during lock-in, the lift coefficient remained fluctuating at low values (Fig. 5b). The similar behavior was observed by Blackburn and Henderson [13] (Fig. 6), although chaotic non-periodic response occurred before the lock-in. The varied parameter of Blackburn and Henderson's simulations was natural frequency of the structure. The Reynolds number was kept constant at the value of 250.

Two Degrees-of-Freedom Motion of Elastically Supported Cylinder at Low Mass Ratios

Although a large number of papers are dedicated to the VIV of elastically supported cylinder in transverse direction to a fluid flow, there are significantly less results published on both inline and transverse vibrations. The schematic representation of such system is shown in Fig. 7.

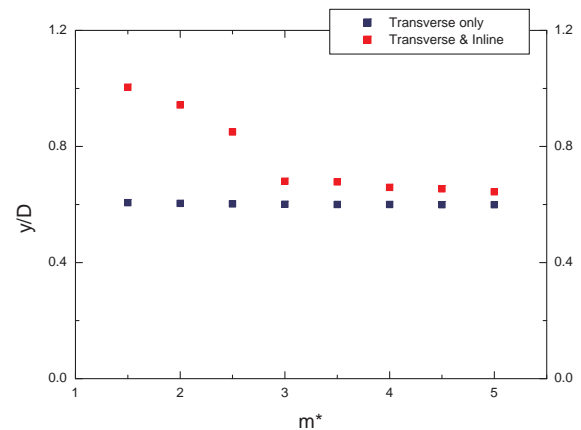


FIGURE 10. COMPARISON OF 1DOF AND 2DOF RESPONSES AT VARIOUS MASS RATIOS.

The sub-critical regime, when the wake is fully turbulent, has been considered next, and the system behaviour for a various mass ratios has been investigated, where particular attention has been paid to low-mass ratio cylinders. Simulations reveal that drag forces influence cross-flow amplitude, and it was found that their impact at resonance becomes more crucial as mass ratio of a cylinder decreases. The amplitude of the cylinder as a function of reduced velocity is presented in Fig. 8 for two values of cylinder's mass ratio. As can be seen on the figure, lower mass ratio cylinder demonstrates significantly larger peak value.

Experimental studies by Jauvtis and Williamson [14] provide data for the fluid-structure interactions when mass ratios are reduced below $m^* = 6$. A new response branch appears in the case of two degrees-of-freedom motion of the structure. It was defined as a "super-upper" branch (Fig. 9). The computational results in current studies agree well with the existence of this branch, however the peak amplitude exhibits lower value than in physical experiments.

Comparison between peak amplitudes of the single degree-of-freedom cylinder and the two degree-of-

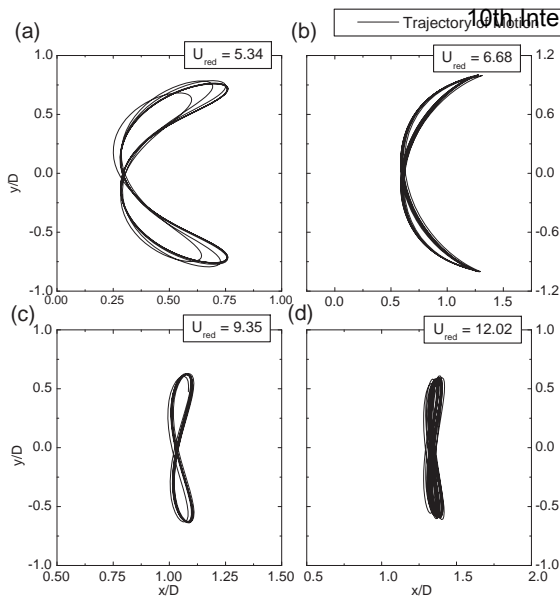


FIGURE 11. TRAJECTORY OF MOTION.

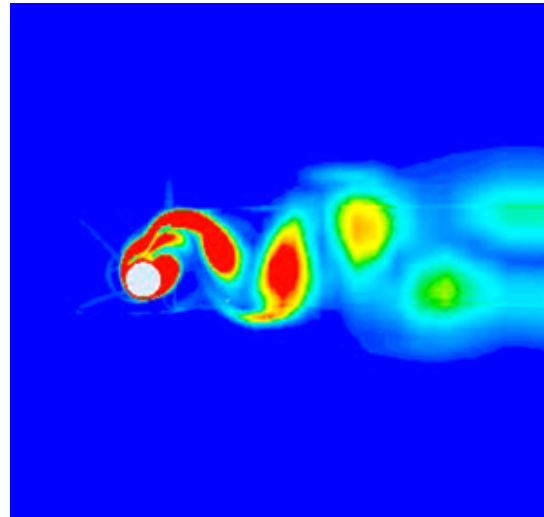


FIGURE 12. VORTICITY CONTOURS. TWO DEGREES-OF-FREEDOM MOTION.

freedom cylinder at various mass ratios have been made and is presented in Fig. 10. It can be seen that, for the ratios below $m^* < 3$, the two degree of freedom cylinder demonstrates the presence of "super-upper" branch. This can be crucial for VIV of cylindrical structures in water as water is an illustrative example where low mass ratio observed in the system.

Thus, the impact of inline vibrations is getting more crucial on cross-flow amplitude as the mass ratio decreases. The trajectory of motion becomes asymmetric to the Y axis and the classic "eight" shape distorts by bending the peak positions of the cylinder in the fluid flow direction (for $m^* = 2$ see Fig. 11). It can be seen in Fig. 12 that a new periodic vortex wake mode occurs and the formation of vortices changes to "2T" according to the terminology that Williamson and Roshko introduced in 1988 [16] (Fig. 13).

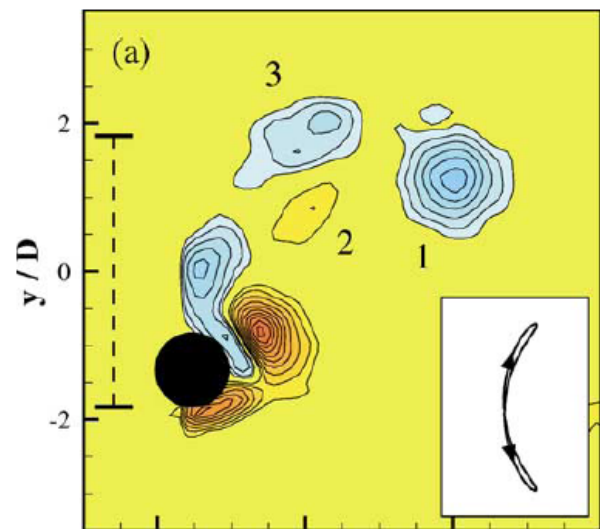


FIGURE 13. "2T" VORTEX WAKE MODE. [14]

CONCLUDING REMARKS

The work is still in progress and the presented CFD models are being expanded towards multiple "strips" in order to observe modes of vibration of the reduced-order structure. For two dimensional simulations it has been obtained that considered CFD models allow to describe adequately the lock-in condition and captures the coupled effect of lift and drag forces on the structure with rather good correspondence to experimental data.

The overall output of the work is aimed towards providing a framework based on the Computational Fluid Dynamics approach and development of novel reduced-order models.

ACKNOWLEDGMENT

This work is supported by the National Subsea Research Institute (NSRI) UK. Authors would like to thank Marko Keber of the University of Aberdeen for valuable discussions and helpful advice.

REFERENCES

- [1] Bishop R. E. D., Hassan A. Y. *The Lift and Drag Forces on a Circular Cylinder in a Flowing Field*. Proc. Roy. Soc. (London) Ser. A, 277, 51-75 1964
- [2] Skop, R. A., and Griffin, O. M. *A Model for the Vortex-Excited Resonant Vibrations of Bluff Bodies*. J. Sound and Vibration 27, 225-233. 1973
- [3] Iwan, W. D., and R. D. Blevins *A Model for Vortex-*

- Induced Oscillation of Structures*. J. Appl. Mech. 41, 581-586. 1974
- [4] Balasubramanian, S., Skop, R.A. *A New Twist on an Old Model for Vortex-Excited Vibrations*. Journal of Fluids and Structures 11, 395-412. 1997
- [5] Skop, R.A., Luo, G. *An Inverse-Direct Method for Predicting the Vortex-Induced Vibrations of Cylinders in Uniform and Nonuniform Flows*. Journal of Fluids and Structures 15, 867-884. 2001
- [6] Krenk, S., Nielsen, S.R.K. *Energy Balanced Double Oscillator Model for Vortex-Induced Vibrations*. ASCE Journal of Engineering Mechanics 125, 263-271. 1999
- [7] Mureithi, N.W., Kanki, H., Nakamura, T. *Bifurcation and Perturbation Analysis of Some Vortex Shedding Models*. Proceedings of the Seventh International Conference on Flow-Induced Vibrations, Luzern, Switzerland. Balkema, Rotterdam, pp. 6168. 2000
- [8] Plaschko, P. *Global Chaos in Flow-Induced Oscillations of Cylinders*. Journal of Fluids and Structures 14, 883-893. 2000
- [9] Facchinetti M. L., de Langre E., Biolley F. *Coupling of Structure and Wake Oscillators in Vortex-Induced Vibrations*. Journal of Fluids and Structures 19, 123-140. 2004
- [10] R. Violette, E. de Langre, J. Szydlowski *Computation of Vortex-Induced Vibrations of Long Structures Using a Wake Oscillator Model: Comparison with DNS and Experiments*. Computers and Structures 85 1134-1141. 2007
- [11] M. Keber, M. Wiercigroch *Dynamics of a Vertical Riser with Weak Structural Nonlinearity Excited by Wakes*. Journal of Sound and Vibration 315, 685-699. 2008
- [12] Robert D. Blevins *Flow-Induced Vibrations*. Litton Educational Publishing, Inc. 1977
- [13] Hugh Blackburn, Ron Henderson *Lock-In Behavior in Simulated Vortex-Induced Vibration*. Experimental Thermal and Fluid Science 12, 184-189. 1996
- [14] C. H. K. Williamson and N. Jauvtis *A High-Amplitude 2T Mode of Vortex-Induced Vibration for a Light Body in XY Motion*. European Journal of Mechanics B/Fluids 23, 107-114. 2004
- [15] C. H. K. Williamson and R. Govardhan *Vortex-Induced Vibrations*. Annual Reviews of Fluid Mechanics, Vol. 36, 413-455. 2004
- [16] C. H. K. Williamson and A. Roshko *Vortex Formation in the Wake of an Oscillating Cylinder*. Journal of Fluids and Structures 2, 355-381. 1988



Experimental Evaluation of Acoustic Resonance at Single Stub Pipe in each Dry and Wet Steam Flow

Yuta Uchiyama¹

Central Research Institute of Electric Power Industry (CRIEPI)
Tokyo, Japan
Email: uchiyama@criepi.denken.or.jp

Ryo Morita

Central Research Institute of Electric Power Industry (CRIEPI)
Tokyo, Japan
Email: ryo@criepi.denken.or.jp

ABSTRACT

Flow-induced acoustic resonances of piping system containing closed side-branches are sometimes encountered in power plants. In U.S. NPP, the steam dryer had been damaged by high cycle fatigue due to acoustic-induced vibration under a power uprating condition. The steam piping systems of actual power plants often have nearly saturated wet steam condition. Although there are several previous studies about acoustic resonance, most of them are not steam flow but air flow. In the present study, the acoustic resonance in steam flow was investigated by conducting experiments under dry and wet steam conditions. Pressure fluctuation at closed end of the single branch pipe and in main steam piping is measured. As a result, it is clarified that resonance amplitude of fluctuating pressure in wet steam was reduced by comparing with that in dry.

NOMENCLATURE

a	speed of sound	[m/s]
C_p	specific heat	[kJ/kgK]
D	diameter of main piping	[m]
d	diameter of branch piping	[m]
f	frequency of pressure fluctuation	[Hz]
f_n	resonance frequency	[Hz]
h	depth of branch piping	[m]
H	enthalpy	[kJ/kg]
Le	end correction	[m]
n	mode number	[-]
P	pressure	[Pa]
P_{rms}	normalized RMS amplitude of fluctuating pressure	[-]
Q	flow rate	[m ³ /s]
r	curvature radius of branch piping	[m]
ρ	density	[kg/m ³]
St	Strouhal number ($= f_n d / U$)	[-]
T	temperature	[K]
U	mean velocity in main piping	[m/s]
x	steam quality	[-]
Subscript		
s	steam (gas phase)	

w	water (liquid phase or droplet)
dry	dry steam condition
wet	wet steam condition
sat	saturated steam condition

INTRODUCTION

Flow-induced acoustic resonances of piping system containing closed side-branches are sometimes encountered in power plants. Acoustic standing waves with large amplitude pressure fluctuation in closed side-branches are excited by the unstable shear layer which separates the mean flow in the main piping from the stagnant fluid in the branch [1, 2]. In U.S. boiling water reactor (BWR), the steam dryer had been damaged by high cycle fatigue due to acoustic-induced vibration under a 17.8% extended power uprating condition [3]. The cause of that is considered as flow-induced acoustic resonance at the branch sections of safety relief valve (SRV) in the main steam (MS) lines (Fig. 1). Velocity of main piping is increased by uprating, and that excites the pressure fluctuations and makes large amplitude resonance at the SRVs, and that propagates to the dryers through MS lines.

Flow-induced acoustic resonance at the single branch piping such as SRV has been investigated by many researchers. It has been clarified that acoustic resonance with large amplitude of pressure fluctuation occurs where the range of Strouhal number St from 0.3 to 0.6 [4-8]. The amplitude of pressure fluctuation at the closed end of the branch is largest around $0.4 < St < 0.44$ [4-8]. Morita et al. have been made flow calculations under the resonance condition by CFD and carried out the acoustic and structure analysis of MSLs and the dryer using the calculation results [4]. However, the amplitude and frequency of fluctuating pressure in wet steam cannot be calculated in directly by CFD though the steam piping systems of actual power plants often have nearly saturated wet steam condition. So, in order to predict or evaluate the acoustic resonance at the branch sections in actual power plants, it is necessary to clarify the characteristics

Address all correspondence to this author¹

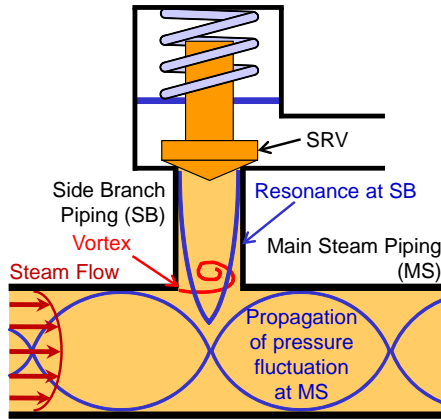


FIGURE 1: SCHEMATIC OF ACOUSTIC RESONANCE AT SIDE BRANCH.

of acoustic resonance in steam flow and effects of steam wetness on the amplitude and frequency of pressure fluctuation. Although there are many other previous studies about acoustic resonance, most of them are not steam flow but air flow.

In the present study, to investigate the acoustic resonance in steam flow, experiments under dry and wet steam conditions, and also under air were conducted. Pressure fluctuation at the closed end of the single branch and in main steam piping was measured. As a result, it is clarified and discussed the effects of steam wetness on the phenomena of acoustic resonance.

EXPERIMENTAL SETUP

Test Facility under steam flow

Figure 2 shows schematic diagram of the test facility under steam flow condition. The facility is mainly consisted of two closed loops; steam loop and cooling water loop. In the steam loop, which is main test loop, a saturated steam is supplied from two boilers, which can be reached up to 1.6 MPa in pressure and 800 kg/h in flow rate. Temperature of saturated steam at 1.6 MPa is about 474 K. The flow rate of supplied steam can be controlled as changing differential pressure across the test section by using automatic and manual pressure control valves. Two silencers are installed at each upstream and downstream of test section to reduce noise from the automatic and manual pressure control valves, and so on. Total flow rate of steam through test section is measured as flow rate of fully condensed water by a heat exchanger, which is measured by Coriolis flow meter at downstream of steam loop.

Steam condition can be regulated dry or wet by using a super heater or wetness control line, respectively. In the wetness control line, the saturated steam is cooled down by cold water through copper coil in the main pipe. Flow rate of the cooling water in the copper coil is regulated by

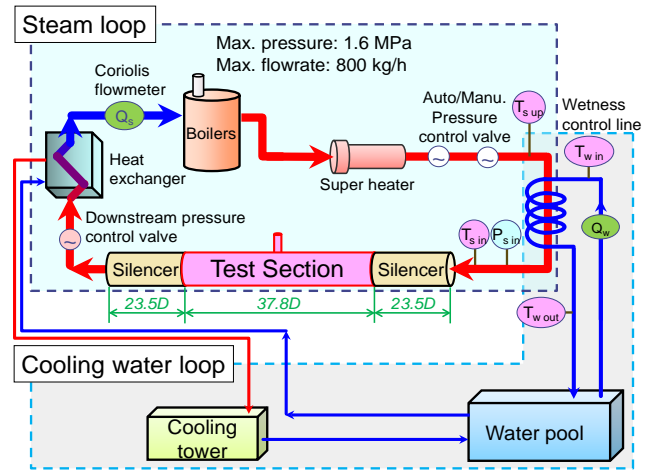


FIGURE 2: SCHEMATIC OF TEST FACILITY UNDER STEAM FLOW.

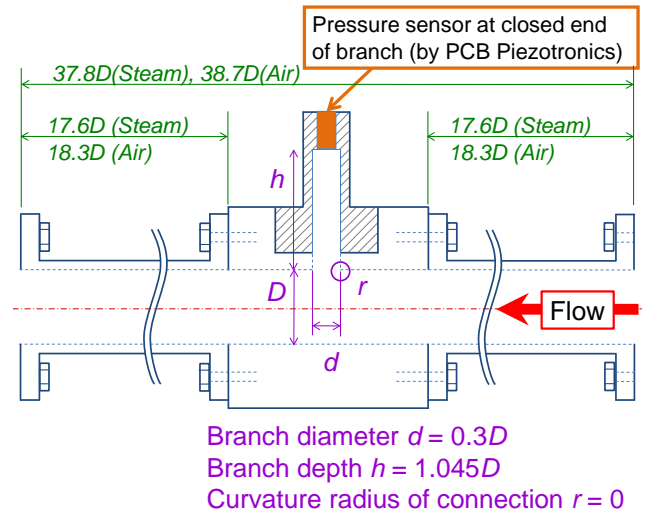


FIGURE 3: SCHEMATIC OF TEST SECTION.

ball valve. By using the flow rate of the cooling water in the copper coil (Q_w) which is measured by electromagnetic flow meter and its inlet and outlet temperature ($T_{w,in}$ and $T_{w,out}$), the enthalpy drawn from the steam in the main line is calculated as

$$\Delta h = \rho_w C_{p,w} Q_w (T_{w,out} - T_{w,in}), \quad (1)$$

where ρ_w and $C_{p,w}$ are calculated by using the international equation of state IAPWS-IF97 [9]. Then, quality of steam is calculated as

$$x = \frac{H - H_{w,sat}}{H_{s,sat} - H_{w,sat}}, \quad (2)$$

where $H_{s,sat}$ and $H_{w,sat}$ are enthalpies of saturated steam and water of inlet condition, respectively, which are calculated by using inlet pressure ($P_{s,in}$) of test section. Quality of steam (x) is varied according to steam enthalpy at inlet of test section (H). If steam condition is saturated in test section, x is equal to 1 since H is enthalpy of

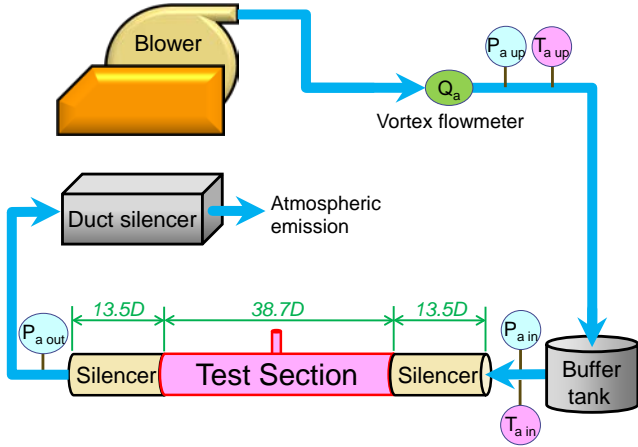


FIGURE 4: SCHEMATIC OF TEST FACILITY UNDER AIR FLOW.

saturated steam (H_{s_sat}). If steam condition is dry, H is calculated as enthalpy of dry steam at inlet of the test section (H_{s_dry}) by P_{s_in} and inlet temperature (T_{s_in}), which is larger than H_{s_sat} so x is larger than 1. If steam condition is wet, H is calculated as enthalpy of wet steam as two phase flow (H_m), as follows,

$$H_m = H_{s_up} - \frac{\Delta h}{Q_s}, \quad (3)$$

where H_{s_up} is enthalpy of incoming steam at upstream of wetness control line. H_m is smaller than H_{s_sat} so x is smaller than 1 under wet steam condition.

Schematic diagram of the test section is shown in Fig. 3. A single branch pipe with $0.3D$ diameter and $1.045D$ depth was installed in the test section, where D is diameter of main piping (42.6 mm). Curvature radius (r) of connection between the main piping and the branch was set at 0 to simplify the phenomena. The test section was made of stainless-steel SUS304.

Test Facility under air flow

Figure 4 shows schematic diagram of the test facility under air flow condition. The facility is consisted a blower, a vortex flow meter, a buffer tank, a test section, two silencers at upstream and downstream of test section and a duct silencer. In the facility, air at almost room temperature and almost atmospheric pressure (a little high) is supplied by the blower, which can be reached up to $900 \text{ m}^3/\text{h}$ in flow rate. The flow rate was regulated by inverter ($\sim 60 \text{ Hz}$) and measured by vortex flow meter. A buffer tank was installed at upstream of test section to reduce turbulence of flow such as swirling. Two silencers were installed at each upstream and downstream of test section to reduce noise from the blower, and so on.

Test section was as same dimension as that of steam flow experiments, which is shown in Fig. 3. It was made of aluminum.

TABLE 1: EXPERIMENTAL CONDITIONS.

	Steam	Air
Steam quality	Dry: 1.06, 1.03 Wet: 0.99, 0.97, 0.90	-
Inlet pressure	0.1 ~ 0.3 MPa	0.1 MPa
Flow rate	80 ~ 800 kg/h	150~800 kg/h
Temperature	Dry: ~ 470 K Wet: ~ 400 K	~ 320 K
Velocity	20 ~ 100 m/s	15 ~ 90 m/s
Strouhal number	0.3 ~ 1.3	0.25 ~ 1.25
$St = f_n d / U$		

Experimental Conditions and Procedure

Experimental conditions are shown in Tab. 1. Experiments were conducted under dry and wet steam condition and under air flow. The quality of steam (x) was 1.06 and 1.03 as dry, 0.99, 0.97 and 0.90 as wet. A series of experiments at each steam quality or air condition was performed by varying (both increasing and decreasing) the velocity in the main pipe flow. It was calculated by measuring the total flow rate, and corrected by measuring the pressure and temperature; the ranges of them are shown in Tab. 1. The range of velocity was about 20 ~ 100 m/s under steam flow and about 15 ~ 90 m/s under air flow. At each velocity, fluctuating pressures at the closed end of the branch and in main steam piping were measured by pressure sensors of piezoelectric devices (PCB Piezotronics). The measurements were repeated 5 times for each velocity condition, sampling time was 1.4 s and sampling rate was 100 kHz on each measurement.

Amplitude of the pressure fluctuation was evaluated as root mean square (RMS) and normalized by using dynamic pressure in main piping flow ($0.5\rho U^2$). Inlet velocity of test section (U) as flow condition was normalized by using resonance frequency (f_n) and diameter of branch (d) as Strouhal number (St), which is defined as

$$St = \frac{f_n d}{U}. \quad (4)$$

The Resonance frequency (f_n) was calculated as the first mode quarter-wave frequency of branch piping depth (h) with an end correction (Le), which is defined as

$$f_n = \frac{a}{4(h + Le)}, \quad (5)$$

where a is speed of sound. The end correction was $0.393d < Le < 0.425d$ corresponding to Reileigh [10]. In present study, $0.4d$ was used as the end correction under air flow (f_n is about 1450 Hz). Under steam flow, it is difficult that f_n is evaluated from Eqn. (5), since it is not cleared that presence or absence of influence on end correction due to a difference in fluid between air and steam. In addition, it was reported that speed of sound in wet steam was different between measurement results and theoretical

isentropic calculation [11, 12]. So, in the present study, resonance frequency of steam flow was defined as dominant frequency at St condition of maximum pressure fluctuation under same steam quality condition. That is, f_n was constant under same steam quality condition in the present study.

EXPERIMENTAL RESULTS AND DISCUSSION

Comparison of Pressure Fluctuation between Dry Steam Flow and Air Flow

Figure 5 shows the time histories of pressure (left figures) and FFT analysis results of fluctuating pressure (right figures) at closed end of the branch under typical St conditions. In Fig. 5, red line shows results of dry steam of $x = 1.03$ and black line shows results of air. Vertical axes of the left and right figures are normalized by dynamic pressure in main piping flow. Horizontal axes of the right figures are frequency ratio, which is normalized by resonance frequency.

Under $St = 0.82$ (Fig. 5 (a)), periodic pressure fluctuations were measured under both dry steam ($x = 1.03$) and air, and dominant frequencies of them were same as f_n of each fluid. It is thought that 2nd mode resonance of quarter-wave frequency was occurred, which two shedding vortices are existed in branch section.

Under $St = 0.58$ (Fig. 5 (b)), periodic pressure fluctuations could not be measured and dominant peaks of fluctuating pressure were disappeared in both fluids. In Fig. 5 (a) and (b), the pressure pulsation from boilers due to regulating low flow rate was also measured, and its period was much longer than that of resonance.

Under both $St = 0.40$ and 0.32 (Fig. 5 (c) and (e)), periodic pressure fluctuations were measured. The amplitudes of them were larger than that of $St = 0.82$. It is thought that 1st mode resonance of quarter-wave frequency was occurred, which one shedding vortex is existed in branch section. The dominant frequencies of fluctuating pressure were almost same but a little different between under $St = 0.40$ and 0.32 . In addition, two peaks of dominant frequency of pressure fluctuation were measured near f_n under $St = 0.36$ (Fig. 5 (d)).

Figure 6 shows the distribution of RMS amplitude of fluctuating pressure in main piping under $St = 0.4$ (Fig. 6 (a)) and 0.32 (Fig. 6 (b)). Horizontal axes are normalized distance from the branch section, and vertical axes are ratio of P_{rms} and normalized by P_{rms} at closed end of the branch. In Fig. 6, the distribution of P_{rms} in main piping was a little different between under $St = 0.4$ (Fig. 6 (a)) and 0.32 (Fig. 6 (b)). So, it is supposed that the changing dominant frequency of pressure fluctuation around $St = 0.36$ in Fig. 5 was occurred due to affection by the interaction between the acoustic standing wave in branch and that in main piping.

Figures 7 and 8 show response curves of RMS amplitude and dominant frequency of fluctuating pressure

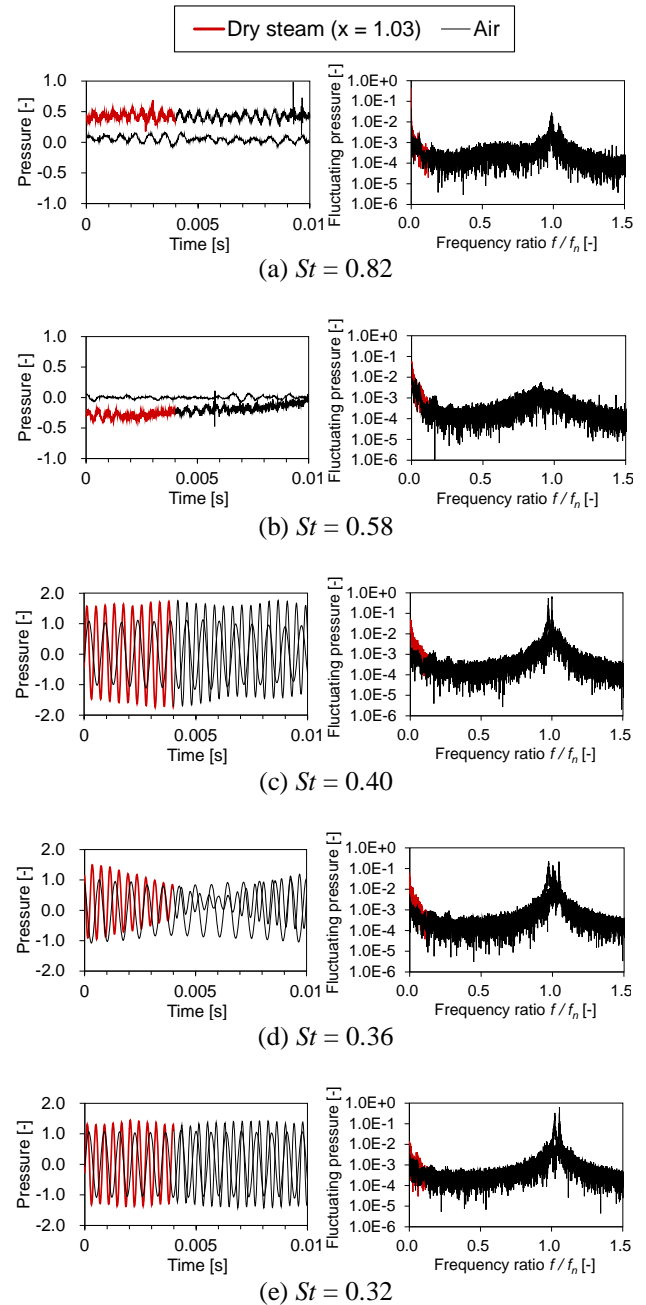


FIGURE 5: TIME HISTORIES (LEFT) AND FFT ANALYSIS RESULTS (RIGHT) OF FLUCTUATING PRESSURE AT CLOSED END OF THE BRANCH UNDER TYPICAL St CONDITIONS.

at closed end of the branch on each velocity under dry steam flow of $x = 1.06$ and 1.03 and under air flow. Horizontal axes in Figs. 7 and 8 are Strouhal number. Vertical axis is normalized RMS amplitude (P_{rms}) in Fig. 7 and frequency ratio which is normalized by f_n in Fig. 8. In Fig. 8, dominant frequency of excitation due to shedding vortex from upstream connection of the branch with a convection speed equal to the average velocity in the shear layer (i.e. near $0.5 U$) according to Martin et al.

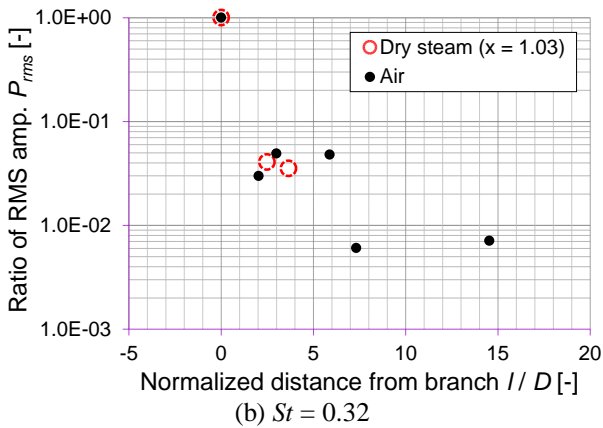
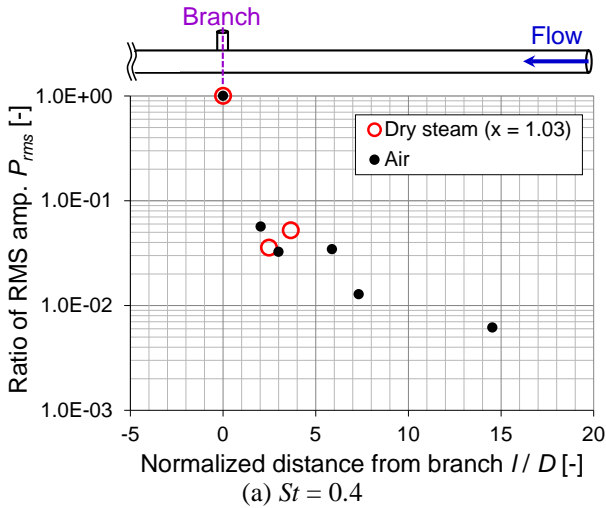


FIGURE 6: DISTRIBUTIONS OF RMS AMPLITUDE OF FLUCTUATING PRESSURE IN MAIN PIPING UNDER TYPICAL St CONDITIONS.

[13] is shown in chain line ($n = 1$) and broken line ($n = 2$), which is calculated as

$$f = 0.5 \left(n - \frac{1}{4} \right) \frac{U}{d}, \quad (6)$$

where n is mode number.

In Fig. 7, RMS amplitudes of both dry steam (in each $x = 1.06$ and 1.03) and air were increased with decreasing Strouhal number (increasing velocity of main piping) within the range of $0.8 < St$. They were decreased with decreasing St within the range of $0.6 < St < 0.8$. In Fig. 8, frequency ratios f/f_n of both dry steam (in each $x = 1.06$ and 1.03) and air were 0.98 within the range of $0.7 < St < 1.0$, that is, the dominant frequencies of pressure fluctuation were approximately equal to resonance frequency and locked-in 2nd mode resonance of quarter-wave frequency ($n = 2$). So, 2nd mode resonance peak of quarter-wave frequency was occurred around $St = 0.8$.

Within the range of $0.4 < St < 0.6$ in Fig. 7, RMS amplitudes were increased significantly with decreasing St . And they were reached maximum around $St = 0.4$.

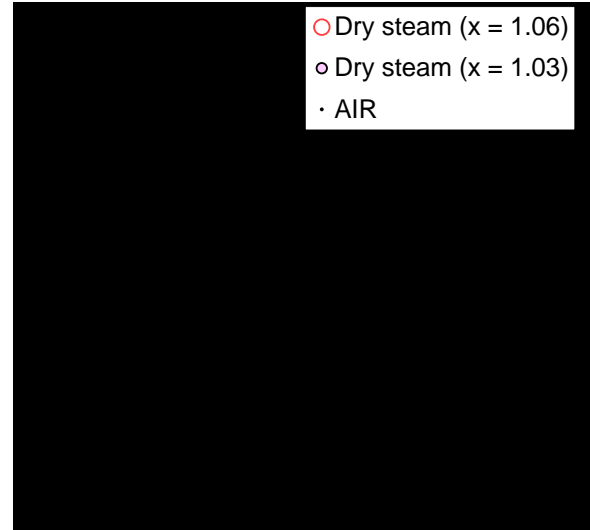


FIGURE 7: RMS AMPLITUDE OF FLUCTUATING PRESSURE AT CLOSED END OF THE BRANCH UNDER DRY STEAM FLOW AND AIR FLOW.

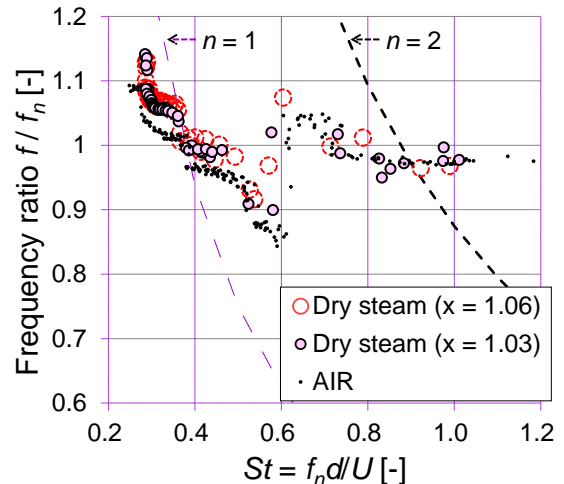


FIGURE 8: FREQUENCY OF FLUCTUATING PRESSURE AT CLOSED END OF THE BRANCH UNDER DRY STEAM FLOW AND AIR FLOW.

The maximum value of P_{rms} was about 1.1 in dry steam (both $x = 1.06$ and 1.03) and was about 0.8 in air, respectively. It is supposed that the difference between maximum P_{rms} in dry steam and that in air was caused by difference of fluid property and material of test section. In addition, the length of the two silencers at upstream and downstream of the test section in air flow ($13.5D$) is shorter than that in steam flow ($23.5D$). So, it is supposed that the noise could not be reduced completely in air flow compared to steam flow. RMS amplitudes were approximately same as the maximum value at $0.45 < St < 0.32$. And they were decreased with decreasing St within the range of $St < 0.32$. In Fig. 8, frequency ratios f/f_n of dry steam (in each $x = 1.06$ and 1.03) were about 1.0 at

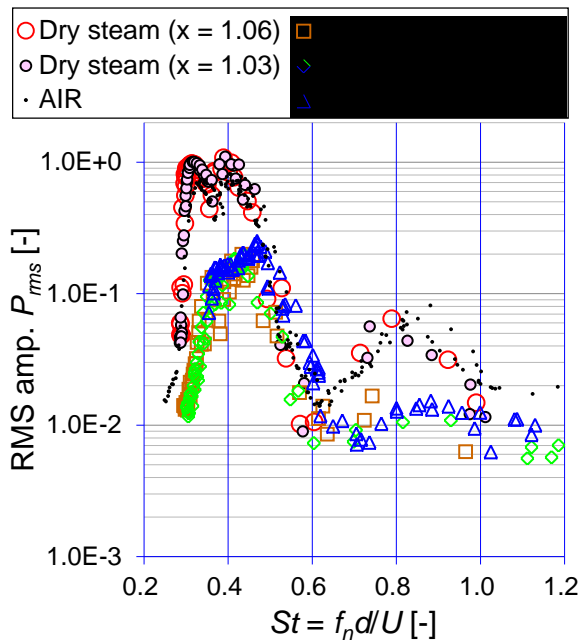


FIGURE 9: COMPARISON OF RMS AMPLITUDE OF FLUCTUATING PRESSURE AT CLOSED END OF THE BRANCH BETWEEN DRY STEAM FLOW AND WET STEAM FLOW.

$0.38 < St < 0.5$, and were about 1.05 at $0.3 < St < 0.38$. Under air flow, f/f_n was about 0.98 at $0.38 < St < 0.5$, and was about 1.02 at $0.3 < St < 0.38$. That is, the dominant frequencies of pressure fluctuation were approximately equal to resonance frequency and locked-in 1st mode resonance of quarter-wave frequency ($n = 1$) under both of dry steam flow and air flow at $0.3 < St < 0.5$. The difference of f/f_n between dry steam and air was caused by the different definition of f_n in present study as previously mentioned. When f_n under dry steam flow was calculated from Eqn. (5) by using $0.4d$ as same value of the end correction as air, calculating f_n was just about 2550 Hz under $x = 1.03$, and the distribution of f/f_n at $0.3 < St < 0.5$ was became as same as that in air in Fig 8.

In Figs. 7 and 8, it was found that the response curves to St of RMS amplitude and dominant frequency of fluctuating pressure in dry steam flow could be evaluated as same as that in air flow.

Comparison of Pressure Fluctuation between Wet Steam Flow and Dry Steam Flow

Figures 9 and 10 show response curves of RMS amplitude and dominant frequency of fluctuating pressure at closed end of the branch on each velocity under wet steam flow ($x = 0.99, 0.97$ and 0.90), dry steam flow ($x = 1.06$ and 1.03) and air flow. Horizontal and vertical axes in Figs. 9 and 10 are same as that in Figs. 7 and 8.

In Fig. 9, RMS amplitudes under wet steam conditions of $x = 0.99, 0.97$ and 0.90 were approximately

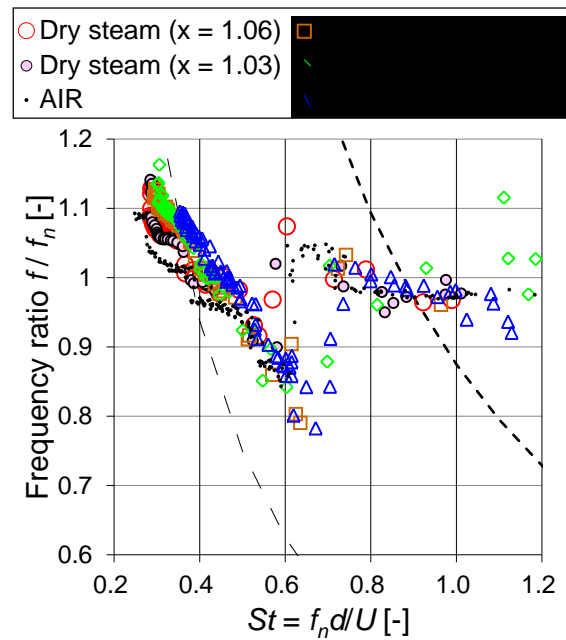


FIGURE 10: COMPARISON OF DOMINANT FREQUENCY OF FLUCTUATING PRESSURE AT CLOSED END OF THE BRANCH BETWEEN DRY STEAM FLOW AND WET STEAM FLOW.

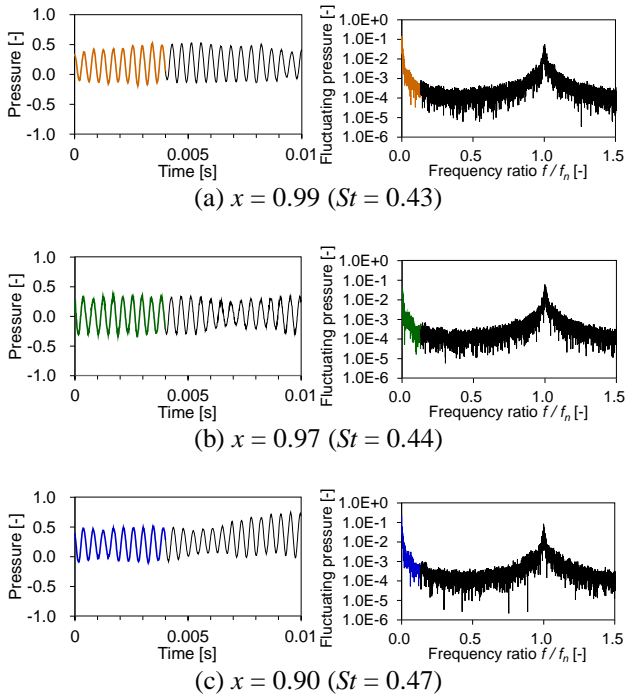
0.01 within the range of $0.62 < St$. 2nd mode resonance peak of quarter-wave frequency was appeared at $0.7 < St < 1.0$ although that was not clearly compared with that in dry steam flow.

Within the range of $0.5 < St < 0.6$ in Fig. 9, RMS amplitudes were increased significantly with decreasing St and the curve of P_{rms} under wet steam condition was almost same as that of dry steam and air. That is supposed to be caused by which frequency ratios f/f_n of wet steam conditions were increased approximately as same as that of dry steam within the range in Fig. 10. There were a little difference of the P_{rms} curves at the range between $x = 0.90$ and the other conditions. In present study, liquid on the main piping wall and slip of velocity between saturated steam as continuous phase and saturated water droplets as discontinuous phase were not considered to estimate the mean velocity in main piping. It is suggested that the difference of the P_{rms} curves at the range between $x = 0.90$ and the other conditions was maybe caused by that.

RMS amplitudes were reached maximum around $St = 0.45$ in Fig. 9. The maximum values of P_{rms} were about 0.2 under each wet steam conditions. The time histories of pressure (left figures) and FFT analysis results of fluctuating pressure (right figures) under St of maximum P_{rms} conditions were shown in Fig 11. Maximum P_{rms} of wet steam was less than about one-fifth of its dry steam condition. It is supposed that the difference of maximum P_{rms} between under wet steam condition and under dry steam condition was caused by attenuation of pressure

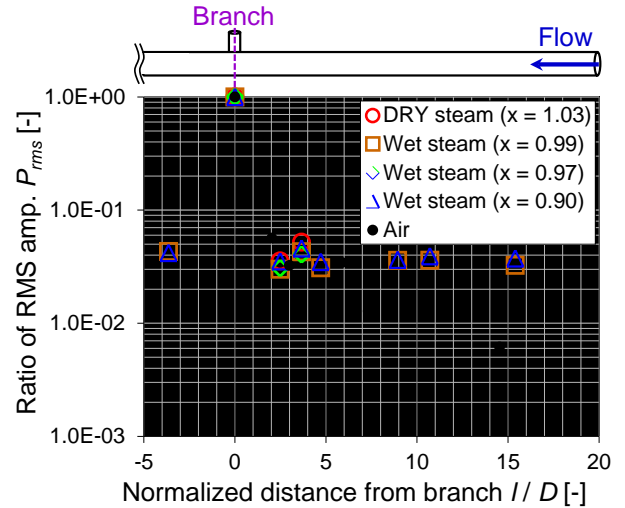
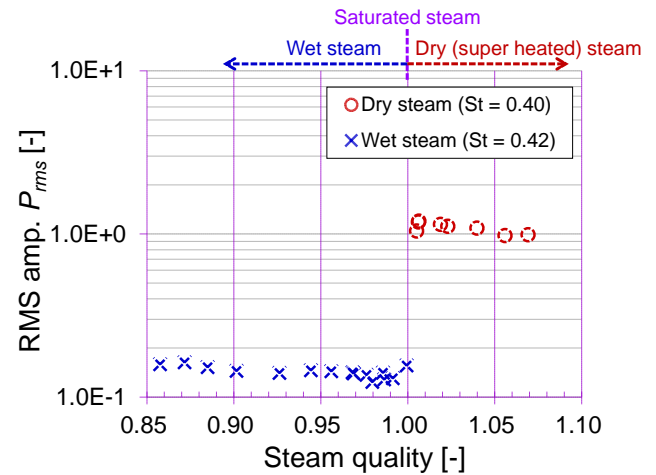
TABLE 2: PROPERTIES OF DROPLET UNDER WET STEAM FLOW EVALUATED BY EXPERIMENTAL EQUATION [15] IN PRESENT EXPERIMENTS.

	$x = 0.99$	$x = 0.97$	$x = 0.90$
D10 diameter	13~27 μm	11~24 μm	10~21 μm
Droplet number	$\sim 1.0 \times 10^{10}$	$\sim 5.0 \times 10^{10}$	$\sim 5.0 \times 10^{11}$
density	Num./ m^3	Num./ m^3	Num./ m^3


FIGURE 11: TIME HISTORIES (LEFT) AND FFT ANALYSIS RESULTS (RIGHT) OF FLUCTUATING PRESSURE AT CLOSED END OF THE BRANCH UNDER St CONDITIONS WITH MAXIMUM AMPLITUDE.

fluctuation in wet steam flow [14]. Phase transition between saturated steam and water droplets was occurred by the pressure fluctuations. And as results of the vaporization and condensation, mass, momentum and energy transfers were occurred. It is just suggested that they were working as damping for pressure propagation in wet steam. In addition, many water droplets were existed in wet steam flow. The D10 diameter and number density of droplet under present experimental wet steam condition evaluating by using experimental equation according to Morita [15] are shown in Tab. 2. It is suggested that these droplets in wet steam may be worked as the obstacle of the pressure propagation.

In Fig. 9, RMS amplitudes were approximately same as the maximum value at $0.35 < St < 0.5$. And they were decreased with decreasing St within the range of $St < 0.35$. In Fig. 10, there were no lock-in at $0.35 < St < 0.5$,


FIGURE 12: DISTRIBUTION OF RMS AMPLITUDE OF FLUCTUATING PRESSURE IN MAIN PIPING UNDER St CONDITION WITH MAXIMUM AMPLITUDE.

FIGURE 13: EFFECT ON STEAM QUALITY ON RMS AMPLITUDE OF FLUCTUATING PRESSURE AT CLOSED END OF THE BRANCH UNDER SAME St CONDITIONS.

which is the range of St being large amplitude of fluctuating pressure. In addition, frequency ratios f/f_n of wet steam (in each $x = 0.99$, 0.97 and 0.90) were increased gradually at the range. It is suggested that the feedback mechanism at branch section was affected by droplets in wet steam.

Figure 12 shows the distribution of RMS amplitude of fluctuating pressure in main piping under St of maximum P_{rms} condition. RMS amplitudes in main piping, which were propagated from branch, were less than one-twentieth of that at closed end of the branch under each wet steam, dry steam and air condition.

Figure 13 shows the distribution of P_{rms} at closed end of the branch under St as approximately same as that of maximum P_{rms} condition in each steam quality ($0.85 < x < 1.07$). P_{rms} in each wet steam condition ($0.85 < x < 1.0$) was less than about one-fifth of that in each dry steam condition ($1.0 < x < 1.07$). It is found that the amplitude of fluctuating pressure in wet steam condition could be predicted conservatively by evaluating as that in dry steam or air in present experimental range of steam quality ($0.85 < x < 1.0$).

CONCLUSIONS

In the present study, in order to investigate the acoustic resonance in steam flow, especially in wet steam, experiments under dry and wet steam conditions, and also under air were conducted. The following conclusions were obtained.

1. Acoustic resonance with large amplitude of pressure fluctuation was occurred where the range of $0.3 < St < 0.6$, and the amplitude of pressure fluctuation at the closed end of the branch was largest around $St = 0.4$ in dry steam and air, these results were same as previous studies. The response curves of RMS amplitude and dominant frequency of fluctuating pressure in dry steam flow was evaluated as approximately same as that in air flow.
2. RMS amplitudes in main piping, which were propagated from branch, were less than one-twentieth of that at closed end of the branch under each wet steam, dry steam and air condition.
3. The response curve of RMS amplitude under wet steam condition where the range of $0.5 < St < 0.6$, that is the range of increasing RMS amplitude significantly with decreasing Strouhal number, was almost same as that of dry steam and air. Resonance with large amplitude of pressure fluctuation in wet steam was occurred where the range of $0.3 < St < 0.6$ as same as that in dry steam, air.
4. Maximum value of RMS amplitude of fluctuating pressure in wet steam flow was less than about one-fifth of that in dry steam flow. In nearly saturated wet steam condition, RMS amplitude was also reduced comparing to that in nearly saturated dry steam. That is suggested to be caused by attenuation of pressure fluctuation due to phase transition between saturated steam and saturated water droplets and the obstacle by existence of droplets on the pressure propagation in wet steam flow.
5. It is found that the amplitude of fluctuating pressure in wet steam could be predicted conservatively by evaluating as that in dry steam or air.

In the future, the attenuation mechanism and effect on fluctuating pressure is evaluated and predicted quantitatively to predict the acoustic resonance in actual plant piping system.

REFERENCES

- [1] Rockwell, D., 1977. "Prediction of Oscillation Frequencies for Unstable Flow Past Cavities", *Transactions of the ASME, Journal of Fluids Engineering*, Vol. 99, Ser. I, Issue 2, pp. 294-300.
- [2] Rockwell, D. and Naudascher, E., 1978. "Review-Self-Sustaining Oscillations of Flow Past Cavities", *Transactions of the ASME, Journal of Fluids Engineering*, Vol. 100, Issue 2, pp. 152-165.
- [3] DeBoo, G., Ramsden, K. and Gesior, R., 2006. "Quad Cities Unit 2 Main Steam Line Acoustic Source Identification and Load Reduction", *Proc. ICONE14*, July, 89903.
- [4] Morita, R., et al., 2011. "Evaluation of Acoustic- and Flow-Induced Vibration of the BWR Main Steam Lines and Dryer", *Journal of Nuclear Science and Technology*, Vol. 48, No. 5, pp. 759-776.
- [5] Weaver, D. S. and MacLeod, G. O., 1999. "Entrance Port Rounding Effects on Acoustic Resonance in Safety Relief Valves", *ASME PVP*, Vol. 389, pp. 291-297.
- [6] Ziada, S., 1993. "A Flow Visualization Study of Flow-Acoustic Coupling at the Mouth of a Resonant Side-Branch", *ASME PVP*, Vol. 258, pp. 35-59.
- [7] Ziada, S. and Shine, S., 1999. "Strouhal Numbers of Flow-Excited Acoustic Resonance of Closed Side Branches", *Journal of Fluids and Structures*, Vol. 13, pp. 127-142.
- [8] Knotts, B. D. and Selamet, A., 2003. "Suppression of Flow-Acoustic Coupling in Side branch Ducts by Interface Modification", *Journal of Sound and Vibration*, Vol. 265, No. 5, pp. 1025-1045.
- [9] IAPWS, 1997, "Release on the IAPWS Industrial Formulation 1997 for the Thermodynamic Properties of Water and Steam".
- [10] Rayleigh, J. S. W., 1945. "The Theory of Sound", Vol. 2, pp. 180-183.
- [11] Collingham, R. E. and Firey, J. C., 1963. "Velocity of Sound Measurements in Wet Steam", *I&EC Process Design and Development*, Vol. 2, No. 3, pp. 197-202.
- [12] England, W. G., Firey, J. C. and Trapp, O. E., 1966. "Additional Velocity of Sound Measurements in Wet Steam", *I&EC Process Design and Development*, Vol. 7, No. 2, pp. 198-202.
- [13] Martin, W., Naudascher, E. and Padmanabhan, M., 1975. "Fluid-Dynamic Excitation involving Flow Instability", *ASCE Journal of the Hydraulics Division*, Vol. 101, Issue 6, pp. 681-698.
- [14] Marble, F. E., 1969. "Some Gasdynamic Problems in the Flow of Condensing Vapors", *Astronautica Acta.*, Vol. 14, pp. 585-614.
- [15] Morita, R., 2011. "Measurement of Droplet Diameter in a high-Speed Wet Steam Flow", *Proceedings of the 16th National Symposium on Power and Energy Symposium, C222*, (in Japanese).



KEY PARAMETERS FOR NOISE GENERATION WITHIN CORRUGATED PIPES

Hugh Goyder

Cranfield University
Shrivenham Swindon SN6 8LA
h.g.d.goyder@cranfield.ac.uk

ABSTRACT

Corrugated pipes have the advantage of being flexible but the disadvantage of generating unacceptable levels of noise. The source of the noise is the oscillation of vortices within the corrugations. For applications that are sensitive to noise it is desirable to have a method for predicting the internal flow rates that cause noise and the level of the noise generated. This paper develops a theoretical model for the noise generation by considering the interaction of an acoustic wave with the vortices. From this model some key parameters emerge that are necessary for the modelling. These include one parameter for the maximum noise produced, which is known from experimental work, and two more which describe the balance of acoustic damping and flow excitation.

NOMENCLATURE

A	Pipe cross-sectional area
D	Pipe diameter
N	Number of pitches in one wavelength
N_o	Number of wavelengths in pipe
R_e	Reynolds number
St	Strouhal number
U_o	Mean pipe flow velocity
U_c	Convection velocity of vortex
c	Speed of sound in pipe
f	Vortex shedding frequency Hz
f_j	Natural frequency in Hz
k	Wavenumber
ℓ	Cavity width
p, p_j	Pressure, modal pressure
q	Volume velocity source
s, s_1, s_2	Dipole source models
w	Corrugation pitch
β	Saturation parameter
γ	Delay parameter
λ	Wavelength
ρ	Fluid density
ζ	Damping ratio
ω	Frequency in radians per second

INTRODUCTION

The oil and gas industry use corrugated pipes to carry gas between the sea bed and platforms. Such pipes are known as risers and can accommodate platform motions because they are flexible. On the sea bed corrugated pipes are used to connect pipework and are known as jumpers. An illustration of a corrugated pipe (taken from ISO 13628-11, 1997) is shown in Figure 1. The corrugations are on the inside of the pipe and are part of a carcass which maintains the circular form of the pipe even when the internal pressure is reduced (e.g. to atmospheric pressure) and the external pressure is large due to the subsea hydrostatic depth.

The corrugations consist of alternate cavities and lands, or plateau regions, which are symmetric about the axis of the pipe. The cavities are therefore a circular groove around the circumference of the pipe. Sometimes these grooves are manufactured to be helical but these still conform well to a circular approximation. Within the cavities the flow is stagnant and thus a shear layer forms at the edge of the cavity between the moving fluid in the pipe and the still fluid in the cavity. This shear layer rolls up into vortices which are ejected from the cavity creating a noise source (see illustration in Figure 2). The noise is typically a pure tone and may have an amplitude sufficient to cause structural vibration in pipework connected to the ends of the corrugated pipe. These structural vibrations can be large enough to cause a fatigue failure after only hours of operation which then results in a gas release. This is always unacceptable and consequently the production of noise from corrugated pipes needs to be fully understood.

This paper looks at the overall behaviour of the corrugated pipe when there are feedback effects between the acoustic waves and the vorticity shed in the cavities. The key problem is to model the feedback between the many thousands of distributed sources and the many acoustic waves within the pipe.

The production of noise from a corrugated pipe seems to have been first identified by Petrie and Huntley [1980] and then by Ziada [1991]. More recent publications are Belfroid et al [2008], Debut Antunes and

Moreira [2008] and Tonon et al. [2010]. A good source of experimental investigations and analysis is available in the thesis of Nakiboglu [2012]. The effect on structural vibration induced by the corrugation noise has been described by Goyder et al [2006].

GENERAL SPECIFICATIONS AND CHARACTERISTICS

Corrugated pipes cover a wide range of lengths from short jumpers of 20 m to long risers of 500 m or more with all lengths producing noise. Typical pipe dimensions are an internal diameter of about 0.2 m with the corrugation width being 5 to 10 mm with a pitch of around 25 mm. The gas within the pipe is typically methane under high pressure with a density of about 100 kg / m^3 . The gas flow velocity is in the range 2 to 15 m/s. The speed of sound can be high at about 400 m/s. The Mach number (ratio of flow velocity to speed of sound) is thus small. The noise is typically a pure tone with a frequency that depends on flow velocity but with values of 100 to 500 Hz. However, it is important to note that there is no known lower or upper frequency bound and in principle any frequency can be produced. In typical cases the wavelength of the noise is large compared to the corrugation width and pitch with there being tens or hundreds of corrugation gaps in a wavelength. The typical wavelength of concern is large compared to the diameter of the pipe so that acoustic modes within the cross-section need not be considered.

The corrugation gap is a helix around the pipe inner wall but will be modelled for simplicity in this paper as a sequence of circular ring gaps as shown in Figure 3.

As the flow rate in a corrugated pipe is increased from zero there is initially no noise until a threshold velocity is crossed. The prediction of this threshold velocity is important because for some operators it marks the maximum flow rate that will be allowed in the pipe. Such operators decide not to take the risk of noise in the pipeline causing vibration and possible pipework fatigue. Other operators decide to allow higher flow rates and to permit noise in the pipe but then take care to assess their pipework for the potential damaging effects of vibration.

As the flow rate is increased beyond the threshold a pure tone is maintained over a range of flows. At some higher flow rate the tone will switch to a new higher frequency in a step like manner. If the flow is increased still further then new higher frequencies will be observed each of which maintains, to a good approximation, the same frequency over a range of flow rates. If the flow rate is decreased the frequencies also decreases stepping down to a lower, frequency as some flow rate is passed. (The step-up and step-down flow rates do not necessarily coincide for increasing and decreasing flows.) The phenomenon whereby the frequency stays at one value despite the changing flowrate is known as lock-on or lock-in.

Each corrugation within the pipe is a noise source that becomes locked-in to the acoustic frequency of the noise. Various experiments have been performed to determine if the noise source acts like a monopole or dipole. Experiments by Tonon et al [2010] and by Nakiboglu [2012] show that the noise is produced at pressure nodes, where the acoustic velocity is a maximum, demonstrating that the source is a dipole.

MODELLING APPROACH

The general acoustic condition described in the last section is that of an acoustic standing wave in the corrugated pipe. The standing wave is associated with a natural frequency which is excited by the vortices produced in the corrugation cavities by the mean flow. The conditions that give rise to a standing wave depend on the terminations of the pipe which are generally open to allow flow but provide a discontinuity at which reflections may occur. An important consideration is the acoustic loss at the discontinuities which determines one source of damping for the acoustic waves. In a long pipe there are many natural frequencies that could be excited by vortex shedding but typically only those few with small damping actually materialize. The determination of acoustic natural frequencies and damping in terms of reflection coefficients has been investigated by Goyder [2010].

The approach taken here is to start by considering the excitation from just one circular corrugation with the source modelled as a dipole. The modelling of the dipole in terms of vortices is considered subsequently and finally the equations are generalised to consider the effect of all the corrugations.

The one dimensional acoustic wave in a pipe can be formulated in the usual manner (see Lighthill [1978] for a good discussion) by considering the equations of mass continuity, momentum and a constitutive relation. The momentum equation when linearised is

$$\frac{\partial u}{\partial t} = -\frac{1}{\rho_0} \frac{\partial p}{\partial x} \quad (1)$$

where u is the acoustic velocity, p the acoustic pressure and ρ_0 the mean fluid density. Time is t and x is the location along the pipe. The acoustic velocity does not include the mean velocity of the pipe, U_0 , which is small compared to the speed of sound and can be ignored.

The speed of sound, c is given by the differential form

$$dp = c^2 d\rho \quad (2)$$

which relate fluctuations in the pressure and density at constant entropy.

The equation of mass conservation contains the source terms. The source is regarded as a volume of fluid which is injected and removed from the main gas at a

point location. The source has a volume velocity q . For the case of a dipole, required here, two volume velocities separated by a distance ε are considered with one injecting fluid while the other removes fluid (subscripts + and -). The equation is

$$\frac{\partial \rho}{\partial t} + \rho_0 \frac{\partial u}{\partial x} = \frac{\rho_0}{A} (q_+ \delta(x - \varepsilon/2) - q_- \delta(x + \varepsilon/2)) \quad (3)$$

$$= \frac{\rho_0}{A} s \delta' x$$

where A is the cross-sectional area of the pipe. The locations for the sources are given as Dirac delta functions. For the second form on the right hand side the two monopole sources are combined into a dipole. The dipole source, s , has the dimensions of volume times length divided by time. The dipole location is given by the derivative of a delta function.

The wave equation is formed by combining Equations 1, 2 and 3 to give

$$\frac{1}{c^2} \frac{\partial^2 p}{\partial t^2} - \frac{\partial^2 p}{\partial x^2} = \frac{\rho}{A} \frac{\partial s}{\partial t} \delta'(x - x_n) \quad (4)$$

where the single acoustic source is located at x_n the position of the n th corrugation along the pipe. Note that in forming the equation the time derivative of the source has been taken.

MODEL FOR ONE CORRUGATION AND ONE RESONANT MODE

The condition in a corrugated pipe generating noise is that of an acoustic standing wave. This condition will be used to develop the wave equation from a partial differential equation into an ordinary differential equation. A cosine wave form may be adopted for the pressure that assumes the space and time variables are separable. This approach assumes that just one acoustic mode, the j th, is being excited by the source. Thus

$$p(t, x) = p_j(t) \cos k_j x \quad (5)$$

here p_j is the time dependent modal pressure. Also, k_j is the wave number which is related to the wavelength, λ_j , the speed of sound, c , and the acoustic natural frequency ω_j in the standard manner namely

$$k_j = \frac{2\pi}{\lambda_j} = \frac{\omega_j}{c} \quad (6)$$

The acoustic natural frequency is in radians per second so that $\omega_j = 2\pi f_j$ where f_j is the acoustic natural frequency in Hz.

By substituting Equation 5 into Equation 4, multiplying by $\cos k_j x$ and integrating over the

wavelength containing the source an ordinary differential equation is formed.

$$\frac{\lambda_j}{2c^2} (\ddot{p}_j + \omega_j^2 p_j) = -\frac{\rho}{A} \frac{\partial s}{\partial t} k_j \sin k_j x_n \quad (7)$$

Note that in this process, as usual, the derivative of the delta function has been replaced by the derivative of the acoustic mode shape evaluated at the location of the source.

The acoustic velocity plays a strong role in the source term and, with the assumption of the acoustic mode shape for pressure, a similar acoustic mode shape may be determined for the acoustic velocity. The velocity mode shape is derived by considering the relationship between pressure and velocity in Equation 1. The acoustic velocity emerges as

$$u(t, x) = u_j(t) \sin k_j x \quad (8)$$

where u_j is the time dependent modal velocity. Further examination of Equation 1 shows that the time dependent modal velocity and pressure are related by

$$\dot{u}_j(t) = \frac{\omega_j}{\rho c} p_j(t) \quad (9)$$

SOURCE MODEL

The noise source is attributed to vortex shedding from the corrugation gaps. Figure 4 illustrates the behaviour. The boundary layer emerges from the leading edge to form a shear layer between the moving fluid above the cavity and the still fluid within the cavity. The shear layer rolls up into discrete vortices which are convected from the leading edge to the trailing edge. There may be one or more vortices in the gap. The relationship between flow velocity and the frequency of the noise generated was first developed by Rossiter [1962] and is given in detail in Howe's textbook [2004]. In each cycle one vortex is formed at the leading edge and one is ejected at the trailing edge. Each vortex is convected by the local velocity U_c which is about 0.4 to 0.6 U_0 where U_0 is the mean velocity in the pipe. Thus the time taken to cross the corrugation gap of width ℓ is ℓ / U_c . If f is the frequency of vortex shedding then this time may be related to the frequency by

$$\frac{\ell}{U_c} = \frac{m}{f} \quad (10)$$

where m is the number of vortices in the gap. This equation may be generalized by allowing for additional delays and, at high Mach numbers, for the effects of the speed of sound. See Howe [2004] for details.

The usual nondimensional group used to characterize the vortex shedding frequency is the Strouhal number

which is given by $St = f\ell / U_0$. Thus the Strouhal number is related to the Rossiter theory by

$$St = \frac{f\ell}{U_0} = m \frac{U_c}{U_0} \quad (11)$$

The above formula has been examined in detail by Belfroid et al. [2007] who largely find agreement but report on the difficulty of defining ℓ exactly particularly when the corrugation edges are rounded. Nakiboglu [2012] obtains consistent results by including the upstream radius in the definition of ℓ .

The vortex shedding is periodic because the flow is self organising. According to Rockwell [2003] and Crighton [1992] the flow in the leading edge is sensitive to perturbations in the overall flow. Thus the violent ejection of a vortex when it arrives at the trailing edge creates perturbations in flow which influence the formation of a vortex at the leading edge.

The flow oscillations, due to the acoustic wave, which is the concern in this paper, also modify the vortex shedding causing lock-on which is the synchronization of the vortex shedding to the acoustic wave. When there are many corrugations they all become synchronized to the local phase of the flow oscillation thus providing many sources and much energy input to the acoustic wave.

The vortex shedding mechanism is a dipole source with a strength that depends on the amplitude of the flow oscillation. For a small acoustic amplitude the source is a destabilising feedback while for a large amplitude it is a stabilising feedback. The balance between the destabilising feedback and the stabilising feedback is an important issue to be modelled in this paper.

The wavelength of the noise is large compared to the size of the cavity and the noise source is thus classified as compact. The consequence is that the mechanism is only a function of the instantaneous local flow velocity and is independent of the pressure or density changes that occur over the length of a whole acoustic wave. The behaviour of the flow in the cavity is thus one of an incompressible fluid.

It is not yet possible to model the fluid mechanics of the vortex shedding process and to extract the dipole source strength (although some progress has been made by Nakiboglu [2012] using computational fluid dynamics). However, an approach based on dimensional analysis and considerations of vortex dynamics provides considerable insight. The key inputs to the dipole source strength are the geometry of the cavity, the vorticity entering at the leading edge from the boundary layer and the flow outside the cavity composed of the mean flow U_0 plus the fluctuating flow due to the presence of the acoustic wave.

The dipole source, s , has dimensions of length to the power of 4 divided by time and is a function of time. A suitable set of parameters to characterise these

dimensions are the area occupied by the cavity on the pipe wall namely, $\pi D \ell$ and the circulation associated with each vortex. The circulation associated with each vortex is easily estimated by noting the rate at which circulation is shed from the wall into the cavity and multiplying by the period of one cycle. The rate of generation of circulation is $U_0^2/2$ for a boundary layer that is taken to be linear, as shown in Figure 4 as B and is larger for the more realistic profile in A . For a 7th power law it is $7U_0^2/8$. The total circulation of a vortex is obtained by multiplying by the period or dividing by the frequency f . The value of the circulation will be taken to be U_0^2/f thus disregarding the factor arising from the boundary layer shape. The model for the dipole now reads

$$s = \frac{\pi D \ell U_0^2}{f} s_1 \left(t f, R_e, \frac{u(t)}{U_0} \right) \quad (12)$$

where the nondimensional function s_1 is shown as depending on time, t , Reynolds number, R_e and the ratio of fluctuating flow velocity to mean flow velocity.

For locked-on conditions the time dependence of the dipole source is determined by the fluctuating flow velocity $u(t)$ due to the acoustic wave. It is assumed that this flow velocity is harmonic with a slowly varying amplitude. A model for the amplitude and phase of the dipole source must be deduced from this velocity.

A phase difference exists between the oscillating flow velocity and the oscillating dipole source. This phase difference is due to the time lag between the interaction of the flow and the sensitive leading edge and the vortex moving across the cavity. Such phase differences have been observed in experiments by Ziada et al. [2003]. In these experiments the flow at the leading edge was perturbed and it was found that the source was enhanced if a delay of 3/7 of a period was applied between the perturbation and flow maximum and suppressed if the delay was 7/8 of a period. The value for the phase lag in the case being considered here is unknown.

The source strength depends on the amplitude of the flow oscillations. Since this is a self excited system it can be expected to have a linear dependence for small amplitudes. This gives rise to the unstable feedback effect. However, since the system is also self-limiting it must have a nonlinear term that provides a stable feedback condition for large amplitudes. These effects can be modelled by expanding the function s_1 in a Taylor series. The inclusion of the delay and the Taylor series terms results in the final model for the source being

$$s = \pi D \ell \frac{U_0^2}{f} \left(\frac{u(t - \gamma/f)}{U_0} - \frac{1}{\beta^2} \left(\frac{u(t - \gamma/f)}{U_0} \right)^3 \right) s_2 \quad (13)$$

where s_2 is independent of time and is just dependant on Reynolds number. The Taylor series has been expanded using odd terms only and includes a liner term and a velocity cubed term. Higher terms could also be included if necessary. However, no even terms are included because when oscillating terms are considered even terms lead to an increase in the mean flow which is not physically possible. Thus, for example, a term in u^2 with an oscillation frequency of ω would lead to a fluctuating velocity of

$$(\hat{u} \cos \omega t)^2 = \frac{1}{2} \hat{u}^2 + \frac{1}{2} \hat{u}^2 \cos 2\omega t$$

where \hat{u} is a slowly varying velocity amplitude. The first term on the right hand side is a constant implying an impossible change to the mean flow. Such terms are rejected. Equation 13 has a new parameter, β , which models the strength of the nonlinear term. It is also a function of Reynolds number. The oscillating velocity includes a term γ/f to represent the phase shift between the oscillations of the acoustic velocity and the dipole.

Two more stages are required before the model for one corrugation is completed. It is necessary to take the time derivative of the source and then to replace the velocity u with the velocity corresponding to the location x_n . Also, use may also be made of Equation 1 to relate the derivative of the velocity to the pressure. With these substitutions the ordinary differential equation for the pressure may be written as Equation 14, which is given in the Appendix due to its length.

SUMMING ALL SOURCES

Equation 14 is a linear differential equation in pressure and it is thus possible to use superposition to determine the response from all the sources. This requires the right hand side to be summed over all the locations x_n were a corrugation is located. If the spacing between corrugations, the pitch, is w and there are an integer number of pitches, say $N = \lambda_j/w$, in a wave length then the sin terms may be written

$$\sin k_j x_n = \sin 2\pi \frac{n}{N} \quad (15)$$

Use may now be made of two trigonometric identities which simplify the summation. Note that the summation is made over one wavelength.

$$\begin{aligned} \sum_{n=0}^N \sin^2 2\pi \frac{n}{N} &= \frac{N}{2} \\ \sum_{n=0}^N \sin^4 2\pi \frac{n}{N} &= \frac{3N}{8} \end{aligned} \quad (16)$$

The result of this superposition is the final model for the corrugated pipe, Equation 17 in the appendix, which

contains N_0 wavelengths. A damping term has also been inserted on the left hand side.

THE COMPLETE MODEL

Figure 5 shows a typical result from a simulation of the model. The simulation solves for Equation 17 and Equation 1 simultaneously. The system is unstable and the amplitude rises to a fixed value as the system saturates. A theoretical analysis shows that the saturation value of the acoustic velocity depends only on β and is given by

$$\frac{\hat{u}}{U_0} = \frac{4}{3} \beta \quad (18)$$

where \hat{u}_j is the amplitude of the acoustic velocity. Experimental observations by Belfroid et al [2009] and Nakiboglu [2012] indicate that \hat{u}_j / U_0 is typically about 0.1 making $\beta = 0.075$. Numerical investigation of the model also shows that it is insensitive to the value of γ so long as $0.1 < \gamma < 0.45$. A value for s_2 is not available in the open literature.

DISCUSSION

The model suggests that although the system is highly complex there are relatively few key parameters. The unknown parameters in Equation 17 are only β , γ , s_2 and ζ . In particular the maximum pressure amplitude is only dependent on β for which the value of 0.075 has been deduced from experiments. The numerical insensitivity to the value of γ , the phase lag, suggests that this parameter is not important. This is reasonable since the pressure is a harmonic function with a slowly varying amplitude which may be considered as the sum of in-phase and out-of-phase components. All that is required for the instability is that there is a component out-of-phase with the pressure.

The conditions for the onset of the noise are much more difficult to investigate. For small amplitudes the damping will oppose the destabilising effect. There are two sources of damping. First damping from within the pipe due to friction with the pipe wall and other viscous thermal effects. Second damping due to losses from the ends of the pipe. Experiments that attempt to separate the destabilising effect from the first type of damping would be very difficult to perform because only a combined effect could be observed. In fact the parameter s_2 could be defined to include such damping effects. With respect to the second source of damping it is interesting to note that as the pipe becomes longer then there are more sources while the proportion of the energy generated lost to the ends remains the same. Thus as a corrugated pipe becomes longer the effect of the ends becomes less important. However, establishing the relative importance of the ends remains to be accomplished.

The assumptions of the model can be divided into two kinds. Those associated with the modelling of the mode and those associated with the modelling of the source. The modelling of the modes is well established and is a basic part of linear acoustics theory. This should have few errors. In contrast the modelling of the noise source is much more difficult. It is probably that empirical measurements will always be necessary and the fact that there is only one key parameter, s_2 , is welcome.

CONCLUSIONS

The following conclusions may be drawn.

1. The growth of the acoustic pressure to a maximum value in a corrugated pipe can be represented by a simple model involving only a few parameters.
2. The maximum acoustic velocity is predicted to increase until it is a simple fraction of the mean velocity. This fraction has been observed in experiments to be about 0.1 of the mean velocity.
3. The prediction of the flow velocity for the onset of noise is problematic because it depends on a balance of energy losses from the system and energy developed by the system. Although a parameter has been identified to characterise this effect no experimental values are available from which it may be deduced.

ACKNOWLEDGMENTS

The author acknowledges the support of Cranfield University in the development of this research.

REFERENCES

- Belfroid PC, Shatto DP, and Peters MCAM "Flow induced pulsations caused by corrugated tubes (2007) ASME PVP, San Antonio, Texas.
- Belfroid SPC, Swindell R, and Tummers R. 2008. "Flow induced pulsations generated in corrugated tubes" 9th International Conference on Flow-Induced Vibration , Prague, Czech Republic, 3 June – 3 July (2008).
- Belfroid SPC, Swindell RJ and Kitney N "Flow Induced Pulsations due to Flexible Risers" Offshore Technology Conference (2009) Houston USA 4-7 May.
- Crighton DG. "The jet-dedge-tone feedback cycle: linear theory for the operating stages." *Journal of Fluid Dynamics* (1992) 234 361-392.
- Debut V, Antunes J and Moreira M "Flow-acoustic interaction in corrugated pipes: time domain simulation of experimental phenomena", 9th International Conference on Flow-Induced Vibration , Prague, Czech Republic, 3 June – 3 July (2008).
- Goyder H.G.D, Armstrong K, Billingham, L , Every M. J., Jee T. P, Swindel R. J., "A full scale test for acoustic fatigue in pipework". ASME PVP (2006) - ICPVT -11-9377
- Goyder HGD "On the modeling of noise generation in corrugated pipes". (2010), ASME Journal of Pressure Vessel Technology, Volume 132, Issue 4, pages 041304
- Graf HR and Ziada S. "Flow Induced Acoustic Resonance in Closed Side Branches: An Experimental Determination of the Excitation Source. ASME PVP Vol 247 (1992)
- Howe MS "Acoustics of Fluid-Structure Interactions", Cambridge University Press, (2004) ISBN 0521 633206
- Howe MS "Mechanism of sound generation by low Mach number flow over a cavity", *Journal of sound and vibration* 273 (2004) 103-123
- ISO 13628-11. "Petroleum and natural gas industries – Design and operation of subsea production systems – Part 11: Flexible pipe systems for subsea and marine applications. (2007) -09 15
- Lighthill J 1978 "Waves in fluids" Cambridge University Press, ISBN -10 0-521-01045-4.
- Nakiboglu G. "Aeroacoustics of corrugated pipes." PhD Thesis Technical University of Eindhoven. (2012) ISBN 978-90-386-3110-3
- Nayfeh A H and Mook DT, "Nonlinear Oscillations", (1979) John Wiley and Sons, Inc, ISBN 0-471-03555-6.
- Petrie A M and Huntley I D "The acoustic output produced by a steady airflow through a corrugated duct" *Journal of Sound and Vibration* Volume 70, Issue 1, 8 May (1980), Pages 1-9.
- Rossiter J E "The effects of cavities on the buffeting of aircraft" Royal Aircraft Establishment Technical Memorandum 754.
- Rockwell D, Lin J-C, Oshkai P, Reiss M and Pollack M, "Shallow cavity flow tone experiments: onset of locked-on states", *Journal of Fluids and Structures* 17 (2003) 381-414.
- Tonon D, Landry BJT, Belfroid SPC, Willems JFH, Hofmans GCJ and Hirschberg A, "Whistling of a pipe system with multiple side branches: Comparison with corrugated pipes" *Journal of Sound and Vibration*, 329, (2010) pp 1007-1024.
- Ziada, S and Buhlmann ET 1991, "Flow induced vibration in long corrugated pipes." International conference on Flow-Induced Vibrations May (1991) Brighton United Kingdom, ImechE, ISBN 85298 764 1
- Ziada S, Ng N and Blake CE. "Flow excited resonances of a confined shallow cavity in a low Mach number flow and its control." *Journal of fluids and structures* (2003) vol 18 pp79-92.

APPENDIX: LONG EQUATIONS

$$\ddot{p}_j + \omega_j^2 p_j = -16 \pi \left(\frac{cN_0 U_0}{D \lambda_j} \right) \left(\frac{\ell}{\lambda_j} \right) \left(\frac{\omega_j}{f} \right) p_j (t - \gamma / f) \sin^2 k_j x_n \left(1 - \frac{3}{\beta^2} \left(\frac{u_j(t - \gamma / f) \sin k_j x_n}{U_0} \right)^2 \right) s_2 \quad (14)$$

$$\ddot{p}_j + 2\zeta\omega_j \dot{p}_j + \omega_j^2 p_j = -16 \pi^2 \left(\frac{N_0 U_0 f_j}{D} \right) \left(\frac{\ell}{w} \right) \left(\frac{f_j}{f} \right) p_j (t - \gamma / f) \left(1 - \frac{9}{4\beta^2} \left(\frac{u_j(t - \gamma / f)}{U_0} \right)^2 \right) s_2 \quad (17)$$

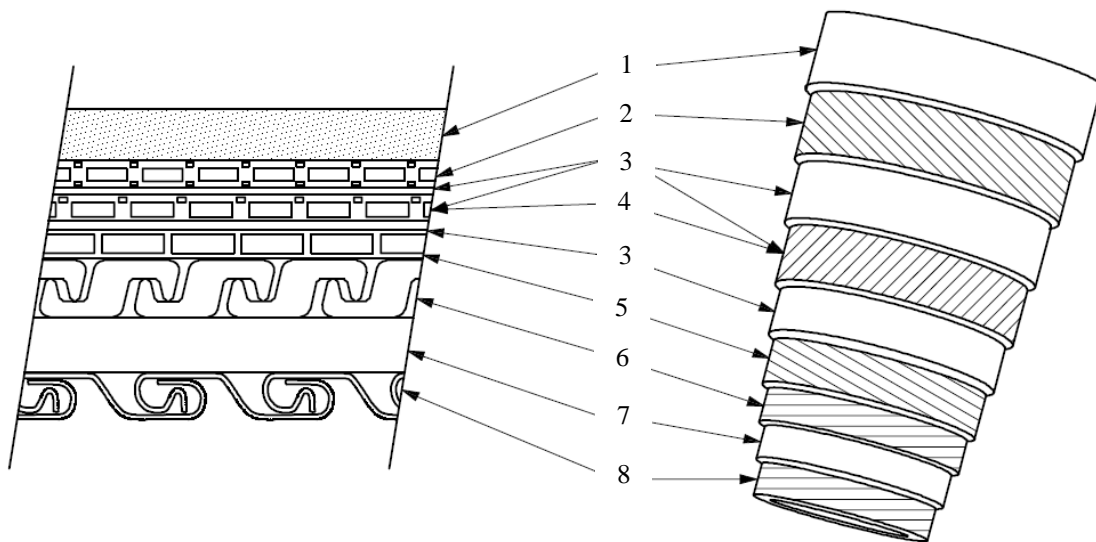


Figure 1. Construction of corrugated pipe. 1. Anti-friction layer, 2. Outer layer of tensile armour, 3. Anti-wear layer, 4. Inner layer of tensile armour, 5. Back-up pressure armour, 6. Interlocked pressure armour, 7. Internal pressure sheath, 8. Carcass.

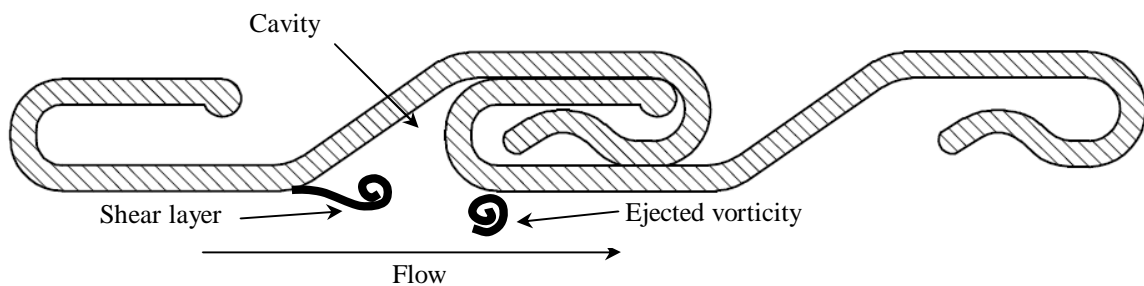


Figure 2. Corrugated pipe carcass showing cavity and shear layer.

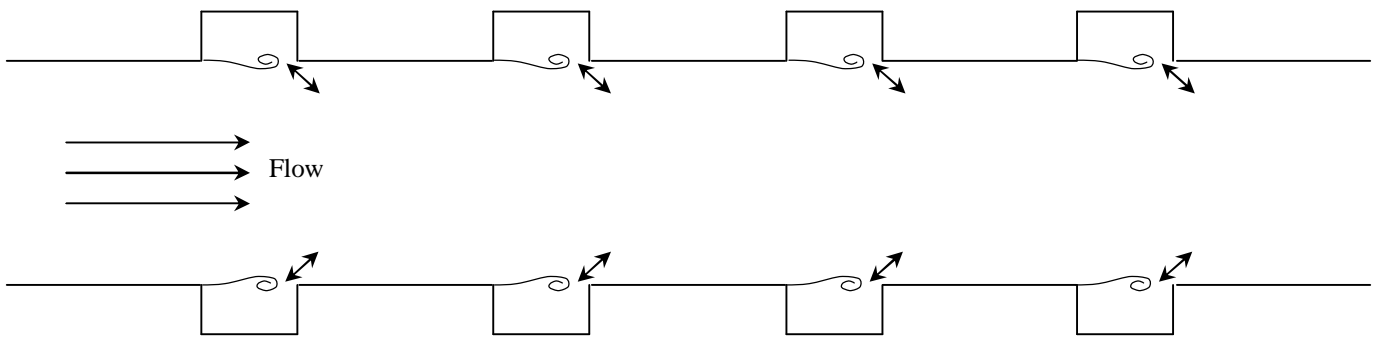


Figure 3. Diagrammatic representation of pipe, flow, cavities and shear layers. The sources are dipoles shown as arrows at the trailing edge.

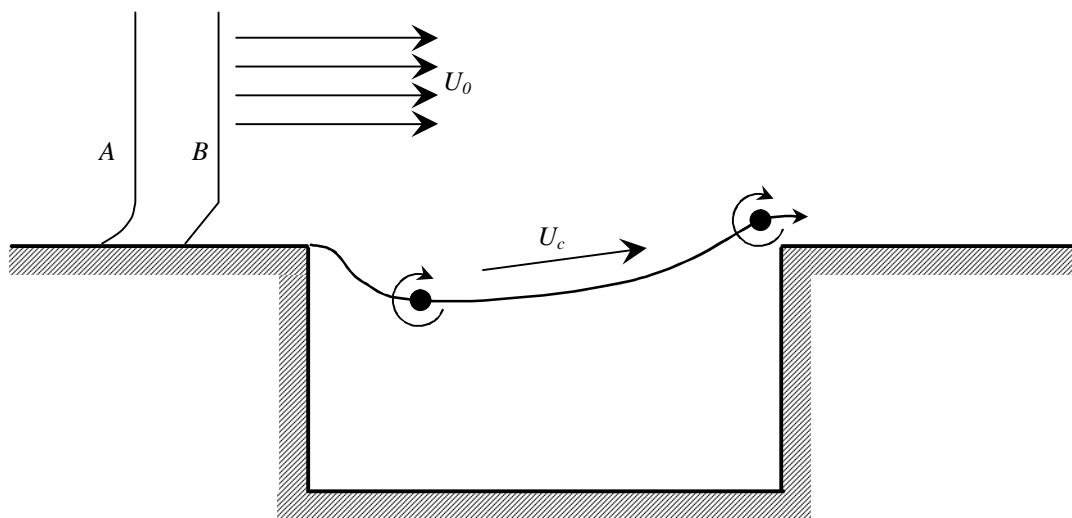


Figure 4. Illustration of vortices within a corrugation. A and B are approximations to the boundary layer set up by the free stream U_0 . The vortices move with typical velocity U_c across the cavity.

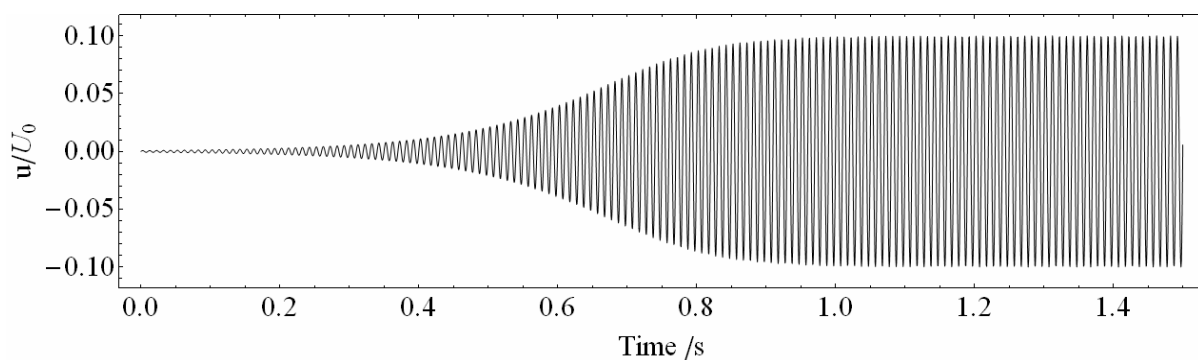


Figure 5. Simulation of Equation 18. $U_0 = 3$ m/s, $f_j = f = 100$ Hz, $\ell/w = 1/3$, $N_0 s_2 = 0.1$, $\beta = 0.075$

ON WHISTLING OF PIPES WITH A CORRUGATED PIPE SEGMENT

Oleksii Rudenko*, Gunes Nakiboglu and Avraham Hirschberg
 Department of Applied Physics, Eindhoven University of Technology,
 Eindhoven 5600 MB, The Netherlands
 Email: o.rudenko@tue.nl

ABSTRACT

A generic experiment is conducted in which a corrugated pipe segment is placed between two smooth pipe segments with open terminations. Such a composite pipe system, widely utilized in industry, can produce high amplitude whistling noises. Experiments with pipes of 1 cm diameter and various lengths of the downstream smooth segment were carried out for flow velocities up to 55 m/s at room conditions. We observed a maximum of whistling amplitude at a critical Strouhal number between 0.36 and 0.43. There is a critical smooth downstream pipe length (much larger than the length of the corrugated pipe segment), which is sufficient to prevent pulsations at room conditions for the pipes considered. A simple model is proposed allowing the prediction of a critical Mach number above which the whistling occurs. Preliminary results focus on the worst-case scenario in which the corrugated segment is placed close to one of the pipe terminations with a high reflection coefficient. In this configuration there is a long downstream smooth pipe and a short upstream smooth pipe.

INTRODUCTION

A corrugated pipe is a tube with a periodically changing diameter. This undulatory shape makes the thin-walled corrugated pipes locally rigid and globally flexible. Various industrial applications benefit from corrugated pipes' utilization ranging from vacuum cleaners to offshore natural gas production [1]. A drawback of corrugated pipes is the production of strong whistling sounds. This whistling is an environmental nuisance and associated vibration can lead to a mechanical failure [2].

In this paper we consider a generic experiment in which a corrugated pipe segment is placed between two smooth pipe segments. The pipe has open terminations.

We report the existence of a critical Mach number, M_{cr} , above which a substantial increase of the whistling amplitude is observed. A simple model is provided explaining this observation.

WHISTLING OF CORRUGATE PIPES

The sound generation in corrugated pipes has been intensely studied [2–15]. The whistling of a corrugated pipe is the result of a coupling between local vortex shedding at the cavities formed by the corrugations and longitudinal acoustic waves traveling along the pipe.

Whistling is a self-sustained oscillation. For relatively short pipes, involving strong acoustical reflections at the pipe ends, the vortex shedding at the upstream edge of the corrugations is triggered by the grazing oscillating velocity u' associated with acoustic standing waves along the pipe. The unsteadiness of the flow at each corrugation results into a fluctuating hydrodynamic force in the direction of the pipe axis. This fluctuating force reinforces the acoustic oscillation. At very small acoustic amplitudes, when the regime is linear, the oscillation amplitude can grow exponentially until a non-linear regime is reached resulting in a saturation of the amplitude, and a steady whistling amplitude is established (limit cycle) [9, 11]. Alternatively, perturbations decay exponentially in time.

The whistling is observed when the travel time of the vortices across the cavity width W of a corrugation matches the oscillation period of the standing wave. This corresponds to a critical Strouhal number,

$$Sr_{cr} = fW/U_{cp}, \quad (1)$$

where f is the oscillation frequency and U_{cp} is the steady flow velocity in the corrugated pipe averaged over the inner cross-section of the pipe. An empirical relation was suggested in Ref. [11] relating the critical Strouhal num-

*Address all correspondence to this author.

ber with the ratio of W/D_{cp} , i.e. the cavity width W to the minimal corrugated pipe diameter D_{cp} :

$$Sr_{cr} \approx 0.58 (W/D_{cp})^{0.2}. \quad (2)$$

The steady whistling amplitude is a result of the balance between the power produced by the sound sources and the power losses.

The acoustic power generated by a single corrugation has been studied by means of computer simulations in [11, 13]. Within the linear approximation (see e.g. [16]), the acoustic source power averaged over a period of acoustic oscillation, $\langle P_{src} \rangle$, scales as $\rho |u'|^2 U_{cp} S_{cp}$, where ρ is the mean fluid density, $|u'|$ is the amplitude of the local grazing acoustic velocity and $S_{cp} = \pi D_{cp}^2/4$ is the minimal cross-section area of the corrugated pipe.

Fig. 1 adopted from the Ref. [13] shows the dependence of the acoustic source power produced by a single cavity on the relative acoustic amplitude, $|u'|/U_{cp}$. This is for a fully developed turbulent flow in a corrugated pipe with a geometry similar to that of the corrugated pipes used in our experiments. The source power was computed for the most intense whistling, i.e. at the critical Strouhal number, which is equal to 0.46 for the present corrugated pipe geometry. The horizontal asymptote in the graph for small $|u'|/U_{cp}$ corresponds to the linear regime.

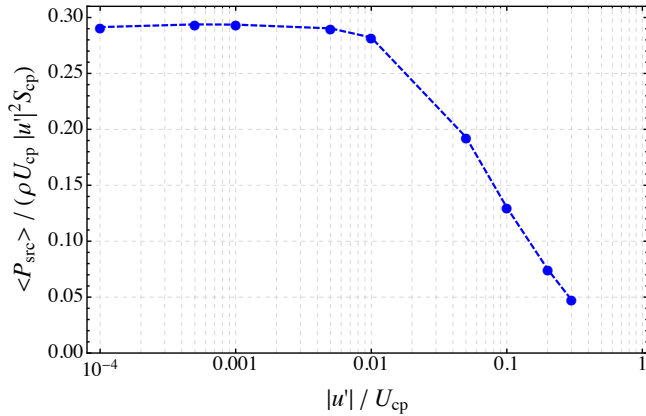


FIGURE 1: SINGLE CORRUGATION DIMENSIONLESS SOURCE POWER VS. RELATIVE PULSATION AMPLITUDE. ADOPTED FROM REF. [13].

EXPERIMENTAL SET-UP

The set-up and the corrugated pipe segment are sketched in Fig. 2. The pipe system consists of a short

upstream smooth pipe segment of length $L_{up} = 59$ mm followed by the corrugated pipe segment of length $L_{cp} = 228$ mm and a downstream smooth pipe segment. Four different lengths of the downstream smooth pipe segment, L_{dn} , were tested: 59 mm, 509 mm, 988 mm and 2009 mm.

The smooth pipe segments are RVS buis UHP 12.7x1.22mm 1.4404 ultron. The inner smooth pipe diameter is $D_{sp} = 10.32$ mm, the outer is 12.7 mm. The corrugated pipe segment is BOA stainless steel corrugated pipe, type PNR made of AISI 316. The number of corrugation is $N = 53$. The pitch (wavelength) of the corrugations is $p = 4.3$ mm corresponding to a cavity width $W \simeq 3p/4 \simeq 3.18$ mm [11]. The depth of the cavities is estimated to be 3 mm. The the outer diameter of corrugated pipe is 16.1 mm and the inner one is $D_{cp} = 10.19$ mm ($D_{cp}/W \simeq 3.18$).

The flow through the pipe is driven by a centrifugal ventilator attached to a settling chamber (volume 0.5 m x 0.5 m x 1.8 m). A 10 cm thick layer of acoustic absorbing material (foam) covers the side-walls of the settling chamber. This avoids acoustic resonances of the settling chamber and approximates free field radiation conditions for the upstream open end (inlet) of the pipe (flanged pipe termination). At the downstream side of the set-up (outlet), the flow leaves the pipe through an un-flanged open pipe termination.

A constant temperature hot wire anemometer is placed on the pipe axis inside the pipe 4 mm upstream of the downstream open pipe termination. The hotwire anemometer was a Dantec 90C10 CTA module installed within a Dantec 90N10 frame. The signal was amplified and low-pass filtered through a low-noise preamplifier (Stanford Research Systems, Model SR560) and sent to the computer via a National Instrument BNC-2090 184 data acquisition board with a 12-bit resolution at a sampling rate of 10 kHz. This calibrated hot-wire provides a measurement of the time dependent velocity $u(t)$, which then is split into a time-averaged velocity U_{cl} at the center-line and a fluctuating (acoustic) velocity of amplitude u' and frequency f .

The acoustic velocity is uniform over the pipe cross-section (outside the viscous boundary layers of thickness $\sqrt{\nu/(\pi f)} < 0.07$ mm, where ν is the kinematic viscosity). The center-line velocity, U_{cl} , is related to the average velocity $U = Q/S_{sp}$ (where Q is the volume flow and $S_{sp} = \pi D_{sp}^2/4$ is the cross-section area of the smooth pipe) by the empirical equation [17]:

$$U \simeq U_{cl} / \left(1 + 1.33\sqrt{Fr}\right), \quad (3)$$

Where the friction factor, Fr , for a smooth pipe is given

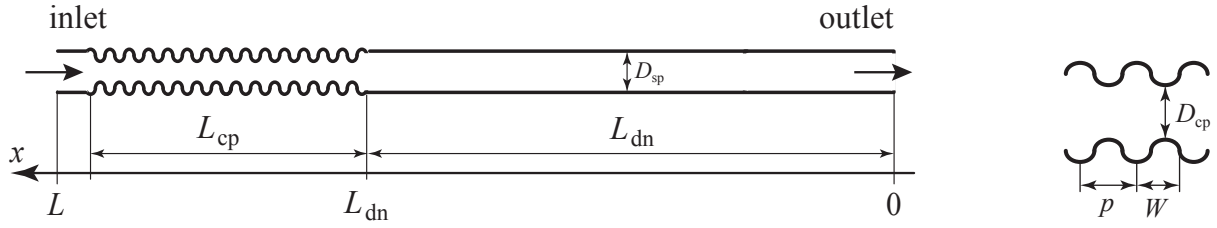


FIGURE 2: EXPERIMENTAL SET-UP & CORRUGATED PIPE GEOMETRY.

by the formula of Blasius [17]:

$$Fr \simeq 0.316Re^{-0.25}, \quad (4)$$

with $Re = UD_{sp}/\nu$ is the Reynolds number. For typical Reynolds numbers in our experiments, $47000 < Re < 64000$, we approximate $U \simeq U_{cl}/1.19$. Due to slight mismatch in the smooth pipe and corrugated pipe diameters, average velocity in corrugated pipe is $U_{cp} = US_{sp}/S_{cp}$. Thus

$$U_{cp} \simeq U_{cl}/a, \quad a = 1.16, \quad (5)$$

i.e. the steady cross-section averaged velocity in the corrugated pipe is about a factor 1.16 lower than the center-line velocity at the end of the downstream smooth pipe segment measured by means of the hot wire.

After establishing a stable flow velocity the hot wire signal was recorded during 30 s at a sample rate of 10 kHz. The amplitude u' of the acoustic velocity fluctuations was determined by carrying a Fast Fourier Transform (FFT) of the hot wire signal and by integrating the energy in the dominating peak (above 20 Hz) over a bandwidth of 10 Hz. Then u' corresponds to an amplitude of a sinusoidal signal with the same energy [10].

In discussing the results, an experiment is denoted by the length of the upstream smooth pipe segment, the length of the corrugated pipe segment and the length of the downstream smooth pipe segment, i.e. (L_{up}, L_{cp}, L_{dn}) . These lengths are rounded and given in millimeters.

RESULTS AND DISCUSSION

Whistling Frequency

In Fig. 3, the Helmholtz number, He , is presented versus the Mach number, M , defined as

$$He \equiv \frac{Lf}{c_0} = \frac{LSr_{cr}}{aW} M, \quad M \equiv \frac{U_{cl}}{c_0}, \quad (6)$$

where $L = L_{up} + L_{cp} + L_{dn}$ is the total length of the composite pipe and $c_0 \simeq 340$ m/s is the speed of sound in the air at room temperature. The symbols in Fig. 3, left, are the experimental data: (black) discs – (6,27,6) configuration, (blue) squares – (6,27,51) configuration and (orange) rhombi – (6,27,99) configuration. The lines are fits of Eq. (6) to the experimental data at the most intense whistling per mode (step or quasi-plateau in the Figure): lower (black) gives critical Strouhal number 0.36, middle (blue) – 0.38 and upper (orange) – 0.43. Note, that the Eq. (2) gives $Sr_{cr} \simeq 0.46$, which is 22% larger than the lowest observed critical Strouhal number. This variation in the critical Strouhal number are not understood and deserve further study. The longest pipe configuration (6,23,201), not shown in the Fig. 3, left, was not whistling in the whole range of Mach numbers reachable with the current set-up.

In agreement with the previous observations [11,13], the Helmholtz number, hence the whistling frequency, changes in a step-wise manner illustrating the coupling of the standing wave (inside the corrugated pipe) with an appropriate hydrodynamic mode of vortex shedding (see [11,13] for more details). In first order approximation, the standing waves correspond to the Helmholtz number changing in steps of 0.5. A stepping close to this is observed in Fig. 3.

Whistling Threshold

In Fig. 3, the relative whistling amplitude, $|u'_0|/U_{cl}$, versus the Mach number is shown. Here $|u'_0|$ is the acoustic velocity amplitude at $x = 0$, i.e. at the downstream end. Observe that the increase in length of the downstream smooth pipe segment leads to an expected decrease in the relative amplitude such that for the configuration (6,27,201), not shown in the Fig. 3. The whistling disappears in the flow range considered in our experiments. There are also noticeable sudden variations in whistling amplitudes for high Mach numbers. These variations might be due to acoustic resonances of the room in which the experiment was conducted. Interesting

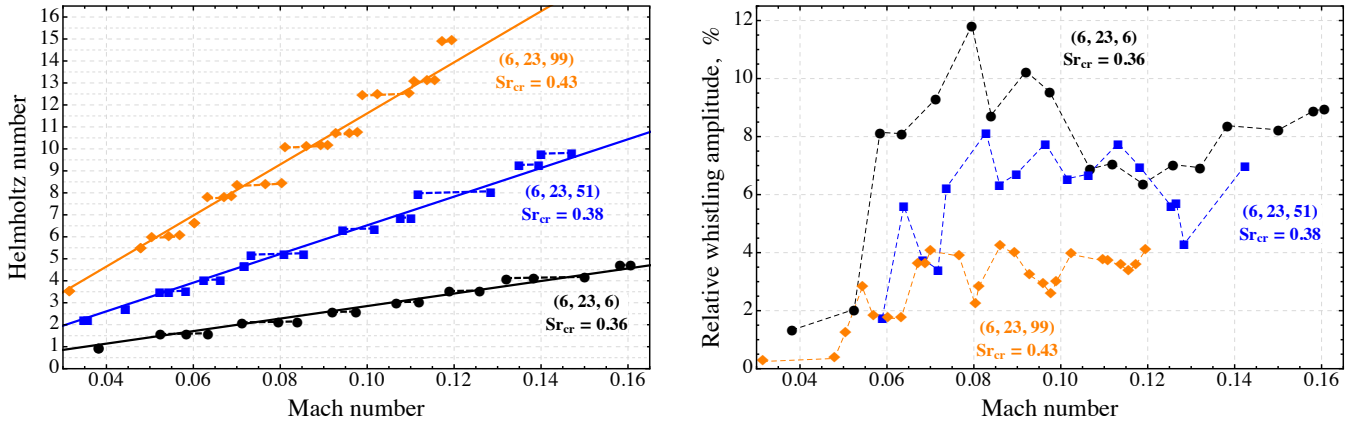


FIGURE 3: LEFT: HELMHOLTZ VS. MACH NUMBER, RIGHT: AMPLITUDE VS. MACH NUMBER.

observation is the existence of a critical Mach number, $M_{cr} \approx 0.05$, below which there is only weak whistling. This is more evident for longer downstream smooth pipe segments.

We try to rationalize the existence of the critical Mach number by the following simple model. We suppose that $L_{up} \ll L_{cp} \ll L_{dn}$, which is very roughly realized in (6,27,99) configuration. For such a configuration one expects a limit behavior in which the upstream open end is strongly reflecting, while the downstream end is almost anechoic. Thus a downstream traveling wave in the long (downstream) smooth pipe segment is a first order approximation. In this approximation the radiation losses of the corrugated pipe are

$$\langle P_{loss} \rangle \simeq \frac{1}{2} \rho c_0 |u'_{dn}|^2 S_{sp}, \quad (7)$$

where $|u'_{dn}|$ is a typical value of the sound velocity amplitude at $x = L_{dn}$. In the limit case of vanishingly small oscillatory perturbation, i.e. for $|u'|/U_{cp} \ll 1$, the linear shear layer instability acts as the sound source. Then a rough estimate for the source power is

$$N \langle P_{src} \rangle \simeq N A \rho |u'|^2 U_{cp} S_{cp}. \quad (8)$$

The single source power $\langle P_{src} \rangle$ is shown in Fig. 1. In the linear regime we have $\langle P_{src} \rangle \simeq A \rho |u'|^2 U_{cp} S_{cp}$ with $A \simeq 0.29$. If the losses overcome the production, the system remains silent. The balance of the losses with production, $\langle P_{src} \rangle_N = \langle P_{loss} \rangle$, determines the threshold for whistling:

$$N A \rho |u'|^2 U_{cp} S_{cp} = \frac{1}{2} \rho c_0 |u'_{dn}|^2 S_{sp}, \quad (9)$$

Assuming $|u'| = |u'_{dn}|$, we find a critical Mach number:

$$M_{cr} = \left(\frac{D_{sp}}{D_{cp}} \right)^2 \frac{a}{2A} \cdot \frac{1}{N}. \quad (10)$$

This is the Mach number below which the system remains silent. For the set-up considered ($N = 53$, $a = 1.16$, $A = 0.29$, $D_{sp}/D_{cp} \simeq 1.01$) we find:

$$M_{cr} \simeq 0.04, \quad (11)$$

which agrees surprisingly well with the experimentally observed value.

It is important to stress that we made a very crude approximation assuming that the grazing oscillatory velocity amplitude, $|u'|$, is uniform through the whole corrugated pipe and equal to $|u'_{dn}|$. In general this is not true. The weakly unstable shear layers amplify the acoustic wave propagating in the corrugated pipe at every corrugation. Hence we expect a non-uniform acoustic velocity along the corrugated pipe segment. Furthermore, a critical Mach number also exists for other pipes configurations including the symmetric one (6,27,6), where a dominating traveling wave in the downstream smooth pipe segment is a poor approximation.

Note that considering damping which is independent of the (mean) flow velocity will result in the prediction of a critical Mach number. Hence a quasi-steady model of frictional losses would not predict such a Mach number. A better quantitative model is required. Nevertheless, even a very simple model indicates the existence of a critical Mach number, which value surprisingly well agrees with the experiment.

CONCLUSIONS

Experiments have been carried out on pipes consisting of three segments: upstream smooth segment, corrugated pipe segment and downstream smooth segment. The length of the last smooth pipe segment was varied. Strong whistling was observed for all the lengths except the longest one at which the system remained silent. This supports the idea that a long enough smooth pipe placed after the corrugated one will keep the system silent since the losses brought by the smooth pipe will overcome the sources power, which are located in the corrugated pipe. However, a very simple model predicts another behavior: the whistling should occur for very long downstream pipes above a critical Mach number.

The recorded dimensionless whistling frequencies (Strouhal numbers) appeared to be in a fair agreement with the earlier findings [11]. A very simple order-of-magnitude estimate predicts surprisingly good the value for the critical Mach number observed in the experiments below which a corrugated pipe segment attached to a long smooth pipe should not whistle.

ACKNOWLEDGMENT

This work was made possible by the contributions of STW Technologiestichting (Project No. STW 1037 08126). The authors wish to thank A. Holten, J. F. H. Willems, H. B. M. Manders, E. Cocq and F. M. R. van Uittert for their contributions to the development of the experiments.

REFERENCES

- [1] Belfroid, S., Shatto, D., and Peters, R., 2007. "Flow induced pulsation caused by corrugated tubes". In Proceeding of ASME Pressure Vessels and Piping Division Conference, San Antonio.
- [2] Ziada, S., and Bühlmann, E., 1991. "Flow induced vibration in long corrugated pipes". In Intl Conference on Flow-Induced Vibrations. IMechE, UK.
- [3] Ziada, S., and Bühlmann, E., 1991. "Multiple side-branches as tone generators". In Proceedings of International Mechanical Engineering Conference, paper, Vol. 416, pp. 435–444.
- [4] Cadwell, L. H., 1994. "Singing corrugated pipes revisited". *American Journal of Physics*, **62**, pp. 224–227.
- [5] Elliott, J., 2005. *Corrugated pipe flow*. Imperial College Press, ch. 11, pp. 207–222.
- [6] Debut, V., Antunes, J., and Moreira, M., 2007. "Experimental study of the flow-excited acoustical lock-in in a corrugated pipe". 14th International Conference on Sound and Vibration.
- [7] Debut, V., Antunes, J., and Moreira, M., 2008. "Flow-acoustic interaction in corrugated pipes: time domain simulation of experimental phenomena". 9th International Conference on Flow-Induced Vibration.
- [8] Nakiboğlu, G., Belfroid, S. P. C., Tonon, D., Willems, J., and Hirschberg, A., 2009. "A parametric study on the whistling of multiple side branch system as a model for corrugated pipes". No. PVP2009-77754, ASME-PVP.
- [9] Tonon, D., Landry, B., Belfroid, S., Willems, J., Hofmans, G., and Hirschberg, A., 2010. "Whistling of a pipe system with multiple side branches: Comparison with corrugated pipes". *Journal of Sound and Vibration*, **329**(8), pp. 1007–1024.
- [10] Nakiboğlu, G., Belfroid, S., Willems, J., and Hirschberg, A., 2010. "Whistling behavior of periodic systems: Corrugated pipes and multiple side branch system". *International Journal of Mechanical Sciences*, **52**(11), pp. 1458–1470.
- [11] Nakiboğlu, G., Belfroid, S. P. C., Golliard, J., and Hirschberg, A., 2011. "On the whistling of corrugated pipes: effect of pipe length and flow profile". *Journal of Fluid Mechanics*, **672**, pp. 78–108.
- [12] Kristiansen, U. R., Mattei, P. O., Pinhede, C., and Amielh, M., 2011. "Experimental study of the influence of low frequency flow modulation on the whistling behavior of a corrugated pipe". *The Journal of the Acoustical Society of America*, **130**, pp. 1851–1855.
- [13] Nakiboğlu, G., Rudenko, O., and Hirschberg, A., 2012. "Aeroacoustics of the swinging corrugated tube: Voice of the dragon". *The Journal of the Acoustical Society of America*, **131**, pp. 749–765.
- [14] Nakiboğlu, G., Manders, H. B. M., and Hirschberg, A. "Aeroacoustic power generated by a compact axisymmetric cavity: prediction of self-sustained oscillation and influence of the depth". *Journal of Fluid Mechanics*, Submitted.
- [15] Nakiboğlu, G., and Hirschberg, A. "Aeroacoustic power generated by multiple compact axisymmetric cavities: Effect of hydrodynamic interference on the sound production". *Physics of Fluids*, Accepted.
- [16] Kop'ev, V., Mironov, M., and Solntseva, V., 2008. "Aeroacoustic interaction in a corrugated duct". *Acoustical Physics*, **54**, pp. 197–203.
- [17] Daugherty, R., Franzini, J., and Finnemore, E., 1989. *Fluid mechanics with engineering applications: SI metric ed.* McGraw-Hill.



Modeling of Combustion Oscillation Experienced in Micro Gas Turbine Combustor Fueled by Biomass Gas

Shigehiko KANEKO

Department of Mechanical Engineering
University of Tokyo
7-3-1 Hongo, Bunkyo-ku, Tokyo, Japan
Email: kaneko@mech.t.u-tokyo.ac.jp

Hosung HWANG

Department of Mechanical Engineering
University of Tokyo
7-3-1 Hongo, Bunkyo-ku, Tokyo, Japan
Email: hhwang@fiv.t.u-tokyo.ac.jp

Daisuke YAMASAKI

Department of Mechanical Engineering
University of Tokyo
7-3-1 Hongo, Bunkyo-ku,
Tokyo, Japan

Tatsuo WATANABE

Department of Mechanical Engineering
University of Tokyo
7-3-1 Hongo, Bunkyo-ku,
Tokyo, Japan

Yudai YAMASAKI

Department of Mechanical Engineering
University of Tokyo
7-3-1 Hongo, Bunkyo-ku,
Tokyo, Japan

ABSTRACT

In this paper, combustion oscillation model capable of explaining the effects of various fuel components contained in biomass gas is presented. This model is an extension based on ignition-delay model, originally proposed by Z. M. Ibrahim for single gas component, where the effect of various fuel components to ignition-delay time has not been considered. We evaluated the ignition-delay time by CHEMKIN and considered the effects of various fuel components. As a result, it was found that H₂ tends to cause unstable thermo acoustic oscillations. Incombustible components, such as CO₂ and N₂ had effects to suppress the combustion oscillation. Also, combustion experiments were performed with quartz premixed combustor system with various fuel components and compared with results calculated based on proposed model

NOMENCLATURE

E	energy in a cycle
L	length of the combustor
Q_{loss}	loss of heat
c	speed of sound
e	acoustic energy
n	heat/pressure interaction index
p	pressure
p'	fluctuation of pressure
q	heat release rate density
q'	heat release rate fluctuation
u	velocity of flow
x_f	flame location

α	amplification/attenuation rate of acoustic energy
γ	specific heat ratio
ρ	density
τ	ignition delay time
ω	angular frequency

INTRODUCTION

Recently, due to the interests for environmental problems, high efficiency and low NO_x emission properties are demanded for gas turbine combustors. Lean premixed combustion, burning air-fuel premixed gas in combustion chamber, has suitable features for modern combustors due to wider range of combustion area and low maximum flame temperature.

Beside of advantages to the lean premixed combustion, its flame has tendency to be unstable, commonly called combustion instability. The combustion instability includes various unstable flame phenomena such as combustion oscillation, blow out, flashback and etc. Combustion oscillation is a thermo-acoustic oscillation phenomenon, caused from thermo-acoustic coupling leads to large scale oscillation of pressure and flow speed.[1].

Biomass gas is considered to be an alternative energy source as renewable energy. In gas turbine industry biomass fuel is able to replace natural gas, conventional fuel. The benefit of using biomass gas as a fuel is environmental feature called carbon neutral. Because the sources of the fuel are plants on the ground, carbon dioxide in the air does not increase. The composition of the biomass gas varies by the sources, producing method. Biomass made from pyrolysis, one of the producing method of biomass fuel, is mainly composed of various components of gases as CH₄, H₂, CO, CO₂, N₂. However, these components in the biomass fuels can affect to combustion oscillation due to different combustion properties of components[2-4]. Besides,

Integrated coal Gasification Combined Cycle (IGCC), has similar fuel composition to pyrolysis gas, needs to be operational with the consideration on the effect of various fuel components.

Z.M. Ibrahim suggested combustion instability predicting model of single composition fuel based on theory of energy transfer between heat and acoustic. Analysis was compared with experimental results showing good match of them[5].

Janus conducted experiments and analytic calculations with various fuel mixtures, inlet temperature, inlet velocity, equivalence ratio. Delay time, summation of mixing time, ignition delay time, is shown as key parameter of combustion oscillation[6].

Santavicca performed combustion experiments with mixed gas of natural gas and hydrogen. The two-dimensional heat distribution of internal combustor and pressure fluctuation was measure. It was shown that heat distribution is closely related with combustion oscillation[2].

Samuelson calculated ignition delay time of IGCC type fuels and confirmed match with experimental results. Proportion of carbon monoxide in methane/carbon monoxide mixture shown little effect on ignition delay time. Besides hydrogen is dominant parameter of various composition fuels[7].

In this paper, the effect of fuel composition to combustion oscillation is investigated and a method for considering fuel composition to combustion oscillation modeling is suggested. Experiments were performed with premixed combustion system with various compositions of fuel.

MODELLING

In this section, analytic method of predicting occurrence of combustion oscillation in various fuel composition. Based on Ibrahim's model, effect of fuel composition is reflected in ignition delay time, which is dominant parameter of the oscillation model. Ignition delay time is calculated with chemical reaction calculation tool, CHEMKIN.

Criterion of Rayleigh

Combustion oscillation is a phenomenon of the thermal acoustic oscillation. Thermal acoustic oscillation is self-excited vibration excited by mutual interaction of pressure, heat release and fluid. Rayleigh's criterion is an equation which associates three factors. Rayleigh's criterion is shown as Eq. (1).

$$\Delta E = \int_L \frac{(\gamma-1)}{\rho c^2} p' \cdot q' dx - Q_{loss} > 0 \quad (1)$$

The equation indicates that the oscillation occurs if pressure fluctuation p' and heat release fluctuation q' is in same phase, and acoustic energy fluctuation in one oscillation cycle ΔE is positive. When ΔE is positive acoustic energy in

combustor increases in every cycle and diverge. In case of $\Delta E < 0$ acoustic energy of combustor converge and preserve stability.

Combustion Oscillation Model

Based on the theory of Rayleigh's criterion, $n - \tau$ model is proposed by Ibrahim[5] to estimate the occurrence of combustion oscillation. Appearance of oscillation is determined by the eigenvalue which can be obtained from conservation of acoustic energy. The oscillation occurs when eigenvalue is positive. Conservation of acoustic energy is written as

$$\frac{\partial e}{\partial t} + \frac{\partial}{\partial x} (p'u') + \frac{\partial}{\partial x} (e\bar{u}) - \Phi = 0 \quad (2)$$

where Φ is dissipating acoustic energy per unit volume, which shows reciprocal action between pressure and heat release. Φ can be written as

$$\Phi = \frac{(\gamma-1)}{\rho c^2} p'q' - \frac{\partial u'}{\partial x} \tau \quad (3)$$

Assuming fundamental mode, the distribution of flow speed, pressure and heat release can be schematically shown as Fig. 1. Flame location, used in following equation, is determined by ignition delay time τ and flow speed u . Solution of acoustic energy can be solved from Eq. (2) and Eq. (3) as follow,

$$\Delta E = e_0 e^{\alpha t}, \alpha_{amp} = n(\gamma-1) \frac{q}{p} \left[\cos\left(\frac{\pi x_f}{2L}\right) \right]^2 \cos(\omega\tau) \quad (4)$$

where α_{amp} is the amplification coefficient. Considering damping effect, α_{damp} is decay rate of the acoustic energy by damping effect, consequently, substantial amplification coefficient can be expressed as $\alpha = \alpha_{amp} - \alpha_{damp}$. Wall

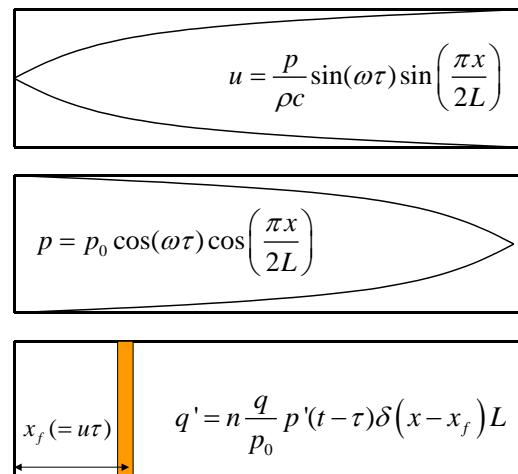


Fig. 1 Schematic illustration of $n - \tau$ model.

damping is the most effective damping element in the combustor. α_{damp} for wall damping is estimated as

$$\alpha_{damp} = \frac{\int_A e_{wall} dA}{2\bar{e}V} \quad (5)$$

Where

$$e_{wall} = \frac{1}{2} \left(\frac{T_{wall}}{T_{comb}} \right)^2 |\bar{u}|^2 \sqrt{\frac{\omega \rho_{wall} \mu_{wall}}{2}} \quad (6)$$

is obtained from time-dependent momentum equation. e_{wall} indicates acoustic energy attenuation at the combustor wall, \bar{e} is average acoustic energy per time. Wall temperature T_{wall} , combustion temperature T_{comb} is assumed as $900^\circ C$. Eq. (6) shows that wall damping is proportional to $\sqrt{\omega}$, which intends higher damping effect at higher frequency, and therefore oscillation is difficult to occur.

Combustion Oscillation Model for Biomass Fuel

The effect of fuel composition to ignition delay time τ was investigated. τ is dominant parameter in $n - \tau$ model, and varies by components of the fuel. Composition of CH_4 , H_2 , CO , CO_2 , N_2 are used to calculate ignition delay time of biomass fuel. Numerical analysis was performed to calculate delay time by CHEMKIN(Reaction Design). GRI-mech 3.0 was used for analyzing chemical reaction mechanism. GRI-mech 3.0 is a detailed chemistry reaction mechanism and

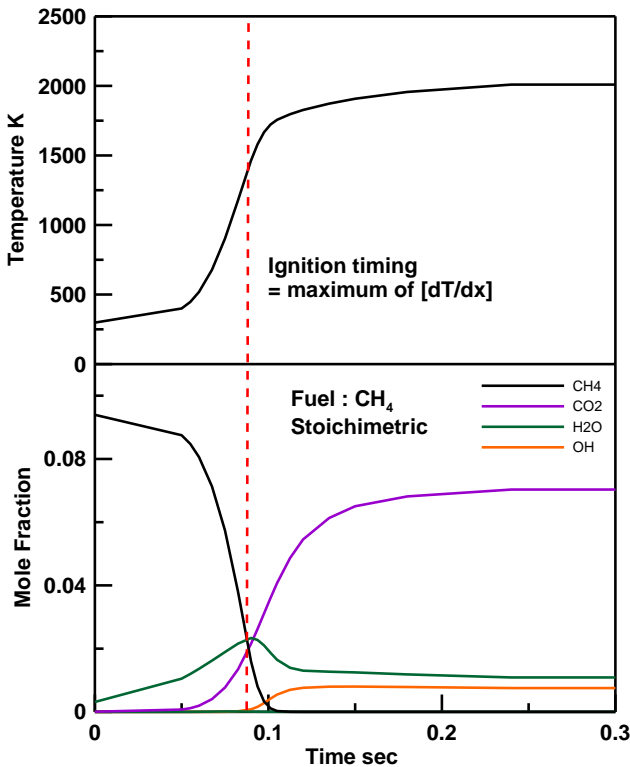


Fig. 2 Calculated ignition delay time of low calorific gas.

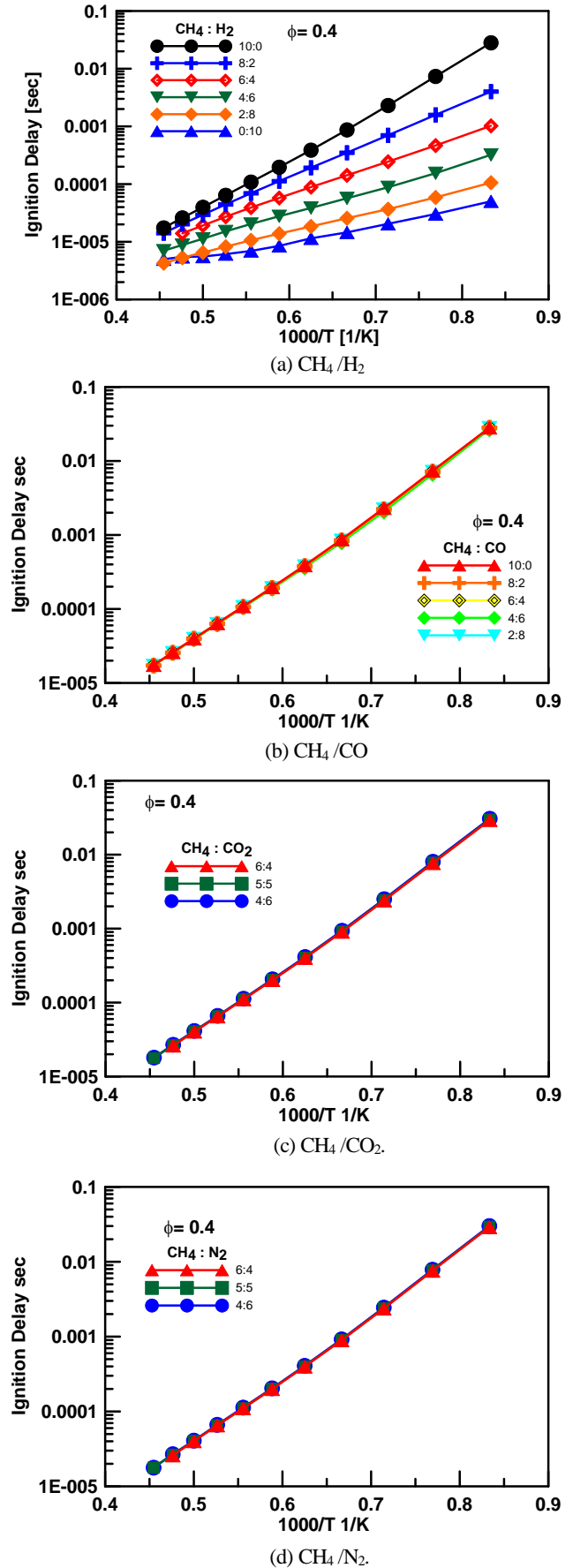


Fig. 3 Effect of fuel composition to ignition delay time.

contains 325 reactions of 53 species.

Chemical reaction is calculated in time periods. For example, reaction of methane in 1[atm] is calculated as Fig.2. Reactant (CH₄) is decreased and products of reaction (CO₂, H₂O) are increased as reaction proceeds. Temperature is also raised by heat of reaction. To determine delay time, period of maximum temperature gradient from beginning of reaction is selected as maximum heat release point during reaction.

The relationship between inlet temperature and ignition delay time of various mixed gas fuel are calculated. To examine each components of biomass fuel, calculation was carried with cases of CH₄ / H₂, CH₄ / CO, CH₄ / N₂, CH₄ / CO₂ mixtures. The result of CH₄/H₂ mixture is shown as Fig. 3 (a). Ignition delay time decreases at higher inlet temperature, due to higher internal energy at initial. Linear relationship between logτ and 1000/T in same composition of fuel is shown well. As proportion of H₂ increases, the graph shows shorter ignition delay time. The difference among CH₄/H₂ mixtures is wider when inlet temperature is low. Delay time of CO, N₂, CO₂ with CH₄ mixture show no difference as composition varies (Fig. 3 (b) (c) (d)). This result shows ignition delay time of biomass fuel is decided by composition of combustible gas : CH₄, H₂, CO. Moreover, proportion of CH₄ and CO has no effect on ignition delay time, Ignition delay time of the fuel is able to be determined from proportion of H₂ in all combustible components in the fuel.

Ignition delay time and 1000/T is in linear relationship as mentioned above. Therefore relationship between ignition delay time τ and combustion temperature can be written as Eq. (7)[8]

$$\tau = c \exp\left(\frac{E}{RT}\right) \tag{7}$$

where *c* is constant, *E* is activation energy, *R* is universal gas constant. To evaluate delay time with combustion temperature, effect of composition to constants *c*, *E* and *R* was examined from the result of ignition delay time of CH₄ and H₂, since CH₄ and H₂ are only components in biomass gas that affects to delay time. From the result of Fig. 3 (a), assuming that relation between *c*, *E/R* and *p_{H2}* are in linear, the constants are approximated by Eq. (8), (9)

$$c = -12.53 p_{H2} + 18.02 \tag{8}$$

$$\frac{E}{R} = 3 \times 10^{-4} p_{H2} - 3 \times 10^{-5} \tag{9}$$

where *p_{H2}* is proportion of H₂ in the fuel.

Amplification rate of acoustic energy α amp in Eq. (4) was calculated with obtained ignition delay time from Eq. (7), (8) and (9). The compositions of fuels, used in calculation are shown in Table 1. The result of ignition delay time is shown as Fig. 4. CH₄/H₂ mixture and pyrolysis shows shorter delay time due to H₂ is included. Delay time of pyrolysis is the shortest, since proportion of H₂ in flammable gases is higher than CH₄/H₂ mixture gas. Amplification rate of acoustic energy are calculated with calculated ignition delay time (Fig. 5). Other constants in Eq.(4) were assumed as *n* = 0.05. *L* = 0.03 m, *p* = 1 atm. Above 0 is unstable area where coefficient of acoustic energy diverges and oscillation occur, under 0 area is stable. Inlet temperature is used for temperature *T* and frequency is determined as resonant frequency 750 Hz (= *c* / 4*L*). Compositions of the fuel were shown as Table 1. The result shows, α of CH₄ single fuel has turned positive at 800°C. But CH₄ with H₂, α conversed at lower temperature than CH₄, 700°C. Lower inlet temperature of premixed gas contains lower heat value, and results in lower heat release rate. As Eq. (4), although low heat release rate decreases amplification of acoustic energy at low temperature, short ignition delay time of H₂ affected the equation to be more high α than CH₄. CO₂ and N₂ had effect of relieving oscillation that, α was under 0 at all the temperature.

Table 1 Components of low carolific gas.

	CH4	H2	CO2	N2	CO
CH4	100				
CH4 / H2	60	40			
CH4 / CO2	60		40		
CH4 / N2	60			40	
pyrolysis	3	30	30	20	17

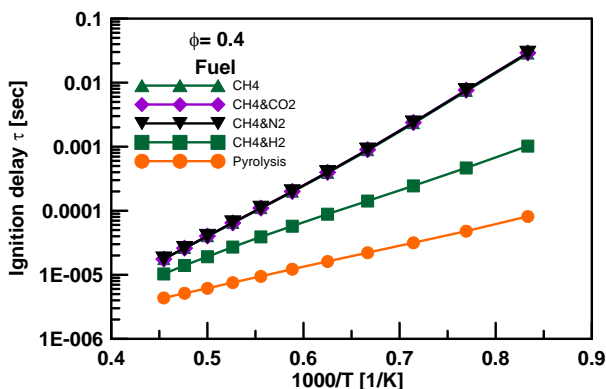


Fig. 4 Calculated ignition delay time of low calorific gas.

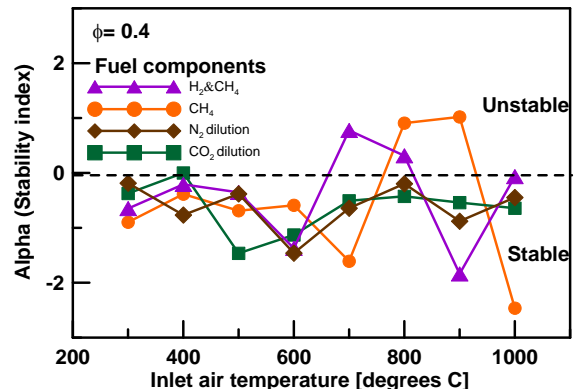


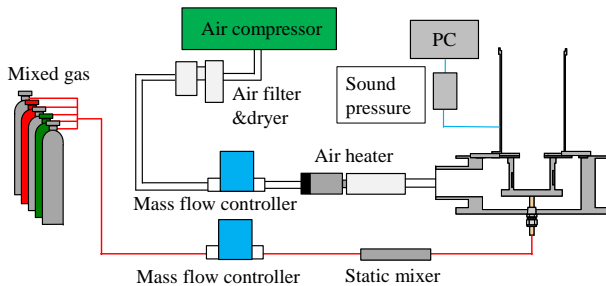
Fig. 5 Calculated stability index of mixed gas.

EXPERIMENT

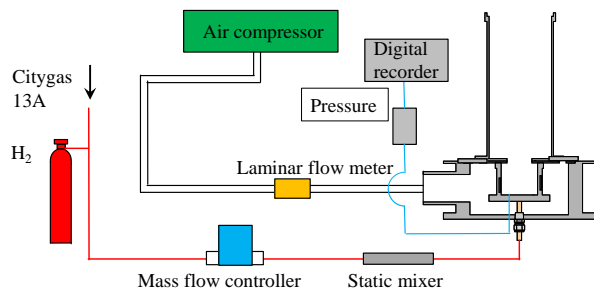
Experiments were carried out to compare with analytic model and verify propriety of the model. The effect of H₂ in fuel and intensity of swirl in internal combustor to combustion oscillation is also investigated. Occurrence of combustion oscillation is measured in sound pressure level or pressure fluctuation.

Experiment Apparatus

Combustion experiments were performed to examine effect of biomass gas composition to combustion oscillation. Schematic experiment rigs and combustors are shown as Fig. 6 and Fig. 7. Two systems are used for the test. Air heater was equipped at System A for variable inlet air temperature and inlet air flow controlled by mass flow controller. Mixed gas of CH₄, H₂, CO, CO₂, N₂ is supplied as fuel. Sound pressure is measured to estimate occurrence of oscillation. The length of combustor is 235 mm and diameter of quartz

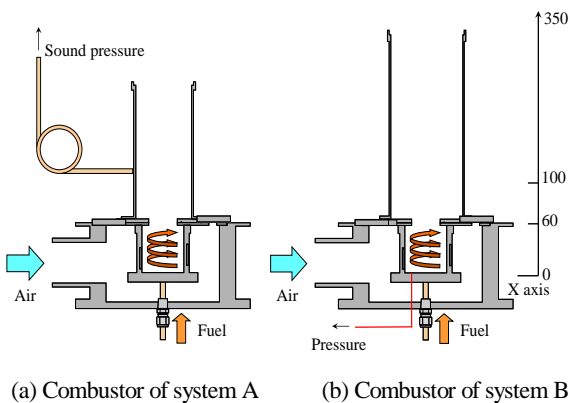


(a) Experiment system A



(b) Experiment system B

Fig. 6 Schematic illustration of experimental rigs.



(a) Combustor of system A

(b) Combustor of system B

Fig. 7 Combustors of experiment system.

liner is 76 mm. By contrast, air heater and mass flow controller for inlet air is removed for system B. Flow of inlet air is measured with laminar flow meter. Mixed gas of city gas 13 A and H₂ is used for the fuel and pressure fluctuation is measured by piezoelectric pressure gauge of internal combustor. Length of combustor is 335mm and diameter of quartz liner is 105.5 mm.

Effect of Inlet Air Temperature and Fuel Composition

The result of sound pressure of internal combustor at various fuel and inlet air temperature is shown in Fig. 8. The test is carried out with system A and the same fuel compositions are used as analytical method, shown as Table 1. Equivalent ratio and input energy were unified as $\phi = 0.4$, $Q_{in} = 276$ kJ/min. Combustion oscillation occurred above 108 dB of sound pressure. Sound pressure tended to be higher with increasing inlet air temperature risen. The

Table 2 Mean temperature of internal combustor

Composition of fuel	Mean temperature [°C]
CH ₄	837.7
CH ₄ & H ₂ 7:3	806.9
CH ₄ & H ₂ 6:4	800.2
CH ₄ & CO ₂	660.3
CH ₄ & N ₂	734.1

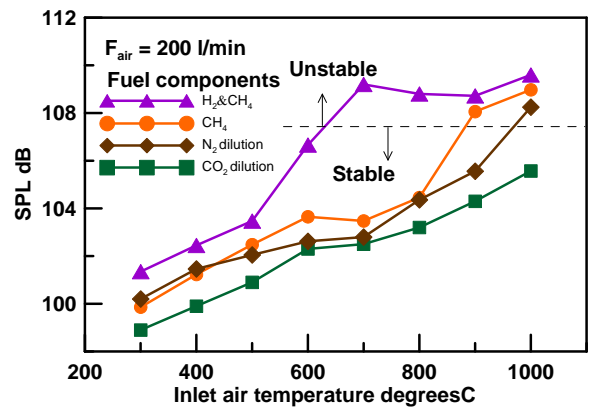


Fig. 8 Experimental result of flame stability.

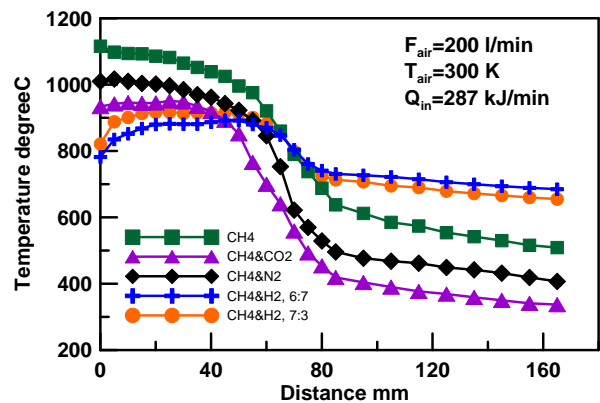


Fig. 9 Internal temperature of combustor.

temperature which flame converted into unstable was at 900 °C with CH₄, 700 °C with mixed gas of H₂ and CH₄. Oscillation did not occur at all range of inlet temperature, if CH₄ was diluted by CO₂ or N₂. This result was very close to the result obtained by the analytical method which was

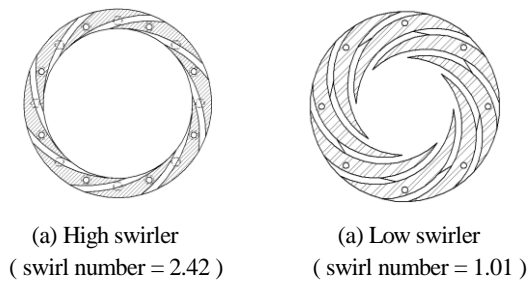


Fig. 10 Schematic illustration of swirlers.

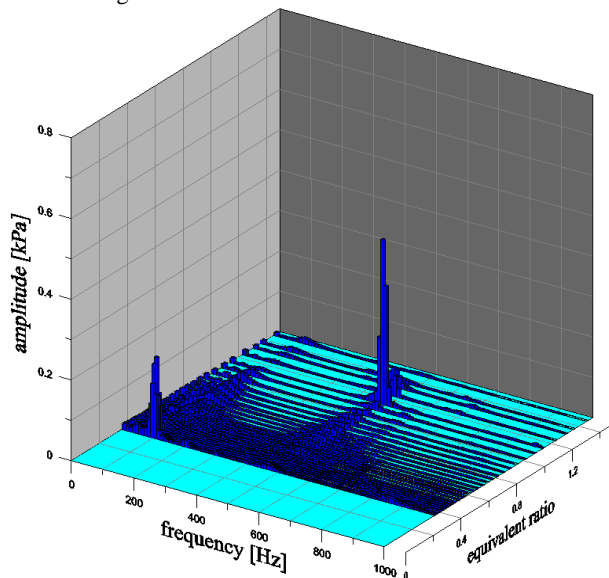
shown as above. Both results show oscillation inducing effect of H₂ and oscillation relieving effect of CO₂ and N₂.

Internal Temperature of Combustor

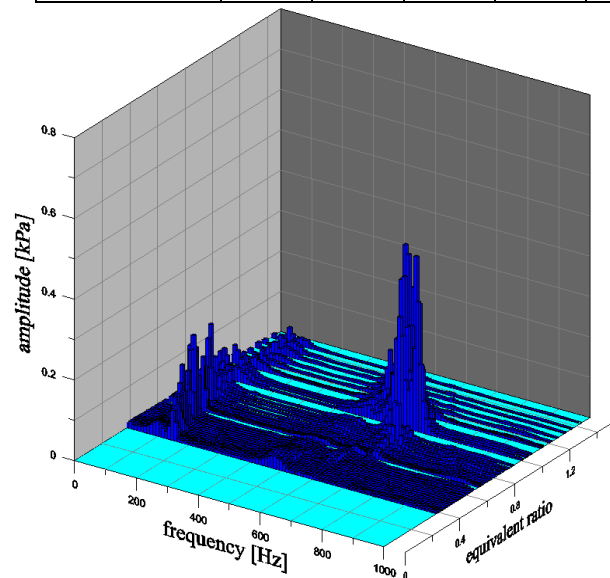
Internal temperature of combustor is measured with R-

Table 3 Experimental conditions.

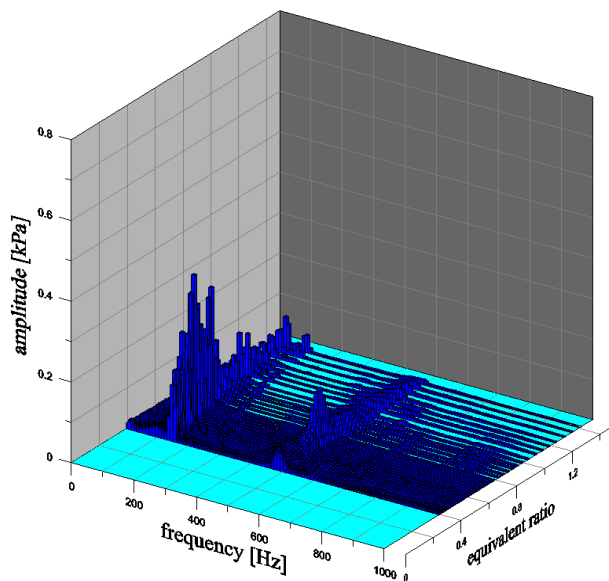
Fuel flow rate [L/min]	50	52	100	103	128
% 13A / %H ₂	100/0	96/4	100/0	96/4	70/30
Heat input [kJ/s]	8.03	8.16	16.17	16.16	16.13



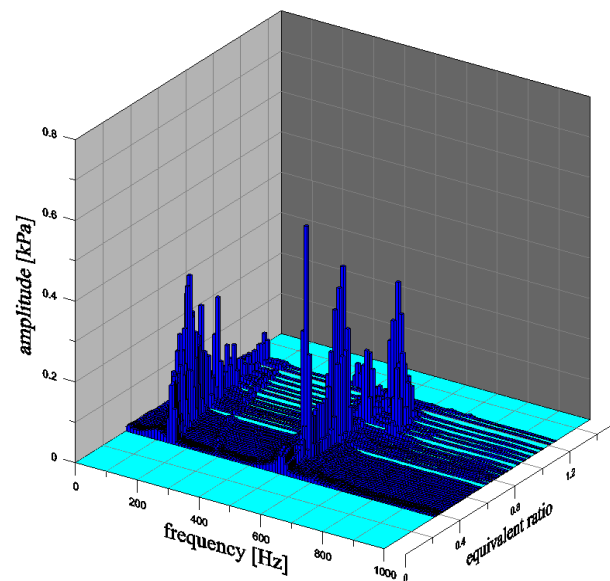
(a) $F_{\text{fuel}} = 50$ L/min, 13A, $Q_{\text{in}} = 8.03$ kJ/s, high swirl



(b) $F_{\text{fuel}} = 100$ L/min, 13A, $Q_{\text{in}} = 16.17$ kJ/s, high swirl



(c) $F_{\text{fuel}} = 103$ L/min, 13A, $Q_{\text{in}} = 16.16$ kJ/s, low swirl



(d) $F_{\text{fuel}} = 128$ L/min, 70% 13A / 30% H₂, $Q_{\text{in}} = 16.13$ kJ/s, low swirl

Fig. 11 Experimental results for 13A / H₂ mixed

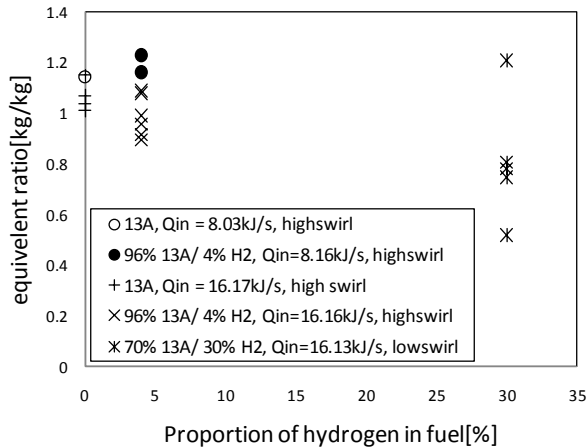


Fig. 12 Relationship between proportion of hydrogen in fuel and combustion oscillation occurred equivalent ratio.

type thermocouple through the center line of combustor. The result is shown in Fig. 9. To identify the location of thermocouple, distance is measured from the bottom of the combustor. Temperature descends radically after 60 mm where the flame holder ends. CH₄ / H₂ mixture shows lower temperature at short distance, because of water vapor is produced by combustion of H₂, which has large specific heat. By the same reason, temperature descending is relieved after 60 mm. Mixed gas with incombustible gas, such as CO₂ and N₂ showed low temperature at all distance. Table 2 shows mean temperature of combustor. H₂ had little effect of descending mean temperature, but CO₂ or N₂ mixed gas show difference about 100 °C or more with CH₄. Low temperature of combusted gas leads to less occurrence of oscillation.

Effect of Equivalence Ratio and Swirl Number

Fig. 10 shows two types of swirler which is used in System B. Low swirler was designed to have smaller inner diameter to get low swirl number by raising axial velocity of flow.

Experimental conditions are shown in Table 3. The fuels were composed of city gas 13A and H₂. Equivalent ratio was controlled by increasing flow rate of the air. Pressure fluctuation was measured by piezoelectric pressure sensor installed on the wall of the bottom at internal combustor and analyzed by fast fourier transform (FFT). The results are shown in Fig. 11. The oscillation at near 100 Hz was confirmed to the influence of air compressor by experiment in non-combustion situation.

Combustion oscillation occurred near 500 Hz, $\phi = 1.14$ (Fig. 11 (a)). The range of the frequency and equivalent ratio was wider at larger heat input (Fig. 11 (b)), since more heat was converted to the pressure fluctuation. Oscillation was diminished by low swirler (Fig. 11 (c)), which has higher axial flow speed. The reason of low fluctuation level is expected that location of flame has changed by axial flow speed and the location affects to the oscillation as seen in Eq. (4). In all condition low swirler was used, combustion oscillation did not occur, except 70% 13A/ 30% H₂. Fig. 10

(d) shows oscillation inducing effect of hydrogen at most of the equivalent ratio range in spite of heat input was same as Fig. 11 (c). Delay time shortens by H₂ as mentioned above, consequently, flame location supposed to be shorter as opposite effect of low swirl number. Fig. 11 shows the relationship between proportion of hydrogen and oscillation occurred equivalent ratio. Without hydrogen, oscillation occurs at narrow range of 1~1.1, but 96% 13A/4% H₂ fuel generates oscillation at 0.9 ~ 1.2. Oscillation was observed at almost all range of operative equivalent ratio, when 70% 13A/30% H₂ fuel is used.

CONCLUSIONS

It was shown that ignition delay time of various composition of fuel was calculated and the delay time was shortened by the effect of hydrogen. Combustion oscillation was induced by hydrogen contained fuel, because of short ignition delay time. Not only increasing level of oscillation, but also oscillation occurring range of equivalent ratio was widen.

Ignition delay time can be estimated by fuel composition, which made possible to consider fuel composition to combustion oscillation model.

Inflammable components such as N₂, CO₂ had effect of relieving oscillation. Lower mean temperature, due to larger specific heat, was effective to reduce oscillation.

Combustion oscillation was tended to occur at high swirl number, whether hydrogen is combined or not.

REFERENCES

- [1] T. C. Lieuwen, V. YANG, Combustion Instabilities in Gas Turbine Engines, AIAA, Reston, USA, (2005).
- [2] D. A. Santavicca, The Effects of Fuel Distribution, Velocity Distribution, and Fuel Composition on Static and Dynamic Instabilities and NO_x Emissions in Lean Premixed Combustors, The Pennsylvania State University, 2007
- [3] M. C. Janus, G. A. Richards, M. J. Yip, E. H. Robey, Effects of Ambient Conditions and Fuel Composition on Combustion Stability, *ASME Turbo Expo*, 1997
- [4] M. Lee, S. Seo, J. Chung et al., Gas turbine combustion performance test of hydrogen and carbon monoxide synthetic gas, *Fuel* 89 (2010) 1485-1491.
- [5] Z. M. Ibrahim, F. A. Williams, and S. G. Buckley, An Acoustic Energy Approach to Modeling Combustion Oscillations, *ASME Turbo Expo 2006: Power for Land, Sea and Air*, 2006.
- [6] M.C.Janus, G.A. Richards, Effects of Ambient Conditions and Fuel Composition on Combustion Stability, *1997 ASME International Gas Turbine (IGTI) Turbo Expo Meeting*, 1997.
- [7] S. Samuelson, Correlation of Ignition Delay with Natural Gas and IGCC Type Fuels, University of California, 2006.
- [8] Y. Mizutani, *Combustion Engineering*, Third Ed. Morikita Publishing Company, Tokyo, Japan, (2002), pp. 61 – pp. 74.

STEEL ROD BREAKING EXCITATION TO IDENTIFY FULL-SCALE TAITNER GATE DYNAMICS

Keiko Anami¹

Division of Mechanical and
Electrical Engineering
Ashikaga Institute of
Technology
Ashikaga, Tochigi, Japan
Email: anami@ashitech.ac.jp

Noriaki Ishii

Department of Mechanical
Engineering
Osaka Electro-
Communication University
Neyagawa, Osaka, Japan
Email: ishii@isc.osakac.ac.jp

Charles W. Knisely

Department of Mechanical
Engineering
Bucknell University
Lewisburg, PA, USA
Email: knisely@bucknell.edu

Takuma Tsuji

Osaka Electro-
Communication University
Neyagawa, Osaka, Japan
Email: d10201@oecu.jp

Tatsuya Oku

Mayekawa Co. Ltd.
Moriya, Ibaraki, Japan
Email: tatsuya-
oku@mayekawa.co.jp

Toshiaki MAKIHATA

Consultant
Takatsuki, Osaka, Japan
Email: makihata@smel.jp

ABSTRACT

Field vibration tests were conducted on operational full-scale Tainter gates in the USA using the tensile failure of a machined steel rod to provide impulsive excitation to the gates. The specific intent of the tests was to advance the state-of-the-art knowledge of the coupled-mode instability mechanism for such gates. The tests provided clear identification of the gates' inherent in-water vibration characteristics; ambient excitation was unable to identify these dynamic characteristics of the gates. Subsequently, the previously developed theoretical analysis was applied to the tested gates to expose an essential dynamic instability for these installations, as well as to provide a framework for the design of a retrofit and an optimized maintenance plan.

INTRODUCTION

Tainter (radial) gates are used world-wide as dam crest gates for regulation and flood release. On July 17, 1995, one of the massive Tainter gates at the Folsom Dam in California experienced failure, possibly as a result of flow-induced vibrations, as described by Ishii (1995). Figure 1 shows the photo just after the gate failure with substantial unrestrained discharge. The gate operator stated that at his position on the catwalk over the gate, he felt a small steady vibration which rapidly intensified. In 1967, a similar Tainter gate failure occurred in Japan. A Tainter gate at the Wachi Dam in Kyoto prefecture, failed suddenly at a small gate opening, and was swept downstream, as described by Ishii & Imaichi (1980) and Ishii, et al. (2011).

Tainter gate failures such as those experienced at the Folsom and Wachi Dams do not happen frequently. However, it is well known that many Tainter gates cannot



Figure 1: Tainter gate failure of an 87-ton gate at the Folsom Dam in California (USA) on July 17, 1995.

be operated at small gate openings, since they are very susceptible to self-excited vibration. In the hopes of preventing a recurrence of such Tainter gate failures, the authors have persistently pursued a rigorous research program. The studies involved laboratory testing of two- and three-dimensional model gates (Anami, et al., 2003; 2006), full-scale field tests on operational gates (Ishii et al., 2009a; 2009b), as well as theoretical analyses (Anami, et al., 2004; 2007). The conclusion from this series of studies was that the underlying mechanism behind the failure of these two gates was an essential dynamic instability to which all Tainter gates may be susceptible (see Anami, 2002).

Clearly, it is imperative to identify gates that do indeed possess susceptibility to this dynamic instability, and subsequently take measures to prevent future failure of these susceptible gates. To assure the complete stability and long-term safe operation of the tremendous number of

¹ 268-1 Omae-cho, Ashikaga, Tochigi 326-8558, Japan

Tainter gates used all over the world, an effective method of distinguishing susceptible gates from unsusceptible gates is absolutely necessary.

This paper presents an effective and reliable method of excitation of Tainter gates, analogous to impact testing of less massive structures. The method permits the identification of the dynamic characteristics of the gate, which are indicative of the gate's potential for dynamic instability. Initially, examples of the use of the steel rod tensile failure method on operational, full-scale Tainter gates are presented. In the testing, low levels of damped vibrations of the Tainter gate in running water were triggered by breaking a small-diameter, machined steel rod attached to the bottom center of the skinplate and anchored to the surface of the dam crest. The steel rod breaking tests permitted the identification of the gate's natural in-water vibration frequencies and mode shapes, as well as, through analysis of these modes shapes and frequencies, the gate's susceptibility to the coupled-mode dynamic instability.

Subsequently, similar measurements undertaken with ambient excitation (without an impulsive input trigger such as that supplied by the steel rod breaking method) show that ambient excitation is incapable of identifying the gate's susceptibility to the coupled-mode dynamic instability mechanism.

A previously developed theoretical analysis is then applied to the tested gates to identify whether the gates, under the operational conditions tested, were susceptible to the essential dynamic instability. Finally, the effect of the magnitude of impulsive excitation, such as that supplied by the breaking of the steel rod, in overcoming friction maintained dynamic stability is demonstrated in a model study.

MECHANISMS OF COUPLED-MODE SELF-EXCITED VIBRATION

Tainter gates dynamics can be characterized by two predominant in-air natural vibration modes as illustrated in Figure 2. One mode is the rigid body vibration of the whole gate about the trunnion pin and other is a streamwise bending vibration mode of the skinplate, as described by Ishii (1995) and Anami et al. (1998). With the gate exposed to flowing water, these two natural vibration modes can couple through inertial and hydrodynamic forces, as documented in Anami, et al. (1998). This type of coupled-mode vibration is accompanied by a fluctuation in the gate's discharge (*i.e.*, a flow rate variation), and is capable of inducing violent, destructive self-excited vibrations.

Figure 3 shows a closed loop energy cycle of the coupled-mode self-excited vibration. If any random excitation triggers the streamwise vibration of the skinplate, the resulting skinplate inertial torque excites the whole gate motion around the trunnion pin. Whole gate rotary motion produces a flow-rate variation, with an accompanying flow-rate-variation pressure. If the bottom end of the skinplate behaves as a press-shut device (a

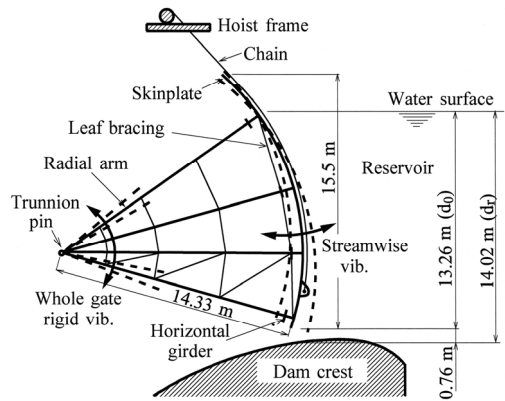


Figure 2: Side view of 87-ton Folsom Dam Tainter gate in California and its inherent vibration modes.

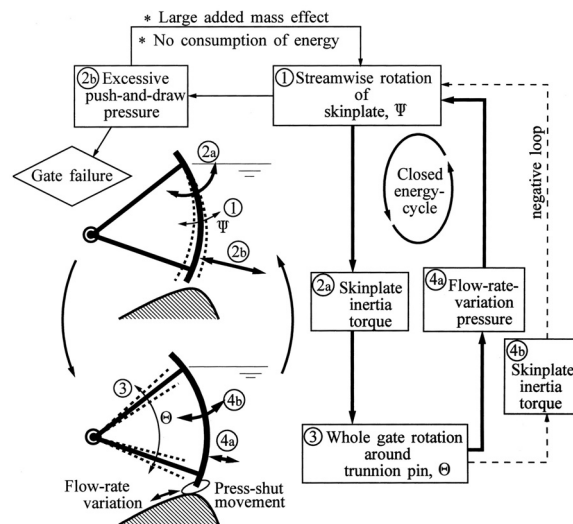


Figure 3: Closed loop energy cycle of coupled-mode flow-induced vibration, possible in Tainter gates.

device that tends to reduce gate opening with increased upstream head), the flow-rate-variation pressure feeds energy back to the skinplate streamwise vibration, thus amplifying its vibration amplitude, which in turn amplifies the torsional vibration around the trunnion pin. This type of coupled-mode self-excited vibration can occur naturally, even if the skinplate is concentric with the trunnion pin.

Of special note in this closed loop energy-cycle is that the streamwise skinplate vibration induces a push-and-draw pressure, which does not consume energy from the vibrating gate, but yields a large added mass effect. With the large added mass, the frequency of the in-air streamwise skinplate vibration mode is substantially reduced in flowing water, often coming dangerously close to the rigid body rotational frequency. If the two frequencies coalesce, the comparatively small amplitude flow-rate variation pressure can spontaneously amplify the amplitude of coupled-mode vibration.

Equations (1) and (2) describe this coupled-mode self-excited vibration:

$$\theta'' + 2\zeta_{a\theta}\theta' + \theta = -\frac{\alpha'_l}{\alpha_s}\psi'' \quad (1)$$

and

$$\begin{aligned} & (1 + \delta_p \alpha_{\psi} \Delta m_{\psi}^*) \psi'' + 2\gamma_{\psi\theta} (\zeta_{a\psi} + \zeta_{f\psi}) \psi' + \gamma_{\psi\theta}^2 \psi \\ & = \alpha_s \left\{ - \left(\alpha_{l\psi} + \sqrt{2} c_f \frac{\alpha_{\psi} \Delta m_{\theta}^*}{r_{sa}} \right) \theta'' + \sqrt{2} c_f \frac{\alpha_{\psi} \Delta c_{\theta}^*}{r_{sa} F_{a\theta}} \theta' \right\} \end{aligned} \quad (2)$$

Equation (1) represents the whole gate rigid-body vibration around the trunnion pin, and the Equation (2) represents the in-water streamwise vibration of the skinplate. The symbols θ and ψ represent the reduced vibration amplitude of the skinplate center and the whole gate around the trunnion pin, respectively.

The hydrodynamic pressure does not appear in Equation (1); the whole gate rigid-body vibration is excited by the inertia torque of the skinplate. On the other hand, the hydrodynamic pressure directly appears in the Equation (2). In Equation (2), the first term on right side represents the energy source that excites the streamwise vibration due to flow-rate variation under the gate (Anami et al., 2000).

The dynamic stability diagram for the gate can be determined from the simultaneous solution of Equations (1) and (2), using numerical computer-simulation to obtain the approximate solutions.

This fundamental mechanism applies not only to skinplate streamwise rotational vibration, but to streamwise parallel vibration of the skinplate. The inertial force caused by the streamwise parallel vibration induces a torque around the trunnion pin. This inertia torque, in turn, drives the whole gate vibration around the trunnion pin.

STEEL ROD BREAKING EXCITATION METHOD

The identification of the in-air and in-water natural vibration characteristics is essential in ascertaining the dynamic stability of Tainter gates. The in-air natural vibration characteristics can be determined by experimental modal analysis using an impact hammer. However, in water, the energy that can be input with an impact hammer is insufficient to determine accurately the in-water natural vibration characteristics, because of the large added mass of the water. To overcome this limitation, the authors proposed using the tensile failure of a machined steel rod (similar to a tensile test specimen) to input sufficient energy to excite the relevant mode shapes and provide accurate, repeatable data with a relatively simple experiment.

To provide a small initial impulsive force on the gate, a machined steel rod with a small diameter was installed between the bottom center of the skinplate and the spillway concrete, as shown in Figure 4. The gate was then gradually raised in a step-wise fashion until the steel rod fixed between the skinplate bottom and the dam crest was loaded past its capacity and broke suddenly. Common dimensions and a photo of the machined steel rod are

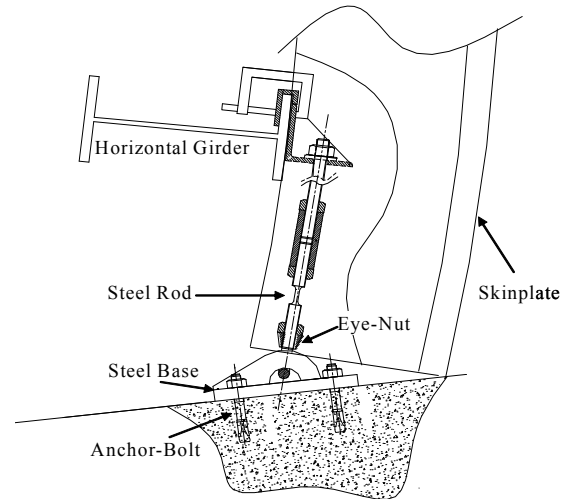
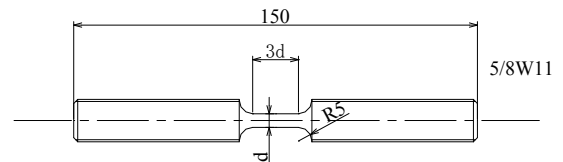


Figure 4: Installation of the steel rod between the skinplate bottom and spillway concrete apron.



(a) Dimensions



(b) Photo

Figure 5: Machined steel rod sample.

shown in Figure 5, where d represents the diameter of the neck of the steel rod, made of S45C steel (contains 0.45 % carbon).

The diameter d of the machined portion of the rod is critical to the method. If the diameter is too small, the impulsive load is insufficient to excite the vibration; if it is too large, too much excitation is provided to the gate and gate lifting system. Therefore, the diameter of the steel rod was carefully determined using the elongation-to-tension-load characteristics of the gate lifting chains. Based on our experience, the elongation of the lifting wires/chains due to the load of the steel rod resistance should not exceed about 1 mm to assure the safety of the gate.

For correct testing, it was essential that the operator stop raising of the gate immediately upon the breaking of the steel rod. A load cell was attached in series with the steel rod to measure the tension load.

TAITER GATE "T"

Results with Steel Rod Breaking Excitation

The field vibration test with the steel rod breaking excitation was undertaken on a 24-ton Tainter gate, as reported by Ishii, et al., (2009a). The upstream water level at the tested condition was close to maximum design level.

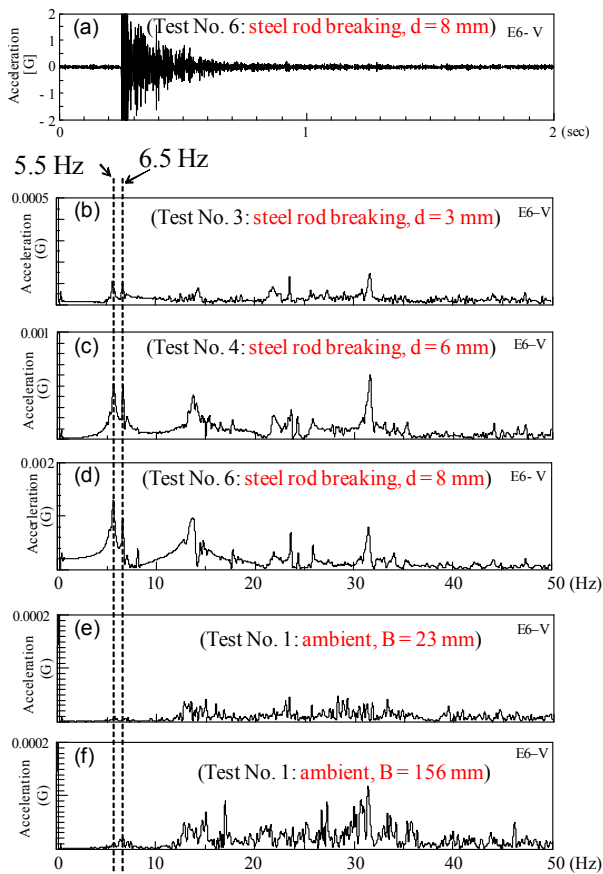


Figure 6: Real time waveforms and frequency power spectrum of Tainter gate "T": (a) Real time waveforms, (b),(c), and (d) acceleration power spectra measured after steel rod breaking excitation; (e) and (f) acceleration power spectra measured with ambient excitation.

The measured acceleration responses at the skinplate center position, triggered by the sudden failure of the steel rod are shown in Figures 6(a) to 6(d). Figure 6(a) shows the real time waveforms of the acceleration response in the vertical direction (tangential direction) at the skinplate bottom center, triggered by the sudden failure of an 8 mm diameter steel rod. The exponentially decaying vibration is evident. Figure 6(b), 6(c), and 6(d) represent the frequency power spectrum of the vertical direction at the skinplate bottom center, triggered by the sudden failure of a 3 mm diameter, a 6 mm diameter, and an 8 mm diameter steel rod, respectively. There are the sharp peaks at 5.5 Hz and at 6.5 Hz, both of which are quite significant when considering movement-induced self-excitation.

The natural vibration mode shapes were analyzed using spatial distributions of the amplitude and phase-lag of the damped vibratory response to the impulsive input provided by the breaking of the steel rod. The amplitude and phase difference data were used to create mode animations of the in-water natural vibrations simulated with a simple BASIC program. Simulated mode shapes are shown in Figure 7.

Figure 7(a) shows the vibration mode of the skinplate streamwise vibration with the frequency of 5.5 Hz. Based

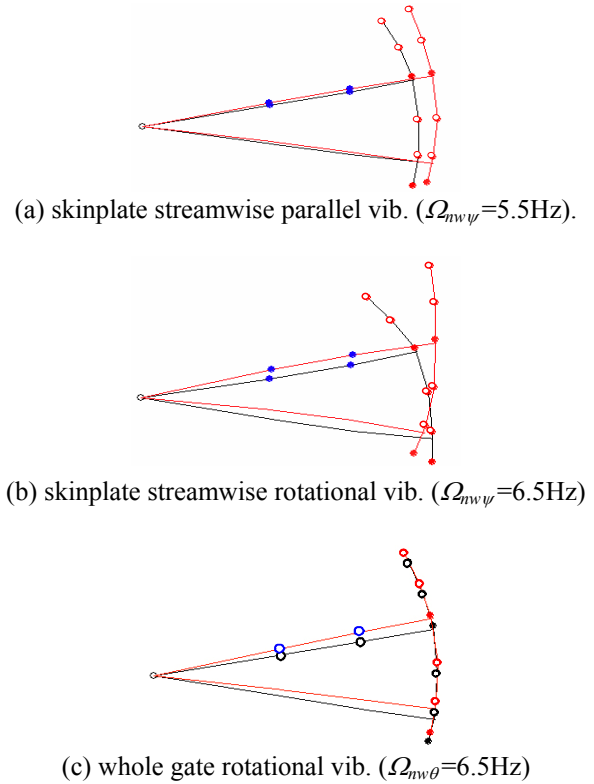


Figure 7: Simulated mode shapes of Tainter gate "T".

on the amplitude and phase modal analysis, the whole skinplate performs a streamwise “parallel vibration” in the press-shut direction (when the skinplate moves in the downstream direction, the whole gate also moves downward). The damping ratio estimated from the power spectra using the half-power method takes a comparatively large value between 0.016 and 0.030. Figure 7(b) and Figure 7(c) show two vibration modes with a frequency of 6.5 Hz. The skinplate undergoes streamwise rotational vibration in Figure 7(b), while vibrating in the tangential direction in Figure 7(c) at the same time, suggesting a streamwise rotational vibration coupled with a vertical vibration. The streamwise rotation center height is about 2.0 m from the bottom of the skinplate. The damping ratios take on small values between 0.011 and 0.015.

It should be noted here that these small damping ratios are due to the internal damping for small amplitude vibrations and do not include any Coulomb damping that would accompany large amplitude vibration.

Comparison of Steel Rod Breaking Excitation with Ambient Excitation

In the past, attempts have been made to measure in-water vibration characteristics by examining the gate’s response to the ambient excitation provided by water discharging through a fixed gate opening. Ambient excitation tests were conducted on gate “T” to assess its suitability in identifying the gate’s natural vibration characteristics.

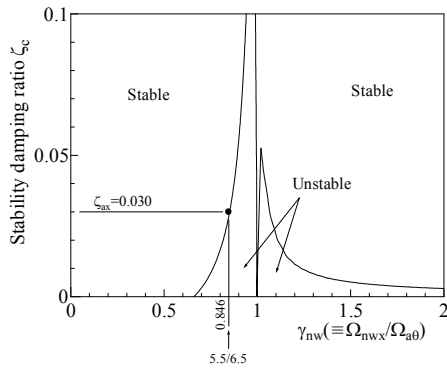
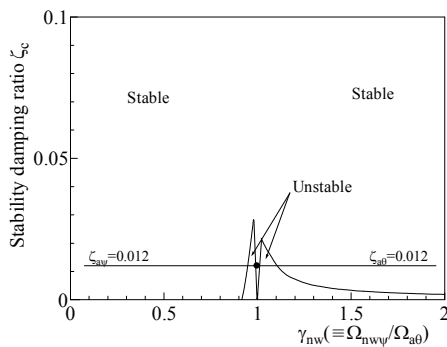

 (a) For coupling of mode M_{X1} and M_Z

 (b) For coupling of mode M_{X2} and M_Z

Figure 8. Dynamic stability criterion diagram for gate “T”

The acceleration power spectra, shown in Figures 6(e) and 6(f), and measured at gate openings of $B = 23$ mm and 156 mm, respectively, show many higher frequency components in the 15 Hz to 40 Hz range. The spectra contain no significant peaks near frequencies that can be identified as modes of gate vibration from dynamic analysis. Therefore, it appears impossible to identify the in-water natural vibration frequencies for the dynamic stability analysis of the gate using ambient excitation.

Dynamic Stability Analysis

The Tainter gate “T” can potentially undergo two different coupled mode vibrations, which are:

- (1) Coupling of the skinplate streamwise parallel vibration “ M_{X1} ” ($\Omega_{wx} = 5.5$ Hz) with the whole gate rigid-body rotational vibration around the trunnion pin “ M_Z ” ($\Omega_{a0} = 6.5$ Hz).
- (2) Coupling of the skinplate streamwise rotational vibration “ M_{X2} ” ($\Omega_{w\psi} = 6.5$ Hz) with the whole gate rigid-body rotational vibration around the trunnion pin “ M_Z ” ($\Omega_{a0} = 6.5$ Hz).

The ratio of the in-water streamwise vibration frequency $\Omega_{wx,\psi}$ to the in-air whole gate rotational vibration frequency Ω_{a0} takes on a value of 0.85 for the first possible coupled-mode vibration, and a value of 1.0 for the second coupling possibility. When this ratio is equal to or slightly less than 1.0, Anami’s (2000) theory predicts a region of potential susceptibility.

The dynamic stability diagram, calculated from the simultaneous numerical solution to Equations (1) and (2), is shown in Figure 8(a) for the coupling of the skinplate parallel vibration mode M_{X1} and the whole gate vibration mode M_Z . The ordinate in the stability diagram is the damping required for complete dynamic stability, and is called the critical damping ratio ζ_c for dynamic stability. The abscissa is the ratio of in-water natural vibration frequency of the parallel mode to the in-air frequency of the rigid body gate vibration, denoted by γ_{nw} . Note the region of very intense dynamic instability that appears when the frequency ratio is just slightly smaller than 1.0.

At the measured values of $\Omega_{nwx} = 5.5$ Hz and $\Omega_{a0} = 6.5$ Hz, the frequency ratio γ_{nw} is 0.846. In addition, the in-air damping ratio was estimated to be $\zeta_{ax} = 0.030$ for the skinplate streamwise parallel vibration. The point defined by these two values is plotted as the filled circle in Figure 8(a). The location of the data point just above the stability curve indicates that the strength of the coupling of the parallel vibration mode with the whole gate rotation mode is insufficient to drive the coupled-mode instability and the gate narrowly escapes instability.

Similar calculations made for the coupling of Modes M_{X2} and M_Z produced the dynamic stability diagram shown in Figure 8(b). The overall level of dynamic instability is far smaller than that of Figure 8(a). The measured frequencies of $\Omega_{nw\psi} = 6.5$ Hz and $\Omega_{a0} = 6.5$ Hz, result in a frequency ratio γ_{nw} of exactly 1.0. The in-air damping ratio is estimated to be 0.012 for the skinplate streamwise rotational vibration. This data pair is again plotted as the filled circle on the stability diagram in Figure 8(b). The location of the data point, just above the stability curve, again indicates a narrow escape from the unstable region.

Based on this analysis, one may conclude that the Tainter gate “T” barely maintained its dynamic stability for the coupling of Mode M_{X1} with M_Z , and Mode M_{X2} with M_Z at the tested condition.

TAINTER GATE “P”

Results with Steel Rod Breaking Excitation

Field vibration tests were undertaken on the 77-ton Tainter gate “P” using steel rod breaking excitation, as reported by Ishii, et al. (2009b). The upstream water level at the tested condition was close to maximum design level.

Figures 9(a) to 9(c) show the acceleration responses at the skinplate, triggered by the sudden failure of a 10-mm diameter steel rod. Figure 9(a) shows the real time waveforms. The damped waveform initiated by the steel rod breaking excitation is evident. The second impact at about 1 sec occurred because the L-bracket fastened to the gate with a pair of C-clamps came loose and fell onto the horizontal girder.

Figure 9(b) and 9(c) show the acceleration power spectrum. There are the sharp peaks at 4.6 Hz and 6.3 Hz in radial direction of Figure 9(b) and 8.3 Hz in vertical

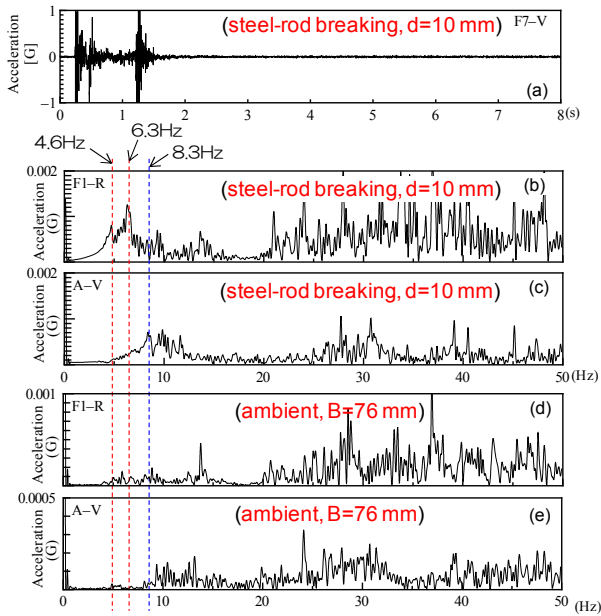


Figure 9: Real time acceleration waveform and power spectra for Tainter gate "P": (a) Real time waveforms; (b) radial and (c) tangential acceleration power spectra for steel rod breaking excitation; (d) radial and (e) tangential acceleration power spectra for ambient excitation.

direction of Figure 9(c), all of which are significant when considering movement-induced self-excitation.

Simulated mode shapes of the skinplate streamwise vibration with the frequency of 4.6 Hz and 6.3 Hz are shown in Figure 10. Figure 10(a) shows the 4.6 Hz vibration, in which the whole skinplate performs a streamwise "parallel vibration" in the press-open direction (when the skinplate moves in the downstream direction, the whole gate moves upward). Figure 10(b) shows the 6.3 Hz vibration, in which the skinplate performs the streamwise rotational vibration with the rotation center height of about 2.03 m from the bottom of the skinplate.

A simulated mode shape for the 8.3 Hz vibration is shown in Figure 10(c). The whole gate performs the rotational vibration around the trunnion pin.

The identified damping ratios for the skinplate streamwise parallel vibration (4.6 Hz) and streamwise rotational vibration (6.3 Hz) are 0.040 and 0.021, respectively, while, the damping ratio for the whole gate vibration around the trunnion pin (8.3 Hz) takes on a somewhat smaller value of 0.018. Of course, these small damping ratios do not including any Coulomb damping.

Comparison of Steel Rod Breaking Excitation with Ambient Excitation

Ambient excitation tests were also conducted on gate "P." The frequency power spectra, shown in Figures 9(d) and 9(e) were measured at a gate opening of $B = 76$ mm. Figure 9(d) shows the radial response spectrum and Figure 9(e) that for the tangential response. Many high frequency components from about 20 Hz to 50 Hz are found in the ambient response spectra, but these are well

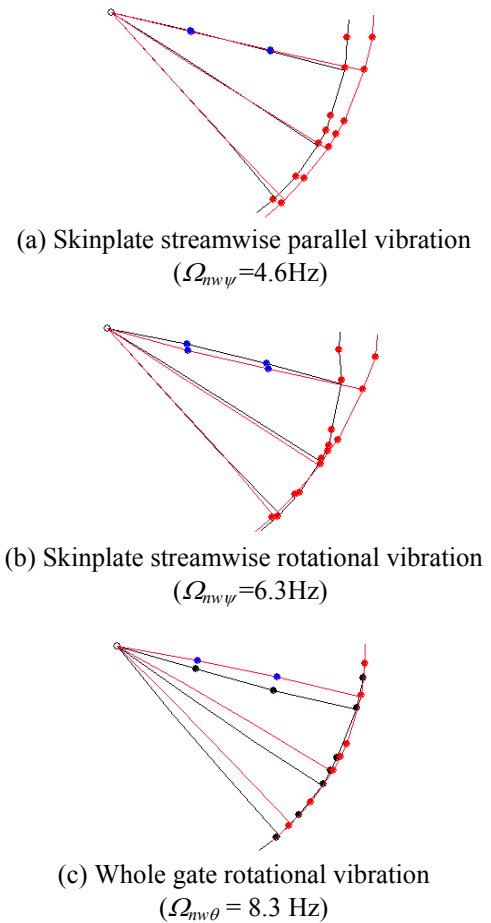
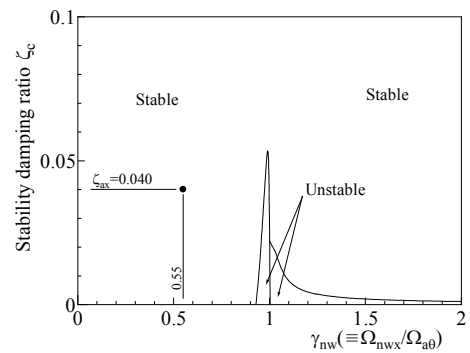
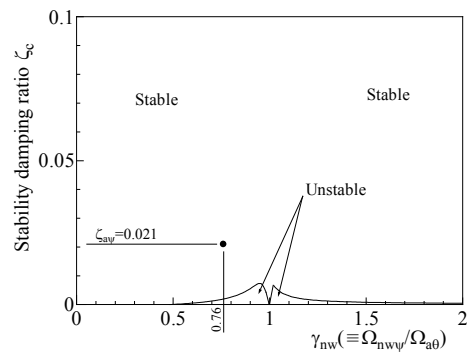


Figure 10: Simulated mode shapes of Tainter gate "P".



(a) For coupling of mode M_{X1} and M_Z



(b) For coupling of mode M_{X2} and M_Z

Figure 11. Dynamic stability diagram for gate "P"

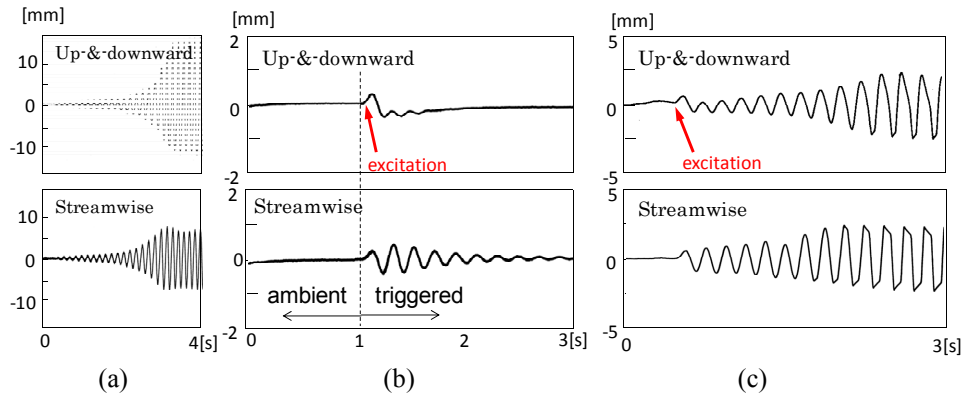


Figure 12: Model test results for friction maintained dynamic stability; (a) Spontaneous vibration without Coulomb friction, (b) ambient vibration (before 1 second) and small displacement trigger, (c) large displacement trigger

beyond the range of the frequency components that are involved in the dynamic instability of the gate. The ambient spectra did not, however, have any substantial low frequency components, making it impossible to identify the in-water natural vibration frequencies. The vibration mode shapes that lead to mode coupling and movement-induced instability (*i.e.*, the coupled-mode dynamic instability that we are investigating) cannot be identified from the ambient excitation tests.

Dynamic Stability Analysis

The Tainter gate "P" can potentially undergo two different coupled-mode vibrations, which are:

- (1) Coupling of the skinplate streamwise parallel vibration " M_{X1} " ($\Omega_{wx} = 4.6$ Hz) with the whole gate rigid-body rotational vibration around the trunnion pin " M_Z " ($\Omega_{a0} = 8.3$ Hz).
- (2) Coupling of the skinplate streamwise rotational vibration " M_{X2} " ($\Omega_{w\psi} = 6.3$ Hz) with the whole gate rigid-body rotational vibration around the trunnion pin " M_Z " ($\Omega_{a0} = 8.3$ Hz).

The dynamic stability diagrams for Tainter gate "P" are shown in Figure 11. Figure 11(a) shows the stability criterion for the coupling of mode M_{X1} with mode M_Z , and Figure 11(b) shows that for the coupling of mode M_{X2} with mode M_Z . In both cases, the plotted data point indicates no susceptibility to coupled-mode instability. Based on this analysis, one may conclude that the Tainter gate "P" is dynamically stable at the tested condition.

MODEL EXPERIMENT OF FRICTION-MAINTAINED DYNAMIC STABILITY

As explained in the previous sections, the in-water natural vibration characteristics of the Tainter gates cannot be determined by ambient excitation. In order to discuss the essential dynamic stability and instability of the gate, it is necessary to conduct tests with impulsive excitation, such as the steel rod breaking tests.

The appearance of dynamic stability of a Tainter gate may be maintained by the damping effect due to Coulomb friction acting on the side seals and on the trunnion pin.

To consider such friction-maintained stability, model experiments were conducted.

The model experiments were conducted on a 1/21-scale 3-dimensional model of the Folsom Dam Tainter gate. Based on a previous study (Anami & Ishii, 2000; 2003), violent coupled-mode self-excited vibrations are expected when the in-water natural vibration frequency of the skinplate streamwise vibration is slightly smaller than the natural vibration frequency of the whole gate rotational vibration around the trunnion pin. Therefore, the vibration frequencies were adjusted, yielding a frequency ratio of skinplate streamwise natural vibration to whole gate natural vibration of 0.96. With this condition, a very intense dynamic instability was observed, as shown in Figure 12(a).

Under this very unstable condition, rubber seals were attached to the sides of the skinplate, to add Coulomb friction damping (that all operational gates possess) to the model gate. When the water was discharged from small gate opening in this state, no vibration occurred, as shown at times before 1 second of Figure 12(b). This trace indicates that the Coulomb friction maintained the appearance of dynamic stability, although the model gate has an essential dynamic instability. This trace is analogous to the measurement on the full-scale gate with ambient excitation.

Under same conditions with the rubber seals in place, a weak vertical displacement trigger was introduced to the model gate. The clearly damped waveforms were measured and a sharp peak at the natural vibration frequency was obtained, as shown after 1 second in Figure 12(b). This is analogous to the measurement state for the steel rod breaking excitation in the full-scale gate.

When the amplitude of the displacement trigger exceeding the threshold value for the Coulomb friction, a violent self-excited vibration is induced in the essentially dynamic unstable gate, as shown in Figure 12(c).

CONCLUSIONS

The field vibration tests on operational Tainter gates using steel rod breaking excitation were conducted to identify the in-water dynamic characteristics of the gate.

Furthermore, a previously established theoretical analysis was applied to the gate, and the dynamic stability and instability of a gate were examined.

Through use of steel rod breaking excitation, it was possible to show that the gates considered here maintained the appearance of dynamic stability due to Coulomb friction. In addition, it was clearly shown that the dynamic characteristics of full-scale gates cannot be accurately identified using ambient excitation.

The authors hope is that their testing methodology can become a standard acceptance test upon the completion of construction of all new gate projects and that it can be used as a tool to identify potential instabilities in all Tainter gate installations around the world in order to assure the long-term safe operation of large-scaled Tainter gates.

ACKNOWLEDGMENTS

The authors wish to acknowledge the financial support provided by the Grants-in-Aid for Scientific Research from Japan Society for the Promotion of Science. The field vibration tests on the full-scale Tainter gates were made possible through the special consideration, understanding, and cooperation of many people related to the gates. The authors wish to express their sincere appreciation to all of these people for their kind contributions.

REFERENCES

- Anami, K., 2002, Flow-Induced Coupled-Mode Self Excited Vibration of Large-Scaled Tainter-Gates, Dissertation submitted to Osaka Electro- Communication University, (in Japanese: Translated into English on Dec. 2005).
- Anami, K. and Ishii, N., 1998 In-Air and In-Water Natural Vibrations of Folsom Dam Radial Gate in California, in *Experimental Mechanics 1 (Advances in design, testing and analysis)* (ed: Allison I.M.), pp. 29-34, Balkema.
- Anami, K. and Ishii, N., 2000, Flow-Induced Dynamic Instability Closely Related to Folsom Dam Tainter-Gate Failure in California, in *Flow-Induced Vibration* (eds: Ziada S. & Staubli T.), pp. 205-212, Balkema.
- Anami, K. and Ishii, N., 2003, Model Tests for Non-Eccentricity Dynamic Instability Closely Related to Folsom Dam Tainter-Gate Failure, *Proc. of ASME Pressure Vessels and Piping Conference*, Vol. 465, pp. 213-221.
- Anami, K., Ishii, N., Knisely, C.W., 2004, Validation of Theoretical Analysis of Tainter Gate Instability Using Full-Scale Field Tests, Proc. of the 8th International Conference on Flow-Induced Vibration, in *Flow Induced Vibration* (eds: De Langre, E. & Axisa, F.), Vol. 1, pp. 409-414.
- Anami, K., Ishii, N., Knisely, C.W., Oku, T., 2007, Field Measurement of Dynamic Instability of a 50-Ton Tainter-Gate, Proc. of 2007 ASME Pressure Vessels and Piping Division Conference, PVP2007-26543 (CD-ROM), ISBN 0-7918-3804-8.
- Anami, K., Ishii, N., Knisely, C. W., Todd, R.V., Oku, T., 2006, Vibration Tests with a 1/13-Scaled 3D Model of Folsom Dam Tainter-Gate and Its Prediction by Theory, Proc. of ASME 6th International Symposium on FSI, AE & FIV+N, Vancouver, Vol. 4, pp. 1127-1134, PVP2006-ICPVT-11-93917(CD-ROM).
- Ishii, N., 1995, Folsom Dam Gate Failure Evaluation and Suggestions, 1st report submitted to U.S. Bureau of Reclamation, Aug. 1995.
- Ishii, N., Anami, K., Knisely, C.W., Oku, T., 2009a, Field Tests Concerning the Dynamic Stability of Tainter Gates at the "T" Dam, Proc. of WaterPower XVI International Conference (CD-ROM), No.188, Spokane, WA . July 27-30.
- Ishii, N., Anami, K., Knisely, C.W., Oku, T., Aslam, M., 2009b, Field Vibration Tests Concerning the Dynamic Stability of Tainter Gates at the "P" Dam, Proc. of Hydro 2009 International Conference (CD-ROM), No.8-10, Lyon, France. October 26-28
- Ishii, N., Anami, K., Knisely, C.W., Tsuji, T., Oku, T., 2011, Tainter Gates - Why Some Fail but Many Do Not -, Proc. of Hydro Vision 2011 International Conference, Paper No. 1J-5 (Online). Sacramento, CA. July 19-22.
- Ishii, N. and Imaichi, K., 1980, Dynamic Instability of Tainter-Gates, in *Practical Experiences with Flow-Induced Vibrations* (Editor: Naudascher, E. & Rockwell, D.), pp. 452-460, Berlin, Springer-Verlag.



MECHANISMS OF INSTABILITY OF SAFETY RELIEF VALVES IN WATER SYSTEMS

Hassan Berro¹

Electricité de France R&D
Analysis in Mechanics and Acoustics Dpt.
Clamart, France
Email: hassan.berro@edf.fr

Pierre Moussou

LaMSID laboratory
UMR CNRS EDF 2832
Clamart, France
Email : pierre.moussou@edf.fr

ABSTRACT

Safety relief valves (SRV) in water systems encounter chatter-type instabilities when partially open. A numerical approach is employed in this work in order to investigate the physical mechanisms behind the unstable dynamics of SRVs near their set pressures. Analysis of the pressure drop through the valve and the fluid forces acting on its disc reveals a dependency, in the harmonic regime, of the oscillation amplitudes on the inlet velocity and the vibration frequency. The inertial and dissipative contributions to the fluid force are investigated over a wide range of frequencies. The results allow to accurately describe the underlying physics which correspond to the fluid response over a wide range of operating conditions.

INTRODUCTION

In hydraulic systems such as pipe networks and vessels, safety relief valves (SRV) play the important role of pressure regulation and control. In emergency situations involving pressure build-ups, SRV's are supposed to open rapidly in order to cause a flow discharge and a singular pressure drop, lowering the pressure down to secure levels.

In the sizing procedure of SRV's, many design aspects are taken into consideration in order to be sure of the lifetime of the valves and their robustness in operation. Several of these aspects are related to the steady-state properties of the valve, i.e. its set pressure, flow capacity, and discharge coefficient. These properties depend mainly on the geometry of the valve and properties of its release spring [1]. In order for SRV's to open instantly, they are designed in such a way that once the set pressure is attained and the valve is slightly open, the force balance on the valve disc, between the hydraulic force on one side and the force from the release spring on the other, is unstable until the valve is completely open. Intermediate equilibrium positions of the disc between fully-closed and fully-open positions are designed to be statically unstable [2]. This instability is not only desirable but can be even thought as indispensable for the good functioning of the SRV.

Instability of a different nature, unfortunately undesirable, may occur during the operation of SRV's. It is the dynamic instability, also known as the "chatter" effect [3, 4]. The basic idea is that for a given set of inlet conditions of flow and pressure, the valve lift undergoes spontaneous self-sustained oscillations at large amplitudes. In order to prevent the occurrence of dynamic instability, empirical rules are still used in the design while the underlying physics are still not completely understood [1, 5, 6]. The most wide-spread explanation of "chatter" is based on the acoustic resonance of the pipe, upstream of the valve, causing synchronized vortex shedding in the main branch [7]. Recent experiments on SRV's showed that they are prone to acoustically-induced instability [2]. In the presence of reverberating acoustic boundary conditions, negative pressure drops could be measured for a range of frequencies. The acoustic instability feeds on the pressure build-up resulting in an amplification of the disc oscillations [8, 9].

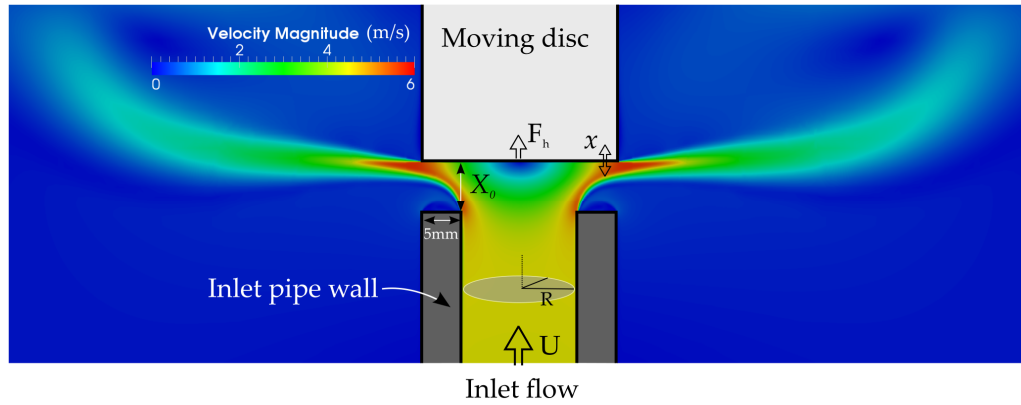
This work aims to improve the understanding of how the valve disc vibrations and the generated fluid forces synchronize causing the chatter instability. A numerical approach based on a finite volume solver in CFD is used with the implementation of mesh deformation to simulate the disc motion [10, 11].

The paper is organized as follows. In the first section, the geometrical model for the SRV is described. In the second section, the static properties of the SRV are explored with steady-state simulations. The results for the more complex dynamic behavior of the SRV are then presented and a comprehensive discussion on the underlying physics is given in section 3. Finally, the paper is concluded in section 4.

MODEL DESCRIPTION

In order to reveal the relationships between the fluid forces acting on the valve disc on one hand and the complex boundary conditions near the dynamic instability on the other, a simplified axisymmetric model of a SRV was chosen as presented in Fig. 1.

Address all correspondence to this author¹


FIGURE 1: SCHEMATIC OF THE SIMPLIFIED SRV MODEL.

Geometrical complications in common SRV designs that were judged irrelevant for the purpose of this study were omitted. The system consists of a disc which partially blocks an inlet water flow through a pipe. The pipe is of a radius $R = 7.5\text{mm}$, and a thickness of 5mm , invariant properties for this study.

In steady flow conditions, the valve lift X_0 and the inlet velocity U are both constant. Since the discharge flow through the valve ($\pi R^2 U$) is given, the system's response is by developing a pressure differential between the lower and upper-streams of the valve. This pressure difference represents the pressure drop through the valve for the chosen inlet velocity U :

$$\Delta P = P_{\text{in}} - P_{\text{out}} = K \left(\frac{\rho U^2}{2} \right) \quad (1)$$

K is a characteristic pressure drop coefficient which depends on the lift X_0 . In the calculations, the exit pressure P_{out} is set to zero in relative units. Measured at the inlet, P_{in} is thus representative of the total pressure drop ΔP through the SRV. The total hydraulic force F_h acting on the valve disc is also calculated. This force, in steady-state conditions, can be expressed as the product of the inlet pressure P_{in} and a certain hydraulic surface S_h :

$$F_h = P_{\text{in}} S_h \quad (2)$$

The simulations were conducted using the multi-purpose finite volume computational fluid dynamics software Code_Saturne [10]. For the simulations presented in this study, a Reynolds-Averaged Navier-Stokes turbulence model (K-omega) was employed. For the dynamic analysis involving forced oscillations of the valve disc, the Arbitrary Lagrangian-Eulerian (ALE) method for mesh deformation was used. More details about this method can be found in Ref. [11]. No cavitation is considered in the framework of this study.

STEADY-STATE CHARACTERISATION

The SRV model is first characterized in terms of its static properties: pressure drop, hydraulic force and hydraulic surface. These properties are calculated for a range of disc lifts and two inlet velocities corresponding to $Re = 10^3$ and $Re = 10^4$.

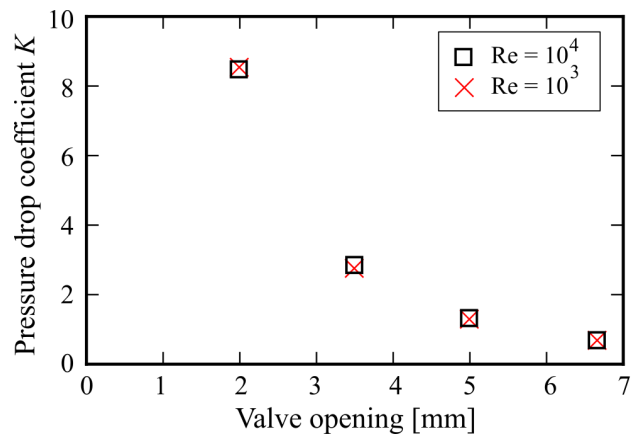

FIGURE 2: PRESSURE DROP COEFFICIENT AS A FUNCTION OF THE VALVE OPENING (LIFT) FOR TWO INLET REYNOLDS NUMBERS.

Figure 2 presents the results of the pressure drop coefficient K as a function of the lift position X_0 for two inlet velocities. For both values of the inlet Reynolds number, the pressure drop coefficient for a given opening was found to be constant. This implicates that the pressure drop characteristics are uniquely dependent on the geometry of the valve during operation, i.e. its opening in this case. As the valve opens, a lower singular pressure drop is measured as K is shown to decrease with the lift (Fig. 2).

A similar effect occurring when the valve opens is shown in Fig. 3, regarding the reduced hydraulic force ($F_h/\pi\rho R^2 U^2$) and pressure drop ($\Delta P/\rho U^2$). The fluid force acting on the valve disc weakens as the disc moves upwards, i.e. near a fully-open configuration.

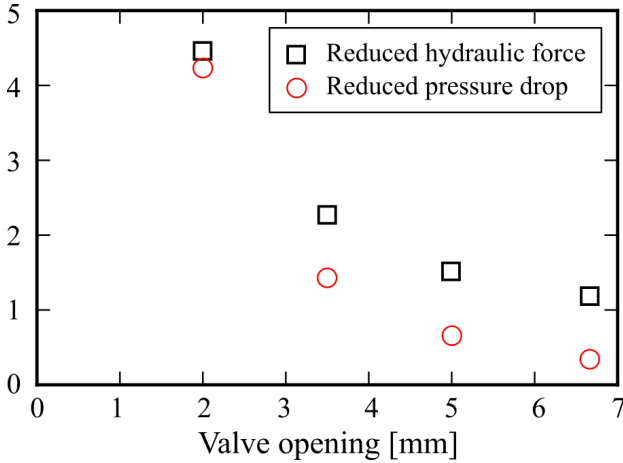


FIGURE 3: REDUCED HYDRAULIC FORCE AND PRESSURE DROP AS A FUNCTION OF THE LIFT. (RE=10⁴)

On the other hand, the reduced hydraulic surface ($S_h/\pi R^2$), calculated according to Eqn. (2) is given in Fig. 4 for two inlet Reynolds numbers. For small openings of the valve, the value is close to unity. The hydraulic surface is thus close to the inner surface of the upstream pipe. As the valve opens, the hydraulic surface increases due to the divergence of the flow beyond the pipe neck. The surface of impact by the fluid on the valve disk thus increases as the latter moves up. The effect of the inlet speed is noticeable in the case of large openings. The impact surface is larger the case of smaller Reynolds number due to the dispersion of the jet over the disc for small impact velocities. Recent experiments dealing with the static characterization of safety relief valves have shown a very similar effect [2].

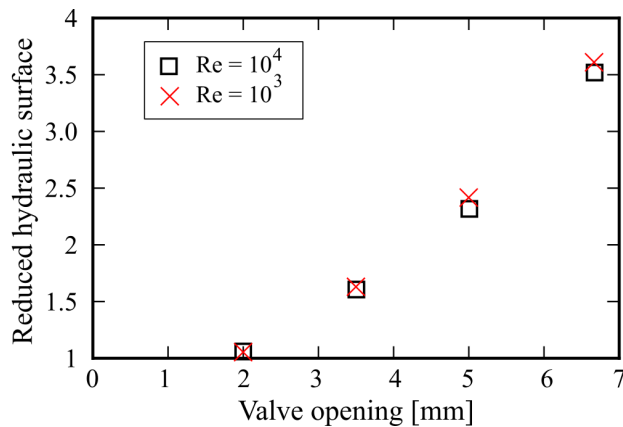


FIGURE 4: REDUCED HYDRAULIC SURFACE AS A FUNCTION OF THE LIFT. (RE=10⁴)

The most important result to be concluded from the steady state characterization of the SRV model is that both the pressure drop and the hydraulic force present negative slopes with respect to the lift in steady-state conditions. Physically, this means that starting from a given lift X_0 , if the disc moves slightly upwards (see Fig.

1), the pressure drop and the fluid force on the disc decrease. This important observation and the results in Figs. 2-4 will be used as elements of discussion for the dynamic calculations of the following section.

DYNAMIC RESPONSE OF THE SAFETY RELIEF VALVE

In order to understand how the SRV behaves in dynamic conditions, a set of simulations were conducted in the unsteady-flow regime providing a large spectrum of responses in force and pressure for frequencies in the range of 20 to 200Hz. Moreover, different operation points were tested which correspond to lift positions $X_0 = 2, 3.5, 5,$ and 6.67 mm (see Fig. 1).

In the harmonic regime, the hydraulic force and the pressure drop can be linearized with respect to the lift and the inlet velocity. Inducing a small amplitude of vibration x of the valve disc about an equilibrium position X_0 , the change in the hydraulic force with respect to its steady-state value is reported. This value is referred to as the unsteady hydraulic force, denoted by f_h . Similarly, the change in the pressure drop through the valve is referred to as the unsteady pressure drop and denoted by δP . In non-dimensional terms, it can be written that:

$$\frac{f_h}{\pi \rho R^2 U^2} = \alpha \frac{u}{U} + \beta \frac{x}{X_0} \quad (3)$$

$$\frac{\delta P}{\rho U^2} = \gamma \frac{u}{U} + \delta \frac{x}{X_0} \quad (4)$$

The complex coefficients ($\alpha, \beta, \gamma,$ and δ) in Eqns. (3) and (4) are calculated for a wide range of frequencies. The knowledge of these coefficients allows gaining insight on the coupled physics that could be behind the instable dynamic behavior observed in experiments. In order to characterize the four coefficients, two sets of unsteady-flow simulations were conducted. In the first set, the inlet velocity was fixed to a $Re = 10^4$ and the disc was set to a sinusoidal motion around an equilibrium position X_0 once a steady flow was established. In the second set of simulations, the position of the disc was held fixed while sinusoidal variations in the inlet velocity were imposed. The frequency of the oscillations was varied in order to characterize the coefficients over a wide spectrum.

Dynamic response to oscillations in the disc position

The results for the first set of simulations (i.e. for oscillating disc) are presented in Figs. 5-10. Note that the results are expressed in terms of a reduced frequency f_{red} in order to compare between the different geometrical configurations (different X_0 's). This reduced frequency is calculated as follows:

$$f_{red} = \frac{f \times T}{U_{out}} \quad (5)$$

In this equation, T is the pipe thickness, and U_{out} is the exit velocity calculated as:

$$U_{out} = \left(\frac{R^2}{2X_0(R + T)} \right) U \quad (6)$$

The real parts of β and δ are given in Figs. 5 and 6. Physically, they represent the in-phase proportionality, with respect to the lift, of the hydraulic force and the pressure drop respectively (see Eqns. (3) and (4)). For instance, a positive value of $real(\beta)$ means that if the disc is moved upwards by a small displacement dx , the hydraulic force, proportional to the lift, increases by a value of $(real(\beta)dx)$. A similar analogy for the pressure drop is valid with δ . The results show that although β and δ increase with the frequency, they actually change sign at a certain frequency.

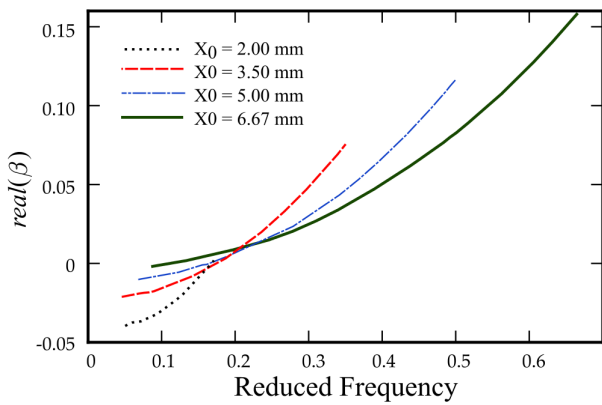


FIGURE 5: IN-PHASE PROPORTIONALITY COEFFICIENT BETWEEN THE HYDRAULIC FORCE AND THE LIFT, AS A FUNCTION OF FREQUENCY FOR DIFFERENT MEAN OPENINGS. (RE=10⁴)

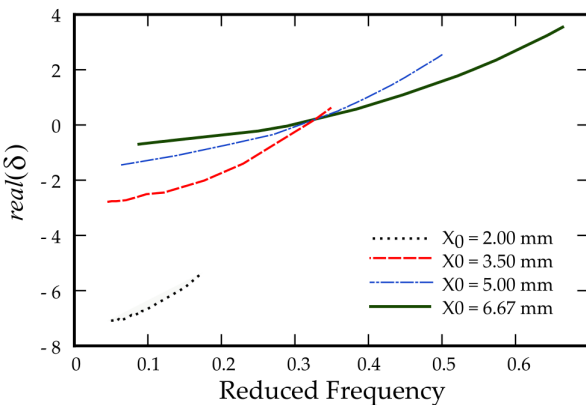


FIGURE 6: IN-PHASE PROPORTIONALITY COEFFICIENT BETWEEN THE PRESSURE DROP AND THE LIFT FOR DIFFERENT EQUILIBRIUM OPENINGS. (RE=10⁴)

For low frequencies, the real parts of β and δ are both negative. This means that a slight increase in the lift results in a decrease in the hydraulic force and the pressure drop, a result perfectly coherent with the steady-state responses presented in Fig. 3 which show a drop in the hydraulic force and pressure with the lift. Moreover, the observed negative slope in Fig. 3 tends to zero for large openings of the valve. This is equally observed in the low-frequency dynamic response.

As the frequency of the oscillations increases, the pseudo-static behavior of low frequencies starts to vanish. The in-phase coefficients of β and δ increase proportionally to the square of the frequency. A new physics thus enters in play at high frequencies; it is that of the added mass effect of the fluid. This explains why the fluid force is proportional to the disc acceleration.

A reduced added mass was calculated as the ratio between the real part of β and the square of the reduced frequency. The results shown in Fig. 7 illustrate that the added mass effect of the fluid is amplified in confined configurations although the onset of the inertial effect is shifted to higher frequencies as shown in Fig. 5.

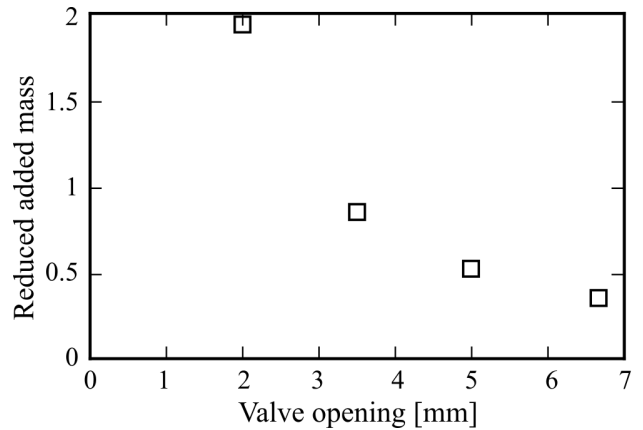


FIGURE 7: REDUCED ADDED MASS OF THE FLUID IN THE HIGH FREQUENCY REGIME AS A FUNCTION OF THE LIFT. (RE=10⁴)

Figure 8 presents the results for the real part of β , obtained for the same equilibrium opening $X_0 = 6.67$ mm but with two different values for the inlet flow velocity, corresponding to $Re = 10^3$ and $Re = 10^4$. One can observe that the inlet speed does not influence the physics of the flow and the nature of the dynamic response of the SRV. The results given for two inlet speeds seem to superpose on a single master curve corresponding to the average lift position X_0 considered. For a given dimensional frequency of oscillations, the inertial effect of added mass is more dominant in the case of reduced flow speeds.

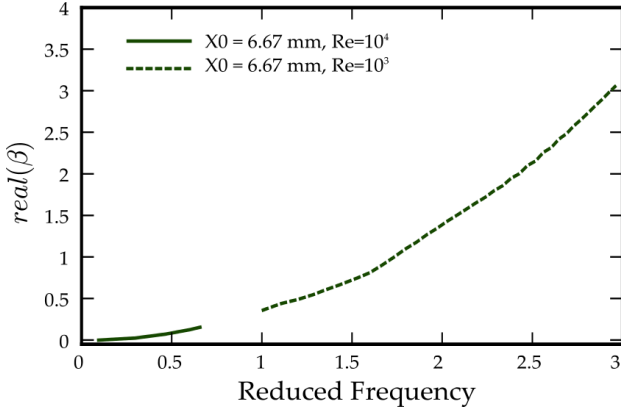


FIGURE 8: REAL PART OF THE FORCE-DISPLACEMENT PROPORTIONALITY COEFFICIENT FOR TWO INLET VELOCITIES.

As for the imaginary parts of β and δ , they are given as functions of the reduced frequency in Figs. 9 and 10. In the harmonic regime, the imaginary parts of these coefficients represent the $(\pi/2)$ out-of-phase proportionality between the force and pressure on one hand and the disc position. In other words, this represents the dissipative effects proportional to \dot{x} , the oscillation velocity of the valve disc. Similar to the analysis done with the real parts of these coefficients, the results in Figs. 9 and 10 allow to distinguish between two zones of dissipative responses.

At low frequencies, dissipation is of a viscous nature which manifests itself with the linear dependence of the imaginary parts of β and δ on frequency. For each value of the average lift position, dissipation can be characterized with the slope of the curve in the linear zone.

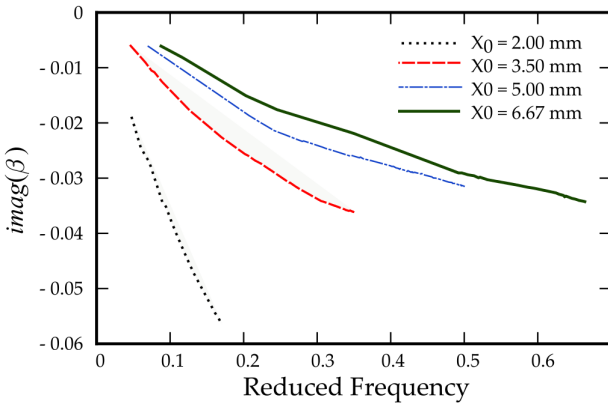


FIGURE 9: IMAGINARY PART OF THE FORCE-DISPLACEMENT PROPORTIONALITY COEFFICIENT FOR DIFFERENT VALVE OPENINGS.

The results in Fig. 10 show that the dissipation is amplified when the valve is nearly closed, i.e. for low values of X_0 . This phenomenon can be explained as being due to the more severe shearing of the fluid in the confined geometry.

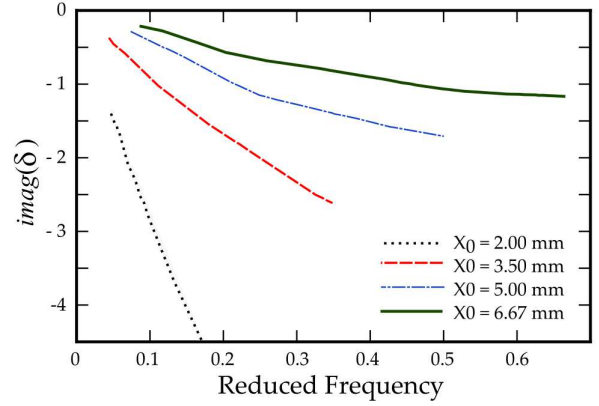


FIGURE 10: IMAGINARY PART OF THE PRESSURE DROP-DISPLACEMENT PROPORTIONALITY COEFFICIENT FOR DIFFERENT VALVE OPENINGS. (RE=10⁴)

Since the fluid considered is Newtonian, the viscous stresses are proportional to the shear rate. The fluid is sheared the highest in the case of 2mm opening. The results shown in Figs. 9 and 10 show that the highest “negative-slope” is encountered with this opening

In order to elaborate more quantitatively on this result, Table 1 presents the value of the dissipation coefficient C_d , calculated as:

$$C_d = \frac{d(\text{imag}(\beta))}{df_{\text{red}}} \quad (7)$$

TABLE 1: DISSIPATION COEFFICIENT AS A FUNCTION OF THE LIFT

$X_0(\text{mm})$	C_d	$X_0 C_d$
2.00	-0.37	-0.74
3.50	-0.15	-0.53
5.00	-0.09	-0.45
6.67	-0.07	-0.48

A very interesting observation is that the dissipation coefficient, multiplied by the valve lift is almost constant for three of the considered valve openings. Since the lift is equal to the height of the exit channel where the fluid is principally sheared, the product of these two quantities should be constant for a given velocity. At the smallest opening other effects, than the simple geometry, seem to play a role in amplifying the fluid shear. A possible physical interpretation could be the more developed negative pressure, observed in the confinement zone for small valve openings, which plays a role in relatively producing a thinner fluid jet through the exit channel.

In the high-frequency regime, complex non-linear effects seem to take place in the system. These effects however remain orders of magnitude inferior to the inertial effects which increase with the square of the frequency.

Dynamic response to oscillations in the inlet flow velocity

In the second set of simulations, the inlet velocity is allowed to vary and the non-dimensional coefficients α and γ were calculated according to Eqns. (3) and (4). A similar analysis of the real and imaginary parts of these coefficients is hereby undertaken. Some care must be taken when evaluating the unsteady pressure difference across the valve, because the upstream pipe contributes to it by a significant amount. In order to provide results which describe the role of the ‘bare’ valve, the pressure difference due to a portion of straight pipe of length H submitted to an accelerating fluid flow is subtracted from the total pressure difference, i.e.,

$$\delta P' = \delta P - \rho H \frac{dU}{dt} \tag{8}$$

where H represents the height of the inlet pipe (see Fig. 1).

Figures 11 and 12 present the results for the real parts of α and γ as a function of the reduced frequency, defined as in Eqn. (5). A positive value of $real(\alpha)$ signifies that for a small increase in the inlet velocity, an increase in the hydraulic force in phase with the velocity is obtained. Similarly, a positive value of $real(\gamma)$ indicates that an increase in the flow velocity results in a pressure build up in the upstream of the valve. In steady flow simulations, the results obtained for different flow velocities (Re) illustrate that the pressure and the fluid force are both proportional to the square of the inlet velocity (Figs. 2 and 4). As a result, a pseudo-static response of the system would be characterized by positive real parts of the non-dimensional coefficients α and γ .

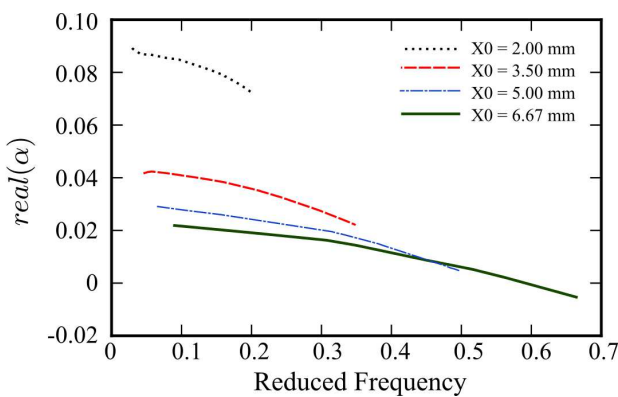


FIGURE 11: REAL PART OF THE FORCE-FLOW VELOCITY PROPORTIONALITY COEFFICIENT FOR DIFFERENT VALVE OPENINGS. ($Re=10^4$)

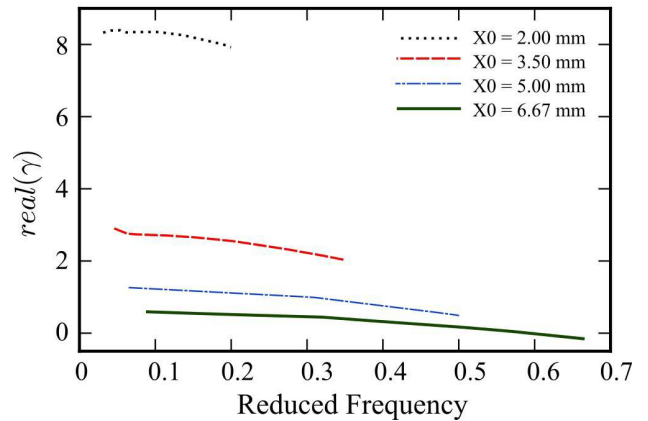


FIGURE 12: REAL PART OF THE PRESSURE-VELOCITY PROPORTIONALITY COEFFICIENT FOR DIFFERENT VALVE OPENINGS. ($Re=10^4$)

It is clear in Figs. 11 and 12 that for values of the reduced frequency below 0.6, the static response remains valid for both the hydraulic force and the pressure drop. A more complex dynamic response is observed for high frequencies and is characterized by the decay of both $real(\gamma)$ and $real(\alpha)$ with the frequency. It seems that for elevated frequencies, a physics of a different nature enters into play, one that produces fluid forces that are no longer dependent on the flow velocity but on the acceleration. This will be shown in the following results regarding the imaginary parts of the proportionality coefficients.

In Fig. 13, the imaginary part of γ is given as a function of the reduced frequency. This coefficient gives valuable information about the proportionality between the pressure difference across the ‘bare’ valve as in Eqn. (8) and the inlet fluid acceleration.

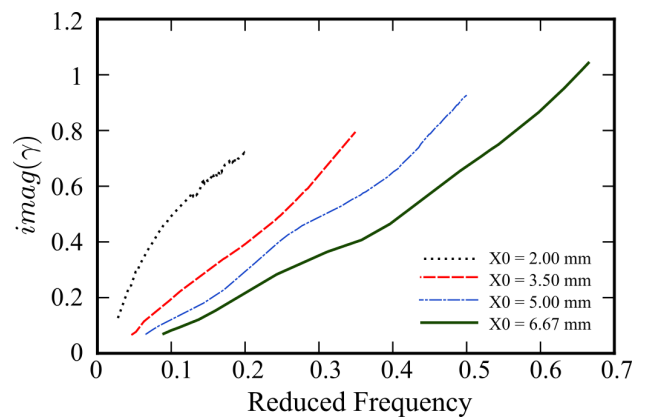


FIGURE 13: IMAGINARY PART OF THE PRESSURE-VELOCITY PROPORTIONALITY COEFFICIENT FOR DIFFERENT VALVE OPENINGS. ($Re=10^4$)

It can be seen that $imag(\gamma)$ is an increasing function of the frequency. This suggests that an inertial effect of added mass enters into play. This effect can be roughly characterized by the slope of the curves in Fig. 13. The inertial effect is found to be more important for confined configurations, i.e. for small valve openings. This result is coherent with the investigations of added mass shown in Fig. 7.

On the other hand, Fig. 14 gives the imaginary part of α given as a function of the reduced frequency. Qualitatively, the response for the hydraulic force seems to differ than that of pressure for low frequencies and in large valve openings. Several non-linear effects seem to be occurring over the range of considered frequencies and operating conditions. Further investigation is needed to identify the nature of the underlying physics for this behavior.

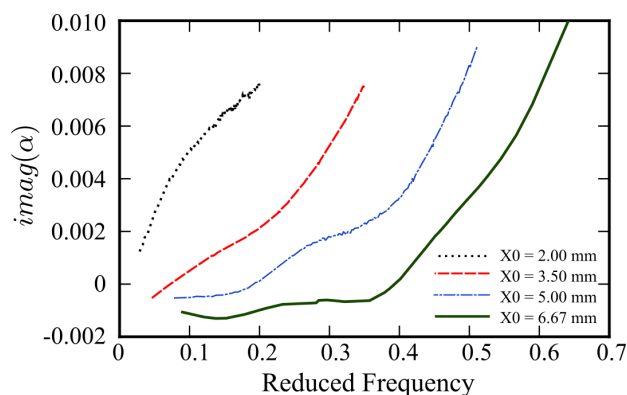


FIGURE 14: IMAGINARY PART OF THE FORCE-VELOCITY PROPORTIONALITY COEFFICIENT FOR DIFFERENT VALVE OPENINGS. ($RE=10^4$)

CONCLUSIONS

In this paper, a numerical approach was used to investigate the physical phenomena influencing the dynamic response of partially open safety relief valves. Several inertial and dissipative aspects were revealed by defining and analyzing 4 non-dimensional coefficients fully describing the fluid force on the valve disc and the pressure drop across the SRV.

A characteristic reduced frequency parameter was used to analyze the results with different geometrical configurations and operating conditions. It was found that a quasi-static description of the SRV remains valid up to a reduced frequency of 0.2, independent of the disc position. Dissipative effects primarily due to the fluid shear at the exit canal were also revealed in this work and appeared clearly up to the same reduced frequency of 0.2. At high frequencies, inertial effects of added mass dominate, the inertial effect being amplified in confined configurations.

The conducted simulations also showed that the fluid force and pressure difference across the valve are influenced by perturbations in the inlet flow. For a range

of frequencies, an inertial effect in the fluid force was observed which can be attributed to the forced acceleration of the fluid in the flow inlet.

The results of this work, quantifying the effects of the occurring physics with simple coefficients, can easily enrich a global dynamic model of an SRV. The comprehensive model can be used not only to predict acoustically-induced instability of safety relief valves but also to explain the physical origin of their onset.

REFERENCES

- [1] Morris, S., 1996. "Liquid flow through safety valves: Diameter ratio effects on discharge coefficients, sizing and stability". *Journal of Loss Prevention in the Process Industries*, **9**(3), pp. 217 – 224.
- [2] Moussou, P., Gibert, R. J., Brasseur, G., Teygeman, C., Ferrari, J., and Rit, J. F., 2010. "Instability of pressure relief valves in water pipes". *Journal of Pressure Vessel Technology*, **132**(4), p. 041308.
- [3] Hayashi, S., Hayase, T., and Kurahashi, T., 1997. "Chaos in a hydraulic control valve". *Journal of Fluids and Structures*, **11**(6), pp. 693 – 716.
- [4] Licskó, G., Champneys, A., and Hos, C., 2009. "Dynamical analysis of a hydraulic pressure relief valve". *Proceedings of the World Congress on Engineering 2009 Vol II*, July.
- [5] Cremers, J., Friedel, L., and Pallaks, B., 2001. "Validated sizing rule against chatter of relief valves during gas service". *Journal of Loss Prevention in the Process Industries*, **14**(4), pp. 261 – 267.
- [6] Frommann, O., and Friedel, L., 1998. "Analysis of safety relief valve chatter induced by pressure waves in gas flow". *Journal of Loss Prevention in the Process Industries*, **11**, pp. 279–290.
- [7] Shigehiko Kaneko, Tomomichi Nakamura, F. I. M. K., and Mureithi, N. W., eds., 2008. *Flow Induced Vibrations - Classifications and Lessons from Practical Experiences*. Elsevier.
- [8] Johnston, D. N., Edge, K. A., and Brunelli, M., 2002. "Impedance and stability characteristics of a relief valve". *Proceedings of the Institution of Mechanical Engineers, Part I: Journal of Systems and Control Engineering*, **216**(5), pp. 371–382.
- [9] Testud, P., Auregan, Y., Moussou, P., and Hirschberg, A., 2009. "The whistling potentiality of an orifice in a confined flow using an energetic criterion". *Journal of Sound and Vibration*, **325**(4-5), pp. 769 – 780.
- [10] Archambeau, F., Namane, M., and Sakiz, M., 2004. "Code saturne: A finite volume code for turbulent flows". *International Journal On Finite Volumes*, **1**(1), pp. 1–62.
- [11] Hirt, C., Amsden, A., and Cook, J., 1974. "An arbitrary lagrangian-eulerian computing method for all flow speeds". *Journal of Computational Physics*, **14**(3), pp. 227 – 253.

A THEORETICAL AND EXPERIMENTAL STUDY OF A DUCKBILL VALVE

J. Wang S. Tullis D.S. Weaver

Department of Mechanical Engineering
McMaster University

1280 Main St W, Hamilton, ON, Canada, L8S4L8

Email: wangj73@mcmaster.ca

ABSTRACT

A fluid-structure interaction (FSI) model was developed to model a duckbill valve (DBV) using shell elements with layered hyperelastic composite materials, and model the fluid as an ideal fluid (potential flow). The simulations were carried out with and without fiber layers, which were modeled as a laminated orthotropic material, to verify the effect of fabric reinforcement. An experimental study in a water tunnel was also carried out to verify the pressure-discharge characteristics, velocity profiles at the valve outlet, and valve opening profiles, predicted by the model. Additionally, flow induced valve oscillation at small openings was studied. In general, the theoretical predictions agree well with the experiment. Comparisons between the simulations and water tunnel results demonstrated that the valve performance was mainly dependent on the mechanics of the rubber bending deformation with lower pressure loadings, while the fabric extension reinforcement becomes dominant with higher pressure loadings.

NOMENCLATURE

A_{in}, A_{out}	– Section area of inlet and outlet
$A(z)$	– Area function
C_{10}, C_{01}, C_{11}	– Three parameters for the Mooney-Rivlin model
I_1, I_2, I_3	– Strain invariants
p	– Arbitrary hydrostatic pressure
P_{in}, P_{out}	– Pressure at inlet and outlet
P_t	– Total pressure
P_s	– Static pressure
$P(z)$	– Pressure function
Q	– Mass flow rate
t_i	– Time, $i=1,2,3,4,5,6$
V	– Velocity
V_{in}, V_{out}	– Velocity at inlet and outlet
W	– Strain energy potential
x, y, z	– x, y, z coordinates
ΔP	– Pressure difference
$\sigma_1, \sigma_2, \sigma_3$	– Principal stresses, $i=1,2,3$
$\lambda_1, \lambda_2, \lambda_3$	– Principle extension ratios

ε_i	– Engineering strains, $i=1,2,3$
ρ	– Fluid density
τ	– Period of cycle

INTRODUCTION

Duckbill valves are widely used as non-return valves for fluid flows with low back pressures. They have the shape of a conical section that narrows to an elongated slit (the duckbill, as seen in Fig.1), with the valve material usually consisting of a fabric reinforced layered rubber composite. Sufficient upstream pressure opens the valve, after which the flow is established, and the valve opening depends on the pressure drop across the valve. Thus, predicting the pressure drop-discharge characteristics is an FSI problem. There are many challenges in developing an effective and predictive model for these valves since the valve material is strongly nonlinear, undergoes very large deformations, and the fully coupled FSI modeling is demanding of computer capabilities. In addition, many of the valves employed in practice are so large that they cannot be tested in a laboratory. This makes the development of a reliable predictive model all the more important.

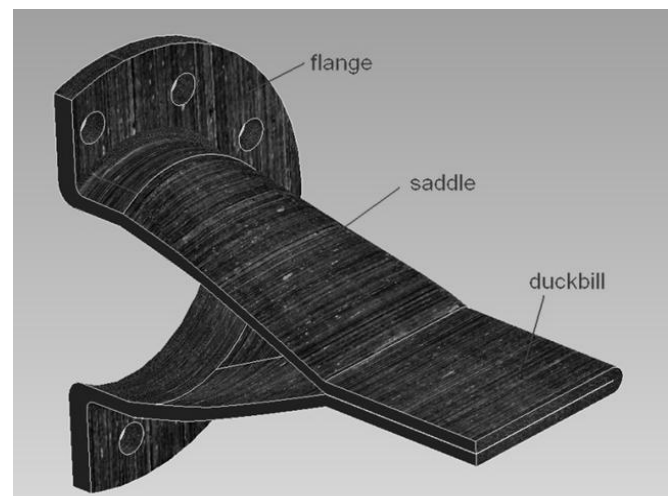


FIGURE 1: GEOMETRY OF DUCKBILL VALVE

However, research studies on the valves are unexpectedly lacking. Few published papers can be found. Some investigations are in the form of internal reports which are not easily found for academic purposes. Chouchaoui [1] conducted a series of tests on the valve composite materials and obtained some necessary parameters for hyperelastic rubber and orthotropically elastic fiber models. He also developed a solid model to simulate the valve deformation under static pressure loadings. However, the solid model worked in a very small pressure range (up to 1.67kPa) and the flow was not coupled. Lee et al. [2, 3, 4] published three papers using theoretical, numerical and experimental methods to investigate the characteristics of a duckbill valve. In reference [2], Lee et al. firstly developed a very simple analytical method to predict the hydraulic performance of a duckbill valve. In their theory, a duckbill valve could be considered as a smooth converging nozzle. By modeling the duckbill valve as a linear elastic rubber membrane coupled with a 1D potential flow model, the deflection and hydraulic performance of the duckbill valve under given pressure drops were calculated. However, the laminated layer structure of the valve materials with fabric reinforcement was excluded in their theory. Therefore, the nonlinearity of the rubber and orthotropic features of the fiber were not evaluated in their study. Lee et al. also conducted a computational fluid dynamics (CFD) simulation and a velocity field measurement to investigate duckbill valve jet flows [3]. The CFD simulation was a static case with $k-\epsilon$ model and focused on the downstream nozzle jet flows, the FSI of duckbill valve flow was not included. In reference [4], Lee et al. carried out a finite element simulation to study the relationship of large elastic deformation to flow variation of a duckbill valve. The valve was modeled by 224 20-node brick elements. The pressure load of potential flow inside the duckbill valve was applied as an inner surface boundary condition of the finite element model. The material of the duckbill valve was assumed to be a single linear material and no fabric reinforcement was modeled. They argued that the valve deformation was mainly dependent on the mechanics of the rubber deformation, and only secondarily on the fabric reinforcement and upstream connection, but this assumption had yet to be justified. In addition, the influence of fluid viscosity on the pressure and velocity fields was not compared with their prediction of 1D potential flow, even though their simulation results were reported to have a good agreement with their experimental data for hydraulic performance.

The present authors [5] developed a more realistic model of a duckbill valve. The valve was considered as a bottom-plane based laminated thick shell structure

with simplified boundary conditions along the duckbill edges. The hyperelastic behavior of the rubber and orthotropy of the fiber reinforcement were included, as were the large valve deformations. The flow was modeled as 1D potential flow similar to that used in reference [4]. The bottom-plane based shell model was beneficial to determine the deformed valve shape for coupling the 1D flow since the bottom-plane was just the interface between the fluid and solid domains. However, its mesh quality became relatively poor at the connection between the saddle and duckbill portions, which limited the driving pressure range from 5kPa to 20kPa. This work also demonstrated the important effects of the fabric layer at higher pressure drops.

In this paper, the shell model is modified using middle-plane based shell elements and the valve geometry becomes relatively smooth. Hence, the mesh quality is greatly improved. The coupling algorithm of the duckbill valve is also improved to be suitable for the middle-plane based shell geometry and the transient opening process is tracked until a steady state opening is achieved. A more precise three-parameter hyperelastic material model is applied to replace the previous two-parameter one. The simulations are carried out with and without orthotropic fiber layers to further verify the effects of the fiber layer. The hydraulic performance of the duckbill valve is predicted by the idea flow model. For purposes of verification, an experimental study in a water tunnel is also carried out to verify the valve performance predicted by the FSI model. The pressure-discharge relations, velocity profiles at the valve outlet, and valve opening profiles are all measured and compared with model predictions. Finally, to study the potential for flow induced vibration phenomena in the valve at small openings, duckbill oscillation is studied using the FSI model with a thicker valve wall and various damping factors for low flow rates.

ANALYSIS METHOD

Layered Shell Structure of DBV

In this paper, three different models are built. In the first model, the composite material is divided into a more detailed sandwich structure than that in the previous model [5], consisting of three internal layers of rubber (1 layer of Styrene-Butadiene Rubber (SBR) and 2 layers of Chloroprene Rubber (CR), 3mm thick per layer), two layers of fabric reinforcement in the middle (Fiber #82 (W-82A), approximately 1mm thick each layer, layered in angles of $\pm 45^\circ$ along the valve longitudinal direction), and one external layer of rubber (Ethylene Propylene Diene Monomer rubber (EPDM), 3mm thick). Thus, the total thickness of the rubber matrix hosting the fabric reinforcement is around 14mm, the same as that of the tested valves in the water tunnel.

In the second model, the fiber layer is excluded and a 2mm CR layer is used in the model. To investigate the flow induced vibration phenomenon of the duckbill valve at small openings, a thicker valve wall is used in the third model to reduce the mesh deformation and increase the stability of the solution. The valve wall is totally 16mm thick and consists of one layer of EPDM and two layers of CR, two layers of woven fabric reinforcement which are the same as in [1, 5], and two layers of SBR. Since the ratios of valve wall thickness to duckbill width are all around 5%, it is reasonable to consider the valve geometries as a moderately thick shell structure [6].

Hyperelasticity and Orthotropic Features of the Valve Materials

Here, the three-parameter Mooney-Rivlin model is applied for the constitutive relations of rubber materials [6, 7, 8, 9]. The form of stored energy function for the Mooney-Rivlin model is given by:

$$W = C_{10}(I_1 - 3) + C_{01}(I_2 - 3) + C_{11}(I_1 - 3)(I_2 - 3) \quad (1)$$

where the strain invariants are defined by

$$\begin{aligned} I_1 &= \lambda_1^2 + \lambda_2^2 + \lambda_3^2 \\ I_2 &= \lambda_1^2 \lambda_2^2 + \lambda_2^2 \lambda_3^2 + \lambda_3^2 \lambda_1^2 \\ I_3 &= \lambda_1^2 \lambda_2^2 \lambda_3^2 = 1 \end{aligned} \quad (2)$$

The principal extension ratios are defined as $\lambda_i = 1 + \varepsilon_i$, ($i=1, 2, 3$), ε_i is the principal value of the engineering strain tensor in the i th direction. $I_3=1$ is required by the incompressibility of rubber.

The material tests of rubber (EPDM, CR, and SBR) and fiber sheets (W-82A), as well as three point bending tests of the composite matrix, were conducted by Axel Products, Inc., USA. while the rubber material curve fitting was processed at McMaster University. Table 1 lists the coefficients of the 3-p Mooney-Rivlin models for SBR, CR and EPDM.

TABLE 1: COEFFICIENTS FOR 3-P MOONEY RIVLIN MODEL

	C10	C01	C11
SBR	-6.55 MPa	7.92 MPa	2.82 MPa
CR	-1.50 MPa	2.11 MPa	0.66 MPa
EPDM	-2.91 MPa	3.66 MPa	1.47 MPa

The stress-strain relations are given by [6, 7, 9]

$$\sigma_i = \lambda_i \left(\frac{\partial W}{\partial I_1} \frac{\partial I_1}{\partial \lambda_i} + \frac{\partial W}{\partial I_2} \frac{\partial I_2}{\partial \lambda_i} \right) - p \quad (3)$$

where σ_i are the principal stresses, $i=1,2,3$, and p is an arbitrary hydrostatic pressure.

The orthotropic properties of unidirectional fabric reinforced resins matrix, W-82A, were evaluated using

the Halpin-Tsai equations based on the warp and weft extension tests. The results are listed in Table 2.

TABLE 2: ORTHOTROPIC PROPERTIES OF FIBER SHEET W-82A

E_x	1555MPa	G_{xy}	2.94MPa	ν_{xy}	0.27
E_y	7.94MPa	G_{xz}	2.94MPa	ν_{xz}	0.27
E_z	7.94MPa	G_{yz}	5.57MPa	ν_{yz}	0.28

where E_x, E_y, E_z are Young's modulus's in x, y, z directions, G_{xy}, G_{xz}, G_{yz} are the shear modulus in each plane, and $\nu_{xy}, \nu_{xz}, \nu_{yz}$ are the Poisson ratio in each direction. The stress and strain linear relations are determined by using Hooke's law.

Flow Model and Fluid Structure Coupling

Figure 2 shows a schematic diagram of the coupled model. Since the valve area is rapidly but smoothly decreasing through the valve tunnel, the flow can be approximated using Bernoulli's equation [10]. A detailed description of the 1D flow model can be found in reference [5]. Generally, the local pressure, $P(z)$, along the valve deflects the valve surface as determined by the valve material properties. This deflection establishes the flow area, $A(z)$, and by mass continuity, the velocity variation through the valve. This velocity determines the pressure which, in turn, controls the valve deflection. Thus, the problem of determining the mass flux through a DBV for a given pressure drop requires a coupled fluid-structure analysis. In the present calculations, an upstream pressure with a small initial opening (say, 0.1mm) is imposed on the valve, the valve deflection is computed, the exit area and flow velocity are determined assuming zero pressure at the outlet and, using mass continuity, the inlet flow velocity is calculated. This velocity and the imposed inlet pressure are used to repeat the calculations iteratively until a steady state is achieved, i.e., for the imposed inlet pressure, when the computed mass flow rate agrees with that assumed for the calculation from the last iteration step.

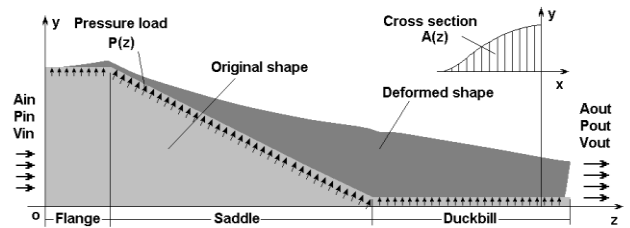


FIGURE 2: SCHEMATIC DIAGRAM OF COUPLED IDEAL FLOW MODEL

In some instances, a stable equilibrium could not be found if valve vibration occurred. In such cases,

structure damping becomes significant in the simulation. By adjusting the damping, the dynamic response of the valve to the flow can be observed for small flow rates, i.e., unsteady duckbill fluttering, and stable limit cycle valve vibrations.

Laminate Shell Elements and Boundary Conditions

ANSYS shell elements can be used to model layered composite materials [11][12]. The element used was a 4-node shell element with six degrees of freedom at each node. The accuracy in modeling rubber-fiber materials is governed by the Mindlin-Reissner shell theory [6]. The layers of shell are defined by the layer thickness, material number, and layer position. The computed result for each layer is recorded during the simulation. Symmetries about the x - z plane and y - z plane are assumed so that only one quarter of the valve about the planes of symmetry is modeled. Figure 3 shows the quadrilateral grids and boundary conditions for the DBV shell model. In the previous model, some quadrilateral grids degenerated to triangular grids due to the curvature of the valve surface, which resulted in poor shapes at large valve deformations. In the present model, all quadrilateral grids are well generated as seen in the figure. There are a total of 1152 layered hyperelastic shell elements and 1225 nodes.

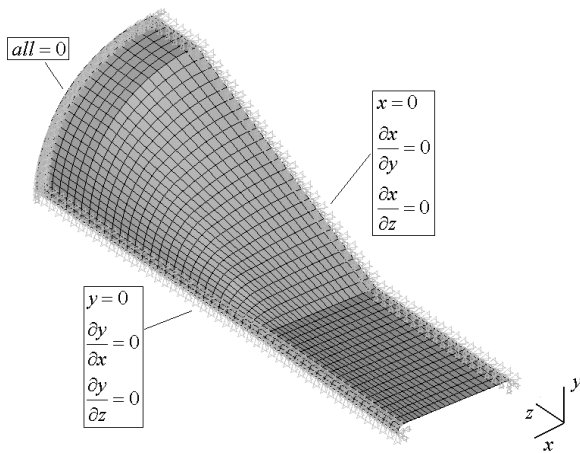


FIGURE 3: FINITE ELEMENT MESH AND BOUNDARY CONDITIONS OF SHELL MODEL

In the previous model, strictly speaking, some rotation in the y - z plane can occur along the side of the duckbill portion, i.e. $\partial y / \partial z \neq 0$. This rotation will be a function of valve opening and the largest near the valve outlet. The shell elements cannot model this behaviour along the valve sides. The error associated with this simplification is expected to be small since only the first row of elements along the sides are fixed.

In the present model, the rotation of the side edge around the z -axis is still fixed. However, there exists a

small arch structure along the side edge of the duckbill portion due to the middle-plane based geometry, which extends the duckbill in the transverse direction and avoids the fixed rotation applied directly on the bottom based side edge. Generally, this arch structure is expected to reduce the above error to a considerable degree.

The ANSYS Parametric Design Language (APDL) code was rewritten for the FSI model. Since the mesh quality was improved in the present model, more stably convergent solutions could be obtained within a wide range of driving pressure drops (from 1kPa to 80kPa).

Water Tunnel Experiment

Figure 4 schematically illustrates the water tunnel and data acquisition system [13]. Water was driven by a pump and flows in a closed pipe loop. A flow straightener/conditioner was used to make the upstream velocity profile uniform and reduce turbulence intensity. The overall flow rate was adjusted by a motor control box and measured by a volume flow meter. Two different but apparently identical valves were used in the water tunnel experiments.

Seven sets of pressure taps (each set with 4 taps equally spaced around the test section pipe) were used to measure the static pressure drops between the set 1 and set 2 to 7, as indicated in Fig. 4. A ball valve system was used to switch on/off between the taps for the measurement of pressure drop ΔP using a differential pressure transducer.

Two Pitot probes were set close to the inlet and outlet of the duckbill valve and could be moved up and down to measure the velocity profiles at the valve inlet and outlet. The inlet velocity was measured using a U-tube manometer due to the lower pressure drop, while the outlet velocity is measured using the differential pressure transducer. The velocity measured by the Pitot probes is defined by:

$$V = \sqrt{\frac{2}{\rho} (P_t - P_s)} \quad (4)$$

where V is velocity, ρ is fluid density, P_t is total pressure and P_s is static pressure.

The output signals from the transducer were amplified by a Validyne CD101 conditioner and transferred to a NI PCI-6024E A/D card, which was plugged in an HP desktop computer. The commercial code, Labview was applied to analyze the digital signals.

Since the deformation of the duckbill valve was essential to evaluate the outlet area-discharge relation, it was measured using five angled ruler scales with sliding probes installed near the valve outlet to determine the valve deformation shape as shown in Fig. 4.

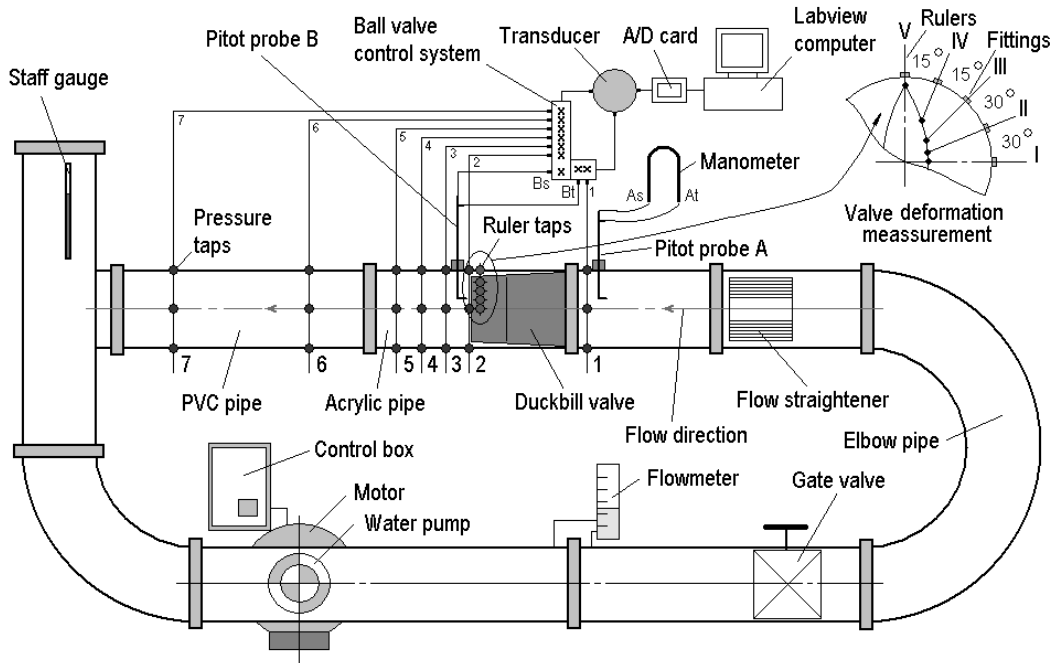


FIGURE 4: SCHEMATIC DIAGRAM OF 12" DIAMETER WATER TUNNEL SYSTEM

RESULTS AND DISCUSSION

Hydraulic Characteristics of DBV

For convenience of comparing the simulations with the experiments, the driving pressure drops of the valve models (with and without fiber layers) were the same as those measured from the water tunnel. Figure 5 shows the relationships between the pressure drops and the mass flow rates for the duckbill valve, including both the theoretical predictions and experimental results. The relationship may be considered roughly linear within a wide pressure range. However, it is seen that a relatively large pressure increase is required to produce a relatively small mass flow rate during the initial opening process (i.e. cases from 0kPa to 6kPa). Recall that this head-discharge characteristic contrasts sharply with rigid valves which typically have a pressure drop which increases with the square of the flow rate.

Interestingly, it is seen that the water tunnel results match well with both the valve models with or without fiber layers at smaller flow rates, but approach the valve model with fiber layers at higher flow rates. This indicates that the valve performance is primarily dependent on the mechanics of the rubber bending deformation under lower pressure loadings, while the fabric extension reinforcement becomes dominant under higher pressure loadings.

This makes sense because the relatively stiffer fiber layer is located near the neutral axis of bending and therefore, will have little influence on bending stiffness but dominates in-plane stretching. It follows that neglect of the fiber layer in modelling valve

deformation due to significant pressure drops could lead to serious errors, contrary to the assumption of Lee, et al [4].

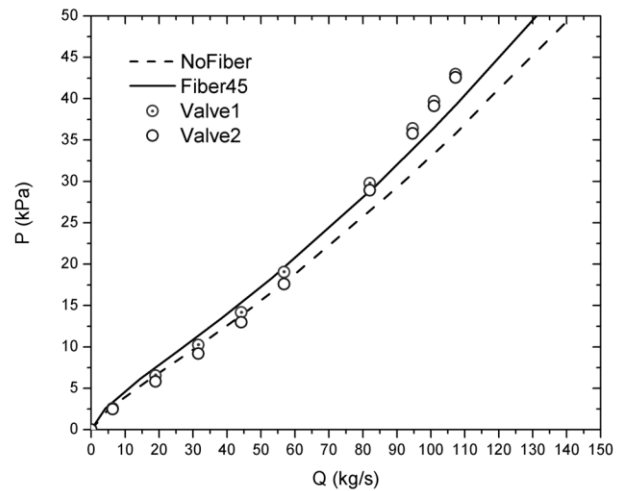


FIGURE 5: PRESSURE DROP-DISCHARGE RELATIONSHIPS

Figure 6 shows the velocity-head relations. It is seen that the 1D predictions agree excellently with the experiment. Static viscous flow models based on the deformed valve shapes predicted by the coupled model were also shown to match well with the 1D predictions indicating the fluid viscosity effect was small in the valve flow.

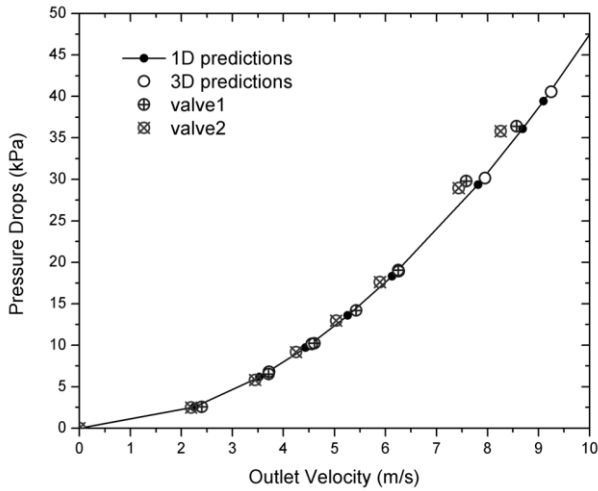


FIGURE 6: OUTLET VELOCITY-PRESSURE DROP RELATIONSHIPS

Valve Deformations

Figure 7 shows the valve opening areas predicted by the coupled model with fiber layers under the increasing pressure drops of 10kPa, 18kPa, and 29kPa. The two measured valve opening deformations are also shown in this figure. Generally, the simulations under predicted the duckbill openings.

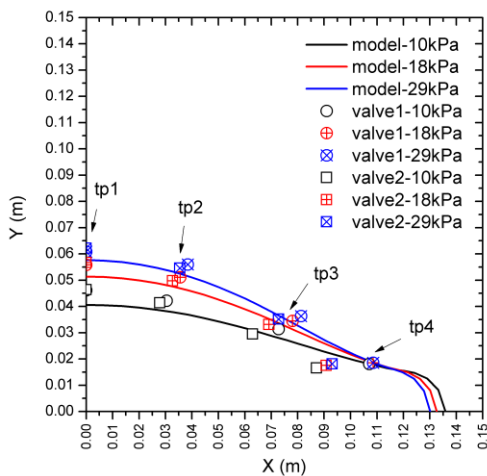


FIGURE 7: DEFORMATION SHAPES OF EXIT AREA UNDER VARIOUS DRIVING PRESSURES

Flow Induced Vibration of DBV

As mentioned above, a valve model with a thicker fiber layer and valve wall was developed to investigate the flow induced valve oscillation at small openings under various damping ratios. The computations were performed for a range of pressures drops ($\Delta P=1\sim 80$ kPa), which corresponds to a flow range of $Q=0.3\sim 145$ kg/s.

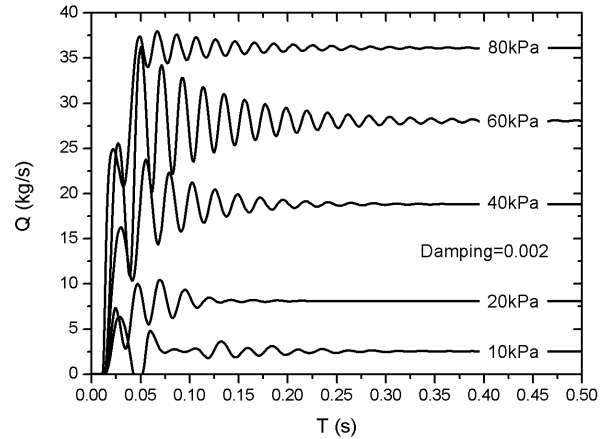


FIGURE 8: STABLE CONVERGENCES OF DUCKBILL VALVE SOLUTIONS

A flow induced vibration often occurs in certain valves at small openings. Weaver and Ziada [14] summarized three mechanisms causing such phenomena, i.e. jet flow inertia, turbulence and acoustic resonance. In the present case, the vibrations are associated with a high velocity jet through the narrow opening of the valve. The results for the transient opening process are shown in Fig. 8 for various suddenly imposed upstream pressures ranging from 10kPa to 80kPa. It is seen that the valve opens quickly, overshoots, and goes through decaying oscillations before the flow asymptotes to the steady flow condition for the assumed upstream pressure. A small damping ratio with a magnitude of 0.002 is applied for each case to accelerate the convergence of iteration. All five cases are convergent within the solution time of 0.5s.

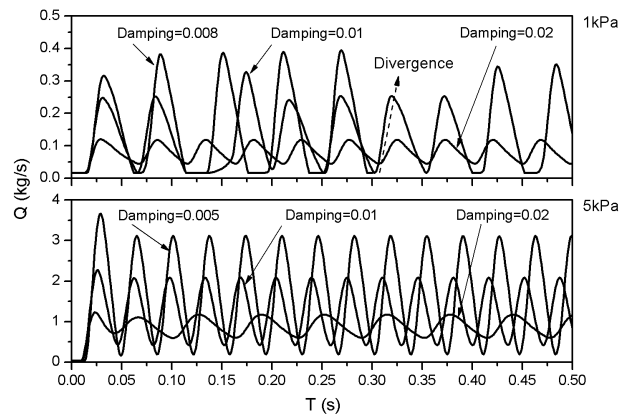


FIGURE 9: FLOW INDUCED VIBRATIONS OF DUCKBILL VALVE AT SMALL OPENINGS FOR SMALL FLOW RATES

Figure 9 shows the predicted valve behavior for the lower pressure drops of 1kPa and 5kPa with three different damping ratios. For the 5kPa case, the valve maintains a steady vibration amplitude after a brief transient. As the damping increases, both the amplitude

and frequency of oscillation decreases. For the 1kPa case, the predicted behaviour is the same as for the 5kPa case when the damping ratio is 0.02. However, for smaller damping, the solution appears unsteady (damping ratio 0.01) or unstable (damping ratio 0.008). The flat portion of the response curves near zero opening indicates that the duckbill is actually flapping shut briefly during its oscillation cycle which leads to numerical stability issues in the simulations. Certainly this is the case for the smallest damping ratios as the predicted divergence of the valve is not physically possible.

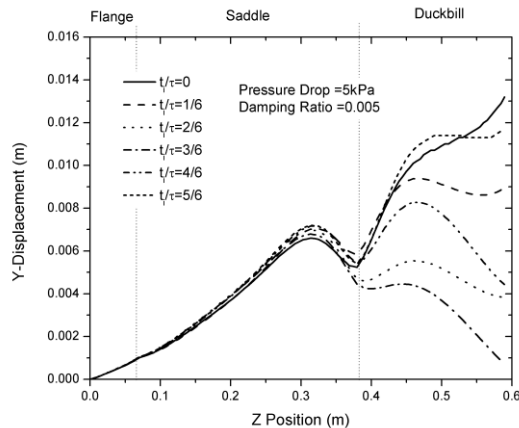


FIGURE 10: CENTERLINE NODE Y-DISPLACEMENTS OF THE VALVE MODEL AT VARIOUS TIMES IN AN OSCILLATION CYCLE

Figure 10 shows the node y -displacements of the pathline at the central symmetric y - z plane of the valve model for the 5kPa case. There are six sets of node displacement curves corresponding to six different times, illustrating that the vibration occurs mainly in the duckbill portion. The latter is seen to have its largest amplitude at the valve exit with a streamwise motion like a travelling wave. This behavior seems reasonable physically but experimental verification is required to ensure that the observations are not due to numerical instability.

CONCLUSIONS

Duckbill valves are non-return valves made of a composite material which deforms to open the valve as the upstream pressure increases. The head-discharge behavior is a fluid-structure interaction problem since the discharge depends on the valve opening which depends on the pressure distribution along the valve produced by the discharge. To design a duckbill valve, a theoretical model is required which will predict the head-discharge characteristics as a function of valve material and geometry.

The particular valves of concern in this study can be very large and are made from laminated, fiber-

reinforced rubber. Thus, the structural problem has strong material nonlinearities as well as geometric nonlinearities due to the large deflections. Clearly, a fully coupled FSI analysis using three dimensional viscous flow would be very challenging and therefore, a simplified approach was sought which treats the essential aspects of the problem in a tractable way.

The DBV was modeled using thick shell finite elements which included the laminates of hyperelastic rubber and orthotropic fiber reinforcement. The FEM was simplified by assuming that the side edges of the valve were clamped. The unsteady Bernoulli equation was used to model the fluid dynamics which enabled a full FSI analysis.

In order to validate the predictions of the FSI simulations, an experimental study was carried out at several mass flow rates. Pressure drops along the water tunnel, valve inlet and outlet velocity profiles, and valve opening deformations were all measured as functions of upstream pressure.

FIV of the valve at small openings was also examined to improve our understanding of valve stability behavior. Some interesting phenomena were observed. The following general conclusions are drawn:

- 1) In spite of its relative simplicity, the 1D unsteady Bernoulli approximation appears adequate for modeling the flow behavior of duckbill valves and makes the fluid-structure interaction simulations much more tractable.
- 2) At relatively small driving pressures, the present model of the laminated rubber including the fiber reinforcement layer seems to over predict the valve stiffness and therefore underestimate the valve discharge for a given pressure. Neglecting the fiber reinforcement in the model produces good agreement with the experiments.
- 3) At relatively high driving pressures, the fiber reinforcement layer plays a dominant role in modeling the large valve deformations and the full laminated rubber with fiber reinforcement model provides valve deformation and discharge characteristics which agree well with experiments.
- 4) At very low driving pressures, the valve openings are very small and the simulations predict valve oscillations. This behavior is very challenging numerically and viscosity effects are probably significant. More theoretical and experimental research is necessary to better understand this behavior.

ACKNOWLEDGMENT

The authors gratefully acknowledge the financial support of the Natural Sciences and Engineering Research Council of Canada (NSERC), the Ontario

Centers of Excellence (OCE), Ontario Graduate Scholarship (OGS), and Elasto-Valve Rubber Products Inc. (EVR). EVR also supplied DBV samples for study and some material data and related literature.

REFERENCES

- [1] Chouchaoui, B., 2001, *Simulating Flow through 8" Duckbill Valve*, Internal Report, EVL001, Windsor Industrial Development Laboratory, Inc., Canada.
- [2] Lee, J.H.W., Wilkinson, D.L., and Wood, I.R., 2001, *On the Head-Discharge Relation of a "Duckbill" Elastomer Check Valve*, *Journal of Hydraulic Research*, Vol.39, No.6, p619~628.
- [3] Lee, J.H.W., Kuang, C.P. and Chan, H.C., 2002, "The Velocity Field of a Duckbill Valve (DBV) Jet in Coflow", 15th ASCE Engineering Mechanics Conference, Columbia University, New York, NY.
- [4] Lee, J.H.W., Lo, S.H. and Lee, K.L., 2004, "Flow Variation of Duckbill Valve Jet in Relation to Large Elastic Deformation", *Journal of Engineering Mechanics*, ASCE, Vol. 130, Issue 8, p971~981.
- [5] Wang, J., Weaver, D.S., and Tullis, S., 2012, "Simplified Fluid-Structural Model for Duckbill Valve Flow", *Journal of Pressure Vessel Technology*, ASME Transactions, Paper in Press.
- [6] ANSYS Inc., 2010, ANSYS and CFX user's manual.
- [7] Treloar, L. R. G., 1958, *The Physics of Rubber Elasticity*, 2nd Edition, Oxford University Press, pp342.
- [8] Mooney, M., 1940, "A Theory of Large Elastic Deformation", *Journal of Applied Physics*, p582~592.
- [9] Rivlin, R.S., 1948, "Large Elastic Deformations of Isotropic Materials", *Philosophical Transactions of The Royal Society*, Vol.241, p379-397.
- [10] Streeter, V.L., and Wylie, E.B., 1985, *Fluid Mechanics*, 8th edition, New York, McGraw Hill.
- [11] Reddy, J.N., 1984, "Exact Solutions of Moderately Thick Laminated Shells", *Journal of Engineering Mechanics*, Vol.110, No.5, p 790~809, May.
- [12] Timoshenko, S. P. and Woinowsky-Krieger, S., 1959, *Theory of Plates and Shells*, 2nd Edition, McGraw-Hill Book Company, pp580.
- [13] Wang, J., 2012, *Water Tunnel Test Report*, Internal Report, Department of Mechanical Engineering, McMaster University, Canada.
- [14] Weaver, D.S. and Ziada, S., 1980, "A Theoretical Model for Self-Excited Vibrations in Hydraulic Gates, Valves and Seals", *Journal of Fluids Engineering*, Transactions of the ASME, Vol. 100, p239-245.



OUTPUT-ONLY IDENTIFICATION OF AN ELASTIC PANEL COUPLED TO A FLUID: MODEL-SCALE AND FULL-SCALE INVESTIGATIONS FOR SHIPS

Daniele Dessi*

Diego D'Orazio

INSEAN

National Research Council of Italy

Rome, Italy

Email: d.dessi@insean.it

ABSTRACT

In this paper the Proper Orthogonal Decomposition (POD) is applied to the identification of elastic plates coupled to fluid (water). The excitation is provided by the turbulent boundary layer wetting the plate on one side and the plate response is measured with an array of twelve accelerometers. Two cases are considered: an aluminum plate mounted at the bottom of a scaled hull model tested in the towing tank and a stiffened steel plate of a ro-ro pax ferry during regular service.

INTRODUCTION

In marine engineering, there is a renovate effort to provide additional insights on the structural behaviour of floating structures. Thus, although the theory of hydroelasticity concerning this kind of coupled fluid-structure systems was essentially established in the eighties, new challenges relative to the application of the governing equations arise as long as advanced vehicles or constructions appear. Indeed, naval architecture has been exploiting experimental investigation as a tool to design ships since a long time. Towing-tank facilities were built at the beginning of last century for studying performances and sea-keeping features of novel hull forms. However, less attention was paid to the analysis of structural aspects because ship weight had never been of concern to the naval architect. Recently, weight reduction has led to more flexible structures that may suffer vibrations. Thus, fatigue analysis has become part of the design process and the correct evaluation of damping a relevant information for that. The investigation of these aspects has motivated not only the need of frequency analysis and

time domain simulation, but also more challenging objectives for experiments in model basins. Indeed, recent advances in measurement techniques and fabrication technology has broadened the capability to design experimental set-ups where scaled models can reproduce, even if partially, the full-scale elastic behavior. Thus, also in marine and ship engineering it is now reasonable to distinguish a research area known as experimental fluid-structure dynamics, where structural identification may play a relevant role in the future.

In previous papers, frequency domain decomposition (FDD) [1] and proper orthogonal decomposition (POD) [2] techniques were applied to floating structures, exploiting the ambient excitation provided by the waves. In this paper, the focus is on identification of the vibration modes of a plate excited by a turbulent boundary layer (TBL) on one side. The TBL is generated by the inflow around a scaled model of a ship towed in the towing tank. The aluminum plate is inserted at the wooden hull bottom through a steel frame that allows clamping of the plate and its response is acquired from 12 accelerometers. The non-stationary and random pressure field provides the so-called ambient excitation necessary for application of modal analysis procedures based on the measurement of the structural response alone. Thus, POD in its standard and modified forms is herein used as an output-only technique to determine the shape of the 'wetted' modes and its associated energy. Even if the plate has constant thickness, the application of POD without supplying information about mass distribution fails to extract the vibration mode shapes because of the mass of the accelerometers. Similarly to what was done in the case of floating structures [2], the use of a slightly different technique, known as band-pass POD (BP-POD), allows

*Address all correspondence to this author.

to overcome this limitation. As a further demonstration of the capability and usefulness of output-only procedures, identification of the first vibration modes of a stiffened hull panel below the waterline of a ferry was carried out and some results are reported at the end of this paper.

IDENTIFICATION TECHNIQUES

Output-only approach to the identification of vibration modes

In last decades, the vibration analysis has taken advantage of a new approach to structural identification, known as operational modal analysis. This approach aims to broaden the field of application of experimental modal testing, lifting the requirement of simultaneous measurements of both the excitation force and the elastic response of the structure.

From a general point of view, the modal analysis allows characterization of the dynamics of linear and time-invariant structures in terms of mode shapes, natural frequencies and modal damping, providing a well established theoretical frame to explain vibrations. Nevertheless, marine structures demand for updating of these coefficients to modal analysis techniques. The main point is that marine structures are coupled to a heavy fluid that, due to the increased fluid inertia and damping, changes significantly the modal behavior of the structure with respect to the dry case. If a linear behavior is assumed, the presence of the fluid can be taken into account by defining the fluid added mass, damping and stiffness terms in the hydroelastic equations. The determination of added mass at rest (zero inflow velocity and absence of surface waves for floating bodies) is quite straightforward and several commercial codes yield wet mode shapes and natural frequencies in agreement with experimental values, provided that dry frequencies were originally accurate. However, the estimation of the overall damping in practical cases may be approximate and there is no *a priori* knowledge of the number of modes necessary to calculate the hydroelastic response, information that becomes critical if reduced order models are sought. Moreover, experimental validation or updating becomes worthwhile also if extreme loading conditions are concerned, like large amplitude motion in severe sea states or high forward speeds.

In the perspective of applying input-output modal analysis, the main concern is to provide an adequate source of excitation in terms of intensity, frequency spectrum and chances to estimate these values. However, this task may be too expensive in the case of large structures, such as a ship. Moreover, it becomes unfeasible if the identification procedure is part of a real-time monitor-

ing system that points to evaluate the modal parameters in operational conditions. For these reason, output-only approaches give the best chance to avoid the restrictions frequently met in experimental modal analysis of marine structures.

Several output-only techniques have been originally developed in last decades or were proposed adapting approaches that were not initially conceived for structural identification. Frequency domain decomposition (Brincker, [3]) or Stochastic Subspace Identification (Overschee and Moor, [4]) are quite popular in modal testing. The first applications of POD in the field of structural dynamics date back to the nineties and were mainly devoted to nonlinear problems. In the field of structural dynamics of linear systems, several papers considered the use of POD as an output-only technique, motivating also some different versions of the original algorithm [5–7]).

The Proper Orthogonal Decomposition

From a general point of view, the POD is a multivariate statistical method that aims to obtain a compact representation of a dataset, regardless of the origin of the data. The POD extracts an orthonormal basis (proper orthogonal modes) to decompose the analyzed dataset, so that the projection of the data onto these basis functions contains as much energy as possible. The method, often called Karhunen-Loeve decomposition from the name of the authors that stated the method [8, 9] has appeared in literature with various names depending on the area of application

Consider a zero-mean scalar random field $w(\mathbf{x}, t)$ with $\mathbf{x} \in \Omega$ (finite domain), expressed in the variable-separated form as an infinite sum of terms

$$w(\mathbf{x}, t) = \sum_{k=1}^{\infty} w_k(t) \psi_k(\mathbf{x}), \quad (1)$$

with $\psi_k(\mathbf{x})$ unknown scalar basis functions. For instance $w(\mathbf{x}, t)$ is the displacement field that satisfies the equation

$$\mu(\mathbf{x}) \ddot{w}(\mathbf{x}, t) + \mathcal{L}w(\mathbf{x}, t) = f(\mathbf{x}, t), \quad (2)$$

where \mathcal{L} defines a linear self adjoint (structural) operator (with respect to given boundary conditions), $\mu(\mathbf{x})$ is the mass per unit area, $f(\mathbf{x}, t)$ is the pressure forcing term and the dots denote differentiation with respect time. From a general point of view, the decomposition of the field $w(\mathbf{x}, t)$ does not require the knowledge of the form of the governing equation. Nevertheless, due to the link that we intend to establish between POMs and LNMs, it is useful

to explain the method with reference to the mechanical problem. Clearly the expansion provided by Eq. (1) is not unique and depends on the choice of the basis functions $\psi_k(\mathbf{x})$. The POD deals with one possible choice of the functions $\psi_k(\mathbf{x})$, based on the criteria of orthogonality between the basis functions and optimality in the least squares sense: fixed a limited number L of functions, they provide an approximated representation of the field that accounts for more energy compared with any other orthogonal function representation.

It can be demonstrated that the optimal basis functions are the solution of the integral equation

$$I(\psi; \lambda) = \int_{\Omega} R(\mathbf{x}, \mathbf{y}) \psi(\mathbf{y}) d\mathbf{y}, = \lambda \psi(\mathbf{x})$$

$$\text{with } R(\mathbf{x}, \mathbf{y}) = \frac{1}{T} \int_0^T w(\mathbf{x}, t) w(\mathbf{y}, t) dt, \quad (3)$$

where $R(\mathbf{x}, \mathbf{y})$ is the time averaged autocorrelation function and λ an eigenvalue. In other words, Eq. (3) defines the optimal basis function as the eigensolutions of the integral operator. Since the eigenvalue problem for $I(\psi; \lambda)$ has to be solved numerically in most cases, it turns out that the POMs can be equivalently determined by applying the POD on the solution $\mathbf{w}(t) \in \mathbb{R}^M$ of the following equation

$$\mathbf{M}\ddot{\mathbf{w}} + \mathbf{K}\mathbf{w} = \mathbf{f}, \quad (4)$$

that represents a suitable discretization of the continuous problem defined by Eq. (2), with \mathbf{M} and \mathbf{K} the mass and stiffness $M \times M$ square matrices of the discretized system, respectively, and M the considered dofs. For instance, one may assume that the i -th component of the vector $\mathbf{w}(t)$ is provided by the evaluation of the field $w(\mathbf{x}, t)$ at the grid node \mathbf{x}_i of a plate. Thus, we look for a decomposition:

$$\mathbf{w}(t) = \sum_{k=1}^L a_k(t) \mathbf{p}^{(k)}, \quad (5)$$

that gives the best representation of the solution \mathbf{w} in the sense already specified for the continuous problem, where the vectors $\mathbf{p}^{(k)} \in \mathbb{R}^M$ denote the POMs. It is useful to introduce the following transformation in Eq. (4),

$$\mathbf{w} = \mathbf{M}^{-1/2} \hat{\mathbf{w}}, \quad (6)$$

thus obtaining

$$\ddot{\hat{\mathbf{w}}} + \hat{\mathbf{K}}\hat{\mathbf{w}} = \hat{\mathbf{f}}, \quad (7)$$

where the matrix $\hat{\mathbf{K}} = \mathbf{M}^{-1/2} \mathbf{K} \mathbf{M}^{-1/2}$ is still symmetric and $\hat{\mathbf{f}} = \mathbf{M}^{-1/2} \mathbf{f}$. Equation (7) defines an undamped mechanical system with uniform mass distribution ($\mathbf{M} = \mathbf{I}$ in this particular case) for which the LNM are directly provided by the POMs. The convergence of POMs to LNM is a key point in the present analysis that has been diffusely treated in a recent paper by Mariani and Dessi [2]. If N ‘observations’ for each of the M components of the vector $\hat{\mathbf{w}}$ are available, let us define a new vector variable, $\hat{\mathbf{w}}^{(m)} = \{\hat{w}_m(t_1), \dots, \hat{w}_m(t_N)\}^T$, that is the sampled time history relative to the m -th component of the vector $\hat{\mathbf{w}}(t)$. Thus, the $N \times M$ response ensemble matrix is constructed as

$$\hat{\mathbf{W}} = [\hat{\mathbf{w}}^{(1)}, \hat{\mathbf{w}}^{(2)}, \dots, \hat{\mathbf{w}}^{(M)}], \quad (8)$$

that allows us to obtain the sample covariance matrix as $\mathbf{R}_{\hat{\mathbf{w}}} = \frac{1}{N} \hat{\mathbf{W}}^T \cdot \hat{\mathbf{W}}$, where the symbol \cdot denotes the inner product, and the POMs are calculated as the eigenvectors of $\mathbf{R}_{\hat{\mathbf{w}}}$, *i.e.*,

$$\mathbf{R}_{\hat{\mathbf{w}}} \hat{\mathbf{p}} = \sigma \hat{\mathbf{p}}, \quad (9)$$

where the eigenvalue σ is the corresponding proper orthogonal value (POV). Considering the system response in its continuous form (Eqs. (2) and (3)), it emerges that the averaged auto-correlation function $R(\mathbf{x}, \mathbf{y})$ and the basis functions $\psi_k(\mathbf{x})$ have been replaced by the $M \times M$ sample covariance matrix $\mathbf{R}_{\hat{\mathbf{w}}}$ and the proper orthogonal vectors $\hat{\mathbf{p}}^{(k)}$, respectively. Each POV gives an indication of the level of excitation of the correspondent POM, being the estimated total energy $\mathcal{E} = \sigma_1 + \dots + \sigma_M$ defined as the norm of the signal and not as mechanical energy. The proper orthogonal coordinate (POC) functions $\hat{a}_k(t)$, relative to the decomposition of the solution $\hat{\mathbf{w}}(t)$ (cfr. Eq. (5)), are:

$$\hat{\mathbf{w}}(t) = \sum_{k=1}^L \hat{a}_k(t) \hat{\mathbf{p}}^{(k)}, \quad (10)$$

and can be defined as a suitable interpolation over the proper coordinate vector $\hat{\mathbf{a}}^{(k)} = \{\hat{a}_k(t_1), \dots, \hat{a}_k(t_N)\}^T$, that is provided as

$$[\hat{\mathbf{a}}^{(1)}, \hat{\mathbf{a}}^{(2)}, \dots, \hat{\mathbf{a}}^{(M)}] = \hat{\mathbf{W}} \cdot \hat{\mathbf{P}}, \quad (11)$$

with $\hat{\mathbf{P}} = [\hat{\mathbf{p}}^{(1)}, \hat{\mathbf{p}}^{(2)}, \dots, \hat{\mathbf{p}}^{(M)}]$. In general, the number of assumed modes L is less or equal than the number of considered response points M . Using Eq. (6) is then possible to obtain the POMs $\mathbf{p}^{(k)}$ relative to Eq. (4).

TABLE 1: MAIN STRUCTURAL PARAMETERS OF THE PLATE.

Length (along x)	l_x	0.35 m
Width (along y)	l_y	0.32 m
Thickness (along z)	t	0.002 m
Density	ρ	2700 Kg/m ³
Young modulus	E	70 GPa
Poisson ratio	ν	0.25

MODEL-SCALE ANALYSIS

Experimental set-up

Acceleration signals relative to plate response excited by the TBL flow provided the data to be processed by POD. The plate is located in the bottom of a wooden hull (see Fig. 1) towed by the carriage at INSEAN towing tank basin in Rome. This experimental set-up allows to have a plate wetted by water on one side alone (bottom side) and dry on the top side where sensors were put on as shown in Fig. 2. The main dimensions of the aluminum plate are reported in Tab. 1. Instead of using glue like silicone to connect the plate to the wooden bottom, it was preferred to build a steel frame to clamp the plate edges. The steel frame was then inserted into a gap made on the bottom and then properly fixed. The first vibration mode of the frame, depicted in Fig. 3, was close to 5 KHz indicating that it is sufficiently rigid with respect to the plate. Finite element analysis confirmed that the dry frequencies of the plate did not exhibit differences larger than 0.5% if the presence of the steel frame was taken into account instead of applying ideal boundary conditions on the plate contour. Indeed, the choice of these ideal boundary conditions to represent correctly the real plate dynamics constitutes a critical point. First, the plate FE model was updated through modal identification (hammer impact test) of the plate itself lying on very soft rubber supports mimicking free boundary conditions. In Tab. 2 the corresponding frequencies, experimentally identified, are reported. Then, identification was carried out on the plate in its final arrangement at the hull bottom, leading to vibration mode frequencies in Tab. 2 slightly less than those relative to the case of the unconstrained plate. Simulations show that these frequencies can be obtained only relaxing the constraint on the rotations along the plate contour, even if very stiff rotational springs are needed. Therefore, the real boundary conditions, even if

TABLE 2: DRY FREQUENCIES OF THE PLATE.

Mode	1-1	1-2	2-1	2-2
Test Case	Hz	Hz	Hz	Hz
Dry on rubber	151.7	295.5	325.8	459.5
Dry on hull	134.7	283.9	323.4	460.5

**FIGURE 1: HULL ARRANGEMENT.**

do not provide perfect clamping of the plate edges, are much more close to clamping than to supporting boundary conditions. In Fig. 2 the sensor layout shows three rows of four accelerometers each. The modal accelerometers are ICP sensors of PCB Electronics for a measurement frequency range above 0.5 Hz. The wires, connecting each sensor to LMS Scadas Mobile acquisition system, were properly disposed using a grid superimposed on the rectangular hole where the metallic frame and the plate were inserted.

Load excitation

The vibrations of the panel are ‘naturally’ induced by the fluctuating pressure field generated by the turbulent boundary layer developed over the hull bottom when the physical model is towed by the towing tank carriage. The power spectral density of the turbulent boundary layer is shown in Fig. 4. The applied pressure field is effective in producing a broad-band excitation suitable to output-only identification techniques like POD. The inflow velocity was varied by setting different carriage speeds.

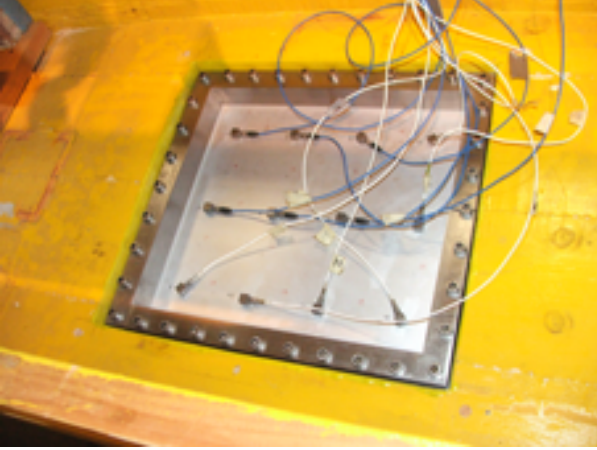


FIGURE 2: DETAIL OF BOTTOM HULL PLATE WITH SENSOR LAYOUT.

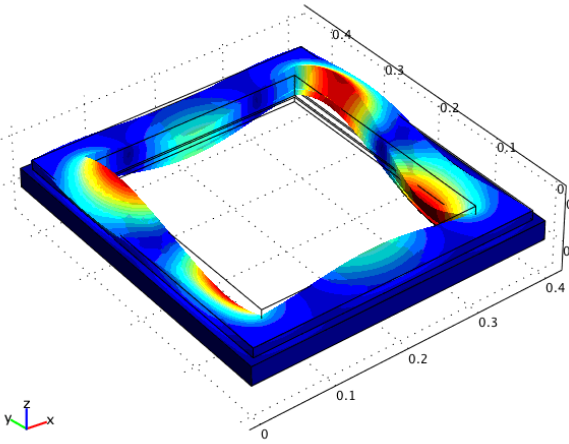


FIGURE 3: 1st STEEL FRAME VIBRATION MODE.

Analysis of accelerations

POD is first applied to the acceleration signals using standard theory. Only the average value is subtracted to raw data and no filtering is applied. Since the vertical acceleration field along the plate can be expanded with respect to the mode shapes $\psi_i(x, y)$, *i.e.*,

$$\dot{w}(x, y, t) = \sum_{i=1}^M \dot{w}_i(t) \psi_i(x, y), \quad (12)$$

the POD provides the same modes obtained processing the displacements (but normalization constants may not be the same). The obtained POV values are listed in Tab. 3, where $\Sigma = \sigma_1 + \sigma_2 + \dots + \sigma_{12}$.

Since the number of measurement points is small, the components of the eigenvectors $\mathbf{p}^{(k)}$ provide low spatial

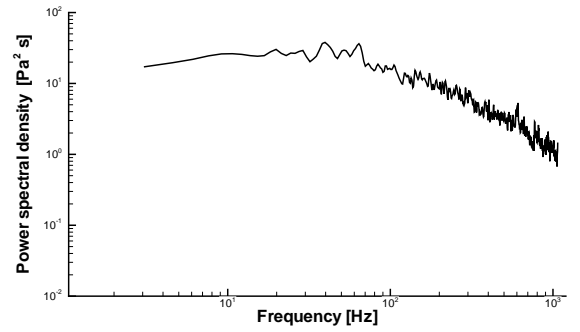


FIGURE 4: POWER SPECTRAL DENSITY OF THE PRESSURE IN THE TURBULENT BOUNDARY LAYER.

TABLE 3: POV OBTAINED FROM RAW ACCELEROMETER DATA.

Mode	σ_i	σ_i/Σ
1	0.040	58.86
2	0.010	14.54
3	0.004	5.76
4	0.003	4.35
5	0.002	2.97
6	0.002	2.69

sampling of mode shapes. The orthogonal grid of measurement points can be extended to cover the plate edges, setting $w_i(t) = 0$ for the virtual dofs along the plate contour. The results both in terms of POVs and POMs do not change ($\sigma_i = 0$ for virtual dofs) but it is a useful way of enhancing the graphical representation of the mode shapes that are then evaluated in 30 points (see Fig. 5).

From inspection of Figs. 5 and 6, where the POM shapes are plotted, it is apparent that the first POM corresponds to the plate mode (1, 1). This mode, on the basis of Tab. 3, collect more than half of all the energy transmitted from the TBL flow to the plate. The same observation applies to the second vibration mode, that is the (2, 1) mode with 14.54% of the overall energy. If identification proceeds further, it is evident that the identified POMs hardly recall the shape of LNMs. The associated energy is slowly decreasing from 5.76% (third POM) to 2.97% (fourth POM). Looking at Fig. 7, it is evident that the identified POMs present similar energy values for $i > 3$.

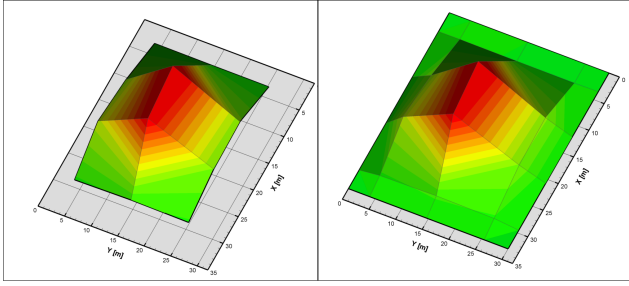


FIGURE 5: 1st POM COMPUTATION WITHOUT (LEFT) AND WITH (RIGHT) INCLUSION OF BCs.

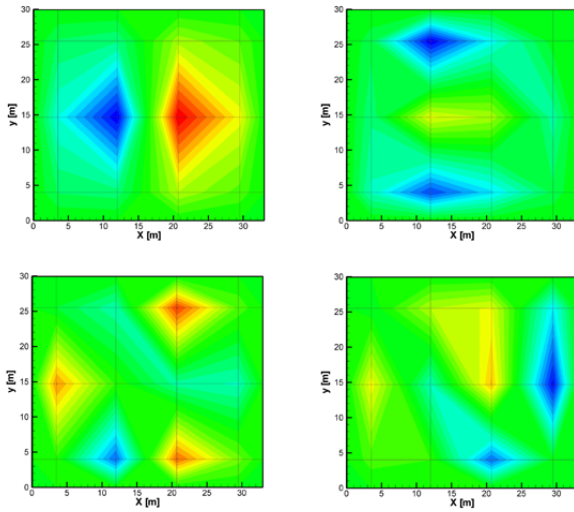


FIGURE 6: 2nd to 4th POM COMPUTATION WITH STANDARD POD.

The explanation for the lack of convergence of the POMs to LNMs can be done considering the application of the covariance matrix to the LNM $\mathbf{z}^{(p)}$, that yields (see [2] for further details):

$$\mathbf{Rz}^{(p)} = \sigma_{pp} D_{pp} \left[\mathbf{z}^{(p)} + \sum_{k=1, k \neq p}^M \frac{\sigma_{kk} D_{kp}}{\sigma_{pp} D_{pp}} \mathbf{z}^{(k)} \right], \quad (13)$$

where $\sigma_{kh} = N^{-1} \mathbf{q}^{(k)} \cdot \mathbf{q}^{(h)}$ and $D_{kh} = \mathbf{z}^{(k)} \cdot \mathbf{z}^{(h)}$, with $\mathbf{q}^{(k)}$ the vector of sampled time-histories of the generalized coordinate $q^{(k)}(t)$. Since the LNMs satisfy the orthogonality relationship with respect to the mass matrix \mathbf{M} , it follows that $D_{kp} \neq 0$ unless $\mathbf{M} = \mathbf{I}$. Nonetheless, it is worth to note that the contribution of the terms in the summation is always negligible for the first POM. In fact, since $\mathbf{p}^{(1)}$ has energy higher than any other POM, $\sigma_{11} \gg \sigma_{kk}$. It means that the POM with highest energy gives always the correspondent LNM. This assumption is not valid for the

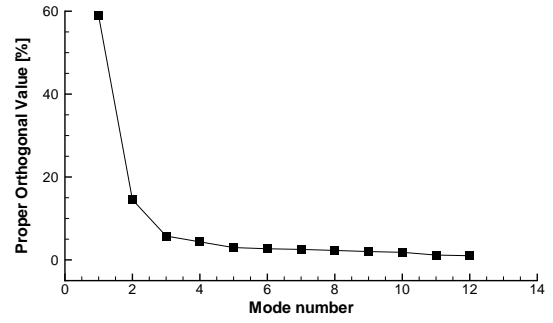


FIGURE 7: POV SPECTRUM EXPRESSED AS PERCENTAGE OF THE OVERALL ENERGY ASSOCIATED TO POMs.

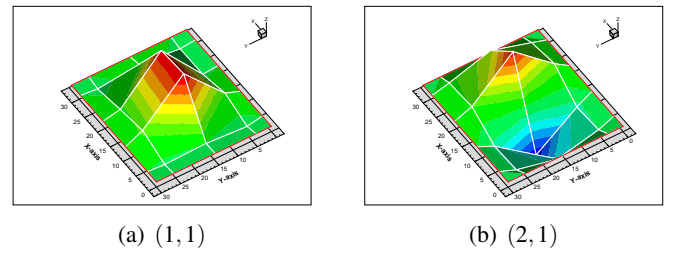


FIGURE 8: 1st AND 2nd POMs WITH BP-POD.

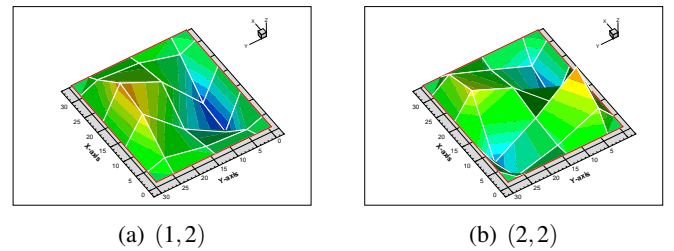


FIGURE 9: 3rd AND 4th POMs WITH BP-POD.

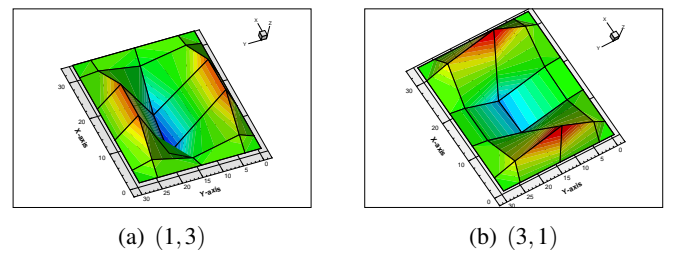


FIGURE 10: 5th AND 6th POMs WITH BP-POD.

second mode but identification was successful anyway. For $p = 2$, one has:

$$\mathbf{Rz}^{(2)} = \sigma_{22} D_{22} \left[\mathbf{z}^{(2)} + \frac{\sigma_{11} D_{12}}{\sigma_{22} D_{22}} \mathbf{z}^{(1)} + \sum_{k=3}^M \frac{\sigma_{kk} D_{k2}}{\sigma_{22} D_{22}} \mathbf{z}^{(k)} \right].$$

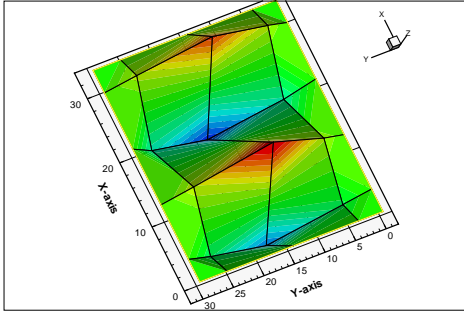


FIGURE 11: 7th POM WITH BP-POD.

In this case, since $\sigma_{11}/\sigma_{22} > 1$, the first LNM $\mathbf{z}^{(1)}$ combines with the second LNM $\mathbf{z}^{(2)}$ unless $D_{12} = \mathbf{z}^{(1)} \cdot \mathbf{z}^{(2)} \simeq 0$ holds, as in the present case. In fact, the mass non-uniformity due accelerometers has a larger effect as long as the order of the vibration mode grows. This effect combines with the observation that POV values of the POMs above the second are similar, preventing to identify POM shapes similar to LNMs for $i > 2$ (cfr. Fig. 6).

The alternative way is to filter the time-histories of the accelerations so as to leave just one mode contribution in the signals and thus to let this mode be (trivially) the mode with highest energy. This procedure, named BP-POD in [2], will be shortly recalled here. From the PSD, averaged over the accelerometer signals, the resonance frequencies are selected and symmetric band-pass filtering around these peaks can be preliminary carried out. By applying for each band the standard POD procedure, the identified plate modes are convergent to LNMs, as shown in Figs. 8-9-10-11.

Next, the sensitivity of this procedure with respect to the amplitude of the bandwidth chosen for filtering is taken into account. In Fig. 12, the different curves represent the percentage of energy relative to the first POV. Of course, this percentage grows if the frequency bands are narrow because other mode contributions are gradually excluded in the time-histories and BP-POD has more chances to be successful. Satisfactory width of the intervals for filtering are obtained for all the modes if $\Delta f \leq 9 \text{ Hz}$. Note that, when the curve is flat in the neighborhood of the maximum, it means that there are more possibilities to define the bandwidth in the neighborhood of the mode resonant frequency.

FULL-SCALE MEASUREMENTS AND IDENTIFICATION

INSEAN-CNR was involved in full-scale trials onboard the ro-ro pax Fortuny vessel within the frame of FP7-SILENV project. Part of the measurements was de-

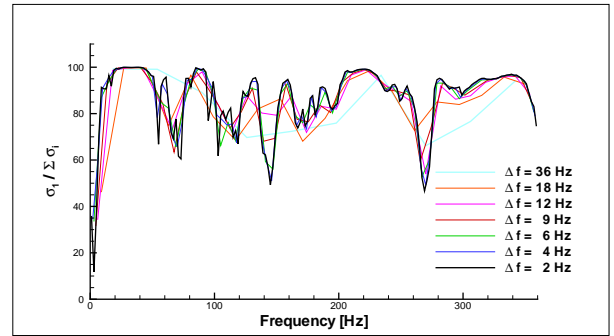


FIGURE 12: DEPENDENCE OF 1st MODE ENERGY PERCENTAGE ON BANDWIDTH OF THE PROCESSED SIGNAL.



FIGURE 13: FORTUNY RO-RO PAX VESSEL.

voted to evaluate the response and to identify the local vibration modes of a hull elastic panel, placed at ship section indicated by the arrow in Fig. 13. The updating of the steel stiffened hull panel, shown in Fig. 14, was intended to improve the FE prediction of the panel mean response to wall pressure fluctuations estimated using universal scaling laws [10]. Eight accelerometers were used with a sampling frequency of 2048 Hz with an acquisition time of about 15 minutes. The panel was entirely wetted and the flow velocity was determined by a forward ship speed of 20 knots. The frequencies are reported in the following Tab. 4 whereas the identified mode shapes are shown in Fig. 15. It is worth to note that the mode shapes are relative to the region where accelerometer were applied, approximately over half the panel.

CONCLUDING REMARKS

In the case of missing mass distribution, the use of a band-pass POD is the only possibility to obtain POMs coinciding with LNMs. In fact, including in the processed signal just one mode at time, there is again the chance to exploit the property that the most excited (and in this case unique) LNM can be identified without the need of providing the mass layout along the plate. Since one mode at time can be identified with this procedure, the orthogo-



FIGURE 14: STIFFENED PANEL OF THE FORTUNY VESSEL.

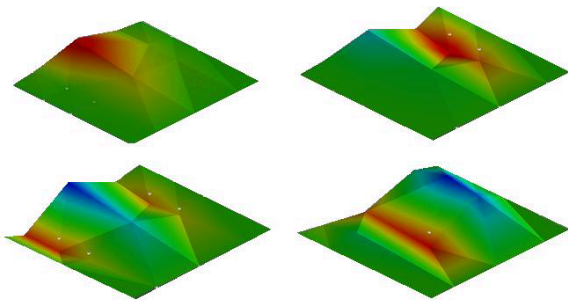


FIGURE 15: IDENTIFIED MODES OF THE STIFFENED PANEL.

TABLE 4: STIFFENED PANEL FREQUENCY AND DAMPING.

Mode	f_i [Hz]	Damping ratio
1	12.5	0.03
2	19.2	0.07
3	21.9	0.02
4	25.8	0.01

nality relationship between the modes can be guaranteed only for those POMs converging to the LNMs (intrinsically orthogonal). However, the drawback in this case is that comparable information about the energy associated to each mode is lost.

ACKNOWLEDGMENT

We would like to thank the FP7-SILENV consortium for which on-board measurements were carried out and ACCIONA Transmediterranea for logistic support.

REFERENCES

[1] Coppotelli, G., Dessi, D., Mariani, R., and Raimondi, M., 2008. “Output-only analysis for modal parameters estimation of an elastically scaled ship”. *Journal of Ship Research*, **52**(1), pp. 71–86.

[2] Mariani, R., and Dessi, D., 2012. “Analysis of the global bending modes of a floating structure using the proper orthogonal decomposition”. *Journal of Fluids and Structures*, **28**(1), pp. 115–134.

[3] Brincker, R., E., C., and Andersen, P. “Why output-only modal testing is a desirable tool for a wide range of practical applications”. In Proceedings of 21th IMAC.

[4] Overschee, P. V., and Moor, B. D., 1996. *Subspace Identification for Linear Systems, Theory, Implementation, Applications*. Kluwer.

[5] Kerschen, G., and Golinval, J. C., 2002. “Physical interpretation of the proper orthogonal modes using the singular value decomposition”. *Journal of Sound and Vibration*, **249**(5), pp. 849–865.

[6] Feeny, B. F., and Liang, Y., 2003. “Interpreting proper orthogonal modes in randomly excited vibration systems”. *Journal of Sound and Vibration*, **265**(5), pp. 953–966.

[7] Chelidze, D., and Zhou, W., 2006. “Smooth orthogonal decomposition-based vibration mode identification”. *Journal of Sound and Vibration*, **292**(3), pp. 461–473.

[8] Karhunen, K., 1946. “Under lineare methoden in der wahrscheinlichkeitsrechnung”. *Annals of Academic Science Fennicae Series, A 1, Math. Phys.*, **37**, pp. 1–79.

[9] Loeve, 1955. *Probability theory*. Von Nostrand, Princeton, New Jersey.

[10] Ciappi, E., Magionesi, F., DeRosa, S., and Franco, F., 2009. “Hydrodynamic and hydroelastic analyses of a plate excited by the turbulent boundary layer”. *Journal of Fluids and Structures*, **25**(2), pp. 321–342.

THE INFLUENCE OF CHANNEL WALLS ON FLAG FLUTTER

Olivier Doaré*

Unité de Mécanique (UME), ENSTA-Paristech
Chemin de la Hunière,
91761, Palaiseau, FRANCE
Email: olivier.doare@ensta-paristech.fr

*Address all correspondence to this author

Christophe Eloy

IRPHE, Université d'Aix-Marseille
49 rue Joliot-Curie,
13013, Marseille, France
Email: eloy@irphe.univ-mrs.fr

ABSTRACT

The effect of confinement of a rectangular channel on the flag flutter instability is investigated, both in terms of waves propagating in the infinite medium (local approach) and in terms of modes in the finite length system (global approach). Using a 1D Euler-Bernoulli model for the plate and a 3D potential flow model for the flow, the problem is solved numerically for various sets of the geometrical parameters to compute the critical velocity for instability as function of the mass ratio. It is found that the proximity of walls parallel and perpendicular the plate affects significantly the plate's dynamics and instability. One main conclusion of this work is that models considering a 2D flow can predict correctly the critical velocity only in specific cases such as large mass ratio, large aspect ratio or very confined plates.

INTRODUCTION

The equilibrium state of a cantilevered plate in an axial flow can become unstable once a critical value of the flow velocity is reached, resulting in oscillations of large amplitude. This phenomenon, referred to as *flag flutter* has been the focus of a large amount of researches, as reported in some recent books and reviews [1, 2]. Among the various linear models that attempted to give a numerical prediction of the critical flow velocity for apparition of flutter instability, one can distinguish three main families. In the first one, a 2D problem is considered, *i.e.* an infinite span plate in a 2D potential flow [3–5]. The approximation done in these models is referred to as *large span* approximation. In the second family, the typical wavelengths of deformation are considered large enough when compared to the typical size of the cross section of the plate, so that the perturbation of the flow at a given cross section depends only on the plate dynamics at this

cross section [6]. These models are referred to as *slender body* models. The third family concerns models that do not consider any of the above approximations, and solve the 3D flow around the plate. This kind of model has shown that there is a strong influence on the aspect ratio of the plate on the critical velocity [7]. Works using similar method followed to study the presence of walls perpendicular to the plate (spanwise confinement) and showed that the critical velocity tends slowly to that predicted by a 2D model when the walls are approached [8]. In the present work, two additional walls, parallel to the plate are considered so that the latter is confined in a rectangular channel flow. The method used in the present paper is the same as developed in previous works [7, 8].

Experimentally, flag flutter has also been intensively investigated. The first experimental studies of the phenomenon are reported in references [3, 9, 10], among others. A consistent review of all experimental studies before 2004 can be found in reference [1]. These studies have shown that although the plate's dynamics is always two-dimensional, the values of the critical velocity predicted by 2D models are always lower than that found experimentally. Comparison with 3D models taking into account the finite aspect ratio of the plate significantly improved the prediction of the critical velocity [7] and a nonlinear model taking into account the initial spanwise curvature [11] explained the origin of the hysteresis observed experimentally. Finally, the effect of walls perpendicular to the plate has been investigated experimentally in reference [12] and results are in good agreement with the model developed in [8].

The paper is organized as follows. In the next section, the problem of a flat plate in a rectangular channel potential flow is formulated. The stability properties of the infinite length problem are then analysed. Next, a finite length system is considered.

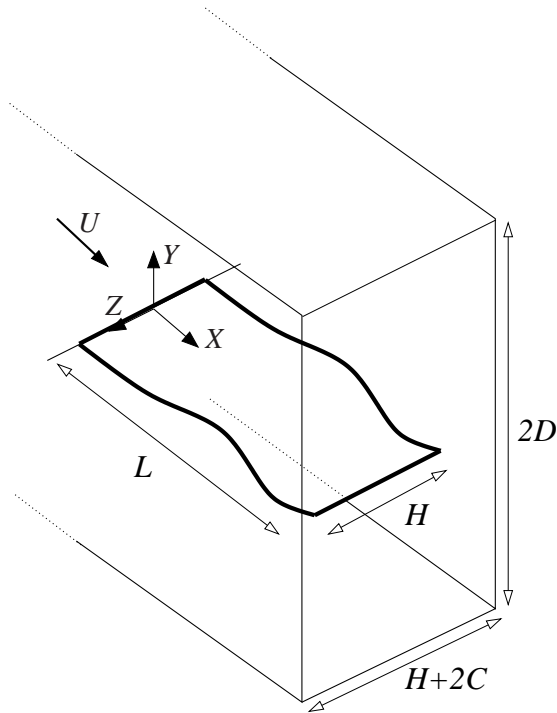


FIGURE 1: Schematic view of a plate in a rectangular channel.

1 FORMULATION OF THE PROBLEM

1.1 Coupled fluid-structure equations

The problem considered in this paper is sketched on Fig. 1. The solid is modeled as a plate of negligible thickness under the Euler-Bernoulli approximation. It is assumed that the deformation does not depend on the spanwise coordinate, so that the linearized equilibrium equation of the coupled fluid-solid system has the following expression:

$$B \frac{\partial^4 W}{\partial X^4} + \mu \frac{\partial^2 W}{\partial T^2} = \langle [P] \rangle, \quad (1)$$

where B is the flexural rigidity per unit length in the spanwise direction of the plate and μ its surface density, $[P]$ stands for the pressure jump between each side of the plate and the angles $\langle \cdot \rangle$ denote the mean value along the span. The surrounding fluid flows at a constant velocity U_0 in the direction X and is modeled using the potential flow approximation. The velocity potential is noted Ψ . Using the following dimensionless variables,

$$x = \frac{2Z}{H}, \quad z = \frac{2Z}{H}, \quad t = \frac{4TB}{\mu H^2}, \quad w = \frac{2W}{H}, \quad (2)$$

$$p = \frac{P}{\rho U^2}, \quad \psi = \Psi \sqrt{\mu/B}, \quad (3)$$

and parameters,

$$m = \frac{\rho_f H}{2\mu}, \quad u = \frac{UH}{2} \sqrt{\frac{\mu}{B}}, \quad c = \frac{2C}{H}, \quad d = \frac{2D}{H}, \quad (4)$$

equation (1) becomes,

$$\frac{\partial^4 w}{\partial x^4} + \frac{\partial^2 w}{\partial t^2} = m \langle [p] \rangle. \quad (5)$$

In the fluid domain, the non-dimensional velocity potential satisfies the Laplace equation,

$$\Delta \psi = 0, \quad (6)$$

with the following boundary conditions:

$$\frac{\partial \psi}{\partial z} = 0 \quad \text{for } |y| = d, \quad (7)$$

$$\frac{\partial \psi}{\partial y} = 0 \quad \text{for } |z| = 1 + c, \quad (8)$$

$$\frac{\partial \psi}{\partial z} = \frac{\partial w}{\partial t} + u \frac{\partial w}{\partial x} \quad \text{on the plate.} \quad (9)$$

The pressure is then linked to the potential through the linearized unsteady Bernoulli equation,

$$p = -\frac{\partial \psi}{\partial t} - u \frac{\partial \psi}{\partial x}. \quad (10)$$

1.2 Problem in the Fourier space

Introducing the Fourier transform in space and time \hat{h} of a function $h(x, t)$,

$$\hat{h}(k, \omega) = \left(\frac{1}{2\pi} \right)^2 \int_{-\infty}^{+\infty} \int_{-\infty}^{+\infty} h(x, t) e^{i\omega t} e^{ikx} dt dx, \quad (11)$$

equation (5) takes the following form in the Fourier space:

$$[k^4 - \omega^2] \hat{w} = -m \langle [\hat{p}] \rangle. \quad (12)$$

A normalized potential $\hat{\phi} = \hat{\psi} / -i(\omega - U_R k) \hat{w}$ is then introduced. Using the unsteady Bernoulli equation (10), the pressure jump may be linked to the displacement and the normalised potential $\hat{\phi}$,

$$\langle [\hat{p}] \rangle = (\omega - uk)^2 \langle [\hat{\phi}] \rangle \hat{w}. \quad (13)$$

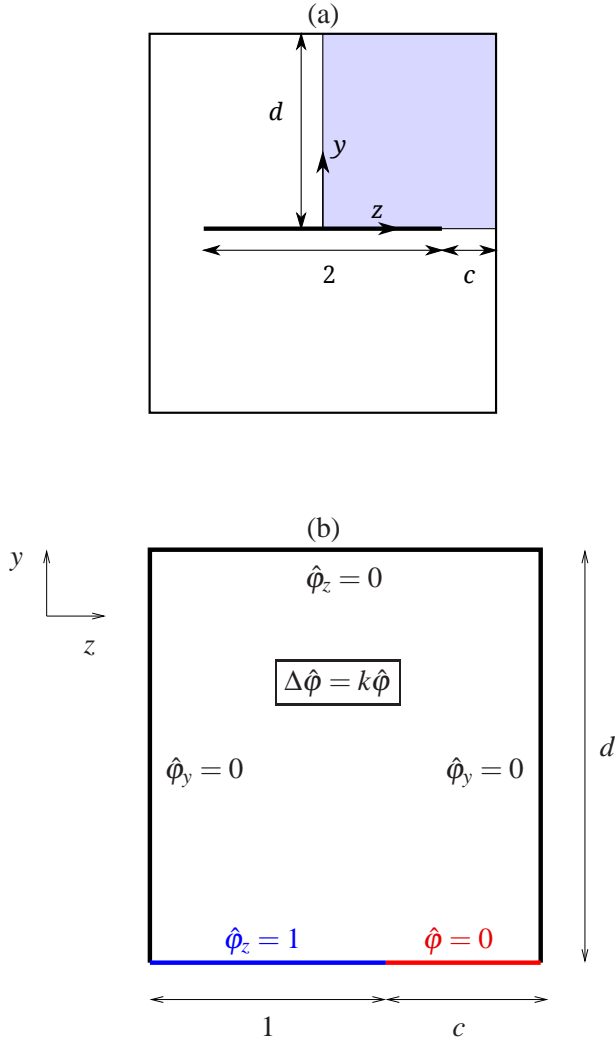


FIGURE 2: (a), complete geometry of the problem in Fourier space; (b), numerical domain and boundary conditions after taking into account symetries of the problem.

The Laplace equation (6) with boundary conditions (7-9) can now be expressed for the normalized velocity potential $\hat{\phi}$. This problem is defined in the plane (y, z) of a cross-section of the plate, as sketched on Fig.2a. It can be shown that this problem is symmetric with respect to the y -axis and skew-symmetric with respect to the z -axis. Hence it can be rewritten in only one quarter of the domain as sketched on Fig.2b,

$$\frac{\partial^2 \hat{\phi}}{\partial y^2} + \frac{\partial^2 \hat{\phi}}{\partial z^2} = k^2 \hat{\phi}, \quad \text{for } z \in [0, 1+c], y \in [0, d] \quad (14)$$

$$\frac{\partial \hat{\phi}}{\partial z} = 1 \quad \text{for } z < 1, y = 0, \quad (15)$$

$$\frac{\partial \hat{\phi}}{\partial z} = 0 \quad \text{for } y = d, \quad (16)$$

$$\frac{\partial \hat{\phi}}{\partial y} = 0 \quad \text{for } z = 1+c \text{ and } z = 0. \quad (17)$$

This last problem depends only on k and the geometrical parameters c and d . Combining equations (12) and (13), the dispersion relation takes the following form,

$$k^4 - \omega^2 = m \frac{2g(k, c, d)}{|k|} (\omega - uk)^2, \quad (18)$$

where $g(k, c, d)$ reads,

$$g(k, c, d) = k \langle \hat{\phi}(y = 0^+) \rangle. \quad (19)$$

In the Fourier space, the work hence consists in obtaining the dispersion relation (18) for a given set of geometrical parameters. To do so, it is necessary to compute the function $g(k, c, d)$ by solving an Helmholtz problem (equation 14). The end of this section is devoted to recall the analytical form of g in various limit cases found in previous studies and present some computational results in the general case.

1.3 Limit cases for the function g found in the litterature

The different limit cases found in the litterature for the function g are presented here. The 2D limit of a plate in an infinite fluid domain is [13],

$$g = 1. \quad (20)$$

The 2D limit of a plate confined by two parallel rigid walls is [14],

$$g = \frac{1}{\tanh(kd)}. \quad (21)$$

The slender-body limit is [15],

$$g = \frac{k\pi}{4}. \quad (22)$$

Using asymptotic expansions of the 2D and slender-body limits, a composite function as been introduced to take into account the influence of a 3D flow around the plate [7],

$$g = 1 - \frac{1}{2k + \exp[(\pi/4 - 2)k]}. \quad (23)$$

In refence [8], a similar approach has been used to develop asymptotic expansions of the 2D and slender-body

limits that take into account the presence of walls perpendicular to the plate (C effect). A composite expansion of these two limits has then been developed, that extends the kernel of equation (23) to take into account spanwise confinement.

1.4 General case of a plate in a rectangular flow: numerical solution

In the general case of the present paper, the Helmholtz equation is solved using the open source finite element software Freefem [16] for given values of c , d and k . The resulting function g is plotted on Fig.3a for a large value of $d = 30$, and values of c in the range $[3 \times 10^{-4}, 3]$. As already reported in a previous work [8], the function g is linear at low values of k and tends to unity at large values of k . When c is large, it is correctly approximated by the infinite fluid domain 3D model [7], equation (23). Typical results when c is large are plotted on Fig.3b. Here, g is well approximated by equation (21) for large values of k while it tends to a linear slender-body type behavior at low values of k . Indeed, the function g is well fitted by a function of the form $g = Ak$ when $k \ll 1$. The value of A is plotted as function of d on Fig.4 for different values of c . When d is small, the value of A does not depend on c and the data is well fitted by,

$$A \simeq 1/3d, \quad d \ll 1. \quad (24)$$

When d is increased, A tends to a constant value which dependence on c has been characterized in a previous work [8],

$$A = \frac{k\pi}{4} \left[1 + 0.805 \ln \left(\frac{c + 0.189}{c} \right) \right]. \quad (25)$$

Now that we have the function $g(k)$, and consequently the dispersion relation, in numerical form for any combination of the numerical parameters, it will be used to compute stability boundaries of the system in two different cases: the infinite case (local instability), for which only the dispersion relation is necessary to characterize the medium, and the finite case (global instability), for which subsequent work is needed, as boundary conditions and the length have to be taken into account. In the following, numerical data will be directly used to compute the different stability limits except at low values of k , where a third order polynomial fit is used.

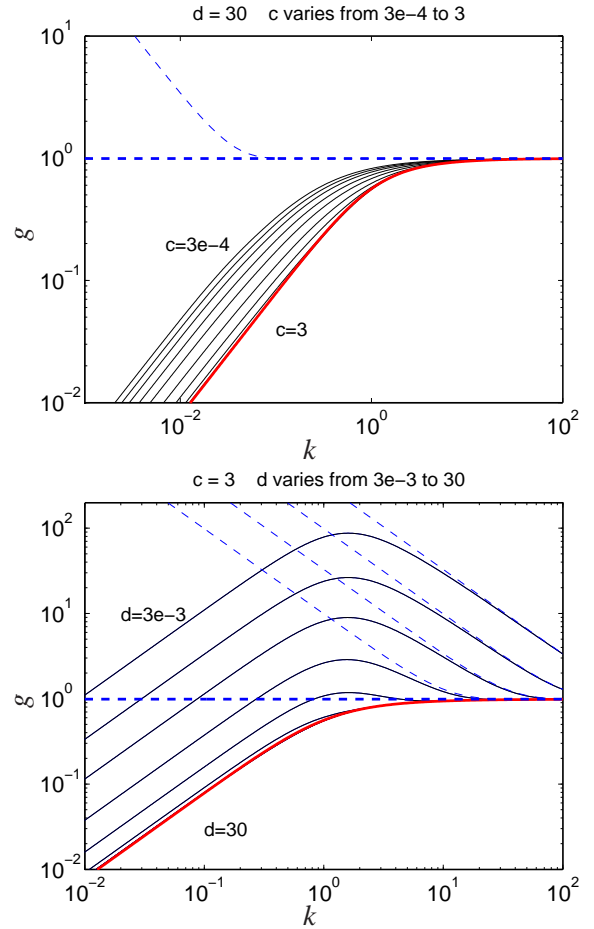


FIGURE 3: Function $g(k)$ computed numerically for various sets of the parameters c and d (solid thin lines) and compared with different limit cases; thick dashed line, equation (20); thin dashed lines, equation (21); thick solid line, equation (23).

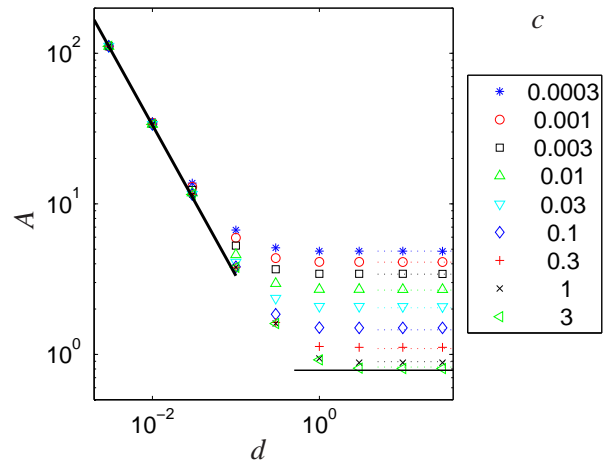


FIGURE 4: Linear coefficient of the slender-body limit (*i.e.* small wavenumbers) as function of d for different values of c . Bold line indicate the limit for low values of d , equation (24), thin line indicates the limit of unconfined flow, $A = \pi/4$ and dotted lines indicate the empirical model developed in reference [8], equation (25).

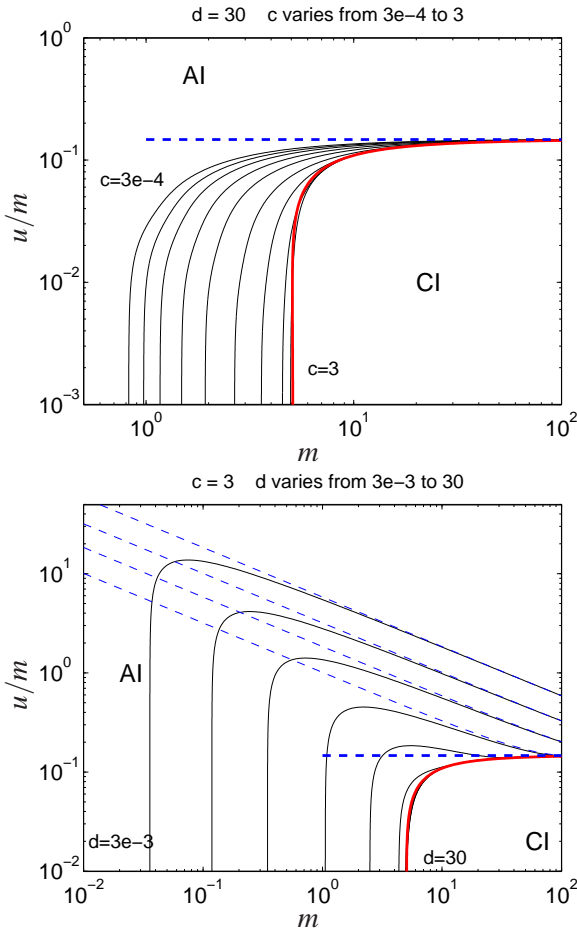


FIGURE 5: Critical curves for transition between convective and absolute instabilities (thin plain line) compared with that given by using g defined in equation (20), thick dashed line, equation (21), thin dashed lines and equation (23), thick solid line.

2 LOCAL STABILITY ANALYSIS

The instability properties of bending waves propagating in an infinite length medium in such channel flow are now studied. In its non-dimensional form, the dispersion relation depends on four parameters, the mass ratio m , the non-dimensional velocity u , the non-dimensional spanwise gap c and the non-dimensional channel height d . The dispersion relation of equation (18) is considered, where the g function is obtained by solving the Helmholtz problem (14-17), as explained in the previous section.

The temporal approach consists in solving the dispersion relation, a second order polynomial for the variable ω , associated to real values of k . If for a least one real value of k , the imaginary part of one root ω is positive, the amplitude of the associated wave $\exp[i(kx - \omega t)]$ grows exponentially with time and the medium is said locally unstable. It can be easily shown that the system bears unstable waves at any value of $u \neq 0$.

However, one may distinguish two cases of wave instability, depending on the long time impulse response of the plate. If the exponentially growing wave packet is advected by the flow, the instability is said *convective*. Conversely, if it grows in place, so that the entire space is ultimately dominated by the instability, the latter is said *absolute*. The concepts of convective and absolute instabilities, and the underlying theory, have been initially introduced in the domain of plasma physics [17] and successfully applied in the particular domain of fluid-structure interaction [13]. In the present paper, a numerical method presented in reference [18] is used to compute the critical curves for transition between convective and absolute instabilities. The results are plotted on Fig.5 in the $(m, u/m)$ plane. On Fig.5a, $d = 30$ and c varies from 3×10^{-4} to 3. On Fig.5b, $c = 3$ and d varies from 3×10^{-3} to 30. All curves share a common limit at large values of m . This limit ($u/m = 0.148$) is that given by a 2D approach, where $g = 1$. It is actually twice the value found by Crighton & Oswell [13] in the case of a compliant panel with a flow on one side only, whereas the flow is on both sides in the present study. It has to be noted that in this context of 3D flow, the 2D limit corresponds to large values of the wavenumber. It is consistent with the fact that when $m \rightarrow \infty$, the wavenumber at which convective to absolute instability transition arises also tends to infinity.

The infinite derivative of all these curves at low values of m corresponds to the opposite limit where the wavenumber at transition is small. This is the slender body limit. In the case of a fluid-conveying pipe, which is properly described by a similar dispersion relation in the slender-body limit, Kulikoskii [19] showed that the transition does not depend on the flow velocity, but only on the mass-ratio. Again, this is consistent with the vertical limit observed on Fig.5: an added mass effect of the channel confinement modifies the mass ratio in the slender-body limit and the asymptotic value of m varies. The more the plate is confined (small c and d), the larger is the added mass. Hence the smaller is the critical value of m . Two additional asymptotic cases are plotted on Fig.5: the curve obtained using an analytical solution of the Helmholtz problem in a 2D case with walls (blue dotted) and the curve obtained considering the 3D flow without walls (thick red). The numerical data tends to these two limits in a consistent manner.

3 GLOBAL STABILITY ANALYSIS

When studying a finite length system during timescales such that boundaries have an influence on the dynamics,

boundary conditions must be taken into account. A plate clamped at $X = 0$ and free at $X = L$ is now considered. The problem is now rescaled using L as a characteristic length, so that the following non-dimensional variables and parameters are introduced,

$$x = \frac{X}{L}, y = \frac{Y}{L}, z = \frac{Z}{L}, w = \frac{W}{L}, t = \frac{UT}{L}, p = \frac{P}{\rho U^2}. \quad (26)$$

$$M^* = \frac{\rho L}{M}, U^* = \sqrt{\frac{M}{B}} LU, H^* = \frac{H}{L}, C^* = \frac{C}{L}, D^* = \frac{D}{L}. \quad (27)$$

In this finite length approach, the dimensionless equation of motion is now

$$\frac{\partial^2 w}{\partial t^2} + \frac{1}{U^{*2}} \frac{\partial^4 w}{\partial x^4} = M^* \langle [p] \rangle, \quad (28)$$

and the clamped-free boundary conditions are

$$w(x=0) = \frac{\partial w}{\partial x} \Big|_{x=0} = \frac{\partial^2 w}{\partial x^2} \Big|_{x=1} = \frac{\partial^2 w}{\partial x^2} \Big|_{x=1} = 0 \quad (29)$$

Stability analysis is done through a modal analysis of the system. By looking for solutions of the problem in the form

$$w(x, t) = \phi(x) e^{i\omega t}, \quad (30)$$

and assuming that pressure forces exerted on the plate can be expressed as linear functions of the displacement w , one end up with a Sturm-Liouville eigenvalue problem that does not have an analytical solution in the general case. If one eigenvalue has a negative imaginary part, the system is unstable, as the temporal evolution of displacement is such that it diverges when time goes to infinity. The corresponding real part gives then the circular frequency. In practice the system has to be put in a form suitable for numerical integration. Equation (13) may be rewritten in the form,

$$\frac{k \hat{p}}{g} = (\omega - k)^2 \hat{w}. \quad (31)$$

Taking the inverse transform of this expression leads to a solution in the form of a convolution integral for the pressure,

$$\frac{1}{2\pi} \int_0^1 p'(v) G(x-v) dv = \left(\frac{\partial}{\partial t} + \frac{\partial}{\partial x} \right)^2 w, \quad (32)$$

where prime denotes for derivation with respect to the axial coordinate and $G(x)$ is the inverse Fourier transform of $1/g(k)$,

$$G(x) = \int_0^\infty \frac{\sin(kx)}{g(k)} dk. \quad (33)$$

It has to be noted that as G diverges when x tends to 0, the Cauchy's principal value of the integral in equation (32) has to be taken. As done in previous papers [7, 8], the displacement is decomposed on the modes of the plate in vacuum $\phi_i(x)$,

$$w(x, t) = e^{i\omega t} \sum_i a_i \phi_i(x). \quad (34)$$

Next, the pressure associated with the mode i is expanded on Chebyshev polynomials of the first kind and assumed to have an inverse square root singularity,

$$p'_i(x) = \sum_j A_{ij} \frac{T_j(2x-1)}{\sqrt{x(1-x)}}. \quad (35)$$

This expansion is then inserted into the integral expression for the pressure (32). A scalar product with Chebyshev polynomials of the second kind $U_k(2x-1)$ is applied. This leads to a linear problem for A_{ij} , which is solved numerically for a given set of the geometrical parameters (C^*, D^*, H^*) . This method necessitates the knowledge of the function $G(x, C^*, D^*, H^*)$. In practice, it is calculated numerically using,

$$G(x) = \frac{1}{x} + G_1(x), \quad (36)$$

with,

$$G_1(x) = \int_0^\infty \sin(kx) \left(\frac{1}{g(k)} - 1 \right) dk. \quad (37)$$

As the integrand tends to zero when k tends to infinity, this integral is easily computed numerically.

Numerical results are now presented. It has to be noted that they involve a significant amount of numerical steps: Helmutz equation using finite elements, numerical inverse Fourier transform, various projections (Chebyshev modes and Galerkin modes) and finally an eigenvalue problem.

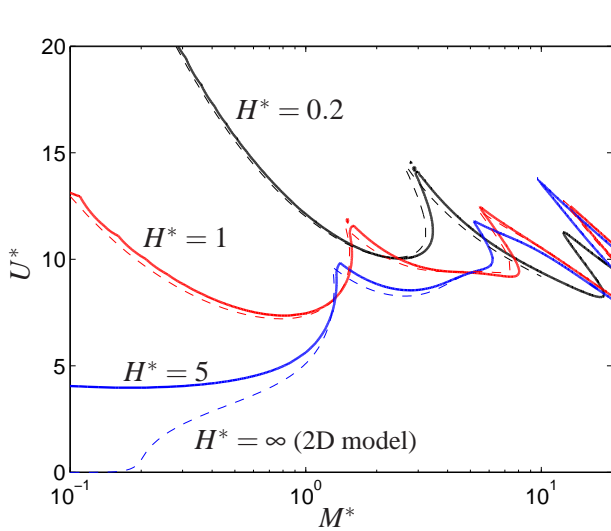


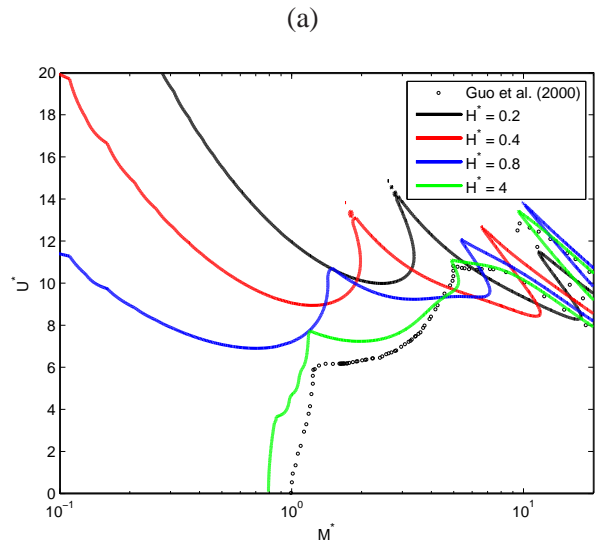
FIGURE 6: Critical curves of marginal stability at $c = 3$ and $d = 30$ obtained by the present numerical method (solid lines), compared to critical curves obtained considering an unbounded flow [7] (dashed lines).

A first set of results is presented on Fig.6. It consists in comparing the critical curves for apparition of instability in the (M^*, U^*) plane when the channel is large, $(c, d) = (3, 30)$, with that of previous studies in an unbounded flow (C^* and $D^* = \infty$). A good agreement is found between the two methods.

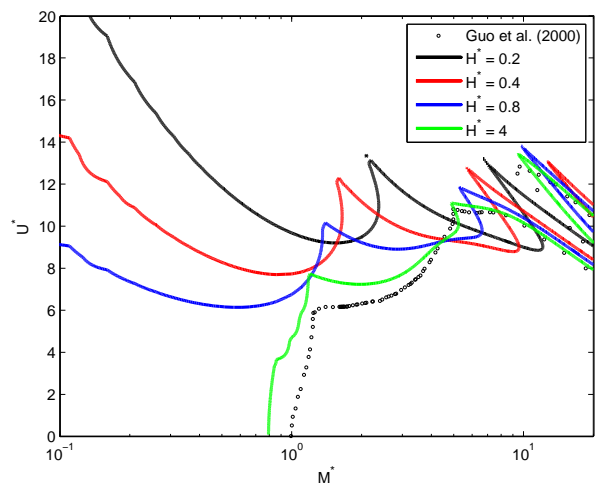
Another comparison is done with results of Guo and Paidoussis [14] for $D^* = 0.2$ on Fig.7a,b. Here again, the critical curves of the present 3D model tend to that predicted by a 2D model when H^* is increased. It appears that the smaller is C^* , the faster is the convergence. The main result of this comparison is that for low values of M^* , the 2D limit of reference [14], can be reached only for very large H^* or very low C^* . This is in practice difficult to achieve experimentally.

DISCUSSION

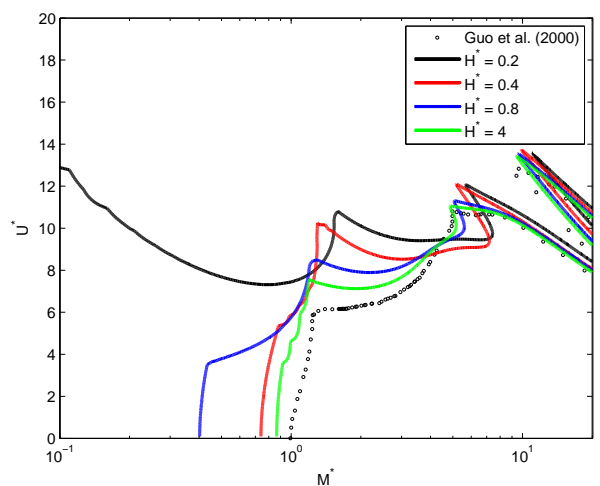
In this article, the influence of the walls of a rectangular channel on the critical velocity for flutter instability has been characterized. Local and global stability analyses have been performed. In the local approach the system is always unstable, provided the fluid is not still. Critical values of the parameters for transition between convective and absolute instabilities have been computed. In a general manner, confinement is found to significantly affect the local stability properties of the medium. Next, global stability of the finite length system has been investigated. The crucial importance of the 3D modeling at low values of the mass ratio has been emphasized. Indeed, it is found that 2D models predict the correct critical velocity



(a)



(b)



(c)

FIGURE 7: Critical curves of marginal stability at $D^* = 0.2$ for different values of H^* , compared with the 2D results of reference [14]; (a) $c = 3$, (b) $c = 0.1$, (c) $c = 0.001$. The small irregularities of the curves are due to imprecisions of the numerical method.

only for high values of the aspect ratio or low values the spanwise and lateral confinements.

When confinement is important, one may wonder if the viscosity has an effect on the instability thresholds. In the case spanwise confinement (small values of C^*), the effect of the existence of a boundary layer has been discussed in reference [12]. In this case, only the edges of the plate are affected by the presence of a boundary layer and the experimental results are found to be in good agreement with the theoretical predictions. Conversely, in the case of significant confinement by walls parallel to the plate (small values of D^*), viscosity may play a more important role. Here the whole surface may be affected by viscous drag and it may be necessary to consider a boundary layer of a Poiseuille-type flow.

Further work is now mainly focused on experiments.

REFERENCES

- [1] Paidoussis, M. P., 2004. *Fluid-structure Interactions. Slender Structures and Axial Flow*, Vol. 2. Academic Press.
- [2] Shelley, M. J., and Zhang, J., 2011. “Flapping and Bending Bodies Interacting with Fluid Flows”. *Annual Review of Fluid Mechanics*, **43**(1), pp. 449–465.
- [3] Kornecki, A., Dowell, E. H., and O’Brien, J., 1976. “On the aeroelastic instability of two-dimensional panels in uniform incompressible flow”. *Journal of Sound and Vibration*, **47**(2), pp. 163–178.
- [4] Huang, L., 1995. “Flutter of cantilevered plates in axial flow”. *Journal of Fluids and Structures*, **9**(2), pp. 127–147.
- [5] Aurégan, Y., and Depollier, C., 1995. “Snoring: Linear stability and in-vitro experiments”. *Journal of Sound and Vibration*, **188**(1), pp. 39–53.
- [6] Lemaitre, C., Hémon, P., and de Langre, E., 2005. “Instability of a long ribbon hanging in axial air flow”. *Journal of Fluids and Structures*, **20**(7), pp. 913–925.
- [7] Eloy, C., Souilliez, C., and Schouveiler, L., 2007. “Flutter of a rectangular plate”. *Journal of Fluids and Structures*, **23**(6), pp. 904–919.
- [8] Doaré, O., Sauzade, M., and Eloy, C., 2011. “Flutter of an elastic plate in a channel flow: Confinement and finite-size effects”. *Journal of Fluids and Structures*, **27**(1), pp. 76–88.
- [9] Taneda, S., 1968. “Waving motions of flags”. *Journal of the Physical Society of Japan*, **24**(2), pp. 392–401.
- [10] Datta, S., and Gottenberg, W., 1975. “Instability of an elastic strip hanging in an airstream”. *Journal of Applied Mechanics*, **42**, pp. 195–198.
- [11] Eloy, C., Kofman, N., and Schouveiler, L., 2012. “The origin of hysteresis in the flag instability”. *Journal of Fluid Mechanics*, **In press**.
- [12] Doaré, O., Mano, D., and Bilbao Ludena, J. C., 2011. “Effect of spanwise confinement on flag flutter: Experimental measurements”. *Physics of Fluids*, **23**, p. 111704.
- [13] Crighton, D., and Oswell, J. E., 1991. “Fluid loading with mean flow. I. Response of an elastic plate to localized excitation”. *Philosophical Transactions of the Royal Society of London A*, **335**, pp. 557–592.
- [14] Guo, C. Q., and Paidoussis, M. P., 2000. “Stability of Rectangular Plates With Free Side-Edges in Two-Dimensional Inviscid Channel Flow”. *Journal of Applied Mechanics*, **67**(1), pp. 171–176.
- [15] Lighthill, M., 1960. “Note on the swimming of slender fish”. *Journal of FLuid Mechanics*, **9**(2), pp. 305–317.
- [16] Hecht, F., and le Hyaric, A. <http://www.freefem.org/ff++/index.htm>.
- [17] Briggs, R. J., 1964. *Electron-Stream Interaction with Plasmas*. The MIT Press.
- [18] de Langre, E., 2002. “Absolutely unstable waves in inviscid hydroelastic systems”. *Journal of Sound and Vibration*, **256**(2), pp. 299–317.
- [19] Kulikovskii, A. G., and Shikina, I. S., 1988. “On the bending oscillations of a long tube filled with moving fluid”. *Izv. Akad. Nauk. ArmSSR, Mekhanika*, **41**(1), pp. 31–39.

FLOW-INDUCED VIBRATIONS OF A FLEXIBLE PANEL IN A BOUNDARY-LAYER FLOW

J. S. Kapor* and A. D. Lucey*

*Fluid Dynamics Research Group, Curtin University of Technology,
GPO Box 1987, Perth, WA 6845, Australia
Email: j.kapor@curtin.edu.au

ABSTRACT

This paper presents the development and use of numerical-simulation methods for the non-linear two-dimensional fluid-structure interaction of flexible panels in both uniform and boundary-layer axial flows. The inviscid system is modelled using a combination of Finite-difference (FDM) and Boundary-element (BEM) methods for the structural and fluid dynamics respectively. This is then used as the platform for the incorporation of a boundary-layer for which rotationality and viscous effects are added using a Discrete-Vortex Method (DVM). Computational costs are reduced massively through the use of a Fast-multipole (FMM), Generalised Minimum Residual (GMRES) and Newton Krylov (NK) methods in an implicit scheme that is mesh free and can efficiently scale to very large problem sizes. The efficiency of the simulation scheme is demonstrated for divergence of flexible panel. Thereafter, it is shown quantitatively that the laminar boundary yields higher critical flow speeds of divergence-onset than those predicted by potential-flow analyses.

INTRODUCTION

We study the two-dimensional fluid-structure interaction (FSI) of a flexible panel subjected to one-sided axial flow. This system has a long history of investigation although the vast majority of studies have assumed potential flow. In such studies it is found that as the (uniform) flow speed is increased, a critical speed is reached at which divergence (or buckling) instability sets in; a further increase to flow speed sees the flexible panel succumb to a violent flutter instability. For simple elastic panels without a spring foundation, the non-linear potential-flow study of Lucey et al. [1] showed that divergence instability saturated at finite amplitude and underwent limit-cycle oscillation. The inclusion of boundary-layer effects in such a problem introduces significant complexity. Established approaches to hydrody-

amic stability (such as the Orr-Sommerfeld equation) are based upon the assumption of both small-amplitude disturbances and an infinitely long wall that permits a continuous spectrum of normal modes to be used to characterise these. Of course, wave-based models have limited utility for predicting nearly static instabilities such as divergence. However, computational methods have been successfully used to overcome these limitations. Davies and Carpenter [2] modelled the FSI of linear deformations of a compliant-wall insert on one side of plane Poiseuille flow while Luo et al. [3] have successfully modelled large-amplitude dynamics of a tensioned membrane in the same system; however, both of these studies are restricted to relatively low Reynolds-number flows.

The overall aim of the present work is to develop a versatile grid-free computational model for the external problem of viscous flow over a flexible wall of finite length and deformation amplitudes for a broad range of Reynolds numbers that include those of transitional boundary layers.

COMPLIANT-WALL MODELLING

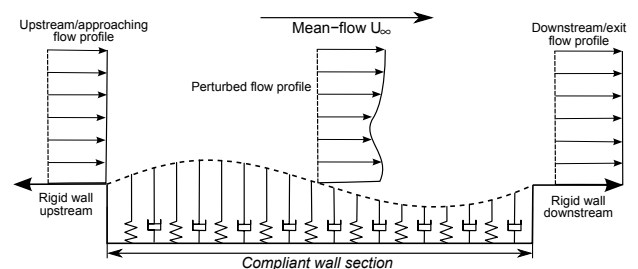


FIGURE 1: SCHEMATIC OF THE FLEXIBLE PANEL INTERACTION WITH A POTENTIAL FLOW.

We begin by introducing a base model for fluid-structure interactions of a flexible panel (or compliant)

wall and an inviscid (equivalent to an infinite Reynolds number) flow as shown in Fig. 1. The compliant-wall is modelled by the one-dimensional (1D), nonlinear, Euler-Bernoulli-Beam model with spring-damper wall backing, presented in [1]. Nonlinearity in the wall is captured through an induced tension term that results from elongation caused by wall curvature. The governing differential equation for the vertical wall motion, $\eta = \eta(x, t)$, is given by,

$$\rho h \frac{\partial^2 \eta}{\partial t^2} + B \frac{\partial^4 \eta}{\partial x^4} - T_l \left(\frac{\partial \eta}{\partial x} \right) \frac{\partial^2 \eta}{\partial x^2} + d \left(\frac{\partial \eta}{\partial t} \right) + k \eta = F(x, t), \quad (1)$$

where ρ is the wall density, h is the thickness, d and k are the damping and spring coefficients in the wall backing and $F(x, t)$ is the force applied at the wall's surface. In addition, B denotes the flexural rigidity of the plate and T_l is the induced tension coefficient given by,

$$B = \frac{Eh^3}{12(1-\nu_p^2)}, \quad (2)$$

$$T_l = \frac{Eh}{L(1-\nu_p^2)} \int_0^L \left(\sqrt{1 - \left(\frac{\partial \eta}{\partial x} \right)^2} - 1 \right) dx, \quad (3)$$

where ν_p refers to Poisson's ratio, E is the elastic modulus and L is the length of the undeformed wall.

A solution to the compliant-wall system is achieved numerically by discretising the continuous wall into N nodes of mass, uniformly spaced in the horizontal direction to allow a second-order, central-difference approximation (from the Finite Difference Method (FDM) [4]) to be used to solve all spatial differentials along with hinged end-conditions. In this work, we look at the transient response obtained from the initial value problem where time integration is achieved through a second-order, implicit, trapezoidal stepping method.

The use of an explicit (or semi-implicit) time-stepping method has been avoided as the numerical stiffness of the equations of motion results in the convergence rate and stability of the problem being highly dependent on wall discretisation and time-step sizes. An increase in spatial discretisation requires a much larger increase in time discretisation to ensure numerical stability, well beyond the necessity for solution accuracy. By using an implicit method, relative time-step sizes no longer impact the numerical stability of the solution [5].

To obtain an implicit solution to our system we find the roots of the system of nonlinear equations in the

form¹ $f(\ddot{\eta}) = 0$. This is achieved using a Newton-Krylov (NK) method [6] that is based upon the use of finite-difference approximations (typically first-order) to the Jacobian-vector product used in Newton's root-finding method. The advantage of this formulation is that one can use a Krylov subspace method, such as the Generalised Minimum Residual method (GMRES) [7], to iteratively determine the vector product. This method is suited to large systems of nonlinear equations because only system function (f) evaluations are required, thus allowing the whole scheme to be conducted in a matrix-free manner. However, for good performance of any iterative Krylov method, the system of equations must be well conditioned. In this work we use a static pre-conditioner that is obtained by generating an approximate sparse Jacobian matrix through finite differences, and providing its inverse using an Incomplete-LU Factorisation.

WALL IN VACUO – ILLUSTRATIVE RESULTS

We demonstrate the behaviour of our flexible panel operating in vacuo as a validation of the NK method and provide a contrast for later immersed systems. The in-vacuo case is implemented in the FSI model by setting the external force on the wall in Eqn. (1) to $F(x, t) = 0$. By initially releasing the wall in its fundamental mode-one position, a plot of wall deformations in time reveals the expected sinusoidal oscillations in Fig. 2. Excellent agreement is found with the theoretical values of oscillation frequency for this and subsequent structural modes.

INVISCID-FLOW COUPLING

For very high Reynolds numbers, the flow can be assumed as being purely inviscid and potential flow used as a very good approximation. The Boundary Element Method (BEM) for potential flow is a technique that has been applied to the nonlinear, compliant-wall, potential-flow FSI problem before in [1] with good success. While the theoretical background of the BEM is not discussed here, it can be obtained from reference texts such as Katz and Plotkin [8]. The BEM in its standard formulation is an 'N-body' method; thus, computational cost scales according to the element numbers by $O(n^2)$. We use the Fast Multipole Method (FMM) [9] to perform all field evaluations in an efficient $O(n \log n)$ matrix-free manner². Boundary-element strengths are obtained by enforcing

¹We interchangeably use condensed notation, $\ddot{\eta} = \frac{\partial^2 \eta}{\partial t^2}$ and $\dot{\eta} = \frac{\partial \eta}{\partial t}$.

²The specific FMM implementation features and performance are available in Kapor et al. [10]

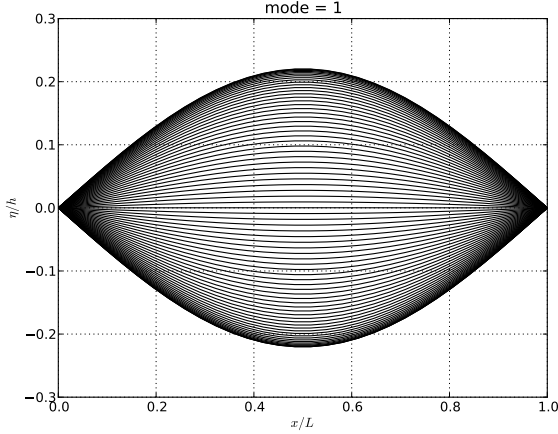


FIGURE 2: SERIES OF PANEL DEFORMATIONS IN TIME FOR THE COMPLIANT-WALL, IN VACUO, AFTER AN INITIALISATION OF ITS FUNDAMENTAL-MODE SHAPE.

the zero normal-velocity boundary condition at the panel midpoints. This is solved using the GMRES in conjunction with the FMM to allow efficient handling of very large BEM systems.

The fluid-wall coupling is achieved by placing the BEM source/sink panels between the FDM mass nodes that follow the wall's motion. Where the fluid flow perturbs under the wall's motion, it offers a response back onto the wall through its corresponding change in pressure. To determine the pressure in the flow field we apply the unsteady Bernoulli equation for potential-flow that is coupled to the wall through the forcing term ($F(x,t)$) of Eqn. (1) as,

$$\begin{aligned} F(x,t) &= -\Delta p(\dot{\eta}, \dot{\eta}, \eta) \\ &= \rho_f \left(-\frac{U_\infty^2}{2} + \frac{\partial \phi}{\partial t} + \frac{U^2 + V^2}{2} \right), \end{aligned} \quad (4)$$

where ρ_f is the fluid density, U_∞ is the undisturbed velocity seen in Fig. 1 and the time differential is solved numerically using a standard, second-order backwards difference approximation. ϕ , U and V are the perturbation velocity potential, horizontal and vertical velocities respectively in the fluid at position x and are obtained using the BEM and evaluating at panel midpoints. Rewriting the full potential-flow FSI system of equations by substi-

tuting Eqn. (4) into Eqn. (1) we have,

$$\begin{aligned} \rho h \frac{\partial^2 \eta}{\partial t^2} + B \frac{\partial^4 \eta}{\partial x^4} - T_l \left(\frac{\partial \eta}{\partial x} \right) \frac{\partial^2 \eta}{\partial x^2} \\ = \rho_f \left(-\frac{U_\infty^2}{2} + \frac{\partial \phi}{\partial t} + \frac{U^2 + V^2}{2} \right). \end{aligned} \quad (5)$$

We note that for the entirety of this work we focus only on walls with both spring backing (k) and damping (d) set to zero. We couple the entire potential-flow pressure implicitly by moving it to the left hand side of Eqn. (5),

$$\begin{aligned} \rho h \frac{\partial^2 \eta}{\partial t^2} + B \frac{\partial^4 \eta}{\partial x^4} - T_l \left(\frac{\partial \eta}{\partial x} \right) \frac{\partial^2 \eta}{\partial x^2} \\ + \rho_f \frac{U_\infty^2}{2} - \rho_f \left(\frac{\partial \phi}{\partial t} - \frac{U^2 + V^2}{2} \right) = 0, \end{aligned} \quad (6)$$

allowing the full FSI system to be solved implicitly in one sweep of the NK scheme [5].

INVISCID FSI – ILLUSTRATIVE RESULTS

We now demonstrate energy-stable, nonlinear divergence instabilities in the potential-flow FSI model. This instability begins with a growth in wall amplitude due to an energy transfer from the fluid caused by a post-divergent flow speed³. The wall amplitude continues to grow until the nonlinear tension provides sufficient force to overcome the energising action of the fluid, at which point it causes a 'snap-back' towards the wall's neutral position. By simulating the case of $\rho_f/\rho_w = 0.385$, akin to water flow over a thin aluminium wall, with a wall thickness ratio of $h/L = 0.01$, a non-dimensional flow speed⁴ of $\Lambda = 61$, we can validate our model to the work of [1]. The system is initiated by releasing the wall from its fundamental mode-shape imposed with an amplitude non-dimensionalised by plate thickness of $A/h = 0.02$. Figures 3a and 3b show a series of wall deformations in non-dimensional time⁵ of a single nonlinear wall oscillation using $N = 64$ mass nodes. Fig. 3c shows the trace of the vertical position in time of the central wall node, illustrating the non-linear oscillatory behaviour that is in good amplitude and frequency agreement with [1].

This FSI case also serves as a means of demonstrating the capability of the presented numerical methods (NK,

³The flow speed from which buckling is induced as a result of the pressure in the fluid exceeding that of the restorative wall forces.

⁴ $\Lambda = \frac{\rho_f U_\infty^2 L^3}{B}$
⁵ $t' = \frac{t}{L} \sqrt{\frac{E}{\rho(1-\nu_p^2)}}$

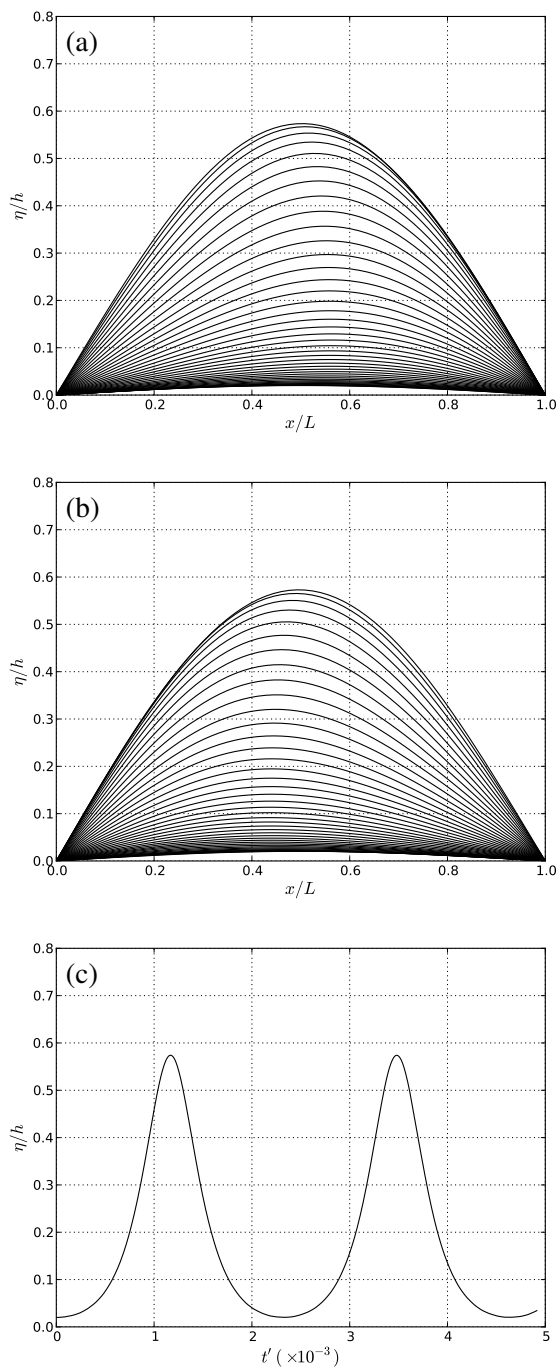


FIGURE 3: SIMULATION OF NON-LINEAR DIVERGENCE INSTABILITY FOR INVISCID WATER FLOW OVER AN ALUMINIUM ($\rho_f/\rho_w = 0.385$) PLATE ($h/L = 0.01$) AT $\Lambda = 61$. SERIES OF WALL DEFORMATIONS IN TIME FOR (a) GROWTH AND (b) DECAY PHASE OF A SINGLE CYCLE, AND (c) PANEL MIDPOINT DISPLACEMENT WITH TIME OVER TWO CYCLES.

BEM, FMM and FDM) for studying numerical systems with a very high level of spatial discretisation or degrees of freedom. We compare the computational effort using an algorithm based on the semi-implicit (SI) method of [1] to that of the present method by varying only the level of spatial (FDM) discretisations, based on the simulation presented in Fig. 3. Figure 4a shows the total computational time required for a full three-oscillation simulation using the SI and NK based algorithms. Computational time has been non-dimensionalised to the wall time required for the SI method using 8 nodes, at $T_{C,N=8} = 18.7s$, achieved on a standard desk-top computer (Intel Q9650 3.0GHz processor). Data for $N = 128$ using the SI scheme was estimated based on previous scaling rates because running this experiment would have been infeasible due to its poor scaling ability. Figure 4b shows a further zoomed scale of Fig. 4a to illustrate the linear scaling of NK scheme. While the SI method offers the fastest computation time for the coarsest spatial discretisations, the NK demonstrates vastly superior scaling from mildly increased levels of discretisation. The brief advantage of the SI method for coarse discretisations can be attributed to the inherent overhead that must be amortised within the NK.

BOUNDARY-LAYER MODELLING

For finite Reynolds-number flows the effects of viscosity such as the no-slip condition, the attendant formation of a boundary-layer velocity profile, and viscous diffusion must be included in the FSI model. We continue to use the BEM to represent the outer (inviscid) flow behaviour while the effects of the boundary-layer are modelled using the grid-free Discrete Vortex Method (DVM), shown in Fig. 5. In this work we use a parallel-boundary layer model [11] that focuses on the perturbations to a boundary layer that has already established a given thickness (δ). In its unperturbed state, the boundary-layer flow can be modelled using a series of flat shear layers, stacked upon one another to represent the different levels of shear that occur in a boundary layer due to the action of viscosity and the no-slip condition. The computational ‘free-field’ is modelled using Gaussian vortices, while far field effects are modelled by semi-infinite vortex sheets that satisfy the parallel boundary-layer assumptions. To mitigate the ‘N-body’ problem of the DVM, all velocity-field calculations are also performed within the FMM framework. To prevent Gaussian vortices overlapping the wall, we use a ‘near-wall’ region that encapsulates what would be the lowest shear layer. The Gaussian vortices of this layer are replaced by linearised representations of zero-

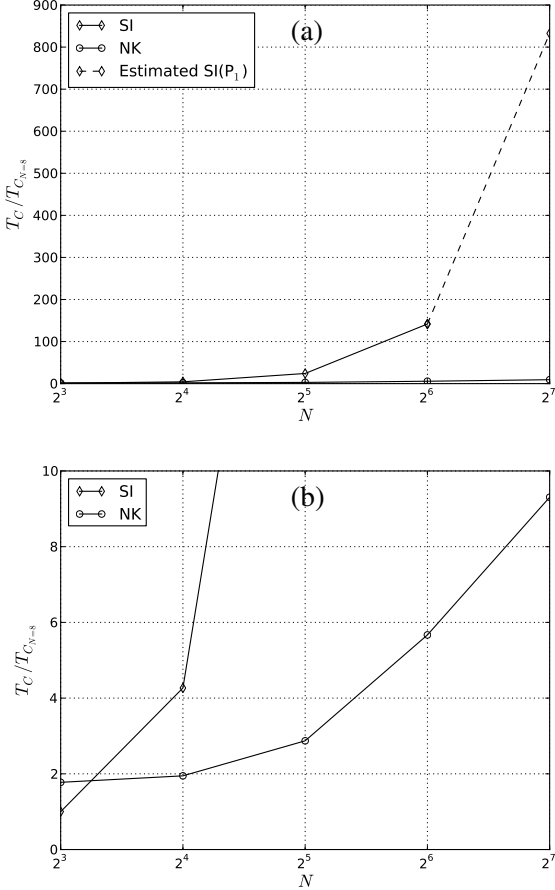


FIGURE 4: RELATIVE COMPUTATIONAL TIME REQUIRED TO COMPLETE THREE NON-LINEAR PANEL OSCILLATIONS OF THE DIVERGENCE INSTABILITY IN FIG. 3 FOR VARYING SPATIAL DISCRETISATIONS. (a) STANDARD VIEW, AND (b) ZOOMED-IN TO EMPHASISE THE NK-SCHEME PERFORMANCE.

order vortex panels who are fixed to the motions of the compliant wall. The model is discretised in the vertical (y) direction based on shear layers with a fixed separation of Δy . The strengths of the shear layers are adjusted to suit the given boundary-layer mean velocity/vorticity profile. Each shear layer is discretised in the horizontal (x) direction by a series of overlapping Gaussian vortices with a spacing of Δx and initial core-sizes of σ . We use a rectangular grid for our initial Lagrangian discretisation, where $\Delta x = \Delta y = h$, with a Gaussian overlap ratio of $\beta = h/\sigma < 1$.

MODELLED VELOCITY PROFILE RESULTS

The mean-flow velocity profile of the unperturbed boundary layer is given by a 4th order Pohlhausen ap-

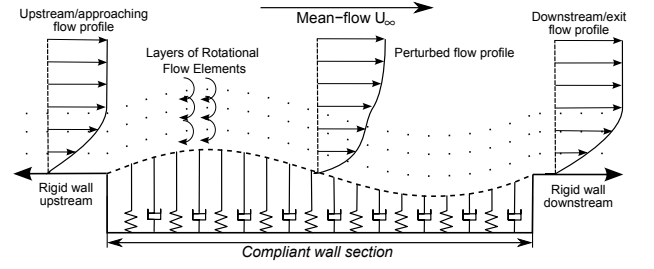


FIGURE 5: SCHEMATIC OF THE FLEXIBLE PANEL INTERACTION WITH A BOUNDARY-LAYER FLOW.

proximation to a laminar Blasius boundary layer,

$$\frac{U}{U_\infty} = 2 \left(\frac{y}{\delta} \right) - 2 \left(\frac{y}{\delta} \right)^3 + \left(\frac{y}{\delta} \right)^4, \quad (7)$$

where y/δ is the normalised vertical position within the boundary layer and U/U_∞ is the stream-wise velocity normalised to the outer-flow speed. To demonstrate the suitability of the DVM to adequately capture the behaviour of the unperturbed Blasius profile, we take a sample of the velocity generated in a vertical slice above a flat wall. With a linearised sub-layer at $y = 0.15\delta$ the simulated velocity profile is compared to the desired Blasius profile in Fig. 6.

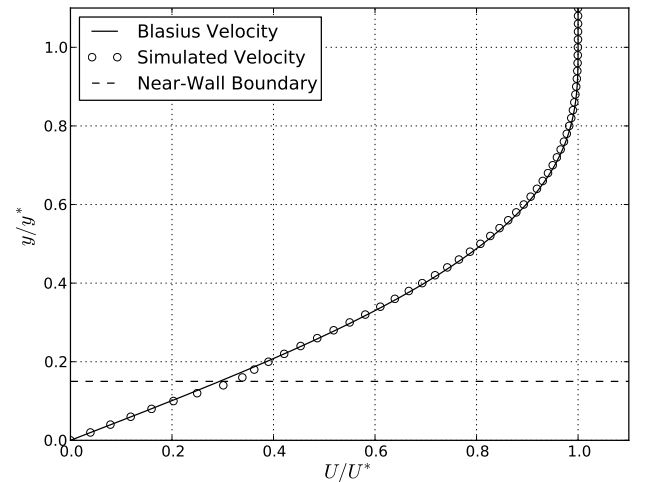


FIGURE 6: UNPERTURBED VELOCITY PROFILE FOR THE DVM-BASED LAMINAR BOUNDARY-LAYER MODEL.

The current arrangement of the DVM captures the desired Blasius velocity profile to a high level of accuracy and results in a numerical error in the displacement thickness of 0.34%.

TRANSIENT FEATURES AND WALL COUPLING

To study the transient behaviour of our boundary-layer model, the vortex particles in the computational ‘free-field’ are time-stepped using a first-order accurate Euler time-stepping scheme. Vorticity injection and deletion occurs in a conservative manner at the domain inlet (left hand side) and exit (right hand side) respectively while vortices are deleted if they convect below the wall. The effects of viscous diffusion are modelled using operator splitting and a viscous core-spreading method [12]. To maintain convection accuracy throughout long-time simulations we use a Lagrangian-grid ‘remapping’ scheme using the GMRES [13].

To model the impact of the movable, impermeable flexible-plate surface, we use the BEM to enforce the zero normal-flow condition with zero-order source/sink panels. The no-slip condition at the wall is enforced using zero-order vortex panels. These elements are superimposed on the source/sink panels and are solved simultaneously with the zero normal-flow condition. The resulting injected vorticity at each time-step is then shed back into the computational domain at the lowest free shear layer.

We obtain the viscous flow pressure (Δp_μ) at the wall through direct numerical integration of the conservation of fluid momentum equations in the y -direction where,

$$\begin{aligned} \Delta p_\mu &= -\frac{\rho_f U_\infty^2}{2} + \int_{+\infty}^{\delta} \frac{\partial p}{\partial y} dy + \int_{\delta}^0 \frac{\partial p}{\partial y} dy \\ &= \Delta p_{\phi, \delta} + \int_{\delta}^0 \left(-\rho_f \left(\frac{\partial V}{\partial t} + U \frac{\partial V}{\partial x} + V \frac{\partial V}{\partial y} \right) \right. \\ &\quad \left. + \mu \left(\frac{\partial^2 V}{\partial x^2} + \frac{\partial^2 V}{\partial y^2} \right) \right) dy. \end{aligned} \quad (8)$$

The integration begins with the potential flow pressure ($\Delta p_{\phi, \delta}$) evaluated at the theoretical boundary of the inviscid outer flow region at $y = \delta$, using the unsteady Bernoulli equation from Eqn. (4). The remaining pressure from the viscous region of flow is integrated down through the boundary layer to the wall. Sufficient samples of the velocity-field (U, V) are taken to enable the approximation of all spatial differentials using a 2nd-order accurate central-difference method.

The viscous-flow pressure is coupled to the complaint wall through the forcing term, $F(x, t) = -\Delta p_\mu(\ddot{\eta}, \dot{\eta}, \eta)$, in Eqn. (1) as,

$$\begin{aligned} \rho h \frac{\partial^2 \eta}{\partial t^2} + B \frac{\partial^4 \eta}{\partial x^4} - T_I \left(\frac{\partial \eta}{\partial x} \right) \frac{\partial^2 \eta}{\partial x^2} \\ = -\Delta p_\mu(\ddot{\eta}, \dot{\eta}, \eta). \end{aligned} \quad (9)$$

The full viscous pressure cannot be coupled implicitly and solved with the existing NK due to the DVM’s extremely high (relative to other components) computational intensity. We instead solve the system numerically by decoupling the left and right hand sides of Eqn. (9) into a semi-implicit solution method. To avoid the inherent instability of a pure semi-implicit method we take a hybrid approach by solving the left hand side of the equation implicitly (with the NK) while the right hand side is treated as a constant that must be iterated until convergence. In scenarios with high-density (relative to the plate density) fluid loading, the convergence behaviour of this scheme rapidly deteriorates. Thus, we apply a ‘conditioner’, $\beta \Delta p_\Phi$, to both sides of the equation that represents a scaled fluid loading of a hypothetical inviscid flow case. This is evaluated with the flow system treated as purely inviscid using the unsteady Bernoulli equation with all rotational/viscous elements turned off. This improves the conditioning of the semi-implicit iterations, increasing the numerical stability and convergence rate. The selection of this ‘conditioner’ is based on reducing the sensitivity of the semi-implicitly coupled pressure to wall acceleration whereby,

$$\left| \frac{\partial (\Delta p_\mu - \beta \Delta p_\Phi)}{\partial \ddot{\eta}} \right| \ll \left| \frac{\partial \Delta p_\mu}{\partial \ddot{\eta}} \right| \quad (10)$$

To further improve convergence rates we adjust the scaling factor (β) dynamically based on the RMS of the inviscid and viscous flow pressures of the previous time-step,

$$\{\beta\}_t = \sqrt{\frac{\sum_{i=1}^N \{\Delta p_\mu\}_{t-1}}{\sum_{i=1}^N \{\Delta p_\Phi\}_{t-1}}}. \quad (11)$$

The resulting NK-SI hybrid system with improved conditioning can be expressed as,

$$\begin{aligned} \underbrace{\left[\rho h \frac{\partial^2 \eta}{\partial t^2} + B \frac{\partial^4 \eta}{\partial x^4} - T_I \left(\frac{\partial \eta}{\partial x} \right) \frac{\partial^2 \eta}{\partial x^2} + \beta \Delta p_\Phi \right]_t}_{\text{Implicit NK}} \\ = \underbrace{\left[-(\Delta p_\mu - \beta \Delta p_\Phi) \right]_{t^*}}_{\text{Semi-Implicit Iteration}} \end{aligned} \quad (12)$$

The right hand side term now represents a viscous correction that is applied to the implicitly coupled potential flow pressure. This is updated after every application of the NK method until convergence is reached ($t^* = t$).

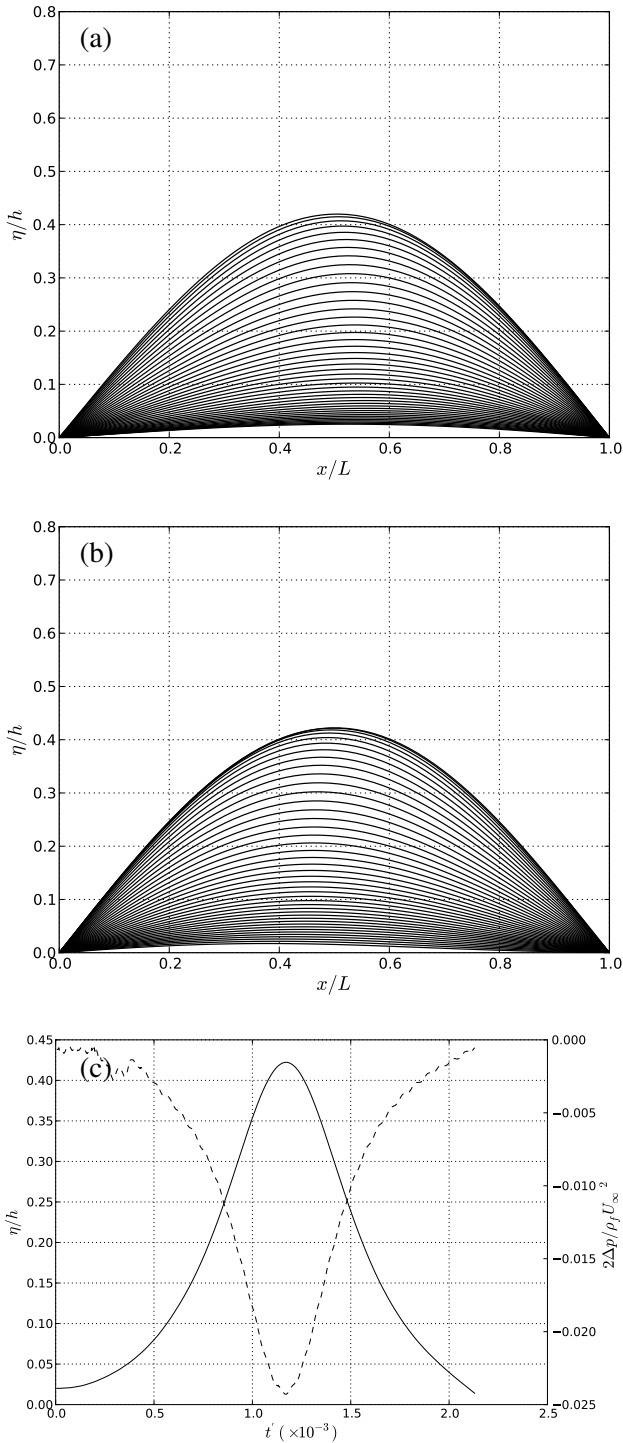


FIGURE 7: SIMULATION OF NON-LINEAR DIVERGENCE INSTABILITY FOR A BOUNDARY-LAYER ($L/\delta = 12.8$) WATER FLOW OVER AN ALUMINIUM ($\rho_f/\rho_w = 0.385$) PLATE ($h/L = 0.01$) AT $\Lambda = 61$. SERIES OF WALL DEFORMATIONS IN TIME FOR (a) GROWTH AND (b) DECAY PHASE OF A SINGLE CYCLE, AND (c) PANEL MIDPOINT DISPLACEMENT AND PRESSURE WITH TIME OVER ONE CYCLE.

BOUNDARY-LAYER FSI – ILLUSTRATIVE RESULTS

Figures 7a and 7b show the nonlinear motion, through one cycle, of a simple elastic panel through divergence occasioned by a boundary-layer flow. The system parameters match that of the previous potential-flow system, with the introduction of a boundary layer thickness of $\delta/L = 0.078$ and a flow viscosity set to that of water. The overall unstable fluid-structure mode is seen to be dominated by the fundamental although slight elements of higher-order mode contribute within its limit-cycle. This behaviour is similar to the potential-flow results of Fig. 3 albeit with a reduced maximum amplitude. Accordingly, the effect of the boundary-layer is to modify, as opposed to change, the divergence of such flexible panels.

Figure 8 illustrates the scaling factor β and the various pressure signals (Δp_μ , $\Delta p_{\Phi,\delta}$ and Δp_Φ) at the wall midpoint in time. Contrary to the expected attenuating

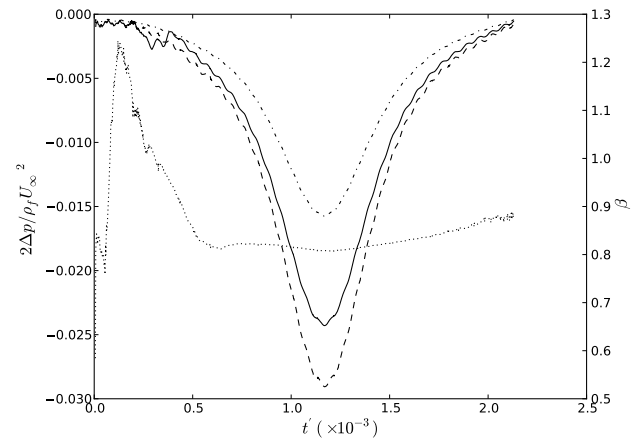


FIGURE 8: MEASURED SCALING RATIO $\{\dots\} \beta$ AND PRESSURE SIGNALS IN TIME FOR $\{\text{SOLID}\} \Delta p_\mu$, $\{-\cdot-\} \Delta p_{\Phi,\delta}$, $\{- -\} \Delta p_\Phi$ FOR THE DIVERGENCE INSTABILITY OF A BOUNDARY-LAYER FLOW.

behaviour, the boundary layer amplifies what would be a potential flow pressure signal for times $t' \approx 0.75$. This artefact is a consequence of the time lag between the impulsive initialisation of the wall and the time it takes for the viscous flow to convect/diffuse the disturbances downstream. Consequently, the first growth cycle of the system varies in intensity to the first decay cycle, allowing the wall to fall below its neutral axis for subsequent nonlinear oscillations. When neglecting the effects of the initial disturbance in the flow field, the viscous pressure slowly varies in the vicinity of 85%–RMS of the theoretical potential-flow pressure, thus reducing the maximum oscillation amplitude when compared to Fig. 3.

This steady-state reduction in pressure will also cause the divergence-onset speed for a boundary-layer flow to increase. To measure this increase, we use an algorithm that iteratively finds the divergence-onset flow speed based on a binary search and Newton-Raphson method. Figure 9 shows the variation of divergence-onset (critical) flow speed with the boundary-layer thickness. The non-dimensional critical flow speed has been normalised with a potential-flow value of $\Lambda_{\Phi,cr} = 41$. Reducing the boundary-layer thickness towards zero is seen to make the critical flow speed asymptote to that of the potential-flow case.

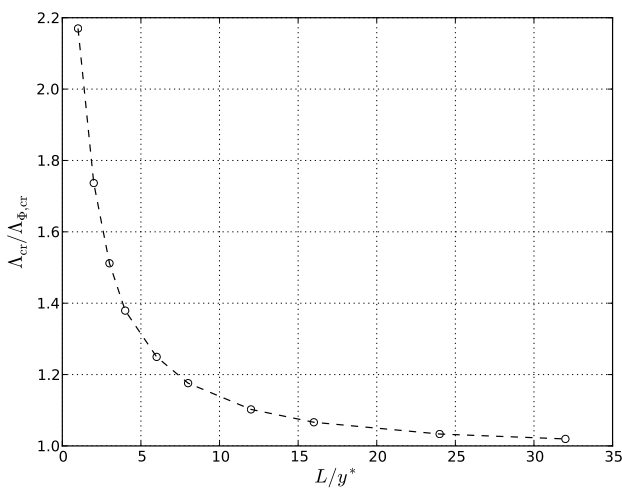


FIGURE 9: DEPENDENCE OF DIVERGENCE-ONSET FLOW SPEED ON BOUNDARY-LAYER THICKNESS.

CONCLUSION

Practicable computational modelling and numerical methods have been developed for the study of the linear two-dimensional fluid-structure interaction of flexible panels in uniform and boundary-layer flows. The key result of the ensuing investigation of panel divergence instability is that potential-flow modelling yields a lower onset flow speed than when boundary-layer shear is included in a full flow model. The present full-flow model also can find application for the simulation of further instabilities such as travelling-wave flutter of a compliant wall and the flow-based Tollmien-Schlichting waves that are responsible for boundary-layer transition in low-disturbance environments.

REFERENCES

- [1] Lucey, A. D., Carpenter, P. W., Cafolla, G. J., and Yang, M., 1997. “The nonlinear hydroelastic behaviour of flexible walls”. *Journal of Fluids and Structures*, **11**, pp. 717–744.
- [2] Davies, C., and Carpenter, P., 1997. “Instabilities in a plane channel flow between compliant walls”. *Journal of Fluid Mechanics*, **352**, pp. 205–243.
- [3] Luo, X., Cai, Z., Li, W., and Pedley, T., 2008. “The cascade structure of linear instability in collapsible channel flows”. *Journal of Fluid Mechanics*, **600**, pp. 45–76.
- [4] Trefethen, L., 1996. *Finite difference and spectral methods for ordinary and partial differential equations*. Cornell University.
- [5] Kapor, J. S., Lucey, A. D., and Pitman, M. W., 2011. “A mesh-free compliant-wall fluid-structure interaction model”. In MODSIM2011, 19th International Congress on Modelling and Simulation. December 2011.
- [6] Knoll, D., and Keyes, D., 2004. “Jacobian-free newton-krylov methods: a survey of approaches and applications”. *Journal of Computational Physics*, **193**(2), pp. 357–397.
- [7] Saad, Y., and Schultz, M., 1986. “Gmres: A generalized minimal residual algorithm for solving non-symmetric linear systems”. *SIAM Journal on scientific and statistical computing*, **7**(3), pp. 856–869.
- [8] Katz, J., and Plotkin, A., 1991. *Low Speed Aerodynamics: From Wing Theory to Panel Methods*. McGraw-Hill.
- [9] Greengard, L., and Rokhlin, V., 1987. “A Fast Algorithm for Particle Simulations”. *Journal of Computational Physics*, **73**, pp. 325–348. help me.
- [10] Kapor, J., Lucey, A., and Pitman, M., 2009. “Boundary-Layer Hydrodynamics using Mesh-Free Modelling”. In 18th World IMACS Congress and MODSIM09 International Congress on Modelling and Simulation. July 2009.
- [11] Kapor, J. S., Lucey, A. D., and Pitman, M. W., 2010. “Fluid-structure interaction using mesh-free modelling”. In Proc. 6th Australasian Congress on Applied Mechanics, 12-15 December, Perth, Australia.
- [12] Leonard, A., 1980. “Vortex methods for flow simulation”. *Journal of Computational Physics*, **37**(3), pp. 289–335.
- [13] Barba, L., Leonard, A., and Allen, C., 2005. “Advances in viscous vortex methods meshless spatial adaption based on radial basis function interpolation”. *International journal for numerical methods in fluids*, **47**(5), pp. 387–421.

EXPERIMENTAL INVESTIGATION INTO VORTEX-INDUCED VIBRATIONS OF YAWED CYLINDERS WITH ONE AND TWO DEGREES-OF-FREEDOM

Guilherme R. Franzini*

Julio R. Meneghini

Fluids and Dynamics Research Group - NDF

POLI

University of São Paulo, Brazil

Rodolfo T. Gonçalves

André L. C. Fajarra[†]

Numerical Offshore Tank - TPN

POLI

University of São Paulo, Brazil

ABSTRACT

Vortex-Induced Vibrations (VIV) experiments were carried out with yawed cylinders. The purpose is investigating the validity of the Independence Principle on properly describing the flow characteristics and the dynamics of structures subjected to oblique flow. Five yaw angles in relation to the direction perpendicular to the free stream velocity were tested, namely $\theta = 0, 10, 20, 30$ and 45 degrees. Both the upstream and downstream orientations were tested. The models were mounted on a leaf spring apparatus that allows experiments with one or two degrees-of-freedom. The Reynolds number based on the component normal to the cylinder axis falls in the range $3 \times 10^3 < Re_n < 1.5 \times 10^4$. Time histories of displacement and hydrodynamic forces were acquired. The results of amplitude and forces coefficients agree very well for yaw angles up to 30° for both one and two degrees-of-freedom experiments. Differences in the results for upstream and downstream were observed and were more evident for the higher yaw angle.

Keywords: Vortex-Induced Vibrations, Experiments, Yawed Cylinders.

INTRODUCTION

The flow around a fixed circular cylinder is one of the most studied problems within the fluids mechanics theme. In this case, the adverse pressure gradient leads to the flow separation, and consequently to the formation of two free shear layers with opposite circulations. Accordingly to the model proposed in [1], the interaction between these free shear layers gives rise to the periodic vortex shedding process with a well defined frequency f_s .

If the cylinder is free to oscillate, the vortex shedding process can be severely affected by the oscillations, as pointed out in the reviews [2,3]. Considering the problem of a rigid cylinder mounted on an elastic support with natural frequency f_N , the lock-in range is the one in which the $f_s \approx f_N$.

As a resonant phenomenon, the Vortex-Induced Vibrations (VIV) present the higher values of amplitude (order of one diameter) at the range of reduced velocity $V_R = U_\infty / f_N D$ (U_∞ is the free stream velocity and D the structural diameter) in which the lock-in is observed. Papers [4–7] consists on comprehensive reviews regarding the Vortex-Induced Vibrations phenomenon.

Up to the 2000s, the VIV investigations focused on the problem of a rigid cylinder assembled onto an elastic base free to oscillate just in the direction transversal to the free-stream (cross-flow direction). Defining the mass parameter $m^* = m_s / m_d$ (m_s is the structural mass and m_d is the mass of fluid displaced by the body), the mass-damping parameter $m^* \zeta$ defines not only the maximum amplitude of oscillation (see [8]) but also the aspect of the response curve.

Considering a system with low $m^* \zeta$, the amplitude plot can be split into initial, upper and lower branches. Each of these branches presents particular characteristics of amplitude/frequency of oscillation, hydrodynamic force coefficients and vortex shedding pattern. Further details regarding these aspects can be found in [9, 10].

Motivated by the new technological demands, since the early 2000s numerous investigations with a rigid cylinder free to oscillate both in the in-line and cross-flow oscillations have been carried out. In this scenario, one of the most striking results indicates that the in-line oscillations strongly affect the cross-flow amplitude only if m^* is below a critical value (see, for example, the parametric

*Corresponding author. Email: gfranzini@usp.br

[†]Presently at MARIN - Maritime Research Institute Netherlands as visiting researcher.

investigations carried out by [11] and [12]). Moreover, as pointed out by [13, 14] in the case of small mass ratio parameter, there is a new branch defined as “*super-upper branch*”, characterized by a vortex pattern in which two triplets of vortex are shed in each cycle of oscillation ($2T$ pattern).

Despite the numerous investigations regarding the flow around a cylinder, the problem with a yawed cylinder placed in a free stream has received much less focus. Aiming at studying this kind of flow, the most common approach is the Independence Principle (IP). The IP states that the flow characteristics depend only on the component of the free stream velocity normal to the cylinder axis. In this work, the yaw angle θ is formed between the cylinder axis and the direction orthogonal to the incoming flow velocity. Positive values of θ refer to the cylinder yawed in downstream orientation, as sketched in FIGURE 1(a).

Theoretical investigations presented in [15] and [16] stress that the IP is a bidimensional approach, i.e., valid under an infinity length cylinder. In this way, there are investigations aimed to check the validity of the IP. Wind tunnel experiments with a tensioned string described in [17] and [18] stressed that the Strouhal number curve is well collapsed by using the IP for values of θ up to 68° .

The experimental investigation described in [19] enlightened some aspects regarding the characteristics of the flow around a fixed and yawed cylinder. The wake angle is very sensitive to the end conditions, and by manipulating the end plate angles, the wake is parallel to the cylinder axis. Moreover, the validity of the IP is intrinsically related to parallel vortex-shedding.

Others aspects that can also be pointed out is the existence of flow regimes depending on the angle θ (see [20]) and the broadening of the spectral distribution with the increase of θ (see [21] and [22]).

Besides the investigations with a stationary yawed cylinder, the forced oscillations were studied either experimentally ([19]) or numerically (see [23] and [24]). Regarding the self-excited oscillations of an yawed cylinder, the experimental investigations carried out by employing both a cantilevered cylinder ([25]) and a rigid cylinder elastically mounted on a one degree-of-freedom support ([26]) showed that the IP very well collapses the reduced velocities in which the lock-in is observed, despite a slight decrease in the maximum amplitude.

The present paper gives continuity to the investigation of VIV on rigid yawed cylinders, for both upstream and downstream orientations. Oscillation amplitudes, as well as force coefficients were evaluated for system constrained to oscillate in one and two degrees-of-freedom

(1DOF and 2DOF respectively).

EXPERIMENTAL ARRANGEMENT

The experiments were carried out at the recirculating water channel facility at NDF, University of São Paulo. The test section has dimensions $0.70 \times 0.70 \times 7.5m$ and can operate with low level of turbulence ($\approx 2\%$) in free stream velocities up to $U_\infty = 0.40m/s$. The displacements were obtained through laser sensors LEUZE model ODSL 8/V4 and the forces were measured by a ATI (Mini40) load cell.

A leaf-spring elastic base was employed for both 1DOF and 2DOF experiments (see Fig.1(b)). This apparatus were designed by using genetic algorithm and Finite Element Method in order to optimize its parameters for running at the NDF experimental facility. The cylinders were made in aluminium with external diameter $D = 44.45mm$.

For each angle of inclination, the model presents its lower edge parallel to the bottom of the channel. The gap between them is lower than $0.2D$. All the experiments were carried out with aspect ratio $L/D \approx 13$ (L is the wet length), mass ratio parameter $m^* = 2.6$ and very low structural damping $\zeta_s \approx 0.1\%$. The range of Reynolds number corrected by using the IP is $3 \times 10^3 < Re_n < 1.5 \times 10^4$.

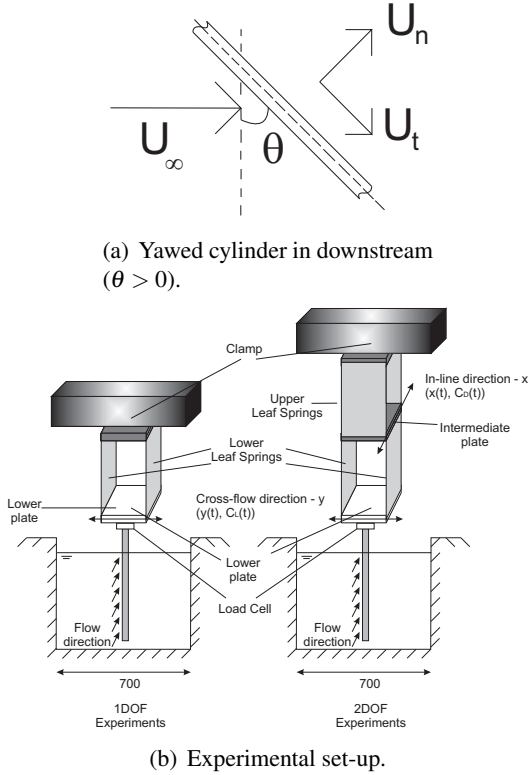
1 ANALYSIS METHODOLOGY

The oscillation amplitudes were calculated by taking the average of the 10% highest peaks recorded in the time history of displacement. The frequencies of oscillation f_{dx} or f_{dy} refer to those with the higher amount of energy in the frequency spectrum. The hydrodynamic forces were normalized by employing the Independence Principle, thus only the component of the free-stream velocity normal to the cylinder axis $U_n = U_\infty \cos \theta$ are considered in equations 1 and 2:

$$C_{D,n}(t) = \frac{2F_D}{\rho U_n^2 DL} = \frac{2F_D}{\rho U_\infty^2 \cos^2 \theta DL} \quad (1)$$

$$C_{L,n}(t) = \frac{2F_L}{\rho U_n^2 DL} = \frac{2F_L}{\rho U_\infty^2 \cos^2 \theta DL} \quad (2)$$

Notice that the use of the IP consists of a correction of the forces coefficients evaluated with the free-stream velocity.


FIGURE 1: SCHEMATIC REPRESENTATIONS.

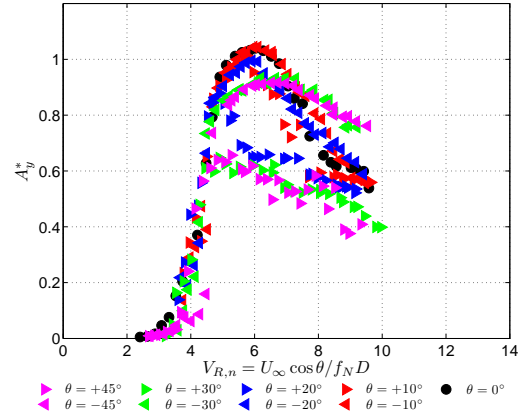
ONE DEGREE-OF-FREEDOM RESULTS

The oscillation amplitude curves for all the experiments is presented in FIGURE 2. The results for the non-yawed cylinder agree very well with the ones obtained with the cylinder in 10 and 20 degrees. At these values of θ and properly considering the values of mass ratio parameter and Reynolds number, the maximum amplitude of oscillation is well compared with the one obtained by using the “modified Griffin plot”, as proposed in [8].

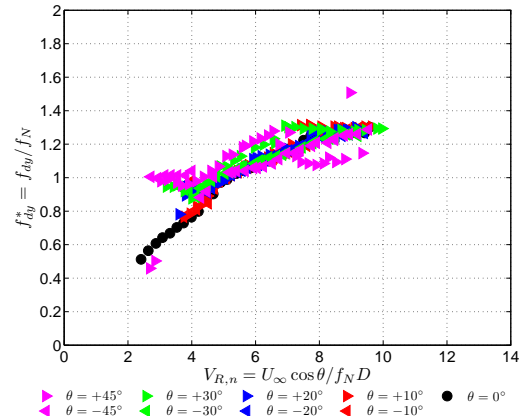
The amplitude plot for $\theta = -30^\circ$ is similar to the case with $\theta = -45^\circ$. In the latter case, the maximum amplitude is slightly lower than the one observed for the cases with $|\theta| \leq 20^\circ$. Besides that, the transition from the “upper branch” to the “lower branch” that occurs at $V_{R,n} \approx 7$ occurs at lower rate.

At this point, an interesting aspect arises. In the case with $|\theta| > 20^\circ$, a difference in the amplitude plot is observed between the cylinder yawed in upstream or downstream orientations, being the oscillation amplitudes consistently higher for the upstream orientations. This difference can be associated to the free-surface aspects, but this aspect deserves a more detailed investigation.

FIGURE 3(a) presents the frequency of oscillation normalized by the natural frequency in still water. As expected, the cases in which there is a good adherence in the amplitude plot, the frequency plot agrees very well.


FIGURE 2: AMPLITUDE OF OSCILLATION (1DOF).

On the other hand, the results for $\theta = +30$ and $+45$, the values of f_{dy}^* are, monotonically with θ , higher than the results for $\theta = 0^\circ$. This can be an indicative of differences in the lock-in process. It is worth mentioning that none of the results follow the classical lock-in concept $f_{dy} \approx 1$ because of the low value of m^* , as stressed, for example, in [6].


FIGURE 3: FREQUENCY OF OSCILLATION (1DOF).

The results of the mean drag coefficient $\overline{C_{D,n}}$ are presented in FIGURE 4(a). The asymptotic result $\overline{C_D},n \approx 1.1$ for $V_{R,n} < 3$ and $V_{R,n} > 8$ is observed here, indicating that the drag amplification occurs at the “upper branch”, albeit the values of $A_y^* \approx 0.5$ at $V_{R,n} \approx 8$.

Similarly to the oscillation amplitude results, the mean drag coefficient decreases monotonically when θ is increased. Notice that the maximum value of the mean drag coefficient for the non yawed cylinder is approximately 3 and occurs at $V_{R,n} \approx 5.8$, corresponding to an amplitude of oscillation close to 1. An analogous analysis can be carried out for the condition $\theta = -45^\circ$, obtain-

ing $\overline{C_{D,n}} \approx 2$, corresponding to an amplitude $A_y^* \approx 0.9$. Taking now $V_{R,n} = 4.5$, i.e, the reduced velocity in which $A_y \approx 0.9$ for no yawed cylinder, the mean drag coefficient is approximately 2.

It is well known that the amplitude of oscillation strongly increases the mean drag coefficient, as stressed in [27] and [10]. Keeping this aspect in mind, the experimental results suggest that the effect of the yaw angle on the mean drag coefficient is caused by the decrease in the amplitude of oscillation in the same manner that occurs for the no yawed cylinder.

The RMS lift force coefficient $C'_{L,n}$ results are presented in FIGURE 4(b). In spite of the differences observed in the amplitude of response curve, there is a very good adherence for all the conditions tested. Despite the different elastic apparatus employed, [26] reported similar behavior for both the lift force coefficient and amplitude of response plot.

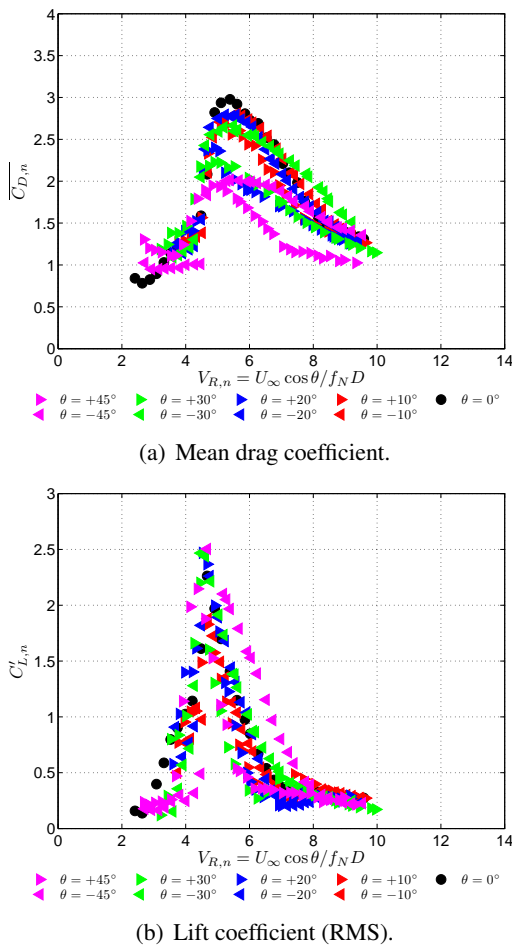


FIGURE 4: FORCE COEFFICIENT (1DOF).

TWO DEGREES-OF-FREEDOM RESULTS

The amplitude of oscillation as a function of the corrected reduced velocity is shown in FIGURE 5. The results for the non-yawed cylinder agrees very well with those presented in [14]. Both the amplitude of in-line (FIGURE 5(a)) and cross-flow (FIGURE 5(b)) oscillations are well collapsed by using the IP for yaw angles up to $|\theta| = 30^\circ$. Moreover, not only the range of reduced velocities is corrected, but also the amplitudes present marked similarity in this range of θ . Notice that, for $\theta = 30^\circ$, there are some differences between the results for upstream and downstream. Considering $\theta = 45^\circ$, this difference becomes more pronounced, being the amplitude for upstream higher than those for downstream.

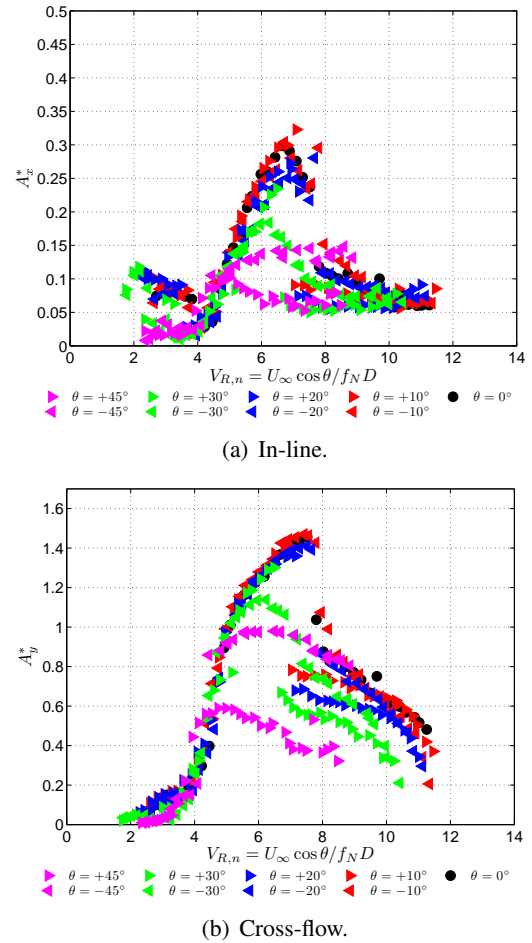


FIGURE 5: AMPLITUDE OF OSCILLATION (2DOF).

FIGURE 6 presents the frequency of response plot. Similarly to the results of amplitude, the cross-flow frequency of oscillation, shown in FIGURE 6(a), the f_{dy}^* plot is very well collapsed for angles up to 30 degrees. As θ is increased from 30° to 45° , the values of $f_{dy}^* = f_{dy}/f_N$

at the “*super upper branch*” gradually depart from the results obtained with small yaw angles, being closer to the ones from the 1DOF experiments.

Besides the low amplitude of in-line oscillations at the “*super upper branch*” for $|\theta| = 45^\circ$, the ratio f_{dx}/f_{dy} is equal to one, as can be found in FIGURE 6(b). As pointed out in [14], the twice in-line frequency is related to the $2T$ vortex pattern, suggesting a change in the vortex patterns caused by the yaw angle. This fact can also explain the lower values of A_y^* if compared to the non-yawed results.

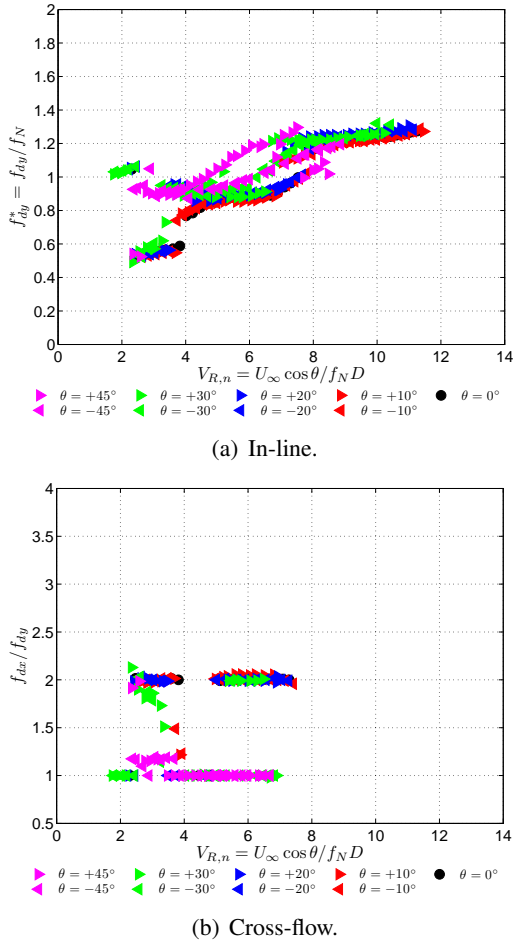


FIGURE 6: FREQUENCY OF OSCILLATION (2DOF).

A more detailed discussion regarding the frequency distribution can be carried out by looking at the time histories at the “*super upper branch*”. FIGURE 8 presents the time histories of displacement for the in-line and cross-flow directions ($x^*(t)$ and $y^*(t)$ respectively) for the conditions $\theta = 0^\circ$ and $\theta = -45^\circ$.

For the no yawed cylinder, the spectrum from the cross-flow time series (FIGURE 7(a)) is clearly narrow-

banded with a dominant frequency $f_{dy} \approx 0.8f_N$. The spectrum obtained from $x^*(t)$ (FIGURE 7(b)) is also narrowbanded, but the dominant frequency is twice the as that for cross-flow one. This aspect leads to the classical 8-shape Lissajous plot characteristic to the “*super upper branch*” as outlined by [14].

In turn, the cross-flow spectrum (FIGURE 8(a)) for $\theta = -45^\circ$ is also narrowbanded, but there is some energy leak to the vicinity of the dominant frequency. This leak is also observed in the in-line spectrum (FIGURE 8(a)), but the dominant frequency is the same as that of the cross-flow oscillation. Thus one can assert that the cylinder yawed at 45 degrees does not reach the “*super upper branch*”, and the vortex shedding pattern is distinct from the $2T$.

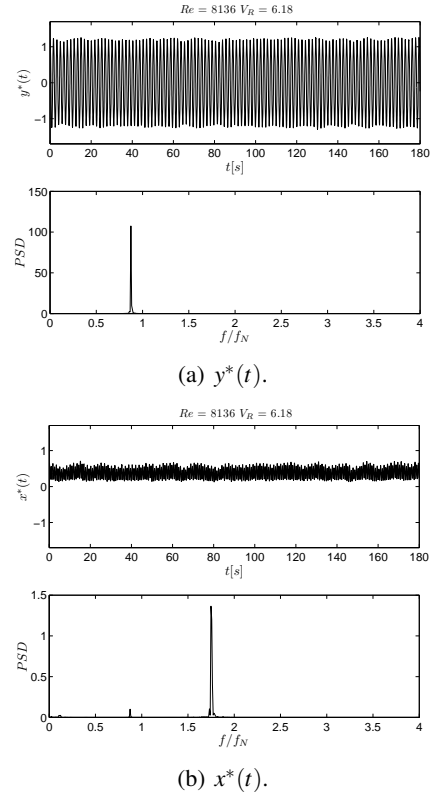
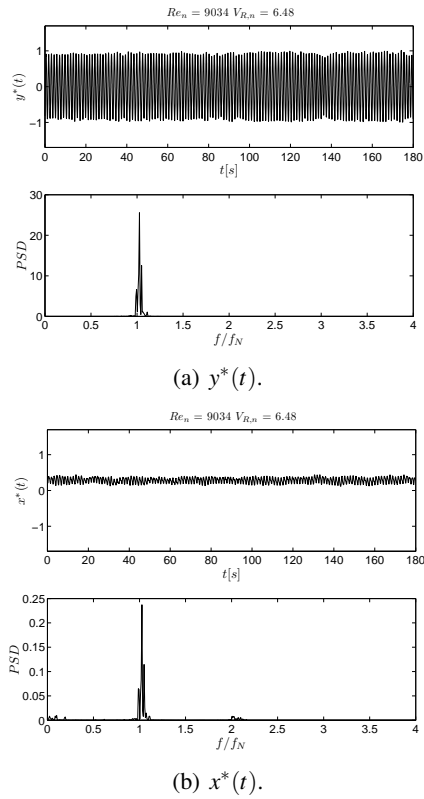
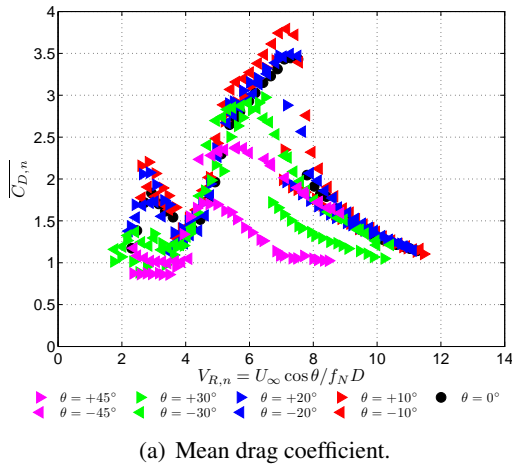


FIGURE 7: TIME HISTORIES - $\theta = 0^\circ$.

Following the methodology adopted in the 1DOF experiments, the hydrodynamic forces were normalized as stated by the IP and the results are presented in FIGURE 9. Similarly to the cross-flow amplitude of response, the maximum mean drag coefficient $\overline{C_{D,n}}$ monotonically decreases by increasing the yaw angle. Notice that the asymptotic results for a fixed cylinder $\overline{C_{D,n}} \approx 1$ is recovered here for $V_{R,n} > 10$. The only exception is the case $\theta = +45^\circ$, and can be explained by the high cross-flow

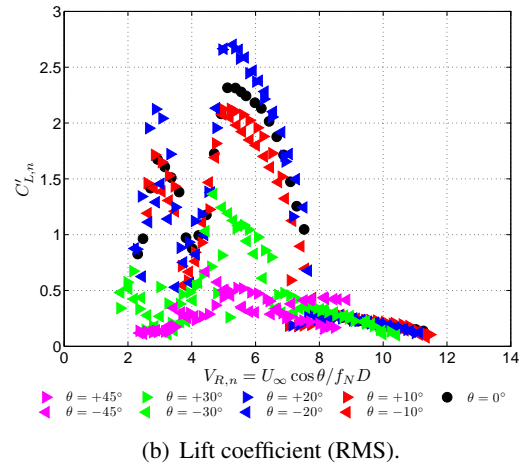

FIGURE 8: TIME HISTORIES - $\theta = -45^\circ$.

amplitude ($A_y^* \approx 0.8$) that amplifies the mean drag force, as pointed out in [27].



Conversely to the results of amplitude and mean drag coefficient, the RMS of the corrected lift force coefficient is no monotonic. It is worth mentioning that no monotonic behavior of the flow characteristics around a fixed yawed cylinder was reported in [20]. Another aspect that should be pointed out is the fact that, although the maximum cross-flow amplitude for 45° reaches 70% of the

peak of A_y^* for $\theta = 0^\circ$, the ratio between the maximum values of $C'_{L,n}$ is close to 30%.


FIGURE 9: FORCE COEFFICIENT (2DOF).

FINAL REMARKS

The results for the yawed cylinder in 1DOF and 2DOF were found to be partially similar to the ones observed for the non yawed case. The Independence Principle (IP) has proved to be useful to correct the range of reduced velocities in which the higher amplitudes of oscillation are observed. Both the amplitudes of oscillations and the forces coefficients present marked similarity for yaw angles up to 20 degrees. For yaw angles higher than 20° , differences between upstream and downstream results arise, and become more pronounced with the increase of θ .

The hydrodynamic forces were evaluated by using the correction proposed by the IP, i.e., employing the component of the free stream velocity normal to the cylinder axis. For the one degree-of-freedom, the dependence of the corrected mean drag coefficient on the amplitude of oscillation is the same for the no yawed cylinder and the cylinder yawed at 45° . The corrected root-mean square lift force coefficient is very similar for all the angles tested.

For the two degrees-of-freedom experiments, the root-mean square lift force coefficient plot is not collapsed by using the IP. The maximum $C'_{L,n}$ for 30° is 30% of the one from the no yawed case, although the maximum amplitude differs only by 30%.

Further works will include flow visualizations using the Particle Image Velocimetry technique aiming at a better description of the wake from yawed cylinders. The

free-surface effects and their relation with the difference between upstream and downstream results is under investigation.

ACKNOWLEDGMENT

The authors acknowledge FAPESP (São Paulo State Research Foundation), CNPq (Brazilian National Council of Scientific and Technological Development), Petrobras (Brazilian oil and gas company) and FINEP (Research and Projects Financing Agency) for the financial support to Vortex-Induced Vibrations (VIV) projects at USP. G.R.F. is also grateful to FAPESP for his PhD scholarship, process 2008/00688 – 4. Special thanks to César Monzu Freire, Ivan Korkischko, Douglas Silva and Reinaldo Marcondes Orselli for their help with the experiments. Prof. Fujarra is grateful to the Brazilian Navy and Maritime Research Institute Netherlands for all support provided during his sabbatical period, 2011 – 2012.

REFERENCES

- [1] Gerrard, J. H., 1966. “The mechanics of the formation region of vortices behind bluff bodies”. *Journal of Fluid Mechanics*, **25**, pp. 401–413.
- [2] Bearman, P. W., 1984. “Vortex shedding from oscillating bluff bodies”. *Annual Review of Fluids Mechanics*, **16**, Jan, pp. 195–222.
- [3] Bearman, P. W., 2011. “Circular cylinders wake and vortex-induced vibrations”. *Journal of Fluids and Structures*, **27**, pp. 648–658.
- [4] Sarpkaya, T., 2004. “A critical review of the intrinsic nature of vortex-induced vibrations”. *Journal of Fluids and Structures*, **19**, pp. 389–447.
- [5] Gabbai, R., and Benaroya, H., 2005. “An overview of modeling and experiments of vortex-induced vibration of circular cylinders”. *Journal of Fluids and Structure*, **282**, pp. 575–616.
- [6] Williamson, C. H. K., and Govardhan, R. N., 2004. “Vortex-induced vibrations”. *Annual Review of Fluids Mechanics*, **36**, pp. 413–455.
- [7] Williamson, C. H. K., and Govardhan, R. N., 2008. “A brief review of recent results in vortex-induced vibrations”. *Journal of Wind Engineering and Industrial Aerodynamics*, **96**, pp. 713–735.
- [8] Govardhan, R. N., and Williamson, C. H. K., 2006. “Defining the “modified griffin plot” in vortex-induced vibration: revealing the effect of reynolds number using controlled damping”. *Journal of Fluid Mechanics*, **561**, pp. 147–180.
- [9] Khalak, A., and Williamson, C. H. K., 1997. “Fluid forces and dynamics of a hydroelastic structure with very low mass and damping”. *Journal of Fluids and Structures*, **11**, pp. 973–982.
- [10] Khalak, A., and Williamson, C. H. K., 1999. “Motions, forces and modes transitions in vortex-induced vibration at low reynolds number”. *Journal of Fluids and Structures*, **13**, pp. 813–851.
- [11] Freire, C. M., and Meneghini, J. R., 2010. “Experimental investigation of viv on a circular cylinder mounted on an articulated elastic base with two degrees-of-freedom”. In IUTAM Symposium on Bluff Bodies Wakes and Vortex-Induced Vibrations - BBVIV6.
- [12] Stappenbelt, B., and Lalji, F., 2008. “Vortex-induced vibration super-upper branch boundaries”. *International Journal of Offshore and Polar Engineering*, **18**, pp. 99–105.
- [13] Jauvtis, N., and Williamson, C. H. K., 2003. “Vortex-induced vibration of a cylinder with two degrees of freedom”. *Journal of Fluids and Structures*, **17**, pp. 1035–1042.
- [14] Jauvtis, N., and Williamson, C. H. K., 2004. “The effect of two degrees of freedom on vortex-induced vibration at low mass and damping”. *Journal of Fluid Mechanics*, **509**, pp. 23–62.
- [15] Sears, W. R., 1948. “The boundary layer of yawed cylinders”. *Journal of Aeronautical Sciences*, **15**, pp. 49–52.
- [16] Marshall, J. S., 2003. “Wake dynamics of yawed cylinder”. *Journal of Fluids Engineering*, **125**, pp. 97–103.
- [17] Hanson, A. R., 1966. “Vortex shedding from yawed cylinders”. *Technical notes AIAA Journal*, **4**, pp. 738–740.
- [18] van Atta, C. W., 1968. “Experiments on vortex shedding from yawed circular cylinders”. *Technical notes AIAA Journal*, **6**, pp. 931–933.
- [19] Ramberg, S. E., 1983. “The effects of yaw and finite length upon vortex wakes of stationary and vibrating circular cylinders”. *Journal of Fluid Mechanics*, **128**, pp. 81–107.
- [20] Snarski, S. R., 2004. “Flow over yawed circular cylinders: Wall pressure spectra and flow regimes”. *Physics of Fluids*, **16**, pp. 344–359.
- [21] Zhou, T., Razali, S. F. M., Zhou, Y., Chua, L., and Cheng, L., 2009. “Dependence of the wake on inclination of a stationary cylinder”. *Experiments in fluids*, **46**, pp. 1125–1138.
- [22] Wang, H. F., Razali, S. F. M., Zhou, T. M., Zhou, Y., and Cheng, L., 2011. “Streamwise evolution of an inclined cylinder wake”. *Experiments in fluids*, **51**, pp. 533–570.

- [23] Lucor, D., and Karniadakis, G. E., 2003. “Effects of oblique inflow in vortex-induced vibrations”. *Flow, Turbulence and Combustion*, **71**, pp. 375–389.
- [24] Willden, R. H. J., and Guerbi, M., 2010. “Vortex dynamics of stationary and oscillating cylinders in yawed flow”. In IUTAM Symposium on Bluff Bodies Wakes and Vortex-Induced Vibrations - BB-VIV6, pp. 47–54.
- [25] King, R., 1977. “Vortex excited oscillations of yawed circular cylinders”. *Journal of Fluids Engineering*, **99**, pp. 495–502.
- [26] Franzini, G. R., Fugarra, A. L. C., Meneghini, J. R., Korkishcko, I., and Franciss, R., 2009. “Experimental investigation of vortex-induced vibration on rigid, smooth and inclined cylinders”. *Journal of Fluids and Structures*, **25**, pp. 742–750.
- [27] Sarpkaya, T., 1995. “Hydrodynamic damping, flow-induced oscillations and biharmonic response”. *Journal of Offshore Mechanics and Artic Engineering*, **117**, pp. 232–238.

KARMAN VORTEX EFFECT ON CROSS FLOW RESPONSE ON NON-YAWED AND YAWED CIRCULAR CYLINDER IN SMOOTH FLOW

Masaru Matsumoto
 Professor Emeritus of Kyoto University,
 Kyoto, Japan
 Email: matsu@brdgeng.gee.kyoto-u.ac.jp

Hiroshi Ishizaki
 President of Hanshin Expressway
 Maintenance and Technology,
 Osaka, Japan

Michio Hashimoto
 Shimizu Corporation,
 Tokyo, Japan

ABSTRACT

In this paper, vortex-induced vibration and galloping instability, which is one of self-controlled cross-flow vibrations, is studied in relation to Karman vortex(KV) of non-yawed and yawed circular cylinder in smooth flow. Vortex of bluff body is classified into conventional KV, impinging shear layer related vortex (IMPV) and motion-induced vortex (MIV), then their mutual fluid dynamic interaction. Unsteady galloping, in particular, is studied to verify the unsteady response of yawed cable with yawed angle of 45° from the point of flow field of flow-reattachment and its undulation effect, basing on the experimental data on rectangular cylinders with various side ratios with fixed splitter plate in a wake. Furthermore, bias flow appearance is introduced in relation to weakened KV.

INTRODUCTION

In this study, Karman vortex is defined as alternative vortex shedding with shedding frequency characterized by Strouhal number for stationary state. Complex vortex characteristics near $V_r=1/St$ has been clarified by Williamson and Roshko[1] and sequentially many studied has carried out, including Laneville and Brika[2] and Zasso, Belloli and Muggiasca[3]. On the other hand, Okajima[4] experimentally obtained $St(D)$ (Strouhal number) of rectangular cylinder with various side ratios, B/D (B :along length, D :depth of body). St changes associated to B/D drastically near $B/D=2.8$ and $B/D=5-6$ corresponding to the change of flow patterns around cylinders, those are steady-separated flow type, unsteady-separated flow type, it means intermittently flow reattaches on the cylinder, and steady flow reattach type. Depending on these flow types, particular vortex exists. Well known KV is generated in steady-separated flow type, on the other hand, IMPV is generated in steady flow reattachment type. In particular, multiple Strouhal numbers exist between $B/D=2$ and 2.8 as shown in Fig.1. At these B/D ranges, conventional KV, simultaneous

symmetrical vortex with twice of St of KV, or IMPV should intermittently appears. On $St(B)$ (defined as fB/V) of IMPV has been verified to be 0.6 for H-shaped sections between $B/D=2$ and 8 by Nakamura, Hirata and Urabe[5] and for rectangular cylinder little bit smaller than 0.6 between $B/D=3$ and 6 by Shimada[4], Nakamura et.al.[5], and Shiraishi and Matsumoto[6]. Fig.2 shows the IMPV of stationary H shaped section with $B/D=5$ (by Nakamura and et.al.[7], the alternative vortex in a wake is almost identical to conventional KV of circular cylinder as shown in Fig.3.

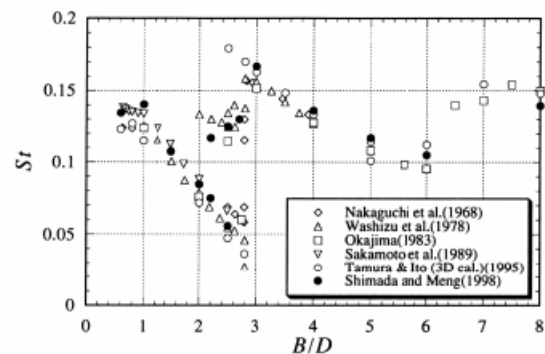


Fig.1 $St(D)$ of rectangular cylinders (Shimada[4])

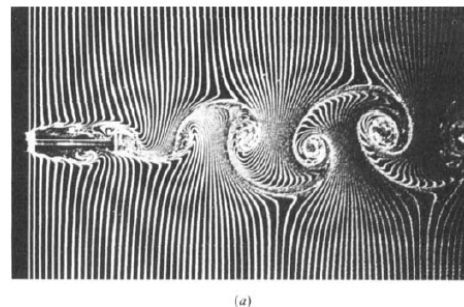


Fig.2 _IMPV of stationary H-shaped cylinder with $B/D=5$ (Nakamura and Nakashima[7])

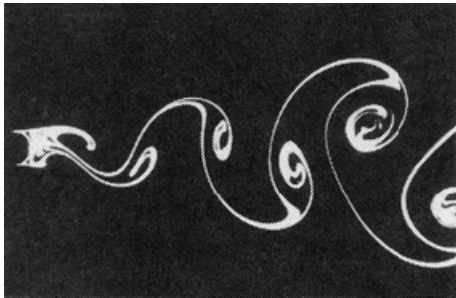
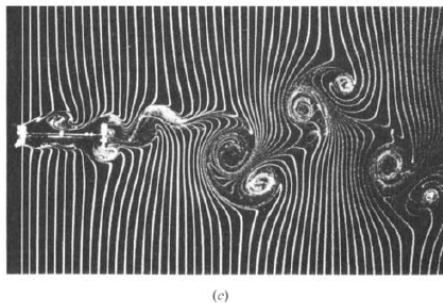
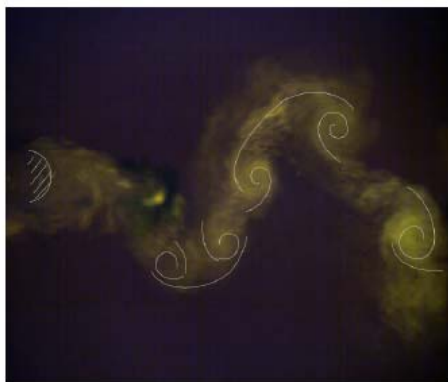


Fig.3 KV of circular cylinder

On the other hand, complex vortex structures, which consist of KV and MIV, of H-shaped section with $B/D=5$ during cross flow forced vibration with $y_0/D=$ at $V_r=$ (by Nakamura and Nakashima[7]) are significantly similar to the ones of circular cylinder at $y_0/D=0.37$ and $V_r=0.965(1/St)$ (Dallaire, Questa-Lavoie, Filion, Laneville and Van Dyke[8]) as shown in Fig.4.



(a) H-shaped cylinder with $B/D=5$ at forced heaving vibration with $y_0/D=0.19D$, $V_r=1.34(1/St)$ (Nakamura and Nakashima[7])



(b) Circular cylinder at heaving forced vibration with $y_0=0.37D$ and $V_r=0.965(1/St)$ (Dallaire, Questa-Lavoie, Filion, Laneville and Van Dyke[8])

Fig.4 complex vortex structures of KV and MIV (for circular cylinder) and of IMPV and MIV (for H-shaped cylinder)

On the galloping instability basing on den Hartog criterion[9], Bearman and Trueman[10] and Nakamura and Tmonari[11] individually clarified the substantial generation mechanism of negative lift slope of bluff bodies, those are "inner circulatory flow", generated by significant fluid interaction between separated shear flow and sharp trailing edge of body (Bearman and Trueman[10]) and "reattachment type pressure distribution flow" (Nakamura and Tomonari[11]), respectively. Negative lift slope is also observed for thin airfoil such as NACA0012 at stalling angle. Rinoue[12] studied in detail on the separation bubble structure of airfoil at angle of attach larger than critical stalling angle, classified into "short bubble" which produces more intensive negative pressure, and "long bubble", which appears by "burst" from "short bubble". The galloping instability of transmission line with snow has been studied on generation of negative lift force in relation to flow reattachment and formation of separation bubble at particular angle of attack. (Shimizu, Oka and Ishihara[13], Matsumiya, Nishihara and Shimizu[14]).

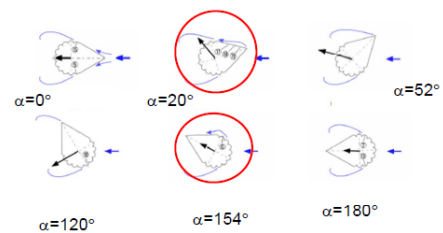
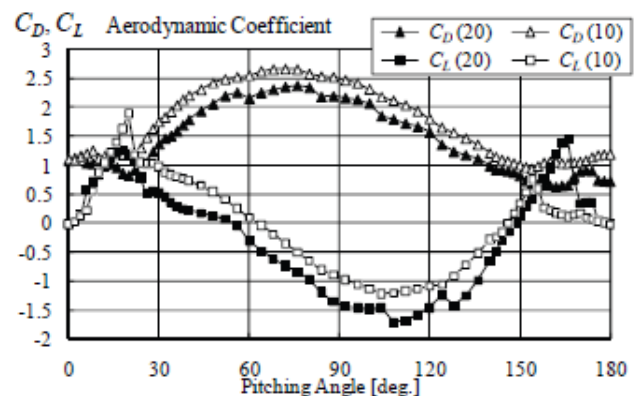


Fig.5 negative lift slope of transmission line with snow caused by flow reattachment (Matsumiya, Nishihara, and Shimizu[14])

These galloping instabilities described above are generated in relation to negative lift slope, that is den Hartog criterion, in another expression, they are "quasi-steady galloping". However, galloping instability can be

excited in no relation to negative lift slope. Rectangular cylinders with less than $B/D=0.75$ at lower reduced velocity than $Vr=1/St$ (Nakamura and Hirata[5]), rectangular cylinders with fixed splitter plate in a wake and yawed or inclined cylinder shows like galloping vibration. First one is called as “Low speed galloping (LSG), and they explained its generation mechanism is non-fluid memory, it means deformed separated shear flow by body motion can generate “flow reattachment pressure distribution flow. For rectangular cylinder with a fixed splitter plate, it has been known that a splitter plate in a wake can make KV weakened/ mitigated, then the undulation flow in near wake can excite galloping by the fluid dynamic unsteady effect as fluid memory, it means phase of flow and body motion. On appearance of cross flow vibration like galloping of yawed/inclined circular cylinder can be excited by axial flow generated in near wake (Matsumoto, Yagi, and et.al.[15]). Furthermore, yawed circular cylinder shows, in unsteady, cross flow response when KV is mitigated (Matsumoto and et.al.[16]). All of these cross flow response are called as “unsteady galloping (UG)” in contrast to “quasi-steady galloping(QG)” On “bias flow” of symmetrical sections has been studied for side-by-side rectangular cylinder (Okajima[17], Alam and Zhou[18], Matsumoto and et.al.[16]), circular cylinder at critical Reynolds number (Recr) (Shewe[19], Macdaonalds[20], Liu[21], Basu[22], Sato[23], Matsumoto[24]), circular cylinder with symmetrical protuberances (Matsumoto[16]), and circular cylinder with movable splitter plate in a wake(Cimbala and Carg[25]) (Assi, Bearman and Kitney[26]).

HYBRID VORTEX STRUCTURES OF CIRCULAR CYLINDER AT NEAR $Vr=1/St$

The unsteady lift forces of circular cylinder under cross flow forced vibration with $f_0=2.5\text{Hz}$, $y_0/D=0.1, 0.2, 0.3, 0.4, 0.5, 0.6, 0.7, 0.75, 0.8, 0.85$ and 0.9 and $0.2at$ near $Vr=St$, with velocity step of $\Delta=0.01\text{m/s}$. wind velocity and amplitude of forced vibration. Therefore the unsteady lift forces at totally 803combinations of amplitude and velocity. The band-passed filtered unsteady forces against KV frequency, $fk\pm 0.2\text{Hz}$ where fk is defined by $St=0.2$.

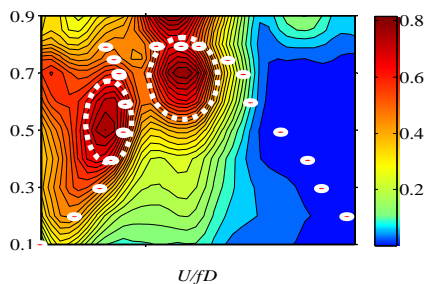


Fig.6. KV component in unsteady lift force of circular cylinder exists during forced vortex-induced vibration (dotted area is intensive KV zone and red small circle indicates V-A diagram obtained from unsteady derivatives $H1^*$)

As shown in Fig.6, KV component clearly exists during forced cross flow vibration. It means KV is not locked in MIV, in general called as lock-in. Therefore “lock-in” phenomenon does not occur in vortex induced vibration, of circular cylinder. Red circle in Fig.6, indicates V-A diagram obtained by unsteady aerodynamic force $H1^*$ as shown in Fig.7.This V-A diagram shows good agreement with the result obtained by Brika and Laneville[28]. From Fig.6, response induced by MIV seems avoiding the intensive KV zone. KV, in consequence, might kick around to MIV as fluid interference. On the other hand, interference of KV on MIV of a circular cylinder can be verified by change of the peak amplitude of MIV vortex-induced vibration under suitably controlled KV intensity in a wake. Perforated splitter plates with opening ratio(OR) from 0% (solid splitter plate) to 100% (without splitter plate) by every 10% pitch were used for changing mitigation level of intensity of KV in near wake. The length of splitter plate is $14D(D=50\text{mm})$ and the gap between cylinder and splitter plate was $0.1D$. (Matsumoto and et.al.[16])

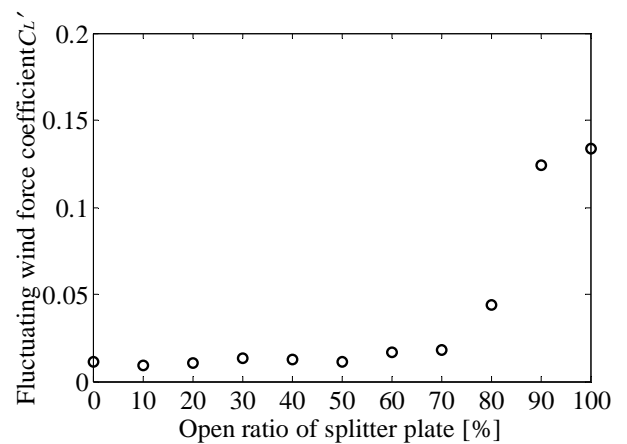
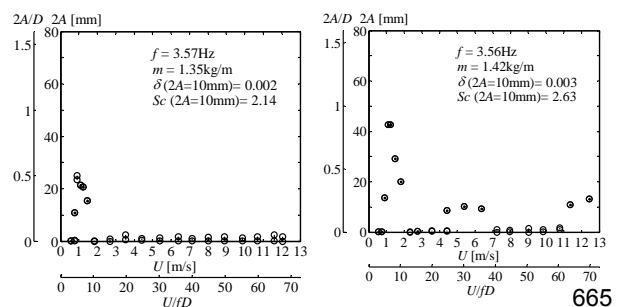


Fig.7 Fluctuating lift force coefficient CL' generated by KV v.s. opening ratio of splitter plate diagram

As shown in Fig. 7, increasing OR of splitter plate, CL' drastically decreases. Then maximum amplitude of MIV vortex-induced vibration increase with OR between $OR=100\%$ and 50%



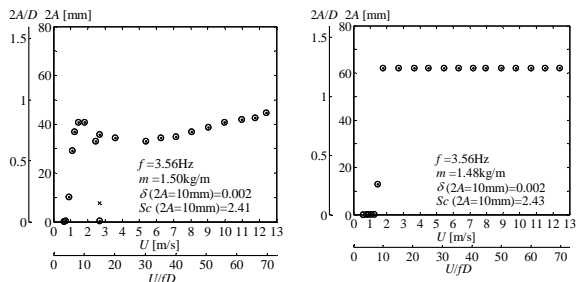


Fig.8 Change of cross-flow response of circular cylinder by change of opening ration of splitter plate(top of right: OR=100%, top of right:OR=70%, bottom of left: OR=40%, bottom of right:OR=0%)

From these results, it is cleared that on the interference between MIV and KV, KV mitigates MIV. This characteristic of KV on MIV is identical feature indicated in Fig.6. On interaction between MIV and IMPV, heaving vortex-induced vibration of a rectangular cylinder with B/D=4 without/with a solid splitter plate with 3B length and 0.1B gap between splitter plate and cylinder. (Matsumoto, Yagi, Tamaki and Tsubota[27]) is not so affected by a splitter plate in a wake as shown in Fig.9. It is natural taking into account of the formation of IMPV on side-face of cylinder, not in a wake. Thus, Interaction between MIV and IMPV might be not significant, however, it should be noted that torsional MIV vortex-induced vibration begins at $Vr=(2/3)(1/0.6)(B/D)$, not at $Vr=(1/0.6)(B/D)$, which is for the one of heaving MIV vortex-induced vibration characterized by IMPV. (Shiraishi and Matsumoto[6])

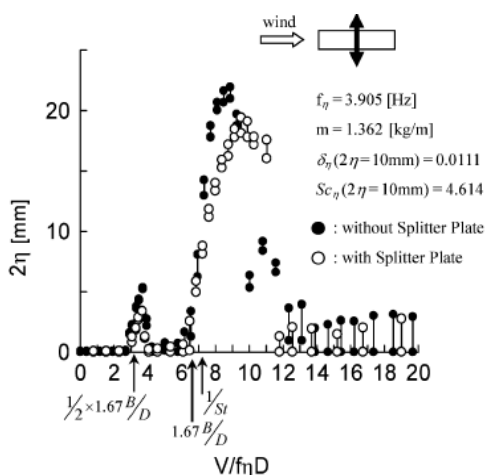


Fig.9 MIV vortex-induced vibration of rectangular cylinder with B/D=4

UNSTEADY GALLOPING

Den Hartog Criterion, that is $dCF/d\alpha < 0$, has been widely well known that it definitely characterizes the appearance of galloping instability. Parkinson succeeded to beautifully explain the non-linear behavior of galloping instability of square cylinder by use of Krylov-Bogoliubov method. (Parkinson and Brooks[28]) However, a rectangular cylinder with B/D=0.3, or B/D=0.4 with a splitter plate shows $dCF > 0$, galloping instability appears. Also in the case of “Low Speed Galloping”(LSG) studied by Nakamura and Hirata[], bluff rectangular cylinders with less than $B/D < 0.75$, show galloping at lower reduced velocity than $Vr=(1/St)$, though not showing $sCF/d\alpha < 0$, as described before. If quasi-steady is satisfied, from the analogy of lift force induced by heaving velocity (dy/dt) between ($dCF/d\alpha$) and Scanlan derivative(Scanlan and Tomko[29]), $H1^*$, associated to heaving velocity, dy/dt , the following formula can be obtained.

$$H1^* = (1/\pi)(-dCF/d\alpha)Vr \quad (1)$$

Where, $Vr = V/b\omega$ (V : wind velocity, b :half chord length, $b=B/2$, ω :circular frequency of heaving motion)

It means $H1^* > 0$ corresponds to $dCF/d\alpha < 0$. In another expression, galloping instability appears when $H1^*$ is positive. $H1^*$ can be directly measured from free vibration test or forced vibration test. Furthermore, comparing $H1^*$ directly measured and the one obtained from equation (1) based on $dCF/d\alpha$ measured from static test, one can discuss how to satisfy quasi-steady condition. Fig.10 shows $dCF/d\alpha$ of rectangular cylinder with B/D between 0.3 and 2.0 without/with splitter plate (with 18D length and 0.06D gap between cylinder and splitter plate). Rectangular cylinders with splitter plate with B/D=0.5, 0.4 and 0.3 shows $dCF/d\alpha > 0$, however they shows $H1^* > 0$, it means galloping appearance. On the other hand, even though rectangular cylinders between B/D=0.6 and B/D=0.9 shows $dCF/d\alpha < 0$, but their absolute values are definitely small, that is almost zero. All of these cylinders with a splitter plate show galloping instability. These data clearly indicate that galloping of these cases can be excited independently den Hartog criterion, therefore galloping of these types can be said to be “unsteady galloping (UG)”, in contrast to “quasi-steady galloping(QG)” characterized by den Hartog criterion. The fluctuating lift coefficient CL' of rectangular cylinders with various sider ratios, B/Ds caused by KV is drastically suppressed by splitter plate as shown in Fig.11 by interruption of fluid communication between two separated shear layers. On generation mechanism of UG of rectangular cylinder with splitter plate, the undulation of separated shear flow from vibrating cylinder, caused by effect of “fluid memory” which should be produced by KV mitigation in near wake, would generate exciting lift

force with significant phase lag between lift and heaving motion of cylinder. LSPG is caused by no fluid memory (Nakamura, Hirata and Urabe[5]). As an example, CF- α diagram and $H1^*$ of rectangular cylinder with $B/D=0.3$ without/with splitter plate are shown in Fig.12.

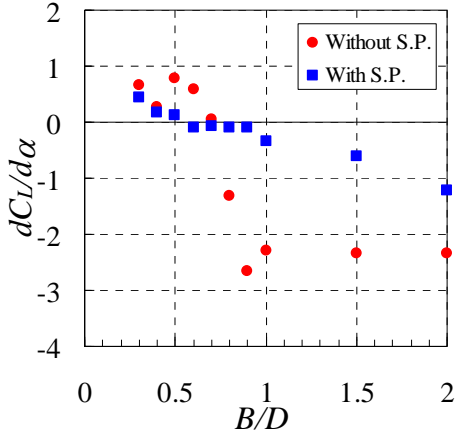


Fig.10. CF- α diagram and their $H1^*$ - V_r diagram of rectangular cylinder without a solid splitter plate and with a splitter plate

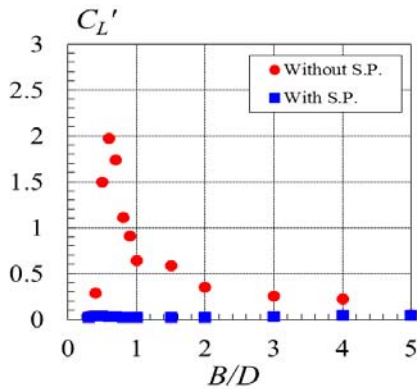
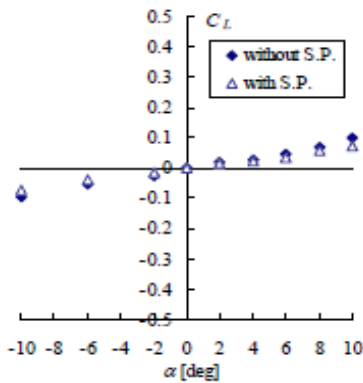
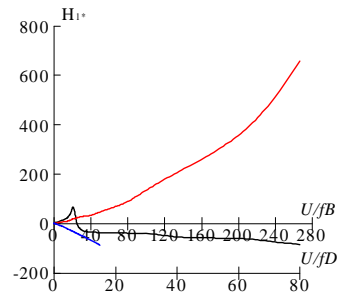


Fig. 11 Fluctuating lift coefficient C_L' generated by KV of rectangular cylinders with various side ratios without/with a splitter plate.



(a) CF- α diagram



(b) $H1^*$ diagram

Fig.12 CF- α diagram and $H1^*$ diagram of a rectangular cylinder with $B/D=0.3$ without(black line)/with(red line) a splitter plate (blue line in Fig.(b) : obtained by Theodorsen Function)

CROSS FLOW RESPONSE OF YAWED CIRCULAR CYLINDER

A yawed circular cylinder with $\beta=45^\circ$ shows galloping instability at high reduced velocity as shown in Fig. 13.

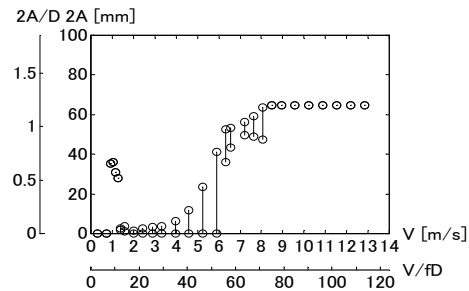
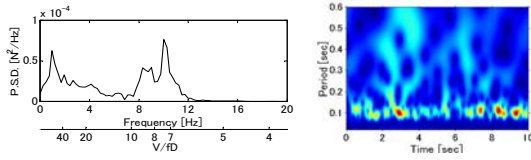


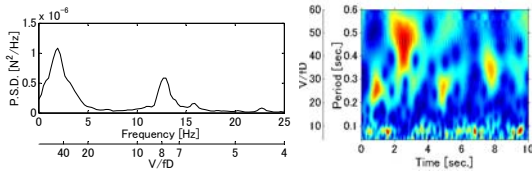
Fig. 13 Cross-flow response of yawed circular cylinder with $\beta=45^\circ$ in smooth flow($Sc=1.138$ at $2y_0/D=0.2$)

The galloping is generated by an intensive axial flow in near wake(Matsumoto[30]). The axial flow in near wake of yawed cable can be simulated by perforated(30% perforation) splitter plate with $4D$ length and $0.1D$ gap between cylinder and splitter plate installed in near wake of non-yawed ($\beta=0^\circ$) cylinder. Fig. 14 shows comparison of PSD and wavelet value of fluctuating lift of yawed($\beta=45^\circ$) cable and non-yawed cylinder($\beta=0^\circ$) with perforated splitter plate. Cross-flow response of non-yawed cylinder with a perforated splitter plate is shown in Fig. 15. Though there are some differences in cross-flow response, this perforated splitter plate might simulate fluid dynamic role of the axial flow from global point of view. Taking into account of generation, by a splitter plate, of $dCF/d\alpha < 0$ but extremely small absolute value of $dCF/d\alpha$ and significant suppression of KV, galloping instability of yawed cylinder and non-yawed cylinder with a perforated splitter plate should be UG. From experiments it has been

clarified that perforated splitter plate to non-yawed cylinder and axial flow generated by yawing angle can remarkably reduce of peak fluctuating lift by KV by less than 1/3000 and 1/100, respectively.



(a) Yawed ($\beta=45^\circ$) cylinder



(b) Non-yawed ($\beta=0^\circ$) cylinder with perforated splitter plate

Fig.14 PSD and wavelet of fluctuating lift of yawed and non-yawed with perforated splitter plate

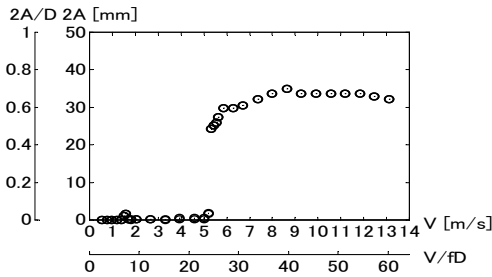
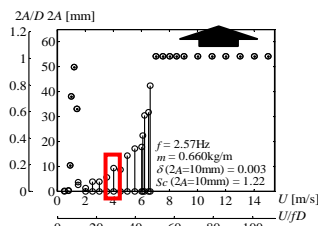


Fig.15 Cross flow response of non-yawed cylinder with perforated splitter plate ($Sc=7.618$ at $2y_0/D=0.2$)



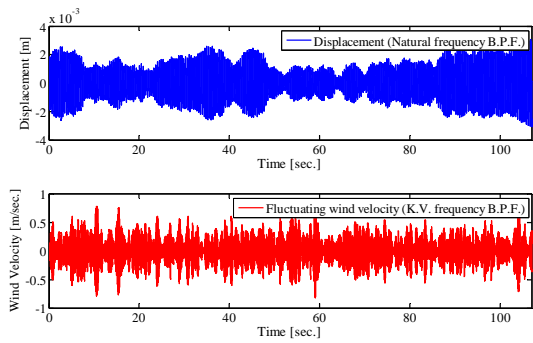
(a) Test view of test of yawed cylinder



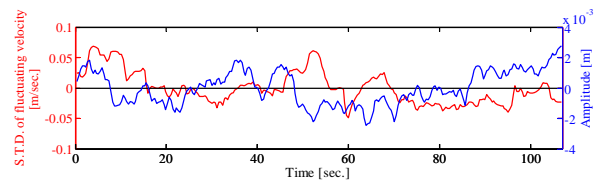
(b) cross flow response of yawed cylinder

Fig.16 Test view and cross-flow response of yawed ($\beta=45^\circ$) circular cylinder

Fig. 16 shows test views of yawed ($\beta=45^\circ$) circular cylinder and its cross flow response. Looking at response with unsteady amplitude near at $V=4\text{m/s}$, response appears when KV is mitigated as indicated in Fig. 17.



(a) cross flow response at $U=4\text{m/s}$ Band-pass filtered by f_0 (2.4-2.8 Hz)(top blue data) and fluctuating velocity in a wake ($U=4\text{m/s}$) Band pass filtered by KV frequency ($f_k=8.0-10.5$)(measured position $x/L=0.25$, $y/D=1.0$, $z/D=1.25$) (bottom red data)



(b) STD subtracted by its mean value of STD in 100sec of fluctuating velocity time-averaged by 5.0sec (f_k B.P.F) :red-solid line, and STD of response amplitude B.S. filtered by f_0 (B.P.F.), subtracted by its mean value in 100 sec: blue broken line

Fig. 17 Cross flow response of yawed($\beta=45^\circ$) cylinder related to unsteady change of KV intensity

The unsteady change of KV intensity must be caused by unsteady characteristics of axial flow in near wake, corresponding to low frequency peak of PSD of lift force shown in Fig. 14(a). The intensity of axial flow becomes intensively, KV must be weaker, then UG can be more sensitively excited. In another expression, unsteady cross flow response at lower reduced velocity than evident galloping appearance might be UG.

Other phenomena related to KV

As the other phenomena related to KV on bluff bodies, “bias flow” for bluff body with symmetrical shape, “bi-stable flow”, and “Bifurcation” characteristics of vortices would be listed. All of these are caused by non-stationary flow separation and reattachment of separated shear layer. Study on these is substantially important to understand the complicate bluff body aerodynamics. However

because of space, these are discussed in another chance.

Conclusion

Conclusion in this paper is as follows:

1. On aerodynamic interaction between KV and MIV of circular cylinder, peak amplitude of vortex induced vibration related to MIV significantly increases with decreasing KV intensity in near wake.
2. On the other hand, on the interaction between IMPV and MIV, peak amplitude of vortex induced vibration related to MIV is less affected by mitigation of KV (alternative vortex shedding) in near wake, because of generation of both vortices on side-face of body.
3. Unsteady galloping (UG) is introduced. UG appears completely free from den Hartog Criterion, and it would be generated by "undulation" of shear separated flow as "fluid memory" under mitigation of KV. Galloping of circular or rectangular cylinders with splitter plate in a wake would be classified to UG. Low Speed Galloping (LSPG) studied by Nakamura might be a kind of UG, though its mechanism is non-fluid memory at lower reduced velocity than $V_r=1/St$.
4. Aerodynamic characteristics of yawed ($\beta=45^\circ$) circular cylinder is caused by axial flow generated in near wake. This axial flow can be simulated by a perforated splitter plate with $4D$ length and 30% perforation for non-yawed cylinder. Then it is verified that the similarity of aerodynamics between yawed ($\beta=45^\circ$) cylinder and non-yawed cylinder with perforated splitter plate in a wake.
5. The unsteady amplitude of cross flow response of yawed cylinder at lower reduced velocity than onset of divergent type galloping would be UG caused by unsteady intensity axial flow in a wake.

ACKNOWLEDGMENTS

The authors would like to acknowledge many former Dr Tomomi Yagi of Kyoto University, graduated students of Kyoto Universities, including Dr. Kotaro Hori, Mr. Kazuki Tsubota, Miss. Uki Kawashima, Mr. Masanori Shima, Mr. Masanobu Tanaka, Mr. Jun Ohya, Mr. Takahiro, Mr. Takahiro Ohishi, Mr. Takao Okada, Mr. Hideaki Hatsuda, Mr. Tomoyuki Nakase, Mr. Kouji Maeta, Mr. Youichi Adachi, for their contribution for wind tunnel tests.

REFERENCES

[1] C.H.K. Williamson and A. Roshko (1988): "Vortex formation in the wake of an oscillating cylinder", *Journal of Fluids and Structures* 2, pp.355-381

[2] A. Laneville and D. Brika (2001): "Experimental Simulation of the Fluid Mechanical Coupling between Transmission Line Conductors", in Proc. of the 4th International Symposium on Cable Dynamics, Montreal, Canada, May 28-30, pp.7-26

[3] A. Zasso, M. Belloli, S. Muggiasca, (2006) "On the pressure and force field on a circular cylinder oscillating in the lock-in region at sub-critical Reynolds number.", In Proc. ASME PVP2006-ICPVT-11

[4] K. Shimada, (1999), "Study on Aerodynamic characteristics of rectangular cylinders based on k- ϵ model and evaluation of their aerodynamic behaviors", Doctor Dissertation, Kyoto University, (in Japanese)

[5] Y. Nakamura, K. Hirata and T. Urabe (1991) "Galloping of Rectangular Cylinders in the Presence of a Splitter Plate", *Journal of Fluids and Structures*, 5, pp.521-549,

[6] N. Shiraishi and M. Matsumoto, (1982), "Study on vortex induced vibrations of bluff bodies", *J. of JSCE*, 322, pp37-50

[7] Y. Nakamura and M. Nakashima (1986), "Vortex Excitation of Prisms with elongated H and T cross sections", *J. of Fluid Mech.*, vol.163, pp 149-169

[8] Dallaire, Questa-Lavoie, Filion, Laneville and Van Dyke, (2004), "Flow Visualization of Critical Events of Vortex Induced Vibrations in the case of a Long Flexible Cylindrical Tube", Proc. of FIV, Paris

[9] J.P. Den Hartog (1956), *Mechanical Vibration*, New York, McGraw-Hill, pp299-305

[10] P.M. Bearman and D.M. Trueman (1972), "An Investigation of the flow around rectangular cylinders", *The Aeronautical Quarterly*, Vol. XXIII, pp1-6

[11] Nakamura, and Y. Tomonari, (1981), "The Aerodynamic Characteristics of D-section Prism in a Smooth and in a Turbulent Flow", *Aeronautical Quarterly*, Vol.32, pp153-168

[12] K. Rinoue, (2003), "Laminar Separation Bubbles formed on Airfoils", *NAGARE (Fluid)* 22, pp15-22 (in Japanese)

[13] M. Shimizu, S. Oka, T. Ishihara, (2006) "Development of Web-Based Ice-Accreted Transmission Line Aerodynamic Analysis System", Proc. of 19th Japan Symposium on Wind Engineering, (in Japanese)

[14] H. Matsumiya, T. Nishihara, M. Shimizu, (2010), "Aerodynamic Characteristics of Ice and Snow accreted Conductors of Overhead Transmission Lines", Proc. of 10th ICWE, Amsterdam, Holland

[15] M. Matsumoto, T. Yagi, H. Hatsuda, K. Shima, M. Tanaka and H. Naito, (2010), "Dry galloping characteristics and its mechanism of inclined/yawed cables", *J of Wind Eng. and Industrial Aerodyn.* 98, pp317-327

[16] M. Matsumoto, M. Hashimoto, T. Yagi, T. Nakase and T. Maeta, (2008), "Study on the role of Karman Vortex on Galloping of Bluff bodies", Proc. of the 9th FIV, Prague

[17] A. Okajima, K. Sugutani and T. Mizota, (1984), "Lift and drag forces on two structures arranged side-by-side in

a uniform flow”, Proc. of Wind Engineering Symposium, (in Japanese)

[18]Md.M,Alam and Y.Zhou, (2008), “Classification of the wake of two side-by-side square cylinders”, Proc. of the 9th FIV, Prague

[19]G.Shewe, (1983), “On the force fluctuating acting on a circular cylinder in cross flow from subcritical up to transcritical Reynolds number”, J. of Fluid Mec. 133, pp 265-285

[20] J.H.G.Macdonald, (2005),”Quasi-Steady Analysis of 2DOF Inclined Cable Galloping in the Critical Reynolds Number Range”, Proc. of 6th ISCD, pp435-442

[21]Q.Liu, Y.Wang, Y.Cheng and W.Ma, (2011), “Reynolds number effect on wind induced vibration of stay cables”, Proc. of the 9th ISCD, Shanghai

[22]R.I.Bass (1985),”Aerodynamic forces on structures of circular cross-sections”, J of Wind Eng. And Industrial Aerodyn., Part I, Vol.21.pp

[23]M.Sato, H.Kanda, H.Suenaga, N.Sudani and M. Shigemi, (1991), “Visualization of separated flow over the circular cylinder at high Reynolds numbers”, Technical Report of National Aerospace Laboratory, TR-1378, pp1-11 (in Japanese)

[24]M.Matsumoto, T.Yagi, T. Shima, M. Tanaka and H.Natito, (2008), “Mechanism and how to suppress wind-induced vibration of inclined cables of cable stayed bridges”, Proc. of 4th International Conf. AWAS08 (key note) pp 75-86,

[25]J.M.Cimbala and S.Garg,(1991), “Flow in the wake of a freely rotatable cylinder with splitter plate”, AIAA Journal, pp1001-1003

[25]C.R.S.Assi, P.W.Bearman and N.Kitney, (2009), “Low drag solutions for suppressing vortex induced vibration of circular cylinders”, JFS 25, pp666-675

[26]D. Brika, A. Laneville: “Vortex-induced vibrations of a long flexible circular cylinder”, Journal of Fluid Mechanics 250, pp.481-508, 1993

[27]M.Matsumoto , T.Yagi, H.Tamaki and T. Tsubota, (2008), “Vortex induced vibration and its effect on torsional flutter instability in the case of B/D=4 rectangular cylinder,” JWEIA 96, pp 971-983

[28]G.V.Parkinson and N.P.H Brooks,(1961), “On the aeolastic instability of bluff cylinders”,Trans., J. of Applied Mechanics, ACME, vol.83

[29]R.H.Scanlan and J.J.Tomko, (1971), “Airfoil and bridge deck flutter derivatives”, J. of Eng. Mech. Divisoin, 97, EM6, ASCE, pp 1717-1737

[30]M.Matsumoto, (2010), “The Role of Axial Flow in Near Wake on the Cross-Flow Vibration of the Inclined Cable of Cable-Stayed Bridges”, Proceedings of ASME 2010 3rd Joint US-European Fluids Engineering Summer Meeting, FEDSM-ICNMM2010



VORTEX-INDUCED VIBRATIONS OF A FLEXIBLE CYLINDER IN INCLINED FLOW

Rémi Bourguet*

Institut de Mécanique des Fluides de Toulouse
Toulouse, France
Email: bourguet@imft.fr

George E. Karniadakis

Brown University
Providence, RI, USA
Email: gk@cfm.brown.edu

Michael S. Triantafyllou

Massachusetts Institute of Technology
Cambridge, MA, USA
Email: mistetri@mit.edu

ABSTRACT

A slender deformable body placed in a cross-flow may exhibit oscillations due to the unsteady forces caused by the vortex formation in its wake. The occurrence of such vortex-induced vibrations for a flexible cylinder of aspect ratio 50 and immersed in a current inclined at 60° with respect to the plane perpendicular to its axis, is investigated by means of direct numerical simulation, at a Reynolds number equal to 500. The analysis of the coupled fluid-structure system behavior shows that the inclined flow properties and resulting forces and structural responses are very similar to the cross-flow problem, where only the component of the oncoming flow velocity normal to the cylinder is considered (no inclination); the independence principle is thus validated in the present case.

INTRODUCTION

A bluff body immersed in a cross-flow is subjected to unsteady forces due to the vortex shedding in its wake. If the body is flexible or flexibly mounted, these forces can lead to vibrations. The phenomenon of vortex-induced vibrations (VIV) occurs in a number of physical problems, especially in the context of long flexible cylindrical structures employed in civil and ocean engineering, such as cables or risers. The case of a rigid circular cylinder free to move, or forced to oscillate within a uniform cross-flow, has shed light on the principal VIV mechanisms [1–4]. It has been shown that self-excited but self-limiting, large amplitude oscillations occur when the vortex shedding and the structural vibration frequencies coincide, a condition of wake-body synchronization referred to as *lock-in*.

Previous works concerning flexibly mounted rigid cylinders have shown that vortex-induced excitation through lock-in may also occur when the body is exposed to an inclined oncoming flow [5], even at angles of inci-

dence larger than 50° [6]. Several studies have investigated the possibility of comparing the inclined flow case to the normal incidence case by considering the component of the oncoming flow velocity normal to the cylinder, thus assuming a negligible impact of the axial flow component [7]. This approach, referred to as *cosine law* or *independence principle* (IP), is not valid for the prediction of the principal flow features (e.g. vortex shedding frequency, fluid force coefficients) at large angles of incidence, in the case of stationary cylinders [8,9].

In contrast, [5,6,9,10] showed that for rigid cylinders oscillating in inclined flow, the use of the IP is appropriate over a wide range of incidence angles, especially for the estimation of the wake-body synchronization window.

The increased complexity of the VIV phenomenon in the case of slender flexible bodies immersed in normal uniform and sheared currents has been analyzed in recent experimental and numerical works [11–15] but the impact of flow inclination in this context still remains to be studied.

The objective of this work is to quantify through high-resolution numerical simulations the influence of the axial component of the flow on the mechanisms of distributed fluid-structure interaction, which were previously studied for the normal incidence case; and to assess the validity of the IP in the case of flexible bodies.

FORMULATION AND NUMERICAL METHOD

The flow past a flexible cylinder of circular cross-section is predicted using direct numerical simulation of the three-dimensional incompressible Navier-Stokes equations. The cylinder of length to diameter aspect ratio 50, pinned at both ends and free to oscillate in both directions, is immersed in a uniform current at 60° of incidence with respect to the plane perpendicular to the cylinder axis. For comparison purpose, a normal incidence case, where the axial component of the oncoming flow is

*Address all correspondence to this author.

removed, is also considered. In the following, all physical variables are non-dimensionalized using the cylinder diameter D and the inflow velocity magnitude U . The Reynolds number (Re) based on D and U is equal to 500.

The cylinder mass ratio, defined as $m = \rho_c / \rho_f D^2$, where ρ_c is the cylinder mass per unit length and ρ_f the fluid density, is set to 6. The constant tension and damping of the structure are designated by T and K . The displacements of the cylinder in the direction of the inflow component normal to the body (in-line direction, x) and in the transverse direction (cross-flow direction, y) are denoted by ζ_x and ζ_y . The sectional drag and lift coefficients are defined as $C_x = 2F_x / \rho_f D U^2$ and $C_y = 2F_y / \rho_f D U^2$, where F_x and F_y are the in-line and cross-flow dimensional fluid forces. The structural dynamics are governed by forced vibrating string equations, expressed as follows in non-dimensional form:

$$\frac{\partial^2 \zeta}{\partial t^2} - \omega^2 \frac{\partial^2 \zeta}{\partial z^2} + \frac{K}{m} \frac{\partial \zeta}{\partial t} = \frac{1}{2} \frac{C}{m}, \quad (1)$$

where $\zeta = [\zeta_x, \zeta_y]^T$ and $C = [C_x, C_y]^T$. t denotes the non-dimensional time variable. The string phase velocity, $\omega = \sqrt{T/m}$ is set equal to 4.55. The structural damping is set equal to zero ($K = 0$) to allow maximum amplitude oscillations.

The parallelized code *Nektar*, based on the spectral/ hp element method [16], is used to solve the coupled fluid-structure system. Validation studies of the numerical method have been reported in previous works concerning similar physical configurations [15, 17]. A boundary-fitted coordinate formulation is used to take into account the cylinder unsteady deformation. The computational domain extends $50D$ downstream, and $20D$ upstream, above, and below the cylinder. A two-dimensional grid of 2175 elements with Jacobi polynomials of order $p = 7$ is used in the (x, y) planes. In the z direction, 1024 planes (512 complex Fourier modes) are used. The present simulations involve approximately 0.6×10^9 degrees of freedom.

STRUCTURAL RESPONSES

The flexible cylinder immersed in inclined flow exhibits large standing wave vibrations in the in-line and cross-flow directions, as illustrated in Fig. 1 by selected time series of the displacements along the span. The root mean square (RMS) values of the displacements are plotted in Fig. 2 for the inclined and normal flow configurations. Similar vibration amplitudes are noted in both cases. The excited structural wavenumbers are also

similar. The ratio between the maximum values of the cross-flow and in-line displacements, equal to 3.5 approximately, is comparable to the values reported in previous studies concerning low-wavenumber vibrations of flexible cylinders in normal currents [18].

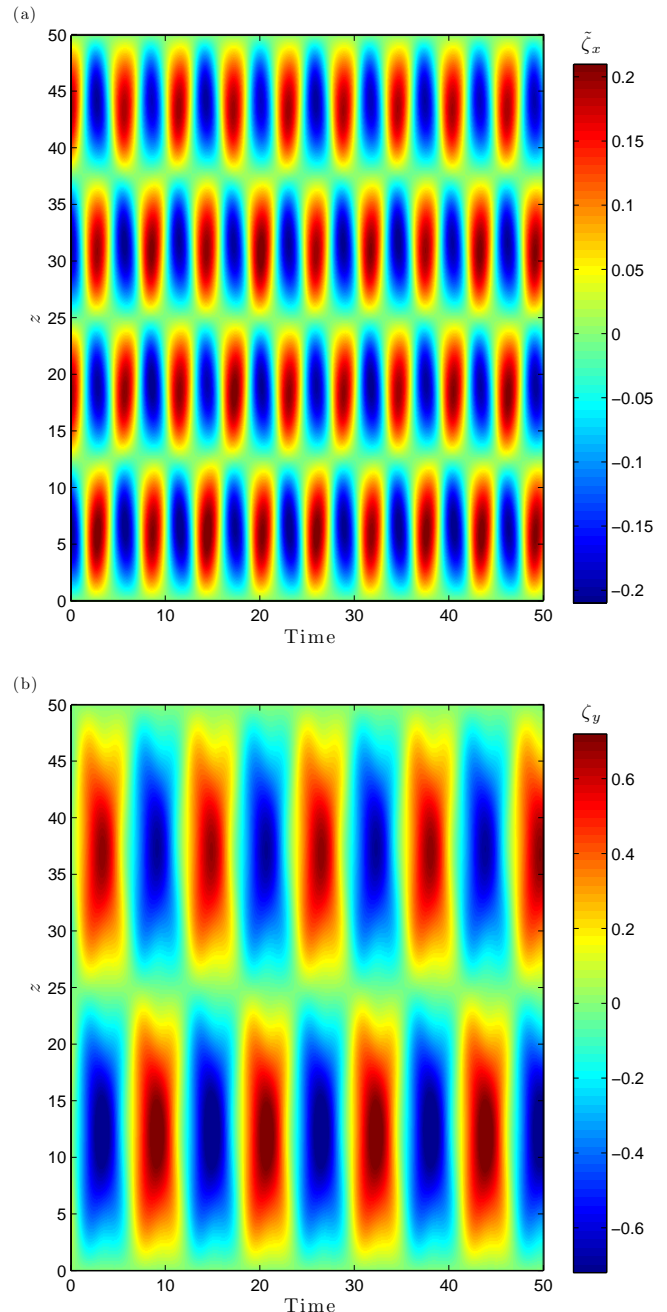


FIGURE 1: TEMPORAL EVOLUTION OF THE (a) IN-LINE DISPLACEMENT FLUCTUATION AND (b) CROSS-FLOW DISPLACEMENT ALONG THE CYLINDER SPAN.

The vibration frequencies, non-dimensionalized us-

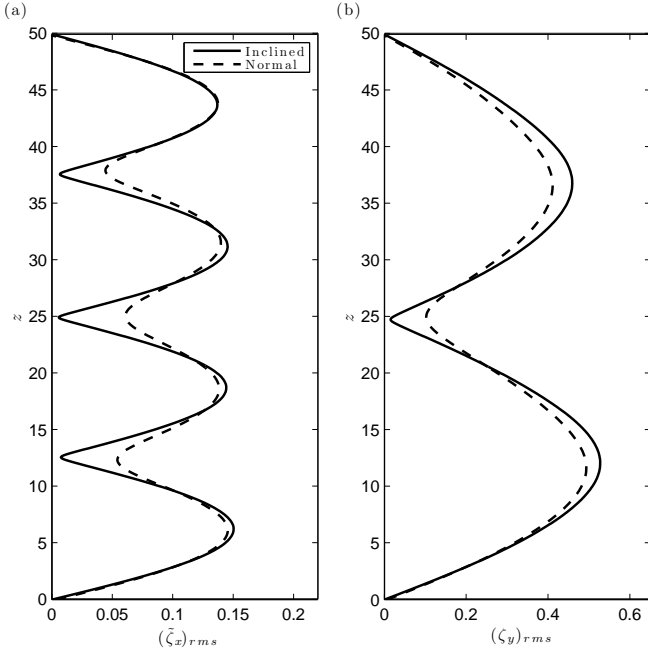


FIGURE 2: RMS VALUE OF THE (a) IN-LINE DISPLACEMENT FLUCTUATION AND (b) CROSS-FLOW DISPLACEMENT ALONG THE CYLINDER SPAN.

ing the magnitude of the normal component of the flow velocity, are analogous in the inclined and normal flow cases, as show in Fig. 3. A frequency ratio of 2 can be noted between the in-line and cross-flow responses. The following dispersion relation may be used to estimate the natural frequency f associated with the structural wavenumber k :

$$f = k\omega \sqrt{\frac{m}{m + \frac{\pi}{4}C_m}}, \quad (2)$$

where C_m is the added mass coefficient induced by the fluid forces in phase with the cylinder acceleration.

The natural frequencies, normalized by the normal flow velocity component, and associated with the in-line and cross-flow excited wavenumbers, for $C_m = 1$, are indicated by red dashed lines in Fig. 3. The actual peaks are close to the estimated natural frequencies.

The phase difference between the in-line and cross-flow displacements controls the shape and orientation of the cylinder trajectories in the plane perpendicular to the span. The phase difference between responses occurring with a frequency ratio of 2 can be defined as $\Phi_{xy} = [\phi_x - 2\phi_y, \text{ mod } 360^\circ]$, where the instantaneous phases of the in-line and cross-flow responses (ϕ_x and ϕ_y , respectively) are determined by means of the Hilbert transform.

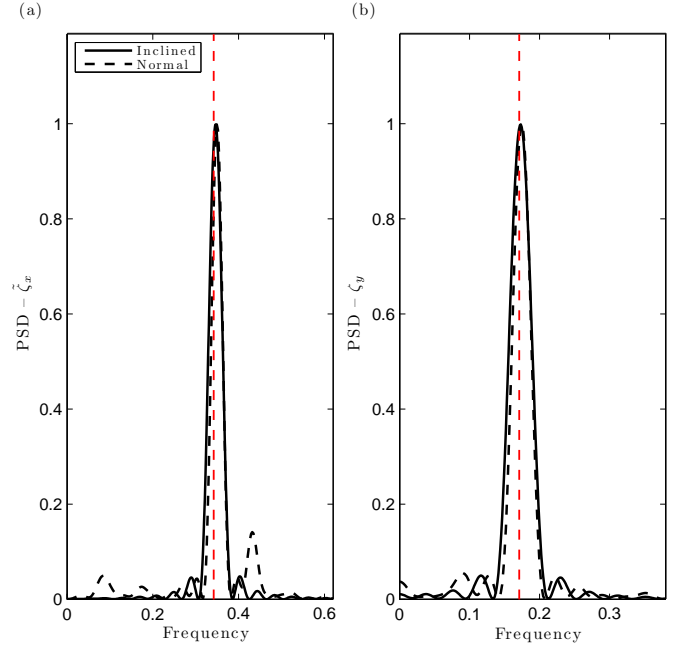


FIGURE 3: SPAN-AVERAGED PSD OF THE (a) IN-LINE DISPLACEMENT FLUCTUATION AND (b) CROSS-FLOW DISPLACEMENT. THE NATURAL FREQUENCIES ASSOCIATED WITH THE EXCITED WAVENUMBERS AND BASED ON THE NORMAL INFLOW VELOCITY ARE INDICATED BY RED DASHED LINES.

Values of Φ_{xy} in the range $0^\circ - 180^\circ$ ($180^\circ - 360^\circ$ respectively) correspond to ‘figure eight’ orbits where the body moves upstream (downstream respectively) when reaching the cross-flow oscillation maxima. These two types of trajectories are referred to as ‘counter-clockwise’ and ‘clockwise’, respectively [19]. The spanwise evolution of the histogram of Φ_{xy} in the inclined flow case is plotted in Fig. 4(a). As expected in the case of standing wave vibrations, the phase difference exhibits a discontinuous spanwise pattern. The structural response is dominated by crescent-shaped orbits ($\Phi_{xy} \approx 0^\circ$, $\Phi_{xy} \approx 180^\circ$). The normal flow case exhibits a very similar synchronization pattern (Fig. 4(b)).

WAKE PATTERNS AND FLUID FORCES

The PSD of the cross-flow component of the flow velocity, v , in the wake, is used to identify the vortex shedding frequency. The span-averaged PSD of v associated with the inclined and normal inflow profiles are presented in Fig. 5. In these plots, the predominant cross-flow vibration frequencies, identified in Fig. 3, are indicated by red dashed lines. In both cases, the vortex formation and the body cross-flow oscillation are synchronized and it can be

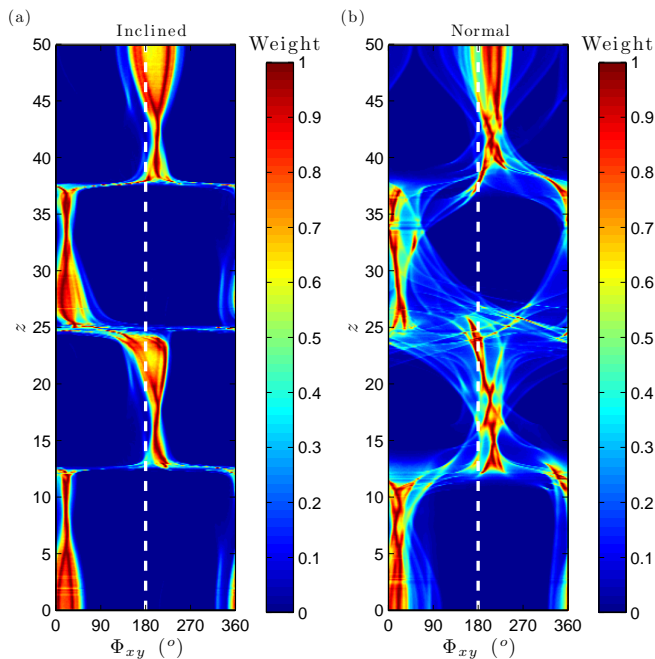


FIGURE 4: HISTOGRAM OF THE IN-LINE/CROSS-FLOW MOTION PHASE DIFFERENCE ALONG THE CYLINDER SPAN, IN THE CASES OF (a) INCLINED AND (b) NORMAL VELOCITY PROFILES. THE LIMIT BETWEEN CLOCKWISE AND COUNTER-CLOCKWISE ORBITS IS INDICATED BY A WHITE DASHED LINE.

verified that the lock-in condition is established along the entire span.

Despite the high angle of incidence, the vortex rows forming downstream of the cylinder remain mainly parallel to the body, and the wake patterns appear similar to those observed in the case of normal flow, as illustrated in Fig. 6 by means of instantaneous iso-surfaces of the spanwise vorticity. This corroborates the observations made in the case of rigid cylinders oscillating under wake-body synchronization condition [9].

The spanwise evolutions of the time-averaged in-line force coefficient and of the RMS value of the cross-flow force coefficient are presented in Fig. 7. In these plots, the fluid forces are non-dimensionalized by the normal component of the inflow velocity. The force coefficients reach high magnitudes compared to the values reported for a stationary cylinder. The span-averaged value of the mean in-line force coefficient is equal to 2.1 in the inclined flow case versus 2 when the inflow axial component is removed. Larger peaks of the cross-flow force coefficient can be identified in the normal flow case; however both cases exhibit relatively similar trends along the span.

The effective in-line and cross-flow added mass co-

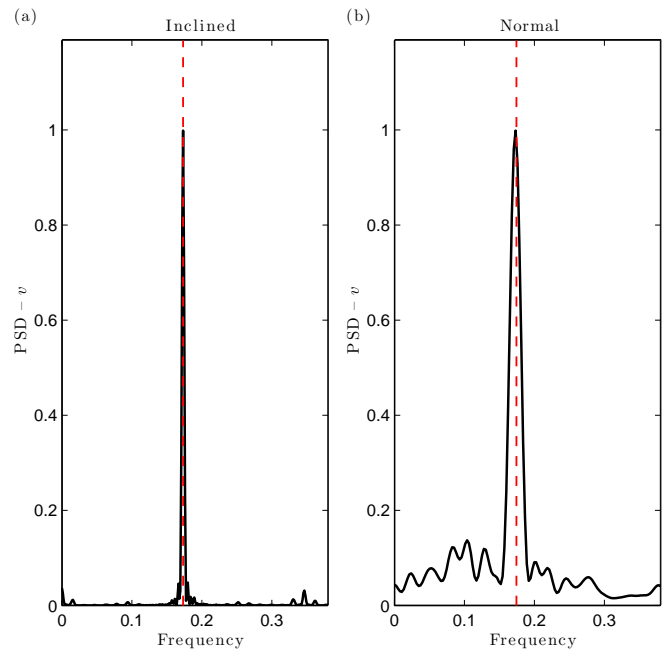


FIGURE 5: SPAN-AVERAGED PSD OF THE CROSS-FLOW COMPONENT OF FLOW VELOCITY IN THE WAKE IN THE CASES OF (a) INCLINED AND (b) NORMAL VELOCITY PROFILES. THE STRUCTURE VIBRATION FREQUENCIES ARE INDICATED BY RED DASHED LINES.

efficients due to the fluid forces in phase with the body acceleration are determined as follows:

$$C_{xm} = -\frac{2}{\pi} \frac{\langle \tilde{C}_x \frac{\partial^2 \tilde{\zeta}_x}{\partial t^2} \rangle}{\langle \left(\frac{\partial^2 \tilde{\zeta}_x}{\partial t^2} \right)^2 \rangle}, \quad C_{ym} = -\frac{2}{\pi} \frac{\langle C_y \frac{\partial^2 \zeta_y}{\partial t^2} \rangle}{\langle \left(\frac{\partial^2 \zeta_y}{\partial t^2} \right)^2 \rangle}. \quad (3)$$

As can be observed in Fig. 8, C_{xm} and C_{ym} exhibit substantial spanwise modulations and comparable behaviors in the inclined and normal flow cases. It is interesting to note that the variability of the effective added mass, and its departure from the potential flow value of 1 in both directions, does not induce significant differences between the excited frequencies and the natural frequencies determined through the dispersion relation (2). Spikes are noted near the local minima of the response envelopes ('nodes') in the inclined flow case. The absence of such spikes in the normal flow case can be related to larger displacement amplitudes in these regions, as can be observed in Fig. 2. The same trend appears for both cases in the spanwise evolution of the effective added mass coefficients, depending on the orientation of the crescent-shaped orbits: in the cross-flow direction, values close to

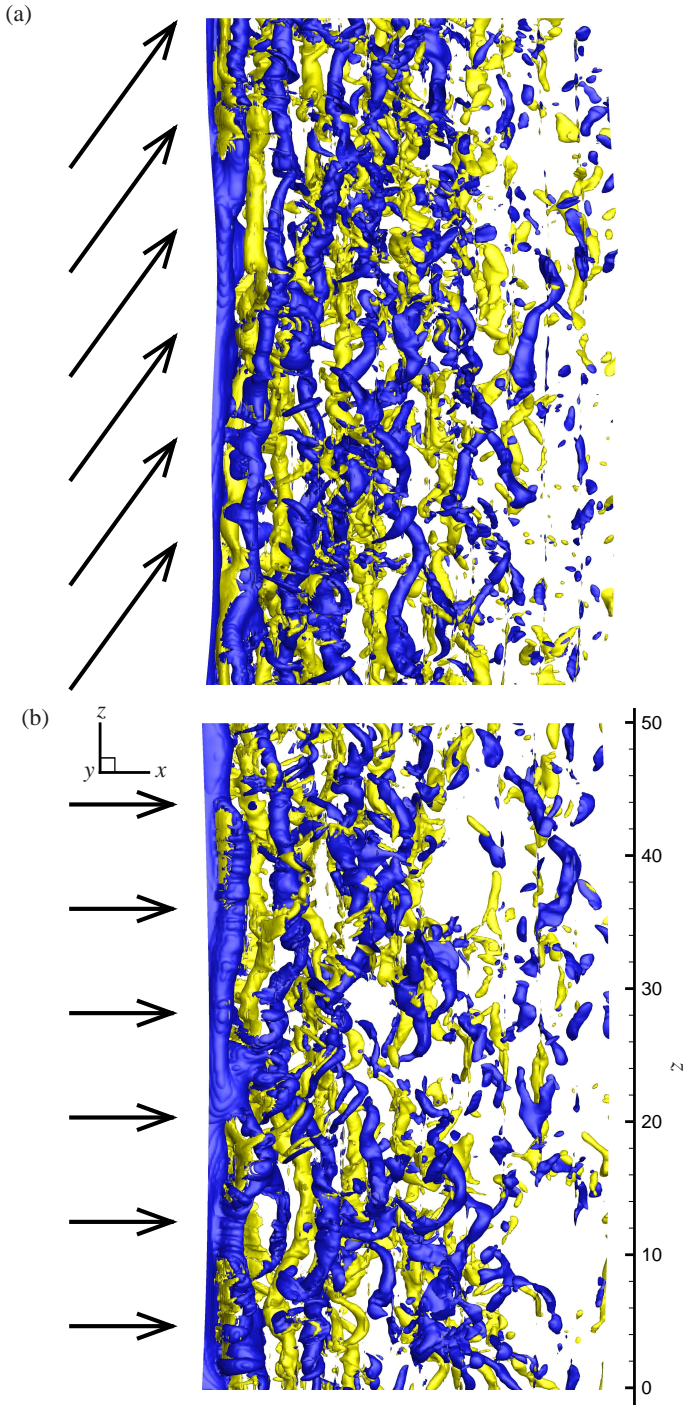


FIGURE 6: INSTANTANEOUS ISO-SURFACES OF THE SPANWISE VORTICITY DOWNSTREAM OF THE CYLINDER ($\omega_z = \pm 0.3$): (a) INCLINED AND (b) NORMAL VELOCITY PROFILES. PART OF THE COMPUTATIONAL DOMAIN IS SHOWN. ARROWS REPRESENT THE ONCOMING FLOW.

1 are reached in regions where $\Phi_{xy} \approx 0^\circ$, while smaller, and even negative values of C_{ym} are noted in zones where $\Phi_{xy} \approx 180^\circ$. Even if less clearly defined, the opposite trend can be noted in the in-line direction.

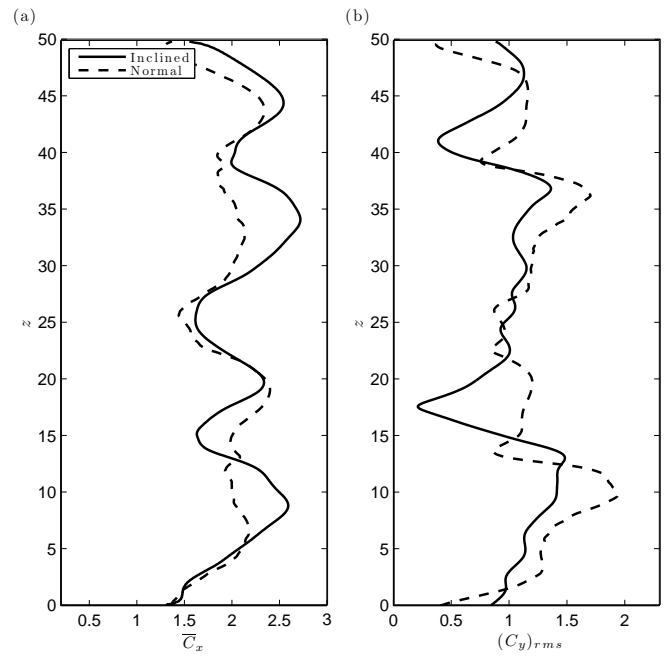


FIGURE 7: (a) TIME-AVERAGED VALUE OF THE IN-LINE FORCE COEFFICIENT AND (b) RMS VALUE OF THE CROSS-FLOW FORCE COEFFICIENT, ALONG THE SPAN. IN THE INCLINED FLOW CASE, THE FORCES ARE NORMALIZED BY THE INFLOW VELOCITY NORMAL COMPONENT.

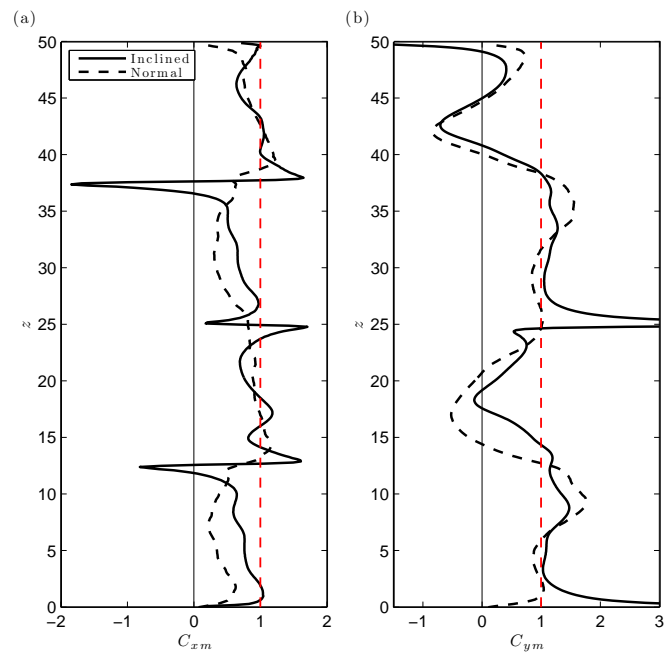


FIGURE 8: ADDED MASS COEFFICIENT IN THE (a) IN-LINE AND (b) CROSS-FLOW DIRECTIONS, ALONG THE SPAN. THE POTENTIAL FLOW VALUE OF 1 IS INDICATED BY A RED DASHED LINE.

SUMMARY

The vortex-induced vibrations of a flexible cylinder, immersed in a current inclined at an angle of 60° , have been investigated by means of direct numerical simulation at a Reynolds number equal to 500. Under the lock-in condition, the structure exhibits large amplitude oscillations in both the in-line and cross-flow directions. Comparison with the corresponding normal incidence case, where the axial component of the oncoming flow is removed, demonstrates the applicability of the independence principle in this context, and the limited impact of the flow axial component on the fluid forces and vibrational responses.

ACKNOWLEDGMENT

The authors wish to acknowledge support from the BP-MIT Major Projects Programme, monitored by M. Tognarelli and P. Beynet; and the Office of Naval Research under Grants N00014-07-1-0135 and N00014-07-1-0446, monitored by T. Swean, Jr.

REFERENCES

- [1] Bearman, P. W., 1984. "Vortex shedding from oscillating bluff bodies". *Annual Review of Fluid Mechanics*, **16**, pp. 195–222.
- [2] Sarpkaya, T., 2004. "A critical review of the intrinsic nature of vortex-induced vibrations". *Journal of Fluids and Structures*, **19**, pp. 389–447.
- [3] Williamson, C. H. K., and Govardhan, R., 2004. "Vortex-induced vibrations". *Annual Review of Fluid Mechanics*, **36**, pp. 413–455.
- [4] Bearman, P. W., 2011. "Circular cylinder wakes and vortex-induced vibrations". *Journal of Fluids and Structures*, **27**, pp. 648–658.
- [5] King, S., 1977. "Vortex excited oscillations of yawed circular cylinders". *Journal of Fluids Engineering*, **99**, pp. 495–502.
- [6] Lucor, D., and Karniadakis, G. E., 2003. "Effects of oblique inflow in vortex-induced vibrations". *Flow, Turbulence and Combustion*, **71**, pp. 375–389.
- [7] Schlichting, H., 1968. *Boundary Layer Theory (sixth edition)*. McGraw-Hill, New York.
- [8] Van Atta, C. W., 1968. "Experiments on vortex shedding from yawed circular cylinders". *AIAA Journal*, **6**, pp. 931–933.
- [9] Ramberg, S. E., 1983. "The effects of yaw and finite length upon the vortex wakes of stationary and vibrating circular cylinders". *Journal of Fluid Mechanics*, **128**, pp. 81–107.
- [10] Franzini, G. R., Fajarra, A. L. C., Meneghini, J. R., Korkischko, I., and Franciss, R., 2009. "Experimental investigation of vortex-induced vibration on rigid, smooth and inclined cylinders". *Journal of Fluids and Structures*, **25**, pp. 742–750.
- [11] Trim, A. D., Braaten, H., Lie, H., and Tognarelli, M. A., 2005. "Experimental investigation of vortex-induced vibration of long marine risers". *Journal of Fluids and Structures*, **21**, pp. 335–361.
- [12] Chaplin, J. R., Bearman, P. W., Huera-Huarte, F. J., and Pattenden, R. J., 2005. "Laboratory measurements of vortex-induced vibrations of a vertical tension riser in a stepped current". *Journal of Fluids and Structures*, **21**, pp. 3–24.
- [13] Vandiver, J. K., Jaiswal, V., and Jhingran, V., 2009. "Insights on vortex-induced, traveling waves on long risers". *Journal of Fluids and Structures*, **25**, pp. 641–653.
- [14] Modarres-Sadeghi, Y., Mukundan, H., Dahl, J. M., Hover, F. S., and Triantafyllou, M. S., 2010. "The effect of higher harmonic forces on fatigue life of marine risers". *Journal of Sound and Vibration*, **329**, pp. 43–55.
- [15] Bourguet, R., Karniadakis, G. E., and Triantafyllou, M. S., 2011. "Vortex-induced vibrations of a long flexible cylinder in shear flow". *Journal of Fluid Mechanics*, **677**, pp. 342–382.
- [16] Karniadakis, G. E., and Sherwin, S., 1999. *Spectral/hp Element Methods for CFD (first edition)*. Oxford University Press, Oxford.
- [17] Evangelinos, C., and Karniadakis, G. E., 1999. "Dynamics and flow structures in the turbulent wake of rigid and flexible cylinders subject to vortex-induced vibrations". *Journal of Fluid Mechanics*, **400**, pp. 91–124.
- [18] Huera-Huarte, F. J., and Bearman, P. W., 2009. "Wake structures and vortex-induced vibrations of a long flexible cylinder part 1: Dynamic response". *Journal of Fluids and Structures*, **25**, pp. 969–990.
- [19] Dahl, J. M., Hover, F. S., Triantafyllou, M. S., Dong, S., and Karniadakis, G. E., 2007. "Resonant vibrations of bluff bodies cause multivortex shedding and high frequency forces". *Physical Review Letters*, **99**, p. 144503.

EXPERIMENTAL RESULTS OF A FLUTTERING PROFILE IN THE WIND TUNNEL

Igor Zolotarev¹

Institute of Thermomechanics AS CR, v.v.i.
Dolejskova 5, 182 00 Prague 8
Czech Republic
Email: igor@it.cas.cz

Václav Vlček

Institute of Thermomechanics AS CR, v.v.i.
Dolejskova 5, 182 00 Prague 8
Czech Republic
Email: vlcek@it.cas.cz

Jan Kozánek

Institute of Thermomechanics AS CR, v.v.i.
Dolejskova 5, 182 00 Prague 8
Czech Republic
Email: kozanek@it.cas.cz

ABSTRACT

The two-dimensional flow patterns around the profile NACA0015 vibrating in self-excitation modes were measured in the wind tunnel by optical methods. The profile with two-degree-of-freedom moved in the vertical direction and rotated around the elastic axis in 1/3 of the profile chord. The Mach numbers for the self-excited vibrations were in the interval 0.2 – 0.45. Results of the interferometric measurement and the profile kinematic movements during the self-oscillations are presented.

INTRODUCTION

Aeroelastic experiments were realized in the subsonic aerodynamic tunnel of the Institute of Thermomechanics AS CR in Nový Knín with a modified NACA0015 profile. The Mach numbers corresponding to the self-excited vibrations were in the range $M = 0.2 - 0.45$ and the Reynolds number range was $(0.25 - 0.54) \cdot 10^6$. The detail description of the experimental setup is in [2] and a schematic arrangement is in Fig. 1. The flow field was measured by interferometric and pneumatic methods, the profile vertical position was indicated by a mechanical sensor.

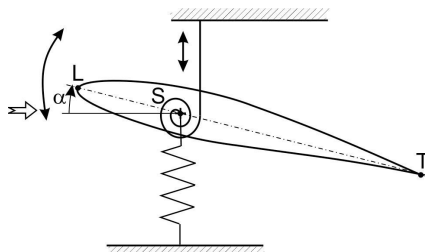


Figure 1: Schematic arrangement of the experiment.

Measured eigenfrequencies for $M = 0$ were 16.4 Hz with 2.0 % damping, 19.3 Hz with 9.3 % damping in

translation mode, and 24.5 Hz with 1.5 % damping, 21.5 Hz with 11.9 % damping in rotation mode, respectively. The Table 1 presents a list of data, setting for various experimental trials in the measurements and evaluated flutter frequencies.

profile (meas. No.)	M [1]	Re [1]	mode	f_0 [Hz]	damping [%]	f [Hz] evaluated	film pict/sec
NACA0015	0	0	translat	16.4	2.0		
(for 2510)	0	0	rotation	24.5	1.5		
NACA0015_2510-06	0.43	$0.52 \cdot 10^6$				19.5	1000
NACA0015	0	0	translat	19.0	9.3		
(for 2662,2663)	0	0	rotation	21.5	11.9		
NACA0015_2662-14	0.33	$0.40 \cdot 10^6$				31.2	500
NACA0015_2662-15	0.30	$0.36 \cdot 10^6$				28.5	1000
NACA0015_2662-16	0.28	$0.34 \cdot 10^6$				27.8	1000
NACA0015_2662-17	0.22	$0.27 \cdot 10^6$				21.2	500
NACA0015_2663-01	0.26	$0.31 \cdot 10^6$				22.7	500
NACA0015_2663-02	0.21	$0.25 \cdot 10^6$				21.7	1000
NACA0015_2663-03	0.38	$0.46 \cdot 10^6$				31.8	1000
NACA0015_2663-04	0.40	$0.48 \cdot 10^6$				32.2	1000
NACA0015_2663-05	0.45	$0.54 \cdot 10^6$				32.2	1000

Table 1: Experimental value sets.

The flow-field around the vibrating profile was measured by Mach-Zehnder interferometer.

EXPERIMENTAL RESULTS

The example of measured interferogram is depicted on Fig. 2, where it is possible to see flow separation beside the whole the upper profile surface.

Address all correspondence to this author¹

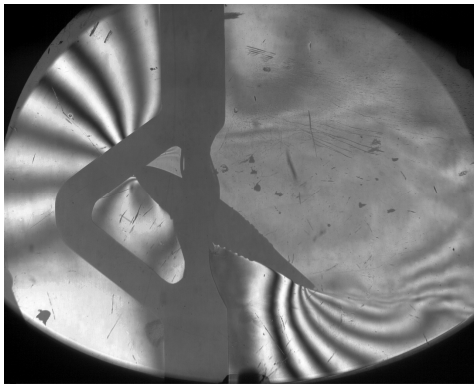


Figure 2: Interferogram of a studied profile.

The arrangement of the system with different eigenfrequencies (corresponding to the translation and rotation motion of the profile) influenced the properties of the flow-field and the mechanical structure interaction. As it is depicted in Fig. 3 by increasing the inflow velocity higher than $M = 0.26$, the separation area is larger and the vibration frequency rises above the both eigenfrequencies identified for $M = 0$. The couple mode flutter found between $M = 0.21$ and $M = 0.26$ is changed to the stall flutter for the bigger Mach numbers. The increase of the vibration level was so high, that at $M = 0.45$ the experiment had to be finished due to the danger of system destruction. The flutter frequency of the vibration in this process increased 1.6 times and the optical measurements showed that the area-wide separation appears during 25% to 50% of the vibration period. In this case we can observe so-called stall flutter [1]. The evaluation of interferograms is described in [3].

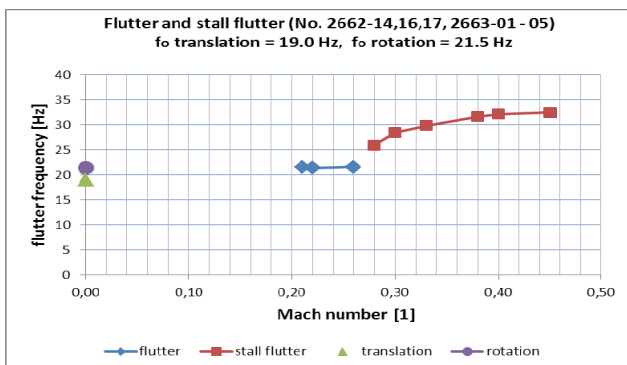


Figure 3: The eigenfrequency changes of the self-excited vibration as a function of the Mach number.

In case of the bigger difference between the eigenfrequencies for translation and rotation modes for $M = 0$ no stall flutter was observed. Fig. 4 illustrates this result: original translation frequency was 16.4 Hz and the rotational frequency was 24.5 Hz, i.e. the difference in this case was 8.1 Hz (about four times more than in previous case shown in Fig. 3). The flutter frequency 19.9 Hz ($M = 0.44$) lies between original profile frequencies measured for $M = 0$. It means that the origin of the aeroelastic instability was in the classic coupled mode flutter with two-degrees of freedom.

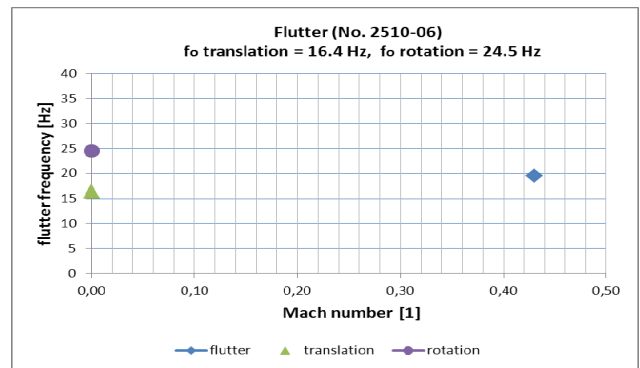


Figure 4: The eigenfrequency changes of the self-excited vibration as a function of the Mach number for the case of bigger difference between the profile eigenfrequencies.

The kinematics of the airfoil motion during one period of the self-excitation is presented in the next Figures 5a) – 5e) for several Mach numbers in increasing order. There is interesting that in Figure 5c), 5d) and 5e) zero angle of attack was achieved at the value 80-85% of the maximal amplitude of the rotation center motion. This was found in the case of the profile with the eigenfrequencies 19,0 Hz without flow ($M = 0$) for translation mode, and 21,5 Hz for rotation mode. On the all figures, the red points inside denote the trajectory of motion of the profile rotation center.

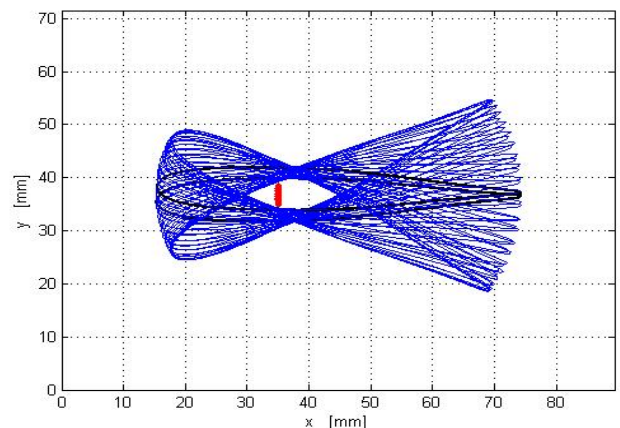


Figure 5a): Profile motion during one period of its self-excited vibration by flutter for $M = 0.21$ (2663-02).

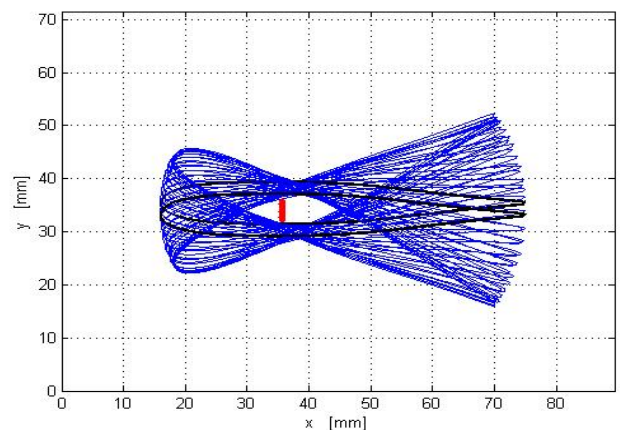


Figure 5b): $M = 0.22$ (2662-17).

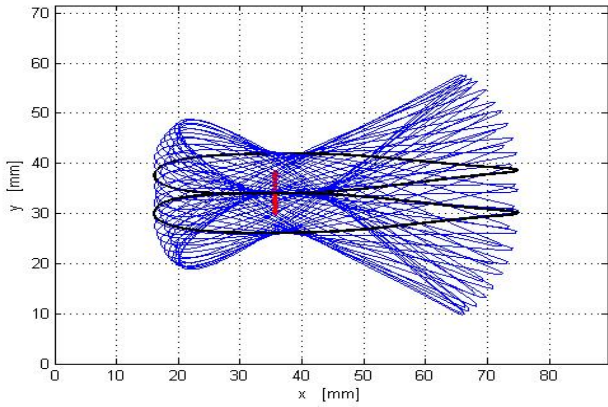


Figure 5c): $M = 0.28$ (2662-16).

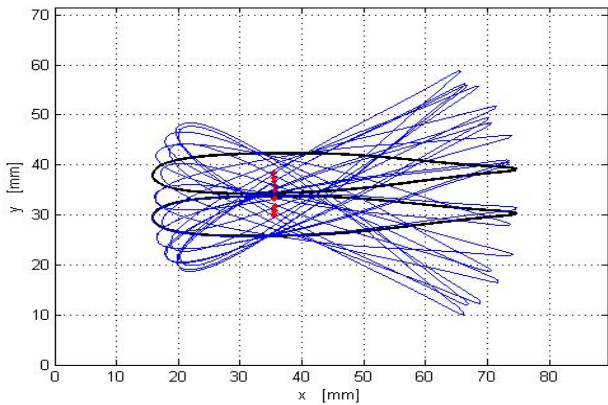


Figure 5d): $M = 0.33$ (2662-14).

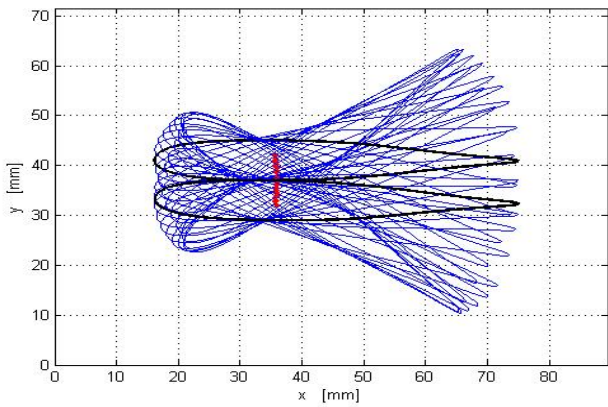


Figure 5e): $M = 0.45$ (2663-05).

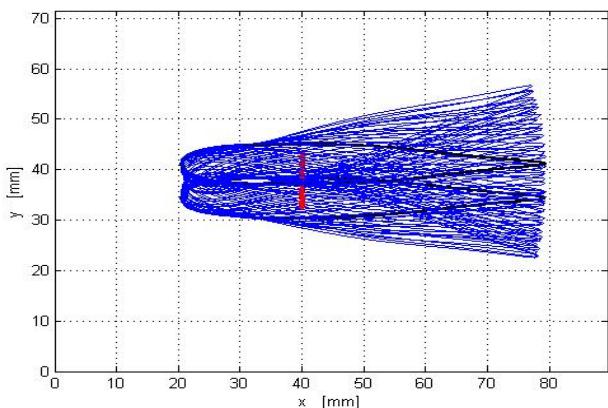


Figure 6: The profile NACA0015, $M = 0.43$.

Figure 6 shows the kinematics of the airfoil motion of the profile for the case bigger difference between profile eigenfrequencies: translation mode – 16.4 Hz (damping 2.0 %), rotation mode 24.5 Hz (damping 1.5 %).

Figures 7a) – 7c) explain the stall flutter arise during the flow velocity increase. On the presented results it is possible to see the jumping between the flutter frequencies with increasing the flow velocity in the interval of Mach numbers 0.25 – 0.35. Outside of this velocity interval the system has properties as follows: unstable by coupled mode flutter is for $M < 0.25$ and by stall flutter for $M > 0.35$.

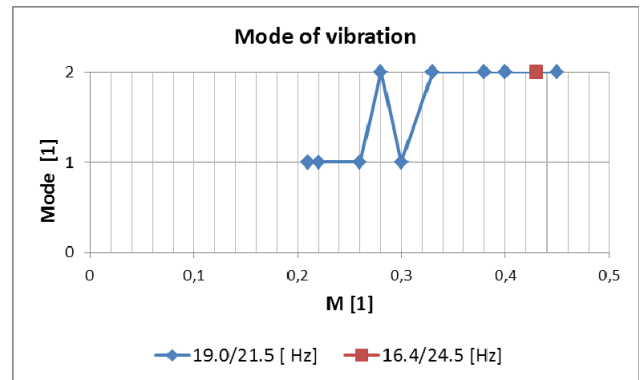


Figure 7a): *Mode of vibration.*

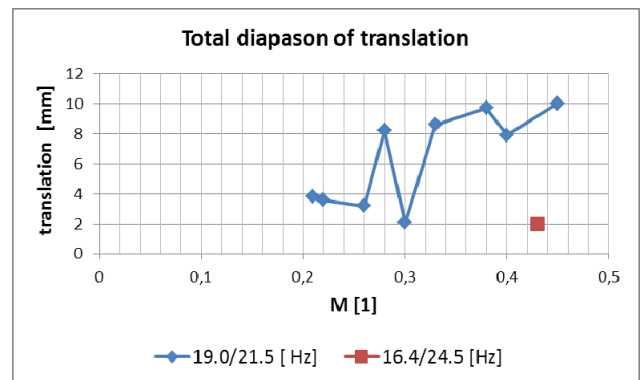


Figure 7b): *Total diapason of translation.*

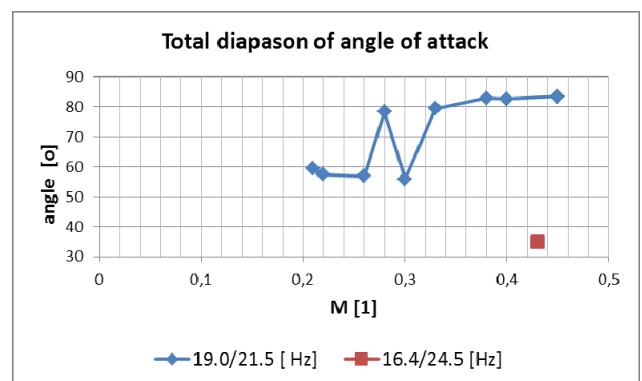


Figure 7c): *Total diapason of angle of attack.*

The motion of the profile during the stall flutter is shown in more detail on Figure 8 for the highest Mach number $M = 0.45$. The point B in the diagram denotes zero angle of attack, the point A denotes the maximal translation and precedes the point B in time. In the point S the profile impacts to some artificial mechanical barrier; a point-line represents the profile trajectory that could be realised in the system without impacts. The points A and C correspond to the maximal translation displacement in positive and negative direction, respectively. The intervals denoted by letters **u** and **d** correspond to the regimes when the whole break of the flow appears on the upper (**u**) and lower (**d**) profile surface, respectively. The maximal positive (point D) and negative (point E) angles of attack correspond to zero profile translation.

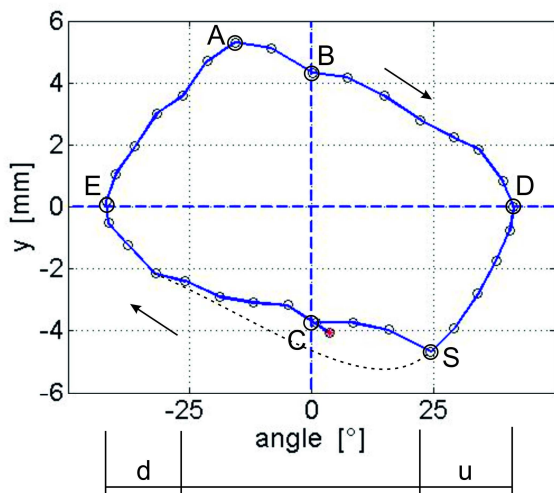


Figure 8: Relation between axis rotation center shift of the profile (vertical, [mm]) and approach angle (horizontal, [°]) for measure No. 2663-05, $M=0.45$, translation frequency for $M = 0$ is 19.0 Hz and rotation frequency is 21.5 Hz.

An example of the phase shift between the translation and rotation of the profile demonstrated in Figure 9.

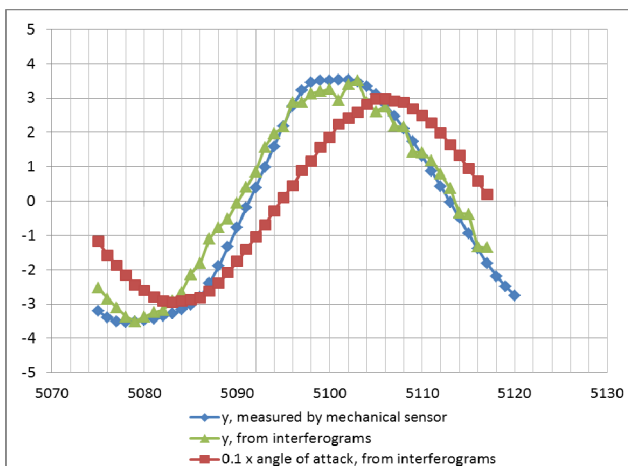


Figure 9: The angle of attack (in [°]) and vertical translation (in 10 time scale, [mm]) on the vertical axis

versus the time (horizontal, [ms]) during one period of the self-excited vibrations, for measurement No. 2663-02, $M=0.21$.

CONCLUSION

Several combinations of experimental parameters were realized during aeroelastic measurements of the self-excited profile vibrations in the Mach number range $M=0.21 - 0.45$. The influence of Mach number on the coupled mode flutter and stall flutter in relation to the difference between the eigenfrequencies corresponding to the translation and rotation motion of the profile was determined.

ACKNOWLEDGMENTS

The authors gratefully acknowledge the Grant Agency of the Czech Republic for supporting this work under Grant No. 101/09/1522 and our colleagues Prof. P. Šafařík, Dr. M. Luxa, Mr. V. Bula, Dr. F. Vaněk, Mr. J. Cibulka, Mr. J. Česal for their kind collaboration.

REFERENCES

- [1] Dowell, Earl H. (Editor) (1995): A Modern Course in Aeroelasticity. Kluwer Academic Publishers, Dordrecht/Boston / London, 3rd edition.
- [2] Vlček, V., Horáček, J., Luxa, M., Veselý, J., Bula, V. (2009) Visualization of unsteady flow around a vibrating profile: experimental set-up and preliminary tests. *Interaction and Feedbacks Proceedings, 2009*, ed. Zolotarev I., Praha, IT AS CR, v.v.i., pp. 75-83, ISBN 978-80-87012-23-9.
- [3] Vlček, V., Kozánek, J. (2010) Preliminary interferometry measurements of flow field around a fluttering NACA0015 profile. *Engineering Mechanics 2010*, ed. Zolotarev I., Svratka, May 10 – 13, 2010, pp. 167-168 (full paper on the CD, ISBN 978-80-87012-26-0).
- [4] Šafařík, P., Vlček, V. (1985): Using interferometric measurements in calculation of aerodynamic forces. *Optical Methods in Dynamics of Fluid and Solids* (editor Píchal M.), Springer Verlag, Berlin, pp. 301-305.
- [5] Vlček, V., Kozánek, J. (2011): Preliminary interferometry measurements of a flow field around fluttering NACA0015 profile. *Acta Technica* 56, 379-387.

NUMERICAL INVESTIGATION OF SELF-SUSTAINED SHOCK OSCILLATION ACOUSTICS

Ciarán J. O'Reilly*

Gunilla Efraimsson

Aeronautical and Vehicle Engineering
KTH Royal Institute of Technology
SE-100 44 Stockholm
Sweden

Johan Hammar

Urban Emborg

Creo Dynamics AB
SE-582 16 Linköping
Sweden

ABSTRACT

A numerical investigation of the sound resultant from a compressible flow about an 18% thick circular-arc aerofoil, for free-stream Mach numbers between $M_\infty = 0.7$ and $M_\infty = 0.82$, and a Reynolds number $Re \approx 10^7$, is presented in this paper. Within this range of parameters, self-sustained shock oscillations may be present on the upper and lower aerofoil surfaces. The transient flow-field was computed by detached-eddy simulation, with the solution used to quantify acoustic sources, defined by Howe's analogy, that are propagated using a wave expansion method. The results were compared with available experimental and numerical results from other studies of the same configuration.

NOMENCLATURE

Variables:

B	total enthalpy
K	reduced frequency ($= \omega b / u_\infty$)
M	Mach number vector
b	aerofoil semi-chord
c	speed of sound
f	frequency
i	imaginary unit
k	wave number ($= \omega / c$)
p	pressure
t	time
\mathbf{u}	velocity vector
\mathbf{v}	wave propagation direction vector
x	distance in x-direction
α	truncation factor
γ	ratio of specific heats
ρ	density

$\boldsymbol{\omega}$ vorticity vector

ω angular frequency

Subscripts and Superscripts:

$\bar{}$ mean values

\prime fluctuating values

$\hat{}$ frequency domain values

∞ free-stream values

INTRODUCTION

Self-sustained shock oscillations on aerofoils at transonic flow conditions are of importance to many applications, as they are associated with flow phenomena such as buffeting, unsteady boundary layer separation and vortex shedding in the trailing-edge region, which are major causes of noise [1]. Comprehensive reviews of the topic have been given by Tijdeman & Seebass [2] and Lee [3]. Despite being the subject of investigation for over fifty years, the physical mechanisms of periodic shock motion are not yet fully understood. However, three typical flow regimes may be classified [4] as attached boundary layer, moving shock wave/turbulent boundary layer interaction and intermittent boundary layer separation.

In addition to experimental studies (see Lee [3] for a full list), there have been many numerical investigations. These simulations have been quite successful in predicting the frequencies of shock oscillation, the onset boundaries, as well as the unsteady pressure fluctuations. Unsteady RANS [5, 6, 7] and hybrid RANS/LES [4, 8] have been used to predict accurately the oscillation frequency and the surface pressure fluctuations.

This transonic flow phenomena not only generates a strong tone at the oscillation frequency, but also leads to increased levels of broadband noise, due to an increase in

*Address all correspondence to this author. Email: ciaran@kth.se

the intensity of wake fluctuations. As shown by Roos and Riddle [9], the surface pressure fluctuations on the aerofoil, induced by the shock, and the velocity fluctuations in the wake are correlated, which is evidence of the coupling between the shock motion and the wake oscillation.

In this paper, the sound from a compressible flow past an 18% thick circular-arc aerofoil is investigated for a Reynolds number $Re \approx 10^7$ and free-stream Mach numbers from $M_\infty = 0.7$ to $M_\infty = 0.82$. These simulation parameters are comparable with those in the experiments of McDevitt *et al.* [10] and Levy [5] and the numerical study of Chen *et al.* [4].

The objective of this work is to gain a better understanding of the sound from this simple 2D transonic configuration with a view to examining more realistic 3D geometries, which may have a similar profile. It is assumed that the sound is generated by the flow separation and wake downstream of the shock. As the surface pressure fluctuations and the wake fluctuations are correlated, it is believed that this will be sufficient to capture the sound generated by this phenomena.

Chen *et al.* [4] showed that the structures of the separated shear layer and the moving shock wave are reasonably well captured using the instantaneous Lamb vector, $(\boldsymbol{\omega} \times \mathbf{u})$, divergence and curl respectively. As the Lamb vector divergence appears as an acoustic source term in Howe's acoustic analogy [11], the acoustics are framed within this analogy for this present work.

The transient flow-field is computed by DES [12], with the solution then being used to quantify acoustic sources defined by Howe's analogy, which are propagated using a WEM [13].

NUMERICAL METHODOLOGY

The numerical investigation was divided into two steps – firstly, flow simulations were made for a transonic flow about the aerofoil, and secondly, acoustic sources were extracted from the flow solution and propagated to the far-field.

Flow Simulations

Transient flow simulations were performed by solving the unsteady Reynolds-averaged Navier Stokes (RANS) equations and by means of a detached-eddy simulation (DES) [12] using the compressible Navier-Stokes solver sonicFoam, which is part of the open-source software package OpenFOAM. DES is a hybrid RANS / large-eddy simulation (LES) method, with RANS used close to walls and LES used in separated regions. For high-Reynolds-number flows, DES is convincingly more

capable presently than either unsteady RANS or LES on their own.

The flow was initially solved using only RANS to obtain an unsteady RANS solution, before the LES scheme was introduced into separated flow regions. The original formulation of DES with the Spalart-Allmaras (SA) model at the walls was used. The equations were discretised using a bounded central scheme on the divergence terms with a gamma scheme [14] and a value of 0.5 to ensure stability and minimise *wiggles* at the shocks. A Crank-Nicholson scheme was used for the time integration. The preconditioned biconjugate gradient method was used to solve the matrix equations. A wave transmissive condition was used to minimise the reflections of waves propagating through the outer boundaries.

Acoustics

It was assumed in this present work that the sound is generated by vorticity inhomogeneities in the flow separation downstream of the shock, and that the shock itself only influences the location of the separation region and the subsequent propagation of acoustic waves. The sound generation and propagation were, therefore, defined using Howe's analogy [15], which describes the acoustic propagation, through a homentropic flow, of fluctuations in the total enthalpy generated by vorticity inhomogeneities. Howe's analogy is

$$\left(D \left(\frac{1}{c^2} D \right) - \frac{1}{\rho} \nabla \cdot (\rho \nabla) \right) B = \frac{1}{\rho} \nabla \cdot (\rho (\boldsymbol{\omega} \times \mathbf{u})) \quad (1)$$

where B is the total enthalpy, which for an ideal gas is $\gamma p / (\gamma - 1) \rho + u^2 / 2$; and D is the operator $(d/dt + \mathbf{u} \cdot \nabla)$. Linearising this equation and replacing the wave operator coefficients with their values in the absence of perturbations gives

$$\left(D_0 \left(\frac{1}{c_0^2} D_0 \right) - \frac{1}{\rho_0} \nabla \cdot (\rho_0 \nabla) \right) B' = \frac{1}{\rho_0} \nabla \cdot (\rho_0 (\boldsymbol{\omega} \times \mathbf{u})') \quad (2)$$

where D_0 is the operator $(d/dt + \mathbf{u}_0 \cdot \nabla)$ and $(\boldsymbol{\omega} \times \mathbf{u})'$ is the perturbed Lamb vector.

Switching to the frequency domain gives this equation as

$$\begin{aligned} \left(L_0 \left(\frac{1}{c_0^2} L_0 \right) - \frac{1}{\rho_0} \nabla \cdot (\rho_0 \nabla) \right) \hat{B} \\ = \text{FFT} \left(\frac{1}{\rho_0} \nabla \cdot (\rho_0 (\boldsymbol{\omega} \times \mathbf{u})') \right) \end{aligned} \quad (3)$$

where L_0 is the frequency domain operator ($i\omega + \mathbf{u}_0 \cdot \nabla$). The source here is evaluated from the time domain solution from the DES. This approach is appealing because, as shown in Chen *et al.* [4], the instantaneous Lamb vector divergence removes the shock from the source.

For the acoustic propagation, the flow is also fixed by introducing a plane of symmetry through the chord of the aerofoil. Although this stops the oscillation of the shock, the sound-producing separated flow region remains. In this way the sources are propagated through a steady background flow. The frequency of the tonal component of the sound field may be determined directly from the DES, with the broadband sound computed from the steady flow.

The propagation of acoustic waves in the near-field was determined using a wave expansion method (WEM). This is a physically-based discretisation method [13], which is suitable for solving wave propagation through inhomogeneous flows. See Ref. [13] for more details.

FLOW RESULTS

Onset of shock motion

Unsteady RANS solutions were computed using three different turbulence models – the one-equation SA, and the two-equations κ - ϵ and SST κ - ω models – in order to assess their influence on the onset of the shock oscillations. The free-stream Mach number was varied from $M_\infty = 0.7$ to $M_\infty = 0.82$. The domain was discretised with a 2D grid, shown in Fig. 1, that had 120 nodes along the chord of the aerofoil. A continuous wall function was used with a distance to the first node of $y^+ \approx 10$ and $y^+ \approx 30$.

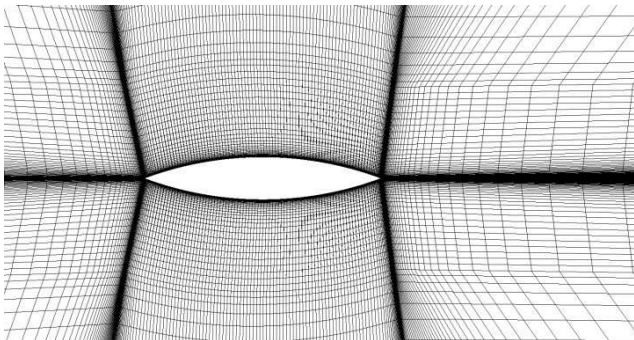


FIGURE 1: 2D GRID USED FOR THE UNSTEADY RANS COMPUTATIONS.

The results are presented in Tab. 1. The κ - ω and

SA models showed similar behaviour giving the onset of the oscillating shock to be at a free-stream Mach number of between $M_\infty = 0.76$ and $M_\infty = 0.77$. With the κ - ϵ model the onset was slightly higher at a Mach number of $M_\infty = 0.79$. An explanation for the higher onset Mach number with the κ - ϵ model remains unknown. The results with the SST κ - ω and SA model are consistent with those presented in [3].

TABLE 1: REDUCED FREQUENCY FOR DIFFERENT MACH NUMBERS. (X) INDICATES THAT NO OSCILLATION IS PRESENT.

Mach	0.76	0.77	0.78	0.79	0.80
SA					
$n = 150, y^+ = 2$		0.44			
$n = 120, y^+ = 10$	X	0.45	0.47	0.49	0.55
$n = 120, y^+ = 30$	X	X	0.45	0.47	
$n = 90, y^+ = 30$	X	X	0.44	0.47	0.55
$n = 60, y^+ = 30$	X	X	0.45	0.58	X
SST κ-ω					
$n = 120, y^+ = 10$	X	0.46	0.47	0.49	0.53
$n = 120, y^+ = 30$	X	X	0.46	0.48	
κ-ϵ					
$n = 120, y^+ = 10$	X	X	X	0.47	
$n = 120, y^+ = 30$	X	X	X	X	

To analyse the shock motion the lift coefficient, based on the force acting on the entire profile, was used. The reduced frequency of the oscillation in the lift coefficient, $K \equiv \omega b / u_\infty$, at the onset free-stream Mach number was similar for the three turbulence models, with $K \approx 0.45$. Previous simulations, reviewed in Lee [3], have shown reduced frequencies from $K = 0.4$ to $K = 0.495$ and measurements of $K = 0.49$.

It was observed in the present results, that the reduced frequency increases as the free-stream Mach number increases until the shocks stabilises at a higher Mach numbers. This is consistent with the shock moving towards the trailing-edge as the Mach number increases. Therefore, the time it takes for the disturbances, which drive the

oscillation, to travel between the shock and trailing-edge decreases, resulting in a higher oscillation frequency.

The oscillating motion of the wake from side to side may be seen in the Mach number contours close to onset conditions in Fig. 2. As a shock is established on one side at about 80% of the chord length, the boundary layer separates towards the trailing-edge, causing a larger wake on that side of the profile. The shock then moves upstream to about 60% of the chord, where it disperses due to a dechambering of the profile on that side as a result of the growth in the separated flow region. As this happens, another shock establishes itself on the other side of the profile at roughly 80% of the chord, and the flow separation and shock movement are repeated on this side. The cyclical loop is closed when the shock is reestablished on the original side. This motion is repeated in a self-sustained manner.

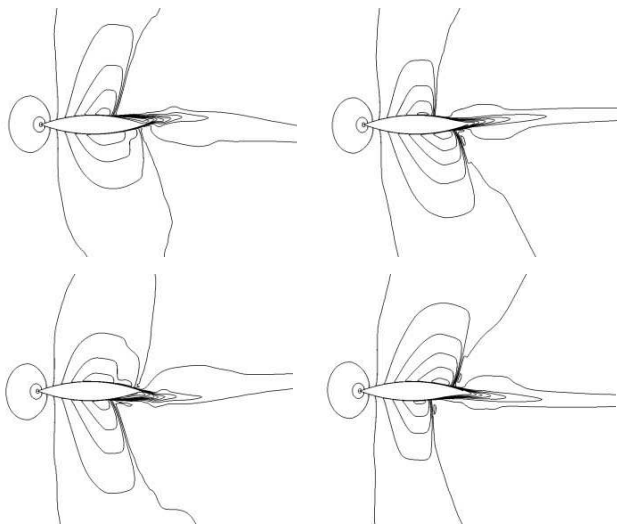


FIGURE 2: CONTOURS OF MACH NUMBER FOR FOUR DIFFERENT TIMES. SA MODEL AND $M_\infty = 0.77$.

As the free-stream Mach number is increased, the pattern of the shock movement is slightly different, as is shown Fig. 3. The shocks starts to move both up and down stream along the chord instead of disappearing at the upstream location as was the case before. The range over the chord of the movement also decreases until the shock stabilises at the offset Mach number.

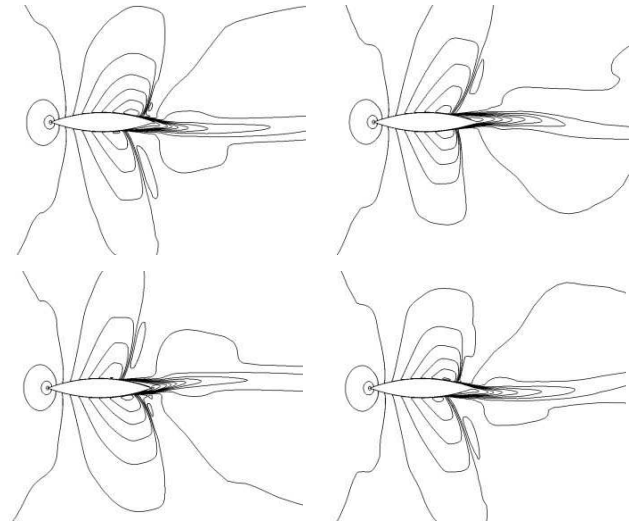


FIGURE 3: CONTOURS OF MACH NUMBER FOR FOUR DIFFERENT TIMES. SA MODEL AND $M_\infty = 0.80$.

Quasi-3D Simulations

A refined grid with $y^+ = 2$, 150 nodes along the chord and an additional 170 nodes in the distance one chord length downstream was used for the DES simulations. This grid is shown in Fig. 4. The span was also discretised with 20 nodes to get a quasi-3D domain with cyclic boundaries. The solution was run for a time of 0.15 seconds with a time-step of 10^{-7} seconds giving a $CFL < 1$. The total simulation time is equivalent to the flow passing the length of the profile approximately 60 times. However due to the low frequency of the oscillations this only gave about 8 periods of the shock motion.

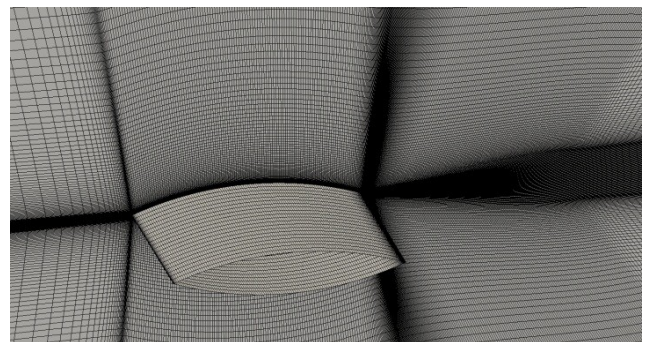


FIGURE 4: QUASI-3D GRID USED FOR THE DES SIMULATIONS.

The shock movement range over the chord was slightly increased in the DES case reaching about 50% of the chord. In Fig. 5 the increased wake flow structure is clearly visible with smaller vortical structures shed at the trailing-edge. These are shed at higher frequency than the shock oscillation frequency and form in the shear layer from the shock induced boundary layer separation. The mean wake movement still shows much resemblance to the results produced by the RANS solutions, with the region of large-scale separation moving from side to side with the shock motion.

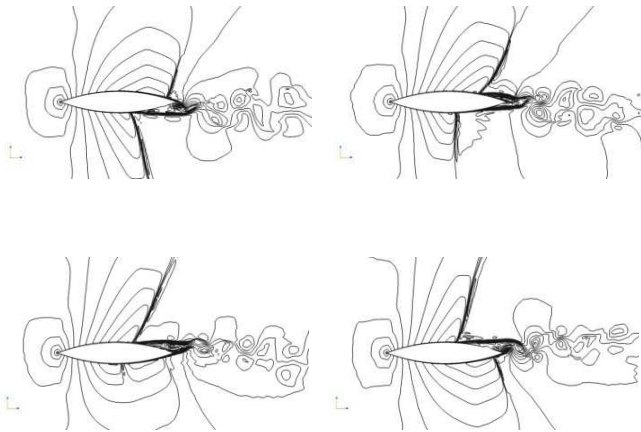


FIGURE 5: VELOCITY CONTOURS OF FOUR TIMESTEPS FROM THE DES SIMULATION.

The reduced frequency was increased with the DES simulation. A Fourier analysis of the lift force coefficient, CL , acting on the profile, shown in Fig. 6, shows a peak at a reduced frequency of $K = 0.47$ compared with $K = 0.44$ from a RANS solution on the same grid. This is in closer agreement with the experimental measurements [3], which gave a reduced frequency of $K = 0.49$.

The presence of small-scale vorticity in the DES solution is evident in Fig. 7, with a much more complex wake formation. The wake structure also appears to be highly three dimensional.

ACOUSTIC RESULTS

Acoustic Sources

The acoustic source is defined by Howe's analogy [15] as the divergence of the Lamb vector. As shown in Chen *et al.* [4], the instantaneous Lamb vector divergence removes this shock from the source as can be seen in Fig. 8, which was computed from the instantaneous

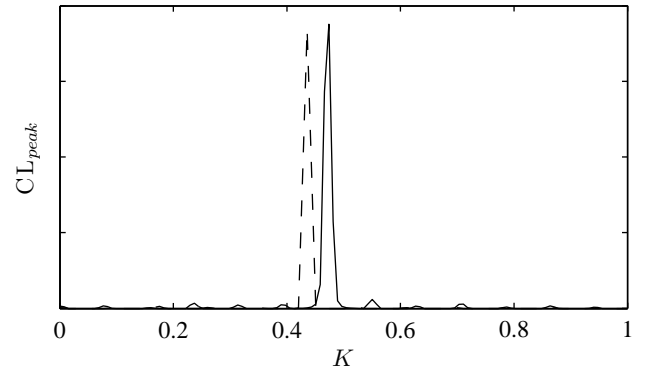


FIGURE 6: SPECTRUM OF THE LIFT FORCE ACTING ON THE PROFILE FROM THE DES (—) AND UNSTEADY RANS (- -) SOLUTIONS.



FIGURE 7: VORTICITY CONTOURS FROM DES SOLUTION.

DES solution.

In the present investigation the shock is fixed for defining the acoustic sources and propagation. This is achieved by imposing a symmetry condition running through the aerofoil chord. A RANS solution was computed for this configuration and the Lamb vector divergence and curl from this solution are shown in Fig. 9. Once again it can be seen that the acoustic source (the divergence of the Lamb vector) does not contain the shock. This source can then be propagated through a flow which contains the shock.

Acoustic Propagation

Numerically propagating waves through a flow with a shock present is quite challenging. This is because commonly used propagation methods, which discretise the domain, require that the Nyquist frequency criteria, of at least 2 points-per-wavelength, is met in order to avoid aliasing. The wave number vector is altered by the flow such that $\mathbf{k} = k/(1 + \mathbf{M} \cdot \mathbf{v})$. This means that wave-fronts propagating into the flow are compressed and so require a greater number of points-per-wavelength. The singularity at $M = 1$ can, therefore, not be included directly.

The strategy employed here to include the shock in

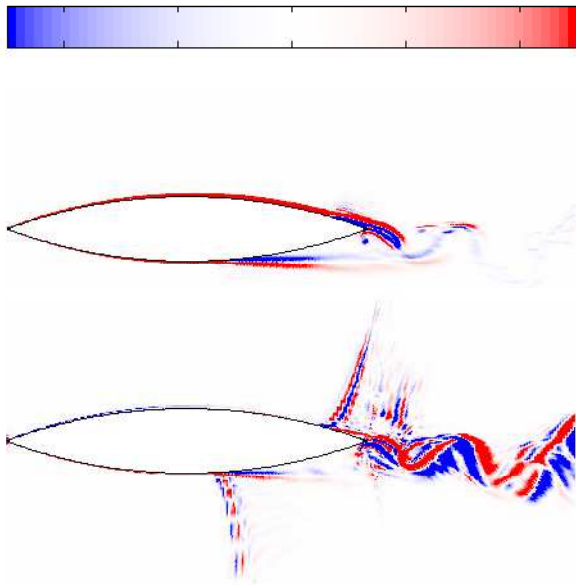


FIGURE 8: THE DIVERGENCE (BOTTOM) AND CURL (TOP) OF THE INSTANTANEOUS LAMB VECTOR.

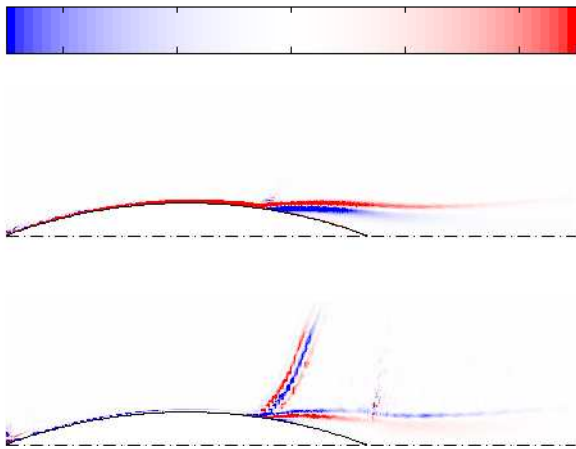


FIGURE 9: THE DIVERGENCE (BOTTOM) AND CURL (TOP) OF THE INSTANTANEOUS LAMB VECTOR WITH A SYMMETRY PLAIN IMPOSED.

the propagation is to truncate the Mach number in the vicinity of $M = 1$. A truncation factor is defined as $\alpha \equiv \min |M - 1|$. Mach number values are rounded to $M = 1 \pm \alpha$ depending on which is nearer.

In order to test this strategy, a 1D solution was computed using the WEM for wave propagating into a flow that increases linearly in amplitude from $M = 0$ to $M = 2$.

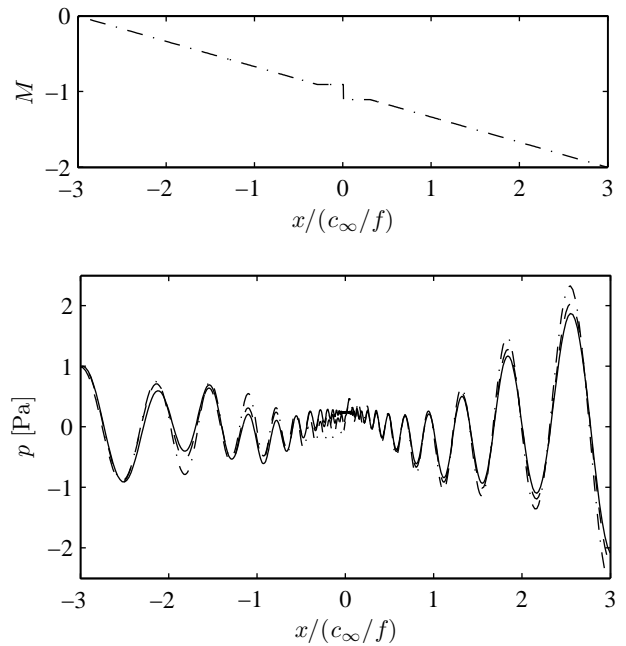


FIGURE 10: 1D PROPAGATION WITH A TRUNCATED TRANSONIC MACH NUMBER PROFILE (TOP) AND THE REAL COMPONENT OF THE PRESSURE (BOTTOM). THE TRUNCATION VALUE IS VARIED FOR $\alpha = 0.01$ (—) ; $\alpha = 0.05$ (- · -), AND $\alpha = 0.1$ (- · ·).

The Mach number truncation, with $\alpha = 0.1$, is visible in the top sub-plot of Fig. 10 at $x/(c_\infty/f) = 0$. The real part of the pressure is also shown in Fig. 10 for varying values of α . The grid is refined so as to ensure that there are a sufficient number of points-per-wavelength. It can be seen that although there is some disagreement locally at $M \approx 1$ the solutions agrees well away from this region. It is, therefore, concluded that with Mach number truncation and local grid refinement, the transonic flow can be included in the acoustic propagation.

Figure 11 shows the mesh used for acoustic propagation about the aerofoil. The mesh is also refined locally near the sonic line, as can be seen in Fig. 11, using an iterative scheme in order to ensure that there are a sufficient number of points-per-wavelength.

The propagation of a point source located at the trailing-edge across the aerofoil with a stationary shock is shown in Fig. 12, again, for varying α values. The frequency here is $K = 2.8$, which is the highest frequency possible with this mesh. This shows some amount of qualitative agreement with the results presented in Lee [16], which used a graphical method for propagation. The directivity shown in Fig. 13 for this configuration shows

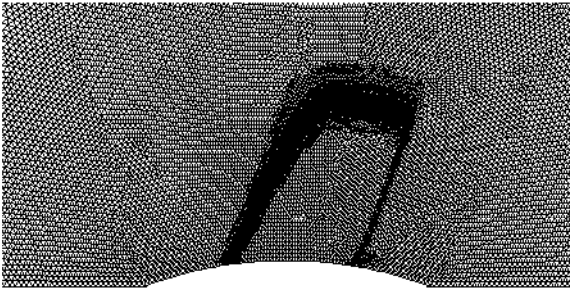


FIGURE 11: LOCALLY REFINED GRID USED FOR THE PROPAGATION.

reasonably good agreement, with a strong lobe between 90° and 120° . The directivity has also been checked for different amounts of mesh refinement and similar results were found. Although some penetration of the supersonic region can be expected [16], for the most part the sound appears to be deflected by the shock into the sideline.

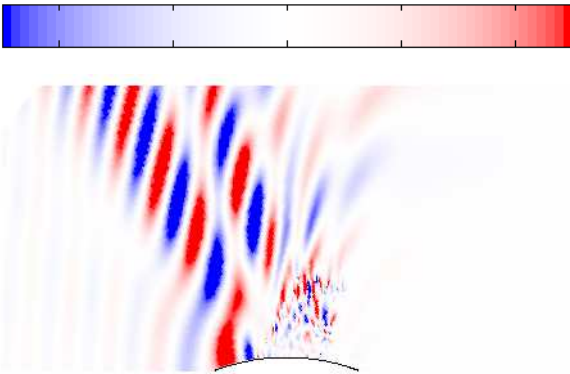


FIGURE 12: CONTOURS OF THE REAL COMPONENT OF THE PRESSURE FROM A POINT SOURCE AT THE TRAILING-EDGE.

As a RANS solution was used for the source definition here, it was not possible to determine a frequency dependent source. As an initial approach, the source shown in Fig. 9 was used to weight an incoherent point source distribution. The result computed at $K = 0.45$ with $\alpha = 0.01$ is shown in Fig. 14. Once again the directivity is strongest in the sideline.

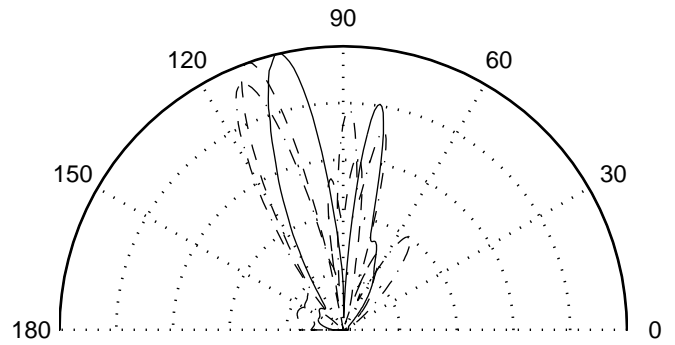


FIGURE 13: ABSOLUTE PRESSURE DIRECTIVITY FROM A POINT SOURCE AT THE TRAILING-EDGE. THE TRUNCATION VALUES ARE $\alpha = 0.01$ (—); $\alpha = 0.05$ (- -), AND $\alpha = 0.1$ (- · -).

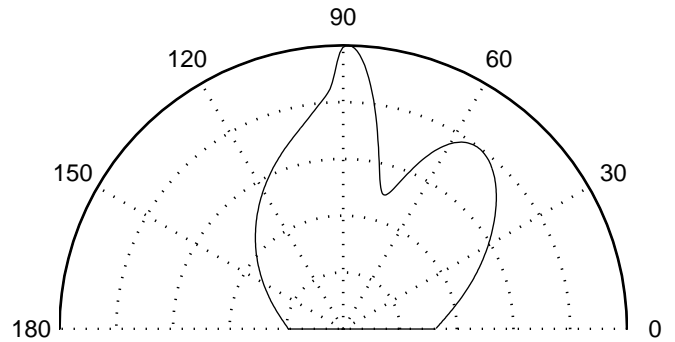


FIGURE 14: ABSOLUTE PRESSURE DIRECTIVITY FROM THE LAMB VECTOR DIVERGENCE SOURCES.

CONCLUDING REMARKS

Self-sustained shock oscillations on an 18% thick circular-arc aerofoil were investigated in this paper. Unsteady RANS and DES computations were performed for a variety of Mach numbers and with different turbulence models. The acoustics were defined by Howe’s analogy and an initial investigation into the propagation of sound generated by vorticity fluctuations in the flow separation and wake downstream of the shock was performed using the WEM.

The onset of shock oscillations was determined to occur between $M_\infty = 0.76$ and $M_\infty = 0.78$ with a shock oscillation frequency of $K \approx 0.45$. This falls within the ranges presented in the literature.

The use of Howe’s analogy to define the acoustics is an attractive approach as it separates the shock from the source region. However, there remains unresolved ques-

tions about the use of this wave operator in an unsteady flow such as is present here.

The transonic flow was included in the discretised propagation method by truncating the Mach number around the singularity at $M = 1$ and refining the mesh in this region. Initial computations appear to give reasonable results but further work is required in order to establish their accuracy.

The fact that the propagation results from both a point source at the trailing-edge and a source distribution give strong sideline directivity, leads to the possibility of simply using trailing-edge point sources for more complex 3D geometries. This would be a computational saving.

ACKNOWLEDGMENT

The authors gratefully acknowledge the support of the Vinnova funded NFFP5 project number 2010-01270.

REFERENCES

- [1] Wang, M., Freund, J. B., and Lele, S. K., 2006. "Computational prediction of flow-generated sound". *Annual Review of Fluid Mechanics*, **38**(1), p. 483.
- [2] Tijdeman, H., and Seebass, R., 1980. "Transonic Flow Past Oscillating Airfoils". *Annual Review of Fluid Mechanics*, **12**(1), p. 181.
- [3] Lee, B., 2001. "Self-sustained shock oscillations on airfoils at transonic speeds". *Progress in Aerospace Sciences*, **37**(2), p. 147.
- [4] Chen, L. W., Xu, C. Y., and Lu, X. Y., 2010. "Numerical investigation of the compressible flow past an aerofoil". *Journal of Fluid Mechanics*, **643**, p. 97.
- [5] Levy, L. L., 1978. "Experimental and computational steady unsteady transonic flows about a thick airfoil". *AIAA Journal*, **16**(6), pp. 564–572.
- [6] Rumsey, C., Sanetrik, M. D., Biedron, R. T., Melson, N., and Parlette, E. B., 1996. "Efficiency and accuracy of time-accurate turbulent Navier-Stokes computations". *Computers & Fluids*, **25**(2), p. 217.
- [7] Thiery, M., and Coustols, E., 2005. "URANS computations of shock-induced oscillations over 2D rigid airfoils: Influence of test section geometry". *Flow, Turbulence and Combustion*, **74**(4), p. 331.
- [8] Deck, S., 2005. "Numerical simulation of transonic buffet over a supercritical airfoil". *AIAA Journal*, **43**(7), pp. 1556–1566.
- [9] Roos, F. W., and Riddle, D. W., 1977. "Measurements of surface-pressure and wake-flow fluctuations in the flow field of a Whitcomb supercritical airfoil". *NASA TN D-8443*.
- [10] McDevitt, J. B., Deiwert, G. S., and Levy, L. L., 1976. "Transonic flow about a thick circular-arc airfoil". *AIAA Journal*, **14**(5), p. 606.
- [11] Howe, M. S., 1975. "Contributions to the theory of aerodynamic sound, with application to excess jet noise and the theory of the flute". *Journal of Fluid Mechanics*, **71**(04), p. 625.
- [12] Spalart, P. R., 2009. "Detached-Eddy Simulation". *Annual Review of Fluid Mechanics*, **41**(1), p. 181.
- [13] Caruthers, J. E., Engels, R. C., and Raviprakash, G. K., 1996. "A wave expansion computational method for discrete frequency acoustics within inhomogeneous flows". *2nd AIAA/CEAS Aeroacoustics Conference (State College, Pennsylvania, USA)*. AIAA 1996-1684.
- [14] Jasak, H., Weller, H. G., and Gosman, A. D., 1999. "High resolution NVD differencing scheme for arbitrarily unstructured meshes". *International Journal for Numerical Methods in Fluids*, **31**, pp. 431–449.
- [15] Howe, M. S., 1998. *Acoustics of fluid-structure interactions*. Cambridge University Press.
- [16] Lee, B. H. K., Jiang, H., and Murty, H., 1994. "Role of Kutta waves on oscillatory shock motion on an airfoil". *AIAA Journal*, **32**(4), p. 789.

ACOUSTIC RESONANCES AND AERODYNAMIC INTERACTIONS IN AN AXIAL COMPRESSOR STATOR STAGE TEST RIG

Benjamin Pardowitz

Ulf Tapken

Lars Enhardt

German Aerospace Center (DLR)

Institute of Propulsion Technology / Engine Acoustics Department

Berlin, Germany

Email: Benjamin.Pardowitz@dlr.de

ABSTRACT

For a noise reduced design of turbomachinery components a detailed understanding of various broadband noise source mechanisms is required. This paper presents an experimental investigation of an *isolated* axial compressor stator stage. The background of our study is the so-called rotating instability (RI), which is one of the major phenomena regarding broadband noise generation at off-design conditions. For the first time characteristic modal structures of the RI are investigated on a set-up without rotating parts. An enhanced analysis technique is used to determine the modal properties, even though their associated amplitudes are significantly smaller than other predominating spectral properties such as resonances. This paper focusses on preliminary studies to identify these resonances caused by geometric features of the whole test set-up. Thus, results can be interpreted with a separation of different noise characteristics in order to identify the RI associated modal patterns.

INTRODUCTION

The predominant noise sources at aeroengines are generated by periodic rotor-stator interaction. A future design needs to more and more consider the acoustic properties of turbomachinery components such as compressors. This requires a detailed understanding of the various broadband noise generation mechanisms in an axial compressor stator stage. The complex three dimensional geometry and flow field make it difficult to separate the different effects and their significance for the overall noise emission. One of the major phenomena in compressors at off-design conditions is the blade tip vortex noise,

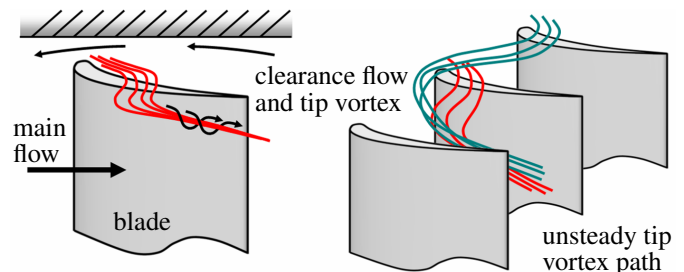


FIGURE 1: UNSTEADY CLEARANCE FLOW CAUSING TIP CLEARANCE NOISE (SEE [1–3]).

which is generated by an aerodynamic phenomenon often referred to as 'rotating instability' (RI) [1–5]. The term RI is used here in accordance with these publications. It should be noted, however, that the RI phenomenon is different from the typical part-span rotating stall in axial compressors. According to [1–5], the RI arises with an increase in blade loading, resulting in a more intense radial clearance vortex. Its vortex path is shifted forward to the leading edge of the subsequent blade and thereby blocks the passage in the clearance region. This blockage redirects the flow, resulting in an increased incidence at the following blades. Its pronounced unsteady characteristics appear over several blade passages and thereby lead to a specific azimuthal structure (see figure 1). Its rotation and narrowband frequency generate typical noise spectra containing several peaks at a regular frequency spacing, measured at the casing wall. Earlier investigations of rotor-stator-stages have shown that each peak of the RI components is associated with a single dominant circumferential mode [3]. This is explained by the transformation from the rotating source frame into the fixed

frame, resulting in a series of peaks corresponding to continuously numbered modes.

Subject of a joint project is the experimental investigation of the RI phenomenon and its associated effects at a single axial compressor stator stage with hub clearance [6]. In order to ensure an exclusive examination of the annular stator cascade, rotating parts were avoided in the test-setup, i.e. the incident swirling flow field was created by upstream nozzle guide vanes. The involved partners investigate the steady and unsteady flow characteristics in regard to the RI, e.g. with hotwire probes, microphones and 2D-High-Speed PIV. In addition, results will be compared with numerically obtained results of delayed detached eddy simulations. Acoustic measurements were carried out with the objective to examine the noise components generated at the *isolated* stator stage, that are associated with both the RI and other dominant noise sources, such as blade incident turbulence noise and trailing edge noise.

It is assumed that aerodynamic interactions between the blade rows and the inflow conditions of the stator-stage as well as the radial and circumferential flow profile play an important role for the RI. However, the situation turned out to be more complex than expected. Several features such as peaks or humps were found in the pressure spectra, which strongly depend on operating conditions. Preliminary analyses revealed a significant impact of acoustic resonances caused by geometric features of the test rig and the upstream piping system of the compressed air supply. High amplitudes at unexpected frequencies quite often occur in experimental acoustic research on turbomachinery components (cf. [7]), but these spectral properties are usually not investigated in detail. The objective of the present paper is to identify spectral components that are associated with test rig resonances, in order to enable the separation of the RI related acoustic parts of interest.

AXIAL COMPRESSOR STATOR STAGE TEST RIG

Experimental investigations were performed on an axial compressor stator stage test rig, shown in figure 2. It consists of five sections without any rotating parts and is operated by TU Berlin¹. In the annular flow duct, there are three consecutive blade rows, each with adjustable flow angles. An inlet nozzle constricts the cylindrical duct (section A). The resulting cross sectional area is kept constant in the following sections B to E with an inner radius of $r_1 = 86$ mm and an outer radius of

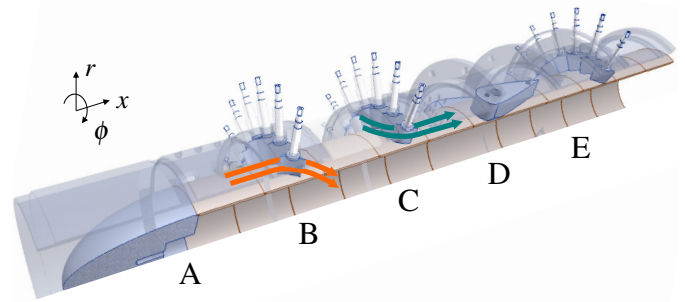


FIGURE 2: AXIAL COMPRESSOR STATOR STAGE TEST RIG WITH SECTIONS A - E.

$r_2 = 120$ mm. The overall test rig length is $L = 1.27$ m. The first blade row turns the flow in positive azimuthal direction (section B) comparable to nozzle guide vanes. Thereby, the inflow conditions of the subsequent compressor blade row (section C) is provided with an intense swirl flow (colored arrows in figure 2 showing the basic flow paths). The incidence angle at the stator blades can be adjusted in a range of -5° to $+21^\circ$. The compressor blades were non-twisted and 2D-contoured with specifically designed, highly loaded profiles, comparable to so-called Controlled Diffusion Airfoils [8]. Supporting struts in the outflow region of the compressor blade row stabilize the hub (section D). Finally, a throttle consisting of unprofiled blades in section E adjusts the overall flow conditions in the duct.

Pressure Air Supply Piping System

Pressurised air is produced by radial compressors and supplied at specific conditions by a variable piping system including a heat exchanger. A simplified scheme is shown in figure 3, a more detailed description is found in [6, 8]. The air is decelerated in the diffuser, cleaned by a filter and straightened in a settling chamber before entering the test rig. The characteristic lengths between test rig, main valves, heat exchanger and radial compressor are approximately 10 to 15 m depending on the used configuration. The pipe diameter is 0.35 m and the settling chamber has a length of approx. 2.2 m and a diameter of 1.0 m. None of the components has an acoustic treatment such as sound absorbers.

Sensor Configuration

Acoustic measurements were performed upstream of the stator row in section C using $1/4''$ condenser microphones (G.R.A.S. type 40BP-S). 30 microphones were placed in a ring wall flush mounted and equidistantly spaced at the outer casing upstream of the stator blades

¹Institute for Aeronautics and Astronautic
Chair for Aero Engines.

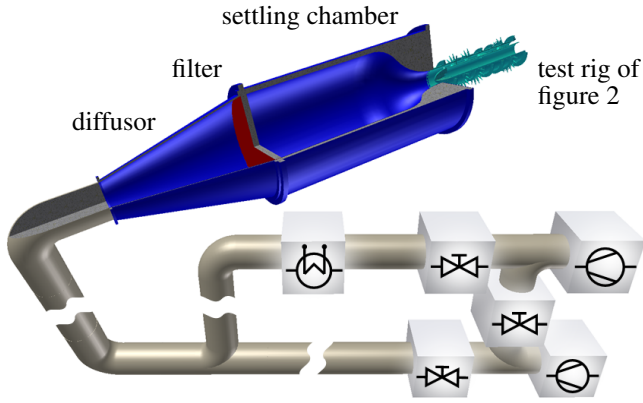


FIGURE 3: TEST RIG WITH AIR SUPPLY SYSTEM.

with 48 mm distance to the leading edge. Five reference sensors (type Endevco 8510C-15) were placed at the inner casing (next to the hub clearance) with 10 mm distance to the leading edge. In addition, there were two microphones as references wall flush mounted on the outer casing in section A. The recording lasted 120 seconds with a sampling frequency of 24 kHz.

Investigations With Axial Traversed Microphones

For a pre-study of the test rig's resonant behaviour, a single noise source was introduced through an aperture in the outer casing between section C and D. Either a speaker producing tonal and broadband noise or a blast pipe were used to excite the natural harmonics of the whole set-up. The resulting pressure field in the test rig was measured both at the installed reference sensors, as well as at five axially traversed microphones with a stepsize of $\Delta x = 20$ mm through section A to E. The traversed microphones were spaced equidistantly around the circumference and measured simultaneously, thus permitted an azimuthal mode analysis at each axial position up to mode orders $m = \pm 2$. All three cases of excitation (either tonal sweep, a high-pass filtered white noise or the pressure air driven noise source) induced similar spectral characteristics. This paper focusses on excitations with the air driven blast pipe only.

In addition to tests without flow, further investigations were performed under more realistic test conditions without blast pipe but with flow conditions at the stator blades. A single microphone (equipped with a 1/4" nosecone) was traversed axially through the test rig at a fixed $\phi = 150^\circ$. The reference microphones were recorded, too. Due to the set nozzle guide vane angle, only sections B to E could be reached.

OVERVIEW OF NOISE SOURCES IN THE TEST RIG

Various noise sources are present in each section of the test rig. The individual blade rows and struts exhibit characteristic spectral properties depending on their geometry, inflow conditions and aerodynamic interactions with adjacent blade rows. Main sources are blade incident turbulence noise, trailing edge noise, flow separation at blades and casing and the hub clearance vortex noise. A summary of these source mechanisms at subsonic compressors is given e.g. by [9]. In general, the relative contribution of a particular noise source significantly varies with the operation conditions. Further, a mutual influence is expected as well as a specific coupling of these sources to resonances of the test facility.

AZIMUTHAL MODE ANALYSIS

For an interpretation of noise source characteristics the azimuthal distribution of the unsteady pressure field is determined. With the upstream 30 microphones as described above, an azimuthal mode analysis is feasible up to mode orders $m = \pm 14$, corresponding to a circumferential resolution of approximately 1.4 passages of the stator row. The unsteady pressure field within a duct at fixed axial and radial positions can be described by a linear superposition of an infinite number of azimuthal modes (cf. [3]):

$$p(\phi, \omega) = \sum_{m=-\infty}^{\infty} A_m e^{im\phi} e^{i\omega t}. \quad (1)$$

A least-square-fit of the sensor data to the analytic model as given in equation (1) delivers frequency-dependent mode amplitudes $A_m(\omega)$. In the case of broadband noise, a statistical description of the modes in terms of mean values and spatial cross-correlation is necessary. Procedures for a circumferential sound field analysis based on cross-spectra have been described by [3, 10–12]. The azimuthal mode decomposition used in this paper is a simplified version of the radial mode decomposition technique described by [11], i.e. the expansion into radial mode orders is omitted, and is including cross spectra of all possible sensor combinations leading to an improved statistical description of the sound field. In brief: If equation 1 is written in matrix form as $\mathbf{p} = \mathbf{G}\mathbf{a}$, with the vector of azimuthal mode amplitudes $\mathbf{a} = (A_{-m}, \dots, A_0, \dots, A_m)$ and the matrix \mathbf{G} of mode transfer functions, then the cross spectral matrix of azimuthal mode amplitudes can be calculated as a least-square estimate by

$$\mathbf{A}_{aa} = \lim_{T \rightarrow \infty} E \left\{ \frac{1}{T} \mathbf{G}^+ \mathbf{p} \mathbf{p}^H (\mathbf{G}^+)^H \right\} \quad (2)$$

Here $\mathbf{G}^+ = (\mathbf{G}^H \mathbf{G})^{-1} \mathbf{G}^H$ denotes the pseudo-inverse of \mathbf{G} . The magnitude A_m of each azimuthal mode can be deduced from the main diagonal of matrix (2).

AXIAL SOUND PRESSURE DISTRIBUTION

Using traversed microphones, axial properties of the sound field in the test rig were studied. Cross spectra in relation to the fixed reference sensor (signal REF) were determined at each axial position x (signal X) by $S_{ref,x} = \lim_{T \rightarrow \infty} E \{ REF \cdot X^* / T \}$ (cf. [10]). An interpretation of these complex spectra with $\Re \{ S_{ref,x} \}$ and $\Im \{ S_{ref,x} \}$ at various frequencies yielded axially dependent properties.

RESULTS

At first spectral characteristics measured at operating conditions are discussed. Figure 4 presents averaged auto power spectra of the 30 microphones in the upstream section of the stator. Here the absolute inflow mach number to the stator blades was kept constant at $M=0.2$ and the incidence angle varies between 0.0° and $+16.0^\circ$. Such a parameter variation corresponds to a change of blade loading in an axial compressor stage. As seen in figure 4, characteristic peaks with varying amplitudes and dominant frequencies occur. The overall noise level increases with the incidence angle, explained by a corresponding higher blade loading. The pronounced peak at approx. 120 Hz remains almost the same, while the peaks between 450 and 800 Hz change their amplitudes and dominant frequencies. A further characteristic signature is observed between 200 and 350 Hz consisting of several peaks of different amplitudes with a frequency spacing of approx. 13 Hz. These peaks vary solely their amplitudes but at constant frequencies.

With the initial motivation of studying different noise source mechanisms of an isolated axial compressor stator stage, these spectra has to be investigated in detail. The objective is to separate the sources and identify the RI associated spectral characteristics. For that purpose, the natural harmonics of the test rig itself are investigated first, and subsequently their dependencies due to the connected pressure air supply system. An additional test case with flow focusses on the test rig resonances under more realistic conditions. Finally, a measurement at conditions where the RI occurs is interpreted with respect to the developed preliminary results.

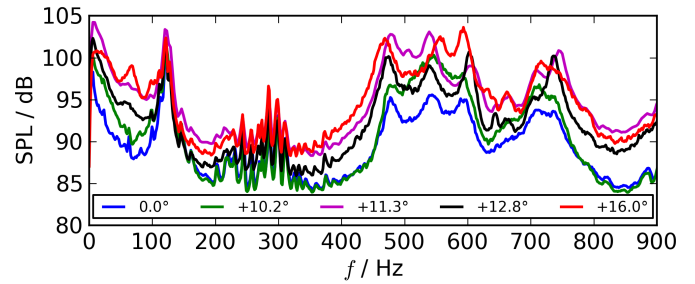


FIGURE 4: SPECTRA MEASURED UPSTREAM OF STATOR ROW C AT VARIOUS INCIDENCE ANGLES.

Resonances without piping system

Earlier studies at this test rig already presumed a significant influence of resonances but without verification [8]. An investigation with an external noise source and axially traversed microphones was performed to support this statement. Properties of the test rig without the pressure air supply piping system were investigated first. An averaged auto power spectrum of five microphones measured at 51 axial positions between 0.0 and 1.0 m is given in figure 5 (top). In the frequency range up to 900 Hz eight pronounced peaks were found. Three subplots in figure 5 show the axial distribution of the corresponding peak frequencies. Given here is the normalized quantity $\Re \{ S_{ref,x} \} / |\Re \{ S_{ref,x} \}|_{max}$ for a single microphone at five frequencies around each peak (same color as the highlighted amplitudes above). Dominant wavelengths of $\lambda = 2 \cdot L / o$, with $o = 1, 2, 3, \dots$ and zero crossings are clearly seen for all selected frequencies corresponding to standing waves in a duct of length L , which here is the overall length of the test rig. For a cylindrical/annular open duct without terminations, the resonance frequencies of azimuthal, radial and longitudinal order m , n and o (with inner and outer radius r_1 and r_2) can be calculated without flow [13]:

$$f_{m,n,o} = \frac{c}{2\pi} \cdot \sqrt{\left(\frac{o \cdot \pi}{L}\right)^2 + \left(\frac{j_{mn}}{r_2}\right)^2} \quad (3)$$

Here j_{mn} denotes the corresponding value of the n -th root of the m -th besselfunction, depending on the inner and outer radius.

Table 1 gives eight calculated resonance frequencies in the range up to 900 Hz using equation 3 (here speed of sound $c = 338$ m/s). In addition, the peak frequencies observed in figure 5 are listed. A comparison of the two reveals a high level of agreement between calculated and measured data for most of the peaks with an error of $< 5\%$. It can easily be verified that the mode orders

TABLE 1: CALCULATED RESONANCES AND MEASURED PEAK FREQUENCIES IN THE TEST RIG.

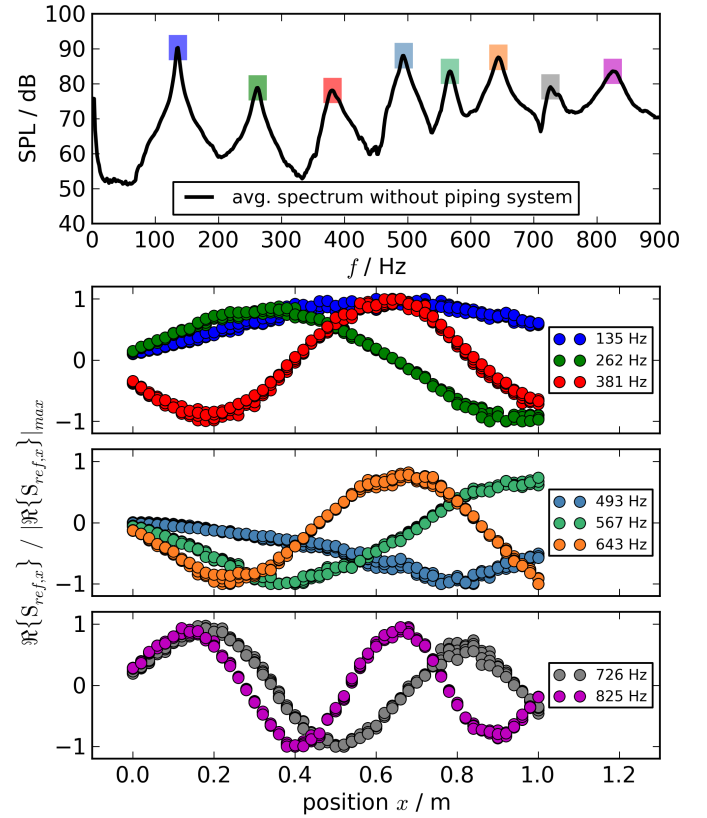
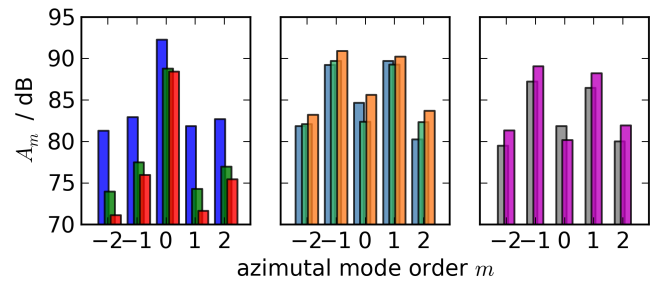
mode order	calculated	measured	deviation
m, n, o	$f_{m,n,o}$ [Hz]	f_{peak} [Hz]	[%]
0, 0, 1	133	135	1.4
0, 0, 2	266	262	1.6
0, 0, 3	399	381	4.8
$\pm 1, 0, 1$	541	493	9.8
$\pm 1, 0, 2$	588	567	3.7
$\pm 1, 0, 3$	659	643	2.5
$\pm 1, 0, 4$	747	726	2.9
$\pm 1, 0, 5$	847	825	2.7

o correspond to the sinusoidal waves depicted in figure 5. A final verification of the results of equation 3 is found in the azimuthal mode amplitudes. Using five traversed microphones, an azimuthal mode analysis at each axial position is feasible up to $m = \pm 2$ (determined with the method described above). The resulting mode amplitudes at these eight frequencies are given in figure 6, colored in correspondence to figure 5. Overall it can be seen that each frequency has either a dominant mode of $m = 0$ or a pair of $m = \pm 1$, as expected for azimuthally standing waves.

In conclusion, although three blade rows and struts are installed in the annular duct, the resonant behaviour is dominated by the overall axial extension of the test rig, which causes all cut-on acoustic modes (m, n) to protrude at multiple frequencies $f_{m,n,o}$.

Resonances with connected piping system

Based on the previous results, the influence of the pressure air supply piping system was determined next. The investigation method introducing a sound source and using five axially traversed microphones was repeated in exactly the same conditions, but with the additional connected piping system. The averaged auto power spectrum is shown on top in figure 7. Compared to figure 6 differences mainly occur in the frequency range from 180 to 480 Hz. In this range many peaks with different amplitudes and a frequency spacing of approx. 13 Hz are measured. This must be due to the ducting of the pressure air supply piping system (see figure 3) with various locations of reflections and characteristic dimensions.


FIGURE 5: AXIAL DISTRIBUTION OF THE SOUND PRESSURE WITHOUT PIPING SYSTEM.

FIGURE 6: AZIMUTHAL MODES AT PEAK FREQUENCIES CORRESPONDING TO FIGURE 5

The cross section changes several times in the settling chamber, the diffusor and the piping system. This situation leads to various reflections superimposing with phase cancellation at specific frequencies, resulting in characteristic amplitude variations (cf. [13]). However, in the range above 480 Hz the spectrum is almost unchanged compared to figure 5. Obviously, azimuthal modes of the order $m > 0$ in the test rig are (almost) not influenced by the piping system, as given by their propagation and reflection properties. An azimuthal mode analysis at the highlighted frequencies reveals a similar result as found

before in figure 6. Derived from this, each peak corresponds to a standing wave with specific azimuthal, radial and longitudinal mode orders comparable to table 1. For validation, the axial distribution of the sound pressure is presented in the same manner as before, given in three subplots in figure 7. A comparison of figure 5 and 7 reveals a high level of accordance, showing sine waves at peak frequencies with $m > 0$ almost with the same wavelengths and zero crossings as without the connected piping system. However, the axial distribution according to the three lowest peaks with $m = 0$ is influenced the most. The different behaviour of modes $m = 0$ and $m \neq 0$ can be explained by the different dependency of their axial wave numbers. The axial wave number of the plane wave mode $m = 0$ keeps constant throughout the whole piping system, so that a definite interference pattern results out of the reflections at the few duct cross-sectional changes. On the other hand the axial wave number of higher order modes vary with each change of the duct cross section. The degree of wave number change hereby depends on the mode cut-on ratio, i. e. in particular modes with lower cut-on ratio as modes $m = \pm 1$ in the observed frequency range exhibit more intense destructive interference.

Overall one can conclude that the piping system exhibits a resonant behaviour only for modes having a very high cut-on ratio throughout the whole piping system, which in the investigated frequency range is true only for mode $m = 0$.

Resonances at idle conditions

Test rig resonances at *idle* conditions of $M = 0.18$ and $\alpha = +12^\circ$ are investigated. Unlike before, many noise sources of various mechanisms are present now, caused by the flow itself. As before, the axial distribution of the sound pressure is of interest, but due to technical restrictions only a single microphone is traversed from 0.32 to 1.0 m (stepsize $\Delta x = 20$ mm). Hence, this investigation and interpretation is based on less measurements and without determining the azimuthal structure. However, the situation is expected to be more complex in the case of flow. The measured averaged auto power spectrum is given on top in figure 8. An increased noise level is observed for all frequencies, plausibly due to the existing various noise sources in each test rig section.

A comparison with figure 7 reveals the recurrence of already identified spectral characteristics: The dominant peak at 120 Hz and amplitude peaks in the range between 180 and 480 Hz with frequency spacing of approx. 13 Hz. However, above 480 Hz various new amplitude peaks or humps are present in an apparently unsystematic manner. For selected peak frequencies (highlighted as be-

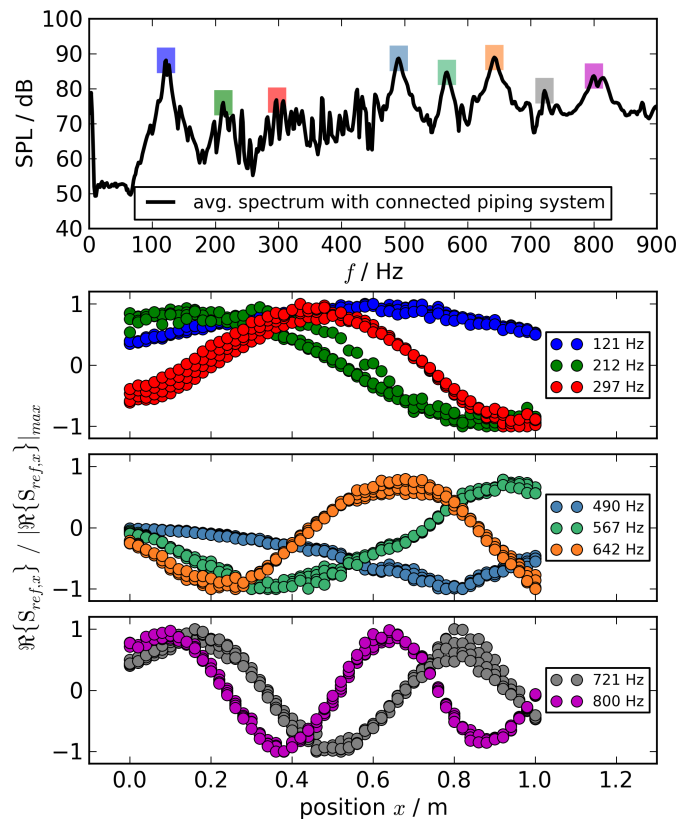


FIGURE 7: AXIAL DISTRIBUTION OF THE SOUND PRESSURE WITH CONNECTED PIPING SYSTEM.

fore), the axial distribution is shown again in the subplots in figure 8. Due to a smaller axial section and the presence of source distributions with different spectral characteristics at various locations, an interpretation is not forthright concerning wavelengths or standing waves in the duct. However, a major influence of the swirling flow can be identified.

It is well-known that a circumferential flow component results in different wave numbers for modes having equal azimuthal order but spinning in respectively opposite direction to the mean flow. As a consequence the resonance frequencies of these modes do not collapse any more, further they do not superpose to an azimuthal standing wavepattern. Thus the spectral diversity is increased already solely by superposition of swirling flow. Unfortunately, this makes a separation of broadband noise sources such as blade incident turbulence noise or trailing edge noise very difficult.

Rotating Instability Components

So far, only simplified cases were investigated to understand various occurring spectral properties. These findings will help to interpret results at conditions $M = 0.2$

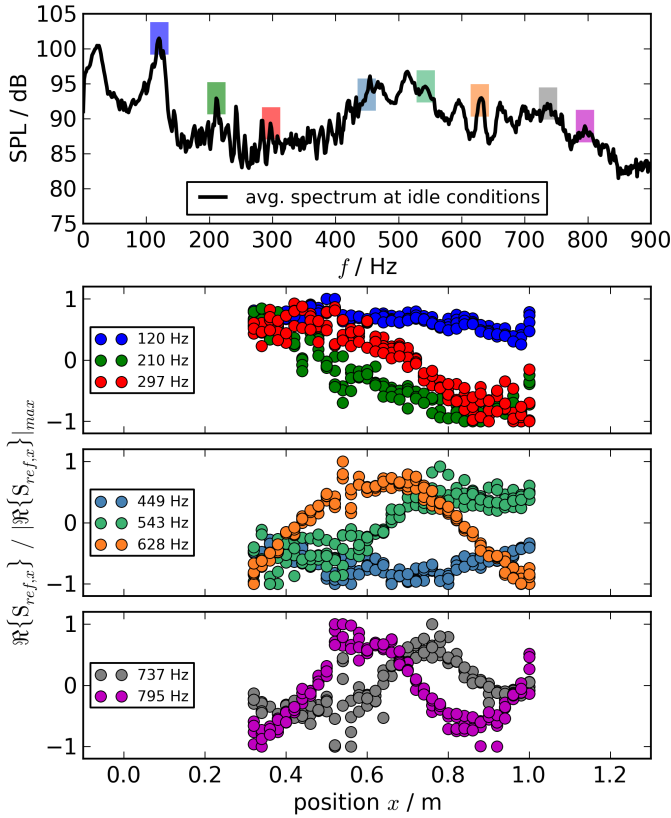


FIGURE 8: AXIAL DISTRIBUTION IN CASE OF IDLE CONDITIONS.

and $\alpha = +12^\circ$ where the RI phenomenon is present. The sound field is now measured with the fixed microphone ring array in the outer casing upstream of the compressor and the additional reference sensors next to the hub clearance. Averaged auto power spectra are shown at the top of figure 9 both for the upstream array (black line), as well as for the reference sensors (red line). The spectrum of the upstream array exhibits the already identified properties, a predominant peak at approx. 120 Hz, various peak amplitudes with frequency spacing of approx. 13 Hz between 200 and 400 Hz and various high amplitudes in the range above 450 Hz, all associated with the test rig resonances. A new spectral characteristic is clearly present at the reference sensors in the near field in the range between 100 and 200 Hz. Narrowband peaks at constant frequency spacings are visible with high amplitudes. In general, an increased noise level is detected at the reference sensors due to unsteady pressure fluctuations next to the hub clearance.

An azimuthal mode analysis was carried out for the microphone ring to get further insight. Selected mode amplitudes are depicted in figure 9 (bottom). The predominant amplitudes of the modes $m = -1, 0, +1$ between

400 and 800 Hz comply with the previous findings of specific resonances at frequencies, at which wavelengths of positive and negative spinning azimuthal modes in a swirl flow match the characteristic length of the test rig. However, more striking are the mode amplitude peaks in the frequency range 80 to 200 Hz with a frequency spacing of approx. $\Delta f = 25$ Hz and subsequent numbered orders from $m = +2$ up to $+8$. Each modal peak corresponds to a peak in the averaged reference spectrum (see red line on top of figure 9 above). This pattern is attributed to the RI phenomenon [3]. In a simplified model it can be described as a rotating narrowband noise source mechanism with characteristic azimuthal dimensions, measured with sensors in a fixed coordinate system [2]. Here the frequency spacing of Δf denotes the rotational frequency of the RI phenomenon. The large differences between the measured amplitudes at the reference sensors and the determined mode amplitudes in the upstream field are explained by an exponential decay of non propagating modes in the duct, where amplitudes of higher mode orders show a greater decay. As a consequence, a characteristic modal signature (with relative amplitudes) is changed with distance to its initial source plane. This behaviour is observed comparing the spectra in the nearfield with the modal pattern measured in the upstream array. In summary, the mode analysis method used here enabled clearly the detection of the RI, although the microphone array is placed in the outer casing upstream of the stator, where RI associated modes have lower amplitudes compared to other predominant spectral properties such as resonances. This constitutes a significant improvement compared to former investigations of the RI using a more simple analysis technique [1–3]. Thus, RI associated modal patterns could be proven for an axial stator with hub clearance for the very first time, similar to studies of rotors with tip clearance.

CONCLUSION

Resonances in test facilities often complicate a separation of the phenomena of interest. Objective of an ongoing study is the detection and characterisation of an aerodynamic rotating instability (RI) and the associated noise caused by an *isolated* axial compressor stator stage. In the present paper the influences of rig resonances on the sound field are dissolved and the characteristic signature of the RI is detected with help of an enhanced azimuthal mode detection for the very first time. The origin of the RI phenomenon was found next to the hub clearance. The modal properties of the RI match former results at rotor-stator stages with tip clearance. Predominant spectral properties caused by resonances due to geometric fea-

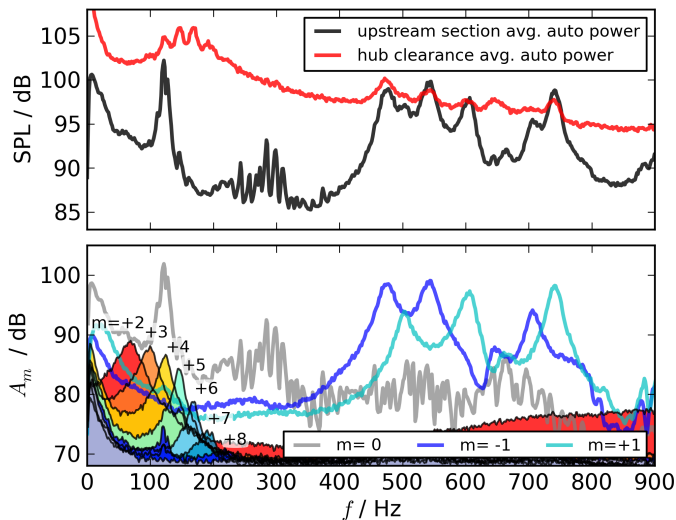


FIGURE 9: AVERAGED SPECTRA AND MODE AMPLITUDES AT TEST CONDITIONS WITH RI.

tures of the test rig and the connected piping system were identified clearly, based on extensive preliminary studies. This helped to interpret the occurring spectral properties. Unfortunately, a separation of the other broadband noise sources such as blade incident turbulence noise or trailing edge noise could not be reached. The analysis method used in this paper allows a clear detection of the RI, even if its associated modes have low amplitudes compared to other predominant spectral properties. Advantages of this analysis technique can be used in case of noisy environments or in a more reliable and earlier detection of the RI, as an assumed stall indicator. As an outlook, the mutual influence of resonances and the RI will be identified. Furthermore, a detailed investigation of the RI source mechanism and the influence of parameters will be conducted, e.g. by determining the temporal properties of each mode. Such investigations will complete the knowledge on the RI phenomenon.

ACKNOWLEDGMENT

The work presented was supported by the German Research Foundation (DFG, project: Flow induced noise in turbomachinery - The rotating instability). The experimental support by our cooperative partners at TU Berlin and helpful discussions are gratefully acknowledged.

REFERENCES

[1] J. März, C. H., and Neise, W., 2001. "An experimental and numerical investigation into the mechanisms

of rotating instability". *Journal of Turbomachinery*, **124**, pp. 367–365.

- [2] Kameier, F., and Neise, W., 1997. "Rotating blade flow instability as a source of noise in axial turbomachines". *Journal of Sound and Vibration*, **203**, June, pp. 833–853.
- [3] J.M. Liu, F. H., and Neise, W., 1996. "On the azimuthal mode structure of rotating blade flow instabilities in axial turbomachines". In 2nd AIAA/CEAS Aeroacoustics Conference; May 1996, State College PA, USA, no. AIAA 96-1741.
- [4] Mugridge, B. D., and Morfey, C. L., 1972. "Sources of noise in axial flow fans". *J. Acoust. Soc. Am.*, **51**, pp. 1411–1426.
- [5] Yamamoto, M., and Imaichi, K., 1982. "Sound power level and noise generation mechanism of axial-flow fans". *Journal of the Acoustical Society of Japan*, **3**, pp. 197–206.
- [6] Ch. Beselt, D. Peitsch, B. P., and Enghardt, L., 2011. "Strömungsinduzierter schall in turbomaschinen - die rotierende instabilität". In German Society for Aeronautics and Astronautics (DGLR), no. ID-241377, pp. 913–923.
- [7] Hellmich, B., 2008. "Acoustic resonance in a high speed axial compressor". PhD Thesis, Gottfried Wilhelm Leibniz University Hannover.
- [8] Ulbricht, I., 2002. "Stabilität des stehenden Ringgitters". PhD Thesis, Technical University Berlin.
- [9] Carolus, T., Schneider, M., and Reese, H., 2007. "Axial flow fan broad-band noise and prediction". *Journal of Sound and Vibration*, **300**(12), pp. 50 – 70.
- [10] Sijtsma, P., and Zillmann, J., 2007. "In-duct and far-field mode detection techniques for engine exhaust noise measurements". In 13th AIAA/CEAS Aeroacoustics Conference, no. 2007-3439.
- [11] Jürgens, W., Tapken, U., Pardowitz, B., Kausche, P., Bennett, G. J., and Enghardt, L., 2010. "Technique to analyze characteristics of turbomachinery broadband noise sources". In 16th AIAA/CEAS Aeroacoustic Conference; 7–9 June 2010, Stockholm, Sweden, no. AIAA 2010-3979.
- [12] Mugridge, B., 1969. "The measurement of spinning acoustic modes generated in an axial flow fan". *Journal of Sound and Vibration*, **10**(2), pp. 227 – 246.
- [13] Jacobsen, F., 2010. Propagation of sound waves in ducts. Progress report, Technical University of Denmark, Ørstedes Plads, DK-2800 Lyngby, Denmark.



EXPERIMENTAL ANALYSIS OF AERODYNAMIC NOISE GENERATION IN A ROTARY CONTROL VALVE

Stefano Malavasi

Department of Environmental, Hydraulic,
Infrastructures and Surveying Engineering
Politecnico di Milano University
Piazza Leonardo da Vinci,32 – 20133 Milano,
Italy
Email: stefano.malavasi@polimi.it

Filippo Carlo Bossi

Department of Environmental, Hydraulic,
Infrastructures and Surveying Engineering
Politecnico di Milano University
Piazza Leonardo da Vinci,32 – 20133 Milano,
Italy
Email: filippo.bossi@polimi.it

ABSTRACT

The high flow capacity of rotary control valves, increases the probability of noise generation in the plant. This paper deals with the experimental analysis of the aerodynamic noise in a rotary control valve. The experimental tests have been performed, according with the International Standards, using a pilot plant with 3" steel pipes feed by an air compression system. The characterization of the noise intensity, vibration and sound pressure has been measured by mean a PCB accelerometer and a sound level meter. Noise measurements were performed closing the test section in an anechoic chamber, expressly designed for this type of investigation. The first results of this analysis allowed the solution of a specific problem of noise generation on a real case and gave significant information on the parameters that affect the aerodynamic noise generation in this type of valves.

NOMENCLATURE

A_p	Pipe area on section 'A' [m ²]
c	Sound speed [m/s]
c_0	Sound speed of a fluid at rest [m/s]
D_p	Differential pressure measured with the pitot tube on section 'A' [Pa]
d	Hole diameter [m]
d	Pipe diameter [m]
f_c	Characteristic frequency of the peak [Hz]
Ma	Mach number [-]
p	Pressure into a fluid flow [Pa]
p_0	Pressure of a fluid at rest [Pa]
p_p	Absolute pressure on section 'A' [Pa]
Q_m	Mass flow rate [kg/s]
SPL	Sound pressure level [dB]
St	Strouhal number [-]
T_{ij}	Lighthill turbulent stress tensor [Pa]
T_p	Temperature on section 'A' [K]
t	Plate thickness [m]
V_p	Flow velocity on section 'A' [m/s]
v_i	Component of fluctuation velocity [m/s]
ε_{ij}	Strain rate tensor [s ⁻¹]

θ	Valve opening angle [°]
μ	Dynamic viscosity [Pa·s]
ρ	Density into a fluid flow [kg/m ³]
ρ_0	Density of a fluid at rest [kg/m ³]
ρ_p	Fluid density on section 'A' [kg/m ³]

INTRODUCTION

The noise level of ducts for fluid transport is a constant problem in many activities that have to do with fluid-dynamic infrastructures, such as pipelines or pneumatic systems, where the generated noise may substantially exceed the limits imposed by law. This is true especially when specific devices, such as control valves, are installed to control the flow. The control of the flow is indeed provided by an abrupt energy dissipation that is obtained through a local increase of the flow turbulence.

According to the Analogy of Lighthill [1-2] the emission of noise in a compressible flow is related to turbulence. The Lighthill's formulation is based on the principle that the turbulence involves the transformation of part of the fluid mechanical energy in sound energy, which propagates in the surrounding as a wave. The idea of Lighthill made an advance in noise knowledge and it is at the basic of the modern Vortex Sound Theory [3]. The effect of turbulence on noise production therefore can be expressed by a particular stress tensor, said Lighthill turbulent stress tensor, in which are considered the contributions of the Reynolds stress, the surplus of momentum and the effects of noise attenuation due to viscosity. T_{ij} expression is presented in Eqn. (1):

$$T_{ij} = \rho v_i v_j + [(p - p_0) - c_0^2 (\rho - \rho_0)] - 2\mu \varepsilon_{ij} \quad (1)$$

Generally, the difficulties in determining the Reynolds stress and the viscosity attenuation allow to evaluate T_{ij} only when those terms are negligible. In this case the sound pressure level is simply given by the transformation of the momentum surplus into pressure fluctuations.



FIGURE 1: 3" MODEL VALVE'S TRIM

Since the Analogy of Lighthill was originally formulated by considering free jets, when the noise of confined flows is investigated, it is necessary to consider other sources of noise in addition to the "free" turbulence, such as: the mechanical response of the structure to the fluid excitation and the whistling effects due to the particular design of the boundary (cavity and holes) [3].

Inside of a pipeline therefore the noise prediction could be a very tricky problem. The turbulent structures can interact each others, with pipeline and control devices or, in the case of supersonic regime, with the shock waves. To each type of interaction a different value of sonic emission could be associated. These sonic emissions have different efficiencies depending on the Mach number of the flow [4]. This allows to explain the sudden reinforcing of a sonic frequency compared to the others and also the simultaneous presence of several characteristic frequencies which may constitute the sound emission. The fluid-structure interactions can also generate reinforcing phenomena, due to resonance, leading to the occurrence of a single-frequency emission (whistle) [5]. This is the case of a flow over a cavity [6-7]. The whistle can be generated at low Mach number and its characteristics change with the cavity shape and flow speed [8].

Despite all the advance of the theoretical knowledge, noise prediction models still remain an open issue. The greatest gap between theory and applications is represented by the turbulence field, which is generally unknown and unpredictable. To overcome this problem, the noise predictions for fluid-dynamic devices are based on theoretical and empirical knowledge validated by experimental evidences (i.e. IEC 60534-8-3 standards). The method proposed by the International Standards however is limited by the range of applicability of the experimental evidences and does not guarantee, in general, a sufficiently accurate estimation of sound pressure levels for equipments different from those experimentally investigated. Specific trims may be particularly noisy under some working conditions or generate an unexpected noisy whistle which brings the noise level over an acceptable limit.

The study presented in this paper originates from a real case of single-frequency noise generated by a gas

pipeline regulated by a rotary control valve with perforated plates inside the trim. Using accelerometers and sound level meters was possible to reconstruct the acoustic field of the pipeline and identify the whistle characteristic emission frequency (ranging from 1170 to 2500 Hz) proportionally increasing with the pipeline flow conditions. In particular the Beamforming technique was used to determine the sonic source. This technique starts from the sound level meter signals, perceived by a microphone array fixed to a frame, whose geometry has to be properly designed, and reconstructs the sound field in each location within a pre-defined region space [9]. As location algorithm was used the Delay & Sum algorithm. It combines (Sum) the acoustic measurements, taking into account the different acoustic paths (Delay) between the suspected source locations and the measurement points [10], the resulting effect is:

- if the focused location corresponds to an actual sound source, the algorithm performs a constructive sum and the output is equal to the actual source SPL;
- if the location doesn't correspond to a source, the sum is destructive and the output is attenuated.

Thanks to the previous information taken on the gas pipeline, it was possible to reproduce the single-frequency noise on a 3" simplify model of the real valve (Fig.1). Moreover, laboratory investigations allowed the study of the influence of different geometrical parameters of the valve, such as: hole's diameters of the perforated plates placed inside the trim and the travel of the valve [11]. The analysis of the experimental evidences will be presented after the experimental setup description.

EXPERIMENTAL SETUP

The experimental tests have been performed, according to the International Standards, using a pilot plant realized at PIBIVIESSE Srl in Nerviano (Italy) (Fig. 2). It has been designed and implemented within a research program between Politecnico of Milano and PIBIVIESSE. The plant, composed with 0.0762 m (3") steel pipes and 10 m long, is fed by an air compressor system able to guarantee pressures up to 9.5 bar at the reference section upstream the test section. Control valves placed upstream and downstream the test section allow the setting of the proper fluid-dynamic conditions for each experimental test. Sections 'A' and 'D' are fixed, while the others can be replaced for testing devices of different diameters. So that, both diameters (of sections and device) are kept constant to maintain flux uniformity. Section 'A' is provided with a pressure tap, a pitot tube and a thermocouple respectively at $52d$, $55d$ and $58d$ of its total length ($60d$). Section 'B' is $30d$ long to avoid any flux interference due to the pitot tube and is equipped with a thermocouple, at $26d$, and a pressure tap, three diameters

farthest. Section 'C' (20d) has four pressure taps (at 3d, 6d, 12d e 15d) and a thermocouple at 9d. The last section is 9d long and both a thermocouple and a pressure tap are set on it. The silenced outlet is at atmospheric pressure.

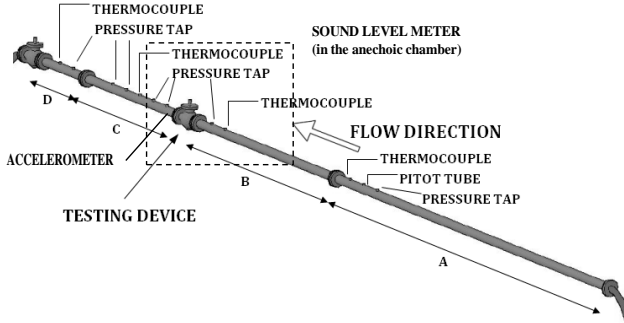


FIGURE 2: EXPERIMENTAL APPARATUS

Measures of pressure, temperature, mass flow rate and noise can be performed on the apparatus. Several instruments have been used during the test; the following provides all the equipment used (precisions are in Tab. 1):

- an high precision absolute pressure transducer 0-10 bar by TecSis mod. P3290S075020;
- two absolute pressure transducer 0-10 bar by TecSis mod. P3276S075801;
- an absolute pressure transducer 0-2 bar by TecSis mod. P3276S075801;
- a differential pressure transducer 0-10000 Pa by Furness Controls mod. 352;
- a differential pressure transducer 0-150 Pa by Furness Controls mod. 352;
- a differential pressure transducer 0-1 bar by Lektra mod. WT2000DP5S;
- four k-type thermocouples;
- a multihole pitot tube by Furness Controls mod. FCO68;
- a single point pitot tube by Furness Controls mod. FCO65;
- a sound level meter by Larson Davis mod. LXT with a 1.27 cm (1/2") microphone by PCB mod. 377B02;
- an accelerometer by PCB mod. 352A60.

The acquisition of each instrument signal is made using the Lab View software, setting the necessary parameters (sampling rate, and transfer functions). The signals of the three instruments on section 'A' are used to determine the mass flow (Q_m) and then, inverting Eqn. (2), the flow velocity is analytically determined in each point where pressure, temperature and pipe area are known.

$$Q_m = \rho_p \cdot A_p \cdot V_p \quad (2)$$

In Equation 2, the subscript 'p' indicates the quantity measured in the pipe section 'A', the flow density and the flow velocity are defined by the following Equations

$$\rho_p = \frac{P_p}{287 \cdot T_p} \quad (3)$$

$$V_p = \sqrt{\frac{2 \cdot D_p}{\rho_p}} \quad (4)$$

and A_p is the area of the pipe. Noise measurements were performed closing the test section in an anechoic chamber and acquiring the accelerometer and sound level meter signals. The sound level meter can perform measures of sound pressure level (dB) and pressure fluctuations.

TABLE 1: INSTRUMENT PRECISION

Instrument	Measurement Range	Precision
TecSis mod. P3276S075801	0-10 bar	0.25% of F.S. ± 0.03 bar
TecSis mod. P3276S075801	0-2 bar	0.25% of F.S. ± 0.03 bar
TecSis mod. P3290S075020	0-10 bar	0.1% of F.S.
Furness Controls Mod. 352	0-150 Pa	0.25% of the lecture for $\Delta p \geq 15$ Pa for $\Delta p < 15$ Pa ± 0.0375 Pa
Furness Controls Mod. 352	0-10000 Pa	0.25% of the lecture for $\Delta p \geq 1000$ Pa for $\Delta p < 1000$ Pa ± 2.5 Pa
Lektra WT2000DP5S	0-1 bar	0.44% F.S.

RESULTS

In this paper are presented the results of an experimental investigation on the acoustic emission due to the interaction between an air flow and coupled perforated plates within a rotary control valve. In each test the pressure upstream the valve was kept constant to 50000 Pa and were changed the mass flow rate, the diameter of the plate holes and the opening angle of the valve.

The first step of the experimental investigation was focus on the reproduction of the whistle evidenced in the gas pipeline on a 3" simplify valve model. After that, within the limit of the experimental set-up, we have investigated the dependence of the single-frequency emission (whistle) on the Mach number, on the holes diameter and on the travel range of the valve.

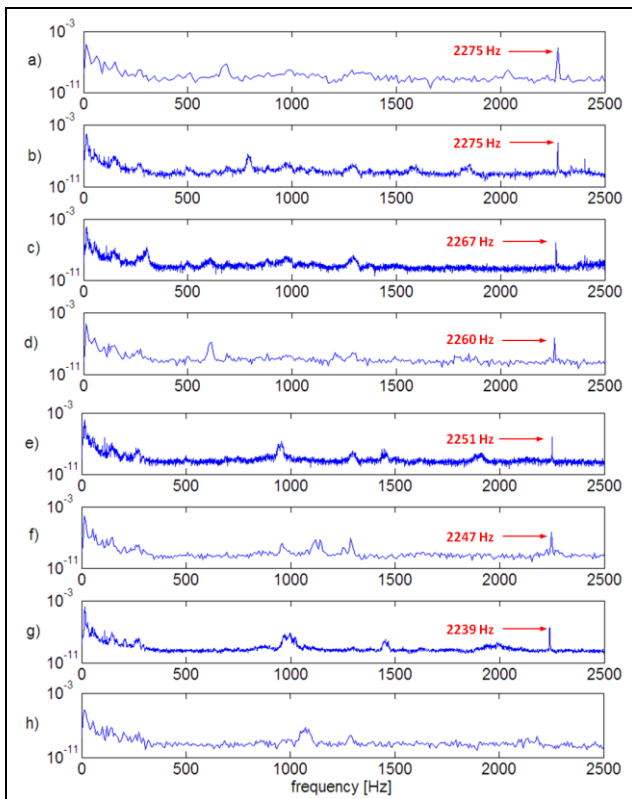


FIGURE 3: PSD OF THE PRESSURE FLUCTUATION SIGNAL FOR $d=0.004\text{m}$, $\theta=90^\circ$, MACH NUMBER: a) 0.091, b) 0.089, c) 0.084, d) 0.078, e) 0.067, f) 0.061, g) 0.052, h) 0.038.

Figure 3 reports the power spectral density (PSD), obtained by Welch’s method, of the pressure fluctuations acquired with the sound level meter placed in the anechoic chamber versus the Mach number of the flow referred to the pipe velocity. The case is set on a full open valve with two perforated plates placed parallel to the flow direction. The plate thickness was of 0.005 m and the holes diameter was $d=0.004\text{m}$. The figure evidences the presence of a well recognizable single-frequency emission (whistle) at about 2275Hz ($\text{Ma}=0.091$). This whistle, which was clearly audible during the lab test evidences the same characteristic frequency of the whistle acquired on the gas pipeline mentioned before. The emission frequency and the intensity, of the whistle of Figure 3, decrease with Mach number and disappear for $\text{Ma}=0.038$. The same behavior was observed by considering the accelerometer signal as it is shown in Figure 4. The parallel analysis of the sound level and accelerometer signals gave us a better understanding and control of the phenomenon. It was repeated for each of the following analysis with comparable results.

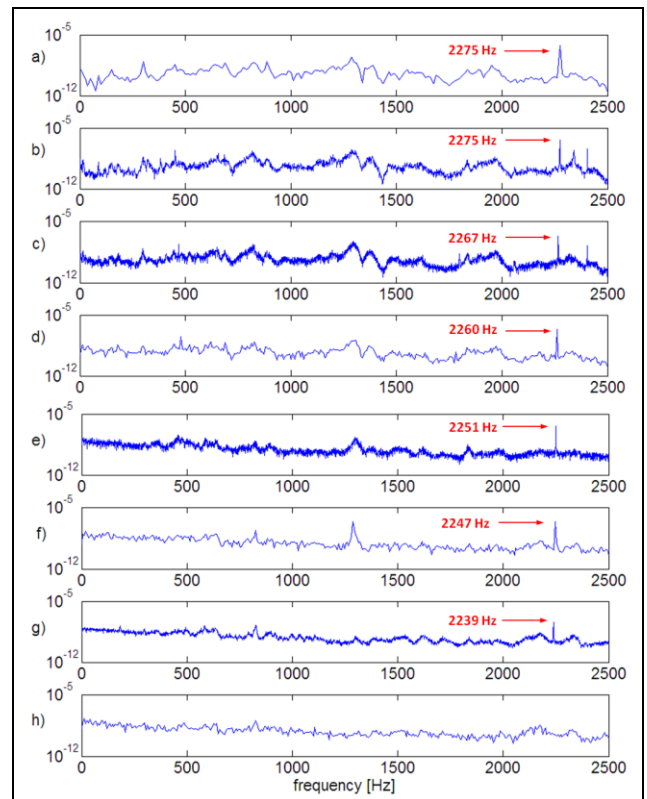


FIGURE 4: PSD OF THE ACCELEROMETER SIGNAL FOR $d=0.004\text{m}$, $\theta=90^\circ$, MACH NUMBER : a) 0.091, b) 0.089, c) 0.084, d) 0.078, e) 0.067, f) 0.061, g) 0.052, h) 0.038.

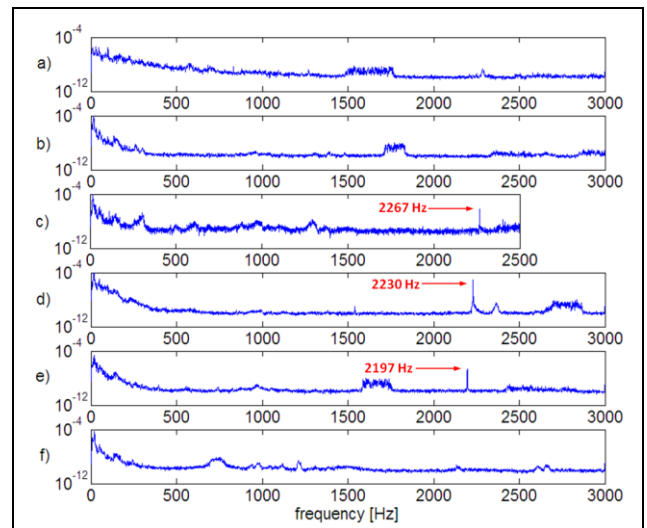


FIGURE 5: PSD OF THE PRESSURE FLUCTUATION SIGNAL FOR $\text{Ma} \approx 0.085$, $\theta = 90^\circ$ FOR: a) no holes, b) $d=0.003\text{m}$, c) $d=0.004\text{m}$, d) $d=0.005\text{m}$, e) $d=0.006\text{m}$ and f) $d=0.008\text{m}$

In Figure 5 is analyzed the influence of the holes dimension on the noise emission for the full open configuration ($\theta = 90^\circ$). For a quasi constant value of the Mach number ($Ma \approx 0.085$) the figure reports the power spectral density (PSD) of the pressure fluctuations for a plate without holes and for 5 different plate with holes of diameters having ranges between $d=0.003\text{m}$ and $d=0.008\text{m}$, maintaining the same porosity. In this cases (Fig.5), the whistle is detected only for a holes diameter equal to 0.004m , 0.005m and 0.006m and, in this range, the frequency of the peak decreases with the increases of the holes diameter. This can be related with the vortex shedding frequency: the greater is the hole the lower is the shedding frequency. Furthermore, while the whistle absence for plates with no holes was predictable, the behavior of $d=0.003$ and 0.008m is unexpected. For $d = 0.008\text{m}$, it could probably be due to the limited flow speed available in the experiment set-up; for $d=0.003\text{m}$ it could be related to the aspect ratio of the holes that changes because we maintained constant the plate thickness.

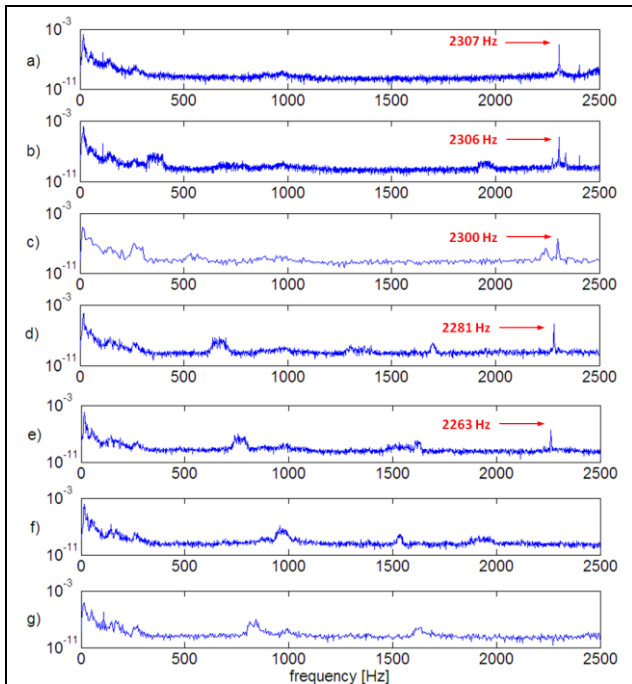


FIGURE 6: PSD OF THE PRESSURE FLUCTUATION SIGNAL FOR $d = 0.004\text{m}$, $\theta = 80^\circ$, MACH NUMBER: a) 0.091, b) 0.089, c) 0.085, d) 0.079, e) 0.068, f) 0.061, g) 0.052

Changing the travel of the valve, it is possible to observe a different behavior of the sonic emission both changing the Mach number and the design of the plates. Figure 6 reports the power spectral density (PSD) of the pressure fluctuations versus the Mach number for the case of travel $\theta = 80^\circ$. On the figure can be observed that the behavior of the position of the noise pick is not very

different by those observed in Figure 3. The position of the pick assumed a greater value than the corresponding pick of Figure 3, but decreasing the Mach number the presence of the whistle disappears before. The whistle is absent for Mach number lower than $Ma=0.079$.

We experimentally investigate same travel lower than $\theta=80^\circ$, but starting to $\theta=70^\circ$ in the experimental range of Mach number available, we did not record the presence of whistles.

The effects of the plate design on the whistle presence are also considered for the case of 80° travel.

As before considered in Figure 5, for a quasi constant value of the Mach number ($Ma \approx 0.085$) the Figure 7 reports the power spectral density (PSD) of the pressure fluctuations for 5 different plates with the same porosity and with the holes of diameters $d=0.003$, 0.004 , 0.005 , 0.006 , 0.008 m . In this case we observe that the frequencies of the whistles increase. Moreover it is possible to observe that in this case a whistle with a significant pick is present also for the case of $d=0.008\text{m}$.

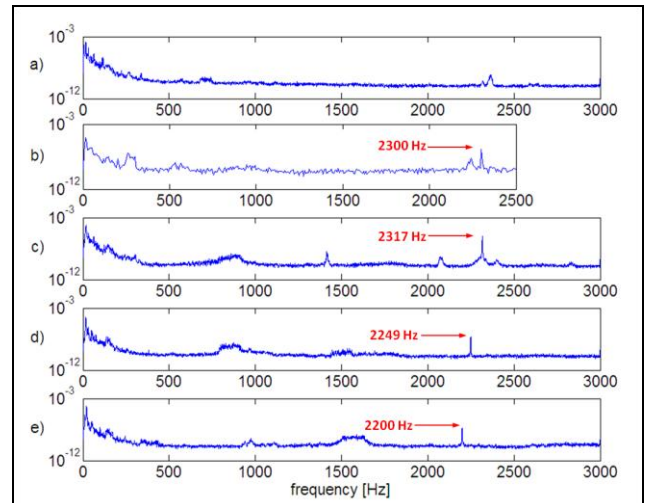


FIGURE 7: PSD OF THE PRESSURE FLUCTUATION SIGNAL FOR $M \approx 0.085$, $\theta = 80^\circ$ FOR: a) $d = 0.003\text{m}$, b) $d=0.004\text{m}$, c) $d=0.005\text{m}$, d) $d=0.006\text{m}$ and e) $d=0.008\text{m}$

Even if, with these first experimental results, we are not able to give a complete description of the phenomenon, some analogies with the phenomenon of flow over cavity can be discussed. As depicted in Figure 8, the flow over a cavity induced vortex generation on the upstream edge (A); when the vortices impacting on the downstream edge of the cavity (B) they generate a sound. The sound waves generated by the impact of the vortices propagate up to the leading edge and increase the vortices generation. The phenomenon is reinforced and therefore gives rise to a particularly intense sound source characterized by a specific frequency.

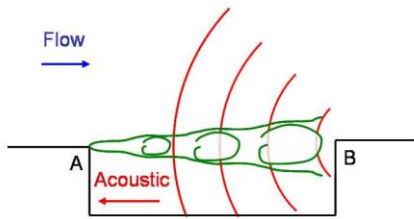


FIGURE 8: WHISTLER MECHANISM PRODUCTION GENERATED BY A FLOW OVER CAVITY

Starting by this analogy, we tried to correlate the frequency peak and the flow speed by means of the Strouhal number based on the frequency of the whistle (f_c), the hole diameter (d) and the flow velocity (V_p) as reported in the following equation:

$$St = \frac{f_c \cdot d}{V_p} \quad (5)$$

Figure 9 shows the behavior of the Strouhal number when the Mach number changes within our experimental range. The legend divides the series on the base of the hole's aspect ratio and on the travel of the valve.

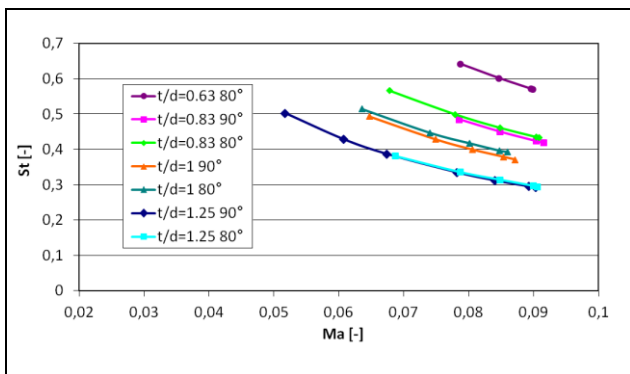


FIGURE 9: STROUHAL NUMBER VERSUS THE MACH NUMBER FOR DIFFERENT HOLE ASPECT RATIO t/d

The minimum Mach values of every series represent the threshold for the whistle perception, the maximum Mach values are the plant limit. The Strouhal number represents the dimension of vortex structures, as result the vortex structure increases proportionally with the diameter and inversely with the Mach. Similar results was found by Rowley et al. [5], though significant differences exist between the respective experiments. In fact, in our case cavities go through the whole plate, there are several holes close together and the plates are coupled.

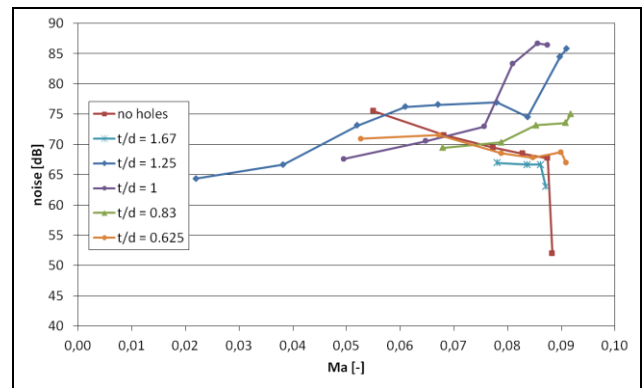


FIGURE 10: SPL FOR $\theta = 90^\circ$ AT DIFFERENT MACH VALUES AND HOLE DIAMETERS

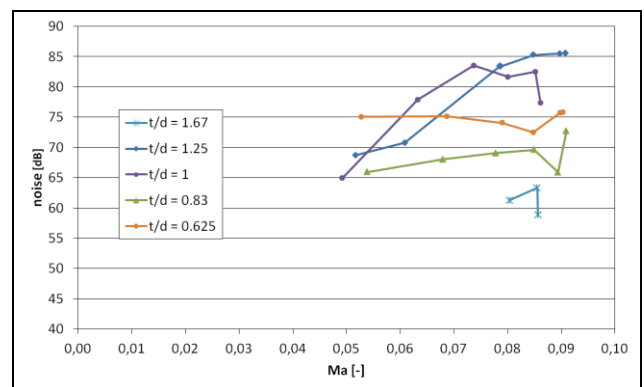


FIGURE 11: SPL FOR $\theta = 80^\circ$ AT DIFFERENT MACH VALUES AND HOLE DIAMETERS

About the overall noise produced by the different configurations, the interpretations of the preliminary records are not so clear. As shown in Figures 10 and 11, it seems that for the whistling cases there is an increase in the SPL detected by the sound level meter but the trend is not always concordant. This can be due to some experimental uncertainties for example related to the correct use of the anechoic chamber (i.e. external noise recorded into the chamber) or to significant differences in the frequency spectrum placed over the 3000 Hz limit imposed by the acquisition frequency that was limited to 6000 Hz by the experimental set-up.

CONCLUSIONS

The experimental analysis has shown that, in the cases considered of control device, the relevance of the fluid-structure interaction is significant and causes the strengthening of a single frequency noise generating a whistle that increases the noise level to unacceptable levels. The results of this work have provided interesting suggestions for the practical solution of specific noise problems which affect this type of device. Moreover, the

dependence of the whistle frequency on the dimension of the hole diameter is a significant result for the optimization of these trims. By the scientific point of view, the geometry of the system should be simplified to better understand the influence of the main significant parameters involved. For example, the use of a single plate and the changing of the plate thickness are the first improvements to be considered on the experimental set-up. Finally, also the use of numerical simulation to study in more detail the flow field generated inside the valves could be important to help the comprehension of the phenomenon.

ACKNOWLEDGMENTS

The authors thank PIBIVIESSE SpA, providing the structure and tools used in laboratory tests, and the Ing. Ilaria Colpo, for the energy devoted to the research.

REFERENCES

- [1] Lighthill, M.J., 1952, "On sound generated aerodynamically. I. General Theory". *Proceedings of the Royal Society of London*, London, United Kingdom, Vol. **211**(1107), pp. 564-587.
- [2] Lighthill, M.J., 1954, "On sound generated aerodynamically. II. Turbulence as a source of sound". *Proceedings of the Royal Society of London*, London, United Kingdom, Vol. **228**(1148), pp. 1-32.
- [3] Howe, M.S., 2003, "Theory of vortex sound", Vol. **33** of *Cambridge texts in applied mathematics*. Cambridge University Press, Cambridge, United Kingdom.
- [4] Bies, D.A. and Hansen, C.H., 2009, "Engineering noise control: Theory and practice", 4th ed. Spon Press, Abingdon, United Kingdom.
- [5] Rowley, C.W., Colonius, T. and Basu, A.J., 2002, "On self-sustained oscillations in two-dimensional compressible flow over rectangular cavities". *Journal of Fluid Mechanics*, Vol. **455**(1), pp. 315-346.
- [6] Howe, M.S., 1997, "Edge, cavity and aperture tones at very low Mach numbers". *Journal of Sound and Vibration*, Vol. **330**, pp. 61-84.
- [7] Howe, M.S., 2004, "Mechanism of sound generation by low Mach number flow over a wall cavity". *Journal of Sound and Vibration*, Vol. **273**(1-2), pp. 103-123.
- [8] Kook, H. and Mongeau, L., 2002, "Analysis of the periodic pressure fluctuations induced by flow over a cavity". *Journal of Sound and Vibration*, Vol. **251**(5), pp. 823-846.
- [9] Cigada, A., Ripamonti, F. and Vanali, M., 2007, "The delay & sum algorithm applied to microphone array measurements: Numerical analysis and experimental validation". *Mechanical System and Signal Processing*, Vol. **21**(6), pp. 2645-2664.
- [10] Cigada, A., et al., 2008, "Moving microphone arrays to reduce spatial aliasing in the beamforming technique: Theoretical background and numerical investigation". *Journal of Acoustical Society of America*, Vol. **124**(6), pp. 3648-3658.
- [11] Colpo, I., 2011, "Valvole di regolazione a sfera: Caratterizzazione fluidodinamica e generazione di rumore aerodinamico". Master Thesis, Politecnico di Milano, Milano.



Experimental and Numerical Investigations of Self-Excited Vibration of Steam Control Valves

Koichi Yonezawa

Graduate School of Engineering Science
Osaka University
1-3, Machikaneyama-cho, Toynaka, Osaka, Japan
Email: yonezawa@me.es.osaka-u.ac.jp

Yoshinobu Tsujimoto

Graduate School of Engineering Science
Osaka University
1-3, Machikaneyama-cho, Toynaka, Osaka Japan

Takahide Endo

Tokyo Electric Power Company
4-1, Egasaki-cho, Tsurumi-ku Yokohama,
Kanagawa, Japan

Kenichi Tezuka

Tokyo Electric Power Company
4-1, Egasaki-cho, Tsurumi-ku Yokohama,
Kanagawa, Japan

ABSTRACT

Experimental and numerical investigations of unsteady transonic flows and flow-induced vibration of venturi type control valves are carried out. For test valves, three kinds of valve heads are examined. With rigidly supported valve heads, unsteady flow characteristics are investigated experimentally and numerically. Results show that the transonic separated jet around the valve head fluctuates with several kinds of fluctuation modes. With flexibly supported valve heads, characteristics of flow-induced vibrations are investigated. Experimental results show that the self-excited valve vibrations can take place at a certain range of operation condition. Numerical simulations are carried out under forced valve head oscillation in order to estimate fluid forces and fluid force moments. Results show that the lateral forces and moments on the valve head may provide negative damping.

NOMENCLATURE

C	Added damping coefficient
A	Valve head displacement in y - z plane
D_s	Valve seat diameter
ε	Valve head whirling radius
ε_L	Valve opening ratio, x_L/D_s
F_n	Fluid force in radial direction
F_t	Fluid force in tangential direction
K	Added stiffness coefficient
M_n	Fluid force moment in radial direction
M_t	Fluid force moment in tangential direction
p_0	Inlet total pressure
p_b	Back pressure
ω	Angular frequency of valve head vibration
x	Coordinate in axial (longitudinal) direction

x_L	Valve head lift
y, z	Coordinates in lateral to x axis
ψ_p	Pressure ratio, p_b/p_0

INTRODUCTION

In nuclear and thermal power plants, various kinds of valves are used. Venturi type valves are adopted for control valves of main steam flow from steam generators to power turbines. The function of the main control valve is to control the steam flow rate during startup and shutdown transients of the power plants. During the throttle operation of the control valve, however, it is known that high level pressure fluctuations may take place due to flow fluctuations around the valve. Such flow fluctuations can cause serious noise and vibration.

Experimental and numerical investigations have been carried out in order to understand unsteady flow characteristics around the valve [1]-[6]. In these studies, it has been clarified that a separated transonic jet around the valve head fluctuates at random and high level pressure pulsations are observed around valve head and valve seat. Shioyama et al.[7] have carried out investigation of characteristics of acoustics and downstream pipe vibrations and have reported that the vibration of the downstream pipe is caused by the resonance of higher order eigen modes of the pipe wall and acoustic modes in the cross section of the pipe. Widel [8] and Zhang [9][10] have reported that valve head support shafts have been damaged by dynamic fluid forces due to flow fluctuations.

Authors have carried out experimental and numerical investigations of a flow-induced vibration of the valve head [6][11]. In these investigations, the valve head is excited with fixed frequencies and displacement amplitudes and dynamic fluid forces are examined. According to both experimental and numerical results, the

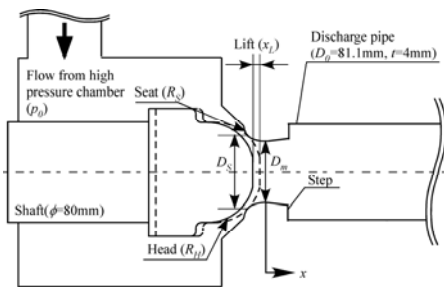


Fig. 1 Test valve with rigid support shaft

Table 1 Dimensions of test valve

Seat diameter, D_s	62.4 mm
Minimum diameter downstream of valve, D_m	52 mm
Diameter of downstream pipe	81.9 mm
Length of downstream pipe	1800mm
Curvature radius of head surface	43.7 mm
Curvature radius of seat surface	12 mm

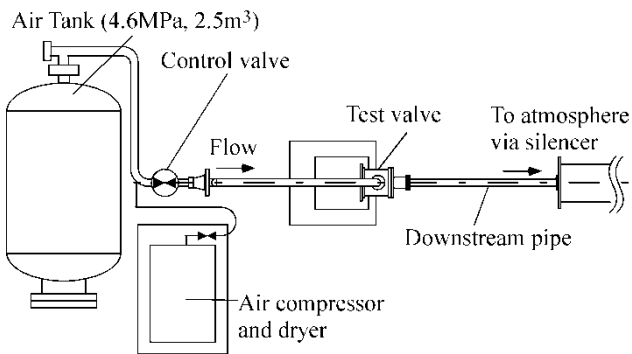


Fig. 2 Test facility

lateral fluid force provides the negative damping. In the present study, influences of valve head contours are discussed by comparing three kinds of valve head. Fundamental flow characteristics around the valve head are examined with rigidly supported valve head. Flow induced vibration of the valve head are observed with flexibly supported valve head. Numerical simulations are carried out in order to clarify characteristics of flow patterns and fluid forces. In addition to fluid forces, influences of fluid force moments are also taken into account.

EXPERIMENTAL SETUP

Schematic of a test valve and main dimensions are shown in Fig. 1 and Table 1. The valve head is supported by the shaft and the flow rate can be adjusted by shifting the valve head. The operation conditions are defined by following two parameters:

$$\epsilon_L = x_L / D_s \quad \dots(1)$$

$$\psi_p = p_0 / p_b \quad \dots(2)$$

ϵ_L in Eq. (1) is valve opening ratio and is defined as the ratio of the valve head opening, x_L and the valve seat

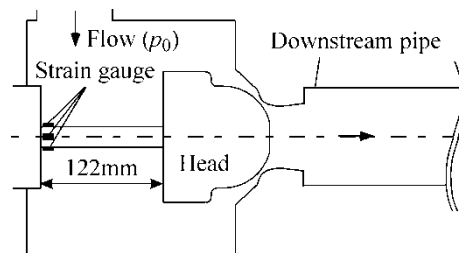


Fig. 3 Test valve with flexible support shaft

Table 2 Specifications of Flexible shafts A and B

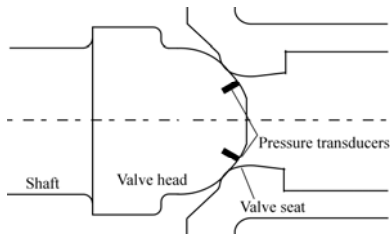
		Shaft A	Shaft B
Inner diameter		10	20
Outer diameter		14	24
Natural frequency	Original valve head	60.8	29.3
	Flat/Wedge valve head	97.7	39.1

diameter, D_s . The pressure ratio ψ_p in Eq. (2) is defined as the ratio of the inlet total pressure, p_0 and back pressure, p_b .

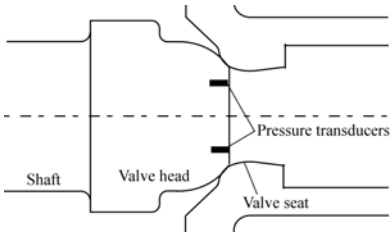
The test facility is shown in Fig. 2. It is a blow-down type wind tunnel. The working fluid is dry air stored in an air tank. The inlet pressure is kept less than 1.0 MPa with a magnetic control valve. The working fluid from the test valve is discharged to atmosphere via a silencer with the diameter of 500mm. The inlet pressure is measured at the side of the valve case with a pressure transducer (Kyowa electronic instruments, PH-10KB). The back pressure is atmospheric.

Two kinds of support shafts are used. The first one is the rigid shaft as shown in Fig. 1. The rigid shaft is made of steel and with the diameter of 80mm. The second shaft is a flexible one which is shown in Fig. 3. Specification of the flexible shaft is shown in Table 2. With the rigid shaft, flow fluctuations without the valve head vibration are observed. With the flexible shaft, the flow-induced vibration of the valve head is observed. With the flexible shaft, the displacement of the valve head is estimated from the strains of the shaft measured with the strain gauges put in the vicinity of shaft root.

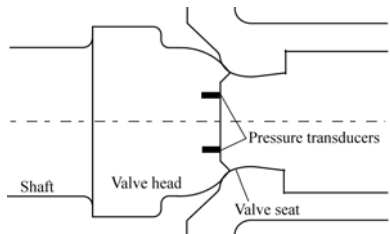
Three valve heads shown in Fig. 4 are used in order to compare the characteristics of flow fluctuation and flow-induced vibration of the valve head. The original valve head in Fig. 4 (a) is similar to the one in the real power plants [7]. The second one in Fig. 4 (b) is named “flat valve head” and is made by cutting the tip of the original valve head. The third one in Fig. 4 (c) is named “wedge valve head” and is made by cutting the flat valve head furthermore. The wedge valve is similar to the modified valve head contour in the study by Araki et al.[1] For these valve heads, the same valve seat is used. Four flush mount pressure taps are located on the valve head surface at each 90 degrees in circumferential direction and are named “A1” through “A4”. Unsteady pressure fluctuations are measured with semiconductor pressure transducers (KULITE, CT-190-100A).



(a) Original valve head

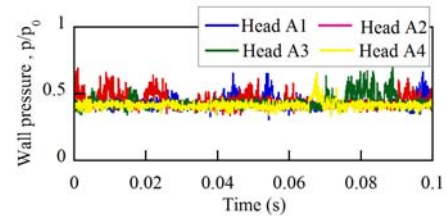


(b) Flat valve head

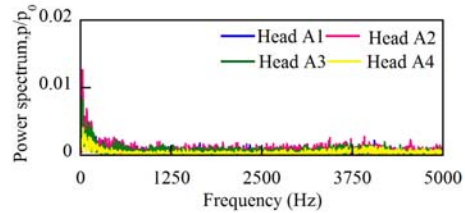


(c) Wedge valve head

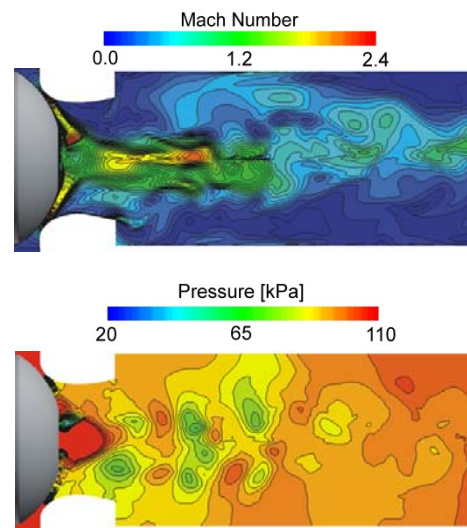
Fig. 4 Three kinds of test valve head



(a) Time history of pressure fluctuation (Measurement)



(b) Spectral analysis (Measurement)



(c) Mach number and pressure distribution (CFD)

 Fig. 5 Random flow fluctuation (Original valve head, $\varepsilon_L=0.046$, $\psi_p=0.51$)

CHARACTERISTIC OF FLOW FLUCTUATION

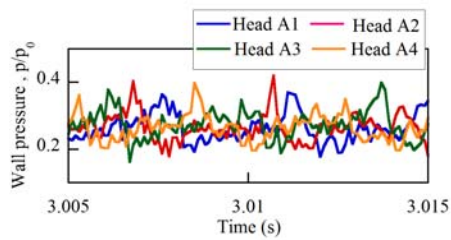
The characteristics of flow fluctuations have been examined with the rigid supported shaft. Unsteady numerical simulations with the validated code [11] were made in order to understand flow pattern around the valve. According to the pressure fluctuation patterns the flow fluctuation patterns are classified into three kinds as follows:

i) Random flow fluctuation

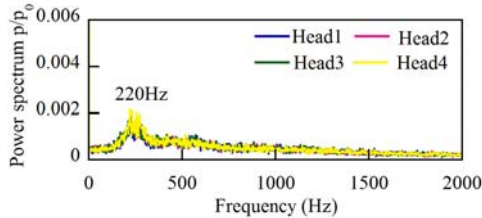
Figure 5 shows experimental and numerical results with the original valve head for a condition at which the random flow fluctuation takes place. The wave forms of pressure fluctuations measured at four points A1 through A4 show random pattern and no spectral peak is observed as shown in Fig. 5 (a) and (b). Similar spectra were obtained from the numerical simulation. Figure 5 (c) shows instantaneous Mach number and pressure distributions obtained by the numerical simulation. The numerical result shows that the pressure fluctuation observed on the valve head surface is caused by the fluctuation of the separated supersonic jet. Around the reattachment point of the separated jet, a high pressure region occurs due to the shock-boundary layer interaction. The random flow fluctuation pattern is also observed in the experiments with the flat valve head and the wedge valve head.

ii) Periodic asymmetric flow fluctuation

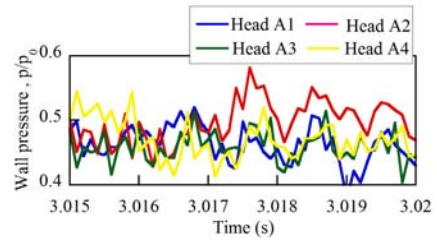
With the flat valve head and the wedge valve head, a periodic pressure fluctuation propagating in the circumferential direction is observed. Time histories and spectra of the pressure fluctuation measured at points A1 through A4 are shown in Fig. 6. According to Fig. 6(a), it can be seen that the pressure peak propagates A4→A3→A2→A1 and amplitudes of the pressure fluctuation are comparable with those of the random flow fluctuation. The spectral analysis in Fig. 6 (b) shows an obvious spectral peak at 220Hz and the phase differences between each two neighboring point have been confirmed to be approximately 90°. Similar spectra were obtained from the numerical simulation. The numerical results in Fig. 6 (c) shows the high pressure region rotates on the valve head associating with the fluctuation of the separated jet in circumferential direction. Such periodic asymmetric flow fluctuation has been observed at low pressure ratios in the experiment with the flat and the wedge valve heads but



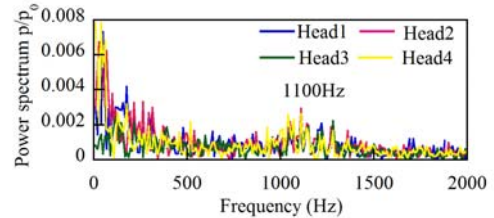
(a) Time history of pressure fluctuation (Measurement)



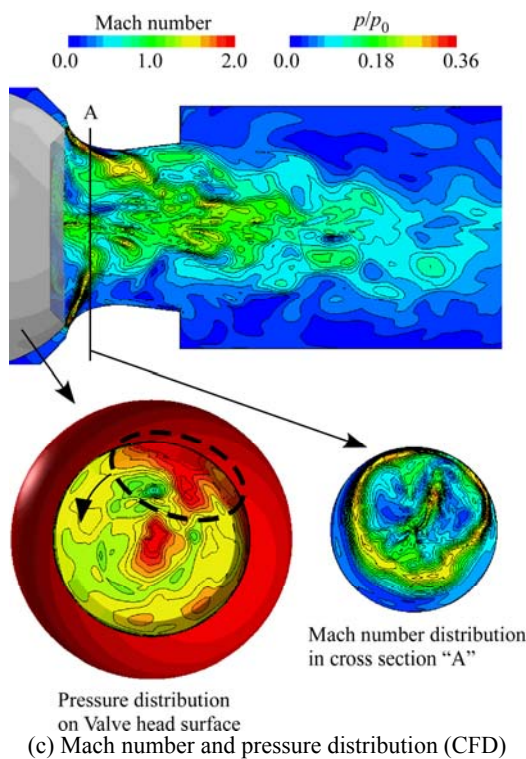
(b) Spectral analysis (Measurement)



(a) Time history of pressure fluctuation (Measurement, $\psi_p=0.50$)



(b) Spectral analysis (Measurement, $\psi_p=0.50$)



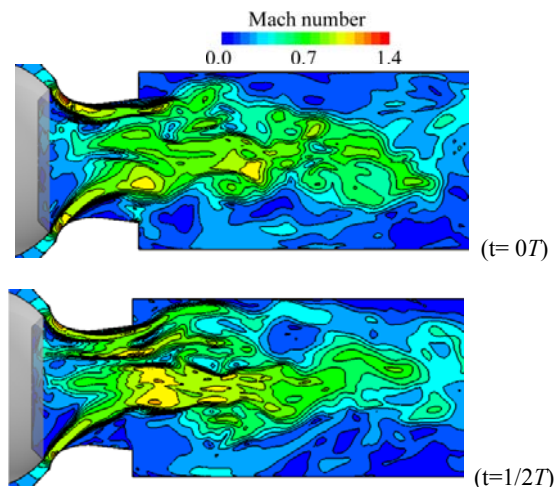
(c) Mach number and pressure distribution (CFD)

Fig. 6 Wall pressure measurement of periodic and asymmetric flow fluctuation. (Wedge valve head, $\epsilon_L=0.025$, $\psi_p=0.3$)

not with the original valve head. Frequencies vary from 100Hz to 500Hz depending on operating conditions. iii) Periodic symmetric flow fluctuation

In Fig. 7, pressure measurements and their spectra shows periodic pressure fluctuation with small phase differences between four points A1-A4. The numerical result shows that the asymmetric separated jet fluctuates in axial direction and the jet directions are almost fixed. Such a flow fluctuation pattern has been observed with the wedge valve head at large valve opening ratios and high pressure ratios. It has been observed that the frequencies increase as pressure ratios decreases from 700 to 1200Hz.

In Fig. 8, flow fluctuation patterns are shown in $\psi_p-\epsilon_L$



(c) Mach number and pressure distribution (CFD, $\psi_p=0.62$, Frequency=1170Hz and period, $T=8.5 \times 10^{-4}$ s)

Fig. 7 Wall pressure measurement of periodic and asymmetric flow fluctuation. (Wedge valve head, $\epsilon_L=0.068$)

plane. For the original valve head, the random flow fluctuation (i) are observed. For the flat and the wedge valve heads, in Fig. 8 (a) and (b), at the pressure ratio lower than the dashed line, the jet separates from the valve head and the valve seat at the pressure ratio lower than the dashed line. At the pressure ratio higher than the dashed line, the flow attaches on the valve seat and the pressure fluctuation level is much lower. For the flat valve head, the periodic pressure fluctuation is observed above the dashed line but the amplitudes are small. The periodic asymmetric flow fluctuation with large amplitude (ii) is observed at the pressure ratio less than and in the vicinity of the dashed line for the flat and the wedge valve heads. The symmetric flow fluctuation (iii) is observed at the large valve opening ratio for the wedge valve head. Comparing three valve heads, the region at which the flow fluctuations take place is the largest for the flat valve head and is the smallest for the wedge valve head. It is confirmed that flow fluctuations are suppressed with the wedge valve head as Araki et al. [1] have reported.

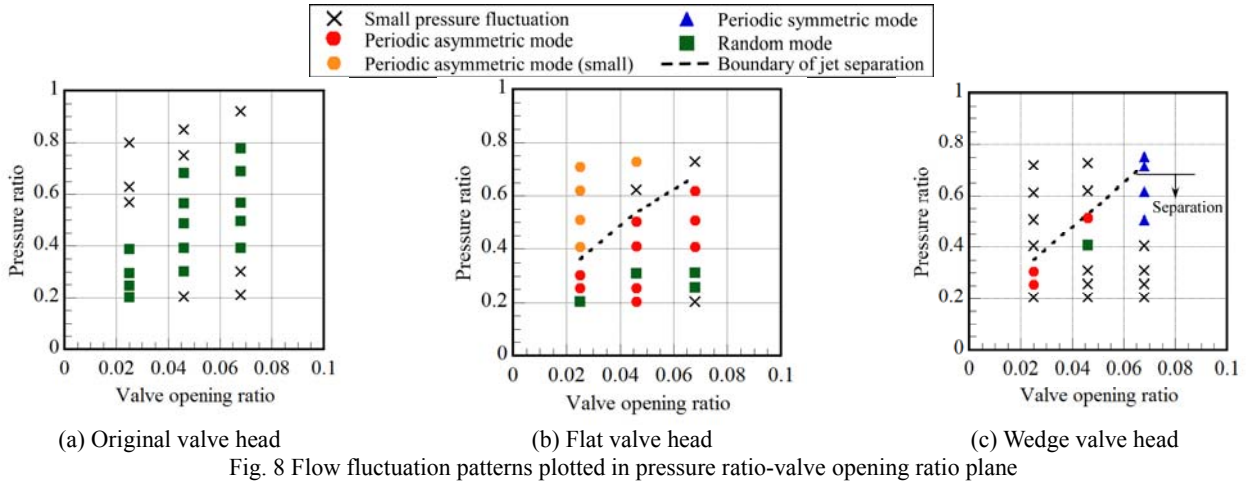
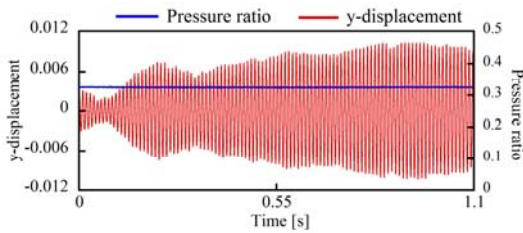
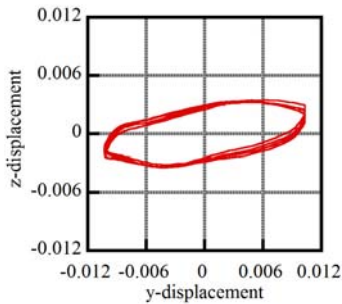


Fig. 8 Flow fluctuation patterns plotted in pressure ratio-valve opening ratio plane



(a) Time histories of valve head displacement and pressure ratio



(b) Lissajous curve of valve head displacement (0.9s - 0.95s)
 Fig. 9 Valve head displacement (Measurement of Wedge valve head at $\varepsilon_L=0.025$, $\psi_p=0.33$ with shaft A, Displacements are normalized by D_s .)

FLOW INDUCED VIBRATION OF VALVE HEAD

As authors have reported previously [6][11], the self-excited valve head vibration can take place due to the flow fluctuation. In the previous study [6][11], experimental and numerical investigations were carried out for the original valve head. Results showed that the random flow fluctuation became periodic due to the valve head vibration. Both experimental and numerical results showed that dynamic fluid forces caused negative damping effects. According to these results, it was concluded that the valve head vibration was self-excited vibration. With the flat and wedge valve heads, similar phenomena are observed as shown in Fig. 9. In this section, influences of valve head contours on the characteristics and mechanisms of the valve head vibration are discussed by comparing the results for the original valve head, flat valve head and wedge valve head.

Figure 10 shows spectra of pressure fluctuations measured with the wedge valve head with the rigid shaft,

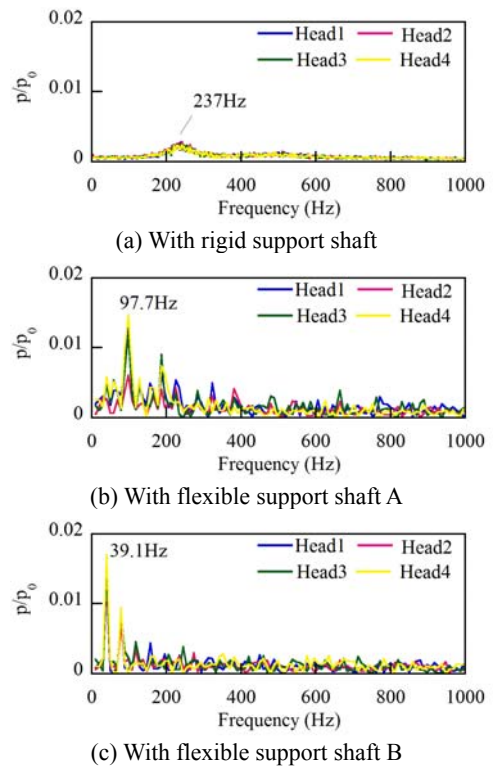
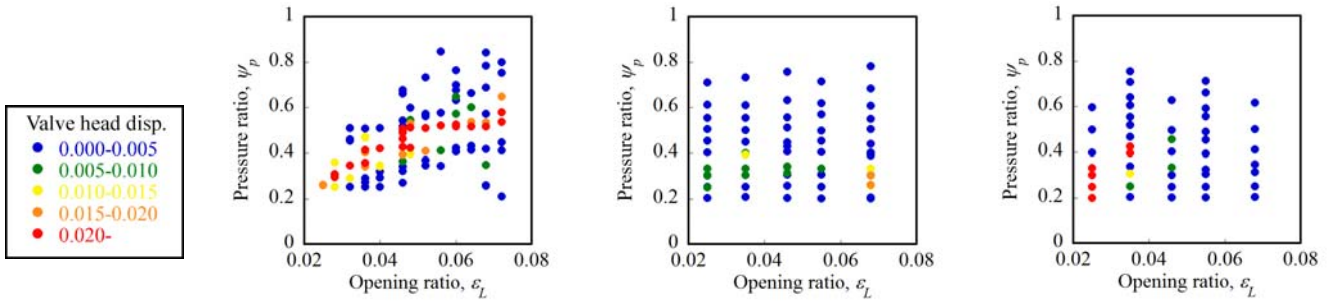


Fig. 10 Spectral analyses of wall pressure and valve head displacement (Measurement of wedge valve head, $\varepsilon_L=0.025$, $\psi_p=0.33$)

flexible shafts A and B. With the rigid shaft, the periodic asymmetric flow fluctuation pattern is observed. With shafts A and B, frequencies of the pressure fluctuation agree with each natural frequency shown in Table 2. The flow fluctuation is locked-in with the valve head vibration.

In Fig. 11, valve head displacement amplitudes are shown in $\psi_p-\varepsilon_L$ plane. Comparing with Fig. 8, the valve head displacement amplitude becomes larger when the flow fluctuation takes place. In Fig. 11, the size of the region with larger displacement amplitude is the largest for the original valve head. For the flat and the wedge valve heads, the displacement amplitude becomes large at the small valve opening ratio and pressure ratio region.



(a) Original valve head (b) Flat valve head (c) Wedge valve head
 Fig. 11 Amplitude of valve head vibration (With shaft B, Displacements are normalized by D_s .)

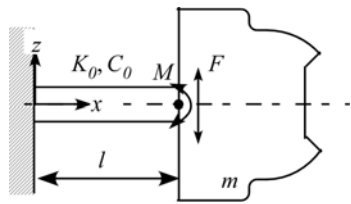


Fig. 12 Schematic of valve head vibration model

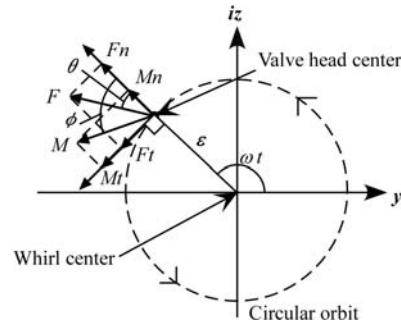


Fig. 14 Fluid force and fluid moment on vibrating valve head in circular trajectory

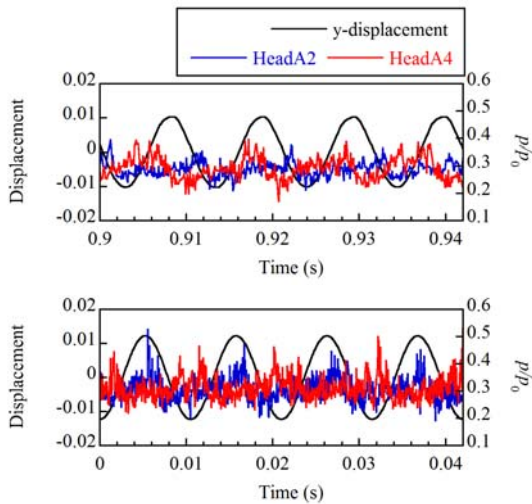


Fig. 13 Valve head displacement and pressure fluctuation (Wedge valve head, $\epsilon_L=0.025$, $\psi_p=0.33$, Freq.=95.2Hz, top: measurement, bottom: numerical result)

The displacement amplitudes for the flat valve head are totally smaller than those for the wedge valve head.

As mentioned in the previous study, the fluid force plays an important role to determine the stability of the valve head vibration. However, it is difficult to estimate the dynamic fluid forces with the present experimental equipment because the additional structural damping effects of the test facility are included. In the present study, fluid forces are evaluated numerically. Numerical simulations are carried out under the forced vibration of the valve head with constant amplitude and frequency. Dynamic fluid forces and moments are evaluated by integrating the surface pressure. The flow-valve head

system is assumed to be a linear system as shown in Fig. 12. The fluid force and fluid force moment are assumed to act at the junction of the shaft and valve head. The shaft root is treated a fixed end. The trajectory of the valve head displacement is assumed to be circular although elliptical in the experiments as shown in Fig. 9.

Experimental and numerical results of the pressure fluctuation at the point A2 and A4 along the valve head displacement in y-direction are shown in Fig. 13. Where, the y-axis directs from the point A2 towards the point A4. Comparing these results, amplitudes of pressure fluctuations are in acceptable agreement. Comparing phase differences between the valve head displacement and pressure fluctuations, pressure fluctuations show the phase lead at the point A4 and the phase lag at the point A2 for both experimental and numerical results. According to this comparison it is considered that the numerical predictions are useful to discuss dynamic fluid force and moment.

The valve head vibration is considered to be caused by fluid force and moment to the support shaft. The equation of motion of the valve head is represented as follows in the circular orbit in complex plane as shown in Fig. 14 [12].

$$m\ddot{\epsilon} + C_0\dot{\epsilon} + K_0\epsilon = F + i\frac{M}{l} \quad (1)$$

Where ϵ is the valve head displacement, C_0 , K_0 are damping and stiffness coefficients of the shaft, F and M are dynamic fluid force and fluid force moment. By assuming amplitudes and frequency of the displacement and fluid forces are constant, ϵ , F , and M are represented as follows.

$$\varepsilon = \varepsilon_0 e^{i\omega t} \quad (2)$$

$$F = F_0 e^{i(\omega t + \theta)} \quad (3)$$

$$M = M_0 e^{i(\omega t + \phi)} \quad (4)$$

By substituting (3), (4) into right hand side of (1), the fluid force and moment are represented as follows.

$$\begin{aligned} F + i\frac{M}{l} &= F_0 e^{i(\omega t + \theta)} + i\frac{M_0}{l} e^{i(\omega t + \phi)} \\ &= \left[\left(F_0 \cos\theta - \frac{M_0}{l} \sin\phi \right) + i \left(F_0 \sin\theta + \frac{M_0}{l} \cos\phi \right) \right] e^{i\omega t} \\ &= \left(F_0 \cos\theta - \frac{M_0}{l} \sin\phi \right) e^{i\omega t} + i \left(F_0 \sin\theta + \frac{M_0}{l} \cos\phi \right) e^{i\omega t} \quad (5) \\ &= \left(F_n - \frac{M_t}{l} \right) \frac{\varepsilon}{\varepsilon_0} + \left(F_t + \frac{M_n}{l} \right) \frac{\dot{\varepsilon}}{\omega \varepsilon_0} \end{aligned}$$

Where, the subscripts n and t means the components normal and tangential to the whirl orbit. Comparing left and right hand sides of Eq. (1), added stiffness and damping coefficients are obtained.

$$K = -\frac{1}{\varepsilon_0} \left(F_n - \frac{M_t}{l} \right) \quad (5)$$

$$C = -\frac{1}{\omega \varepsilon_0} \left(F_t + \frac{M_n}{l} \right) \quad (6)$$

Consequently the equation of motion of the valve head is obtained.

$$m\ddot{\varepsilon} + (C_0 + C)\dot{\varepsilon} + (K_0 + K)\varepsilon = 0 \quad (7)$$

When $(F_t + M_n/l) > 0$, added damping coefficient C becomes negative and the flow around the valve head would enhance the valve head vibration.

Numerical evaluation of dynamic fluid forces and fluid force moments are presented in Fig. 15 with the wedge valve head at $\varepsilon_L=0.025$, $\psi_p=0.33$. At this condition, the valve head vibration with large displacement amplitudes is observed as shown in Fig. 11. In Fig. 15, mean values of F_t and M_t/l are 0.011 and 0.006, respectively. Therefore, the mean added damping coefficient is negative and this agrees with the observation in Fig. 11.

Figure 16 shows the result with the wedge valve head at $\varepsilon_L=0.025$, $\psi_p=0.6$. Mean values of F_t and M_t/l are 0.0052 and 0.0004, respectively. Although the added damping coefficient becomes negative, the absolute values are much smaller than in Fig. 15. Actually, in Fig. 11, the displacement amplitude is small. This may be because the total damping coefficient $C_0 + C$ is not negative.

Figure 17 shows the result with the original valve head at $\varepsilon_L=0.068$, $\psi_p=0.4$. Mean values of F_t and M_t/l are 0.0078 and 0.0008, respectively. Comparing with the wedge valve head shown in Fig. 15, F_t is the same level but the M_t/l is much smaller.

According to these results, negative damping effects

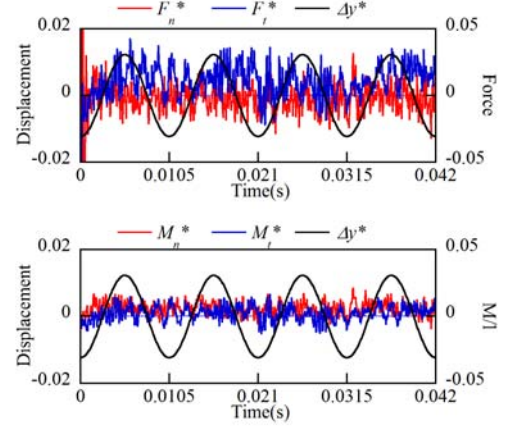


Fig. 15 Dynamic fluid force and fluid moment (Wedge valve head, $\varepsilon_L=0.025$, $\psi_p=0.33$, Numerical result, Freq.=95.2Hz)

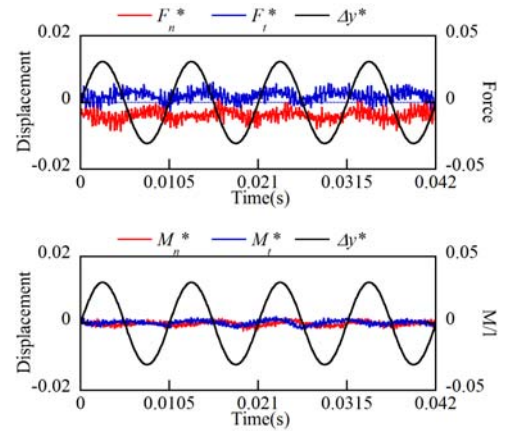


Fig. 16 Dynamic fluid force and fluid moment (Wedge valve head, $\varepsilon_L=0.025$, $\psi_p=0.62$, Numerical result, Freq.=95.2Hz)

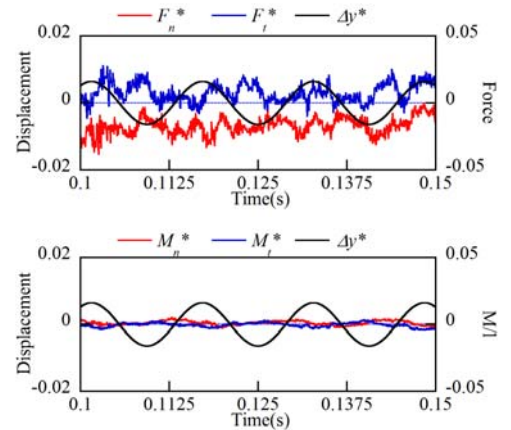


Fig. 17 Dynamic fluid force and fluid moment (Original valve head, $\varepsilon_L=0.068$, $\psi_p=0.4$, Numerical result, Freq.=64Hz)

are mainly caused by fluid forces and the contribution of the fluid force moment is smaller. Schematics of the pressure distribution and the fluid force are shown in Fig. 18. For the original valve head, the lateral fluid force occurs due to the pressure imbalance. For the flat valve head, the lateral fluid force cannot become large because the top of the valve head is normal to the center

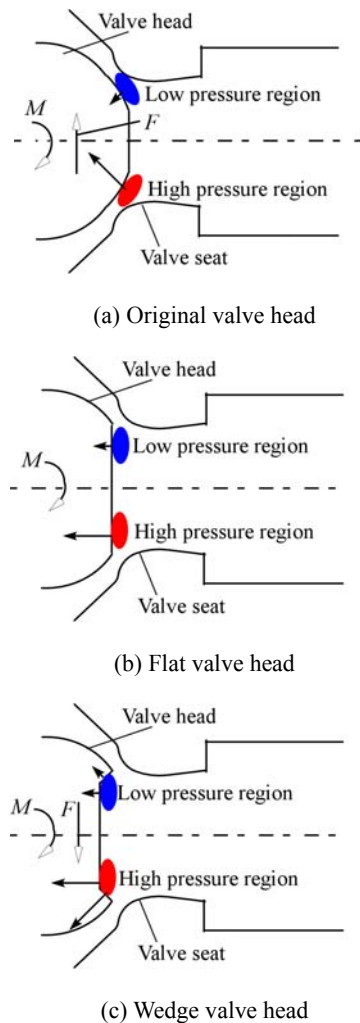


Fig. 18 Relationship between asymmetric pressure distribution and dynamic fluid force and moment

axis. The pressure imbalance cause only the fluid force moment. For the wedge valve head, the lateral force occurs due to the pressure imbalance on the inner side of the wedge part as shown in Fig. 18 (c). Therefore, the displacement amplitude of the valve head vibration can be large for the original and wedge valve heads because of lateral fluid forces. The displacement amplitude does not become large for the flat valve without the lateral fluid force in spite of occurrences of the pressure fluctuation with large amplitude in wide region of the operation condition as shown in Fig. 8.

CONCLUSIONS

Effects of valve head contours on characteristics of flow fluctuations and valve head vibrations are discussed by comparing three kinds of valve heads. With rigidly supported valve heads, the wedge valve head is the most effective to suppress the flow fluctuation. With flexibly supported valve heads, the flat valve head is the most effective to suppress the valve head vibration. In order to discuss the stability of the valve head, dynamic fluid forces and fluid force moments are evaluated numerically. Results show that the lateral fluid force is the main cause

of the negative damping force. The contribution of the fluid force moment is not large.

REFERENCES

- [1] Araki, T., Okamoto, Y. and Ootomo, F., 1981. "Fluid-Induced Vibration of Steam Control Valves (In Japanese)," Toshiba review, 36(7), pp. 648-656.
- [2] Jibiki, K., 2000, "Fluctuation of Steam Control Valve (In Japanese)," Turbomachinery, 28(4), pp. 225-229.
- [3] Morita R., Inada F., Mori M., Tezuka K., and Tsujimoto Y., 2007. "CFD Simulations and Experiments of Flow Fluctuations Around a Steam Control Valve," ASME J. Fluids Eng., 129(48), pp. 48-57.
- [4] Yonezawa, K., Terachi, Y., Nakajima, T., Tsujimoto, Y., Tezuka, K., Mori, M., Morita, R., and Inada, F., 2010. "A Two-Dimensional Study of Transonic Flow Characteristics in Steam Control Valve for Power Plant", Int. J. Fluid Machinery and Systems, 3(1), pp.58-66.
- [5] Morita, R., Inada, F., Mori, M., Tezuka, K. and Tsujimoto, Y., 2005. "Flow Induced Vibration of a Steam Control Valve," ASME Paper No. PVP2005-71334.
- [6] Yonezawa, K., Tsujimoto, Y., Tezuka, K., Mori, M., Morita, R., and Inada, F., 2008. "Transonic Flow Vibration in a Steam Control Valve for a Power Plant," Flow Induced Vibration, Zolotarev, I. and Horáček, J., eds., Institute of Thermomechanics, Prague, pp. 599-604.
- [7] Shioyama, T., Asakura, D., Kobayashi, T., Iseki, T. and Hosaka, H., 1995. "Coupling Vibration between Pipe Wall and Internal Higher-Order Acoustic Wave Caused by Valve Choking (In Japanese)," Trans. JSME, Ser. B, 61(589), pp. 3450-3455.
- [8] Widel, K.-E., 1980. "Governing Valve Vibrations in a Large Steam Turbine," Practical Experiences with Flow-Induced Vibrations, Springer-Verlag, New York, 320-322.
- [9] Zhang, D and Engeda, A., 2003. "Venturi Valves for Steam Turbines and Improved Design Consideration," Proceedings of the Institution of Mechanical Engineers, Part A: Journal of Power and Energy, 217 (2), 219-230.
- [10] Zhang, D, Engeda, A., Hardin, J. R., and Aungier, R. H., 2004. "Experimental Study of Steam Turbine Control Valves," Proceedings of the Institution of Mechanical Engineers, Part A: Journal of Power and Energy, 218 (5), 493-507.
- [11] Yonezawa, K., Ogi, K., Takino, T., Tsujimoto, Y., Tezuka, K., Morita, R., and Inada, F., 2010. "Experimental and Numerical Investigation of Flow Induced Vibration of Steam Control Valve," ASME Paper FEDSM-ICNMM2010-30676.
- [12] Song, B., Horiguchi, H., Ma, Z., and Tsujimoto, Y., 2010, "Rotordynamic Moment on the Backshroud of a Francis Turbine Runner Under Whirling Motion," ASME Journal of Fluids Engineering, Vol. 132, pp. 071102_1-071102_9.



EFFECTS OF INTERNAL PIPE GEOMETRY ON ACOUSTIC DIAMETRAL MODES IN A STEAM CONTROL VALVE

Oleksandr Barannyk¹

Institute for Integrated Energy Systems
Department of Mechanical Engineering
University of Victoria
Victoria, BC V8W 3P6,
Canada

Email: barannyk@me.uvic.ca

Peter Oshkai

Institute for Integrated Energy Systems
Department of Mechanical Engineering
University of Victoria
Victoria, BC V8W 3P6,
Canada

Email: poshkai@me.uvic.ca

ABSTRACT

In the present study, the effects of the internal pipe geometry immediately upstream and downstream of the shallow cavity on the characteristics of partially-trapped diametral acoustic modes is investigated. The mode shapes were calculated numerically by solving a Helmholtz equation in a 3D domain corresponding to the internal geometry of the pipe and the cavity. The experimentally obtained pressure data were used to determine the amplitude of pressure. The present results are in good agreement with the results reported in earlier studies for an axisymmetric cavity mounted in a pipe with a uniform cross-section. As the angle of the converging-diverging section of the main pipeline in the vicinity of the cavity increased, the trapped behavior of the acoustic diametral modes diminished, and additional antinodes of the acoustic pressure wave were observed in the main pipeline.

INTRODUCTION

A steam delivery system in a thermal power station consists of multiple pipes that involve gate valves and high pressure orifices that disrupt the smooth flow. When steam or air flow passes over the cavity formed by the seat of a gate valve mounted in a circular pipe, flow separation leads to formation of an unsteady shear layer over the opening of the cavity. Coupling of the shear layer oscillations with the acoustic standing waves, that are formed within and in the vicinity of the cavity, often results in loud tonal noise and high levels of pipe vibration [1, 2]. Detailed reviews of noise and vibration generation can be found, for example, in [3-6].

This paper investigates the flow-excited resonances of the acoustic diametral modes of a gate valve used in a thermal power plant. The seat of a typical valve forms a shallow cavity in the main pipeline. When the frequency of the shear layer oscillation coincides with the

natural frequency of a diametral acoustic mode, of a circular axisymmetric cavity, strong flow-acoustic resonance has been documented [7-9]. When the resonance occurs, the interaction between the standing acoustic waves and the transverse (cross-flow) shear layer oscillations results in the generation of the net positive acoustic power generation during each period of the oscillation. This power contributes to the increase of the amplitude of the acoustic oscillations and, in turn, to the radiated noise.

The original work that served as a basis for the current study was reported in [1, 2]. This investigation was aimed on reducing the steam line noise and vibration at a thermal power plant on a scaled model of an inline gate valve. The authors tested a variety of practical cavity, gate and seat configurations using air as the flowing fluid. It was found that the noise generating mechanism was associated with vortex shedding over the valve seat cavity coupled with an acoustic transverse mode in the valve throat. In addition, a 15° chamfered angle, which was machined into the valve seat rings, upstream and downstream of the cavity, lead to complete elimination of the tonal noise.

Also related to the present study are investigations reported in [7, 9, 10], where a simplified system consisting of a shallow axisymmetric cavity mounted in a pipeline with a circular cross-section was considered. Those studies were aimed at understanding the excitation mechanism of the trapped acoustic diametral modes, as well as their azimuthal behavior. It was shown by the authors, that for the all tested configurations, flow coupling with acoustic diametral modes was a dominant phenomenon at relatively low Mach numbers. It was found that the pulsation amplitude

Address all correspondence to this author¹

during resonance was increased as the cavity was made deeper or shorter. The authors also concluded that the acoustic diametral modes, coupled with the flow, are likely to spin when the cavity-duct system has a perfectly axisymmetric geometry.

The so-called trapped modes are generally confined to the cavity and its immediate vicinity. The trapped modes are typically associated with negligible radiation losses. Existence of trapped modes in a system is of great importance for practical applications, because these modes can typically be easily excited by external forcing. In [11], the existence of an infinite sequence of trapped modes was proven for cylindrical ducts. The authors in [10], compared numerically obtained resonances for several model configurations with analytically calculated embedded trapped modes. The lock-on in two-dimensional models of a butterfly and ball-type valves were also investigated.

The objective of the proposed work is to develop a methodology for effective control of flow-induced noise caused by gate valves in a wide variety of piping systems. Specific emphasis was on characterisation of the role of key geometric parameters, such as the angle of the converging-diverging section of the main pipeline upstream and downstream of the valve. These geometric components are indicated in the isometric schematic shown in Figure 1.

GATE VALVE GEOMETRY

The computational domain used in the present numerical investigation represents a variation of the experimental apparatus that was used in the previous studies by the Atomic Energy of Canada Limited (AECL) [1, 2]. The focus of the current study is on the effects of the internal pipe geometry immediately upstream and downstream of the shallow cavity formed by the valve seat on the characteristics of partially-trapped acoustic diametral modes. In particular, the objective is to investigate how the geometry of the convergent/divergent section of the main pipeline affects the spatial structure of the partially-trapped modes and the degree of their propagation into the main pipeline.

The major geometric parameters are defined in Figure 2. The four geometries considered in the current study are characterized by different convergence/divergence angles α . These geometries are referred to as follows: $G_1: \alpha=0^\circ$, $G_2: \alpha=5^\circ$, $G_3: \alpha=8^\circ$, $G_4: \alpha=11.2^\circ$. In all four cases, the following parameters were kept constant: $D_1=72\text{mm}$, $D_2=47.2\text{mm}$, $D_3=54.3\text{mm}$, $L_1=6.1\text{mm}$, $L_2=21.3\text{mm}$, $h=3.55\text{mm}$. The valve model, shown in

Figure 1, was connected, on both ends, to 1m long straight pipes with a circular cross-section.

GOVERNING EQUATIONS AND BOUNDARY CONDITIONS

Sound waves in a lossless medium, without dipole and monopole sources, are governed by the following equation for the pressure p :

$$\frac{1}{\rho c^2} \frac{\partial^2 p}{\partial t^2} + \nabla \cdot \left(\frac{1}{\rho} \nabla p \right) = 0, \quad (1)$$

where ρ is the density of the medium, p is the acoustic pressure, and c is the speed of sound. Considering a time harmonic acoustic waves of frequency ω , the pressure associated with this type of waves varies with time as

$$p(\mathbf{x}, t) = p(\mathbf{x})e^{i\omega t}, \quad (2)$$

here $\omega = 2\pi f$ is the angular frequency (rad/s). After substituting (2) into (1) one obtains a Helmholtz equation:

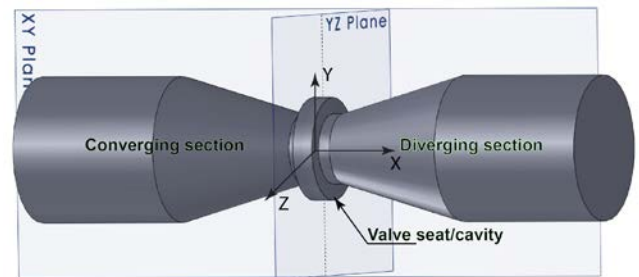


Figure 1: Schematic of the valve model.

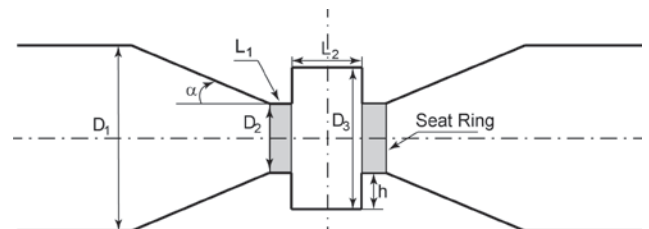


Figure 2: Schematic of the pipeline-cavity geometry.

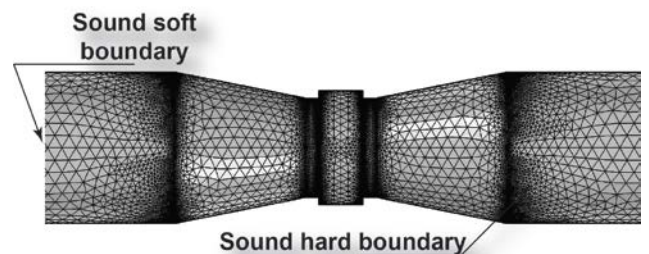


Figure 3: Schematic of the computational domain.

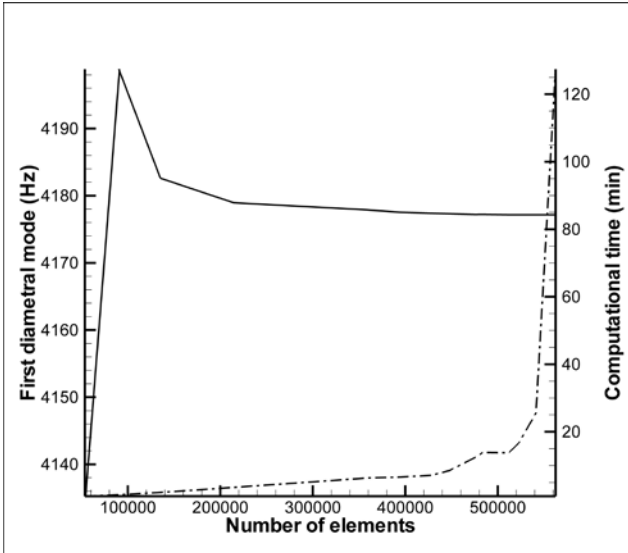


Figure 4: Computed frequency of the first diametral mode and computational time as functions of the total number of mesh elements.

$$\nabla \cdot \left(\frac{1}{\rho} (\nabla p) \right) - \frac{\omega^2 p}{\rho c^2} = 0. \quad (3)$$

By introducing the eigenvalue $\lambda = i2\pi f = i\omega$, equation (3) can be treated as an eigenvalue problem, and the eigenfrequencies with the correspondent eigenmodes can be obtained. In the case of the pipeline-cavity system, the eigenvalues represent the resonant frequencies, and the corresponding eigenfunctions represent the acoustic mode shapes.

Figure 3 shows a schematic of the computational domain and the grid. The boundary conditions on all solid surfaces corresponded to the sound hard walls, i.e. the normal derivative of the pressure was equal to zero on the boundaries. The inlet/outlet boundary conditions corresponded to the sound soft boundaries, i.e. to zero acoustic pressure.

DOMAIN DISCRETIZATION AND MESH INDEPENDENCE

The finite-element package COMSOL 4.2a was employed to solve the eigenvalue problem corresponding to the governing equation (3).

The computational domain was discretized using a 4-node tetrahedral mesh with minimal element size of 1.2mm which yielded a total number of 522,766 elements. A close-up of the generated mesh is shown in Figure 3. With the singularities associated with the sharp edges of the cavity were removed by replacing the sharp corners with the radii of 0.2mm.

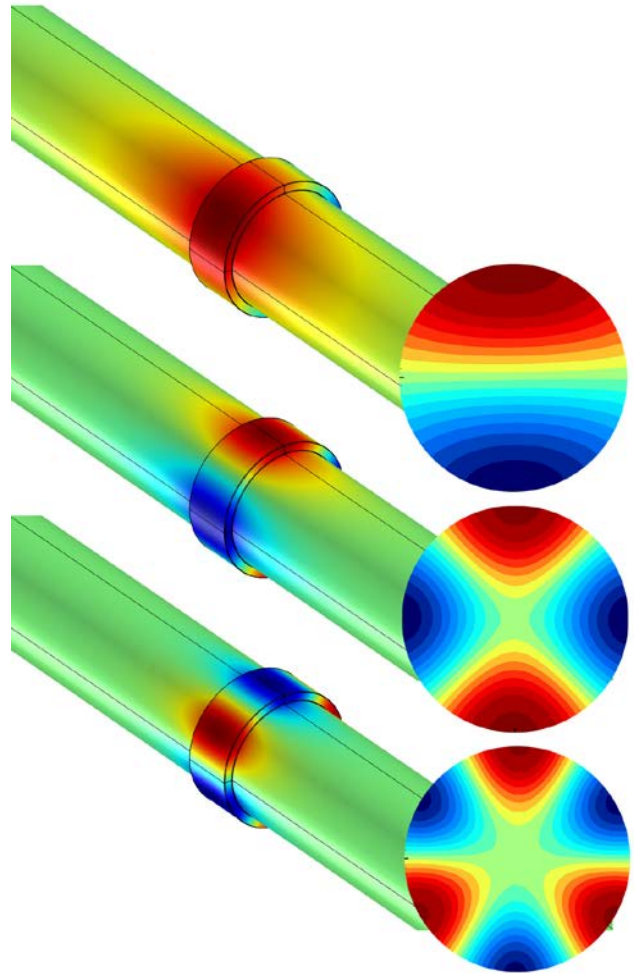


Figure 5: Pressure distributions corresponding to geometry G₁: (a) first diametral mode ($f_1^D = 4141$); (b) second diametral mode ($f_2^D = 6665$); (c) third diametral mode ($f_3^D = 8973$)

The numerical solutions were tested for mesh independence by performing successive refinements of the grid and monitoring the numerical values of the simulated frequencies. Convergence of up to three decimal places was achieved for grids with 522,766 elements and above. The corresponding computational time was approximately equal to 16 minutes per simulation on a single processor. These grids corresponded to at least 31 elements per wave length associated with the maximum simulated frequency of approximately 9kHz. The results of the mesh independence study are shown in Figure 4.

Geometry	$f_{\text{numerical}}$, Hz	$f_{\text{experimental}}$, Hz
G1	$f_1^D = 4141$ $f_2^D = 6665$ $f_3^D = 8973$	N/A
G2	$f_1^D = 4125$ $f_2^D = 6648$ $f_3^D = 8984$	$f_1^D = 4127$ $f_2^D = 6547$ $f_3^D = 8992$
G3	$f_1^D = 4191$ $f_2^D = 6644$ $f_3^D = 8996$	$f_1^D = 4113$ $f_2^D = 6616$ $f_3^D = 8964$
G4	$f_1^D = 4181$ $f_2^D = 6632$ $f_3^D = 8985$	$f_1^D = 4079$ $f_2^D = 6662$ $f_3^D = 9052$

Table 1: Numerical and experimental lock-on frequencies

The numerical model was validated against the published experimental results corresponding to a shallow axisymmetric cavity mounted in a pipeline with a circular cross-section [7]. The simulated frequencies were in good agreement with the experimental values in [7]. For example, the numerical simulation yielded the frequency of the first diametral mode of 1285 Hz, which is close to the experimentally-observed value of 1269 Hz.

RESULTS AND DISCUSSION

In addition to the numerical results presented herein, a series of experiments were performed using physical models corresponding to the configurations described above using air as a working fluid [12]. The acoustic pressure was measured at the bottom wall of the cavity for a range of inflow velocities. The pressure signals were analyzed in terms of their characteristic frequencies and amplitudes.

In Table 1, frequencies obtained from the numerical simulations are compared to those observed in the experiments. Here, f_i^D refers to the i^{th} acoustic diametral mode. The numerical results, which correspond to the no-flow condition, are in good agreement with the measured, flow-excited frequencies.

Major experimental highlights

In Figure 6, the experimentally obtained pressure spectra is shown as the inflow velocity was increased from 8 m/s to 29.4 m/s. The data corresponds to the case of the shallow axisymmetric cavity and the geometry G₄ with $\alpha=11.2^\circ$.

The dominant spectral peaks correspond to acoustically-coupled flow regimes that occurred when the frequencies of the hydrodynamic shear layer oscillations matched the frequencies of the diametral acoustic mode of

the axisymmetric cavity. These results indicate that the highest peak in Figure 6 corresponds to the second acoustic diametral mode ($f = 6665$ Hz).

From Figure 6 one can see that the maximum amplitude of acoustic oscillation is increased as the mean flow velocity increased up to $U=19.4$ m/s, followed by a rapid decrease at $U=22$ m/s. The pressure amplitude increased again as the inflow velocity increased from 22 m/s to 29.4 m/s. Thus, the maximum pressure amplitudes for the geometry G₄ were observed at the inflow velocities of $U=19.4$ m/s and $U=29.4$ m/s. For larger values of the angle of the converging/diverging pipe section, the noticeable decrease in the values of maximum pressure was achieved. Moreover, the lock-on frequency remained approximately constant throughout the entire velocity range employed in this experiment.

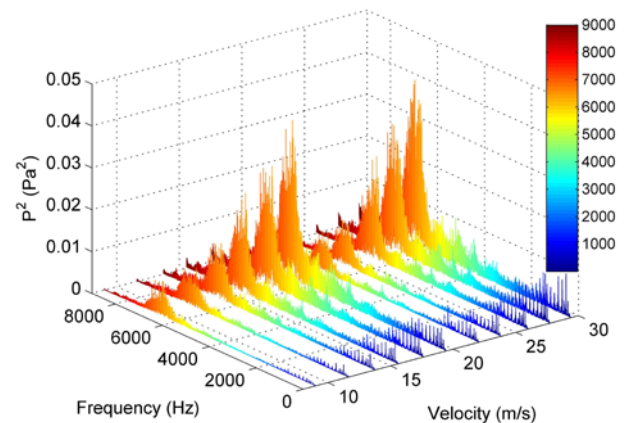


Figure 6: Power spectrum of pressure as a function of the inflow velocity for geometry G₄

Effect of the convergence/divergence angle

In this section, the effect of the convergence/divergence angle α on the the acoustic pressure distribution corresponding to the (partially-) trapped modes is discussed. Based on the published results [2, 7, 8], it is expected that shallow, axisymmetric cavities are capable of producing high-amplitude narrow-band, high-frequency noise, which implies flow-induced excitation of highly trapped modes. In this section, the experimentally obtained pressure data were used to determine the amplitude of pressure of the mode shape of the appropriate diametral mode.

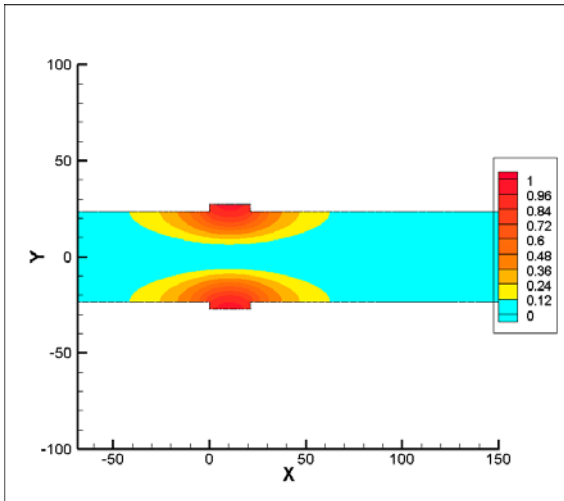


Figure 7: Mode shape of the second diametral mode for geometry G1

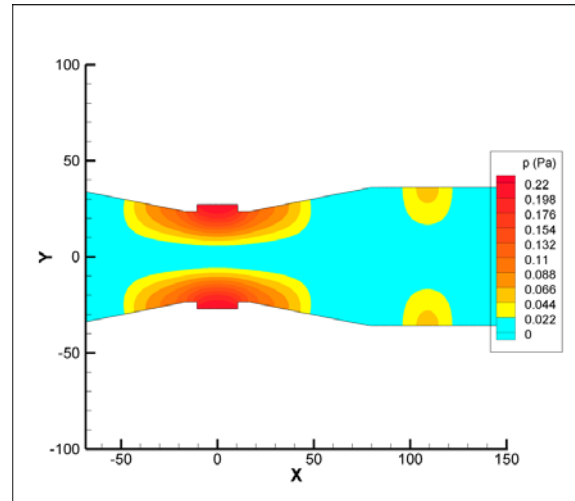


Figure 10: Mode shape of the second diametral mode for geometry G4

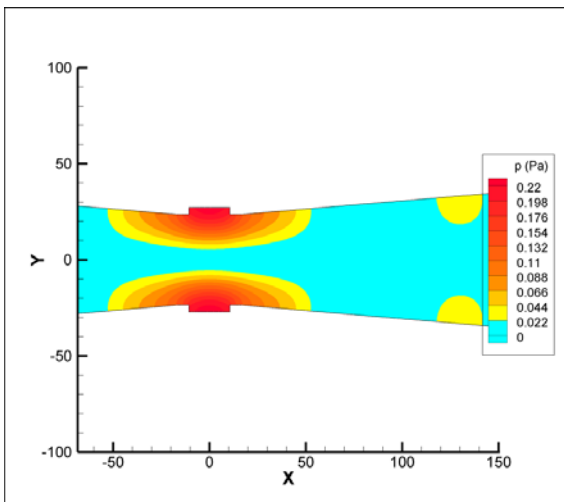


Figure 8: Mode shape of the second diametral mode for geometry G2

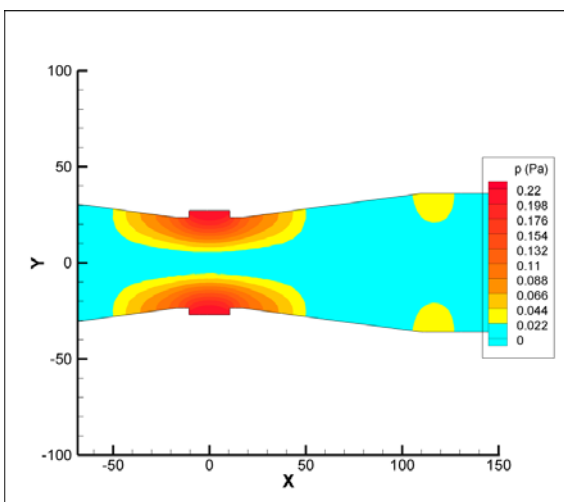


Figure 9: Mode shape of the second diametral mode for geometry G3

Figure 5 shows the pressure amplitude distributions corresponding to the first three diametral acoustic modes for geometry G_1 . The first three diametral modes are trapped in the vicinity of the cavity, i.e. pressure levels in the main pipeline, away from the cavity are negligible. This feature is in agreement with the published results [7, 9]. The higher modes are highly concentrated around the cavity. In other words, they correspond to lower levels of radiation into the main pipeline, compared to the lower modes.

For all modes, the maximum pressure occurred at the bottom wall of the cavity, at $x = 0$ (as defined in Figure 5). The cross-sections of the mode shapes in the YZ plane located at $x = 0$ show that the pressure distribution at the bottom wall of the cavity, along its circumference, corresponded to a sinusoidal function with respect to the azimuthal position. The first mode corresponded to one period of the sinusoid around the entire cavity, while the second and the third modes corresponded to two and three periods, respectively. These results follow the general trend established in the earlier investigations [7, 9].

Figures 7 through 10 illustrate the effect of the geometry of the main pipeline in the vicinity of the cavity on the degree of confinement of the second diametral mode. As the characteristic angle of the converging/diverging pipe section, α , was changed from 0° to 11.2° (corresponding to geometries G_1 through G_4) the levels of radiation of pressure into the main pipeline increased. In other words, the degree of confinement of the first diametral mode diminished.

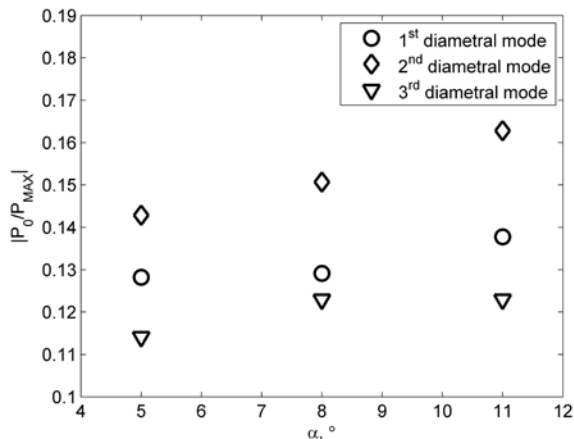


Figure 11: The effect of the geometry of the main pipeline in the vicinity of the cavity on the degree of confinement of the first three diametral modes.

Qualitatively, this trend can be observed in Figures 7 -10 by noting the occurrence of the secondary pressure peaks in the main pipeline for the cases of higher α . This trend is similar for higher-order diametral modes (not shown).

The degree of mode confinement, or, inversely, the level of radiation, of a mode was quantified in terms of the magnitude of the secondary peak closest to the cavity, P_0 relative to the magnitude of the primary peak, P_{max} . The values of P_{max} were taken from experimental study[12]. The ratio P_0/P_{max} as a function of α is plotted in Figure 12. The decreased confinement of the diametral modes with increasing convergence/divergence angle is in agreement with the results of the experimental study. Specifically, increasing α resulted in a decrease of the strength of the flow-tone lock-on, which is an indication of the increased radiation losses.

CONCLUSIONS

Numerical simulations of the frequencies and the corresponding mode shapes of the diametral modes of the gate valve model were performed for a range of the main pipeline geometries. It was shown that increasing the characteristic angles of the converging/diverging section that was located in the vicinity of the valve seat cavity resulted in the increased radiation of acoustic pressure into the main duct. These result are in agreement with the experimental study that demonstrated a corresponding decrease in the strength of the flow-induced resonance.

ACKNOWLEDGMENTS

The authors wish to thank the Atomic Energy of Canada Limited (AECL) for providing the original experimental model of the gate valve and the Natural

Sciences and Engineering Research Council of Canada (NSERC) for providing funding for financial support.

REFERENCES

1. Janzen, V.P., et al., *Acoustic noise reduction in large-diameter steam-line gate valves*. Proceedings of the Asme Pressure Vessels and Piping Conference 2007, Vol 4: Fluid-Structure Interaction, ed. M. Moatamedi. 2008. 513-522.
2. Smith, B.A.W. and B.V. Luloff, *The effect of seat geometry on gate valve noise*. Journal of Pressure Vessel Technology-Transactions of the Asme, 2000. **122**(4): p. 401-407.
3. Rockwell, D. and E. Naudascher, *Review - self-sustaining oscillations of flow past cavities*. Journal of Fluids Engineering-Transactions of the Asme, 1978. **100**(2): p. 152-165.
4. Ziada, S. and E.T. Buhlmann, *Self-excited resonances of 2 side-branches in close proximity*. Journal of Fluids and Structures, 1992. **6**(5): p. 583-601.
5. Kriesels, P.C., et al., *Flow induced pulsation in pipe systems*. Flow-Induced Vibration, ed. P.W. Bearman. 1995. 505-514.
6. Bruggeman, J.C., et al., *Flow Induced Pulsations in Gas Transport Systems: Analysis of the Influence of Closed Side Branches*. Journal of Fluids Engineering, 1989. **111**(4): p. 484-491.
7. Aly, K. and S. Ziada, *Flow-excited resonance of trapped modes of ducted shallow cavities*. Journal of Fluids and Structures, 2010. **26**(1): p. 92-120.
8. Rockwell, D., et al., *Shallow cavity flow tone experiments: onset of locked-on states*. Journal of Fluids and Structures, 2003. **17**(3): p. 381-414.
9. Aly, K. and S. Ziada, *Azimuthal behaviour of flow-excited diametral modes of internal shallow cavities*. Journal of Sound and Vibration, 2011. **330**(15): p. 3666-3683.
10. Duan, Y.T., et al., *Complex resonances and trapped modes in ducted domains*. Journal of Fluid Mechanics, 2007. **571**: p. 119-147.
11. Linton, C.M. and M. McIver, *Trapped modes in cylindrical waveguides*. Quarterly Journal of Mechanics and Applied Mathematics, 1998. **51**: p. 389-412.
12. Barannyk, O. and P. Oshkai, *Experimental investigation of flow-acoustic coupling In gate valves*. 10th International Conference on Flow-Induced Vibration (& Flow-Induced Noise), 2012.



THREE-DIMENSIONAL DYNAMICS OF LONG PIPES TOWED UNDERWATER

Mojtaba Kheiri*
 Michael P. Païdoussis
 Marco Amabili

Department of Mechanical Engineering
 McGill University
 817 Sherbrooke Street West
 Montreal, QC, Canada H3A 0C3
 Email: mojtaba.kheiri@mail.mcgill.ca

Bogdan I. Epureanu

Department of Mechanical Engineering
 University of Michigan
 Ann Arbor, MI, USA
 Email: epureanu@umich.edu

ABSTRACT

In this paper, three-dimensional equations of motion are derived for the dynamics of long pipes towed underwater. The pipeline is flexibly connected to the towing and trailing vessels via cables at its upstream and downstream ends. The cables are modelled as springs and the body is assumed to have null buoyancy. The linearized equations of motion and the boundary conditions are discretized via a finite difference technique and are solved by using a time integration method. Some results, including an Argand diagram and a set of deformation and time-trace diagrams, are presented for a typical long pipe.

INTRODUCTION

The main interest in the study of dynamics of pipes towed underwater comes from a specific application: instead of welding individual lengths of pipe *in situ*, on a ship or platform, to the desired overall length for offshore use (where the pipe length can be very large, in the kilometer range), the pipe is welded on land, near the shore; it is then towed underwater, suitably buoyed, to the desired location; see, for example, [1] and [2] and Fig. 1.

The basic system is similar to several other underwater towed systems, such as acoustic streamers used for oil/gas exploration (see, e.g., [3]), umbilical cables for underwater vehicles connected to surface vessels (e.g., [4]), and the Dracone barges used for sea-transport of lighter than sea-water fluid cargo (e.g., [5] and [6]). The main difference of all these from the pipe problem is in the end-conditions; whereas acoustic streamers and Dracones are free at the downstream end and umbilicals are attached to the towed vessel, the ends of a towed pipe system are flex-

ibly attached to cables connected upstream to the towing vessel and downstream to a trailing vessel. The purpose of the trailing vessel is to ensure that currents do not result in unduly large motions of the pipe; one scenario to be avoided is the pipe breaking surface in front of unsuspecting vessels crossing its path. For the same reason it is important to establish that no instabilities, or more generally no large motions, are allowed; which means that the dynamics of the system has to be studied carefully.

There have been many studies of various aspects of the dynamics of flexible cylinders towed underwater; see, e.g., [6]. In most, two dimensional (2-D) motions are considered and cross-flow due to currents is neglected, e.g. [7–9]. Although a sufficiently long pipe may justifiably be modelled as a cable – in effect neglecting flexural rigidity relative to tension – the model is then not suitable for studying both long and relatively short pipes towed underwater. Moreover, in all these studies the cylinder is not attached fore and aft as in the pipe system.

In this paper, a simplified model is considered for 3-D motions of a pipe towed underwater in the configuration shown in Fig. 1, generally subjected to both axial flow (due to the towing) and cross-flow (due to cross-currents). Then, a finite difference scheme is used to spatially discretize the linearized unsteady equations of motion. The resultant set of time-domain ODEs are solved by using the DIVPAG routine of Fortran IMSL library. Finally, numerical results are presented for the case of purely axial flow and long pipes.

THE EQUATIONS OF MOTION

Definitions and the basic model

The pipe, of diameter \hat{D} and length \hat{L} , is modelled as a uniform, neutrally buoyant Euler-Bernoulli beam, towed

*Address all correspondence to this author.

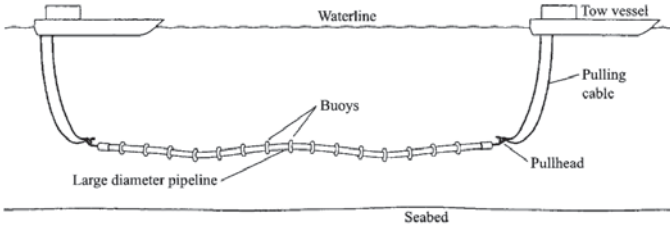


FIGURE 1: LARGE DIAMETER (64 in.) TOWED PIPELINE FOR USE IN DEEP OCEAN STORAGE OF LIQUID CO₂ [1].

underwater, as in Fig. 1. The hydrodynamic forces acting on it, in the absence of cross-flow, are obtained in the manner described in [6, 7, 10, 11]. Here it is important to note that there is an error in the derivation in [7], important for long systems, which has subsequently been corrected [6].

Basically, an element of the pipe is subjected to (i) inviscid hydrodynamic forces $\hat{F}_{A_y} \delta \hat{x}$ and $\hat{F}_{A_z} \delta \hat{x}$ in the two transverse directions \hat{y} and \hat{z} , the axial direction along which the pipe is towed being denoted by \hat{x} , and (ii) viscous forces in the longitudinal direction $\hat{F}_L \delta \hat{x}$, and in the transverse normal directions $\hat{F}_{N_y} \delta \hat{x}$ and $\hat{F}_{N_z} \delta \hat{x}$, the hat denoting a dimensional quantity throughout. The former are obtained from Lighthill's work [12], while the latter from Taylor's [13]. Thus, in their simplest form:

$$\hat{F}_{A_y} = \hat{\rho} \hat{A} \left(\frac{\partial}{\partial \hat{t}} + \hat{U}_x \frac{\partial}{\partial \hat{x}} \right)^2 \hat{v}, \quad (1)$$

$$\hat{F}_{N_y} = \frac{1}{2} \hat{\rho} \hat{D} \hat{U}_x^2 (C_f \sin i + C_{D_p} \sin^2 i), \quad (2)$$

$$\hat{F}_L = \frac{1}{2} \hat{\rho} \hat{D} \hat{U}_x^2 C_f \cos i, \quad (3)$$

where $\hat{\rho}$ is the fluid density, \hat{A} the external mean cross-sectional area of the pipe, \hat{U}_x the axial flow velocity (towing speed), \hat{v} the displacement in the \hat{y} -direction, C_f and C_{D_p} are frictional and form drag coefficients, and i is the angle of incidence at location \hat{x} ; e.g., for planar motion, $i = \tan^{-1}(\partial \hat{v} / \partial \hat{x}) + \tan^{-1}[(\partial \hat{v} / \partial \hat{t}) / \hat{U}_x]$. Considering an element of the body with the forces acting on it, the equations of motion may be written as

$$\hat{E} \hat{I} \frac{\partial^4 \hat{v}}{\partial \hat{x}^4} + \hat{F}_{A_y} + \hat{F}_{N_y} - \hat{F}_L \frac{\partial \hat{v}}{\partial \hat{x}} - \frac{\partial}{\partial \hat{x}} \left(\hat{T} \frac{\partial \hat{v}}{\partial \hat{x}} \right) + \hat{m} \frac{\partial^2 \hat{v}}{\partial \hat{t}^2} = 0, \quad (4)$$

with a similar one for the \hat{z} -direction, where

$$\frac{\partial \hat{T}}{\partial \hat{x}} + \hat{F}_L = 0, \quad (5)$$

in which it has been assumed that the deflections in the \hat{y} - and \hat{z} -direction, \hat{v} and \hat{w} , respectively, are small, of $O(\hat{\epsilon})$ (with $\hat{\epsilon} = O(\hat{D}) \ll \hat{L}$). Quantities of $O(\hat{\epsilon}^2)$ have been neglected here, as well as in what follows; i.e., a linearized set of equations will eventually be obtained.

These equations are modified by the presence of a cross-current. It is assumed that the cross-flow velocity \hat{U}_z is sufficiently small relative to the towing speed for flow separation not to take place. Hence, the main effect of the cross-flow is to modify the frictional forces acting on the cylinder, notably the angle of incidence i .

The cables to the towing and trailing vessels are modelled as shown in Fig. 2. The springs are attached as shown to points in the (x, z) -plane at one end, and to the pipe at the other. Hence, the boundary conditions may be expressed as

$$\begin{aligned} \hat{E} \hat{I} \frac{\partial^3 \hat{v}}{\partial \hat{x}^3} + \hat{a}_{1,y}^{(1)} \frac{\partial \hat{v}}{\partial \hat{x}} + \hat{a}_{2,y}^{(1)} \hat{v} + \hat{a}_{3,y}^{(1)} \hat{w} &= \hat{a}_{4,y}^{(1)}, \\ \hat{E} \hat{I} \frac{\partial^3 \hat{w}}{\partial \hat{x}^3} + \hat{a}_{1,z}^{(1)} \frac{\partial \hat{w}}{\partial \hat{x}} + \hat{a}_{2,z}^{(1)} \hat{v} + \hat{a}_{3,z}^{(1)} \hat{w} &= \hat{a}_{4,z}^{(1)}, \end{aligned} \quad (6)$$

$$\begin{aligned} \hat{E} \hat{I} \frac{\partial^3 \hat{v}}{\partial \hat{x}^3} + \hat{a}_{1,y}^{(2)} \frac{\partial \hat{v}}{\partial \hat{x}} + \hat{a}_{2,y}^{(2)} \hat{v} + \hat{a}_{3,y}^{(2)} \hat{w} &= \hat{a}_{4,y}^{(2)}, \\ \hat{E} \hat{I} \frac{\partial^3 \hat{w}}{\partial \hat{x}^3} + \hat{a}_{1,z}^{(2)} \frac{\partial \hat{w}}{\partial \hat{x}} + \hat{a}_{2,z}^{(2)} \hat{v} + \hat{a}_{3,z}^{(2)} \hat{w} &= \hat{a}_{4,z}^{(2)}, \end{aligned} \quad (7)$$

respectively, at the upstream and downstream ends, and

$$\hat{E} \hat{I} \frac{\partial^2 \hat{v}}{\partial \hat{x}^2} = \hat{E} \hat{I} \frac{\partial^2 \hat{w}}{\partial \hat{x}^2} = 0 \quad (8)$$

at both ends, where $\hat{a}_i^{(1)}$ ($i = 1..4$) are the coefficients associated with the upstream end and $\hat{a}_i^{(2)}$ ($i = 1..4$) are associated with the pipe downstream end.

Nondimensionalization

We introduce the following length and time scales

$$\hat{\ell} = [(\pi \hat{D})^2 \hat{L}]^{1/3} \quad \text{and} \quad \hat{\tau} = [(\hat{m} + \hat{\rho} \hat{A}) \hat{\ell}^4 / \hat{E} \hat{I}]^{1/2}, \quad (9)$$

and hence define

$$\begin{aligned} x &= \frac{\hat{x}}{\hat{\ell}}, \quad v^* = \frac{\hat{v}}{\hat{\ell}}, \quad w^* = \frac{\hat{w}}{\hat{\ell}}, \quad t = \frac{\hat{t}}{\hat{\tau}}, \\ \beta &= \frac{\hat{\rho} \hat{A}}{\hat{\rho} \hat{A} + \hat{m}}, \quad T^* = \frac{\hat{T} \hat{\ell}^2}{\hat{E} \hat{I}}, \quad \varepsilon = \frac{\hat{\ell}}{\hat{D}}, \end{aligned} \quad (10)$$

$$U = \left(\frac{\hat{\rho} \hat{A}}{\hat{E} \hat{I}} \right)^{1/2} \hat{U} \hat{\ell}, \quad c_f = \frac{4}{\pi} C_f, \quad c_{D_p} = \frac{4}{\pi} C_{D_p};$$

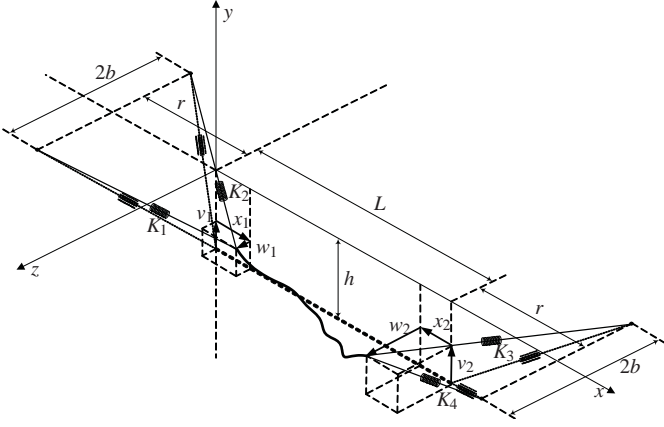


FIGURE 2: DIAGRAMMATIC VIEW OF THE TOWED PIPE, SHOWING THE SPRINGS MODELLING THE CABLE ATTACHMENTS TO THE SURFACE VESSELS.

note that ε here is different from \hat{L}/\hat{D} as in previous papers [7,10,11]. With these quantities, using also equations (1) and (5), the equations of motion take the form

$$\frac{\partial^4 v^*}{\partial x^4} + U_x^2 \frac{\partial^2 v^*}{\partial x^2} + 2\beta^{1/2} U_x \frac{\partial^2 v^*}{\partial x \partial t} - T^* \frac{\partial^2 v^*}{\partial x^2} + F_{N_y}^* + \frac{\partial^2 v^*}{\partial t^2} = 0, \quad (11)$$

$$\frac{\partial^4 w^*}{\partial x^4} + U_x^2 \frac{\partial^2 w^*}{\partial x^2} + 2\beta^{1/2} U_x \frac{\partial^2 w^*}{\partial x \partial t} - T^* \frac{\partial^2 w^*}{\partial x^2} + F_{N_z}^* + \frac{\partial^2 w^*}{\partial t^2} = 0, \quad (12)$$

where T^* , $F_{N_y}^*$ and $F_{N_z}^*$ are generally nonlinear.

Linearization

It is assumed that the cross-current, if one exists, occurs in the horizontal, (x, z) -plane. Hence, deflections from the stretched-straight configuration in the z -plane comprise a steady component $\bar{w} \sim O(\varepsilon)$ and an unsteady one $w \sim O(\varepsilon)$; in the vertical, (x, y) -plane, however, no steady deflection arises. Hence, we have

$$w^* = \bar{w} + w, \quad v^* = v. \quad (13)$$

The equations for the frictional forces may be linearized to

$$\begin{aligned} F_{N_y}^* &= \frac{1}{2} U_x^2 \varepsilon c_f \left(\frac{\partial v}{\partial x} + \frac{\beta^{1/2}}{U_x} \frac{\partial v}{\partial t} \right) + \frac{1}{2} \varepsilon c_d \beta^{1/2} \frac{\partial v}{\partial t}, \\ F_{N_z}^* &= \bar{F}_{N_z} + \frac{1}{2} U_x^2 \varepsilon c_f \left(\frac{\partial w}{\partial x} + \frac{\beta^{1/2}}{U_x} \frac{\partial w}{\partial t} \right) + \frac{1}{2} \varepsilon c_d \beta^{1/2} \frac{\partial w}{\partial t}, \\ F_L^* &= \frac{1}{2} U_x^2 \varepsilon c_f, \end{aligned} \quad (14)$$

where c_d is the zero-flow normal coefficient; \bar{F}_{N_z} is the steady part of $F_{N_z}^*$ and is given as ¹

$$\bar{F}_{N_z} = \frac{1}{2} U_x^2 \varepsilon c_f \frac{d\bar{w}}{dx} + \frac{1}{2} U_x U_z \varepsilon c_f + \frac{1}{2} U_z \varepsilon c_d. \quad (15)$$

The procedure to find reasonable values of c_d for a long cylinder oscillating in quiescent fluid can be found in [6]. The linearized steady tension in the pipe (\bar{T}) can also be obtained from equations (5) and (14) as

$$\bar{T}(x) = \bar{T}_1 - \frac{1}{2} U_x^2 \varepsilon c_f (x - x_1), \quad (16)$$

in which \bar{T}_1 is the steady tension at the pipe upstream end, $x = x_1$ (see Fig. 2).

Steady-state and unsteady equations

In the absence of a cross-flow, the pipe lies in its stretched-straight configuration. If, however, $U_z \neq 0$, then the (x, z) -plane equilibrium is determined via

$$\begin{aligned} \frac{d^4 \bar{w}}{dx^4} + (U_x^2 - \bar{T}) \frac{d^2 \bar{w}}{dx^2} + \frac{1}{2} U_x^2 \varepsilon c_f \frac{d\bar{w}}{dx} + \frac{1}{2} U_x U_z \varepsilon c_f \\ + \frac{1}{2} U_z \varepsilon c_d = 0. \end{aligned} \quad (17)$$

The unsteady motions are governed by

$$\begin{aligned} \frac{\partial^4 v}{\partial x^4} + (U_x^2 - \bar{T}) \frac{\partial^2 v}{\partial x^2} + 2\beta^{1/2} U_x \frac{\partial^2 v}{\partial x \partial t} + \frac{1}{2} U_x^2 \varepsilon c_f \frac{\partial v}{\partial x} \\ + \left(\frac{1}{2} U_x \varepsilon c_f \beta^{1/2} + \frac{1}{2} \varepsilon c_d \beta^{1/2} \right) \frac{\partial v}{\partial t} + \frac{\partial^2 v}{\partial t^2} = 0, \end{aligned} \quad (18)$$

$$\begin{aligned} \frac{\partial^4 w}{\partial x^4} + (U_x^2 - \bar{T}) \frac{\partial^2 w}{\partial x^2} + 2\beta^{1/2} U_x \frac{\partial^2 w}{\partial x \partial t} + \frac{1}{2} U_x^2 \varepsilon c_f \frac{\partial w}{\partial x} \\ + \left(\frac{1}{2} U_x \varepsilon c_f \beta^{1/2} + \frac{1}{2} \varepsilon c_d \beta^{1/2} \right) \frac{\partial w}{\partial t} + \frac{\partial^2 w}{\partial t^2} = 0. \end{aligned} \quad (19)$$

Boundary motions and final equations

The complete formulation of the problem is complicated by the fact that neither end of the pipe is fixed. Here, the boundary motions are defined, and then the final equations of motion and boundary conditions obtained.

¹The unsteady part of F_L^* has been neglected since it is of $O(\varepsilon^2)$.

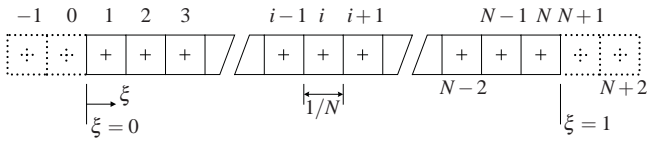


FIGURE 3: THE SPATIAL DISCRETIZATION OF THE BODY.

Let x_0 be the steady-state axial deflection due to cross-currents, and x_1 and x_2 be the unsteady axial deflections associated with lateral motions. To have an independent variable which varies from 0 to 1, regardless of pipe deflection, we define a new axial variable

$$\xi = \frac{x - x_1}{L - x_0 - x_1 - x_2} = \alpha(x - x_1). \quad (20)$$

If there is no cross-current ($U_z = 0$); hence $\bar{w} = 0$, and the equations in the y - and z -direction become identical, and only one needs to be solved. The equation of motion in the z -direction may be written as

$$\alpha^4 \frac{\partial^4 w}{\partial \xi^4} + (c_1 \alpha^2 + c_2 \alpha \xi) \frac{\partial^2 w}{\partial \xi^2} + c_3 \alpha \frac{\partial^2 w}{\partial \xi \partial t} + c_4 \alpha \frac{\partial w}{\partial \xi} + c_5 \frac{\partial w}{\partial t} + \frac{\partial^2 w}{\partial t^2} = 0, \quad (21)$$

where $c_1 = U_x^2 - \bar{T}_1$, $c_2 = \frac{1}{2} \epsilon c_f U_x^2$, $c_3 = 2\beta^{1/2} U_x$, $c_4 = c_2$ and $c_5 = \frac{1}{2} U_x \epsilon c_f \beta^{1/2} + \frac{1}{2} \epsilon c_d \beta^{1/2}$.

The boundary conditions may be simplified to

$$\frac{\partial^2 w}{\partial \xi^2} \Big|_{\xi=0} = \frac{\partial^2 w}{\partial \xi^2} \Big|_{\xi=1} = 0; \quad (22)$$

$$\begin{aligned} (\alpha^3 \frac{\partial^3 w}{\partial \xi^3} + \alpha a_{1,z}^{(1)} \frac{\partial w}{\partial \xi} + a_{3,z}^{(1)} w - a_{4,z}^{(1)}) \Big|_{\xi=0} &= 0, \\ (\alpha^3 \frac{\partial^3 w}{\partial \xi^3} + \alpha a_{1,z}^{(2)} \frac{\partial w}{\partial \xi} + a_{3,z}^{(2)} w - a_{4,z}^{(2)}) \Big|_{\xi=1} &= 0. \end{aligned} \quad (23)$$

Discretization

Following [14] and [15] we use the central finite difference method to spatially discretize the equation of motion and the boundary conditions. In order to apply the method, the body is assumed to be divided into N elements. As seen from Fig. 3, the mesh points are taken at

the centre of each element. Using the central finite difference approximations for derivatives, the equation of motion becomes

$$\begin{aligned} \left(\frac{\partial U}{\partial t}\right)_i &= -\left(\frac{c_3 \alpha}{2h}\right) U_{i+1} - c_5 U_i + \left(\frac{c_3 \alpha}{2h}\right) U_{i-1} - \left(\frac{\alpha}{h}\right)^4 Y_{i+2} \\ &+ \left[\frac{-c_4 \alpha}{2h} - \frac{(c_1 \alpha^2 + c_2 \alpha \xi_i)}{h^2} + 4\left(\frac{\alpha}{h}\right)^4\right] Y_{i+1} \\ &+ \left[\frac{2(c_1 \alpha^2 + c_2 \alpha \xi_i)}{h^2} - 6\left(\frac{\alpha}{h}\right)^4\right] Y_i \\ &+ \left[\left(\frac{c_4 \alpha}{2h}\right) - \frac{(c_1 \alpha^2 + c_2 \alpha \xi_i)}{h^2} + 4\left(\frac{\alpha}{h}\right)^4\right] Y_{i-1} - \left(\frac{\alpha}{h}\right)^4 Y_{i-2}, \\ \left(\frac{\partial Y}{\partial t}\right)_i &= U_i. \end{aligned} \quad (24)$$

where $h = 1/N$, Y_i is the transverse displacement (w) at the i th element and $U_i = (\partial Y / \partial t)_i$.

As seen from Fig. 3, the unknowns, e.g. Y_0 , Y_{-1} and U_0 , are not associated with the real mesh points and should be determined as functions of unknowns associated with the real mesh points, i.e. Y_i , U_i ($i = 1..N$). This is done through the boundary conditions.

Following closely the procedure developed in [15] and after considerable manipulation, the following expressions are obtained from the boundary conditions given in equations (22) and (23):

$$\begin{aligned} Y_{-1} &= (1 + c_0) Y_1 - (1 + d_0) Y_2 + g_0, \\ Y_0 &= c_0 Y_1 - d_0 Y_2 + g_0, \quad U_0 = c_0 U_1 - d_0 U_2, \end{aligned} \quad (25)$$

$$\begin{aligned} Y_{N+2} &= (1 + c_1) Y_N - (1 + d_1) Y_{N-1} + g_1, \\ Y_{N+1} &= c_1 Y_N - d_1 Y_{N-1} + g_1, \quad U_{N+1} = c_1 U_N - d_1 U_{N-1}, \end{aligned} \quad (26)$$

where, after some manipulations, the coefficients can be found from equations (22) and (23).

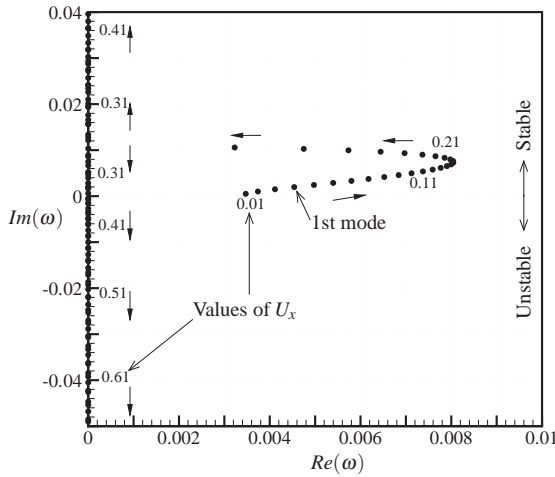
Equation (24), after applying the expressions given in equations (25) and (26), may be cast in first-order form:

$$\dot{X} = AX + B, \quad (27)$$

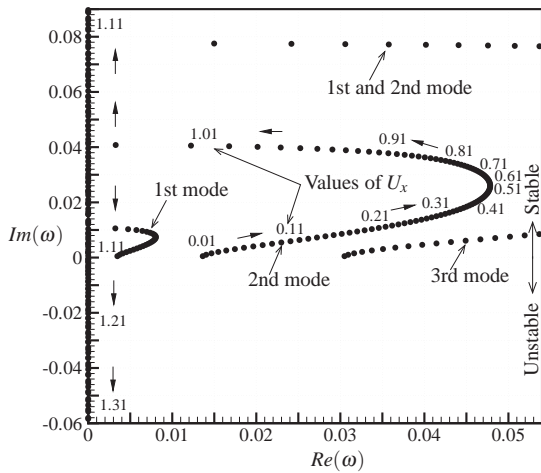
where $X = [U_1 \ U_2 \ \dots \ U_N \ Y_1 \ Y_2 \ \dots \ Y_N]^T$ and $(\dot{\ }) = \partial(\) / \partial t$. Equation (27) may be solved numerically by using one of several available mathematical packages, such as DIV-PAG of IMSL Library and ODE functions of MATLAB.

NUMERICAL RESULTS FOR LONG PIPES

Here, the dynamics of very long pipes, as in real applications, are discussed. The pipes considered are 500 m to 3000 m long, and made of stainless steel. The diameter



(a)



(b)

FIGURE 4: A TYPICAL ARGAND DIAGRAM FOR A LONG PIPE ($\hat{L} = 2000$ m), SHOWING THE EVOLUTION OF (a) THE FIRST MODE, (b) THE SECOND MODE, (c) THE THIRD MODE, and (d) THE COUPLED-MODE.

and thickness of the pipes chosen are based on standard values found in real applications.

It may easily be shown that, if $\hat{K}_1 = \hat{K}_2$ and $\hat{K}_3 = \hat{K}_4$, B in equation (27) vanishes and, therefore, $\dot{X} = AX$, which is a standard eigenvalue problem. By solving this problem the system behaviour can be determined.

Here the solutions are presented as plots of the evolution of the generally complex system eigenfrequencies (ω) in Argand diagrams, i.e. in a plane where the abscissa and the ordinate correspond to the real and imaginary part of the eigenfrequencies ($Re(\omega)$ and $Im(\omega)$), respectively, as a system parameter varies. A typical Argand diagram,

which displays the evolution of ω as the nondimensional flow velocity (U_x) is varied, for a long pipe ($\hat{L} = 2000$ m) is given in Fig. 4 for three modes; the lowest one is called here “first mode” and the second lowest “second mode” etc. As seen from Fig. 4(a-c), small flow velocities damp free motions of the pipe ($Im(\omega) > 0$). For sufficiently high flow velocities, the frequencies of all three modes successively become purely imaginary, bifurcating on the $Im(\omega)$ -axis. The frequency associated with one branch of each mode eventually vanishes altogether, indicating the onset of static divergence (buckling) via a pitchfork bifurcation.

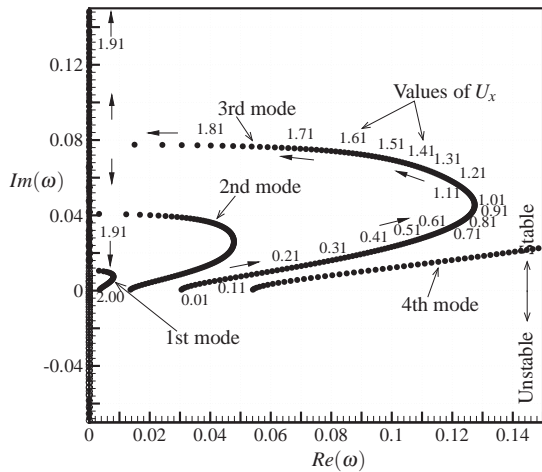
The first divergence occurs at $U_x \simeq 0.35$, in the first mode, followed at $U_x \simeq 1.12$ by divergence in the second mode. However, as shown in Fig. 4d, at higher flow velocity, $U_x \simeq 1.59$, the negative branches of the first- and second-mode loci coalesce and leave the axis at a point where $Im(\omega) < 0$, indicating the onset of coupled-mode flutter. The other branches of these modes also coalesce, leaving the axis where $Im(\omega) > 0$, as shown in the top part of Fig. 4b. Finally, at $U_x \simeq 1.99$ there is divergence in the third mode (see Fig. 4c).

In order to also visually display the dynamical behaviour of a long pipe, the shape of the same pipe as above is plotted along time for $U_x = 0.35$, 0.60 and 1.65 in the (a) part of Figs. 5 to 7. Also, the corresponding time trace of a specific point of the pipe is given for each of the flow velocities in the (b) part of the figures. For long pipes the deflections of the mid-pipe position ($\xi = 0.5$), normally used in the case of short systems with supported ends, may not be a good choice for properly illustrating the dynamical behaviour of the system. In fact, a previous study on long cantilevered cylinders subjected to axial flow [16] shows that the corresponding deflections to divergence and flutter of such systems are confined to a small downstream region of the body. For this reason, the time traces are obtained for a point located at $\xi = 0.8$.

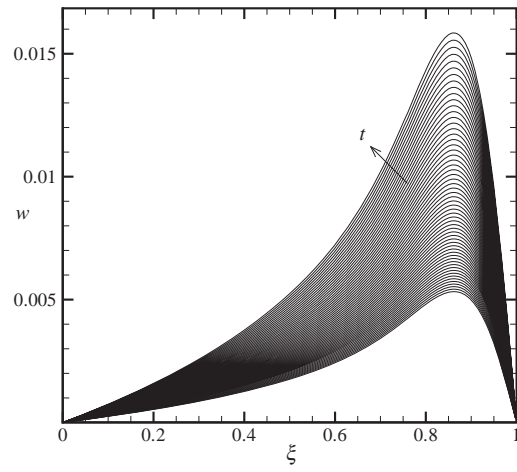
The dynamical behaviour of the pipe slightly after the onset of divergence ($U_x = 0.35$) is shown in Fig. 5. It is seen in Fig. 5a that the pipe takes the first-mode form of a simply supported (pinned-pinned) beam but with the antinode shifted toward the downstream end; the deformation amplitude increases with time.

As seen from Fig. 6a (for $U_x = 0.60$), no appreciable deformation occurs over most of the length of the body; it is limited to a finite portion, about 20% of the pipe length, close to the pipe trailing end.

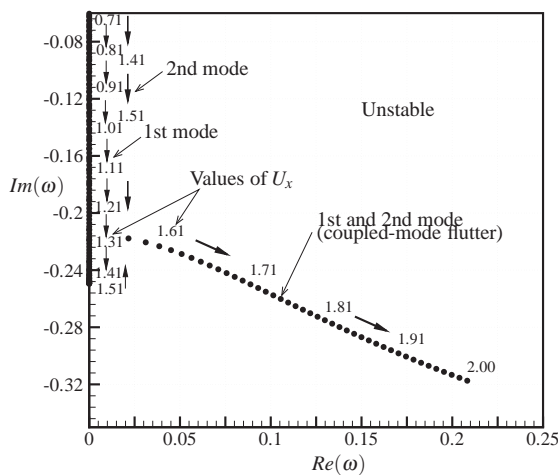
The pipe shape and the time trace for the point at $\xi = 0.8$ just after the onset of flutter are presented in Fig. 7. As seen in Fig. 7(a,c), the pipe oscillations increase with time dramatically, and they are confined to a small part



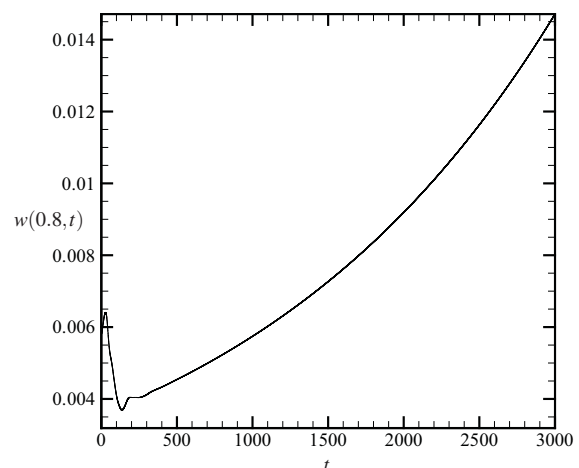
(c)



(a)



(d)



(b)

FIGURE 4: (Continued.)

FIGURE 5: TYPICAL RESULTS FOR A “LONG PIPE”, SHOWING (a) THE SHAPE OF THE PIPE SLIGHTLY AFTER THE ONSET OF DIVERGENCE, AND (b) THE TIME TRACE OF PIPE DEFORMATION AT $\xi = 0.8$; $U_x = 0.35$.

close to the pipe downstream end.

Accurate conclusions on how the pipe surface roughness (the skin friction coefficient, c_f) can change the onset of instabilities for long pipes may be reached by considering Fig. 8(a,b) where the dimensional critical flow velocities for divergence (\hat{U}_{cd}) and flutter (\hat{U}_{cf}) of a long pipe are presented as a function \hat{L} for different values of c_f . As seen from the figure, increasing c_f can significantly push both the static and dynamic instability margins toward higher values of flow velocity. For example, \hat{U}_{cd} changes (as \hat{L} changes) approximately between 10 kn and 30 kn for $c_f = 0.0025$, while it changes between 26 kn and 42 kn for $c_f = 0.0080$. For \hat{U}_{cf} , these values are approximately between 36 kn and 60 kn for $c_f = 0.0025$ and between 104 kn and 116 kn for $c_f = 0.0080$. Obviously,

increasing c_f , increases the skin friction-induced tension in the pipe, making it more stable.

As can also be seen from this figure, for long enough pipelines, \hat{U}_{cd} and \hat{U}_{cf} show little change as \hat{L} varies. This holds for almost all values of c_f considered here.

CONCLUSION

The numerical results obtained for long pipes confirm that both divergence and flutter may arise for such systems in the course of towing. For very long pipes, the instability thresholds are only weakly dependent on the pipe length. It was also found that the instabilities

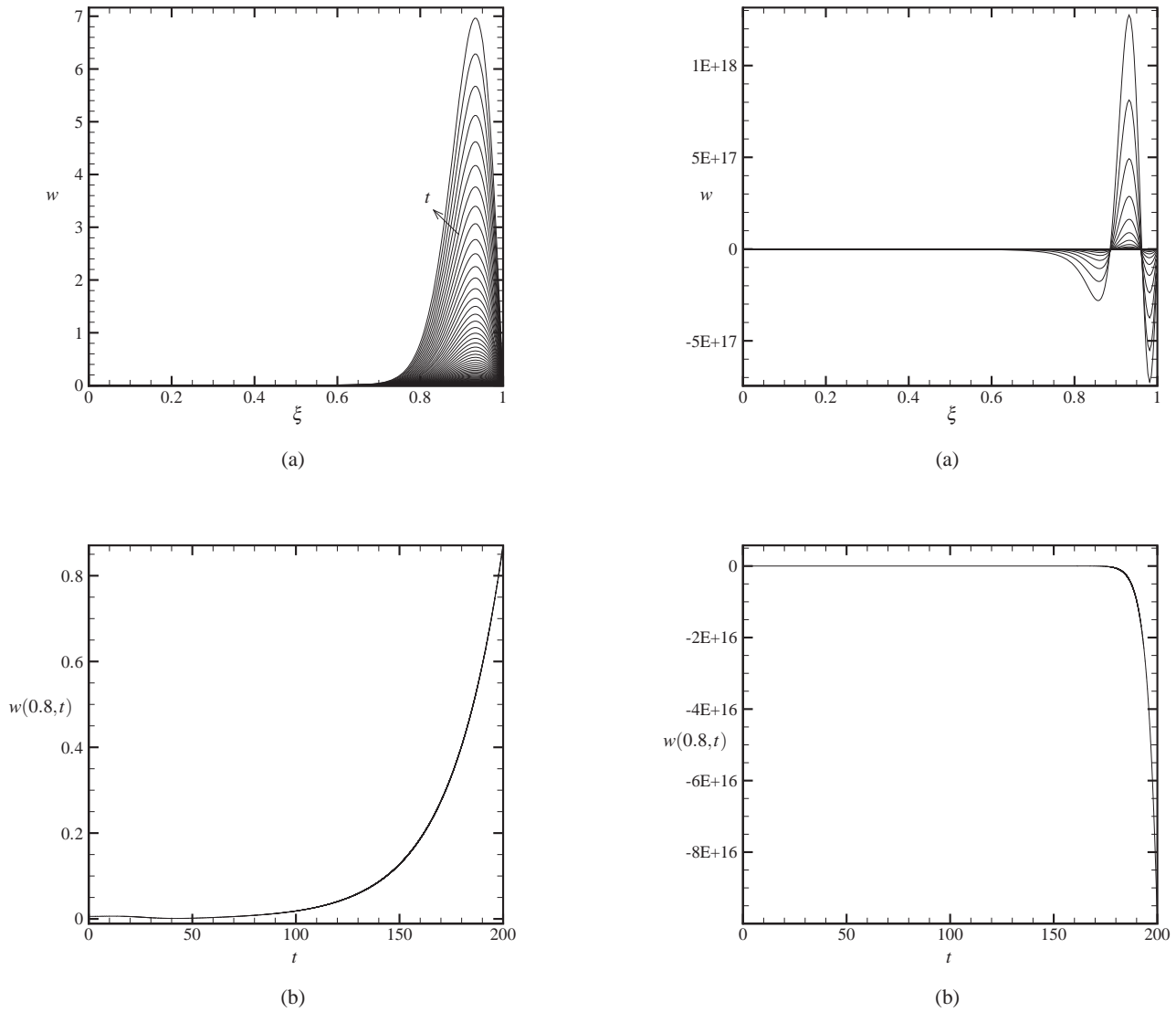


FIGURE 6: TYPICAL RESULTS FOR A “LONG PIPE”, SHOWING (a) THE SHAPE OF THE PIPE, AND (b) THE TIME TRACE OF PIPE DEFORMATION AT $\xi = 0.8$; $U_x = 0.60$.

may be suppressed by using rough surface pipes, but this would significantly increase the drag force acting on the pipe and therefore the required towing power. The deformation results also suggest that special attention should be paid to a finite downstream portion, about 20% of the overall length, to which the pipe deformation seems to be confined. The effect of cross-currents could also be examined using the equations obtained in this study; however, this and other such interesting investigations are left for the future.

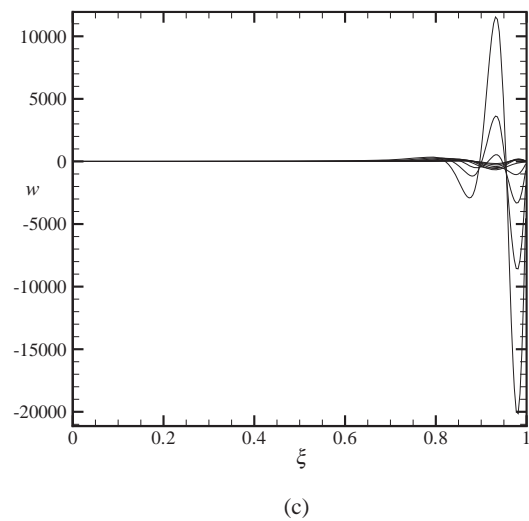


FIGURE 7: (a) THE SHAPE OF THE FLUTTERING “LONG PIPE” (b) THE TIME TRACE OF PIPE DEFORMATION AT $\xi = 0.8$, AND (c) THE PIPE SHAPE FOR SOME OF THE EARLY CYCLES OF OSCILLATION; $U_x = 1.65$.

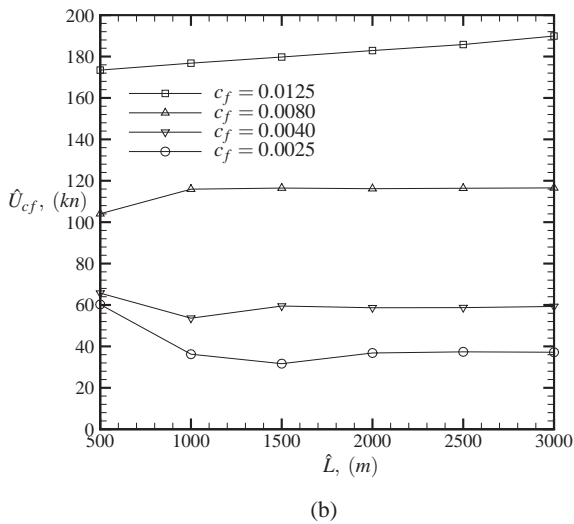
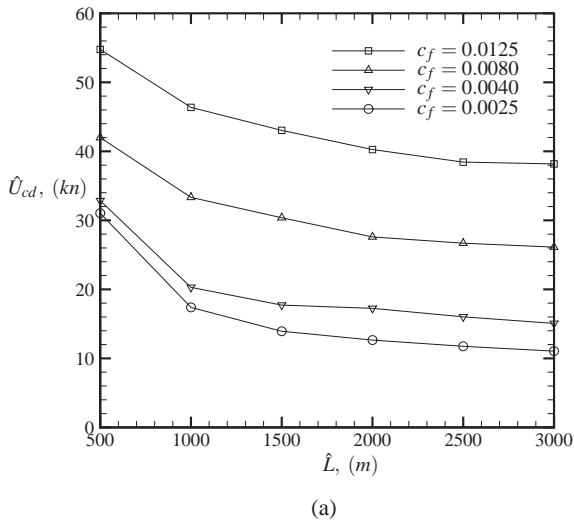


FIGURE 8: THE VARIATION OF CRITICAL FLOW VELOCITY (a) FOR DIVERGENCE (\hat{U}_{cd}), AND (b) FOR FLUTTER (\hat{U}_{cf}), VERSUS THE PIPE LENGTH FOR DIFFERENT VALUES OF SKIN FRICTION (c_f).

ACKNOWLEDGMENT

The support to this research by NSERC of Canada is gratefully acknowledged. The first author is also grateful to the Faculty of Engineering of McGill University for a McGill Engineering Doctoral Award for his PhD studies.

REFERENCES

[1] Sarv, H., and John, J., 2000. "Technical and economical aspects of large-scale storage CO₂ in deep oceans". In Proceedings 25th International Technical Conference on Coal Utilization and Fuel Systems, Vol. 1, Paper MTI 00-03.
 [2] Kyriakides, S., and Corona, E., 2007. *Mechanics of*

Offshore Pipelines, Vol. 1: Buckling and Collapse. Oxford: Elsevier Academic Press.

[3] Telford, W. M., Geldart, L. P., Sheriff, R. E., and Keys, D. A., 1976. *Applied Geophysics*. Chapter 4. Cambridge: Cambridge University Press.
 [4] Choo, Y. I., and Casarella, M. J., 1973. "A survey of analytical methods for dynamic simulation of cable-body systems". *Journal of Hydraulics*, **7**, pp. 137–144.
 [5] Hawthorne, W. R., 1961. "The early development of the dracone flexible barge". *Proceedings of the Institution of Mechanical Engineers*, **175**, pp. 52–83.
 [6] Paidoussis, M. P., 2004. *Fluid-Structure Interactions: Slender Structures and Axial Flow*, Vol. 2. Oxford: Elsevier Academic Press.
 [7] Paidoussis, M. P., 1968. "Stability of towed, totally submerged flexible cylinders". *Journal of Fluid Mechanics*, **34**, pp. 273–297.
 [8] Dowling, A. P., 1988. "The dynamics of towed flexible cylinders. part 1: neutrally buoyant elements". *Journal of Fluid Mechanics*, **187**, pp. 507–532.
 [9] Dowling, A. P., 1988. "The dynamics of towed flexible cylinders. part 2: negatively buoyant elements". *Journal of Fluid Mechanics*, **187**, pp. 533–571.
 [10] Paidoussis, M. P., 1970. "Stability of submerged towed cylinders". In Eight Symposium on Naval Hydrodynamics: Hydrodynamics in the Ocean Environment, pp. 981–1016.
 [11] Paidoussis, M. P., 1973. "Dynamics of cylindrical structures subjected to axial flow". *Journal of Sound and Vibration*, **29**, pp. 365–385.
 [12] Lighthill, M. J., 1960. "Note on the swimming of slender fish". *Journal of Fluid Mechanics*, **9**, pp. 305–317.
 [13] Taylor, G. I., 1952. "Analysis of the swimming of long and narrow animals". *Proceedings of the Royal Society (London)*, **A214**, pp. 158–183.
 [14] Iwatsubo, T., Saigo, M., and Sugiyama, Y., 1973. "Parametric instability of clamped-clamped and clamped-simply supported columns under periodic axial load". *Journal of Sound and Vibration*, **30**(1), pp. 65–77.
 [15] Sugiyama, Y., Kashima, K., and Kawagoe, H., 1976. "On an unduly simplified model in the non-conservative problems of elastic stability". *Journal of Sound and Vibration*, **45**(2), pp. 237–247.
 [16] de Langre, E., Paidoussis, M. P., Doaré, O., and Modarres-Sadeghi, Y., 2007. "Flutter of long flexible cylinders in axial flow". *Journal of Fluid Mechanics*, **571**, pp. 371–389.

NORMAL FORCES EXERTED UPON A LONG OSCILLATING CYLINDER IN AN AXIAL FLOW

Lise Divaret*
Olivier Cadot
Olivier Doaré

Unité de Mécanique (UME), ENSTA ParisTech
Chemin de la Hunière
91761 Palaiseau, France
Email: lise.divaret@ensta-paristech.fr

Pierre Moussou
Julien Berland
LaMSiD

UMR CNRS/EDF/CEA 2832,
Clamart, France

ABSTRACT

Cylinders oscillating laterally in axial flows are known to experience a high level of damping. The normal forces exerted upon an oscillating cylinder depends on the axial velocity U and the angle $\alpha(t)$ between the lateral and axial velocities. Two types of experiments have been performed: in the first one, a cylinder is arranged in an axial flow and oscillates at small amplitudes, in the second one, a cylinder is arranged in an oblique flow at small angles. The variation of normal forces with the axial velocity U and the angle $\alpha(t)$ is studied and the added mass and damping coefficients identified. For small angles, the experiment results show a linear variation of the normal forces with the axial velocity and the angle.

INTRODUCTION

A fuel assembly comprises an array of fuel rods maintained by grids and subjected to an axial flow. A description of the forces exerted upon a cylinder oscillating laterally in an axial flow is useful in the nuclear engineering to represent the forces on a fuel assembly during an earthquake. In order to understand physical phenomena involved, the behavior of only one cylinder oscillating in axial flow is investigated in this paper.

The study is focused on the normal force, which is the force component in the direction of the oscillation and orthogonal to the axis of the cylinder. The normal force depends both on the axial flow and the lateral flow velocities.

A quasi-steady approach can be developed if the characteristic velocity of the fluid-solid interface is small compared to the mean flow velocity. The instantaneous

drag force exerted on a cylinder oscillating laterally in an axial flow is equivalent to the one exerted on a cylinder placed in an oblique flow.

The normal force for a cylinder oscillating in a fluid at rest has been described by Morison [2] as the sum of an added mass force and a drag force. The added mass is a concept [8] which presents the advantage of reducing all the inertial forces to one single coefficient. The Morison expansion can serve as a basis for the description of the forces exerted upon a cylinder oscillating in a axial flow. In the case of a cylinder placed in an oblique flow, Taylor [1], showed that for oblique flow with angles greater than 20° , the axial component of the velocity has no influence. Ersdal [3] brings out three different cases: for angles lower than 5° , it is not possible to hold the cross flow principle, for angles between 5° and 20° , it is possible to hold the cross flow principle but in taking into account the state of the boundary layer and beyond 20° the cross flow principle can hold.

The objective of this paper is to analyze the results of experiments carried out at small angles, for both an oscillating cylinder and a cylinder in an oblique flow. The cross flow principle [1] can be used when the boundary layers is laminar: in this case, the lateral force depends only on the lateral velocity. As the cross flow principle cannot hold to small angle cases, the variation of the normal force with the axial and lateral velocities will be carefully studied. A description of the normal forces at small angles will be discussed.

THEORETICAL BACKGROUND

It has been known for long that a single cylinder oscillating in a fluid at rest undergoes inertial and drag fluid

*Address all correspondence to this author.

forces. For low amplitudes and low frequencies, when the flow is laminar and bi-dimensional, Stokes [4] analytically calculated in 1851 the normal force by neglecting the convective term in the Navier-Stokes equations. He showed that the normal force is the sum of an inertial term proportional to the acceleration and of a drag term due to the velocity.

For higher amplitudes and higher frequencies, the flow pattern becomes more complex: separated flow regions can appear downstream and the flow can exhibit vortex shedding. In this case, the normal force values differ from the Stokes analytical solution which is based on an unseparated flow. Morison [2, 5] found that the expansion of the normal force in inertial and drag terms is still relevant and of practical interest, even for larger amplitudes or higher frequencies. In Morison's expansion, the inertial force is defined as the component of the force proportional to the acceleration and the drag force as the dissipative component of the force, which depends on the velocity. This expansion is classically used to describe the normal forces by unit length for a cylinder oscillating in a fluid at rest [6].

$$F_N^{Morison} = -C_m \frac{\rho_f \pi D^2}{4} \frac{d\dot{X}}{dt} - \frac{1}{2} \rho_f D C_d |\dot{X}| \dot{X} \quad (1)$$

The drag of a cylinder oscillating in an axial flow is known to increase with the axial velocity. It is possible to evaluate the drag forces exerted on a cylinder oscillating in an axial flow either with a dynamic or a steady oblique flow representation. The transition from a representation to the other is classically found in the literature [3, 7]. Most of the experiments have been carried out with a cylinder in a steady oblique flow as the good accuracy is easier to reach. As it is essential to the analysis, the relationship between the oscillator and the steady oblique flow representations is detailed in the following paragraph.

In the oscillator representation, where a cylinder oscillates in an axial flow, the drag can be extracted from the force signal as the dissipative component of the force. In the steady oblique flow representation, a fixed cylinder is placed in an oblique flow. The figures 1 and 2 show the two different setups. In the oscillating cylinder setup, \dot{X} is the cylinder velocity, A is the amplitude of the oscillations, f the frequency and in the oblique flow setup, the angle between the incoming flow and the cylinder axis is α . In both cases, U is the incoming flow velocity. The knowledge of the drag force exerted on the



FIGURE 1: CYLINDER OSCILLATING Laterally IN AN AXIAL FLOW WITH A VELOCITY U

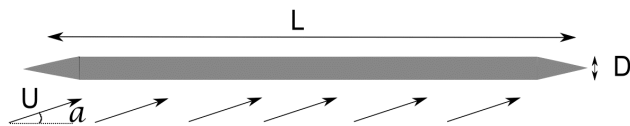


FIGURE 2: CYLINDER IN AN OBLIQUE FLOW WITH A VELOCITY U AND AN ANGLE α

cylinder can be related to the instantaneous drag force in the oscillating cylinder approach. An oscillating cylinder in an axial flow can indeed be seen as a cylinder placed in an oblique flow of velocity U and angle α with the axial component of the velocity $U \cos \alpha$ equal to the axial velocity and the lateral component $U \sin \alpha$ equal to the instantaneous oscillation velocity. The two approaches are equivalent for $\tan \alpha \approx \alpha$, which means for lateral velocities much lower than the axial velocity. This equivalence also supposes that the oscillation frequencies are very small, in a sense defined thereafter.

For a cylinder oscillating at low amplitudes in an axial flow, two characteristic times of convection can be built: the ratio of the diameter to the axial velocity and the ratio of the cylinder length to the axial velocity. In the absence of three-dimensional effects, only the ratio of the diameter to the axial velocity makes sense and can be compared to the oscillation period. If the flow is two-dimensional and the characteristic time D/U is lower than the oscillation period, an expansion in powers of $j\omega$ in the frequency domain becomes relevant. Then the fluid force exerted on the cylinder can be written as the sum of a term proportional to $j\omega$ and a term proportional to $-\omega^2$, where $\omega = 2\pi f$ is the angular frequency. A linearization of the force with the displacement leads to write the force as the sum of a force component in phase with the cylinder acceleration and a component in phase with the cylinder velocity. This second-order expansion is a Morison-like expansion, widespread to axial flow. The added mass can be defined from the first term of the expansion as the mass of fluid which would generate through its acceleration an unsteady force equal to the inertial force. The second term is a damping term. The variation of the two terms with the axial velocity has to be determined.

The scientific literature provides very few data about

cylinders oscillating in an axial flow. Taylor [1] summed up the results of Relf and Powell for a cylinder placed in an oblique flow in an air tunnel at angles between 10° and 90° . In the experiment, the normal force measured is proportional to the square of the lateral component of the velocity. In other words, the normal force measured for an cylinder placed in an oblique flow of velocity U and angle α is the same as the one which would be measured for the same cylinder placed in a cross flow of velocity $U \sin(\alpha)$:

$$F_N = \frac{1}{2} C_d \rho_f D (U \sin(\alpha))^2. \quad (2)$$

This result is called the cross flow principle. According to the equation (2), the drag coefficient C_d is around 1.1. This result is however valid only for angles higher than 20° .

Ersdal & Faltinsen [3] carried out experiments with a cylinder mounted on a towed carriage. The cylinder was towed at a constant velocity and angle α and the normal force was measured. The experiments have been performed by steps of 1 or 2 degrees. Results similar to those of Taylor for angles beyond 20° were provided. For angles between 5° and 20° , a transition in the state of the boundary layer was observed: the boundary layer which is laminar for high angles becomes turbulent. In practical terms, it means that the cross flow principle can hold as in the equation (2), but the drag coefficient is lower in this case than for a laminar boundary layer. Ersdal measured a drag coefficient $C_d \approx 0.8$

For angles lower than 5° , the cross flow principle does not hold. Ersdal shows that the normal force is proportional to the lateral velocity $U \sin(\alpha)$.

$$F_N = \frac{1}{2} C_d \rho_f D U^2 \sin(\alpha) \quad (3)$$

Ersdal & Faltinsen [3] also carried out experiments with an oscillating cylinder in an axial flow at amplitude $A/D = 1, 2, 3$. The variation of the added mass coefficient with the axial velocity has not been studied in details especially at small angles. An average value of the added mass coefficient $C_m = 1.02$ is found for a maximum instantaneous angle α_{max} such as $\tan \alpha_{max} = A\omega/U$ with α_{max} between 3° and 40° .

In the present work, the description of the fluid forces is focused on the normal component of the force. For a

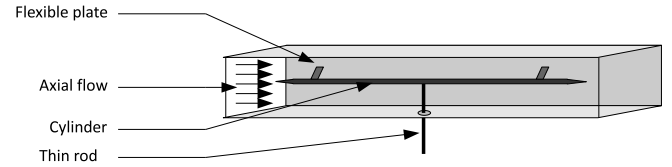


FIGURE 3: SKETCH OF THE FREE OSCILLATION EXPERIMENT IN A WATER TUNNEL

cylinder oscillating in a fluid at rest or in an axial flow, the normal force is the in-line force in the direction of the cylinder motion. For a cylinder in an oblique flow, the normal force F_N is the component of the fluid force in a direction orthogonal to the cylinder axis and in the plane of the flow direction and the cylinder axis (figures 1 and 2).

Experiments are carried out with both an oscillating cylinder in axial flow and a cylinder in a steady oblique flow. The investigations are focused on the quasi-axial flows, i.e at small angles. The mass and drag coefficients obtained with the two setups are compared.

As the experiments with an oscillating cylinder described in this paper are carried out at small angles, the Morison expansion has been modified to take into account Ersdal's and Taylor's results [3, 7]:

$$F_N = -C_m \frac{\rho_f \pi D^2}{4} \frac{d\dot{X}}{dt} - \frac{1}{2} \rho_f D C_d U \dot{X}. \quad (4)$$

Other terms could be added in the expansion but would not bring more information.

EXPERIMENTAL PROCEDURE

Device

The first series of experiments are performed in a water tunnel. A brass cylinder is arranged in the middle of the duct and fixed to one wall of the tunnel with two flexible plates. The cylinder has a diameter $D = 0.01$ m and a length $L = 0.55$ m, the plates are 0.025×0.01 m large and have a thickness of 0.001 m, and the tunnel has a section $S = 0.08 \times 0.15$ m. Both ends of the cylinder are cone-shaped to avoid flow separation when it is placed in the axial flow. The axial flow velocity in the tunnel can vary from 0.5 m.s^{-1} to 9.0 m.s^{-1} . The natural frequency of the system is around $f = 7.8$ Hz. The displacement of the cylinder is measured by an high speed optical micrometer. The cylinder is moved aside from its equilibrium

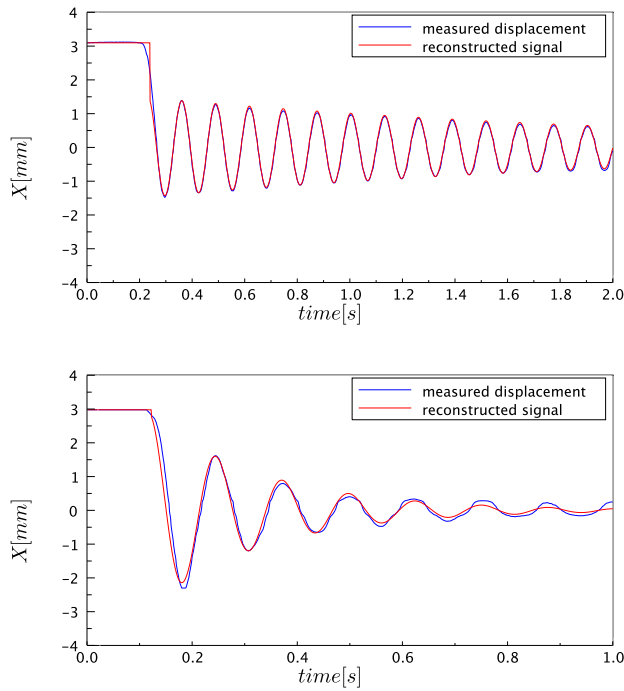


FIGURE 4: CYLINDER DISPLACEMENT AND DAMPED EXPONENTIAL SIGNAL FOR $U = 0.7$ M/S AND $U = 6.3$ M/S ($f = 7.8$ Hz)

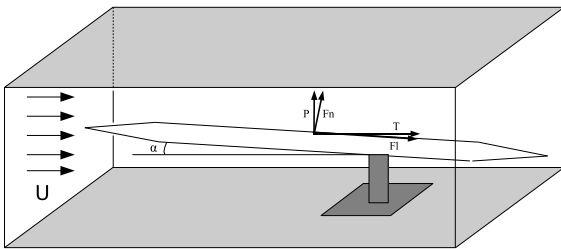


FIGURE 5: SKETCH OF THE EXPERIMENT IN OBLIQUE FLOW IN AN AIR TUNNEL

position with a thin rod going through a water-tight hole in the tunnel wall. The rod is suddenly removed and the cylinder oscillates around its equilibrium position. The experiment is repeated for axial velocities between 0.53 and 9 m/s. Figure 4 shows an example of displacement signals of the cylinder for axial velocities $U = 0.7$ m/s and $U = 6.3$ m/s.

PIV measurements have been carried out in order to check if there are three dimensional effects. Except for $U < 2.5$ m/s, where the lateral and axial velocities are in a range of comparable values, the axial flow is parallel and there is no flow separation along the cylinder.

In the second series of experiments performed in an air tunnel, a wood cylinder is placed obliquely to the air

flow with an angle α . The length of the cylinder is $L = 1.5$ m and its diameter $D = 0.02$ m. The cylinder is fixed with a shaped piece to a bi-dimensional scale to measure the normal and longitudinal forces. As for the experiment in the water tunnel, the ends of the cylinder are also cone-shaped. The horizontal position of the cylinder ($\alpha = 0$) is the position where there is no normal force: $F_N = 0$. The range of pitch investigated spans over 10° : from 0° to 10° by 0.5° .

Signal processing

In the experiments in the water tunnel, the displacement signal of the cylinder (Fig. 4) can be fitted with a damped exponential signal (Eq. 5). A fair agreement between the measured signal and the following reconstructed signal with a damped exponential is obtained.

$$X(t) = X_0 e^{-\xi \omega (t-t_0)} \cos[\omega(t-t_0) + \phi] \quad (5)$$

The oscillation frequency $f = \omega/(2\pi)$ and the damping rate ξ are calculated for each pseudo-period of the displacement signal $X(t)$. As the amplitude of the oscillation decreases with time, it is shown that for such amplitude range $A < 0.3D$ the oscillation frequency and the damping rate do not depend on the amplitude. Furthermore, another measurement is done in air, without axial velocity and will be used to evaluate the added mass by comparison with the measures in water.

The oscillation frequency f and the damping rate ξ are represented in figure 6. It turns out that the damping linearly increases with the axial velocity.

It is assumed that the system can be described by a linear oscillator equation [9]:

$$M_{cyl} \ddot{X} + C \dot{X} + K_{lam} X = F_N. \quad (6)$$

In the equation 6, C is the damping of the structure, M_{cyl} the cylinder mass, K_{lam} the two flexible plate stiffness, and F_N the fluid forces in the normal direction. The agreed description is the Morison-like expansion (Eq. 4) for small angles. By solving the system, the added mass and the drag coefficients C_m and C_d can be expressed as functions of the measured oscillation frequency f , the added mass M_a and the damping rate ξ .

For the experiments in the air tunnel, the normal and longitudinal forces are measured for each angle α . The measurements last at least 3 minutes with a sampling frequency $f_s = 1000$ Hz and the results are averaged.

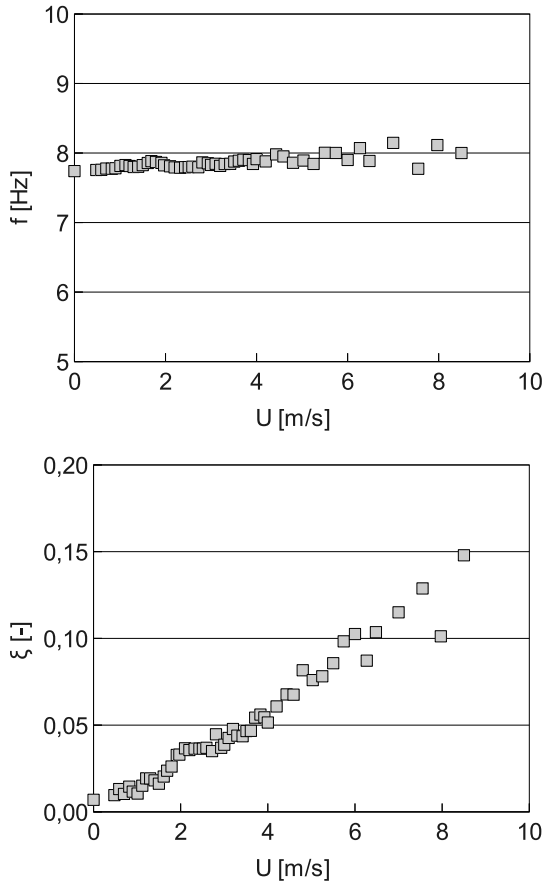


FIGURE 6: FREQUENCY f AND DAMPING RATE ξ VS AXIAL VELOCITY. PRESENT EXPERIMENTS IN WATER TUNNEL

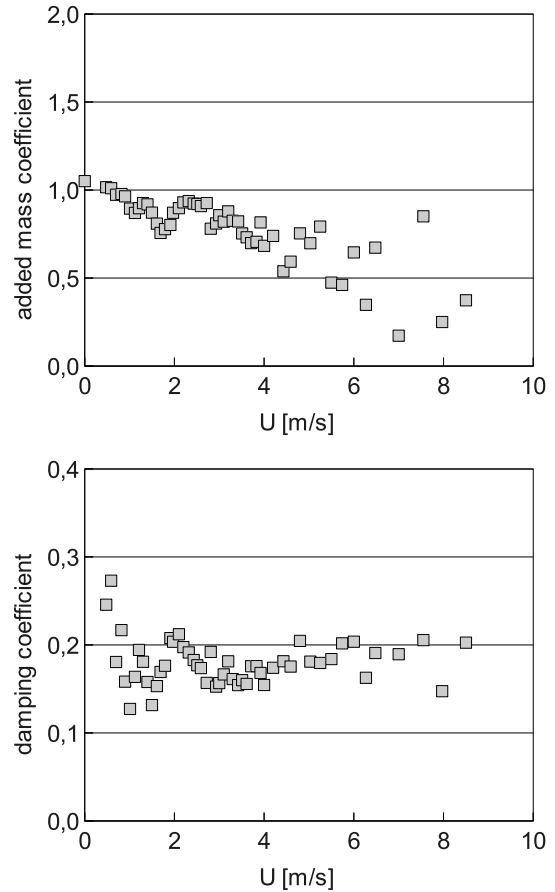


FIGURE 7: ADDED MASS AND DRAG COEFFICIENTS C_m C_d VS AXIAL VELOCITY U

RESULTS

The results of the experiments in the water tunnel are reported in figure 7. The variation of the added mass and damping coefficients is studied for axial velocities ranging from 0.53 to 9 m/s. The added mass does not vary a lot at low axial velocities. At higher axial velocities the accuracy is low and further experiments are needed. Furthermore there is no significant variation of the drag coefficient with the axial velocity for axial velocities higher than 1.5 m/s, where the instantaneous angles are lower than few degrees. For example at a velocity of 1.5 m/s, the maximal equivalent angle of a cylinder in an oblique flow, obtained for the maximal lateral velocity during the first oscillation, is lower than 6° . Hence, for axial velocities larger than 1.5 m/s, the drag component of the Morison-like expansion is relevant. For axial velocities below 1.5 m/s, the amplitude of the first oscillations is too large and a description based on the cross flow principle could give more accurate results for the first oscillations. The decrease of the added mass component with the axial velocity is still to explain.

Figures 8 and 9 shows the normal force coefficient at low pitch angles for the experiment in the air tunnel with two different normalisations. The present experiments have been repeated at three different axial velocities and are indexed with the Reynolds number associated to the incoming flow velocity: $Re = DU/\nu$. The results of the present experiments, carried out at Reynolds numbers between $Re = 19 \cdot 10^3$ and $Re = 32 \cdot 10^3$, are compared to the experimental data of Taylor ($Re = 7 \cdot 10^3$) and Ersdal & Faltinsen [3] (Re between $48 \cdot 10^3$ and $120 \cdot 10^3$).

A zoom at the small angles (Fig. 9) shows a fair agreement between the present experiments and the data of Ersdal & Faltinsen [3]. The discrepancy observed for the angles lower than 2° is probably due to the uncertainty measurement for small values of the force. The linearity of the normal force with the angle can be called into questions beyond 6° . Moreover, the results do not seem to depend on the Reynolds number. In figure 8, the normal force is normalized with the product of the axial and lateral velocities. The present experimental data and

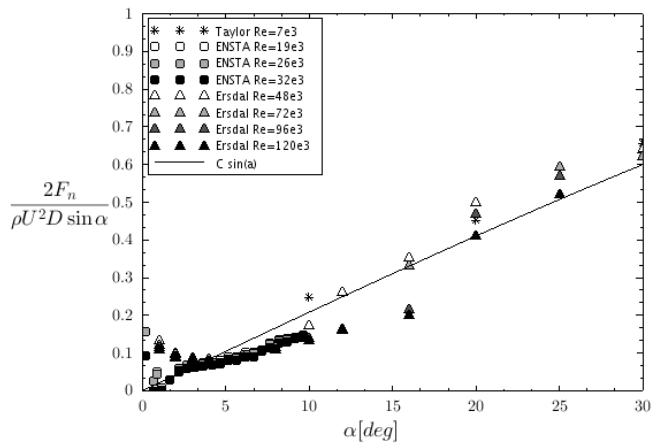


FIGURE 8: NORMAL FORCE COEFFICIENT NORMALIZED WITH THE PRODUCT OF THE AXIAL AND LATERAL VELOCITIES VS ANGLE. * EXPERIMENTAL DATA OF TAYLOR, \square PRESENT EXPERIMENTAL DATA, \triangle EXPERIMENTAL DATA OF ERSDAL, - CROSS FLOW PRINCIPLE.

the experimental data of previous work [1, 3] are plotted together with the cross flow principle description. The results show that the cross flow principle cannot hold at small angles and that the normalisation with the product of the axial and lateral velocities is satisfying at angles below 6° . In the angle range where the transition between the turbulent and laminar states of the boundary layer is observed (for α between 10° and 20°), the experimental data of Ersdal & Faltinsen [3] shows that the normal force highly depends on the Reynolds number. This becomes less true for the cross flow principle area (for α beyond 20°).

For small angles, Ersdal & Faltinsen [3] showed that the normal force was too large to be only due to wall friction. Other mechanism are involved to create the normal force and have to be determined. In the experiments in the air tunnel, the lift and drag forces P and T are measured simultaneously. Both are plotted in figure 10 for the three Reynolds numbers of the experiment. It is shown that the drag force depends on the Reynolds number for small angles ($\alpha < 6^\circ$) and is almost constant between 0° and 10° . The lift force linearly increases between 0° and 6° and becomes non-linear beyond 6° . The Reynolds number has not a significant influence on the lift force.

The lift and drag forces are of the same order and their contribution to the normal force reads:

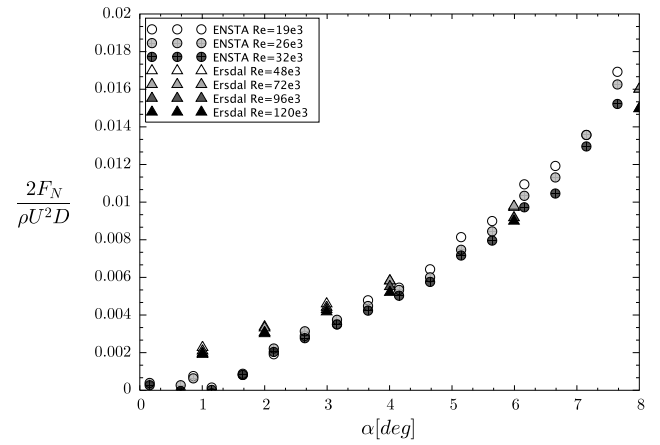


FIGURE 9: NORMAL FORCE COEFFICIENT NORMALIZED WITH THE SQUARE OF THE AXIAL VELOCITY VS ANGLE FOR $\alpha < 8^\circ$. \circ PRESENT EXPERIMENTAL DATA \triangle EXPERIMENTAL DATA OF ERSDAL.

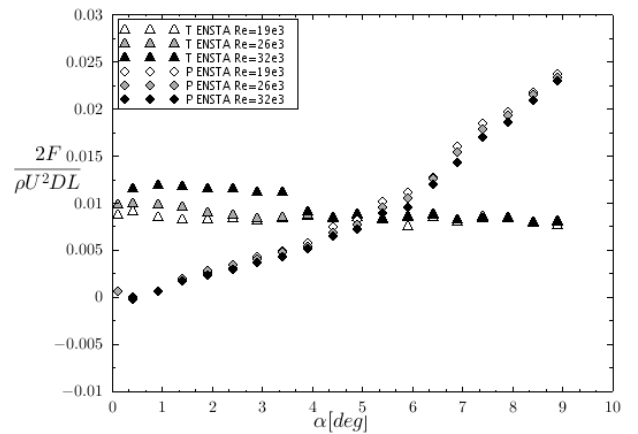


FIGURE 10: LIFT (\diamond) AND DRAG (\triangle) FORCES VS ANGLE FOR A CYLINDER IN OBLIQUE FLOW, PRESENT EXPERIMENTS.

$$F_N = P(\alpha)\cos\alpha + T(\alpha)\sin\alpha. \quad (7)$$

Hence the normal force is mainly due to a lift force for which the origin has to be determined.

The results of the experiments realized with the cylinder in oblique flow can be used to build a quasi-steady representation. At small angles, it has been shown that

the normal force mainly correspond to a lift and is proportional to the angle. Figure 8 highlights that the coefficient C_d can be taken as constant at small angles with an average value around 0.1. In the dynamic case, the drag term of the normal force expansion (Equation 4) can be written as function of the instantaneous angle $\alpha(t) \approx \dot{X}/U$ at small angles. The formulation of the normal force in the oscillating cylinder case is:

$$F_N = -C_m \frac{\rho_f \pi D^2}{4} \frac{d\dot{X}}{dt} - \frac{1}{2} \rho_f D C_d U^2 \alpha(t). \quad (8)$$

The drag term of the expansion correspond to the one of the oblique cylinder case. Then the two coefficients C_d identify the same term of the normal force and can be directly compared.

In figure 7, small angles configurations correspond to large axial velocities as the initial displacement is always the same. The average value of C_d for axial velocities $U > 1.5$ m/s is around 0.18. The two coefficients found with the oscillating cylinder and the oblique cylinder experiments differ with almost a factor 2. This difference can be explained by the low accuracy of the measurements at small angles or by the influence of the ends of the cylinders.

CONCLUSION

The experimental results for the normal force exerted on a cylinder in an oblique steady flow are consistent with the results obtained by Ersdal & Faltinsen [3]. It is found that at small angles the normal force is proportional to both axial and lateral velocities. The experiments with an oscillating cylinder in an axial flow also show that the damping component of the normal force is proportional to the axial velocity and to the lateral velocity.

At small angles and low oscillation frequencies, the two approaches are equivalent and the damping coefficients C_d can be compared. The values of the damping coefficient differ between the two experiments: in the oscillator setup, $C_d = 0.1$ and in the steady oblique flow setup, $C_d = 0.18$. End effects could be responsible for this difference and further work is needed to evaluate their contribution to the normal force.

For a cylinder oscillating in an axial flow at a low ratio of the lateral velocity to the axial velocity, the present work showed that the cross flow principle cannot hold: the normal force depends not only on the lateral velocity but also on the axial flow. Then, the expansions classically used to describe the normal force has to be modified

to take into account the axial flow. The modified expansion proposed in the equation (4) provides a fair description of the damping term of the normal forces.

Further work is needed to better understand the variation of the added mass with the experiment parameters. The velocity pattern should be investigated with high speed PIV.

REFERENCES

- [1] Taylor, G., 1952. "Analysis of the swimming of long and narrow animals". *Proceedings Royal Society of London*, **214**, pp. 158–183.
- [2] J.R. Morison, M.P. O'Brien, J. J., and Schaaf, S., 1950. "The force exerted by surface waves on piles". *Petroleum Transactions, AIME*, **189**, pp. 149–154.
- [3] Ersdal, S., and Faltinsen, O., 2006. "Normal forces on cylinders in near-axial flow". *Journal of Fluids and Structures*, **22**(8), pp. 1057 – 1077.
- [4] Stokes, G. G., 1851. "On the Effect of the Internal Friction of Fluids on the Motion of Pendulums". *Transactions of the Cambridge Philosophical Society*, **9**, p. 8.
- [5] Sarpkaya, T., 2001. "On the force decompositions of Lighthill and Morison". *Journal of Fluids and Structures*, **15**, pp. 227–233.
- [6] Sarpkaya, T., 1986. "Force on a circular cylinder in viscous oscillatory flow at low keulegan-carpenenter numbers". *Journal of Fluid Mechanics*, **165**, pp. 61–71.
- [7] Païdoussis, M., 2004. *Fluid-structure interactions: slender structures and axial flow*. Fluid-structure interactions. Academic Press.
- [8] Sarpkaya, T., 2004. "A critical review of the intrinsic nature of vortex-induced vibrations". *Journal of Fluids and Structures*, **19**(4), pp. 389 – 447.
- [9] Blevins, R., 1990. *Flow-induced vibration*. Van Nostrand Reinhold.

ENERGY HARVESTING FROM AXIAL FLOW INDUCED INSTABILITIES IN SLENDER STRUCTURES

Kiran Singh* Sébastien Michelin[†] Emmanuel de Langre

Department of Mechanics, LadHyX

École Polytechnique, Palaiseau, France

Email: sebastien.michelin@ladhyx.polytechnique.fr

ABSTRACT

In this work we examine the prospects for harvesting energy from flutter instabilities of a slender, flexible cylinder in an axial flow stream. We couple the fluid-solid model and include energy harvesting as curvature based damping. In the first instance we model the reduced order system comprising of an articulated rigid cylinder pair with discrete springs and dampers and demonstrate the scope for harvesting energy from flutter instabilities. Extending the study to a continuously varying system confirms the scope for energy harvesting. The numerical models are employed to find the optimal damping distributions and we see that the two configurations give very different results. We examine the subtle differences between the two apparently canonical configurations that lead to these differing optimals.

INTRODUCTION

The projected growth in global energy demands strongly motivates the interest in energy harvesting concepts, where the idea is to harness unconventional and previously untapped sources of energy. Concepts range from energy harvesting from tidal currents [1] and ocean waves [2] to energy scavenging from ambient vibrations in structures such as buildings and bridges and oscillatory motion of wheels in automobiles or turbines in engines to power sensors and mobile electronic devices [3]. Energy harvesting from fluid-structure interactions (FSI) include concepts such as vortex induced vibrations (VIV) of bluff bodies in a cross-flow [4], resonant vibrations induced in aerofoils mounted on elastic supports [5] and flutter of flexible plates [6, 7]. In this work we focus on harvesting

energy from flutter instabilities of slender structures in an axial flow.

The classical description of flutter instabilities is self-sustained oscillations that arise due to the unstable coupling of fluid dynamic pressure and structural bending modes, where for undamped structures the critical speed at flutter onset depends on fluid as well as structural properties [8]. Flapping flags [9, 10] and fluttering panels [11] in a steady flow fall under the broad category of external flow based instabilities. Recent work by de Langre *et al.* [12] examined the onset and evolution of fluid-induced instabilities in slender structures (also see [13]).

In this work our objective is to evaluate the scope for harvesting energy from fluttering slender elastic structures. From the perspective of the fluid-solid system, energy harvesters act essentially as an energy sink, and in line with the theoretical point of view of this work, are modelled as curvature based damping. Noting that for the undamped case the reduced order system is a canonical model for a continuously varying system [14], in [15] we examined the scope to harvest energy in fluttering structures using a reduced-order model of a pair of slender cylinders connected with a curvature-based spring-damper pair. In [16] we analysed the continuous energy harvester configuration consisting of an elastic beam with a non-uniform distribution of damping. These studies led to the surprising result that the optimal for the bi-articulated configuration (peak damping at the fixed end) is very different from the continuous optimal (a damping distribution increasing with distance from the fixed end). In this paper we interpret and reconcile the results from these two harvester configurations.

This paper is organised as follows: we first examine the reduced order system and briefly develop the governing equations for a nonlinear articulated spring-damper-cylinder pair. We develop the fluid dynamics model for a

*Present address: OCCAM, Maths Institute, 24-29 St Giles, Oxford OX13LB, UK

[†]author for correspondence

slender flexible structure, which includes the inviscid and viscous drag components. The power harvested is computed numerically and results from the numerical optimisation study are examined. Next we consider the continuous configuration: we develop the governing equations and model for nonlinear damping distributions and examine the optimal linear damping distribution. Finally we examine the origin of the subtle differences in configuration between the discrete and continuous systems, which lead to the different optimals.

BI-ARTICULATED SYSTEM

We consider the planar motion of a pair of rigid cylinders: the first cylinder is allowed to rotate about the fixed joint O and is connected to the second cylinder through the articulation P (see Fig. 1). These articulated joints give us a two degree of freedom configuration where θ_1 , θ_2 are the angles through which the first and second cylinders rotate about an axis perpendicular to plane $(\mathbf{e}_x, \mathbf{e}_y)$ at joints O and P respectively. The energy harvesters are modelled as viscous dashpots with damping coefficients (c_1, c_2) , and we seek the combination that corresponds to the peak power. Cylinders of cross-sectional area A , are modelled with equal lengths, L , torsional spring stiffness, K , and mass per unit length, $\rho_s A$. The slender structure is immersed in a stream of fluid of density ρ moving at mean speed U_∞ , the motion of the structure is confined to the $(\mathbf{e}_x, \mathbf{e}_y)$ plane.

In this section we develop the system of equations required to model the fluid-structure system combined with the dampers/energy harvesters. Since fully developed flutter is a nonlinear phenomenon, the equations of motion are developed for large rotation angles. We nondimensionalise the system of equations in terms of the characteristic length, L , mass, $\rho_s AL$, and time, $t^* = (\rho_s AL^3/K)^{1/2}$, the nondimensional flow speed is given as

$$u = U_\infty (\rho_s AL/K)^{1/2}. \quad (1)$$

Governing equations

We apply the conservation of momentum principle to derive the equations of motion for the pair of rotating rigid cylinders in contact [17]. This requires that the rates of change of linear momentum ($d\mathbf{p}/dt = m\dot{\mathbf{r}}$) and angular momentum ($d\mathbf{l}/dt = \partial(\mathbf{r} \wedge m\dot{\mathbf{r}})/\partial t$) respectively balance the external forces and torques acting on a rigid body of mass m , instantaneously at position vector \mathbf{r} (defined with respect to the fixed origin). Momentum balance leads to

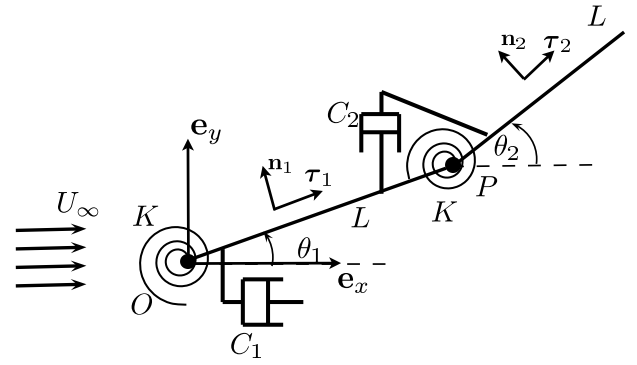


FIGURE 1: Model of the bi-articulated cylindrical energy harvester (see text for description).

a pair of equations that in vector form give:

$$\frac{d\mathbf{L}}{dt} = \mathbf{T}_k(\mathbf{X}) + \mathbf{T}_c(\dot{\mathbf{X}}) + \mathbf{T}_f(\mathbf{X}, \dot{\mathbf{X}}, \ddot{\mathbf{X}}). \quad (2)$$

\mathbf{L} is the angular momentum vector for the bi-articulated cylindrical system that balances the external forces and torques. \mathbf{T}_k and \mathbf{T}_c are the system stiffness and damping torques, respectively, and \mathbf{T}_f corresponds to the torque generated due to the locally acting fluid-dynamic force \mathbf{f} . These expressions are defined in (12)-(15) (see [15] for a complete derivation). Solutions are sought in terms of variable $\mathbf{X} = [\theta_1, \theta_2]^T$, where the dotted terms are differentiated in time.

Fluid dynamic model

For slender structures of diameter $D \ll L$, the fluid force, \mathbf{f} , can be decomposed into the reactive and resistive components, respectively \mathbf{f}^i and \mathbf{f}^v . The reactive force \mathbf{f}^i is obtained from Lighthill's Large Amplitude Elongated Body Theory [18] as:

$$\mathbf{f}^i = -m_a \left(\frac{\partial(u_n \mathbf{n})}{\partial t} - \frac{\partial(u_n u_\tau \mathbf{n})}{\partial s} + \frac{1}{2} \frac{\partial(u_n^2 \boldsymbol{\tau})}{\partial s} \right), \quad (3)$$

and \mathbf{f}^v is obtained from Taylor's resistive force theory [19]:

$$\mathbf{f}^v = \frac{M^*}{2} (C_f u_\tau \mathbf{u} - C_d u_n |u_n| \mathbf{n}), \quad (4)$$

where $\mathbf{u} = u_\tau \boldsymbol{\tau} + u_n \mathbf{n}$ is the solid's local velocity relative to the incoming flow. We define the nondimensional mass

ratio, $M^* = \rho DL / \rho_s A$, and nondimensional added mass, $m_a = M_a / \rho_s A$, with M_a as the dimensional added mass per unit length. For details on the fluid model refer to [15, 16] and references cited therein. In the remainder of the paper, we assume a neutrally buoyant circular cylinder ($\rho = \rho_s$, $A = \pi D^2 / 4$, $m_a = 1$) with $D/L = 0.1$ ($M^* \approx 12.7$) for all subsequent calculations.

Model of energy harvesting

As noted energy harvesters are modelled in this system as viscous dashpots, with nondimensionalised coefficient c_i . To quantify the energy harvesting action we parametrise damping coefficients, c_i , and compute the nondimensional power harvested:

$$\mathcal{P} = \frac{\mathcal{P}}{\rho D L U_\infty^3} = c_1 \langle \dot{\theta}_1^2 \rangle + c_2 \langle (\dot{\theta}_2 - \dot{\theta}_1)^2 \rangle, \quad (5)$$

where \mathcal{P} is the mean dimensional harvested power and operator $\langle \cdot \rangle$ indicates time-averaging over a limit cycle oscillation of period T . In the next section we seek optimal values of the damping coefficients that yield maximum harvested power, \mathcal{P} .

Results:

Eqn. (2) corresponds to a pair of second-order nonlinear ordinary differential equations in time with variables θ_1 , θ_2 . The equations are solved numerically using a Runge-Kutta `ode45` solver in MATLAB with a relative error tolerance of 10^{-6} . We fix the flow speed as $u = 2.45$, calculations are initiated with a perturbation from the rest state, the integration is stopped if either condition $\bar{\theta} < \pi/2$ or $|\theta_i| < \pi/2$ is violated.

Flutter instabilities in the undamped system

Prior to the analysis of energy harvesting we examine the flutter response of the undamped system ($c_i = 0$) in the absence of fluid dissipation ($C_f = C_d = 0$) and in Fig. 2(a) we show the system response to increasing flow speed, u . We calculate a critical flow speed of $u^{cr} \approx 2.13$, below which the fluid acts to damp out disturbances imparted to the system. At u^{cr} the system undergoes a Hopf bifurcation and at higher velocities we see steady flutter oscillations. A physical picture of these oscillations are indicated in Fig. 2(b) where we superimpose snapshots of the bi-articulated cylinder at different instants during the oscillation cycle.

Power harvesting We now introduce structural damping in the configuration and calculate the power \mathcal{P}

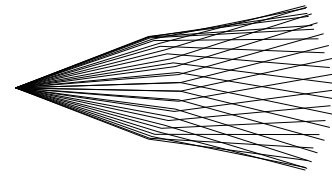
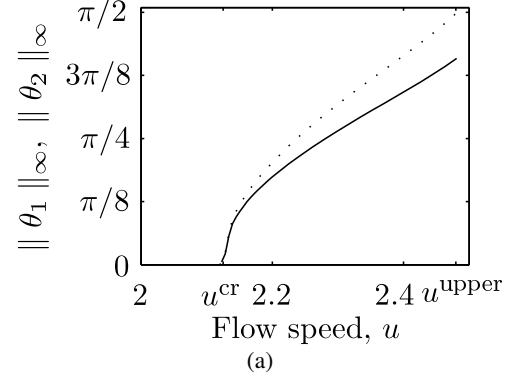


FIGURE 2: (a) Flutter amplitude dependence on the bifurcation parameter, u (θ_2 : solid curves; θ_1 : dotted curves). (b) Flutter response indicated by superimposed snapshots at discrete time instants during a limit cycle period (at $u = 2.2$).

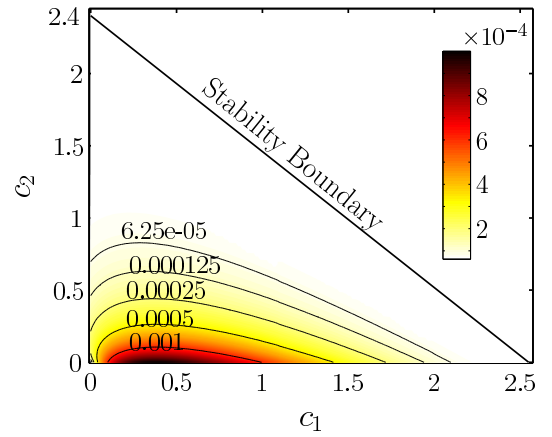


FIGURE 3: Power dependence on damping coefficients c_1 and c_2 (at $u = 2.45$, $C_f = 0.01$, $C_d = 1.0$).

for combinations of (c_1, c_2) that yield limit cycle oscillations. We fix the flow speed at $u = 2.45$, and select representative values for the drag coefficients ($C_f = 0.01$, $C_d = 1.0$).

In Fig. 3 we plot the power map in the (c_1, c_2) -parameter space; also indicated is the stability boundary

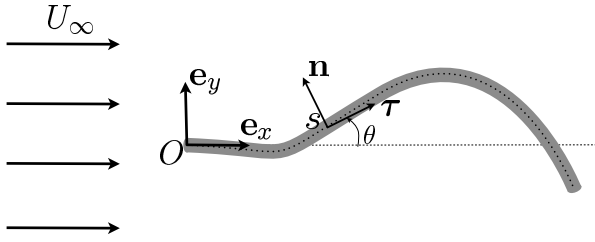


FIGURE 4: Model of the continuously varying energy harvesting system (see text for description).

that shows combinations of damping coefficients above which flutter oscillations are damped out. A key point to note is that peak power lies on the c_1 axis, indicating that a dashpot at the moving articulation is far less effective in harvesting power than one at the fixed end. The expression (5) indicates that structural damping increases the proportion of power harvested, however the very process of energy harvesting necessarily mitigates the oscillatory response. The challenge is in identifying an optimal balance between these competing effects.

The results show the scope for harvesting energy from slender fluttering structures. For this system the optimal configuration that maximises power is one with harvesters concentrated at the fixed end of the configuration, and this result is invariant to variations in flow speed, mass ratio (m_a) and viscous drag coefficients. In the next section we use these insights to examine a fluttering beam with a continuous distribution of damping.

CONTINUOUS SLENDER STRUCTURE

We consider a cantilevered (clamped-free, fixed at O) slender structure (see Fig. 4) of length L with crosswise dimension D , density ρ_s , stiffness B , and nonuniformly varying structural damping $B^*(s)$. The equations for the continuous system, are nondimensionalised by the system scales: ρ , L , U_∞ .

Governing equations

The flexible structure is modelled as an inextensible Euler-Bernoulli beam, where $\mathbf{r}(s)$ is the position vector in the fixed coordinate system ($\mathbf{e}_x, \mathbf{e}_y$), and s is the curvilinear coordinate. At each point along the beam, the orientation $\theta(s, t)$ is defined as the angle of the tangent vector $\boldsymbol{\tau}(s)$ with the horizontal; \mathbf{n} is the local normal. The nonlinear equation of motion for the beam subjected to a fluid

force, \mathbf{F} , is:

$$\frac{1}{M^*} \frac{\partial^2 \mathbf{r}}{\partial t^2} = \frac{\partial}{\partial s} \left\{ \mathbf{v} \boldsymbol{\tau} - \frac{1}{M^* U_\infty^2} \left[\frac{\partial^2 \theta}{\partial s^2} + \frac{\partial}{\partial s} \left(\xi(s) \frac{\partial^2 \theta}{\partial s \partial t} \right) \right] \mathbf{n} \right\} + \mathbf{F}, \quad (6)$$

where the inextensibility condition $\partial \mathbf{r} / \partial s = \boldsymbol{\tau}$ is satisfied with the internal tension, $\mathbf{v}(s, t)$. The nondimensional damping is given by $\xi(s) = U_\infty B^*(s) / (BL)$. The clamped-free boundary conditions must also be satisfied, namely at the fixed end ($s = 0$):

$$\theta = 0, \quad \mathbf{r} = 0, \quad (7)$$

and at the free end ($s = 1$):

$$\frac{\partial \theta}{\partial s} + \xi \frac{\partial^2 \theta}{\partial s \partial t} = 0, \quad \frac{\partial^2 \theta}{\partial s^2} + \frac{\partial}{\partial s} \left(\xi \frac{\partial^2 \theta}{\partial s \partial t} \right) = 0, \quad \mathbf{v} = 0. \quad (8)$$

For consistency with the bi-articulated system we define an equivalent nondimensional flow speed, $U^* = U_\infty L (\rho_s A / B)^{1/2}$; as before A is the cross-sectional area of the structure, and M^* the nondimensional mass ratio. We employ the same fluid model as for the discrete system (3)-(4), the nondimensionalised fluid forces for the two configurations are related by $\mathbf{F} = (\mathbf{f}^i + \mathbf{f}^v) / M^*$. Moreover in [15] we found that friction drag has a rather small effect on the system response; therefore here we only include the parasitic drag ($C_f = 0$, $C_d = 1$).

Energy harvester model

The energy harvesting is modelled as strain-based damping $\xi(s)$, and we obtain a similar expression for nondimensional power harvested at the damper as for the discrete case:

$$\mathcal{P} = \frac{\mathcal{P}}{\rho D L U_\infty^3} = \frac{1}{M^* U_\infty^2} \int_0^1 \xi(s) \langle \dot{\kappa}^2 \rangle ds, \quad (9)$$

where as before \mathcal{P} is the mean dimensional harvested power, and $\dot{\kappa}$ is the time derivative of the local curvature κ . We characterise the intensity and distribution of damping with:

$$\xi_0 = \int_0^1 \xi(s) ds, \quad \text{and} \quad \tilde{\xi}(s) = \xi(s) / \xi_0. \quad (10)$$

Eqn. (10) allows us to independently evaluate the impact on the system response of the amount of damping (ξ_0) and its distribution in the structure.

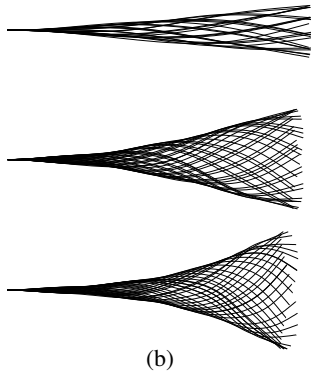
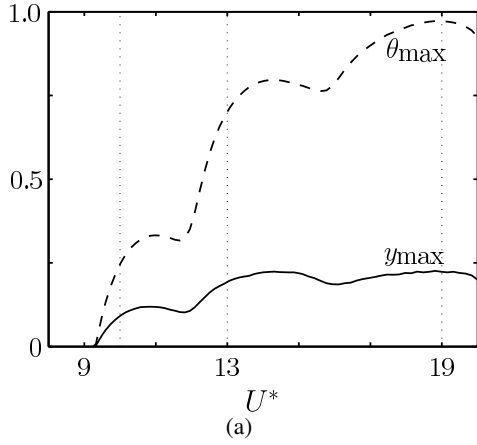


FIGURE 5: (a) Maximum deflection y_{\max} (solid) and orientation θ_{\max} (dashed) of the free end as a function of flow speed U^* . (b) Snapshots of the beam response for $U^* = 10, 13$ and 19 (from top to bottom).

Results

Numerical model Expanding θ in terms of orthogonal Chebyshev polynomials in s , Eq. (6) is solved numerically together with Eqs. (7)–(8), using an iterative second-order implicit method in time [20]. In the numerical implementation the beam and the fluid are initially at rest; the flow speed is ramped up to its steady state value and a small perturbation is applied to the vertical flow, and at each time step we ensure conservation of energy is satisfied within an acceptable tolerance (see [16] for details).

Flutter response for an undamped beam As for the discrete case we first examine the undamped flutter response and plot the system response for increasing nondimensional flow speed in Fig. 5. The critical flow speed at which flutter ensues is verified from linear stability analysis. For the energy harvesting computations we choose a flow speed of $U^* = 13$.

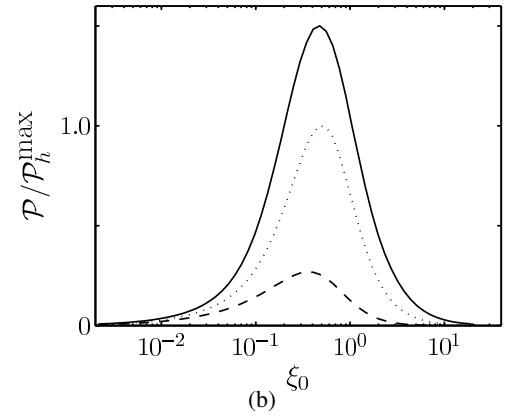
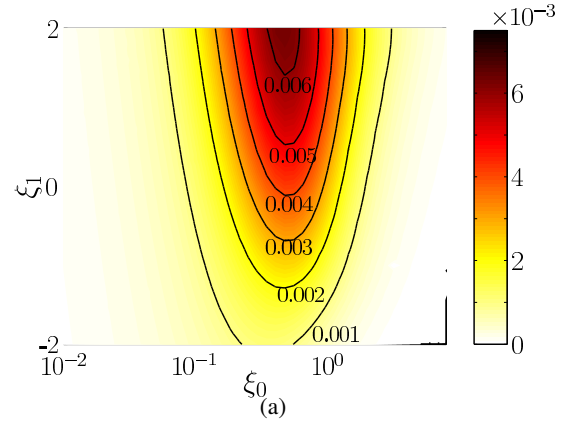


FIGURE 6: Power computations for a linear damping distribution (11): (a) Power contours \mathcal{P} for varying ξ_0 and ξ_1 . (b) Rescaled harvested power $\mathcal{P}/\mathcal{P}_h^{\max}$ as a function of the damping intensity ξ_0 for linearly decreasing ($\xi_1 = -2$, dashed), constant ($\xi_1 = 0$, dotted) and linearly increasing ($\xi_1 = 2$, solid) damping distributions.

Model of energy harvesting Based on the results from the bi-articulated configuration we seek distributions that are allowed to vary along the length of the beam. Here we examine a simple nonhomogeneous distribution of damping of the form:

$$\xi(s) = \xi_0(1 + \xi_1(s - 1/2)) \quad (11)$$

characterised by two coefficients, the total damping, $10^{-3} < \xi_0 < 10$, and slope, $-2 \leq \xi_1 \leq 2$. Operating on the (ξ_0, ξ_1) -parameter space, Fig. 6(a) shows the variation of harvested power \mathcal{P} . In Fig. 6(b) we plot the rescaled power $\mathcal{P}/\mathcal{P}_h^{\max}$, where \mathcal{P}_h^{\max} is the peak harvested power for a constant distribution of damping ($\xi_1 = 0$). The figure shows that for $\xi_1 = 2$ the peak harvested power is enhanced by almost 50% compared to the constant distribution case. Thus the optimal linear damping distribution is one that increases with distance from the free end.

We note that the function family (11) corresponds physically to a dispersed distribution, and the damping is significant over the entire length of the structure. Inspired by the discrete optimal that has damping concentrated at the fixed end, in [16] we optimised on a family of Gaussian distributions, where the mean position on the beam and the Gaussian spread were the optimisation parameters. Despite these different families of functions we converged on a dispersed distribution that confirms the results in Fig. 6. Therefore in contrast to the bi-articulated system, for a continuously varying system we find that a dispersed distribution of damping generates higher peak power than a focused distribution.

COMPARISONS AND CONTRASTS: Discrete vs. continuous systems

In this work, we considered the possibility of harvesting energy from a slender body fluttering in an axial flow, in particular the impact of harvester-distribution on the performance of the system and resulting optimisation strategies. To this end, a simplified fluid-solid model was proposed with energy harvesting represented as curvature based damping.

We first investigated the reduced-order system comprising of a spring-damper-cylinder pair in an axial flow stream. The model demonstrates the scope for energy harvesting, furthermore we find that a single harvester positioned at the fixed end can optimally extract power from the system. Conversely, an additional dashpot at the moving articulation suppresses the flutter instability and considerably diminishes the total harvested power. An investigation of the continuously varying system confirms the scope to harvest energy. However we find that to maximally harvest power, damping that is dispersed along the length of the beam is superior to a focused distribution. Furthermore, an increasing distribution of damping enhances the peak harvested power by approximately 50%, over that for a constant distribution.

To reconcile the differing optimal solutions between these two apparently canonical systems, we note that curvature in the system drives the instability for both configurations. Whilst the bi-articulated system has only one source of instability (the second articulation), deformations can occur all along the length of the beam in the continuous system. As damping acts to suppress the instability locally, for the continuous system the flutter instability can be maintained as long as the fluttering beam can adapt to locally rigidify the structure at the position of high damping. Conversely for the discrete case where there is one sole source of curvature that sustains the flut-

ter instability in the entire system, oscillations are quickly suppressed if damping is added at the same curvature. Thus although the system response to damping is identical in both systems, a careful examination of the dynamics of the different configurations is necessary to predict the optimal harvester distribution.

ACKNOWLEDGMENT

The authors gratefully acknowledge the support of Electricité de France (EDF) for their support through the “Chaire Energies Durables” at Ecole Polytechnique. S. M. was also supported by a Marie Curie International Reintegration Grant within the 7th European Community Framework Program.

REFERENCES

- [1] Westwood, A., 2004. “Ocean power: Wave and tidal energy review”. *Refocus*, **5**, pp. 50 – 55.
- [2] Falcao, A., 2010. “Wave energy utilization: A review of the technologies”. *Renew. Sust. Energ. Rev.*, **10**, pp. 899–918.
- [3] Anton, S., and Sodano, H., 2007. “A review of power harvesting using piezoelectric materials (2003-2006)”. *Smart Mater. Struct.*, **16**, pp. 1–21.
- [4] Grouthier, C., Michelin, S., and de Langre, E., 2012. Optimal energy harvesting by vortex-induced vibrations in cables. pre-print, arXiv:1203.0236v1.
- [5] Peng, Z., and Zhu, Q., 2009. “Energy harvesting through flow-induced oscillations of a foil”. *Phys. Fluids*, **21**, p. 123602.
- [6] Tang, L., Païdoussis, M., and Jiang, J., 2009. “Cantilevered flexible plates in axial flow: Energy transfer and the concept of flutter-mill”. *Journal of Sound and Vibration*, **326**, pp. 263–276.
- [7] Doaré, O., and Michelin, S., 2011. “Piezoelectric energy harvesting from flutter instability: Local/global linear stability and efficiency”. *J. Fluids Struct.*, **27**, pp. 1357–1375.
- [8] Païdoussis, M. P., 2004. *Fluid-Structure Interactions: Slender structures and axial Flow, Volume 2*. London: Elsevier Academic Press.
- [9] Alben, S., and Shelley, M., 2008. “Flapping states of a flag in an inviscid fluid: bistability and the transition to chaos”. *Phys. Rev. Lett.*, **100**, p. 074301.
- [10] Michelin, S., Llewellyn Smith, S. G., and Glover, B., 2008. “Vortex shedding model of a flapping flag”. *J. Fluid Mech.*, **617**, pp. 1–10.
- [11] Crighton, D. G., and Oswell, J. E., 1991. “Fluid loading with mean flow. (I). Response of an elastic

plate to localized excitation”. *Philos. Trans. R. Soc. London, A*, **335**, pp. 557–592.

- [12] de Langre, E., Doaré, O., Païdoussis, M. P., and Modarres-Sadeghi, Y., 2007. “Flutter of long flexible cylinders in axial flow”. *J. Fluid Mech.*, **571**, pp. 371–389.
- [13] Païdoussis, M. P., Grinevich, E., Adamovic, D., and Semler, C., 2002. “Linear and nonlinear dynamics of cantilevered cylinders in axial flow. Part 1. Physical dynamics”. *J. Fluids Struct.*, **16**, pp. 691–713.
- [14] Païdoussis, M. P., 1998. *Fluid-Structure Interactions: Slender structures and axial flow, Volume 1*. London: Academic Press.
- [15] Singh, K., Michelin, S., and de Langre, E., 2012. “Energy harvesting from fluid-elastic instabilities of a cylinder”. *J. Fluids Struct.*, **30**, pp. 159–172.
- [16] Singh, K., Michelin, S., and de Langre, E., 2012. “Effect of damping on flutter in axial flow and optimal energy harvesting”. (*under review*).
- [17] Landau, L. D., and Lifshitz, E. M., 1976. *Mechanics*, third ed., Vol. Volume 1 of Course of Theoretical Physics. Elsevier Ltd.
- [18] Lighthill, M. J., 1971. “Large-amplitude elongated-body theory of fish locomotion”. *Proc. R. Soc. B*, **179**, pp. 125–138.
- [19] Taylor, G. I., 1952. “Analysis of the swimming of long and narrow animals”. *Proc. R. Soc. A*, **214**, pp. 158–183.
- [20] Alben, S., 2009. “Simulating the dynamics of flexible bodies and vortex sheets”. *J. Comp. Phys.*, **228**, pp. 2587–2603.

Appendix A: Expressions for the discrete system

The terms in Eqs. (2) are defined in this section. We define the rate of change of angular momentum about point P and O respectively as:

$$\begin{aligned} \dot{L}^P &= \left(\frac{\ddot{\theta}_2}{3} + \frac{\dot{\theta}_1}{2} \cos(\theta_2 - \theta_1) + \frac{\dot{\theta}_1^2}{2} \sin(\theta_2 - \theta_1) \right), \\ \dot{L}^O &= \dot{L}^P + \left(\frac{4\dot{\theta}_1}{3} + \frac{\ddot{\theta}_2}{2} \cos(\theta_2 - \theta_1) - \frac{\dot{\theta}_2^2}{2} \sin(\theta_2 - \theta_1) \right), \end{aligned} \quad (12)$$

and $d\mathbf{L}/dt = [\dot{L}^O - \dot{L}^P, \dot{L}^P]^T$. Note that this recombination of the two equations leads to significantly simpler expressions.

The contribution from the restoring torsional springs is linear thus the angular moment transferred to the joints

is given as,

$$\begin{aligned} T_k^P &= -(\theta_2 - \theta_1), \\ T_k^O &= -\theta_1 = T_k^P - (\theta_2 - \theta_1). \end{aligned} \quad (13)$$

and $\mathbf{T}_k = [T_k^O - T_k^P, T_k^P]^T$.

From the Kelvin-Voigt model the angular moment transferred to the joints for dampers with coefficients, c_1 and c_2 at P and O respectively are:

$$\begin{aligned} T_c^P &= -c_2(\dot{\theta}_2 - \dot{\theta}_1), \\ T_c^O &= -c_1\dot{\theta}_1, \\ &= T_c^P - (c_1\dot{\theta}_1 - c_2(\dot{\theta}_2 - \dot{\theta}_1)), \end{aligned} \quad (14)$$

and $\mathbf{T}_c = [T_c^O - T_c^P, T_c^P]^T$.

Fluid torque vector $\mathbf{T}_f = \mathbf{T}_{f,v} + \mathbf{T}_{f,i}$, where the first term is the contribution from the viscous drag or resistive forces and the second term is the inviscid or reactive force contribution. For brevity we do not include the viscous components. The contribution of the reactive flow forces to the fluid torques at the two articulations is given by,

$$\begin{aligned} T_{f,i}^P &= -m_a \left\{ \dot{\theta}_1 \left(\frac{\dot{\theta}_1}{2} - \dot{\theta}_2 \right) \sin(\theta_2 - \theta_1) + \frac{\ddot{\theta}_1}{2} \cos(\theta_2 - \theta_1) \right. \\ &\quad \left. + \frac{\ddot{\theta}_2}{3} + u \cos \theta_2 \dot{\theta}_2 \right\}, \\ T_{f,i}^O &= T_{f,i}^P - m_a \left\{ \ddot{\theta}_1 \left(\frac{1}{3} + \cos^2(\theta_2 - \theta_1) \right) + \frac{\ddot{\theta}_2}{2} \cos(\theta_2 - \theta_1) \right. \\ &\quad \left. + \dot{\theta}_1 \left(\frac{\dot{\theta}_1}{2} - \dot{\theta}_2 \right) \sin 2(\theta_2 - \theta_1) \right. \\ &\quad \left. + u [\dot{\theta}_1 \cos \theta_1 + 2\dot{\theta}_2 \cos \theta_2 \cos(\theta_2 - \theta_1)] \right\} + T^{\text{jump}}, \end{aligned} \quad (15)$$

where m_a is the nondimensionalised added mass. T^{jump} is the contribution of the inviscid fluid dynamics over the corner, P , is:

$$T^{\text{jump}} = -m_a (a_o + a_1 u + a_2 u^2) \quad (16)$$

where

$$\begin{aligned}
 a_o &= \frac{\dot{\theta}_1^2}{2} \left(-\cos^2(\theta_2 - \theta_1) \sin(\theta_2 - \theta_1) \right), \\
 a_1 &= \dot{\theta}_1 \left(\cos^2(\theta_2 - \theta_1) \cos \theta_2 - \cos \theta_1 \right) \\
 a_2 &= \frac{1}{2} \left(\sin \theta_2 \cos \theta_1 + \frac{1}{2} \sin 2\theta_2 \cos(\theta_2 - \theta_1) \right. \\
 &\quad \left. - \sin 2\theta_1 \right) \quad (17)
 \end{aligned}$$

and the inviscid fluid moment vector is,

$$\mathbf{T}_{f,i} = [T_{f,i}^o - T_{f,i}^p, T_{f,i}^p]^T.$$

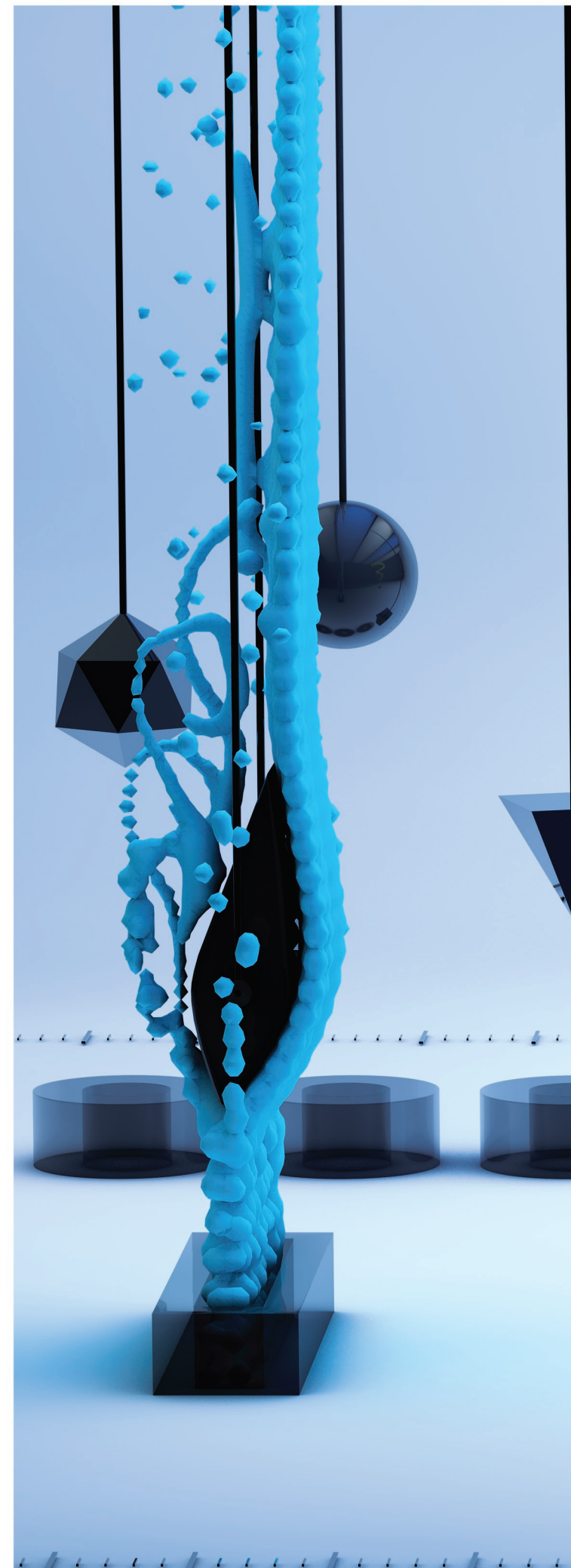
AUTHORS INDEX

Åbom, M.	243	Bouris, D.	473
Amabili, M.	1, 719	Broc, D.	439
Amandolese, X.	61	Buitrago, A.	35
Anagnostopoulos, P.	423	Béguin, C.	489
Anami, K.	607	Cadot, O.	353, 727
Anderson, J. B.	337	Cagney, N.	465
Antunes, J.	313, 481	Carmo, B.	369
Aouag, M. L.	453	Chang, G.	15
Arthurs, D.	27	Choquel, M.	61
Assi, G. R. . S.	543	D'Orazio, D.	631
Astolfi, J.	67	Daou, M.	453
Aydin, B. T.	283	Dedes, A.	473
Balabani, S.	465	Delaune, X.	313, 481
Barannyk, O.	415, 713	Deniset, F.	67
Baranyi, L.	361	Desbonnets, Q.	439
Becker, S.	407	Dessi, D.	631
Belfroid, S.	49, 115, 531, 537	de Langre, E.	291, 735
Bennett, G.	267, 275	de Paula, A. V.	499
Berland, J.	353, 727	Divaret, L.	353, 727
Berro, H.	615	Doaré, O.	211, 639, 727
Berton, M.	171	Efrainsson, G.	243, 681
Boccaccio, E.	391	Ekmekci, A.	283
Bodén, H.	187	El Bouzidi, S.	107
Boersma, B. J.	115	Eloy, C.	639
Boij, S.	243	Emborg, U.	681
Borsoi, L.	313, 481	Endo, T.	705
Bossi, F. C.	697	Enghardt, L.	689
Bouabdallah, A.	453	Epureanu, B. I.	719
Bourguet, R.	671	Étienne, S.	489

Feistauer, M.	147	Hémon, P.	165
Finnegan, S.	251	Ishihara, K.	43
Floyd, M. . R.	195	Ishii, N.	607
Franzini, G. R.	561, 655	Ishizaki, H.	663
Freire, C. M.	543	Izuchi, H.	523
Fujarra, A. L. . C.	561, 655	Jain, A.	555
Fujita, K.	375	Jakobsen, K. G.	515
Fujita, Y.	99	Janzen, V.	195
Gaugain, F.	67	Joost, G.	179
Giordano, E.	259	Joshi, A.	283
Golliard, J.	49, 179, 531	Kalfas, A. I.	259
González Díez, N.	179, 531	Kaneko, S.	599
González, L.	139	Kapor, J. S.	647
Gonçalves, R. T.	561, 655	Karlsson, M.	171
Gotou, A.	375	Karniadakis, G. . E.	671
Goyder, H.	585	Kato, M.	55, 399
Grouthier, C.	291	Keogh, D.	91
Haj Ghayesh, M.	1	Khalifa, A.	83
Hamdouni, A.	431	Kheiri, M.	719
Hammar, J.	681	Kierkegaard, A.	171, 243
Han, Y.	195	Knisely, C. W.	607
Hanchi, S.	453	Kojima, S.	55
Hashimoto, M.	663	Konrath, R.	307
Hassan, M.	107, 337	Konstantinidis, E.	457, 473
Hayashi, I.	523	Korkischko, I.	307, 543
Hirooka, E.	55	Kozanek, J.	677
Hirschberg, A.	49, 593	Kritikos, K.	259
Holmberg, A.	171	Lalonde, V.	321
Horáček, J.	147	Lam, G. C. Y.	235
Howell, R. M.	219	Leung, R. C. . K.	235
Huera-Huarte, F.	139	Levy, B.	123
Hwang, H.	599	Liberge, E.	431

Liu, Y. Z.	123	Oyakawa, T.	99
Longatte, E.	431	Paak, M.	383
Lucey, A. D.	203, 219, 647	Paduano, C.	227
MacDonald, J. H. . G.	155	Paidoussis, M. P.	1, 383, 719
Maekawa, A.	55, 399	Pardowitz, B.	689
Makihata, T.	607	Patnaik, B. S. V.	299, 345
Malavasi, S.	697	Pavlovskaia, E.	569
Margnat, F.	35	Pellegrino, A.	75
Marino, L.	21	Pettigrew, M. J.	321, 489, 507
Matsumoto, M.	663	Piteau, P.	313, 481
Meneghini, J. R.	307, 561, 655	Pitman, M. W.	203
Meskill, C.	75, 91, 227, 251	Pomarède, M.	431
Michelin, S.	61, 211, 291, 735	Postnikov, A.	569
Minorikawa, G.	523	Remans, D.	537
Misra, A. K.	383	Ricciardi, G.	391
Modarres-Sadeghi, Y.	15, 555	Richard, J.	7
Mohany, A.	337	Riedelmeier, S.	407
Morita, R.	577	Rodriguez Verdugo, F.	267, 275
Moussou, P.	353, 615, 727	Romano, G. P.	21
Mureithi, N.	329, 489, 507	Ross, A.	321
Möller, S. V.	131, 499	Rudenko, O.	49, 593
Nakamura, T.	99	Sakakibara, T.	55
Nakiboglu, G.	49, 593	Sanchis, A.	515
Nennie, E.	537	Sawadogo, T.	329
Ni, Y.	99	Schlücker, E.	407
Nikitas, N.	155	Sears, D. . F.	195
Nishiguchi, M.	523	Seitanis, S.	423
O'Reilly, C. J.	681	Sigrist, J.	67, 431
Oku, T.	607	Silveira, R. S.	131
Omrani, S. P.	115, 531	Singh, K.	735
Oshkai, P.	415, 713	Sinibaldi, G.	21
Oualli, H.	453	Siozos-Rousoulis, L.	259

Smith, B. . A. . W.	195
Sridhar, M.	345
Srinil, N.	543
Steindl, A.	7
Stephens, D. B.	267
Subhash Reddy, M.	299
Sváček, P.	147
Takahashi, T.	55, 399
Tan, B. H.	203
Tang, S.	235
Tantot, N.	259
Tapken, U.	689
Tezuka, K.	705
Torigoe, Y.	55
Triantafyllou, M. . S.	671
Tsuji, T.	55, 399, 607
Tsujimoto, Y.	705
Tullis, S.	623
Twerda, A.	115
Uchiyama, Y.	577
van Bokhorst, E.	537
Vclek, V.	677
Wang, J.	623
Watanabe, T.	599
Weaver, D. S.	83, 623
Whan, T.	195
Wiercigroch, M.	569
Yamasaki, D.	599
Yamasaki, Y.	599
Yonezawa, K.	705
Zhou, L.	187
Ziada, S.	27, 83
Zolotarev, I.	677



Flow-Induced Vibration and Noise, and the physical parameters which control them, are of significant importance to design engineers and operators of systems in a wide range of industries ranging from aerospace, automotive and civil engineering to marine structures, electricity generation and chemical processing. The potential of these phenomena to cause catastrophic failure to engineering systems and unacceptably high levels of environmental and occupational noise has motivated significant effort to understand and mitigate these problems in the interests of human safety. FIV2012 is the tenth in a series of international conferences on Flow-Induced Vibration which started at Keswick in 1973. These proceedings present almost 100 papers on the current research of some of the most experienced researchers in the field working in both academia and industry.